# A World-Class University-Industry Consortium for Wind Energy Research, Education, and Workforce Development

# Final Technical Report

**DOE Award Number:** DE-EE0002979

**Project Period:** January 15, 2010 to August 1, 2012

**Principle Investigator:**
Dr. Mohammad Shahidehpour, Director
Galvin Center for Electricity Innovation
Email: ms@iit.edu
Phone: 312-567-5737

Illinois Institute of Technology
3300 South Federal Street
Chicago, IL 60616-3793

**Project Team Members (in Alphabetical Order):**
Acciona Wind Energy USA, Alstom Grid, Dakota Power, Electric Power Research Institute, EnerNex, Innovative Technology Applications Company, Intellergy, Intelligent Power Solutions, Invenergy, Keyworks, McCoy Energy, S&C Electric, SmartSignal (Now GE Intelligent Platforms), Southern Illinois University, Three Point Square, University of Chicago, Wiedman Power System Consulting

## October 30, 2012

# Acknowledgment

This report is based upon the work supported by the U. S. Department of Energy under Award Number DE-EE0002979. On behalf of the Consortium members of this project, I would like to thank the U.S. Department of Energy for making this study possible. The many tasks of this two-year study could not have been completed without the dedicated effort of all Consortium members. We look forward to continuing our technical and educational collaborations, and utilize the expertise developed as part of this study, beyond the completion of the proposed tasks.

Mohammad Shahidehpour, Principal Investigator
Bodine Chair Professor and Director
Robert W. Galvin Center for Electricity Innovation
Illinois Institute of Technology
Chicago, IL 60616

## Disclaimer

# Table of Contents

# List of Acronyms

| | |
|---|---|
| A/D | Analog/Digital |
| AC | Alternating Current |
| ADS | Acoustic Data Surface |
| AEP | Annual Energy Production |
| AGC | Automatic Generation Control |
| AMR | Adaptive Mesh Refinement |
| AWC | Atlantic Wind Connection |
| BLDC | Brushless Direct Current |
| CCM | Cross Correlation Matrix |
| CF | Capacity Factor |
| CFD | Computational Fluid Dynamics |
| CLSC | CLEAN-SC, CLEAN based on source coherence |
| CO2 | Carbon Dioxide |
| COE | Cost of energy |
| ComEd | Commonwealth Edison |
| CP | Power Capture |
| CSC | Current Source Converter |
| CSM | Cross Spectral Matrix |
| CTW | Catch the Wind, Inc. |
| CVP | Continuously Variable Planetary |
| CVT | Continuously Variable Transmission |
| DAMAS | Deconvolution Approach for the Mapping of Acoustic Sources |
| DAS | Delay and Sum |
| DAS | Data Acquisition System |
| DB | Database |
| DC | Direct Current |
| DCF | Domain Connectivity Function |
| DFIG | Doubly Fed Induction Generator |
| DFIM | Doubly Fed Induction Machine |
| DH | High Duty Cycle |
| DL | Low Duty Cycle |
| DNR | Illinois Department of Natural Resources |
| DOE | Department of Energy |
| DOF | Degree-Of-Freedom |
| DP | Dakota Power |
| DP (filter) | Filter Differential Pressure |
| DPM | Lagrangian Discrete Phase Model |
| DSP | Digital Signal Processing |
| DTF | Dynamometer Test Facility |
| ECE | Electrical and Computer Engineering |

| | |
|---|---|
| ECEDHA | Electrical and Computer Engineering Department Heads Association |
| EMF | Electric and Magnetic Fields |
| EMS | Energy Management System |
| EPRI | Electric Power Research Institute |
| FDBF | Frequency Domain Beamforming |
| FEA | Finite Element Analysis |
| FEMM | Finite Element Magnetics Method |
| FERC | Federal Energy Regulatory Commission |
| FFT | Fast Fourier Transform |
| GE | General Electric |
| GENCO | Generation Company |
| GIS | Geographical Information System |
| GMP | Geometry Manipulation Protocol |
| GUI | Graphical User Interface |
| GW | giga-watt |
| GWh | giga-watt-hour |
| HAWT | Horizontal-Axis Wind-Turbine |
| HVAC | Heating, Ventilation, & Air Conditioning |
| Hz | Hertz |
| I/O | Input/Output |
| IEC | International Electrotechnical Commission |
| IEEE | The Institute of Electrical and Electronics Engineers |
| IG | Induction Generator |
| IGBT | Insulated Gate Bipolar Transistors |
| IIT | Illinois Institute of Technology |
| IM | Induction Motor |
| IPPSC | Intelligent Perfect Power System Controller |
| IPRO | Interprofessional Project |
| IPS | Intelligent Power Solutions, LLC |
| ISO | Independent System Operator |
| IT | Information Technology |
| ITAC | Innovative Technology Applications Company, LLC |
| ITP | Incidental Take Permit |
| KERI | Korea Electrotechnology Research Institute |
| kV | kilo-volt |
| kW | kilo-watt |
| kWh | kilo-watt-hour |
| LIDAR | Light Detection And Ranging |
| LMP | Locational Marginal Price |
| LWS | Laser Wind Sensor |
| MB | mega-byte |
| MISO | Midwest Independent System Operator |
| MMAE | Mechanical, Materials, and Aerospace Engineering |

| | |
|---|---|
| MMS | Market Management System |
| MOSFET | Metal–Oxide–Semiconductor Field-Effect Transistor |
| MS | Microsoft |
| MTEP | MISO Transmission Expansion Planning |
| MTS | Modular Tower System |
| MUT | Machine Under Test |
| MW | mega-watt |
| MWh | mega-watt-hour |
| NASA | National Aeronautics and Space Administration |
| NEMA | National Electrical Manufacturers Association |
| NERC | North American Electric Reliability Corporation |
| NETCS | National Electric Transmission Congestion Study |
| NFAC | National Full-Scale Aerodynamics Complex |
| NPT | National Pipe Thread Tapered Thread |
| NREL | National Renewable Energy Laboratory |
| OCS | Optical Control System |
| OEM | Original Equipment Manufacturer |
| OTS | Office of Technical Services |
| PCB | Printed Circuit Board |
| PHEV | Plug-in Hybrid Electric Vehicle |
| PI | Principal Investigator |
| PJM | Pennsylvania-New Jersey-Maryland |
| PLC | Programmable Logic Controller |
| PM | Permanent Magnet |
| PMSM | Permanent Magnet Synchronous Motor |
| PMU | Phasor Measurement Units |
| POMS | POwer Market Simulator |
| PV | Photovoltaic |
| PWM | Pulse With Modulation |
| RFP | Request for Proposal |
| ROR | reduced-order representation |
| RPM | Revolutions Per Minute |
| SA | Supervisor Agent |
| SCADA | Supervisory Control and Data Acquisition System |
| SCUC | Security-Constrained Unit Commitment |
| SIU | Southern Illinois University |
| SMI | Standard Module Interface |
| SOC | State of Charge |
| SPIV | Stereoscopic Particle Image Velocimetry |
| SPL | Sound Pressure Level |
| SQL | Structured Query Language |
| SR | Switched Reluctance |
| SRDCM | Switch Reluctance DC Machine |

| | |
|---|---|
| SRM | Switched Reluctance Machine |
| SST | Shear-Stress Transport |
| SUP | Special Use Permits |
| SVPWM | Space Vector Pulse Width Modulation |
| THD | Total Harmonic Distortion |
| TSR | Tip Speed Ratio |
| TW | terra-watt |
| TWh | terra-watt-hour |
| USB | Universal Serial Bus |
| V2G | Vehicle to Grid |
| VAR | Volt-Amp-Reactive |
| VLAN | Virtual Local Area Network |
| VOF | Eulerian Volume of Fluid Model |
| VPN | Virtual Private Network |
| VPPC | Vehicle Power and Propulsion Conference |
| VSC | Voltage Source Converter |
| WECS | Wind Energy Conversion Systems |
| WFMS | Wind Farm Management System |
| WG | Wind Generation |
| WINS | Wind INtegration Simulator |
| WISER | IIT Wanger Institute for Sustainable Energy Research |
| WPP | Wind Power Plants |
| WTC | Wind Turbine Contract |
| WTG | Wind Turbine Generator |
| WTGU | Wind Turbine Generating Unit |
| XML | Extensible Markup Language |

# List of Figures

# List of Tables

# List of Appendices

## Executive Summary

Since January 2010, the Illinois Institute of Technology (IIT), with an ABET accredited engineering program, has led an extensive effort in forming a world-class wind energy consortium (the Consortium) of multiple universities (domestic and international) and multiple industry participants (all types of wind energy stakeholders) to perform focused research and development on critical wind energy challenges identified in the "20% Wind Energy by 2030" report, including wind technology challenge, grid system integration, and workforce development. During the two-year project period, the consortium members have developed control algorithms for enhancing the reliability of wind turbine components. The consortium members have developed advanced operation and planning tools for accommodating the high penetration of variable wind energy. The consortium members have developed extensive education and research programs for educating the stakeholders on critical issues related to the wind energy research and development.

More specifically,

- The Consortium procured a 1.5MW GE wind unit by working with the world leading wind energy developer, Invenergy, which is headquartered in Chicago, in September 2010. The Consortium also installed advanced instrumentation on the turbine and performed relevant turbine reliability studies.

- The Consortium, by working with Viryd Technologies, installed an 8kW Viryd wind unit (the Lab Unit) at an engineering lab at IIT in September 2010 and an 8kW Viryd wind unit (the Field Unit) at the Stuart Field on IIT's main campus in July 2011, and performed relevant turbine reliability studies. IIT's existing microgrid provides a unique opportunity to see how local wind turbine generation might affect the microgrid.

- The consortium performed research on turbine reliability including (1) Predictive Analytics to Improve Wind Turbine Reliability; (2) Improve Wind Turbine Power Output and Reduce Dynamic Stress Loading Through Advanced Wind Sensing Technology; (3) Use High Magnetic Density Turbine Generator as Non-rare Earth Power Dense Alternative; (4) Survivable Operation of Three Phase AC Drives in Wind Generator Systems; (5) Localization of Wind Turbine Noise Sources Using a Compact Microphone Array; (6) Wind Turbine Acoustics - Numerical Studies; and (7) Performance of Wind Turbines in Rainy Conditions. The consortium performed research on wind integration including (1) Analysis of 2030 Large-Scale Wind Energy Integration in the Eastern Interconnection; (2) Large-scale Analysis of 2018 Wind Energy Integration in the Eastern U.S. Interconnection; (3) Integration of Non-dispatchable Resources in Electricity Markets; (4) Integration of Wind Unit with Microgrid. The consortium research resulted in
    - 36 papers
    - 36 presentations
    - 13 PhD degrees
    - 9 MS degrees
    - 7 awards

- The education and outreach activities on wind energy included (1) Wind Energy Training Facility Development; (2) Wind Energy Course Development; (3) Wind Energy Outreach.

    1) The wind energy training facility is located at the Robert W. Galvin Center for Electricity Innovation at IIT. The Galvin Center brings together faculty, students, researchers, industry, government, innovators, and entrepreneurs to collaborate to improve the reliability, security and efficiency of the electric grid and overcome obstacles to the national adoption and implementation of sustainable energy.

    2) For the Wind Energy Outreach, the Center for Electricity Innovation hosted the 2010 meeting of the Consortium members on September 30, 2010 and the 2011 meeting on July 19, 2011 on IIT's main campus in Chicago. Ribbon Cutting Events were held to commemorate the installation of the 1.5MW GE Wind Unit and the 8kW Viryd Wind Unit (the Field Unit) at the 2011 meeting. In addition, the Center for Electricity Innovation hosted the first Great Lakes Symposium on Smart Grid and the New Energy Economy on October 18-19, 2011 and the second on September 24-26, 2012 on IIT's main campus in Chicago. The Symposium featured keynote and plenary sessions, technical presentations, and tutorials by international experts on renewable energy applications.

# 1. Introduction

The Illinois Institute of Technology (IIT) was awarded by the U.S. Department of Energy to lead an extensive effort in forming a world-class wind energy consortium (the Consortium) of multiple universities (domestic and international) and multiple industry participants (all types of wind energy stakeholders) to perform focused research and development on critical wind energy challenges identified in the "20% Wind Energy by 2030" report, including wind technology challenge, grid system integration, and workforce development.

The project started in January 2010 and ended in August 2012. The Principle Investigator of this project is Dr. Mohammad Shahidehpour, Director of the Robert W. Galvin Center for Electricity Innovation at IIT. The Project Team Members (in Alphabetical Order) include Acciona Wind Energy USA, Alstom Grid, Dakota Power, Electric Power Research Institute, EnerNex, Innovative Technology Applications Company, Intellergy, Intelligent Power Solutions, Invenergy, Keyworks, McCoy Energy, S&C Electric, SmartSignal (Now GE Intelligent Platforms), Southern Illinois University, Three Point Square, University of Chicago, Wiedman Power System Consulting.

**Project Objectives.** The Consortium's research and development objectives are focused on addressing several challenges identified in the "20% Wind Energy by 2030" report, i.e., wind technology, grid system integration, and workforce development. In particular, (1) The consortium members will develop control algorithms for enhancing the reliability of wind turbine components; (2) The consortium members will develop advanced operation and planning tools for accommodating the high penetration of intermittent wind energy in electric power utility systems. (3) The consortium members will educate the stakeholders on critical issues related to the wind energy research and development. (4) The world-class wind energy education and research programs developed by the consortium will outlast the proposed two-year period of the project.

**Project Scope.** The project will be performed in phases. In Phase 1, the consortium members will procure a utility-scale wind turbine at a wind farm and install a small wind turbine at IIT. In Phase 2, the consortium members will perform research on the wind turbine reliability. In Phase 3, the consortium members will perform wind energy related research and development to facilitate the integration of wind into the electric power grid system. In Phase 4, the consortium members will engage in the workforce development for wind energy research, design, and integration.

**Summary of Project Activities.** During the two-year project period since January 2010, the consortium members have developed control algorithms for enhancing the reliability of wind turbine components. The consortium members have developed advanced operation and planning tools for accommodating the high penetration of variable wind energy. The consortium members have developed extensive education and research programs for educating the stakeholders on critical issues related to the wind energy research and development. In summary,

- The Consortium procured one utility-grade wind unit and two small wind units. Specifically, the Consortium procured a 1.5MW GE wind unit by working with the world leading wind energy developer, Invenergy, which is headquartered in Chicago, in September 2010. The Consortium

also installed advanced instrumentation on the turbine and performed relevant turbine reliability studies. The site for the wind unit is Invenergy's Grand Ridge wind farmin Illinois. The Consortium, by working with Viryd Technologies, installed an 8kW Viryd wind unit (the Lab Unit) at an engineering lab at IIT in September 2010 and an 8kW Viryd wind unit (the Field Unit) at the Stuart Field on IIT's main campus in July 2011, and performed relevant turbine reliability studies. The operation of the Field Unit is also monitored by the Phasor Measurement Unit (PMU) in the nearby Stuart Building. The Consortium commemorated the installations at the July 20, 2011 ribbon-cutting ceremony.

- The Consortium's researches on turbine reliability included (1) Predictive Analytics to Improve Wind Turbine Reliability; (2) Improve Wind Turbine Power Output and Reduce Dynamic Stress Loading Through Advanced Wind Sensing Technology; (3) Use High Magnetic Density Turbine Generator as Non-rare Earth Power Dense Alternative; (4) Survivable Operation of Three Phase AC Drives in Wind Generator Systems; (5) Localization of Wind Turbine Noise Sources Using a Compact Microphone Array; (6) Wind Turbine Acoustics - Numerical Studies; and (7) Performance of Wind Turbines in Rainy Conditions.
- The Consortium's researches on wind integration included (1) Analysis of 2030 Large-Scale Wind Energy Integration in the Eastern Interconnection; (2) Large-scale Analysis of 2018 Wind Energy Integration in the Eastern U.S. Interconnection; (3) Integration of Non-dispatchable Resources in Electricity Markets; (4) Integration of Wind Unit with Microgrid.
- The Consortium's education and outreach activities on wind energy included (1) Wind Energy Training Facility Development; (2) Wind Energy Course Development; (3) Wind Energy Outreach.

## 2. Background

Illinois Institute of Technology (IIT), with an ABET accredited engineering program, has led an extensive effort in forming a world-class wind energy consortium (the Consortium) of multiple universities (domestic and international) and multiple industry participants (all types of wind energy stakeholders) to perform focused research and development on critical wind energy challenges identified in the "20% Wind Energy by 2030" report, including wind technology challenge, grid system integration, and workforce development.

The Consortium worked with the world leading wind energy developer, Invenergy, which is headquartered in Chicago, to procure a 1.5MW GE wind unit, and perform relevant turbine reliability studies. The site for the wind unit is the Invenergy's wind farm at the LaSalle County (adjacent to Marseilles), Illinois. The site which is within the 50 mile of IIT is an NREL Class 3 or better wind site as verified by multiple years of onsite data. The Invenergy's extensive experience in the deployment and operation of large numbers of wind turbines in the United States provided guidance to the Consortium for conducting world-class wind energy research and development. The Consortium also worked with the world-leading small wind turbine manufacturer, Viryd Technologies, to procure and install an 8KW Viryd wind unit at the IIT campus. Viryd also provided the second turbine to IIT which is installed in one of the engineering laboratories and used for performing relevant turbine reliability studies. IIT also utilized the two Viryd turbines on its campus to promote the public awareness on wind energy.

The Consortium consists of a world-class leading team and advisory board. The principal investigator (PI) is Dr. Mohammad Shahidehpour, who is the Bodine Distinguished Professor of IIT's ECE Department and the Director of the Robert W. Galvin Center for Electricity Innovation at IIT. He has a 30-year experience in electric power system research. Dr. Shahidehpour was the VP for Publications of the IEEE Power and Energy Society and had facilitated the publication of two new and very prestigious IEEE Transactions on Sustainable Energy and Smart Grid. Dr. Shahidehpour is also leading a DOE-funded Perfect Power project at IIT with a total budget of $13,000,000, a DOE-funded Wind Integration project with a two-year budget of $750,000, a DOE-funded Smart Grid Workforce Development project with a total budget of $12,000,000, and several NSF-funded projects on wind energy research and utilization.

The Consortium is led by IIT, which has a long history of offering one of the finest electrical power programs since 1930's. Other university consortium members include the world-renowned **University of Chicago**, as well as **Southern Illinois University** and four internationally prestigious universities with a strong wind energy program: **University of Castilla-La Mancha (Spain), University of São Paulo (Brazil), Aristotle University of Thessaloniki (Greece), and Polytechnic University of Bucharest (Romania)**. The international faculty and student members participated at the consortium workshops and shared their innovative ideas with American counterparts. The industry consortium members include all types of wind energy stakeholders: **wind turbine companies** (GE Energy, Viryd Technologies, Acciona Wind Energy USA), **wind energy developers** (Invenergy, Pampa Energia Eolica (Brazil), PS Wind Management (Romania)), **power transmission system operators** (ComEd/Exelon, ISO New England, British Columbia Transmission Corporation), **wind energy control device manufacturers and software companies** (Boeing Advanced Global Services & Support, Honeywell, Dakota Power, EnerNex Corporation,

SmartSignal Corporation, Innovation Technology Applications Company) and **energy system consultants** (Electric Power Research Institute, AREVA T&D, Keyworks, Intelligent Power Solutions, McCoy Energy, Wiedman Power System Consulting).

**Members of the *World-Class Wind Energy Consortium***

| **University Members** | **Point of Contact (Professor)** |
|---|---|
| Illinois Institute of Technology (Lead) | Mohammad Shahidehpour, (ms@iit.edu) |
| University of Chicago | John Birge, (john.birge@chicagobooth.edu) |
| Southern Illinois University | Morteza Daneshdoost, (daneshdo@siu.edu) |
| University of Castilla - La Mancha (Spain) | Antonio Conejo, (Antonio.Conejo@uclm.es) |
| University of São Paulo (Brazil) | Newton Bretas, (ngbretas@sc.usp.br) |
| Aristotle University of Thessaloniki (Greece) | Anastasio Bakirtzis, (bakiana@eng.auth.gr) |
| Polytechnic University of Bucharest (Romania) | Mircea Eremia, (eremia1@yahoo.com) |
| **National Labs Members** | **Point of Contact** |
| Argonne National Laboratory | Jianhui Wang, CEEESA (jianhui.wang@anl.gov) |
| National Renewable Energy Laboratory | Fort Felker, Director of the National Wind Technology Center, (fort.felker@nrel.gov) |
| Sandia National Laboratory | Matthew Barone, Wind Energy Technology (mbarone@sandia.gov) |
| **Industry Members** | **Point of Contact** |
| ***Wind Turbine Companies*** | |
| GE Energy | Steve Moffitt, Account Executive (steven.moffitt@ge.com) |
| Viryd Technologies, Inc. | John Langdon, CEO (jlangdon@viryd.com) |
| Acciona Wind Energy USA | Frank Bristol, Director of Transmission (fbristol@acciona-na.com) |
| ***Wind Energy Developers*** | |
| Invenergy, LLC | Michael Polsky, President and CEO (MPolsky@invenergyllc.com) |
| Pampa Energia Eolica (Brazil) | Edgar Pereira, Director (edgar@pampaeolica.com.br) |
| PS Wind Management (Romania) | Radu Popoiu, Managing Director (rpopoiu@vivalex.ro) |

| | |
|---|---|
| ***Power Transmission System Operators*** | |
| ComEd/Exelon | Terence Donnelly, COO (terence.donnelly@ComEd.com) |
| ISO New England | Eugene Litvinov, Director of Business Architecture and Technology (elitvinov@iso-ne.com) |
| British Columbia Transmission Corporation | Ebrahim Vaahedi, CTO (Ebrahim.Vaahedi@bctc.com) |
| ***Wind Energy Control Devices and Software Companies*** | |
| Honeywell | Tariq Samad, Corporate Fellow (tariq.samad@honeywell.com) |
| Dakota Power | Richard Gowen, President (dick@dplwed.com) |
| EnerNex Corporation | Erich Gunther, Chairman and CTO (erich@enernex.com) |
| SmartSignal Corporation | David R Bell, VP Application Engineering David.Bell@ge.com |
| Innovation Technology Applications Company | Alan Cain, President (abcain@itacllc.com) |
| ***Energy System Consultants*** | |
| Keyworks | Kurt Yeager, President and CEO (KYEAGER@epri.com) |
| Electric Power Research Institute | Don Von Dollen, Program Manager, IntelliGrid (DVONDOLL@epri.com) |
| AREVA T&D | Jay Giri, Director of Power System Technology and Strategic Initiatives (jay.giri@areva-td.com) |
| Intelligent Power Solutions | John Kelly, President (jkelly@ippconnect.com) |
| McCoy Energy | Paul McCoy, President (Pdpdm@aol.com) |
| Wiedman Power System Consulting | Thomas Wiedman, President (twieds@aol.com) |

IIT Faculty Participants

| **Faculty Name** | **Department** | **Area of Expertise Related to Wind Energy Research** |
|---|---|---|
| Mohammad Shahidehpour, PI (ms@iit.edu) | Electrical and Computer Engineering | Wind energy unit integration and optimization |
| Hamid Arastoopour (arastoopour@iit.edu) | Wanger Institute for Sustainability and Energy Research | Turbine design optimization using computational fluid dynamics |
| Zuyi Li (lizu@iit.edu) | Electrical and Computer Engineering | Wind integration and deployment |
| Ali Emadi (emadi@iit.edu) | Electrical and Computer Engineering | Wind turbine control and operation |
| Alireza Khaligh (khaligh@ece.iit.edu) | Electrical and Computer Engineering | Power electronic applications to wind turbine control |
| Mahesh Krishnamurthy (kmahesh@ece.iit.edu) | Electrical and Computer Engineering | Turbine health monitoring and diagnosis |
| Ganesh Raman (ramanar@iit.edu) | Mechanical, Materials and Aerospace Engineering | Optimal turbine design and noise reduction |
| Dietmar Rempfer (rempfer@iit.edu) | Mechanical, Materials and Aerospace Engineering | Wind energy prediction and optimal ramping events |
| Candace Wark (wark@iit.edu) | Mechanical, Materials and Aerospace Engineering | Turbine design optimization using computational fluid dynamics |
| Peter Land (land@iit.edu) | College of Architecture | High-rise building retrofitting with wind turbine |
| Navid Sabbaghi (nsabbagh@stuart.iit.edu) | Stuart School of Business | Economics of wind integration and environment impacts |

# 3. Results and Discussions

## 3.1 Consortium Wind Unit Installation

### 3.1.1 Wind Unit Installation at Grand Ridge, Illinois

#### *A. Wind Unit Procurement*

We proposed the installation of a 1.5MW GE wind unit at the Grand Ridge wind facility located near Marseilles, Illinois. The facility is owned by Invenergy, a Chicago-based wind energy developer, which has installed 140 similar wind units and is planning to install additional units at the location. It was planned that Invenergy will procure the test wind turbine within 6 months of the date of the award and install the test wind turbine within 12 months of the date of the award.

In April 2010 (three months after the date of the ward), it had become apparent that there would be a significant delay in the installation of a new unit, primarily due to environmental and permitting issues for a new unit. In particular, the Illinois Department of Natural Resources (DNR) had a consulting role in determining Special Use Permits (SUP) in the state of Illinois. For the next phase of the Grand Ridge facility, which had not yet been constructed, DNR had recommended that Invenergy sought a state Incidental Take Permit (ITP) that would allow for Indiana Bat takes. This recommendation was weighed by the County that would issue the SUP. A state ITP had an estimated lead time of at least 6 months and a Federal ITP had a lead time of about 2 years. DNR did not recommend an ITP for previous phases of Grand Ridge facility, which were permitted in 2008 and 2009. This change reflected a rising concern across the country for the Indiana Bat. In addition to being Federally listed as endangered, Indiana Bats (as well as other bat species) were facing further threat from the White Nose Syndrome (http://www.fws.gov/northeast/wnsabout.html).

IIT then decided to acquire an existing unit at Grand Ridge. The proposed existing unit for acquiring was Unit #139. The installation of Unit #139 was completed in December 2009 and the unit was in operation for a few months. The Consortium designated Invenergy as the entity to install test equipment on the turbine in order to perform all proposed research tasks.

The consortium felt that the overall impact of the acquiring an existing unit was much bigger than waiting to get the permit and having the purchase and installation happen in unknown periods, which could be well beyond the two-year project period. Such acquisition allowed all proposed research tasks to be completed according to schedule, and more importantly, allowed the economic and job benefits required by the Recovery Act to occur in a timely fashion. Additional benefits would result from such acquisition. For instance, the interconnection of the wind unit with the real grid would make any research results more practical and meaningful.

Per the approval of the DOE and the mutual agreement between IIT and Invenergy, a Wind Turbine Sale Agreement (Agreement) was signed on September 27, 2010. The Agreement enabled IIT to purchase and own the unit while Invenergy maintained the unit and provided an electrical generation interconnection to the grid.

The purchased GE Wind Turbine Generator (WTG) includes (1) Nacelle: 1.5MW SLE, which includes generator, main shaft, bearings, drive train couplings, rotor hub, gearbox (with oil and cold weather fixtures allowing the unit to withstand design loads at -40C), generator cooling system, hydraulic system, yaw drive system, blade pitch mechanism including drive motors and control system, wind speed and direction sensors, lightning protection system, braking system, instrumentation, and other related components; (2) Tower: 80m MTS 3-section with T-flange, which includes 80m three section steel tower with T-flange base for bolting to concrete foundation. Tower internals include ladders, platforms, power cabling (with all necessary terminations), fall protection, lighting and other items; (3) Blade set: 77 meter rotor diameter, which includes three fiberglass epoxy resin blades; (4) Controller; (5) Hub; (6) Control and data documentation systems: The turbine will report data back to the Central GE SCADA and PI systems for storage. The turbine will also accept commands from the SCADA system and Wind Farm Management System (WFMS) to keep the power and voltage requirements of the site in balance and compliant with NERC, ComEd and PJM. These systems themselves are excluded from the Agreement, however all data related to the WTC being purchased (including the right to access the same) will be owned by IIT.


**Figure 1: Screenshots of IIT Wind Turbine at Grand Ridge Wind Farm**

### *B. GE 1.5MW Wind Turbine*

The 1.5SLE/XLE 60Hz is a three bladed, upwind, horizontal-axis wind turbine with a rotor diameter of 77/82.5 m, respectively. The turbine rotor and nacelle are mounted on top of a tubular tower. Different hub heights are available. The machine employs active yaw control (designed to steer the machine with respect to the wind direction), active blade pitch control (designed to regulate turbine rotor speed), and a generator/power electronic converter system.

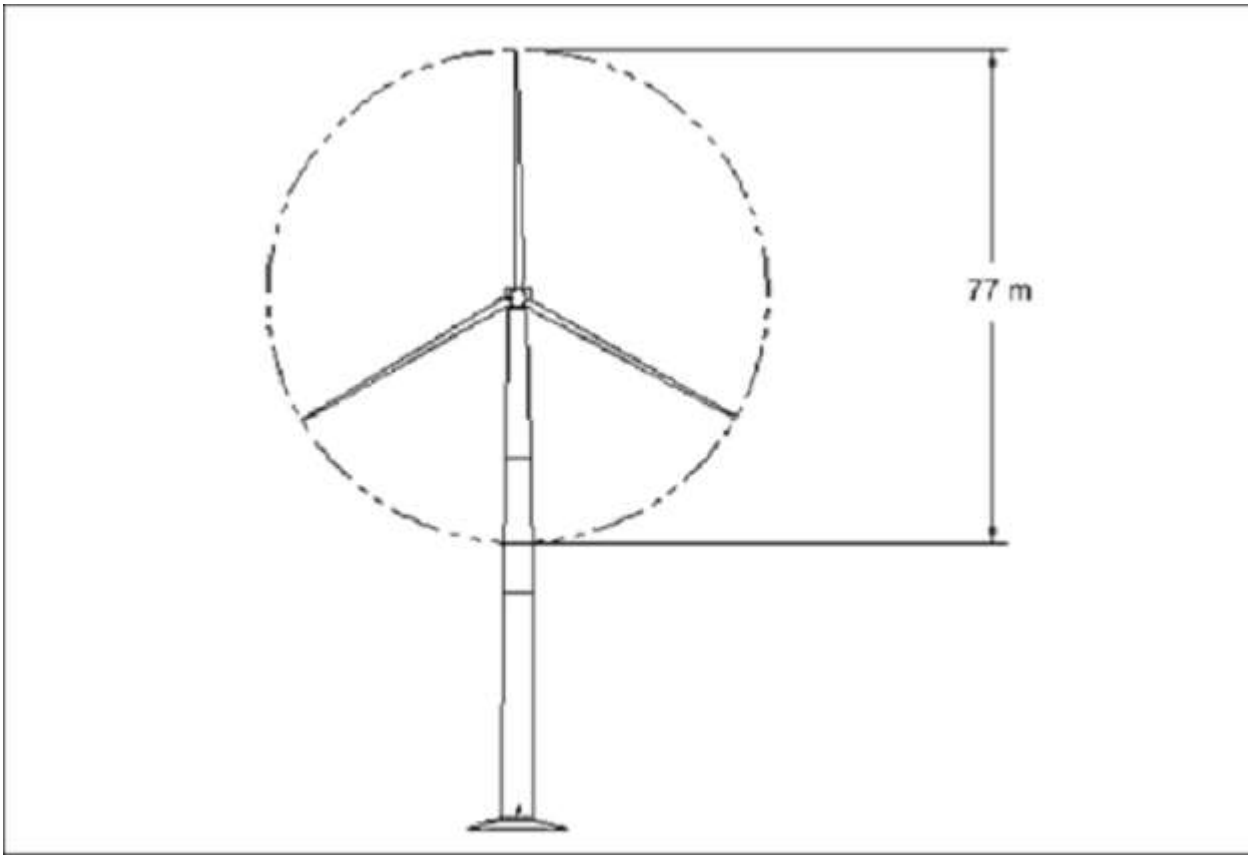


**Figure 2: GE Energy 1.5SLE/XLE 60Hz Wind Turbine Generator**

The wind turbine features a distributed drive train design wherein the major drive train components including main shaft bearing, gearbox, generator, yaw drives, and control panel are attached to a bedplate.

**Rotor**

The sle/xle rotor diameter is 77/82.5 m, resulting in a swept area of 4,657/5,346 m2, and is designed to operate between 10 and 20/9 and 18 revolutions per minute (rpm). Rotor speed is regulated by a combination of blade pitch angle adjustment and generator/converter torque control. The rotor spins in a clock-wise direction under normal operating conditions when viewed from an upwind location. Full blade pitch angle range is approximately 90 degrees, with the zero degree position being with the blade flat to the prevailing wind. The blades being pitched to a full feather pitch angle of approximately 90

degrees accomplishes aerodynamic braking of the rotor; whereby the blades “spill” the wind thus limiting rotor speed.

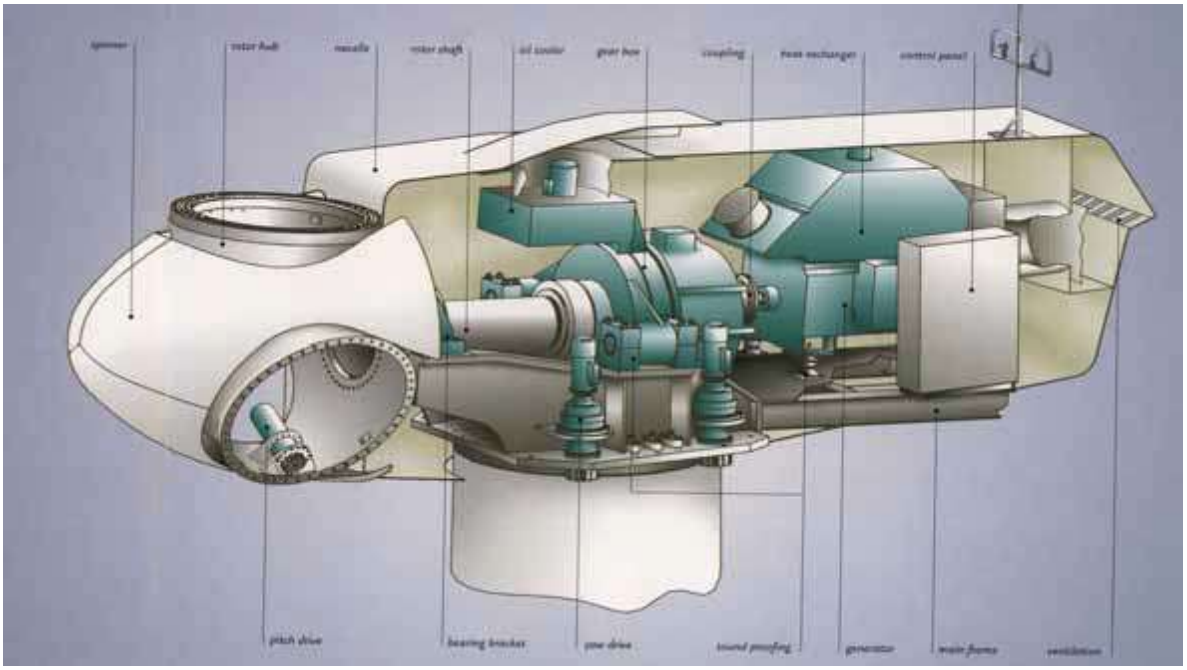

**Figure 3: GE Energy 1.5SLE/XLE 60Hz Wind Turbine Nacelle Layout**

**Blades**

There are three rotor blades used on each GE Energy 1.5SLE/XLE 60Hz wind turbine. The airfoils transition along the blade span with the thicker airfoils being located inboard towards the blade root (hub) and gradually tapering to thinner cross sections out towards the blade tip.

**Blade Pitch Control System**

The rotor utilizes three (one for each blade) independent electric pitch motors and controllers to provide adjustment of the blade pitch angle during operation. Blade pitch angle is adjusted by an electric drive that is mounted inside the rotor hub and is coupled to a ring gear mounted to the inner race of the blade pitch bearing. GE’s active-pitch controller enables the wind turbine rotor to regulate speed, when above rated wind speed, by allowing the blade to “spill” excess aerodynamic lift. Energy from wind gusts below rated wind speed is captured by allowing the rotor to speed up, transforming this gust energy into kinetic energy that may then be extracted from the rotor. Independent back-up units are provided to power each individual blade pitch system to feather the blades and shut down the machine in the event of a grid line outage or other fault. By having all three blades outfitted with independent pitch systems, redundancy of individual blade aerodynamic braking capability is provided.

**Hub**

The hub is used to connect the three rotor blades to the turbine main shaft. The hub also houses the three electric blade pitch systems and is mounted directly to the main shaft. Access to the inside of the hub is provided through a hatch

**Gearbox**

The gearbox in the wind turbine is designed to transmit power between the low-rpm turbine rotor and high-rpm electric generator. The gearbox is a multi-stage planetary/helical design. The gearbox is mounted to the machine bedplate. The gearbox mounting is designed such that it minimizes the vibration and noise transfer to the bedplate. A parking brake is mounted on the high-speed shaft of the gearbox. The gearbox is lubricated by a forced lubrication system and a filter maintains oil cleanliness.

**Bearings**

The blade pitch bearing is designed to allow the blade to pitch about a span-wise pitch axis. The inner race of the blade pitch bearing is outfitted with a blade drive gear that enables the blade to be driven in pitch by an electric gear-driven motor/controller. The main shaft bearing is a roller bearing mounted in an arrangement designed to provide bearing and alignment of the internal gearing shafts and accommodate radial and axial loads.

**Brake System**

The electrically actuated individual blade pitch systems act as the main braking system for the wind turbine. Braking under normal operating conditions is accomplished by feathering the blades out of the wind. Any single feathered rotor blade is designed to slow the rotor, and each rotor blade has its own back up to provide power to the electric drive in the event of a grid line loss. The turbine is also equipped with a mechanical brake located at the output (high speed) shaft of the gearbox. This brake is only applied as an auxiliary brake to the main aerodynamic brake and to prevent rotation of the machinery as required by certain service activities.

**Generator**

The generator is a doubly fed induction type. The generator is mounted to the bedplate and the mounting is designed so as to reduce vibration and noise transfer to the bedplate.

**Gearbox/generator Coupling**

Designed to protect the drive train from excessive torque loads, a special coupling is provided between the generator and gearbox output shaft, which is equipped with a torque-limiting device sized to keep the maximum allowable torque below the maximum design limit of the drive train torque.

**Yaw System**

The bearing attached between the nacelle and tower facilitates yaw motion. Yaw drives (with brakes that engage when the drive is disabled) mesh with the gear of the yaw bearing and steer the machine to track the wind in yaw. The automatic yaw brakes engage in order to prevent the yaw drives from seeing peak loads from any turbulent wind. The controller activates the yaw drives to align the nacelle to the wind direction based on the wind vane sensor mounted on the top of the nacelle. A sensor provides a record of nacelle yaw position and cable twisting. After the sensor detects excessive rotation in one direction, the controller automatically brings the rotor to a complete stop, untwists the cable by counter-yawing of the nacelle, and restarts the wind turbine.

**Tower**

The wind turbine is mounted on top of a tubular tower, which is manufactured in sections from steel plates. Access to the turbine is through a steel door at the base of the tower. Service platforms are provided. A ladder provides access to the nacelle and also supports a fall arrest safety system. Interior lights are installed at critical points from the base of the tower to the tower top.

**Nacelle**

The nacelle houses the main components of the wind turbine generator. Access from the tower into the nacelle is through the bottom of the nacelle. The nacelle is ventilated, and illuminated with electric light. A hatch provides access to the blades and hub.

**Anemometer, Wind Vane, and Lightning Rod**

An anemometer, wind vane, and lightning rod are mounted on top of the nacelle housing. Access to these devices is accomplished through the hatch in the nacelle.

**Lightning Protection**

The rotor blades are equipped with lightning receptors mounted in the blade. The turbine is grounded and shielded to protect against lightning, however, lightning is an unpredictable force of nature and it is possible that a lightning strike could damage various components notwithstanding the lightning protection employed in the machine.

**Wind Turbine Control System**

The wind turbine machine can be controlled locally either automatically or manually. Control signals can also be sent from a remote computer via a Supervisory Control and Data Acquisition System (SCADA) (purchased separately), with local lockout capability provided at the turbine controller. Service switches at the tower top prevent service personnel at the bottom of the tower from operating certain systems of the turbine while service personnel are in the nacelle. To override any machine operation, emergency-stop buttons located in the tower base and in the nacelle can be activated to stop the turbine in the event of an emergency.

**Power Converter**

The wind turbine uses a power converter system that consists of a converter on the rotor side, a DC intermediate circuit, and a power inverter on the grid side. This allows for variable rotor speed while keeping in synchronization with the grid frequency. The converter system consists of a power module and associated electrical equipment. Variable output frequency of the converter allows variable speed operation of the generator. The technical data for rotor, pitch system, and operational limits are shown in the following tables. The yaw rate is 0.5 degree / s.

**Table 1: Technical Data for the 1.5MW GE Wind Turbine: Rotor**

| | |
|---|---|
| Diameter | 77/82.5 m |
| Number of blades | 3 |
| Swept area | 4,657/5,346 m2 |
| Rotor speed range | 10 – 20/9 – 18 rpm |
| Rotational direction | Clockwise looking downwind |
| Maximum tip speed | 73.8 m/s |
| Orientation | Upwind |
| Speed regulation | Pitch control |
| Aerodynamic brakes | Full feathering |

**Table 2: Technical Data for the 1.5MW GE Wind Turbine: Pitch System**

| | |
|---|---|
| Principle | Independent blade pitch control |
| Actuation | Individual electric drive |

**Table 3: Operational Limits of the 1.5MW GE Wind Turbine**

| | |
|---|---|
| Height above sea level | Maximum 2500 m. See notes in section “Maximum standard ambient temperature” below. |
| Minimum standard ambient temperature (operational/survival) | Standard Weather Package: -15°C / -20°C<br>Cold Weather Package: -30°C / -40°C<br>(Switching on takes place with a hysteresis of 5°C after a cold temperature trip) |
| Maximum standard ambient temperature (operational/survival) | +40°C / +50°C<br>The turbine has a feature by which the maximum output is reduced if the component temperatures approach specified thresholds, such that turbine trips are minimized. This feature is especially beneficial for higher altitudes, since the heat transfer properties of air are diminished with decreased density. Note that the units are not “derated” per any specific site conditions; the unit’s reaction related to this feature is based solely on sensor temperatures. |
| Wind conditions according to IEC 61400 for the standard temperature range | Standard Weather Package:<br>8.5 m/s @ 18 % turbulence @ 15 m/s<br>Cold Weather Package:<br>8.5 m/s @ 16% turbulence @ 15 m/s |
| Maximum extreme gust (10 min) according to IEC 61400 | Standard Weather Package: 39.3 m/s<br>Cold Weather Package 37.2 m/s |
| Maximum extreme gust (3 s) according to IEC 61400 | Standard Weather Package: 55 m/s<br>Cold Weather Package: 52 m/s |

As a leading global provider of energy products and services, GE continues to invest heavily in advancing its 1.5 MW wind turbine product line. With a core focus on reliability, efficiency, and multi- generational product advancements, GE's 1.5 MW wind turbine is the most widely used turbine in its class. GE's WindBOOST control system upgrade is a unique offering in the wind industry and the latest addition to the 1.5 MW platform, which helps increase the annual energy production (AEP) of a wind plant by allowing increased power output (kW) under certain conditions. This advancement helps increase the return on wind plant investments for our customers. The WindBOOST control system is offered as an option available on new and existing 1.5 MW SLE 60 Hz wind turbine generators with 80 m towers. The WindBOOST control system uses smart control algorithms to assess ambient conditions and calculates an increase in rotational speed of the turbine to maximize AEP. This additional speed increases output power by 100 kW from 1500 kW to 1600 kW. The WindBOOST control system also provides grid stability by allowing the turbine to maintain –0.9 to 0.9 Power Factor during operation. The maximum reactive power of the turbine is maintained by reducing additional output of the WindBOOST control system when grid conditions demand reactive power.

This transition is handled by the control system and returns the turbine to full additional power when grid Volt-Amp-Reactive (VAR) demand is satisfied. GE's WindBOOST control system is designed to minimize changes to turbine hardware components. This can reduce downtime during installation of this product. The WindBOOST control system is operator friendly, SCADA controlled, and can be remotely accessed to turn the feature on or off. Major features and benefits include

- Up to 4% increased annual energy output, resulting in higher return on investment
- Flexibility to increase power production when rates are highest
- Patent-pending control technology for optimum rotational speed, resulting in increased energy production
- Remote capability to turn feature on and off at the turbine level
- Increased power output while maintaining grid stability
- During Noise Reduction Operation WindBOOST control system is not active.

GE has developed controls to improve stall mitigation of the turbines during blade icing. Improved power output is achieved with optimized pitch controls, and minimizing the effects of icing on blade stall reduces potential blade vibrations. Snow and ice accretion on wind turbine blades is common for units located in winter climates. Winter blade ice-fouling can produce aerodynamic stall resulting in reduced power output (See Figure 4). Turbine operation with blade stall can also lead to increased blade vibration levels. In rare cases, blade vibrations at a resonant frequency can lead to blade damage. Anti-stall operation is accomplished with a blade tip speed ratio (TSR) algorithm executed by the PLC. The TSR pitch control algorithm intends to maximize power capture (CP) for the rotor while minimizing the risk of blade stall (See Figure 5). The tip speed ratio is calculated from turbine rotor speed and anemometer wind speed inputs. The modified pitch control scheme applies primarily for operation of the turbine during rated winds or higher. Annualized increase of energy production of approximately 1 to 3% can be achieved for sites with 4 to 6 months winter weather opportunity.

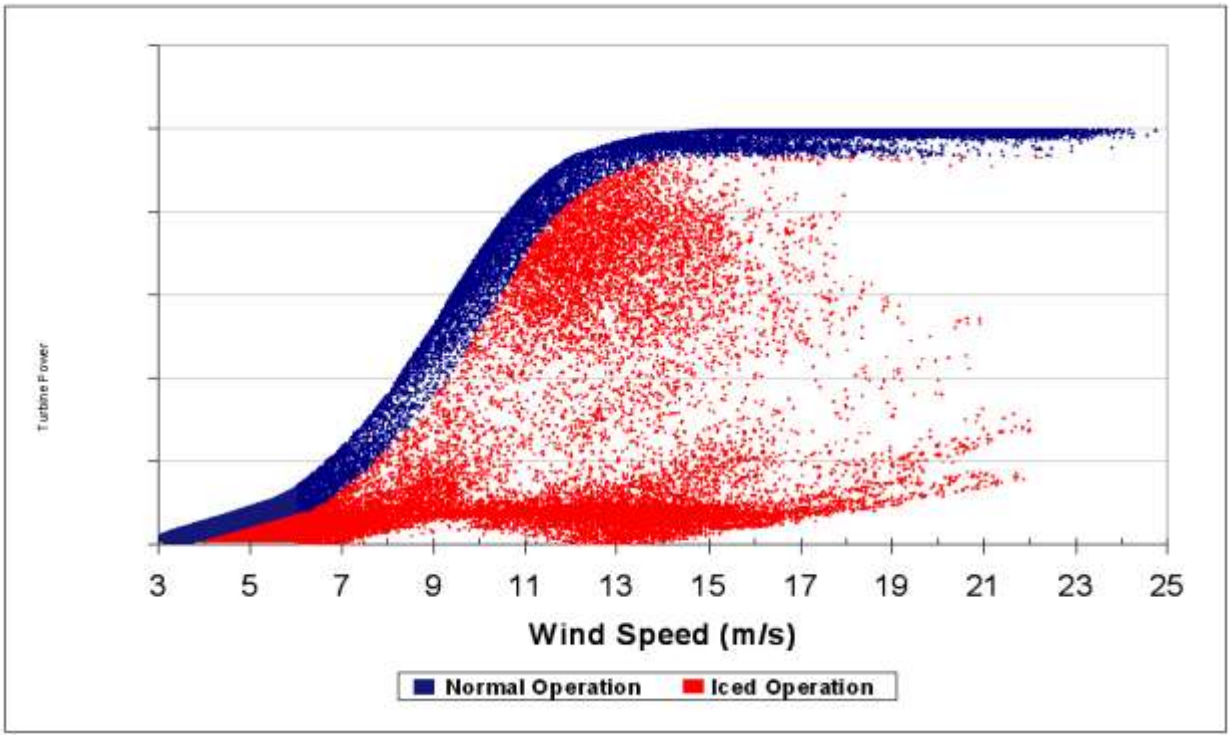


**Figure 4: Power performance for winter operation**

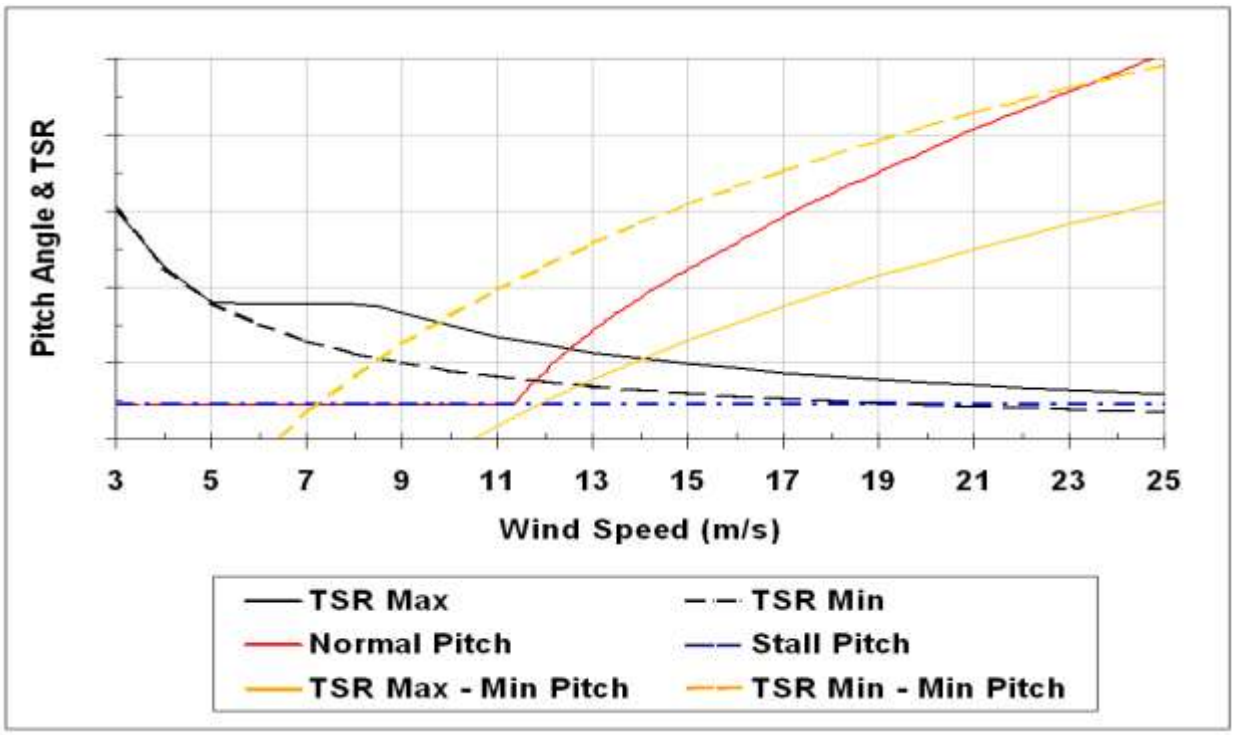


**Figure 5: TSR pitch control schedule**

### 3.1.2 Wind Unit Installation at IIT

IIT installed two 8kW Viryd Wind Turbine on campus which are used extensively for research and education. In the following we discuss the specifications of the Viryd unit and elaborate on the specifics of the two installations at IIT.

#### *A. Viryd 8kW Wind Turbine*

The Viryd Wind Turbine features a Continuously Variable Transmission (CVT) technology which is defined by its inventors as the next major advancement in the production of practical, clean energy from wind. A variable wind turbine is recognized as the best way of wind energy practical by maximizing efficiency and minimizing production cost. The Viryd Wind Turbine is also known, in general, as Wind Energy Conversion Systems (WECS).

At the heart of Viryd wind turbine technology is the NuVinci® Continuously Variable Planetary (CVP) transmission. This class of CVT technology and innovative energy management system now provides a solution that can make wind energy a more viable alternative by dramatically increasing power production at all wind speeds, greatly reducing system and maintenance costs, and significantly lowering the cost of energy Viryd utilizes NuVinci® continuously variable planetary (CVP) technology to provide benefits that reduce the cost of energy (COE) for wind turbines. Developed by Fallbrook Technologies Inc., NuVinci CVP technology is suitable for use in a wide variety of applications from automobiles to bicycles to wind turbines of all sizes. Viryd has an exclusive license from Fallbrook for the use of NuVinci technology in wind energy applications.

*NuVinci* technology for wind improves energy capture and can reduce both capital costs, and ongoing operations and maintenance. By increasing energy capture, reducing cost, and providing greater reliability, the Viryd system has the lowest cost of energy (COE) of any competitive system.

The *NuVinci* CVP provides automatic and continuously variable ratio change that changes rotor speed as wind speed changes. This enables the rotor to maintain high efficiency at all wind speeds. If a rotor spins too fast or slow its efficiency drops. Traditional small wind turbines suffer from varying rotor speeds at each wind speed, and all of these rotor speeds except for one produces losses in efficiency. A few small wind turbines, called constant speed wind turbines, have only one rotor speed no matter what the wind speed. These turbines suffer losses in efficiency at all wind speeds except for one (design speed or design condition).

| TURBINE | |
|---|---|
| System | 3 blade, horizontal axis, upwind |
| Rated Power | 8 kW at 10 m/s (23 mph)* |
| Control | Wireless internet accessible |
| Cut-in wind speed | 4.5 m/s (10 mph) |
| Cut-out wind speed | 25 m/s (56 mph) |
| Survival wind speed | 59 m/s (132 mph) |
| **ROTOR** | |
| Size | 8 m (26') diameter |
| Swept Area | 50 m² (541 ft²) |
| Material | Fiberglass with foam core |
| Yaw | Passive yaw, furling not required |
| Power Regulation | Stall control aerodynamic braking |
| Speed | Variable speed – 50 to 150 RPM |
| **GENERATOR** | |
| Type | Grid connected, induction generator |
| Output | 60 Hz, 240 Volts, Single Phase |
| Inverter | None |
| **TOWER** | |
| Standard | 24m (80') guyed, tilt-up, tubular |
| Optional Styles | Guyed or free-standing lattice or tubular |
| Optional Heights | 18m (60'), 30m (100'), 36m (120') |
| **SAFETY** | |
| Brake | Fail-safe, mechanical |
| Certifications | UL 1741/IEEE 1547 |
| Automatic Shut-Down | High wind, grid failure, overspeed |
| **QUALITY** | |
| Design Life | 20 year minimum design life |
| Warranty | 5 years |

*NOTE: V8000 actually achieves rated power at less than 11 m/s


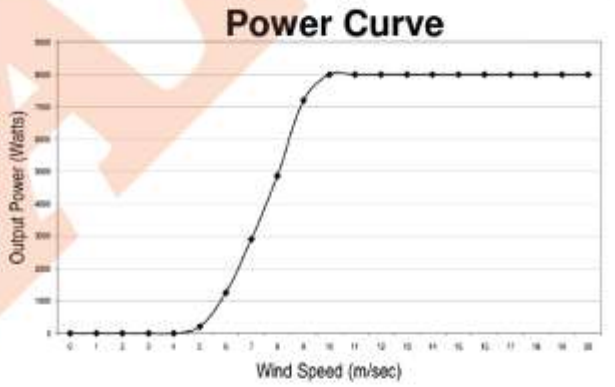


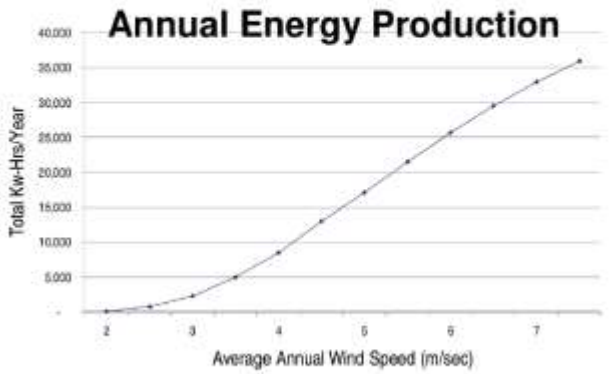


NOTE: Wind speed measured on standard Met tower at 10m, Power is at standard hub height of 24m

**Figure 6: Viryd 8KW Wind Turbine Technical Specification**

**Table 4: Viryd 8000 Technical Datasheet**

| Turbine | |
|---|---|
| System | 3 blades, horizontal axis, upwind |
| Rated power | 8 kW at 10 m/s (23 mph) |
| Control | |
| Cut-in wind speed | 4.5 m/s (10 mph) |
| Cut-out wind speed | 25 m/s (56 mph) |
| Survival wind speed | 59 m/s (132 mph) |
| Rotor | |
| Size | 8 m (26') diameter |
| Swept area | 50 m2 (541 ft2) |
| Material | Fiberglass with foam core |
| Yaw | Passive yaw, furling not required |
| Power regulation | Stall control aerodynamic braking |
| Speed | Variable speed - 50 to 150 rpm |
| Generator | |
| Type | Grid connected, induction generator |
| Output | 60 Hz, 240 volts, single phase |
| Inverter | None |
| Tower | |
| Standard | 24 m (80') guyed, tilt-up tubular |
| Optional styles | Guyed or free-standing lattice or tubular |
| Optional heights | 18 m (60'), 30 m (100'), 36 m (120') |
| Safety | |
| Brake | Fail-safe, mechanical |
| Certifications | UL 1741/IEEE 1547 |
| Automatic shut-down | High wind, grid failure, overspeed |
| Quality | |
| Design life | 20 year minimum |
| Warranty | 5 years |

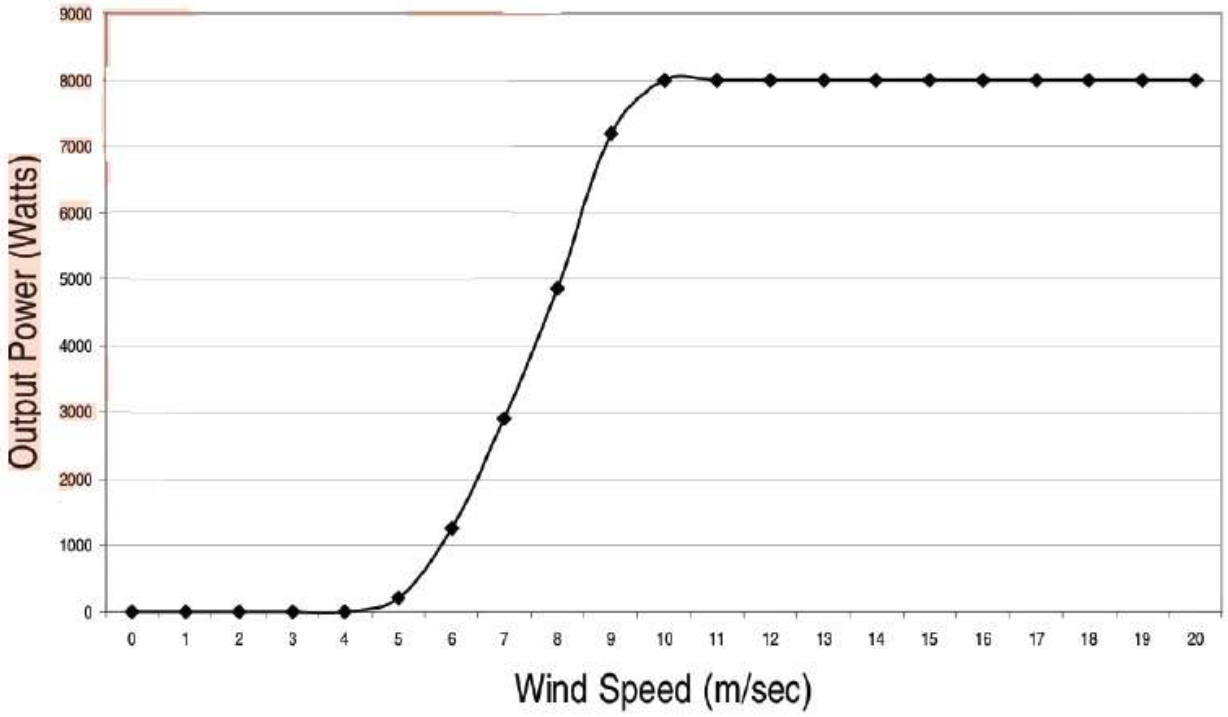


**Figure 7: Viryd 8KW Wind Turbine Power Curve**

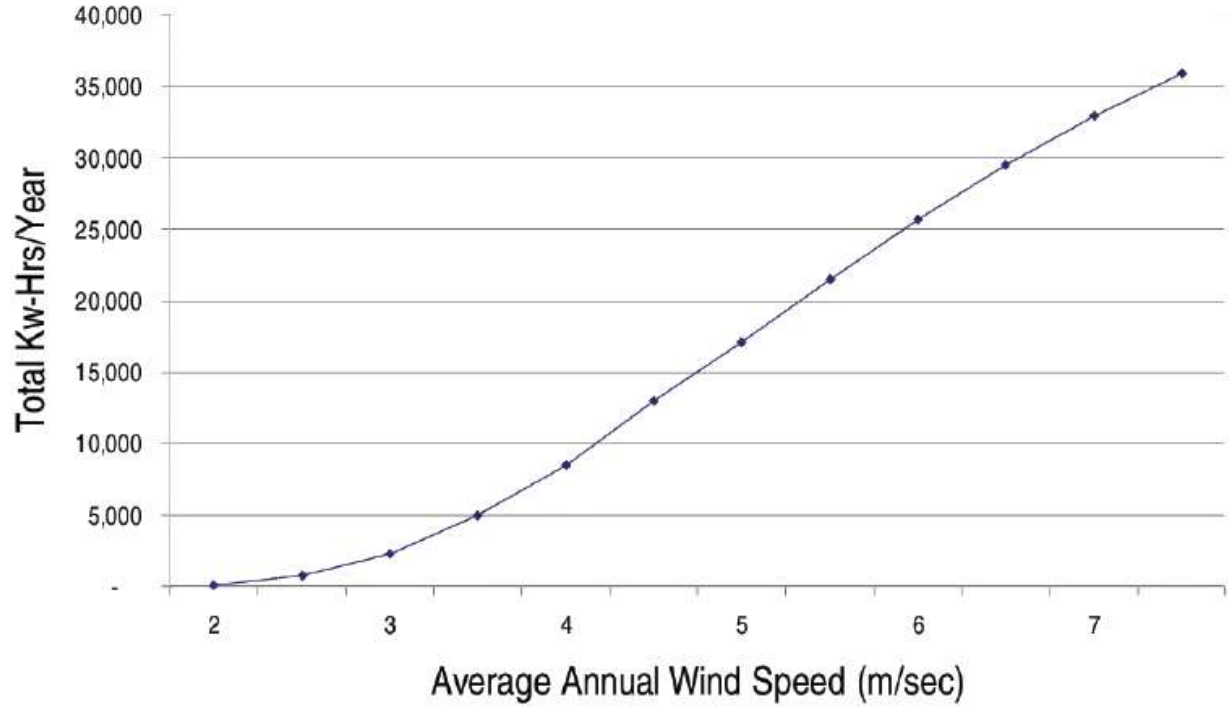


**Figure 8: Viryd 8KW Wind Turbine Annual Energy Production**


**Figure 9: Cross-Section and Components of the Viryd Wind Turbine**

The *NuVinci* CVP is the only technology that can produce and maintain the ideal rotor speed for every wind speed. The result is that wind turbines equipped with the NuVinci CVP capture more energy than traditional systems.

High winds produce too much power and can damage wind turbine drive trains. All wind turbines face the problem of how to handle excess power destroying the generator and other components in high winds.

Most small wind turbines employ a crude method called passive furling, which turns the rotor out of the wind when wind speeds are too high. Passive furl is unreliable because wind direction can suddenly change, hitting the rotor straight on during high winds. Small wind turbines compensate for this problem and inherently inaccurate furling by including a safety margin in their passive furl systems. The result is that small wind turbines that use passive furl actually see power production decrease in high winds.

Another method used to control excess power in high winds is called passive stall. With this method, the rotor blades transition to stall in high winds and become inefficient. The result is that wind turbines employing passive stall also produce less power in high winds.

The *NuVinci* CVP can precisely slow the rotor in high winds, shedding the exact amount of power necessary to maintain peak energy production, and capture more energy from the wind.

The unique ability of the *NuVinci* CVP to control rotor speed allows the use of a larger rotor than competing systems. Larger rotors exacerbate the problem of too much power entering the drive train from gusts and high winds. Because the *NuVinci* CVP can precisely control rotor speed, it can use a rotor with approximately 20% more area, resulting in nearly 20% more energy capture.

Variable speed small wind turbines use an inefficient device called an inverter to produce grid acceptable electricity. Good inverters, which advertise efficiencies up to 96%, are actually about 86% efficient when the time spent shut down or not producing power is considered. A gust in high winds can cause an inverter to shut down to prevent damage, and typically the inverter will remain off for a

programmed period of time (~ 5 minutes). A gust at low winds will cause an inverter to turn on, when the low wind speed can't produce power. An inverter will draw power during this standby time.

The *NuVinc*i CVP doesn't need an inverter because it can shift with wind speed changes, allowing it to eliminate the ~ 14% losses from the inverter and capture more energy from the wind than competing systems.

Viryd systems eliminate the inverter which is prone to failure from the variable and harsh conditions produced by the wind. Downtime from inverter failures is expensive, and troubleshooting the source can be difficult. Often a professional must be hired or the entire inverter needs to be replaced. If the source of failure is found, replacement parts can often have long lead times.

Gusts produce torque spikes which can damage wind turbine drive trains. The NuVinci CVP is a compliant device that spreads the torque spike over time. It can also accelerate the rotor to reduce the torque spike. This ability to absorb torque spikes smoothens the variable effects of the wind and helps keep the Viryd system operating longer and without interruption.

### *B. Viryd Lab Unit Installation at IIT*

Viryd Technologies designed, built, tried out and debugged, shipped, installed and trained IIT personnel on a bench top Viryd wind turbine drivetrain system (Figure 10). The system provided by Viryd included all components that are in the Viryd 8000 wind turbine along with additional instrumentation required to run the tests detailed below. This bench top system was designed for use in experimentation and configured to allow several tests to be conducted and for additional tests to be added in the future.

Test Stand includes:

- Test Stand Base
- Mounting System for the Viryd 8000 drivetrain
- Drive motor and Variable frequency drive
- Gear Box (sized to allow system to mimic rotor)
- Coupling to connect drive system to drivetrain
- Inertia (wheel or gearbox)
- Labview DAQ System for operating the drive motor and variable speed drive as well as any instrumentation to e collected and analyzed in the DAQ
- Personal Computer
- Labview software license to be discussed if IIT has current license
- Labview application software configured to conduct several pre-determined tests

Drivetrain includes:

- Viryd 8000W drivetrain including speed increaser- Brake- NuVinci CVP- Generator
- All Viryd 8000 Electrical components, controls and software installed in a NEMA 4 enclosure including a Zigbee wireless communications card.
- All Heat Exchanger and fluid transport
- All pressure and temperature measurements will use a thermistor por pressure transducer as opposed to the normal pressure switch and thermistor

- 1 torque transducer at the input to the drivetrain
- 1 torque transducer at the output of the NuVinci CVP
- Voltage and current probes
- Wattmeter
- Electrical connections will be made at the electrical panel as NO Slip rings will be supplied with this system

Software is provided to perform the following tests: The software will be configured with a graphical user interface to operate the tests below. This interface will be configurable for future testing.

- Static power sweeps – Input static power levels and vary NuVinci CVP ratio manually. Maximize output power for each input power condition
- Component level efficiency testing versus speed, torque or power
- Static power sweeps to measure system level efficiency at varying Nuvinci CVP ratio
- Static power sweeps to measure NuVinci CVP lubrication temperate and generator temperature
- Dynamic wind simulations with capability to modify wind speed, turbulence intensity and wind cycle duration
- Power quality including power factor, THD versus output power
- Cumulative output power for various duty cycles and set-ups
- Error log file (continuous)
- Software to remotely monitor system via wireless network

Additional testing or instrumentation that has been added in addition to the baseline proposal:

- Speed Increaser oil temperature. Solution will be a pipe plug thermocouple capable of 0-250C temperature range. Adapter from speed increaser to NPT fitting will also be supplied.
- Accelerometers mounted in various areas to measure vibration in multiple axis. Solution will be tri-axial accelerometers mounted in 2 locations as well as required cable and signal conditioners.
- Pressure measurements if NuVinci CVP. Solution will utilize a Honeywell Sensotech pressure transducer for measuring the pressure at the input side of the NuVinci CVP.
- Obtain bearing “signature” analysis which could be used as a baseline and compared to as time and testing accumulate. Solution initially will be to have a discrete analysis completed on the system to establish the baseline signatures of all rotating components. These baselines will be documented with the machine for future analysis and if automated data collection and analysis system shall be added
- Ability to simulate very high ambient temperature conditions. Solution is to build an insulated containment system to capture the waste heat being rejected by the components. It can be calculated that the waste heat will allow for the system to reach temperature of 125F or higher similar to that inside a nacelle in an extreme warm environment.

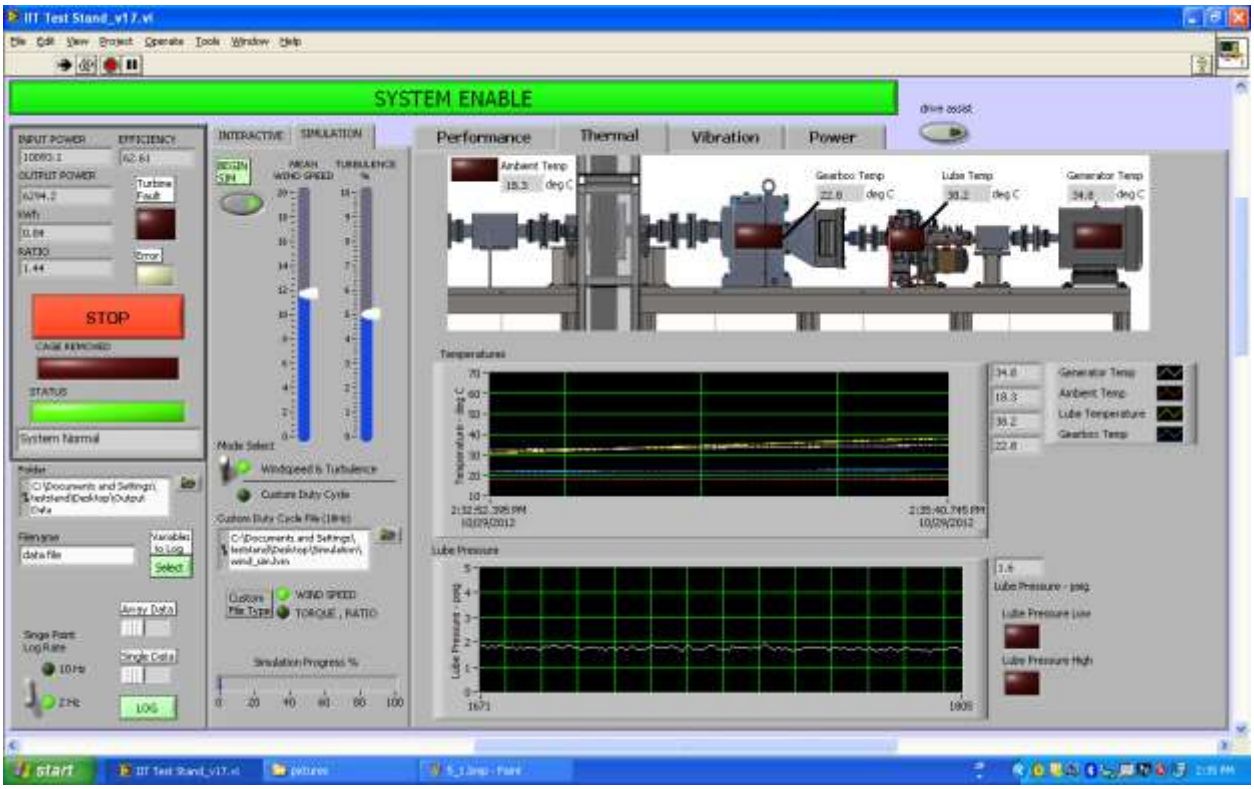


Figure 11Figure 11 and Figure 12 show screenshots of the software monitoring the Lab Field Unit regarding Performance, Thermal, Vibration, and Power.

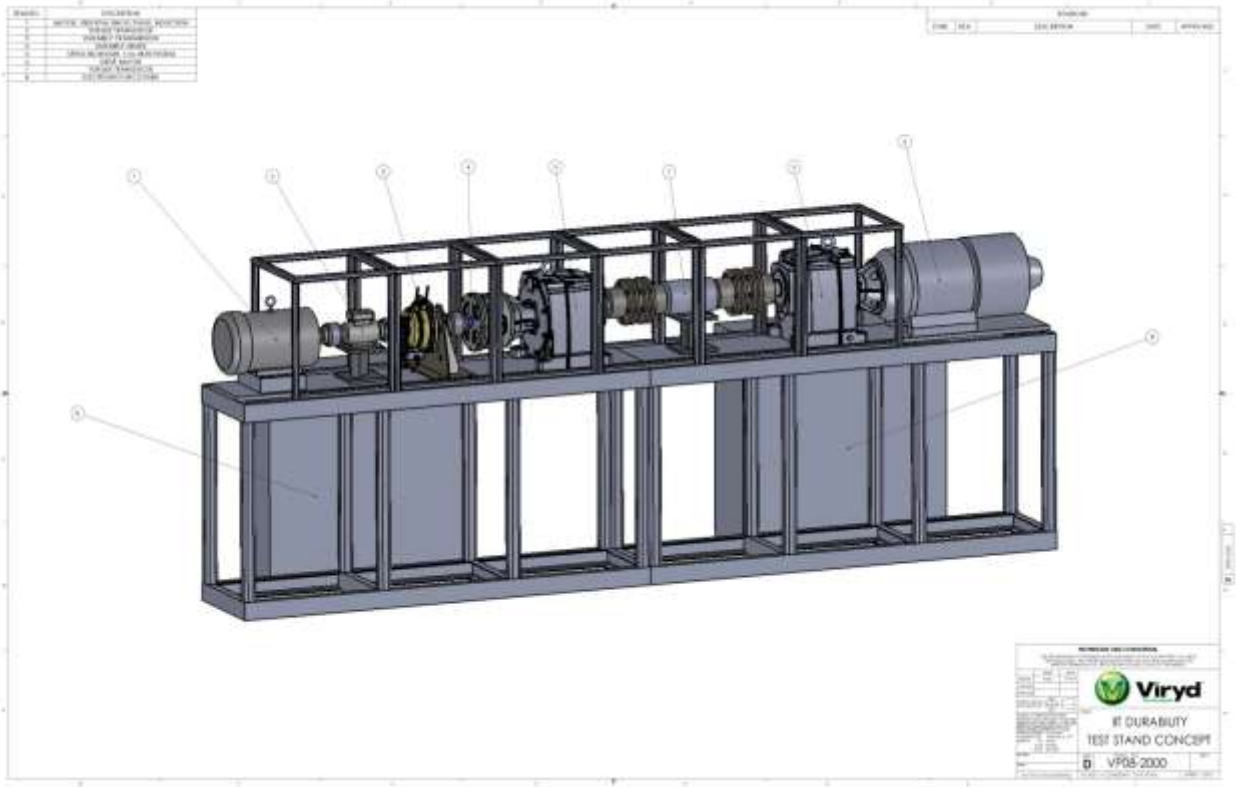


**Figure 10: Viryd 8kW Unit Fully Instrumented and Designed for the IIT Lab**

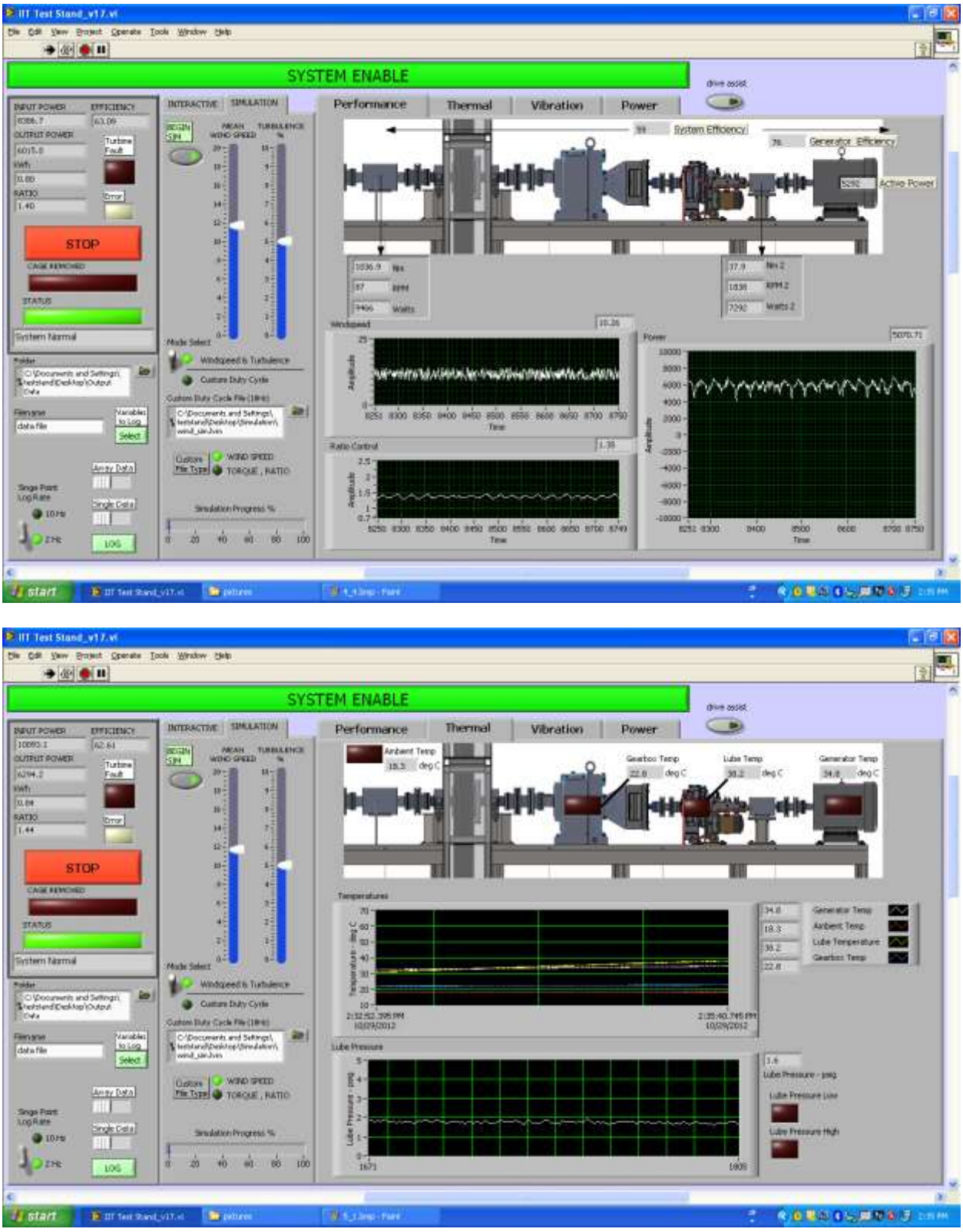


**Figure 11: Screenshot of the Lab Unit**

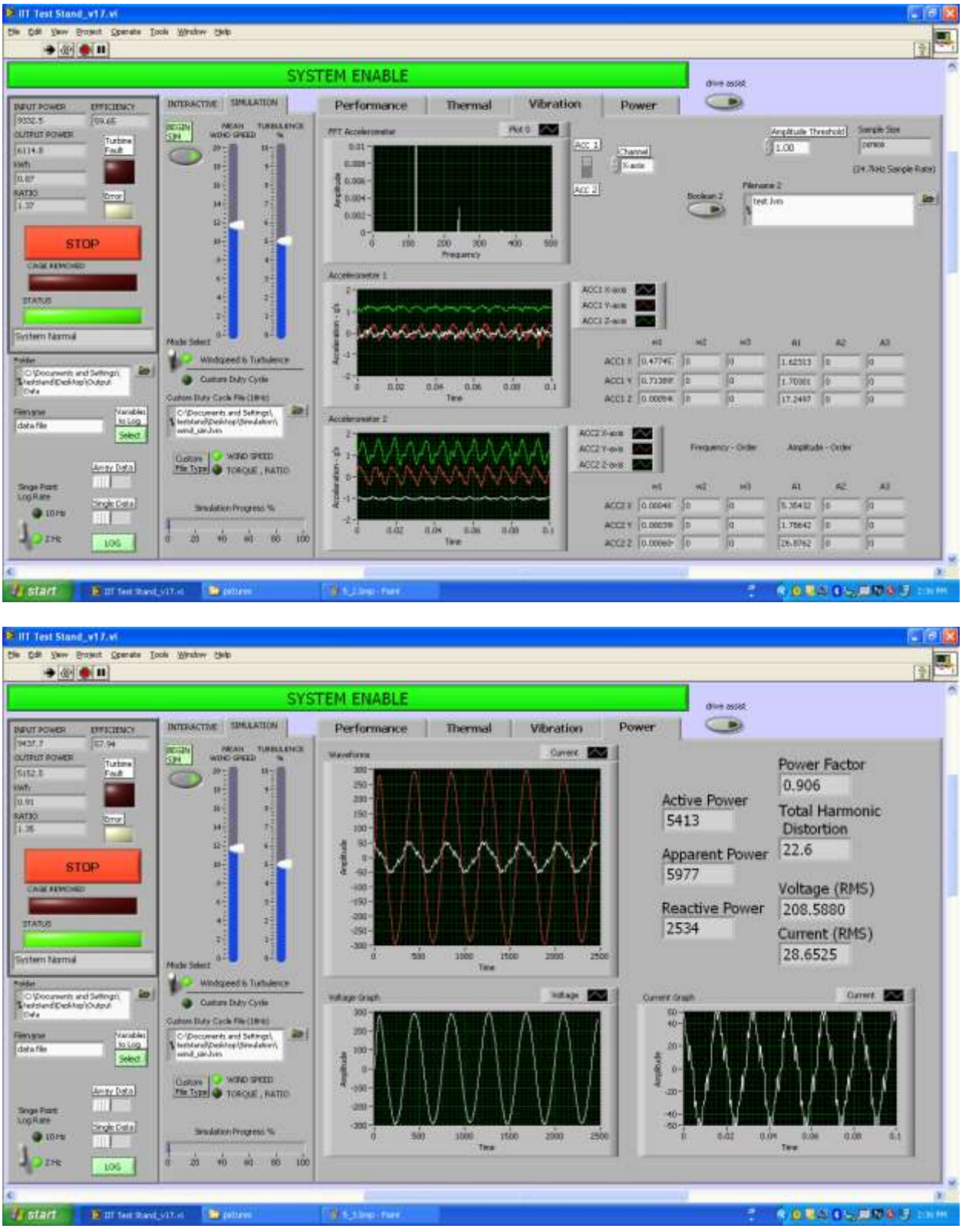


**Figure 12: Screenshot of the Lab Unit**

### C. *Viryd Field Unit Installation at IIT*

IIT installed a wind turbine in the field, which is very similar to the lab unit. This installation enables us to run experiments on the lab unit and then try to validate and correlate data on the actual turbine running in the field. There are also "real world" circumstances in the field that are hard to model in the lab, and the researches can take these into account.

The turbine was installed in mid-2011 at the IIT soccer filed (Figure 13) which would provide easy access to the machine, as well as help promote the University's effort surrounding wind and alternative energy. The unit is an 8kW Single Phase Wind Turbine – Upwind with Induction Generation and Custom Designed 4m Stall-Regulated Blades. The tower is 80' Hydraulic Monopole Tower, which can be brought down for maintenance without a crane.

**Figure 13: Viryd 8kW Unit Installed at the IIT Soccer Field**

Project Timeline: The building permit was initiated in November, 2010 and granted on June 9, 2011. The installation was delayed by two weeks due to rain. The entire system is completed and signed off on July 19, 2011. Note that the city permit process took about 8 months vs. wind turbine on-site installation 3 weeks.


**Figure 14: Installation Chronology for the Viryd 8kW Unit at the IIT Soccer Field**

Figure 16 shows a screenshot of the software monitoring the Field Unit and Figure 15 shows the recent wind speed and wind power output as well as some statistics for the Field Unit.

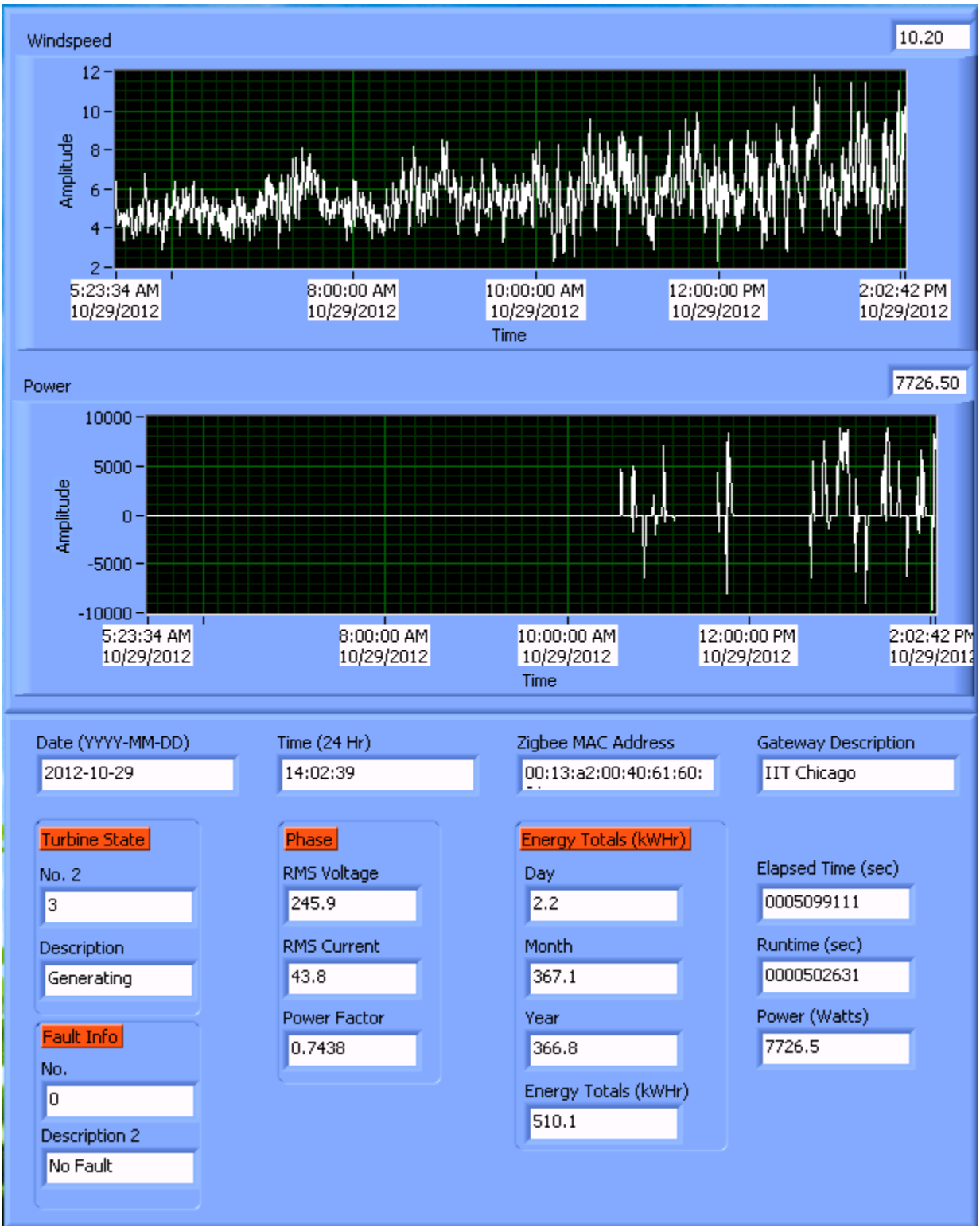


**Figure 15: Display of the Wind Speed and Power Output for the Field Unit**

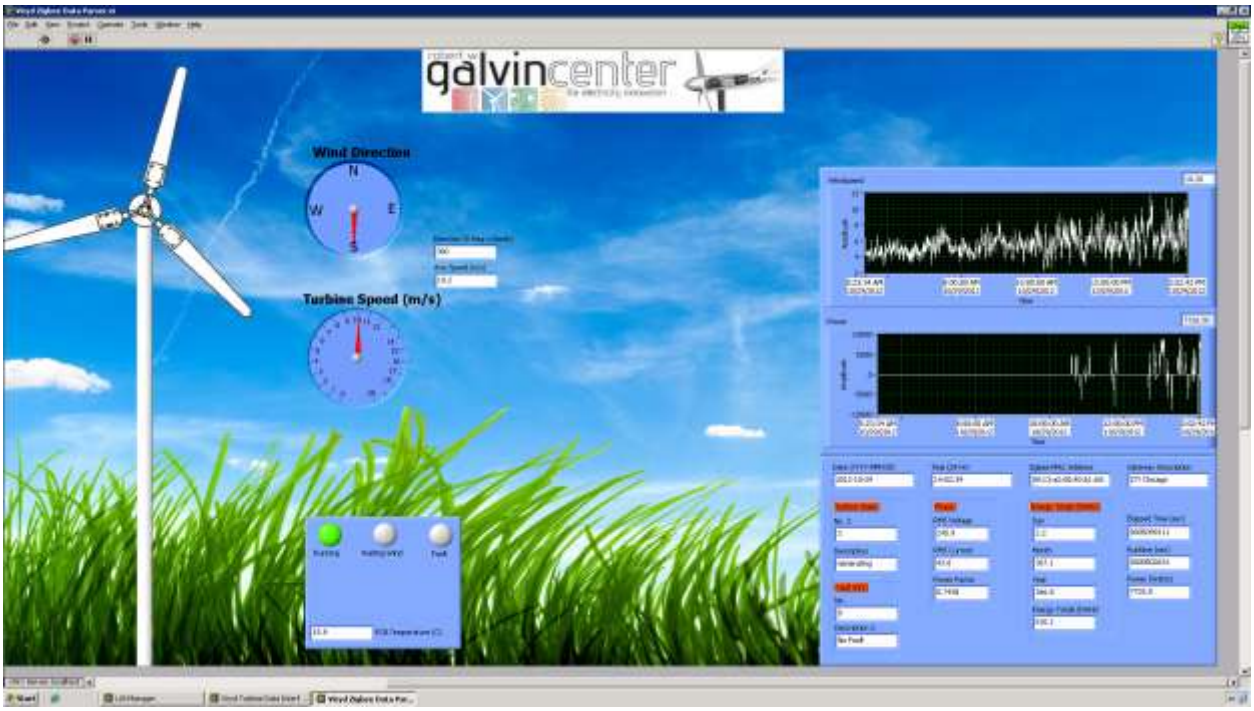


**Figure 16: Screenshot of the Software Monitoring the Field Unit**

## 3.2 Wind Energy Research and Development

### 3.2.1 Wind Turbine Research

#### *A. Predictive Analytics to Improve Wind Turbine Reliability*

IIT entered into an agreement with SmartSignal Corporation in early 2010. This agreement brought SmartSignal into a consortium arrangement with IIT and Invenergy. Under these terms, SmartSignal provided overall project management as well as specific system designs, software licenses, and staging hardware in support of SmartSignal's Epi-center Predictive Analytic software. SmartSignal was subsequently purchased by General Electric Company in January 2011.

The scope of the project was to implement SmartSignal Epi-center Predictive Analytic software on the IIT's Grand Ridge Wind Turbine #139 and design, specify, procure and install additional sensors which provide supplemental information to enhance the predictive analytic capabilities in support of Wind Turbine Reliability Research.

The purpose of this project was to determine an optimal set of add-on instrumentation and analytical techniques that can improve the existing state of the art emerging problem detection and be cost effective for broad deployment across large fleets of WTG's. A specific focus on gearbox issues was identified. The goals of this project were to evaluate a range of advanced instrumentation for early detection of gearbox problems including:

- Installation costs
- WTG interface and integration issues

- Determine sensor reliability in WTG environment
- Determine suitability for detection of WTG gearbox problems in real-time
- Develop a least-cost deployment approach for existing WTG assets
- Suitability of sensor data into real-time predictive analytic approaches

The overall project approach is as follows:

- Identify a range of possible instrumentation technologies
- Install multiple technologies on test WTG
- Collect real-time data
- Build SmartSignal Predictive Analytic models with data and assess correlation and ability of models to detect changes in sensed parameters using simulated faults injected into the data stream.
- Perform cost analysis for fleet deployment
- Make recommendation of instrumentation for broader sample fleet deployment

A key concept to also be evaluated during the project is the presumption that precise diagnostics from the analysis of the real-time data will not be required, as long as most failure modes can be detected in some fashion. The assumption is once it is determined there is a possible emerging problem, additional on-machine analysis methods can be used (e.g. oil sampling, boroscoping, supplemental vibration analysis, etc.) to isolate the problem and assess further operational risk.

A monitoring center was established on the IIT campus utilizing the SmartSignal Epi-center Predictive Analytic software and a video camera for visual condition monitoring of wind turbine #139. This monitoring center was linked via a Hardware VPN to the Proficy historian in the data acquisition and storage system at the Grand Ridge Energy Center. A link to the Proficy historian from the existing plant historian enables the existing sensor data to be forwarded to the monitoring center for analysis. Analytical models of this wind turbine utilizing the Similarity Based Modeling technique with the existing sensor data are installed in the monitoring center. The existing sensors will be supplemented with additional sensors measuring gear box oil temperatures, pressures, and contamination levels. The blade pitch motor currents and temperatures will be added to the data transferred from the plant historian to the Proficy historian. This additional information will be incorporated into the models in various combinations to develop the best model configuration.

Designated IIT personnel will be trained in the creation, modification and interpretation of the models. Asset Intelligence will assist in the advanced theoretical aspects of the research as requested. The initial planning phase of the project included network development and identification of hardware and software necessary to support the IT needs of the project. Key milestones were identified. After discussion with Invenergy and relying on SmartSignal's experience in monitoring wind farms across North America and Europe, a strategic set of additional sensors was identified, an overall IT network was agreed upon.

The next step was to execute the project according to plan. Component specifications were developed, work was assigned according to the work breakdown structure to various entities according to their capabilities, including identifying external resources necessary to supplement the consortium members'

own resources. The required purchases were separated into two phases; first to establish the IT infrastructure and activate the SmartSignal Predictive Analytic software and second, to incorporate the additional sensors into the analytic models.

Once component compatibility was established, purchase orders were placed. A trip to the wind turbine was made with the suppliers to install and activate the network servers and software. The servers supporting the analytic software were installed and commissioned on the IIT campus. After server validation, the SmartSignal predictive analytic software was installed. A data feed was established from the wind farm to the campus. The wind turbine models were activated in September and began processing data from the turbine. We now had the established baseline 'industry standard' predictive analytics.

As the sensor orders were being placed a new component vendor emerged with an offer to provide their product at no cost on a trial basis, including modified mounting hardware customized for this application. This change was accepted in principle and is currently being finalized. Invenergy personnel will be performing the sensor installation with factory specialists consulting as necessary.

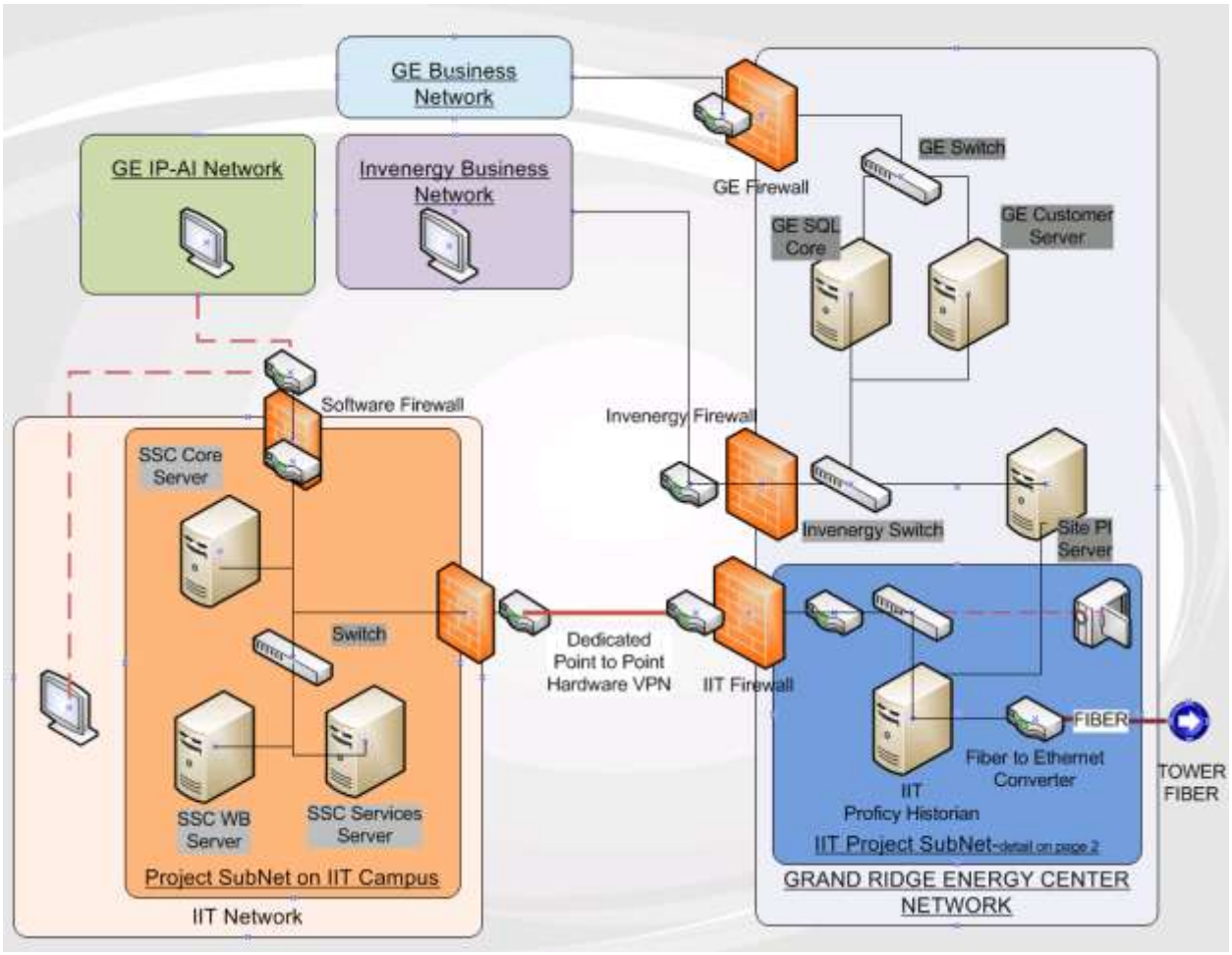


**Figure 17: IIT – Invenergy – SmartSignal Wind Project: Overall Network Arrangement**

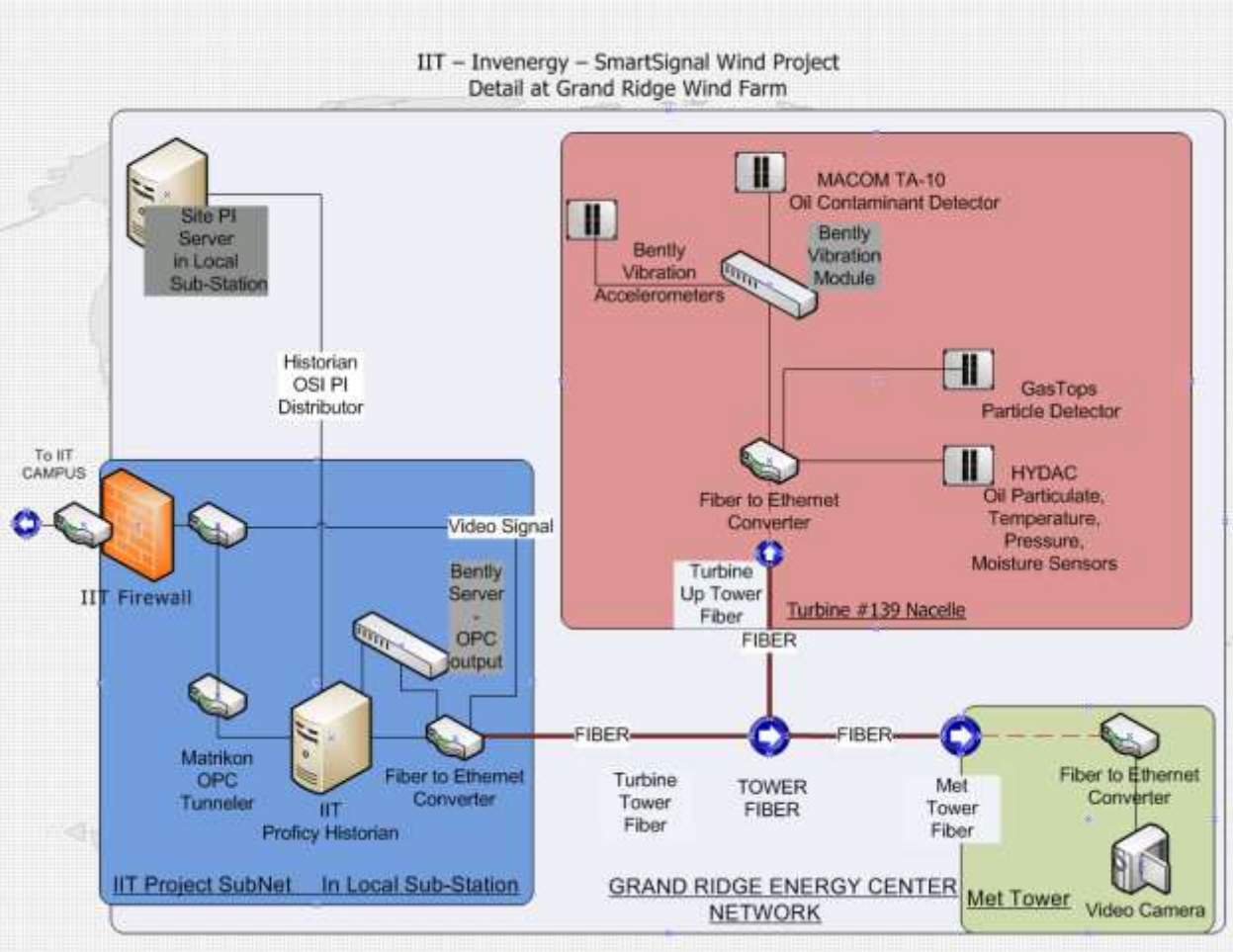


**Figure 18: IIT – Invenergy – SmartSignal Wind Project: Detail at Grand Ridge Wind Farm**

Once the new sensors are all delivered we will plan and execute a trip uptower to install and activate the sensors. As they are activated their output signals will be routed to the Proficy historian and made available to the SmartSignal predictive analytics software for inclusion into the models and further research.

Upon the completion of the project, the Consortium has (1) installed the GE ADAPT vibrations system; (2) installed the Lube Oil System Monitoring Sensors; (3) installed associated software and hardware to acquire the data and communicate the information to IIT main campus; (4) installed associate software and hardware to receive the data at IIT main campus, capture the data in a historian, and support the Proficy SmartSignal Software; (5) created a SmartSignal Condition Monitoring model using the OEM standard available sensors plus the additional sensors.

The GE ADAPT vibrations system provides vibration indication on the:

- Generator Outboard Bearing
- Generator Inboard Bearing
- High Speed gear Box bearing

- Intermediate Speed Gearbox bearing
- Planetary Stage bearing
- Main Bearing

The Lube Oil System Monitoring Sensors Include

- MaCom Particulate Counter, which provides Ferrous and Non-Ferrous Particulate Count from 101-200 um, from 201-300 um, from 301-400 um, from 401-500 um, from 501-600 um, from 601-700 um, from 701-800 um
- HYDAC Particulate Counter (Sensor and Bracket donated by HYDAC), which provides Ferrous and Non-Ferrous Particulate count for the last 10 minutes. With additional equipment, this unit also has the capability to provide ferrous and non-ferrous totals by particulate size.
- Gastop MetalScan Particulate Sensor, which provides Particulate Count for the last 10 minutes (Both ferrous and non-ferrous together)
- Cooler Inlet temperature (HYDAC)
- Cooler Outlet temperature (HYDAC)
- Filter Differential Pressure

Items that can be identified using the standard OEM Sensors include:

- Yaw control issues
- Blade Pitch Control Issues
- Bearing temperature issues
- Power Related issues such as phase imbalance and shorts
- Nacelle Temperature Issues
- Control Box temperature Issues (Affects the electronics)
- Turbine Efficiency Issues.

Items that can be identified using the Newly Installed Sensors include:

- Better indication of bearing health through direct measurement of vibration. It is expected that the SmartSignal model will identify the early indication of bearing issues such that tower climbs can be limited and more effective. Once identified via SmartSignal, a deeper analysis of the vibrations issues can conducted via the Adapt System.
- Direct Measurement of the count of metal particulate in the oil system. This is an indication of damage to the gears and is traditionally measured by climbing the tower and taking oil samples. Three different particulate counters were installed to allow the comparison between manufacturer capabilities. There particulate counters may differ in their ability to detect particulate, ability to filter unwanted counts (i.e.: entrained air bubbles), and the ability to provide detailed information (i.e.: ferrous verses nonferrous counts, particulate count by size)
- Directly measure filter DP. Filter DP will provide an indication of the condition of the oil filter. Additionally, measuring filter dp may provide an inexpensive alternative to installing a particulate counter (i.e.: If the filter dp increases at a faster rate, it can be assumed that there is more particulate in the oil.)
- Cooler inlet and outlet temperature. Cooler differential temperature can provide an indication of the health of the cooler (plugging) and the effectiveness of the oil cooler.

In summary, the monitoring center has been established on the campus. The video camera is in place and functional. The SmartSignal Epi-center software is installed and active. The data acquisition and storage system has been established and linked to the campus. The models are connected to the data store and active on the campus servers.

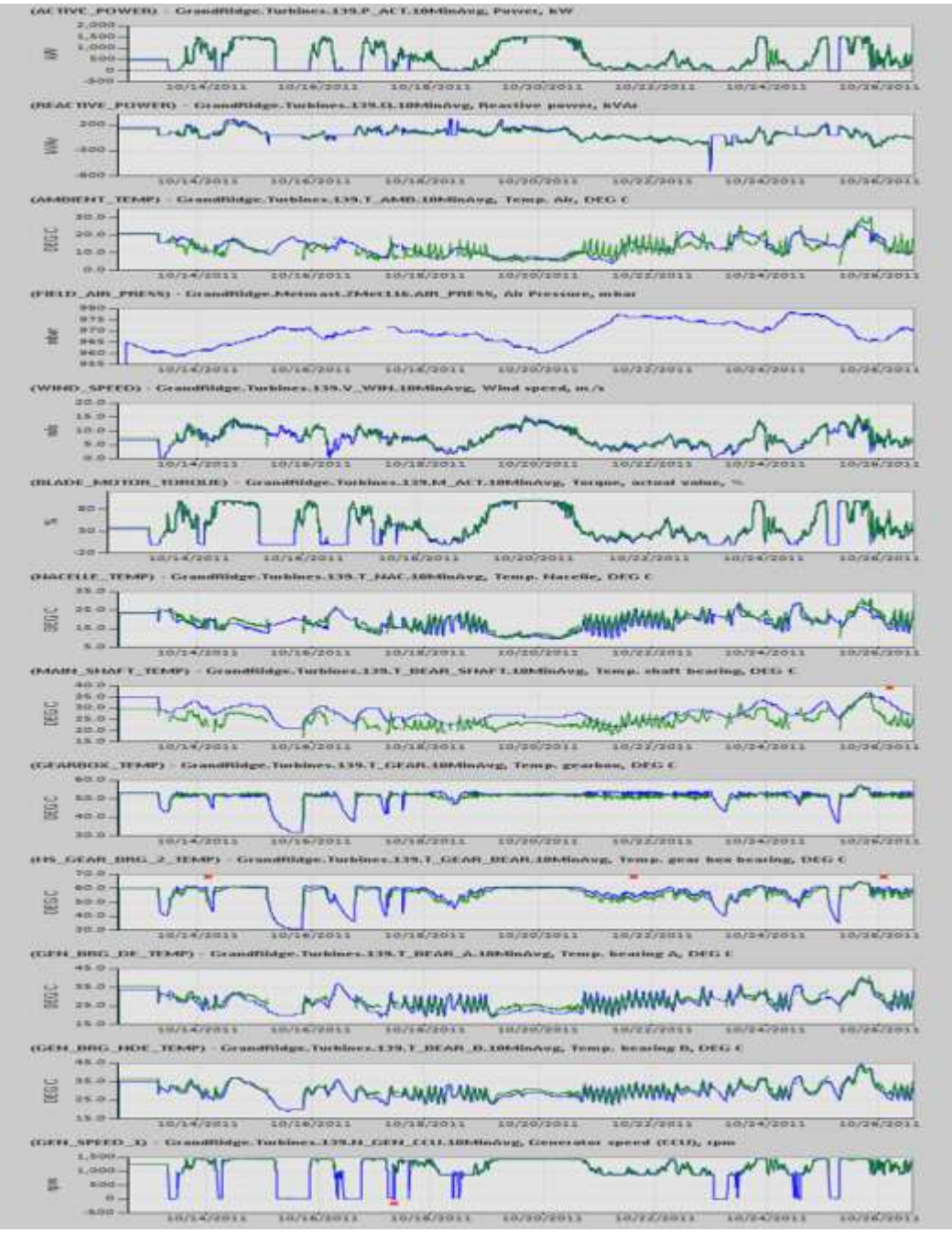

**Figure 19: Sample SmartSignal Predictive Analytics Display**

**Figure 20: Sample SmartSignal Software Display**

The Green lines represent the predicted values, the blue lines represent the actual current values, and the red XXX represent significant deviations of actual from estimate, alerting the analyst to further investigate the situation.

### *B. Improve Wind Turbine Power Output and Reduce Dynamic Stress Loading Through Advanced Wind Sensing Technology*

Discussed in this section is a vision for moving from where the industry is today to the progressive improvements now attainable for future wind turbine control. Given that wind turbines have to operate through the dynamics of uncertain and imperfect airflow, sensors and controls can make a major contribution to performance and profitability. The existence of nacelle-mounted look-ahead laser wind sensors, capable of not only high data rates but also of various schemes to map the inflow, leads to the developmental path discussed below and illustrated in the diagram below. Incremental improvements in turbine efficiency and stress control are expected at each stage leading to an optimized control/sensor suite.

**Why Is It Needed?**

Collecting wind data at the rear of the wind turbine nacelle results in several significant compromises. First, both the effect of the bluff body of the nacelle itself and the blade blockage effects on the airflow have to be corrected using wind speed dependent transfer functions. These empirical correction factors do not account for any flow regimes other than perfect yaw alignment, so in periods of even the slightest misalignment to the wind, the transfer function no longer accurately corrects the measurement. Secondly, the flow encountered at the rear of the nacelle is heavily affected by the wash or wake of the passing blades. Current practice is to use long (up to 10 minute) rolling or binned averages to smooth

out the wake impulses. Not only is this imprecise, it also disguises actual fluctuations in the wind and drastically affects the response time of the control system. Thirdly, the information measured at the rear of the turbine is obtained after the air mass has passed the turbine. There is therefore no possible way to have proactive, anticipatory or feed-forward control using this data.

Installation of strain measurement into the blades, towers, shafting or other components gives an indication of operating conditions. These stresses and strains can be linked to a feedback control loop. While this provides one direct measurement of the turbine's interaction with the wind, it only generates a sensed control trigger after the mechanisms have already experienced excess stress and strain. Stress and vibration data is difficult to use for discerning whether a yaw or blade pitch correction is needed. Using strain feedback, the duration of this undesirable condition can be reduced, but events still use up the finite fatigue life of the components prematurely. This approach also increases the cost of the blades and other instrumented components.

**Improving Yaw Control Brings Big Gains**

The addition of a forward measuring laser wind sensor provides the control system accurate wind direction information in the undisturbed flow as it approaches the wind turbine. Tests using just this more accurate wind direction information have demonstrated both significant increased power output and reduced stresses from better alignment to the wind. A forward-looking laser not only provides a more accurate flow direction, but the absence of blade wake effects allows this information to be fed to the control system without long averaging periods.

Less averaging informs the control system of the actual flow dynamics as they occur. By virtue of the laser wind sensor measuring wind at various ranges in front of the wind turbine, control actions gain anticipatory data for feedforward controlling. This can be implemented as merely a timing advantage to reduce lag in yaw corrections, as well as the ability to track wind changes and gusts to determine not only their predicted time of arrival at the wind turbine, but also to inform the control logic with information on the "depth" or duration of an approaching gust.

**Intelligent Blade Pitch Adds More Benefit**

A laser wind sensor looking ahead in the inflow can also provide the blade pitch control logic with wind speed changes and wind speed gusts before they arrive at the blades. This information also can allow estimation of the precise arrival timing to correlate with the reaction times of the pitch control mechanism. The result is a reduction of time spent at a suboptimal blade angle to the flow and experiencing unexpected loads or stress.

Laser wind sensors can be designed to provide multiple measurement points simultaneously at known locations in the inflow to provide spatial flow mapping at multiple ranges. With this spatial wind speed and direction information, the shear and veer of the flow in the inflow can be determined in real time. The pitch control of each blade can then be timed to the sweep angle so that it is optimized based on the spatial wind conditions it is actually passing through. While laser wind direction data can greatly improve the alignment with the wind over time, the relatively slow yaw response of the large nacelle mass compared to the rates of wind direction change results in transients of misalignment which can be

addressed with individual blade pitch adjustments to minimize the vibration caused by the leading/following blade effects. This is similar in concept to the blade pitch adjustments made on helicopters to compensate for the relative airspeed of leading/following blades in forward flight.

**What Does The Future Hold?**

While current turbine designs are based on unitary blades that account for the span-wise (radially) differences of flow and moment with taper and twist, those designs are based on the assumption of a uniform flow field perfectly normal to the plane of the blade rotation. In fact, as a result of spatial and temporal wind speed and direction variations, the flow field at any point in time is not truly uniform in the radial direction. Even informed individual blade pitch control has to select a best compromise angle of attack for the entire blade length and does not have the ability to handle span-wise flow differences. With real-time spatial wind speed and direction data from a laser sensor, high response rate aerodynamic devices along the blade span could be actuated to correspond to local relative wind. This could be implemented using various flaps, jets, or tabs as developed for aircraft wings or rigid sails. Combined with the other control advances, this stage represents an optimization of active controls.

Ever-increasing sophistication is projected for wind turbine sensors and controls with resultant step-wise increases in efficiency and reductions of undesirable stresses. Wind turbine control practice can begin to catch up to university research and aerospace now that forward-looking laser wind sensors can provide the needed wind accuracy, timeliness, data rates, and spatial mapping. It is time for the wind energy industry to start gaining the power performance and stress reduction advantages.

**Forward Looking Laser Technology**

The Vindicator® laser wind sensor (LWS) is a ‘next generation’ wind sensor for utility-scale wind turbines. From its position on top of the nacelle, it determines the wind speed and direction in the undisturbed air 250 meters in front of the turbine. As a result, the unit can provide the control system with a predictive, three-dimensional view of actual conditions which allows you to optimize wind turbine performance.

By delivering a more precise and accurate picture of wind speed and direction, the Vindicator® LWS increases wind power output and reduces wear and tear on system components. For example, wind data measured in front of the turbine allows the control system to make proactive decisions about yaw angle and adjustment. Staying in alignment with the wind will significantly increase power output and dramatically reduce turbine stress. It can also adjust blade pitch in anticipation of sudden stress events such as high winds or sudden drops in production due to low wind conditions.

With the accurate predictive data delivered by the Vindicator® LWS, the control system can work smarter to increase efficiency, improve blade alignment, make better pitch decisions and reduce overall system stress, which will extend turbine life and cut maintenance costs.

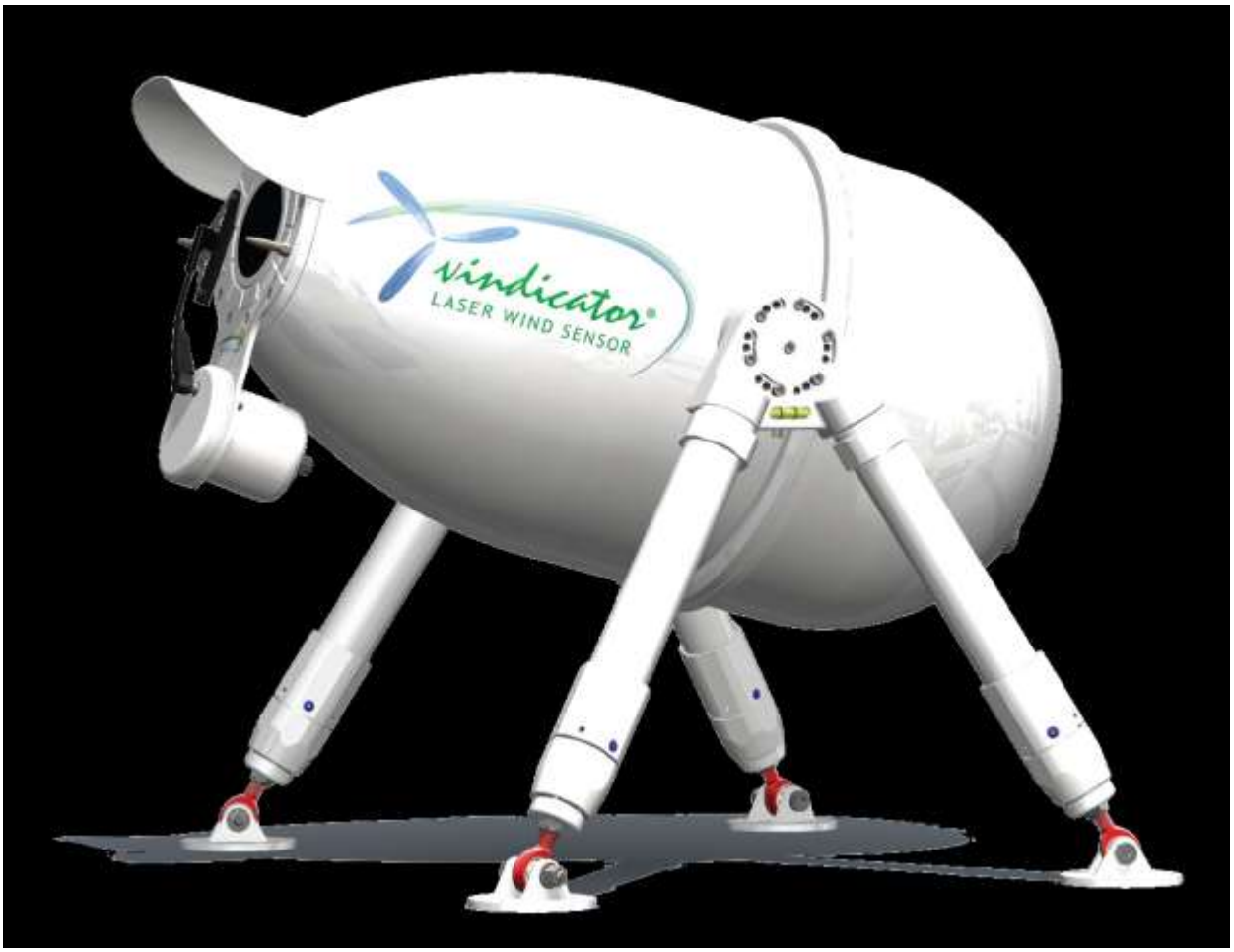


**Figure 21: Catch the Wind Vindicator® Laser Wind Sensor**

### B1. Wind Measurement and Power

The wind is a curious creature, blowing this way and that. Mathematicians would say that wind is a classic example of chaos. If asked about the wind, a surfer would simply shrug and say that waves are crazy, too. This powerful, but also quirky creature, the breeze that makes a child smile- this is what we must capture.

Our world needs us, the wind turbine industry, to produce power, cleanly, efficiently and at low cost. The contribution of this project to the wind industry is to use our understanding of optics to provide a fundamentally deeper understanding of the wind resource - to produce substantial, repeatable increases in the output power of wind turbines.

**Synopsis**

An Optical Control System (OCS), beta-version, is tested upon an operating utility scale wind turbine. The turbine was operated in four regimes; legacy yaw control (sonic anemometer) and three OCS control regimes. The behavior of the sonic anemometer, measuring both speed and wind angle, is studied. The uptime of the OCS is studied. Power curves in the four regimes are compared.

The data set is large, approximately 500 MB, composed of 335,000 data points taken at 1 second spacing. SAS JMP used as the statistical analytic tool. The dataset includes output from the OCS, two sonic anemometers (giving both wind speed and wind direction), turbine state, ambient temperature, output power, and absolute yaw position.

**The Ideal Wind Turbine**

Wind has a mind of its own; it is turbulent, has shear, changes direction, and changes velocity.

An ideal wind turbine needs to be pointed in the right direction, with its blades set at the correct angle to the wind. When a gust approaches, an ideal turbine will take actions to avoid damage. Practically, this means that the turbine has sufficient wind data to properly adjust blade pitch and yaw, is equipped with adjustable pitch and yaw, and has a control architecture that is sufficiently sophisticated to translate wind data into the appropriate turbine actions.

To properly adjust the pitch of all of the blades at the same time ("collective" pitch control) requires an accurate understanding of the average wind speed approaching the entire spatial plane of the blades of the turbine.

To properly adjust the pitch of each blade individually ("individual" pitch control) requires both rapid pitch adjustment and an accurate mapping of the variance (either modeled or measured directly) of the wind speed incident upon the turbine. A discussion of 2-D mapping is outside of the scope of this discussion.

Correct yaw adjustment implies that the turbine understands the direction of the wind, as it approaches the blades of the turbine. As an aside, we note that most analysis of a wind turbine, particular work on advanced control algorithms and controller analysis and design tend to begin with an a priori assumption that the there is no yaw misalignment. The data collected in this work, regardless of which control algorithm is used, clearly demonstrated that the assumption of no yaw misalignment is not valid.

Gust avoidance is possible when the turbine knows the wind speed and direction that will hit the wind turbine, with enough warning time to take actions to avoid damage.

**Current State of the Art**

***Speed Measurement***

Wind turbines today use anemometers, mounted on the rear of the nacelle, to measure wind speed. Although these are high quality wind measurement devices, they cannot be mounted in front of the turbine and, hence, must operate in the turbulent air that has already passed through the turbine blades, which has little resemblance to the wind condition in front of the blades. Figure 22 shows the raw output of a sonic anemometer in action. The horizontal axis is recorded seconds, with the figure capturing 10 minutes of operation. This particular turbine model has two sonic anemometers; Figure 22 only shows the output of one of the two sonic anemometers. Throughout this Section, the sonic anemometers are referred to as A1 and A2.

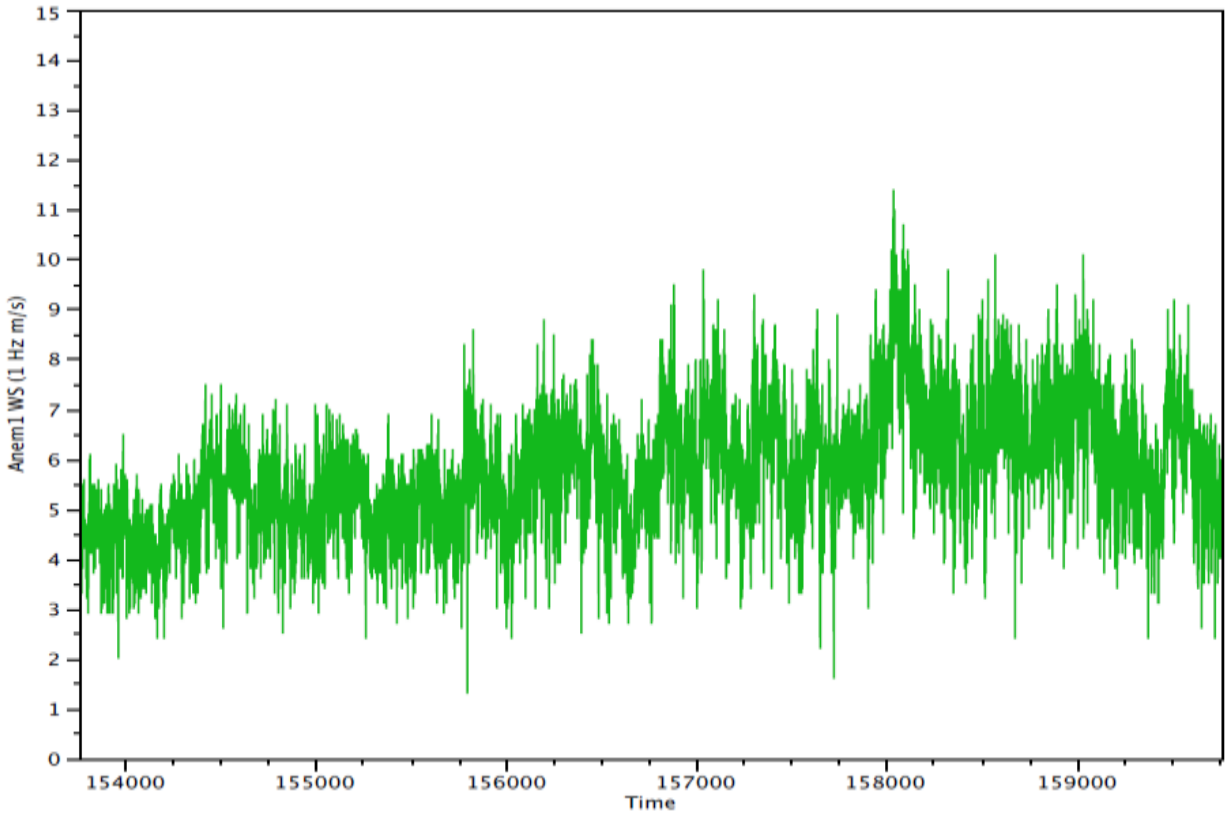


**Figure 22: The data of a sonic anemometer, mounted on the rear of the nacelle of an operating wind turbine.**

*(The data is taken each second of operation. The period shown here covers a 10 minute interval.)*

While this data is extremely noisy, much of that noise comes from the turbulence effects of the turbine blades as the wind passes through them. Stated differently, if this sonic anemometer were measuring undisturbed air, the data would be more accurate and much less noisy. This can be seen in Figure 23, where we show the wind speed data measured in front of the turbine, where the wind is free of these turbulence effects. This data, also taken each second of operation, and without any averaging external to the system, is taken using our Vindicator® Optical Control System, or more simply the "OCS". As the OCS utilizes a pulsed laser operating with a pulse repetition rate much higher than 1 Hz, internal averaging is used prior to the 1 Hz output. The industry deals with noisy sonic anemometer data quite pragmatically by averaging the wind data output of the sonic anemometer over time. This is effective in smoothing the data, but requires fairly lengthy averaging times to produce data of sufficient quality to make control decisions. Figure 24 shows a comparison of the OCS output, from Figure 23 above, compared to the outputs of the sonic anemometers, where the sonic anemometer data is averaged over 60 seconds to smooth the data.

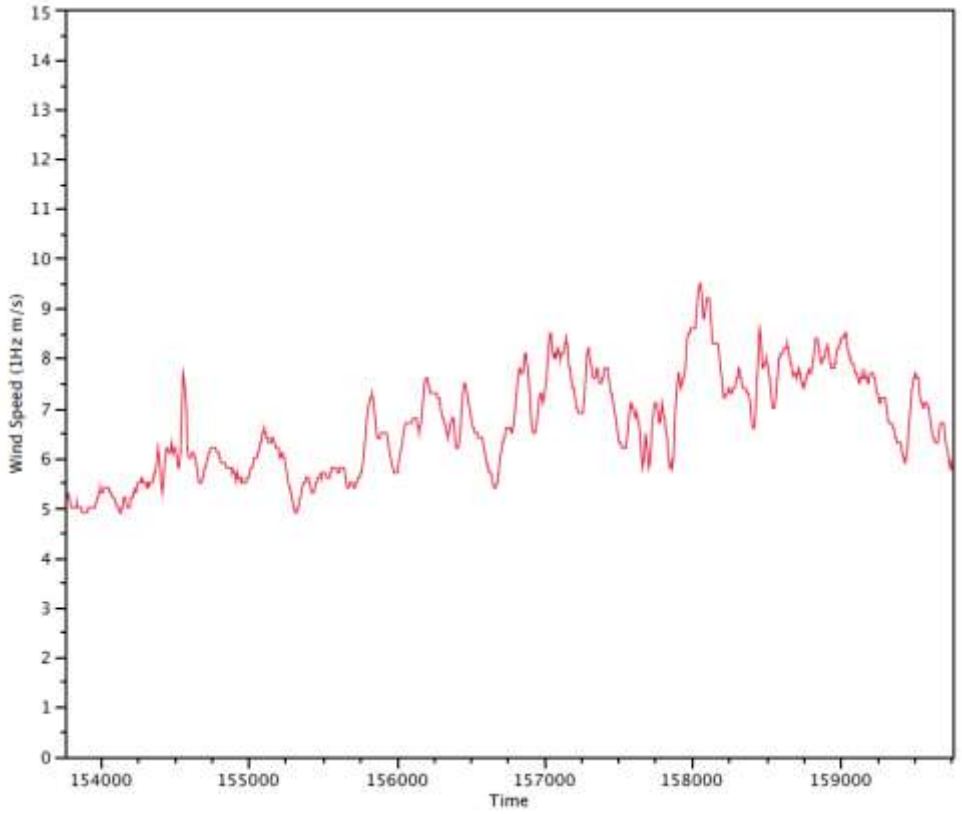


**Figure 23: The wind speed in front of the turbine, measured with the OCS.**

*(This data is also taken each second, un- averaged, with a 10-minute period of operation shown.)*

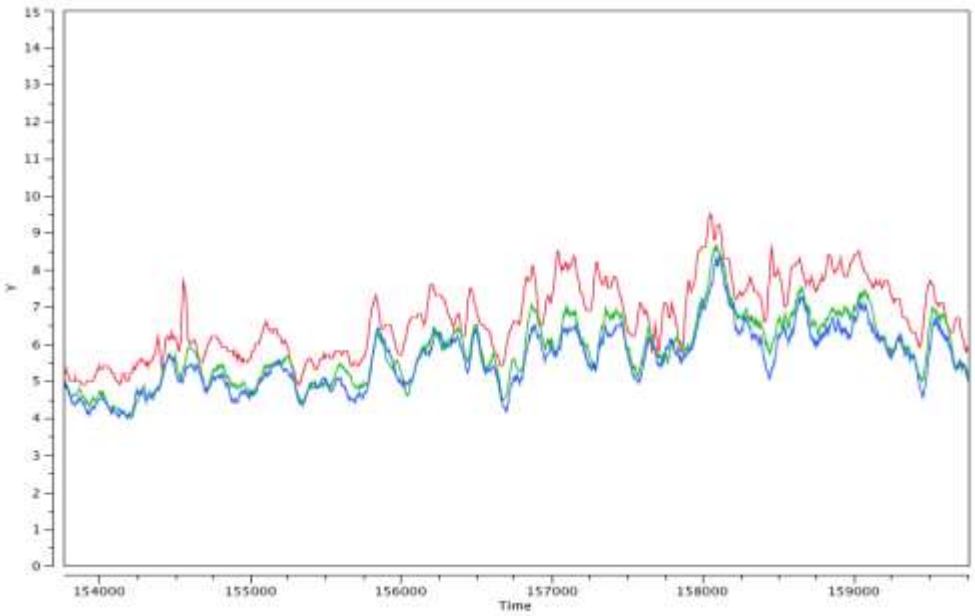


**Figure 24: Outputs of the sonic anemometers**

*(The blue and green lines are the outputs of the sonic anemometers, averaged over a 60 second period, with the vertical axis representing wind speed in meters per second. The correlation between the two sonic anemometers is quite respectable. The sonic anemometers show lower wind velocity than the OCS, as is expected due to the fact that the turbine has extracted power from the wind.)*

Figure 24 shows fairly clearly several effects. First, the mean wind speed measured by the sonic anemometers is made much more usable by averaging. Sudden gusts of wind, however, are lost by this averaging as indicated at approximate time 154500 in Figure 24. As expected, since the OCS is measuring the wind in front of the turbine, the OCS captures changes in wind speed slightly ahead of the sonic anemometers.

Second, the wind speed as recorded by the sonic anemometers is significantly lower than the OCS measurement over the same period of time. The OCS is detecting wind behavior well in front of the turbine. As such, the operational state of the turbine has no impact upon the OCS wind speed measurement, or equivalently, the actual wind speed that is being measured.

The fact that wind speed as recorded by the sonic anemometer on the rear of the nacelle is lower than the OCS is actually expected from first principles: as the turbine extracts power from the wind, the velocity of the wind decreases.

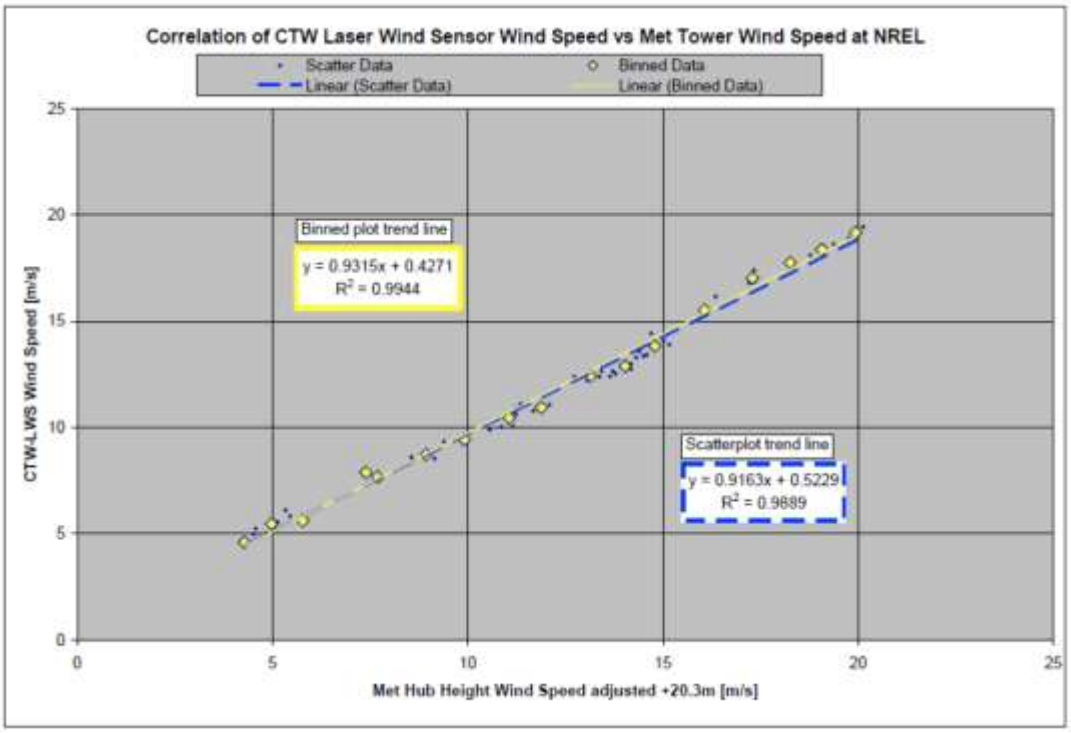


**Figure 25: Experimental LIDAR data.**

*(The comparison is with a calibrated met tower. R^2 is ~0.99. Data in collaboration with NREL.)*

Our experience with the OCS is that it shows excellent correlation to calibrated metrological (met) towers whose measurements, like the OCS, are unaffected by the turbulence effect of turbine blades. This has been demonstrated several times now. For reference we show wind speed data taken in collaboration with the U.S. Department of Energy's National Renewable Energy Laboratory (NREL). This level of correlation is consistent with our OCS wind measurement performance in other met tower comparisons. If the reader is interested in a more holistic write-up of experimental LIDAR/met tower correlations, please contact CTW directly.

Following this argument, at wind speeds so low that the turbine blades cease to spin, the well-calibrated sonic anemometer should be accurate. In Region II, where the power extracted rises with wind speed, the sonic anemometer error is expected to increase. In Region III, where the power extracted from the wind is approximately constant since the turbine is operating at its rated power, the velocity error of the sonic anemometer should begin decreasing with increasing wind speed, since the amount of power being extracted from the wind is roughly constant until the cut-off wind speed is reached. Stated differently, the wind speed detected by the sonic anemometers is observed to be, as expected, dependent upon the output power of the turbine.

This effect is borne out in Figure 26. The correlation of sonic anemometer to the free wind speed is not symmetric, and, as expected, is skewed to lower velocity, with this asymmetry particularly apparent in Region II.

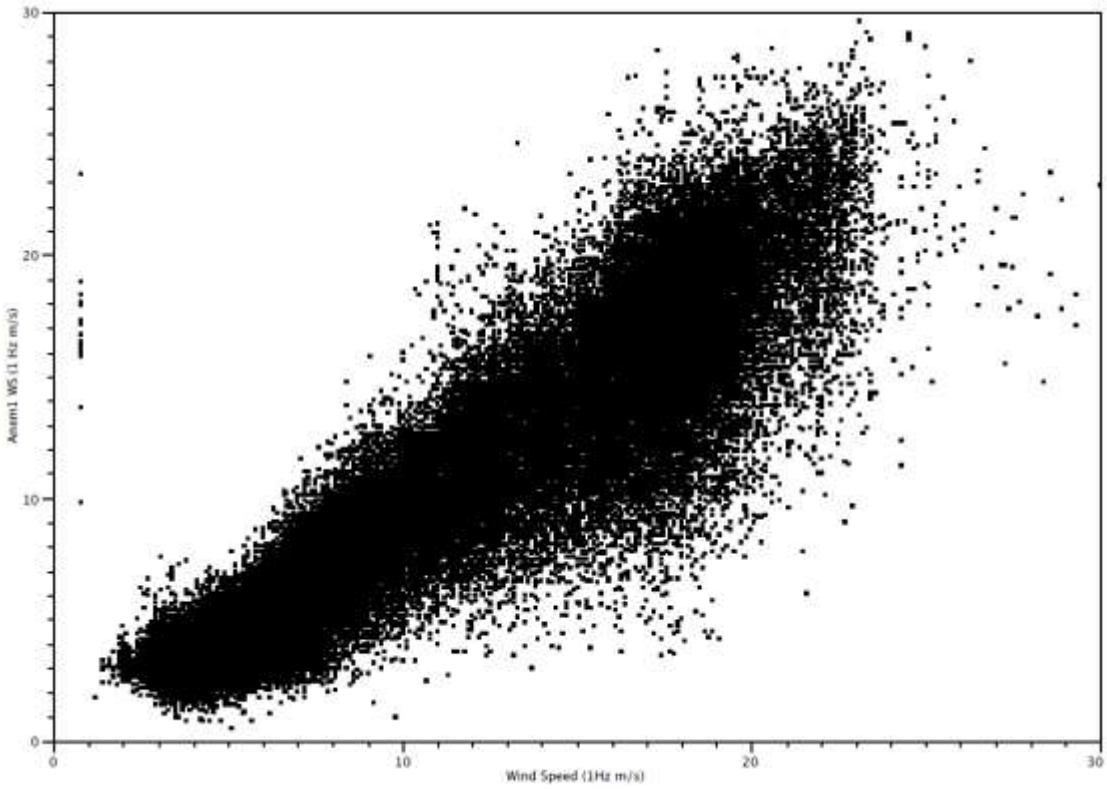


**Figure 26: The correlation between the wind speed behind the turbine blades and the free wind**

*(Wind speed behind the turbine blades measured by the sonic anemometer, and the free wind measured by the OCS)*

Next, we examine the wind speed correlations between the free wind measurements (OCS) and the post-rotor wind speed measurements (taken by the two sonic anemometers, noted as A1 and A2) when they are in different control regimes (i.e, we look at the correlations when the turbine is under OCS control versus when the turbine is under legacy control). All correlations between the different wind speed measurement devices improve under OCS control. It is our hypothesis that OCS controls the angular yaw of the turbine such that the actual angle error is reduced, and that the sonic anemometers' measurement is closest to the free wind when they are not additionally perturbed by cross-winds due to angular yaw misalignment. Again, it is noted that rotor blades are generally designed assuming zero yaw angle. Off-axis wind may increase loading on the blades, but this loading would be out of plane such that torque may actually be reduced while lift and drag may increase.

| R^2 | Turbine Control | |
|---|---|---|
| Speed | Legacy | OCS |
| A1 & A2 | 0.991 | 0.995 |
| A1 & OCS | 0.947 | 0.975 |
| A2 & OCS | 0.946 | 0.976 |

**Figure 27: The correlations between the different measurement tools.**

*(The correlations improve when the turbine is under OCS control.)*
In addition to the correlations between the various wind measurement devices improving under OCS control, the difference between wind speed as measured in front of the wind turbine by the OCS, and, in the rear of the turbine by the sonic anemometer as averaged for "smoothing" effects, also decreases under OCS control and, conversely, increases under legacy control. A real-time plot of this is shown below, where, even before the sonic anemometer data is processed, or "smoothed", it is clear that the wind measurement correlation between the OCS and the sonic anemometer is worsened under sonic anemometer control, with the sonic anemometer recording a generally lower wind speed for the post-turbine wind than the free wind speed recorded by the OCS. This effect may be due to the fact that the wind turbine is operating, on average, more out of alignment with the wind when under legacy control, and, therefore, the blades somewhat "shield" off-axis wind (i.e., the sonic anemometer behind the turbine is measuring the projection of the wind along the axis of the wind turbine).

*(In general, the sonic anemometers record a lower wind speed behind the turbine blades than the wind speed recorded by the OCS in front of the turbine, as expected from physical arguments. However, this difference increases when the turbine is under legacy control.)*

The difference in wind speed measurements can be shown quite simply. Figure 8 shows the linear fits of an average of the two anemometers vs. the wind as measured by the OCS. Under legacy control, the wind speed measured by the anemometers is lower than when under OCS control. We believe that the wind speed measurement of the anemometer, relative to the OCS, drops as the turbine is taken off of alignment with the wind.

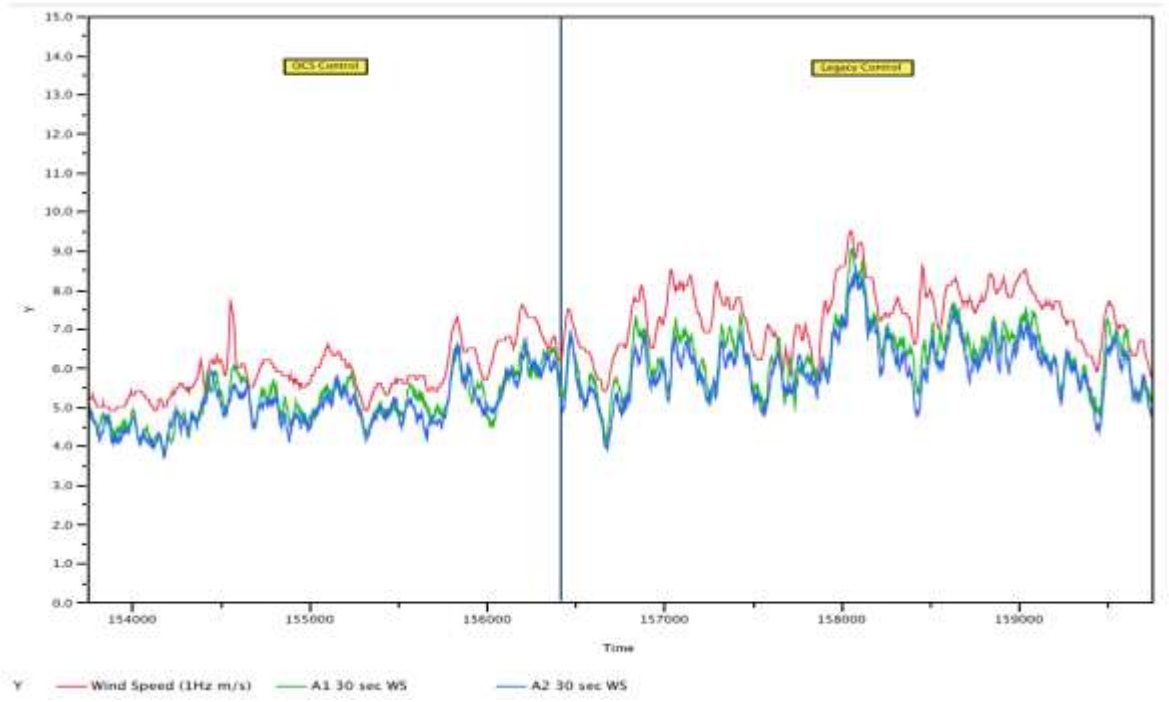


**Figure 28: A plot of real-time wind speed measured by the OCS and both sonic anemometers.**

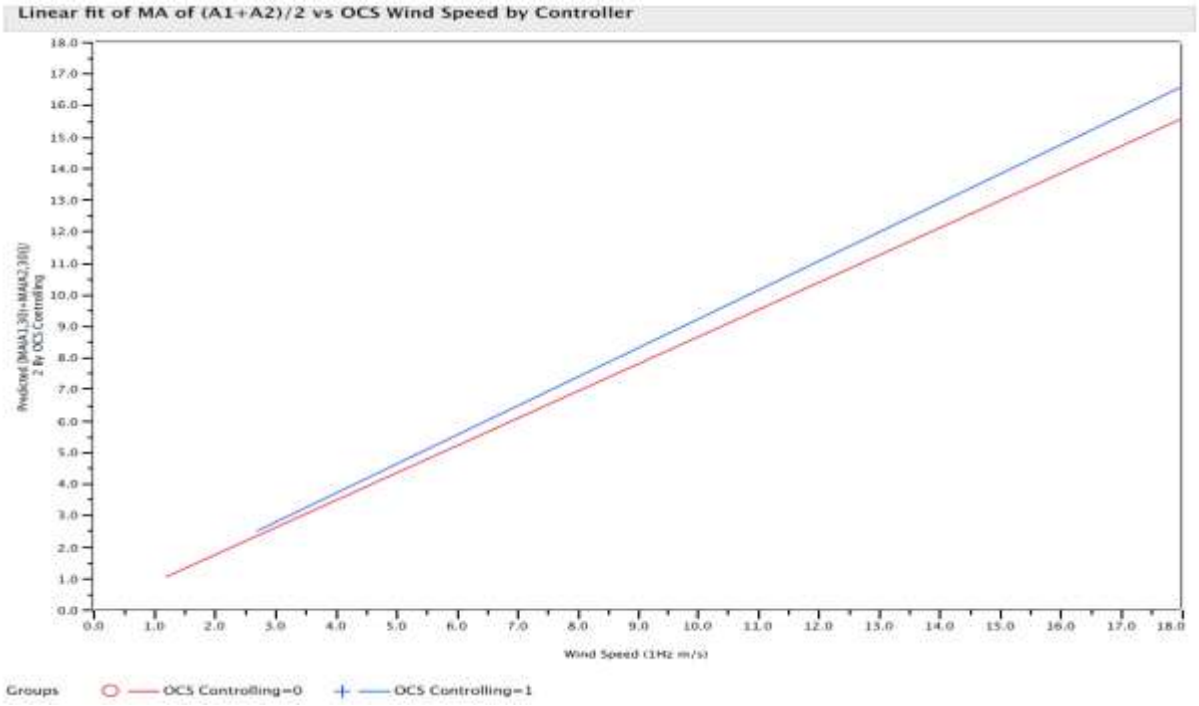


**Figure 29: The fitted curves of wind speed as measured by the anemometer and the OCS.**

**Key Points**

- The region at the rear of the nacelle is very turbulent. Wind speed measured within this environment is noisy, and cannot be directly used in controlling the wind turbine. Averaging can be

used to make the outputs of the sonic anemometer(s) useful; however, rapid changes in wind speed are lost.

- Wind speed data from the OCS is real-time, less noisy and does not require further averaging to be usable.
- The operation of the turbine decreases the accuracy and usability of the wind speed measurements that the sonic anemometer records. This effect is most pronounced in Region II.
- The correlation between all wind speed measurement devices improves under OCS control. The wind speed detected by the sonic anemometers is lower, as expected, than the free wind speed. However, the wind speed measured by the legacy system is even lower relative to the OCS when the system is under legacy control.

***Measurement of Wind Angle***

The wind turbine under study here uses a sonic anemometer to measure the angle of the wind relative to the turbine. For ease of discussion, throughout this document, when we refer to angular measurement, we use the term wind vane. Figure 30 shows the raw output of a sonic wind vane (one of two) in operation.

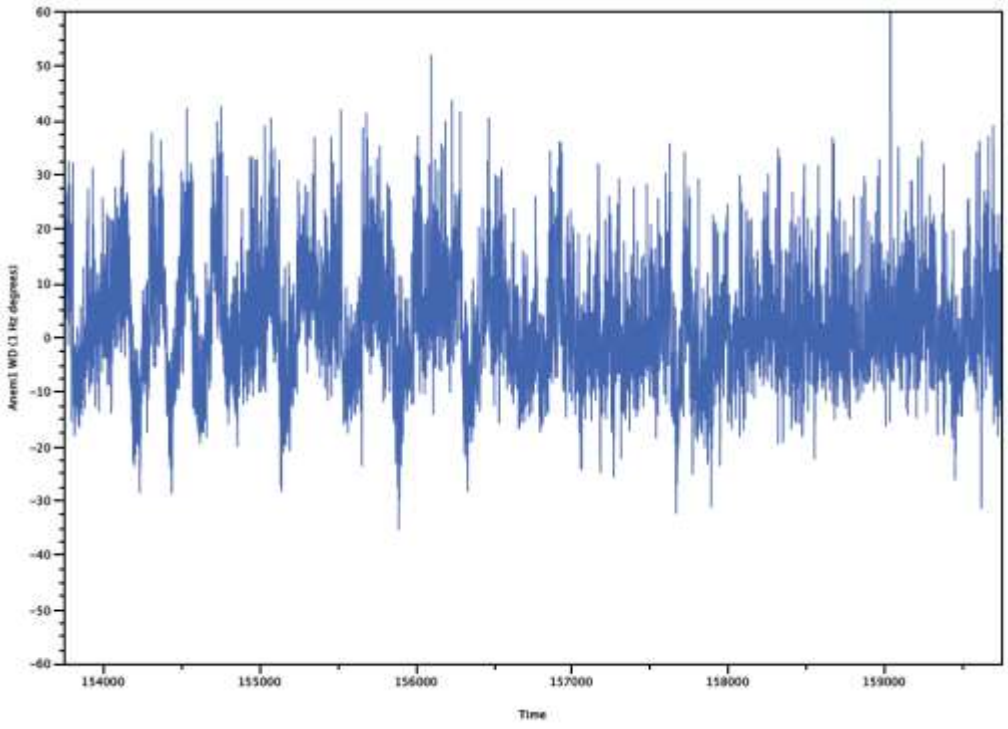


**Figure 30: The wind angle, measured each second, of a sonic wind vane mounted at the rear of the nacelle.**

We now examine the correlation between the wind angle relative to the turbine, as measured by the two sonic wind vanes and the OCS (which measures the wind direction in front of the turbine). In general, the correlation between the two sonic wind vanes (V1 and V2) is reasonable. However, the correlation between the sonic wind vanes and the measured angle of the free wind is marginal. All

correlations improve under OCS control. These correlations, as measured by the figure of merit R^2, are shown in Figure 31.

| R^2 | Turbine Control | |
|---|---|---|
| Angle | Legacy | OCS |
| V1 & V2 | 0.991 | 0.995 |
| V1 & OCS | 0.947 | 0.975 |
| V2 & OCS | 0.946 | 0.976 |

**Figure 31: The correlations between the sonic wind vanes and the OCS when measuring wind angle.**

*(The correlations all improve under OCS control.)*

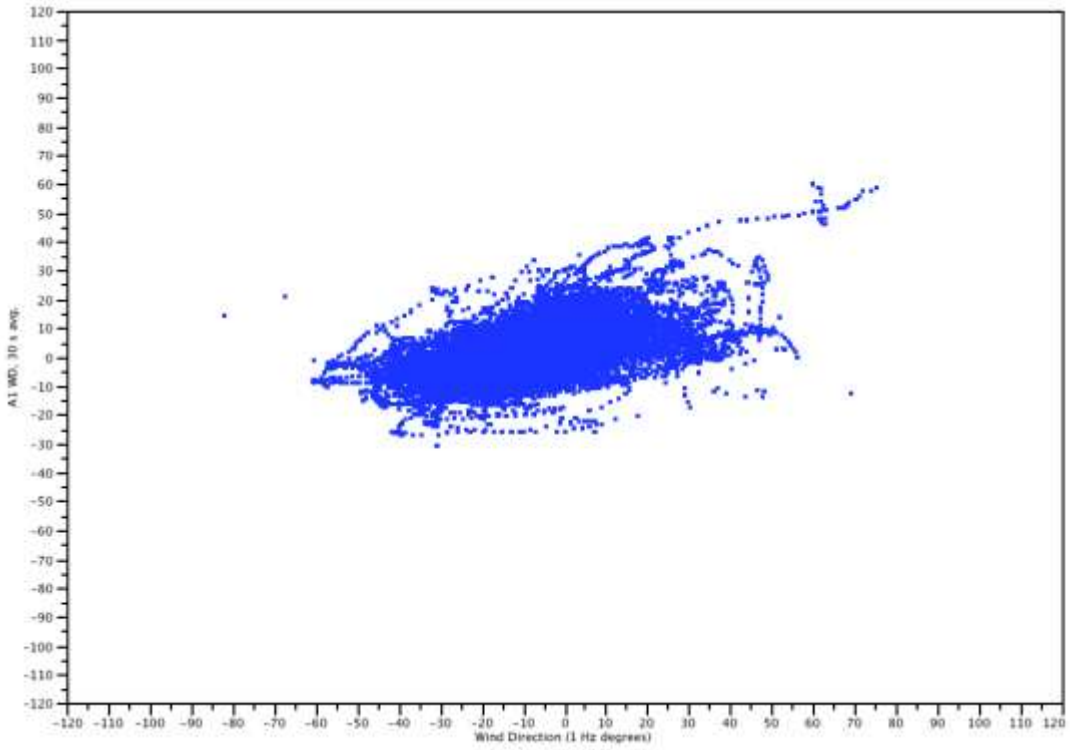


**Figure 32: Scatter plot of wind angles relative to the turbine measured by a single sonic wind vane plotted against the wind angle measured by the OCS, while under legacy control.**

*(R^2 is 0.56. The sonic wind vane measurement is suppressed relative to the measurement of the free wind direction, with the correlation slope)*

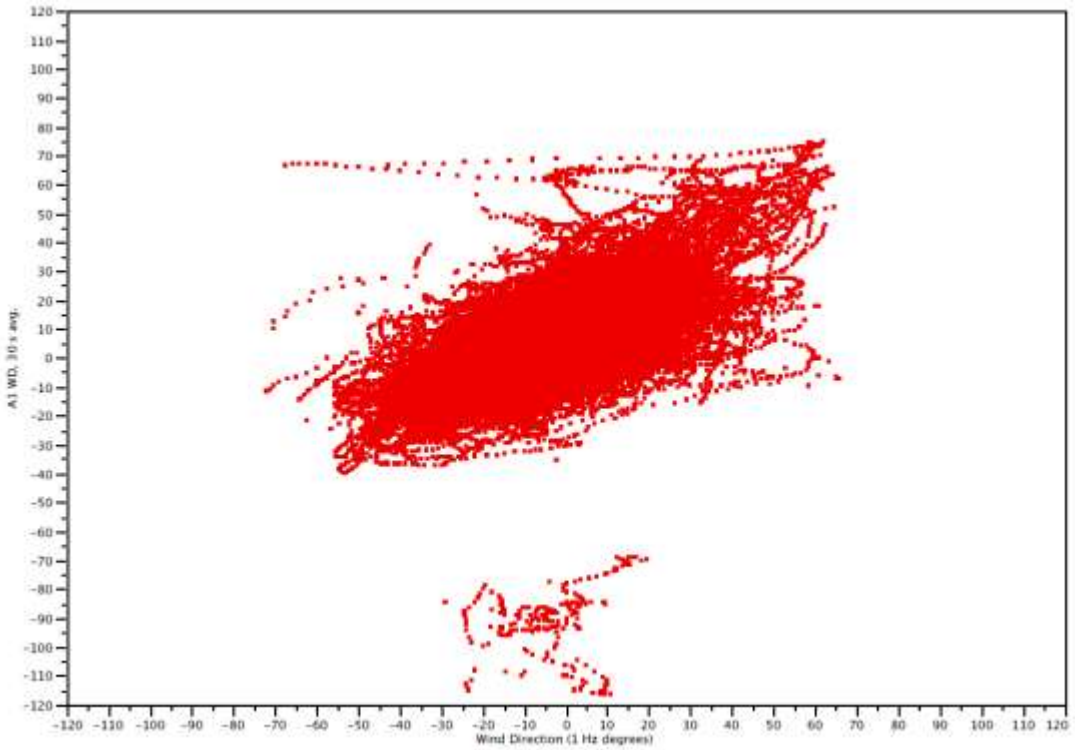


**Figure 33: The scatter plot of wind angles of a turbine measured by a single sonic wind vane plotted against the wind angle measured by the OCS, while the turbine is under OCS control.**

*(R^2 is 0.63. Here, the average yaw angle of the turbine is approximately zero. The sonic wind vane measurement is more tightly correlated to the free flowing wind direction, and the ratio of angle measured by the sonic wind vane to the OCS is closer to unity.)*

Two things are now clearly observed. First, the measurements of the angular devices all display superior correlation when the turbine is being controlled by the OCS. Second, the slope of angle measured by the sonic wind vane to the OCS measurement is closer to unity when the turbine is being controlled by the OCS.

There is an aggregation of points, in the lower portion of Figure 12, where the OCS is measuring small angles, while the sonic wind vane is measuring an angle almost orthogonal. This data set is being investigated.

**Key Points**

- The region at the rear of the nacelle is very turbulent. Wind angles measured within this environment are noisy, and can not be directly used in controlling the wind turbine. Time averaging improves this.
- The correlations, and directionality, of wind angle as measured by the sonic wind vane and OCS are substantially improved while the turbine is under OCS control.

**Measurement Asymmetry**

To further investigate the disparity between the angles measured by the sonic wind vane and the OCS, we simply generated a scatter plot of power generated vs. measured angle. In this comparison, we are showing all data, whether the system was controlled by the legacy system or the OCS.

If we plot power vs. OCS angle, we see a distribution with a rather flat top, being limited by the rated power of the turbine, roughly centered at angle = 0, with the distributions being rather symmetric around zero. This distribution is what would be intuitively expected.

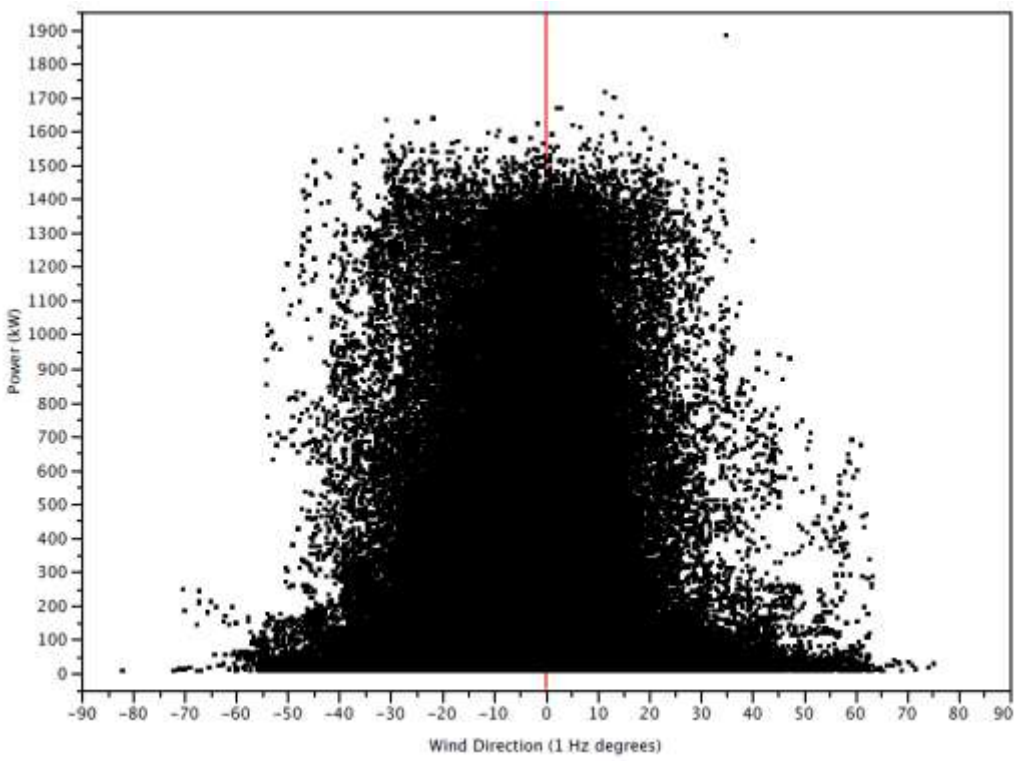


**Figure 34: A scatter plot of output power vs. angle as measured by the OCS.**

*(All operational conditions are shown, including both legacy and OCS control regimes. The distribution is centered at zero and is roughly symmetric.)*

Similar data taken with sonic wind vanes measuring wind angle is very different. The distribution is not symmetric, and is in fact skewed strongly in one direction. The amount of "skewedness", including the degree of angular offset, changes with output power, i.e., the angular error of the sonic wind vane is a function of the power, which is related to wind speed. We will discuss later why the apparent angle of the wind, and the wind speed, which should be independent of turbine power, is functionally related to the output power of the wind turbine, making yaw control difficult. However, this is fairly easy to understand intuitively since a gigantic fan (i.e., the blades of the wind turbine) is creating vigorous wind patterns that are a function of blade pitch, angle of attack and actual wind velocity. Stated differently, a large signal error is imposed upon the sonic anemometer, and that error is not constant, but is a function of wind turbine operation, making removal of that systematic error difficult.

**Key Points**

- The distribution of output powers is centered and symmetric for the OCS. A yaw control algorithm designed to minimize the measured angle of the OCS would maximize turbine power.
- The distribution of output powers is neither centered nor symmetric for the sonic wind vane. The amount of angular offset appears to be a function of output power, and by extension, wind speed.
- Because the yaw angle error of the post-turbine wind, as measured by the sonic wind vanes, is a function of power and wind speed, it is much more complicated to design and test effective control algorithms.

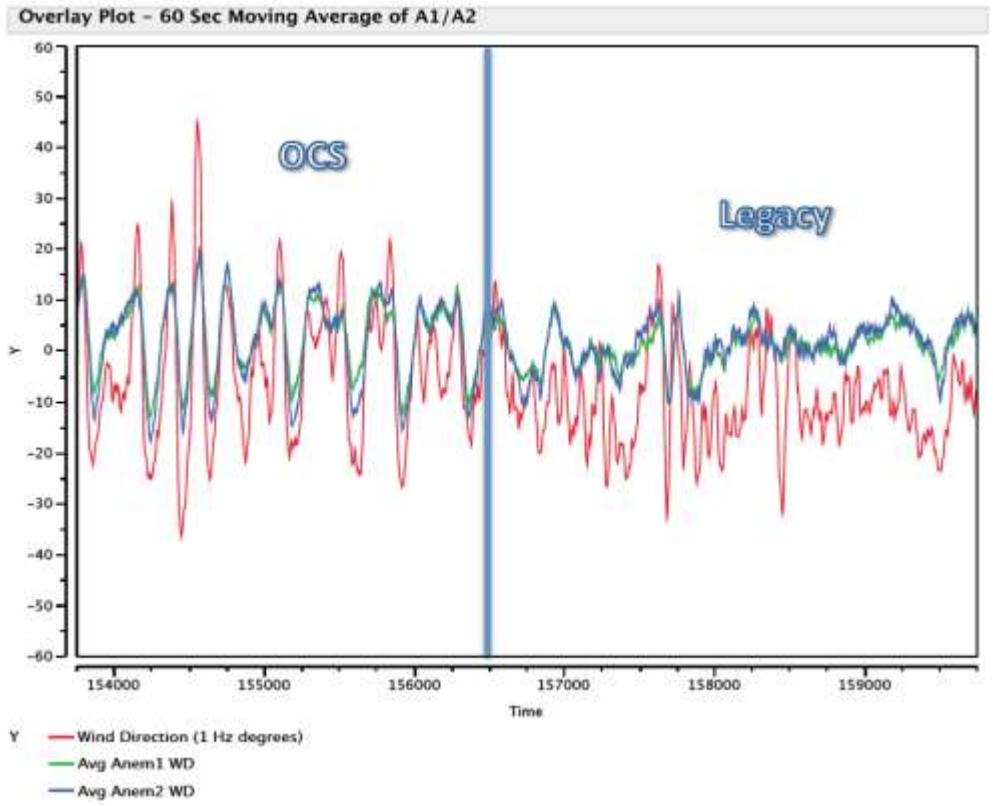


**Figure 35: A comparison of measured wind angles.**

*(In the left portion, with generally good correlation, is data taken with the turbine under OCS control. Conversely, in the right portion, with substantially poorer correlation, is data taken with the legacy control. The red trace is the OCS, the blue and green traces are the sonic anemometer)*

Previously we noted that the wind angle correlations for both sonic wind vanes and OCS improved when the turbine was operating under OCS control. The arguments presented above help explain this. However, the difference in these correlations is quite striking to look at in real time. Figure 35 shows a time period of approximately 6000 seconds (1.6 hours) in which the turbine is first under control of the OCS and then under the control of the sonic wind vane. While the sonic wind vane does miss some of the rapid changes in wind angle, the tracking between the OCS and the sonic wind vanes is generally

good while under OCS control. By contrast, when under the control of the legacy sonic wind vanes, substantial differences appear between the OCS, which is measuring undisturbed air, and the sonic wind vanes, which are in air disturbed by the rotating blades.

**Uptime**

In general, the LIDAR world refrains from discussing device uptime. This is intellectually bankrupt, because if the system is not up and running, it can't control the turbine. If the OCS cannot control the turbine, it obviously generates exactly zero extra power. Within this uptime demonstration, the OCS was in operation a minority of the time as shown in the following figure.

Beta units from CTW did not demonstrate good uptime performance. CTW Generation II, or G2, units, with improvement in both design and manufacturing, have radically improved signal-to-noise (SNR) performance, which directly translates into significantly better uptime. While no measurement will have 100% uptime, we believe that the G2 and subsequent versions of the OCS will have uptime approaching 100%, as demonstrated by recent field results. This study employed a beta OSC unit, which experienced a low system uptime. This is shown below.

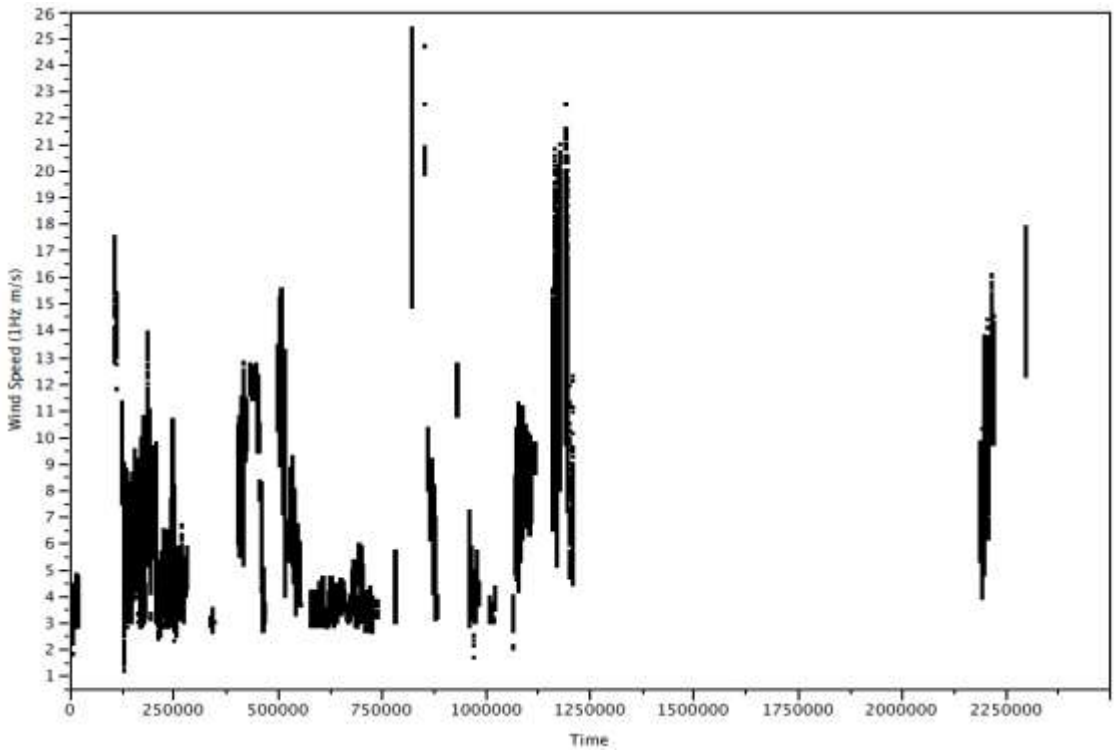


**Figure 36: A scatter plot of all wind speed measurements of a turbine from the beta version of the OCS over a period approximately 30 days.**

*(The OCS exhibited uptime of 33%.)*

In order to track the uptime of the OCS, which we believe is a critical figure of merit for any sensing system, we computed an up-time figure, defined as the total amount of time the OCS was operating divided by the total time the turbine was operational. Up-time for this beta unit was 33%.

**Key Point:**

- The beta version of the OCS used in this study had poor uptime of only 33%.
- The redesigned optical system now used in the G2 version of the OCS has demonstrated uptime in the field approaching 100%.

**Turbine Power Production**

Instead of just starting the discussion of turbine power production with a comparison of the scatter plots that lead to power curves, we instead begin by looking at what the output power of the wind turbine looks like over time.

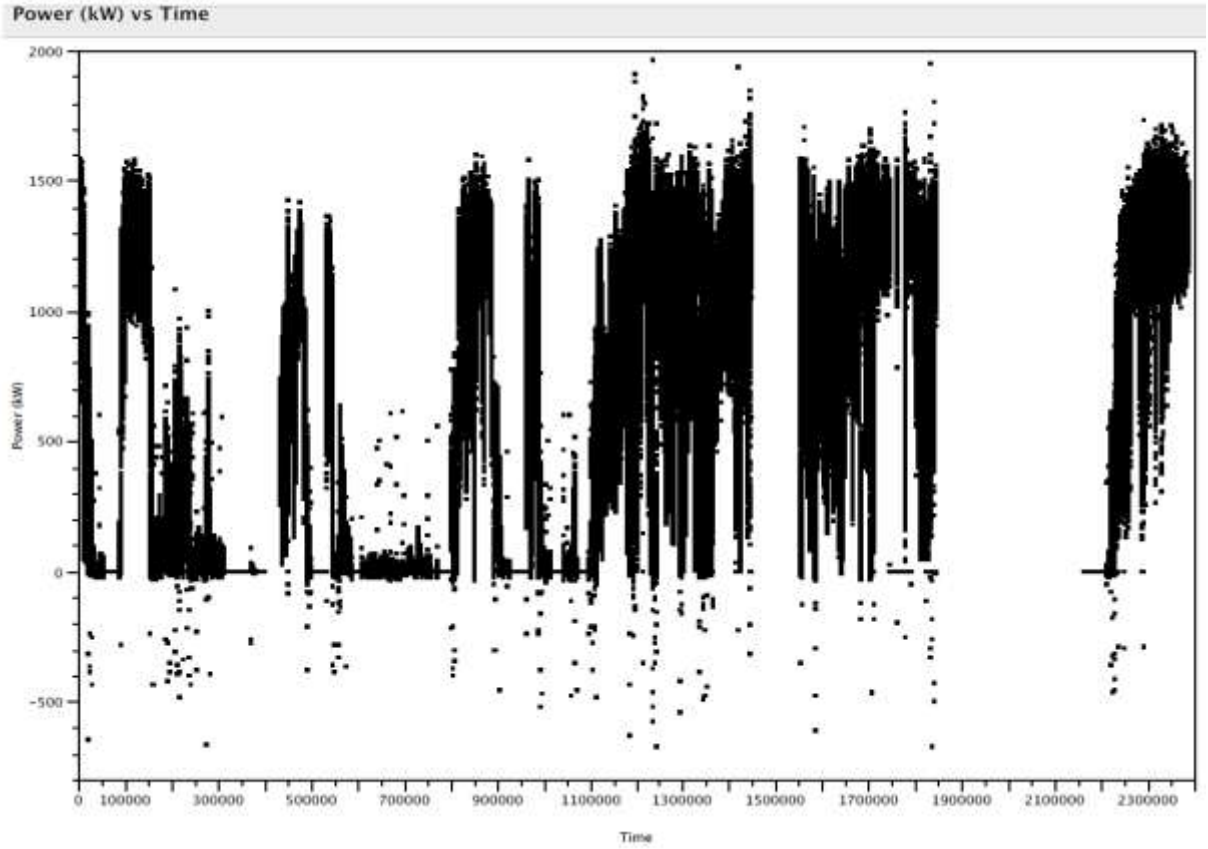


**Figure 37: The output power of the turbine during the entire period of study.**

In Figure 34, we show all power data for the full period of operation for the turbine, whether the turbine was operating under the control of the legacy sonic anemometer or the OCS. This data shows periods of good output and also periods of minimal or zero output. In addition, there are many data points where the turbine output power is shown to be negative. We don't fully understand negative power production in turbines, but do note this data. In Figure 38, we show 100 seconds of power output data for the same wind turbine. The data was surprising; within that timeframe, the power output of the turbine fluctuated from 400 kW to 160 kW, with +/- 50% changes in power output occurring within seconds. As an aside, we understand that the wind can change very quickly. These changes in wind speed drive substantial torque fluctuation which yield rapid changes in power output. That being said,

the electrical generation properties of wind turbines are outside of our area of expertise, and as such, we now move onto the calculation of the actual power curves.

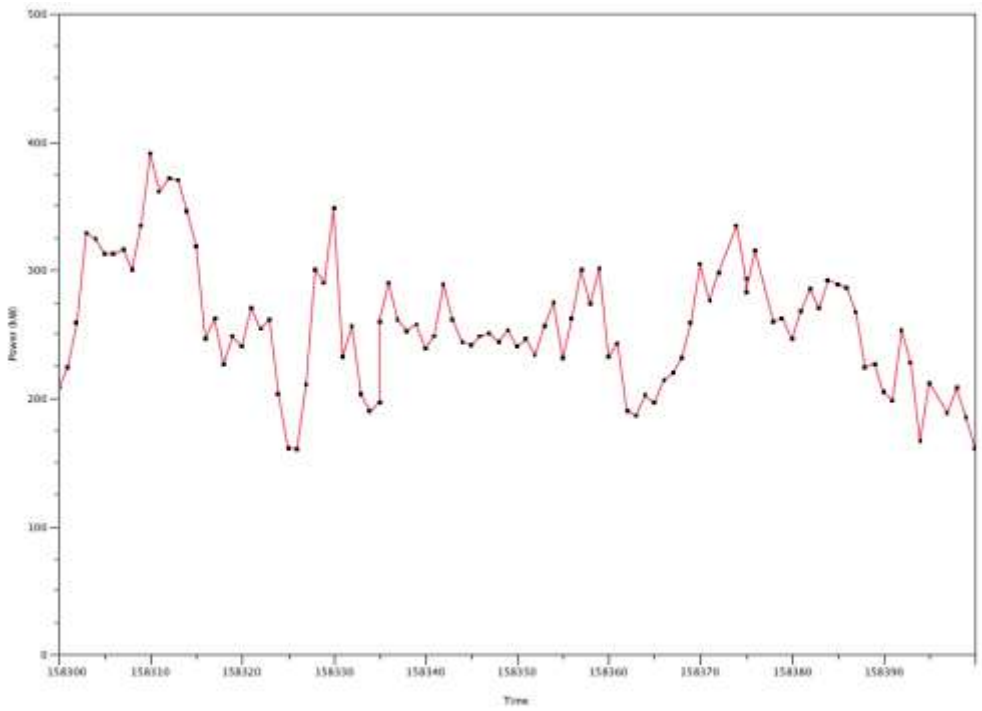

**Figure 38: The power output of the turbine, at one-second intervals, over a 100 second period.**

***Power Curves***

Before we begin here, it is important to tackle a simple question: what device should we use as the reference point for wind speed? We start with the philosophy of the IEC standard which uses met towers to measure the undisturbed wind in front of the turbine. Based upon this philosophy, the OCS, which measures air in front of the turbine, is the correct choice.

On the one hand, the industry has experience with the sonic anemometers measuring the disturbed air after the turbine propellers. However, the sonic anemometer measurement is strongly related to power output (i.e., is not an independent variable), leading to all sorts of non-linear effects. The anemometer understates actual wind speed, thereby exaggerating the efficiency of the turbine. The data of this report clearly demonstrates the deficiencies of using a measurement device in the middle of the rotor turbulence as the benchmark for power curve computation.

Thus, to align with IEC standards, the correct benchmark measurement is that of the free- flowing wind in front of the turbine nacelle. In cases where met towers are available, we believe that a met tower is a convenient, non-controversial choice. However, given the excellent correlation that the OCS shown to have with met towers, we chose the OCS wind speed measurement as the power curve benchmark.

We start by showing the power curve of the turbine operating in legacy mode. The curve is fitted to a generalized logistics (Richards' curve) function. The generalized logistic curve or function, also known as

Richards' curve is a widely-used and flexible sigmoid function for growth modeling. Other curves could have been used, but the function matches the general shape of the power curve well and is well known in the statistical world.

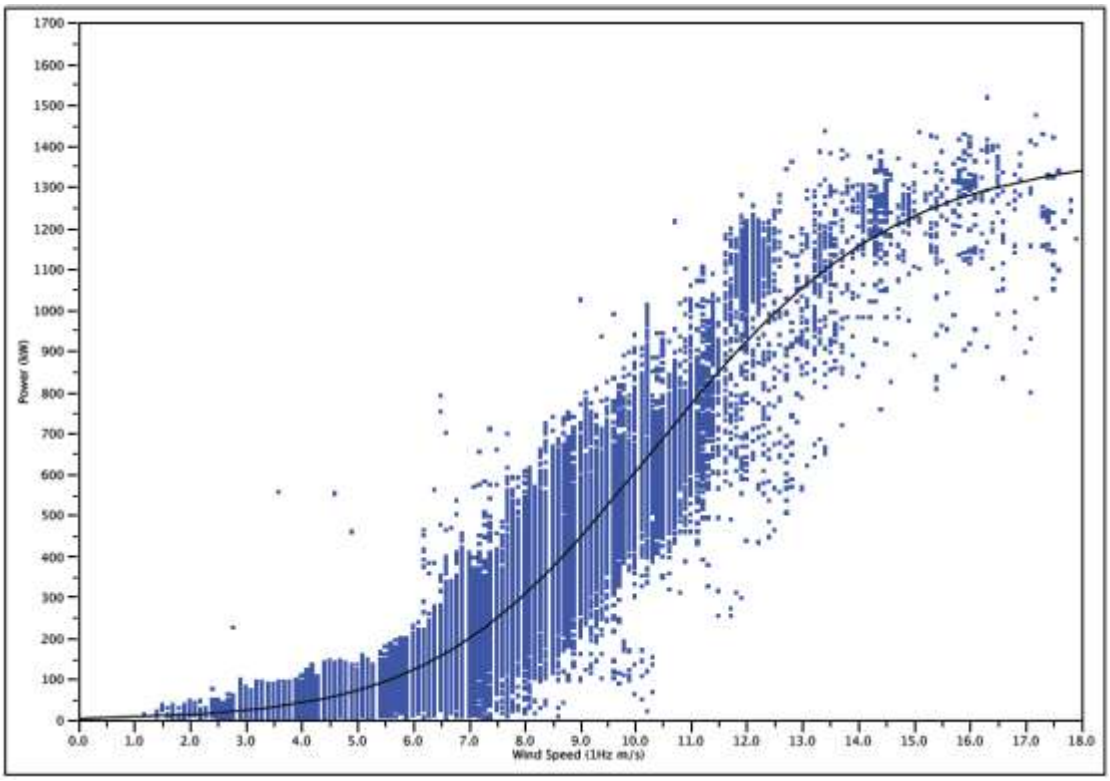


**Figure 39: A scatter plot of power output vs. wind speed.**

*(The turbine is under legacy sonic anemometer control mode, with the free wind speed in front of the turbine, on the horizontal axis, as measured by the OCS. The data is fitted to a Richards' function.)*

Next, we show the performance of the same turbine under OCS control. Please note that the OCS has three modes, and the data captures all three OCS modes. These three modes are proprietary to CTW, and the specifics of the differences between these modes of operation will not be discussed within this document.

There is a cut-off of wind data at about 3 m/s in the OCS modes. The system is effectively only recording data in a power-on status, after cut-in.

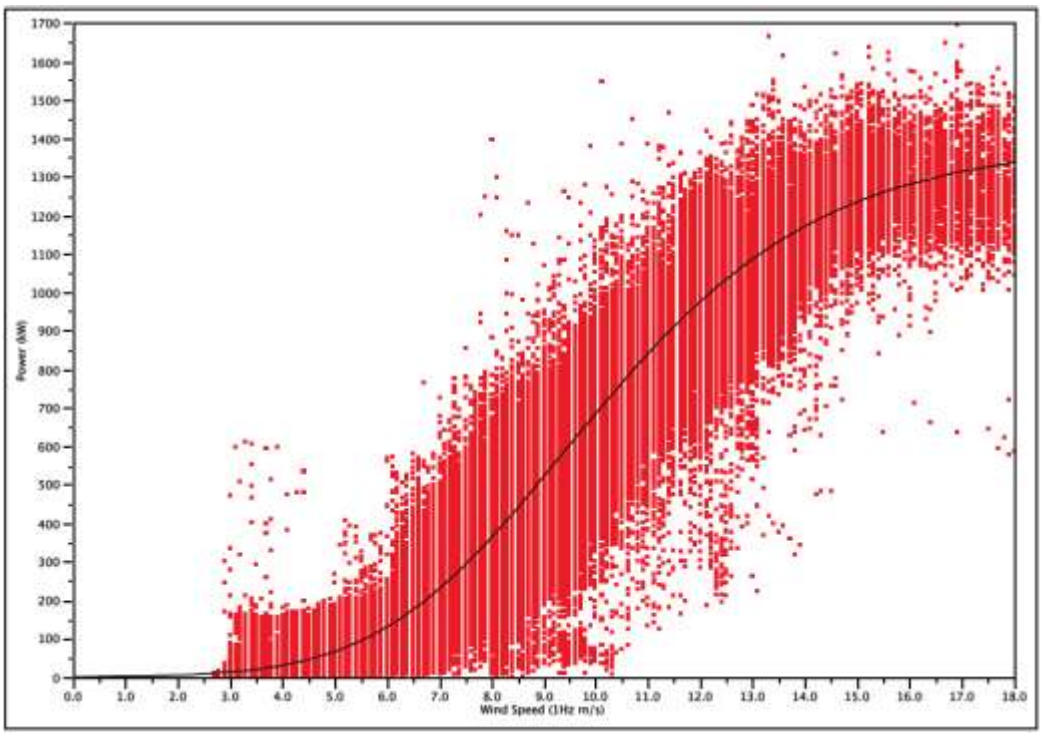


**Figure 40: A scatter plot of output power vs. wind speed.**

*(The free wind speed in front of the turbine, on the horizontal axis, as measured by the OCS. The data is for the turbine under one of three OCS control modes. The data is fitted to a Richards' function.)*

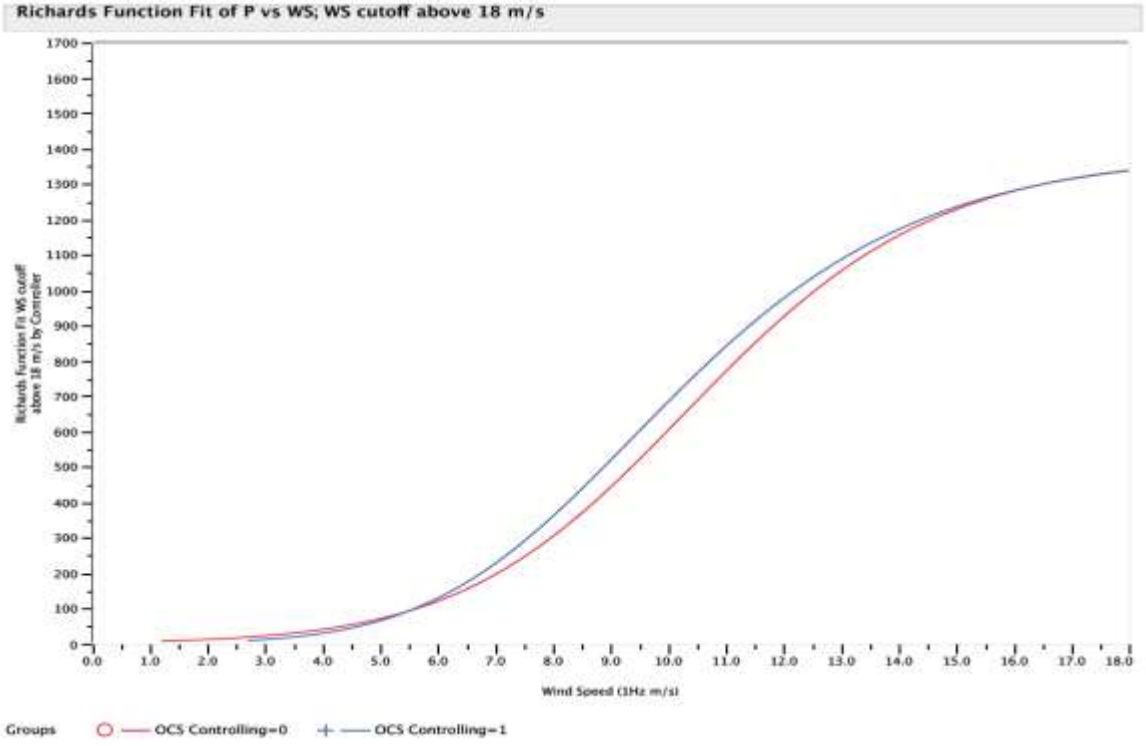


**Figure 41: The fitted functions for legacy (red curve) and OCS (all three control modes) (blue curve).**

*(The OCS generates substantial increases in power throughout Region II.)*

We then show the two fitted functions together: with the OCS controlling the turbine and with the sonic anemometer controlling the turbine. The OCS control generates extra power throughout Region II. However, the OCS control situation operated in three proprietary modes. These modes had substantially different performance. The following table lists the results of this experiment in terms of anticipated increases in energy production, and, for a turbine producing $0.5M of revenue a year, the actual increase in annual revenue.

| | | Control Method | | |
|---|---|---|---|---|
| ***% AEP Improvement*** | Legacy | 3 | 2 | 1 |
| Uptime = 100% | 0.00 | 0.50% | 7.60% | 15.00% |
| Uptime = 35% | 0.00 | 0.18% | 2.66% | 5.25% |
| | | | | |
| Assume Turbine Revenue = $500K/yr | | Control Method | | |
| ***Additional Turbine Revenue/Yr*** | Legacy | 3 | 2 | 1 |
| Uptime = 100% | 0 | $ 2.50 | $ 38.00 | $ 75.00 |
| Uptime = 35% | 0 | $ 0.88 | $ 13.30 | $ 26.25 |

**Figure 42: The tabulated results of the various control methods.**

*(The OCS increased energy production in all cases. The increases varied from less than a one percent increase, which is in the noise of the experiment, to a substantial 15% increase in energy production)*

To illustrate the more dramatic power increases of Mode 1, the fitted curves for Legacy control and OCS Mode 1 control are shown in Figure 40.

**Conclusions**

The behavior of wind speed and angle measurements for a utility scale turbine, taken in front of the turbine by the OCS, and following the turbine blades by sonic anemometers and sonic wind vanes, respectively, are compared.

The measurements in the perturbed air are very noisy, and, even after averaging, are so heavily affected by the operation of the turbine that they present very substantial control theory problems when considered as inputs to a control algorithm for turbine yaw.

The free wind measurements may be used without secondary processing, such as averaging. By examining the output power of the turbine, we conclude that the alignment of the turbine under OCS control is significantly better than under legacy control.

The OCS operated in three modes. Averaged over all modes, the OCS improved the output power of the turbine by ~10% when it was operating. The highest performance enhancement occurred when the turbine was operated in OCS Mode 1, where a 15% improvement in energy production was shown against the wind distribution of the location when the OCS was operating.

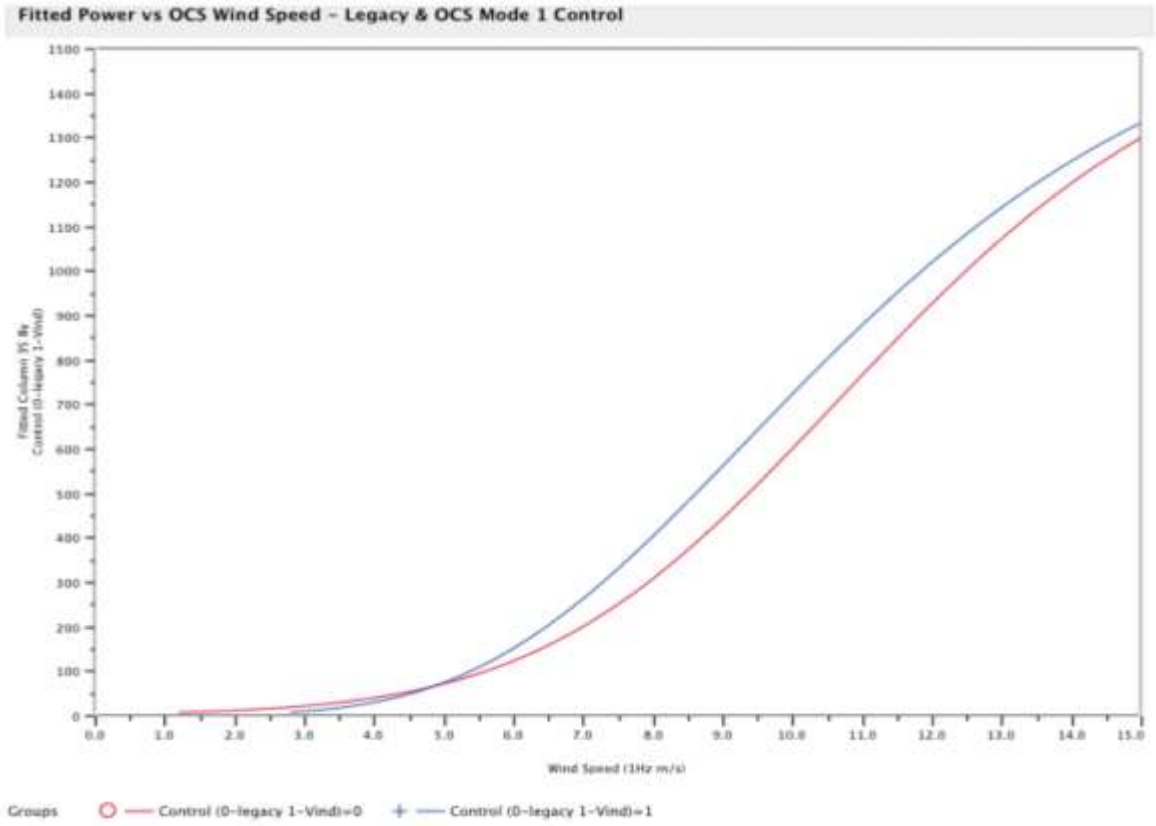


**Figure 43: The fitted functions for legacy (red curve) and OCS Mode 1 (blue curve).**

*(This control mode generated a 15% increase in energy production using the measured wind distribution of this turbine location.)*

The beta version OCS had substantial periods of time when it was not collecting good data, and by extension, was not controlling the turbine. This is being improved in the G2 version of the OCS. For the period of time studied here, the uptime of the beta OCS was 33%. In future G2 units, we anticipate that the uptime of the device will be close to 100%.

## B2. Analysis of Traditional Yaw Measurements

**Limitations of Post-Rotor Yaw Measurements**

In a recent analysis we demonstrated two key points. We demonstrated that the wind speed measurement of the post-rotor anemometer had an error related to the wash produced by the rotating blades. As such, free wind measurements are much better to determine wind speed for calculating the output power curves of turbines than the wind speed measurements via nacelle-mounted anemometers.

*In general, the industry does accept that the speed measurement of an anemometer located in the post-rotor flow is flawed, and that measurement of the wind in front of the turbine is superior.*

The second was that by switching to yaw control based upon free wind characteristics real and substantial power increases can be achieved.

*In general, the industry is dubious of the amount of extra power that can be generated by changing yaw control.*

A reading of the literature suggests that yaw angle isn't nearly as exciting as pitch control. Perhaps that's because yaw is sort of like yawn? Maybe it's because the industry thinks the vanes behind the turbine are nicely calibrated and believes the simple COS^3 math and doesn't see how it could really matter all that much. Or perhaps the turbine manufacturers just don't like to talk about how silly it is to point a multi-million dollar turbine based upon measuring the wind direction right after a gigantic spinning propeller?

However, when yaw is not set properly, power is lost, but more importantly, stresses are placed onto turbines. Because of the potential magnitude of the economics of these issues, we believe spending some time asking fundamental questions about yaw, and then using actual data from field turbines to try to answer these questions, might be of some benefit to the operators of wind turbines trying to maximize their economic viability.

In this section, we look in greater detail at the yaw angle of the turbine relative to the wind.

**Key questions**

- Based upon data from the nacelle-mounted measurement system, what are the characteristics of the current yaw measurement system?
- Does the rotating vortex post-rotor have an effect on measurement of yaw angle?
- Can rotor-induced errors in yaw measurements be corrected so that a good control system can be designed?

Our world needs us, the wind turbine industry, to produce power, cleanly, efficiently and at low cost. Here at BlueScout, our contribution to the wind industry is to use our understanding of optics to provide a fundamentally deeper understanding of the wind resource – to produce substantial, repeatable increases in the output power of wind turbines.

An Optical Control System (OCS), Generation I, is mounted upon an operating utility scale wind turbine. The yaw angle of the turbine is studied in a variety of different ways to better understand the physics of basing control decisions upon measurements of the post-rotor flow.

The data set is large, approximately 500 MB, composed of 335,000 data points taken at 1 second spacing. SAS JMP used as the statistical analytic tool. The dataset includes output from the OCS, two sonic anemometers (giving both wind speed and wind direction), turbine state, ambient temperature, output power, and absolute yaw position.

A wind turbine produces the most power when it is pointed directly in the wind. As the turbine moves away from facing the wind, two things happen- it produces less power and endures more mechanical stress.

Let's begin by looking at the distribution of output power against the measured wind angle. We start with the data from the OCS.

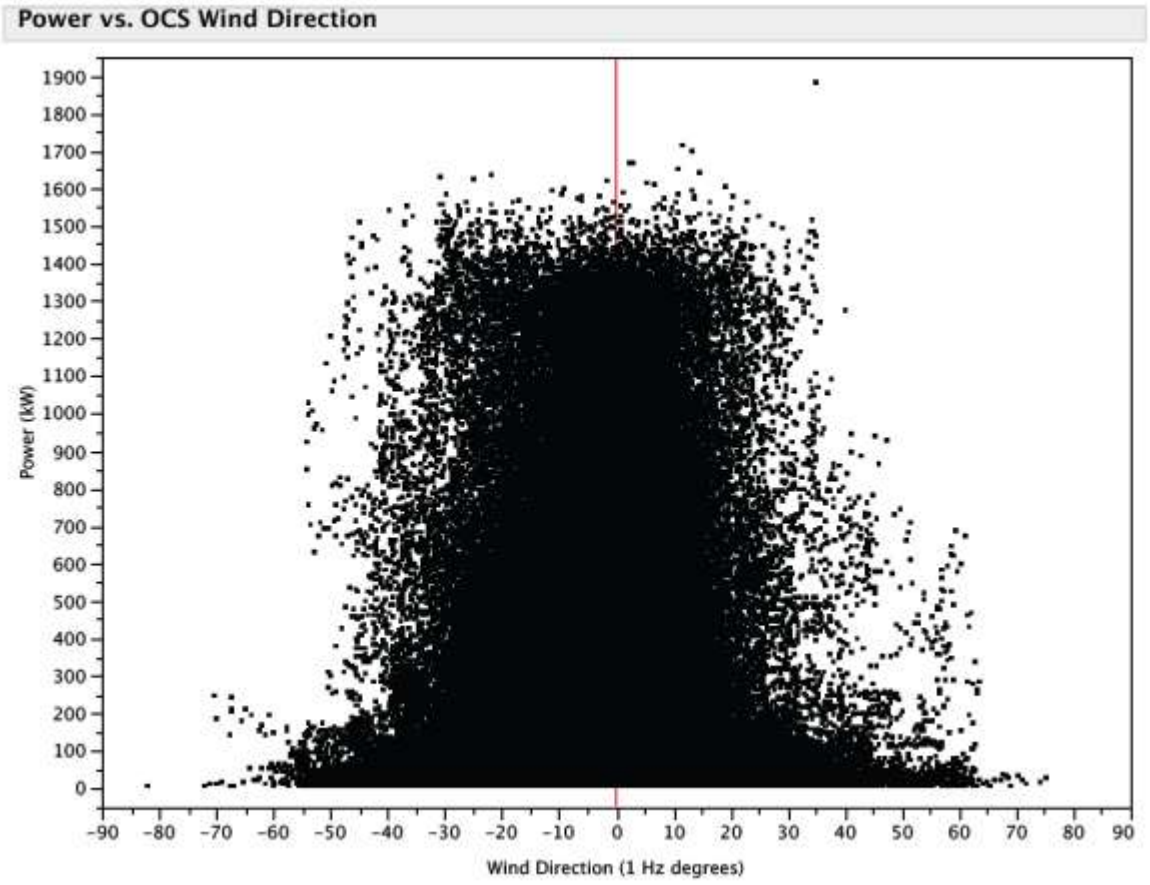


**Figure 44: A scatter plot of the output power of the turbine vs. wind angle as measured by the OCS.**

In general, the data of Figure 44 fits our intuition. The measured output power is roughly capped at 1.5 MW. The power of the turbine falls off as the angle of the wind relative to the turbine (yaw error) increases. The data is symmetric, and roughly centered at zero.

Now the same data set is used to do a scatter plot with the angle being measured by one of the sonic anemometers. Again, the power peaks at about 1.5 MW. Again, the power falls off as the post-rotor angle increases. The scatter plot is narrower than what is measured in the free stream. The data set is not symmetric, with the center of power distribution now being ~10-15 degrees. Further, the amount of angular offset changes with turbine power. Finally, the measurement of post-rotor angle shows very sparse data for angles less than -30 degrees.

This section focuses upon understanding this behavior in greater detail.

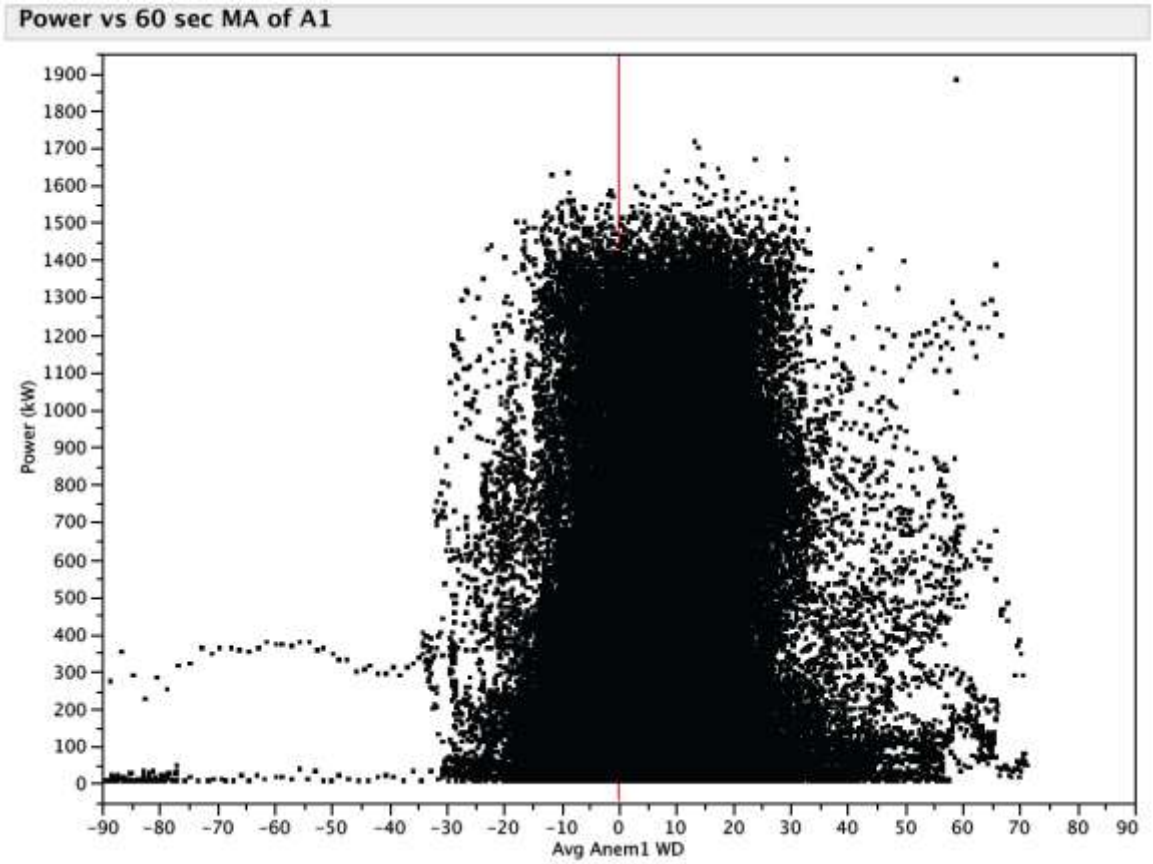


**Figure 45: A scatter plot of power vs. post-rotor wind angle measured by the anemometer.**

*(The data is not symmetric, with the center of the distribution being offset by ~10 degrees.)*

**Post-Rotor Yaw Measurements**

Let's start with basics. The turbine is going to produce the most power when it faces the wind. The fundamental task of yaw control is to aim the turbine into the wind. We look first at the distribution of wind angles, as judged by post-rotor wind as measured by the sonic anemometer, while the legacy yaw control is operating the turbine. In this work, we do not look to the OCS to judge the legacy control system, rather we look closely at the post-rotor measurements and use very simple physical arguments to understand the efficacy of trying to figure out a yaw angle while sitting in the vortex of the rotor.

It should be noted that when we do compare the OCS to the legacy measurement system, that comparison compares two different attributes. The first is the type of measurement device. While the physics of wind measurement with LIDAR are a bit different than measurements based upon a physical wind vane or an acoustic anemometer, we believe that each of these devices can be calibrated and do a fine job of measuring wind characteristics. The second, and we believe much more significant, is the physical position of the wind that is being measured. The sonic anemometer (or wind vane) is behind the rotor. As such, it is situated in place with a constant rotational bias. This effect, where the direction of the airflow is partially due to the wind and partially due to the rotating blades is one of the items that we wish to investigate in this paper.

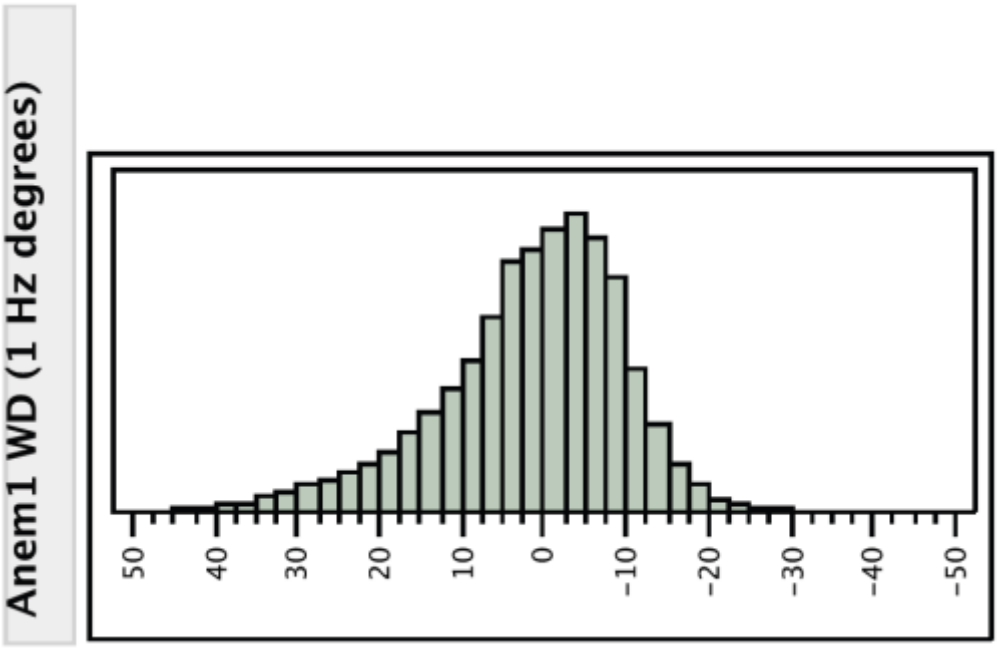


**Figure 46: The measured distribution of wind angles, as measured in the post-rotor wind flow.**

*(The bottom is degrees. The distribution has mean and median of 1.55 and 0 degrees, respectively. The standard deviation is 11.3 degrees.)*

Figure 46 shows the distribution of yaw angles, as measured by the acoustic anemometer. In looking at this distribution, we note that the mean and median are very well centered, at 1.55 degrees and 0 degrees, respectively. The standard deviation is 11.3 degrees. The distribution is not symmetric, as one would expect for a device in the rotor wash of the turbine. This implies that the measurement system is non-linear with respect to wind angle.

Figure 47 shows the same distribution, under legacy control, but now measured by the OCS on the free wind in front of the turbine. This distribution is roughly symmetric, but is now centered about 8 degrees off of the zero axis of the OCS.

**Key Points**

- The legacy control does a good job of centering the yaw angle as judged by post-rotor wind measured by the sonic anemometer. The yaw angle is measured to be asymmetric, with standard deviation of ~11.3 degrees.
- Under legacy control, the OCS measures a free-wind angle distribution that is about as broad as distribution measured by the sonic anemometer, but centered at -7.8 degrees. This distribution is symmetric.

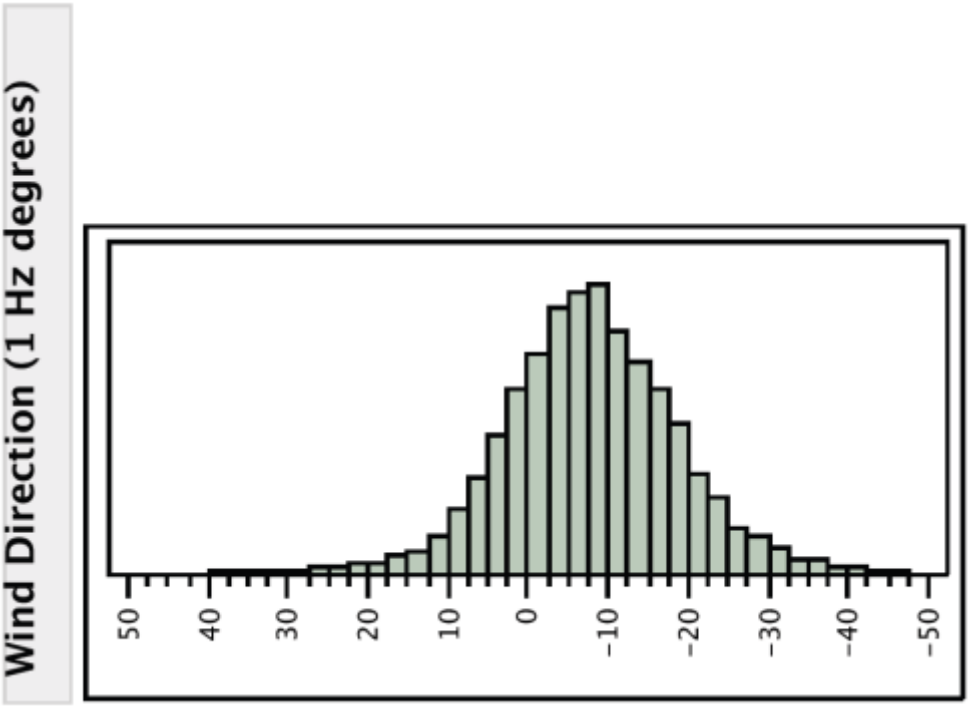


**Figure 47: The distribution of yaw angles with respect to the free wind, as measured by the OCS.**

*(The turbine is under legacy control. The distribution is roughly symmetric. The mean of the distribution is -7.8 degrees, with a standard deviation of 11.8 degrees.)*

Now we consider the distributions when the turbine sets yaw based on the free wind angle in front of the turbine as measured by the OCS. We again start with the yaw-angle measured post-rotor by the sonic anemometer.

As the anemometer is measuring wind in the rotating rotor wash, the measurement shows asymmetry. The distribution is shifted away from zero and is substantially broadened. Given that the distribution of yaw angle, as measured by the post rotor flow, is worsened under OCS control, the turbine should produce less power under OCS control if the post rotor yaw measurement is correct. The yaw angle distributions, using the free wind in front of the turbine as measured by the OCS, is shown below. The distribution is still symmetric, but is now much better centered, with a distribution that is substantially narrower than when the turbine is under legacy control. Given that the distribution of yaw angle, as measured by the free wind flow, is improved under OCS control, the turbine should produce more power under OCS control if the OCS measurements are correct.

The curious reader says, “whoa! Those paragraphs can’t both be right!” While we don’t wish this paper to deal with power production under different control regimes, the fact that the yaw angle distributions are very different when controlled differently does imply that the power that will be extracted from the wind, and the mechanical wear and tear upon the turbine, will be different in the different control regimes (i.e., under OCS control or legacy control). *Spoken bluntly, yaw control does matter*.

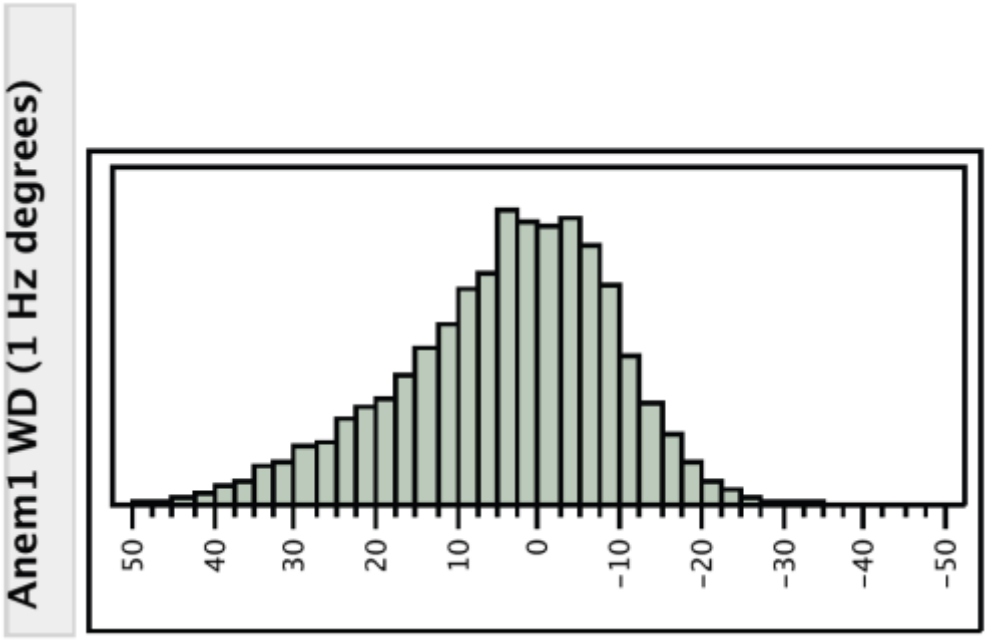


**Figure 48: The distribution of yaw angles, measured in the post-rotor flow by the sonic anemometer.**

*(The distribution is still asymmetry, as before, but the mean of the distribution has been shifted to 4.2 degrees. Under OCS control the distribution measured by the anemometer significantly broadens, with standard deviation increasing to 13.6 degrees.)*

**Key points**

- Under OCS control, the distribution of yaw angle, as measured by the OCS, is center at ~0 degrees and is made substantially narrower.
- Under OCS control, the distribution of yaw angle, as measured post-rotor, is moved away from being centered at zero, and is substantially broadened.
- The yaw distributions, as measured by either the OCS or the legacy post- rotor anemometer, change substantially between the two control schemes. Because yaw angle directly impacts the performance of the wind turbine the performance of the turbine will be different under OCS control than legacy control.

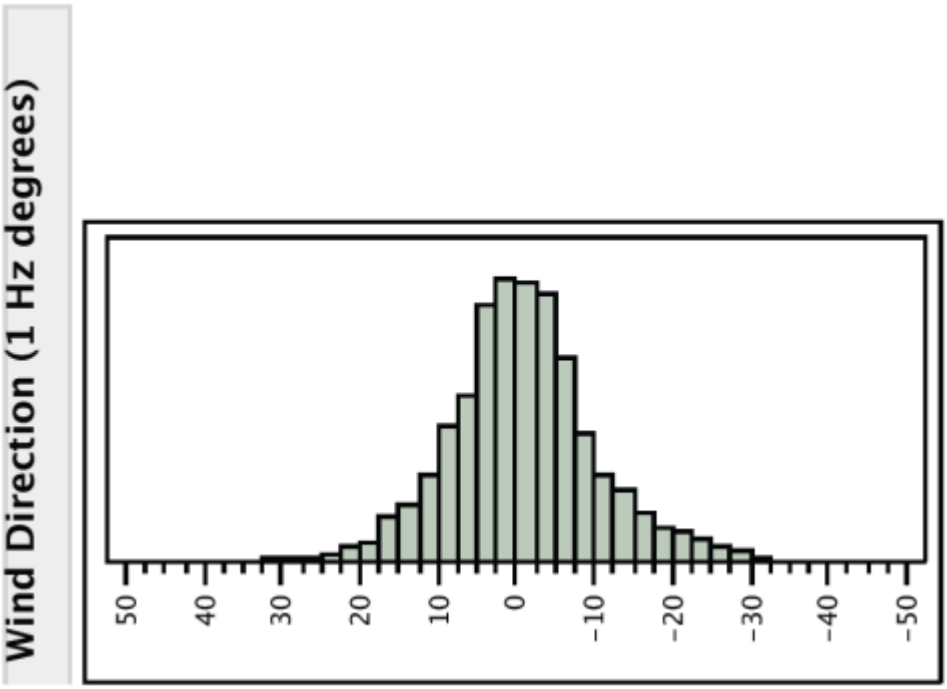


**Figure 49: The distribution of yaw angles, based upon the free wind in front of the turbine as measured by the OCS.**

*(The distribution is shifted, with the mean now at -0.9 degrees. The distribution of yaw angle is substantially narrower, with standard deviation now down to 9.7 degrees.)*

**Practical Yaw Optimization Using Post-Rotor Yaw Measurements**

It is tempting to look at the data just presented and think that a neat controls protocol could fix up the problems associated with a control algorithm based upon post-rotor wind measurements.

To investigate this, we begin by grouping the data into angular buckets, -25 to -15, -15 to -5, -5 to 5, 5 to 15, 15 to 25, and 25 to 35 degrees. Next, we compute power curves for each angular group. For clarity, this is shown by coloring the data points by which angular bucket they fall into as shown below.

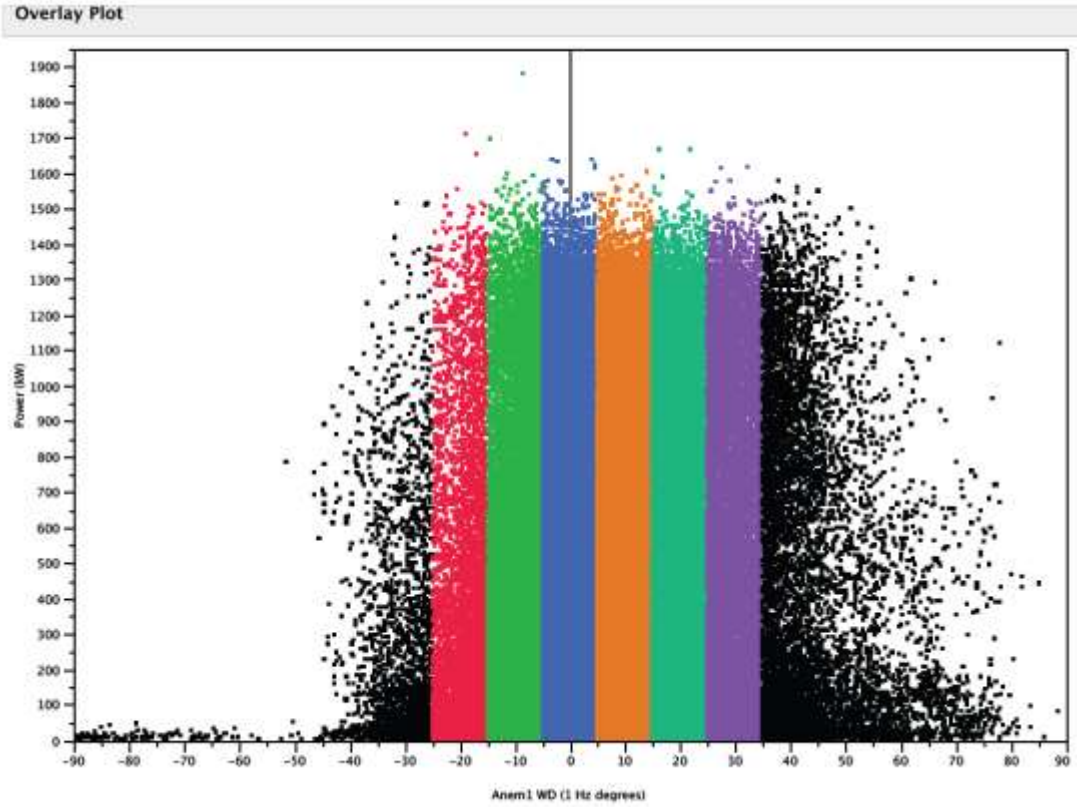


**Figure 50: The scatterplot of wind angle as measured by the post-rotor anemometer.**

*(The color-coding of the data points indicates the angle bins.)*

We next cut power curves for each of the angle buckets. As expected, the efficiency of the turbine changes with angle. However, the angle where maximum power occurs changes with output power as shown in the following figure. Given that the turbine always produces maximum power with a zero yaw angle, we conclude that the anemometer has an angular error that is dependent upon wind speed, and that a simple offset is not capable of fixing the post-rotor yaw angle error.

For this turbine, the optimum angle for power extraction, as measured by the sonic anemometer, varies with power. Obviously, the true “optimal” angle, with respect to the free wind in front of the turbine, is zero degrees, implying that a wind measurement device in the post-rotor turbulence has a rotor-induced error, at a true angle of zero degrees to the turbine, which is dependent upon the operational state of the turbine. This angular error has variance of approximately 40 degrees over the operation of this turbine.

Thus, the measurement of yaw angle is non-linear with respect to both yaw angle and wind speed.

For this turbine, the post-rotor error crosses zero at ~10 m/s wind speed. In heavy wind, the legacy turbine control will be misaligned to the wind by ~20 degrees.

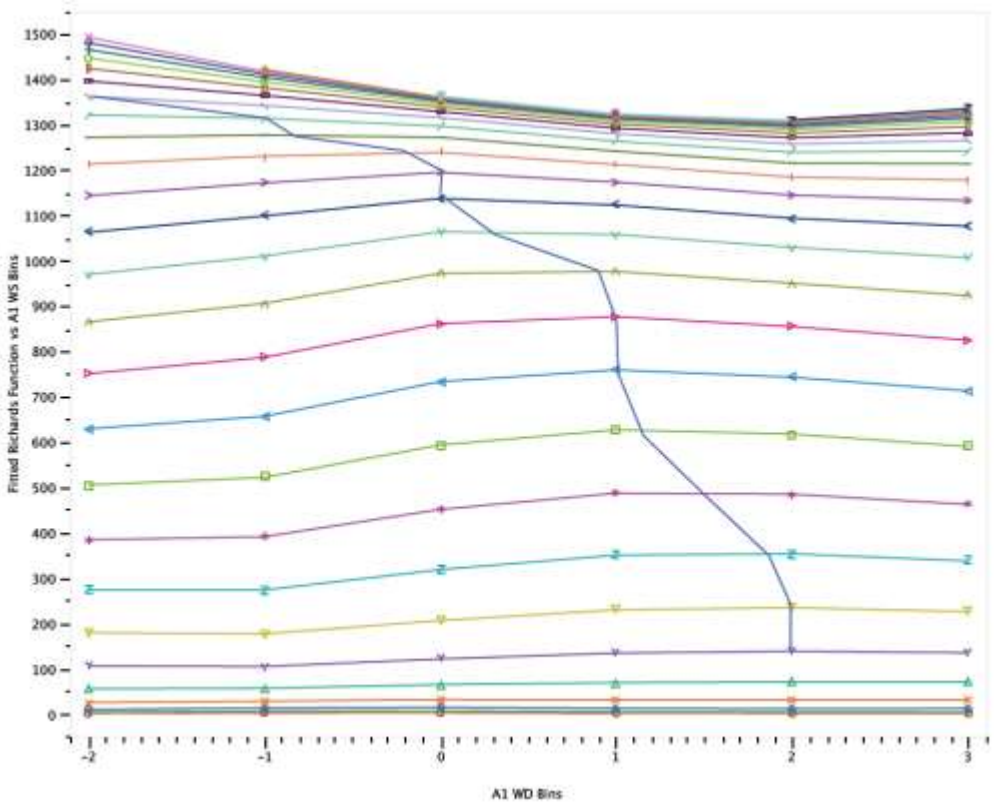


**Figure 51: A contour plot showing curves of constant wind speed.**

*(The blue line indicates the angle of maximum power production. Each integer unit on the X-axis corresponds to 10 degrees, indicating that the angle of maximum power varies substantially.)*

**Key Points**

- The rotation of the blades induces an error into the measurement of yaw angle. This error changes as the wind speed increases. The turbine has no way of sensing this error.
- There is no magic offset angle for the anemometer. A control algorithm that uses a constant offset angle to optimize power based upon post-rotor wind measurements will sub-optimize the power production.
- In moderate to heavy wind, the turbine is misaligned to the wind by ~20 degrees, resulting in increased operational stresses.
- These conclusions are based simply upon the legacy post-rotor sonic anemometer and upon the idea that turbine power is maximized at zero yaw angle.

## B3. Yaw Control Optimization

**Overview**

It is widely believed in the wind industry that improvements in yaw control can only produce a small improvement in output power. This belief simultaneously exists with an acknowledgement that attempting measure wind characteristics in the turbulent post-rotor wind is problematic.

It has been shown, on a variety of turbines, that power increases can be achieved when improved wind angle information is fed into the yaw control systems of turbines. However, this early work typically uses the legacy control strategy of the turbine. In truth, turbine manufacturers have invested considerable time and thought into developing yaw control strategies that compensate for the errors of the post-rotor measurement system. However, those strategies typically include long averaging times and allow considerable variance in yaw before correcting the yaw angle of the turbine.

Accurately measuring the incoming wind properties, with dramatically reduced noise, means that different control strategies can be considered for yaw control. Put most simply, beyond the gains achieved by simply feeding better information into the legacy control system, how much extra power can really be generated by employing control strategies that take advantage of the improvement in wind information?

This work takes real data from an operating turbine under the yaw control of the Optical Control System (OCS). The summary describes the methodology used in the simulation and the results of the parametric study for the two control parameters of wind direction moving average time and yaw direction threshold. Power performance increases and turbine yaw actuation times are presented. For unlimited yaw activity, a power increase of about 6% is demonstrated. If yaw activity is limited to 8%, it was found that an additional 3% power gain may be achieved with settings for the site/turbine installation evaluated in the study at a moving average time for the wind direction of 60 seconds and a yaw direction threshold of 8 degrees.

**Methodology**

A simulation was developed in order to estimate optimal control parameters for the OCS. The simulation and model were developed in MATLAB and Simulink, the model being presented in Figure 52. The design of this controller model was based on existing turbine yaw algorithms: the system utilizes a moving average of the wind direction as measured by the nacelle anemometry and begins yawing when the moving average exceeds a specific threshold. The turbine continues to yaw until the moving average of the direction error is zero degrees. Both the moving average time and the direction error threshold are parameters in the simulation.

The input to the simulation is the sum of the OCS measured wind direction on an operational wind turbine (wind direction relative to the nacelle) and the turbine nacelle position. This sum is a measure of the wind direction relative to north, and represents the wind field to which the turbine is exposed in time. The data utilized to run these simulations is real data from an installation of an OCS on an

operational turbine. The data set includes OCS variables, such as wind speed and direction, as well as the nacelle orientation and power production.

The simulation models how this actual turbine will react to this changing wind field based on the turbine's yaw rate, and the two parameters of moving average time and yaw error threshold. The output of the simulation is the yaw actuation of the turbine and an estimate of the local wind direction error to which the rotor is exposed. The yaw actuation data allows for calculation of number of yaw events and time yawing. The wind field measurements from the OCS upwind of the turbine are propagated to the turbine assuming a constant convection velocity equal to the mean velocity of the sample data being processed. Utilizing the wind from north data and the current simulated nacelle position, and assuming the time to convect to the rotor from the OCS measurement locations, a local rotor wind direction error can be calculated. This data allows for statistics of the instantaneous yaw error and estimates of power production to be determined. Power production is modeled as the cos3 of the local rotor wind direction error. This relationship comes from the argument that the effective wind speed for power production is the cube of the normal component of the wind to the rotor. The relative power production is proportional to cos3 of the wind direction error, so the cos3 of the convected wind direction error is the metric for performance increase in this study.

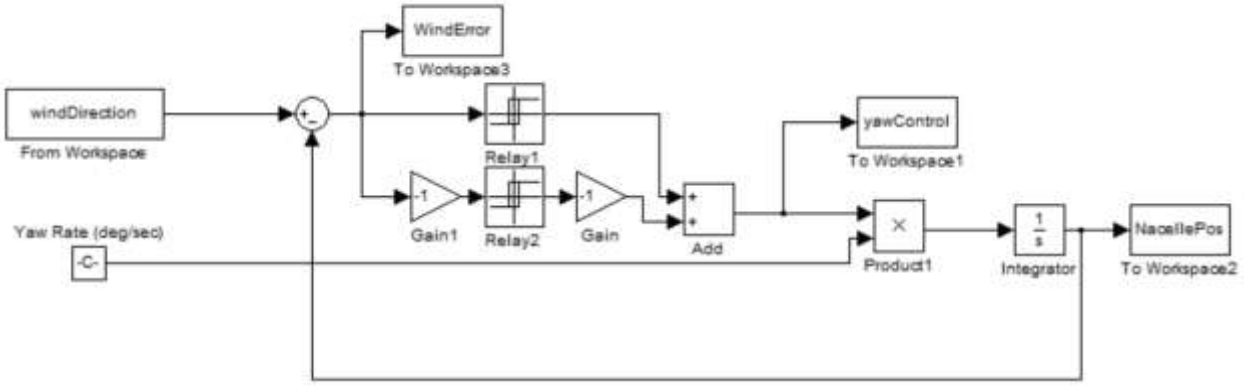


**Figure 52: Simulink model of the yaw control system.**

## Results

A parametric study was conducted using the simulation for a variety of moving average times and yaw threshold values. The simulation assumes that the power produced by the turbine is proportional to the cos3 of the wind direction error at the rotor, so this value is used as the metric for power performance improvement. Results of this study can be seen in Figure 53 and Figure 54. Figure 53 demonstrates how the cos3 of the yaw error varies with the two-parameter settings. Figure 54 demonstrates how the fraction of time yawing changes with the two-parameter settings. In looking at these curves, as the moving average time is decreased and the yaw dead-band is tightened, both the relative power captured and the amount of time yawing increase. This is as expected: the turbine is more accurately tracking the wind, especially smaller turbulent scales, such that the local rotor wind direction error is reduced, but at the cost of much more yaw actuation. Figure 53 also demonstrates that there is an upper limit to this benefit in power capture given the upwind nature of the measurements. Once the

moving average time becomes small enough, the phase lag this introduces is smaller than the convection time from the OCS measurement volume, such that the controller is introducing an error by yawing too soon. This is more evidence that these studies should be more rigorous in being done at specific speed regimes, and that the parameter settings will probably be optimized with a scheduling routine to account for this phase issue.

Given these results, a recommend set of parameters where there is moderate power performance gain, while limiting the increase in yaw actuation, would put the moving average time around 60 seconds, and the yaw direction threshold at 8 degrees. This would be an increase in power performance of roughly 3% while changing the time yawing from about 5% of time yawing to roughly 8%. Again, performing this study while focusing on differing wind regimes would be beneficial, as a representative power curve showing the relative increase with scheduled parameters could also be developed.

Note that this is optimization of the OCS. The OCS has greatly improved performance over legacy control systems with existing nacelle anemometry at any of the parameter settings in the range demonstrated in this study.

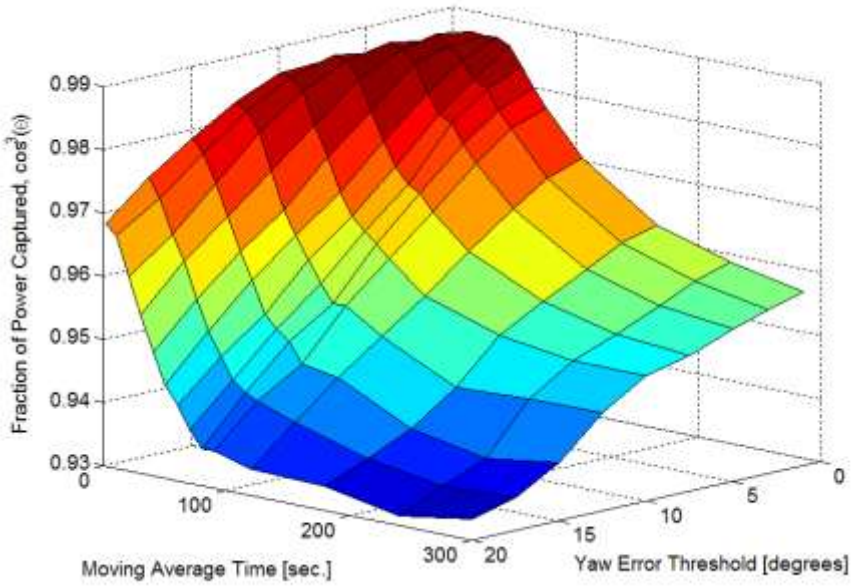


**Figure 53: Surface plot of the representative power improvement based on the model of cos3 of wind direction error at the rotor versus the two parameters: yaw threshold and moving average time.**

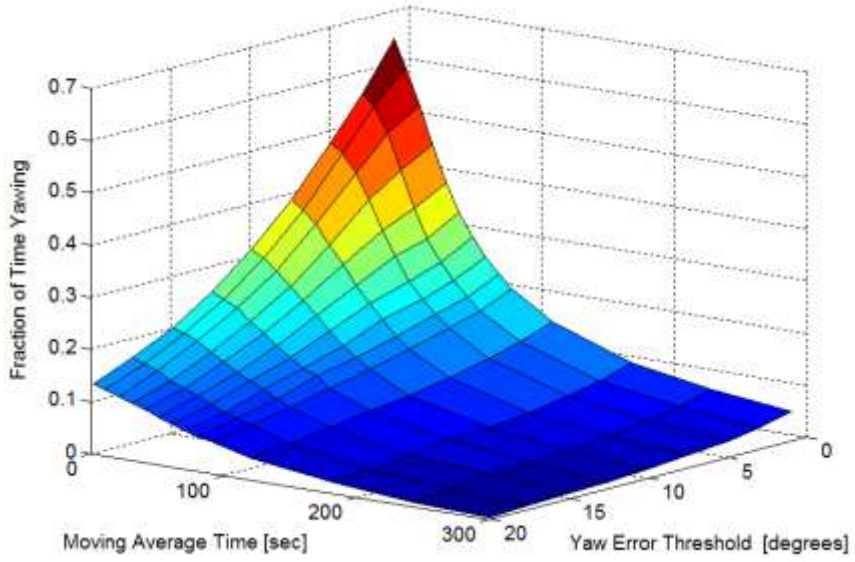


**Figure 54: Surface plot of the fraction of time yawing versus the two parameters: yaw threshold and moving average time.**

**Discussion and Further Work**

The results presented here are mean results over all wind speeds. The model for power performance of the cos3 of the wind direction error is only applicable below rated power. The performance increase may vary depending on wind speed. The simulation could be run taking speed regimes in to account, which may lead to scheduling of parameters for different wind speeds.

This simulation is run using local wind data and turbine characteristics. Parameters may vary by time of year (seasonal weather patterns), or by nominal wind direction (local properties – terrain, etc. – which may affect turbulence), as well as for turbine model (unique yaw rates). A schedule of parameters could be developed if optimal parameters were found to vary for these changing conditions (such as scheduling by wind sector). Historical MET data from the original site assessment could be utilized to do this work, but this would ignore the local affects the turbine has on the inflow wind. The data used for this study had the benefit of an OCS installed on an operational wind turbine, so blockage/induced flow effects are present in the real inflow measured data.

This simulation is based on a simple turbine control algorithm. More advanced algorithms could be developed and implemented. The same processes as described in this study could be utilized, where the Simulink model has more capability. More complexity could also be added for scheduling yaw rates (variable yaw rate machines), as well as scheduling the given parameter settings. The overall algorithm could also be modified, where the simple on/off relay model is replaced. Manufacturers could also modify the physical yaw actuation systems to allow for different control strategies, such that the controller is not limited by the amount of time yawing. This research is currently ongoing in order to best utilize the novel optical control system. Implementation of such algorithms is relatively simple, as these are simply software changes in existing control hardware implementations.

## B4. Turbine Controller Integration

Turbine Model: GE 1.5 SLE

The Optical Control System (OCS) is designed to improve turbine performance by enhancing alignment of the turbine with approaching wind while maintaining or enhancing the overall safety and reliability of the turbine. The OCS utilizes state of the art laser sensors to detect the approaching wind before it reaches the rotor, and commands yaw actuations of the nacelle in order to reduce yaw error. More timely and accurate alignment with the wind leads to improved power capture. This document describes the integration concept of the OCS, with emphasis on mechanisms that maintain safe control of the turbine.

The OCS is designed to take over the yaw actuation of the turbine utilizing the LIDAR for accurate and look-ahead wind data. In this control configuration the OCS utilizes a Bachmann Programmable Logic Controller (PLC) as the basis of the design. This system has a processor module, Ethernet ports, and digital I/O modules that allow it to easily interface with the legacy GE central controller, the laser sensor unit, and the digital hardware of the turbine.

There are two primary modes of operation of the system: automatic control and bypass mode. In automatic control, the OCS utilizes the laser wind sensor to align the nacelle with the approaching wind. In this mode, the system outputs signals to the legacy controller that mimic a mean zero wind direction error – this results in the turbine operating as normal, but without the legacy system providing any yaw actuation commands to the yaw brakes or motors. The OCS then sends its own yaw commands to the yaw brakes and yaw motors to track the wind. In bypass mode, all of the digital signals are passed directly through the system, such that the OCS acts like it is not present. In bypass, the legacy controls all yaw activity.

**Communication**

***Ethernet: TCP & SMI***

The PLC communicates to the laser sensor via Modbus-TCP over a local Ethernet network. The messages the OCS monitors include wind speed, direction, status of the laser system, and validity of the measurements at the various range gates.

The OCS for GE 1.5 SLE integrations makes use of Bachmann PLC components. Bachmann PLC systems are designed for industrial control systems, and the BlueScout solution mirrors the GE 1.5 controller strategy. Utilization of a Bachmann PLC allows for the BlueScout controller to directly communicate with the GE PLC utilizing the Standard Module Interface (SMI) libraries supplied by Bachmann. The BlueScout PLC can directly read internal variables from the turbine so that it has knowledge of the operating conditions of the turbine.

The OCS has a Modbus server running for data capture. Internal values of the OCS are recorded along with performance data such as wind speed, direction, and power.

***Digital I/O***

The OCS makes use of digital Input and Output lines in order to intercept or monitor the following signals from the turbine controller and turbine hardware:

- Yaw brakes
- Yaw motors
- Wind Vane
- Yaw teeth counters

The yaw teeth counters are only read in by the OCS, but are still physically connected to the turbine controller. The OCS sends these teeth counts to the legacy controller – this ensures the legacy controller always has accurate knowledge of the absolute nacelle position.

The digital signals are connected to the OCS via a set of controlled relays. The normal states of the relays pass the original signals to and from the legacy controller and the turbine hardware. Only when in automatic mode are the relays engaged in order to intercept signals and feed OCS derived values to the legacy controller and turbine hardware. This also ensures that any issues with the OCS PLC (or the powering off of the PLC) result in the turbine returning to legacy control so that OCS does not adversely affect turbine performance or safety.

**State Machine**

There are four states for the OCS controller: Initialize, Auto, Bypass, and Fault (see Figure 55 and Table 5 for state transitions). The Initialize state acts as a default initialization state and dictates transitions at startup of the OCS, or when the system returns from the Fault state. The Auto state is when the OCS is directly controlling the yaw of the turbine. The Bypass state acts as if the OCS is not present. The Fault state is when there is any fault detected with the BlueScout OCS (not with the turbine controller; a fault of the legacy controller will result in the system switching to Bypass mode). In the three states of Initialize, Bypass, and Fault, the relays for the interception of digital I/O signals are in the default state, and the turbine is wired as if the OCS is not present. The faults that are monitored by the OCS are:

- Untwisting Right
- Untwisting Left
- Yaw drive end position
- Timeout yaw count
- Wrong yaw drive direction
- Yaw end switch activated
- Yaw motors over temperature
- OCS Communications Fault
- SMI Fault
- Wind Direction Limit
- OCS Wind Measurement Status
- UPS alarm
- UPS battery mode

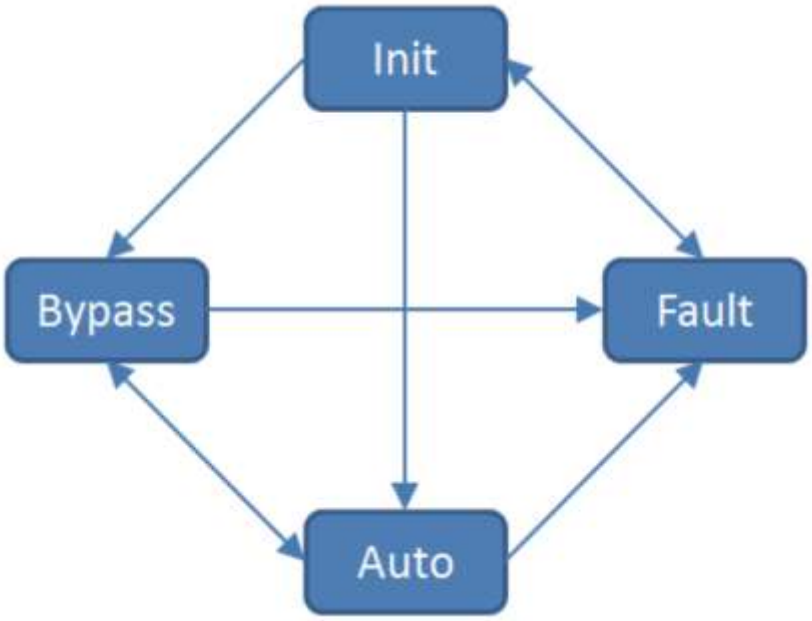


**Figure 55: State diagram for the OCS, showing the direction of state transitions.**

**Table 5: State table for the OCS, demonstrating logic for state transitions.**

| State Transitions From -> To | Init | Bypass | Auto | Fault |
|---|---|---|---|---|
| Init | | No Entry | No Entry | No Fault |
| Bypass | NOT bFault AND (Par_bBypass OR (Par_bSwitchBtwControllers AND bSwitchBtwCtrlsBypass)) OR NOT bLoadOperation | | NOT bLoadOperation OR IN_bYawToTheLeft_CC OR IN_bYawToTheRight_CC OR IN_bYawBrakes12_CC OR IN_bYawBrakes34_CC OR bFlagAvoidRunaway OR Par_bBypass OR (Par_bSwitchBtwControllers AND bSwitchBtwCtrlsBypass) | No Entry |
| Auto | Ton_CentralCtrlYaws.Q bLoadOperation AND NOT Par_bBypass AND NOT bFault AND NOT(Par_bSwitchBtwControllers AND bSwitchBtwCtrlsBypass) | NOT bFlagAvoidRunaway AND NOT OUT_bYawToTheLeft AND NOT OUT_bYawToTheRight AND bLoadOperation AND NOT(Par_bSwitchBtwControllers AND bSwitchBtwCtrlsBypass) AND NOT Par_bBypass AND Ton_CentralCtrlYaws.Q | | No Entry |
| Fault | Fault | Fault | Fault | |

**States Summary**

Initialize: The system enters this state upon start up. If the turbine is in load operation (status = 2 and turbine is generating power) and the turbine has yawed to reset its current position since the PLC last went in to Auto mode, then the system will transition to Auto mode. If the bypass parameter is enabled, then the Auto state will be overridden, and the system will stay in Bypass mode. If the switching parameter is enabled and the timer is currently in Bypass mode, the system will not transition to Auto,

but will transition to Bypass. If any faults are detected internally to the OCS, the system transitions to the Fault state. The digital I/O relays are disengaged and the turbine is functioning as normal.

- **Auto**: The system will utilize the laser wind sensor to track the wind and will command the yaw brakes and motors. Zero error vane signals are sent to the legacy controller to prevent the turbine from yawing. If the legacy controller does command a yaw, for any reason, the system will transition to bypass mode and pass through the yaw commands. If the turbine status changes away from a value of 2 or it is not producing power (indicating a potential issue with the turbine), the system will transition to Bypass mode. If the switching parameter is enabled, and the period for the Bypass mode is enabled, the system will transition to Bypass. If the OCS detects that it tries to yaw beyond the parameter 11.13 value, the Avoid Runaway flag will be triggered, and the system will transition to Bypass mode until the turbine resets its current yaw position.
- **Bypass**: The system will disengage the relays and the turbine will perform in its original configuration. If the OCS does not have the Bypass parameter set, the turbine is not currently yawing, the turbine is in load operation (no alarms), the turbine has yawed such that it has reset its current yaw position for the yaw runaway alarm (since the last time in the Auto state), and the system is not switching between controllers with the timer currently set for the Bypass sate, then the system will transition to the Auto state. If a fault is detected, the system will transition to the Fault state.
- **Fault**: This state lets the OCS know that an internal fault has been detected and records the fault in the system's Modbus data. In practice, this state acts like Bypass, in that the relays are disengaged and the turbine is essentially in its original configuration. The Fault state allows for safe handling of the OCS interface and insures the system is only able to control the yaw systems when safely in the Auto state. The system transitions to Initialize when the faults clear.

**Summary**

The OCS is designed to increase turbine performance while maintaining conservative safety requirements. When in OCS control, the system utilizes an advanced laser measurement device to drive the nacelle yaw motors to more accurately align the nacelle with the approaching wind direction.

The OCS control architecture is designed to only take control when both the turbine and the OCS are operating well and without any indication of issue. In all situations where either the turbine or the OCS exhibits any cautionary signals, turbine control is returned to the legacy system until these system issues are resolved and the OCS has worked through the Initialize state. This control strategy allows the turbine to maintain all of its current functionality regarding safety monitoring.

### *C. Phasor Measurement Units Installation*

Phasor Measurement Units (PMUs) provide GPS time stamped voltage and current samples with one phasor sample per cycle (60 samples per sec). Accordingly, PMUs provide detailed load models for individual buildings and detailed power measurements for renewable and distributed sources. The 8KW field wind unit is connected to IIT's Stuart Building, which is located within the Loop 1 of the IIT microgrid. PMUs are installed in the Stuart Building to enable engineers to develop more accurate load models, which is one of the most significant sources of uncertainty in understanding, predicting and controlling power delivery network behavior. The load characterization application will develop both static and dynamic load models to facilitate reliable and secure operation of the Perfect Power system, which is especially valuable under islanding conditions.


**Figure 56: Phasor Measurement Unit (PMU) Installed at IIT's Stuart Building**

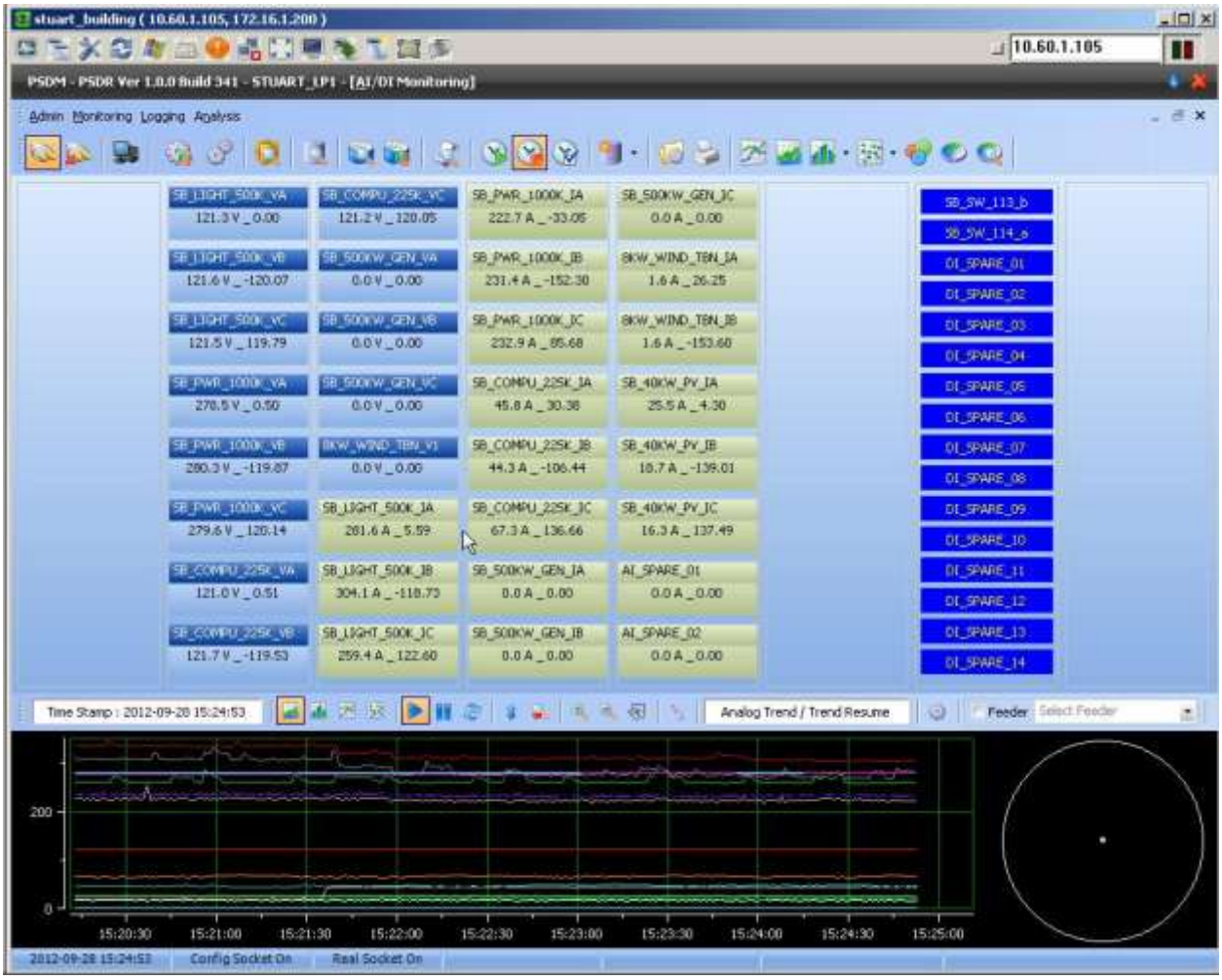


**Figure 57: Stuart Building PMU data showing the building transformer loads, wind turbine, and PV system**

### *D. Use High Magnetic Density Turbine Generator as Non-rare Earth Power Dense Alternative*

Dakota Power, LLC (DP) is developing unique electric drive and power generation systems. This project provides for the application of DP technology to the generation of electricity from wind power. DP technology provides a non-rare earth power dense alternative for the operation of wind turbines. DP is integrating switched reluctance technologies with other sources of magnetic energy to produce high-performance electrical machines. The DP technology has the potential to provide a lightweight, low-cost wind turbine for residential and light industrial applications.

DP is developing next-generation light weight electric drive systems for military and civilian applications through a Cooperative Agreement with the Army Research Office (ARO). This project provides for the application of DP electrical machine technology to the generation of electricity from wind. This report

provides a comprehensive summary of the development of DP switched reluctance technology and the potential for its application to the generation of electricity from wind.

The process for the development of DP switched reluctance technology includes the transition of a concept for a machine through design and simulation using advanced FEA software. DP provides commercially developed Maxwell FEA simulation software to validate the potential performance of each proposed design. The optimal design, including the specific geometry, stator winding turns and current, is then fabricated to provide a prototype test machine. The performance of each prototype machine is tested and evaluated through the capabilities of the DP Dynamometer Test Facility (DTF). The resulting performance information is analyzed and incorporated into subsequent developments of the DP switched reluctance technology.

DP has evaluated the potential for switched reluctance technology to provide a non-rare earth direct drive wind turbine. This section includes the development of a switched reluctance machine to validate the performance of DP short path switched reluctance technology for application as residential wind turbines.

DP has developed a Quick Machine software program to support the introduction of switched reluctance technology in the development of wind turbines and other machine applications. The QuickMachine software provides an approximate result as compared to the detailed design produced with hours of computation with the Maxwell FEA software. The QuickMachine software facilitates the application of the principles of switched reluctance technology to the development of residential wind turbines.

### D1. Generation of Electrical Energy from Wind

Increasing global demand for energy has placed new emphasis on the development of alternative sources of energy. The United States Department of Energy identified the major target of producing 20% of the nation's electrical energy needs from wind by 2030.

There are two main targets that have been identified for wind energy. A report by the National Renewable Energy Laboratory (NREL) estimated the need for more than 300 GW to achieve the 20% wind target by 2030. The NREL report identified the need for the wind industry to produce 16,000 MW per year to achieve the 2030 target. The increasing role of wind in the generation of electrical energy as reported by the Energy Information Administration is shown in Figure 58. While this figure illustrates the results of the significant technological advances that have enabled the development of large wind turbines, wind farms, and expanding electrical distribution grids, there are challenges to the continued growth of wind turbines. The distribution of wind resources in the United States as shown in Figure 59 provides for the potential generation of electrical energy along the coasts and in the middle of the country. This distribution of wind resources highlights the challenge of delivering electrical energy generated by wind to the users who are located outside of the areas of concentration when resources are available. The development of wind generating capacity in the middle of the United States is hampered by the existing transmission grids that have traditionally served the rural farmland region.

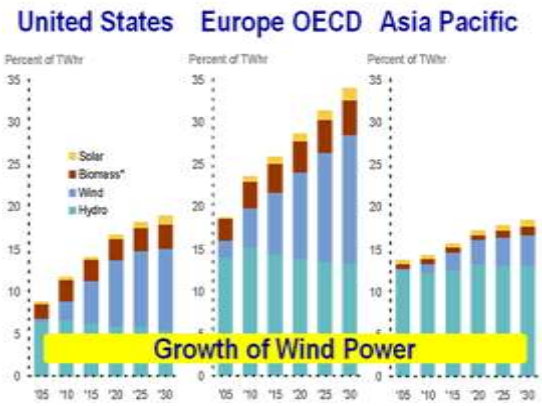


**Figure 58: Growth of Wind Power**

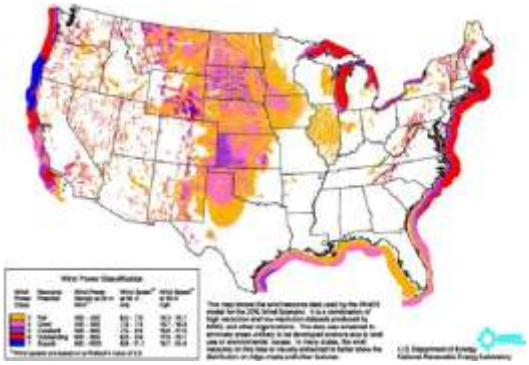

**Figure 59: Distribution of Wind Resource**

**Figure 60: Transmission Grid for 400 GW**

The expansion of electrical distribution is a priority to transport electrical energy generated to population centers. The effective development of wind as a source of electrical energy requires the development of a high-capacity country-wide electric power grid such as illustrated in green in Figure 60.

Additionally, there is increasing global interest in the generation of electric energy from large wind turbines located offshore. These turbines would provide electrical power to population centers located on the coast and through the new grid to areas of low population density. As the preparation of wind farms of large wind turbines in areas of high wind resources is being developed, there is also growing interest in the development of residential and small industrial wind turbines.

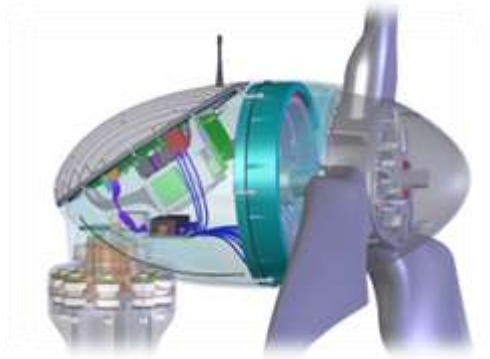

**Figure 61: Skystream Residential Wind Turbine**

While there are commercially available electrical generators to produce electrical energy for residential and small industrial applications as shown in Figure 61, there is growing interest in the potential of new electrical machine technologies to improve the conversion of wind to electricity. The use of a new switched reluctance technology, being developed by Dakota Power, has the potential to reduce the cost of the production and distribution of electrical energy generated by small-scale wind turbines. With the increased availability of residential and small industrial wind turbines, it is possible to significantly expand access to wind resources without the need for significant increase in the capacity of the local electrical grid.

The need for gearboxes to convert the relatively low rotation rate of wind to the more efficient higher rotation rate of induction generators is both a significant initial investment and an on-going maintenance cost. Technologies, such as permanent magnet generators and switched reluctance generators, that have the capability to provide a direct drive for converting wind energy to electrical energy. There is interest in the application of direct drive technologies to large wind turbines, particularly wind turbines used in off-shore wind farms. The potential use of direct drive switched reluctance technology for residential and small industrial applications has the advantage of lower weight and cost relative to permanent magnet machines.

The non-rare earth Dakota Power switched reluctance technologies provide an option to the growing concerns for the availability of rare earth materials currently supplied through China. The potential of unique new capabilities for residential and small industrial wind turbines through the use of DP switched reluctance technologies offers a significant new approach to expanding the electrical energy available from wind.

### D2. Switched Reluctance Technology

DP switched reluctance machine (SRM) technology employs the fundamental principal of reluctance motion will be created to minimize the separation of two pieces of iron or other ferromagnetic material when placed in a magnetic field. SRM technology converts magnetic energy into rotational torque through reluctance alignment of the salient pole of a fixed machine stator with the salient pole of a movable rotor.

Electrical energy is applied to a pole of the stator through current flowing through a coil of wire wound around that pole. The current flowing through the stator coil creates the magnetic field that induces the movement of the rotor. Figure 62 illustrates the salient poles of a stator. Figure 63 illustrates the salient poles of the rotor. Figure 64 illustrates the relationship of the salient poles of the stator with the poles of a rotor in a typical switched reluctance machine.

Since it is intended that the rotor will rotate, there is an air gap between the poles of the stator and the rotor. The magnetic path from the pole of the stator to the pole of the rotor travels through the air gap. Torque is produced by the reluctance action between the magnetically energized stator pole and rotor pole. The rotation torque is transmitted through the shaft at the center of the rotor.

Figure 65 is an end view of a switched reluctance machine with the housing removed showing the coil windings of the stator, the rotor, and the output shaft. The coils of wire placed around each of the stator poles provide magnetic fields essential to the operation of the switched reluctance machine.

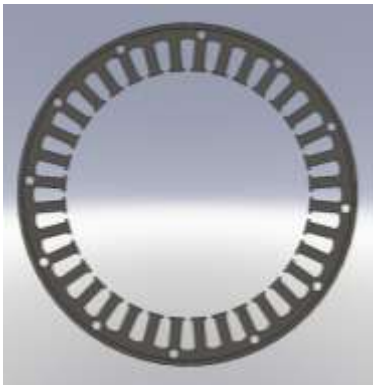

**Figure 62: Stator salient poles**

**Figure 63: Rotor salient poles**

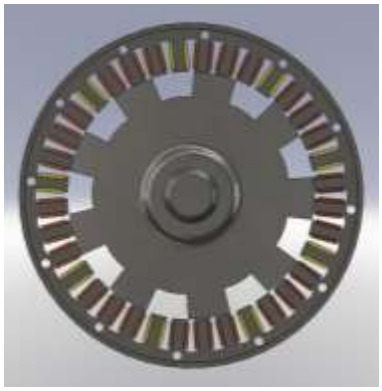

**Figure 64: Stator and rotor poles separated by air gap**

**Figure 65: End of a Switched Reluctance Machine**

The principle of magnetic field reluctance was applied to motors and generators over 150 years ago. Early switched reluctance machines controlled the switching of current to the stator windings with a mechanical switch. However, the mechanical switching system was incapable of responding to the need

for higher speed rotation which led to the development of other motor technologies, including brushed DC and AC inductance motors. The development of electronic switches, such as Insulated Gate Bipolar Transistors (IGBT), with capability to control significant electrical current has led to a resurgence of interest in switched reluctance technology. The capability to embed low-cost, high-performance microprocessors to control the switching of stator current is enabling the design and development of unique switched reluctance machines for applications as motors, generators, and electric drive systems, including residential wind turbines.

Figure 66 illustrates the magnetic field created between poles of the stator and rotor. The full flux of the stator is transmitted to the rotor through the increasing alignment between the stator in rotor across the air gap interface. The red areas of Figure 66 depict the high intensity of the flux density of the magnetic field with the initial alignment of the stator and rotor poles. The reluctance principal will cause the rotation of the rotor until there's equal distribution of the magnetic flux across the interface between the rotor and stator. The rotor rotates so that the center line of the rotor equals the center line of the stator, which is termed the fully aligned position. In the fully aligned position, there is no longer an inequality to provide a reluctance force to create motion.

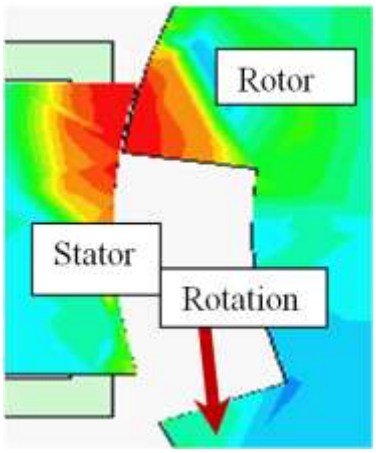


**Figure 66: Magnetic Field Produced by Stator Coil**

To achieve continuous rotation the magnetic field created by current in the stator coil must be switched to the stator pole in which the rotation of the rotor is approaching alignment. The ability to achieve switched reluctance across the stator and rotor poles requires accurate sensing of the location of the rotor pole relative to the stator pole. The ability to control the switching of current in the stator is essential to operating switched reluctance machine as a motor or as a generator. DP has developed a proprietary sensor system to sense the location of a rotor pole relative to the adjacent stator pole. The DP switched reluctance technology includes the development of embedded microprocessor control systems to switch the stator coil current to maximize the performance of DP switched reluctance machines.

Switched reluctance machines offer several advantages over conventional motor and generator technologies. The low cost of manufacturing the stator and the rotor is an advantage of switched

reluctance machines. The rotor has no windings or permanent magnets, and therefore can operate at high speed. Additionally, switched reluctance machines have the capability to operate as a direct drive machine which eliminates the need for a gearbox. Operation as a direct drive makes switched reluctance technology an attractive option for wind turbine generation of electrical energy. Direct drive operation has the potential to reduce the cost of manufacturing and maintenance of wind turbines, particularly residential wind turbines.

The ability to operate without permanent magnets, particularly rare earth permanent magnets, provides switched reluctance machines both advantages and challenges. The elimination of rare earth materials enables switched reluctance machines to operate at increased levels of temperature without the degradation of magnetic flux at Curie temperatures. However, the lack of the higher levels of magnetic flux of permanent magnets presents the challenge of achieving increased power densities comparable to rare earth permanent magnet machines. DP is developing processes for the integration of additional sources of magnetic fields to increase the specific power performance of switched reluctance machines. DP is evaluating applications of switched reluctance as a direct drive wind turbine, as vehicle traction motors, and as an electrical generator powered by a high-speed light weight combustion turbine

### D3. Prototype development

Dakota Power (DP) provides an environment for the enhancement of the performance and application of switched reluctance machine technology. The DP process of design, simulation, fabrication, test, and evaluation has produced prototypes of potential major developments in the application of switched reluctance technology. The DP prototype development process includes the capability for a full FEA simulation of the magnetic fields of a potential design. DP has acquired Maxwell computer software that includes the ability to simulate the both the electrical and magnetic operation of a potential switched reluctance machine.

Once the potential prototype design is optimized to provide the target power density and efficiency, the design is fabricated. The prototype development includes the design of stator, rotor, and the switching control system. DP has facilities to both fabricate a proposed machine design and evaluate the performance of the resulting prototype machine. The DP Dynamometer Test Facility (DTF) has the capability to evaluate prototype machines with output power up to 10 hp and speeds up to 10,000 RPM. The results of the development of each DP prototype machine continue to extend the understanding of switched reluctance and associated technologies.

Table 6 provides a summary of the prototypes developed by DP. The initial prototypes evolved from a patented proof of concept electric drive system prepared by the inventor, Dr. William Hughes. DP has designed 12 prototype switch reluctance machines. The prototypes developed include a range of potential switched reluctance technologies including axial and radial flux paths. The axial flux path prototypes have a path that includes dual stators separated by a DC field coil. The radial flux path prototypes have a single stator and employ a short flux path that does not pass through the shaft of the rotor. These prototypes provided a understanding of switched reluctance operation that led to concepts for unique designs for lightweight switched reluctance motors and generators.

**Table 6: Dakota Power Switched Reluctance Technology**

| Model | Type | Flux Path | Stator Poles | Phases | Rotor | Status |
|---|---|---|---|---|---|---|
| Hughes-1 | SRDCM | Axial | 12 Pole | 3 Phase | 6 Lobe | Built by Hughes 2006 |
| Hughes-2 | SRDCM | Axial | 12 Pole | 3 Phase | 6 Lobe | Built by Hughes 2006 |
| DP-01 | SRDCM | Axial | 9 Pole | 4 Phase | 9 Lobe | Built by DP 02/10 |
| DP-02 | SRDCM | Axial | 9 Pole | 4 Phase | 9 Lobe | Built by DP 10/10 |
| DP-03 | SRDCM | Axial | 12 Pole | 3 Phase | 6 Lobe | Built by DP 12/10 |
| DP-04 | SRDCM | Axial | 9 Pole | 4 Phase | 18 Lobe | Built by DP 01/11 |
| DP-05 | SRM | Axial | 2 Pole | 4 Phase | 6 Segment | Built by DP 02/11 |
| DP-06 | SRM | Radial (Short) | 18 Pole | 2 Phase | 18 Lobe | Built by DP 02/11 |
| DP-07 | SRM | Radial (Short) | 12 Pole | 3 Phase | 12 Lobe | Design completed |
| DP-08 | IPM | Radial | 6 Pole | 3 Phase | 6 Lobe / NdFeB | Built by DP 03/11 |
| DP-09 | IPM | Radial | 6 Pole | 3 Phase | 6 Lobe / Ceramic | Built by DP 04/11 |
| DP-10 | SRM | Radial | 20 Pole | 5 Phase | 18 Lobe | Pending Testing |
| DP-11 | SRM | Radial | 12 Pole | 2 Phase | 6 Lobe | Pending Testing |
| DP-12 | SRM | Radial | 12 Pole | 3 Phase | 10 Lobe | Pending Testing |

The DP-06 prototype is designed to operate as a symmetrical machine with two phases. This symmetrical design demonstrates potential for providing optimal power density and efficiency as a residential wind turbine. DP-10, he a lightweight version of DP-06 has the potential to an ideal residential wind turbine machine.

Prototypes developed by DP are evaluated using the DP Dynamometer Test Facility (DTF). The evaluations both the performance of machines built by DP and the performance of purchased commercially available machines. The DTF has the capability to provide test results in the to document the performance of each Machine Under Test (MUT). The DTF also has the capability to test machines as both motors and generators. DP has developed standardized test and evaluation procedures to measure and record the performance data of each MUT.

Figure 67 shows DP-06 mounted in the DTF. The DP testing and evaluation procedure combines data collected from the MUT with data recorded by the engineers performing the test. The DP standardized test and evaluation procedure includes the ability to display the collected data in graphs that present information about torque, speed, and efficiency of a MUT. The data collected during the evaluation of a MUT enables adjustment of the initiation of switching of current to the stator coil relative to the position of the rotating stator pole which will result in the optimization of power density and efficiency.

**Figure 67: Dakota Power machine DP-06 mounted in the Dynamometer Test Facility**

Figure 68 is a comparison of the peak specific power of DP-06 with the peak specific power of other commercial switched reluctance motors, arranged from the highest to the lowest value. The DP-06 peak specific power of .67 kW/kg compares favorably with the peak specific power of .69 kW/kg produced by the Danahar switched reluctance motor.

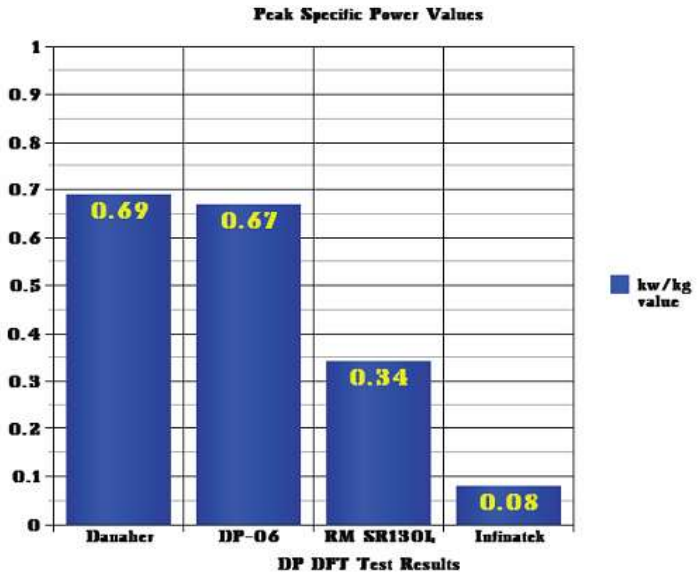


**Figure 68: Comparison of peak specific power of DP-06 of .67 kW /kg to peak specific power of commercial machines**

The test and evaluation of DP-06 identified the potential for enhancements in the control of the switching of current to stator coils in response to the location of an approaching rotor pole. Additionally, the availability of new high speed compact IGBT modules provides the opportunity to expand the capability to evaluate the performance of the DP switched reluctance technology machines throughout the full range of the capabilities of the DTF. Figure 69 shows the new fabricated IGBT circuit board with capability to provide operation with a stator coil current of 90 A and system bus voltage by up to 600 V. The upgrade of the IGBT stator current drivers also provided the opportunity to expand the

microprocessor memory and to implement additional software code to enhance the feedback operation of DP switched reluctance machines.


**Figure 69: IGBT power driver board**

Figure 69 shows one of the six IGBT stator drive circuit boards for providing stator coil current for DP switched reluctance machines. The lower two-thirds of the circuit board provides the operation of the power IGBT and stator current. The top one-third of the circuit board provides the interface connections with the microprocessor in software code.

It is anticipated that the DP-06 will be fully evaluated as a switched reluctance machine in October 2011 and the results will be documented at this location in this report. The DTF will be configured with the capability to dissipate generated electric energy for operation as a generator. DP-06 will be tested and evaluated as a generator with the potential to be a prototype of a switched reluctance wind turbine in November 2011.

### D4. Switched reluctance generation

The DP switched reluctance machine will operate as a motor or generator depending on the timing of the switching of stator current. Figure 70 is a schematic diagram for the two phase control circuit for DP-06. The high current IGBT power switches are identified as S1, S2, S3, and S4. The stator coils are designated as Phase 1 and Phase 2. Current is provided to the stator coils of Phase 1 when the IGBT S1 and S2 are switched to the “on” state. The IGBT current flowing through the stator coils of Phase 1 will cause the rotation of the rotor. The IGBT S1 is switched between the “on” and “off” states to provide Pulse With Modulation (PWM), which in conjunction with the capability to control the voltage across the stator coils, provides control of the introduction of current to energize the inductance of the stator coils.

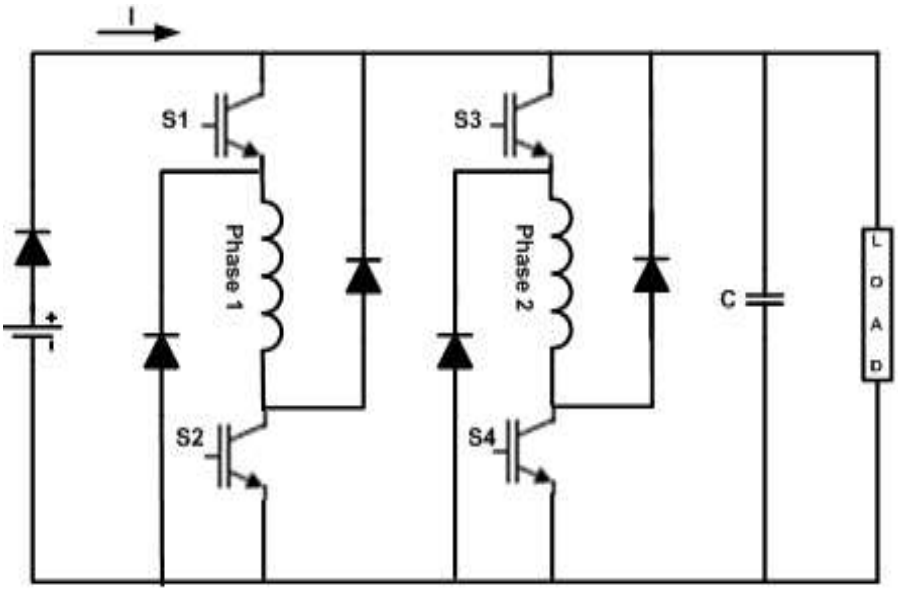


**Figure 70: Schematic diagram for DP 06**

Figure 71 is a diagram of the current of the stator coil for three electrical cycles of a switched reluctance machine operating as a generator. The middle cycle of Figure 71 illustrates the desired change in stator current as the pole of the rotor rotates through a full electrical cycle. At the beginning electric cycle, the stator current is switched "on" and the stator current transfers energy to create a magnetic field in the stator coil creating a reluctance force to cause the rotor to rotate. As the rotor and stator reach full alignment, the stator coil achieves maximum inductance with maximum stator current. In addition to current flowing to the stator, current also charges the capacitor and provides power to the load. The IGBT S1 and S2 are switched to the "off" state and current continues to flow through the stator coil producing magnetic flux. The continued rotation of the rotor through the magnetic flux generates a current through the stator for the remainder of the electrical cycle. As the rotor moves to alignment with the next pole of the stator, IGBT S3 and S4 are switched "on" and the cycle is repeated.

By changing the timing of the IGBTs, DP switched reluctance machines can be operated as generators. A diagram of the circuit used for operating the two phase DP-06 as a generator is shown in Figure 70.

Figure 71 shows an example of phase current with respect to time for a generating cycle. The IGBTs are switched on while the rotor is aligning with the stator. This is necessary to increase the current through the phase and create magnetic flux. Shortly after alignment, the desired phase current is reached and the IGBTs are switched off. At this point, the current in the phase windings flows back into the upper bus. While the rotor is unaligning, the back emf caused by the rotation of the shaft and the magnetic flux maintains the level of current flowing through the phase windings, thus electricity is generated and approaches zero and the current in the phase windings decreases.

The evaluation of DP-06 to function as a switch reluctance generator is projected to be completed the first half of November 2011. The results of this evaluation will be included in the final version of this report.

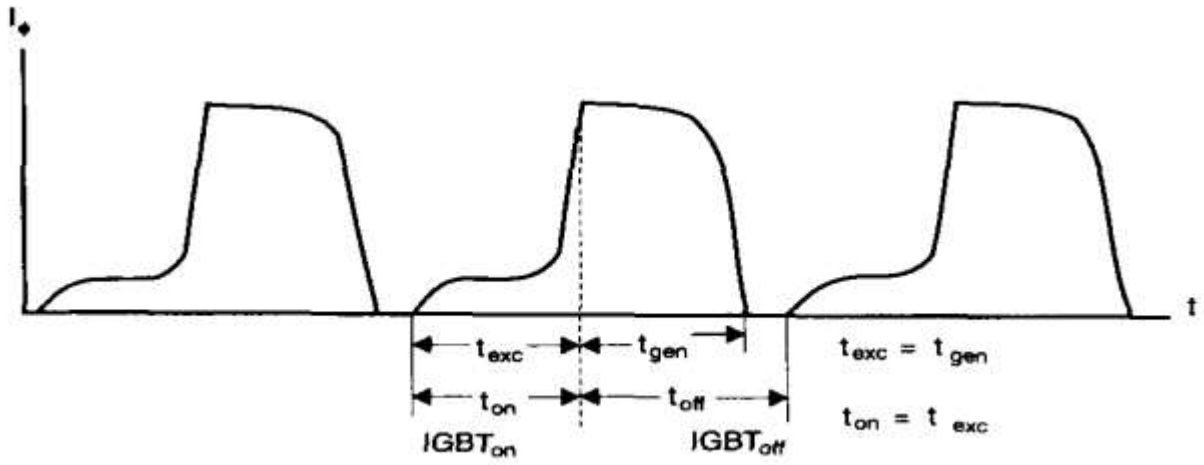


**Figure 71: Stator current diagram for generating electricity**

### D5. Lightweight wind turbine

The development of a light weight electric drive system is a major objective of the DP research and development program. Studies of the Maxwell FEA simulation of the magnetic flux show the variability in the flux density of the magnetic field. In concept, it will be possible to remove the portion of the stator with minimum flux density, thereby reducing the weight of the stator, without significantly impacting the performance of the motor. The reduction in the weight of the stator will produce a lighter weight machine and higher specific power.

Figure 72 is a graphic of a Maxwell simulation showing the variability in the field density on the left for DP-12, a three phase short path reluctance machine. The reduced level of flux in the stator between the energized poles to provide the short path magnetic field led to the removal of this portion the stator in DP-10 as shown in the simulation on the right.

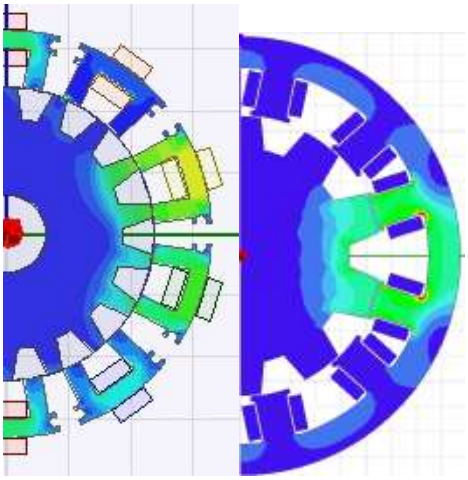

**Figure 72: Maxwell plot showing the stator reduced flux density**

Figure 73 is a graphic of the stator and rotor of DP-10 with a 20 pole stator and 10 pole rotor. The DP-10 is designed as a lightweight version of DP-06. The stator of DP-10 consists of 10 segmented sections mechanically linked through an aluminum frame. The windings of this stator are distributed on each of the segments of the stator. The 10 pole rotor of DP-10 has the same outside diameter as the rotor of DP-06. The DP-10 is an asynchronous five phase motor. The Maxwell FEA simulation of the DP-10 indicates the performance should be equivalent to DP-06 and the reduction in weight will result in an increase in specific power. In addition to reducing the weight of the motor, the segmented stator has a potential advantage of reducing the cost of winding stator coils.

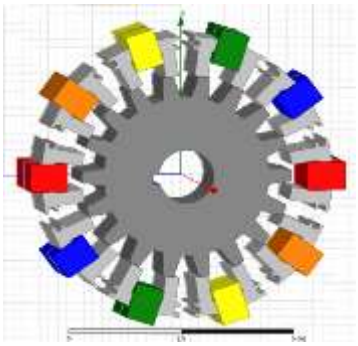

**Figure 73: The DP-10 lightweight segmented stator**

Figure 74 shows the coil winding of a stator segment of DP-10. While a traditional stator requires the insertion of windings around each stator pole, the stator windings of the DP-10 segmented stator are wound directly on each segment. Each DP-10 stator coil segment is wound with 35 turns of 17 gauge magnet wire. Each of the 10 stator segmented coil windings provide the magnetic flux for the pole pairs of each of the five phases of DP-10.

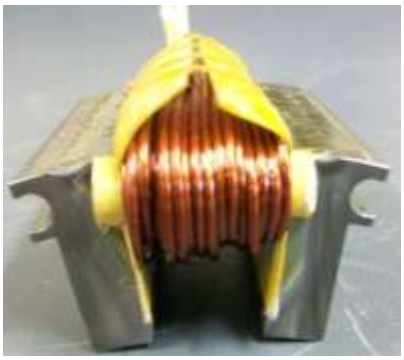

**Figure 74: DP-10 stator stack wound with 35 turns of 17gauge magnet wire**

Figure 75 is a Solid Works drawing of the assembled DP-10 motor. The wound stator segments are shown as salient poles on the circumference of the motor. The DP-10 will be evaluated in November 2011.

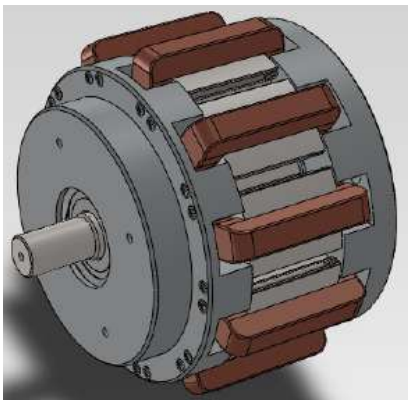

**Figure 75: Model of an assembled DP-10 showing the segmented windings**

### D6. Scalability of switched reluctance

The development of DP technology includes demonstration of the capability to scale switched reluctance technology to produce prototype machines of various diameters, length, torque, and efficiency. In order to provide a baseline for comparing potential changes in performance with changes in the size of new prototype machines, DP-06 has been designated as the baseline machine.

Two of the test prototype machines have been designed with an outside diameter of 3.5 inches, length of 4.25 inches and weight of 7 pounds. DP-11 is designed as a radial short path synchronous two phase switched reluctance machine equivalent to DP-06. DP-12 is designed as a radial short path asynchronous switched reluctance machine with identical size and weight of DP-11.

DP-11 has 12 stator poles and 6 rotor poles to provide a synchronous two phase motor. DP-06 is also a synchronous two phase motor, but it has 36 stator poles and 18 rotor poles. The one third fewer stator and rotor poles of the DP-11 and DP-12 machines is the result of the need for sufficient space between the adjacent stator poles for the insertion of the stator windings.

As a comparison, the DP-06 has a stator winding of 16 turns of parallel 19 gauge wires. DP-06 has an outside diameter of 7.5 inches, length of 6 inches, and weight of 25 pounds. DP-11, with reduced volume for stator winding, has a stator winding of 56 turns of 23 gauge wire. The Maxwell FEA simulations of DP-11 and DP-12 project specific power and efficiency equivalent to DP-06.

DP-12 has the same physical dimensions as DP-11 but is configured as a three-phase switched reluctance machine. Figure 76 shows the results of the Maxwell simulation of DP-12, and illustrates the unique asymmetrical stator geometry designed to provide high specific power and efficiency in the performance of this machine. Figure 77 is a graph of the phase current of DP-12 and illustrates the switching sequence of the three phases of this machine to function as a switched reluctance generator.

It is anticipated that the scalability test and evaluation of DP-11. DP-12 will be completed in November of 2011 and the results will be included in the final report.

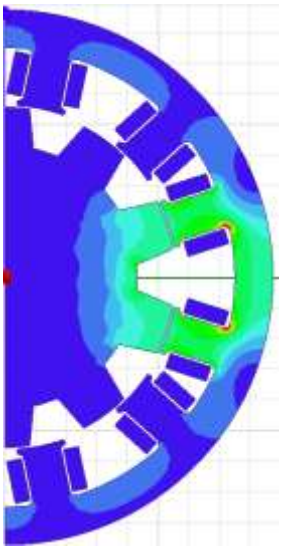

**Figure 76: Maxwell plot of DP-12 illustrating the unique geometry of the poles of the stator**

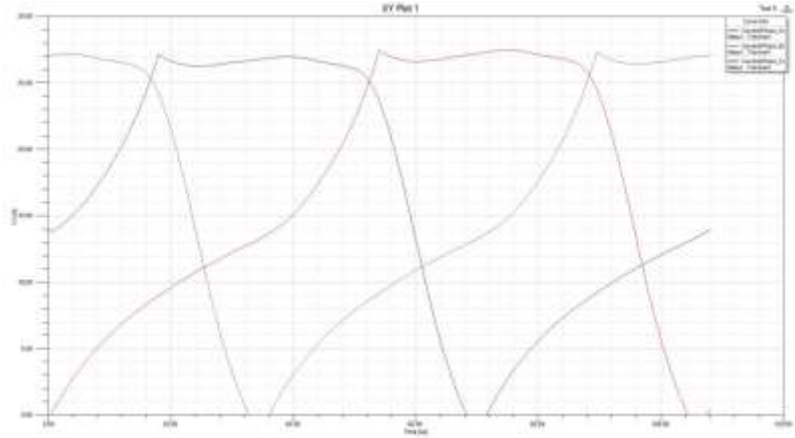

**Figure 77: Plot of the Maxwell simulation of the stator current of the three phases of DP-12 with operation as a switched reluctance generator**

### D7. Quick machine

In support of this project, DP has developed a software program for the design of switched reluctance machines. The software is intended to assist users to apply the principles a switch reluctance machines and produce a prototype design. The goal of the Quick Machine software is to provide “quick” design results in comparison to the longer time required to produce a more detailed design using Maxwell or other FEA software. The Quick Machine software will be made available free for open source use through the DP website in the final report of this contract.

The Quick Machine software has the capability to design the geometry of the stator and rotor of a switched reluctance machine and to provide a simulation of the operation of the machine. The following section provides an introduction to the operation of the Quick Machine. The manual describing the full

details of the operation of the Quick Machine software is provided in Appendix B. The Quick Machine program will be available to download at the website for Dakota Power at the www.dplwed.com.

Quick Machines operation begins with the provision of three sets of parameters:

- Geometric Parameters – the physical dimensions of the machine
- Electric Parameters – the electrical components of the machine (phase windings and switching circuit)
- Material Parameters – the materials used in the machine

Once the geometric parameters are loaded, an interactive figure of the machine will appear. Figure 78 shows the DP-06 modeled inside Quick Machine. The rotor of the interactive figure can be rotated by clicking and dragging any rotor lobe – this allows the user to visualize the design, and helps in defining the switching circuit.

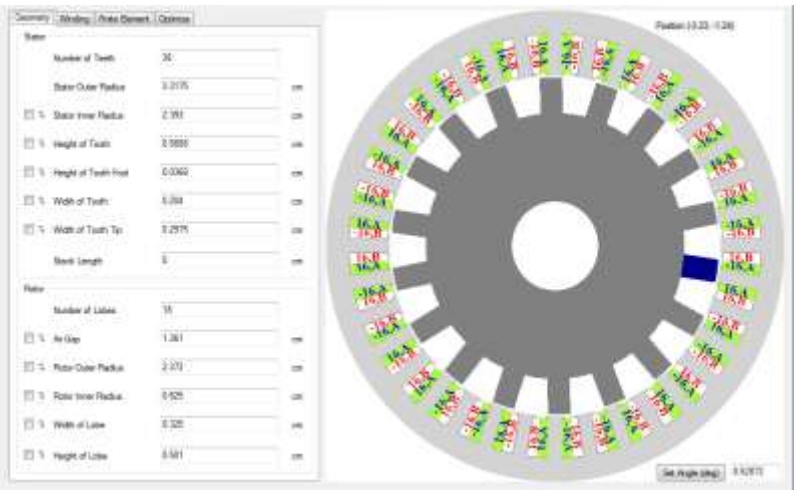

**Figure 78: Quick Machine model of DP-06.**

*(The figure on the right is interactive – clicking and dragging a rotor lobe will cause the rotor to rotate)*

Quick Machine uses an auto phasing algorithm that automatically sets the electrical components. The algorithm creates the phases based on the symmetry of the motor, then designs the switching circuit to produce maximum torque – given a rotor position, the switching circuit will fire all phases that produce a clockwise torque. With the auto phase algorithm the user can create a model in a matter of seconds. If the design requires a more customized phase set up and switching circuit, there is an option to design the phases manually – this option allows the user to explicitly set their phases, winding configurations, and firing angles.

Once the model is created, it is exported to an open source FEA program called Finite Element Magnetics Method (FEMM). FEMM is a widely used FEA simulator, and is the primary FEA tool in a number of research papers. Once the model is exported to FEMM, it performs a static finite element

analysis. This analysis provides the user with a graph of the flux densities and flux path, as well as calculations of torque, inductance, flux linkage, etc. Figure 79 shows an FEMM analysis of DP-06.

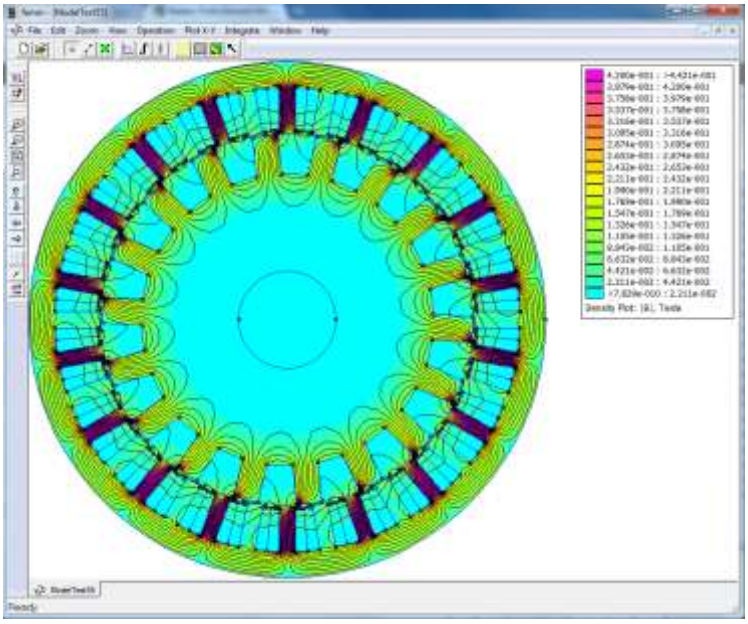

**Figure 79: FEMM simulation of DP – 06.**

*(The solid lines show the flux path, while the colors indicate the flux densities)*

The most powerful feature of Quick Machine is its ability to optimize a geometry by iterating the value of any number of parameters. This parametric sweep is performed given a list of parameters, each containing a start, end, and increment value. To execute the sweep, Quick Machine creates a model for each permutation in the sweep and sends it to FEMM for analysis. FEMM has a scripting interface that provides a list of commands; these commands can be used to specify the output of an FEMM simulation (i.e. torque, inductance, flux linkage, etc.). Quick Machine uses user input to generate a script of the above commands, and controls the output of FEMM with this script. This allows the user to customize the FEMM analysis for each parametric sweep. Once each permutation is analyzed, a single data file is created. Excel or MATLAB (or a similar program) can be used for further analysis.

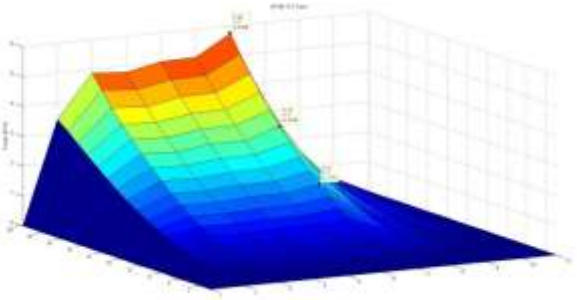

**Figure 80: MATLAB plot of a parametric sweep of the current and rotor angle – Z Axis torque**

Quick Machine allows the user to optimize any of the input parameters – including the electrical parameters. Figure 80 shows an example MATLAB plot of data created by Quick Machine iterating the phase current and rotor angle of DP-06. The analysis shown on Figure 80 is a combination of 200 simulations with a combined computation time of approximately one hour on a quad core 2GHz processor. The same analysis was performed using Maxwell – the Maxwell simulations gave similar results; however the 200 Maxwell simulations took a combined computation time of 13.3 hours.

## *E. Survivable Operation of Three Phase AC Drives in Wind Generator Systems*

### E1. Introduction: Advantages and Challenges of Wind Energy

Wind energy has gained increasing popularity over recent years due to the depletion of natural resources and the increasing concern about our environment. According to the data from Department of Energy (DOE) and American Wind Energy Association of the United States, as shown in Figure 81, the installed wind power generation capacity of the US has increased from 2,500 MW in 2000 to more than 35,000 MW in 2009. As of 2009, 26 states have more than 100 MW installed and more states will join the 100 MW club in the near future. In addition, as shown in Figure 82, wind energy takes 50% of all renewable electricity and reaches 1.8% of all the electricity generated in the US in 2009. Also, in report [**1**] of DOE, wind energy is targeted to reach 20% of all electricity generated in the US by 2030. In this scenario, enough energy can be extracted from wind to replace 11% natural gas consumption and 18% coal consumption, which could reduce 25% of the CO2 emissions and 17% water consumption in electric sectors in 2030. From these data, it can be easily noticed that there is global trend to replace conventional unhealthy energy generation modes with wind energy generation. Though the initial investment for the installation of wind farm might be large, this kind of energy generation mode is profitable and environment-friendly in the long run.

Although wind energy has a promising future, several challenges exist that hinder the wide-spread acceptance of this technology. These challenges including materials, manufacturing, transportation, initial investment and wind turbine stability etc. Wind turbine stability is one of the main concerns in the development of wind energy. Wind turbine faults happen frequently after installation. As shown in Figure 83 [1], the designed life-span for a wind turbine is 20 years. During this time period, the most frequent failure in the wind generator is in its sensor and control unit failure which begin to occur around 2.5 years right after the warranty. Though the repair cost is relatively cheap compared to other failures, frequent stops can significantly reduce the effectiveness of the generator and cause large loss of revenue. The gearbox might only last for 6 years without any problem, but after that, it begins to have faults and the risk of failure is increasing as time goes on. Unfortunately, the gearbox is one of the most expensive components in wind plant and its failure will cause the longest downtime of the wind plant [**2**], [**3**]. Besides, motors and switchgear can last for 6 years. The generator bearings begin to have faults around 11 years. Yaw drive and pitch drive can be used for 10 years etc. Based on the above data and analysis, it can be noticed that the low reliability of wind turbine components greatly hinder the development of wind energy.

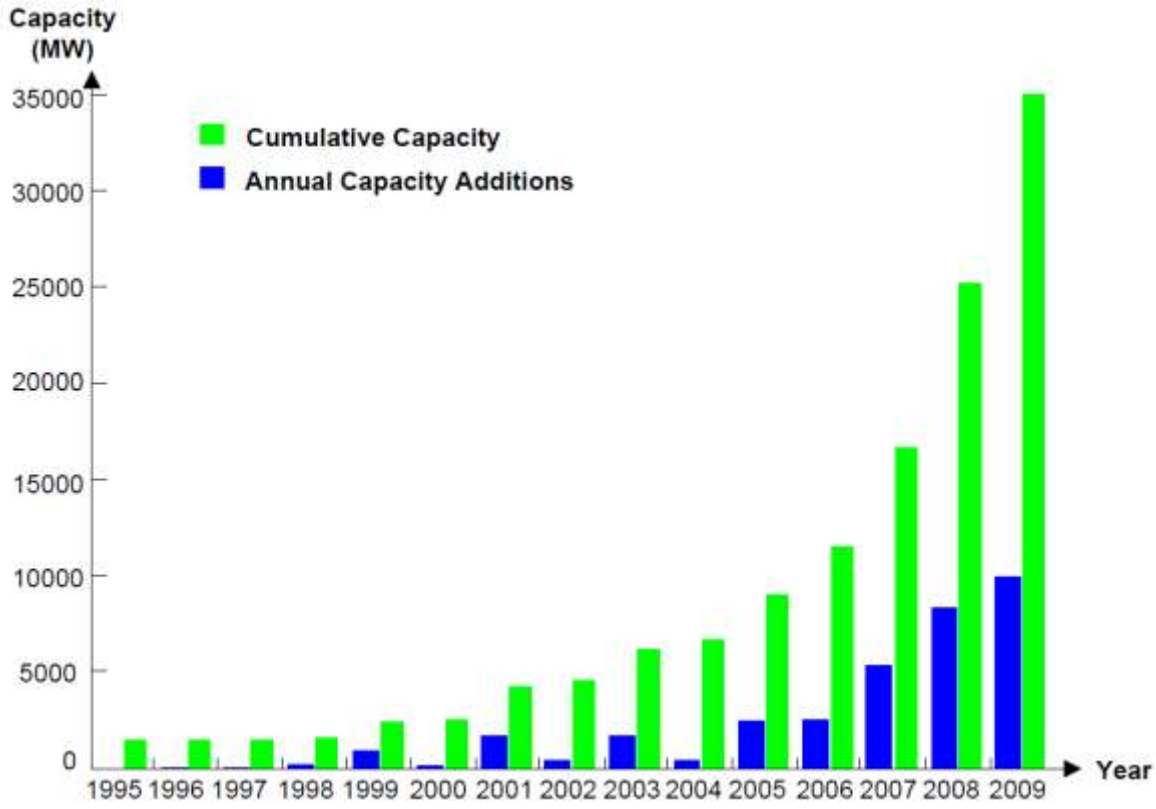


**Figure 81: US annual and cumulative wind power capacity growth [1]**

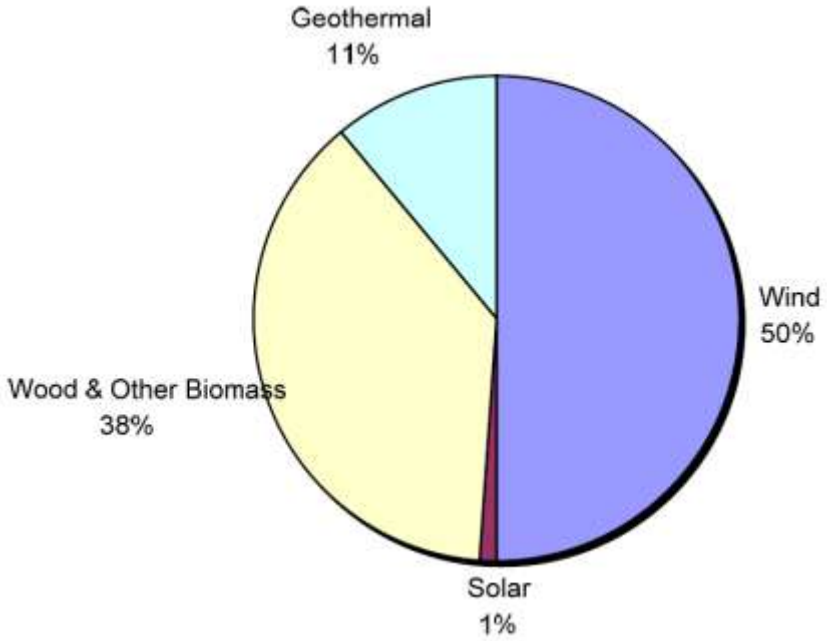


**Figure 82: Percentage of renewable electricity [1]**

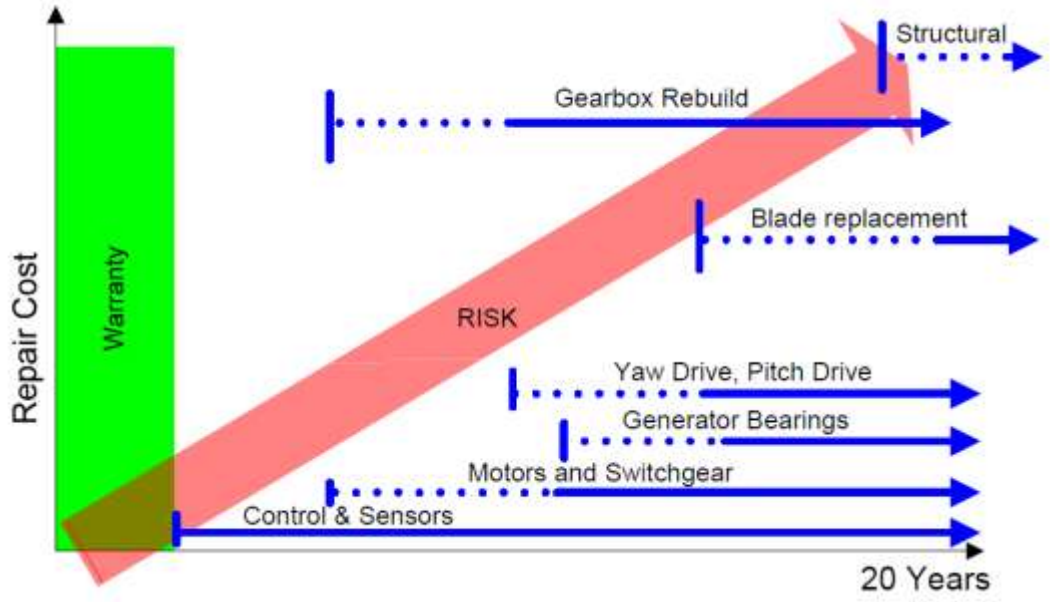


**Figure 83: Unplanned repair cost and risk of failure with wind plant age [1]**

Induction machine is one of the most popular machines in industry due to its robustness and low maintenance. Similarly, this machine is also widely used in all power levels of wind power applications. However, the control of induction motor (IM) and induction generator (IG) is complicated. In order to maximize the performance of induction machine, vector control is often utilized to decouple the flux and torque and control them individually. This control method usually requires complex control routines, fast processing unit and multiple system feedbacks including three phase current sensors. However, as shown in Figure 83, the most unreliable part of the wind plant is the control and sensors. Frequent sensor failures or even the drift of system parameters can result in unscheduled maintenance issues that require the unit to be frequently stopped, leading to a reduced power yield. In addition, unscheduled maintenance often results in longer downtime and causes reduction of availability of the wind generator especially for those wind turbines located offshore or in remote areas.

In order to enhance the reliability of the wind generator system, a novel simplified control strategy, state switching control, has been proposed and implemented for the induction machine in both motoring mode and generating mode, which have never been done before. This control method requires low signal processing need, low memory capacity and no current sensor. Therefore, it is a simple, cost-effective and very reliable control strategy. By utilizing this control method, system is only allowed to operate at two different duty cycles of PWMs which are given to the PWM rectifier and produces phase voltages with different magnitudes. Meanwhile, the frequency of the phase voltages is derived from the reference speed. By switching between these two states, different torque can be generated at the generator side, which leads to precise speed regulation and output power control.

Based on the simplified control strategy, a survivable control algorithm for wind generators is further proposed in order to deal with the failure of sensors (mainly for current sensors). The concept of survivable drive is that when system is healthy, the induction generator is often controlled by

sophisticated control algorithms such as vector control. When sensor fault happens, the wind plant can survive and the generator can be controlled by state switching control strategy and still be operated with relative lower but acceptable performance. Survivable drive is very useful for wind turbines when sensor fault happens. This ability ensures the power production and greatly reduce the lost of revenue.

Besides, the idea of survivable drive can be extended to Brushless Permanent Magnet Machine. Brushless PMSM is also one of the popular machines for wind power application due to its high power density. However, the potential failure possibility of current sensor will also cause stability problems to Brushless PMSM generator system. By utilizing the survivable algorithm and state switching control, the failure of current sensor can be tolerated, which greatly improves the reliability of the PMSM generator systems.

This section consists of six parts. Section E1 introduces the advantages of wind energy and the benefit in increasing wind plant installations in the US in recent years. This chapter then discusses current challenges in the reliability of wind generators and introduces the concept of a survivable generator drives in the event of failure of current sensors. Section E2 offers an overview of the common faults of different components of a wind generator setup. It identifies faults that are most frequent and ones that are most fatal causing the longest downtime with expensive repair costs. Section E3 presents a fundamental description of an induction machine model. In addition, converter topologies and generator control methods which are often used in wind plants are explained. Section E4 describes the principle and performance of a state switching control strategy for induction machine. As a backup control strategy, a novel state switching control method is proposed and implemented on hardware to control the induction machine without relying on current feedback. Simulation and hardware results are included to verify the feasibility of this method. Section E5 proposes a survivable drive algorithm for induction machine in wind power application when there is a failure of in current sensor(s). First, the principle and implementation of a sensor failure detection method is introduced. Then, implementation of vector control as a main control strategy for induction machine is introduced. After that, a change in control algorithm is proposed when sensor failure occurs. In addition, a controller smooth transition method is designed to ensure the seamless controller transition without stopping the system and causing speed vibration. Detailed simulation and hardware results are included to validate these methods. Section E6 concludes achievements in this research and identifies future work.

## E2. Current Existing Faults for Wind Power Generator Systems and Corresponding Solutions

Wind energy has a promising future. However, wind turbine has many challenges in its reliability. Different components of a wind plant have different failure rates. As shown in Figure 84 [**1**], the electrical faults take more than 50% in fault rates and sensor faults take 9%. Such a high failure rate greatly hinders the development of wind energy. Detailed information regarding certain failures and their corresponding fault tolerant solutions is presented in the following sections.

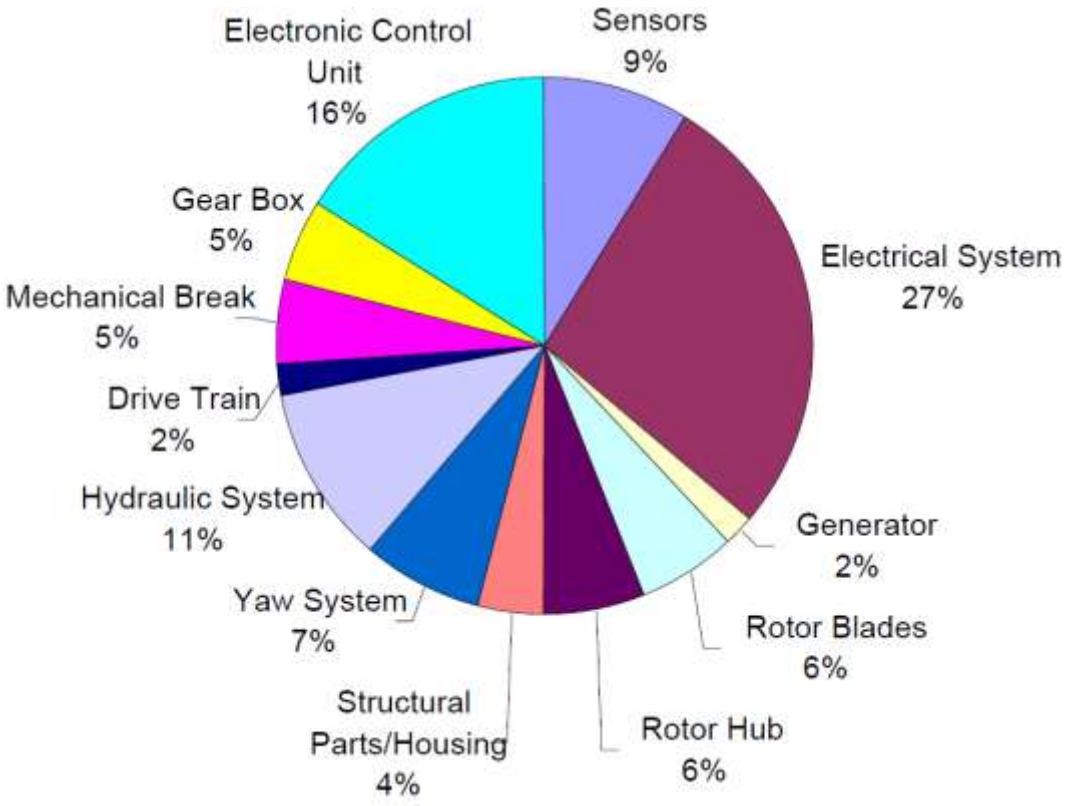


**Figure 84: Failure rate of different component in wind turbine [1]**

In wind turbine applications, converter failure happens much more frequently than any other wind turbine faults. In paper [**4**], it pointed out that the MTBF (Mean Time between Failures) of a conventional converter (or inverter) is 20,800 hours (about 2.4 years) which is too short for wind power applications. The topology of a conventional converter can be displayed in Figure 85. The right side is connected to the three-phase generator and the left side is connected to the DC link. In between them, six IGBT switches with six parallel diodes forms three converter legs which are connected to different machine phases independently. Converter fault can be single switch failure (open circuit or short circuit) or two-switch failure—usually one leg is open circuit or short circuit. All of these faults are fatal and will cause the wind turbine system to be shut down. Since unscheduled maintenances experience relatively longer period. It leads to the decrease of power production and availability of healthy wind turbines.

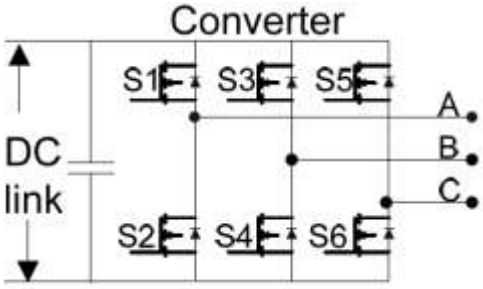


**Figure 85: Typical topology of converter**

Fault-tolerant strategy for inverter failure is introduced in paper [**5**], which is also applicable to converter failure. In [**5**], the inverter fault is tolerated by introducing the forth leg to conventional inverter. As shown in Figure 86, the forth leg (Switch S7 & S8) is added to the conventional inverter with its middle point connected to the neutral of the three phase AC machine. When inverter failure happens, the faulty leg is isolated while the forth leg is activated. As a result, one phase of the AC machine connected to the faulty leg is also isolated and the machine is operating with the rest two phases. The advantage of this inverter topology is that it can handle single switch open-circuit or short-circuit fault and one leg open-circuit fault. If additional isolating devices are added to inverter legs, one leg short-circuit fault can also be tolerated. The torque performance under fault condition is claimed to be the same as a healthy machine by proper compensating the phase current of the machine. However, this method has some disadvantages in practical applications. Inverter fault must be detected quickly and isolated immediately. Otherwise, it will cause severe damage to the machine and other electrical components. The challenge is how to detect and isolate the inverter leg failure fast enough before causing undesirable troubles. In addition, in order to maintain same torque performance after failure happens, the current flowing through the rest two phases and inverter legs increased especially for the fourth leg (the maximum current flowing through the forth leg is near three times greater than conventional inverter). As a result, high power rating switches are required compared with conventional inverter, which will increase the cost of hardware.

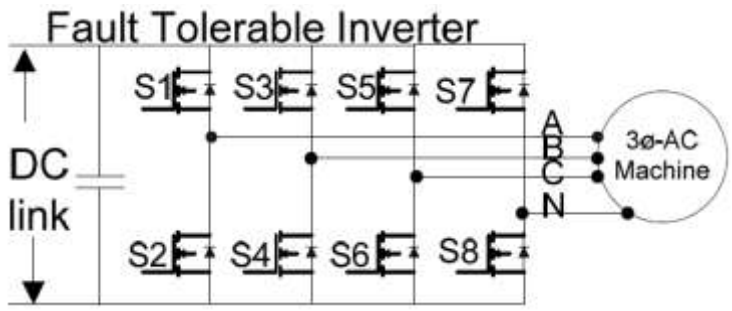


**Figure 86: Four-leg fault tolerant inverter**

In paper [**4**], several voltage source redundant inverter topologies are presented and their reliabilities are discussed and compared with the conventional inverter. Two redundant inverter topologies are shown in Figure 87. Instead of using two switches, multiple switches are used to form one leg of the inverter.

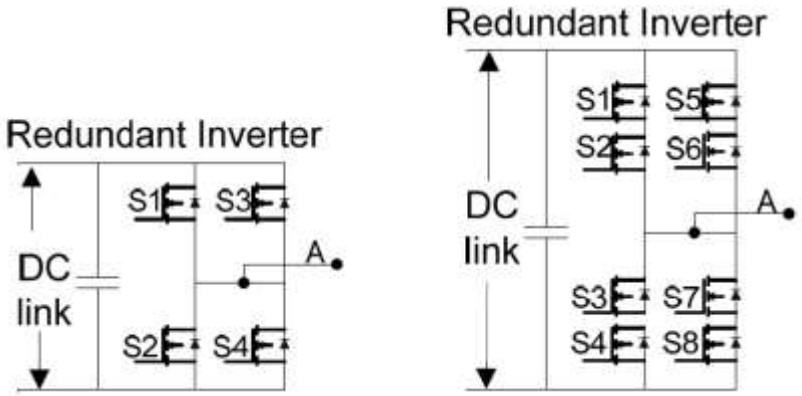


**Figure 87: Redundant inverter topology**

By using redundant inverter topologies, the reliability will increase obviously for short term operation (around several hundreds of hours) compared with conventional inverter. However, for long term operation (longer than 80,000 hours), the reliability tend to become the same. Since the reliability of the redundant converter doesn't change very much for long term operation, this method is not recommended for wind turbine application to improve the converter reliability.

In wind power generation, a bunch of sensors work together to provide feedbacks regarding the conditions of a wind turbine. These feedbacks can be used to control the efficiency of the wind turbine system and ensure its safety. The control of generator and power electronics requires current sensors and voltage sensors. The control of electric drive also need speed or position sensors. Besides, temperature sensors monitor the temperature of different part of the wind turbine such as the generator and the gearbox. Vibration sensors sense the vibration of the transmission as well as the wind turbine tower to avoid possible damages caused by large vibration. Therefore, sensors are necessary for the operation of a wind turbine. A sudden sensor failure will decrease the system performance and even lead to system malfunction, which is harmful to the availability of the wind turbines. Among these sensors, voltage sensors, current sensors and speed sensor (or position sensor) plays more fundamental roles in a wind turbine system. They provide basic information about the generated voltage, current and their frequency. The failure of these sensors might lead to uncontrolled power which is harmful to the system and the grid. In addition, these sensor outputs are often used in close-loop control strategies such as Field Oriented Control and constant V/f Control. If one of these sensors is in fault condition, these control strategies cannot perform correctly since basic feedbacks are missing. Therefore, in order to improve the reliability of the system and prevent unscheduled shutdown, sensor fault detection and compensation method are often adopted. 1) Current sensor and voltage sensor failure

In literature [**6**], current sensor failure is detected and isolated using three-phase current balancing test. Under normal operation, the sum of the measured three-phase currents is very small (near zero). If one of the current sensors is in fault condition, this value will change dramatically. Therefore, by comparing the sum of measured currents with a small threshold value, the current fault can be detected. Then, the faulty current is identified and compensated by fuzzy logic state observer. The observer basically estimates the stator flux and phase current which is then used to replace the faulty current and

reconfigure the control loops. Similar method can be found in literature [**7**] and [**8**]. This technique for tolerating the current sensor failure also applies to three-phase voltage sensor because these voltage signals have the same characteristics.

In paper [**9**], the failure of sensor is tolerated by reducing the performance of the control using control strategies that requires fewer sensors. As a result, one can toggle between different control strategies based on the availability of the sensors. For example, if all voltage sensors, current sensors and position sensor are available, sophisticated control strategies can be employed to enhance the performance of the system such as Field Oriented Control and Direct Torque Control. If only voltage sensor is good, constant V/f method can be used to control the induction machine.

In paper [**10**], the failure of phase current sensor is tolerated by eliminating the phase that the faulty current sensor belongs to. As shown in Figure 86. The PMSM machine can be operated with the rest two phases and with the natural point connected to the forth leg of the inverter. The torque performance is claimed to be the same with the three-phase machine using this method. 2) Speed or position sensor failure

In wind power generation, position information is typically required to calculate the shaft speed of the machine in order to control it properly and employ Maximum Power Point Tracking (MPPT) schemes. As a result, the failure of the speed or position sensor often leads to system malfunction and unscheduled shutdown. Sensorless techniques are often used to handle the position sensor failure. Large amount of literatures are dealing with different kind of sensorless techniques including Motional-EMF based prediction [**11**], [**12**], Inductance variation based prediction [**13**] and FluxLinkage variation based prediction [**14**] etc. These sensorless methods can be employed to handle the position sensor failure. However, the performance of sensorless method is poor in low speed conditions.

The gearbox is a mechanical device which connects the low-speed shaft and thegenerator. Gearbox is indispensable for indirect drive wind turbines due to the high rotating speed requirement of generators. Usually, it can speed up to 1500rpm (50Hz) to 1800rpm (60Hz). The lifetime expectation of a wind turbine is around 20 years. However, according to literature [**15**], [**2**], the current existing gearboxes can only last for 7 years on average, which is far less than the designed lifetime objective. Worse still, gearbox is the most expensive part of the wind turbine system and the most responsive component for the wind turbine down time. Replacing a gearbox and lubrication will cost 38% of the total budget of the entire wind turbine and make the wind turbine stop for a long time [**2**]. This down time data can be displayed in Figure 88.

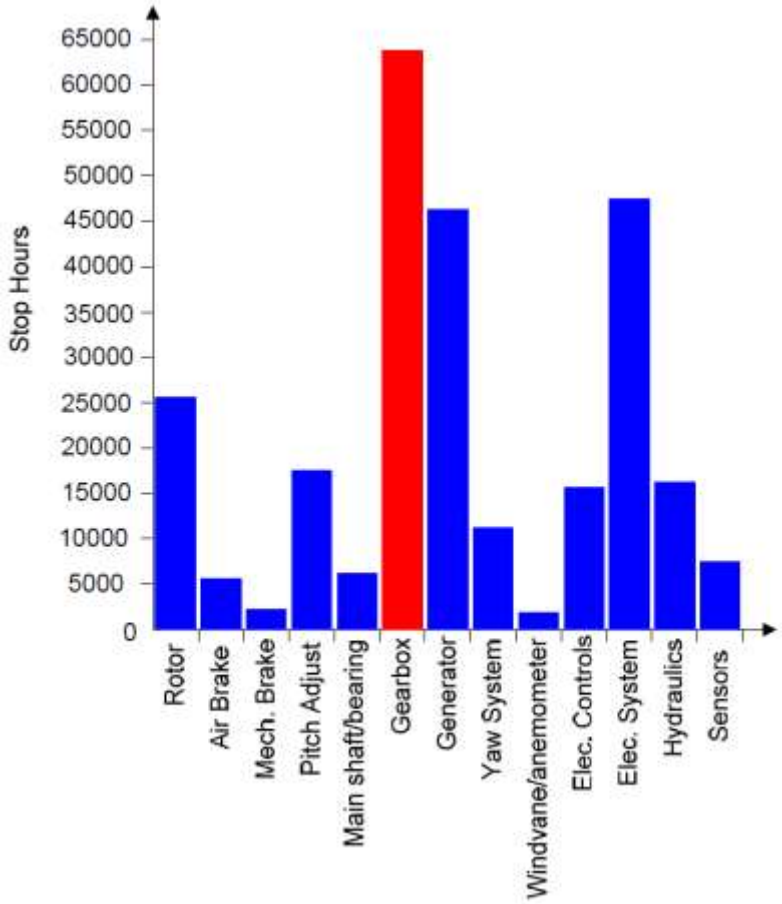


**Figure 88: Wind turbine down time caused by component failure [2]**

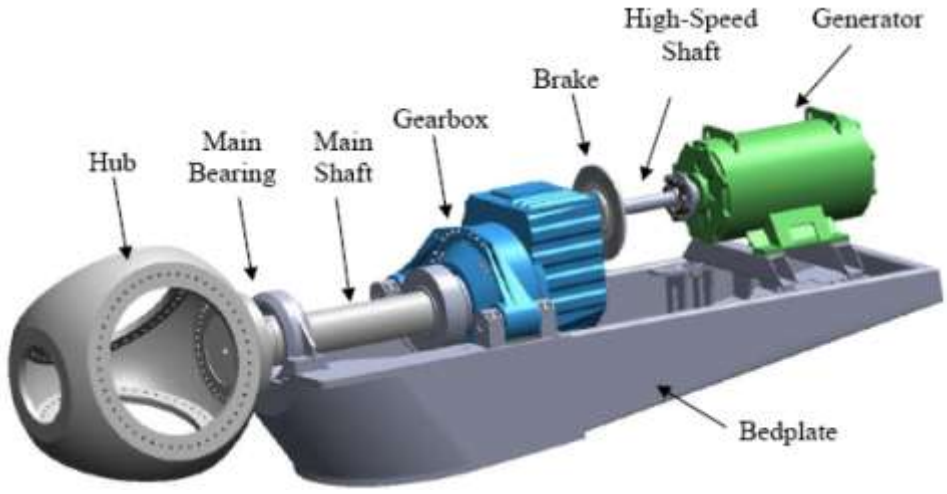


**Figure 89: Conventional drive train of wind turbine [2]**

The fundamental reasons for the failure of gearboxes are still not clear. But certain reasons can be estimated from observations and software simulation [**3**].

1) Improper design of wind turbine gearboxes without considering the complicate load conditions. This is primary due to the lack of communication between gearbox manufactures and wind turbine designers.

2) Non-torsional load is transferred between different components of the drive train including the gearbox. Non-torsional of the drive train load is introduced by the conventional rotor support structure. As shown in Figure 89, the gearbox not only performs mechanical acceleration, but also works as a rotor support of heavy wind blades. This kind of rotor support structure hastens the wearing of the gearbox.

3) The quality of bearings is essential for the health of the gearbox. If the bearing is broken or even worn due to strain, there will be a misalignment in the drive train which will cause damage to the gearbox.

4) Improper installation and lubrication problems will also cause damage to the gearbox.

Gearbox failure is fatal. But there are no fault tolerant strategies till now. Certain methods can be used to increase the reliability of the gearbox according to the above mentioned causes.

1) Redesign the gearbox according to the practical load conditions of the wind turbines. National Renewable Energy Laboratory (NREL) of the US has lunched several projects aim to improve the reliability of the gearbox of wind turbine.

2) Redesign the rotor support structure and eliminate the non-torsional load in the drive train. Actually, wind turbine designers begin to try new structures. As shown in Figure 90 [**15**], the rotor which connected to the hub and heavy blades is supported by the wind turbine tower instead of the gearbox. As a result, non-torsional load can be eliminated from the drivetrain.

3) Ensure the quality of the bearing and enhance the communication between wind turbine designers and bearing suppliers.

4) Direct drive is also an option to fundamentally solve the gearbox problem since this kind of wind turbine structure eliminates the gearbox and the generator is directly connected to the wind turbine shaft, as shown in Figure 91. However, this method requires a generator with large diameter and increased number of poles due to the low speed of the shaft, which will not only significantly increase the cost of the generator but also make the control strategy complicate if the generator working in variable speed generating mode. Moreover, the failure rate of the converter in the direct drive wind turbines is much higher than in the indirect drive wind turbines [**16**]. Therefore, direct drive wind turbines still have a long way to go before replacing the indirect drive wind turbines.

Other failures including generator failure, yaw drive failure, pitch failure, rotor blade failure and structural failure etc. Failure rates of most of these failures are smaller then those introduced in the previous part of this chapter. In addition, most of these failures cannot be tolerated. As a result, detailed information regarding these faults will not be introduced.

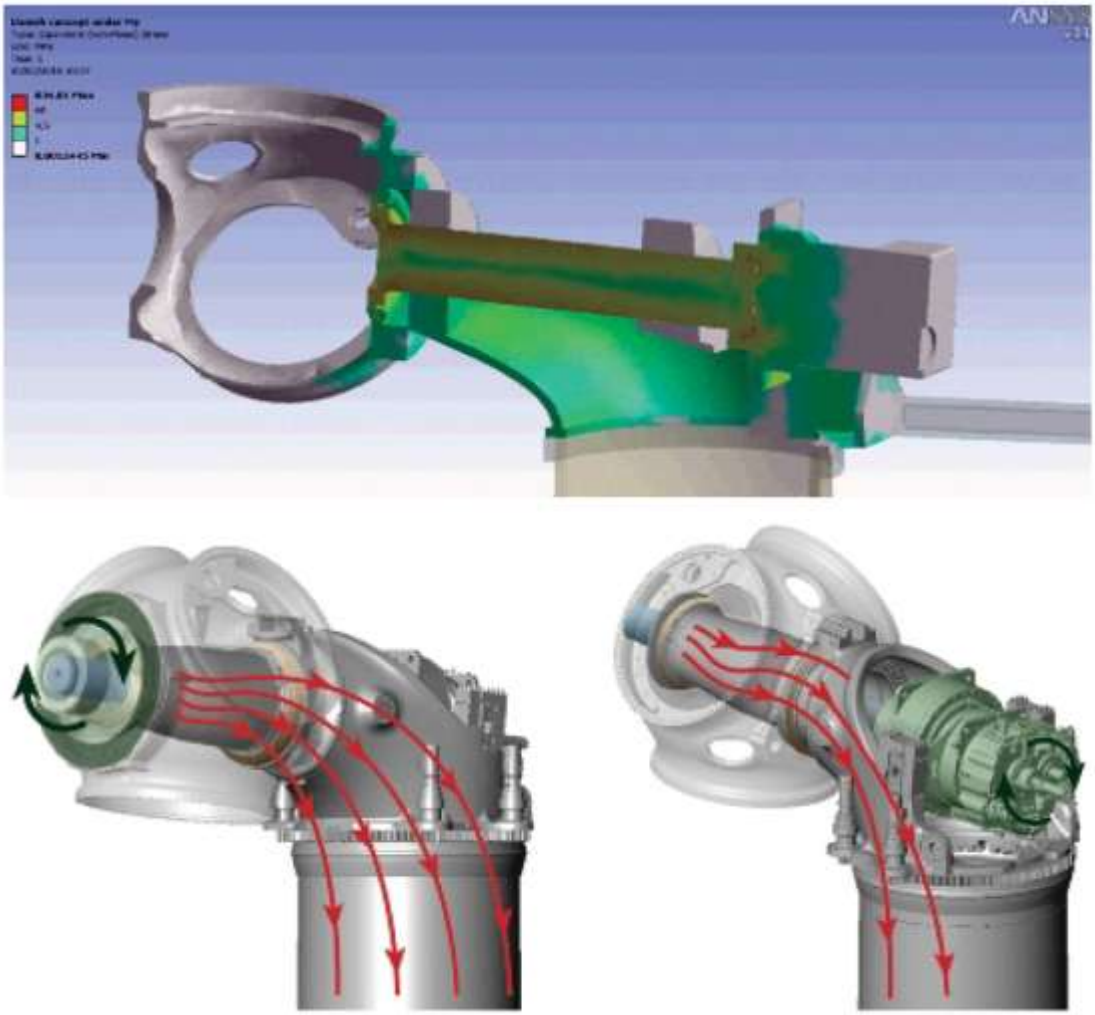

**Figure 90: Tower supported rotor configuration [15]**

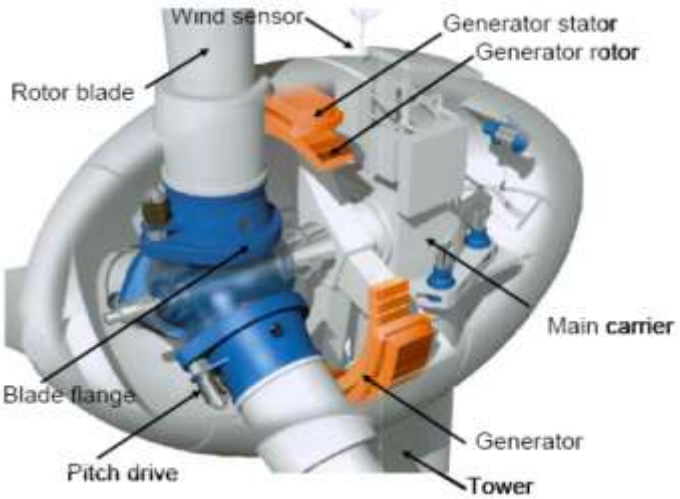


**Figure 91: Direct drive wind turbine configuration [2]**

In this section, several types of component failures are introduced and their corresponding fault tolerant solutions are discussed. Electrical faults take the highest percentage of failure rate. While mechanical faults often causes longest downtime and cannot be tolerated.

### E3. Fundamentals of Induction Machine Drive

Induction machines are popular due to their robustness, cheap price and low maintenance. They can be found in wind turbines at almost all power levels. For small power level, squirrel cage induction machines are often utilized. For medium and high power level, wound rotor induction machines (Double Fed Induction Machine) are often employed.

One of the commonly used induction machine model is the synchronous rotating reference frames model. The equivalent circuit of this induction machine model can be displayed in Figure 92. According to equivalent circuit, the mathematical model of the induction machine can be derived and expressed in equations (1) to (5). Mechanical system of the induction machine can be expressed in equation (6) and (7).

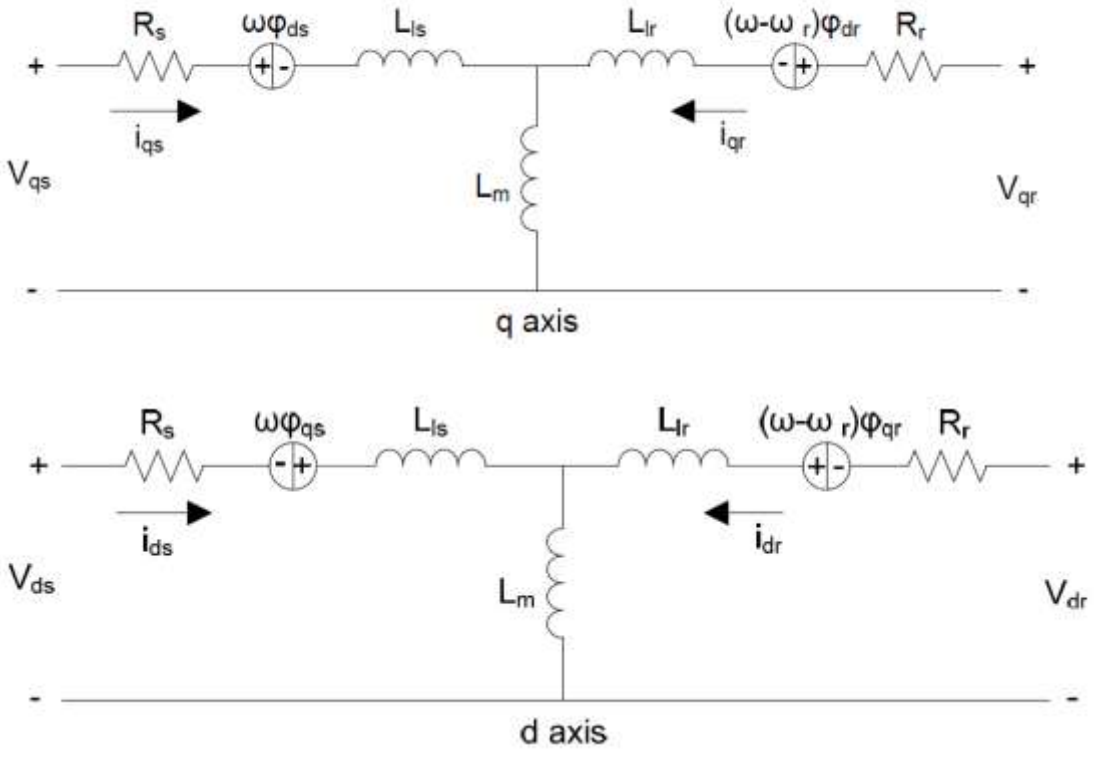


**Figure 92: Equivalent circuit of induction machine in d-q axis**

$$V_{qs} = R_s i_{qs} + \frac{d}{dt}\varphi_{qs} + \omega\varphi_{ds} \quad \textbf{(1)}$$

$$V_{ds} = R_s i_{ds} + \frac{d}{dt}\varphi_{ds} - \omega\varphi_{qs} \quad (2)$$

$$V_{qr} = R_r i_{qr} + \frac{d}{dt}\varphi_{qr} + (\omega - \omega_r)\varphi_{dr} \quad (3)$$

$$V_{dr} = R_r i_{dr} + \frac{d}{dt}\varphi_{dr} - (\omega - \omega_r)\varphi_{qr} \quad (4)$$

$$T_e = 1.5p(\varphi_{ds} i_{qs} - \varphi_{qs} i_{ds}) \quad (5)$$

$$\frac{d}{dt}\omega_m = \frac{1}{2H}(T_e - F\omega_m - T_m) \quad (6)$$

$$\frac{d}{dt}\theta_m = \omega_m \quad (7)$$

where

$$\varphi_{qs} = L_s i_{qs} + L_m i_{qr}$$

$$\varphi_{ds} = L_s i_{ds} + L_m i_{dr}$$

$$\varphi_{qr} = L_r i_{qr} + L_m i_{qs}$$

$$\varphi_{dr} = L_r i_{dr} + L_m i_{ds}$$

$$L_s = L_{ls} + L_m$$

$$L_r = L_{lr} + L_m$$

The converter topologies for induction machine drives can be grouped into two major categories. One is passive converter and the other is active converter.

The topology of a commonly used passive converter is shown in Figure 93. This topology is often used when the generator is operating at constant speed. For example, an induction generator is often required to operate at 1500rpm synchronous speed when its output is directly connected to the grid with 50Hz frequency. In such a circumstance, shaft speed of the generator is maintained by the

mechanical part of the wind turbine instead of the converter. This topology can also be found in some direct drive wind turbine. In this case, the shaft speed of the generator is not constant, which results in the change of the DC link voltage. As a result, an active inverter is often required after the passive converter stage to convert DC power into three phase power for sending to the grid.

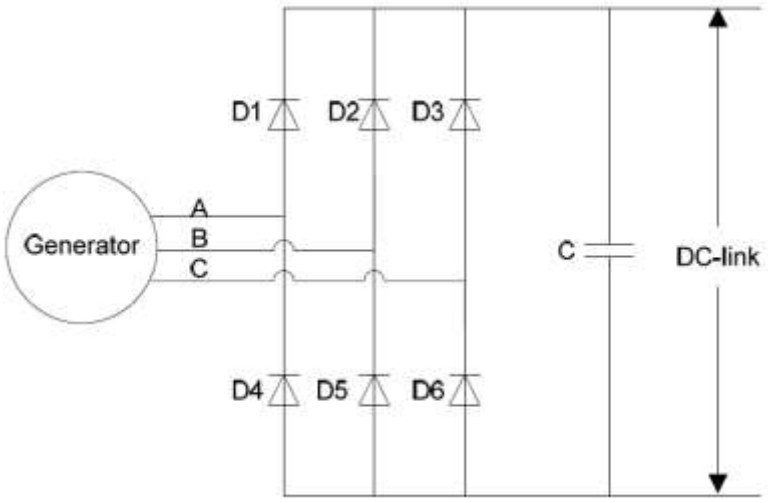


**Figure 93: Passive converter topology**

The topology of a typical active converter is illustrated in Figure 94, in which active components (IGBT or MOSFET) are used instead of diodes. In this topology, power flow can be bidirectional. Power can flow from generator side to the source and vise versa. As a result, this topology is extremely popular in Hybrid Vehicle applications. Active converters are also popular in wind power application, since the use of an active converter allows the generator torque to be properly controlled. By manipulating the generator torque, shaft speed of the generator can be controlled. This ability is very useful in direct drive wind turbines since the maximum power point is related to specific shaft speeds.

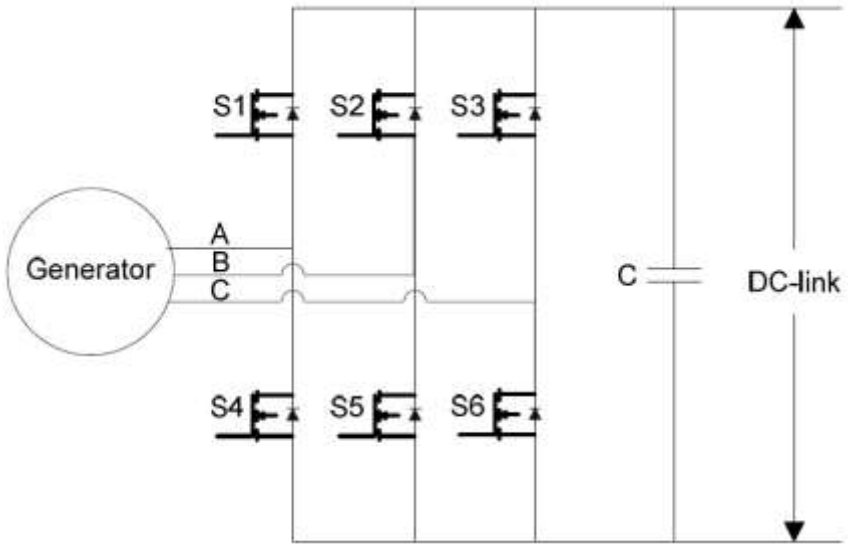

**Figure 94: Active converter topology**

In order to control induction machine properly and efficiently, different kinds of control strategies emerged in the past. Among these control strategies, most commonly used control strategies are constant V/f control and vector control.

Constant V/f control [**17**], [**18**] is popular for induction machine mainly because of its simplicity. In general purpose applications, most constant V/f controls are open-looped and control the voltage and frequency proportionally. By applying a specific phase voltage and frequency to induction machine, it can work at a desired speed. However, the speed control of conventional constant V/f controls lacks accuracy due to the existence of the rotor slip. When load increases or frequency decreases, rotor slip increases. This results in the increase of error between reference speed and actual speed. In order to deal with these problems, stator voltage boost [**19**], [**20**], [**21**] and slip compensation methods [**20**], [**21**] are often used. However, these methods increase the complexity of the system and require additional voltage or current sensors.

Vector control [**22**], [**23**], [**24**] has gained popularity over the last three decades due to its high efficiency and better transient performance. This method controls the flux and torque of induction machine separately and makes it work as a DC machine. Vector control turns out to be the most efficient and promising control strategy for induction machine. However, the implementation of vector control is complicated and expensive. It not only requires fast computation speed devices such as DSP and FPGA, but also additional sensors including current sensors and position sensor.

In this section, the basic model and the equivalent circuit of induction machine and permanent magnet machine is introduced individually. In addition, two typical converter topologies are explained including passive converter and active converter.

### E4. State Switching Control as a Back Up Control Strategy for Three Phase AC Machine

Current sensor failure is one of the most frequent faults in wind plants. A back up control strategy is required to continue operating the system. Otherwise, wind plant has to be shut down. State switching control is one of the simplest control methods which only need speed feedback. In other words, if current sensors are in faulty condition, system can still be operated with state switching control. State switching control is a variation of digital control method which is first designed to control BLDC, Switch Reluctance Machines (SR) and DC-DC converters. In this report, a state switching control method is proposed and applied on induction machine. The performance of this control method is highly acceptable.

In recent years, digital control has been proposed in [**25**], [**26**], [**27**], and [**28**]. This control method is extremely simple and very effective for many applications, such as BLDC, SR control and DC-DC converter control. In this method, two different states (state “High” and state “Low”) are predefined, these states can be voltage, current and PWM duty cycle. Then, state is switching between these two states by comparing the actual output value with the reference value. As a result, the system output can be well regulated. Therefore, there is no need for any massive computation controllers or even PI controllers. Only a comparator is required for the implementation.

Digital control has been found effective in several applications. This section presents the realization and implementation of state switching control technique for induction machine. The proposed state switching control method is based on six-step drive method [**17**] which is a basic drive technique for induction machine. By integrating PWM signals to gate signals of traditional six-step drive, a PWM based six-step drive method is derived. Then, by defining two different duty cycle for those PWMs, two phase voltages with different magnitudes (VH or VL) can be obtained. At the same time, by defining the frequency of the phase voltage according to given reference speed, the state switching control method for induction machine can be realized. By using this method, the induction machine system is only allowed to operate at a high duty cycle (DH) or low duty cycle (DL) which corresponds to VH and VL respectively. Speed regulation is achieved by defining the frequency of the phase voltage according the given reference speed and then switching between these two different duty cycles. Therefore, this controller is extremely simple. This technique also reduces the cost and complexity of hardware implementation. Simulation and experiment results regarding the speed response, change of duty cycle and phase current are included in this chapter to prove the effectiveness of the proposed approach.

For a three phase induction machine, the most frequently used driver topology is the three phase inverter which can be illustrated in Figure 95. This inverter includes six switches (MOSFETs or IGBTs) and six freewheeling diodes. By applying specific signals to these switches, induction machine can be operated properly.

Six-step drive method [**17**] is one of the simplest methods to drive the induction machine. Gate signals from the inverter are shown in Figure 96. In every electrical circle, each switch is turned on for 180 electrical degrees. The switching status of the upper and lower switches of each phase is always complementary in order to avoid short circuit. At the same time, for different phases, switching statuses are 120 electrical degrees phase shifted from each other. In other words, only three switches are turned on for every 60 electrical degrees. Two in high side and one in low side, or one in high side and two in low side. Therefore, for a wye-connected three phase induction machine, three six-stepped and quasi-sine phase voltages can be formed in the stator winding of the induction machine. These phase voltages are illustrated in Figure 96.

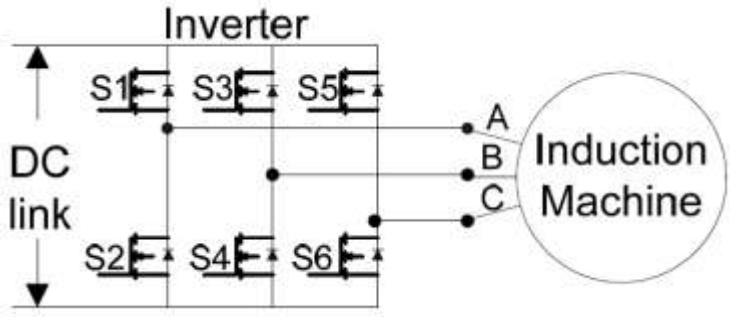


**Figure 95: Inverter for induction machine**

The implementation of the six-step drive method is also very simple. The electrical cycle is first divided into six equivalent regions with 60 degrees each. Then, each region corresponds to a specific

combination of switching status. These combinations can be described in Table 7. Finally, by generating these gate signals and applying them to the inverter with proper frequency, the induction machine can be operated.

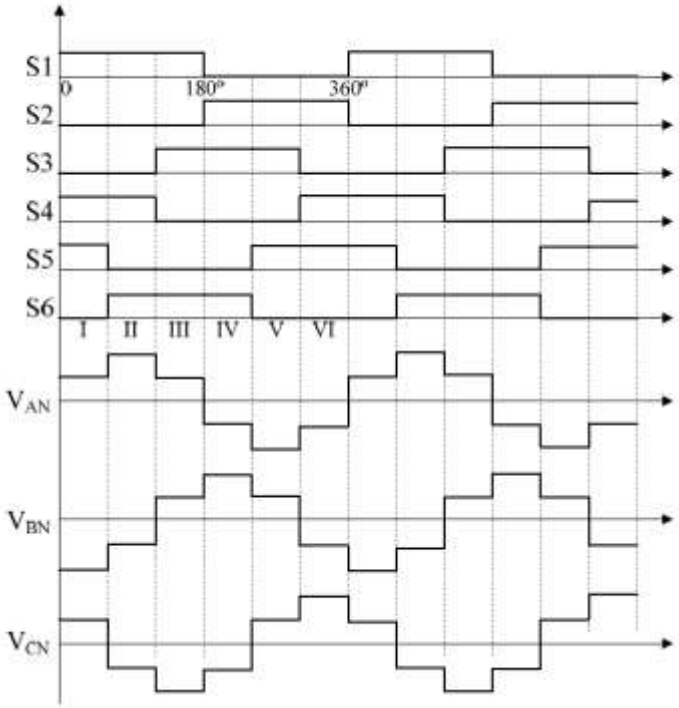


**Figure 96: Six-Step waveform**

**Table 7: Switching Status for Different Regions of Six-step Drive Method**

| Region No. | Switch Status | | | | | |
|---|---|---|---|---|---|---|
| | S1 | S2 | S3 | S4 | S5 | S6 |
| I | ON | OFF | OFF | ON | ON | OFF |
| II | ON | OFF | OFF | ON | OFF | ON |
| III | ON | OFF | ON | OFF | OFF | ON |
| IV | OFF | ON | ON | OFF | OFF | ON |
| V | OFF | ON | ON | OFF | ON | OFF |
| VI | OFF | ON | OFF | ON | ON | OFF |

Speed control of induction machine involves two parameters–the magnitude and frequency of the applied voltage across the phase winding. The frequency of the applied phase voltage mainly determines the shaft speed of the induction machine. This relationship can be explained in the following equations.

$$\omega_s = \frac{2\pi f_s}{P} \quad (8)$$

$$\omega_r = \omega_s(1-s) \quad (9)$$

where ωs is the synchronous speed of the induction machine in rad/s, fs is the frequency of the applied phase voltage in Hz, P is the number of pole pairs, ωr is the speed of the shaft in rad/s and s is the slip rate.

By changing the frequency of the phase voltage, the synchronous speed can be changed. At the same time, the variation of the synchronous speed results in the change of the shaft speed since shaft speed is very close to the synchronous speed at steady-state. Therefore, the shaft speed can be determined mainly by the frequency of the phase voltage. On the other hand, if the reference speed of the shaft is defined, we can also obtain the frequency of the applied phase voltage using equation (8) and (9).

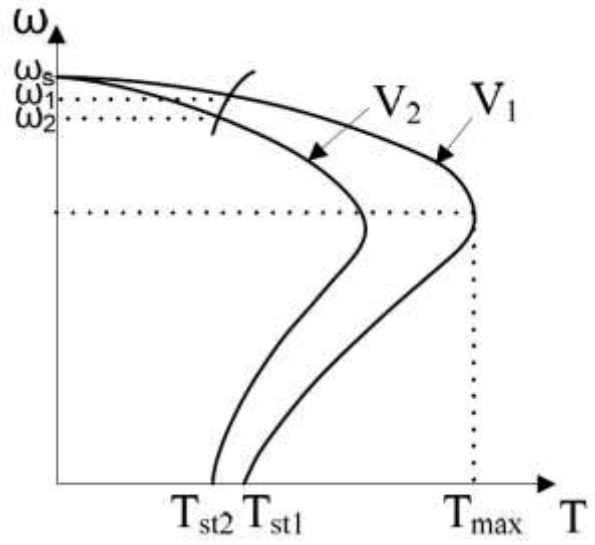


**Figure 97: Speed torque characteristics at different voltage level**

The magnitude of the applied phase voltage is also a factor which could affect the shaft speed. This relationship is shown in Figure 97 [**29**]. If the magnitude of the applied phase voltages is increased (V1>V2), the torque performance of the induction machine will be changed, as a result, the shaft speed will increase slightly (ω1>ω2), but the synchronous speed will be the same.

Based on the above analysis as well as the six-step drive method, a state transition control technique can be designed and expressed in Figure 98. According to the reference speed (ωref), the applied phase frequency can be defined using equation (8) and (9) if slip is approximated to be constant (roughly 5% in this case). By applying this frequency to the induction machine with proper magnitude of the phase voltage, shaft speed can be obtained, which is close to the reference. Then, by comparing the actual speed to the reference speed, the magnitude of the phase voltage can be switched between high

voltage level (VH) and low voltage level (VL). As a result, the actual speed (ωact) of the induction machine can be regulated accurately.

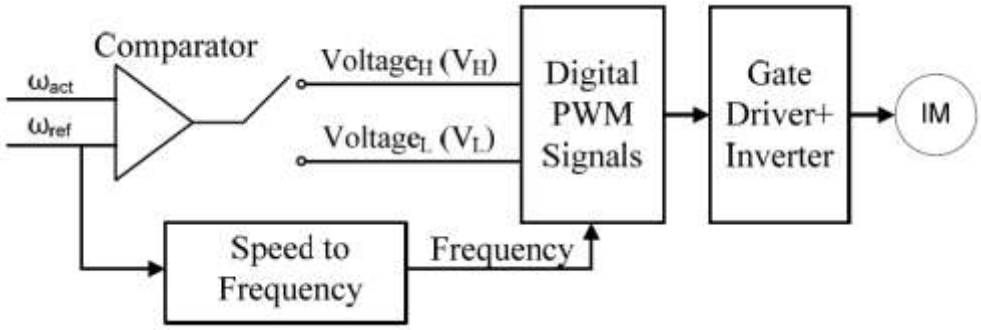


**Figure 98: Principle of state transition control of induction machine**

The change of the magnitude of the applied phase voltage is done by a new drive method—PWM six-step drive method. As shown in Figure 99, compared to traditional six-step drive method which is shown in Figure 96, switches are given PWM gate signals instead of turning them "ON" all the time for 60 electrical degrees. As a result, in Figure 99, the phase voltages are also PWM shaped if the load is resistive. Therefore, by changing the duty cycle of the PWM, the magnitude of the phase voltage of the induction machine could be changed.

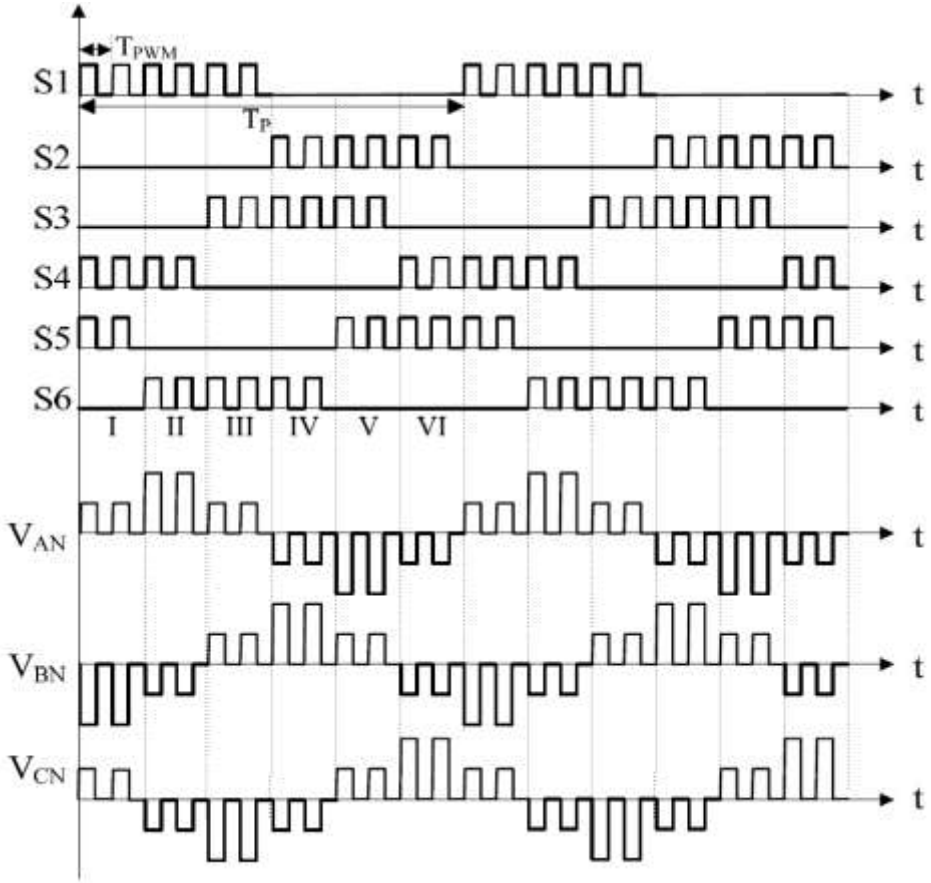

**Figure 99: PWM six-step waveform**

Therefore, the principle of the state transition control of induction machine can be shown in Figure 100 and concluded as follow:

1) The reference speed determines the frequency of the applied phase voltage. In our case, it determines the frequency of the six-step waveform.

2) The duty cycle (dL or dH) of the PWM is determined by comparing the actual speed (ωact) with the reference speed (ωref). The frequency of the PWM is set to 5 kHz in our case.

**Table 8: Switching Status of PWM Six-step Drive Method**

| Region No. | Switch Status | | | | | |
|---|---|---|---|---|---|---|
| | S1 | S2 | S3 | S4 | S5 | S6 |
| I | PWM | OFF | OFF | PWM | PWM | OFF |
| II | PWM | OFF | OFF | PWM | OFF | PWM |
| III | PWM | OFF | PWM | OFF | OFF | PWM |
| IV | OFF | PWM | PWM | OFF | OFF | PWM |
| V | OFF | PWM | PWM | OFF | PWM | OFF |
| VI | OFF | PWM | OFF | PWM | PWM | OFF |

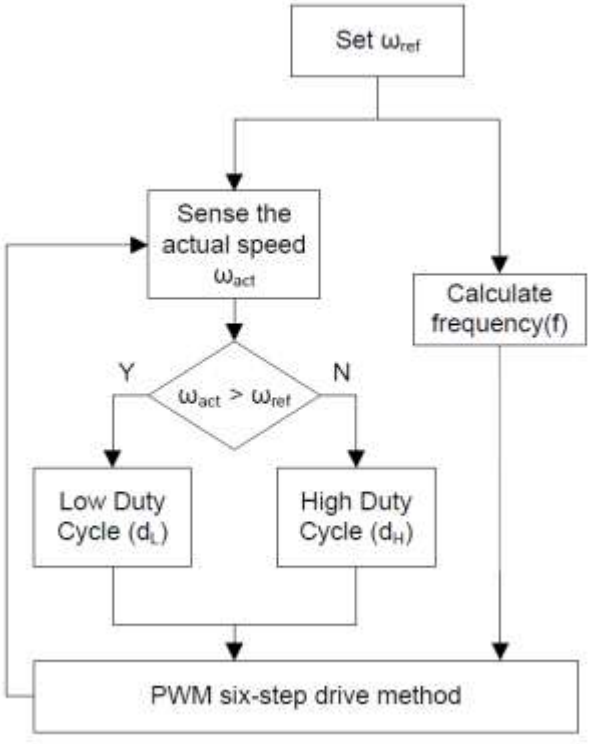


**Figure 100: Principle of state transition control of induction machine**

In order to design the controller, operating conditions for the induction machine and load conditions must be defined to calculate the frequency (which also defines TP of switch signals in Figure 99 and duty cycle of PWM (dL & dH). However, the first step is to find the relationship between angular velocity and operating parameters under steady-state conditions. From the torque equation, we have

$$T_e = J\frac{d\omega_m}{dt} + b\omega_m + T_L \tag{10}$$

Where Te is the generated electromagnetic torque, ωm is the rotor speed in rad/s, J is the rotor moment of inertia, b is the viscous friction constant and TL is the load torque.

The rotor induced torque of the induction machine is

$$T_e = \frac{3V_s^2 R_2 / s}{\omega_{syn}\left[\left(R_1 + R_2/s\right)^2 + \left(X_1 + X_2\right)^2\right]} \tag{11}$$

Where Vs is the magnitude of the applied phase voltage, ωsyn is the synchronous speed of the induction machine in rad/s, s is the slip, R1 and X1 refers to the stator impedance, R2 and X2 refers to the rotor impedance.

Substituting (11) into (10), we get

$$\frac{3V_s^2 R_2 / s}{\omega_{syn}\left[\left(R_1 + R_2/s\right)^2 + \left(X_1 + X_2\right)^2\right]} = J\frac{d\omega_m}{dt} + b\omega_m + T_L \tag{12}$$

(4.5)

At steady state, the shaft speed ωm and the slip s is constant. Meanwhile, stator and rotor impedances are also constant. As a result, (13) can be simplified as

$$k\frac{V_s^2}{\omega_{syn}} = b\omega_{mss} + T_L \tag{13}$$

Where ωmss is the rotor steady state speed and

$$k = \frac{3R_2 / s}{\left[\left(R_1 + R_2/s\right)^2 + \left(X_1 + X_2\right)^2\right]}$$

Therefore, the relationship between voltage magnitude and rotor speed can be obtained as

$$V_s = \sqrt{\frac{(b\omega_{mss} + T_L)\omega_{syn}}{k}} \quad (14)$$

In six step method, the magnitude of the applied phase voltage Vs is 2/3 of the DC link voltage VDC. If the duty cycle of the PWM is d, we get

$$\frac{2}{3} dV_{DC} = \sqrt{\frac{(b\omega_{mss} + T_L)\omega_{syn}}{k}} \quad (15)$$

Therefore, the relationship between the duty cycle and the rotor speed of the induction machine can be expressed as

$$d = \frac{3\sqrt{\frac{(b\omega_{mss} + T_L)\omega_{syn}}{k}}}{2V_{DC}} \quad (16)$$

From (16), the duty cycle is a function of the desired steady-state rotor speed. It can be used to find the necessary duty cycle to produce ωH and ωL. Let

$$d(\omega_{mss} = \omega_H) = d_H \quad (17)$$

$$d(\omega_{mss} = \omega_L) = d_L \quad (18)$$

Meanwhile, the frequency of the applied voltage can be calculated using (19) which is derived from (8) and (9). Slip is considered as a constant which equals to 5% in our simulation and experiment.

$$f = \frac{\omega_{ref} P}{2\pi(1-s)} \quad (19)$$

To obtain ωH, ωsyn can be calculated since slip is set to a constant value, which also determines the phase voltage frequency using (19). According to (16), the duty cycle of PWM must be equal to dH. Similarly, in order to obtain ωL, the duty cycle of PWM must be equal to dL.

Therefore, the state switching controller for induction machine can be implemented in the following procedure.

1) Find the following parameters of the induction machine from the manufacture's datasheet.

R1 and X1: Stator impedance

R2 and X2: Rotor impedance

b: Friction constant

2) Define the desired operating speed and specify the load torque TL. Specify ωH and ωL to cover the desired speed range.

3) Set slip to constant values for simplicity (5% in our case)

4) Use (16) to determine the values of dH and dL base on ωH and ωL.

5) Use (19) to calculate the frequency of the phase voltage (which also determines TP of switch signals in Figure 99)

At steady state, speed ripple is closely related to the sampling time. In order to minimize the speed ripple, the relationship between sampling time and speed ripple need to be defined. According to the torque equation listed in equation (10), we have the following differential equation:

$$\frac{d\omega_m}{dt} + \frac{b}{J}\omega_m = \frac{T_e - T_L}{J} \tag{20}$$

The speed response can be calculated as (21) by solving the above differential equation.

$$\omega_m(t) = \frac{T_e - T_L}{b} + Ce^{-\frac{b}{J}t} \tag{21}$$

where C is a constant. Suppose the steady state speed response can be shown in Figure 101, the upper side maximum speed ripple (ΔωH) happens after time t1 and the lower side maximum speed ripple (ΔωL) happens after t2.

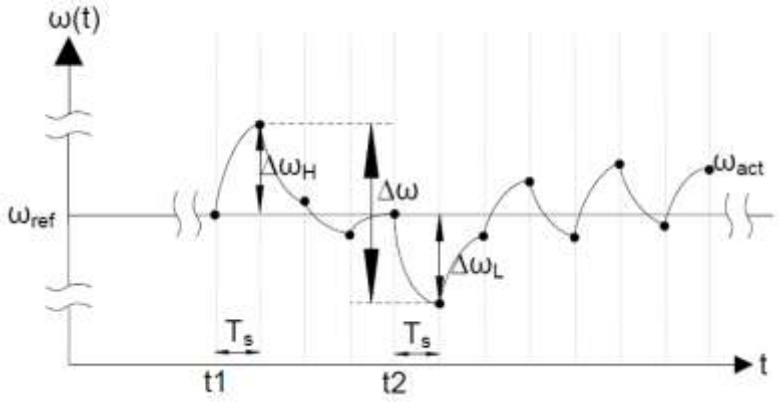


**Figure 101: Speed response in steady state**

At time t1, we have

$$\omega_m(t1) = \omega_{ref} = \frac{T_{e1} - T_L}{b} + Ce^{-\frac{b}{J}t1} \quad (22)$$

We get,

$$C = (\omega_{ref} - \frac{T_{e1} - T_L}{b})e^{\frac{b}{J}t1} \quad (23)$$

Therefore, at time t1+Ts,

$$\omega_m(t1 + T_s) = \frac{T_{e1} - T_L}{b} + (\omega_{ref} - \frac{T_{e1} - T_L}{b})e^{-\frac{b}{J}T_s} \quad (24)$$

$$\omega_m(t1 + T_s) = \omega_{ref} + \Delta\omega_H \quad (25)$$

During the sampling time period after t1, speed is increasing. We can define

$$T_{e1} - T_L = \Delta T_{em} \ (\Delta T_{em} > 0)$$

to get,

$$\Delta\omega_H = \frac{\Delta T_{em}}{b} + (\omega_{ref} - \frac{\Delta T_{em}}{b})e^{-\frac{b}{J}T_s} - \omega_{ref} \quad (26)$$

Similarly, at time t2,

$$\omega_m(t2) = \omega_{ref} = \frac{T_{e2} - T_L}{b} + Ce^{-\frac{b}{J}t2} \quad (27)$$

We get,

$$C = (\omega_{ref} - \frac{T_{e2} - T_L}{b})e^{\frac{b}{J}t2} \quad (28)$$

Meanwhile, at time t2+Ts,

$$\omega_m(t2 + T_s) = \frac{T_{e2} - T_L}{b} + (\omega_{ref} - \frac{T_{e2} - T_L}{b})e^{-\frac{b}{J}T_s} \quad (29)$$

$$\omega_m(t2+T_s)=\omega_{ref}-\Delta\omega_L \tag{30}$$

During the sampling time period after t2, speed is decreasing. Defining

$$T_{e2}-T_L=-\Delta T_{em}$$

we get,

$$\Delta\omega_L=\frac{\Delta T_{em}}{b}-(\omega_{ref}+\frac{\Delta T_{em}}{b})e^{-\frac{b}{J}T_s}+\omega_{ref} \tag{31}$$

Since

$$\Delta\omega=\Delta\omega_H+\Delta\omega_L$$

we have

$$\Delta\omega=2\frac{\Delta T_{em}}{b}(1-e^{-\frac{b}{J}T_s}) \tag{32}$$

As a result, we get the expression given in (33):

$$T_S=-\tau_m\ln\left(1-\frac{\Delta\omega}{2\omega_{\max}}\right) \tag{33}$$

where

$\tau_m$ is the mechanical time constant and ωmax is the maximum speed under no load condition.

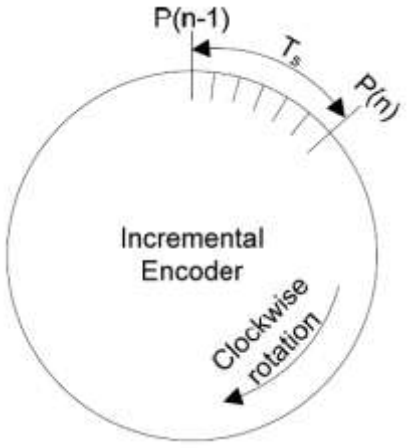


**Figure 102: Instantaneous speed read from an incremental encoder**

From (33), it can be seen that the smaller the sampling time results in better the speed tracking performance. However, in practical applications, speed tracking results is also limited by the resolution of the speed sensor. Suppose the encoder can generate Ptotal pulse per revolution and the speed of the shaft is ω rpm. The number of pulses generated in one second is ωPtotal/60. Therefore, the minimum sampling time (only one pulse can be detected within this sampling period) at speed ω is,

$$T_{S\_\min} = \frac{60}{\omega P_{total}} \tag{34}$$

This sampling time is often too small, which can cause significant instantaneous speed error. If an incremental encoder is used, instantaneous speed is defined in terms of pulses generated divided by its sampling time Ts and encoder's pulses-per-revolution Ptotal. This can be shown in Figure 102 and equations (35) and (36).

$$\omega(n) = 60\frac{P_{act}}{P_{total}T_s} \tag{35}$$

$$P_{act} = P(n) - P(n-1) \tag{36}$$

Where Pact is the actual pulses generated by the encoder during a sampling time Ts. Then, the speed error between reference speed and actual speed is,

$$e(n) = \omega_{ref}(n) - \omega_{act}(n) \tag{37}$$

$$e(n) = \frac{60}{P_{total}T_s}(P_{ref} - P_{act}) \tag{38}$$

In (38), Pref is reference pulses generated during each sampling time Ts. In order to minimize the instantaneous speed error, pulse error should be kept small (|Pref –Pact|=1) while sampling time Ts should be maintained as large as possible. This can be proved by experimental results shown in Figure 103 and Figure 104. Figure 103 and Figure 104 shows the instantaneous speed tracking error of the proposed state switching control under no load condition when reference speed is 1025rpm. Figure 103 shows that when sampling frequency is 5 kHz, the minimum pulse variation is one pulse which corresponds to 73.2 rpm in speed error (Ptotal =4096 pulses in our case). However, as shown in Figure 104, if the sampling frequency is increased to 10 kHz, the pulse variation stays at the minimum value (one pulse). But instantaneous speed error increases to 146.5 rpm since the sample time is half of the previous case. The detailed speed error versus sampling time under different conditions is plotted in Figure 105 through experiments. A range of sampling time (from 0.2ms to 2.8ms) is defined which ensures the performance of state switching control. In our case, 1ms (1kHz) is chosen as the sampling time, which not only ensures the speed tracking performance of state switching control, but also guarantees the fast response of the control strategy.

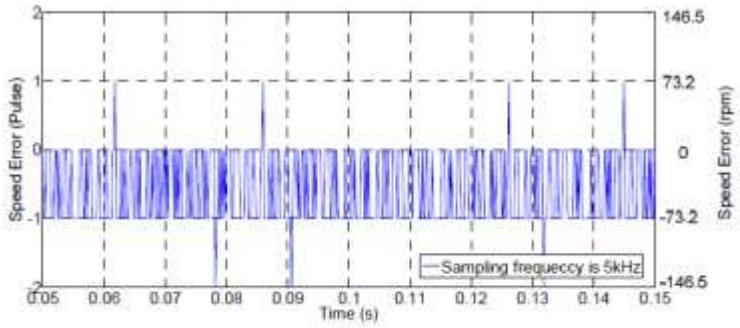


**Figure 103: Speed error when sampling frequency is 5kHz**

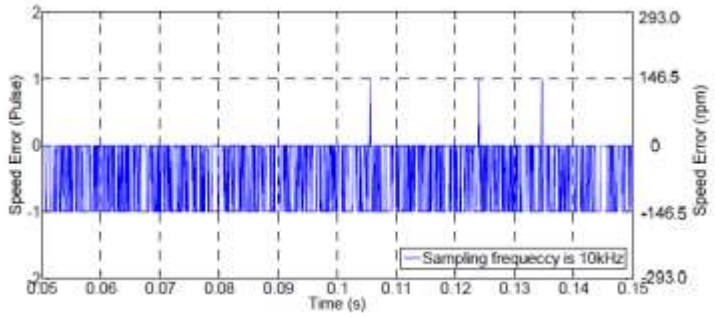


**Figure 104: Speed error when sampling frequency is 10kHz**

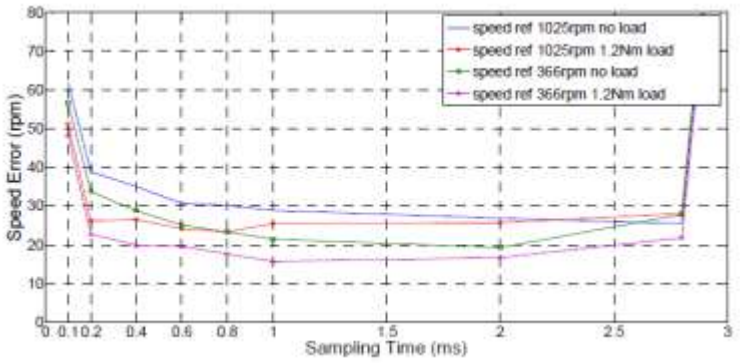


**Figure 105: Speed error under different conditions**

In practical implementation, deadband must be added to switch signals shown in Figure 99. Otherwise, it might cause short circuit when region changes and damage power components. For example, as shown in Figure 99, when region change from region I to region II, S5 tries to change from PWM to OFF state. At the same time, S6 tries to change from OFF state to PWM state. For safety consideration, S5 must be turned OFF before S6 is turned ON. As a result, deadband is required to be inserted into these signals. The insertion of deadband to switch signals can be easily done by turning OFF all the switches at the instant when transition of region occurs. The modified PWM six step waveforms can be illustrated in Figure 106 with deadband in red circles. However, this results in significant spikes in phase voltages during region transition moment. Figure 107 shows measured phase voltage and phase current in the

induction machine when gate signals in Figure 106 is applied to the switches with duty cycle of PWM equals to 100%. The six-stepped phase voltage can be clearly noticed and large spikes exist during region transition instant. These spikes are induced due to the rapid change of current flowing back to the source when all the switches are turned OFF. In order to eliminate these spikes, further improvement can be done by turning OFF two switches during transition. The improved gate signals are shown in Figure 108 with deadband in red circles. This time only two switches will be turned OFF during each transition. Figure 109 shows the hardware results of phase current and phase voltage with reduced spikes.

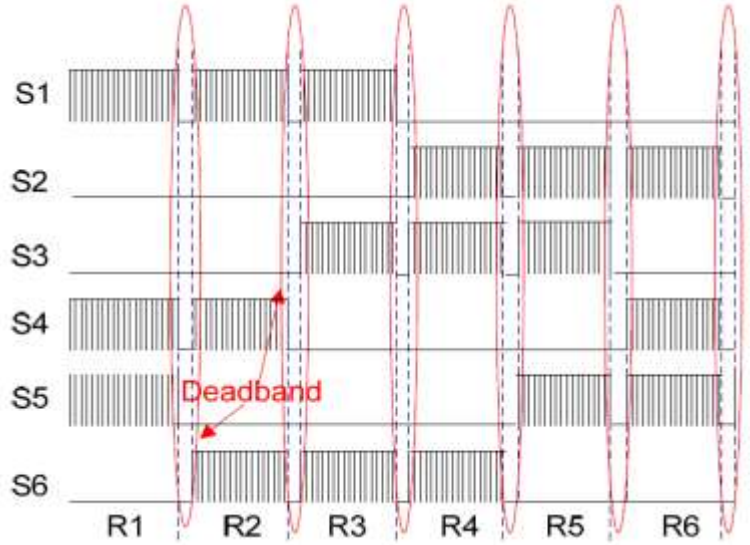


**Figure 106: PWM six-step waveform with deadband**

In order to verify the feasibility of the proposed state transition control of induction machine, simulation is implemented in Matlab/Simulink. The block diagram of the proposed state transition control of induction machine in simulation is shown in Figure 110, in which a 60Hz, 4 pole induction machine is used with a rated speed of 1725rpm.

Figure 111 shows the speed response of the proposed digitally controlled induction machine. Although the actual speed has a little oscillation during starting period, it quickly settles down and precisely tracks the reference speed.

Figure 112 to Figure 114 is simulation results in steady-state. Figure 112 shows the steady-state speed of the induction machine. The speed error between reference speed and actual speed is very small. Figure 113 shows the change of duty cycle during steady-state. Figure 114 shows the phase current of the induction machine.

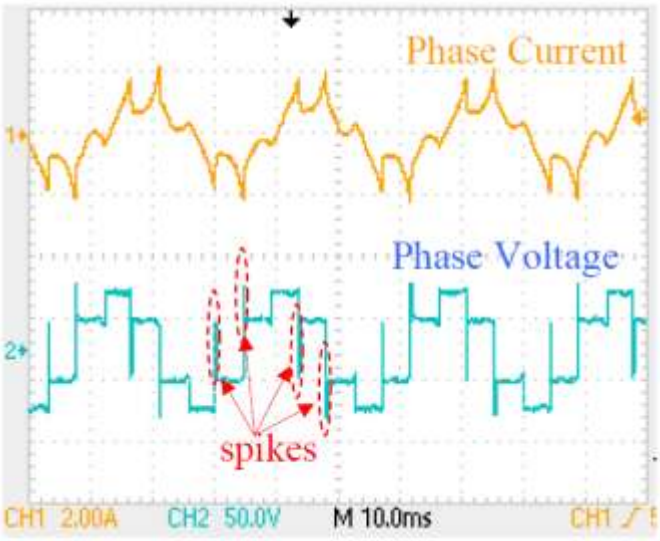


**Figure 107: Induction Machine Phase Voltage with spikes**

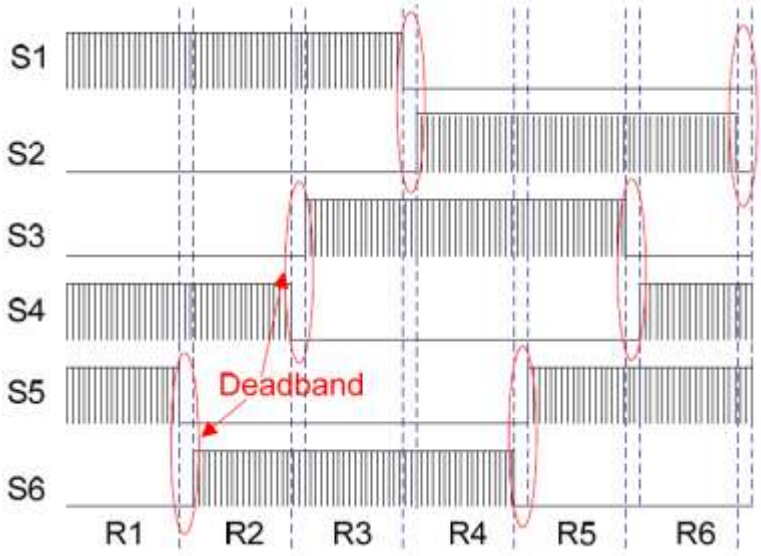


**Figure 108: PWM six-step waveform with deadband**

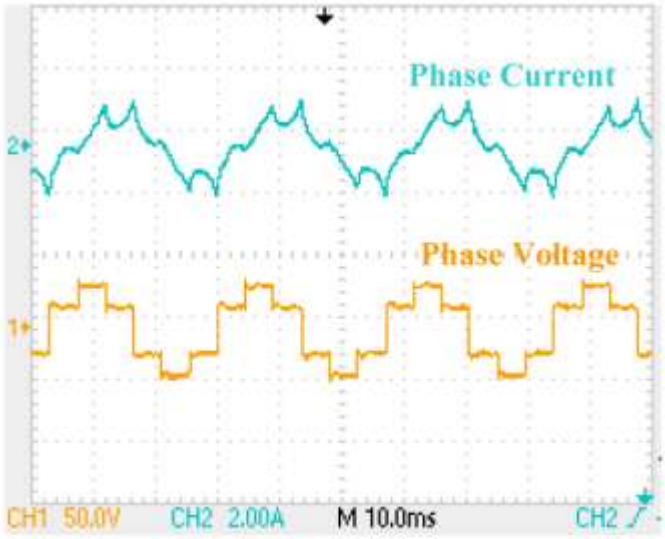


**Figure 109: PWM six-step waveform with deadband**

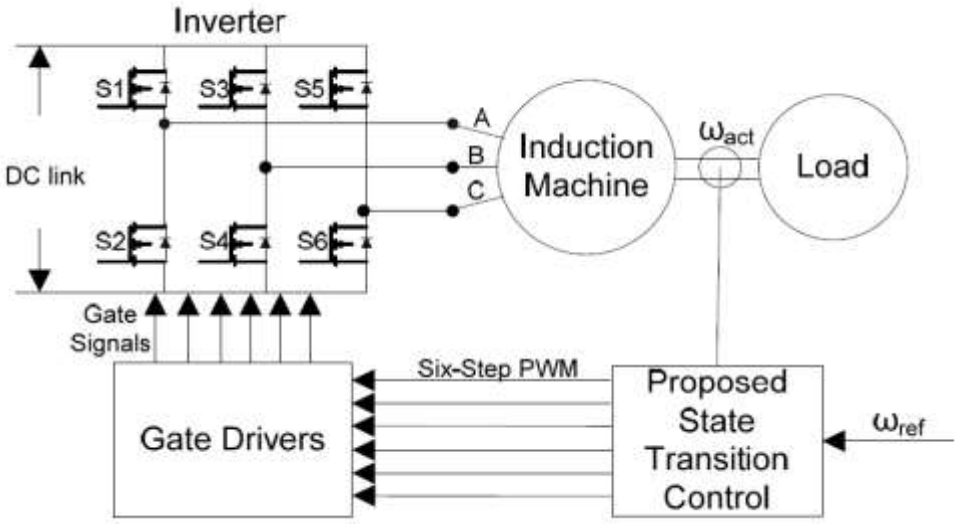


**Figure 110: Block diagram of the proposed state transition control of Induction Machine**

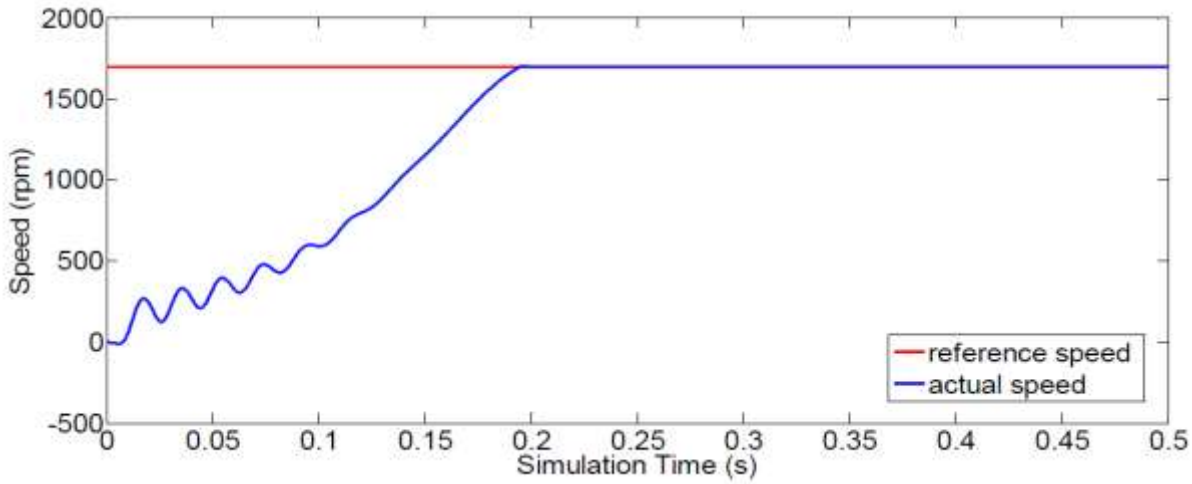


**Figure 111: Speed response of the state transition control of induction machine**

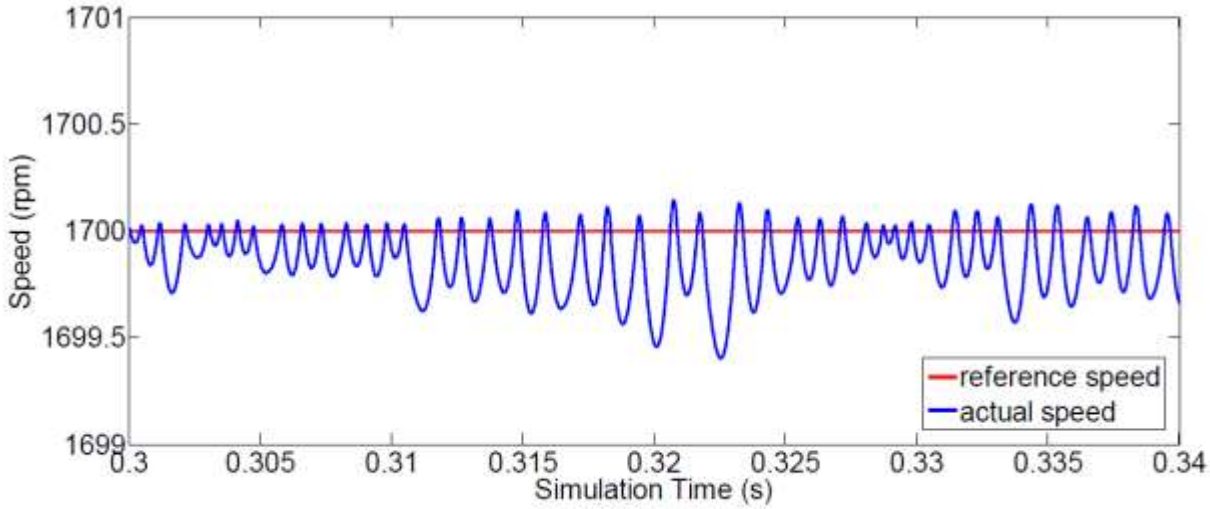


**Figure 112: Speed response in steady-state**

In order to verify the effectiveness of the proposed state transition control method for induction machine as well as its simulation results, an experimental setup has been developed which is shown in Figure 115. It includes a DC power supply, a TMS320F2812 based DSP controller, three phase inverter and gate drivers, voltage and current sensors, a torque sensor, an induction machine and a PM DC Load. Specifications regarding the induction machine and the PM DC load are listed in Table 9.

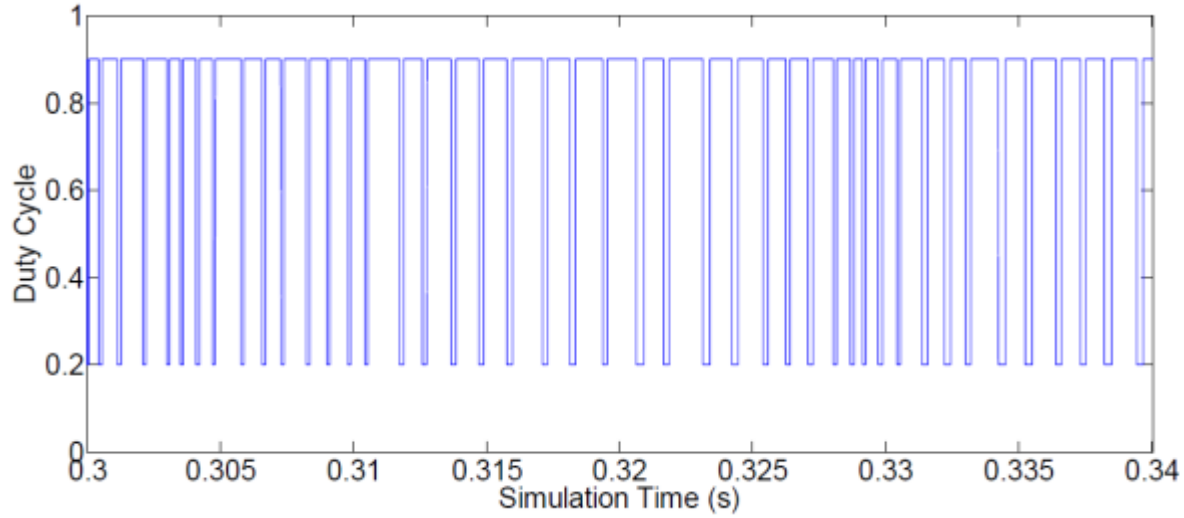


**Figure 113: Change of duty cycle in steady-state**

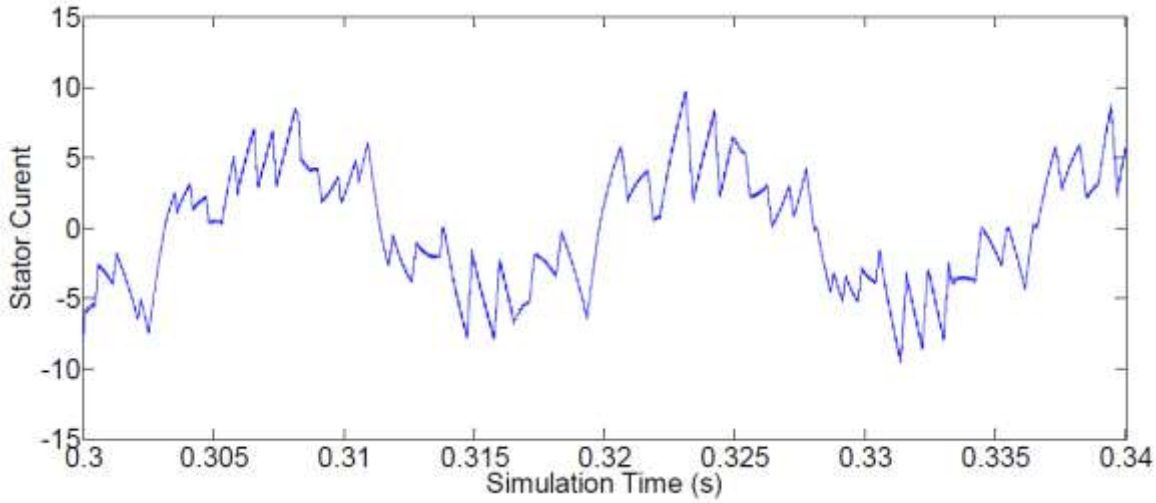


**Figure 114: State current in steady-state**

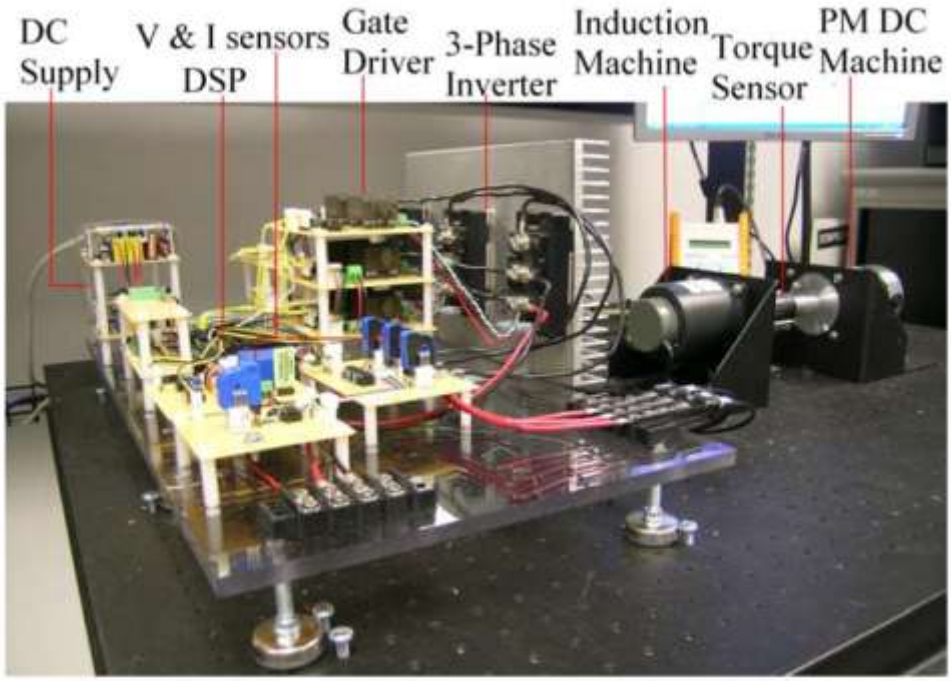


**Figure 115: Hardware setup for experimental verification of proposed state transition control strategy of an Induction Machine**

**Table 9: Parameters of the Induction Machine and DC Brush Load Used**

| | Induction Machine | PM DC Load |
|---|---|---|
| Rated Power | 130 watts | 250 watts |
| Rated RPM | 3396 | 4000 |
| Rated Volts | 30VAC | 42V |
| Rated Current | 3.93 A/phase | 8.4 A/phase |
| No. of poles | 4 | 2 |
| No. of phases | 3 | N/A |

Figure 116 to Figure 123 show experimental results obtained from the setup under different operating conditions. Figure 116 shows the speed response of the induction machine when reference speed is 2850rpm (84% of the rated speed) and load is 0.15Nm. Figure 117 shows the corresponding duty cycle. From these two figures, we find out that the speed response can be divided into two regions: acceleration and steady state (constant speed). During acceleration, a constant high duty cycle PWM is applied to the induction machine since the reference speed is greater than actual speed. During steady state, the duty cycle of PWM begins to switch between high duty cycle and low duty cycle since the actual speed is varying about the reference speed. The current profile during the acceleration is shown in Figure 118 and the current profile during the steady state is shown in Figure 119.

Similarly, Figure 120 and Figure 121 show results when the reference speed is 2250rpm (66% of the rated speed) and 1125rpm (33% of the rated speed) respectively and load is 0.15Nm. From these figures, it can be noticed that the proposed state transition control method has a wide range of speed control capability.

In order to test the performance of the control strategy for sensitivity to change in operating conditions, a step change in reference speed was applied to the machine. Figure 122 and Figure 123 shows the response of the induction machine when reference speed was changed.

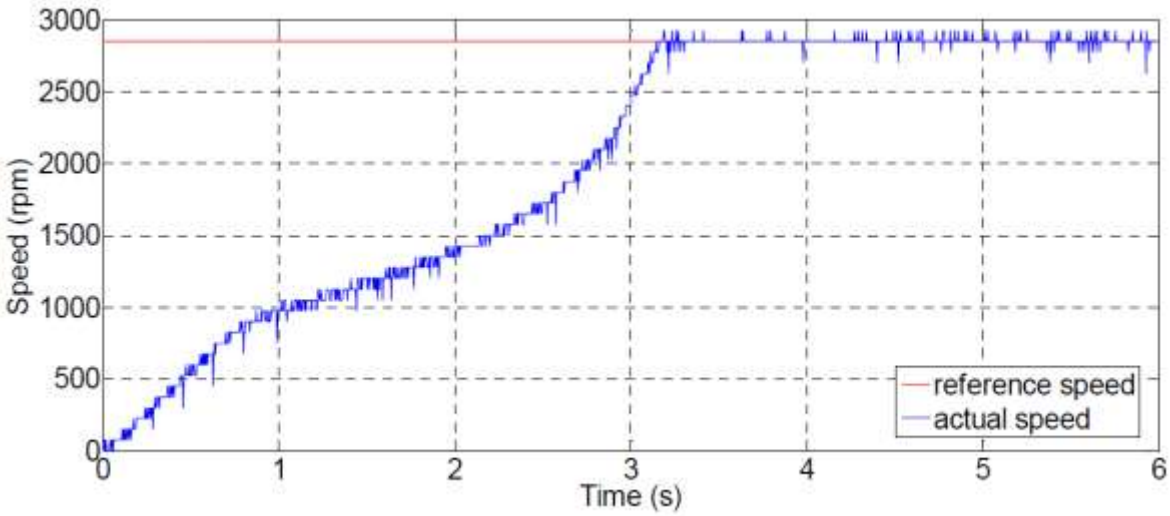


**Figure 116: Speed response when reference speed is 2850rpm**

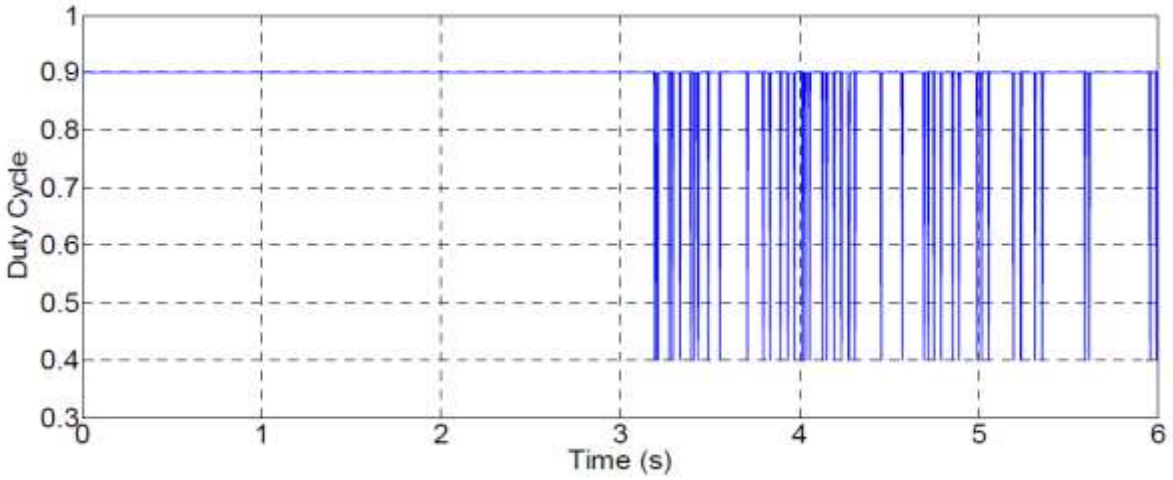


**Figure 117: PWM duty cycle profile when reference speed is 2850rpm**

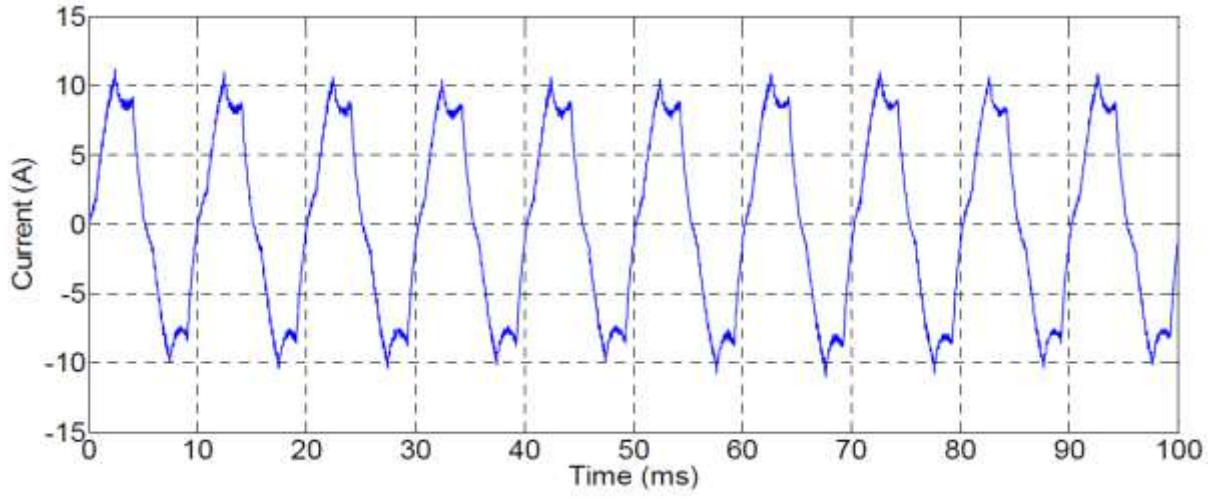


**Figure 118: Phase current of Induction machine during start-up when reference speed is 2850rpm**

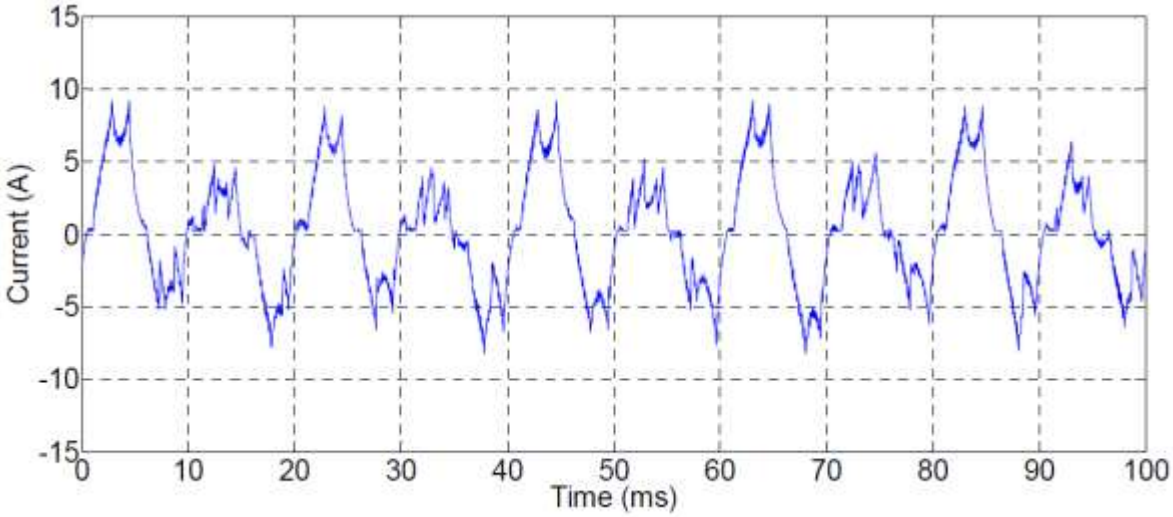


**Figure 119: Phase current of Induction Machine during steady-state when reference speed is 2850rpm**

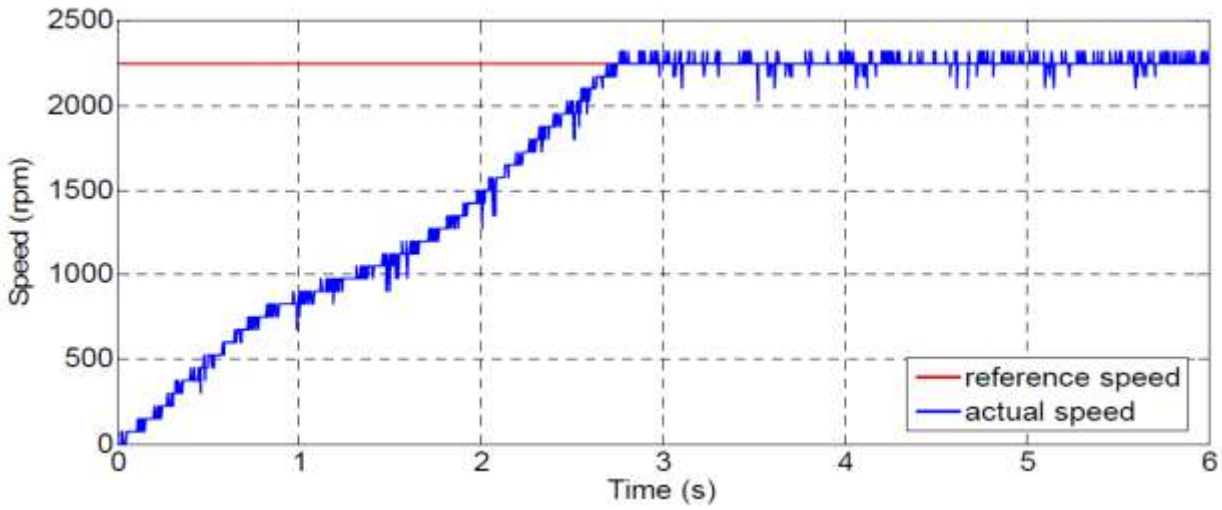


**Figure 120: Speed response when reference speed is 2250rpm**

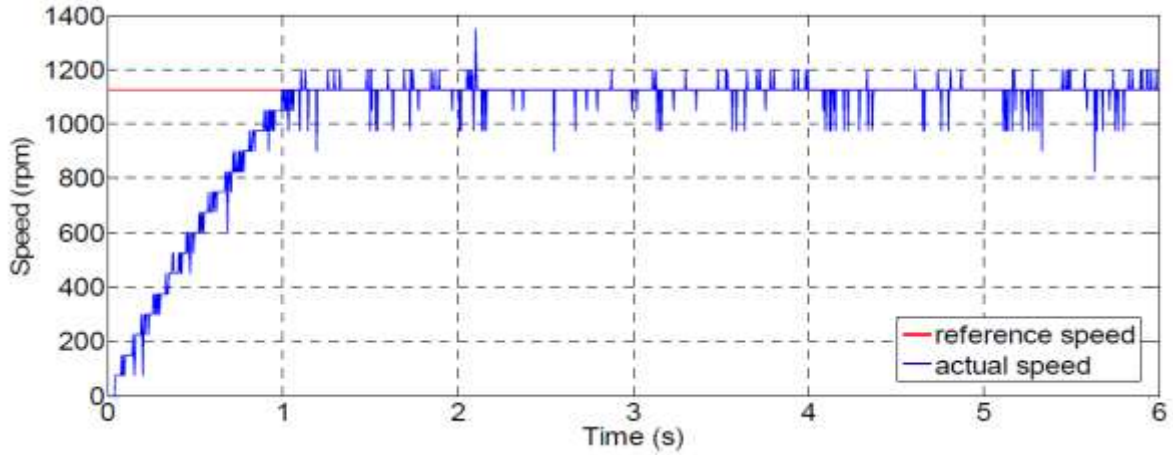


**Figure 121: Speed response when reference speed is 1125rpm**

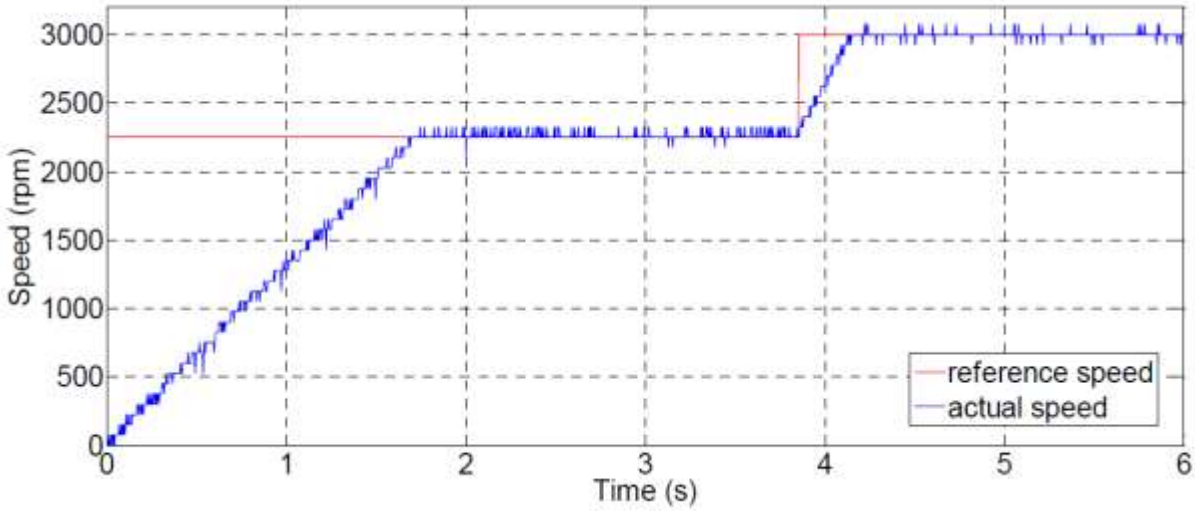


**Figure 122: Step change of speed from 2250rpm to 3000rpm**

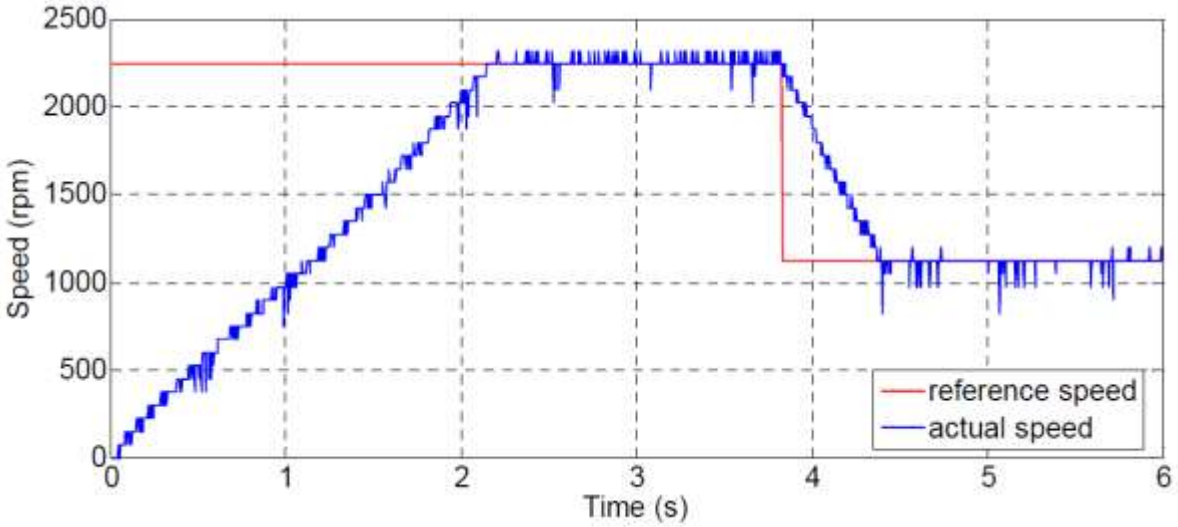


**Figure 123: Step change of speed from 2250rpm to 1125rpm**

From the results obtained, it can be seen that the speed ripple was found in an acceptable range under different conditions. This shows the effectiveness of the control scheme. In addition, the system responds to any change in speed command within an acceptable time period.

In order to further validate the effectiveness of the proposed state switching control. The experimental setup has been upgraded to PCB boards with kilowatt level induction machine installed which is shown in Figure 124. It includes a 3kW PM DC Load, a 2.2kW induction machine, a speed encoder, a TMS320F2812 based DSP controller, three-phase inverter and gate drivers. Specifications of the induction machine and the PM Dynamometer are listed in Table 10.

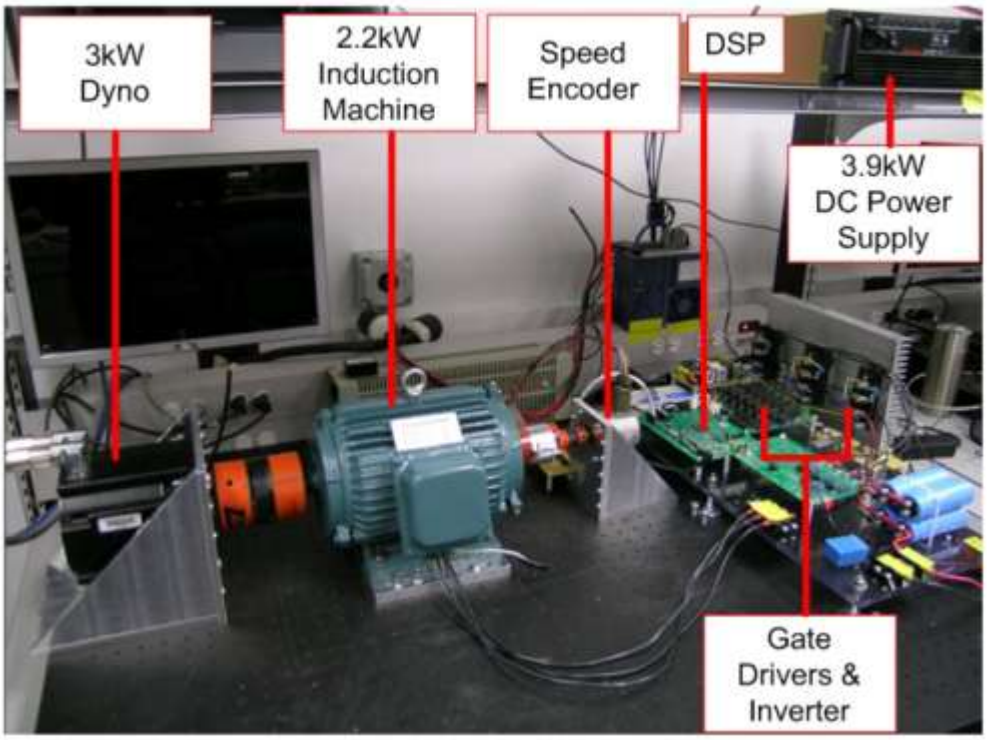


**Figure 124: Hardware setup for experimental verification of proposed state switching**

**Table 10: Parameters of the Induction Machine and DC Brush Load Used**

| | Induction Machine | PM Dyno |
|---|---|---|
| Rated Power | 2.2kW | 3 kW |
| Rated RPM | 1420 | 6000 |
| Rated Volts | 380/Y Conn. | 640DC |
| Rated Current | 5A/phase | 12.4A/phase |
| No. of poles | 4 | N/A |
| No. of phases | 3 | 3 |

Figure 125 to Figure 132 show experimental results obtained from the setup under different operating conditions. Figure 125 shows the speed response of the induction machine when reference speed is 1025rpm under a load torque of 1Nm. It can be seen that the actual speed of the induction machine quickly settles down to the reference and tracks precisely without any overshoots, which verifies fast dynamic response of this control method. Figure 126 shows the phase current profile and the change of PWM duty cycle between DH and DL. As mentioned previously, presence of harmonics in the phase current is the main trade-off in the implementation of this control technique.

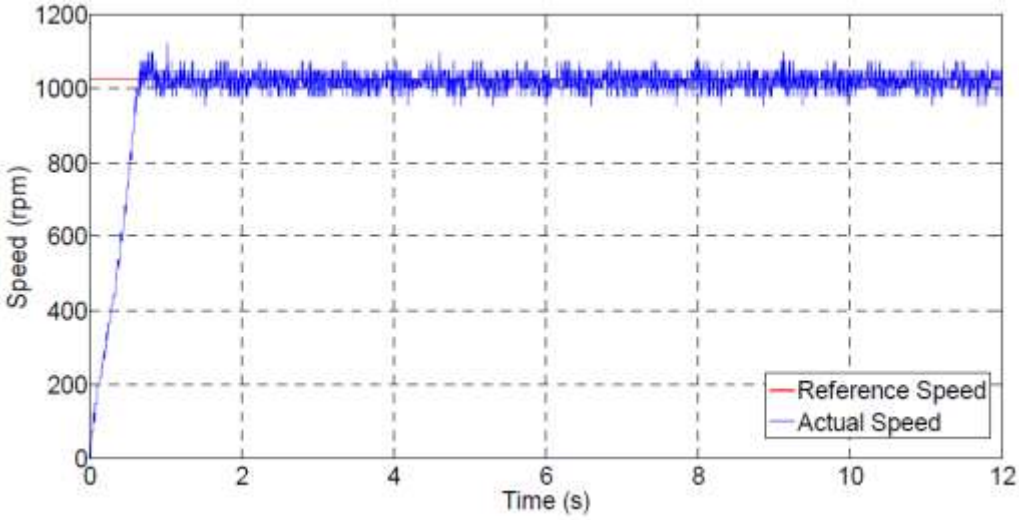


**Figure 125: Speed response when reference speed is 1025rpm and load torque is 1Nm**

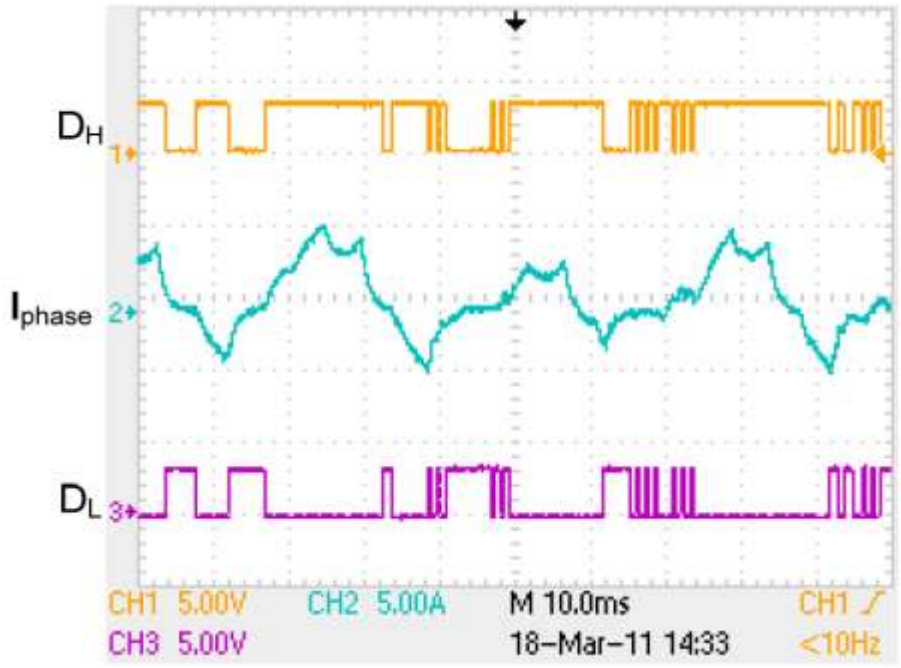


**Figure 126: Phase current and change of PWM duty cycle when reference speed is 1025rpm**

Similarly, Figure 127 and Figure 128 show results when reference speed is 366rpm and load is 1Nm. From these figures, it can be noticed that the proposed state switching control method also has a wide range of speed regulation capability.

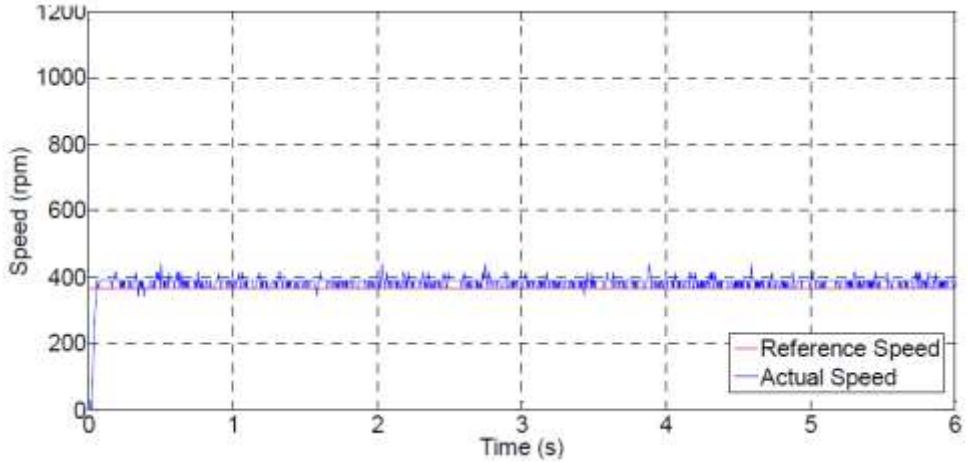


**Figure 127: Speed response when reference speed is 366rpm and load torque is 1Nm**

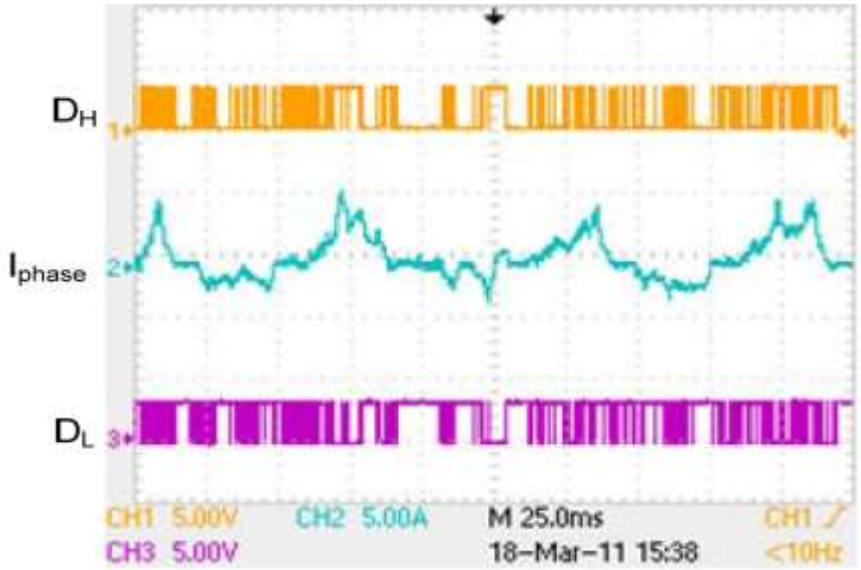


**Figure 128: Phase current and change of PWM duty cycle when reference speed is 366rpm**

In order to test the performance of the control strategy for sensitivity to change in operating conditions, a step change in load torque and reference speed was applied to the machine. Figure 129 shows the speed response of the induction machine when load torque was changed from 0.5Nm to 1.5Nm. Figure 130 and Figure 131 shows the phase current, change of PWM duty cycle before and after torque change respectively. Figure 132 shows the speed response of the induction machine when reference speed was changed from 1025rpm to 366rpm (load torque is 1Nm). The measured results show that the proposed control strategy allows the system to respond to any change in speed command within an acceptable time period.

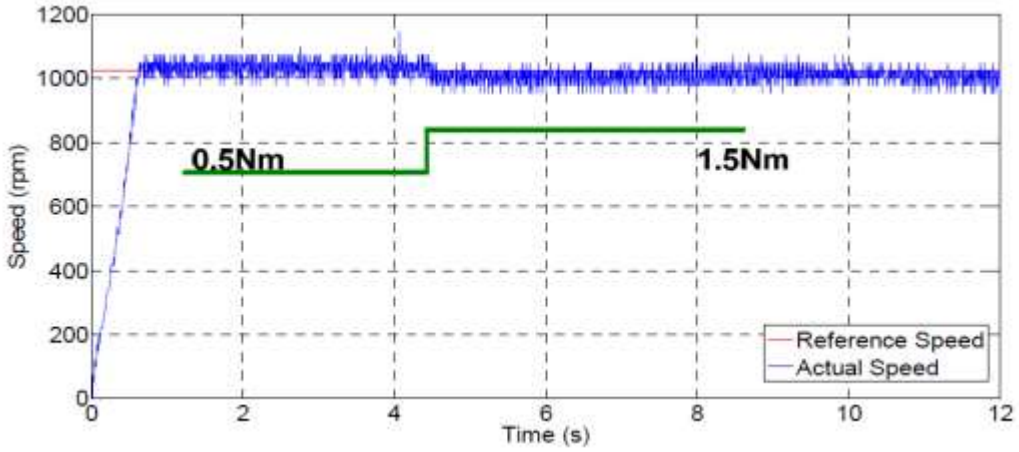


**Figure 129: Speed response when reference speed is 1025rpm and load torque changes from 0.5Nm to 1.5Nm**

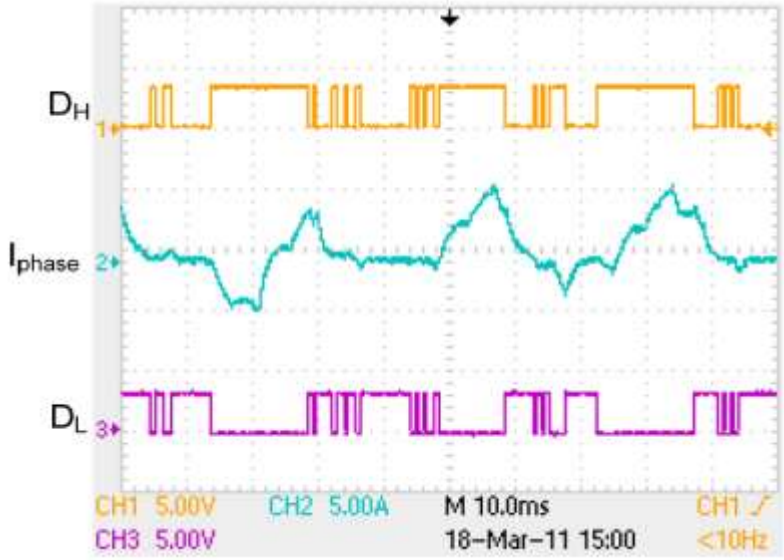


**Figure 130: Phase current and change of PWM duty cycle when load torque is 0.5Nm**

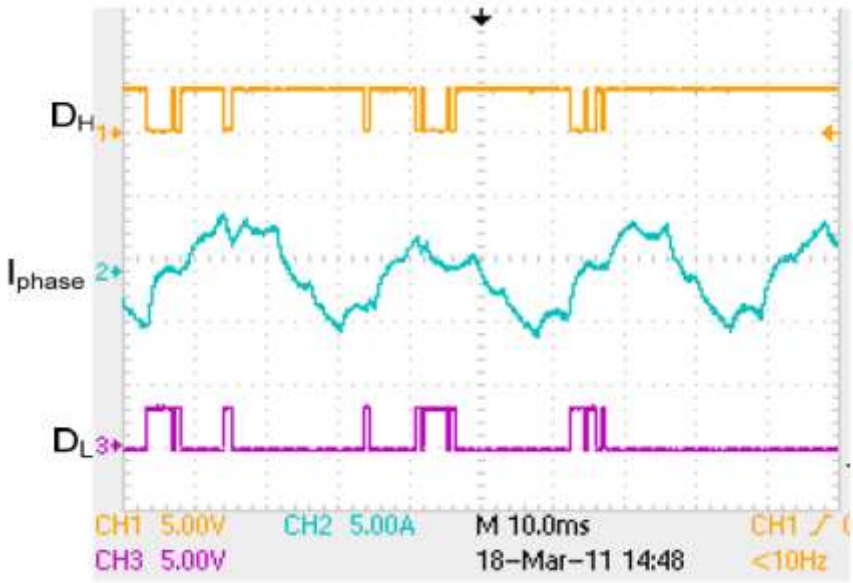


**Figure 131: Phase current and change of PWM duty cycle when load torque is 1.5Nm**

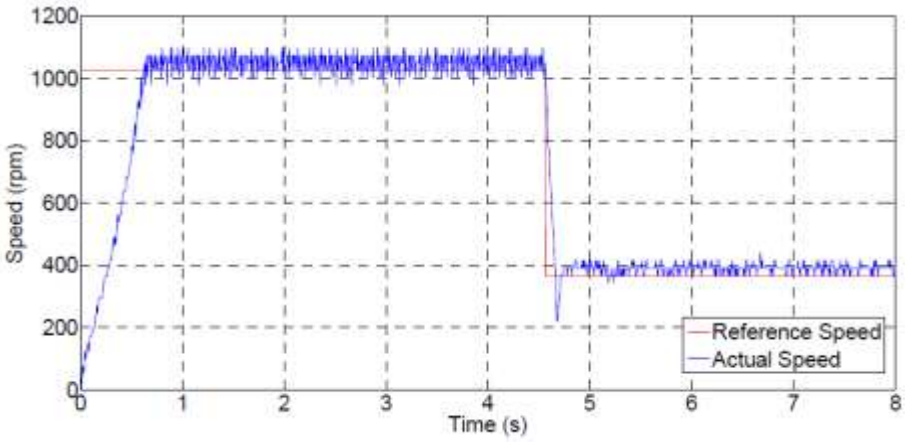


**Figure 132: Speed response when reference speed changes from 1025rpm to 366rpm**

The block diagram of the proposed state transition control of induction generator in Simulink is shown in Figure 133. A 60Hz, 4 pole induction machine is used with a rated speed of 1725rpm. Two different PWM duty cycles are defined at 30% and 90%. Simulation results are shown in Figure 134 and Figure 135. Figure 134 shows the speed response of the proposed digitally controlled induction machine. The speed quickly settles down and precisely tracks the reference speed. Figure 135 shows the steady-state speed error between reference speed and actual speed and the corresponding duty cycle adjustment.

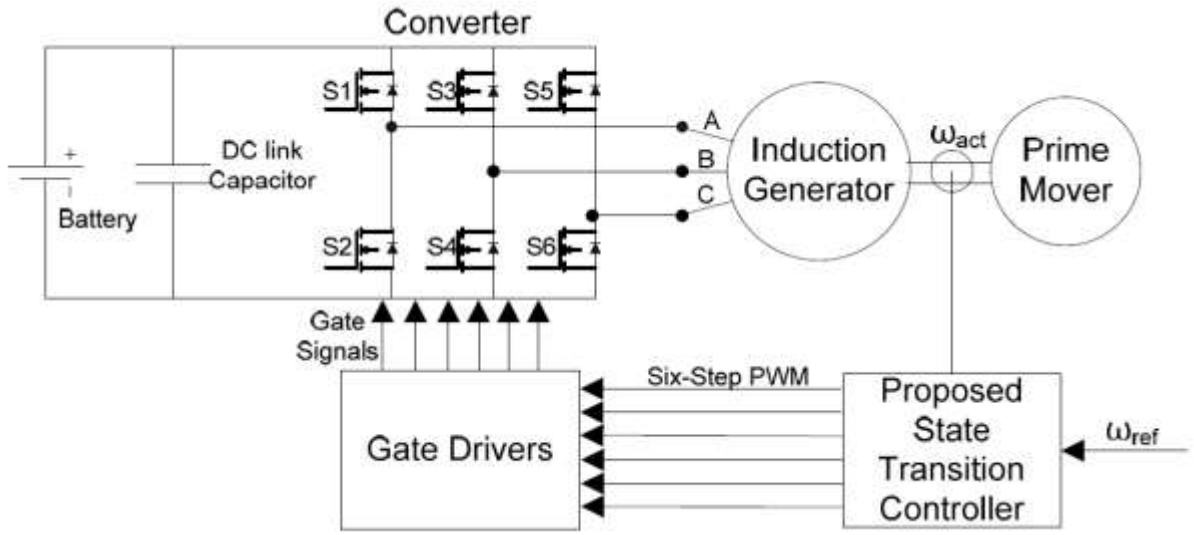


**Figure 133: Block diagram of state transition control of Induction Generator**

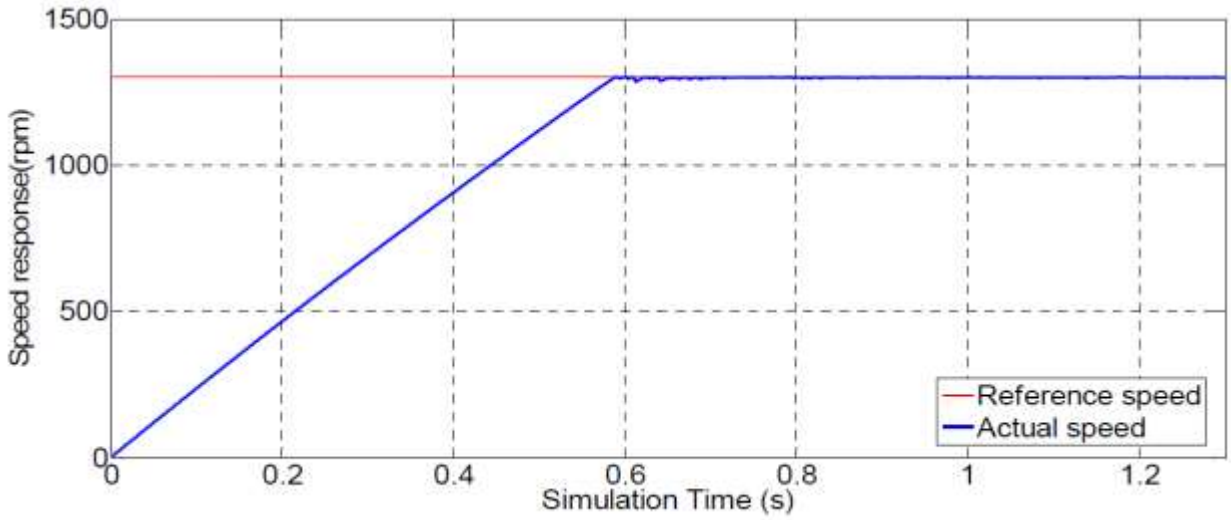


**Figure 134: Speed response of the induction generator**

The proposed state switching control method for induction generator is verified on the 2.3kW induction machine setup, as shown in Figure 136. Figure 137 to Figure 145 show experimental results obtained from the setup under different operating conditions. Figure 137 shows the speed response of the induction generator when reference speed is set to 1025rpm and the torque of prime mover is 1Nm. Since the prime mover is turned on before starting the induction generator, initial speed at startup increases to 1500rpm. Once the induction generator is started and state switching control is applied, speed quickly settles down to the reference speed with a steady state error lower than 7%. Figure 138 shows the generated DC link voltage and DC link current flowing into the dump resistor and the change of duty cycle between DH and DL. It is clear that the average DC link current is positive which confirms the operation of the IM in generating mode. Figure 139 shows the steady state phase current as well as

the change of duty cycle. It can be observed that the phase current has significant harmonics which is the main trade-off in the implementation of this control technique.

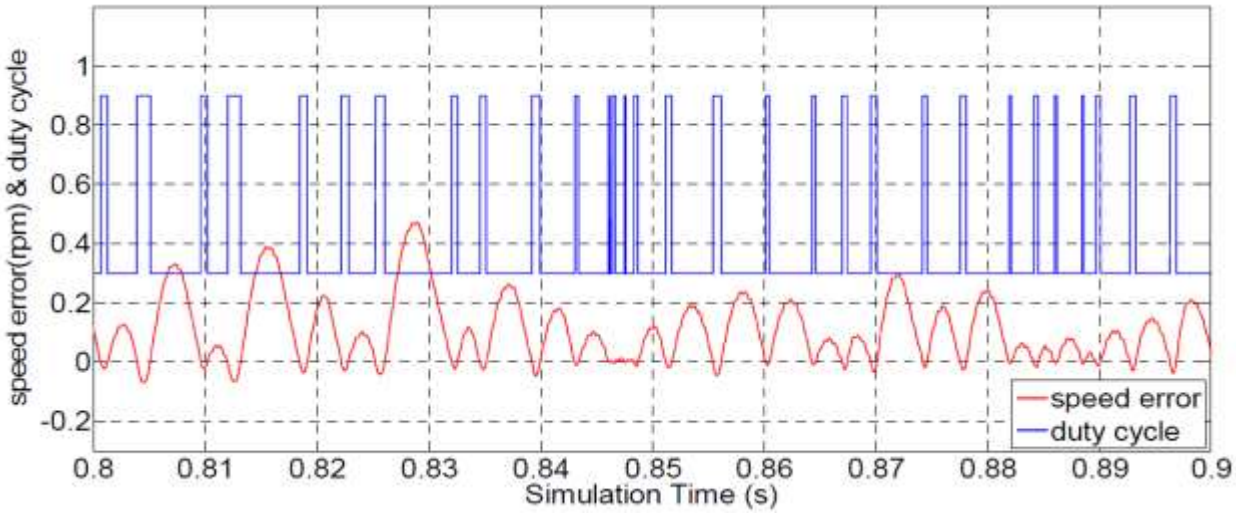


**Figure 135: Steady state error and change of duty cycle**

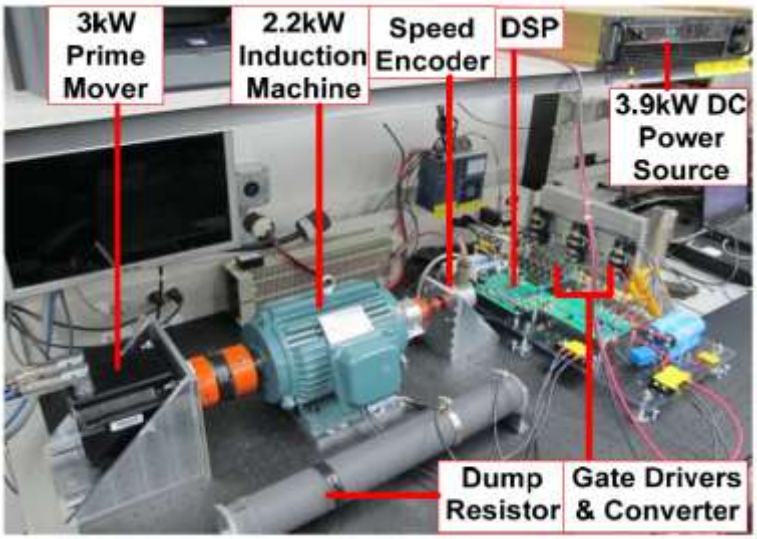


**Figure 136: Hardware setup for experimental verification of proposed state switching control strategy of an Induction Generator**

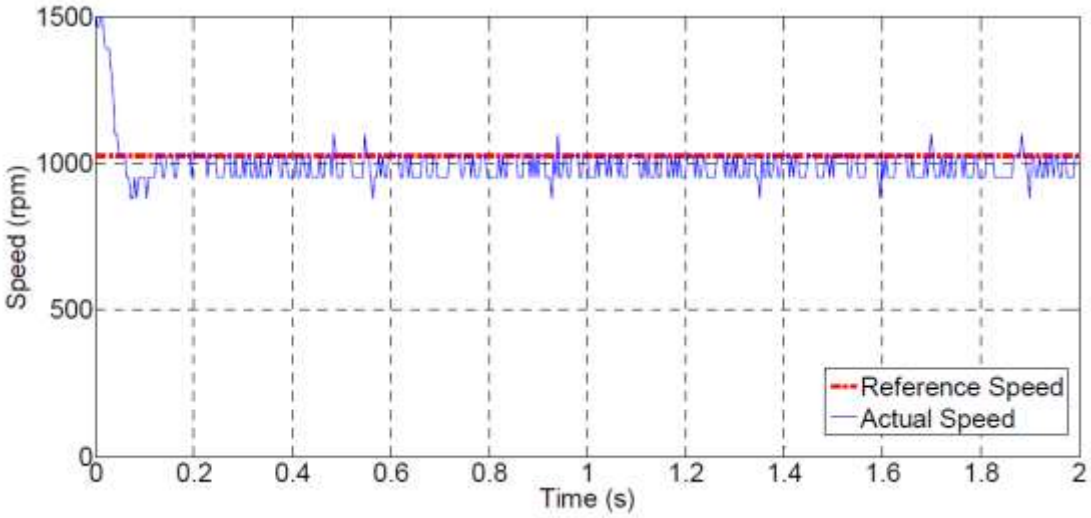


**Figure 137: Speed response when reference speed is 1025 rpm**

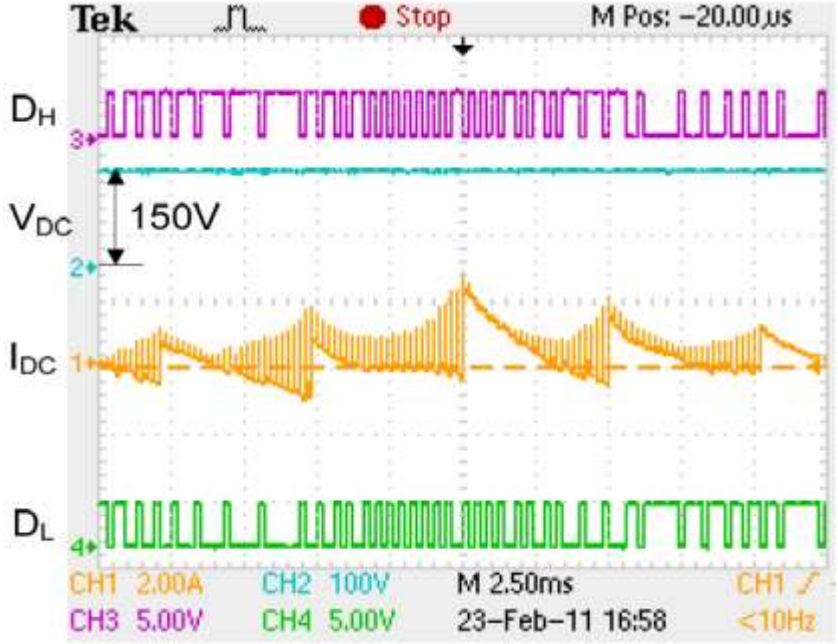


**Figure 138: DC link voltage, current and change of duty cycle**


**Figure 139: Phase current and change of duty cycle**

Figure 140 to Figure 142 show results when the reference speed is 586rpm and the prime mover torque is 1Nm. Figure 140 shows the speed response of the induction generator. The initial speed is 1150rpm before exciting the induction generator. After the induction generator is excited, shaft speed quickly goes down and tracks the reference speed. Figure 141 shows the DC link voltage and DC link current flowing into the dump resistor and the change of duty cycle. Figure 142 shows the steady state phase current and the change of duty cycle. From these figures, it can be noticed that the proposed state switching control method also has a good speed tracking performance at relatively low speeds.

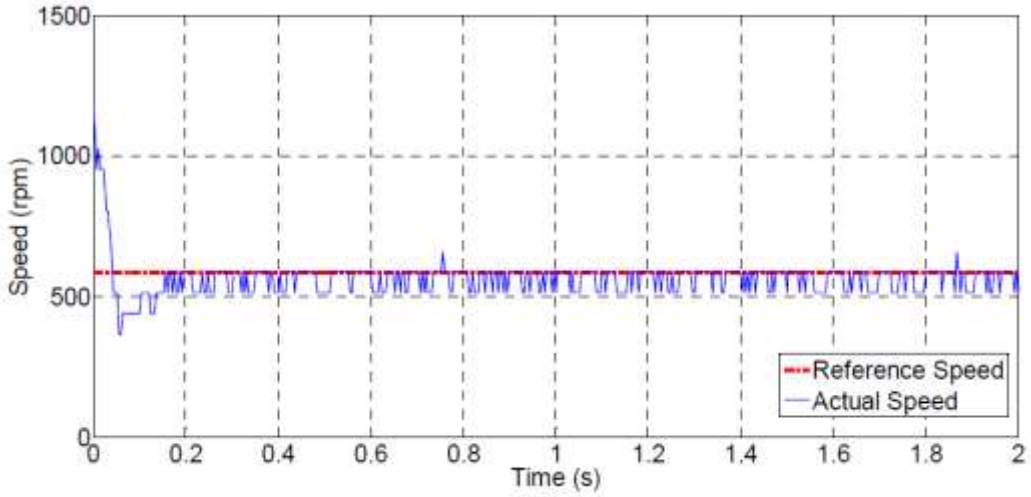


**Figure 140: Speed response when reference speed is 586rpm**

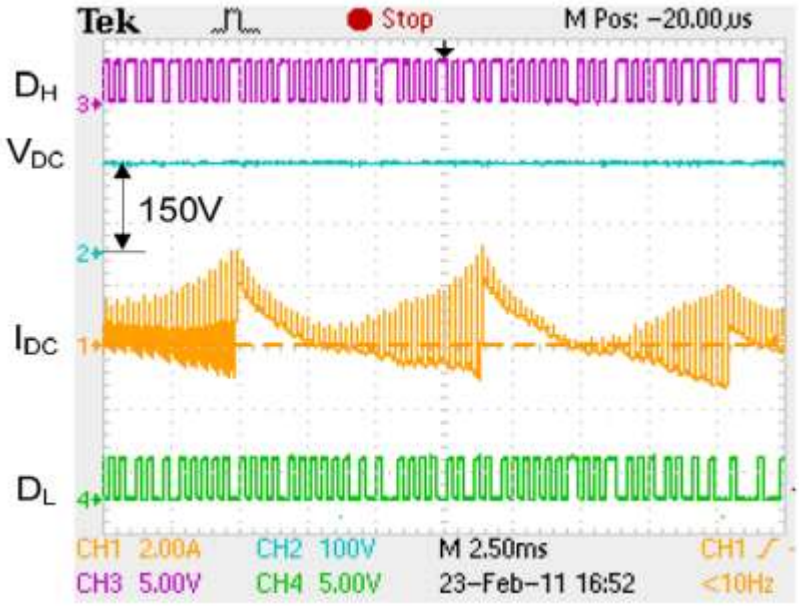


**Figure 141: DC link voltage, current and change of duty cycle**

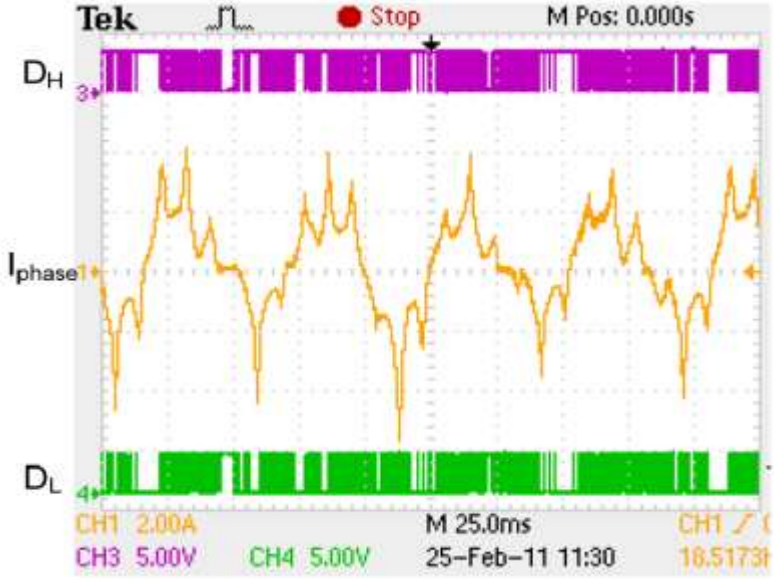


**Figure 142: Phase current and change of duty cycle**

The speed response and the generated DC link voltage and current for a step change in torque from 1Nm to 2Nm from the prime mover are shown in Figure 143 and Figure 144 respectively. It is clear that when the prime mover torque becomes larger, more power is generated and transmitted to the dump resistor. In addition, a step change of reference speed is also applied to the machine. Figure 145 shows the speed response of the induction generator when reference speed changes from 1025rpm to 586rpm. The actual speed again can track the reference speed precisely.

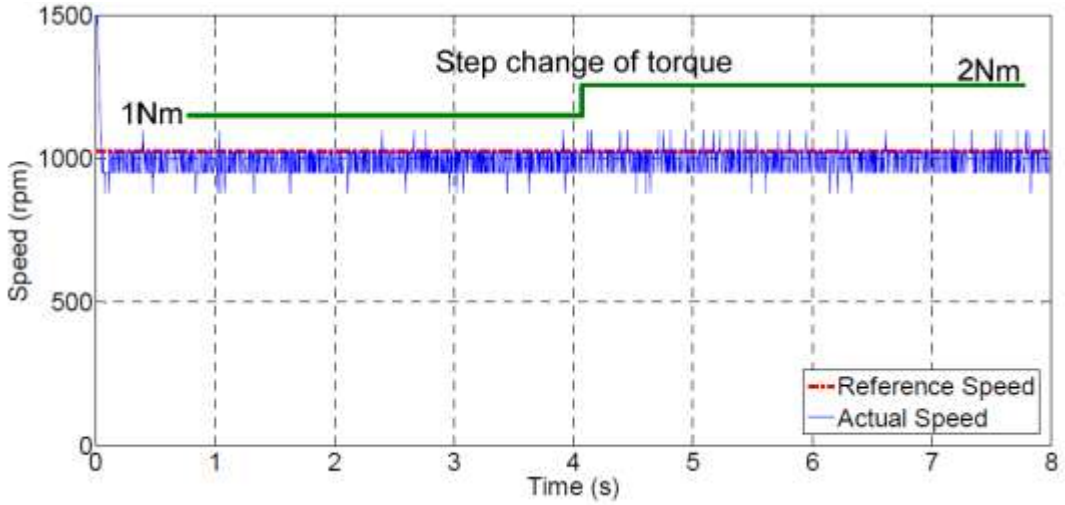


**Figure 143: Speed response under step change of prime mover torque**

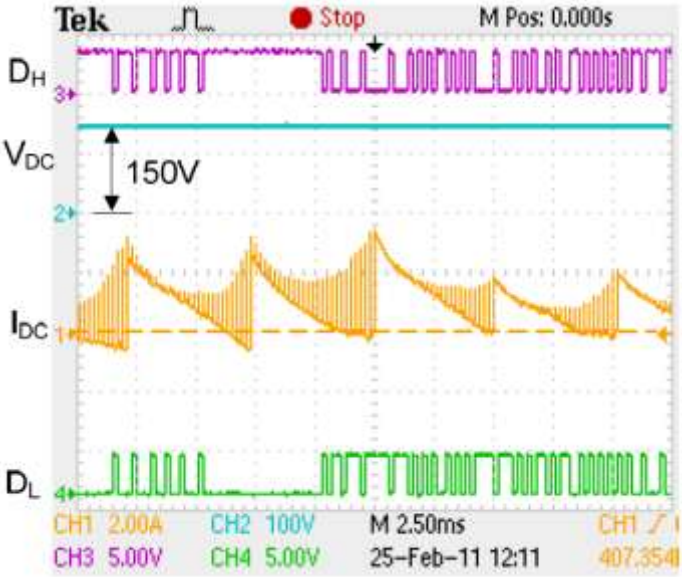


**Figure 144: DC link voltage, current and change of duty cycle at 2Nm**

In this section, state switching control is designed and implemented for induction machine. From simulation results and some hardware results, it can be found that state switching control can control three-phase AC machine with highly acceptable performance but requires least system information. Therefore, state switching control can be a very good option to work as a back-up control strategy.

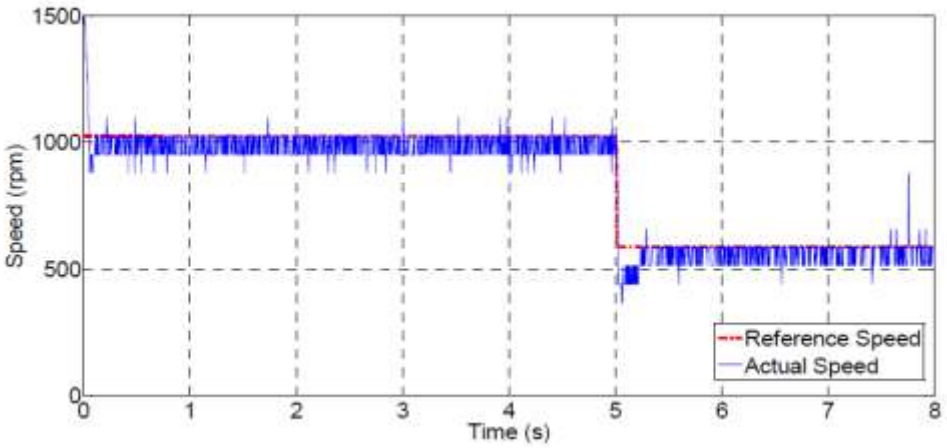


**Figure 145: Speed response under step change of reference speed**

### E5. Survivable Operation of Induction Machine

Survivable operation of electric machines is required in wind power generation especially for those wind turbines located in remote areas. Failure of current sensors could bring the wind generator to a standstill and cause reduction of wind plant availability in the absence of immediate maintenance or redundancies, which in turn, could affect the overall stability of the power system. This section proposes a technique for survivable operation of three-phase Induction Machine drives in the event of current sensor failure by switching from vector control to state switching control with smooth transition strategy. A simple current sensor failure detection method keeps monitoring the conditions of current sensors and can trigger a fault flag if current sensor fails. Simulation and experimental results are included to show the effectiveness of the proposed strategy.

The proposed survivable drive for IM is illustrated in Figure 146. The basic idea is that if system is healthy, vector control is activated to regulate the speed and maximize the performance based on three-phase current feedbacks and one speed feedback. At the same time, a fault detection algorithm continuously monitors the health of vector controlled IM system. If the system shows signs of failure owing to a fault in current sensor(s), the fault detection algorithm can sense it. Vector control is then disabled and state switching control is activated to continue regulating the IM speed only using speed feedback. Therefore, the rules that the survivable drive algorithm follows are extremely simple and are ideally suited for hardware implementation. It can be represented in terms of one “IF ELSE” statement.

IF, Fault Detection = 0

Vector Control = Enable;

State Switching Control = Disable.

Else,

Vector Control = Disable;

State Switching Control = Enable.

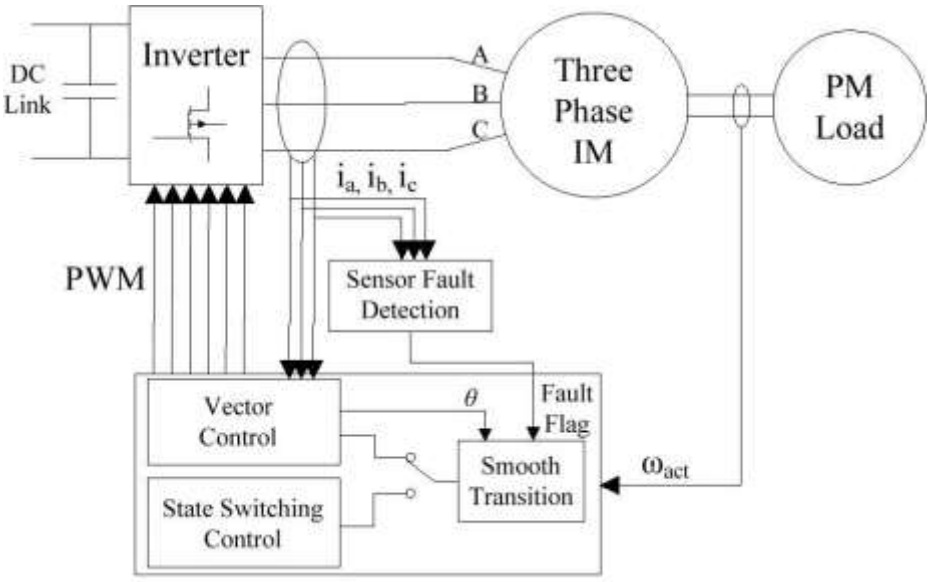


**Figure 146: Proposed survivable drive for three-phase IM**

The current sensor failure detection method presented in this report is based on the Kirchhoff's law. The sum of all three phase currents (Isum) equals zero. If current sensor fails, this value changes dramatically. Theoretically, sensor failure detection can be achieved by comparing Isum to zero, which is applicable in Simulink. However, in practical applications, Isum usually is a small value which oscillates around zero, as shown in Figure 147. Therefore, a threshold value (Ith) which is larger than |Isum| needs to be defined to monitor the health of current sensors. If |Isum| exceeds the threshold value, a fault flag is generated.

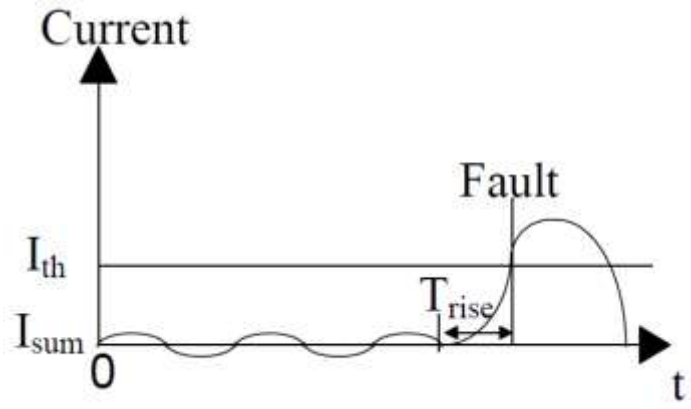


**Figure 147: Basic principle of current sensor failure detection**

The definition of this threshold value (Ith) is subject to the output voltage type of current sensor—with DC offset or without DC offset.

Current Sensor without DC Offset: the relationship between input current and output voltage signal can be expressed in equation (39), while equation (40) is used to calculate the input current in microprocessor (DSP).

$$V_{out} = \frac{1}{k} I_{in} \quad \textbf{(39)}$$

$$I_{calc} = kV_{out} \quad \textbf{(40)}$$

Where Vout refers to the output voltage signal of the current sensor, Iin is the input current. Icals is the calculated value of input current. With this kind of current sensors, Vout will be zero when current sensor fails. As a result, Isum becomes the sum of the remaining current sensors' outputs, which usually is a sinusoidal waveform with its magnitude significantly larger than the value of Isum in normal condition. As shown in Figure 148, in order to quickly detect the failure of current sensor, the threshold value (Ith) should be defined slightly greater than the maximum possible value of |Isum| for the purpose of minimizing the rise time Trise of |Isum| to generate a fault signal. The maximum possible |Isum| can be found by running the IM under different load conditions. It must be mentioned that this method is not applicable when all current sensors fail simultaneously since Isum remains zero in this case. This fault can be detected by comparing |Ia +Ib| to Ith. The fault detection logic for current sensor without DC offset can be shown in Figure 148.

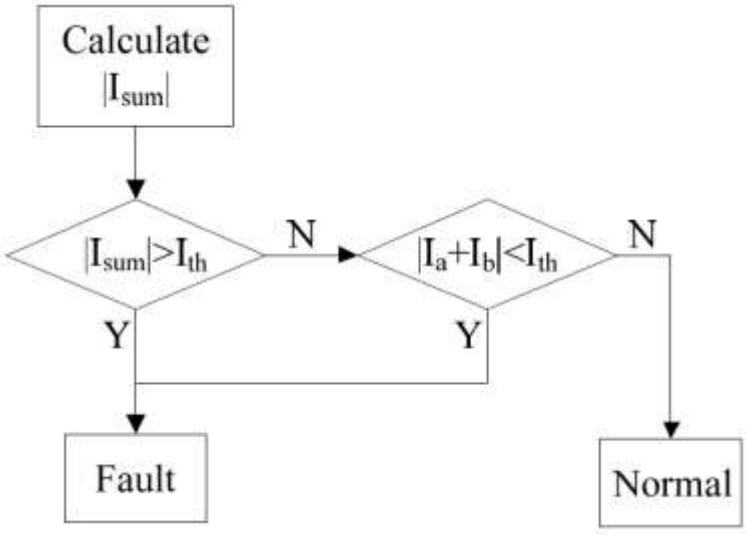


**Figure 148: Current sensor failure detection method (without DC offset)**

Current Sensor with DC Offset: Similarly, the current sensor with DC offset equals to kDC functions as (41) while equation (42) is implemented in DSP to calculate the input current.

$$V_{out} = \frac{1}{k} I_{in} + k_{DC} \quad (41)$$

$$I_{calc} = k(V_{out} - k_{DC}) \quad (42)$$

With this kind of current sensor, the threshold value (Ith) is much easier to define. This is because when a current sensor fails, Vout becomes zero, which leads to a sudden increase in the DSP-calculated current |Icalc| (|Icalc|= k*kDC). Therefore, Ith can be defined slightly smaller than k*kDC. If the value of Ith is greater than k*kDC, a fault signal is generated. In this paper, current sensors with DC offset are used. Current sensor used in this paper is LTS 25-NP with its DC offset equals to 1.875V. Three current sensors' output is calibrated in the DSP using the flowing equations.

$$I_a = 0.0123(V_{a\_adc} - 2310) \quad (43)$$

$$I_b = 0.01236(V_{b\_adc} - 2180) \quad (44)$$

$$I_c = 0.01244(V_{c\_adc} - 2200) \quad (45)$$

$$|I_{sum}| = |I_a + I_b + I_c| \quad (46)$$

where Vadc is the analog to digital conversion result of Vout and the range of current sensor output in normal conditions is within ±15A. Based on the above equations, current sensor failure, the resultant |Isum| as well as the definition of Ith are presented in Table 11. The threshold value Ith is set to 20A which can be used to detect all possible current sensor failures.

**Table 11: Sensor Failure and Parameters**

| No. of Current Sensor Fails | Failed Phase Current Sensor(s) | Failed Current Sensor(s) Output (A) | \|Isum\| (A) | Ith (A) |
|---|---|---|---|---|
| 1 | a | 28.4 | ≥28.4 | |
| | b | 26.9 | ≥26.9 | |
| | c | 27.4 | ≥27.4 | |
| 2 | a & b | 55.3 | ≥55.3 | 20 |
| | a & c | 55.8 | ≥55.8 | |
| | b & c | 54.3 | ≥54.3 | |
| 3 | a & b & c | 82.7 | ≥82.7 | |

Experimental results from sensor failure detection are shown in Figure 149, in which (a) stands for single sensor failure, |Isum| exceed the value of Ith at 3s and trigger the fault flag. Similarly, (b) and (c) represents two and three current sensor failure respectively.

The vector control module implemented in this paper is a conventional vector control scheme which relies on three-phase current feedbacks (ia, ib and ic) and one rotor speed feedback (ωact). As shown in Figure 150, three phase currents (ia, ib and ic) are transformed into stator d-q axis currents (isd and isq) using Clarke and Park transformation (equations (47) and (48)) based on rotor flux angle (θ). This rotor flux angle is estimated by the rotor flux estimator based on d-q axis currents (isd and isq) and rotor speed (ωact). A speed control loop calculates the q axis reference current (isq*) by comparing the actual rotor speed (ωact) to the reference rotor speed (ωref). Two stator d-q axis current control loops calculate stator d-q axis voltages (Usd and Usq) which are then be transformed into voltages (Uα and Uβ) in stator stationary reference frame using inverse Park transformation. Uα and Uβ are then sent to the Space Vector PWM module (SVPWM) to generate the desired switching signals.

$$\begin{bmatrix} i_\alpha \\ i_\beta \end{bmatrix} = \sqrt{\frac{2}{3}} \begin{bmatrix} 1 & -\frac{1}{2} & -\frac{1}{2} \\ 0 & \frac{\sqrt{3}}{2} & -\frac{\sqrt{3}}{2} \end{bmatrix} \begin{bmatrix} i_a \\ i_b \\ i_c \end{bmatrix} \quad (47)$$

$$\begin{bmatrix} i_d \\ i_q \end{bmatrix} = \begin{bmatrix} \cos\theta & \sin\theta \\ -\sin\theta & \cos\theta \end{bmatrix} \begin{bmatrix} i_\alpha \\ i_\beta \end{bmatrix} \quad (48)$$

Decoupling of d-q axis current components requires accurate position information of the rotor flux-linkages at every instant. Unlike PMSM, this position cannot be obtained directly from speed or poison sensors due to the existence of slip. Rotor flux estimator therefore is necessary and essential, which is also one of the most challenge parts in implementing vector control. The rotor flux estimator is shown in Figure 151 and expressed mathematically by equations **Error! Reference source not found.** to **Error! Reference source not found.**.

$$\lambda_{rd} = \frac{L_m}{1 + s\tau_r} i_{sd} \quad (49)$$

$$\omega_{da} = \frac{L_m}{\lambda_{rd}\tau_r} i_{sq} \quad (50)$$

$$\omega_d = \omega_{da} + \omega_m \quad (51)$$

$$\theta = 0 + \int_0^t \omega_d(\tau) d\tau \quad (52)$$

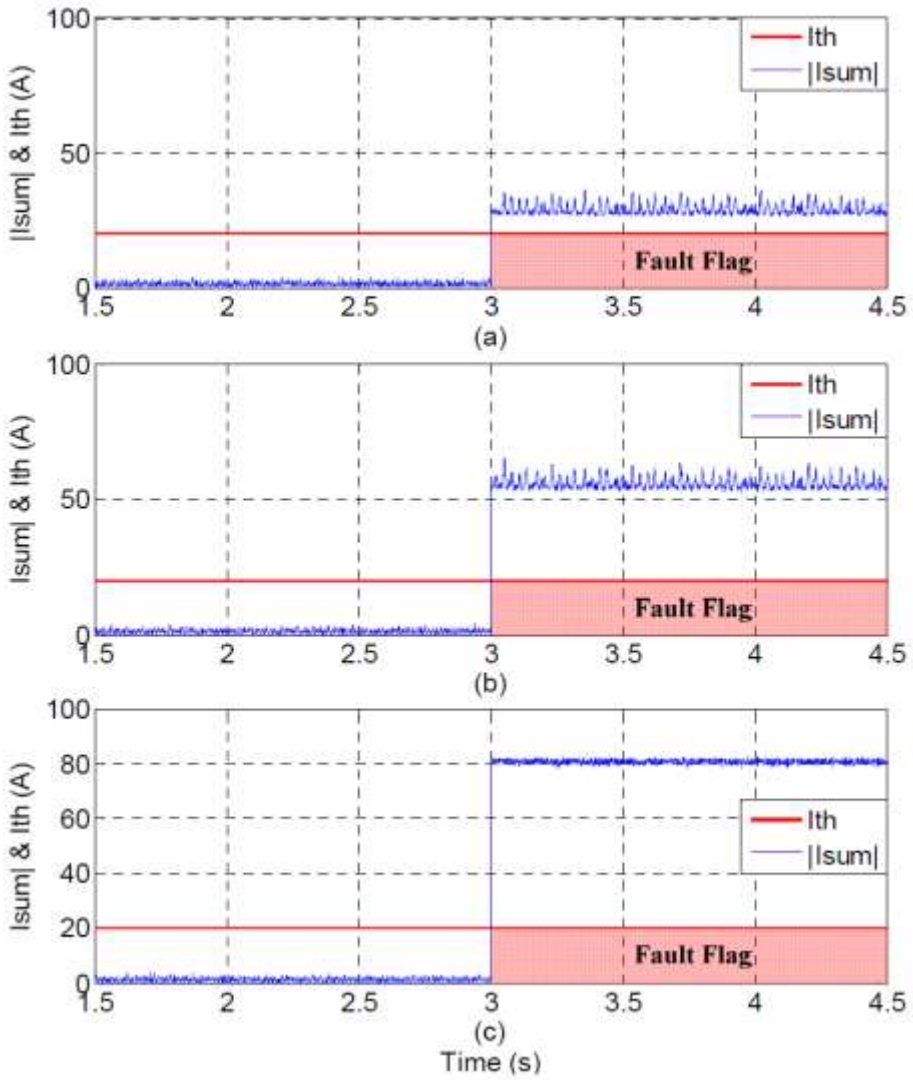


**Figure 149: |Isum| of three phase currents under different number of current sensor failure**

*One current sensor failed at 3s (b) Two current sensors failed simultaneously at 3s (c) Three current sensor failed simultaneously at 3s*

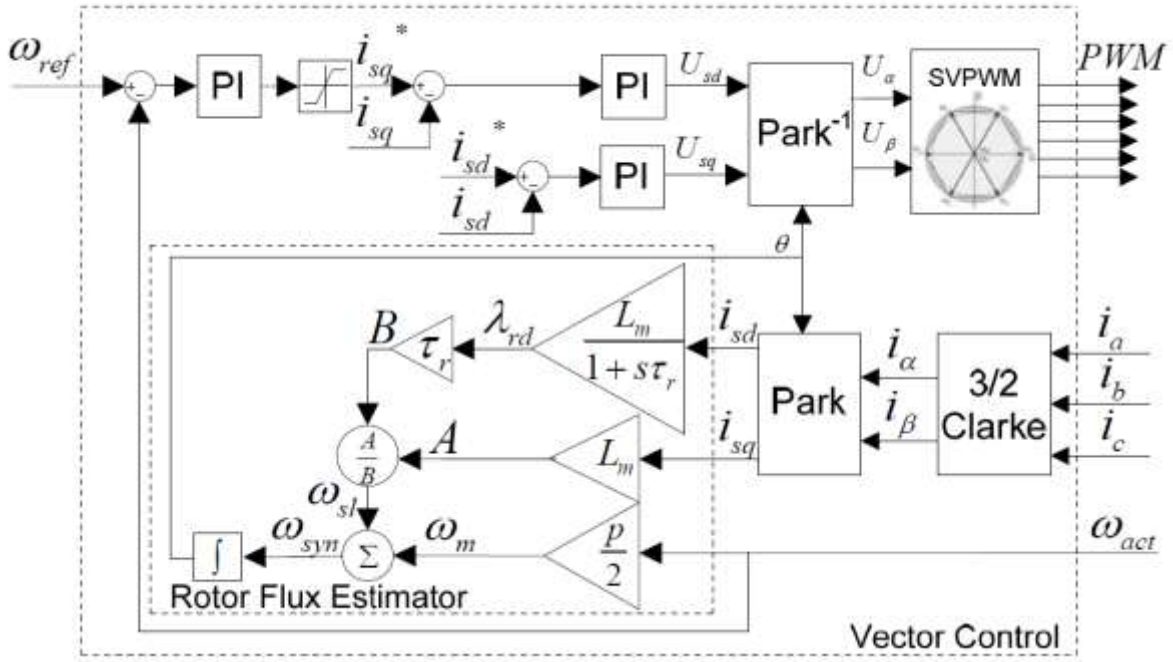


**Figure 150: Block diagram of vector control**

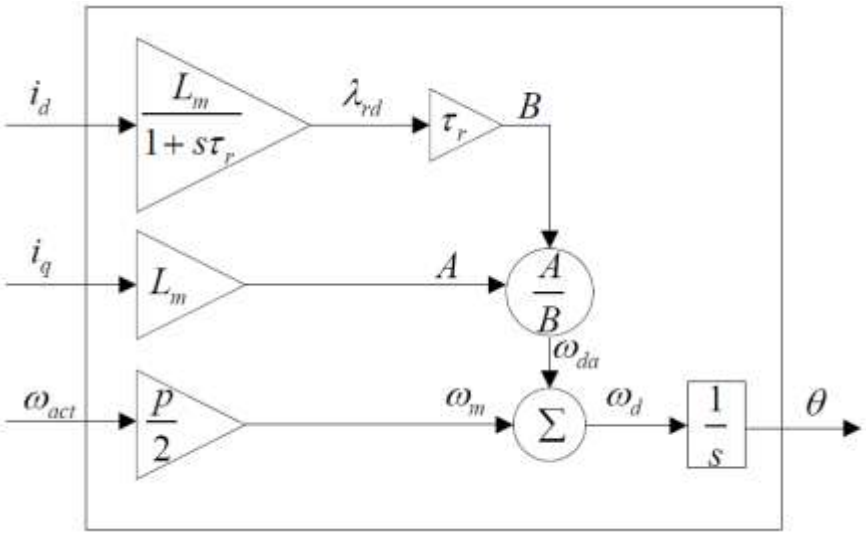

**Figure 151: Rotor flux position estimation**

In hardware implementation, the above equations need to be discretized. Before that, equation **Error! Reference source not found.** is first transformed into a time-domain equation (53).

$$\frac{d\lambda_{rd}}{dt} = \frac{L_m}{\tau_r} i_d - \frac{1}{\tau_r} \lambda_{rd} \tag{53}$$

Then, (53) can be discretized into (54),

$$\frac{\lambda_{rd}[k] - \lambda_{rd}[k-1]}{T} = \frac{L_m}{\tau_r} i_d[k] - \frac{1}{\tau_r} \lambda_{rd}[k] \tag{54}$$

Where T is the sampling step time, k is the current step and k-1 refers to the previous step. As a result, rotor flux estimation can be expressed in the flowing equations and can be easily transformed into C-code for DSP.

$$\frac{\lambda_{rd}[k] - \lambda_{rd}[k-1]}{T} = \frac{L_m}{\tau_r} i_d[k] - \frac{1}{\tau_r} \lambda_{rd}[k] \tag{55}$$

$$\omega_{da}[k] = \frac{L_m}{\tau_r \lambda_{rd}[k]} i_q[k] \tag{56}$$

$$\theta_{da}[k] = \omega_{da}[k]T + \theta_{da}[k-1] \tag{57}$$

$$\theta_m[k] = \omega_m[k]T + \theta_m[k-1] \tag{58}$$

$$\theta[k] = \theta_{da}[k] + \theta_m[k] \tag{59}$$

Space Vector Pulse Width Modulation (SVPWM) has become a popular PWM technique for voltage source inverter fed three-phase AC machines. SVPWM has two main advantages over conventional SPWM. One advantage is that the voltages and currents created by SVPWM have fewer harmonics. The other one is that the DC link voltage usage of SVPWM is higher than SPWM. The detailed principle will not be explained in this dissertation. But the realization of SVPWM in real application is introduced as follow.

According to the previous section, we know that the inputs of the SVPWM of module are Uα and Uβ, as shown in Figure 150. Based on these two values, the following steps show how to implement SVPWM in real applications.

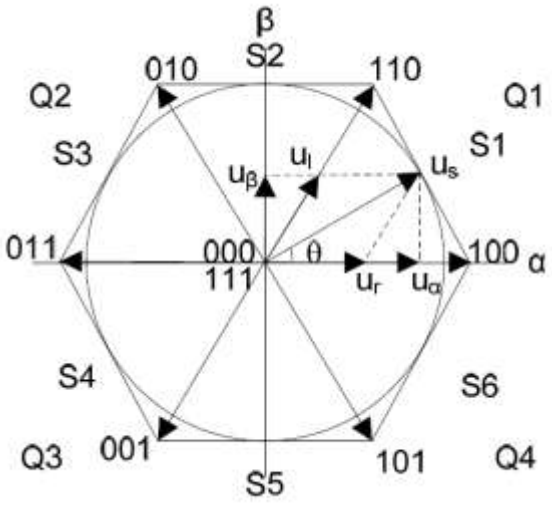


**Figure 152: Voltage vector space**

**Table 12: The relationship between P and sector number**

| P | 1 | 2 | 3 | 4 | 5 | 6 |
|---|---|---|---|---|---|---|
| Sector | S2 | S6 | S1 | S4 | S3 | S5 |

Step 1: Determine which sector the voltage vector belongs to. In order to do so, following equations can be used to get the value of P and the sector number can be obtained according to Table 12.

$$B_0 = U_\beta \tag{60}$$

$$B_1 = U_\alpha \sin\frac{\pi}{3} - U_\beta \sin\frac{\pi}{6} \tag{61}$$

$$B_2 = -U_\alpha \sin\frac{\pi}{3} - U_\beta \sin\frac{\pi}{6} \tag{62}$$

$$P = 4sign(B_2) + 2sign(B_1) + sign(B_0) \tag{63}$$

Step 2: Calculate |ur|, |ul|and |usmax|.

After sector number is calculated, two adjacent switch vectors can be defined for specific voltage vector. Then, based on the value of Uα and Uβ, Ur and Ul can be determined by geometric calculations. Ur and Ul stands for voltage vectors that locate on two adjacent switch vectors, which can be used to determine the switch time for these two switch vectors. Take the case shown in Figure for example, voltage vector Us is located in sector 1, which is formed by Uα and Uβ. Since Ur and Ul forms the same voltage vector Us, their modulus can be calculated using the flowing two equations.

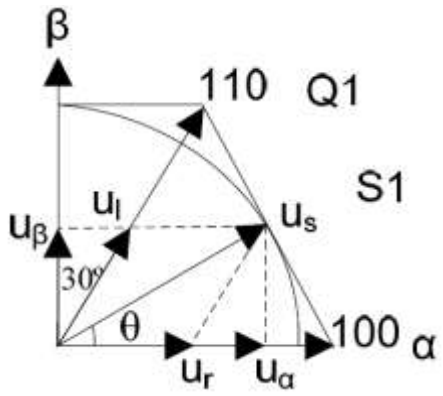


**Figure 153: Ur and Ul Calculation**

$$|U_r| = |U_\alpha| - |U_\beta| \tan\frac{\pi}{6} \tag{64}$$

$$|U_l| = \frac{|U_\beta|}{\cos\frac{\pi}{6}} \tag{65}$$

Similarly, the value of |Ur |and |Ul | for other sectors can be concluded in Table 13.

**Table 13: |Ur| and | Ul| calculation table**

| | | \|Ur\| | \| Ul\| |
|---|---|---|---|
| S1 | Q1 | b | c |
| S2 | Q1 | a | -b |
| | Q2 | -b | a |
| S3 | Q2 | c | b |
| S4 | Q3 | b | c |
| S5 | Q3 | a | -b |
| | Q4 | -b | a |
| S6 | Q4 | c | b |
| $a = \|U_\alpha\| + \frac{1}{\sqrt{3}}\|U_\beta\|,\ b = \|U_\alpha\| - \frac{1}{\sqrt{3}}\|U_\beta\|,\ c = \frac{2}{\sqrt{3}}\|U_\beta\|$ S: Sector; Q: Quadrant | | | |

|Ur| and | Ul| can be determined according to Table 7. For S2 and S5, there are two groups of values for |Ur| and |Ul|. In order to determine which group will be assigned to |Ur| and | Ul|. We need to know which quadrant the voltage vector is located. This can be done by examine the value of Uα. For example, for S2, if Uα>0, the voltage vector is located in Q1, otherwise, it is located in Q2.

The maximum modulus (amplitude) of voltage vector is 2UDC/3 (UDC is the amplitude of the DC link voltage). However, in practical applications, in order to reduce harmonics in the output voltage, the hexagon area is not used. Only the area of the inner circle which touches the hexagon is used, as shown in Figure 154. The maximum usable DC link voltage with lowest phase current harmonics is:

$$\left|U_{s\max}\right| = \frac{1}{\sqrt{3}} U_{DC} \tag{66}$$

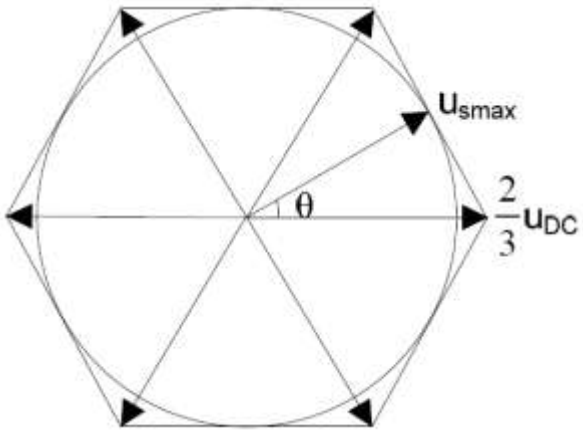


**Figure 154: Usable area for the voltage vector us**

Step 3: Calculate Tr, Tl and T0.

These values Tr, Tl and T0 determine the turn ON time of corresponding voltage vectors. The relationship between these values can be expressed in equations (67) to (70) and Figure 5.10.

$$T_r = T_p \frac{\left|u_r\right|}{\left|u_{s\max}\right|} \tag{67}$$

$$T_l = T_p \frac{\left|u_l\right|}{\left|u_{s\max}\right|} \tag{68}$$

$$T_0 = \frac{T_p^* - T_r - T_l}{2} \quad (69)$$

$$T_p = \frac{\sqrt{3}}{2} T_p^* \quad (70)$$

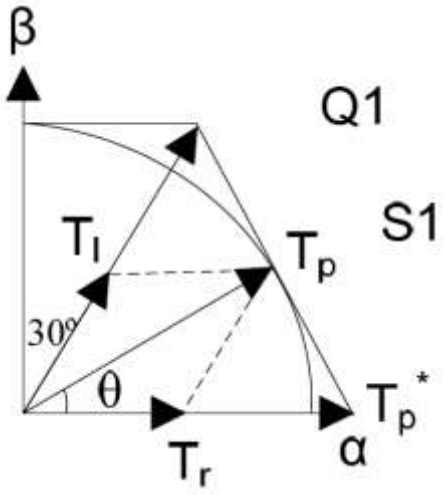


**Figure 155: Tr and Tl calculation**

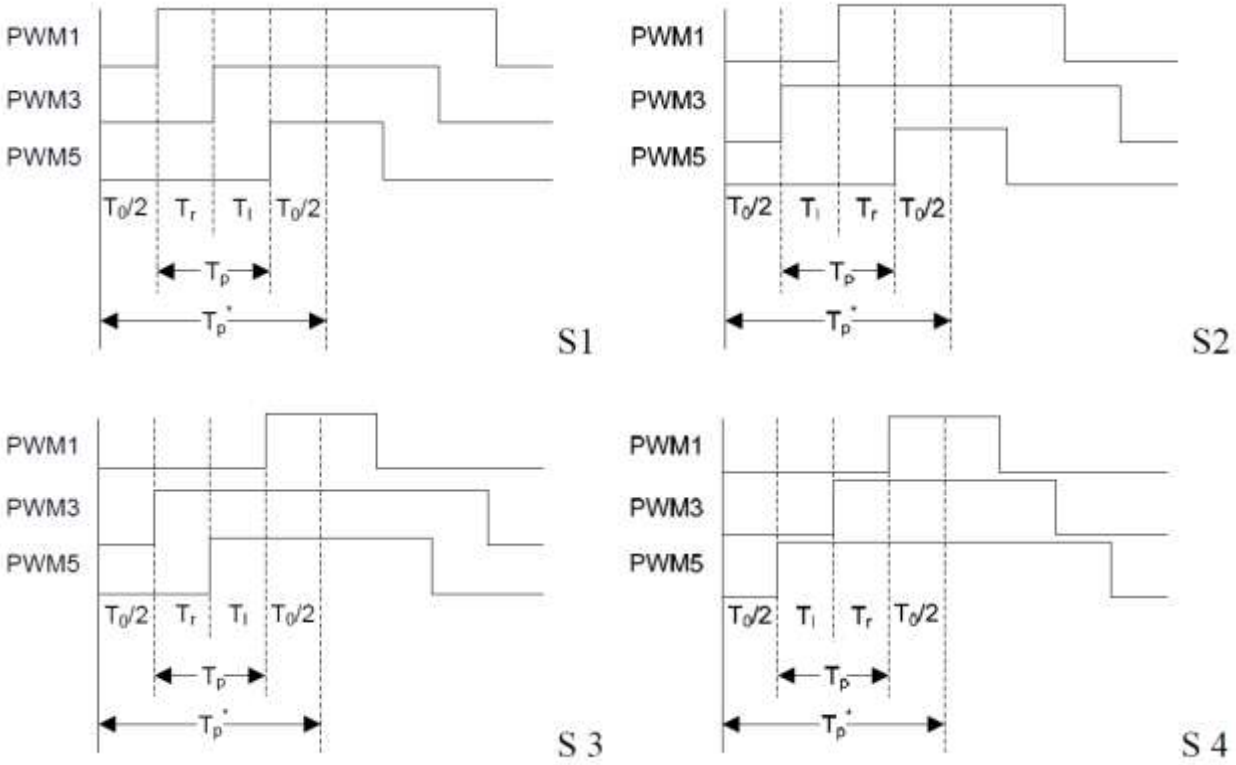

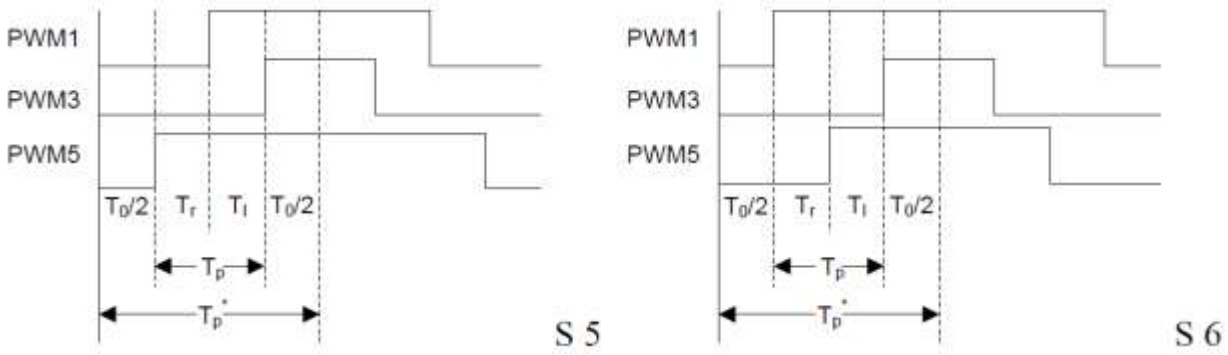


**Figure 156: Relationship between switching time variables**

Step 4: Limit Uα, Uβ or Tr, Tl proportionally

Two input parameters Uα and Uβ of the SVPM module are calculated from other modules of vector control. During startup or when the load increases, system might generates two large Uα and Uβ which forms a very large voltage vector Us that exceed the range of the hexagon, as shown in Figure 157. The result is that two large turn-on time Tr and Tl (Tr+Tl >$Tp^*$ ) is required for switch vector 100 and 110. However, it is not achievable physically. What need to be done is to either limit Uα, Uβ or limit Tr, Tl.

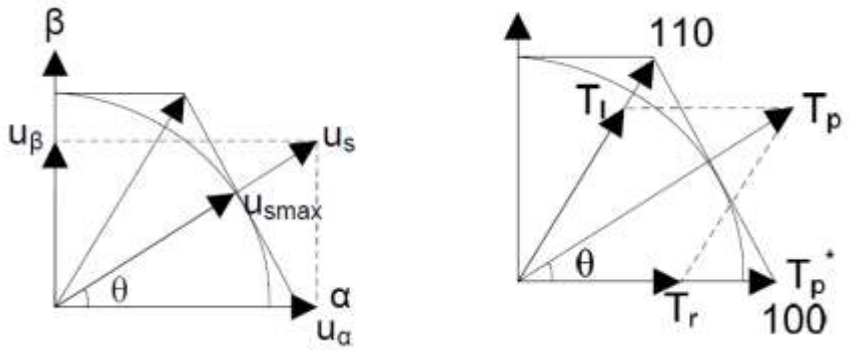


**Figure 157: Limit voltage vector**

If system is required to have lowest harmonics in its current and lowest vibration in its torque performance even during startup or load increase, input value of Uα, Uβ need to be limited proportionally. By doing so, the voltage vector will stay inside the inscribed circle with its modulus be equal or lesser than Usmax. Flowing two equations need to be implemented when Us is larger than Usmax.

$$U_\alpha^{'} = U_\alpha \frac{U_{s\max}}{U_s} = U_\alpha \frac{\frac{1}{\sqrt{3}} U_{DC}}{\sqrt{U_\alpha^{\,2} + U_\beta^{\,2}}} \quad (71)$$

$$U_\beta^{'} = U_\beta \frac{U_{s\max}}{U_s} = U_\beta \frac{\frac{1}{\sqrt{3}} U_{DC}}{\sqrt{U_\alpha^{\,2} + U_\beta^{\,2}}} \tag{72}$$

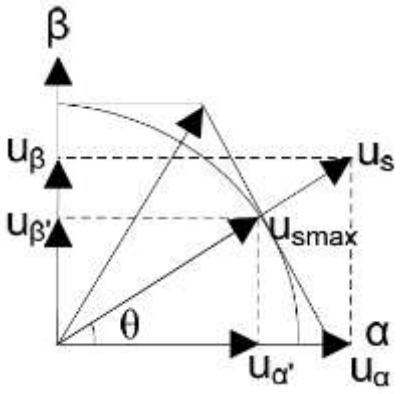


**Figure 158: Limit voltage vector within the inscribed circle**

If system is required to respond faster during startup or load increase and have better DC link voltage usage, Tr and Tl is limited proportionally instead of Uα, Uβ. When the sum of Tr and Tl is greater than $Tp^*$ (Tr+Tl >Tp ), following two equations are need to be implemented. By doing so, the voltage vector will cover the whole hexagon which maximize the usage of the DC link voltage. During startup or when load increases, the voltage vector can goes to the region that exceeds the inscribed circle of the hexagon, which is also called "Over Modulation". Disadvantage of over modulation is that it will create harmonics for phase current and result in torque vibration. Simulation results regarding the vector controlled induction machine in motoring mode can be shown in Figure 160 to Figure 162. Figure 160 shows the speed response of the induction machine under vector control. The speed quickly settles down and precisely tracks the reference speed. The torque performance of the induction machine under vector control is shown in Figure 161. Step change of reference torque can be tracked. In addition, the phase current can be illustrated in Figure 162.

$$T_r^{'} = T_r \frac{T_p^{*}}{T_r + T_l} \tag{73}$$

$$T_l^{'} = T_l \frac{T_p^{*}}{T_r + T_l} \tag{74}$$

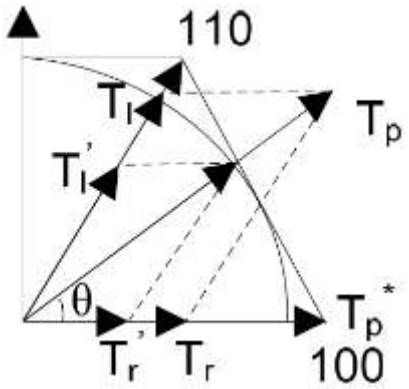


**Figure 159: Limit voltage vector within the hexgon**

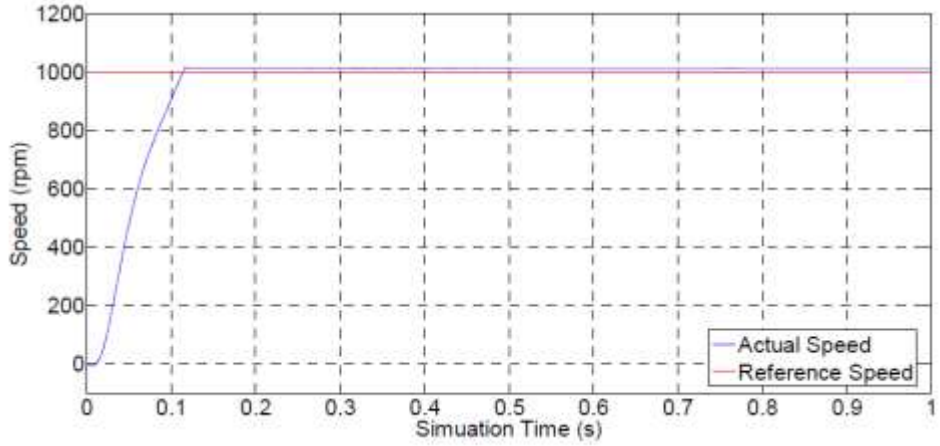


**Figure 160: Speed response of vector controlled induction motor**

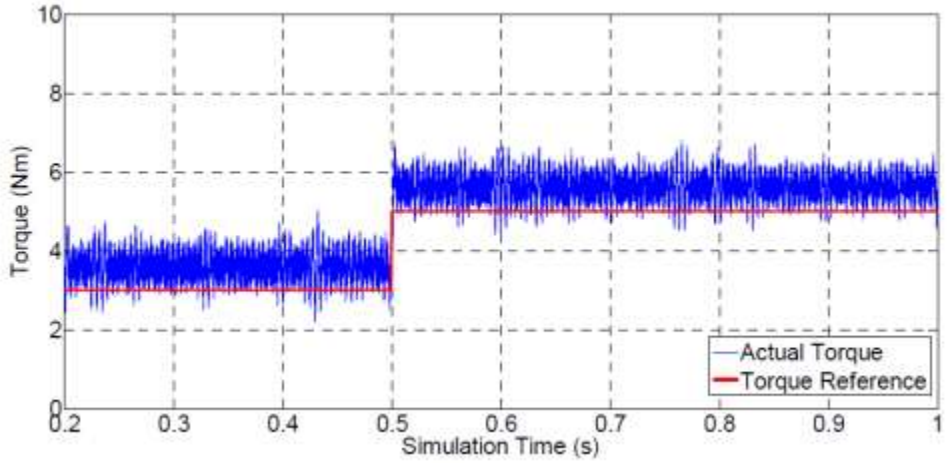


**Figure 161: Torque performance of vector controlled induction motor**

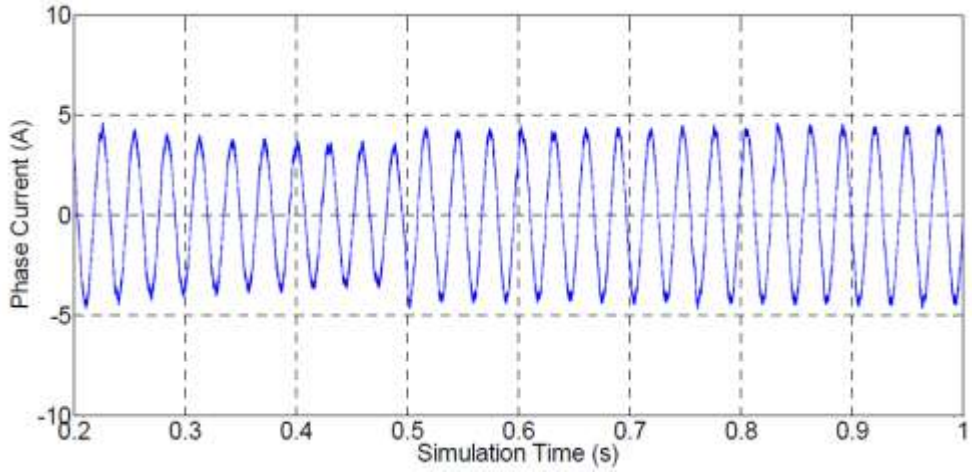


**Figure 162: Phase current of vector controlled induction motor**

Simulation results regarding the vector controlled induction machine in generating mode can be shown in Figure 163 to Figure 166. Figure 163 to Figure 165 shows speed, torque and current performance in generating mode. Figure 166 shows the generated DC link current flowing to the battery.

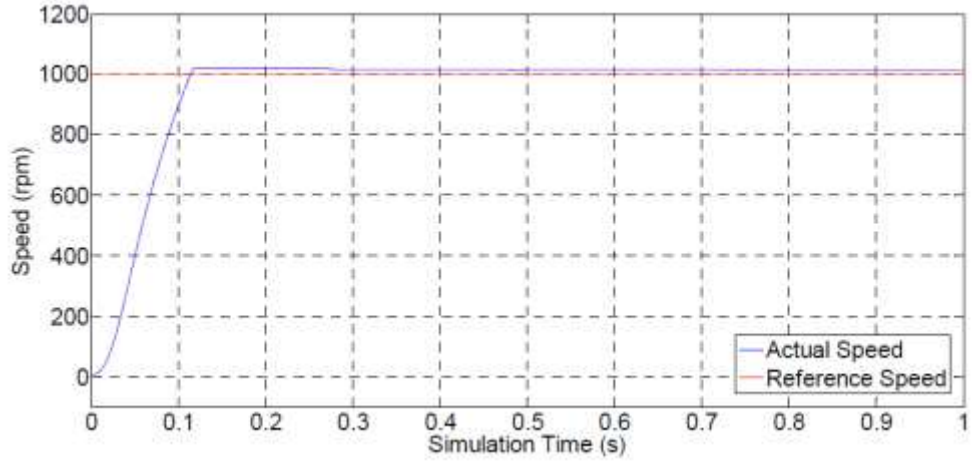


**Figure 163: Speed response of vector controlled induction generator**

The transition strategy for survivable operation proposed in this paper is described as follows-when current sensor failure occurs, vector control is disabled and state switching control is enabled. The smoothness of the controller transition greatly depends on how state switching control fires its switches at the very beginning. As shown in Figure 167, firing the wrong subsequent switches will cause undesired braking torque which could lead to large speed dip and even cause mechanical damage. In fact, this phenomenon can be explained using voltage space vector. As shown in Figure 168, under vector control, the desired voltage vector Us which rotates around the circle inside the hexagon of voltage space creates a smooth rotating rotor flux λrd (Suppose the rotation is anticlockwise).

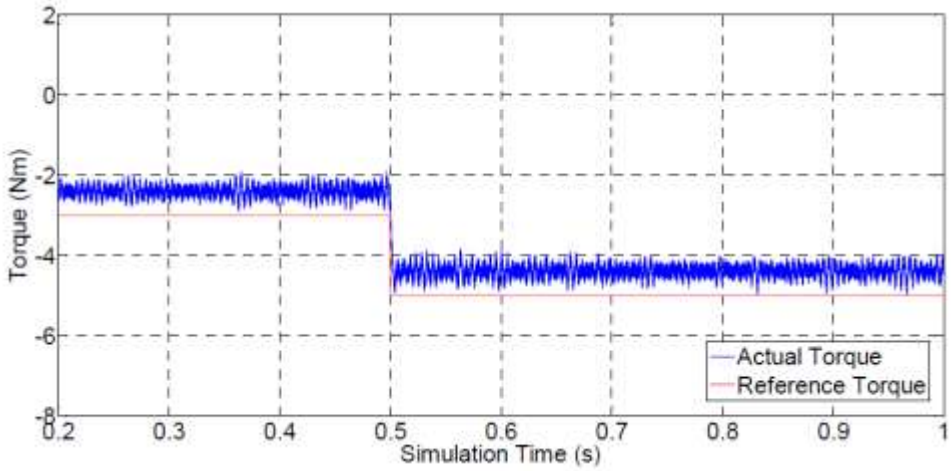


**Figure 164: Torque performance of vector controlled induction generator**

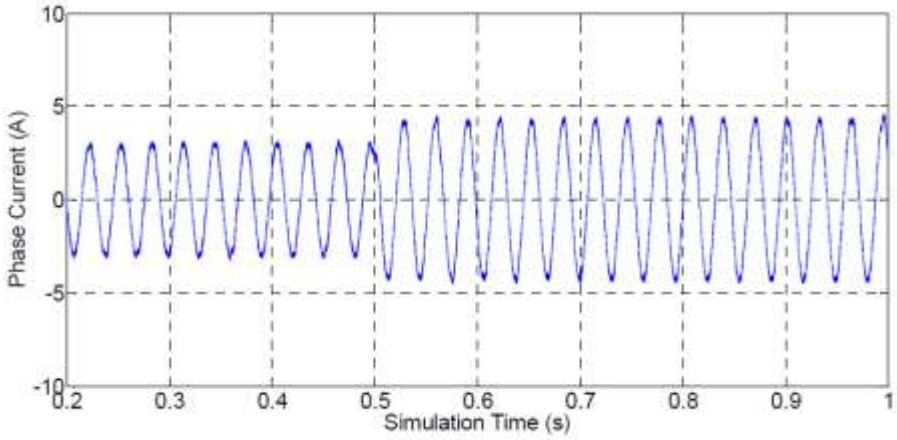


**Figure 165: Phase current of vector controlled induction generator**

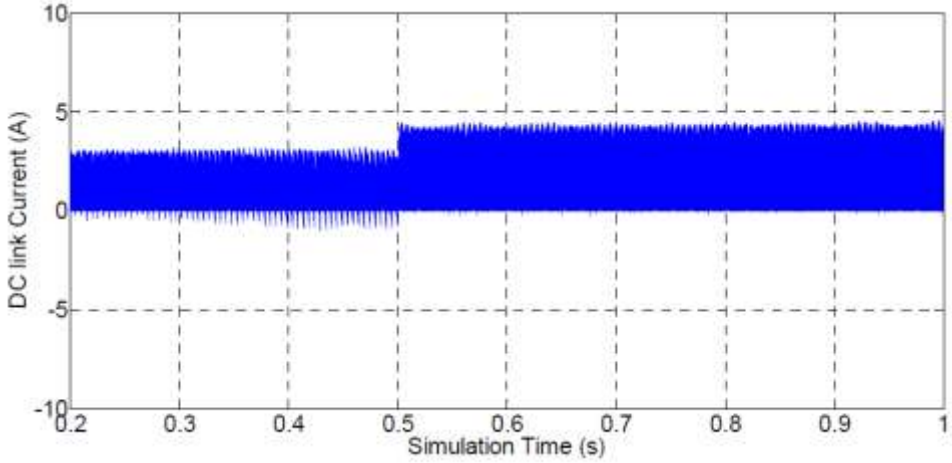


**Figure 166: The generated DC link current flowing into the battery**

This voltage vector Us should always be perpendicular to the rotor flux λrd. If at the moment of vector control failure, we assume that the rotor flux position is located in sector 6 and has an angle of θ with α-axis, the next desired voltage vector Us should be located in sector 1 and have a angle of 90º-θ with α-axis. However, if the initial position of the voltage vector Us' generated by state switching control is located in the right side of the dotted line along the direction of rotor flux position, a negative braking torque will be generated which will cause phenomenon shown in Figure 167.

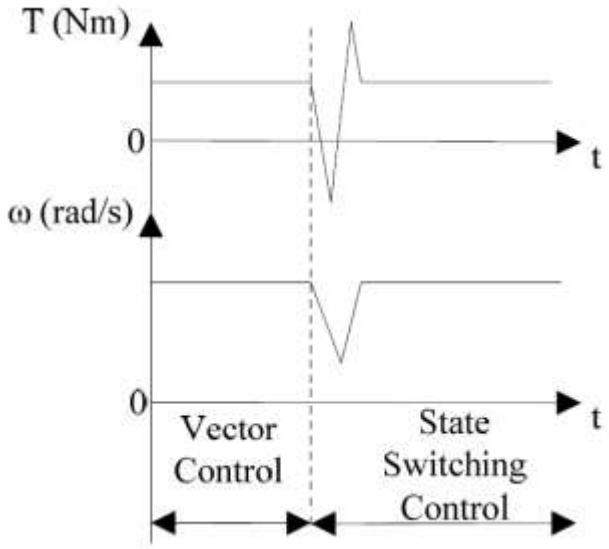


**Figure 167: Braking torque and speed dip caused by misfiring of switches**

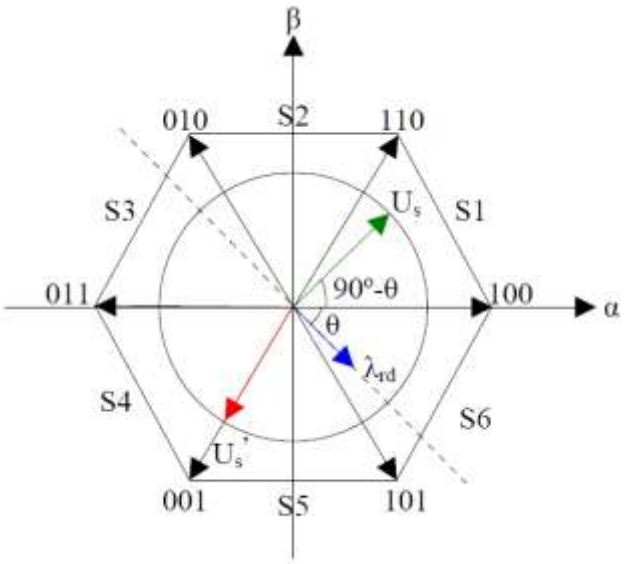


**Figure 168: Phasor diagram of rotor flux angle and voltage vector**

Therefore, in order to obtain a smooth transition, the initial voltage vector Us' of state switching control should be placed as close as possible to Us in sector 1. Since state switching control uses PWM

integrated six-step drive methods. Only voltage vectors located at $0^{o}$(100), $60^{o}$(110), $120^{o}$(010), $180^{o}$(011), $240^{o}$(001) and $300^{o}$(101) can be used. In this case, the $60^{o}$(110) voltage vector is the best option to achieve a smooth transition from vector control to state switching control. Based on the above analysis, the following steps should be implemented in order to achieve a smooth transition from vector control to state switching control.

1) When current sensor failure detection mechanism senses the failure of current sensors and vector control is going to be disabled, the rotor flux angle θ should be saved to determine the initial voltage vector for the subsequent state switching control.

2) Based on the rotor flux angle θ, the initial voltage vector of state switching control can be concluded in the following Table 14.

**Table 14: Initial Voltage Vectors for State Switching Control Based on Rotor Flux Angle**

| Rotor Flux Angle (θ) | Initial Voltage Vector (Us') |
|---|---|
| 0°~60° | 120° (010) |
| 60°~120° | 180° (011) |
| 120°~180° | 240° (001) |
| 180°~240° | 300° (101) |
| 240°~300° | 0° (100) |
| 300°~360° | 60° (110) |

In order to verify the feasibility of the proposed survivable operation of IM in the event of current sensor failure, simulation is implemented in Matlab/Simulink. The block diagram of the survivable operation of IM is the same as the one shown in Figure 146, in which a 3kW, 60Hz, 4 pole induction machine is used with a rated speed of 1725rpm.

Figure 169 shows results of the first simulation without smooth transition strategy. Speed regulation of IM is done by vector control and the output of the current sensor is a sinusoidal waveform when system is healthy. The failure of current sensor happens at 0.505s by manually disabling the sensor and the output becomes zero. At the same time, the fault signal is triggered by the current sensor fault detection mechanism and the control strategy is toggled from vector control to state switching control. Due to the lack of smooth transition technique, a significant braking torque is induced at the moment of transition, which causes a large speed dip in speed response. After that, state switching control take over the control and precisely regulate the speed.

Figure 170 shows results of the second simulation with smooth transition strategy employed. Similarly, the failure of the current sensor happens at 0.505s and the control strategy is switched from vector control to state switching control. This time, speed regulation is not influenced by the controller transition and keeps tracking the reference precisely without any dips. The torque has a small drop during transition due to discontinuous voltage vectors of six-step method, but it quickly recovers so it doesn't affect the speed. In order to verify the effectiveness of the proposed survivable operation of

induction machine as well as its simulation results, experiments were carried out on the same hardware setup displayed in Figure 124 without adding additional hardware. Parameters regarding the 2.2kW induction machine are listed in Table 15. Hardware results of survivable operation of induction machine in motoring mode are shown in Figure 171 to Figure 172. Once the fault flag is triggered, the survivable algorithm will be activated to cancel the current sensor dependence, in which the vector control will be disabled and the state switching control will be enabled. At the same time, a smooth transition strategy will take place to ensure the smoothness of the transition process. Experiment results are shown in Figure 171 and Figure 172. Figure 171 shows the results when the reference speed is 1000rpm at 1Nm load condition. Sensor failure happens at 3s and the fault flag is trigger which is shown in Figure 171 (a). Figure 171 (b) shows how smooth transition is achieved.

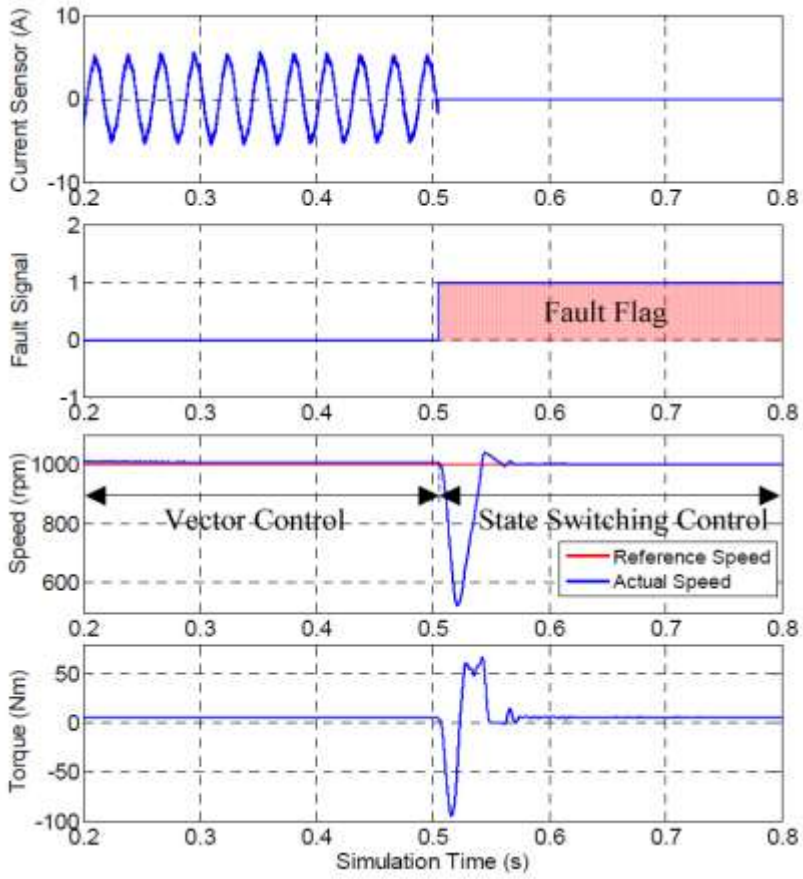


**Figure 169: Survivable operation of IM without smooth transition strategy**

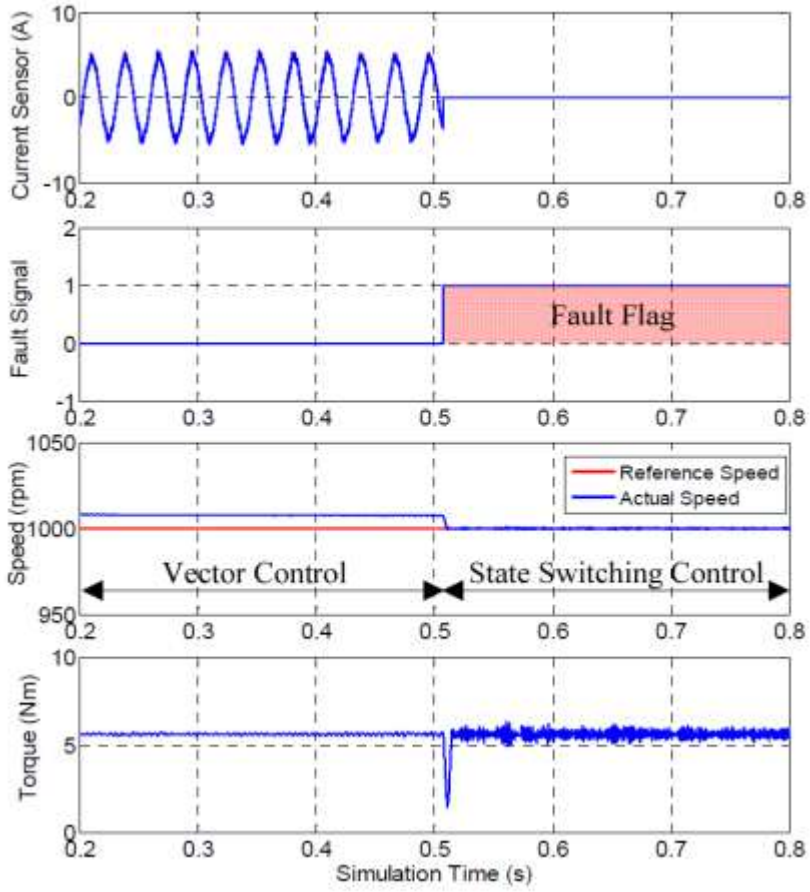


**Figure 170: Survivable operation of IM with smooth transition strategy**

**Table 15: Induction Motor Parameters**

| Symbol | Parameters | Values |
|---|---|---|
| Rs(Ω) | Stator Resistance | 2.9 |
| Ls(mH) | Stator Inductance | 245.7 |
| Rr(Ω) | Rotor Resistance | 2.1 |
| Lr(mH) | Rotor Inductance | 253.2 |
| Lm(mH) | Mutual Inductance | 238.4 |

The red dotted line represents the rotor flux angle (0~360º) estimated by vector control. The blue solid line is the voltage vector which always leads 90º under vector control. At the moment of transition, the rotor flux angle (143.7º) is saved as the starting point for state switching control, based on this value and Table 8, the 240º (001) voltage vector is chose as the first step of the consecutive state switching control. After that, voltage vector is moving in the six-step style. Figure 171 (c) illustrates continue operating of IM after sensor failure happens. It can be noticed that speed is precisely regulated without any dips during and after controller transition. Therefore, both smooth transition and survivable operation is achieved. Figure 171 (d) shows the three-phase current waveforms before and after controller transition.

When vector control is active, phase currents are sinusoidal waveforms with high system efficiency and low noise. When state switching control is activated, phase currents are distorted with harmonics due to the lack of current monitoring. As a result, system efficiency is lower than vector control, but the speed regulation is highly acceptable.

Similarly, Figure 172 shows experiment results when reference speed is 500rpm and load torque is 1Nm. Sensor failure happens at 3s. Figure 172 (a) shows the fault flag triggered by the sensor failure detection mechanism. Figure 172 (b) illustrates the smooth transition of voltage vector based on rotor flux angle. Figure 172 (c) displays the capability speed tracking at relative low speed. Figure 172 (d) shows the phase current waveforms before and after transition.

Survivable operation of induction machine in generating mode was carried out on the same setup displayed in Figure 136 without adding additional hardware. Hardware results regarding the survivable operation of induction generator is shown in Figure 173. The reference speed of the induction generator is 1000rpm and the prime mover torque is 1Nm. As shown in Figure 173 (a), fault flag is triggered by the current sensor failure event. Figure 173 (b) shows how state switching control picks up an optimal voltage vector based the previous rotor flux position. Figure 173 (c) shows the entire speed response in which speed is not influence at the moment of controller transition. Figure 173 (d) and € shows phase current waveforms before and after sensor fails. Figure 173 (f) and (g) shows the generated DC link current before and after controller transition respectively.

In this section, the survivable operation technique has been introduced for the continuous operation of induction machine in the event of current sensor failure. A current sensor failure detection mechanism is used to monitor the conditions of current sensors and trigger the fault flag if current sensor fails. Vector control has been implemented as the strategy typically chosen for optimizing performance when the system is healthy. A simplified state switching control has been proposed and implemented to take over the control when the fault flag is triggered. Since this technique does not require any additional hardware and is not computationally intense, it is very suitable for survivable operation and can be embedded in the processor without overloading it. In addition to the state-switching strategy, a strategy has been implemented for smooth transition to avoid braking torque and any significant fluctuations in speed. Simulation and experimental results verify the effectiveness of this method.

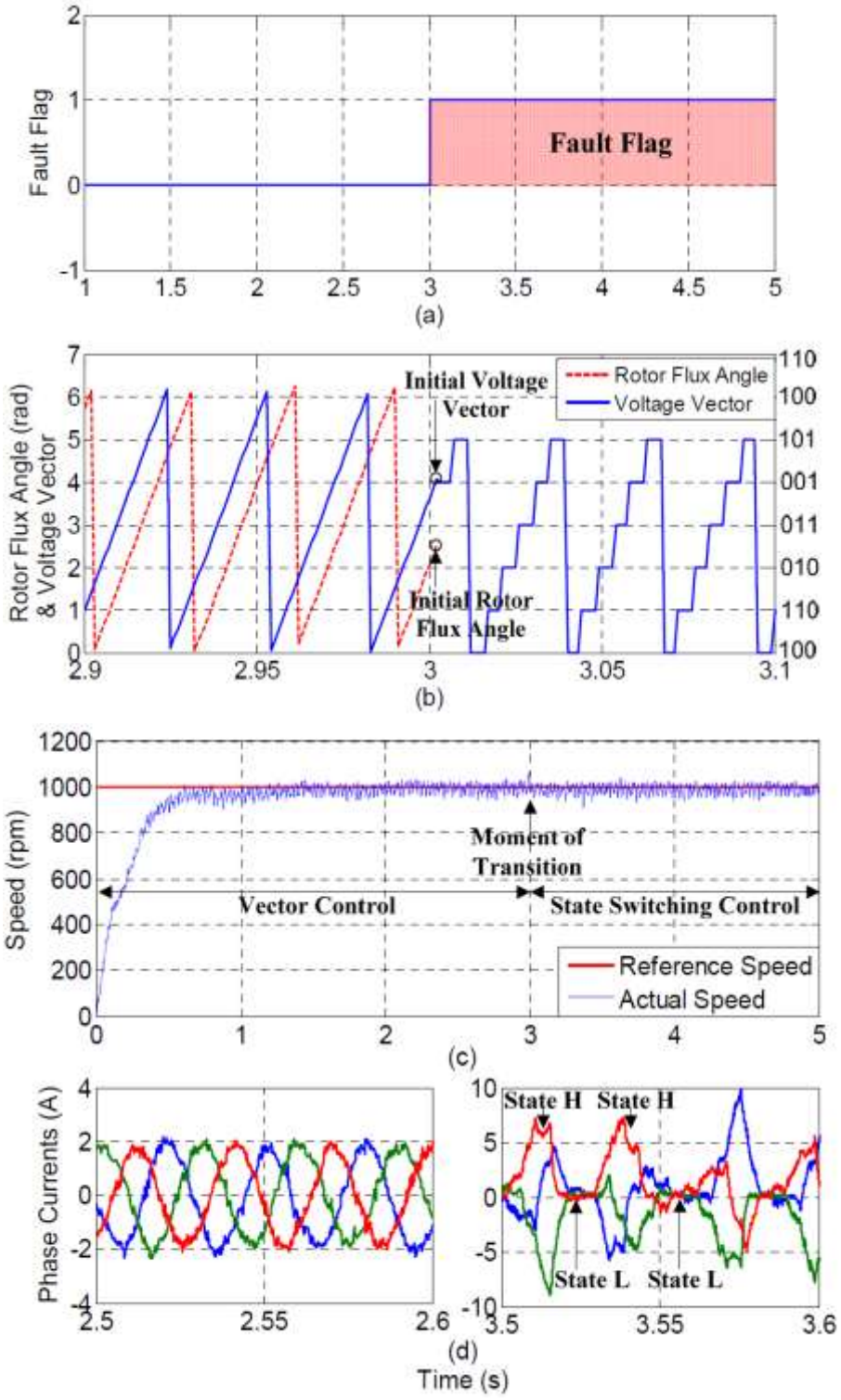


**Figure 171: Experimental results of survivable operation of IM in the event of current sensor failure with smooth transition strategy (speed ref 1000rpm, load torque 1Nm)**

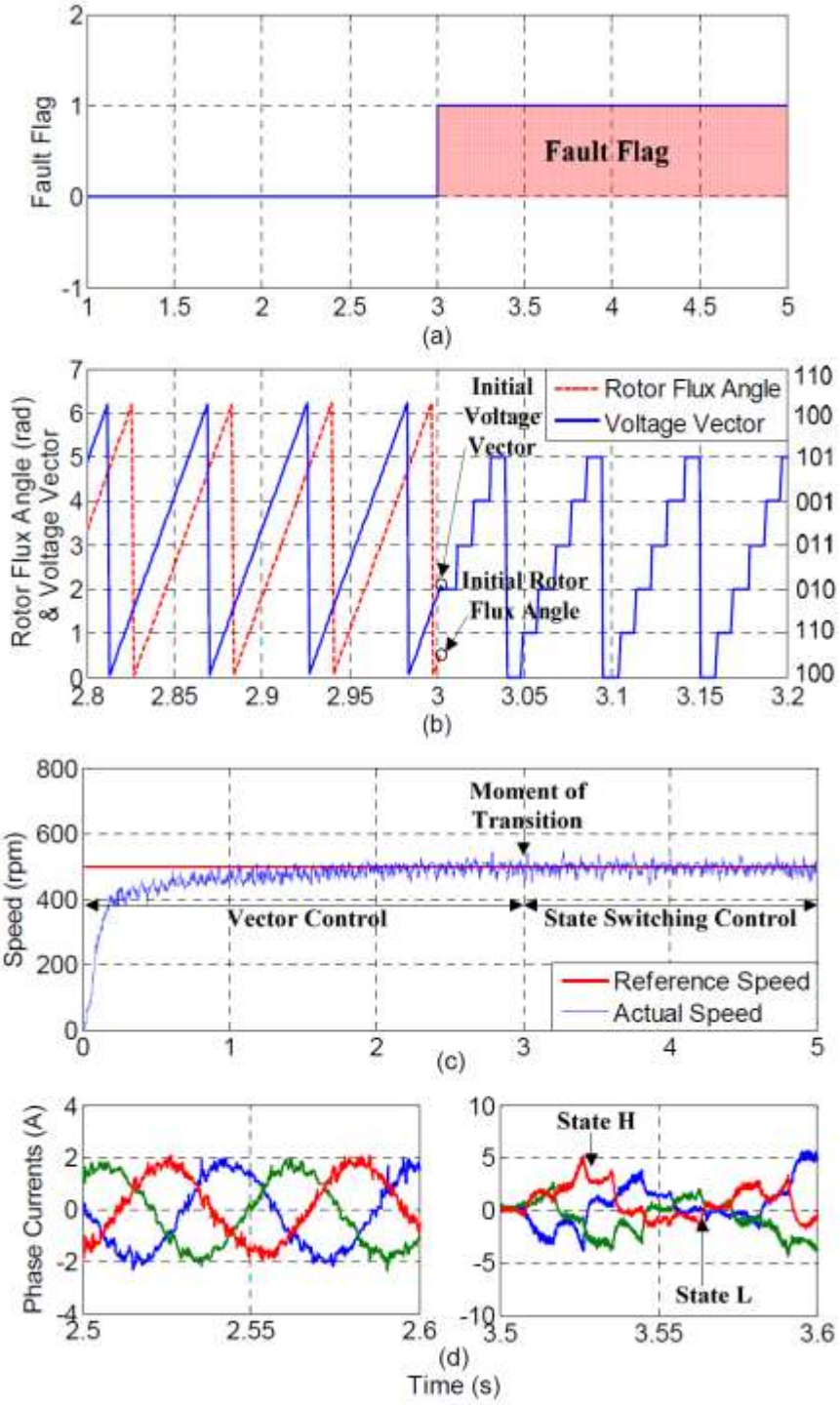


**Figure 172: Experimental results of survivable operation of IM in the event of current sensor failure with smooth transition strategy (speed ref 500rpm, load torque 1Nm)**

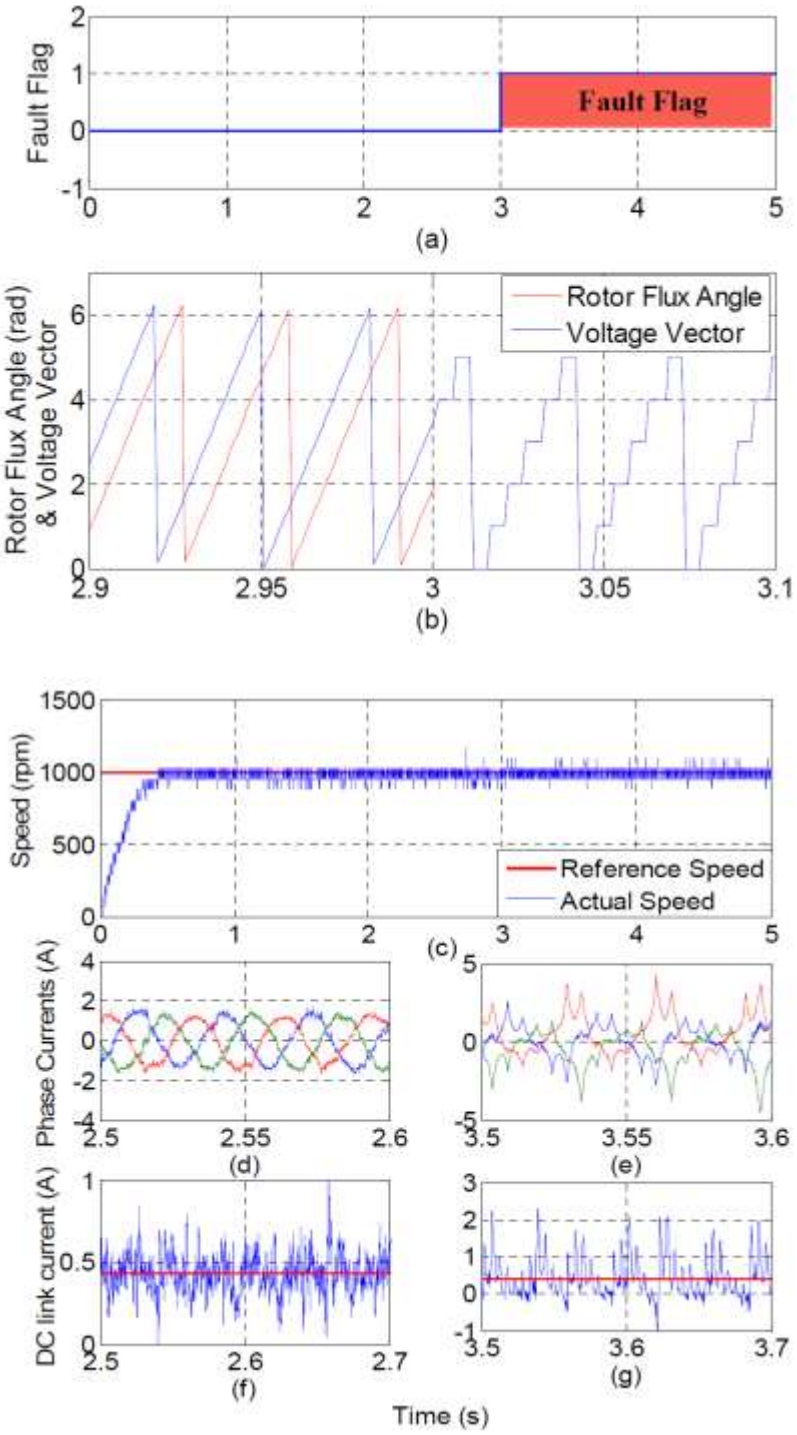


**Figure 173: Experimental results of survivable operation of IG in the event of current sensor failure with smooth transition strategy (speed ref 1000rpm, load torque 1Nm)**

### E6. Conclusions and Future Work

In this section, a survivable drive method is proposed to handle the current sensor failure and continue operating the wind turbine when current fault happens. Vector control is implemented and used control

the three-phase AC machine when system is healthy. When current fault happens, a current sensor failure detection mechanism is used to generator a fault signal which can trigger the transition from vector control to a simplified control method. In this section, a simplified control method—state transition control is proposed for induction machine to work as a backup control strategy. Simulation and experimental results are provided in this section to show the effectiveness of the proposed survivable drive method. More simulations and experiments are undergoing and more results will be provided in future reports. Future work includes

- Extensively test survivable operation of induction machine in generating mode and compare the efficiency before and after controller transition.
- Extend the survivable operation algorithm to PMSM machine in both motoring mode and generating mode.

### *F. Wind Turbines Acoustics – Localization of Wind Turbine Noise Sources*

**Localization of wind turbine noise sources on a 1.5 MW production scale wind turbine using a compact microphone array**

The primary objective of the current work was to study the behavior of various beamforming algorithms and use that understanding to locate various noise sources on a production scale 1.5 MW wind turbine located in a wind farm using a compact microphone array. The sound sources in the wind turbine include both mechanical and aerodynamic noise. The sources on the wind turbine are mostly broadband and are moving sources. The beamforming algorithms were validated in the laboratory using three speakers which could produce both coherent and incoherent noise. The spacing between the three speakers could be changed on a speaker frame. The microphone array was also tested on a moving source. The microphone array was then used to measure the wind turbine noise to locate aerodynamic and mechanical noise sources. Measurements were also made on a small wind turbine drive train simulator. This report includes a detailed discussion of all these experimental results.

In the United States, officials responsible for energy policy have been exhibiting renewed interest in wind energy as an alternate power source that is clean and renewable. One of the important factors determining the approval of a site permit for wind turbines is the level of wind turbine noise. Many researchers have spent the past decade in trying to understand wind turbine noise and developing various techniques to reduce them. In order to better understand the noise generated from the wind turbines we would need to localize the source of various types of noise. Using a single microphone one can only obtain a quantitative value (sound pressure level, SPL) of the noise. The use of multiple microphone array along with the use of beamforming will help us connect the different types of noise generated by the wind turbine to their respective components of mechanical/aerodynamic parts. Properly utilized, arrays are powerful tools that can often be used to extract noise source radiation information in circumstances where other measurement techniques may fail. Some of the widely used beamforming algorithms are Delay and Sum (DAS) beamformer, Classical Frequency Domain Beamforming (FDBF), deconvolution approach for the mapping of acoustic sources [**30**] (DAMAS), modified DAMAS [**31**], [**32**], (DAMAS2), CLEAN based on spatial source coherence [**33**] (CLEAN-SC) and TIDY. The use of basic beamformers like FDBF and DAS require very large arrays (of the order of 4 $m^2$) for

localizing the sources on a 1.5 MW production wind turbine. The requirement of large array spread over a large area serves as a major drawback of using this technique. Our idea was to use a compact microphone array along with advanced beamforming algorithms such as CLEAN-SC and TIDY to locate the wind turbine noise sources. This served as the objective for the current work. This report is a documentation of our effort to study the principles behind the advanced algorithms and conduct a thorough validation of these algorithms on a compact microphone array using coherent and incoherent sources. The quantification experiments were done before measurements on full scale unit at the wind farm.

### F1. Wind turbine noise

Wind turbines generate both aerodynamic and mechanical noise from its various components (see Figure 174(a)). Aerodynamic noise includes low-frequency sound, in-flow turbulence sound, and airfoil self- noise. The cylindrical tower can produce additional noise due to vortex shedding in various regimes. Mechanical sources include sound from the gearbox, generator, yaw drives, cooling fans, and hydraulics. Even though wind turbines have become much quieter over the years, their sound is still an important siting (installation site selection) criterion. Mechanical sounds originate from the relative motion of mechanical components and dynamic response among them. Examples of mechanical sound sources include the gear box that houses gears that connect the low speed shaft to the high speed shaft. Typically the rotor blade rotations occur at 30-60 rotations per minute (rpm). These rotations are transmitted to the high speed shaft at 1000-1800 rpm and during the process noise is produced by the gears and the high speed shaft. Aerodynamic broadband sound is typically the largest component of wind turbine acoustic emissions. It originates from air flow around the blades. Figure 174(b) shows a number of complex fluid dynamic phenomena occurring, each of which might generate sound. Aerodynamic sound generally increases with rotor speed and the noise producing mechanisms can be divided into three groups: *Low Frequency Sound, Inflow Turbulence and Airfoil Self Noise.* [**34**], [**35**]

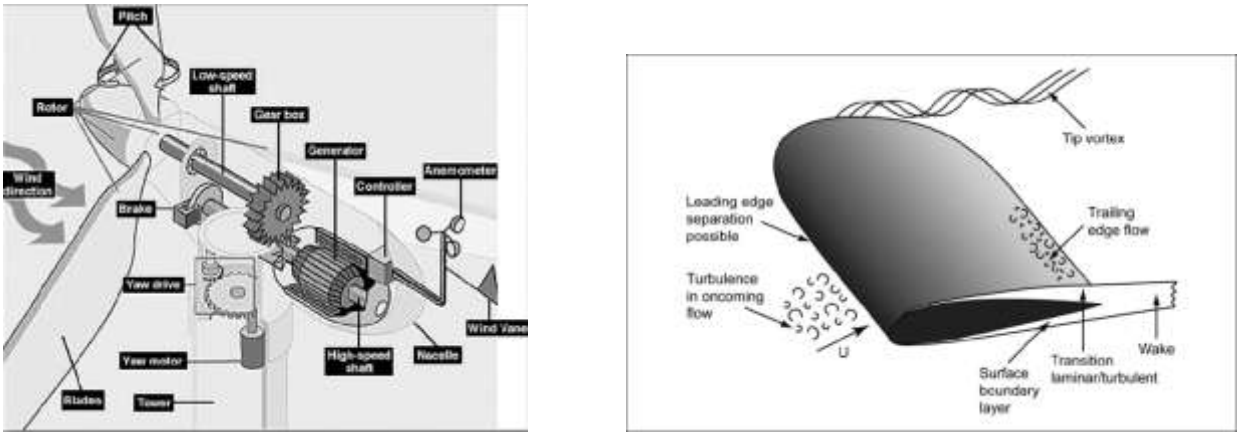


**(a)** (b)

**Figure 174: Schematic of (a) components of a wind turbine and (b) Noise producing mechanisms on a rotor blade.**

**(a) components of a wind turbine. Source: US Department of Energy (http://www1.eere.energy.gov/windandhydro/images/illust_large_turbine.gif) and (b) Noise producing mechanisms on a rotor blade (as described in [34]).**

### F2. Beamforming

The use of phased arrays provides very valuable information about the sources of wind turbine noise at various operating conditions. The very first step after acquiring data from the phased array system for every beamforming algorithm considered is the computation of cross spectral matrix (CSM). The pressure time series of each microphone is divided into B blocks and the FFT of each block is computed after applying a suitable spectral window. Then each element of the CSM is calculated via sample averaging. Since the locations of the sources are unknown in practice, a scanning grid that covers a region of interest with a certain resolution is formed and every point of this grid is considered as a potential source whose corresponding sound pressure level at the array center is estimated. This results in a beam forming map representing the acoustic source distribution in the region of interest. DAMAS attempts to estimate the true signal powers from the contaminated DAS results by constructing a linear system of equations that relate the DAS estimates at every scanning point to the signal powers at every scanning point. It utilizes the iterative Gauss-Seidel method. A potential drawback of this is computation time. DAMAS2 solves this problem by calculating the point spread function only once and using the same for all the points in the scanning grid. Another widely used method is the CLEAN-SC which iteratively builds up the beamform maps corresponding to the dominant sources using the previously estimated signal powers. TIDY is philosophically similar to CLEAN-SC, but it works in the time domain using the cross correlation matrix (CCM) instead of the frequency domain with CSM.

### F3. Calibration of microphone array

The microphone array had to be tested for its accuracy using four different beamforming algorithms namely FDBF, DMS2, CLSC and TIDY. The array was tested for many possible conditions such as,

- Single and multiple sources
- Stationary and moving sources
- Coherent and incoherent sources
- Broadband and tonal noise

The compact microphone array system with integral preamplifiers and a built-in camera developed by OptiNav was tested and used for the experiments. The signal from the microphone array is acquired by an A/D converter which has 24 I/O audio interfaces. A MAGMA express box handles the task of interfacing the PCI 424 card to the computer. A USB cable connects the camera to a USB port on the computer. The sound sources for this experiment were produced using three 4 ohm dual cone speaker with a maximum power of 60 W connected to a dedicated amplifier which received input from a white/tonal noise generator. The speakers were mounted on a rectangular frame support which had 21 different mounting locations each separated by distance of one inch (see Figure 175(a)). One speaker was mounted at the center most location on the frame, referred to as the $0^{th}$ position. The other two

speakers were mounted on the frame at a distance of 9 inches, both to the left and right of the 0th position, and the setup was referred to as 9_0_9. The amplitude of the speakers were individually controlled by dedicated amplifiers. Before the experiments were conducted three different amplitude levels were selected, a low amplitude (69-71 dB), one mid amplitude (75-77 dB) and a high amplitude (82-84 dB). For ease of reference these three amplitude cases were assigned a number; low amplitude case- '2', mid amplitude case- '4' and high amplitude case- '6'. The speaker switched off case was assigned a '0'. For example, if the center speaker was fed with high amplitude input and the other two speakers were switched off then the case was referred to as 9.0_0.6_9.0. Similarly if the right and left speaker were fed with high amplitude input and the center one was switched off then it was referred to as 9.6_0.0_9.6. This nomenclature will be used throughout the report. A Coherent source scenario was created by feeding the three amplifiers with input from the same white noise generator whereas three different white noise generators were used to feed the amplifiers in the incoherent case. The data acquired from the microphone array was then processed through four different beamforming algorithms namely the Frequency Domain Beamforming (FDBF), DAMAS (DMS2), CLEAN-SC (CLSC) and TIDY. A single 0.25" B&K 4939 microphone with a flat response from 1 Hz – 100 kHz was used for acquiring acoustic data for comparison with the results obtained from the microphone array. The microphone was positioned such that it was located exactly at the center of the microphone array. The calibration of the microphone was done using a piston phone which emits sound at 250 Hz at an amplitude of 124 dB.

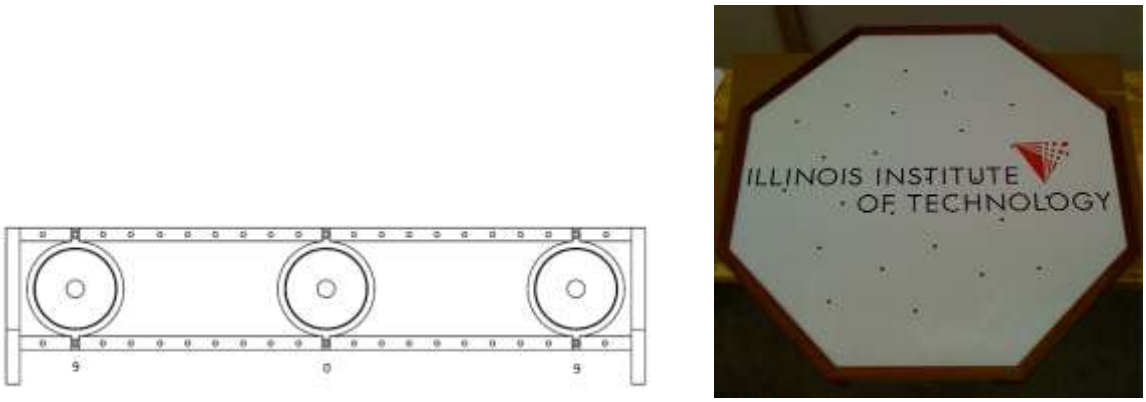


**(a)** (b)

**Figure 175: Schematic of (a) the speaker arranged on the rectangular frame support at the 9_0_9 position and (b) the microphone array.**

The microphone array was tested for a single source where only one speaker is switched on. The input signal to the speaker was a broadband noise signal. Three frequency ranges were examined: 972.5-1020.3 Hz, 2174.6-2299.3 Hz and 5777.0-6120.6 Hz. The results for the 9.0_0.6_9.0 case for the above mentioned frequency ranges are shown in Figure 176. It was observed that the FDBF and DMS2 give a very broad map for the source at low frequency (<2000 Hz) whereas the TIDY and CLSC give a clean map compared to the other beamformers. As we increase the frequency of the source the beamformers' performance gets better. It has to be mentioned that the results obtained are for the particular

arrangement of microphones on the array being tested. The spectrum obtained by the beamforming algorithms is compared with that of a calibrated single microphone. The spectra for the cases 9.0_0.2_9.0, 9.0_0.4_9.0 and 9.0_0.6_9.0 are shown in Figure 177. We observed that the spectra from the single microphone matched well with that of the microphone array.

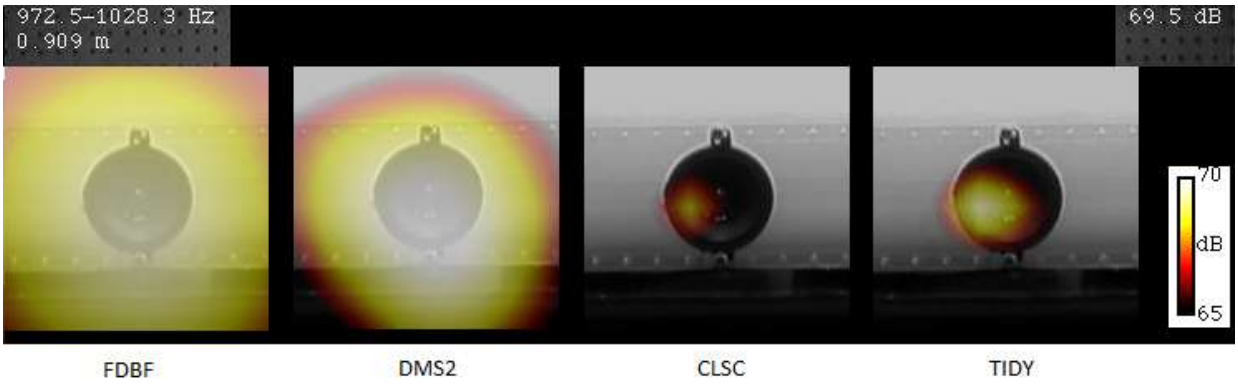


(a)

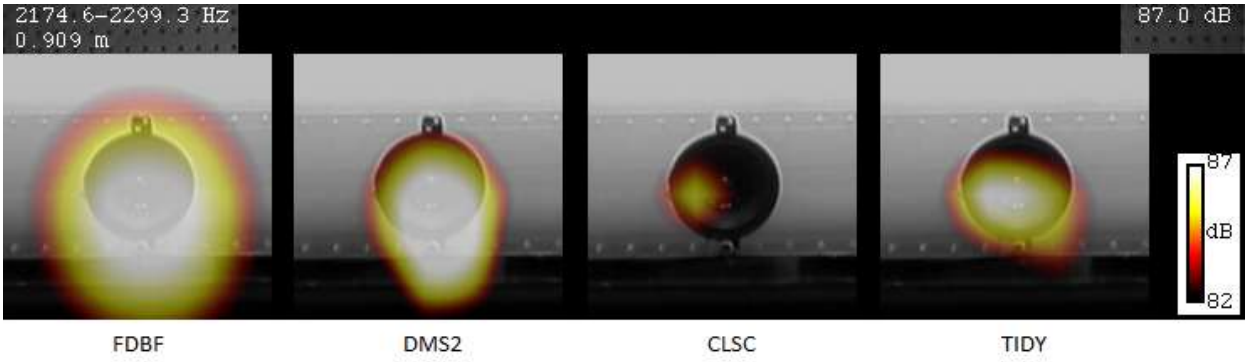


(b)

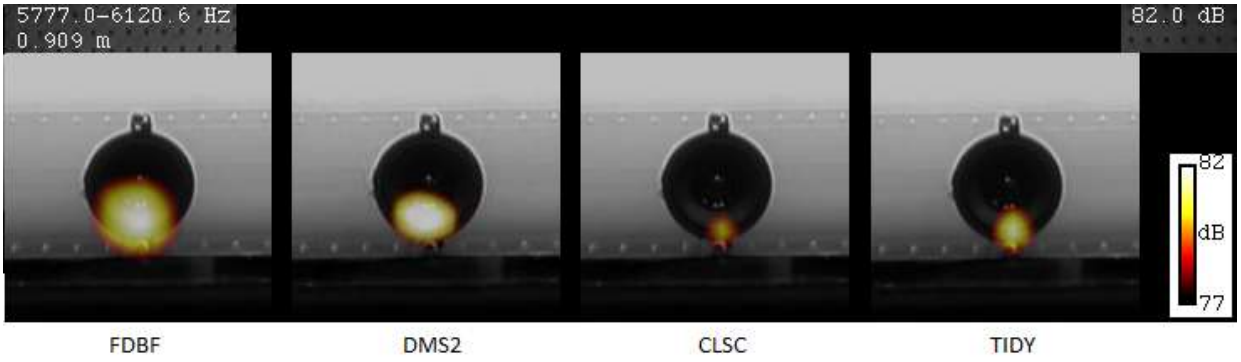


©

**Figure 176: Beamform maps of narrowband frequency ranging between**

**(a) 972.5-1028.3 Hz, (b) 2174.6-2299.3 Hz and (c) 5777-6120.6 Hz.**

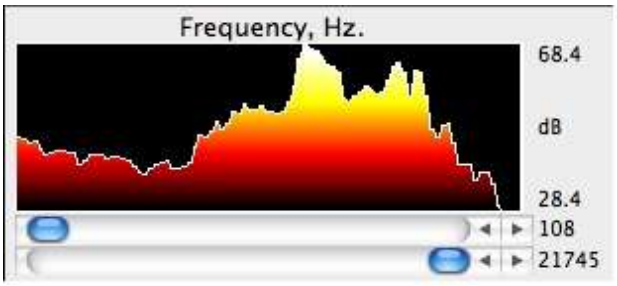


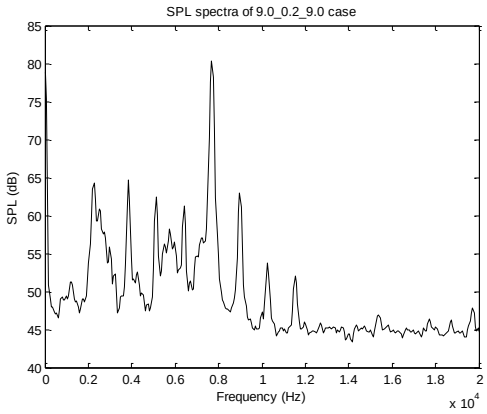


(a)

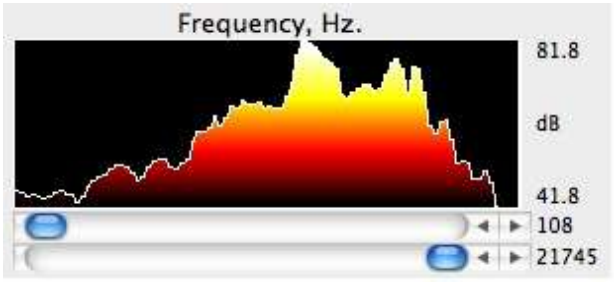


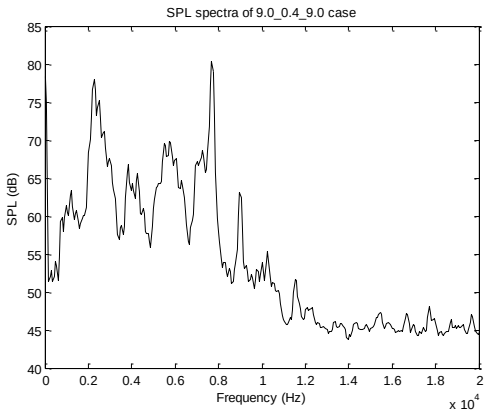


(b)

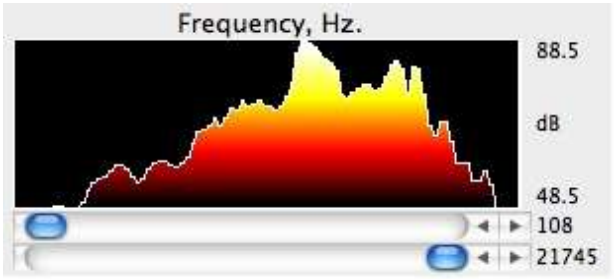


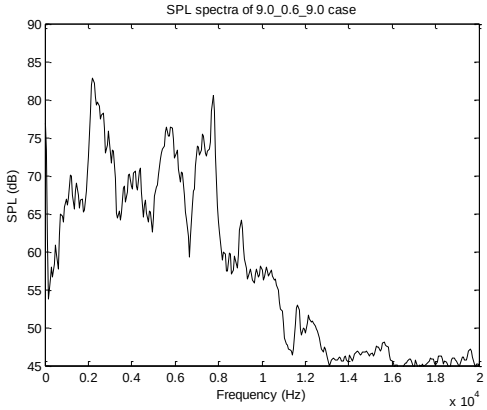


©

**Figure 177: Sound pressure level spectra from the microphone array and single microphone respectively of the cases**

**(a) 9.0_0.2_9.0, (b) 9.0_0.4_9.0 and (c) 9.0_0.6_9.0.**

The ability of the microphone array to locate multiple sources was examined in the next set of validation experiments. In this particular case we used two sources both at the same amplitude level 6 separated by a distance of 18 inches (9.6_0.0_9.6). In order to understand the behavior of the beamforming algorithms when exposed to coherent and incoherent sound sources we fed the speakers with both coherent and incoherent signals. The beamform maps for this case are shown in Figure 178. In this particular analysis the frequency band of interest was chosen to be 2292.3-2431.5 Hz and the dynamic range was chosen to be 10 dB. We observed that the FDBF, DMS2 and TIDY algorithms whose formulation was based on incoherent sources was able to pick up both the sources in both incoherent and coherent cases. The CLSC algorithm is formulated to pick out the highest of the coherent sources as evident from our results. Also in the incoherent case the CLSC was able to locate both the sources. The cleanest map was given by the CLSC followed by TIDY then DMS2 and finally FDBF.

In the next set of validation experiments the number of sources and the distance of separation were the same as the latter case whereas the amplitude of the two sources was different. The idea behind this experiment was to check the beamformers' ability to locate sources of different amplitudes. Figure 179 shows the beamform maps of the case 9.6_0.0_9.4 both for coherent and incoherent cases. We observed that all the beamforming algorithms were able to distinguish the two sources. In this case the difference in amplitude was about 8 dB. It was observed that the beamforming algorithms were able to locate the two sources with an amplitude difference of up to 12 dB beyond which they were not able to distinguish the sources clearly.

The number of sources was then increased to three separated by a distance of 9 inches from each other. The amplitude of the sources was the same and both incoherent and coherent cases were tested. The beamform maps of the case 9.6_0.6_9.6 are shown in Figure 180. We observed that for the frequency range of interest the beamforming algorithms were able to locate the three sources. In case of FDBF and DMS2 we observe that when the sources are coherent the algorithms tend to merge sources together. The CLSC algorithm locates only a single maximum amplitude source in the coherent case true to its formulation. The TIDY algorithm was able to locate all the three sources in both the incoherent and coherent case.

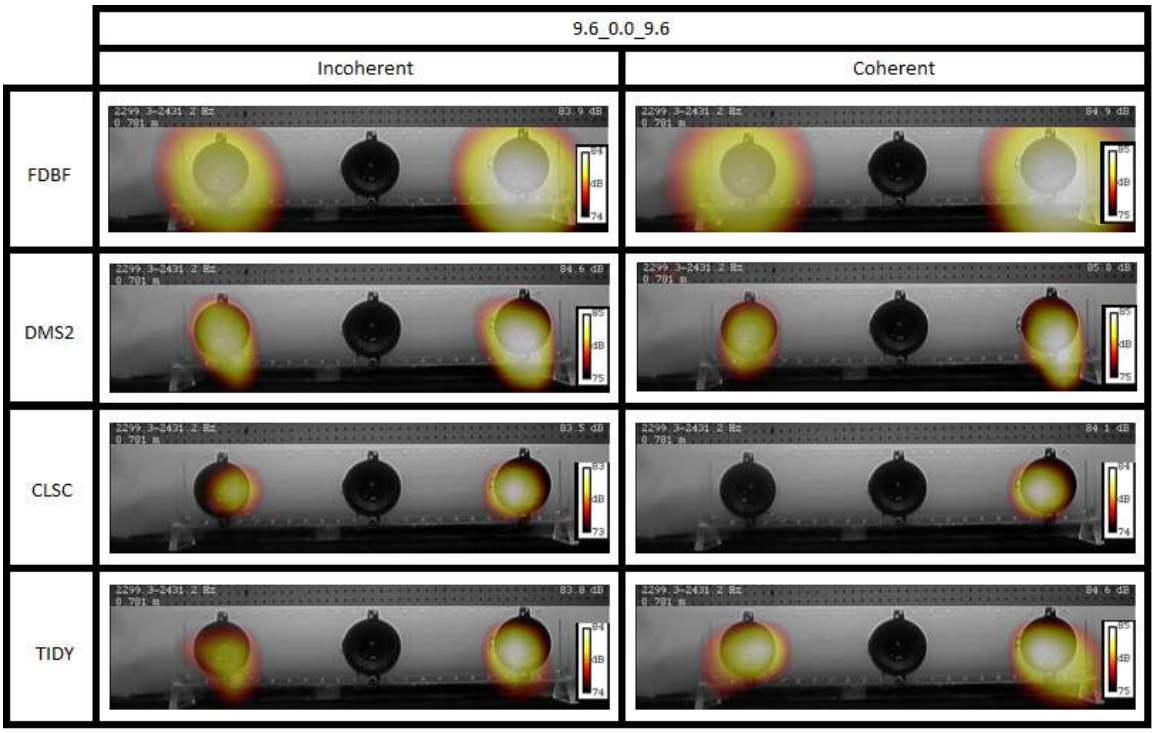


**Figure 178: Comparison of beamform maps obtained from FDBF, DMS2, CLSC and TIDY for multiple incoherent and coherent sources of the same amplitude (9.6_0.0_9.6).**

As the aerodynamic sources on a wind turbine are moving sources, we used one of the speakers suspended from a rod which could be oscillated to study a moving source. The frequency range of interest here was a broadband range 1371.2-5146.6 Hz (as the primary sources on wind turbine are broadband in nature). In order to measure broadband noise the only advanced algorithm is TIDY. The beamform map for the oscillating source is shown in Figure 181. We observe that TIDY is able to locate the source as it is in its motion. As before with increase in the frequency range the beamform maps gets cleaner and sharper.

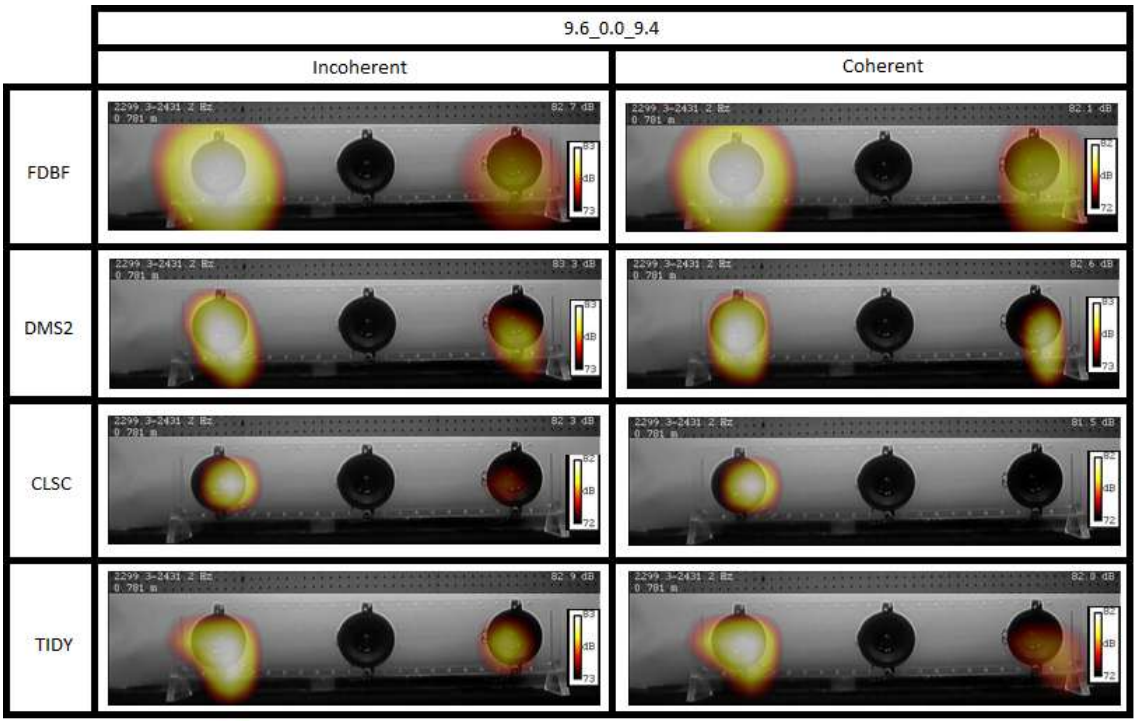


**Figure 179: Comparison of beamform maps obtained from FDBF, DMS2, CLSC and TIDY for multiple incoherent and coherent sources of different amplitude (9.6_0.0_9.4).**

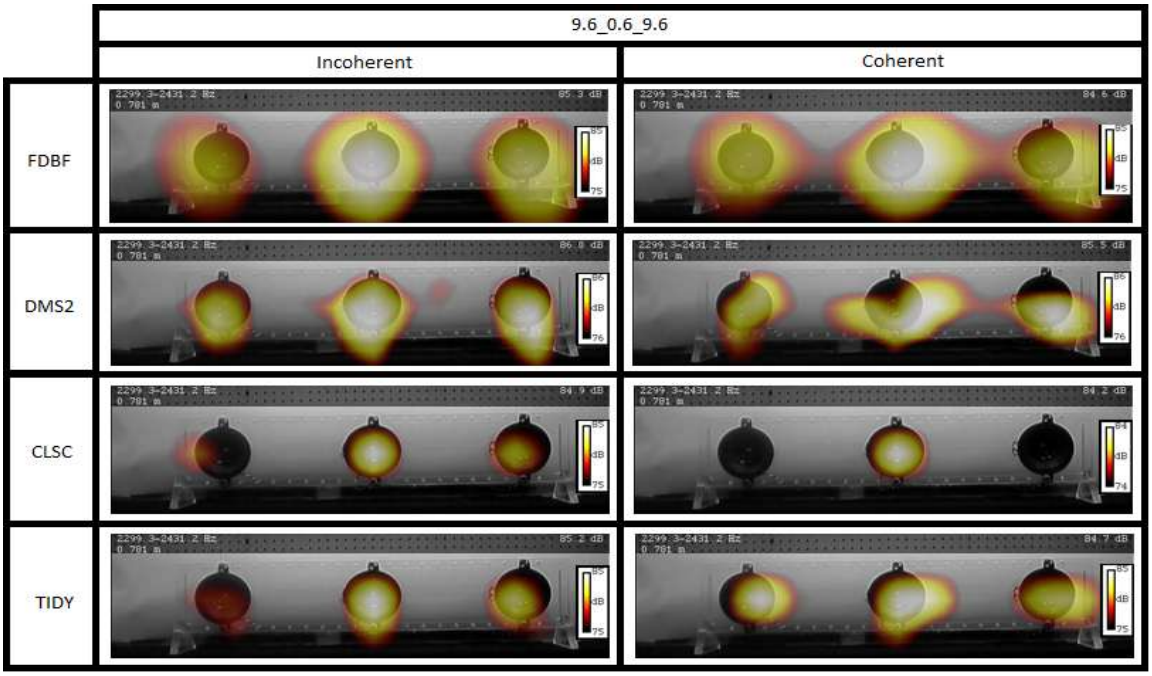


**Figure 180: Comparison of beamform maps obtained from FDBF, DMS2, CLSC and TIDY for three incoherent and coherent sources of the same amplitude (9.6_0.6_9.6).**

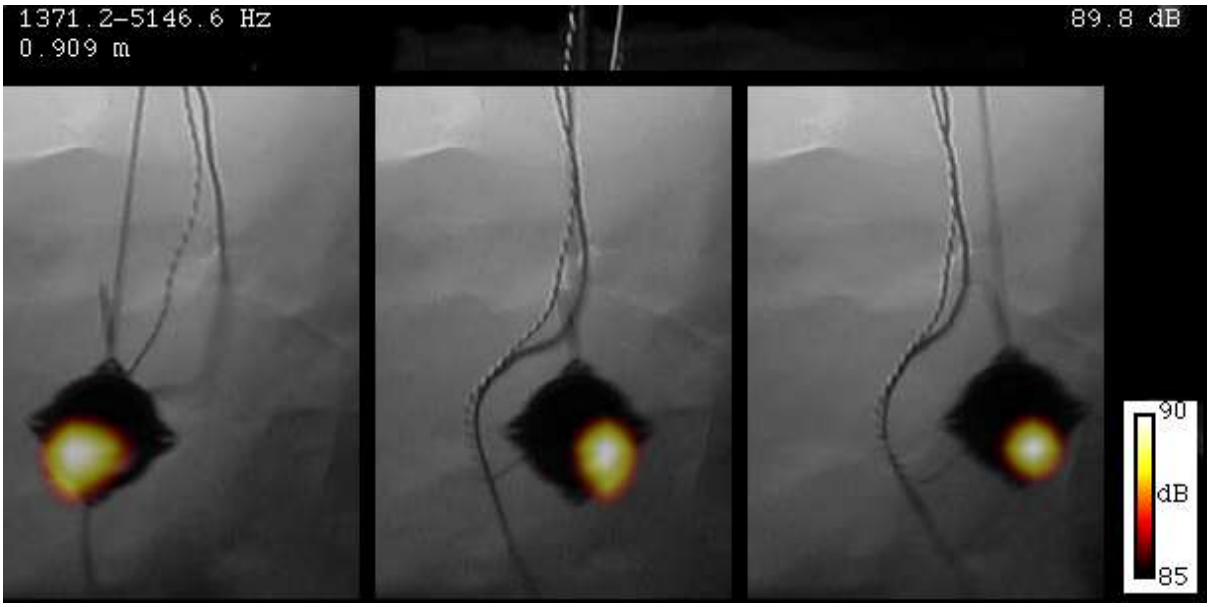


**Figure 181: Beamform map of a single oscillating source at three different positions during oscillation obtained using TIDY.**

### F4. Wind Turbine Noise Measurement

The objective of this part of the study was to use a compact microphone array along with the use of advanced beamforming algorithms to successfully measure and locate sources on a production scale 1.5 MW wind turbine located at a wind farm.

As a part of this project the university (under DOE sponsorship) purchased a GE 1.5 MW wind turbine. The picture of this wind turbine is shown in Figure 182. This wind had a hub height of 85m with the rotor diameter of 77m. The turbine has a variable rotor speed of 10.4 to 10.4 rpm. The rated wind speed of this turbine is 12 m/s. The wind turbine is located at the Invenergy farm at Grand Ridge Illinois. In addition, to study the noise from the mechanical parts in the nacelle, a Viryd 8kW wind turbine drive train simulator which can simulate various wind conditions was used. The drive train consists of four part namely, Gear box, brake, CVP and Generator. This drive train is attached to a fly wheel which is in turn connected to a drive side with gearbox and a motor controlled by a user program. The program allows the user to input various parameters such as the wind speed and turbulence level. Based on which the drive motor will be given the appropriate amount of current to simulate the wind conditions. The picture of the wind turbine drive train is shown in Figure 187. The distance from the base of the wind turbine to the array was measured to be 85 m.

**Figure 182: The GE 1.5 MW wind turbine located at the Invenergy wind farm in Grand Ridge, Illinois.**

The wind turbine noise was first measured using a conventional beamforming algorithm, the delay and sum (DAS) beamformer. The beamform map for this case is shown in Figure 183. We observed that the DAS beamformer produced a smeared sound pressure level (SPL) map that covered the entire wind turbine. It was not possible to distinguish between the different aerodynamic and mechanical source of noise from the wind turbine. Next, the noise from the same the wind turbine was measured using an advanced algorithm, TIDY. The beamform map for this case is shown in Figure 184. We observed that the TIDY beamformer was able to distinguish the various noise sources on the wind turbine. The noise around the edge of the rotor blades are the blade tip vortex noise. The noise at the nacelle of the wind turbine is mainly produced by mechanical sources. Figure 185 shows the beamform map of wind turbine noise using TIDY at a particular instant in time during its rotation. We can clearly indentify the mechanical noise that arises inside the nacelle and the aerodynamic noise from the blade tip.

The important application of using the microphone array to measure wind turbine noise is that we could detect changes that arise due to various components and various modes of operation of the wind turbine. For instance we measured the noise due to yaw motor when it was operational. The particular wind turbine under interest has a unique technology which is known as the catch the wind. This technology detects the wind speed and direction up to 300 ft in front of the wind turbine and turns the nacelle to the direction of the wind. This is made possible by the yaw motors in the wind turbine. Figure 186(a) shows the time series of the microphone array measuring the noise from the wind turbine. In this particular case we see the yaw motor in action. The frequency of interest in this particular case was 1087-1149 Hz. We see that there is an increased amplitude for a particular period of the time series. This is due to the yaw motor. In Figure 186(b) we observe the amplitude of the noise from the nacelle to be about 7.7 dB. From Figure 186(c) we observe that in the case where the yaw motor is operational the

noise increases to up to 24.3 dB at the particular frequency of interest. This is an increase of about 16 dB in the nacelle.

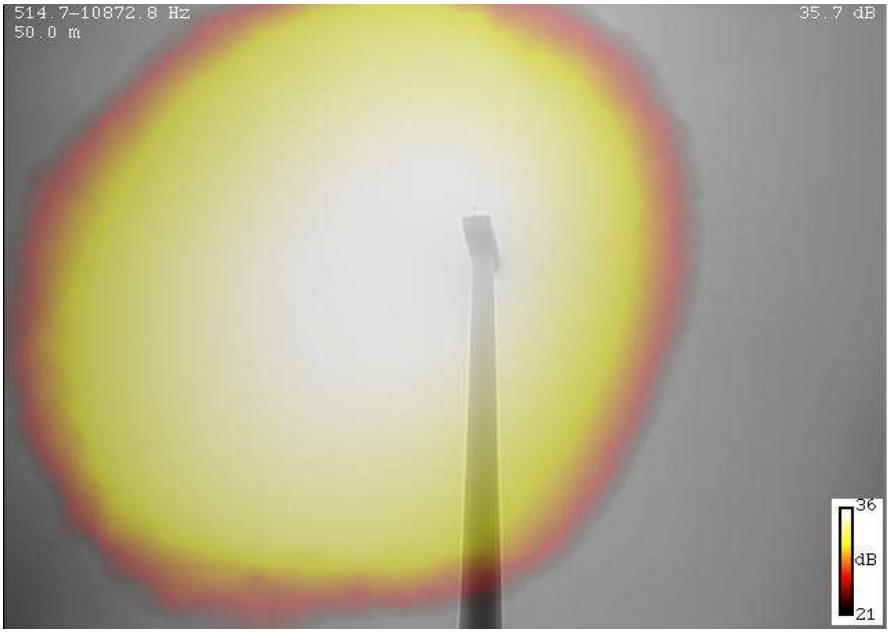


**Figure 183: Beamform map of the GE 1.5 MW wind turbine using DAS.**

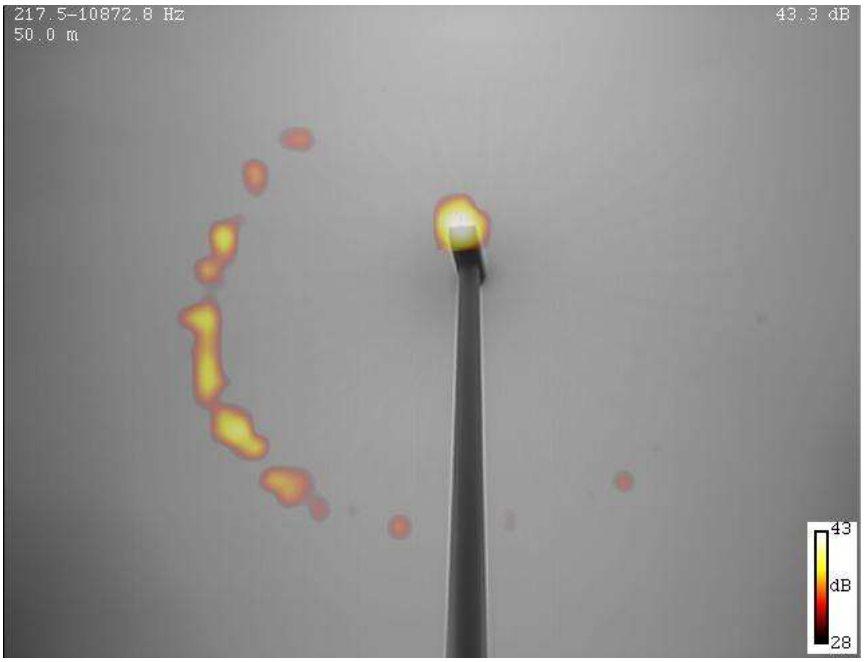


**Figure 184: Beamform map of the GE 1.5 MW wind turbine using TIDY.**


**Figure 185: Beamform map of the GE 1.5 MW wind turbine using TIDY at a particular instant of time during its rotation.**

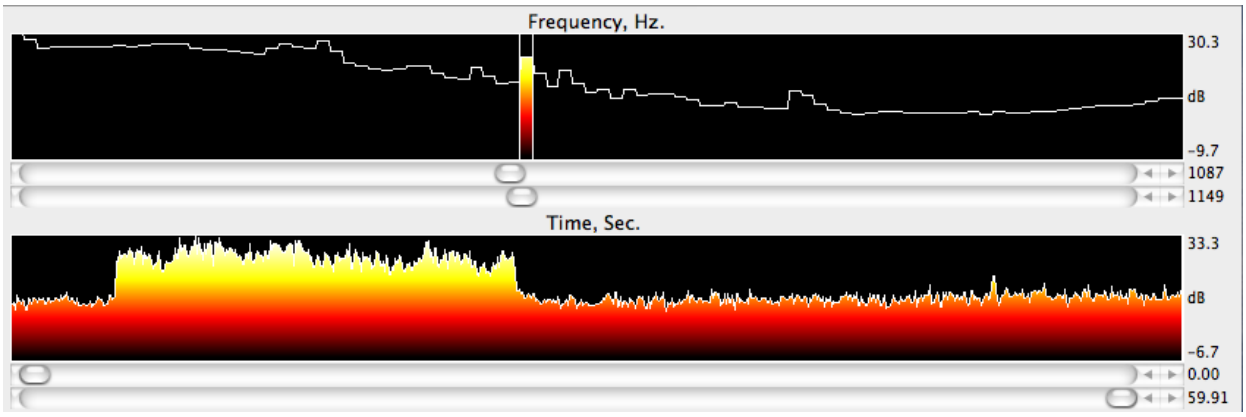


(a)

(a) (c)

**Figure 186: Schematic of. (a) time series of the wind turbine noise measured using the microphone array showing the increase in amplitude due to yaw motor, (b) the beamform map (TIDY) showing the nacelle noise at 1087-1149 Hz when the yaw motors are not operational and (c) the beamform map (TIDY) showing the nacelle noise at 1087-1149 Hz when the yaw motors are operational.**

In order to study in detail the noise produced inside a nacelle, measurements were conducted on the Viryd 8kW wind turbine drive train simulator. The beamform map of the gearbox at a wind speed of 6 m/s and 0% turbulence level using TIDY is shown in Figure 188. The frequency of interest was chosen to be 164-2056 Hz and the microphone array was placed 0.6 m away from the drive train. We observe that in this particular frequency of interest the noise from the drive train was about 75.7 dB. The gear box and the generator produces considerable amount of noise. The beamfrom map for the generator using TIDY for the same wind conditions are shown in Figure 189. We observe that for the frequency range of interest chosen the noise produced by generator is about 72.5 dB. At frequencies above 3000 Hz we observed that the CVP was producing a considerable amount of noise. The beamform map of the CVP using TIDY with the same wind conditions is shown in Figure 190. We observe that the noise produced by CVP was about 66.6 dB for the frequency of interest considered.


**Figure 187: Viryd 8 kW wind turbine drive train simulator.**

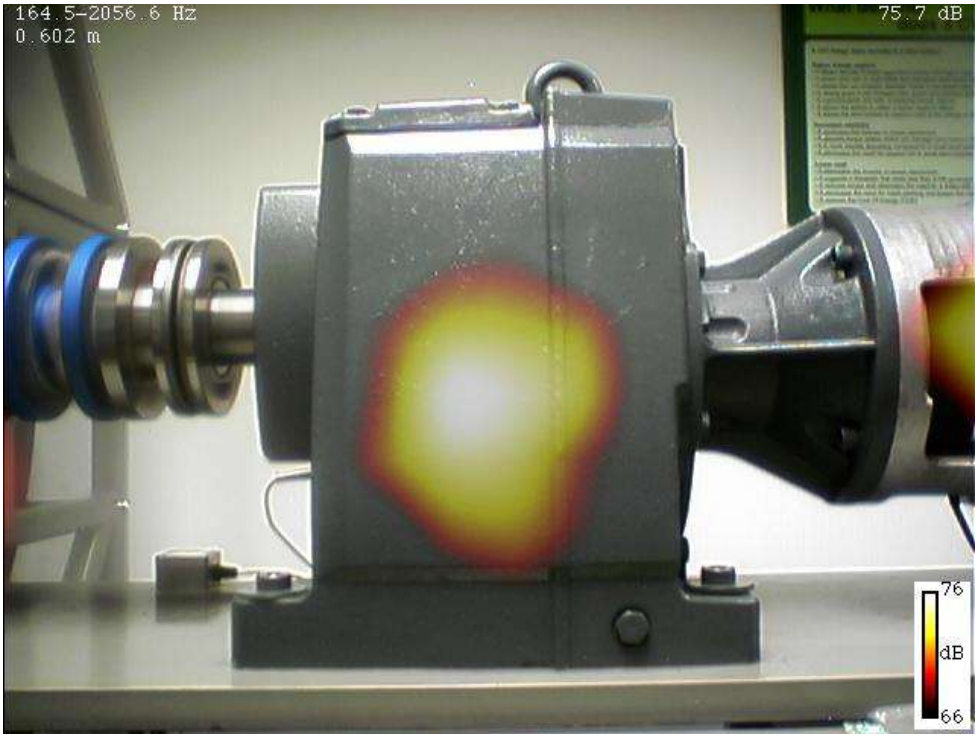


**Figure 188: Beamform map of the gearbox at wind speed 6 m/s and turbulence 0% using TIDY.**


**Figure 189: Beamform map of the gearbox at wind speed 6 m/s and turbulence 0% using TIDY.**

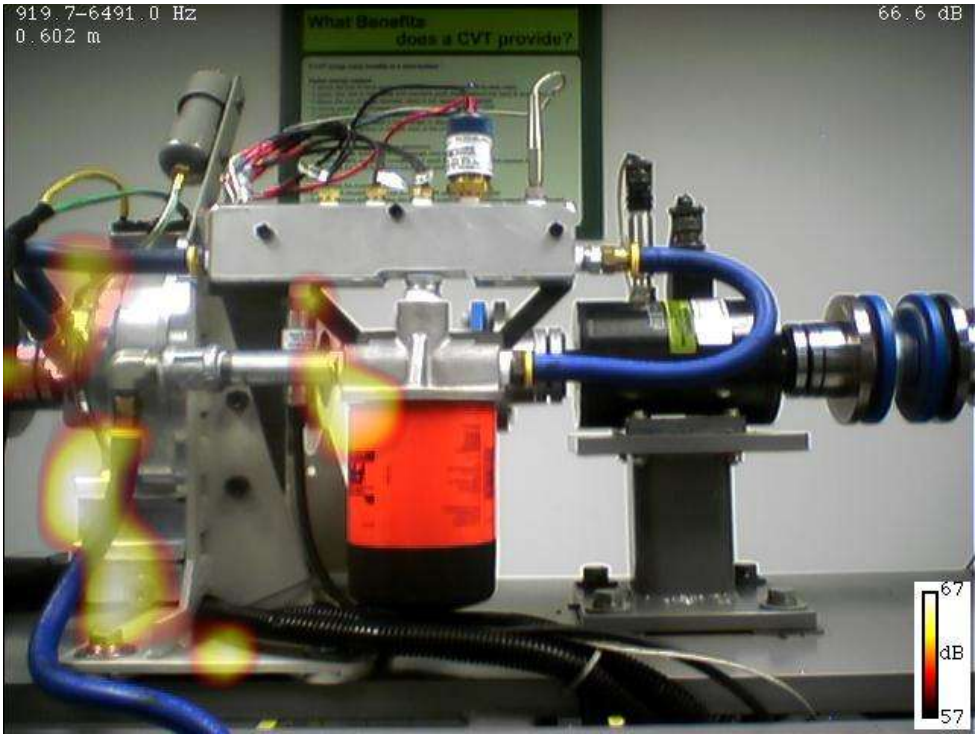


**Figure 190: Beamform map of the CVP at wind speed 6 m/s and turbulence 0% using TIDY.**

### F5. Summary and Future Possibilities

The results of the initial calibration of the array provided us with the knowledge of how various beamforming algorithms behave on exposure to different types on noise sources. The FDBF, DM2 and CLSC were all limited to narrowband analysis whereas DAS and TIDY could be used for broadband analysis. Even though the FDBF, DMS2 and TIDY beamformers were all formulated on the assumption of incoherent sources, they were able to locate coherent sources as well. TIDY, however, produced cleaner spectrum map than FDBF and DMS2. The CLSC beamformer was formulated to pick the maximum of the coherent sources as evident from our experimental results. The CLSC however was able to locate the incoherent sources too. In terms of the frequency of the source, for the particular array and the distance of the source from the array, the microphone array was able to clearly locate the sources above 1000 Hz. The distance of source separation for which the beamformers were able to separate the sources was about 6-8 inches from each other for the frequency range of 1000 – 4000 Hz. From the study it was clear that there was no single algorithm that was perfect for measuring wind turbine noise. In order to study the narrow band sources CLSC was the best algorithm and for broadband analysis TIDY was the best. In view of moving sources TIDY provided the best results again.

From the results of actual wind turbine measurements, it was evident that the compact microphone array was effectively able to separate various noise sources, both mechanical and aerodynamic, produced by the wind turbine. The results from the GE 1.5 MW wind turbine show the potential of the microphone array by effectively separating the blade tip vortex noise and the nacelle mechanical noise. Further we were able to separate out the yaw motor noise which was a narrow band source. The results from the Viryd 8kW wind turbine drive train simulator show that using the microphone array we could further separate the mechanical noise in the nacelle to its particular components such as the gearbox, cooling fan and the generator. In this particular case we were able to separate out the noise components from the gearbox, CVP and generator.

From the detailed study we conducted, we have realized our objective of studying various beamforming algorithms and using them to locate the noise sources on a wind turbine with a compact array. This demonstrates the potential of the microphone arrays in the future of wind turbine noise management. We could use this tool to further investigate the different types of aerodynamic noise that arise on the blade such as the blade tip noise and the trailing edge noise. A lot of interest has been shown in recent years to study these noise sources. This could provide valuable information on modifying the blade configuration to further reduce the aerodynamic noise. Also measurements could be made on a variety of wind turbines such as smaller urban wind turbine and larger wind turbines. One other possible application for the microphone array is to use them as a health monitoring tool for the wind turbine.

## *G. Wind Turbine Acoustics – Numerical Studies*

Modern industrial economies are heavily reliant on electricity. As a result, developing and maintaining a sufficient supply of affordable and reliable power is a priority for every nation. At the same time, a number of factors have combined to stimulate increased interest in more “environmentally friendly” methods of power generation, such as wind or solar. With the currently ongoing political turmoil in the Middle East and the recent Fukushima nuclear accident, this interest is only increasing.

This work involves the numerical simulation of the flow around wind turbines and investigating the acoustic field associated with the unsteady fluid behavior. This section discusses the progress made in this work, the analysis methods used, and the results obtained.

### G1. Numerical Methods

The current methodology combines the abilities of three different numerical tools to predict the unsteady flow around a wind turbine, the resulting acoustics, and an analysis of the noise sources. The Navier-Stokes equations are solved using the OVERFLOW solver to obtain an unsteady flow field in the vicinity of the turbine. Data from this solution is then fed into the PSU-WOPWOP Ffowcs-Williams Hawkings solver to predict the farfield acoustics. This prediction is used to record sound levels at virtual microphone locations, and this information is fed into the Beamform Interactive software package which is used to analyze the data using a variety of beamforming methods.

This methodology is referred to as the "synthetic array technique" as it uses numerical methods to perform an analysis identical to that used for experimental data from microphone arrays. A similar technique was successfully used in a previous joint effort for the acoustics of an airfoil with a blunt trailing edge.

The CFD code used for this work was version 2.2 of the OVERFLOW solver, which is the latest release of this widely used code from NASA Langley [**36**], [**37**]. This software is a state-of-the-art Navier-Stokes solver for structured meshes. The original OVERFLOW code has long been used successfully for a wide variety of Reynolds-averaged Navier-Stokes (RANS) simulations [**38**], [**39**], [**40**].

OVERFLOW 2.2 solves the time-dependent Navier-Stokes equations in an implicit manner on overset structured meshes. The compressible form of the equations are solved in conservative form on a curvilinear coordinate system.

Recent additions to the code make it particularly attractive for the work reported here [**41**], [**42**], [**43**].

With version 2, OVERFLOW introduced the OVERFLOW-D mode (originally from the code of the same name by Robert Meakin). Compared to the regular mode of operation, this mode requires some additional input files and NAMELIST input, but what it enables is the use of internal mesh assembly algorithms (called "Domain Connectivity Function"—DCF) for simulations with moving meshes. This obviates the need for an external mesh assembly package (such as PEGSUS or SUGGAR).

OVERFLOW-D mode also allows automatic off-body mesh generation. When used in this fashion, Cartesian outer meshes can be automatically generated prior to mesh assembly using DCF. Only the near-body meshes must be provided to the code.

For the current work, the code was run in "OVERFLOW-D" mode. Thus, OVERFLOW's internal mesh motion, hole cutting, and block coupling algorithms were used. In addition, automatic off-body mesh generation with mesh adaption was used throughout the run.

Similar to OVERFLOW-D mode, OVERFLOW now has a built-in 6-DOF (six degree-of-freedom) mesh motion module called the "Geometry Manipulation Protocol" (GMP). GMP is a protocol for specifying

geometric hierarchies and associated rigid-body motion. OVERFLOW currently implements only a subset of the larger GMP, but this capability is more than sufficient for the current work, and eliminates the need for an external mesh motion package.

With GMP, two files are used to set up mesh motion parameters for a simulation. For a case like this, which has a simple prescribed motion for the rotor meshes, the configuration is quite simple. First, a file named "Config.xml" is used to identify which meshes are associated with each other, assign labels to these groupings (called "components"), and specify an initial orientation for each component. The Config.xml file for the wind turbine case consists of the following:

```
<?xml version='1.0' encoding='utf-8'?>
<Configuration AngleUnit="degree">
  <Component Name="Rotor" Type="struc">
    <Data> Grid List=1-12 </Data>
    <Transform>
      <Rotate Center="0.,0.,0." Axis="0.,0.,1." Angle="-45." />
    </Transform>
  </Component>

  <Component Name="Tower" Type="struc">
    <Data> Grid List=13 </Data>
    <Transform>
      <Rotate Center="0.,0.,0." Axis="0.,0.,1." Angle="0." />
    </Transform>
  </Component>

  <Component Name="Nacelle" Type="struc">
    <Data> Grid List=14-16 </Data>
    <Transform>
      <Rotate Center="0.,0.,0." Axis="0.,0.,1." Angle="0." />
    </Transform>
  </Component>

</Configuration>
```

The above file identifies three different components: "Rotor", "Tower", and "Nacelle". The near-body meshes (blocks 1-16) are each assigned to one of the three components. The rotor is identified as being initially at the negative 45 degree position.

The prescribed motion is then specified using a second XML file: Scenario.xml:

```
<?xml version='1.0' encoding='utf-8'?>
<Scenario AngleUnit="radian">
 <Prescribed Component="Rotor" Start="0" Duration="100000">
```

```
  <Rotate Center="0.,0.,0." Axis="0.,0.,1." Speed="-0.198846689" Frame="parent" />
 </Prescribed>

 <Prescribed Component="Tower" Start="100000" Duration="0">
  <Rotate Center="0.,0.,0." Axis="0.,0.,1." Speed="0." Frame="parent" />
 </Prescribed>

 <Prescribed Component="Nacelle" Start="100000" Duration="0">
  <Rotate Center="0.,0.,0." Axis="0.,0.,1." Speed="0." Frame="parent" />
 </Prescribed>

</Scenario>
```

The above XML specifies that the "Rotor" component (defined in Config.xml) is rotating about the *z*-axis at a constant speed of approximately -0.199 radians per non-dimensional time unit. The motion starts at the beginning of the simulation, and continues, effectively, forever (technically, the motion would stop at non-dimensional time of 100,000). The other two components (the "Tower" and the "Nacelle") are both set as stationary.

Another extremely useful capability of the OVERFLOW solver is Adaptive Mesh Refinement (AMR). This is the ability to adapt the off-body Cartesian meshes (generated using the OVERFLOW-D mode discussed above) to better resolve the propagation of flow features away from the near-body meshes. The initial off-body Cartesian mesh generation algorithm produces a multi-block configuration where the blocks surrounding the near-body meshes closely match the resolution of those near-body meshes. Away from the near-body meshes, however, the resolution coarsens until, near the farfield boundaries, the mesh spacing exceeds one meter in each direction.

The initial configuration is perfectly suitable for starting the simulation, but as the run progresses, the vortices shed from the rotor (as well as from the nacelle and tower) will be dissipated due to the lack of mesh resolution unless the computational mesh is refined in the necessary regions. Likewise, because the rotor is constantly sweeping through space, there may be regions which at one time require refinement, but which later do not need it.

The traditional approach to such a situation is to generate a mesh which is refined everywhere that might ever need such refinement throughout the entire simulation. This typically results in a huge mesh (in terms of number of points). Furthermore, such meshes almost always have one of two significant drawbacks. In the first case, the flow features of interest do not always move exactly as expected, and thus some may move beyond the refined region of the mesh (and thus fail to propagate correctly). In the other case, meshes are often over-refined, or finely spaced in regions which do not need them. This results in a significantly increased run time for the simulation.

OVERFLOW's mesh adaption algorithm allows the off-body mesh to be refined and/or coarsened as the solution progresses. Our initial wind turbine simulations did not employ the adaptive mesh refinement

algorithm, and a consequence of this was that the unsteady features in the flow were largely dissipated once they had propagated more than one radius downstream.

The results reported here did use the AMR algorithm, and because of this, the unsteady flow features were successfully propagated much further downstream. For the current work, vorticity magnitude was used to trigger the adaption sensor. Mesh refinement was performed every 40 time steps for the cases reported here, which corresponds to every five degrees of rotation of the rotor.

One drawback of the AMR algorithm is that, while it is more efficient than refining the mesh everywhere, it still results in a significant increase in mesh size. In this case, the baseline mesh had approximately 17 million points, but with AMR, the runs reported here ultimately used meshes which had between 40 and 55 million points on any given time step.

After our initial results with AMR (which are reported here) were obtained, it was discovered that the settings we used were not ideal. Preliminary tests using the most recent version of OVERFLOW (version 2.2c) and the recommended AMR settings indicate that the mesh size can quickly grow too large for the limited resources on ITAC's in-house compute cluster. When two or three levels of refinement were permitted, the mesh grew so quickly in size that the ITAC cluster was unable to capture even 90 degrees of rotation of the rotor before the run crashed. Even when limiting the number of off-body refinement levels to one, the total number of mesh points climbs to more than 100 million on more than 2000 blocks by the time a complete revolution of the rotor has been modeled.

The solver was run with a second order implicit scheme in time in conjunction with a dual time marching method to obtain a time-accurate solution. Six sub-iterations per time step were used to synchronize the boundaries with the interior flow and better allow for signals to propagate between computational mesh blocks.

A second order central difference method was used for the explicit convective terms on the near-body meshes, with spectral-radius based smoothing to prevent spurious oscillations. Our initial simulations used the same algorithm for the off-body meshes, and did not make use of the adaptive mesh refinement capability. Based on those results, however, the more recent simulations discussed here employed, for the off-body meshes, both AMR and a $4^{th}$ order central scheme with a higher-order filter to prevent the build-up of spurious oscillations. Since the majority of the flow domain contains very low speed flow (compared to the typical aircraft external flow situations for which OVERFLOW was originally designed), a Low Mach number preconditioning algorithm was used to stabilize the code.

An SST turbulence model was used in the near-body meshes (with Delayed Detached Eddy Simulation), but the off-body meshes were run inviscid. The turbulence model convective terms were solved second order.

The PSU-WOPWOP code is based on the concept of an acoustic analogy. The acoustic analogy was introduced by Lighthill [**44**] in his seminal paper on sound generated aerodynamically. In an acoustic analogy the equations of motion are rearranged into the form of a wave propagator and equivalent

sources. This pioneering work introduced the concept of convective amplification and Doppler frequency shift.

Lilley [**45**] introduced an acoustic analogy in which the wave propagator included the effects of mean shear and density gradients. In the case of a parallel shear flow the equivalent sources are all at least second order in the turbulent fluctuations. Noise prediction methods based on Lilley's equation generally use steady calculations of the flow development, such as provided by a RANS-based Navier-Stokes solver. These are used to set the length and time scales of the turbulence. Examples include methods for jets developed by Khavaran et al. [**46**] and Khavaran [**47**].

In their 1969 paper, Ffowcs Williams and Hawkings [**48**] utilized the powerful technique of generalized function theory to an extension to the Lighthill acoustic analogy that enabled them to consider the noise generated by surfaces in arbitrary motion. The FW–H equation is an exact rearrangement of the continuity equation and the Navier–Stokes equations into the form of an inhomogeneous wave equation with two surface source terms (monopole and dipole) and a volume source term (quadrupole). Although the quadrupole source contribution is insignificant in many subsonic applications with solid surfaces, it is the only noise source term in the original Lighthill acoustic analogy and is particularly relevant for jet noise. Even so, the quadrupole source term in the FW–H equation is a volume source term, therefore it is considerably more expensive to evaluate than the surface source terms.

Although originally pointed out by Ffowcs Williams and Hawkings, the usefulness of the FW–H equation as a Kirchhoff type equation was demonstrated by Brentner and Farassat [**49**]. In this application, the fictitious surface used in the derivation of the FW–H is located not on a solid body, as in the classical implementation, but rather surrounding all the relevant noise sources. Thus the integration surface (or acoustic data surface) is a fictitious surface (like a control volume) located in the fluid; hence, this application of the FW–H is called the permeable (or porous) surface formulation because fluid may flow through the surface. With all the significant acoustic sources contained inside the surface, the volume quadrupole term does not need to be computed – saving substantial computational effort. The permeable surface formulation has become a valuable noise prediction tool primarily because CFD has advanced sufficiently to provide the time-dependent flow field solution on the integration surface with high spatial and temporal fidelity, as required by the permeable surface formulation of the FW–H.

PSU-WOPWOP is a general purpose Ffowcs Williams–Hawkings (FW-H) solver developed at The Pennsylvania State University by Dr. Brentner and his research team [**50**], [**51**], [**52**], [**53**]. The code was originally developed to compute the noise of rotorcraft in maneuvering flight, but was developed using an object-oriented design in the Fortran 95 language in a very general manner. Both the classical and permeable surface formulations of the FW-H equation [**54**], as expressed by Farassat's Formulation 1A [**55**], [**56**], have been implemented in the code and have been thoroughly tested.

The PSU-WOPWOP code has extensive source motion capability—originating from its roots as a maneuver noise prediction tool. The integration surfaces (solid or permeable) may be either rigid or flexible. PSU-WOPWOP predicts the acoustic pressure time history in the near and far fields, for either stationary or arbitrarily moving observers. PSU-WOPWOP also has significant output signal processing

to convert the acoustic pressure time history into acoustic spectra, including narrow band spectra, $1/n^{th}$ octave bands, etc. The code's output processing also includes the ability to filter the data over arbitrary frequency ranges and include various types of windowing functions for the frequency domain processing.

PSU-WOPWOP has recently been upgraded to predict the acoustic pressure gradient at arbitrary observer locations [**57**], [**58**]. The acoustic pressure gradient is an input to either frequency or time domain acoustic scattering codes, which then can predict the scattered field when rigid bodies are in the vicinity of the noise predicted by PSU-WOPWOP. PSU-WOPWOP has been used for rotor noise prediction, landing gear noise prediction, acoustic scattering, prediction of trailing edge noise, and jet noise.

In the current work, the permeable integration surfaces (also referred to as acoustic data surfaces or ADS) will be used for the FW-H noise prediction. PSU-WOPWOP will require the time-dependent location of the surfaces along with the time dependent specification of density, momentum and pressure at each of the surface mesh points.

The computation of the acoustic pressure at a large number of observer positions, as might be used, for example, in an extensive phased array, should be very efficient because PSU-WOPWOP uses an observer parallel implementation, employed via the Message Passing Interfaces (MPI). This parallelism effectively sends the acoustic computation for each observer to single processor on a computer cluster, up to the number of processors available. As the processors become free, a new observer position is sent to the processor, keeping all the processors busy until the entire job is done. PSU-WOPWOP has previously been coupled with OVERFLOW and several other CFD codes using a file-based method, which is relatively easy to implement and should be ideal for this project.

Given that OVERFLOW can accurately compute the wind turbine near-field, and that PSU-WOPWOP can compute the acoustic farfield, it remains to enable the two separate solvers to communicate with each other. There are several possibilities for doing this; three of these have been identified and evaluated for the current wind turbine work.

One option is to try to obtain and use a utility which takes data from surface meshes, as processed by MIXSUR, to create the input needed by PSU-WOPWOP. The drawback to this approach is that the primary acoustic sources for this case are expected to be off-body (associated with separated regions of the flow). As such, a FWH surface on the blade surface will not properly enclose these regions, and their contribution will be lost.

To overcome this limitation, a second possibility is to create a "pringle can" mesh around the spinning blade (avoiding any intersection with the hub or mast) and use OVERFLOW's "Acoustic Data Surface" (ADS) capability to save data on it. This data can then be converted for later processing with PSU-WOPWOP. A utility would have to be created to perform this conversion. Also, when the ADS is inserted into the CFD mesh, the solution file must be somehow modified to add some form of initial conditions or else the solution must be restarted from scratch. Either option requires expenditure of additional time and resources.

A third option, and the one which appears to best fit the requirements of the current work, is to use OVERFLOW's capability to save solution data in specified regions of the flow (the "SPLITM" controls). By selecting an appropriate set of surfaces, a reasonable integration surface can be assembled around the spinning blade. The SPLITM data can then be assembled into the "patch file" (containing the surface mesh data at each time step) and "flow data file" (containing the density, momentum, and pressure on the surface at each time step) needed by PSUWOPWOP.

Using SPLITM means that no additional mesh needs to be generated, and no special manipulation of the restart solution file is required to insert initial conditions for the surfaces. Thus, this is the approach which we have taken.

There are two drawbacks to the SPLITM approach. One is that OVERFLOW saves a separate file for each SPLITM surface specified. Also, a new file is created every time the SPLITM data is output to the disk. Since each SPLITM surface must come from only one block, multiple surfaces (twelve, in fact) were required in order to construct the FWH surface. As a result, a full run of the wind turbine case will result in over 150K files which must be processed.

A new utility was written to semi-automatically assemble all of these SPLITM files into the patch and flow data files which PSU-WOPWOP reads.

Beamfom Interactive is a commercial product of OptiNav, Inc. for processing microphone array data. There are several different modules in Beamform Interactive, which allow the user to apply various beamforming methods to analyze the data. The most basic method is the "Conventional Beamforming" algorithm. This is a high speed, wide band implementation of the classical formula. An "Enhanced Resolution" variant of the classical beamforming technique is also available. This approach weights cross spectral matrix elements to improve resolution. Another algorithm available is DAMAS2. This is a high-speed version of DAMAS which employs an FFT for improved processing speed. It also used a nonuniform mesh to avoid problems with the PSF model. The CLEAN-SC method is an implementation of Sijitsma's algorithm [**33**], which is another deconvolution-based approach to beamforming. Finally, TIDY is an OptiNav method, related to CLEAN-SC, which allows analysis with unlimited bandwidth.

### G2. Previous Application of the Synthetic Array Technique

As mentioned above, ITAC has previously worked with Dr. Dougherty and Profs. Brentner and Morris to couple a CFD solver with PSU-WOPWOP and Beamform Interactive to obtain insights into acoustic noise sources. This work was performed in the context of a NASA-sponsored Phase I SBIR. While the full analysis process has not been completed for the current wind turbine work, it was successfully demonstrated on an airfoil with a blunt trailing edge (specifically, a truncated NACA 0012 airfoil). The results of that work are repeated here to illustrate the potential of the approach for current wind turbine work.

Given the solution on the specified FWH integration surface(s) for the truncated airfoil test case), PSU-WOPWOP predicted acoustic data at "observer" locations corresponding to phased array microphone locations. The microphone array used for the proof-of-concept work was based on coordinates

provided by the NASA customer as representative of their MADA arrays. Figure 192 shows the array layout, with two microphones noted in particular.

The spectra predicted at these two locations are shown in Figure 193 and Figure 194. Microphone 1 identifies a peak near 5 kHz, which corresponds to the drag peak for this case. Microphone 23, on the other hand, picks up both the lower frequency peak associated with lift and the drag-related peak.

Three array views of the trailing edge segment (simulated by the CFD) were used. The first view (the "side" view) positioned the array 1.39 meters to the side of the airfoil, looking down the trailing edge, with the center of the array aligned with the trailing edge of the airfoil (see Figure 195). The second view was a "top" view, with the array positioned above the sliver of airfoil section which was simulated and looking down at the trailing edge (as shown in Figure 196). Again, the array was positioned 1.39 meters from the airfoil. The final view was the "back" view, shown in Figure 197, in which the array was positioned 1.39 meters aft of the airfoil trailing edge and faced upstream.

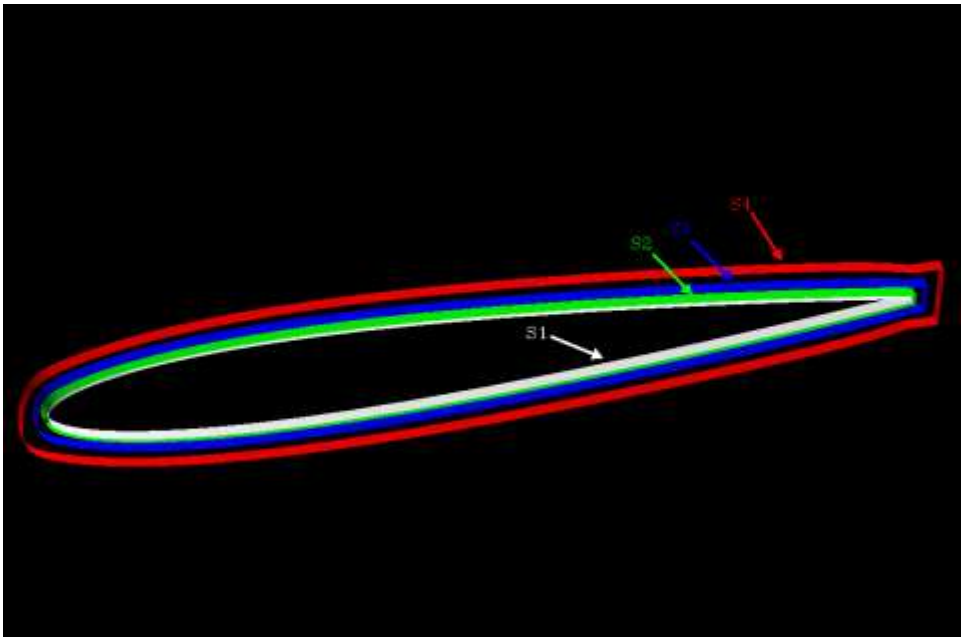


**Figure 191: Locations of Ffowcs Williams-Hawkings surfaces at which data was saved in the unsteady 3-D case**

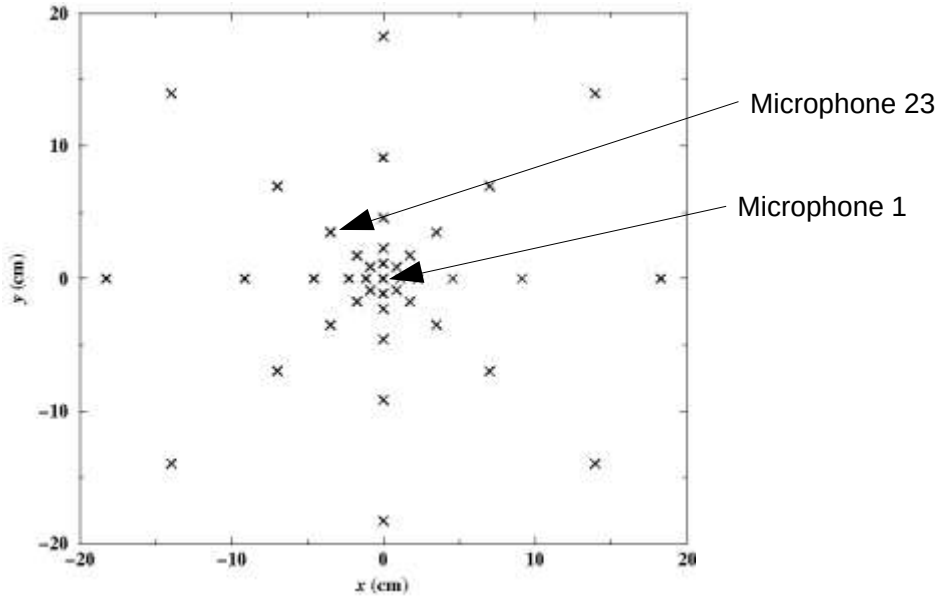


**Figure 192: Arrangement of the synthetic microphone array used for the Phase I work**

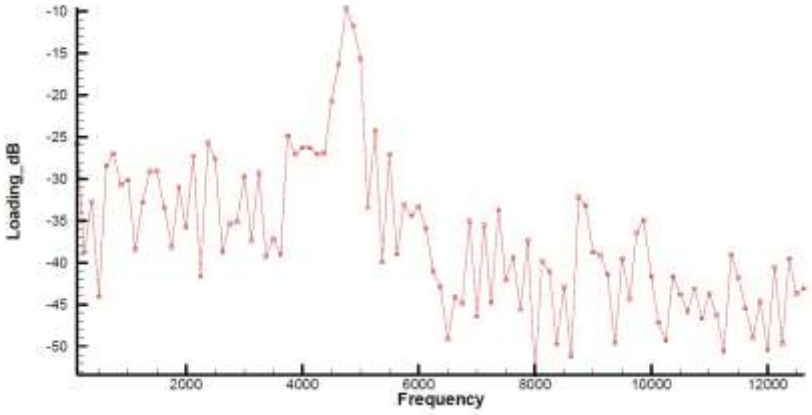


**Figure 193: Spectra predicted by PSU-WOPWOP at Microphone 1 location**

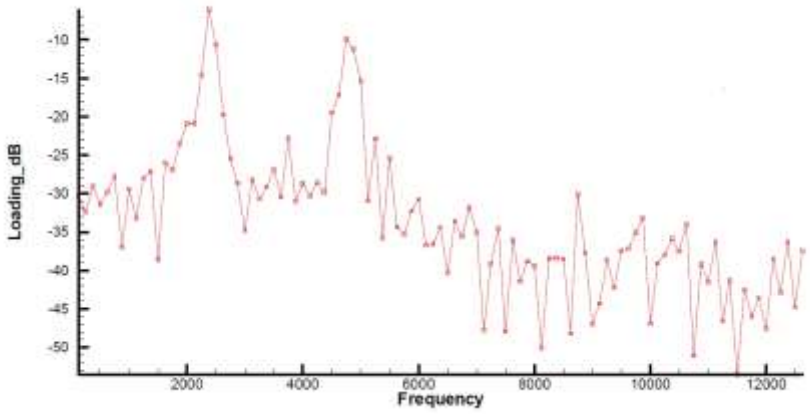


**Figure 194: Spectra predicted by PSU-WOPWOP at microphone 23 location**

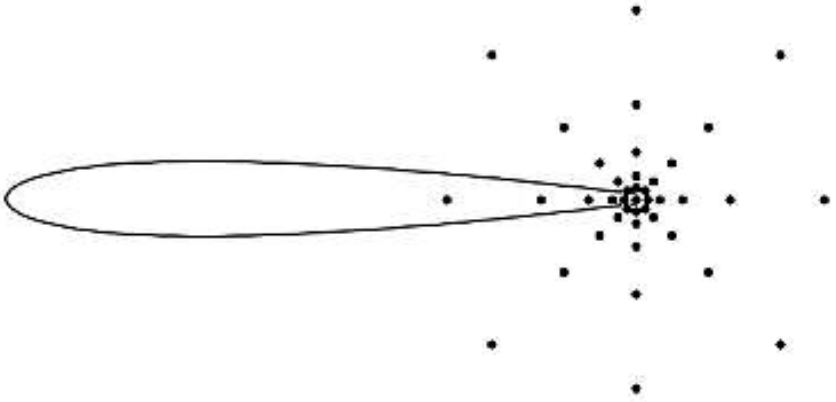

**Figure 195: "Side view" orientation of the microphone array**

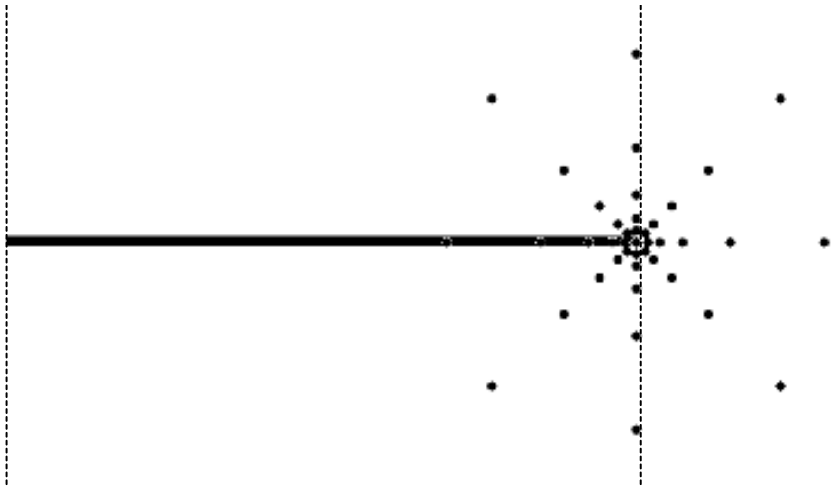

**Figure 196: "Top view" orientation of the microphone array**

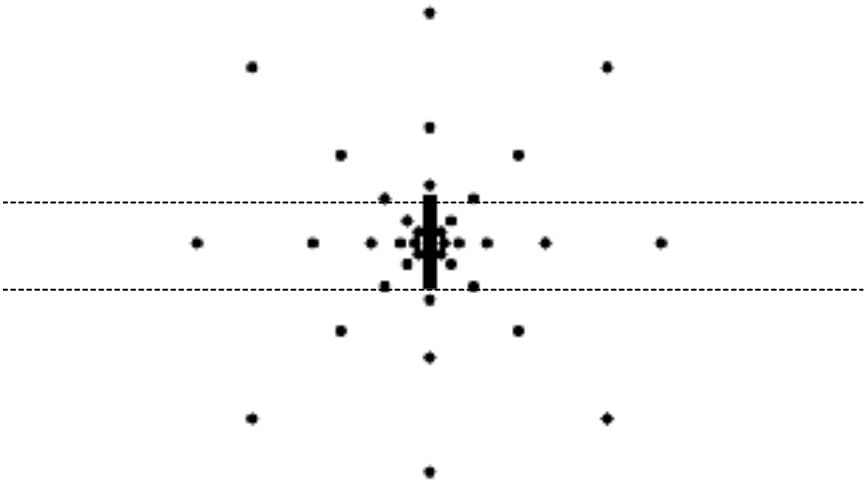

**Figure 197: "Back view" orientation of the microphone array**

The average array spectra detected from the three different viewpoints are shown in Figure 198. Note that the "back view" detects the peak frequency to be around 5 kHz, while the other two views show the 2.5 kHz peak having the largest amplitude.

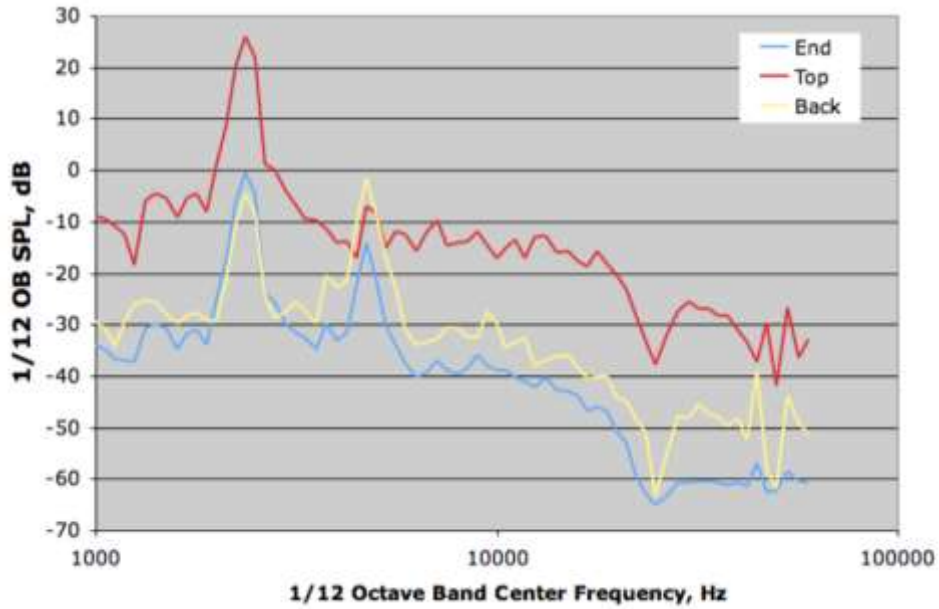


**Figure 198: Average array spectra computed at the three different array positions**

Several beamforming methods in OptiNav's "Beamform Interactive" product were used to analyze the data from PSU-WOPWOP. The first set of results look at the "side view" data and focus on the frequencies in the vicinity of the 5 kHz peak. The frequency range used for these results is indicated in Figure 199. A monopole-oriented analysis was used for these results.

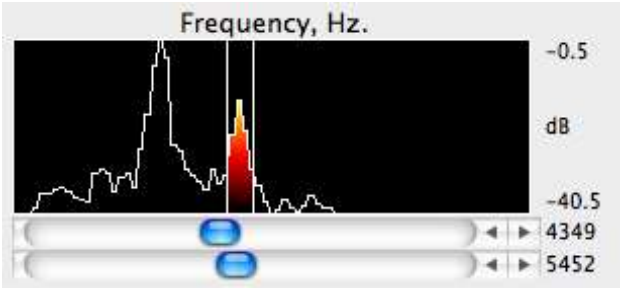


**Figure 199: Frequency range used for monopole-oriented analysis of 5kHz peak**

Figure 200 to Figure 204 show the predicted noise sources using the various algorithms. Conventional beamforming, shown in Figure 200, shows a large region centered about the trailing edge. When the enhanced resolution conventional beamforming variant is used, the region identified as containing the noise sources is somewhat reduced in size, as shown in Figure 201. This algorithm achieves enhanced resolution by weighting cross spectral matrix elements. When applying the DAMAS2 algorithm, the source region is predicted even smaller (shown in Figure 202). DAMAS2 is a high speed version of DAMAS which uses an FFT algorithm for improved performance and nonuniform meshes to avoid problems with the PSF model. In Figure 203, the CLEAN-SC algorithm (Sijtsma's algorithm [**33**]) predicts a slightly smaller source region. OptiNav's TIDY algorithm result, shown in Figure 204, shows the source extending further downstream than either DAMAS2 or CLEAN-SC. Since the integration surfaces used by PSU-WOPWOP to predict the sound measured by the microphone array was on the airfoil surface, and since the computational mesh only resolved significant unsteadiness in the vicinity of the trailing edge, these figures indicate that, as expected, DAMAS2, CLEAN-SC, and TIDY are better able to predict the source location than conventional beamforming techniques.

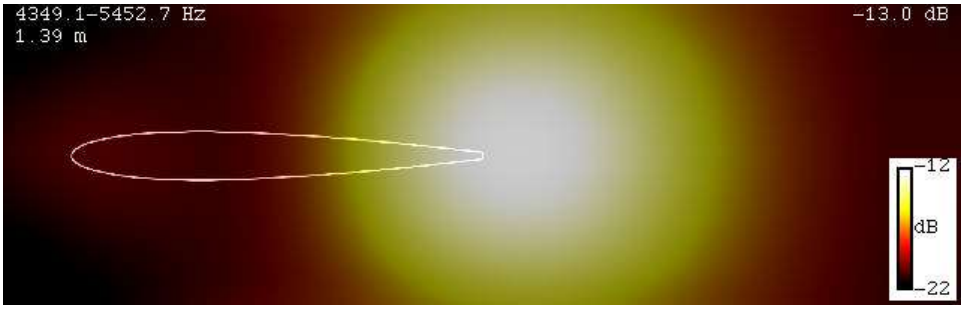


**Figure 200: Noise sources identified by conventional beamforming**

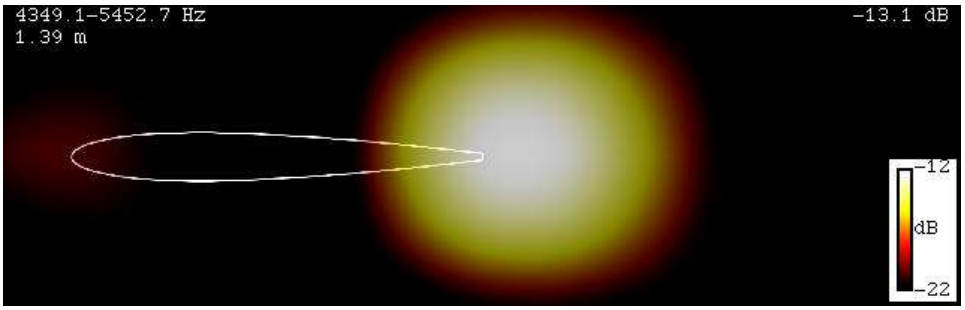


**Figure 201: Noise sources identified by conventional beamforming with enhanced resolution**

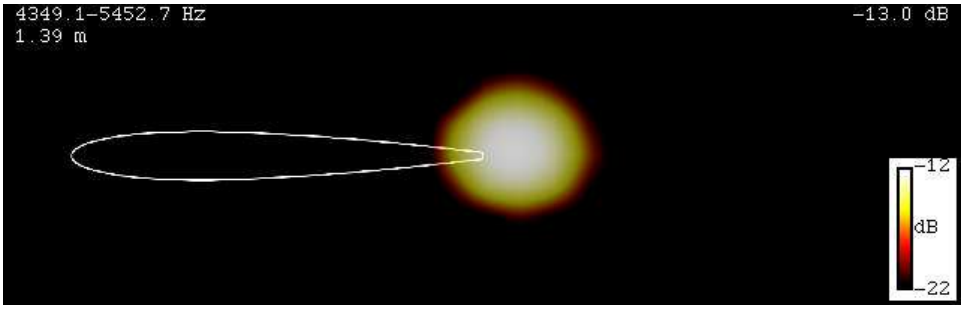


**Figure 202: Noise sources identified using the DAMAS2 algorithm**

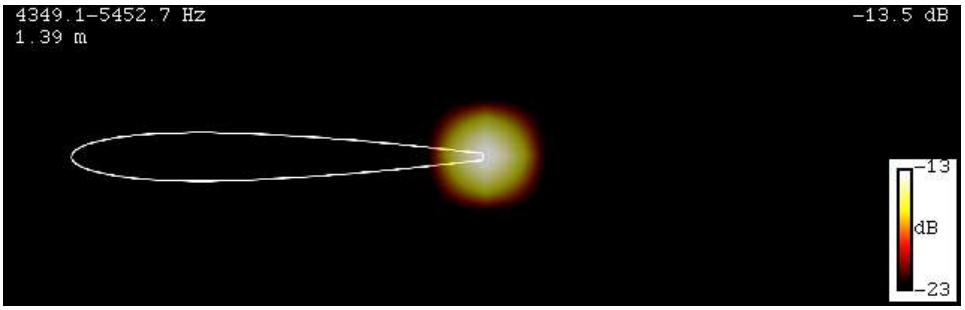


**Figure 203: Noise sources identified using the CLEAN-SC method**

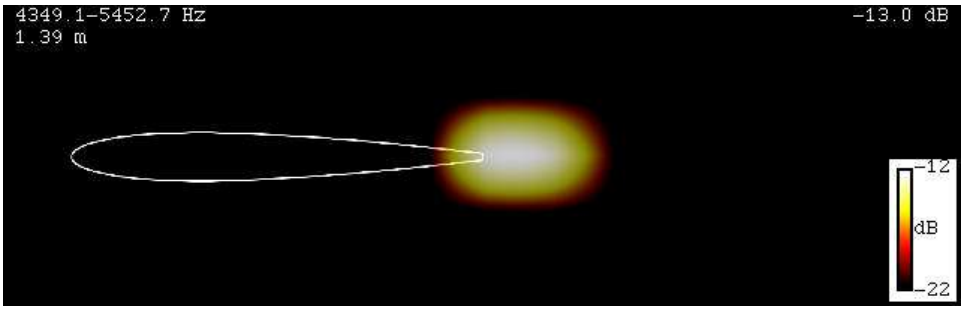


**Figure 204: Noise sources identified using OptiNav's TIDY algorithm**

In the next set of plots, the results of the low frequency peak analysis are presented. This analysis was performed using dipole-based methods. The frequency range used here is illustrated in Figure 205.

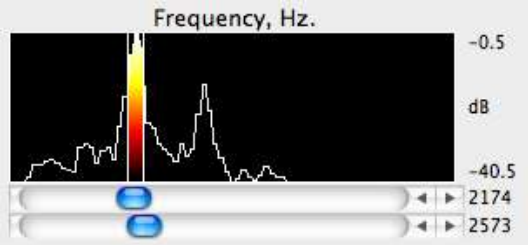


**Figure 205: Frequency range used for monopole-oriented analysis of 2.5kHz peak**

The predicted low frequency peak noise source regions, as determined by various methodologies, are shown in Figure 206 to Figure 209. Again, the conventional beamforming methods (Figure 206 and Figure 207) indicate a much larger source region, whereas the deconvolution-based methods, DAMAS2 and TIDY, are able to focus more tightly on the trailing edge region, as shown in Figure 208 and Figure 209.

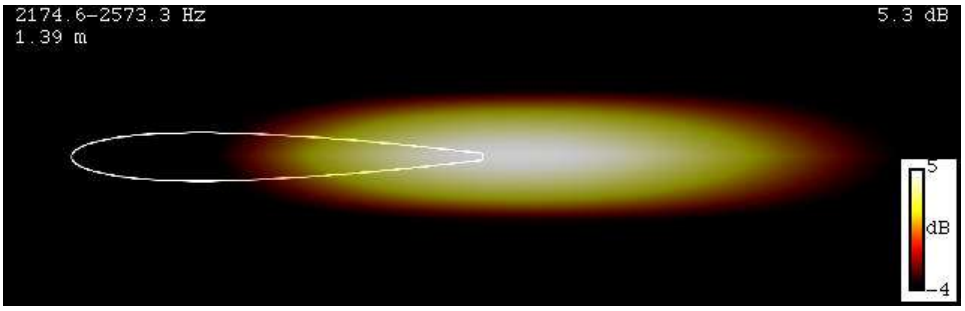


**Figure 206: Low frequency peak noise sources identified using conventional beamforming**

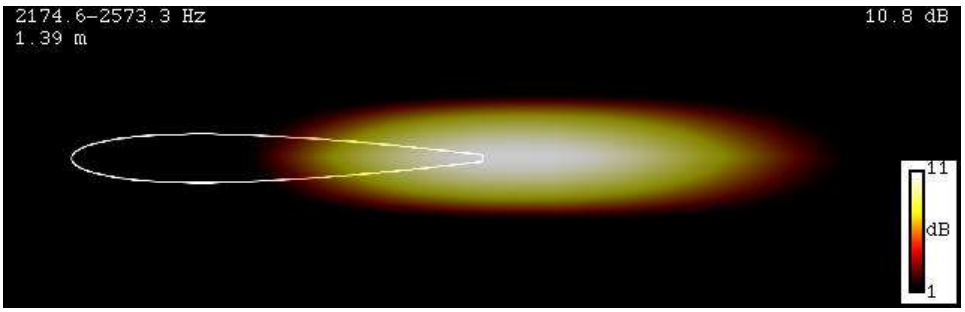


**Figure 207: Low frequency peak noise sources identified using conventional beamforming with enhanced resolution**

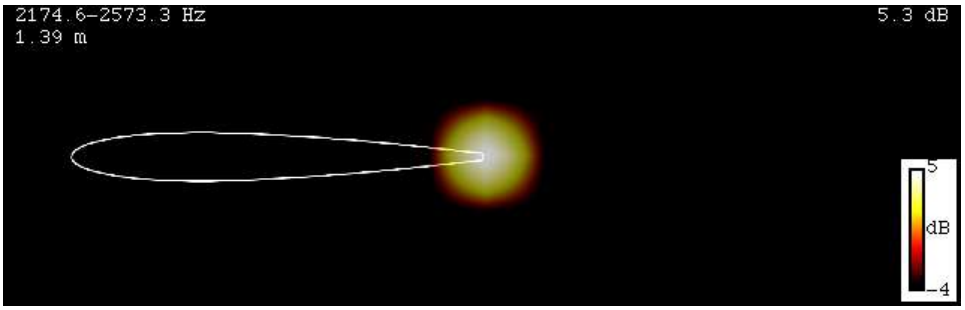


**Figure 208: Low frequency peak noise sources identified using DAMAS2**

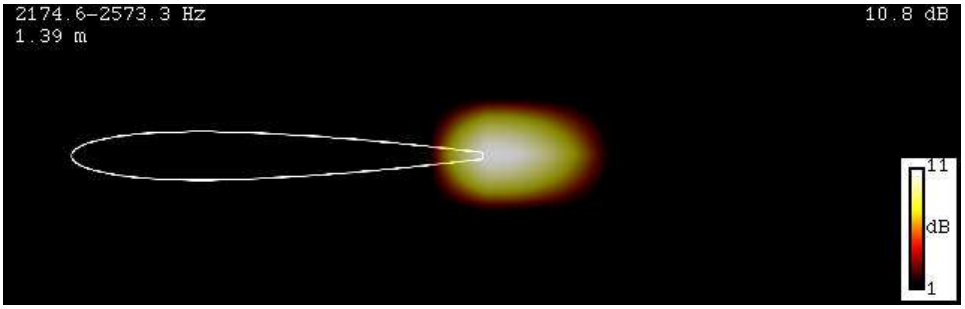


**Figure 209: Low frequency peak noise sources identified using TIDY**

The next set of results are from the analysis of the data taken by the array in the "top view" position. Figure 210 shows the results from a wide-band analysis using conventional beamforming. One strength of the TIDY algorithm is its ability to process data with unlimited bandwidth. Thus, the results of a wide-band analysis of the same data using the TIDY algorithm are shown in Figure 211. Compared to the conventional beamforming approach, TIDY predicts a much tighter region of noise, which is what one would expect, given the knowledge of the CFD data used to create the synthetic array.

The above analysis was followed up with a series of investigations using TIDY which focused on different frequency bands. Figure 212 looks at the frequencies surrounding a secondary peak in the vicinity of 1.4 kHz. Again, the sound sources are detected just aft of the trailing edge.

Figure 213 shows the noise sources responsible for the primary peak at 2500 Hz. Again, TIDY indicates that these sources are located in the vicinity of the trailing edge and just aft of it. The same is true of the secondary peak at 5 kHz, shown in Figure 214.

In Figure 215, which examines the sources of another secondary peak near 7 kHz, some sources are detected on the surface of the airfoil upstream of the trailing edge. Given the limitations of the computational mesh used in the CFD simulations, it is unlikely that this is an accurate reflection of the simulated physics, nor is the similar prediction shows in Figure 216 for a range of higher frequencies.

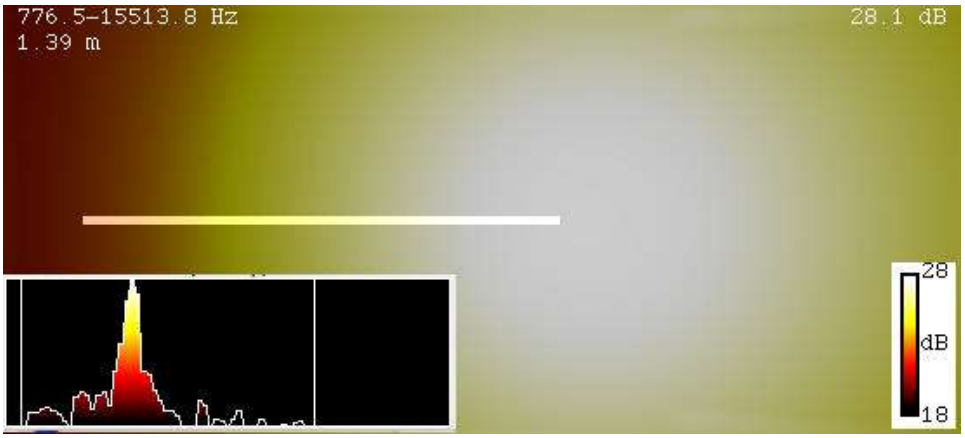


**Figure 210: Wide frequency band processing results using conventional beamforming**

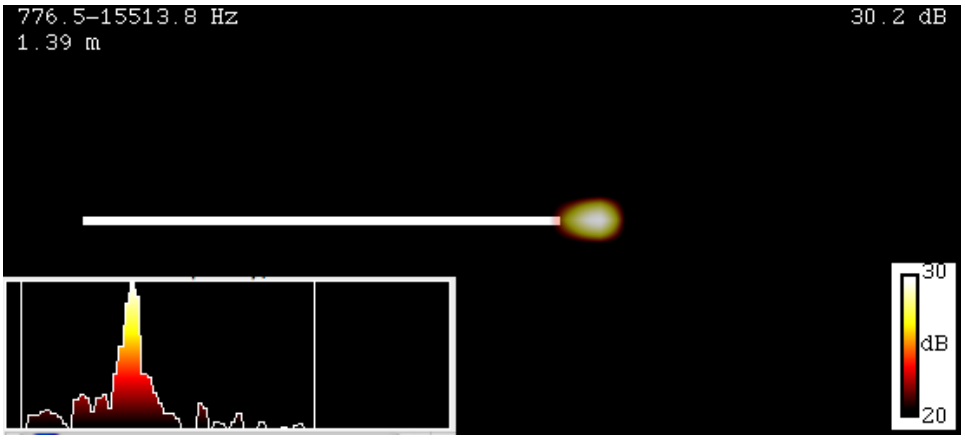


**Figure 211: Wide frequency band processing results using TIDY**

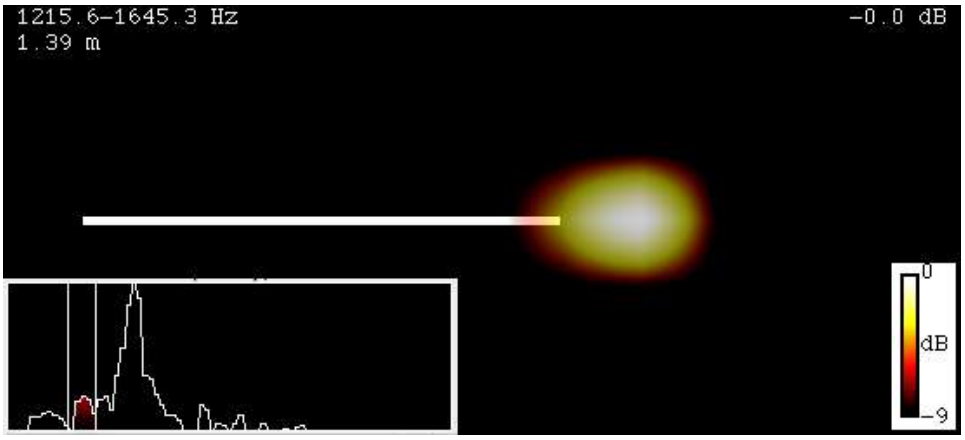


**Figure 212: TIDY analysis of top view data in a frequency band centered on secondary peak near 1.4 kHz**

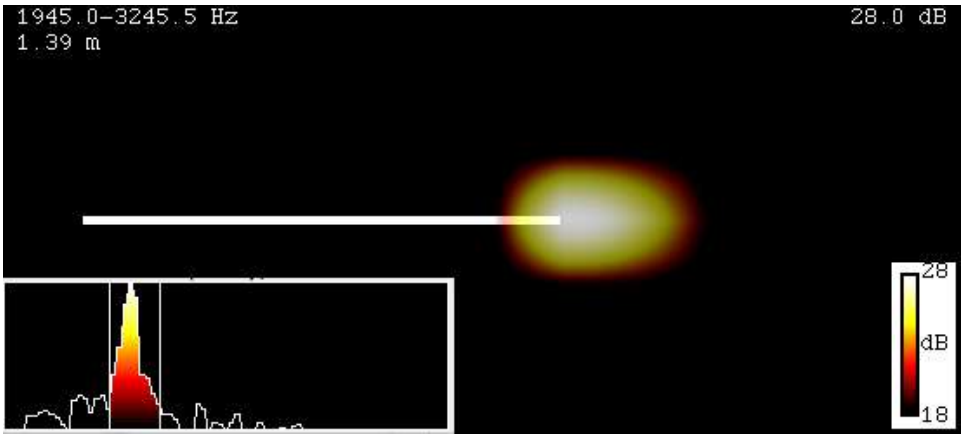


**Figure 213: TIDY analysis of top view data in a frequency band centered on primary peak near 2.5 kHz**

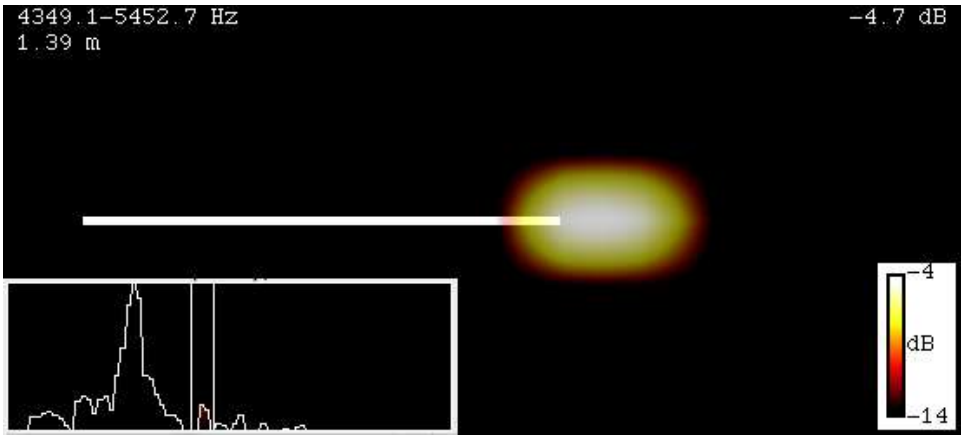


**Figure 214: TIDY analysis of top view data in a frequency band centered on secondary peak near 5 kHz**

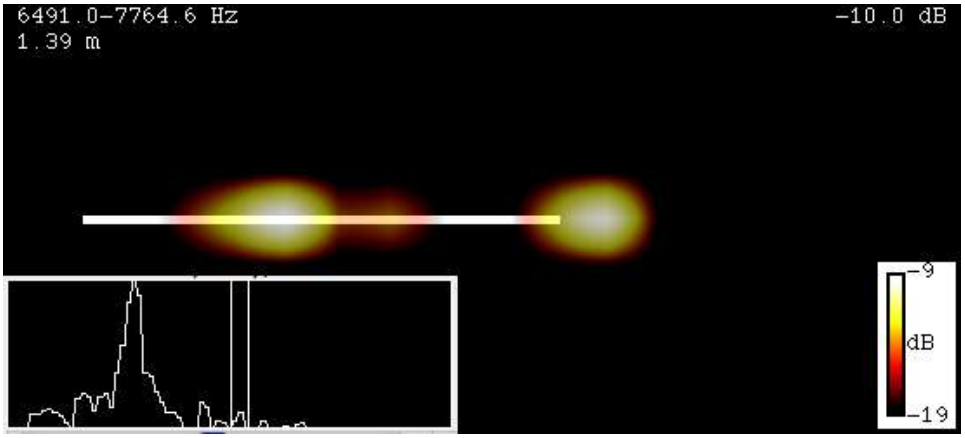


**Figure 215: TIDY analysis of top view data in a frequency band centered on secondary peak near 7 kHz**

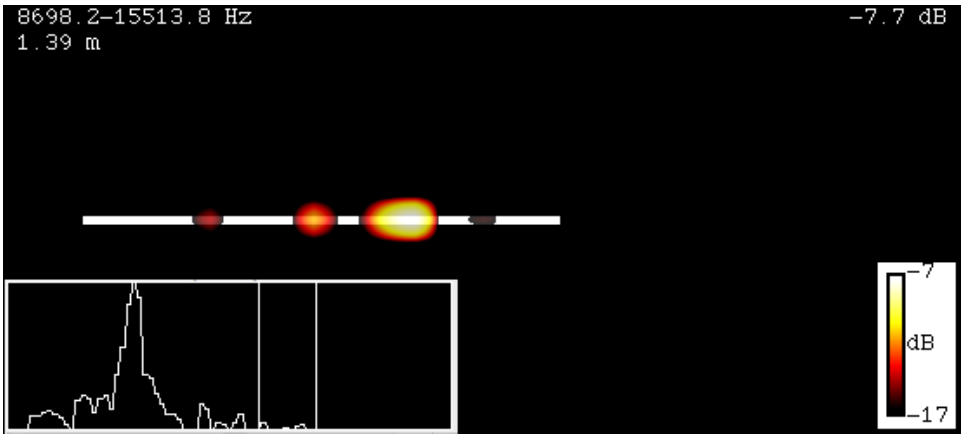


**Figure 216: TIDY analysis of top view data in a frequency band between 8 and 15 kHz**

The final set of beamforming results comes from positioning the synthetic array downstream of the trailing edge and looking upstream at the trailing edge. The analysis was conducted using 1/3 octave bands. All of these results employed TIDY beamforming algorithm. Except where noted, a monopole-oriented analysis was used. Figure 217 shows the results of the relatively lower frequency bands (up to 2.8 kHz). The off-body noise sources identified in the lower frequency bands are almost certainly non-physical, given the methodology employed to generate the acoustic measurements being analyzed. Note that the two highest frequency bands on this plot are clearly of a dipole nature. Figure 218 continues this analysis and presents results from frequency bands up to 44 kHz. At the highest frequencies, one can again see some non-physical results.

The results of the beamforming analysis are summarized in Figure 219. Much of the data is consistent with the dramatic vortex shedding behind trailing edge which was observed in the CFD. The spectral analysis of the flow quantities was consistent with theories of lift and drag dipoles.

In general, we consider this proof-of-concept application of the synthetic array technique a success. The lower-frequency tone (the lift dipole) was indeed seen by the beamforming analysis to have a dipole spatial structure. The higher frequency (2x) tone, which presumably corresponds to the drag dipole, was observed from the side and the back, but the dipole character was not evident. Sources were also seen forward of the trailing edge at high frequencies.

We expect that applying the synthetic array technique to the wind turbine problem will provide results of similar or better quality. The airfoil case was limited by the thin spanwise dimension which could be modeled on the then-available computational resources. The wind turbine case, on the other hand, includes the full rotor geometry, as well as the nacelle, mast, and ground plane. While the spanwise resolution of the rotor is not perfect, it is sufficient to resolve significant instabilities, including those which we believe to be responsible for the most intense acoustics.

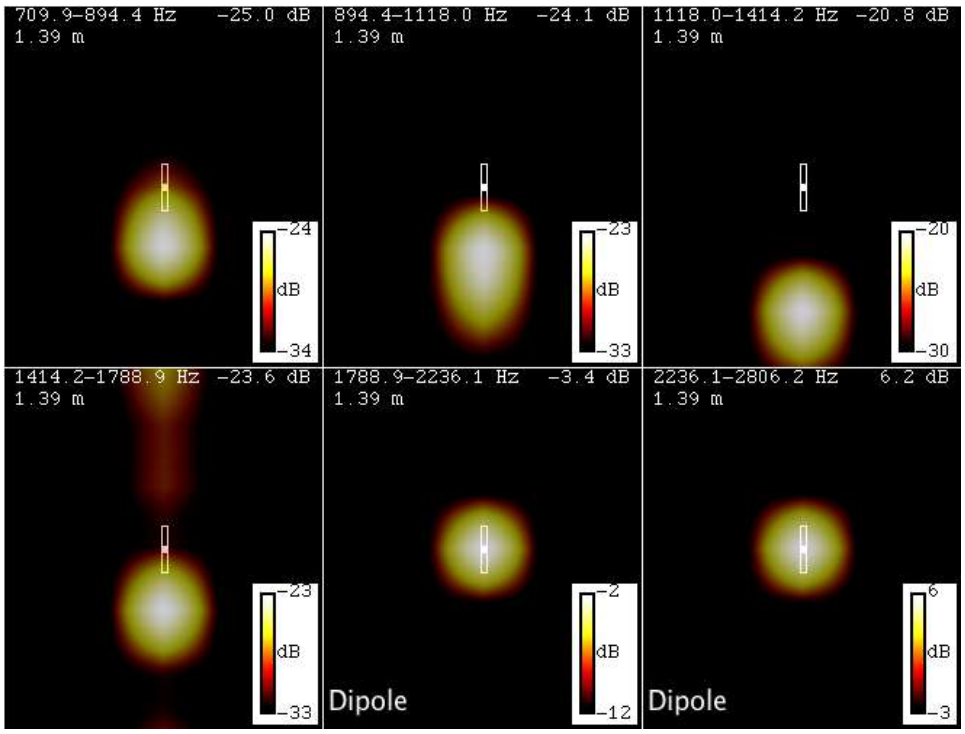


**Figure 217: TIDY analysis of 1/3 octave lower frequency bands with the synthetic array in the "back view" position**

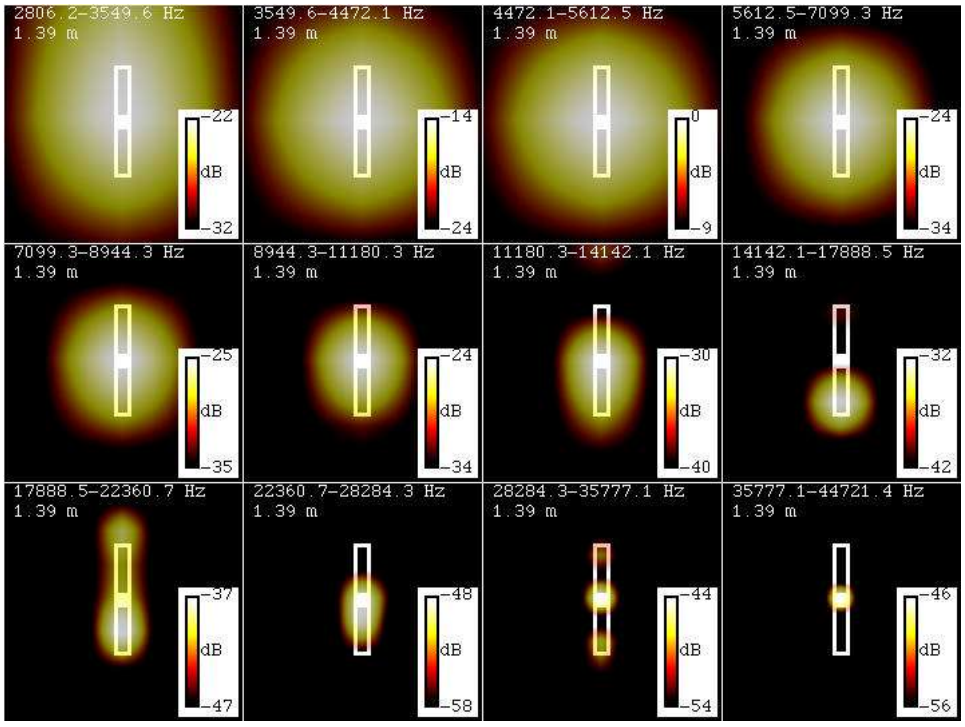


**Figure 218: TIDY analysis of 1/3 octave higher frequency bands with the synthetic array in the "back view" position**

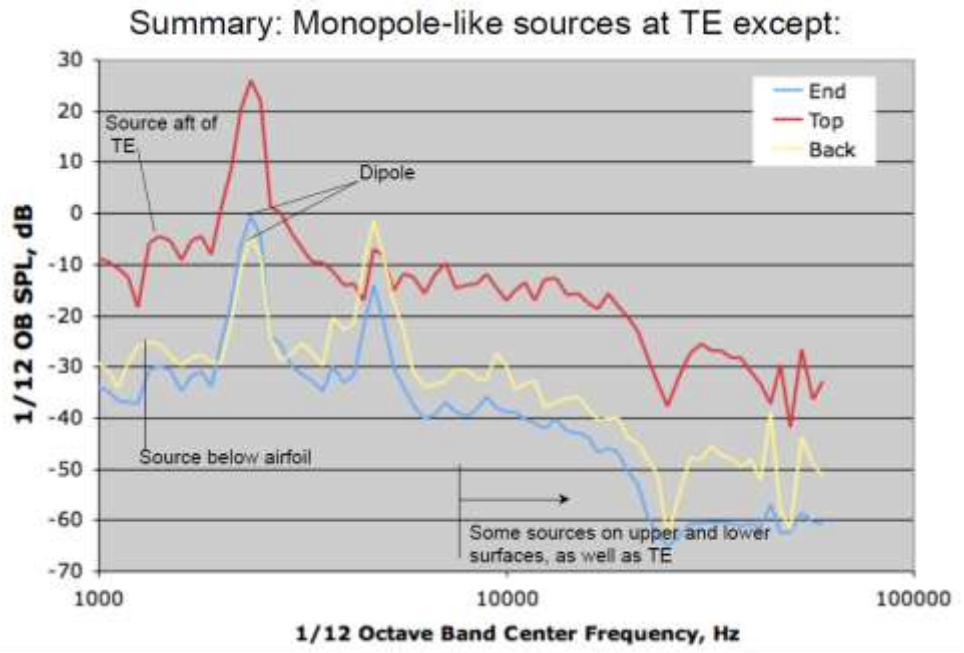


**Figure 219: Summary of beamforming analysis results**

### G3. Problem Identification

The configuration used for the current work is based on the U.S. Department of Energy National Renewable Energy Laboratory (NREL) 10m diameter research wind turbine, shown in Figure 30. This device has been field tested field-tested in various configurations since 1989 at DOE's National Wind Technology Center located near Boulder, Colorado. It has been operated in outdoor atmospheric turbulent wind conditions up to 31 m/s (70 mph), and has been exposed to winds above 65 m/s (145 mph) with the rotor parked. Test data have been made available to the research community through International Energy Agency Annex XIV and Annex XVIII. Reports summarizing results of the atmospheric turbine tests have demonstrated the extremely complex dynamic nature of the typical wind turbine operating environment. Highly turbulent wind and sheared inflow conditions are major factors that contribute to the complexity.

Some of these issues have been addressed by testing the device in NASA's 24.4 by 36.6 meter (80' by 120') wind tunnel. This tunnel is part of the National Full-Scale Aerodynamics Complex (NFAC) which is located at the NASA Ames Research Center in Moffett Field. Testing in a controlled wind tunnel environment eliminates many of the uncertainties of a field test, and the resulting data provide information from which a significant portion of the complex inflow-induced operating environment is removed.

The current work seeks to accomplish a similar reduction in uncertainty, in that, even more than a wind tunnel, a numerical experiment can isolate specific features of interest. For example, in the current work, the turbine geometry is assumed to be rigid. Also, the effects of tunnel walls and/or unsteady inflow conditions are eliminated.

**Figure 220: The NREL 10m research wind turbine**

***Computational Mesh***

A near-body computational mesh for the NREL wind turbine geometry was obtained from Drs. Chris Stone and Marilyn Smith, who developed the mesh under contract from the National Science Foundation. The blade tip pitch was four degrees. This original mesh consisted of 2.6 million points in 16 blocks. As mentioned above, the OVERFLOW-D option to automatically generate Cartesian off-body meshes was employed to fill in the remainder of the flow domain.

The basic layout of the geometry is shown in Figure 221. As the figure shows, the mast and the generator housing were included in the simulation, but the other features shown in Figure 220 were not (most notably the shaft and the cone-like structure attached to the front of it).

A close-up of the surface mesh in the rotor tip region is shown in Figure 222. The mesh is clustered toward the leading edge, trailing edge, and the tip, but away from these regions, the spanwise spacing of points becomes fairly large, considering the nature of the acoustics we wish to resolve. If more computational resources were available, this is one aspect of the mesh which would have been modified in order to better resolve the unsteady shedding. The present mesh does capture significant unsteadiness, however, as will be shown below, since a large portion of the flow features of interest are generated at the blade tips or aft of the trailing edges.

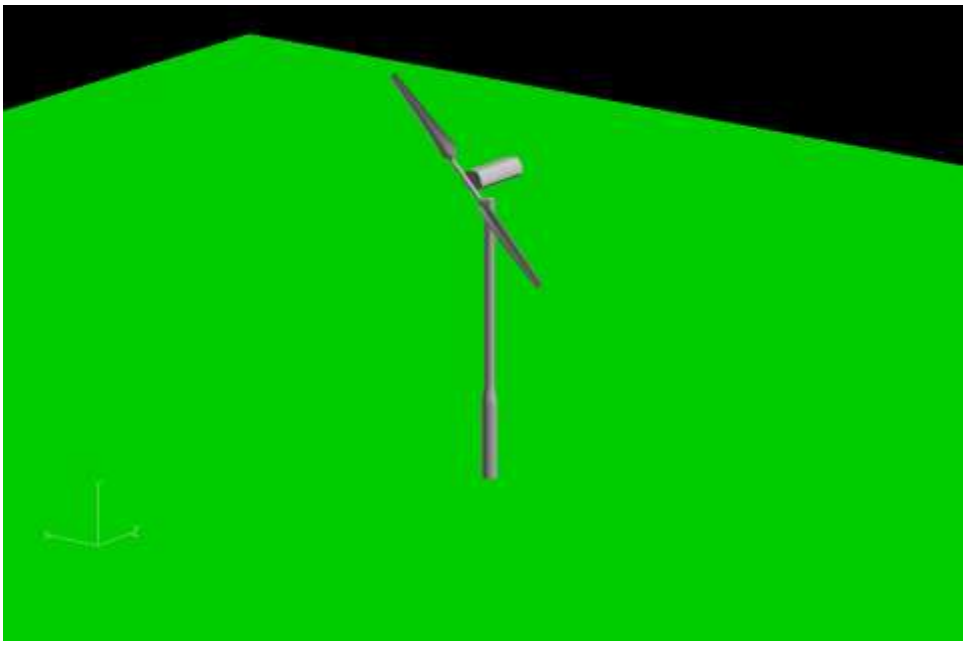

**Figure 221: Simulated NREL 10 m research wind turbine geometry (solid surfaces)**

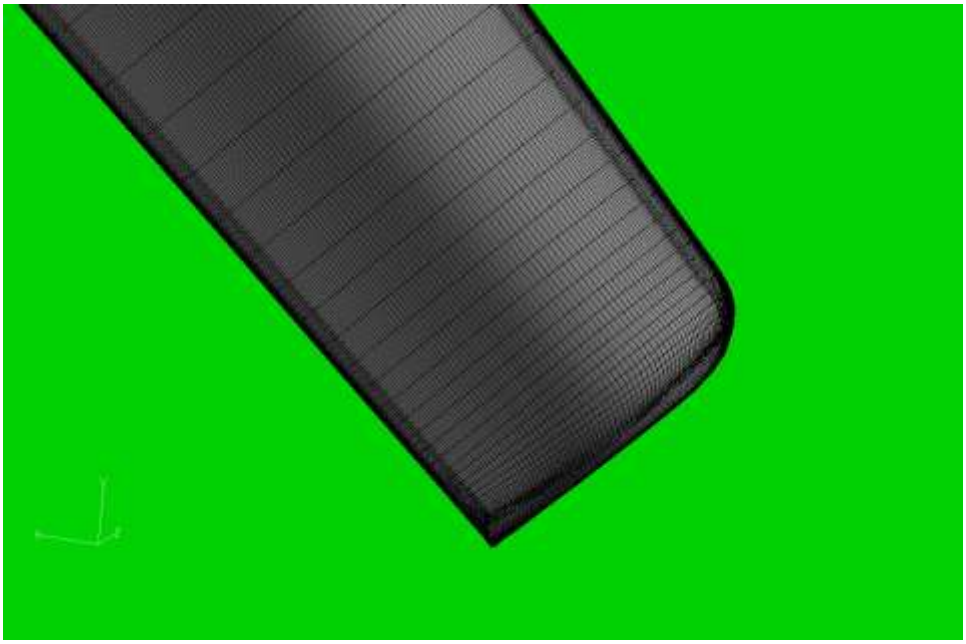

**Figure 222: Surface computational mesh in the blade tip region of the NREL 10 m research wind turbine**

Figure 223 shows a similar plot to Figure 222, but for the surface mesh near the rotor hub. Again, the spanwise spacing of points is somewhat coarse, but the surface mesh does have good resolution along the chord and also normal to the surface (not shown).

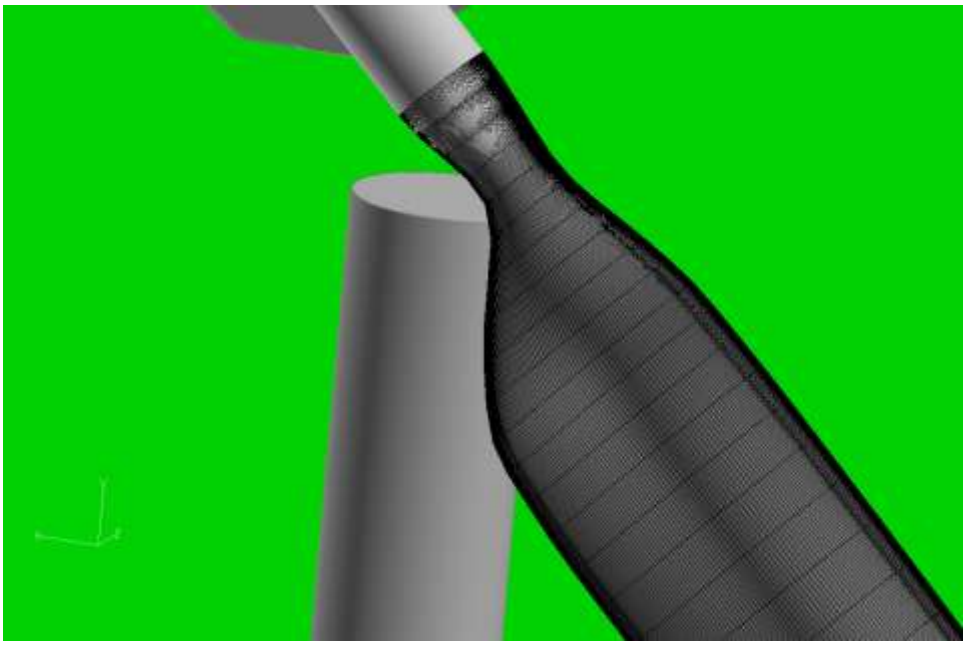

**Figure 223: Surface computational mesh in the blade near-hub region of the NREL 10 m research wind turbine**

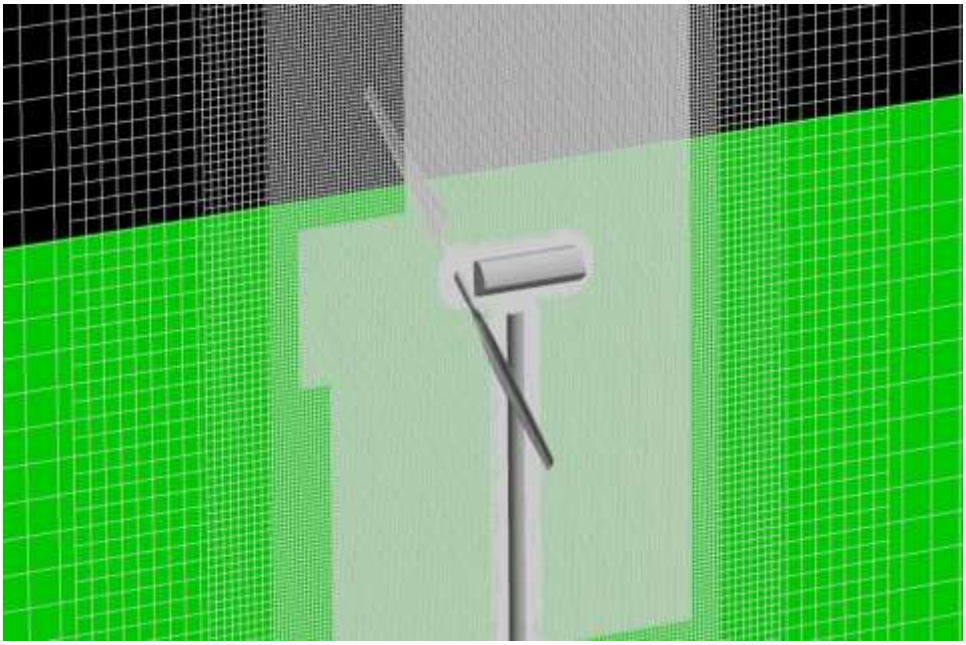

**Figure 224: Cross-section through the centerline of the mesh near the start of the simulation (after 8 time steps)**

A cross-section of the computational mesh through the centerline of the turbine is shown in Figure 224. In this view, the automatically generated off-body Cartesian meshes are readily seen. As the flow has only advanced for eight time steps at this point (one degree of blade rotation), the automatic mesh refinement algorithm has not modified the initial Cartesian meshes. Recall that AMR is used only every forty time steps (five degrees of blade rotation).

The need for the automatic mesh refinement is clearly seen in Figure 34, where, beyond about three meters aft of the nacelle, the mesh becomes too coarse to resolve any significant unsteadiness.

### G4. Results

The simulated case corresponds to a 7 meters per second constant inflow velocity. The reference Mach number, based on tip speed, was 0.11158. The Reynolds number was 2.67 million.

The flowfield solution has been advanced for a total of 5,488 time steps (over multiple runs), with a solution saved every 16 steps. For the fixed time step which was used, this corresponds to solutions saved at every two degrees of rotation, and a total rotation for the blades of 686 degrees. The following plots were made using the final state (at step 5,488).

Note that, because of the automatic mesh refinement, the original 30.5 million point mesh (in 68 blocks) became a 1028 block mesh with more than 46 million points. Further, had the simulation continued, the point count would have increased still more, because the unsteady flowfield still had not propagated to the edges of the domain.

Figure 225 shows a centerline cross-section of the mesh at the final step run thus far (step 5488). For clarity, the plot shows only every other point in each direction. The region where the adaptive mesh refinement has been active is clearly visible and corresponds closely to the extent that the solver has propagated the 210ertical structures shed from the turbine.

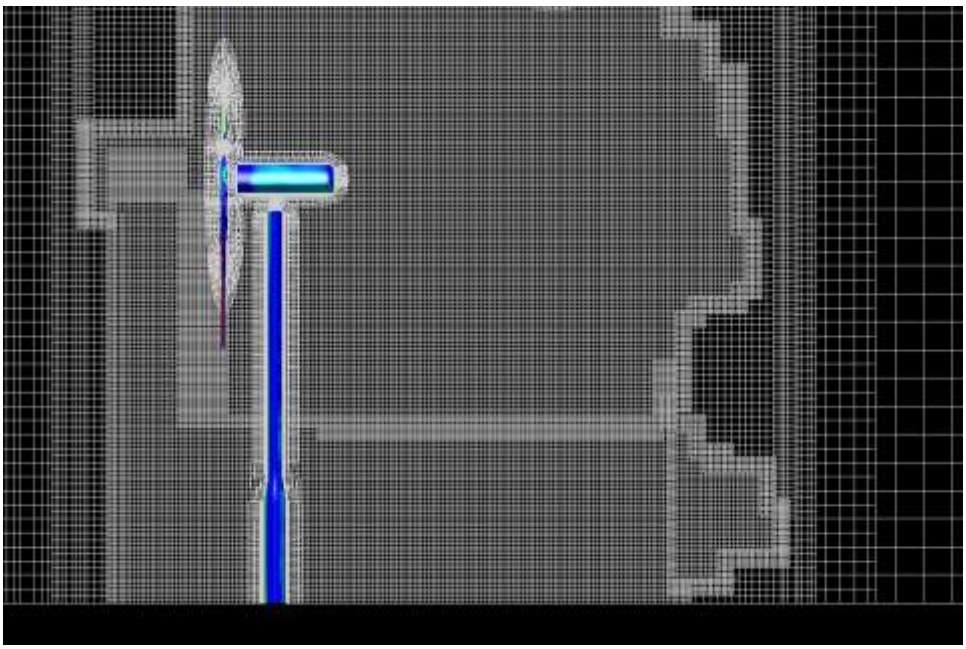

**Figure 225: Mesh cross-section along centerline after 5488 steps (every other point plotted)**

Figure 226 shows the surface pressure on the wind turbine and the ground plane. While faint, the traces of a Karman vortex street can be seen on the ground plane downstream of the mast.

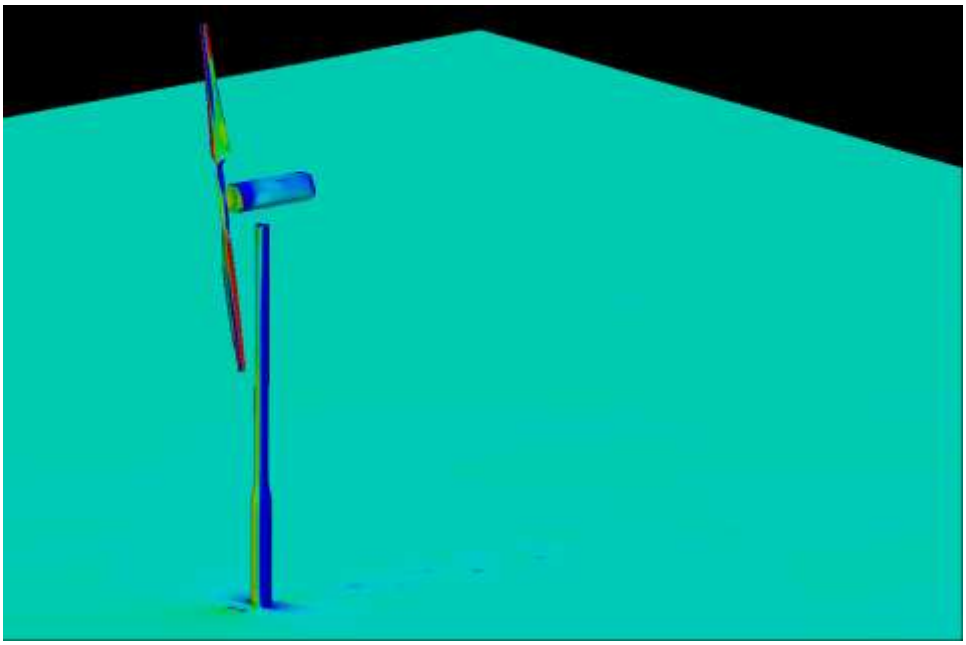

**Figure 226: Computed surface pressures on the 10 meter wind turbine**

The nature of the unsteady flowfield downstream of the rotor is somewhat more apparent in Figure 227, which shows streamlines of flow around turbine. The effect of the moving rotors is apparent in the coiling of the streamlines downstream of the turbine housing.

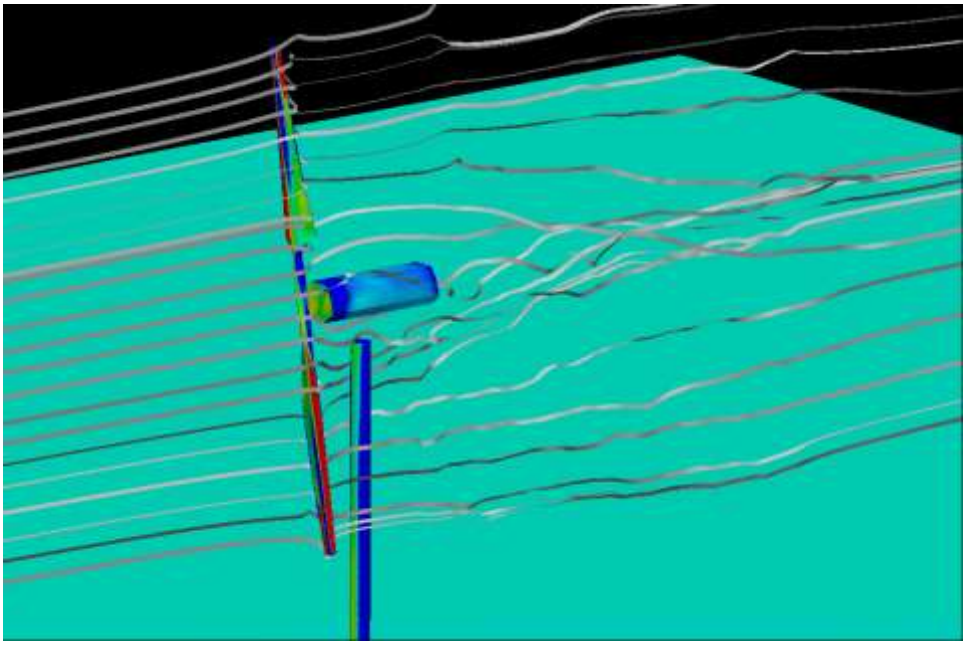

**Figure 227: Streamlines of flow around the wind turbine rotor**

Figure 228 shows an iso-surface of vorticity magnitude. Here, the tip vortices shed as the rotor spins are clearly visible, as are the 211ertical structures shed off the mast. Numerous smaller structures are also seen throughout the downstream region.

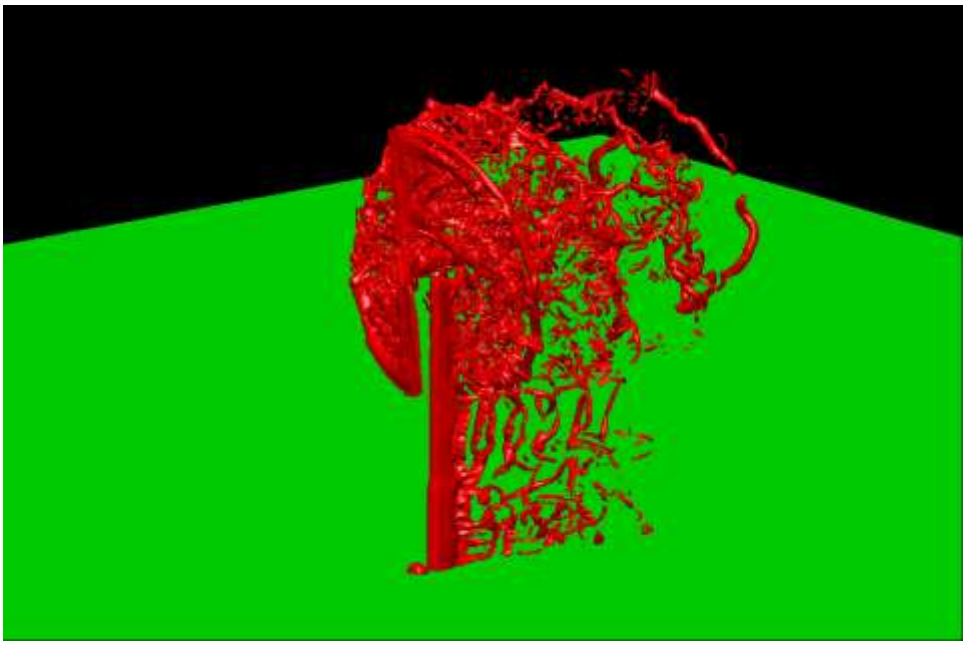

**Figure 228: Iso-surface of vorticity magnitude in the flow around the wind turbine**

Note that, without automatic mesh refinement, these flow features would not be so well resolved. The initial attempts to run this problem, which did not use AMR, were only able to resolve unsteady features for about half the downstream distance shown here. Further note that this does not represent the limit of OVERFLOW's capabilities, since the vorticity observed here includes the initial transients, which have not yet propagated out of the domain. It thus appears that, to the extent the near-body meshes are able to generate the 212ertical structures, the off-body Cartesian meshes with AMR are able to propagate them. Also note that the above results were obtained using sub-optimal settings for the AMR algorithm.

An integration of the forces and moments over the entire wind turbine structure, including the mast and nacelle was performed. The technique used was not exact, in that the overlapping meshes used by the OVERFLOW simulation were not precisely accounted for. The results, however, are expected to be proportional to the actual loads, and can thus be used to determine whether or not a time-dependent loading is being predicted.

The coordinate system for this simulation had the oncoming wind blowing in the positive *z* direction. The *y*-axis points in the vertical direction, and the *x*-axis points to the left when facing the front of the turbine. The force (in arbitrary units) in the *z*-direction is shown in Figure 229 as a function of solution time steps. Recall that the timestep is such that the rotor sweeps out one degree every eight steps. Thus, 2880 steps are required for a full 360 degree sweep. The history plotted in Figure 39 therefore represents only about two full rotations of the rotor. Clearly, the load is trending to some sort of asymptotic value, but it is not clear whether or not any ongoing periodicity will be resolved in this component of the force.

The vertical and side-force components as a function of time are shown in Figure 230, along with their combined magnitudes. All of these quantities show a clear unsteadiness, and there are also hints that some sort of periodicity may be setting up. At this point, however, the simulation has not run far enough to detect the presence of harmonics with any certainty.

The moments on the wind turbine about the base of the mast, have been plotted as a function of time step count in Figure 231. As with the previous plots, a clear time dependence is observed, and there are hints of some sort of periodicity setting up, but until the solution is run farther, it is not possible to draw too many conclusions.

Hints of this vortex street can still be seen in the wake higher above the ground plane, such as that shown in Figure 233. In regions behind where the rotor sweeps, the helical structures created by the vortices shed from the blade tips and trailing edges become more dominant. Note the region of strong vorticity which has just been shed from the rotor as one of the blades reached its lowest point the sweep.

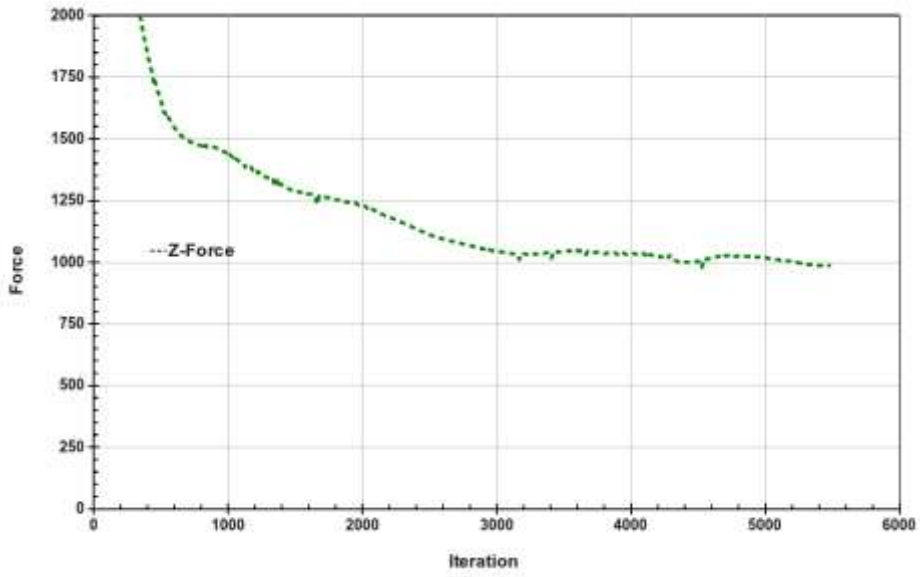


**Figure 229: Streamwise force on wind turbine as a function of time step**

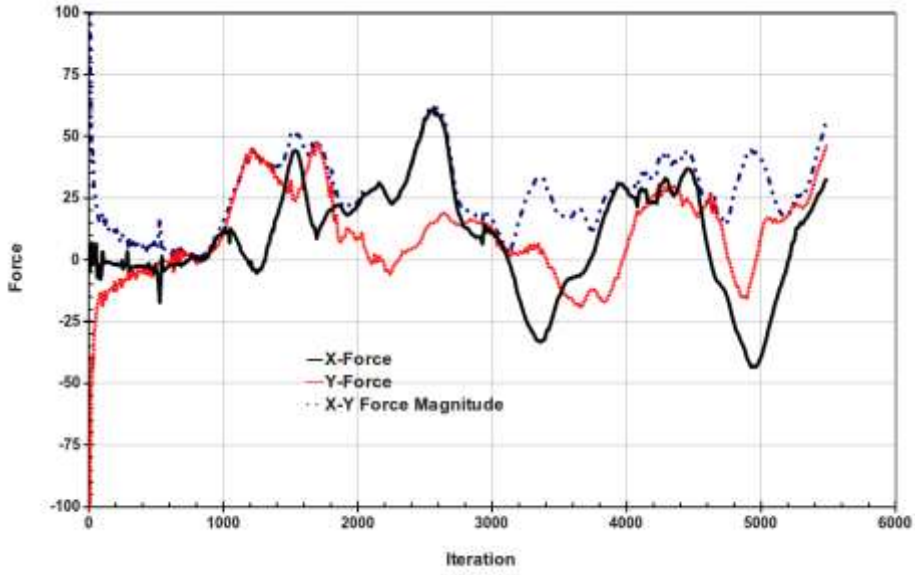


**Figure 230: History of forces normal to the streamwise direction on the wind turbine simulation**

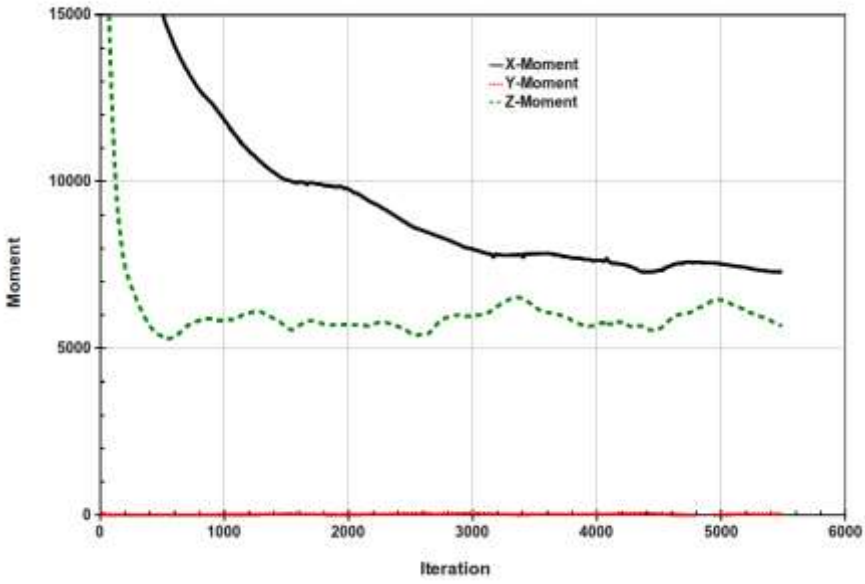


**Figure 231: Moments about the base of the wind turbine mast as a function of time**

Another way to look at the unsteadiness in the flow is to examine the vorticity in the wake at various points. The plot of vorticity magnitude in Figure 232 shows that, below the level swept by the rotor, the wake behind the mast takes on a Karman vortex street structure.

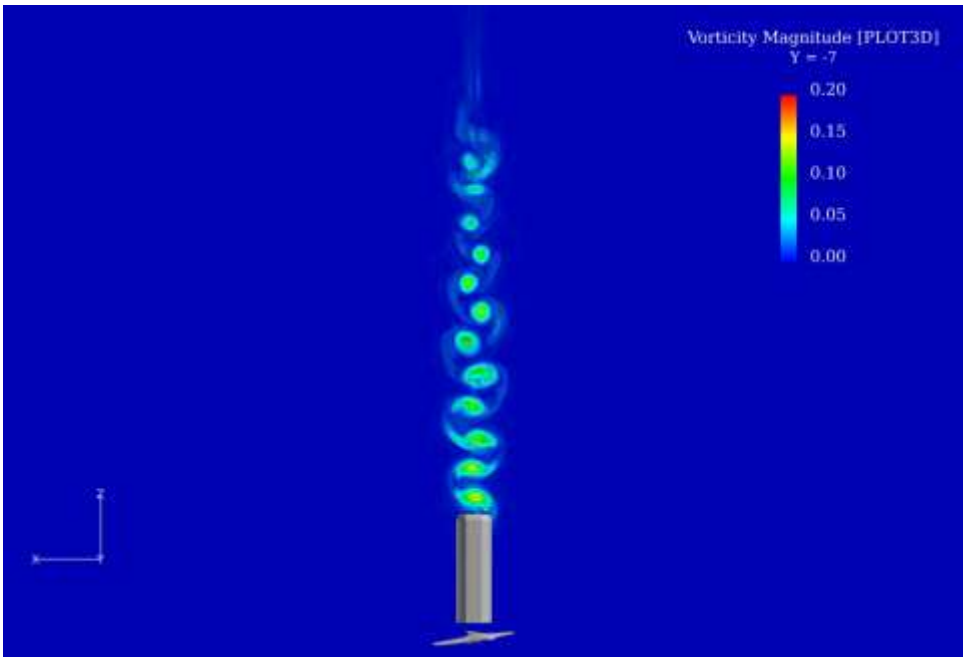


**Figure 232: Vorticity magnitude behind the wind turbine mast five meters above the ground plane**

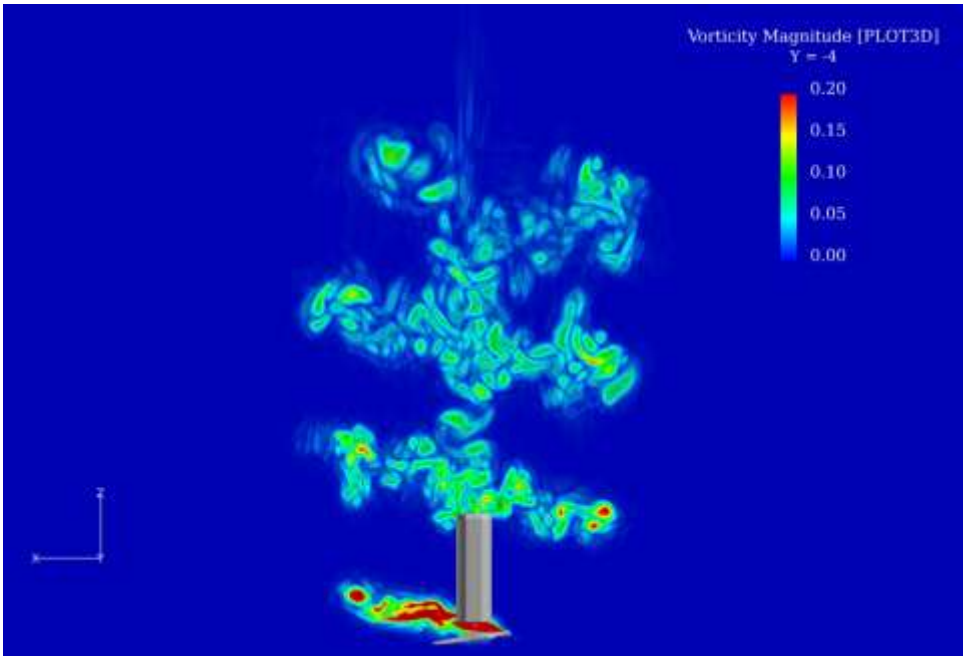


**Figure 233: Vorticity magnitude on a constant-y plane one meter above the lower limit of the rotor sweep**

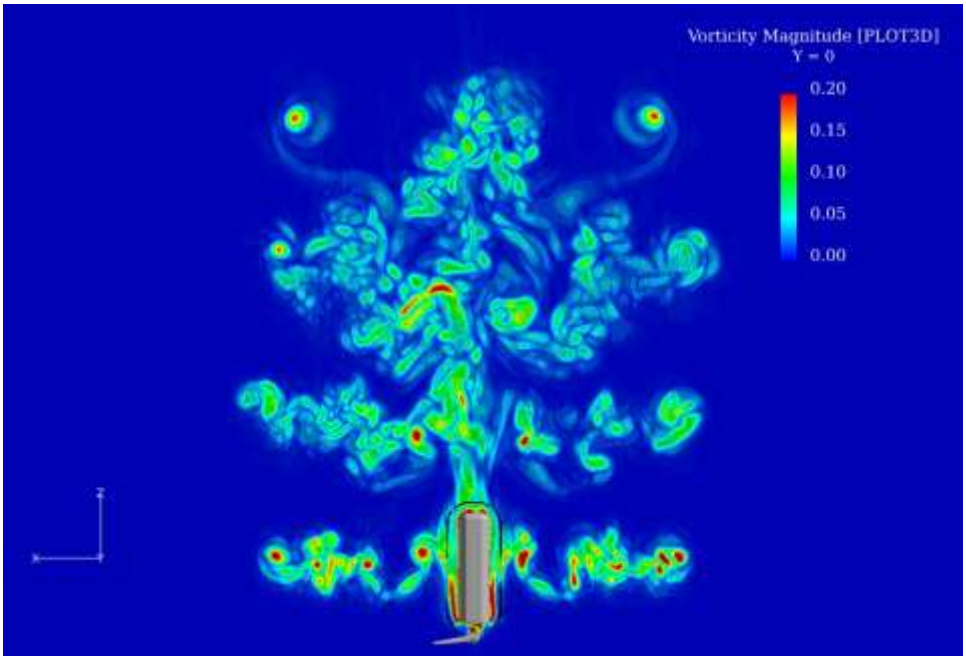


**Figure 234: Vorticity magnitude on a constant-y plane through the nacelle centerline**

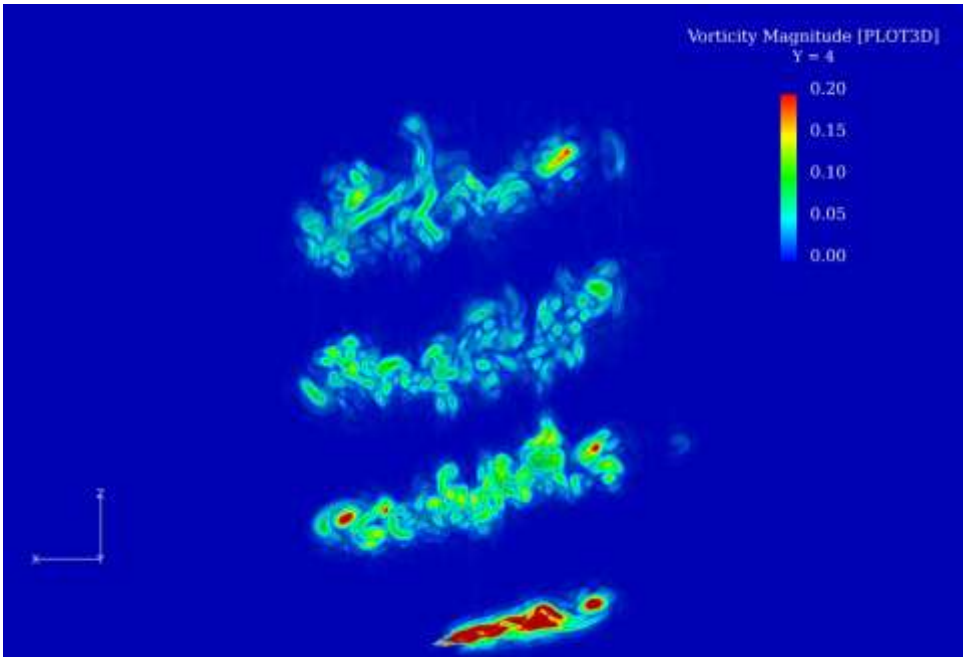


**Figure 235: Vorticity magnitude on a constant-y plane one meter below the upper limit of the rotor sweep**

The vorticity magnitude contours shown in Figure 234 are plotted on a horizontal cut through the nacelle centerline (and the rotor hub). The starting vortices are clearly visible at the top of the plot (not having had enough time to propagate beyond the domain. The complex wake vortex interactions are clearly visible. The "gap" visible surrounding the nacelle region in this plot is due to the decision to only

plot at interior points, and not plot contours at fringe points, in order to minimize the plotting of overlapping contours due to the overlapping computational meshes used by the OVERFLOW solver. As such, the gap is a numerical artifact, and does not represent any discontinuity in the solution.

The final plane of vorticity magnitude contours is shown in Figure 235. This plane is positioned four meters above the rotor hub (one meter below the maximum height swept by the rotor). This plot is very similar to Figure 233, but lacks the wake from the mast. Again, the simulation predicts a complex interaction of the wake and tip vortices shed from the rotor.

Vortical structures such as those visualized in the preceding Figures are associated with noise emission, but the acoustic field itself consists, of course, of pressure fluctuations. The pressure field is shown in Figure 236 on the same horizontal plane where vorticity magnitude was plotted in Figure 233. The pressure footprints of the 217ertical structures are clearly evident, but in addition, there are traces of what appear to be acoustical waves radiating away from the turbine and the wake.

Note that, because of the low speed of the flow, the pressure variations in the flow are close to the limits of what can be resolved due to the numerical precision of the calculation. This is a known phenomenon of low speed flows, and is the reason why low Mach number preconditioning was used for these simulations. The fine-grained oscillations observed in the pressure contours are believed to be largely due to the precision limitations, along with the effects of the changing resolution of the overlapping computational meshes, possibly incomplete convergence of the subiteration process, and the lack of dissipation in the fourth order scheme used away from the near-body computational mesh blocks.

To highlight the acoustical field, the pressure gradient magnitude has been plotted in Figure 237 on the $y = -4$ plane. This plot clearly shows the radiating pressure waves centered on the rotor. The noise which was present in the pressure field contours is magnified when the gradient is computed. In addition, slight differences in the predicted gradient in overlapping regions results in a noisier appearance to the contours than the flowfield actually warrants.

Also, it should be noted, both for this plot and the vorticity magnitude contours, that the gradients for these quantities are being computed by the flow visualization package using a different algorithm (and boundary conditions) than that used by the OVERFLOW solver for the actual solution. Despite this limitation, the values shown in the plots should be reasonably close to the “actual” values seen by the CFD solver.

A view of the pressure gradient magnitude on a plane upstream of the rotor is shown in Figure 238. Here, the radiating waves are again clearly visible. In addition, pressure waves can be seen reflecting from the ground plane. The regions of elevated pressure gradient magnitude appear to be related to the rotor position (which is almost vertical at this point in the simulation). We believe that these also correspond to regions of increased noise production.

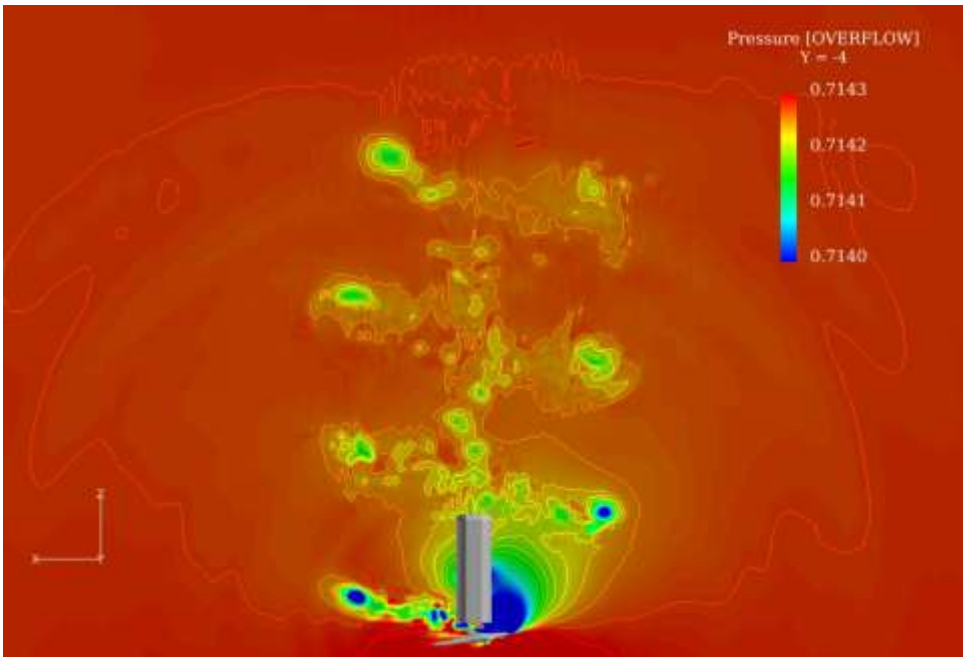


**Figure 236: Pressure on a constant-y plane one meter above the lower limit of the rotor sweep**

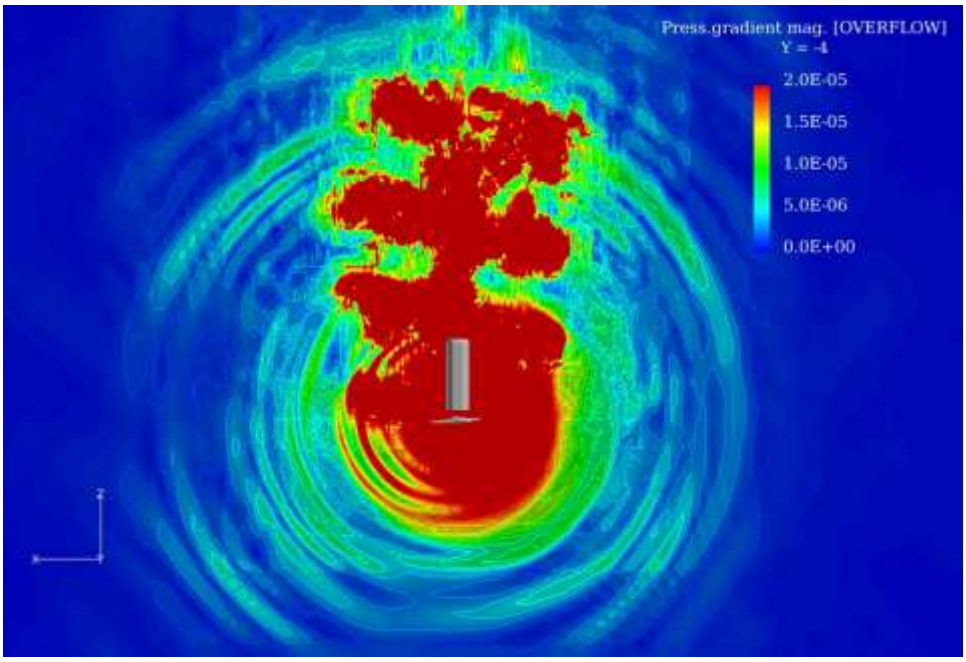


**Figure 237: Magnitude of pressure gradient on a constant-y plane**

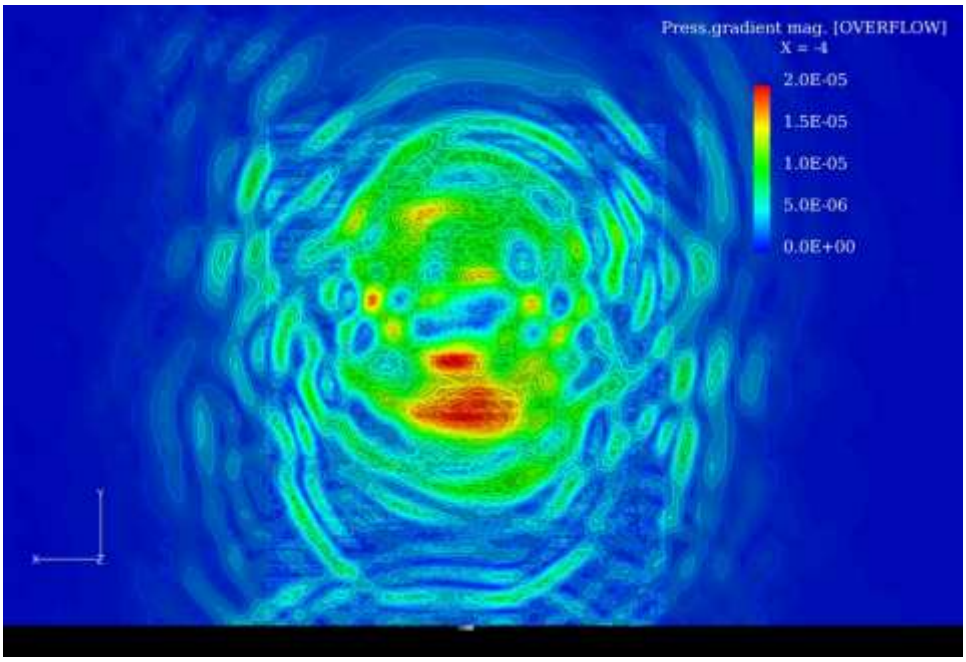


**Figure 238: Magnitude of pressure gradient on a constant-x plane upstream of the rotor**

### G5. Conclusions

All of the pieces have been assembled to enable a full acoustic analysis of the flow around an operational wind turbine. The OVERFLOW code solves the unsteady Navier-Stokes equations to predict the acoustic near-field. The near-field data is used by the PSU-WOPWOP Ffowcs-Williams Hawking solver to propagate the acoustic field to the farfield. Farfield data is then recorded at locations corresponding to a microphone array, and this data is processed using the Beamform Interactive analysis software.

Demonstrations of each of these pieces were presented above, and work is ongoing to finish the complete analysis for the NREL 10 meter wind turbine test case. The identified shortcomings of the current results largely involve the limitations of the CFD solution.

The case is currently being rerun using the recommended AMR settings. Limited computational resources, however, require that we permit only a single level of refinement. With increased computational resources, two or three levels of refinement might be possible, which would greatly enhance the ability of the solver to propagate the unsteady 219ertical flow in the rotor wakes. More available computer resources would also allow the resolution of the near-body computational meshes to be improved, with a corresponding improvement to the predicted acoustic near-field. Due to the nature of the synthetic array technique, an improved CFD solution leads directly to an improved prediction of farfield noise and noise source location.

### *H. Performance of Wind Turbines in Rainy Conditions*

Notations used in this section are listed as follows.

| | |
|---|---|
| $C_{b2}$ | Constant in Spalart-Allmaras turbulence model |
| $d_p$ | particle diameter |
| $D_\omega$ | cross-diffusion term |
| $F_D$ | drag force on particle |
| $\widetilde{G_k}$ | generation of turbulence kinetic energy |
| $G_v$ | production of turbulent viscosity |
| $G_\omega$ | generation of $\omega$ |
| $g_x$ | gravitational acceleration |
| $k$ | turbulence kinetic energy |
| $m_p$ | parcel mass |
| $p$ | static pressure |
| $Re$ | relative Reynolds number |
| $S_{\alpha_q}$ | source term to phase $q$ |
| $u$ | free stream velocity |
| $u_i$ | air velocity |
| $u_p$ | particle velocity |
| $\bar{v}$ | air velocity |
| V | volume of the impinging cell |
| $y^+$ | non-dimensional wall distance |
| $Y_v$ | destruction of turbulent viscosity |
| $Y_k$ | dissipation of $k$ |
| $Y_\omega$ | dissipation of $\omega$ |
| $\alpha_q$ | volume fraction of phase $q$ |
| $\Gamma_k$ | effective diffusivity of $k$ |
| $\Gamma_\omega$ | effective diffusivity of $\omega$ |
| $\Delta t$ | time interval of continuous phase solver |
| $\mu$ | air viscosity |
| $\upsilon$ | molecular kinematic viscosity |
| $\rho$ | air density |
| $\rho_P$ | particle density |
| $\rho_q$ | density of phase $q$ |
| $\sigma_{\bar{v}}$ | Constant in Spalart-Allmaras turbulence model |
| $\bar{\bar{\tau}}$ | stress tensor |
| $\omega$ | specific dissipation rate |

Global climate change, increasing concentration of greenhouse gases in the atmosphere, and depletion of fossil fuel reserves have significantly increased demand for alternative energy. Wind energy is one of the most promising alternative energy sources due to its relatively lower cost, water consumption, and environmental effects.

Performance of a typical wind turbine is continuously influenced by the surrounding environmental conditions. Performance losses due to the sand-laden winds and dust accumulation, in arid regions, or insect debris build-up on the blades of the wind turbine, in tropical regions, have been reported by many researchers. Corten and Veldkamp [**59**] reported near 25% power losses on wind farms in California due to the accumulated insect debris on the leading edge of the wind turbine blades; while a performance loss of 50% has been reported due to the dust accumulation and increased roughness of the blades surface [**60**].

Moreover, other meteorological phenomena such as air moisture, rains, and, in the cloud regions, ice formation on the blades, could influence the performance of the wind turbine due to the impact on the geometry of the blades, increasing load on the blades, or vibrations caused by ice shedding [**61**], [**62**], [**63**], [**64**], [**65**], [**66**].

Investigating the effect of these phenomena is necessary to improve the design and performance of the wind turbines. Although there are a handful of studies on the performance of the airfoils under icing conditions, both in aviation and wind turbine applications, the same studies under heavy rain conditions were limited to the aviation applications [**67**], [**68**], [**69**], [**70**].

In work conducted by Valentine and Decker [**68**], the performance of the NACA64-210 airfoil under rain conditions was studied using the Lagrangian method. They had estimated a performance loss due to the decreasing boundary layer momentum absorbed by splashed back droplets, which shows only a fraction of the airfoil performance loss due to rain. Other researchers had estimated the impact of water film formation resulting in up to 83% degradation of the airfoil performance [**69**]. Therefore, study of the performance of the wind turbine under heavy rain conditions seems necessary as turbine efficiency is a critical component of the overall economic justification for a potential wind farm.

Moreover, wind turbine design and corresponding economic projections depend on accurate aerodynamic airfoil data and advanced design tools including extensive experimental data for lift, drag and moment coefficients, and computational fluid dynamics (CFD) analysis [**71**].

The objective of this study is to develop a numerical model for assessing and analyzing the performance of a horizontal-axis wind-turbine (HAWT) in the presence of rain droplets under heavy rain conditions using computational fluid dynamics (CFD) for multiphase flow systems [**72**].

## H1. Approach

The CFD was chosen to obtain a comprehensive tool for design, scale-up, and performance evaluation of wind turbines, and also to overcome the lack of experimental data on the performance of wind turbines in rainy conditions. A set of benchmarking CFD simulations was performed, both in two and three dimensions. The simulation results were compared with the available experimental data for single phase flow in the literature to refine our CFD model. Then, the single-phase simulation results were used as a baseline to calculate the impact of rain on the performance of the wind turbine.

To summarize our approach, we can categorize the performed simulations into the following case studies:

**Case 1: Simulation of single-phase flow around a 2-D airfoil**

Initially, a single-phase CFD simulation was performed for a S809 airfoil which is a 21% thick, laminar-flow airfoil designed specifically for HAWT applications by the U.S. National Renewable Energy Laboratory (NREL) [**73**]. The S809 airfoil profile is shown in Figure 239. The blade sections were analyzed at different angles of attack using a two-dimensional CFD model and the results were compared with the available wind tunnel experimental data obtained using a low-turbulence wind tunnel at the Delft University of Technology. The results of these tests are reported by Somers [**73**]. Our main goal here was to test the available turbulence models in the commercial CFD code, ANSYS Fluent 13.0, and choose the most appropriate turbulence model for our simulations. We are also aware of some approximations of the standard turbulence models in predicting laminar to turbulence transition and flow separation at higher angles of attack; however, the improvement of turbulence models will be the subject of future research.

**Case 2: Simulation of 3-D wind turbine using a single-phase flow model**

A set of single phase three dimensional simulations based on the aerodynamic experiments of the U.S. National Renewable Energy Laboratory (NREL-Phase II) was performed to predict the power output of the wind turbine at different wind velocities. Figure 240 shows the test configuration of the simulated NREL-Phase II with an untwisted blade turbine. At this step, the validity of our model in prediction of the wind turbine performance in a rotating 3-D model has been verified.

**Case 3: Simulation of two phase flow around a 2-D airfoil**

In this case, the aforementioned 2-D model in case 1 was used as a base for our 2-D multiphase simulation to capture the water layer formation over the airfoil in presence of rain droplets. To model this phenomenon a novel approach by coupling a Lagrangian Discrete Phase Model (DPM) and an Eulerian Volume of Fluid Model (VOF) has been utilized. The effect of the formed water film was investigated on the aerodynamic performance of the airfoil.

**Case 4: Simulation of 3-D wind turbine using a multi-phase flow model**

This case is the subject of our future work and is not presented here.

Details and results of our simulations will be presented in the next sections followed by a summary and the scope of future work.

A commercial Computational Fluid Dynamics (CFD) code, ANSYS FLUENT 13.0, was selected to conduct our numerical simulation studies. ANSYS FLUENT is a CFD software package used to simulate fluid flow problems. It uses the finite-volume method to solve the governing equations, as presented in the Table 1, for a fluid flow on a discretized domain (mesh). Geometry and mesh generation were done using ICEM software, which is the pre-processor bundled with FLUENT. A two-dimensional mesh for case 1 and case 3 was built based on a unit length S809 airfoil using a C-type unstructured grid with a refined boundary layer region.

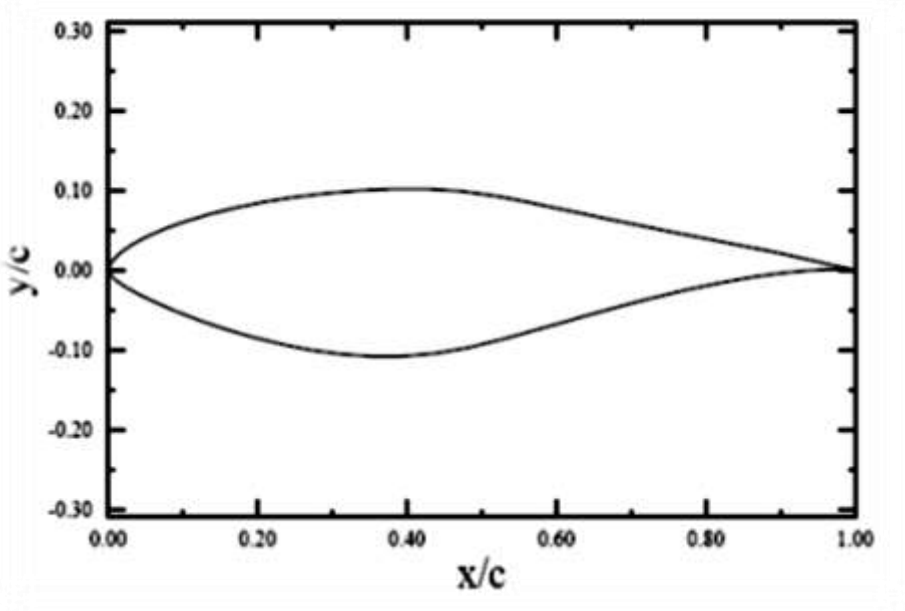


**Figure 239: S809 airfoil profile**

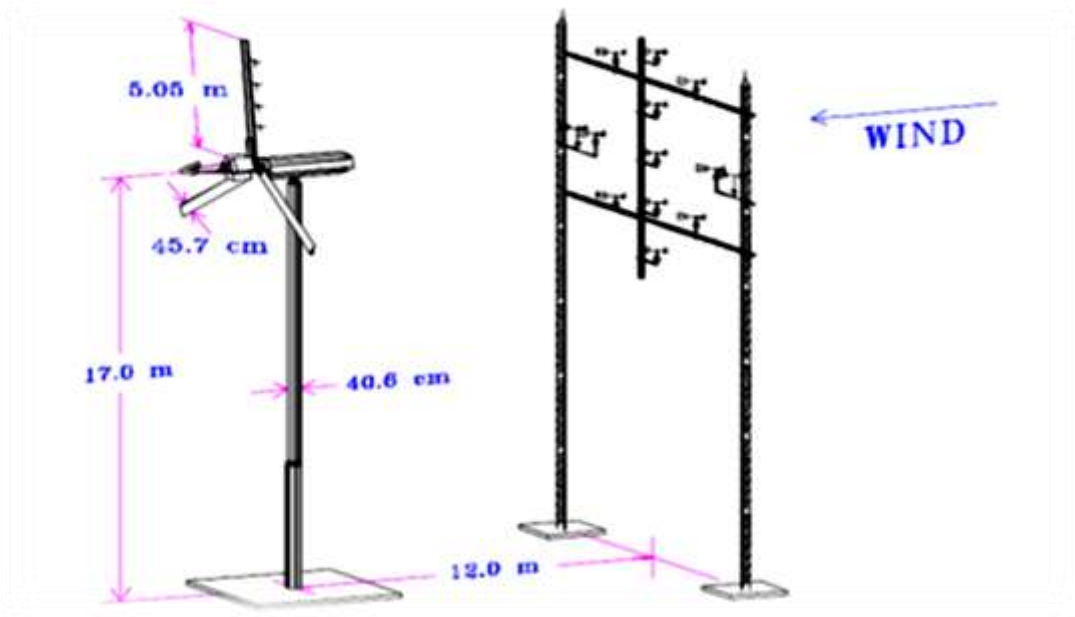


**Figure 240: NREL: Phase II (untwisted blade) test configuration**

We used approximately 180,000 cells in the domain and the boundary layer was refined so that the required cell thickness for resolving the turbulence flow near the wall was provided (i.e. $y^+ <1$). The computational domain is extended 10 chord lengths from the leading edge and 13 chord lengths from the trailing edge of the airfoil. All the simulations were performed at a Reynolds number of $2\times10^6$. The mesh for the two-dimensional domain and the refined boundary layer around the airfoil are shown in the Figure 241 and Figure 242, respectively.

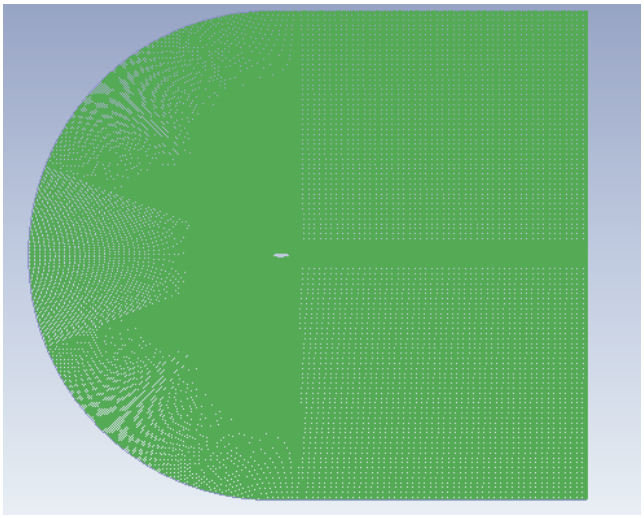

**Figure 241: 2-D mesh for calculation**

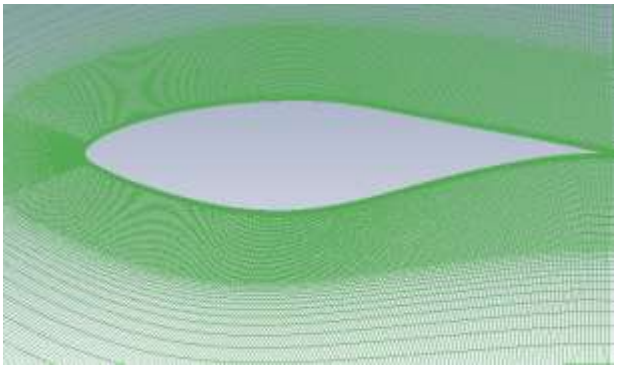

**Figure 242: Refined boundary layer**

The simulations for case 3 were performed based on the aerodynamic experiments of the U.S. National Renewable Energy Laboratory (NREL-Phase II). Due to periodic configuration, only one third of the domain and the 3-blade turbine (Figure 243) were considered for the calculations to reduce the computational cost.

A spherical domain measuring 40 m in diameter was adopted for our simulation as shown in Figure 244. A tetra mesh with 0.48 million cells was generated as shown in Figure 245. A rotational reference frame was employed and the rotational speed was set to be 72 rpm in order to be in line with NREL's field experiments. In all the cases, grid resolution ensures the grid independent solution.

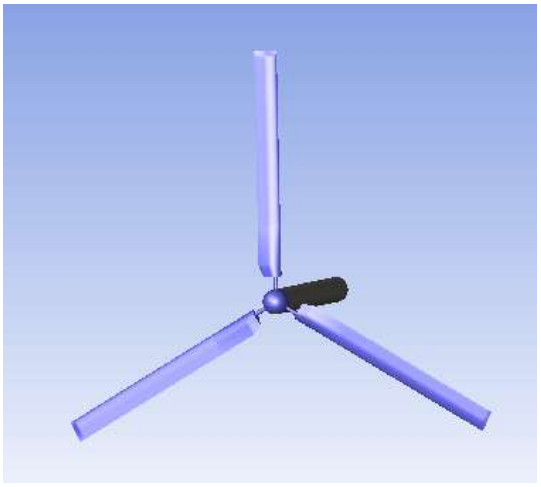

Figure 243: 3-D model of the turbine

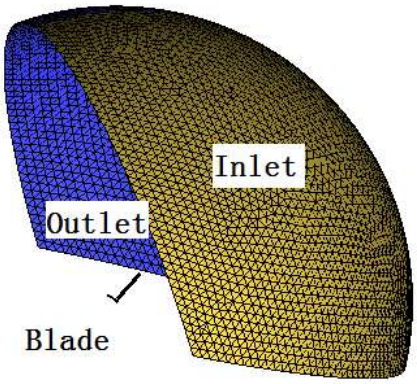


Figure 244: 3-D computational domain

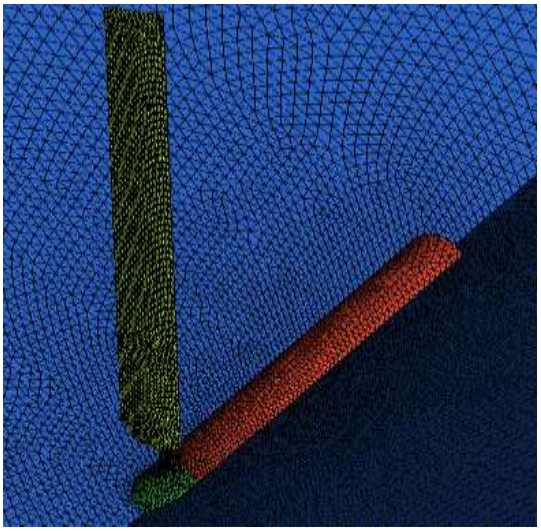

Figure 245: 3-D mesh

**Table 16: Summary of Governing Equations**

A. Single Phase Conservation Equations

Conservation of Mass

$$\frac{\partial \rho}{\partial t} + \nabla \cdot (\rho \bar{v}) = 0$$

Conservation of Momentum

$$\frac{\partial}{\partial t}(\rho \bar{v}) + \nabla \cdot (\rho \bar{v} \bar{v}) = -\nabla p + \nabla \cdot (\bar{\bar{\tau}})$$

$$\bar{\bar{\tau}} = \mu[(\nabla \bar{v} + \nabla \bar{v}^T)]$$

B. Turbulent Models

Spalart-Allmaras Model

$$\frac{\partial}{\partial t}(\rho \tilde{v}) + \frac{\partial}{\partial x_i}(\rho \tilde{v} u_i) = G_v + \frac{1}{\sigma_{\tilde{v}}}\left[\frac{\partial}{\partial x_j}\left\{(\mu + \rho \tilde{v})\frac{\partial \tilde{v}}{\partial x_j}\right\} + C_{b2}\rho\left(\frac{\partial \tilde{v}}{\partial x_j}\right)^2\right] - Y_v$$

SST k-ω Model

$$\frac{\partial}{\partial t}(\rho k) + \frac{\partial}{\partial x_i}(\rho k u_i) = \frac{\partial}{\partial x_j}\left(\Gamma_k \frac{\partial k}{\partial x_j}\right) + \widetilde{G_k} - Y_k$$

$$\frac{\partial}{\partial t}(\rho \omega) + \frac{\partial}{\partial x_i}(\rho \omega u_i) = \frac{\partial}{\partial x_j}\left(\Gamma_\omega \frac{\partial \omega}{\partial x_j}\right) + G_\omega - Y_\omega + D_\omega$$

C. Discrete Phase Model (DPM) Governing Equations

Particle Force Balance

$$\frac{du_p}{dt} = F_D(u - u_p) + \frac{g_x(\rho_P - \rho)}{\rho_P}$$

$$F_D = \frac{18\mu C_d\, Re}{\rho_P d_p^2\, 24}, \qquad Re = \frac{\rho d_p |u_p - u|}{\mu}$$

D. Volume of Fluid (VOF) Conservation Equations

Continuity Equation

$$\frac{\partial}{\partial t}(\alpha_q \rho_q) + \nabla \cdot (\alpha_q \rho_q \bar{v}_q) = S_{\alpha_q}$$

Momentum Equation based on shared-filed approximation

$$\frac{\partial}{\partial t}(\rho\bar{v}) + \nabla\cdot(\rho\bar{v}\bar{v}) = -\nabla p + \nabla\cdot[\mu(\nabla\bar{v} + \nabla\bar{v}^T)] + \rho\bar{g}$$

Source Term for coupling DPM and VOF

$$S_\alpha = \frac{m_p}{V\Delta t}$$

---

To simulate flow around the airfoil, we are dealing with a wall-bounded turbulent flow which is affected by the presence of a no-slip boundary condition at the airfoil surface. The numerical treatment of the near-wall flow directly impacts the fidelity of numerical solutions due to the large gradients of solution variables. Therefore, resolving the flow in the near-wall region is necessary in our simulation. Among the available turbulent models in ANSYS Fluent 13.0, the *k-ε* models, the RSM, and the LES model are primarily valid for turbulent core flows (i.e., the flow in the regions somewhat far from walls). The Spalart-Allmaras and *k-ω* models were designed to be applied throughout the boundary layer, provided that the near-wall mesh resolution is sufficient. In this study, we solved Navier-Stocks equations along with two different turbulence models, the Spalart-Allmaras and *SST k-ω* models.

The Spalart-Allmaras model is a one-equation model that solves for the kinematic eddy viscosity. It was developed for aerodynamic flows with a low-Reynolds-number requiring a fine mesh for the viscosity affected region of boundary layer ($y^+$ <1). The transport equation for $\bar{v}$ is

$$\frac{\partial}{\partial t}(\rho\bar{v}) + \frac{\partial}{\partial x_i}(\rho\bar{v}u_i) = G_v + \frac{1}{\sigma_{\bar{v}}}\left[\frac{\partial}{\partial x_j}\left\{(\mu + \rho\bar{v})\frac{\partial\bar{v}}{\partial x_j}\right\} + C_{b2}\rho\left(\frac{\partial\bar{v}}{\partial x_j}\right)^2\right] - Y_v \quad \textbf{(75)}$$

Where $G_v$ is the production of turbulent viscosity, $Y_v$ is the destruction of turbulent viscosity that occurs in the near-wall region due to wall blocking and viscous damping. $\sigma_{\bar{v}}$ and $C_{b2}$ are the constants and $v$ is the molecular kinematic viscosity.

The shear-stress transport (SST) *k-ω* model was developed to blend the accuracy and robustness of *k-ω* model in the near-wall region with the free-stream independence of the *k-ε* model in the far field. To convert the *k-ε* model to the *k-ω* model in the near wall region, standard *k-ω* model and *k-ε* models are both multiplied by a blending function and added together. The blending function is designed to activate the *k-ω* model in the near-wall region and activates *k-ε* model away from the surface.

The transport equations are given

$$\frac{\partial}{\partial t}(\rho k) + \frac{\partial}{\partial x_i}(\rho k u_i) = \frac{\partial}{\partial x_j}\left(\Gamma_k\frac{\partial k}{\partial x_j}\right) + \widetilde{G_k} - Y_k \quad \textbf{(76)}$$

$$\frac{\partial}{\partial t}(\rho\omega) + \frac{\partial}{\partial x_i}(\rho\omega u_i) = \frac{\partial}{\partial x_j}\left(\Gamma_\omega\frac{\partial\omega}{\partial x_j}\right) + G_\omega - Y_\omega + D_\omega \quad \textbf{(77)}$$

The term $\widetilde{G_k}$ represents the generation of turbulence kinetic energy due to mean velocity gradients. $G_\omega$ is the generation of $\omega$, while $\Gamma_k$ and $\Gamma_\omega$ represent the effective diffusivity of *k* and $\omega$. $Y_k$ and $Y_\omega$ are the dissipation of *k* and $\omega$ respectively and $D_\omega$ is the cross-diffusion term.

More details about these two models could be found in the literature [**74**], [**75**], and [**76**].

In this study, we utilized a coupled Lagrangian-Eulerian approach to model the water layer formation on the airfoil due to the rain. A Lagrangian discrete phase model was used for tracking the rain droplets and a Eulerian approach was employed for tracking the interface and water film accumulation. *SST k-ω* turbulence model was used for the turbulence since it gives more accurate results for wind turbine simulations based on our simulation results of part 1 and also the work of Pape and Lecanu [**77**].

Droplet trajectories are calculated by the parcel approach. Each parcel represents several physical droplets with the same diameter being convected by a common velocity. The injection condition was based on Dunham's study [**67**]. Once the parcel is injected into the domain, a Lagrangian force balance for that is solved and the trajectory of that parcel is updated at each time step. For simplicity, it is assumed that all the parcels have the same initial velocity and diameter. A rain fall rate of 1800 mm/h and a Reynolds number of $2\times10^6$ was used for all the simulations. The droplet diameter was set to 6mm based on the droplet size distribution reported by Markowitz et al. [**78**].

The key assumption in our simulations is the transformation of the rain droplets into the liquid elements of water film. We assumed that once a parcel impinges on a wall or pre-formed water film, it acts as a mass source for the film and will add to the mass of the film. Then, the volume fraction and momentum balance of the film are calculated using a Eulerian Volume of Fluid model with the Geo-Reconstruct scheme. The Geo-Reconstruct scheme is able to resolve the sharp interface between the water layer and air flow. However, the required time step is relatively small. For this reason a variable time step method was employed to change the time step size while keeping the courant number in a reasonable range. The calculation is based on a pressure-based solver using the implicit body force treatment to account for the effect of gravity. The same approach has been used by Arienti et al. [**79**] to model fuel atomization process in combustion devices.

The computational mesh is the same as the mesh we used for the single-phase simulations. A very fine layer was built along the airfoil surface in order to capture the thin film formation on the airfoil. In addition, an 8 $m^2$ injection surface was defined 3m above the airfoil.

The governing equations for the multiphase flow around the airfoil are based on part D of Table 16. The force balance equation for the parcels in discrete phase model is

$$\frac{du_p}{dt} = F_D\left(u - u_p\right) + \frac{g_x(\rho_P - \rho)}{\rho_P} \quad \textbf{(78)}$$

where $F_D\left(u - u_p\right)$ is the drag force per unit particle mass and

$$F_D = \frac{18\mu C_d\, Re}{\rho_P d_p^2\, 24} \quad \textbf{(79)}$$

$u$ is the fluid phase velocity, $u_p$ is the parcel velocity, $\mu$ is the fluid viscosity, $\rho$ is the fluid density, $\rho_P$is the particle density and $d_p$ is the particle diameter.

The equations for the Volume of Fluid model are the Continuity equation and Navier-Stokes equations based on the shared-field approximation:

$$\frac{\partial}{\partial t}\left(\alpha_q \rho_q\right) + \nabla \cdot \left(\alpha_q \rho_q \bar{v}_q\right) = S_{\alpha_q} \quad \textbf{(80)}$$

$$\frac{\partial}{\partial t}(\rho \bar{v}) + \nabla \cdot (\rho \bar{v} \bar{v}) = -\nabla p + \nabla \cdot [\mu(\nabla \bar{v} + \nabla \bar{v}^T)] + \rho \bar{g} \quad \textbf{(81)}$$

$$S_\alpha = \frac{m_p}{V \Delta t} \quad \textbf{(82)}$$

$\alpha_q$ is the volume fraction of phase $q$, $\rho_q$ is the density of phase $q$, $\bar{v}_q$ is the velocity and $S_{\alpha_q}$ is the source term due to particle impingement. Where $m_p$ is the mass of the particle, $V$ is the volume of impinging cell and $\Delta t$ is the time step size of continuous phase solver. $\rho$ and $\mu$ are the density and viscosity of mixture and are changing with the volume fraction.

## H2. Results and Discussion

**Case 1: Simulation of single-phase flow around a 2-D airfoil**

In this section, the results of the 2-D benchmarking simulation of Case 1 are presented. The comparison between the calculated Lift and Drag coefficients is considered, as the main measures of the aerodynamics performance of the airfoil. The comparison between the calculated lift and drag coefficients using the two turbulence models with the wind tunnel experiments of the Delft University of Technology is presented in Figure 246 and Figure 247.

As shown in Figure 246, at angles of attack higher than 14.24, the airfoil experienced a degradation of performance due to a decrease in lift coefficient. The *SST k-ω* model outperformed the Spalart-Allmaras model by predicting this degradation. However, this model is over predicting the lift coefficient at higher angles of attack. This is in line with the results of a previous study by Pape and Lecano concluding that the *SST k-ω* model is more suitable for wind turbine simulations [**77**]. In addition, we could not get a converged solution with the Spalart-Allmaras model at angles of attack higher than 14.24.

Figure 247 shows that the Spalart-Allmaras and *SST k-ω* models both are in a good agreement with the experiments in the calculation of the drag coefficient; however, both models under predict the drag at angles of attack greater than 9.22 degree.

Figure 248 shows the velocity contour around the airfoil under different angle of attacks calculated with the *SST k-ω* model. By increasing the angle of attack, the stagnation point goes downward and boundary layer separation starts at an angle of attack of 9.22 degree. As the angle of attack increases, the separation point moves toward the leading edge.

In summary, both the calculated lift and drag coefficients using our CFD model are in a reasonable agreement with the experiments up to an angle of attack of 9.22, while the flow is attached. At higher angles of attack when the boundary layer separation begins, the model over predicts the lift and under predicts the drag, possibly due to under predicting boundary layer separation.

Based on the above-mentioned results, the *SST k-ω* model was chosen as the turbulence model for further simulations.

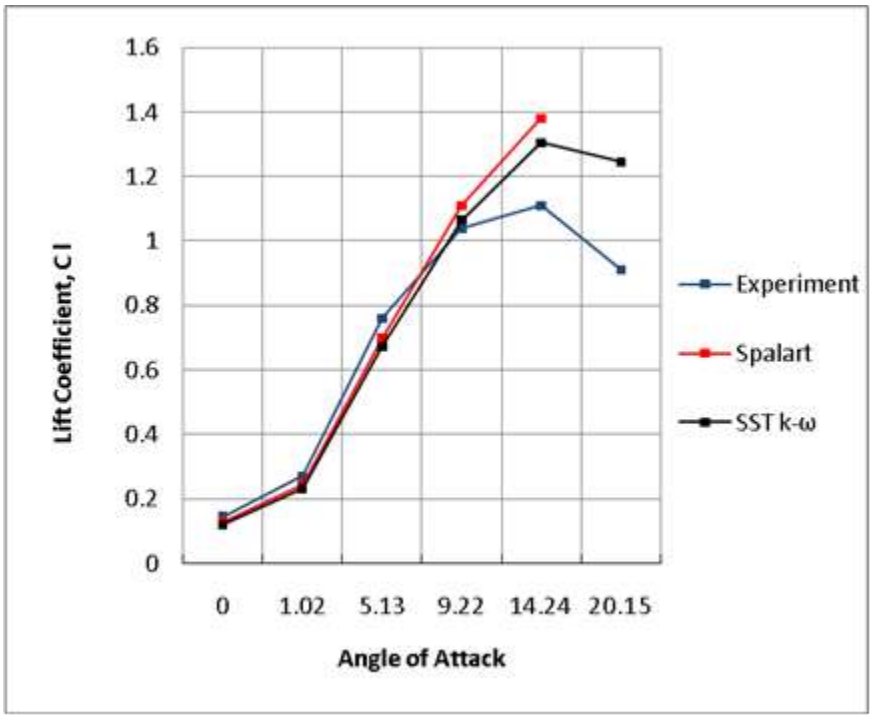


**Figure 246: S809 Lift coefficients at different AoA**

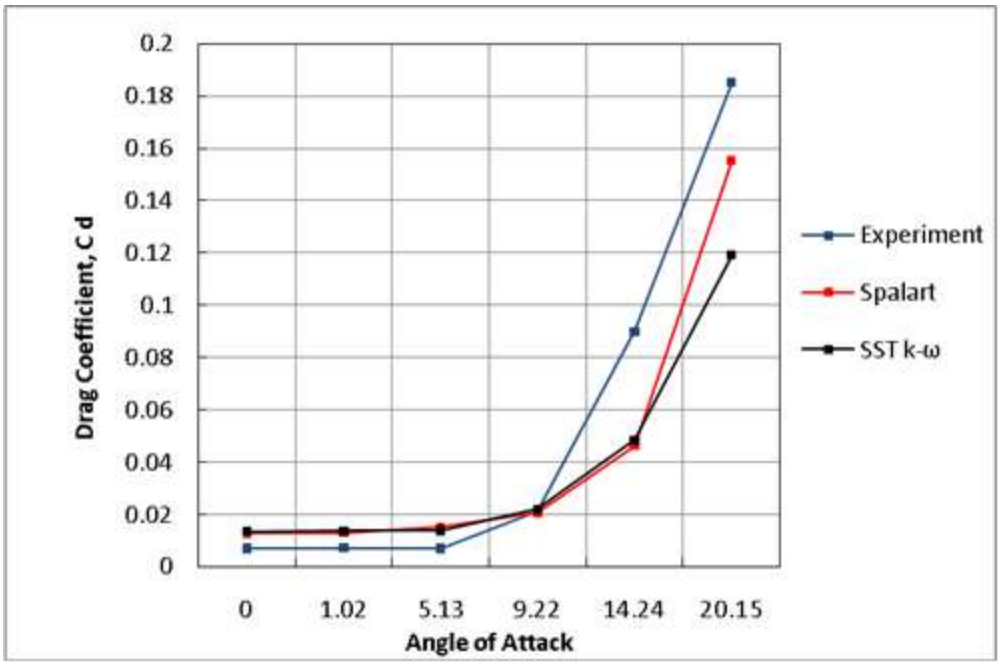


**Figure 247: S809 Drag coefficients at different AoA**

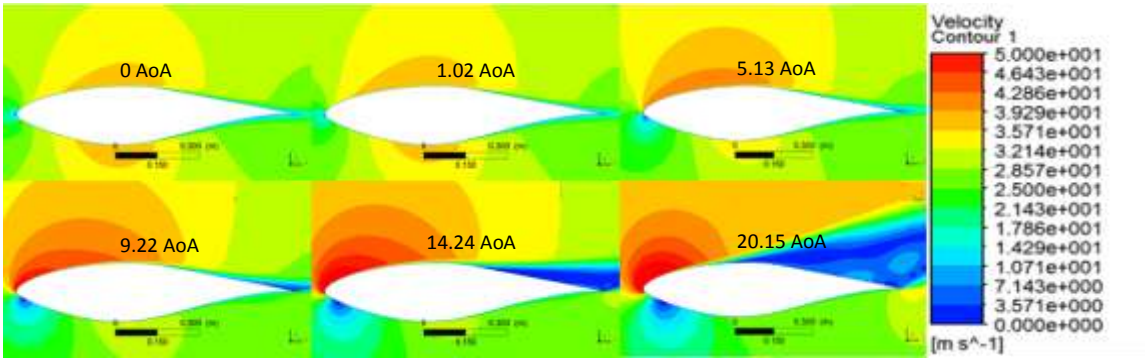


**Figure 248: Velocity contour near the airfoil**

**Case 2: Simulation of 3-D wind turbine using a single phase flow model**

In our 3-D simulations of Case 2, the torque of the turbine had been monitored during the simulations at different wind speed. Constant rotational speed is maintained during the operation of wind turbine to provide a steady power output. The shaft power could be related to the torque simply by

$$Total\ Shaft\ Power(kW) = \frac{Torque(N \cdot m) \times 2\pi \times rotational\ speed(rpm)}{60000} \times 3 \qquad (83)$$

The comparison between calculated shaft power and experimental data of the NREL-phase II field experiments for different wind speeds is presented in Figure 249. For wind velocity lower than 17 m/s, the simulation results show a very good agreement with the experimental data. For the higher wind velocities, the power output is slightly under predicted using our CFD model which could be due to the not fully resolved turbulence flow at higher wind velocities.

**Case 3: Simulation of two phase flow around a 2-D airfoil**

In our model, two processes are being considered during the formation of water film:

1. Accumulation of the water on the airfoil due to the rain
2. Stripping off of the film due to the wind shear stress

When the accumulation and stripping off processes on the surface of an airfoil balance each other, the system will reach a quasi-steady state and a thin layer of water film could be observed on the airfoil surface.

Figure 250 shows the accumulation of water on the trailing edge of the airfoil. At an angle of attack of zero, the formation of a bump by the film on the upper surface near the trailing edge is captured by the simulation. As the angle of attack increases, the "bump" moves toward the leading edge and less water is accumulated on the upper surface of the airfoil. We can define a "detach" point where water film detached from the upper face of the airfoil. As shown in Figure 250, the detach point moves towards leading edge with increasing angle of attack. These results are in qualitative agreement with the behavior of splashed water droplets distribution presented in Valentine and Decker's study [**68**].

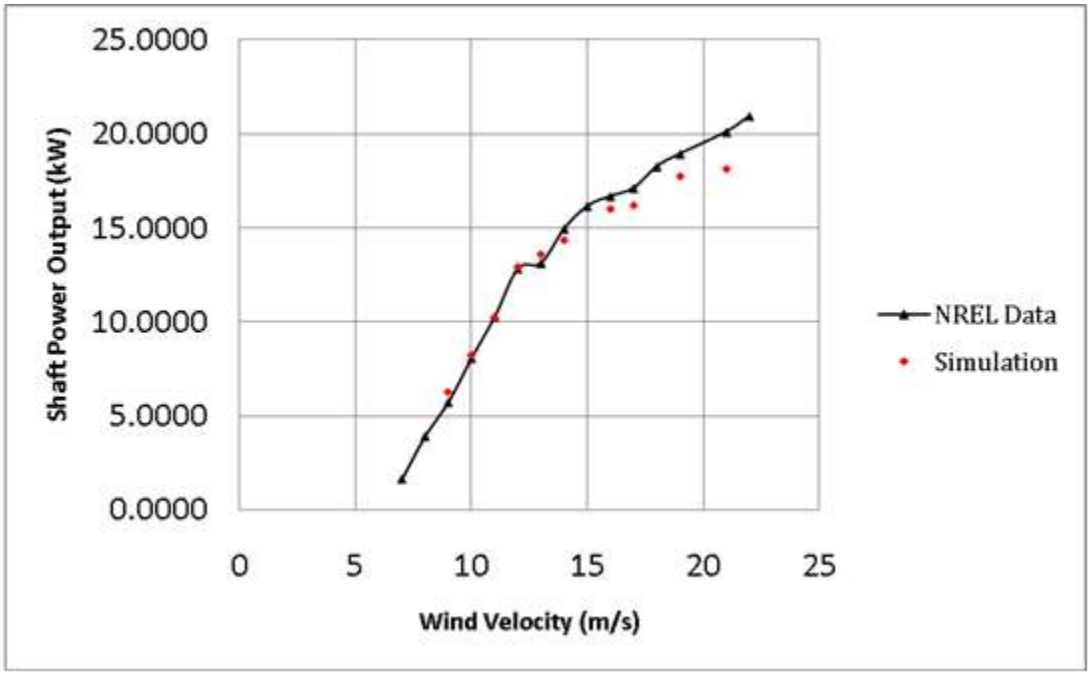


**Figure 249: Power output vs. wind speed**

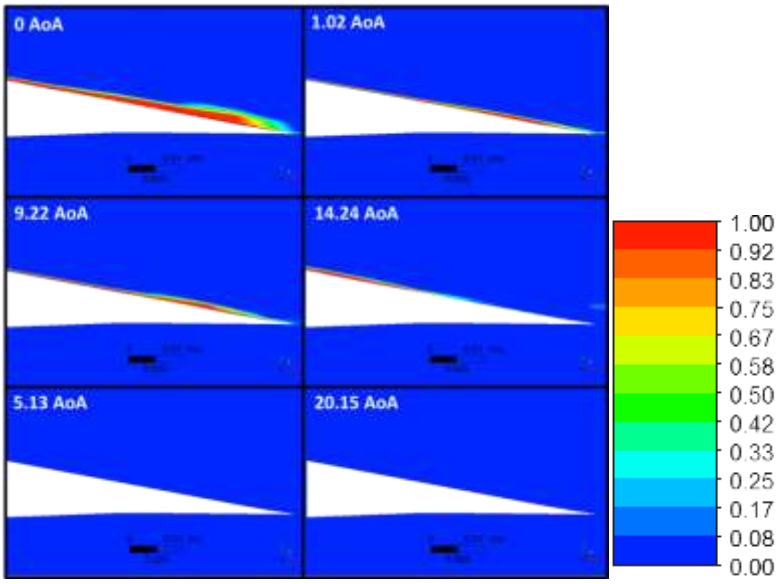


**Figure 250: Contours of the water volume fraction on the trailing edge of the airfoil for different angles of attack shows accumulation of water on the airfoil**

**The accumulation of water on the leading edge is not significant due to the high shear stress that moves the film toward either trailing edge or off the blade. Since we applied a transient simulation and shape of water film changes with time, the lift and drag coefficients fluctuate in a small range. The time averaged values of lift and drag coefficients has been used for performance analysis of the airfoil. Water film formation due to rain affects airfoil performance coefficients (see Table 17 and**

Table 18 and Figure 251 and Figure 252).

The simulation showed the lift coefficient decreases up to 34% due to the film formation, while the drag coefficient increases up to 40 percent for 5 different angles of attack. On average, the airfoil experienced a 12% loss in lift and a 30% increase in drag. Maximum lift coefficient loss appears at a 0 degree angle of attack and the degradation in lift decreases as the angle of attack increases. This is due to less water accumulation on the upper surface of the airfoil as shown in Figure 250.

Table 19 and Figure 253 show the Lift-to-Drag ratio as a measure of the airfoil performance for different angles of attack. The results show a significant degradation of airfoil performance due to the film formation with a maximum value of 48% and an average of 31%. The captured water film by our simulations is homogeneous and no wavy shape of the film has been captured. Our simulation results are in line with the behavior of an airfoil with wettable surface in rainy condition reported by Hansman and Barsotti [**70**]. They also studied the impact on performance of the airfoils with different surface materials and found that the airfoil with non-wettable materials experiences the most severe degradation in performance due to the surface tension effect.

Comparisons between the calculated pressure coefficient distribution with rain and without rain are presented in Figure 254. The difference in pressure coefficient distribution on the airfoil surfaces

indicates the appearance of a water layer. The water accumulation on the upper surface causes an increase in the pressure on the upper surface and leads to the degradation in the lift coefficient.

**Table 17: Degradation of Lift Coefficient due to the Rain at Different Angles of Attack**

| Angle of Attack | No Rain | Rain | Absolute Difference | Percentage Difference |
|---|---|---|---|---|
| 0 | 0.12022 | 0.07889 | -0.04133 | -34.38% |
| 1.02 | 0.23237 | 0.181171 | -0.0512 | -22.03% |
| 5.13 | 0.67224 | 0.611387 | -0.06085 | -9.05% |
| 9.22 | 1.0655 | 1.045239 | -0.02026 | -1.90% |
| 14.24 | 1.3044 | 1.295126 | -0.00927 | -0.71% |
| 20.15 | 1.2452 | 1.198291 | -0.04691 | -3.77% |

**Table 18: Increase of Drag Coefficient due to the Rain at Different Angles of Attack**

| Angle of Attack | No Rain | Rain | Absolute Difference | Percentage Difference |
|---|---|---|---|---|
| 0 | 0.01347 | 0.016918 | 0.00345 | 25.60% |
| 1.02 | 0.013688 | 0.017408 | 0.00372 | 27.18% |
| 5.13 | 0.013874 | 0.019667 | 0.00579 | 41.75% |
| 9.22 | 0.021966 | 0.031529 | 0.00956 | 43.54% |
| 14.24 | 0.048426 | 0.054785 | 0.00636 | 13.13% |
| 20.15 | 0.11915 | 0.149746 | 0.0306 | 25.68% |

**Table 19: Lift-to-Drag Ratio**

| Angle of Attack | No Rain | Rain | Difference |
|---|---|---|---|
| 0 | 8.925019 | 4.663081 | -47.75% |
| 1.02 | 16.97618 | 10.40734 | -38.69% |
| 5.13 | 48.45322 | 31.08695 | -35.84% |
| 9.22 | 48.50678 | 33.15167 | -31.66% |
| 14.24 | 26.93594 | 23.64016 | -12.24% |
| 20.15 | 10.45069 | 8.002157 | -23.43% |

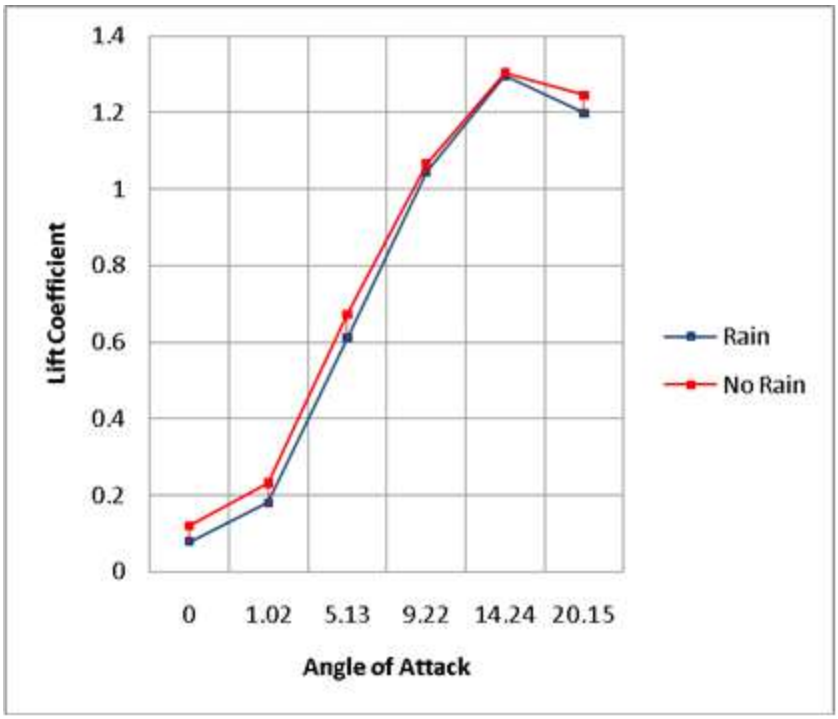


**Figure 251: Comparison of lift coefficients at different angles of attack with and without rain**

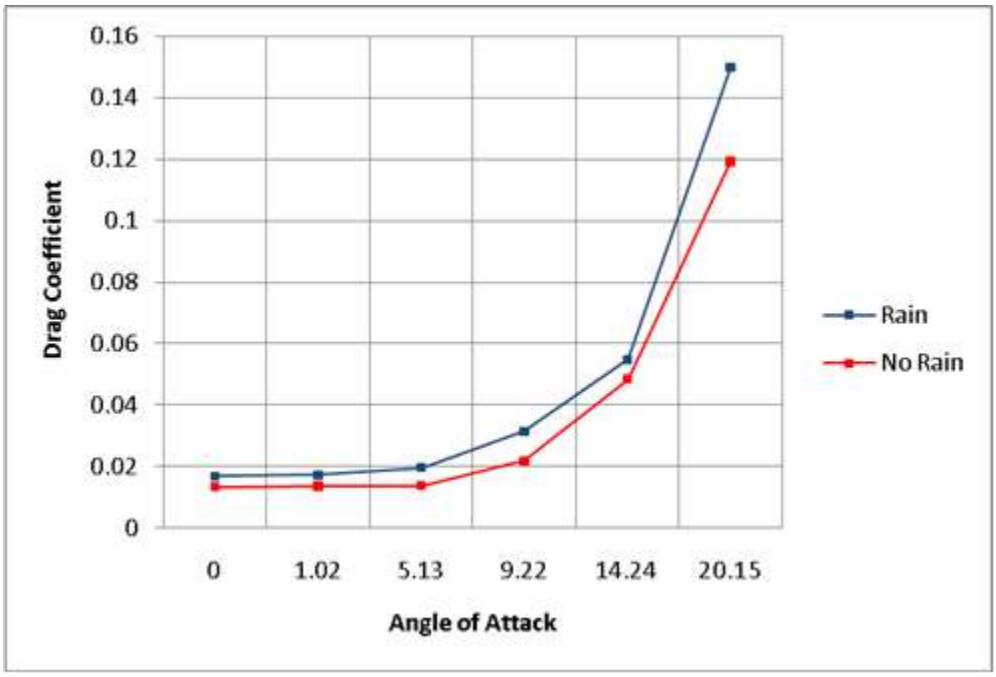


**Figure 252: Comparison of drag coefficients at different angles of attack with and without rain**

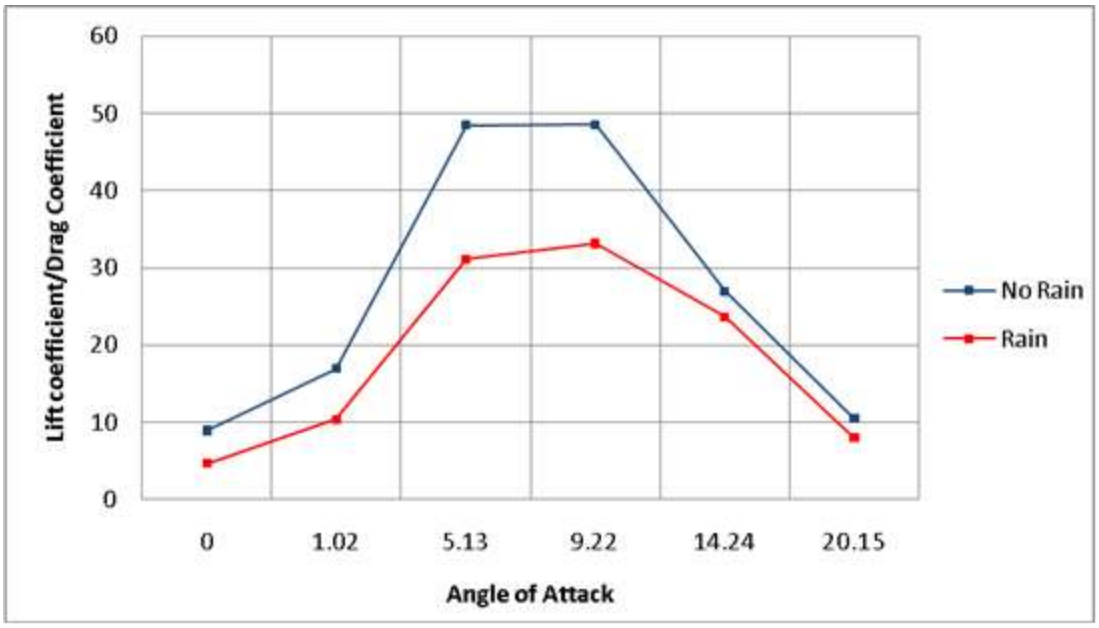


**Figure 253: Lift-to-drag ratio at different angles of attack with and without rain**

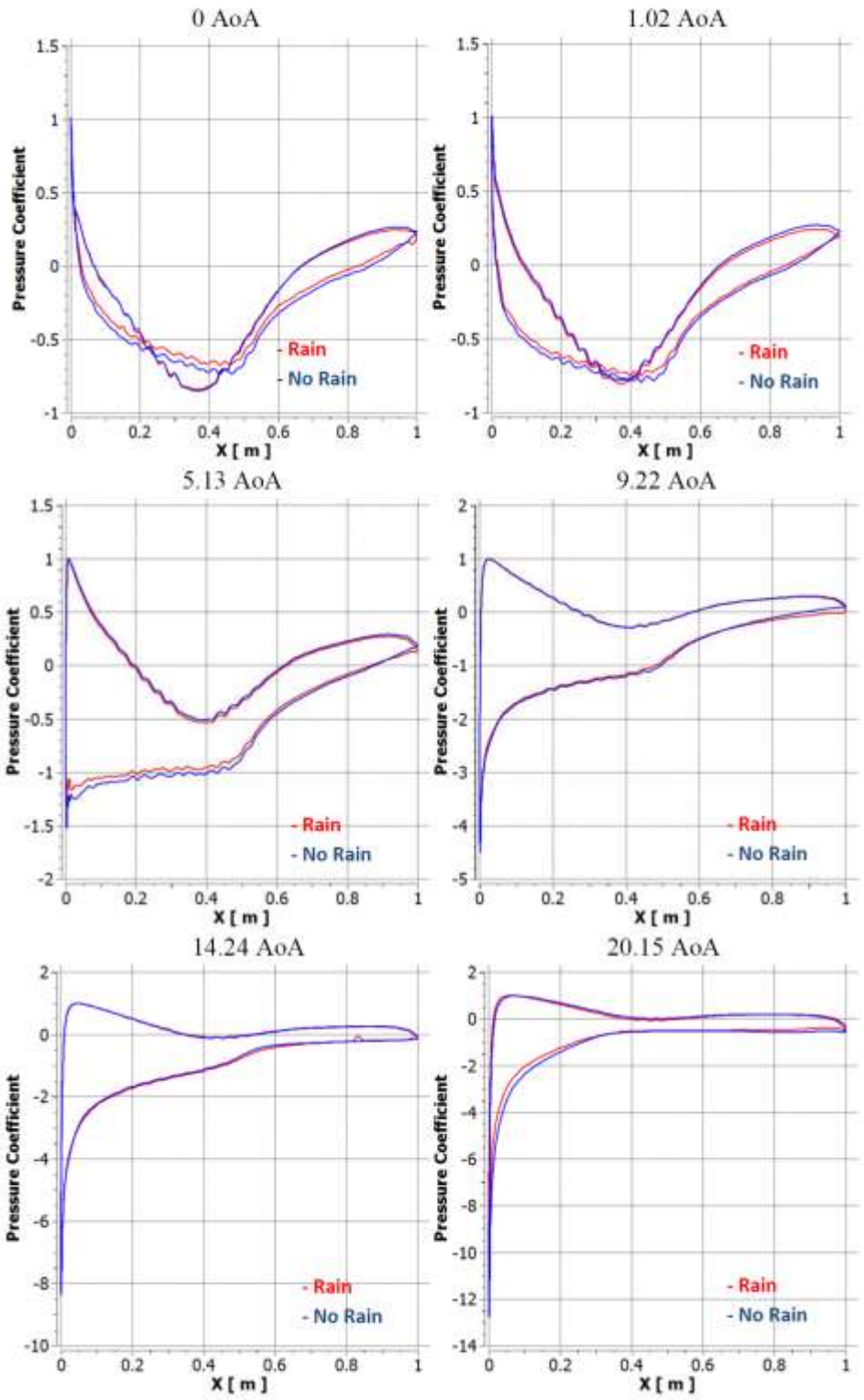


**Figure 254: Comparison between pressure coefficient distribution on the airfoil at different angles of attack with and without rain**

### H3. Summary and Conclusion

We used the CFD approach to assess and predict the performance of a horizontal-axis-wind-turbine (HAWT). Initially a set of single-phase benchmarking CFD simulations was performed in 2-D and 3-D and the results were compared with the available experimental data in the literature to refine our CFD model. Then, the single phase simulation results were used as a baseline to calculate the impact of rain on the performance of the wind turbine.

To capture the water film formation over the airfoil, a new coupled Lagrangian-Eulerian approach was employed. By capturing the shape and position of the accumulated water film, we estimated the performance loss caused by the formation of the water film. The results of this study could help designers to minimize the impact of rain on the new generation of wind turbines.

Our future work is geared toward adding the effect of splash back of droplets in our model and considering the effect of surface tension on the water film formation. In addition, we are going to apply our Lagrangian-Eulerian model in a three-dimensional case and calculate the performance of the horizontal-axis-wind-turbine in a heavy rain condition.

## 3.2.2 Wind Energy Integration

### *A. Analysis of 2030 Large-Scale Wind Energy Integration in the U.S. Eastern Interconnection*

A simulation of the 2030 load forecast in the Eastern Interconnection suggests that large-scale wind energy integration will have a major impact on the hourly commitment and dispatch of gas and coal units, especially at off-peak load hours. While fuel price alterations will have major impacts on the system production cost, load variation will have a larger impact and potential carbon costs will have the greatest impact.

Wind energy is an important component of the future energy portfolio throughout the world. In the United States, wind energy is expected to provide 20% of the electricity by 2030 [**1**], [**80**], [**81**]. However, the electricity market would require a detail simulation of the adequacy of energy portfolio before integrating the large-scale wind energy into the existing power systems.

The Eastern Interconnection is the largest interconnection in the world with more than 5,000 generating units and about 70,000 branches. The National Renewable Energy Laboratory initiated a study in 2008 to examine the impact of 20-30% wind energy penetration in the Eastern Interconnection [**82**]. The western wind and solar integration study in 2007 examined the operational impact of 35% renewable energy penetration in the Western Interconnection [**83**]. The impact of wind integration on power system operations is analyzed further in [**84**], [**85**].

An hourly unit commitment and economic dispatch model for analyzing large-scale power system operations was represented in [**86**]. A follow-up optimization-based SCUC model [**87**], [**88**], [**89**] was presented in [**90**] which took into account the intermittency and volatility of wind power generation and transmission network constraints.

In this section, we focus on studying the large-scale security-constrained wind energy integration in the Eastern Interconnection in 2030. The wind energy sites are analyzed and the impact of large-scale wind integration on existing generation resources and production costs are studied. Fuel price sensitivity, wind energy production sensitivity, load growth sensitivity, carbon cost sensitivity, and load management strategies are considered and analyzed in this chapter for the large-scale wind energy integration.

The rest of this section is organized as follows. Section A1 describes the proposed methodology, assumption and relevant evaluation metrics. Section A2 presents the wind energy integration study results for the Eastern Interconnections. The conclusions drawn from the study is provided in Section A3.

## A1. Methodology for Wind Energy Integration

At Illinois Institute of Technology (IIT), we had developed over the years an efficient decision tool called POMS [**91**] for the day-ahead scheduling of large scale power systems. The expansion of POMS, which is referred to as WINS (Wind INtegration Simulator), is considered in this study to support the collaborative planning, analysis, and implementation of the large-scale wind energy integrations in the United States. The WINS architecture is depicted in Figure 255.

WINS applies unit commitment to simulate large-scale wind energy integrations in the hourly power system operation. The application of WINS in this chapter analyzes the impact of large-scale wind energy integration in the year 2030 on production costs, unit commitment, and dispatch of generation resources in the Eastern Interconnection. For the purpose of this energy adequacy study, we do not consider transmission constraints in this chapter. We use wind data given in [**82**]. A brief description of the wind data is given in [**92**]. The wind uncertainty is simulated by sensitivity analyses applied to the wind energy integration Scenarios.

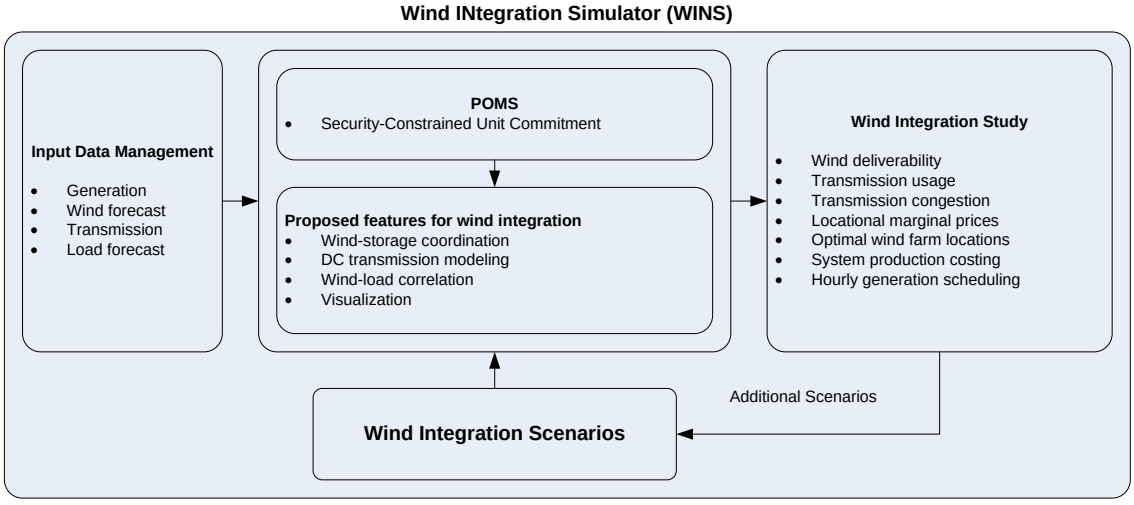


**Figure 255: Framework of WINS**

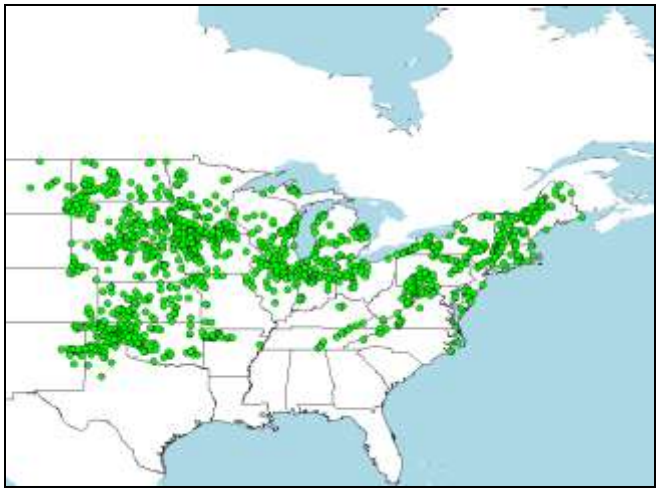

**Figure 256: Potential Wind Sites in the Eastern Interconnection**

**Input Data**

It is estimated that approximately 225GW of wind power generation is required to supply the 20%, and 330GW is required to supply the 30% of the total energy by 2024 in the Eastern Interconnection [**82**]. In this chapter, we utilize the land-based time series wind simulation results [**82**]. The potential land-based wind sites in the Eastern Interconnection are shown in Figure 256 for about 580GW of wind power generation capacity. The figure shows that there are potential wind sites with rich wind resources in the central parts of the United States.

In this study, we consider a 1.28% annual load growth rate which is based on the MTEP 2008 data. The hourly load distribution shown in Figure 257 is based on the MISO's hourly load profile in 2007 [**93**]. In Figure 257, peak load hours appear in July and August. The power flow solution is used for calculating the hourly load distribution at each bus.

Fuel prices are assumed to increase at an annual rate of 4% for oil and gas, 2% for coal, and 3% for nuclear fuel based on the fuel price given in 2008 [**93**].

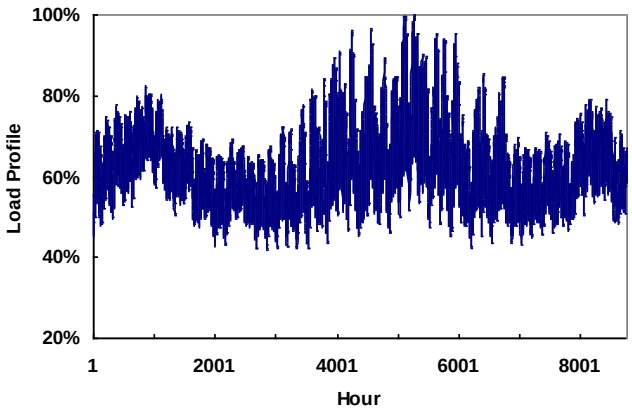


**Figure 257: Annual Hourly Load Profile**

**Evaluation Metrics**

The evaluation criteria and metrics used in the simulations are defined as follows.

**Wind Energy Availability**. The available wind energy is treated as dispatchable in WINS simulations. Here,

$$P_A = \sum_{t=1}^{T} \sum_{i=1}^{NG} p_i^{\max} w_{it} \quad \textbf{(84)}$$

where *T* represents the number of hours in a period (e.g., one year), *NG* represents the number of wind generators/farms, $p_i^{\max}$ is the nominal capacity of wind generator/farm *i*, $w_{it}$ represents the wind power profile *i* at time *t*, $P_A$ represents the system wind availability in the given study period.

We assume the available wind energy is much less than the total system load in the Eastern Interconnection. Therefore, the total available wind energy is to be dispatched without any curtailment.

**Percentage of Wind Energy Contribution**. This metric is to evaluate the percentage of wind energy contribution to the total energy utilized for supplying the load in the power system.

$$= \frac{Wind\ \ Ener\quad gy}{Total\ \ Ene\quad rgy} * 100\ \ \% \quad \textbf{(85)}$$

## A2. Numerical Results

In this section, we utilize WINS to simulate the wind integration in the Eastern Interconnection of the United States based on the methodology presented in Section A1.

**Level of Wind Integration**

We simulate the hourly power system operation using WINS for a given wind power capacity factor (CF). Four scenarios are studied as follows.

- Scenario 1: No wind integration
- Scenario 2: Wind energy integration with a minimum 40% CF
- Scenario 3: Wind energy integration with a minimum 30% CF
- Scenario 4: Integration of all potential wind energy sites

**Scenario 1: No wind integration**. This is the base case in which the hourly loads will be served by fossil fuel and hydro units. Figure 258 shows the hourly production cost which is $217.5 billion per year with an average production cost of $45.64/MWh. The production cost will not change linearly with the hourly load fluctuations. Hydro units will have zero costs and be scheduled first to serve hourly loads or reserves; then cheaper units such as nuclear, coal, and large oil will be committed as loads pick up, and finally expensive units such as gas and oil will be committed to supply hourly loads. A higher production cost will occur at annual peak hours of 5000-5500 (i.e., July and August.) The production cost at peak

hours (6AM-10PM) will be $177.8 billion and the production cost at off-peak hours (11PM-5AM) will be $39.7 billion. The average production costs at peak/off-peak hours are $50.2/MWh and $32.5/MWh. The average production cost at peak load hours is higher when expensive generators are committed and dispatched.

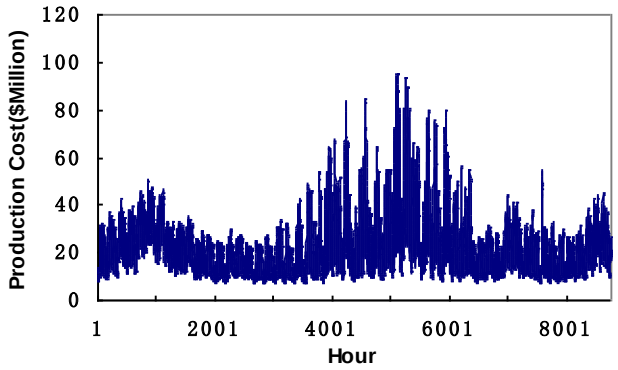


**Figure 258: Hourly Production Cost without Wind Integration**

**Scenario 2: Integration of Wind Energy Sites with a minimum 40% CF**. There are 399 of such potential wind energy sites with a total wind generation capacity of 230.5GW. The largest annual CF is 49%. Figure 259 shows the 399 potential wind energy sites in the Eastern Interconnection in which wind energy resources are mainly located remotely in the central region of the United States. The total available wind energy with a minimum 40% CF in that region is 845.2TWh.

The 2030 energy forecast in the Eastern Interconnection is 4,783.2TWh which indicates that the potential wind energy is about 17.67% of the total energy portfolio. We assume the wind energy has zero fuel cost and transmission congestion is not considered. So the entire available wind energy will be dispatched to satisfy the hourly load.

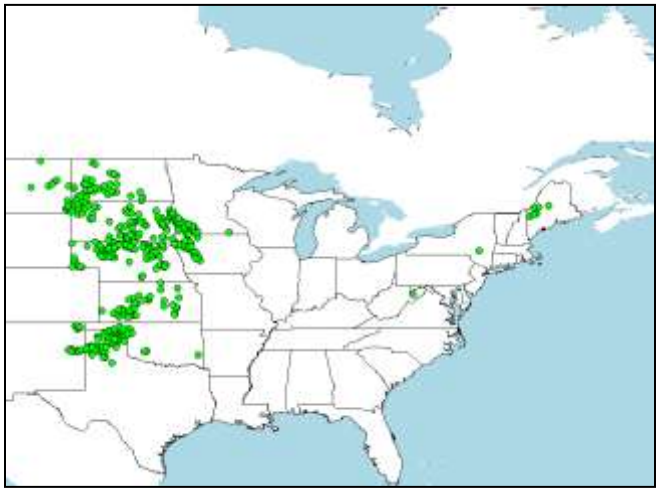

**Figure 259: Potential Wind Sites with CF ≥ 40%**

Figure 260 shows the monthly wind energy in 2030. The wind energy resources are mostly available in spring or winner; however, peak loads occur in summer. January has the highest level of available wind

energy of 86.4TWh which amounts to 21.11% of the total energy. March has the highest percentage for wind energy contribution (21.53%) because the load is lower than that of January. The available wind energy is scarce in August while the highest level of load occurs in this month. So August represents the month with the least available wind energy and the percentage of wind energy contribution (i.e., 57.5TWh and 12.2%) to the total energy portfolio.

Figure 261 shows the wind energy contribution at peak and off-peak hours. The figure shows that the wind is usually rich at night as compared with that in the day time especially in the summer. The hourly average wind energy at peak/off-peak hours are 2.27TWh and 2.69TWh in August, and the percentages of wind energy contribution are 10.88% and 16.22% respectively.

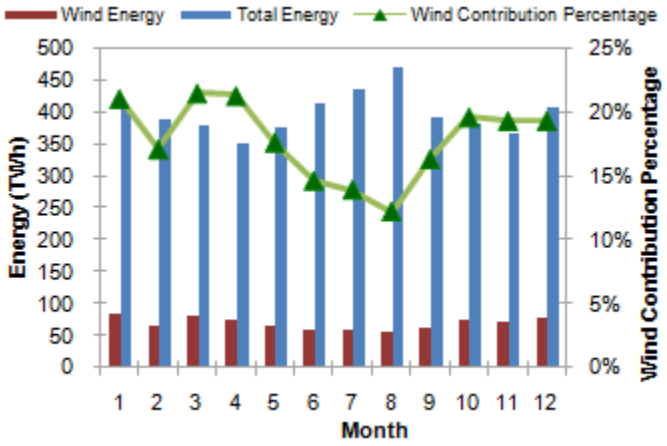


**Figure 260: Monthly Wind Energy and its Contribution to Total Energy in Scenario 2**

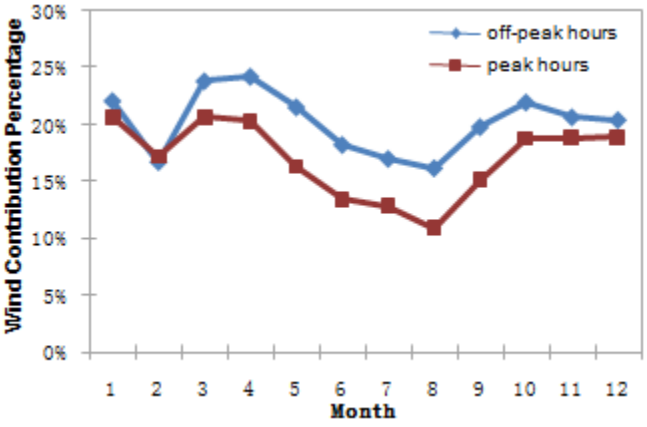


**Figure 261: Wind Energy Contribution at Peak/Off-Peak Hours in Scenario 2**

Figure 262 shows the hourly production cost. Compared to Figure 258, the production cost is lower when the large-scale wind energy is integrated. The annual production cost is $130.4 billion, which is about $87.1 billion less than that in Scenario 1. The annual average production cost decreases from $45.64/MWh to $27.25/MWh when the wind energy is integrated. Here, the production costs at peak/off-peak hours are $107.1 billion and $23.2 billion, and the average production cost at peak/off-

peak hours are 30.1$/MWh and 18.9$/MWh respectively. The average production cost is lower in this Scenario at peak/off-peak hours.

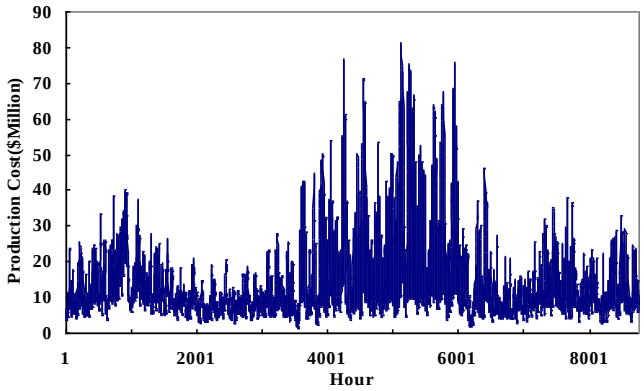


**Figure 262: Hourly Production Cost in Scenario 2**

**Scenario 3: Integration of Wind Sites with a Minimum 30% CF**. In this case, 972 wind sites are introduced in Figure 263 with a total capacity of 481.5GW. Compared to Figure 259, additional wind energy sites located in Wisconsin, Illinois, Indiana, and other sites are considered in this Scenario.

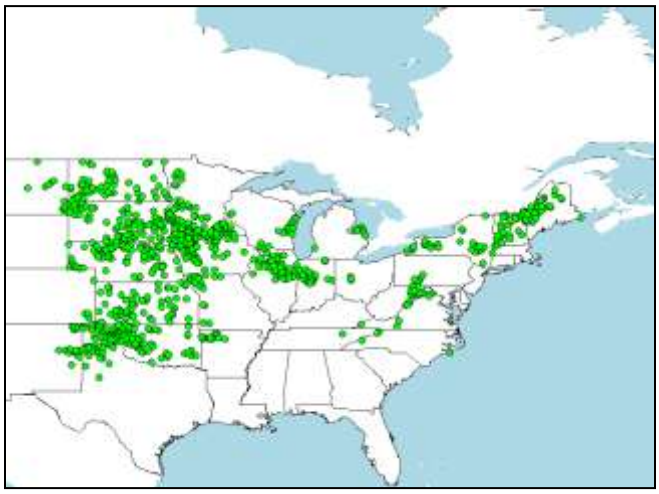

**Figure 263: Potential Wind Sites with CF ≥ 30%**

Figure 264 shows the annual wind energy contribution is 1,596TW which amounts to 33.37% percentage of the energy portfolio. Figure 265 shows the monthly wind energy contribution at peak/off-peak hours. Compared to the simulation results in Scenario 2, 573 additional potential wind energy sites with a 251GW of capacity are added here with a lower CF between 30% and 40%. In this case, the added wind capacity is 108.9% (i.e., 481.5GW VS 230.5GW) while the wind energy contribution increases about 88.85% (i.e., 33.37% VS 17.67%).

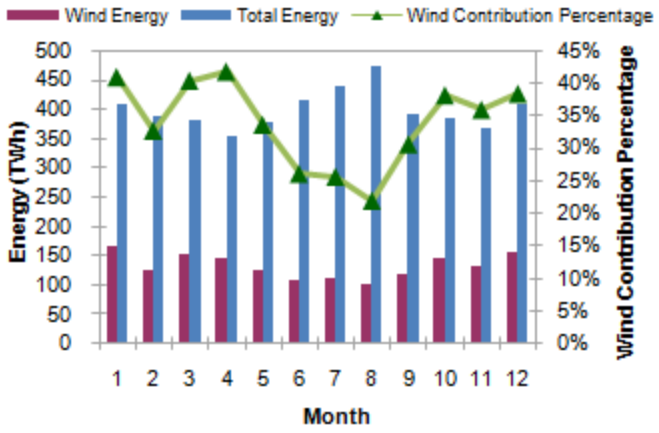


**Figure 264: Monthly Wind Energy and its Contribution to Total Energy in Scenario 3**

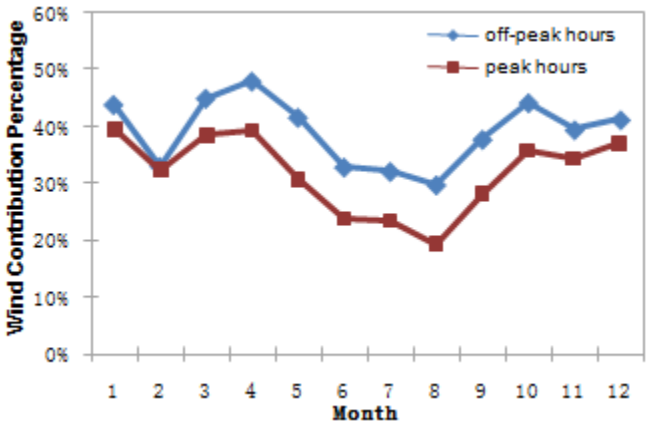


**Figure 265: Wind Contribution at Peak/Off-Peak Hours in Scenario 3**

The production cost in Figure 266 is $86.8 billion with an average hourly production cost of 18.14$/MWh. The average production costs at peak/off-peak hours are 20.33$/MWh and 11.33$/MWh, respectively.

**Scenario 4: Integration of All Potential Wind Sites**. There are 1,326 wind energy sites in the Eastern Interconnection with a total capacity of 580 GW. Figure 267 shows the monthly wind energy production and wind energy contribution. The annual wind energy production is about 1,816TWh and the annual percentage of wind energy contribution is about 38%. In this case, the minimum wind energy contribution will be more than 20% of the system load.

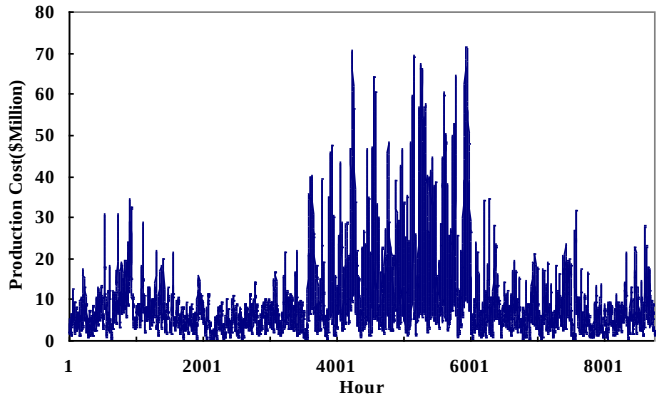


**Figure 266: Hourly Production Cost in Scenario 3**

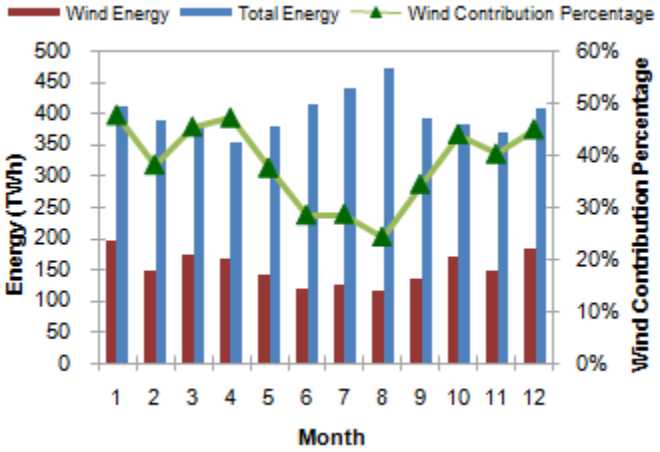


**Figure 267: Monthly Wind Energy and its Contribution to Total Energy in Scenario 4**

Figure 268 shows the percentage of wind energy contribution at peak/off-peak hours. Here, the wind energy contribution to the total energy at peak hours in August is 21.33%, which is also the lowest period for the wind energy production. The wind energy in this period is 75.83TWh as compared to 38.67TWh in Scenario 2 and 68.52TWh in Scenario 3. The annual production cost is $77 billion. Figure 269 shows the hourly production cost with an average production cost of $16.1/MWh, and peak/off-peak average production costs of $18.19/MWh and $10.04/MWh respectively. Compared to the simulation results in Scenarios 1-3, the production costs has dropped here as more wind energy sites are added. Figure 270 shows the wind energy contribution in all four Scenarios. Here, the gas unit production has decreased as more wind energy is considered. Also, the energy supplied by coal units is lower which is replaced by the integrated wind energy units. Figure 271-Figure 273 show the energy supplied by gas, coal and wind units in four Scenarios. These figures show that wind energy will replace some of the fossil energy especially at off-peak hours in the Eastern Interconnection.

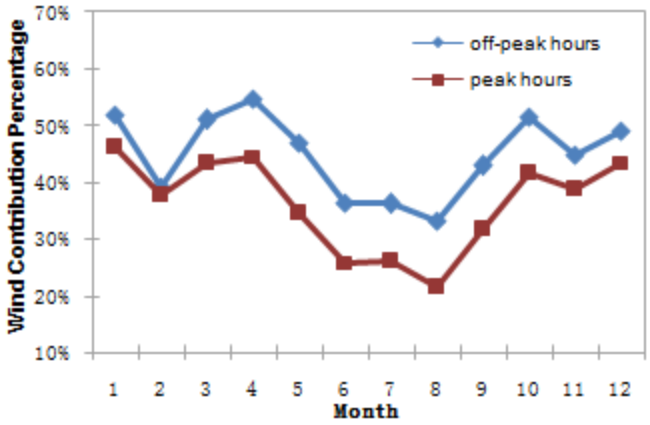


**Figure 268: Wind Energy Contribution at Peak/Off-Peak Hours in Scenario 4**

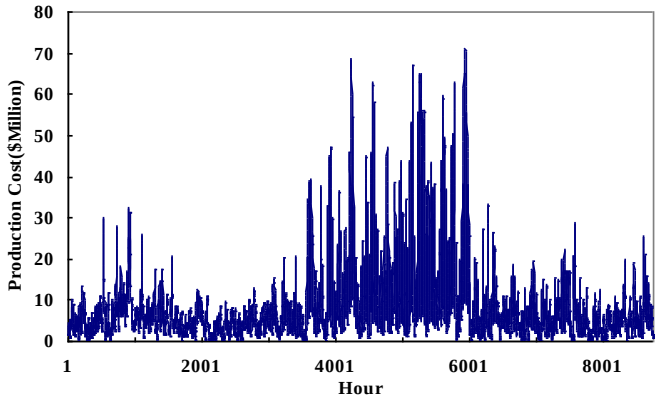


**Figure 269: Hourly Production Cost in Scenario 4**

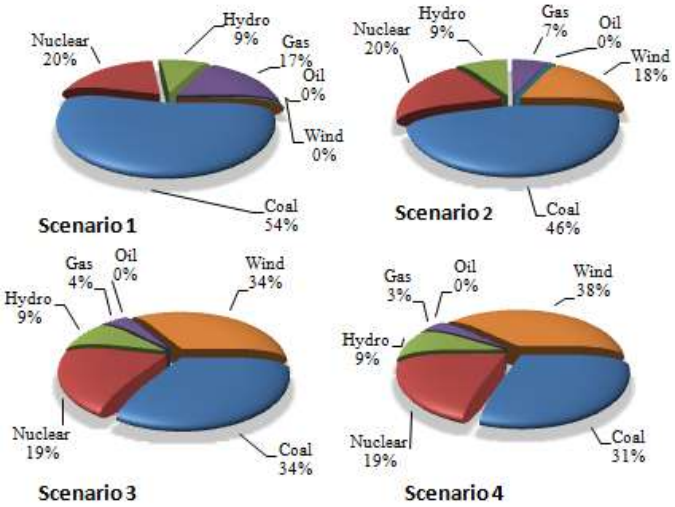


**Figure 270: Energy Portfolio in Wind Integration Scenarios**

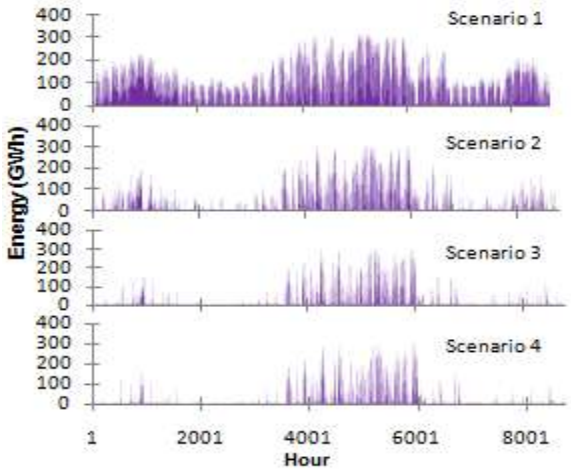


**Figure 271: Hourly Energy Provided by Gas Units in Wind Integration Scenarios**

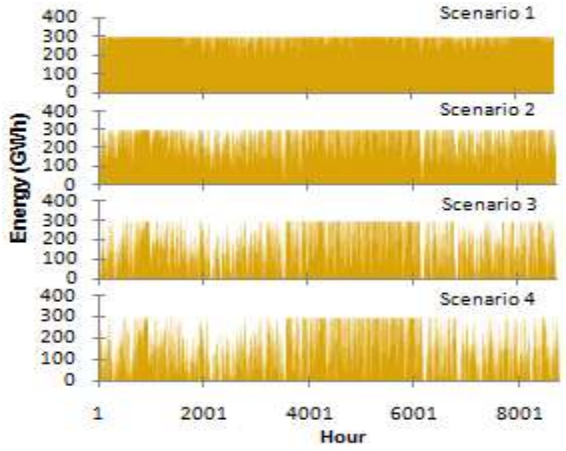


**Figure 272: Hourly Energy Provided by Coal Units in Wind Integration Scenarios**

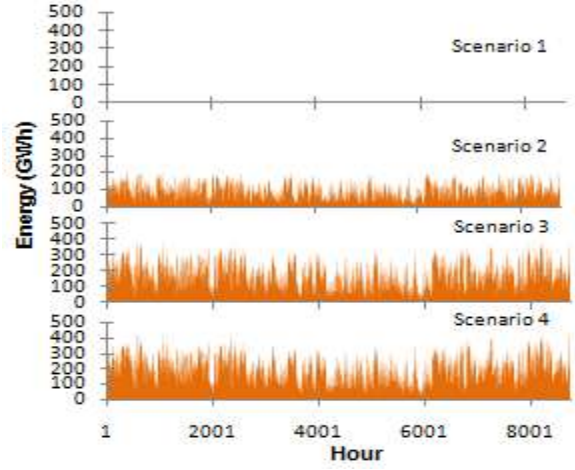


**Figure 273: Hourly Wind Energy in Wind Integration Scenarios**

Figure 274 show the annual commitment results of existing power plants in four Scenarios, in which red dots represents the power plants in which at least one unit is committed for a minimum of one hour per year. Also, blue dots show the plants which will be off throughout the year as more wind energy is integrated in the Eastern Interconnection.

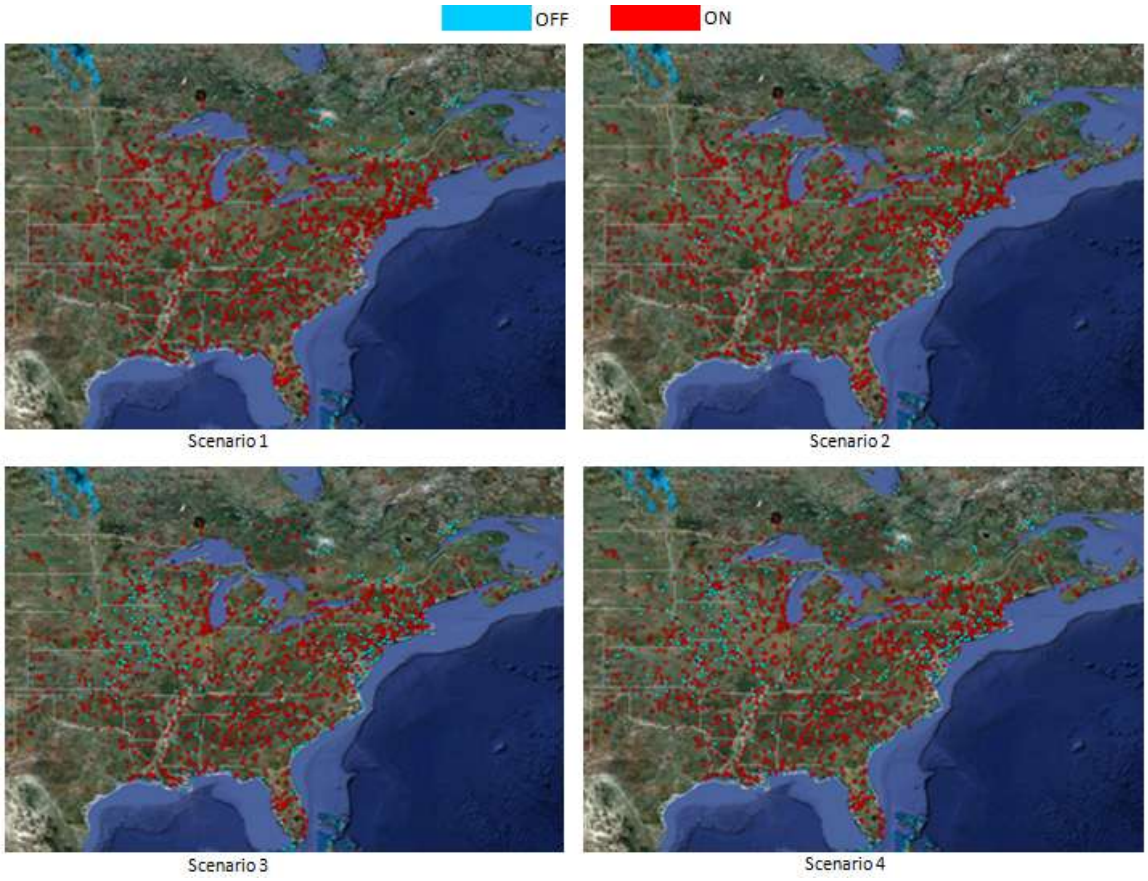


**Figure 274: Unit Commitment Result in Wind Integration Scenarios**

**Sensitivity Analysis**

There are several uncertain factors in the Eastern Interconnection, including fuel price, hourly wind speed, hourly loads, and carbon costs, which could have major impacts on the large-scale wind energy integration and the energy portfolio. It is perceived that the accurate forecast for some of these factors might not be readily available. In this section, we apply sensitivity analyses, based on the simulation results for Scenario 2 to study the impact of fluctuations in such factors on the wind energy integration and the annual energy portfolio in the Eastern Interconnection. The simulation results for Scenario 2 are considered as the base case in this Section.

***Fuel Price Sensitivity***

We apply the sensitivity analysis to the WINS simulation results for 2030, given for Scenario 2, in which the potential wind energy sites with a minimum CF of 40% and a total energy contribution of 17.67% (which is close to the expected 20% wind contribution in 2030) were considered. The following four scenarios would consider the impact of fuel price forecast.

- Scenario 5: Actual fuel price would be 20% lower than the forecast
- Scenario 6: Actual fuel price would be 10% lower than the forecast
- Scenario 7: Actual fuel price would be 10% higher than the forecast
- Scenario 8: Actual fuel price would be 20% higher than the forecast

As expected, the fuel price escalation has no impact on the wind energy dispatch since the wind energy has a zero price and will always be dispatched. The production cost in Figure 275 will increase as fuel price increases. The increase in fuel price at peak hours will have a more pronounced impact on the production cost as more expensive units are committed.

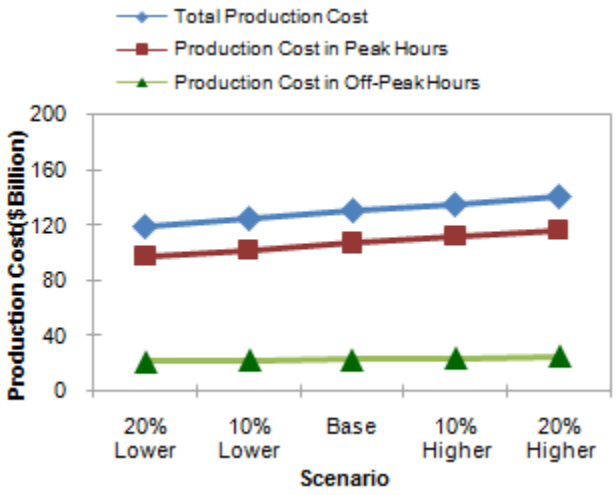


**Figure 275: Production Cost in Fuel Cost Scenarios**

***Wind Energy Output Sensitivity Analysis***

We apply the sensitivity analysis to the 2030 simulation results for Scenario 2. Four scenarios are studied as follows.

- Scenario 9: Actual wind energy production is 20% lower than the forecast
- Scenario 10: Actual wind energy production is 10% lower than the forecast
- Scenario 11: Actual wind energy production is 10% higher than the forecast
- Scenario 12: Actual wind energy production is 20% higher than the forecast

Figure 276 shows that the wind energy contribution to the total energy production is about 20% when the actual wind energy is 10% percent higher than that in the base case. Figure 277 shows that the total production cost decreases with the added wind energy production. Again, the production cost is more sensitive to the wind energy production at peak hours.

Figure 278 shows the energy portfolios in all four Scenarios. The energy produced by gas and coal units will decrease as the wind energy production is higher. Similar to that in Figure 276, the wind energy contribution is increased from 14% to 22%. The unit commitment and hourly generation dispatch show a similar pattern as that for Scenario 2.

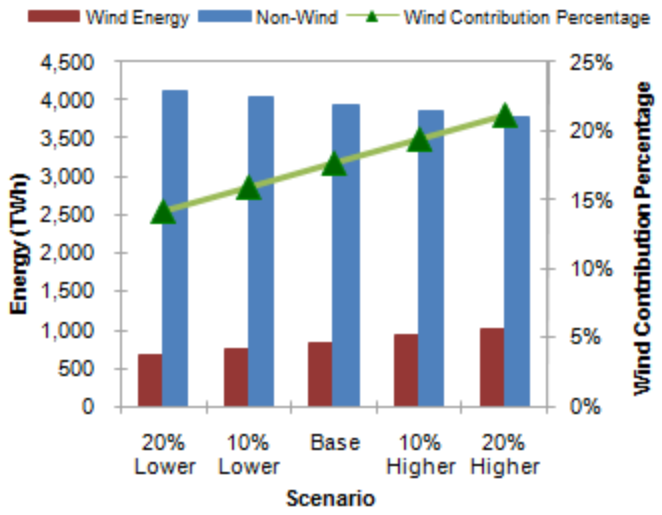


**Figure 276: Wind/Non-Wind Energy for Wind Energy Scenarios**

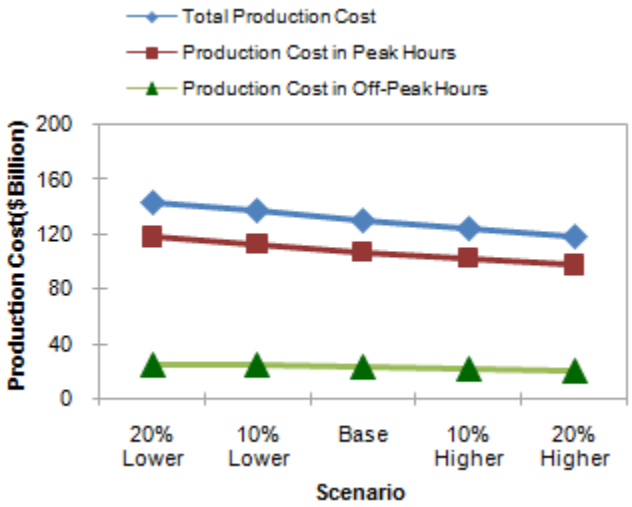


**Figure 277: Production Cost for Wind Energy Scenarios**

***Load Sensitivity Analysis***

In this section, we study the impact of load forecast errors on the WINS base case simulation results for Scenario 2. We do the sensitivity analysis based the load forecast in 2030. Four scenarios are studied as follows.

- Scenario 13: Actual load is 20% lower than the forecast
- Scenario 14: Actual load is 10% lower than the forecast
- Scenario 15: Actual load is 10% higher than the forecast
- Scenario 16: Actual load is 20% higher than the forecast

The wind energy contribution, depicted in Figure 279, shows a 19.62% contribution to the total energy production in Scenario 14 when the actual load is 10% lower than the forecast. The wind energy

contribution will decline as the actual load escalates because the additional load will be served by other types of units.

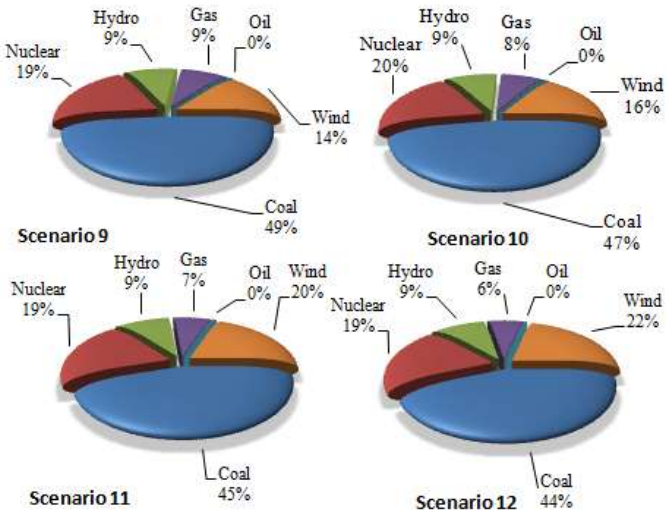


**Figure 278: Energy Portfolio in Wind Energy Scenarios**

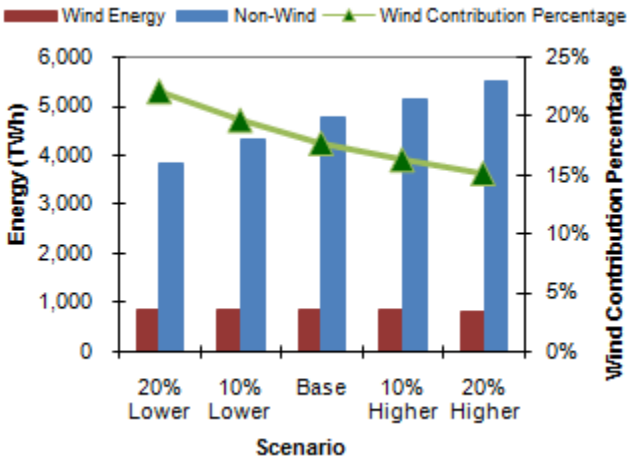


**Figure 279: Wind/Non-Wind Energy in Load Scenarios**

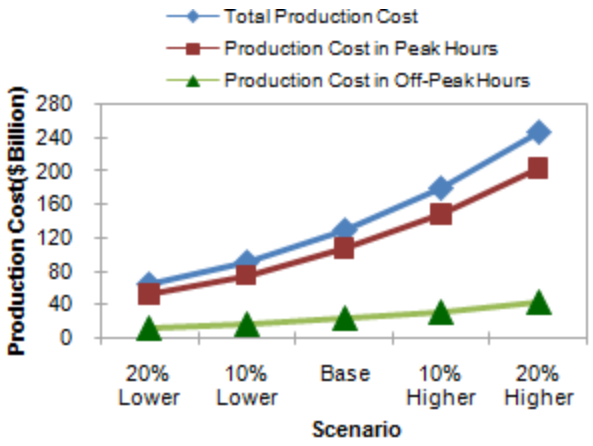


**Figure 280: Production Cost in Load Scenarios**

The production costs in Figure 280 show that the system load will have the largest impact on production costs. Here, the production cost increases a lot between Scenarios 13 and 16. The production cost at peak hours is more sensitive to load variations.

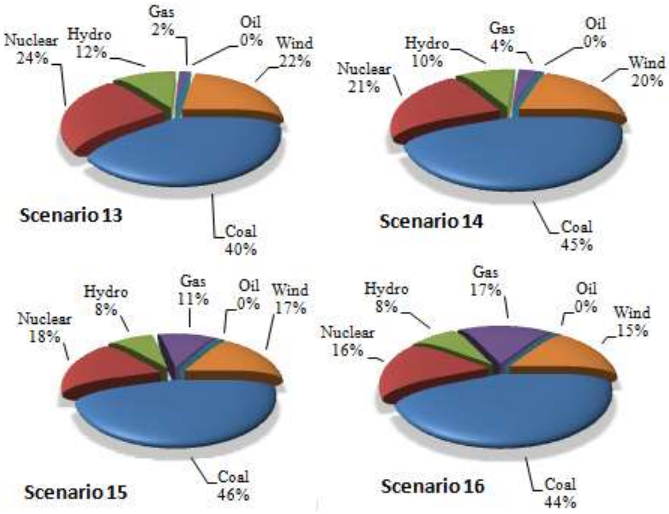


**Figure 281: Energy Portfolio in Load Scenarios**

Figure 281 shows the energy contribution in the given four Scenarios. The nuclear, hydro, and wind unit with their inexpensive fuel will supply much of the hourly load. However, their contributions will decline as the system load increases. Compared with the base case of Scenario 2, the energy contributions by gas and coal units, especially those supplied by gas units, will decrease as we reduce the system load. Furthermore, the contribution of gas units to the energy portfolio will increase from 7% in the base case (for Scenario 2) to 11% in Scenario 15 and 17% in Scenario 16 as we increase the system load, which means that the additional load is mainly supplied by gas units.

Figure 282 and Figure 283 show the hourly energy supplied by gas and coal units. In Figure 282, the energy supplied by gas units has increased as compared to that in Scenarios 13-14 especially at peak hours. In Scenario 13, gas units are mainly committed and dispatched at peak hours.

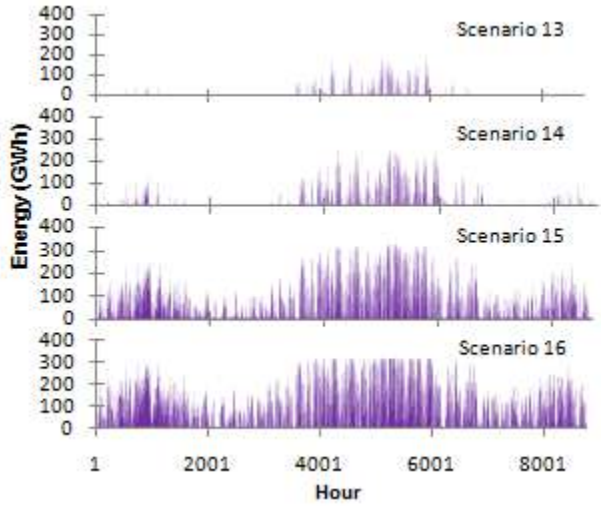


**Figure 282: Hourly Energy Provided by Gas Units in Load Scenarios**

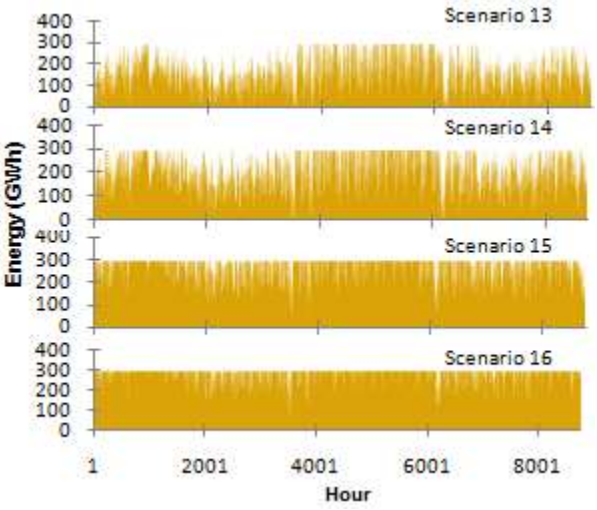


**Figure 283: Hourly Energy Provided by Coal Units in Load Scenarios**

Figure 284 shows that the load variation would have the largest impact on the commitment and the dispatch of generating units as compared to the fluctuation in fuel price or wind energy production. The commitment based on Scenarios 13-14 shows that many of the existing units will never be committed as hourly loads are lowered. On the other hand, almost all existing units will be committed when the hourly loads are higher than the forecast in Scenarios 15-16. The results indicate that the load management could introduce large incentives for improving the system operation bottlenecks and decreasing the operation costs.

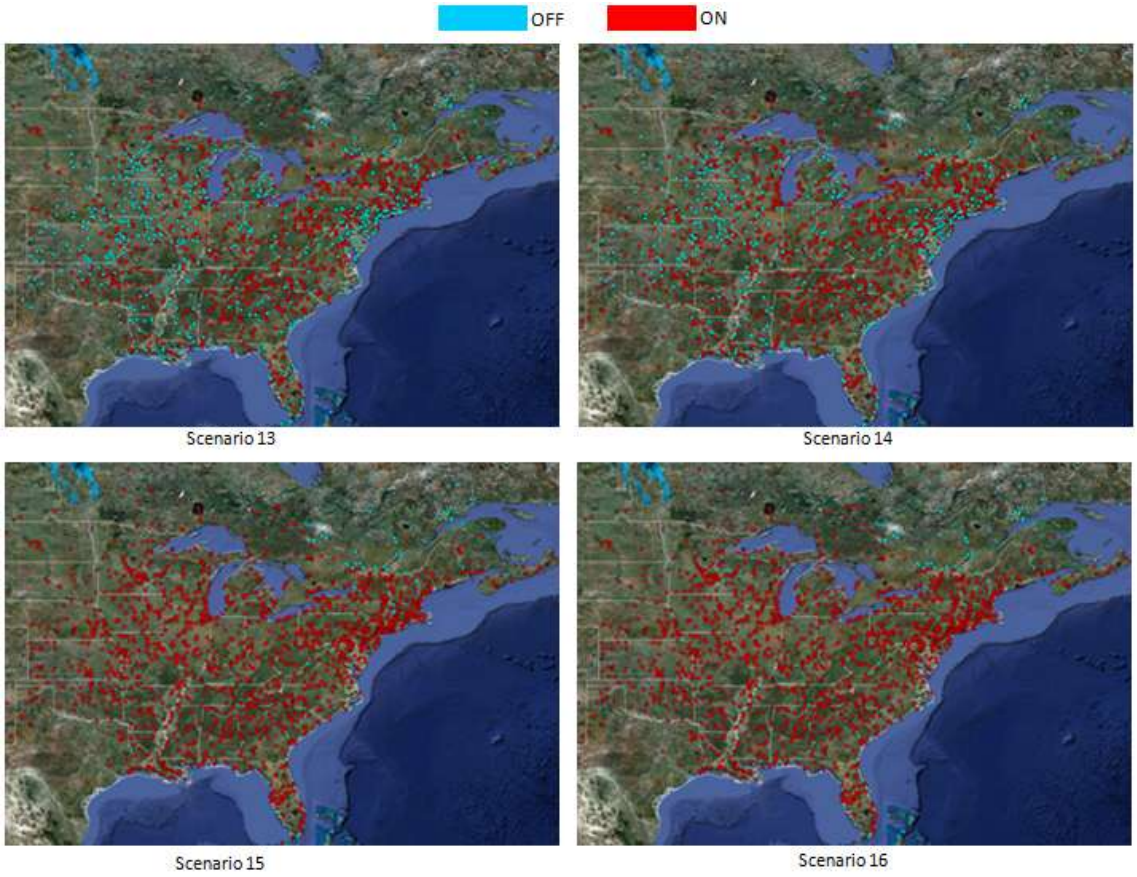


**Figure 284: Unit Commitment Result in Load Scenarios**

***Carbon Cost Sensitivity Analysis***

Higher carbon cost can be used as an incentive for promoting the development of clean, efficient or environmentally friendly power generation portfolios [**94**]. The carbon cost data given in [**94**] is considered here as the low carbon cost scenario. The high carbon cost scenario would consider a carbon cost that is doubled. In this section, we consider wind energy sites with CF ≥ 40% and CF ≥ 30% for analyzing the following four scenarios.

- Scenario 17: Low carbon cost with a minimum 40% CF for wind energy sites
- Scenario 18: High carbon cost with a minimum 40% CF wind energy sites
- Scenario 19: Low carbon cost with a minimum 30% CF wind energy sites
- Scenario 20: High carbon cost with a minimum 30% CF wind energy sites

The variations in carbon cost will not change the wind energy contribution to the energy portfolio. The production costs for all four Scenarios are $406.8 billion, $638 billion, $285.7 billion, and $448 billion. Therefore, the total production costs with higher carbon cost would be much higher. For example, the average production cost at peak/off-peak load hours are $89.5/MWh and $71.7/MWh in Scenario 17, and $140/MWh and $113.5/MWh in Scenario 18.

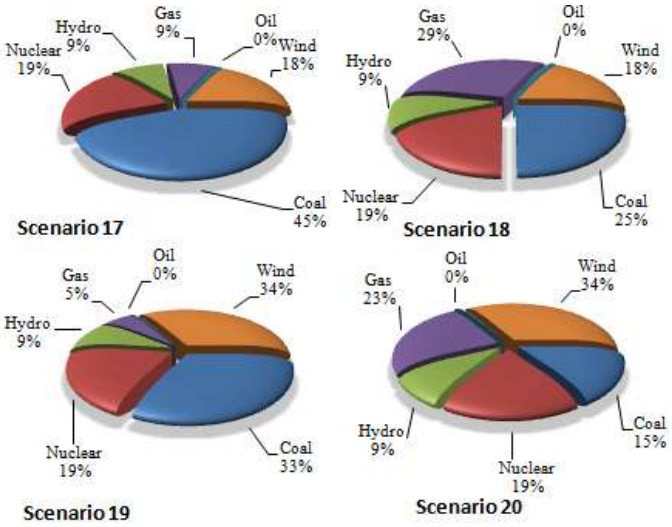


**Figure 285: Hourly Energy Portfolio in Carbon Cost Scenarios**

Figure 285 shows the energy portfolios in carbon cost Scenarios in which the high carbon cost will have a major impact on the energy supplied by gas and coal units. Since coal prices are lower than gas prices, the energy supplied by coal units does not change much in the low carbon cost Scenarios. The energy supplied by gas units increases from 9% in low carbon cost scenario (Scenario 17) to 29% in high carbon cost scenario (Scenario 18) while that of coal decreases from 45% to 25%. Similar results are obtained when we consider wind units with a minimum 30% CF.

Figure 286 and Figure 287 show the hourly energy supplied by gas and coal units, which is consistent with that of Figure 285. Here, gas units would be committed and dispatched in most hours with high carbon costs.

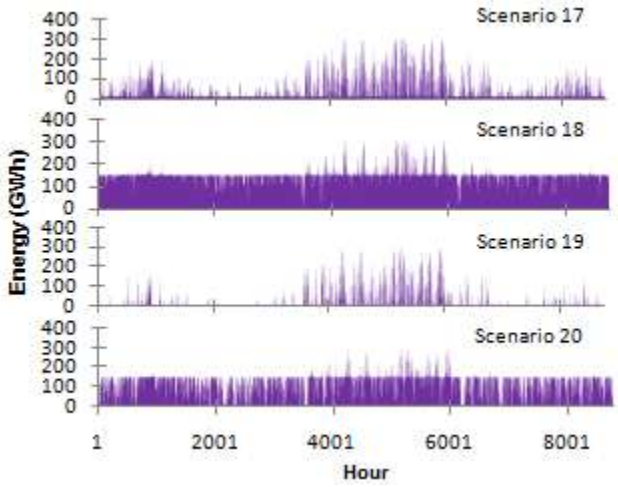


**Figure 286: Hourly Energy Provided by Gas Units in Carbon Cost Scenarios**

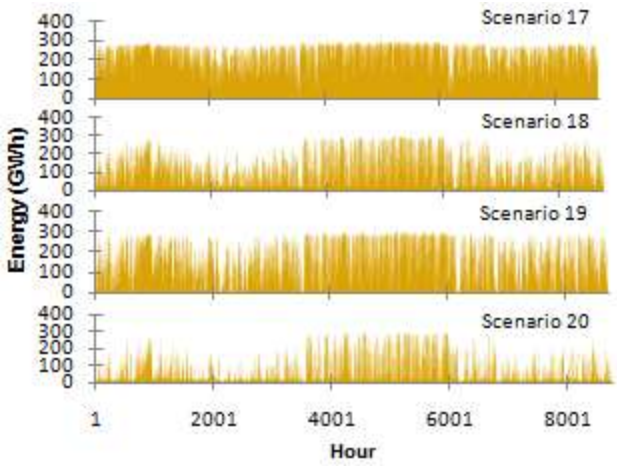


**Figure 287: Hourly Energy Provided by Coal Units in Carbon Cost Scenarios**

**Load Management by Introducing Load Shedding**

As presented for Load Sensitivity Analysis, the hourly load variations would have a major impact on the WINS simulation results. In this section, we consider load shedding as an option to manage the system operation more efficiently at peak hours. For instance, if the hourly load is higher than 80% of annual peak load, we would set it at 80%. Three scenarios are considered as follows.

- Scenario 21: No wind energy is considered when the load shedding is applied
- Scenario 22: Wind energy with a minimum CF of 40% is considered when the load shedding is applied
- Scenario 23: Wind energy with a minimum CF of 30% is considered when the load shedding is applied

Figure 288 shows the energy production portfolios for the three load shedding Scenarios.

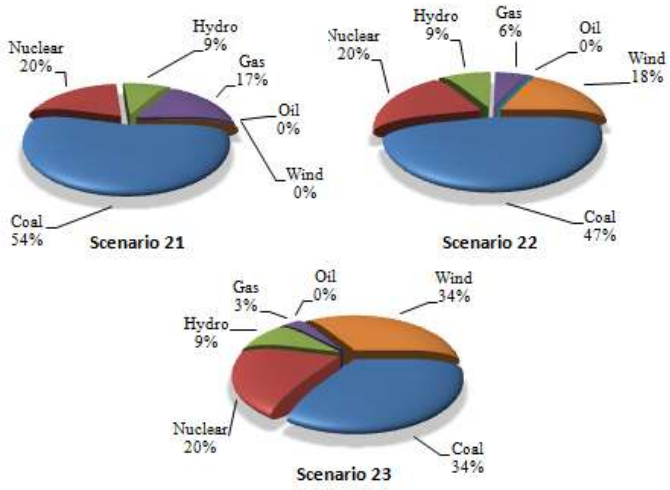


**Figure 288: Energy Portfolio in Load Shedding Scenarios**

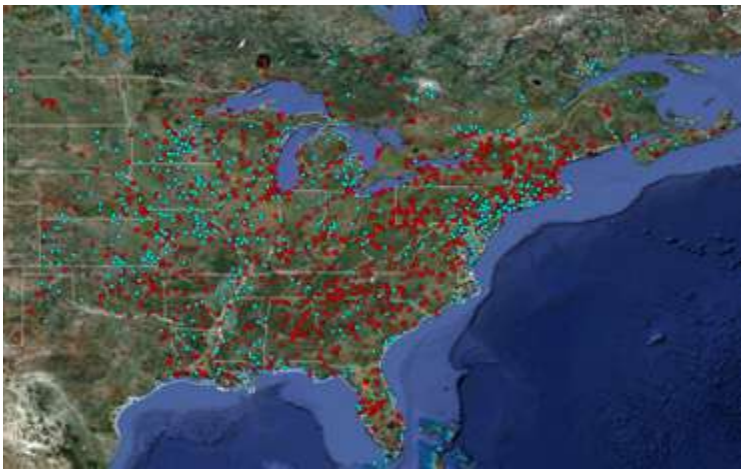

**Figure 289: Unit Commitment Result in Scenario 21**

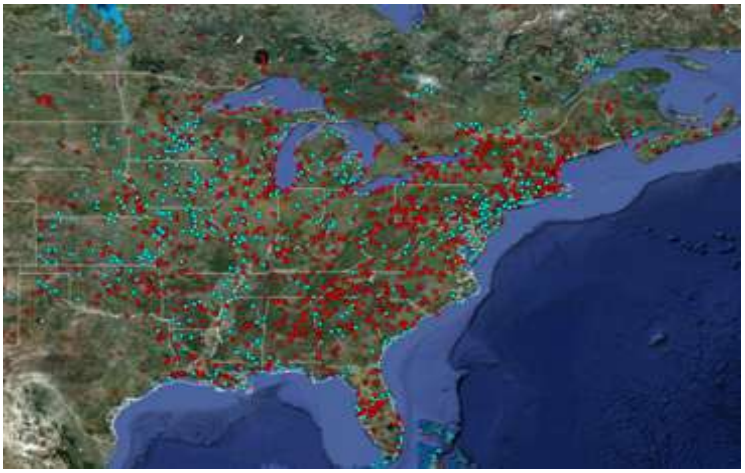

**Figure 290: Unit Commitment Result in Scenario 22**

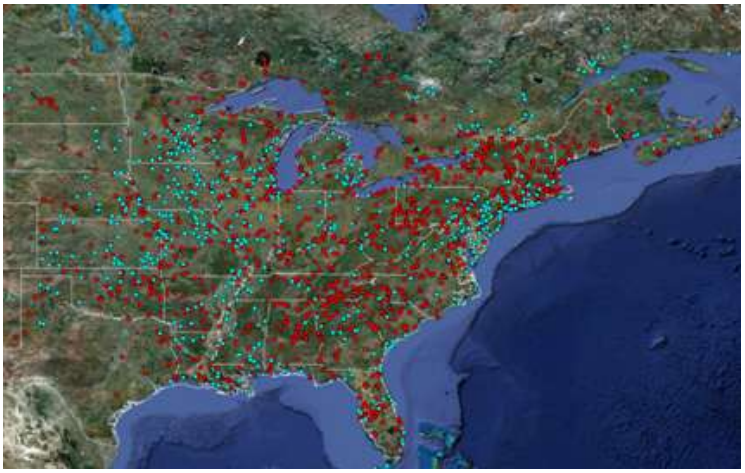

**Figure 291: Unit Commitment Result in Scenario 23**

Figure 289-Figure 291 show that the load shedding will alter the unit commitment as compared to those in Figure 274. Here, more gas units are turned off at peak hours when load shedding is applied. Here, there are about 1,200 gas units which would never be committed again when load shedding is considered as compared to those of the Scenarios 1, 2, and 3. These results are similar to those for load variation analysis given in Scenarios 13 and 14.

Figure 292 shows the hourly energy supplied by gas units in which the gas unit dispatch is lower because of the load shedding at peak hours. Load shedding has almost no impact on the hourly dispatch of coal units, as coal units are committed to serve the base load.

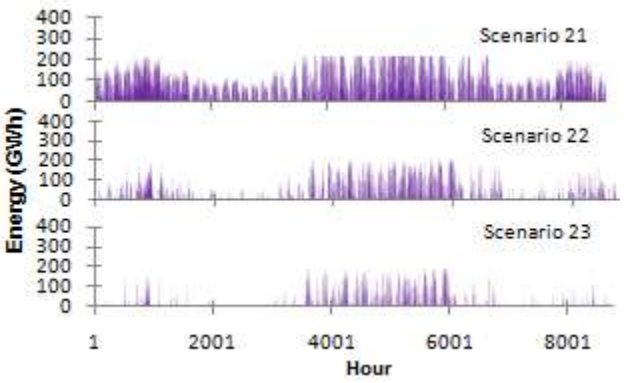


**Figure 292: Hourly Energy Provided by Gas Units in Load Shedding Scenarios**

### A3. Conclusions

In this section, a comprehensive large-scale wind energy integration analysis is considered which is based on the 2030 load forecast in the Eastern Interconnection of the United States. Here, transmission constraints are not considered when studying the wind energy portfolios. The wind energy integration is studied based on the capacity factors of potential wind sites. Wind energy contributions to peak/off-peak annual production costs are studied based on the WINS simulation results. The sensitivity of fuel costs, wind energy production, hourly loads, carbon costs, and load management are analyzed in the wind energy integration Scenarios. The wind energy integration simulation results and their sensitivities are summarized in Table 20. Here, the contribution of wind energy to the 5 Scenarios is about 20% or higher.

**Table 20: Summary of Simulation Results in All Scenarios**

| Scenario | Wind Capacity (GW) | Wind Generation (TWh) | Wind Contribution Percentage (%) | Production Cost ($ Billion) | Average Production Cost ($/MWh) |
|---|---|---|---|---|---|
| 1 | 0 | 0 | 0 | 217.5 | 45.64 |
| 2 | 230.5 | 845.2 | 17.67 | 130.4 | 27.25 |
| 3 | 481.5 | 1,596 | **33.37** | 86.8 | 18.14 |
| 4 | 580 | 1,816 | **38** | 77 | 16.10 |
| 5 | 230.5 | 845.2 | 17.67 | 118.9 | 24.87 |
| 6 | 230.5 | 845.2 | 17.67 | 124.7 | 26.06 |
| 7 | 230.5 | 845.2 | 17.67 | 135.7 | 28.36 |
| 8 | 230.5 | 845.2 | 17.67 | 141.7 | 29.63 |
| 9 | 230.5 | 676.1 | 14.14 | 143.7 | 30.03 |
| 10 | 230.5 | 760.6 | 15.9 | 136.8 | 28.59 |
| 11 | 230.5 | 929.7 | 19.44 | 130.4 | 25.99 |
| 12 | 230.5 | 1014 | **21.20** | 124.3 | 24.80 |
| 13 | 230.5 | 845.2 | **22.07** | 64 | 16.73 |
| 14 | 230.5 | 845.2 | 19.62 | 91.6 | 21.27 |
| 15 | 230.5 | 845.2 | 16.29 | 178.5 | 34.65 |
| 16 | 230.5 | 845.2 | 15.12 | 245.9 | 44.54 |
| 17 | 230.5 | 845.2 | 17.67 | 406.8 | 84.97 |
| 18 | 230.5 | 845.2 | 17.67 | 638 | 133.3 |
| 19 | 481.5 | 1,596 | 17.67 | 285.7 | 69.68 |
| 20 | 481.5 | 1,596 | 17.67 | 448 | 93.59 |
| 21 | 0 | 0 | 0 | 208.7 | 44 |
| 22 | 230.5 | 845.2 | 17.81 | 123 | 25.9 |
| 23 | 481.5 | 1,596 | **33.53** | 80.6 | 16.97 |

### *B. Large-scale Analysis of 2018 Wind Energy Integration in the U.S. Eastern Interconnection*

This section presents the hourly simulation results for the year 2018 with the large-scale wind energy integration in the Eastern Interconnection of the United States. A simulator referred to as WINS (Wind INtegration Simulator) is developed for this annual study. The wind energy integrations in the year 2018 are simulated using the hourly security-constrained unit commitment (SCUC) in WINS. The generation portfolio for supplying the hourly load in 2018 is developed with/without transmission network constraints. The sensitivities to the 2018 wind energy integration are carried out for fuel price, wind energy availability, load growth, carbon cost, and hourly load management strategies. The hourly production cost, generation credit, load payment, levelized congestion cost, LMPs, and wind energy contribution, are calculated and analyzed.

The U.S. Eastern Interconnection is the largest interconnection in the world with more than 5,000 generating units and about 45,000 transmission lines. The National Renewable Energy Laboratory (NREL) performed a study in 2008 to examine the impact of 20-30% wind energy integration in the Eastern Interconnection [**82**]. The western wind and solar integration study in 2007 examined the operational impact of 35% renewable energy penetration [**83**]. The impact of wind energy integration on power system operations is analyzed further in [**84**], [**85**]. An hourly unit commitment and economic dispatch model for analyzing large-scale power system operations was represented in [**86**]. A follow-up optimization-based security-constrained unit commitment (SCUC) model [**87**], [**89**] was presented in [**90**] which took into account the intermittency of wind power generation and transmission network constraints. A comprehensive adequacy analysis of energy production portfolio for 2030 was presented in [**95**]. The adequacy study in [**95**] did not consider transmission constraints as locations for the 2030 wind generation unit installations were not provided.

In this section, we focus on studying the 2018 large-scale wind energy integration in the Eastern Interconnection. The impact of large-scale wind energy integration on existing generation resources, production costs, LMPs, generation credits, load payments, transmission utilization, and wind energy deliverability are studied. The sensitivity of wind integration to fuel price, wind energy availability, load growth, carbon cost, and load management strategies is analyzed in this paper.

The rest of the section is organized as follows. Section B1 describes the proposed methodology, assumption and relevant evaluation metrics. Section B2 presents the wind energy integration study results for the Eastern Interconnections. The conclusions drawn from the study are provided in Section B3.

## B1. Methodology for Wind Energy Integration

POMS (Power Market Simulator) is an efficient decision tool for the day-ahead scheduling of large-scale power systems which has been utilized in transmission congestion analysis for the Eastern Interconnection in [**91**]. WINS (Wind Integration Simulator) is the expansion of POMS in order to support the collaborative planning and implementation of the large-scale wind energy integration in the United States [**95**]. WINS applies SCUC to simulate the large-scale wind energy integration in the hourly power system operation. The application of WINS in this paper will analyze the impact of 2018 large-scale wind energy integration in the Eastern Interconnection.

**Input Data**

The generation and transmission data used in this study are based on the 2018 planning data in MTEP 08 (MISO Transmission Expansion Planning) [**93**]. We consider a 1.28% annual load growth which is based on the MTEP 08 assumptions. The hourly load distribution shown in Figure 293 is based on the MISO's hourly load profile in 2007.

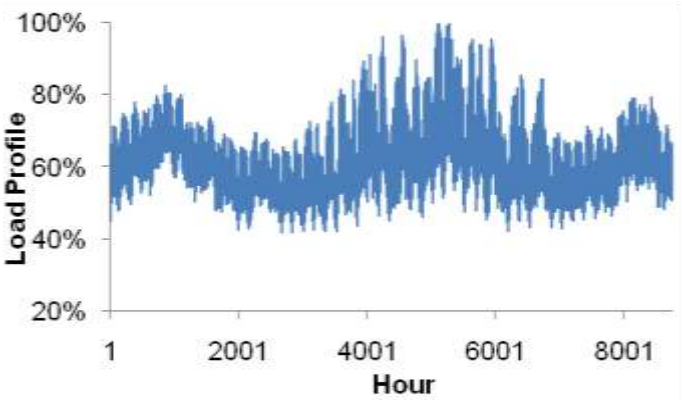


**Figure 293: Annual Hourly Load Profile**

In Figure 293, peak loads appear in July and August. The power flow solution is used for calculating the hourly bus load distribution. The wind unit data for the 2018 WINS simulation are based on MTEP assumptions for 2018 and the hourly wind profiles are provided by the land-based time series wind simulation results [**82**]. The hourly wind profiles based on geographical locations are considered for wind generation units. Fuel prices are assumed to increase at an annual rate of 4% for oil and gas, 2% for coal, and 3% for nuclear fuel based on the fuel price given in 2008 [**93**].

**Evaluation Metrics**

The evaluation criteria and metrics used in this study are defined as follows.

*Wind Energy Availability*

The available wind energy is treated as dispatchable in WINS simulations. Here,

$$P_A = \sum_{t=1}^{T} \sum_{i=1}^{NW} p_i^{\max} w_{it} \quad \textbf{(86)}$$

where *T* represents the number of hours in a period (e.g., one year), *NW* represents the number of wind generators/farms, $p_i^{\max}$ is the nominal capacity of wind generator/farm *i*, $w_{it}$ represents the wind power generation profile for generator/ farm *i* at time *t*, $P_A$ represents the available wind energy for dispatch that is subject to transmission constraints.

*Percentage of Wind Energy Contribution*

This metric will evaluate the percentage of the wind energy contribution to the total energy for supplying the load in the power system.

$$= \frac{Wind\ Ener\quad gy}{Total\ Ene\quad rgy} * 100\ \% \quad \textbf{(87)}$$

*Production Cost*

$$\text{Production Cost} = \sum_{t=1}^{T} \sum_{i=1}^{NG} F_i(P_{i,t}) \quad \textbf{(88)}$$

where *NG* is the number of generators, $P_{i,t}$ is the dispatch of generator *i* at period *t*, $F_i(.)$ is the production cost function of generator *i*.

*Generation Credit*

$$\text{Generation Credit} = \sum_{t=1}^{T} \sum_{i=1}^{NG} LMP_{i,t} * P_{i,t} \quad \textbf{(89)}$$

where $LMP_{i,t}$ is the LMP at generator bus *i* at period *t*.

*Load Payment*

$$\text{Load Payment} = \sum_{t=1}^{T} \sum_{j=1}^{ND} LMP_{j,t} * D_{j,t} \quad \textbf{(90)}$$

where *ND* is the number of load buses; $LMP_{j,t}$ represents the LMP of load bus *j* at period *t*; $D_{j,t}$ represents the load at bus *j* at period *t*.

*Transmission Utilization*

$$= \frac{\sum_{t=1}^{T} |flow_{i,t}|}{T * Cap_i} * 100\ \% \quad \textbf{(91)}$$

where $flow_{i,t}$ is the power flow on line *i* at period *t*; $Cap_i$ is the capacity of line *i*. The transmission utilization could also be calculated based on voltage level of transmission line.

*Levelized Congestion Cost*

This metric represents the levelized congestion cost.

$$= \frac{(\text{Load Payment} - \text{Generation Credit})}{\text{Load Payment}} * 100\ \% \quad \textbf{(92)}$$

*Transmitted Energy*

$$= \sum_{i=1}^{NL} \sum_{t=1}^{T} |flow_{i,t}| \quad \textbf{(93)}$$

where *NL* represents the number of transmission lines. The transmitted energy is calculated for transmission lines grouped by voltage level (i.e., 230kV, 345kV, 500kV, and 765kV).

*Levelized Energy Flow*

$$= \frac{\sum_{i=1}^{NL} \sum_{t=1}^{T} | \, flow_{i,t} \, |}{T * NL} \quad (94)$$

It is the averaged value of transmitted energy at a given voltage level.

## B2. Numerical Results

In this section, we utilize WINS to simulate the 2018 wind integration in the Eastern Interconnection of the United States based on the methodology presented in Section B1.

**Wind Integration Reference Cases**

We simulate the hourly power system operation using WINS. Four scenarios are studied as follows.

- Scenario 1: All wind unit generation and transmission constraints are excluded in 2018
- Scenario 2: All wind unit generation is excluded in 2018 while transmission constraints are considered
- Scenario 3: The 2018 wind unit integration is considered while all transmission constraints are excluded
- Scenario 4: The 2018 wind unit integration and transmission constraints are considered

These four scenarios are discussed here.

**Scenario 1: All wind unit generation and transmission constraints are excluded in 2018**. This is the reference case in which the hourly loads will be served by fossil fuel and hydro units without considering any wind energy or transmission constraint in 2018. Figure 294 shows the hourly production cost which is $92.25 billion per year with an average production cost of $22.4/MWh. The production cost will not change linearly with hourly load fluctuations. Hydro units will have zero costs and be scheduled first to serve hourly loads or reserves; then cheaper units such as nuclear, coal, and large oil will be committed, and finally expensive units such as gas and oil will be committed to supply hourly loads. A higher production cost will occur at annual peak hours of 5,000–5,500 (i.e., July and August of 2018). The total production cost at peak hours (6 AM–10 PM) is $74.04 billion and that at off-peak hours (11 PM–5 AM) is $18.21 billion. The average production costs at peak/off-peak hours are $24.2/MWh and $17.3/MWh. The average production cost at peak load hours is higher when expensive generators are committed and dispatched.

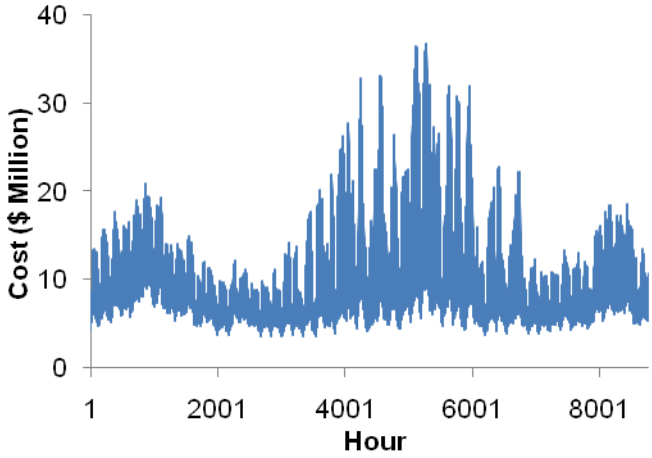


**Figure 294: The 2018 Hourly Production Cost in Scenario 1**

**Scenario 2: All wind unit generation is excluded in 2018 while transmission constraints are considered**. Figure 295 shows the hourly production cost. Compared to Figure 294, the production cost is higher when transmission constraints are taken into account. The annual production cost is $106.1 billion with an average production cost of $25.93/MWh. The production costs at peak and off-peak hours are $84.1 billion and $24.04 billion respectively. The average production costs at peak and off-peak hours are $27.49/MWh and $20.98/MWh respectively. Compared with Scenario 1, the production cost will increase by 15.06% when considering transmission constraints. The annual average LMPs based on the 2018 WINS simulation are shown in Figure 296. The annual average LMP in this scenario is $61.77/MWh. Without any wind energy integration, LMPs are lower in the northwest and a small area in New England, and are higher in the New York region.

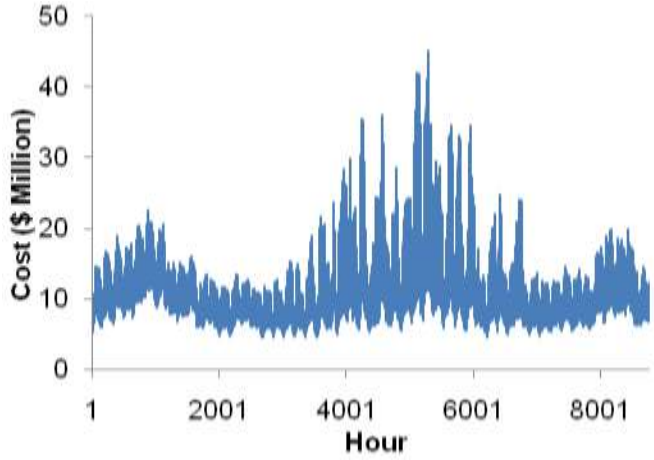


**Figure 295: The 2018 Hourly Production Cost in Scenario 2**

Figure 297 shows the monthly generation credit, load payment and production cost in Scenario 2. All three curves show a pattern similar to that of load profile in Figure 293. The incremental difference between the two curves shows the congestion cost. The annual generation credit, load payment and levelized congestion cost in 2018 are $254.2 billion, $270.7 billion, and 6.1% respectively.

**Scenario 3: The 2018 wind unit integration is considered while all transmission constraints are excluded**. Figure 298 shows the hourly production cost in Scenario 3. The annual production cost is $77.95 billion with an average production cost of $18.96/MWh. The production cost at peak and off-peak hours are $62.67 and $15.27 billion, respectively. Figure 298, the average production costs at peak and off-peak hours are $20.48/MWh and $14.54/MWh. Compared to Scenario 1, the production cost is 15.5% lower after taking into account the wind energy integration because wind energy is treated as zero fuel cost generation resource. Figure 299 shows the monthly wind energy in 2018 without considering transmission constraints. The wind energy resources are mostly available in spring and winter; however, peak loads occur in summer. January has the highest level of available wind energy of 27.8 TWh, which amounts to 7.9%, of the total energy. The wind energy is scarce in August when the highest level of annual load occurs. The available wind energy in August and the wind energy contribution (dispatch) to the total energy production portfolio are 16.8 TWh and 4.1% respectively. The annual wind energy contribution to the energy production portfolio is 6.5%.

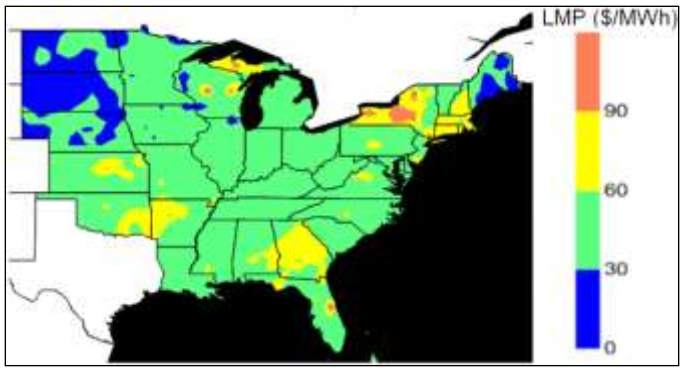


**Figure 296: The 2018 Annual Average LMPs in Scenario 2**

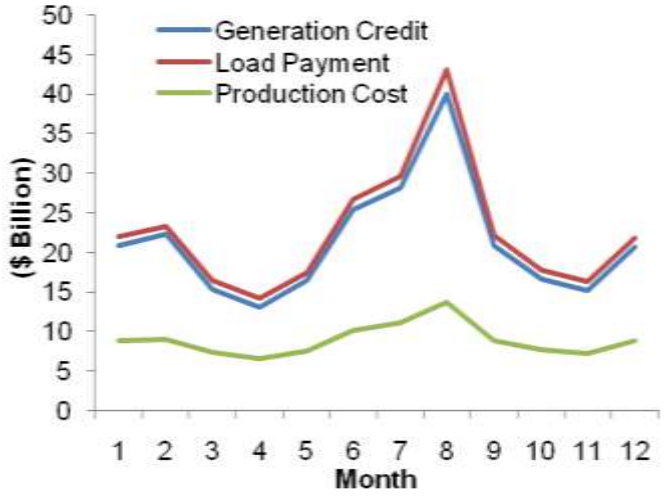


**Figure 297: Monthly Generation Credit, Load Payment and Production Cost in Scenario 2**

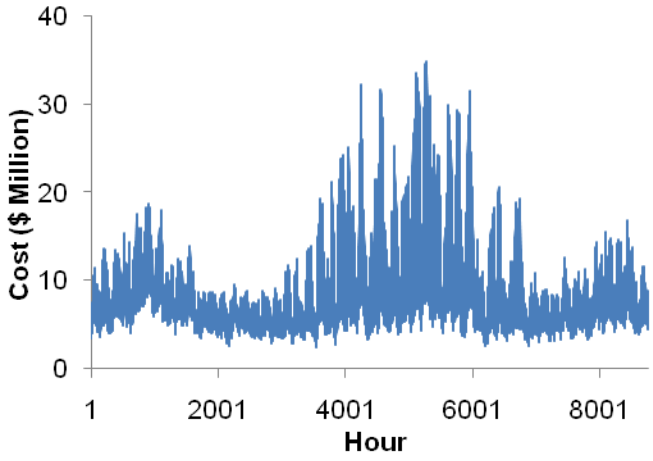


**Figure 298: The 2018 Hourly Production Cost in Scenario 3**

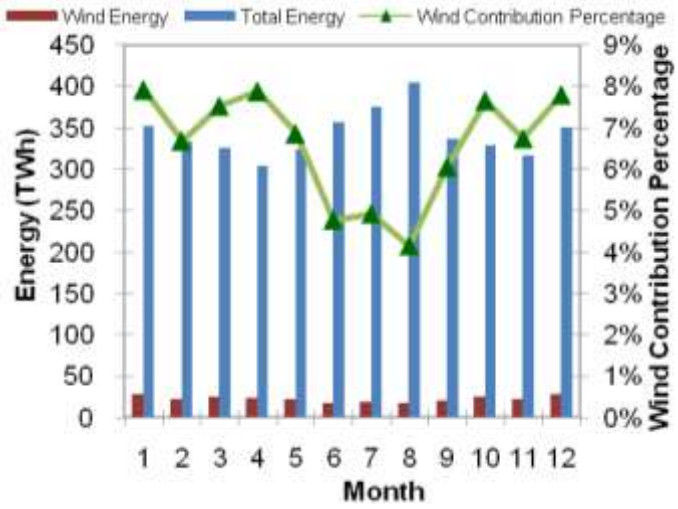


**Figure 299: Monthly Available Wind Energy and its Contribution in Scenario 3**

**Scenario 4: The 2018 wind unit integration and transmission constraints are considered**. Figure 300 shows the hourly production cost in which the annual production cost amounts to $99.39 billion with an average production cost of $24.18/MWh. The production costs at peak and off-peak hours are $78.76 billion and $20.63 billion respectively. The average production costs at peak and off- peak hours are $25.74/MWh and $19.63/MWh. Compared to Scenario 3, the production cost is 27.5% higher with the consideration of transmission constraints because transmission constraints would limit the flow from cheap and largely concentrated generation resources to load centers. Compared with the results in Scenario 2, the production cost is 6.8% lower when the wind energy is included. The production cost shows a higher sensitivity to the additional transmission constraints than to higher levels of wind energy integration.

Figure 301 shows the monthly wind energy in 2018 considering transmission constraints. December has the highest level of dispatched wind energy of 20.4 TWh, which amounts to 5.8% of the total energy supply. August represents the month with the least dispatched wind energy again (i.e., 13TWh and

3.2%). The annual wind energy contribution is 4.8%. Hence, about 26.1% of the available wind energy is curtailed due to transmission constraints.

Figure 302 represents the monthly available and dispatched wind energy in Scenario 4. Transmission constraints would limit the wind energy delivery to 73.88%. Here, 69.8TWh of wind energy is curtailed due to transmission congestion. The highest wind energy curtailment which is 7.46TWh occurs in January 2018. Figure 303 shows the monthly generation credit, load payment and production cost in Scenario 4. The annual generation credit, load payment and levelized congestion cost are $232.9 billion, $253.1 billion, and 7.97% respectively. All three indicators in Figure 303 exhibit a pattern similar to that in Figure 297.

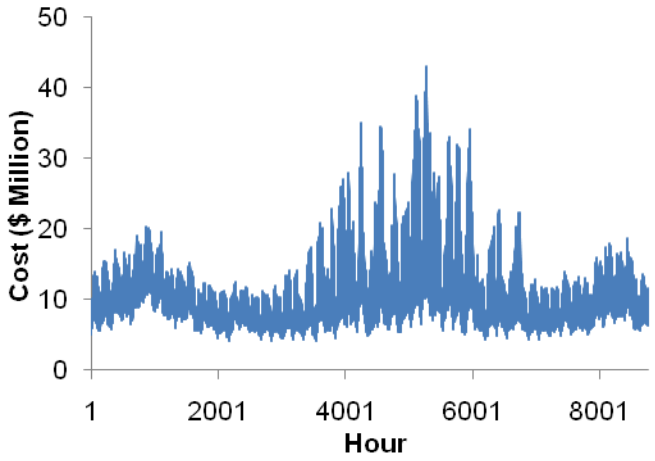


**Figure 300: The 2018 Hourly Production Cost in Scenario 4**

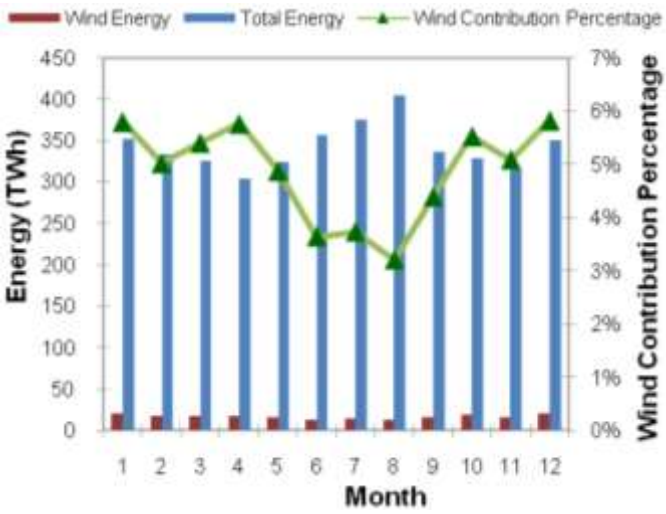


**Figure 301: Monthly Wind Energy and its Contribution in Scenario 4**

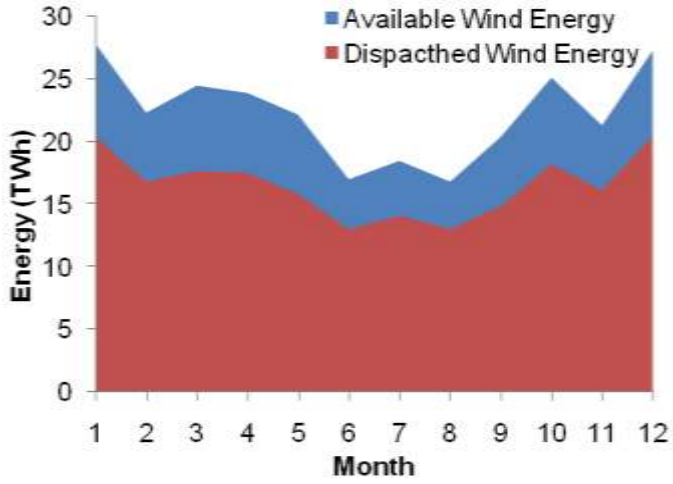


**Figure 302: The 2018 Monthly Available and Dispatched Wind Energy**

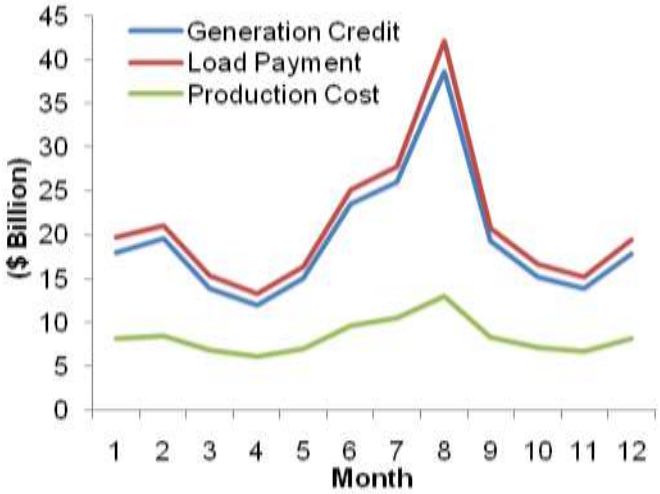


**Figure 303: Monthly Generation Credit, Load Payment and Production Cost in Scenario 4**

Compared to Scenario 2, generation credit and load payment quantities are reduced in this scenario when the wind energy is integrated; however, the levelized congestion cost increases from 6.1% to 7.97% which indicates that the wind integration will cause more congestion if there is no transmission expansion planning considered at the same time.

The annual average LMPs in Scenario 4 are shown in Figure 304. With the wind energy integration, LMPs in the northwest region drop which is due to rich wind energy resources in that region. The LMPs in New York, New England, and Florida are higher which demonstrate transmission congestion in those regions. The annual average LMP is $54.49/MWh which is lower than that in Scenario 2. Figure 304 shows a higher regional price increment than that in Figure 296 which is consistent with the higher levelized congestion cost in Scenario 4.

Figure 305 shows the energy production portfolio in all four Scenarios. Here, the gas unit production would increase as transmission constraints are considered. The energy supplied by coal units is

decreased, when transmission constraints are taken into account, which is replaced by the energy supplied by gas or wind generation units. Figure 306-Figure 308 show the energy supplied by gas, coal and wind units in four scenarios. With transmission constraints in place, more gas units are commitment and dispatched, less coal units are dispatched, and wind energy is partly curtailed. These figures show that wind energy will partly replace the fossil energy production especially at off-peak hours when the wind energy is mostly available in the Eastern Interconnection.

Figure 309 depicts the transmission utilization (see (6)) in 2018 at various voltage levels with and without the wind energy integration. The 500kV transmission system shows the highest utilization level at both scenarios. The transmission utilization at 765kV level is lower than those at other voltage levels (i.e., 230kV, 345kV and 500kV). In Figure 309, the 765 kV transmission utilization with the wind energy integration is lower than that of other voltages which indicates that the wind energy is transmitted mostly at 500kV, 345kV, and 230kV transmission levels.

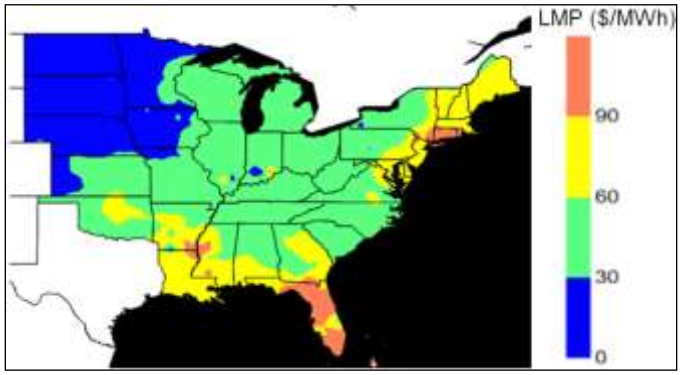


**Figure 304: Annual Average LMPs in Scenario 4**

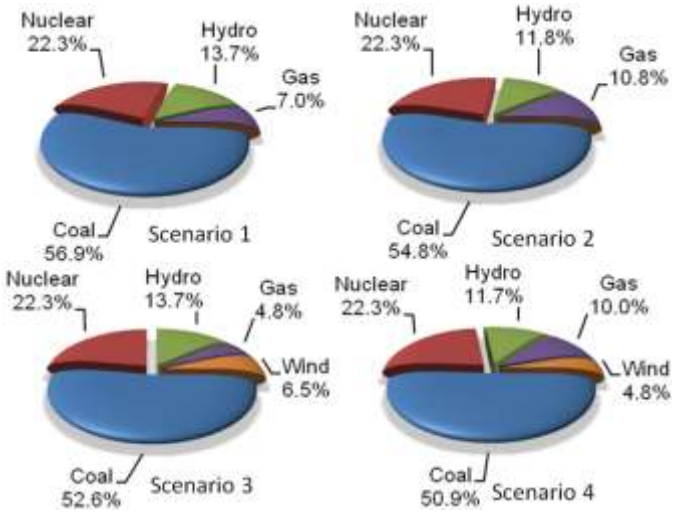


**Figure 305: Energy Production Portfolios in Scenarios 1-4**

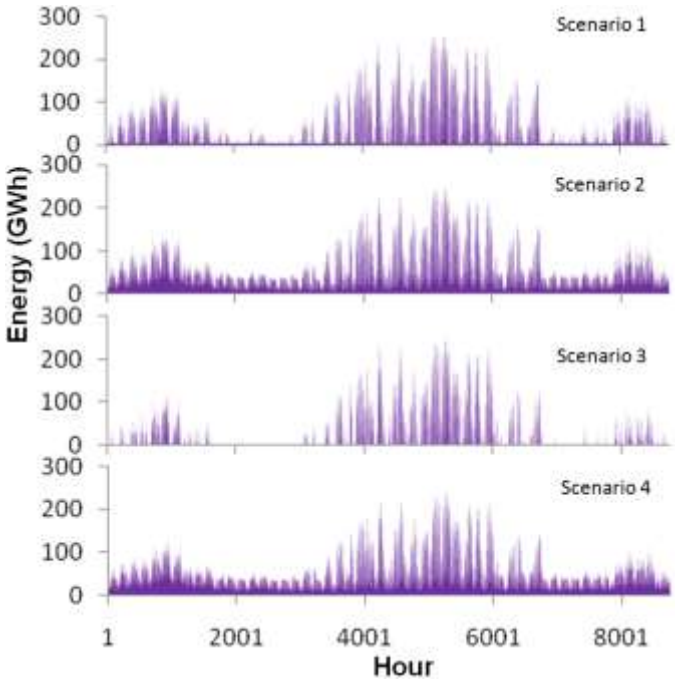


**Figure 306: Hourly Energy Provided by Gas Units in Scenarios 1-4**

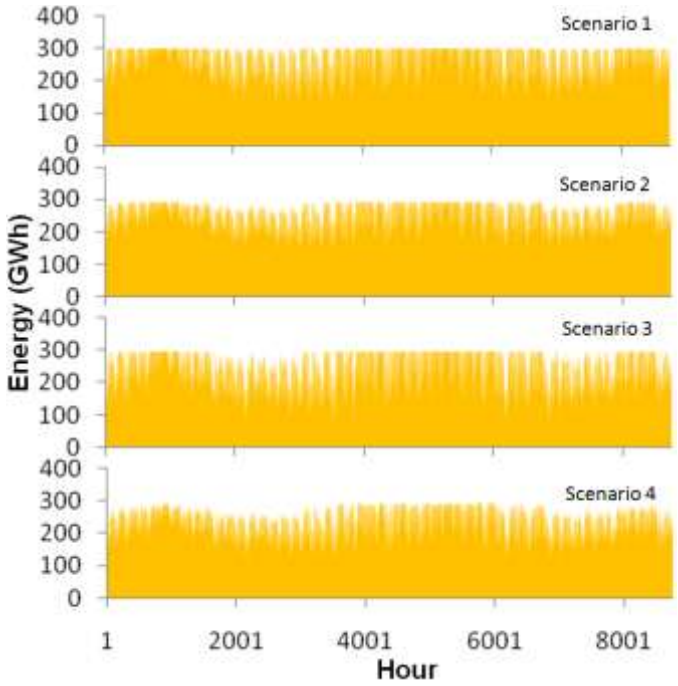


**Figure 307: Hourly Energy Provided by Coal Units in Scenarios 1-4**

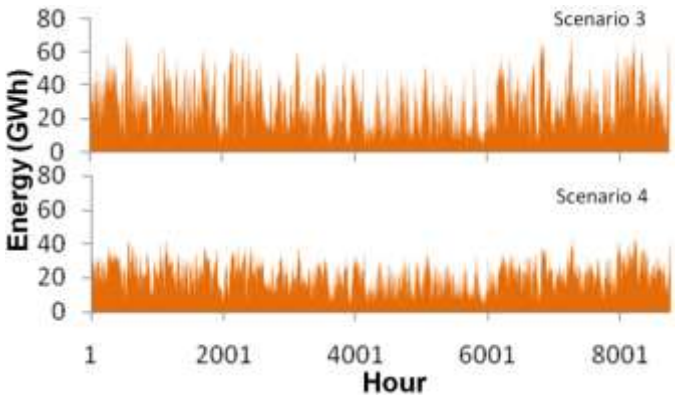


**Figure 308: Hourly Wind Energy in Scenarios 2 and 4**

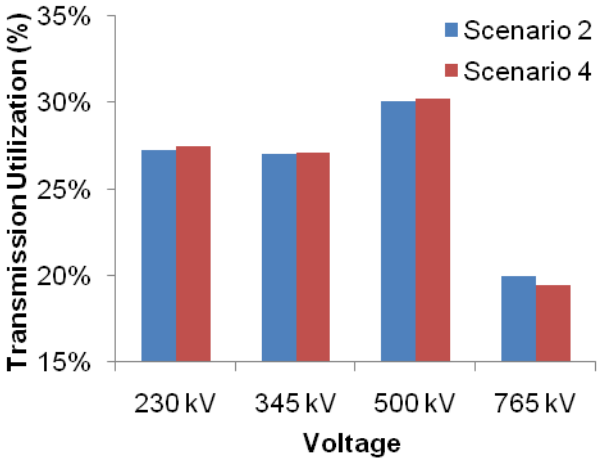


**Figure 309: Transmission Utilization with/without Wind Energy Integration**

Figure 310 shows the sum of hourly transmitted energy in 2018. The 230kV transmission lines will transmit the most energy in the Eastern Interconnection. As shown in Figure 310, the 765kV transmission lines will only transmit a small portion of the total energy because there are fewer of such lines in the Eastern Interconnection. Figure 311 shows the levelized energy flow over a year in 2018. The largest levelized energy flow would be on 765kV transmission lines which is due to the higher capacity offered by such lines. In Figure 311, the levelized energy flow at the 500kV level is close to that in 765kV and higher than that in lower voltage levels (230kV, 345kV).

Figure 312 shows the annual commitment of existing power plants in 2018 in which red dots represent power plants in which at least one unit is committed for a minimum of one hour per year. Also, blue dots show the plants which will be off throughout the year as more wind energy is integrated in the Eastern Interconnection.

**Sensitivity Analysis**

There are several uncertain parameters in large-scale power systems including fuel price, wind speed, hourly load, and carbon tax, which could have major impacts on the large-scale wind energy integration. These parameters may not be accurately forecasted for 2018. So, we apply sensitivity analyses to the

WINS simulation results given for Scenario 4 to study the impact of variations in such parameters on the wind energy integration. The WINS simulation results for Scenario 4 are treated as the base case.

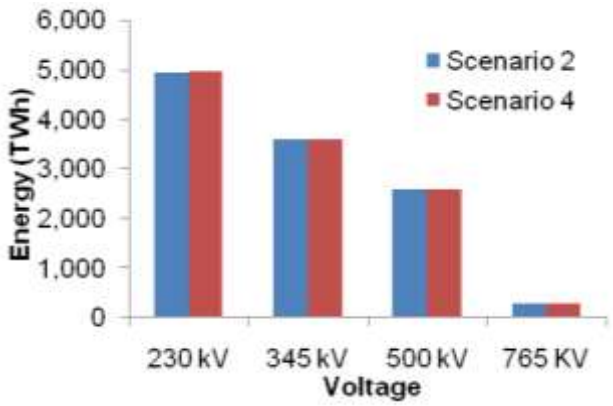


**Figure 310: Transmitted Energy in 2018 with/without Wind Integration**

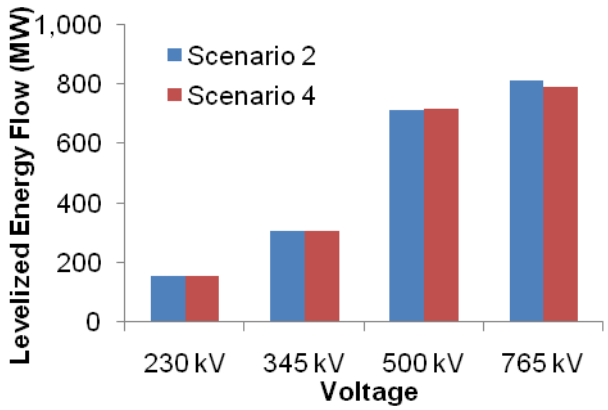


**Figure 311: Levelized Energy Flow in 2018 with/without Wind Integration**

***Fuel Price Sensitivity***

We apply the sensitivity analysis based on the WINS simulation results for Scenario 4. The wind energy integration was considered in transmission-constrained Eastern Interconnection. Generally, oil and gas prices are more volatile, while nuclear and coal prices are more settled. The following four scenarios are considered for analyzing the sensitivity of the WINS results to the fuel price volatility:

- Scenario 5: Oil and gas prices are 20% lower than the forecast
- Scenario 6: Oil and gas prices are 10% lower than the forecast
- Scenario 7: Oil and gas prices are 10% higher than the forecast
- Scenario 8: Oil and gas prices are 20% higher than the forecast

Figure 313 shows the production cost, generation credit, load payments and annual average LMP of four fuel price scenarios which are compared with the base case scenario results. The difference between load payments and generation credits represents the congestion cost in the Eastern Interconnection.

The production cost, generation credit, load payments, and LMPs in all scenarios will increase as fuel price goes up.

Figure 314 shows the levelized congestion cost and wind energy contribution in the four scenarios. In Figure 314, higher oil and gas prices would cause more transmission congestion which would limit the flow from cheaper and concentrated generation resources to load centers. In this case, the wind energy contribution will be slightly lower when fuel prices are higher. The reason is that more of large coal units will be used in such cases which could cause additional congestion for utilizing wind energy units. The fuel price volatility would have no impact on wind energy dispatch if transmission constraints are not taken into account [**95**].

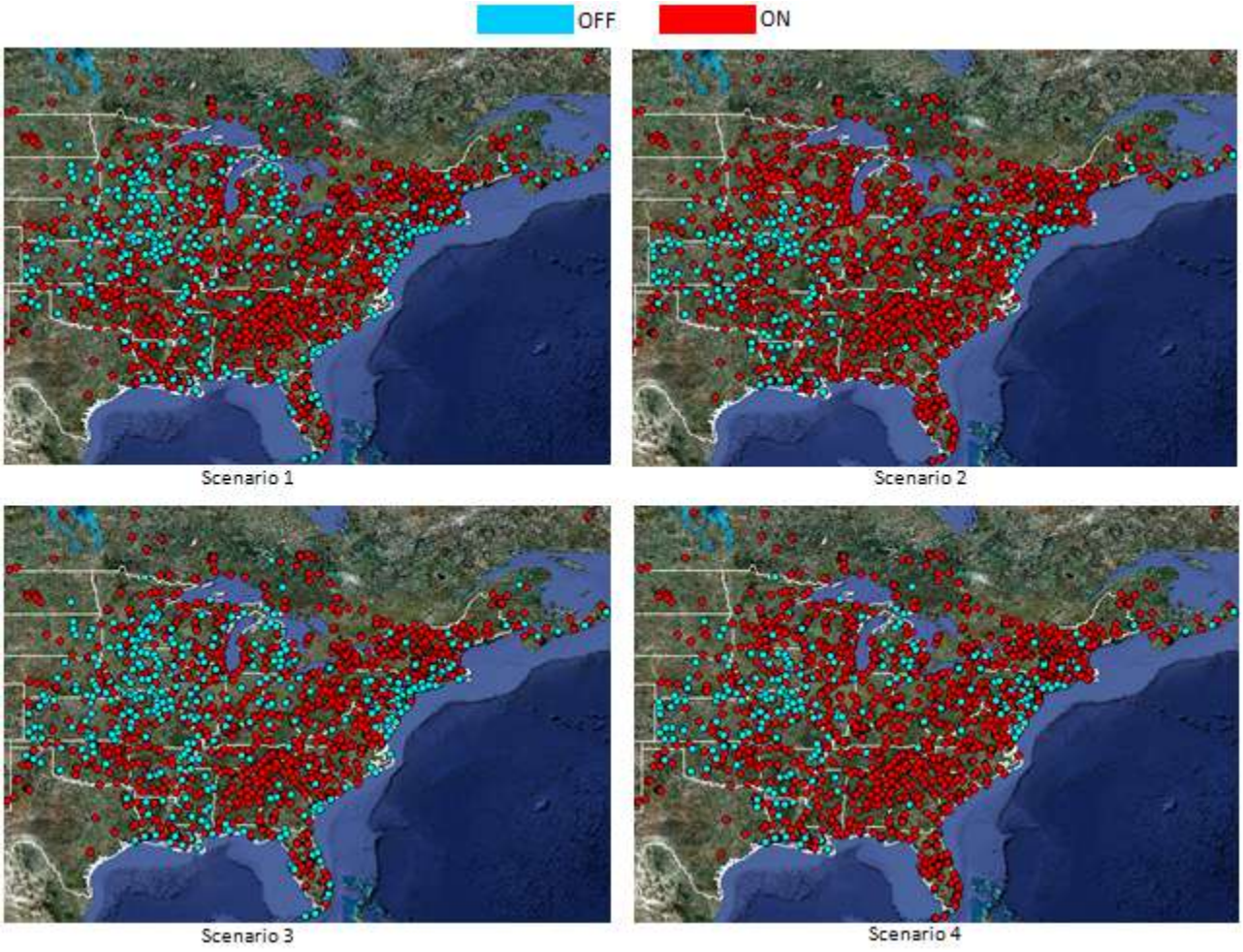


**Figure 312: Annual Unit Commitment in Scenarios 1-4**

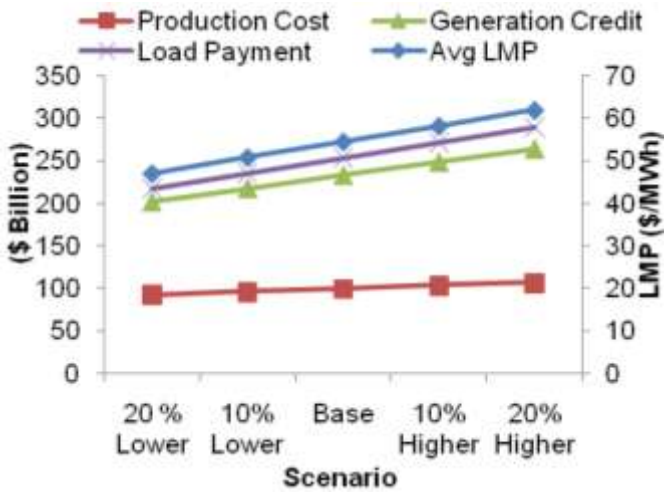


**Figure 313: Economic Metrics in Fuel Price Scenarios**

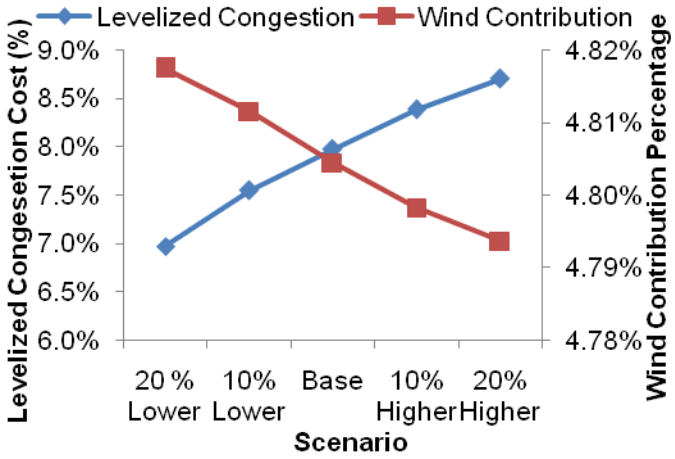


**Figure 314: Levelized Congestion Cost and Wind Energy Contribution in Fuel Price Scenarios**

***Wind Energy Contribution Sensitivity Analysis***

We implement the sensitivity analysis based the 2018 WINS simulation results for Scenario 4. Four scenarios are considered as follows.

- Scenario 9: Available wind energy is 20% lower
- Scenario 10: Available wind energy is 10% lower
- Scenario 11: Available wind energy is 10% higher
- Scenario 12: Available wind energy is 20% higher

Figure 315 shows the 2018 production cost, generation credit, load payments, and annual average LMP in the four wind production scenarios. As expected, the economic metrics will be more favorable as more wind energy is dispatched. Figure 316 shows the levelized congestion cost and wind energy contribution in the four wind energy production scenarios. Wind energy is assumed as a zero fuel cost resource, so the transmission system will try to deliver all the available wind energy to load centers.

Hence, higher wind energy production scenarios could cause additional transmission congestion. Figure 316 shows a higher wind energy contribution to the energy production portfolio and higher congestion in the Eastern Interconnection as more wind energy is made available.

Figure 317 shows the energy production portfolio in four wind energy production scenarios. The energy produced by gas and coal units will decrease as additional wind energy is made available.

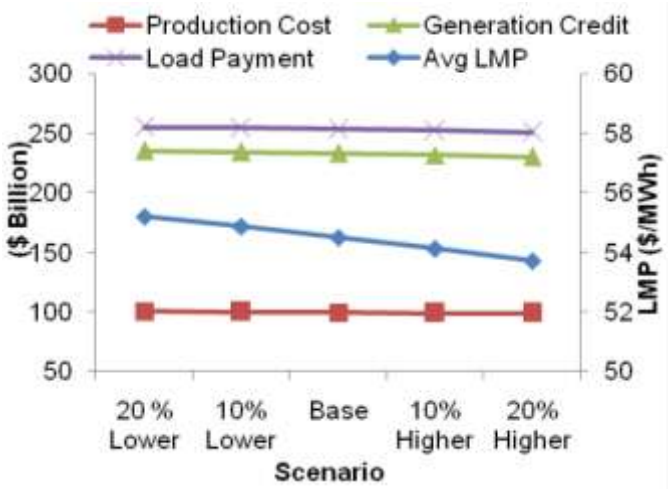


**Figure 315: Economic Metrics for Available Wind Energy Scenarios**

***Load Variations Sensitivity Analysis***

In this section, we carry out the load forecast sensitivity analysis based the 2018 load forecast. The WINS simulation results for Scenario 4 are treated as base case. Four load sensitivity scenarios are studied as follows.

- Scenario 13: Total load is 5% lower than the forecast
- Scenario 14: Total load is 3% lower than the forecast
- Scenario 15: Total load is 3% higher than the forecast
- Scenario 16: Total load is 5% higher than the forecast

Figure 318 shows the production cost, generation credit, load payment, and annual average LMP in the four load sensitivity scenarios which are compared with the base case scenario. In Figure 318, as compared with Figure 313 and Figure 315, the system load variations will have a larger impact on production costs, generation credit, load payment, and LMPs. Also, generation credit and load payment demonstrate a higher sensitivity than the production cost to load variations. Similar to the results in [**95**], Figure 319 shows that the system load variations will have the highest impact among the listed parameters on the commitment and dispatch of generating units. The unit commitment results based on Scenarios 13-14 shows that many generation units may never be committed again in 2018 as hourly loads drop.

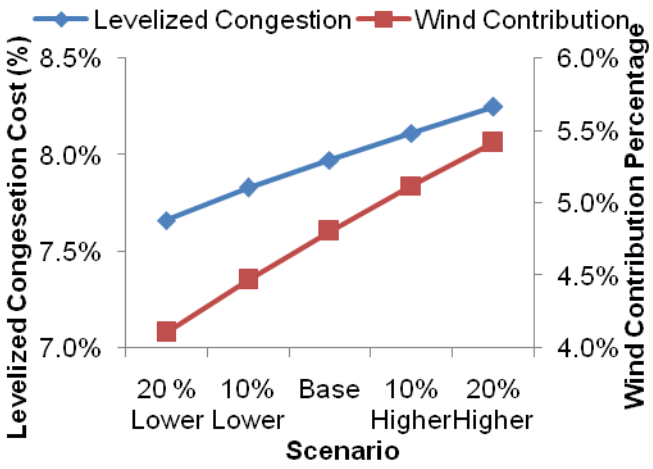


**Figure 316: Levelized Congestion Cost and Wind Contribution in Wind Energy Scenarios**

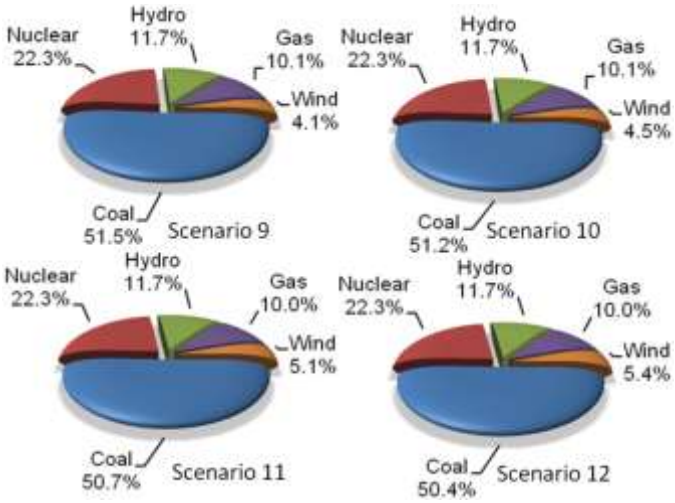


**Figure 317: Energy Production Portfolios in Wind Energy Production Scenarios**

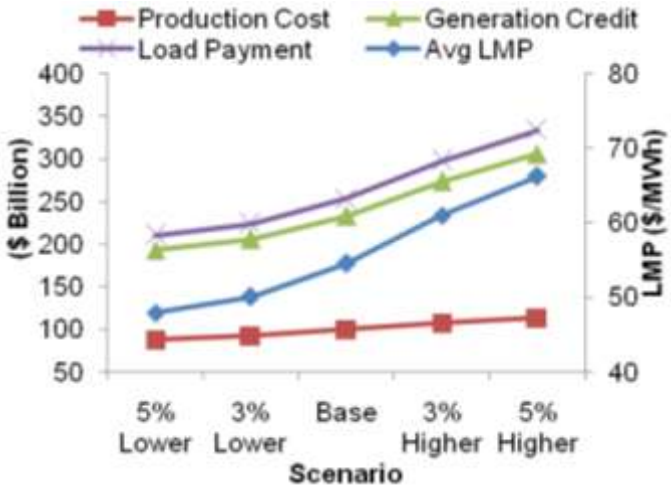


**Figure 318: Economic Metrics in Load Scenarios**

On the other hand, additional units are committed when the system load is higher. The results indicate that the hourly load management and demand response could introduce major alternatives for improving the system operation bottlenecks and enhancing the economic metrics of power systems in the Eastern Interconnection.

Figure 320 shows the levelized congestion cost and wind energy contribution in four load scenarios. The wind energy contribution will decrease as the system load increases because the additional load is served mainly by fossil generation units. The congestion cost for the four load scenarios are $17.47 billion, $18.05 billion, $24.20 billion and $28.03 billion respectively, which will increase with higher system loads. However, the levelized congestion cost in Figure 320 demonstrates a mixed result which is not increasing monotonically with the bus load level. The reason is that both generation credits and load payments are used to calculate the levelized congestion cost (7). However, generation credits and load payments which are determined by bus LMPs do not change uniformly with the bus load increments.

Figure 321 shows the energy contribution portfolio in the four load sensitivity scenarios. The cheaper nuclear, hydro, and wind generation units will supply much of the hourly load. However, their contributions will decline as load increases. Compared with the base case of Scenario 4, the energy contribution portfolio by gas and coal units, especially those supplied by gas units, will decrease as we lower the system load.

Furthermore, the contribution of gas units to the energy production portfolio will increase from 10% in the base case (Scenario 4) to 11.1% in Scenario 15 and 11.8% in Scenario 16 as we increase the system load. This observation shows that the additional load is mainly supplied by gas units.

***Carbon Cost Sensitivity Analysis***

Additional carbon cost can be used as an incentive for promoting the development of clean, efficient, and environmentally-friendly generation resource [**96**]. Two Scenarios are studied in this section as follows.

- Scenario 17: Low Carbon cost at $30/ton
- Scenario 18: High Carbon cost at $60/ton

Figure 322 shows the production cost, generation credit and load payment in carbon cost scenarios. All three economic parameters will be much higher than those in the base case when carbon costs are applied. Figure 323 shows the levelized congestion cost, wind energy contribution and annual average LMP for the base scenario and two carbon cost scenarios. It is observed that the higher carbon cost will reduce the levelized congestion cost because higher carbon costs could reduce fuel price increments between cheap generation resources (coal) and expensive generation resources (gas). The annual average LMP could increase a lot when the carbon cost is higher. Figure 324 shows the energy production portfolios in carbon cost scenarios in which the high carbon cost will have a major impact on the energy supplied by gas and coal units. Since coal prices are lower than gas prices, the energy supplied by coal units does not change much in the low carbon cost scenarios.

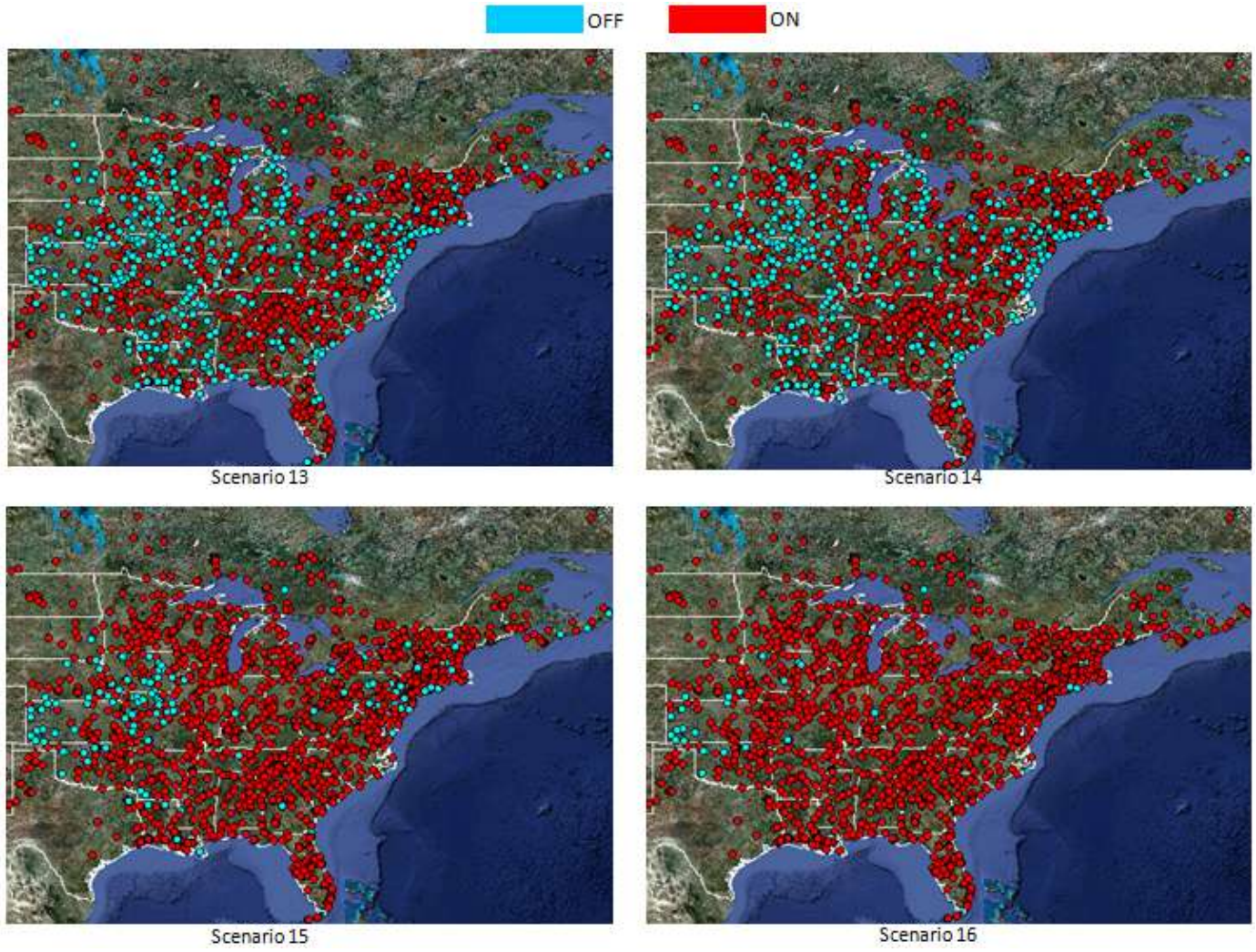


**Figure 319: Annual Unit Commitment in Load Variation Scenarios**

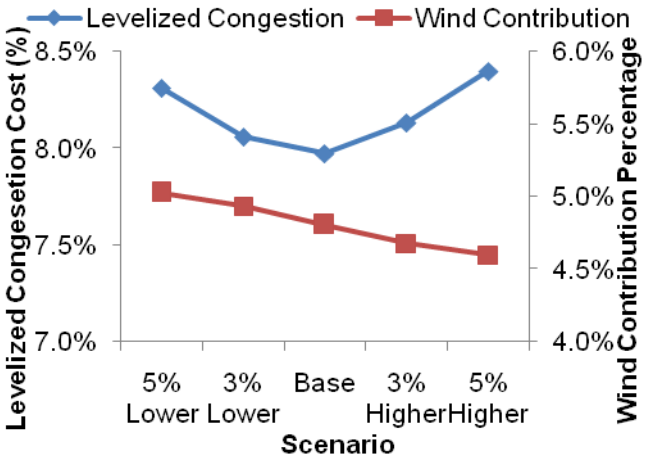


**Figure 320: Levelized Congestion Cost and Wind Contribution in Load Scenarios**

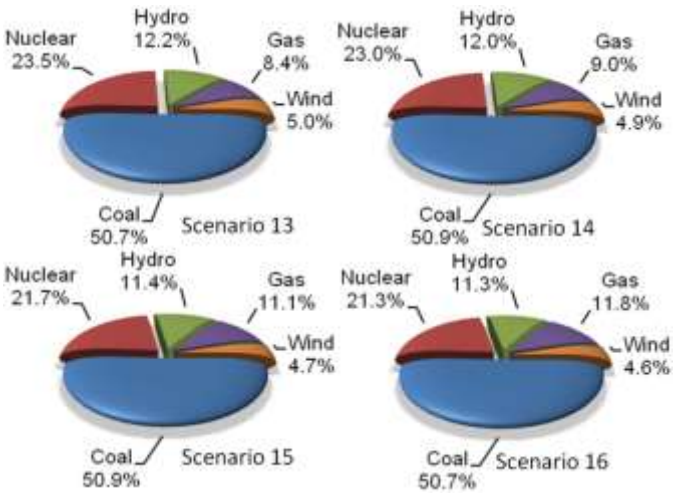


**Figure 321: Energy Production Portfolios in Load Scenarios**

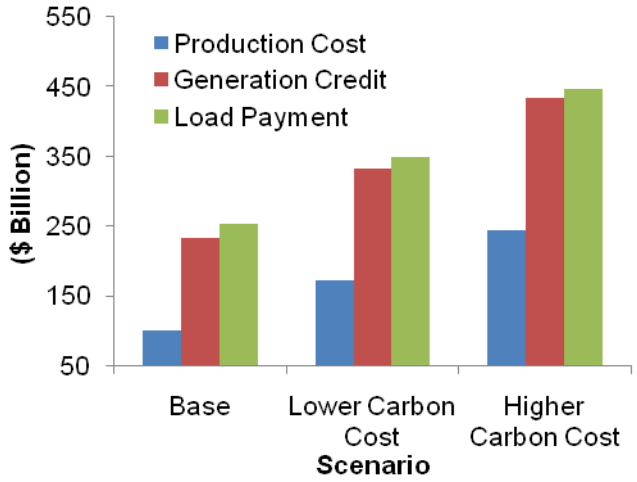


**Figure 322: Economic Factors in Carbon Cost Scenarios**

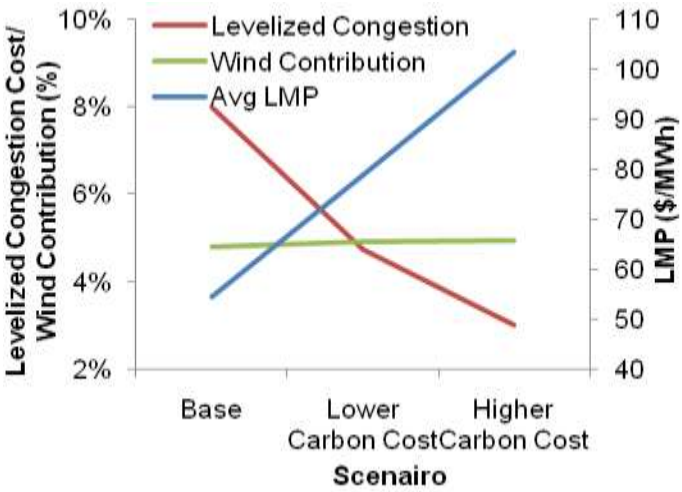


**Figure 323: Levelized Congestion Cost, Wind Contribution, and LMP in Carbon Cost Scenarios**

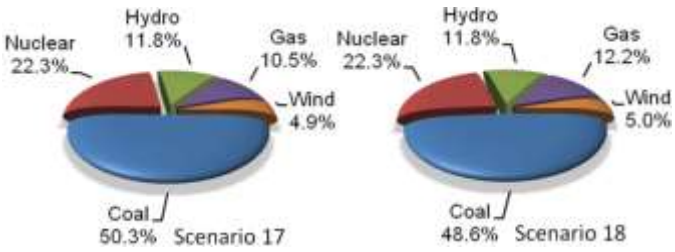


**Figure 324: Energy Production Portfolios in Carbon Cost Scenarios**

The energy supplied by gas units increases from 10.5% in Scenario 17 to 12.2% in Scenario 18 while that of coal decreases from 50.3% to 48.6%. Additional wind energy will be dispatched when the high carbon cost mitigates the transmission congestion. The wind energy contribution will be higher when the carbon cost increases. In this case, the wind energy contribution will increase from 4.8% in the base case (Scenario 4), to 4.9% in the low carbon cost scenario (Scenario 17) and 5.0% in the high carbon cost scenario (Scenario 18).

**Load Management in 2018**

As presented in section on load sensitivity analysis, the hourly load variations will have a major impact on the WINS simulation results. In this section, we consider load shedding at peak hours, i.e., if the hourly load at peak hour is higher than 80% of the annual peak load. In essence, the hourly load will be subject to demand response and set at 80% of annual peak load. One scenario is studied as follows.

- Scenario 19: Wind energy integration with possible load shedding

Figure 325 shows the production cost, generation credit and load payment for the base case and the load shedding scenario. All three economic factors will be lower with the load shedding implementation. Load shedding will almost have no impact on the hourly dispatch of coal units as coal units are committed to serve the base load.

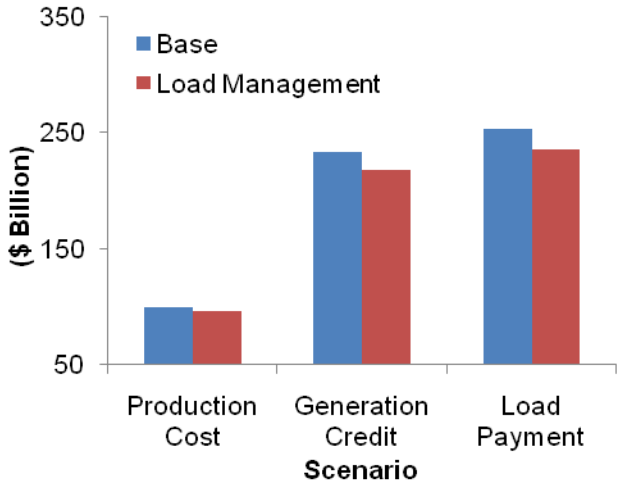


**Figure 325: Economic Factors in Load Shedding Scenario**

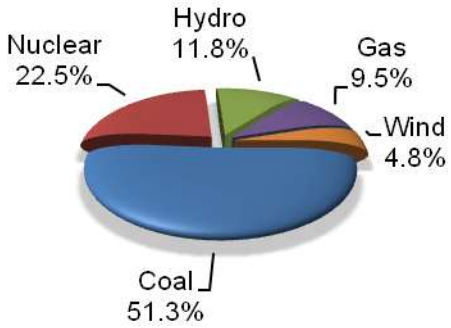


**Figure 326: Energy Production Portfolios in Load Shedding Scenario**

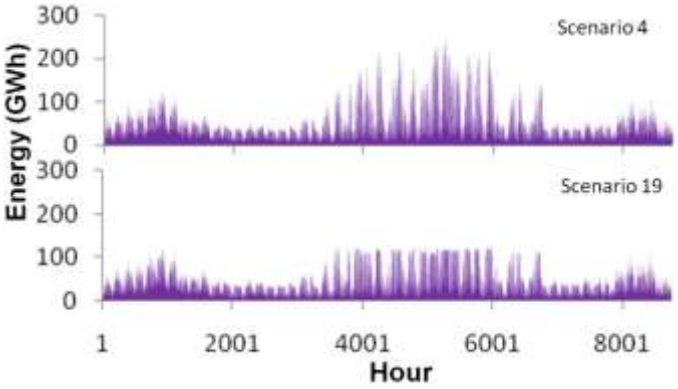


**Figure 327: Energy Provided by Load Shedding Scenario**

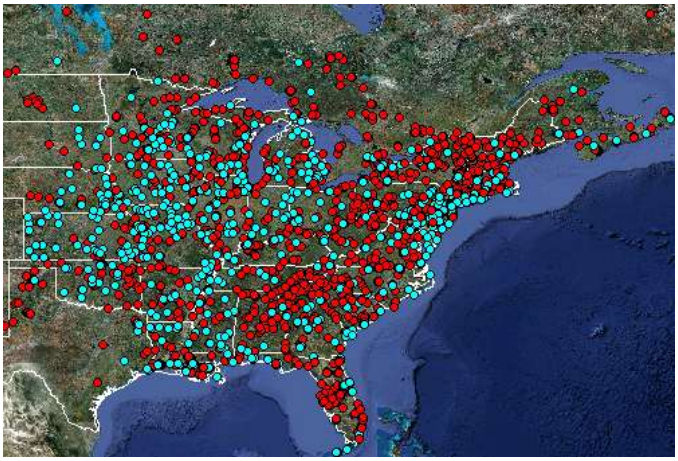

**Figure 328: Annual Unit Commitment in Scenario 19**

Figure 326 shows the energy production portfolios for the load shedding scenario. Figure 327 shows the hourly energy supplied by gas units in which the gas unit dispatch is lower due to load shedding at peak load hours. Figure 328 shows that the load shedding will alter the unit commitment as compared to that

of Scenario 4 shown in Figure 312. Here, additional gas units (1,700) are turned off at peak hours when the load shedding is applied.

### B3. Conclusions

In this section, a comprehensive large-scale wind energy integration analysis is implemented based on the 2018 load forecast in the Eastern Interconnection of the United States. The wind energy integration with/without transmission constraints are studied and analyzed. The sensitivity of fuel price, wind energy production, load, carbon cost, and load shedding are implemented to study the impact of volatility of major parameters on the WINS simulation results. 19 Scenarios are studied and analyzed. The main observations based on the simulations are listed as follows:

- Production cost is more sensitive to transmission constraints than to wind energy integration.
- The location of wind energy integration could have an impact on the wind energy dispatch in the hourly generation portfolio.
- The addition of wind generation units at certain locations in the Eastern Interconnection may cause additional transmission congestion.
- In 2018, the replacement of coal units by wind energy at certain locations could mitigate transmission congestion.
- Wind energy is often available and can replace fossil energy at off-peak load hours. During certain seasons when wind is unavailable, wind energy supply could be replaced by fossil energy.
- In 2018, wind energy is transmitted mostly at 500kV, 345kV, and 230kV transmission levels while the 765kV transmission is utilized less by wind generation units.
- Higher costs for gas and oil will result in additional transmission congestion as power systems try to use cheaper coal units located centrally in fewer geographical spots. Such limited utilizations of centrally located resources may also limit the available dispatch of wind generating units.
- Higher levels of wind energy integration could result in higher levelzied congestion costs when wind generation units, located at few geographical spots, try to supply a significant level of load.
- Carbon cost demonstrates the highest impact on the 2018 simulation results. Higher carbon costs will be instrumental in mitigating the regional transmission congestion in the Eastern Interconnection.
- Load forecast uncertainty will have a larger impact on the 2018 simulation results as compared to fluctuations in fuel prices or possible levels of wind energy integration.
- The levelized congestion cost may not increase monotonically with higher levels of bus loads.
- Peak load shaving will have a major impact on the commitment and dispatch of gas units because peak loads are mostly supplied by such units

The WINS simulation results shows that lowering the hourly volatility of load profile by introducing smart grid, additional distribution automation for the utilization of demand response, and the large-scale integration of wind energy and storage could lower the transmission congestion and improve the economics and the optimal operation of power systems in the Eastern Interconnection of the United States.

### C. *Integration of Non-dispatchable Resources in Electricity Markets*

The electricity market structure, involving generally a pool, a futures market and a bilateral trading floor, was designed before the large integration of non-dispatchable sources, particularly wind power. There is a need to address the suitability of the current electricity market structure for producers relying on non-dispatchable energy sources. Considering the intrinsic variability and uncertainty of the production level of non-dispatchable sources, appropriate changes in the current market structure are needed to adapt such structure to an increasingly non-dispatchable generation mix. To efficiently integrate non-dispatchable production, the questions below regarding market design and organization need to be answered:

- Which is the most appropriate time framework to clear short-term electricity markets? Is it a day-ahead horizon as today, or a shorter one?
- Should the algorithms to clear such markets be deterministic or stochastic? How should prices be derived?
- How much reserves should be scheduled to cope with the variable and uncertain nature of renewable non-dispatchable producers? Who should pay for such reserves?
- How the transmission infrastructure should be expanded and operated to avoid bottlenecks that hider the integration of renewable non-dispatchable resources?

The features of wind-dominated systems are listed as follows.

- Wind and demand correlation: Negative correlation (no good)
- Wind power dispersion: Geographical dispersion beneficial (production smoothing)
- Transmission network dependency: Network bottlenecks lead to wind spillage
- Increasing uncertainty: Need of volatility protection
- Wind zero fuel cost: Hydro + wind + nuclear may lead to zero or negative prices

The required improvements of wind-dominated systems include

- Encourage demand-side management: Load control from the demand side.
- Incorporate new loads: Controllable loads (plug-in cars)
- Promote electricity storage: Pumped-storage and others (compressed air)
- Achieve flexible thermal generation: Load-following units.
- Carry out wind technology upgrading: More flexible and controllable wind turbines
- Ensure optimal use & expansion of networks: Avoiding bottlenecks is a must
- Update tools for ISOs: Tools adapted to uncertain wind power behavior
- Redesign ancillary services: Reserve, regulation, voltage control, etc.
- Improve market-clearing tools
- Improve the market design

Specific issues are

- A non-dispatchable producer needs to establish an effective offering strategy in the pool.

- The market operator should use a stochastic clearing mechanism.
- The market operator needs to set up an efficient balancing market to cover production deviations.
- The regulator may need to restructure the markets within the pool.
- The ISO should determine the amount of reserve & its cost.

The specific market problems for wind producer regarding how to offer include

- How to represent the uncertainty pertaining to prices and wind production?
- Where to sell? In the day-ahead market, or rather in the adjustment markets?
- How to build hourly offer curves?
- Is it convenient to control the financial risk on a daily basis?

The specific market problems for market operator regarding the balancing market include

- How should the balancing market be organized?
- In which manner should deviations be penalized?
- How should deviations helping to offset the net system imbalance be considered?
- Which is the behavior of deviation prices?

The specific market problems for market operator regarding pool auctions include

- Is it appropriate to simultaneously clear energy and reserve markets?
- Is it economically reasonable to establish a deterministic reserve level?
- Is it feasible and socially acceptable to implement a probabilistic reserve level?
- How should prices for energy and reserve be derived?
- How to deal with non-convex prices?

The specific market problems for regulator adjustment markets include

- How many adjustment markets should be available?
- Is the day-ahead market still needed?
- Should the trade in adjustment markets be capped?

The specific market problems for ISOs regarding reserve determination and valuation include

- At which level of nondispatchable penetration are additional reserves needed?
- How the reserve level/cost increases as the nondispatchable power increases?
- How the variability level of the nondispatchable sources affects the reserve level/cost?
- Who should pay for the additional reserves needed as a result of integrating nondispatchable producers?

The implications for modeling include

- A redesign of the different markets in the pool might be needed as the level of wind power increases.
- Stochastic market clearing algorithms involving energy and reserve are needed.
- The stochastic nature of reserve and energy prices should be properly modeled.
- Locational issues need to be properly taken into account, because network bottlenecks may seriously hamper the advantages of wind power.
- Reserve determination and valuation are crucial for an efficient and fair cost allocation.

### *D. Integration of Wind Unit with Microgrid*

This section discusses the data gathering and software integration of an 8kW Viryd Wind Turbine installed on the main campus. The primary purpose for installing this wind turbine was to increase public awareness of renewable energy technologies and thus the primary objective of this effort was to gather data from the wind turbine and make real time data viewable on campus, something that is not typically available for Viryd Wind Turbine Installations. A secondary objective in this work was to model and predict wind turbine output and compare the predictions to actual wind turbine data. This predictive modeling will be important as wind turbine penetration increases. IIT's existing microgrid provides a unique opportunity to see how local wind turbine generation might affect the microgrid.

#### D1. Background

Viryd typically supplies wind turbines with a data logger that accumulates real time data in a log file and transmits the data when the accumulator is full to one of Viryd's data servers. Viryd then uses this data for their purposes such as performance models and determining the condition of the wind turbine. This project required a modified approach so that real time data could be viewed on campus. This approach will be discussed in latter sections but it is important to note that the real time data view will be accomplished through IIT's microgrid master controller.

IIT's microgrid master controller, also called the Intelligent Perfect Power System Controller (IPPSC) is intended to coordinate the energy systems on the campus. An overview of the IPPSC is shown in Figure 329. The specific energy systems at IIT include existing onsite generation consisting of two 4MW gas turbines, several diesel and natural gas backup generators, renewable Solar PV generation, an intelligent electric distribution system consisting of intelligent sectionalized loops, building control systems which typically control lighting and HVAC systems within the buildings and a building metering system which measures the electric loads of the buildings. The primary scope of the IPPSC's control is:

- Campus and Building Load Prediction
- Turbine, Engine Generator and Solar PV Output Prediction
- Load management and coordination for Island Mode and Demand Response events
- Generation dispatching based on potential threats and dynamic market pricing
- Threat detection such as lightning detection or voltage sags

Modifications made to the IPPSC, as a result of this research effort, will have to allow for real time wind turbine data to be collected and stored for viewing through the IPPSC GUI interface. In order to meet the secondary objective of the project, the wind turbine modeling would theoretically account for the combined variability of both Solar PV and Wind, and will have to allow operation when the campus is in

island mode and is operating solely on the installed campus generation. Though the impact of both Wind and Solar PV resources installed at IIT will likely be relatively small compared to the campus's total load, an effort will be made to account for scenarios with a much larger portion of wind resources.

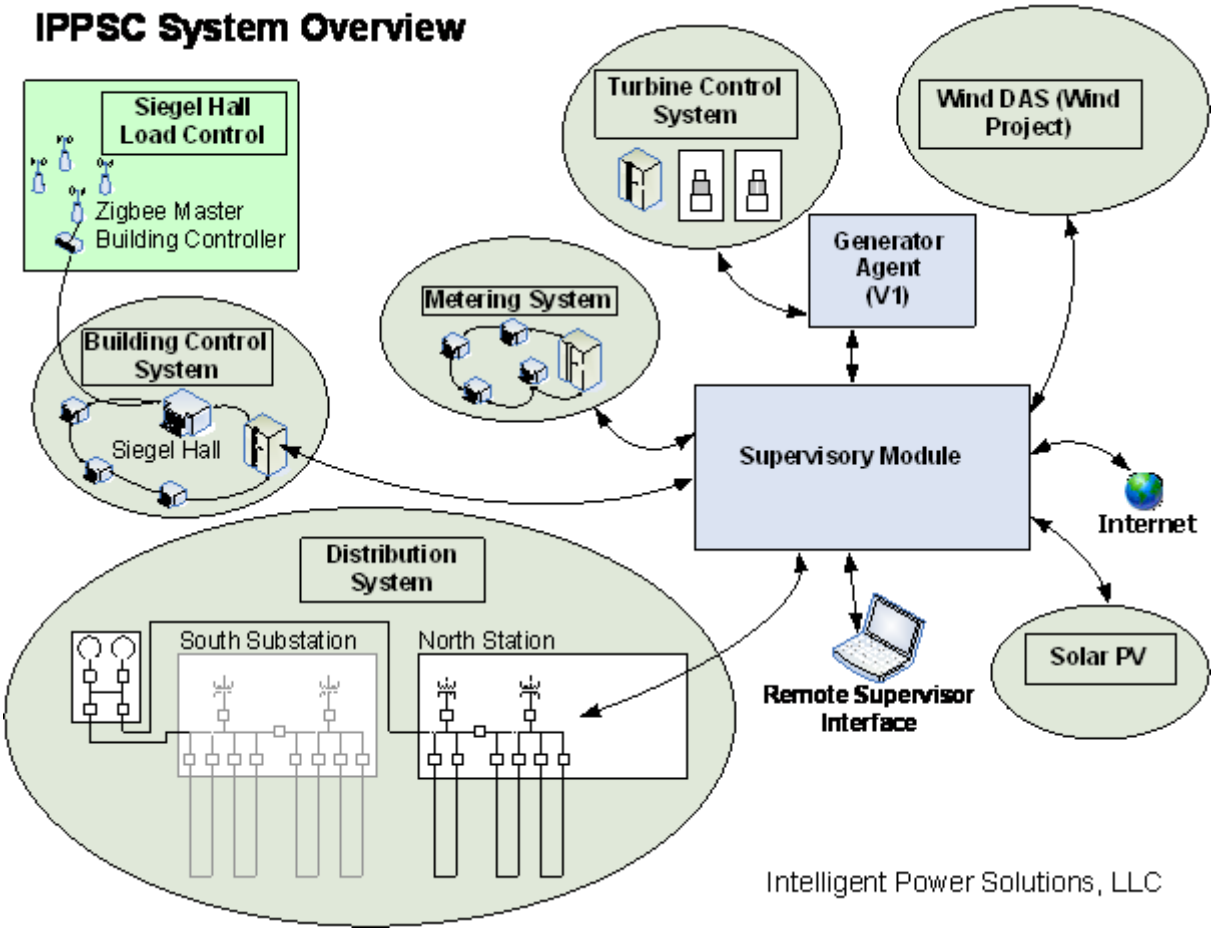


**Figure 329: Overview of IPPSC**

### D2. Approach

As mentioned, the Viryd data logger is typically setup to log data and periodically post it to its data servers for future analysis and typically do not supply a real time data interface. As such Viryd modified the programming in their data logger to push real time data out to the IPPSC in addition to pushing logged data out to their own servers. A sketch showing the two communication schemes is shown in Figure 330.

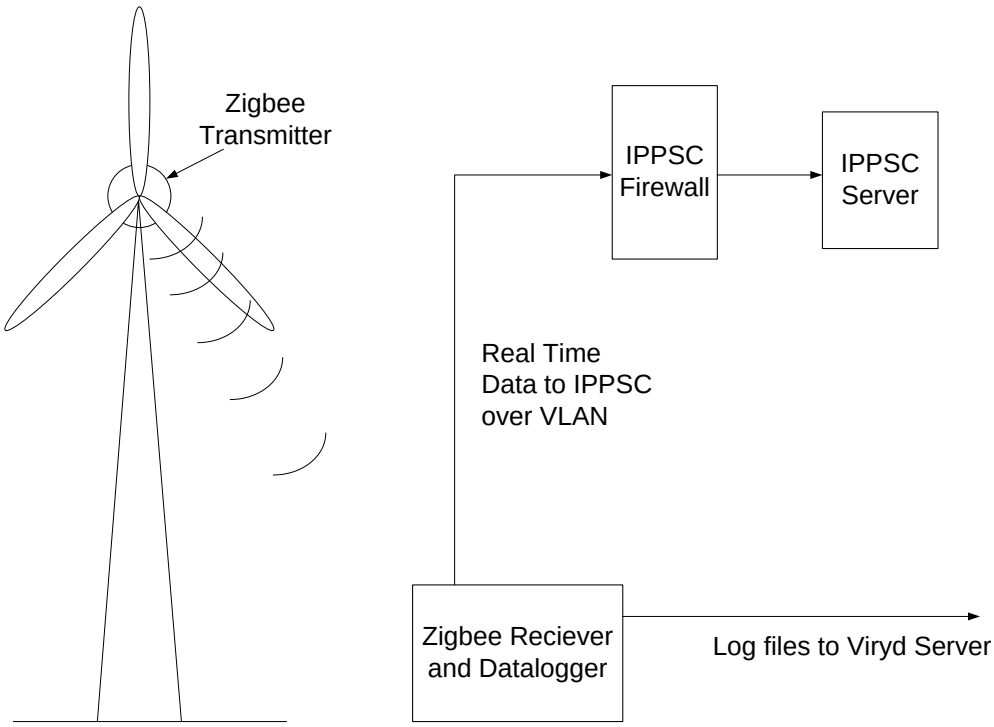


**Figure 330: Viryd Data Logger Communications**

Several studies have been made regarding the integration of utility scale wind project in to the grid. To a lesser extent, wind integration studies have been conducted on small scale wind projects. In the course of this effort, the project team attempted to glean as much as possible from studies regarding utility scale integration but took note of exceptions that might apply to small scale projects with microgrids. The project team proposed software changes to the IPPSC based on the results of this literature research and is working to implement these changes before the end of the related contract.

### D3. Findings from Wind Integration Studies

Wind integration studies reveal several issues that were categorized into 4 areas:

- Large Variation in Wind Generator Output
- High Wind Generator Ramp Rates
- Power Factor
- Prediction Wind Generator Output

Brief descriptions of some of the main issues are given below. Some of the issues reviewed were considered less relevant to a microgrid and some of the issues are more critical.

**Large Variation in Wind Output**

Obviously, there can be large variations in wind output as wind output is primarily based on wind speed. Wind speed can vary significantly on gusty days and it can be more constant on other days. Wind speed variability is also dependent on the wind direction because local effects. In addition to output variation due to wind speed, wind output does not always correlate with wind speed due to more localized

effects such as wakes from buildings, trees and terrain. Wind output can also depend on a lesser extent on barometric pressure, air temperature and wind direction. These effects can be taken into account when possible.

Because of the variations in wind output, wind energy resources are not typically viewed as a good capacity resource. Instead they are viewed as an alternative source of energy that can be used to offset fossil fuels. Several wind integration studies have indicated that systems with large wind generation require higher spinning reserve requirement than systems without wind generation and therefore to some extent incur higher cost due to the higher reserve requirement and the higher maintenance costs of maintaining these reserves that are subject to higher output variations.

One study suggested that wind output variations are smoothed out in large wind farms as not every unit gets the same gust of wind at the same time. This would indicate that the worst case is installation of a single wind generator or just a few wind generators that don't benefit of smoothing.

**High Wind Generator Ramp Rates**

In addition to large output variations, wind generators can have high ramp rates meaning the rate at which the output changes is large. Wind generation is subject to large output changes in a short amount of time. Most generators, be it a coal plant, gas turbine, or hydroelectric dam have ramp rates defined by the nature of the equipment, due to mainly inertia and control lag, so their ramp rates are much better known. As it turns out on a utility scale, a hydroelectric dam has one of the highest ramp rates and is one of the few generation resources that can match the ramp rates of wind generation. High wind generation ramp rates create additional problems for the grid. Normally, the generation on the grid has to match the variation in loads caused by consumers. This type of generator is known as a load follower. Grids with wind generation require the load followers to match the variations in both load and wind energy.

There are two reasons for high wind ramp rates. One is that the speed of the wind can change rapidly, especially if the wind turbine is in an eddy cause by an obstruction from a mountain, tree or building. The steadiness of the wind often depends on the wind direction due to the lack of or presence of an obstruction in the wind direction. The other reason for high ramp rates is that the power of the wind, that is the theoretical power that can be captured by a wind turbine, is a cubic function of the wind speed. To illustrate this effect, if the wind speed changes from 10 meter per second to 5 meters per second, the wind power will drop to 1/8 of the power output at 10 meters per second. Additionally, the wind speed needs to only drop from 10 meters per second to 8 meters per second (20%) to reduce the wind power in half.

One way to reduce the impact of high wind generator ramp rates is to use energy storage such as flywheels and batteries, to provide energy when the wind generator is reducing output quickly, and to store energy when the wind generator is ramping up output quickly. Energy storage can also smooth out wind generator output variation but this will require much larger energy storage devices. The energy storage requirements required for reducing the wind energy ramp rates require energy storage

over much shorter time periods than what would be required for smoothing wind output variations over an entire day.

**Power Factor and Voltages**

Most wind generators use induction generators which required reactive voltage support from the grid. Newer induction generators reduce this requirement but still require power factor adjustment on the utility and transmission operator side of the grid and can consume valuable grid resources. Wind turbines with DC generators and inverters do not have this problem.

**Prediction of Wind Generator Output**

Prediction wind generator output has additional issues. As mentioned, power does not always correlate with wind speed. For instance if a model of a wind turbine's output is made assuming a uniform velocity flow field (constant velocity through the axis of the wind turbine) through the wind turbine, then "dirty" air will reduce the wind turbine's performance. Some factors that can cause deviations from a uniform flow field assumption are upward or downward components of wind direction that can be caused by the site or convection and wakes from nearby objects or wind turbines. Predicting the wind turbine, or wind farms output requires that a good model of wind output be made for each site and possibly each wind generator if they are dispersed throughout the campus. A good model will should account for the factors mentioned above. Another source of error is the fact that actual wind speed and direction do not always match predicted wind speed and direction. Large wind farms subscribe to sophisticated wind prediction services that can update predictions in shortened time intervals. This offering may not be practical for a microgrid depending on the price of such services. Additionally, results from these services are not perfect. Because of the cubic relationship between wind speed and wind power mentioned above, a seemingly small error in wind speed can lead to fairly large errors in wind output predictions.

Wind farms also use wind predictions to predict the ramp rates of wind generators. Since ramp rates can be dependent on local conditions prediction models should be site specific.

ISOs tend to use three time frames for wind predictions. A long term time frame might be from 48 to 168 hours ahead. A medium term forecast might be from 6 to 48 hours ahead and short term forecast might be from 5 to 10 minutes ahead to 6 hours ahead. The California ISO also required that meteorological data and wind turbine output data be transmitted to them every 4 seconds.

**Other Issues**

Transmission and distribution constraints should be considered for wind farms. The system operator needs to make sure that the transmission and distribution circuits have enough margin to handle load variations, and generator output variations on the circuits carrying power from the wind farm. For the same reasons, circuits on the microgrid should also be monitored to ensure that the local cables have enough margin to handle generator and load variations.

Another concern is that the issues associated with wind generation may be compounded when the system, circuit, or microgrid also have solar energy resources that can cause additional variations in generation output.

### D4. Recommendations for Local Wind Integration in to Microgrids

When integrating local wind generation into a microgrid, the microgrid master controller should be able to mitigate all of the issues mention above. The functional requirements are given below.

**Large Variation in Wind Generator Output.** When the campus or microgrid is connected to the grid, variation in electrical output can be mitigated by the utility supply. This is not an option available to wind farms. Typical utility interconnection agreements require that a certain amount of power shall always be imported to the site to make sure that the onsite generation never back feeds the grid. In the case of IIT, the utility should factor wind variability into the interconnection agreement particularly if the rated output is significant relative to the campus's load. IIT will find out what the specific requirements are when they apply for an interconnect agreement but the microgrid master controller really does not need to account for this while in grid parallel mode. However, when the campus is in island mode, the load following capabilities of the campus generators will have to account for the additional variability. This should be factored into the reserve power requirement for the generators and be a considered in the microgrid master controller when reserve power requirements are calculated in real time.

**High Wind Generator Ramp Rates.** As with load variations, high ramp rates can be mitigated by the utility when the campus is operating parallel to the grid. When operating in island mode, the campus generation will have to account for the high ramp rates of the wind turbine. IIT's campus generation consists of two 4 MW gas turbines. Currently IIT is not planning a large scale deployment of wind on campus but, if a large scale deployment of wind were to be considered at IIT, the ramp rate specification of these turbines should be compared to the expect ramp rates of the wind turbine. In the event that IIT's gas turbine and wind turbine ramp rates are determined to not be compatible, additional measures would have to be taken. For an example, an energy storage system designed to reduce the ramp rates of a particular wind turbine would have to have a control system closely tied and integrated with the wind turbine and its controls. So the other option, if the ramp rates are found to not be compatible, would be to curtail the wind turbine when the campus is in island mode. The latter would be the least expensive option.

**Power Factor.** A small wind turbine should not cause much of an issue when the campus is in grid parallel or island mode. However, if the campus were to add a high percentage of wind turbines generation compared to the campus load, special provisions may be required. Depending on local utility rules, the campus may be required to add equipment for adjusting the power factor. It may be more effective to use a wind turbine with an inverter. When the campus is in island mode, the amount of wind resources that can be used in this mode would depend on the amount of wind generation installed, the power factor of the wind generation, the power factor characteristics of the campus loads, and the power factor capabilities of the campus's gas turbines.

**Prediction Wind Generator Output.** When the campus is operating parallel to the grid, the wind output predictions are not necessarily critical. As part of the research though, the project team was interested in working on models to predict wind output and ramp rates for the campus. The microgrid master controller, which is still in development, will have the capability to model the campus loads based on meteorological conditions and campus schedules. This modeling capability can be adapted to model the wind generation output as well as ramp rates. In island mode, wind generation output predictions become more critical as the percentage of wind generation versus campus load increases. The modeling capability already mentioned should help in this case.

A list of suggested features put together for a microgrid master controller designed to handle a large portion of wind generation on campus. Further analysis and experimentation would have to be performed to define what a large portion is, but for now it is estimated that it is somewhere near 20 to 30% of the campus load. Due to the limited scope and funding for this part of the project, these features will not necessarily be implemented into the IPPSC. Based on the research described above, the microgrid master controller should ideally:

- Have the capability to make adjustments to the campus's reserve power requirements when wind generation is added to the system when the campus is in island mode. These adjustments could be manual or automatically calculated based on the size of the wind generation resources and models of the wind generation resource output and ramp rates.
- Have the capability to curtail wind generation when the campus is in island mode and the wind generation ramp rates are not compatible with the rest of the campus. This feature would require that master controller can send control signals to the wind turbine to curtail its output. To do so, the turbine controls would have to be modified to allow for remote control. Alternatively, the campus could use energy storage to help manage the ramp rate issues associated with the wind turbine. In this case, the energy storage controls would have to be closely coupled with wind turbine models to help determine the optimal charge state of the energy storage system. Dump resistors may also be required as a way to dissipate excess energy.
- Should be able to model and a make short term predictions of wind generation output and ramp rate predictions based on meteorological conditions measured at the site.
- Should be able to model and a make long term predictions of wind generation output and ramp rate predictions based on NOAA weather predictions available over the internet.
- Should be able to make campus load ramp rate predictions based on campus meteorological predictions.
- Should be able to monitor real time wind generation output and distribution circuit power flows on the campus to ensure that circuits do not become overloaded. The controller should have the ability to curtail wind if necessary. This is more critical for higher levels on wind energy installations on campus.

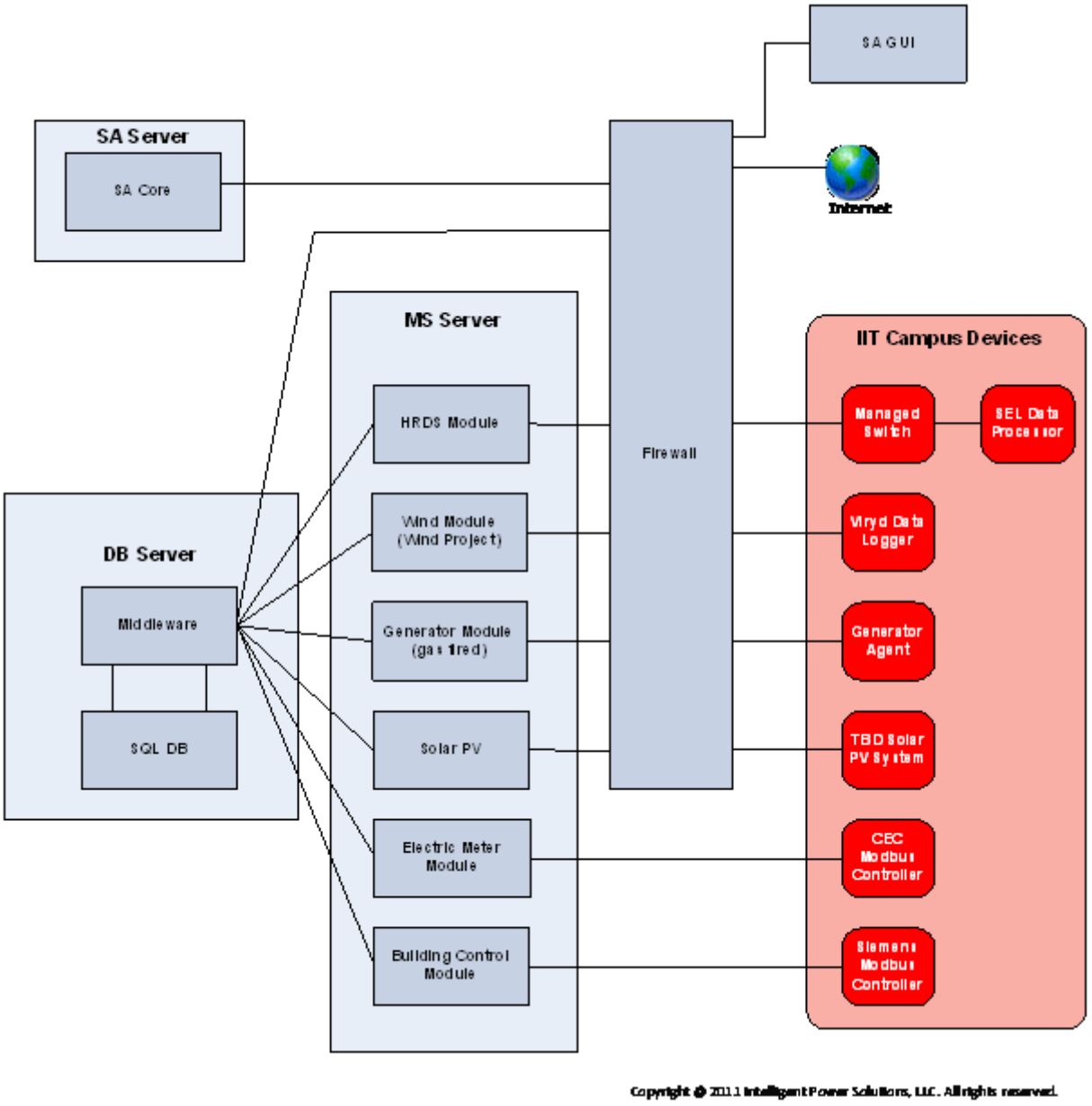


**Figure 331: IPPSC Servers and Software Modules**

### D5. IPPSC Implementation and Integration

A more in depth description for the IPPSC software is shown in Figure 331. The IPPSC software resides on 3 different servers that operate behind the IPPSC firewall. The software is distributed on the servers for load management and for redundancy. If one of the servers goes down, the functions will be distributed between the two remaining servers. The database server will host a MS SQL database and middleware used to store and retrieve data from the database. The middleware uses a web services interface for transferring XML data to and from the database. The SA core, which is the Supervisor Agent (SA) core, operates on its own server. The SA core is the brains of the IPPSC and is responsible for the decision making and modeling making for the IPPSC. Currently the GUI (graphic user interface) for

the IPPSC, also called the SA GUI, communicates directly with the SA Core. In future revisions, the SA GUI will interact only with the middleware on the database server.

The MS server hosts several different modules that communicate with various devices at IIT. Specific to this project, the Wind Turbine Module collects data from the Viryd data logger and then sends it to the middleware by transferring XML data. The Wind Turbine Module transfer both real time data every few seconds and 15 minute averaged data every fifteen minutes. The real time data is used primarily for viewing the real time status of the wind turbine and the 15 minute data is used for data modeling of longer periods of time.

In order to integrate the wind turbine data into the IPPSC, it is necessary to modify the software specification, test the software modifications, and make sure that the campus network could handle the data communications from the wind turbine data logger to the Wind Turbine Module shown in Figure 331.

The project team procured and configured a firewall to setup a VLAN for securely transferring data to the IPPSC. This sounds like a simple effort, but the work had to be coordinated with several departments with IIT's OTS.

The Wind Turbine Module was written to receive data from the Viryd data logger. Viryd helped out in this effort by supplying a subroutine, written in Labview, to listen for data communications from the Viryd data logger and to parse it out into separate parameters. Functions were added around Viryd's data listener to accumulate the data into 15 minute averages and to convert it to and XML format readable by the IPPSC's middleware. An example of the wind turbine XML data is shown in the appendix. The Wind Turbine Module was written in Labview.

Example of the Wind Turbine Module XML that will be sent every 5 seconds

```
<Wind_Turbine_Data>
  <Current_Wind_Turbine_Data>
    <Index>0</Index>
    <Time_Stamp_String>09/28/11 02:21:06 PM</Time_Stamp_String>
    <Power_Output>1.5906138892429</Power_Output>
    <Power_Factor>0.88845417557357</Power_Factor>
    <Wind_Speed>13.414981866903</Wind_Speed>
    <Wind_Direction>259.6584167354</Wind_Direction>
    <Wind_Temperature>67.866002551997</Wind_Temperature>
    <State_Index>3</State_Index>
    <Fault_Number>5</Fault_Number>
    <Data_Okay>true</Data_Okay>
  </Current_Wind_Turbine_Data>
</Wind_Turbine_Data>
```

Example of the Wind Turbine Module XML that will be sent every 15 minutes

```
<Wind_Turbine_Data>
 <Current_Wind_Turbine_Data>
  <Index>0</Index>
  <Time_Stamp_String>09/28/11 02:12:03 PM</Time_Stamp_String>
  <Power_Output>5.8518867140121</Power_Output>
  <Power_Factor>1.0829881900052</Power_Factor>
  <Wind_Speed>77.284238904113</Wind_Speed>
  <Wind_Direction>370.96102237804</Wind_Direction>
  <Wind_Temperature>69.974370191443</Wind_Temperature>
  <State_Index>5</State_Index>
  <Fault_Number>2</Fault_Number>
  <Data_Okay>true</Data_Okay>
 </Current_Wind_Turbine_Data>
 <_15_Min__Wind_Turbine_Data>
  <Index>0</Index>
  <Time_Stamp_String>09/28/11 02:12:03 PM</Time_Stamp_String>
  <Power_Output>5.9756798295702</Power_Output>
  <Power_Factor>1.156556307218</Power_Factor>
  <Wind_Speed>68.331191820848</Wind_Speed>
  <Wind_Direction>433.21311222641</Wind_Direction>
  <Wind_Temperature>87.259401237249</Wind_Temperature>
  <State_Index>4</State_Index>
  <Fault_Number>2</Fault_Number>
  <Data_Okay>true</Data_Okay>
 </_15_Min__Wind_Turbine_Data>
</Wind_Turbine_Data>
```

In addition to developing the Wind Turbine Module, the IPPSC middleware was modified to accept the XML data from the Wind Turbine Module and write it to the database. New procedures in the middleware were also written to retrieve real time and 15 minute average wind turbine data from the database. IPPSC's middleware was written in C# which provides an easy interface into Microsoft's .NET functions in Windows.

The stored procedures in the database that retrieves actual and forecasted data from the National Weather Service were modified. These procedures request data from NWS web servers and store the data in the IPPSC database. The procedures are scheduled to run in the database scheduler. The stored procedures and the database were modified to gather data and forecasts for humidity, wind speed, and wind direction. These are in addition to the temperature, cloud cover, and parametric pressure data that was already programmed to be collected. The stored procedures were also improved to eliminate

sporadic errors found when communicating with the NWS web services, which would periodically report back random errors when data was requested.

A new GUI screen was developed to display the wind turbine data and relevant weather predictions on the same page. A screen shot of this display is shown in Figure 332. The GUI was written in Labview.

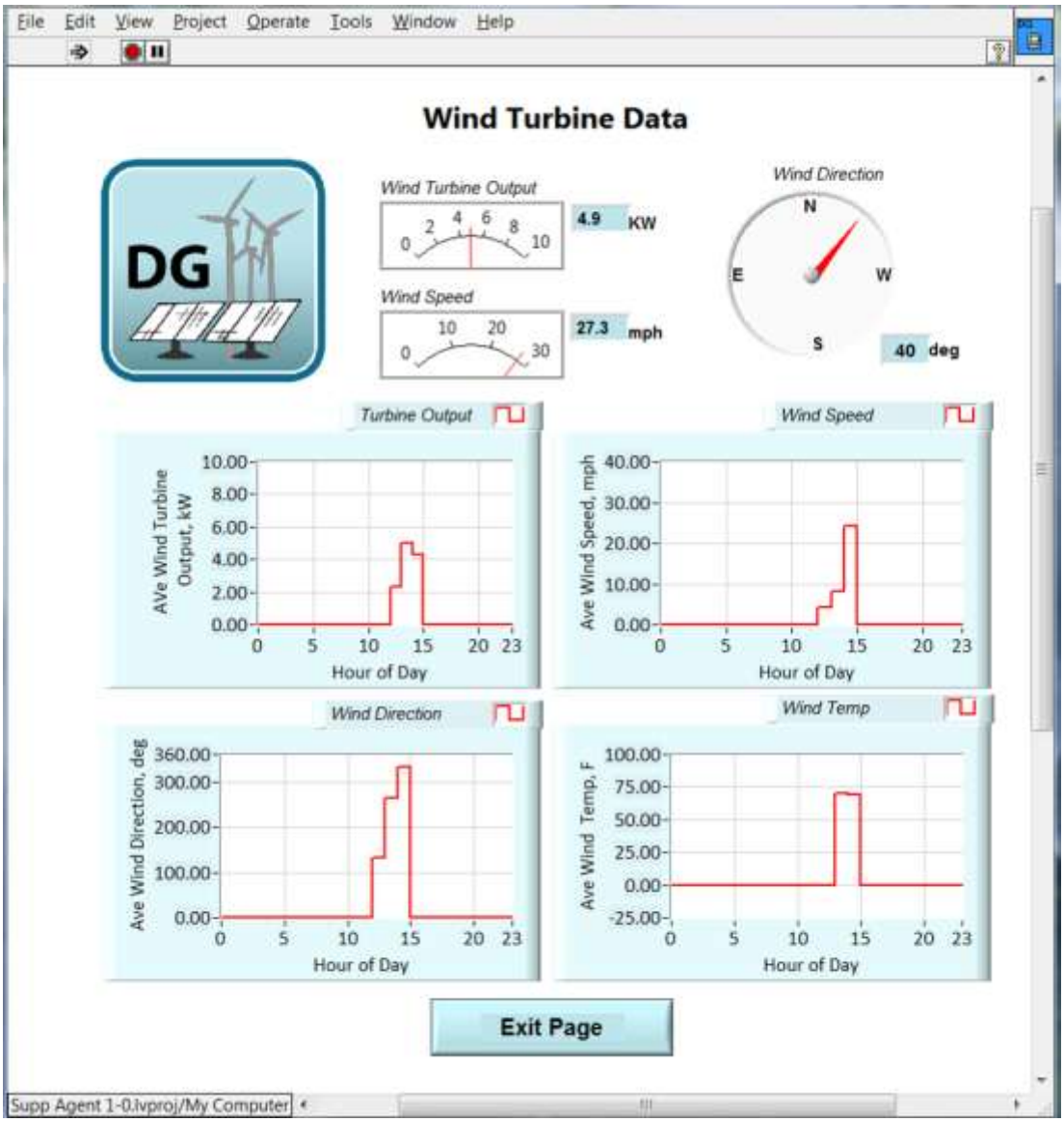


**Figure 332: Screen Shot of IPPSC Wind Turbine Page**

## D6. Conclusions and Recommendations

A review of wind integration studies revealed several issues to consider in integrating wind energy resources in to IIT's microgrid. Since IIT to date has added only an 8 kW wind turbine on campus, these issue are not really severe enough to worry about. However, if the campus were to add a much higher percentage of the wind power, for example 20 to 30% relative to the campus's load, these issues should

be considered. The point of this research is to study these effects on a small wind turbine and to project how to handle these issues in a larger deployment of wind on campus.

In the interest of evaluating concerns with a large deployment of wind within the campus's microgrid, four categories of issues that might be of concern were identified:

- Large Variation in Wind Generator Output
- High Wind Generator Ramp Rates
- Power Factor
- Prediction Wind Generator Output

Microgrid master controller requirements were specified to help mitigate these issues, though some of the issues, such as power factor have more to do the details of the installation rather than the microgrid controls. The microgrid master controller requirements for wind integration are summarized below and pertain mostly when the campus is operating in island mode. When the campus is operating parallel to the grid, the utility supply will mitigate these issues for the campus and these issues will likely be passed on to the utility. The utility interconnection agreement for the wind turbines will likely address the issues in this case. The summarized list of microgrid master control requirements are:

- Make short term on long term predictions of wind output and ramp rates.
- Make adjustments to the campus reserve power requirements when operating in island mode.
- Be able to curtail wind power when wind intermittency and ramp rates as required to ensure the campus's power reliability and safety.
- Monitor distribution circuit power flows and curtail wind power if necessary to reduce over loading.

Non-controller issues that should be considered are:

- Though not necessary for installing the planed 8kW wind turbine on campus, in an larger scale deployment of wind on campus, the turbine ramp rate requirements should be evaluated against the expected ramp rates for the wind turbines to determine how much installed wind generation might start to cause ramp rate related issues on campus.

## 3.3 Wind Energy Education and Outreach

### 3.3.1 Wind Energy Training Facility Development

To fulfill our project tasks on workforce training and education, the project team erected a permanent facility at IIT for Workforce Training and Education on Sustainable Energy and Smart Grid. IIT secured funds from the State of Illinois to renovate the 16,000 sqft of space for establishing the proposed facility. This project provided funds to furnish the facility with the state-of-the-art equipment to offer a world-class training and education on sustainable energy at IIT. The proposed facility will provide training on sustainable energy to various sectors including power industry employees, union workers, high school teachers, the public, and students through instructor-led and internet-based training courses. The floor plan of the training facility is shown in Figure 333.

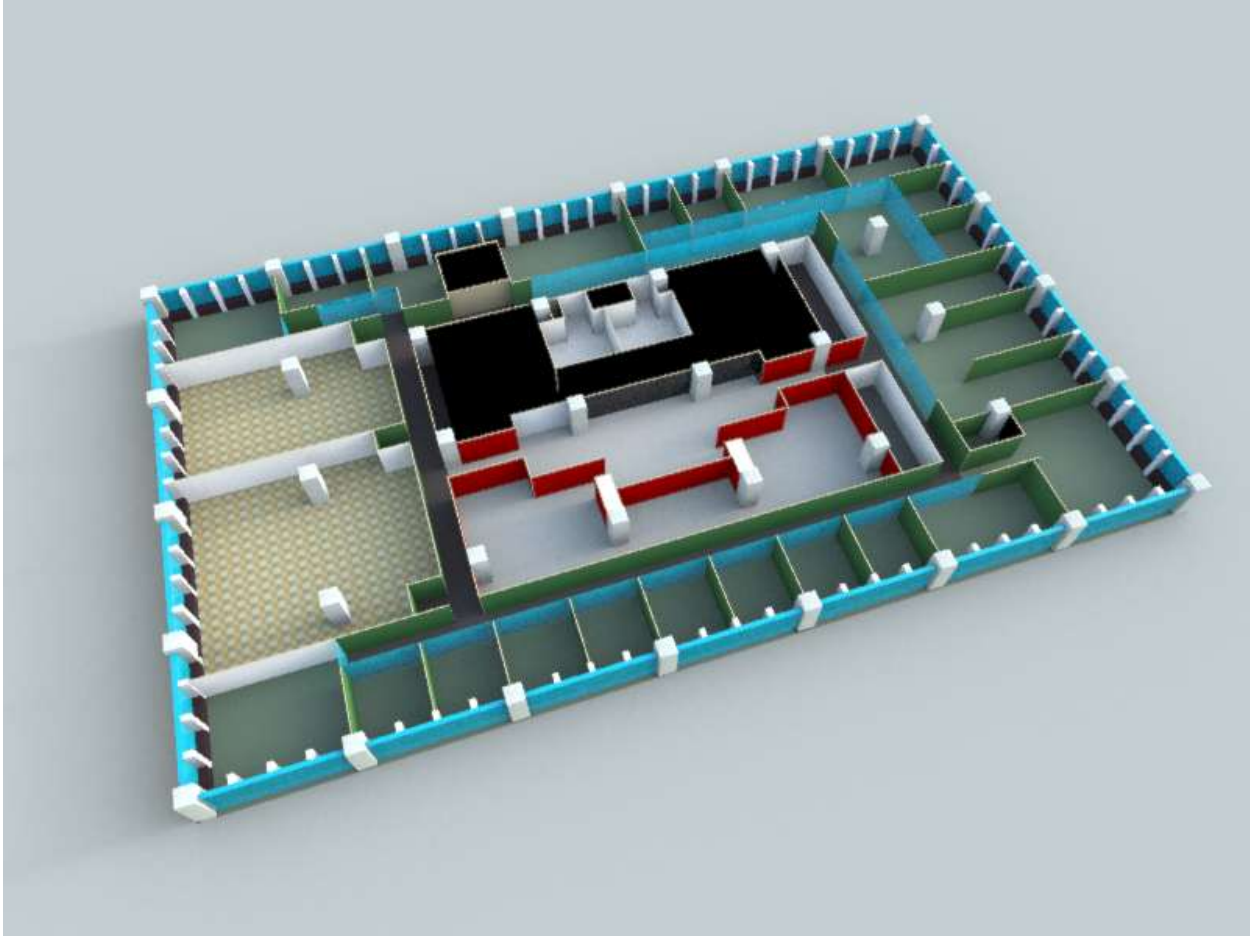

**Figure 333: Floor plan of the training facility**

### *A. Robert W. Galvin Center for Electricity Innovation*

In 2010, Illinois Institute of Technology launched the Robert W. Galvin Center for Electricity Innovation, whose mission is to pursue groundbreaking work in the generation, transmission, distribution, management and consumption of electricity. The Galvin Center brings together faculty, students, researchers, industry, government, innovators, and entrepreneurs to collaborate to improve the reliability, security and efficiency of the electric grid and overcome obstacles to the national adoption and implementation of the Smart Grid. The center brings together researchers, industry, government, and innovators to "plug-in" to IIT's smart microgrid, research laboratories and technology park, creating a hub – or sandbox – for new innovations in advanced grid technology. IIT and the Galvin Center have become leaders of the Smart Grid technological revolution by building the first ever fully-functional Perfect Power system, a smart grid demonstration project, on IIT's Main Campus in Chicago.

- Pioneering Perfect Power – IIT and the Galvin Center have become leaders of the Smart Grid technological revolution by building the first ever fully-functional Perfect Power system, a smart grid demonstration project, on IIT's Main Campus in Chicago. The project eliminates blackouts, allows for "islanding" of the campus from the broader grid, integration of renewable energy and battery storage, and introduction of advanced smart buildings technology for energy efficiency. The Galvin

Center leadership is working with entities across the world to replicate and scale the microgrid model for communities, military bases, corporate parks, sports facilities, and other universities.

- IIT "Living Laboratory" for clean tech – IIT and the Galvin Center have transformed the IIT campus into a "Living Laboratory" for energy projects. This approach integrates advanced new technology demonstrations in visible locations with hands-on research and education opportunities for students and faculty. The technologies demonstrated as part of this approach include: building automation and control, master controller systems, rooftop solar, a wind turbine, electric vehicle charging stations, and large-scale batter storage.

- Smart Grid Workforce Training – The Galvin Center recently completed construction of a state-of-the-art facility to house its Smart Grid Education and Workforce Training Center. The 16,000-square-foot center contains offices, exhibition rooms, classrooms and student workrooms, acting as a living lab for Smart Grid and microgrid technology and education. The Center is engaging thousands of workers and students to accelerating the adoption of energy efficiency, renewable energy, and smart grid technologies across the world.

- IIT Wind Consortium – In 2009, the Galvin Center leadership was awarded a $9 million grant from the U.S. Department of Energy to establish a University-Industry Consortium for wind energy research and education. The Galvin Center leadership was also awarded $750,000 from DOE to study wind integration into the U.S. grid. The Consortium has engaged 50 companies and 8 universities in the U.S. and around the world in technological advances related to the next generation of wind energy manufacturing.

- Illinois Smart Grid Regional Innovation Cluster – IIT is leading the development of an innovation platform for Smart Grid technology that was awarded $1.5 million from the Small Business Administration. The Center is providing technical and business support to speed new Smart Grid technologies on the path to commercialization in Illinois.

- Global Smart Grid Technology Partnership – In 2011, the Galvin Center launched the Illinois-Korea Smart Grid R&D Collaboration, a joint international collaboration to accelerate the technological development of smart grid in Chicago. The Korea industries have awarded the Galvin Center a $2.5 million project for the installation of phasor measurement units (PMUs) at the IIT's microgrid. This partnership is intended to stimulate new interactions among stakeholders in Chicago and Korea and bring additional manufacturing jobs to Illinois.

The Galvin Center has led more than $40 million in projects with funding from the government and private sectors for research and development in microgrids, smart grid technology, and sustainable energy. All of these projects have been completed on-time and within budget. IIT has designated the campus as a "Living Laboratory" for smart grid, microgrid, and other energy technologies, training facility staff and other personnel on the operation, maintenance and repair of these and new technologies. This innovative partnership between facility managers and a research unit is one of the first of its kind in the U.S.

**State-of-the-Art Facility.** In January 2012, the Galvin Center completed and moved into a new, state-of-the-art facility designed to house its Smart Grid, microgrid and energy research, demonstration and education activities. Located on the 16th floor of the IIT Tower, the 16,000-square-foot center contains offices, exhibition rooms, classrooms and student workrooms, acting as a hands-on experience center for Smart Grid, microgrid and energy technology and education. The $3 million project was funded by the State of Illinois, U.S. Department of Energy and IIT.

**Figure 334: State-of-the-art facility at the Galvin Center**

**Perfect Power System.** In 2011, the Galvin Center completed the world's first Perfect Power System on its main campus in Chicago. Inspired by the leadership of Bob Galvin, the center's premier project is the development of the nation's first Perfect Power microgrid at IIT. When fully completed in the next year, the $14 million project has equipped IIT's microgrid with a new high-reliability distribution system for enhancing reliability, the ability to integrate new sustainable energy sources (roof-top solar panels, wind generation units, flow batteries and charging stations for electric vehicles), and smart building automation technology (building controllers, Zigbee sensors, controllable loads) for energy efficiency and demand response. The high-reliability distribution system was completed in 2011, allowing IIT to eliminate blackouts.

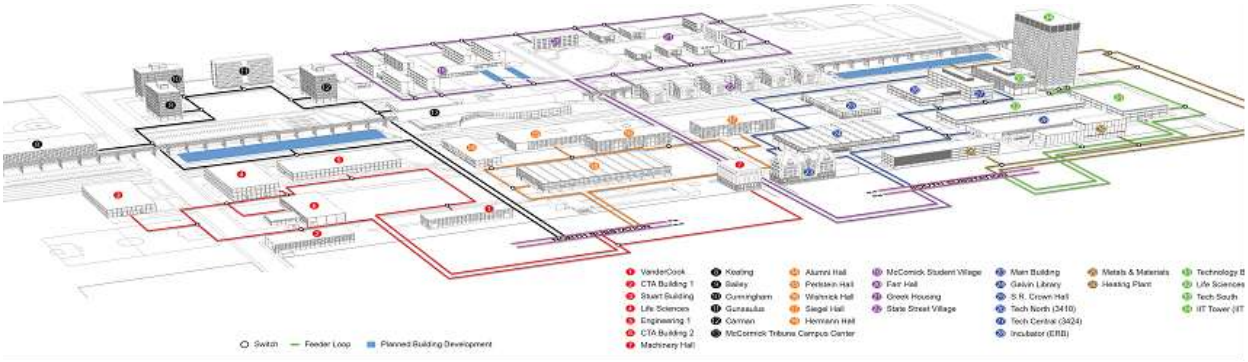

**Figure 335: IIT Perfect Power System overview**

**Electric Vehicle Charging Stations.** In 2012, the Galvin Center completed the installation of 7 Electric Vehicle charging stations on its main campus in Chicago. The installation includes 6 "Level 2" charging stations for 5-hour EV charging, and one of the first DC Quick Charge EV charging stations in the country, which can charge a vehicle in 20-30 minutes. The $120,000 project was funded by the U.S. Department of Energy and private partners.

**Figure 336: IIT Electric Vehicle Charging Stations**

**Rooftop Solar.** In 2012, the Galvin Center completed the installation of a 60 kW of rooftop solar on two campus buildings: Siegel Hall and Stuart Building. The $440,000 project was funded by the U.S. Department of Energy, the State of Illinois and private partners.

**Figure 337: IIT Rooftop Solar Installation**

**Large-Scale Battery Storage.** In 2012, the Galvin Center completed the installation of a next-generation smart grid-capable large-scale battery project on IIT's microgrid testbed for demonstration and evaluation. Produced by the ZBB Corporation, the 500 kWh zinc-bromide flow battery will be the first-of-its-kind in the U.S., demonstrating the ability of microgrid systems to island, coordinate peak load management and peak shaving, and provide backup power. The $1,000,000 project was funded by the U.S. Department of Energy, with cost-share provided by ZBB Corporation.

**Figure 338: IIT Large-scale Battery Storage**

### *B. WINS: Wind Integration Simulator*

Wind Integration Simulator (WINS) is a decision tool that can facilitate the analyses for the integration of 20% or more wind energy. The development of WINS is funded by the U.S. Department of Energy and completed at Illinois Institute of Technology (IIT). WINS explores innovative solutions for continuing reliable operation of existing grid with the most economic integration of additional wind energy. WINS offers scheduling of wind power across interties and adopting new transmission for wind integration. WINS represents advanced features for the modeling and simulation of energy storage, DC transmission lines, hourly wind availability and system reserves, transmission utilization and congestion studies, optimal production costing and nodal price calculations, and advanced visualization techniques for representing the hourly results and facilitates operator training for wind integration. WINS represents a major expansion of a very efficient decision tool called Power Market Simulator (POMS), which was developed by IIT and has been used extensively for power system studies for decades. POMS offers outstanding features for power market simulation which will be embedded into WINS. WINS focuses on augmenting the existing power utility capabilities to support collaborative planning, analysis, and implementation of wind integration. In particular, WINS provides the following superiorities:

- An integrated framework is included in WINS for the comprehensive modeling of DC transmission configurations, including mono-pole, bi-pole, tri-pole, back-to-back, and multi-terminal connection, as well as AC/DC converter models including current source converters (CSC) and voltage source converters (VSC).
- An existing shortcoming of traditional decision tools for wind integration is the limited availability of user interface, i.e., decision results are often text-based demonstrations. WINS includes a powerful visualization tool and user interface capability for transmission analyses, planning, and assessment,

which will be of great interest to power market participants, power system planners and operators, and state and federal regulatory entities.

- WINS can handle extended transmission models for wind integration studies. WINS models include limitations on transmission flow as well as bus voltage for analyzing power system states. The existing decision tools often consider transmission flow constraints (dc power flow) alone which could result in the over-utilization of existing resources when analyzing wind integration.

The input WINS data include (1) generation data (unit type, capacity, availability; cost information; unit operating constraints such as max/min capacities, ramping up/down rates, min on/off times, maximum number of start-ups); (2) wind data (8760 hourly profile); (3) transmission data (network topology, line parameters, control transformers, normal/contingency limits for line flows and bus voltages); and (4) load data (hourly load and distribution, demand bids and load shedding cost and data).

WINS simulates the actual market operations which is based on the security-constrained unit commitment (SCUC) with full AC transmission and voltage constraints considered. The computational engine of WINS is written in Microsoft Visual C++, and the Graphical User Interface (GUI) is written in Microsoft Visual C# and ASP.NET. The database is based on ORACLE and can be extended to include other database formats as well. Microsoft Excel is used for the downloading reports.

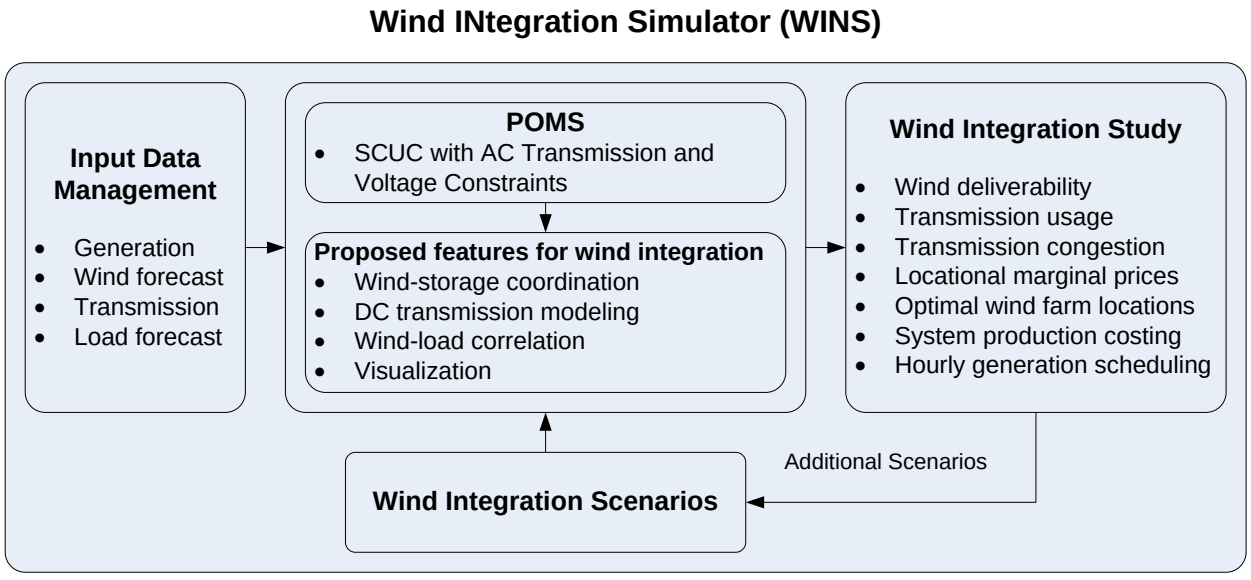


**Figure 339: Architecture for the Design and the Implementation of WINS**

### *C. Situation Awareness at Control Center: e-terravision*

e-terravision is a system that was jointly developed by Alstom Grid with major utilities, a situation awareness expert, and in partnership with Microsoft for the use of the latest graphics technology. This system addresses the need for enhanced situation awareness in control centers. e-terravision is a relatively new product suite whose main purpose is to supplement control rooms with higher-level

decision support capability using visualizations for improving situation awareness. E-terravision complements Energy Management System (EMS) and Market Management System (MMS) user interfaces.

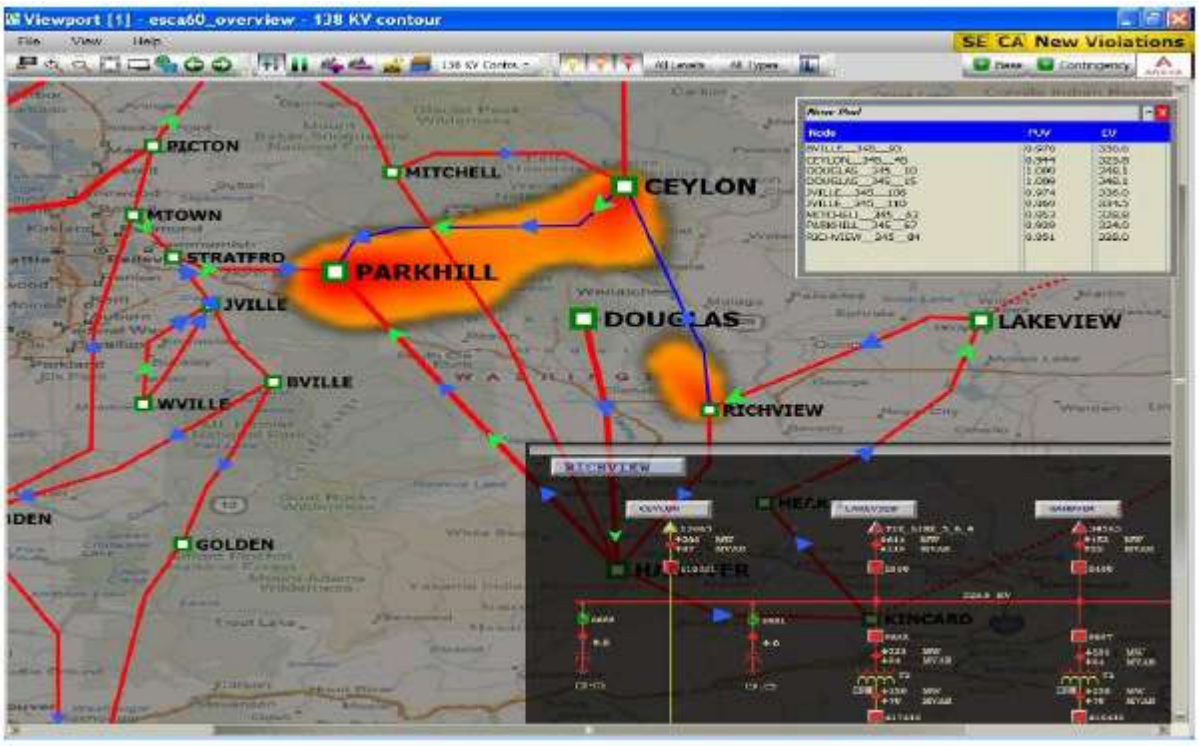


**Figure 340: Enhanced Situation Awareness in Control Centers**

The goals for e-terravision are to implement a control center "situation awareness" framework and tools to:

- Mitigate operational risks
- Present wide-area and "big picture" views of the system
- Assist in ensuring system reliability
- Increase the productivity of control center resources

With e-terravision, control room, operators can:

- Monitor the transmission network with large overviews,
- Assess the grid's reliability using advanced visualization,
- Perform predictive analysis, and
- Prioritize corrective actions.

### 3.3.2 Wind Energy Course Development

#### *A. Engage Undergraduates in Wind Energy Research*

##### A1. Interprofessional Projects at Illinois Institute of Technology

The Interprofessional Project (IPRO) course at IIT is a general education requirement. Specifically, all undergraduates must participate in at least two interprofessional project experiences to receive their respective Bachelor's degree. The IPRO program is described at http://ipro.iit.edu/about: "The IPRO program joins together students from various academic disciplines to work as a team to tackle a real-world problem. Students from architecture, engineering, and humanities may create low-cost shelter solutions, or chemistry, business, and law students may develop best practices in CO2-reducing technologies. Such experiential learning reinforces traditional education methods, providing students a richer academic experience. Each IPRO course is organized as a team of 5-15 students from sophomore to graduate level. All projects are designed with goals that can be completed in one semester. However, many projects continue over multiple semesters and years, with continuing areas of investigation. No two semesters are ever alike." "Teamwork, innovation, and complex problem-solving skills make successful professionals—and reflect the overall performance of their organizations. Since 1995, the IPRO team project course at IIT has been teaching students how to excel in the workplace by providing them the practical tools that can make a difference in their professional and personal lives."

##### A2. Integration of Plug-in Hybrid Electric Vehicles and Renewable Energy Systems

The purpose of the research project is to investigate the economic effects of the integration of wind power generation systems and PHEVs. For wind generations it is important to investigate factors that impact the generation of wind, like location of the wind farm, speeds of wind in the specific location, type of turbine and its characteristics. In the case of PHEVs a significant research on driving habits, type of battery and its life will be pursued. The final goal of the research is to determine the effectiveness of the method on lowering the operational cost by analyzing various cases which introduce the use of PHEVs into the power generation system. The results obtained from the research will serve targeted markets including, but not limited to, automotive industry, wind power generation industry, and utility companies. The advancement of alternative energy technology will also benefit the environment.

**Organization and Approach**

The problem of creating a basic model for the purpose of studying the effects of the integration of PHEVs and wind energy is split into four parts; wind energy, PHEVs, power generation costs, and creation of an objective function to minimize the operational cost of the model. These four parts are split up between the members of the group, who are responsible for researching their topic and reporting back to the team.

The first three parts require finding the necessary data regarding the topic. Analysis of how the data is to be used in the objective function, namely as a cost function or power curve, is determined. This determination requires deciding which variables are pertinent to the topic.

Conclusions for the initial three parts of the approach are used in the formulation of the objective function. The objective function is subsequently utilized to determine the effectiveness and feasibility of integration of PHEVs with wind energy.

Wind is one of the most important renewable energies used to generate electric energy. Wind energy is clean, renewable, and a potentially cost efficient method for energy production. The American Wind Energy Association AWEA notes that "wind power is one of the fastest growing methods of electricity generation in the United States. Approximately 40 % of all new generation capacity contributing to the power grid in the United States was from wind power projects in the recent years." [**97**] The U.S. Department of Energy's goal is to have 20% wind power generation by 2030 [**1**].

The downside of wind energy is that wind is typically intermittent. When wind is present, the laws of thermodynamics state that it is not possible to translate all the kinetic energy in wind into the same amount of electrical energy. Moreover, the implementation of more wind power to the grid will create storage problems. Wind will inevitably be available when electricity demand is low. Ideally, there would be a method or apparatus for storing the wind energy for use when electricity demand is low. PHEVs are a potential solution to the electrical energy storage problem.

When studying wind generation, it is important to take into account different variables such as, the speed of wind in a determined place, turbine location, and turbine characteristics. For the project's investigated system the above stated variables have been analyzed. The analysis of the problem has allowed for assumptions regarding some of the variables as constants to permit the simulation of a scenario to determine the feasibility of wind energy. The variables analyzed are described below.

A wind map is a useful tool to locate the areas of the United States where the winds are the highest. This map bases its determination of particular areas on the wind's annual average speed and power. For the study of this particular research project, an urban area of Chicago, Illinois is the focus of the group research interest for the simulation. Figure 341 shows the map of wind speeds at 80 meters above the ground level for Illinois [**98**]. Chicago is indicated as the spot where the turbines are going to be sitting.

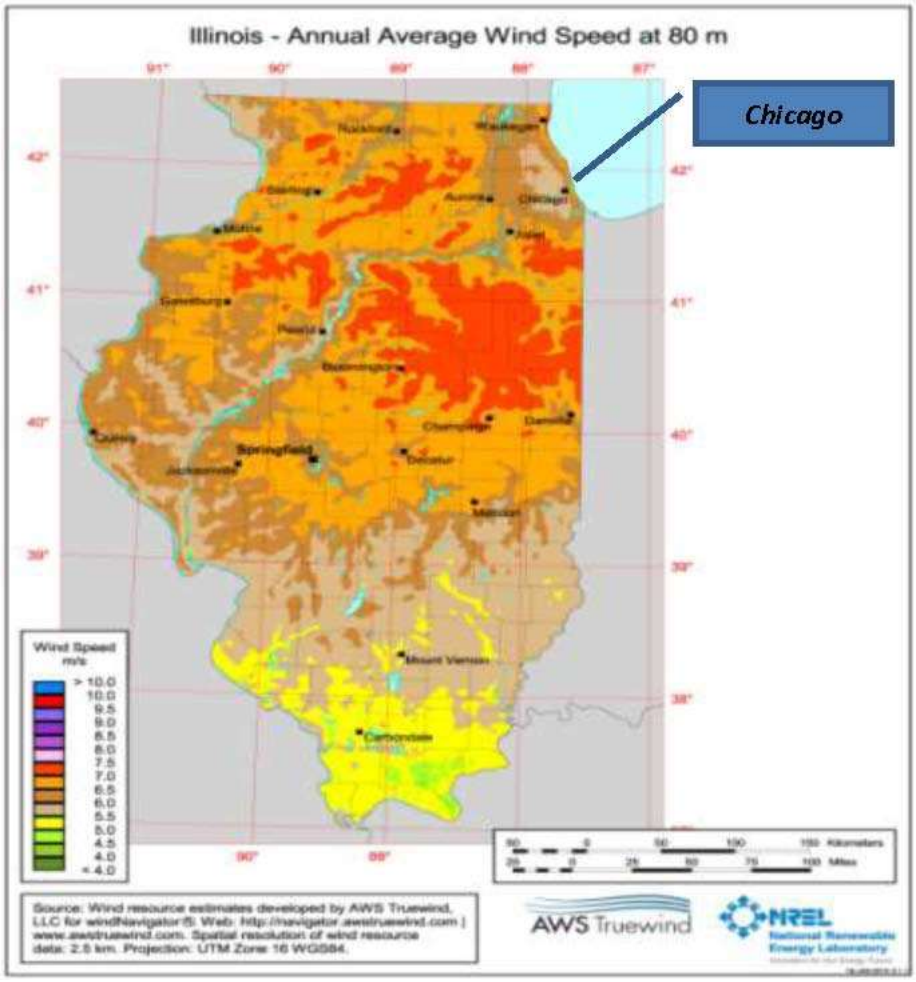


**Figure 341: Wind map supplied by the U.S. Department of Energy**

Having determined the location of a wind turbine, it is now possible to determine the friction coefficient and the roughness length which enables calculation of wind speed. The friction coefficient is a quantity that is used to quantify the resistance that an object imparts on wind flow. Obtaining the values of friction coefficient will allow for calculation of the wind speed at ground level. These values are taken into account when forecasting wind speeds. Since friction coefficient is already included in the forecast calculated data, it is not necessary for the research to obtain the friction coefficient value at this point. The research uses a 24 hour wind forecast to determine the wind speed per hour. The data will be considered for the months in which the winds are at their yearly average speeds. This speed forecast gives the speeds at ground level in the Chicago urban area. Table 21 shows the wind speed forecasted values.

**Table 21: 24 hour forecasted wind speeds.**

| Time | Wind Speed [mph] | Wind Speed at Ground Level [m/s] |
|---|---|---|
| **12am** | 8 | 3.576 |
| **1am** | 8 | 3.576 |
| **2am** | 8 | 3.576 |
| **3am** | 8 | 3.576 |
| **4am** | 8 | 3.576 |
| **5am** | 9 | 4.023 |
| **6am** | 9 | 4.023 |
| **7am** | 9 | 4.023 |
| **8am** | 9 | 4.023 |
| **9am** | 9 | 4.023 |
| **10am** | 8 | 3.576 |
| **11am** | 8 | 3.576 |
| **12pm** | 8 | 3.576 |
| **1pm** | 8 | 3.576 |
| **2pm** | 8 | 3.576 |
| **3pm** | 10 | 4.47 |
| **4pm** | 10 | 4.47 |
| **5pm** | 10 | 4.47 |
| **6pm** | 10 | 4.47 |
| **7pm** | 11 | 4.917 |
| **8pm** | 11 | 4.917 |
| **9pm** | 11 | 4.917 |
| **10pm** | 8 | 3.576 |
| **11pm** | 8 | 3.576 |
| ***Average*** | *8.917* | *3.986* |

The roughness length (z) [meters] depends on the terrain where the wind turbines are located. Roughness length is used to find hourly wind speed 80 meters above ground level. The values of roughness length are tabulated according to terrain conditions and roughness class. The terrain conditions are the characteristics of the various places where the turbines can be located. The roughness class is the rating of the terrain in ascending form. A value of zero is assigned to less rough terrain such as a water surface. A value of four is assigned the roughest terrain such as a dense urban area or forest. For the case of urban districts and farm lands with many windbreaks (obstacles) the roughness length is equal to 0.4 meters.

The equation to calculate the wind at a height above the ground level is shown below.

$$v = v_{ref} \frac{\ln \frac{z}{z_0}}{\ln \frac{z_{ref}}{z_0}} \quad (95)$$

Where,
v is wind speed at height z above ground level;
z is height above ground level for the desired velocity (v);
z0 is roughness length in the current wind direction;
zref is the height where the exact wind speed, vref, is known.

Table 22 shows the values of wind speed at 80 meters above ground level.

The Vestas V90 wind turbine is selected for research analysis. The performance, mechanical, and physical characteristics are listed in Table 23.

The maximum power that wind can produce in a determined area depends on blade size of the turbine and density of air. Note that the values of maximum power do not take into account the losses incurred from transformation of kinetic energy to electrical energy.

The following equation shows the maximum wind power equation.

$$P_{total} = \frac{1}{2} \cdot \rho \cdot R^2 \cdot \pi \cdot v_b^3 \quad (96)$$

Where,

ρ is the air density;
R is the radius of the blades;
vb are the wind speeds after and before passing through the turbine.

Wind turbines cannot absorb all the wind available in a certain location. Equation 3 calculates the turbine's captured power.

$$P_{total} = \frac{1}{2} \cdot \rho \cdot c_p \cdot R^2 \cdot \pi \cdot v_b^3 \quad (97)$$

Where cp is the power coefficient.

The power coefficient is the ratio of the electrical output power of the wind turbine to the total (potential) wind power. The values of the power coefficient depend on the type of turbine and are usually provided by turbine manufactures. For this specific case the power coefficient is 0.44.

The turbine does not output more than is specified by the generator. Therefore, 1.8 MW is the maximum power that the turbine used for this case of study can provide. In order not to surpass this value most turbines have mechanisms which prevents excessive angular velocity thereby preventing

mechanical failure of the turbine. One mechanism used is the pitch control which rotates around the turbines longitudinal axis of the blades to control the amount of wind energy captured.

The maximum power output for the simulation is set to 75 MW. 42 Vestas V90 turbines are required to produce 75 MW

$$\frac{75\ MW}{1.8\ \frac{MW}{turbine}} = 42\ turbines$$

Table 24 shows the maximum power, the captured power and the power produced by 42 turbines in a 24 hour window. Figure 342 shows the Power Output curve for 42 turbines outputting a maximum of 75 MW.

A PHEV is a vehicle that uses both an internal combustion engine and an electric motor, which utilizes an externally or internally charged battery. The distance the battery can solely drive the car is referred to as the All Electric Range (AER). The type of car that is focused on in this project is termed PHEV40, which has an AER of forty (40) miles. Another type of PHEV is the PHEV20, which can drive the car solely on the battery for approximately twenty (20) miles. The PHEV40 will be used for the reasons listed below.

- There are statistics from the University of Michigan Transportation Research Institute (UMTRI) that show the average distance traveled per day for Americans is about 40 miles with a standard deviation of about 10 miles.
- The current price for low-weight lithium ion batteries for use in PHEVs is relatively high: $400-700/kWh [**97**]. Therefore, the maximum battery pack size is limited, but this may change in the future as technology reduces battery cost.
    - Low weight batteries are preferred because the weight of the car has a great impact on the energy efficiency, and therefore, AER range of the vehicle.

A measure of the battery is its State of Charge (SOC), which is the percentage that the battery is charged. A battery cycle is defined as fully charging and discharging a battery, from its manufactured minimum SOC to maximum SOC. Batteries that go through too many cycles too often will have a reduced capacity and battery life. In order to increase the battery life, the usable SOC of the battery is limited to only half of its capacity. The model used in analysis is the Chevrolet Volt. Some specifications for the Chevrolet Volt are listed below [**99**]:

- Total battery size of 16 kWh
- SOC range of 0.3 to 0.85
- Battery energy range of 4.8 kWh to 13.6 kWh, which reflects the SOC range

**Table 22: 24 hour wind speed values at 80 meters above ground level.**

| Time | Wind Speed [mph] | Wind Speed at Ground Level [m/s] | V @ 80 m above ground [m/s] |
|---|---|---|---|
| **12am** | 8 | 3.576 | 8.058 |
| **1am** | 8 | 3.576 | 8.058 |
| **2am** | 8 | 3.576 | 8.058 |
| **3am** | 8 | 3.576 | 8.058 |
| **4am** | 8 | 3.576 | 8.058 |
| **5am** | 9 | 4.023 | 9.066 |
| **6am** | 9 | 4.023 | 9.066 |
| **7am** | 9 | 4.023 | 9.066 |
| **8am** | 9 | 4.023 | 9.066 |
| **9am** | 9 | 4.023 | 9.066 |
| **10am** | 8 | 3.576 | 8.058 |
| **11am** | 8 | 3.576 | 8.058 |
| **12pm** | 8 | 3.576 | 8.058 |
| **1pm** | 8 | 3.576 | 8.058 |
| **2pm** | 8 | 3.576 | 8.058 |
| **3pm** | 10 | 4.47 | 10.073 |
| **4pm** | 10 | 4.47 | 10.073 |
| **5pm** | 10 | 4.47 | 10.073 |
| **6pm** | 10 | 4.47 | 10.073 |
| **7pm** | 11 | 4.917 | 11.08 |
| **8pm** | 11 | 4.917 | 11.08 |
| **9pm** | 11 | 4.917 | 11.08 |
| **10pm** | 8 | 3.576 | 8.058 |
| **11pm** | 8 | 3.576 | 8.058 |
| ***Average*** | *8.917* | *3.986* | *8.982* |

**Table 23: Vestas V90 wind turbine characteristics.**

| Model | Capacity [MW] | Blade Length [m] | Hub Height [m] | Total Height [m] | Area Swept by blades [$m^2$] | RPM Range | Maximum Blade Tip Speed [m/s] | Rated Wind Speed [m/s] |
|---|---|---|---|---|---|---|---|---|
| Vestas V90 | 1.8 | 45 | 80 | 125 | 6,362 | 8.8-14.9 | 70 | 11 |

**Table 24: Maximum power, captured power, and produced power by 42 turbines.**

| Time | Wind Speed [mph] | Wind Speed at Ground Level [m/s] | V @ 80 m above ground [m/s] | P [MW] | Pcaptured [MW] | P output [MW] | nominal P @ 42 turbines [MW] | Pcaptured @ 42 turbines [MW] |
|---|---|---|---|---|---|---|---|---|
| **12am** | 8 | 3.576 | 8.058 | 2.041 | 0.898 | 0.898 | 85.712 | 37.713 |
| **1am** | 8 | 3.576 | 8.058 | 2.041 | 0.898 | 0.898 | 85.712 | 37.713 |
| **2am** | 8 | 3.576 | 8.058 | 2.041 | 0.898 | 0.898 | 85.712 | 37.713 |
| **3am** | 8 | 3.576 | 8.058 | 2.041 | 0.898 | 0.898 | 85.712 | 37.713 |
| **4am** | 8 | 3.576 | 8.058 | 2.041 | 0.898 | 898 | 85.712 | 37.713 |
| **5am** | 9 | 4.023 | 9.066 | 2.906 | 1.279 | 1.279 | 122.039 | 53.697 |
| **6am** | 9 | 4.023 | 9.066 | 2.906 | 1.279 | 1.279 | 122.039 | 53.697 |
| **7am** | 9 | 4.023 | 9.066 | 2.906 | 1.279 | 1.279 | 122.039 | 53.697 |
| **8am** | 9 | 4.023 | 9.066 | 2.906 | 1.279 | 1.279 | 122.039 | 53.697 |
| **9am** | 9 | 4.023 | 9.066 | 2.906 | 1.279 | 1.279 | 122.039 | 53.697 |
| **10am** | 8 | 3.576 | 8.058 | 2.041 | 0.898 | 0.898 | 85.712 | 37.713 |
| **11am** | 8 | 3.576 | 8.058 | 2.041 | 0.898 | 0.898 | 85.712 | 37.713 |
| **12pm** | 8 | 3.576 | 8.058 | 2.041 | 0.898 | 0.898 | 85.712 | 37.713 |
| **1pm** | 8 | 3.576 | 8.058 | 2.041 | 0.898 | 0.898 | 85.712 | 37.713 |
| **2pm** | 8 | 3.576 | 8.058 | 2.041 | 0.898 | 0.898 | 85.712 | 37.713 |
| **3pm** | 10 | 4.47 | 10.073 | 3.986 | 1.754 | 1.754 | 167.406 | 73.659 |
| **4pm** | 10 | 4.47 | 10.073 | 3.986 | 1.754 | 1.754 | 167.406 | 73.659 |
| **5pm** | 10 | 4.47 | 10.073 | 3.986 | 1.754 | 1.754 | 167.406 | 73.659 |
| **6pm** | 10 | 4.47 | 10.073 | 3.986 | 1.754 | 1.754 | 167.406 | 73.659 |
| **7pm** | 11 | 4.917 | 11.08 | 5.305 | 2.334 | 1.8 | 222.818 | 75.6 |
| **8pm** | 11 | 4.917 | 11.08 | 5.305 | 2.334 | 1.8 | 222.818 | 75.6 |
| **9pm** | 11 | 4.917 | 11.08 | 5.305 | 2.334 | 1.8 | 222.818 | 75.6 |
| **10pm** | 8 | 3.576 | 8.058 | 2.041 | 0.898 | 0.898 | 85.712 | 37.713 |
| **11pm** | 8 | 3.576 | 8.058 | 2.041 | 0.898 | 0.898 | 85.712 | 37.713 |
| ***Average*** | *8.917* | *3.986* | *8.982* | *2.953* | *1.299* | *1.233* | *124.034* | *51.77* |

The large size of the PHEVs battery allows it to be used as an energy storage system; when not in use, the PHEV can be used to feed energy back into the power grid. This interaction of the vehicle with the power grid called Vehicle to grid (V2G) technology. V2G used during peak grid demand hours can reduce the cost of the grid operations but will also increase the cycling rate of the battery, reducing its capacity and life. The Chevrolet Volt is able to charge at two speeds; fast and slow. Fast charging occurs at 240V and takes 3 hours to charge the battery from minimum SOC to maximum SOC. Slow charging

occurs at 120V and takes 8 hours to charge the battery. Slow charging is the charging rate assumed for analysis simulations.

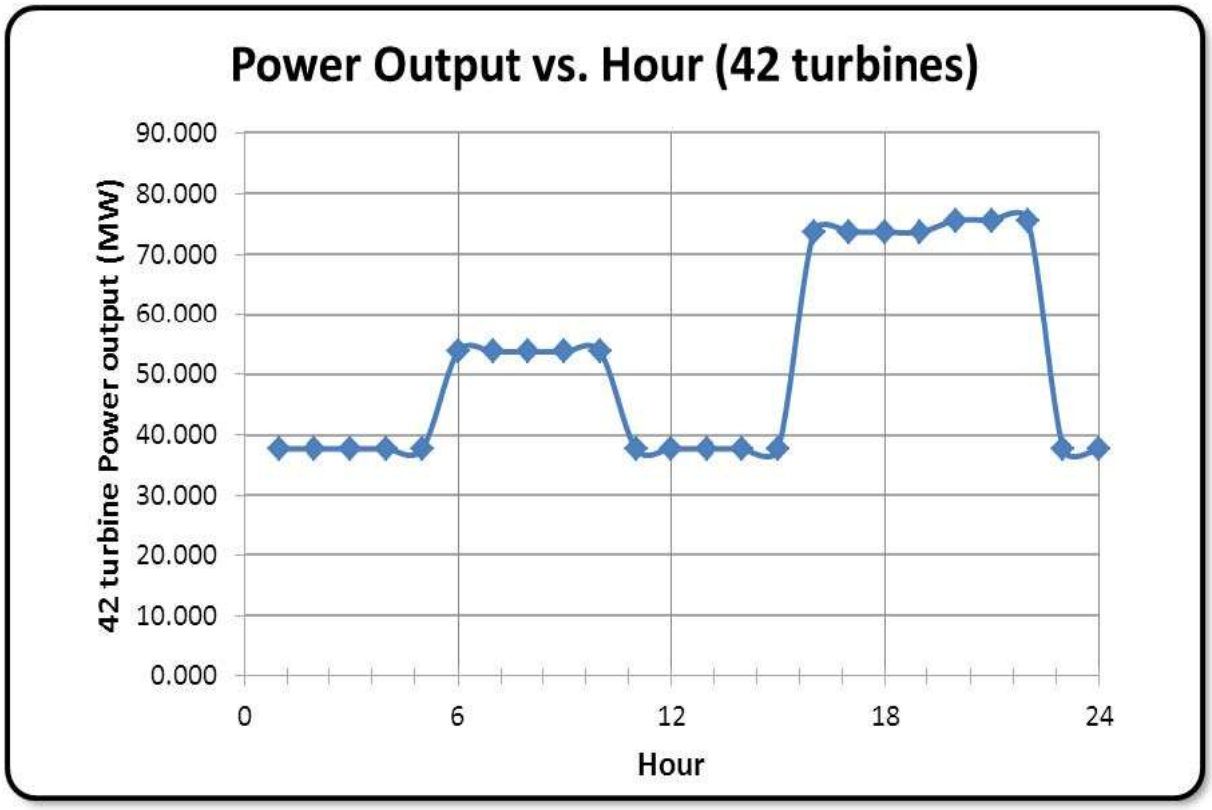


**Figure 342: Power output vs. Hour for 42 turbines.**

In order to derive an objective function with which to optimize the operational cost of the integrated PHEV and wind energy system, it is necessary to come up with several scenarios describing PHEV charging times and times that the PHEV would utilize V2G. The scenarios are created assuming the fleet of PHEVs leave home charging stations and travel to work between the hours of 8:00 am and 10:00 am and return home between the hours of 5:00 pm and 7:00 pm. The scenarios are varied by assuming certain percentages of the fleet would have differing states of charge and are discharging or charging during different parts of the day. From these scenarios an hourly load curve is generated for the PHEVs. Using the PHEV's load curve, the objective function is used to simulate the associated operational costs.

The power system optimal operational cost is the least amount of cost used to create electrical power to satisfy the load demand in a specific time. The power system operational cost is different from one generator to the other generator based on the type and the efficiency of energy convergence.

To compare and find the best optimal operational cost, objective function is used. The objective function is a function that enables to find the optimum value (either largest or smallest) by comparing all possible situations. However, the objective function is only effective on a linear function.

In this case the objective function is used to find the minimum operational cost spent by operating 3 conventional generators and 42 wind generators (wind farm). It is assumed that there is no operational cost for wind generators because they are the renewable resources. The cost functions of each generators is given in a polynomial way; $fG1 = c + b*X + a*X^2$ (the cost function for the 1st generator). In our case the coefficients of cost function, a, b, and c, are given but it can be obtained by analyzing the cost vs. time graph. The coefficients of cost function for generators are shown in Table 25.

**Table 25: The coefficients of cost function for generators**

| Unit | a [$/MW$^2$] | b [$/MW] | c [$/h] | $P_{min}$ [MW] | $P_{max}$ [MW] |
|---|---|---|---|---|---|
| G1 | 0.099 | 6.589 | 211.4 | 100 | 320 |
| G2 | 0.203 | 7.629 | 217.4 | 10 | 160 |
| G3 | 0.494 | 10.07 | 102.8 | 10 | 100 |
| Wind | 0 | 0 | 0 | 37.7 | 75.6 |

**Table 26: Linearized cost functions for generators**

| Dispatch | Gen1 | Gen2 | Gen3 |
|---|---|---|---|
| P1(MW) | 100 | 10 | 10 |
| F1($) | 1860.3 | 313.99 | 252.9 |
| P2(MW) | 120 | 30 | 30 |
| F2($) | 2427.68 | 628.97 | 849.5 |
| P3(MW) | 140 | 50 | 50 |
| F3($) | 3074.26 | 1106.35 | 1841.3 |
| P4(MW) | 160 | 70 | 70 |
| F4($) | 3800.04 | 1746.13 | 3228.3 |
| P5(MW) | 180 | 90 | 90 |
| F5($) | 4605.02 | 2548.31 | 5010.5 |
| P6(MW) | 200 | 110 | 110 |
| F6($) | 5489.2 | 3512.89 | 7187.9 |
| P7(MW) | 220 | 130 | |
| F7($) | 6452.58 | 4639.87 | |
| P8(MW) | 240 | 150 | |
| F8($) | 7495.16 | 5929.25 | |
| P9(MW) | 260 | 170 | |
| F9($) | 8616.94 | 7381.03 | |
| P10(MW) | 280 | | |
| F10($) | 9817.92 | | |
| P11(MW) | 300 | | |
| F11($) | 11098.1 | | |

| | | | |
|---|---|---|---|
| **P12(MW)** | 320 | | |
| **F12($)** | 12457.48 | | |

**Table 27: Slopes of the linearized cost functions for generators**

| Segment | Gen1 | Gen2 | Gen3 |
|---|---|---|---|
| **1** | 28.369 | 15.749 | 29.83 |
| **2** | 32.329 | 23.869 | 49.59 |
| **3** | 36.289 | 31.989 | 69.35 |
| **4** | 40.249 | 40.109 | 89.11 |
| **5** | 44.209 | 48.229 | 108.87 |
| **6** | 48.169 | 56.349 | |
| **7** | 52.129 | 64.469 | |
| **8** | 56.089 | 72.589 | |
| **9** | 60.049 | | |
| **10** | 64.009 | | |
| **11** | 67.969 | | |

At first, the power capacity should be divided as a certain value and the cost should be measured by each segments. In our case, we divided each segments by 20 MW power generations. We assumed all the generators are operating (never shutting down) so each generators are analyzed from the minimum power generations. The wind generators are not analyzed because of the assumption that there is no operational cost. The data is shown on Table 26.

Secondly, using the data from the Table 26, it is possible to calculate the gradient on each segment Table 27. At last, linear cost function is obtained. For example, the cost function for the 1$^{st}$ generator can be re-written as fG1 = 1860.3 + 28.369*X1,1 + 32.329*X1,2 + 36.289*X1,3 + 40.249*X1,4 + 44.209*X1,5 + 48.169*X1,6 + 52.129*X1,7 + 56.089*X1,8 + 60.049*X1,9 + 64.009*X1,10 + 67.969*X1,11. The code to find the minimum operational cost is attached on the appendix.

**Analysis and Findings**

The four cases that utilize PHEVs are labeled as Scenario 1, Scenario 2, Scenario 3, and Scenario 4. These scenarios were developed as a way to test the operational cost on the grid due to the introduction of PHEVs. The factors that affect the operational cost include the time of charging of the PHEVs and the time of V2G of the PHEVs. These PHEVs move around the six-bus system as fleets, with a total fleet size of ten thousand (10,000) units. We have designated bus 6 as the homes of the owners of the PHEVs and bus 4 as the workplace of the owners of the PHEVs. All cars stay at home at night, go to work in the afternoon, and come back home in the evening.

Throughout the research we analyzed 6 different scenarios to find the effectiveness of integrating wind energy and PHEV to the current system. All the scenarios are analyzed in a 6-bus system shown in Figure 343. The 6-bus system is the most commonly used system to simulate the real world. As you can see from the diagram below, we have 2 load bus, 2 generator bus, 1 wind generator & load bus, 1 generator & load bus. PHEV moves from one bus to the other bus. We assumed that there is no fault in the system, there is no transmission line loss, and there is no operational cost for wind power generation.

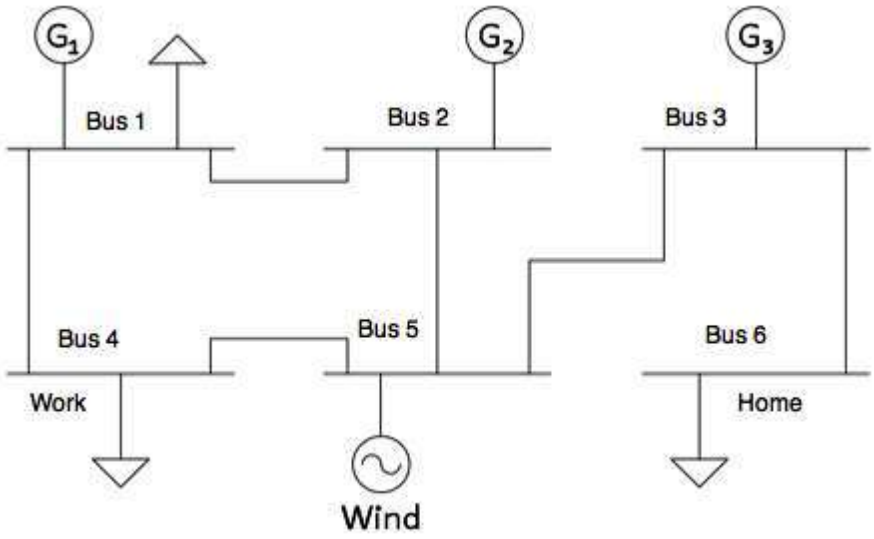


**Figure 343: One-line Diagram of the 6-bus System**

In this analysis, we are going to analyze the result in two ways. At first, we are going to observe how peak hour changes as wind energy and PHEV are integrated. Secondly, we are going to observe the total operational cost and find the best scenario based on it. The first scenario is the 6 bus system that doesn't have any wind energy. We are investigating the following scenarios:

Scenario 1: No wind
Scenario 2: Only wind
Scenario 3: PHEVs, no V2G, and night G2V (grid-to-vehicle)
Scenario 4: PHEVs, day time V2G, and night G2V
Scenario 5: PHEVs, evening V2G, and night G2V
Scenario 6: PHEVs, afternoon G2V, evening V2G, and night G2V

The peak demand is between 8:00pm to 10:00pm. The average load demand in an hour at this area is 261MW. As we said, we are going to observe how this peak demand changes as wind energy and PHEVs are integrated. Besides, we can also observe the patterns of power generation in 24 hours. For example from 2:00am to7:00am, 1$^{st}$ generator supplies 120MW, 2$^{nd}$ generator supplies 50MW, 3$^{rd}$ generator supplies from 22 MW to 26MW depending on the time.

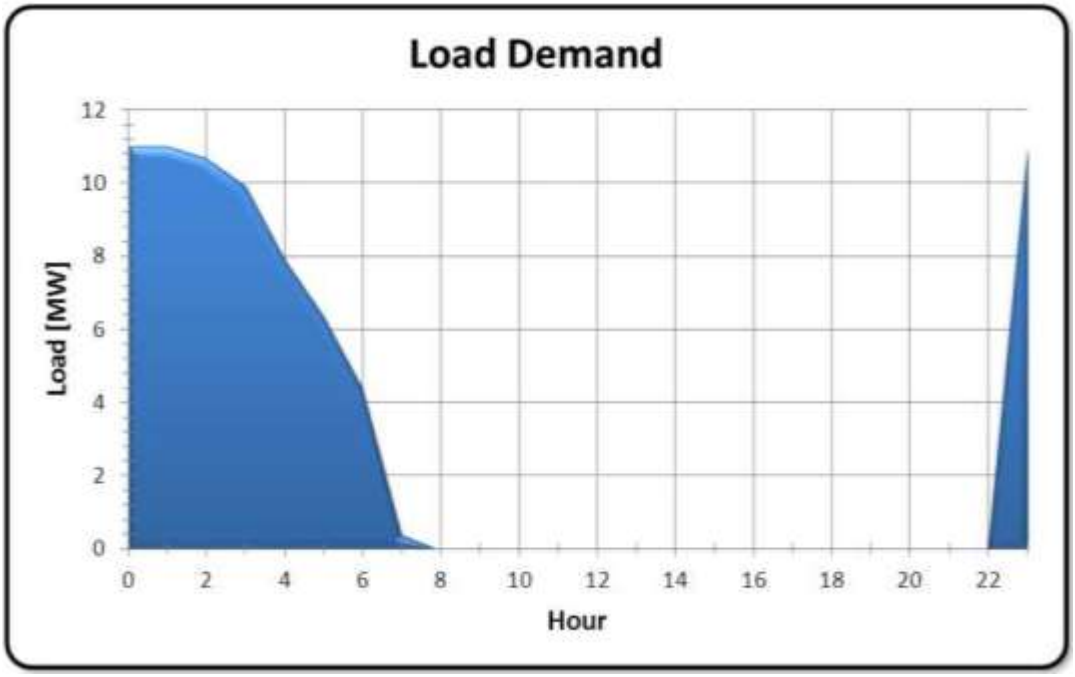


**Figure 344: Scenario 3 PHEV Load Demand**

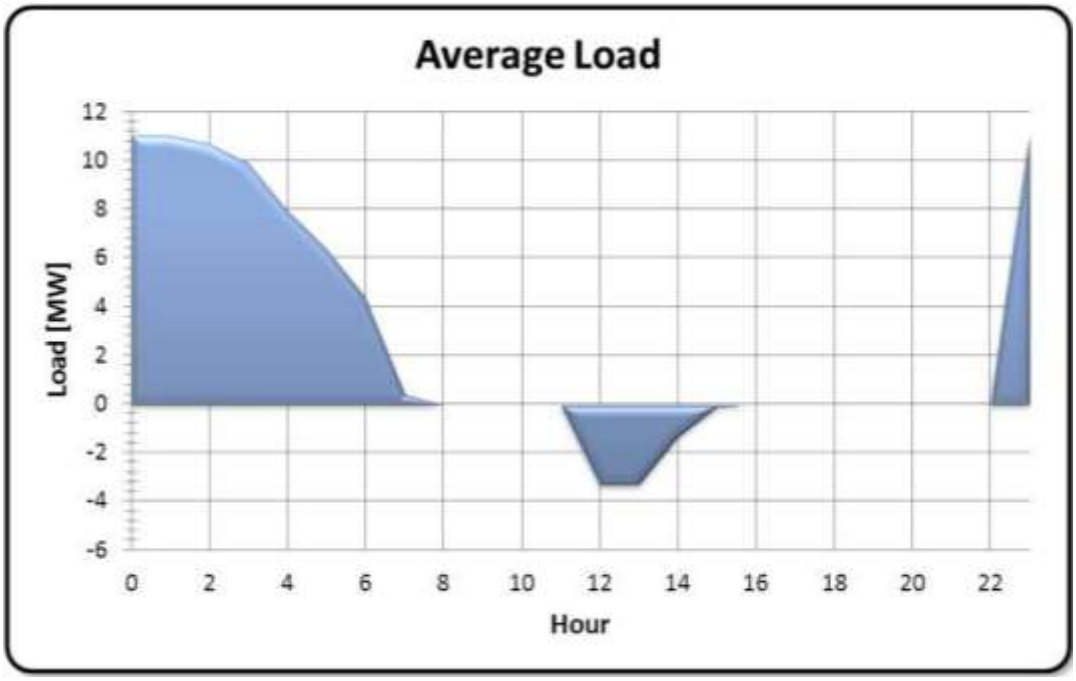


**Figure 345: Scenario 4 PHEV Load Demand**

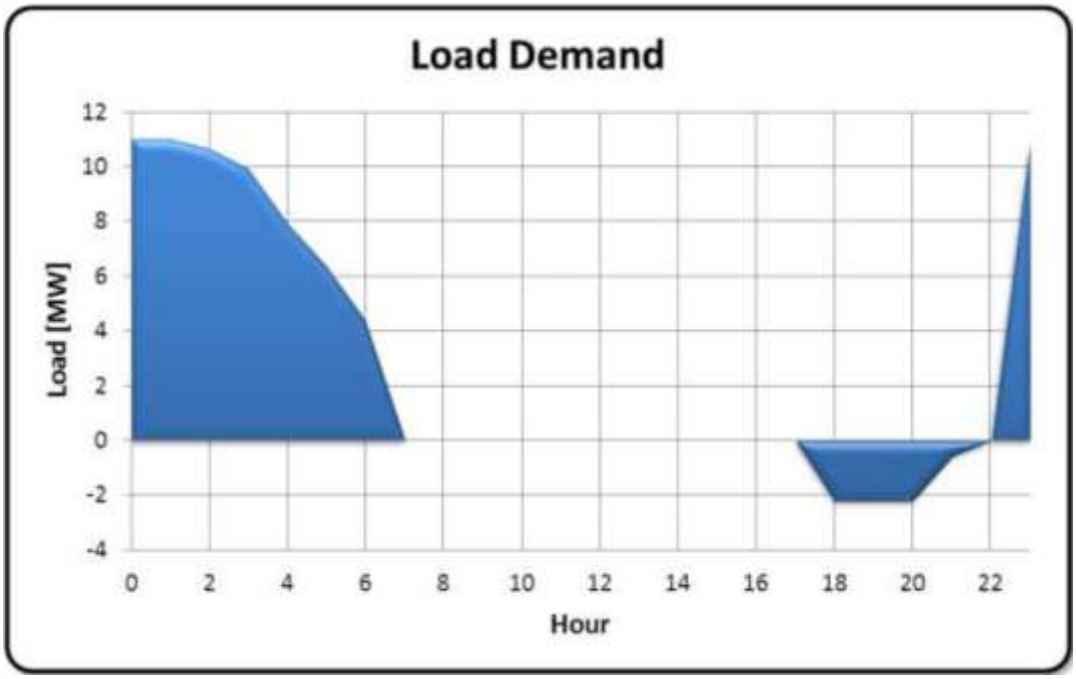


**Figure 346: Scenario 5 PHEV Load Demand**

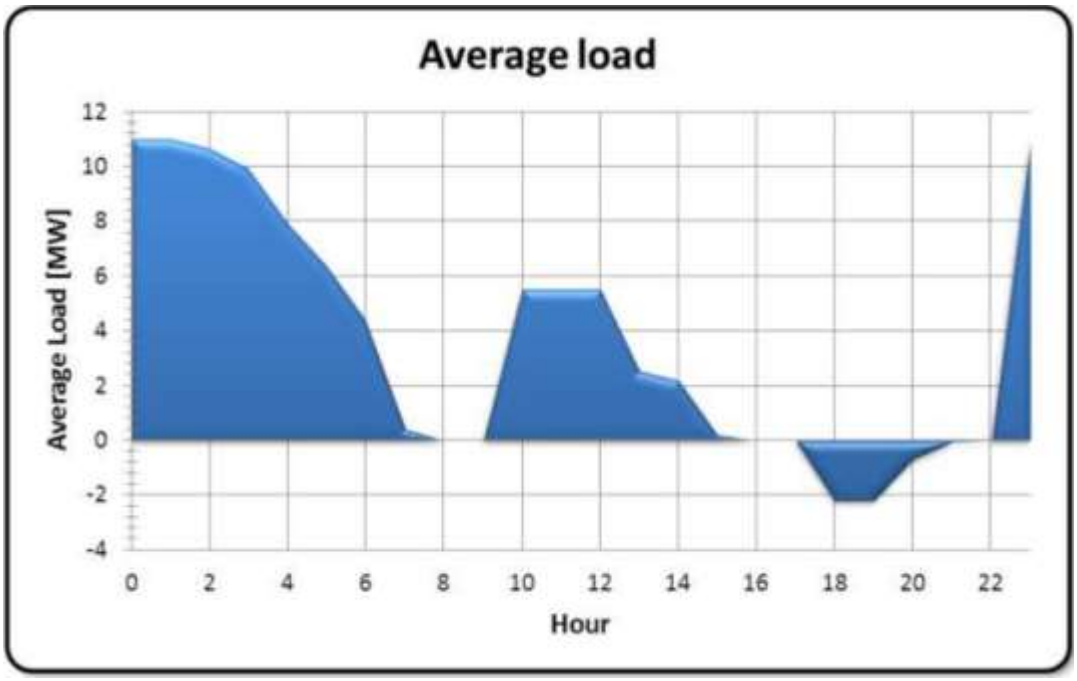


**Figure 347: Scenario 6 PHEV Load Demand**

It is shown that the cheapest way to generate 1MW after the 1st generator reaches 120MWand 2nd generator reaches 50 MW would be the generation from the 3rd generator. However, once the 3rd

generator reaches 30 MW generation and the 1st generator reaches 120 MW, the 2nd generator creates more power to satisfy the load demand (8:00am to 10:00am). In this analysis, we are going to focus on only the first part which is analyzing the peak demand.

The second scenario is the 6 bus system that does have only wind energy. The peak demand supplied by conventional units, which is between 8:00pm to 10:00pm, is delayed to 10:00pm to 1:00am because wind farm is added (The peak demand defines the amount greater than 140MW). The average load demand in an hour at this area is 154.6MW. In other word, adding wind energy relieves the stress to supply the power from the conventional units. From now on, the peak demand and the average load demand imply the values subtracting the amount supplied by wind energy. Besides, there is one more peak demand between 10:00am to 3:00 pm. The average load demand in an hour at this area is 151.2MW. The peak demand is reduced about 90MW which is 34.5% of the peak demand from the first scenario.

The third scenario has the same as peak demand as the second scenario. The first peak demand is between 10:00pm to 1:00am. The average load demand in an hour at this area is 161.9MW. The average load demand should be higher than the second scenario because we are starting to do G2V at night time. The second peak demand is between 10:00am to 3:00pm. The average load demand in an hour at this area is 151.2MW.

The first peak demand for the fourth scenario is between 10:00pm to 1:00am. The average load demand in an hour at this area is 161.9MW. The second peak demand is between 10:00am to 3:00pm. The average load demand in an hour at this area is 149.6MW. The reason for the decrease is because there is an afternoon V2G.

The first peak demand for the fifth scenario is between 10:00pm to 1:00am. The average load demand in an hour at this area is 161.9MW. The second peak demand is between 10:00am to 3:00pm. The average load demand in an hour at this area is 151.2MW. In this scenario, there is an evening V2G instead of afternoon V2G. Therefore, the average load demand is higher than the one from the fourth scenario.

The first peak demand sixth scenario is between 10:00pm to 1:00am. The average load demand in an hour at this area is 161.9MW. The second peak demand is between 10:00am to 3:00pm. The average load demand is 155.4MW. The reason for the increase is the afternoon V2G around 10:00am to 3:00pm.

In other word, by adding wind energy and PHEV, the peak demand have not been changed but it released the stress of the conventional units by 38.0% (comparing the first peak demand between scenario1 and scenario4).

Secondly, we are going to compare the total operational cost in each scenario and find the best scenario based on it. As you can see from Figure 348, the optimal operational cost dropped significantly when we added wind generation. No operational or installation cost for wind generation is assumed. In other words, wind generation acts like a free source so theoretically adding wind generation should reduce the operational cost. In the analyzed case, the total operational cost diminished by $37,590.35 which is

30.8% of the power generation without wind generation. The total power generation without wind and PHEV for one day is estimated to be 5308 MW. However, wind generation creates 1242.5 MW for one day which is 23.4% of total generation. Therefore, introducing 23.4% of wind generation reduced 30.8% of total operational cost.

As you can see from the Figure 349, the best scenario is the fourth scenario because it shows the least operational cost. The fourth scenario utilizes charging at night time (11pm ~ 7 am) and discharging at day time (12 pm ~ 3 pm). The total operational cost at this time is estimated as $85,953.03. The least efficient way of charging and discharging PHEVs is the fourth scenario. The sixth scenario utilizes charging at night time (11pm ~ 7am) and also day time (10 am ~ 3pm) and discharge during the late afternoon (6pm ~ 9pm). The total operation cost in this case is estimated as $86,681.53 which is $728.50 more expensive than the worst case. While this is a small difference between two cases, if the system is expanded to, a 150 bus system, there would be a significant difference between the two scenarios.

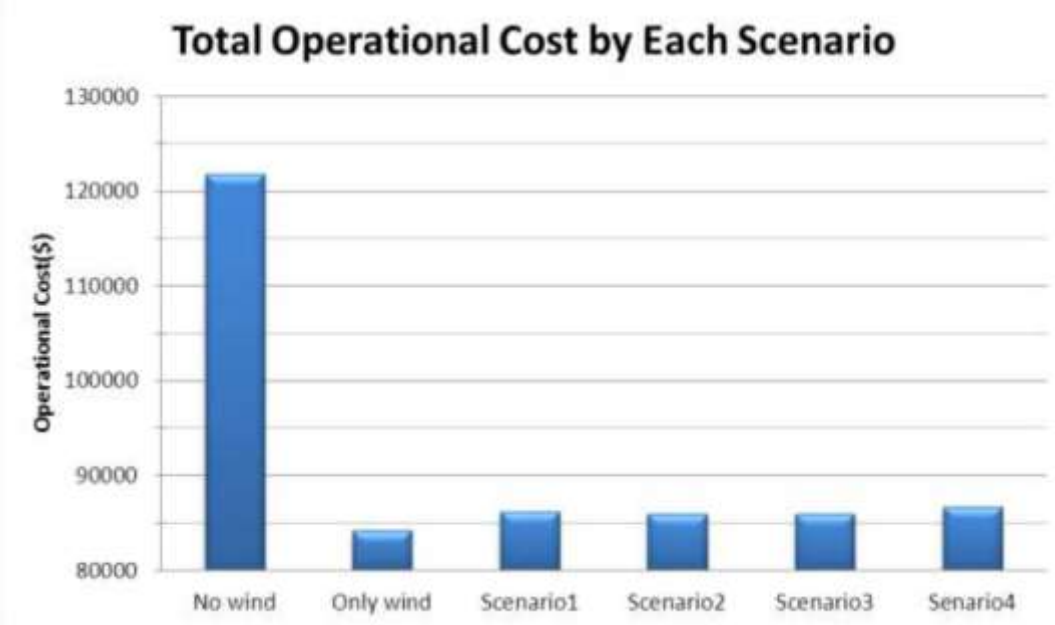


**Figure 348: Total operational cost.**

The fourth scenario utilizes charging at night time (11pm ~ 7 am) and discharging at day time (12 pm ~ 3 pm). The total operational cost at this time is estimated as $85,953.03. The least efficient way of charging and discharging PHEVs is the fourth scenario. The sixth scenario utilizes charging at night time (11pm ~ 7am) and also day time (10 am ~ 3pm) and discharge during the late afternoon (6pm ~ 9pm). The total operation cost in this case is estimated as $86,681.53 which is $728.50 more expensive than the worst case. While this is a small difference between two cases, if the system is expanded to, a 150 bus system, there would be a significant difference between the two scenarios.

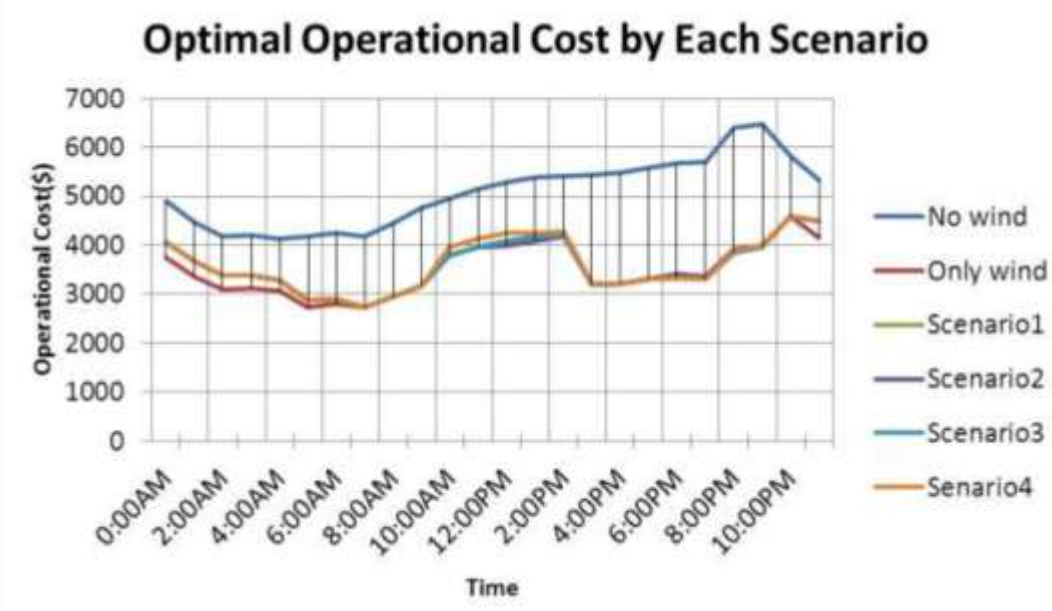


**Figure 349: Optimal operational cost.**

**Conclusions and Recommendations**

This IPRO team has researched the factors affecting the integration of renewable energy systems and PHEVs in the future. Wind power is expected to provide a 20% generation of all energy produced in the US and the introduction of PHEVs into the market will increase demand for electric power. Wind power was found to reduce the operational cost of the grid considerably, due to wind power's negligible operational cost relative to other power generation methods. There is the potential for reducing the operational cost of the grid by PHEVs being charged at night and utilizing the V2G feature during peak power demand on the grid. Our case simulations showed that the second scenario provided the optimal operational cost with respect to the charging times of the PHEVs. This scenario has the PHEVs utilizing charging at night time (11pm ~ 7 am) and V2G discharging at day time (12 pm ~ 3 pm), Our simulation may be improved in the future by including and/or simulating the following features:

- Simulation of more than 6 buses
- Operational cost of the PHEV batteries due to V2G (cycling)
- More scenarios of PHEV charging situations
- The feasibility of using PHEVs as an electric storage system to mitigate the natural inconsistencies of wind generated power can be investigated.

Our analysis was sufficient to provide us with answers to the question of how to integrate renewable energy systems and PHEVs.

### A3. Modeling of Building Integrated Wind Turbine Modules

One of the tasks of this DOE project was to "Engage Undergraduate Students in Wind Energy Research". IPRO 323 was developed in response to this task and is currently in its second semester with plans for continuing on into next year. The overall goal for the students enrolled in IPRO 323 is to develop a

methodology for designing and developing building-integrated wind turbine modules so that more urban environments will see wind power as a viable alternate energy source. The project plan that the students' enrolled in the course developed was to investigate designing a surface shape integrated onto the roof and/or facades of buildings to increase the power output of building mounted wind turbines. This goal of course requires the understanding of the fluid dynamics/aerodynamics of wind turbines and also the architectural, social, public, safety and environmental issues associated with integrating wind turbines into urban environments. Therefore the IPRO course will benefit from the experience and knowledge of students enrolled in various academic majors at IIT. Several undergraduate disciplines have representation on the team: Architecture, Mechanical Engineering, Aerospace Engineering, Materials Science and Engineering, Electrical Engineering and Architectural Engineering. This diverse mix of students working on one project provides a unique and interesting learning environment not typical of conventional undergraduate education.

**Organization and Approach**

Each semester the IPRO team was divided into several subdivisions in order to achieve the IPRO 323 goals. These subdivisions included research and development, wind tunnel testing, computational fluid dynamics, and architectural analysis. The research and development team investigated the best methods for conducting the research and analysis with specific emphasis on the development of the prototype and testing components. The wind tunnel team was responsible for conducting the experiments, as well as analyzing the data. The computational fluid dynamics team was in charge of working with the experimental team to help guide the testing parameters and analysis of the data. The architectural analysis team was responsible for determining whether the theoretical power output measurements were viable for an urban high-rise building as well as determining how the finished product would be integrated into the structure taking into account the social, public and safety issues.

The research team read through a number of articles in order to determine the best experimentation method. The discussion of testing an actual model scale wind turbine versus a simulated (i.e., actuator disc) wind turbine resulted in the conclusion that because of the time and cost limitations for IPRO 323, creating a real turbine and calculating the actual power output of the turbine would not be practical. It was decided that for the first semester or two the goal would be focused on the building shape rather than the wind turbine design. Therefore, the class decided to adopt an idea that other investigators have used which is to use a porous plate (actuator disc) to simulate a wind turbine. Aubrun, et al. [**100**] tested a 3-blade wind turbine by using a porous disc to investigate the wind turbine wake characteristics. The idea behind this 'mock turbine' is that it acts as a drag source and creates a pressure drop across the porous plate similar to the pressure drop across an actual spinning turbine.

The fluid mechanics/aerodynamics describing the behavior of wind turbines was researched with emphasis on the main mechanisms responsible for optimized power output. Articles describing the well accepted Betz' limit [**101**], proved very useful in the selection of the porous plate. It was decided that the students would simulate an "ideal wind turbine" from an aerodynamics point of view (as in the Betz' limit) by suitably choosing the porosity of the porous plate to provide the same pressure drop across the plate as one would see with an "ideal wind turbine".

After the porosity was determined, the students' focused on shaping the surface that the "wind turbine" would be placed upon in addition to determining what type of data would be acquired in the wind tunnel. The goal being: by shaping the surface (both upstream and/or downstream) of the wind turbine an increase in power output could be achieved. They determined that the most important measurements to take would be of the velocity and static pressures at several locations upstream and downstream of the porous plate in addition to several height locations off the surface. Measurements of velocity and pressure would allow the data analysis to be done to determine the effects of the surface shape on the theoretical power output of the wind turbine module.

Several hurdles had to be overcome by the students to get to the stage of taking any data. The experiments were designed and fabricated from scratch which included determining what equipment was necessary, how to use the equipment and fabrication of model support structures. Several pieces of instrumentation also required calibration in addition to the writing and testing of data acquisition software. The Computational Fluid Dynamics team used FLUENT to numerically analyze the fluid flow in the wind tunnel/porous plate configuration. This was seen as a complement to the experimental work with the goal being that the students would get the FLUENT code set up with the appropriate turbulence model along with appropriate boundary and initial conditions. With that in place the investigation of the optimum shape could proceed at a faster pace since changing the shape in the computational code and testing it would be faster than fabricating and testing several shapes in the wind tunnel. This would help narrow down the range of shapes to be tested in the wind tunnel.

The architectural analysis team had two major responsibilities involving the end product of this semester's IPRO. The first was to design a structure integrating the wind turbine in such a way that the final design would be aesthetically pleasing and it was also important for the architects to consider the material used to create the surface design, noise and safety implications among other factors. The interactions from turbine to turbine for designs incorporating several on one building must also be taken into account. With these in mind, they were able to design several three-dimensional renderings of possible ways the wind turbine modules could be incorporated in typical urban buildings.

The second goal of the architectural analysis team was to gather information in regards to energy and power consumption of average high-rise office buildings, and to relate these to the power output of the wind turbine module designed by the engineers. They were compared to the theoretical power output calculated from the experimental data in order to determine whether the proposed turbine design would be viable.

**Results from Students Work**

For the first several weeks the students' in the wind tunnel team as well as the research and development team secured, learned to use and calibrated the necessary instrumentation, software and equipment:

- DigiTec Temperature Sensor, Model: 5810, S/N: 65360672
- Validyne, Model: DP45-34, S/N: 43444. Demodulator, Model: CD15, S/N: 109352
- Engineering Corp Pressure Transducer, Model: DP103-10, S/N: 67548 10310N1S4D

- Keithley Autoranging Multimeter
- Pertec Peripheral Corp. Traverse System Motors, Model: PSX01 PWR.SUP, S/N: 2552
- National Instruments DAQ: 16-Input 16-bit, Model: USB 6221, S/N: E88779
- Dwyer Microtector Manometer, Model: 23-206
- M.V. Morkovin Wind Tunnel at Illinois Institute of Technology
- Pitot Tubes
    - Labview 8
    - Matlab 7.4.0 (R2007a)
    - Microsoft Excel

The porous (perforated) plate was the first component to be tested since the goal was to simulate an ideal wind turbine. In order to achieve the pressure drop associated with an ideal turbine the porosity of the plate needed to be tailored for that condition. Velocity measurements were taken at various streamwise (horizontal) and vertical locations behind the plate. Based on the Betz' limit [**101**] for an ideal wind turbine it is well known how the velocity and static pressure distributions should develop downstream of an ideal turbine.

Description of Betz' Limit

A wind turbine's ideal efficiency can be derived using Betz' Law. By analyzing the fluid dynamics through an "actuator disc" the limit for power output can be obtained using conservation of mass and momentum and Bernoulli's equation.

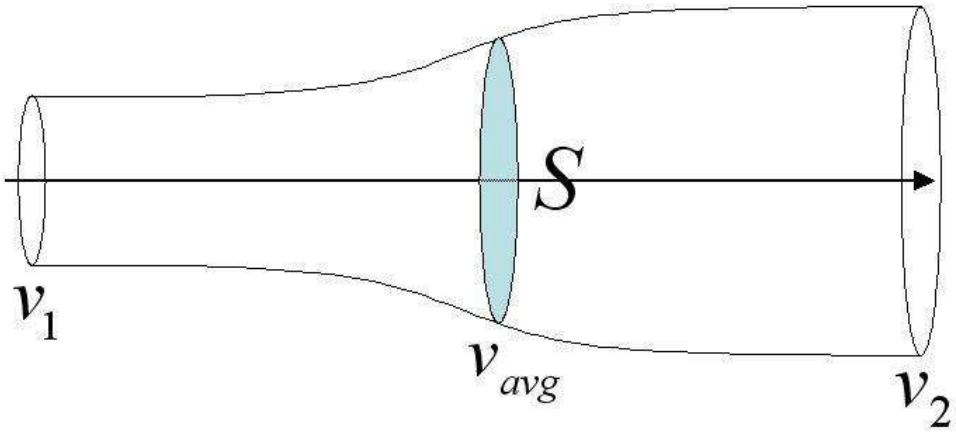


**Figure 350: Schematic representation of flow through an actuator disc.**

Bernoulli's equation can be applied to two points along a streamline for incompressible, steady and frictionless flow. For this case we can apply Bernoulli's equation from point 1 which is far upstream of the turbine where the velocity and pressure are $V_1$ and $P_1$ respectively, to a point just upstream of the disc where the velocity is some $V_{avg}$ and the pressure is $P_A$. We can again apply Bernoulli's equation from a point just downstream of the disc where the velocity and pressure are $V_{avg}$ and $P_B$ respectively, to

a point far downstream of the turbine where the velocity and pressure are $V_2$ and $P_2$ respectively. This analysis will result in giving us the pressure drop across the turbine which can then be related to the power output as:

$$Power = (P_A - P_B)A_t V_{avg} \quad \textbf{(98)}$$

where $A_t$ is the area of the rotor, $P_A$ is the pressure just before the rotor, $P_B$ is the pressure just after the rotor, and $V_{avg}$ is the average velocity at the rotor. From conservation of mass,

$$A_1 V_1 = A_t V_{avg} = A_2 V_2. \quad \textbf{(99)}$$

Using conservation of momentum and noting that $P_1 = P_2$, the force on the fluid caused by the rotor can be calculated as:

$$F = \dot{m}\Delta V = \rho A V(V_1 - V_2) = (P_A - P_B)A_t \quad \textbf{(100)}$$

Using Bernoulli's equation for the fluid flow before and after the rotor yields equations 4a and 4b respectively,

$$P_1 + \frac{1}{2}\rho V_1^2 = P_A + \frac{1}{2}\rho v_{avg}^2 \quad \textbf{(101)}$$

$$P_2 + \frac{1}{2}\rho V_2^2 = P_B + \frac{1}{2}\rho v_{avg}^2 \quad \textbf{(102)}$$

Combining equations (99) through (102) provides,

$$P_A - P_B = \frac{1}{2}\rho(v_1^2 - v_2^2) = \frac{\dot{m}}{A_t}(v_1 - v_2) = \rho v_{avg}(v_1 - v_2) \quad \textbf{(103)}$$

Therefore, it can be shown that the average velocity at the rotor is simply the arithmetic mean of the velocity far upstream and far downstream of the rotor.

$$V_{avg} = \frac{1}{2}(V_1 + V_2) \quad \textbf{(104)}$$

Finally, the efficiency can be given from the following equation:

$$\eta = \frac{Power}{\frac{1}{2}\rho A_t v_1^3} \quad \textbf{(105)}$$

Plotting the velocity ratio versus efficiency, results in :

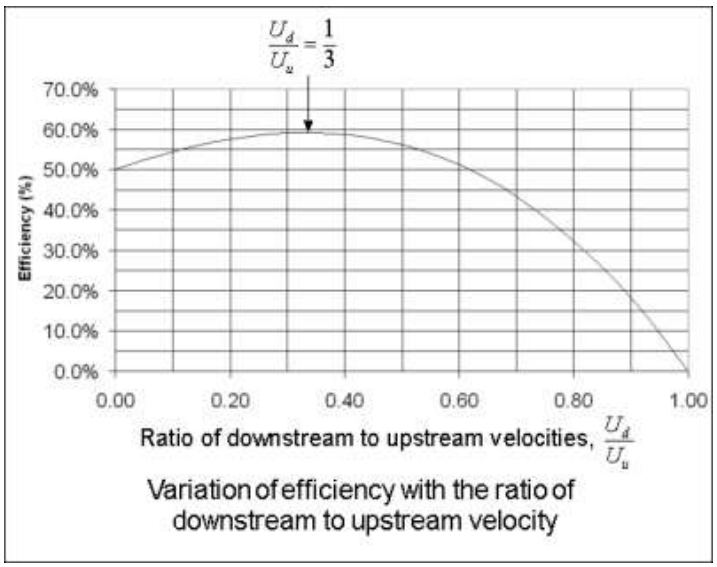


**Figure 351: Plot of velocity ratios versus efficiency**

(from http://www.wind-power-program.com/betz.htm)

It is apparent from this plot that the highest efficiency occurs when the lowest downstream velocity is a third of the free stream velocity before the rotor ($V_1$). This efficiency is calculated to be 59.3%.

Determining Plate Porosity

The next step for the wind tunnel team was to determine the porosity of the porous plate needed to simulate an ideal wind turbine. That is, what porosity will result in a $V_m/V_1 = 1/3$ where $V_m$ is the minimum downstream velocity which will be determined from wind tunnel tests? For a too porous of a plate the pressure drop would be too small ($V_m/V_1 > 1/3$) and would simulate a very inefficient turbine and conversely if the porous plate were too dense the pressure drop would be very large ($V_m/V_1 < 1/3$) and indicative of a wind turbine exceeding the Betz' limit. Therefore, the porosity of the plate was adjusted until the experimental measurements indicated that we had achieved the desired velocity and static pressure distributions close to those predicted with the Betz' theory. These results would then be compared with those for the cases where the surface shape was modified. Figure 352 is a photograph of the porous plate mounted in the test section of the wind tunnel. The direction of flow is from right to left and two Pitot-static tubes can be seen just downstream of the porous pate. The Pitot-static tubes provide for both pressure measurements and velocity measurements in the wind tunnel. The traverse mechanism is also seen in the photograph and for the results shown in Figure 353, one of the Pitot-static tubes was secured to the traverse mechanism in order to move the Pitot-static probe to various x and y locations with respect to the porous plate. The x direction is defined as the streamwise location with respect to the plate whereas the y location is the wall-normal (vertical) distance as measured from the wind tunnel floor. In Figure 353 the minimum value for the velocity is seen to occur around y ≈ .86 which indicates the centerline of the porous plate. The flow velocity increases away from the centerline and for large enough y locations the velocity would be approximately that of the free stream value. The

velocity is also a function of distance from the porous plate and is consistent with those from earlier investigations, see Castro [**102**].

**Figure 352: Photograph depicting porous plate set-up in wind tunnel**

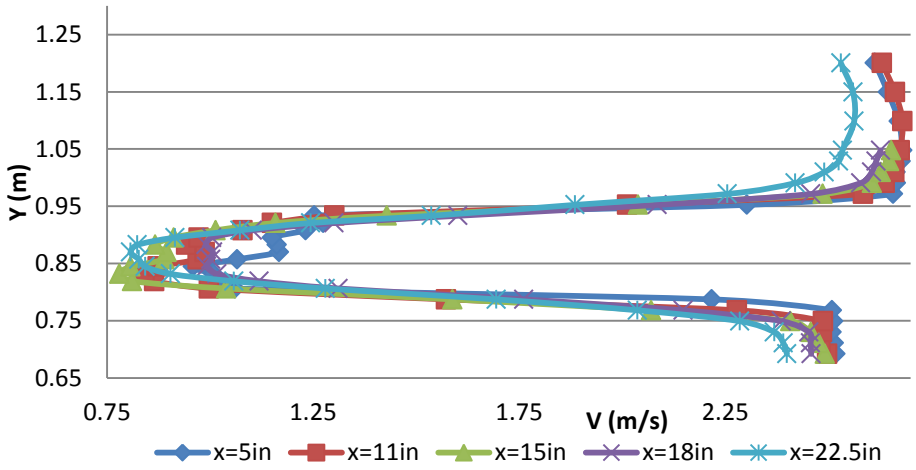


**Figure 353: Velocity profiles downstream of a porous plate for several streamwise and vertical locations.**

These velocity profiles were acquired for several mesh porosities and for several streamwise locations. $V_m$ is determined for each porosity by looking for the minimum value of the velocity on the centerline (y

≈ .86) as a function of streamwise location. The plot shown in Figure 354 is the value of the velocity on the centerline normalized with the far upstream velocity for a porous plate with a 62.3% porosity. This porosity was shown to provide the closest results to the Betz' limit for the range of plates investigated; namely, by plotting the velocity on the centerline (y ≈ 0.86m) normalized by the approach wind speed, $U_o$, as a function of x/c, where c is the chord length (height) of the porous plate, the lowest velocity reached downstream of the mesh is in the 1/3 range. The students' results compare well with previous published work done in the 70's on flow downstream of perforated plates by Castro [**102**].

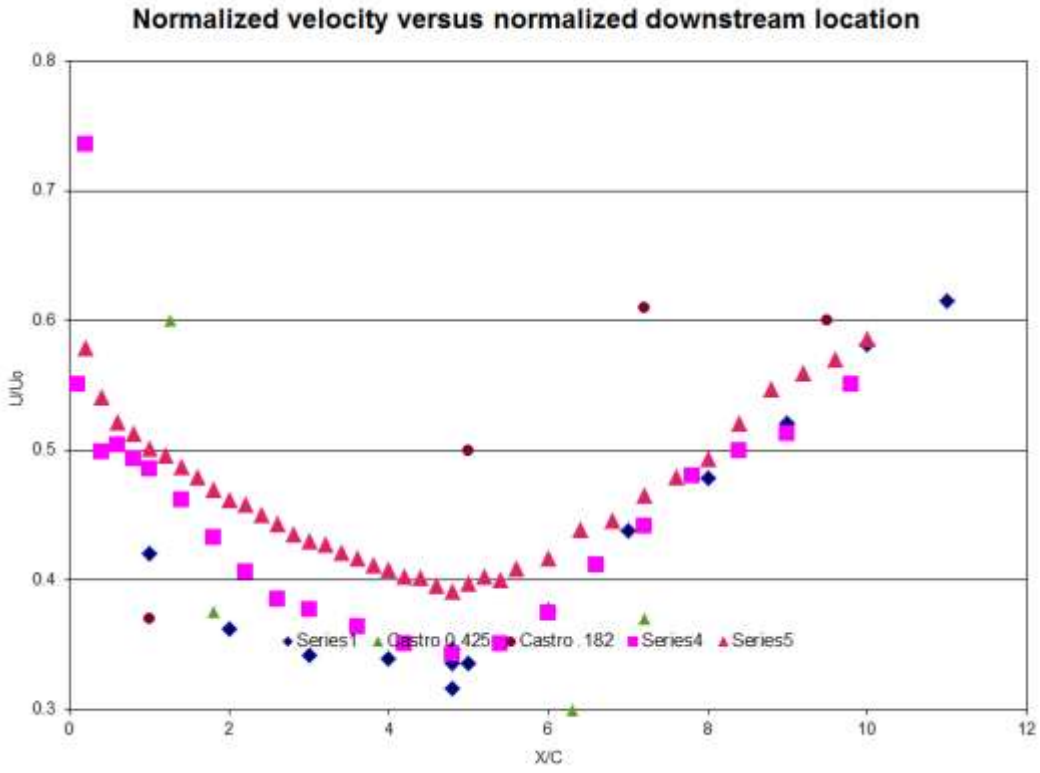


**Figure 354: Normalized Velocity as a function of normalized streamwise distance for a 62.3% porous plate.**

Surface Shape Modification

After the porosity was determined, the attention was directed on shaping the surface that the "wind turbine" would be placed upon with the goal being that by shaping the surface (both upstream and/or downstream) of the wind turbine an increase in power output could be achieved. For this experiment on the "ideal wind turbine" this change in power output would be measured by a change in static pressure across the turbine: $Power = \Delta P V_{avg} A_t$ where $V_{avg}$ is the flow speed, $A_t$ is the plate surface area and $\Delta P = (P_A - P_B)$. Figure 355 is a photograph of the first modified surface shape to be tested with the porous plate installed in the wind tunnel. The first shape tested was simply a Gaussian shape. It can be seen in Figure 355 that there is a Pitot-static tube on each side of the perforated plate facing the oncoming airflow. The actual fabricated shape can be seen, as well as the final perforated plate with the

correct size and porosity. Data were taken with the mesh at 1 inch above the centerline of the shape and at various locations downstream of the shape centerline. Those locations were 0 inches, 0.75 inches, 1 inch, and 5 inches as shown schematically in Figure 356.

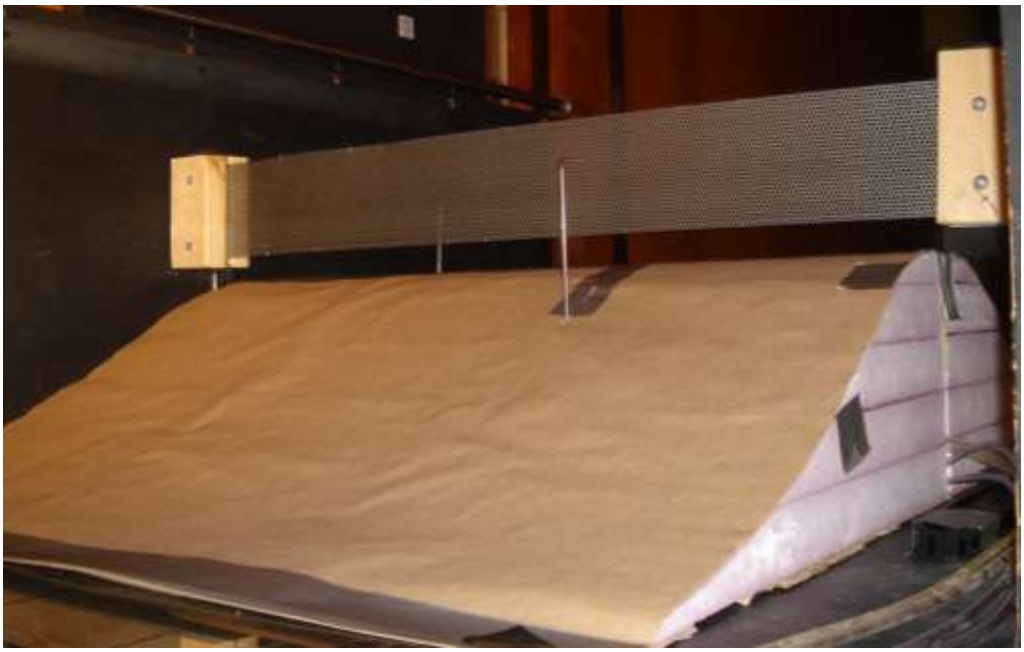

**Figure 355: Photograph of Porous plate and surface shape in wind tunnel.**

The $\Delta P$ was measured and the theoretical power was calculated for different flow speeds in the wind tunnel the various plate locations shown in Figure 356. The results are given below in Figure 357 where the power output is compared against the condition with a flat surface (no shape). The architectural analysis team was responsible for investigating power consumption levels in urban environments, determining how surface integrated wind modules could be integrated into architectural structures all while taking into account the social, public and safety issues. In addition rough cost estimates for implementing these structures into buildings was also performed by this group. Urban environments currently use over 66% of the world's energy. In the US, buildings represent 50% of the total national energy consumption and 77% of electricity use. It is also important to mention that 30% of energy production and 67.5% of all electrical energy is lost with current infrastructure, deeming them inefficient and wasteful [5].

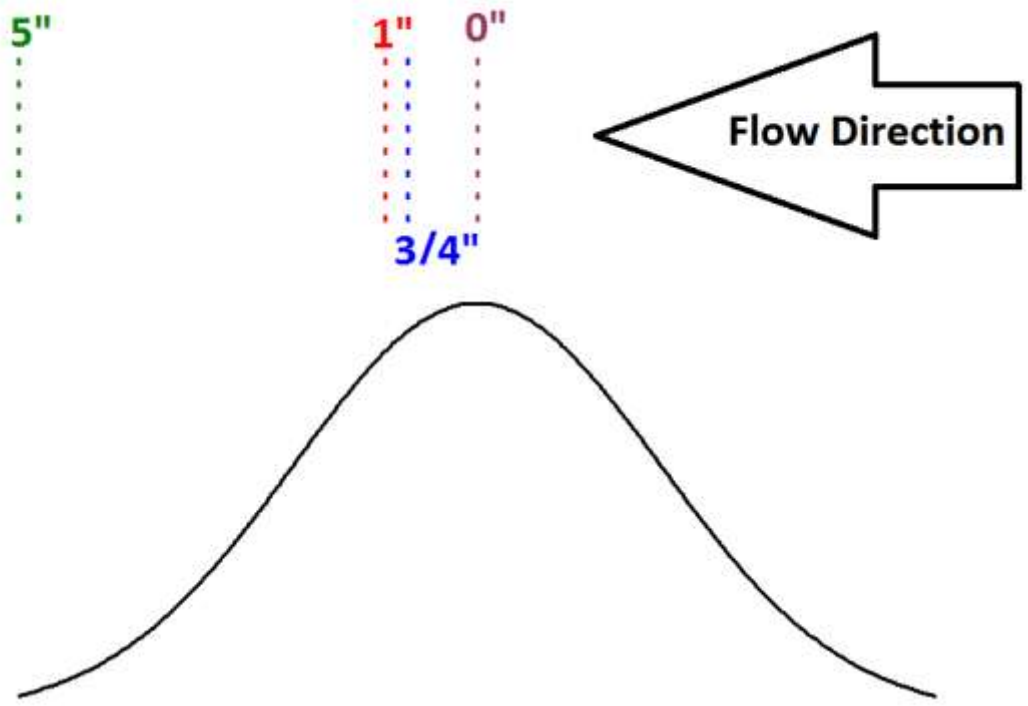


**Figure 356: Schematic illustrating several porous plate testing locations.**

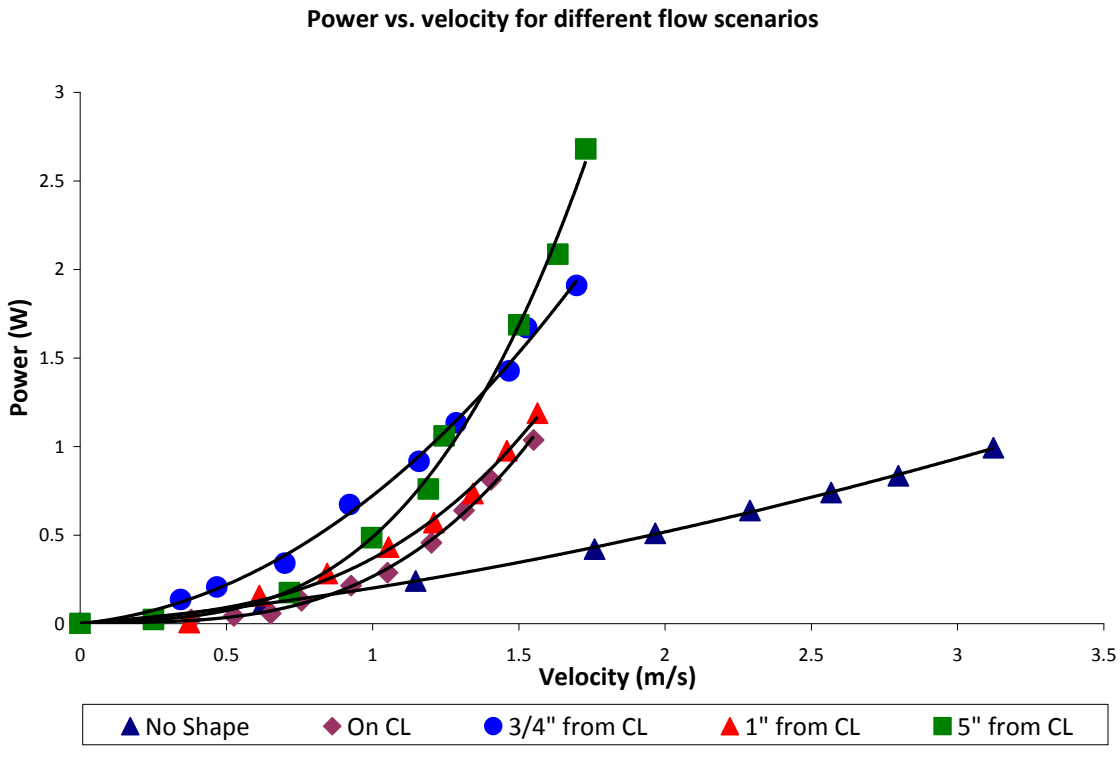


**Figure 357: Power output for various wind speeds and mesh locations.**

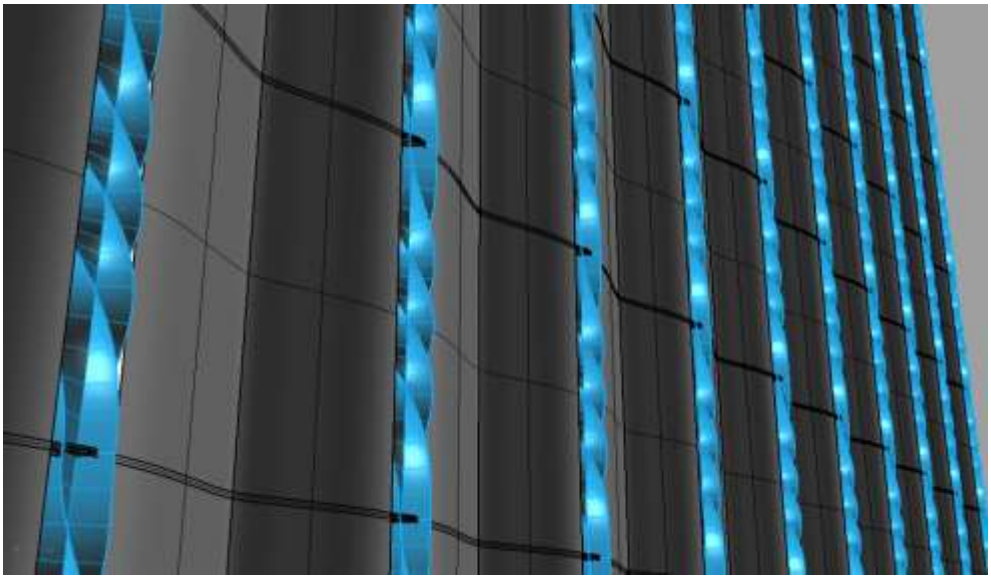

**Figure 358: Surface Design with helical turbines located at the center of each shape.**

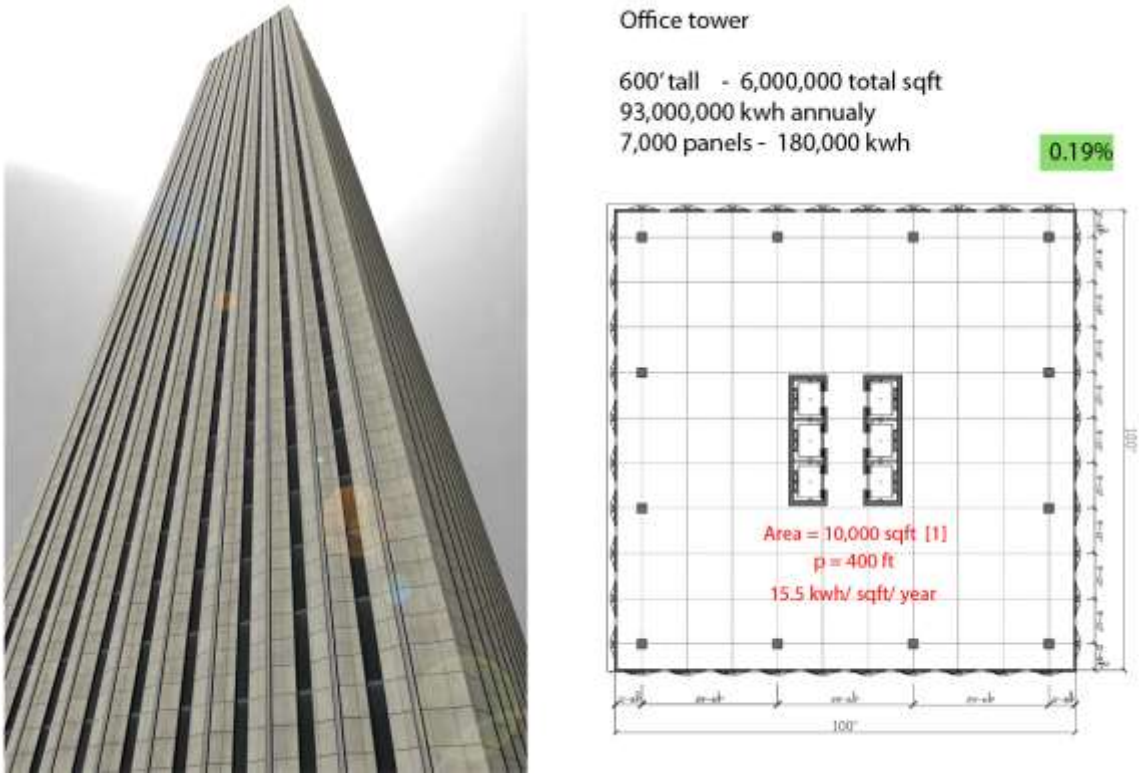


**Figure 359: Example of a high-rise building with the surface design implemented vertically along the sides of the building**

**Figure 360: Example of shorter buildings with the surface shape designed to cover the roof.**

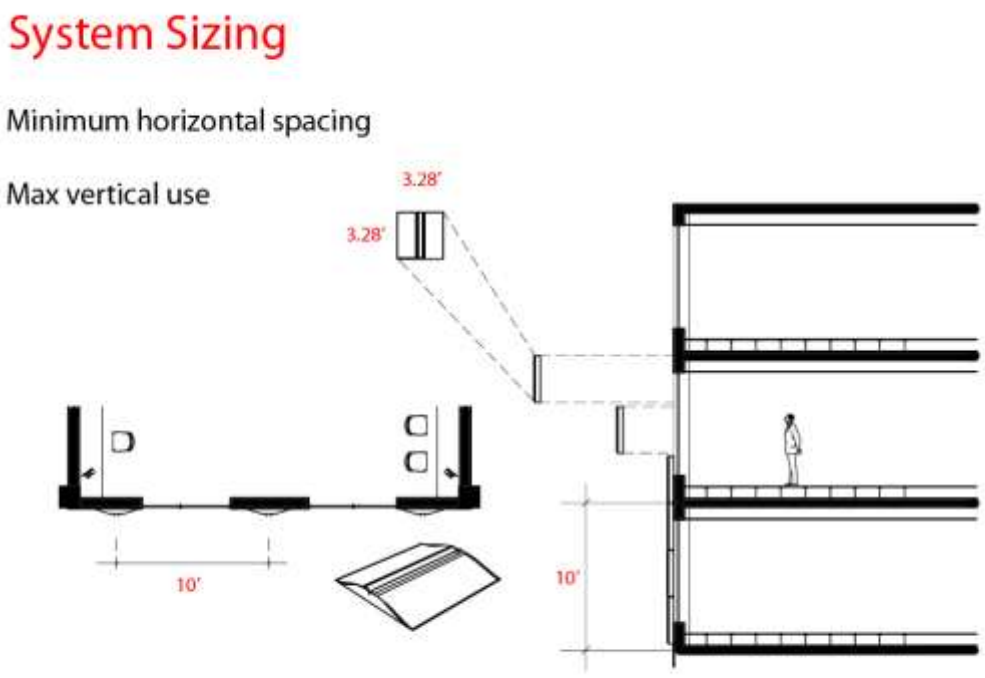


**Figure 361: A schematic of a building with the wind turbine surface design integrated onto the side.**

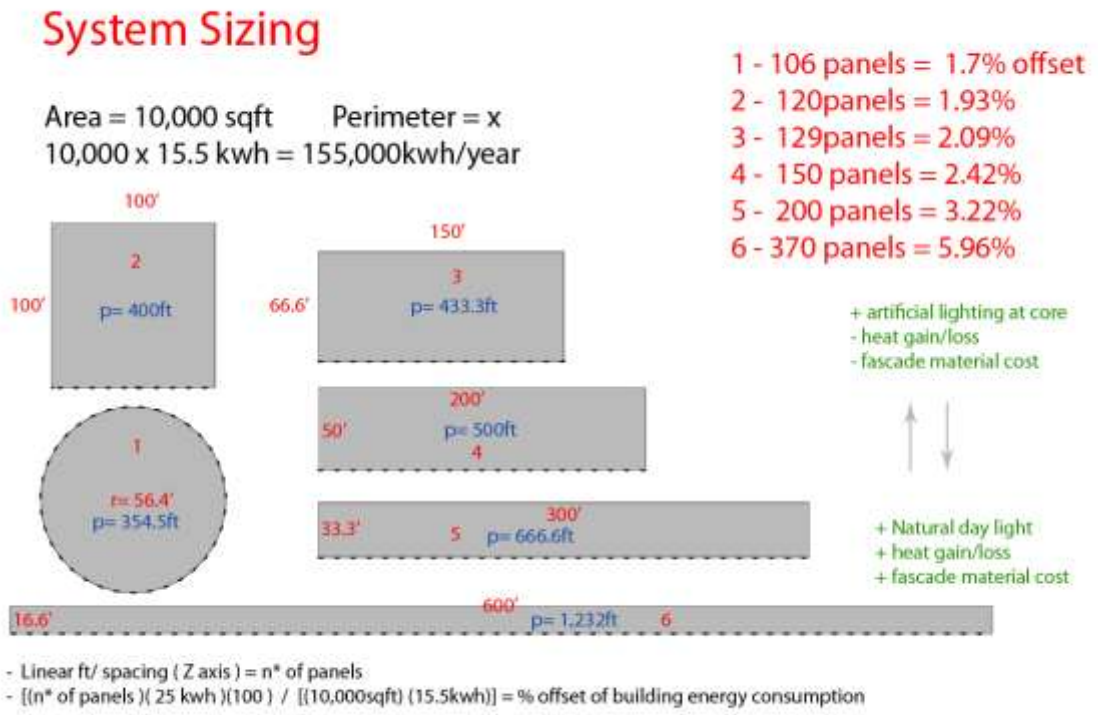


**Figure 362: An example of buildings with the same area and different perimeters.**

Studies indicate that urbanization causes an increase in $CO_2$ emissions as countries shift from using $CO_2$-neutral energy sources to $CO_2$-intensive energy sources in urban areas [6]. In addition to this, projections indicate that cities are likely to increase their share in global energy consumption to 73% by 2030 and 87% in the U.S. alone [**103**]. Some three-dimensional architectural renderings were created to visualize the surface of a building with surface integrated wind turbines and are shown below. An analysis of the surface area of building sides, sizing and spacing was done to determine the most efficient architectural set-up for the wind turbine modules. The Power consumption of typical urban buildings was researched, which was important in the architectural analysis to assess the percentage of power a series of surface mount wind turbines would produce for a typical urban building.

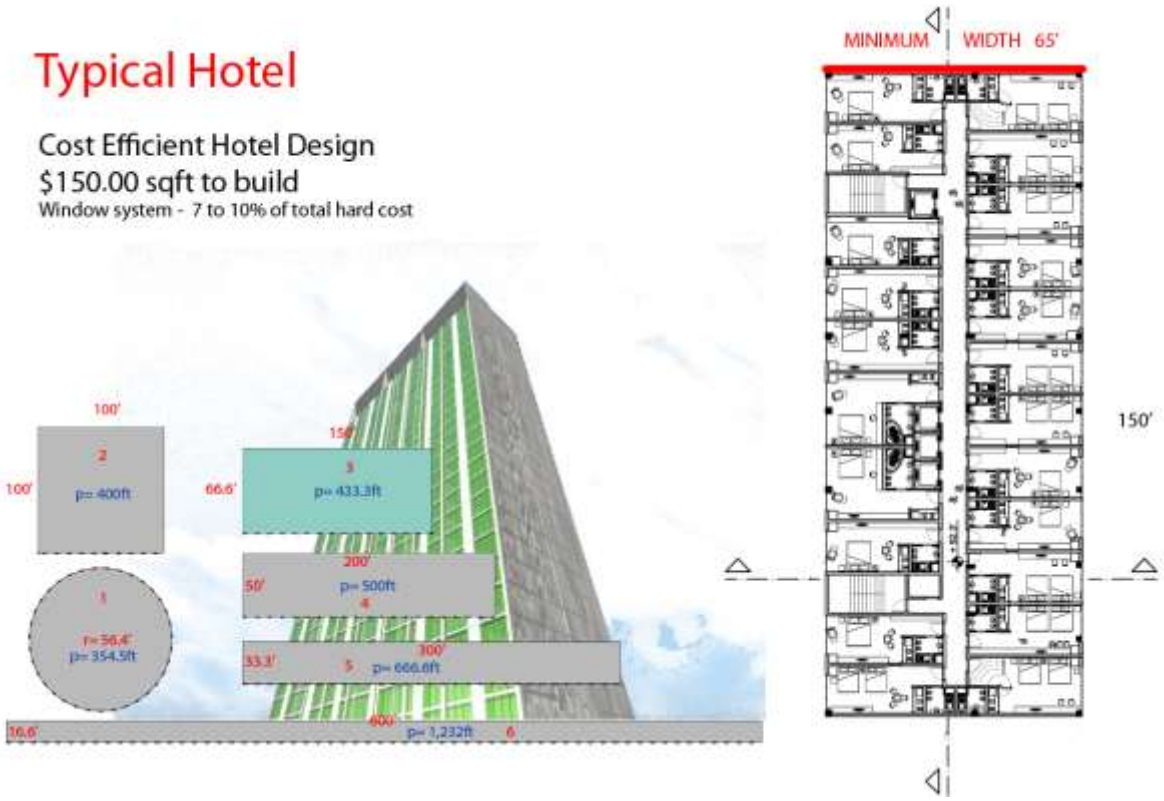


**Figure 363: Analysis of hotel design and building perimeter.**

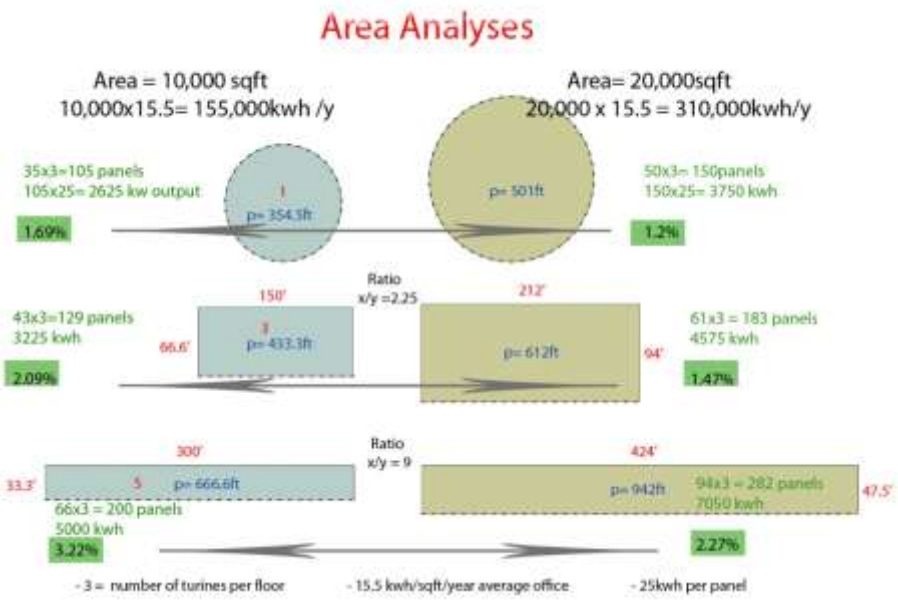


**Figure 364: Analysis of power consumption for different sized buildings.**

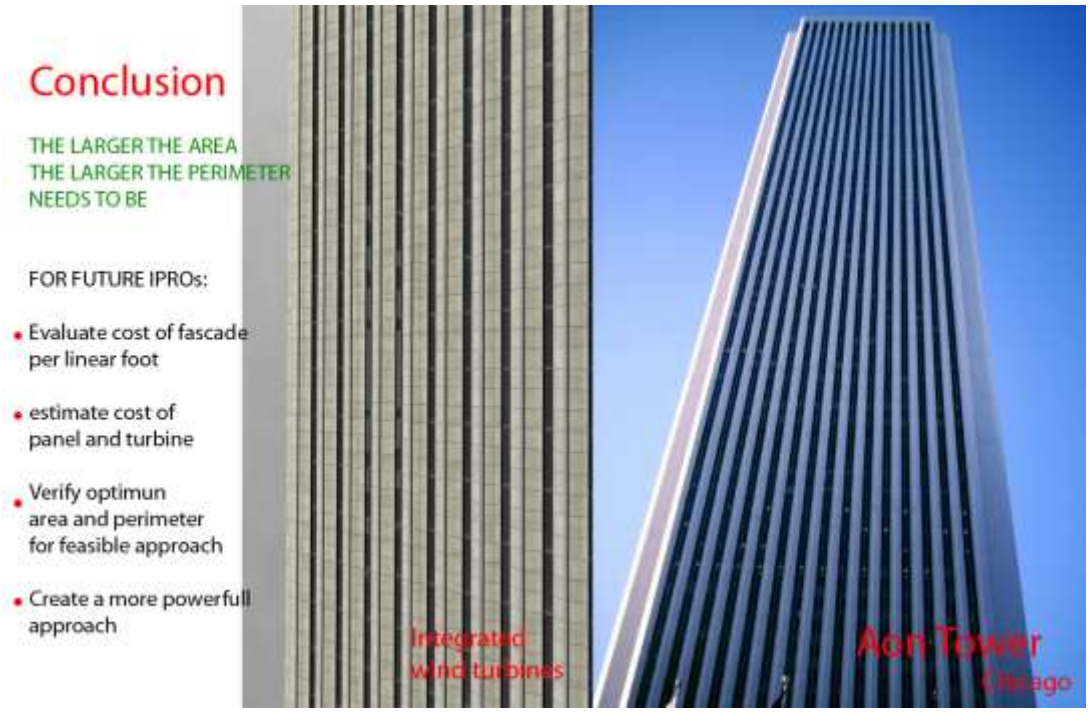


**Figure 365: Recommendations for future architectural research in IPRO 323.**

Another aspect the architectural research team had to consider was the power output at different wind speeds, and the average wind speeds in Chicago at different building heights. Calculations were made using the data gathered for the current surface design prototype and an ideal wind turbine, assuming that the ideal Betz' limit of 59.3% of the wind power was extracted and used by the turbines, and that the air density is 1.225 kg/m$^3$. The area used for the calculations was 0.137 m$^2$, which was the area of the perforated plate tested. The calculated values are as follows:

**Table 28: Annual power output for increasing wind speeds typical of urban environments.**

| Wind Speed (m/s) | Wind Speed (mi/hr) | Annual Power (kW-hr/m$^2$) | Annual Power (kW-hr) |
|---|---|---|---|
| 5 | 11.2 | 398 | 54.53 |
| 10 | 22.4 | 3182 | 435.9 |
| 15 | 33.6 | 10,740 | 1471 |

Another major task for the architecture team was to come up with estimations of how much it would cost to implement these structures onto urban buildings. After some research, estimated prices for fabricating one surface mount structure with a wind turbine are as follows:

- Tubular aluminum frame
  - Approx. 45' of ¾" sq. tubing $50
  - Welded $15
- Molded plastic upper $5

- Turbine body
  - Solid paddle $10
  - Solid savonious $20
  - Membrane paddle/savonious $30
- Magnetic generator $100
- Transformer $70
- Total $300

This cost estimates the price of only one component being implemented on a building; however, to produce useful energy, many of these structures must be implemented on the same building just as many horizontal axis wind turbines are installed in fields of wind farms.

**Conclusion and Future Work**

During the Spring 2011 semester, the students worked mainly on developing the methodology, setting up the experiments and investigating various aspects of incorporating wind energy into urban architectural structures. The data gathered showed promising results, in that there is a significant change in the pressure drop across an "ideal wind turbine" when the surface shape is modified.

During the Fall 2011 semester the students needed to move their experimental setup to a different wind tunnel test section which consumed approximately 3-4 weeks. For the remaining weeks, the main goal for the wind tunnel team is to test various surface shapes to determine which surface shape would optimize power output. The architectural team is further investigating various possibilities for incorporating these wind models into an urban environment and also is discussing with IIT facilities the possibility of placing an actual wind turbine model on the roof of IITRI.

With renewable energy becoming an increasingly desirable source, wind power is among the most sought after technologies at present. The development of wind turbines in rural areas has been steadily increasing in the past decades, but the overall goal of IPRO 323 is to develop a way to integrate efficient wind turbines into an urban environment where energy is most heavily consumed. With the help of engineers, architects, and industrialists, wind energy in large cities will become a common technology.

### A4. Capstone Senior Design Project at Southern Illinois University

This course is designed to teach senior level students about team approach to engineering projects. The students are expected to understand and analyze RFPs (Request for Proposals), identify tasks, develop team organization, and assignment of tasks. In addition as part of their work, they are required to have a work plan and time schedule. The projects must have: feasibility analysis, team approach in engineering projects, understanding and analyzing a request for proposals, identification of tasks, assignment of tasks and team organization, work plan and time scheduling, feasibility analysis and cost-benefit analysis, ethics and professionalism issues related to engineering projects in general and to the specific project assigned, team coordination and documentation of team member efforts, documentation of team communications and the team decision making processes, development, presentation and defense of the final proposal for the assigned project.

Each semester, a number of projects are posted and students are asked to pick one and submit a proposal for their choice of project. The following description of project was posted as an RFP for senior level students.

Create a Z-scale model of a 3-phase power generation and distribution system. This model will have the following areas: residential, commercial, industrial, coal-fired generation, and wind generation. This will be a dynamic model where the user can specify the real and reactive power demand from the residential, commercial, and industrial loads as analog inputs, the wind input from a fan, and the state of various power factor correcting capacitor banks. The system will respond by showing the real and reactive power generated by the coal fired power plant and the wind farm required to supply the specified loads. Additionally the model will report the current on each distribution line and the voltage at each end of each distribution line. The inputs from the user will be analog and the currents, voltages, and powers will be displayed as analog values. The values will be determined by a microprocessor using equations that describe the load flow of the power system.

The finished project will require:

- A set of power equations that describe the behavior of the system
- A set of appropriate limits for each input for each of the various loads
- A fan to use to simulate the wind and turn the wind turbine(s)
- An animated Z-scale model that shows light and/or action for the user selected demand for each load type
- A suitable way for the user to input the desired demands
- A suitable way to display the voltages and currents associated with the load flow on the lines
- A suitable way to display the power produced by the wind farm and the coal-fired plant
- A carrying case to transport the system

The objective of this project is to simulate a 3-phase power generation and distribution system to incorporate wind energy as a supplemental source. The system will be a portable Z-scale model on a scale of 1:220. This single-phase model will be used to demonstrate 3-phase power to an audience at conferences or high schools. This model will have the following areas: residential, commercial, industrial, coal-fired generation, and wind generation. This will be a dynamic model where the user can specify the real and reactive power demand from the residential, commercial, and industrial loads. The wind speed will utilize a controlled fan, and the power factor will be corrected by capacitor banks automatically by an SVC. The system will respond by showing the real and reactive power generated by the coal fired power plant and the wind farm required to supply the specified loads. Additionally the model will report the line current, power flows, bus voltage and power, and display their values. These values will be calculated by a microprocessor using power equations.

Description:

The power system display will be 2’ x 4’ in dimensions. The system for this project is composed of three main parts: power sources, control station, and the power loads. The system will be a five-bus system

utilizing relays and breakers. Figure 366 is the diagram of the control system. Figure 367 is a diagram of power system.

Power Sources: There are two types of power sources: the coal-fired generation station and the wind generation station. The coal-fired generation will be the main source of power for the town. Under windy conditions, the windmill will begin to produce power so that the coal plant's output will be decreased. A fan will be used to simulate high-wind and low-wind conditions. During low- or no- wind conditions, the town will run solely on power obtained from the coal plant. An inverter circuit will be connected to the windmill to invert the dc power to ac power. The system will function on 110V.

Control Station: The main component for the control station will be an Arduino microprocessor for switch control. Arduino is a tool for making computers that can sense and control more of the physical world than your desktop computer. It is a physical computing platform based on a simple microcontroller board, and a development environment for writing software for the board. It can be used to develop interactive objects, taking inputs from a variety of switches or sensors, and controlling a variety of lights, motors, and other physical outputs. The Arduino programming language is an implementation of Wiring, a similar physical computing platform, which is based on the Processing multimedia programming environment. There are many reasons why Arduino is preferable over other microcontroller devices:

- Inexpensive: Arduino boards are relatively inexpensive compared to other microcontroller platforms. The least expensive version of the Arduino module can be assembled by hand, and even the pre-assembled Arduino modules cost less than $50.
- Cross-platform: The Arduino software runs on Windows, Macintosh OSX, and Linux operating systems. Most microcontroller systems are limited to Windows.
- Simple programming environment: The Arduino programming environment is easy to use.
- Open source and extensible software and hardware: The Arduino software is published as open source tools and the language can be expanded through C++ libraries. Hence, people wanting to understand the technical details can make the leap from Arduino to the AVR C programming language on which it's based.

The user will utilize a laptop/tablet to input values and limits to the power system model and the outputs will be displayed on Matlab/Simulink graphical user interface (GUI). The power system simulation involves modeling power generation equipment, planning the integration of power plants onto the electric grid, and performing generator control system parameter estimation. MATLAB and Simulink will be used to perform critical power system simulation and optimization tasks such as simulating performance against grid code, ensuring production goals are met, and automating control system parameter estimation to meet regulatory requirements.

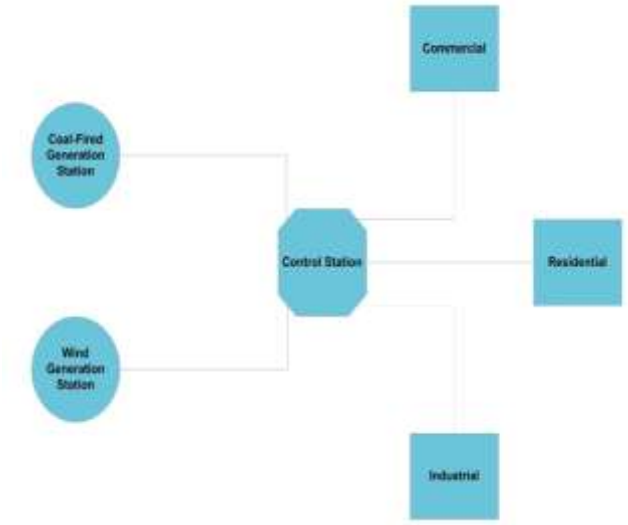


**Figure 366: Control System Diagram**

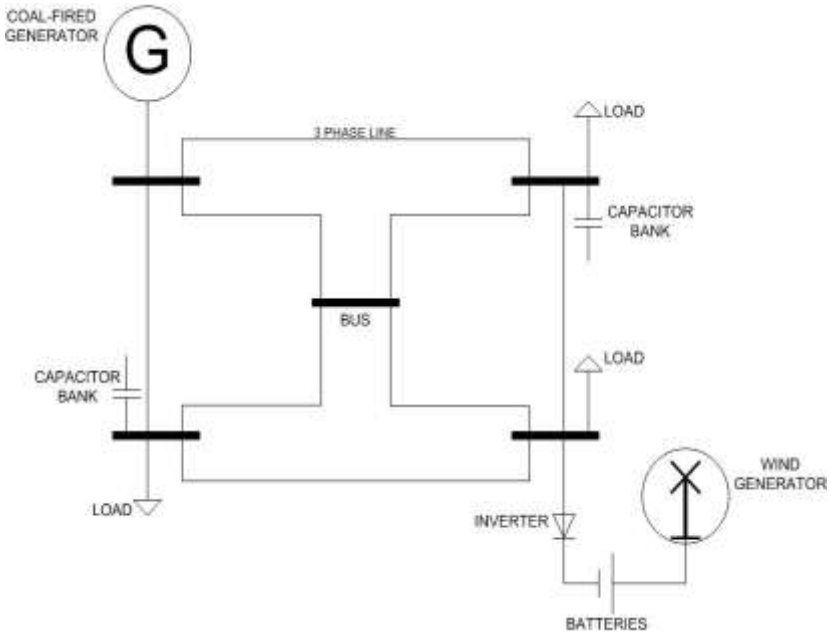


**Figure 367: Power System Diagram**

A Simulink Support Package for Arduino will be used to create an application that will run autonomously on the Arduino board. We will simulate and visualize our application on the host computer. This will allow us to communicate with Simulink on the host computer for testing, and read from and write to the Arduino's analog and digital I/O channels.

Power Loads: There will be three types of loads: residential, commercial, and manufacturing. The residential will operate on real power (large resistance and low induction). A capacitor bank will be used to increase the power factor. No substations or transformers will be used.

### A5. Wind Energy Research Course at Southern Illinois University

This course which is delivered during the summer has been redesigned recently to introduce the concept of Clean Energy Resources. The course is not restricted to ECE students and has been very popular between all students from different disciplines. Upon completion of this course students are supposed to be able to:

- Understand the energy supply and demand patterns for the United States and the world. Calculate energy consumption based on historic data, and future consumption based on past and predicted growth rates. Know the time until the reserve is depleted.
- Understand the basic laws and the role of all clean resources of energy, such as, wind, solar, hydro, oceanic, tidal, fuel cell, waste, and clean coal technology.
- Appreciate the social and economic issues, including public acceptance and economics of all alternative energy sources. Appreciate the role of government regulations and world events on energy utilization.
- Research and investigate issues related to energy resources of a specific energy source.

### A6. Add Wind Energy Component to Traditional Course at Southern Illinois University

Course description of ECE-456 Embedded Control and Mechatronics lectures: Introduction to mechatronic systems, systems modeling and simulation, sensors and actuators, real-time interfacing, DSPs and micro-controllers, analysis of sampled-data systems, z-transform, digital control design techniques, emulation method, direct method, industrial applications.

This course is delivered once a year, in spring semester. It has been recently redesigned to introduce model-based control design techniques for embedded mechatronic systems using microcontrollers and Mathworks toolboxes, and has been offered twice a year so far. The course is offered to ECE senior undergraduate and graduate students. However, it is also open to students with appropriate background from other disciplines.

In the redesigned course, a number of recorded webinars from Mathworks, on the subject of modeling and control of wind turbines, have been presented in the lectures to expose the students to wind energy as an alternative energy source and to explore the techniques for modeling and control of turbines for harvesting this energy. The webinars include:

- Modeling a Wind Turbine Using MathWorks Tools, 53:00 minutes
- Designing Pitch and Yaw Actuators for Wind Turbines, 36:00 minutes
- Determining Mechanical Loads for Wind Turbines, 34:00 minutes
- Designing Control Systems for Wind Turbines, 34:00 minutes

The integration of webinars in some of the class lecture has been received well by the students.

### *B. Develop Graduate Courses in Wind Energy*

#### B1. Elements of Sustainable Energy at Illinois Institute of Technology

This course covers cross-disciplinary subjects on sustainable energy that relate to energy generation, transmission, distribution, and delivery as well as theories, technologies, design, policies, and integration of sustainable energy. Topics include wind energy, solar energy, biomass, hydro, nuclear energy, and ocean energy. Focus will be on the integration of sustainable energy into the electric power grid, the impact of sustainable energy on electricity market operation, and the environmental impact of sustainable energy. The syllabus of this course is as follows.

#### B2. Elements of Smart Grid at Illinois Institute of Technology

This course covers cross-disciplinary subjects on smart grid that relates to energy generation, transmission, distribution, and delivery as well as theories, technologies, design, policies, and implementation of smart grid. Topics include: smart sensing, communication, and control in energy systems; advanced metering infrastructure; energy management in buildings and home automation; smart grid applications to plug-in vehicles and low-carbon transportation alternatives; cyber and physical security systems; microgrids and distributed energy resources; demand response and real-time pricing; and intelligent and outage management systems. The syllabus of this course is as follows.

#### B3. Wind Energy Power Systems at Southern Illinois University

This course, which is in the area of wind energy (wind turbine control, wind power generation, smart grid, etc.), has been developed and is being offered as part of the ECE Department Curriculum at graduate level. The catalog description of the course is as follows: “The course introduces graduate students to advanced configurations of wind energy power systems with an in-depth treatment of their control and protection. Wind speed and power relations, basic design of wind energy power systems, synchronous and induction generators, power inverters, generator drives-control modes, interface with the power grid-system modeling, stability, control and protection.” The syllabus of this course is as follows.

**ECE 580 – Elements of Sustainable Energy, Fall 2010**

**Class Meetings**: 6:25-9:05 PM, Tuesday; Location: Wishnick Hall 115

**Instructor**: Zuyi Li, PHD; Office: Room 223, Siegel Hall; Phone: (312) 567-5259; E-mail: lizu@iit.edu

**Office hours**: 3-5PM, Tuesday, or by appointment.

**Textbook**: No textbook is required

**References**

- Gilbert Masters, Renewable and Efficient Electric Power Systems, Wiley, 2004.
- Leon Freris and David Infield, Renewable Energy in Power Systems, Wiley, 2008.
- U.S. Department of Energy, 20% Wind Energy by 2030, 2008.
- Selected papers from the IEEE and other journal publications and conference proceedings.

**Grading**

Homework: 50%

Exam: 20%

Research Paper: 30%

The exam is open-book and open-notes.

A: [85, 100]

B: [70, 85)

C: [60, 70)

E: [0, 60)

**Course Schedules (subject to change)**

| | | |
|---|---|---|
| Week 1 | August 24 | Introduction to Sustainable Energy |
| Week 2 | August 31 | Renewable Energy Technologies |
| Week 3 | September 7 | Variability of Renewable Energy |
| Week 4 | September 14 | Operational Issues of Renewable Energy (1) |
| Week 5 | September 21 | Operational Issues of Renewable Energy (2) |
| Week 6 | September 28 | Operational Issues of Renewable Energy (3) |
| Week 7 | October 5 | Planning Issues of Renewable Energy (1) |
| Week 8 | October 12 | Planning Issues of Renewable Energy (2) |
| Week 9 | October 19 | Planning Issues of Renewable Energy (3) |
| Week 10 | October 26 | **Exam** |
| Week 11 | November 2 | Other Issues Related to Sustainable Energy (1) |
| Week 12 | November 9 | Other Issues Related to Sustainable Energy (2) |
| Week 13 | November 16 | Other Issues Related to Sustainable Energy (3)<br>Presentation of Research Paper (1) |
| Week 14 | November 23 | Presentation of Research Paper (2) |
| Week 15 | November 30 | Presentation of Research Paper (3) |
| Week 16 | Final Exam Week | Research Paper Due |

**ECE 581 – Elements of Smart Grid, Fall 2010**

**Class**: W-F 10:00- 11:15 am; Location: PH 131

**Instructor**: Professor Mohammad Shahidehpour, 222 SH, (312) 567-5737, ms@iit.edu

**Office Hours**: W and F 2-3 pm (or by appointment)

**Grading**: HW: 30%, Class participation: 10%, Midterm exam: 25%, Final: 35%

Homework Assignments: Students must review the power point slides before attending the lecture. I will distribute eight technical papers throughout the semester. Students are required to summarize each paper and write a review on the paper within two weeks. Midterm and final exams will include questions on class presentations and the technical papers. Exams will be open book.

**Course Schedules**

August 25 Mohammad Shahidehpour Professor, IIT
August 27 Steve Blume President, Applied Professional Training
September 1 Mohammad Shahidehpour Professor, IIT
September 3 Christian Herzog President, Software Technologies Group
September 8 John Kelly President, IPS Corporation
September 10 Al Stevens Director, S&C Electric Company
September 15 Ken Zduneck Professor, IIT
September 17 Tony Metke Distinguished Member of Technical Staff, Motorola
September 22 Kui Ren Professor, IIT
September 24 Jim Gagnard President, Smart Signal
September 29 Terry Schuster Director, Energy Connect
September 30 Mohammad Shahidehpour Wind Energy Conference
October 1 Mohammad Shahidehpour Perfect Power Presentation
October 6 Robert Holz Director, Smart Lab
October 8 Tom Hulsebosch West Monroe Partners
October 13 Alireza Khaligh Professor, IIT
October 15 Joshua Milberg Deputy Commissioner, City of Chicago
October 20 Ali Emadi Professor, IIT
October 22 Midterm Exam Midterm Exam
October 27 Paul McCoy President, TransElect
October 29 Tim Stojka CEO, Fast Heat
November 3 Yang Xu Professor, IIT
November 5 Terence Donnelly Senior VP, ComEd
November 10 Mohammad Shahidehpour Professor, IIT
November 12 Mark Pruitt Director, Illinois Power Agency
November 17 Kevin Dennis VP, ZBB Energy
November 19 Tom Overbye Professor, University of Illinois
December 1 Farrokh Rahimi VP, Open Access Technology International
December 3 Mohammad Shahidehpour Professor, IIT
Final Exam

**ECE 5813 Wind Energy Power Systems, Spring 2011**

**Instructor**: C.J. Hatziadoniu, Professor: ENGR-E221; (618) 453-7036; hatz@siu.edu.

**Office Hours**: TR 10:00-11:30.

**Lectures**: TR 03:35-04:50 at ENGR-A0210.

**Objectives**: To introduce graduate students to the principles of electric power generation from the wind and to present issues related to the planning, design and control and protection of a wind generation system.

**Description**: Planning of wind farms, mechanical component design, electrical component design, wind generator to network interface, control and protection of wind generators.

**Text**: Grid Integration of Wind Energy Conversion Systems, 2nd Edition, by Siegfried Heier, translation by Rachel Waddington, Willey and Sons. ISBN: 978-0-470-86899-7.

**Reference**: Wind and Solar Power Systems, by Mukund R. Patel, CRC Press, 1999, ISBN 0-8493-1605-7. IEEE and IET Transactions, Class notes.

**Class work**: Three design projects.

**Grading**: Letter grade assignment is done according to the rule, A>=90>B>=80>C>=70>D>=60>F.

**Topic by Lecture** (with the corresponding text/reference book chapters) based on 75-min lectures:

1. Wind energy power plants (Chapter 1/1, 2 lectures).
2. Wind energy planning and economics (Chapter 6/(2,4,15,16), 6 lectures);
3. Power extraction from wind and energy conversion, Wind turbines, basic mechanical system design (Chapter 2/5, 4 lectures).
4. Synchronous and induction generators (Chapter 3/6, 5 lectures).
5. Power electronic converters and drive systems (Chapter 4/(7,11), notes, 4 lectures).
6. Grid-connected generators-grid interface; control and protection (Chapter 4/13, 5 lectures);
7. Generator monitoring and supervisory control, interactions with the power grid (Chapter 5, 4 lectures).
8. Examples of practical systems and bench marks (2 lectures).

### *C. Develop Professional Training Courses in Wind Energy*

A Short Course on Wind Energy Technology, Interconnection and Integration

Wind power is an abundant, widely distributed energy resource that has zero fuel cost, zero emissions and zero water use. Wind power is the fastest growing form of generation in the world today, growing worldwide at the rate of 22.5% more than in 2009. Today, there is over 40.2 GW of wind capacity installed in the US, and over 194.4 GW of total wind capacity installed worldwide. American wind power is a mainstream electricity generation source and has been responsible for 35 percent of all new electric generating capacity over the last four years-more than coal and nuclear combined. In U.S. 38 states now have utility-scale wind projects, and 14 states have now installed more than 1,000 MW of wind power.

Wind turbine technology evolved remarkably over the past 20 years. The newer turbines have increased output and reduced generation costs with tall towers and longer blades. The newer machines also has better availability factor than that of coal and nuclear plants. Wind energy is one of the lowest priced renewable energy technologies available today, costing between 4 and 6 cents per kilowatt-hour. Moreover, a decline in the prices of wind turbines was observed which was due to (1) improved turbine technology, as witnessed by the recent and continued growth in average hub heights and rotor diameters, and (2) favorable terms for turbine purchasers, including reduced turbine delivery lead times, lesser need for large frame-agreement orders, initial operations and maintenance (O&M) contract durations that have increased from an average of 2-5 to 5-10 years, improved warranty terms, and more-stringent performance guarantees.

Despite growing demand for wind energy, the present technology still present significant challenges. Wind's challenges are largely related to its variable nature which can change by the season, day, hour and minute. For electricity grid operators the variability of wind, sometimes too much wind is blowing and at others too little, makes it difficult to integrate wind into a grid that was not designed for fluctuations.

Wind technology behaves differently than the conventional generating technologies and therefore in order to properly study and evaluate the impact of wind on power systems it is essential to understand its characteristics. This short course will provide an introduction to the underlying technology of wind turbine generators and wind power plants, how they are modeled for power system analysis purposes for planning and operating studies, and an introduction to using actual models in simulation programs.

This course is intended to provide the necessary background for engineers and researchers by addressing various aspects of interconnecting wind power plants into electric power systems. The study course is designed to provide knowledge on the state-of-the-art of wind-technology and wind-integration related issues.

The study course will mainly discuss insights on dealing with high wind power penetration levels in North America networks. In addition, a brief summary on the European wind energy performance is also presented.

This course is targeted towards power systems engineering and management personnel from utilities, RTOs, ISOs, and ITCs as well as consultants, manufacturers and developers involved with the evaluation and planning of the interconnection and operation of new wind plants. The students and professors who are working in the field of wind energy and technology will also benefit from this study course.

The wind study course is divided in 11 sessions which will be covered in 3 days. The sessions will begin at 10.00 AM each day. The duration of each session will be 45 minutes. At the end of each day attendees will be given an opportunity to raise any topics for discussion. The Course Outline is as follows.

**Day 1: Introduction to Wind Energy and Technology**

| | |
|---|---|
| 10.00 AM to 10.45 AM | Session 1: Wind Energy Outlook in 2010<br>• Growth of wind energy, market barriers & technology development |
| 10.50 AM to 11.15 AM | Coffee Break |
| 11.15 AM to 12.00 PM | Session 2: Wind Turbine Technology and Control – Part 1<br>• Components of wind turbine, power generation from wind, & different types of turbines |
| 12.00 PM to 2.00 PM | Lunch Break |
| 2.00 PM to 2.45 PM | Session 3: Wind Turbine Technology and Control – Part 2<br>• Control sub-systems, mechanical speed control, and generator configuration/control |
| 2.50 PM to 3.15 PM | Coffee Break |
| 3.15 PM to 4.00 PM | Session 4: Wind Plant Design<br>• Components of wind power plant |
| 3.15 PM to 4.00 PM | Q&A Session/Discussion |

**Day 2: Modeling and Grid Interconnection**

| | |
|---|---|
| 10.00 AM to 10.45 AM | Session 5: Modeling and Simulation<br>• Modeling of wind turbines for power flow, dynamic and short circuit studies |
| 10.50 AM to 11.15 AM | Coffee Break |
| 11.15 AM to 12.00 PM | Session 6: Introduction to Grid Codes<br>• Summary of North American and European grid codes |
| 12.00 PM to 2.00 PM | Lunch Break |
| 2.00 PM to 2.45 PM | Session 7: Interconnection Case Studies<br>• Steady state, transient and dynamic studies |
| 2.50 PM to 3.15 PM | Coffee Break |
| 3.15 PM to 4.00 PM | Q&A Session/Discussion |

**Day 3: Wind Plant Integration**

| | |
|---|---|
| 10.00 AM to 10.45 AM | Session 8: Power System Operation<br>• AGC, EMS, SCADA, control performance metrics, ancillary service requirements, operations planning |
| 10.50 AM to 11.15 AM | Coffee Break |
| 11.15 AM to 12.00 PM | Session 9: Impact of Wind Energy on Power System Operation<br>• Wind power characteristics & uncertainties, Wind forecasting methods, and tools |
| 12.00 PM to 2.00 PM | Lunch Break |
| 2.00 PM to 2.45 PM | Session 10: Wind Integration Case Studies<br>• Cost of wind integration |
| 2.50 PM to 3.15 PM | Coffee Break |
| 3.15 PM to 4.00 PM | Session 11: Capacity Value and Ancillary Services<br>• System adequacy, and methods for calculating capacity credit |
| 4.00 PM to 4.30 PM | Q&A Session/Discussion |

### 3.3.3 Wind Energy Outreach

#### *A. First Consortium Conference, September 30, 2010*

On September 30, 2010, IIT's Center for Electricity Innovation hosted the 2010 meeting of the Consortium members on IIT's main campus in Chicago. The schedule for the day is as follows:

8:00-8:30 am Registration and Introduction
8:30-10:45 Discussion on implementation of the DOE-funded Wind Consortium project
10:45-12:00 Tour of the DOE-funded projects at IIT
12:00-1:00 pm Lunch
1:00-3:00 Symposium on Future of Wind Power Event
3:00-4:00 Reception

**MORNING SESSION**

The morning session will include presentations by consortium members and discussions of ongoing tasks. The discussions will be followed up by a tour of the DOE-funded projects at IIT.

**Presentations (8:30-10:15 am)**

Mohammad Shahidehpour, IIT
Frank Bristol, Acciona
Jim Gagnard, SmartSignal
Alan Cain, Innovation Technology Applications, and Ganesh Raman, IIT
Greg Rouse and John Kelly, Intelligent Power Solutions
Alireza Khaligh, IIT
Richard Gowen, Dakota Power
Zuyi Li, IIT
John Birge, University of Chicago

**Discussion (10:15-10:45 am)**

All Consortium members

**Tour of the IIT Projects (10:45-12:00 noon)**

- Wind Turbine Installations. The wind energy consortium tasks include the installation of two 8-kW wind units at IIT for research and education. The first unit already installed in one of the laboratories at IIT will be demonstrated as part of the campus tour.
- Perfect Power Smart Microgrid. IIT has been working on a DOE-funded perfect power project since 2008. The project is converting IIT to a microgrid for enhancing reliability, sustainability, and efficiency of its electricity grid. A tabletop model of the campus buildings is developed and a demonstration of the perfect power concept will be presented to the consortium members and guests.

**Lunch (12:00 noon-1:00 pm) at McCormick Tribune Campus Center**

**AFTERNOON SESSION**

**Symposium on Future of Wind Power (1:00-3:00 pm)**

The symposium will bring industry and government leaders together to discuss breakthrough technologies, innovations, and implementation developments in the industry. The state of the Wind Energy industry in the United States is facing numerous challenges, from wildlife and zoning concerns to the deficiencies of our nation's electric transmission grid. Yet, the industry is also being presented with new opportunities, from the country's first offshore wind farms, to new smart grid technologies that allow better integration of intermittent power into the grid.

Symposium Speakers:

Brian Connor – U.S. Department of Energy
Sonny Garg – President, Exelon Power & Senior Vice President, Exelon Generation
Michael Polsky – President/CEO, Invenergy
Paul McCoy – President, Trans-Elect
Kurt Yeager – Former President, EPRI / Executive Director, Galvin Electricity Initiative
Joshua Milberg - First Deputy Commissioner, City of Chicago Department of Environment

**Reception (3:00-4:00 pm)**

### *B. Second Wind Consortium Conference, July 20, 2011*

On July 20, 2011, IIT's Center for Electricity Innovation hosted the 2011 meeting of the Consortium members on IIT's main campus in Chicago. The schedule for the day is as follows:

**7:45-8:00 am Continental Breakfast**

**Introduction and Welcome Remarks**

8:00-8:10 Mohammad Shahidehpour, PI, DOE Wind Consortium Project
8:10-8:15 Brian Connor, U.S. Department of Energy
8:15-8:20 Dave Loomis, Chair, Illinois Wind Working Group Annual Conference

**Wind Energy Integration in the Eastern Interconnection**

8:20-8:30 Paul McCoy, McCoy Energy and AWC
8:30-8:40 Aidan Tuohy, EPRI
8:40-8:45 Zuyi Li, Electrical and Computer Engineering Department, IIT
8:45-8:55 Panel Discussion

**Wind Energy Installation at IIT**

8:55-9:05 Marty Price, Viryd
9:05-9:15 C.S. Choi, KERI / Alex Flueck, IIT
9:15-9:25 Greg Rouse, IPS
9:25-9:35 Panel Discussion
9:35-9:50 BREAK

**Wind Energy Research and Development**

9:50-10:00 Richard Gowen, Dakota Power
10:00-10:10 Jay Giri, Alstom
10:10-10:20 David Chiesa, S&C
10:20-10:30 Panel Discussion

**Wind Energy Education and Workforce Development**

10:30-10:40 Hamid Arastoopour, Chemical & Biological Engineering Department, IIT
10:40-10:50 Ganesh Raman, MMAE Department, IIT
10:50-11:00 Bob Zavadil, EnerNex
11:00-11:10 Alireza Khaligh, ECE Department, IIT / Dietmar Rempfer, MMAE Department, IIT
11:10-11:20 Panel Discussion

**Wind Energy Installation at Grand Ridge**

11:20-11:30 Dave Parta, Smart Signal
11:30-11:40 Steve Moffitt, GE
11:40-11:50 Bill Fetzer, Catch the Wind
11:50-12:00 Panel Discussion
12:00 Closing

**12:15 pm Ribbon Cutting Event – 8kW Wind Unit at IIT**

Hamid Arastoopour, WISER (Moderator)
Mohammad Shahidehpour, Robert Galvin Center for Electricity Innovation
Brian Connor, U.S. Department of Energy
Robert Galvin, Galvin Electricity Initiative
Marty Price, Viryd
Michael Polsky, Invenergy

Kurt Yeager, Galvin Electricity Initiative
Terry Frigo, IIT

**2:30 pm Ribbon Cutting Event – 1.5MW IIT Wind Unit at Grand Ridge, Illinois**
Andrew Barbeau, IIT (Moderator)
Mohammad Shahidehpour, Robert Galvin Center for Electricity Innovation
Gary Nowakowski, U.S. Department of Energy
Stacy Kacek, Smart Signal
Bill Fetzer, Catch the Wind
James Rafferty, Invenergy

**5:30 pm Adjourn**

### *C. Great Lakes Symposium on Smart Grid and the New Energy Economy 2011*

The first Great Lakes Symposium on Smart Grid and the New Energy Economy was held on October 18-19, 2011 on IIT's main campus. The symposium was presented by the Midwestern Governors Association, Illinois Science & Technology Coalition, Illinois Institute of Technology, Galvin Electricity Initiative, Citizens Utility Board, Environmental Defense Fund, Clean Energy Trust, UL, S&C Electric Company, Northwestern University, Argonne National Laboratory, Sierra Club, and Illinois Manufacturing Extension Center. The symposium was sponsored by Commonwealth Edison, Eaton Corporation, General Electric, Silver Spring Networks, and the Joyce Foundation. The agenda of the symposium is as follows.

## TUESDAY, OCTOBER 18, 2011

**Master of Ceremonies: Dr. Mohammad Shahidehpour**
Director of the Robert W. Galvin Center for Electricity Innovation, Illinois Institute of Technology

**Welcome and Keynote — AUDITORIUM**

| | |
|---|---|
| 8 – 8:50 a.m. | **Registration in Lobby/Gallery** |
| 9 – 9:10 a.m. | **Welcome**<br>**Hon. Rahm Emanuel, Mayor, City of Chicago** |
| 9:10 – 10 a.m. | **Keynote: Smart Grid and the New Energy Economy**<br>**Ellen Alberding**, President, Joyce Foundation<br>**Scott Lang**, President and CEO, Silver Spring Networks<br>**Luke Clemente**, General Manager of Metering & Sensing Systems, GE Energy's Digital Energy Services |
| 10 – 10:15 a.m. | **Leveraging the Convening Power of the PUC**<br>**Doug Scott**, Chairman, Illinois Commerce Commission |

## MORNING SESSION

| | EXPO CENTER | AUDITORIUM |
|---|---|---|
| | Midwest Policy Summit | Consumer Track: Path to Perfect Power |
| 10:30 a.m. – Noon | How Can Smart Grid Technologies Increase the Efficiency between Transmission and Distribution?<br>• Moderator: Mark Brownstein, Chief Counsel of the Energy Program, Environmental Defense Fund<br>• Philip Moeller, Commissioner, Federal Energy Regulatory Commission<br>• Vladimir Koritarov, Deputy Director of the Center for Energy, Environmental and Economic Systems Analysis, Argonne National Laboratory<br>• Chantal Hendrzak, Director of Applied Solutions, PJM<br>• Paul Centolella, Commissioner, Public Utilities Commission of Ohio | Leading Practices for Ensuring Consumer Empowerment<br>• Moderator: Brewster McCracken, Executive Director, Pecan Street Inc.<br>• Eric Dresselhuys, Executive Vice President and Chief Marketing Officer, Silver Spring Networks<br>• Dr. Kristin B. Zimmerman, Manager of Advanced Technology Infrastructure, General Motors Research and Development Center<br>• Dr. Louay Eldada, Chief Science Officer, VP Global R&D, SunEdison |

**LUNCHEON EXECUTIVE PANEL: The Pursuit of Quality and Innovation — BALLROOM**

Noon – 1:30 p.m.

Moderator: **Jim Buckman**, Quality Advisor, Galvin Electricity Initiative
**Michael Niggli**, President and CEO, San Diego Gas & Electric
**Anne Pramaggiore**, President and COO, ComEd
**Teri Ivaniszyn**, Senior Director of Corporate Excellence, Florida Power & Light

## AFTERNOON SESSION

| | EXPO CENTER | AUDITORIUM |
|---|---|---|
| | **Innovation and Economic Opportunity Track** | **Consumer Track: Path to Perfect Power** |
| 1:30 – 3 p.m. | **Smart Grid and Energy Business Leadership Roundtable**<br>• **Session Kick-Off: A Futurist Point of View:** Michael J. Meehan, Senior Principal Consultant, KEMA<br>• **Integration of Renewable Resources/Energy Storage:** Jay Marhoefer, CEO, Intelligent Generation; Chris Walti, Power Originator, Acciona Energy<br>• **Smart Buildings:** Chris Thomas, Policy Director, Citizens Utility Board; Peter Scarpelli, Vice President of Global Leader of Energy Services, CB Richard Ellis<br>• **Electrified Transportation:** Paul H. Pebbles, Global Electrification Product Manager, OnStar®; Sam Ori, Director of Policy, The Electrification Coalition<br>• **Home/Community Adoption:** Jonathan "JT" Thompson, Smart Appliance Utility Leader, GE Appliances – Home and Business Solutions; Rep. Daniel Biss, Illinois State Representative, 17th District | **Leading Practices for Grid Safety, Reliability and Power Quality**<br>• Moderator: Mike Edmonds, Vice President of Strategic Solutions, S&C Electric Company<br>• David Wade, EVP and COO, Electric Power Board of Chattanooga, Tenn.<br>• Mark Curran, Director of Public Utilities – Electric, City of Naperville, Ill.<br>• Greg Blake, Global Smart Grid Sales Director, GE Energy's Digital Energy Services<br>• Terence Donnelly, Executive Vice President of Operations, ComEd |
| | **Midwest Policy Summit** | **Innovation and Economic Opportunity Track** |
| 3:15 – 4:15 p.m. | **Articulating the Benefits of Smart Grid**<br>• Suzanne Malec-McKenna, Former Commissioner, City of Chicago Department of Environment<br>• David Kolata, Executive Director, Citizens Utility Board<br>• Michael Gregerson, Energy Consultant, Great Plains Institute<br>• Beth Soholt, Director, Wind on the Wires<br>• Jacqueline Voiles, Director of Regulatory Affairs, Ameren Illinois<br>• Wade Malcolm, Global Senior Director for Smart Grid Operations Technology, Accenture | **Innovative Marketplace Quick Pitch Competition**<br>**JUDGES:**<br>• Doug Dillie, Director of Smart Grid Solutions, Eaton Corporation<br>• Mark Zhu, Investment Professional, DTE Energy Ventures<br>• Paul H. Pebbles, Global Electrification Product Manager, OnStar®<br>• Chris Walti, Power Originator, Acciona Energy<br>• Kerri Breen, Principal, Arsenal Venture Partners<br>• Rob Schultz, Senior Director, IllinoisVENTURES<br>• Teresa Esser, General Partner, Capital Midwest Fund<br>• Sam Hogg, Director of Venture Development, NextEnergy<br>• Kirk Colburn, Managing Director, SURGE<br>• Rep. Robyn Gabel, Illinois State Representative, 18th District<br>• Steve Moffitt, Account Executive, GE |
| 4:15 – 4:30 p.m. | **BREAK** | |
| 4:30 – 5:30 p.m. | **Midwest Smart Grid Pilots: Realizing the Economic Value of Smart Grid**<br>• Moderator: Matthew Summy, President, Illinois Science and Technology Coalition<br>• Nic Stover, Regional Sales Director, Northwest, EnerNOC | |

4:30 – 5:30 p.m. **Midwest Smart Grid Pilots: Realizing the Economic Value of Smart Grid** (Continued)

- Shaun Summerville, Marketing Program Manager, DTE Energy
- Dan Francis, Manager of gridSMART Policy, American Electric Power
- DeWayne Todd, Corporate Compliance and Regulatory Affairs, Warrick Primary Metals

**NETWORKING RECEPTION: 5:30 – 7 p.m.**

## WEDNESDAY, OCTOBER 19, 2011

### Keynote: Smart Grid and Climate Change

9 – 10 a.m. Michael Brune, Executive Director, Sierra Club

## MORNING SESSION

| | EXPO CENTER | AUDITORIUM | ARMOUR DINING ROOM |
|---|---|---|---|
| | Midwest Policy Summit | Consumer Track: Path to Perfect Power | Innovation and Economic Opportunity Track |
| 10 – 11 a.m. | **Developing Good Smart Grid Policy**<br>• Moderator: Lauren Navarro, Attorney, Environmental Defense Fund<br>• Phyllis Reha, Vice Chair, Minnesota Public Utilities Commission | **Leading Practices for Integrating Clean and Efficient Power**<br>• Moderator: John Kelly, Executive Director, Galvin Electricity Initiative<br>• Sue Tierney, Managing Principle, Analysis Group<br>• Mike Bull, Manager of Environmental Policy, Xcel Energy<br>• Shawn Marshall, Executive Director, Lean Energy<br>• Tom Barwin, Village Manager, Oak Park | **Growing the Smart Grid Regional Innovation Cluster Workshop**<br>• Matthew Summy, President, Illinois Science and Technology Coalition<br>• Dan Bowman, Principal, PricewaterhouseCoopers PRTM Management Consulting<br>• Oliver Hazimeh, Principal, PricewaterhouseCoopers PRTM Management Consulting<br>• Jared Racine, Senior Associate, PricewaterhouseCoopers PRTM Management Consulting |
| 11 a.m. – Noon | **Developing Great Midwest Smart Grid Strategies**<br>• Moderator: Miriam Horn, Director, Smart Grid Initiatives, Environmental Defense Fund<br>• Ed Miller, Environment Program Manager, Joyce Foundation<br>• Tom Catania, Vice President of Government Relations, Whirlpool<br>• Ade Dosunmu, Senior Director of Strategic Markets, Comverge | | |

**LUNCHEON: Midwest Energy Leadership Awards**

Noon – 1:30 p.m. Luncheon and Awards Presentation

**1:30 – 3 p.m. Tour of the Perfect Power Microgrid at Illinois Institute of Technology**

### *D. Great Lakes Symposium on Smart Grid and the New Energy Economy 2012*

On September 24-26, 2012, the Robert W. Galvin Center for Electricity Innovation will host the second annual Great Lakes Symposium on Smart Grid and the New Energy Economy, on the Illinois Institute of Technology's campus in Chicago. The Symposium will feature keynote and plenary sessions, technical presentations, and tutorials by international experts on smart grid applications. The Symposium is a one-of-a-kind event that breaks new ground in smart grid design and development and showcases smart grid best practices from around the country along with new technologies and ideas that are spurring innovation, growing state economies, reducing emissions and empowering consumers to conserve and save. Participants will have the opportunity to engage thought leaders on key policy questions, identify investment and job creation opportunities, and learn about projects already underway.

The symposium was technically sponsored by the Robert W. Galvin Center for Electricity Innovation and the IEEE Power and Energy Society. The symposium was financially sponsored by Commonwealth Edison, Environmental Defense Fund, Silver Spring Networks, Ameren Illinois, Eaton Corporation, Landis+Gyr, S&C Electric Company, the Joyce Foundation, OSIsoft, and General Electric. The agenda of the symposium is as follows.

## MONDAY | SEPTEMBER 24, 2012

### MONDAY MORNING

8:30 a.m. – Noon

SHORT COURSES

1. **Introduction to Smart Grids and Smart Grid Roadmaps**
   Room: Hermann Lounge
2. **How Today's Grid is Evolving for the 21st Century**
   Room: Hermann Hall – Trustee Dining Room
3. **Microgrids – Designing Their Role in Smart Grid**
   Room: Hermann Hall – 007

# MONDAY | SEPTEMBER 24, 2012

## MONDAY AFTERNOON

1:30 pm – 2:00 pm

**4. Introduction and Welcome Remarks**
**Hermann Hall Ballroom**

- Mohammad Shahidehpour, Chair, Great Lakes Symposium on Smart Grid and the New Energy Economy
- Noel Schulz, President, IEEE Power and Energy Society

2:00 pm – 3:00 pm

**5. Plenary Session: Illinois Smart Grid Deployment**
**Hermann Hall Ballroom**

- Chair: Wanda Reder, S&C Electric
- Anne Pramaggiore, President and CEO, ComEd
- Richard Mark, President and CEO, Ameren Illinois
- Scott Lang, President and CEO, Silver Spring Networks

3:00 pm – 3:30 pm

**AFTERNOON BREAK**
**Expo Room**

3:30 pm – 5:15 pm

**6. Panel Session: Military Microgrids**
**Hermann Hall Ballroom**

- Chair: Tom Podlesak, US Army
- Robert Lasseter, University of Wisconsin-Madison
- Tristan Glenwright, Boeing
- Tarek Abdalla, U.S. Army Engineer Research and Development Center
- Gary Wetzel, S&C Electric
- Doug Houseman, EnerNex

**7. Panel Session: Electric Vehicles and Mobility in Energy Systems**
**McCormick Tribune Campus Center (MTCC) Auditorium**

- Chair: Sharon Feigon, CEO, I-GO Cars
- Gary Rackliffe, ABB
- Abas Goodarzi, US Hybrid
- Mike McMahan, ComEd
- Ramteen Sioshansi, Ohio State University
- Michael Abba, Ameren

**8. Panel Session: Smart Grid Cyber Security and Data Management**
**McCormick Tribune Campus Center (MTCC) Ballroom**

- Chair: Erich Gunther, EnerNex
- Tony Metke, Motorola Solutions
- Joseph Giampapa, Carnegie Mellon University
- Alfonso Valdes, University of Illinois
- Michael Manske, West Monroe Partners

**9. Panel Session: Transmission Planning Issues for Variable Energy Resources**
**Armour Dining Room**

- Chair: Paul McCoy, McCoy Energy Consulting
- Marcelino Madrigal, World Bank
- Beth Soholt , Wind on the Wires
- John Moore, Sustainable FERC Project
- Julija Matevosyan, ERCOT
- Scott Deffenderfer, Ameren

**10. Paper Session: Advanced Distribution Systems**
**Alumni Lounge**

- Chair: Amin Khodaei, University of Houston
- *Electricity Fraud Detection by Incorporating PV System Using Support Vector Machines*
  Yonghe Guo and Chee-Wooi Ten, Michigan Technological University
- *An Analytical Approach for Reliability Evaluation of Aged Distribution Systems*
  Masood Parvania, Mahmud Fotuhi-Firuzabad, Sharif University of Technology
- *Online Management Framework for Distribution System with Wind Generation*
  Bhairavi Pandya and Chee-Wooi Ten, Michigan Technological University

5:30 pm – 7:00 pm

**EVENING RECEPTION**
**Expo Room**

# TUESDAY | SEPTEMBER 25, 2012

## TUESDAY MORNING

8:00 am – 8:30 am

**BREAKFAST**
**Expo Room**

8:30 am – 9:00 am

**11. Keynote Speaker: Michael Polsky, President and CEO, Invenergy**
**Hermann Hall Ballroom**

9:00 am – 10:00 am

**12. Plenary Session: Offshore Wind at Great Lakes**
**Hermann Hall Ballroom**

- Chair: The Honorable Robyn Gabel, Representative, 18th District, Evanston, Illinois
- Lorry Wagner, President of LEEDCo
- Jack Darin, Sierra Club
- Mary Ann Christopher, Esq., Law Office of Mary Ann Christopher

10:00 am – 10:30 a.m.

**MORNING BREAK**
**Expo Room**

10:30 am – 12:15 pm

**13. Panel Session: Wind Turbine Operation and Control**
**McCormick Tribune Campus Center (MTCC) Auditorium**

- Chair: Bill Fetzer, VP, BlueScout Technologies
- Don Doan, GE Intelligent Platforms (Smart Signal)
- Aidan Tuohy, EPRI
- Steve Moffitt, GE Energy

**14. Panel Session: Power System Operations: EV Infrastructure and Smart Distributed Systems**
**Hermann Hall Ballroom**

- Chair: Kate Tomford, Illinois Department of Commerce and Economic Opportunity
- Stephanie Cox, Ecotality
- Ted Bohn, Argonne National Laboratory
- Johan Enslin, University of North Carolina
- Paul Myrda, EPRI

**15. Panel Session: Smart Homes, Electric Vehicles and Demand Response**
**Armour Dining Room**

- Chair: Jianhui Wang, Argonne National Laboratory
- Vladimir Koritarov, Argonne National Laboratory
- Marty Cohen, Board Chairman, Illinois Science and Energy Innovation Fund
- John Finnigan, Environmental Defense Fund
- Prakash Thimmapuram, Argonne National Laboratory
- Zhi Zhou, Argonne National Laboratory

**16. Panel Session: Solar Energy Integration**
**McCormick Tribune Campus Center (MTCC) Ballroom**

- Chair: Mark Handy, KenJiva Energy Systems
- Jeff Smith, West Monroe Partners
- Madeleine Weil, SoCore Energy
- Tom Tansy, SunSpec Alliance

**17. Paper Session: Impacts of PHEV on Transportation and Energy Systems**
**Alumni Lounge**

- Chair: Kuilin Zhang, Argonne National Laboratory
- *An Information System for Electric Vehicle Charging Infrastructure Deployment*
  Diego Klabjan and Timothy Sweda, Northwestern University
- *An Analysis of Car and SUV Daytime Parking for Potential Charging of Plug-in Electric Vehicles*
  Yan Zhou, Argonne National Laboratory
- *Dynamics of PEV Driving and Charging Behavior under Intelligent Energy Management Systems*
  Kuilin Zhang, Argonne National Laboratory

# TUESDAY | SEPTEMBER 25, 2012

## TUESDAY AFTERNOON

12:15 pm – 1:30 pm

**18. Luncheon Keynote Speaker**

**Expo Room**

- Chair: Alex Flueck, Illinois Institute of Technology
- Presenter: Mani Venkata, Principal Scientist, Alstom

1:30 pm – 3:00 pm

**19. Plenary Session: Great Lakes Forum on Regulatory Policy**

**Hermann Hall Auditorium**

- Chair: Joshu Milberg, Willdan Energy
- Andre Porter, Ohio Public Utility Commission
- Eric Callisto, Wisconsin Public Utility Commission
- Ed Miller, Program Manager, Joyce Foundation

3:00 pm – 3:30 pm

**AFTERNOON BREAK**

**Expo Room**

3:30 pm – 5:15 pm

**20. Panel Session: Microgrid Planning and Operation**

**Hermann Hall Auditorium**

- Chair: Shay Bahramirad, S&C Electric
- Mani Venkata, Alstom
- Maryam Saeedifard, Purdue University
- Ernst Camm, S&C Electric
- Steve Pullins, Horizon Energy Group
- Mike Presutti, Agentis

**21. Panel Session: Electric Vehicle Manufacturing in Great Lakes States**

**Armour Dining Room**

- Chair: Steve Johanns, Eaton
- John Wirtz, Eaton Business Unit Manager
- Angela Strand, Chief Marketing Officer, Smith Electric
- Ron Prosser, CEO, Green Charge Networks and Chair, Smart Grid on the U.S.–China Clean Energy Forum
- John Shen, University of Central Florida

**22. Panel Session: Smart Grid Workforce Training and Education**

**McCormick Tribune Campus Center (MTCC) Auditorium**

- Chair: Bruce Hamilton, President, Adica and Smart Grid Network
- Gary Blank, Vice-President, IEEE-USA
- Marge Anderson, Executive Vice President, Energy Center of Wisconsin
- Julie Elzanati, Executive Director, Illinois Green Economy Network
- Matt Shields, Workforce Development Agency, State of Michigan

**23. Panel Session: Geomagnetic Disturbances on the Power Grid**

**McCormick Tribune Campus Center (MTCC) Ballroom**

- Chair: Tom Overbye, University of Illinois
- David Wojtczak, ATC
- Scott Dahman, PowerWorld Corporation
- Alan Engelmann, ComEd
- Tom Overbye, University of Illinois

**24. Paper Session: Smart Grid: Policy, Regulation and Customer Engagement**

**Alumni Lounge**

- Chair: Alex Tang, Clean Energy Trust
- *Regulation, Competition, and New Technology Adoption: Applying the Bell Doctrine to Retail Electricity Markets*

  Lynne Kiesling, Northwestern University
- *Customer Privacy & The Smart Grid: Where the Policy Debate Presently Stands & the Strategic Steps Utilities Should be Taking Today*

  Will McNamara, West Monroe Partners
- *Infinite-horizon Economic MPC for HVAC systems with Active Thermal Energy Storage*

  David Mendoza-Serrano and Donald Chmielewski, Illinois Institute of Technology
- *Communicating to Engage the Modern Customer in the New Energy Economy*

  David Tilson, West Monroe Partners

5:30 pm – 6:15 pm

**NETWORKING RECEPTION**

**Gallery Lounge**

6:15 pm – 8:00 pm

**25. Dinner and Keynote Session**

- Speaker: Alan Wendorf, Chairman, President, and CEO, Sargent and Lundy

# WEDNESDAY | SEPTEMBER 26, 2012

## WEDNESDAY MORNING

8:00 am – 8:30 am

**BREAKFAST**

**Expo Room**

8:30 am – 9:00 am

**26. Keynote Speech**

**Hermann Hall Ballroom**

- Chair: Peter Sauer, University of Illinois
- Presenter: Wanda Reder, Vice President, S&C

9:00 am – 10:00 am

**27. Plenary Session: Recovery Act Demonstrations of Smart Grid Development**

**Hermann Hall Ballroom**

- Chair: Joseph Paladino, U.S. Department of Energy
- Jim Hull, DTE
- Olga Geynisman, City of Naperville
- Barry Feldman, Indianapolis Power and Light

10:00 am – 10:30 a.m.

**MORNING BREAK**

**Expo Room**

10:30 am – 12:15 pm

**28. Panel Session: Microgrid Storage**

**McCormick Tribune Campus Center (MTCC) Auditorium**

- Chair: Troy Miller, S&C
- Tony Siebert, ZBB Energy Corporation
- James J. Greenberger, National Alliance for Advanced Technology Batteries
- Henry Louie, Seattle University
- Mitch Mabrey, Dow Kokam

**29. Panel Session: Utilizing Smart Grid Test Beds in Illinois**

**McCormick Tribune Campus Center (MTCC) Ballroom**

- Chair: Robert Greenlee, Illinois Science & Technology Coalition
- Joseph Clair, Illinois Institute of Technology
- Timothy Yardley, University of Illinois
- David Pope, Village of Oak Park
- Rod Hilburn, Ameren

**30. Panel Session: Customer Engagement and Empowerment**

**Hermann Hall Ballroom**

- Chair: Scott Binnings, Patton Boggs
- Michael Murray, Lucid Design Group
- Val Jensen, ComEd
- David Hodgson, UK Trade & Investment
- Tom Wieser, PaceControls

**31. Panel Session: Storage for Power System Operation**

**Armour Dining Room**

- Chair: Caisheng Wang, Wayne State University
- Daniel Lindenmeyer, Infineon
- Anurag K Srivastava, Washington State University
- Roland Kibler, NextEnergy
- Piyush Desai, Danfoss

**32. Paper Session: Smart Grid Monitoring and Cyber Security**

**Alumni Lounge**

- Chair: Zuyi Li, Illinois institute of Technology
- *Video Monitoring Solutions for Utilities – Using video to make a Grid Smarter*

  John McClean, Powerstream Inc.
  Anselm Viswasam, Systems with Intelligence, Inc.
- *How Electrical System Monitoring Improves Facility Efficiency, Reliability and Safety*

  Dave Loucks, Eaton Corporation, Greg Reed, University of Pittsburgh
- *Substation Cybersecurity Architectural Design*

  Pingal Sapkota and Chee-Wooi Ten, Michigan Technological University

# WEDNESDAY | SEPTEMBER 26, 2012

## WEDNESDAY AFTERNOON

12:15 pm – 1:30 pm

**33. Luncheon Keynote Speaker**
**Expo Room**
- Chair: Andrew Barbeau, Robert W. Galvin Center, Illinois Institute of Technology
- Presenter: Arlene Juracek, Director, Illinois Power Agency at State of Illinois

1:30 pm – 3:00 pm

**34. Plenary Session: Shifting Smart Grid focus to Customer Driven Performance Outcomes**
**Hermann Hall Ballroom**
- Chair: John Kelly, Perfect Power Institute
- Farokh Rahimi, OATI
- Austin Montgomery, Carnegie Mellon University
- Dave Roberts, OSIsoft
- Paul Alvarez, Wired Group

3:00 pm – 3:30 pm

**AFTERNOON BREAK**
**Expo Room**

3:30 pm – 5:15 pm

**35. Panel Session: Smart Grid Innovation in Great Lakes Region**
**Hermann Hall Ballroom**
- Chair: Karen Weigert, City of Chicago
- Jay Marhoefer, Intelligent Generation
- Scott Henneberry, Schneider Electric
- Dan Francis, American Electric Power
- Jett Tackbary, West Monroe Partners

**36. Panel Session: Community Choice Aggregation: Progress and Promise**
**McCormick Tribune Campus Center (MTCC) Auditorium**
- Chair: Mark Pruitt, Power Bureau
- Ghida Neukirch, Buffalo Grove Deputy Village Manager
- Maria Fields, Joule Assets
- David Kolata, Citizens Utility Board
- Kris Torvik, Wired Group

**37. Panel Session: Smart Homes and Distributed Generation**
**McCormick Tribune Campus Center (MTCC) Ballroom**
- Chair: Joyce Coffee, Edelman
- Colin Meehan, Environmental Defense Fund
- Paul Navratil, University of Texas
- Charles O'Donnell, Siemens
- George Thomas, Contemporary Controls

**38. Panel Session: Future of Nuclear**
**Armour Dining Room**
- Chair: Michael Corradini, American Nuclear Society
- Jack Grobe, Exelon Nuclear Partners
- Alexander Marion, Nuclear Energy Institute.
- Yoon Il Chang, Argonne National Laboratory
- Scott Bond, Ameren

**39. Paper Session: Power System Planning**
**Alumni Lounge**
- Chair: Lei Wu, Clarkson University
- *Probabilistic Production Cost Simulation and Reliability Evaluation of Composite Power System Including Renewable Generators*
  Jintaek Lim, Jinhwan Jang and Jaeseok Choi, Gyeongsang National University, South Korea
  Keonghee Cho, Korea Economic Research Institute (KERI), South Korea
  Junmin Cha, Daejin University, South Korea
- *A Hybrid Method for Long-Term Transmission Lines Expansion in Large-Scale Electric Grids*
  Mohammad Albaijat, University of California at Davis
  Kaveh Aflaki, Illinois Institute of Technology
- *Coordinated Expansion Planning of Generation and Transmission Systems Considering Outage Cost*
  Jintaek Lim, Jinhwan Jang and Jaeseok Choi, Gyeongsang National University, South Korea
  Donghoon Jeon, Korea Electric Power Corporation (KEPCO), South Korea

# 4. Accomplishments

## 4.1 Award

1) Dr. Mohammad Shahidehpour received the IEEE Power and Energy Society Outstanding Power Engineering Educator Award (For leadership in the power engineering field and contributions to the engineering profession and engineering education) in 2012.
2) Dr. Mohammad Shahidehpour Technologist of the Year Award from the Illinois Technology Association (Presented to the individual whose talent has championed true technology innovation, either through new application of existing technology or the development of technology to achieve a truly unique product or service) in 2011
3) Dr. Mohammad Shahidehpour received the Outstanding Engineer Award, IEEE Power and Energy Society Chicago Chapter (for significant leadership and contributions towards IIT's Prefect power microgrid, the IIT's wind consortium, and the IIT's Smart Grid Education and Workforce Development) in 2011
4) In the 27th Annual Conference of the ECEDHA (Electrical and Computer Engineering Department Heads Association) on March 14, 2011, IIT's Center for Electricity Innovation, the principal unit performing this DOE project, won the Innovation Award from ECEDHA (single award) for establishing the Illinois Institute of Technology as a global leader in microgrids, smart grid technology, and sustainable energy. Below is a copy of the citation.
5) Dr. Mohammad Shahidehpour received IIT's First Research Leadership Award (in Recognition of Outstanding Accomplishments in Developing Strong Research Collaborations and Large Scale Research Projects) in 2010
6) Dr. Mohammad Shahidehpour received the Distinguished Service Award, IEEE Power &Energy Society (For serving as General Chair of the 2012 IEEE Innovative Smart Grid Conference)
7) Dr. Mohammad Shahidehpour received the Distinguished Service Award, IEEE Power & Energy Society (For serving as VP of Publications) in 2011

ECEDHA

*Electrical and Computer Engineering Department Heads Association*

2010 Innovative Program Award

presented to

Mohammad Shahidehpour
Illinois Institute of Technology

for the Center for Electricity Innovation
Establishing the Illinois Institute of Technology as a global leader in microgrids,
smart grid technology, and sustainable energy

*Presented at the 27th Annual Conference of the ECEDHA*

Ed Schlesinger
ECEDHA President
2010-2011

Phoenix, Arizona
March 14, 2011

## 4.2 List of Presentations

### 4.2.1 Presentations at the First Consortium Conference

September 30, 2010, Illinois Institute of Technology

1) A World-class University-Industry Consortium for Wind Energy Research, Education, and Workforce Development, Mohammad Shahidehpour, Illinois Institute of Technology
2) Acciona and Its Support for Consortium, Frank Bristol, Acciona
3) SmartSignal and Its Collaboration with the IIT Wind Energy Consortium, Jim Gagnard, SmartSignal
4) Acoustics of Wind Turbine, Alan Cain, Innovation Technology Applications
5) Acoustic Measurements using Phased Arrays, Ganesh Raman, Illinois Institute of Technology
6) Wind Management Tool for the IIT Wind Project, Greg Rouse, Intelligent Power Solutions

7) IPRO 311 – Integration of Plug-in Hybrid Electric Vehicles and Renewable Energy Systems, Alireza Khaligh, Illinois Institute of Technology

8) Next Generation Lightweight Electric Drive Systems, Richard Gowen, Dakota Power

9) Wind Energy Class Offering at the Illinois Institute of Technology, Zuyi Li, Illinois Institute of Technology

10) Impact of Wind Forecasting Precision on Unit Commitment and Network Control, John Birge, University of Chicago

11) DOE Educational Program Wind University Consortia, Brian Connor – U.S. Department of Energy

12) Smart Transmission Making a Smart Grid Smarter, Paul McCoy, Trans-Elect Development Company

### 4.2.2 Presentations at the Second Wind Consortium Conference

July 20, 2011, Illinois Institute of Technology

13) Overview of the Center for Renewable Energy, David G. Loomis, Illinois State University

14) A Big Step Toward Energy Independence, Paul McCoy, Atlantic Wind Connection

15) Integrating Midwest Wind Energy into Southeast Electricity Markets, Aidan Tuohy, Electric Power Research Institute

16) Advanced Wind Integration Study, Zuyi Li, Illinois Institute of Technology

17) Viryd Technologies Overview & Installation, Alan Hays, Viryd Technologies

18) Perfect Power @ IIT and Local Area Measurement System, Alex Flueck, Illinois Institute of Technology

19) Microgrid Master Controller & Wind Management Tool, Greg Rouse, Intelligent Power Solutions

20) DP Switched Reluctance Technology, Richard Gowen, Dakota Power

21) Impacts of Wind Power on Grid Operations, Jay Giri, Alstom Grid

22) Wind Energy & Perfect Power, David Chiesa, S&C Electric Company

23) CFD Simulation of a Horizontal Axis Wind Turbine, Hamid Arastoopour, Illinois Institute of Technology

24) Acoustic Phased Array Measurements of Wind Turbines, Ganesh Raman, Illinois Institute of Technology

25) Development of a Comprehensive Tutorial on Wind Energy Technology, Interconnection & Integration, Bob Zavadil, EnerNex

26) IPRO 323: Modeling of Building-Integrated Wind Turbine Modules, Dietmar Rempfer, Illinois Institute of Technology

27) Advancing Wind Power in Illinois-Emerging Technologies, Dave Parta, GE Intelligent Platforms

28) GE Energy 1.5 MW Wind Turbine, IIT Grand Ridge Discussion, Steve Moffitt, GE

29) Vindicator® Laser Wind Turbine Control System, Bill Fetzer, Catch the Wind

### 4.2.3 Other Presentations

30) Market Clearing under Uncertainty, Antonio J. Conejo, University of Castilla – La Mancha, Spain, January 2011, at Illinois Institute of Technology

31) Integrating Non-dispatchable Producers (Wind) in Electricity Markets, Antonio J. Conejo, University of Castilla – La Mancha, Spain, January 2011, at Illinois Institute of Technology

32) Improving Efficiency and Reliability of Drivetrain Components by Smart Surface and Lubrication Engineering, Ali Erdemir, Argonne National Laboratory, February 2011

33) Vindicator® Laser Wind Sensor, The Future of Wind Sensing Technology, Scripted Tech Brief, Catch the Wind, 2011

34) Energy: The Road Ahead, Richard Gowen, Keynote address at the Energy Summit held at West Point Military Academy, April 2011

35) Large-Scale Simulation of Electric Power Systems for Wind Integration, PhD Final Defense, Wei Tian, Illinois Institute of Technology, August 2011

36) A World-class University-Industry Consortium for Wind Energy Research, Education, and Workforce Development , Mohammad Shahidehpour, IEEE Power and Energy Society General Meeting 2010, held in Minneapolis, Minnesota, July 2011

## 4.3 List of Videos

1) IIT Wind Turbine Ribbon Cutting Ceremony, Illinois Institute of Technology

2) Viryd Test-stand at IIT Laboratory, Illinois Institute of Technology, Viryd Technologies

3) IIT Wind Turbine (1.5MW GE) at Grand Ridge, Illinois Institute of Technology

4) IIT Wind Turbine (8kW Viryd) at Soccer Field, Illinois Institute of Technology

5) Switch Reluctance DC Machine (SRDCM) Exploded Animation, Dakota Power

## 4.4 List of Theses

### 4.4.1 Ph.D. Dissertations

1) Mohammad Khodayar, Coordination of Storage with Renewable Energy Resources in Power Systems, Illinois Institute of Technology, July 2012

Abstract: The ever-increasing penetration of variable wind energy in power systems affects the hourly dispatch of thermal power generation in electricity markets. The coordination of wind power generation units with pumped-storage hydro (PS) generation could relieve the variability of wind energy and increase its hourly dispatchability. Chapter 2 proposes a coordination methodology for wind and pumped-storage hydro (PS) units in the day-ahead operation planning of power systems. With coordination, the PS unit can offset intrahour wind energy imbalances (i.e., deviations from hourly schedules) and minimize wind energy curtailments. The variability of wind energy, which makes it non-dispatchable and difficult to control, could bring significant challenges to power system operators. In Chapter 3, the wind-PS coordination is based on the application of stochastic security-constrained unit commitment (Stochastic SCUC). In this study, the hourly bus- level coordinated scheduling of wind energy and PS is compared with the system-level coordinated operation strategies in the day-ahead scheduling of power systems.

From GENCO point of view volatility of wind generation can reduce the profit in day-ahead market by imposing potential imbalance charges. In Chapter 4 day-ahead price-based scheduling strategy for the coordination of wind and storage units in a generating company (GENCO) is proposed. The proposed strategy is based on the stochastic price-based unit commitment (PBUC) which considers volatilities in day-ahead intra-hour market prices and wind power generation when scheduling wind and storage units. The proposed approach firms up the hourly sum of wind and storage unit generation, and mitigate potential wind energy imbalance charges for GENCOs in electricity markets. Although the proposed approach applies to any kind of storage, we consider the pumped-storage hydro (PS) unit in this study.

The increased utilization of PEVs, which consume electricity rather than fossil fuel for driving, offers unique economic and environmental opportunities, and brings out new challenges to electric power system operation and planning. The storage capability of PEVs could help power systems mitigate the variability of renewable energy sources and reduce grid operation costs. Vehicle-to-grid (V2G) enables PEVs to have bi-directional power flows once they are connected to the grid, i.e., they can either inject power to, and draw power from, the grid which adds further complexity to power system operations. PEVs signify customers' random behavior when considering their driving patterns, locational energy

requirements, topological grid interconnections, and other constraints imposed by the consumers. The proposed approach in Chapter 5 evaluates the effect of integrating a large number of electric vehicles (EVs) on power grid operation and control. The EV fleets could serve as electricity load when drawing energy from the grid and as energy storage (vehicle-to-grid) when delivering energy to the grid. Two operating modes for EV fleets were considered which are consumer-controlled and grid-controlled. The power grid generation mix represents a multitude of units including thermal, hydro, and wind. In this chapter, the impact of EV battery utilization on offsetting the hourly intermittency of wind generation units in transmission-constrained power grids is evaluated. Moreover, the effect of charging/discharging schedule of EV batteries and consumer driving requirements on the optimal hourly transmission-constrained commitment and dispatch of generation units in the day-ahead scheduling is investigated. The hourly solution of the proposed method will minimize the cost of supplying the hourly load while satisfying the temporal constraints of individual components in power grids.

In Chapter 6 the coordinated integration of aggregated plug-in electric vehicle (PEV) fleets and renewable energy sources (wind energy) in power systems is studied by stochastic security-constrained unit commitment (Stochastic SCUC) model, which minimizes the expected grid operation cost while considering the random behavior of the many PEVs. PEVs are mobile and distributed devices with deferrable options for the supply/utilization of energy at various times and locations. Numerical tests demonstrate the effectiveness of the proposed approach for analyzing the impact of PEVs on the grid operation cost and hourly wind energy dispatch.

Microgrid is composed of distributed energy resources (DER) including distributed generation (DG), controllable loads, and storage. Microgrids could satisfy hourly demands economically according to power quality and reliability (PQR) requirements. Other objectives in a microgrid could include the reduction in distribution system losses and increase in the efficiency of the combined heat and power (CHP) supply. In Chapter 7, the role of high reliability distribution system (HRDS) in microgrid operations is evaluated. HRDS, which offers a higher operation reliability and fewer outages in microgrids, is applied to looped networks in distribution systems. The storage system would enhance the microgrid reliability while offering hourly ancillary services and demand response for reducing operation costs. The HRDS implemented at Illinois Institute of Technology (IIT) is used as a case study along with the local DER to increase the load point reliability and decrease the operation cost of the microgrid. The outage frequency and duration indices are measured at the microgrid level and the customer level, and the potential system enhancements are discussed at the IIT microgrid.

2) Kaveh Aflaki, Large Scale Integration of Sustainable Energy and Congestion Management in the Western Interconnection, Illinois Institute of Technology, July 2012

Abstract: Sustainable energy is the maintainable type of energy that meets the needs of the present for generating electricity without compromising the ability of future generations to meet their needs. In electricity generation, implementing sustainable energy sources for generating electricity is one of the critical and the most inevitable challenging topics. Sustainable energy resources for generating electricity which is some cases called renewable energy are wind, solar, hydro, and geothermal energy. Furthermore, sustainable energy is a term which is use for techniques to improve energy efficiency as

well in some of the researches. Wind and solar energy are the fastest growing sustainable energy sources that can be used as alternatives to the pollution generated from other electricity production in the United States. When the Department of Energy, (DOE), announced its vision for a 20% wind and a 5% solar energy contribution to electricity generation by the year 2030 in the United States, most of the research centers, national laboratories, and universities shifted their priorities to do research on different aspects of wind and solar energy. Furthermore, greenhouse gas reduction led to Carbon Tax policies for pollution generating units, which boosted the combined efforts at wind and solar energy research as well as their implementation. The DOE, as well as different recovery acts enacted at the state level, emphasize the expectation of an increased level of wind, solar, and other renewable energy sources so that together they will provide 30% of the total U.S. electricity consumed nationwide by 2030. The utilization of sustainable energy sources like wind and solar energy will offer great socioeconomic benefits reductions in power plant emissions and the supply of zero cost electricity.

Large scale wind and solar energy integration to the bulk grid could introduce inevitable challenges to regional transmission and generation systems. The most important challenges for transmission system are the congestion analysis of the grid and planning for transmission expansion to transfer the zero cost generated electricity to different electricity markets. The other big challenge is competition of current generation units in the electricity market. Current generators in the grid based on where they are located want to compete and participate in the electricity markets. However, generators like coal units are generating tons of carbon dioxide. Coming policies regarding carbon tax and adding high level of sustainable sources to the bulk grid force them to retire. This thesis addresses the congestion identification and management, optimization, simulation and analysis of large scale electric power systems in different scenarios for high level of wind and solar energy integration and related transmission expansion issues.

This thesis brings a new method used to study transmission congestions in Western Interconnection of the United States. The process involved Security-Constrained Unit Commitment (SCUC) formulation applying its results for analysis of transmission congestion. The proposed SCUC tool for these analyses is referred to as Power Market Simulator, POMS, which is being developed in the Electrical and Computer Engineering Department of Illinois Institute of Technology. With the help of POMS, all congested branches are shown on a Geographical Information System, GIS, synchronized map. In next step all congested branches are compared with two results; the National Electric Transmission Congestion Study, NETCS published by the U.S. Department of Energy in December 2009; and the annual 2009 report of Transmission Expansion Planning Policy committee, TEPPC, of Western Electricity Coordinating Council, WECC. Moreover, POMS allowed calculation of LMP for the entire WECC which was not considered in the report of NETCS.

This thesis presents results and findings in simulation of the system operation in the Western Interconnection of the United States with the inclusion of large-scale wind and solar power penetration into the grid for year 2030. For this study, a simulator is developed and implemented as a Wind Integration Simulator, WINS, in the Galvin Center for Electricity Innovation at the Illinois Institute of Technology (IIT). In WINS high level wind and solar energy with the forecasted wind and solar time series profiles were added to the bulk grid of WECC. Their impact on different existing types of generation

plants is studied. WINS utilize Security-Constrained Unit Commitment (SCUC) to simulate the wind and solar energy penetration. The bulk system of western interconnection which is coordinated and promoted by WECC and is the second largest bulk grid in the three interconnections of the North America primarily used as a case study for this thesis. High transmission capacities assumed accessible to all generation resources that mean the transmission constraints are relaxed. Moreover, none of the current bilateral contracts for WECC are considered. WINS uses hourly forecasted profiles of the wind and solar energy for an economic dispatch of the units. The production costs, wind and solar power contributions in peak load hours and off-peak load hours are also calculated and studied for this thesis. The sensitivity of the fuel prices, wind turbine power output, load volatility and demand side management as well as carbon tax are analyzed in different possible scenarios.

In order to incorporate large scale of wind and solar energy into a bulk electricity grid footprint, planned transmission expansion showed need to take place. Transmission expansion reduces grid congestion and balances Locational Marginal Prices (LMP). This thesis explores the advancements in high-performance computing and visual analytics of economic-based transmission expansion in the Western Electricity Coordinating Council (WECC). This expansion is based on 2018 and 2029 forecasted data. An advanced congestion analysis is proposed using WINS for optimization, simulation and visualization of the results. It identifies transmission congestions and different area average bus LMP, and expands the transmission system while accommodating large scale wind and solar energy to achieve the Department of Energy's (DOE) renewable energy vision for year 2030. In wind and solar integration studies, WINS applies annual wind energy forecast data as individual generation profile curves for each defined wind and solar farm units in the Security-Constrained Unit Commitment (SCUC) problem. WINS applies the SCUC engine to solve optimization issues caused by network constraints. Results are visualized on the Geographical Information System (GIS) format map. An iterative transmission expansion analysis, based on the average marginal prices for each area, is used to identify the minimum WECC transmission lines required. By using WINS, the transmission congestion and transmission expansion analysis results are visualized on a map of North America.

3) Xiaodong Shi, Survivable Operation of Three Phase AC Drives in Wind Generator Systems, Illinois Institute of Technology, May 2012

Abstract: Recent years have seen significant popularity in the use of wind generators owing to the depletion of natural resources and growing concerns about our environment. However, this development has raised issues concerning reliability of the wind turbine components. Among these faults, failure of current sensors is one of most common fault that can bring the wind generator to a standstill and lead to reduction in power yielded. In addition, unscheduled maintenance often results in longer downtime and causes reduction of wind plant availability especially for those wind turbines located offshore or in remote areas.

This dissertation proposes a survivable drive method to continue to operate the wind turbine in spite of current sensor failure. One of the common control strategies for the optimal of three-phase AC generators is vector control. Therefore, vector control method is implemented in this dissertation for both induction machine and Brushless PMSM. In order to achieve survivability when current sensor fault

happens, a simple and effective method which doesn't rely on current feedbacks is required as a backup control strategy. For this purpose, a state transition control strategy is proposed for an induction machine and a Brushless Permanent Magnet Machine. In addition, a current sensor failure detection method is designed to trigger the transition. Simulation and experimental results have been presented to prove feasibility and demonstrate the effectiveness of the proposed strategy.

4) Yao Da, Novel Fault Diagnostic Technique And Universal Sensor For Permanent Magnet Electric Machines Using Search Coils, Illinois Institute of Technology, May 2012

Abstract: Over the past decade, permanent magnet synchronous machines (PMSMs) have gained significant popularity in industry, such as wind turbines and electric vehicles, owing to their high efficiency, high output power to volume ratio, and high torque to current ratio. In these mission critical applications, an unexpected fault or failure of the machine could lead to very high repair or replacement cost, or even catastrophic system failure. Therefore a robust and reliable health monitoring and fault diagnostic approach is desired, which could help in scheduling preventive maintenance to lengthen their lifespan and avoid machine failure. This dissertation presents a novel multi-faults diagnostic approach using search coils. These search coils are wound around armature teeth, so they typically need to be installed during manufacturing. But its immunity to high frequency harmonics makes it suitable for inverter/rectifier fed motors or generators, such as wind turbines and automotive systems. In addition, this method does not require the knowledge of proprietary constructional details of the machine. Since the electromagnetic flux is directly measured in this method, it provides much more information than any other scheme: the direction of eccentricity and the location of shorted windings. Furthermore, this method is also capable of evaluating the severity of each fault, which is of significant importance in mission critical applications such as automotive, aerospace and military applications. In addition to these uses, the search coils can be used as a universal sensor to estimate phase current or rotor position, which are critical information in a PMSM close-loop control, which allow it to work as a backup sensor for fault tolerant operation. The proposed fault detection scheme and universal sensor concept have been tested under several scenarios with Finite Element Analysis and experimentally validated.

5) Jie Li, Optimal Behavior Modeling and Analysis of Electricity Market Participants, Illinois Institute of Technology, May 2012

Abstract: In restructured electricity power markets, competition among market participants is a key issue of concern for both the ISO (Independent System Operator) and the market participants themselves. This dissertation analyzes the market behavior of both the generation side and demand side participants, and provides solution guidelines for devising effective competition strategies for market players' profit maximization objectives.

Generation side is the most competitive part in the electricity market with the unbundling of generation, transmission and distribution. Acting as self-interested entities, GENCOs (Generation Companies) are seeking effective and computationally efficient methodology for generation resource scheduling, while keeping its financial risks at acceptable levels when constituting bidding strategies. To help GENCOs

achieve such goal, this dissertation propose a game theory based supply function like bidding model to construct the optimal bidding strategies in both energy and ancillary service markets.

On the demand side, demand participation in the electricity market has already been advocated for a long time for its benefit to the entire market and the society as a whole. This dissertation focuses on a specific large electricity consumer type – Internet Data Center (IDC). By analyzing the unique energy consumption pattern for different IDC applications, this dissertation devises effective electric demand management solution, and quantifies the demand response effect of IDC on the electricity market.

6) Yanling Yuan, Load Redistribution Attacks and Protection Strategy in Electric Power Systems, Illinois Institute of Technology, May 2012

Abstract: Electric power systems have evolved over the past century to the largest and the most complex cyber-physical systems. With the development of Smart Grid, cyber security has becoming an area of growing concern. The well functioning of state estimation, which provides faithful estimation of the real-time physical system information based on a large number of distributed meter measurements, is of paramount importance for maintain stable and secure system operation. False data injection attack, which is against state estimation through SCADA network, has recently attracted wide research interest. This paper further develops the concept of load redistribution attack, a special type of false data injection attack. The physical and market impact of load redistribution (LR) attacks are quantitatively analyzed in this thesis.

Since LR attacks can successfully bypass bad data detection and manipulate the state estimation outcome, Security constrained economic dispatch (SCED) based on the false estimated state would lead the system into a false secure and optimal operating state. The physical damaging effects of LR attacks are analyzed thoroughly in this thesis. Based on the damaging effect analysis, two different attacking goals are differentiated from the adversary's perspective, i.e., immediate attacking goal and delayed attacking goal. For the immediate attacking goal, a max-min attacker-defender model is proposed to identify the most damaging immediate LR attack. Different algorithms are used to solve this bi-level optimization problem. For the delayed attacking goal, a tri-level model is proposed and solved to identity the most damaging delayed LR attack. This paper is a first attempt to formalize the physic impact of false data injection attacks on the system operation and control.

Recent research examined the possible economic impact of false data injection attacks against state estimation in electric power market operations. False data injection attacks, by manipulating the state estimation, can manipulate the nodal price of ex-post real-time market. In conjunction with virtual bidding, these integrity attacks can lead to consistent financial profit for the attacker. This thesis further this study by quantifying the economic impact of LR attacks to the market operation of power systems. A convex model is developed under the mechanism of virtual bidding to compute the optimal injection of LR attack and the optimal selection of nodal pairs for virtual power, which gains the most profit from the attackers' perspective.

This thesis investigates the construction of LR attacks against AC state estimation. A practical procedure is proposed to construct an effective LR attack that can bypass the bad data detection (BBD) in AC state estimation, while having great damaging effect to the physical and market operation of power systems.

The quantitative impact analysis of LR attacks provides an in-depth insight on effective attack prevention with limited protection resource budget. This thesis also proposes the theory and criterion of protecting the system from the damage of a specific LR attack, considering the existence of stochastic measurement error. Effective protection strategies can then be designed to defeat the attacker's attempt.

7) Wei Tian, Large-scale Simulation of Electric Power Systems for Wind Integration, Illinois Institute of Technology, July 2011

Abstract: The utilization of wind energy will pose great socioeconomic benefits with reductions in power plant emissions and the supply of zero cost energy; however, large-scale wind energy integration could introduce inevitable challenges to regional transmission systems and hourly system operations. This thesis addresses the congestion identification, simulation and analysis of large-scale electric power systems in different scenarios, large-scale wind energy integration and related transmission expansion issues.

A methodology based on the security-constrained unit commitment (SCUC) is applied to analyze the transmission congestions in the Eastern Interconnection of the United States. The identified congestions are visualized along with the Geographical Information System (GIS) data and compared with the results in National Electric Transmission Congestion Study (NETCS) published by the Department of Energy of the United States in 2006. The study also provides the locational marginal price (LMP) information in the Eastern Interconnection, which is not available in the NETCS report.

This thesis implements a comprehensive simulation and scenario analysis of the Illinois electric power system for the year 2011. Possible scenarios representing electrical load sensitivities to economic growth, fuel price variations, and the impact of carbon cost, are studied.

This thesis presents the hourly simulation results for the large-scale wind energy integration in the Eastern Interconnection of the United States. An hourly unit commitment is applied for the simulation of the economics of wind energy integration in the year 2030. The energy portfolio for supplying the hourly load in 2030 is developed based on wind integration levels. The sensitivities of fuel price, wind energy quantity, load forecast, carbon cost, and load management to the proposed 2030 wind integration are studied.

This thesis identifies transmission congestions and expands the existing transmission system in the Eastern Interconnection of the United States for accommodating a large-scale integration of wind energy. Violated transmission flows which would cause the infeasibility of hourly SCUC are identified. An iterative transmission expansion analysis is implemented to identify the minimum required additions to the Eastern Interconnection for mitigating hourly transmission congestions.

8) Bruno Monnier, Three Dimensional Flow Structures and Turbulence Distribution in an Urban Environment, Illinois Institute of Technology, December 2010

Abstract: Understanding and controlling the dispersion of pollutants and contaminants in urban areas has become a major focus recently. Field measurements, numerical studies, and wind tunnel experiments have increased in number. Specifically, there is a growing need for a spatio-temporal description of such complex flow fields under well-controlled conditions, typically obtained in wind tunnel experiments. The reduced scale model of interest is a 4 by 3 array of cuboid blocks in an experimentally modeled, neutrally stratified, atmospheric boundary-layer. The use of Stereoscopic Particle Image Velocimetry (SPIV) allows for a three-dimensional description of this urban flow. A large amount of SPIV data is collected upstream and in each middle street of the urban environment allowing for a study of the flow evolution from street to street. Valuable information about the flow structures are presented along with the mechanisms responsible for contaminant transport and dispersion. The effects of small incidence angles of the incoming flow with respect to the urban array and the effects of streamwise spacing between streets on the flow characteristics are investigated. A major observation from this work is that a strong channeling effect is observed for incidence angles as small as 4.5◦ and is found to be comparable in strength to that observed in other investigations for much larger angles. A coupling between this channeling effect and the structures responsible for contaminant transport is revealed.

An innovative method using sparse measurements to estimate the continuous temporal evolution of the dominant structures in the flow is investigated. Proper Orthogonal Decomposition is used to obtain a reduced-order representation (ROR) of the flow field. Sparse velocity measurements within the domain serve as input to measurement models that provide an estimation of the ROR of the velocity field. This ROR of the flow field could be regarded as the first that provides a temporal evolution of a spatially well-resolved flow field in a complex geometry. Finally, a linear state-space model is used to describe the continuous temporal evolution of the ROR of the velocity field which is of primary importance with respect to contaminant tracking at the urban scale.

9) Mark E. Carlos, An Analysis of Wind Power Plant Site Prospecting in the Central United States, Southern Illinois University, December 2010

Abstract: Rapid deployment of terrestrial wind power plants (WPPs) is a function of accurate identification of areas suitable for WPPs. Efficient WPP site prospecting not only decreases installation lead time, but also reduces site selection expenses and provides faster reductions of greenhouse gas emissions. Combining conventional predictor variables, such as wind strength and proximity to transmission lines, with nonconventional socioeconomic and demographic predictor variables, will result in improved identification of suitable counties for WPPs and therefore accelerate the site prospecting phase of wind power plant deployment. Existing and under-construction American terrestrial WPPs located in the top 12 windiest states (230 as of June 2009) plus 178 potential countylevel predictor variables are introduced to logistic regression with stepwise selection and a random sampling validation methodology to identify influential predictor variables. In addition to the wind resource and proximity to electricity transmission lines, existence of a Renewable Portfolio Standard, the population density within

a 200 mile radius of the county center, median home values, and farm land area in the county are the four strongest nonconventional predictors (Hosmer and Lemeshowχ 2 = 9.1250, N = 1009, df = 8, p = 0.3319, -2LogLikelihood = 619.521). Evaluation of the final model using multiple statistics, including the Heidke skill score (0.2647), confirms overall model predictive skill. The model identifies the existence of 238 suitable counties in the twelve state region that do not possess WPPs (~73% validated overall accuracy) and eliminates 654 counties that are not classified as suitable for WPPs. The 238 counties identified by the model represent ideal counties for further exploration of WPP development and possible transmission line construction. The results of this study will therefore allow faster integration of renewable energy sources and limit climate change impacts from increasing atmospheric greenhouse gas concentrations.

10) Amin Khodaei, Optimal Transmission Switching in Power System Operation and Planning, Illinois Institute of Technology, December 2010

Abstract: Transmission networks are traditionally considered as fixed assets where market-based changes in transmission states are not considered by power system operators. However, system operators consider changes in transmission states by adjusting the network topology for security purposes. The adjustment in transmission state, known as transmission switching (TS), could mitigate transmission flow violations, manage congestion, enhance power system security and adjust bus voltage levels. TS, as a market tool, could potentially affect power generation dispatch and commitment and improve power system economics.

This dissertation presents the formulations and the methodologies for combining the security as well as the economic features of TS. The TS applications are incorporated into the DC model of security-constrained unit commitment (SCUC) for the day-ahead power system scheduling. The dissertation will also consider the AC solution of SCUC for TS applications. The TS application to the AC network solution will enhance the reactive power flow for mitigating any bus voltage violations. The power system operation results are compared based on the AC and the DC power network solutions and the results are discussed. TS applications are also considered in the security-constrained power system planning in which various network planning options are considered for improving the short-term TS solutions. The TS solutions will improve the real power flow and provide security and the economic feedbacks to the planning module on how the long-term planning alternatives can be improved. The results are discussed and additional recommendations are made for future TS studies in power systems.

11) Shaghayegh Bahramirad, Design and Implementation of Hydrokinetic Run-of-River Turbines, Illinois Institute of Technology, December 2010

Abstract: The restructured electric power system considers load as a constant value and that the forecasted load value should be satisfied under any circumstances. Therefore, the competition was among generators that submit strategic bids to the ISO (independent system operator) to supply the forecasted load. The market clearing price is set by the marginal price of the last accepted generator to satisfy the fixed load. Thus the demand-side has no role in the market clearing and price setting process. Furthermore, price spikes might occur when the demand-side has no role in setting electricity prices, so

generators have no incentive to bid close to their marginal cost which would lead to bids that are much higher than actual generation costs. This behavior would lead to volatile market prices that are far from the perfectly competitive prices. The demand-side participation may reduce the system load during peak periods, which is a more economical way to respond to generation capacity shortages. Using demand-side also mitigates the potential to exercise market power, which is caused by price manipulations of generation companies. The price manipulations mainly occur when the generation schedule is obtained through the minimization of total operating cost, i.e. no load-side participation is considered. An increase in demand-side participation would have benefits for individual consumers and the entire electricity market. Demand-side participation would include distributed generation, on-site storage, and demand response. This dissertation discusses two aspects of demand side participation; distributed generation and demand response. Hydrokinetic energy as an example of distributed generation has been studied. A hydrokinetic turbine has been designed and a sensitivity analysis has been performed with an optimal placement of turbines in a hydrokinetic farm. In addition, demand response in a day ahead market clearing process has been investigated.

12) Cong Liu, Interdependency of Gas and Electricity in Restructured Power Systems, Illinois Institute of Technology, July 2010

Abstract: The electric power generation relies increasingly on the natural gas supply system as additional natural gas-fired power plants are installed in restructured power systems. In this context, the economics and the reliability of electric power and natural gas systems will impact one another. This dissertation addresses the interdependency of electricity and natural gas systems and proposes an integrated approach for the operation and the scheduling of the coupled energy systems.

The dissertation considers combined-cycle gas turbine units (CCGTs) as key elements for linking electric power and natural gas systems and proposes mode and component models for representing CCGTs. The component and mode models are used in scheduling of CCGTs by mixed-integer programming (MIP).

The dissertation proposes two integrated short-term scheduling models. The first one is from the viewpoint of the ISO (Independent System Operator) which proposes a security-based methodology for the unit commitment solution when considering the natural gas transmission system and contracts. The proposed solution applies a Benders decomposition method to incorporate the natural gas transmission feasibility check subproblem in the security-constrained unit commitment (SCUC) solution. The second integrated model considers a joint-operator for the coordinated scheduling of the interdependent electric power and natural gas systems. The integrated operator utilizes an augmented Lagrangian relaxation (LR) based model for the coordinated least-cost allocation of natural gas resources to individual gas loads and generating power plants.

The natural gas flow exhibits remarkable differences with the electric power flow because of the slow response of the former system and storage nature of pipelines. The dissertation also proposes an integrated short-term scheduling model with the transient state natural gas flow formulations which is represented by a group of partial differential equations and nonlinear algebraic equations. In this

dissertation, the implicit finite difference method is adopted to approximate partial differential equations into algebraic difference equations.

13) Saeed Kamalini, Security Constrained Expansion Planning of Fast-Response Units for Wind Integration, Illinois Institute of Technology, July 2010

Abstract: The increasing socio-environmental concerns have persuaded decision makers to support large integrations of WG (Wind Generation) in power systems. Renewable generation is fuel-free and clean which would reduce the cost of electricity production and delivery. On the other hand, WG is volatile and intermittent. WG uncertainties could decrease the expected payoff of a GENCO (Generation Company) and possibly reduce the investors' interest in the WG capacity planning. Chapters 2 and 3 in this study have developed sophisticated mechanisms for proper WG expansions. Chapter 4 discusses that proper long-term and mid-term operations planning which would include the simulation of power system uncertainties could provide a wider range of global options for managing the reliability and economics in power systems operations. From a power system's viewpoint, WG fluctuations could lead to additional system reserve requirements and the adoption of fast-response units for reliability purposes which would result in higher operation costs. Indeed, such conflicts between reliability and economics are inevitable in competitive environments. The optimal capacity expansion of renewable generation and fast-response capacity is the main theme of this dissertation. Chapter 5 discusses that the large integration of WG would also affect other generation resources including fossil fuel based and hydro units. A proper long-term or mid-term operation planning study is required to investigate the coordination of various generation resources.

This dissertation offers algorithms for managing tradeoffs between profitability and reliability. The dissertation discusses assumptions, functions, and methodologies for the large integration of WG that would maximize profits of self-interested GENCOs and enhance the power system operation reliability at the presence of uncertainties.

### 4.4.2 M.S. Theses

1) Ming Cai, Modeling and Numerical Simulation of Wind Turbine Performance in Rainy Conditions Using a Multiphase Flow Approach, Illinois Institute of Technology, May 2012

Abstract: Wind energy is becoming one of the key renewable sources of energy in the United States and the world due to its environmental and economic advantages and absence of water requirements. The performance of a wind turbine is largely affected by surrounding environments and the total power output of a wind farm is closely related to meteorological phenomena such as rain and icing. Investigating the effects of these phenomena is necessary to improve the design and performance of the wind turbines. In this research, we focused on the study of wind turbine performance in rainy conditions as the stepping stone to the future study of icing. We applied Computational Fluid Dynamics (CFD) technology to investigate the impact of rain on wind turbines. A novel model coupling the Lagrangian

method with the Eulerian method was developed. The rain droplet was tracked in the Lagrangian frame due to its discrete nature, and the film formed on the wind turbine was simulated with the Eulerian Volume of Fluid Model (VOF). The performance loss and impact on the flow field were also studied. Numerical studies have been conducted on 2-Dimensional S809 airfoils and 3- Dimensional Horizontal Axial Wind Turbines (HAWT). The performance loss under heavy rain conditions was observed and the flow field was analyzed. The impact of air moisture content on wind turbine performance was also studied using our 3-D model. Due to the lack of experimental data on wind turbine performance under heavy rain conditions, our coupled two phase flow model was applied to a NACA 64-210 airfoil to compare with the experimental data in rainy conditions. Simulation results using our model showed good agreement with the experimental data.

2) Hirenkumar Patel, Analysis of Mechanical Noise Generation in Wind Turbine Drive Train, Illinois Institute of Technology, May 2012

Abstract: The research work presented here is a part of a project, funded by U.S. Department of Energy to study mechanical noise generated by a wind turbine drive train. In our study a Viryd 8 kW wind turbine drive train test bed located at the Illinois Institute of Technology was used. Various wind speeds and turbulence levels could be simulated using a computer program that is used to control the test bed. Acoustic measurements were carried out using a single microphone and a microphone array. The microphone array was used to localize noise sources on the drive train. Various beamforming algorithms such as FDBF, DAMAS2, CLSC, DAS and TIDY were used to study the noise sources. Qualification experiments using synthetic sources showed that \Clean based on spatial coherence" beamforming algorithm localizes noise sources very accurately for narrowband frequency analysis and TIDY was found to work best for broadband analysis. The resolution of the beamform maps improved for higher frequencies of interest (>700 Hz). The continuous variable planetary (CVP) gearbox, which is a proprietary gearbox by Viryd was used in the drive train to optimize the generator rotational speed. An interesting trend was observed in active power generated for the wind speeds greater than 10 m/s, where the power does not increase significantly as it is regulated at 6000 Watts. CVP speed ratio, ratio of input rotational speed to output rotational speed of CVP, was also found to be having similar effect after wind speed reaches a value of 10 m/s. Vibrations of the drive train test bed were studied using accelerometers. It was observed that the test bed was vibrating at a fundamental frequency of 120 Hz, with harmonics of decreasing amplitude at 240 and 360 Hz. Vibrations in all degrees of motion were found to be occurring at similar frequencies. Acoustic beamforming using a microphone array showed that the test bed was a dominant noise source at the same frequencies. Initially the entire test bed was covered by a Plexi-glass casing for safety reasons. It was found that the glass casing affected the microphone array measurements as the noise produced by the components had no direct path to the array. Almost all the measured noise was refracted through the gaps between the glass casing and the stretcher holding it, that led to spurious microphone array results. As a result of this, the experiments were conducted without the glass casing. It was discovered after the experiments that the glass casing not only affects the path of sound but the amplitude is also affected. The components of the drive train namely gearbox, brake, CVP and generator, were found to be emitting sound at various discrete frequencies ranging from 165 to 3885 Hz. They were also found to be emitting broadband noise, where

gearbox and generator were found to be most dominant noise sources. We were able to separate each noise source on a complex wind turbine drive train that contributed to the mechanical noise generation from a wind turbine.

3) Jing Guo, Control Of Doubly-Fed Induction Generator For Wind Application, Illinois Institute of Technology, May 2012

Abstract: With growing concerns over environmental pollution and globe warming, renewable energy has received considerable attention as an alternative energy resource of electricity production. Because of the immense potential of wind energy on the earth, wind power generation has gained significant popularity over recent years. From this research, it has been concluded that there is a constant need to reduce the size and rating of power electronic converters, improve efficiency of the electromechanical system and make the system more reliable by eliminating the gearbox. This thesis analyzes a doubly fed induction generator (DFIG) drive system for distributed wind generation systems. The structure of a doubly fed induction generator is similar to that of an induction generator. To illustrate the operation principle and control strategy of a DFIG clearly, the fundamentals and control principle of an induction generator have been discussed. For DFIG control, two closed control loops are designed-active power control loop and rotor speed control loop; and they can be switched between each other. By utilizing active power control loop, the output power of the system can be regulated to meet different customer requirements and their dependence on grid electricity can be eliminated, therefore the cost and the power loss on transmission lines can be reduced. On the other hand, by switching to the speed control loop, the system can extract maximum power at different wind speeds, and any extra power can either be stored or sold to the utility for profit. To validate the proposed concept, Finite Element Analysis (FEA) models of a doubly fed induction generator and an induction generator have been built and simulated using the software Magnet®; furthermore, the control systems of these two generators are implemented and simulated in a Matlab/Simulink environment. Finally, a Magnet and Matlab/Simulink co-simulation has been performed for the DFIG. By analyzing the simulation results, the differences between the doubly-fed induction generator and an induction generator have been demonstrated.

4) Udit Goyal, Computational Techniques for Wind Turbine Power Prediction, Illinois Institute of Technology, December 2011

Abstract: Wind energy is expected to play an important role in meeting the ever- increasing energy requirements and reducing our dependence on conventional sources of energy. Wind turbines are broadly classified as horizontal-axis and vertical-axis depending upon the orientation of the rotor shaft relative to the wind direction. Considerable research has been carried out on horizontal-axis wind turbines, which today are sophisticated and efficient electro-mechanical systems. Continuous research and development in areas of electronics, controls and instrumentation aids in the advancements of this technology. From an aerodynamic point of view the Betz limit is known to impose theoretical limit on the power extraction of propellers. The momentum balance equations show that the maximum of 59.3 percent of free-stream energy can be extracted by propellers. This limit, however is not well de fined, particularly when considering diff user and nozzle-augmented wind turbines with local flow accelerations. In this study the actuator disk approach is used to model the momentum loss across a

wind turbine rotor and simulate the Betz limit using Fluent software. This approach is subsequently applied to study the coefficient of performance expected from different user and nozzle-augmented wind turbines. Vertical-axis wind turbines, on the other hand, are still not completely understood in terms of blade aerodynamics and are the focus of various research studies. Large variations in angle of attack and wake evolution downstream of the blade have a time-dependent effect on the blade forces, instantaneous torque and hence the coefficient of power of the turbine. Since Navier-Stokes solutions for vertical- axis wind turbines are expensive and complicated, various low-cost models have been developed based on momentum balance such as single, double and double multiple-streamtube formulations. These models, however, use static lift and drag data for the airfoils as inputs, neglecting the unsteady effects on aerodynamic coefficients. In the present study, an alternative approach based on the panel method is explored further for developing a low-cost computational method for simulating the aerodynamics of vertical-axis wind turbines. At each time step an airfoil is represented as a combination of source and vortex distributions which induce a potential in the flow field. A time-stepping mechanism is implemented satisfying the Kutta and the Kelvin Helmholtz condition for the wake evolution behind the rotating blades. The effect of this vortex evolution on the aerodynamic forces on the airfoil is studied, focusing on the coefficient of performance (Cp) of the blade. Results show a decrease in Cp values till the wake attains a quasi-steady state. A comparison study is performed with other computational models, showing the importance of the wake evolution in time. An optimization of the blade pitch angle is also performed by defining a composite variable pitch function in order to improve the torque and hence the instantaneous power from the blades.

5) Chandrahas Aserkar, Induction Motor Modeling For Electromechanical Dynamic Simulation and Electromagnetic Transient Simulation, Illinois Institute of Technology, December 2011

Abstract: The initial part of this research work focuses on distribution power flow for agent based distribution systems. Power flow analysis is an essential tool for power system planning and operation. Traditionally, most distribution systems are radial or weakly meshed types. Faced with the power markets of today, increasing requirements for reliability and ongoing distributed generation have meant that the structure of the distribution systems has become more complex. Also, with the advent of smart-grid technology, distribution automation and micro-grids, the distribution systems are focusing towards distributed control with the use of smart switches via agents. Thus the need for power flow analysis in such systems becomes more important than before. The forward-backward sweep method is a very popular method for distribution power-flow analysis. But, the traditional forward-backward sweep method focuses on the load flow solution based on the bus-injection to branch-current (BIBC) matrix, which is calculated considering the network topology. For distribution systems focusing on distributed control, the complete distribution network topology is unknown to any one agent and hence the complete BIBC matrix is not formed. Rather, the property of these agents to communicate with each other is exploited to obtain the power flow solution. Here, we focus on altering the network topology based algorithm for forward-backward sweep method so as to make it suitable for agent based distribution systems. The later part of this research work focuses on development of induction motor load models for transient dynamic stability simulators (TS) and electromagnetic transient simulators (EMT), to study the voltage stability of power systems. A Transient Stability simulator runs at a larger

time step and is used to study relatively slower dynamics in the system. On the other hand, an Electromagnetic Transient simulator uses a smaller time step to capture the fast dynamics in the system. A combined TS-EMT simulator attempts to model the bulk of the system as a slowly varying dynamic system and a small portion of the system for which the fast dynamics are to be studied, with an electromagnetic transient model. Load modeling is a very important aspect for studying power system stability. Power system stability is the property of a power system that insures the system remains in electromechanical equilibrium throughout any normal and abnormal operating conditions. It is thus defined as the ability of designated synchronous machines in the system to remain in synchronism with one another following disturbance at various locations in the system. It also indicates the ability of induction motors in the system to maintain electrical torque to carry the load following these disturbances. This research work provides a detailed modeling of the induction motor for electromechanical as well as electromagnetic transient simulations and uses them to study the effects of composite load models on power system voltage stability.

6) Joan Camprubi, Sustainable Stadium: Qatar 2022, Illinois Institute of Technology, July 2011

Abstract: This thesis tries to evaluate in general terms which are the energy needs and concerns for a sustainable soccer field planned to be built for the next 2022 Qatar World Cup. To face the issue about the high temperatures and to reduce the electricity waste and greenhouse effect, several renewable energies such as solar, wind, heat pumps or piezoelectric energies would be taken into account. Some economic concerns and other approximations have been done in order to achieve a general overview of the impact of solar and wind energy to feed the stadiums grid and also make some profits at the same time that geothermal heat pumps can help to decrease air conditioning costs and piezoelectric energy can be tested and included as a future prospective to look after. Moreover is an opportunity to show to the entire world that a sustainable stadium with 8.6MW of solar and 1.6MW of wind power is feasible and Qatar could decrease their oil dependence.

7) Naglaa Elashry, Modeling and Simulation of Wind Power Generation Using Kites, Southern Illinois University, May 2011

Abstract: This thesis presents the modeling and simulation of wind energy generators, denoted as KiteGen, which employ power kites to capture high altitude wind power. A simple kite model is used to describe the system's dynamics. A simple structure for KiteGen is investigated through simulation. The Simscape and SimMechanics toolboxes (under Matlab) are used to develop the simulation model of the system. Linearized model of the system as well as its reduced order models are found using Matlab/Simulink and control toolbox to determine the stability, controllability and observability of the system for the purpose of control design.

8) Emad Elhaji, Impact of Wind Turbine on Power System Voltage Stability, Southern Illinois University, May 2011

Abstract: This thesis discusses the impact of WTGUs on the IEEE 26-bus power system voltage stability. The effect of WTGUs is studied by increasing the real generated power and real and reactive load power by factor (1+delta_lambda), where delta_lambda is incremental in the loading factor until reaching the

voltages on the buses to the point of collapse. The lowest voltage bus in the system is a critical bus that WTGUs will be connected on it. The WTGUs are Farm of wind turbines that are connected to the system. Two types of WTGUs are discussed in this thesis. The first type of WTGU that discus is the fixed speed wind turbine. There are two types of fixed speed wind turbines: pitch angle regulated, and stall regulated. The pitch angle regulated fixed speed wind turbine is focused in this study. The second type of WTGU is the semi-variable speed wind turbine.

The models of WTGUs for both types (pitch angle regulated, and semivariable speed) are used to calculate the reactive power that will be added to the system, but real power is known from manufacture. The real and reactive powers for both WTGUs are dependent on the wind speed, wind turbine characteristic, parameters for induction generator and terminal voltage.

One of the most important parts in this thesis is the sensitivity analysis. The main concept of the sensitivity is the slope of the voltage profile at specific loading factor lambda. In this part, the study is focused on the effect of increasing the real generated power and real and reactive loaded power on the critical bus.

9) Erik Ela, “Advanced Interaction between Day-Ahead Markets and Unit Commitment Methods with High Wind Power Penetrations,” ECE Department, Illinois Institute of Technology, May 2010.

Abstract: Recent trends in the power and electrical energy industry have seen tremendous growth in the amount of installed wind power plants for use in power generation. Concerns of climate change and the availability of fossil fuels have stimulated interest in providing increasing amounts of renewable energy. Many countries see wind power as a major contributor to the total renewable energy mix. Wind power plants have a collection of wind turbine generators that convert the power of the wind into electrical energy. The plants can cover vast areas and can have wind speeds that are variable both geographically and temporally. This variability in wind speed that leads to variability in wind power production makes wind power generation a unique source of power generation.

The power system is very complex in nature. When restructuring of the industry began, innovative ways of administering a market had to be thought of so that the laws of economics do not clash with the laws of physics. When the first energy markets were being designed, wind power held a very small fraction of the participants in the market and its unique characteristics were not anticipated. Since wind power has grown in recent years, wind power forecasting has become an essential tool to assist in its integration. This research attempts to step back to see if the current process of integrating wind power and wind power forecasts into the unit commitment and day-ahead markets is efficient. It then evaluates novel ideas from prior research to improve this process and how these new methods could be integrated into the current market structures.

## 4.5 List of Papers and Reports

### 4.5.1 Journal Publications

1) Wei Tian, Mohammad Shahidehpour, Zuyi Li, Analysis of 2030 Large-Scale Wind Energy Integration in the Eastern Interconnection Using WINS, The Electricity Journal, Volume 24, Issue 8, October 2011, Pages 71-87

Abstract: A simulation of the 2030 load forecast in the Eastern Interconnection suggests that large-scale wind energy integration will have a major impact on the hourly commitment and dispatch of gas and coal units, especially at off-peak load hours. While fuel price alterations will have major impacts on the system production cost, load variation will have a larger impact and potential carbon costs will have the greatest impact.

2) S. Kamalinia, M. Shahidehpour, and A. Khodaei, "Security-constrained expansion planning of fast-response units for wind integration," Electric Power Systems Research, vol.81, no.1, pp.107-116, January 2011

Abstract: This paper proposes a stochastic expansion planning of fast-response thermal units for the large-scale integration of wind generation (WG). The paper assumes that the wind integration level is given and considers the short-term thermal constraints and the volatility of wind units in the planning of fast-response thermal units. Random outages of generating units and transmission lines as well as hourly load and wind speed forecast errors are modeled in Monte Carlo scenarios. The Monte Carlo simplification methods are introduced to handle large-scale stochastic expansion planning as a tradeoff between the solution accuracy and the calculation time. The proposed security-constrained approach can be used by an ISO or a regulatory body to secure the optimal planning of power systems while the WG integration is increasing. The effectiveness of the proposed approach is demonstrated through numerical simulations.

3) S. Kamalinia and M. Shahidehpour, "Generation expansion planning in wind-thermal power systems," IET Generation, Transmission & Distribution, vol.4, no.8, pp.940-951, August 2010

Abstract: The intermittency and volatility of wind generation (WG) would require additional upward and downward reserves, as well as enhanced ramping capabilities in power systems. This paper investigates the optimal expansion planning of fast-response generating capacity (e.g., gas-fired units) to accommodate the uncertainty of WG. The study utilizes a MIP-based security-constrained unit commitment (SCUC) for analyzing operational and reliability issues related to the proposed optimization problem. Numerical experiments signify the effectiveness of the proposed method.

4) M. Khodayar, M. Barati, and M. Shahidehpour, "Integration of High Reliability Distribution System in Microgrid Operation," IEEE Transactions on Smart Grid, Vol. 3, 2012

Abstract: In this paper, the application of high reliability distribution system (HRDS) in the economic operation of a microgrid is studied. HRDS, which offers higher operation reliability and fewer outages in

microgrids, is applied to looped networks in distribution systems. The microgrid model in this study is composed of distributed energy resources (DER) including distributed generation (DG), controllable loads, and storage. The microgrid would utilize the local DER as well as the main grid for supplying its hourly load economically which is subject to power quality and reliability requirements. The HRDS implemented at Illinois Institute of Technology (IIT) is used as a case study along with the local DER to increase the load point reliability and decrease the operation cost of the IIT microgrid. The availability of distribution lines, main grid supply, and microgrid generation is considered using the Markov chain Monte Carlo simulation in the microgrid scenarios. The reliability indices based on frequency and duration of outages are measured at the microgrid level and the load point level, and the potential system enhancements are discussed for improving the economic operation of the IIT microgrid.

5) A. Khodaei, M. Shahidehpour, "Microgrid-based Co-optimization of Generation and Transmission Planning in Power Systems," IEEE Transactions on Power Systems, Vol. 27, 2012

Abstract: This paper presents an algorithm for the microgrid planning as an alternative to the co-optimization of generation and transmission expansion planning in electric power systems. The integration of microgrids in distribution systems will offer a decentralized control of local resources for satisfying the network reliability and the power quality required by local loads. The objective in this paper is to minimize the total system planning cost comprising investment and operation costs of local microgrids, the co-optimized planning of large generating units and transmission lines, and the expected cost of unserved energy. The cost of unserved energy reflects the cost of load shedding which is added to the objective function for reliability considerations. The microgrid-based co-optimization planning problem is decomposed into a planning problem and annual reliability subproblem. The optimal integer planning decisions calculated in the planning problem will be examined against the system reliability limits in the subproblem and the planning decisions will be revised using proper feasibility cuts if the annual reliability limits are violated. Numerical simulations demonstrate the effectiveness of the proposed microgrid-based co-optimization planning in power systems and explore the economic and reliability merits of microgrid planning as compared to grid-based generation and transmission upgrades.

6) M. Khodayar and M. Shahidehpour, "Stochastic Price-based Coordination of Intra-hour Wind Energy and Storage in a Generation Company," IEEE Transactions on Sustainable Energy, 2012

Abstract: This paper develops a day-ahead price-based scheduling strategy for the coordination of wind and storage units in a generating company (GENCO). The proposed strategy is based on the stochastic price-based unit commitment (PBUC) which considers volatilities in day-ahead intra-hour market prices and wind power generation when scheduling wind and storage units. The proposed approach firms up the hourly sum of wind and storage unit generation, and mitigate potential wind energy imbalance charges for GENCOs in electricity markets. Although the proposed approach applies to any kind of storage, we consider the pumped-storage hydro (PS) unit in this study. Numerical examples illustrate a GENCO's day-ahead coordinated scheduling results for wind and PS units.

7) H. Wu, M. Shahidehpour, and A. Al-Abdulwahab, “Hourly Demand Response in Day-ahead Scheduling for Managing the Variability of Renewable Energy,” IET Journal on Generation, Transmission & Distribution, 2012

Abstract: This paper proposes a stochastic optimization model for the day-ahead scheduling in power systems, which incorporates the hourly demand response (DR) for managing the variability of renewable energy sources (RES). DR considers physical and operating constraints of the hourly demand for economic and reliability responses. The proposed stochastic day-ahead scheduling algorithm considers random outages of system components and forecast errors for hourly loads and RES. The Monte Carlo simulation (MCS) is applied to create stochastic security-constrained unit commitment (SCUC) scenarios for the day-ahead scheduling. A general purpose MILP software is employed to solve the stochastic SCUC problem. Numerical results in the paper demonstrate the benefits of applying DR to the proposed day-ahead scheduling with variable renewable energy sources.

8) A. Khodaei, M. Shahidehpour, L. Wu, and Z. Li, “Coordination of Short-Term Operation Constraints in Multi-Area Expansion Planning,” IEEE Transactions on Power Systems, Vol. 27, 2012

Abstract: This paper presents a comprehensive expansion planning algorithm of generation and transmission components in multi-area power systems. The objective is to minimize the total system cost in the planning horizon, comprising investment and operation costs and salvage values subject to long-term system reliability and short-term operation constraints. The multi-area expansion planning problem is decomposed into a planning problem and annual reliability subproblems. The planning decisions calculated in the planning problem would also satisfy the short-term operation constraints. A detailed model of thermal and hydro units is considered using the mixed-integer programming (MIP) formulation. In addition, a multi-state representation for the expansion planning of renewable energy units is explored. The proposed approach considers customers’ demand response as an option for reducing the short-term operation costs. The planning problem solution is applied to the annual reliability indices subproblems which examine system reliability indices as a post-processor. If the reliability limit is not satisfied, additional reliability constraints will be introduced which are based on the sensitivity of system reliability index to investment decisions. The new reliability constraints are added to the next iterations of the planning problem to govern the revised plan for the optimal expansion. Numerical simulations indicate the effectiveness of the proposed approach for solving the operation-constrained multi-area expansion planning problem of practical power systems.

9) C. Sahin, M. Shahidehpour, I. Erkmen, “Allocation of Hourly Reserve versus Demand Response for Security-Constrained Scheduling of Stochastic Wind Energy,” IEEE Transactions on Sustainable Energy, 2012

Abstract: This paper presents a stochastic method for the hourly scheduling of optimal reserves when the hourly forecast errors of wind energy and load are considered. The approach utilizes the stochastic security-constrained unit commitment (SCUC) model and a two-stage stochastic programming for the day-ahead scheduling of wind energy and conventional units with N-1 contingencies. The effect of

aggregated hourly demand (DR) response is considered as a means of mitigating transmission violations when uncertainties are considered. The proposed mixed-integer programming (MIP) model applies the Monte Carlo method for representing the hourly wind energy and system load forecast errors. A 6-bus, 118-bus, and the Northwest region of Turkish electric power network are considered to demonstrate the effectiveness of the proposed day-ahead stochastic scheduling method in power systems.

10) M. Khodayar, L. Wu, and M. Shahidehpour, "Hourly Coordination of Electric Vehicle Operation and Volatile Wind Power Generation in SCUC," IEEE Transactions on Smart Grid, Vol. 3, No. 3, pp. 1271-1279, Sept. 2012

Abstract: In this paper, the coordinated integration of aggregated plug-in electric vehicle (PEV) fleets and renewable energy sources (wind energy) in power systems is studied by stochastic security-constrained unit commitment (Stochastic SCUC) model, which minimizes the expected grid operation cost while considering the random behavior of the many PEVs. PEVs are mobile and distributed devices with deferrable options for the supply/utilization of energy at various times and locations. The increased utilization of PEVs, which consume electricity rather than fossil fuel for driving, offers unique economic and environmental opportunities, and brings out new challenges to electric power system operation and planning. The storage capability of PEVs could help power systems mitigate the variability of renewable energy sources and reduce grid operation costs. Vehicle-to-grid (V2G) enables PEVs to have bi-directional power flows once they are connected to the grid, i.e., they can either inject power to, and draw power from, the grid which adds further complexity to power system operations. PEVs signify customers' random behavior when considering their driving patterns, locational energy requirements, topological grid interconnections, and other constraints imposed by the consumers. Numerical tests demonstrate the effectiveness of the proposed approach for analyzing the impact of PEVs on the grid operation cost and hourly wind energy dispatch.

11) A. Lotfjou, Y. Fu, and M. Shahidehpour, "Hybrid AC/DC Transmission Expansion Planning," IEEE Transactions on Power Delivery, Vol. 27, No. 3, pp. 1620-1628, July 2012

Abstract: This paper proposes a hybrid algorithm for the AC/DC transmission expansion planning (TEP). The stochastic simulation method would consider random outages of generating units and AC/DC transmission lines as well as load forecast errors. The mixed-integer linear programming problem is decomposed into a master planning problem with integer investment decision variables and subproblems which examine the feasibility of master planning solution and calculate the optimal operation schedule over the planning horizon. The independent system operator (ISO) would utilize the proposed method to select the optimal set of AC/DC transmission lines for satisfying TEP criteria: supplying load forecasts, minimizing investment costs, and optimizing market operations. The proposed set of DC transmission system may use either current source converters (CSCs) or voltages source converters (VSCs). Numerical examples illustrate the effectiveness of the proposed TEP model.

12) L. Abreu, M. Khodayar, M. Shahidehpour, L. Wu, "Risk-Constrained Coordination of Cascaded Hydro Units with Volatile Wind Power Generation" IEEE Transactions on Sustainable Energy, Vol. 3, No. 3, pp. 359-368, July 2012

Abstract: This paper presents a stochastic hourly coordination strategy for wind units and cascaded hydro generation as storage to firm up the hourly dispatch in a generating company (GENCO). The proposed strategy is based on the stochastic price-based unit commitment (Stochastic PBUC) formulation which includes wind energy imbalance charges. The forecast errors of electricity market price and wind speed are simulated with the Monte Carlo method via a scenario approach. The risk-aversion constraints are considered for limiting a GENCO's financial risks when considering uncertain wind power generation. The proposed optimization model is solved by mixed- integer linear programming (MIP) and illustrative examples examine the effectiveness of the proposed risk-based coordination model for optimizing a GENCO's payoff.

13) C. Sahin, M. Shahidehpour, and I. Erkmen "Generation Risk Assessment in Volatile Conditions with Wind, Hydro, and Natural Gas Units" Applied Energy, Vol. 96, pp. 4-11, Aug. 2012

Abstract: This paper studies a generating company (GENCO)'s midterm (a few months to a year) scheduling payoffs and risks in volatile operating conditions. The proposed algorithm considers the integration of intermittent wind units into a GENCO's generation assets and coordinates the GENCO's hourly wind generation schedule with that of natural gas (NG) units (with volatile gas prices) and hydro units (with water inflow forecast) for maximizing the GENCO's payoff. The proposed midterm GENCO model applies market price forecasts to the risk-constrained stochastic price-based unit commitment (PBUC) for calculating the GENCO's risk in energy and ancillary services markets. The proposed PBUC minimizes the cost of a) NG contracts, storage, startup and shutdown, b) startup and shutdown of cascaded hydro units, and c) penalty for defaulting on the scheduled power delivery. Simulation results show that the diversification of generating assets including bilateral contracts (BCs) could enhance the GENCO's midterm planning by increasing the expected payoff and decreasing the financial risk.

14) L. Wu, M. Shahidehpour, and Z. Li, "Comparison of Scenario-Based and Interval Optimization Approaches to Stochastic SCUC," IEEE Transactions on Power Systems, Vol. 27, No. 2, pp. 913-921, May 2012

Abstract: This paper compares applications of scenario-based and interval optimization approaches to stochastic security- constrained unit commitment (Stochastic SCUC). The uncertainty of wind power generation is considered in this study to compare the two approaches, while other types of uncertainty can be addressed similarly. For the simulation of uncertainty, the scenario-based approach considers the Monte Carlo (MC) method, while lower and upper bounds are adopted in the interval optimization. The Stochastic SCUC problem is formulated as a mixed-integer linear programming (MIP) problem and solved using the two approaches. The scenario-based solutions are insensitive to the number of scenarios, but present additional computation burdens. The interval optimization solution requires less computation and automatically generates lower and upper bounds for the operation cost and generation dispatch, but its optimal solution is very sensitive to the uncertainty interval. The numerical results on a 6-bus system and the modified IEEE 118-bus system show the attributes of the two approaches for solving the Stochastic SCUC problem. Several convergence acceleration options are also discussed for overcoming the computation obstacles in the scenario-based approach.

15) A. Khodaei and M. Shahidehpour, “Security-Constrained Transmission Switching with Voltage Constraints,” International Journal of Electrical Power and Energy Systems, Vol. 35, No. 1, pp. 74-82, Feb. 2012

Abstract: Transmission switching (TS) would play a vital role in the security and economics of electric power systems. The application of TS to the AC model of security-constrained unit commitment (SCUC) for the day-ahead scheduling is presented in this paper. The proposed AC model of SCUC with TS would include real and reactive power flow constraints which increase the controllability of base case and contingency solutions with voltage constraints. A general FACTS model is introduced for the reactive power management in SCUC which is based on the power injection model (PIM). A modified Newton-Raphson power flow model is introduced in the proposed SCUC with TS in which line flows are considered as variables. The proposed AC network model is compared with the DC network model (without voltage constraints) for enhancing the power network controllability and minimizing the operation cost. The case studies exhibit the effectiveness of the TS application to SCUC with AC network constraints.

16) A. Khodaei, M. Shahidehpour, and S. Bahramirad, “SCUC With Hourly Demand Response Considering Intertemporal Load Characteristics,” IEEE Transactions on Smart Grid, Vol. 2, No. 3, pp. 564-571, Sept. 2011

Abstract: In this paper, the hourly demand response (DR) is incorporated into security-constrained unit commitment (SCUC) for economic and security purposes. SCUC considers fixed and responsive loads. Unlike fixed hourly loads, responsive loads are modeled with their inter-temporal characteristics. The responsive loads linked to hourly market prices can be curtailed or shifted to other operating hours. The study results show that DR could shave the peak load, reduce the system operating cost, reduce fuel consumptions and carbon footprints, and reduce the transmission congestion by reshaping the hourly load profile. Numerical simulations in this paper exhibit the effectiveness of the proposed approach.

17) L. Wu and M. Shahidehpour, “Optimal Coordination of Stochastic Hydro and Natural Gas Supplies in Midterm Operation of Power Systems,” IET Journal on Generation, Transmission & Distribution, Vol. 5, No. 5, pp. 577-587, May 2011

Abstract: This paper presents a stochastic security-constrained unit commitment (SCUC) model for the optimization of coordinated midterm water and natural gas supplies. The stochastic model considers random outages of system components, load forecast errors, and water inflow uncertainty, which are modeled as scenarios in the Monte Carlo (MC) simulation. Water resources may be used in winter to cover gas unit outages caused by an insufficient gas supply. However, those hydro units may not then be available for peak load shaving in the following summer if the summer happens to be a dry season. Thus, water reservoirs would have to be utilized efficiently throughout the year to provide substantial cost reductions while maintaining the power system reliability. The proposed model also considers the impact of midterm scheduling of water and gas on the power system reliability. Reliability indices are incorporated in the hourly unit commitment problem. The stochastic problem is formulated as a two-stage optimization where the first stage optimizes the short-term water and gas usages and the second

stage considers the midterm schedule. Numerical simulations indicate the effectiveness of the proposed stochastic approach for the optimal scheduling of midterm water and gas usages.

18) C. Liu, M. Shahidehpour, J. Wang, “Coordinated Scheduling of Electricity and Natural Gas Infrastructures with a Transient Model for Natural Gas Flow,” Chaos (American Institute of Physics), Vol. 21, pp. 025102-1 through 025102-12 , May 2011

Abstract: This paper focuses on transient characteristics of natural gas flow in the coordinated scheduling of security-constrained electricity and natural gas infrastructures. The paper takes into account the slow transient process in the natural gas transmission systems. Considering their transient characteristics, natural gas transmission systems are modeled as a set of partial differential equations (PDEs) and algebraic equations. An implicit finite difference method is applied to approximate PDEs by difference equations. The coordinated scheduling of electricity and natural gas systems is described as a bi-level programming formulation from the independent system operator’s viewpoint. The objective of the upper-level problem is to minimize the operating cost of electric power systems while the natural gas scheduling optimization problem is nested within the lower-level problem. Numerical examples are presented to verify the effectiveness of the proposed solution and to compare the solutions for steady-state and transient models of natural gas transmission systems.

19) C. Sahin, Z. Li, M. Shahidehpour, and I. Erkmen, "Impact of Natural Gas System on Risk-Constrained Midterm Hydrothermal Scheduling,” IEEE Transactions on Power Systems, Vol. 26, No. 2, pp. 520-531, May 2011

Abstract: This paper studies the impact of natural gas (NG) contracts and constraints on a GENCO’s midterm risk-constrained hydrothermal scheduling problem. The NG contracts and constraints are modeled as a set of linear equations. The proposed model utilizes the stochastic price-based unit commitment (PBUC). The PBUC hourly solution considers uncertainties of market prices for energy and ancillary services, uncertainties of natural water inflows, and random NG infrastructure interruptions in Monte-Carlo scenarios. Illustrative examples analyze the GENCO’s risk levels when considering midterm schedules for generating units, target payoffs, and usages of water inflow, NG and other thermal resources. Simulation results show that a GENCO’s midterm schedules and financial risks could be impacted significantly with the consideration of NG contracts and constraints.

20) A. Lotfjou, M. Shahidehpour, and Y. Fu, “Hourly Scheduling of DC Transmission Lines in SCUC With Voltage Source Converters,” IEEE Transactions on Power Delivery, Vol. 26, No. 2, pp. 650-660, April 2011

Abstract: This paper presents the modeling of high voltage direct current (DC) transmission systems with voltage source converters (VSCs) in security-constrained unit commitment (SCUC). The impact of VSC-DC transmission system on the economics and the security of integrated AC/DC transmission systems is discussed. The nonlinear AC/DC equations are linearized and the Newton-Raphson method is utilized to solve the linearized network in the base case and contingencies. The SCUC solution will determine the optimal hourly schedule of controllable VSC-DC transmission systems in electricity markets. Numerical examples show the efficiency of the proposed model.

21) C. Liu, M. Shahidehpour, and J. Wang, "Application of Augmented Lagrangian Relaxation to Coordinated Scheduling of Interdependent Hydrothermal Power and Natural Gas Systems," IET Journal on Generation, Transmission & Distribution, Vol. 4, No. 12, pp. 1314–1325 Dec. 2010

Abstract: This paper proposes an optimization model for the coordinated scheduling of interdependent electric power and natural gas transmission systems from a joint operator's viewpoint. The objective is to minimize the coordinated social cost while satisfying network and temporal constraints of the two interdependent systems. The joint operator will coordinate hourly schedules to supply natural gas to loads or generate electric power. We consider the application of LR or augmented LR to relax the coupling constraints of the two systems. The Lagrangian dual is decomposed into the security-constrained unit commitment subproblem with the hydro coordination (SCUC) and the natural gas allocation subproblem. The application of LR for solving the coordinated problem could cause oscillations in the dual solution which is due to the nonconvex characteristics of the coordinated problem represented by integer variables and network constraints. Moreover, with slight changes in multiplier values, the linear cost function of the natural gas well may result in a cycling behavior of the gas well output between its max and min limits. To avoid numerical oscillations and improve the solution quality, the augmented LR with a piecewise linear approximation of quadratic penalty terms and the block descent coordination (BDC) technique are proposed. We consider the 6-bus with 7-node and the 118-bus with 14-node systems to verify that the applicability of the proposed method to the coordinated scheduling of electric power and natural gas transmission systems.

22) A. Khodaei and M. Shahidehpour, Y. Fu, "Transmission Switching in Security-Constrained Unit Commitment," IEEE Transactions on Power Systems, Vol. 25, No. 4, pp. 1937-1945, Nov. 2010

Abstract: Transmission switching (TS) is introduced in security-constrained unit commitment (SCUC) for alleviating transmission violations and reducing operating costs. The SCUC problem is decomposed into the unit commitment (UC) master problem and the TS subproblem. The UC master problem finds the optimal hourly schedule of generating units. The TS subproblem uses this solution for transmission switching to find the optimal dispatch of units when considering network constraints. The TS subproblem also examines contingencies and identifies required changes to the UC master problem solution when contingencies cannot be mitigated in the TS subproblem. To propose a practical TS model, the standing phase angle difference limit is considered and relevant constraints are added to the TS subproblem. The case studies exhibit the effectiveness of the proposed approach.

23) L. Wu and M. Shahidehpour, Y. Fu, "Security-Constrained Generation and Transmission Outage Scheduling with Uncertainties," IEEE Transactions on Power Systems, Vol. 25, No. 3, pp. 1674-1685, Aug. 2010

Abstract: This study presents a stochastic model for the Independent System Operator's (ISO's) optimal coordinated long-term maintenance scheduling of generation units and transmission lines with short-term security-constrained unit commitment (SCUC). Random disturbances of power systems including forced outages of generation units and transmission lines, load forecast errors, and fuel price fluctuations are modeled as scenario trees using the Monte Carlo simulation. Lagrangian relaxation (LR)

is applied to separate the coordinated optimization problem into long-term equipment maintenance (LTEM) and stochastic long-term SCUC (LTSCUC) subproblems. For the stochastic LTSCUC subproblem, scenario bundle constraints are relaxed via LR and the optimization problem is decomposed into deterministic LTSCUC problems. LR is applied to each deterministic LTSCUC to relax long-term fuel and emission limits and decompose the problem into short-term SCUC subproblems. The decomposition is further applied to short-term SCUC subproblems for separating hourly unit commitment and transmission network constraints. The unit commitment is formulated as a mixed-integer programming (MIP) problem and solved by the branch-and-cut method using CPLEX. The outcome of this study includes the hourly scheduling of outages of generation units and transmission lines, which corresponds to the optimal generation unit commitment and dispatch, and transmission flows. The hourly schedules minimize the total cost of operation and maintenance and satisfy long-term and short-term constraints of generation units and transmission network with the inclusion of power system uncertainty. A modified IEEE-118 bus system is used to exhibit the effectiveness of the proposed scheduling approach.

24) A. Khodaei and M. Shahidehpour, S. Kamalinia, "Transmission Switching in Expansion Planning," IEEE Transactions on Power Systems, Vol. 25, No. 3, pp. 1722-1733, Aug. 2010

Abstract: Transmission switching (TS) is introduced to add flexibility to the transmission and generation capacity expansion planning problem. TS could improve the performance of the capacity expansion planning model and reduce the total planning cost. The capacity expansion planning problem is decomposed into a master problem and two subproblems. The master problem utilizes the candidate set for additional generating unit and transmission capacity investments to find the optimal plan throughout the planning horizon. The subproblems use the optimal plan, apply transmission switching to relieve any transmission flow violations, and calculate the optimal dispatch of generating units. The transmission network contingencies are also considered in the subproblems. The case studies exhibit the effectiveness of the proposed expansion planning approach.

25) O. Tor, A. Guven, and M. Shahidehpour, "Promoting the Investment on IPPs for Optimal Grid Planning," IEEE Transactions on Power Systems, Vol. 25, No. 3, pp. 1743-1750, Aug. 2010

Abstract: This paper presents a transmission expansion planning (TEP) model which coordinates investment decisions in monopolistic transmission and decentralized generator sectors. The proposed planning approach gauges transmission congestion and security constraints with respect to transmission investments while promoting investments on independent power produces (IPPs) through incentive payments. The paper includes discussions on incentive mechanisms and prioritization among qualified IPPs for several planning scenarios. Such incentives might be necessary to trigger investments on IPPs earlier than those projected by the decentralized generation system, when the power system security is threatened. The proposed planning approach would optimize the sum of transmission investments, incentive payments to IPPs, and congestion costs along the planning horizon. The case studies illustrate how the proposed planning algorithm could be utilized in order to determine incentive payments to candidate generators when necessary, and prioritize such incentives among multiple IPP candidates.

26) L. Wu and M. Shahidehpour, “A Hybrid Model for Price Forecasting,” IEEE Transactions on Power Systems, Vol. 25, No. 3, pp. 1519-1530, Aug. 2010

Abstract: This paper presents a hybrid time-series and adaptive wavelet neural network (AWNN) model for the day-ahead electricity market clearing price forecast. Instead of using price series, one-period continuously compounded return series is used to achieve more attractive statistical properties. The autoregressive moving average with exogenous variables (ARMAX) model is used to catch the linear relationship between price return series and explanatory variable load series, the generalized autoregressive conditional heteroscedastic (GARCH) model is used to unveil the heteroscedastic character of residuals, and AWNN is used to present the non-linear, non-stationary impact of load series on electricity prices. The Monte Carlo method is adopted to generate more evenly distributed random numbers used for time series and AWNN models to accelerate the convergence. Several criteria such as average mean absolute percentage error (AMAPE) and the variance of forecast errors are used to assess the model and measure the forecasting accuracy. Illustrative price forecasting examples of the PJM market are presented to show the efficiency of the proposed method.

27) L. Wu and M. Shahidehpour, Y. Fu, “Accelerating the Benders Decomposition for Network-Constrained Unit Commitment Problems,” Energy Systems, Vol. 1, pp. 339-376, July 2010

Abstract: This study presents an optimization method by generating multiple strong Benders cuts for accelerating the convergence of Benders Decomposition (BD) when solving the network-constrained generation unit commitment (NCUC) problem. In NCUC, dc transmission network evaluation subproblems are highly degenerate, which would lead to many dual optimal solutions. Furthermore, the classical BD cuts are often low-density which involve only a limited number of decision variables in the master problem. Therefore, the dual optimal solutions and the corresponding Benders cuts are of crucial importance for improving the efficiency of the BD algorithm. The proposed method would generate multiple strong Benders cuts, which are pareto optimal, among candidates from multiple dual optimal solutions. Such cuts would be high-density in comparison with low-density cuts produced by the classical BD. The proposed multiple strong Benders cuts are efficient in terms of reducing the total iteration number and the overall computing time. The high-density cuts may restrict the feasible region of the master unit commitment (UC) problem in each iteration as they incorporate more decision variables in each Benders cut. The multiple strong Benders cuts would accordingly reduce the iteration number and overall computing time. Numerical tests demonstrate the efficiency of the proposed multiple strong Benders cuts method in comparison with the classical BD algorithm and the linear sensitivity factors (LSF) method. The proposed method can be extended to other applications of BD for solving the large-scale optimization problems in power systems operation, maintenance, and planning.

28) C. Liu, M. Shahidehpour, and L. Wu, “Extended Benders Decomposition for Two-Stage SCUC, IEEE Transactions on Power Systems, Vol. 25, No. 2, pp. 1192-1194, May 2010

Abstract: This paper presents the solution of a two-stage security-constrained unit commitment (SCUC) problem. The proposed SCUC model could include integer variables at the second stage. A framework of extended Benders decomposition with linear feasibility and optimality cuts is proposed for the solution

of mixed-integer programming (MIP) problems at both stages. Test results show the effectiveness of the proposed methodology.

29) S. Kamalinia and M. Shahidehpour, "Capacity Adequacy Calculation by Considering Locational Capacity Prices," IET Journal on Generation, Transmission & Distribution, Vol. 4, No. 3, pp. 376-385, Feb. 2010

Abstract: A proper investment mechanism is required in restructured power systems to secure the adequacy of installed capacity by encouraging investments on generation and transmission expansions. In this paper, we propose a locational capacity price (LCP) model along with multi-level load bidding curves, which reflect the effectiveness of the market-based capacity payment and at the same time, prohibits the capacity withholding and the exercising of market power. The purpose of capacity expansion decision is analyzed and compared with three other market design options, i.e., energy only, capacity payment, and installed capacity. The case studies show that the proposed LCP method provides proper investment signals in capacity-constrained locations. The proposed LCP method also provides signals to system operators to alleviate transmission congestions economically using proper operation strategies in power systems.

30) A. Lotfjou and M. Shahidehpour, "Security-Constrained Unit Commitment with AC/DC Transmission Systems," IEEE Transactions on Power Systems, Vol. 25, No. 1, pp. 531-543, Feb. 2010

Abstract: This paper presents the solution of security- constraint unit commitment (SCUC) problem with a detailed representation of high voltage direct current (DC) transmission system with current source converter (CSC). We find an economic operation and control strategy for AC and CSC-DC transmission systems by solving the SCUC problem with AC/DC transmission constraints. The presented model is decomposed into a master problem for the solution of hourly unit commitment (UC) problem and subproblems that examine the security (branch flows and bus voltages) of integrated AC/DC transmission systems. The solution of transmission security check subproblem is based on linear programming (LP) which minimizes AC bus mismatches subjected to AC/DC transmission security constraints. The iterative SCUC solution coordinates the power transfer on the DC transmission system for enhancing the economics and the security of AC transmission system. The numerical tests illustrated the efficiency of the proposed model.

### 4.5.2 Conference Publications

1) Wei Tian, Zuyi Li, Mohammad Shahidehpour, "Transmission Congestion Analysis in the Eastern Interconnection using POMS," IEEE Power and Energy Society General Meeting, July 2010, Minneapolis, Minnesota.

Abstract: A methodology based on the security-constrained unit commitment (SCUC) is applied to analyze the transmission congestion in the Eastern Interconnection of the United States for 2008 and 2018. The proposed SCUC tool for this study is referred to as the POwer Market Simulator (POMS). The

identified congestions are visualized along with the Geographical Information System (GIS) data and compared with the results published by the U.S. Department of Energy's National Electric Transmission Congestion Study (NETCS) in 2006. The POMS study also provides the locational marginal price (LMP) information in the Eastern Interconnection, which is not available in the NETCS report. The POMS simulation results for representing congested branches and LMPs could be applied to the future transmission expansion planning studies.

2) Ganesh Raman, Mahesh Krishnamurthy, Rakesh C Ramachandran, Clement Pereira, Xiaodong Shi, Yong Jiang, Martin Price, and Matthew Arnold, Test bed for acoustic assessment of small wind turbine drive-trains, Fourth International Meeting on Wind Turbine Noise, Rome, Italy, 12-14 April 2011

Abstract: This paper describes a test facility for acoustic assessment of small wind turbine drive trains. The wind turbine drive train chosen for our facility was that of a 8 kW horizontal axis wind turbine (Viryd 8000). The facility has a drive side and a turbine side. On the drive side, a drive motor is connected through a gearbox to a flywheel that compensates for the absence of the blades. The turbine side includes the entire driveline of the wind turbine. The system can simulate inflow wind speed and turbulence. The system also includes accelerometers and torque sensors. For the acoustic assessment both single microphones and an array of 24 microphones were used. Various beamforming algorithms were used for source localization. These include classical beamforming (FDBF), deconvolution approaches for mapping acoustic sources (DAMAS2), CLEAN based on source coherence (CLSC) and TIDY. The array was calibrated and validated for both coherent and incoherent sources. Acoustic measurements from the fully functional drive train test facility are presented for a few operating conditions. Further tests in the facility will be conducted to assess wind turbine drive train acoustics and vibration for various wind velocities and turbulence levels. The facility will also be used to develop techniques for the minimization of sound and vibration from small wind turbine drive trains.

3) Xiaodong Shi; Serradilla, J.P.; Krishnamurthy, M.; , "A back EMF-based rotor position prediction in Permanent Magnet machines for survivable wind generator systems," IECON 2010 - 36th Annual Conference on IEEE Industrial Electronics Society , vol., no., pp.778-783, 7-10 Nov. 2010

Abstract: In wind power generators, position information is often required for tracking maximum power point as well as implementing control strategies for the Permanent Magnet (PM) generator. For such a system, failure of position sensor could potentially lead to major fault or require the system to be shut down. This could cause significant economic losses and also require unscheduled maintenance. This paper proposes a new sensorless position estimation approach to track position of the PM machine using the back EMF if the position sensor fails. This technique can also be used to provide initial rotor position for the proper implementation of a fall-back strategy. This technique can also be extended to detect position information at low speeds. Simulation and experimental results have been presented showing the effectiveness the proposed scheme and validate the claims presented.

4) Xiaodong Shi; Krishnamurthy, M.; , "Concept and implementation of a simplified speed control strategy for survivable induction motor drives," Industrial Electronics (ISIE), 2011 IEEE International Symposium on , vol., no., pp.556-561, 27-30 June 2011

Abstract: Induction machine is one of the most widely used machines in residential and industrial applications. Traditional drive methods for induction machines such as vector control usually require complex control routines, fast processing unit and multiple system status feedbacks. The complexity of these methods greatly reduces the reliability of the system since the failure of the sensor or even the drift of system parameters could potentially result in system malfunction. This creates the need for a simple, cost-effective and reliable control strategy as a backup to continue operation of the system in case of failure of current and voltage feedback sensors. In this paper, an effective, yet simple and low-cost state switching control technique is proposed and implemented for a three phase squirrel cage induction machine system. This state switching control operates at two specific duty cycles of PWM which produces phase voltages with different magnitudes across the phase windings. At the same time, the frequency of phase voltages is derived from the reference speed. By switching between these two states, precise speed regulation can be achieved. This new control method makes the controller extremely simple in design and implementation for induction machine. Simulation and experimental results are included in this paper to validate our claims.

5) Yao Da; Xiaodong Shi; Krishnamurthy, M.; , "Health monitoring, fault diagnosis and failure prognosis techniques for Brushless Permanent Magnet Machines," Vehicle Power and Propulsion Conference (VPPC), 2011 IEEE , vol., no., pp.1-7, 6-9 Sept. 2011

Abstract: Over the past few years, many researchers have been attracted by the challenges of electrical machines' fault diagnosis and condition monitoring, which provide early warnings that could help schedule necessary maintenance to avoid catastrophic consequence. With advancements in the use of rare-earth magnets, Brushless Permanent Magnet Machines are widely used in industry recently, which has led to the development of numerous fault diagnosis techniques. Considerable papers have presented reviews and compared condition monitoring and fault diagnosis methods for induction machines, but none for Brushless Permanent Magnet Machines. To make a difference, this paper presents a comprehensive survey of modern research advancements and state-of-the-art in health monitoring, fault diagnosis and prognosis techniques for Brushless Permanent Magnet Machines. The symptoms of each type of fault and the principles of diagnosis process are also described and discussed.

6) Xiaodong Shi; Krishnamurthy, M.; , "A simplified state switching control strategy for survivable variable-speed induction generators," Electric Machines & Drives Conference (IEMDC), 2011 IEEE International , vol., no., pp.182-187, 15-18 May 2011

Abstract: Induction machines are one of the most widely used electric machines in wind power applications. However, the control of an induction generator is complicated if advanced control strategy is employed in order to maximize the performance. Also, the complexity of advanced control strategies and their high demand on hardware and sensors can lower the overall reliability of the generator system and potentially result in system malfunction, leading to unscheduled maintenance and power yield

reduction. In this paper, an effective, yet simple and low-cost state switching control technique is proposed and implemented as a backup control strategy in case of control or sensor failure. This state switching control system is only allowed to operate at two different duty cycles of PWM which produces phase voltages with different magnitudes. At the same time, the frequency of the phase voltages is derived from the reference speed. By switching between these two states, precise speed regulation can be achieved. Owing to its simplicity, the control strategy can be implemented on a low cost FPGA or embedded into existing controllers for use as a backup strategy. In addition since it does not require the use of current sensors, it is very suitable for survivable operation. Simulation and experimental results are included to validate our claims.

7) Nelson, C. C., Cain, A. B., Raman, G., Dougherty, R., Brentner, K. S., and Morris, P. J., “Numerical Studies of Wind Turbine Acoustics,” 50th AIAA Aerospace Sciences Meeting including the New Horizons Forum and Aerospace Exposition, Nashville, Tennessee, January 9-12, 2012. DOI: 10.2514/6.2012-6

### 4.5.3 Manuscripts in Preparation

1) Xiaodong Shi; Krishnamurthy, M.; , "Concept and implementation of a simplified speed control strategy for survivable induction motor drives," submitted to IEEE Transactions on Industrial Electronics.

Abstract: Induction machines are one of the most widely used machines in residential and industrial applications. Traditional drive methods for induction machines, such as vector control, usually require complex control routines, fast processing unit and multiple system status feedbacks. These methods require the use of several current and position sensors for high grade operation. Failure of current sensor or even the drift of system parameters could potentially result in system malfunction. This creates the need for a simple, cost-effective and reliable control strategy as a backup control strategy to continue operation in case of failure of current and voltage sensors. In this paper, an effective, yet simple and low-cost state switching control technique is proposed for a three phase squirrel cage induction machine system. This state switching control system operates at two specific duty cycles of PWM which produces phase voltages with different magnitudes across the phase windings. At the same time, the frequency of phase voltages is derived from the reference speed. By switching between these two states, precise speed regulation can be achieved. This new control method makes the controller extremely simple in design and implementation for induction machine. Simulation and experimental results are included in this paper to validate our claims.

2) Xiaodong Shi; Krishnamurthy, M.; , "Implementation of a Simple Survivable Strategy for Three-Phase Induction Motor Drives with Smooth Control Transition," Submitted to IEEE Transactions on Power Electronics.

Abstract: Continuous operation of electric machines is required in most mission critical applications. Failure of current sensors could lead to catastrophic faults in the absence of immediate maintenance or redundancies, which in turn, could increase cost of the overall system. This paper proposes a technique for survivable operation of three-phase Induction Motor (IM) drives in the event of current sensor failure by switching from vector control to a simplified, novel state switching control with smooth transition strategy. A simple but effective current sensor failure detection mechanism keeps monitoring the conditions of current sensors and can trigger a fault flag if current sensor fails. Simulation and experimental results, including current sensor failure detection, speed and torque response, voltage vector continuity and phase current waveforms, are included to show the effectiveness of the proposed strategy.

3) Wei Tian, Mohammad Shahidehpour, Zuyi Li, Large-scale Analysis of 2018 Wind Energy Integration in the Eastern U.S. Interconnection, Submitted to The Electricity Journal

Abstract: This paper presents the hourly simulation results for the year 2018 with the large-scale wind energy integration in the Eastern Interconnection of the United States. A simulator referred to as WINS (Wind INtegration Simulator) is developed for this annual study. The wind energy integrations in the year 2018 are simulated using the hourly security-constrained unit commitment (SCUC) in WINS. The generation portfolio for supplying the hourly load in 2018 is developed with/without transmission network constraints. The sensitivities to the 2018 wind energy integration are carried out for fuel price, wind energy availability, load growth, carbon cost, and hourly load management strategies. The hourly production cost, generation credit, load payment, levelized congestion cost, LMPs, and wind energy contribution, are calculated and analyzed.

### 4.5.4 Unpublished Reports

1) Richard Gown, Wind Electrical Generation with a Unique High Magnetic Density Turbine Generator, Dakota Power, October 2011

Dakota Power, LLC (DP) is developing unique electric drive and power generation systems. The DP sub-contract with Illinois Institute of Technology (IIT) provides for the application of DP technology to the generation of electricity from wind power. DP technology provides a non-rare earth power dense alternative for the operation of wind turbines. DP is integrating switched reluctance technologies with other sources of magnetic energy to produce high-performance electrical machines. The DP technology has the potential to provide a lightweight, low-cost wind turbine for residential and light industrial applications.

DP is developing next-generation light weight electric drive systems for military and civilian applications through a Cooperative Agreement with the Army Research Office (ARO). This sub-contract with IIT provides for the application of DP electrical machine technology to the generation of electricity from wind. This report provides a comprehensive summary of the development of DP switched reluctance technology and the potential for its application to the generation of electricity from wind.

The process for the development of DP switched reluctance technology includes the transition of a concept for a machine through design and simulation using advanced FEA software. DP provides commercially developed Maxwell FEA simulation software to validate the potential performance of each proposed design. The optimal design, including the specific geometry, stator winding turns and current, is then fabricated to provide a prototype test machine. The performance of each prototype machine is tested and evaluated through the capabilities of the DP Dynamometer Test Facility (DTF). The resulting performance information is analyzed and incorporated into subsequent developments of the DP switched reluctance technology.

DP has evaluated the potential for switched reluctance technology to provide a non-rare earth direct drive wind turbine. This report includes the development of a switched reluctance machine to validate the performance of DP short path switched reluctance technology for application as residential wind turbines.

DP has developed a Quick Machine software program to support the introduction of switched reluctance technology in the development of wind turbines and other machine applications. The Quick Machine software provides an approximate result as compared to the detailed design produced with hours of computation with the Maxwell FEA software. The QuickMachine software facilitates the application of the principles of switched reluctance technology to the development of residential wind turbines.

This report includes a bibliography of the extensive published studies, papers, and information about the technologies, policies, laws, and regulations for the development of wind turbines. The information for this bibliography has supported the development of switched reluctance technology for the generation of electricity by wind turbines.

2) Ming Cai, Emadoddin Abbasi, and Hamid Arastoopour, “A Report on Wind Energy Research,” Illinois Institute of Technology, October 2011

The objective of this study is to develop a numerical model for assessing and analyzing the performance of a horizontal-axis wind-turbine (HAWT) in the presence of rain droplets under heavy rain conditions using computational fluid dynamics (CFD) for multiphase flow systems.

The CFD was chosen to obtain a comprehensive tool for design, scale-up, and performance evaluation of wind turbines, and also to overcome the lack of experimental data on the performance of wind turbines in rainy conditions. A set of benchmarking CFD simulations was performed, both in two and three dimensions. The simulation results were compared with the available experimental data for single phase flow in the literature to refine our CFD model. Then, the single-phase simulation results were used as a baseline to calculate the impact of rain on the performance of the wind turbine.

By capturing the shape and position of the accumulated water film, we estimated the performance loss caused by the formation of the water film. The results of this study could help designers to minimize the impact of rain on the new generation of wind turbines.

Our future work is geared toward adding the effect of splash back of droplets in our model and considering the effect of surface tension on the water film formation. In addition, we are going to apply our Lagrangian-Eulerian model in a three-dimensional case and calculate the performance of the horizontal-axis-wind-turbine in a heavy rain condition.

3) Greg Rouse, Software Integration for Small Wind Turbine into IIT's Microgrid, Intelligent Power Solutions, LLC, October 2011

In this work, Intelligent Power Solutions, LLC (IPS) assisted IIT with data gathering and software integration of an 8kW Viryd Wind Turbine installed on the main campus. The primary purpose for installing this wind turbine was to increase public awareness of renewable energy technologies and thus the primary objective of this effort was to gather data from the wind turbine and make real time data viewable on campus, something that is not typically available for Viryd Wind Turbine Installations. A secondary objective in this work was to model and predict wind turbine output and compare the predictions to actual wind turbine data. This predictive modeling will be important as wind turbine penetration increases. IIT's existing microgrid provides a unique opportunity to see how local wind turbine generation might affect the microgrid.

Under this project IPS was able to modified IIT's microgrid master control software called the Intelligent Perfect Power Supervisory Controller (IPPSC) software for displaying and reporting wind turbine data and developed graphical user interface screens for displaying this data. These screens will be accessible on campus for user to be able to login and see real time turbine performance data and trends. IPS developed and adapted artificial neural network algorithms for modeling the wind turbine performance. These models are intended to be used for predicting the wind turbine's performance in the future will be important for the operational planning required for integrating wind turbine generation resources within a microgrid.

4) Christopher C. Nelson, Alan B. Cain, Ganesh Raman, Tom Chan, Michael Saunders, Jay Noble, and Robert Engeln, Robert Dougherty, Kenneth S. Brentner, and Philip J. Morris, "Numerical Studies of Wind Turbine Acoustics," Innovative Technology Applications Company, LLC, Illinois Institute of Technology, Tecplot, Inc., OptiNav, Inc., Penn State University, October 2011

Innovative Technology Applications Company, LLC (ITAC) is currently working as part of an Illinois Institute of Technology (IIT) led team to investigate various aspects of wind power generation. ITAC's portion of this work involves the numerical simulation of the flow around wind turbines and investigating the acoustic field associated with the unsteady fluid behavior. This report discusses the progress made in this work, the analysis methods used, and the results obtained.

The current methodology combines the abilities of three different numerical tools to predict the unsteady flow around a wind turbine, the resulting acoustics, and an analysis of the noise sources. The Navier-Stokes equations are solved using the OVERFLOW solver to obtain an unsteady flow field in the vicinity of the turbine. Data from this solution is then fed into the PSU-WOPWOP Ffowcs-Williams Hawkings solver to predict the farfield acoustics. This prediction is used to record sound levels at virtual microphone locations, and this information is fed into the Beamform Interactive software package

which is used to analyze the data using a variety of beamforming methods. This methodology is referred to as the "synthetic array technique" as it uses numerical methods to perform an analysis identical to that used for experimental data from microphone arrays.

5) Ganesh Raman, Mahesh Krishnamurthy, Rakesh C. Ramachandran, Hirenkumar Patel, Localization of Wind Turbine Noise Sources On a 1.5 MW Production Scale Wind Turbine Using a Compact Microphone Array, Illinois Institute of Technology, October 2011

The primary objective of the current work was to study the behavior of various beamforming algorithms and use that understanding to locate various noise sources on a production scale 1.5 MW wind turbine located in a wind farm using a compact microphone array. The sound sources in the wind turbine include both mechanical and aerodynamic noise. The sources on the wind turbine are mostly broadband and are moving sources. The beamforming algorithms were validated in the laboratory using three speakers which could produce both coherent and incoherent noise. The spacing between the three speakers could be changed on a speaker frame. The microphone array was also tested on a moving source. The microphone array was then used to measure the wind turbine noise to locate aerodynamic and mechanical noise sources. Measurements were also made on a small wind turbine drive train simulator. This report includes a detailed discussion of all these experimental results.

6) Candace Wark and Dietmar Rempfer, Engaging Undergraduate Students in Wind Energy Research Through IIT's Interprofessional Project Course (IPRO), Illinois Institute of Technology, October 2011

One of the tasks of this DOE grant (Task 10.0) was to "Engage Undergraduate Students in Wind Energy Research". IPRO 323 was developed in response to this task and is currently in its second semester with plans for continuing on into next year. The overall goal for the students enrolled in IPRO 323 is to develop a methodology for designing and developing building-integrated wind turbine modules so that more urban environments will see wind power as a viable alternate energy source. The project plan that the students' enrolled in the course developed was to investigate designing a surface shape integrated onto the roof and/or facades of buildings to increase the power output of building mounted wind turbines. This goal of course requires the understanding of the fluid dynamics/aerodynamics of wind turbines and also the architectural, social, public, safety and environmental issues associated with integrating wind turbines into urban environments. Therefore the IPRO course will benefit from the experience and knowledge of students enrolled in various academic majors at IIT. Several undergraduate disciplines have representation on the team: Architecture, Mechanical Engineering, Aerospace Engineering, Materials Science and Engineering, Electrical Engineering and Architectural Engineering. This diverse mix of students working on one project provides a unique and interesting learning environment not typical of conventional undergraduate education.

## 4.6 List of Courses

### 4.6.1 Undergraduate Courses

#### *A. IPRO 311 – Integration of Plug-in Hybrid Electric Vehicles and Renewable Energy Systems*

Illinois Institute of Technology, Fall 2010

The purpose of the research project is to investigate the economic effects of the integration of wind power generation systems and PHEVs. For wind generations it is important to investigate factors that impact the generation of wind, like location of the wind farm, speeds of wind in the specific location, type of turbine and its characteristics. In the case of PHEVs a significant research on driving habits, type of battery and its life will be pursued. The final goal of the research is to determine the effectiveness of the method on lowering the operational cost by analyzing various cases which introduce the use of PHEVs into the power generation system. The results obtained from the research will serve targeted markets including, but not limited to, automotive industry, wind power generation industry, and utility companies. The advancement of alternative energy technology will also benefit the environment.

#### *B. IPRO 323 – Modeling of Building Integrated Wind Turbine Modules*

Illinois Institute of Technology, Spring 2011

Being able to adapt cities to include onsite renewable technologies is of vital importance. IPRO 323 hopes to design a device that will reduce the reliance on fossil fuels in urban areas. This device will unite wind energy and high-rise buildings. Building-integrated wind turbine technology is not commonly used at the moment and research and development is required. The goal of IPRO 323 is to effectively integrate wind turbines and buildings with harmony as to not disturb the social and natural environments of the city, and to produce the maximum amount of power possible. This can be done by designing a surface shape to integrate onto buildings that will accelerate the velocity, and thus increase the power output of the wind turbines implemented on the shapes. In IPRO 323, it is not only important to understand the fluid dynamics of wind flow and energy to increase turbine efficiency, but to understand how it can be applied to urban environments and integrated onto current buildings to create architecturally efficient and aesthetically pleasing building-integrated wind turbine modules.

#### *C. ECE 456 – Embedded Control and Mechatronics*

Southern Illinois University

Introduction to mechatronic systems, systems modeling and simulation, sensors and actuators, real-time interfacing, DSPs and micro-controllers, analysis of sampled-data systems, z-transform, digital control design techniques, emulation method, direct method, industrial applications. This course is delivered once a year, in spring semester. It has been recently redesigned to introduce model-based control design techniques for embedded mechatronic systems using microcontrollers and Mathworks toolboxes, and has been offered twice a year so far. The course is offered to ECE senior undergraduate and graduate students. However, it is also open to students with appropriate background from other disciplines. In the redesigned course, a number of recorded webinars from Mathworks, on the subject of

modeling and control of wind turbines, have been presented in the lectures to expose the students to wind energy as an alternative energy source and to explore the techniques for modeling and control of turbines for harvesting this energy. The webinars include: (1) Modeling a Wind Turbine Using MathWorks Tools, 53:00 minutes; (2) Designing Pitch and Yaw Actuators for Wind Turbines, 36:00 minutes; (3) Determining Mechanical Loads for Wind Turbines, 34:00 minutes; (4) Designing Control Systems For Wind Turbines, 34:00 minutes. The integration of webinars in some of the class lecture has been received well by the students.

#### *D. ECE 486 – Wind Energy Research Paper*

Southern Illinois University

This course is not restricted to ECE students and has been very popular between all students from different disciplines. Upon completion of this course students are supposed to be able to: (1) Understand the energy supply and demand patterns for the United States and the world. Calculate energy consumption based on historic data, and future consumption based on past and predicted growth rates. Know the time until the reserve is depleted. (2) Understand the basic laws and the role of all clean resources of energy, such as, wind, solar, hydro, oceanic, tidal, fuel cell, waste, and clean coal technology. (3) Appreciate the social and economic issues, including public acceptance and economics of all alternative energy sources. Appreciate the role of government regulations and world events on energy utilization. (4) Research and investigate issues related to energy resources of a specific energy source.

#### *E. ECE 495 – Capstone Senior Design Project*

Southern Illinois University

This course is designed to teach senior level students about team approach to engineering projects. The students are expected to understand and analyze RFPs (Request for Proposals), identify tasks, develop team organization, and assignment of tasks. In addition as part of their work, they are required to have a work plan and time schedule. The projects must have: feasibility analysis, team approach in engineering projects, understanding and analyzing a request for proposals, identification of tasks, assignment of tasks and team organization, work plan and time scheduling, feasibility analysis and cost-benefit analysis, ethics and professionalism issues related to engineering projects in general and to the specific project assigned, team coordination and documentation of team member efforts, documentation of team communications and the team decision making processes, development, presentation and defense of the final proposal for the assigned project.

### 4.6.2 Graduate Courses

#### *A. ECE 580 – Elements of Sustainable Energy*

Illinois Institute of Technology, Fall 2010

This course covers cross-disciplinary subjects on sustainable energy that relate to energy generation, transmission, distribution, and delivery as well as theories, technologies, design, policies, and integration of sustainable energy. Topics include wind energy, solar energy, biomass, hydro, nuclear energy, and

ocean energy. Focus will be on the integration of sustainable energy into the electric power grid, the impact of sustainable energy on electricity market operation, and the environmental impact of sustainable energy.

#### *B. ECE 581 – Elements of Smart Grid*

Illinois Institute of Technology, Fall 2010

This course covers cross-disciplinary subjects on smart grid that relates to energy generation, transmission, distribution, and delivery as well as theories, technologies, design, policies, and implementation of smart grid. Topics include: smart sensing, communication, and control in energy systems; advanced metering infrastructure; energy management in buildings and home automation; smart grid applications to plug-in vehicles and low-carbon transportation alternatives; cyber and physical security systems; microgrids and distributed energy resources; demand response and real-time pricing; and intelligent and outage management systems.

#### *C. ECE 581 – Wind Energy Power Systems*

Southern Illinois University

The course introduces graduate students to advanced configurations of wind energy power systems with an in-depth treatment of their control and protection. Wind speed and power relations, basic design of wind energy power systems, synchronous and induction generators, power inverters, generator drives-control modes, interface with the power grid-system modeling, stability, control and protection.

### 4.6.3 Professional Course

#### *A. Wind Energy Technology, Interconnection & Integration*

EnerNex

This course is intended to provide the necessary background for engineers and researchers by addressing various aspects of interconnecting wind power plants into electric power systems. The study course is designed to provide knowledge on the state-of-the-art of wind-technology and wind-integration related issues. The study course will mainly discuss insights on dealing with high wind power penetration levels in North America networks. In addition, a brief summary on the European wind energy performance is also presented. This course is targeted towards power systems engineering and management personnel from utilities, RTOs, ISOs, and ITCs as well as consultants, manufacturers and developers involved with the evaluation and planning of the interconnection and operation of new wind plants. The students and professors who are working in the field of wind energy and technology will also benefit from this study course. This course is divided in 11 sessions which will be covered in 3 days. The sessions will begin at 10.00 AM each day. The duration of each session will be 45 minutes. At the end of each day attendees will be given an opportunity to raise any topics for discussion.

# 5. Conclusions

The consortium members have developed extensive education and research programs for educating the stakeholders on critical issues related to the wind energy research and development.

The Consortium procured one utility-grade wind unit and two small wind units. Specifically

- The Consortium procured a 1.5MW GE wind unit by working with the world leading wind energy developer, Invenergy, which is headquartered in Chicago, in September 2010. The Consortium also installed advanced instrumentation on the turbine and performed relevant turbine reliability studies. The site for the wind unit is Invenergy's Grand Ridge wind farm in Illinois. Invenergy's extensive experience in the deployment and operation of large numbers of wind turbines in the United States provided guidance to the Consortium for conducting world-class wind energy research and development. Upon the completion of the project, the Consortium has (1) installed the GE ADAPT vibrations system; (2) installed the Lube Oil System Monitoring Sensors; (3) installed associated software and hardware to acquire the data and communicate the information to IIT main campus; (4) installed associate software and hardware to receive the data at IIT main campus, capture the data in a historian, and support the Proficy SmartSignal Software; (5) created a SmartSignal Condition Monitoring model using the OEM standard available sensors plus the additional sensors; (6) installed Vindicator® laser wind sensor (LWS), which is a next generation wind sensor for utility-scale wind turbines. The Consortium commemorated the installation at the July 20, 2011 ribbon-cutting ceremony.
- The Consortium, by working with Viryd Technologies, installed an 8kW Viryd wind unit (the Lab Unit) at an engineering lab at IIT in September 2010 and an 8kW Viryd wind unit (the Field Unit) at the Stuart Field on IIT's main campus in July 2011, and performed relevant turbine reliability studies. The Lab Unit is a "bench top" wind turbine drivetrain system including all components that are in the Field Unit along with additional instrumentation. This "bench top" system is designed for use in experimentation and configured to allow several tests to be conducted and for additional tests to be added in the future. The Field Unit is very similar to the Lab Unit, which enable the Consortium members to run experiments on the Lab unit and then try to validate and correlate data on the actual turbine running in the field. The field installation provides easy access to the machine, as well as helps promote the Consortium's effort in wind and sustainable energy. The operation of the Field Unit is also monitored by the Phasor Measurement Unit (PMU) in the nearby Stuart Building. The PMU provides GPS time stamped voltage and current samples with one phasor sample per cycle (60 samples per sec) and, accordingly, detailed power measurements for the Field Unit.

Researches on turbine reliability included (1) Predictive Analytics to Improve Wind Turbine Reliability; (2) Improve Wind Turbine Power Output and Reduce Dynamic Stress Loading Through Advanced Wind Sensing Technology; (3) Use High Magnetic Density Turbine Generator as Non-rare Earth Power Dense Alternative; (4) Survivable Operation of Three Phase AC Drives in Wind Generator Systems; (5) Localization of Wind Turbine Noise Sources Using a Compact Microphone Array; (6) Wind Turbine Acoustics - Numerical Studies; and (7) Performance of Wind Turbines in Rainy Conditions. Specifically,

- The advanced instrumentation on the 1.5MW wind unit and associated software systems can be used to identify items including yaw control issues, blade pitch control issues, bearing temperature issues, power related issues such as phase imbalance and shorts, nacelle temperature issues, control box temperature issues, and turbine efficiency issues. The advanced instrumentation also provides (1) better indication of bearing health through direct measurement of vibration; (2) direct measurement of the count of metal particulate in the oil system, which is an indication of damage to the gears and is traditionally measured by climbing the tower and taking oil samples; (3) direct measurement of filter differential pressure, which provides an indication of the condition of the oil filter, and additionally, an inexpensive alternative to installing a particulate counter; (4) cooler inlet and outlet temperature, which provides an indication of the health of the cooler (plugging) and the effectiveness of the oil cooler. The SmartSignal EPI*Center software detects, diagnoses, and prioritizes developing mechanical and instrumentation turbine failures. The software analyzes in real time all the data collected in the nacelle and detects and notifies impending problems, allowing owners to focus on fixing problems early and efficiently.
- The intelligent wind sensing technology, the Vindicator® laser wind sensor (LWS) installed on top of the nacelle, determines the wind speed and direction in the undisturbed air 250 meters in front of the turbine. As a result, it can provide the control system with a predictive, three-dimensional view of actual conditions which allows the optimization of wind turbine performance. The optical control system (OCS) is designed to increase turbine performance while maintaining conservative safety requirements. When in OCS control, the system utilizes an advanced laser measurement device to drive the nacelle yaw motors to more accurately align the nacelle with the approaching wind direction. The OCS control architecture is designed to only take control when both the turbine and the OCS are operating well and without any indication of issue. In all situations where either the turbine or the OCS exhibits any cautionary signals, turbine control is returned to the legacy system until these system issues are resolved and the OCS has worked through the Initialize state. This control strategy allows the turbine to maintain all of its current functionality regarding safety monitoring.
- The Dakota Power (DP) technology provides a non-rare earth power dense alternative for the operation of wind turbines. This technology integrates switched reluctance technologies with other sources of magnetic energy to produce high-performance electrical machines. This technology has the potential to provide a lightweight, low-cost wind turbine for residential and light industrial applications. The process for the development of the DP switched reluctance technology includes the transition of a concept for a machine through design and simulation using advanced FEA software. A commercially developed Maxwell FEA simulation software is provided to validate the potential performance of each proposed design. The optimal design, including the specific geometry, stator winding turns and current, is then fabricated to provide a prototype test machine. The performance of each prototype machine is tested and evaluated through Dynamometer Test Facility (DTF). The resulting performance information is analyzed and incorporated into subsequent developments of the DP switched reluctance technology. A

Quick Machine software program has been developed to support the introduction of switched reluctance technology in the development of wind turbines and other machine applications.

- A survivable drive method is proposed to handle the current sensor failure and continue operating the wind turbine when current fault happens. Vector control is implemented and used to control the three-phase AC machine when system is healthy. When current fault happens, a current sensor failure detection mechanism is used to generator a fault signal which can trigger the transition from vector control to a simplified control method. The simplified control method, which is a state transition control, is proposed for induction machine to work as a backup control strategy. Simulation and experimental results have demonstrated the effectiveness of the proposed survivable drive method.
- A major drawback of the use of basic beamformers for localizing the noise sources on a 1.5 MW production wind turbine is that requires a large array spread over a large area serves. The propsoed idea was to use a compact microphone array along with advanced beamforming to locate the wind turbine noise sources. The results of the initial calibration of the array provided the knowledge of how various beamforming algorithms behave on exposure to different types on noise sources. From the results of actual wind turbine measurements, it was evident that the compact microphone array was effectively able to separate various noise sources, both mechanical and aerodynamic, produced by the wind turbine. The results from the GE 1.5 MW wind turbine show the potential of the microphone array by effectively separating the blade tip vortex noise, the nacelle mechanical noise, and the yaw motor noise (a narrow band source). The results from the Viryd 8kW wind turbine drive train simulator show that the use of the microphone array could separate the mechanical noise in the nacelle to its particular components such as the gearbox, cooling fan and the generator.
- Numerical simulation of the flow around wind turbines was performed for investigating the acoustic field associated with the unsteady fluid behavior. Numerical studies enable a full acoustic analysis of the flow around an operational wind turbine. The OVERFLOW code solves the unsteady Navier-Stokes equations to predict the acoustic near-field. The near-field data is used by the PSU-WOPWOP Ffowcs-Williams Hawking solver to propagate the acoustic field to the farfield. Farfield data is then recorded at locations corresponding to a microphone array, and this data is processed using the Beamform Interactive analysis software.
- A numerical model was developed for assessing and analyzing the performance of a horizontal-axis wind-turbine (HAWT) in the presence of rain droplets under heavy rain conditions using computational fluid dynamics (CFD) for multiphase flow systems. Initially a set of single-phase benchmarking CFD simulations was performed in 2-D and 3-D and the results were compared with the available experimental data in the literature to refine the CFD model. Then, the single phase simulation results were used as a baseline to calculate the impact of rain on the performance of the wind turbine. To capture the water film formation over the airfoil, a new coupled Lagrangian-Eulerian approach was employed. The performance loss caused by the formation of the water film was estimated by capturing the shape and position of the accumulated water film. The results of this study could help designers to minimize the impact of rain on the new generation of wind turbines.

Researches on wind integration included (1) Analysis of 2030 Large-Scale Wind Energy Integration in the Eastern Interconnection; (2) Large-scale Analysis of 2018 Wind Energy Integration in the Eastern U.S. Interconnection; (3) Integration of Non-dispatchable Resources in Electricity Markets; (4) Integration of Wind Unit with Microgrid. Specifically,

- A comprehensive large-scale wind energy integration analysis is considered which is based on the 2030 load forecast in the Eastern Interconnection of the United States. This study is performed using a software called WINS. In this study, transmission constraints are not considered when studying the wind energy portfolios. The wind energy integration is studied based on the capacity factors of potential wind sites. Wind energy contributions to peak/off-peak annual production costs are studied based on the WINS simulation results. The sensitivity of fuel costs, wind energy production, hourly loads, carbon costs, and load management are analyzed in the wind energy integration Scenarios. The results of the study suggest that large-scale wind energy integration will have a major impact on the hourly commitment and dispatch of gas and coal units, especially at off-peak load hours. While fuel price alterations will have major impacts on the system production cost, load variation will have a larger impact and potential carbon costs will have the greatest impact.
- A comprehensive large-scale wind energy integration analysis is implemented based on the 2018 load forecast in the Eastern Interconnection of the United States. This study is performed using a software called WINS. The wind energy integration with/without transmission constraints are studied and analyzed. The sensitivity of fuel price, wind energy production, load, carbon cost, and load shedding are implemented to study the impact of volatility of major parameters on the WINS simulation results. 19 Scenarios are studied and analyzed. The main observations based on the simulations are listed as follows: (1) Production cost is more sensitive to transmission constraints than to wind energy integration; (2) The location of wind energy integration could have an impact on the wind energy dispatch in the hourly generation portfolio; (3) The addition of wind generation units at certain locations in the Eastern Interconnection may cause additional transmission congestion; (4) In 2018, the replacement of coal units by wind energy at certain locations could mitigate transmission congestion; (5) Wind energy is often available and can replace fossil energy at off-peak load hours. During certain seasons when wind is unavailable, wind energy supply could be replaced by fossil energy; (6) In 2018, wind energy is transmitted mostly at 500kV, 345kV, and 230kV transmission levels while the 765kV transmission is utilized less by wind generation units; (7) Higher costs for gas and oil will result in additional transmission congestion as power systems try to use cheaper coal units located centrally in fewer geographical spots. Such limited utilizations of centrally located resources may also limit the available dispatch of wind generating units; (8) Higher levels of wind energy integration could result in higher levelzied congestion costs when wind generation units, located at few geographical spots, try to supply a significant level of load; (9) Carbon cost demonstrates the highest impact on the 2018 simulation results. Higher carbon costs will be instrumental in mitigating the regional transmission congestion in the Eastern Interconnection; (10) Load forecast uncertainty will have a larger impact on the 2018 simulation results as compared to fluctuations in fuel prices or possible levels of wind energy integration; (11) The levelized

congestion cost may not increase monotonically with higher levels of bus loads; (12) Peak load shaving will have a major impact on the commitment and dispatch of gas units because peak loads are mostly supplied by such units. The WINS simulation results shows that lowering the hourly volatility of load profile by introducing smart grid, additional distribution automation for the utilization of demand response, and the large-scale integration of wind energy and storage could lower the transmission congestion and improve the economics and the optimal operation of power systems in the Eastern Interconnection of the United States.

- The electricity market structure, involving generally a pool, a futures market and a bilateral trading floor, was designed before the large integration of non-dispatchable sources, particularly wind power. There is a need to address the suitability of the current electricity market structure for producers relying on non-dispatchable energy sources. Considering the intrinsic variability and uncertainty of the production level of non-dispatchable sources, appropriate changes in the current market structure are needed to adapt such structure to an increasingly non-dispatchable generation mix. To efficiently integrate non-dispatchable production, this study presented the questions below regarding market design and organization need to be answered: (1) Which is the most appropriate time framework to clear short-term electricity markets? Is it a day-ahead horizon as today, or a shorter one? (2) Should the algorithms to clear such markets be deterministic or stochastic? How should prices be derived? (3) How much reserves should be scheduled to cope with the variable and uncertain nature of renewable non-dispatchable producers? Who should pay for such reserves? (4) How the transmission infrastructure should be expanded and operated to avoid bottlenecks that hider the integration of renewable non-dispatchable resources?
- IIT's existing microgrid provides a unique opportunity to see how local wind turbine generation might affect the microgrid. The microgrid master controller requirements for wind integration are investigated and pertain mostly when the microgrid is operating in island mode. The summarized list of microgrid master control requirements are: (1) Make short term on long term predictions of wind output and ramp rates; (2) Make adjustments to the microgrid reserve power requirements when operating in island mode; (3) Be able to curtail wind power when wind intermittency and ramp rates as required to ensure the microgrid's power reliability and safety; (4) Monitor distribution circuit power flows and curtail wind power if necessary to reduce over loading.

The education and outreach activities on wind energy included (1) Wind Energy Training Facility Development; (2) Wind Energy Course Development; (3) Wind Energy Outreach. Specifically,

- To fulfill the mission on workforce training and education, the Consortium erected a permanent facility at IIT for Workforce Training and Education on Sustainable Energy and Smart Grid. IIT secured funds from the State of Illinois to renovate the 16,000 sqft of space for establishing the facility. This project provided funds to furnish the facility with the state-of-the-art equipment to offer a world-class training and education on sustainable energy at IIT. The facility has provided and will continue to provide training on sustainable energy to various sectors including power

industry employees, union workers, high school teachers, the public, and students through instructor-led and internet-based training courses.

- Undergraduate students were engaged in the research on wind energy. The Interprofessional Project (IPRO) “Integration of Plug-in Hybrid Electric Vehicles and Renewable Energy Systems” at IIT engaged undergraduate students to investigate the economic effects of the integration of wind power generation systems and Plug-in Hybrid Electric Vehicles (PHEVs). The IPRO “Modeling of Building Integrated Wind Turbine Modules” at IIT engaged undergraduate students to develop a methodology for designing and developing building-integrated wind turbine modules so that more urban environments will see wind power as a viable alternate energy source. The Capstone Senior Design Project at Southern Illinois University (SIU) is designed to teach senior level students about team approach to engineering projects. The students were asked to create a model of a 3-phase power generation and distribution system including residential, commercial, industrial, coal-fired generation, and wind generation. The students were to understand and analyze RFPs (Request for Proposals), identify tasks, develop team organization, and assignment of tasks. A Wind Energy Research Course was also offered at SIU to introduce the concept of Clean Energy Resources. The course is not restricted to ECE students and has been very popular between all students from different disciplines.
- Graduate Courses in Wind Energy were developed and offered at both IIT and SIU. The course “Elements of Sustainable Energy” at IIT covers cross-disciplinary subjects on sustainable energy that relate to energy generation, transmission, distribution, and delivery as well as theories, technologies, design, policies, and integration of sustainable energy. Topics include wind energy, solar energy, biomass, hydro, nuclear energy, and ocean energy. Focus was on the integration of sustainable energy into the electric power grid, the impact of sustainable energy on electricity market operation, and the environmental impact of sustainable energy. The course “Elements of Smart Grid” at IIT covers cross-disciplinary subjects on smart grid that relates to energy generation, transmission, distribution, and delivery as well as theories, technologies, design, policies, and implementation of smart grid. Topics include: smart sensing, communication, and control in energy systems; advanced metering infrastructure; energy management in buildings and home automation; smart grid applications to plug-in vehicles and low-carbon transportation alternatives; cyber and physical security systems; microgrids and distributed energy resources; demand response and real-time pricing; and intelligent and outage management systems. The course “Wind Energy Power Systems” at SIU introduces graduate students to advanced configurations of wind energy power systems with an in-depth treatment of their control and protection. Topics include wind speed and power relations, basic design of wind energy power systems, synchronous and induction generators, power inverters, generator drives-control modes, interface with the power grid-system modeling, stability, control and protection.
- A Short Course on “Wind Energy Technology, Interconnection and Integration” was developed to provide an introduction to the underlying technology of wind turbine generators and wind power plants, how they are modeled for power system analysis purposes for planning and operating studies, and an introduction to using actual models in simulation programs. This course is targeted towards power systems engineering and management personnel from

utilities, RTOs, ISOs, and ITCs as well as consultants, manufacturers and developers involved with the evaluation and planning of the interconnection and operation of new wind plants. The students and professors who are working in the field of wind energy and technology will also benefit from this study course.

- IIT's Center for Electricity Innovation hosted the 2010 meeting of the Consortium members On September 30, 2010 and the 2011 meeting on July 19, 2011 on IIT's main campus in Chicago. Ribbon Cutting Events were held to commemorate the installation of the 1.5MW GE Wind Unit and the 8kW Viryd Wind Unit (the Field Unit) at the 2011 meeting.
- IIT's Center for Electricity Innovation hosted the first Great Lakes Symposium on Smart Grid and the New Energy Economy on October 18-19, 2011 and the second on September 24-26, 2012 on IIT's main campus in Chicago. The Symposium featured keynote and plenary sessions, technical presentations, and tutorials by international experts on smart grid and renewable energy applications. The Symposium is a one-of-a-kind event that breaks new ground in smart grid and renewable energy design and development and showcases smart grid and renewable energy best practices from around the country along with new technologies and ideas that are spurring innovation, growing state economies, reducing emissions and empowering consumers to conserve and save. Participants had the opportunity to engage thought leaders on key policy questions, identify investment and job creation opportunities, and learn about projects already underway.

# 6. Recommendations

The Consortium would like to make the following recommendations based on the research and development performed in this project.

- While current turbine designs are based on unitary blades that account for the span-wise (radially) differences of flow and moment with taper and twist, those designs are based on the assumption of a uniform flow field perfectly normal to the plane of the blade rotation. In fact, as a result of spatial and temporal wind speed and direction variations, the flow field at any point in time is not truly uniform in the radial direction. Even informed individual blade pitch control has to select a best compromise angle of attack for the entire blade length and does not have the ability to handle span-wise flow differences. With real-time spatial wind speed and direction data from a laser sensor, high response rate aerodynamic devices along the blade span could be actuated to correspond to local relative wind. This could be implemented using various flaps, jets, or tabs as developed for aircraft wings or rigid sails. Combined with the other control advances, this stage represents an optimization of active controls. Ever-increasing sophistication is projected for wind turbine sensors and controls with resultant step-wise increases in efficiency and reductions of undesirable stresses. Wind turbine control practice can begin to catch up to university research and aerospace now that forward-looking laser wind sensors can provide the needed wind accuracy, timeliness, data rates, and spatial mapping. It is time for the wind energy industry to start gaining the power performance and stress reduction advantages.
- The DP technology represents next-generation light weight electric drive systems for military and civilian applications. The same DP electrical machine technology can be applied to the generation of electricity from wind. The DP technology provides a non-rare earth power dense alternative for the operation of wind turbines by integrating switched reluctance technologies with other sources of magnetic energy to produce high-performance electrical machines. The DP technology has the potential to provide a lightweight, low-cost wind turbine for residential and light industrial applications.
- A survivable drive method can be used to handle the current sensor failure and continue operating the wind turbine when current fault happens. Vector control is implemented and used control the three-phase AC machine when system is healthy. When current fault happens, a current sensor failure detection mechanism is used to generator a fault signal which can trigger the transition from vector control to a simplified control method. A simplified control method—state transition control can work as a backup control strategy for induction machine.
- The compact microphone array can be used to separate various noise sources, both mechanical and aerodynamic, produced by the wind turbine. Various beamforming algorithms can be used to locate the noise sources on a wind turbine with a compact array. This demonstrates the potential of the microphone arrays in the future of wind turbine noise management. This tool can be further used to investigate the different types of aerodynamic noise that arise on the blade such as the blade tip noise and the trailing edge noise. This could provide valuable information on modifying the blade configuration to further reduce the aerodynamic noise. One other possible application for the microphone array is to use them as a health monitoring tool for the wind turbine.

- A full acoustic analysis of the flow around an operational wind turbine can be enabled by assembling several components. The OVERFLOW code can be used to solve the unsteady Navier-Stokes equations to predict the acoustic near-field. The near-field data can be used by the PSU-WOPWOP Ffowcs-Williams Hawking solver to propagate the acoustic field to the farfield. Farfield data can be then recorded at locations corresponding to a microphone array and processed using the Beamform Interactive analysis software.
- A coupled Lagrangian-Eulerian approach can be employed to capture the water film formation over the airfoil. The performance loss caused by the formation of the water film can be estimated by capturing the shape and position of the accumulated water film. The results could help designers to minimize the impact of rain on the new generation of wind turbines. Future work can be geared toward adding the effect of splash back of droplets in the model and considering the effect of surface tension on the water film formation. In addition, the Lagrangian-Eulerian model could be applied in a three-dimensional case and calculate the performance of the horizontal-axis-wind-turbine in a heavy rain condition.
- The WINS software can be applied to perform a comprehensive large-scale wind energy integration analysis with/without transmission constraints. The sensitivity analyses of fuel price, wind energy production, load, carbon cost, and load shedding should be implemented to study the impact of volatility of major parameters on the simulated wind integration results.
- The electricity market structure, involving generally a pool, a futures market and a bilateral trading floor, was designed before the large integration of non-dispatchable sources, particularly wind power. There is a need to address the suitability of the current electricity market structure for producers relying on non-dispatchable energy sources. Considering the intrinsic variability and uncertainty of the production level of non-dispatchable sources, appropriate changes in the current market structure are needed to adapt such structure to an increasingly non-dispatchable generation mix. To efficiently integrate non-dispatchable production, the following questions regarding market design and organization need to be answered: (1) Which is the most appropriate time framework to clear short-term electricity markets? Is it a day-ahead horizon as today, or a shorter one? (2) Should the algorithms to clear such markets be deterministic or stochastic? How should prices be derived? (3) How much reserves should be scheduled to cope with the variable and uncertain nature of renewable non-dispatchable producers? Who should pay for such reserves? (4) How the transmission infrastructure should be expanded and operated to avoid bottlenecks that hider the integration of renewable non-dispatchable resources?
- The impact of wind turbine generation on microgrid operation should be considered especially when the microgrid is operating in island mode. A list of microgrid master control requirements are: (1) Make short term on long term predictions of wind output and ramp rates; (2) Make adjustments to the microgrid reserve power requirements when operating in island mode; (3) Be able to curtail wind power when wind intermittency and ramp rates as required to ensure the microgrid's power reliability and safety; (4) Monitor distribution circuit power flows and curtail wind power if necessary to reduce over loading.

## References


[1] NREL. (2008) 20% Wind Energy by 2030: Increasing Wind Energy's Contribution to U.S. Electricity supply. [Online]. http://www.nrel.gov/docs/fy08osti/41869.pdf

[2] F. Oyague, "Gearbox Modeling and Load Simulation of a Baseline 750-kW Wind Turbine Using State-of-the-Art Simulation Codes," 2009.

[3] W. Musial, S. Butterfield, and B. McNiff, "Improving Wind Turbine Gearbox Reliability," 2007.

[4] A. Julian and G. Oriti, "A Comparison of Redundant Inverter Topologies to Improve Voltage Source Inverter Reliability," in *2006 IEEE Industry Applications Conference*, 2006, pp. 1674-1678.

[5] S. Bolognani, M. Zordan, and M. Zigliotto, "Experimental fault-tolerant control of a PMSM drive," *IEEE Transactions on Industrial Electronics*, vol. 47, pp. 1134-1141, 2000.

[6] K. Lee and J. Ryu, "Instrument fault detection and compensation scheme for direct torque controlled induction motor drives," *IEEE Proceedings - Control Theory and Applications*, vol. 150, pp. 376-382, 2003.

[7] L. Baghli, P. Poure, and A. Rezzoug, "Sensor fault detection for fault tolerant vector controlled induction machine," in *2005 European Conference on Power Electronics and Applications*, 2005.

[8] K. Rothenhagen and F. Fuchs, "Current Sensor Fault Detection, Isolation, and Reconfiguration for Doubly Fed Induction Generators," *IEEE Transactions on Industrial Electronics*, vol. 56, pp. 4239-4245, 2009.

[9] R. Sepe, B. Fahimi, C. Morrison, and J. Miller, "Fault tolerant operation of induction motor drives with automatic controller reconfiguration," in *IEEE International Electric Machines and Drives Conference*, 2001, pp. 156-162.

[10] O. Wallmark, L. Harnefors, and O. Carlson, "Control Algorithms for a Fault-Tolerant PMSM Drive," *IEEE Transactions on Industrial Electronics*, vol. 54, pp. 1973-1980, 2007.

[11] K. Iizuka, H. Uzuhashi, M. Kano, T. Endo, and K. Mohri, "Microcomputer Control for Sensorless Brushless Motor," *IEEE Transactions on Industry Applications*, vol. IA-21, pp. 595-601, 1985.

[12] Xiaodong Shi, J. Serradilla, and M. Krishnamurthy, "A back EMF-based rotor position prediction in Permanent Magnet machines for survivable wind generator systems," in *IECON 2010 - 36th Annual Conference on IEEE Industrial Electronics Society*, 2010, pp. 778-783.

[13] M. Krishnamurthy, C. Edrington, and B. Fahimi, "Prediction of rotor position at standstill and rotating shaft conditions in switched reluctance machines," *IEEE Transactions on Power Electronics*, vol. 21, pp. 225-233, 2006.

[14] P. Acarnley and J. Watson, "Review of position-sensorless operation of brushless permanent-magnet machines," *IEEE Transactions on Industrial Electronics*, vol. 53, pp. 352-362, 2006.

[15] P. Jordi and A. Beaumont. (2010, June) Wind Turbine Gearbox Reliability: The impact of rotor support. [Online]. http://www.renewableenergyworld.com/rea/news/article/2010/06/wind-

turbine-gearbox-reliability

[16] P.J. Tavnet, G.J.W. Van Bussel, and F. Spinato, "Machine and Converter Reliabilities in Wind Turbines," in *The 3rd IET International Conference on Power Electronics, Machines and Drives*, 2006, pp. 127-130.

[17] R. Krishnan, *Electric Motor Drives: Modeling, Analysis, and Control*.: Prentice Hall, 2001.

[18] R. Ueda, T. Sonoda, K. Koga, and M. Ichikawa, "Stability analysis in induction motor driven by V/f controlled general-purpose inverter," *IEEE Transactions on Industry Applications*, vol. 28, pp. 472-481, 1992.

[19] Rongfeng Yang, Wei Chen, Yong Yu, and Dianguo Xu, "A novel V/F control system based on stator voltage oriented method," in *International Conference on Electrical Machines and Systems*, 2008, pp. 83-87.

[20] A. Munoz-Garcia, T. Lipo, and D. Novotny, "A new induction motor V/f control method capable of high-performance regulation at low speeds," *IEEE Transactions on Industry Applications*, vol. 34, pp. 813-821, 1998.

[21] M. Tsuji, Shuo Chen, S. Hamasaki, Xiaodan Zhao, and E. Yamada, "A novel V/f control of induction motors for wide and precise speed operation," in *International Symposium on Power Electronics, Electrical Drives, Automation and Motion*, 2008.

[22] J. Santisteban and R. Stephan, "Vector control methods for induction machines: an overview," *IEEE Transactions on Education*, vol. 44, pp. 170-175, 2001.

[23] S. Wade, M. Dunnigan, and B. Williams, "Modeling and simulation of induction machine vector control with rotor resistance identification," *IEEE Transactions on Power Electronics*, vol. 12, pp. 495-506, 1997.

[24] Yen-Shin Lai, "Machine modeling and universal controller for vector-controlled induction motor drives," *IEEE Transactions on Energy Conversion*, vol. 18, pp. 23-32, 2003.

[25] A. Sathyan, N. Milivojevic, Young-Joo Lee, M. Krishnamurthy, and A. Emadi, "An FPGA-Based Novel Digital PWM Control Scheme for BLDC Motor Drives," *IEEE Transactions on Industrial Electronics*, vol. 56, pp. 3040-3049, 2009.

[26] F. Rodriguez and A. Emadi, "A Novel Digital Control Technique for Brushless DC Motor Drives," *IEEE Transactions on Industrial Electronics*, vol. 54, pp. 2365-2373, 2007.

[27] A. Khaligh et al., "Digital Control of an Isolated Active Hybrid Fuel Cell/Li-Ion Battery Power Supply," *IEEE Transactions on Vehicular Technology*, vol. 56, pp. 3709-3721, 2007.

[28] A. Khaligh and A. Emadi, "Pulse Adjustment, a Novel Digital Control Technique, for Control of a DC-DC Buck-Boost Converter Operating in Discontinuous Conduction Mode and Driving Constant Power Loads," in *IEEE Vehicle Power and Propulsion Conference*, 2006.

[29] M. El-Sharkawi, *Fundamentals of Electric Drives*.: CL-Engineering, 2000.

[30] T. F. Brooks and W. M. Humphreys, "A deconvolution approach for the mapping of acoustic sources (DAMAS) determined from phased microphone arrays," *Journal of Sound and Vibration*, vol. 294, pp. 856-879, July 2006.

[31] R.P Dougherty, "Extensions of DAMAS and benefits and limitations of deconvolution in beamforming," in *AIAA–2005–2961*, 2005.

[32] R.P. Dougherty and G.G. Podboy, "Improved phased array imaging of a model jet," in *AIAA Paper 2009-3186*, Miami, FL, May 2009.

[33] P. Sijtsma, "CLEAN based on spatial source coherence," *International Journal of Aeroacoustics*, vol. 6, no. 4, p. 357–374, 2007.

[34] Ganesh Raman, "Wind turbines: clean, renewable and quiet?," *Noise & Vibration Worldwide*, vol. 40, pp. 15-21, November 2009.

[35] Ganesh Raman, "Advances in measuring noise from wind turbines," *Noise & Vibration Worldwide*, vol. 41, pp. 19-25, April 2010.

[36] M. Kandula and P. G. Buning, "Implementation of LU-SGS Algorithm and Roe Upwinding Scheme in OVERFLOW Thin-Layer Navier-Stokes Code," in *AIAA Paper 1994-2357*, 1994.

[37] D. Jesperson, T. Pulliam, and P. Buning, "Recent enhancements to OVERFLOW," in *AIAA Paper 1997-0644*, 1997.

[38] J. C. Vassberg, P. G. Buning, and C. L. Rumsey, "Drag prediction for the DLR-F4 wing/body using OVERFLOW and CFL3D on an overset mesh," in *AIAA Paper 2002-0840*, 2002.

[39] E. Bounajem, "Prediction of business jet airloads using the OVERFLOW Navier-Stokes code," in *AIAA Paper 2001-1004*, 2001.

[40] M. E. Olsen and D. K. Prabhu, "Application of OVERFLOW to hypersonic perfect gas flowfields," in *AIAA Paper 2001-2664*, 2001.

[41] P. G. Buning, R. J. Gomez, and W. I. Scallion, "CFD Approaches for Separation of Wing-Body Stage Separation," in *AIAA Paper 2004-4838*, 2004.

[42] R. Nichols, R. Tramel, and P. Buning, "Solver and Turbulence Model Upgrades to OVERFLOW 2 for Unsteady and High-Speed Applications," in *AIAA Paper 2006-2824*, 2006.

[43] R. Nichols, R. Tramel, and P. Buning, "Evaluation of Two High Order WENO Schemes," in *AIAA Paper 2007-3920*, 2007.

[44] M. J. Lighthill, "On Sound Generated Aerodynamically: I. General Theory," *Proc. Roy. Soc. Lond. A*, vol. 211, pp. 564-587, 1952.

[45] G. M. Lilley, "On the Noise from Jets," *Noise Mechanisms*, pp. AGARD-CP-131, 13.1-13.12, 1974.

[46] A. Khavaran, E. A. Krejsa, and C. M. Kim, "Computation of Supersonic Jet Mixing Noise for an Axisymmetric Convergent Divergent Nozzle," *J. of Aircraft*, vol. 31, no. 3, pp. 603-609, 1994.

[47] A. Khavaran, "Role of Anisotropy in Turbulent Mixing Noise," *AIAA Journal*, vol. 37, no. 7, pp. 832-841, 1999.

[48] J. E. Ffowcs Williams and D. L. Hawkings, "Sound Generated by Turbulence and Surfaces in Arbitrary Motion," *Philosophical Transactions of the Royal Society*, vol. A264, no. 1151, pp. 321-342, 1969.

[49] K.S. Brentner and F. Farassat, "An analytical comparison of the acoustic analogy and Kirchhoff formulation for moving surfaces," *AIAA Journal*, vol. 36, no. 8, pp. 1379-1386, 1998.

[50] G. A. Brès, "Modeling the noise of arbitrary maneuvering rotorcraft: Analysis and implementation of the PSU-WOPWOP noise prediction code," The Pennsylvania State University, M.S. Thesis 2002.

[51] G. Perez, "Investigation of the influence of maneuver on rotorcraft noise," The Pennsylvania State University, M.S. Thesis 2002.

[52] K. S. Brentner, G. Perez, G. A. Brès, and H. E. Jones, "Maneuvering Rotorcraft Noise Prediction," *Journal of Sound and Vibration*, vol. 39, no. 3-5, pp. 719-738, 2003.

[53] C. Hennes, L. Lopes, and J. Shirey, "PSUWOPWOP User's Manual," The Pennsylvania State University, University Park, PA, 2009.

[54] Kenneth S Brentner and Farassat F., "Modeling Aerodynamically Generated Sound of Helicopter Rotors," *Progress in Aerospace Sciences*, vol. 39, no. 2-3, pp. 83-120, 2003.

[55] F. Farassat and G. P. Succi, "The Prediction of Helicopter Discrete Frequency Noise," *Vertica*, vol. 7, no. 4, pp. 309-320, 1983.

[56] F. Farassat, "Derivation of Formulations 1 and 1A of Farassat," 2007.

[57] S. Lee, K. S. Brentner, F. Farassat, and P. J. Morris, "Analytic Formulation and Numerical Implementation of an Acoustic Pressure Gradient Prediction," *Journal of Sound and Vibration*, vol. 319, no. 3-5, pp. 1200-1221, 2009.

[58] S. Lee, "Prediction of Acoustic Scattering in the Time Domain and Its Applications to Rotorcraft Noise," The Pennsylvania State University, PhD Dissertation 2009.

[59] G.P. Corten and H.F. Veldkamp, "Insects can halve wind turbine power," *Nature*, vol. 412, pp. 42-43, 2002.

[60] M.G. Khalfallah and A.M. Koliub, "Effect of dust on the performance of wind turbines," *Desalination*, pp. 209-220, 2007.

[61] M.B. Bragg, G.M. Gregorek, and J.D. Lee, "Airfoil Aerodynamics in Icing Conditions," *Journal of Aircraft*, vol. 23, no. 1, 1986.

[62] S. Lee and M.B. Bragg, "Experimental investigation of simulated large-droplet ice shapes on airfoil aerodynamics," *Journal of Aircraft*, vol. 36, no. 5, 1999.

[63] F. De Gregorio, "Aerodynamic Performance Degradation Induced by Ice Accretion. PIV Technique Assessment in Icing Wind Tunnel," *Topics in Applied Physics*, vol. 112, pp. 396-417, 2008.

[64] J. J. Chung and H. E. Addy, "A Numerical Evaluation of Icing Effects on a Natural Laminar Flow Airfoil," in *AIAA–2000–0096*, 2000.

[65] W. J. Jasinski, S. C. Noe, M. S. Selig, and M. B. Bragg, "Wind turbine performance under icing conditions," in *AIAA paper 97-0977, 35rd Aerospace Sciences Meeting & Exhibit*, 1997.

[66] S. Lee, H.S. Kim, and M.B. Bragg, "Investigation of Factors that Influence Iced- Airfoil Aerodynamics," in *AIAA paper 2000-0099, 38rd Aerospace Sciences Meeting & Exhibit*, 2000.

[67] R.E., Jr. Dunham, "The Potential Influence of Rain on Airfoil Performance," Rhode-Saint Genese, Belgium, 1987.

[68] J.R. Valenine and R.A. Decker, "A Largrangian-Eularian Scheme for Flow around an Airfoil in Rain," *Int. J. Multiphase Flow*, vol. 21, no. 4, pp. 639-648, 1995.

[69] T. Wan and S.W. Wu, "Aerodynamic Analysis under Influence of Heavy Rain," in *24th International Congress of the Aeronautical Sciences*, 2004.

[70] R. J. Jr Hansman and M.F. Barsotti, "Surface Wetting Effects on a Laminar Flow Airfoil in Simulated Heavy Rain," *J. Aircraft*, vol. 22, no. 12, 1985.

[71] H. Arastoopour, "Numerical Simulation and Experimental Analysis of Gas/solid Flow Systems: 1999 Flour Daniel Plenary Lecture," *Powder Technology Journal*, vol. 119, pp. 59-67, 2001.

[72] H. Iddir and H. Arastoopour, "Modeling of Multi-Type Particle Flow Using Kinetic Theory Approach," *AIChE Journal*, vol. 51, no. 6, pp. 1620-1632, 2005.

[73] D. M. Somers, "Design and Experimental Results for the S809 Airfoil," Golden, CO, 1997.

[74] P. Spalart and S. Allmaras, "A one-equation turbulence model for aerodynamic flows," 1992.

[75] F. R. Menter, "Two-Equation Eddy-Viscosity Turbulence Models for Engineering Applications," *AIAA Journal*, vol. 32, no. 8, pp. 1598-1605, August 1994.

[76] D. C. Wilcox, "Turbulence Modeling for CFD," La Canada, California, 1998.

[77] A.L. Pape and J. Lecanu, "3D Navier-Stokes Computations of a Stall-regulated Wind Turbine," *Wind Energy*, vol. 7, pp. 309-324, 2004.

[78] A.H. Markowitz, "Raindrop Size Distribution Expressions," 1976.

[79] M. Arienti et al., "Modeling Wall Film Formation and Breakup Using an Intergraded Interface-Tracking/Discrete-Phase Approach," *J. of Engineering for Gas Turbines and Power*, 2011.

[80] DOE. (2009) Wind Technologies Market report. [Online]. http://www1.eere.energy.gov/windandhydro/./2009_wind_technologies_market_report.pdf

[81] IEA. (2010) IEA Wind Energy Annual Report 2009. [Online]. http://www.ieawind.org/AnnualReports_PDF/2009.html

[82] NREL. (2010) Eastern Wind Integration and Transmission Study. [Online]. http://www.nrel.gov/wind/systemsintegration/ewits.html

[83] NREL. (2010) Western Wind and Solar Integration Study. [Online]. http://www.nrel.gov/wind/systemsintegration/wwsis.html

[84] B. Parsons et al., "Grid impacts of wind power: A summary of recent studies in the United States," *Wind Energy*, vol. 1, no. 7, pp. 87-108, 2004.

[85] J. C. Smith, M. R. Milligan, E. A. DeMeo, and B. Parsons, "Utility wind integration and operating impact state of the art," *IEEE Trans. Power Syst.*, vol. 22, no. 3, pp. 900-908, 2007.

[86] M. Shahidehpour, H. Yamin, and Z., Li, *Market Operations in Electric Power Systems*. New York: Wiley, 2002.

[87] Y. Fu, M. Shahidehpour, and Z. Li, "Security-constrained Unit Commitment with AC Constraints," *IEEE Trans. Power Syst.*, vol. 20, no. 2, pp. 1001-1013, 2005.

[88] Y. Fu, M. Shahidehpour, and Z. Li, "AC contingency dispatch based on security-constraints unit commitment," *IEEE Trans. Power Syst.*, vol. 21, no. 2, pp. 897-908, 2006.

[89] L. Wu, M. Shahidehpour, and T. Li, "Stochastic Security-Constrained Unit Commitment," *IEEE Trans. on Power Syst.*, vol. 22, no. 2, pp. 800-811, 2007.

[90] J. Wang, M. Shahidehpour, and Z. Li, "Security-Constrained Unit Commitment with Volatile Wind Power Generation," *IEEE Trans. Power Syst.*, vol. 23, no. 3, pp. 1319-1327, 2008.

[91] W. Tian, Z. Li, and M. Shahidehpour, "Transmission Congestion Analysis in the Eastern Interconnection using POMS," in *IEEE Power Eng. Soc. General Meeting*, Minneapolis, MN, 2010.

[92] J. E. Schmidt, "A Statistical Analysis of Wind Power in the Eastern Interconnect of the United States," in *IEEE Power Eng. Soc. General Meeting*, Minneapolis, MN, 2010.

[93] MISO. Expansion Planning. [Online]. http://www.midwestiso.org/page/Expansion+Planning

[94] EIA. (2011) Electric Power Monthly. [Online]. http://www.eia.doe.gov/cneaf/electricity/epm/table4_2.html

[95] W. Tian, M. Shahidehpour, and Z. Li, "Analysis of 2030 Large-Scale Wind Energy Integration in the Eastern Interconnection Using WINS," *The Electricity Journal*, vol. 24, pp. 71-87, 2011.

[96] EIA. (2011) Fuel and Energy Source Codes and Emission Coefficients. [Online]. http://www.eia.doe.gov/oiaf/1605/coefficients.html

[97] AWEA. Utilities & Wind Power, 1996-2010. [Online]. http://www.awea.org/la_utilitywind.cfm

[98] DOE. Illinois Wind Map & Resource Potential, 2010. [Online]. http://www.windpoweringamerica.gov/wind_resource_maps.asp?stateab=il

[99] GM. Volt 2011. [Online]. http://gm-volt.com/full-specifications/

[100] S. Aubrun, S. Loyer, and G. Espana. Experimental study on the wind turbine wake meandering with the help of a non-rotating simplified model and of a rotating model. [Online]. http://www.wind-power-program.com/betz.htm

[101] A. Betz, *Introduction to the Theory of Flow Machines*. Oxford: Pergamon Press, 1966.

[102] I.P. Castro, "Wake Characteristics of two-dimensional perforated plates normal to an airstream," *Journal of Fluid Mechanics*, vol. 46, no. 3, pp. 599-609, 1971.

[103] OECD. [Online]. http://www.oecd.org/home/0,2987,en_2649_201185_1_1_1_1_1,00.html

[104] Keliang Zhou and Danwei Wang, "Relationship between space-vector modulation and three-phase carrier-based PWM: a comprehensive analysis [three-phase inverters]," *IEEE Transactions on Industrial Electronics*, vol. 49, pp. 186-196, 2002.

[105] Zuo-xia Xing, "Damping Control Study of the Drive Train of a Double Fed induction Generator Wind Turbine," in *International Conference on Energy and Environment Technology*, 2009.

[106] W. Wong, H. Chao, D. Julian, P. Lindberg, and S. Kolluri, "Transmission Planning in a Deregulated Environment," in *IEEE Trans. and Distr. Conference*, vol. 1, 1999, pp. 350-355.

[107] Wikipedia. PID Controllers. [Online]. http://en.wikipedia.org/wiki/PID_controller

[108] Wikipedia. Dynamometer. [Online]. http://en.wikipedia.org/wiki/Dynamometer

[109] Wikipedia. Aeroelasticity. [Online]. http://en.wikipedia.org/wiki/Aeroelasticity

[110] Rick Wallace, "Plug-In Vehicle and Infrastructure Workshop," Washington, D.C., 2010.

[111] A. Tuohy, P. Meibom, E. Denny, and M. O'Malley, "Unit Commitment for Systems with Significant Wind Penetration," *IEEE Trans. Power Syst.*, vol. 24, no. 2, pp. 592-601, 2009.

[112] O. Tor, A. Guven, and M. Shahidehpour, "Congestion-Driven Transmission Planning Considering the Impact of Generator Expansion," *IEEE Trans. Power Syst.*, vol. 23, no. 2, pp. 781-789, 2008.

[113] S. Shinnaka, S. Takeuchi, A. Kitajima, F. Eguchi, and H. Haruki, "Frequency-hybrid vector control for sensorless induction motor and its application to electric vehicle drive," in *Sixteenth Annual IEEE Applied Power Electronics Conference and Exposition*, vol. 1, 2001, pp. 32-39.

[114] Shiyi Shao, E. Abdi, F. Barati, and R. McMahon, "Stator-Flux-Oriented Vector Control for Brushless Doubly Fed Induction Generator," *IEEE Transactions on Industrial Electronics*, vol. 56, pp. 4220-4228, 2009.

[115] Kersti Schroeder, "A fibre Bragg grating sensor system monitors operational load in a wind turbine rotor blade," *Measurement Science and Technology Journal* , vol. 17, p. 1167–1172, 2006.

[116] A. Rudkevich, K. Egilmez, M. Liu, P. Murti, and T. Overbye, "Identification and congestion analysis of transmission corridors of the Eastern Interconnection," in *The 40th Hawaii International Conference on System Sciences*, 2007.

[117] Anthony L. Rogers, "Wind Turbine Noise Issues: A White Paper," Amherts, MA ,.

[118] A. Pullen and Sawyer. S., *Global Wind 2007 Report*. Brussels, Belgium: GWEC, May 2008.

[119] K. Porter and Rogers J., "Central Wind Power Forecasting Programs in North America by Regional Transmission Organizations and Electric Utilities," December 2009.

[120] K. Parks, P. Denholm, and T Markel, "Costs and Emissions Associated with Plug-In Hybrid Electric Vehicle Charging in the Xcel Energy Colorado Service Territory," 2007.

[121] M. Oloomi, H. Shanechi, G. Balzer, and M. Shahidehpour, "Transmission planning approaches in restructured power systems," in *IEEE Power Eng. Soc. Power Tech. Conf.*, Bologna, Italy, 2003.

[122] S. Ogasawara, H. Akagi, and A. Nabae, "The generalized theory of indirect vector control for AC machines," *IEEE Transactions on Industry Applications*, vol. 24, pp. 470-478, 1988.

[123] Barack Obama and Joe Biden, Barack Obama and Joe Biden: New Energy for America, 2008.

[124] NERC. (2002) Reliability Assessment 2002–2011. [Online]. http://www.hks.harvard.edu/hepg/Papers/NERC_reliability.assessment_2002-2011.pdf

[125] NERC. [Online]. http://www.nerc.com

[126] M. Mohseni, S. Islam, and M. Masoum, "Enhanced Hysteresis-Based Current Regulators in Vector Control of DFIG Wind Turbines," *IEEE Transactions on Power Electronics*, vol. 26, pp. 223-234, 2011.

[127] N. Mohan, *Advanced Electric Drives: Analysis, Control and Modeling Using Simulink*.: Mnpere, 2001.

[128] Timothy McCoy, "Active Control of Rotor Aerodynamics and Geometry: Status, Methods, and preliminary Results, Global Energy Concepts," in *44th AIAA Aerospace Sciences Meeting and Exhibit*, Reno, Nevada, 2006.

[129] P. Maghouli, S. Hosseini, M. Buygi, and M. Shahidehpour, "A Multi-Objective Framework for Transmission Expansion Planning in Deregulated Environments," *IEEE Trans. Power Syst.*, vol. 24, no. 2, pp. 1051-1061, 2009.

[130] Guillaume Lethe, "Simulating dynamics, durability, and noise emissions of Wind Turbines in a Single CAE environment," *Journal of Mechanical Science and Technology*, 2009.

[131] C. Lee, K. Ng, J. Zhong, and F. Wu, "Transmission expansion planning from past to future," in *IEEE Power Eng. Soc. Power System Conf. Expo.*, Atlanta, GA, 2006.

[132] Richard Lawson, "Developing a realistic and balanced United States Electric Power Generation portfolio," 2010.

[133] G. Lattore, R. Cruz, J. Areiza, and A. Villegas, "Classification of publications and models on transmission expansion planning," *IEEE Trans. Power Syst.*, vol. 18, no. 2, pp. 938-946, 2006.

[134] Argonne National Lab. (2009) Wind Power Forecasting: State-of-the-Art 2009. [Online]. http://www.dis.anl.gov/pubs/65613.pdf

[135] Lars Kroldrup, "Gains in Global Wind Capacity," February 15, 2010.

[136] Neil Kelly, "Turbsim," 2010.

[137] N.D. Kelly, "The Impact of Coherent Turbulence on Wind Turbine Aeroelastic Response and Its Simulation," in *National Wind Technology Center, Conference Paper, NREL/CP-500-38074*, 2005.

[138] R. Jobing, F. van der Merwe, and M. Kamper, "Digital implementation of bus clamped space vector

modulation," *IEEE Transactions on Energy Conversion*, vol. 9, pp. 344-348, 1994.

[139] Hannele Holttinen, "Impacts of Large Amounts of Wind Power on Design and Operation of Power Systems, Results of IEA Collaboration," in *8th International Workshop on Large Scale Integration of Wind Power into Power Systems as well as of Transmission Networks of Offshore Wind Farms*, Bremen, 2009.

[140] Yassin Hassan, "Large Eddy Simulation," 2010.

[141] G. Hamoud and I. Bradley, "Assessment of transmission congestion cost and locational marginal pricing in a competitive electricity market," *IEEE Trans. Power Syst.*, vol. 19, no. 2, pp. 769-775, 2004.

[142] GWEC. (2011) Global Wind Report Annual Market Update 2010. [Online]. http://www.gwec.net

[143] Terje Gjengedal, "System Control of Large Scale Wind power by Use of Automatic Generation Control (AGC)," Oslo, Norway, 2000.

[144] M. Gibescu, "Case Study for the Integration of 12 GW Wind Power in the Ductch Power System by 2020," in *IEEE Power & Energy Society General Meeting*, Calgary, 2009.

[145] R. Gallego, A. Monticelli, and R. Romero, "Comparative studies on non-convex optimization methods for transmission network expansion planning," *IEEE Trans. on power Syst.*, vol. 13, no. 3, pp. 822-828, 1998.

[146] L. Gaines and R. Cuenca, "Costs of Lithium-Ion Batteries for Vehicles," Argonne, Illinois,.

[147] Y. Fu, M. Shahidehpour, and Z. Li, "Long-term security-constrained unit commitment: hybrid Dantzig–Wolfe decomposition and subgradient approach," *IEEE Trans. Power Syst.*, vol. 20, no. 4, pp. 2093-2106, 2005.

[148] Erik Ela, "The Evolution of Wind Power Integration Studies: Past, Present, and Future," 2009.

[149] EIPC. [Online]. http://www.eipconline.com/

[150] EIA. International Energy Statistics.

[151] EIA. International Energy Annual 2006.

[152] D. Dang, "A Multi-objective Optimal Nonlinear Control of Variable Speed Wind Turbine," in *IEEE International Conference on Control and Automation*, New Zealand, 2009.

[153] S. Chapman, *Electric Machinery and Power System Fundamentals*.: McGraw-Hill Science/Engineering/Math, 2001.

[154] C. Chan, "The state of the art of electric and hybrid vehicles," *Proceedings of the IEEE*, vol. 90, pp. 247-275, 2002.

[155] D. Casadei, G. Serra, and K. Tani, "Implementation of a direct control algorithm for induction motors based on discrete space vector modulation," *IEEE Transactions on Power Electronics*, vol. 15, pp. 769-777, 2000.

[156] R. Cardenas and R. Pena, "Sensorless vector control of induction machines for variable-speed wind energy applications," *IEEE Transactions on Energy Conversion*, vol. 19, pp. 196-205, 2004.

[157] R. Cardenas, R. Pena, G. Asher, and J. Clare, "Control strategies for enhanced power smoothing in wind energy systems using a flywheel driven by a vector-controlled induction machine," *IEEE Transactions on Industrial Electronics*, vol. 48, pp. 625-635, 2001.

[158] S. Bowes and Yen-Shin Lai, "The relationship between space-vector modulation and regular-sampled PWM," *IEEE Transactions on Industrial Electronics*, vol. 44, pp. 670-679, 1997.

[159] Audun Botterund, "Wind Power Forecasting in U.S. Electricity Markets," *The Electricity Journal*, no. 3, April 2010.

[160] Calo Bottaso, "Aero-servo-elastic modeling and control of wind turbines using finite-element multibody procedures," in *ECCOMAS Multibody Dynamics 2005 Thematic Conference*, Madrid, Spain, 2006.

[161] AWEO. Size Specifications, 2003-2006. [Online]. http://www.aweo.org/windmodels.html

[162] C. Alvarez, "Custom Power Systems and Software Platforms for Wind Farms under Volateg Dips Situations," 2004.

[163] Daniel J. Alberts, *Addressing Wind Turbine Noise*.: Lawrence Technological University, 2006.

[164] AWS. [Online]. http://navigator.awstruewind.com

[165] Architecture2030. Architecture 2030. [Online]. http://www.architecture2030.org/

[166] DOE. (2009) Assessment of Historical Transmission Congestion in the Eastern Interconnection. [Online]. http://congestion09.anl.gov/documents/docs/EasternInterconnection.pdf

[167] DOE. (2008) Buildings Energy Data Book. [Online]. http://buildingsdatabook.eren.doe.gov/

[168] CAISO, "CAISO Integration of Renewable Resources," November 2007.

[169] Chris Woodford, "Dynamometer Testing," 2010. [Online]. http://www.explainthatstuff.com/dynamometer-wind-turbine-test.jpg

[170] GCC. (2010) Green Car Congress. [Online]. http://www.greencarcongress.com/resources.html

[171] DOE. Greenhouse Gases.

[172] DOE. (2006) National Electric Transmission Congestion Study. [Online]. http://nietc.anl.gov/congestionstudy/index.cfm

[173] DOE. (2009) National Electric Transmission Congestion Study. [Online]. http://congestion09.anl.gov/index.cfm

[174] ICC. (2010) Office of Retail Market Development Annual Report of 2010. [Online]. http://www.icc.illinois.gov/downloads/public/2010ORMDSection20110report.pdf

[175] DOE. (March 2006) Power Technologies Energy Data Book. [Online]. http://www.nrel.gov/analysis/power_databook/

[176] OSA. PowrSym3. [Online]. http://www.powrcast.com/products.htm

[177] DOE. (2005) Section 1221(a) of the Energy Policy Act of 2005. [Online]. http://www.oe.energy.gov/epa_sec1221.htm

[178] GE, "Technical Requirements for Wind Generation Interconnection and Integration," 2009.

[179] UWIG, "Utility Wind Integration State of the Art," Reston, VA, May 2006.

[180] Viryd. (2010) Viryd 8000 Technical Datasheet. [Online]. http://www.viryd.com/technology.htm

[181] NI. (2010) Wind turbine Control methods. [Online]. http://zone.ni.com/devzone/cda/tut/p/id/8189

[182] WWEA. (2011) World Energy Report 2010. [Online]. http://www.wwindea.org/home/images/stories/pdfs/worldwindenergyreport2010_s.pdf

[183] Herbert Girardet. Regenerative Cities. [Online]. http://www.worldfuturecouncil.org/fileadmin/user_upload/papers/WFC_Regenerative_Cities_web_final.pdf

# Appendices

**Appendix A: Project Summary Presentation**

- Mohammad Shahidehpour, "A World-Class University-Industry Consortium for Wind Energy Research, Education, and Workforce Development," 2012.

**Appendix B: Grand Ridge Wind Unit Video Clip**

**Appendix C: Journal and Conference Publications**

1) Wei Tian, Mohammad Shahidehpour, Zuyi Li, Analysis of 2030 Large-Scale Wind Energy Integration in the Eastern Interconnection Using WINS, The Electricity Journal, Volume 24, Issue 8, October 2011, Pages 71-87
2) S. Kamalinia, M. Shahidehpour, and A. Khodaei, "Security-constrained expansion planning of fast-response units for wind integration," Electric Power Systems Research, vol.81, no.1, pp.107-116, January 2011
3) S. Kamalinia and M. Shahidehpour, "Generation expansion planning in wind-thermal power systems," IET Generation, Transmission & Distribution, vol.4, no.8, pp.940-951, August 2010
4) M. Khodayar, M. Barati, and M. Shahidehpour, "Integration of High Reliability Distribution System in Microgrid Operation," IEEE Transactions on Smart Grid, Vol. 3, 2012
5) A. Khodaei, M. Shahidehpour, "Microgrid-based Co-optimization of Generation and Transmission Planning in Power Systems," IEEE Transactions on Power Systems, Vol. 27, 2012
6) M. Khodayar and M. Shahidehpour, "Stochastic Price-based Coordination of Intra-hour Wind Energy and Storage in a Generation Company," IEEE Transactions on Sustainable Energy, 2012
7) H. Wu, M. Shahidehpour, and A. Al-Abdulwahab, "Hourly Demand Response in Day-ahead Scheduling for Managing the Variability of Renewable Energy," IET Journal on Generation, Transmission & Distribution, 2012
8) A. Khodaei, M. Shahidehpour, L. Wu, and Z. Li, "Coordination of Short-Term Operation Constraints in Multi-Area Expansion Planning," IEEE Transactions on Power Systems, Vol. 27, 2012
9) C. Sahin, M. Shahidehpour, I. Erkmen, "Allocation of Hourly Reserve versus Demand Response for Security-Constrained Scheduling of Stochastic Wind Energy," IEEE Transactions on Sustainable Energy, 2012
10) M. Khodayar, L. Wu, and M. Shahidehpour, "Hourly Coordination of Electric Vehicle Operation and Volatile Wind Power Generation in SCUC," IEEE Transactions on Smart Grid, Vol. 3, No. 3, pp. 1271-1279, Sept. 2012

11) A. Lotfjou, Y. Fu, and M. Shahidehpour, “Hybrid AC/DC Transmission Expansion Planning,” IEEE Transactions on Power Delivery, Vol. 27, No. 3, pp. 1620-1628, July 2012
12) L. Abreu, M. Khodayar, M. Shahidehpour, L. Wu, “Risk-Constrained Coordination of Cascaded Hydro Units with Volatile Wind Power Generation” IEEE Transactions on Sustainable Energy, Vol. 3, No. 3, pp. 359-368, July 2012
13) C. Sahin, M. Shahidehpour, and I. Erkmen "Generation Risk Assessment in Volatile Conditions with Wind, Hydro, and Natural Gas Units" Applied Energy, Vol. 96, pp. 4-11, Aug. 2012
14) L. Wu, M. Shahidehpour, and Z. Li, “Comparison of Scenario-Based and Interval Optimization Approaches to Stochastic SCUC,” IEEE Transactions on Power Systems, Vol. 27, No. 2, pp. 913-921, May 2012
15) A. Khodaei and M. Shahidehpour, “Security-Constrained Transmission Switching with Voltage Constraints,” International Journal of Electrical Power and Energy Systems, Vol. 35, No. 1, pp. 74-82, Feb. 2012
16) A. Khodaei, M. Shahidehpour, and S. Bahramirad, “SCUC With Hourly Demand Response Considering Intertemporal Load Characteristics,” IEEE Transactions on Smart Grid, Vol. 2, No. 3, pp. 564-571, Sept. 2011
17) L. Wu and M. Shahidehpour, “Optimal Coordination of Stochastic Hydro and Natural Gas Supplies in Midterm Operation of Power Systems,” IET Journal on Generation, Transmission & Distribution, Vol. 5, No. 5, pp. 577-587, May 2011
18) C. Liu, M. Shahidehpour, J. Wang, “Coordinated Scheduling of Electricity and Natural Gas Infrastructures with a Transient Model for Natural Gas Flow,” Chaos (American Institute of Physics), Vol. 21, pp. 025102-1 through 025102-12 , May 2011
19) C. Sahin, Z. Li, M. Shahidehpour, and I. Erkmen, "Impact of Natural Gas System on Risk-Constrained Midterm Hydrothermal Scheduling,” IEEE Transactions on Power Systems, Vol. 26, No. 2, pp. 520-531, May 2011
20) A. Lotfjou, M. Shahidehpour, and Y. Fu, “Hourly Scheduling of DC Transmission Lines in SCUC With Voltage Source Converters,” IEEE Transactions on Power Delivery, Vol. 26, No. 2, pp. 650-660, April 2011
21) C. Liu, M. Shahidehpour, and J. Wang, “Application of Augmented Lagrangian Relaxation to Coordinated Scheduling of Interdependent Hydrothermal Power and Natural Gas Systems,” IET Journal on Generation, Transmission & Distribution, Vol. 4, No. 12, pp. 1314–1325 Dec. 2010
22) A. Khodaei and M. Shahidehpour, Y. Fu, “Transmission Switching in Security-Constrained Unit Commitment,” IEEE Transactions on Power Systems, Vol. 25, No. 4, pp. 1937-1945, Nov. 2010
23) L. Wu and M. Shahidehpour, Y. Fu, “Security-Constrained Generation and Transmission Outage Scheduling with Uncertainties,” IEEE Transactions on Power Systems, Vol. 25, No. 3, pp. 1674-1685, Aug. 2010
24) A. Khodaei and M. Shahidehpour, S. Kamalinia, “Transmission Switching in Expansion Planning,” IEEE Transactions on Power Systems, Vol. 25, No. 3, pp. 1722-1733, Aug. 2010

25) O. Tor, A. Guven, and M. Shahidehpour, “Promoting the Investment on IPPs for Optimal Grid Planning,” IEEE Transactions on Power Systems, Vol. 25, No. 3, pp. 1743-1750, Aug. 2010
26) L. Wu and M. Shahidehpour, “A Hybrid Model for Price Forecasting,” IEEE Transactions on Power Systems, Vol. 25, No. 3, pp. 1519-1530, Aug. 2010
27) L. Wu and M. Shahidehpour, Y. Fu, “Accelerating the Benders Decomposition for Network-Constrained Unit Commitment Problems,” Energy Systems, Vol. 1, pp. 339-376, July 2010
28) C. Liu, M. Shahidehpour, and L. Wu, “Extended Benders Decomposition for Two-Stage SCUC, IEEE Transactions on Power Systems, Vol. 25, No. 2, pp. 1192-1194, May 2010
29) S. Kamalinia and M. Shahidehpour, “Capacity Adequacy Calculation by Considering Locational Capacity Prices,” IET Journal on Generation, Transmission & Distribution, Vol. 4, No. 3, pp. 376-385, Feb. 2010
30) A. Lotfjou and M. Shahidehpour, “Security-Constrained Unit Commitment with AC/DC Transmission Systems,” IEEE Transactions on Power Systems, Vol. 25, No. 1, pp. 531-543, Feb. 2010
31) Wei Tian, Zuyi Li, Mohammad Shahidehpour, “Transmission Congestion Analysis in the Eastern Interconnection using POMS,” IEEE Power and Energy Society General Meeting, July 2010, Minneapolis, Minnesota.
32) Ganesh Raman, Mahesh Krishnamurthy, Rakesh C Ramachandran, Clement Pereira, Xiaodong Shi, Yong Jiang, Martin Price, and Matthew Arnold, Test bed for acoustic assessment of small wind turbine drive-trains, Fourth International Meeting on Wind Turbine Noise, Rome, Italy, 12-14 April 2011
33) Xiaodong Shi; Serradilla, J.P.; Krishnamurthy, M.; , "A back EMF-based rotor position prediction in Permanent Magnet machines for survivable wind generator systems," IECON 2010 - 36th Annual Conference on IEEE Industrial Electronics Society , vol., no., pp.778-783, 7-10 Nov. 2010
34) Xiaodong Shi; Krishnamurthy, M.; , "Concept and implementation of a simplified speed control strategy for survivable induction motor drives," Industrial Electronics (ISIE), 2011 IEEE International Symposium on , vol., no., pp.556-561, 27-30 June 2011
35) Yao Da; Xiaodong Shi; Krishnamurthy, M.; , "Health monitoring, fault diagnosis and failure prognosis techniques for Brushless Permanent Magnet Machines," Vehicle Power and Propulsion Conference (VPPC), 2011 IEEE , vol., no., pp.1-7, 6-9 Sept. 2011
36) Xiaodong Shi; Krishnamurthy, M.; , "A simplified state switching control strategy for survivable variable-speed induction generators," Electric Machines & Drives Conference (IEMDC), 2011 IEEE International , vol., no., pp.182-187, 15-18 May 2011

ILLINOIS INSTITUTE OF TECHNOLOGY

# A World-Class University-Industry Consortium for Wind Energy Research, Education, and Workforce Development

**Lead Organization:** Illinois Institute of Technology

**Principal Investigator:** Mohammad Shahidehpour

2012

ILLINOIS INSTITUTE OF TECHNOLOGY

# Project Objectives

The consortium's research and development objectives will be focused on addressing several challenges identified in the "20% Wind Energy by 2030" report:

**1) Wind Technology.** The consortium members will develop control algorithms for enhancing the reliability of wind turbine components.

**2) Grid System Integration.** The consortium members will develop advanced operation and planning tools for accommodating the high penetration of intermittent wind energy in electric power utility systems.

**3) Research & Development.** The consortium members will educate the stakeholders on critical issues related to the wind energy research and development.

**4) Workforce Development.** The world-class wind energy education and research programs developed by the consortium will outlast the proposed two-year period of the project.

**Members of the *World-Class Wind Energy Consortium***

| **University Members** | **Point of Contact** |
|---|---|
| Illinois Institute of Technology (Lead) | , Professor |
| University of Chicago | John Birge, Professor |
| Southern Illinois University | Morteza Daneshdoost, Professor |
| University of Castilla - La Mancha (Spain) | Antonio Conejo, Professor |
| University of São Paulo (Brazil) | Newton Bretas, Professor |
| Aristotle University of Thessaloniki (Greece) | Anastasio Bakirtzis, Professor |
| Polytechnic University of Bucharest (Romania) | Mircea Eremia, Professor |
| | |
| **National Labs Members** | **Point of Contact** |
| Argonne National Laboratory | Jianhui Wang, Center for Energy and Economics |
| National Renewable Energy Laboratory | Erik Ela, National Wind Technology Center |
| **Industry Members** | **Point of Contact** |
| ***Wind Turbine Companies*** | |
| GE Energy | Steve Moffitt, Account Executive |
| Viryd Technologies, Inc. | Matt Arnold |
| Acciona Wind Energy | Frank Bristol, Director of Transmission |
| ***Wind Energy Developers*** | |
| Invenergy, LLC | Michael Polsky, President and CEO |
| Energia Eolica () | Edgar Pereira, Director |
| PS Wind Management () | Radu Popoiu, Managing Director |
| ***Power Transmission System Operators*** | |
| ComEd/Exelon | Terence Donnelly, Senior Vice President |
| ISO New | Eugene Litvinov, Director of Business Architecture and Technology |
| British Columbia Transmission Corporation | Ebrahim Vaahedi, CTO |
| ***Wind Energy Control Devices and Software Companies*** | |
| Dakota Power | Richard Gowen, President |
| EnerNex Corporation | Erich Gunther, Chairman and CTO |
| SmartSignal Corporation | James Gagnard, President and CEO |
| Innovation Technology Applications Company | Alan Cain, President |
| ***Energy System Consultants*** | |
| Keyworks | Kurt Yeager, President and CEO |
| Electric Power Research Institute | Brooks, Daniel, |
| AREVA T&D | Jay Giri, Director of Power System Technology |
| Intelligent Power Solutions | John Kelly, President |
| McCoy Energy | Paul McCoy, President |
| Wiedman Power System Consulting | Thomas Wiedman, President |

ILLINOIS INSTITUTE OF TECHNOLOGY

# Task 1.0 Procure a 1.5MW GE Test Wind Turbine

- The purchase agreement was signed by Invenergy on September 28, 2010.
- We commemorated the installation at the July 20, 2011 ribbon-cutting ceremony.

ILLINOIS INSTITUTE OF TECHNOLOGY

# Task 2.0 Install an 8KW Viryd Test Wind Turbine

- 8KW lab wind unit was installed at IIT in September, 2010.

ILLINOIS INSTITUTE OF TECHNOLOGY

# Task 3.0 Install a Small Wind Turbine for Public Awareness

- Groundbreaking ceremony on March 30, 2011.
- We celebrated the installation at the July 20, 2011 ribbon-cutting ceremony

ILLINOIS INSTITUTE OF TECHNOLOGY

# Task 3.0 Install a Small Wind Turbine for Public Awareness

ILLINOIS INSTITUTE OF TECHNOLOGY

# Task 4.0 GE Wind Turbine Reliability Study

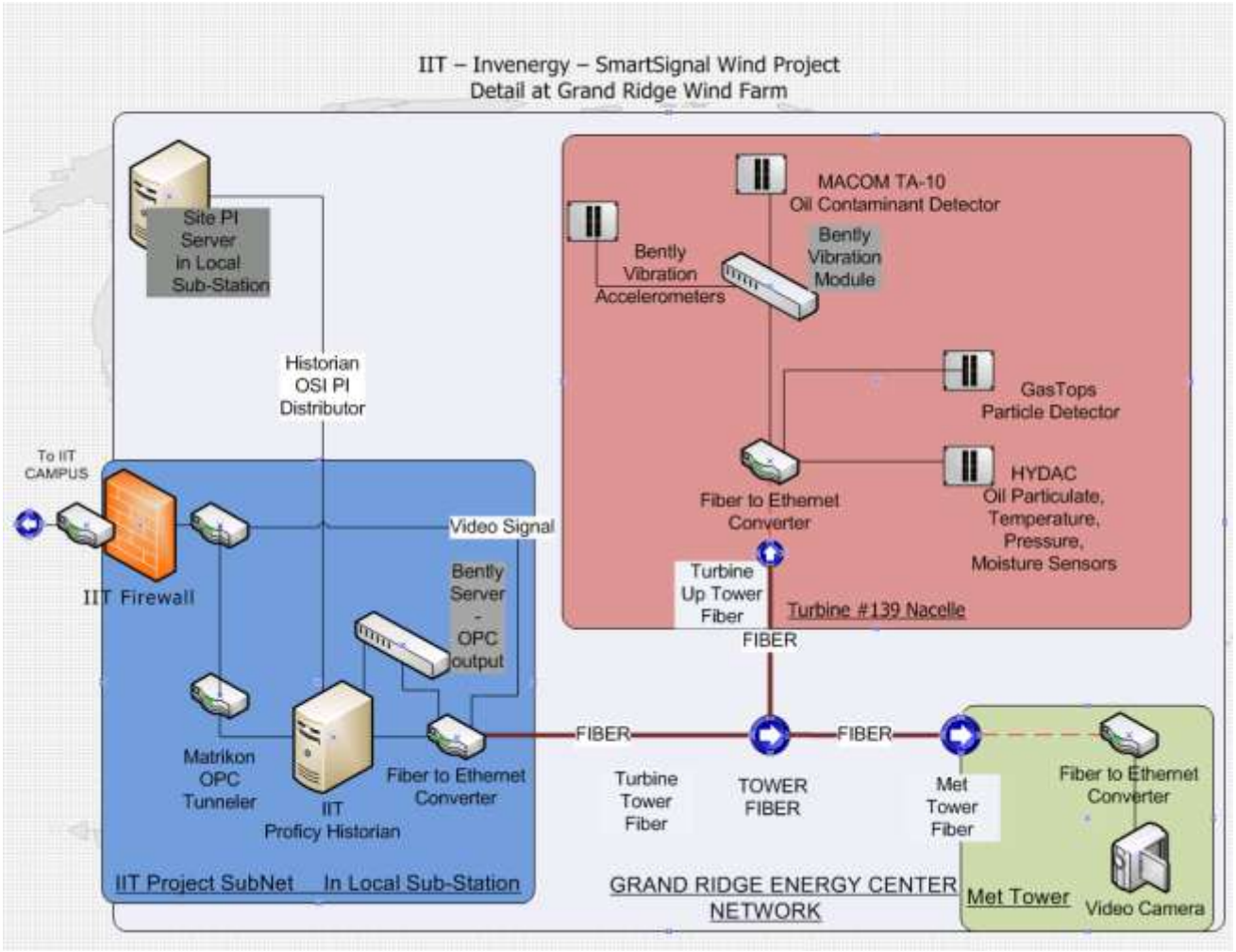

ILLINOIS INSTITUTE OF TECHNOLOGY

# Task 4.0 GE Wind Turbine Reliability Study

The Green lines represent the predicted values, the blue lines represent the actual current values, and the red XXX represent significant deviations of actual from estimate, alerting the analyst to further investigate the situation.

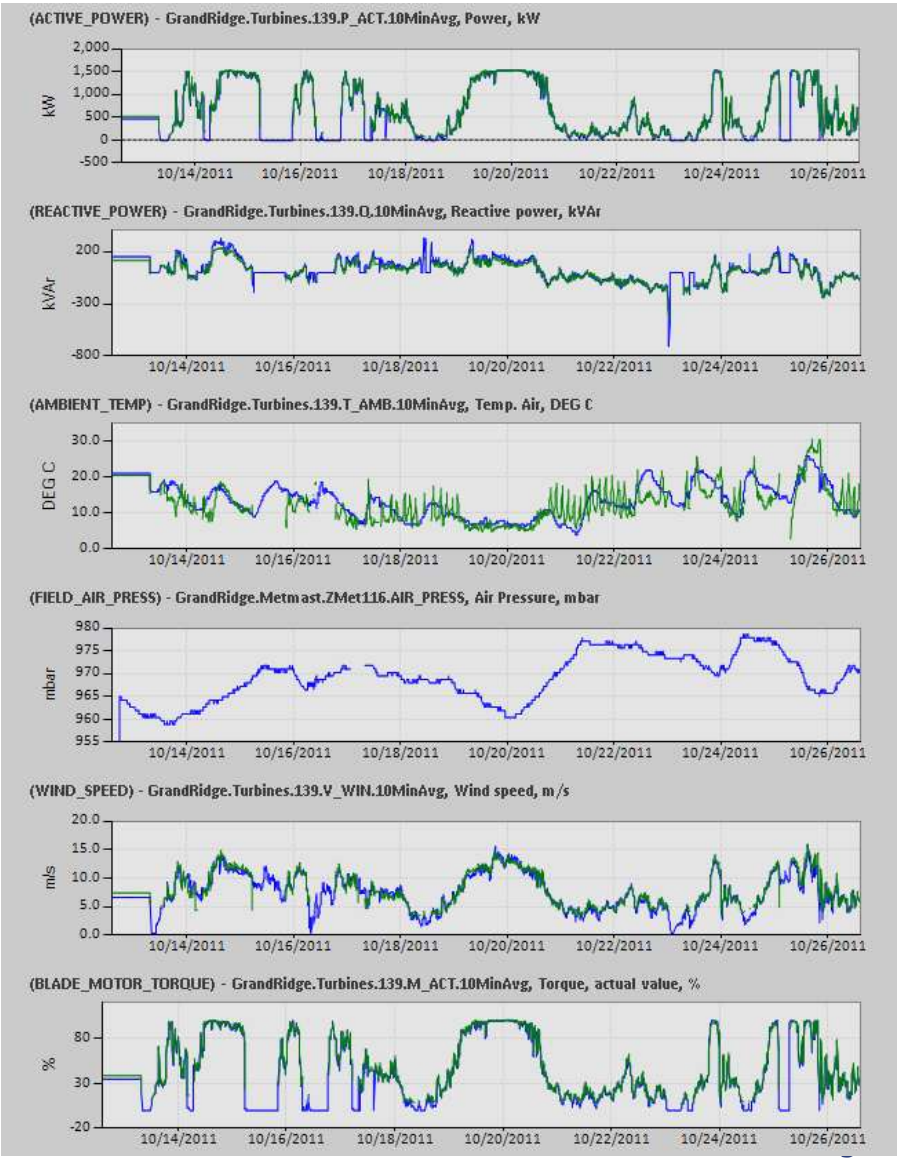

ILLINOIS INSTITUTE OF TECHNOLOGY

# Task 4.0 GE Wind Turbine Reliability Study

The Green lines represent the predicted values, the blue lines represent the actual current values, and the red XXX represent significant deviations of actual from estimate, alerting the analyst to further investigate
the situation.

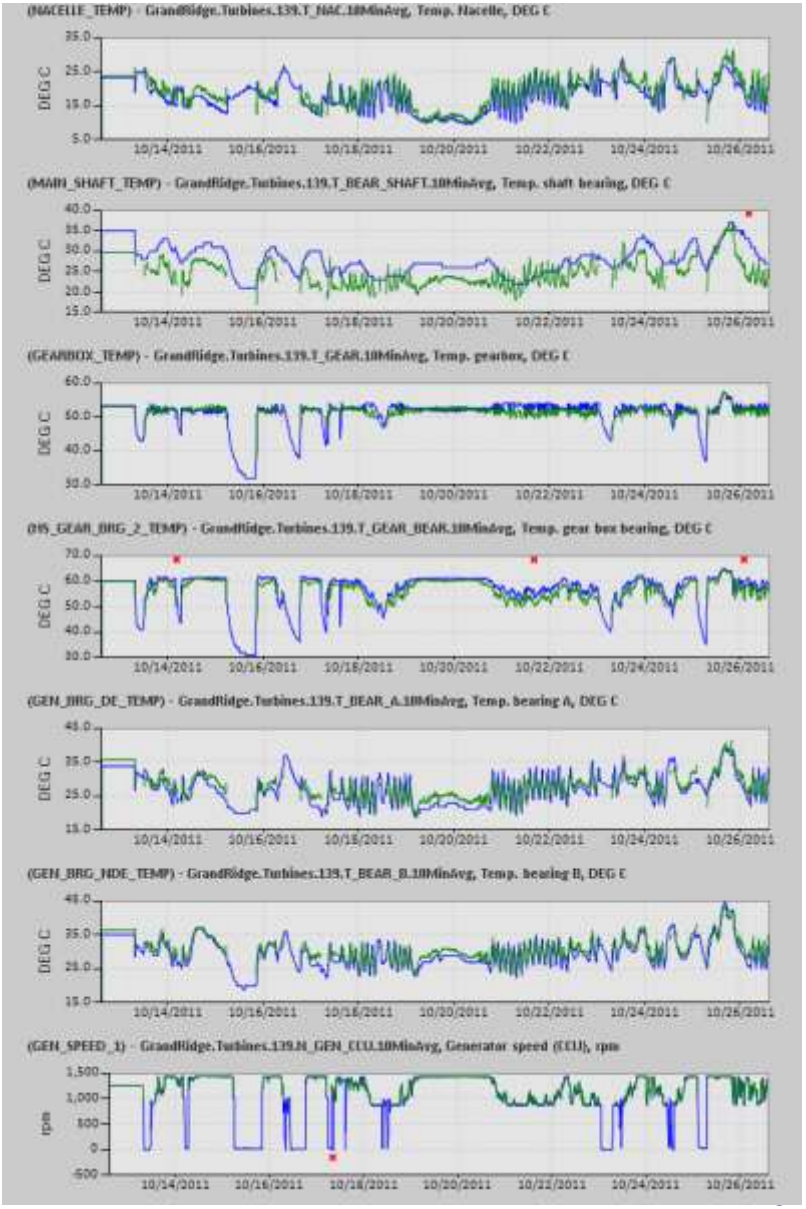

# Task 4.0 GE Wind Turbine Reliability Study

- Deployment of Catch the Wind's Laser Wind Sensor (LWS)
  - In this research project, the LWS measures the wind out in front of the turbine blades using laser Doppler velocimeter technology, and use this information to change the yaw angle of the turbine to more accurately align the turbine with the direction of the wind.
  - The yaw control would be revised by working around the GE control system to replace the anemometer/wind vane data with data from the LWS, while preserving the functionality of all the existing safety mechanisms.

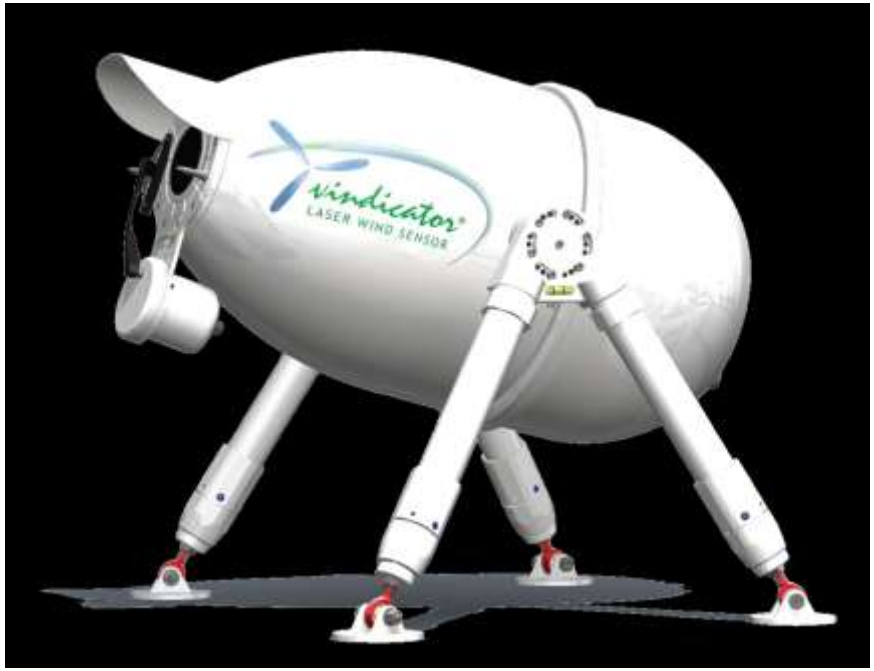

ILLINOIS INSTITUTE OF TECHNOLOGY

# Task 5.0 Viryd Wind Turbine Reliability Study

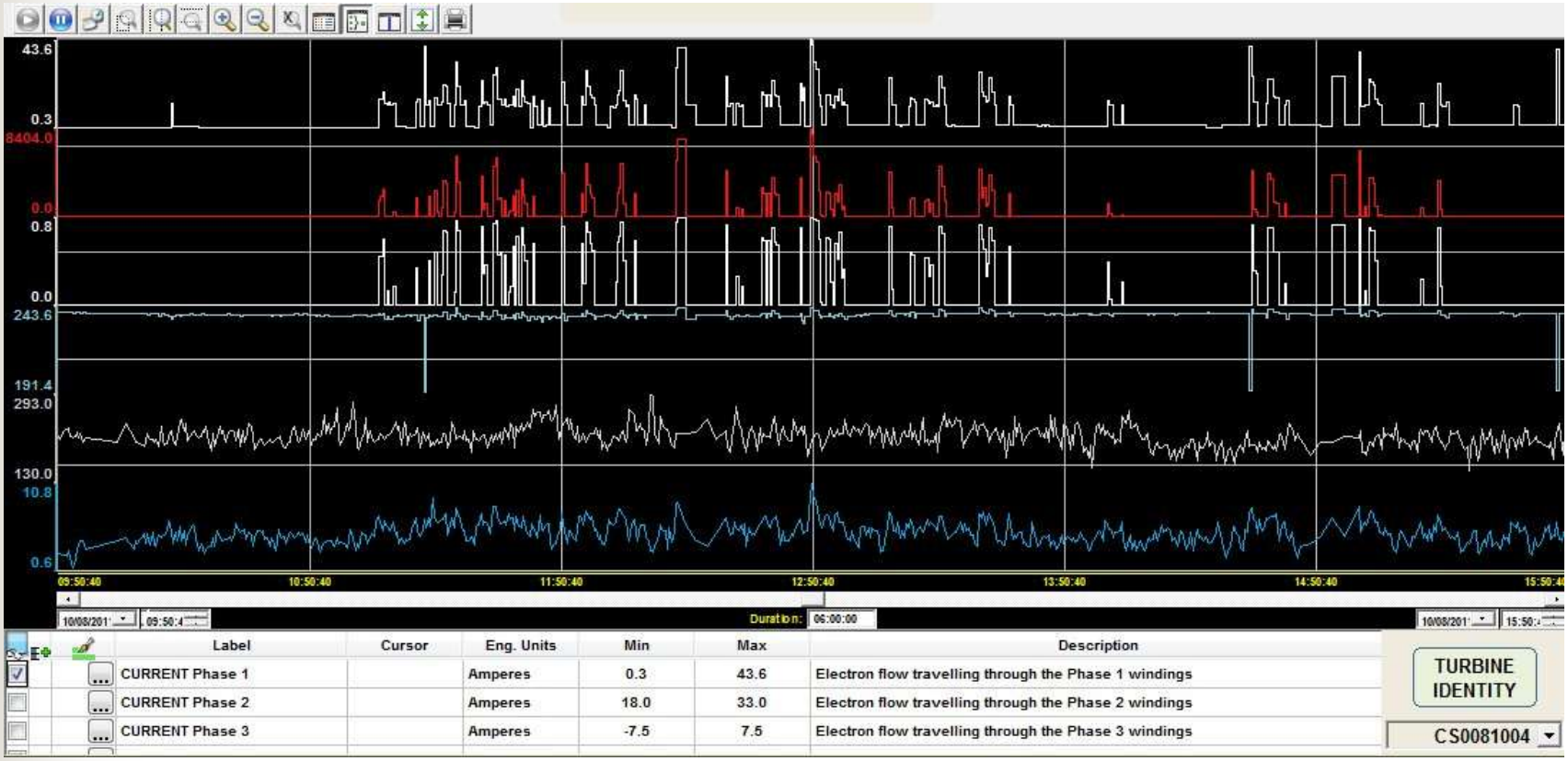

ILLINOIS INSTITUTE OF TECHNOLOGY

# Task 6.0 Noise Reduction in Wind Turbine Design through Fluid Dynamics and Acoustics

ILLINOIS INSTITUTE OF TECHNOLOGY

# Task 6.0 Noise Reduction in Wind Turbine Design through Fluid Dynamics and Acoustics

- Ganesh Raman, Mahesh Krishnamurthy, “Localization of Wind Turbine Noise Sources on a 1.5 MW Production Scale Wind Turbine Using a Compact Microphone Array,” Illinois Institute of Technology

ILLINOIS INSTITUTE OF TECHNOLOGY

# Task 6.0 Noise Reduction in Wind Turbine Design

- Innovative Technology Applications Company, "Numerical Studies of Wind Turbine Acoustics,"

Figure 38: Iso-surface of vorticity magnitude in the flow around the wind turbine

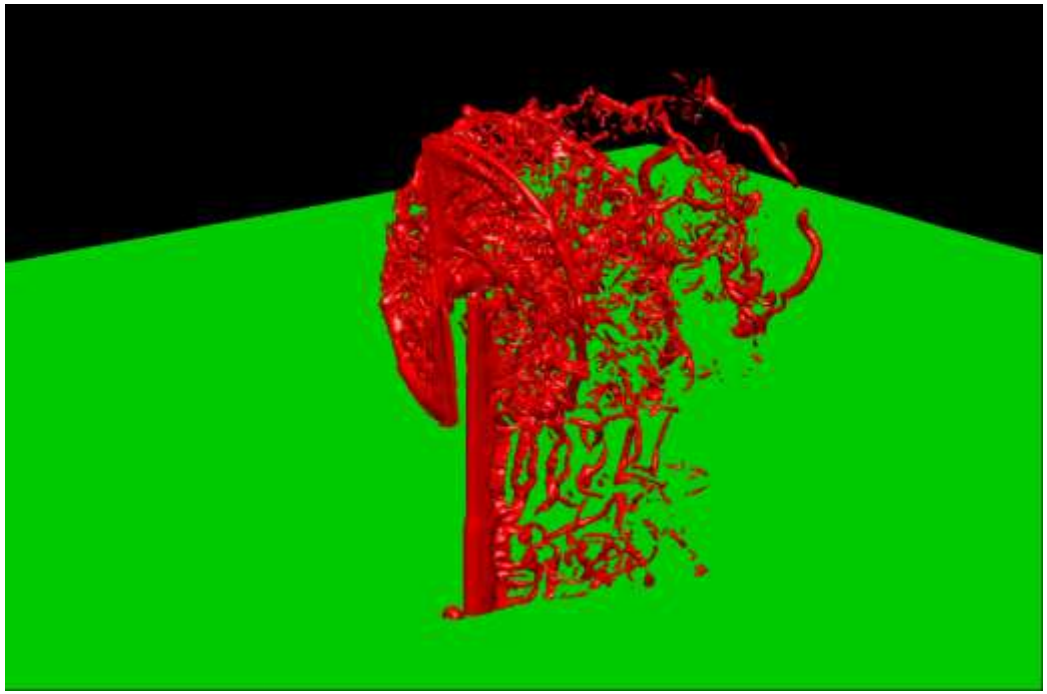

ILLINOIS INSTITUTE OF TECHNOLOGY

# Task 8.0 Advanced Wind Integration Study

- Wind integration studies for the Eastern Interconnection
  - 23 scenarios are represented
    - Scenarios 1-4: no wind, wind CF>=40%, wind CF>=30%, all candidate wind sites
    - Scenarios 5-8: fuel prices 20% higher, 10% higher, 10% lower, 20% lower
    - Scenarios 9-12: wind power 20% higher, 10% higher, 10% lower, 20% lower
    - Scenarios 13-16: forecasted load 20% higher, 10% higher, 10% lower, 20% lower
    - Scenarios 17-20: low and high carbon taxes
    - Scenarios 21-23: load management

ILLINOIS INSTITUTE OF TECHNOLOGY

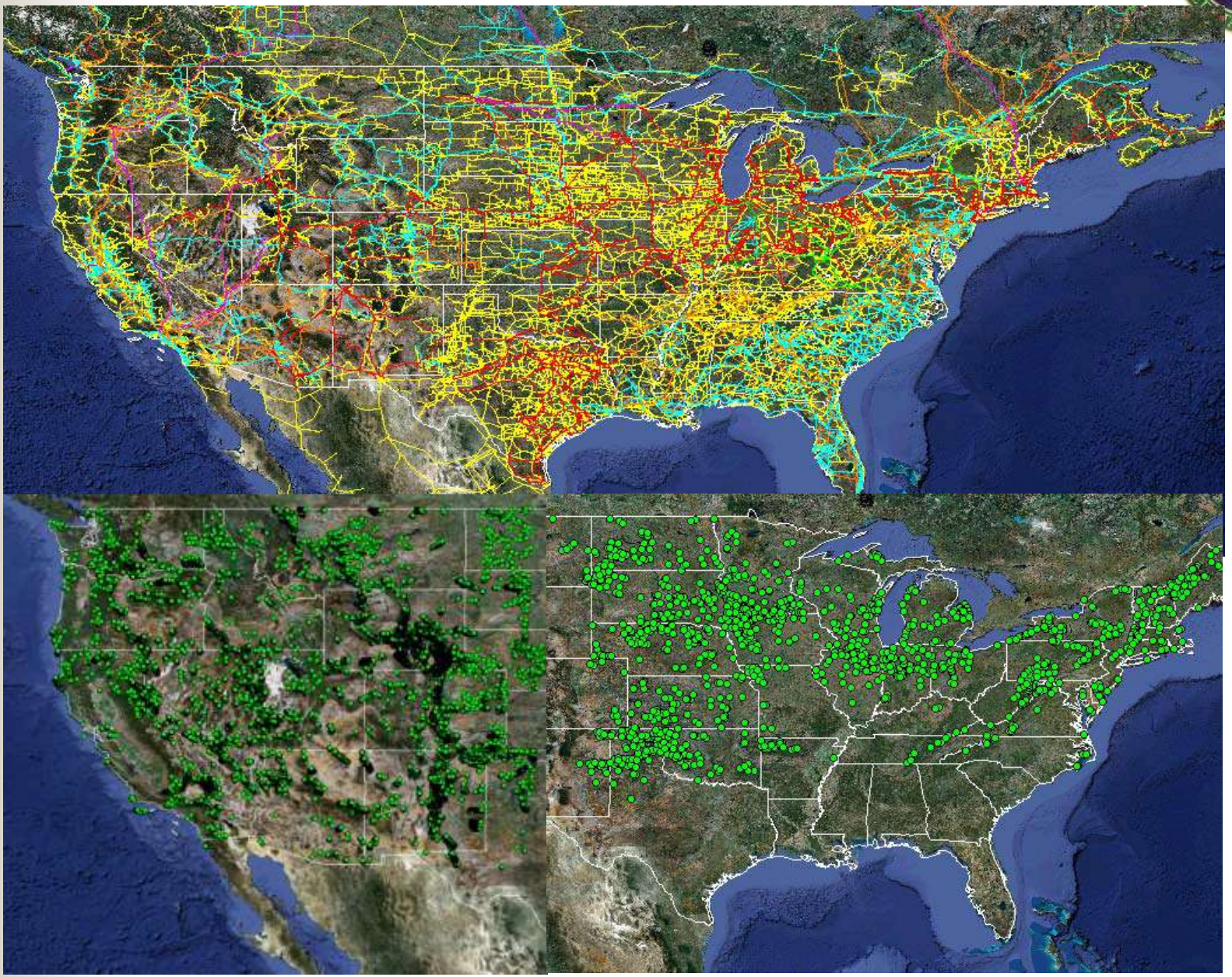

ILLINOIS INSTITUTE OF TECHNOLOGY

# Scenario 3: 30% Wind (Cap. Factor>=30%)

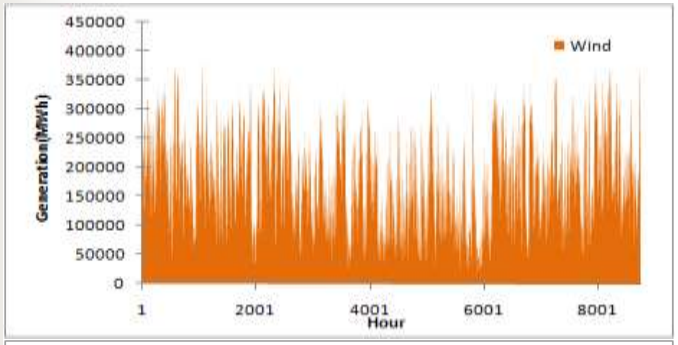


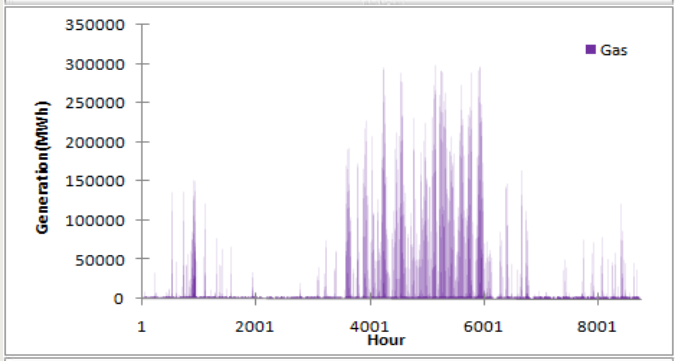


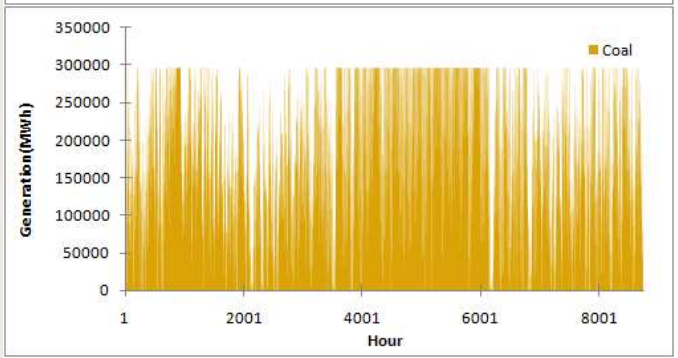


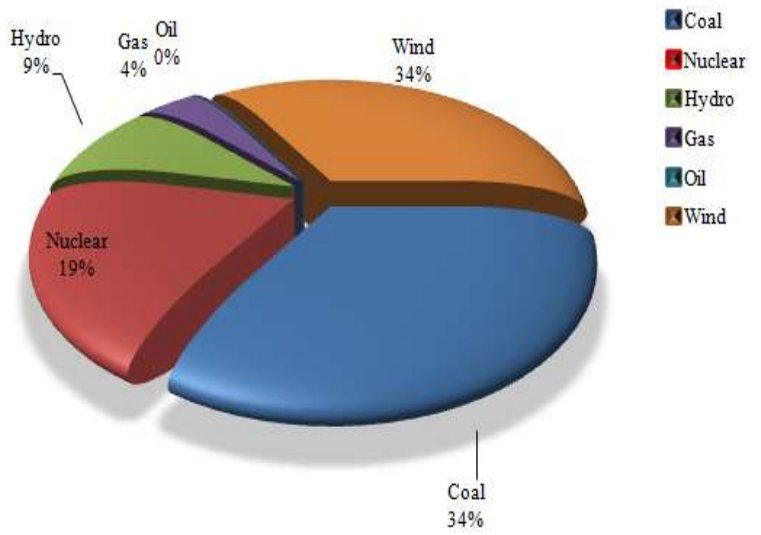


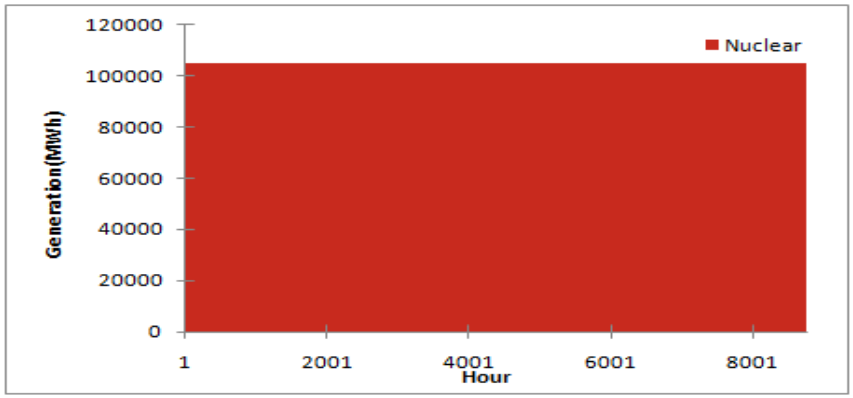

ILLINOIS INSTITUTE OF TECHNOLOGY

# Load Sensitivity Analysis

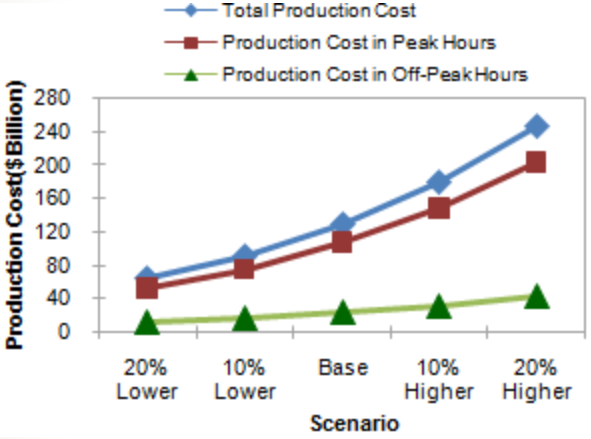


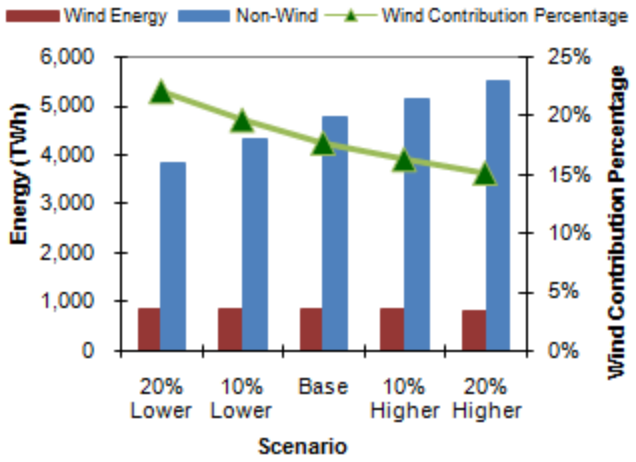


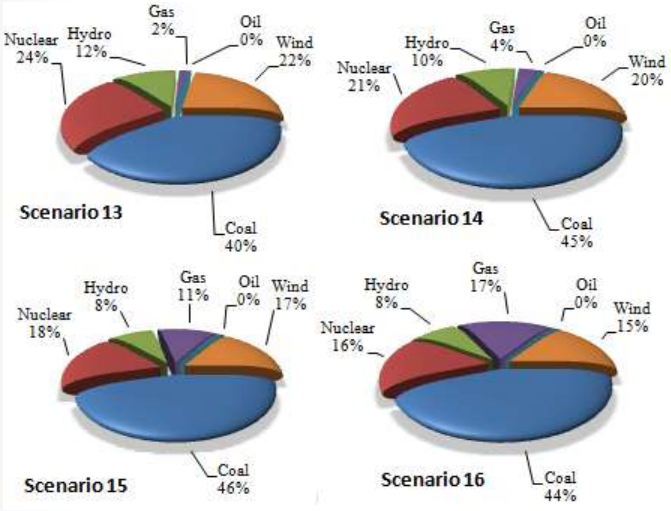


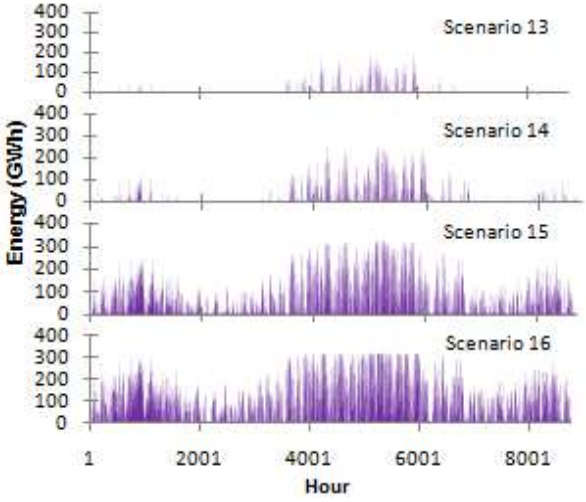

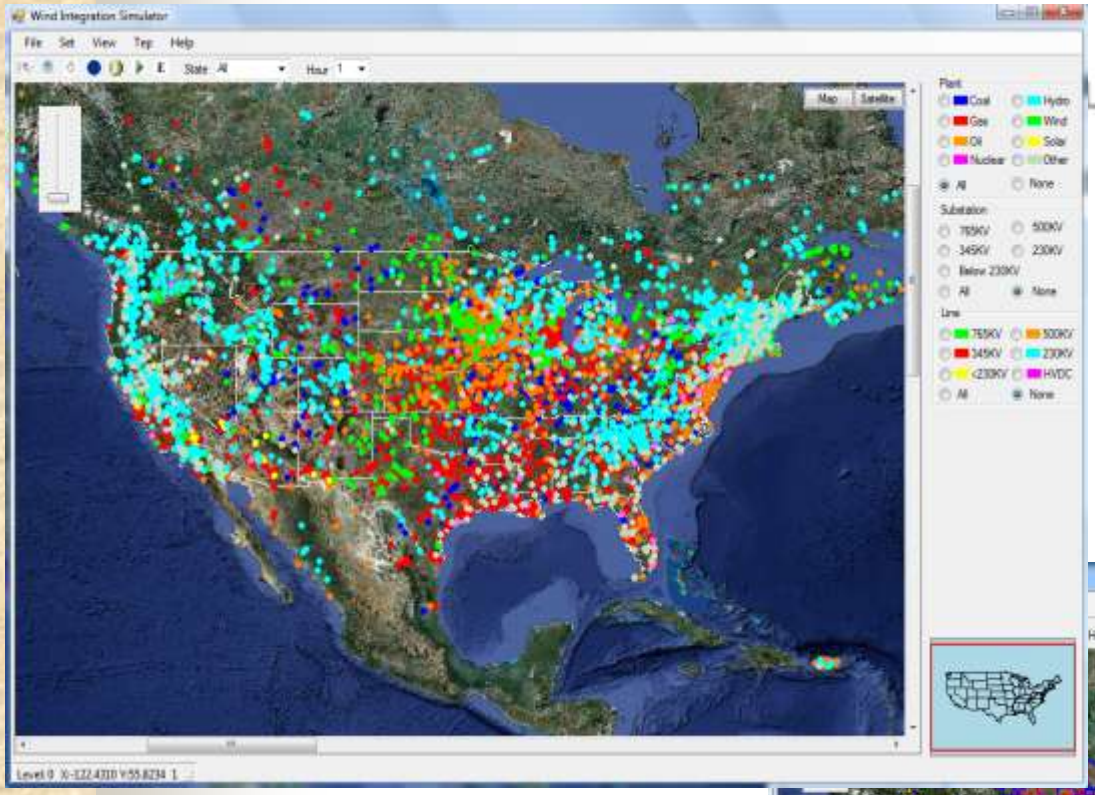
Wind Integration Simulator
File Set View Tep Help
State All
Hour 1
Map Satellite
Plant
Coal Hydro
Gas Wind
Oil Solar
Nuclear Other
All None
Substation
765KV 500KV
345KV 230KV
Below 230KV
All None
Line
765KV 500KV
345KV 230KV
<230KV HVDC
All None

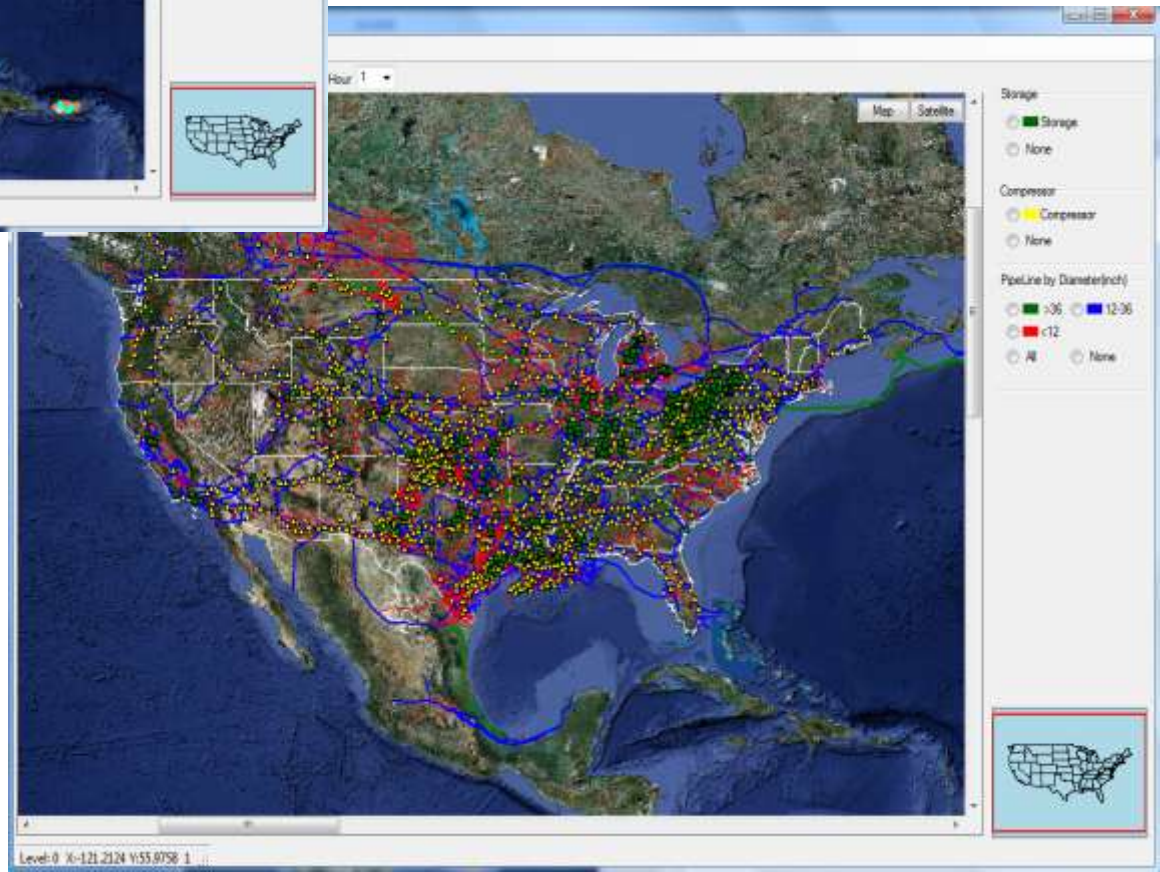
Hour 1
Map Satellite
Storage
Storage
None
Compressor
Compressor
None
PipeLine by Diameter(inch)
>36 12-36
<12
All None

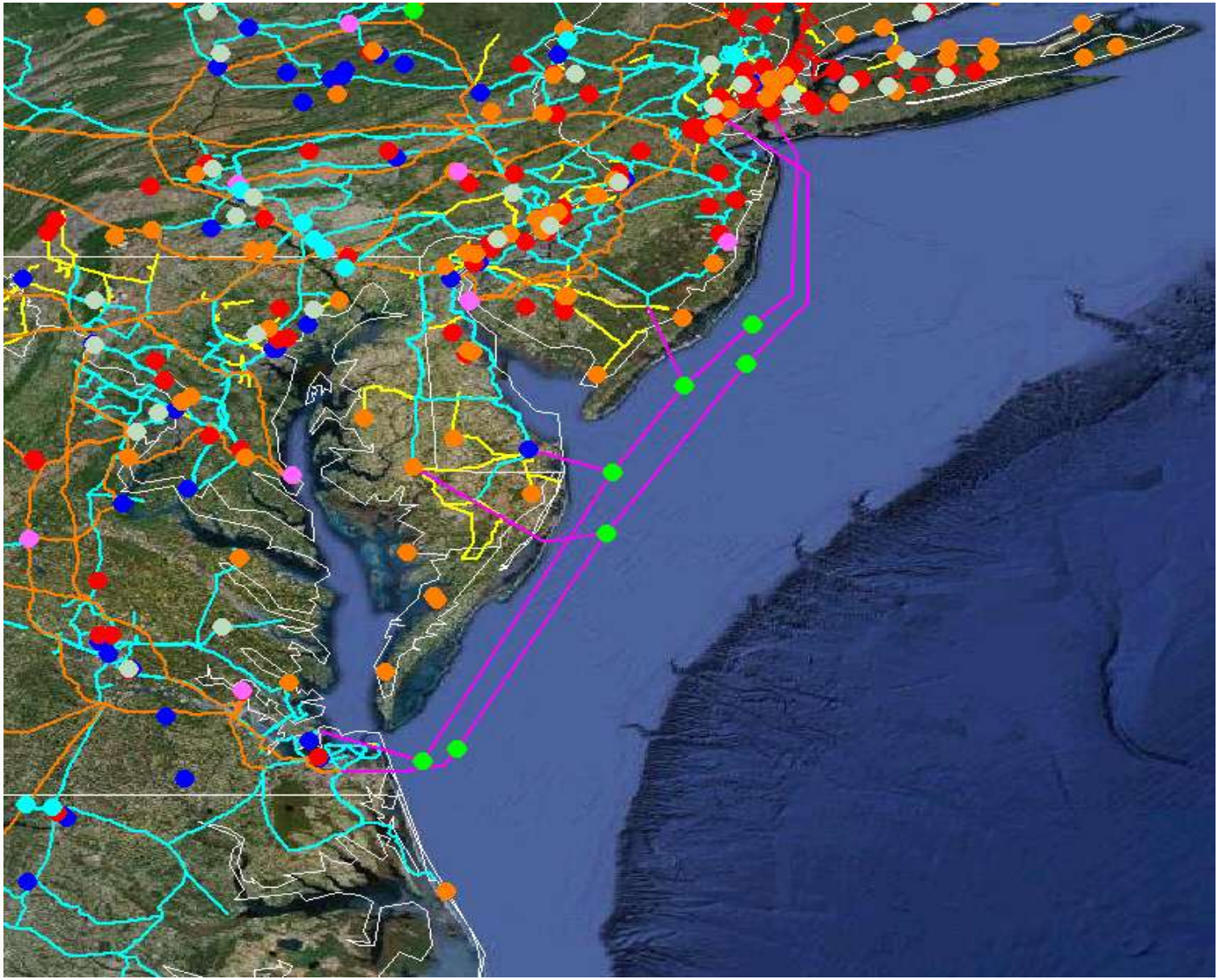

ILLINOIS INSTITUTE OF TECHNOLOGY

| without Offshore Wind Integration | with Offshore Wind Integration |
|---|---|

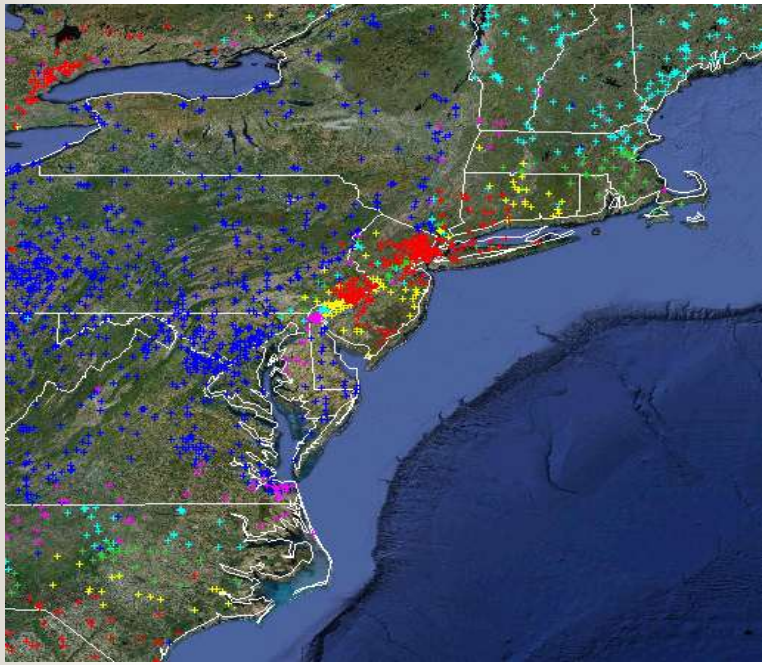

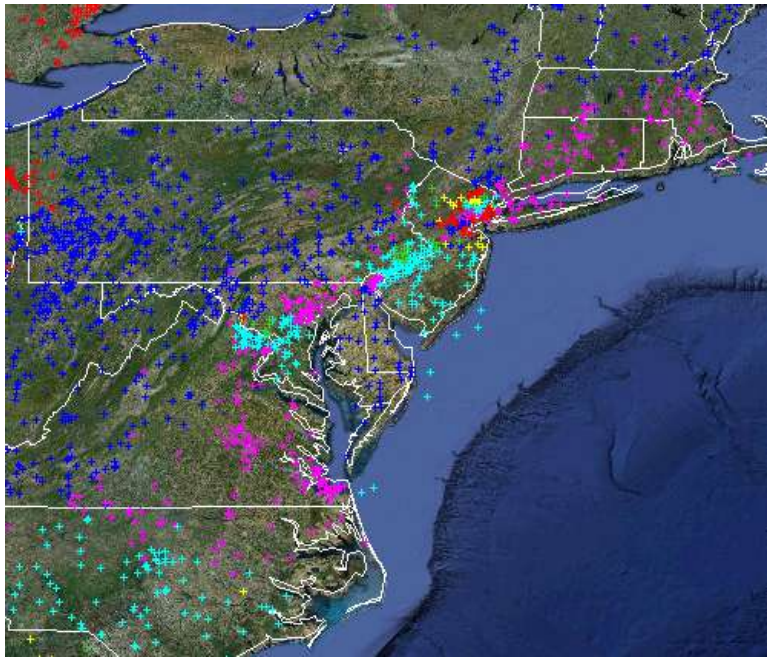

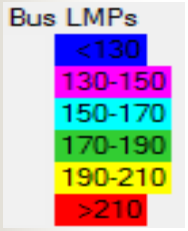

# Task 9.0 International Collaboration on Wind Energy Research

- The first wind energy conference was held at IIT's main campus on September 30, 2010.

**Fall 2010 Meeting**

**A World-Class University-Industry Consortium for Wind Energy Research, Education, and Workforce Development**

September 30, 2010
McCormick Tribune Campus Center Ballroom, Illinois Institute of Technology
3201 S. State Street, Chicago, IL
http://www.iit.edu/about/directions_main_campus.shtml

Illinois Institute of Technology was awarded an $8M grant from the U.S. Department of Energy to establish a University-Industry Consortium for Wind Energy Research, Education, and Workforce Development. http://www.iit.edu/department/publicaffairs/newsroom/article_viewer_do.php?articleID=386. On September 30, 2010, IIT's Center for Electricity Innovation and Wanger Institute for Sustainable Energy Research (WISER) are hosting the Fall 2010 meeting of the Consortium members on IIT's main campus in Chicago. The schedule for the day is as follows:

| | |
|---|---|
| 8:00-8:30 am | Registration and Introduction |
| 8:30-10:45 | Discussion on implementation of the DOE-funded Wind Consortium project |
| 10:45-12:00 | Tour of the DOE-funded projects at IIT |
| 12:00-1:00 pm | Lunch |
| 1:00-3:00 | Symposium on Future of Wind Power Event |
| 3:00-4:00 | Reception |

**MORNING SESSION**

The morning session will include presentations by consortium members and discussions of ongoing tasks. The discussions will be followed up by a tour of the DOE-funded projects at IIT.

**Presentations (8:30-10:15 am)**

Mohammad Shahidehpour, IIT
Frank Bristol, Accona
Jim Gagnard, SmartSignal
Alan Cain, Innovation Technology Applications, and Ganesh Raman, IIT
Greg Rouse and John Kelly, Intelligent Power Solutions
Ahsaas Khaligh, IIT
Richard Cowen, Dakota Power
Zuyi Li, IIT
John Birge, University of Chicago

**Discussion (10:15-10:45 am)**

All Consortium members

**Tour of the IIT Projects (10:45-12:00 noon)**

- **Wind Turbine Installations.** The wind energy consortium tasks include the installation of two 8-kW wind units at IIT for research and education. The first unit already installed in one of the laboratories at IIT will be demonstrated as part of the campus tour.
- **Perfect Power Smart Microgrid.** IIT has been working on a DOE-funded perfect power project since 2008. The project is converting IIT to a microgrid for enhancing reliability, sustainability, and efficiency of its electricity grid. A tabletop model of the campus buildings is developed and a demonstration of the perfect power concept will be presented to the consortium members and guests.

**Lunch (12:00 noon-1:00 pm) at McCormick Tribune Campus Center**

**Symposium on Wind Energy Research, Education, and Workforce Development**

**(1:00- 3:00 pm) September 30, 2010**

**McCormick Tribune Campus Center Ballroom, Illinois Institute of Technology**
**3201 S. State Street, Chicago, IL**
http://www.iit.edu/about/directions_main_campus.shtml

The symposium will bring industry and government leaders together to discuss breakthrough technologies, innovations, and implementation developments in the wind industry. The state of the wind energy industry in the United States is facing numerous challenges, from wildlife and zoning concerns to the deficiencies of our nation's electric transmission grid. Yet, the industry is also being presented with new opportunities, from the country's first offshore wind farms, to new smart grid technologies that allow better integration of intermittent power into the grid.

Symposium Speakers:

Brian Connor – U.S. Department of Energy
Sonny Garg – President, Exelon Power & Senior Vice President, Exelon Generation
Michael Polsky – President/CEO, Invenergy
Paul McCoy – President, Trans-Elect
Kurt Yeager – Former President, EPRI / Executive Director, Galvin Electricity Initiative
Joshua Millsberg - First Deputy Commissioner, City of Chicago Department of Environment

**Reception (3:00-4:00 pm)**


EXIT

ILLINOIS INSTITUTE OF TECHNOLOGY

# Task 9.0 International Collaboration on Wind Energy Research

- The Second Wind Energy Conference was held at IIT's main campus on Wednesday, July 20, 2011
  - 7:45-8:00 am Continental Breakfast
  - 8:00-8:20 am Introduction and Welcome Remarks
  - 8:20-8:55 am Wind Energy Integration in the Eastern Interconnection
  - 8:55-9:35 am Wind Energy Installation at IIT
  - 9:50-10:30 am Wind Energy Research and Development
  - 10:30-11:20 am Wind Energy Education and Workforce Development
  - 11:20-12:00 Wind Energy Installation at Grand Ridge
  - 12:15 pm Ribbon Cutting Event – 8kW Wind Unit at IIT
  - 2:30 pm Ribbon Cutting Event – 1.5MW IIT Wind Unit at Grand Ridge, Illinois

ILLINOIS INSTITUTE OF TECHNOLOGY

ILLINOIS INSTITUTE OF TECHNOLOGY

# Task 9.0 International Collaboration on Wind Energy Research

- Advancing Wind Power in Illinois Conference


**Advancing Wind Power in Illinois Conference**
**Thursday and Friday, July 21-22, 2011**

At Illinois Institute of Technology
Main Campus, Hermann Hall
3241 S. Federal Street, Chicago, IL 60616

Conference Co-Hosted by:
Center for Renewable Energy at Illinois State University and
Galvin Center for Electricity Innovation at Illinois Institute of Technology

ILLINOIS INSTITUTE OF TECHNOLOGY

# Task 9.0 International Collaboration on Wind Energy Research

- **Great Lakes Symposium on Smart Grid and the New Energy Economy**
  - *October 18-19, 2011 | Illinois Institute of Technology, Chicago, IL*

ILLINOIS INSTITUTE OF TECHNOLOGY

# Great Lakes Symposium on Smart Grid and the New Energy Economy – October 18, 19

ILLINOIS INSTITUTE OF TECHNOLOGY

# Great Lakes Symposium on Smart Grid and the New Energy Economy – October 18, 19

# Task 9.0 International Collaboration on Wind Energy Research

- IEEE Symposium on Smart Grid and Sustainable Energy Vision
  - In November 2011, IIT sponsored an IEEE Symposium which was attended by several engineers and scientists to discuss and prepare a position paper on the IEEE/PES vision for smart grid. One of the major components of the position paper will be the vision for wind energy design, manufacturing, integration, and operation and its relation to smart grid.

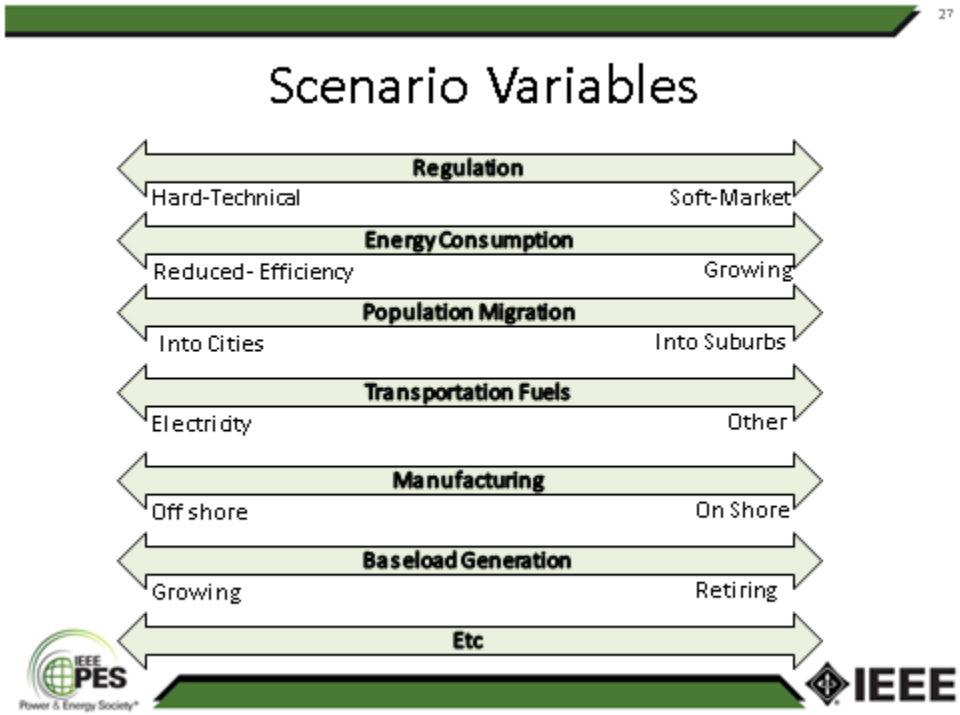

# Task 9.0 International Collaboration on Wind Energy Research

- Professor Antonio Conejo of University of Castilla – La Mancha, (Spain) visited IIT in January 2011 to discuss the international collaboration with the IIT Wind Consortium.
- Dr. Roberto Ferrero (Regulatory Agency of San Juan, Argentina) Visited IIT in January 2011 to discuss the international collaboration with the IIT Wind Consortium.

ILLINOIS INSTITUTE OF TECHNOLOGY

# Task 10.0 Engage Undergraduate Students in Wind Energy Research

- IPRO Courses at IIT
- IPRO 311 – Integration of Plug-in Hybrid Electric Vehicles and Renewable Energy Systems (Fall 2010)
  - The purpose of this project is to investigate the economic effects of the integration of wind power generation systems and PHEVs. The results obtained from the research will serve targeted markets including, but not limited to, automotive industry, wind power generation industry, and utility companies.
- IPRO 323 – Modeling of Building Integrated Wind Turbine Modules (Spring 2011)
  - The goal of this project is to effectively integrate wind turbines and buildings with harmony as to not disturb the social and natural environments of the city, and to produce the maximum amount of power possible.

ILLINOIS INSTITUTE OF TECHNOLOGY

# Task 10.0 Engage Undergraduate Students in Wind Energy Research

- Renewable Energy Courses Offered at Southern Illinois University
  - ECE 456 – Embedded Control and Mechatronics lectures
    - Modeling a Wind Turbine Using MathWorks Tools, Designing Pitch and Yaw Actuators for Wind Turbines, Determining Mechanical Loads for Wind Turbines, Designing Control Systems For Wind Turbines
  - ECE 486 – Wind Energy Research
    - This course which is delivered during the summer has been redesigned recently to introduce the concept of Clean Energy Resources.
  - ECE 495 – Capstone Senior Design Project
    - Create a Z-scale model of a 3-phase power generation and distribution system. This model will have the following areas: residential, commercial, industrial, coal-fired generation, and wind generation. This will be a dynamic model where the user can specify the real and reactive power demand from the residential, commercial, and industrial loads as analog inputs, the wind input, and the state of various power factor correcting capacitor banks.

ILLINOIS INSTITUTE OF TECHNOLOGY

# Task 12.0 Offer Degree Program and Certificates on Wind Energy

- Graduate Level Courses Offered at IIT
  - ECE 580 – Elements of Sustainable Energy (Fall 2010)
    - Introduction to Sustainable Energy, Renewable Energy Technologies, Variability of Renewable Energy, Operational Issues of Renewable Energy, Planning Issues of Renewable Energy
  - ECE 581 – Elements of Smart Grid (Fall 2010)
    - Smart Grid, Microgrids, Distributed and Renewable Generation, Building Energy Management System, Communication/AMI/Security, Smart Transmission System, PHEV and Electric Storage, Future of Smart Grid
- Graduate Level Courses Offered at Southern Illinois University
  - ECE 581 – Wind Energy Power Systems
    - The course introduces graduate students to advanced configurations of wind energy power systems with an in-depth treatment of their control and protection. Wind speed and power relations, basic design of wind energy power systems, synchronous and induction generators, power inverters, generator drives-control modes, interface with the power grid-system modeling, stability, control and protection.

ILLINOIS INSTITUTE OF TECHNOLOGY

# Task 12.0 Offer Degree Program and Certificates on Wind Energy

- Short Course on Wind Energy
  - EnerNex in Collaboration with IIT: Short Course on Wind Energy Technology, Interconnection & Integration
  - Day 1: Introduction to Wind Energy and Technology
    - Session 1: Wind Energy Outlook in 2010
    - Session 2: Wind Turbine Technology and Control – Part 1
    - Session 3: Wind Turbine Technology and Control – Part 2
    - Session 4: Wind Plant Design
  - Day 2: Modeling and Grid Interconnection
    - Session 5: Modeling and Simulation
    - Session 6: Introduction to Grid Codes
    - Session 7: Interconnection Case Studies

# Graduate Degrees Completed at IIT

- PhD Degrees
  - Wei Tian, Large-scale Simulation Of Electric Power Systems For Wind Integration
    - Developed an algorithm for analyzing the impact of wind integration on transmission planning and operation in the Eastern Interconnection.
  - Saeed Kamalini, Security Constrained Expansion Planning of Fast-Response Units for Wind Integration
    - Developed a optimization algorithm for wind generation planning
  - Bruno Monnier, Three Dimensional Flow Structures And Turbulence Distribution In An Urban Environment
    - Developed an algorithm for studying the impact of small wind structures on new architectural designs.
- Master's Degree
  - Joan Camprubi, Sustainable Stadium, Qatar 2022
    - Developed an architectural model for a sports stadium with wind generating units

ILLINOIS INSTITUTE OF TECHNOLOGY

# Graduate Degrees Completed at SIU

- PhD Degrees
  - Mark E. Carlos, An Analysis Of Wind Power Plant Site Prospecting In The Central United States
    - Develped a model to identify the existence of 238 suitable counties in the twelve state region that do not possess WPPs and eliminates 654 counties that are not classified as suitable for WPPs.
- Master Degrees
  - Naglaa Elashry, Modeling And Simulation Of Wind Power Generation Using Kites
    - Developed modeling and simulation of wind energy generators, denoted as KiteGen, which employ power kites to capture high altitude wind power.
  - Emad Elhaji, Impact Of Wind Turbine On Power System Voltage Stability
    - Developed a model on the impact of WTGUs on the power system voltage stability.

ILLINOIS INSTITUTE OF TECHNOLOGY

# Research Outcomes

- Ming Cai, Emadoddin Abbasi, and Hamid Arastoopour, “Wind Energy Research,” Illinois Institute of Technology
  - The objective of this study is to develop a numerical model for assessing and analyzing the performance of a horizontal-axis wind-turbine (HAWT) in the presence of rain droplets under heavy rain conditions using computational fluid dynamics (CFD) for multiphase flow systems.

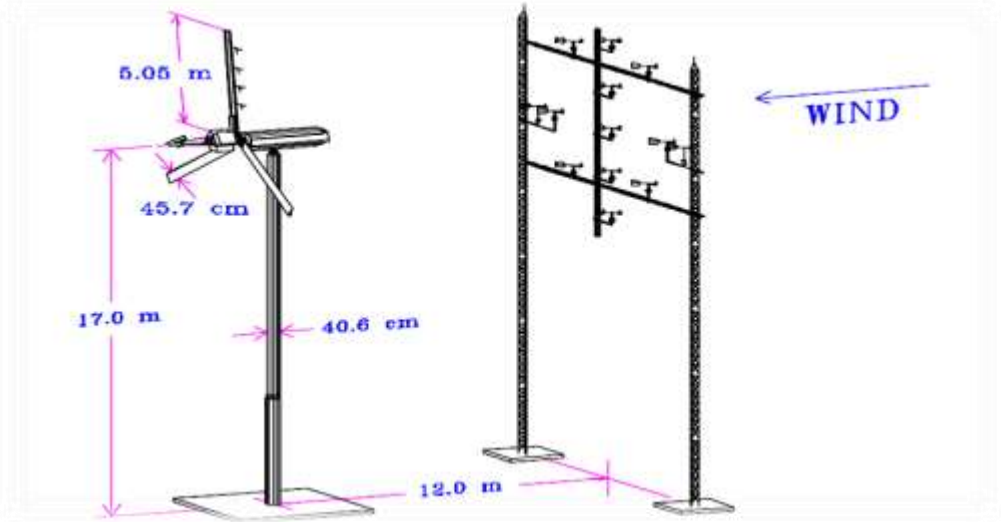

# Research Outcomes

- Xiaodong Shi, Mahesh Krishnamurthy, “Survivable Operation Of Three Phase AC Drives In Wind Generator Systems,” Illinois Institute of Technology

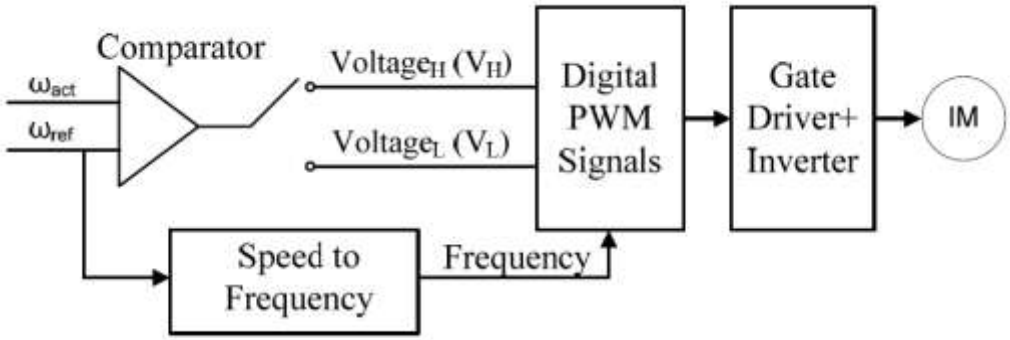


Figure 4.4. Principle of state transition control of induction machine

# Research Outcomes

- Xiaodong Shi, Jorge Pineiro Serradilla and Mahesh Krishnamurthy, “A Back EMF-based Rotor Position Prediction in Permanent Magnet Machines for Survivable Wind Generator Systems,” Ilinois Institute of Technology

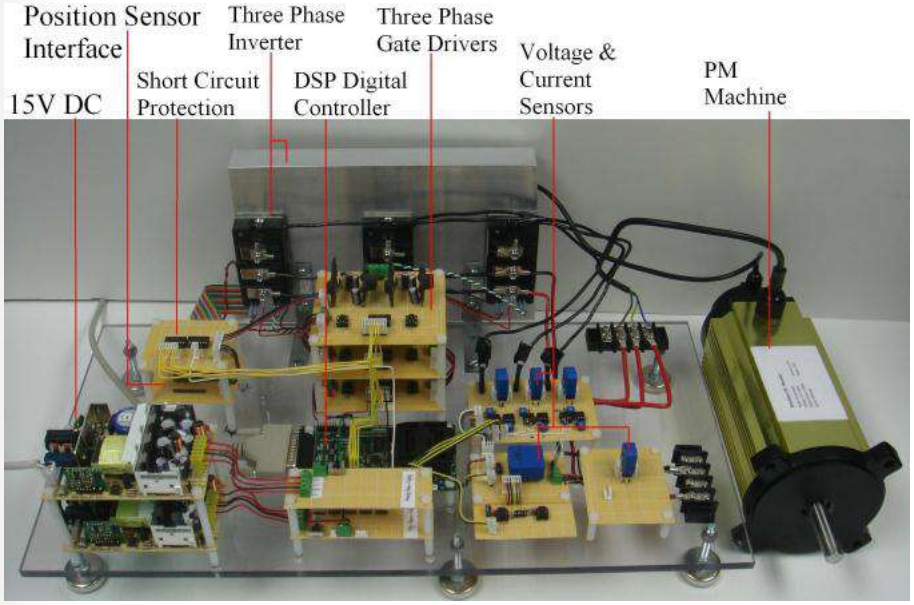


Fig. 8. Compositions of the Experimental setup

# Research Outcomes

- Richard J. Gowen, “Wind Electrical Generation with a Unique High Magnetic Density Turbine Generator,” Dakota Power

Figure 10 - Dakota Power machine DP-06 mounted in the Dynamometer Test Facility

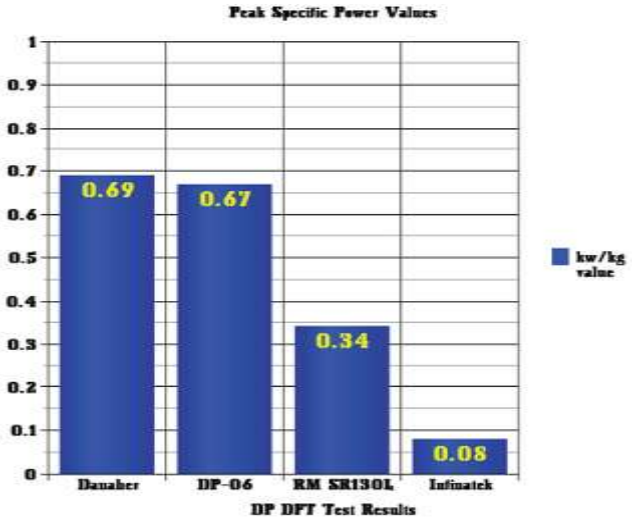


Figure 11 - Comparison of peak specific power of DP-06 of .67 kW /kg to peak specific power of commercial machines

ILLINOIS INSTITUTE OF TECHNOLOGY

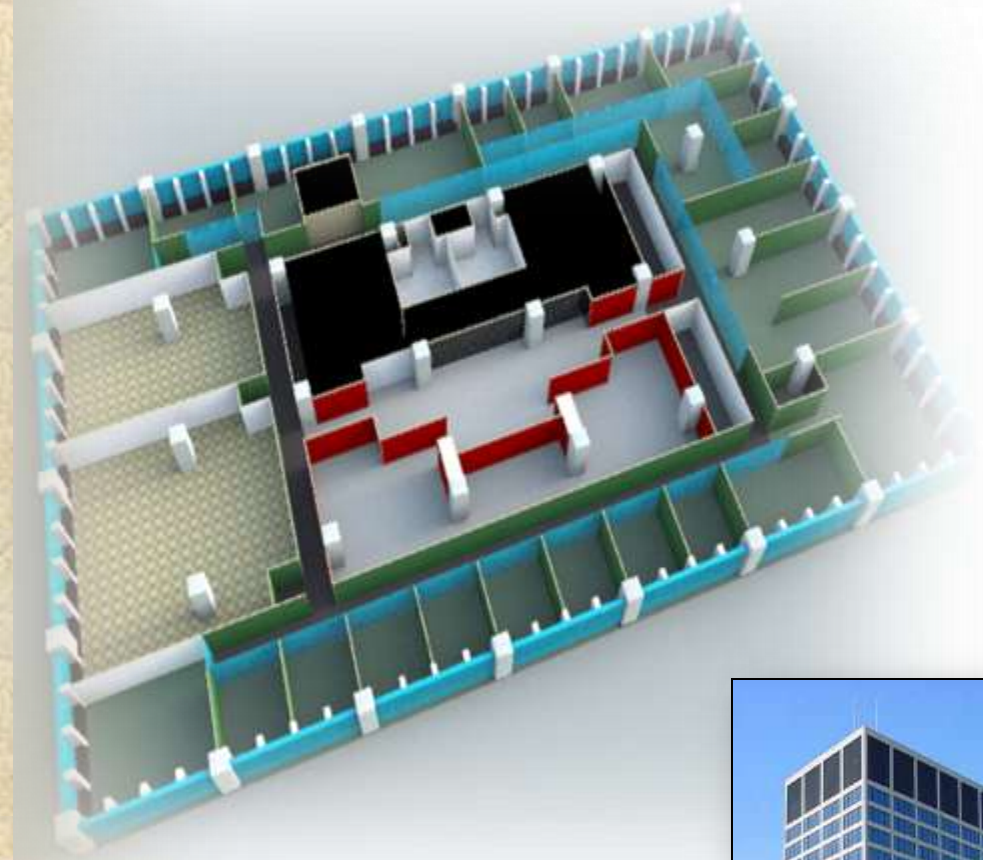

ILLINOIS INSTITUTE OF TECHNOLOGY

# Galvin Center for Electricity Innovation

- Groundbreaking in February 2011

ILLINOIS INSTITUTE OF TECHNOLOGY

# Mayor of Chicago Visit to the Center – January 4, 2012

ILLINOIS INSTITUTE OF TECHNOLOGY

# Mayor of Chicago Visit to the Center – January 4, 2012

ILLINOIS INSTITUTE OF TECHNOLOGY

ILLINOIS INSTITUTE OF TECHNOLOGY

# Microgrid at Illinois Institute of Technology

- In 2008, Illinois Institute of Technology entered into a $12 million partnership with the Department of Energy to build the first-ever Perfect Power microgrid.

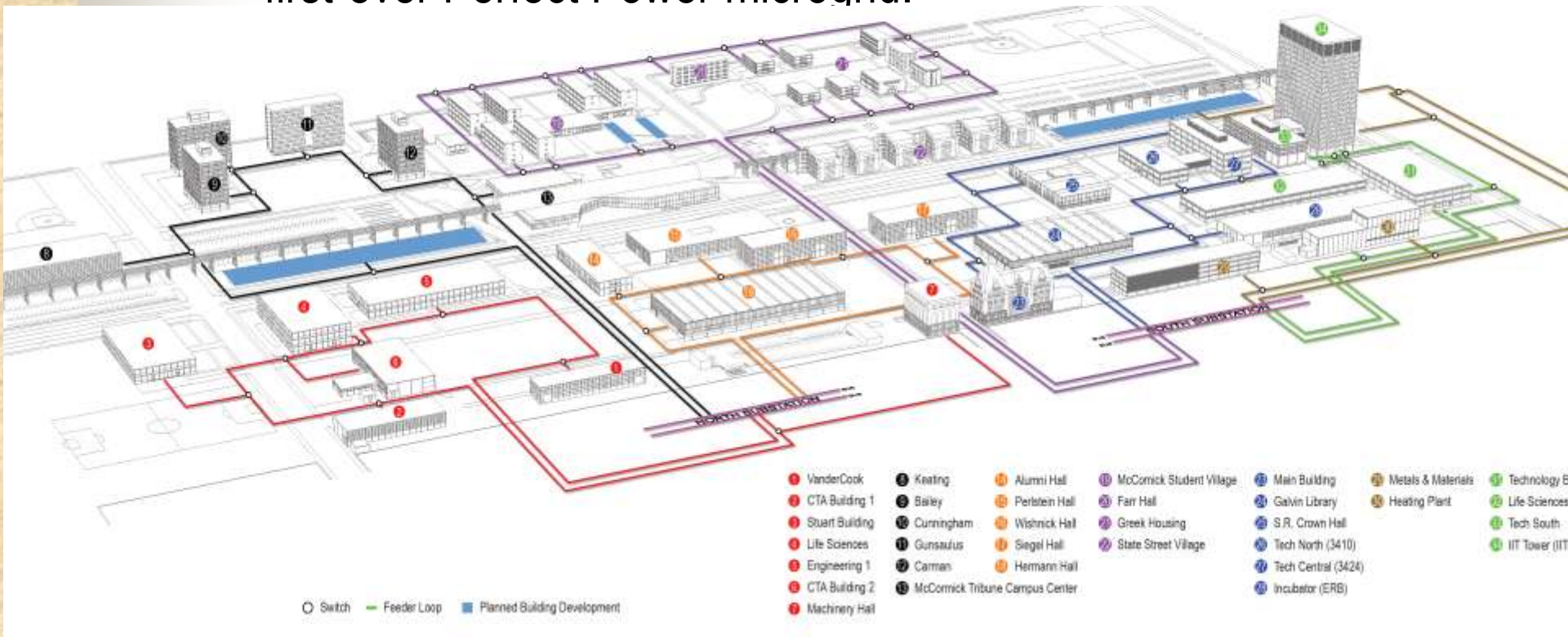

# Research Outcomes

- Greg Rouse, “Software Integration for Small Wind Turbine into IIT’s Microgrid,” Intelligent Power Solutions

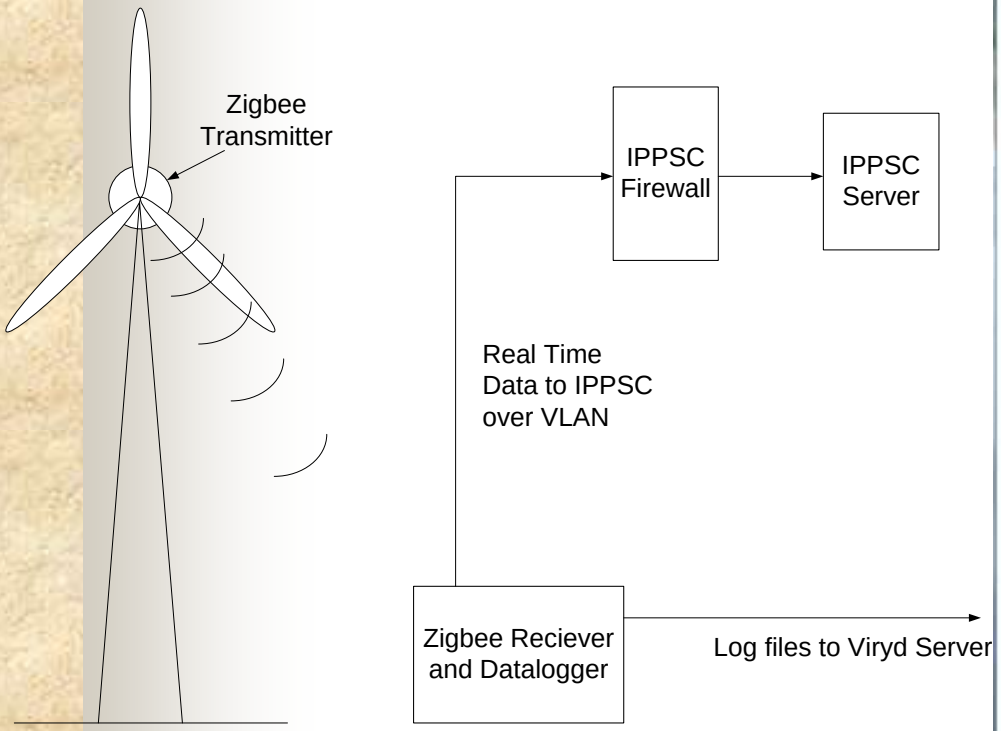


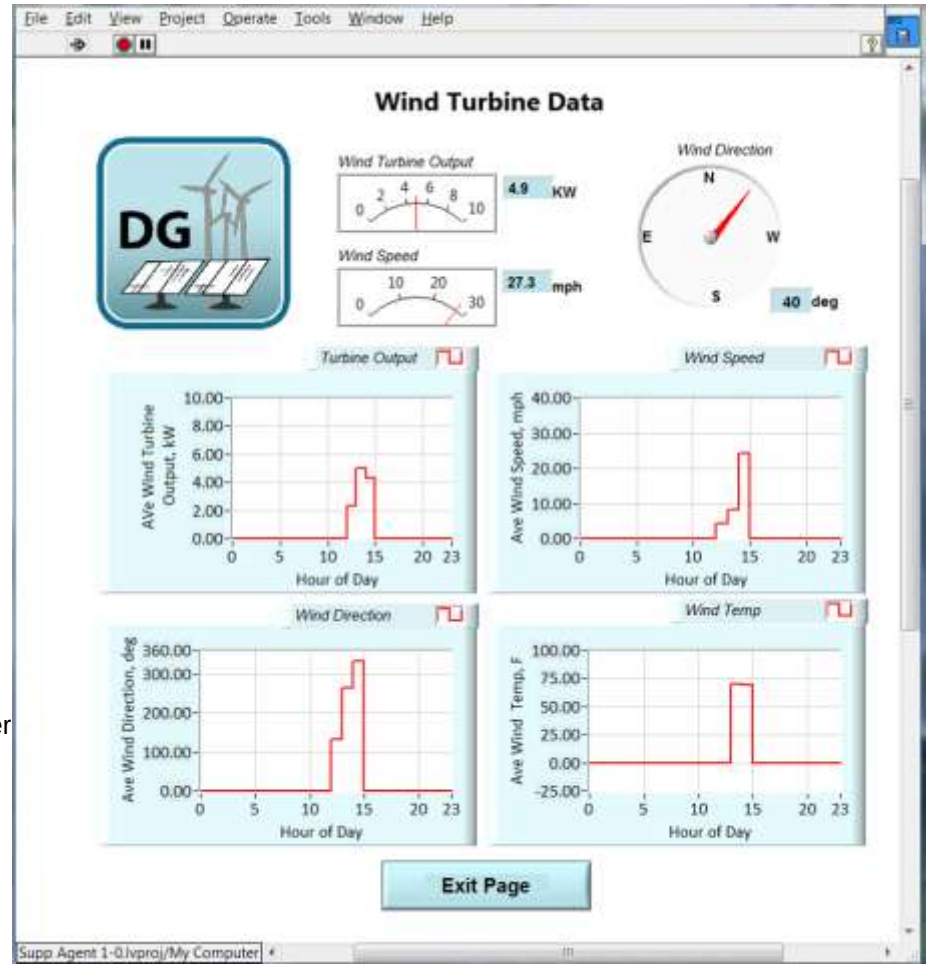

ILLINOIS INSTITUTE OF TECHNOLOGY

# Roof top Solar Panels

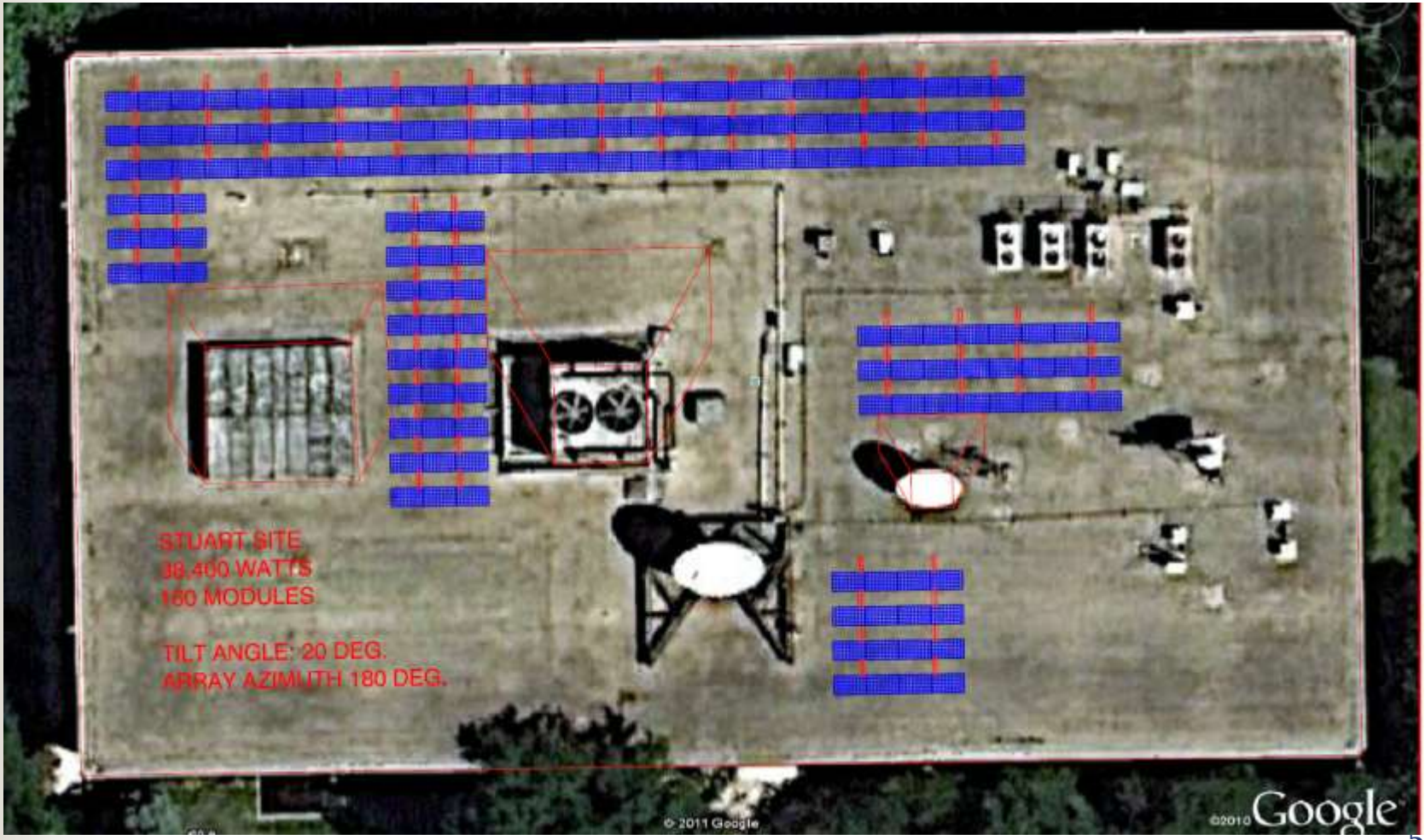

# Battery and Charging Station Installation

# Battery and Charging Station Installation

# Battery and Charging Station Installation

ILLINOIS INSTITUTE OF TECHNOLOGY

# Battery and Charging Station Installation – Ongoing

# IIT-KERI PMU Project

Campus Microgrid
Illinois Institute of Technology

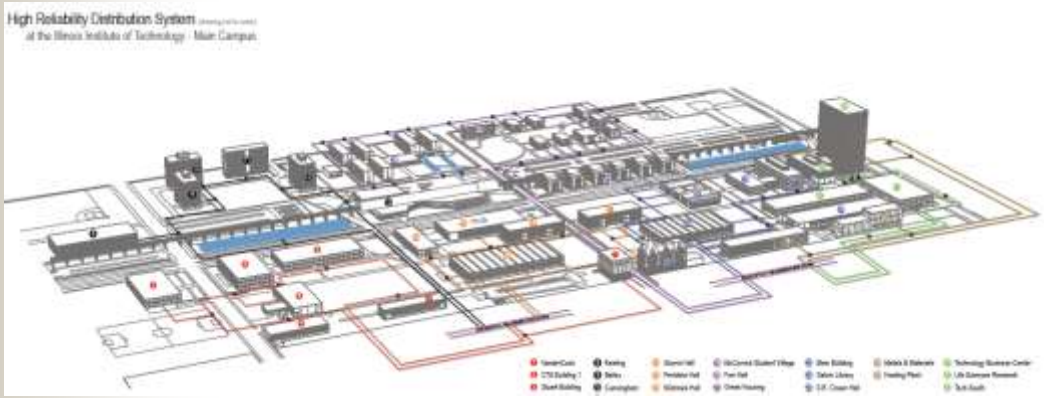


Smart PMU

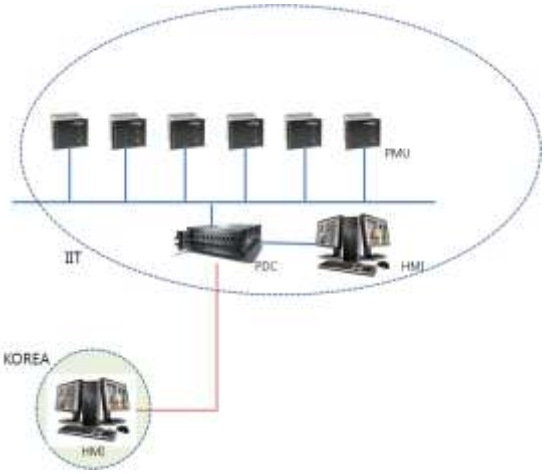


- PMU Demonstration for microgrid application
- LAMS for Campus Microgrid field test
- Enlarge PMU application field & Enhance microgrid technology

ILLINOIS INSTITUTE OF TECHNOLOGY

# Master Controller

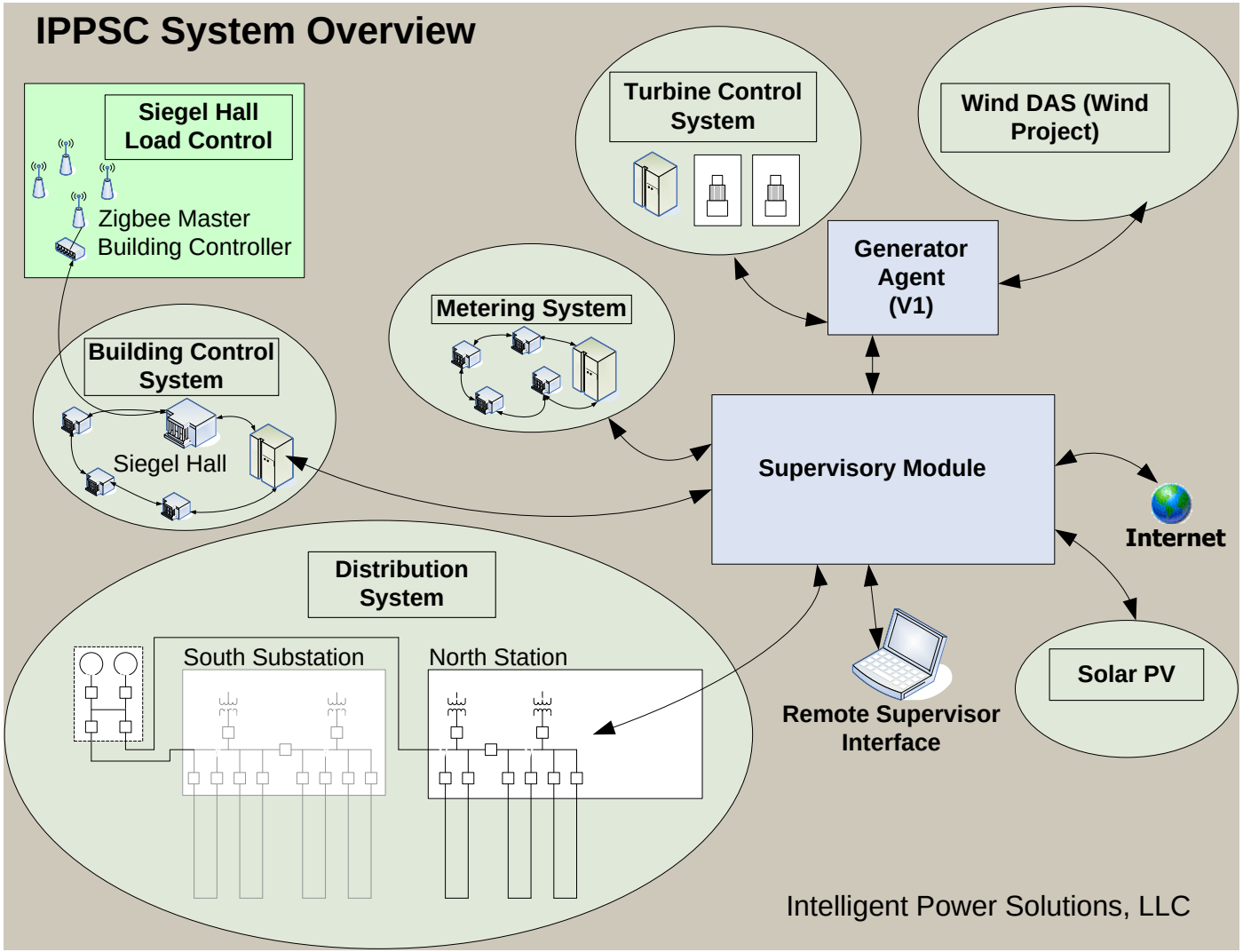

ILLINOIS INSTITUTE OF TECHNOLOGY

# ECEDHA

*Electrical and Computer Engineering Department Heads Association*

## 2010 Innovative Program Award

presented to

## Mohammad Shahidehpour
### Illinois Institute of Technology

for the Center for Electricity Innovation
Establishing the Illinois Institute of Technology as a global leader in microgrids, smart grid technology, and sustainable energy

*Presented at the 27th Annual Conference of the ECEDHA*

Ed Schlesinger
ECEDHA President
2010-2011

Phoenix, Arizona
March 14, 2011

ILLINOIS INSTITUTE OF TECHNOLOGY

## Upcoming Event

# 2012 U.S. Department of Energy Microgrid Workshop

## Illinois Institute of Technology

## July 30-31, 2012

ILLINOIS INSTITUTE OF TECHNOLOGY

## Upcoming Event

# 2012 Great Lake Symposium on Smart Grid and the New Energy Economy

## Illinois Institute of Technology

## September 24-26, 2012

# Proposed Activities

- Research on 1.5MW unit
  - Utilize the more accurate wind measurement from Catch the Wind package to optimize turbine control
  - Noise reduction (Ganesh Raman and Innovative Technology Applications Company)
  - Health monitoring (Smart Signal)
  - Study the stability impact on local grid (Shanechi research)
  - Study the economic impact on local grid (LMP and IPA type of research)
- Research on 8KW unit
  - Improve the reliability of small wind turbine
  - Integrate small wind units into microgrid, and coordinate with battery storage and electric vehicle charging stations

# Proposed Activities

- Annual workshop
  - Expand the annual consortium meeting under the Great Lakes Symposium on Smart Grid and the New Energy Economy
  - Support student to attend the Symposium (free accommodation)
- Short courses
  - Elements of Sustainable Energy to be offered at the IIT Galvin Center for Electricity Innovation
  - IIT IPRO course to support undergraduate research
- Wind energy seminar series
  - Domestic scholars
  - International scholars

# Analysis of 2030 Large-Scale Wind Energy Integration in the Eastern Interconnection Using WINS

*A simulation of the 2030 load forecast in the Eastern Interconnection suggests that large-scale wind energy integration will have a major impact on the hourly commitment and dispatch of gas and coal units, especially at off-peak load hours. While fuel price alterations will have major impacts on the system production cost, load variation will have a larger impact and potential carbon costs will have the greatest impact.*

*Wei Tian, Mohammad Shahidehpour and Zuyi Li*

**Wei Tian** *received his B.S. degree in Mathematics from Shandong University in 2001, M.S. degree in System Engineering from Xi'an Jiaotong University, China, in 2004, and Ph.D. degree from the Illinois Institute of Technology, Chicago, in 2011. He is a visiting scientist at the Robert W. Galvin Center for Electricity Initiative at IIT. His research interests include power system restructuring and long-range planning.*

**Mohammad Shahidehpour** *is the Bodine Chair Professor and Director of the Robert W. Galvin Center for Electricity Initiative at the Illinois Institute of Technology. He is the recipient of the 2011 Innovation Award from the Association of Electrical and Computer Engineering Department Heads.*

**Zuyi Li** *received his B.S. degree in Electrical Engineering from Shanghai Jiaotong University in 1995, M.S. degree in E.E. from Tsinghua University, China, in 1998 and Ph.D. degree in E.E. from IIT in 2002. Presently, he is an Associate Professor in the ECE Department at IIT.*

*This study was funded in part by the U.S. Department of Energy, grants nos. DE-EE 0002979 and DE-EE 0001380.000.*

## I. Introduction

Wind energy is an important component of the future energy production portfolio throughout the world. In the United States, wind energy is expected to provide 20 percent of the U.S. energy production portfolio by 2030 [1–3]. However, the electricity market requires a detailed simulation of the economics and the adequacy of the energy production portfolio before large-scale wind energy can be integrated into existing power systems.

The U.S. Eastern Interconnection is the largest interconnection in the world with more than 5,000 generating units and about 70,000 branches. The National Renewable Energy Laboratory (NREL) initiated a study in 2008 to examine the impact of 20–30 percent wind

  doi:/10.1016/j.tej.2011.09.002 

energy integration in the Eastern Interconnection [4]. The western wind and solar integration study in 2007 examined the operational impact of 35 percent renewable energy penetration [5]. The impact of wind energy integration on power system operations is analyzed further in [6,7,15]. An hourly unit commitment and economic dispatch model for analyzing large-scale power system operations was represented in [8]. A follow-up optimization-based security-constrained unit commitment (SCUC) model [16–18] was presented in [9] which took into account the intermittency and volatility of wind power generation and transmission network constraints.

In this article, we focus on large-scale wind energy integration in the Eastern Interconnection in 2030. The wind energy sites are analyzed and the impact of large-scale wind energy integration on existing generation resources and production costs is studied. Fuel price sensitivity, wind energy production sensitivity, load growth sensitivity, carbon cost sensitivity, and load management strategies are considered and analyzed for large-scale wind energy integration.

The rest of the article is organized as follows. Section II describes the proposed methodology, assumptions, and relevant evaluation metrics. Section III presents the wind energy integration study results for the Eastern Interconnection. The conclusions drawn from the study are provided in Section IV.

## II. Methodology for Wind Energy Integration

### A. WINS

At the Illinois Institute of Technology (IIT), we had developed over the years an efficient decision tool called POMS (POwer Market Simulator) [10] for the day-ahead scheduling of large-scale power systems. The expansion of POMS, which is referred to as WINS (Wind INtegration Simulator), is considered in this study to support the collaborative planning, analysis, and implementation of large-scale wind energy integration in the United States. The WINS architecture is depicted in **Figure 1**. WINS applies unit commitment to simulate large-scale wind energy integrations in the hourly power system operation. The application of WINS in this article analyzes the impact of large-scale wind energy integration in the year 2030 on production costs, unit commitment, and dispatch of generation resources in the Eastern Interconnection. For the purpose of this energy adequacy study, we do not consider transmission constraints in this article. We use the wind data given in [4]. A brief description of the wind data is given in [12]. The wind forecast uncertainty is simulated in this article by

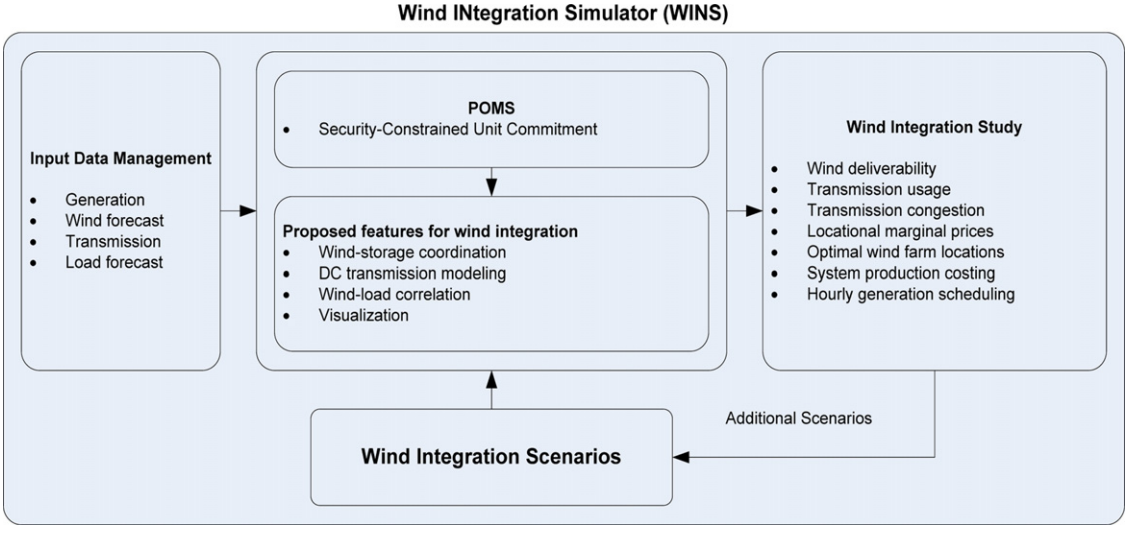


**Figure 1:** Framework of WINS

 1040-6190/$–see front matter  doi:/10.1016/j.tej.2011.09.002 

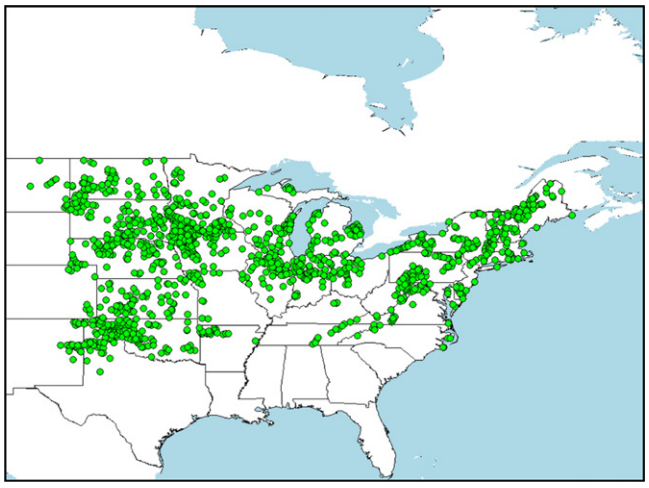

**Figure 2:** Potential Wind Sites in the Eastern Interconnection

sensitivity analyses applied to the wind energy integration Scenarios.

### B. Input data

It is estimated that approximately 225 GW of wind power generation is required to supply 20 percent, and 330 GW is required to supply 30 percent, of the total energy by 2024 in the Eastern Interconnection [4]. In this article, we utilize the land-based time series wind simulation results [4]. The potential land-based wind sites in the Eastern Interconnection are shown in **Figure 2** for about 580 GW of wind power generation capacity. The figure shows that there are potential wind energy sites with rich wind resources in the central part of the United States. In this study, we consider a 1.28 percent annual load growth rate which is based on the MTEP 08 (MISO Transmission Expansion Planning) assumptions. The hourly load distribution shown in **Figure 3** is based on the MISO's hourly load profile in 2007. In Figure 3, peak loads appear in July and August. The power flow solution is used for calculating the hourly load distribution at each bus. Fuel prices are assumed to increase at an annual rate of 4 percent for oil and gas, 2 percent for coal, and 3 percent for nuclear fuel based on the fuel price given in 2008 [13].

### C. Evaluation metrics

The evaluation criteria and metrics used in our simulations are defined as follows.

#### *1. Wind Energy Availability*

The available wind energy is treated as dispatchable in WINS simulations. Here,

$$(1) P_A = \sum_{t=1}^{T} \sum_{i=1}^{NG} p_i^{\max} w_{it} \text{ where } T$$

represents the number of hours in a period (e.g., one year), $NG$ represents the number of wind generators/farms, $p_i^{\max}$ is the

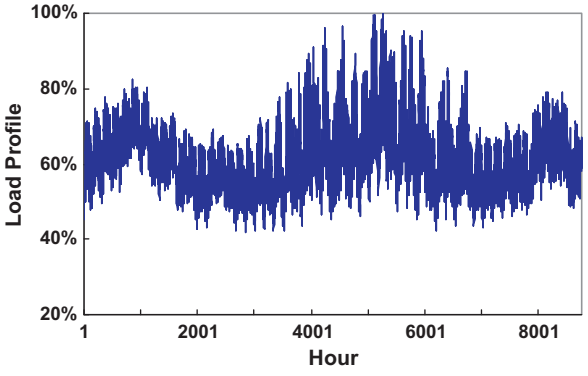


**Figure 3:** Annual Hourly Load Profile

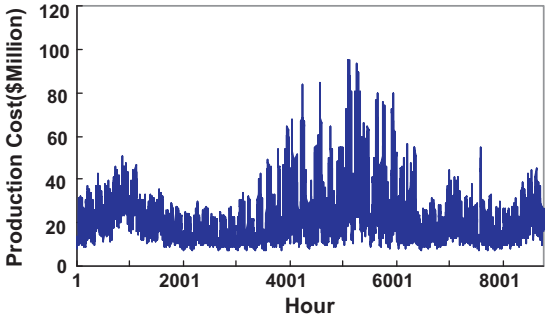


**Figure 4:** Hourly Production Cost Without Wind Integration

nominal capacity of wind generator/farm $i$, $w_{it}$ represents the wind power generation $i$ at time $t$, $P_A$ represents the system wind energy availability in the given study period.

We assume the available wind energy is much less than the total system load in the Eastern Interconnection. Therefore, the total available wind energy is to be dispatchable without any curtailment.

*2. Percentage of Wind Energy Contribution*

This metric (2) is to evaluate the percentage of wind energy contribution to the total energy utilized for supplying the load in the power system.

$$= \frac{\text{Wind Energy}}{\text{Total Energy}} \times 100\% \qquad (2)$$

## III. Numerical Results

In this section, we utilize WINS to simulate the wind energy integration in the Eastern Interconnection of the United States based on the methodology presented in Section II.

### A. Level of wind energy integration

We simulate the hourly power system operation using WINS for a given wind power capacity factor (CF). Four Scenarios are studied as follows.

Scenario 1: No wind energy integration is considered.

Scenario 2: Wind energy integration with a minimum CF of 40 percent is considered.

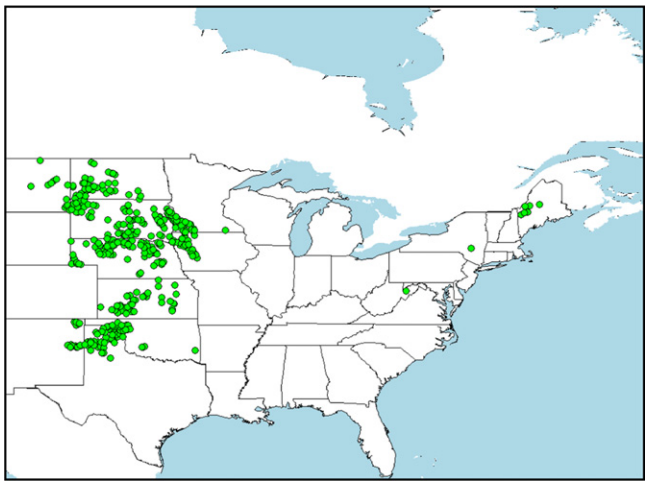

**Figure 5:** Potential Wind Sites with CF $\geq$40%

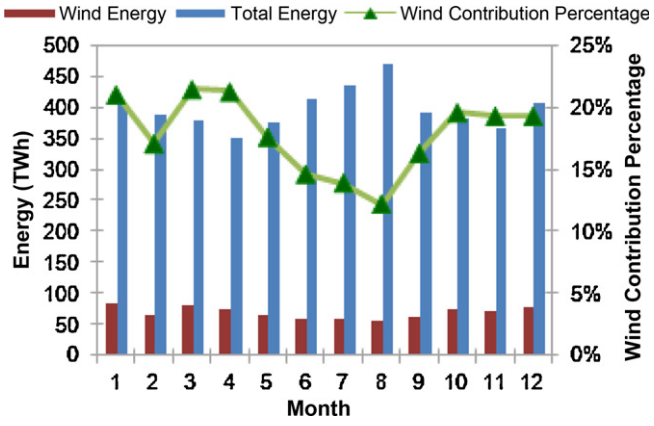


**Figure 6:** Monthly Wind Energy and its Contribution to Total Energy

Scenario 3: Wind energy integration with a minimum CF of 30 percent is considered.

Scenario 4: Wind energy integration in all potential sites is considered.

*1. No Wind Integration*

This is the base case in which the hourly loads will be served by fossil fuel and hydro units. **Figure 4** shows the hourly production cost which is $217.5

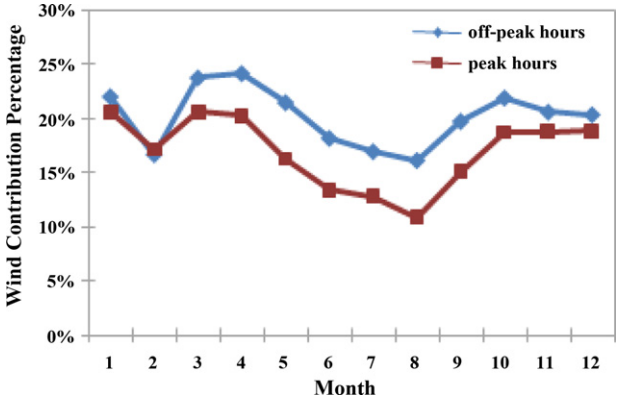


**Figure 7:** Wind Energy Contribution at Peak/Off-Peak Hours

 1040-6190/$–see front matter  doi:/10.1016/j.tej.2011.09.002 

billion per year with an average production cost of $45.64/MWh. The production cost will not change linearly with the hourly load fluctuations. Hydro units will have zero costs and be scheduled first to serve hourly loads or reserves; then cheaper units such as nuclear, coal, and large oil will be committed as loads pick up, and finally expensive units such as gas and oil will be committed to supply hourly loads. A higher production cost will occur at annual peak hours of 5,000–5,500 (i.e., July and August). The production cost at peak hours (6 AM–10 PM) will be $177.8 billion and the production cost at off-peak hours (11 PM–5 AM) will be $39.7 billion. The average production costs at peak/off-peak hours are $50.2/MWh and $32.5/MWh. The average production cost at peak load hours is higher when expensive generators are committed and dispatched.

### 2. *Integration of Wind Energy Sites with a Minimum CF of 40 Percent*

There are 399 such potential wind energy sites with a total wind generation capacity of 230.5 GW. The largest annual CF is 49 percent. **Figure 5** shows the 399 potential wind energy sites in the Eastern Interconnection in which wind energy resources are mainly located remotely in the central region of the United States. The total available wind energy with a minimum 40 percent CF in that region is 845.2 TWh.

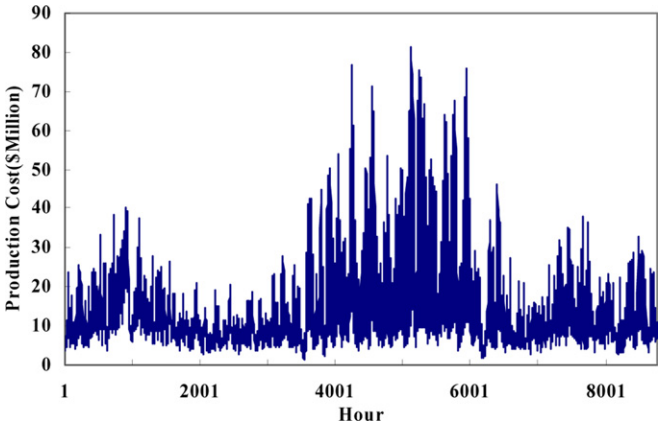


**Figure 8:** Hourly Production Cost in Scenario 2

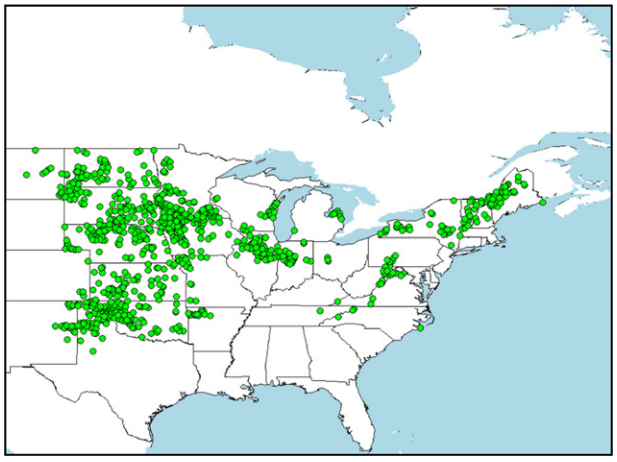

**Figure 9:** Potential Wind Sites with CF $\geq$30%

The 2030 energy forecast in the Eastern Interconnection is 4,783.2 TWh, which indicates that the potential wind energy is about 17.67 percent of the total energy production portfolio. We assume the wind energy has zero fuel cost and transmission congestion is not considered. So the entire available wind energy

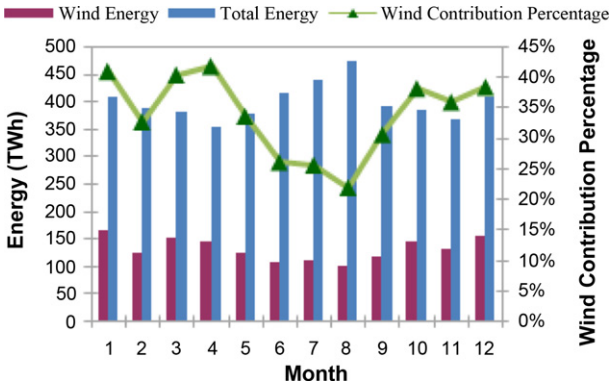


**Figure 10:** Monthly Wind Energy and its Contribution to Total Energy

will be dispatched to satisfy the hourly load. **Figure 6** shows the monthly wind energy in 2030. The wind energy resources are mostly available in spring and winter; however, peak loads occur in summer. January has the highest level of available wind energy of 86.4 TWh, which amounts to 21.11 percent, of the total energy. March has the highest percentage for wind energy contribution (21.53 percent) because the load is lower than that of January. The available wind energy is scarce in August while the highest level of load occurs in this month. So August represents the month with the least available wind energy and the percentage of wind energy contribution (i.e., 57.5 TWh and 12.2 percent) to the total energy production portfolio.

**Figure 7** shows the wind energy contribution at peak and off-peak hours. The figure shows that the wind is usually rich at night as compared with that in the daytime, especially in the summer. The hourly average wind energy at peak/off-peak hours are 2.27 TWh and 2.69 TWh in August, and the percentages of wind energy contribution are 10.88 percent and 16.22 percent, respectively. **Figure 8** shows the hourly production cost. Compared to Figure 4, the production cost is lower when the large-scale wind energy is integrated. The annual production cost is $130.4 billion, which is about $87.1 billion less than that in Scenario 1. The annual average production cost decreases from $45.64/MWh to $27.25/MWh when the wind energy is integrated. Here, the production costs at peak/off-peak hours are $107.1 billion and $23.2 billion, and the average production cost at peak/off-peak hours are $30.1/MWh and $18.9/MWh respectively. The average production cost is lower in this Scenario at peak/off-peak hours.

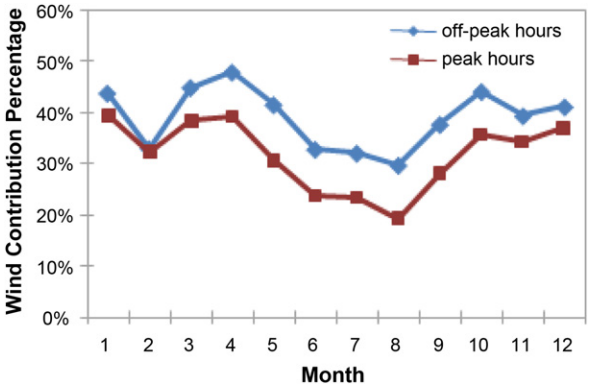


**Figure 11:** Wind Energy Contribution at Peak/Off-Peak Hours

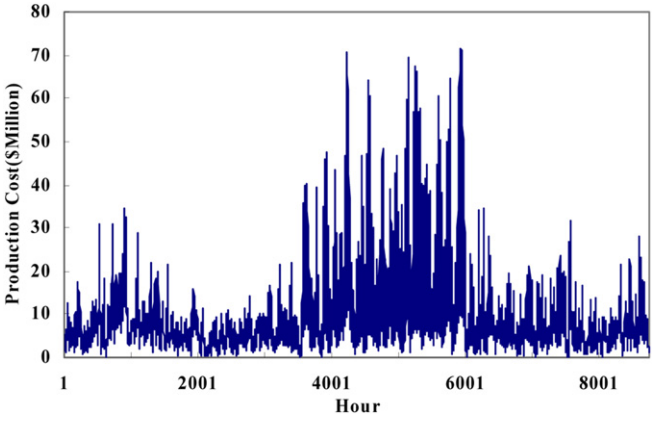


**Figure 12:** Hourly Production Cost in Scenario 3

### *3. Integration of Wind Energy Sites with a Minimum CF of 30 Percent*

In this case, 972 wind sites are introduced in **Figure 9** with a total

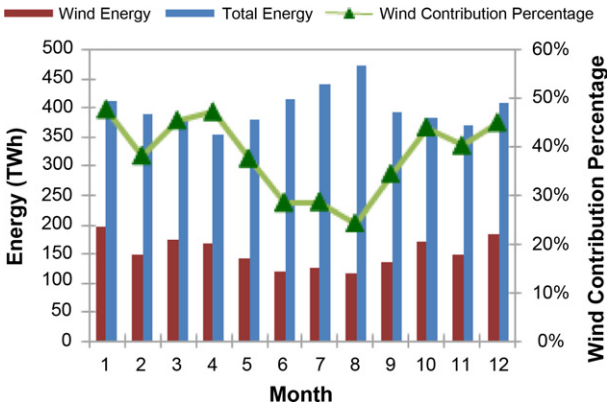


**Figure 13:** Monthly Wind Energy and its Contribution to Total Energy

 1040-6190/$–see front matter  doi:/10.1016/j.tej.2011.09.002 

capacity of 481.5 GW. Compared to Figure 5, additional wind energy sites located in Wisconsin, Illinois, Indiana, and other regions are considered in this Scenario. **Figure 10** shows that the annual wind energy contribution is 1,596 TW, which amounts to 33.37 percent of the total energy production portfolio. **Figure 11** shows the monthly wind energy contribution at peak/off-peak hours. Compared to the simulation results in Scenario 2, 573 additional potential wind energy sites with a total capacity of 251 GW are added here with a CF between 30 percent and 40 percent. In this case, the added wind generation capacity is 108.9 percent (i.e., 481.5 GW vs. 230.5 GW) while the added wind energy contribution is about 88.85 percent (i.e., 33.37 percent vs. 17.67 percent). The production cost in **Figure 12** is $86.8 billion with an average hourly production cost of $18.14/MWh. The average production costs at peak/off-peak hours are $20.33/MWh and $11.33/MWh, respectively.

### *4. Integration in All Potential Wind Energy Sites*

There are 1,326 wind energy sites in the Eastern Interconnection with a total capacity of 580 GW. **Figure 13** shows the monthly wind energy production and wind energy contribution. The annual wind energy production is about 1,816 TWh and the annual percentage of wind energy contribution is about 38 percent. In this case, the minimum wind

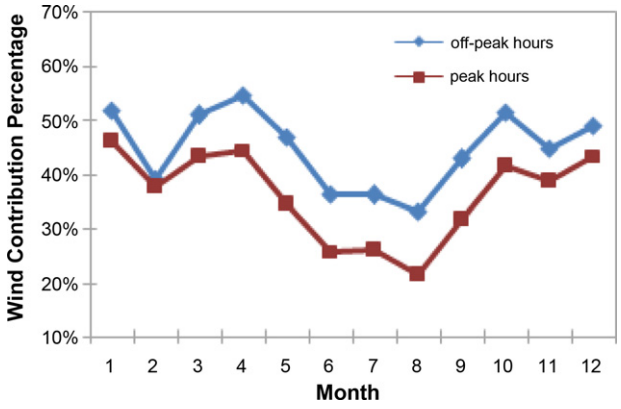


**Figure 14:** Wind Energy Contribution at Peak/Off-Peak Hours

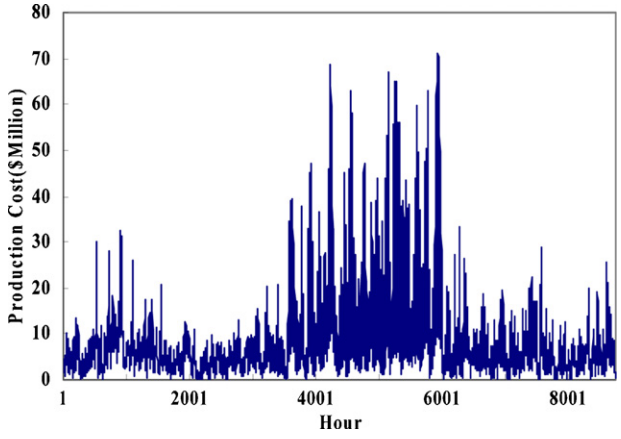


**Figure 15:** Hourly Production Cost in Scenario 4

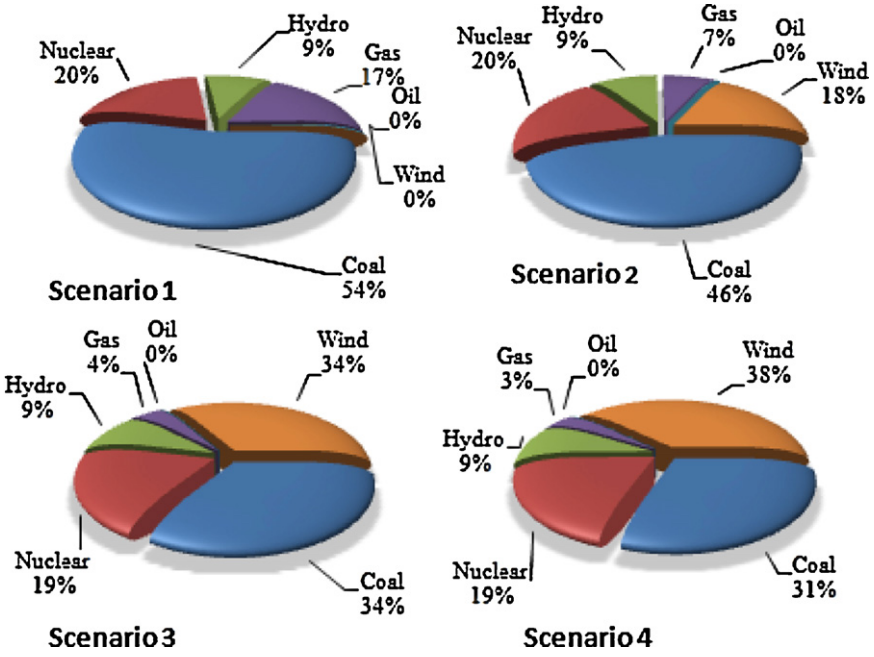


**Figure 16:** Energy Production Portfolios in Wind Integration Scenarios

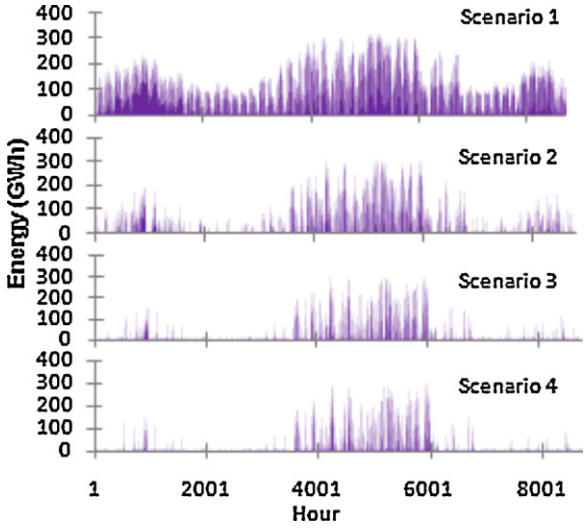


**Figure 17:** Energy Provided by Gas Units in Wind Integration Scenarios

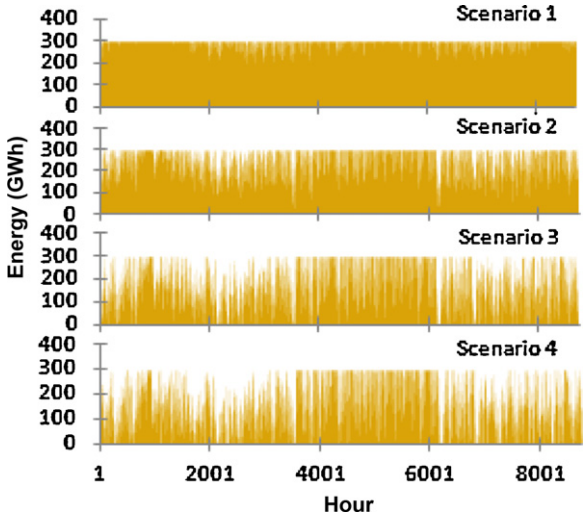


**Figure 18:** Energy Provided by Coal Units in Wind Integration Scenarios

energy contribution will be more than 20 percent of the system load. **Figure 14** shows the percentage of wind energy contribution at peak/off-peak hours. Here, the wind energy contribution to the total energy at peak hours in August is 21.33 percent, which is also the lowest period for the wind energy production. The wind energy in this period is 75.83 TWh as compared to 38.67 TWh in Scenario 2 and 68.52 TWh in Scenario 3. The annual production cost is $77 billion.

**Figure 15** shows the hourly production cost with an average production cost of $16.1/MWh, and peak/off-peak average production costs of $18.19/MWh and $10.04/MWh, respectively. Compared to the simulation results in Scenarios 1–3, the production costs has dropped here as more wind energy sites are added. **Figure 16** shows the wind energy contribution in all four Scenarios. Here, the gas unit production has decreased as more wind energy is considered. Also, the energy supplied by coal units is lower as they are replaced by the integrated wind energy units. Figures 17–19 show the energy supplied by gas, coal, and wind units in four Scenarios. These figures show that wind energy will replace some of the fossil energy especially at off-peak hours in the Eastern Interconnection. **Figure 20** show the annual commitment results of existing power plants in four Scenarios, in which red dots represents the power plants in

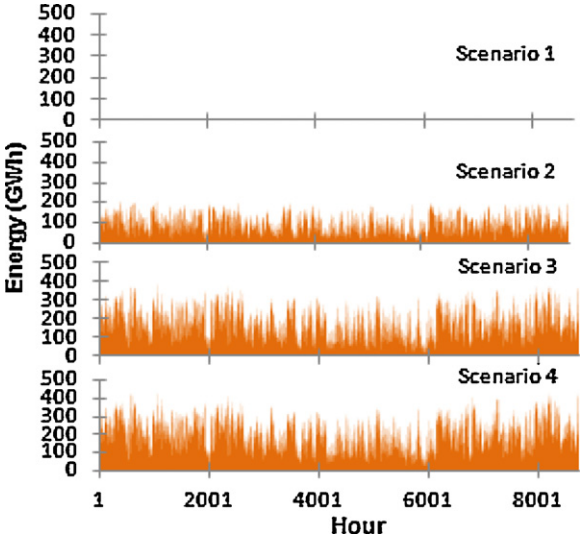


**Figure 19:** Hourly Wind Energy in Wind Integration Scenarios

 1040-6190/$–see front matter  doi:/10.1016/j.tej.2011.09.002 

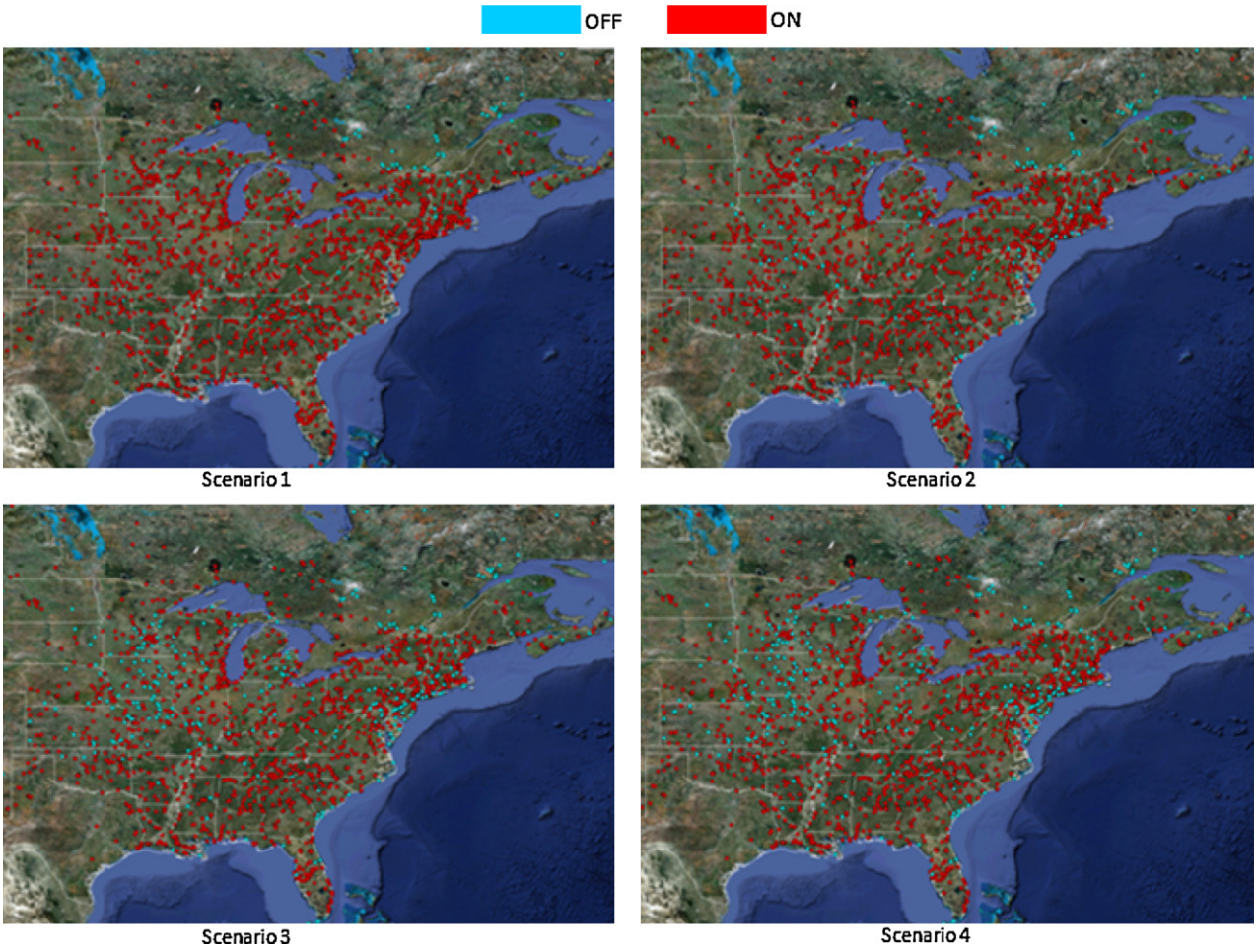


**Figure 20:** Unit Commitment Results in Wind Integration Scenarios

which at least one unit is committed for a minimum of one hour per year. Also, blue dots show the plants which will be off throughout the year as more wind energy is integrated in the Eastern Interconnection.

### B. Sensitivity analysis

There are several uncertain energy factors in the Eastern Interconnection, including fuel prices, hourly wind speed [11], hourly loads, and carbon costs, which could have major impacts on the large-scale wind energy integration and the energy production portfolio. It is perceived that an accurate forecast for some of these factors might not be readily available. In this section, we apply sensitivity analyses, based on our simulation results given in Section A2, to study the impact of fluctuations in such factors on the wind energy integration and the annual energy production portfolio in the

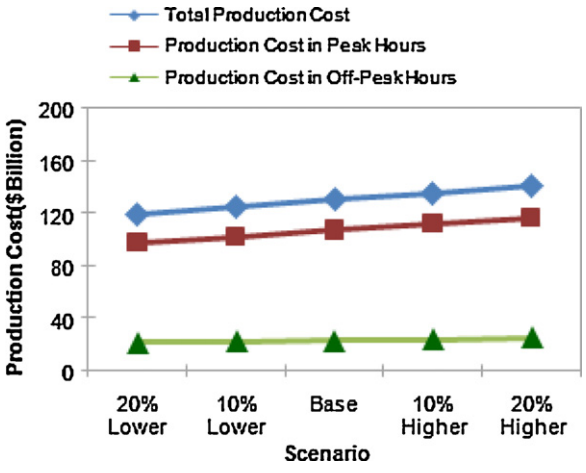


**Figure 21:** Production Costs in Fuel Cost Scenarios

 1040-6190/$–see front matter  doi:/10.1016/j.tej.2011.09.002 

Eastern Interconnection. The simulation results given in Section A2 are considered as the base case in this section.

### 1. *Fuel Price Sensitivity*

We apply the sensitivity analysis to the WINS simulation results for 2030, given in Section A2, in which the potential wind energy sites with a minimum CF of 40 percent and a total energy contribution of 17.67 percent (which is close to the expected 20 percent wind contribution in 2030) were considered. The following four Scenarios would consider the impact of fuel price forecast.

Scenario 5: Actual fuel price is 20 percent lower than the forecast
Scenario 6: Actual fuel price is 10 percent lower than the forecast
Scenario 7: Actual fuel price is 10 percent higher than the forecast
Scenario 8: Actual fuel price is 20 percent higher than the forecast

As expected, the fuel price escalation has no impact on the wind energy dispatch since the wind energy has a zero price and will always be dispatched. However, the production cost in **Figure 21** will increase as fuel prices increase. The increase in fuel price at peak hours will have a more pronounced impact on the production cost as more expensive units will be committed.

### 2. *Wind Energy Production Sensitivity Analysis*

We apply the sensitivity analysis to the 2030 simulation results in Section A2. Four Scenarios are studied as follows.

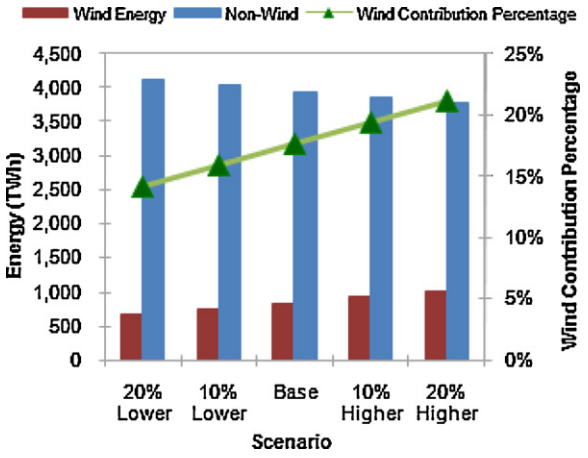


**Figure 22:** Wind/Non-Wind Energy in Wind Energy Scenarios

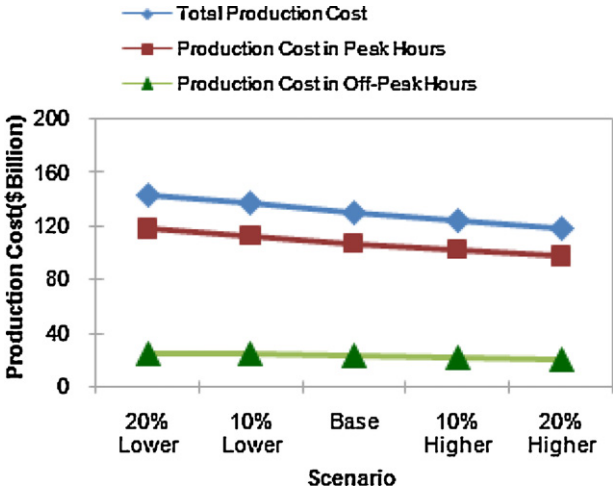


**Figure 23:** Production Cost in Wind Energy Production Scenarios

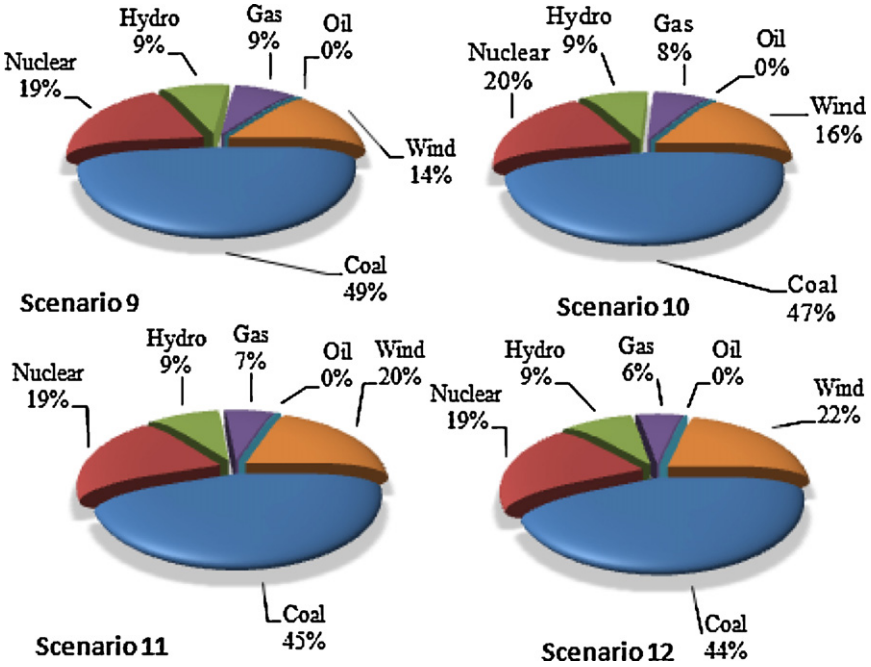


**Figure 24:** Energy Production Portfolios in Wind Energy Production Scenarios

 1040-6190/$–see front matter  doi:/10.1016/j.tej.2011.09.002 

Scenario 9: Actual wind energy production is 20 percent lower than the forecast
Scenario 10: Actual wind energy production is 10 percent lower than the forecast
Scenario 11: Actual wind energy production is 10 percent higher than the forecast
Scenario 12: Actual wind energy production is 20 percent higher than the forecast

**Figure 22** shows that the wind energy contribution to the total energy production is about 20 percent when the actual wind energy is 10 percent higher than that in the base case. **Figure 23** shows that the total production cost decreases with the added wind energy production. Again, the production cost is more sensitive to the wind energy production at peak hours. **Figure 24** shows the energy production portfolios in all four Scenarios. The energy produced by gas and coal units will decrease as the wind energy production is higher. Similar to that in Figure 22, the wind energy contribution is increased from 14 percent to 22 percent. The unit commitment and hourly generation dispatch show a similar pattern as that in Section A2.

### 3. *Load Sensitivity Analysis*

In this section, we study the impact of load forecast errors on the WINS base case simulation results in Section A2. We do the sensitivity analysis based the load forecast in 2030. Four Scenarios are studied as follows.

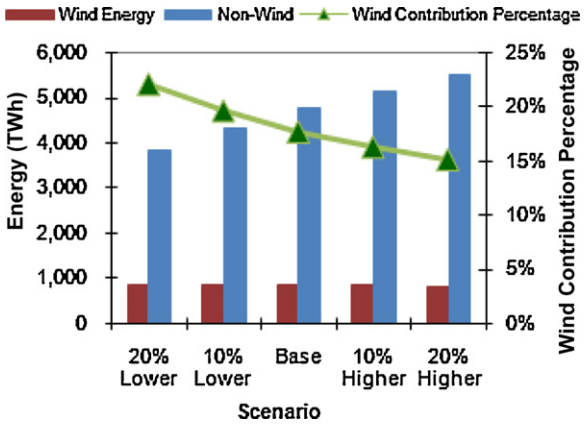


**Figure 25:** Wind/Non-Wind Energy in Load Scenarios

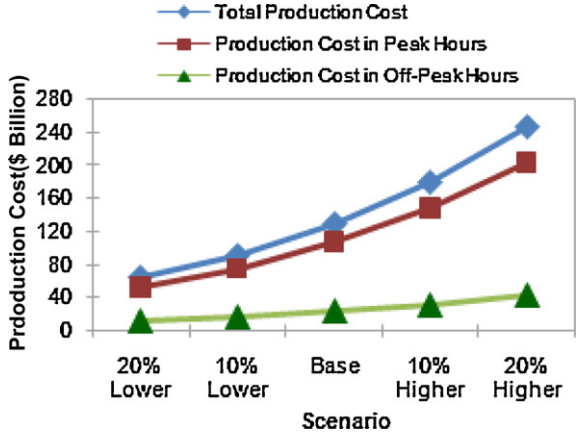


**Figure 26:** Production Cost in Load Scenarios

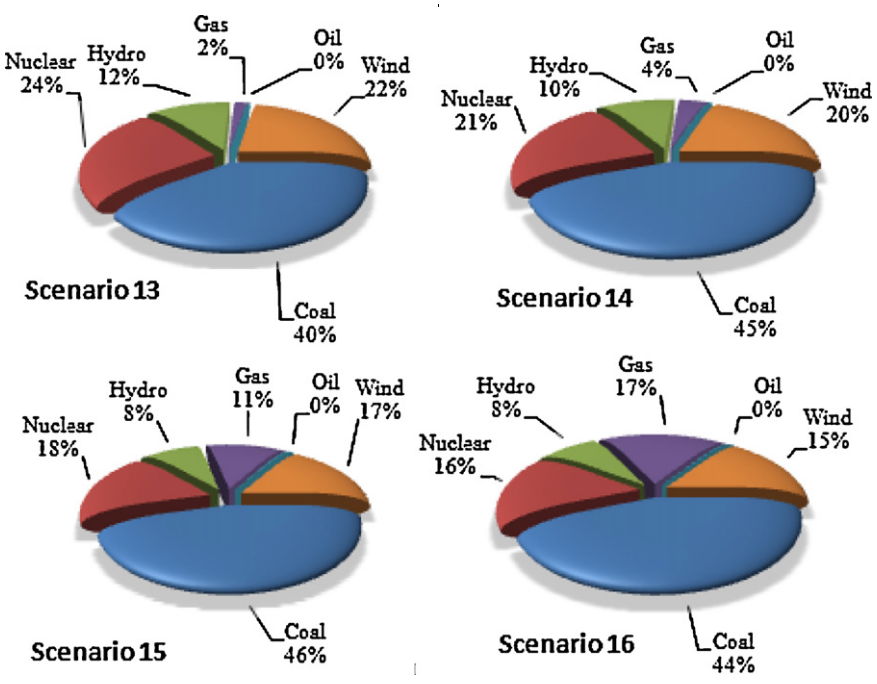


**Figure 27:** Energy Production Portfolios in Load Variation Scenarios

Scenario 13: Actual load is 20 percent lower than the forecast
Scenario 14: Actual load is 10 percent lower than the forecast
Scenario 15: Actual load is 10 percent higher than the forecast
Scenario 16: Actual load is 20 percent higher than the forecast

The wind energy contribution, depicted in **Figure 25**, shows a 19.62 percent contribution to the total energy production in Scenario 14 when the actual load is 10 percent lower than the forecast. The wind energy contribution will decline as the actual load escalates because the additional load will be served by other types of units. The production costs in **Figure 26**, as compared to those in Sections B1 and B2, show that the system load will have the largest impact on production costs. Here, the production cost increases a lot between Scenarios 13 and 16. The production cost at peak hours is more sensitive to load variations.

**Figure 27** shows the energy contribution in the given four Scenarios. The nuclear, hydro, and wind unit with their inexpensive fuel will supply much of the hourly load. However, their contributions will decline as the system load increases. Compared with the base case in Section A2, the energy contributions by gas and coal units, especially those supplied by gas units, will decrease as we reduce the system load. Furthermore, the contribution of gas units to the energy production portfolio will increase from 7 percent in the base case (A2) to 11 percent in Scenario 15 and 17 percent in Scenario 16 as we increase the system load, which means that the additional load is mainly supplied by gas units.

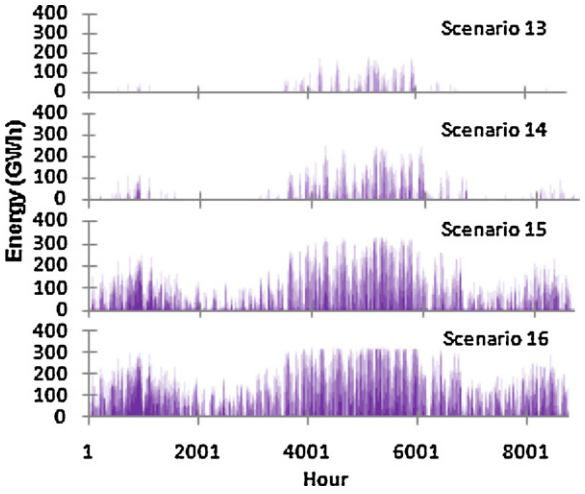


**Figure 28:** Hourly Energy Provided by Gas Units in Load Variation Scenarios

Figures 28 and 29 show the hourly energy supplied by gas and coal units. In **Figure 28**, the energy supplied by gas units has increased as compared to that in Scenarios 13–14 especially at peak hours. In Scenario 13, gas units are mainly committed and dispatched at peak hours. **Figure 30** shows that the load variation would have the largest impact on the commitment and the dispatch of generating units as compared to the fluctuation in fuel price or wind energy production. The commitment based on Scenarios 13–14 shows that many of the existing units will never be committed as hourly loads are lowered. On the other hand, almost all existing units will be committed when the hourly loads are higher than the forecast in Scenarios 15–16. The results indicate that the load management could introduce

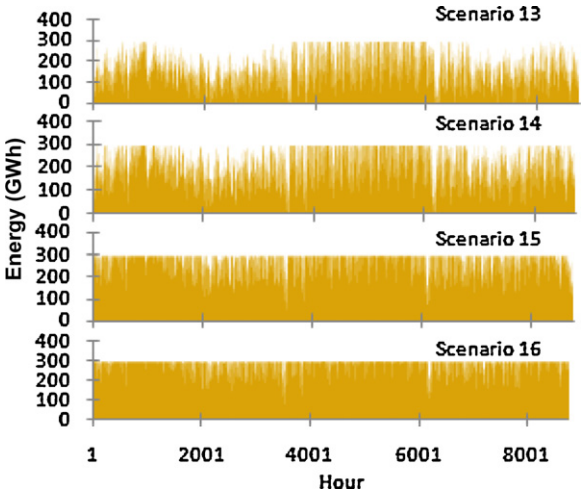


**Figure 29:** Hourly Energy Provided by Coal Units in Load Variation Scenarios

 1040-6190/$–see front matter  doi:/10.1016/j.tej.2011.09.002 

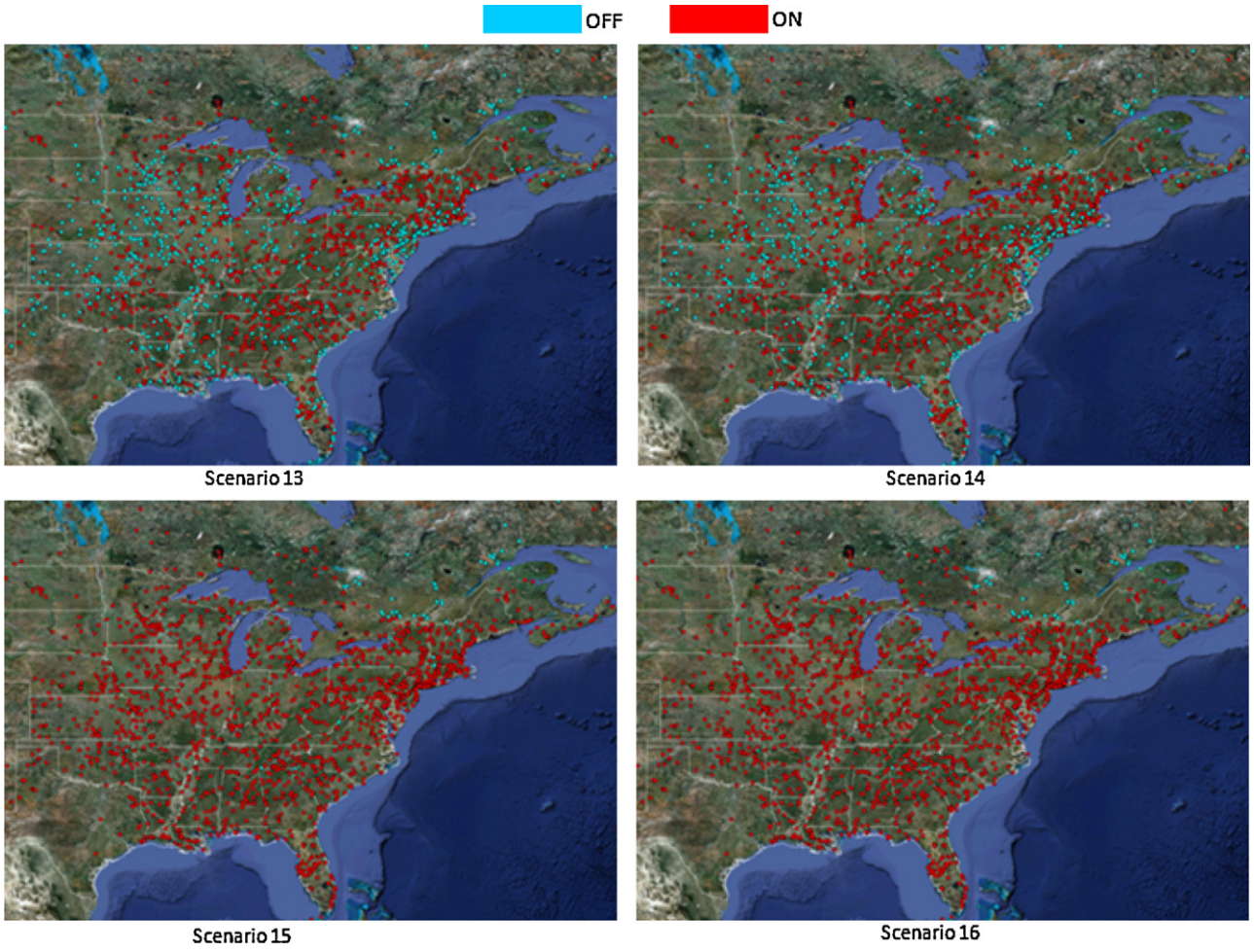


**Figure 30:** Unit Commitment Results in Load Variation Scenarios

large incentives for improving the system operation bottlenecks and decreasing the operation costs.

### *4. Carbon Cost Sensitivity Analysis*

Higher carbon cost can be used as an incentive for promoting the development of clean, efficient or environmentally friendly power generation portfolios [14]. The carbon cost data given in [14] is considered here as the low-carbon-cost Scenario. The high carbon cost Scenario would consider a carbon cost that is doubled. In this section, we consider wind energy sites with CF ≥40% and CF ≥30% for

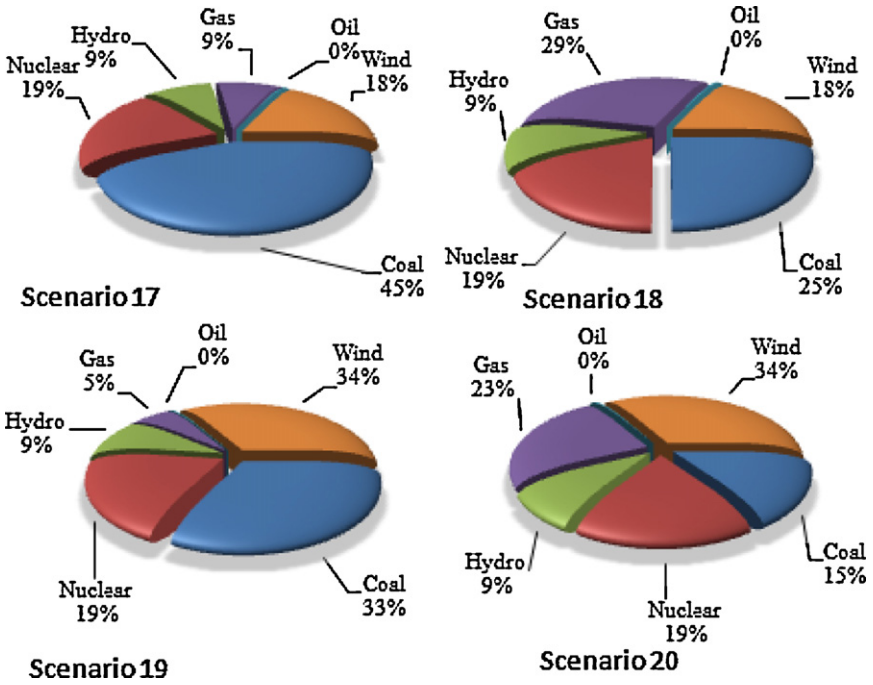


**Figure 31:** Energy Production Portfolios in Carbon Cost Scenarios

analyzing the following four Scenarios.

Scenario 17: Low carbon cost is considered with a minimum CF of 40 percent for wind units

Scenario 18: High carbon cost is considered with a minimum CF of 40 percent for wind units

Scenario 19: Low carbon cost is considered with a minimum CF of 30 percent for wind units

Scenario 20: High carbon cost is considered with a minimum CF of 30 percent for wind units.

The variations in carbon cost will not change the wind energy contribution to the energy production portfolio. However, the total production cost will be much higher when we apply a higher carbon cost. The production costs for four Scenarios are $406.8 billion, $638 billion, $285.7 billion, and $448 billion. The average production cost at peak/off-peak load hours are $89.5/MWh and $71.7/MWh in Scenario 17, and $140/MWh and $113.5/MWh in Scenario 18.

**Figure 31** shows the energy production portfolios in carbon cost Scenarios in which the high carbon cost will have a major impact on the energy supplied by gas and coal units. Since coal prices are lower than gas prices, the energy supplied by coal units does not change much in the low-carbon-cost Scenarios. The energy supplied by gas units increases from 9 percent in Scenario 17 to 29 percent in Scenario 18 while that of coal decreases from 45 percent to 25 percent. Similar results are obtained in Scenarios 19 and 20 when we consider wind units

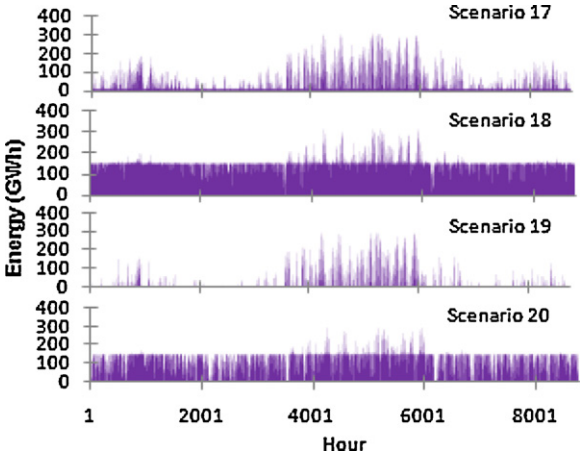


**Figure 32:** Energy Provided by Gas Units in Carbon Cost Scenarios

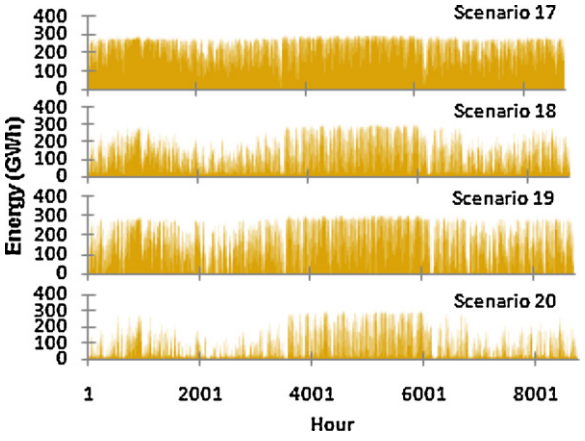


**Figure 33:** Energy Provided by Coal Units in Carbon Cost Scenarios

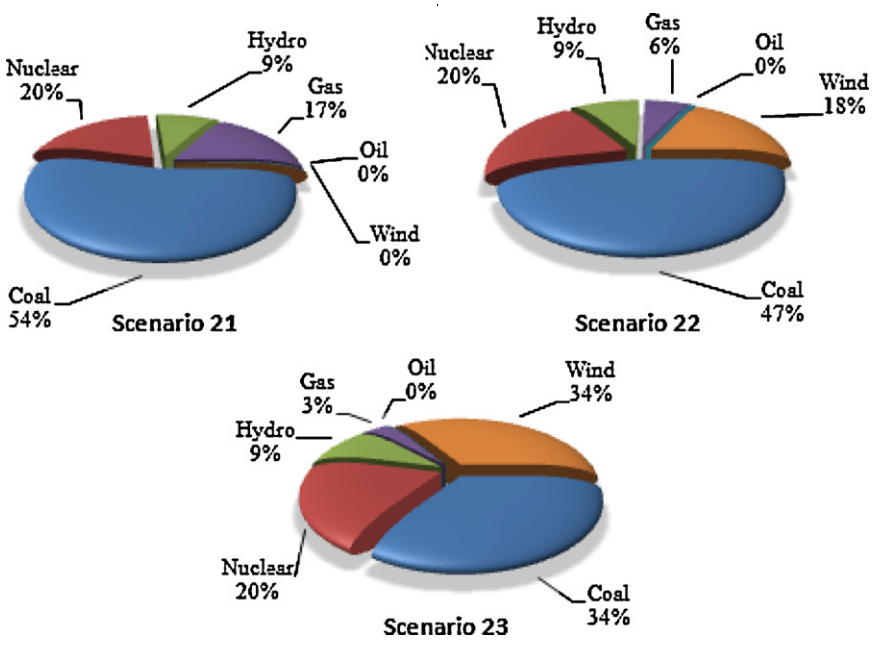


**Figure 34:** Energy Production Portfolios in Load Shedding Scenarios

 1040-6190/$–see front matter  doi:/10.1016/j.tej.2011.09.002 

with a minimum CF of 30 percent. Figures 32 and 33 show the hourly energy supplied by gas and coal units, which are consistent with that of Figure 31. Here, gas units would be committed and dispatched in most hours when we consider high carbon costs.

### C. Load management by introducing load shedding

As presented in Section B3, the hourly load variations would have a major impact on the WINS simulation results. In this section, we consider load shedding as an option to manage the system operation more efficiently at peak hours. For instance, if the hourly load were higher than 80 percent of the annual peak load, we would set it at 80 percent. Three Scenarios are considered as follows.

Scenario 21: Wind energy is not considered when load shedding is applied

Scenario 22: Wind energy with a minimum CF of 40 percent is considered when load shedding is applied

Scenario 23: Wind energy with a minimum CF of 30 percent is considered when load shedding is applied

**Figure 34** shows the energy production portfolios for the three load shedding Scenarios. **Figures 35–37** show that the load shedding will alter the unit commitment as compared to those in Figure 20. Here, more gas units are turned off at peak hours when load shedding is applied. Here, there are about 1,200 gas units which would never be committed again when load shedding is considered as compared to those of the Scenarios 1, 2, and 3 in Section A. These results are similar to those for load variation analysis given in Scenarios 13 and 14 (Section B3). **Figure 38** shows the hourly energy supplied by gas units in which the gas unit dispatch is lower because of the load shedding at peak hours.

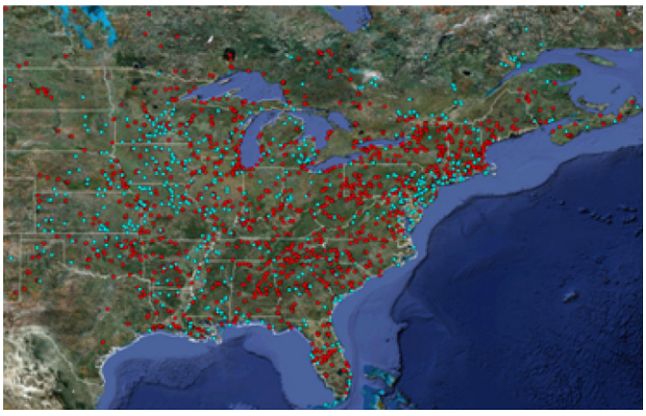

**Figure 35:** Unit Commitment Results in Scenario 21

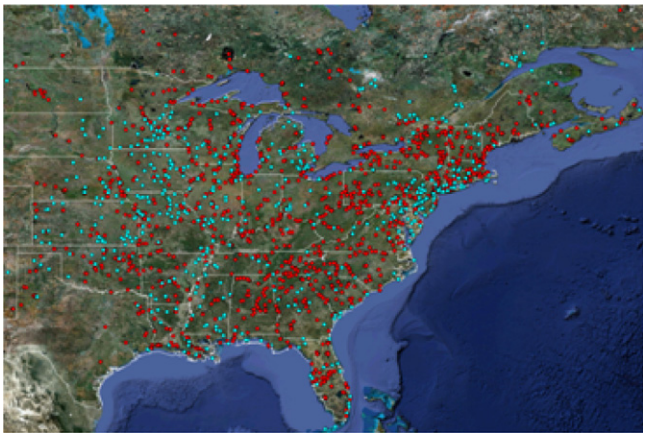

**Figure 36:** Unit Commitment Results in Scenario 22

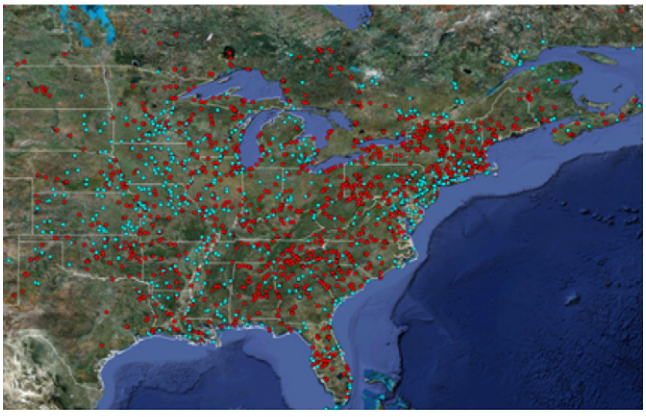

**Figure 37:** Unit Commitment Results in Scenario 23

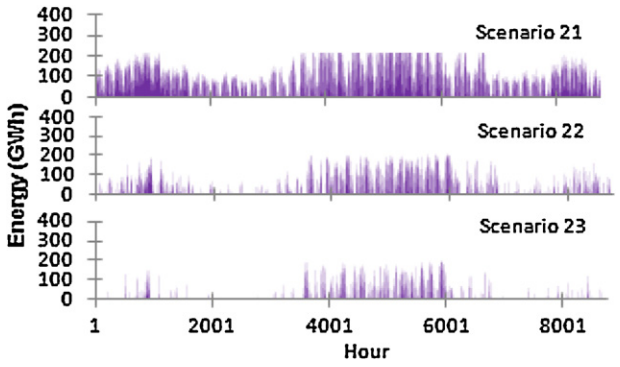


**Figure 38:** Energy Provided by Gas Units

Load shedding has almost no impact on the hourly dispatch of coal units, as coal units are committed to serve the base load.

## IV. Concluding Remarks

In this article, a comprehensive large-scale wind energy integration analysis is considered

**Table 1:** Summary of Simulations in All Scenarios

| Scenarios | Wind Capacity (GW) | Wind Energy (TWh) | Wind Energy Contribution (%) | Production Cost ($ Billion) | Average Production Cost ($/MWh) |
|---|---|---|---|---|---|
| No wind | 0 | 0 | 0 | 217.5 | 45.64 |
| *CF* ≥40% | 230.5 | 845.2 | 17.67 | 130.4 | 27.25 |
| *CF* ≥30% | 481.5 | 1,596 | 33.37 | 86.8 | 18.14 |
| All Wind | 580 | 1,816 | 38 | 77 | 16.10 |
| Fuel price sensitivity | | | | | |
| 20% lower | 230.5 | 845.2 | 17.67 | 118.9 | 24.87 |
| 10% lower | | 845.2 | 17.67 | 124.7 | 26.06 |
| 10% higher | | 845.2 | 17.67 | 135.7 | 28.36 |
| 20% higher | | 845.2 | 17.67 | 141.7 | 29.63 |
| Wind gen. sensitivity | | | | | |
| 20% lower | | 676.1 | 14.14 | 143.7 | 30.03 |
| 10% lower | | 760.6 | 15.9 | 136.8 | 28.59 |
| 10% higher | | 929.7 | 19.44 | 130.4 | 25.99 |
| 20% higher | | 1014 | 21.20 | 124.3 | 24.80 |
| Load sensitivity | | | | | |
| 20% lower | | 845.2 | 22.07 | 64 | 16.73 |
| 10% lower | | 845.2 | 19.62 | 91.6 | 21.27 |
| 10% higher | | 845.2 | 16.29 | 178.5 | 34.65 |
| 20% higher | | 845.2 | 15.12 | 245.9 | 44.54 |
| Carbon cost sensitivity | | | | | |
| Low carbon cost with 40% wind | 230.5 | 845.2 | 17.67 | 406.8 | 84.97 |
| High carbon cost with 40% wind | 230.5 | 845.2 | 17.67 | 638 | 133.3 |
| Low carbon cost with 30% wind | 481.5 | 1,596 | 17.67 | 285.7 | 69.68 |
| High carbon cost with 30% wind | 481.5 | 1,596 | 17.67 | 448 | 93.59 |
| Load management | | | | | |
| No wind energy with load shedding | 0 | 0 | 0 | 208.7 | 44 |
| Min 40% CF wind with load shedding | 230.5 | 845.2 | 17.81 | 123 | 25.9 |
| Min 30% CF wind with load shedding | 481.5 | 1,596 | 33.53 | 80.6 | 16.97 |

 1040-6190/$–see front matter , doi:/10.1016/j.tej.2011.09.002 

which is based on the simulation of the 2030 load forecast in the Eastern Interconnection of the United States. The wind energy integration simulation results and their sensitivities are summarized in **Table 1**. Here, transmission constraints are not considered when studying the wind energy production portfolios because the 2030 wind integration sites are not specified in the proposed wind energy data. Accordingly, the contribution of wind energy to the five Scenarios listed in Table 1 is about 20 percent or higher.

The 2030 simulation results show that large-scale wind energy integration will have a major impact on the hourly commitment and the dispatch of gas and coal units, especially at off-peak load hours, since the wind energy is generally rich at such hours. More gas and coal units will be replaced by wind energy as wind units at candidate wind sites are integrated into the grid, and the system production cost will decrease along with the wind energy integration. The fuel price sensitivity simulation shows that fuel price alterations will have major impacts on the system production cost. However, load variation will have a larger impact on the simulation results. Potential carbon costs will have the largest impact on simulation results. Here, production costs will rise significantly with increasing the carbon costs, and more gas units and fewer coal units will be committed and dispatched as carbon costs increase. Peak load shaving and demand response will have a major impact on the hourly commitment and dispatch of gas units because peak loads are mainly supplied by gas units. Also, load deferrals and smoothing out the daily load profile by introducing Smart Grid technologies (e.g., storage) will notably improve the economics and enhance the operation of power systems.■

**References**


[1] U.S. Department of Energy, 2009 Wind Technologies Market report, Aug. 2010, at http://www1.eere.energy.gov/windandhydro/pdfs/2009_wind_technologies_market_report.pdf

[2] U.S. National Renewable Energy Laboratory, *20% Wind Energy by 2030: Increasing Wind Energy's Contribution to U.S. Electricity Supply*, at http://www.nrel.gov/docs/fy08osti/41869.pdf

[3] International Energy Agency, *IEA Wind Energy Annual Report 2009*, July 2010, at http://www.ieawind.org/AnnualReports_PDF/2009.html

[4] Eastern Wind Integration and Transmission Study, at http://www.nrel.gov/wind/systemsintegration/ewits.html

[5] Western Wind and Solar Integration Study, at http://www.nrel.gov/wind/systemsintegration/wwsis.html

[6] B. Parsons, M. Milligan, B. Zavadil, D. Brooks, B. Kirby, K. Dragoon and J. Caldwell, 2004, *Grid Impacts of Wind Power: A Summary of Recent Studies in the United States*, Wind Energy, 7 at 87–108.

[7] J.C. Smith, M.R. Milligan, E.A. DeMeo and B. Parsons, Aug. 2007, *Utility Wind Energy Integration and Operating Impact State of the Art*, IEEE Trans. Power Syst., 22 (3) at 900–908.

[8] M. Shahidehpour, H. Yamin and Z. Li, Market Operations in Electric Power Systems (New York: Wiley, 2002).

[9] J. Wang, M. Shahidehpour and Z. Li, Aug. 2008, *Security-Constrained Unit Commitment with Volatile Wind Power Generation*, IEEE Trans. Power Syst., 23 (3) at 1319–1327.

[10] W. Tian, Z. Li and M. Shahidehpour, Transmission Congestion Analysis in the Eastern Interconnection Using POMS, in: Proc. IEEE Power Eng. Soc. General Meeting, Minneapolis, July 26–29, 2010.

[11] Argonne National Lab, Wind Power Forecasting: State-of-the-Art, 2009, at http://www.dis.anl.gov/pubs/65613.pdf.

[12] J.E. Schmidt, A Statistical Analysis of Wind Power in the Eastern Interconnect of the United States, in: Proc. IEEE Power Eng. Soc. General Meeting, Minneapolis, July 26–29, 2010.

[13] Midwest ISO Planning, at http://www.midwestiso.org/page/Expansion+ Planning.

[14] U.S. Department of Energy, Fuel and Energy Source Codes and Emission Coefficients, at http://www.eia.doe.gov/oiaf/1605/coefficients.html.

[15] A. Tuohy, P. Meibom, E. Denny, M. and and O'Malley, May 2009, *Unit Commitment for Systems with Significant Wind Penetration*, IEEE Trans. Power Syst., 24 at 592–601.

[16] L. Wu, M. Shahidehpour and T. Li, May 2007, *Stochastic Security-Constrained Unit Commitment*, IEEE Trans. on Power Syst., 22 (2) at 800–811.

[17] Y. Fu, M. Shahidehpour and Z. Li, Aug. 2005, *Security-Constrained Unit Commitment with AC Constraints*, IEEE Trans. Power Syst., 20 (3) at 1538–1550.

[18] Y. Fu, M. Shahidehpour and Z. Li, May 2006, *AC Contingency Dispatch Based on Security-Constrained Unit Commitment*, IEEE Trans. Power Syst., 21 (2) at 897–908.


 , doi:/10.1016/j.tej.2011.09.002 

Electric Power Systems Research 81 (2011) 107–116

Contents lists available at ScienceDirect

Electric Power Systems Research

journal homepage: www.elsevier.com/locate/epsr

# Security-constrained expansion planning of fast-response units for wind integration☆

Saeed Kamalinia, Mohammad Shahidehpour*, Amin Khodaei

*Electrical and Computer Engineering Department, Illinois Institute of Technology, United States*

ARTICLE INFO

*Article history:*
Received 18 June 2010
Received in revised form 18 July 2010
Accepted 20 July 2010
Available online 14 August 2010

*Keywords:*
Wind generation (WG)
Fast-response generating units
Generation expansion planning
Security-constrained unit commitment (SCUC)

ABSTRACT

This paper proposes a stochastic expansion planning of fast-response thermal units for the large-scale integration of wind generation (WG). The paper assumes that the WG integration level is given and considers the short-term thermal constraints and the volatility of wind units in the planning of fast-response thermal units. The new fast-response units are proposed by market participants. The security-constrained expansion planning approach will be used by an ISO or a regulatory body to secure the optimal planning of the participants' proposed fast-response units with the WG integration. Random outages of generating units and transmission lines as well as hourly load and wind speed forecast errors are modeled in Monte Carlo scenarios. The Monte Carlo simplification methods are introduced to handle large-scale stochastic expansion planning as a tradeoff between the solution accuracy and the calculation time. The effectiveness of the proposed approach is demonstrated through numerical simulations.



## 1. Introduction

The increasing socio-environmental concerns have persuaded governments to support large integrations of renewable generation in power systems by introducing mandatory Renewable Portfolio Standards (RPS) or equivalent policies [1]. The large integration of intermittent wind generation (WG) in power systems has necessitated the inclusion of more innovative and sophisticated approaches in power system operation and planning [2].

In this paper, the intermittency refers to a situation where the power output of WG is less than a minimum amount over an extended time. While the volatility points out to smaller WG fluctuations in a shorter time. A major challenge in power systems is to determine the optimal availability of reserves to compensate WG uncertainties. Without a sufficient supply of reserves, the power system may not be able to provide short-term ramping support to contain large WG variability. However, the real-time allocation of a large sum of reserves may not be feasible when considering the economics and the security of power systems. Here, the allocation of excessive thermal reserves could further increase the operating costs while thermal reserves supplied by remote generating units may not be readily accessible due to transmission constraints.

The deterministic allocation of thermal reserves (e.g., largest generation unit in the system or certain percentages of load and WG) may offer a sub-optimal solution. Large integrations of intermittent WG could further contribute to the vulnerability of power systems [3–5]. Hence, it is necessary to apply stochastic optimization methods to address major WG integration concerns such as the coordinated expansion of WG and fast-response generation units, uncertain nature of systems with WG units, and short-term operating constraints of power systems.

The operation planning of WG integration is proposed in Ref. [6]. The reliability of composite generation and transmission system with a large-scale WG integration is investigated in Ref. [7]. The Monte Carlo simulation is used in Ref. [8] to investigate the effect of wind and load forecast errors on the power system expansion planning.

However, only a few studies in the literature considered the complicated operation issues in the WG expansion planning problem. The problem in Ref. [9] provides a nonlinear wind-thermal model and applies the evolutionary programming to large-scale power systems. A coordinated wind-thermal dispatch is presented in Ref. [10] by applying the direct search method to the WG integration. A combination of branch and bound and dynamic programming is considered in Ref. [11] for a coordinated economic dispatch of wind and thermal units in isolated power systems. The impact of transmission lines on the WG expansion is discussed in Ref. [12]. The approach considers additional zonal reserves because of the WG uncertainty. The incorporation of the WG model in the optimal economic dispatch is discussed in Ref. [13]. The study in Ref. [14] considers the short-term operation along with the long-term

☆ This work is supported in part by DOE grants DE-EE 0002979 and DE-EE 0001380.000 and the NSF grant ECCS-0801853.

* Corresponding author.
*E-mail address:* ms@iit.edu (M. Shahidehpour).

0378-7796/$ – see front matter © 2010 Elsevier B.V. All rights reserved.
doi:10.1016/j.epsr.2010.07.017

planning, where renewable energy resources are operated along with conventional generating systems to satisfy certain objectives. A comprehensive study of the operation of power systems when considering the WG integration is presented in Ref. [15]. The study shows that, at the present time, frequency control is not a significant challenge when integrating WG into large power systems. However, such issues will become more of a challenge for systems with large penetrations of WG. Recently, North American Electric Reliability Corporation (NERC) released a report on the planning and the operation of power systems with large sums of WG [16].

This paper proposes a stochastic expansion planning of fast-response thermal units for the large-scale integration of WG. The level of WG integration is assumed to be given. The site and the year of installation of fast-response units are proposed by the participants. The ISO does not plan any generating units. Rather the ISO would acknowledge and optimize the proposed planning of fast-response units that would provide both the reserve capacity and the fast ramping required for large WG integrations. The fast-response units in the paper assumed to have the ability to reach their maximum capacity in a short period. The inclusion of the hourly unit commitment is essential when considering the WG variations and ramping constraints. The paper considers the short-term thermal constraints and the volatility of wind units in the planning model and applies a decomposition model for utilizing the hourly unit commitment states. Random outages of generating units and transmission lines as well as load and wind speed forecast errors are modeled in scenarios using the Monte Carlo simulation. The Monte Carlo simplification methods are introduced to handle large-scale the stochastic expansion planning as a tradeoff between accuracy and calculation time. The proposed stochastic generation expansion planning approach would inherently form a large-scale optimization problem and a decomposition method is used to alleviate the calculation burdens. The application of mixed-integer programming (MIP) presents attractive features including a fast convergence, simplicity of the model, linearity of constraints, and the ability to handle large-scale problems [17]. The approach can be used by an ISO or a regulatory body to secure the optimal planning of fast-response units proposed by market participants while considering the large-scale WG integration. The contribution of the paper is to consider and utilize new fast-response generating units in power systems that would accommodate large WG integrations. The impact of WG dispersion (i.e., centralized or distributed) on the power system operation and planning is investigated. The planning problem, when considering the WG uncertainty, would present a large-scale problem with major computation burdens. Several improvements in decomposition and modeling are considered in this paper to make the proposed approach more practical.

Other alternatives such as the demand response and the application of storage systems may accommodate the WG uncertainty. However, such alternatives are usually available in small quantities as compared with large WG variations in power systems [18,19]. The application of responsive demands may incur additional investments on communication facilities between the supply and the demand [20].

The rest of this paper is organized as follows. Section 2 describes the modeling of uncertainties in the proposed model. Section 3 presents the framework and the decomposition procedure applied to the model. Section 4 provides a detailed formulation of the problem and the solution methodology. Section 5 presents and discusses the case studies for a six-bus system and the IEEE 118-bus system over a 10-year planning period. The conclusions drawn from the case studies are provided in Section 6.

## 2. Uncertainty in power system planning

The uncertainty can be categorized into (1) the participant level uncertainty which includes fuel availability and emission costs, discount rates, investment costs, competition, etc., and (2) the ISO level uncertainty which includes random component outages and load and wind forecast errors. The financial risks are usually included in the market participant portfolio optimization [21]. As this paper assumes that the investors have already submitted their expansion planning proposals to the ISO, the participant level uncertainty is not considered. Accordingly, the ISO's uncertainty is considered in scenarios to maintain the reliability index at an acceptable level. The ISO assumes the stochastic behavior of power systems corresponding to component outages and load and wind forecast errors by deploying an optimal level of generation reserves. The embedded expansion planning risk, assumed to be undertaken by the ISO, is modeled in Section 4 by adding the cost of imaginary units to the ISO's objective function.

The Monte Carlo (MC) simulation method is adopted to simulate random characteristics of power systems. The proposed stochastic planning model would consider multiple scenarios in the Monte Carlo simulation [23,24]. To address the uncertainty of WG, we assume the wind power is subject to a Weibull distribution. The detailed modeling of WG uncertainty with a Weibull distribution is provided in Refs. [13,22]. The Monte Carlo simulation will generate a large number of scenarios considering wind speed forecast errors. In each scenario, the hourly WG is considered to be given.

To consider random outages of generators and transmission lines, we use UX and UY vectors in the Monte Carlo simulation, which $UX_{iht} = 1$ indicates that the $i$th generator is available in year $t$ and scheduling period $h$ while $UX_{iht} = 0$ indicates otherwise. Likewise, $UY_{jht} = 1$ indicates that the $j$th transmission line is available in year $t$ and scheduling period $h$ while $UY_{jht} = 0$ indicates otherwise [23].

To consider load forecast errors, the annual peak load forecast is expressed as the base load times the annual growth rate. The annual growth rate consists of an average growth rate and a random component. Normally distributed random components are assumed to be added to the average growth rates in order to reflect an uncertain economic growth or weather changes in the load forecast [24]. The hourly load at each bus is then determined based on the annual system peak load using given load distribution factors.

Each scenario is assigned a probability of occurrence, PRs, that is one divided by the number of generated scenarios. The number of scenarios has a substantial impact on the computational requirements for solving scenario-based optimization models. Therefore, using an effective scenario reduction method could be very essential for solving large-scale systems [25]. The reduction technique is a scenario-based approximation with a smaller number of scenarios and a reasonably good approximation of original system. Therefore, we determine a subset of scenarios and a probability measure based on the subset that is the closest to the initial probability distribution in terms of probability metrics. The General Algebraic Modeling System (GAMS) is used in this study. GAMS provides a tool called SCENRED for scenario reduction and modeling random data processes. These scenario reduction algorithms provided by SCENRED determine a scenario subset (of prescribed cardinality or accuracy) and assign optimal probabilities to the preserved scenarios [26].

## 3. Planning model description

Fig. 1 depicts the proposed planning model. The Benders decomposition is used to decompose the planning problem into the optimal investment plan as master problem, and

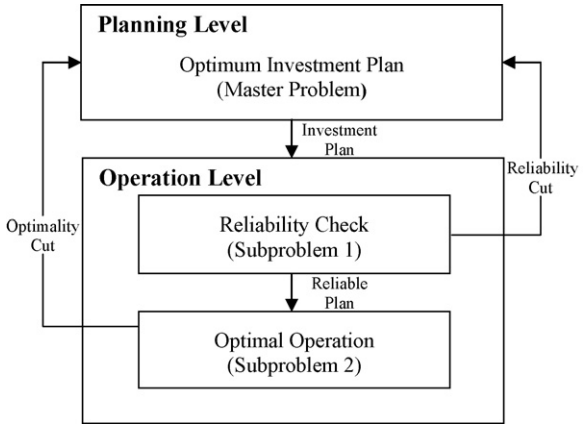


**Fig. 1.** The ISO's proposed planning framework.

the reliability and the optimal operation as two subproblems. The optimality of Benders decomposition as well as its applicability to power system problems is discussed in Refs. [27–30].

It is assumed that the level of wind integration is already known by the ISO. The large WG integration could aggravate the reliability of power systems if non-wind units cannot adequately support WG variations. The fast-response units are planned in this study to tackle such uncertainties. On the other hand, the emission associated with fast-response gas units may negatively contribute to the overall goal of WG expansion. Therefore, the proposed study would determine the optimal mix of generation which would also satisfy the system reliability.

In Fig. 1, the candidate set of fast-response generating units is provided to the ISO by market participants. Although, the ISO is not making any investment decisions, it would maintain the system reliability along with the minimum social cost (i.e., total operation and investment cost) to enhanced the market operation. The optimal investment plan of the new generating units is determined in the ISO's master problem. The objective of the master problem is to minimize the total investment cost of new generating units while considering the planning constraints. The planning constraints include capital investment funds, the maximum number of units, and the construction time of candidate units. The lower bound of the objective function is also obtained in the master problem and used further to check the optimality of the proposed plan. In addition to the planning constraints, the cuts generated in the subproblems are considered in the master problem. All binary variables are considered in the master problem and all constraints are linear. The master problem is a mixed-integer linear programming (MILP) problem. Commitment states are adjusted in the master problem through the cuts provided by reliability and optimal operation subproblems.

The reliability check subproblem examines the plan proposed by the master problem for the feasibility of system reliability constraints. This subproblem would satisfy the power balance in every bus while preserving the transmission security and physical constraints of generating units. In the case of feasibility violations, a reliability cut will be formed and added to the master problem for solving the next iteration of the planning problem. This iterative process will continue until a reliable plan is calculated. Once the system reliability is feasible, the optimal operation subproblem will consider the optimality of the proposed plan. The iterative process will continue until the given convergence criterion is satisfied.

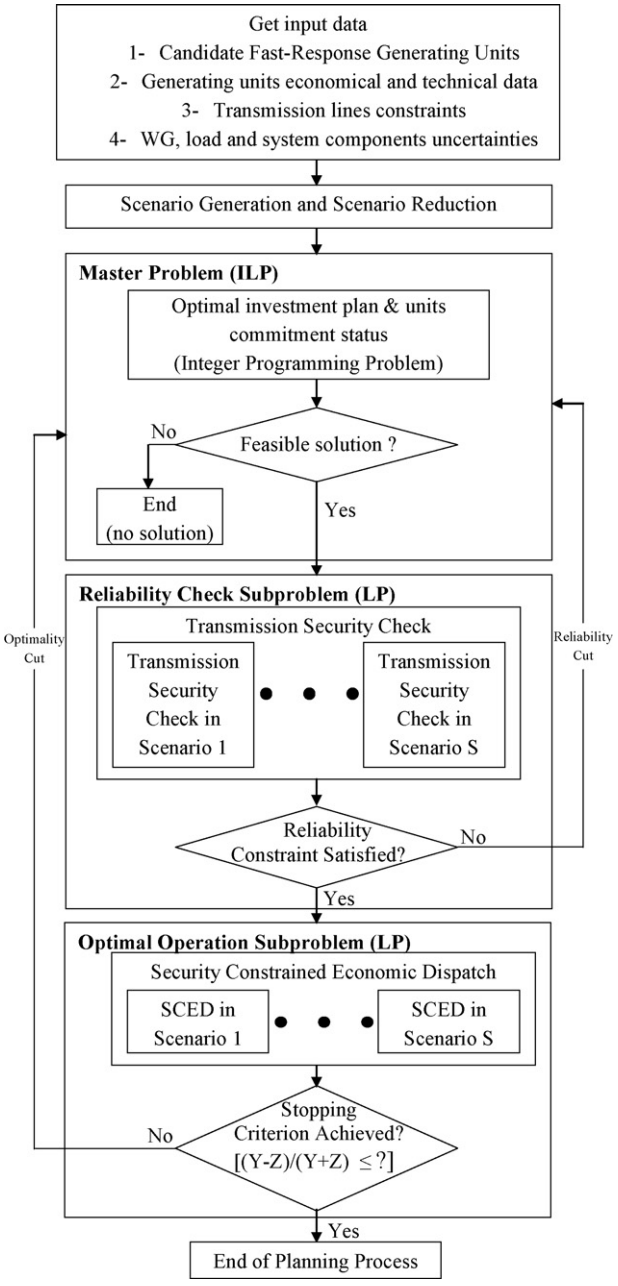


**Fig. 2.** Flowchart of the ISO's proposed planning problem.

## 4. Formulation and solution methodology

The ISO's proposed objective of security-constrained planning is to minimize the total cost of planning (1) while satisfying the planning and the operation constraints:

$$Y = \sum_{t=1}^{NT}\sum_{i=1}^{NG} \frac{PIC_{it}(GX_{it} - GX_{i(t-1)})}{(1+d)^{(t-1)}} + \sum_{s=1}^{NS} PR_s \sum_{t=1}^{NT}\sum_{h=1}^{NH}\sum_{i=1}^{NG} \frac{DT_{ht} PO_{iht} P_{ihts}}{(1+d)^{(t-1)}} \quad (1)$$

Fig. 2 depicts the flowchart of the decomposed planning problem. The solution steps are listed as follows:

Step 1 (scenario generation): We assume that the list of fast-response thermal units is provided by the participants as an input data to the ISO. The initial information provided to the ISO includes investment candidate units of individual participants, forced outages of generating units and transmission lines, as well as load and wind speed forecast errors. A set of scenarios is created using the Monte Carlo simulation. The stochastic long-term planning problem is inherently large. So, the scenario reduction is utilized to establish a tradeoff between the execution time and the accuracy of the long-term planning solution.

Step 2 (master problem): The proposed model consists of an MILP master problem and two LP subproblems. The master problem provides the optimal investment plan, while the subproblems provide the reliability check and the optimal market operation. The optimal investment plan is determined in the master problem, where the objective is to minimize the investment cost of new fast-response generating units (2).

$$Min\ Z$$

$$Z \geq \sum_{t=1}^{NT}\sum_{i=1}^{NG} \frac{PIC_{it}(GX_{it} - GX_{i(t-1)})}{(1+d)^{(t-1)}} \tag{2}$$

This objective is subject to planning constraints for new units, which include the construction time (3), the installation status (4), and the commitment state of such fast-response units (5):

$$GX_{it} = 0 \text{ if } t < CT_i \tag{3}$$

$$GX_{i(t-1)} \leq GX_{it} \tag{4}$$

$$I_{iht} \leq GX_{it} \tag{5}$$

The master problem solution consists of the optimal investment plan, commitment state of new units, and the lower bound of the planning objective function. At the first iteration there are no system constraints on commitment states of the units; so random values are assigned to these variables. However, in the subsequent iterations the Benders cuts from the reliability check and the optimal operation subproblems establish the constraints on the unit states. The proper initial values for $I$ could reduce the solution time. If an infeasibility problem occurs (i.e., no solution is found in Fig. 2), the ISO would consider preventive actions including load curtailments or the additional incentives provided to participants for extra capacity expansions.

Step 3 (reliability check subproblem): After determining the optimal plan, $G\hat{X}_{it}$, and commitment states, $\hat{I}_{iht}$, of generating units in the master problem, the reliability check subproblem will minimize the system violations based on the master solution. Slack variables are considered in the power balance constraint, where the objective (6) is to minimize these slack variables. The objective function (6) is subject to nodal power balance constraint (7), generating unit installation status (8), commitment states (9) which are determined in the master problem, generating limits (10), DC power flow (11), transmission lines limits (12), and ramping constraints (13) and (14):

$$Min \quad W_{ts}^{r} = \sum_{h=1}^{NH}\sum_{b=1}^{NB}(SL_{bhts,1}^{r} + SL_{bhts,2}^{r}) \tag{6}$$

S.t.

$$P_{hbts} - \sum_{j\in J_b} PL_{jbts} + SL_{bhts,1} - SL_{bhts,2} = PD_{bhts} \tag{7}$$

$$GX_{its} = G\hat{X}_{it} \quad \lambda_{its} \tag{8}$$

$$I_{ihts} = \hat{I}_{iht} \quad \mu_{ihts} \tag{9}$$

$$P_{\min,i} I_{iht} UX_{ihts} \leq P_{ihts} \leq P_{\max,i} I_{iht} UX_{ihts} \tag{10}$$

$$PL_{jhts} - \frac{\theta_{jmhts} - \theta_{jnhts}}{x_j} = (1 - U_{jhts})M \tag{11}$$

$$|PL_{jhts}| \leq PL_{\max,j} UY_{jhts} \tag{12}$$

$$P_{ihts} - P_{i(h-1)ts} \leq [1 - I_{ihts}(1 - I_{i(h-1)ts})]RU_i + I_{ihts}(1 - I_{i(h-1)ts})P_{\min,i} \tag{13}$$

$$P_{i(h-1)ts} - P_{ihts} \leq [1 - I_{i(h-1)ts}(1 - I_{ihts})]RD_i + I_{i(h-1)ts}(1 - I_{ihts})P_{\min,i} \tag{14}$$

The stochastic planning solution would satisfy the long-term reliability index, i.e., loss of energy probability (LOEP). A Benders cut at iteration $r$ is generated and the corresponding reliability signal is sent to the master problem when the LOEP at hour $h$ in year $t$ is larger than the target LOEP. LOEP is applied as a constraint to limit the amount of unsupplied hourly load. The yearly sum would satisfy the annual LOEP. However, the benefit of using the hourly index is that it would prevent any large-scale load shedding at certain hours. The LOEP at hour $h$ in year $t$ is calculated by dividing the expected generation deficit, $SL_{bhts,1}^{r}$, in (6) by the expected load at hour $h$ in year $t$. The reliability constraint in (15) would also enforce generation surplus, $SL_{bhts,2}^{r}$, to be zero. If either constraint in (15) is not satisfied, the Benders cut (16) will be generated:

$$\begin{cases} \sum_{h=1}^{NH}\sum_{b=1}^{NB} SL_{bhts,2}^{r} = 0 \\ \sum_{s=1}^{NS}\left(PR_s \sum_{b=1}^{NB} SL_{bhts,1}^{r}\right) \Big/ \sum_{s=1}^{NS}(PR_s L_{hts}) \leq \text{LOEP}_{ht} \end{cases} \tag{15}$$

$$\sum_{s=1}^{NS}(PR_s W_{ts}^{r}) + \sum_{s=1}^{NS}\sum_{i=1}^{NG} PR_s \lambda_{its}(GX_{its} - G\hat{X}_{it}) + \sum_{s=1}^{NS}\sum_{i=1}^{NG}\sum_{h=1}^{NH} PR_s \mu_{ihts}(I_{ihts} - \hat{I}_{iht}) \leq \sum_{s=1}^{NS}\sum_{h=1}^{NH} \text{LOEP}_{ht} \cdot PR_s \cdot L_{hts} \tag{16}$$

The Benders cut (16) represents the coupled information on the existing unit commitment state and the candidate unit installation status. The cut indicates that the violation can be mitigated by readjusting the master's investment plan in year $t$.

Step 4 (optimal operation subproblem): The objective of the optimal operation subproblem is to maximize the social welfare based on submitted bids for generation and demand. The social welfare is defined as the difference between consumption payments, based on accepted bids, and production costs. Security-constrained economic dispatch (SCED) is utilized to model the optimal operation subproblem which checks the optimality of the proposed solution.

When the power demand is inelastic, the objective function is to minimize the system cost for the given investment plan and the unit commitment state (17). In some scenarios, generating unit and transmission line outages can cause solution infeasibility. To calculate the price in such cases, imaginary generating units (IMP) are assumed to supply the deficient energy at high prices as represented below. The energy supplied by the IMPs represents the expected unsupplied energy (EUE):

$$Min \quad V_s^q = \sum_{t=1}^{NT}\sum_{h=1}^{NH}\sum_{i=1}^{NG}\frac{DT_{ht}PO_{iht}P_{ihts}}{(1+d)^{(t-1)}} + \sum_{t=1}^{NT}\sum_{h=1}^{NH}\sum_{b=1}^{NB}\frac{DT_{ht}IMC_{bht}IMP_{bhts}}{(1+d)^{(t-1)}} \tag{17}$$

S.t.

$$\sum_{i=1}^{NG}P_{ihbts} + \sum_{b=1}^{NB}IMP_{bhts} = \sum_{b=1}^{NB}PD_{bhts} \tag{18}$$

$$\mathbf{A}\cdot\mathbf{P} - \mathbf{B}\cdot\mathbf{PD} + \mathbf{IMP} \le \mathbf{K}\cdot\mathbf{PL} \tag{19}$$

$$0 \le IMP_{bhts} \quad \forall b \tag{20}$$

The optimal operation objective is subject to physical constraints, which are similar to the reliability check subproblem (8)–(14). The solution of this subproblem provides the upper bound of the objective function in the master problem. This upper bound is used to check the optimality of the solution. If the proposed plan is not optimal, the Benders cut (21) will be formed and added to the master problem for the next iteration.

$$Z \ge \sum_{s=1}^{NS}PR_sV_s^q + \sum_{t=1}^{NT}\sum_{i=1}^{NG}\frac{PIC_{it}(GX_{its} - GX_{i(t-1)s})}{(1+d)^{(t-1)}} + \sum_{s=1}^{NS}PR_s\sum_{t=1}^{NT}\sum_{i=1}^{NG}\lambda_{its}(GX_{its} - G\hat{X}_{it}) + \sum_{s=1}^{NS}PR_s\sum_{t=1}^{NT}\sum_{h=1}^{NH}\sum_{i=1}^{NG}\mu_{ihts}(I_{ihts} - \hat{I}_{iht}) \tag{21}$$

The important feature of the Benders decomposition is the availability of upper and lower bounds to the optimal solution at each iteration. These bounds are used as an effective convergence criterion. The convergence criterion is given as

$$\frac{Y-Z}{Y+Z} < \varepsilon \tag{22}$$

where $\varepsilon$ is a small positive number which shows the predefined threshold to accept the solution as optimal.

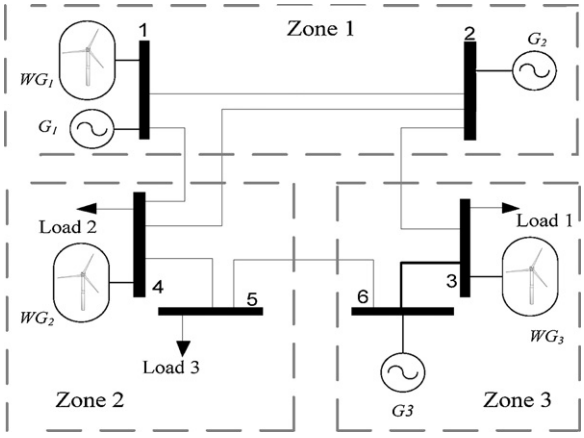


**Fig. 3.** Six-bus system.

**Table 1**
Existing generator data.

| Generator | Capacity (MW) | Ramp up/down (MW/h) | Operating cost coefficient ($/MWh) |
|---|---|---|---|
| $G_1$ | 250 | 20 | 13.5 |
| $G_2$ | 100 | 30 | 22.6 |
| $G_3$ | 50 | 20 | 17.6 |

## 5. Numerical simulations

In this section, two case studies are presented. In Section 6.1, different aspects of centralized and distributed WG expansion are investigated.

Two case studies consisting of a six-bus system and the IEEE 118-bus system are analyzed to illustrate the performance of the proposed method. The model is implemented on a 2.4-GHz server with a 64 GB of memory with the CPLEX solver. Using the six-bus system, centralized and distributed WG expansions are discussed. The IEEE 118-bus system is selected to investigate the effect of transmission constraints on the proposed expansion planning model. This study will consider the planning of fast-response thermal generating units for a given level of WG integration.

### 5.1. Six-bus system

This system is shown in Fig. 3 [31]. Based on wind speed forecasts, three wind zones are defined in the system with the WG capacity factors of 47%, 39% and 32%, respectively. The capacity factor of a WG is the ratio of the actual available wind power generation over a given period (e.g., 1 year) to its output if it had operated at full nameplate capacity the entire time. A 10-year planning horizon is considered for this study. The system data are given in Tables 1 and 2. The base-case annual peak load forecast is listed in Table 3. This load is distributed with the ratio of 50%, 30% and 20% among buses 3, 4 and 5, respectively. It is assumed that the load has the same distribution factor in the

**Table 2**
Transmission line data.

| Line number | From bus number | To bus number | Reactance (Ω) | Capacity (MW) |
|---|---|---|---|---|
| 1 | 1 | 2 | 0.17 | 200 |
| 2 | 2 | 3 | 0.137 | 100 |
| 3 | 1 | 4 | 0.258 | 100 |
| 4 | 2 | 4 | 0.197 | 100 |
| 5 | 4 | 5 | 0.137 | 100 |
| 6 | 5 | 6 | 0.14 | 100 |
| 7 | 3 | 6 | 0.118 | 100 |

**Table 3**
Forecasted annual peak load of six-bus system.

| Year | 1 | 2 | 3 | 4 | 5 | 6 | 7 | 8 | 9 | 10 |
|---|---|---|---|---|---|---|---|---|---|---|
| Peak load (MW) | 256 | 262 | 269 | 276 | 283 | 290 | 297 | 304 | 312 | 320 |

**Table 4**
Candidate fast-response generating units in six-bus system.

| Bus number | Capacity (MW) | Ramp up/down (MW/h) | Operating cost coefficient ($/MWh) | Investment cost (k$/MW) |
|---|---|---|---|---|
| 1 | 30 | 30 | 18.3 | 1050 |
| 2 | 30 | 30 | 20.9 | 959 |
| 3 | 30 | 30 | 22.5 | 847 |
| 4 | 30 | 30 | 24.55 | 780.5 |
| 5 | 30 | 30 | 26.4 | 700 |
| 6 | 30 | 30 | 28.1 | 577.5 |

entire planning period. The annual peak load forecast is the base load (i.e., 256 MW) times the annual growth rate (i.e., 2.5% per year). The random component of the peak load and energy demand growth rate is assumed to have a normal distribution with a zero mean and standard deviation of 0.01. The hourly load distribution factor and the hourly wind generation forecast are provided in http://motor.ece.iit.edu/data/6bus_Hourly_Data.xls.

Table 4 shows the candidate generating unit data. The hourly cost of wind generation is negligible. The WG capacity is 120 MW which is centralized (i.e., Case 1) and distributed (Cases 2–4). Five cases are studied as follows:

*Case 1*: Planning with WG centered at bus 1.
*Case 2*: Planning with WG distributed at buses 1, 3 and 4.
*Case 3*: WG in Case 2 with the outage of line 5–6 in year 8.
*Case 4*: WG in Case 2 with the outage of unit 3 in year 8.
*Case 5*: WG in Case 2 with the simultaneous outages in Cases 3 and 4.

*Case 1*: In this case, the proposed WG capacity is aggregated at bus 1 located in zone 1 with the best wind speed pattern. In this case a 120 MW WG with a capacity factor of 47% is added in the first year of planning period at bus 1. The shortcoming of such a plan is that large wind speed variations at bus 1 may not be compensated by other generating units. The proposed method is used to find the results shown in Table 5. WG and the cheaper existing unit 1 are committed at all hours while the existing unit 2 is used at peak hours to satisfy the remaining load and minimize the operating cost. The total investment and operating costs are $178.15M while the operating cost is $73.75M. In this case, at the beginning, the candidate unit 1 is installed at bus 1 and the candidate unit 3 is introduced at bus 3 which is the system's largest load center. The other three candidate units in Table 5 are added in later years when the WG capacity and loads are increased. Another significant deficit of such centralized solution could be the lack of enough transmission access [32].

*Case 2*: We disaggregate the WG capacity in Case 1 to represent three WG units located at different zones as depicted in Fig. 3. Each WG has a capacity of 40 MW and the WG capacity factor in the two remote areas, i.e., zones 2 and 3, are less than that in zone 1 (i.e., site in Case 1). Table 6 shows the candidate unit installation year. Similar to Case 1, candidate units 2 and 3 are installed in years 5 and 1, respectively. However, the installation of candidate unit 1 at bus 1 is delayed until year 7. The average generation of $WG_1$ located at bus 1 is 9 MW (i.e., 22.5% of $WG_1$ capacity) while there is no congestion on lines 1 and 3. The reason the low-cost $WG_1$ is dispatched below its capacity factor in some periods is the system ramping constraint. Therefore, after the installation of the fast-response unit in year 7, the average generation of $WG_1$ increases to 17 MW (i.e., 42.5% of $WG_1$ capacity). This amount is less than $WG_1$ capacity factor (i.e., 47%), which is due to transmission and operating constraints (i.e., thermal generating units min generation limit, system ramping and min on/off constraints, etc.). Compared to Case 1, the total investment and operating costs decrease to $142.91M while the operating cost increases to $80.07M.

**Table 5**
Candidate fast-response unit installation year: Case 1.

| Unit | 1 | 2 | 3 | 4 | 5 | 6 |
|---|---|---|---|---|---|---|
| Year | 1 | 5 | 1 | 5 | 7 | – |

**Table 6**
Candidate generating units installation year: Case 2.

| Unit | 1 | 2 | 3 | 4 | 5 | 6 |
|---|---|---|---|---|---|---|
| Year | 7 | 5 | 1 | – | – | – |

In Case 2 the total WG utilization decreases by 24% as compared to Case 1, which is because of the lower capacity factor in zones 2 and 3. A lower WG utilization would result in the dispatch of more expensive thermal units and the increase in operating costs. If we could set the capacity factor of zones 2 and 3 to be the same as that in zone 1 (i.e., 47%) the operating cost would decrease to $71.95M. Fig. 4 depicts operation and investment costs as a function of WG capacity. The initial point in Fig. 4 is associated with the current level of WG penetration. Here, the operation cost would decrease as the investment cost on fast-response generating units increases. Based on social cost results, it is concluded that the optimal increase in WG capacity is 20% (i.e., it would result in the minimum social cost).

While zones 2 and 3 have lower WG capacity factors, the dispersion of WG in the three locations would cause a significant decrease in the total cost and a more utilization of available low-cost WG. The reason for such cost reductions is that the intermittency of WG in one zone may be compensated by available WGs in the other zones. Accordingly, a smaller fast-response generation capacity would be needed for reliability purposes.

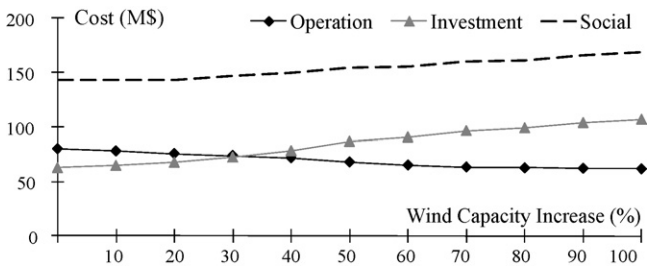


**Fig. 4.** System operation cost and fast-response unit investment cost vs. WG capacity.

**Table 7**
Candidate generating units installation year: Case 3.

| Unit | 1 | 2 | 3 | 4 | 5 | 6 |
|---|---|---|---|---|---|---|
| Year | 7 | 5 | 1 | 10 | 8 | – |

**Table 8**
Candidate generating units installation year: Case 4.

| Unit | 1 | 2 | 3 | 4 | 5 | 6 |
|---|---|---|---|---|---|---|
| Year | 7 | 5 | 1 | 8 | – | – |

*Case 3*: The outage of line 5–6 at the peak-load period in the year 8 is considered in this case. Similar to Case 2, the candidate generating units 3, 2 and 1 are installed in years 1, 5 and 7, respectively as shown in Table 7. In addition, as a preventive action, candidate units 5 and 4 are installed in years 8 and 10, respectively. The outage of line 5–6 decreases the transmission access between zones 2 and 3. Therefore, the addition of candidate units 4 and 5 would be necessary at zone 2. Compared to Case 2, the total cost has increased to \$163.65M.

*Case 4*: The outage of unit 3 in the peak-load period in the year 8 would change the plan proposed in Case 2. New generating units 3, 2 and 1 are again added in years 1, 5 and 7, respectively as shown in Table 8. In addition, the installation of candidate unit 4 in year 8 is a preventive action to compensate the possible outage of unit 3. This preventive action increases the planning cost to \$154.94M and the operating cost to \$80.08M.

**Table 9**
Candidate generating units installation year: Case 5.

| Unit | 1 | 2 | 3 | 4 | 5 | 6 |
|---|---|---|---|---|---|---|
| Year | 7 | 7 | 1 | 8 | 8 | – |

*Case 5*: Simultaneous outages of line 5–6 and generating unit 3 at peak and off-peak periods in the year 8 are considered respectively. Similar to previous cases, the candidate unit 1 is installed in year 1. Candidate units 4 and 5 are installed in the year 8 as shown in Table 9 to compensate the system's possible outage. The total cost increases to \$164.31M, which is the highest among all the cases, while the operating cost does not change significantly as compared to Cases 4 and 5.

### 5.2. IEEE 118-bus

A modified 118-bus system in Fig. 5 is used in this case. The test data and the single line diagram are provided in http://motor.ece.iit.edu/data/IEEE118bus_data_figure.xls. The system has 54 units, 186 branches, 14 capacitors, 9 tap-changing transformers, and 91 demand sides. The peak load of initial year is 3733 MW. The system is tested in a 10-year time horizon to

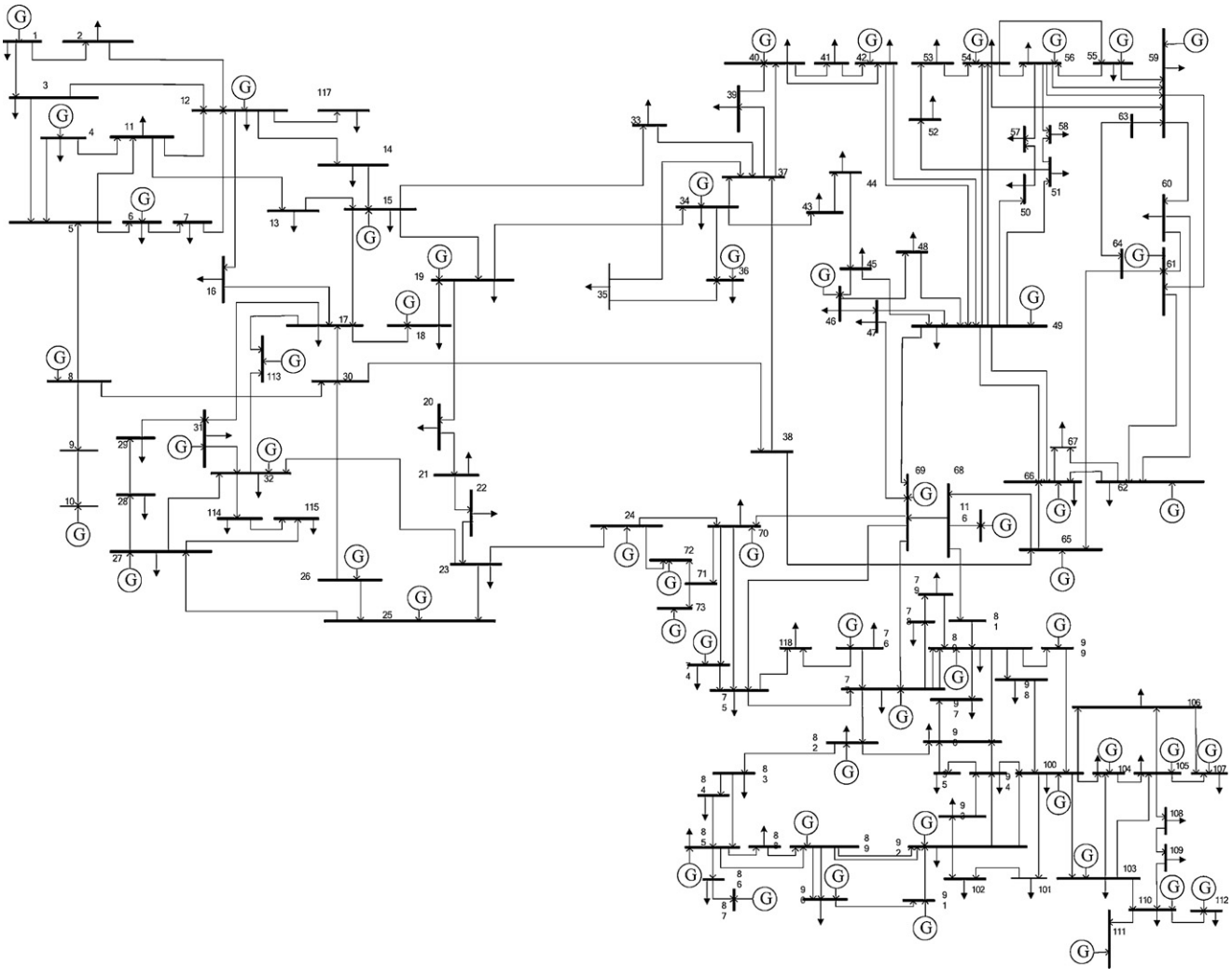

**Fig. 5.** One-line diagram of IEEE 118-bus system.

**Table 10**
WG data and network connection year.

| WG | Bus number | Capacity (MW) | Wind capacity factor (%) | Network connection year |
|---|---|---|---|---|
| 1 | 1 | 150 | 39 | 1 |
| 2 | 2 | 200 | 37 | 3 |
| 3 | 3 | 250 | 36 | 5 |
| 4 | 11 | 250 | 35 | 7 |
| 5 | 13 | 300 | 34 | 9 |

demonstrate the stochastic long-term planning solution. The average annual peak load growth rate is assumed to be 5%. The random component of the peak load and energy demand growth rate is assumed to have a normal distribution with a zero mean and standard deviation of 0.01. The discount rate is 10% which is used in the calculation of net present value of new generating units and the operating cost of existing units during the planning period. The convergence criterion $\varepsilon$ is 0.1%. The planning period includes hours in which the WG variation is significant. The target LOEP is 5% at all hours. Five WGs are to be connected to the grid, which is based on the predefined schedule given in Table 10. The candidate fast-response generating unit data are presented in Table 11.

The low-discrepancy Monte Carlo simulation method is used to create 1000 scenarios, each representing possible component outages, load forecast errors, and wind speed volatilities. The computation time for the scenario-based problem depends on the number of scenarios. Therefore, using the scenario reduction method, the number of scenarios is reduced from 1000 to 10 as a tradeoff between the computation time and the solution accuracy. Table 12 shows the scenario weights after the reduction. We consider four test cases categorized into deterministic (Cases 1 and 2) and stochastic (Case 3 and 4) cases as follows.

*Case 1*: Transmission-constrained deterministic case.
*Case 2*: Deterministic case without transmission constraints.
*Case 3*: Transmission-constrained stochastic case.
*Case 4*: Stochastic case without transmission constraints.

Table 13 shows the installation year of candidate units. In Case 3, the candidate unit 5 is installed in year 5 to handle uncertainties. Compared to Case 1, the candidate generating units 2 and 9 are installed a year earlier in Case 3. Additional fast-response generating unit would have to be installed earlier in the stochastic cases (Cases 3 and 4) as compared to the deterministic cases (Cases 1 and 2). This is because of the random outages of generation units and transmission lines as well as load and wind forecast errors.

Table 14 shows the planning and operating costs in four cases. The costs in Case 3 are higher than those in Case 1 by $43.287M and $2.871M, respectively. The costs are higher when uncertainties are considered as additional generating units and transmission lines would be installed. The operating and planning costs could be decreased when transmission constraints are relaxed (Cases 2 and 4). Here, the system can handle more WG variations if a sufficient transmission access is available. Therefore, a coordinated generation-transmission planning would be necessary for a high integration of WG.

The CPU time is about 5 h for one scenario in Case 3 (i.e., the most computationally intensive case). Table 15 lists the computation time for different convergence criteria. With the possible short-cuts introduced in Section 6, the CPU time could be further reduced to less than 2 h.

**Table 12**
Weight of each scenario after scenario reduction (%).

| Scenario | 1 | 2 | 3 | 4 | 5 | 6 | 7 | 8 | 9 | 10 |
|---|---|---|---|---|---|---|---|---|---|---|
| Weight | 5.3 | 0.1 | 0.1 | 0.1 | 61.2 | 3.9 | 4.4 | 0.1 | 5.0 | 19.8 |

**Table 13**
Candidate unit installation year.

| Unit number | 1 | 2 | 3 | 4 | 5 | 6 | 7 | 8 | 9 | 10 |
|---|---|---|---|---|---|---|---|---|---|---|
| Case 1 | 8 | 8 | 9 | – | – | 1 | 1 | 1 | 7 | 8 |
| Case2 | – | – | – | – | – | 1 | 1 | 6 | – | – |
| Case 3 | 8 | 7 | 9 | – | 5 | 1 | 1 | 1 | 6 | 8 |
| Case 4 | – | – | – | – | 5 | 1 | 1 | 6 | – | – |

**Table 14**
Total planning and operating costs.

| Case | Planning cost (billion$) | Operating cost (billion$) |
|---|---|---|
| Case 1 | 2.149 | 1.516 |
| Case 2 | 1.834 | 1.489 |
| Case 3 | 2.192 | 1.518 |
| Case 4 | 1.877 | 1.490 |

**Table 15**
Computation time for one scenario in each iteration.

| Convergence criterion value (%) | Computation time for one scenario (h) |
|---|---|
| 0.001 | 5.41 |
| 0.01 | 5.29 |
| 0.05 | 5.21 |
| 0.1 | 4.93 |
| 10 | 4.57 |

## 6. Discussions and conclusions

A stochastic planning method is proposed for the fast-response generating units in power systems with large WG integrations. In this paper, we assume that market participants would individually submit their candidate list of units to the ISO. It is the responsibility of the ISO to determine which candidates would violate the system reliability by considering the power system constraints. In this

**Table 11**
Candidate fast-response generating units in 118-bus system.

| Unit number | Bus number | Capacity (MW) | Ramp up/down (MW/h) | Operating cost coefficient ($/MWh) | Investment cost (Thousand $/MW) |
|---|---|---|---|---|---|
| 1 | 35 | 100 | 100 | 17.5 | 1050 |
| 2 | 41 | 100 | 100 | 18 | 945 |
| 3 | 45 | 100 | 100 | 18.5 | 840 |
| 4 | 60 | 100 | 100 | 19.5 | 735 |
| 5 | 75 | 100 | 100 | 20 | 630 |
| 6 | 94 | 150 | 150 | 13.5 | 945 |
| 7 | 95 | 150 | 150 | 14.5 | 875 |
| 8 | 96 | 150 | 150 | 15.5 | 770 |
| 9 | 98 | 150 | 150 | 16 | 665 |
| 10 | 118 | 150 | 150 | 16.5 | 595 |

paper, the ISO does not make any investments. Rather it maintains the reliability of the system. Although, the proposed expansion model is for fast-response units, the same approach can be utilized for the capacity expansion planning of any kind of generating units or transmission lines. The Monte Carlo simulation and the scenario reduction techniques are applied for representing the random outages of generating units and transmission lines, and load and wind speed forecast errors. Scenarios would add a dimension to the planning problem that could make the large-scale expansion planning problem more complex and computationally impractical. Hence, the Benders decomposition is utilized for the decomposition of the problem into tractable easy-to-solve subproblems at each period.

The numerical experiments show that the fast-response units can improve the reliability of power systems in the case of large integration of volatile WG. The merits of proposed stochastic approach include the provision of reliable decision signals to planners and regulators on the long-term capacity expansion planning. It is also observed that the transmission access has a significant impact on the generation expansion especially when there is a large wind integration. The results show that a coordinated generation-transmission planning can significantly improve the WG integration.

A few short-cuts are introduced to speed up the solution. These short-cuts are listed as follows:

- Limit the hours under study: power systems may not face large wind variations on the hourly basis. Wind variations at many hours may also be compensated by the existing generation redispatch. So, we could select certain hours for analyses at which the incremental wind generation in two subsequent hours is larger than a percentage of the generation at the given hours. To ensure the capacity adequacy, the peak load hours are always added to the study.
- Limit the committable units: generating units may be classified as always ON, always OFF and committable units [33]. Intrinsically, peak loads will utilize Always OFF units and base loads utilize Always ON units. We determine the status of committable units by iterations between the master and the subproblems.

## Appendix A. List of symbols

| | |
|---|---|
| $b$ | index of bus |
| $t$ | index of planning year |
| $h$ | index of subperiod |
| $i$ | index of generating unit |
| $j$ | index of transmission line |
| $s$ | index of scenario |
| $r$,$q$ | index of iteration number |

*Parameters and variables*

| | |
|---|---|
| $CT_i$ | construction time of candidate unit $i$ |
| $d$ | discount rate |
| $DT_{ht}$ | duration of subperiod $h$ in year $t$, e.g., 1 h |
| $Gx_{its}$ | installation status of generating unit $i$ in year $t$ and scenario $s$, 1 if installed, otherwise 0 |
| $I_{ihts}$ | commitment state of generating unit $i$ in subperiod $h$ of year $t$ in scenario $s$, 1 means on and 0 means off |
| $j_b$ | preserved set of branches connected to bus $b$ |
| $IMP_{bhts}$ | dispatched capacity of imaginary unit at bus $b$ in subperiod $h$ of year $t$ in scenario $s$ |
| $IMC_{bht}$ | cost of imaginary unit at bus $b$ in subperiod $h$ of year $t$ |
| $L_{hts}$ | load in subperiod $h$ of year $t$ in scenario $s$ |
| LOEP | target LOEP, reliability criterion |
| $NB$ | number of buses |
| $NT$ | number of years |
| $NG$ | number of generating units |
| $NH$ | number of subperiods |
| $NS$ | number of scenarios |
| $PIC_{it}$ | investment cost of unit $i$ at year $t$ |
| $PD_{bhts}$ | load at bus $b$ in subperiod $h$ at year $t$ in scenario $s$ |
| $PR_s$ | probability of scenario s |
| $PL_{jhts}$ | real power flow of transmission line $j$ in subperiod $h$ of year $t$ in scenario $s$ |
| $P_{ihts}$ | generation dispatch of unit $i$ in subperiod $h$ of year $t$ in scenario $s$ |
| $PO_i$ | operating cost of generating unit $i$ |
| $RU_i$, $RD_i$ | ramping up/down limit of unit $i$ |
| $SL^r_{bhts}$ | slack variable for bus b in subperiod $h$ of year $t$ in scenario $s$ |
| $UY_{jhts}$ | transmission lines availability status of transmission line $j$ subperiod $h$ of year $t$ in scenario $s$, 0 if in outage, otherwise 1 |
| $UX_{ihts}$ | generators availability status of unit $i$ in subperiod $h$ of year $t$ in scenario $s$, 0 if in outage, otherwise 1 |

*Matrices and vectors*

| | |
|---|---|
| **A** | bus-unit incidence matrix |
| **B** | bus-load incidence matrix |
| **IMP** | dispatched capacity of imaginary unit vector |
| **K** | bus-branch incidence matrix |
| **P** | real power output vector |
| **PD** | load vector |

## References


[1] Renewable Portfolio Standards in the United States, Lawrence Berkeley National Laboratory, 2008.
[2] J. Wang, M. Shahidehpour, Z. Li, Security-constrained unit commitment with volatile wind power generation, IEEE Trans. Power Syst. 23 (3) (2008) 1319–1327.
[3] A.G. Bakirtzis, P.S. Dokopoulos, Short term generation scheduling in a small autonomous system with unconventional energy sources, IEEE Trans. Power Syst. 3 (3) (1998) 1230–1236.
[4] E.S. Gavanidou, A.G. Bakirtzis, P.S. Dokopoulos, A probabilistic method for the evaluation of the performance of wind-diesel energy systems, IEEE Trans. Power Syst. 7 (3) (1992) 418–425.
[5] M. Bouzguenda, S. Rahman, Value analysis of intermittent generation sources from the system operations perspective, IEEE Trans. Energy Convers. 8 (3) (1993) 484–490.
[6] K.F. Schenk, S. Chan, Incorporation and impact of a wind energy conversion system in generation expansion planning, IEEE Trans. PAS PAS-100 (12) (1981) 4710–4718.
[7] R. Billinton, Y. Gao, R. Karki, Composite system adequacy assessment incorporating large-scale wind energy conversion systems considering wind speed correlation, IEEE Trans. Power Syst. 24 (3) (2009).
[8] H. Yu, C.Y. Chung, K.P. Wong, J.H. Zhang, A chance constrained transmission network expansion planning method with consideration of load and wind farm uncertainties, IEEE Trans. Power Syst. 24 (3) (2009) 1568–1576.
[9] T.Y. Lee, Optimal spinning reserve for a wind-thermal power system using EIPSO, IEEE Trans. Power Syst. 22 (4) (2007) 1612–1621.
[10] C.L. Chen, T.Y. Lee, R.M. Jan, Optimal wind–thermal coordination dispatch in isolated power systems with large integration of wind capacity, Energy Convers. Manage. 47 (18–19) (2006) 3456–3472.
[11] C.L. Chen, Optimal wind–thermal generating unit commitment, IEEE Trans. Power Syst. 23 (1) (2008) 273–279.
[12] C.L. Chen, T.Y. Lee, Impact analysis of transmission capacity constraints on wind power penetration and production cost in generation dispatch, in: Int. Conference on Intelligent Systems Applications to Power Systems, ISAP, 2007.
[13] J. Hetzer, D.C. Yu, K. Bhattarai, An economic dispatch model incorporating wind power, IEEE Trans. Energy Convers. 23 (2) (2008) 603–611.
[14] S.A. Farghal, M.R. Abdel Aziz, Generation expansion planning including the renewable energy sources, IEEE Trans. Power Syst. 3 (3) (1988) 816–822.
[15] H. Holttinen, et al., Design and operation of power systems with large amounts of wind power, IEA WIND Task 25, Phase one 2006-08 Final Report, 2009.
[16] Accommodating High Levels of Variable Generation, North American Electric Reliability Corporation (NERC), Special Report, 2009.
[17] Y. Fu, M. Shahidehpour, Z. Li, Security-constrained unit commitment with AC constraints, IEEE Trans. Power Syst. 20 (2) (2005) 1001–1013.
[18] V. Hamidi, F. Li, L. Yao, M. Bazargan, Domestic demand side management for increasing the value of wind, in: Int. Conf. on Electricity Distribution, CICED, 2008, pp. 1–10.

[19] L. Leclercq, C. Saudemont, B. Robyns, G. Cimuca, M.M. Radulescu, Flywheel energy storage system to improve the integration of wind generators into a network, in: Proc. of the 5th Int. Symp. on Advanced Electromechanical Motion Syst., vol. 2, 2003, pp. 641–646.
[20] V. Hamidi, F. Li, F. Robinson, Responsive demand in networks with high penetration of wind power, in: IEEE/PES Trans. and Dist. Conf. and Exp., 2008, pp. 1–7.
[21] S. Awerbuch, Portfolio-Based Electricity Generation Planning: Policy Implications for Renewable and Energy Security, Mitigation and Adaptation Strategies for Global Change 11 (3) (2006) 693–710.
[22] X. Liu, S. Islam, Reliability evaluation of a wind-diesel hybrid power system with battery bank using discrete wind speed frame analysis, in: Conf. on the Probabilistic Methods Applied to Power Systems, KTH, 2006.
[23] L. Wu, M. Shahidehpour, T. Li, Stochastic security-constrained unit commitment, IEEE Trans. Power Syst. 22 (2) (2007) 800–811.
[24] J.H. Roh, M. Shahidehpour, L. Wu, Market-based generation and transmission planning with uncertainties, IEEE Trans. Power Syst. 24 (3) (2009) 1587–1598.
[25] J. Dupačová, N. Gröwe-Kuska, W. Römisch, Scenario reduction in stochastic programming: an approach using probability metrics, Math. Program., Ser. A 95 (2003) 493–511.
[26] GAMS/SCENRED Documentation. http://www.gams.com/docs/document.htm.
[27] A.M. Geoffrion, Generalized benders decomposition, J. Optim. Theory Appl. 10 (4) (1972) 237–261.
[28] M. Shahidehpour, V. Ramesh, Nonlinear programming algorithms and decomposition strategies for OPF, in: IEEE/PES Tutorial on Optimal Power Flow, IEEE Press, Piscataway, NJ, 1996.
[29] H. Ma, M. Shahidehpour, Transmission constrained unit commitment based on benders decomposition, Electr. Power Energy Syst. 20 (4) (1998) 287–329.
[30] M. Shahidehpour, Y. Fu, Benders decomposition, IEEE Power Energy Mag. 3 (2) (2005) 20–21.
[31] Y. Fu, M. Shahidehpour, Z. Li, AC contingency dispatch based on security-constrained unit commitment, IEEE Trans. Power Syst. 21 (2) (2006) 897–908.
[32] R. Piwko, D. Osborn, R. Gramlich, G. Jordan, D. Hawkins, K. Porter, Wind energy delivery issues, IEEE Power Energy Mag. 3 (6) (2005).
[33] Y. Fu, M. Shahidehpour, Fast SCUC for large-scale power systems, IEEE Trans. Power Syst. 22 (4) (2007) 2144–2151.

Published in IET Generation, Transmission & Distribution
Received on 7th December 2009
Revised on 22nd February 2010
doi: 10.1049/iet-gtd.2009.0695

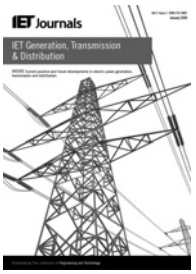

ISSN 1751-8687

# Generation expansion planning in wind-thermal power systems

*S. Kamalinia M. Shahidehpour*

*Electrical and Computer Engineering Department, Illinois Institute of Technology, Chicago, IL, USA*
*E-mail: ms@iit.edu*

**Abstract:** The intermittency and volatility of wind generation (WG) would require additional upward and downward reserves, as well as enhanced ramping capabilities in power systems. This study investigates the optimal expansion planning of fast-response generating capacity (e.g. gas-fired units) to accommodate the uncertainty of WG. The study utilises a mixed integer programming-based security-constrained unit commitment for analysing operational and reliability issues related to the proposed optimisation problem. Numerical experiments signify the effectiveness of the proposed method.

## Nomenclature

The symbols used in this paper are classified into indices, parameters and variables as follows.

### *Indexes*

| | |
|---|---|
| $t$ | index of planning time |
| $i$ | index of thermal unit |
| $g$ | index of gas-fired unit |
| $w$ | index of wind generator (WG) |
| cm | index of compressor |
| $s$ | index of scenario |

### *Parameters and variables*

| | |
|---|---|
| PO | operation cost of generating unit |
| PIC | investment cost |
| NT | number of times under study |
| NI | number of thermal generation units |
| NG | number of gas-fired units |
| NW | number of WGs |
| NS | number of scenarios |
| $I$ | unit commitment schedule vector |
| $F_i(\cdot)$ | fuel cost function of thermal generation unit |
| $F_g(\cdot)$ | operating cost function of gas-fired units |
| $F_w(\cdot)$ | operating cost function of WG |
| $P$ | generation dispatch of a unit |
| $GX_g$ | installation status of candidate gas-fired unit $g$, 1 if installed, otherwise 0 |
| wf | weighting factor (represents energy not served cost a percentage of social cost) |
| CENS | cost of energy not served |
| $a$, $b$, $c$ | coefficients of thermal unit cost function |
| $ga$, $gb$, $gc$ | gas consumption coefficients of compressor |
| $gc$ | cost of natural gas contract |
| $C_{\text{cm}}$ | cost of natural gas consumption of a compressor |
| HP | horsepower of compressor |
| $\rho_{\text{gas}}$ | price of natural gas |
| $f_{\text{gas}}$ | natural gas consumption of gas-fired unit |
| LS | amount of scheduled load shedding |
| EENS | expected energy not served |
| VOLL | value of lost load |
| PR($Z_s$) | individual probability of forced outage of $Z_s$ (MW) |
| $Z_s$ | load shedding in the $s$th contingency scenario |
| $\text{EC}_s$ | energy curtailed due to forced outage of $Z_s$ MW |
| $D$ | power system demand |
| GL | total generation capacity of power system |
| USR, DSR | system up/down spinning reserve requirement without the WG uncertainty |

| | |
|---|---|
| $ASR_U$, $ASR_D$ | coefficients of up/down spinning reserve due to the WG uncertainty |
| $US_{it}$, $DS_{it}$ | up/down spinning reserve of unit $i$ at time $t$ |
| $RU_i$, $RD_i$ | ramp up/down limit of unit $i$ |
| $d$% | percentage of unit capacity available for reserve |
| MSR | maximum sustained ramp rate (MW/min) |
| $X_{it}^{on}$, $X_{it}^{off}$ | period that unit $i$ has been on/off at time $t$ |
| $T_i^{on}$, $T_i^{off}$ | minimum up/down time of unit $i$ |
| $\kappa$, $\eta$ | Weibull's probability distribution function shape and scale parameter |
| $v$, $v_{CI}$, $v_{CO}$, $v_R$ | instantaneous, cut-in, cut-out and rated wind speed |
| $P_w^*$ | available WG power |
| PW | system's total WG |
| SRC | system total ramping capability |
| SRCD | system ramp down capability without gas-fired unit contribution |
| SRCU | system ramp up capability without gas-fired unit contribution |

# 1 Introduction

Wind generation (WG) emerges with new challenges in power systems. In practice, WG large forecasting errors are not uncommon [1, 2]. Therefore the volatile nature of WG would require a more sophisticated approach to the planning and operation of power systems [3, 4]. During the last decade, the capital cost of WG has substantially decreased, which has made WG a serious contender among generation resources [5, 6]. The environmental concerns have also persuaded governments to impose additional restrictions such as production tax credit (PTC) on carbon production and enhanced standards and initiatives such as renewable portfolio standard (RPS) and regional greenhouse gas initiative (RGGI) for expanding renewable energy generation [7].

The intermittent nature of WG would create a planning challenge for calculating the optimal size of reserve and generation ramping that could guarantee a reliable supply of load. The WG penetration could result in power system vulnerabilities, if ancillary services are not scheduled properly [3, 4]. The additional reserves must also be co-ordinated with ramping requirements in order to respond to WG interruptions quickly. Temporary solutions like the utilisation of storage systems or additional power exchanges with adjacent power systems have been considered. However, the most effective solution for responding to the volatility and intermittency of WG is the use of fast-response conventional generation systems for compensating the WG shortcomings [8].

Several publications have addressed the WG integration in power systems. The impact of large-scale WG on the scheduling of conventional generation is investigated when considering the operation cost and reliability of the system [8]. The impact of wind forecasting errors on power system operations is discussed in [1] by applying different unit commitment models. In [9] by applying the Monte-Carlo simulation, a security-constrained unit commitment algorithm has been developed that takes into account the intermittency and variability of wind power generation. An economic dispatch model was developed in [10] by applying genetic algorithm. The incorporation of wind energy conversion system in power system unit commitment and economic dispatch was discussed in [11]. A co-ordinated wind-thermal dispatch using direct search method was presented in [12]. A combination of branch and bound and dynamic programming algorithms was developed in [13] to model the co-ordinated economic dispatch of wind and thermal generation in isolated power systems. The impact of transmission capacity on the WG expansion was discussed in [14], which considered additional zonal reserves for an uncertain WG. The adequacy of power systems with WG was evaluated in [15]. A few articles investigated the utilisation of demand response for the reliability enhancement when considering the WG uncertainty [16–18]. The main problem with such approaches is that the amount of interruptible load is usually small as compared with drastic WG changes. However, very few articles considered power system operation issues in the WG expansion planning.

This paper presents a co-ordinated wind-thermal planning framework for managing hourly WG operation issues. We utilise fast-response generating units to respond to the unpredictability of WG. The quick-start and high ramping capability of fast-response generating units allows units to reach a maximum capacity in a short time. This is a NP-complete non-convex large-scale mixed-integer optimisation problem [19]. A mixed-integer linear programming (MILP) algorithm is utilised which presents attractive features, including short convergence time, simplicity of algorithm, linearity of constraints and ability to handle large-scale problems. In our proposed stochastic resource planning problem, each possible system state is represented by a scenario. The consideration of power system component outages and the WG volatility along with the load forecast uncertainty could results in a large number of scenarios. The number of scenarios would have a substantial impact on computational requirements. So, we determine a subset of scenarios and a probability measure based on this subset that is the closest to the initial probability distribution in terms of probability metrics.

The rest of this paper is organised as follows. Section 2 briefly introduces mathematical model of wind generators. Section 3 presents problem formulation and the objective function. Incorporation of WG in optimal scheduling model with the prevailing constraints is provided in Section 4. Stochastic planning is discussed in Section 5. Section 6

presents a numerical experiments and results. Lastly, in Section 7, the conclusions drawn from the studies are provided.

## 2 Mathematical model of wind generators

The wind speed distribution is modelled by the Weibull probability distribution function (PDF) [20–22] as

$$f(v) = \frac{\kappa}{\lambda}\left(\frac{v}{\lambda}\right)^{\kappa-1} \cdot \exp\left[-\left(\frac{v}{\lambda}\right)^{k}\right] \quad (\kappa > 0, v > 0, \lambda > 0) \quad (1)$$

We assume the WG volatility is subject to a Weibull PDF, that is, $f(v)$, where $k$ is the shape factor based on historical data and $\lambda$ is the scale factor which represents the forecasted WG.

Various methods for estimating Weibull's parameters are discussed in [23–25]. The power output of a wind turbine [26, 27] is given as

$$P_{\text{wt}}^{*} = \begin{cases} P_{\text{w}}^{\max}\dfrac{v^{\kappa} - v_{\text{CI}}^{\kappa}}{v_{R}^{\kappa} - v_{\text{CI}}^{\kappa}} & (v_{\text{CI}} \le v \le v_{\text{R}}) \\ P_{\text{w}}^{\max} & (v_{\text{R}} \le v \le v_{\text{CO}}) \\ 0 & (v < v_{\text{CI}} \text{ and } v > v_{\text{CO}}) \end{cases} \quad (2)$$

There is a small cost associated with WG operations. The market price of WG is determined based on bilateral contracts or locational marginal prices. Upper and lower WG are constrained by the physical characteristics of WG units as well as the optimal operation of power systems.

## 3 Mathematical formulation

The power system's objective (3) is to minimise the social cost (operating cost of existing generation units plus investment costs of new gas-fired units for catering to WG uncertainty). This objective is subject to unit and system constraints, including new unit installation status and commitment states (6) and (7), thermal and gas-fired unit cost function (8) and (9), fuel and compressor costs in gas-fired units (10) and (11), contingency condition (12)–(16), system constraints (17)–(19), generating unit physical constraints (20)–(29), WG constraints (30)–(33) and system ramping capability (34)–(36). The planned WG capacity is assumed to be known based on a given criterion such as the RPS plan.

### 3.1 Objective function

$$\text{Min PO} + \text{PIC} \quad (3)$$

such that

$$\text{PO} = \sum_{s=1}^{\text{NS}}\sum_{t=1}^{\text{NT}}\left\{\sum_{i=1}^{\text{NI}}[F_i(P_{its})I_{its}] + \sum_{g=1}^{\text{NG}}[F_g(P_{gts})I_{gts}] + \sum_{w=1}^{\text{NW}}[F_w(P_{wts})] + \text{wf} \times \text{CENS}_{ts}\right\} \quad (4)$$

$$\text{PIC} = \sum_{g=1}^{\text{NG}} IC_g P_{\max,g} GX_{gt} \quad (5)$$

$$GX_{g(t-1)} \le GX_{gt} \quad (6)$$

$$I_{gts} \le GX_{gt} \quad (7)$$

$$F_i(P_{it}) = a_i + b_i P_{its} + c_i P_{its}^2 \quad (8)$$

$$F_g(P_{gts}) = gc_{ts} + C_{\text{cm},ts} \quad (9)$$

$$gc_{ts} = \rho_{\text{gas},t} f_{\text{gas},gts} \quad (10)$$

$$C_{\text{cm},ts} = ga + gb\text{HP}_{\text{cm},s} + gc\text{HP}_{\text{cm},s}^2 \quad (11)$$

$$\text{CENS}_{ts} = \text{EENS}_{ts} \times \text{VOLL} \quad (12)$$

$$\text{EENS}_{t} \le \text{EENS}^{\max} \quad (13)$$

$$\text{EENS}_{t} = \sum_{s}(\text{PR}(Z_{ts})\text{EC}_{ts}) \quad (14)$$

$$\text{EC}_{ts} = \begin{cases} D_t - (GL_{ts} - Z_{ts}), & \text{when } D_{ts} > GL_{ts} - Z_{ts} \\ 0, & \text{otherwise} \end{cases} \quad (15)$$

$$\text{GL}_{ts} = \sum_{i=1}^{\text{NI}} P_{its}^{\max} + \sum_{g=1}^{\text{NG}} P_{gts}^{\max} + \sum_{w=1}^{\text{NW}} P_{wts}^{\max} \quad (16)$$

### 3.2 Power system constraints ($\forall t = 1, \ldots, DT$)

#### 3.2.1 Power balance constraint

$$\sum_{i=1}^{\text{NI}} P_{its} I_{its} + \sum_{g=1}^{\text{NG}} P_{gts} I_{gts} + \sum_{w=1}^{\text{NW}} P_{wts} = D_{ts} \quad (17)$$

Load shedding could be considered in the case of contingencies.

#### 3.2.2 System up/down spinning reserve requirements:

$$\sum_{i=1}^{\text{NI}} \text{US}_{its} I_{its} + \sum_{g=1}^{\text{NG}} \text{US}_{gts} GX_{gt} \ge \text{USR}_t + \text{ASR}_U\left(\sum_{w=1}^{\text{NW}} P_{wts}\right) \quad (18)$$

$$\sum_{i=1}^{\text{NI}} \text{DS}_{its} I_{its} + \sum_{g=1}^{\text{NG}} \text{DS}_{gts} I_{gts} \ge \text{DSR}_t + \text{ASR}_D\left(\sum_{w=1}^{\text{NW}} P_{w}^{\max} - \sum_{w=1}^{\text{NW}} P_{wts}\right) \quad (19)$$

Equations (18) and (19) indicate that the system would require hourly up/down spinning reserves for responding to WG uncertainties. Extra reserve requirements are in proportion



IET Gener. Transm. Distrib., 2010, Vol. 4, Iss. 8, pp. 940–951
doi: 10.1049/iet-gtd.2009.0695

to estimated hourly WGs, which are represented by $ASR_U$ and $ASR_D$ factors. Fast-response gas-fired generation units can enhance the system's up/down reserve requirements as discussed here. Theoretically, if the number of scenarios be large enough, then the reserve requirement can be neglected, that is, the reserve parameters (USR, DSR, $ASR_U$ and $ASR_D$) would take smaller values. However, in practice there is always a trade-off between accuracy and speed. Therefore here we considered a combination of scenario-based and regulatory reserve constrained models.

### 3.3 Thermal and gas-fired generating unit constraints

#### 3.3.1 Generation capacity limit

$$P_i^{\min} I_{its} \le P_{its} \le P_i^{\max} I_{its} \tag{20}$$

$$0 \le P_{gts} \le P_g^{\max} I_{gts} \tag{21}$$

#### 3.3.2 Up/down 10-min spinning reserve contribution

$$\mathrm{US}_{its} = \mathrm{Min}\{d\% \times P_i^{\max}, 10 \times \mathrm{MSR}_i, P_i^{\max} - P_{its}\} \tag{22}$$

$$\mathrm{DS}_{its} = \mathrm{Min}\{d\% \times P_i^{\max}, 10 \times \mathrm{MSR}_i, P_{its} - P_i^{\min}\} \tag{23}$$

#### 3.3.3 Ramping up/down constraints

$$P_{its} - P_{i(t-1)s} \le [1 - I_{its} \times (1 - I_{i(t-1)s})]\mathrm{RU}_{its} + I_{its}(1 - I_{i(t-1)s})P_i^{\min} \tag{24}$$

In (24) and (26), the assumption is that the thermal units can start-up/shutdown only at their minimum generation limit.

$$\mathrm{RU}_{its} = \mathrm{Min}\{\mathrm{RU}_i, P_i^{\max} - P_{its}\} \tag{25}$$

$$P_{i(t-1)s} - P_{its} \le [1 - I_{i(t-1)s} \times (1 - I_{its})]\mathrm{RD}_{its} + I_{i(t-1)s}(1 - I_{its})P_i^{\min} \tag{26}$$

$$\mathrm{RD}_{its} = \mathrm{Min}\{\mathrm{RD}_i, P_{its} - P_i^{\min}\} \tag{27}$$

#### 3.3.4 Minimum up/down time constraints

$$(X_{i(t-1)s}^{\mathrm{on}} - T_i^{\mathrm{on}}) \times (I_{i(t-1)s} - I_{its}) \ge 0 \tag{28}$$

$$(X_{i(t-1)s}^{\mathrm{off}} - T_i^{\mathrm{off}}) \times (I_{its} - I_{i(t-1)s}) \ge 0 \tag{29}$$

## 4 Wind generator constraints

WGs incur additional constraints to optimal scheduling problem. Three constraints could limit the available WG as follows:

1. Wind velocity (2)
2. System spinning reserve (32)
3. System maximum ramping capability (33)

$$0 \le P_{wts} \le P_{wts}^* \tag{30}$$

$$\mathrm{PW}_{ts} = \sum_{w=1}^{\mathrm{NW}} P_{wts} \tag{31}$$

Using (18) and (31), the system up-spinning reserve limit is linked with the maximum available WG as

$$\mathrm{PW}_{ts} \le \frac{\sum_{i=1}^{\mathrm{NI}} (\mathrm{US}_{its} I_{its}) + \sum_{g=1}^{\mathrm{NG}} \mathrm{US}_{gts} GX_{gt} - \mathrm{USR}_t}{\mathrm{ASR}_U} \tag{32}$$

The hourly system ramping capability is linked to the hourly change in the WG output as

$$|\mathrm{PW}_{ts} - \mathrm{PW}_{(t-1)s}| \le \mathrm{SRC}_{ts} \tag{33}$$

where (see (34))

and

$$\mathrm{SRCD}_{ts} = \sum_{i=1}^{\mathrm{NI}} [\mathrm{Min}(60 \times \mathrm{RD}_i, P_{i(t-1)s} - P_i^{\min})] \tag{35}$$

$$\mathrm{SRCU}_{ts} = \sum_{i=1}^{\mathrm{NI}} [\mathrm{Min}(60 \times \mathrm{RU}_i, P_i^{\max} - P_{i(t-1)s})] \tag{36}$$

Here $\Sigma P_{gs}$ is the total planning candidate gas-fired generation. $GX_{gt}$ is the decision variable for the required gas-fired generation to compensate WG deficiencies. Equation (35) forms a non-linear constraint. Therefore to keep the problem in linear conditions, this constraint is linearised by using auxiliary binary variables discussed in Section 10.1 (Appendix). The problem in (4)–(36) in addition to DC network security constraints provided in [28] is solved at all scenarios as explained in the following section.

$$\mathrm{SRC}_{ts} = \begin{cases} \mathrm{SRC}_{ts} + \sum_{g=1}^{\mathrm{NG}} P_{gs} GX_{gt}, & \text{if } \mathrm{PW}_{ts} \ge \mathrm{PW}_{(t-1)s} \\ \mathrm{SRCU}_{ts} + \sum_{g=1}^{\mathrm{NG}} (P_g^{\max} - P_{gts}) GX_{gt}, & \text{if } \mathrm{PW}_{ts} \le \mathrm{PW}_{(t-1)s} \end{cases} \tag{34}$$

## 5 Stochastic planning solution

The Monte-Carlo simulation along with a scenario reduction technique is applied to generate scenarios that simulate random characteristics of system components. The stochastic model is proposed which considers outages of generator and transmission system components as well as the uncertainty of load and available wind forecasts in the proposed scenarios. A set of possible scenarios is considered for modelling the uncertainties in the long-term planning problem. We assign a weight, PRs, to each scenario that would reflect the probability of the occurrence of the scenario. The WG planning would form a large-scale problem when considering operating constraints. Hence the Monte-Carlo simulation method is well-suited for such an application because the number of samples for a given accuracy level is independent of system size. A detailed formulation of Monte-Carlo approach for creating scenarios in power system operation with uncertainties can be found in [29, 30].

To address the volatility of WG, we assume the wind power is subject to a Weibull distribution, that is, $W(k, \lambda)$ where $k$ is the shape factor achieved from historical data and $\lambda$ is the scale factor which represents the forecasted WG. The Monte-Carlo simulation will generate a large number of scenarios subject to a Weibull distribution. A probability is assigned to each scenario, that is, one divided by the number of generated scenarios. In each scenario, an hourly random wind power generation is considered which is based on the forecasted wind power generation.

The simulation of power system component outages, volatility of WG and uncertainty of load forecast would result in a large number of scenarios. On the other hand, the large number of scenarios would have a substantial impact on the computational requirements of the scenario-based optimisation model. Therefore using an effective scenario reduction method would be very essential for large-scale systems [29]. The reduction technique would present a scenario-based approximation with a smaller number of scenarios for a reasonably good representation of the original system. So, we determine a subset of scenarios and a probability measure based on the subset that is the closest to the initial probability distribution in terms of probability metrics. A general algebraic modelling system (GAMS) is used in this study. GAMS provides a tool called SCENRED for scenario reduction. The scenario reduction algorithm provided by SCENRED determines a scenario subset (of prescribed cardinality or accuracy) and assigns optimal probabilities to the preserved scenarios [31].

## 6 Numerical results

In this section, two case studies are presented. In Section 6.1, different aspects of centralised and distributed expansion of WG are discussed. The purpose is to investigate the planning of fast-response gas-fired generation units to compensate WG uncertainties. In this paper, we assumed that market participants (e.g. GENCOs) already expressed their willingness to install new generation units by submitting the proposals to the ISO. Therefore ISO's role is to accept the proposals which benefit the system the most. In Section 6.2, a six-bus test system is selected to investigate the effect of network constraints on the proposed hybrid expansion planning. The spinning reserve parameters are $ASR_U = 20\%$, $ASR_D = 50\%$, $wf = 1$ and $VOLL = 1000$ \$/MWh. The WG parameters are $v_{CI} = 5$, $v_R = 15$ and $v_{CO} = 45$ m/s and the Weibull wind speed PDF is assumed to have $k = 2$ and $\lambda = 20$. Wind farms are assumed to operate with a negligible cost. In the following numerical experiments, the effect of gas transmission network is not considered. However, when the penetration of gas-fired units increases in the system, the impact of gas transmission network could be significant. This is the subject of our future research. The problem is coded in the GAMS with CPLEX 11.0 solver on a 2.4 GHz server computer with 64 GB memory.

### 6.1 Centralised and distributed wind models

The study period is one year with hourly simulations. The base-case load profile and the system data are given in Section 10.2 (Appendix). USR is assumed to be 10% of the load. The computation time for the scenario-based problem depends on the number of scenarios. The scenario reduction method would reduce the total number of scenarios from 100 to 10 as a trade-off between the solution speed and accuracy. Table 1 shows the weights of each scenario after reduction. The WG in power systems is simulated in four possible modes as follows.

*6.1.1 Centralised planning: Wind unit only planning:* WG expansion is concentrated in a limited area. The WG intermittency could result in higher load shedding if system reserves/ramping cannot accommodate large changes in WG. The other shortcoming of centralised investment could be the lack of large access to transmission capacity [32], which is beyond the scope of this discussion. Table 2 shows the simulation results for three different wind patterns in the zone without the addition of any gas-fired units. In this case, the installed wind capacity is 90 MW and the total thermal generation is 525 MW.

**Table 1** Weight of each scenario after scenario reduction

| Scenario | 1 | 2 | 3 | 4 | 5 | 6 | 7 | 8 | 9 | 10 |
|---|---|---|---|---|---|---|---|---|---|---|
| Weight, % | 5.1 | 0.1 | 0.1 | 0.1 | 61.2 | 4.1 | 6.9 | 0.1 | 4.8 | 17.5 |



*IET Gener. Transm. Distrib.*, 2010, Vol. 4, Iss. 8, pp. 940–951
doi: 10.1049/iet-gtd.2009.0695

**Table 2** Centralised WG without gas-fired generation expansion

| Capacity factor, % | Social cost, M$/year | |
|---|---|---|
| | With load shedding | Without load shedding |
| 39 | 46.81 | infeasible |
| 45 | 45.85 | infeasible |
| 55 | 44.4 | 44.4 |

The capacity factor of a WG is the ratio of the actual power generation over a given period to its output if it had operated at full nameplate capacity the entire time. In Table 2, when the WG capacity factor is not large enough the solution is infeasible because the gas-fired generation capacity is not increased accordingly. This is because the existing generation units cannot provide the required spinning reserve or the system ramping capability is not sufficient to accommodate the WG fluctuations. However, a higher WG capacity factor would offer a more robust power system. If the load shedding is allowed, a feasible solution is possible at higher operating costs.

*Combined wind and gas-fired unit planning:* To maintain a secure operation, the combined wind-thermal planning is investigated in a centralised case. The capacity factor of WG is 39%. In this case, there is an option of installing new gas-fired units to prevent emergency load shedding. One of the major challenges would be determining the optimal reserve and its associated gas-fired unit capacity. Fast-response units provide large ramping rates which enhance the SRC along with the available 10-min spinning reserve. On the other hand, the cost of these units is usually high (e.g. annualised investment cost of $100 k/MW is assumed). The stochastic solution provides a total objective value of $51.95 M/year. The social cost is higher than that of the previous case when the cost of gas-fired capacity expansion is considered. However, this extra cost would benefit the social welfare by not enforcing the service curtailment to the consumers. The gas-fired unit is installed on 24th June, which is the beginning of hot season with higher hourly demands. Furthermore, the WG output would experience more fluctuations in the summer months, that is, wind speed is smaller and there would be high possibility that the WG output falls to zero ($v < v_{CI}$).

### 6.1.2 Dispersed planning: *Wind unit only planning:*

WG farms located in a limited geographical area could increase the risk of power shortages at certain periods when the wind is not available. On the other hand, WG farms dispersed at several zones may impose additional financial risks if some of those locations possess a low quality wind. In such cases, local authorities may provide additional incentives to investors, such as easier transmission access or faster grid connection time, to encourage the dispersion of wind farms. Indeed, the diverged planning option would result in higher system reliability if the wind is more readily available at individual zones. Assume that there are three wind farms in separate zones, each with a capacity of 30 MW (total wind capacity is the same as that in the centralised case, see Section 6.1.1) and WG capacity factor in the two remote zones are 37 and 36% which are less than that in the local site (39%).

Fig. 1 depicts the average WG variation in a 24-hour period of the operation in aforementioned three zones. Comparing with the case in Section 6.1.1 (Wind unit only planning), someone would learn that wind shortages in one zone could be covered by those in other zones (e.g. in Fig. 1 wind speed is low at hour 11 in zone 1, whereas it is higher in zones 2 and 3). Therefore the probability of large WG deficits is reduced. The study results show that the social cost is $47.06 M/year and no gas-fired capacity expansion is needed. Despite the fact that the total capacity factor in remote zones are less than 39% (as was in the centralised zone), the cost decreases as compared to that in the centralised case. Therefore not only the WG capacity factor is an important factor in locating new wind farms, but also distance to the existing ones can significantly affect system reliability.

In another study, the available generation capacity is on outage by 20% and load shedding is considered at the cost of 1000 $/MWh. Here, the available thermal and WG capacity is higher than the peak-load of 503.42 MW and the social cost is $117.14M. This is because the available WG is significantly less than its rated value in most periods. The fast-response gas-fired generation is considered next.

*Combined wind and gas-fired unit planning:* As discussed in Section 6.1.2 (Wind unit only planning), when WG farms are dispersed geographically, the optimal solution may not require any gas-fired capacity expansions. However, the expansion of fast-response gas-fired units will provide spinning reserves and ramping requirements when considering the existing thermal unit outages. Table 3 shows the results of existing generation capacity outages. In Table 3, the larger rate of capacity outage would result

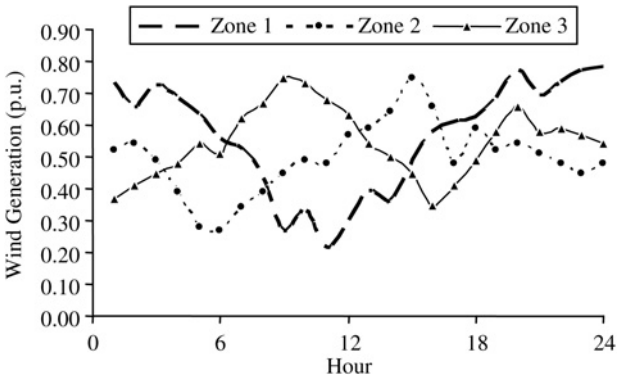


**Figure 1** *24-hour average WG in three zones*

**Table 3** Changes in social costs when resources are on outage

| Capacity outage | Gas-fired installation period, hours/month | Social cost, M$ |
|---|---|---|
| thermal by 20% | 212/January | 57.35 |
| thermal by 10% | 4096/May | 52.66 |
| thermal by 5% | 4910/July | 51.69 |

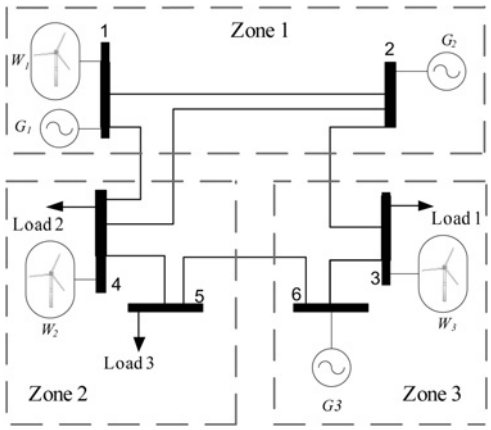


**Figure 2** *Six-bus system single diagram*

**Table 4** WGs expansion plan in six-bus test case system

| Bus number | WG capacity, MW | Grid connection time, year | Wind zone | Wind zone capacity factor, % |
|---|---|---|---|---|
| 1 | 80 | 1 | 1 | 45 |
| 4 | 60 | 3 | 2 | 40 |
| 3 | 40 | 5 | 3 | 35 |

in the earlier generation capacity expansion as well as higher social costs.

The wind speed pattern has a substantial impact on fast-response generation expansion. The generation capacity expansion needs to be enhanced when the WG capacity factor is less than expectation. If we decrease the capacity factor in the three zones to 30, 28 and 27%, respectively, generation expansion will occur at hour 4913 while the social cost increase to $53.05M.

**Table 6** Weights of each scenario after scenario reduction

| Scenario | 1 | 2 | 3 | 4 | 5 | 6 |
|---|---|---|---|---|---|---|
| Weight | 0.05 | 0.08 | 0.23 | 0.04 | 0.06 | 0.24 |
| Scenario | 7 | 8 | 9 | 10 | 11 | 12 |
| Weight | 0.05 | 0.045 | 0.045 | 0.015 | 0.045 | 0.1 |

## 6.2 Six-bus test case

This case demonstrates the effectiveness of the proposed approach for solving the optimal planning problem in a transmission-constrained power system. The optimal capacity of gas-fired generation units associated with the WG uncertainty is investigated. In addition, the impact of WG expansion on power system operation is studied. The system is shown in Fig. 2 [33] and the system data are provided in Section 10.3 (Appendix). The planning period is five years and WGs come into service at the beginning of each planning year according to the plan given in Table 4. The maximum load is 505 MW and the average load is 300 MW in the initial year of study, which is increased 5% annually in the base-case scenario. The candidate gas-fired generating units are given in Table 5. The scenario weights after reduction are shown in Table 6.

*6.2.1 Fast-response generating units requirement:* Table 7 summarises the generating unit installation schedule in the planning period. The earliest installed fast-response unit is unit 4. This unit shows a balance of investment and operating costs. Furthermore, this generation unit is located at load bus 4 where WG 2 is installed in year 4. However, with an increase in WG penetration and transmission capacity limitations, extra fast-response units are installed in the last planning year. The candidate generation unit 6 is installed at bus 6

**Table 5** Candidate fast-response gas-fired generation units

| Bus number | Capacity, MW | Investment cost, k$/MW/year | Operating cost, k$/MWh | MSR, MW/min | Ramp up/down, MW/h | *d*% |
|---|---|---|---|---|---|---|
| 1 | 50 | 65 | 15 | 8 | 100 | 80 |
| 2 | 50 | 60 | 18 | 8 | 100 | 80 |
| 3 | 50 | 55 | 18 | 8 | 100 | 80 |
| 4 | 50 | 50 | 21 | 8 | 100 | 80 |
| 5 | 50 | 45 | 23 | 8 | 100 | 80 |
| 6 | 50 | 40 | 24 | 8 | 100 | 80 |




doi: 10.1049/iet-gtd.2009.0695

**Table 7** Generating units installation time

| Unit | 1 | 2 | 3 | 4 | 5 | 6 |
|---|---|---|---|---|---|---|
| Hour (year/month) | 40 357 (5/August) | — | 39 974 (5/July) | 31 213 (4/July) | – | 39 973 (5/July) |

in the summer of year 5. At the same time, candidate unit 3 is added to the load bus 3. In addition, candidate unit 1 is installed at bus 1 where the largest WG is located. The major reason for adding this gas-fired unit at a later period, while it has the lowest operating cost, is that the bus 1 in zone 1 has a favourable wind speed, which would reduce the necessity of adding fast-response unit.

*6.2.2 Sensitivity analysis of spinning reserve and social cost:* In Table 7, the fast-response units are installed to compensate the WG uncertainty which would increase the required spinning reserve capacity. The experiments demonstrate changes in system parameters as a result of WG capacity expansion. Fig. 3 depicts variations in average up/down spinning reserve requirements when WG penetration increases. Here the base case (Section 6.2.1) represents zero percent wind capacity increase. $ASR_D$ is assumed to be larger than $ASR_U$, so the down spinning reserve is more influenced by the WG penetration. Hence, the down spinning reserve variation curve has a larger gradient as compared to that of the up-spinning reserve.

Increase in WG penetration would change reserve requirements and consequently affects generation scheduling. Different approaches used in literatures aimed to obtain optimal reserve requirements [34–36]. However, determining optimal amount of reserve requirements which consider

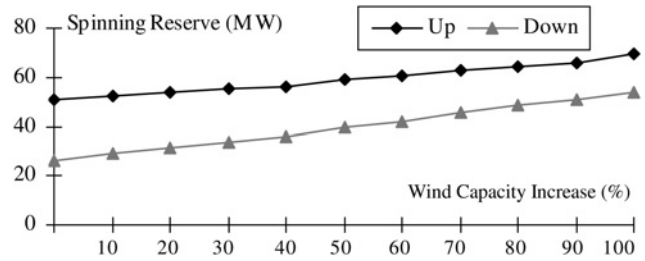


**Figure 3** *Average Up/down spinning reserve by increasing the WG capacity*

security and economy of the system is still an open question. This deserves to be the subject of a separate paper, especially when there is large wind power penetration in the system. Based on the proposed approach, the amount of reserve requirement is directly influenced by $ASR_U$ and $ASR_D$ parameters. Therefore finding optimal values of these parameters would be essential. Fig. 4 depicts variation of the production, energy not served (ENS) and total operating (OP) costs when reserve parameter change. As the study shows, the minimum operating cost is obtained when $ASR_U = 1.1$ (i.e. roughly 5.5 times the wind to thermal installed capacity ratio). In the similar study, minimum OP is obtained when $ASR_D = 2$ (i.e. roughly 10 times the wind to thermal installed capacity ratio). However, the value of these parameters may change in different systems and with various wind speed pattern.

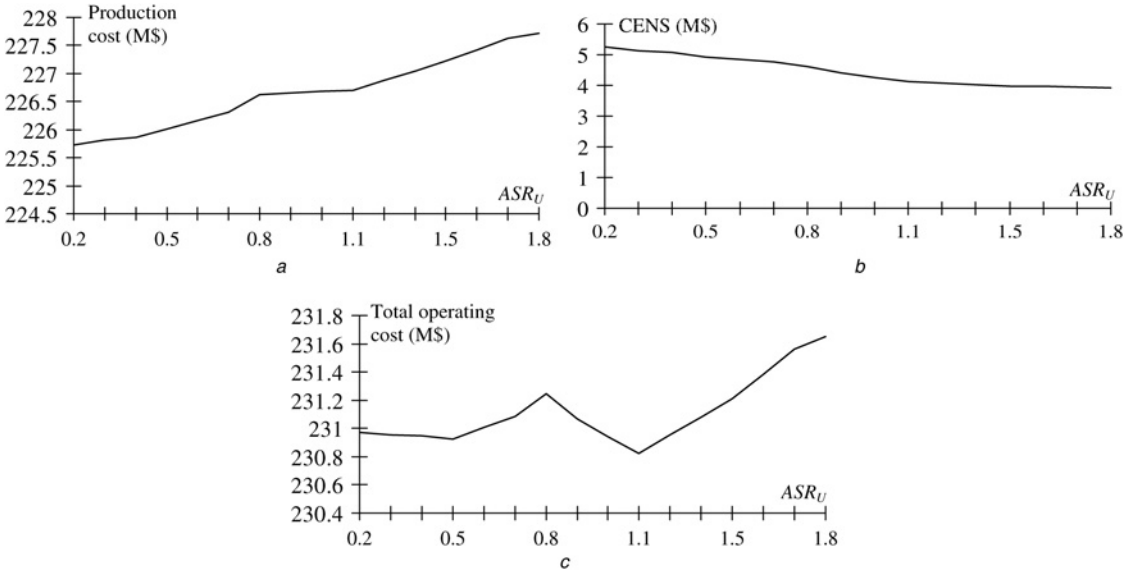


**Figure 4** *The effect of the variation of reserve parameter on system costs*

*a* Production
*b* ENS
*c* Total operation costs variation for change of $ASR_U$

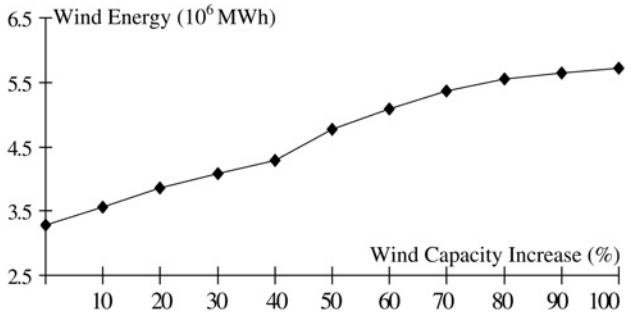


**Figure 5** *WG variation by increasing the WG capacity*

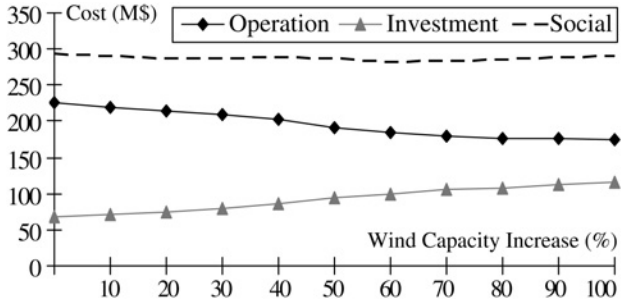


**Figure 6** *Cost variations by increasing the WG capacity*

Fig. 5 shows the WG (MWh) addition as a result of the WG capacity (MW) expansion. However, the WG gradient decreases gradually since the system reserve and ramping capability would constrain WG. On the other hand, system may not have the capability (reserve, ramping etc.) of absorbing the whole available WG when the wind penetration is significant. Hence, fast-response units are installed when WG capacity increases by 40%. However, WG cannot increase further when the WG capacity is increased beyond 80% which is due to transmission constraints.

In Fig. 6, operation costs decrease by increasing the WG capacity. On the other hand, fast-response units are installed at additional costs to compensate the WG uncertainty. Therefore the optimal social cost provides planners with a trade-off for the optimal WG capacity expansion. In this case, the minimum social cost is \$282.72M which is achieved when the WG capacity increases by 60%.

# 7 Conclusions

A stochastic model for long-term generation scheduling problem is proposed in this paper. Scenario-based approach along with modified reserve and ramping constraints are modelled considering trade-off between accuracy and calculation time. Fast-response generating unit expansion is considered to alleviate WG uncertainty impacts on system reliability.

In many countries, the expansion planning of renewable energy resources is usually based on pre-scheduled or regulatory plans. We assume the WG expansion plan is given, and utilise gas-fired units as candidates to cater to the volatility and intermittency of WGs. The proposed long-term scheduling considers operating issues (e.g. system reserves and ramping of thermal units) for enhancing the system reliability. The fast-response units are costly and may contribute to emission. The optimal size and type of these units are determined in the proposed approach. Case studies showed the effectiveness of the proposed model and the effects of system component outages and load and WG uncertainties on generation capacity expansion plans and costs. Numerical experiments showed that fast-response units can improve the reliability of power systems with a large penetration of volatile WG, especially in the limited geographical area. The size of the problem becomes too large when considering detailed operation constraints, and the calculation time would increase. In such cases, proper simplifications, for example, decomposition methods or parallel simulation can be utilised for large system solutions.

# 8 Acknowledgments

This work is supported in part by the US Department of Energy grant number DE-EE 0001380.000 and the US National Science Foundation grant number NSF ECCS-0801853.

# 9 References

[1] WANG J., BOTTERUD A., MIRANDA V., MONTEIRO C., SHEBLE G.: 'Impact of wind power forecasting on unit commitment and dispatch'. 8th Int. Workshop on Large-Scale Integration of Wind Power into Power Systems, Bremen, Germany, 2009

[2] BOTTERUD A., WANG J., MONTEIRO C., MIRANDA V.: 'Wind power forecasting and electricity market operations'. The 32nd IAEE Int. Conf., San Francisco, California, 2009

[3] BAKIRTZIS A.G., DOKOPOULOS P.S.: 'Short term generation scheduling in a small autonomous system with unconventional energy sources', *IEEE Trans. Power Syst.*, 1988, **3**, (3), pp. 1230–1236

[4] GAVANIDOU E.S., BAKIRTZIS A.G., DOKOPOULOS P.S.: 'A probabilistic method for the evaluation of the performance of wind–diesel energy systems', *IEEE Trans. Power Syst.*, 1992, **7**, (3), pp. 418–425

[5] BERRY D.: 'Innovation and the price of wind energy in the US', *Energy Policy*, 2009, **37**, (11), pp. 4493–4499

[6] KIRBY B., MILLIGAN M.R.: 'Facilitating wind development: the importance of electric industry structure', *Electr. J.*, 2008, **21**, (3), pp. 40–54




doi: 10.1049/iet-gtd.2009.0695

[7] PLATTS J.E.: 'Impact of regional greenhouse gas initiative and renewable portfolio standards on power system planning'. Power Engineering Society General Meeting, 2006

[8] UMMELS B.C., GIBESCU M., PELGRUM E., KLING W.L., BRAND A.J.: 'Impacts of wind power on thermal generation unit commitment and dispatch', *IEEE Trans. Energy Convers.*, 2007, **22**, (1), pp. 44–51

[9] WANG J., SHAHIDEHPOUR M., LI Z.: 'Security-constrained unit commitment with volatile wind power generation', *IEEE Trans. Power Syst.*, 2008, **23**, (3), pp. 1319–1327

[10] YONG L., TAO S.: 'Economic dispatch of power system incorporating international wind power plant'. Power Engineering Conf. (IPEC), 2007, pp. 159–162

[11] SCHLUETER R.A., PARK G.L., LOTFALIAN M., SHAYANFAR H., DORSEY J.: 'Modification of power system operation for significant wind generation penetration', *IEEE Trans. Power Appar. Syst.*, 1983, **102**, (1), pp. 153–161

[12] CHEN C.L., LEE T.Y., JAN R.M.: 'Optimal wind–thermal co-ordination dispatch in isolated power systems with large integration of wind capacity', *Energy Convers. Manage.*, 2006, **47**, (18), pp. 3456–3472

[13] CHEN C.L.: 'Optimal wind–thermal generating unit commitment', *IEEE Trans. Power Syst.*, 2008, **23**, (1), pp. 273–279

[14] CHEN C.L., LEE T.Y.: 'Impact analysis of transmission capacity constraints on wind power penetration and production cost in generation dispatch'. Int. Conf. Intelligent Systems Applications to Power Systems, ISAP, 2007

[15] BILLINTON R., BAI G.: 'Generating capacity adequacy associated with wind energy', *IEEE Trans. Power Syst.*, 2004, **9**, (3), pp. 641–646

[16] GOEL L., WU Q., WANG P.: 'Reliability enhancement of a deregulated power system considering demand response'. IEEE/PES General Meeting, 2006

[17] HAMIDI V., LI F., ROBINSON F.: 'Responsive demand in networks with high penetration of wind power'. IEEE/PES Transmission and Distribution Conf. and Exposition, 2008, pp. 1–7

[18] HAMIDI V., LI F., YAO L., BAZARGAN M.: 'Domestic demand side management for increasing the value of wind'. Int. Conf. Electricity Distribution, CICED, 2008, pp. 1–10

[19] FU Y., SHAHIDEHPOUR M., LI Z.: 'Security-constrained unit commitment with AC constraints', *IEEE Trans. Power Syst.*, 2005, **20**, (2), pp. 1001–1013

[20] PAPAEFTHYMIOU G., KLÖCKL B.: 'MCMC for wind power simulation', *IEEE Trans. Energy Convers.*, 2008, **23**, (1), pp. 234–240

[21] ALHUSEIN M.A., ABU-LEIYAH O., INAYATULLAH G.A.: 'Combined system of renewable energy for grid-connected advanced communities', *J. Renew. Energy*, 1993, **3**, (6), pp. 563–566

[22] JOHNSON G.L.: 'Wind energy systems' (Prentice-Hall, 1985)

[23] PATEL M.R.: 'Wind and solar power systems' (FL CRC Press, Boca Raton, 1999)

[24] JUSTUS C.G., HARGRAVES W.R., MIKHAIL A., GRABER D.: 'Methods for estimating wind speed frequency distributions', *J. Appl. Meteorol.*, 1978, **17**, (3), pp. 350–353

[25] SEGURO J.V., LAMBERT T.W.: 'Modern estimation of the parameters of the Weibull wind speed distribution for wind energy analysis', *J. Wind Engng. Ind. Aerodyn.*, 2000, **85**, (1), pp. 75–84

[26] BOROWY B.S., SALAMEH A.M.: 'Optimum photovoltaic array size for a hybrid wind/PV system', *IEEE Trans. Energy Convers.*, 1994, **9**, (3), pp. 482–488

[27] GAVANIDOU E.S., BAKIRTZIS A.G.: 'Design of a standalone system with renewable energy sources using trade-off methods', *IEEE Trans. Energy Convers.*, 1992, **7**, (1), pp. 42–48

[28] SHAHIDEHPOUR M., YAMIN H., LI Z.: 'Market operations in electric power systems' (Wiley, New York, 2002)

[29] WU L., SHAHIDEHPOUR M., LI T.: 'Stochastic security-constrained unit commitment', *IEEE Trans. Power Syst.*, 2007, **22**, (2), pp. 800–811

[30] DUPAČOVÁ J., GRÖWE-KUSKA N., RÖMISCH W.: 'Scenario reduction in stochastic programming an approach using probability metrics', *Math. Program.*, 2003, **95**, pp. 493–511

[31] GAMS/SCENRED Documentation. Available at www.gams.com/docs/document.htm

[32] JACOBBS M.B.: 'Transmission recommendations for high wind penetration'. Power Engineering Society General Meeting, 2007

[33] FU Y., SHAHIDEHPOUR M., LI Z.: 'AC contingency dispatch based on security-constrained unit commitment', *IEEE Trans. Power Syst.*, 2006, **21**, (2), pp. 897–908

[34] GOOI H.B., MENDES D.P., BELL K.R.W., KIRSCHEN D.S.: 'Optimal scheduling of spinning reserve', *IEEE Trans. Power Syst.*, 1999, **14**, (4), pp. 1485–1490

[35] WANG J.X., WANG X.F., WU Y.: 'Operating reserve model in the power market', *IEEE Trans. Power Syst.*, 2005, **20**, (1), pp. 223–229

[36] ORTEGA-VAZQUEZ M.A., KIRSCHEN D.S.: 'Estimating the spinning reserve requirements in systems with significant wind power generation penetration', *IEEE Trans. Power Syst.*, 2009, **24**, (1), pp. 114–124

# 10 Appendix

## 10.1 Linearising non-linear constraint using auxiliary binary variables

Equation (34) represents a non-linear conditional constraint which is modelled in MILP by using an auxiliary integer variable approach presented in Table 8. Table 8 shows that (34) conditional non-linear constraints can be modelled by linear constraints as follows

$$\mathrm{PW}_t - \mathrm{PW}_{t-1} \le (m-\varepsilon)\delta + \varepsilon \tag{37}$$

$$\mathrm{SCR}_t - \mathrm{SRCU}_t - \sum_{g=1}^{\mathrm{NG}} (P_g^{\max} - P_{gt}) \le M(1-\delta) \tag{38}$$

$$\mathrm{SCR}_t - \mathrm{SRCU}_t - \sum_{g=1}^{\mathrm{NG}} (P_g^{\max} - P_{gt}) \ge m(1-\delta) \tag{39}$$

**Table 8** MILP representation of conditions

| # | Condition | Represented by |
|---|---|---|
| 1 | $\sum_j a_j x_j \le b \rightarrow \delta = 1$ | $\sum a_j x_j - (m-\varepsilon)\delta \ge b + \varepsilon$ |
| 2 | $\delta = 1 \rightarrow \sum_j a_j x_j = b$ | $\sum a_j x_j + M\delta \le M + b$ |
| | | $\sum a_j x_j + m\delta \ge m + b$ |
| 3 | $\sum_j a_j x_j \ge b \rightarrow \delta = 0$ | $\sum a_j x_j + (M+\varepsilon)\delta \le M + b$ |
| 4 | $\delta = 0 \rightarrow \sum_j a_j x_j = b$ | $\sum a_j x_j - M\delta \le b$ |
| | | $\sum a_j x_j - m\delta \ge b$ |

**Table 9** Generation data

| Unit type | Capacity, MW | Ramp-up/ down, MW/h | MSR, MW/min | *d*% | Levelised investment cost, k$/MW/year | FOR, % |
|---|---|---|---|---|---|---|
| thermal | 525 | 180 | 6 | 50 | existing unit | 5 |
| gas | 100 | 300 | 10 | 40 | 100 | 5 |
| wind | 90 | 90 | 0 | 0 | existing unit | 0 |

**Table 10** Load profile

| Months | Total, GWh | Average, MW | Peak, MW |
|---|---|---|---|
| January | 239.45 | 321.42 | 413.74 |
| February | 209.82 | 312.23 | 403.81 |
| March | 223.62 | 300.56 | 388.47 |
| April | 196.62 | 273.09 | 351.59 |
| May | 204.82 | 275.29 | 394.36 |
| June | 226.82 | 315.02 | 466.41 |
| July | 228.14 | 306.63 | 499.66 |
| August | 249.26 | 335.02 | 503.42 |
| September | 208.97 | 292.11 | 429.61 |
| October | 208.16 | 279.78 | 359.77 |
| November | 203.43 | 283.05 | 377.92 |
| December | 222.98 | 299.70 | 414.55 |

**Table 11** Six-bus system generation data

| Bus number | Capacity, MW | Ramp up/ down, MW/h | MSR, MW/ min | *d*% | FOR, % |
|---|---|---|---|---|---|
| 1 | 180 | 60 | 2 | 50 | 5 |
| 2 | 130 | 60 | 2 | 50 | 5 |
| 6 | 100 | 60 | 2 | 50 | 5 |

**Table 12** Six-bus system transmission data

| Line number | From bus | To bus | Reactance, Ω | Capacity, MW |
|---|---|---|---|---|
| 1 | 1 | 2 | 0.17 | 130 |
| 2 | 2 | 3 | 0.037 | 120 |
| 3 | 1 | 4 | 0.258 | 170 |
| 4 | 2 | 4 | 0.197 | 140 |
| 5 | 4 | 5 | 0.037 | 100 |
| 6 | 5 | 6 | 0.14 | 170 |
| 7 | 3 | 6 | 0.018 | 160 |




doi: 10.1049/iet-gtd.2009.0695

$$\mathrm{PW}_t - \mathrm{PW}_{t-1} \leq M - (m + \varepsilon)\delta \tag{40}$$

$$\mathrm{SCR}_t - \mathrm{SRCD}_t - \sum_{g=1}^{\mathrm{NG}} P_{gt} \leq M\delta \tag{41}$$

$$\mathrm{SCR}_t - \mathrm{SRCD}_t - \sum_{g=1}^{\mathrm{NG}} P_{gt} \geq m\delta \tag{42}$$

where $M$ is an upper bound and $m$ is a lower bound for the expression $(\Sigma_j a_j x_j - b)$ and $\varepsilon$ is a small tolerance value.

## 10.2. Data for centralised and distributed cases

Generation data and load profile are given in Tables 9 and 10.

## 10.3 Six-bus system data

Six-bus system data are given in Tables 11 and 12.

# Integration of High Reliability Distribution System in Microgrid Operation

Mohammad E. Khodayar, *Member, IEEE*, Masoud Barati, Mohammad Shahidehpour, *Fellow, IEEE*

***Abstract*— In this paper, the application of high reliability distribution system (HRDS) in the economic operation of a microgrid is studied. HRDS, which offers higher operation reliability and fewer outages in microgrids, is applied to looped networks in distribution systems. The microgrid model in this study is composed of distributed energy resources (DER) including distributed generation (DG), controllable loads, and storage. The microgrid would utilize the local DER as well as the main grid for supplying its hourly load economically which is subject to power quality and reliability requirements. The HRDS implemented at Illinois Institute of Technology (IIT) is used as a case study along with the local DER to increase the load point reliability and decrease the operation cost of the IIT microgrid. The availability of distribution lines, main grid supply, and microgrid generation is considered using the Markov chain Monte Carlo simulation in the microgrid scenarios. The reliability indices based on frequency and duration of outages are measured at the microgrid level and the load point level, and the potential system enhancements are discussed for improving the economic operation of the IIT microgrid.**

***Index Terms*— Microgrid economics, high reliability distribution system, storage, stochastic security constrained unit commitment**

## NOMENCLATURE

### Variables

| | |
|---|---|
| $E_{k,t}^{(.)}$ | Available energy in storage unit *k* at time *t* |
| $F_{c,(.)}$ | Production cost function of a DG unit |
| $g$ | Denote the main grid connection |
| $i$ | Denote a DG unit |
| $k$ | Denote a storage unit |
| $I_{(.)}^{(.)}$ | Unit status; 1 means on and 0 means off |
| $I_{c,(.)}^{(.)}$ | Indicator of storage unit in charging mode |
| $I_{dc,(.)}^{(.)}$ | Indicator of storage unit in discharging mode |
| $j, o$ | Index of bus |
| $P_{(.)}^{(.)}$ | Dispatch of a unit/grid generation |
| $P_{c,(.)}^{(.)}, P_{dc,(.)}^{(.)}$ | Charge/discharge power of storage unit |
| $P_{j,(.)}^{d,(.)}, Q_{j,(.)}^{d,(.)}$ | Real/reactive served load at bus *j* |
| $P_{j,(.)}^{inj,(.)}, Q_{j,(.)}^{inj,(.)}$ | Real/reactive injection at bus *j* |
| $PL_{j,o}^{(.)}$ | Real power flow between buses *j* and *o* |
| $Q_{(.)}^{(.)}$ | Reactive power generation of a unit |
| $QL_{j,o}^{(.)}$ | Reactive power flow between buses *j* and *o* |
| $s$ | Denote a scenario |
| $SD_{(.)}^{(.)}$ | Shutdown cost of a generation unit |
| $SL_{j,o}^{(.)}$ | Apparent power flow between buses *j* and *o* |
| $SU_{(.)}^{(.)}$ | Startup cost of a generation unit |
| $t$ | Hour index |
| $V_{j,t}^{s}$ | Voltage of bus *j* at hour *t* in scenario *s* |
| $\theta_{(.)}^{(.)}$ | Bus voltage angle |

### Constants

| | |
|---|---|
| $B_{(.)}^{(.)}$ | Imaginary part of microgrid admittance matrix |
| $b_{j,o}^{(.)}$ | Susceptance of the branch between buses *j* and *o* |
| $CS_i, CD_i$ | Startup/Shut down cost of the thermal DG unit *i* |
| $D_j^{(.)}$ | Set of units/loads which are connected to bus *j* |
| $E_k^{\min}, E_k^{\max}$ | Min/max energy stored in storage unit *k* |
| $E0_k, ET_k$ | Initial and terminal energy stored in storage unit *k* |
| $G_{(.)}^{(.)}$ | Real part of microgrid admittance matrix |
| $g_{j,o}^{(.)}$ | Conductance of the branch between buses *j* and *o* |
| $NB$ | Total number of buses in the system |
| $NT$ | Total number of hours under study |
| $p^s$ | Probability of scenario *s* |
| $P_{(.)}^{\min}, P_{(.)}^{\max}$ | Min/max generation capacity |
| $P_{c,k}^{\min}, P_{c,k}^{\max}$ | Min/max charging capacity of storage unit *k* |
| $P_{dc,k}^{\min}, P_{dc,k}^{\max}$ | Min/max discharging capacity of storage unit *k* |
| $P_{D,t}$ | Total microgrid load |
| $P_{j,(.)}^{D}$ | Load at bus *j* |
| $Q_{(.)}^{\min}, Q_{(.)}^{\max}$ | Min/max reactive power capacity of unit |
| $r_{j,o}, x_{j,o}$ | Line resistance & reactance between buses *j* and o |
| $SL_{o,j}^{\max}$ | Maximum line capacity between buses *j* and *o* |
| $U_{j,o}^{(.)}$ | Line availability between buses *j* and *o* |
| $UX_{(.)}^{(.)}$ | Generation availability, 1 if available, otherwise 0 |
| $VOLL$ | Value of lost load |

This project is funded in part by the U.S. Department of Energy Grant # DE-FC26-08NT02875. The authors are with Electrical and Computer Engineering Department, Illinois Institute of Technology, Chicago, IL 60616 USA. (e-mails: mkhodaya@iit.edu, mbarati@iit.edu and ms@iit.edu).

$y_{j,o}$ Admittance connected between buses *j* and *o*

$\rho_t$ Hourly price of the grid supply

$\eta_k$ Charge/discharge cycle efficiency of storage unit *k*

## I. INTRODUCTION

MICROGRIDS are considered as viable options for the electrification in university campuses, military installations, and other locations where the main grid expansion is either impossible or has no economic justification [1]. The operation and control of microgrids with distributed energy resources (DER) could also reduce the transmission burden on a power utility system. DER in a microgrid could include combined heat and power (CHP), photovoltaic (PV), small wind turbines (WT), heat or electricity storage, and controllable loads. DER applications increase the efficiency of energy supply and reduce the electricity delivery cost and carbon footprint in a microgrid. DER applications could also make it possible to impose intentional islanding in microgrids [2]. The proximity of generation to loads in microgrids could improve the power quality and reliability (PQR) at load points.

The emergence of microgrids in power utility systems has raised additional technical, economical, and regulatory challenges [3]. Matching generation and load to maintain the frequency and managing reactive power to regulate voltages and minimize losses are important issues in microgrid operations especially when microgrids are operated in an island mode. Storage devices including batteries, super-capacitors, and flywheels are used to match generation with load in microgrids. Storage can supply generation deficiencies, reduce load surges by providing ride-through capability for short periods [4], reduce network losses [5], and improve the protection system by contributing to fault currents [6].

The operation and control of automated switches can improve PQR indices in microgrids. Proper control signals would ensure the economics and the security of microgrids in grid-connected and island modes. Control schemes in microgrids include hierarchical and decentralized controls. The decentralized control facilitates distributed control and management of large complex systems by offering small autonomous systems referred to as agents. However, decentralized control requires significant experimentation with coordination before implementation and could introduce security challenges [7]. In [8], the economic operation of microgrids is evaluated by incorporating a hierarchical control. Hierarchical control is performed by a master controller which matches generation and load for real and reactive power control. The voltage-reactive power and frequency-real power characteristics of DGs would provide the required real and reactive power to adjust the voltage and frequency in microgrids. The master controller is responsible for maintaining the frequency in a microgrid by adjusting DG according to their frequency droop characteristics, utilizing storage, and load shedding. Moreover, voltage control strategies can be utilized by the master controller considering the voltage/reactive power droop of DGs so that there would be no reactive circulating currents among such resources. The Kyotango microgrid project in Japan is an example of hierarchically controlled microgrid [1]. In [9]-[11], the role of power sharing is evaluated to regulate the frequency and the voltage in microgrids.

From the reliability point of view, microgrids can provide higher reliability and power quality at load points. The proximity of DG and load could decrease the duration and the frequency of outages as well as the level of energy not supplied at a microgrid [12]-[13]; however, the microgrid topology could play a crucial role in supplying the microgrid loads with diverse reliability requirements. In a grid-connected mode, outages of the main grid could lead to the microgrid islanding. In the island mode, the master controller relies on the microgrid generation and storage to balance the load with generation and prevent load curtailments. The load-supply balancing in an islanded microgrid could depend on the load priority and reliability requirements. In [14], the effect of load-supply mismatch on the microgrid reliability indices is evaluated by incorporating the stochastic nature of DGs. Ref. [15] addresses the load serving sequence in microgrids considering load point reliability indices.

This paper will evaluate the effect of HRDS switches and storage facilities on increasing the reliability indices in looped distribution systems. HRDS is introduced and applied to the IIT microgrid and the improvements on reliability indices are evaluated. The proposed reliability indices include the system average interruption frequency index (SAIFI), system average interruption duration index (SAIDI), customer average interruption duration index (CAIDI), customer average interruption frequency index (CAIFI), expected energy not supplied (EENS), and loss of load expectation (LOLE). The numerical results show that the integration of HRDS switches will help improve the reliability indices in a microgrid. Moreover, it is shown that integrating storage will not only improve the reliability indices in a microgrid but also reduce the operation cost at consumer levels. Section II introduces the HRDS and automatic switches. Section III presents the mathematical formulation and the solution methodology for the optimal operation and control of microgrids. Section IV presents an overview of the IIT microgrid and Section V discusses the optimal operation and control of IIT microgrid and evaluates the effect of HRDS on the IIT microgrid and consumer reliability indices. The conclusions are presented in Section VI.

## II. HIGH RELIABILITY DISTRIBUTION SYSTEM

The implementation of microgrid loops is made possible by the use of automatic switches in HRDS. An example of HRDS is to apply Vista switches, equipped with $SF_6$ gas insulated fault interrupters, manufactured by the S&C Electric Company. HRDS switches can sense the cable faults and isolate the faulted section with no impact on other sections in a microgrid. The master controller will monitor the status of each HRDS switch using the supervisory control and data acquisition (SCADA) system. The master controller is responsible for economic operation of the microgrid based on signals received from switches on the status of distribution branches. Fig.1 shows the sample microgrid network with a

traditional protection scheme. Fig. 2 shows the HRDS implementation.

Comparing Figs. 1 and 2, it is clear that any line outages in microgrid shown in Fig. 1 will lead to load interruptions. In Fig. 1, if a fault occurs on the line connecting buses 2 and 3, the switches 4 and 5 will open and the load at buses 3 and 4 will be interrupted. In Fig. 2, if a fault occurs on the line connecting buses 2 and 3, switches 4 and 5 detect the fault according to the fault current direction and clear the fault without any interruptions to the loads at buses 3 and 4. Hence, loads will remain in service. In this case, all switches remain closed except S4 and S5. By incorporating the fiber optic technology for the communications between switches and fast response directional relays, the fault in Fig. 2 is cleared in less than 6 cycles (0.1 sec) which will not be sensed by the other microgrid loads.

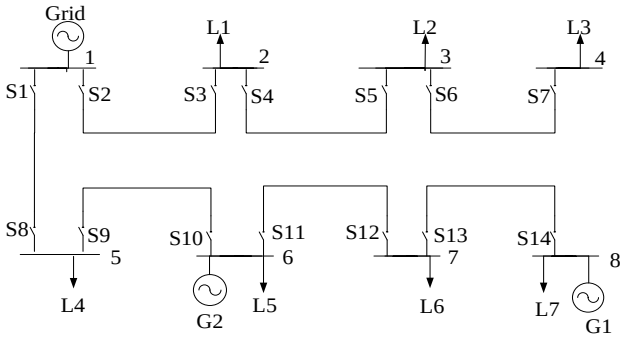


Fig. 1 Sample of a microgrid without HRDS switches

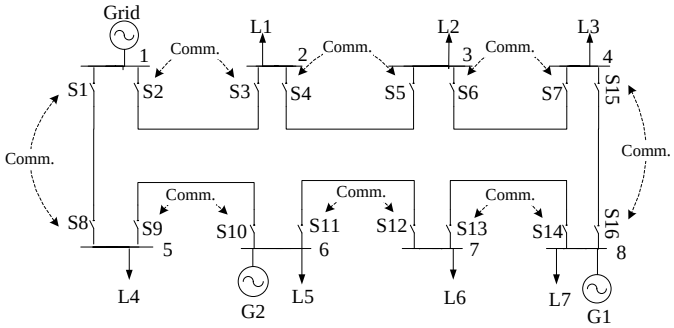


Fig. 2 Sample of a microgrid with HRDS switches

The relays incorporated in HRDS switchgears provide permissive over-reaching transfer trip (POTT) and directional comparison blocking (DCB) protection. Before isolation, POTT monitors the direction of over-current relays on both sides of the cable to confirm that there is a fault. DCB acts as a backup protection system which tends to isolate the fault once the short circuit current is sensed by switches; however, POTT sends blocking signals if a fault is not occurred between the switches. As a backup protection scheme, DCB is always active in the microgrid even if the distribution system is open-looped. Fiber optics is used as a communication medium between relays and switches. The fiber optic communication system is capable of transferring the information in less than 2 msec which enables the main protection system to clear the fault in less than 6 cycles. The backup non-directional over current protection will operate if the primary protection scheme or the communication system fails.

## III. Optimal Operation of Microgrids

At steady state, the microgrid master controller will minimize the operation cost of DG, including startup and shut down costs, the cost of energy supplied by the main grid, and penalty costs (i.e., value of lost load) associated with the microgrid load curtailments. The optimal solution is subject to microgrid and the main grid constraints. The master controller will create an islanded microgrid in the case of grid contingencies and supply the microgrid loads by the local microgrid generation.

In this paper, a stochastic security-constrained unit commitment formulation is proposed for the master controller which is solved using the mixed-integer programming (MIP) model for the microgrid generation, grid supply and battery storage. The master controller objective and constraints are shown in (1)-(25). The load balance constraint is shown in (2). The mismatch represents the lost load, which is minimized in the objective function by penalizing the value of lost load. (3)-(4) represent the startup and shutdown costs of local generation. The real and reactive power generation constraints by the local and the main grid generation are shown in (5)-(8), respectively. The substation transformers/breakers will limit the energy trades with the main grid. Microgrid outages could further constrain such trades.

The microgrid storage will store energy when the market price of electricity is low and supply energy to the microgrid when the hourly market price is high. The storage constraints are shown in (9)-(16). The dispatch of storage unit is represented by (9). The constraint on the storage commitment is represented by (10) and charge/discharge capacity limits are shown in (11)-(12). The reactive power supplied by power electronic interface of the storage unit is shown in (13) [20]. The available energy at hour *t* is shown in (14) which is dependent on the available energy at hour *(t-1)* and the charged/discharged energy at hour *t*. In (14), the hourly charged/dischaged energy is restricted by the charge/discharge cycle efficiency of the storage unit. The limitation on stored energy which is represented by min/max state of charge of the storage unit is represented by (15) and (16). The net injected real/reactive power at each bus is shown in (17)-(18). Eq. (19) shows the admittance of distribution lines. The linearized formulation of real/reactive power injections are given in (20)-(21). Eq. (22)-(23) show the linearized formulation of real and reactive line flow and (24) represents the apparent power flow through the distribution line. Here, $\zeta_{j,o}^{t,s}$ is an auxiliary parameter, which is dependent on the load power factor as calculated in Appendix. The constraint on apparent power flow which is enforced by the line capacity is shown in (25).

Random outages are considered in the main grid and the microgrid. The Monte Carlo representation of outages is applied and the Latin Hypercube Sampling (LHS) technique is used to develop a large number of scenarios with equal probabilities. A two-state Markov chain process is utilized to represent microgrid outages according to the microgrid component outage and repair rates. The scenario reduction technique is applied to reduce the number of generated scenarios to an acceptable level with the corresponding

probabilities. Scenario reduction will eliminate the low probability scenarios and bundle scenarios that are close in terms of statistical metrics [16]-[18].

The MIP formulation in each scenario is decomposed into a master problem and several subproblems based on the linear programming duality theory [21]. In each scenario, the master problem determines the hourly unit commitment and dispatch solution of generation and storage facilities while the subproblems will check the distribution network constraints. In the case of violations, Benders cuts are generated and added to the master problem. The master problem is solved with the new constraints and the network constraints are checked in the next step. This iterative process will continue until there is no further transmission violation [21]-[23].

$$Min \sum_s p^s \begin{Bmatrix} \sum_t \sum_i \left( F^s_{c,i}(P^s_{i,t}) + SU^s_{i,t} + SD^s_{i,t} \right) + \\ \rho_t \cdot P^s_{g,t} + VOLL.(\sum_t \sum_j P^D_{j,t} - P^{d,s}_{j,t}) \end{Bmatrix} \quad (1)$$

s.t.

$$\sum_i P^s_{i,t} + P^s_{g,t} + \sum_k P^s_{k,t} = \sum_j P^{d,s}_{j,t} \quad (2)$$

$$SU^s_{i,t} \geq CS_i \cdot (I^s_{i,t} - I^s_{i,t-1}) \quad (3)$$

$$SD^s_{i,t} \geq CD_i \cdot (I^s_{i,t-1} - I^s_{i,t}) \quad (4)$$

$$P^{\min}_i \cdot UX^s_{i,t} \cdot I^s_{i,t} \leq P^s_{i,t} \leq P^{\max}_i \cdot UX^s_{i,t} \cdot I^s_{i,t} \quad (5)$$

$$P^{\min}_g \cdot UX^s_{g,t} \leq P^s_{g,t} \leq P^{\max}_g \cdot UX^s_{g,t} \quad (6)$$

$$Q^{\min}_i \cdot I^s_{i,t} \cdot UX^s_{i,t} \leq Q^s_{i,t} \leq Q^{\max}_i \cdot I^s_{i,t} \cdot UX^s_{i,t} \quad (7)$$

$$Q^{\min}_{grid} \cdot UX^s_{g,t} \leq Q^s_{g,t} \leq Q^{\max}_{grid} \cdot UX^s_{g,t} \quad (8)$$

$$P^s_{k,t} = P^s_{dc,k,t} - P^s_{c,k,t} \quad (9)$$

$$I^s_{dc,k,t} + I^s_{c,k,t} \leq 1 \quad (10)$$

$$I^s_{c,k,t} \cdot P^{\min}_{c,k} \leq P^s_{c,k,t} \leq I^s_{c,k,t} \cdot P^{\max}_{c,k} \quad (11)$$

$$I^s_{dc,k,t} \cdot P^{\min}_{dc,k} \leq P^s_{dc,k,t} \leq I^s_{dc,k,t} \cdot P^{\max}_{dc,k} \quad (12)$$

$$Q^{\min}_k \cdot (I^s_{dc,k,t} + I^s_{c,k,t}) \leq Q^s_{k,t} \leq Q^{\max}_k \cdot (I^s_{dc,k,t} + I^s_{c,k,t}) \quad (13)$$

$$E^s_{k,t} = E^s_{k,t-1} - (P^s_{dc,k,t} - \eta_k \cdot P^s_{c,k,t}) \quad (14)$$

$$E^{\min}_k \leq E^s_{k,t} \leq E^{\max}_k \quad (15)$$

$$E_{k,0} = E_{k,NT} \quad (16)$$

$$\sum_{i \in D^i_j} P^s_{i,t} + \sum_{g \in D^g_j} P^s_{g,t} + \sum_{k \in D^k_j} P^s_{k,t} - \sum_{d \in D^d_j} P^{d,s}_{D,t} = P^{inj,s}_{j,t} \quad (17)$$

$$\sum_{i \in D^i_j} Q^s_{i,t} + \sum_{g \in D^g_j} Q^s_{g,t} + \sum_{k \in D^k_j} Q^s_{k,t} - \sum_{d \in D^d_j} Q^{d,s}_{D,t} = Q^{inj,s}_{j,t} \quad (18)$$

$$y^{t,s}_{o,j} = g^{t,s}_{o,j} + Jb^{t,s}_{o,j} = \frac{r_{o,j} \cdot U^{t,s}_{o,j}}{r^2_{o,j} + x^2_{o,j}} - J \frac{x_{o,j} \cdot U^{t,s}_{o,j}}{r^2_{o,j} + x^2_{o,j}} \quad (19)$$

$$P^{inj,s}_{j,t} = (2V^s_{j,t} - 1) \cdot G^{t,s}_{j,j} + \sum_{o(j \neq o)}^{NB} G^{t,s}_{j,o}(V^s_{j,t} + V^s_{o,t} - 1) + B^{t,s}_{j,o}(\theta^s_{j,t} - \theta^s_{o,t}) \quad (20)$$

$$Q^{inj,s}_{j,t} = -(2V^s_{j,t} - 1) \cdot B^{t,s}_{j,j} + \sum_{o(j \neq o)}^{NB} -B^{t,s}_{j,o}(V^s_{j,t} + V^s_{o,t} - 1) + G^{t,s}_{j,o}(\theta^s_{j,t} - \theta^s_{o,t}) \quad (21)$$

$$PL^{t,s}_{j,o} = G^{t,s}_{j,o}(V^{t,s}_j - V^{t,s}_o) + B^{t,s}_{j,o}(\theta^{t,s}_j - \theta^{t,s}_o) \quad (22)$$

$$QL^{t,s}_{j,o} = B^{t,s}_{j,o}(V^{t,s}_o - V^{t,s}_j) + G^{t,s}_{j,o}(\theta^{t,s}_j - \theta^{t,s}_o) \quad (23)$$

$$SL^{t,s}_{j,o} = PL^{t,s}_{j,o} + \xi^{t,s}_{j,o} \cdot QL^{t,s}_{j,o} \quad (24)$$

$$\left| SL^{t,s}_{j,o} \right| \leq SL^{\max}_{j,o} \quad (25)$$

## IV. The Perfect Power System - IIT Microgrid

In 2004-2006, the underground distribution system at IIT suffered 12 unplanned power outages which disrupted academic and administrative activities and damaged several operation and research equipment. The outages were due to partial or complete loss of the utility supply and malfunctions of aged cables and other distribution components at IIT. The lack of system redundancy and the unavailability of replacement components prolonged the outage durations at IIT. In 2005, the Galvin Electricity Initiative lead a campaign to implement a perfect power system at IIT with the objective of establishing a microgrid that is environmentally friendly, fuel efficient, robust, and resilient with a self-healing capability. The microgrid at IIT empowers the campus consumers, in response to the real time price of electricity, to control daily power consumptions. IIT microgrid enhances its operation reliability by applying a real-time reconfiguration of power distribution assets, real-time islanding of critical loads, and real-time optimization of power supply resources.

Fig. 3 shows the configuration of the ComEd distribution network (main grid) that feeds the IIT microgrid. IIT is supplied by three 12.47 KV circuits fed from the ComEd Fisk substation. The peak load at IIT is approximately 10 MW. The IIT's 4.16 KV distribution system consists of 12.47/4.16 kV transformers, supply/feeder breakers and building transformers. Siegel Hall is the pilot building for the perfect power demonstration which is fed through the primary - which is backed up by a secondary (redundant) - feeder equipped with automatic switch. The voltage is further stepped down to 120 V in the building.

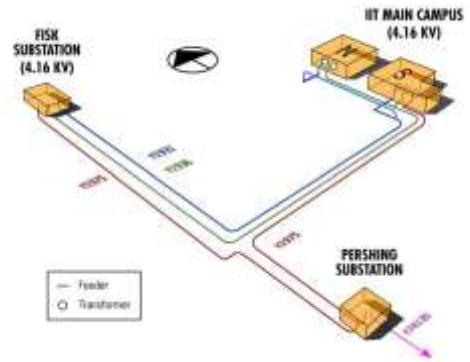


Fig. 3 ComEd system configuration feeding IIT substations [24]

In Fig. 4, the IIT microgrid consists of seven loops. The North Substation feeds three loops while the South Substation supplies energy to the remaining loops. Each building is supplied by redundant feeders which are normally energized to ensure that the building is fed by an alternate path in the case of an outage.

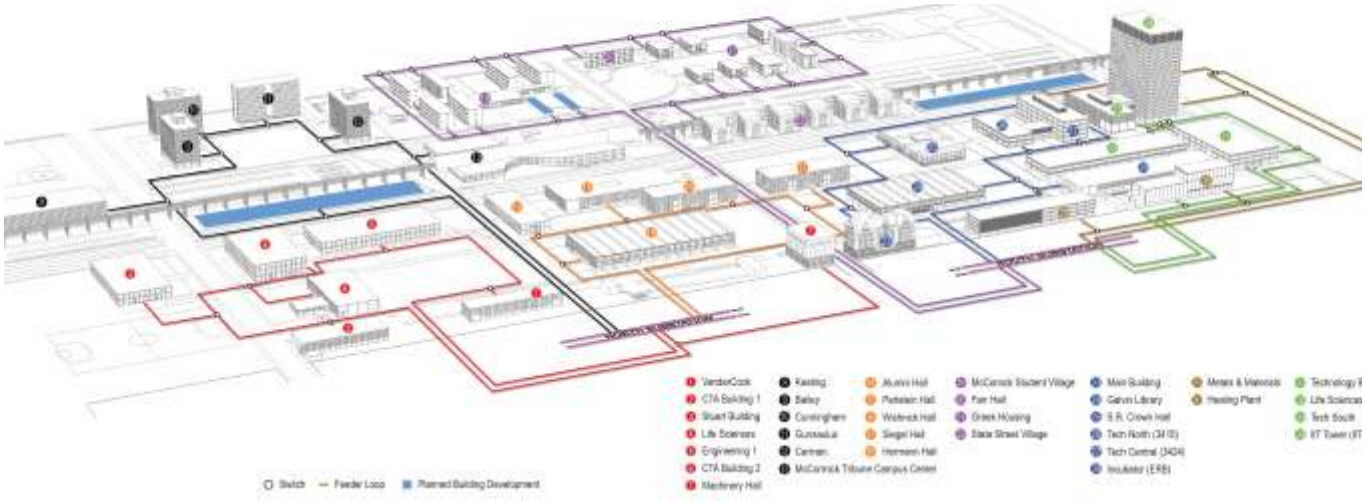

Fig. 4. IIT distribution system layout based on HRDS

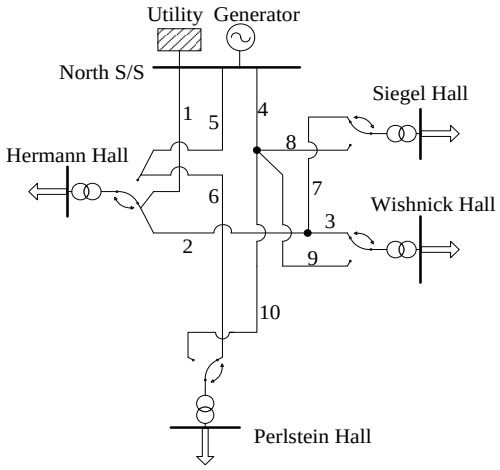


Fig. 5 Third loop layout without HRDS switches

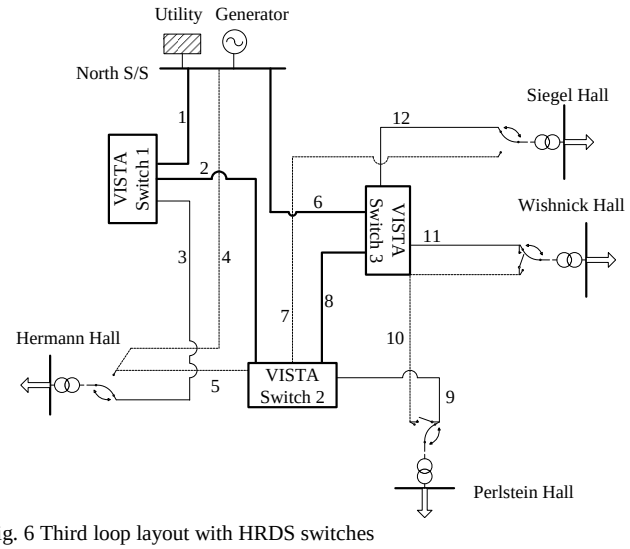


Fig. 6 Third loop layout with HRDS switches

The HRDS at IIT utilizes Vista underground closed loop fault-clearing switchgear with SEL-351 directional over-current protection relays. The fault isolation takes place in a quarter of a cycle by automatic breakers. The communication system is via fiber optic cables which facilitate the coordination between switches.

In Fig. 4, the third loop which is connected to the North Substation consists of five buildings including Hermann Hall, Wishnick Hall, Siegel Hall, Perlstein Hall, and Alumni Hall. Figs. 5 and 6 show the third loop with and without HRDS switches. It is also assumed that the redundant cables in Figs. 5 and 6 will be available when the primary feeding cable has failed. The load at Perlstein and Alumni Hall are aggregated as the Perlstein Hall load. In Fig. 5, an outage will result in downstream load curtailments until the manual switching restores the loads. Since the transfer switches are manually operated, the estimated time for manual source transfer at the building feeder is about three hours. In Fig. 6, the HRDS switches at load points provide uninterruptable load serving capability. Here, buildings are referred to as customers throughout the paper.

The IIT microgrid generation includes combustion microturbines connected to the North Substation as well as renewable energy sources. The IIT microgrid is equipped with an 8 MW gas-fired power plant which includes two 4 MW Rolls Royce gas turbines. The microgrid generation could be used for reliability and economic improvements in the main grid-connected and the island modes.

Renewable energy sources include wind and solar generation. An 8 kW Viryd wind turbine is installed on the north side of the campus in the Stuart soccer field. 60 kW of PV cells are installed on two building rooftops to supply portions of campus load. A 500 kWh ZBB storage is installed on campus to increase the reliability and efficiency of the IIT microgrid. Moreover, several electric vehicle charging stations are deployed on campus to utilize the microgrid energy storage and provide green energy for on campus electric vehicles.

A major element of the IIT microgrid is its master controller. Master controller applies a hierarchical control via SCADA to ensure reliable and economic operations of the IIT microgrid. It also coordinates the operation of HRDS controllers, on-site generation, storage, and individual building controllers [25]. Intelligent switching and advanced coordination technologies of master controller through communication systems facilitates rapid fault assessments and isolations in the IIT microgrid [24]. Fig. 7 shows the overview of the control tasks performed by master controller at IIT.

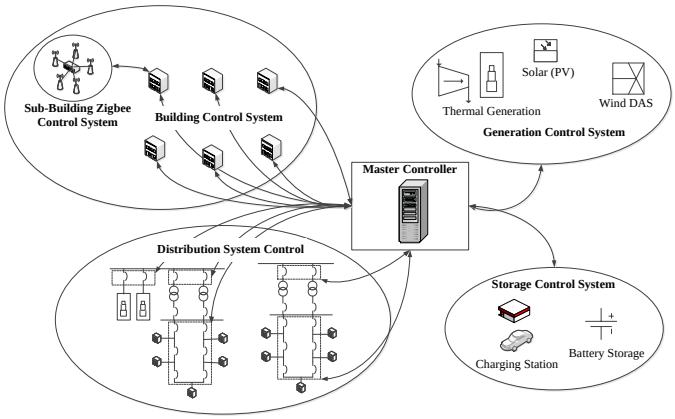


Fig. 7 Overview of the master controller system

The IIT microgrid participates in real-time electricity markets. Once the real-time price exceeds 7-8 cents per kWh (marginal cost of microgrid generation), the microgrid generation could serve the IIT load. The on-site generation can provide demand response and increase the reliability. The provision of spinning reserve and day ahead load response is also offered by master controller by managing microgrid generation, storage, controllable loads, power quality devices and smart switches.

## V. Simulation of IIT Microgrid Operation

The master controller simulation at steady state and in contingencies (with and without HRDS) is considered. The simulation period is one year. The maximum loads at Hermann, Siegel, Wishnick, and Perlstein Halls are 289 kW, 167 kW, 272 kW and 513 kW, respectively. The typical Hermann Hall load is shown in Fig. 8, in which the weekend load is approximately 30% of that of weekdays.

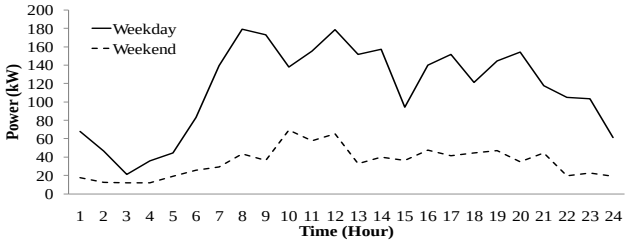


Fig. 8 Load pattern in Hermann Hall

Tables I and II show the IIT distribution system characteristics with and without HRDS respectively. The line numbers are shown in Figs. 5 and 6. It is assumed that the backup lines are always available once they are energized to serve the loads. For example, in Fig. 5, once Lines 1, 2 or 3 fail, the Wishnick Hall load is served through Lines 4 and 9. Here, the microgrid generation capacity is 1 MW. The mean time to failure (MTTF) for the microgrid generation and grid supply is 1,200 hours and the mean time to repair (MTTR) of microgrid generation and grid supply is 25 hours. For simplicity, the charge/discharge efficiency and the availability of storage and HRDS switches are assumed to be 100%. The maximum charge/discharge rate of the 500 kWh ZBB storage unit is 250 kW/h.

The stochastic solution of microgrid provides the expected economic and reliability indices once HRDS switches and storage are integrated into the IIT microgrid. The availability of distribution lines, grid supply, and microgrid generation is considered in scenarios using the Markov chain Monte Carlo (MCMC) simulation. The Monte Carlo simulation is applied to generate a large number of scenarios. The scenario reduction is applied to select 10 scenarios corresponding to Figs. 5 and 6 with their assigned probabilities. The reliability indices of microgrid are calculated and compared with and without HRDS switches. In the following, the contribution of master controller, HRDS, and storage to the reliability and the optimality of microgrid are evaluated for the eighth scenario, followed by a discussion on the results in other scenarios.

Table I Cable characteristic at IIT microgrid with HRDS

| Line ID | Resistance (Ω/1000 ft) | Inductance (Ω/1000 ft) | Length (ft.) | Failure Rate (/yr) | MTTR (hr) | MTTF (hr) |
|---|---|---|---|---|---|---|
| 1 | 0.028 | 0.037 | 159.2 | 0.2866 | 20 | 30,565 |
| 2 | 0.028 | 0.037 | 435.9 | 0.7846 | 20 | 11,164 |
| 3 | 0.028 | 0.037 | 144.5 | 0.2601 | 20 | 33,679 |
| 4 | 0.028 | 0.037 | 261.3 | - | - | - |
| 5 | 0.028 | 0.037 | 584 | - | - | - |
| 6 | 0.028 | 0.037 | 1,409.9 | 2.5378 | 20 | 3,451 |
| 7 | 0.028 | 0.037 | 755.7 | - | - | - |
| 8 | 0.028 | 0.037 | 452.7 | 0.8148 | 20 | 10,751 |
| 9 | 0.028 | 0.037 | 65.7 | 0.1182 | 20 | 74,111 |
| 10 | 0.028 | 0.037 | 376.8 | - | - | - |
| 11 | 0.028 | 0.037 | 99.4 | 0.1789 | 20 | 48,965 |
| 12 | 0.028 | 0.037 | 76.0 | 0.1368 | 20 | 64,035 |

Table II Cable characteristic at IIT microgrid without HRDS

| Line ID | Resistance (Ω/1000 ft) | Inductance (Ω/1000 ft) | Length (ft.) | Failure Rate (/yr) | MTTR (hr) | MTTF (hr) |
|---|---|---|---|---|---|---|
| 1 | 0.028 | 0.037 | 145.8 | 0.2624 | 20 | 33,384 |
| 2 | 0.028 | 0.037 | 382.6 | 0.6886 | 20 | 12,721 |
| 3 | 0.028 | 0.037 | 100.5 | 0.1809 | 20 | 48,424 |
| 4 | 0.028 | 0.037 | 758.1 | - | - | - |
| 5 | 0.028 | 0.037 | 182.6 | 0.3286 | 20 | 26,658 |
| 6 | 0.028 | 0.037 | 407.9 | 0.7342 | 20 | 11,931 |
| 7 | 0.028 | 0.037 | 250.0 | 0.45 | 20 | 19,466 |
| 8 | 0.028 | 0.037 | 238.5 | - | - | - |
| 9 | 0.028 | 0.037 | 92.6 | - | - | - |
| 10 | 0.028 | 0.037 | 30 | - | - | - |

In the following two options for the modeling of campus microgrid are studied. Option A applies a deterministic operation by considering the eighth scenario as the only alternative for the microgrid operation, and option B analyzes the stochastic behavior of the IIT microgrid.

### *A. Deterministic Operation of Microgrid*

In this case, one scenario is closely analyzed and the effect of HRDS and the storage system on the microgrid reliability indices is evaluated. The following cases are studied:

Case 1: IIT microgrid is not equipped with HRDS switches (Fig. 5)

Case 2: IIT microgrid is equipped with HRDS switches (Fig. 6)

Case 3: IIT microgrid is equipped with HRDS switches and the storage system which is located next to Hermann Hall.

Table III shows the annual incidents with HRDS in the eighth scenario. The table shows that the first grid outage took place in the second day at hour 6 with two-hour duration while the second outage occurred on the fifth day which required a two-day repair. In the eighth scenario, there are five cable outages in the system equipped with HRDS switches while there is only one cable outage in the system without HRDS switches. Without HRDS, line L6 failed on the 224th day at hour 23 and was restored on the 225th day at hour 6. The outages of the main grid and DG are the same in both systems. In this scenario, we could have additional outages with HRDS because there are more components in a loop; however, the loads have never been interrupted.

Table III IIT microgrid with HRDS (start and end date of outage, day/hr)

| | Grid | Power Plant | L1 | L2 | L6 | L8 |
|---|---|---|---|---|---|---|
| First Outage | 2/6-2/8 | 88/19-88/21 | 212/12-212/18 | 7/6-8/16 | 67/17-69/1 | 59/20 |
| Second Outage | 5/1-7/6 | 146/11-147/7 | - | - | 174/14-175/12 | - |
| Third Outage | 38/10-39/21 | 334/13-336/23 | - | - | - | - |
| Fourth Outage | 193/9-194/10 | 337/20-338/17 | - | - | - | - |
| Fifth Outage | 201/18-202/9 | 343/22-345/1 | - | - | - | - |
| Sixth Outage | 280/12-280/19 | - | - | - | - | - |
| Seventh Outage | 284/13-289/17 | - | - | - | - | - |
| Eighth Outage | 311/18-311/23 | - | - | - | - | - |

*a) Economic Operation of Microgrid*

The microgrid operation cost includes the cost of main grid energy transactions (in both directions), cost of microgrid energy supply, and curtailment costs (value of lost load.) The operation cost of storage is assumed negligible. When the hourly market price of energy is higher than the marginal cost of microgrid generation, the microgrid could supply its excess energy to the main grid for reducing its operation cost. The main grid electricity prices in this study are based on historical hourly electricity prices of commercial customers [26].

Proper protective devices are located in the microgrid at the point of common coupling (PCC) which enables bi-directional power flows. The failure rate of the grid indicates the failure rate of the interface facilities at PCC. It is assumed that the price of electricity for trading with the grid is the same as the grid LMP at PCC.

The microgrid outages could result in the loss of revenue estimated at 80$/kWh (value of lost load) which covers the replacement cost of the damaged equipment (campus facilities as well as those in laboratories), personnel and administrative cost of restoring and sustaining research and educational experiments, cost of aggravation associated with disrupted academic classes, laboratories, and any other major campus events such as open houses and conferences that are interrupted by microgrid outages.

The annual operation cost in Case 1 is 140,497$/yr. The HRDS implementation reduces the operation cost to 126,644$/yr. The use of storage will further reduce the annual operation cost to 119,236$/yr by performing demand response and taking daily market price fluctuations into account. The lost loads in the three Cases are 173.236, 0, and 0 kWh/yr, respectively.

Fig. 9 shows the microgrid energy flow on the 23rd day of the year. Here the energy drawn from the main grid is stored at the storage when the main grid hourly prices are low (hours 4, 5, 16 and 17) and deployed once the main grid prices are high (hours 10, 11, 19 and 20.) The main grid prices in Fig. 9 are not high enough to trigger the local microgrid generation. The lowest prices at the microgrid occurs at hours 4 and 5 (2.4 ¢/kWh) which increase to 3.5 and 3.6 ¢/kWh at hours 10 and 11, respectively. This cycle is repeated at hours 16-17 and 19-20.

Fig. 10 shows the energy supply to the microgrid on the 217th day (summer day) when the main grid electricity prices are higher. Here, the local microgrid generation is dispatched at hour 10 when the main grid prices are higher than 6¢/kWh. The microgrid revenue for a single day energy sale is $473.699.

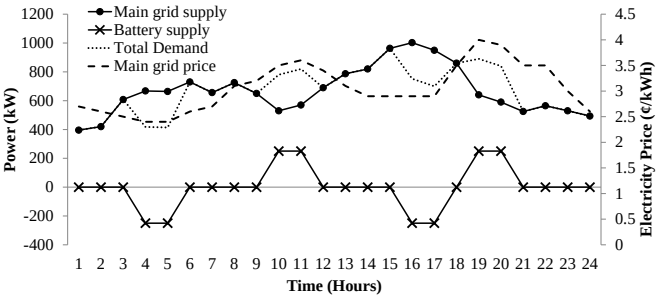


Fig. 9 Storage and the main grid supply on the 23rd day.

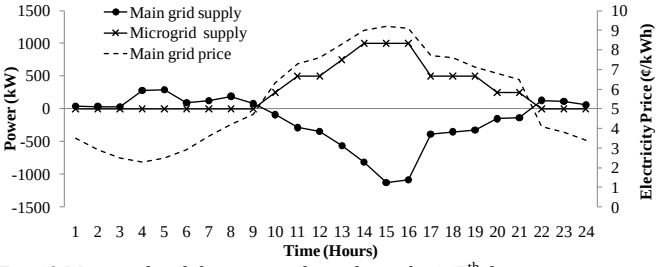


Fig. 10 Microgrid and the main grid supply on the 217th day.

*b) Microgrid Reliability Evaluation*

In this case, interruption indices for consumers and the entire microgrid are evaluated. There are four customers in the third loop. In Case 1, there is a single load interruption in Perlstein Hall, so SAIFI and CAIFI are 0.25 (interruption/customer.yr) and 1 (interruption/affected customer.yr) respectively. The outage duration is 3 hours and SAIDI and CAIDI are 0.75 (hrs/customer.yr) and 3 (hrs/customer interruption.yr) respectively. In Case 2, no microgrid outages occur which decreases SAIFI, CAIFI, SAIDI and CAIDI to zero. Likewise, in Case 3, SAIFI, CAIFI, SAIDI and CAIDI are zero.

The results show that the HRDS integration will decrease the microgrid outage duration and frequency in Case 2, and lower the microgrid SAIFI, SAIDI, CAIDI and CAIFI. In Cases 2 and 3, we could have additional outages with HRDS because there are more components in a loop; however, the loads would never be interrupted as shown in Table IV. In the eighth scenario, there is only one outage at L6 in Case 1 which lasts 9 hours. Since the manual switching takes 3 hours and the

building is fed by the redundant path after manual switching, this event leads to a 3 hour outage and 173.236 kWh energy not supplied in Perlstein Hall. The EENS and LOLE in this case are 173.236 kWh/yr and 3 hours/yr respectively. In Cases 2 and 3 there are 5 cable outages which lasted 103 hours; however, these events did not interrupt the served loads because of HRDS.

Table IV. Annual energy not supplied at load points

| | Hermann Hall (kWh/yr) | Siegel Hall (kWh/yr) | Wishnick Hall (kWh/yr) | Perlstein Hall (kWh/yr) |
|---|---|---|---|---|
| Case1 | 0 | 0 | 0 | 173.236 |
| Case 2 | 0 | 0 | 0 | 0 |
| Case 3 | 0 | 0 | 0 | 0 |

### *B. Stochastic Solution of Microgrid Operation*

*a) Operation Cost*

A scenario reduction technique was applied to select 10 scenarios from a large number of scenarios generated by the MCMC method [27], [28]. The scenario reduction algorithms include fast backward, fast forward/backward and fast backward/backward methods [28]. The algorithms are chosen according to the size of the stochastic problem and the required solution accuracy. For large scenario trees, the fast forward method provides a more accurate solution with a longer processing time. In this paper, a fast backward/forward method is used for the scenario reduction. The probabilities of 10 stochastic scenarios are shown in Table V.

Table V. Probability of stochastic scenarios after scenario reduction

| Scenario No. | 1 | 2 | 3 | 4 | 5 |
|---|---|---|---|---|---|
| Probability | 0.107 | 0.119 | 0.126 | 0.0326 | 0.084 |
| Scenario No. | 6 | 7 | 8 | 9 | 10 |
| Probability | 0.125 | 0.092 | 0.108 | 0.0964 | 0.11 |

Table VI. Operation cost of stochastic scenarios in Case 1

| Scenario No. | 1 | 2 | 3 | 4 | 5 |
|---|---|---|---|---|---|
| Operation Cost ($/yr) | 182,655 | 191,727 | 154,340 | 730,330 | 232,863 |
| Scenario No. | 6 | 7 | 8 | 9 | 10 |
| Operation Cost ($/yr) | 226,398 | 192,773 | 140,497 | 238,694 | 303,518 |

Table VII. Operation cost of stochastic scenarios in Case 2

| Scenario No. | 1 | 2 | 3 | 4 | 5 |
|---|---|---|---|---|---|
| Operation Cost ($/yr) | 127,087 | 125,041 | 125,750 | 609,400 | 124,609 |
| Scenario No. | 6 | 7 | 8 | 9 | 10 |
| Operation Cost ($/yr) | 127,544 | 127,861 | 126,644 | 152,777 | 146,649 |

Table VIII. Operation cost of scenarios in Case 3

| Scenario No. | 1 | 2 | 3 | 4 | 5 |
|---|---|---|---|---|---|
| Operation Cost ($/yr) | 119,525 | 117,513 | 118,223 | 549,537 | 117,108 |
| Scenario No. | 6 | 7 | 8 | 9 | 10 |
| Operation Cost ($/yr) | 120,045 | 119,109 | 119,236 | 122,157 | 120,968 |

The operation costs of scenarios are shown in Tables VI-VIII. Here, the operation cost of Case 2 is lower than that in Case 1 in all scenarios because HRDS can reduce the energy not supplied and its respective penalties. The storage will also reduce the duration of microgrid load curtailments and the annual energy not supplied. Comparing Tables VIII and VII, it is shown that the cost in Case 3 is decreased as compared to that in Case 2. The expected operation costs in Cases 1-3 are 224,073$/yr, 146,899$/yr and 120,038$/yr respectively. The estimated saving at the IIT microgrid with HRDS installed at all seven loops is 621,867$/yr.

*b) Microgrid Reliability indices*

Tables IX-XI show the microgrid system and customer interruption indices in stochastic scenarios. Table X shows the HRDS reduces SAIFI and SAIDI; however, it may not decrease CAIDI and CAIFI consistently. In the seventh scenario, CAIFI is not reduced in Case 2 because fewer outages will affect fewer customers proportionally which leads to an equal frequency of interruption per affected customer per year. In Case 1, there are 3 outages which affect 3 customers. In Case 2, there is a single outage which affected one customer; hence the CAIFI in Cases 1 and 2 are equal. In the fourth scenario, CAIDI in Case 2 is increased as compared to Case 1. The reason for a higher CAIDI is that the frequency of interruption drops faster than the duration of interruption; hence the duration of interruption per affected customer per year is higher.

Table IX. Microgrid and consumer interruption indices in Case 1

| Scenario No. | 1 | 2 | 3 | 4 | 5 |
|---|---|---|---|---|---|
| SAIFI (int./cust.yr) | 0.25 | 1.25 | 0.5 | 3.5 | 1.5 |
| SAIDI (hr/ cust. yr) | 0.75 | 2.25 | 1.5 | 18 | 3.75 |
| CAIFI (int./aff. cust. yr) | 1 | 1.25 | 1 | 3.5 | 3 |
| CAIDI (hr/cust. int. yr) | 3 | 1.8 | 3 | 5.14 | 2.5 |
| Scenario No. | 6 | 7 | 8 | 9 | 10 |
| SAIFI (int./cust.yr) | 1.25 | 0.75 | 0.25 | 2.5 | 2.25 |
| SAIDI (hr/ cust. yr) | 3.75 | 1.75 | 0.75 | 5.25 | 5.75 |
| CAIFI (int./aff. cust. yr) | 1.66 | 1 | 1 | 3.33 | 2.25 |
| CAIDI (hr/cust. int. yr) | 3 | 2.33 | 3 | 2.1 | 2.55 |

Table X. Microgrid and consumer interruption indices in Case 2

| Scenario No. | 1 | 2 | 3 | 4 | 5 |
|---|---|---|---|---|---|
| SAIFI (int./cust.yr) | 0 | 0 | 0 | 1.75 | 0 |
| SAIDI (hr/ cust. yr) | 0 | 0 | 0 | 12.75 | 0 |
| CAIFI (int./aff. cust. yr) | 0 | 0 | 0 | 1.75 | 0 |
| CAIDI (hr/cust. int. yr) | 0 | 0 | 0 | 7.28 | 0 |
| Scenario No. | 6 | 7 | 8 | 9 | 10 |
| SAIFI (int./cust.yr) | 0 | 0.25 | 0 | 0.75 | 0.25 |
| SAIDI (hr/ cust. yr) | 0 | 0.25 | 0 | 1 | 0.5 |
| CAIFI (int./aff. cust. yr) | 0 | 1 | 0 | 1 | 1 |
| CAIDI (hr/cust. int. yr) | 0 | 1 | 0 | 1.33 | 2 |

Table XI. Microgrid and consumer interruption indices in Case 3

| Scenario No. | 1 | 2 | 3 | 4 | 5 |
|---|---|---|---|---|---|
| SAIFI (int./cust.yr) | 0 | 0 | 0 | 1.25 | 0 |
| SAIDI (hr/ cust. yr) | 0 | 0 | 0 | 11.25 | 0 |
| CAIFI (int./aff. cust. yr) | 0 | 0 | 0 | 1.25 | 0 |
| CAIDI (hr/cust. int. yr) | 0 | 0 | 0 | 9 | 0 |
| Scenario No. | 6 | 7 | 8 | 9 | 10 |
| SAIFI (int./cust.yr) | 0 | 0 | 0 | 0 | 0 |
| SAIDI (hr/ cust. yr) | 0 | 0 | 0 | 0 | 0 |
| CAIFI (int./aff. cust. yr) | 0 | 0 | 0 | 0 | 0 |
| CAIDI (hr/cust. int. yr) | 0 | 0 | 0 | 0 | 0 |

In Case 2, the duration of interruption is 51 hours/yr and the frequency of interruptions is 7, while in Case 1, the duration of interruption is 72 hours and the frequency of interruption is 14. Although the frequency of interruption is decreased by a half, the duration of interruption is not decreased proportionally, leaving a higher CAIDI in Case 2. In Case 2, most scenarios have lower CAIDI and CAIFI than those in Case 1. Although it is not shown, CAIFI can also be higher in some scenarios in Case 2, as compared to that in Case 1, if the number of outages and the affected customers are not reduced proportionally. CAIDI is dependent on the duration and the frequency of outages. In some scenarios, CAIDI is higher because the

frequency and the duration of outages are not reduced proportionally. So the HRDS implementation will lead to shorter frequency and duration for outages with lower SAIFI and SAIDI.

Table XII. Energy not supplied at load points in Case 1 (kWh/yr)

| Scenario No. | 1 | 2 | 3 | 4 | 5 |
|---|---|---|---|---|---|
| Hermann Hall | 0 | 56.662 | 0 | 1,413.705 | 0 |
| Wishnick Hall | 0 | 495.024 | 0 | 1,951.124 | 0 |
| Siegel Hall | 0 | 32.803 | 292.129 | 1,370.819 | 404.838 |
| Perlstein Hall | 694.830 | 249.597 | 65.467 | 2,802.999 | 948.843 |
| Total | 694.830 | 834.086 | 357.596 | 7,538.647 | 1,353.681 |
| Scenario No. | 6 | 7 | 8 | 9 | 10 |
| Hermann Hall | 172.573 | 0 | 0 | 0 | 437.242 |
| Wishnick Hall | 658.611 | 17.793 | 0 | 622.114 | 1,129.902 |
| Siegel Hall | 405.045 | 84.496 | 0 | 645.066 | 580.567 |
| Perlstein Hall | 0 | 903.08 | 173.236 | 96.612 | 42.08 |
| Total | 1,236.229 | 1,005.369 | 173.236 | 1,363.792 | 2,189.791 |

Table XIII. Energy not supplied at load points in Case 2 (kWh/yr)

| Scenario No. | 1 | 2 | 3 | 4 | 5 |
|---|---|---|---|---|---|
| Hermann Hall | 0 | 0 | 0 | 1,451.496 | 0 |
| Wishnick Hall | 0 | 0 | 0 | 1,356.101 | 0 |
| Siegel Hall | 0 | 0 | 0 | 791.003 | 0 |
| Perlstein Hall | 0 | 0 | 0 | 2,427.678 | 0 |
| Total | 0 | 0 | 0 | 6,026.278 | 0 |
| Scenario No. | 6 | 7 | 8 | 9 | 10 |
| Hermann Hall | 0 | 17.793 | 0 | 61.401 | 227.972 |
| Wishnick Hall | 0 | 0 | 0 | 68.201 | 0 |
| Siegel Hall | 0 | 0 | 0 | 159.771 | 0 |
| Perlstein Hall | 0 | 0 | 0 | 0 | 0 |
| Total | 0 | 17.793 | 0 | 289.373 | 227.972 |

Table XIV. Energy not supplied at load points in Case 3 (kWh/yr)

| Scenario No. | 1 | 2 | 3 | 4 | 5 |
|---|---|---|---|---|---|
| Hermann Hall | 0 | 0 | 0 | 1,248.662 | 0 |
| Wishnick Hall | 0 | 0 | 0 | 1,017.405 | 0 |
| Siegel Hall | 0 | 0 | 0 | 769.404 | 0 |
| Perlstein Hall | 0 | 0 | 0 | 2,335.710 | 0 |
| Total | 0 | 0 | 0 | 5,371.181 | 0 |
| Scenario No. | 6 | 7 | 8 | 9 | 10 |
| Hermann Hall | 0 | 0 | 0 | 0 | 0 |
| Wishnick Hall | 0 | 0 | 0 | 0 | 0 |
| Siegel Hall | 0 | 0 | 0 | 0 | 0 |
| Perlstein Hall | 0 | 0 | 0 | 0 | 0 |
| Total | 0 | 0 | 0 | 0 | 0 |

Table XV. Total outage duration in Cases and Scenarios (hr/yr)

| Scenario No. | 1 | 2 | 3 | 4 | 5 |
|---|---|---|---|---|---|
| Case 1 | 3 | 9 | 6 | 72 | 15 |
| Case 2 | 0 | 0 | 0 | 51 | 0 |
| Case 3 | 0 | 0 | 0 | 45 | 0 |
| Scenario No. | 6 | 7 | 8 | 9 | 10 |
| Case 1 | 15 | 7 | 3 | 21 | 23 |
| Case 2 | 0 | 1 | 0 | 4 | 2 |
| Case 3 | 0 | 0 | 0 | 0 | 0 |

Table XVI. Expected reliability and economic indices

| Case | 1 | 2 | 3 |
|---|---|---|---|
| Exp. SAIFI (int./cust.yr) | 1.22 | 0.18 | 0.04 |
| Exp. SAIDI (hr/ cust. yr) | 3.29 | 0.59 | 0.37 |
| Exp. CAIFI (int./aff. cust. yr) | 1.73 | 0.36 | 0.04 |
| Exp. CAIDI (hr/cust. int. yr) | 2.69 | 0.68 | 0.29 |
| Exp. Operation Cost ($/yr) | 224,073 | 146,899 | 120,038 |
| Exp. Energy not Supplied (kWh/yr) | 1,216.21 | 251.07 | 175.10 |
| LOLE (hr/yr) | 13.153 | 2.360 | 1.467 |

In Case 3, SAIFI, SAIDI and CAIFI are reduced as compared to that in Case 2; however, CAIDI in the fourth scenario is higher. In this scenario, there are 7 outages in Case 2 as compared to 5 outages in Case 3, and the outage duration is dropped from 51 hours in Case 2 to 45 hours in Case 3. Hence, CAIDI is higher in Case 3 since the duration of interruption drops more slowly than its frequency.

In Table XII, scenario 4 corresponds to a generation failure when the grid fails. In this case, the storage unit would supply the load partially which is supplemented by the microgrid load curtailment. Table V shows a lower probability in this case.

Although interruption frequency indices are lower, the integration of microgrid storage may not decrease SAIFI and CAIFI in all scenarios since the storage will lower the unserved load rather than the frequency of interruptions. However, the expected SAIFI and CAIFI will be lower when the storage is implemented. When the storage is introduced, SAIFI, SAIDI, CAIFI and CAIDI are lowered to zero in Scenarios 7, 9 and 10, which shows that the storage can eliminate the energy not supplied. In summary, SAIDI and SAIFI are lowered in all scenarios once the HRDS is installed and SAIDI is lower with the microgrid storage in place.

Table XVI shows lower expected SAIFI, SAIDI, CAIFI and CAIDI when HRDS is implemented and demonstrates an enhance reliability when the storage is used. Tables XII-XIV show the energy not supplied. As expected, Case 3 shows the lower energy not supplied in each scenario due to storage. HRDS will lead to lower energy not supplied with the lowest expected energy not supplied in Case 3 followed by that of Case 2.

Storage can also reduce the LOLE in microgrids. In Table XV, Case 3 demonstrates the lowest outage hours followed by that in Case 2. The LOLE in Cases 1-3 are 13.15, 2.36, and 1.47 hr/yr which are reduced with HRDS switches and storage. Here, microgrid load shedding occurs when the main grid supply is unavailable. Table XVI shows the enhancements in Cases 2 and 3.

## VI. Conclusions

In this paper, reliability and economic indices of a microgrid equipped with HRDS switches is analyzed. The simulation of the IIT microgrid is presented and the contributions are highlighted as follows:

- The stochastic AC network formulation for the master controller is offered to solve the hourly unit commitment and economic dispatch in microgrids.
- The role of local generation, main grid, and energy storage on the economic operation of microgrids is considered and the enhanced reliability indices at load points are calculated.
- Storage can reduce the operation cost of a microgrid by performing demand response and avoiding emergency load curtailments. Storage helps mitigate the expected interruption duration and frequency and improves the customer reliability in microgrids.
- HRDS is used for the evaluation of reliability and economic indices in microgrids which are compared to those in traditional distribution systems.
- The implementation of HRDS and automatic switches can reduce the expected frequency and the duration of interruptions and the expected energy not supplied in microgrids. HRDS can also reduce the expected operation

cost of a microgrid by mitigating emergency load curtailments and reducing the value of lost loads.

- Microgrid reliability indices are calculated with/without HRDS.
- It is estimated that the expected operation cost at the IIT microgrid would be lowered by $621,867 annually by integrating HRDS; the storage can further reduce the operation cost by $109,220.

## APPENDIX

$\zeta_{j,o}^{t,s}$, derived here, is an auxiliary parameter which is dependent on the load power factor. The apparent power flow through the line is written as:

$$SL_{j,o}^{t,s} = \sqrt{(PL_{j,o}^{t,s})^2 + (QL_{j,o}^{t,s})^2} \tag{A1}$$

$$SL_{j,o}^{t,s} = PL_{j,o}^{t,s} \cdot \sqrt{1 + \left( \frac{QL_{j,o}^{t,s}}{PL_{j,o}^{t,s}} \right)^2} \tag{A2}$$

Using Taylor series:

$$SL_{j,o}^{t,s} = PL_{j,o}^{t,s} \cdot \left( 1 + \frac{1}{2} \cdot \left( \frac{QL_{j,o}^{t,s}}{PL_{j,o}^{t,s}} \right)^2 \right) \tag{A3}$$

$$SL_{j,o}^{t,s} = PL_{j,o}^{t,s} + \frac{1}{2} \cdot QL_{j,o}^{t,s} \cdot \tan \theta_{j,o}^{t,s} \tag{A4}$$

where

$$\xi_{j,o}^{t,s} = \frac{1}{2} \cdot \tan \theta_{j,o}^{t,s} \tag{A5}$$

$$\theta_{j,o}^{t,s} = \tan^{-1} \left( \frac{Q_j^{t,s} + Q_o^{t,s}}{P_j^{t,s} + P_o^{t,s}} \right) \tag{A6}$$

## REFERENCES


[1] G. Venkataramanan, C. Marnay, "A larger role for microgrids," *IEEE Power and Energy Mag.*, vol. 6, no. 3, May 2008.

[2] N. Hatziargyriou, H. Asano, M. R. Iravani, and C. Marnay, "Microgrids: An Overview of Ongoing Research, Development and Demonstration Projects," *IEEE Power and Energy Mag.*, vol. 5, no. 4, Jul./Aug. 2007.

[3] B. Kroposki, R. Lasseter, T. Ise, S. Morozumi, S. Papathanassiou, and N. Hatziargyriou, "Making microgrids work," *IEEE Power and Energy Mag.* vol. 6, no. 3, May 2008.

[4] J. Kim, J. Jeon, S. Kim, C. Cho, J. H. Park, H. Kim, K. Nam, "Cooperative control strategy of energy storage system and microsources for stabilizing the microgrid during islanded operation," *IEEE Trans. On Power Electronics*, vol. 25, no. 12, Sep. 2010.

[5] U. Kwhannet, N. Sinsuphun, U. Leeton and T. Kulworawanichpong, "Impact of energy storage in microgrid systems with DGs," in *Proc. International conference on power system technology (POWERCON)*, Hangzhou, Oct. 2010.

[6] N. Jayawarna, C. Jones, M. Barnes, N. Jenkins, "Operating microgrid energy storage control during network faults," IEEE International Conference on Systems Engineering, San Antonio, Texas, Apr. 2007.

[7] K. E. Nygard, et. al., "Decision support independence in a smart grid," *in Proc. Second International Conference on Smart Grids, Green Communications and IT Energy-aware Technologies*, pp. 69-74, Mar. 2012.

[8] A. G. Tsikalakis, N. D. Hatziargyriou, "Centralized control for optimizing microgrids operation," *IEEE Trans. on Energy Conversion*, vol. 23, no. 1, Mar. 2008.

[9] J. A. P. Lopes, C. L. Moreira, A. G. Madureria, "Defining control strategies for microgrids islanded operation," *IEEE Trans. Power Syst.*, vol. 12, no. 2, May 2006.

[10] S. Ahn, J. Park, I. Chung, S. Moon, S. Kang, S. Nam, "Power-sharing method of multiple distributed generators considering control modes and configurations of a microgrid," *IEEE Trans. on Power Delivery*, vol. 25, no. 3, Jul. 2010.

[11] F. Katiraei, M. R. Iravani, "Power management strategies for a microgrid with multiple distributed generation units," *IEEE Trans. Power Syst.*, vol. 21, no. 4, Nov. 2006.

[12] P. Jahangiri, M. Fotuhi-Firuzabad, "Reliability assessment of distributed system with distributed generation," in *Proc. IEEE 2nd Conference on Power and Energy, PECon*, pp. 1551-1556, Dec.2008.

[13] M. Fotuhi-Firuzabad, A. Rajabi-Ghahnavie, "An analytical method to consider DG impacts on distribution system reliability," in *Proc. IEEE Transmission and Distribution Conference and Exhibition*, pp. 1-6, Aug. 2005.

[14] S. Kennedy, M. Marden, "Reliability of islanded microgrids with stochastic generation and prioritized load," IEEE Powertech, Bucharest, Jun. 2009.

[15] I. Bae and J. Kim, "Reliability evaluation of customers in a microgrid", *IEEE Trans. Power Syst.*, vol. 23, no. 3, Aug. 2008.

[16] R. Billinton and R. Allan, *Reliability Evaluation of Power Systems*, Second Edition, London: Plenum Publishing Corporation, New York 1996.

[17] L. Wu, M. Shahidehpour, and T. Li, "Stochastic security-constrained unit commitment," *IEEE Trans. Power Syst.*, vol. 22, no. 2, pp. 800-811, May. 2007.

[18] L. Wu, M. Shahidehpour, and Z. Li, "GENCO's risk-constrained hydrothermal scheduling," *IEEE Trans. Power Syst.*, vol. 23, no. 4, pp. 1847-1858, Nov. 2008.

[19] P. Glasserman, *Monte Carlo Method in Financial Engineering*, Springer, New York, 2003.

[20] C. E. Lin, Y. S. Shiao, C. L. Huang, P. S. Sung, "A real and reactive power control approach for battery energy storage system," *IEEE Trans. Power Syst.*, vol. 7, no. 3, pp. 1132-1140, 1992.

[21] M. Shahidehpour and Y. Fu, "Benders decomposition: applying Benders decomposition to power systems," *IEEE Power and Energy Magazine*, vol. 3, no. 2, pp. 20-21, March 2005

[22] Y. Fu, M. Shahidehpour, and Z. Li, "Security-constrained unit commitment with ac constraints," *IEEE Trans. on Power Systems*, vol. 20, no. 3, pp. 1538-1550, Aug. 2005.

[23] Y. Fu, M. Shahidehpour, and Z. Li, "AC contingency dispatch based on security-constrained unit commitment," *IEEE Trans. on Power Systems*, vol. 21, no. 2, pp. 897-908, May 2006.

[24] A. Flueck, Z. Li, "Destination: perfection", *IEEE Power and Energy Magazine*, vol. 6, no. 6, pp. 36-47, Nov. 2008.

[25] *IIT perfect power prototype final report*, Endurant Energy, Oct. 2007. [Online]. Available: http://www.galvinpower.org

[26] ComEd residential real-time price (RRTP) of electricity in Chicago [Online]. Available: http://www.thewattspot.com/.

[27] J. Dupačová, N. Gröwe-Kuska, and W. Römisch, "Scenario reduction in stochastic programming: An approach using probability metrics," *Math. Program.*, ser. A 95, pp. 493–511, 2003.

[28] GAMS/SCENRED Documentation. [Online]. Available: http://www.gams.com/docs/document.htm.


## BIOGRAPHIES

**Mohammad E Khodayar** (S'09) received his MS degree in electrical engineering from Sharif University of Technology, Tehran, Iran in 2006. He is a Ph.D student in electrical engineering at Illinois Institute of Technology. His research interests include power system operation and planning.

**Masoud Barati** (S'09) is a Ph.D. student in the Electrical and Computer Engineering Department at the Illinois Institute of Technology. His research interests include operation and economics in smart grid.

**Mohammad Shahidehpour** (F'01) is the Bodine Professor and Director of the Robert W. Galvin Center for Electricity Innovation at Illinois Institute of Technology. He is an Honorary Professor in the King Abdulaziz University in Saudi Arabia, North China Electric Power University, and Sharif University of Technology in Iran.

# Microgrid-based Co-optimization of Generation and Transmission Planning in Power Systems

Amin Khodaei, *Member, IEEE* and Mohammad Shahidehpour, *Fellow, IEEE*

***Abstract*— This paper presents an algorithm for the microgrid planning as an alternative to the co-optimization of generation and transmission expansion planning in electric power systems. The integration of microgrids in distribution systems will offer a decentralized control of local resources for satisfying the network reliability and the power quality required by local loads. The objective in this paper is to minimize the total system planning cost comprising investment and operation costs of local microgrids, the co-optimized planning of large generating units and transmission lines, and the expected cost of unserved energy. The cost of unserved energy reflects the cost of load shedding which is added to the objective function for reliability considerations. The microgrid-based co-optimization planning problem is decomposed into a planning problem and annual reliability subproblem. The optimal integer planning decisions calculated in the planning problem will be examined against the system reliability limits in the subproblem and the planning decisions will be revised using proper feasibility cuts if the annual reliability limits are violated. Numerical simulations demonstrate the effectiveness of the proposed microgrid-based co-optimization planning in power systems and explore the economic and reliability merits of microgrid planning as compared to grid-based generation and transmission upgrades.**

***Index Terms*— Power system expansion planning, microgrids, co-optimization of transmission and generation planning, Annual reliability**

## NOMENCLATURE

***Indices:***

| | |
|---|---|
| $b$ | Index for load blocks |
| $h$ | Index for periods |
| $i$ | Index for generating units |
| $l$ | Index for transmission lines |
| $m$ | Index for buses |
| $q$ | Index for microgrids |
| $s$ | Superscript for scenarios |
| $t$ | Index for years |
| $\wedge$ | Index for calculated variables |

***Sets:***

| | |
|---|---|
| $CG$ | Set of candidate generating units |
| $CL$ | Set of candidate transmission lines |
| $EG$ | Set of existing generating units |
| $EL$ | Set of existing transmission lines |
| $N_m$ | Set of components connected to bus $m$ |

***Parameters:***

| | |
|---|---|
| $B$ | Bus-line incidence matrix |
| $CC$ | Capital cost |
| $d$ | Discount rate |
| $D$ | HV bus load demand |
| $DT$ | Duration time |
| $M$ | Large positive constant |
| $NQ$ | Maximum number of microgrid installations |
| $PD$ | Microgrid load demand |
| $pr$ | Probability |
| $T$ | Number of years in the planning horizon |
| $T^{com}$ | Commissioning year |
| $UX$ | Contingency state of generating units |
| $UY$ | Contingency state of transmission lines |
| $VOLL$ | Value of lost load |
| $x$ | Reactance of line |
| $\kappa$ | Coefficient of present-worth value |
| $\gamma$ | Salvage factor |

***Variables:***

| | |
|---|---|
| $C$ | Total investment and operation cost |
| $CR$ | Cost of unserved energy |
| $EENS$ | Expected energy not served |
| $LS$ | Load shedding |
| $OC$ | Operation cost |
| $P$ | Unit generation |
| $PL$ | Line flow |
| $PM$ | Microgrid local generation |
| $u$ | Microgrid investment state |
| $y$ | Line investment state |
| $z$ | Unit investment state |
| $\omega$ | System load curtailment |
| $\theta$ | Voltage angle |
| $\lambda, \mu, \pi$ | Dual variables |

## I. INTRODUCTION

Microgrids generate, distribute and regulate the flow of electricity to local customers, representing a modern small-scale power system with a high degree of flexibility and efficiency in both supply and demand sectors [1]-[5]. Technically, a microgrid is a system with at least one distributed energy resource (DER) and one demand which can be islanded from the main power distribution system. In

A. Khodaei is with the Department of Electrical and Computer Engineering, University of Houston, Houston, TX 77004 USA (email: akhodaei@central.uh.edu). M. Shahidehpour is with the Robert W. Galvin Center for Electricity Innovation, Illinois Institute of Technology, Chicago, IL 60616 USA (e-mail: ms@iit.edu). This study was funded in part by the DOE Award # DE-FC26-08NT02875.

practice, microgrids are introduced to address the emergence of a large number of DERs in distribution systems and to ensure secure and optimal operations of potentially islanded power grids.

A microgrid is considered as a controllable aggregated load from a utility's point of view. The hourly operation of a microgrid is controlled by the microgrid master controller instead of a central dispatch provided by the utility. The DERs located within a microgrid differ from conventional power plants as they possess a smaller capacity, are directly connected to the microgrid distribution network, and could be customized to supply local load requirements [6].

The benefits of a microgrid include the improved reliability by introducing self-healing at the local distribution network, higher power quality by managing local loads, reduction in carbon emission by the diversification of energy sources, economic operation by reducing T&D costs, utilization of less costly renewable energy sources, and offering energy efficiency by responding to real-time market prices [7]-[10].

The salient feature of a microgrid is its ability to be islanded from the main grid by upstream switches at the point of common coupling (PCC). Islanding could be introduced for economic as well as reliability purposes. During main grid disturbances, microgrid is transferred from the grid-connected to the islanded mode and a reliable and uninterrupted supply of consumer loads is offered by local generation resources. The microgrid master controller would offer the optimal operation by maintaining the frequency and voltages within permissible ranges. The islanded microgrid would be resynchronized with the main grid once the disturbance is removed [11]-[13].

Microgrid alternatives to the traditional T&D expansion could reduce the total planning cost and increase the system reliability with a local control option for lowering the possibility of load shedding. Microgrids offer a lower construction time and are regarded as viable options for reducing the transmission congestion when large investments on new generation and transmission facilities are not forthcoming [14]-[18].

Previous power system planning studies investigated generation and transmission expansion planning methodologies in a vertically integrated power system (where a centralized generation and transmission expansion is performed), and a market-based environment (where proposed generation and transmission expansion planning options are coordinated) [19]-[29]. However, existing planning approaches did not consider the impact of microgrid installations on the power system expansion.

This paper utilizes a co-optimization approach to the generation and transmission expansion planning which also considers the most suitable locations for microgrid installations in a power system. The proposed approach considers short-term operation constraints in conjunction with the co-optimization planning of generation and transmission. The proposed microgrid-based co-optimization approach will simulate the iterative and the interactive planning coordination among generation companies, transmission companies, and the ISO in a competitive electricity market.

The proposed microgrid-based co-optimization planning is a mixed-integer programming (MIP) problem. The optimal cost of reliability is considered as an objective and the acceptable reliability level is modeled as a constraint. The Monte Carlo simulation is applied to simulate random component outages and a scenario reduction method is applied as a tradeoff between the computation time and the solution accuracy. The random outages of system components are considered in the calculation of annual expected energy not supplied (EENS).

The rest of the paper is organized as follows. Section II discusses the microgrid architecture and introduces microgrid components. Section III proposes the microgrid-based planning model, while Section IV presents the problem formulation. Section V presents illustrative examples to show the proposed model applied to a standard power system. Discussion on the features of the proposed model and concluding remarks are provided in Sections VI and VII, respectively.

## II. Microgrid Model

Fig. 1 depicts a typical microgrid configuration, where DERs are connected to loads through low voltage (LV) and medium voltage (MV) distribution networks. The PCC circuit breaker enables the microgrid islanding. The integration of DERs facilitates bidirectional electricity flows in the distribution network.

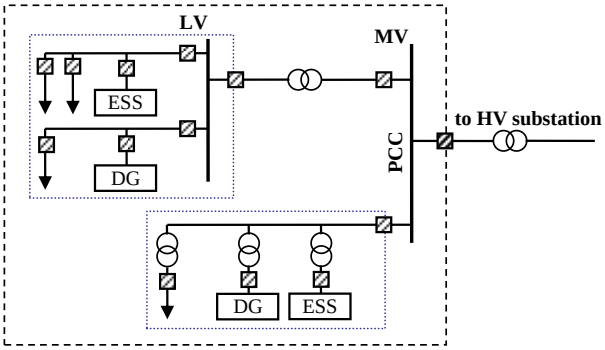


Fig. 1 A typical microgrid architecture (DG: distributed generation, ESS: energy storage system, PCC: point of common coupling)

The microgrids could be interconnected to form a cluster of microgrids. In this fashion, the loads in each microgrid would be supplied from several interconnected microgrids using a common distribution network. The interconnected microgrids would achieve greater stability and controllability as well as enhanced redundancy to ensure the supply reliability. The interconnection of microgrids significantly reduces the complexity in the control and operation of hundreds of individual DERs. DERs would seamlessly control power and provide required energy to local loads in the interconnection. We assume that DERs and loads are coordinated such that the microgrid generation is used solely to satisfy the interconnected microgrid loads or stored in the energy storage system. DERs in a microgrid are not designed to continuously generate power for supplying the main grid. By allowing such power transfers, the power system could further rely on the DER generation in lieu of large generation expansion planning. Thus, microgrids are regarded as controllable loads

in this study and no power generation is injected to the main grid from the interconnected microgrids. A microgrid may include several DERs with variable generation profiles; however, in this study, we assume DERs are aggregated in a cluster of microgrids for supplying local loads in which a microgrid is regarded a controllable load with a more settled hourly profile from the ISO's point of view. The intermittency of DERs inside a microgrid would require additional scenario generation to model DER operation. We assume the distribution network expansion is internalized as part of the microgrid cluster which would not be the ISO's concern.

## III. Proposed Microgrid-Based Planning Model

Fig. 2 depicts the proposed microgrid-based planning model. We assume candidate microgrids installed at designated buses would normally be operated in a grid-connected mode. In the case of a main grid disturbance, however, the microgrid would switch over to an islanded mode to satisfy local loads. The investments are analyzed on an annual basis. A year is decomposed into multiple periods and the load duration curve (LDC) is utilized with load blocks at each period. The number and the duration of load blocks are considered as a tradeoff between the accuracy and the computation burden in the proposed planning model. The load forecast at every block in every period of the planning horizon is met by system operation and expansion planning decisions.

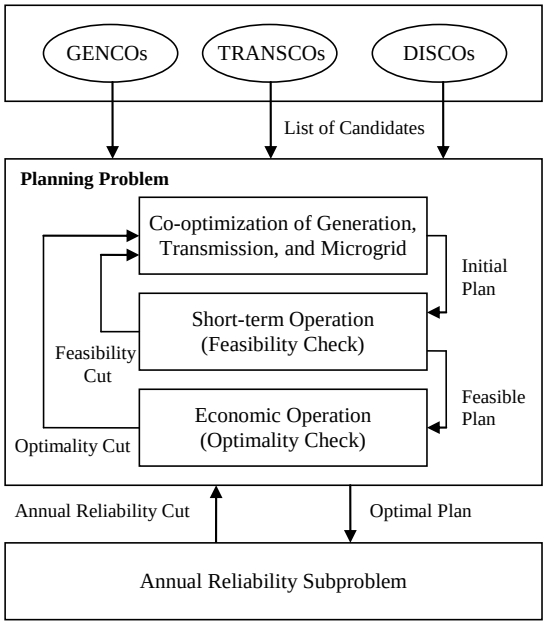


Fig. 2 Proposed microgrid-based co-optimization planning model

The planning problem in Fig. 2 co-optimizes the least-cost options of candidate generating units, transmission lines, and microgrids for supplying the load forecast and satisfying prevailing operation and planning constraints. The objective comprises investment costs and salvage values for new resources, operation costs of generating units and microgrids, and the cost of unserved energy.

A decomposition is applied in Fig. 2 to coordinate the operation and planning constraints as part of the co-optimization scheme. The decomposition would separate the planning problem into a co-optimization of generation, transmission and microgrid, a short-term operation subproblem (which checks the transmission network constraints in the proposed plan) and an economic operation subproblem (which finds the optimal system operation based on the proposed plan). If the feasibility or the optimality check fails, proper cuts are generated in the corresponding subproblems and added to the next iteration of co-optimization of generation, transmission and microgrid. This iterative process will continue until a secure and optimal expansion planning solution is achieved.

## IV. Microgrid-Based Planning Problem Formulation

### A. Planning Problem

The objective of the proposed microgrid-based planning problem is to minimize the total planning cost throughout the planning horizon as shown in (1)

$$Min \quad \sum_t \sum_i \kappa_t C_{it} + \sum_t \sum_l \kappa_t C_{lt} + \sum_t \sum_m \sum_q \kappa_t C_{qmt} + \sum_t \kappa_t CR_t \qquad (1)$$

Here, $\kappa_t = 1/(1+d)^{t-1}$ is the present-worth value coefficient. The objective includes investment and operation costs associated with new generating units, transmission lines, and microgrids, in addition to the cost of unserved energy. The objective is evaluated in terms of discounted costs, where discount rates are incorporated in the present-worth cost components. A higher discount rate would affect investments as candidates with higher investment costs become inferior. The cost of unserved energy in the objective would represent the economics of system reliability.

Equations (2)-(5) define cost terms used in the objective function. The generation costs (2) include the investment cost of new generating units and the operation cost of existing and installed units. The operation cost includes fuel and maintenance costs. The investment cost of new transmission lines is represented by (3). The salvage value, i.e., the percentage of depreciation of the initial investment, is included in the investment cost to represent the monetary value of the installed resource at the end of the planning horizon. $\kappa_T$ is the worth value coefficient of the resources at the end of the planning horizon.

$$C_{it} = CC_i P_i^{\max} (z_{it} - z_{i(t-1)}) - \frac{\kappa_T}{\kappa_t} \gamma_{it} CC_i P_i^{\max} (z_{it} - z_{i(t-1)}) + \sum_h \sum_b DT_{bht} OC_i P_{ibht} \qquad (2)$$

$$C_{lt} = CC_l PL_l^{\max} (y_{lt} - y_{l(t-1)}) - \frac{\kappa_T}{\kappa_t} \gamma_{lt} CC_l PL_l^{\max} (y_{lt} - y_{l(t-1)}) \qquad (3)$$

$$C_{qmt} = CC_{qm} (PM_{qmt}^{\max} u_{qmt} - PM_{qm(t-1)}^{\max} u_{qm(t-1)}) - \frac{\kappa_T}{\kappa_t} \gamma_{qmt} CC_{qm} (PM_{qmt}^{\max} u_{qmt} - PM_{qm(t-1)}^{\max} u_{qm(t-1)}) + \sum_h \sum_b DT_{bht} OC_{qm} PM_{qmbht} \qquad (4)$$

$$CR_t = VOLL_t EENS_t \qquad (5)$$

The candidate generating units and transmission lines will

be commissioned once the planning, the detailed engineering design, and the construction work are completed. The commissioning time is dependent on the type and the size of the unit (6)-(7). Once a candidate generating unit or transmission line is installed, its investment state will be fixed at 1 for the remaining years in the planning horizon (8)-(9).

$$z_{it} = 0 \qquad \forall i \in CG,\ \forall t < T_i^{\text{com}} \tag{6}$$

$$y_{lt} = 0 \qquad \forall l \in CL,\ \forall t < T_l^{\text{com}} \tag{7}$$

$$z_{i(t-1)} \le z_{it} \qquad \forall i \in CG,\ \forall t \tag{8}$$

$$y_{l(t-1)} \le y_{lt} \qquad \forall l \in CL,\ \forall t \tag{9}$$

The investment and operation costs of a microgrid would depend on the size and the type of DERs used in the microgrid. The microgrid investment cost is assumed to be a linear function of its generation capacity. The operation cost is obtained based on the microgrid generation dispatch. The total planning cost of the microgrid is the sum of its investment and operation costs minus its salvage value (4).

The bus load supply is limited to the associated microgrid generation capacity (10)-(11). The microgrid would shift seamlessly from grid-connected to the islanded mode for supplying local loads. The microgrid generation (12) would either supply loads at associated microgrids or be stored at local storage facilities (rather than feeding the main grid loads). A microgrid could be subject to further expansion (13) to supply the local load forecast. Microgrids are interconnected to form a cluster so that the required reserve in one microgrid could be supplied by the interconnected microgrids where DERs would seamlessly provide the required energy to local loads in the interconnection. In a case that a microgrid is not interconnected to other microgrids, (10) would be modified to increase the installed capacity and further consider the required spinning reserve.

$$PM_{qmt}^{\max} = \underset{h,b}{Max}\left\{PD_{qmbht}\right\} \qquad \forall q, \forall m, \forall t \tag{10}$$

$$PM_{qmbht} \le PM_{qmt}^{\max} u_{qmt} \qquad \forall q, \forall m, \forall b, \forall h, \forall t \tag{11}$$

$$\sum_{q} (PM_{qmbht} - PD_{qmbht}) \le 0 \qquad \forall m, \forall b, \forall h, \forall t \tag{12}$$

$$u_{qm(t-1)} \le u_{qmt} \qquad \forall q, \forall m, \forall t \tag{13}$$

The cost of unserved energy defined by (5) is obtained based on EENS and the value of lost load (VOLL). EENS is calculated in the subproblem and added in each iteration to the planning problem. The EENS in the first iteration is the base case system reliability. VOLL, which is the load shedding price for compensating customers, depends on several factors including the types of customers, the amount and the duration of load interruption, and the time of outage. A higher VOLL corresponds to lower load shedding [30]-[31]. VOLL is given as an input to our model.

The proposed co-optimization expansion planning objective is subject to prevailing operation constraints, such as the limits on generation, fuel, ramping, emission, etc., and transmission network constraints [32]-[33]. A dc power flow is used, where it is assumed that the voltage related concerns would be handled by the microgrid master controller. Additional details on the decomposition of the planning problem are found in [34]-[37].

### *B. Role of Annual Reliability*

Once the optimal planning decisions for microgrids and the main grid are made in the planning problem, the new system topology is sent to the subproblems to calculate the annual EENS. The annual reliability calculation at load block *b*, period *h*, year *t* and scenario *s* is formulated in (14)-(28).

The objective (14) is to minimize the load curtailment for balancing purposes in the case of system component outages [38]. Equation (15) defines the load balance at each system bus incorporating load shedding variable. The dual variables are obtained in (16)-(18) to represent the incremental reduction in load curtailments with regards to system investments. The dual variables are used to generate investment signals for consequent iterations of the planning problem. The existing and candidate generating unit capacity limits are defined by (19)-(20), respectively. Constraints on existing transmission lines are imposed by (21)-(22), while those of candidate transmission lines are (23)-(24). The microgrid generation is limited by (25), while that of a cluster of microgrids in limited by (26). Load shedding is limited by (27). The phase angle of the reference bus is set to zero by (28).

$$Min \quad \omega_{bht}^{s} = \sum_{m} (LS_{mbht}^{s}) \tag{14}$$

$$\sum_{i \in N_m} P_{ibht}^{s} + \sum_{l \in N_m} PL_{lbht}^{s} + \sum_{q} PM_{qmbht}^{s} + LS_{mbht}^{s} = D_{mbht} \qquad \forall m \tag{15}$$

$$z_{it} = \hat{z}_{it} \quad \leftrightarrow \quad \lambda_{it}^{s} \qquad \forall i \in CG \tag{16}$$

$$y_{lt} = \hat{y}_{lt} \quad \leftrightarrow \quad \mu_{lt}^{s} \qquad \forall l \in CL \tag{17}$$

$$u_{qmt} = \hat{u}_{qmt} \quad \leftrightarrow \quad \pi_{qmt}^{s} \qquad \forall q \tag{18}$$

$$0 \le P_{ibht}^{s} \le P_i^{\max} UX_{ibht}^{s} \qquad \forall i \in EG \tag{19}$$

$$0 \le P_{ibht}^{s} \le P_i^{\max} UX_{ibht}^{s} z_{it} \qquad \forall i \in CG \tag{20}$$

$$\left| PL_{lbht}^{s} - \sum_{m} B_{l,m} \theta_{mbht}^{s} \right| x_l \le M\,(1 - UY_{lbht}^{s}) \qquad \forall l \in EL \tag{21}$$

$$\left| PL_{lbht}^{s} \right| \le PL_l^{\max} UY_{lbht}^{s} \qquad \forall l \in EL \tag{22}$$

$$\left| PL_{lbht}^{s} - \sum_{m} B_{l,m} \theta_{mbht}^{s} \right| x_l \le M\,(1 - UY_{lbht}^{s}) + M\,(1 - y_{lt}) \qquad \forall l \in CL \tag{23}$$

$$\left| PL_{lbht}^{s} \right| \le PL_l^{\max} UY_{lbht}^{s} y_{lt} \qquad \forall l \in CL \tag{24}$$

$$0 \le PM_{qmbht}^{s} \le PM_{qmt}^{\max} u_{qmt} \qquad \forall q \tag{25}$$

$$\sum_{q} (PM_{qmbht}^{s} - PD_{qmbht}^{s}) \le 0 \qquad \forall m \tag{26}$$

$$0 \le LS_{mbht}^{s} \le PD_{mbht} \qquad \forall m \tag{27}$$

$$\theta_{mbht}^{s} = 0 \qquad m = \text{Ref} \tag{28}$$

In the above formulation, the constraints on candidate generating unit, transmission line, and microgrids include the associated binary variables determined in the planning problem. The contingency state of generating units and

transmission lines are included in the set of constraints. The Monte Carlo simulation is applied to model the random outages of generating units and transmission lines [39]-[40]. Moreover, a scenario reduction method is adopted as a tradeoff between the computational burden and the modeling accuracy. An outage in a microgrid will be compensated by adjacent microgrids rather than the main grid. The annual EENS for a system of microgrids is calculated as

$$EENS_t = \sum_h \sum_b \sum_s pr^s DT_{bht} \omega^s_{bht} \qquad \forall t \tag{29}$$

If the EENS limit is violated, reliability constraints (30)-(31) are generated and added to the planning problem for promoting investments on new generating units, transmission lines, and microgrids.

$$EENS_t = \sum_h \sum_b \sum_s pr^s DT_{bht} \omega^s_{bht} + \sum_s \sum_{i \in CG} pr^s \lambda^s_{it} (z_{it} - \hat{z}_{it}) + \sum_s \sum_{l \in CL} pr^s \mu^s_{lt} (y_{lt} - \hat{y}_{lt}) + \sum_s \sum_q \sum_m pr^s \pi^s_{qmt} (u_{qmt} - \hat{u}_{qmt}) \quad \forall t \tag{30}$$

$$EENS_t \le EENS_t^{\text{target}} \qquad \forall t \tag{31}$$

where $\lambda$, $\mu$, and $\pi$ are dual values of constraints (16)-(18), respectively. In addition, the reliability constraints facilitate the calculation of cost of unserved energy in the planning problem. The iterative procedure will continue until an optimal plan is calculated.

## V. Numerical Simulations of the Planning Problem

A modified IEEE 118-bus system is used to demonstrate the application of the proposed model for microgrid-based co-optimization of generation and transmission planning. The system has 118 buses, 54 units and 186 branches. The data are given in motor.ece.iit.edu/data/MicrogridPlanning.xls. A set of 16 candidate generating units and 8 candidate transmission lines are considered. Forced outage rates of generating units and transmission lines are 4% and 1%, respectively. A 20-year planning horizon is considered. Each planning year is divided into 12 monthly periods. The monthly load is divided into three load blocks representing off-peak, intermediate and peak loads. The quantity and the duration of load blocks may vary in each period within each year. The planning is performed annually while the operation is carried out for each load block. The VOLL is \$10/kWh and the discount rate is 5%.

There are no limitations on annual investments or the number of microgrids, generating units or transmission lines that could be installed annually. The initial system peak load is 5400 MW with an annual load growth rate of 2.9%. Table I shows annual peak load forecasts. The initial available generation capacity is 5,850 MW. The EENS limit of 150 MWh is considered for the first planning year. The EENS limit is increased 2.9% annually as shown in Table II. The total EENS for the entire planning horizon is limited to 3,990 MWh.

We assume microgrids can be installed at any system buses with an investment cost of \$2000/kW and operation cost of \$1/MWh for microgrids [41]. The Monte Carlo simulation is applied to generate scenarios and simulate random outages of system components. Each possible system state is represented by a scenario. A uniformly distributed random number from 0 to 1 is sampled for representing the outages of generating units and transmission lines. If the random number is less than the associated forced outage rate, the corresponding generating unit or transmission line is on outage, otherwise it is in service [39]-[40]. The scenario reduction is applied which reduces the number of scenarios from 1000 to 12 and the corresponding probabilities are demonstrated in Table III. The probability metrics based scenario reduction method [39] is applied in this paper. The proposed planning method is implemented on a 2.4-GHz personal computer using CPLEX 11.0 [42].

TABLE I
ANNUAL PEAK LOAD FORECAST

| Year | 1 | 2 | 3 | 4 | 5 |
|---|---|---|---|---|---|
| Peak Load (MW) | 4000 | 4116 | 4235 | 4385 | 4485 |
| Year | 6 | 7 | 8 | 9 | 10 |
| Peak Load (MW) | 4615 | 4748 | 4886 | 5028 | 5174 |
| Year | 11 | 12 | 13 | 14 | 15 |
| Peak Load (MW) | 5324 | 5478 | 5637 | 5800 | 5969 |
| Year | 16 | 17 | 18 | 19 | 20 |
| Peak Load (MW) | 6142 | 6320 | 6503 | 6692 | 6886 |

TABLE II
ANNUAL EENS LIMIT

| Year | 1 | 2 | 3 | 4 | 5 |
|---|---|---|---|---|---|
| EENS (MWh) | 150.00 | 154.35 | 158.83 | 163.43 | 168.17 |
| Year | 6 | 7 | 8 | 9 | 10 |
| EENS (MWh) | 173.05 | 178.07 | 183.23 | 188.54 | 194.01 |
| Year | 11 | 12 | 13 | 14 | 15 |
| EENS (MWh) | 199.64 | 205.43 | 211.39 | 217.52 | 223.82 |
| Year | 16 | 17 | 18 | 19 | 20 |
| EENS (MWh) | 230.31 | 236.99 | 243.87 | 250.94 | 258.22 |

TABLE III
PROBABILITIES OF SCENARIOS AFTER SCENARIO REDUCTION

| Scenario | 1 | 2 | 3 | 4 | 5 | 6 |
|---|---|---|---|---|---|---|
| Probability | 0.6103 | 0.0330 | 0.0273 | 0.0317 | 0.0497 | 0.0357 |
| Scenario | 7 | 8 | 9 | 10 | 11 | 12 |
| Probability | 0.0293 | 0.0250 | 0.0383 | 0.0347 | 0.0430 | 0.0420 |

The following cases are studied:

**Case 0:** Base case planning of the main grid generating units

**Case 1:** Co-optimization planning of the main grid generating units and transmission lines

**Case 2:** Co-optimization planning of the main grid generating units with microgrids

**Case 3:** Co-optimization planning of the main grid generating units and transmission lines with microgrids

**Case 0:** The existing system cannot satisfy the load growth in the planning horizon. The existing generation capacity is larger than the load in years 1-14; however, the system is unable to meet the load and satisfy the reliability requirements together in years 5-20. In years 5-20, the annual EENS limit is violated and additional load shedding is unavoidable. Accordingly, generating units 1-7 and 9-11 are installed by the proposed planning problem to meet the forecasted load. However, the expanded generation capacity does not satisfy system reliability requirements in the subproblems. Although, the original EENS is reduced once the new units are installed, the new EENS would violate the EENS limit in years 5-20. In this case, additional units would violate the EENS limit when the transmission network is congested.

**Case 1:** The 20-year co-optimization planning of the main grid generation and transmission expansion planning is applied without any microgrid installations. The candidate generating units and transmission lines installation years are shown in Tables IV and V, respectively. The installed generation capacity at the end of the planning horizon is 7,590 MW with a total planning cost of $4.496B. The total EENS is 862.47 MWh and the cost of unserved energy is $4M. Load shedding occurs partially at buses 1,4,35,59,60,95 and 117. The load shedding in this case is an economic option that is offered by the planning solution. In this case, the proposed load shedding would replace the installation of candidate units 14-16.

TABLE IV
CANDIDATE UNITS AND INSTALLATION YEARS

| Candidate Unit | Bus | Capacity (MW) | Inv. Cost ($/kW) | Comm. (year) | Case 1 | Case 2 | Case 3 |
|---|---|---|---|---|---|---|---|
| 1 | 5 | 200 | 750 | 10 | 14 | 20 | 14 |
| 2 | 12 | 200 | 750 | 10 | 11 | 16 | 11 |
| 3 | 25 | 200 | 750 | 10 | 17 | - | - |
| 4 | 26 | 200 | 750 | 10 | 20 | - | - |
| 5 | 80 | 200 | 750 | 10 | 15 | 20 | 19 |
| 6 | 89 | 200 | 750 | 10 | 13 | 20 | 20 |
| 7 | 18 | 100 | 400 | 6 | 19 | 11 | - |
| 8 | 32 | 100 | 400 | 6 | 20 | 15 | - |
| 9 | 55 | 100 | 400 | 6 | 17 | - | - |
| 10 | 56 | 100 | 400 | 6 | 19 | - | - |
| 11 | 62 | 100 | 400 | 6 | 18 | - | - |
| 12 | 78 | 20 | 200 | 3 | 20 | - | - |
| 13 | 78 | 20 | 200 | 3 | 20 | - | - |
| 14 | 78 | 20 | 200 | 3 | - | - | - |
| 15 | 95 | 20 | 200 | 3 | - | - | - |
| 16 | 95 | 20 | 200 | 3 | - | - | - |

TABLE V
CANDIDATE LINES AND INSTALLATION YEARS

| Candidate Line | From Bus | To Bus | Capacity (MW) | Inv. Cost ($/kW) | Comm. (year) | Case 1 | Case 2 | Case 3 |
|---|---|---|---|---|---|---|---|---|
| 1 | 8 | 5 | 200 | 267 | 5 | 5 | - | 5 |
| 2 | 11 | 12 | 100 | 196 | 4 | - | - | - |
| 3 | 26 | 30 | 200 | 860 | 5 | - | - | - |
| 4 | 38 | 37 | 200 | 375 | 5 | 15 | - | - |
| 5 | 77 | 78 | 100 | 124 | 4 | - | - | - |
| 6 | 94 | 100 | 100 | 580 | 4 | 20 | - | - |
| 7 | 99 | 100 | 100 | 813 | 4 | - | - | - |
| 8 | 17 | 113 | 100 | 301 | 4 | - | - | - |

**Case 2**: The co-optimization planning of microgrids and the main grid generation is considered. Table VI summarizes the total planning cost along with the expected cost of unserved energy. In Case 2, 42 microgrids are installed and a partial load shedding is applied to buses 4,59,60, and 82. Table IV shows that the microgrid installations would eliminate the requirement for the installation of generating units 3, 4 and 9-16. The total EENS is 1047.37 MWh which entails to a higher load shedding as compared to that in Case 1. In Case 1, we considered the installation of candidate transmission line 1 which would reduce the congestion on the existing line 4-5, and accordingly reduce the load shedding at bus 4. However in Case 2, a higher total EENS occurs when no microgrid is installed at bus 4. As will be discussed in Case 3, the system will consider the installation of a transmission line in order to reduce EENS.

The total investment cost is increased and the total operation cost is decreased in Case 2 as compared to Case 1. The proposed microgrid installations will mitigate the congestion on transmission lines 2-12, 23-25 and 84-85. The generation supply by less expensive units will be increased in a less congested grid and the operation cost will be reduced. The installed microgrid capacity at the end of the planning horizon would supply 30% of the associated peak load, which shows that the majority of loads will be satisfied by the main grid generation. In this case, the total planning cost is lowered by 1.36% to $4.435B as compared to that in Case 1, which suggests that the Case 2 provides a more economical solution with a higher EENS.

Fig. 3 illustrates the total planning cost and the cost of unserved energy as a function of the microgrid capital cost. The microgrid capital cost depends on the type and the location of DER. A less expensive microgrid will result in a higher number of microgrid installations which will reduce the level of load shedding and the cost of unserved energy. In addition, fewer generating units will be installed at the main grid level. A microgrid with a capital cost of $1000/kW will result in the installation of 5 generating units and 52 microgrids, while a microgrid with a capital cost of $3000/kW will result in the installation of 9 generating units and 12 microgrids. Fig. 3 illustrates that the investment cost is a decisive factor in microgrid installations, though microgrids will offer low operation costs for supplying local loads. As microgrid investment costs increase, it will be more economical to build a candidate generating unit at the main grid level and/or consider additional load shedding as microgrid installations become inferior.

TABLE VI
SUMMARY OF SYSTEM COSTS ($BILLION)
(G: GENERATING UNIT, T: TRANSMISSION LINE, M: MICROGRID)

| Costs ($Billion) | Case 1 | | | Case 2 | | | Case 3 | | |
|---|---|---|---|---|---|---|---|---|---|
| | G | T | M | G | T | M | G | T | M |
| Investment Cost | 0.225 | 0.052 | - | 0.062 | - | 0.435 | 0.115 | 0.036 | 0.221 |
| Operation Cost | 4.215 | - | - | 3.916 | - | 0.017 | 4.045 | - | 0.009 |
| Unserved Energy Cost | 0.004 | | | 0.005 | | | 0.003 | | |
| Total Planning Cost | 4.496 | | | 4.435 | | | 4.429 | | |

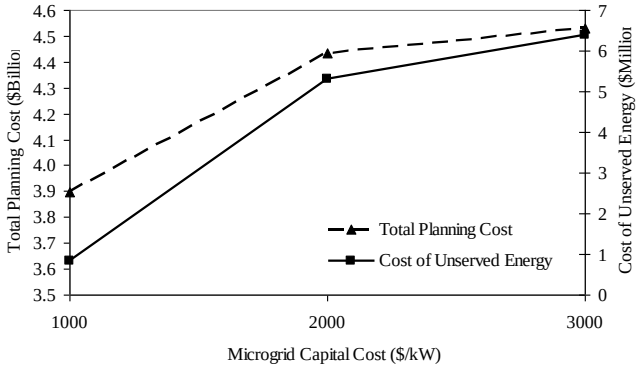


Fig. 3 Cost of planning and unserved energy as a function of microgrid capital cost

In this paper, VOLL is fixed at $10/kWh at all buses. However, VOLL depends on the types of customers, the amount and the duration of load interruptions, and the time in which the interruption occurs [43]. VOLL, which would impact the unserved energy, would accordingly influence microgrid investments. Fig. 4 illustrates the total planning cost

and the cost of unserved energy as a function of VOLL. Fig. 4 shows that smaller VOLL will result in higher unserved energy. On the other hand, higher VOLL will reduce the system EENS and the cost of unserved energy which corresponds to a higher investment in system planning. Therefore, VOLL will control the expected level of load shedding at each load bus. When VOLL is \$10/kWh, load will be partially curtailed at buses 4,36,59,60,82,93,94. As VOLL increases to \$20/kWh, more microgrids are installed and the load shedding is dropped at buses 36,93,94. When VOLL is \$30/kWh, an additional microgrid is installed at bus 62. So, higher VOLL will results in additional microgrid investments.

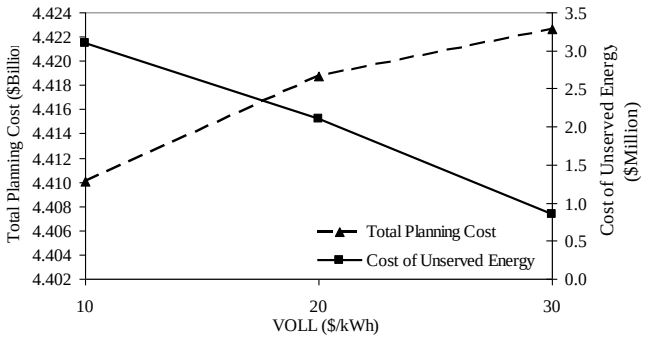


Fig. 4 Total planning cost and cost of unserved energy as a function of VOLL

**Case 3:** A co-optimization expansion planning is considered for the microgrids and the main grid generating units and transmission lines. Table IV shows that only 4 units are installed. Transmission line 1 is installed at year 5 to reduce the congestion on existing line 4-5, enhance generation of unit 1 (at bus 5) and reduce load shedding in bus 4. The low capital cost of this candidate transmission line makes it a more viable investment option as compared to a microgrid installation at bus 4. It is presumed that the microgrids will be installed in a year. As the commissioning time of generating units and transmission lines are large, several microgrids are installed in years 1-4 to reduce the system EENS and meet the system reliability requirements. In this case, a total of 31 microgrids are installed in the planning horizon and transmission line flows are altered as compared to previous cases.

The transmission congestion on lines 4-5, 15-17, 23-25, 84-85 and 17-113 is mitigated. The total planning cost is less by 1.49% as compared to that in Case 1 and 0.13% as compared to that in Case 2. The presented result indicates that higher reliability and economic milestones are attainable in a co-optimization planning of the main grid and microgrids.

The microgrids represent the aggregation of several buses and, as such, can be installed at any main grid regions. In the given system, bus 117 represents a remote bus which is interconnected with the rest of the system through a single transmission line. The annual peak load at this bus in year 1 is 4 MW which increases to 6.88 MW in year 20. The lack of enough generation at this bus, following the line outage, will result in the curtailment of the entire load. The outage of this single line may result in an expected unserved energy of 643.48 MWh (when peak load with probability of 0.042 occurs in a scenario). The load shedding at this bus may be reduced by the installation of either a second transmission line to connect this bus to the rest of the system or a microgrid at this remote bus location. The first option may feature high installation costs and large commissioning time of the transmission line. Therefore, a microgrid is considered as a quick and efficient solution to this curtailment problem.

Next, we would limit the number of microgrid installations to *NQ*, where $\sum_m u_{qmt} \le NQ, \forall t$ in order to provide an insight on a reasonable number of microgrid installations, how microgrid installations would affect the operation and reliability results, and the most suitable buses for microgrid installations, the expansion planning problem. Table VII summarizes the results. The necessary investments on generating units and transmission lines will drop when a higher number of microgrids are installed at proper locations. The locations and the number of microgrids will depend on the maximum number of microgrids that can potentially be installed. The microgrid installations could reduce the annual EENS. However, the total EENS will not change monotonically with the number of installed microgrids. Comparing the load shedding level in Cases 1 and 2 with the number of installed microgrids in Table VII, it is clear that the majority of microgrids are installed at buses where load shedding occurs (i.e., buses 1,35,60,95). There are a few other buses with load shedding (i.e. buses 4,59,82) where microgrids are not ultimately installed. The additional dispatch of generating unit at the main grid level would mitigate the load shedding at these buses. Therefore, microgrids are primarily installed at buses where the load shedding is eminent and local generating units are insufficient to supply the designated load.

TABLE VII
SUMMARY OF MICROGRID INSTALLATIONS

| Max. No. of Microgrids | Microgrid Installations | Unit Installations | Line Installations | Total EENS (MWh) |
|---|---|---|---|---|
| 1 | 60 | 1-11 | 1, 4, 6 | 958 |
| 2 | 35, 95 | 1-13 | 1, 4, 6 | 1209 |
| 3 | 1, 35, 60 | 1-11 | 1, 4 | 862 |
| 4 | 35, 39, 41, 60 | 1-3, 5-11 | 1, 4 | 968 |
| 5 | 35, 39, 41, 45, 60 | 1-3, 5-11 | 1, 4 | 1055 |
| 6 | 1, 35, 39, 41, 60, 83 | 1-3, 5-7, 9-11 | 1, 4 | 526 |
| 7 | 1, 11, 35, 39, 41, 45, 60 | 1-3, 5-7, 9-11 | 1, 4 | 380 |
| 8 | 1, 11, 35, 39, 41, 45, 60, 95 | 1-3, 5-7, 9-10 | 1, 4 | 707 |
| 9 | 1, 11, 35, 39, 41, 45, 60, 88, 95 | 1, 2, 4-7, 10, 11 | 1, 4 | 1208 |
| 10 | 1, 13, 33, 35, 39, 41, 45, 60, 83, 95 | 1-3, 4-9 | 1 | 822 |

## VI. DISCUSSIONS

Microgrids increase the system reliability (by reducing load shedding and enhancing the local controls) and improve the system economics (by reducing system congestion, enhancing the operation of less expensive units, and reducing the need for additional generation and transmission investments). Specific features of the proposed microgrid-based co-optimization

planning of generation and transmission are listed as follows:

- Co-optimization expansion planning: The microgrid-based planning incorporates a co-optimization planning of generation and transmission. The microgrid investment decisions are made as planning alternatives to those of generation and transmission.
- Stochastic Planning Approach: A stochastic approach is applied to the proposed co-optimization planning approach to calculate the system reliability criterion. The stochastic planning employs the Monte Carlo simulation for the modeling of random outages of system components. The stochastic planning approach considers the microgrid as an alternative for enhancing the system reliability when considering the main grid contingencies.
- Enhancements in system operation: The generation and transmission upgrades are subject to large commissioning time and depend on the availability of geographical locations in the main grid; however, microgrids could be installed quickly in any selected system buses, providing a quick and efficient solution to the system reliability requirements.
- Optimal location of microgrids: All system buses are considered as potential options for microgrid installations. Most suitable buses for the installation of microgrids are located at constrained geographical locations which are often subject to hourly load curtailments.
- Economics of microgrids: Despite higher capital investment requirements, microgrids offer economic benefits to power systems. Microgrids could lower the cost of supplying the local loads by reducing the network congestion and enhancing the utilization of less expensive units in power systems.
- Economics of load shedding: A high VOLL in the proposed planning approach would justify the microgrid installation, while for lower VOLLs the economics of load shedding could be comparable with those of a microgrid installation.
- Computational efficiency: Microgrid-based co-optimization planning would include additional binary and continuous variables associated with microgrid investments and operations. In order to reduce the computational burdens, the reliability requirements are examined in annual reliability subproblems as post-processor, which would reduce the size of the microgrid-based planning problem and makes it possible to apply the approach to large-scale planning problems.

## VII. Conclusions

A microgrid-based co-optimization planning model considering the power system reliability and economic criteria was proposed. An efficient formulation of the microgrid installation was proposed, incorporating investment and operation costs of microgrids. The proposed problem considered the annual reliability as a planning criterion. The solution of the planning problem was obtained by minimizing the investment and operation costs of generating units, transmission lines and microgrids, as well as the cost of unserved energy. The problem utilized the proposed plan to calculate the system annual reliability index and compare it with the targeted EENS value. In the case of violations, reliability constraints were formed and added to the next iteration of the planning problem. The proposed model was analyzed further through numerical simulations, where it was shown that microgrid investments in the power system can provide significant reliability and economic benefits and are viable options for system upgrades when large investments on new generation and transmission facilities are not forthcoming.

## References


[1] M. Shahidehpour, "Role of smart microgrid in a perfect power system," *IEEE Power and Energy Society Gen. Meeting*, 2010.

[2] A. Flueck, Z. Li, "Destination perfection," *IEEE Power and Energy Mag*., vol. 6, no. 6, pp 36-47, Nov./Dec. 2008.

[3] M. Shahidehpour and J. Clair, "A functional microgrid for enhancing reliability, sustainability, and energy efficiency," *Electricity Journal*, Oct. 2012.

[4] S. Bahramirad, W. Reder, and A. Khodaei, "Reliability-constrained optimal sizing of energy storage system in a microgrid," *IEEE Trans. Smart Grid*, accepted for publication.

[5] N. Hatziargyriou, H. Asano, M.R. Iravani, and C. Marnay, "Microgrids: An overview of ongoing research, development and demonstration projects," *IEEE Power and Energy Mag.*, vol. 5, no. 4, Jul./Aug. 2007.

[6] A.G. Tsikalakis, N.D. Hatziargyriou, "Centralized control for optimizing microgrids operation," *IEEE Trans. Energy Conversion*, vol. 23, no. 1, Mar. 2008.

[7] B. Kroposki, R. Lasseter, T. Ise, S. Morozumi, S. Papathanassiou, and N. Hatziargyriou, "Making microgrids work," *IEEE Power and Energy Mag.* vol. 6, no. 3, May 2008.

[8] I. Bae and J. Kim, "Reliability evaluation of customers in a microgrid", *IEEE Trans. Power Syst.*, vol. 23, no. 3, Aug. 2008.

[9] M. Khodayar, M. Barati, and M. Shahidehpour, "Integration of high reliability distribution system in microgrid operation," *IEEE Trans. Smart Grid*, vol. 3, 2012.

[10] S. Kennedy, M. Marden, "Reliability of islanded microgrids with stochastic generation and prioritized load," *IEEE Powertech, Bucharest*, Jun. 2009.

[11] F. Katiraei, M.R. Iravani, "Power management strategies for a microgrid with multiple distributed generation units," *IEEE Trans. Power Syst.*, vol. 21, no. 4, Nov. 2006.

[12] C. Hou X. Hu, D. Hui, "Hierarchical control techniques applied in micro-grid," *IEEE Conf. on Power Syst. Tech. (POWERCON)*, Hangzhou, Oct. 2010.

[13] A.G. Tsikalakis, N.D. Hatziargyriou, "Centralized control for optimizing microgrids" *IEEE Trans. Energy Conv*., vol. 23, no. 1, pp. 241-248 2008.

[14] M. Shahidehpour, "Global broadcast - transmission planning in restructured systems," *IEEE Power Eng Mag.*, vol. 5, no. 5, pp. 18-20, Sep./Oct. 2007.

[15] S. de la Torre, A. J. Conejo, and J. Contreras, "Transmission expansion planning in electricity markets," *IEEE Trans. Power. Syst.*, vol. 23, no. 1, pp. 238-248, Feb. 2008.

[16] M. Shahidehpour, H. Yamin, and Z. Y. Li, *Market Operations in Electric Power Systems*. New York: Wiley, 2002.

[17] O.B. Tor, A.N. Guven, and M. Shahidehpour, "Congestion-driven transmission planning considering the impact of generator expansion," *IEEE Trans. Power Syst.*, vol. 23, no.2, pp. 781-789, May. 2008.

[18] Federal Energy Management Program, "Using distributed energy resources, a how-to guide for federal facility managers," DOE/GO-102002-1520, US Department of Energy, May 2002.

[19] S. Binato, M. V. Pereira, and S. Granville, "A new Benders decomposition approach to solve power transmission network design problems," *IEEE Trans. Power Syst.*, vol. 16, pp. 235–240, May 2001.

[20] G. B. Shrestha and P. A. J. Fonseka, "Congestion-driven transmission expansion in competitive power markets," *IEEE Trans. Power Syst.*, vol. 19, pp. 1658-1665, Aug. 2004.

[21] M. Buygi, G. Balzer, H. Shanechi, and M. Shahidehpour, "Market-based transmission expansion planning", *IEEE Trans. Power Syst.*, vol. 19, no. 4,2060-2067, Nov. 2004
[22] J. Choi, A. A. El-Keib and T. Tran, "A fuzzy branch and bound-based transmission system expansion planning for the highest satisfaction level of the decision maker," *IEEE Trans. Power Syst.*, vol. 20, pp. 476-484, Feb. 2005.
[23] M. Lu, Z.Y. Dong and T. K. Saha, "A framework for transmission planning in a competitive electricity market," *Transmission and Distribution Conference and Exhibition*, Asia and Pacific, pp. 1-6, Aug. 2005.
[24] P. Sánchez-Martín, A. Ramos and J. F. Alonso, "Probabilistic midterm transmission planning in a liberalized market," *IEEE Trans. Power Syst.*, vol. 20, no. 4, pp. 2135-2142, Nov. 2005.
[25] A.H. van der Weijde and B.F. Hobbs, "Transmission planning under uncertainty: A two-stage stochastic modeling approach," *Proceedings 7th Int. Conf. European Energy Market (EEM)*, 2010.
[26] J. McCalley, E. Ibanez, G. Yang, K. Gkritza, D. Aliprantis, W. Lizhi, A. Somani, and R. Brown, R, "National long-term investment planning for energy and transportation systems," *Proceedings IEEE Power and Energy Society General Meeting*, 2010.
[27] A.S.D. Braga and J. T. Saraiva, "A multiyear dynamic approach for transmission expansion planning and long-term marginal costs computation," *IEEE Trans. Power Syst.*, vol. 20, pp. 1631-1639, Aug. 2005.
[28] L.P. Garces, A.J. Conejo, R. Garcia-Bertrand and R. Romero, "A bilevel approach to transmission expansion planning within a market environment," *IEEE Trans. Power Syst.*, vol. 24, no. 3, pp. 1513-1522, Aug.. 2009.
[29] A. Khodaei, M. Shahidehpour, L. Wu, Z. Li, "Coordination of short-term operation constraints in multi-area expansion planning," *IEEE Trans. on Power Syst.*, In Press, 2012.
[30] C.K. Woo and R.L. Pupp, "Cost of service disruptions to electricity consumers," *Int. J. Energy*, vol. 17, no. 2, pp. 109–126, 1992.
[31] Y.L. Mok and T.S. Chung, "Prediction of domestic, industrial and commercial interruption costs by relational approach," *in Proc. 4th Int. Conf. Advances in Power System Control, Operation and Management*, Nov. 1997, vol. 1, pp. 209–215.
[32] J.H. Roh, M. Shahidehpour, and Y. Fu, "Security-constrained resource planning in electricity markets," *IEEE Trans. Power Syst.*, vol. 22, no. 2, pp. 812-820, May 2007.
[33] B. Alizadeh and S. Jadid, "Reliability constrained coordination of generation and transmission expansion planning in power systems using mixed integer programming," *IET Gen. Trans. Distr.*, vol. 5, no. 9, pp. 948-960, Sep. 2011.
[34] A. Khodaei, M. Shahidehpour, and S. Kamalinia, "Transmission switching in expansion planning," *IEEE Trans. Power Syst.*, vol. 25, no. 3, pp. 1722-1733, Aug. 2010.
[35] O.B. Tor, A.N. Guven and M. Shahidehpour, "Promoting the investment on IPPs for optimal grid planning," *IEEE Trans. on Power Systems*, vol. 25 no. 3, pp. 1743-1750, Aug. 2010.
[36] J.H. Roh, M. Shahidehpour, and Y. Fu, "Market-based coordination of transmission and generation capacity planning," *IEEE Trans. Power Syst.*, vol. 22, no. 4, pp. 1406-1419, Nov. 2007.
[37] A.J. Conejo, E. Castillo, R. Mínguez, and R. García-Bertrand, *Decomposition Techniques in Mathematical Programming*, Springer, 2006.
[38] W. Li, *Risk Assessment of Power Systems: Models, Methods, and Applications*, IEEE Press/Wiley, 2005.
[39] L. Wu, M. Shahidehpour, and T. Li, "Stochastic security-constrained unit commitment," *IEEE Trans. Power Syst.*, vol. 22, no. 2, pp. 800–811, May 2007.
[40] J. Dupa˘cová, N. Gröwe-Kuska, and W. Römisch, "Scenario reduction in stochastic programming: An approach using probability metrics," *Math. Program.*, vol. A 95, pp. 493–511, 2003.
[41] "Using distributed energy resources, A how-to guide for federal facility managers," U.S. Dept. of Energy [Online]. Available: http://www1.eere.energy.gov/femp/pdfs/31570.pdf
[42] ILOG CPLEX, ILOG CPLEX Homepage 2009 [Online]. Available: http://www.ilog.com
[43] M. J. Sullivan and D. M. Keane, "Outage Cost Estimation Guidebook," *EPRI Research Project 2878-04 Final Report*, Dec. 1995.

## BIOGRAPHIES

**Amin Khodaei** (M'11) received the B.S. degree from the University of Tehran, Iran, in 2005, the M.S. degree from the Sharif University of Technology, Tehran, Iran, in 2007, and the Ph.D. degree from the Illinois Institute of Technology (IIT), Chicago, in 2010, all in electrical engineering. He was a visiting faculty (2010-2012) in the Robert W. Galvin Center for Electricity Innovation at IIT. He joined the University of Houston in 2012 as an assistant professor. His research interests include operation planning and economics of electric power systems.

**Mohammad Shahidehpour** (F'01) is the Bodine Chair Professor and Director of Robert W. Galvin Center for Electricity Innovation at Illinois Institute of Technology. Dr. Shahidehpour is the recipient of the Honorary Doctorate for the Polytechnic University of Bucharest in Romania. He is a Research Professor at King Abdulaziz University in Jeddah, Saudi Arabia, and Honorary Professor in North China Electric Power University in Beijing and Sharif University in Tehran. Dr. Shahidehpour is an IEEE Distinguished Lecturer, Chair of the 2012 IEEE Innovative Smart Grid Technologies Conference, Chair of the 2012 Great Lakes Symposium on Smart Grid and the New Energy Economy, and the Editor-in-Chief of the IEEE Transactions on Smart Grid. He is the recipient of the 2012 IEEE PES Outstanding Power Engineering Educator Award.

# Stochastic Price-based Coordination of Intra-hour Wind Energy and Storage in a Generation Company

Mohammad Khodayar, *Member*, Mohammad Shahidehpour, *Fellow, IEEE*

***Abstract* —This paper develops a day-ahead price-based scheduling strategy for the coordination of wind and storage units in a generating company (GENCO). The proposed strategy is based on the stochastic price-based unit commitment (PBUC) for the scheduling of wind energy and storage units, which considers volatilities in day-ahead intra-hour market prices and wind power generation. The proposed approach firms up the hourly sum of wind and storage unit generation, and mitigate potential wind energy imbalance charges for participating GENCOs in electricity markets. Although the proposed approach would apply to any kind of storage, we consider the pumped-storage hydro (PS) unit as an example in this study. Numerical examples illustrate a GENCO's day-ahead coordinated scheduling results for wind and PS units.**

***Index Terms* — Variable wind power generation, pumped-storage hydro units, GENCOs, Stochastic PBUC, day-ahead market.**

## NOMENCLATURE

***Indices:***

| | |
|---|---|
| $h$ | Index for PS units |
| $k$ | Index for intra-hour intervals |
| $s$ | Index for scenarios |
| $t$ | Index for hourly scheduling periods |
| $w$ | Index for wind energy units |

***Functions:***

| | |
|---|---|
| $F_{g,h}$ | Water to power conversion function of PS unit $h$ in generation mode |
| $F_{p,h}$ | Water to power conversion function of PS unit $h$ in pump mode |

***Variables:***

| | |
|---|---|
| $I_{g,h,t}$ | Commitment status of PS unit $h$ in generation mode at hour $t$ (binary variable, 0: not in generation mode, 1: in generation mode) |
| $I_{i,h,t}$ | Commitment status of PS unit $h$ in idle mode at hour $t$ (binary variable, 0: not in idle mode, 1: in idle mode) |
| $I_{p,h,t}$ | Commitment status of PS unit $h$ in pump mode at hour $t$ (binary variable, 0: not in pump mode, 1: in pump mode) |
| $P_{h,t}$ | Generation dispatch of PS unit $h$ at hour $t$ (MW) |
| $P_{C,h,t}$ | Coordinated generation dispatch of PS unit $h$ and its coordinated wind energy units at hour $t$ (MW) |
| $P^{s}_{(.),t,k}$ | Generation dispatch of unit at hour $t$ and intra-hour $k$ in scenario $s$ (MW) |
| $P^{s}_{g,h,t,k}$ | Generation dispatch of PS unit $h$ in generation mode at hour $t$ and intra-hour $k$ in scenario $s$ (MW) |
| $P^{s}_{p,h,t,k}$ | Output power of PS unit $h$ in pump mode at hour $t$ and intra-hour $k$ in scenario $s$ (MW) |
| $P_{w,t}$ | Generation dispatch of wind energy unit $w$ at hour $t$ (MW) |
| $P^{s}_{\Delta,(.),t,k}$ | Power imbalance of unit at hour $t$ and intra-hour $k$ in scenario $s$ (MW) |
| $P^{s}_{\Delta,C,h,t,k}$ | Deviation of coordinated dispatch of wind-PS at hour $t$ and intra-hour $k$ in scenario $s$ (MW) |
| $P^{c,s}_{w,t,k}$ | Wind power curtailment of wind energy unit $w$ at hour $t$ and intra-hour $k$ in scenario $s$ (MW) |
| $q^{s}_{h,t,k}$ | Net water flow rate of PS unit $h$ at hour $t$ and intra-hour $k$ in scenario $s$ (Hm³/h) |
| $q^{s}_{g,h,t,k}$ | Water flow rate of PS unit $h$ in generation mode at hour $t$ and intra-hour $k$ in scenario $s$ (Hm³/h) |
| $q^{s}_{p,h,t,k}$ | Water flow rate of PS unit $h$ in pump mode at hour $t$ and intra-hour $k$ in scenario $s$ (Hm³/h) |
| $V^{s}_{h,t,k}$ | Reservoir volume of PS unit $h$ at hour $t$ intra-hour $k$ in scenario $s$ (Hm³) |
| $y_{g,h,t}$ | Generation startup indicator of PS unit $h$ at hour $t$ |
| $z_{g,h,t}$ | Generation shutdown indicator of PS unit $h$ at hour $t$ |
| $y_{p,h,t}$ | Pumping startup indicator of PS unit $h$ at hour $t$ |
| $z_{p,h,t}$ | Pumping shutdown indicator of PS unit $h$ at hour $t$ |

***Constants:***

| | |
|---|---|
| $NH$ | Number of PS units |
| $NK$ | Number of intra-hour intervals in one hour |
| $NS$ | Number of scenarios |
| $NT$ | Number of hours |
| $NW$ | Number of wind energy units |
| $p^{s}$ | Probability of scenario $s$ |
| $P^{f,s}_{w,t,k}$ | Forecasted generation of wind energy unit $w$ at hour $t$ and intra-hour $k$ in scenario $s$ (MW) |

This project is partially supported by the NSF grant ECCS-0801853 and the U.S. Department of Energy grants DE-EE 0002979 and DE-EE 0001380.000. The authors are with the Robert W. galvin Center for Electricity Innovation, Illinois Institute of Technology, Chicago, IL 60616 USA (e-mail: mkhodaya@iit.edu, ms@iit.edu)

$q_{g,h}^{\max}, q_{g,h}^{\min}$ Max/min water flow rates of PS unit *h* in generation mode (Hm³/h)

$q_{p,h}^{\max}, q_{p,h}^{\min}$ Max/min water flow rates of PS unit *h* in pump mode (Hm³/h)

$RU_{g,h}, RD_{g,h}$ Ramp up/down rate limits of PS unit *h* in generation mode (MW/h)

$RU_{p,h}, RD_{p,h}$ Ramp up/down rate limits of PS unit *h* in pump mode (MW/h)

$S_{C,h}$ Set of wind energy units coordinated with PS unit *h*

$V_h^{\max}, V_h^{\min}$ Max/min reservoir volume of PS unit *h* (Hm³)

$\rho_{BP}$ Energy balancing price ($/MWh)

$\rho_{DA,t}^{s}$ Day-ahead energy price at hour $t$ in scenario *s* ($/MWh)

$\rho_{DA,t,k}^{s}$ Day-ahead energy price at hour $t$ and intra-hour *k* in scenario *s* ($/MWh)

## I. Introduction

GENCOs with wind energy units could incur imbalance energy charges in real-time markets due to uninstructed deviations of wind power generation from the day-ahead schedule. In practice, wind energy units participate in day-ahead markets as price takers by offering hourly generation quantities that are based on wind speed forecasts [1].

State-of-the-art forecasting models are able to predict the hourly wind power generation with a mean absolute error in the range of 15–20% of the installed capacity of a wind farm [2]. Such errors may considerably lower the payoff of GENCOs when the scheduled wind power generation cannot be delivered in real-time. Furthermore, the intermittency of wind power generation could make it difficult for wind energy units to take advantage of differences in daily locational marginal prices (LMPs) [3]-[5]. The coordination of energy storage with wind energy is a promising strategy since it not only reduces imbalance energy charges but also improves the dispatchability of wind power generation [6]-[13].

An optimal PS bidding strategy is proposed in [14] which is based on the forecasted market clearing price (MCP) in a competitive electricity market. However, the coordination of energy storage and intermittent wind energy would need to be further addressed. An optimization approach to procure the hourly operation strategy of wind farms located near a small PS generation in a day-ahead energy market is proposed in [15]. In [16], the optimal operation of wind energy unit and PS is investigated from a GENCO's viewpoint considering the volatility of hourly wind power generation and electricity prices in a day-ahead electricity market. The proposed optimization model includes a stochastic analysis of PS and wind power generation in coordinated and uncoordinated schemes. However, the market price volatility and intra-hour fluctuations of wind energy would need to be further addressed [17].

Hourly or intra-hourly variations of load and wind power generation will impose load following and regulation charges on power systems [18]. Imbalance energy charges imposed on wind energy units would compensate the corresponding load following and regulation charges borne by the power system.

In this paper, we apply the stochastic price based unit commitment (PBUC) to the day-ahead coordinated scheduling of PS and wind energy units in a GENCO [19],[20]. The coordination, depicted in Fig. 1, would firm-up the hourly wind power generation and increase the payoff of wind energy units by mitigating imbalance energy charges. The stochastic PBUC considers day-ahead market price and wind power generation forecast errors in Monte Carlo scenarios. We divide the hourly scheduling period into *k* intra-hour intervals The auto-regressive moving average (ARMA) time series is used to simulate the intra-hour wind speed variations [21]. Artificial Neural Network (ANN) is used to represent the intra-hour price forecasts [22].

The rest of this paper is organized as follows. The stochastic PBUC formulation with wind-PS unit coordination is presented in section II. Illustrative example and conclusions are provided in sections III and IV, respectively.

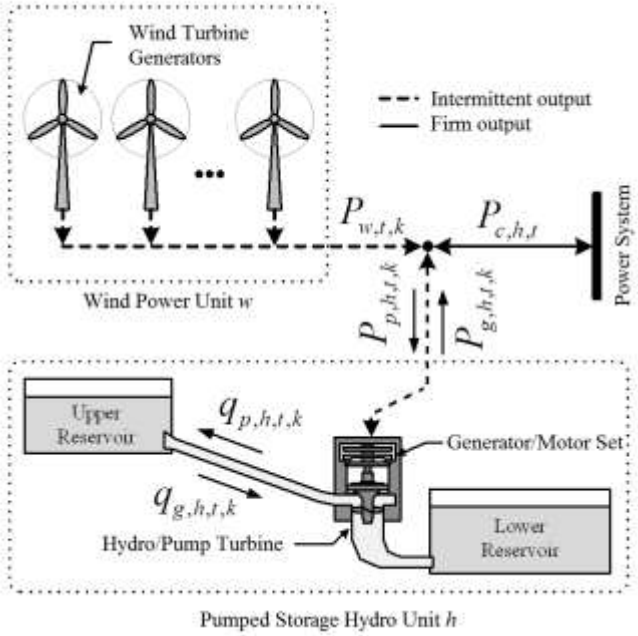


Fig. 1 Coordination of wind energy and PS units

## II. Stochastic PBUC for Wind-PS Unit Coordination

The PBUC formulation with wind-PS unit coordination is presented in this section as a stochastic optimization problem. In this paper, we assume the forecasts for day-ahead hourly energy prices as well as intra-hourly energy price and wind power generation are available. The wind power generation forecast is procured by incorporating power curve of wind turbine and wind speed time series. The wind speed time series is procured by Markov chain with the probability transition matrix. The probability transition matrix is a square matrix which defines probabilities of transiting from one wind speed category to others. Each wind speed category defines a wind speed range represented by its respective mean value. The probability transition matrix is either constructed by using historical data or by incorporating the characteristics of the probability distribution of the wind speed. Considering the

Weibull distribution function and the autocorrelation factor for the wind speed time series, the probability transition matrix is procured by incorporating an initial probability vector, a weighting matrix and a normalizing vector [23]. Once the probability transition matrix is acquired, Markov chain simulation is used to procure the wind speed time series. In the next step, the diurnal pattern strength is applied to the acquired time series. The diurnal pattern strength which has a sinusoidal form signifies the daily pattern of wind speed. The peak value indicates the ratio of the maximum wind speed to the average wind speed. The wind speed forecast error is further represented by ARMA which is applied to the procured time series [24],[25].

The time series for the market price forecast is procured by using the historical data and ANN. In this paper, the intra-hour (5-min) historical data of the ISO New England is procured [26]. The Monte Carlo simulation method is applied for generating scenarios. The computation burden in the scenario-based optimization is highly dependent on the number of scenarios. The basic idea of scenario reduction is to eliminate low-probability and bundle similar scenarios [27]-[30]. After scenario reduction, each scenario $s$ is associated with a probability $p^s$. The scenario input to the stochastic PBUC includes the day-ahead hourly energy price, day-ahead intra-hour energy price, and intra-hour wind power generation.

The stochastic optimization is decomposed into a master MIP problem and several linear programming (LP) sub-problems. Once a solution for master problem is procured, the sub-problems check the volume constraints of PS hydro units in scenarios. In case of any violation in scenarios, Benders cuts are generated and fed back to the master problem. The decomposition methodology is shown in Fig. 2.

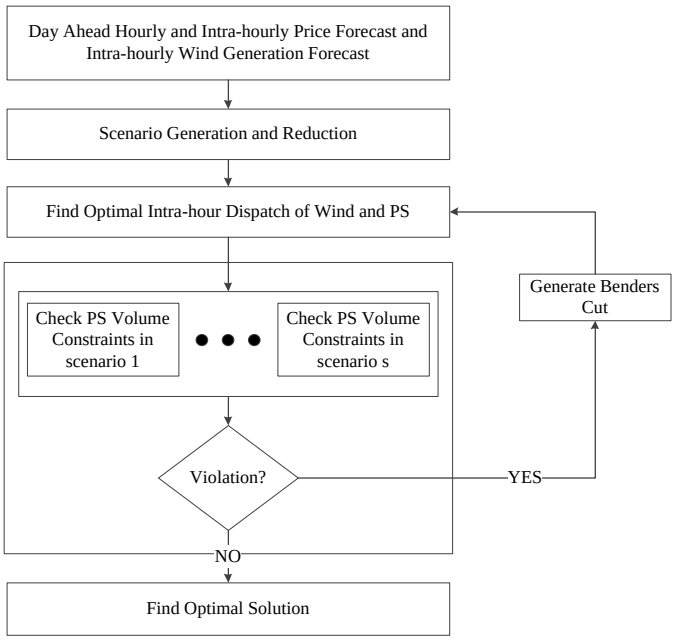


Fig. 2. Proposed GENCO's Stochastic PBUC solution

The stochastic PBUC formulation with wind-PS unit coordination is represented by (1)-(28). The objective function (1) maximizes the expected payoff of the coordinated wind-PS schedule which is represented in (2), (3). The rest of the constraints include wind energy unit constraints (4)-(6) and PS unit constraints (7)-(28). The expected day-ahead payoff (1) represents the weighted revenue from day-ahead energy sales based on day-ahead hourly energy prices, day-ahead intra-hourly prices and coordinated wind-PS hourly and intra-hourly schedules.

$$\max \sum_{s=1}^{NS} p^s \cdot \left[ \sum_{h=1}^{NH} \sum_{t=1}^{NT} (\rho_{DA,t}^s \cdot P_{C,h,t}) \right] + p^s \cdot \left[ \frac{1}{NK} \sum_{h=1}^{NH} \sum_{t=1}^{NT} \sum_{k=1}^{NK} (\rho_{DA,t,k}^s \cdot P_{\Delta,C,h,t,k}^s) \right] - p^s \cdot \left[ \frac{1}{NK} \sum_{h=1}^{NH} \sum_{t=1}^{NT} \sum_{k=1}^{NK} \rho_{BP} \cdot \left| P_{\Delta,C,h,t,k}^s \right| \right] \quad (1)$$

s.t.

$$P_{C,h,t} = \sum_{w \in S_{C,h}} P_{w,t} + P_{h,t} \qquad \forall h, \forall t \quad (2)$$

$$P_{\Delta,C,h,t,k}^s = P_{\Delta,w,t,k}^s + P_{\Delta,h,t,k}^s \qquad \forall h, \forall t, \forall k, \forall s, \forall w \in S_{C,h} \quad (3)$$

$$P_{\Delta,w,t,k}^s = P_{w,t,k}^s - P_{w,t} \qquad \forall w, \forall t, \forall k, \forall s \quad (4)$$

$$P_{w,t,k}^s = P_{w,t,k}^{f,s} - P_{w,t,k}^{c,s} \qquad \forall w, \forall t, \forall k, \forall s \quad (5)$$

$$P_{w,t} \le \sum_{s=1}^{NS} p^s \cdot \frac{1}{NK} \sum_{k=1}^{NK} P_{w,t,k}^{f,s} \qquad \forall w, \forall t, \forall k, \forall s \quad (6)$$

$$P_{h,t,k}^s = P_{g,h,t,k}^s - P_{p,h,t,k}^s \qquad \forall h, \forall t, \forall k, \forall s \quad (7)$$

$$P_{\Delta,h,t,k}^s = P_{h,t,k}^s - P_{h,t} \qquad \forall h, \forall t, \forall k, \forall s \quad (8)$$

$$P_{g,h,t,k}^s = F_{g,h}(q_{g,h,t,k}^s) \qquad \forall h, \forall t, \forall k, \forall s \quad (9)$$

$$P_{p,h,t,k}^s = F_{p,h}(q_{p,h,t,k}^s) \qquad \forall h, \forall t, \forall k, \forall s \quad (10)$$

$$-RD_{g,h} / NK \le P_{g,h,t,(k+1)}^s - P_{g,h,t,k}^s \le RU_{g,h} / NK \qquad \forall h, \forall t, \forall k \in [1, NK-1] \quad (11)$$

$$P_{g,h,t+1,1}^s - P_{g,h,t,NK}^s \le (RU_{g,h} / NK)(1 - y_{g,h,t+1}) + F(q_{g,h}^{\min}) \cdot y_{g,h,t+1} \qquad \forall h, \forall t, \forall s \quad (12)$$

$$(-RD_{g,h} / NK)(1 - z_{g,h,t+1}) - F(q_{g,h}^{\min}) \cdot z_{g,h,t+1} \le P_{g,h,t+1,1}^s - P_{g,h,t,NK}^s \qquad \forall h, \forall t, \forall s \quad (13)$$

$$-RD_{p,h} / NK \le P_{p,h,t,(k+1)}^s - P_{p,h,t,k}^s \le RU_{p,h} / NK \qquad \forall h, \forall t, \forall k \in [1, NK-1] \quad (14)$$

$$P_{p,h,t+1,1}^s - P_{p,h,t,NK}^s \le (RU_{p,h} / NK)(1 - y_{p,h,t+1}) + F(q_{p,h}^{\min}) \cdot y_{p,h,t+1} \qquad \forall h, \forall t, \forall s \quad (15)$$

$$(-RD_{p,h} / NK)(1 - z_{p,h,t+1}) - F(q_{p,h}^{\min}) \cdot z_{p,h,t+1} \le P_{p,h,t+1,1}^s - P_{p,h,t,NK}^s \qquad \forall h, \forall t, \forall s \quad (16)$$

$$z_{g,h,t} + y_{g,h,t} \le 1 \quad (17)$$

$$y_{g,h,t} - z_{g,h,t} = I_{g,h,t} - I_{g,h,t-1} \quad (18)$$

$$z_{p,h,t} + y_{p,h,t} \le 1 \quad (19)$$

$$y_{p,h,t} - z_{p,h,t} = I_{p,h,t} - I_{p,h,t-1} \quad (20)$$

$$q_{h,t,k}^s = q_{g,h,t,k}^s - q_{p,h,t,k}^s \qquad \forall h, \forall t, \forall k, \forall s \quad (21)$$

$$q_{g,h}^{\min} \cdot I_{g,h,t} \le q_{g,h,t,k}^s \le q_{g,h}^{\max} \cdot I_{g,h,t} \qquad \forall h, \forall t, \forall k, \forall s \quad (22)$$

$$q_{p,h}^{\min} \cdot I_{p,h,t} \le q_{p,h,t,k}^s \le q_{p,h}^{\max} \cdot I_{p,h,t} \qquad \forall h, \forall t, \forall k, \forall s \quad (23)$$

$$I_{g,h,t} + I_{p,h,t} + I_{i,h,t} = 1 \qquad \forall h, \forall t \quad (24)$$

$$V^s_{h,t,k} = V^s_{h,t,k-1} - \frac{1}{NK} q^s_{h,t,k} \qquad \forall h, \forall t, \forall k \in [2, NK], \forall s \quad (25)$$

$$V^s_{h,t,1} = V^s_{h,(t-1),NK} - \frac{1}{NK} q^s_{h,t,1} \qquad \forall h, \forall t, \forall s \quad (26)$$

$$V_h^{\min} \le V^s_{h,t,k} \le V_h^{\max} \qquad \forall h, \forall t, \forall k, \forall s \quad (27)$$

$$V^s_{h,0,NK} = V^s_{h,NT,NK} \qquad \forall h, \forall s \quad (28)$$

The first part in (1) represents the expected day-ahead revenue for the coordinated wind-PS dispatch. The second part represents the incurred expected cost in the day-ahead market based on the day-ahead intra-hour energy price and the deviation of intra-hour wind-PS dispatch from the day-ahead hourly schedule. As shown in (2), the coordinated dispatch is the cumulative dispatch of wind energy and PS units. Here, $P_{C,h,t}$ is the hourly PBUC schedule that a GENCO would submit to the ISO in the day-ahead market. The wind-PS power imbalance is the difference between the day-ahead hourly schedule and the intra-hour output. The GENCO gets paid extra if the intra-hour energy delivery is higher than the hourly day-ahead schedule, and pays to the ISO otherwise. The third term in (1) represents imbalance energy charges for the uninstructed deviation of the coordinated wind-PS power from the hourly day-ahead schedule caused by the intra-hour volatility of wind and PS power generation [31],[32].

As shown in (1), the GENCO pays balancing charges based on the energy balancing price and the absolute value of deviation. Once the energy balancing price is high enough, there would be no deviation from the hourly coordinated schedule of wind-PS units and no imbalance energy charge would incur in the day-ahead market. As shown in the numerical cases, the energy balancing price could play a major role in the GENCO's scheduling decision. Note that, the energy balancing price can be different for excesses and shortages of the scheduled coordinated power. For the sake of simplicity we assume in this paper that the two prices are the same.

In this paper, only the hourly schedule for energy is considered; however, ancillary services could also be included. Moreover, the operation cost of PS units, which include startup and shutdown costs caused by the wear and tear of turbines, are ignored. Note that a PS unit can be coordinated with several wind energy units as shown in (2), where $S_{C,h}$ contains wind energy units coordinated with a PS unit *h*. Eq. (3) represents the deviation of intra-hour coordinated dispatch of wind-PS from the day-ahead hourly schedule.

Eq. (4) represents the deviation of day-ahead intra-hour wind power generation from the hourly generation schedule. The intra-hourly wind curtailment is represented in (5) where the wind power forecast is a function of forecasted wind speed. The wind power generation is zero when the wind speed is below the cut-in and above the cut-out levels and it is procured by incorporating the wind turbine power curve as the wind speed is between the cut-in and cut-out limits. The actual wind power that is delivered to the power system in scenario *s* is equal to the Monte Carlo simulated wind power generation minus the non-negative curtailed wind power. In order to maintain the generation/load balance, the wind power generation may also be curtailed at the ISO's request. The hourly wind power dispatch in (6) is limited by the expected hourly wind power forecast.

Eqs. (7)-(28) represent the PS unit constraints at intra-hour levels. A PS unit has multiple operating modes including generation, pump, and idle. Each mode is modeled as a pseudo unit with ramping up/down rate limits, water balance equations, and reservoir limits. Pseudo units corresponding to the same PS unit are mutually exclusive [20].

Eq. (7) shows that the net intra-hour dispatch of a PS unit is either the power output in the generation mode or the negative of the consumed power in the pump mode. The deviation of intra-hour dispatch from the hourly dispatch is shown in (8). The water to power conversion functions are presented in (9)-(10) for the generation mode and the pump mode, respectively. The ramp up/down constraints for the intra-hour operation are shown in (11)-(20). The net intra-hour water flow rate is defined in (21) as the difference between intra-hour generation and pump flow rates, which are constrained by respective lower and upper flow rates in (22)-(23).

Since the switching between operation modes (i.e., generation, pump, idle) would take time, we assume that a PS unit cannot change its operation mode within the same hour. The intra-hour generation dispatch of a PS unit can vary every 10 minutes but its operation mode must be retained for the entire hour. Eq. (24) shows that the pump, generation, and idle modes are mutually exclusive.

The intra-hour water volume in the PS reservoir shown in (25) is dependent on its previous intra-hour value and the net water flow in the present intra-hour. In particular, the volume in the first intra-hour of each hour shown in (26) is dependent on the volume in the last intra-hour of the previous hour and the present net water flow rate. Here, (25)-(26) represent PS reservoirs with no external flows. This implies that the sum of upstream and downstream reservoir volumes is constant; thus, only one reservoir volume (either the upstream or the downstream) is considered. The volume at each intra-hour is bound to be between min/max values as shown in (27). Eq. (28) imposes volume limits at the beginning and the end of the period. For the sake of simplicity, the initial and the terminal volumes of reservoirs are assumed to be the same in this paper so that the simulation can be performed using the same assumptions for the next day. The hourly constraints for PS unit are included in the formulation by representing the same set of constraints (9), (10) and (21)-(28) and changing the intra-hour indices with the hourly ones.

Eqs. (1)-(28) represent the coordinated wind-PS formulation, which is converted into a master problem with several sub-problems as shown in Fig. 2. The master problem is a mixed-integer linear programming (MILP) optimization problem and the sub-problems are LP problems which are solved by the CPLEX MILP/LP solver. The optimization result is the coordinated wind-PS unit schedule that a GENCO would submit to the ISO. For comparison, we calculate the dispatch of wind and PS units independently (without wind-PS unit coordination). In this case, a GENCO would submit to the

ISO a separate schedule for wind energy and PS units. The stochastic PBUC formulation for PS and wind energy units without wind-PS unit coordination is presented in (29), which maximizes the expected payoff of PS and wind energy units separately subjected to the respective unit constraints.

$$\max \sum_{s=1}^{NS} p^s \cdot [\sum_{w=1}^{NW}\sum_{t=1}^{NT}(\rho^s_{DA,t}\cdot P_{w,t}) + \frac{1}{NK}\sum_{w=1}^{NW}\sum_{t=1}^{NT}\sum_{k=1}^{NK}(\rho^s_{DA,t,k}\cdot P^s_{\Delta,w,t,k}) - \frac{1}{NK}\sum_{w=1}^{NW}\sum_{t=1}^{NT}\sum_{k=1}^{NK}\rho_{BP}\cdot\left|P^s_{\Delta,w,t,k}\right| + \sum_{h=1}^{NH}\sum_{t=1}^{NT}(\rho^s_{DA,t}\cdot P_{h,t}) + \frac{1}{NK}\sum_{h=1}^{NH}\sum_{t=1}^{NT}\sum_{k=1}^{NK}(\rho^s_{DA,t,k}\cdot P^s_{\Delta,h,t,k}) - \frac{1}{NK}\sum_{h=1}^{NH}\sum_{t=1}^{NT}\sum_{k=1}^{NK}\rho_{BP}\cdot\left|P^s_{\Delta,h,t,k}\right|] \quad (29)$$

In this formulation, the payoff of wind and PS units are presented as autonomous terms in the objective function. The first part in (29) represents the day-ahead revenue for wind energy unit *w*. The second part represents the incurred cost in the day-ahead market based on the intra-hour energy price and the deviation of intra-hour wind power from the day-ahead hourly schedule. As shown in (4), the wind power imbalance is the difference between the hourly day-ahead schedule and the actual intra-hour output. Hence, the GENCO gets paid if the intra-hourly energy delivery is higher than the hourly day-ahead schedule, and pays to the ISO otherwise. The third part in (29) represents imbalance energy charges for the uninstructed deviation of delivered wind power from the day-ahead schedule caused by wind power generation variations. As shown, GENCO pays balancing charges based on the energy balancing price and the absolute value of deviation. Similar terms for the PS generation are presented in (29). The objective function is maximized subjected to the constraints (4)-(28) which were presented before.

## III. Numerical Examples

To illustrate the proposed PBUC model, we consider a GENCO that has a single wind energy unit and a single PS unit and participates in the day-ahead energy market. The capacity of the wind energy unit is 150 MW and the operating characteristics of the PS unit are provided in Table I. The input to the proposed model includes the day-ahead hourly and intra-hourly forecasted market price and wind power. The output is the GENCO's coordinated and uncoordinated generation dispatch schedule for wind and PS units.

To consider forecast errors in electricity market prices, we generate 10,000 scenarios using ANN based on the hourly and intra-hourly historical data of energy price in the market [26]. The forecasted wind power is procured by synthesizing wind speed time series and adding the wind speed forecast error using the ARMA method. The forecasted wind power generation is procured by applying the power curve of wind turbine. The 10,000 scenarios are then reduced to 13 scenarios using scenario reduction techniques [29], [30]. The 13 scenarios in 10-minute intra-hour intervals for the forecasted energy price and wind power are depicted in Figs. 3 and 4, respectively. The day-ahead hourly energy price is procured by using the historical data of day-ahead energy prices. The day-ahead hourly forecasted wind power generation is calculated as the expected average intra-hourly wind power generation as indicated on right hand side of (6).

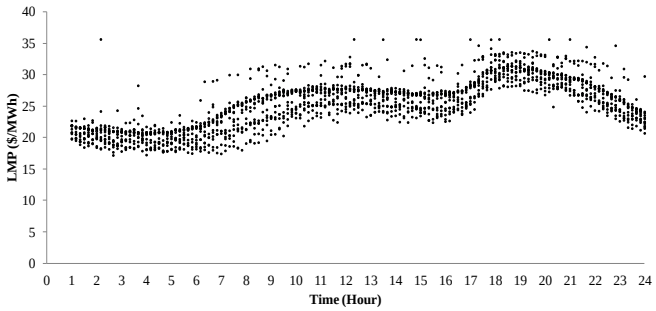


Fig. 3 Forecasted intra-hourly energy price in 13 scenarios

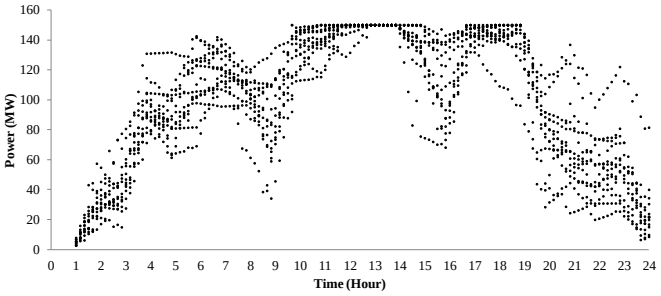


Fig. 4 Forecasted intra-hour wind power generation in 13 scenarios

Four cases are studied in this section. In deterministic Cases 1 and 3, the scenario with highest probability represents the forecasted hourly and intra-hourly energy price and wind power. In stochastic Cases 2 and 4, 13 scenarios are considered for energy price and wind power generation. The considered cases are as follows:

Case 1: Deterministic solution without any unit coordination
Case 2: Stochastic solution without any unit coordination
Case 3: Deterministic solution with wind-PS unit coordination
Case 4: Stochastic solution with wind-PS unit coordination

TABLE I
OPERATING CHARACTERISTICS OF THE PS UNIT

| | | |
|---|---|---|
| Generation Mode | Minimum Discharge Rate | 0.1 Hm³/h |
| | Maximum Discharge Rate | 1.5 Hm³/h |
| | Maximum Power Output | 240 MW |
| | Minimum Power Output | 16 MW |
| | Ramp Up/Down Rate | 250 MW/h |
| Pump Mode | Minimum Discharge Rate | 0.1 Hm³/h |
| | Maximum Discharge Rate | 1.5 Hm³/h |
| | Maximum Power Output | 300 MW |
| | Minimum Power Output | 20 MW |
| | Ramp Up/Down Rate | 250 MW/h |
| Reservoir Volume | Maximum Volume | 20 Hm³ |
| | Minimum Volume | 3 Hm³ |

The four Cases are analyzed with respect to the GENCO's payoff, unit commitment, and generation dispatch as follows:

*1) Payoff analysis*

Table II shows the total payoff, the wind energy unit payoff, and the PS unit payoff for Cases 1 and 3, and expected payoffs for Cases 2 and 4 once the energy balancing prices is 30 $/MWh . In this table, the imbalance charges incurred in Cases 3 and 4 were divided equally between the wind energy and PS units. Tables III and IV show the impact of energy balancing price in Cases 1-4 on the total payoff. Based on the results given in Tables II-IV, we offer the following observations.

The first observation is that a stochastic model in comparison with the deterministic solution would result in a

lower total payoff and wind energy and PS unit payoffs. For the wind energy unit, if there is no wind-PS coordination and 30 $/MWh energy balancing price is incurred, the payoff in Case 1 is $113,580.42 and the expected payoff in the Case 2 is $92,482.09. The difference between the two payoffs is $21,098.33. The same comparison is applied to Cases 3 and 4 in which the difference between the stochastic and deterministic payoffs is $17,958.96.

For the uncoordinated wind energy and PS units, the differences in total payoff are $28,792.75 and $27,012.37 in Cases 1-2 and Cases 3-4, which show a 20.6% and 18.9% reduction in the total payoff, respectively. In Table II, The deterministic case represents a perfect forecast (i.e., zero forecast error) which indicates that a more accurate forecast would result in higher payoffs. If the deterministic solution of Case 1 is applied to Case 2; the wind, PS and total payoff are $91,102.651, $17,485.763 and $97,798.822, respectively. The payoffs are higher in Case 2 which indicate the value of stochastic solution. The same applies to Cases 3-4 in which the total payoff in stochastic solution is higher by $1,702.813.

The second observation is that the payoffs for wind energy and PS units and the wind-PS coordination are higher than those in the non-coordinated strategy. Table II shows the payoffs for wind energy and PS units and wind-PS are increased from Case 1 to Case 3 by 1.4%, 5.3% and 2.1%, respectively. In the stochastic solution, the payoffs for wind energy and PS units and wind-PS coordination are increased from Case 2 to Case 4 by 5.1%, 0.2% and 4.3%, respectively. Here, the coordination can increase the payoff by reducing the intra-hour imbalance charges in the day-ahead market.

TABLE II
EXPECTED PAYOFFS ($)

| Case | Total | Wind Unit | PS Unit |
|---|---|---|---|
| 1 | 139,563.5 | 113,580.42 | 25,983.11 |
| 2 | 110,770.8 | 92,482.10 | 18,288.68 |
| 3 | 142,568.9 | 115,192.74 | 27,376.16 |
| 4 | 115,556.5 | 97,233.78 | 18,322.75 |

The third observation is that, as the energy balancing price increases, imbalance energy charges become more expensive and wind power generation curtailment becomes preferable to avoid higher imbalance energy charges. Wind power generation curtailments reduce the day-ahead generation dispatch and decrease the day-ahead energy revenue. Figs. 5 and 6 show the total payoff and day ahead total sales revenue in Cases 1-4 with respect to energy imbalance charges. The increase in energy balancing price would decrease the day-ahead energy sale revenues when more conservative day-ahead generation schedules are submitted and the total payoff would decrease accordingly.

TABLE III
IMPACT OF ENERGY BALANCING PRICE ON PAYOFFS IN CASE 1

| Balancing Price ($/MWh) | Day Ahead Energy Sale Revenue ($) | Day Ahead Revenue Adjustment ($) | DA Imbalance Charge ($) | Payoff ($) |
|---|---|---|---|---|
| 0 | 149,598.75 | 4,934.05 | 0 | 154,532.8 |
| 40 | 145,317.83 | -1,781.29 | -5,493.97 | 138,042.6 |
| 80 | 141,718.44 | -1,300.58 | -6,710.33 | 133,707.5 |
| 120 | 138,554.00 | -890.29 | -6,621.07 | 131,042.6 |
| 160 | 136,701.14 | -562.10 | -6,974.67 | 129,164.4 |

TABLE IV
IMPACT OF ENERGY BALANCING PRICE ON PAYOFFS IN CASE 3

| Balancing Price ($/MWh) | DA Energy Sale Revenue ($) | DA Revenue Adjustment ($) | DA Imbalance Charge ($) | Payoff ($) |
|---|---|---|---|---|
| 0 | 149,598.75 | 4,934.04 | 0 | 154,532.8 |
| 40 | 145,417.30 | -1,395.75 | -2,005.83 | 142,015.7 |
| 80 | 143,853.97 | -889.10 | -2,494.40 | 140,470.5 |
| 120 | 141,823.83 | -402.11 | -1,669.13 | 139,752.6 |
| 160 | 139,546.51 | 0 | 0 | 139,546.5 |

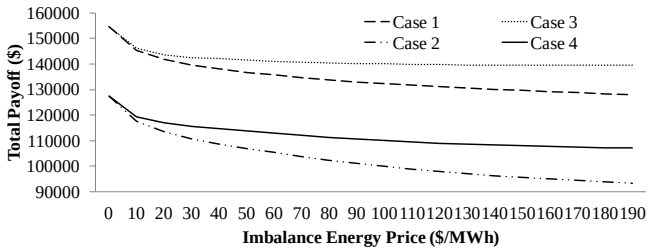


Fig. 5 Total payoff with respect to balancing price

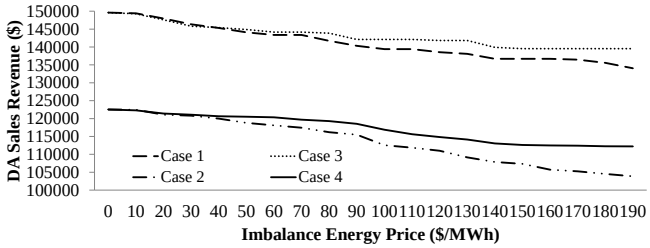


Fig. 6 Day ahead sales revenue with respect to balancing price

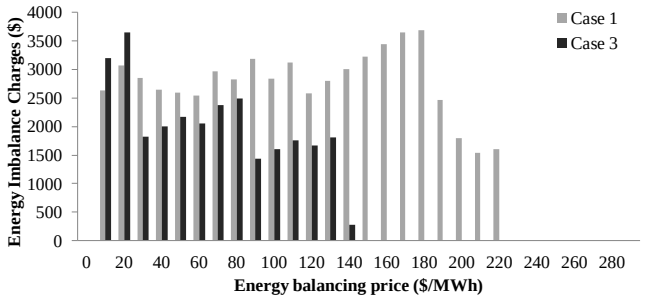


Fig. 7 Energy imbalance charges with respect to energy balancing price

The fourth observation is that, as energy balancing prices increase, the wind-PS coordination would result in lower imbalance charges. Comparing Table III and IV, the difference in day-ahead energy imbalance charges is increased between Cases 1 and 3 as the balancing price increases.

In Fig. 7, for energy balancing prices that are less than 20 $/MWh, the energy imbalance charges in coordinated cases will increase with the energy balancing price. In this case, imbalance charges will be compensated by intra-hour energy sales. For energy balancing prices that are higher than 30 $/MWh, the wind-PS coordination will decrease the energy imbalance charges.

In Fig. 7, the energy imbalance charge in Case 3 is zero if the energy balancing price reaches 150 $/MWh; however, the imbalance charges are higher in uncoordinated cases and will reach zero when the energy balancing price is 230$/MWh. Hence the wind-PS coordination is less susceptible to high energy balancing prices and would decrease the imbalance

charges more rapidly than the uncoordinated operation schemes.

The balancing price plays an important role in determining the day-ahead payoff of a GENCO. The monthly average energy balancing price may become higher than the spot price in certain cases [32],[33]. As energy balancing prices increase, the difference in day-ahead energy sales and intra-hour imbalance charges will increase from Case 1 to Case 3. Once the balancing price is zero, the payoffs in Cases 1 and 3 would become the same; however the payoff in Case 3 is more resilient as energy balancing prices increase.

*2) Unit commitment and generation dispatch*

The hourly unit commitment for PS is given in Table V. In Cases 1 and 3, the PS unit pumps at hours 1-8 and 23-24 when the energy price is relatively low (see Fig. 3), and generates between hours 9-22 when the energy price is relatively high. Comparing Cases 4 and 2 in which the forecast error is considered, the wind-PS unit coordination would change the unit commitment at hour 22 as shown in Table V. The inclusion of forecast errors may alter the PS unit schedule as shown by comparing Case 3 with Case 4.

In Table V, there is a difference between Cases 3 and 4 at low and high price hours of 9 and 22. In Case 3, the PS unit will generate at those hours while it would switch to pumping in Case 4 to increase the expected payoff.

TABLE V
HOURLY COMMITMENT SCHEDULE OF THE PS UNIT

| PS | Hours (1-24) | | | | | | | | | | | | | | | | | | | | | | | |
|---|---|---|---|---|---|---|---|---|---|---|---|---|---|---|---|---|---|---|---|---|---|---|---|---|
| Case 1 | -1 | -1 | -1 | -1 | -1 | -1 | -1 | -1 | 1 | 1 | 1 | 1 | 1 | 1 | 1 | 1 | 1 | 1 | 1 | 1 | 1 | -1 | -1 |
| Case 2 | -1 | -1 | -1 | -1 | -1 | -1 | -1 | -1 | -1 | 1 | 1 | 1 | 1 | 1 | 1 | 1 | 1 | 1 | 1 | 1 | **1** | -1 | -1 |
| Case 3 | -1 | -1 | -1 | -1 | -1 | -1 | -1 | -1 | 1 | 1 | 1 | 1 | 1 | 1 | 1 | 1 | 1 | 1 | 1 | 1 | 1 | -1 | -1 |
| Case 4 | -1 | -1 | -1 | -1 | -1 | -1 | -1 | -1 | -1 | 1 | 1 | 1 | 1 | 1 | 1 | 1 | 1 | 1 | 1 | 1 | **-1** | -1 | -1 |

We offer the following observations which are based on the results presented in Fig. 8 and Table VI.

The first observation is that additional curtailments may be necessary when considering market price and wind speed forecast errors. The wind energy curtailments in Cases 1-4 are 60.554, 140.737, 58.261 and 90.099 MWh, respectively. The stochastic case has a higher wind energy curtailment because a GENCO would be more conservative in submitting the generation schedule as it considers the outcome of different scenarios. Comparing Cases 1 and 3 and Cases 2 and 4 in Fig. 8, it is clear that the coordination will help reduce the wind curtailment once the energy balancing price is increased.

The second observation is that according to Table VI, the scheduled PS dispatch is reduced by 4.47MWh from Case 1 to Case 3 which indicates the effect of wind-PS coordination and the efficiency of PS units in reducing the total dispatched energy. The same notion is applied to the stochastic solution as the PS energy dispatch is reduced by 22.85 MWh from Case 2 to Case 4. The coordination tends to reduce the total generation dispatch. In the deterministic solution, the hourly coordinated dispatch is reduced slightly from 1,870MWh in Case 1 to 1,865MWh in Case 3. The net reduction is caused by a frequent use of the PS unit to compensate the intra-hour variations of wind power generation. The effect is a lower generation because of the difference in water to power conversion curves of pumping and generation. Also, the coordinated dispatched energy was decreased from 1,923.25 MWh in Case 2 to 1,902.36 MWh in Case 4. However, the payoff was increased by 4.32%.

The third observation is that the scheduled wind power generation is increased in coordinated cases. The total dispatched wind energy in Cases 1-4 are 2,262.53, 2,346.92, 2,262.53 and 2,348.81 MWh respectively. The reduction in the uncoordinated operation is caused by imposing energy balancing price and intra-hour energy price. Note that the energy balancing price is 30$/MWh in all four cases. The curtailment of wind power generation in Cases 1-4 would increase as the energy balancing price was increased, which would lead to lower payoffs.

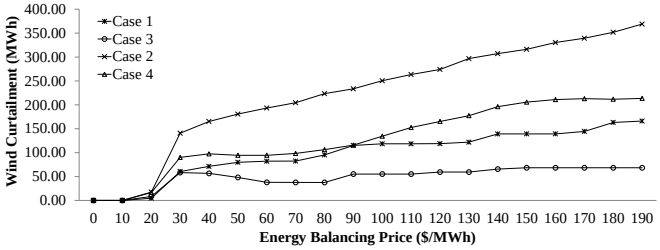


Fig. 8 Wind curtailment with respect to energy balancing price

TABLE VI
DAY AHEAD HOURLY WIND AND PS UNIT DISPATCH (MWH)

| Hour | Case 1 | | | Case 3 | | |
|---|---|---|---|---|---|---|
| | **Total** | **Wind** | **PS** | **Total** | **Wind** | **PS** |
| 1 | -280.00 | 20.01 | -300 | -276.1 | 20.01 | -296.10 |
| 2 | -259.80 | 40.20 | -300 | -257.36 | 40.2 | -297.56 |
| 3 | -223.65 | 76.36 | -300 | -222.57 | 76.36 | -298.92 |
| 4 | -212.83 | 87.17 | -300 | -212.83 | 87.172 | -300 |
| 5 | -206.32 | 93.68 | -300 | -203.41 | 93.68 | -297.09 |
| 6 | -150.94 | 107.39 | -258.3 | -155.22 | 107.39 | -262.61 |
| 7 | 37.310 | 98.98 | -61.67 | 13.99 | 98.98 | -84.98 |
| 8 | 60.420 | 80.42 | -20 | 52.57 | 80.42 | -27.85 |
| 9 | 117.46 | 101.46 | 16 | 130.94 | 101.46 | 29.48 |
| 10 | 189.81 | 132.14 | 57.67 | 180.26 | 132.14 | 48.115 |
| 11 | 262.21 | 146.17 | 116 | 255.13 | 146.17 | 108.97 |
| 12 | 349.38 | 150.00 | 199.4 | 338.47 | 150 | 188.47 |
| 13 | 307.40 | 149.69 | 157.7 | 296.72 | 149.69 | 147.03 |
| 14 | 254.85 | 138.81 | 11.04 | 253.08 | 138.81 | 114.27 |
| 15 | 182.11 | 107.73 | 74.38 | 203.35 | 107.73 | 95.61 |
| 16 | 152.88 | 120.17 | 32.71 | 171.55 | 120.17 | 51.38 |
| 17 | 217.15 | 142.77 | 74.38 | 213.14 | 142.77 | 70.37 |
| 18 | 259.90 | 143.86 | 116.0 | 255.12 | 143.86 | 111.26 |
| 19 | 341.76 | 101.76 | 240 | 341.76 | 101.76 | 240 |
| 20 | 306.43 | 66.43 | 240 | 306.42 | 66.43 | 240 |
| 21 | 166.11 | 51.11 | 115 | 175.22 | 51.11 | 124.11 |
| 22 | 63.68 | 47.68 | 16 | 67.71 | 47.68 | 20.03 |
| 23 | -31.41 | 30.26 | -61.67 | -21.03 | 30.26 | -51.29 |
| 24 | -34.21 | 28.29 | -62.50 | -41.66 | 28.29 | -69.95 |
| Total | 1,869.70 | 2,262.53 | -392.8 | 1,865.26 | 2,262.53 | -397.27 |

| Hour | Case 2 | | | Case 4 | | |
|---|---|---|---|---|---|---|
| | **Total** | **Wind** | **PS** | **Total** | **Wind** | **PS** |
| 1 | -283.47 | 16.53 | -300 | -274.828 | 16.53 | -291.36 |
| 2 | -263.09 | 36.911 | -300 | -256.23 | 36.91 | -293.14 |
| 3 | -223.67 | 76.327 | -300 | -218.63 | 76.33 | -294.95 |
| 4 | -208.14 | 91.86 | -300 | -206.24 | 93.75 | -300 |
| 5 | -198.72 | 101.28 | -300 | -198.72 | 101.28 | -300 |
| 6 | -181.74 | 118.26 | -300 | -168.92 | 118.26 | -287.17 |
| 7 | -63.420 | 111.58 | -175 | -54.09 | 111.58 | -165.66 |
| 8 | 29.500 | 91.17 | -61.67 | 21.68 | 91.17 | -69.49 |
| 9 | 91.910 | 111.91 | -20 | 84.89 | 111.91 | -27.018 |

| | | | | | | |
|---|---|---|---|---|---|---|
| 10 | 152.53 | 136.53 | 16 | 162.19 | 136.53 | 25.659 |
| 11 | 202.43 | 144.77 | 57.67 | 248.87 | 144.77 | 104.12 |
| 12 | 249.04 | 149.71 | 99.33 | 332.22 | 149.71 | 182.51 |
| 13 | 290.95 | 149.95 | 141 | 373.81 | 149.95 | 223.85 |
| 14 | 309.8 | 139.13 | 170.67 | 330.17 | 139.13 | 191.04 |
| 15 | 243.26 | 114.26 | 129 | 279.96 | 114.26 | 165.70 |
| 16 | 241.33 | 126.33 | 115 | 246.74 | 126.33 | 120.40 |
| 17 | 298.60 | 141.94 | 156.67 | 254.61 | 141.94 | 112.67 |
| 18 | 338.90 | 140.57 | 198.33 | 296.27 | 140.57 | 155.7 |
| 19 | 339.1 | 99.1 | 240 | 331.76 | 99.10 | 232.66 |
| 20 | 308.2 | 68.2 | 240 | 296.17 | 68.20 | 227.97 |
| 21 | 172.77 | 57.77 | 115 | 101.30 | 57.77 | 43.52 |
| 22 | 70.595 | 54.59 | 16 | 15.56 | 54.595 | -39.035 |
| 23 | 16.875 | 36.87 | -20 | -70.14 | 36.875 | -107.02 |
| 24 | -10.305 | 31.36 | -41.67 | -26.05 | 31.362 | -57.408 |
| Total | 1,923.25 | 2,346.92 | -423.6 | 1,902.36 | 2,348.81 | -446.45 |

## IV. Conclusions

We proposed a stochastic PBUC solution strategy for the intra-hour coordination of wind-PS units when considering the intra-hour wind energy and market price forecast errors in a GENCO. The numerical example shows the effect of coordination in deterministic and stochastic case studies. The results show that PS units can be coordinated with wind energy units in order to firm up the wind power generation and to take advantage of electricity price volatilities. The imbalance energy charges can reduce a GENCO's expected payoffs which can be fixed by the wind-PS unit coordination. The merits of coordination are more significant as energy balancing price are increased. Thus, the proposed wind-PS unit coordination provides a hedging mechanism to protect GENCOs against wind speed variations. The major contributions of the paper are listed as follows:

- The intra-hour variation of wind power generation is modeled and the PS coordination is proposed to firm the total hourly wind-PS generation.
- The intra-hour variation of energy price is considered for maximizing the GENCO's expected payoff which includes imbalance energy charges and additional intra-hour costs.
- The forecast errors for energy price and wind power are modeled and their impacts on the hourly commitment, generation dispatch, and payoffs are considered.

## References


[1] J. Wu, X. Guan, X. Zhou, and Y. Zhou, "Estimation and characteristic analysis of aggregated generation of geographically distributed wind farms," in *Proc. 2011 IEEE Power Engineering Society General Meeting*, pp. 1-6, Jul. 2011.

[2] D. Lew, M. Milligan, G. Jordan and R. Piwko, "The value of wind power forecasting," in *Proc. 91st American Meteorological Society Annual Meeting, The Second Conference on Weather, Climate and New Energy Economy*, Jan. 2011.

[3] *ERCOT Wind Impact / Integration Analysis, Phase 1 Review: Variability and Predictability* [On-line], Electric Reliability Council of Texas (ERCOT), ROS Wind A/S Task Force Meeting, Oct. 2007.

[4] *ERCOT Wind Impact / Integration Analysis, Phase 2 Review: Ancillary Services Requirements* [On-line], Electric Reliability Council of Texas (ERCOT), Wind Impact Task Force Meeting, Feb. 2008.

[5] J. Wang, M. Shahidehpour, and Z. Li, "Security-constrained unit commitment with volatile wind power generation," *IEEE Trans. on Power Syst.*, vol. 23, no. 3, pp. 1319-1327, Jul. 2008.

[6] T. Hennessy, and M. Kuntz, "The multiple benefits of integrating electricity storage with wind energy," in *Proc. 2005 IEEE Power Engineering Society General Meeting*, vol. 2, pp. 1952-1954, Jun. 2005.

[7] R. B. Schainker, "Executive overview: energy storage options for a sustainable energy future," In *Proc. 2004 IEEE Power Engineering Society General Meeting*, vol. 2, pp. 2309-2314, Jun. 2004

[8] The Multiple Benefits of Integrating the VRB-ESS with Wind Energy Producers - a Case Study in MWH Applications [On-line], VRB Power Systems Inc., Vancouver, Canada, Mar. 2007.

[9] D. Hawkins, "Achieving California's 20% renewable portfolio standard," California Independent System Operator Renewable Integration Study, Sep. 2007.

[10] J. M. Morales, A. J. Conejo, and J. Perez-Ruiz, "Short-term trading for a wind power producer," *IEEE Trans. on Power Syst.*,vol. 25, no. 1, pp. 554-564, Feb. 2010.

[11] P.B. Eriksen, T. Ackermann, H. Abildgaard, P. Smith, W. Winter, and J. Rodriguez Garcia, "System operation with high wind penetration," *IEEE Power and Energy Magazine*, vol. 3 , no. 6, pp. 65-74, Nov.-Dec. 2005.

[12] J. M. Morales, A. J. Conejo and J. Perez-Ruiz, "Economic valuation of reserves in power systems with high penetration of wind power," *IEEE Trans. on Power Syst.*,vol. 24, no. 2, pp. 900-910, May. 2009.

[13] M. Ahlstrom, L. Jones, R. Zavadil, and W. Grant, "The future of wind forecasting and utility operations," *IEEE Power Energy Mag.*, vol. 3, no. 6, pp. 57–64, Nov./Dec. 2005.

[14] N. Lu, J. H. Chow, and A. A. Desrochers, "Pumped-storage hydro-turbine bidding strategies in a competitive electricity market," *IEEE Trans. Power Syst.*, vol. 19, no.2, pp. 834-841, May 2004.

[15] E. D. Castronuovo and J. A. P. Lopes, "On the optimization of the daily operation of a wind-hydro power plant," *IEEE Trans. on Power Systems*, vol.19, no. 3, pp. 1599-1606, Aug. 2004.

[16] J. Garcia-Gonzalez, R. M. Ruiz de la Muela, L. M. Santos and A. M. Gonzalez, "Stochastic joint optimization of wind generation and pumped-storage units in an electricity market," *IEEE Trans. Power Syst*, vol. 23, no. 2, pp. 460-468, May 2008.

[17] International Energy Agency. (2005, June). *Variability of Wind Power and Other Renewables-Management options and strategies*, [online] www.uwig.org/IEA_Report_on_variability.pdf

[18] B. Parson, M. Milligan, B. Zavadil, D. Brooks, B. Kirby, K. Dragoon, J. Caldwell, "Grid impacts of wind power: a summary of recent studies in the united states", *Wind Energy*, vol. 7, no. 2, pp. 87-108, May 2004.

[19] M. Shahidehpour, H. Yamin and Z. Li, "Market operation in electric power systems: forecasting, scheduling and risk management", Wiley-IEEE press, 2002.

[20] T. Li and M. Shahidehpour, "Price-based unit commitment: a case of Lagrangian relaxation versus mixed integer programming," *IEEE Trans. Power Syst.*, vol. 20, pp.2015-2025, Nov. 2005.

[21] R. Billinton, B. Karki, R. Karki, and G. Ramakrishna, "Unit commitment risk analysis of wind integrated power systems," *IEEE Trans. Power Syst.*, vol. 24, no. 2, pp. 930-939, May 2009.

[22] F. Gao, X. H. Guan, X. R. Cao, and A. Papalexopoulos, "Forecasting power market clearing price and quantity usage using a neural network method," in *Proc. IEEE Power Eng. Soc. Summer Meeting*, Seattle, WA, pp. 2183-2188, Jul. 2000.

[23] J. F. Manwell, et al. "Hybrid2- a hybrid system simulation model theory manual," Renewable Energy Research Laboratory, Department of Mechanical Engineering, University of Massachusetts, Jun. 2006.

[24] L. Söder, "Simulation of wind speed forecast errors for operation planning of multiarea power systems," in *Proc. Probabilistic Methods Applied to Power Systems, 2004 International Conference on*, pp. 723-728, 12-16 Sep. 2004.

[25] A. Boone, "Simulation of short-term wind speed forecast errors using a multi-variate ARMA (1,1) time-series model," Master Thesis, KTH 2005.

[26] ISO New England five-minute LMPs historical data [online] http://www.iso-ne.com/markets/hst_rpts/hstRpts.do?category=Fivemin

[27] L. Wu, M. Shahidehpour, and T. Li, "Stochastic security-constrained unit commitment," *IEEE Trans. on Power Syst.*, vol.22, no.2, pp. 800-811, May 2007.

[28] L. Wu, M. Shahidehpour, and T. Li, "GENCO's risk-based maintenance outage scheduling," *IEEE Trans. on Power Syst.*, vol.23, no.1, pp.127-136, Feb. 2008.

[29] J. Dupa˘cová, N. Gröwe-Kuska, and W. Römisch, "Scenario reduction in stochastic programming: An approach using probability metrics," *Math. Program.*, ser. A 95, pp. 493–511, 2003.
[30] GAMS/SCENRED Documentation. [Online]. Available: http://www.gams.com/docs/document.htm.
[31] *Wind Power and Electricity Markets - A living summary of markets and market rules for wind energy and capacity in North America* [On-line] Utility Wind Integration Group, Market Operation and Transmission Policy Best Practices Users Group, Sep. 2007.
[32] *2006 State of the Market Report: Volume II* [On-line], PJM Interconnection, Market Monitoring Unit, pp. 151-158, Mar. 2007.
[33] M. Zima-Bo˘ckarjova, J. Matevoysan, M. Zima, and L. Söder, "Sharing of profit from coordinated operation planning and bidding of hydro and wind power," *IEEE Trans. Power Syst.*, vol. 25, no. 3, pp. 1663-1673, Aug. 2010.

## BIOGRAPHIES

**Mohammad E Khodayar** (S'09) received his MS degree in electrical engineering from Sharif University of Technology, Tehran, Iran in 2006. He is a Ph.D student in electrical engineering at Illinois Institute of Technology. His research interests include power system operation and planning.

**Mohammad Shahidehpour** (F'01) is the Bodine Professor and Director of the Robert W. Galvin Center for Electricity Innovation at Illinois Institute of Technology. He is an Honorary Professor in the King Abdulaziz University in Saudi Arabia, North China Electric Power University, and Sharif University of Technology in Iran.

# Hourly Demand Response in Day-ahead Scheduling for Managing the Variability of Renewable Energy

Hongyu Wu, Mohammad Shahidehpour, and Ahmed Al-Abdulwahab

The first author is with the Robert W. Galvin Center for Electricity Innovation at Illinois Institute of Technology. The second author is with the Robert W. Galvin Center for Electricity Innovation at Illinois Institute of Technology and the ECE Department at King Abdulaziz University, Jeddah, Saudi Arabia. The third author is with the ECE Department at King Abdulaziz University. This study was funded in part by the DOE Award # DE-FC26-08NT02875.

Abstract—This paper proposes a stochastic optimization model for the day-ahead scheduling in power systems, which incorporates the hourly demand response (DR) for managing the variability of renewable energy sources (RES). DR considers physical and operating constraints of the hourly demand for economic and reliability responses. The proposed stochastic day-ahead scheduling algorithm considers random outages of system components and forecast errors for hourly loads and RES. The Monte Carlo simulation (MCS) is applied to create stochastic security-constrained unit commitment (SCUC) scenarios for the day-ahead scheduling. A general purpose MILP software is employed to solve the stochastic SCUC problem. Numerical results in the paper demonstrate the benefits of applying DR to the proposed day-ahead scheduling with variable renewable energy sources.

Index Terms - Hourly demand response, day-ahead scheduling, variable renewable energy sources, load forecast errors, network contingencies, stochastic SCUC.

## NOMENCLATURE

*Parameters:*

| | |
|---|---|
| $N_T$ | Number of time periods |
| $N_G$ | Number of available generators |
| $N_B$ | Number of buses |
| $N_D$ | Number of renewable energy sources |
| $N_J$ | Number of batteries |
| $N_S$ | Number of scenarios |
| $t$ | Index for time periods, $t = 1, 2, \cdots, N_T$. |
| $i$ | Index for generators, $i = 1, 2, \cdots, N_G$. |
| $b$ | Index for buses, $b = 1, 2, \cdots, N_B$ |
| $k$ | Index for renewable sources, $k = 1, 2, \cdots, N_D$. |
| $j$ | Index for batteries, $j = 1, 2, \cdots, N_J$. |
| $s$ | Index for scenarios, $s = 1, 2, \cdots, N_S$. |
| $l$ | Index for available transmission lines |
| $NB^D_{b,t}$ | Number of blocks of energy demand by bus *b* at time *t* |
| $NB^G_{i,t}$ | Number of blocks of supply bid offered by generator *i* at time *t* |
| $P_s$ | Probability of scenario *s* |
| $NL_i$ | No-load cost of generator *i*, in $ |
| $\lambda D_{n,b,t}$ | Marginal benefit of the *n*-th block of the bid at bus *b* and time *t*, in $/MW |
| $\lambda G_{m,i,t}$ | Marginal production cost of the *m*-th block of generator *i* at time *t*, in $/MW |
| $VOLL_{b,t}$ | Value of lost load at bus *b* at time *t*, in $ |
| $RCAP_t$ | System reserve requirement at time *t*, in MW |

$P_i^{max}$ Upper generation limit of unit *i*, in MW

$\Gamma_{(\cdot)}^{(\cdot)}$ Shift factor

$DR_{b,t}^{min}$ Minimum curtailed load at bus *b* and time *t*, in MW

$DR_{b,t}^{max}$ Maximum curtailed load at bus *b* and time *t*, in MW

$D_{b,t}^{max}$ Maximum load at but *b* at time *t*, in MW

$\Delta G_i$ Maximum ramp up/down rate of generator *i*, in MW/min

$\Delta D_b$ Pick-up or drop-off rate of load at bus b

$X_{b,t-1}^{on}$ ON time of load at bus *b* at time *t*-1, in hour

$X_{b,t-1}^{off}$ OFF time of load at bus *b* at time *t*-1, in hour

$UT_b$ Minimum ON time of load at bus *b*, in hour

$DT_b$ Minimum OFF time of load at bus *b*, in hour

$E_b^{max}$ Maximum energy change at but *b* in the scheduling horizon, in MW

$\underline{q}_j^c$ Minimum charge of storage *j*, in MW

$\overline{q}_j^c$ Maximum charge of storage *j*, in MW

$\underline{q}_j^d$ Minimum discharge of storage *j*, in MW

$\overline{q}_j^d$ Maximum discharge of storage *j*, in MW

$\underline{e}_j$ Minimum state of storage *j*, in MW

$\overline{e}_j$ Capacity of storage *j*, in MW

$\tau$ Reserve responsive time, usually in 10 minute

$\eta$ Period span, usually in hour

$\lambda_{(\cdot)}$ Mean time to failure for system component, in hour

$\mu_{(\cdot)}$ Mean time to repair for system component, in hour

*Variables:*

$d_{n,b,t}^s$ Demand in the *n*-th block of the stepwise demand bid at bus *b* at time *t* in scenario *s*, in MWh

$p_{m,i,t}^s$ Generation in the *m*-th block of piecewise linear output by generator *i* at time *t* in scenario *s*, in MW

$S_{i,t}(\cdot)$ Start-up or shut-down cost of unit *i* at time *t*, in $

$X_{i,t}$ Time periods when unit *i* has been ON or OFF at time *t*, in hour

$DL_{b,t}^s$ Loss of load at bus *b* at time *t* in scenario *s*, in MW

$p_{i,t}^s$ Dispatch of generator *i* at time *t* in scenario *s*, in MW

$g_{k,t}^s$ Dispatch of renewable source *k* at time *t* in scenario *s*, in MW

$q_{j,t}^s$ Charge (-) or discharge (+) of storage *j* at time *t* in scenario s, in MW

$C_{j,t}^s$ State of charge (SOC) of storage *j* at time *t* in scenario s, in %

$DE_{b,t}$ Expected price-responsive load at bus *b* at time *t*, in MW

$DB_{b,t}^s$ Customer base load at bus *b* at time *t* in scenario *s*, in MW

$DR_{b,t}^s$ Adjustable load of bus *b* at time *t* in scenario *s*, in MW

$RU^{s}_{i,t}$ Reserve provided by generator *i* at time *t* in scenario *s*, in MW

$RB^{s}_{j,t}$ Reserve provided by storage *j* at time *t* in scenario *s*, in MW

$z_{i,t}$ Commitment Status of thermal generator *i* at time *t*; 1 for ON and 0 for OFF

$y^{s}_{b,t}$ State of curtailment at but *b* at time *t* in scenario *s*; 1 when curtailed and 0 otherwise

# I. INTRODUCTION

The hourly demand response (DR) program in electricity markets could provide significant benefits to market participants and customers. Such benefits include lower hourly market prices, lower volatility in hourly market prices, enhanced system reliability, and a smaller chance for the market power exertion by generating companies (GENCO), as customers play a more active role in power system operations. DR offers incentives for lowering electricity usage at times when electricity prices are high or when the power system reliability is in question [1]-[3]. DR becomes more attractive to customers and ISOs as electricity demands, fuel prices, and the quest for achieving a higher system reliability increase.

The DR program includes reliability and economic considerations. In the reliability DR program, participating customers are paid incentives for measured baseline load reductions during contingency conditions [2]. In the economic DR program, participating consumers would curtail hourly loads voluntarily in response to market prices. In this case, customers would shift their less critical hourly loads to periods which would balance potential cost savings against customer inconvenience [4]-[8]. The efficient market dynamics are represented by incorporating both DR programs into the market clearing process.

The integration of renewable energy sources (RES) into power systems could reduce transmission losses and congestion by dispersing power generation, improve the system reliability, defer infrastructure upgrades by the installation of local power supply, reduce carbon footprint by customizing the use of RES, and improve the system efficiency by enhancing the power quality according to customer requirements [9]-[11]. However, the widespread usage of variable RES could be problematic for power system operations [12],[13].

The simulation-based approach is generally applied when considering RES. A set of power production scenarios with their probabilities is introduced to handle uncertainties [14]. The stochastic unit commitment and dispatch with high wind penetration are examined for rolling planning with scenario trees [15]. Rolling planning is carried out for rescheduling which is based on the most up-to-date wind forecasts and existing schedules [16]. A methodology is proposed to determine the required level of spinning and non-spinning reserves with a high penetration of wind power [17]. The Monte Carlo simulation (MCS) method is applied to evaluate the performance of grid-connected wind turbine generators (WTGs) [18],[19]. WTGs are modeled as energy limited units by using a load modification technique [20]. Reliability indices are developed for hybrid solar-wind generation systems [21].

This paper proposes a short-term stochastic SCUC model for day-ahead markets which incorporates a coordinated DR and storage program for managing variable RES, random outages of generating units and transmission lines, and load and wind forecast errors. Both economic and reliability DR programs are considered in the presented DR model. The operating characteristics of loads include stepwise price bids and physical constraints of loads. The scenario reduction is adopted in MCS as a tradeoff between calculation speed and solution accuracy. A general purpose MILP software is employed to solve the stochastic SCUC problem.

The rest of paper is organized as follows. The market clearing mechanism is provided in Section II. The Monte Carlo simulation method for simulating the stochastic SCUC is described in Section III. The mathematical formulation of the stochastic SCUC problem is proposed in Section IV. Numerical testing results are presented and analyzed in Section V. The observation and the concluding remarks are provided in Section VI and Section VII, respectively.

# II. PROPOSED MARKET CLEARING MECHANISM

## *A. Day-ahead Market*

The ISO received bids from market participants including load aggregators and DR providers (DRP), and clears the market by optimizing the hourly dispatch of individual generating units over a scheduling horizon. The day-ahead schedule will maximize the social welfare while satisfying system-wide limits and operating constraints of individual market participants.

## *B. DR Program*

In the proposed DR model, loads include the customer base load (CBL) and the price responsive load (PRL). CBL is forecasted based on the historical data; for example, the customer's average electricity usage in the curtailment bid period during the 10 days prior to the day when the bid was submitted [22]. The economic DR may include blocks of hourly PRL bids with corresponding prices. The hourly constraints may include expected price-responsive load, minimum/maximum curtailable load, maximum load pick-up/drop-off rate and minimum up/down time of load curtailment. PRL can be curtailed or shifted to other time periods for economic reasons as scheduled by ISO in the day-ahead market. The proposed model allows customers to participate in reliability DR program. The CBL of participating customers could be curtailed in the case of a system emergency. Customers are required to submit the maximum loss of load and the value of lost load (VOLL) to the DA market and the load curtailment will be scheduled by ISO. Unlike the PRL in economic DR, the loss of load is involuntary [23],[24]. If load shedding occurs, customers will get

compensated equivalent to the amount of lost load multiplied by the corresponding VOLL.

Both DR programs offer operation reserves to the ancillary service market. The energy and reserve markets are scheduled and cleared simultaneously through MILP in the proposed model.

## III. Monte Carlo Simulation for Stochastic SCUC

The stochastic SCUC in our proposed model includes the following:

### A. Renewable Energy Sources

We disregard for simplicity the correlation of load and RES and treated them independently in the scheduling horizon. Suppose the random photovoltaic array (PVA) output follows a Beta distribution and the random WTG output follows a Weibull distribution at each time period [25]. The continuous probability distribution functions (PDFs) are approximated by a discrete distribution. Let $PVA_t$ and $WTG_t$ denote discrete probability distributions for PVA and WTG outputs at time *t*, respectively. Then:

$$PVA_t = [\{s_t^n, P(s_t^n)\}],\ n = 1, 2, \ldots, NS_t \quad (1)$$

$$WTG_t = [\{w_t^n, P(w_t^n)\}],\ n = 1, 2, \ldots, NW_t \quad (2)$$

where $NS_t$ and $NW_t$ are the total number of discrete output levels in $PVA_t$ and $WTG_t$, respectively; $s_t^n$ and $w_t^n$ are the *n-th* discrete levels of PVA and WTG outputs at time stage *t*, respectively; $P(s_t^n)$ and $P(w_t^n)$ are probabilities of occurrence with respect to $s_t^n$ and $w_t^n$, which can be calculated based on their probability density functions (PDFs).

We divide the entire scheduling horizon into several time stages in which each stage spans several hours. For each time stage, several scenarios are created based on historical data in which PVA and WTG outputs are different from the corresponding forecasts. The probability of each scenario at each stage is calculated as its weight based on the PDF. The weight for the final-stage scenario is obtained by multiplying corresponding weights along the scenario tree. The stochastic output of PVA or WTG is then represented by possible scenarios with their corresponding probability.

### B. Monte Carlo Simulation

The number of samples needed for a given accuracy level is irrelevant to the system size; so the Monte Carlo simulation method is suitable for representing the uncertainty in large-scale optimization problems. MCS includes random outages of generating units and transmission lines [26],[27] as well as CBL forecast errors which represent variations around the forecasts at each time stage. The CBL forecast errors are represented by normal distribution functions in which the mean values are the forecasts and the standard deviations are percentages of the mean values. The outages of generator and transmission line are simulated based on forced outage rates and repair rates [27]. In each scenario, a sampling method [26] is used to determine the 0/1 value of system component availability. Scenario reduction is adopted as a tradeoff between computational burden and modeling accuracy in large-scale DR scheduling problems [28]. The probability metrics based on the scenario reduction method is applied.

## IV. Stochastic Problem Formulation and Constraints

We assume electricity market participants are independent bidders who bid at their respective marginal costs. ISO calculates the hourly SCUC and DR schedule, and hourly locational marginal prices (LMPs). The problem objective and constraints are formulated as follows:

### A. Objective Function

The objective of the proposed SCUC problem is to determine the day-ahead hourly schedule of generating units and hourly DR schedule such that the expected total social welfare is maximized. The social welfare is defined as the sum of consumer surplus and the producer surplus as shown in Fig. 1. The objective function is expressed as follows:

$$\begin{aligned}\max \sum_{s=1}^{N_S} P_s \{ & \sum_{t=1}^{N_T} \sum_{b=1}^{N_B} \sum_{n=1}^{NB_{j,t}^D} \lambda D_{n,b,t} d_{n,b,t}^s \\ & - \sum_{t=1}^{N_T} \sum_{i=1}^{N_G} [\sum_{m=1}^{NB_{i,t}^G} \lambda G_{m,i,t} p_{m,i,t}^s + NL_i z_{i,t} + S_{i,t}(X_{i,t}, z_{i,t})] \\ & - \sum_{t=1}^{N_T} \sum_{b=1}^{N_B} VOLL_{b,t} * DL_{b,t}^s \}\end{aligned} \quad (3)$$

The first term in the objective function (3) is the customer gross surplus and the second term is the generation cost of thermal units, which includes fuel cost, no-load cost, and piecewise linear start-up and shut-down cost. The third term represents the cost of load curtailment. The objective is subject to the following individual scenario constraints.

### B. System and Unit Constraints

Constraints (4), (6) and (8) are on power balance, system reserve, and transmission flows, respectively. Constraints (5) and (7)

show unit spinning reserve and line flows, respectively. Other physical constraints of generating units are generating unit limits, ramp rate limits, and min up/down time limits [1],[29],[30].

$$\sum_{i=1}^{N_G}\sum_{m=1}^{NB_{i,t}^{G}} p_{m,i,t}^{s} + \sum_{k=1}^{N_D} g_{k,t}^{s} + \sum_{j=1}^{N_J} q_{j,t}^{s} - \sum_{b=1}^{N_B} (DE_{b,t} - DR_{b,t}^{s}) = 0, \ \forall t, \forall s. \quad (4)$$

$$RU_{i,t}^{s} = z_{i,t} \cdot \min\{P_i^{\max} - p_{i,t}^{s}, \ \Delta G_i \cdot \tau\}, \ \forall i, \forall t, \forall s. \quad (5)$$

$$\sum_{i=1}^{N_G} RU_{i,t}^{s} + \sum_{j=1}^{N_J} RB_{j,t}^{s} + \sum_{b=1}^{N_B} DR_{b,t}^{s} \geq RCAP_t, \ \forall t, \forall s. \quad (6)$$

$$F_{l,t}^{s} = \sum_{i=1}^{N_G} \Gamma_{l,i}^{G} \sum_{m=1}^{NB_{i,t}^{G}} p_{m,i,t}^{s} + \sum_{k=1}^{N_D} \Gamma_{l,k}^{D} g_{k,t}^{s} + \sum_{j=1}^{N_J} \Gamma_{l,j}^{J} q_{j,t}^{s} - \sum_{b=1}^{N_B} \Gamma_{l,b}^{L} (DE_{b,t} - DR_{b,t}^{s}), \ \forall l, \forall t, \forall s. \quad (7)$$

$$-\overline{F}_l \leq F_{l,t}^{s} \leq \overline{F}_l, \ \forall l, \forall t, \forall s. \quad (8)$$

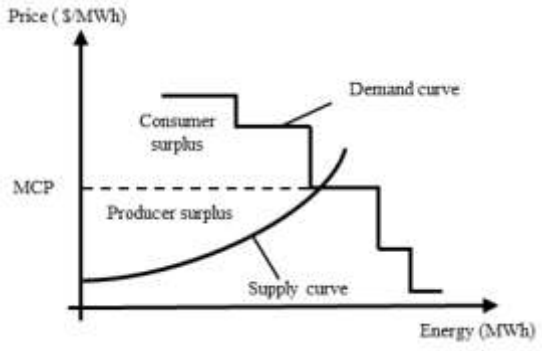


Fig. 1. Net social welfare and market equilibrium

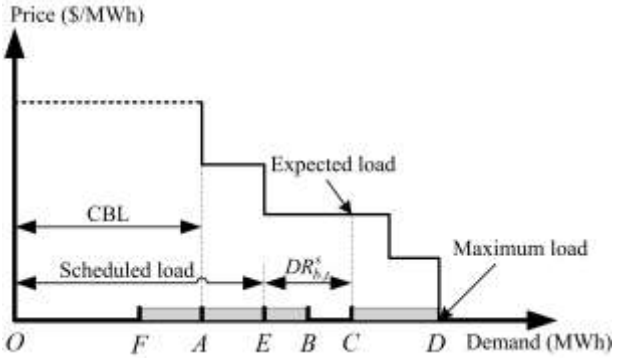


Fig. 2. Stepwise demand response bid

### *C. DR Constraints*

Fig. 2 shows a stepwise DR bid in which OA, OC, and OD represent the customer base load, the expected price-responsive load, and the maximum hourly load, respectively. CB and CF are the minimum and maximum load curtailment, respectively. OE denotes the customer load scheduled by ISO in the day-ahead market. Point E (end point of the scheduled load) would be located within two zones of FB and CD as highlighted in Fig. 2. The price-responsive load can be curtailed or shifted to another time period for satisfying system economic or reliability constraints. The ratio of available price-responsive load to the expected price-responsive load is defined as load participation factor (LPF), which is expressed as $LPF = AC/OC$ in Fig. 2. A higher LPF indicates a higher price elasticity of demand and more curtailable loads. $DR_{b,t}^{s}$ is the adjustable load of bus *b* at time *t* in scenario *s* which is calculated as the difference between the expected price-responsive load and the scheduled load as shown in Fig. 2. Decision variables in the proposed DR model are $DR_{b,t}^{s}$ and its 0-1 state. $DR_{b,t}^{s}$ is positive when the load is shifted out from bus *b* at time *t*, and negative when the load is shifted to bus *b* at time *t*.

The demand response constraints are listed in (9)-(15). The correlation between block demand and total demand is given in (9). The limit on curtailable load is provided in (10), which may either reflect physical load limits or be imposed by ISO. The loss of load constraint is shown in (11), which indicates that loss of load could occur if and only if all price-responsive loads are completely curtailed. Limits on pick-up/drop-off rate of load, min up/down time for load curtailment and allowable change of bus load across schedule horizon are given in (12)-(15), respectively. Constraint (12) would restrict the rate of customer load changes between any two successive hours. Constraint (13) indicates the minimum number of hours that a load would be curtailed. Constraint (14) shows the minimum number of hours when the load would be supplied. Constraint (15) would limit the total number of load curtailments in the scheduling horizon. By setting $E_b^{\max}$ to 0 in (15), the curtailed load at certain time periods will be fully shifted to other periods.

$$\sum_{n=1}^{NB_{j,t}^{D}} d_{n,b,t}^{s} = DE_{b,t} - DR_{b,t}^{s}, \ \forall b, \forall t, \forall s. \quad (9)$$

$$\begin{cases} DR_{b,t}^{\min} y_{b,t}^{s} \leq DR_{b,t}^{s} \leq DR_{b,t}^{\max} y_{b,t}^{s}, \ if \ DR_{b,t}^{s} \geq 0 \\ DR_{b,t}^{s} \geq DE_{b,t} - D_{b,t}^{\max} \qquad , \ else \end{cases} \forall b, \forall t, \forall s. \quad (10)$$

$$DL_{b,t}^{s} = \max\{DB_{b,t}^{s} - (DE_{b,t} - DR_{b,t}^{s}), \ 0\}, \ \forall b, \forall t, \forall s. \quad (11)$$

$$|(DE_{b,t} - DR_{b,t}^{s}) - (DE_{b,t-1} - DR_{b,t-1}^{s})| \leq \Delta D_b, \ \forall b, \ t = 2, \ 3, \ldots, N_T, \forall s. \quad (12)$$

$$(X^{s,on}_{b,t-1} - UT_b)(y^s_{b,t-1} - y^s_{b,t}) \geq 0,\ \forall b, t = 2,\ 3, \ldots, N_T, \forall s. \quad (13)$$

$$(X^{s,off}_{b,t-1} - DT_b)(y^s_{b,t} - y^s_{b,t-1}) \geq 0,\ \forall b, t = 2,\ 3, \ldots, N_T, \forall s. \quad (14)$$

$$0 \leq \sum_{t=1}^{N_T} DR^s_{b,t} \leq E^{\max}_b,\ \forall b, \forall t, \forall s. \quad (15)$$

D. *Storage Constraints*

We assume the power system is equipped with a storage with the following constrains: input and output limits of storage, SOC dynamics, SOC limits, initial/final SOC, and reserve contribution of storage are given in (16)-(20), respectively [31]. In (16), $q^s_{j,t}$ is negative when storage is charging, positive when the storage is discharging, and 0 when the storage is not functional. Constraint (20) indicates that reserve provided by storage is the minimum of its existing capacity and the maximum discharge.

$$q^s_{j,t} \in \{0, [-\overline{q}^c_j, -\underline{q}^c_j], [\underline{q}^d_j, \overline{q}^d_j]\},\ \forall j, \forall t, \forall s. \quad (16)$$

$$C^s_{j,t} = C^s_{j,t-1} - q^s_{j,t} \cdot \eta / \overline{e}_j,\ \forall j, \forall t = 2, 3, \ldots, N_T, \forall s. \quad (17)$$

$$\underline{C}_j = \frac{\underline{e}_j}{\overline{e}_j} \leq C^s_{j,t} \leq 1,\ \forall j, \forall t, \forall s. \quad (18)$$

$$C^s_{j,0} = C^0_j,\ C^s_{j,T} = C^T_j, \forall j, \forall s. \quad (19)$$

$$RB^s_{j,t} = \tau \cdot \min\{C^s_{j,t} * \overline{e}_j,\ \overline{q}^d_j\},\ \forall j, \forall t, \forall s. \quad (20)$$

Here, (4)-(20) are constraints that are related to individual scenarios. In each scenario, the availability of system components is represented by a set of input parameters in the proposed optimization formulation. For the purpose of presentation, this additional set of variables is not introduced in the SCUC formulation. Thermal units are formulated as non-quick start units with hourly scenario commitments which are the same as those in the base case. However, the dispatch of individual committed thermal units in scenarios could be altered in response to scenario realizations. The final dispatch of a thermal unit is its expected dispatch which is the corresponding weighted average solution of all possible scenarios.

## V. Numerical Solution for the Proposed Problem

Numerical cases are studied for a modified 6-bus system and a modified IEEE 118-bus system. The MILP model (3)-(20) is solved using the ILOG CPLEX 11.0 [32] in Microsoft Visual C# .NET on an Intel Xeon Sever with 64GB RAM. The DR program is implemented at all load buses and curtailed load will be shifted to other periods. The hourly price-responsive loads consist of a single energy block with a bidding price of 20$/MWh. The system reserve requirement is set as the largest generating unit capacity.

### *A. The Modified 6-bus System*

The modified 6-bus system, shown in Fig. 3, has three thermal units, one WTG, and seven transmission lines. The characteristics of generators, transmission lines and the expected hourly loads are listed in Table I, Tables II and III, respectively.

TABLE I
GENERATORS' DATA FOR 6-BUS SYSTEM

| U | Pmax (MW) | Pmin (MW) | Initial Status (h) | Min Down (h) | Min Up (h) | Ramp (MW /h) | $\lambda_i$ (h) | $\mu_i$ (h) |
|---|---|---|---|---|---|---|---|---|
| G1 | 220 | 100 | 4 | 4 | 4 | 30 | 23.6 | 0.4 |
| G2 | 100 | 10 | -3 | 3 | 2 | 50 | 23.7 | 0.3 |
| G3 | 20 | 10 | -1 | 1 | 1 | 20 | 23.8 | 0.2 |

TABLE II
TRANSMISSION LINE DATA FOR 6-BUS SYSTEM

| Line No. | From Bus | To Bus | X (pu) | Flow Limit (MW) | $\lambda_l$ (h) | $\mu_l$ (h) |
|---|---|---|---|---|---|---|
| 1 | 1 | 2 | 0.170 | 200 | 23.5 | 0.5 |
| 2 | 1 | 4 | 0.258 | 100 | 23.7 | 0.3 |
| 3 | 2 | 3 | 0.037 | 100 | 23.6 | 0.4 |
| 4 | 2 | 4 | 0.197 | 100 | 23.6 | 0.4 |
| 5 | 3 | 6 | 0.018 | 100 | 23.7 | 0.3 |
| 6 | 4 | 5 | 0.037 | 100 | 23.6 | 0.4 |
| 7 | 5 | 6 | 0.140 | 100 | 23.8 | 0.2 |

TABLE III
EXPECTED HOURLY LOAD FOR 6-BUS SYSTEM

| H | Load (MWh) | H | Load (MWh) | H | Load (MWh) | H | Load (MWh) |
|---|---|---|---|---|---|---|---|
| 1 | 175.19 | 7 | 168.39 | 13 | 242.18 | 19 | 245.97 |
| 2 | 165.15 | 8 | 177.60 | 14 | 243.60 | 20 | 237.35 |
| 3 | 158.67 | 9 | 186.81 | 15 | 248.86 | 21 | 237.31 |
| 4 | 154.73 | 10 | 206.96 | 16 | 255.79 | 22 | 215.67 |
| 5 | 155.06 | 11 | 228.61 | 17 | 256.00 | 23 | 185.93 |

| | | | | | | | |
|---|---|---|---|---|---|---|---|
| 6 | 160.48 | 12 | 236.10 | 18 | 246.74 | 24 | 195.60 |

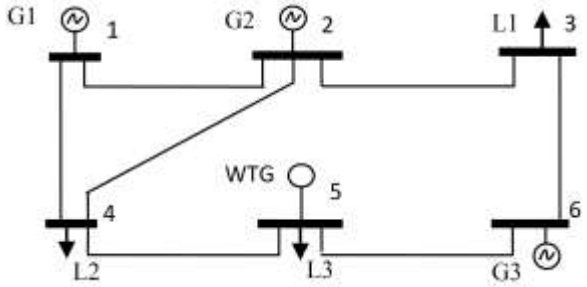

Fig.3. One line diagram of 6-bus system

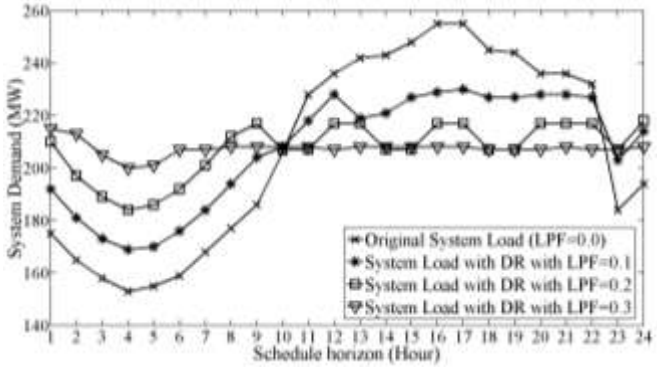

Fig 4. Actual and shifted loads

Three cases are studied to illustrate the impact of DR program on the RES variability in the day-ahead scheduling:

Case 1: DR is considered at all load buses.
Case 2: Combined DR and WTG variability is considered.
Case 3: Effect of DR, WTG variability, and storage on hourly LMPs is compared.
These cases are discussed as follows:

***Case 1***: Economic DR program is considered at all load buses. Fig. 4 shows the hourly system demand with several LPFs. At peak hours, the hourly load profile will be more flat as LPF increases. In Fig. 4, the load profile with LPF=0.3 is almost flat during Hours 6-24, and the standard deviation of hourly load is reduced from 101 MW to 18 MW at 0.3 LPF. A flat load profile corresponds to lower LMPs, lower transmission congestion, and lower system production cost. Also, power system operations will be more efficient since the hourly demand fluctuations are less frequent [2]. We assume a large WTG is located at Bus 5 with its deterministic hourly profile shown in Fig. 5. With a higher LPF, the system load profile will be increasingly close to the WTG profile. In an extreme case, when LPF=0.9, the system load profile would almost match that of WTG in which the peak load is shifted to other hours when the WTG output reaches its peak.

***Case 2***: In this case, economic DR at all load buses and variable WTG output at Bus 5 are included. The forecasted hourly WTG output is based on http://www.nrel.gov/. The 24-hour scheduling horizon is divided into 4 time stages when each time stage spans 6 hours. For each time stage, 5 scenarios including the forecasted output are considered in which the probability of each scenario is calculated according to the PDF of Weibull distribution. For simplicity, the variance is fixed during the horizon. There are $5^4$ =625 scenarios and each scenario represents a possible WTG output. The scenario reduction method is not applied to this small system. The MCS convergence characteristics for the WTG output and the value of objective function in the 625 scenarios are shown in Fig. 6. The relative error is given as $(1.96 \times S_Y / \sqrt{M}) / \bar{Y} \times 100\%$ , where $S_Y$ , $M$ and $\bar{Y}$ are standard deviation, number of scenarios, and expected value of variable $Y$ under 95% confidence interval, respectively. In Fig. 6, the relative error of the total WTG output with 625 simulations is less than 1.5%, while the relative error of objective function is less than 0.2%. Moreover, the relative errors are within 2% after the initial 250 simulations.

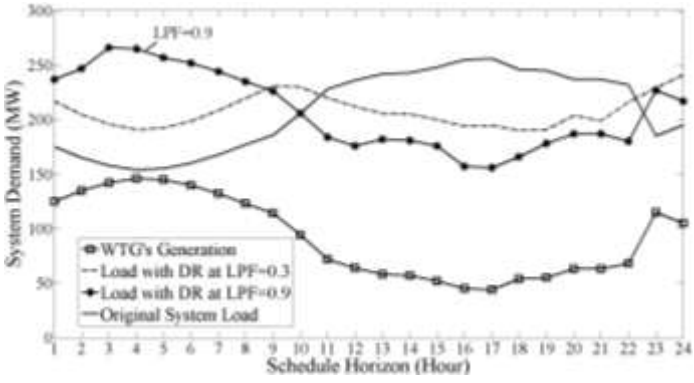

Fig. 5 Comparison of WTG output

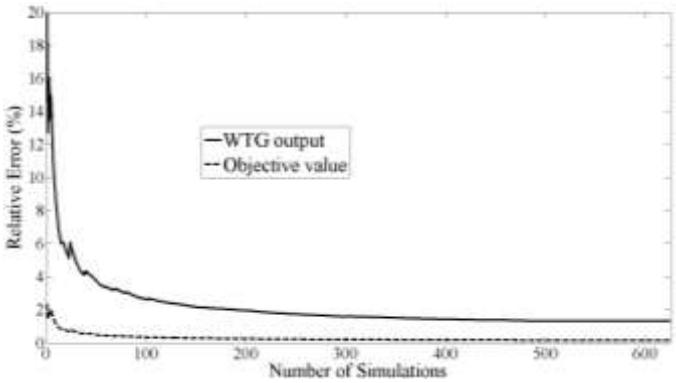

Fig. 6. Convergence characteristic of MCS

***Case 3***: In this case, the effects of considering DR, WTG variability, and storage on the hourly LMP are discussed. We study the

following four scenarios in this case:

Scenario 3.1: Base case without considering WTG or DR.
Scenario 3.2: A variable WTG is considered at Bus 5. The MCS with 625 scenarios used in Case 2 is adopted here.
Scenario 3.3: An aggregated and large storage (e.g., pumped storage hydro) located at Bus 5 is added to Scenario 3.2 in order to show explicitly the effect of the storage on hourly LMP profile. The storage parameters are listed in Table IV.
Scenario 3.4: DR is considered at Bus 5 based on Scenario 3.2. For comparison, the upper bound of hourly price-responsive load is set to the maximum charge/discharge in Table IV. The pick-up/drop-off rate limits of loads and the minimum up/down times are not considered for load curtailment.

LMPs at bus 5 in the four scenarios are compared in Fig. 7. Here, the LMPs in Scenario 3.1 spike at Hours 12-21. In Scenario 3.2, the time period is shortened to Hours 14-19. However, the peak-valley difference of LMPs becomes larger due to the WTG variability. The price spike in Scenarios 3.3 is mitigated as the storage shifts peak loads to off-peak hours. Scenario 3.4 shows a smoother LMP profile with 1.20$/MWh of peak-valley LMP difference by shifting loads to off-peak hours. The LMP fluctuations in Scenario 3.4 are reduced as compared to those in Scenario 3.3. A large storage is less effective than DR in reducing the volatility of hourly LMP because the charging of storage may be limited at off-peak hours. Fig. 8 shows the expected hourly storage output versus the expected LMP in Scenario 3.3. Here, the storage is charging during low LMP hours and discharging when the LMP is high.

TABLE IV
STORAGE DATA FOR 6-BUS SYSTEM

| Capacity (MWh) | Max Charge (MW) | Min Charge (MW) | Max Discharge (MW) | Min Discharge (MW) | Initial SOC (%) | Final SOC (%) |
|---|---|---|---|---|---|---|
| 300 | 50 | 30 | 50 | 30 | 20 | 20 |

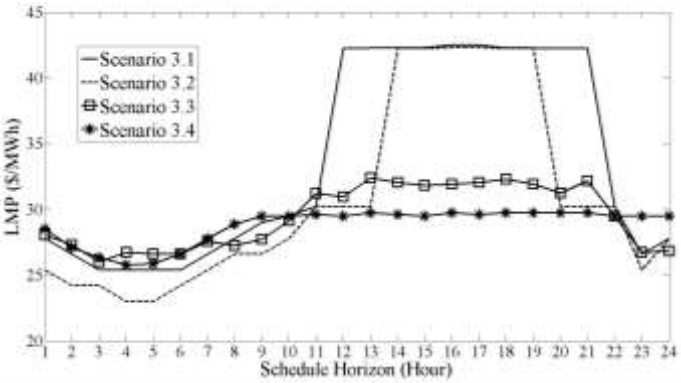

Fig. 7. LMPs at Bus 5

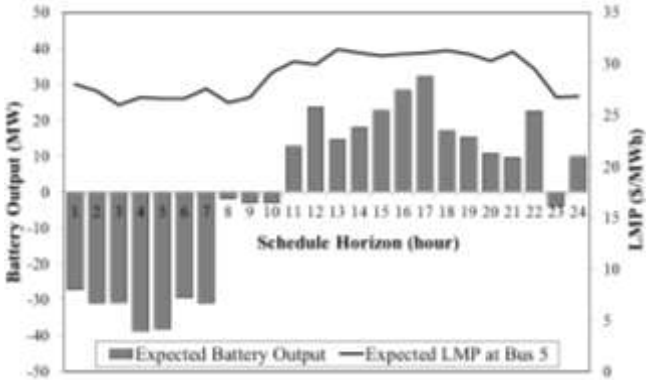

Fig. 8. Hourly storage charges versus LMP at Bus 5

*B. The Modified IEEE 118-Bus System*

The IEEE-118 bus system has 54 thermal generators, 186 branches, 91 load buses. The parameters of generators, transmission network, and load profiles are given in [1] . Economic and reliability DR programs at all load buses, random outages of generating unit and transmission lines, load forecast errors, and variable RES, and aggregated storage system are considered. There are 3 RES including 2 WTGs (at Buses 15,54) and 1 PVA (at Bus 96). A storage with parameters listed in Table IV is installed at buses with RES. The hourly WTG forecast is provided at http://www.nrel.gov/. VOLL is set at 100$/MWh. The hourly load forecast error is represented by ±5% of the CBL forecast. We generate 1800 scenarios and reduce the number to 185 by scenario reduction.

Table V lists the results in which EXP is the expected value and RERR is the relative error. Here, the expected average LMP is 19.06±0.23 $/MWh with a 0.2 LPF and 20% load shedding. Note that the 19.06±0.23 shows that 5% of LMPs will be beyond the given interval of ±0.23. The smaller the confidence interval, the more accurate the expectation will be. In spite of high VOLL, the load shedding occurs at certain scenarios with transmission line outages. In such scenarios, the average LMP is much higher than that of the base case. In Table V, the expected average LMP decreases from 19.06 $/MWh to 18.73 $/MWh as LPF increases from 0.2 to 0.3. In this case, more operating reserves are made available with a higher LPF. The results suggest that the benefit of larger economic DR is more significant when considering system contingencies. The total CPU time is 6.2 hours when 185 scenarios are applied. The relative errors of operating cost and average LMP are less than 2% as listed in Table V. The relative errors will be smaller and the accuracy will be higher if more scenarios are introduced. In such cases, parallel computation can be further adopted in each scenario to reduce the total CPU time.

TABLE V
DR RESULTS WITH 3 RES (95% CONFIDENCE INTERVAL)

| 20% Load | LPF=0.2 | LPF=0.3 |
|---|---|---|

| Shedding | Operating Cost ($) | Average LMP ($/MWh) | Operating Cost ($) | Average LMP ($/MWh) |
|---|---|---|---|---|
| **EXP** | 1660250 ±22937 | 19.06 ±0.23 | 1652905±25193 | 18.73 ±0.11 |
| **RERR** | 1.38% | 1.21% | 1.52% | 0.59% |

Fig. 9 shows the reduction in operating costs, average LMPs, and load payments as a function of RES contribution, which are compared with the base SCUC (without DR or RES.) In Fig. 9, the reduction in economic metrics increases almost linearly as RES contribution increases. When incorporating a 3.7% RES contribution and a 20% DR, the system operating cost, average LMP and load payment are reduced by 6.93%, 17.77% and 20.71%, respectively. Fig. 10 shows the variation of economic metrics with LPFs when the RES contribution is 3.7%. Comparing Figs. 9 and 10, it is seen DR has a higher impact on the reduction of average LMP and load payment, but RES has a higher impact on the reduction of operating cost. The contribution of DR, RES and storage to the average LMP reduction is shown in Fig. 11. In this case, DR is the leading factor in contributing to the 64.3% reduction in the average LMP, which is followed by those of WTG (18.2%), storage (10.4%) and PVA (7.1%).

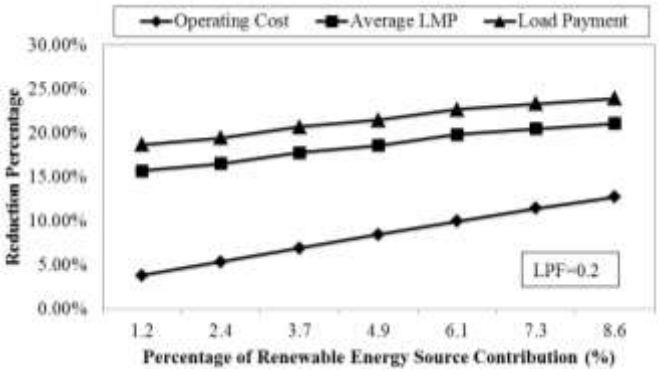


Fig. 9. Economic metrics versus RES

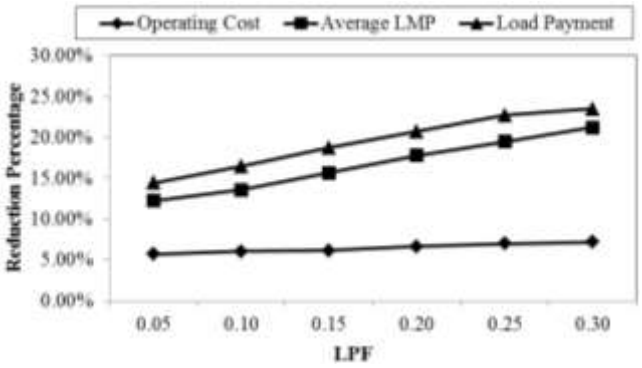


Fig. 10. Economic metrics versus LPF

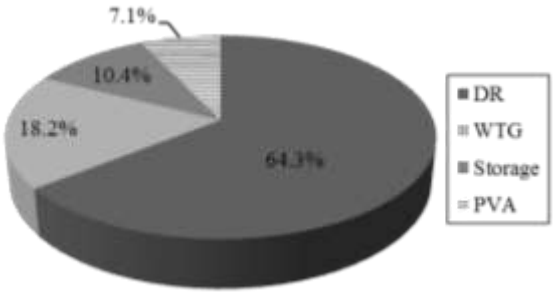


Fig. 11. Contribution percentages to average LMP reduction

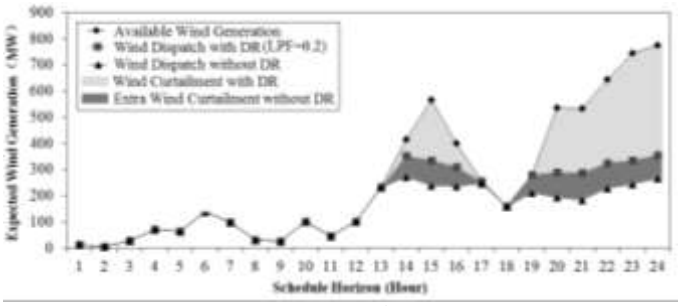


Fig. 12. Expected dispatch of WTG at bus 54

TABLE VI
EFFECT OF DR ON WIND ENERGY IN THE SYSTEM

| EXP | Without DR | With DR (LPF=0.2) |
|---|---|---|
| **Total Wind Curtailment (MWh)** | 6948 | 4958 |
| **Wind Penetration (%)** | 13.4 | 17.3 |

In Fig. 12, WTG curtailments with or without DR at bus 54 are compared. The expected available wind energy in this case is 24,631 MWh, which is 21.7% of the total daily energy demand. The available wind generation represents the upper limit of actual wind dispatch and the difference between the upper limit and the actual dispatch is defined as wind curtailment. In Fig. 12, the available wind generation is dispatched without any curtailment at Hours 1-13, 18 when the hourly available wind generation is below 232 MW. The lightly shaded area in Fig. 12 shows wind curtailment when considering a 20% DR at Bus 54. Here, wind curtailment is higher at Hours 14-17, 19-24 when the available wind generation is higher than 256MW. The flows on Lines 77 and 78, which connect Buses 54-55 and Buses 54-56, reach their respective limits during those curtailment hours. However, when DR is applied, Bus 54 faces a higher wind curtailment without DR, which is represented by darker shade in Fig. 12. This is because the corresponding load can be shifted between hours. Table VI shows the DR effect on reducing the system wind curtailment. Here, a 20% DR at every load bus would reduce the wind curtailment from 6,948 MWh to 4,958 MWh, while the wind penetration is increased from 13.4% to 17.3%.

## VI. OBSERVATIONS

We list the observations below based on our numerical results.

1. Economic DR offers a flat load profile which leads to lower LMPs, lower transmission congestion, and lower system operating cost. Economic DR benefits are more significant when considering system contingencies. Reliability DR provides a chance to maintain the system security.
2. DR has a more significant impact than RES on lowering average LMPs and load payments; RES has a more significant impact than DR on reducing operating costs. DR increases the wind penetration by reducing wind curtailments.
3. The storage system is less effective than DR on lowering the hourly LMP fluctuations which is due to the physical limitation of storage. When compared with RES and storage systems, DR is more effective in reducing average LMPs.

## VII. CONCLUSIONS

In this paper, we proposes a stochastic optimization model for the day-ahead power system scheduling which incorporates the hourly DR for managing the variability of RES. Physical and operating constraints of hourly demand are considered in DR for economic and reliability responses. The MCS creates multiple scenarios for representing possible realizations of uncertainty. Random outages of system components and forecast errors for hourly load and RES are included in MCS. Numerical results demonstrate that DR offers a flat load profile which leads to lower transmission congestions, lower system operating costs and lower LMPs. In addition, DR is the leading factor for lowering LMPs, which outperforms the utilization of generation resources such as RES and storage. DR increases wind penetration in terms of reducing wind curtailments, which make DR an effective tool for managing the variability of RES.

## REFERENCES


[1] M. Shahidehpour, H. Yamin, and Z. Y. Li, *Market Operations in Electric Power Systems*. New York: Wiley, 2002.

[2] M.H. Albadi, E.F. El-Saadany. "A summary of demand response in electricity markets," *Elect. Power. Syst. Res.*, vol. 78, no. 11, pp. 1989-1996, Nov. 2008.

[3] U.S. Department of Energy, Benefits of Demand Response in Electricity Markets and Recommendations for Achieving Them, 2006.

[4] A. J. Conejo, J. M. Morales, and L. Baringo. "Real-time demand response model," *IEEE Trans. Smart Grid*, vol. 1, no. 3, pp. 236-242, Dec. 2010.

[5] J. Wang, C. Bloyd, Z. Hu and Z. Tan, "Demand response in China", *Int. J. Energy*, vol. 35, no. 4, pp. 1592-1597, April 2010.

[6] A. Khodaei, M. Shahidehpour, and S. Bahramirad, "SCUC with hourly demand response considering intertemporal load characteristics," *IEEE Trans. Smart Grid*, vol. 2, no. 3, pp. 564-571, Sept. 2011.

[7] K. Herter, P. McAuliffe, and A. Rosenfeld, "An exploratory analysis of California residential customer response to critical peak pricing of electricity," *Energy*, vol. 32, no. 1, pp. 25-34, Jan. 2007.

[8] S. Valero, M. Ortiz, C. Senabre, et al. "Methods for customer and demand response policies selection in new electricity markets," *IET Gen. Transm. Distrib.*, vol. 1, no. 1, pp. 104-110, Jan. 2007.

[9] B.C. Ummels, M. Gibescu, E. Pelgrum, W.L. Kling, and A.J. Brand, "Impacts of wind power on thermal generation unit commitment and dispatch," *IEEE Trans. on Energy Conversion*, vol. 22, no. 1, pp. 44-51, 2007.

[10] Y. M. Atwa, E. F. El-Saadany, M. M. A. Salama, et al, "Optimal renewable resources mix for distribution system energy loss minimization," *IEEE Trans. Power Syst*., vol. 25, no. 1, pp. 360-370, Feb. 2010.

[11] L. F. Ochoa and G. P. Harrison, "Minimizing energy losses: optimal accommodation and smart operation of renewable distributed generation," *IEEE Trans. Power Syst.*, vol. 26, no. 1, pp. 198-205, Feb. 2011.

[12] H.H.D. Mangueira, O.R. Saavedra, and J.E.O. Pessanha, "Impact of wind generation on the dispatch of the system: A fuzzy approach," *International Journal of Electrical Power & Energy Systems*, vol. 30, no. 1, pp. 67-72, 2008.

[13] A.G. Tsikalakis, N.D. Hatziargyriou, Y.A. Katsigiannis, and P.S. Georgilakis, "Impact of Wind Power Forecasting Error Bias on the Economic Operation of Autonomous Power Systems," *Wind Energy*, vol. 12, no. 4, pp. 315-331, 2009.

[14] G. Celli and F. Pilo, "MV network planning under uncertainties on distributed generation penetration," in *Proc. 2001 IEEE PES Summer Meeting*, vol. 1, pp. 485-490.

[15] A. Tuohy, P. Meibom, E. Denny, and M. O'Malley, "Unit commitment for systems with significant wind penetration," *IEEE Trans. on Power Systems*, vol. 24, no. 2, pp. 592-601, May 2009.

[16] P. Meibom, R. Barth, B. Hasche, et al, "Stochastic optimization model to study the operational impacts of high wind penetrations in Ireland", *IEEE Trans. on Power Systems*, vol. 26, no. 3, pp. 1367-1379, Aug. 2011.

[17] J. M. Morales, A. J. Conejo, J. Perez Ruiz, "Economic valuation of reserves in power systems with high penetration of wind power", *IEEE Trans. on Power Systems*. vol. 24, no. 2, pp. 900-910, May 2009.

[18] G. Desrochers, M. Blanchard, and S. Sud, "A Monte Carlo simulation method for the economic assessment of the contribution of wind energy to power systems," *IEEE Trans. Energy Convers.*, vol. EC-1, no. 4, pp. 50–56, Dec. 1986.

[19] R. Billinton, H. Chen, and R. Ghajar, "A sequential simulation technique for adequacy evaluation of generating systems including wind energy," *IEEE Trans. Energy Convers.*, vol. 11, no. 4, pp. 728–734, Dec. 1996.

[20] R. Billinton and A. A. Chowdhury, "Incorporation of wind energy conversion systems in conventional generating capacity adequacy assessment," *Proc. Inst. Elect. Eng.-C*, vol. 139, no. 1, pp. 47–56, Jan. 1992.
[21] G. Tina, S. Gagliano, and S. Raiti, "Hybrid solar/wind power system probabilistic modelling for long-term performance assessment," Sol. Energy, vol. 80, no. 5, pp. 578–588, May 2006
[22] Day-Ahead Demand Response Program Manual at NYISO, Available at http://www.nyiso.com/public/webdocs/products/demand_response/day_ahead/dadrp_mnl.pdf.
[23] F. Bouffard, F. D. Galiana, A. J. Conejo, "Market-Clearing With Stochastic Security--Part I: Formulation", *IEEE Trans. on Power Systems*. vol. 20, no. 4, pp. 1818-1826. Nov. 2005.
[24] F. Bouffard, F. D. Galiana, A. J. Conejo, "Market-Clearing With Stochastic Security--Part II: Case Studies", *IEEE Trans. on Power Systems*, vol. 20, no. 4, pp. 1827-1835. Nov. 2005.
[25] S.H. Karaki, R.B. Chedid and R. Ramadan, "Probabilistic performance assessment of autonomous solar-wind energy conversion systems," *IEEE Trans. Energy Convers.*, vol. 14, no. 3, pp. 766-772, Sep. 1999.
[26] L. Wu, M. Shahidehpour, and T. Li, "Stochastic security-constrained unit commitment," *IEEE Trans. Power Syst*., vol. 22, no. 2, pp. 800–811, May 2007.
[27] J. Valenzuela and M. Mazumdar, "Monte Carlo computation of power generation production costs under operating constraints," *IEEE Trans. Power Syst*., vol. 16, pp. 671–677, Nov. 2001.
[28] J. Dupa˘cová, N. Gröwe-Kuska, and W. Römisch, "Scenario reduction in stochastic programming: An approach using probability metrics," *Math. Program.*, vol. A 95, pp. 493–511, 2003.
[29] H. Wu, X. Guan, Q. Zhai, et al, "A systematic method for constructing feasible solution to SCUC problem with analytical feasibility conditions," *IEEE Trans. Power Syst*., vol. 27, no. 1, pp.526-534, Feb. 2012.
[30] Y. Fu, M. Shahidehpour. "Fast SCUC for large-scale power systems," *IEEE Trans. Power Syst.*, vol.22, no.4, pp. 2144-2151, Nov. 2007.
[31] X. Guan, Z. Xu and Q. Jia, "Energy-efficient buildings facilitated by Microgriod," *IEEE Trans. Smart Grid*, vol.1, no.3, pp. 2144-2151, Dec. 2010.
[32] ILOG CPLEX, ILOG CPLEX Homepage 2009 [Online]. Available at http://www.ilog.com

## BIOGRAPHIES

**Hongyu Wu** (M'09) received his B.S. degree in Energy and Power engineering and Ph.D. degree at the System Engineering from Xi'an Jiaotong University, China in 2003 and 2011, respectively. Currently, he is a Visiting Faculty in the Robert W. Galvin Center for Electricity Innovation at Illinois Institute of Technology, USA. His research interests include optimization of large-scale systems and scheduling in the deregulated electric power market.

**Mohammad Shahidehpour** (F'01) is the Bodine Chair Professor and Director of Robert W. Galvin Center for Electricity Innovation at IIT. Dr. Shahidehpour is the recipient of the Honorary Doctorate for the Polytechnic University of Bucharest in Romania. He is a Research Professor at King Abdulaziz University in Jeddah, Saudi Arabia, and Honorary Professor in North China Electric Power University in Beijing and Sharif University in Tehran.

**Ahmed Al-Abdulwahab** is an Associate Professor in the Department of Electrical Engineering and Computer Engineering at King Abdulaziz University. He has been a consultant to the Electricity and Co-Generation Regulatory Authority in Saudi Arabia and a visiting scientist at Kinectrics and the University of Manchester. His field of interest includes power system planning and reliability evaluations. He received his PhD degree in Electrical Engineering from the University of Saskatchewan.

# Coordination of Short-Term Operation Constraints in Multi-Area Expansion Planning

Amin Khodaei, *Member, IEEE*, Mohammad Shahidehpour, *Fellow, IEEE*, Lei Wu, *Member, IEEE*, and Zuyi Li, *Senior Member, IEEE*

***Abstract*—This paper presents a comprehensive expansion planning algorithm of generation and transmission components in multi-area power systems. The objective is to minimize the total system cost in the planning horizon, comprising investment and operation costs and salvage values subject to long-term system reliability and short-term operation constraints. The multi-area expansion planning problem is decomposed into a planning problem and annual reliability subproblems. The planning decisions calculated in the planning problem would also satisfy the short-term operation constraints. A detailed model of thermal and hydro units is considered using the mixed-integer programming (MIP) formulation. In addition, a multi-state representation for the expansion planning of renewable energy units is explored. The proposed approach considers customers' demand response as an option for reducing the short-term operation costs. The planning problem solution is applied to the annual reliability indices subproblems which examine system reliability indices as a post-processor. If the reliability limit is not satisfied, additional reliability constraints will be introduced which are based on the sensitivity of system reliability index to investment decisions. The new reliability constraints are added to the next iterations of the planning problem to govern the revised plan for the optimal expansion. Numerical simulations indicate the effectiveness of the proposed approach for solving the operation-constrained multi-area expansion planning problem of practical power systems.**

***Index Terms*—Multi-area expansion planning, coordinated transmission and generation expansion planning, coordinated long-term and short-term planning, renewable generation planning, demand response, reliability constraints.**

## NOMENCLATURE

### *Indices:*

| | |
|---|---|
| $a$ | Index for area |
| $b$ | Index for load blocks |
| $f$ , $v$ | Superscripts for fixed and variable O&M costs |
| $g$ , $p$ | Superscripts for generating and pumping modes of pumped-storage unit |
| $h$ | Index for period |
| $i$ | Index for generating units |
| $l$ | Index for transmission line |
| $m$ | Index for bus |
| $n$ | Index for fuel type |
| $s$ | Superscript for units in a group |
| $t$ | Index for year |
| $\wedge$ | Index for calculated variables |

### *Sets:*

| | |
|---|---|
| $A$ | Set of system components in an area |
| $CG$ | Set of candidate generating units |
| $CH$ , $CT$ | Set of candidate hydro and thermal units |
| $CL$ | Set of candidate transmission lines |
| $EG$ | Set of existing generating units |
| $EH$ , $ET$ | Set of existing hydro and thermal units |
| $EL$ | Set of existing transmission lines |

### *Parameters:*

| | |
|---|---|
| $B$ | Bus-line incidence matrix |
| $BL$ | Bus load percentage |
| $CC$ | Capital cost |
| $d$ | Discount rate |
| $DB$ | Percentage of responsive load |
| $DR$ | Demand response bid |
| $DT$ | Duration time |
| $E$ | Energy limit of pumped-storage unit |
| $EL$ | Emission limit |
| $EM$ | Emission rate |
| $FL$ | Fuel limit |
| $FP$ | Fuel price |
| $OM$ | O&M cost |
| $PD$ | Load demand |
| $r$ | Unit spinning reserve |
| $R$ | System spinning reserve requirement |
| $T$ | Number of years in the scheduling horizon |
| $T^{\text{com}}$ | Commissioning year |
| $T^{\text{Re}}$ | Retirement year |
| $x$ | Reactance of line |
| $\eta$ | Efficiency of pumped-storage unit |
| $\kappa$ | Coefficient of present-worth value |
| $\gamma$ | Salvage factor |
| $\vartheta$ | Ratio of hours in a load block to the hours in the associated period |

### *Variables:*

| | |
|---|---|
| $CU$ | Curtailed load |
| $F$ | Fuel function |

A. Khodaei, M. Shahidehpour, and Z. Li are with Electrical and Computer Engineering Department, Illinois Institute of Technology, Chicago, IL 60616 USA (e-mail: akhodaei@iit.edu; ms@iit.edu; lizu@iit.edu). L. Wu is with Electrical and Computer Engineering Department, Clarkson University, Potsdam, NY 13699 USA (e-mail: lwu@clarkson.edu).

| | |
|---|---|
| $I$ | Commitment state |
| $IC$ | Total investment cost |
| $LOLE$ | System loss of load expectation |
| $OC$ | Total operation cost |
| $P$ | Unit generation |
| $PL$ | Line flow |
| $PN$ | Unit generation associated with a specific fuel type |
| $Q^g$ | Generating power of pumped-storage unit |
| $Q^p$ | Pumping power of pumped-storage unit |
| $SP$ | Energy of pumped-storage unit |
| $ST$ | Stored power of large reservoir unit |
| $SV$ | Total salvage value |
| $u^g$ | Generating state of pumped-storage unit |
| $u^p$ | Pumping state of pumped-storage unit |
| $y$ | Line investment state |
| $z$ | Unit investment state |
| $\theta$ | Voltage angle |
| $\xi$ | Fuel permission state |

## I. Introduction

POWER system expansion planning determines the optimal size, time and location of additional generating units and transmission lines for facilitating economic, secure, and reliable operations of a power grid [1]-[3]. Various optimization techniques were considered which shared a common objective: minimize planning and operation costs over the planning horizon. These techniques include mathematical or heuristic approaches to the expansion planning problem [4]-[12].

In the traditional integrated resource planning approaches, a vertically integrated utility would utilize an integrated approach to determine the preferred plan for the installation of new resources. However, the market-based expansion planning considers self-interested participants, coordinates the participants' planning strategies, and analyzes the associated risks based on prevailing uncertainties [13],[14].

In multi-area power systems, the coordination between the generation and transmission expansion planning would become more critical as it could enhance the reliability of individual areas as well as that of the entire system. The transmission cost represents a small portion of the total cost of delivering electricity to multi-area consumers. However, any transmission investment could yield benefits much more than its planning cost in such cases. To encourage the participation in expansion planning opportunities, power market authorities identify long-term demand forecasts, pinpoint potential resource planning alternatives, and demonstrate revenue options for participants in such ventures. The multi-area resource planning proposals are studied and analyzed by the market authorities with respect to cost and reliability for the optimal development of additional generation and transmission capacity in the multi-area expansion planning horizon [15]-[18].

Although market-based planning is applicable to restructured power systems, the coordinated expansion planning of generation and transmission is exercised in many parts of the world. The reasons for utilizing a coordinated approach are twofold: first, the governments in many countries would still have jurisdictions over power system planning criteria, in which a full privatization in the generation sector is not conceivable and the transmission sector is excluded from any privatization. In other words, the private sector follows tight regulations on generation and transmission planning, and a state entity is overseeing the expansion planning. Second, power systems are often operated and controlled by a single entity in certain countries which are irrespective of individual asset ownerships in the grid. Hence, independent planning decisions are made by market participants who may not have much authority on the daily operation and control of interconnected power systems. The coordinated planning of power systems is exercised primarily for balancing the generation and load, delivering appropriate responses to system events, and preventing unintentional islanding of large interconnections.

A coordinated multi-area expansion planning of transmission and generation components in power systems is proposed in this paper. The approach considers the short-term power system operation strategies in multi-area expansion planning which could reduce the impact of outages, promote affordable and stable market prices, and encourage investments on cleaner and more efficient power plants. A computationally viable approach is developed for considering multi-area system reliability constraints in multi-area expansion planning, where annual reliability subproblems are introduced. The system reliability criterion would be checked in the subproblems and, if not met, additional multi-area reliability constraints are considered and added for revising the power system investment decisions and improving the system reliability to desired levels. The solution of the proposed coordinated model provides annual multi-area plans in the multi-year planning horizon including generation and transmission expansion plans, and advises system planners on the optimal size, location, installation time, and fuel type of new generating units based on transmission limitation, reliability requirements, system operation criteria, and additional economic and environmental constraints.

The proposed multi-area expansion planning algorithm is applicable to both traditional unbundled power systems and the market-based environment. In the market-based environment, the proposed approach is an ISO model which would simulate the interactive coordination of transmission and generation expansion planning [19],[20]. The generation and transmission companies would individually submit their candidate lists of new components to the system operator. It is the responsibility of the system operator to optimally determine appropriate candidates for the least-cost planning while considering long-term reliability and short-term operation constraints. The approach considers the impact of additional renewable energy sources and consumers' hourly demand response on enhancing the long-term planning decisions in multi-area power systems.

The rest of the paper is organized as follows. Section II presents the model outline of the proposed approach, while Section III presents the detailed formulation. Section IV presents illustrative examples to show the proposed model applied to a practical power system. Discussion on the features of the proposed model and concluding remarks are provided in Sections V and VI, respectively.

## II. Multi-Area Expansion Planning Model

Fig. 1 depicts the proposed multi-area expansion planning model. For large-scale applications, the multi-area expansion planning problem is decomposed into a planning problem and annual reliability subproblems for each year which are treated as a post- processor for the planning problem. The planning problem minimizes the total system cost, comprising planning for new resources and operation costs for the entire system, while considering prevailing unit and system constraints. Planning costs include investment costs and salvage values. Operation costs include fuel costs and operation & maintenance (O&M) costs of thermal, hydro and renewable units.

In Fig. 1, the planning problem is formulated and solved by commercial solvers as an integrated MIP problem. A decomposition could otherwise be applied to reduce the execution time of the proposed planning problem and ensure its applicability to practical systems [18],[21]. The decomposition would separate the planning problem into a master problem, a reliability check subproblem (which checks the transmission network constraints in the proposed plan) and an optimal operation subproblem (which finds the optimal system operation based on the proposed plan). Whenever the reliability or optimality check fails, proper cuts are generated in the corresponding subproblems and added to the next iteration of master problem. This iterative process continues until a secure and optimal expansion planning solution is achieved.

The planning problem finds the least-cost set of candidate generating units and transmission lines to be added to the multi-area system in order to meet load forecasts and satisfy prevailing constraints. Considering the power system operation in the multi-area expansion planning problem, the proposed model provides at each period the solution for generating unit dispatch, capacity factor, fuel consumption, fuel consumption cost, fixed and variable O&M costs, and the cumulative emission level for each unit along with the multi-area network flows.

In Fig. 1, the solution of the planning problem is applied to annual Reliability subproblems for calculating the system reliability index, i.e. loss of load expectation (LOLE). If the stated annual reliability criterion is not satisfied in the subproblems, a reliability constraint based on the sensitivity of LOLE to the current investment decisions is generated and added to the next iteration of the planning problem. This new reliability constraint will govern the investment plan of subsequent iterations to achieve the desired system reliability requirement. The iterative process in Fig. 1 will continue until the reliability criterion is satisfied in the entire planning horizon.

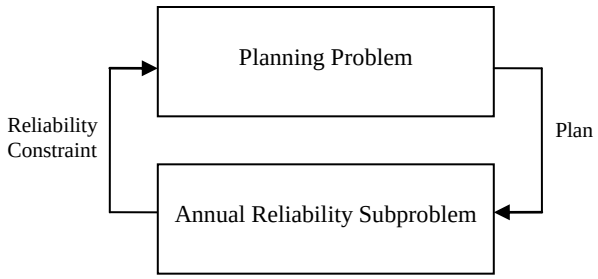


Fig. 1 Proposed multi-area expansion planning model

The multi-area investments are analyzed on an annual basis, i.e. each planned candidate unit or line would be considered for the installation at the beginning of each year. For the system operation, however, every year is decomposed into periods, and each period includes several load blocks. The load duration curve (LDC) method is utilized to consider system load variations and construct load blocks at each period. This long-term option is a practical version of considering hourly chronological loads with an acceptable level of accuracy. The number and the duration of load blocks will represent a tradeoff between the accuracy and the computation burden in the proposed model.

Various types of generators including thermal units (coal, gas, and nuclear), hydro units (run-of-river, large reservoir, and pumped-storage), and renewable units are modeled in this study. Renewable units are modeled as multi-state units to facilitate the system reliability calculation while assuring the modeling accuracy.

The load forecast at every block in every period of the planning horizon will be met by proper multi-area system expansion planning and operation decisions. The system reserve requirements are modeled considering the reserve capability of individual thermal and hydro units.

## III. Formulation of Multi-Area Expansion Planning

The proposed multi-area expansion planning minimizes the total system cost throughout the planning horizon (1). The investment cost required for the installation of new generating units and transmission lines is a function of the capital cost ($/MW) and the available capacity for investment (2). The capacity of individual candidate units and lines is fixed. Operation costs include fuel costs of thermal units, O&M costs of thermal, hydro and renewable units, and demand response of curtailable loads (3). The cost of demand response (i.e., negative generation) is the demand response bid multiplied by the curtailed load, which is paid to consumers for load management. The salvage value (or the residual value) is the future value in terms of percentage of depreciation of the initial investment. In our proposed model, salvage value is the value of installed resource at the end of the planning horizon (4). A higher salvage factor for a commodity indicates a lower depreciation by the end of the planning horizon. The objective is evaluated in terms of discounted costs, in which the discount rate is incorporated in the present-worth value of cost components. A higher discount rate in (5) would affect the investment as resources with higher investment costs become inferior. To calculate the salvage value, $\kappa_t$ is replaced with $\kappa_T$ to reflect the commodity value at the end of the planning horizon. *T* represents the number of planning years.

$$Min \quad IC + OC - SV \tag{1}$$

$$IC = \sum_t \sum_{i \in CG} \kappa_t CC_i P_i^{\max} (z_{it} - z_{i(t-1)}) + \sum_t \sum_{l \in CL} \kappa_t CC_l PL_l^{\max} (y_{lt} - y_{l(t-1)}) \tag{2}$$

$$OC = \sum_t \sum_h \sum_b \sum_{i\in\{ET,CT\}} \sum_n \kappa_t DT_{bht} FP_{it}^{n} F_{ibht}^{n} + \sum_t \sum_h \sum_b \sum_i \kappa_t DT_{bht} OM_i^{v} P_{ibht} + \sum_t \sum_h \sum_b \sum_i \kappa_t OM_i^{f} P_i^{\max} I_{ibht} \vartheta_b - \sum_t \sum_h \sum_b \sum_m \kappa_t DR_{mht} CU_{mbht} \quad (3)$$

$$SV = \kappa_T \sum_t \sum_{i\in CG} \gamma_{it} CC_i P_i^{\max} (z_{it} - z_{i(t-1)}) + \kappa_T \sum_t \sum_{l\in CL} \gamma_{lt} CC_l PL_l^{\max} (y_{lt} - y_{l(t-1)}) \quad (4)$$

$$\kappa_t = \frac{1}{(1+d)^{t-1}} \qquad \forall t \quad (5)$$

The proposed multi-area expansion planning objective is subject to the following practical constraints:

### A. System Operation Constraints

The load balance constraint (6) requires that the power generated in an area plus the net power injected by transmission lines satisfy the area load minus the curtailed load. The system reserve requirement (7) ensures that the reserve provided by thermal and hydro units satisfies the system spinning reserve requirement. The load curtailment limit (8) ensures that the load curtailment is limited to the designated responsive loads.

$$\sum_{i\in A_a} P_{ibht} + \sum_l B_{a,l} PL_{lbht} = \sum_{m\in A_a} PD_{mbht} - \sum_{m\in A_a} CU_{mbht} \qquad \forall a, \forall b, \forall h, \forall t \quad (6)$$

$$\sum_{i\in\{ET,CT\}} r_i P_i^{\max} I_{ibht} + \sum_{i\in\{EH,CH\}} (P_i^{\max} - P_{ibht}) I_{ibht} \geq R_{bht} \qquad \forall b, \forall h, \forall t \quad (7)$$

$$CU_{mbht} \leq DB_{mht} PD_{mbht} \qquad \forall m, \forall b, \forall h, \forall t \quad (8)$$

### B. Commissioning Time and Installation Constraints

A commissioning time is imposed before any new installations for exchanging the planning information between multi-area system operators and generation and transmission investors. This time is required to obtain necessary approvals on planning and detailed engineering design and construction work, which is dependent on the type and the size of the new installations. A candidate unit or transmission line cannot be installed before its commissioning time is elapsed (9)-(10). Once a candidate generating unit or transmission line is installed, its investment state will be fixed as 1 for the remaining years in the planning horizon (11)-(12). Generating units cannot be committed or dispatched until they are installed (13). A retired generating unit cannot be operated any longer (14).

$$z_{it} = 0 \qquad \forall i \in CG, \forall t < T_i^{\text{com}} \quad (9)$$

$$y_{lt} = 0 \qquad \forall l \in CL, \forall t < T_l^{\text{com}} \quad (10)$$

$$z_{i(t-1)} \leq z_{it} \qquad \forall i \in CG, \forall t \quad (11)$$

$$y_{l(t-1)} \leq y_{lt} \qquad \forall l \in CL, \forall t \quad (12)$$

$$I_{ibht} \leq z_{it} \qquad \forall i \in CG, \forall b, \forall h, \forall t \quad (13)$$

$$I_{ibht} = 0 \qquad \forall i \in EG, \forall b, \forall h, \forall t > T_i^{\text{Re}} \quad (14)$$

### C. Thermal Units Constraints

Thermal units are subject to limits on min/max capacity, fuel, emission, and scheduled maintenance. The commitment status of thermal units is considered as part of the min/max capacity limit (15), for an accurate modeling of unit commitment in multi-area power system operations. The proposed multi-area model supports any number of fuel types for new and existing generating units. Thermal units might use alternate or standby fuels as long as the primary fuel is used up. The unit generation dispatch is the sum of its generation by each fuel type (16). Each fuel type would satisfy its min/max limits (17). For the primary fuel, $\xi_{it}^{1} = 1$. Likewise, the fuel permission state of the next fuel type would be set to 1 by (18) for switching to the next fuel type. The fuel function of a generating unit is obtained based on min/max heat values and heat rate of the generating unit. The total annual emission of each thermal unit is restricted by (19). Scheduled maintenance would limit the unit commitment and dispatch (20). In addition, group limits are considered which would represent multi-area expansion planning constraints such as total fuel and emission limits of a system (21)-(22).

$$P_i^{\min} I_{ibht} \leq P_{ibht} \leq P_i^{\max} I_{ibht} \qquad \forall i \in \{ET,CT\}, \forall b, \forall h, \forall t \quad (15)$$

$$P_{ibht} = \sum_n PN_{ibht}^{n} \qquad \forall i \in \{ET,CT\}, \forall b, \forall h, \forall t \quad (16)$$

$$FL_{it}^{n,\min} \xi_{it}^{n} \leq \sum_h \sum_b DT_{bht} F_{ibht}^{n} \leq FL_{it}^{n,\max} \xi_{it}^{n} \qquad \forall i \in \{ET,CT\}, \forall n, \forall t \quad (17)$$

$$\sum_h \sum_b DT_{bht} F_{ibht}^{n} \geq FL_{it}^{n,\max} \xi_{it}^{n+1} \qquad \forall i \in \{ET,CT\}, \forall n, \forall t \quad (18)$$

$$\sum_h \sum_b \sum_n EM_i^{n} DT_{bht} PN_{ibht}^{n} \leq EL_{it}^{\max} \qquad \forall i \in \{ET,CT\}, \forall t \quad (19)$$

$$\sum_h \sum_b DT_{bht} P_{ibht} \leq P_i^{\max} (\sum_h \sum_b DT_{bht} - SM_i * 24) \qquad \forall i \in \{ET,CT\}, \forall t \quad (20)$$

$$\sum_h \sum_b \sum_{i\in S} \sum_n EM_i^{n} DT_{bht} PN_{ibht}^{n} \leq EL_t^{s,\max} \qquad \forall t \quad (21)$$

$$FL_t^{s,\min} \leq \sum_h \sum_b \sum_{i\in S} \sum_n DT_{bht} F_{ibht}^{n} \leq FL_t^{s,\max} \qquad \forall t \quad (22)$$

### D. Hydro Units Constraints

Three types of hydro units including run-of-river, large reservoirs, and pumped-storage are modeled in our algorithm. For run-of-river hydro units, min/max generation capacity limits and min/max energy limits per period are shown in (23) and (24), respectively. The run-of-river hydro unit has no storage, so $ST_{iht} = 0$.

Existing large reservoir hydro units are modeled by (23)-(27). Similar to run-of-river hydro units, (23) defines min/max capacity limits and (24) defines min/max energy limits available per period. The stored energy is restricted by the reservoir storage capacity (25). The stored energy at various periods is coupled so that the energy is not consumed before it is stored (26). The total stored energy at the end of each planning year is zero (27), i.e. the stored energy annually is converted into generation. For large-reservoir hydro candidate units, (24)-(25) are replaced with (28)-(29) to incorporate the investment variable $z_{it}$.

$$P_i^{\min} I_{ibht} \le P_{ibht} \le P_i^{\max} I_{ibht} \quad \forall i \in \{EH, CH\}, \forall b, \forall h, \forall t \tag{23}$$

$$E_{ih}^{\min} \le \sum_b DT_{bht} P_{ibht} + ST_{iht} \le E_{ih}^{\max} \quad \forall i \in EH, \forall h, \forall t \tag{24}$$

$$-ST_{ih}^{\max} \le ST_{iht} \le ST_{ih}^{\max} \quad \forall i \in EH, \forall h, \forall t \tag{25}$$

$$0 \le \sum_{h'<h} ST_{ih't} \le ST_{ih}^{\max} \quad \forall i \in \{EH, CH\}, \forall h, \forall t \tag{26}$$

$$\sum_h ST_{iht} = 0 \quad \forall i \in \{EH, CH\}, \forall t \tag{27}$$

$$E_{ih}^{\min} z_{it} \le \sum_b DT_{bht} P_{ibht} + ST_{iht} \le E_{ih}^{\max} z_{it} \quad \forall i \in CH, \forall h, \forall t \tag{28}$$

$$-ST_{ih}^{\max} z_{it} \le ST_{iht} \le ST_{ih}^{\max} z_{it} \quad \forall i \in CH, \forall h, \forall t \tag{29}$$

Pumped-storage hydro units are modeled by (30)-(38). A pumped-storage unit has three operation modes which are generating, pumping, and idling modes. The pumped-storage unit is a load when in pumping mode (30). Generating and pumping modes are subject to min/max capacity limits (31) and (32). At each time point, the unit can only be operated at one of its modes, which is denoted by (33). If $u_{ibht}^{p} = 1$, the unit is pumping, and if $u_{ibht}^{g} = 1$, the unit is generating. If both binary variables are zeros, the unit is in idling mode. The constraint is further extended to consider the relationship of operation modes and the investment status of candidate units (34). The stored energy is calculated based on the energy stored at pumping mode minus the energy consumed in the generating mode (35). The stored energy is less than the maximum storage capacity (36). The stored energy in blocks is coupled so that the energy can only be consumed after it is stored (37). The total stored energy by the end of each period is zero (38).

$$P_{ibht} = Q_{ibht}^{g} - Q_{ibht}^{p} \quad \forall i \in \{EH, CH\}, \forall b, \forall h, \forall t \tag{30}$$

$$Q_i^{g,\min} u_{ibht}^{g} \le Q_{ibht}^{g} \le Q_i^{g,\max} u_{ibht}^{g} \quad \forall i \in \{EH, CH\}, \forall b, \forall h, \forall t \tag{31}$$

$$Q_i^{p,\min} u_{ibht}^{p} \le Q_{ibht}^{p} \le Q_i^{p,\max} u_{ibht}^{p} \quad \forall i \in \{EH, CH\}, \forall b, \forall h, \forall t \tag{32}$$

$$u_{ibht}^{p} + u_{ibht}^{g} \le 1 \quad \forall i \in EH, \forall b, \forall h, \forall t \tag{33}$$

$$u_{ibht}^{p} + u_{ibht}^{g} \le z_{it} \quad \forall i \in CH, \forall b, \forall h, \forall t \tag{34}$$

$$SP_{ibht} = \eta_i DT_{bht} Q_{ibht}^{p} - DT_{bht} Q_{ibht}^{g} \quad \forall i \in \{EH, CH\}, \forall b, \forall h, \forall t \tag{35}$$

$$-SP_i^{\max} \le SP_{ibht} \le SP_i^{\max} \quad \forall i \in \{EH, CH\}, \forall b, \forall h, \forall t \tag{36}$$

$$0 \le \sum_{b'<b} SP_{ib'ht} \le SP_i^{\max} \quad \forall i \in \{EH, CH\}, \forall b, \forall h, \forall t \tag{37}$$

$$\sum_b SP_{ibht} = 0 \quad \forall i \in \{EH, CH\}, \forall h, \forall t \tag{38}$$

### *E. Renewable Unit Constraints*

A large integration of intermittent renewable sources could challenge the reliability of multi-area power systems. The significant challenge appears in expansion planning when the additional renewable sources must guarantee a reliable supply of energy to loads [22]. The generation pattern for each renewable unit is determined by its forecasted value. Thus, the generation value is considered as constant in the load balance equation. Several approaches can be applied to renewable unit generation forecast. For instance, wind speed can be forecasted by historical data or simulated by the Weibull probability distribution function; the generation pattern for wind generating units would then be obtained by applying the wind speed quantity to the power curve of each wind turbine [23].

The renewable energy forecast would also define the pattern for the availability of such units. To consider intermittent units in reliability assessments, their respective generation output should remain above a particular minimum generation level for a specified time period (i.e., persistence time.) A persistence time is assumed for each generation level of a unit. Each minimum generation level is compared to the forecasted renewable generation pattern. The periods are identified in which the forecasted renewable generation is higher than the minimum generation level and continues for at least the persistence time. The sum of all such periods divided by the total generation time for a renewable unit would represent the associated availability of the given generation level. This procedure will be repeated for all generation levels between the min and max generation to determine a generation model for an intermittent generating unit. The renewable unit would be represented as a multi-state unit with a given availability for each state. These states are applied in the reliability calculation using the same method as that for non-intermittent generating units [24].

### *F. Transmission Network Constraints*

The multi-area power system is partitioned into geographical areas, which are connected through transmission lines. The existing line flows are modeled by (39)-(40). For candidate lines, however, the power flow depends on the installation state of the line (41)-(42). If the line is not installed, (41) is relaxed and (42) sets the line flow to zero. Once a line is installed, it will no longer be treated as a candidate line. The voltage angle of the area incorporating slack bus is set to zero (43).

$$PL_{lbht} = \sum_a B_{l,a} \theta_{abht} \Big/ x_l \quad \forall l \in EL, \forall b, \forall h, \forall t \tag{39}$$

$$-PL_l^{\max} \le PL_{lbht} \le PL_l^{\max} \quad \forall l \in EL, \forall b, \forall h, \forall t \tag{40}$$

$$\left| PL_{lbht} - \sum_a B_{l,a} \theta_{abht} \Big/ x_l \right| \le M(1 - z_{lt}) \quad \forall l \in CL, \forall b, \forall h, \forall t \tag{41}$$

$$\left| PL_{lbht} \right| \le PL_l^{\max} z_{lt} \quad \forall l \in CL, \forall b, \forall h, \forall t \tag{42}$$

$$\theta_{abht} = 0 \quad \forall a = \text{Ref}, \forall b, \forall h, \forall t \tag{43}$$

### *G. Multi-Area System Reliability Criterion*

Once the multi-area expansion planning decisions are made in the planning problem, the new topology with generating unit and transmission line investments is sent to the subproblems where annual LOLEs are calculated as a post-processor. The LOLE calculation utilizes the component forced outage rate [17]. If the system LOLE in a year is larger than the LOLE limit, a reliability constraint is generated in the subproblem and added to the next iteration of the planning problem. The reliability constraint is based on the sensitivity of changes in the system LOLE with respect to changes in each investment decision

(44)-(48).

$$\Delta LOLE_{at} = \sum_{i \in CG} \left( LOLE^{(1)}_{at,i} - LOLE^{(0)}_{at,i} \right) \Delta z_{it} + \sum_{l \in CL} \left( LOLE^{(1)}_{at,l} - LOLE^{(0)}_{at,l} \right) \Delta y_{lt} \quad \forall a, \forall t \tag{44}$$

$$\Delta z_{it} = z_{it} - \hat{z}_{it} \quad \forall i \in CG, \forall t \tag{45}$$

$$\Delta y_{lt} = y_{lt} - \hat{y}_{lt} \quad \forall l \in CL, \forall t \tag{46}$$

$LOLE^{(1)}_{at,i}$ is for an installed unit *i* and $LOLE^{(0)}_{at,i}$ is for a candidate generating unit *i*, which is not installed. Here, $LOLE^{(1)}_{at,i} - LOLE^{(0)}_{at,i}$ represents the incremental change in the LOLE of area *a* when the investment decision for unit *i* is changed. Similarly, $LOLE^{(1)}_{at,l} - LOLE^{(0)}_{at,l}$ represents the change in the LOLE of area *a* when the investment decision for line *l* is changed. The reliability constraint (47) will be included in the next planning iteration.

$$\hat{LOLE}_{at} + \Delta LOLE_{at} \le LOLE^{target}_{at} \quad \forall a, \forall t \tag{47}$$

## IV. Numerical Simulations

The proposed multi-area expansion planning model is applied to a power system with 43 thermal units, 9 hydro units, and 2 renewable units. The system is partitioned into 7 areas interconnected by 8 tie-lines. Transmission congestion in each single area is ignored.

A set of 23 candidate units (including 16 thermal and 7 hydro units) and 4 candidate lines are considered in Fig. 2. A 20-year planning horizon is considered. Each planning year is divided into six 2-month periods, and six load blocks are considered in each period. Load blocks equally divide the loads between min/max values in each period, and the duration of each block is determined accordingly. The quantity and duration of load blocks may change in each period within each year. The planning is performed annually while the operation is carried out for each load block.

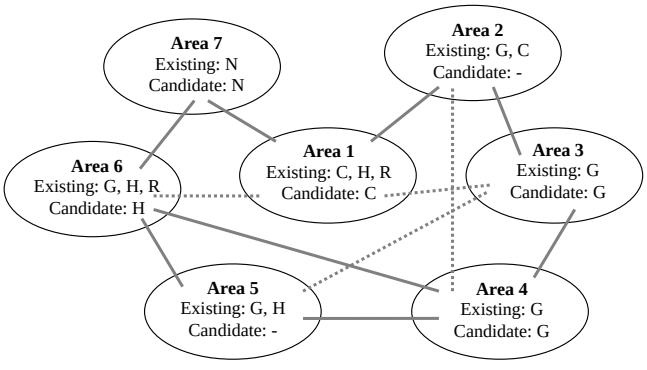


Fig. 2 Multi-area system (C: coal, G: gas, N: nuclear, H: hydro, R: renewable).

In the proposed multi-area model, there are no limitations on annual investments or the number of units and lines that could be installed annually. The discount rate is 5%. The spinning reserve requirement is 5% of the load in each block. The initial multi-area system load is 8,976 MW with an average load growth rate of 2.6%. The initial available generation capacity is 20,430 MW, which decreases due to the retirement of units. By the end of the planning horizon, 11 units will be retired, which reduce the generation capacity to 17,980 MW. LOLE of one day per year is considered as the reliability criterion in all areas. The proposed multi-area expansion planning method is implemented on a 2.4-GHz personal computer using CPLEX 11.0 [25].

These cases are discussed as follows:

**Case 1**: The 20-year generation expansion planning is performed in each area without considering any transfer capability among multi-areas. The expansion planning candidates in Tables I and II are intended to ensure an adequate supply of load in each area and satisfy the area reliability criterion. In Case 1, each area in Fig. 2 would supply its own load and satisfy its reliability requirements without any regards to the overall system reliability. As a result, less economical units 4-6 (in area 3) are installed, which result in higher investments and operation costs.

TABLE I
CANDIDATE UNIT INSTALLATION YEAR

| Candidate Unit | Type | Area | Capacity (MW) | FOR | Case 1 | Case 2 | Case 3 |
|---|---|---|---|---|---|---|---|
| 1 | Gas | 3 | 240 | 0.04 | - | 11 | 11 |
| 2 | Gas | 3 | 240 | 0.04 | - | 6 | 6 |
| 3 | Gas | 3 | 240 | 0.04 | - | - | - |
| 4 | Gas | 3 | 350 | 0.04 | 1 | 20 | - |
| 5 | Gas | 3 | 350 | 0.04 | 1 | - | 20 |
| 6 | Gas | 3 | 350 | 0.04 | 1 | - | - |
| 7 | Gas | 4 | 750 | 0.04 | 20 | 15 | 15 |
| 8 | Gas | 4 | 750 | 0.04 | 1 | 15 | 17 |
| 9 | Gas | 4 | 750 | 0.04 | 3 | - | - |
| 10 | Coal | 1 | 1000 | 0.06 | - | - | 2 |
| 11 | Coal | 1 | 1000 | 0.06 | - | - | - |
| 12 | Coal | 1 | 1000 | 0.06 | 1 | - | - |
| 13 | Nuclear | 7 | 1000 | 0.04 | 1 | 1 | 1 |
| 14 | Nuclear | 7 | 1000 | 0.04 | 1 | 1 | 1 |
| 15 | Nuclear | 7 | 1000 | 0.04 | - | 1 | 1 |
| 16 | Nuclear | 7 | 1000 | 0.04 | 1 | 1 | 1 |
| 17 | Hydro | 6 | 50 | 0.01 | 1 | 1 | 1 |
| 18 | Hydro | 6 | 250 | 0.01 | 1 | 1 | 1 |
| 19 | Hydro | 6 | 380 | 0.01 | 1 | 1 | 1 |
| 20 | Hydro | 6 | 275 | 0.01 | 1 | 1 | 1 |
| 21 | Hydro | 6 | 400 | 0.01 | 1 | 1 | 1 |
| 22 | Hydro | 6 | 400 | 0.01 | 1 | 1 | 1 |
| 23 | Hydro | 6 | 400 | 0.01 | 1 | 1 | 1 |

TABLE II
CANDIDATE LINE INSTALLATION YEAR

| Candidate Line | From Area | To Area | Capacity (MW) | FOR | Case 1 | Case 2 | Case 3 |
|---|---|---|---|---|---|---|---|
| 1 | 1 | 6 | 2000 | 0.002 | - | - | 4 |
| 2 | 1 | 3 | 2000 | 0.002 | - | - | 1 |
| 3 | 3 | 5 | 2000 | 0.002 | - | - | 1 |
| 4 | 2 | 4 | 2000 | 0.002 | - | - | - |

TABLE III
INSTALLED CAPACITY IN EACH AREA AND THE SYSTEM (MW)

| | Case 1 | Case 2 | Case 3 |
|---|---|---|---|
| Area 1 | 4380 | 3380 | 4380 |
| Area 2 | 4200 | 4200 | 4200 |
| Area 3 | 3450 | 3230 | 3230 |
| Area 4 | 4850 | 4100 | 4100 |
| Area 5 | 2850 | 2850 | 2850 |
| Area 6 | 3705 | 3705 | 3705 |
| Area 7 | 4000 | 5000 | 5000 |
| System | 27435 | 26465 | 27465 |

The installed area capacity and LOLEs at the end of the planning horizon are shown in Tables III and IV, respectively. The total system cost is $505.16B and the investment cost is only 4.62% of the total system cost.

TABLE IV
LOLE IN EACH AREA AND THE SYSTEM (DAY/YEAR)

| | Case 1 | Case 2 | Case 3 |
|---|---|---|---|
| Area 1 | 0.00326 | 0.05431 | 0.00345 |
| Area 2 | 0.28790 | 0.28790 | 0.28790 |
| Area 3 | 0.11476 | 0.68759 | 0.68759 |
| Area 4 | 0.00704 | 0.10360 | 0.10360 |
| Area 5 | 0.69304 | 0.69304 | 0.68604 |
| Area 6 | 0.00001 | 0.00001 | 0.00001 |
| Area 7 | 0.64735 | 0.04164 | 0.04164 |
| System | - | 0.000008 | 0.0000011 |

TABLE V
SUMMARY OF SYSTEM COSTS

| | Case 1 | Case 2 | Case 3 |
|---|---|---|---|
| Investment Cost ($Billion) | 23.311 | 21.110 | 25.517 |
| Operation Cost ($Billion) | 482.275 | 299.958 | 289.181 |
| Salvage Value ($Billion) | 0.422 | 0.402 | 0.474 |
| Total Planning Cost ($Billion) | 505.164 | 320.666 | 314.224 |

**Case 2**: A multi-area generation planning model with transmission network constraints is considered. Table IV shows that all areas have met the given reliability criterion. Here, areas with higher levels of reliability would assist those with generation shortfalls. Compared to Case 1, an economical unit is installed at area 7 instead of less economical units at areas 3 and 4. The assisting area 7 would compensate the capacity deficiency in other areas and reduce the overall generation dispatch cost. In Table V, the total system planning cost for investment and operation is $320.66B, which shows a 36.52% reduction as compared to that in Case 1. Here, both investment and operation costs are reduced.

**Case 3**: The coordination between the generation and transmission planning is considered in the constrained multi-area power systems. Candidate lines 1, 2 and 3 are installed which would mitigate the congestion in line 1-2 and facilitate the dispatch of economical units in area 1. By installing the candidate line 1, area 1 would also install and utilize the economic unit 10. As a result, area 1 would meet its reliability requirement without any support from area 7 and would also support other areas to compensate their capacity deficiency. Table V shows that the total system cost is $314.22B, which is 37.80% lower than that of Case 1, and 2.01% lower than that of Case 2. The transmission investment cost in this case is $2.57B, which represents a small portion of the total cost of multi-area expansion planning. Table V also shows that the proposed solution reduces the operation cost by about $10.77B as compared with that in Case 2 which yields higher benefits than its investment cost. The annual installed capacity in Cases 1, 2 and 3 are shown in Fig. 3 in which a higher installed capacity is required in Case 1 for maintaining the same level of reliability. The installation of unit 10 in Case 3 would result in a higher installed capacity as compared to that in Case 2; however, the installation would provide significant economical benefits by low cost power generation.

The effect of renewable sources is further studied by adding 9 candidate wind units to area 4. All candidate wind units are installed at the first year of planning. However, additional non-wind units would be installed to alleviate the intermittency issue of wind units. The additional units may not be economically justifiable; however, they would be required for maintaining the area reliability. The total operation cost after the installation of wind units drops to $287.83B, which is 8.39% lower than that in Case 3. However, the investment cost increases by 9.34% with the installation of additional thermal units for managing the wind generation intermittency.

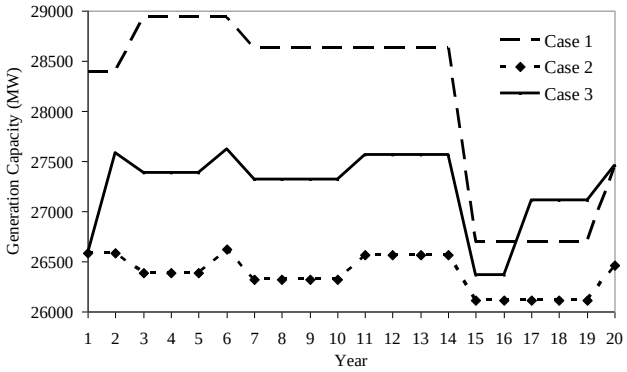


Fig. 3 Generation capacity

In Case 3, if the emission constraint on coal units is further considered, more gas units will be installed in the multi-area system. The additional gas units will result in a higher installed capacity and a lower LOLE. Most of the installed gas units are located in area 4 so the candidate line 4 will be installed to mitigate transmission congestion. The installation of gas units will increase the system operation and investment costs, but will lower the emission and facilitate the installation of intermittent wind generating units.

In Cases 1-3, the multi-area expansion planning is performed annually while the operation is carried out for load blocks. There are no limitations on load block durations which could extend from hours to months. The choice will be a tradeoff between the accuracy and the computation time in the proposed model. However, the duration of load blocks could play a key role when considering the short-term system operation. To address this issue in the multi-area expansion planning, annual peak loads are considered in which short-term operation constraints are ignored. In this case, the minimum LOLE requirement in areas 2 and 5 would not be met despite the possibility of receiving assistance from other areas and considering additional generating unit installations. The investment cost of generating units would be 6.67% higher when the short-term operation constraints are not considered.

**Case 4:** Gas-fired generating units have become favorable commodities in power systems because of their economic benefits, operation flexibility, and low environmental impacts. Gas-fired units provide a linkage between natural gas and electric power systems. Therefore, limitations on natural gas supply might affect power system operations. To consider the

interdependency of gas and electricity, an annual gas supply limit of 150 mmscfd is considered in this case. Here, gas supply in years 2 and 3 (164.88 and 213.14 mmscfd, respectively) is insufficient which is compensated by coal units. All the candidate lines are installed to enhance the coal unit dispatch located in area 1. The total system cost is 0.66% higher than that in Case 3 which is due to the installation of more expensive coal units.

## V. Discussions

The specific features of the proposed multi-area expansion planning model are listed as follows:

- Lower investment costs: Fewer units are to be installed for reliability requirements because the interconnected areas would maintain a desired level of reliability in the multi-area system.
- Lower operation costs: The interconnected areas would facilitate the economic transfer of low cost generation to areas with higher load demands.
- Accurate models: Load blocks are used for load modeling (instead of peak loads), and comprehensive models are considered for generating units and transmission lines in the short-term system operation.
- Practical results: The multi-area generation and transmission coordination is considered in operation and planning stages. Moreover, reliability requirements are considered based on random outages of generating units and transmission lines.
- Computation efficiency: The reliability requirements are incorporated in the multi-area expansion planning model by introducing annual reliability subproblems in Fig. 1. The proposed decomposition will reduce the size of the coordinated problem and add minute computation burdens to the multi-area expansion planning problem.

## VI. Conclusions

An efficient and comprehensive multi-area model for the coordinated expansion planning with the consideration of system reliability constraints was proposed. The multi-area expansion planning problem was decomposed into a planning problem and annual reliability subproblems for each year. The planning problem found the expansion plan by considering candidate units and lines. The subproblems utilized the proposed plan to calculate the system annual reliability index and compared it to the target value. In case of violations, reliability constraints were formed and added to the next iteration of the planning problem. A complete formulation of this multi-area model was presented, incorporating models for thermal, hydro and renewable units, along with a multi-area transmission network, so that the readers can replicate the model. The proposed multi-area model was analyzed further through numerical simulations, where it was shown that the solution of the coordinated multi-area expansion planning is applicable to practical power systems. The coordinated multi-area expansion planning enhanced the solutions by considering the impact of transmission constraints on system adequacy and reliability, and further guaranteed a reliable and optimal solution.

## References


[1] M. Shahidehpour, "Global broadcast - transmission planning in restructured systems," *IEEE Power Eng Mag.*, vol. 5, no. 5, pp. 18-20, Sep./Oct. 2007.

[2] S. de la Torre, A. J. Conejo, and J. Contreras, "Transmission expansion planning in electricity markets," *IEEE Trans. Power. Syst.*, vol. 23, no. 1, pp. 238-248, Feb. 2008.

[3] L. P. Garces, A. J. Conejo, R. Garcia-Bertrand, and R. Romero, "A bilevel approach to transmission expansion planning within a market environment," *IEEE Trans. Power Syst.*, vol. 24, no. 3, pp. 1513-1522, Aug. 2009.

[4] J. Choi, A. A. El-Keib, and T. Tran, "A fuzzy branch and bound-based transmission system expansion planning for the highest satisfaction level of the decision maker," *IEEE Trans. Power Syst.*, vol. 20, no. 1, pp. 476-484, Feb. 2005.

[5] J. Choi, T. Tran, A. A. El-Keib, R. Thomas, H.S. Oh, and R. Billinton, "A method for transmission expansion system expansion planning considering probabilistic reliability criteria," *IEEE Trans. Power Syst*., vol. 20, no. 3, pp. 1606-1615, Aug. 2005.

[6] O. B. Tor, A. N. Guven, and M. Shahidehpour, "Congestion-driven transmission planning considering the impact of generator expansion," *IEEE Trans. Power Syst.*, vol. 23, no.2, pp. 781-789, May. 2008.

[7] S. Binato, M. V. Pereira, and S. Granville, "A new Benders decomposition approach to solve power transmission network design problems," *IEEE Trans. Power Syst.*, vol. 16, no. 2, pp. 235-240, May 2001.

[8] P. Sánchez-Martín, A. Ramos, and J. F. Alonso, "Probabilistic midterm transmission planning in a liberalized market," *IEEE Trans. Power Syst.*, vol. 20, no. 4, pp. 2135-2142, Nov. 2005.

[9] E. L. Silva, H. A. Gil, and J. M. Areiza, "Transmission network expansion planning under an improved genetic algorithm," *IEEE Trans. Power Syst.*, vol. 15, no. 3, pp. 1168-1175, Aug. 2000.

[10] A. S. D. Braga and J. T. Saraiva, "A multiyear dynamic approach for transmission expansion planning and long-term marginal costs computation," *IEEE Trans. Power Syst.*, vol. 20, no. 3, pp. 1631-1639, Aug. 2005.

[11] J. Contreras and F. F. Wu, "Coalition formation in transmission expansion planning," *IEEE Trans. Power Syst.*, vol. 14, no. 3, pp. 1144-1152, Aug. 1999.

[12] T. De la Torre, J. W. Feltes, T. G. S. Roman, and H. M. Merril, "Deregulation, privatization, and competition: transmission planning under uncertainty," *IEEE Trans. Power Syst.*, vol. 14, no. 2, pp. 460-465, May 1999.

[13] M. O. Buygi, M. Shahidehpour, H. M. Shanechi, and G. Balzer, "Market based transmission expansion planning: stakeholders' desires," in Proc. 2004 *IEEE Int. Conf. on Electric Utility Deregulation, Restructuring and Power Technologies*, vol. 2, pp. 433-438.

[14] J. H. Roh, M. Shahidehpour, and Y. Fu, "Security-constrained resource planning in electricity markets," *IEEE Trans. Power Syst.*, vol. 22, no. 2, pp. 812-820, May 2007.

[15] B. Alizadeh and S. Jadid, "Reliability constrained coordination of generation and transmission expansion planning in power systems using mixed integer programming," *IET Gen. Trans. Distr.*, vol. 5, no. 9, pp. 948-960, Sep. 2011.

[16] M. O. Buygi, G. Balzer, H. M. Shanechi, and M. Shahidehpour, "Market-based transmission expansion planning", *IEEE Trans. Power Syst.*, vol. 19, no. 4, pp. 2060-2067, Nov. 2004.

[17] R. Billinton, and R.N. Allan, *Reliability of Power Systems*, second edition, New York: Plenum Publishing, 1996.

[18] A. Khodaei, M. Shahidehpour, and S. Kamalinia, "Transmission switching in expansion planning," *IEEE Trans. Power Syst.*, vol. 25, no. 3, pp. 1722-1733, Aug. 2010.

[19] O. B. Tor, A. N. Guven and M. Shahidehpour, "Promoting the Investment on IPPs for Optimal Grid Planning," *IEEE Trans. on Power Systems*, vol. 25 no. 3, pp. 1743-1750, Aug. 2010.

[20] J. H. Roh, M. Shahidehpour, and Y. Fu, "Market-based coordination of transmission and generation capacity planning," *IEEE Trans. Power Syst.*, vol. 22, no. 4, pp. 1406-1419, Nov. 2007.

[21] A.J. Conejo, E. Castillo, R. Mínguez, and R. García-Bertrand,

*Decomposition Techniques in Mathematical Programming*, Springer, 2006.
[22] S. Kamalinia, M. Shahidehpour, and A. Khodaei, "Security-constrained expansion planning of fast-response units for wind integration," *Elect. Power Syst. Res.*, vol. 81, no. 1, pp. 107-116, Jan. 2011.
[23] M. R. Patel, *Wind and Solar Power Systems*, CRC Press, 1999.
[24] R. N. Allan, P. Djapic, and G. Strbac, "Assessing the contribution of distributed generation to system security," *Int. Conf. on Prob. Meth. App. Power Syst.*, pp. 1-6, 2006.
[25] ILOG CPLEX, ILOG CPLEX Homepage 2009 [Online]. Available: http://www.ilog.com.

## BIOGRAPHIES

**Amin Khodaei** (M'11) received the B.S. degree from the University of Tehran, Iran, in 2005, the M.S. degree from the Sharif University of Technology, Tehran, Iran, in 2007, and the Ph.D. degree from the Illinois Institute of Technology (IIT), Chicago, in 2010, all in electrical engineering. He is currently a Senior Research Associate in the Electrical and Computer Engineering Department, Illinois Institute of Technology. His research interests include operation and economics of power systems.

**Mohammad Shahidehpour** (F'01) is the Bodine Chair Professor and Director of Robert W. Galvin Center for Electricity Innovation at IIT. Dr. Shahidehpour is the recipient of the Honorary Doctorate for the Polytechnic University of Bucharest in Romania. He is the recipient of 2011 Technologist of the Year Award from the Illinois Technology Association, Engineer of the Year Award from the IEEE/PES Chicago Section, and the Innovation Award from the Association of Electrical and Computer Engineering Department Heads in the United States.

**Lei Wu** (M'07) received his B.S. in Electrical Engineering and M.S. in Systems Engineering from Xi'an Jiaotong University, China, in 2001 and 2004, respectively, and Ph.D. degree in EE from IIT in 2008. Presently, he is an Assistant Professor in the ECE Department at Clarkson University. His research interests include power systems operation and economics.

**Zuyi Li** (SM'09) received the B.S. and M.S. degrees from Shanghai Jiaotong University, Shanghai, China, in 1995 and 1998, respectively, and the Ph.D. degree from IIT, Chicago, in 2002, all in electrical engineering. Presently, he is an Associate Professor in the ECE Department at IIT. He is the Co-PI of $40M grants and contracts on energy and sustainability. Dr. Li is the coauthor of *Market Operations in Electric Power Systems* (New York: Wiley, 2002).

# Allocation of Hourly Reserve versus Demand Response for Security-Constrained Scheduling of Stochastic Wind Energy

Cem Sahin, *Member*, *IEEE*, Mohammad Shahidehpour, *Fellow*, *IEEE* , Ismet Erkmen,[1]

***Abstract*—This paper presents a stochastic method for the hourly scheduling of optimal reserves when the hourly forecast errors of wind energy and load are considered. The approach utilizes the stochastic security-constrained unit commitment (SCUC) model and a two-stage stochastic programming for the day-ahead scheduling of wind energy and conventional units with N-1 contingencies. The effect of aggregated hourly demand (DR) response is considered as a means of mitigating transmission violations when uncertainties are considered. The proposed mixed-integer programming (MIP) model applies the Monte Carlo method for representing the hourly wind energy and system load forecast errors. A 6-bus, 118-bus, and the Northwest region of Turkish electric power network are considered to demonstrate the effectiveness of the proposed day-ahead stochastic scheduling method in power systems.**

***Index Terms*— Stochastic security-constrained unit commitment, wind energy, hourly reserves, demand response, load and wind forecast errors, random contingencies.**

## NOMENCLATURE

**Indices:**

| | |
|---|---|
| $d$ | Index of load |
| $i$ | Index of non-wind energy generating units |
| $r$ | Index of DRPs |
| $s$ | Index of scenarios |
| $t$ | Index of time period (hour) |
| $k$ | Index of DR provider bid segments |
| $w$ | Index of wind energy units |

**Dimensions:**

| | |
|---|---|
| $NC$ | Number of *N-1*contingencies |
| $ND$ | Number of system loads |
| $NDR$ | Number of DRPs |
| $NG$ | Number of non-wind generating units |
| $NS$ | Total number of scenarios including contingencies and wind, load forecast error scenarios |
| $NT$ | Number of hours |
| $NQ_r$ | Number of bidding segments |
| $NW$ | Number of wind energy units |

**Constraints:**

| | |
|---|---|
| $C_{net}$ | Generalized network constraints in base case and wind, load scenarios |

**Variables:**

| | |
|---|---|
| $C_{DRR,r}$ | Cost of scheduling DRR by DRP $r$ |
| $C_{EDRR,r}$ | Cost of utilizing scheduled DRR by DRP $r$ |
| $DRR_{rt}$ | Scheduled DR by DRP $r$ at time $t$ |
| $DRR_{rts}$ | Deployed DR by DRP $r$ at time $t$ in scenario $s$ |
| $F_{c,i}$ | Bid-based energy cost function of unit $i$ |
| $F_{RR,i}$ | Bid-based cost function of unit $i$ regulation reserve |
| $F_{SR,i}$ | Bid-based cost function of unit $i$ spinning reserve |
| $I$ | Commitment state |
| $P$ | Power generation |
| $P_{IMB}$ | Power generation in regulation interval |
| $P_{\Psi,wts}$ | Wind generation of unit $w$ at time $t$ and scenario $s$ |
| $P_{curt,wts}$ | Curtailed wind generation of unit $w$ at time $t$ and scenario $s$ |
| $RR$ | Regulation reserve |
| $RR_d$ | Scheduled regulation-down reserve |
| $RR_{its}$ | Deployed regulation reserve of unit $i$ at time $t$ in scenario $s$ |
| $RR_u$ | Scheduled regulation-up reserve |
| $SR$ | Deployed spinning reserve |
| $SR_d$ | Scheduled spinning-down reserve |
| $SR_{its}$ | Deployed spinning reserve by unit $i$ at time $t$ in scenario $s$ |
| $SR_u$ | Scheduled spinning-up reserve |
| $SD$ | Shutdown cost |
| $SU$ | Startup cost |
| $u^k_{rts}$ | Binary variable (1 if point $k$ of offer package DRP $r$ at time $t$ in scenario $s$ is utilized, 0 otherwise) |
| $U^k_{rt}$ | Binary variable (takes the value 1 if point $k$ of offer package DRP $r$ at time $t$ is scheduled, 0 otherwise) |
| $y_{it}$ | Startup indicator (1 if unit $i$ is started up at time $t$) |
| $z_{it}$ | Shut down indicator (1 if unit $i$ is shut down at time $t$) |
| $\psi_{wts}$ | Speed of wind energy unit $w$ at hour $t$ in scenario $s$ |

**Constants:**

| | |
|---|---|
| $A_w$ | Area swept by the rotor of wind energy unit $w$ |
| $c_{P,w}$ | Power coefficient of wind energy unit $w$ |
| $cc^k_{rt}$ | Scheduling cost of point $k$ of offer package DRP $r$ at time $t$ |
| $c_{curt,wts}$ | Cost of 1MWh wind power curtailment from wind generator $w$ at time $t$ |
| $DR$ | Ramp down limit |
| $ec^k_{rt}$ | Deployment cost of point $k$ of scheduled offer by DRP $r$ at time $t$ |
| $l_d$ | Involuntary load shedding at load $d$ |
| $MD_i$ | Minimum down time for unit $i$ |
| $MU_i$ | Minimum up time for unit $i$ |

Cem Sahin and Ismet Erkmen are with the ECE Department, Middle East Technical University (cem.sahin@uzay.tubitak.gov.tr,erkmen@metu.edu.tr). M. Shahidehpour is with the ECE Department at Illinois Institute of Technology (ms@iit.edu)

$p_s$ Probability of scenario *s* of wind and load uncertainty
$P_{D,d}$ Power demand at load *d*
$P_{max}$ Maximum power generation of unit *i*
$P_{min}$ Minimum power generation of unit *i*
$q_r^k$ *k* th discrete DRR value of the bid of DRP *r*
$\rho_{air,w}$ Air density at region where wind unit *w* is located
$\rho_{\alpha,i}$ Capacity cost of reserve type $\alpha$ for unit *i*
$TD_{i0}$ Number of hours unit *i* has been offline initially
$TU_{i0}$ Number of hours unit *i* has been online initially
$v_{CI,w}$ Cut-in wind speed of wind energy unit *w*
$v_{CO,w}$ Cut-out wind speed of wind energy unit *w*
$v_{R,w}$ Rated wind speed of wind energy unit *w*
$VOLL_d$ Value of lost load at load *d*
*UR* Ramp up limit
$\Delta_S$ Allowed system load imbalance for the *N-1* contingency in scenario *s*

**Abbreviations:**

*DR* Demand Response
*DRR* Demand Response Reserve
*DRP* Demand Response Provider

## I. Introduction

As the renewable energy integration in power systems evolves, the cost of supplying ancillary services becomes more prevalent with respect to operating decisions [1]. Wind energy is the fastest growing type of renewable energy due to its clean and indigenous nature. On the other hand, the installed wind capacity is not readily dispatchable due to its intermittent nature [2]-[7]. The effect of wind energy forecast errors is considered in the network-constrained market-clearing problem using a two-stage stochastic programming model in [8]. The first contribution of this paper is that it calculates the hourly reserves for addressing load and wind energy forecast errors in a stochastic framework while considering *N-1* contingencies in power networks.

DR is a tariff that would encourage lower electricity consumptions [9]-[11]. DR can be motivated by either providing end-users with time-varying rates or giving incentives to such costumers to reduce loads at times when the electricity market price is high or the system reliability is at stake. The time-varying rates require an advanced measurement and communication infrastructure in order to convey real-time prices to end-use consumers, while the incentives are more suitable for a faster adaptation of electricity markets. DR provides financial incentives to customers who also benefit from lower hourly demands [12]-[16]. The second contribution of this paper would model the hourly DR in a discrete form in order to reflect the market behavior in an uncertain environment.

We propose a stochastic model in which wind and load forecast errors are addressed through Monte-Carlo based scenarios in a two-stage stochastic programming model. The component outages are considered in an *N-1* contingency model. To address the computation complexity, the problem is decomposed into a master problem to solve the UC and reserve schedules, and subproblems for considering the network security, for pre-selected *N-1* contingencies, and load and wind forecast error scenarios. At the same time, DR is considered for managing hourly violations and reducing the cost of supplying the load. Load shedding is utilized whenever its contribution to lowing the stochastic cost is higher than that of allocating additional generating reserves. The proposed method would be used by an ISO or a vertical integrated utility to address the stochastic cost of security. The stochastic cost of security is defined as the difference between the scheduling cost of deterministic SCUC and that of considering uncertainties.

The rest of the paper is organized as follows. Mathematical models of DR and simulation of wind and load forecast error are discussed in Section II. The energy and A/S market clearing problem is introduced in Section III. Case studies are given in Section IV. Section V concludes this paper.

## II. DR, Load, and Wind Energy Models

### A. Demand Response Model

Demand response is formulated using a MIP formulation to fit the SCUC model. The bid should be in a discrete form since the DRP (demand response provider) represents an aggregated DR of end-users. (1)-(2) in the following represent the scheduled demand response reserve (DRR) of DRP *r* at the time interval *t* and the related capacity cost. The value of $q^0_r$ would be greater than the minimum amount determined by the ISO. (3)-(4) give the actual DRR utilized by DRP *r* in scenario *s* at time *t*, and the associated energy cost. A graphical representation of (1)-(5) is given in Fig. 1.

$$DRR_{rt} = q_r^0 U_{rt}^0 + \sum_{k=1}^{NQ_r} \lambda_r^k U_{rt}^k \quad \forall r, \forall t \tag{1}$$

$$C_{DRR,rt} = cc_{rt}^0 q_r^0 U_{rt}^0 + \sum_{k=1}^{NQ_r} cc_{rt}^k \lambda_r^k U_{rt}^k \quad \forall r, \forall t \tag{2}$$

$$DRR_{rts} = q_r^0 u_{rts}^0 + \sum_{k=1}^{NQ_r} \lambda_r^k u_{rts}^k \quad \forall r, \forall t, \forall s \tag{3}$$

$$C_{EDRR,rts} = ec_{rt}^0 q_r^0 u_{rts}^0 + \sum_{k=1}^{NQ_r} ec_{rt}^k \lambda_r^k u_{rts}^k \quad \forall r, \forall t, \forall s \tag{4}$$

$$\lambda_r^k = q_r^k - q_r^{k-1} \quad \forall r \tag{5}$$

In Fig. 1, "x" denotes a schedule *k* (i.e., $U^0_{rt}$, $U^1_{rt}$, $U^2_{rt}$, $U^3_{rt}$=1, and $U^4_{rt}$=0), and "+" denotes the discrete DR offer *k* deployed in scenario *s* (i.e. $u^0_{rts}$, $u^1_{rts}$=1$_t$ and $u^2_{rts}$, $u^3_{rts}$, $u^4_{rts}$=0).

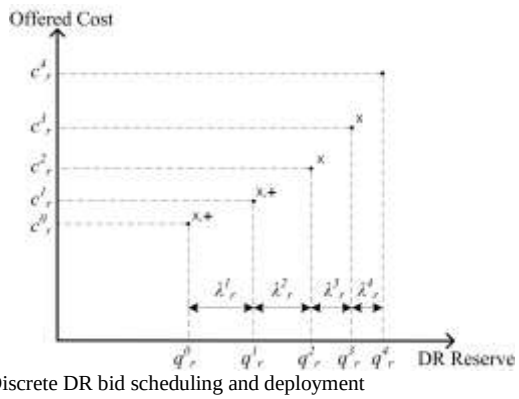


Fig. 1. Discrete DR bid scheduling and deployment

### B. Wind Energy and Load Simulation

This section discusses the modeling of forecast error scenarios for wind energy and system load which will be used in Monte Carlo simulations. The nonlinear wind speed to power conversion curve is given in (6) and $P_{\psi,wts}$ is given as an input to the algorithm. The wind power generation $w$ is subject to (7):

$$P_{\psi,wts}\left(\psi_{wts}\right)=\begin{cases}0 & \text{if } \psi_{wts} < v_{CI,w}\\ 0.5 c_{p,w}\cdot\rho_{air,w}\cdot A_w\cdot(\psi_{wts})^3 & \text{if } v_{CI,w}\le\psi_{wts}<v_{R,w}\\ P_{R,w} & \text{if } v_{R,w}\le\psi_{wts}<v_{CO,w}\\ 0 & \text{if } \psi_{wts}\ge v_{CO,w}\end{cases} \quad \forall w,\forall s \tag{6}$$

$$I_{wts}\cdot P_{\min,w}\le P_{wts}\le I_{wts}\cdot P_{\psi,wts}\left(\psi_{wts}\right) \quad \forall k,\forall s \tag{7}$$

The auto-regressive moving average (ARMA) based approach [17] provides scenarios for representing wind energy forecast errors. The wind energy forecast errors are simulated using ARMA series. The obtained ARMA series is sampled in order to obtain the forecast errors at each time step $t$ in each scenario $s$. The corresponding available wind power is obtained via (6). The system load forecast error at time $t$ is subject to a normal distribution $N(P_{Dt0}',\sigma^2)$, where $P_{Dt0}$ is the forecasted system load at time $t$ and $\sigma$ is the load volatility. The system load distribution is sampled for scenario $s$ at time $t$. The autocorrelation of the load forecast error model is assumed to be zero. The wind and load uncertainties are assumed independent.

## III. Security-Constrained Wind Energy Scheduling

### A. Objective Function

SCUC is modeled as an optimization problem for calculating the hourly unit commitment schedule at minimum production cost without compromising the system reliability. The regulation reserve is considered for following the short-term variations in the hourly customer demand or the scheduled generation, in order to maintain the system frequency within a permissible range. Spinning reserve is the unloaded generating capacity that can ramp up/down in 10 minutes. DR is assumed to be in the class of spinning reserves [1]. There are four terms in the SCUC objective function (8).

$$\begin{aligned}\min \sum_{t=1}^{NT}\Bigg\{&\sum_{i=1}^{NG}\begin{bmatrix}F_{c,i}(P_{it0})\\ +F_{RR,i}(RR_{u,it})+F_{RR,i}(RR_{d,it})\\ +F_{SR,i}(SR_{u,it})+F_{SR,i}(SR_{d,it})\\ +SU_{it}+SD_{it}\end{bmatrix}\\ &+\sum_{r=1}^{NDR}C_{DRR,rt}+\sum_{w=1}^{NW}P_{curt,wt0}\cdot c_{curt,wt0}\\ &+\sum_{s=NC+1}^{NS}p_s\Bigg\{\begin{bmatrix}\sum_{i=1}^{NG}(F_{c,i}(P_{its})-F_{c,i}(P_{it0}))\\ +\sum_{r=1}^{NDR}C_{EDRR,rts}+\sum_{d=1}^{ND}VOLL_d\cdot l_{dts}\\ +\sum_{w=1}^{NW}P_{curt,wts}\cdot c_{curt,wts}\end{bmatrix}\Bigg\}\Bigg\}\end{aligned} \tag{8}$$

The first term is composed of base case generation and reserve costs, and startup and shutdown costs. The second term is the capacity allocation cost corresponding to demand response. The third term is the cost of base case wind energy curtailment. The last term is the expected cost of deployment of regulation and spinning reserves, cost of deployment of DR reserves, cost of involuntary load shedding, and cost of wind curtailment for wind and load forecast scenarios. The scenarios $s=1$ to $NC$ represent $N-1$ contingencies and $s= NC+1$ to $NS$ represent the wind and load forecast error scenarios.

We use a two-stage stochastic programming with recourse [18] in which the first stage variables are commitment states ($I_{it}$), base case generations ($P_{it0}$ ,$P_{wt0}$), wind curtailments ($c_{curt,wt0}$), and scheduled regulation and spinning reserves ($RR_{u,it}$, $RR_{d,it}$, $SR_{u,it}$, $SR_{d,it}$), and DRPs at hour $t$ ($DRR_{rt}$). The second stage variables are scenario power generations ($P_{IMB,its}$, $P_{its}$, $P_{wts}$), deployed regulation and spinning reserves ($RR_{its}$, $SR_{its}$) and deployed DRPs ($DRR_{rts}$), wind curtailments ($c_{curt,wts}$), and involuntary load shedding ($l_{dts}$) for scenario $s$ and hour $t$.

The first stage variables are determined prior to the realization of uncertainties. The objective function is subject to the base case, $N-1$ contingencies, and wind and load forecast error scenario constraints in (9)-(20). The $N-1$ contingencies would only apply to the base case. The cost of deploying reserves for the $N-1$ contingencies is not considered in the objective function since the algorithm considers such contingencies as constraints and guarantees the scheduling of necessary generating reserves to respond to the $N-1$ contingencies without shedding any loads. Wind and load forecast errors are considered in scenarios ($s= NC+1$ to $NS$) for scheduling the hourly reserves.

### B. Base Case Constraints

Power balance equation for the base case is given in (9). Load shedding is not allowed for the base case, since the available generation capacity would utilize the load.

$$\sum_{i=1}^{NG}P_{it0}+\sum_{i=1}^{NW}P_{wt0}=\sum_{d=1}^{ND}P_{D,dt0} \quad \forall t \tag{9}$$

Unit generation and reserve constraints and wind power curtailment

$$\begin{aligned}&P_{it0}+RR_{u,it}+SR_{u,it}\le P_{\max,i}\cdot I_{it}\\ &P_{it0}-RR_{d,it}-SR_{d,it}\ge P_{\min,i}\cdot I_{it}\\ &0\le RR_{u,it}\le RR_{\max,i}\\ &0\le RR_{d,it}\le RR_{\max,i}\\ &0\le SR_{u,it}\le SR_{\max,i}\\ &0\le SR_{d,it}\le SR_{\max,i} \quad \forall i,\forall t\\ &0\le DRR_{rt}\le DRR_{\max,r} \quad \forall r,\forall t\\ &0\le P_{wt0}\le P_{\psi,wt0} \quad \forall w,\forall t\\ &P_{curt,wt0}=P_{\psi,wt0}-P_{wt0} \quad \forall w,\forall t\end{aligned} \tag{10}$$

Ramp up and down limits

$$\begin{aligned}&P_{it0}-P_{i(t-1)0}\le(1-y_{it})UR_i+y_{it}P_{\min,i}\\ &P_{i(t-1)0}-P_{it0}\le(1-z_{it})DR_i+z_{it}P_{\min,i}\\ &y_{it}-z_{it}=I_{it}-I_{i(t-1)}\\ &y_{it}+z_{it}\le 1 \quad \forall i,\forall t\end{aligned} \tag{11}$$

Minimum on/off time limits

$$UT_i = \max\{0, \min[NT, (MU_i - TU_{i0})I_{i0}]\}$$

$$\sum_{t=1}^{UT_i} (1 - I_{it}) = 0 \quad \forall i$$

$$\sum_{m=t}^{t+MU_i-1} I_{im} \geq MU_i y_{it} \quad \forall i, \forall t = UT_i + 1,..., NT - MU_i + 1$$

$$\sum_{m=t}^{NT} (I_{im} - y_{it}) \geq 0 \quad \forall i, \forall t = NT - MU_i + 2,..., NT$$

$$DT_i = \max\{0, \min[NT, (MD_i - TD_{i0})(1 - I_{i0})]\}$$

$$\sum_{t=1}^{DT_i} I_{it} = 0 \quad \forall i$$

$$\sum_{m=t}^{t+MD_i-1} (1 - I_{im}) \geq MD_i z_{it}$$

$$\forall i, \forall t = DT_i + 1,..., NT - MD_i + 1$$

$$\sum_{m=t}^{NT} (1 - I_{im} - z_{it}) \geq 0 \quad \forall i, \forall t = NT - MD_i + 2,..., NT \qquad (12)$$

Fuel and emission limits of thermal units can be added as in [19]. The generalized network constraints refer to network constraints in the base case and scenarios [20].

$$C_{net}(P_{it0}, P_{wt0}) \leq 0 \quad , \forall t \qquad (13)$$

### *C. N-1 contingency and Wind-Load Scenario Constraints*

Here (14) and (15) indicate that the system load in scenario *s* is supplied by generation, reserves, DRRs, and involuntary load shedding.

$$\sum_{i=1}^{NG} P_{its} + \sum_{r=1}^{NDR} DRR_{rts} + \sum_{d=1}^{ND} l_{dts} + \sum_{w=1}^{NW} P_{wts} = \sum_{d=1}^{ND} P_{D,dts}$$

$$\forall t, \forall s \qquad (14)$$

$$P_{its} = P_{it0} + RR_{its} + SR_{its} \quad \forall i, \forall t, \forall s \qquad (15)$$

$P_{its}$= 0 for every *t* if generator *i* is on outage at scenario *s*. The deployed reserves and involuntary load shedding in scenario *s* are determined based on the scheduled generation capacities. The wind energy delivery in scenario *s* at time *t* is limited by the available wind generation.

$$-RR_{d,it} \leq RR_{its} \leq RR_{u,it} \quad \forall i, \forall t, \forall s$$

$$-SR_{d,it} \leq SR_{its} \leq SR_{u,it} \quad \forall i, \forall t, \forall s$$

$$-DRR_{d,rt} \leq DRR_{rts} \leq DRR_{u,rt} \quad \forall r, \forall t, \forall s$$

$$0 \leq P_{wts} \leq P_{\psi,wts} \quad \forall w, \forall t, \forall s$$

$$P_{curt,wts} = P_{\psi,wts} - P_{wts} \quad \forall w, \forall t, \forall s$$

$$0 \leq l_{dts} \leq l_{dt,\max} \quad \forall d, \forall t, \forall s$$

$$l_{dts} = 0 \quad \forall d, \forall t, s = \{1,..., NC\} \qquad (16)$$

The involuntary load shedding variables are set to zero for the first iteration of *N-1* contingency calculations so that consumers can utilize all available generation resources. However, if a few scenarios remain to be infeasible, the involuntary load shedding will be made available in the following iterations as an option for mitigating the scenario violations. The ramp limit for non-wind energy units in scenario *s* is

$$P_{its} - P_{i(t-1)s} \leq (1 - y_{it})UR_i + y_{it}P_{\min,i}$$

$$P_{i(t-1)s} - P_{its} \leq (1 - z_{it})DR_i + z_{it}P_{\min,i} \quad \forall i, \forall t, \forall s \qquad (17)$$

Once a contingency occurs, the system load is defined in (18) as the total load minus the allowable system load imbalance Δ. The amount of system load imbalance is defined by the type of the contingency for an acceptable range of frequency changes [21]. The regulation reserve is considered in (18)-(19) for supplying the load in contingencies.

$$\sum_{i=1}^{NG} P_{IMB,its} + \sum_{r=1}^{NDR} DRR_{rts} + \sum_{w=1}^{NW} P_{wts} \geq \sum_{d=1}^{ND} P_{D,dts} - \Delta_s$$

$$\forall s \in \{1,..., NC\}, \forall t \qquad (18)$$

$$P_{IMB,its} = P_{it0} + RR_{its} \quad \forall i, \forall s \in \{1,..., NC\}, \forall t \qquad (19)$$

The network constraints in scenario *s* are represented by

$$C_{net}(P_{its}, P_{wts}, RR_{its}, SR_{its}, DRR_{rts}, l_{dts}) \leq 0 \quad \forall t, \forall s \qquad (20)$$

If there is a line outage in scenario *s*, (20) will incorporate the required changes in generator and load incidence matrices and the corresponding line flows [22].

## IV. Proposed Solution Methodology

The proposed MIP problem is represented by the objective function (8), subject to constraints (9)-(20). For large systems with many possible contingencies and wind and load forecast errors, the problem might be intractable due to the increased size of constraints and variables. Therefore, we resort to decomposition as shown in Fig. 2. The algorithm depicts the application of Benders decomposition to the solution of the proposed scheduling problem.

The master UC problem includes first and second-stage variables described in Section III-A plus the network cuts (21) for the base case and scenarios.

$$C_{net}(P_{it0}, P_{wt0}) \leq 0 \quad \forall t$$

$$C_{net}(P_{its}, P_{wts}, RR_{its}, SR_{its}, DRR_{rts}, l_{dts}) \leq 0 \quad \forall t, \forall s \qquad (21)$$

The dc power network subproblems consider the master problem solution to detect flow violations and send cuts to the master UC problem as necessary [20].

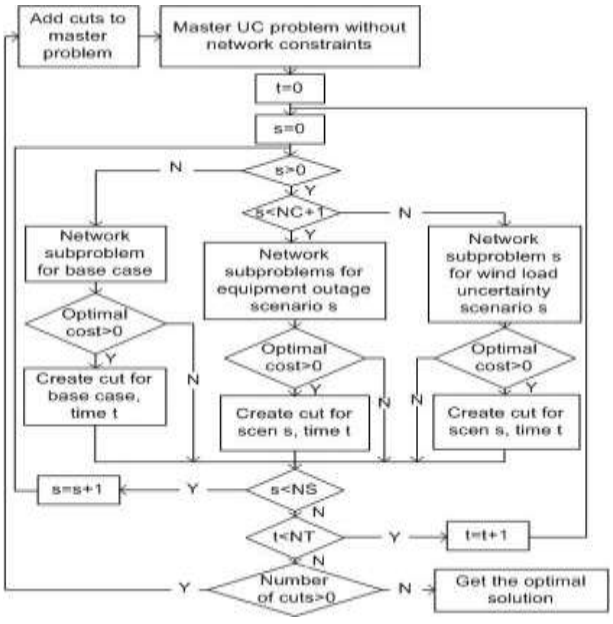


Fig. 2. Flowchart of the proposed scheduling algorithm

## V. Case Studies

The proposed algorithm is applied to a six-bus system to capture the essential characteristics of the algorithm, and to the modified IEEE-118 bus system to assess the performance of the proposed solution. The method is also applied to the northwest region of the Turkish electric power market.

### A. Six-Bus System

The six-bus system data are given in [3] in which a wind energy unit with a maximum power output of 20MW is added at bus 6. The one-line diagram of the system is given in Fig. 3. The system has three thermal units, four transmission lines, two tap-changing transformers, and one phase shifter for MW control. The generation units from cheapest to most expensive are G1, G2, and G3. The regulation reserve prices are 14, 13 and 11 \$/MW, spinning reserve prices are 11, 10 and 8 \$/MW for three units respectively. Flow limits of lines are 200, 150, 150, 100MW for lines 1-2, 1-4, 2-4, 5-6 respectively.

DRP bids include three discrete points with $q^k_r$ of 1.8MW, 3.6MW and 5.4MW, and $cc^k_{rt}$ of 10, 13 and 16 \$/MW respectively at each time interval. The deployment cost $ec^k_{rt}$ is 10 \$/MW and the *VOLL* is 450 \$/MWh at each load bus. The scenario reduction tool of the General Algebraic Modeling System (GAMS) is used in which the reduction method is set to the Mix of Fast Backward/Forward methods [23]. Initially there were 1500 Monte Carlo scenarios with even probabilities (1/1500) which are reduced to 10 scenarios with a relative distance of 75%. The relative distance would be 70% and 83% when the Monte Carlo scenarios are reduced to 50 and 9 scenarios, respectively [24].

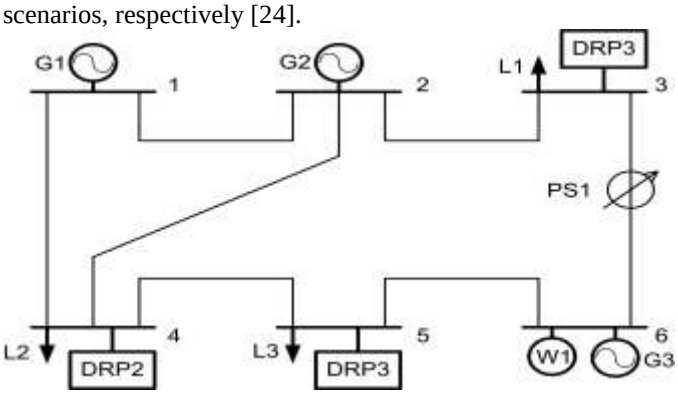


Fig. 3. One-line diagram for six-bus system

TABLE I
PROBABILITY OF SCENARIOS AFTER SCENARIO REDUCTION

| **Scenario** | 1 | 2 | 3 | 4 | 5 |
|---|---|---|---|---|---|
| **Probability** | 0.26 | 0.12 | 0.08 | 0.07 | 0.14 |
| **Scenario** | 6 | 7 | 8 | 9 | 10 |
| **Probability** | 0.09 | 0.02 | 0.07 | 0.07 | 0.08 |

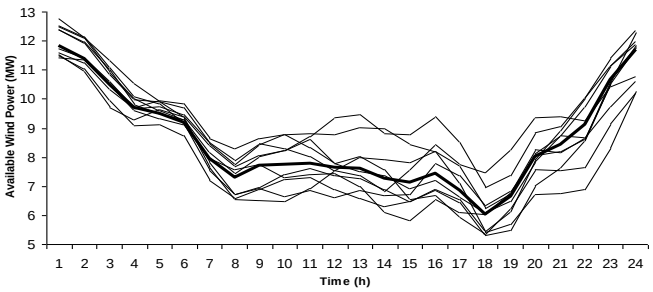


Fig. 4. Wind power forecast and scenarios

The wind curtailment cost is 50 \$/MW which is higher than the largest marginal cost of the given thermal units. The standard deviation of wind forecast error will gradually increase from 0 to 6.5% of the forecast from $t$=0 to 24. The standard deviation of the system load forecast error is 3% of the load forecast at each time interval. The probability of scenarios is given in Table I. The forecasted wind and its error scenarios are depicted in Fig. 4. The following three case studies are considered:

Case 1: Deterministic case (without network contingencies).
Case 2: Stochastic wind and load forecast errors in Case 1.
Case 3: *N-1* contingencies in Case 2.

*Case 1*: This case provides a reference in which no contingency or uncertainty is considered. The total system operation cost is \$99,061. Table II depicts the scheduling of three thermal units and the wind energy units. The available wind energy is fully utilized since the wind energy units are assumed to be price-takers. G1 is scheduled at all hours since it is the cheapest unit. G2 is committed in the first hour due to min up constraints. G2 is scheduled to generate between hours 11-21, while G3 is scheduled between 13-19, since these are the next expensive units in the ascending order. No reserves or DR are scheduled in the base case.

TABLE II
CASE 1 GENERATION DISPATCH (MW)

| **Hour** | **G1** | **G2** | **G3** | **W1** |
|---|---|---|---|---|
| 1 | 161.88 | 10 | 0 | 11.82 |
| 2 | 162.05 | 0 | 0 | 11.4 |
| 3 | 156.33 | 0 | 0 | 10.51 |
| 4 | 153.13 | 0 | 0 | 9.7 |
| 5 | 153.67 | 0 | 0 | 9.49 |
| 6 | 159.51 | 0 | 0 | 9.18 |
| 7 | 173.91 | 0 | 0 | 7.95 |
| 8 | 191.92 | 0 | 0 | 7.3 |
| 9 | 206.97 | 0 | 0 | 7.7 |
| 10 | 218.79 | 0 | 0 | 7.75 |
| 11 | 230 | 0 | 0.4 | 7.79 |
| 12 | 230 | 0 | 8.16 | 7.66 |
| 13 | 230 | 10 | 4.42 | 7.61 |
| 14 | 230 | 10 | 6.19 | 7.28 |
| 15 | 230 | 11.71 | 10 | 7.12 |
| 16 | 230 | 18.47 | 10 | 7.43 |
| 17 | 230 | 19.27 | 10 | 6.85 |
| 18 | 230 | 10.64 | 10 | 6.04 |
| 19 | 230 | 10 | 9.25 | 6.64 |
| 20 | 230 | 0 | 9.08 | 8.02 |
| 21 | 230 | 0 | 8.61 | 8.44 |
| 22 | 227.57 | 0 | 0 | 9.11 |
| 23 | 199.39 | 0 | 0 | 10.68 |
| 24 | 194 | 0 | 0 | 11.68 |

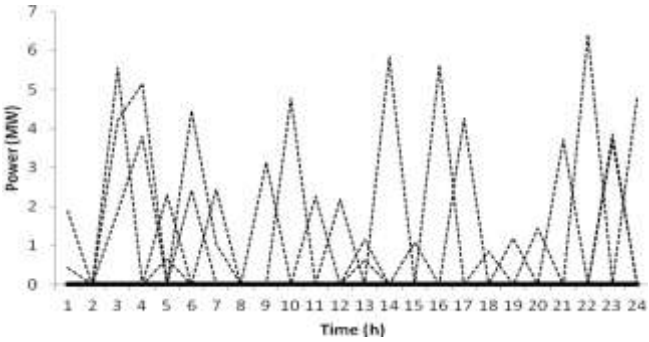


Fig. 5. Wind generation curtailments in Case II Solid line: zero curtailment at base case. Dotted line: wind energy curtailments in scenarios.

*Case 2*: This case includes wind and load forecast errors which are considered through the Monte-Carlo scenarios. The total system cost increases to $104,431. The base case dispatch is identical to that of Case 1. Fig. 5 depicts the wind power curtailments in the base case and scenarios. The algorithm curtails small amounts of wind in order to not utilize expensive regulation and spinning-down reserves. However, it should be noted that wind power curtailment might not be allowed in certain cases. The algorithm does not schedule regulation reserves in Case 2 other than 1.12 MW for hour 12 and 2 MW for hour 19 from G3. The spinning reserve dispatch and DR are given in Table III. These are the maximum deployable reserves available to the scenarios. Involuntary load shedding of 790, 50, 1450, 470, 120 and 7010 kWh is utilized in scenarios 1,2,3,4,5,7 respectively. The maximum load shedding occurs in the 7th scenario with the smallest probability. The expected system cost in Case II will increase to $104,592 when the involuntary load shedding is not allowed. The day-ahead system cost without DRR is $104,973 which will be reduced once DRR replaces the expensive units.

TABLE III
CASE 2 RESERVE DISPATCH (MW)

| Hour | $SR_u$ | | | $SR_d$ | | | DR | | |
|---|---|---|---|---|---|---|---|---|---|
| | G1 | G2 | G3 | G1 | G2 | G3 | DRP1 | DRP2 | DRP3 |
| 1 | 5.07 | 0 | 0 | 4.83 | 0 | 0 | 0 | 0 | 0 |
| 2 | 8.55 | 0 | 0 | 7.04 | 0 | 0 | 0 | 0 | 0 |
| 3 | 5.38 | 0 | 0 | 2.29 | 0 | 0 | 0 | 0 | 0 |
| 4 | 5.77 | 0 | 0 | 2.21 | 0 | 0 | 0 | 0 | 0 |
| 5 | 7.87 | 0 | 0 | 2.28 | 0 | 0 | 0 | 0 | 0 |
| 6 | 4.51 | 0 | 0 | 0.88 | 0 | 0 | 0 | 0 | 0 |
| 7 | 10.82 | 0 | 0 | 4.81 | 0 | 0 | 0 | 0 | 0 |
| 8 | 4.12 | 0 | 0 | 4.56 | 0 | 0 | 0 | 0 | 0 |
| 9 | 7.98 | 0 | 0 | 4.36 | 0 | 0 | 0 | 0 | 0 |
| 10 | 4.66 | 0 | 0 | 2.35 | 0 | 0 | 0 | 0 | 0 |
| 11 | 1.51 | 0 | 6.67 | 2.73 | 0 | 1.9 | 0 | 0 | 0 |
| 12 | 0 | 0 | 1.67 | 0 | 0 | 6.67 | 1.8 | 1.8 | 1.8 |
| 13 | 0 | 0 | 5.43 | 0 | 0 | 4.42 | 0 | 0 | 1.8 |
| 14 | 0 | 2.32 | 6.67 | 0 | 2.85 | 0.32 | 0 | 0 | 0 |
| 15 | 0 | 6.06 | 1.05 | 0 | 2.76 | 6.67 | 0 | 0 | 0 |
| 16 | 0 | 7.59 | 0.02 | 0 | 8.5 | 0 | 0 | 0 | 0 |
| 17 | 0 | 12.31 | 0 | 0 | 3.06 | 0 | 0 | 0 | 0 |
| 18 | 0 | 8.41 | 0 | 0 | 0.64 | 3.4 | 0 | 0 | 0 |
| 19 | 0 | 0 | 0.75 | 0 | 0 | 6.67 | 3.6 | 3.6 | 3.6 |
| 20 | 0 | 0 | 0.92 | 0 | 0 | 6.67 | 0 | 0 | 1.8 |
| 21 | 0 | 0 | 1.39 | 0 | 0 | 6.67 | 5.4 | 5.4 | 5.4 |
| 22 | 3.34 | 0 | 6.67 | 0 | 0 | 2.37 | 0 | 0 | 0 |
| 23 | 13.83 | 0 | 0 | 3.98 | 0 | 0 | 0 | 0 | 0 |
| 24 | 4.34 | 0 | 0 | 6.63 | 0 | 0 | 0 | 0 | 0 |

*Case 3*: Two *N-1* contingencies of G3 and the transmission line (between buses 3-6) are considered along with the 10 wind and load forecast scenarios. The system cost increases to $105,848 in Case 3 with an expected involuntary load shedding of 138.2kWh. The involuntary load shedding in this case is due to infeasibilities in wind and load scenarios. The DR schedule is identical to that in Case 2. The reserve dispatch for Case 3 is given in Table IV. The expensive regulation reserve is deployed for managing contingencies. The wind generation in the base Case 3 is curtailed, similar to that in Case 2, to consider the *N-1* contingencies. When DRR is not allowed, the optimal expected system cost is $106,041 with an expected involuntary load shedding of 20kWh.

*Sensitivity Analysis:* A sensitivity analysis is performed to evaluate the effect of wind and load forecast errors. Fig. 6 depicts the error levels versus the expected costs. In order to compare the effect of wind and load forecast errors, the standard deviation of wind is normalized by the maximum capacity of wind energy unit and the standard deviation of load is normalized by the maximum system load. First the system load forecast error is fixed to that of Case 3 (3%) and wind forecast error is varied starting from that of Case 3 (6.5%) to 32%. We observe that the wind forecast error does not affect the expected system cost significantly due to the limited availability of wind generation. Then the wind forecast error is fixed to that of Case 3 (6.5%) and the system load forecast error is varied starting from that of Case 3 (3%) to 12%. The expected system cost increases sharply due to the allocation and the deployment of additional reserves to respond to the increasing volatility of the system load.

TABLE IV
CASE 3 RESERVE DISPATCH (MW)

| Hour | $RR_u$ | | $SR_u$ | | | $SR_d$ | | |
|---|---|---|---|---|---|---|---|---|
| | G2 | G3 | G1 | G2 | G3 | G1 | G2 | G3 |
| 1 | 0 | 0 | 5.07 | 0 | 0 | 4.83 | 0 | 0 |
| 2 | 0 | 0 | 8.55 | 0 | 0 | 7.04 | 0 | 0 |
| 3 | 0 | 0 | 5.38 | 0 | 0 | 2.29 | 0 | 0 |
| 4 | 0 | 0 | 5.77 | 0 | 0 | 2.21 | 0 | 0 |
| 5 | 0 | 0 | 7.87 | 0 | 0 | 2.28 | 0 | 0 |
| 6 | 0 | 0 | 4.51 | 0 | 0 | 0.88 | 0 | 0 |
| 7 | 0 | 0 | 10.82 | 0 | 0 | 4.81 | 0 | 0 |
| 8 | 0 | 0 | 4.12 | 0 | 0 | 4.56 | 0 | 0 |
| 9 | 0 | 0 | 7.98 | 0 | 0 | 4.36 | 0 | 0 |
| 10 | 0 | 0 | 4.66 | 0 | 0 | 2.35 | 0 | 0 |
| 11 | 0 | 0 | 8.17 | 0 | 0 | 4.63 | 0 | 0 |
| 12 | 0 | 0 | 1.84 | 4.83 | 0 | 7.78 | 0 | 0 |
| 13 | 3.33 | 0 | 0 | 0 | 6.67 | 3.95 | 1.08 | 0.01 |
| 14 | 3.32 | 0 | 0 | 0 | 6.67 | 3.8 | 2.87 | 0 |
| 15 | 8.05 | 0 | 0 | 0 | 1.95 | 6.85 | 3.66 | 0 |
| 16 | 10 | 0 | 0 | 0 | 0 | 6.79 | 8.47 | 0 |
| 17 | 10 | 0 | 0.35 | 1.96 | 0 | 7.32 | 0 | 0 |
| 18 | 9.78 | 0 | 0 | 0 | 0.22 | 4.02 | 0.86 | 0 |
| 19 | 3.33 | 0 | 0 | 0 | 6.67 | 3.54 | 5.92 | 0 |
| 20 | 0 | 0 | 0 | 0 | 3.56 | 6.23 | 0 | 0 |
| 21 | 0 | 3.02 | 1.39 | 0 | 6.67 | 6.7 | 0 | 0 |
| 22 | 0 | 0 | 2.43 | 0 | 0 | 2.37 | 0 | 0 |
| 23 | 0 | 0 | 13.83 | 0 | 0 | 3.98 | 0 | 0 |
| 24 | 0 | 0 | 4.34 | 0 | 0 | 6.63 | 0 | 0 |

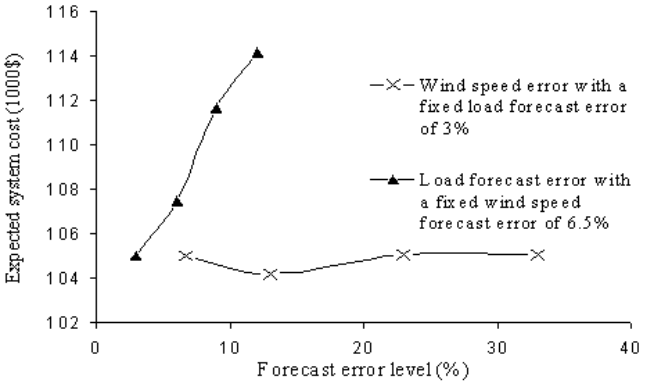


Fig. 6. Expected system cost versus wind energy and load forecast errors

Fig. 7 depicts the expected cost of uncertainty at each wind penetration level when the standard deviation of system load forecast error is 3%. The wind penetration refers to the installed capacity, and the hourly mean production is proportional to the installed capacity. Here, for a lower wind

penetration, the sensitivity of the expected system cost to wind energy forecast error is insignificant. This is because the required reserve would be low as the uncertainty is increased at the limited penetration level of 20 MW. However, the expected cost would increase for a higher penetration level as the forecast error is increased.

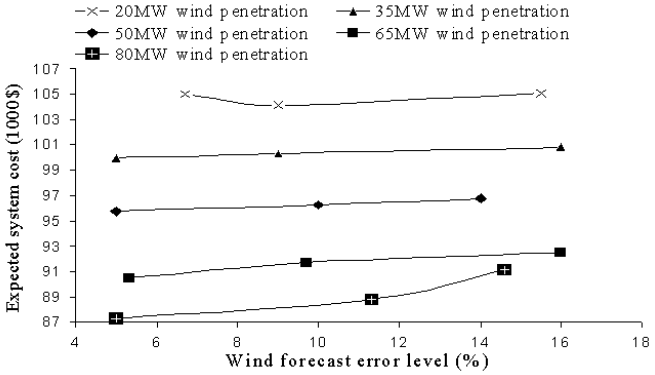


Fig. 7. Expected system cost with the wind penetration level

### B. Modified IEEE 118-Bus System

The Modified IEEE 118-Bus system is used to evaluate the efficiency of the proposed method. There are 186 branches and 91 loads. Three wind energy units are added to the 54 existing units. There are 50 DRPs at certain load buses which provide bids to the reserve market. The VOLL is 400 $/MWh at each load bus. Seven *N-1* contingencies include the outage of generators at buses 77, 82, 105, 113 and the outage of lines 17-113, 114-115 and 17-113. The wind and load forecast errors are represented by 1500 Monte Carlo scenarios. The number of scenarios is reduced to 12 by using forward-backwards scenario reduction techniques [23]. The data are available at motor.ece.iit.edu/data/Data_118_Bus.pdf. Table V shows the generation units with allocated reserves, $RR_{u,it}$, $RR_{d,it}$, $SR_{u,it}$, $SR_{d,it}$ . Here, the $RR_{u,it}$, $RR_{d,it}$, $SR_{u,it}$, $SR_{d,it}$ values for the listed units are positive for at least one hour in 24 hours.

TABLE V
RESERVE ALLOCATION AMONG UNITS IN THE 118-BUS SYSTEM CASE

| | Regulation Up | Spinning Up | Spinning Down |
|---|---|---|---|
| Considering Demand Response | - | 7, 29, 34, 39, 43, 45, 47, 51 | 5, 7, 10, 19, 22, 26, 27, 29, 30, 34, 39, 40, 43, 45, 47, 51, 52 |
| No Demand Response | 4, 7, 19, 22, 23, 26, 28, 30, 40 | 7, 10, 11, 14, 19, 22, 26, 27, 29, 30, 34, 35, 36, 37, 39, 40, 43, 45, 47, 48, 51, 52, 53 | 7, 10, 19, 22, 26, 27, 29, 30, 34, 36, 39, 40, 43, 45, 47, 48, 51, 52 |

The total expected system cost is $1,270,517 without DR. The allocated reserves include 155 MWh of regulation-up, 3076 MWh of spinning-up, and 2204 MWh of spinning-down reserve. No involuntary load shedding is deployed. When DR is considered, the expected cost reduces to $1,263,126, and expensive regulation reserve capacity is not allocated. The spinning-up reserve is reduced to 251MWh while the spinning-down reserve remains nearly the same at 2376 MWh. 2987 MWh of DR is allocated using DRPs for contingency and wind and load forecast error scenarios whenever they are cheaper than spinning-up reserve bids. Similar to the case without DR, no involuntary load shedding is allocated. The solution curtailed 182.27MWh of wind energy for accommodating *N-1* contingencies and forecast errors in both cases. The solution time in the latter case is 1 hour, 42 minutes, with an Intel Xeon 2.4GHz CPU and 64 GB of RAM.

*Scalability Analysis:* This analysis evaluates the performance when the number of *N-1* contingencies and the error forecast uncertainty are increased. Here, two tests are performed. First, three *N-1* contingencies are considered with 12, 18, and 24 forecast error scenarios. The change in the solution time is observed. Second, *N-1* contingencies are changed to 3, 7, and 11 while the number of forecast error scenarios is kept at 12. The results are presented in Table VI and Fig. 8. Here, the slope of the solution time is decreased as the number of contingencies and the level of uncertainties are increased. This is because some scenarios would require higher reserve allocations, and once the situation with these scenarios are resolved, the additional scenarios might not require much further reserve allocations. Besides, the performance is more sensitive to the number of *N-1* contingencies since one contingency could introduce more constraints to the problem.

### C. Northwest Region of Turkish Power System

Turkey has taken major steps towards building the country's electricity market since the enactment of Turkish Electricity Market Law in 2001 [25]. In this section, the proposed model is applied to the northwest region of the Turkish Power System which includes large industrial activities. The proposed scheduling model would study the coordination of hourly reserve and DR requirements when wind and load forecast uncertainties are considered. The subsystem depicted in Fig. 9 is composed of 173 buses, 28 thermal generating units, 66 branches, and 131 transformers.

TABLE VI
SCALABILITY ANALYSIS

| *N-1* Contingencies | Uncertainty Scenarios | Variables | Equality Constraints | Inequality Constraints |
|---|---|---|---|---|
| 3 | 12 | 422,640 | 111,552 | 146,088 |
| | 18 | 583,488 | 157,776 | 199,944 |
| | 24 | 744,336 | 204,000 | 253,800 |
| 3 | 12 | 422,640 | 111,552 | 146,088 |
| 7 | | 519,504 | 131,856 | 181,800 |
| 11 | | 616,368 | 152,160 | 217,512 |

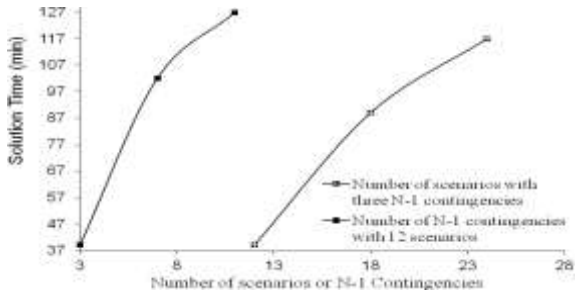


Fig. 8. Solution time versus *N-1 c*ontingency or uncertainty scenarios

Two *N-1* contingencies are considered as the outages of one of the generators at bus NUHENERJI_A and the transmission line COLAKOGLU-KROMANCELIK. 1500 scenarios are created to simulate wind and load forecast errors which are reduced to 12 scenarios. The standard deviations for wind and load forecaster error are 6.5%, and 4% respectively. Considerable industrial loads appear at buses DILISKELESI, COLAKOGLU, ICMELER, DUDULLU and GEBZEOSB.

These loads are mostly composed of shipyards, steel mills, and cement manufacturing facilities in an industrial zone.

Three 100 MW wind farms are located at three buses SILE, KARAMURSEL and YALOVA, which have considerable wind potential. Detailed data are included in motor.ece.iit.edu/data/Data_TR.pdf. Six DRP buses are DILISKELESI, COLAKOGLU, DUDULLU, KOSEKOY, KUCUKBAKKAL, and GEBZEOSB, with both residential and industrial loads. For instance, cement factories could curtail consumption and shift production when required by the ISO. The DRP bids are 7, 14, and 21 MW at 7, 9, and 11 $/MW and the deployment prices at 17.5, 22.5, 27.5 $/MW respectively.

The expected day-ahead system cost without DRR is $559,039 while the cost reduces to $549,289 when DRR is considered. The wind curtailment is 78.38MWh in both cases (see Table VII). DRR replaces 870 MWh of spinning-up, 915 MWh of spinning-down, and 44 MWh of regulation-up reserves, and reduces the costs by $9,750. The DRPs are paid a total of $17,045, for participating in the DRR program.

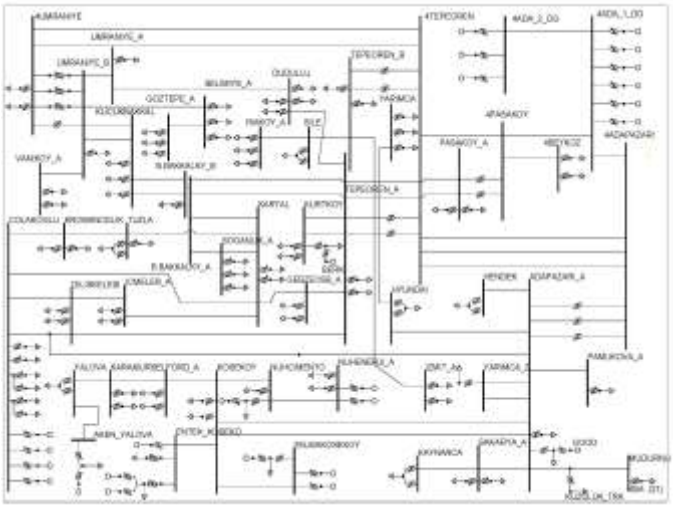

Fig. 9. Northwest region of Turkish Electric Power Network

TABLE VII
ALLOCATED DRRS (MW) OF DRPS

| Hour | | 1 | 2 | 3 | 4 | 5 | 6 | 7 | 8 | 9 | 10 | 11 | 12 |
|---|---|---|---|---|---|---|---|---|---|---|---|---|---|
| DRP | 1 | 7 | 0 | 0 | 0 | 7 | 7 | 7 | 7 | 7 | 7 | 7 | 7 |
| | 2 | 7 | 0 | 7 | 0 | 0 | 0 | 0 | 14 | 7 | 7 | 7 | 7 |
| | 3 | 0 | 7 | 7 | 0 | 0 | 0 | 7 | 14 | 14 | 0 | 14 | 14 |
| | 4 | 7 | 7 | 0 | 0 | 7 | 0 | 0 | 7 | 7 | 7 | 7 | 7 |
| | 5 | 0 | 7 | 7 | 0 | 0 | 0 | 0 | 14 | 7 | 7 | 7 | 7 |
| | 6 | 7 | 0 | 7 | 0 | 0 | 7 | 7 | 14 | 7 | 7 | 7 | 7 |
| **Hour** | | **13** | **14** | **15** | **16** | **17** | **18** | **19** | **20** | **21** | **22** | **23** | **24** |
| DRP | 1 | 7 | 0 | 7 | 7 | 7 | 7 | 7 | 14 | 21 | 0 | 7 | 0 |
| | 2 | 7 | 7 | 7 | 7 | 7 | 7 | 7 | 14 | 14 | 7 | 7 | 0 |
| | 3 | 14 | 14 | 14 | 14 | 14 | 14 | 14 | 14 | 14 | 7 | 14 | 14 |
| | 4 | 7 | 7 | 7 | 7 | 7 | 7 | 7 | 0 | 0 | 0 | 7 | 0 |
| | 5 | 7 | 7 | 7 | 7 | 7 | 7 | 7 | 7 | 7 | 7 | 7 | 7 |
| | 6 | 7 | 7 | 7 | 7 | 7 | 7 | 7 | 14 | 14 | 7 | 7 | 0 |

## VI. CONCLUSIONS

The proposed method is used to analyze the effect of *N-1* contingencies, wind and load uncertainties and DRP bids in the hourly generation scheduling. The proposed algorithm curtails the wind generation in scenarios in order to not allocate expensive regulation and spinning-down reserves. The sensitivity analyses show that the expected system cost is more sensitive to load forecast errors. The effect of wind forecast error depends on the wind penetration level. The system cost decreases as the wind penetration increases since the operating cost of wind energy units is neglected. However, the expected cost increases considerably with the increasing wind forecast errors. A scalability analysis is performed which shows that the rate of change in the solution time decreases sharply as the number of considered contingencies is increased or wind and load volatilities are higher. Furthermore, it is observed that the solution performance is more sensitive to the number of contingencies since contingencies could add more variables and constraints to the problem. It is also shown that the integration of DR at proper locations and periods would reduce the cost of the security-based power system scheduling.

## REFERENCES


[1] M. Shahidehpour, H. Yamin, and Z.Y. Li, *Market Operations in Electric Power Systems, John Wiley &Sons, Inc.*, New York, 2002

[2] Global Wind 2008 Report, GWEC, Global Wind Energy Council [On-line]. Brussels, Belgium. Available: http://www.gwec.net

[3] J. Wang, M. Shahidehpour, and Z. Li, "Security-Constrained Unit Commitment With Volatile Wind Power Generation," *IEEE Trans. Power Syst.*, Vol. 23, no. 4, pp. 1319 – 1327, Aug. 2008

[4] E. D. Castronuovo and J. A. Pecas-Lopes, "On the optimization of the daily operation of a wind-hydro power plant," IEEE Trans. Power Syst., vol. 19, no. 3, pp. 1599–1606, Aug. 2004.

[5] B. C. Ummels, M. Gibescu, E. Pelgrum, W. L. Kling, and A. J. Brand, "Impacts of wind power on thermal generation unit commitment and dispatch," IEEE Trans. Energy Convers., vol. 22, no. 1, pp. 44–51, Mar. 2007.

[6] Y.V. Makarov, C. Loutan, J. Ma, P. de Mello, "Operational Impacts of Wind Generation on California Power Systems," IEEE Trans. on Power Systems, Vol. 24, No. XX, pp. 1039 - 1050, May 2009

[7] A. Fabbri, T. Gomez San Roman, J. Rivier Abbad, and V. H. M. Quezada, "Assessment of the cost associated with wind generation prediction errors in a liberalized electricity market," IEEE Trans. Power Syst., vol. 20, no. 3, pp. 1440–1446, Aug. 2005.

[8] J. M. Morales, A. J. Conejo, and J. Pérez-Ruiz, "Economic Valuation of Reserves in Power Systems With High Penetration of Wind Power," *IEEE Trans. on Power Syst.*, Vol. 24, No. 2, pp. 900-911, May 2009

[9] U.S. Department of Energy, "Benefits of Demand Response in Electricity Markets and Recommendations for Achieving Them", Feb. 2006

[10] F. Boshell and O.P. Veloza, "Review of Developed Demand Side Management Programs Including Different Concepts and their Results," IEEE/PES Transmission and Distribution Conference and Exposition: Latin America, 2008

[11] F. Rahimi, "Overview of Demand Response programs at different ISOs/RTOs," in Proceedings of IEEE/PES Power Systems Conference and Exposition, 2009

[12] M. Parvania, M. Fotuhi-Firuzabad, "Demand Response Scheduling by Stochastic SCUC," *IEEE Trans. Smart Grid.*, Vol. 1, no. 1, pp. 89–98, June 2010

[13] W. Uturbey and A. S. Costa "Dynamic Optimal Power Flow Approach to Account for Consumer Response in Short Term Hydrothermal Coordination Studies," *IET Gener. Transm. Distrib*., Vol. 1, No. 3, pp. 414–421, May 2007

[14] D. Mennit, F. Costanzo, N. Scordino, and N. Sorrentino, "Purchase-Bidding Strategies of an Energy Coalition With Demand-Response Capabilities," *IEEE Trans. Power Syst.*, vol. 24, no. 3, pp. 1241–1255, August 2009

[15] C-L Su, and D. Kirschen, "Quantifying the Effect of Demand Response on Electricity Markets," *IEEE Trans. Power Syst.*, vol. 24, no. 3, pp. 1199–1207, August 2009

[16] Q. Zhang, and X. Wang, "Quantifying Hedge Contract Characterization and Risk-Constrained Electricity Procurement," *IEEE Trans. Power Syst.*, vol. 24, no. 3, pp. 1547–1558, August 2009

[17] L. Soder, "Simulation of wind speed forecast errors for operation planning of multiarea power systems," in Proc. Probabilistic Methods Applied to Power Systems, 2004 International Conference on , pp. 723-728, 12-16 Sep. 2004

[18] J. R. Birge and F. Louveaux, *Introduction to Stochastic Programming. New York: Springer*, 1997

[19] Y. Fu, M. Shahidehpour, and Z. Li, "AC contingency dispatch based on security-constrained unit commitment," IEEE Trans. Power Syst., vol. 21, no. 2, pp. 897–908, May 2006
[20] M. Shahidehpour and Y. Fu "Benders decomposition: applying Benders decomposition to power systems," IEEE Power and Energy Magazine, vol. 3, issue. 2, pp. 20, March 2005
[21] A. Wood and B. Wollenberg, Power Generation Operation and Control, 2nd ed. New York: Wiley, 1996
[22] J. Wang, M. Shahidehpour, and Z. Li, "Contingency-Constrained Reserve Requirements in Joint Energy and Ancillary Services Auction," *IEEE Trans. Power Syst.*, vol. 24, no. 3, pp. 1457–1468, August 2009
[23] GAMS — The Solver Manuals, GAMS Development Corporation, [On-line] Washington, DC, USA. Available: www.gams.com/
[24] H. Heitsch, W. Romisch, "Scenario Reduction Algorithms in Stochastic Programming," Computational Optimization and Applications, Vol 24, Issue 2-3, pp. 187-206, Feb-March 2003
[25] C. Sahin and M. Shahidehpour, "Interdependence of NG and Electricity Infrastructures in Turkey," in Proceedings of 2009 IEEE PES General Meeting, Calgary, Canada

## BIBLIOGRAPHIES

**Cem Sahin** received M.S. and Ph.D. degrees in electrical engineering from Middle East Technical University (METU), Turkey, in 2003 and 2010, respectively. He was a visiting scientist in the Robert W. Galvin Center for Electricity Innovation at IIT in 2009. His research interests include power systems optimization, wind energy integration, and power markets.

**Mohammad Shahidehpour** (F'01) is the Bodine Chair Professor and Director of Robert W. Galvin Center for Electricity Innovation at IIT. Dr. Shahidehpour is a Research Professor at the King Abdulaziz University in Saudi Arabia and Honorary Professor at Sharif University of Technology in Iran and North China Electric Power University in China.

**Ismet Erkmen** is the Chairman in the Electrical and Computer Engineering Department at Middle East Technical University (METU), Ankara -Turkey. His research interests are control of large-scale systems and power systems optimization.

# Hourly Coordination of Electric Vehicle Operation and Volatile Wind Power Generation in SCUC

Mohammad E. Khodayar, *Student Member, IEEE,* Lei Wu, *Member*, *IEEE*, Mohammad Shahidehpour, *Fellow*, *IEEE*

***Abstract*— In this paper, the coordinated integration of aggregated plug-in electric vehicle (PEV) fleets and renewable energy sources (wind energy) in power systems is studied by stochastic security-constrained unit commitment (Stochastic SCUC) model, which minimizes the expected grid operation cost while considering the random behavior of the many PEVs. PEVs are mobile and distributed devices with deferrable options for the supply/utilization of energy at various times and locations. The increased utilization of PEVs, which consume electricity rather than fossil fuel for driving, offers unique economic and environmental opportunities, and brings out new challenges to electric power system operation and planning. The storage capability of PEVs could help power systems mitigate the variability of renewable energy sources and reduce grid operation costs. Vehicle-to-grid (V2G) enables PEVs to have bi-directional power flows once they are connected to the grid, i.e., they can either inject power to, and draw power from, the grid which adds further complexity to power system operations. PEVs signify customers' random behavior when considering their driving patterns, locational energy requirements, topological grid interconnections, and other constraints imposed by the consumers. Numerical tests demonstrate the effectiveness of the proposed approach for analyzing the impact of PEVs on the grid operation cost and hourly wind energy dispatch.**

***Index Terms*—Plug-in electric vehicles, renewable energy sources, V2G, load aggregation, stochastic security-constrained unit commitment.**

## NOMENCLATURE

### Variables

| | |
|---|---|
| $b, j, o$ | Index of bus |
| $C_{(.)}^{(.)}$ | Operation cost of PEV fleet |
| $E_{v,t}^{(.)}$ | Available energy in batteries of fleet $v$ at time $t$ |
| $E_{v,t}^{net}$ | Net discharged energy of PEV fleet $v$ at time $t$ |
| $F_{c,(\cdot)}, F_{c,(\cdot)}^{r}$ | Production/availability cost function of a thermal unit |
| $_i$ | Denotes a thermal unit |
| $I_{(\cdot)}^{(\cdot)}$ | Unit status indicator, 1 means on and 0 means off |
| $I_{c,(.)}^{(.)}$ | Indicator of PEV fleet in charging mode |
| $I_{dc,(.)}^{(.)}$ | Indicator of PEV fleet in discharging mode |
| $I_{i,(.)}^{(.)}$ | Indicator of PEV fleet in idle mode |
| $k$ | Denotes a hydro unit |
| $l$ | Index of transmission line |
| $m$ | Denotes a segment of curves |
| $P_{(\cdot)}^{(\cdot)}$ | Generation of a unit |
| $P_{d,w,t}^{(\cdot)}$ | Power generation curtailed of wind unit $w$ at hour $t$ |
| $P_{c,(.)}^{(.)}, P_{dc,(.)}^{(.)}$ | Charge/discharge power of PEV fleet |
| $P_{m,(.)}^{(.)}$ | Charge/discharge power rate at segment $m$ |
| $PL_{l,t}^{(.)}$ | Real power flow on line $l$ at hour $t$ |
| $s$ | Denotes a scenario |
| $SD_{(.)}^{(.)}$ | Shutdown cost of a unit |
| $SU_{(.)}^{(.)}$ | Startup cost of a unit |
| $t$ | Hour index |
| $v$ | Denotes a PEV fleet |
| $w$ | Denotes a wind unit |
| $\theta_{(.)}^{(.)}$ | Bus angle |
| $\Delta_{(.)}^{\max}$ | Maximum permissible power adjustment of a unit |

### Constants:

| | |
|---|---|
| $B_{b,t}^{(.)}$ | Set of units which are connected to bus $b$ at time $t$ |
| $b_{m,(.)}$ | Slope of segment $m$ in linearized charge/discharge curve |
| $CD_k, CS_k$ | Shutdown/startup cost of hydro unit $k$ |
| $D_b$ | Set of loads which are connected to bus $b$ |
| $DR_{v,t}^{s}$ | Energy for PEV $v$ to drive at time $t$ in scenario $s$ |
| $E_v^{\min}, E_v^{\max}$ | Min/max energy stored in batteries of PEV fleet $v$ |
| $E0_v, ET_v$ | Initial and terminal stored energy in PEV fleet $v$ |
| $L_{f,b}, L_{t,b}$ | Set of lines starting from/ending at bus $b$ |
| $N_{v,t}$ | Status of grid connection of fleet $v$ at time $t$ |
| $NE_v^s$ | Ratio of the number of PEVs in fleet $v$ in scenario $s$ to the number of base case PEVs |
| $NT$ | Number of hours under study |
| $p^b$ | Probability of the base case solution |
| $p^s$ | Probability of scenario $s$ |

M. E. Khodayar and M. Shahidehpour are with the Electrical and Computer Engineering Department, Illinois Institute of Technology, Chicago, IL 60616 USA. (e-mail: mkhodaya@iit.edu, ms@iit.edu). L. Wu is with the Electrical and Computer Engineering Department, Clarkson University, Potsdam, NY 13699 USA. (e-mail: lwu@clarkson.edu).

| | |
|---|---|
| $P_{(.)}^{\min}, P_{(.)}^{\max}$ | Min/max generation capacity |
| $P_{c,v}^{\min}, P_{c,v}^{\max}$ | Min/max charging capacity of PEV fleet $v$ |
| $P_{dc,v}^{\min}, P_{dc,v}^{\max}$ | Min/max discharging capacity of PEV fleet $v$ |
| $P_{D,(.)}^{(.)}$ | Total system demand |
| $P_{f,w,t}^{(.)}$ | Forecasted wind power of wind unit $w$ at hour $t$ |
| $P_{m,v}^{\max}$ | Maximum power output at segment $m$ in charging/ discharging cost curve of PEV fleet $v$ |
| $PL_l^{\max}$ | Maximum capacity of line $l$ |
| $\hat{T}$ | Time in which the charging state is set to a value |
| $UX_{(\cdot)}^{(\cdot)}$, $UY_{(\cdot)}^{(\cdot)}$ | Outage status, 1 if available, and otherwise 0 |
| $X_{jo}$ | Inductance of a line between buses $j$ and $o$ |
| $\eta_v$ | Cycle charging efficiency of PEV fleet |

## I. Introduction

Plug-in electric vehicles (PEVs) represent hourly distributed and mobile demands in power systems which could also provide distributed storage to power grids [1],[2]. The aggregated storage capability of PEVs can help shift the hourly generation portfolio and reduce grid operation costs. Hence, a dramatic increase in the number of PEVs could have a major impact on power system operations. Once aggregated at the distribution level, the distribution company (DISCO) will submit the information on marginal cost, storage capacity, and location of PEV fleets to the ISO for participation in the day-ahead market.

Wind energy is the fastest growing renewable energy resource [3]. The large penetration of wind energy could decrease the operation cost and the emission of hazardous gases from fossil plants. However, the variability of wind energy could impose adverse effects on the dynamic and static security of power systems. [4]-[5] studied the integration of storage for mitigating the effect of hourly wind energy variability on power systems. Likewise, V2G could offer ancillary services and reduce operation costs in power systems.

References [6]-[8] focused on storage technologies and power electronic grid-connection interfaces for facilitating large-scale adoptions of PEVs. Economic potentials of PEVs for participating in regulation services were investigated in [9]. The role of PEV in the integration of renewable energy resources was addressed in [10]. The integration of PEV in power systems was investigated in [11] and major issues for the V2G implementation were discussed. The electricity market issues of PEV integration were presented in [12].

Unlike conventional storage capabilities, the grid-connection storage topography of PEVs may change during the daily operation of power systems. PEVs consume energy according to their driving requirements. In addition, the total PEV energy drawn from the grid could be much larger than the energy injected to the grid [13]-[16]. While most of the previous studies addressed the economic aspects of integrating PEVs to power systems, they lack the transmission system security consideration offered by the PEV interconnection and its daily profile in power systems.

The contributions of this paper include the modeling of large scale PEV integration as mobile distributed load and storage facilities and their impacts on the optimal operation of security-constrained power systems. The study considers physical limitations of power systems, hourly load and wind energy uncertainties, and random outages of generation and transmission components in PEV integration.

The rest of the paper is as follows. Section II discusses the proposed Stochastic SCUC formulation. Section III illustrates the effectiveness of the proposed methodology by a 6-bus system and the IEEE 118-bus system. Detailed discussions and conclusions are presented in Sections IV and V, respectively.

## II. Proposed Stochastic SCUC Formulation

PEV fleet characteristics include starting locations and destinations of PEV fleets, departure and arrival times at designated locations, and PEV charging locations and patterns which could be bundled into power system operations. A random number of PEVs is assumed for each fleet. The state of charge (SOC), energy consumption, and min/max capacity of a PEV fleet is a function of the number of PEVs and their operating characteristics. SOC is the ratio of available energy to maximum storable energy in the battery. The available energy in the PEV battery is computed by multiplying the given SOC by the maximum storable energy in the battery. The energy consumption in a fleet, which is a parameter, depends on the number of PEVs and their energy requirements. The driving habits in a fleet would determine the charging/discharging patterns of aggregated PEVs.

The proposed formulation is a stochastic optimization problem in which the wind energy and load forecast errors, power system component outages, number of PEVs in a fleet and their energy requirements are considered as variables. The proposed solution determines the hourly unit commitment and dispatch of generating units and charge/discharge states of PEV fleets.

The Monte Carlo simulation method is utilized in the proposed stochastic model. Random outages in power systems are represented by incorporating probability distribution functions and forced outage rates. Load forecast errors, PEV energy consumption patterns, and the number of PEVs in a fleet are represented by truncated normal distribution functions in which the mean values are the forecasts and the standard deviations are percentages of the mean values [17]-[18]. Wind speed variations are simulated by the Weibull distribution function, auto correlation factor and diurnal pattern [19], and wind generation is procured by incorporating the wind turbine power curve and wind speed at wind sites. Forward and backward algorithms are developed to reduce the number of scenarios with an acceptable accuracy [20]-[21]. The convex operation cost of aggregated PEVs would depend on the number of vehicles and charging/discharging cycles [9].

The proposed Stochastic SCUC is a mixed-integer programming (MIP) optimization problem. The objective (1) is to minimize the grid operation cost subject to system and unit constraints (2)-(28). The objective function includes the base case operation cost, in which the forecasted quantities of load, wind, and hydro are incorporated, and outages of generators and

transmission lines are not considered. We also consider in the objective function the availability cost for providing spinning reserve in Monte Carlo scenarios. The availability cost refers to the payment to generators that provide reserves. The provision of reserve is exercised as a corrective action by generators in response to the realization of uncertainties. It is assumed that the generators can provide corrective actions, which are restricted by their ramp up/down limitations. The availability cost is considered as one third of the marginal cost of a generating unit [22]. The objective function further includes the expected cost of corrective actions in scenarios for accommodating uncertainties. In this formulation, load curtailment is not acceptable in scenarios, and the system should serve the load in the base case and all scenarios. Alternatively, load curtailment could have been considered by adding the respective penalty factor to the objective function. Thermal units are formulated as non-quick start units, so their scenario commitment status is the same as that in the base case. Thus, there is no need to introduce extra startup/ shutdown costs in scenarios.

The system and generating unit constraints in the base case are shown in (2)-(14). Detailed thermal unit constraints are available in [23]. Hydro unit constraints are provided in [24]. Wind curtailment constraint is shown in (2) in which the sum of dispatched and curtailed wind power is the same as the wind power forecast. The wind curtailment occurs when there is an insufficient ramping down capability of thermal units or a significant transmission congestion for utilizing the available wind power in power systems. The base case PEV fleet constraints are shown in (3)-(10). The net hourly absorbed/delivered energy is given in (3), which shows that the difference in the energy gained from the grid/stored in the aggregated PEV battery and the energy delivered back to the grid from the PEV is quantified by the charging cycle efficiency of the aggregated PEV. The hourly charge/discharge/idle modes of fleets which are mutually exclusive are given in (4). Charge/discharge power constraints are given in (5)-(6). The hourly energy balance in PEV batteries is given in (7). The given parameter $N_{v,t}$ indicates connectivity of PEV fleet to the system. Once a PEV fleet is connected to the power system (i.e., $N_{v,t}=1$), the aggregated battery is either charged by drawing power from the grid (5), or discharged by injecting power to the grid (6). If the PEV fleet is not plugged-in (i.e., $N_{v,t}=0$), the charging/discharging power will be zero according to (4)-(6). The energy capacity limit of each fleet is presented in (8)-(9). The piecewise linear representation of convex charge/discharge cost curve of PEV batteries is shown in (10), which represents the depth of discharge and cycles to failure of the battery for calculating the cost of energy drawn or delivered by PEV batteries. As the depth of aggregated battery discharge increases, the number of cycles to failure would decrease. This indicates a higher cost for charging/discharging of the battery because the total energy stored by/drawn from the battery during its lifetime will decrease for a fixed battery price [9], [11]. Hence, the operation cost of aggregated PEV has a direct correlation with the depth of charging/discharging batteries [12]. The nonlinear battery charging/discharging cost curves are piecewise linearized for consideration in the proposed MIP formulation. A tighter piecewise linear approximation was presented in the authors' previous work [25]. In the consumer-controlled scheme, the aggregated SOC of PEVs is set to be fixed at specific operation periods (11). It is assumed that the SOC is at 100% when a PEV fleet is leaving the station. (12)-(14) represent the base case dc power flow constraints.

The PEV fleet scenario constraints are shown in (15)-(23) and the consumer-controlled scenario scheme is represented by (24). The wind scenario constraint includes a set similar to (2), except base case variables are replaced by scenario variables. The scenario corrective action is enforced by (25) where the hourly cost of corrective action, $F^r_{c,i}\left(\Delta^{\max}_{i,t}\right)$, is included in (1). (26)-(28) represent dc power flow constraints for each Monte Carlo scenario. The grid connection of PEV fleet at time $t$ is represented by $B^v_{b,t}$ in (26).

$$Min\left[\sum_t\sum_i\left(p^b\cdot F_{c,i}(P_{i,t})+SU_{i,t}+SD_{i,t}\right)+\sum_t\sum_k\left(SU_{k,t}+SD_{k,t}\right)+\sum_t\sum_v C_{v,t}\right]+\left[\sum_t\sum_i\left(F^r_{c,i}\left(\Delta^{\max}_{i,t}\right)\right)\right] \quad (1)$$

$$+\sum_s p^s\cdot\left[\sum_t\sum_i F_{c,i}\left(P^s_{i,t}\right)+\sum_t\sum_k\left(SU^s_{k,t}+SD^s_{k,t}\right)+\sum_t\sum_v C^s_{v,t}\right]$$

s.t.

$$P_{w,t}+P_{d,w,t}=P_{f,w,t} \quad (2)$$

$$E^{net}_{v,t}=P_{dc,v,t}-\eta_v\cdot P_{c,v,t} \quad (3)$$

$$P_{v,t}=P_{dc,v,t}-P_{c,v,t}$$

$$I_{dc,v,t}+I_{c,v,t}+I_{i,v,t}=N_{v,t} \quad (4)$$

$$I_{c,v,t}\cdot P^{\min}_{c,v}\le P_{c,v,t}\le I_{c,v,t}\cdot P^{\max}_{c,v} \quad (5)$$

$$I_{dc,v,t}\cdot P^{\min}_{dc,v}\le P_{dc,v,t}\le I_{dc,v,t}\cdot P^{\max}_{dc,v} \quad (6)$$

$$E_{v,t}=E_{v,t-1}-E^{net}_{v,t}-(1-N_{v,t})\cdot DR_{v,t} \quad (7)$$

$$E^{\min}_v\le E_{v,t}\le E^{\max}_v \quad (8)$$

$$E_{v,0}=E_{v,NT} \quad (9)$$

$$C_{v,t}=N_{v,t}\cdot\left(\sum_m b_{m,v}\cdot P_{m,v,t}\right)$$

$$0\le P_{m,v,t}\le P^{\max}_{m,v} \quad (10)$$

$$N_{v,t}\cdot\left|E_{v,t}-E_{v,t-1}\right|=\sum_m P_{m,v,t}$$

$$E_{v,\hat{T}}=E^{\max}_v \quad (11)$$

$$\sum_{i\in B^i_b}P_{i,t}+\sum_{w\in B^w_b}P_{w,t}+\sum_{v\in B^v_{b,t}}P_{v,t}+\sum_{k\in B^k_b}P_{k,t}=\sum_{d\in D_b}P^d_{D,t}+\sum_{l\in L_{f,b}}PL_{l,t}-\sum_{l\in L_{t,b}}PL_{l,t} \quad (12)$$

$$PL_{l,t}=\left(\theta_{j,t}-\theta_{o,t}\right)/X_{jo} \quad (13)$$

$$\left|PL_{l,t}\right|\le PL^{\max}_l \quad (14)$$

$$C^s_{v,t}=N_{v,t}\cdot\left(\sum_m b_{m,v}\cdot P^s_{m,v,t}\right)$$

$$0\le P^s_{m,v,t}\le P^{\max}_{m,v}\cdot NE^s_v \quad (15)$$

$$N_{v,t}\cdot\left|E^s_{v,t}-E^s_{v,t-1}\right|=\sum_m P^s_{m,v,t}$$

$$E_{v,t}^{net,s} = P_{dc,v,t}^{s} - \eta_v \cdot P_{c,v,t}^{s} \tag{16}$$

$$I_{dc,v,t}^{s} + I_{c,v,t}^{s} + I_{i,v,t}^{s} = N_{v,t} \tag{17}$$

$$N_{v,t} \cdot I_{c,v,t}^{s} P_{c,v}^{\min} \cdot NE_v^s \le P_{c,v,t}^{s} \le N_{v,t} \cdot I_{c,v,t}^{s} P_{c,v}^{\max} \cdot NE_v^s \tag{18}$$

$$N_{v,t} \cdot I_{dc,v,t}^{s} P_{dc,v}^{\min} \cdot NE_v^s \le P_{dc,v,t}^{s} \le N_{v,t} \cdot I_{dc,v,t}^{s} P_{dc,v}^{\max} \cdot NE_v^s \tag{19}$$

$$E_{v,t}^{s} = E_{v,t-1}^{s} - E_{v,t}^{net,s} - \left(1 - N_{v,t}\right) \cdot DR_{v,t}^{s} \cdot NE_v^s \tag{20}$$

$$E_v^{\min} \cdot NE_v^s \le E_{v,t}^{s} \le E_v^{\max} \cdot NE_v^s \tag{21}$$

$$E_{v,0}^{s} = E_{v,NT}^{s} = E_{v0} \cdot NE_v^s \tag{22}$$

$$P_{v,t}^{s} = P_{dc,v,t}^{s} - P_{c,v,t}^{s} \tag{23}$$

$$P_{v,\hat{T}}^{s} = E_v^{\max} \cdot NE_v^s \tag{24}$$

$$-\Delta_{i,t}^{\max} \le P_{i,t}^{s} - UX_{i,t}^{s} \cdot P_{i,t} \le \Delta_{i,t}^{\max}$$
$$P_i^{\min} \cdot UX_{i,t}^{s} \cdot I_{i,t} \le P_{i,t}^{s} \le P_i^{\max} \cdot UX_{i,t}^{s} \cdot I_{i,t} \tag{25}$$

$$\sum_{i \in B_b^i} P_{i,t}^{s} + \sum_{w \in B_b^w} P_{w,t}^{s} + \sum_{v \in B_{b,t}^v} P_{v,t}^{s} + \sum_{k \in B_b^k} P_{k,t}^{s} = \sum_{d \in D_b} P_{D,t}^{d,s} + \sum_{l \in L_{f,b}} PL_{l,t}^{s} - \sum_{l \in L_{t,b}} PL_{l,t}^{s} \tag{26}$$

$$-M \cdot \left(1 - UY_{l,t}^{s}\right) \le PL_{l,t}^{s} - \left(\theta_{j,t} - \theta_{o,t}\right) / X_{jo} \le M \cdot \left(1 - UY_{l,t}^{s}\right) \tag{27}$$

$$-PL_l^{\max} UY_{l,t}^{s} \le PL_{l,t}^{s} \le PL_l^{\max} UY_{l,t}^{s} \tag{28}$$

Considering the grid complexity along with the stochastic nature and the mobility of V2G, the proposed optimization problem in (1)-(28) represents a large-scale, non-convex, non-deterministic polynomial-time hard (NP-hard) problem [26].

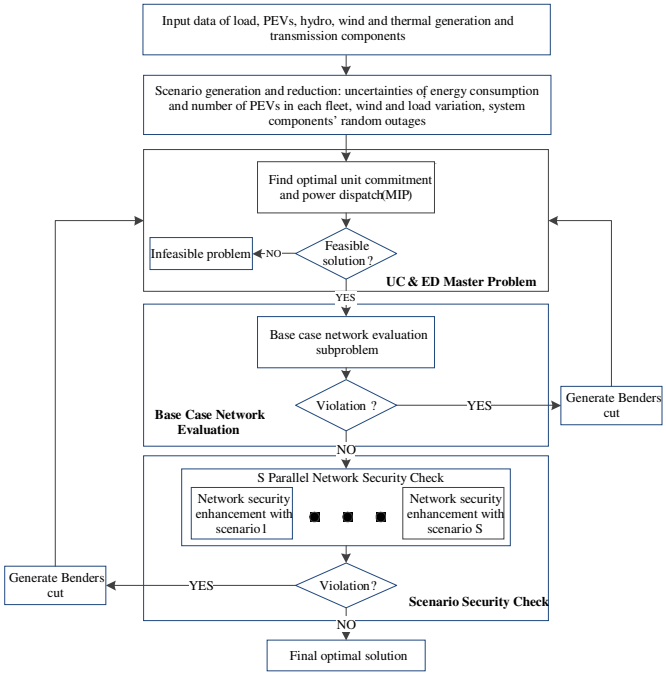


Fig. 1. Proposed Stochastic SCUC with PEV integration in power systems

The solution to the original problem in such cases would be an intractable task without decomposition. The problem is decomposed into a master MIP problem and several linear programming (LP) subproblems. After the master problem is solved, the subproblems check the network constraints in the base case and all scenarios. Network evaluations for the base case and all scenarios are independent which can be optimized in parallel. Benders cuts are generated and fed back to the master problem to mitigate any violation encountered in the base case or any scenario. The decomposition and respective formulation is shown in Fig. 1.

## III. Case Studies

In this section, a 6-bus power system and the 118-bus power system are studied to demonstrate the effectiveness of the proposed approach for analyzing the impact of aggregated PEVs on operation cost, wind curtailment, and optimal unit commitment and dispatch of generation facilities including thermal, hydro, and wind units along with PEV fleets.

### A. 6-Bus Power System

A 6-bus power system shown in Fig. 2 is considered to study the integration of PEVs into the power grid. Generators and transmission line data are shown in Tables I and II, respectively. PEVs in various locations are categorized into different fleets based on their driving characteristics. The available energy, max/min capacity and charge/discharge power of individual vehicles are aggregated in PEV fleet characteristics representing max/min capacities, SOC, and max/min charging/discharging capabilities. Tables III and IV show five fleets in the power system. The charging efficiency of a fleet is 85% which is the ratio of energy stored in the battery to the energy drawn from the grid.

TABLE I
THERMAL UNIT CHARACTERISTICS

| Unit | a ($/MW$^2$) | b ($/MW) | c ($/h) | $P_{min}$ (MW) | $P_{max}$ (MW) | SU ($) | SD ($) | Min. Up (h) | Min Dn. (h) |
|---|---|---|---|---|---|---|---|---|---|
| G1 | 0.099 | 6.589 | 211.4 | 100 | 320 | 100 | 50 | 4 | 3 |
| G2 | 0.203 | 7.629 | 217.4 | 10 | 160 | 200 | 40 | 3 | 2 |
| G3 | 0.494 | 10.07 | 102.8 | 10 | 100 | 80 | 10 | 1 | 1 |

TABLE II
TRANSMISSION LINE CHARACTERISTICS

| Line ID | From Bus | To Bus | Impedance (p.u) | Capacity (MW) |
|---|---|---|---|---|
| 1 | 1 | 2 | 0.170 | 65 |
| 2 | 1 | 4 | 0.258 | 70 |
| 3 | 2 | 4 | 0.197 | 40 |
| 4 | 5 | 6 | 0.140 | 40 |
| 5 | 3 | 6 | 0.018 | 75 |
| 6 | 2 | 3 | 0.037 | 80 |
| 7 | 4 | 5 | 0.037 | 65 |

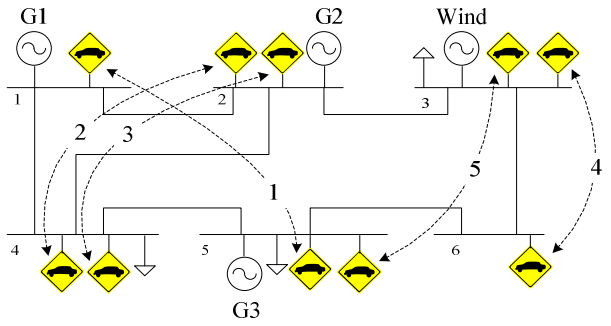


Fig. 2. 6-bus power system

TABLE III
PEV FLEET CHARACTERISTICS

| PEV fleet No. | Min Cap. (MWh) | Max Cap. (MWh) | Min Charge/ Discharge (kW) | Max Charge/ Discharge (MW) | a ($/MW$^2$) | b ($/MW) | c ($/h) |
|---|---|---|---|---|---|---|---|

| | | | | | | | |
|---|---|---|---|---|---|---|---|
| 1 | 13.152 | 65.76 | 7.3/6.2 | 24.8/21.08 | 0.17 | 8.21 | 0 |
| 2 | 10.96 | 54.8 | 7.3/6.2 | 14.58/12.4 | 0.20 | 8.21 | 0 |
| 3 | 5.48 | 27.4 | 7.3/6.2 | 7.29/6.2 | 0.41 | 8.21 | 0 |
| 4 | 8.768 | 43.84 | 7.3/6.2 | 11.67/9.92 | 0.25 | 8.21 | 0 |
| 5 | 10.96 | 54.8 | 7.3/6.2 | 14.58/12.4 | 0.20 | 8.21 | 0 |

TABLE IV
PEV FLEET TRAVEL CHARACTERISTICS

| PEV fleet No. | Number of PEVs | First Trip | | | | Second Trip | | | |
|---|---|---|---|---|---|---|---|---|---|
| | | Departure | | Arrival | | Departure | | Arrival | |
| | | Time | Bus | Time | Bus | Time | Bus | Time | Bus |
| 1 | 3,400 | 6:00 | 5 | 8:00 | 1 | 17:00 | 1 | 19:00 | 5 |
| 2 | 2,000 | 7:00 | 4 | 8:00 | 2 | 16:00 | 2 | 17:00 | 4 |
| 3 | 1,000 | 5:00 | 4 | 7:00 | 2 | 16:00 | 2 | 18:00 | 4 |
| 4 | 1,600 | 5:00 | 6 | 6:00 | 3 | 17:00 | 3 | 18:00 | 6 |
| 5 | 2,000 | 7:00 | 5 | 9:00 | 3 | 18:00 | 3 | 20:00 | 5 |

The PEV fleets have different energy requirements. The annual driving distance by a PEV fleet is 12,000 miles with a 32.88 miles average per day [10], [27]. The energy required by a PEV is 9 kWh/day with an average 3.65 miles/kWh [9]. So, the hourly energy required by the fleets is 7.65, 9.00, 2.25, 7.20 and 4.50 MWh, respectively. We assume the required energy for driving in one direction is the same as that of returning to the starting point. The installed wind capacity is 75 MW, which is about 30% of the system peak load with an hourly average wind generation of 11.7%.

We consider two modes of operation. In the grid-controlled mode, PEV charge/discharge decisions are made by power system operators based on the system operation and driving requirements. In the consumer-controlled scheme, SOCs at certain hours are adjusted to represent consumer charging/ discharging requirements. The following four cases are considered to evaluate the impact of PEVs on the optimal operation of power systems:

Case 1: Deterministic Solution – Grid-Controlled mode

Case 2: Deterministic Solution – Consumer-Controlled mode

Case 3: Stochastic Solution – Grid-Controlled mode

Case 4: Stochastic Solution – Consumer-Controlled mode

### *1) Case 1: Deterministic Solution – Grid-Controlled mode*

The system load, wind generation and driving requirements are the same as forecasts. The operation cost is $115,541.36 and the wind curtailment is 0 MWh. Table V shows the charge/ discharge mode of PEV fleets in which the aggregated V2G enables a cheaper energy delivery at peak hours. In Table V, the first fleet at bus 5 will inject power to the grid at hour 5 when the bus LMP is higher. The fleet will charge PEV at bus 1 rather than bus 5. Likewise, the fifth fleet will not charge/discharge when connected to bus 5 as both the lowest and the highest LMPs occur on bus 3. In Fig. 3 the maximum LMP is 121.6 $/MWh at bus 3. The LMPs at buses 3 and 5 are higher at hours 3, 5 and 16-18. The fourth and fifth fleets in Table V are discharged at hours 16, and 16-17, respectively to take advantage of higher LMPs on bus 3. Table VI shows the hourly commitment of generators in which the third generator is not committed for the first six hours in the morning.

The grid operation cost and wind curtailment will increase to $117,424.15 and 1.2 MWh, respectively, if the aggregated PEVs are stationary (i.e., always connected to the same bus.) These quantities will decrease when PEVs are mobile in the grid. The mobility of PEVs could enhance the optimal generation while satisfying the fleet requirements. However, constraints imposed by consumers on the energy required for driving a vehicle, maximum storage capacity, and SOC could limit the optimal grid operation. For example, the fourth fleet departs bus 6 in the morning with an SOC of 36.4% and returns in the evening with an SOC of 74.8%. This indicates that the energy is transferred from bus 3 to bus 6 via the fourth fleet.

PEVs may reduce the operation cost by storing energy in one bus without transferring the energy elsewhere. The SOC of the fifth fleet when departing and returning to bus 5 is 36.4%, and the power exchange occurs when the PEV is connected to bus 3. Fig. 4 shows the generation dispatch in which the standard deviation of generation dispatch for Generators 1-3 is 16.1, 10.8 and 11.2 MW, respectively.

TABLE V
POWER DISPATCH OF PEVS IN GRID CONTROLLED SCHEME (MW)

| Fleet | Hours (1-12) | | | | | | | | | | | |
|---|---|---|---|---|---|---|---|---|---|---|---|---|
| 1 | 0 | 0 | 0 | 0 | 0.72 | 0 | 0 | -0.01 | 0 | 0 | 0 | -5.9 |
| 2 | -7.0 | 0 | 0 | 0 | 0 | -0.47 | 0 | -12.9 | -7.98 | 0 | 0 | 0 |
| 3 | 0 | 0 | 0 | 0 | 0 | 0 | -7.29 | -3.29 | 0 | 0 | 0 | 0 |
| 4 | 0 | -0.99 | 1.96 | -0.96 | 0 | -11.6 | -11.6 | -10.3 | 0 | 0 | 0 | 5.49 |
| 5 | 0 | 0 | 0 | 0 | 0 | 0 | 0 | 0 | -11.2 | 0 | 0 | 0 |
| Fleet | Hours (13-24) | | | | | | | | | | | |
| 1 | 0 | -15.4 | 0 | -15.4 | 0 | 0 | 0 | 0 | 0 | 0 | 0 | 0 |
| 2 | -12.9 | 0 | 0 | 0 | 12.4 | 7.50 | 0 | 0 | 0 | 0 | -3.25 | 0 |
| 3 | -6.45 | 0 | 0 | 0 | 0 | 5.48 | 0 | 0 | 0 | 0 | 0 | 0 |
| 4 | -11.6 | 0 | -2.39 | 3.86 | 0 | 9.92 | -0.08 | 2.14 | 3.57 | -1.71 | 2.40 | 0 |
| 5 | -14.6 | -11.8 | -10.9 | 10.9 | 12.4 | 0 | 0 | 0 | 0 | 0 | 0 | 0 |

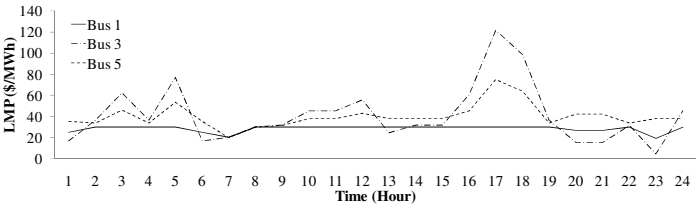


Fig. 3. LMPs in Case 1

TABLE VI
COMMITMENT STATUS IN GRID CONTROLLED SCHEME OF CASE 1

| Unit | Hours (1-24) | | | | | | | | | | | | | | | | | | | | | | | |
|---|---|---|---|---|---|---|---|---|---|---|---|---|---|---|---|---|---|---|---|---|---|---|---|---|
| G1 | 1 | 1 | 1 | 1 | 1 | 1 | 1 | 1 | 1 | 1 | 1 | 1 | 1 | 1 | 1 | 1 | 1 | 1 | 1 | 1 | 1 | 1 | 1 | 1 |
| G2 | 1 | 1 | 1 | 1 | 1 | 1 | 1 | 1 | 1 | 1 | 1 | 1 | 1 | 1 | 1 | 1 | 1 | 1 | 1 | 1 | 1 | 1 | 1 | 1 |
| G3 | 0 | 0 | 0 | 0 | 0 | 0 | 1 | 1 | 1 | 1 | 1 | 1 | 1 | 1 | 1 | 1 | 1 | 1 | 1 | 1 | 1 | 1 | 1 | 1 |

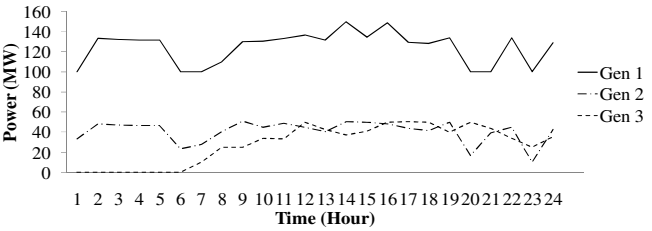


Fig. 4. Hourly dispatch of generators in Case 1

### *2) Case 2: Deterministic Solution – Consumer-Controlled mode*

The grid operation cost increases to $119,084.33 as the consumer-controlled mode imposes further constraints on charge/discharge of PEVs. Table VII shows the dispatch of PEV fleets. The wind curtailment is 0 MWh. Comparing Tables VII and V, it is clear that the required SOC at the departure time will cause the fleet to draw more energy from the grid. Unlike

Case 1, the fifth fleet at bus 5 is charged at hours 1 and 6 to set the desired SOC at the departure time. Table VIII shows the hourly commitment of thermal generators in which G3 is committed at additional hours as compared to Case 1. Table IX shows a higher LMP and congestion at peak hours in the consumer-controlled scheme.

Fig. 5 shows the generation dispatch profile in which the standard deviations of generation dispatch for Generators 1-3 are 14, 10.4 and 20 MW, respectively. So the generation profile of the most expensive generator (Gen. 3) in Case 1 is smoother than that in Case 2. Hence, a flexible PEV control can reduce the volatility when integrating renewable resources into the grid. The generation dispatch volatility could increase the grid operation cost due to turbine wear and tear.

TABLE VII
HOURLY POWER DISPATCH OF PEVS IN CASE 2 (MW)

| Fleet | Hours (1-12) | | | | | | | | | | | |
|---|---|---|---|---|---|---|---|---|---|---|---|---|
| 1 | -8.23 | 0 | 0 | 0 | -9.76 | 0 | 0 | -1.72 | -0.01 | 0 | 0 | 0 |
| 2 | -9.59 | 0 | 0 | 0 | 0 | -12.3 | 0 | 0 | 0 | 0 | 0 | 0 |
| 3 | -5.29 | 0 | 0 | 0 | 0 | 0 | -5.29 | 0 | 0 | 0 | 0 | 0 |
| 4 | 0 | -10.3 | -4.33 | -10.3 | 0 | -8.47 | 0 | 0 | 0 | 1.93 | 0 | 5.49 |
| 5 | -10.6 | 0 | 0 | 0 | 0 | -0.01 | 0 | 0 | 0 | 1.96 | 0 | 0 |
| Fleet | Hours (13-24) | | | | | | | | | | | |
| 1 | 0 | 0 | -0.81 | -15.4 | 0 | 0 | 0 | 0 | 0 | 0 | 0 | 0 |
| 2 | -10.6 | 0 | 0 | 0 | 12.4 | 0 | 0 | 0 | 0 | 0 | -3.25 | 0 |
| 3 | 0 | 0 | 0 | 0 | 0 | 0 | 0 | 0 | 0 | 0 | 0 | 0 |
| 4 | -8.73 | 0 | 0 | 0 | 0 | 6.68 | -2.93 | 2.14 | 5.282 | 0 | 2.403 | 0 |
| 5 | -12.9 | 0 | 0 | 0 | 0 | 0 | 0 | 0 | 0 | 0 | 0 | 0 |

TABLE VIII
HOURLY COMMITMENT IN CONSUMER CONTROLLED SCHEME OF CASE 2

| Unit | Hours (1-24) | | | | | | | | | | | | | | | | | | | | | | | |
|---|---|---|---|---|---|---|---|---|---|---|---|---|---|---|---|---|---|---|---|---|---|---|---|---|
| G1 | 1 | 1 | 1 | 1 | 1 | 1 | 1 | 1 | 1 | 1 | 1 | 1 | 1 | 1 | 1 | 1 | 1 | 1 | 1 | 1 | 1 | 1 | 1 | 1 |
| G2 | 1 | 1 | 1 | 1 | 1 | 1 | 1 | 1 | 1 | 1 | 1 | 1 | 1 | 1 | 1 | 1 | 1 | 1 | 1 | 1 | 1 | 1 | 1 | 1 |
| G3 | 1 | 1 | 1 | 1 | 1 | 1 | 1 | 1 | 1 | 1 | 1 | 1 | 1 | 1 | 1 | 1 | 1 | 1 | 1 | 1 | 1 | 1 | 1 | 1 |

TABLE IX
MAXIMUM LMPS ($/MWH)

| Bus | Case 1 | Case 2 |
|---|---|---|
| 1 | 30.0 | 30.0 |
| 2 | 32.0 | 32.0 |
| 3 | 121.6 | 336.0 |
| 4 | 64.1 | 137.9 |
| 5 | 75.0 | 175.5 |
| 6 | 116.3 | 317.7 |

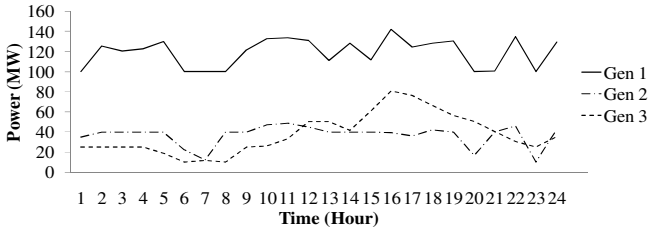


Fig. 5. Hourly dispatch in consumer-controlled scheme in Case 2

### 3) *Case 3: Stochastic Solution – Grid-Controlled mode*

In this case, load and wind forecast errors, generation and transmission outages, and the number of PEVs in a fleet and their energy requirements are considered random. The load forecast error follows a normal distribution with a mean value equal to the forecasted load and standard deviation of 5%. The forecast error of energy consumption for driving and the number of PEVs in a fleet follow a normal distribution with mean values equal to the forecast as shown in Tables III and IV, and the standard deviation of 5% and 20% of the mean values, respectively. The wind generation forecast is procured based on the typical wind power curve and generated wind speed data. The mean daily wind speed is 10 m/s, which follows a Weibull distribution function with Weibull coefficient equal to 2.1.

The deterministic solution applied to the proposed stochastic model would result in the operation cost and the expected demand mismatch penalty of $129,184.989 and $25,146, respectively. While in the stochastic solution, the operation cost and demand mismatch penalty are $128,174.713 and $20,913, respectively. Hence, the stochastic solution would lower the operating cost by $5,243.276 (i.e., 129,184.989+25,146-128,174.713-20,913), which is the value of stochastic programming.

In Table X, a case with higher transmission line capacities is considered to avoid any demand mismatch due to transmission congestions. In this case, the grid operation cost in the base case is $113,454.555 and the availability cost of the system is $1,789.359, while the wind curtailment in the base case and the expected wind curtailment in scenarios are 117.32 MWh and 40.762 MWh, respectively. Table XI shows the hourly commitment of thermal units in which the third unit is not committed for 7 hours.

TABLE X
TRANSMISSION LINE CHARACTERISTICS

| Line ID | From Bus | To Bus | Capacity(MW) | FOR |
|---|---|---|---|---|
| 1 | 1 | 2 | 97 | 1% |
| 2 | 1 | 4 | 100 | 1% |
| 3 | 2 | 4 | 113 | 1% |
| 4 | 5 | 6 | 81 | 1% |
| 5 | 3 | 6 | 121 | 1% |
| 6 | 2 | 3 | 111 | 1% |
| 7 | 4 | 5 | 103 | 1% |

TABLE XI
HOURLY COMMITMENT IN CASE 3

| Unit | Hours (1-24) | | | | | | | | | | | | | | | | | | | | | | | |
|---|---|---|---|---|---|---|---|---|---|---|---|---|---|---|---|---|---|---|---|---|---|---|---|---|
| G1 | 1 | 1 | 1 | 1 | 1 | 1 | 1 | 1 | 1 | 1 | 1 | 1 | 1 | 1 | 1 | 1 | 1 | 1 | 1 | 1 | 1 | 1 | 1 | 1 |
| G2 | 1 | 1 | 1 | 1 | 1 | 1 | 1 | 1 | 1 | 1 | 1 | 1 | 1 | 1 | 1 | 1 | 1 | 1 | 1 | 1 | 1 | 1 | 1 | 1 |
| G3 | 0 | 0 | 0 | 0 | 0 | 0 | 0 | 0 | 0 | 0 | 1 | 1 | 1 | 1 | 1 | 1 | 1 | 1 | 1 | 1 | 1 | 1 | 1 | 1 |

### 4) *Case 4: Stochastic Solution – Consumer-Controlled mode*

Like Case 2, the consumers set the SOC of PEVs prior to departure. In this case, the base case operation cost and availability cost are $114,498.69 and $2,108 while the wind curtailment in the base case and the expected wind curtailment in scenarios are 121.097 MWh and 40.816 MWh, respectively. Here, the base case operation cost, availability cost and wind curtailment are increased as compared to those in Case 3. Table XII shows the hourly commitment of generators that are different from those in Case 3. The hourly commitment of G3 is increased by two hours in this case.

TABLE XII
HOURLY COMMITMENT IN CASE 4

| Unit | Hours (1-24) | | | | | | | | | | | | | | | | | | | | | | | |
|---|---|---|---|---|---|---|---|---|---|---|---|---|---|---|---|---|---|---|---|---|---|---|---|---|
| G1 | 1 | 1 | 1 | 1 | 1 | 1 | 1 | 1 | 1 | 1 | 1 | 1 | 1 | 1 | 1 | 1 | 1 | 1 | 1 | 1 | 1 | 1 | 1 | 1 |
| G2 | 1 | 1 | 1 | 1 | 1 | 1 | 1 | 1 | 1 | 1 | 1 | 1 | 1 | 1 | 1 | 1 | 1 | 1 | 1 | 1 | 1 | 1 | 1 | 1 |
| G3 | 0 | 0 | 0 | 0 | 0 | 1 | 0 | 0 | 0 | 1 | 1 | 1 | 1 | 1 | 1 | 1 | 1 | 1 | 1 | 1 | 1 | 1 | 1 | 1 |

## B. *118-Bus Power System*

In this case, the modified IEEE 118-bus system shown in http://motor.ece.iit.edu/EV/118.emf is considered. Five 150

MW wind generation sites are considered on buses 12, 31, 66, 72 and 100, respectively. Table XIII shows the intermittent wind speed information. A total of 100,000 PEVs are divided into 5 fleets based on their driving patterns. The PEVs in fleets are 34,000, 20,000, 10,000, 16,000 and 20,000, respectively. Table XIV shows the fleet characteristics. The fleet travel schedules are similar to those in the previous case study. The same four cases discussed in the 6-bus system are considered.

Table XV shows the optimal base case cost and wind curtailment in each case. Table XVI shows the expected wind curtailment and the availability cost in Cases 3 and 4. In the grid-controlled scheme, the expected wind curtailment and availability cost are lower. Table XVII shows the operation cost. Comparing Cases 3 and 4, the operation costs are higher in the consumer-controlled scheme because of introducing additional constraints. The results are consistent with that in the previous case study. The CPU in this case is about 58 h on a 3.6 GHz personal computer with CPLEX 12.1. Parallel processing of a larger server with multiple CPUs or several large servers could reduce the computation time. In addition, practical considerations for the implementation of PEV in a specific power system could introduce additional short cuts for reducing the computation time. The grid operation cost will decrease with larger size PEV storage. However, the primary goal of PEV fleets is transportation rather than the provision of ancillary services in power grids.

TABLE XIII
WIND SPEED PROFILE AT SITES

| | site 1 | site 2 | site 3 | site 4 | site 5 |
|---|---|---|---|---|---|
| Weibull Coefficient | 1.17 | 2.03 | 2.19 | 2.9 | 2.26 |
| Auto Correlation Factor | 0.761 | 0.943 | 0.957 | 0.88 | 0.928 |
| Diurnal Wind Pattern | 0.11 | 0.0944 | 0.0969 | 0.0196 | 0.0668 |
| Hour of Peak Wind Speed | 24 | 14 | 13 | 20 | 22 |

TABLE XIV
PEV FLEET CHARACTERISTICS

| PEV Fleet | Min Energy (MWh) | Max Energy (MWh) | Charge/Discharge Min (kW) | Charge/Discharge Max (MW) | a ($/MW$^2$) | B ($/MW) | c ($/h) |
|---|---|---|---|---|---|---|---|
| 1 | 131.52 | 986.4 | 7.3/6.2 | 248/210.8 | 0.57 | 27.35 | 0 |
| 2 | 109.6 | 822 | 7.3/6.2 | 145.8/124 | 0.68 | 27.35 | 0 |
| 3 | 54.8 | 411 | 7.3/6.2 | 72.9/62 | 1.36 | 27.35 | 0 |
| 4 | 87.68 | 657.6 | 7.3/6.2 | 116.7/99.2 | 0.85 | 27.35 | 0 |
| 5 | 109.6 | 822 | 7.3/6.2 | 145.8/124 | 0.68 | 27.35 | 0 |

TABLE XV
RESULTS FOR FOUR CASES (BASE CASE)

| Case | Cost ($) | Wind Curtailment (MWh) |
|---|---|---|
| 1 | 1,323,982 | 305.456 |
| 2 | 1,327,672 | 348.572 |
| 3 | 1,352,637 | 178.216 |
| 4 | 1,357,843 | 169.145 |

TABLE XVI
EXPECTED SCENARIO RESULTS FOR CASES 3 AND 4

| Case | Avail. Cost ($) | Exp. Wind Curtail (MWh) |
|---|---|---|
| 3 | 12,649.754 | 328.57 |
| 4 | 14,289.818 | 367.28 |

TABLE XVII
SCENARIO COSTS IN CASES 3 AND 4 ($)

| Scenario | Case 3 | Case 4 |
|---|---|---|
| 1 | 1,371,254 | 1,378,357 |
| 2 | 1,457,163 | 1,466,943 |
| 3 | 1,408,596 | 1,414,523 |
| 4 | 1,369,053 | 1,374,058 |
| 5 | 1,413,558 | 1,414,729 |
| 6 | 1,423,133 | 1,427,015 |
| 7 | 1,428,505 | 1,429,073 |
| 8 | 1,374,482 | 1,378,838 |
| 9 | 1,411,435 | 1,415,783 |
| 10 | 1,444,603 | 1,444,894 |
| 11 | 1,397,722 | 1,401,078 |
| 12 | 1,408,407 | 1,419,582 |

Fig. 6 shows the relationship between the PEV storage capacity, the charging/discharging cost, and the grid operation cost. The battery capacity factor shows the size of the battery as a percentage of a nominal battery capacity. The operation cost factor (OCF) shows the charging/discharging cost as a percentage of nominal cost for battery operation. In Fig 6, grid operation cost decreases as OCF is reduced. Also, the grid operation cost decreases as PEV battery capacity factor increases. Unlike the grid-controlled scheme, the increase in PEV storage capacity may not reduce the grid operation cost in the consumer-controlled scheme. The SOC constraints may restrict the V2G reduction of the grid operation cost. Fig. 6 shows that the increase in PEV charging/ discharging costs will restrict the PEV storage participation to the operation cost reduction. The PEV contribution to the operation cost reduction may not be significant in an unconstrained (no transmission congestion) power system and system operators may consider dispatching more expensive units rather than using PEV fleets as storage.

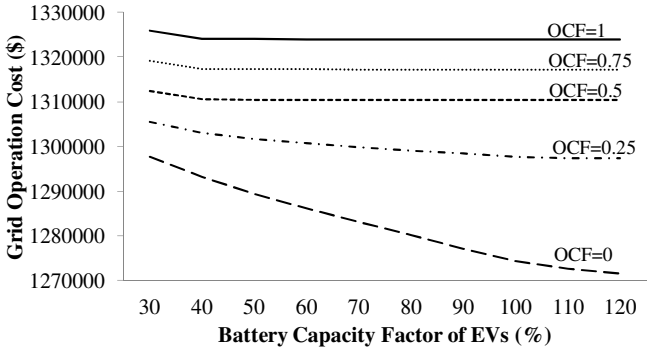


Fig. 6. Grid operation cost in a grid-controlled scheme

## IV. DISCUSSIONS

The integration of PEVs will introduce distributed and mobile demands and storage in power systems. The mobility of PEV fleets will impose additional operation constraints and introduce benefits for supplying critical power system loads in specific locations and periods. The variability of renewable generation resources may also be managed properly by charging/discharging capability of mobile PEV fleets.

Once PEVs are connected to the grid, they can draw energy, store it in batteries, and inject it back to the grid at other times and locations in order to decrease grid operation costs. Once in the V2G mode, PEVs can transfer energy between locations and contribute to the provision of ancillary services and congestion mitigation in transmission systems. Hence, V2G can help ISOs lower grid operation costs by taking advantage of the fact that the stored energy in PEVs can be transmitted between locations without obeying power flow rules.

However, PEV utilization in power systems could introduce additional obstacles and limitations. One issue is that the cost of storing and delivering energy by PEV for reducing power system operation costs may not be much cheaper than that of energy supplied by the grid. The higher charging/discharging cycles may reduce the battery life and impose further

limitations on PEV operations as a vehicle. Moreover, PEV storage requirements as a vehicle could impose further restrictions on the grid utilization of PEV storage. Another challenge is the availability of PEV at certain hours and locations as storage when PEV is mobile. The driving patterns and the number of vehicles in each fleet can alter the characteristics of ancillary services provided by PEV fleets. However, the transmission congestion cost over an extended period could far exceed the PEV storage cost.

## V. CONCLUSIONS

In this paper, the impact of integrating PEV fleets into power systems is evaluated. The proposed stochastic model incorporates the modeling of PEV fleets according to the power system and PEV fleet constraints and requirements. The contributions of the paper include:

- The PEV fleet modeling in power systems is considered using the MIP formulation.
- The detailed power transmission system modeling and transmission constraints are included in the model.
- The integration of high penetration of renewable generation resources in power systems is considered.
- The uncertainties imposed by PEV fleets, renewable energy resources, and transmission and generation components are included.
- The operation schemes of PEV fleets and their impacts on power system operations are considered.
- The impact of PEV on thermal generation profile in power systems is evaluated.

It is shown that the PEV mobility can efficiently transfer energy throughout the network. PEVs can also help reduce the grid operation cost by providing energy storage for renewable energy resources. The PEV charging/discharging costs, limited storage capacity, required energy for driving PEV, and the SOC constraints imposed by consumers will further restrict the reduction in grid operation costs. When consumers set the SOC of PEVs, the grid operation costs will increase and PEV capabilities for transferring energy between locations will be limited.

## REFERENCES


[1] Reducing Greenhouse Gas Emissions from U.S. Transportation available online: www.pewclimate.org/docUploads/ustransp.pdf.

[2] H. Lund and W. Kempton, "Integration of renewable energy into the transport and electricity sectors through V2G," *Energy Policy*, vol. 36, no. 9, pp. 3578-3587, Sep. 2008.

[3] *Global Wind 2008 Report, GWEC, Global Wind Energy Council,* http://www.gwec.net/fileadmin/documents/Global%20Wind%202008%20Report.pdf.

[4] B.C. Ummels, E. Pelgrum, and W.L. Kling, "Integration of large-scale wind power and use of energy storage in the Netherlands' electricity supply," *IET Renewable Power Generation,* vol. 2, no. 1, pp. 34-46, Mar. 2008.

[5] M. Lu, C. Chang, W. Lee, and L. Wang, "Combining the wind power generation system with energy storage equipment," *IEEE Trans. On Industry Applications,* vol. 45, no. 6, pp. 2109-2115, Nov. 2009.

[6] Y. Lee, A. Khaligh, and A. Emadi, "Advanced integrated bi-directional AC/DC and DC/DC converter for plug-in hybrid electric vehicles," *IEEE Trans. on Vehicular Technology,* vol. 58, no. 8, pp. 3970-3980, Oct. 2009.

[7] S.S. Raghavan, O.C. Onar, and A. Khaligh, "Power electronic interfaces for future plug-in transportation systems," *IEEE Power Electronics Society Newsletter*, vol. 24, no. 3, pp. 23-26, Jul. 2010.

[8] S.M. Lukic, J. Cao, R.C. Bansal, R. Rodriguez, and A. Emadi, "Energy storage systems for automotive applications," *IEEE Trans. Ind. Electron.,* vol. 55, no. 6, pp. 2258-2267, Jun. 2008.

[9] J. Tomić and W. Kempton, "Using fleets of electric-drive vehicles for grid support," *Journal of Power Sources,* vol. 168, no. 2, pp. 459-468, Jun. 2007.

[10] A. Saber and G. Venayagamoorthy, "Plug-in vehicles and renewable energy sources for cost and emission reduction," *IEEE Trans. Ind. Electron.*, to be published.

[11] W. Kempton and J. Tomić, "Vehicle to gird power implementation: from stabilizing the grid to supporting large-scale renewable energy," *Journal of Power Sources*, vol. 144, no. 1, pp. 280-294, Apr. 2005.

[12] W. Kempton and J. Tomić, "Vehicle-to-grid power fundamentals: calculating capacity and net revenue," *Journal of Power Sources,* vol. 144, no. 1, pp. 268-279, Jun. 2005.

[13] M. Korpas, R. Hildrum, and A.T. Holen, "Operation and sizing of energy storage for wind power plants in a market system," in *Proc. 14th PSCC*, Sevilla, Spain, Jun. 2002.

[14] E.D. Castronuovo and J.A.P. Lopes, "Wind and small-hydro generation. an optimization approach for daily integrated operation," in *Proc. 2003 EWEA*, Madrid, Spain, Jun. 2003.

[15] E.D. Castronuovo and J.A.P. Lopes, "On the optimization of the daily operation of a wind-hydro power plant," *IEEE Trans. On Power Systems*, vol. 19, no. 3, pp. 1599-1606, Aug. 2004.

[16] E.D. Castronuovo and J.A.P. Lopes, "Bounding active power generation of a wind-hydro power plant," in *Proc. 2004 International Conference on Probabilistic Methods Applied to Power Systems,* pp. 705-710, Sep. 2004.

[17] R. Billinton and R. Allan, *Reliability Evaluation of Power Systems*, Second Edition, London: Plenum Publishing Corporation, New York 1996.

[18] W.H. Greene, *Econometric Analysis*, 5th Edition, Prentice Hall, 2003.

[19] J.F. Manwell, J.G. McGowan, and A.L. Rogers, *Wind Energy Explained,* Wiley, New York, 2002.

[20] J. Dupačová, N. Gröwe-Kuska, and W. Römisch, "Scenario reduction in stochastic programming: An approach using probability metrics," *Math. Program.*, ser. A 95, pp. 493-511, 2003.

[21] GAMS/SCENRED Documentation. [Online]. Available: http://www.gams.com/docs/document.htm.

[22] D. Gan and E. Litvinov, "Energy and reserve market design with explicit consideration to lost opportunity costs," *IEEE Trans. On Power Systems,* vol. 18, no. 1, Feb. 2003.

[23] L. Wu, M. Shahidehpour, and T. Li, "Stochastic security-constrained unit commitment," *IEEE Trans. On Power Systems*, vol. 22, no. 2, pp. 800-811, May 2007.

[24] T. Li and M. Shahidehpour, "Price-based unit commitment: a case of Lagrangian relaxation versus mixed integer programming," *IEEE Trans. On Power Systems,* vol. 20, no. 4, pp. 2015-2025, Nov. 2005.

[25] L. Wu, "A Tighter Piecewise Linear Approximation of Quadratic Cost Curves for Unit Commitment Problems," *IEEE Trans. on Power Systems*, Vol. 26, No. 4, pp. 2581-2583, 2011.

[26] X. Guan, Q. Zhai and A. Papalexopoulos, "Optimization based methods for unit commitment: Lagrangian relaxation versus general mixed integer programming," *IEEE Power Engineering Society Meeting,* vol. 2, Jul. 2003.

[27] C. Roe, A.P. Meliopoulos, J. Meisel, and T. Overbye, "Power system level impacts of plug-in hybrid electric vehicles using simulation data," *IEEE Energy 2030,* Atlanta, GA USA, 17-18 Nov. 2008.


## BIOGRAPHIES

**Mohammad E. Khodayar** (S'09) received his BS and MS degree in Electrical Engineering from Amirkabir University of Technology (Tehran Polytechnic) and Sharif University of Technology respectively. Presently he is PhD student in Electrical Engineering at Illinois Institute of Technology, USA.

**Lei Wu** (M'07) received his BS in Electrical Engineering and MS in Systems Engineering from Xi'an Jiaotong University, China, in 2001 and 2004, respectively, and Ph.D. in EE from Illinois Institute of Technology, USA, in 2008. Presently, he is an Assistant Professor in the ECE Department at Clarkson University. His research interests include power systems restructuring and reliability.

**Mohammad Shahidehpour** (F'01) is the Bodine Professor and Director of the Robert W. Galvin Center for Electricity Innovation at Illinois Institute of Technology. He is an Honorary Professor in the King Abdulaziz University in Saudi Arabia, North China Electric Power University, and Sharif University of Technology in Iran.

# Hybrid AC/DC Transmission Expansion Planning

Azim Lotfjou, *Member, IEEE,* Yong Fu, *Member, IEEE,* and Mohammad Shahidehpour, *Fellow, IEEE*

***Abstract*—This paper proposes a hybrid algorithm for the AC/DC transmission expansion planning (TEP). The stochastic simulation method would consider random outages of generating units and AC/DC transmission lines as well as load forecast errors. The mixed-integer linear programming problem is decomposed into a master planning problem with integer investment decision variables and subproblems which examine the feasibility of master planning solution and calculate the optimal operation schedule over the planning horizon. The independent system operator (ISO) would utilize the proposed method to select the optimal set of AC/DC transmission lines for satisfying TEP criteria: supplying load forecasts, minimizing investment costs, and optimizing market operations. The proposed set of DC transmission system may use either current source converters (CSCs) or voltages source converters (VSCs). Numerical examples illustrate the effectiveness of the proposed TEP model.**

*Index Terms*—**DC transmission lines, transmission expansion planning, reliability, optimal system operation**

## NOMENCLATURE

### Indices:

| | |
|---|---|
| $b$ | Index for bus |
| $e$ | Index for subperiod |
| $h$ | Index for DC converter |
| $i$ | Index for unit |
| $j$ | Index for AC lines |
| $k$ | Index for DC transmission system |
| $l$ | Index for a DC line |
| $m$ , $n$ | Starting and ending buses of AC lines |
| $s$ | Index of scenario |
| $t$ | Index for year |

### Parameters:

| | |
|---|---|
| $Bid_{tei}$ | Bid price of unit $i$ at subperiod $e$ in year $t$ |
| $CJ$ | Number of AC candidate lines |
| $CK$ | Number of DC candidate transmission systems |
| $d$ | Discount rate |
| $D_{ste}$ | Load block at subperiod $e$ in year $t$ for scenario $s$ |
| $DT_{te}$ | Number of hours at subperiod $e$ in year $t$ |
| $EJ$ | Number of existing AC lines |
| $EK$ | Number of existing DC transmission systems |
| $IC_j^C$ | Investment cost of the candidate AC line $j$ |
| $IC_{dc,k}^C$ | Investment cost of the candidate DC transmission system $k$ |
| $LOEP$ | Loss of energy probability |
| $LSC_{teb}$ | Load shedding price of load $b$ at subperiod $e$ in year $t$ |
| $M$ | A large positive constant value (e.g. 10e+8) |
| $NB$ | Number of buses |
| $NE$ | Number of subperiods |
| $NI$ | Number of units |
| $NS$ | Number of scenarios |
| $NT$ | Number of planning years |
| $x_j$ | Reactance of AC line j |
| $P_{dc,h}^{Min}$ , $P_{dc,h}^{Max}$ | Minimum and maximum active power transfer of converter $h$ |
| $P_i^{Min}$ , $P_i^{Max}$ | Minimum and maximum generation output of generating unit $i$ |
| $PL_j^{Max}$ | Maximum power flow limit of AC line $j$ |
| $\Pr_s$ | Probability of scenario $s$ |
| **A** | AC bus-unit incidence matrix |
| **B** | AC bus-load incidence matrix |
| **C** | AC bus-converter incidence matrix |
| **K** | AC bus-AC line incidence matrix |

### Variables:

| | |
|---|---|
| $LS_{steb}$ | Load shedding of bus $b$ at subperiod $e$ in year $t$ for scenario $s$ |
| $P_{dc,h}$ | Active power withdrawal of converter $h$ |
| $P_{stei}$ | Generation dispatch of the unit $i$ at subperiod $e$ in year $t$ for scenario $s$ |
| $PL_j$ | Active power flow of AC line $j$ |
| $PL_{dc,l}$ | Active power flow of DC line $l$ |
| $WF$ , $WO$ | Objective function for reliability check and optimal operation subproblems |
| $Y_{jt}$ | Installation status of the candidate AC line $j$ in year $t$ (1 if installed, otherwise 0) |

Azim Lotfjou is with Genscape Inc. in Boston, MA. Mohammad Shahidehpour is with the Robert W. Galvin Center at Illinois Institute of Technology. Yong Fu is with the Department of Electrical and Computer Engineering, Mississippi State University, MS 39759 USA. This study was funded in part by the U.S. Department of Energy Grants # DE-EE 0002979 and DE-EE 0001380.000.

| | |
|---|---|
| $Y_{dc,kt}$ | Installation status for the candidate DC system $k$ in year $t$ (1 if installed, otherwise 0) |
| $Z_{lower}$ | Lower bound for TEP objective function |
| $Z^{upper}$ | Upper bound for TEP objective function |
| $\theta$ | AC voltage angle |
| $\eta$ , $\pi$ | Dual variables of equality constraints |
| **D** | Vector of bus loads |
| **LS** | Vector of curtailed loads |
| **P** | Active power output vector of generating units |
| $\mathbf{P}_{dc}$ | Active power flow vector of DC converters |
| **PL** | Active power flow vector of AC lines |

**Others:**

| | |
|---|---|
| ^ | Given variables |
| $C$ | Candidate AC/DC line |
| $E$ | Existing AC/DC line |

## I. Introduction

HIGH voltage direct current (HVDC) transmission technology has salient characteristics in comparison with AC transmission, such as the bulk power delivery through underground or under marine cables, low power losses for long distance transmissions, asynchronous connection of AC systems, and stabilization of AC systems in contingencies [1]-[2]. DC transmission is utilized for its power flow controllability which can enhance economic operations, mitigate grid congestion, and prevent cascading outages. DC transmission system is the favorable option for delivering renewable energy from remote sites (e.g., off-shore wind) to load center. Such features have accelerated the deployment of DC transmission in restructured electric power systems.

In contrast to generation expansion planning (GEP) that is mainly driven by market forces, TEP is still regulated and managed by independent system operators (ISOs) in electricity markets. Transmission companies (TRANSCOs) recover their investment from transmission tariffs set by ISOs.

Although there are numerous publications on the optimal expansion planning of AC transmission systems in electricity markets [3]-[16], few studies have investigated the expansion planning of AC/DC transmission systems. References [17] and [18] emphasized that DC transmission systems represent an inevitable TEP alternative in competitive electricity markets. Reference [19] presented two-terminal and multi-terminal DC transmission system (MTDC) planning. MTDC configurations have higher installation costs for providing sophisticated control schemes. These complex control systems will guarantee a reliable operation of DC transmission systems over possible ranges of AC system operations. In order to effectively integrate DC transmission with AC power systems, a comprehensive TEP model would need to be developed for quantifying the benefits of such expansion projects.

In this paper, we focus on the reliability and the economic assessment of TEP. In order to justify the motivation for AC/DC TEP, a simple case study is considered to examine the economic benefits of controllable DC transmission, which is an important factor in the AC/DC TEP projects. Fig. 1 illustrates a three-bus system with three generating units and two existing AC transmission lines. An additional 300-km AC/DC transmission line extended between buses 2 and 3 will be needed to supply the load of 1,350 MW at bus 3. As such the length of DC line is less than the "break-even distance of 600-800 km" [1] and it would be logical to choose an AC line with the investment cost of $190 M instead of a DC line with the investment cost of $320 M. However, Table I shows that if we select the AC line extending from bus 2 to bus 3, cheap generating unit 1 will only be dispatched at 960.69 MW which is less than its capacity of 1200 MW, due to the 600 MW limit on line 1-3. The expensive unit 3 is turned on alternatively to supply the 118.64 MW of load. However, if we select the controllable DC line between buses 2-3, the cheap generating unit 1 will be dispatched at its capacity which will allow more power transfer through the DC line. It is no longer necessary to turn on the expensive generating unit 3 and the total operating cost will be reduced from the $24,915 (AC option) to $20,844 (DC option).

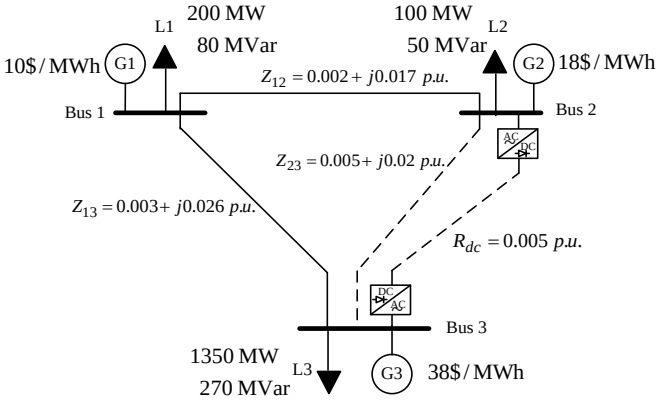


Fig. 1. Three-bus system

TABLE I OPERATION WITH AC LINE 2-3 AND DC LINE 2-3 OPTIONS

| Items | Capacity | With AC Line 2-3 | With DC Line 2-3 |
|---|---|---|---|
| G1 | 300 – 1200 MW | 960.69 MW | 1184.41 MW |
| G2 | 100 – 600 MW | 600 MW | 500 MW |
| G3 | 100 – 300 MW | 118.64 MW | 0 MW |
| Line 1-2 | 500 MW | 160.69 MW | 384.23 MW |
| Line 1-3 | 600 MW | 600 MW | 600 MW |
| Line 2-3 | 900 MW | 660.26 MW | 781.56 MW |
| System Operating Cost ($) | | $24,915 | $20,844 |

For simplicity, we assume that the total load of 1650 MW is averaged hourly throughout the entire year. So, the total annual saving due to the DC transmission selection is about $35.66 M ((24,915 - 20,844) × 8760), which means that the DC operation will pay off the difference (i.e., $320M - $190 M= $130M) in 4 years (4× $35.66M = $142.64M > $130M). Therefore, it would be logical based on economics to select the DC transmission over an AC alternative.

This paper discusses a stochastic TEP approach to AC/DC transmission investment while considering transmission reliability constraints. The proposed model would investigate

the most economical AC/DC TEP by considering the investment cost of transmission facilities, system operation and load shedding costs, and physical system constraints. It is assumed that the information on GEP and the hourly load forecast is available. Random component outages and load forecast errors are taken into account in the stochastic simulation for the AC/DC TEP. The proposed TEP uses the decomposition optimization approach in which binding constraints are incorporated in the ISO's reliability check and optimal market operation subproblems.

The rest of this paper is organized as follows. Section II models the DC transmission system for a dc power flow analysis. Proposed ISO's TEP and formulations are thoroughly discussed in section III. Numerical examples are given in section IV. We summarize our conclusions in section V.

## II. Modeling of DC Transmission System

In general, a DC transmission system consists of two or more converters (rectifiers and inverters), and one or more DC lines that link the converters [20-21]. Different converter technologies such as CSCs and VSCs are utilized in DC transmission systems. Possible DC transmission system converter configurations include monopolar, bi-pole and tri-pole. However, based on the number of converter stations, the HVDC systems can be classified into back-to-back, two-terminal and multi-terminal connections. In this study, we focus on the monopolar two-terminal and multi-terminal DC configuration for TEP. The proposed mathematical model may be easily expanded to any other DC configurations or operating modes.

The DC transmission system shown in Fig. 2 has two converters linked through a DC transmission. To simplify the model of DC link, we assume the total DC terminal withdrawals is zero which means power losses in DC terminals and lines are neglected. Consequently, considering converters 1 and 2 and DC line *l* in Fig. 2,

$$P_{dc,1} + P_{dc,2} = 0 \tag{1}$$

For each converter 1 or 2,

$$\begin{cases} P_{dc,h}^{Min} \le P_{dc,h} \le P_{dc,h}^{Max} & \text{Rectifier} \\ -P_{dc,h}^{Max} \le P_{dc,h} \le -P_{dc,h}^{Min} & \text{Inverter} \end{cases} \tag{2}$$

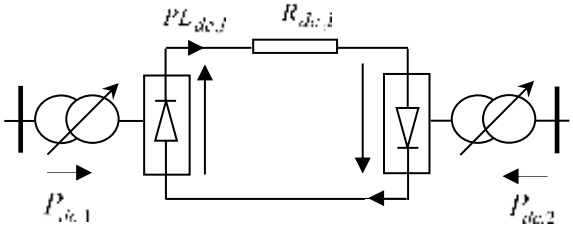


Fig. 2. A monopolar two-terminal DC transmission system

Here, $P_{dc,h} > 0$ indicates a rectifier operation. For the two-terminal DC system, the DC line loading is equal to the inverter power. Applying this model to CSC-DC systems, the dc current is unidirectional and the flow direction is changed by reversing the polarity of DC voltage. However, in VSC-DC systems, the dc voltage is unidirectional and the flow direction is changed by reversing the dc current. For CSC-DC systems, the operation at zero power requires a special design which produces high valve losses and harmonic currents. However, in VSC-DC systems, the operation at zero power produces low losses which makes VSC a more favorable option for DC connections up to 200 MW. For a MTDC system with DC lines $l$ and converters $h$ shown in Fig. 3,

$$\sum_{h} P_{dc,h} = 0 \tag{3}$$

The set of (2)-(3) would model the DC transmission systems in dc power flow analyses and later will be used in the network reliability check subproblem.

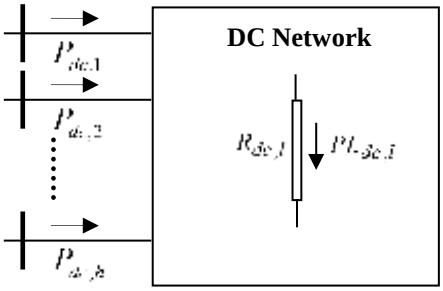


Fig. 3. A multi-terminal DC transmission system

## III. AC/DC Transmission Planning Methodology

Fig. 4 shows the proposed ISO's optimal AC/DC TEP algorithm. At first, TRANSCOs submit AC/DC transmission expansion proposals to the ISO. The ISO executes the proposed TEP algorithm to find the least cost investment plans over the TEP time horizon. Every planning year is divided into multiple subperiods. In Fig. 4, Benders reliability cuts will be generated in the case of reliability violations in any subperiods, which are passed along to the master planning problem to change the previous TEP decisions. Once all existing violations are removed, the optimal market operation will be executed to find an upper bound for the TEP problem.

In the optimal operation subproblem, the ISO executes the security-constrained economic dispatch (SCED) with DC lines modeled as constant injections at sending and receiving terminals. If the ISO's TEP stopping criteria cannot be satisfied based on the optimal operation results, Benders optimality cuts will be introduced to change the master planning decisions. This iterative process will continue until a feasible and optimal TEP schedule is obtained. If the ISO's TEP problem cannot converge after several iterations, there would be no feasible TEP schedules based on the given AC/DC transmission candidates. At this time, the ISO may request the participants to revise the candidate list, stop the TEP process, or make other decisions based on market expansion policies. The ISO may also apply load shedding to find a feasible solution based on the loss of energy probability (LOEP) requirement.

In this paper, the scenario analysis for the strategic TEP is implemented using the stochastic simulation method. This simulation is used to examine the AC/DC TEP performance based on random component outages and load forecast errors. The formulations of individual problems/subproblems are discussed as follows.

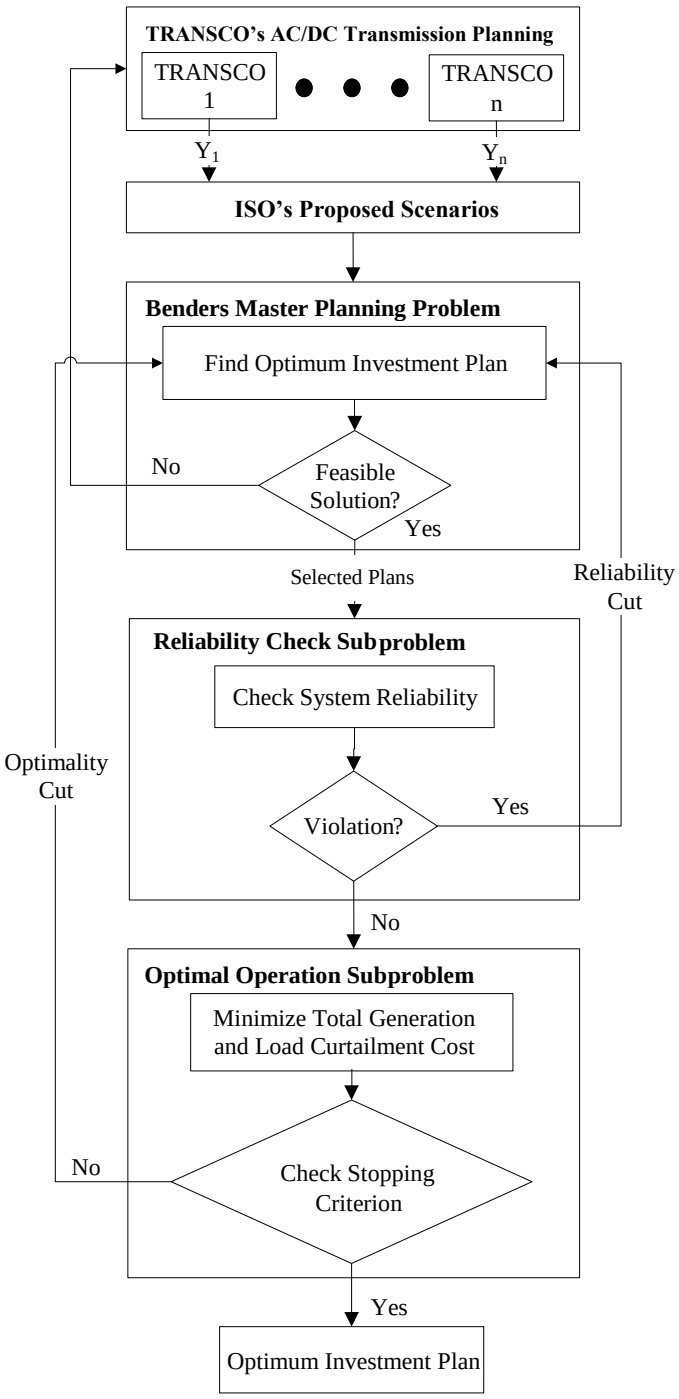


Fig. 4. Flowchart of the proposed hybrid AC/DC TEP model

### A. Objective of the ISO in TEP Problem

The ISO's objective in the proposed TEP problem is to minimize the total investment, operation and load shedding costs for the AC/DC transmission systems. The objective function is given in (4) in which all costs are considered as net present values. The first term in (4) expresses the total investment cost for AC/DC TEP proposals. The second term in (4) is the total expected operation cost which is the sum of generation dispatch multiplied by bidding prices for all units. The third term in (4) is the total expected load curtailment cost over the planning time horizon. The approximate maintenance cost over the project life span may be added to (4). The investment and maintenance costs of DC transmission systems depend on the level of reliability requirements [22].

$$\begin{aligned} Min\ Z^{upper} = & \sum_{t}^{NT}\left(\frac{\sum_{j}^{CJ} IC_{j}^{C} * Y_{jt} + \sum_{k}^{CK} IC_{dc,k}^{C} * Y_{dc,kt}}{(1+d)^{(t-1)}}\right) \\ & + \sum_{s}^{NS}\sum_{t}^{NT}\sum_{e}^{NE}\sum_{i}^{NI}\left(\Pr_{s}\frac{DT_{te} * P_{stei} * Bid_{tei}}{(1+d)^{(t-1)}}\right) \\ & + \sum_{s}^{NS}\sum_{t}^{NT}\sum_{e}^{NE}\sum_{b}^{NB}\left(\Pr_{s}\frac{DT_{te} * LS_{steb} * LSC_{teb}}{(1+d)^{(t-1)}}\right) \end{aligned} \quad (4)$$

### B. Formulation of Transmission Planning Master Problem

The Benders master planning problem in Fig. 4 is formulated as,

$$Min \quad Z_{lower} \quad (5)$$

$$s.t. \quad Z_{lower} \geq \sum_{t}^{NT}\left(\frac{\sum_{j}^{CJ} IC_{j}^{C} * Y_{jt} + \sum_{k}^{CK} IC_{dc,k}^{C} * Y_{dc,kt}}{(1+d)^{(t-1)}}\right) \quad (6)$$

$$Y_{jt} \leq Y_{j(t+1)} \qquad \forall j, \forall t \quad (7)$$

$$Y_{dc,kt} \leq Y_{dc,k(t+1)} \qquad \forall k, \forall t \quad (8)$$

The investment cost of AC transmission lines depends on the voltage level, length of the line, line flow capacity, and financial issues such as discount rates. The investment cost of DC transmission systems depends on DC system configuration, number of terminals, rating of each terminal, and converter type (CSC or VSC). Once the ISO obtains the initial transmission planning schedule, the network reliability check subproblem will be used to mitigate AC/DC transmission reliability violations. The network reliability check is formulated next. Once a feasible master planning problem is obtained, the network reliability is examined in the next section.

### C. Formulation of Reliability Check Subproblem

In this subproblem, the ISO minimizes the load curtailment at load buses by adjusting generation outputs and DC converter flows. The ISO's reliability check subproblem for the $s^{th}$ scenario at subperiod $e$ in year $t$ is formulated in (9)-(21). The ISO checks the network reliability for all scenarios in different years and subperiods. The equations (10) and (11) represent the transmission planning schedules given by the planning master problem. The set of (12)-(21) represents real power balance at AC buses, each DC system equality constraints, real power flows through existing and candidate AC lines, flow limit of existing and candidate AC lines, flow limit of existing and candidate DC converters, generation limit of each generating unit, and the reference bus angle, respectively.

$$Min \quad WF_{ste} = \mathbf{1}^{\mathbf{T}} \cdot \mathbf{LS} \tag{9}$$

*s.t.*

$$Y_{stej} = \hat{Y}_{jt} \qquad \eta_{stej} \qquad \forall\ j \tag{10}$$

$$Y_{dc,stek} = \hat{Y}_{dc,kt} \qquad \eta_{stek} \qquad \forall\ k \tag{11}$$

$$\mathbf{K} \cdot \mathbf{PL}_{s} + \mathbf{C} \cdot \mathbf{P}_{\mathbf{dc},s} + \mathbf{S}_{\mathbf{1},s} - \mathbf{S}_{\mathbf{2},s} = \mathbf{A} \cdot \mathbf{P}_{s} - \mathbf{B} \cdot \mathbf{D}_{s} \tag{12}$$

$$\sum_{h} P_{dc,h} = 0 \tag{13}$$

$$PL^{E}_{stej} = \frac{(\theta_{stem} - \theta_{sten})}{x^{E}_{j}} \qquad \forall j \tag{14}$$

$$\begin{cases} PL^{C}_{stej} - \dfrac{(\theta_{stem} - \theta_{sten})}{x^{C}_{j}} \le M * (1 - Y_{stej}) \\ PL^{C}_{stej} - \dfrac{(\theta_{stem} - \theta_{sten})}{x^{C}_{j}} \ge -M * (1 - Y_{stej}) \end{cases} \qquad \forall j \tag{15}$$

$$-PL^{E,Max}_{j} \le PL^{E}_{stej} \le PL^{E,Max}_{j} \qquad \forall\ j \tag{16}$$

$$-PL^{C,Max}_{j} \cdot Y_{stej} \le PL^{C}_{stej} \le PL^{C,Max}_{j} \cdot Y_{stej} \qquad \forall\ j \tag{17}$$

$$\begin{cases} P^{E,Min}_{dc,h} \le P^{E}_{dc,steh} \le P^{E,Max}_{dc,h} & \text{Rect.} \\ -P^{E,Max}_{dc,h} \le P^{E}_{dc,steh} \le -P^{E,Min}_{dc,h} & \text{Inv.} \end{cases} \qquad \forall h \tag{18}$$

$$\begin{cases} P^{C,Min}_{dc,h} * Y_{dc,stek} \le P^{C}_{dc,steh} \le P^{C,Max}_{dc,h} * Y_{dc,stek} & \text{Rect.} \\ -P^{C,Max}_{dc,h} * Y_{dc,stek} \le P^{C}_{dc,steh} \le -P^{C,\min}_{dc,h} * Y_{dc,stek} & \text{Inv.} \end{cases} \qquad \forall h \tag{19}$$

$$P^{Min}_{i} \le P_{stei} \le P^{Max}_{i} \qquad \forall i \tag{20}$$

$$\theta_{ref,ste} = 0 \tag{21}$$

If the loss of energy probability (LOEP) in (22) is not satisfied in all scenarios and at each subperiod, the Benders reliability cut (23) will be generated and added to the Benders master planning problem presented in (5)-(8).

$$\sum_{s}^{NS} (\Pr_{s} * WF_{ste}) / \sum_{s}^{NS} (\Pr_{s} * DT_{te} * D_{ste}) \le LOEP \tag{22}$$

$$\begin{aligned} &\sum_{s}^{NS} (\Pr_{s} * WF_{ste}) + \sum_{s}^{NS} \left( \Pr_{s} \sum_{j}^{NJ} \eta_{stej} * (Y_{jt} - \hat{Y}_{jt}) \right) \\ &+ \sum_{s}^{NS} \left( \Pr_{s} \sum_{k}^{NK} \eta_{stek} * (Y_{dc,kt} - \hat{Y}_{dc,kt}) \right) \\ &\le LOEP * \sum_{s}^{NS} (\Pr_{s} * DT_{te} * D_{ste}) \end{aligned} \tag{23}$$

Once the network reliability is managed, the ISO examines the optimality of selected schemes as presented in the next section.

### *D. Formulation of Optimal Operation Subproblem*

The objective of the optimal operation subproblem is to minimize the operation and load curtailment costs based on submitted bids and contracts. The ISO's optimal operation for each scenario and each subperiod is formulated as follows.

$$\begin{aligned} Min \quad WO_{ste} = &\sum_{i}^{NI} \frac{DT_{te} * P_{stei} * Bid_{tei}}{(1+d)^{(t-1)}} \\ &+ \sum_{b}^{NB} \frac{DT_{te} * LS_{steb} * LSC_{teb}}{(1+d)^{(t-1)}} \end{aligned} \tag{24}$$

*s.t.*

$$Y_{stej} = \hat{Y}_{jt} \qquad \pi_{stej} \qquad \forall\ j \tag{25}$$

$$Y_{dc,stek} = \hat{Y}_{dc,kt} \qquad \pi_{stek} \qquad \forall\ k \tag{26}$$

And, constraints (12)-(21) are taken into account. Similarly, (25) and (26) represent the transmission planning schedule obtained from the Benders master planning problem. Once the ISO obtains an optimal solution for all scenarios at all subperiods, the ISO calculates the objective function (4) to get $Z^{upper}$. Then, the stopping criterion (27) will be checked.

$$\frac{\left(Z^{upper} - Z_{lower}\right)}{Z_{lower}} \le \varepsilon \tag{27}$$

If the stopping criterion (27) is not satisfied, a Benders optimality cut (28) will be added to the Benders master planning problem presented in (5)-(8).

$$\begin{aligned} Z_{lower} \ge &\sum_{t}^{NT} \left( \frac{\sum_{j}^{CJ} IC_{j} \times Y_{jt} + \sum_{k}^{CK} IC_{dc,k} \times Y_{dc,kt}}{(1+d)^{(t-1)}} \right) \\ &+ \sum_{s}^{NS} (\Pr_{s} * WO_{ste}) + \sum_{s}^{NS} \left( \Pr_{s} \sum_{t}^{NT} \sum_{e}^{NE} \sum_{j}^{NJ} \pi_{stej} (Y_{jt} - \hat{Y}_{jt}) \right) \\ &+ \sum_{s}^{NS} \left( \Pr_{s} \sum_{t}^{NT} \sum_{e}^{NE} \sum_{k}^{NK} \pi_{stek} (Y_{kt} - \hat{Y}_{kt}) \right) \end{aligned} \tag{28}$$

This iterative process will continue until a feasible and optimal AC/DC TEP schedule is obtained.

## IV. Case Studies

A six-bus system and the modified IEEE 118-bus system are studied to show the effectiveness of the proposed hybrid AC/DC TEP. The choice of VSC or CSC lines is based on the system performance and economic evaluation. We assume that two-terminal and MTDC transmission systems have similar converter ratings at sending and receiving terminals. The discount rate is 10%. The total permissible load shedding is 1000 MW over the entire planning period. AC/DC line installations are considered at the beginning of each planning year. The stopping criterion $\varepsilon$ is 0.05%. All cases are solved using CPLEX 12.0 on a dual core 2.66 GHz CPUs personal computer.

### *A. Six-bus System*

A six-bus system is shown in Fig. 5. The pertinent data for the transmission network and generating units are listed in Tables II and III, respectively. The bidding strategy of units is assumed to be fixed. Table IV shows the load forecast for the entire planning period of 10 years. Load distribution factors are 0.2, 0.4 and 0.4 for loads at buses 3-5, respectively. There

is no generation expansion considered in this system and the network contains AC transmission at the beginning of planning period.

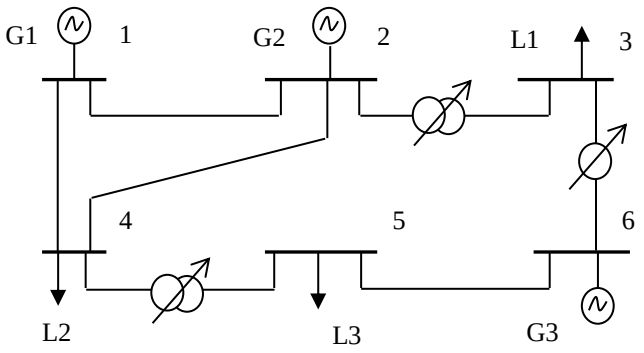


Fig. 5. The six-bus system

Tables V and VI show the AC/DC transmission candidates. These candidates are selected based on SCUC results in [23] to link cheap generation stations to high load centers. In this case study, all DC transmission candidates are two-terminal DC systems. We do not consider uncertainties in Case A.

In the summer of first planning year (subperiod 2 of Yr. 1), the 2,560MW load cannot be served based on the existing transmission network capacity. Consequently, AC/DC transmission candidates listed in Tables V and VI are utilized to find the feasible and most economical TEP. The final AC/DC TEP results listed in Table VII indicates that the candidate lines AC2, AC3 and DC3 are installed in years 8, 1, and 4, respectively to serve the increasing loads at minimum cost. The proposed solution avoids the potential load shedding and transmission violations over the entire planning horizon.

Based on the TEP optimal solution given in Table VII, the AC2 is selected as the least cost plan in the first planning year. The installation of AC2 would secure the network operation for all subperiods in the planning years 1-3. However, there would still be a line flow violation in the summer of the 4$^{th}$ year (subperiod 2 of Yr. 4). In this year, if we only consider the investment cost of AC/DC transmission candidates, AC3 will be selected for installation as it removes transmission network bottlenecks at the lowest installation cost. However, DC3 is selected instead because its total investment and operational cost savings over the entire planning period are higher than those of candidate AC3. DC3 is a fully controllable DC line that can reduce the congestion in parallel AC lines and decrease the operation cost. Based on TEP schedules in Table VII, the net present values of investment and operation costs over a 10 year planning period are \$101.9M and \$104.2M respectively without requiring any load shedding.

Based on general thoughts [1], [2], DC lines are often recommended over AC lines when DC lines are longer than the break-even length of the line. However, the results of this case study, in which all DC transmission candidates are shorter than break-even-distance, demonstrate the impact of market on TEP analyses. In a market driven TEP, short DC lines could be more attractive than AC lines. Hence, in congested regions and large urban areas, DC transmission systems are often the preferred TEP choice for mitigating congestion, decreasing the operation costs, and reducing consumer payments [24].

TABLE II
TRANSMISSION LINE DATA

| Line No. | From Bus | To Bus | X (pu) | Flow Limit (MW) |
|---|---|---|---|---|
| 1 | 1 | 2 | 0.17 | 700 |
| 2 | 1 | 4 | 0.258 | 700 |
| 3 | 2 | 4 | 0.097 | 800 |
| 4 | 2 | 3 | 0.037 | 600 |
| 5 | 3 | 6 | 0.018 | 800 |
| 6 | 4 | 5 | 0.037 | 500 |
| 7 | 5 | 6 | 0.014 | 500 |

TABLE III
GENERATOR DATA

| Unit | Bus No. | $P_{min}$ (MW) | $P_{max}$ (MW) | Bid (\$/MWh) |
|---|---|---|---|---|
| G1 | 1 | 100 | 1200 | 13 |
| G2 | 2 | 200 | 2500 | 32 |
| G3 | 6 | 100 | 1300 | 17 |

TABLE IV
LOAD FORECAST OVER THE 10 YEAR PLANNING PERIOD (MW)

| Subperiods | Yr. 1 (MW) | Yr. 2 (MW) | Yr. 3 (MW) | Yr. 4 (MW) | Yr. 5 (MW) |
|---|---|---|---|---|---|
| **Subperiod 1** | 1800 | 1890 | 1980 | 2080 | 2190 |
| **Subperiod 2** | 2560 | 2690 | 2820 | 2960 | 3110 |
| **Subperiod 3** | 2100 | 2210 | 2320 | 2430 | 2550 |
| **Subperiod 4** | 2330 | 2450 | 2570 | 2700 | 2830 |
| **Subperiods** | **Yr. 6 (MW)** | **Yr. 7 (MW)** | **Yr. 8 (MW)** | **Yr. 9 (MW)** | **Yr. 10 (MW)** |
| **Subperiod 1** | 2300 | 2410 | 2530 | 2660 | 2790 |
| **Subperiod 2** | 3270 | 3430 | 3600 | 3780 | 3970 |
| **Subperiod 3** | 2680 | 2810 | 2950 | 3100 | 3260 |
| **Subperiod 4** | 2970 | 3120 | 3280 | 3440 | 3610 |

TABLE V
CANDIDATE AC TRANSMISSION LINES FOR SIX BUS SYSTEM

| Line | From | To | X (pu) | Length (Mile) | Flow limit (MW) | Investment Cost (Thousand \$/year) |
|---|---|---|---|---|---|---|
| **AC1** | 1 | 5 | 0.2 | 140 | 700 | 7900 |
| **AC2** | 2 | 5 | 0.15 | 150 | 700 | 8400 |
| **AC3** | 4 | 6 | 0.24 | 160 | 700 | 9800 |

TABLE VI
CANDIDATE DC TRANSMISSION SYSTEMS FOR SIX BUS SYSTEM

| System | From | To | Length (Mile) | Converters 1 & 2 Capacity (MW) | Investment Cost (Thousand \$/year) |
|---|---|---|---|---|---|
| **DC1** | 1 | 5 | 140 | 700 | 11300 |
| **DC2** | 2 | 5 | 150 | 700 | 12000 |
| **DC3** | 4 | 6 | 160 | 700 | 11000 |

Table VII
AC/DC TRANSMISSION LINES SCHEDULED TO BE INSTALLED

| Candidate | AC1 | AC2 | AC3 | DC1 | DC2 | DC3 |
|---|---|---|---|---|---|---|
| **Year** | 8 | 1 | - | - | - | 4 |

### *B. IEEE 118-bus System*

A modified IEEE 118–bus system presented in Fig. 6 has 54 units, 186 branches, and 91 demand sides. This larger system is selected to evaluate the proposed TEP algorithm. The 118-bus system data is given in http://motor.ece.iit.edu/DC/Planning/IEEE118.xls where 25 AC, 25 DC and 15 MTDC candidates are suggested for a 15-year TEP. Fig. 7 shows the schematic diagram of two-terminal DC transmission candidates (on the left) and MTDC transmission candidates (on the right). Random scenarios are created by the Monte Carlo simulation. The scenario reduction technique [25] is applied to reduce the number of scenarios which are listed in Table IX. We assumed that load distribution factors at all buses are fixed and all loads have the same annual growth rate of 2%. The total demand through first to fourth quarters of the first planning year are 4219 MW, 6000 MW, 4922 MW and 5461 MW, respectively. We use bus LMP differences to select TEP candidates. The additional AC/DC lines would mitigate the line congestion or transfer power from a low-LMP bus, with access to cheap generation, to a high-LMP bus supplied by expansive generating units. The cost of adding a 100MW AC line is $1.2 M/mile. The cost of adding a 100MW DC system includes $20M for two converter terminals ($10M per each) and $1M/mile for the line.

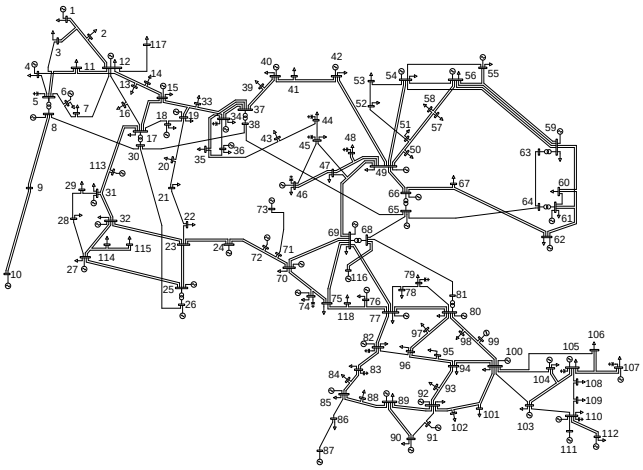

Fig. 6 The modified IEEE 118-bus system

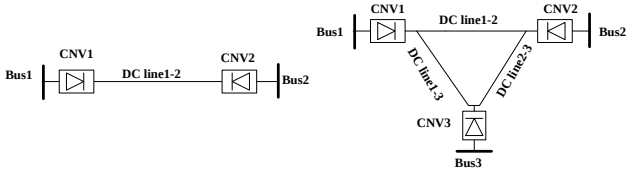


Fig. 7 Two-terminal DC (left) and MTDC (right) candidates

The following two cases are studied

**Case 1:** TEP without considering any uncertainties

**Case 2:** TEP with pre-defined scenarios

**Case 1**: This is the base case power system. The existing system cannot supply the load in years 11-15 without the expansion of existing transmission system. For instance, at year 15, the load curtailment at bus 59 is 9.35MW which is due to the congested AC line 59-63. The load curtailment is not allowed at the base case, so the AC line 49-59 is installed in year 10 to minimize the total investment and operation costs during years 10-15 and mitigate the transmission system bottlenecks in year 11. Though candidate lines AC 5-10, DC 5-10, MTDC 5-10-26 and MTDC 5-10-30 can be installed to solve the load shedding at bus 5, the operation and investment costs are minimized when the AC candidate line 6-113 is installed to supply the load at bus 5. Similarly, the DC candidate line 60-80 is installed on this year to transfer the cheap power from unit 36 at bus 80 to a load center at bus 60, remove the congestion, and avoid the load curtailment at bus 59. Table X shows that 5 AC, 4 DC and 2 MTDC transmission systems are selected out of 25 AC, 25 DC and 15 MTDC candidates. In this case, the net present values of investment and operation costs are $7.14M and $198.43M, respectively.

**Case 2:** In this case, most AC/DC transmission installations occur between years 11-15 for supplying the higher demand. When evaluating the transmission reliability for the pre-defined scenarios, the load shedding may be applied to find a feasible solution based on a permissible LOEP. For instance, 23.61MW of load is curtailed when the scenario S2 (i.e., AC line 8 is on outage at certain subperiods) is considered. Table XI shows that 19 AC and 6 DC transmission lines are installed. The net present values are $2.49M and $205.19M for investment and operation costs, respectively. The difference in total costs between this Case and Case 1 is $2.11M which is the cost of maintaining the transmission system reliability.

TABLE IX
LIST OF OUTAGE SCENARIOS IN IEEE 118 BUS SYSTEM

| Scenario | Element | Outage Season and Year | Probability |
|---|---|---|---|
| **Base Case (S1)** | - | - | 0.9536 |
| **S2** | Line 8 | Winter, Year 6 & Fall, Year 14 | 0.0068 |
| **S3** | Line 37 | Spring, Year 10 | 0.0068 |
| **S4** | Line 52 | Summer, Year 8 | 0.0068 |
| **S5** | Line 161 | Winter, Year 12 | 0.0068 |
| **S6** | Line 150 | Fall, Year 11 | 0.0068 |
| **S7** | Unit 5 | Summer, Year 6 | 0.0031 |
| **S8** | Unit 24 | Fall, Year 12 | 0.0031 |
| **S9** | Unit 29 | Winter, Year 13 | 0.0031 |
| **S10** | Unit 51 | Summer, Year 15 | 0.0031 |

TABLE X
SCHEDULED TRANSMISSION LINES IN CASE 1

| Line Type | From Bus | To Bus (1) | To Bus (2) | Investment Cost (Thousand $) | Inst. Year |
|---|---|---|---|---|---|
| **AC** | 6 | 113 | - | 272 | 13 |
| **AC** | 10 | 17 | - | 496 | 14 |
| **AC** | 15 | 113 | - | 258 | 15 |
| **AC** | 22 | 46 | - | 258 | 15 |
| **AC** | 49 | 59 | - | 242 | 10 |
| **DC** | 7 | 113 | - | 1560 | 15 |
| **DC** | 20 | 26 | - | 1747 | 15 |
| **DC** | 22 | 46 | - | 1548 | 14 |
| **DC** | 60 | 80 | - | 2420 | 13 |
| **MTDC** | 21 | 32 | 36 | 2460 | 14 |
| **MTDC** | 42 | 46 | 54 | 3073 | 15 |

TABLE XI
SCHEDULED TRANSMISSION LINE IN CASE 2

| Line Type | From Bus | To Bus | Investment Cost (Thousand $) | Inst. Year |
|---|---|---|---|---|
| **AC** | 5 | 10 | 624 | 15 |
| **AC** | 7 | 10 | 496 | 15 |
| **AC** | 7 | 113 | 272 | 12 |
| **AC** | 10 | 17 | 496 | 15 |
| **AC** | 10 | 29 | 258 | 15 |
| **AC** | 13 | 17 | 350 | 14 |
| **AC** | 15 | 113 | 258 | 15 |
| **AC** | 17 | 25 | 688 | 14 |
| **AC** | 17 | 33 | 244 | 14 |
| **AC** | 18 | 37 | 258 | 14 |
| **AC** | 22 | 46 | 258 | 13 |
| **AC** | 24 | 26 | 394 | 15 |
| **AC** | 25 | 33 | 496 | 15 |
| **AC** | 30 | 36 | 258 | 14 |
| **AC** | 49 | 59 | 242 | 11 |
| **AC** | 59 | 67 | 242 | 15 |
| **AC** | 59 | 66 | 320 | 13 |
| **AC** | 60 | 80 | 1304 | 15 |
| **AC** | 65 | 69 | 128 | 15 |
| **DC** | 10 | 28 | 1548 | 14 |
| **DC** | 25 | 33 | 1747 | 14 |
| **DC** | 49 | 59 | 1535 | 14 |
| **DC** | 59 | 67 | 1535 | 13 |
| **DC** | 59 | 66 | 1600 | 13 |
| **DC** | 60 | 80 | 2420 | 15 |

## V. CONCLUSIONS

A hybrid AC/DC TEP model was developed to minimize the total investment, operation, and load shedding costs in restructured power systems. Numerical examples emphasized the fact that an optimal TEP should consider both AC and DC transmission candidates that would guarantee the security and the economics of the reinforced transmission system in the base case and critical contingency situations. The TEP model presented in this paper could include all kinds of DC transmission configurations. Numerical examples show the possibility of additional savings based on the installation of DC transmission systems as compared with AC transmission systems. Such studies rationalize the high cost of installing DC transmission systems or replacing existing AC lines with DC systems in a given right of way. Therefore, the importance of the break-even distance concept should not be over-addressed in TEP studies, since the controllability of DC line flow among other factors are important in the selection of AC/DC transmission systems. In addition, the proposed TEP approach can consider the integration of remotely located, variable and large-scale renewable energy. Considering the unpredictable characteristic of wind energy, the scenario-based simulation representing a range of wind energy forecasts, can be incorporated in the proposed model as we identify a reliable and cost-effective AC/DC TEP strategy.

## REFERENCES


[1] K. R. Padiyar, *HVDC Power Transmission*, New York, Wiley, 1990.

[2] V. K. Sood, *HVDC and Facts Controllers*, Netherlands: Springer, 2004.

[3] J. Roh, M. Shahidehpour, and Y. Fu, "Security-Constrained Resource Planning in Electricity Markets," *IEEE Transaction on Power Systems*, Vol. 22, No. 3, pp. 812 – 820, May 2007.

[4] S. Lee, "For the Good of the Whole," *IEEE Power and Energy Magazine*, vol. 5, no. 5, pp. 24 – 35, 2007.

[5] Z. Xu, Z. Dong, K. P. Wong, "A Hybrid Planning Method for Transmission Networks in a Deregulated Environment," *IEEE Transactions on Power Systems*, vol. 21, no. 2, pp. 925-932, May 2006.

[6] J. Roh, M. Shahidehpour, Y. Fu, "Market-Based Coordination of Transmission and Generation Capacity Planning," *IEEE Transactions on Power System*, vol. 22, no. 4, pp. 1406-1419, Nov. 2007.

[7] L. Garces, A. Conejo, R. Garcia-Bertrand, and R. Romero, "A Bilevel Approach to Transmission Expansion Planning Within a Market Environment," *IEEE Transaction on Power Systems*, vol. 24, no. 3, pp. 1513-1522, 2009.

[8] T. De la Torre, J. Feltes, T. Gomez San Roman, and H. Merrill "Deregulation, Privatization, and Competition: Transmission Planning under Uncertainty," *IEEE transactions on power systems*, vol. 14, no. 2, pp. 460-465, May 1999.

[9] P. Maghouli, S. Hosseini, M. Buygi, and M. Shahidehpour, "A Multi-Objective Framework for Transmission Expansion Planning in Deregulated Environments," *IEEE Transactions on Power System*, Vol. 24, No. 2, pp. 1051-1061, May. 2009.

[10] M. Buygi, G. Blazer, M. Shanechi, and M. Shahidehpour, "Market-Based Transmission Expansion Planning," *IEEE Transactions on Power System*, vol. 19, no. 4, pp. 2060-2067, Nov. 2004.

[11] O. Tor, A. Guven, and M. Shahidehpour, "Congestion-Driven Transmission Planning Considering the Impact of Generator Expansion," *IEEE Transactions on Power Systems*, vol. 23, no. 2, pp. 781-790-137, May. 2008.

[12] P. Sanchez-Martin, A. Ramos, and J. Alonso, "Probabilistic Midterm Transmission Planning in a Liberalized Market," *IEEE Transactions on Power System*, vol. 20, no. 4, pp. 2135-2142, Nov. 2005.

[13] A. Khodaei, M Shahidehpour, and S. Kamalinia, "Transmission Switching in Expansion Planning," *IEEE Transactions on Power System*, vol. 25, no. 3, pp. 1722-1733, Aug. 2010.

[14] P. Maghouli, S. Hosseini, M. Oloomi Buygi, and M. Shahidehpour, "A Scenario-Based Multi-Objective Model for Multi-Stage Transmission Expansion Planning," IEEE Transactions on Power Systems, Vol. 26, 2011.

[15] M. Oloomi, H. Shanechi, G. Balzer, M. Shahidehpour, N. Pariz, "Network Planning in Unbundled Power Systems," IEEE Transactions on Power Systems, Vol. 21, No. 3, pp. 1379-1387, Aug. 2006.

[16] O. Tor, A. Guven, and M. Shahidehpour, "Promoting the Investment on IPPs for Optimal Grid Planning," IEEE Transactions on Power Systems, Vol. 25, No. 3, pp. 1743-1750, Aug. 2010.

[17] M. Henderson, J. Gagnon, and D. Bertagnolli, "Planning Issues for HVDC," in Proceedings of *IEEE Power System Conference and Exposition*, Oct-Nov. 2006.

[18] S. Wang, J. Zhu, L. Trinh, and J. Pan, "Economic Assessment of HVDC Project in Deregulated Energy Markets," in Proceedings of *Electric Utility Deregulation and Restructuring and Power Technologies (DRPT 2008)*, China, April 2008.

[19] R. Hauth, P. Tatro, B. Railing, B. Johnson, J. Stewart, J. Fink, "HVDC Power Transmission Technology Assessment", *Oak Ridge National Laboratory Report*, May 1997.

[20] A. Lotfjou, M. Shahidehpour, and Y. Fu, "Security-Constrained Unit Commitment with AC/DC Transmission Systems," *IEEE Transactions on Power Systems*, vol. 25, no. 1, Feb 2010.

[21] A. Lotfjou, M. Shahidehpour, and Y. Fu, "Scheduling of DC Transmission Lines in SCUC with Voltage Source Converter," *IEEE Transactions on Power Delivery*, vol. 26, no. 2, pp. 650-660, April 2011.

[22] J. Cochrane, M. Emerson, J. Donhaue, and G. Wolf, "A Survey of HVDC Operating and Maintenance Practices and Their Impact on Reliability and Performance," *IEEE Transactions of Power Delivery*, vol. 11, no. 1, pp. 504-518, Jan. 1996.

[23] Y. Fu, M. Shahidehpour, Z. Li, "Security-Constrained Unit Commitment With AC Constraints", *IEEE Transactions of Power Systems*, vol. 20, no. 3, pp. 1538-1550Aug. 2005.

[24] "Cross Sound HVDC Cable Project", *TransÉnergie U.S. Ltd.*, Vol. 1 of 2, Oct. 2001.

[25] J. Roh, M. Shahidehpour, and L. Wu, "Market-based Generation and Transmission Planning with Uncertainties," IEEE Transactions on Power Systems, Vol. 24, No. 3, pp. 1587-1598, August 2009.

## BIOGRAPHIES

**Azim Lotfjou** (S'07) received his BS and MS in electrical engineering from Sharif University of Technology, Iran, in 2001 and 2004, respectively, and Ph.D. degree in EE from Illinois Institute of Technology, USA, in 2008. Presently, he is with the power market development group at Genscape Business in Boston, MA. His research interests include power systems restructuring and HVDC transmission applications.

**Yong Fu** (M'05) received his BS and MS in E.E. from Shanghai Jiaotong University, China, in 1997 and 2002, respectively and Ph.D degree in E.E. from Illinois Institute of Technology, USA, in 2006. From 2006 to 2009, he was a senior research associate at the Robert W. Galvin Center for Electricity Innovation at Illinois Institute of Technology. Presently, he is an assistant professor in the Department of Electrical and Computer Engineering at Mississippi State University.

**Mohammad Shahidehpour** (F'01) is the Bodine Professor and Director of the Director of the Robert W. Galvin Center for Electricity Innovation at Illinois Institute of Technology. He is the recipient of the 2009 Honorary Doctorate for the Polytechnic University of Bucharest in Romania. He is a Research Professor at the King Abdulaziz University in Saudi Arabia and Honorary Professor at Sharif University of Technology in Iran and North China Electric Power University in China. Dr. Shahidehpour is an IEEE Distinguished Lecturer.

# Risk-Constrained Coordination of Cascaded Hydro Units with Volatile Wind Power Generation

Lisias V. Abreu, *Member, IEEE*, Mohammad E. Khodayar, *Student Member, IEEE*, Mohammad Shahidehpour, *Fellow*, *IEEE*, Lei Wu, *Member*, *IEEE*

***Abstract* — This paper presents a stochastic hourly coordination strategy for wind units and cascaded hydro generation as storage to firm up the hourly dispatch in a generating company (GENCO). The proposed strategy is based on the stochastic price-based unit commitment (Stochastic PBUC) formulation which includes wind energy imbalance charges. The forecast errors of electricity market price and wind speed are simulated with the Monte Carlo method via a scenario approach. The risk-aversion constraints are considered for limiting a GENCO's financial risks when considering uncertain wind power generation. The proposed optimization model is solved by mixed-integer linear programming (MIP) and illustrative examples examine the effectiveness of the proposed risk-based coordination model for optimizing a GENCO's payoff.**

***Index Terms* — Cascaded hydro and wind coordination, risk-aversion, stochastic price-based unit commitment**

## NOMENCLATURE

### *Variables:*

| | |
|---|---|
| $EDR$ | Expected downside risk ($) |
| $h$ , $h'$ | Denote a cascaded hydro unit |
| $I_{ht}$ | Commitment status of hydro unit $h$ at hour $t$ |
| $k$ | Denote an intrahour interval |
| $P_{C,ht}$ | Coordinated generation dispatch corresponding to hydro unit $h$ at hour $t$ (MW) |
| $PF^{s}$ | Payoff of scenario $s$ ($) |
| $P_{ht}$ | Dispatch of hydro unit $h$ at hour $t$ (MW) |
| $P^{s}_{htk}$ | Dispatch of hydro unit $h$ at hour $t$ and intrahour interval $k$ in scenario $s$ (MW) |
| $P_{wt}$ | Dispatch of wind unit $w$ at hour $t$ (MW) |
| $P^{s}_{wtk}$ | Dispatch of wind unit $w$ at hour $t$ and intrahour $k$ in scenario $s$ (MW) |
| $P^{c,s}_{wtk}$ | Curtailed wind power of wind unit $w$ at hour $t$ and intrahour interval $k$ in scenario $s$ (MW) |
| $P^{s}_{\Delta,wtk}$ | Imbalance power of wind unit $w$ at hour $t$ and intrahour interval $k$ in scenario $s$ (MW) |
| $P^{s}_{\lvert\Delta\rvert,wtk}$ | Absolute imbalance power of unit $w$ at hour $t$ and intrahour interval $k$ in scenario $s$ (MW) |
| $q_{ht}$ | Water discharge of hydro unit $h$ at hour $t$ (Hm$^3$/h) |
| $q^{s}_{htk}$ | Discharge of hydro unit $h$ at hour $t$ and intrahour interval $k$ in scenario $s$ (Hm$^3$/h) |
| $q_{d,h(t-\tau)}$ | Discharge to hydro unit $h$ from upstream hydro units with the delay time $\tau$ at time $t$ (Hm$^3$/h) |
| $R^{s}$ | Downside risk of scenario $s$ ($) |
| $r_{ht}$ | Natural inflow of hydro unit $h$ at hour $t$ (Hm$^3$/h) |
| $s$ | Denote a scenario |
| $s_{ht}$ | Spillage of hydro unit $h$ at hour $t$ in scenario $s$ (Hm$^3$/h) |
| $t$ | Hour index |
| $v_{ht}$ | Reservoir volume of hydro unit $h$ at hour $t$ (Hm$^3$) |
| $w$ | Denote a wind unit |
| $y_{ht}$ , $z_{ht}$ | Operation status/shutdown indicator of hydro unit $h$ at hour $t$ |
| $\delta^{s}_{\Delta,wtk}$ , $\delta^{s}$ | Auxiliary binary variables |

### *Constants:*

| | |
|---|---|
| $\overline{EDR}$ | Targeted expected downside risk target ($) |
| $F_h()$ | Water-to-power conversion curve of hydro unit $h$ |
| $NK$ | Number of intrahour intervals |
| $NS$ | Number of scenarios |
| $p^{s}$ | Probability of scenario $s$ |
| $P^{\min}_{h}$ , $P^{\max}_{h}$ | Min/Max generation of hydro unit $h$ |
| $P^{f,s}_{wtk}$ | Forecasted wind power of unit $w$ at hour $t$ and intrahour interval $k$ in scenario $s$ (MW) |
| $P^{f}_{wt}$ | Forecasted wind power unit $w$ at hour $t$ (MW) |
| $q^{\min}_{h}$ , $q^{\max}_{h}$ | Min/Max discharge limits of hydro unit $h$ (Hm$^3$/h) |
| $RC_h$ | Geographic reservoir connection vector of hydro unit $h$ |
| $rc_{h-h'}$ | Binary variable representing the direct cascaded configuration of hydro units $h$ and $h'$ |
| $RU_h$ , $RD_h$ | Ramp up/down limits of hydro unit $h$ (MW/min) |
| $SU_h$ , $SD_h$ | Start-up/shutdown cost of hydro unit $h$ ($) |
| $S_{C,h}$ | Set of wind units in coordination with hydro unit $h$ |
| $s^{\min}_{h}$ , $s^{\max}_{h}$ | Min/Max spillage limits of hydro unit $h$ (Hm$^3$/h) |
| $T_0$ | Target payoff of a GENCO ($) |
| $V^{\min}_{h}$ , $V^{\max}_{h}$ | Min/Max reservoir volume limits of hydro unit $h$ |

This project is partially supported by the NSF grant ECCS-0801853 and the U.S. Department of Energy grants DE-EE 0002979 and DE-EE 0001380.000. The first three authors are with the Electrical and Computer Engineering Department, Illinois Institute of Technology, Chicago, IL 60616 USA. (e-mail: lisias@ieee.org, mkhodaya@iit.edu, ms@iit.edu). Lei Wu is with the Electrical and Computer Engineering Department, Clarkson University, Potsdam, NY 13699 USA. (e-mail: lwu@clarkson.edu).

| | |
|---|---|
| | ($Hm^3$) |
| $V_{0,h}$ , $V_{NT,h}$ | Initial/terminal water reservoir of hydro unit *h* ($Hm^3$) |
| $X(t)$ | Wind forecast error at time *t* |
| $Z(t)$ | Random Gaussian variable with the mean equal to zero and corresponding standard deviation |
| $\alpha$ , $\beta$ | ARMA constants |
| $\rho^{s}_{\mathrm{BP}}$ | Energy balancing price in scenario *s* ($/MWh) |
| $\rho^{s}_{\mathrm{DA},\,t}$ | Day-ahead energy market price at hour *t* in scenario *s* ($/MWh) |
| $\rho^{s}_{\mathrm{RT},\,tk}$ | Real-time market price at hour *t* and intrahour interval *k* in scenario *s* ($/MWh) |

## I. Introduction

GENCO's objective is to maximize profit through market participation. Price-based unit commitment (PBUC) is a decision tool that is used by GENCOs for procuring the optimal generation bids and/or self-scheduling decisions in day-ahead by considering market price forecasts. However, GENCOs, as market participants, have no obligation to balance supply with loads. Independent system operators (ISOs) use a security-constrained unit commitment (SCUC) tool that would utilize the submitted bids to clear the day-ahead market . ISOs balance supply with loads in a secure and economic fashion.

Usually, the perfect information on the day-ahead market price and wind speed is not available. Thus, GENCOs apply a stochastic model for forecasting hourly wind speed and market price. A stochastic PBUC model is then utilized that would maximize the GENCO's payoff while minimizing its financial risks. The GENCO's payoff consists of energy sales minus the cost of energy production and imbalance penalties. The cost of imbalance energy could reduce the GENCO's potential payoff if the real-time energy dispatch does not match that of day ahead.

The GENCO's finances may be subject to major risks when considering wind energy forecast errors. In general, the daily pattern for wind energy may not coincide with that of electricity demand. Wind energy imbalance charges may be incurred if the real-time wind energy differs from the day-ahead schedule [1]-[10]. The lack of dispatchability of installed wind energy capacity would make it difficult for GENCOs to take advantage of daily differences in electricity prices.

The wind energy forecast errors could also have a major impact on the secure operation of power systems. The ISO may consider preventive and corrective actions for managing the secure operation of power systems with intermittent and volatile wind energy [11]. A stochastic model was applied in [12] to examine the impact of high penetration of wind energy on power system operations. The auto-regressive moving average (ARMA) time series model was considered in [13] to simulate the wind speed volatility. A deterministic PBUC was applied for developing fossil unit bidding strategies [14]-[16]. A stochastic PBUC solution was presented in [17]-[18] for formulating power market dynamics.

This paper proposes a risk-constrained day-ahead coordination strategy for wind and cascaded hydro (storage) units in a GENCO. Wind energy variations could occur within minutes while the day-ahead schedule is hourly; so an intrahour-based model is proposed in this paper to firm up the coordinated wind and hydro generation. The paper shows that the fast ramping and storage capabilities of cascaded hydro units could compensate wind energy volatilities. The Monte Carlo simulation is used to generate scenarios, and scenario reduction techniques are applied to eliminate low-probability scenarios and bundle similar ones to identify a limited number of effective scenarios while maintaining a reasonably good approximation of the original system [19].The advantage of applying the Monte Carlo simulation resides in the fact that the required number of samples for a given accuracy level is independent of the system uncertainty dimension, and therefore is suitable for the simulation of power systems with a large number of uncertainties.

Scenario reduction algorithms include the fast backward method, the fast backward/forward method, and the fast backward/backward method [19]-[20]. The algorithms have different computational performance, and the chosen of algorithms for a certain problem depends on the size of the problem and the required solution accuracy. For large scenario trees, the fast backward method would provide the best computational performance with the worst accuracy. The results of the fast forward method are more accurate at the cost of longer computational time. In this paper, the fast backward/ forward method is selected to reduce the number of scenarios.

The day-ahead hourly market clearing prices (MCPs) are provided as input and the uncertainty of MCPs is represented via scenarios using time series [17],[18]. There is no transmission congestion considered between wind and hydro unit locations (i.e., day-ahead hourly prices are the same for wind and hydro units.) The real-time energy balancing prices are announced daily by the ISO [21]. The energy balancing cost is the daily cost of deviation in the real-time dispatch of market entities, which is allocated as credit to other generating units for supplying energy deviations, or as credit to real-time system demand for enhancing the system reliability.

The rest of the paper is organized as follows. Section II provides the stochastic PBUC formulation with the wind-hydro intrahour coordination. Section III illustrates the proposed formulation in two examples and conclusion is presented in section IV.

## II. Stochastic PBUC Formulation

The objective of PBUC is to maximize a GENCO's payoff, which is the revenue from the sales of energy or bilateral contracts minus the operation cost of GENCO. The operation cost includes the production cost, start-up/shut down costs, and imbalance energy charges incurred by wind energy variations. In this paper, we focus on the coordination strategy of wind and hydro units, thus the hourly scheduling of other types of generating units (thermal, combined-cycle, and pumped-storage units) is not discussed [17]-[18].

In the proposed stochastic PBUC problem, there are first and second stage variables. A first stage variable is stated as a

decision variable which is made before uncertainties are disclosed, that is, yielding identical values in all scenarios such as $P_{C,\,ht}$. A second stage variable is scenario dependent, which can be an intrahour variable depending on *t*, *k*, and *s* such as $P^{s}_{\Delta,wtk}$. The stochastic PBUC formulation is discussed next for the wind-hydro coordination.

### *A. Uncoordinated Scheduling of Wind and Hydro Units*

The stochastic PBUC would maximize the GENCO's expected payoff (1) subject to prevailing constraints. The first term in the objective function is the revenue from hydro and wind energy sales to day-ahead markets. The second term represents the operation cost of hydro units which includes startup and shutdown costs. The imbalance charges for wind units included in the last two terms of (1) are $P^{s}_{\Delta,wtk}$ paid based on $\rho^{s}_{RT,tk}$ and $P^{s}_{|\Delta|,wtk}$ paid based on $\rho^{s}_{BP}$.

Since the coordinated scheduling of cascaded hydro and wind units is not considered here, the objective function of hydro-wind can be decoupled into two independent optimization problems. The water to power curve of hydro unit $h$, expressed in (2), is generally a non-linear, non-convex curve [22], in which the hydro power generation has a nonlinear correlation with the water flow through the turbine and water head. Using auxiliary binary variables, the non-convex water to power curve can be converted into the piecewise linearized model and incorporated into the proposed MIP formulation [18], [22]-[23]. There are two popular methods used in power industry for solving such MIP models including the branch-and-bound/branch-and-cut and Lagrangian Relaxation [24]. The advantages of branch-and-bound/branch-and-cut over the Lagrangian Relaxation approach for solving the MIP-based PBUC problem was discussed in details in [25]. It was shown that the branch-and-bound/branch-and-cut based method would procure near-optimal/good-enough solution with enhanced modeling and convergence acceleration strategies.

Other constraints include water discharge limits (3), reservoir volume (4), initial and terminal reservoir volume (5), water balance constraints for cascaded hydro units (6), and water spillage limits (7). Minimum on/off time and ramping up/down constraints are given in [17]-[18]. In (6), $RC_h$ is the geographic reservoir connection vector with binary elements $rc_{h-h'}$, $rc_{h-h'}=1$ if the hydro unit $h'$ is a direct up stream of unit $h$; otherwise $rc_{h-h'}=0$. In addition, $q^{s}_{\mathrm{d},h(t-\tau)}$ in (8) represents the delayed water discharge to the hydro unit $h$ from upstream hydro units.

Since wind speed variations could occur within minutes, the intrahour variations of wind generation is integrated into the proposed scheduling model. In this paper, the wind speed forecast is procured by the Markov chain with the probability transition matrix. Wind speed values are classified into several categories represented by the mean value at each group. The probability transition matrix can either be obtained by historical data or by probability distribution parameters of the wind speed. Using the Weibull distribution function and the autocorrelation factor, the probability transition matrix is procured by composing an initial probability vector, a weighting matrix and a normalizing vector [26]. The probability transition matrix, which is a square matrix, defines probabilities of transiting from one wind speed category to other wind speed categories. Once the probability transition matrix is built, the wind speed time series can be procured with the Markov chain method. The wind speed forecast error is further represented by ARMA [27],[28]. Since the number of time steps for one day is not large enough (144 time steps for one day considering 10-min interval), the synthesized time series may have mean and standard deviations that are different from the corresponding values in the Weibull distribution function. Thus, the mean and the standard deviation are adjusted to procure the desired wind speed time series. The diurnal pattern strength which represents the daily pattern of wind speed is applied to the time series. The diurnal pattern has the sinusoidal form, in which the peak value indicates the ratio of the maximum wind speed to the average wind speed. The intrahour-based wind unit constraints include hourly and intrahour power generation schedule (9) and generation limits (10)-(11). The available wind energy is calculated using the wind speed forecast and used as input to PBUC. (12)-(15) incorporate $P^{s}_{|\Delta|,wtk}$ in the stochastic PBUC problem where $M$ is a large positive number.

$$\text{maximize} \quad \sum_{s=1}^{NS} p^{s}.PF^{s}$$

$$= \sum_{s=1}^{NS} p^{s}\cdot\left[\begin{array}{l}\sum_{h}\sum_{t}\rho^{s}_{DA,\,t}\cdot P_{ht}+\sum_{w}\sum_{t}\rho^{s}_{DA,\,t}\cdot P_{wt}-\sum_{h}\sum_{t}\left(y_{ht}.SU_{h}+z_{ht}\cdot SD_{h}\right)\\ -\sum_{w}\sum_{t}\left(\frac{1}{NK}\cdot\sum_{k}\rho^{s}_{RT,\,tk}\cdot P^{s}_{\Delta,wtk}+\frac{1}{NK}\cdot\rho^{s}_{BP}\cdot\sum_{k}P^{s}_{|\Delta|,wtk}\right)\end{array}\right] \tag{1}$$

$$P_{ht} = F_h(q_{ht}) \tag{2}$$

$$q^{\min}_{h}\cdot I_{ht} \le q_{ht} \le q^{\max}_{h}\cdot I_{ht} \tag{3}$$

$$V^{\min}_{h} \le v_{ht} \le V^{\max}_{h} \tag{4}$$

$$V_{h(0)} = V_{0,h} \qquad V_{h(NT)} = V_{NT,h} \tag{5}$$

$$v_{h(t+1)} = v_{ht} + RC_h\cdot q_{\mathrm{d},h(t-\tau)} - q_{ht} + r_{ht} - s_{ht} \tag{6}$$

$$s^{\min}_{h} \le s_{ht} \le s^{\max}_{h} \tag{7}$$

$$q_{\mathrm{d},h(t-\tau)} = \left[q_{1t}\cdots q_{(h-1)t}\quad 0\quad q_{(h+1)t}\cdots q_{NH_i t}\right] \tag{8}$$

$$P_{wt} = P^{s}_{wtk} + P^{s}_{\Delta,wtk} \tag{9}$$

$$0 \le P_{wt} \le P^{f}_{wt} \tag{10}$$

$$0 \le P^{s}_{wtk} \le P^{f,s}_{wtk} \tag{11}$$

$$P^{s}_{|\Delta|,wtk} - P^{s}_{\Delta,wtk} \ge 0 \tag{12}$$

$$P^{s}_{|\Delta|,wtk} + P^{s}_{\Delta,wtk} \ge 0 \tag{13}$$

$$P^{s}_{|\Delta|,wtk} - P^{s}_{\Delta,wtk} \le \mathrm{M}\cdot\delta^{s}_{\Delta,wtk} \tag{14}$$

$$P^{s}_{|\Delta|,wtk} + P^{s}_{\Delta,wtk} \le \mathrm{M}\cdot\left[1-\delta^{s}_{\Delta,wtk}\right] \tag{15}$$

### B. Coordinated Scheduling of Wind and Hydro Units

In this case, the coordinated scheduling of cascaded hydro unit with one or more wind units is considered for providing an hourly firm power dispatch. The first term in (16) shows the GENCO's revenue and the second term represents the operation cost of hydro unit. Since the hourly wind generation is firm, the imbalance energy charge will be zero. The unit commitment (UC) of hydro and wind units determines the hourly on/off status, and the generation dispatch provides a 10-minute solution. Thus, by coordination, the sum of intrahour wind $P^{s}_{wtk}$ and hydro $P^{s}_{htk}$ generation is equal to the hourly generation dispatch $P_{C,ht}$ (17). Note that $P_{C,ht}$ is a scenario-independent first-stage decision variable, which is calculated before uncertainties are imposed. The wind power ($P^{f}_{wtk}$) is dependent on the wind speed forecast. The wind power generation follows the power curve of the wind turbine, which is zero below the cut-in or above the cut-out speeds.

$$\text{maximize} \quad \sum_{s=1}^{NS} p^{s}.PF^{s} = \sum_{s=1}^{NS} p^{s}\cdot\left[\sum_{h}\sum_{t}\rho^{s}_{DA,t}\cdot P_{C,ht} - \sum_{h}\sum_{t}\left(y_{ht}.SU_{h} + z_{ht}\cdot SD_{h}\right)\right] \tag{16}$$

$$P_{C,ht} = \sum_{w\in S_{C,h}} P^{s}_{wtk} + P^{s}_{htk} \tag{17}$$

$$P^{s}_{wtk} = P^{s,f}_{wtk} - P^{c,s}_{wtk} \qquad \forall w, \forall t, \forall k, \forall s \tag{18}$$

$$q^{\min}_{h}\cdot I_{ht} \le q^{s}_{htk} \le q^{\max}_{h}\cdot I_{ht} \tag{19}$$

$$P^{s}_{ht(k+1)} - P^{s}_{htk} \le 60\cdot RU_{h}/NK \qquad P^{s}_{htk} - P^{s}_{ht(k+1)} \le 60\cdot RD_{h}/NK \tag{20}$$

$$I_{ht} - I_{h(t-1)} = z_{ht} - y_{ht} \tag{21}$$

$$z_{ht} + y_{ht} \le 1 \tag{22}$$

$$P^{s}_{htk} = F_{h}(q^{s}_{htk}) \tag{23}$$

$$V^{\min}_{h} \le v^{s}_{htk} \le V^{\max}_{h} \tag{24}$$

$$V^{s}_{h,0,NK} = V_{0,h} \qquad V^{s}_{h,NT,NK} = V_{NT,h} \tag{25}$$

$$v^{s}_{htk} = v^{s}_{ht(k-1)} + \frac{1}{NK}\cdot\left(RC_{h}\cdot q^{s}_{d,h(t-\tau)k} - q^{s}_{htk} + r_{htk} - s^{s}_{htk}\right) \qquad \forall h, \forall t, \forall k\in[2,NK], \forall s \tag{26}$$

$$v^{s}_{ht1} = v^{s}_{h(t-1)NK} + \frac{1}{NK}\cdot\left(RC_{h}\cdot q^{s}_{d,h(t-\tau)1} - q^{s}_{ht1} + r_{ht1} - s^{s}_{ht1}\right) \qquad \forall h, \forall t, \forall s \tag{27}$$

$$s^{\min}_{h} \le s^{s}_{htk} \le s^{s}_{h}{}^{\max} \tag{28}$$

$$q^{s}_{d,h(t-\tau)k} = \left[q^{s}_{1tk} \cdots q^{s}_{(h-1)tk} \quad 0 \quad q^{s}_{(h+1)tk} \cdots q^{s}_{NH_{t}tk}\right] \tag{29}$$

In (18), the intrahour wind power in scenario $s$ ($P^{s}_{wtk}$) is equal to the wind power forecast ($P^{f,s}_{wtk}$) minus the non-negative curtailed wind power ($P^{c,s}_{wtk}$). The intrahour hydro power generation $P^{s}_{htk}$ is dependent on the water discharge rate which is subject to the discharge limit (19). Ramping limits (20) show that the hydro power increment in two consecutive intrahours is limited. The wind-hydro coordination with sufficient ramping provides complimentary power from cascaded hydro units to wind units to make $P^{s}_{\Delta,wtk} = 0$ for all wind units in $S_{C,h}$. In (21)-(22), the hourly hydro unit commitment is related to startup and shutdown indicators.

The intrahour hydro power generation is dependent on water discharge in (23). The intrahour reservoir volume constraints of hydro units are given in (24)-(25). The intrahour reservoir volume in (26) is dependent on its previous intrahour value, discharge water flow in the present intrahour, inflow water flow from upstream hydro unit, inflow water flow, and spillage in each intrahour. In (27), the volume in the first intrahour of each hour is dependent on the volume in the last intrahour of the previous hour, the present net water flow rate, spillage, inflow and inflow from upstream hydro units. The intrahour quantities in (28)-(29) are similar to (7)-(8).

### C. Risk Assessment

A GENCO would be concerned with the risk associated with its payoff when considering market price uncertainties [17]-[18]. Suppose the GENCO's day-ahead target payoff is $T_0$. The payoff risk given in (30) is associated with the failure to meet the target payoff. The linear expression of risk (30) is represented in (31) by auxiliary binary variables.

$$R^{s} = \begin{cases} T_0 - PF^{s} & \text{, if } PF^{s} < T_0 \\ 0 & \text{, otherwise} \end{cases} \tag{30}$$

$$0 \le R^{s} - \left[T_0 - PF^{s}\right] \le M\cdot\left[1-\delta^{s}\right] \qquad 0 \le R^{s} \le M\cdot\delta^{s} \tag{31}$$

Here, the expected downside risk is smaller than the accepted risk level. If a GENCO is not satisfied with its payoff that is below the target, an upper expected downside risk given in (32) will be appended into the PBUC formulation.

$$EDR = E\left(R^{s}\right) = \sum_{s=1}^{NS} p^{s}\cdot R^{s} \le \overline{EDR} \tag{32}$$

Hence, the original risk-neutral model is turned into a risk-constrained model by including (31)-(32). The objective is to calculate the expected payoff while keeping the expected downside risk within an acceptable range. The target $\overline{EDR}$ should be carefully designed since a tight constraint on the expected downside risk (i.e., relatively low risk $\overline{EDR}$ or high targeted payoff) could result in an infeasible solution.

### D. Risk-based Stochastic PBUC Solution

The proposed stochastic PBUC for the cascaded hydro and wind unit coordination is solved by a MIP package (CPLEX).

The deterministic PBUC solution is obtained when uncertain variables are replaced by their forecasts. If the transmission network is considered, the dimension of the stochastic PBUC can increase significantly. The solution techniques based on the Benders' decomposition are considered to deal with large-scale systems by decomposing the problem into tractable master UC and hourly network evaluation subproblems [29]-[30].

## III. Numerical Examples

In this section, two case studies are illustrated to investigate

coordinated and uncoordinated scheduling strategies in the GENCO's portfolio with cascaded hydro and wind units. We assume no transmission congestion among wind and hydro units since they belong to the same GENCO. Detailed hydro unit data are given in Table I where $a, b, c$ are the quadratic, linear and constant coefficients of water-to-power conversion curves respectively. The errors in market price forecast (i.e. day-ahead MCPs and energy balancing price) and the wind energy forecast uncertainty are simulated via 10,000 scenarios using the Monte Carlo simulation, and efficient algorithms are used to reduce the number of scenarios [19]-[20]. In the following, a three-hour ahead case and a day-ahead case are studied.

### *A. THREE-HOUR AHEAD SCHEDULING*

Table I shows the system data in which a 3-hour coordination of hydro unit H1 is considered with a 200 MW wind generating unit. Table II shows the six cases in which risk constraints are not included. The forecasts for wind and day-ahead MCP and their respective forecast errors are given in Figs. 1 and 2. Based on the available forecasting techniques, the wind speed forecast would have a larger error (i.e., 10%-20%) than the price forecast (less than 10%); thus a higher standard deviation is used to represent wind speed forecast errors.

TABLE I CHARACTERISTICS OF CASCADED HYDRO UNITS

| Description | H1 | H2 | H3 | H4 | H5 | H6 | H7 |
|---|---|---|---|---|---|---|---|
| $P_{\min,h}$ (MW) | 9.0 | 4.0 | 17.0 | 30.0 | 9.0 | 2.0 | 19.0 |
| $P_{\max,h}$ (MW) | 70.0 | 70.0 | 115.0 | 194.0 | 80.0 | 60.0 | 120.0 |
| $RD_h$ (MW/min) | 1.17 | 1.17 | 1.92 | 3.23 | 1.33 | 1.00 | 2.00 |
| $RU_h$ (MW/min) | 1.17 | 1.17 | 1.92 | 3.23 | 1.33 | 1.00 | 2.00 |
| $a$ (MW/(Hm$^3$/h)$^2$) | -42 | -30 | -12.5 | -31 | -38.8 | -31.2 | -14.4 |
| $b$ (MW/(Hm$^3$/h)) | 113 | 106.2 | 78.8 | 155.1 | 121.75 | 98.42 | 85.5 |
| $c$ (MW) | -1.82 | -6.0 | 7.26 | 7.5 | -2.64 | -7.23 | 6.45 |
| $q_{\min,h}$ (Hm³/h) | 0.1 | 0.1 | 0.13 | 0.15 | 0.1 | 0.1 | 0.15 |
| $q_{\max,h}$ (Hm³/h) | 1.0 | 1.0 | 2.0 | 2.0 | 1.0 | 1.0 | 2.0 |
| $r_h$ (Hm³/h) | 0.4 | 0.3 | 0.2 | 0.3 | 0.3 | 0.2 | 0.12 |
| $s_{\min,h}$ (Hm³/h) | 0.1 | 0.1 | 0.2 | 0.2 | 0.1 | 0.1 | 0.2 |
| $s_{\max,h}$ (Hm³/h) | 1.0 | 1.0 | 2.0 | 2.0 | 1.0 | 1.0 | 2.0 |
| $V_{0,h}$ (Hm³) | 10.0 | 8.0 | 17.0 | 11.0 | 10.0 | 9.0 | 18.0 |
| $V_{NT,h}$ (Hm³) | 10.0 | 8.0 | 17.0 | 11.0 | 10.0 | 9.0 | 18.0 |
| $V_{\min,h}$ (Hm³) | 7.0 | 4.0 | 10.0 | 7.0 | 6.0 | 5.0 | 12.0 |
| $V_{\max,h}$ (Hm³) | 15.0 | 13.0 | 24.0 | 16.0 | 16.0 | 14.0 | 30.0 |
| Catchment Index | 1 | 1 | 1 | 1 | 2 | 2 | 2 |
| Upstream Unit | - | - | H2,H1 | H3 | - | H5 | H6 |
| Downstream Unit | H3 | H3 | H4 | - | H6 | H7 | - |
| Delay Time | 2 | 2 | 2 | 2 | 2 | 2 | 2 |

TABLE II THREE-HOUR AHEAD CASES

| Case | Coordinate | Stochastic | Energy Balancing Price ($/MWh) |
|---|---|---|---|
| 1 | No | No | 5.00 |
| 2 | No | Yes | 5.00 |
| 3 | No | No | 50.00 |
| 4 | No | Yes | 50.00 |
| 5 | Yes | No | - |
| 6 | Yes | Yes | - |

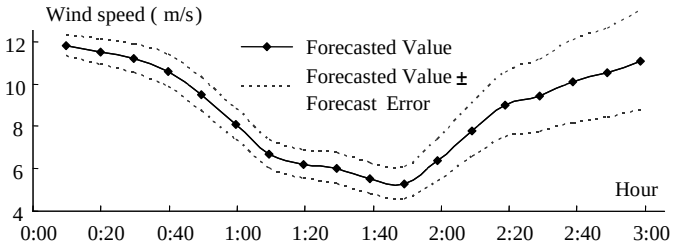

Fig. 1 Wind speed forecast

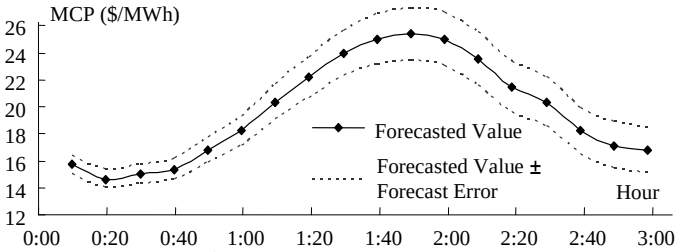

Fig. 2 Day-ahead MCP forecast

The wind speed forecast follows the Weibull distribution function, with the Weibull constant equal to 2 and the average wind speed equal to 9.1 m/s. The 3-hour pattern strength is 0.34 at the peak hour 3, which is the ratio of the peak wind speed to the average wind speed during the 3-hour period. ARMA model is used to simulate the wind speed forecast error [27]-[28]. Since the autocorrelation factor (ACF) and partial autocorrelation factor (PACF) decrease dramatically as the time lag increases, a lower order ARMA (1,1) represented in (33) is used.

$$X(t,k) = \alpha \cdot X(t,k-1) + \beta \cdot Z(t,k-1) + Z(t,k) \qquad k \in [2, NK]$$
$$X(t,1) = \alpha \cdot X(t-1, NK) + \beta \cdot Z(t-1, NK) + Z(t,1) \qquad (33)$$

ARMA constants can be procured by minimizing the difference in the root mean square error (RMSE) between the simulated ARMA model and the wind speed measurement data [28]. In this paper, it is assumed that the ARMA constants are $\alpha = 0.88, \beta = -0.34$. The standard deviation represented by the truncated Gaussian distribution function $[-\sigma, +\sigma]$ in which $\sigma$ ranges from 3% of the wind speed forecast for a 10-minute lag time to 11% of the wind speed forecast for a 3-hour lag time, which shows that the forecast error increases linearly in the forecast horizon. Once a large number of scenarios are generated, the boundary levels are derived by the maximum deviations of wind speed scenarios located above/below the forecast as shown in Fig. 1.

Similarly, autoregressive integrated moving average (ARIMA) is used to procure the price forecast error, which is a non-stationary stochastic process. The non-stationary forecasted time series can be represented by periodic and stationary time series. In this case, the trend of periodic component is shown in Fig. 2, while the standard deviation of the stationary component represented by the truncated Gaussian distribution function $[-\sigma, +\sigma]$ is 1% for a 10-min lag and 5% for a 3-hour lag [31]. The standard deviation of stationary components increases linearly with the time-lag. The 3-hour pattern strength is 0.28, and the peak price hour is 1:50. The average price is 19$/MWh. The boundary levels in Fig. 2 show the maximum deviation of random variables located above/below the forecast at each time interval.

The number of scenarios is reduced to 3 with the corresponding probabilities of 0.5188, 0.1822, and 0.2990, respectively. The probabilities are procured by eliminating scenarios with very low probabilities and bundling scenarios that are very close in terms of statistical metrics [19]-[20]. The simulation results are compared in coordinated and uncoordinated scheduling cases. The payoffs for Cases 1-6 are summarized in Table III with a target payoff of $6,000. The

results are discussed as follows.

TABLE III PAYOFFS IN THE THREE-HOUR AHEAD PROBLEM ($)

| | Case 1 | Case 2 | Case 3 | Case 4 | Case 5 | Case 6 |
|---|---|---|---|---|---|---|
| Imbalance Costs | 1,395 | 1,598 | 3,055 | 933 | 0 | 0 |
| Wind Energy Sales | 6,153 | 6,280 | 4,354 | 4,348 | 4,529 | 4,713 |
| Wind Energy Payoff | 4,758 | 4,682 | 1,299 | 3,415 | 4,529 | 4,713 |
| Hydro Energy Payoff | 2,111 | 2,275 | 2,111 | 2,275 | 2,098 | 1,637 |
| Total Payoff | 6,869 | 6,957 | 3,410 | 5,690 | 6,627 | 6,350 |
| EDR | 45 | 19 | 2,584 | 348 | 230 | 0 |

*A1) Uncoordinated scheduling of wind and hydro units*

Figs. 2-6 show the dispatch results for the uncoordinated scheduling Cases 1-4 listed in Table II. In Cases 1 and 2, the imbalance energy charges have a smaller impact on payoff since the energy balancing price is 5 $/MWh which is much lower than average MCPs.

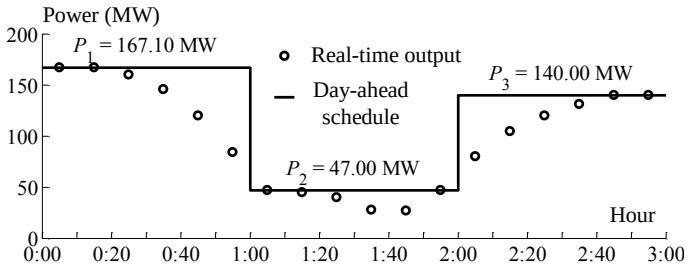


Fig. 3 Three-hour ahead schedule in Case 1

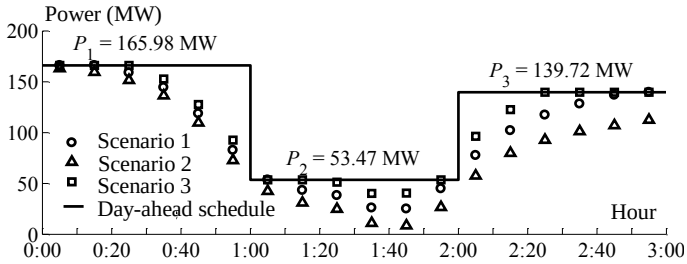


Fig. 4 Three-hour ahead schedule in Case 2

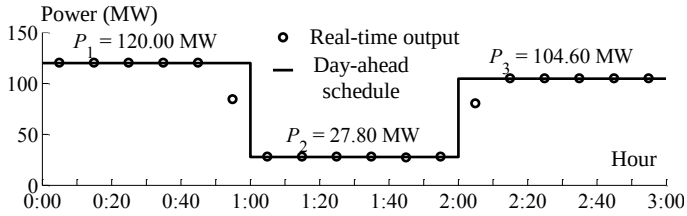


Fig. 5 Three-hour ahead schedule in Case 3

We offer the following observations.

- *Deterministic versus stochastic scheduling solutions*

The imbalance energy, its cost, and the wind energy curtailment are higher in the stochastic solution. Figs. 3-4 show that there are 3.27 MWh and 6.21 MWh of curtailments in Cases 1 and 2, respectively. Comparing Cases 3 and 4, the imbalance energy in Case 3 is 10.22 MWh while it increases to 13.13 MWh in Case 4. The imbalance energy charge in Case 3 is $711.55 which increases to $933.02 in Case 4. Figs. 5-6 show 59.98 and 63.30 MWh of curtailment in Case 3 and 4 respectively. At certain intrahours, the wind power generation is not the same as its hourly dispatch which indicates that the wind power is curtailed to minimize imbalance energy charges. Table III shows that the stochastic scheduling solutions would lead to higher payoffs in the uncoordinated cases. The hydro unit payoff is also increased in the stochastic solutions; however, the wind unit payoff calculated by the energy balancing price increases from Case 3 to 4, and decreases from Case 1 to 2. The deterministic payoffs and imbalance energy costs in Table III are forecast values which are procured by applying deterministic values to uncertain parameters in the market.

- *Impact of energy balancing price on imbalance energy*

As the energy balancing price increases, the imbalance energy decreases. Here, the imbalance energy is decreased from 55.20 MWh in Case 1 to 10.22 MWh in Case 3. The same applies to Cases 2 and 4.

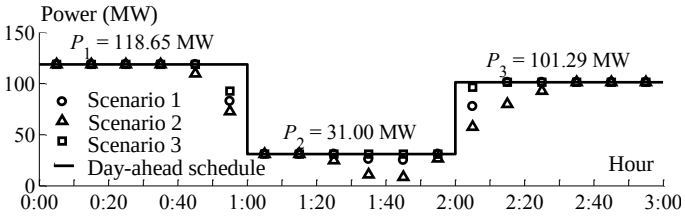


Fig. 6 Three-hour ahead schedule in Case 4

- *Impact of energy balancing price on wind energy curtailment*

Comparing Cases 1 and 2 with Cases 3 and 4, it is seen that higher energy balancing price increases the wind energy curtailment to avoid imbalance energy charges. The wind energy curtailment increases from 3.27 MWh in Case 1 to 59.98 MWh in Case 3. A similar observation can be procured for stochastic Cases 2 and 4.

- *Impact of energy balancing price on total payoff*

Table III shows a lower payoff when the energy balancing price is higher. A lower payoff occurs when the wind energy unit payoff is lowered due to the imposed energy balancing price. The comparison shows that the stochastic scheduling solution demonstrates a higher payoff once energy balancing prices are higher. The increase in payoff from Case 1 to Case 2 is 1.3% while the increase in payoff from Case 3 to Case 4 is 66.8%.

- *EDR in deterministic and stochastic cases*

The EDR of the deterministic solution measures the risk of the deterministic solution in terms of scenarios. The EDR for a target payoff of $6,000 is $45.62 for the deterministic solution (Case 1) and $19.50 for the stochastic solution (Case 2). The difference of $26.12 shows a lower risk for the stochastic scheduling solution. Thus, the stochastic solution would increase the total payoff and decrease the financial risks as compared with the deterministic scheduling solution.

*A2) Coordinated wind and cascaded hydro units*

Cases 5 and 6 investigate the benefits of coordinated dispatch of cascaded hydro and wind units. In comparison with Cases 1-4, imbalance energy charges are not incurred in Cases 5 and 6 since the scheduling coordination of wind and cascaded hydro units will firm up the output and $P^{s}_{\Delta,wtk}$ is zero. The following observations are deducted by comparing coordinated and uncoordinated scheduling cases.

- *Impact of stochastic analysis*

Figs. 7 and 8 show a wind energy curtailment of 12.42 MWh and 37.08 MWh in Cases 5 and 6. Again, the wind energy curtailment is higher in the stochastic scheduling cases.

- *Impact on the total payoff and risk*

The coordinated Cases 5 and 6 in Table III show that the stochastic solution would result in lower risks and total payoffs. In Table III, although the downside risk is decreased in the stochastic solution, the total payoff is decreased by 4.2%. In addition, the cascaded hydro unit payoffs are decreased in the coordinated scheduling cases. Hence, the scheduling coordination may not be economically beneficial for cascaded hydro units. Comparing Cases 4 and 6, it is shown that higher energy balancing prices will lower the risk and increase the expected payoff with the coordination. However, Cases 2 and 6 show that the coordination may not improve the GENCO's expected payoff in a lower energy balancing price.

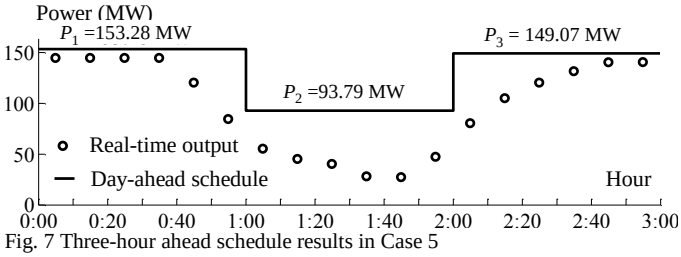


Fig. 7 Three-hour ahead schedule results in Case 5

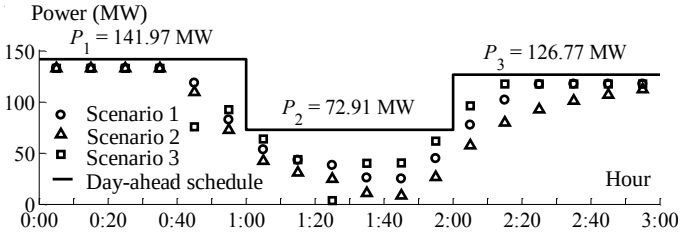


Fig. 8 Three-hour ahead schedule results in Case 6

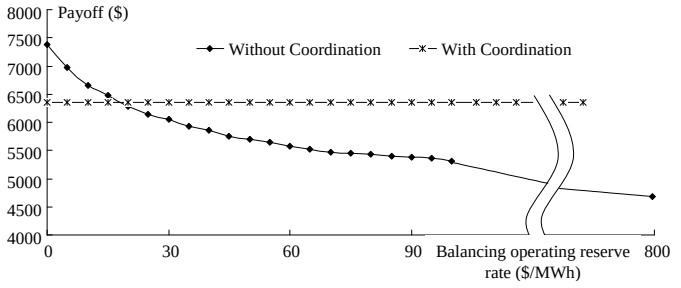


Fig. 9 Payoffs with energy balancing price

Fig. 9 presents the payoffs in Cases 4 and 6. For the uncoordinated Case 4, the expected payoff decreases with an increase in energy balancing price until the price is high enough to eliminate wind power deviations; so the payoff is the highest at the zero energy balancing price. In this case, the maximum expected payoff is \$7,374.06 at $\rho_{BP}$ = 0 \$/MWh, and the minimum payoff is \$4,619.51 starting roughly at $\rho_{BP}$ = 800 \$/MWh. In the coordinated Case 6, the expected payoff is constant since the energy balancing prices have no impact on payoffs. The uncoordinated and coordinated scheduling cases are equally profitable in Fig. 9 where the two curves cross ($\rho_{BP}$ = 18.2\$/MWh). Thus, the coordination provides a higher return when the energy balancing price is higher than 18.2\$/MWh.

### *B. DAY-AHEAD SCHEDULING*

We consider the day-ahead schedule in a GENCO with 3 wind farms (W1-W3) and 7 hydro units in two catchments (H1-H4 in catchment 1 and H5-H7 in catchment 2). The wind farm capacities are 200MW, 200MW and 250MW, respectively and the wind power curves are shown in Fig. 10. We assume W1 and W2 are located near catchment 1 and W3 is close to catchment 2. Thus, the coordinated scheduling of W1-H2, W2-H3, and W3-H6 is considered.

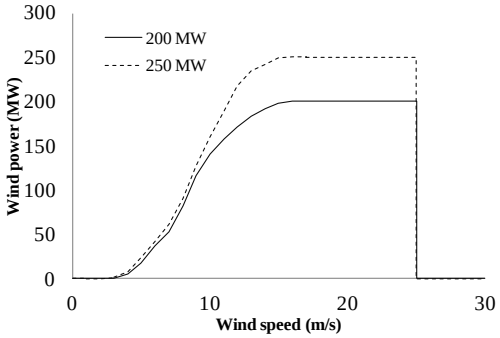


Fig. 10 wind turbine power curves

The hydro unit characteristics are given in Table I, and market prices and wind speeds are forecasted as discussed before. 10,000 scenarios are generated originally and 30 are retained after scenario reduction. In this case study, the standard deviation of forecast error of wind speeds increases linearly from 3% of forecasted wind speed for the 1-hour lag time to 11% of forecasted wind speed for the 24-hours lag time. The diurnal strength pattern is 0.34 with the average wind speed 9.1 m/s and hour of peak wind speed of 24. The wind generation forecast error of W3 is shown in Fig. 11. Here, the wind power forecast error is higher than that of the wind speed because of non-linear and non-convex characteristics of the wind turbine power curve. Alternatively, the forecast error of wind generation can be simulated by fat tailed Beta distribution function in which the parameters are dependent on wind generation levels [32].

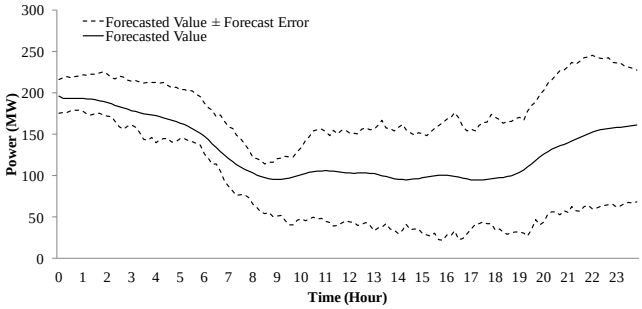


Fig. 11 Wind power forecast error of W3

TABLE IV CASES CONSIDERED IN THE DAY-AHEAD SCHEDULING

| Case | Coordination | W1 | W2 | W3 | Stochastic | Risk-Constrained |
|---|---|---|---|---|---|---|
| 1 | No | - | - | - | Yes | No |
| 2 | No | - | - | - | Yes | Yes |
| 3 | Yes | H2 | H3 | H6 | Yes | No |
| 4 | Yes | H2 | H3 | H6 | Yes | Yes |

The wind generation forecast error is procured based on the wind speed forecast error and four cases are studied as shown in Table IV. The energy balancing price of 30$/MWh is used in all four cases and risk constraint is imposed as given in Table IV. The stochastic PBUC has 160,010 continuous variables, 18,576 binary variables, and 171,685 constraints, which is solved in about 30 seconds with an Intel 2.13 GHz personal computer. The impact of coordination and risk constraints are evaluated on the GENCO's hourly scheduling, generation dispatch, and payoff. The results are discussed as follows.

- *Impact on unit commitment (UC)*

Tables V-VIII show the UC results for units H2, H5 and H6 in Cases 1-4. Comparing Cases 2-4 with Case 1, the hourly unit commitment changes are highlighted in Tables VI-VIII. The changes in Table VI are due to the inclusion of risk constraint. The UC solutions for units H2 and H6 are changed to satisfy the $\overline{EDR}$ limit for the given target payoff at the cost of lowering the payoff. The changes listed in Table VII are due to coordination. Similar to Case 2, the changes listed in Table VIII are due to risk constraints and coordination in Case 4. Since H5 is located on the upstream of H6 with a water discharge flow delay time of 2 hours, the scheduling coordination of W3-H6 when considering the risk constraint would require the commitment of H5 at hour 4 as opposed to hour 2. H5 is shutdown at the end of the day to satisfy terminal reservoir requirements. In Case 4, H2 and H6 are committed at all hours for coordination with wind units.

TABLE V UC FOR H2, H5 AND H6 IN CASE 1

| Unit | Hours (1-24) | | | | | | | | | | | | | | | | | | | | | | | |
|---|---|---|---|---|---|---|---|---|---|---|---|---|---|---|---|---|---|---|---|---|---|---|---|---|
| H2 | 0 | 0 | 0 | 0 | 1 | 0 | 0 | 1 | 1 | 1 | 1 | 1 | 1 | 1 | 1 | 1 | 1 | 1 | 1 | 1 | 1 | 0 | 0 | 0 |
| H5 | 1 | 1 | 1 | 0 | 1 | 1 | 1 | 1 | 1 | 1 | 1 | 1 | 1 | 1 | 1 | 1 | 1 | 1 | 1 | 1 | 1 | 1 | 0 | 0 |
| H6 | 0 | 1 | 1 | 0 | 1 | 0 | 1 | 1 | 1 | 1 | 1 | 1 | 1 | 1 | 1 | 1 | 1 | 1 | 1 | 1 | 1 | 1 | 0 | 0 |

TABLE VI UC FOR H2, H5 AND H6 IN CASE 2

| Unit | Hours (1-24) | | | | | | | | | | | | | | | | | | | | | | | |
|---|---|---|---|---|---|---|---|---|---|---|---|---|---|---|---|---|---|---|---|---|---|---|---|---|
| H2 | 0 | 0 | 0 | 0 | **0** | 0 | 0 | 1 | 1 | 1 | 1 | 1 | 1 | 1 | 1 | 1 | 1 | 1 | 1 | 1 | **1** | 0 | 0 |
| H5 | 1 | 1 | 1 | 0 | 1 | 1 | 1 | 1 | 1 | 1 | 1 | 1 | 1 | 1 | 1 | 1 | 1 | 1 | 1 | 1 | 1 | 1 | 0 | 0 |
| H6 | **1** | 1 | 1 | 0 | 1 | 0 | 1 | 1 | 1 | 1 | 1 | 1 | 1 | 1 | 1 | 1 | 1 | 1 | 1 | 1 | 1 | 1 | 0 | 0 |

TABLE VII UC FOR H2, H5 AND H6 IN CASE 3

| Unit | Hours (1-24) | | | | | | | | | | | | | | | | | | | | | | | |
|---|---|---|---|---|---|---|---|---|---|---|---|---|---|---|---|---|---|---|---|---|---|---|---|---|
| H2 | **1** | **1** | **1** | **1** | 1 | **1** | **1** | 1 | 1 | 1 | 1 | 1 | 1 | 1 | 1 | 1 | 1 | 1 | 1 | 1 | **1** | **1** | **1** |
| H5 | 1 | 1 | 1 | 0 | 1 | 1 | 1 | 1 | 1 | 1 | 1 | 1 | 1 | 1 | 1 | 1 | 1 | 1 | 1 | 1 | 1 | 0 | 0 |
| H6 | **1** | 1 | 1 | **1** | 1 | **1** | 1 | 1 | 1 | 1 | 1 | 1 | 1 | 1 | 1 | 1 | 1 | 1 | 1 | 1 | 1 | **1** | **1** |

TABLE VIII UC FOR H2, H5 AND H6 IN CASE 4

| Unit | Hours (1-24) | | | | | | | | | | | | | | | | | | | | | | | |
|---|---|---|---|---|---|---|---|---|---|---|---|---|---|---|---|---|---|---|---|---|---|---|---|---|
| H2 | **1** | **1** | **1** | **1** | 1 | **1** | **1** | 1 | 1 | 1 | 1 | 1 | 1 | 1 | 1 | 1 | 1 | 1 | 1 | 1 | **1** | **1** | **1** |
| H5 | 1 | **0** | 1 | **1** | 1 | 1 | 1 | 1 | 1 | 1 | 1 | 1 | 1 | 1 | 1 | 1 | 1 | 1 | 1 | 1 | 1 | 0 | 0 |
| H6 | **1** | 1 | 1 | **1** | 1 | **1** | 1 | 1 | 1 | 1 | 1 | 1 | 1 | 1 | 1 | 1 | 1 | 1 | 1 | 1 | 1 | **1** | **1** |

- *Impact on generation dispatch*

Figs. 12-13 show the generation dispatch of W1 in Cases 1 and 3. The generation dispatch of W1 in Cases 2 and 4 have similar trends and thus are not presented here. As expected, the generation dispatch follows the trend in wind energy scenarios. Without any coordination, the optimal generation dispatch incurs an average wind power curtailment of 12.99 MW. The expected wind energy imbalance is 27.58 MWh for W1. With coordination, the average wind power curtailment is 3 MW which is 76.9% lower than that without coordination. The hydro unit generation is represented by the distance between dots and the generation dispatch curve. There is no imbalance wind energy because hydro units provide intrahour power to complement the wind unit generation.

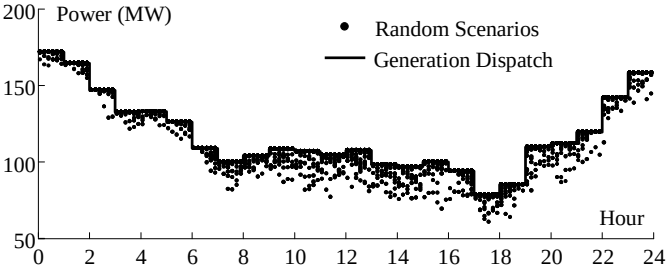

Fig. 12 Day-ahead generation dispatch of W1 in Case 1

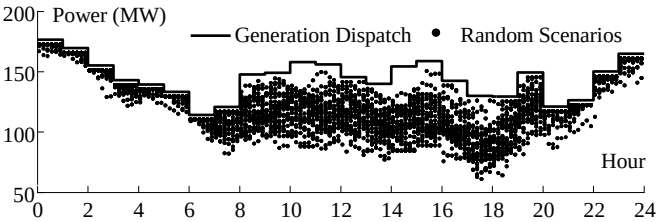

Fig. 13 Day-ahead generation dispatch of W1 in Case 3

- *Impact on payoff*

Table IX shows expected payoffs and downside risks with a target payoff of $900,000. If the expected downside risk of $7,648 in Case 1 is unacceptable, the GENCO can control the associated risk level with the proposed method. In order to obtain the minimum allowable downside risk, the risk will be penalized in the objective function with a large penalty factor. Accordingly, the minimum downside risk is $6,855 with an expected payoff of $896,730. In Case 2, an acceptable risk level is $7,000 with a payoff of $897,498. In comparison with Case 1, the risk is reduced by (7,648 – 7,000) / 7,648 = 8.48% at the cost of reducing the expected payoff by ($897,956 – $897,498) / 897,956 = 0.05%.

In Case 3, EDR is $3,082 with an expected payoff of $914,083. The minimum EDR is $2,997 with an expected payoff of $913,747 which is procured by penalizing the risk into the objective. In Case 4, we set the maximum EDR to $3,000 and obtain an expected payoff of $913,756, which shows a reduction in risk of 2.66% at the cost of 0.04% reduction in payoff, as compared to Case 3.

Table IX shows that the scheduling coordination will increase the expected payoff and decrease the downside risk. By setting EDR in an acceptable range in Cases 2 and 4, the expected payoff in the coordinated Case 4 will be higher. Table IX shows that the acceptable EDR in Case 4 is far less than that in Case 2; hence scheduling coordination will decrease EDR and increase the expected payoff.

TABLE IX EXPECTED PAYOFF AND DOWNSIDE RISK FOR ALL CASES ($)

| Case | Expected Payoff | Downside Risk |
|---|---|---|
| 1 | 897,956 | 7,648 |
| 2 | 897,498 | 7,000 |
| 3 | 914,083 | 3,082 |
| 4 | 913,756 | 3,000 |

## IV. Conclusions

The proposed study and its results demonstrate that the scheduling coordination of cascaded hydro and wind units can firm up wind energy, increase expected payoffs, and reduce downside risks of GENCOs. When wind and hydro units are not coordinated, energy balancing prices would affect the generation dispatch decisions. Also, the expected payoff will decrease when the energy balancing price is increased. It is shown that depending on the energy balancing price, the payoff in uncoordinated hydro and wind unit cases may be larger than that in coordinated cases. Hence, the GENCO may decide to schedule cascaded hydro and wind units in either coordinated or uncoordinated configurations, which depends on the accuracy of forecast of the day-ahead energy balancing price. The wind energy curtailment will increase with energy balancing prices, in order to avoid imbalance energy charges. Thus, the coordination of wind and hydro scheduling would lower the wind curtailment and increase the GENCO's payoff by mitigating the imbalance energy charges. The coordination will result in lower wind curtailment in both stochastic and deterministic scheduling solutions. It is shown that the hydro unit payoffs will decrease once they are coordinated with wind energy units. However, eliminating the imbalance energy charges for wind energy units in coordinated cases could increase the total payoff of a GENCO at certain energy balancing prices.

The stochastic scheduling solution would lower the GENCO's expected downside risk as compared to the deterministic scheduling solution. In addition, in uncoordinated cases, the stochastic scheduling solution will result in higher payoffs for a GENCO as compared to the deterministic scheduling solution.

Other storage technologies, such as the vanadium redox-flow battery (VRB) storage and pumped-storage hydro, may also be used to firm up wind energy. However, storage efficiency cycle, storage capacity, reservoir balance, and limited number of charge/discharge cycles per day could increase wind power curtailments and limit the GENCO's payoffs.

## References


[1] A. Pullen and M. Eneland, *Global Wind 2006 Report, GWEC, Global Wind Energy Council*, Brussels, Belgium. May 2007. Available: http://www.gwec.net/index.php?id=78.

[2] International Energy Agency. (2005, June). *Variability of Wind Power and Other Renewables-Management options and strategies* [on-line]. Available: http://www.awea.org/policy/regulatory_policy/transmission_documents/iea_report_variability_wind.pdf.

[3] P.B. Eriksen, T. Ackermann, H. Abildgaard, P. Smith, W. Winter and J. Rodriguez Garcia, "System operation with high wind penetration," *IEEE Power and Energy Magazine*, vol. 3 , no. 6, pp. 65-74, Nov.-Dec. 2005.

[4] M. Ahlstrom, L. Jones, R. Zavadil, and W. Grant, "The future of wind forecasting and utility operations," *IEEE Power and Energy Magazine*, vol.3, no.6, pp. 57-64, Nov.-Dec. 2005.

[5] G. Kariniotakis, et al., "Next generation forecasting tools for the optimal management of wind generation," in *Proc. International Conference on Probabilistic Methods Applied to Power Systems*, pp. 1-6, Jun. 2006.

[6] I. Sánchez, "Short-term prediction of wind energy production", *International Journal of Forecasting*, vol. 22, no.1, pp. 43-56, Jan. 2006.

[7] *ERCOT Wind Impact / Integration Analysis, Phase 1 Review: Variability and Predictability*, ROS Wind A/S Task Force Meeting, Oct. 2007. http://www.ercot.com/meetings/ros/keydocs/2007/1022/Variablity_and_ Predictability_draft_dlvd_2a.zip.

[8] *ERCOT Wind Impact / Integration Analysis, Phase 2 Review: Ancillary Services Requirements*, Wind Impact Task Force Meeting, Feb. 2008. http://www.ercot.com/meetings/ros/keydocs/2008/0201/ERCOT_AS-Ph2_d7.pdf.

[9] T. Hennessy and M. Kuntz, "The multiple benefits of integrating electricity storage with wind energy," in *Proc. 2005 IEEE Power Engineering Society General Meeting*, vol. 2, pp. 1952-1954, Jun. 2005.

[10] J.C. Smith, M. Milligan, E.A. DeMeo and B. Parsons, "Utility wind integration and operating impact state of the art," *IEEE Trans. Power Syst.*, vol. 22, no. 3, pp.782-789, 2007.

[11] J. Wang, M. Shahidehpour, and Z. Li, "Security-constrained unit commitment with volatile wind power generation," *IEEE Trans. Power Syst.*, vol. 23, no. 3, pp. 1319-1327, Aug. 2008.

[12] A. Tuohy, P. Meibom, E. Denny, and M. O'Malley, "Unit commitment for systems with significant wind penetration," *IEEE Trans. Power Syst.*, vol. 24, no. 2, pp. 592-601, May 2009.

[13] R. Billinton, B. Karki, R. Karki, and G. Ramakrishna, "Unit commitment risk analysis of wind integrated power systems," *IEEE Trans. Power Syst.*, vol. 24, no. 2, pp. 930-939, May 2009.

[14] M. Shahidehpour, H. Yamin, and Z. Li, *Market Operations in Electric Power Systems.* New York: Wiley, 2002.

[15] T. Li and M. Shahidehpour, "Strategic bidding of transmission-constrained GENCOs with incomplete information," *IEEE Trans. Power Syst.*, vol. 20, no. 1, pp.437-447, Feb. 2005.

[16] J. M. Arroyo and A.J. Conejo, "Optimal response of a power generator to energy, AGC, and reserve pool-based markets," *IEEE Trans. Power Syst.*, vol. 17, no. 2, pp. 404-410, May 2002.

[17] T. Li and M. Shahidehpour, "Risk-constrained bidding strategy with stochastic unit commitment," *IEEE Trans. Power Syst.*, vol. 22, no. 1, pp.449- 458, Feb. 2007.

[18] L. Wu, M. Shahidehpour, and Z. Li, "GENCO's risk-constrained hydrothermal scheduling," *IEEE Trans. on Power Systems*, vol.23, no. 4, pp. 1847-1858, Nov. 2008.

[19] J. Dupacová, N. Gröwe-Kuska, and W. Römisch, "Scenario reduction in stochastic programming: An approach using probability metrics," *Math. Program.*, ser. A 95, pp. 493–511, 2003.

[20] GAMS/SCENRED Documentation. [Online]. Available: http://www.gams.com/docs/document.htm.

[21] *2006 State of the Market Report: Volume II*, PJM Interconnection, Market Monitoring Unit, pp. 151-158, Mar. 2007. http://www2.pjm.com/markets/market-monitor/downloads/mmu-reports/2006-som-volume-ii.pdf.

[22] S. Mariano, M. Calado, and L. Ferreira, "Dispatch of head dependent hydro units: modeling of optimal generation in electricity market," *IEEE Power Tech 2009 Bucharest*, June 2009.

[23] S. Bisanovic, M. Hajro, and M. Dlakic, "Hydrothermal self-scheduling problem in a day-ahead electricity market," *Electric Power System Research*, vol. 78, no. 9, pp. 1579-1596, Sep. 2008.

[24] X. Guan, E. Ni, R. Li, and P. B. Lu,"An optimization-based algorithm for scheduling hydrothermal power systems with cascaded reservoirs and discrete hydro constraints," *IEEE Trans. Power Syst.*, vol. 12, no. 4, pp. 1775-1780, Nov. 1997.

[25] T. Li and M. Shahidehpour, "Price-based unit commitment: a case of Lagrangian relaxation versus mixed integer programming," *IEEE Trans. on Power Systems*, vol.20, no. 4, pp. 2015-2025, Nov. 2005.

[26] J. F. Manwell, et al. "Hybrid2- a hybrid system simulation model theory manual," Renewable Energy Research Laboratory, Department of Mechanical Engineering, University of Massachusetts, Jun. 2006.

[27] L. Söder, "Simulation of wind speed forecast errors for operation planning of multiarea power systems," in *Proc. Probabilistic Methods Applied to Power Systems, 2004 International Conference on*, pp. 723-728, 12-16 Sep. 2004.

[28] A. Boone, "Simulation of short-term wind speed forecast errors using a multi-variate ARMA (1,1) time-series model," Master Thesis, KTH 2005.

[29] M. Shahidehpour and Y. Fu, "Benders decomposition - applying Benders decomposition to power systems," *IEEE Power & Energy Magazine* vol. 3, no. 2, pp. 20-21, Mar. 2005.

[30] L. Wu and M. Shahidehpour, "Accelerating the Benders decomposition for network-constrained unit commitment problems," *Energy Systems*, Vol. 1, no. 3, pp. 339-376, Jul. 2010.

[31] M. Zhou, Z. Yan, and G. Li, "An ARIMA approach to forecasting electricity price with accuracy improvement by predicted errors," *IEEE*

*Power Engineering Society general meeting*, vol. 1, pp. 233-238, Jun. 2004.

[32] H. Bludzuweit, J.A. Dominguez-Navarro, and A. Llombart, "Statistical analysis of wind power forecast error," *IEEE Trans. Power Syst.*, vol. 23, pp. 983-991, Aug. 2008.

## BIOGRAPHIES

**Lisias V. L. Abreu** (M'05) received his Ph.D. degree in electrical engineering from Illinois Institute of Technology in 2008. He is currently employed by GE Energy.

**Mohammad E. Khodayar** (S'09) received his BS and MS degree in Electrical Engineering from Amirkabir University of Technology (Tehran Polytechnic) and Sharif University of Technology respectively. Presently he is PhD student in Electrical Engineering at Illinois Institute of Technology, USA. His research interests include renewable energies, electricity markets and power system operation and control.

**Mohammad Shahidehpour** (F'01) is the Bodine Professor and Director of the Robert W. Galvin Center for Electricity Innovation at Illinois Institute of Technology. Dr. Shahidehpour is the recipient of the Honorary Doctorate for the Polytechnic University of Bucharest in Romania. He is an Honorary Professor in the North China Electric Power University and the Sharif University in Iran.

**Lei Wu** (M'07) received his BS in Electrical Engineering and MS in Systems Engineering from Xi'an Jiaotong University, China, in 2001 and 2004, respectively, and Ph.D. in EE from Illinois Institute of Technology, USA, in 2008. He was a Senior Research Associate in the ECE Department at Illinois Institute of Technology from 2008 to 2010. Presently, he is an Assistant Professor in the ECE Department at Clarkson University. His research interests include power systems restructuring and reliability.

Applied Energy 96 (2012) 4–11

Contents lists available at SciVerse ScienceDirect

Applied Energy

journal homepage: www.elsevier.com/locate/apenergy

# Generation risk assessment in volatile conditions with wind, hydro, and natural gas units

Cem Sahin [a,*], Mohammad Shahidehpour [b], Ismet Erkmen [c]

[a] Power Systems Department, Space Technologies Research Institute, TUBITAK, METU Campus, Ankara, Turkey
[b] ECE Department, Illinois Institute of Technology, United States
[c] EEE Department, Middle East Technical University, Turkey

ARTICLE INFO

*Article history:*
Received 14 April 2011
Received in revised form 8 September 2011
Accepted 1 November 2011
Available online 30 November 2011

*Keywords:*
Stochastic price-based unit commitment
Financial and physical risks
Wind unit generation
Hydro unit constraints
Natural gas constraints
Bilateral energy contracts

ABSTRACT

This paper studies a generating company (GENCO)'s midterm (a few months to a year) scheduling payoffs and risks in volatile operating conditions. The proposed algorithm considers the integration of intermittent wind units into a GENCO's generation assets and coordinates the GENCO's hourly wind generation schedule with that of natural gas (NG) units (with volatile gas prices) and hydro units (with water inflow forecast) for maximizing the GENCO's payoff. The proposed midterm GENCO model applies market price forecasts to the risk-constrained stochastic price-based unit commitment (PBUC) for calculating the GENCO's risk in energy and ancillary services markets. The proposed PBUC minimizes the cost of (a) NG contracts, storage, startup and shutdown, (b) startup and shutdown of cascaded hydro units, and (c) penalty for defaulting on the scheduled power delivery. Simulation results show that the diversification of generating assets including bilateral contracts (BCs) could enhance the GENCO's midterm planning by increasing the expected payoff and decreasing the financial risk.



## 1. Introduction

Generating companies (GENCOs) are self-interested entities in restructured power systems, which are responsible for the midterm operation planning of their respective generating units. This paper proposes an optimization framework for a GENCO's midterm coordinated operation planning with wind, hydro, and NG units.

When considering the volatility of NG prices, it is imperative to include the NG transmission system and the uncertainties related to NG transmission system interruptions, which could further impose limits on the availability of NG and the scheduling of NG-fired units by GENCOs. Ref. [1] presented the impact of NG infrastructure contingencies on power system operations and discussed the role of renewable resources on reducing the dependence of electricity infrastructure on the NG infrastructure. Ref. [2] presented an integrated model for assessing the impact of electricity and NG networks on power system security. The integrated model incorporated the simplified linear NG network constraints into the optimal solution of SCUC. Ref. [3] included nonlinear NG network equations in the security-constrained unit commitment (SCUC) problem using a decomposition approach. Ref. [4] proposed a component-based model for the scheduling of combined-cycle gas units by mixed-integer programming. Ref. [5] considered a linear NG network model for representing NG network constraints and interruption uncertainties in evaluating GENCO's risk.

Wind power is the fastest growing renewable energy resource since it is clean, indigenous, fast to deploy and economically competitive with other generation types. However, the intermittent and volatile nature of wind energy should be properly modeled in operational planning analyses. The stochastic SCUC solution with integrated wind energy has usually focused on the short-term operation planning. The effect of wind energy uncertainty on the day-ahead planning was included in SCUC [6]. The impact of wind generation on regulation and load following was analyzed in [7]. Ref. [8] studied the impact of high wind penetration on the day-ahead scheduling. Ref. [9] investigated the short-term wind energy forecast errors on the day-ahead generation scheduling. However, a GENCO would be concerned with its midterm risks when inexpensive and volatile wind units are utilized. The proposed algorithm for the midterm operation planning of a GENCO would consider the volatility of wind units when minimizing the risk of forecast errors for water inflows in hydro units and market prices of electricity and gas.

Forward BCs may hedge GENCO's volatilities. However, a large BC in a volatile environment could expose GENCOs to high penalty payments for defaulting on contracts. In [10], a stochastic decision framework for energy procurement of large customers was proposed. The supply portfolio was optimized considering uncertain pool prices, BCs, and self generation. CVaR was used to formulate risks, and the risk term was added to the objective function with

* Corresponding author. Tel.: +90 5337493205.
*E-mail addresses:* cem.sahin@uzay.tubitak.gov.tr (C. Sahin), ms@iit.edu (M. Shahidehpour), erkmen@metu.edu.tr (I. Erkmen).

0306-2619/$ - see front matter © 2011 Elsevier Ltd. All rights reserved.
doi:10.1016/j.apenergy.2011.11.007

**Nomenclature**

*Indices*

| | |
|---|---|
| $h$ | index of hydro units |
| $j$ | index of NG units |
| $l$ | index of hydro catchments |
| $n$ | index of NG contracts |
| $s$ | index of scenarios |
| $t$ | index of time in BC period (h) |
| $u$ | index of NG storage facilities |
| $w$ | index of wind units |
| $z$ | index of BC periods |

*Dimensions*

| | |
|---|---|
| $NCM$ | number of hydro catchments |
| $NGC$ | number of NG contracts |
| $NNG$ | number of NG-fueled units |
| $NGS$ | number of NG storage facilities |
| $NH_l$ | number of hydro units of a hydro catchment $l$ |
| $NS$ | number of scenarios |
| $NT$ | number of hours |
| $NW$ | number of wind units |
| $NZ$ | number of BC periods under study |

*Sets*

| | |
|---|---|
| $SBC$ | set of units assigned to honor a BC |
| $ST_z$ | set of hours for the BC period $z$ |

*Variables*

| | |
|---|---|
| $C_{ns}$ | cost of NG usage from contract $n$ in scenario $s$ |
| $C_{pen,zs}$ | penalty for deficient BC in period $z$ |
| $C_{us}$ | cost of NG usage from storage facility $u$ in scenario $s$ |
| $E_{bc,z}$ | BC in period $z$ |
| $E_{bc,\max}$ | upper energy limit for the flexible BC |
| $E_{bc,\min}$ | lower energy limit for the flexible BC |
| $E_{def,zs}$ | deficient BC in period in scenario $s$ |
| $E_{del,zs}$ | delivered BC in period z and scenario $s$ |
| $I$ | commitment state |
| $OR$ | operating reserve |
| $P$ | power generation |
| $P_{\Psi,wts}$ | wind generation of unit $w$ at time $t$ and scenario s |
| $P_{bc}$ | power generation to satisfy BC |
| $PF_s$ | GENCO's payoff in scenario $s$ |
| $R_{bc,z}$ | BC revenue in period $z$ |
| $RISK_s$ | GENCO's downside risk in scenario $s$ |
| $SD$ | shutdown cost |
| $SR$ | spinning reserve |
| $SU$ | startup cost |
| $TP$ | generation capacity offered to a day-ahead market |
| $W_{zs}$ | binary index indicating that the GENCO is defaulting on its BC at period $z$ under scenario $s$ |
| $\lambda$ | lagrange multiplier |
| $\psi_{wts}$ | stochastic speed of wind unit $w$ at hour $t$ in scenario $s$ |

*Constants*

| | |
|---|---|
| $A_w$ | area swept by the rotor of wind unit $w$ |
| $c_{P,w}$ | power coefficient of wind unit $w$ |
| $\underline{EDR}$ | expected downside risk |
| $\overline{EDR}$ | upper limit for expected downside risk |
| $p_s$ | probability for a scenario $s$ |
| $T_0$ | target payoff of a GENCO |
| $\rho_{air,w}$ | density of air at region where wind unit $w$ is located |
| $\rho_{bc}$ | BC price |
| $\rho_{g,ts}$ | market price for energy at time $t$ in scenario $s$ |
| $\rho_{or,ts}$ | market price for operating reserve at time $t$ in scenario $s$ |
| $\rho_{pen}$ | penalty price for a deficient BC |
| $\rho_{sr,ts}$ | market price for spinning reserve at time $t$ in scenario $s$ |
| $v_{CI,w}$ | cut-in wind speed of wind unit $w$ |
| $v_{CO,w}$ | cut-out wind speed of wind unit $w$ |
| $v_{R,w}$ | rated wind speed of wind unit $w$ |

a weight factor to address tradeoffs between cost and risk minimization. Ref. [11] presented the optimal bidding strategy as a nonlinear mathematical program with equilibrium constraints. The GENCO's payoff was maximized and expected offers, uncertain system loads, and BCs were modeled as constraints.

In this paper, we consider the simultaneous coordination of BC with several inexpensive but uncertain units in a GENCO for hedging payoffs. The proposed model, which is an extension of [5], considers the uncertain wind model and utilizes the risk-constrained stochastic PBUC framework. A GENCO with uncertain wind, hydro, and NG resources would use the proposed midterm planning for analyzing market risks and coordinating the hourly commitment schedules with BCs for maximizing the GENCO's financial payoffs.

The paper is organized as follows. The risk-based mathematical model is described in Section 2. The MIP-based PBUC solution is introduced in Section 3. Case studies are given in Section 4. Section 5 concludes this paper.

## 2. Risk-based MIP model

This section starts with defining the objective function of the risk-based MIP model. Then the unit, BC coordination and risk constraints are described.

### 2.1. Objective function

The stochastic operational planning problem is modeled using Monte-Carlo scenarios. The objective (1) is to maximize the expected payoffs over all scenarios. The payoff is the difference between revenues and expenses. The revenue (2) is due to sales of energy, spinning reserves, and operating reserves by NG, cascaded hydro, and wind units and the income from BC sales. The cost (3) includes that of (i) NG contracts, storage, startup and shutdown of NG units; (ii) startup and shutdown for cascaded hydro units; (iii) penalty for defaulting on the scheduled generation delivery.

$$\text{Max}\sum_{s=1}^{NS} p_s \cdot PF_s = \sum_{s=1}^{NS} p_s \cdot \{REVENUE_s - COST_s\} \tag{1}$$

where

$$\begin{aligned} REVENUE_s = &\sum_{j=1}^{NNG}\sum_{t=1}^{NT}[\rho_{g,ts}\cdot TP_{jts} + \rho_{sr,ts}\cdot SR_{jts} + \rho_{or,ts}\cdot OR_{jts}] \\ &+ \sum_{l=1}^{NCM}\sum_{h=1}^{NH_l}\sum_{t=1}^{NT}[\rho_{g,ts}TP_{hts} + \rho_{sr,ts}\cdot SR_{hts} + \rho_{or,ts}\cdot OR_{hts}] \\ &+ \sum_{w=1}^{NW}\sum_{t=1}^{NT}[\rho_{g,ts}\cdot TP_{wts} + \rho_{sr,ts}\cdot SR_{wts} + \rho_{or,ts}\cdot OR_{wts}] + \sum_{z=1}^{NZ} R_{bc,z} \end{aligned} \tag{2}$$

and

$$\begin{aligned} COST_s = &\sum_{n=1}^{NGC} C_{ns} + \sum_{u=1}^{NGS} C_{us} + \sum_{j=1}^{NNG}\sum_{t=1}^{NT}[SU_{jts} + SD_{jts}] \\ &+ \sum_{l=1}^{NCM}\sum_{h=1}^{NH_l}\sum_{t=1}^{NT}[SU_{hts} + SD_{hts}] + \sum_{z=1}^{NZ} C_{pen,zs} \end{aligned} \tag{3}$$

### 2.2. Unit constraints

The mathematical formulation for cascaded hydro, NG units, NG infrastructure constraints and wind units constraints are given as follows:

- Cascaded Hydro Constraints
  - (a) Generator availability constraint.
  - (b) Energy and ancillary services supplied.
  - (c) Water-to-power conversion.
  - (d) Operating regions (water discharge limits).
  - (e) Reservoir volume limits.
  - (f) Initial and terminal reservoir volumes.
  - (g) Water balance constraint.
  - (h) Minimum on/off time and ramping up/down constraints.
- NG Unit Constraints
  - (a) Generator availability constraint.
  - (b) Fuel consumption and emission allowance constraints for groups of NG units.
  - (c) Energy and ancillary services supplied.
  - (d) Minimum on/off time and ramping up/down constraints.
- NG Infrastructure Constraints

The hourly and yearly linear network flow models considering limits on pipelines, sub-areas, power plants, and units are adopted for the midterm stochastic model. The detailed description for the constraints regarding NG units, NG contracts, infrastructure and cascaded hydro units could be found in [5] and [13].

- Wind Unit Constraints

The nonlinear wind speed to power conversion curve is given in (4) and $P_{\psi,wts}$ is given as an input. The wind generation $w$ is subject to (5)

$$P_{\psi,wts}(\psi_{wts}) = \begin{cases} 0 & \text{if } \psi_{wts} < v_{\mathrm{CI},w} \\ 0.5 c_{\mathrm{p},w} \cdot \rho_{\mathrm{air},w} \cdot A_w \cdot (\psi_{wts})^3 & \text{if } v_{\mathrm{CI},w} \leqslant \psi_{wts} < v_{\mathrm{R},w} \\ P_{\mathrm{R},w} & \text{if } v_{\mathrm{R},w} \leqslant \psi_{wts} < v_{\mathrm{CO},w} \\ 0 & \text{if } \psi_{wts} \geqslant v_{\mathrm{CO},w} \end{cases} \forall w,\ \forall s \quad (4)$$

$$I_{wts} \cdot P_{\min,w} \leqslant P_{wts} \leqslant I_{wts} \cdot P_{\psi,wts}(\psi_{wts}) \quad \forall k, \forall s \quad (5)$$

The auto-regressive moving average (ARMA) based approach [12] would provide wind energy scenarios forecasts. The wind power forecast errors are simulated using ARMA series. The series parameters are fitted via an optimization algorithm considering the difference between old hourly forecasts and actual realized values. The obtained ARMA series is sampled in order to obtain the forecast errors for each time step $t$ for each scenario $s$. Finally, the wind power Monte-Carlo scenarios are taken to be the sum of the wind power forecasts and the sampled wind power forecast errors for the study horizon. The wind forecast and three Monte Carlo weekly wind power scenarios are depicted in Fig. 1.

### 2.3. Bilateral contracts and coordination

BC, transacted by external generating entities, can be either physical or financial. BC characteristics include:

(1) $NZ$: 52 weeks for a one year study;
(2) $\rho_{pen}$: BC penalty price ($/MW h) over the contract length.

A flexible $E_{bc,z}$ at period $z$ given in (6) can be adjusted by a GENCO for enhancing its payoff.

$$E_{bc,\min} \leqslant E_{bc,z} \leqslant E_{bc,\max}, \quad \forall z \quad (6)$$

A flat case is represented by $E_{bc,min} = E_{bc,z} = E_{bc,max}$. Accordingly, the GENCO receives a payment of $R_{bc,z}$ as

$$R_{bc,z} = \rho_{bc}.E_{bc,z}, \quad \forall z \quad (7)$$

GENCOs can offer excess generation to the day-ahead market as shown in the first three terms of (2). The GENCO's penalty payment is represented by the last term of (3) if the GENCO defaults on its BC given in following equation:

$$E_{def,zs} = \max\{0, (E_{bc,z} - E_{del,zs})\}, \quad \forall z,\ \forall s \quad (8)$$

The MIP formulation of (8) would use an external binary variable $W$, where

$$0 \leqslant E_{def,zs} - [E_{bc,z} - E_{del,zs}] \leqslant M \cdot [1 - W_{zs}]$$

$$0 \leqslant E_{def,zs} \leqslant M \cdot W_{zs}, \quad \forall z,\ \forall s \quad (9)$$

Here $M$ is a large positive number and $W_{zs}$ is the binary index which is equal to 1 when $E_{bc,z} \geqslant E_{del,zs}$, and is 0 otherwise. The penalty $C_{pen,zs}$ is given as

$$C_{pen,zs} = \rho_{pen}.E_{def,zs}, \quad \forall z,\ \forall s \quad (10)$$

Since the penalty is considered in the objective function, (11) would replace (9) to simplify the presentation.

$$[E_{bc,z} - E_{del,zs}] \leqslant E_{def,zs}, 0 \leqslant E_{def,zs}, \quad \forall z,\ \forall s \quad (11)$$

At the optimal solution, one of the constraints in (11) is binding. Multiple generating units in a GENCO could be considered for satisfying BC as given in the following equation

$$\sum_{j\in SBC} \sum_{t\in ST_z} P_{bc,jts} + \sum_{h\in SBC} \sum_{t\in ST_z} P_{bc,hts} + \sum_{w\in SBC} \sum_{t\in ST_z} P_{bc,wts} = E_{del,zs}, \quad \forall z,\ \forall s \quad (12)$$

The BC coordination would be based on the level of uncertainty, i.e. a wind unit dispatch could be coordinated with NG units, which are also subject to NG interruption and NG price uncertainty. A typical generating unit dispatch (13) includes its BC supply and the energy offered to the day-ahead market at time $t$ under contract period $z$ and scenario $s$.

$$P_{bc,jts} + TP_{jts} = P_{jts}, \quad \forall z,\ \forall s,\ \forall t \in ST_z \quad (13)$$

### 2.4. Consideration of financial risk

The stochastic formulation described above is a risk-neutral model that is only concerned with the optimization of expected payoff. However, a GENCO may also be concerned with its risk. A GENCO may set a target payoff $T_0$ and the risk associated with its decision is measured by the failure to meet the target. If the payoff for a scenario is larger than the target, the associated downside risk is zero; otherwise, it is the difference between the payoff and its target as

$$RISK_s = \max\{0, T_0 - PF_s\}, \quad \forall s \quad (14)$$

The expected downside risk should be lower than a target risk,

$$\sum_{s=1}^{NS} p_s.RISK_s \leqslant \overline{EDR} \quad (15)$$

subject to risk constraints given in [14].

## 3. Solution method

The objective function (1) is subject to constraints (2)-(15) as given above. The original problem is first relaxed from risk

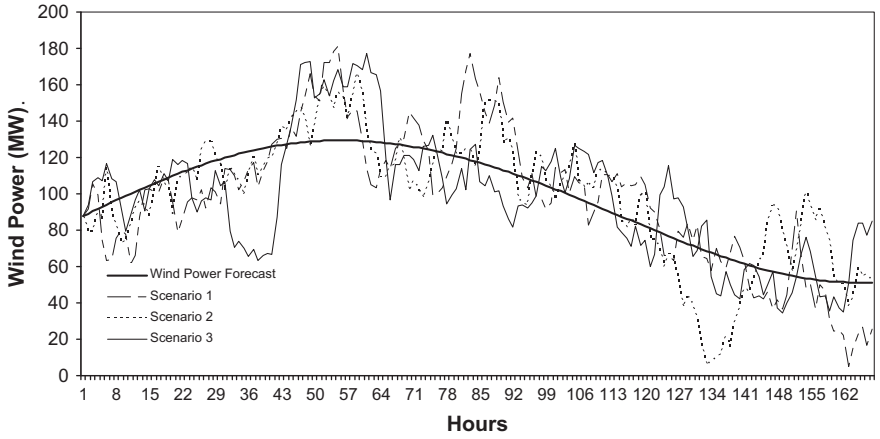


**Fig. 1.** Wind power forecasts and Monte Carlo simulations.

constraints using Lagrangian multipliers. Then, it is decomposed into subproblems for NG, hydro, and wind units [5]. The algorithm flowchart is shown in Fig. 2. The subproblems for NG, cascaded hydro, and wind units are solved in parallel when the coupling risk constraint is relaxed. Each subproblem related to an individual unit is solved to maximize the expected payoff of all scenarios in the entire study horizon. The Lagrange multipliers are updated using the subgradient method and iterations continue until the difference between the objective functions in two consecutive iterations is smaller than a predefined threshold and an optimal or suboptimal solution is reached.

The GENCO's risk evaluation problem is solved by assuming an initial target payoff without considering risk constraints. The proposed solution would include the expected risk level. If the risk were not within the GENCO's tolerance, the GENCO would add the risk-constraints. The process will continue until the difference between the objective function values in two consecutive iterations is smaller than a predefined threshold. If the risk were still out of GENCO's tolerance, the GENCO would decrease its target payoff and repeat the process. The Lagrange multipliers of the risk-neutral solution are recorded and set at the beginning of risk-constrained algorithm to decrease the solution time of the risk-constrained case. Further discussions on the solution method is provided in [5].

## 4. Case studies

We first present a 3-h example to introduce the coordination for one wind and one NG unit. A more realistic example considering a GENCO with 8 NG, 4 cascaded hydro units, and 3 wind units will also be discussed.

### 4.1. Three-hour example

Consider a 3-h example of a GENCO with one wind and one NG unit. There are two scenarios with a 50% probability for each scenario. Assume wind forecasts of 100 MW, 150 MW, 170 MW at hours 1–3 in the first scenario, and 80 MW, 130 MW, 150 MW at hours 1–3 in the second scenario. The NG unit has a generation cost of \$19/MW h with min/max capacity of 55 MW and 200 MW, respectively. The day-ahead energy prices are \$20/MW h and \$15/MW h for scenarios 1 and 2, respectively. The following cases are studied:

Case 1: No coordination of generating units and no BC.
Case 2: Fixed BC without coordination of units.
Case 3: Wind-NG unit coordination with a fixed BC.
Case 4: Wind-NG unit coordination with an optimized BC.

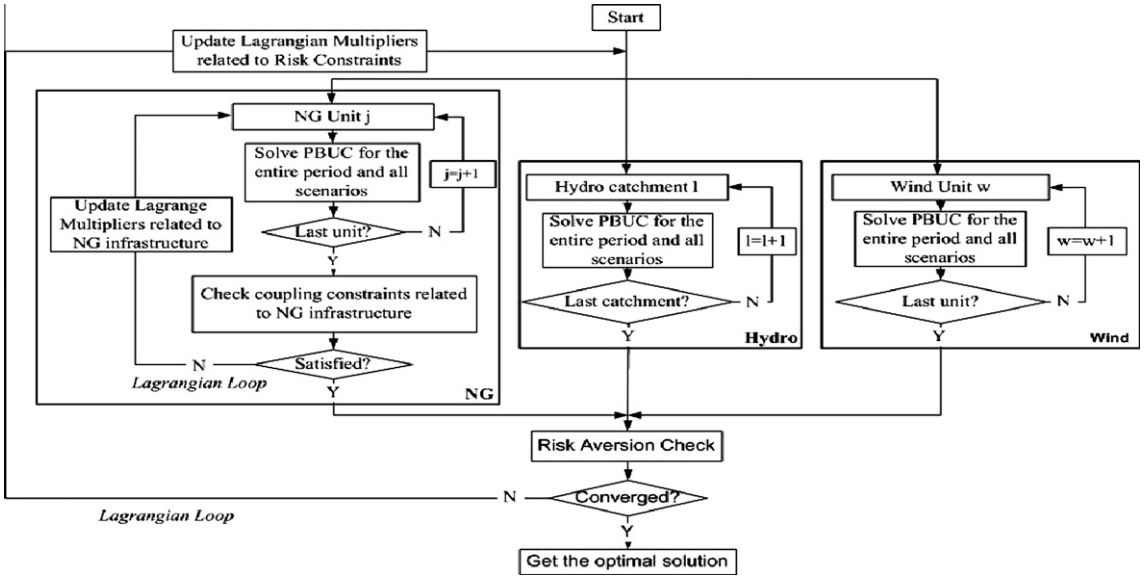


**Fig. 2.** Flowchart of the MIP solution method.

#### 4.1.1. Case 1

This case serves as the base case. All available wind energy is utilized since the NG unit is profitable only in the first scenario when the given scenario day-ahead energy prices and NG unit generation cost is considered. The expected payoff is \$6900 in Table 1 and the target payoff is the same as the expected payoff with a downside risk of \$750. This target payoff is used in the following cases.

#### 4.1.2. Case 2

A BC of 400 MW h with an energy price of \$18/MW h and penalty price of \$30/MW h is added. The hourly schedule based on PBUC is given in Table 2. The BC price is lower than that of energy in scenario 1 and higher in scenario 2. Since there is no coordination between wind and NG units, the GENCO uses the wind unit to supply BC and uses BC to hedge its expected payoff when the NG unit generation is offered to the day-ahead market. The available energy is 420 MW h in scenario 1 and 360 MW h in scenario 2. Since BC is 400 MW h, the excess 20 MW h in scenario 1 is offered to the day-ahead market, while a penalty is paid in scenario 2 for the 40 MW h deficiency. The expected payoff in Case 2 drops to \$6800 due to the penalty payment, while the downside risk is lowered to \$450 when BC is utilized so that the GENCO is not exposed to market volatilities in scenario 2.

#### 4.1.3. Case 3

The NG and wind units are coordinated in Table 3. Here the NG unit provides a means of satisfying the BC energy when the availability of wind generation is uncertain. The expected payoff increases to \$7090 and the downside risk is decreased to \$260. The inexpensive wind unit is scheduled in both scenarios as in previous Cases. In Scenario 1, the NG unit is fully dispatched and offered to the day-ahead market since its generation cost is cheaper than the market price. In Scenario 2, the NG unit with a minimum capacity of 55 MW is committed at hour 1 to supply the deficient BC of 40 MW h, and its excess 15 MW h is offered to the day-ahead market.

#### 4.1.4. Case 4

The potential BC energy is varied between 200 and 600 MW h and the optimal BC is calculated at 525 MW h. The expected payoff is \$7132.5 while the downside risk is increased slightly to \$292.5. The hourly unit schedules are given in Table 4. The NG unit is committed at all hours in coordination with the wind unit to satisfy BC and offer the excess energy to the day-ahead market. The NG unit is only profitable in Scenario 1. However, the additional energy required by BC would require the commitment of NG unit at hours 2 and 3 with a higher expected payoff than that in Case 3. A higher BC limit would increase the GENCO's expected payoff.

#### 4.1.5. Discussions

The expected payoffs and risks are summarized in Table 5. The available wind energy is utilized in all 4 Cases. The NG unit is not scheduled in Cases 1 and 2 since it is not profitable. The NG unit is coordinated with the wind unit in Scenario 2 of Case 3 to prevent penalty payments. The NG unit is committed at all hours in Case 4 for supplying the additional BC. The expected payoff is the highest in Case 4 for introducing a higher BC. The downside risk is increased in Case 4 since the GENCO makes a lower payoff in Scenario 2 to boost the payoff in Scenario 1 and increase the expected payoff. The risk could be reduced in Case 4 by introducing additional risk constraints. The wind-NG coordination and the corresponding BC optimization increase the expected payoff and decrease the expected risk by preventing the GENCO from exposure to volatile day-ahead market prices.

### 4.2. One-year example

A GENCO with 8 NG, 4 cascaded hydro and 3 wind units is analyzed to demonstrate the results. The units are hourly scheduled for the whole one-year period using the proposed algorithm. The forecast errors of day-ahead market prices, natural water inflows, and wind speed are considered. It is assumed that there are no transmission constraints and all units are subject to uniform hourly market prices. The NG infrastructure is shown in Fig. 3. The NG units fed by Pipeline 1 are located in two zones. The yearly NG supply from Zone 1 is limited to 37,200 MMCF. NG contracts are shown in Table 6. The yearly constraint for Pipeline 1 is 155,000 MMCF. The detailed generating unit data, and market prices for energy and ancillary services are given in http://motor.ece.iit.edu/data/WindBCPBUC. The Monte Carlo method is used to initially generate 100 scenarios, which are reduced to 12 final scenarios since the objective function does not change much based on this number of scenarios [15]. A 2% of the nominal power of wind unit (i.e., 4 MW) is used in scenarios as the standard deviation of wind forecast error. The study cases are listed in Table 7.

In Cases 2 and 3, the weekly BC energy is fixed at 50,750 MW h. In Case 4, BC energy is varied between 28,000 and 58,500 MW h for calculating the optimal weekly BC. The BC energy price is 46 \$/MW h and the penalty price for deficient energy is 200 \$/MW h. The risk neutral algorithm without the risk constraints is run first for each case. If the financial risk value is greater than zero for a specific case, the risk constrained algorithm is run to reduce the risk.

#### 4.2.1. Case 1

The PBUC algorithm is applied to schedule the GENCO units considering hourly market prices, natural water inflows, and available wind generation. There is no BC and coordination in this case which means that all of the GENCO's units are separately scheduled considering only the hourly energy market price forecasts. When the risk-neutral algorithm is considered, the expected payoff is \$312,025,369 and the downside risk is \$5335,124 with a probability of 0.46. The individual payoff of NG, hydro, and wind units are calculated as \$102,843,689, \$98,896,229 and \$110,285,448, respectively. When the downside risk is considered as constraint, the downside risk is decreased by 3.97% to \$5123,521. The expected payoff would drop by 0.09% to decrease the expected downside risk.

**Table 1**
Optimal schedule with No BCs and no coordination.

| | Hours | $t = 1$ | $t = 2$ | $t = 3$ |
|---|---|---|---|---|
| Scenario 1 | Available Wind Power | 100 | 150 | 170 |
| | NG unit dispatch | 0 | 0 | 0 |
| Scenario 2 | Available Wind Power | 80 | 130 | 150 |
| | NG unit dispatch | 0 | 0 | 0 |
| Expected payoff | | \$6900 = 20 * 420 * 50% + 15 * 360 * 50% | | |

**Table 2**
Optimal schedule with 400 MW h BC and no coordination.

| | Hours | $t = 1$ | $t = 2$ | $t = 3$ |
|---|---|---|---|---|
| Scenario 1 | Available Wind Power | 100 | 150 | 170 |
| | NG unit dispatch | 0 | 0 | 0 |
| Scenario 2 | Available Wind Power | 80 | 130 | 150 |
| | NG unit dispatch | 0 | 0 | 0 |
| BC (MW) | | 400 | | |
| Expected payoff | | $\$6800 = (400 * 18 + 20 * 20) * 50\% + (400 * 18–30 * 40) * 50\%$ | | |

**Table 3**
Optimal schedule of 400 MW h BC with wind-NG coordination.

| | Hours | $t = 1$ | $t = 2$ | $t = 3$ |
|---|---|---|---|---|
| Scenario 1 | Available wind power | 100 | 150 | 170 |
| | NG unit dispatch | 200 | 0 | 0 |
| Scenario 2 | Available wind power | 80 | 130 | 150 |
| | NG unit dispatch | 55 | 0 | 0 |
| BC (MW) | | 400 | | |
| Expected payoff | | $\$7090 = (400 * 18 + 220 * 20 + 200 * (-19)) * 50\% + (400 * 18 + 15 * 15–55 * 19) * 50\%$ | | |

**Table 4**
Optimal schedule of BC with wind-NG coordination.

| | Hours | $t = 1$ | $t = 2$ | $t = 3$ |
|---|---|---|---|---|
| Scenario 1 | Available Wind Power | 100 | 150 | 170 |
| | NG unit dispatch | 200 | 200 | 200 |
| Scenario 2 | Available Wind Power | 80 | 130 | 150 |
| | NG unit dispatch | 55 | 55 | 55 |
| BC (MW) | | 400 | | |
| Expected payoff | | $\$7132.5 = (525 * 18 + 495 * 20–200 * 3 * 19) * 50\% + (525 * 18–55 * 3 * 19) * 50\%$ | | |

**Table 5**
Three hours payoff and risk summary.

| Cases | Expected payoff ($) | Expected risk ($) |
|---|---|---|
| 1: No wind-NG coordination and No BC | 6900 | 750 |
| 2: No Wind-NG coordination with fixed BC | 6800 | 450 |
| 3: Wind-NG coordination with fixed BC | 7090 | 260 |
| 4: Wind-NG coordination with optimized BC | 7132.5 | 292.5 |

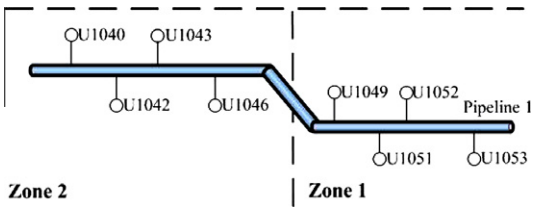


**Fig. 3.** NG infrastructure.

*4.2.2. Case 2*

The hydro units are considered for supplying the weekly BC in 1 year. The GENCO makes penalty payments at certain weeks when water inflows are lower. This condition leads to a negative payoff of \$69,913,914 for hydro units. The expected payoff drops by 54% to \$143,215,223 in comparison to that in Case 1. The downside risk increases to \$168,784,777 that is due to penalty payments. The hydro units are supposed to deliver 2639 GW h of BC energy in 52 weeks. However, due to water shortages the GENCO is subject to penalty payments. When hydro units supply BC, the expected payoff drops as compared to that in Case 1 and scenario payoffs are below the target. The risk constraints are not considered since the expected payoff is well below the target.

**Table 6**
NG Contracts.

| Pipeline # | Contract # | Type | Amount (MMCF) | Cost or price |
|---|---|---|---|---|
| 1 | 1 | Firm | 36,000 | \$70,200,000 |
| 1 | 2 | Interruptible | 117,500 | \$2170/MMCF |

*4.2.3. Case 3*

One NG unit is coordinated with cascaded hydro units for delivering a fixed weekly BC. The expected payoffs for NG and hydro units are calculated as \$106,080,484 and \$98,984,802, while the wind schedule remains unchanged when the risk neutral case is considered. The hydro unit payoff increases by \$168,898,716 when one NG unit is considered additionally to satisfy BC and prevent penalty payments. The added NG would relax the reliance on uncertain water inflows for supplying BC. The total NG units payoff increases by \$3236,795; however, the payoff of individual NG units could decrease based on day-ahead and BC prices as in the 3-h example. The coordination of NG and hydro units would decrease

**Table 7**
1 Year study cases.

| Case | Coordination of units | BC Energy |
|---|---|---|
| 1 | – | None |
| 2 | 4 Hydro | Fixed |
| 3 | 4 Hydro + 1 NG | Fixed |
| 4 | 4 Hydro + 1 NG + 3 Wind | Fixed |
| 5 | 4 Hydro + 1 NG + 3 Wind | Optimized |

the risk by 49.4% to $2702,192 as compared to that in Case 1 when a risk-neutral algorithm is considered. This case indicates that the BC's constant price and energy would reduce the GENCO's financial risk when NG units with given fuel conditions is added to the BC coordination. The NG unit would supply BCs in the case of water shortages. The risk could be further decreased by considering risk as a constraint in the formulation as will be shown in Table 8.

*4.2.4. Case 4*

Wind units are further added to the coordination of 4 cascaded hydro and 1 NG unit. The expected payoff increases to $333,540,888. The payoffs for NG, hydro, and wind units are $110,038,248, $102,830,699,and $120,671,941, respectively. The wind units would increase payoffs by supplying BC and offering energy to the day-ahead market. Hence, the coordination would enhance the GENCO's midterm scheduling and lead to higher payoffs and lower risks.

Fig. 4 shows that the wind forecast error has a crucial impact on a GENCO's financial risk. Here, the target payoff is updated to $333,000,000 since the coordination has increased the expected payoff in Case 4. In Fig. 4, the financial risk is $ 2954,180 when wind forecast error is taken zero. In this case, the uncertainty of water inflow and market price is considered. The risk increases as a nonlinear response to the higher uncertainty. The lowest achievable downside risk is $11,584,835 for a 5% standard deviation. In Fig. 4, if the number of coordinated NG units is increased to 5, the downside risk would be lower. Here, the additional NG units would increase the chance of mitigating financial risks pertaining to wind units. The lowest achievable downside risk is reduced to $5619,520. Moreover, the NG schedule is analyzed as we increase the wind uncertainty in the 4 Hydro, 1 Wind, and 5 NG case.

Fig. 5 depicts the NG utilization as a function of wind forecast error. The figure shows that there is higher utilization as wind uncertainty increases. It becomes more profitable to schedule the additional NG in order to satisfy BC and maximize the payoff. In addition, NG utilization is lowered for a fixed 1% standard deviation of wind forecast error in order to minimize the risk in the risk-constrained case. However, reduction in NG utilization is less significant as we increase the wind uncertainty, since the

**Table 8**
Comparison of cases 1–5 results (Target Payoff ıs $312,000,000).

| | Risk neutral results ($) | | Risk constrained results ($) | |
|---|---|---|---|---|
| Coordination of units | Expected payoff | Downside risk | Expected payoff | Downside risk |
| 1: No Coordination and No BC | 312,025,369 | 5335,124 | 311,752,084 | 5123,521 |
| 2: 4 Hydro | 143,215,223 | 168,784,777 | – | – |
| 3: 4 Hydro + 1 NG | 315,350,734 | 2702,192 | 315,077,937 | 2529,455 |
| 4: 4 Hydro + 1 NG + 3 Wind | 333,540,888 | 0 | 333,540,888 | 0 |
| 5: 4 Hydro + 1 NG + 3 Wind, Variable BC | 334,308,722 | 0 | 334,308,722 | 0 |

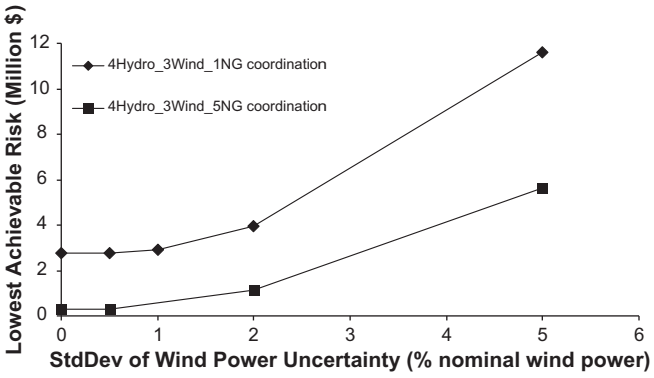


**Fig. 4.** Financial risks versus wind forecast errors for coordination cases.

additional NG units cannot lower the risk effectively. Consequently, GENCO would have to update its target payoff. A higher level of NG is utilized for 10% uncertainty as compared with the 1% case even though the total delivered energy is lower. This is because the NG units are committed at additional hours in the 10% case but produce less energy resulting in a lower total energy.

*4.2.5. Case 5*

In addition to the coordination in Case 4, the weekly BC energy is varied here between 28,000 and 58,500 MW h. The expected payoff increases to $334,308,722. Fig. 6 shows the optimal weekly BC energy in which the BC is higher (lower) in weeks with lower (higher) day-ahead energy price forecasts.

*4.2.6. Discussions*

The results are summarized in Table 8. In Case 1, the generation is offered only to the day-ahead market with a target payoff of

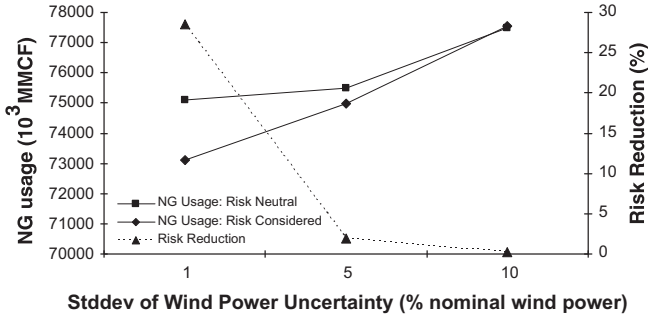


**Fig. 5.** Total NG utilization versus wind forecast errors.

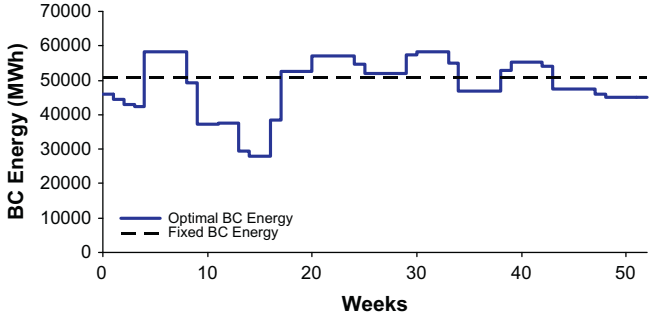


**Fig. 6.** Optimal BC energy.

$312,000,000. When hydro units are committed to satisfy the BC in Case 2, the expected payoff decreases since water inflow resources are insufficient, and the GENCO is subject to penalty payments if NG and wind unit schedules are the same as those in Case 1. One NG unit is coordinated with cascaded hydro units in Case 3 when the expected payoff is higher than that in Case 1 with a lower financial risk. The coordination will avoid penalty payments and offer energy to the day-ahead market when it is profitable. The wind units are also coordinated in Case 4 which increases the flexibility to satisfy the BC energy and leads to a higher expected payoff and zero downside risk. In Case 5, the weekly BC energy is optimized in one year. Table 8 shows that the BC coordination will reduce risks and increase expected payoffs when compared to Case 1. Notice that all of the GENCO's units are scheduled in each case, the difference between cases is the units considered in BC coordination. These units are given in "Coordination of Units" column of Table 8.

## 5. Conclusions

A small system demonstration is included to introduce the concept of coordination. Case studies show that BCs could adversely affect the expected payoff and financial risk of the GENCO when only hydro units with uncertain water inflows are considered. The expected payoff increases and the financial risk decreases with the addition of NG and wind units to the coordination. The observations are given as follows:

- Wind forecast uncertainty has a major impact on the midterm operation of power systems. A GENCO should utilize accurate forecasting tools to obtain a sound financial perspective since the financial risk increases nonlinearly with increments in wind power forecast uncertainty.
- Forward BCs could hedge GENCOs' risks when GENCOs are subject to volatile market prices.
- NG units would add flexibility for satisfying BCs in the midterm operation planning.
- A GENCO could utilize the proposed PBUC algorithm in a volatile environment to calculate its highest expected payoff in coordination with BCs.
- NG utilization increases in the risk-neutral case as the wind uncertainty increases. In the risk-constrained case, when the wind uncertainty is lower, the NG utilization is decreased in order to decrease the financial risk. However, a lower NG is not utilized when wind uncertainties are higher. GENCO should determine its target payoff carefully when the wind uncertainty is higher.
- GENCOs can use the proposed algorithm for the midterm planning of generating assets and bidding strategies.

## References

[1] Shahidehpour M, Fu Y, Wiedman T. Impact of natural gas infrastructure on electric power systems. IEEE Proc 2005;93(5):1042–56.
[2] Li T, Shahidehpour M. Interdependency of natural gas network and power system security. IEEE Trans Power Syst 2008;23(4):1817–24.
[3] Liu C, Shahidehpour M, Li Z. Security-constrained unit commitment with natural gas transmission constraints. IEEE Trans Power Syst 2009;24.
[4] Liu C, Shahidehpour M, Li Z. Component and mode models for the short-term scheduling of combined-cycle units. IEEE Trans Power Syst 2009;24:976–90.
[5] Sahin C, Li Z, Shahidehpour M, Erkmen I. Impact of natural gas system on risk-constrained midterm hydrothermal scheduling. IEEE Trans Power Syst 2011;26(2):520–31.
[6] Wang J, Shahidehpour M, Li Z. Security-constrained unit commitment with volatile wind power generation. IEEE Trans Power Syst 2008;23(4):1319–27.
[7] Makarov YV, Loutan C, Ma J, de Mello P. Operational impacts of wind generation on California power systems. IEEE Trans Power Syst 2009;24(20):1039–50.
[8] Tuohy A, Meibom P, Denny E, O'Malley M. Unit commitment for systems with significant wind penetration. IEEE Trans Power Syst 2009;24(2):592–601.
[9] Wang J, Botterud A, Miranda V, Monteiro C, Sheble G. Impact of wind power forecasting on unit commitment and dispatch. In: 8th International workshop on large-scale integration of wind power into power systems, Bremen, Germany, October 2009.
[10] Carrion M, Philpott AB, Conejo AJ, Arroyo JM. A stochastic programming approach to electric energy procurement for large consumers. IEEE Trans Power Syst 2007;22(2):744–54.
[11] Bakirtzis AG, Ziogos NP, Tellidou AC, Bakirtzis GA. Electricity producer offering strategies in day-ahead energy market with step-wise offers. IEEE Trans Power Syst 2007;22(4):1804–18.
[12] Soder L, Simulation of wind speed forecast errors for operation planning of multiarea power systems. In: 2004 International conference on proceedings of the probabilistic methods applied to power systems, vols. 12–16; 2004. p. 723–8.
[13] Wu L, Shahidehpour M. GENCO's risk-constrained hydrothermal scheduling. IEEE Trans Power Syst 2008;23(4):1847–58.
[14] Wu L, Shahidehpour M, Li T. GENCO's risk-based maintenance outage scheduling. IEEE Trans Power Syst 2008;23(1):127–36.
[15] Dupačová J, Gröwe-Kuska N, Römisch W. Scenario reduction in stochastic programming: an approach using probability metrics. Math Program, Ser A 2003;95:493–511.

# Comparison of Scenario-Based and Interval Optimization Approaches to Stochastic SCUC

Lei Wu, *Member, IEEE*, Mohammad Shahidehpour, *Fellow, IEEE*, and Zuyi Li, *Senior Member, IEEE*

***Abstract*—This paper compares applications of scenario-based and interval optimization approaches to stochastic security-constrained unit commitment (Stochastic SCUC). The uncertainty of wind power generation is considered in this study to compare the two approaches, while other types of uncertainty can be addressed similarly. For the simulation of uncertainty, the scenario-based approach considers the Monte Carlo (MC) method, while lower and upper bounds are adopted in the interval optimization. The Stochastic SCUC problem is formulated as a mixed-integer linear programming (MIP) problem and solved using the two approaches. The scenario-based solutions are insensitive to the number of scenarios, but present additional computation burdens. The interval optimization solution requires less computation and automatically generates lower and upper bounds for the operation cost and generation dispatch, but its optimal solution is very sensitive to the uncertainty interval. The numerical results on a six-bus system and the modified IEEE 118-bus system show the attributes of the two approaches for solving the Stochastic SCUC problem. Several convergence acceleration options are also discussed for overcoming the computation obstacles in the scenario-based approach.**

***Index Terms*—Interval optimization, scenario-based approach, stochastic SCUC.**

## NOMENCLATURE

**Variables**:

| | |
|---|---|
| $i$ | Index of thermal units. |
| $I_{it}$ | Commitment of unit $i$ at time $t$. |
| $k$ | Index of curve segments. |
| $P_{ikt}$ | Dispatch of unit $i$ at time $t$ at segment $k$. |
| $\Delta P^s_{ikt}$ | Corrective dispatch capability of unit $i$ at time $t$ at segment $k$ in scenario $s$. |
| $P_{it}$ | Power dispatch of unit $i$ at time $t$. |
| $P_{wt}$ | Power dispatch of wind unit $w$ at time $t$. |
| $s$ | Index of scenarios. |
| $s^{(\cdot)}_{(\cdot)}$ | Slack variable. |
| $SU_{it}, SD_{it}$ | Startup/shutdown cost of unit $i$ at time $t$. |
| $t$ | Index of hours. |
| $w$ | Index of wind generation units. |
| $\theta^s_t$ | Production cost of scenario $s$ at time $t$. |
| $\lambda, \mu$ | Dual variables. |
| $\hat{\cdot}$ | Solution to variable. |
| $(\cdot)^s$ | Variable related to scenario $s$. |
| $(\cdot)^{\pm}$ | Interval variable. |

**Constants**:

| | |
|---|---|
| $c_{ik}$ | Incremental cost for segment $k$ of unit $i$. |
| $N_i$ | No load cost of unit $i$. |
| $p^s$ | Probability of scenario $s$. |
| $P_{Dt}$ | System load at time $t$. |
| $P^-_{f,wt}$ | Interval numbers for the pessimistic wind scenario. |
| $P^+_{f,wt}$ | Interval numbers for the optimistic wind scenario. |
| $P^{min}_i$ | Minimum capacity of unit $i$. |
| $P^{max}_i$ | Maximum capacity of unit $i$. |
| $P^{\max}_{ik}$ | Power capacity of segment $k$ of unit $i$. |
| $P_{f,wt}$ | Generation forecast for wind unit $w$ at time $t$. |
| $R^{up}_i, R^{dn}_i$ | Up/down limits for corrective dispatch of unit $i$. |

**Matrices and Vectors**:

| | |
|---|---|
| $\mathbf{K_P}, \mathbf{K_D}$ | Bus-generator/bus-load incidence matrix. |
| $\mathbf{PL^{max}}$ | Vector of upper limit for power flow. |
| $\mathbf{SF}$ | Shift factor matrix. |

Manuscript received April 16, 2011; revised June 22, 2011; accepted August 08, 2011. Date of publication October 18, 2011; date of current version April 18, 2012. This work was supported in part by the U.S. Department of Energy Grants # DE-EE 0001380.000 and DE-EE 0002979. Paper no. TPWRS-00339-2011.

L. Wu is with the Electrical and Computer Engineering Department, Clarkson University, Potsdam, NY 13699 USA (e-mail: lwu@clarkson.edu).

M. Shahidehpour and Z. Li are with the Electrical and Computer Engineering Department, Illinois Institute of Technology, Chicago, IL 60616 USA (e-mail: ms@iit.edu; lizu@iit.edu).

Digital Object Identifier 10.1109/TPWRS.2011.2164947

## I. Introduction

THE wind generation uncertainty and price-sensitive demand response (DR) introduce new challenges for managing the operational security of electric power systems. Operational data from wind power plants in Denmark [1], Finland [2], and Germany [3] show that the hourly wind energy may often swing by about 20% of its installed capacity within a short span of time. Such fluctuations make it a challenging task to accurately forecast the short-term wind power generation. State-of-the-art forecasting techniques can predict the wind farm aggregated power generation for the next several hours with a forecast error of 5%–20% of the installed capacity [4], [5]. With DR, the price-sensitive load forecasting would require additional price-related inputs. However, price forecast errors of 5%–20% are not uncommon [6]–[8], which will further deteriorate the accuracy of price-sensitive load forecasts.

The modern power systems would have to plan for alternate backup generation in case the day-ahead wind power generation forecast does not materialize or the real-time consumption deviates a lot from the DR-based load forecasts. When the wind power penetration reaches a critical level, the dependency of power systems to wind power generation could inevitably result in additional supply risks associated with the variability of wind speed. Furthermore, when DR reaches a critical market level, the inaccuracy of price-sensitive load forecast could inevitably pose real-time electricity balance risks.

The impact of uncertainty on the operational security of power systems is of fundamental importance when multiple uncertain factors are integrated into power systems. The operational security of power systems can be addressed via Stochastic SCUC. In this paper, the uncertainty of wind power generation is considered in Stochastic SCUC and two distinct solution approaches are compared for maintaining the operational security of power systems.

The first one is the scenario-based approach, in which multiple scenarios are generated to simulate the possible realization of uncertainties. With presumed probability distribution functions, scenarios are generated by the sampling method or the direct discretization of uncertain parameters. Reference [9] presented an effective AC corrective/preventive contingency dispatch for the SCUC model to minimize the system operation cost while maintaining the system security. Reference [10] explored a decentralized solution to the security-constrained optimal power flow problem for large interconnected multi-area power systems. Reference [11] proposed an analytically-sufficient condition for system demand and network parameters to manage security constraints in SCUC. Reference [12] used the N-K contingency criterion to study the impact of random generator outages on power system security. With the assumption that the load forecast uncertainty follows a normal distribution, [13] discretized the normal distribution into intervals and used mid-points as well as probabilities of individual intervals to represent load point uncertainties. References [14]–[16] studied the impact of random generator outages and load forecast errors on unit commitment (UC) via sample scenario trees. References [17] and [18] studied the impact of the high penetration wind power generation on UC, in which the wind forecast uncertainty was simulated via scenarios sampled from certain probability distributions.

A key issue in the scenario-based approach is to generate scenarios that would truly reflect the probabilistic characteristics of system uncertainties. Scenario-generation methods include MC sampling, moment matching principles, and methods motivated by stability analysis. A general survey of scenario tree algorithms is provided in [19]. The scenario-based approach acknowledges a given probability distribution for simulating uncertainties. A large number of scenarios are usually generated in order to achieve an acceptable solution accuracy, which could increase the scale and the computation burden significantly.

The second approach to Stochastic SCUC is the interval optimization. Instead of sampling scenarios, the interval optimization uses confidence intervals in terms of upper and lower bounds to represent the uncertainty spectrum, and derives optimistic and pessimistic solutions for satisfying the system security requirements. The interval optimization does not require a presumed probability distribution for uncertainties, since interval numbers are acceptable for uncertain inputs [20]–[22]. Reference [23] used the interval optimization to study the impact of bus load uncertainty on system security. The solution was obtained by transforming the problem into two extreme deterministic subproblems corresponding to upper and lower bounds of desired objective function values. Decision alternatives were derived by adjusting decision variables within their solution intervals. Although explicit probability distributions are not required in the interval optimization, the uncertainty intervals would need to be carefully selected. A narrow confidence interval may not cover the entire uncertainty spectrum and, in turn, lead to a UC solution that would not correspond to all possible uncertain situations. On the other hand, a wide interval could lead to pessimistic solutions which would not utilize system resources efficiently and be of limited use to system operators.

The chance-constrained UC was used in [24] to study the load uncertainty by specifying a probability at which stochastic constraints would hold. Usually, such chance constraints are nonconvex and generally intractable. The solution to the chance-constrained UC problem could be obtained by sampling scenarios to approximate the true distribution of random variables, or converting it to a sequence of deterministic UC problems which converge to the solution of the chance-constrained UC. The problem scale and the computation burden of the two options would be comparable to those of scenario-based and interval optimization approaches, respectively.

An efficient solution of Stochastic SCUC problem may often lack a rigorous representation of uncertainty when considering complex operating details of generating units and large-scale transmission networks. In this paper, the Stochastic SCUC problem is studied and the wind power generation uncertainty is considered by applying scenario-based and interval optimization approaches. The scenario-based approach generates multiple scenarios by the MC method to simulate the wind power generation uncertainty. In addition to the base case operation cost, the scenario-based approach minimizes expected costs of corrective actions. The interval optimization uses interval numbers, in terms of lower and upper bounds, to

represent the wind power generation uncertainty. The major contribution of this paper is to compare the two approaches to the solution of Stochastic SCUC to address the power system security.

The rest of the paper is organized as follows. Sections II and III present the scenario-based and interval optimization approaches. Section IV applies a six-bus system and the modified IEEE 118-bus system to compare the two approaches. Several convergence acceleration options are discussed in Section V, and the conclusion is drawn in Section VI.

## II. Scenario-Based Stochastic SCUC

### A. Scenario-Based Stochastic SCUC Formulation

A large number of scenarios are generated to simulate wind speed uncertainty, which would follow the Weibull probability distribution function with the autocorrelation factor and diurnal pattern [25]. The hourly wind energy is procured according to the power curve of wind turbines and hourly wind speed. Other statistical distributions can be similarly considered. The low-discrepancy Latin Hypercube Sampling (LHS) technique is adopted for decreasing the variance of simple MC simulation. Each scenario is assigned a probability that is one divided by the number of scenarios. The scenario reduction technique is adopted to aggregate close scenarios by measuring the distance between scenarios based on the probability metrics and eliminate scenarios with very low probabilities for reducing the scale of the stochastic model and the computation effort [26], [27]. Other scenario reduction techniques may also be adopted including measuring the impact of each scenario on the objective by pre-solving single scenario problems [28], the target/moment matching which matches specified statistical properties [29], and the worst-case scenario probability study which assigns different sets of probabilities by experts and considers the worse scenario [30].

The objective (1) is to minimize the cost of supplying the hourly load in the base case (which includes the no-load cost, startup cost, shutdown cost, and the energy production cost) plus the expected corrective dispatch cost of scenarios, while satisfying various system and unit constraints. The sum of probabilities for all scenarios is equal to one. That is, $\sum_s p^s = 1$. Startup and shutdown costs are considered as time varying variables, which are functions of the number of hours a generating unit has been off and on, respectively [36]. In this paper, only non-quick start generating units are considered in order to facilitate the comparison of the two optimization approaches. That is, in each time interval of the base case and in all scenarios, each generating unit would have the same UC decisions. The formulation for quick-start units can also be included in the formulation [35]. By defining $P^s_{ikt}$ as the power generation of unit $i$ at time $t$, segment $k$, and scenario $s$, which satisfies $P^s_{ikt} = P_{ikt} + \Delta P^s_{ikt}$, (1) is equivalently converted to (2):

$$Min \quad \sum_t \sum_i \left[ N_i \cdot I_{it} + SU_{it} + SD_{it} + \sum_k c_{ik} \cdot P_{ikt} \right] + \sum_s p^s \cdot \sum_t \sum_i \left[ \sum_k c_{ik} \cdot \Delta P^s_{ikt} \right] \tag{1}$$

$$Min \quad \sum_t \sum_i [N_i \cdot I_{it} + SU_{it} + SD_{it}] + \sum_s p^s \cdot \sum_t \sum_i \left[ \sum_k c_{ik} \cdot P^s_{ikt} \right] \tag{2}$$

subject to the following constraints.

*Constraints for the Base Case:* Base case constraints include the system load balance (3). In addition, system reserve requirements are implicitly represented by deviations in the dispatch solutions of the base case and scenarios, and will be optimally determined via preventive and corrective actions. Generating unit constraints include capacity limits of thermal units (4) and power generation limits of wind power generation units (5):

$$\sum_i P_{it} + \sum_w P_{wt} = P_{Dt} \tag{3}$$

$$P^{\min}_i \cdot I_{it} \le P_{it} \le P^{\max}_i \cdot I_{it}$$

$$P_{it} = \sum_k P_{ikt} \qquad 0 \le P_{ikt} \le P^{\max}_{ik} \cdot I_{it} \tag{4}$$

$$0 \le P_{wt} \le P_{f,wt}. \tag{5}$$

Other unit constraints include minimum on/off time, ramping up/down rate, reserve capacity, and fuel and/or emission limitations [31], [32]. Other types of units, such as combined-cycle gas turbine, cascaded hydro, and pumped-storage units, can also be considered. Transmission network constraints include branch flow limits (6), which is enforced in the base case to guarantee the network security of power systems operation:

$$\mathbf{-PL^{max}} \le \mathbf{SF} \cdot (\mathbf{K_P} \cdot \mathbf{P_t} - \mathbf{K_D} \cdot \mathbf{P_{Dt}}) \le \mathbf{PL^{max}}. \tag{6}$$

*Constraints for Each Scenario:* Constraints for each scenario include the system load balance (7), generation limits of thermal and wind power units (8), and dispatch adjustment capabilities of generating units (9), which are restricted by the dispatch in the base case by ramping up/down rate limits. Transmission network constraints (10) are enforced in each scenario to guarantee the network security:

$$\sum_i P^s_{it} + \sum_w P^s_{wt} = P_{Dt} \tag{7}$$

$$P^{\min}_i \cdot I_{it} \le P^s_{it} \le P^{\max}_i \cdot I_{it}$$

$$P^s_{it} = \sum_k P^s_{ikt} \qquad 0 \le P^s_{ikt} \le P^{\max}_{ik} \cdot I_{it}$$

$$P^s_{wt} \le P^s_{f,wt} \tag{8}$$

$$P^s_{it} - P_{it} \le R^{up}_i \cdot I_{it}$$

$$P_{it} - P^s_{it} \le R^{dn}_i \cdot I_{it} \tag{9}$$

$$\mathbf{-PL^{max}} \le \mathbf{SF} \cdot (\mathbf{K_P} \cdot \mathbf{P^s_t} - \mathbf{K_D} \cdot \mathbf{P_{Dt}}) \le \mathbf{PL^{max}}. \tag{10}$$

Other unit constraints include minimum on/off time, ramping up/down rate, reserve capacity, and fuel and/or emission limitations. The detailed formulation is not included in the paper, which can be obtained in the authors' previous work [31], [32]. However, ramping limits between two successive time intervals in each scenario is not considered because it is assumed that the scenarios at successive time intervals are independent. That is, the scenario $s$ at hour $t$ is not necessarily a consequence of

the scenario $s$ at hour $(t-1)$. In addition, the proposed Stochastic SCUC is an hourly based model; thus, it is reasonable to assume that there is enough time to adjust the system back to the base case operation status at hour $t$. Thus, ramping constraints are used to guarantee the secure and economic transfer of system operation status between two successive time intervals in the base, and from the base case to all scenarios at each hour, but not between two successive time intervals in each scenario. In the proposed decomposition framework, the ramping constraints between two successive time intervals in the base is considered in the master UC problem (11), and the ramping constraints between the base case and each hourly scenario is considered in the hourly scenario feasibility and optimality check subproblems (14) and (16).

### B. Solution Methodology

The scenario-based Stochastic SCUC model in (2)–(10) is a large-scale, non-convex, non-deterministic polynomial-time hard (NP-hard) problem. The corresponding solution for large-scale systems would be an intractable task without decomposition. The Benders decomposition (BD) is adopted to decompose the Stochastic SCUC problem into one master problem and several tractable subproblems for each scenario.

*1) Master Unit Commitment Problem:* The master UC problem (11) is to minimize the operation cost of the base case with respect to constraints (3)–(5) and other unit constraints mentioned above:

$$Min \quad \sum_t \sum_i [N_i \cdot I_{it} + SU_{it} + SD_{it}] + \sum_s p^s \cdot \sum_t \theta_t^s. \quad (11)$$

*2) Hourly Network Evaluation for the Base Case:* The hourly network evaluation subproblem (12) checks possible network violations of the master UC solution for the base case. If the objective value $\hat{s}_t$ of (12) is larger than the predefined threshold, a feasibility cut (13) will be utilized:

$$\begin{aligned} &Min\ s_t \\ &S.t. -1 \cdot s_t \le \mathbf{PL^{max}} - \mathbf{SF} \cdot (\mathbf{K_P} \cdot \hat{\mathbf{P}}_\mathbf{t} - \mathbf{K_D} \cdot \mathbf{P_{Dt}}) \quad \boldsymbol{\lambda}_{\mathbf{1,t}} \\ &\qquad -1 \cdot s_t \le \mathbf{PL^{max}} + \mathbf{SF} \cdot (\mathbf{K_P} \cdot \hat{\mathbf{P}}_\mathbf{t} - \mathbf{K_D} \cdot \mathbf{P_{Dt}}) \quad \boldsymbol{\lambda}_{\mathbf{2,t}} \\ &\quad 0 \le s_t \qquad (12) \\ &-(\boldsymbol{\lambda}_{\mathbf{1,t}} - \boldsymbol{\lambda}_{\mathbf{2,t}})^T \cdot \mathbf{K_P} \cdot (\mathbf{P_t} - \hat{\mathbf{P}}_\mathbf{t}) + \hat{s}_t \le 0. \qquad (13) \end{aligned}$$

*3) Hourly Feasibility Check for Each Scenario:* The hourly feasibility check subproblem (14) checks possible violations of the master UC solution in each scenario. If the objective value $\hat{S}_t^s$ in (14) is larger than the predefined threshold, a feasibility cut (15) will be utilized:

$$\begin{aligned} &Min\ S_t^s = s_t^s + s_{1t}^s + s_{2t}^s \\ &S.t. \mathbf{SF} \cdot (\mathbf{K_P} \cdot \mathbf{P_t^s} - \mathbf{K_D} \cdot \mathbf{P_{Dt}}) - 1 \cdot s_t^s \le \mathbf{PL^{max}} \\ &\quad -\mathbf{SF} \cdot (\mathbf{K_P} \cdot \mathbf{P_t^s} - \mathbf{K_D} \cdot \mathbf{P_{Dt}}) - 1 \cdot s_t^s \le \mathbf{PL^{max}} \\ &\quad \sum_i P_{it}^s + \sum_w P_{wt}^s + s_{1t}^s - s_{2t}^s = P_{Dt} \\ &\quad P_{it}^s \le R_i^{up} \cdot \hat{I}_{it} + \hat{P}_{it} \qquad \lambda_{1,it}^s \\ &\quad -P_{it}^s \le R_i^{dn} \cdot \hat{I}_{it} - \hat{P}_{it} \qquad \lambda_{2,it}^s \\ &\quad P_{it}^s \le P_i^{\max} \cdot \hat{I}_{it} \qquad \mu_{1,it}^s \\ &\quad -P_{it}^s \le -P_i^{\min} \cdot \hat{I}_{it} \qquad \mu_{2,it}^s \\ &\quad P_{wt}^s \le P_{f,wt}^s \\ &\quad 0 \le s_t^s, s_{1t}^s, s_{2t}^s \qquad (14) \\ &\sum_i \left[ \left( \hat{\lambda}_{1,it}^s - \hat{\lambda}_{2,it}^s \right) \cdot (P_{it} - \hat{P}_{it}) \right. \\ &\quad + \left( \hat{\lambda}_{1,it}^s \cdot R_i^{up} + \hat{\lambda}_{2,it}^s \cdot R_i^{dn} + \hat{\mu}_{1,it}^s \cdot P_i^{\max} \right. \\ &\quad \left. \left. -\hat{\mu}_{2,it}^s \cdot P_i^{\min} \right) \cdot (I_{it} - \hat{I}_{it}) \right] + \hat{S}_t^s \le 0. \qquad (15) \end{aligned}$$

*4) Optimality Check for Each Scenario:* The optimality check subproblem (16) checks the optimality of master UC solution in each scenario. If the objective value $\hat{W}_t^s$ in (16) is larger than the corrective dispatch cost $\hat{\theta}_t^s$ obtained from the master problem, the optimality cut (17) will be utilized:

$$\begin{aligned} &Min \quad W_t^s = \sum_i \left[ \sum_k c_{ik} \cdot P_{ikt}^s \right] \\ &S.t. -\mathbf{PL^{max}} \le \mathbf{SF} \cdot (\mathbf{K_P} \cdot \hat{\mathbf{P}}_\mathbf{t} - \mathbf{K_D} \cdot \mathbf{P_{Dt}}) \le \mathbf{PL^{max}} \\ &\quad P_{it}^s \le R_i^{up} \cdot \hat{I}_{it} + \hat{P}_{it} \qquad \lambda_{1,it}^s \\ &\quad -P_{it}^s \le R_i^{dn} \cdot \hat{I}_{it} - \hat{P}_{it} \qquad \lambda_{2,it}^s \\ &\quad P_{it}^s \le P_i^{\max} \cdot \hat{I}_{it} \qquad \mu_{1,it}^s \\ &\quad -P_{it}^s \le -P_i^{\min} \cdot \hat{I}_{it} \qquad \mu_{2,it}^s \\ &\quad P_{it}^s - \sum_k P_{ikt}^s = 0 \\ &\quad P_{wt}^s \le P_{f,wt}^s \qquad (16) \\ &\theta_t^s \ge \hat{W}_t^s + \sum_i \left[ \left( \hat{\lambda}_{1,it}^s \cdot R_i^{up} + \hat{\lambda}_{2,it}^s \cdot R_i^{dn} \right. \right. \\ &\qquad \left. + \hat{\mu}_{1,it}^s \cdot P_i^{\max} - \hat{\mu}_{2,it}^s \cdot P_i^{\min} \right) \cdot (I_{it} - \hat{I}_{it}) \\ &\qquad \left. + \left( \hat{\lambda}_{1,it}^s - \hat{\lambda}_{2,it}^s \right) \cdot (P_{it} - \hat{P}_{it}) \right]. \qquad (17) \end{aligned}$$

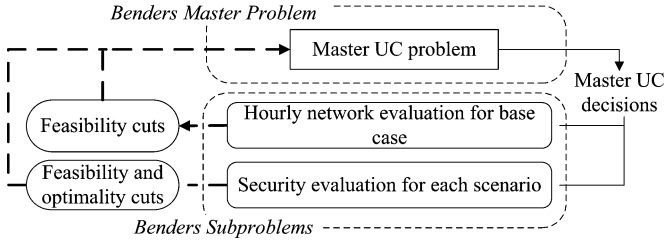


Fig. 1. Scenario-based approach.

Fig. 1 shows the flowchart of the scenario-based Stochastic SCUC solution. The master UC problem (11) is solved first. The hourly UC and dispatch solutions are then passed on to the hourly network evaluation subproblems (12). The subproblems will examine the feasibility of the master solution. If a subproblem is infeasible which violates the remaining constraints, a corresponding feasibility cut (13) will be generated and added to the next calculation of master problem. The hourly UC and dispatch solutions are also passed on to the hourly security evaluation subproblem (14) and the optimality evaluation subproblem (16) in each scenario. If a scenario subproblem is infeasible, a corresponding feasibility cut (15) will be generated. If the optimal objective $\hat{W}_t^s$ is larger than the corrective dispatch cost

$\hat{\theta}_t^s$, an optimality cut (17) will be generated and added to the next iteration of the master problem. The iterative process will stop when the master solution satisfies feasibility and optimality checks.

## III. Interval Optimization for Stochastic SCUC

The scenario-based approach in Section II holds a presumption that the wind speed uncertainty follows a certain probability distribution. However, the wind speed distribution is often more complex. In addition, a huge number of scenarios are needed in order to achieve an acceptable solution accuracy, which could increase the scale and the computation burden of the stochastic problem. In this section, the interval optimization is adopted as an alternative for the Stochastic SCUC solution with the consideration of wind power generation uncertainty.

The objective of the interval optimization approach is to minimize the cost of supplying the hourly load in the base case (18). Different from the scenario-based approach, the interval optimization approach does not hold any presumptions on probability distributions. The expected corrective dispatch costs are not explicitly included in the objective function. Instead, the impact of uncertainty on operation costs is reflected via the operation cost interval:

$$Min \quad \sum_t \sum_i \left[ \sum_k c_{ik} \cdot P_{ikt} + N_i \cdot I_{it} + SU_{it} + SD_{it} \right]. \tag{18}$$

The base case constraints are (3)–(6) and constraints describing the wind power generation uncertainty are given in (19)–(21) with interval variables $P_{it}^{\pm}$ and $P_{wt}^{\pm}$. In (20), the uncertainty interval is derived from a forecasting model [34]. If the forecasting model does not provide such functionality, the uncertainty interval can be formulated using a percentage of the forecast value around such forecast value, i.e., $(1 \pm \alpha)$. The value of $\alpha$ ranges from 0 to 1, for controlling the level of uncertainty under consideration:

$$\sum_i P_{it}^{\pm} + \sum_w P_{wt}^{\pm} = P_{Dt} \tag{19}$$

$$P_{it} - R_i^{up} \cdot I_{it} \le P_{it}^{\pm} \le P_{it} + R_i^{up} \cdot I_{it}$$

$$P_i^{\min} \cdot I_{it} \le P_{it}^{\pm} \le P_i^{\max} \cdot I_{it}$$

$$P_{wt}^{\pm} \le \left[ P_{f,wt}^{-}, P_{f,wt}^{+} \right] \tag{20}$$

$$-\mathbf{PL^{max}} \le \mathbf{SF} \cdot \left( \mathbf{K_P} \cdot \mathbf{P_t^{\pm}} - \mathbf{K_D} \cdot \mathbf{P_{Dt}} \right) \le \mathbf{PL^{max}}. \tag{21}$$

### A. Feasibility Check for the Interval Optimization Subproblem

In (22), the largest violation would occur when the available wind power generation is at its minimum $P_{f,wt}^{-}$. Thus, by checking the worst case (23), if the objective value $S_t^{-}$ is larger than the predefined threshold, a feasibility cut (24) will be utilized. Otherwise, if $S_t^{-}$ is smaller than the predefined threshold, the worst case is feasible. Thus, all other cases will be feasible:

$$Min \quad s_t^{\pm} + s_{1t}^{\pm} + s_{2t}^{\pm}$$

$$S.t. \mathbf{SF} \cdot \left( \mathbf{K_P} \cdot \mathbf{P_t^{\pm}} - \mathbf{K_D} \cdot \mathbf{P_{Dt}} \right) - 1 \cdot s_t^{\pm} \le \mathbf{PL^{max}}$$

$$-\mathbf{SF} \cdot \left( \mathbf{K_P} \cdot \mathbf{P_t^{\pm}} - \mathbf{K_D} \cdot \mathbf{P_{Dt}} \right) - 1 \cdot s_t^{\pm} \le \mathbf{PL^{max}}$$

$$\sum_i P_{it}^{\pm} + \sum_w P_{wt}^{\pm} + s_{1t}^{\pm} - s_{2t}^{\pm} = P_{Dt}$$

$$\hat{P}_{it} - R_i^{up} \cdot \hat{I}_{it} \le P_{it}^{\pm} \le \hat{P}_{it} + R_i^{up} \cdot \hat{I}_{it}$$

$$P_i^{\min} \cdot \hat{I}_{it} \le P_{it}^{\pm} \le P_i^{\max} \cdot \hat{I}_{it}$$

$$P_{wt}^{\pm} \le \left[ P_{f,wt}^{-}, P_{f,wt}^{+} \right]$$

$$0 \le s_t^{\pm}, s_{1t}^{\pm}, s_{2t}^{\pm}. \tag{22}$$

### B. Confidence Intervals

The interval optimization derives the power generation confidence interval $[\hat{P}_{it}^{-}, \hat{P}_{it}^{+}]$ for each unit $i$ at each hour $t$, and the confidence interval $[\sum_t \sum_i (\sum_k c_{ik} \cdot \hat{P}_{ikt}^{-} + N_i \cdot \hat{I}_{it} + \hat{SU}_{it} + \hat{SD}_{it}), \sum_t \sum_i (\sum_k c_{ik} \cdot \hat{P}_{ikt}^{+} + N_i \cdot \hat{I}_{it} + \hat{SU}_{it} + \hat{SD}_{it})]$ of the total operation cost, in response to wind power generation uncertainty. The unique feature of the interval optimization is that it uses confidence interval numbers to simulate uncertainty, without considering any assumptions on probability distributions, and derives optimistic and pessimistic solutions for satisfying the security and economic requirements of power systems:

$$Min \quad S_t^{-} = s_t^{-} + s_{1t}^{-} + s_{2t}^{-}$$

$$S.t. \mathbf{SF} \cdot \left( \mathbf{K_P} \cdot \mathbf{P_t^{-}} - \mathbf{K_D} \cdot \mathbf{P_{Dt}} \right) - 1 \cdot s_t^{-} \le \mathbf{PL^{max}}$$

$$-\mathbf{SF} \cdot \left( \mathbf{K_P} \cdot \mathbf{P_t^{-}} - \mathbf{K_D} \cdot \mathbf{P_{Dt}} \right) - 1 \cdot s_t^{-} \le \mathbf{PL^{max}}$$

$$\sum_i P_{it}^{-} + \sum_w P_{wt}^{-} + s_{1t}^{-} - s_{2t}^{-} = P_{Dt}$$

$$P_{it}^{-} \le R_i^{up} \cdot \hat{I}_{it} + \hat{P}_{it} \qquad \lambda_{1,it}^{-}$$

$$-P_{it}^{-} \le R_i^{dn} \cdot \hat{I}_{it} - \hat{P}_{it} \qquad \lambda_{2,it}^{-}$$

$$P_{it}^{-} \le P_i^{\max} \cdot \hat{I}_{it} \qquad \mu_{1,it}^{-}$$

$$-P_{it}^{-} \le -P_i^{\min} \cdot \hat{I}_{it} \qquad \mu_{2,it}^{-}$$

$$P_{wt}^{-} \le P_{f,wt}^{-}$$

$$0 \le s_t^{-}, s_{1t}^{-}, s_{2t}^{-} \tag{23}$$

$$\sum_i \Big[ \left( \hat{\lambda}_{1,it}^{-} - \hat{\lambda}_{2,it}^{-} \right) \cdot (P_{it} - \hat{P}_{it}) + \left( \hat{\lambda}_{1,it}^{-} \cdot R_i^{up} + \hat{\lambda}_{2,it}^{-} \cdot R_i^{dn} + \hat{\mu}_{1,it}^{-} \cdot P_i^{\max} - \hat{\mu}_{2,it}^{-} \cdot P_i^{\min} \right) \cdot (I_{it} - \hat{I}_{it}) \Big] + \hat{S}_t^{-} \le 0. \tag{24}$$

## IV. Case Studies

A six-bus system and the modified IEEE 118-bus system are used to analyze scenario-based and interval optimization approaches to Stochastic SCUC. The case studies utilize CPLEX 12.1.0 on an Intel Core i7 2.67-GHz personal computer.

### A. Six-Bus System

The six-bus system shown in Fig. 2 is used to illustrate the proposed study, which has three regular thermal generators and one wind farm [31]. Corrective dispatch capabilities of the three

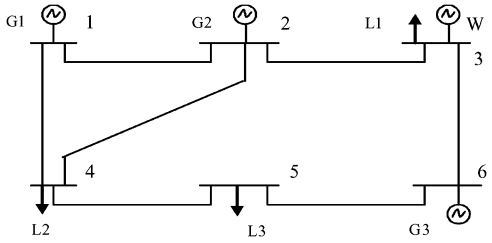


Fig. 2. One-line diagram of the six-bus system.

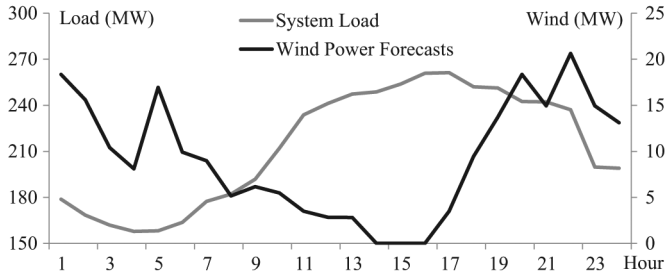


Fig. 3. 24-h load profile and wind power generation forecasts.

TABLE I
INTERVAL OPTIMIZATION RESULTS IN CASE 1

| | Cost ($) | G1 (MW) | G2 (MW) | G3 (MW) | Wind (MW) |
|---|---|---|---|---|---|
| Base case | 3,305.38 | 163.24 | 0 | 0 | 15.52 |
| Pessimistic | 3,496.68 | 172.40 | 0 | 0 | 6.36 |
| Optimistic | 3,114.34 | 154.08 | 0 | 0 | 24.68 |

TABLE II
SCENARIO-BASED RESULTS IN CASE 1 (REDUCED 100 SCENARIOS)

| | Cost ($) | G1 (MW) | G2 (MW) | G3 (MW) | Wind (MW) |
|---|---|---|---|---|---|
| Base case | 3437.19 | 169.60 | 0 | 0 | 9.16 |
| Corrective action | -75.12 | 160.43-178.76 | 0 | 0 | 0-18.33 |

TABLE III
INTERVAL OPTIMIZATION RESULTS FOR 40% WIND VOLATILITY IN CASE 1

| | Cost ($) | G1 (MW) | G2 (MW) | G3 (MW) | Wind (MW) |
|---|---|---|---|---|---|
| Base case | 3,437.84 | 169.60 | 0 | 0 | 9.16 |
| Pessimistic | 3,632.93 | 178.76 | 0 | 0 | 0 |
| Optimistic | 3,246.79 | 160.44 | 0 | 0 | 18.32 |

thermal units are 9.16 MW, 8.33 MW, and 3.33 MW, respectively. The system load profile and wind power generation forecasts for the 24 h are shown in Fig. 3. The wind power generation is calculated based on wind speed forecasts and wind turbine power curves, where the cut-in, rated, and cut-out wind speeds are 5 m/s, 14 m/s, and 24 m/s, respectively. The total installed wind power generation capacity is 60 MW, which represents 14.63% of the total system generation capacity. Two cases are studied here:

Case 1) Stochastic SCUC study at hour 1.
Case 2) The 24-h Stochastic SCUC study.

*Case 1:* The Stochastic SCUC is studied at hour 1, which is a high wind and low load hour. The wind speed forecast is 9.44 m/s, which corresponds to the wind power generation of 18.39 MW. The system load is 178.76 MW.

First, the interval optimization approach for the Stochastic SCUC problem is studied, in which the wind power generation uncertainty is considered as 20% of its installed capacity, i.e., $60 * 20\% = 12$ MW. That is, the available wind power generation in the pessimistic case is $(18.39 - 12)$ MW, and $(18.39 + 12)$ MW in the optimistic case. The Stochastic SCUC solution with the interval optimization approach is shown in Table I. The economic operation strategy while satisfying the operational security under both pessimistic and optimistic cases is to switch on the G1 unit only and adopt wind power generation of 15.52 MW, 6.36 MW, and 24.68 MW in the base case, pessimistic case, and optimistic case, respectively. In this case, the corrective dispatch capability of G1 can balance the wind power generation uncertainty and securely transfer the system operation status from the base case to both pessimistic and optimistic cases. The interval optimization method also provides an operation cost interval of [$3114.34, $3496.68].

Second, the scenario-based approach is used to study the Stochastic SCUC. The wind speed is assumed to follow the Weibull distribution and its uncertainty is simulated via 10 000 scenarios. The scenario reduction is used to reduce the scale and the computation time of the stochastic model. Table II shows the results with the reduced 100 scenarios. The expected operation cost is $3362.07, which includes the base case cost of $3437.19 and the expected corrective dispatch cost of $-75.12.

In the interval optimization approach with 20% wind power generation uncertainty, 6.36 MW wind power generation is available in the pessimistic case. This makes it possible to adopt 15.52 MW wind power generation in the base case, with a corrective dispatch of 9.16 MW provided by G1. In comparison, the scenario-based approach includes scenarios with wind speeds lower than the cut-in value, which derives 0 MW wind power output. In order to securely transfer the system operation status from the base case to scenarios, the base case would dispatch 9.16 MW of wind power generation, which leads to a higher base case cost than that of the interval optimization.

The sensitivity analysis is performed for the two approaches. Table III shows the interval optimization results when the wind power generation uncertainty is assumed to be 40% of the installed wind power generation capacity, i.e., $40\% * 60 = 24$ MW. In this situation, the pessimistic case will have 0 MW wind power output, which adopts 9.16 MW wind power generation in the base case and derives the same base case result as that of the scenario-based approach in Table II. This study shows that the interval optimization solution is very sensitive to the presumed wind uncertainty interval. Fig. 4 shows the operation cost for all 100 scenarios and the operation cost intervals for the interval optimization approach. All scenario costs fall within the lower and upper bounds derived from the interval optimization, which indicates that when the wind uncertainty interval is properly set, the interval optimization could provide accurate operation cost boundaries to cover possible scenarios in the scenario-based approach.

Table IV shows the expected corrective dispatch costs of different tests in the scenario-based approach. For all tests, the base case UC results are the same as those in Table II. In Table IV, the tests with different number of original scenarios and the

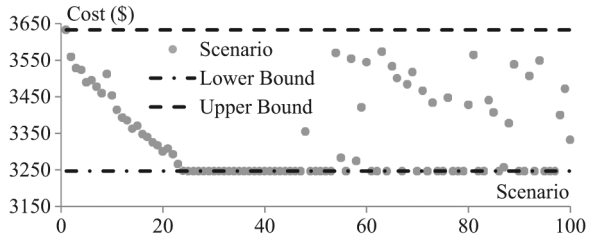


Fig. 4. Scenario operation costs and the operation cost interval.

TABLE IV
EXPECTED CORRECTIVE DISPATCH COSTS IN CASE 1 ($)

| | # of scenarios after scenario reduction | | |
|---|---|---|---|
| # of original scenarios | 5 | 10 | 100 |
| 1,000 | -70.47 | -74.91 | -74.92 |
| 10,000 | -70.78 | -75.15 | -75.12 |
| 10,000 (Another sample) | -70.75 | -75.10 | -75.12 |

TABLE V
RESULTS FOR EACH SCENARIO IN CASE 1 (REDUCED FIVE SCENARIOS)

| | S1 | S2 | S3 | S4 | S5 |
|---|---|---|---|---|---|
| Probability | 0.171 | 0.211 | 0.346 | 0.113 | 0.159 |
| Available wind power (MW) | 0 | 29.76 | 59.82 | 3.44 | 12.72 |
| Adopted wind power (MW) | 0 | 18.33 | 18.33 | 3.44 | 12.72 |
| Scenario cost ($) | 3,632.93 | 3,246.79 | 3,246.79 | 3,559.20 | 3,363.75 |
| Corrective cost ($) | 195.43 | -190.40 | -190.40 | 122.01 | -73.44 |

same number of reduced scenarios have close expected corrective dispatch costs. In addition, ten appears to be an appropriate number of scenarios since their expected corrective dispatch costs are quite close to those of 100 scenarios; though the cost of five scenarios deviates a lot. Furthermore, the last two rows of Table IV show that the expected corrective dispatch costs of another 10 000 sample test are quite close to those of the first 10 000 scenario sample test, which shows that the expected corrective dispatch costs are stable for different scenario samples. Table IV shows that, in this case, the expected corrective dispatch costs are all negative for different tests. This is because in most scenarios, the amount of wind power generation adopted is higher than that of the base case. Thus, less generation from regular thermal units is needed and the scenario operation cost is lower than that of the base case. Table V shows the test results with reduced five scenarios. In this study, scenarios 2, 3, and 5 would adopt more wind power generation and correspondingly have lower scenario operation costs than the base case. The total probability of scenarios 2, 3, and 5 is $0.211 + 0.346 + 0.159 = 0.716$, which brings out the negative expected corrective dispatch cost of $\$-70.47$.

*Case 2:* The 24-h Stochastic SCUC is studied in this case. Tables VI and VII show the 24-h Stochastic SCUC results with the interval optimization and the scenario-based approaches, respectively. Table VI show that the expected operation costs of test cases, given in Table VII, fall in the operation cost interval of [$100 048.78, $109 294.13]. Table VII again shows that ten would be an appropriate number of scenarios in this case since

TABLE VI
INTERVAL OPTIMIZATION RESULTS IN CASE 2

| | Base case | Pessimistic | Optimistic |
|---|---|---|---|
| Cost ($) | 105,595.50 | 109,294.13 | 100,048.78 |

TABLE VII
SCENARIO-BASED RESULTS IN CASE 2 ($)

| # of scenarios after reduction | 5 | 10 | 100 |
|---|---|---|---|
| Expected cost for the first run | 102,270.05 | 103,887.93 | 104,295.86 |
| Expected cost for the second run | 102,294.87 | 103,835.80 | 104,273.27 |

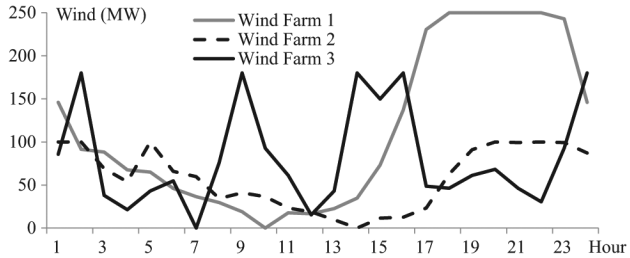


Fig. 5. Wind power generation forecasts for the three wind farms.

TABLE VIII
INTERVAL OPTIMIZATION RESULTS FOR 24 H ($)

| Wind Uncertainty | Base case | Pessimistic | Optimistic |
|---|---|---|---|
| 15% | 2,006,689.78 | 2,032,250.47 | 1,968,175.55 |
| 25% | 2,006,844.22 | 2,042,033.43 | 1,944,019.38 |

TABLE IX
SCENARIO-BASED RESULTS FOR 24 H ($)

| # of scenarios after reduction | 5 | 10 | 100 |
|---|---|---|---|
| Expected cost for the first run | 1,969,428.82 | 1,970,747.87 | 1,969,768.34 |
| Expected cost for the second run | 1,971,080.53 | 1,970,771.70 | 1,969,547.27 |

their costs are close to those of 100 scenarios (i.e., the differences are $(104\,295.86 - 103\,887.93)/104\,295.86 = 0.39\%$ and $(104\,273.27 - 103\,835.80)/104\,273.27 = 0.42\%$). In addition, the expected costs are stable with different replications (i.e., the differences are $(102\,270.05 - 102\,294.87)/102\,270.05 = -0.024\%$, $(103\,887.93 - 103\,835.80)/103\,887.93 = 0.05\%$, and $(104\,295.86 - 104\,273.27)/104\,295.86 = 0.022\%$).

### *B. IEEE 118-Bus System*

The modified IEEE 118-bus system with 54 thermal units, three wind farms, and 186 branches is studied. The peak load is 7200 MW with detailed generator and transmission network data given in [31]. The 24-h wind power generation forecasts for the three geographically dispersed wind farms are shown in Fig. 5.

Table VIII shows operation costs of the base case, the pessimistic case, and the optimistic case for the entire 24 h, when the wind power uncertainty is considered to be 15% and 25% of the total installed wind power generation capacity, respectively. Table IX shows operation costs of test cases with 10 000 original scenarios for the scenario-based approach. In comparison, the scenario-based solutions are more rigid, i.e., the optimal objectives values are approximately the same in test cases. However, the objective intervals in the interval optimization

deviate a lot as the wind power uncertainty interval is changed. When the wind power uncertainty is increased from 15% to 25%, the costs of pessimistic and optimistic cases would change by $(2\,042\,033.43 - 2\,032\,250.74)/2\,032\,250.74 = 0.48\%$ and $(1\,944\,019.38 - 1\,968\,175.55)/1\,968\,175.55 = -1.23\%$ although the base case costs are close. In comparison, changes in the expected operation costs of test cases are within 0.084% in the scenario-based approach.

The interval optimization approach takes five iterations with a computation time of 73 s to reach the optimal solution. For the scenario-based approach, with the reduced ten scenarios, it takes seven iterations with a computation time of 178 s. For reduced 100 scenarios, it needs 20 iterations with the total computation time of 2108 s. Since the Stochastic SCUC is an NP-hard problem, the increase in the number of scenarios will dramatically increase the computation burden. In comparison, the computation time for the interval optimization is equivalent to that of a scenario-based approach with the consideration of only two scenarios.

## V. Acceleration Strategy

The computation burden of the scenario-based approach for the Stochastic SCUC problem may be improved by applying the following options:

1) Tighten the master UC problem formulation (11). It is conceivable that the inclusion of system reserve requirement and/or a few scenarios in the first iteration of the master UC problem would result in a better initial UC solution.
2) Make use of the specific structure of Stochastic SCUC problem in certain cases for eliminating optimality cuts. An alternative partition strategy enabled by the combination of (11) and (16) as the master problem may eliminate the need for optimality cuts and require fewer iterations, when a combined optimization of the MIP problem (11) and (16) is possible.
3) Adopt acceleration strategies proposed for the deterministic SCUC [11], [32]. Reference [11] proposed a necessary and sufficient condition to identify and eliminate inactive security constraints in the SCUC problem, for reducing the problem scale and the computation burden. Reference [32] explored a reasonable operational strategy for fixing and unlocking generating units at each SCUC iteration, to control the iterative SCUC solution efficiently and accelerate the execution.
4) Generate multiple strong cuts to accelerate the convergence of the Benders decomposition approach [33]. Multiple strong cuts would restrict the feasible region of the master UC problem at each iteration and, in turn, result in a significant reduction in the number of iterations and the necessary CPU time for computation. Subproblems for generating additional cuts can be executed in parallel, which would not introduce any extra computation time.

## VI. Conclusions

The impact of various uncertainties on the operational security of power systems is becoming more important, as more uncertainty factors are integrated into power systems. This paper evaluates the scenario-based approach and the interval optimization approach for the Stochastic SCUC solution with the consideration of uncertain wind power generation. A six-bus system and the modified IEEE 118-bus system are studied to evaluate the two approaches. The scenario-based approach provides more stable solutions. However, the scenario-based approach may come with larger problem scales and higher computation burdens. A few convergence acceleration options are referred to in the paper for overcoming the computation obstacles of the scenario-based approach. More research on this issue will be required in the future. The interval optimization approach requires less computation time to generate lower and upper bounds automatically for the objective value. However, its optimal solution is very sensitive to the uncertainty interval. In addition, the interval optimization may not be suitable for simulating discrete uncertain variables such as random outages of generators and transmission lines in power systems.

## References


[1] D. Milborrow, Penalties for Intermittent Sources of Energy. [Online]. Available: http://www.piu.gov.uk.

[2] H. Holttinen, Hourly Wind Power Variations and Their Impact on the Nordic Power System Operation, 2003. [Online]. Available: http://www.vtt.fi/renewables/windenergy/hh_lic_thesis_finalpub.pdf.

[3] Institut fur Solare Energieversorgungstechnik, Wind Energy Report, Germany, 2004.

[4] S. Walson, "Fresh forecasts," *Power Engineer*, vol. 19, no. 2, pp. 36–38, May 2005.

[5] I. Sánchez, "Short-term prediction of wind energy production," *Int. J. Forecast.*, vol. 22, no. 1, pp. 43–56, Jan. 2006.

[6] A. J. Conejo, M. A. Plazas, R. Espínola, and A. B. Molina, "Day-ahead electricity price forecasting using the wavelet transform and ARIMA models," *IEEE Trans. Power Syst.*, vol. 20, no. 2, pp. 1035–1042, May 2005.

[7] P. Mandal, T. Senjyu, N. Urasaki, T. Fundabashi, and A. K. Srivastava, "A novel approach to forecast electricity price for PJM using neural network and similar days method," *IEEE Trans. Power Syst.*, vol. 22, no. 4, pp. 2058–2065, Nov. 2007.

[8] L. Wu and M. Shahidehpour, "A hybrid model for day-ahead price forecasting," *IEEE Trans. Power Syst.*, vol. 25, no. 3, pp. 1519–1530, Aug. 2010.

[9] Y. Fu, M. Shahidehpour, and Z. Li, "AC contingency dispatch based on security-constrained unit commitment," *IEEE Trans. Power Syst.*, vol. 21, no. 2, pp. 897–908, May 2006.

[10] P. N. Biskas and A. G. Bakirtzis, "Decentralised security constrained DC-OPF of interconnected power systems," *Proc. Inst. Elect. Eng., Gen., Transm., Distrib.*, vol. 151, no. 6, pp. 747–754, Nov. 2004.

[11] Q. Zhai, X. Guan, J. Cheng, and H. Wu, "Fast identification of inactive security constraints in SCUC problems," *IEEE Trans. Power Syst.*, vol. 25, no. 4, pp. 1946–1954, Nov. 2010.

[12] A. T. Saric, F. H. Murphy, A. L. Soyster, and A. M. Stankovic, "Two-stage stochastic programming model for market clearing with contingencies," *IEEE Trans. Power Syst.*, vol. 24, no. 3, pp. 1266–1278, Aug. 2009.

[13] R. Billinton and R. Allan, *Reliability Evaluation of Power Systems*, 2nd ed. London, U.K.: Pitman Advanced, 1996.

[14] J. Valenzuela and M. Mazumda, "Monte Carlo computation of power generation production costs under operation constraints," *IEEE Trans. Power Syst.*, vol. 16, no. 4, pp. 671–677, Nov. 2001.

[15] P. Carpentier, G. Cohen, J. C. Culioli, and A. Renaud, "Stochastic optimization of unit commitment: A new decomposition framework," *IEEE Trans. Power Syst.*, vol. 11, no. 2, pp. 1067–1073, May 1996.

[16] S. Takriti, J. R. Birge, and E. Long, "A stochastic model for the unit commitment problem," *IEEE Trans. Power Syst.*, vol. 11, no. 3, pp. 1497–1508, Aug. 1996.

[17] A. Tuohy, P. Meibom, E. Denny, and M. O'Malley, "Unit commitment for systems with significant wind penetration," *IEEE Trans. Power Syst.*, vol. 24, no. 2, pp. 592–601, May 2009.

[18] E. M. Constantinescu, V. M. Zavala, M. Rocklin, S. Lee, and M. Anitescu, "A computational framework for uncertainty quantification and stochastic optimization in unit commitment with wind power generation," *IEEE Trans. Power Syst.*, vol. 26, no. 1, pp. 431–441, Feb. 2011.

[19] J. Dupacova, G. Consigli, and S. W. Wallace, "Scenarios for multistage stochastic programs," *Ann. Oper. Res.*, vol. 100, pp. 25–53, 2000.
[20] Z. Wang and F. L. Alvarado, "Interval arithmetic in power flow analysis," *IEEE Trans. Power Syst.*, vol. 7, no. 3, pp. 1341–1349, Aug. 1992.
[21] A. T. Saric and A. M. Stankovic, "An application of interval analysis and optimization to electric energy markets," *IEEE Trans. Power Syst.*, vol. 21, no. 2, pp. 515–523, May 2006.
[22] P. Zhang and W. Li, "Boundary analysis of distribution reliability and economic assessment," *IEEE Trans. Power Syst.*, vol. 25, no. 2, pp. 714–721, May 2010.
[23] Y. Wang, Q. Xia, and C. Wang, "Unit commitment with volatile node injections by using interval optimization," *IEEE Trans. Power Syst.*, vol. 26, no. 3, pp. 1705–1713, Aug. 2011.
[24] U. A. Ozturk, M. Mazumdar, and B. A. Norman, "A solution to the stochastic unit commitment problem using chance constrained programming," *IEEE Trans. Power Syst.*, vol. 19, no. 3, pp. 1589–1598, Aug. 2004.
[25] J. F. Manwell, J. G. McGowan, and A. L. Rogers, *Wind Energy Explained*. New York: Wiley, 2002.
[26] J. Dupačoý, N. Gröwe-Kuska, and W. Römisch, "Scenario reduction in stochastic programming: An approach using probability metrics," *Math. Program.*, vol. 95, no. 3, pp. 493–511, Mar. 2003.
[27] N. Gröwe-Kuska, H. Heitsch, and W. Römisch, "Scenario reduction and scenario tree construction for power management problems," in *Proc. IEEE Power Tech Conf.*, Bologna, Italy, Jun. 2003, vol. 3, pp. 23–26.
[28] J. M. Morales, S. Pineda, A. J. Conejo, and M. Carrion, "Scenario reduction for futures market trading in electricity markets," *IEEE Trans. Power Syst.*, vol. 24, no. 2, pp. 878–888, May 2009.
[29] M. Kaut and S. W. Wallace, "Evaluation of scenario-generation methods for stochastic programming," *Stochastic Program.*, vol. 3, no. 2, pp. 257–271, May 2007.
[30] S. Takriti and S. Ahmed, Managing Short-Term Electricity Contracts Under Uncertainty: A Minimax Approach, Georgia Inst. Technol., Atlanta, GA, 2002, Tech. Rep.
[31] L. Wu, M. Shahidehpour, and T. Li, "Stochastic security-constrained unit commitment," *IEEE Trans. Power Syst.*, vol. 22, no. 2, pp. 800–811, May 2007.
[32] Y. Fu and M. Shahidehpour, "Fast SCUC for large-scale power systems," *IEEE Trans. Power Syst.*, vol. 22, no. 4, pp. 2144–2151, Nov. 2007.
[33] L. Wu and M. Shahidehpour, "Accelerating Benders decomposition for network-constrained unit commitment problems," *Energy Syst.*, vol. 1, no. 3, pp. 339–376, Aug. 2010.
[34] J. Zhao, Z. Dong, Z. Xu, and K. Wong, "A statistical approach for interval forecasting of the electricity price," *IEEE Trans. Power Syst.*, vol. 23, no. 2, pp. 267–276, May 2008.
[35] L. Wu, M. Shahidehpour, and C. Liu, "MIP-based post-contingency corrective action with quick-start units," *IEEE Trans. Power Syst.*, vol. 24, no. 4, pp. 1898–1899, Nov. 2009.
[36] T. Li and M. Shahidehpour, "Price-based unit commitment: A case of Lagrangian relaxation versus mixed integer programming," *IEEE Trans. Power Syst.*, vol. 20, no. 4, pp. 2015–2025, Nov. 2005.

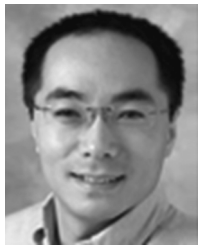

**Lei Wu** (M'07) received the B.S. degree in electrical engineering and the M.S. degree in systems engineering from Xi'an Jiaotong University, Xi'an, China, in 2001 and 2004, respectively, and the Ph.D. degree in electrical engineering from the Illinois Institute of Technology, Chicago, in 2008.

Presently, he is an Assistant Professor in the Electrical and Computer Engineering Department at Clarkson University, Potsdam, NY. His research interests include power systems operation and economics.

**Mohammad Shahidehpour** (F'01) is the Bodine Chair Professor and Director of Galvin Center for Electricity Innovation at the Illinois Institute of Technology, Chicago.

Dr. Shahidehpour is the recipient of the Honorary Doctorate for the Polytechnic University of Bucharest in Romania. He is the recipient of 2011 Technologist of the Year Award from the Illinois Technology Association, Engineer of the Year Award from the IEEE/PES Chicago Section, and the Innovation Award from the Association of Electrical and Computer Engineering Department Heads in the U.S.

**Zuyi Li** (M'01–SM'09) received the B.S. and M.S. degrees from Shanghai Jiaotong University, Shanghai, China, in 1995 and 1998, respectively, and the Ph.D. degree from the Illinois Institute of Technology (IIT), Chicago, in 2002, all in electrical engineering.

Presently, he is an Associate Professor in the Electrical and Computer Engineering Department at IIT. He is the Co-PI of $40 M grants and contracts on energy and sustainability. He is the coauthor of *Market Operations in Electric Power Systems* (New York: Wiley, 2002).

# Security-Constrained Transmission Switching with Voltage Constraints

Amin Khodaei and Mohammad Shahidehpour, ECE Department, Illinois Institute of Technology

This work was supported in part by the United States Department of Energy Grant # DE-EE 0001380.000.

*Abstract*— Transmission switching (TS) would play a vital role in the security and economics of electric power systems. The application of TS to the AC model of security-constrained unit commitment (SCUC) for the day-ahead scheduling is presented in this paper. The proposed AC model of SCUC with TS would include real and reactive power flow constraints which increase the controllability of base case and contingency solutions with voltage constraints. A general FACTS model is introduced for the reactive power management in SCUC which is based on the power injection model (PIM). A modified Newton-Raphson power flow model is introduced in the proposed SCUC with TS in which line flows are considered as variables. The proposed AC network model is compared with the DC network model for enhancing the power network controllability and minimizing the operation cost. The case studies exhibit the effectiveness of the TS application to SCUC with AC network constraints.

*Keywords:* Transmission switching, Security-constrained unit commitment, Voltage Constraints, FACTS devices.

## NOMENCLATURE

***Indices:***

| | |
|---|---|
| $b, m, n$ | Indices for bus |
| $c$ | Index for contingency |
| $i$ | Index for generator |
| $l$ | Index for line |
| $ns$ | Index for non-switchable line |
| $s$ | Index for switchable line |

| | |
|---|---|
| $Sh$ | Superscript for shunt power injections |
| $Se$ | Superscript for series power injections |
| $t$ | Index for time |

***Sets:***

| | |
|---|---|
| $L_b$ | Set of lines connected to bus $b$ |
| $U_b$ | Set of units connected to bus $b$ |

***Parameters:***

| | |
|---|---|
| $M$ | Large positive constant |
| $NB$ | Number of buses |
| $NG$ | Number of units |
| $NNS$ | Number of non-switchable lines |
| $NS$ | Number of switchable lines |
| $NT$ | Number of time periods |
| $PL_l^{\max}$ | Real power flow limit of line $l$ |
| $Q_i^{\min}, Q_i^{\max}$ | Reactive power generation limits of unit $i$ |
| $UX_{it}$ | Contingency state of unit $i$ at time $t$ |
| $UY_{lt}$ | Contingency state of line $l$ at time $t$ |
| $V_b^{\min}, V_b^{\max}$ | Voltage magnitude limits of bus $b$ |
| $\alpha_b$ | Power injection coefficient of FACTS device |
| $\delta_{lt}$ | Standing phase angle difference limit of line $l$ at time $t$ |
| $\Lambda_{it}$ | Permissible real power adjustment of unit $i$ at time $t$ |

***Variables:***

| | |
|---|---|
| $I_{it}$ | Commitment state of unit $i$ at time $t$ |
| $MP_{bt,1}, MP_{bt,2}$ | Slack variables for real power mismatch in bus $b$ at time $t$ |
| $MQ_{bt,1}, MQ_{bt,2}$ | Slack variables for reactive power mismatch in bus $b$ at time $t$ |
| $P_{it}$ | Real power generation of unit $i$ at time $t$ |
| $PF_{bt}$ | Real power injection in bus $b$ at time $t$ due to FACTS device |

| | |
|---|---|
| $PL_{lt}$ | Real power flow of line *l* at time *t* |
| $Q_{it}$ | Reactive power generation of unit *i* at time *t* |
| $QF_{bt}$ | Reactive power injection in bus *b* at time *t* due to FACTS device |
| $QL_{lt}$ | Reactive power flow of line *l* at time *t* |
| $V_{bt}$ | Voltage magnitude of bus *b* at time *t* |
| $w_t$ | Total mismatch at time *t* |
| $z_{lt}$ | Switching state of line *l* at time *t* |
| $\theta_{bt}$ | Voltage angle of bus *b* at time *t* |
| $\psi_{it}, \mu_{lt}, \pi_{it}$ | Dual variables |

***Symbols:***

| | |
|---|---|
| $\wedge$ | Given variables |

***Matrices and Vectors:***

| | |
|---|---|
| $\mathbf{1}$ | Vector of ones |
| $\mathbf{A, B, C, D}$ | Jacobian matrices |
| $\mathbf{dP}_0$ | Real power mismatch vector |
| $\mathbf{dQ}_0$ | Reactive power mismatch vector |
| $\mathbf{MP}_1, \mathbf{MP}_2$ | Vector of slack variables for real power mismatch |
| $\mathbf{MQ}_1, \mathbf{MQ}_2$ | Vector of slack variables for reactive power mismatch |
| $\mathbf{X}$ | Bus-Line incidence matrix |
| $\mathbf{Y}$ | Bus-Unit incidence matrix |
| $\mathbf{\Delta P}$ | Real power generation increment vector |
| $\mathbf{\Delta PL}$ | Real power flow increment vector |
| $\mathbf{\Delta PL}^{min}, \mathbf{\Delta PL}^{max}$ | Real power flow lower and upper increment vectors |
| $\mathbf{\Delta Q}$ | Reactive power generation increment vector |
| $\mathbf{\Delta Q}^{min}, \mathbf{\Delta Q}^{max}$ | Reactive power generation lower and upper increment vectors |
| $\mathbf{\Delta QL}$ | Reactive power flow increment vector |
| $\mathbf{\Delta V}$ | Bus voltage increment vector |

$\Delta V^{min}, \Delta V^{max}$ Bus voltage lower and upper increment vectors

$\Delta\theta$ Bus phase angle increment vector

$\Delta\Lambda^{min}, \Delta\Lambda^{max}$ Real power generation adjustment lower and upper increment vectors

## 1. INTRODUCTION

Recent market design proposals consider a more active role for transmission owners. Incentives are provided for transmission owners to increase investments in transmission and to utilize transmission lines more efficiently. Considering that building new transmission lines to meet the growing demand is a difficult and time-consuming task, the more efficient use of the existing transmission network would be a valuable alternative. Transmission switching (TS) is an efficient approach to utilize the power gird more comprehensively. TS will take specific transmission lines temporarily out of service in order to benefit from the modified network topology. This capability will be considered primarily for the newly installed transmission lines in the electricity market. TS has gained further attention since the FERC order 890 has called for an economic utilization of transmission capacity and hence made TS more favorable for economic purposes. The independent system operator (ISO) may apply TS as a corrective action for mitigating transmission flow violations [1]-[4], as a congestion management tool [5], for enhancing the power system security [6]-[9], and improving the system economics while maintain the security constraints [10]. TS would manage topology changes which could affect nodal prices, load payments, generation revenues, congestion costs, and flowgate prices. It can also improve the solution of the capacity expansion planning problem while providing economic benefits [11]-[12].

Much of the previous studies considered the TS for real power flow adjustments. In this paper, the optimal TS is considered for mitigating both transmission flow and bus voltage violations in the security-constrained unit commitment (SCUC) problem. To consider voltage constraints, a modified Newton–Raphson model is utilized which will satisfy the base case and contingency constraints. The proposed SCUC solution uses the Benders decomposition to decompose the model into a master problem and two subproblems [13]-[17]. A general model of FACTS devices is incorporated into the proposed SCUC formulations, which is capable of modeling all types of series, shunt or series-shunt FACTS devices. These features will add a comprehensive perspective to the SCUC formulation for TS applications.

Fig. 1 depicts the flowchart of the proposed SCUC model with AC network constraints. Benders decomposition is utilized to decompose the SCUC problem into smaller and easier to solve subproblems. The master problem uses the available market information to find the optimal hourly schedule of units (UC) by considering the prevailing UC constraints [18]-[20]. The hourly solution of UC is used in the subproblems to examine the AC network constraints. The TS ability of lines is considered and FACTS devices are incorporated in the subproblems if violations are detected. TS binary variables are determined via UC and

consequently, they are considered as constant values in the subproblems. Given the unit and line schedule by the UC solution, the Subproblem 1 will check the base case network feasibility. In this subproblem, slack variables for real and reactive power mismatches are minimized based on line flow and FACTS device adjustments. The proposed Benders cut incorporates slack variables for the real and reactive power mismatch that is mitigated by recalculating the unit and line schedules. A converged base case power flow will be achieved based on the UC results. The Contingencies Network Check subproblem uses the UC solution for the base case to check the system security in case of contingencies. Using AC power flow equations, both real and reactive power mismatches are minimized in this subproblem. It is required to limit the standing phase angle difference to safeguard the rotor shaft. Different approaches are proposed to obtain the minimum generation redispatch in a reasonable time for desired standing phase angles [21]-[26]. This problem which is inevitable in restoration practices may also occur in the normal operation of power systems when attempting to reclose a single line that is a part of a transmission loop [23]. To present a practical TS model, the standing phase angle difference limit of switchable lines is formulated in our proposed model.

FACTS devices are incorporated here in the SCUC model. FACTS devices are traditionally modeled by a voltage (current) source model (VSM). VSM formulates the device according to the operating conditions, thus representing the device intuitively. However, it destroys the symmetric characteristics of the admittance matrix and may cause oscillations in the power flow solution in successive iterations. A more common approach, as used in this paper, is to utilize power injection model (PIM). The PIM is derived from VSM, in which real and reactive power injections are considered as independent control variables, as shown in Fig. 2. Using PIM, the symmetric characteristics of admittance matrix is kept and the oscillations in the power flow solution are mitigated. Due to advantages of the PIM, this model were extended to almost all FACTS devices and used in most of the researches on operation and control of power systems with FACTS devices. Table 1 represents the required PIM components for modeling different FACTS devices. The power injections are only interim results, where they would be converted to the corresponding VSM parameters once the solution is obtained. The control parameters and the required conversion to obtain control parameters from PIM components are not listed in the table since it can be found in the literature.

The rest of the paper is organized as follows. Section 2 presents the formulation of the problem. Section 3 conducts the numerical simulations and in detail discusses results obtained for the IEEE 118-bus system. Finally, concluding remarks are drawn in Section 4.

## 2. SECURITY-CONSTRAINED REACTIVE POWER FORMULATION

The step by step procedure for the solution of the proposed SCUC model is given as follows.

*2.1. UC (Optimal Hourly Schedule of Units)*

The UC solution provides the hourly generation dispatch and the state of switchable lines in both base case and contingencies. At the first iteration of the problem, there is no constraint on switchable lines states. So, random initial values might be assigned to these variables. However, in our approach we consider that all lines are in service at the first iteration. In subsequent iterations, the Benders cuts from the subproblems establish more constraints on switchable lines states. Although the switchable lines states are determined in the master problem, they are actually governed by Benders cuts stemmed out of the subproblems. Mixed-integer programming (MIP) is used to formulate the UC problem.

*2.2. Network Check (General Formulation)*

In the Base Case and Contingencies Network Check subproblems, a linearized AC power flow based on Newton-Raphson method is performed to check the existence of a converged solution. The general formulation of this linearized power flow in matrix form is expressed by (1)-(8).

$$\mathbf{Min}\ \ \mathbf{w}(\hat{\mathbf{I}},\hat{\mathbf{P}}) = \mathbf{1}^{\mathbf{T}}(\mathbf{MP}_{\mathbf{1}} + \mathbf{MP}_{\mathbf{2}}) + \mathbf{1}^{\mathbf{T}}(\mathbf{MQ}_{\mathbf{1}} + \mathbf{MQ}_{\mathbf{2}}) \tag{1}$$

$$\begin{bmatrix} \mathbf{Y} * \mathbf{\Delta P} \\ \mathbf{Y} * \mathbf{\Delta Q} \end{bmatrix} - \begin{bmatrix} \mathbf{X} * \mathbf{\Delta PL} \\ \mathbf{X} * \mathbf{\Delta QL} \end{bmatrix} + \begin{bmatrix} \mathbf{MP}_{\mathbf{1}} \\ \mathbf{MQ}_{\mathbf{1}} \end{bmatrix} - \begin{bmatrix} \mathbf{MP}_{\mathbf{2}} \\ \mathbf{MQ}_{\mathbf{2}} \end{bmatrix} = \begin{bmatrix} \mathbf{dP}_{\mathbf{0}} \\ \mathbf{dQ}_{\mathbf{0}} \end{bmatrix} \tag{2}$$

$$\begin{bmatrix} \mathbf{\Delta PL} \\ \mathbf{\Delta QL} \end{bmatrix} = \begin{bmatrix} \mathbf{A} & \mathbf{B} \\ \mathbf{C} & \mathbf{D} \end{bmatrix} \begin{bmatrix} \mathbf{\Delta\theta} \\ \mathbf{\Delta V} \end{bmatrix} \tag{3}$$

$$\mathbf{\Delta Q}^{\mathbf{min}} \le \mathbf{\Delta Q} \le \mathbf{\Delta Q}^{\mathbf{max}} \tag{4}$$

$$\mathbf{\Delta PL}^{\mathbf{min}} \le \mathbf{\Delta PL} \le \mathbf{\Delta PL}^{\mathbf{max}} \tag{5}$$

$$\mathbf{\Delta V}^{\mathbf{min}} \le \mathbf{\Delta V} \le \mathbf{\Delta V}^{\mathbf{max}} \tag{6}$$

$$\mathbf{\Delta P} = \mathbf{0} \tag{7}$$

$$\mathbf{\Delta\Lambda}^{\mathbf{min}} \le \mathbf{\Delta P} \le \mathbf{\Delta\Lambda}^{\mathbf{max}} \tag{8}$$

The AC power flow will converge when real and reactive power mismatches at each bus are zero. The objective function (1) minimizes the slack variables for real and reactive power mismatches in the system (2). In this formulation, instead of using the common form of Jacobian matrix [27], the line real and reactive power flows are incorporated in the power balance equation. The line flows are linked to power injections/withdrawals at the associated buses. The line flows are calculated based on bus voltage magnitudes and angles as presented by (3). This modification does not change the basic power flow formulation while it enables the modeling of network topology adjustments. Parallel lines are modeled efficiently since the real and reactive power flows of each line are considered as problem variables. Limits on reactive power generation, line real power flow and bus voltage

magnitudes are presented by (4)-(6), respectively. In the Base Case Network Check, the limit on real power generation (7) is applied to all units except that of slack bus to compensate for power loss mismatch. In the Contingencies Network Check, (8) is applied to consider the unit real power generation adjustments in contingencies. Using the proposed AC power flow equations, the network topology adjustments, i.e. transmission line switching and contingency, can simply be applied by modifying (3). Using the proposed formulation, the power injections due to FACTS devices are added to (2) and unit contingencies are considered by modifying (4) and (8). Further details on the proposed MIP formulation are provided in the following subsection.

### *2.3. Network Check (Detailed Formulation)*

Once the initial unit and line schedule is determined by the UC problem, the Base Case Network Check subproblem is solved for 24 hours. In this subproblem, slack variables for real and reactive power mismatches at various buses are considered for minimization to check whether a converged AC power flow solution can be obtained based on UC results.

$$Min \quad w_t^c = \sum_{b=1}^{NB} (MP_{bt,1}^c + MP_{bt,2}^c) + \sum_{b=1}^{NB} (MQ_{bt,1}^c + MQ_{bt,2}^c) \tag{9}$$

The constraints are given as follows.

$$z_{lt}^c = \hat{z}_{lt}^c \qquad \leftrightarrow \qquad \mu_{lt}^c \qquad (l = 1,..., NS) \tag{10}$$

$$\sum_{i \in U_b} \Delta P_{it}^c - \sum_{l \in L_b^s} \Delta PL_{lt}^{sc} - \sum_{l \in L_b^{ns}} \Delta PL_{lt}^{nsc} + MP_{bt,1}^c - MP_{bt,2}^c = dP_{0bt}^c \qquad (b = 1,..., NB) \tag{11}$$

$$\sum_{i \in U_b} \Delta Q_{it}^c - \sum_{l \in L_b^s} \Delta QL_{lt}^{sc} - \sum_{l \in L_b^{ns}} \Delta QL_{lt}^{nsc} + MQ_{bt,1}^c - MQ_{bt,1}^c = dQ_{0bt}^c \qquad (b = 1,..., NB) \tag{12}$$

$$\Delta Q_{it}^{c\min} \hat{I}_{it} \le \Delta Q_{it}^c \le \Delta Q_{it}^{c\max} \hat{I}_{it} \quad \leftrightarrow \quad \underline{\psi}_{it}^c, \overline{\psi}_{it}^c \qquad (i = 1,..., NG) \tag{13}$$

$$\Delta V_{bt}^{c\min} \le \Delta V_{bt}^c \le \Delta V_{bt}^{c\max} \qquad (b = 1,..., NB) \tag{14}$$

$$\Delta PL_{lt}^{nsc} - \sum_{b=1}^{NB} \frac{\partial PL_{lt}^{nsc}}{\partial \theta_{bt}^c} \Delta \theta_{bt}^c - \sum_{b=1}^{NB} \frac{\partial PL_{lt}^{nsc}}{\partial V_{bt}^c} \Delta V_{bt}^c \le M (1 - UY_{lt}^c) \qquad (l = 1,..., NNS) \tag{15}$$

$$\Delta PL_{lt}^{nsc} - \sum_{b=1}^{NB} \frac{\partial PL_{lt}^{nsc}}{\partial \theta_{bt}^c} \Delta \theta_{bt}^c - \sum_{b=1}^{NB} \frac{\partial PL_{lt}^{nsc}}{\partial V_{bt}^c} \Delta V_{bt}^c \ge -M (1 - UY_{lt}^c) \qquad (l = 1,..., NNS) \tag{16}$$

$$-\Delta PL_{lt}^{c\max} UY_{lt}^c \le \Delta PL_{lt}^{nsc} \le \Delta PL_{lt}^{c\max} UY_{lt}^c \qquad (l = 1,..., NNS) \tag{17}$$

$$\Delta QL_{lt}^{nsc} - \sum_{b=1}^{NB} \frac{\partial QL_{lt}^{nsc}}{\partial \theta_{bt}^c} \Delta \theta_{bt}^c - \sum_{b=1}^{NB} \frac{\partial QL_{lt}^{nsc}}{\partial V_{bt}^c} \Delta V_{bt}^c \le M (1 - UY_{lt}^c) \qquad (l = 1,..., NNS) \tag{18}$$

$$\Delta QL_{lt}^{nsc} - \sum_{b=1}^{NB} \frac{\partial QL_{lt}^{nsc}}{\partial \theta_{bt}^c} \Delta \theta_{bt}^c - \sum_{b=1}^{NB} \frac{\partial QL_{lt}^{nsc}}{\partial V_{bt}^c} \Delta V_{bt}^c \ge -M (1 - UY_{lt}^c) \qquad (l = 1,..., NNS) \tag{19}$$

$$\Delta PL_{lt}^{sc} - \sum_{b=1}^{NB} \frac{\partial PL_{lt}^{sc}}{\partial \theta_{bt}^{c}} \Delta \theta_{bt}^{c} - \sum_{b=1}^{NB} \frac{\partial PL_{lt}^{sc}}{\partial V_{bt}^{c}} \Delta V_{bt}^{c} \le M\,(2 - z_{lt}^{c} - UY_{lt}^{c}) \qquad (l = 1,..., NS) \tag{20}$$

$$\Delta PL_{lt}^{sc} - \sum_{b=1}^{NB} \frac{\partial PL_{lt}^{sc}}{\partial \theta_{bt}^{c}} \Delta \theta_{bt}^{c} - \sum_{b=1}^{NB} \frac{\partial PL_{lt}^{sc}}{\partial V_{bt}^{c}} \Delta V_{bt}^{c} \ge -M\,(2 - z_{lt}^{c} - UY_{lt}^{c}) \qquad (l = 1,..., NS) \tag{21}$$

$$-\Delta PL_{lt}^{c\max} z_{lt}^{c} UY_{lt}^{c} \le \Delta PL_{lt}^{sc} \le \Delta PL_{lt}^{c\max} z_{lt}^{c} UY_{lt}^{c} \qquad (l = 1,..., NS) \tag{22}$$

$$\Delta QL_{lt}^{sc} - \sum_{b=1}^{NB} \frac{\partial QL_{lt}^{sc}}{\partial \theta_{bt}^{c}} \Delta \theta_{bt}^{c} - \sum_{b=1}^{NB} \frac{\partial QL_{lt}^{sc}}{\partial V_{bt}^{c}} \Delta V_{bt}^{c} \le M\,(2 - z_{lt}^{c} - UY_{lt}^{c}) \qquad (l = 1,..., NS) \tag{23}$$

$$\Delta QL_{lt}^{sc} - \sum_{b=1}^{NB} \frac{\partial QL_{lt}^{sc}}{\partial \theta_{bt}^{c}} \Delta \theta_{bt}^{c} - \sum_{b=1}^{NB} \frac{\partial QL_{lt}^{sc}}{\partial V_{bt}^{c}} \Delta V_{bt}^{c} \ge -M\,(2 - z_{lt}^{c} - UY_{lt}^{c}) \qquad (l = 1,..., NS) \tag{24}$$

$$-Mz_{lt}^{c} UY_{lt}^{c} \le \Delta QL_{lt}^{sc} \le Mz_{lt}^{c} UY_{lt}^{c} \qquad (l = 1,..., NS) \tag{25}$$

$$\Delta \delta_{lt}^{c\min} \le \Delta \theta_{mt}^{c} - \Delta \theta_{nt}^{c} \le \Delta \delta_{lt}^{c\max} \tag{26}$$

In (10), $\hat{z}_{lt}^{c}$ is the fixed value calculated by UC for Benders cuts. In power mismatch equations (11)-(12), slack variables would model system violations. Slack variables can be considered as virtual generators/loads that are added to each bus to mitigate mismatches. The right hand-side of (11) and (12) are the present value of power mismatch. Limits on reactive power generations and bus voltage magnitudes are presented by (13) and (14), respectively. The change in real and reactive power flows of non-switchable lines are obtained by (15)-(19). Considering the state of each switchable line, the change in switchable line flows are obtained by (20)-(25). These changes are used to update flows of switchable and non-switchable lines. The standing phase angle difference constraint is considered by (26). Note that *c=0* denotes the base case. In (10) and (13), the double arrow refers to the duality of the equality constraint, where $\mu^{c}_{lt}$ and $\psi^{c}_{it}$ represent the dual variable (simplex multiplier) of these constraints. Mathematically, a dual variable represents the marginal increment/decrement of the objective value when the variable is changed. When the state of the switchable line is zero the real power flow equation of that line will be relaxed by (20) and (21). Similarly, the reactive power flow equation will be relaxed by (23) and (24). In addition, the change in real and reactive power flows of that line will be set to zero by (22) and (25), respectively. So, the switched line will be completely removed from the system. *M* is a large positive constant and is calculated as proposed in [12].

For the base case, (27) is added to consider limits on real power generation. This constraint applies to all units except that of the slack bus, which is relaxed to compensate power loss calculations.

$$\Delta P_{it}^{0} = 0 \leftrightarrow \pi_{it}^{0} \qquad (i = 2,..., NG) \tag{27}$$

In the case of contingencies, the adjustment range for unit generation at contingency with respect to the base case generation is considered. This constraint is presented by (28).

$$\Delta\Lambda_{it}^{\min} \le \Delta P_{it}^{c} \le \Delta\Lambda_{it}^{\max} \quad \leftrightarrow \quad \underline{\pi}_{it}^{c}, \overline{\pi}_{it}^{c} \qquad (i = 2,..., NG) \tag{28}$$

In (28), only contingencies are considered, i.e. $c \ge 1$. For the limits on allowable post-contingency power generation redispatch we would have

$$\Delta\Lambda_{it}^{\max} = \Lambda_i - (P_{it}^{c} - P_{it}^{0}) \tag{29}$$

$$\Delta\Lambda_{it}^{\min} = -\Lambda_i - (P_{it}^{c} - P_{it}^{0}) \tag{30}$$

These limits define the maximum allowable adjustments of power generation output in case of contingencies. In the proposed formulation, small changes in state and control variables are subject to variable limits (31)-(36).

$$\Delta Q_{it}^{c\min} = Q_i^{\min} - Q_{it}^{c} \tag{31}$$

$$\Delta Q_{it}^{c\max} = Q_i^{\max} - Q_{it}^{c} \tag{32}$$

$$\Delta V_{bt}^{c\min} = V_b^{\min} - V_{bt}^{c} \tag{33}$$

$$\Delta V_{bt}^{c\max} = V_b^{\max} - V_{bt}^{c} \tag{34}$$

$$\Delta PL_{lt}^{c\min} = -PL_l^{\max} - PL_{lt}^{c} \tag{35}$$

$$\Delta PL_{lt}^{c\max} = PL_l^{\max} - PL_{lt}^{c} \tag{36}$$

The limits on standing phase angle difference are given as (37)-(40).

$$\Delta\delta_{lt}^{0\min} = \delta_l^{\max} - (\theta_{mt}^{0} - \theta_{nt}^{0}) + Mz_{l(t-1)}^{0} + M(1 - z_{lt}^{0}) \tag{37}$$

$$\Delta\delta_{lt}^{0\max} = \delta_l^{\max} - (\theta_{mt}^{0} - \theta_{nt}^{0}) + Mz_{l(t-1)}^{0} + M(1 - z_{lt}^{0}) \tag{38}$$

$$\Delta\delta_{lt}^{c\max} = Min \begin{Bmatrix} \delta_l^{\max} - (\theta_{mt}^{c} - \theta_{nt}^{c}) + Mz_{l(t-1)}^{c} + M(1 - z_{lt}^{c}), \\ \delta_l^{\max} - (\theta_{mt} - \theta_{nt}) + Mz_{lt} + M(1 - z_{lt}^{c}) \end{Bmatrix} \tag{39}$$

$$\Delta\delta_{lt}^{c\min} = -Max \begin{Bmatrix} \delta_l^{\max} + (\theta_{mt}^{c} - \theta_{nt}^{c}) + Mz_{l(t-1)}^{c} + M(1 - z_{lt}^{c}), \\ \delta_l^{\max} + (\theta_{mt} - \theta_{nt}) + Mz_{lt} + M(1 - z_{lt}^{c}) \end{Bmatrix} \tag{40}$$

In (39) and (40), where $c \ge 1$, the minimum and the maximum allowable changes in the standing phase angle difference would depend on the state of a switchable line in successive hours. In the case of contingencies, minimum and maximum allowable changes in the standing phase angle difference are determined based on two different modes of operation. The first mode represents the switchable line state at successive hours in that contingency, where excessive standing phase angle difference may exist when closing the line. The second mode represents the transition from the base case to a contingency. When a line is off at the base case and is switched back on in a contingency case, the standing phase angle difference of the line is checked. We

calculate the proper limits on changes of standing phase angle difference by comparing the values in these two modes.

To consider FACTS devices, (11) and (12) are modified since the proposed injections only appear in power mismatch equations at each bus. So, (11) is replaced by (41) and (12) is replaced by (42).

$$\sum_{i\in I_b}\Delta P_{it}^{c}-\sum_{l\in L_b^s}\Delta PL_{lt}^{sc}-\sum_{l\in L_b^{ns}}\Delta PL_{lt}^{nsc}+\sum_{b\in B_b}\alpha_{b,1}\Delta PF_{bt}^{Se,c}+MP_{bt,1}^{c}-MP_{bt,1}^{c}=dP_{0bt}^{c}\qquad (b=1,...,\ NB) \tag{41}$$

$$\sum_{i\in I_b}\Delta Q_{it}^{c}-\sum_{l\in L_b^s}\Delta QL_{lt}^{sc}-\sum_{l\in L_b^{ns}}\Delta QL_{lt}^{nsc}+\sum_{b\in B_b}\alpha_{b,2}\Delta QF_{bt}^{Se,c}+\sum_{b\in B_b}\alpha_{b,3}\Delta QF_{bt}^{Sh,c}+MQ_{bt,1}^{c}-MQ_{bt,1}^{c}=dQ_{0bt}^{c}\qquad (b=1,...,\ NB) \tag{42}$$

In the above formulations, coefficients are set to represent certain types of FACTS devices as follows [28]-[29]

Shunt controller: $\alpha_1=0,\quad \alpha_2=0,\quad \alpha_3=1$

Series controller: $\alpha_1=1,\quad \alpha_2=0,\quad \alpha_3=0$

Shunt-Series controller: $\alpha_1=1,\quad \alpha_2=1,\quad \alpha_3=1$

In every iteration, the FACTS control parameter limits are converted into associated PIM values for satisfying the operating constraints.

In the Base Case Network Check, if the total mismatch is greater than zero, the Benders cut (43) is formed and added to the master problem for the next iteration. The violation indicates that the existing UC solution cannot provide a feasible AC power flow solution. The required dual values that would generate cuts are obtained from (27) for power generation, from (13) for commitment state, and from (10) for switchable lines states.

$$\hat{w}_t^{0}+\sum_{i=1}^{NG}\pi_{it}^{0}(P_{it}^{0}I_{it}-\hat{P}_{it}^{0}\hat{I}_{it})+\sum_{i=1}^{NG}(\overline{\psi}_{it}^{0}Q_i^{\max}-\underline{\psi}_{it}^{0}Q_i^{\min})(I_{it}-\hat{I}_{it})+\sum_{l=1}^{NL}\mu_{lt}^{0}(z_{lt}^{0}-\hat{z}_{lt}^{0})\le 0 \tag{43}$$

where $\hat{w}_t^{0}$ is the current value of (9) in the base case. The number of Benders cuts is equal to the number of hours with power flow violations. These cuts provide proper signals for the convergence of AC power flow by re-calculating the hourly UC, dispatch, and the state of switchable lines in the next UC iteration. This iterative process stops when the base case violations are mitigated. In this case, the problem proceeds to the next step to consider different contingencies. In the Contingencies Network Check, if the total mismatch is greater than zero, the Benders cut (44) will be formed for the associated contingency in that hour and added to the UC for the next iteration.

$$\hat{w}_t^{c}+\sum_{i=1}^{NG}(\overline{\pi}_{it}^{c}-\underline{\pi}_{it}^{c})(P_{it}^{0}-\hat{P}_{it}^{0})+\sum_{i=1}^{NG}(\overline{\psi}_{it}^{c}Q_i^{\max}-\underline{\psi}_{it}^{c}Q_i^{\min})(I_{it}-\hat{I}_{it})+\sum_{l=1}^{NL}\mu_{lt}^{c}(z_{lt}^{c}-\hat{z}_{lt}^{c})\le 0 \tag{44}$$

where $\hat{w}_t^{c}$ is the current value of (9) in the case of contingencies. The following iterative procedure would provide the solution to the subproblems:

1) Calculate initial bus mismatches based on the UC solution and initial system states and settings.

2) Use linear programming (LP) to minimize (9) and calculate changes in system state and control variables (i.e., $\Delta Q$, $\Delta\theta$, $\Delta V$).

3) Update state and control variables, and calculate bus mismatches.

4) Again use LP to minimize (9) and calculate changes in the system state and control variables. If the difference between current and previous iterative changes is less than a specified threshold, stop the process. Otherwise, go back to Step 3.

## 3. NUMERICAL SIMULATIONS

A modified IEEE 118-bus system, shown in Fig. 3, is analyzed to illustrate the performance of the proposed model. The proposed model was implemented on a 2.4-GHz personal computer using CPLEX 11.0 [30]. This system has 118 buses, 54 units and 186 branches. The data for this system is found in motor.ece.iit.edu/data/SCUC_118test.xls. Twenty lines are considered switchable as shown in Table 2. Outages of unit 28, line 80-81, and line 85-89 are considered as credible contingencies. Standing phase angle difference limit of 20 degrees is considered for switchable lines. Three cases are considered as follows:

Case 1: Base case UC without network constraints

Case 2: Consider real network constraints in the SCUC solution with TS (DC solution)

Case 3: Consider real and reactive network constraints in the SCUC solution with TS (AC solution)

**Case 1:** In this case, UC will determine the base case schedule of units, when disregarding the network constraints. Seventeen units are committed at various hours to satisfy the forecasted load. Thirteen economical units are considered as base units, which are committed at the entire scheduling horizon. The other more expensive units are committed whenever necessary to meet the changes in the system load. The UC solution is obtained in 20s with a total operating cost of $792,509.

**Case 2:** In this case, the hourly SCUC solution is considered with the DC model of the network. The unit schedule is shown in Table 3. In DC network model, voltage magnitudes at system buses are set to 1 and lines resistances are assumed to be zero. Consequently, the reactive load, reactive power generation capability of units and reactive power flow in the system are disregarded. The hourly schedule is quite different from that of Case 1, where the schedule for eleven units is changed. Most changes have occurred at the peak hour, i.e. hour 16, and its adjacent hours. At these hours, units 14, 19, 30, 34, 35 and 37 are turned on and unit 40 is turned off. Here, the generating unit 40 is turned off for economic reasons. The switchable line states are changed during scheduling hours to mitigate the system congestion and consequently increase the dispatch of economical units. The base case schedule for switchable lines is shown in Table 4, where seventeen switchable lines have changed their hourly states. Lines 90, 115 and 153 are in service at every hour, so their switching capability is not used in the problem solution. At the peak hour, only lines 75 and 164 are switched off to decrease the flow on lines 7, 9, 129, when all other lines are utilized to

supply loads. The system contingencies are handled with corrective actions (generation redispatch and TS). The standing phase angle difference of switched lines is checked whenever a line is switched back on, e.g., hour 7 for line 3, hours 7 and 11 for line 12, and so on. Here, none of the lines would exceed their standing phase angle difference limits, so it would be possible to switch the lines back as scheduled. The total operating cost is $802,170, which shows a 1.22% increase in cost in comparison to that in Case 1. This increase is due to consideration of DC model of the network. This DC solution is obtained in 60s.

**Case 3:** In this case, the hourly SCUC solution is considered with the AC model of the network. The AC network model would include real and reactive power constraints. The constraints on bus voltage magnitudes are considered in this case. Table 3 highlights the revised hourly state of twenty units as compared to those in Case 2. In this case, most solution changes have occurred close to peak hours, except for units 43 and 44. Unit 43 is on at every hour to prevent voltage drops at buses 93, 94 and 102, and unit 44 is off for economic reasons. The switchable line schedule is shown in Table 5. Fifteen lines are switched hourly to satisfy the system constraints. The other five lines are switched at some hours. TS would increase the power transfer capability that could lead to hourly UC changes. TS would also adjust bus voltages and the reactive power dispatch of generating units by changing the network topology. The additional reactive power generated at the peak hour would lead to an overall increase in bus voltage magnitudes. At the peak hour, the smallest voltage magnitude is 0.97 at buses 44, 45, 109 and 118. On the other hand, 17 buses have already reached their upper limits which are adjusted subsequently by TS. TS would also influence voltages at other hours; however these changes do not have a significant effect on the system voltage profile as voltage magnitudes remain within their permissible limits. Fig. 4 depicts the voltage profile at bus 88 with and without TS. The bus is connected to generating units 38 and 40 at buses 85 and 89. Therefore, the two generating units would have the highest impact on the adjustment of voltage at bus 88. However, unit 38 is off and will not have an impact on the voltage at bus 88. We consider two alternatives as follows.

- Without TS: Unit 40 is committed at hours 9-18. In this case, the voltage magnitude at bus 88 is at its lower limit at hours 3-6 and close to its upper limit at hours 10 and 13-18. At hour 9, the voltage magnitude at bus 88 increases when unit 40 is committed. At hour 11, the voltage at bus 88 is affected by the change in the UC schedule. At hours 13-18, the voltage magnitude at bus 88 is close to its upper limit. At hours 19-24, the voltage at bus 88 drops because unit 40 which is the local source of voltage adjustment, is not in service.
- With TS: Unit 40 is committed at hours 10-22. In this case, the voltage at bus 88 is increased slightly at hours 3-7. The voltage magnitude at bus 88 increases at hour 10 when unit 40 is turned on. The UC adjustments at hour 11 would lead to a voltage magnitude drop at bus 88. At hours 13-14, the reactive power generation of unit 40 would increase the voltage magnitude at bus 88, while the TS application at hours 15-18 would decrease the voltage. The lower real and reactive power generation of unit 40 would decrease the reactive power flow on line 137 and voltage magnitude at bus 88. The commitment

of Unit 40 at hours 20-22 would supply the real and reactive power generation which would lead to an increase in the voltage magnitude at bus 88.

TS in Case 3 would provide a better chance for voltage adjustments especially at peak hour. At the peak hours, the additional real and reactive power generation supply the higher load. Using TS, voltage magnitudes could be lowered at peak hours which would increase the dispatch of less expensive units for supplying the load.

In Case 3, nine FACTS devices are considered with tap-changing and phase-shifting capabilities. The FACTS devices are modeled using the proposed PIM. In Case 2, where the DC network constraints are considered, the phase-shifting capability of FACTS devices will adjust the real power flow in the associated lines. In Case 3, the FACTS devices would also modify reactive power flows and accordingly adjust bus voltage levels. The FACTS devices generate a counterflow to decrease the power flow on the associated line and therefore increase the transfer capability of the line. The installed FACTS device at line 107 is between buses 68 and 69. The voltage at bus 69 is adjusted by the generating unit located at 29. Without the FACTS device at line 107, the voltage drop might occur at bus 68 mostly at peak hours. However, the reactive power injection to bus 68 increases the bus 68 voltage and prevents voltage violations. Fig. 5 shows the voltage profile of bus 68 with and without FACTS at line 107. Without the FACTS device, voltages are adjusted by the neighboring units 27, 29 and 54. Here, unit 54 is not committed while units 27 and 29 are always committed. The reactive power generation of units 27 and 29 is increased for adjusting the voltage level at bus 68, which would also increase the reactive power flow at connecting lines 104 and 107. The solid line in Fig. 5 shows the adjusted hourly voltage at bus 68. Comparing the two voltage profiles, the voltage deviation is smaller when FACTS devices are in place. So, the FACTS device could reduce the real and reactive power dispatch of units, decrease line flows, and enhance the use of TS. Similar to Case 2, TS would prevent the violation of standing phase angle difference limits. Hence, line flows and bus voltage magnitudes are within their limits when supplying the reactive loads. The total operating cost is $824,342, which is calculated in 162seconds.

## 4. CONCLUSIONS

TS was incorporated into the SCUC problem with AC network constraints. To enhance the proposed AC solution of SCUC, FACTS devices were considered. A PIM was used to model the effect of FACTS devices in the AC power flow, using real and reactive power injections to system buses. We concluded that the TS applications would enhance the hourly SCUC solution when considering reactive and voltage constraints. In addition, the incorporation of FACTS devices would further enhance the proposed AC solution of SCUC. The incorporation of AC network constraints would increase the total operating cost and the execution time, which is regarded as a trade-off between more accurate and faster SCUC solutions.

## REFERENCES


[1] Shahidehpour M, Yamin H, Li Z. Market operations in electric power systems. New York: Wiley; 2002.

[2] Conejo AJ, Castillo E, Mínguez R, García-Bertrand R. Decomposition techniques in mathematical programming. Springer; 2006.

[3] Bakirtzis A, Meliopoulos A. Incorporation of switching operation in power system corrective control computations. IEEE Trans Power Syst 1987;7(8):669-76.

[4] Rahimi F, Zhang M, Hobbs B. Competitive transmission path assessment for local market power mitigation. Power Eng Soc Gen Meeting 2007.

[5] Granelli G, Montagna M, Zanellini F, Bresesti P, Vailati R, Innorta M. Optimal network reconfiguration for congestion management by deterministic and genetic algorithms. Electr. Power Syst Res 2006;76:549-56.

[6] Schnyder G, Glavitsch H. Integrated security control using an optimal power flow and switching concepts. IEEE Trans Power Syst 1988;3(2):782-90.

[7] Schnyder G, Glavitsch H. Security enhancement using an optimal switching power flow. IEEE Trans Power Syst 1990;5(2):674-81.

[8] Rolim JG, Machado LJB. A study of the use of corrective switching in transmission systems. IEEE Trans Power Syst 1999;14(1):336-41.

[9] Wang J, Shahidehpour M, Li Z. Security-constrained unit commitment with volatile wind power generation. IEEE Trans Power Syst 2008;23(3):1319-27.

[10] Khodaei A, Shahidehpour M. Transmission switching in security-constrained unit commitment. IEEE Trans Power Syst 2010;25(4):1937-45.

[11] Tor OB, Guven AN, Shahidehpour M. Congestion-driven transmission planning considering the impact of generator expansion. IEEE Trans Power Syst 2008;23(2):781-9.

[12] Khodaei A, Shahidehpour M, Kamalinia S. Transmission switching in expansion planning. IEEE Trans Power Syst 2010;25(3):1722-33.

[13] Fu Y, Shahidehpour M, Li Z. Security-constrained unit commitment with AC constraints. IEEE Trans Power Syst 2005;20(3):1538-50.

[14] Shahidehpour M, Fu Y. Benders Decomposition. IEEE Power and Energ Mag 2005;3(2).

[15] Chung KH, Kim BH, Hur D. Multi-area generation scheduling algorithm with regionally distributed optimal power flow using alternating direction method. Int J Electr Power Energy Syst (2011). In Press, doi:10.1016/j.ijepes.2010.11.013.

[16] Ma H, Shahidehpour M. Transmission constrained unit commitment based on Benders decomposition. Elect. Power Energy Syst 1998;20(4):287-94.

[17] Geoffrion AM. Generalized Benders decomposition. J. Optim Theory Appl 1972;10(4).

[18] Wood AJ, Wollenberg BF. Power generation, operation and control. New York: Wiley; 1984.

[19] Senthil Kumar V, Mohan MR. Solution to security constrained unit commitment problem using genetic algorithm. Int J Electr Power Energy Syst (2010);32(2):117-25.

[20] Frangioni A, Gentile C, Lacalandra F. Sequential Lagrangian-MILP approaches for Unit Commitment problems. Int J Electr Power Energy Syst (2011);33(3):585-93.

[21] Martins N, Oliviera EJ, Moreira WC, Pereira JLR, Fontoura RM. Redispatch to reduce rotor shaft impacts upon transmission loop closure. IEEE Trans Power Syst 2008;23(2):592-600.

[22] Nagata T, Sasaki H, Yokoyama R. Power system restoration by joint usage of expert system and mathematical programming approach. IEEE Trans Power Syst 1995;10(3):1473-9.

[23] Wunderlich S, Adibi MM, Fischl R, Nwankpa COD. An approach to standing phase angle reduction. IEEE Trans Power Syst 1994;9(1):470-8.

[24] Hazarika D, Sinhá AK. Standing phase angle reduction for power system restoration. Proc Inst Elect Eng, Gen Trans Distr 1998;145(1).

[25] Hazarika D, Sinhá AK. An algorithm for standing phase angle reduction for power system restoration. IEEE Trans Power Syst 1999;14(4):1213-8.

[26] Martins N, Oliveira EJ, Pereira JLR, Ferreira LCA. Reducing standing phase angles via interior point optimum power flow for improved system restoration. Proc. Power Syst Conf Expo 2004, New York.

[27] Kulworawanichpong T. Simplified Newton–Raphson power-flow solution method. Int J Electr Power Energy Syst (2010);32(6):551-8.

[28] Xiao Y, Song YH, Sun YZ. Versatile model for power flow control using FACTS devices. Power Elect and Motion Cont Conf 2000.

[29] Lai LL, Ma JT. Power flow control in FACTS using evolutionary programming. IEEE Intern Conf on Evol Comp 1995.

[30] The ILOG CPLEX Website, 2006. [Online]. Available: http://www. ilog.com.

Figure Captions:

Fig. 1 Flowchart of SCUC with TS for reactive power management

Fig. 2 Power injection model of FACTS devices

Fig. 3 IEEE 118-bus system

Fig. 4 Voltage profile at bus 88

Fig. 5 Voltage profile at bus 68

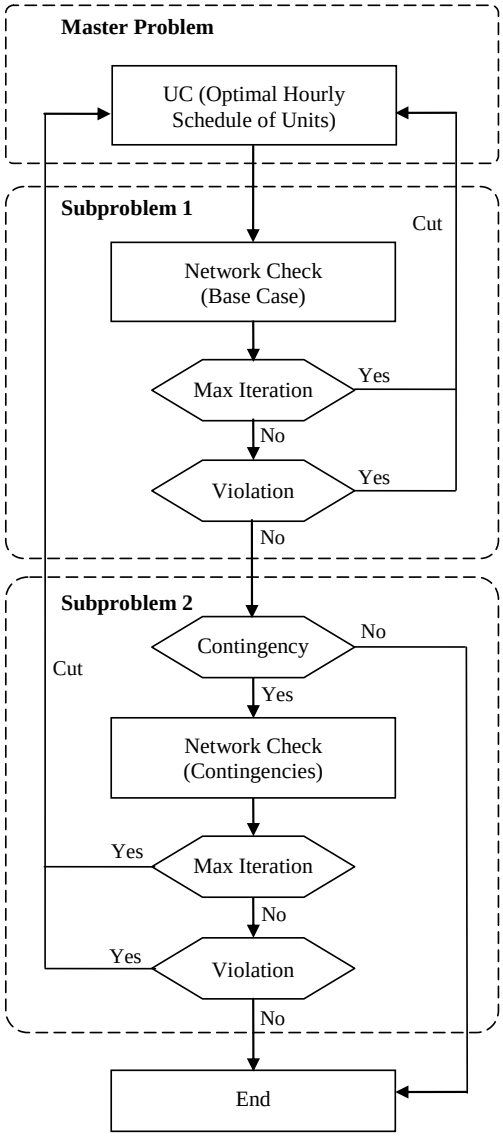


Fig. 1 Flowchart of SCUC with TS for reactive power management

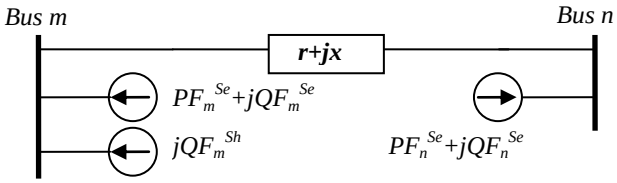


Fig. 2 Power injection model of FACTS devices

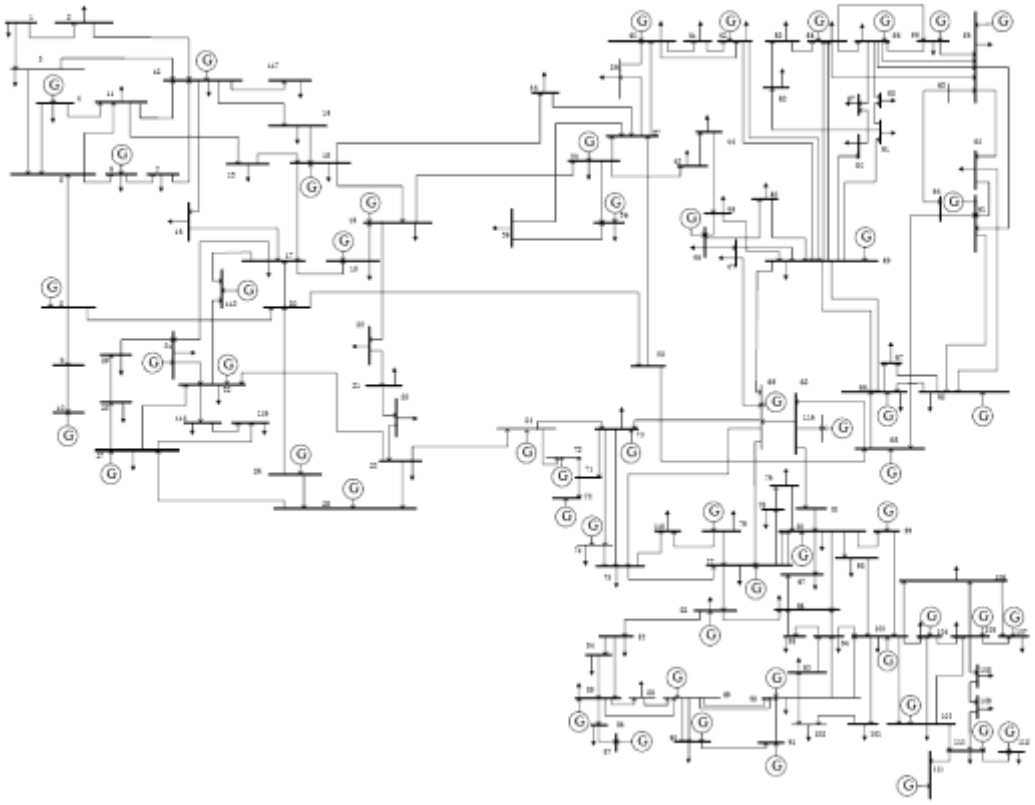

Fig. 3 IEEE 118-bus system

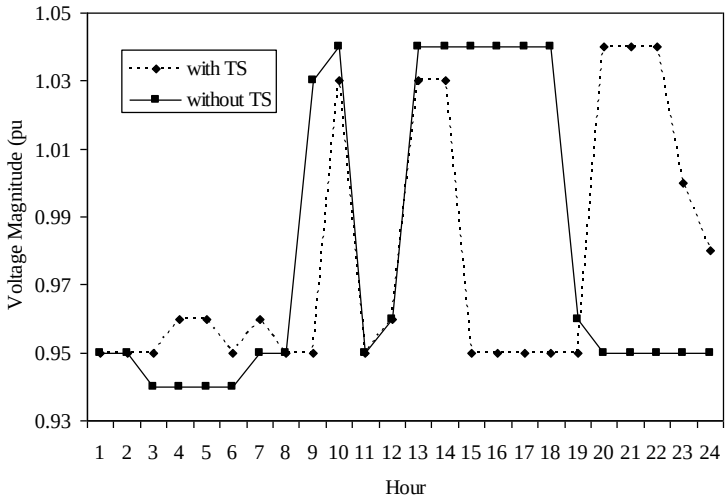


Fig. 4 Voltage profile at bus 88

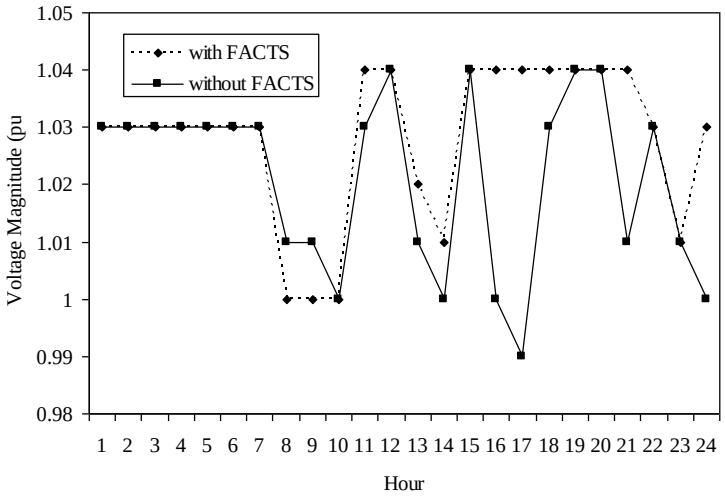


Fig. 5 Voltage profile at bus 68

Table Titles:

Table 1 Power Injection Model Components of FACTS devices

| **Controller Type** | **FACTS Device** | **Steady State Function** | **Control Variable** |
|---|---|---|---|
| Series | TCPS | Real power flow control | $PF^{Se}$ |
| | TCSC | | |
| | SSSC | | |
| Shunt | SVC | Voltage regulation | $QF^{Sh}$ |
| | STATCOM | | |
| Shunt-Series | UPFC | Real and reactive power flow control | $PF^{Se}$, $QF^{Se}$, $QF^{Sh}$ |
| | | Voltage regulation | |

Table 2 Switchable Line Data

| Line No. | From Bus | To Bus | R (pu) | X (pu) | Charging (pu) | Flow limit (MW) |
|---|---|---|---|---|---|---|
| 3 | 4 | 5 | 0.002 | 0.008 | 0.002 | 500 |
| 12 | 11 | 12 | 0.006 | 0.020 | 0.005 | 100 |
| 16 | 11 | 13 | 0.022 | 0.073 | 0.019 | 100 |
| 23 | 17 | 18 | 0.012 | 0.051 | 0.013 | 100 |
| 30 | 23 | 24 | 0.014 | 0.049 | 0.050 | 100 |
| 40 | 29 | 31 | 0.011 | 0.033 | 0.008 | 100 |
| 43 | 27 | 32 | 0.023 | 0.076 | 0.019 | 100 |
| 59 | 43 | 44 | 0.061 | 0.245 | 0.061 | 100 |
| 67 | 42 | 49 | 0.072 | 0.323 | 0.086 | 100 |
| 75 | 49 | 54 | 0.073 | 0.289 | 0.074 | 100 |
| 78 | 54 | 56 | 0.003 | 0.010 | 0.007 | 100 |
| 90 | 60 | 61 | 0.003 | 0.014 | 0.015 | 500 |
| 100 | 62 | 66 | 0.048 | 0.218 | 0.058 | 100 |
| 115 | 70 | 75 | 0.043 | 0.141 | 0.036 | 100 |
| 151 | 80 | 97 | 0.018 | 0.093 | 0.025 | 100 |
| 153 | 80 | 99 | 0.045 | 0.206 | 0.055 | 100 |
| 159 | 99 | 100 | 0.018 | 0.081 | 0.022 | 100 |
| 164 | 100 | 104 | 0.045 | 0.204 | 0.054 | 100 |
| 167 | 100 | 106 | 0.061 | 0.229 | 0.062 | 100 |
| 181 | 27 | 115 | 0.016 | 0.074 | 0.020 | 100 |

Table 3 UC Schedule of IEEE 118-Bus System in Case 2

| Unit | Hours (1-24) |
|---|---|
| 1-3 | 0 0 0 0 0 0 0 0 0 0 0 0 0 0 0 0 0 0 0 0 0 0 0 0 |
| 4 | 0 0 0 0 0 0 0 0 0 1 1 1 1 1 1 1 1 1 1 1 1 1 1 1 |
| 5 | 1 1 1 1 1 1 1 1 1 1 1 1 1 1 1 1 1 1 1 1 1 1 1 1 |
| 6 | 0 0 0 0 0 0 0 0 0 0 0 0 0 0 0 0 0 0 0 0 0 0 0 0 |
| 7 | 0 0 0 0 0 0 0 0 0 0 0 0 0 0 0 0 0 0 0 0 0 0 0 0 |
| 8-9 | 0 0 0 0 0 0 0 0 0 0 0 0 0 0 0 0 0 0 0 0 0 0 0 0 |
| 10-11 | 1 1 1 1 1 1 1 1 1 1 1 1 1 1 1 1 1 1 1 1 1 1 1 1 |
| 12-13 | 0 0 0 0 0 0 0 0 0 0 0 0 0 0 0 0 0 0 0 0 0 0 0 0 |
| 14 | 0 0 0 0 0 0 0 0 0 0 0 0 1 1 1 1 1 0 0 0 0 0 0 0 |
| 15 | 0 0 0 0 0 0 0 0 0 0 0 0 0 0 0 0 0 0 0 0 0 0 0 0 |
| 16 | 0 0 0 0 0 0 0 0 0 0 0 0 0 0 0 0 0 0 0 0 0 0 0 0 |
| 17-18 | 0 0 0 0 0 0 0 0 0 0 0 0 0 0 0 0 0 0 0 0 0 0 0 0 |
| 19 | 0 0 0 0 0 0 0 0 0 0 0 0 0 0 0 0 1 1 1 1 1 0 0 0 |
| 20-21 | 1 1 1 1 1 1 1 1 1 1 1 1 1 1 1 1 1 1 1 1 1 1 1 1 |
| 22 | 0 0 0 0 0 0 0 0 0 0 0 0 0 0 0 0 0 0 0 0 0 0 0 0 |
| 23 | 0 0 0 0 0 0 0 0 0 0 0 0 0 0 0 0 0 0 0 0 0 0 0 0 |
| 24-25 | 1 1 1 1 1 1 1 1 1 1 1 1 1 1 1 1 1 1 1 1 1 1 1 1 |
| 26 | 0 0 0 0 0 0 0 0 0 0 0 0 0 0 0 0 0 0 0 0 0 0 0 0 |
| 27-29 | 1 1 1 1 1 1 1 1 1 1 1 1 1 1 1 1 1 1 1 1 1 1 1 1 |
| 30 | 0 0 0 0 0 0 0 0 0 0 0 1 1 1 1 1 1 1 1 1 1 1 0 0 |
| 31 | 0 0 0 0 0 0 0 0 0 0 0 0 0 0 0 0 0 0 0 0 0 0 0 0 |
| 32-33 | 0 0 0 0 0 0 0 0 0 0 0 0 0 0 0 0 0 0 0 0 0 0 0 0 |
| 34 | 0 0 0 0 0 0 0 0 0 0 0 0 0 0 1 1 1 1 1 0 0 0 0 0 |
| 35 | 0 0 0 0 0 0 0 0 0 0 0 0 0 1 1 1 1 1 1 0 0 0 0 0 |
| 36 | 0 0 0 0 0 0 0 0 0 0 1 1 1 1 1 1 1 1 1 1 1 1 1 0 |
| 37 | 0 0 0 0 0 0 0 0 0 0 0 0 1 1 1 1 1 1 1 1 1 1 0 0 |
| 38 | 0 0 0 0 0 0 0 0 0 0 0 0 0 0 0 0 0 0 0 0 0 0 0 0 |
| 39 | 1 1 1 1 1 1 1 1 1 1 1 1 1 1 1 1 1 1 1 1 1 1 1 1 |
| 40 | 0 0 0 0 0 0 0 0 0 0 0 0 0 0 0 0 0 0 0 0 0 0 0 0 |
| 41-42 | 0 0 0 0 0 0 0 0 0 0 0 0 0 0 0 0 0 0 0 0 0 0 0 0 |
| 43 | 0 0 0 0 0 0 0 0 0 0 0 1 1 1 1 1 1 1 1 1 1 1 0 0 |
| 44 | 1 1 1 1 1 1 1 1 1 1 1 1 1 1 1 1 1 1 1 1 1 1 1 1 |
| 45 | 1 1 1 1 1 1 1 1 1 1 1 1 1 1 1 1 1 1 1 1 1 1 1 1 |
| 46-47 | 0 0 0 0 0 0 0 0 0 0 0 0 0 0 0 0 0 0 0 0 0 0 0 0 |
| 48 | 0 0 0 0 0 0 0 0 0 0 0 0 0 0 0 0 0 0 0 0 0 0 0 0 |
| 49 | 0 0 0 0 0 0 0 0 0 0 0 0 0 0 0 0 0 0 0 0 0 0 0 0 |
| 50-51 | 0 0 0 0 0 0 0 0 0 0 0 0 0 0 0 0 0 0 0 0 0 0 0 0 |
| 52 | 0 0 0 0 0 0 0 0 0 0 0 0 0 0 0 0 0 0 0 0 0 0 0 0 |
| 53 | 0 0 0 0 0 0 0 0 0 0 0 0 0 0 0 0 0 0 0 0 0 0 0 0 |
| 54 | 0 0 0 0 0 0 0 0 0 0 0 0 0 0 0 0 0 0 0 0 0 0 0 0 |

Table 4 Switchable Line Schedule of IEEE 118-Bus System in Case 2

| Line | Hours (1-24) |
|---|---|
| 3 | 1 1 1 1 1 0 1 1 1 1 1 1 1 1 1 1 1 1 1 1 1 1 1 1 |
| 12 | 1 1 1 1 1 0 1 1 0 0 1 1 1 1 1 1 1 1 1 1 1 1 1 0 |
| 16 | 1 1 0 0 0 1 1 1 1 1 1 1 1 1 1 1 1 1 1 1 1 1 1 1 |
| 23 | 1 1 1 1 1 0 1 1 1 1 1 1 1 1 1 1 1 1 1 1 1 1 1 1 |
| 30 | 0 0 0 0 0 0 1 0 0 0 1 0 0 0 0 0 1 0 0 0 0 0 0 1 1 |
| 40 | 0 1 1 1 1 0 0 0 0 0 1 0 0 0 0 0 1 0 0 0 0 0 0 1 1 |
| 43 | 1 1 1 1 1 0 1 1 1 1 1 1 1 1 1 1 1 1 1 1 1 1 1 1 |
| 59 | 1 1 1 1 1 1 1 1 0 0 0 0 0 0 0 1 0 0 0 0 0 0 0 1 |
| 67 | 1 0 1 1 1 1 1 1 1 1 1 1 1 1 1 1 0 1 1 1 1 1 1 1 |
| 75 | 0 0 1 1 1 1 0 0 0 0 0 0 0 0 0 0 0 0 0 0 0 0 0 0 |
| 78 | 0 0 1 0 0 0 0 0 0 0 0 0 0 0 0 1 0 0 0 0 0 0 0 0 |
| 90 | 1 1 1 1 1 1 1 1 1 1 1 1 1 1 1 1 1 1 1 1 1 1 1 1 |
| 100 | 1 1 1 1 1 1 1 1 1 1 1 0 0 0 0 1 1 0 0 0 0 1 1 1 |
| 115 | 1 1 1 1 1 1 1 1 1 1 1 1 1 1 1 1 1 1 1 1 1 1 1 1 |
| 151 | 0 1 0 1 0 1 0 0 0 0 0 1 1 1 1 1 0 1 1 1 1 0 0 0 |
| 153 | 1 1 1 1 1 1 1 1 1 1 1 1 1 1 1 1 1 1 1 1 1 1 1 1 |
| 159 | 1 0 0 0 0 0 0 0 1 1 1 0 1 1 1 1 1 1 1 1 1 1 0 0 |
| 164 | 1 0 0 0 0 0 1 0 0 1 0 0 0 0 0 0 0 0 0 0 1 0 1 0 0 0 |
| 167 | 0 1 1 1 1 1 1 1 1 1 1 1 1 0 1 1 0 1 1 1 1 0 0 1 |
| 181 | 1 1 1 1 1 0 1 1 1 1 1 1 1 1 1 1 1 1 1 1 1 1 1 1 |

Table 5 Switchable Line Schedule of IEEE 118-Bus System in Case 3

| Line | Hours (1-24) |
|---|---|
| 3 | 1 1 1 1 1 1 1 1 0 1 0 1 1 1 1 1 1 1 1 1 1 1 1 0 |
| 12 | 1 1 1 1 1 1 1 1 1 0 1 0 1 0 0 0 0 0 0 1 0 1 1 1 0 |
| 16 | 1 1 1 1 1 1 0 1 0 1 0 0 0 0 0 0 0 0 0 0 0 0 1 0 |
| 23 | 0 0 0 0 0 0 0 0 0 0 0 0 0 0 0 0 0 0 0 0 0 0 0 0 0 |
| 30 | 0 0 0 0 0 0 0 0 0 0 0 0 0 0 0 0 0 0 0 0 0 0 0 0 0 |
| 40 | 0 0 0 0 0 0 0 0 0 0 0 0 0 0 0 0 0 0 0 0 0 0 0 0 0 |
| 43 | 0 0 0 0 0 0 0 0 0 0 0 0 0 0 0 0 0 0 0 0 0 0 0 0 0 |
| 59 | 0 0 0 0 0 0 0 0 0 0 0 0 0 0 0 0 0 0 0 0 0 0 0 0 0 |
| 67 | 0 0 0 0 0 0 0 0 0 0 0 0 0 0 0 0 0 0 0 0 0 0 0 0 0 |
| 75 | 0 0 0 0 0 0 0 0 0 0 0 0 0 0 0 0 0 0 0 0 0 0 0 0 0 |
| 78 | 0 0 0 0 0 0 0 0 0 0 0 0 0 0 0 0 0 0 0 0 0 0 0 0 0 |
| 90 | 0 0 0 0 0 0 0 0 0 0 0 0 0 0 0 0 0 0 0 0 0 0 0 0 0 |
| 100 | 0 0 0 0 0 0 0 0 0 0 0 0 0 0 0 0 0 0 0 0 0 0 0 0 0 |
| 115 | 0 0 0 0 0 0 0 0 0 0 0 0 0 0 0 0 0 0 0 0 0 0 0 0 0 |
| 151 | 0 0 0 0 0 0 0 0 0 0 0 0 0 0 0 0 0 0 0 0 0 0 0 0 0 |
| 153 | 0 0 0 0 0 0 0 0 0 0 0 0 0 0 0 0 0 0 0 0 0 0 0 0 0 |
| 159 | 0 0 0 0 0 0 0 0 0 0 0 0 0 0 0 0 0 0 0 0 0 0 0 0 0 |
| 164 | 1 1 1 1 1 1 1 1 1 1 1 1 1 1 1 1 1 1 1 1 1 1 1 0 0 |
| 167 | 1 1 1 1 1 1 1 1 1 1 1 1 1 1 1 1 1 1 1 1 1 1 1 0 0 |
| 181 | 0 0 0 0 0 0 0 0 0 0 0 0 0 0 0 0 0 0 0 0 0 0 0 0 0 |

# SCUC with Hourly Demand Response Considering Inter-temporal Load Characteristics

Amin Khodaei, *Member, IEEE* and Mohammad Shahidehpour, *Fellow, IEEE*

***Abstract*— In this paper, the hourly demand response (DR) is incorporated into security-constrained unit commitment (SCUC) for economic and security purposes. SCUC considers fixed and responsive loads. Unlike fixed hourly loads, responsive loads are modeled with their inter-temporal characteristics. The responsive loads linked to hourly market prices can be curtailed or shifted to other operating hours. The study results show that DR could shave the peak load, reduce the system operating cost, reduce fuel consumptions and carbon footprints, and reduce the transmission congestion by reshaping the hourly load profile. Numerical simulations in this paper exhibit the effectiveness of the proposed approach.**

***Index Terms*—Demand response, Security constrained unit commitment, Real time prices**

***Indices:***

| | |
|---|---|
| $b$ | Index for bus |
| $i$ | Index for unit |
| $t$ | Index for time |

***Sets:***

| | |
|---|---|
| $f$ | Superscript for fixed loads |
| $r$ | Superscript for responsive loads |

***Parameters:***

| | |
|---|---|
| $NB$ | Number of buses |
| $NG$ | Number of units |
| $NT$ | Number of time periods (hours) |
| $EX_b^{\max}$ | Max curtailable daily load at bus $b$ |
| $D_{bt}^{f}$ | Fixed load at bus $b$ at time $t$ |
| $D_{bt}^{r,\max}$ | Submitted responsive load at bus $b$ at time $t$ |
| $DX_{bt}^{\min}$ | Min curtailable load at bus $b$ at time $t$ |
| $DR_b$ | Drop off rate of load at bus $b$ |
| $UR_b$ | Pickup rate of load at bus $b$ |
| $UT_b$ | Min up time of load at bus $b$ |
| $DT_b$ | Min off time of load at bus $b$ |
| $X_{bt}^{on}$ | ON time of load at bus $b$ and time $t$ |
| $X_{bt}^{off}$ | OFF time of load at bus $b$ at time $t$ |

***Variables:***

| | |
|---|---|
| $CB_{bt}$ | Consumption benefit at bus $b$ at time $t$ |
| $D_{bt}$ | Load at bus $b$ at time $t$ |
| $D_{bt}^{r}$ | Responsive load at bus $b$ at time $t$ |
| $GC_{it}$ | Generation cost of unit $i$ at time $t$ |
| $I_{it}$ | Commitment state of unit $i$ at time $t$ |
| $P_{it}$ | Generation of unit $i$ at time $t$ |
| $v_{bt}$ | Curtailment state of load at bus $b$ at time $t$ |
| $w_t$ | Power mismatch at time $t$ |
| $\mu_{bt}, \pi_{it}$ | Dual variables |

***Symbols:***

| | |
|---|---|
| $\wedge$ | Given variables |

The authors are with Electrical and Computer Engineering Department, Illinois Institute of Technology, Chicago, IL 60616 USA (e-mail: akhodaei@iit.edu; ms@iit.edu).

## I. Introduction

IN RESTRUCTURED power systems, the independent system operator (ISO) would schedule available system resources to satisfy the hourly system load and maintain the system security at the least operating cost [1]-[2]. The hourly system load could be fixed in the day-ahead scheduling. The participating generating companies would submit strategic bids to the ISO to supply the hourly load forecast [3]. The market clearing price would be set by the marginal price of the last scheduled generator for satisfying the hourly fixed load. Hence, the demand-side would have no role in the market clearing and price setting. Some of drawbacks of the lack demand-side participation in power markets could include large price spikes, congested transmission lines, higher fuel consumptions and carbon footprints, lack of sufficient generation resources in particular at peak hours, and exercise of market power [4]-[8].

Price spikes might occur when the demand-side has no role in setting electricity prices, so generators would have no incentive to bid close to their marginal costs which could lead to bids that are much higher than actual generation costs. This behavior could lead to volatile market prices that are away from perfectly competitive prices. In addition, price spikes might happen when generation reserves are lower during peak demand hours. To compensate generation shortages at peak hours, generators with high marginal costs are installed to supply peak demands, which could result in a significant underutilization of such generators at off-peak periods.

Demand-side participation could be very effective in such circumstances. Demand-side participation may reduce the load at peak periods, which is a more economical way to respond to generation and transmission capacity constraints. The demand-side participation could also mitigate price manipulations

which could otherwise lead to market power exercises. The price manipulations could occur when the hourly generation dispatch is calculated by minimizing the total operating cost (without considering any demand-side participation.) An increase in the demand-side participation could benefit individual customers and ultimately the entire electricity market.

Demand-side participation could include distributed generation, on-site storage, and demand response (DR). DR is considered more specifically in this paper. DR includes the reduction or deferral of hourly consumptions in response to higher market prices or market incentives [4]-[5]. DR could include the emergency DR and the economic DR. Emergency DR will reduce the load temporarily in response to an emergency grid condition initiated by a request from system operators. This type of DR is not frequently used and not considered in this paper. Economic DR will reduce the load voluntarily by electricity customers and in response to market prices. In restructured power systems, nodal prices vary with time and location; so electricity customers could adjust their load profiles in response to electricity price volatilities. Customers could curtail loads in such circumstances. However, load curtailments are usually undesirable. Customers would rather shift less critical loads to hours with more moderate prices [9]-[13]. All customers would, however, benefit from lowered market prices as shifting five to eight percent of the consumption to off-peak hours and shedding additional four to seven percent of peak demand could save U.S. customers about $15 billion a year [14].

Fig. 1 depicts the energy market operation in a restructured power system. Generation and transmission companies provide the ISO with the available generating unit and transmission line information. The load serving entity (LSE) which acts as an aggregator for customer loads provides the load data to the ISO. The customers do not directly participate in DR programs and the curtailment service provider (CSP) acts on behalf of such customers. CSP obtains load curtailment data from customers and submits DR bids to the ISO. In addition, it provides customers with curtailment options and saving opportunities, in day-ahead and real-time markets, based on forecasted prices. Note that an LSE or electric distribution company (EDC) could act as a CSP. The ISO runs the day-ahead security-constrained unit commitment (SCUC) based on the prevailing constraints to find the optimal hourly schedule of generating units and loads.

The challenge here is to incorporate DR into the market clearing process to achieve the most efficient market dynamics [16]-[17]. [13] incorporated DR within auction rules using an iterative approach. An auction algorithm to implicitly allow DR is developed in [17], but the periods for reducing loads or recovering the saved energy are fixed. In [18] an alternative market-clearing tool is proposed for maximizing the social welfare in which customers submit bids for energy purchases. In [19] a multi-round auction algorithm is introduced in which market participants would modify their bids until an equilibrium is reached. The iterative algorithm may cause market price oscillations. In [20] load constraints are incorporated into day-ahead auctions using an hourly bidding mechanism. However, most of temporal constraints of loads and transmission constraints are disregarded. [21] quantifies the effect of DR on electricity markets in which the load shifting behavior of customers is considered in a centralized market-clearing mechanism. In [22] the elasticity of demand is incorporated in a centralized market-clearing process. [23] further explored the approach proposed in [22] using a unit commitment (UC) instead of optimal power flow calculation for market clearing. The iterative process used in [22] integrates the market price computation with the elasticity of demand price. In [24] the iterative market-clearing process proposed in [22]-[23] is revisited and convergence problems encountered in those approaches were alleviated.

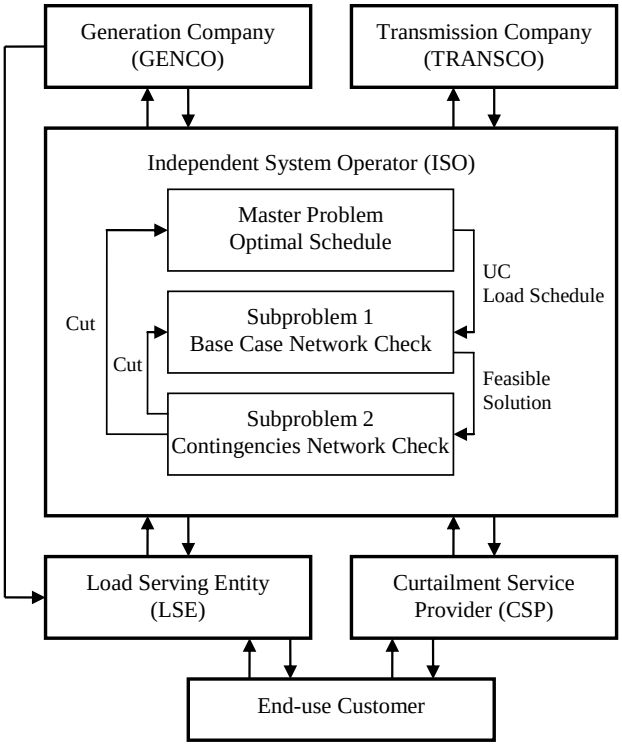


Fig. 1 Energy market components

In general, either a direct approach or an iterative approach is used when considering DR in market clearing processes. The iterative approaches use the elasticity of demand price to adjust the load demand. However, convergence problems may occur in the iterative process which would be time-consuming; it could also be difficult to guarantee the existence of a feasible solution. Direct methods do not accurately model the shifting of responsive loads which could have a significant impact on market-clearing results. In addition, these approaches do not consider operating constraints of DR nor do they consider transmission constraints.

In this paper, we propose a DR model for market clearing. Responsive loads are considered which can be curtailed or shifted in time for economical reasons. The operating characteristics of loads including bids, hourly profile, and temporal characteristics, are considered which are submitted to the ISO. An hourly SCUC is applied for market clearing (see Fig. 1) in which the network feasibility in the base case and contingencies are taken into account. So the impact of DR on

the hourly operation and control of constrained power systems is considered in the proposed approach.

The rest of the paper is organized as follows. Section II outlines the proposed day-ahead market clearing model, while Section III formulates the problem. The numerical studies are provided in Section IV, the observations are listed in Section V and the paper is concluded in Section VI.

## II. Day-Ahead Market Clearing Model

The proposed market-clearing process with DR is presented in this section.

### A. Market clearing process

We assume both generators and loads could submit complex offers and bids to the ISO. Complex load bids include multiple bid sections with inter-temporal load constraints. When considering simple generation offers and load bids, the market-clearing price is the cross section of aggregated load and generation quantities. In our approach, transmission constraints are considered in the base case and contingencies. The objective would be to maximize the social welfare, i.e. consumption payments minus generation costs. The hourly SCUC schedule for complex bids would demonstrate the optimal commitment and dispatch of generating units and the hourly DR based on submitted offers and bids.

### B. Load bids

DR bids include hourly fixed and responsive load bids. Fixed loads are price-takers which are satisfied at the market-clearing price. The responsive load price would drop with increasing the load quantity. A responsive load bid consists of hourly quantity and price of load which are subject to the following constraints [25]-[26]:

- Minimum up/down time limits
- Load pickup/drop rates
- Minimum hourly curtailment
- Maximum daily curtailment

Minimum up time defines the number of consecutive hours that the load would have to be supplied once it is restored. Minimum down time represents the minimum number of consecutive hours that a load would be off once curtailed. Load pickup/drop rates represent the ramping capability for restoring/curtailing loads. These rates identify the rate at which a customer would change its consumption. The minimum hourly curtailment defines the lower limit for the allowable hourly curtailment. The minimum load curtailment may either reflect physical load limits or be imposed by system operators whereby smaller responsive loads could not participate in markets. The maximum daily curtailment would restrict the total load curtailment in the scheduling horizon. A feasible hourly schedule for responsive loads is calculated using these physical constraints.

### C. Hourly SCUC Solution with DR

The proposed flowchart is depicted in Fig. 1. The solution of the master problem consists of optimal day-ahead commitment and dispatch schedule of generating units and loads. The solution of the master problem is applied to the subproblem 1 to check the feasibility of the system when considering the base case transmission system constraints. In the case of violations, hourly Benders cuts are generated and added to the master problem in the next iteration. This iterative process will continue until an optimal base case solution is achieved. The solution of the master problem is further used in the subproblem 2 to check the system feasibility in the case of contingencies. In the case of violations, Benders cut is added to the next iteration of the master problem. This iterative process will continue until the system security constraints are satisfied. The Benders cuts in this problem would include one additional variable, i.e. load quantity, as we solve the SCUC problem [27]-[31].

## III. Formulation of SCUC with DR

The SCUC formulation in the master problem and two subproblems is presented in the following.

### A. Master Problem

The objective of the master problem is to determine the day-ahead schedule of generating units and loads in order to maximize the system social welfare while satisfying the prevailing unit, load and system constraints. The objective is shown in (1):

$$Max \sum_{t=1}^{NT}\sum_{b=1}^{NB} CB_{bt}(D_{bt}) - \sum_{t=1}^{NT}\sum_{i=1}^{NG} GC_{it}(P_{it}) \quad (1)$$

The objective is to maximize the system social welfare, which is the consumption benefit minus the generation cost. This objective is subject to power balance constraint (2)

$$\sum_{i=1}^{NG} P_{it} - \sum_{b=1}^{NB} D_{bt} = 0 \qquad (t = 1,..., NT) \quad (2)$$

In (2), both generation and load are considered as variables. Other system constraints include system spinning/operating reserve requirements, system fuel limits, and system emission limits. Unit constraints include unit output limits, unit spinning/operating reserve limit, ramp up/down rate limits, min up/down time limits, fuel limits, and emission limits.

The bus load consists of fixed and responsive terms (3). The fixed load term should be fully satisfied. The responsive load term can be curtailed or shifted to another operating hour when the electricity price is cheaper. The cost of supplying the fixed load is not considered. Therefore, the objective function of SCUC would only include responsive load bids.

$$D_{bt} = D_{bt}^{f} + D_{bt}^{r} \qquad (b = 1,..., NB)(t = 1,..., NT) \quad (3)$$

A typical DR bid curve is depicted in Fig. 2 which includes fixed and step-wise responsive load bids. The fixed load, minimum load curtailment, and maximum level of responsive load submitted to the ISO are denoted by *A*, *B* and *C*, respectively in Fig. 2. The responsive load constraints are formulated as follows.

$$[D_{bt}^{r,\max} - DX_{bt}^{\min} - D_{bt}^{r}]v_{bt} \geq 0 \qquad (b = 1,..., NB)(t = 1,..., NT) \quad (4)$$

$$D_{bt}^{r} v_{bt} \geq 0 \qquad (b = 1,..., NB)(t = 1,..., NT) \quad (5)$$

$$[D_{bt}^{r} - D_{bt}^{r,\max}][1 - v_{bt}] \geq 0 \qquad (b = 1,..., NB)(t = 1,..., NT) \quad (6)$$

$$D_{bt}^{r} - D_{b(t-1)}^{r} \leq UR_{b} \qquad (b = 1,..., NB)(t = 1,..., NT) \quad (7)$$

$$D^{r}_{b(t-1)} - D^{r}_{bt} \le DR_b \quad (b = 1,..., NB)(t = 1,..., NT) \quad (8)$$

$$[X^{on}_{b(t-1)} - UT_b][v_{b(t-1)} - v_{bt}] \ge 0 \quad (b = 1,..., NB)(t = 1,..., NT) \quad (9)$$

$$[X^{off}_{b(t-1)} - DT_b][v_{bt} - v_{b(t-1)}] \ge 0 \quad (b = 1,..., NB)(t = 1,..., NT) \quad (10)$$

$$\sum_{t=1}^{NT} (D^{r,\max}_{bt} - D^{r}_{bt}) \le EX^{\max}_{b} \quad (b = 1,..., NB) \quad (11)$$

In this formulation, the responsive load, i.e. $D^{r}_{bt}$, and the curtailment state of load, i.e. $v_{bt}$, are variables. The curtailment state is 1 when the load is curtailed and is 0 otherwise. The curtailed load is the difference between the maximum and the scheduled responsive loads. The curtailed load is larger than the minimum load curtailment. Since the curtailed load is not directly considered in the formulation, its associated constraints are represented by the responsive load. The possible cases are listed as follows:

- The proposed curtailed load is less than the minimum load curtailment. In this case the minimum load curtailment constraint (4) would be imposed. The scheduled responsive load would be the submitted responsive load minus the minimum load curtailment.
- The proposed curtailed load is larger than the minimum load curtailment: in this case, constraint (5) would ensure that the scheduled responsive load is nonnegative.
- Load is not curtailed: in this case the submitted responsive load will be scheduled. Constraint (6) would be enforced and loads will be shifted to this hour.

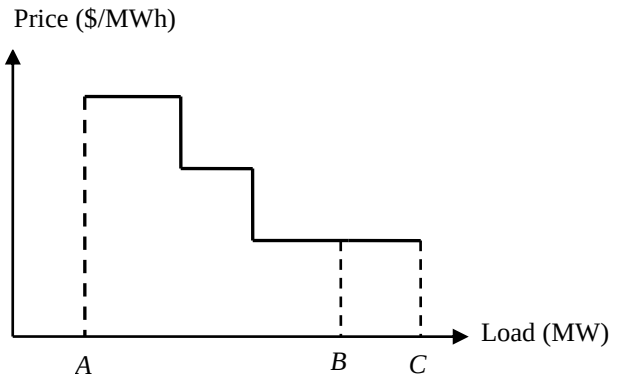


Fig. 2 DR bid curve

The hourly load pickup/drop rates constraints (7)-(8) would limit the rate of load changes between any two successive hours. The minimum load up/down time constraints (9)-(10) indicate that the minimum number of hours when the load cannot be curtailed/restored. Constraint (11) restricts the total daily load curtailment. The hourly load curtailment is the difference between the submitted responsive load and the scheduled responsive load. This term is positive when the load is curtailed, negative when the load is shifted to that hour, and zero when there is no load curtailment or shifting at that hour. Using this constraint, responsive loads may be shifted or curtailed.

### *B. SCUC Subproblems*

The solution of the master problem, i.e. the hourly unit commitment and dispatch as well as load schedule, is used in the base case and contingencies network check subproblems to examine the feasibility of the master solution for satisfying the network security. The objective of the subproblems is to minimize power mismatches in all system buses. In the case of violations, hourly cuts (12) are provided to the UC problem as

$$\hat{w}_t + \sum_{i=1}^{NG} \pi_{it}(P_{it} I_{it} - \hat{P}_{it} \hat{I}_{it}) + \sum_{b=1}^{NB} \mu_{bt}(D_{bt} - \hat{D}_{bt}) \le 0 \quad (12)$$

Here, $\hat{w}_t$ denotes the current bus power mismatch in the base case; $\pi_{it}$ and $\mu_{bt}$ are respectively the dual variables of hourly unit dispatch and load balance equations. The second and third terms respectively represent the change in the objective value (power mismatch) when the unit schedule and load schedule are changed. The cut indicates that current violations in the base case can be mitigated by recalculating the schedule of units and loads. In the case of contingencies, corrective actions are introduced by generation redispatch. In the case of violations, the hourly cuts for the UC problem are

$$\hat{w}_t + \sum_{i=1}^{NG} (\overline{\pi}_{it} - \underline{\pi}_{it})(P_{it} - \hat{P}_{it}) + \sum_{b=1}^{NB} \mu_{bt}(D_{bt} - \hat{D}_{bt}) \le 0 \quad (13)$$

Here, $\overline{\pi}_{it}$ and $\underline{\pi}_{it}$ are dual variables of hourly generation redispatch constraints and $\mu_{bt}$ is the dual variable of load balance equation; $\hat{w}_t$ denotes the current bus power mismatch in the case of contingencies and the second and third terms respectively represent changes in the objective value (power mismatch) when the unit dispatch and load schedule are changed.

The iterative process between the master problem and subproblems continues until all contingencies are handled properly and system security conditions in the base case and contingencies are satisfied [25].

## IV. Numerical Simulations and Discussions

A modified IEEE 118-bus system is analyzed to illustrate the performance of the proposed method. The proposed method was implemented on a 2.4-GHz personal computer using CPLEX 11.0 [32]. The system has 118 buses, 54 units and 186 branches. The data for this system is given in motor.ece.iit.edu/data/SCUC_118test.xls. The following cases are considered for analyzing the effect of DR in SCUC.

### *A. DR considered at a single bus*

Bus 59 is considered as the bus with DR. 10% of the total load in this bus is considered as responsive while the rest is fixed. A single-step consumption bid of 20$/MWh is considered for the responsive load. The minimum and maximum hourly load curtailment of 5 MW and 150 MW are considered for this load. The minimum up and down times are 4 hours and the load pickup and drop rates are considered large enough to allow any load changes in successive hours. The following cases are considered:

Case 0: Base case SCUC with no DR
Case 1: DR in Case 0 (with load curtailment)
Case 2: DR in Case 0 (with load shifting)

**Case 0:** We assume that the load is fixed (DR is not considered) in SCUC. The calculated total operating cost in

this case is $1,046,785.81. Forty five units are committed and the load at bus 59 is fully satisfied.

**Case 1:** In this case, 10% of the hourly load at bus 59 is considered as responsive load. Assume that this load can only be curtailed (cannot be shifted.) Accordingly, the operating cost is dropped to $1,042,325.48 (i.e., 0.43% decrease in the operating cost.) The actual and curtailed loads at bus 59 are depicted in Fig. 3. The load curtailment occurs at hours 14-19. The curtailment at hour 14 is 14.4 MW. At hours 15-19, the curtailed load is 26.9, 27.7, 27.7, 26.7 and 26.6 MW, respectively, which are equal to maximum hourly curtailable loads, and the total load curtailment is equal to the daily curtailment limit of 150 MW. The hourly load curtailment occurs near the peak hour which changes the scheduled unit commitment when units 2 and 9 are turned off. The total saving at bus 59 is $16,265.50 with a 4460.33 MBtu saving in fuel consumption.

**Case 2:** Fig. 4 depicts the application load shifting at bus 59. The load at hours 12-19 is shifted. However, the total energy consumption at bus 59 is not changed. The minimum load of 5 MW was shifted at hour 12. Load shifting changes the unit commitment schedule when nine expensive units are no longer committed at the peak hour. The total operating cost is $1,044,998.12 (i.e., 0.17% decrease) which is larger than that of Case 1 when the load was curtailed. The total saving in load consumption at bus 59 is $10378.15 with a 1787.69 MBtu saving in fuel consumption.

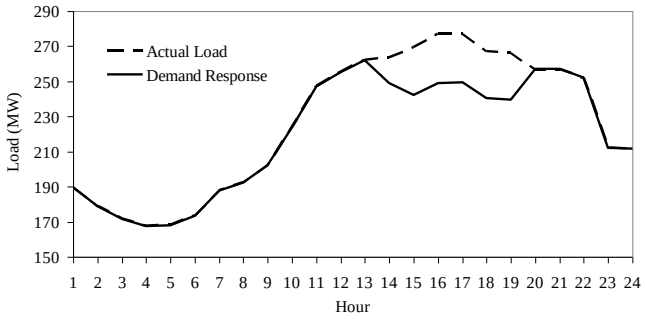


Fig. 3 Load at bus 59 with load curtailment

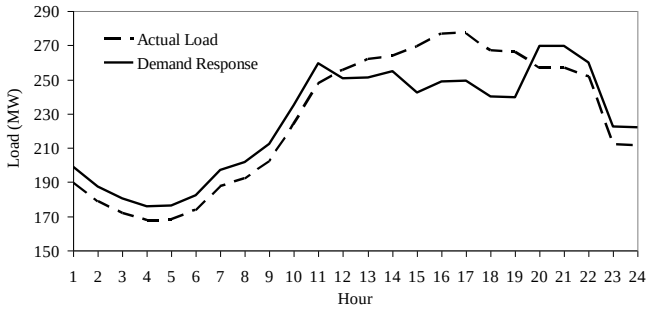


Fig. 4 Load at bus 59 with load shifting

In Cases 1 and 2, the average system LMP is decreased in four hours. The average system LMP in Cases 0 and 1 are compared in Fig. 5. The hourly LMP in the entire scheduling horizon is affected, although the load curtailment is at hours 14-19. Here, a less congested network flows would result in lower LMPs. The average system LMP in Case 2 is fairly similar to that of Case 1, while the LMP at hours 21 and 22 is slightly higher. The load shifting could mitigate price spikes and lower the average system LMP as efficiently as load curtailment.

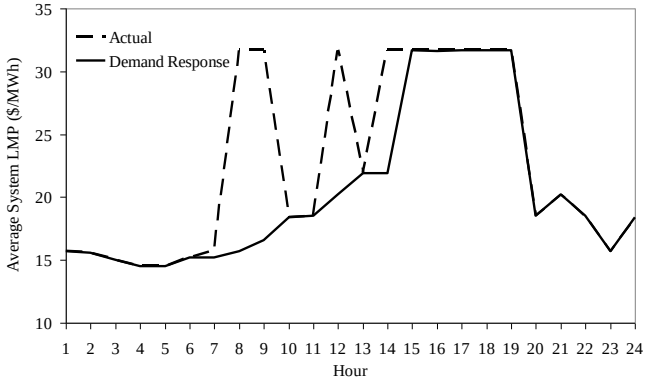


Fig. 5 Average system LMP

### *B. DR considered at all buses*

In this case, DR (load shifting) is considered at all buses when calculating the hourly SCUC. The load is shifted from 0% to 20% with steps of 5%. Here, 20% means that one fifth of the hourly load may be shifted. Four cases are considered as follows:

Case 0: SCUC solution with DR
Case 1: SCED solution with DR
Case 2: Effect of contingencies on Case 0
Case 3: Effect of load pickup/drop rates on Case 0

**Case 0:** In Table I, the number of committed units and the total operating cost are reduced as we shift more loads away from peak hours. In Table I, the largest cost drop occurs during the first 5% step with a 1.32% reduction in the cost.

TABLE I
SCUC RESULTS WITH A VARIETY OF DR

| Responsive load (%) | Total operating cost ($) | Number of committed units | Hourly load average | Hourly load standard deviation |
|---|---|---|---|---|
| 0 | 1,046,785.89 | 45 | 3,048.10 | 537.67 |
| 5 | 1,033,506.86 | 33 | 3,048.10 | 346.68 |
| 10 | 1,030,887.89 | 29 | 3,048.10 | 200.31 |
| 15 | 1,030,191.46 | 25 | 3,048.10 | 70.86 |
| 20 | 1,030,018.28 | 23 | 3,048.10 | 22.09 |

Without any load shifts, 44 units are committed with 15 units operating as base units. With a 5% DR, the number of committed units is decreased to 34 with 16 units operating as base units. The number of committed units would decrease progressively in this case with more units operating as base unit. The hourly load average (total daily load divided by 24) is fixed as curtailment is not considered. However the standard deviation is reduced as we shift more loads which would result in a flatter load profile (i.e., hourly system load gets closer to the average load.) In Fig. 6, the 20% load shift is compared with the actual system load. The small change at hour 7 is due to the commitment of unit 19, which is the latest committed unit. The total shifted load is 5,711 MW which is shifted from hours 11-22 to hours 1-10 and 23-24. With a flat load profile, there will be no need to commit expensive units at peak hours.

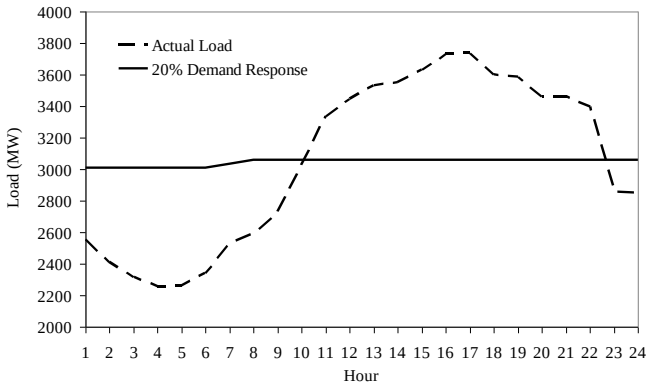


Fig. 6 Actual and shifted system loads

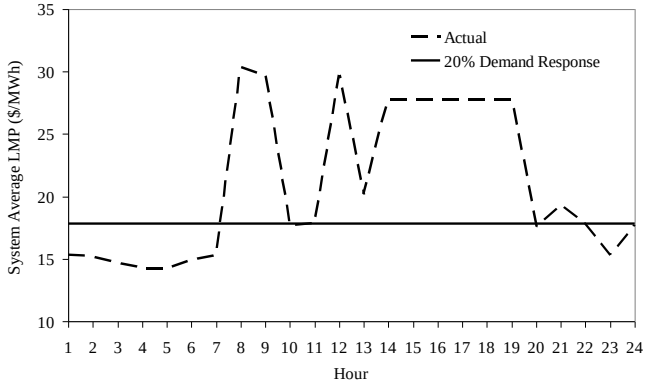


Fig. 7 Average system LMP

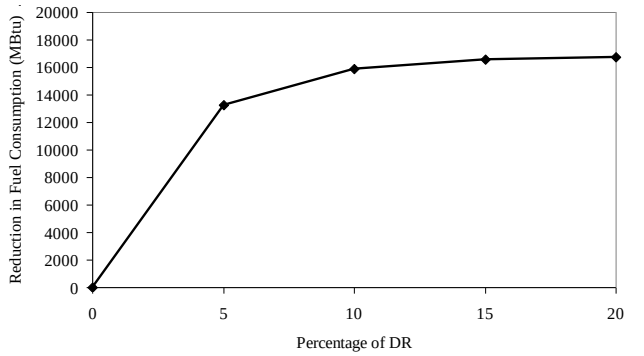


Fig. 8 Reduction in fuel consumption

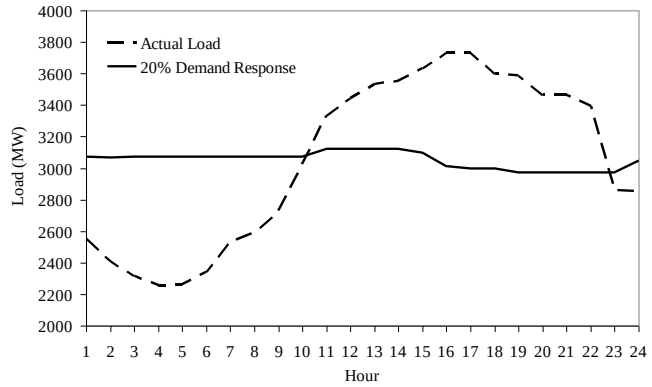


Fig. 9 Actual and shifted system load in the case of contingencies

Here, by shifting loads to off-peak hours, line flows decrease at peak hours (i.e., less congestion) and increase at off-peak hours. The average LMP depicted in Fig. 7 which is much more flat with possible load shifts. The reduction in fuel consumption is shown in Fig. 8.

**Case 1:** In Case 0, there was an iterative process in the SCUC solution in which the UC solution was modified in each iteration in order to optimize the DR solution. Here, we fix the base case UC results in Table 1 and utilize an SCED with the 20% DR. Accordingly, a unit dispatch is obtained with a total operating cost of $1,039,343.61 which is 0.9% higher than that of the SCUC result. The standard deviation is 400 MW with a total load shift of 1,529 MW. Here the cost is higher because the fixed UC solution would restrict the load shifts and the DR benefits presented in Case 0.

**Case 2:** Three possible contingencies including the outages of unit 10 and line 120 at peak hour and the outage of unit 19 at hour 5 are considered. Accordingly, the original unit commitment is adjusted and loads are shifted as preventive actions. However, possible corrective actions would be handled by the hourly generation dispatch and load curtailments. If we do not shift any loads, 48 units are committed to satisfy the load with a total operating cost of $1,060,349.50. When we consider a 20% load shift, the total operating cost is reduced to $1,035,364.42 in which only 25 units are committed. The hourly load standard deviation is 60 MW, which is larger than that of Case 0. This is due to the commitment of additional units at hours with contingency. Unit 23 is committed at hours 15-19 to handle the outage of unit 10; also unit 16 is committed at the entire scheduling horizon. Accordingly the dispatch of units and load shifts are modified. In UC, units 10, 19, and 23 are partially committed while the other committed units are always on. By shifting loads, the partially committed units will be loaded additionally and, as shown in Fig. 9, the load profile will not be as flat.

**Case 3:** In this case load pickup/drop rates of 0.5 MW/min are considered. The SCUC with 20% DR is solved. The load pickup/drop rates would reduce the responsiveness of loads in seventeen buses as compared to Case 0. Accordingly, the load schedule in the entire system is changed to compensate the reduced load shifting capability of affected buses. The total operating cost is slightly increased as the total savings for loads subject to pickup/drop rates are decreased. This decrease in savings is due to fewer load shifting. Fig. 10 shows the DR solution which is compared with the actual system load.

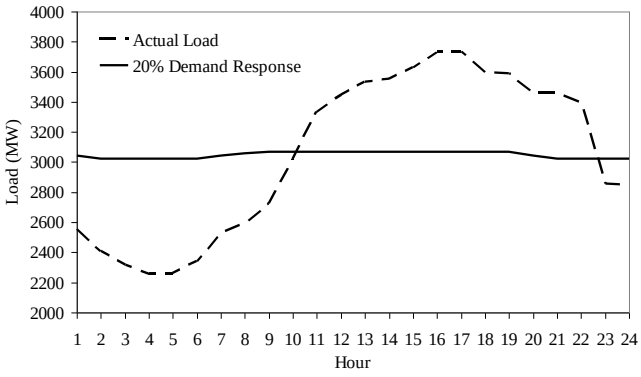


Fig. 10 Actual and shifted system load with load pickup/drop rates

In Fig. 11, the responsive load of bus 54 could change much faster when load pickup/drop rates are not considered. The load changes are as high as 59 MW (between hours 11 and 12 and hours 12 and 13). However when considering the load pickup and drop rates, the responsive load would only change 30 MW from hour 8 to hour 9 and from hour 9 to hour 10.

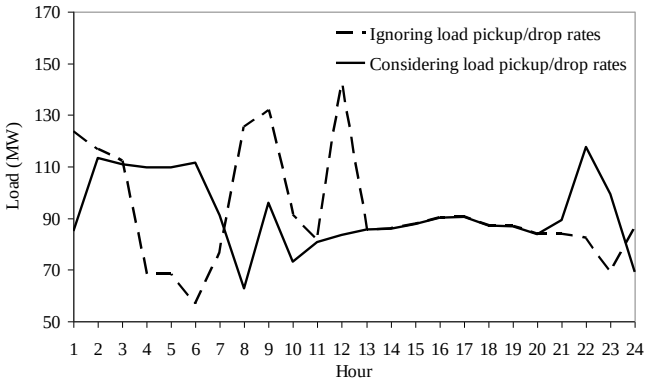


Fig. 11 Effect of load pickup/drop rates on responsive load at bus 54

## V. Observations

Using the studied cases, we list the DR advantages as follows:

- Peak demand reduction. This reduction was by either curtailing peak demands or shifting peak demands to off-peak hours. The peak load reduction would mitigate price spikes and enhanced economical dispatch.
- Reduction in the average system LMP. Changes in DR-based hourly load profile could modify the hourly unit commitment and power flows, and accordingly reduce bus LMPs.
- Social benefits of DR. Any DR applications to a fraction of buses could provide benefits to the entire power system and all market participants.
- DR in day-ahead. DR application was more beneficial to SCUC than to SCED. The corresponding adjustments to SCUC would enhance the flexibility and the efficiency of market operations.
- Higher DR. Additional level of DR would lead to better SCUC results and a more flat hourly load profile. However, merits of very large DR were not as significant.
- Impact of DR on power system operation. A higher DR would lead to lower fuel consumptions and reduced carbon footprint in power systems.

## VI. Conclusions

The ability to curtail or shift loads at peak periods could reduce the energy cost and require few on/off commitment of generating units. In this paper a comprehensive formulation is proposed to model the DR in the clearing process of electricity markets. The application of DR to SCUC would effectively incorporate responsive loads in the day-ahead market operations. Physical constraints of responsive loads along with generation units and transmission lines were considered. Such constraints were considered in base case and contingency operations of the system. The benefits of DR were demonstrated as viable options for managing the load growth in electric power systems.

## References


[1] M. Shahidehpour, H. Yamin, and Z. Y. Li, Market Operations in Electric Power Systems. New York: Wiley, 2002.

[2] A.J. Conejo, E. Castillo, R. Mínguez, and R. García-Bertrand, Decomposition Techniques in Mathematical Programming, *Springer*, 2006.

[3] A. G. Bakirtzis, N. P. Ziogos, A. C. Tellidou, G. A. Bakirtzis, "Electricity producer offering strategies in day-ahead energy market with step-wise offers", *IEEE Trans. on Power Syst.* vol. 22, no. 4, pp. 1804-1818, Nov. 2007.

[4] R. L. Earle, "Demand elasticity in the California power exchange day-ahead market," *Elect. J.*, vol. 13, no. 8, pp. 59–65, Sep. 2000.

[5] R. H. Patrick and F. A. Wolak, "Real-time pricing and demand side participation in restructured electricity markets," in *Proc. Conf. Retail Participation in Competitive Power Markets*, 2001.

[6] A. C. Tellidou, A. G. Bakirtzis, "Demand Response in Electricity Markets," in *Proc. 15th International Conference on Intelligent System Applications to Power Systems*, pp. 1 – 6, 2009.

[7] S. Rassenti, V. Smith, and B. Wilson, "Controlling market power and price spikes in electricity networks: Demand-side bidding," *Proc. Nat. Acad. Sci.*, vol. 100, no. 5, pp. 2998–3003, May 2003.

[8] S. Borenstein, J. Bushnell, and F.Wolak, "Measuring market inefficiencies in California's restructured wholesale electricity market," *Amer. Econ. Rev.*, vol. 92, no. 5, pp. 1376–1405, 2002.

[9] A.K. David and Y.C. Lee, "Dynamic tariffs: theory of utility-consumer interaction," *IEEE Trans. Power Syst.* vol. 4, no. 3, pp. 904-911, Aug. 1989.

[10] A.K. David and Y.Z. Li, "Consumer rationality assumptions in the real-time pricing of electricity," *IEE Proc. Gener. Transm. Distrib.* vol. 139, no. 4, pp. 315–322, 1992.

[11] A.K. David and Y.Z. Li, "Effect of inter-temporal factors on the real time pricing of electricity," *IEEE Trans. Power Syst.* vol. 8, no. 1, pp. 44-52, Feb. 1993.

[12] R. Rajaraman, J.V. Sarlashkar and F.L. Alvarado, "The effect of demand elasticity on security prices for the poolco and multi-lateral contract models," *IEEE Trans. Power Syst.* vol. 12, no. 3, pp 1177-1184, Aug. 1997.

[13] L. Goel, Q. Wu and P. Wang, "Nodal price volatility reduction and reliability enhancement of restructured power systems considering demand–price elasticity," *Elec. Power. Syst. Res.*, vol. 78, pp. 1655-1663, 2008

[14] J.A. Colledge, J. Hicks, J.B. Robb and D. Wagle. "Power by the minute," McKinsey Quarterly, no. 1, pp. 73-81, Jan. 2002.

[15] FERC Staff, "Assessment of demand response and advanced metering," Federal Energy Regulatory Commission, Aug. 2006.

[16] T. Li and M. Shahidehpour, "Strategic Bidding of Transmission-Constrained GENCOs with Incomplete Information," *IEEE Trans. Power Syst.* vol. 20, no. 1, pp. 437 – 447, Feb. 2005

[17] H.Y. Yamin and M. Shahidehpour, "Risk and Profit in Self-Scheduling for GenCos," *IEEE Trans. Power Syst.* vol. 19, no. 4, pp. 2104-2105, Nov. 2004

[18] J. M. Arroyo and A. J. Conejo, "Multi-period auction for a pool-based electricity market," *IEEE Trans. Power Syst.*, vol. 17, no. 4, pp. 1225–1231, Nov. 2002.

[19] J. Contreras, O. Candiles, J. I. de la Fuente, and T. Gomez, "Auction design in day-ahead electricity markets," *IEEE Trans. Power Syst.*, vol. 16, no. 3, pp. 409–417, Aug. 2001.

[20] C. L. Su and D. Kirschen, "Direct participation of demand-side in a pool-based electricity market," *Power Syst. Tech.*, vol. 31, no. 20, pp. 7–14, Oct. 2007.

[21] C. L. Su and D. Kirschen, Quantifying the effect of demand response on electricity markets," *IEEE Trans. Power Syst.*, vol. 24, no. 3, pp. 1199–1207, Aug. 2009.

[22] A. K. David and Y. Z. Li, "Consumer rationality assumptions in the real-time pricing of electricity," *IEE Proceedings*, pt. C, vol. 139, no. 4, pp. 315–322, July 1992.

[23] D.S. Kirschen, G. Strbac, P. Cumperayot and D. de Paiva Mendes, "Factoring the elasticity of demand in electricity prices," *IEEE Trans. Power Syst.* vol. 15, no. 2, pp. 612-617, May 2000.

[24] J. Wang, S. Kennedy and J. Kirtley, "A new wholesale bidding mechanism for enhanced demand response in smart grids," In *Innovative Smart Grid Tech. Conf (ISGT)*, 2010
[25] Y. Fu, M. Shahidehpour and Z. Li, "Security-constrained unit commitment with AC constraints," *IEEE Trans. Power Syst.*, vol. 20, no. 3, pp. 1538–1550, Aug. 2005.
[26] M. Shahidehpour and Y. Fu, "Benders decomposition," *IEEE Power and Energy Mag.*, vol. 3, no. 2, pp. 20-21, March 2005.
[27] M. Shahidehpour and V. Ramesh, "Nonlinear programming algorithms and decomposition strategies for OPF," *IEEE/PES Tutorial on Optimal Power Flow*. Piscataway, NJ: IEEE Press, 1996.
[28] H. Ma and M. Shahidehpour, "Transmission constrained unit commitment based on Benders decomposition," *Elect. Power Energy Syst.*, vol. 20, no. 4, pp. 287–294, Apr. 1998.
[29] A. M. Geoffrion, "Generalized Benders decomposition," *J. Optim Theory Appl.*, vol. 10, no. 4, pp. 237–261, 1972.
[30] Dispatchable load operating guide, 2008 [Online]. Available: http://www.ieso.ca.
[31] CAISO demand response resource user guide, 2007 [Online]. Available: http://www.caiso.com.
[32] ILOG CPLEX. ILOG CPLEX homepage, 2009 [Online]. Available: http://www.ilog.com.

# Optimal Coordination of Stochastic Hydro and Natural Gas Supplies in Midterm Operation of Power Systems

Lei Wu, *Member, IEEE*, and Mohammad Shahidehpour, *Fellow, IEEE*

***Abstract*—This paper presents a stochastic security-constrained unit commitment (SCUC) model for the optimization of coordinated midterm water and natural gas supplies. The stochastic model considers random outages of system components, load forecast errors, and water inflow uncertainty, which are modeled as scenarios in the Monte Carlo (MC) simulation. Water resources may be used in winter to cover gas unit outages caused by an insufficient gas supply. However, those hydro units may not then be available for peak load shaving in the following summer if the summer happens to be a dry season. Thus, water reservoirs would have to be utilized efficiently throughout the year to provide substantial cost reductions while maintaining the power system reliability. The proposed model also considers the impact of midterm security-constrained scheduling of water and gas on the power system reliability. Accordingly, hourly SCUC is incorporated in the reliability calculation. The proposed stochastic problem is formulated as a two-stage optimization in which the first stage optimizes the water and gas usages in the first month and the second stage considers the schedule via multiple scenarios in the following eleven months. Numerical simulations indicate the effectiveness of the proposed stochastic approach for the optimal scheduling of midterm water and gas usages.**

**Keywords: Midterm water and natural gas supplies, power system reliability, stochastic security-constrained unit commitment**

## NOMENCLATURE

**Variables:**

| | |
|---|---|
| $b$ , $c$ | Index of bus/catchment |
| $F_c(\cdot)$ | Production cost function of a unit |
| $h$ , $i$ | Index of hydro/thermal unit |
| $I_{itp}^s$ , $P_{itp}^s$ | Commitment state and real power generation of thermal unit $i$ at time $t$ at period $p$ in scenario $s$ |
| $j,k$ | Index of iteration |
| $LS_{btp,m}^s$ | Load shedding quantity of contract $m$ at bus $b$ at time $t$ at period $p$ in scenario $s$ |
| $m$ | Index of curve segments |
| $p$ , $t$ | Index of period, and hours in each period |
| $SU_{itp}^s$ , $SD_{itp}^s$ | Startup/shutdown cost of thermal unit $i$ at time $t$ at period $p$ in scenario $s$ |
| $V_{htp}^s$ | Reservoir volume of hydro unit $h$ at time $t$ at period $p$ in scenario $s$ |
| $\beta$ | Lagrangian multiplier |
| $\gamma_{ctp}^s$ | Global parameter for catchment $c$ describing its depletion policy at time $t$ at period $p$ in scenario $s$ |
| $\gamma_{h,m}$ | Global parameter corresponding to hydro unit $h$ at segment $m$ in linearized depletion curve |
| $\delta_{h,m}$ | Indicates whether hydro unit $h$ is operated at segment $m$ in linearized depletion curve |
| $v_{h,m}$ | Volume of segment $m$ in linearized depletion curve for hydro unit $h$ |

**Constants:**

| | |
|---|---|
| $IC_{h,m}$ | Slope of segment $m$ in linearized depletion curve for hydro unit $h$ |
| $NB$ , $NC$ | Number of buses/catchments |

Lei Wu is with the Electrical and Computer Engineering Department at Clarkson University. Mohammad Shahidehpour is with the Electrical and Computer Engineering Department at Illinois Institute of Technology, USA. (E-mail: lwu@clarkson.edu, ms@iit.edu). This work was suppoted in part by the NSF grant ECCS-0801853.

| | |
|---|---|
| $NG$ , $NH$ | Number of thermal/hydro units |
| $NH_c$ | Number of hydro units belongs to catchment $c$ |
| $NPD$ , $NPS$ | Number of periods at the first/second stage under study |
| $NM_b$ | Number load shedding contracts at bus $b$ |
| $NS$ | Number of scenarios |
| $NT$ | Number of hours at each period |
| $p^s$ | Probability of scenario s |
| $PL^s_{tp}$ | System load at time $t$ at period $p$ in scenario $s$ |
| $pv^s_{b,m}$ | Value of lost load (VOLL) corresponding to segment $m$ of bus $b$ in scenario $s$ |
| $V_{h,\max}$ , $V_{h,\min}$ | Upper/lower limit of reservoir volume of hydro unit $h$ |
| $V_{h,m}$ | Upper volume limit of segment $m$ in linearized depletion curve for hydro unit $h$ |

Note: Corresponding variables are also considered for hydro units by changing index $i$ to $h$.

# 1 INTRODUCTION

In restructured power systems, ISOs maintain the power system reliability when supplying the hourly load at minimum cost [1]. In this environment, the interdependency of natural gas and electric power systems could affect the security and the economics of power systems. For instance, in winter months when residential usages of gas increases in some regions, there may be an insufficient level of gas available for gas-fired generating units. Hydro units could be used in such occasions in order to avoid electric load curtailments. However, if the following spring season happens to be dry, water reservoirs utilized in the previous winter would not be replenished. Thus insufficient water resources could lead to the inability of hydro units to supply summer peak loads. In order to minimize peak load curtailments in the coming summer months, water usage has to be limited in the winter by committing more expensive thermal units.

The uncertainty of water inflow introduces a relationship between present and future reservoir operation decisions in a cascaded hydro system as shown in Figure 1. Here, at the optimal point, future and current water values are equal. Water values are calculated as incremental/decremental costs for reducing/adding stored water at the final level in the current period.

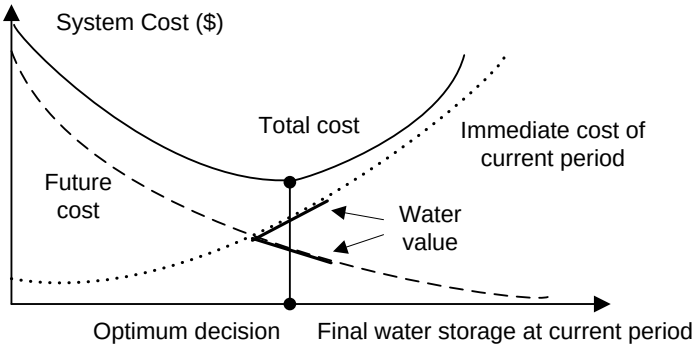


Figure 1 Immediate and future costs versus final water storage

The midterm (i.e., several months to one year) optimization of cascaded hydro units is a difficult task because a reservoir's operation strategy may affect downstream reservoirs' energy production and water quantity. In addition, large dimensions, temporal, and stochastic characteristics of cascaded hydro systems would require fairly accurate solutions with reasonably low computation costs. In [3] and [4], the storage capacity of cascaded reservoirs in a system was aggregated into a single composite reservoir which reduced the number of state variables for long-term studies. The storage and release policies for each reservoir were then disaggregated using heuristic rules. The main drawback of the single composite reservoir model lies in the difficulty to derive feasible/optimal operation policies for individual reservoirs from the aggregate policy. [5] proposed a linear marginal cost model to optimize the long-term hydro unit scheduling, which was derived from the composite marginal cost function of a thermal system. The difficulty would be to derive the composite thermal cost function, especially when incorporating the power transmission network. An overview of the state-of-the-art optimal operation of cascaded reservoir systems was given in [6].

The gas transmission system may affect the operation of power systems with gas-fired generation units. Pressure losses, pipeline contingencies, lack of storage or gas supply disruptions may lead to forced outages of multiple

gas-fired units or generation deration. Such events could dramatically increase the power system operating costs and transmission congestion and jeopardize its security [7]. The scheduling of gas-fired combined cycle units could represent a complicated optimization problem because such units could have multiple operating configurations based on the number and the status of combustion and steam turbines. [8] presented an optimization method for establishing the state space diagram of combined cycle units and applying dynamic programming and Lagrangian relaxation to the security-constrained short-term scheduling of power systems with gas-fired combined cycle units. Nonlinear optimization models for the integrated operation of gas and power systems were discussed in [9], [10]. The impact of gas transmission charges on power markets was discussed in [11]. [12] proposed an integrated model for assessing the impact of interdependency of electricity and gas networks on power system security. The gas network is modeled by considering daily and hourly limits on pipelines, sub-areas, plants, and generating units. [13] proposed an integrated model for UC with gas transmission constraints, which were formulated as nonlinear equations and solved by a Newton-Raphson method. Successive Benders Decomposition (BD) was applied to separate the gas transmission feasibility check subproblem from UC problem. The same methodology is applied here to incorporate gas network constraints into the power system optimal operation problem.

The midterm water allocation could impact the reliability of power systems. [14] modeled hydro unit production using two different methods, i.e., through peak shaving or by dispatching hydro units against the equivalent load duration curve (ELDC). It concluded that the ELDC-based approach would generally result in lower production costs and higher reliability by applying hydro units to cover thermal unit outages. [15] incorporated reliability into a UC framework by developing loss-of-load-expectation (LOLE) and expected-energy-not-served that provided useful information on long-term operating decisions. Additional details on reliability evaluation methods were given in [16].

In this paper, the reliability assessment of power systems is analyzed for the midterm optimal water and gas usages. Since the midterm operation of cascaded reservoirs is coupled in time and space, there is a trade-off between operating cost and supply reliability. Because it is impossible to have prior knowledge of future water inflows, power and gas loads, as well as power system disturbances, this trade-off can only be expressed on a stochastic basis. Uncertainties are simulated by the MC method and a scenario-based technique is applied to keep the trade-off between computation time and accuracy. The stochastic SCUC is used in which the scheduling horizon is decoupled into periodic stages (i.e., several weeks to one month) [17]. The periodic operation policy would determine, at the beginning of each period, how much water should be used or stored for the future use. The predefined operation rules are adopted to approximate the actual depletion policy of reservoirs located in a catchment, which would simplify the coupling constraints among successive periods and take advantage of the decomposition procedure. The problem is formulated as a two-stage stochastic programming model for the optimization period of one year, with the first stage optimizing the operation for the first month and the second stage for the remaining eleven months for simulating the midterm operation via scenarios. In this paper, SCUC would satisfy the hourly electricity and gas network constraints in the base case and all simulated scenarios. Reliability-based solution derived from the proposed two-stage model satisfies the hourly electricity and gas network security constraints and provides sufficient water and gas supply for minimizing the load shedding in the entire midterm horizon. Midterm period refers to the scheduling horizon of several months to one year, short-term refers to several hours to several weeks, and long-term covers several years.

The rest of the paper is organized as follows. Section 2 presents the solution methodology of the stochastic model. Section 3 presents and discusses a 6-bus system and a modified IEEE 118-bus system, and the conclusion is drawn in Section 4.

## 2 Stochastic Midterm Model

The proposed stochastic optimization problem for analyzing the power system reliability and improving the operational efficiency of water and gas usages in a midterm horizon is formulated as a two-stage stochastic model. The objective, formulated in (1), is to minimize the social cost including operation cost (i.e., production cost, startup and shutdown costs of individual units) and the possible load shedding cost for the entire midterm horizon.

$$\min \sum_{p=1}^{NPD} \sum_{t=1}^{NT} \left\{ \sum_{i=1}^{NG} \left[ F_c\left(P_{itp}\right) \cdot I_{itp} + SU_{itp} + SD_{itp} \right] + \sum_{h=1}^{NH} SU_{htp} + \sum_{b=1}^{NB} \sum_{m=1}^{NM_b} pv_{b,m} \cdot LS_{btp,m} \right\} + \sum_{s=1}^{NS} p^s \cdot \sum_{p=1+NPD}^{NPS+NPD} \sum_{t=1}^{NT} \left\{ \sum_{i=1}^{NG} \left[ F_c\left(P_{itp}^s\right) \cdot I_{itp}^s + SU_{itp}^s + SD_{itp}^s \right] + \sum_{h=1}^{NH} SU_{htp}^s + \sum_{b=1}^{NB} \sum_{m=1}^{NM_b} pv_{b,m}^s \cdot LS_{btp,m}^s \right\} \quad (1)$$

The concept of utilizing scenarios adds another dimension to the solution that is different from that of the deterministic midterm UC planning model. The set of constraints includes:

- System power balance constraint.
- Individual generator constraints for various types of units, including ramping up/down rate limits, minimum on/off time limits, generation unit capacity limits, etc.
- Individual cascaded hydro unit constraints, including reserve volume limits, water balance constraint, water discharge limits, etc. We set the initial and the terminal volumes to be the same in a one year horizon to avoid excessive water usage. For the midterm hydro operation, the water usage in the current month is coordinated with that of future months in order to avoid excessive water use in the current month which could lead to the lack of sufficient water supply in future months.
- Power transmission constraints including dc network constraints and phase shifter angles limits.
- Natural gas transmission constraints including gas contract limits, gas usage limits, pipeline and compressor transmission capability limits, etc.
- Reliability constraints including load shedding limits at each bus and each time period in each scenario, and LOLE limits.
- Reservoir volume coupling constraints for two consecutive periods, which indicates that the terminal volume at the end of previous period should be the initial volume at the beginning of successive period.

Detailed formulations of constraints for the system and individual generators are found in [17], cascaded hydro system formulation in [18], reliability formulation in [15], and gas network formulation in [13]. The contributions of this paper reside in the formulation of midterm hydro reservoir operation, the optimization and the coordination of midterm water and natural gas usage, and the proposed solution methodology for the complex midterm scheduling problem by fully utilizing the capabilities of state-of-the-art mixed-integer programming, Lagrangian relaxation, and Benders decomposition techniques.

### *2.1 Scenario Techniques with MC*

A set of scenarios is generated by MC for simulating power system uncertainties, including random outages of system components, electric and gas load forecast errors, and uncertainties associated with water inflows. The advantage of applying MC is that the simulation accuracy of MC depends on the number of samples rather than the dimension of uncertainty in each scenario. Therefore MC is suitable for power systems with large dimensions of uncertainty.

A two-state continuous-time Markov chain model is applied to simulate component outages in each scenario and UC states are calculated by solving the stochastic SCUC problem. The parameters used for MC are failure and repair rates of each power system component. The water inflow to a reservoir follows a discrete Markov chain, which is independent of inflows to other reservoirs, thus the spatially independent log-normal random variable correlated in time with a first-order lag is used to simulate the water inflow. The detailed formulations are provided in [17],[18]. The future power load and gas load uncertainty is represented by a truncated normal distribution with a probability density function shown in (2). The distribution is divided into a discrete number of intervals (i.e., $\mu$, $\mu\pm\sigma$, $\mu\pm2\sigma$, $\mu\pm3\sigma$, etc) and the load in the mid-point of each interval represents the probability of the interval, where $\mu$ is the forecasted load and $\sigma$ is the known standard deviation.

The Latin Hypercube Sampling (LHS) is developed to generate multi-dimensional random numbers to compose a set of scenarios. The scenario reduction can reduce the computational time by eliminating scenarios with very low probabilities and bundling scenarios that are very close in terms of statistical metrics [17]-[19].

$$f(x)=\begin{cases}0 & x<\mu-3.5\sigma \quad or \quad x>\mu+3.5\sigma \\ \dfrac{1}{\alpha\sqrt{2\pi}\,\sigma}\cdot e^{-\frac{(x-\mu)^2}{2\sigma^2}} & \mu-3.5\sigma\le x\le\mu+3.5\sigma\end{cases} \quad (2)$$

$$where \quad \alpha=\int_{\mu-3.5\sigma}^{\mu+3.5\sigma}\frac{1}{\sqrt{2\pi}\,\sigma}\cdot e^{-\frac{(x-\mu)^2}{2\sigma^2}}dx$$

*2.2 Midterm Reservoir Operation Rules*

Simplified operation rules that approximate the depletion policy of cascaded reservoirs may be used to estimate the energy production [20]. The adopted operation rules define the volume of each reservoir $v_h$ in a catchment as a function of $\gamma_c$ corresponding to catchment $c$. That is, a set of curves is adopted for describing the relationship between the global parameter (one global parameter per catchment) and each reservoir volume in the catchment as

$$V_h=\Psi(\gamma_c) \qquad \forall h\in c \quad (3)$$

The operation rule is given based on historical inflow records or nonlinear optimization model [21]. As shown in Figure 2, the operation rule does not have to represent a convex curve.

The following two formulations can be applied for MIP modeling of non-convex operation rule curves. Numbers of integer variables and constraints are often regarded as good indicators of computational difficulty of MIP models [23]. Considering a $NV_h$ segments curve shown in Figure 2, Formulation 1 is based on the type 1 Special Ordered Set (SOS1), which forms variables within which only one is non-zero and would facilitate the branching process of branch-and-bound method for a faster convergence [22]-[23]. Different from Formulation 1 which introduces integer variables corresponding to each of $NV_h$ segments, Formulation 2 includes integer variables corresponding to each of $NV_h-1$ intermediate points, thus containing less integer variables than Formulation 1. The number of variables and constraints are listed in Table 1 for comparison. Although Formulation 1 introduces one more integer variable than Formulation 2, there would be $NV_h$ nodes in either case by the branch-and-bound tree in the worst case. A MIP model is often easier to solve by expanding a limited number of constraints, which provides a tighter approximated MIP formulation and will be used in the tree search strategy. Based on our experience with different formulations for large systems, Formulation 2 is tighter and converges faster and used in this paper.

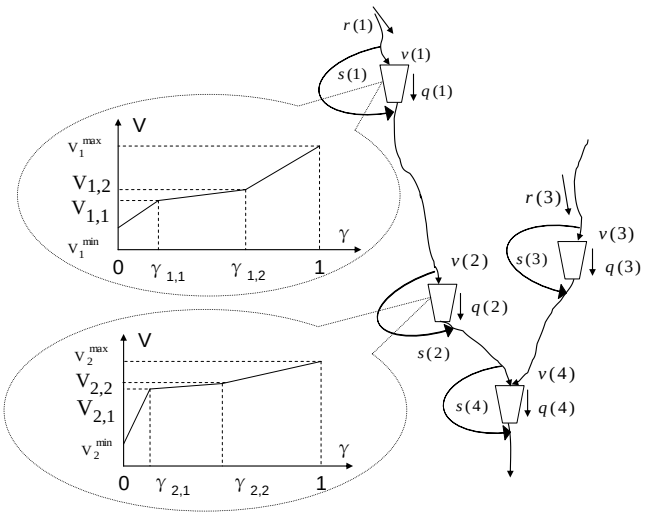


Figure 2 Depletion curves for a catchment

Table 1 Comparison of MIP formulations

| | Formulation 1 | Formulation 2 |
|---|---|---|
| Number of Integer Variables | $NV_h$ | $NV_h-1$ |
| Number of Total Variables | $2\cdot NV_h+2$ | $2\cdot NV_h+1$ |
| Number of Equality Constraints | 3 | 2 |
| Number of Inequality Constraints (limits of variables do not count in) | $NV_h$ | $2\cdot NV_h-2$ |

*Formulation 1:*

$$
\begin{aligned}
&V_h = V_{h,\min} \cdot \delta_{h,1} + \sum_{m=2}^{NV_h} V_{h,m-1} \cdot \delta_{h,m} + \sum_{m=1}^{NV_h} IC_{h,m} \cdot v_{h,m} \\
&\gamma_c = 0 \cdot \delta_{h,1} + \sum_{m=2}^{NV_h} \gamma_{h,m-1} \cdot \delta_{h,m} + \sum_{m=1}^{NV_h} v_{h,m} \\
&\sum_{m=1}^{NV_h} \delta_{h,m} = 1 \qquad \delta_{h,m} \in \{0,1\} \\
&0 \le v_{h,1} \le (\gamma_{h,1} - 0) \cdot \delta_{h,1} \\
&0 \le v_{h,m} \le (\gamma_{h,m} - \gamma_{h,m-1}) \cdot \delta_{h,m} \quad m \in \{2, \cdots, NV_h - 1\} \\
&0 \le v_{h,NV_h} \le (1 - \gamma_{h,NV_h-1}) \cdot \delta_{h,NV_h}
\end{aligned}
\tag{4}
$$

*Formulation 2:*

$$
\begin{aligned}
&V_h = V_{h,\min} + \sum_{m=1}^{NV_h} IC_{h,m} \cdot v_{h,m} \\
&\gamma_c = 0 + \sum_{m=1}^{NV_h} v_{h,m} \\
&(\gamma_{h,1} - 0) \cdot \delta_{h,1} \le v_{h,1} \le (\gamma_{h,1} - 0) \\
&(\gamma_{h,m} - \gamma_{h,m-1}) \cdot \delta_{h,m} \le v_{h,m} \le (\gamma_{h,m} - \gamma_{h,m-1}) \cdot \delta_{h,m-1} \\
&\qquad\qquad m \in [2, NV_h - 1] \\
&0 \le v_{h,NV_h} \le (1 - \gamma_{h,NV_h-1}) \cdot \delta_{h,NV_h-1} \\
&\delta_{h,m} \in \{0,1\}
\end{aligned}
\tag{5}
$$

### *2.3 Proposed Stochastic Solution*

Scenarios add another dimension to the proposed solution of midterm model, which makes the proposed two-stage stochastic problem very large and computationally impractical. A proper decomposition procedure is necessary for decomposing the problem into tractable easy-to-solve subproblems for each period.

In order to consider midterm optimal water usage, reservoir volume coupling constraints between consecutive periods would need to be considered, which states that the terminal volume of one period would be the same as the initial volume of the next period. Thus, the midterm horizon is divided into several periods, with the relaxation of reservoir volume coupling limits for linking successive periods. Other coupling constraints, such as ramping up/down rate limits, minimum on/off time constraints and delayed water discharge from upper reservoirs to lowers, which link successive periods, are managed based on one of the following two strategies:

1) Constraints linking successive periods will be ignored. Accordingly, the short-term UC problem can be solved for each period independently. The application of parallel processing will speed up the solution. However, the accuracy may suffer slightly.

2) Short-term UC subproblems are solved sequentially. That is, the results of the short-term UC for the first period provide initial conditions for the second period. In this case, constraints linking successive periods will be satisfied within each period by UC.

The difference between the two alternatives signifies the tradeoff between speed and accuracy. In this paper, we adopt the second alternative. The reservoir volume which links successive periods is relaxed by introducing artificially duplicated variables of common variables in (6). In (6) the first constraint and third constraint correspond to the reservoir volume coupling constraint between successive periods at the first stage and second stage, respectively, and the second constraint is for the coupling constraint between the last period of the first stage and the first period of the second stage. Based on the midterm reservoir operation rule discussed earlier, (6) is substituted by (7) by using $\gamma_c$ for each catchment $c$.

The introduction of global parameter $\gamma_c$, which uniformly adjusts reservoir volumes in a catchment, reduces the number of coupling constraints that are to be relaxed from $NH \cdot [(NPD - 1) + NS + NS \cdot (NPS - 1)]$ in (6) to $NC \cdot [(NPD - 1) + NS + NS \cdot (NPS - 1)]$ in (7). By introducing a set of Lagrangian multipliers, coupling constraints (7) are relaxed and the Lagrangian dual function of the original problem (1) is formulated as (8). (8) can be easily separated into tractable subproblems, (9)-(11), corresponding to periods at the first stage and (12)-(14) corresponding to periods of each scenario at the second-stage. A decomposition approach is used for solving each subproblem with respected to constraints discussed at the beginning of this Section 2.

$$V_{hNTp} = V_{h0(p+1)} \quad \forall h, \forall p \in \{1, \cdots, NPD - 1\}$$

$$V_{hNTp} = V^{s}_{h0(p+1)} \quad \forall s, \forall h, p = NPD \tag{6}$$

$$V^{s}_{hNTp} = V^{s}_{h0(p+1)} \quad \forall s, \forall h, \forall p \in \left\{ \begin{matrix} NPD + 1, \cdots, \\ NPD + NPS - 1 \end{matrix} \right\}$$

$$\gamma_{cNTp} = \gamma_{c0(p+1)} \quad \forall c, \forall p \in \{1, \cdots, NPD - 1\}$$

$$\gamma_{cNTp} = \gamma^{s}_{c0(p+1)} \quad \forall s, \forall c, p = NPD \tag{7}$$

$$\gamma^{s}_{cNTp} = \gamma^{s}_{c0(p+1)} \quad \forall s, \forall c, \forall p \in \left\{ \begin{matrix} NPD + 1, \cdots, \\ NPD + NPS - 1 \end{matrix} \right\}$$

$$L(\beta) = \min \sum_{p=1}^{NPD} \sum_{t=1}^{NT} \left\{ \sum_{i=1}^{NG} \left[ F_c\left(P_{itp}\right) \cdot I_{itp} + SU_{itp} + SD_{itp} \right] + \sum_{h=1}^{NH} SU_{htp} + \sum_{b=1}^{NB} \sum_{m=1}^{NM_b} pv_{b,m} \cdot LS_{btp,m} \right\}$$

$$+ \sum_{s=1}^{NS} p^{s} \cdot \sum_{p=1+NPD}^{NPS+NPD} \sum_{t=1}^{NT} \left\{ \sum_{i=1}^{NG} \left[ F_c\left(P^{s}_{itp}\right) \cdot I^{s}_{itp} + SU^{s}_{itp} + SD^{s}_{itp} \right] + \sum_{h=1}^{NH} SU^{s}_{htp} + \sum_{b=1}^{NB} \sum_{m=1}^{NM_b} pv^{s}_{b,m} \cdot LS^{s}_{btp,m} \right\} \tag{8}$$

$$+ \sum_{c=1}^{NC} \left\{ \begin{matrix} \sum_{p=1}^{NPD-1} \beta_{cp} \cdot \left(\gamma_{cNTp} - \gamma_{c0(p+1)}\right) + \sum_{s=1}^{NS} \beta^{s}_{c} \cdot \left(\gamma_{cNTNPD} - \gamma^{s}_{c0(NPD+1)}\right) + \\ \sum_{s=1}^{NS} \sum_{p=1+NPD}^{NPS+NPD-1} \beta^{s}_{cp} \cdot \left(\gamma^{s}_{cNTp} - \gamma^{s}_{c0(p+1)}\right) \end{matrix} \right\}$$

$$\min \sum_{t=1}^{NT} \left\{ \begin{matrix} \sum_{i=1}^{NG} \left[ F_c\left(P_{it1}\right) \cdot I_{it1} + SU_{it1} + SD_{it1} \right] \\ + \sum_{h=1}^{NH} SU_{ht1} + \sum_{b=1}^{NB} \sum_{m=1}^{NM_b} pv_{b,m} \cdot LS_{bt1,m} \end{matrix} \right\} + \sum_{c=1}^{NC} \beta_{c1} \cdot \gamma_{cNT1} \tag{9}$$

$$\min \sum_{t=1}^{NT} \left\{ \begin{matrix} \sum_{i=1}^{NG} \left[ F_c\left(P_{itp}\right) \cdot I_{itp} + SU_{itp} + SD_{itp} \right] \\ + \sum_{h=1}^{NH} SU_{htp} + \sum_{b=1}^{NB} \sum_{m=1}^{NM_b} pv_{b,m} \cdot LS_{btp,m} \end{matrix} \right\} + \sum_{c=1}^{NC} \left\{ \beta_{cp} \cdot \gamma_{cNTp} - \beta_{c(p-1)} \cdot \gamma_{c0p} \right\} \tag{10}$$

$$\forall p \in \{2, \cdots, NPD - 1\}$$

The approach applies BD for separating UC in the master problem from the dc network and the gas network se curity check in subproblems. Successive linear programming is applied to solve the gas transmission feasibility c heck. If any electric power network or gas network violations arise, corresponding Benders cuts are formed and a dded to the master problem for solving the next iteration [13].

$$\min \sum_{t=1}^{NT} \left\{ \begin{matrix} \sum_{i=1}^{NG} \left[ F_c\left(P_{itp}\right) \cdot I_{itp} + SU_{itp} + SD_{itp} \right] \\ + \sum_{h=1}^{NH} SU_{htp} + \sum_{b=1}^{NB} \sum_{m=1}^{NM_b} pv_{b,m} \cdot LS_{btp,m} \end{matrix} \right\} + \sum_{c=1}^{NC} \left\{ \sum_{s=1}^{NS} \beta^{s}_{c} \cdot \gamma_{cNTp} - \beta_{c(p-1)} \cdot \gamma_{c0p} \right\} \qquad p = NPD \tag{11}$$

$$\min \; p^{s} \cdot \sum_{t=1}^{NT} \left\{ \begin{matrix} \sum_{i=1}^{NG} \left[ F_c\left(P^{s}_{itp}\right) \cdot I^{s}_{itp} + SU^{s}_{itp} + SD^{s}_{itp} \right] + \\ \sum_{h=1}^{NH} SU^{s}_{htp} + \sum_{b=1}^{NB} \sum_{m=1}^{NM_b} pv^{s}_{b,m} \cdot LS^{s}_{btp,m} \end{matrix} \right\} + \sum_{c=1}^{NC} \left\{ \beta^{s}_{cp} \cdot \gamma^{s}_{cNTp} - \beta^{s}_{c} \cdot \gamma^{s}_{c0p} \right\} \qquad p = NPD + 1 \tag{12}$$

$$\min \; p^{s} \cdot \sum_{t=1}^{NT} \left\{ \begin{matrix} \sum_{i=1}^{NG} \left[ F_c\left(P^{s}_{it1}\right) \cdot I^{s}_{it1} + SU^{s}_{it1} + SD^{s}_{it1} \right] + \\ \sum_{h=1}^{NH} SU^{s}_{ht1} + \sum_{b=1}^{NB} \sum_{m=1}^{NM_b} pv^{s}_{b,m} \cdot LS^{s}_{bt1,m} \end{matrix} \right\} + \sum_{c=1}^{NC} \left\{ \beta^{s}_{cp} \cdot \gamma^{s}_{cNTp} - \beta^{s}_{c(p-1)} \cdot \gamma^{s}_{c0p} \right\} \tag{13}$$

$$\forall p \in \{NPD + 2, \cdots, NPD + NPS - 1\}$$

$$\min \; p^{s} \cdot \sum_{t=1}^{NT} \left\{ \begin{matrix} \sum_{i=1}^{NG} \left[ F_c\left(P^{s}_{itp}\right) \cdot I^{s}_{itp} + SU^{s}_{itp} + SD^{s}_{itp} \right] + \\ \sum_{h=1}^{NH} SU^{s}_{htp} + \sum_{b=1}^{NB} \sum_{m=1}^{NM_b} pv^{s}_{b,m} \cdot LS^{s}_{btp,m} \end{matrix} \right\} - \sum_{c=1}^{NC} \beta^{s}_{c(p-1)} \cdot \gamma^{s}_{c0p} \qquad p = NPD + NPS \tag{14}$$

Since Lagrangian dual function is non-differentiable, the standard subgradient method would result in a slow convergence. A proximal Bundle method is used, which diminishes the unstable behavior of cutting-plane algorithm and speeds up the convergence process by adding the trust region philosophy [24],[25].

First $\overline{\beta} = \left\{ \overline{\beta}_{cp}, \overline{\beta}^{s}_{c}, \overline{\beta}^{s}_{cp} \right\}$ is selected among the current set of available solutions, which is typically the one that provides the largest $L(\beta)$. The quadratic problem (15) is solved to find $\beta^{k} = \left\{ \beta^{k}_{cp}, \beta^{k,s}_{c}, \beta^{k,s}_{cp} \right\}$ for the next iteration, where $\Delta^{j}$ is the linearization error. Here, $\|\|$ is the Euclidean norm and $\alpha^{k}$ is an iteration-variant positive parameter, called the trust-region parameter, which decides the region that can be trusted as an approximation for $L(\beta)$.

Several issues are discussed here for an efficient bundle algorithm, including the dynamic choice of parameter $\alpha^{k}$, updating strategy for the current point $\overline{\beta}$, and stopping criterion. At each iteration, $k$, the current point $\overline{\beta}$ will be shifted to $\beta^{k}$ only if (16) is satisfied, and $\alpha^{k}$ for the next iteration will be increased to enlarge the trust region if (17) is not satisfied.

Otherwise, the current solution of iteration $k$ is added to the bundle if $\Delta^{k}$ is small compared with a predefined threshold. If the condition is not satisfied, we discard the solution of this iteration and reduce $\alpha^{k}$ to shrink the trust region for solving (15) again. The $\alpha^{k}$ updating strategy is as follows:

- Predefine lower and upper bounds of $\alpha$, $\alpha Min$ and $\alpha Max$ as $\alpha^{0} = \left(\alpha^{0}_{Min} + \alpha^{0}_{Max}\right)/2$, $\alpha^{0}_{Min} = \alpha Min$, $\alpha^{0}_{Max} = \alpha Max$.
- For each iteration $k$, set $\alpha^{k}_{Min} = \alpha^{k-1}$ if $\alpha^{k}$ is to be increased; otherwise set $\alpha^{k}_{Max} = \alpha^{k-1}$ and the new $\alpha^{k}$ will be calculated as $\alpha^{k} = \left(\alpha^{k}_{Min} + \alpha^{k}_{Max}\right)/2$.

$$\max_{\beta^{k}_{cp}, \beta^{k,s}_{c}, \beta^{k,s}_{cp}} \left\{ EV^{k} - \frac{1}{2 \cdot \alpha^{k}} \left\| \beta^{k} - \overline{\beta} \right\|^{2} \right\}$$

$$s.t.$$

$$EV^{k} \le \Delta^{j} + \sum_{c=1}^{NC} \left\{ \begin{array}{l} \sum_{p=1}^{NPD-1} \left(\beta_{cp} - \overline{\beta}_{cp}\right) \cdot \left(\gamma^{j}_{cNTp} - \gamma^{j}_{c0(p+1)}\right) + \\ \sum_{s=1}^{NS} \left(\beta^{s}_{c} - \overline{\beta}^{s}_{c}\right) \cdot \left(\gamma^{j}_{cNTNPD} - \gamma^{j,s}_{c0(NPD+1)}\right) + \\ \sum_{s=1}^{NS} \sum_{p=1+NPD}^{NPS+NPD-1} \left(\beta^{s}_{cp} - \overline{\beta}^{s}_{cp}\right) \cdot \left(\gamma^{j,s}_{cNTp} - \gamma^{j,s}_{c0(p+1)}\right) \end{array} \right\} \quad (15)$$

$$\Delta^{j} = L\left(\beta^{j}\right) - L\left(\overline{\beta}\right) + \sum_{c=1}^{NC} \left\{ \begin{array}{l} \sum_{p=1}^{NPD-1} \left(\overline{\beta}_{cp} - \beta^{j}_{cp}\right) \cdot \left(\gamma^{j}_{cNTp} - \gamma^{j}_{c0(p+1)}\right) + \\ \sum_{s=1}^{NS} \left(\overline{\beta}^{s}_{c} - \beta^{j,s}_{c}\right) \cdot \left(\gamma^{j}_{cNTNPD} - \gamma^{j,s}_{c0(NPD+1)}\right) + \\ \sum_{s=1}^{NS} \sum_{p=1+NPD}^{NPS+NPD-1} \left(\overline{\beta}^{s}_{cp} - \beta^{j,s}_{cp}\right) \cdot \left(\gamma^{j,s}_{cNTp} - \gamma^{j,s}_{c0(p+1)}\right) \end{array} \right\}$$

$$\left[L\left(\beta^{k}\right) - L\left(\overline{\beta}\right)\right] \Big/ L\left(\overline{\beta}\right) \ge \varepsilon_{1} \quad (16)$$

$$\sum_{c=1}^{NC} \left\{ \begin{array}{l} \sum_{p=1}^{NPD-1} \left(\beta^{k}_{cp} - \overline{\beta}_{cp}\right) \cdot \left(\gamma^{k}_{cNTp} - \gamma^{k}_{c0(p+1)}\right) + \\ \sum_{s=1}^{NS} \left(\beta^{k,s}_{c} - \overline{\beta}^{s}_{c}\right) \cdot \left(\gamma^{k}_{cNTNPD} - \gamma^{k,s}_{c0(1+NPD)}\right) + \\ \sum_{s=1}^{NS} \sum_{p=1+NPD}^{NPS+NPD-1} \left(\beta^{k,s}_{cp} - \overline{\beta}^{s}_{cp}\right) \cdot \left(\gamma^{k,s}_{cNTp} - \gamma^{k,s}_{c0(p+1)}\right) \end{array} \right\} \le \varepsilon_{2} \quad (17)$$

The process stops when the Lagrangian multiplier difference between two successive iterations is smaller than the predefined threshold $\varepsilon_{3}$ in (18). The solution that satisfies the stopping criterion may not satisfy the relaxed constraints (6)-(7). (19) calculates the degree of violation of relaxed constraints (6)-(7). A feasible solution is constructed by heuristically adjusting the initial and terminal reservoir volumes at each period based on the system

load at successive periods (20)-(22), which are calculated and used as limits for the problem optimization at the final run. Because $\Delta V$ is small when the stopping criterion is met, and reservoirs have spillage capability, the final run will not encounter infeasibility by minor adjustments of reservoir volumes (20)-(22).

$$\left\| \beta^{k} - \overline{\beta} \right\|^{2} = \sum_{c=1}^{NC} \left\{ \sum_{p=1}^{NPD-1} \left( \beta_{cp}^{k} - \overline{\beta}_{cp} \right)^{2} + \sum_{s=1}^{NS} \left( \beta_{c}^{k,s} - \overline{\beta}_{c}^{s} \right)^{2} + \sum_{s=1}^{NS} \sum_{p=1+NPD}^{NPS+NPD-1} \left( \beta_{cp}^{k,s} - \overline{\beta}_{cp}^{s} \right)^{2} \right\} \le \varepsilon_{3} \quad (18)$$

$$\Delta V = \sqrt{\sum_{h=1}^{NH} \left\{ \sum_{p=1}^{NPD-1} \left( V_{hNTp} - V_{h0(p+1)} \right)^{2} + \sum_{s=1}^{NS} \left( V_{hNTNPD} - V_{h0(1+NPD)}^{s} \right)^{2} + \sum_{s=1}^{NS} \sum_{p=1+NPD}^{NPS+NPD-1} \left( V_{hNTp}^{s} - V_{h0(p+1)}^{s} \right)^{2} \right\}} \quad (19)$$

$$V_{hNTp}^{F} = V_{h0(p+1)}^{F} = V_{hNTp}^{k} + \left( V_{h0(p+1)}^{k} - V_{hNTp}^{k} \right) \cdot \frac{\sum_{t} PL_{tp}}{\sum_{t} PL_{tp} + \sum_{t} PL_{t(p+1)}} \qquad \forall p \in \{1, \cdots, NPD-1\} \quad (20)$$

$$V_{hNTp}^{F} = V_{h0(p+1)}^{F} = V_{hNTp}^{k} + \left( \sum_{s} p^{s} \cdot V_{h0(p+1)}^{k,s} - V_{hNTp}^{k} \right) \cdot \frac{\sum_{t} PL_{tp}}{\sum_{t} PL_{tp} + \sum_{s} p^{s} \cdot \left( \sum_{t} PL_{t(p+1)}^{s} \right)} \qquad p = NPD \quad (21)$$

$$V_{hNTp}^{F,s} = V_{h0(p+1)}^{F,s} = V_{hNTp}^{k,s} + \left( V_{h0(p+1)}^{k,s} - V_{hNTp}^{k,s} \right) \cdot \frac{\sum_{t} PL_{tp}^{s}}{\sum_{t} PL_{tp}^{s} + \sum_{t} PL_{t(p+1)}^{s}} \qquad \forall p \in \left\{ NPD+1, \cdots, NPD+NPS-1 \right\} \quad (22)$$

Figure 3 shows the solution strategy for decomposing the large-scale problem into tractable easy-to-solve subpr oblems. With the relaxation of reservoir volume coupling constraints by introducing Lagrangian multipliers, the midterm problem is divided into several short-term subproblems, corresponding to the period in the first stage an d periods in the second stage for each scenario. For each short-term SCUC subproblem, Benders decomposition i s applied for separating UC in the master problem from the hourly dc network and gas network evaluation in subp roblems. If any electric power network or gas network violations arise, corresponding Benders cuts are formed an d added to the master problem for solving the next iteration [13]. After obtaining the hydro schedules from the sh ort-term operation subproblems, the coupling constraints of reservoir volume are checked. If the constraints are vi olated, the corresponding Lagrangian multipliers are updated. The Lagrangian iterations will continue until a near optimal solution is reached, and the final feasible solution is constructed by heuristically adjusting the initial and terminal reservoir volumes at each period.

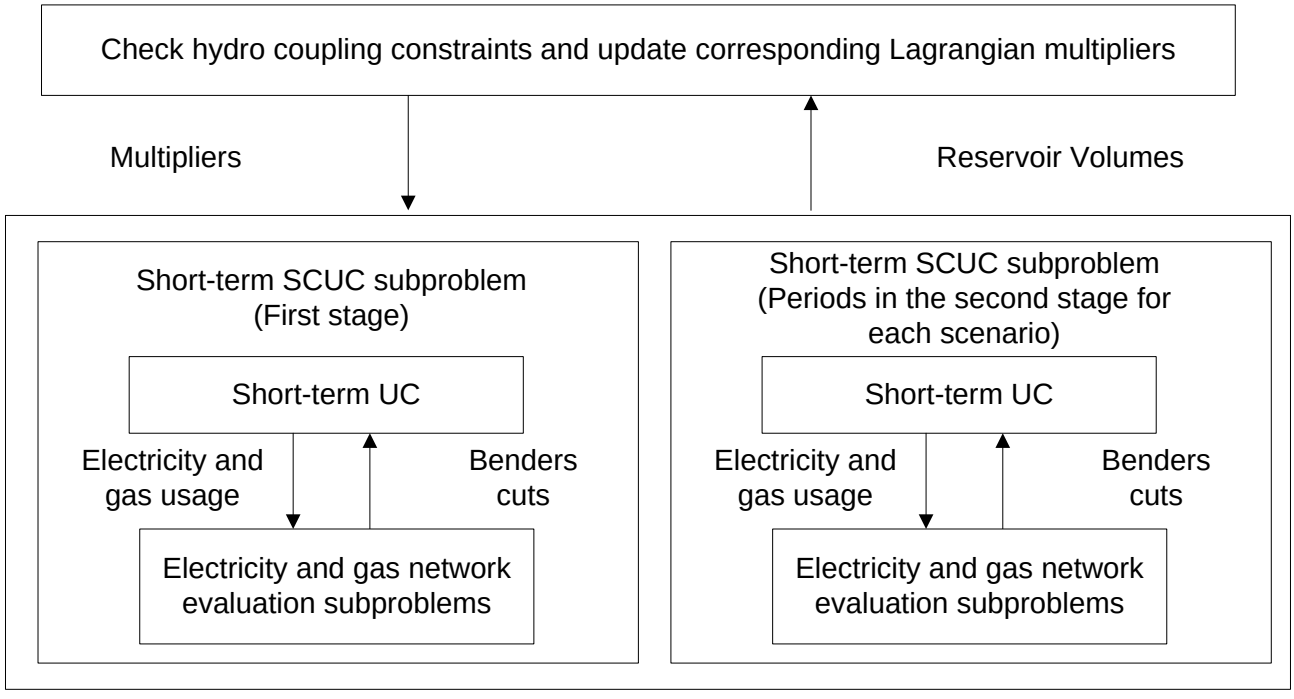


Figure 3 Optimization and coordination for the midterm operation planning with optimal usage for water and natural gas

## 3 CASE STUDY

A 6-bus system and the IEEE 118-bus system are considered to demonstrate the proposed approach for the optimal scheduling of midterm water and gas usages.

### 3.1. 6-bus system

The 6-bus system in Figure 4 is used to illustrate the proposed method. The system has three gas-fired units, one hydro unit and seven transmission lines. The hydro unit data are shown in Table 2. Other detailed generator, transmission line and gas network data are given in [13]. Failure and repair rates for transmission lines are 0.0671 failures/year and 0.9329 repairs/year.

Failure and repair rates for generating units are listed in Table 3. The system is tested for a one-year case (from November to the following October) with the annual peak power load of 330MW and annual peak gas load of 6,000 kcf. Figure 5 shows the weekly peak loads as a percentage of annual peak load. The maximum allowable load shedding is set to be the load value at the designated bus, with a VOLL of 5,000$/MWh for the first 10 percent of the load and 2,000$/MWh for the remaining. For the 6-bus system, each period refers to a month. Thus, the first stage contains one period and the second stage contains eleven periods in each scenario.

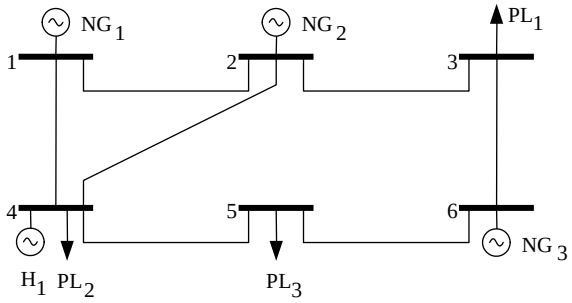


Figure 4 One-line diagram of six-bus example

Table 2 Parameters of hydro unit

| Efficiency | h0 | α | Discharge Max (*$10^4$ $m^3$) | Discharge Min (*$10^4$ $m^3$) |
|---|---|---|---|---|
| 8.091 | 0.857 | 0.0001315 | 10 | 1 |
| Pmin (MW) | Pmax (MW) | Ramp (MW/h) | Min On(h) | Min Off (h) |
| 9 | 80 | 60 | 1 | 1 |
| Volume Min (*$10^4$ $m^3$) | Volume Max (*$10^4$ $m^3$) | Initial Volume (*$10^4$ $m^3$) | Terminal Volume (*$10^4$ $m^3$) | Initial hour |
| 60 | 1000 | 1000 | 1000 | 1 |
| Operation Rule | | | | |
| Global Parameter | 0 | 0.25 | 0.75 | 1 |
| Volume (*$10^4$ $m^3$) | 60 | 250 | 800 | 1000 |

Table 3 Failure and repair rates of generators

| Units | NG1 | NG2 | NG3 | H1 |
|---|---|---|---|---|
| Failure Rate (failures/year) | 0.0307 | 0.0286 | 0.0259 | 0.0262 |
| Repair Rate (repairs/year) | 2.4444 | 2.2749 | 2.0622 | 2.0893 |

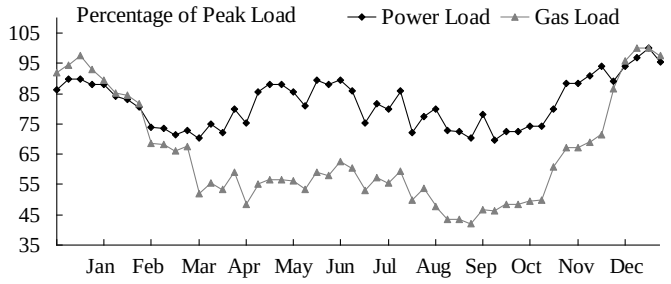


Figure 5 Weekly peak loads as a percentage of annually peak load

Two cases are studied to illustrate the effect of midterm water and gas optimal usages on power system reliability:

**Case 1:** A deterministic solution in the winter season is presented and its impact on the system reliability is discussed, where forced outage rates are assumed to be negligible and the power and gas loads given in Figure 5 are used. The uncertainty of water inflow is not considered, thus the terminal reservoir volume is not restricted. The optimization of deterministic model utilizes as much water as possible to supplement the gas usage in the winter season (November-January with highest gas loads). The impact of the deterministic solution on the system reliability is considered by optimizing a scenario-based stochastic model for the remaining months of

February-October by utilizing terminal volumes at the end of January as the initial condition.
The computation time for the scenario-based problem depends on the number of scenarios. The scenario reduction method would reduce the total number of scenarios from 100 to 12 as a tradeoff between calculation speed and solution accuracy. Table 4 shows the weights of each scenario after reduction. The results of the first three months in Case 1 are presented in Table 5.

Table 4 Weights of each scenario after scenario reduction

| Scenario | 1 | 2 | 3 | 4 | 5 | 6 |
|---|---|---|---|---|---|---|
| Weight | 0.07 | 0.075 | 0.18 | 0.035 | 0.065 | 0.24 |
| Scenario | 7 | 8 | 9 | 10 | 11 | 12 |
| Weight | 0.07 | 0.045 | 0.045 | 0.01 | 0.04 | 0.125 |

Table 5 Results for the first 3 months in Case 1

| | | |
|---|---|---|
| Social Cost ($) | | 12,141,356.75 |
| LS (MWh) | | 411.42 |
| # of Hours LS Occurs | | 56 |
| Volume at the end of each month ($*10^4$ $m^3$) | 11 | 860.34 |
| | 12 | 65.83 |
| | 1 | 60.00 |

Due to the limited capability of gas network, the gas required by gas-fired generating units cannot be transported to corresponding nodes by the gas transmission system. The water resource is the alternative energy to cover the load. It is shown that most of the water reservoir is used in December because of the highest demand by gas loads shown in Figure 5. The terminal reservoir volume at the end of winter reaches its minimum value of $60*10^4$ $m^3$ because the terminal reservoir volume is not restricted and the water resource in the reservoir is used as much as possible. We use the terminal volume at the end of winter, as the initial condition for the following seasons, and 1000 $*10^4$ $m^3$ as the terminal volume for the remaining 9 months. The resulting social cost and load shedding for each scenario is listed in Table 6. Based on results presented in Tables 6 and 7, the social cost is $39,585,164.34 (i.e. 12,141,356.75 + 27,443,807.59) with a load shedding of 460.91MWh. The annual load shedding is 96.465 hours.

Table 6 Results for the following seasons based on Case 1

| Scenario | Social Cost ($) | LS (MWh) | # of LS Hours |
|---|---|---|---|
| 1 | 27,659,311.07 | 53.62 | 57 |
| 2 | 27,425,028.63 | 37.29 | 35 |
| 3 | 27,678,604.15 | 53.10 | 39 |
| 4 | 27,551,233.52 | 54.52 | 43 |
| 5 | 27,296,860.88 | 38.91 | 47 |
| 6 | 27,672,777.70 | 43.15 | 29 |
| 7 | 27,608,847.21 | 57.60 | 48 |
| 8 | 28,646,885.12 | 45.15 | 40 |
| 9 | 26,587,588.48 | 43.03 | 33 |
| 10 | 28,715,483.62 | 76.87 | 54 |
| 11 | 27,667,616.62 | 57.55 | 50 |
| 12 | 26,212,352.22 | 60.16 | 49 |
| Expected | 27,443,807.59 | 49.49 | 40.465 |

**Case 2:** The proposed two-stage stochastic optimization model is discussed. The first-stage covers the first month and the second-stage includes the remaining 11 months via scenarios. The uncertainties of system component availability, power and gas load levels, and water inflows are considered. Table 7 shows that by the midterm stochastic optimization of water and gas usages, one can optimally allocate the water resource to enhance the system reliability. In comparison with Case 1, load shedding is reduced from 460.91MWh to 440.90 MWh. The annual load shedding is reduced from 96.465 hours to 71.07 hours. The reservoir water, previously utilized fully in Case 1, is now partly allocated to the summer for peak-shaving. The social cost in comparison to Case 1 is reduced by 5.08% (i.e., 39,585,164.34 – 37,572,145.9 / 39,585,164.34.)

For this Case, the period for the first-stage and periods corresponding to each scenario in the second-stage are solved sequentially. The CPU time consumed for one scenario is about 15 minutes, and about 60 hours (i.e., No. of scenarios * No. of iterations * 15 minutes) for the entire two-stage stochastic programming on a 3.2 GHz Pentium 4 personal computer. However, parallel computing applied to scenarios would rapidly reduce the CPU time to 5 hours.

Figure 6 shows the optimal monthly water resource allocations for Case 1 and two scenarios of Case 2, representing a wet and a dry weather. In Case 1, the reservoir water is used fully when the future water inflow situation is not considered. Two scenarios, a dry and a wet year, presented in Figure 6 show that when the uncertainty of water inflow is considered, the water used in winter would have to be limited in order to cover the summer peaks. Figure 6 shows that reservoir volumes for wet and dry scenarios are decreased in June since the water is discharged for peak load shaving. That is, the terminal volumes at the end of January are higher than that of Case 1 to cover a possible dry summer season. Figure 6 shows that for the dry scenario, the water usage in November through January is strictly limited with the limited reservoir refilling. This is due to the less available water resource in January through April. The results reveal the necessity of incorporating a two-stage stochastic optimization model for the midterm water and gas management to enhance the system reliability.

Table 7 Results for Case 2

| First-stage solution | | | |
|---|---|---|---|
| Social Cost | | | 3,473,861.69 |
| LS (MWh) | | | 0 |
| # of LS Hours | | | 0 |
| Terminal Volume (*$10^4$ $m^3$) | | | 984.29 |
| Second-stage solution | | | |
| Scenario | Social Cost ($) | LS (MWh) | # of LS Hours |
| 1 | 34,234,442.97 | 426.7466 | 82 |
| 2 | 33,745,037.61 | 447.1278 | 58 |
| 3 | 34,337,516.25 | 436.0846 | 63 |
| 4 | 33,707,806.17 | 426.1430 | 66 |
| 5 | 33,513,715.31 | 422.8795 | 72 |
| 6 | 33,985,407.29 | 446.8944 | 64 |
| 7 | 34,046,856.81 | 452.2434 | 69 |
| 8 | 35,486,860.11 | 432.0145 | 79 |
| 9 | 33,888,175.90 | 423.6509 | 71 |
| 10 | 36,731,962.03 | 444.9300 | 94 |
| 11 | 33,916,433.81 | 452.5987 | 88 |
| 12 | 33,971,571.38 | 452.9742 | 90 |
| Expected | 34,098,284.21 | 440.9000 | 71.07 |

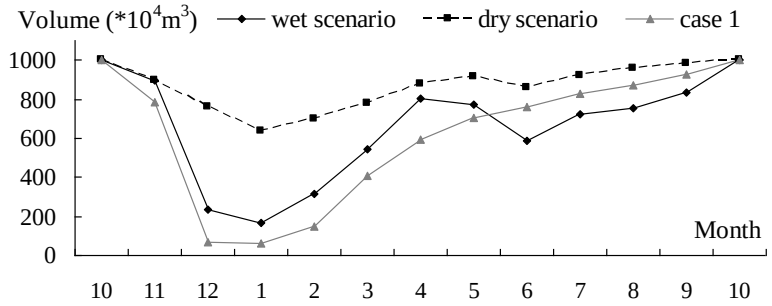


Figure 6 Terminal volumes at the end of each month

In order to demonstrate the convergence process, Figure 7 presents the iterative Lagrangian function. After 20 iterations, we found a solution of $12,081,574.76 which satisfies the stopping criterion (18). By applying the heuristic adjustments (20)-(22), the final social cost is $12,141,356.75. Figure 7 shows the better performance of bundle method in comparison with that of the subgradient method. Figure 8 shows the degree of constraints violation as calculated in (19). The violation in bundle method is reduced much faster than that in the subgradient method, implying that the feasibility is further improved. A better schedule is obtained, which needs less modification in the heuristics process for deriving a final feasible solution.

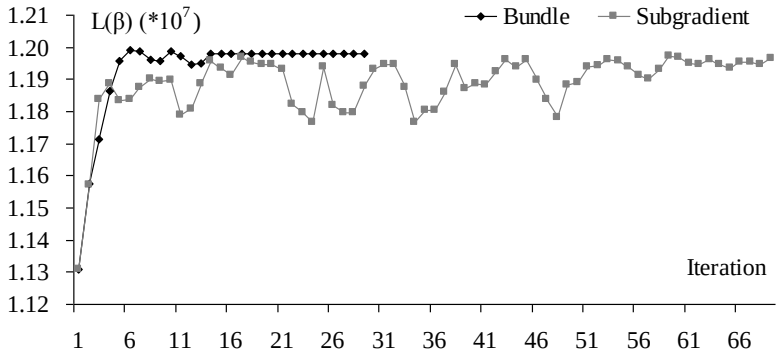


Figure 7 Iterative values of L(β) in Case 1

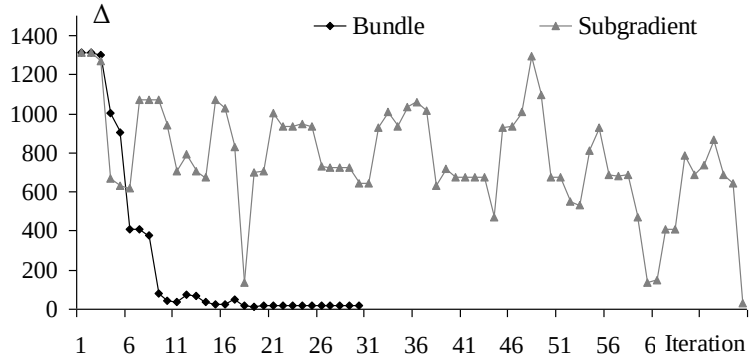


Figure 8 Iterative values of reservoir coupling violation in Case 1

### 3.2. IEEE 118-bus system

A modified IEEE 118-bus system is studied with 54 fossil units, 12 gas-fired units, 7 hydro units, 186 branches, and 91 demand sides. The peak load is 8,600 MW. Hydro units 1-4 belong to one catchment and units 5-7 belong to the second catchment. Detailed generator, transmission line and gas network data are found in [13],[17]. For the 118-bus system, since it is impossible to run a monthly SCUC at one shot, each period refers to a time span of one week. Thus, the first stage contains four periods and the second stage contains remaining 48 periods in each scenario. The probability of each scenario is shown in Table 8. The same two cases in the 6-bus system are considered again. Tables 9-10 present the solution of Case 1 with a social cost of $167,505,857.79 for the winter season. Without considering the water inflow uncertainty, terminal reservoir volumes are limited to their corresponding minimum values. Adopting these terminal volumes as initial conditions for the following seasons, the future social cost is $498,438,128.63 with the load shedding of 10,220.87 MWh. Table 11 shows the optimal two-stage stochastic solution with uncertainties. The load shedding is reduced from 16,036.86 MWh to 14,988.16 (i.e., 1,641.65+13,346.51) MWh. The optimal allocation of water reservoirs for the midterm horizon reduces the social cost by 2.83% (i.e., ((498,438,128.63+167,505,857.79) – (54,915,796.54+592,150,917.73))/ (498,438,128.63+ 167,505,857.79)) which shows that by considering uncertainties in the optimization of water and gas usages in a midterm horizon, one can optimally allocate water resource to enhance the system reliability.

Table 8 Weight of each scenario after scenario reduction

| Scenario | 1 | 2 | 3 | 4 | 5 | 6 |
|---|---|---|---|---|---|---|
| Weight | 0.05 | 0.075 | 0.125 | 0.07 | 0.09 | 0.185 |
| Scenario | 7 | 8 | 9 | 10 | 11 | 12 |
| Weight | 0.065 | 0.07 | 0.06 | 0.05 | 0.05 | 0.11 |

Table 9 Results for the first 3 months of Case 1

| | | | |
|---|---|---|---|
| Social Cost ($) | | | 167,505,857.79 |
| Load Shedding (MWh) | | | 5,815.99 |
| Volume at the end of each month (*10^4 m^3) | Hydro Unit 1 | 11 | 789.521400 |
| | | 12 | 100.576885 |
| | | 1 | 70 |
| | Hydro Unit 5 | 11 | 814.661521 |
| | | 12 | 110.595936 |
| | | 1 | 60 |

Table 10 Results in the following seasons based on results of Case 1

| Scenario | Social Cost ($) | LS (MWh) | Scenario | Social Cost ($) | LS (MWh) |
|---|---|---|---|---|---|
| 1 | 469,781,501.38 | 9,623.66 | 7 | 551,316,220.46 | 8,995.90 |

| | | | | | |
|---|---|---|---|---|---|
| 2 | 546,776,969.21 | 12,474.30 | 8 | 444,484,699.84 | 9,254.63 |
| 3 | 475,292,113.82 | 9,213.25 | 9 | 449,050,768.81 | 10,892.67 |
| 4 | 482,963,151.36 | 10,474.21 | 10 | 472,859,825.43 | 10,474.37 |
| 5 | 480,598,672.06 | 9,264.79 | 11 | 579,381,075.70 | 8,973.25 |
| 6 | 555,092,475.68 | 11,376.21 | 12 | 438,829,845.99 | 10,203.03 |
| Expected Cost | 498,438,128.63 | | Expected LS | | 10,220.87 |

Table 11 Results of Case 2

| First-stage solution (November) | | | | | |
|---|---|---|---|---|---|
| Social Cost | $54,915,796.54 | | | | |
| LS (MWh) | 1,641.65 | | | | |
| Terminal Volume ($*10^4$ $m^3$) | Hydro Unit 1 443.985 | Hydro Unit 5 524.97 | | | |
| Second-stage solution (December – October) | | | | | |
| Scen | Social Cost ($) | LS (MWh) | Scen | Social Cost ($) | LS (MWh) |
| 1 | 569,348,058.64 | 12,709.49 | 7 | 638,250,719.88 | 12,140.42 |
| 2 | 631,623,855.91 | 15,675.10 | 8 | 553,314,423.24 | 12,541.41 |
| 3 | 575,609,207.51 | 12,374.16 | 9 | 548,171,522.09 | 14,049.00 |
| 4 | 573,665,664.86 | 13,381.57 | 10 | 579,617,496.76 | 13,207.50 |
| 5 | 571,984,423.07 | 12,647.78 | 11 | 659,318,818.53 | 12,121.87 |
| 6 | 639,399,045.85 | 14,535.15 | 12 | 539,828,573.25 | 13,165.35 |
| Expected Cost | 592,150,917.73 | | Expected LS | | 13,346.51 |

## 4 CONCLUSIONS

This paper proposed a two-stage stochastic programming model for the optimization of midterm water and gas usage with uncertainties. The probabilistic reliability criteria, which are measured by the expected load shedding quantity and number of hours that load shedding happens, are incorporated into the midterm stochastic UC problem, in which both the power and the gas network security constraints are checked. The optimal mid-term water usage allocation is achieved by introducing reservoir operation rules with a global operation parameter for the whole catchment. The optimal operating point is based on the minimum social cost which includes operating and load shedding costs. The contributions of this work resides in the formulation of midterm hydro reservoir operation, the optimization and coordination for the midterm water and natural gas usages, and the proposed solution methodology for the complex midterm scheduling problem by fully utilizing the capabilities of state-of-the-art mixed-integer programming, Lagrangian relaxation, and Benders decomposition techniques. The optimal point is influenced by the unavailability of power system components, power and gas load levels, and water inflows, which are accurately simulated via multiple scenarios by the Monte Carlo method. The results reveal that water management policies have a major impact on the system reliability. The system reliability is significantly improved by efficiently adjusting the water usage in a midterm horizon. In this regard, the water usage is optimally distributed throughout the midterm horizon. The study shows that the proposed two-stage stochastic optimization model can improve the power system reliability and decrease the social cost by optimally allocating water and gas usages in a midterm horizon.

## REFERENCES


[1] M. Shahidehpour, H. Yamin, and Z. Y. Li: 'Market operations in electric power systems,' John Wiley & Sons, Inc., New York, 2002.

[2] EIA: 'Annual energy review 2007,' http://www.eia.doe.gov/emeu/aer/.

[3] N.V. Arvanitidis and J. Rosing: 'Composite representation of a multireservoir hydroelectric power system,' IEEE Trans. Power App. And Syst., 1970, 89, (2), pp.319-326.

[4] N.V. Arvanitidis and J. Rosing: 'Optimal operation of multireservoir systems using a composite representation,' IEEE Trans. Power App. And Syst., 1970, 89, (2), pp.327-335.

[5] Z. Yu, F.T. Sparrow, and B.H. Bowen: 'A new long-term hydro production scheduling method for maximizing the profit of hydroelectric systems,' IEEE Trans. Power Syst., 1998, 13, (1), pp. 66-71.

[6] J.W. Labadie: 'Optimal operation of multireservoir systems: state-of-the-art review,' J. Water Resour. Plng. And Mgmt. 2004, 130, (2), pp. 93-111.

[7] M. Shahidehpour, Y. Fu, and T. Wiedman: 'Impact of natural gas infrastructure on electric power systems,' IEEE Proceedings, 2005, 93, (5), pp. 1042-1056.

[8] B. Lu and M. Shahidehpour: 'Short-term scheduling of combined cycle units,' IEEE Trans. Power Syst., 2004, 19, (3), pp. 1616-1625.
[9] J. Munoz, N. Jimenez-Redondo, J. Perez-Ruiz, and J. Barquin: 'Natural gas network modeling for power systems reliability studies,' Proceedings of IEEE/PES General Meeting, 2003, 4, pp. 23-26.
[10] S. An, Q. Li, and T.W. Gedra: 'Natural gas and electricity optimal power flow,' Proceedings of IEEE/PES Transmission and Distribution Conference and Exposition, 2003, 1, pp. 7-12.
[11] M. S. Morais and J. W. Marangon Lima: 'Natural gas network pricing and its influence on electricity and gas markets,' 2003 IEEE Bologna PowerTech Conference, June 23-26, Bologna, Italy.
[12] T. Li and M. Shahidehpour: 'Interdependency of natural gas network and power system security,' IEEE Trans. Power Syst., 2008, 23, (4), pp. 1817-1824.
[13] C. Liu, M. Shahidehpour, Z. Li, and M. Fotuhi-Firuzabad: 'Security-constrained unit commitment with natural gas transmission constraints,' IEEE Trans. Power Syst., 2009, 24, (3), pp. 1523-1536.
[14] K. Staschus, A. Bell, and E. Cashman: 'Usable Hydro Capacity and Electric Utility Production Simulation and Reliability Calculations,' IEEE Trans. Power Syst., 1990, 5, (2), pp. 531-538.
[15] L. Wu, M. Shahidehpour, and T. Li: 'Cost of reliability analysis based on stochastic unit commitment,' IEEE Trans. Power Syst., 2008, 23, (3), pp. 1364-1374.
[16] R. Billinton and R. Allan: 'Reliability evaluation of power systems,' 2nd edn, London: Plenum Publishing Corporation, New York 1996.
[17] L. Wu, M. Shahidehpour, and T. Li: 'Stochastic security-constrained unit commitment,' IEEE Trans. Power Syst., 2007, 22, (2), pp. 800-811.
[18] L. Wu, M. Shahidehpour, and Z. Li: 'GENCO's risk-constrained hydrothermal scheduling,' IEEE Trans. Power Syst., 2008, 23, (4), pp. 1847-1858.
[19] G. Paul: 'Monte carlo method in financial engineering,' Springer, New York, 2003.
[20] L.A. Terry, M.V.F. Pereira, T.A.A. Neto, L.F.C.A. Silva, and P.R.H. Sales: 'Coordinating the energy generation of the Brazilian national hydrothermal electrical generating system,' Interfaces, 1986, 16, (1), pp.16-38.
[21] S. Soares and A.A.F.M. Carneiro: 'Reservoir operation rules for hydroelectric power system optimization,' Athens Power Tech. 93 Proceedings. Joint International Power Conference, 1993, 2, pp. 965-969.
[22] E.M.L. Beale and J.A. Tomlin: 'Special facilities in a general mathematical programming system for non-convex problems using ordered sets of variables,' Proceedings of the 5th International Conference on Operations Research, Tavistock, London, 1969.
[23] H. P. Williams: 'Model building in mathematical programming,' 4th edn, John Wiley & Sons, 1999.
[24] J.-B. Hiriart-Urruty and C. Lemaréchal: 'Convex analysis and minimization algorithm,' 2, Springer-Verlag, 1993.
[25] H. Schramm and J. Zowe: 'A version of the bundle idea for minimizing a nonsmooth function: conceptual idea, convergence analysis, numerical results,' SIAM J. Optimization, 1992, 2, (1), pp. 121-152.

## BIOGRAPHIES

Lei Wu (M'07) received his BS and MS degrees in E.E. from Xi'an Jiaotong University, China, in 2001 and 2004, respectively, and Ph.D. degree in EE from Illinois Institute of Technology, USA, in 2008. He was a visiting professor in the ECE Department at Illinois Institute of Technology in 2008-2010. Presently, he is an Assistant Professor in the Electrical and Computer Engineering Department at Clarkson University. His research interests include power systems restructuring and reliability.

Mohammad Shahidehpour (F'01) is Carl Bodine Professor in the Electrical and Computer Engineering Department at Illinois Institute of Technology. Dr. Shahidehpour is the recipient of the Honorary Doctorate for the Polytechnic University of Bucharest in Romania. He is an Honorary Professor in the North China Electric Power University and the Sharif University in Iran.

# Coordinated scheduling of electricity and natural gas infrastructures with a transient model for natural gas flow

Cong Liu,[1,2,a)] Mohammad Shahidehpour,[1,b)] and Jianhui Wang[2,c)]
[1]*Electrical and Computer Engineering Department, Illinois Institute of Technology, Chicago, Illinois 60616, USA*
[2]*Decision and Information Sciences Division, Argonne National Laboratory, Illinois 60439, USA*

(Received 18 January 2011; accepted 27 May 2011; published online 28 June 2011)

This paper focuses on transient characteristics of natural gas flow in the coordinated scheduling of security-constrained electricity and natural gas infrastructures. The paper takes into account the slow transient process in the natural gas transmission systems. Considering their transient characteristics, natural gas transmission systems are modeled as a set of partial differential equations (PDEs) and algebraic equations. An implicit finite difference method is applied to approximate PDEs by difference equations. The coordinated scheduling of electricity and natural gas systems is described as a bi-level programming formulation from the independent system operator's viewpoint. The objective of the upper-level problem is to minimize the operating cost of electric power systems while the natural gas scheduling optimization problem is nested within the lower-level problem. Numerical examples are presented to verify the effectiveness of the proposed solution and to compare the solutions for steady-state and transient models of natural gas transmission systems. © *2011 American Institute of Physics*. [doi:10.1063/1.3600761]

**The electricity and natural gas infrastructures are highly intertwined[1–6] today as more and more gas-fired units have been introduced into power systems and installed, along with an increasing number of high-pressure natural gas pipelines. The security and economics of coupled infrastructures are interdependent.[1–3] Using purely topological metrics to analyze their interdependency can lead to misleading results.[4] Cascaded failures of energy systems may be due to a variety of reasons. One of the most important causes is inaccurate scheduling and decision making so that the system cannot handle variations of loads and severe disturbances. The security-constrained, coordinated scheduling of two coupled energy systems is critical to mitigating the hidden security risks of energy systems, to preventing cascaded failures, and to realizing savings in their operating costs. However, natural gas and electric power flows usually travel through networks via different speeds and illustrate distinct physical characteristics. Hence, we model the electric power and natural gas systems differently but in a coupled manner. The numerical results show that the steady-state natural gas flow model would neglect the built-in storage capabilities of pipelines and the slower travelling speeds of natural gas flows, which may result in impractical or suboptimal schedules in the short-term coordinated scheduling of electricity and natural gas infrastructures.**

## I. INTRODUCTION

The adequacy and availability of natural gas fuel will directly affect the generation unit commitment (UC), dispatch, operating costs, as well as reliability of electric power systems.[5,6] The electric power system is special in the sense that real-time balance between generation and load is required under both normal and fault condition. When contingencies occur, the operators can call gas-fired units that can respond quickly to address the imbalances in comparison with slow-start coal-fired and nuclear units. If the imbalances between generation and load are not eliminated immediately, the frequency of the power system will increase or decrease, which may lead to the loss of stability of the system through electromechanical and electromagnetic transients. More importantly, voltage collapses and loss of synchronization of more generators will increase the likelihood of a blackout. Therefore, adequacy of natural gas fuel is very critical to ensure the power system reliability and to prevent the cascaded failure of power systems.

However, in most cases, gas-fired generating units hold interruptible transportation contracts that would treat the units as preferential curtailment candidates. The natural gas drawn by gas-fired generating units with interruptible transportation contracts would be limited or curtailed once the congestion in natural gas transmission systems has occurred or gas wells have reached their maximum discharge. Moreover, the operation of new gas turbine units or combined-cycle gas turbine units would usually depend on high gas pressure. Hence, electric generators are more susceptible to pressure drops than are other natural gas loads.[7] Even if the priority of natural gas delivery for gas-fired generating units was the same as that of other natural gas loads, the weaker

[a)]E-mail: cliu35@iit.edu & liuc@anl.gov
[b)]E-mail: ms@iit.edu
[c)]E-mail: jianhui.wang@anl.gov

 

ability of gas-fired generating units to manage pressure drops would make the natural gas curtailment more evident.

Many networks, such as energy, biology, and social relationship, are multi-layer interdependent networks. The loss of a part of links and nodes in one network may lead to a forced outage in another network.[2] The failure of components in the second network in turn may lead to a malfunction of additional nodes in the first network. Eventually, the interdependent networks may lose their functions completely. Similarly, any disruption in natural gas supply could have a significant impact on several gas-fired power plants and results in more critical outages than traditional contingencies in power systems. Outages of several gas-fired generators can result in the loss of operating reserves, real-time imbalances between load and generation, and an adverse effect on the system frequency. If necessary, operators would have to adopt load shedding to prevent any collapse in electric power system operations. References 5 and 10 offer examples of preliminary results on the impact of pipeline contingencies on power systems. Moreover, compressors, control devices, and other facilities in natural gas transmission systems are dependent on electricity. Load shedding or interruption of electricity may in turn lead to the failure of a fraction of natural gas system.

In order to satisfy the requirements of gas-fired generating units and other natural gas loads within a reasonable pressure range,[7,8] the natural gas transmission system would have to schedule gas wells and compressors in advance and manage line-pack resources. "Line pack" is related to the amount of additional natural gas stored in a pipeline as a result of maintaining above-normal pressure in the pipeline.[7,9] As such, line pack is analogous to reserves in power systems and is essential in enabling pipelines to handle large swings in natural gas loads, such as the fast ramp up of gas-fired generating units during peak hours and power system contingencies.

In the last ten years, several articles proposed state-of-the-art strategies to model the two interdependent infrastructures.[10–14] However, many of the previous studies focused on the steady-state formulation of electric power and natural gas transmission systems. Such formulations neglected a significant distinction to be made in the traveling speeds of natural gas and electric power flows, as well as the line-pack capacities of interstate pipelines.

This paper concentrates on the development of a methodology for the coordinated scheduling of interdependent power and natural gas transmission systems that are based on a transient-state model of natural gas flows. The paper focuses on slow transient processes—that is, in terms of hours or minutes—caused by natural gas load swings. In the proposed formulation, interstate natural gas pipelines are described by a set of partial differential equations (PDEs) instead of by steady-state Weymouth equations. The implicit finite difference method is adopted to approximate PDEs with algebraic difference equations. As a result, natural gas flows are coupled in space and time. The paper presents a bi-level model shown in Fig. 1 for coordination between natural gas operators and the independent system operator (ISO). Constraints on natural gas supply contracts are directly included in the UC problem. When an optimal UC schedule is obtained without violating power transmission constraints, the hourly natural gas demands of gas-fired generating units will be submitted to natural gas system operators, in the lower-level problem, for checking the feasibility of natural gas transmission constraints. If any violations are detected in natural gas transmission constraints, corresponding energy constraints (Benders-like cuts) are formed and fed back to the ISO for the next iteration of the coordination problem. The cut, which represents shortages in the natural gas supply or congestion in the gas transmission system, would limit the fuel consumed by gas-fired generating units. If the natural gas transmission check is feasible, the natural gas consumed by gas-fired generating units, as well as the security-constrained unit commitment (SCUC) solution, are final. The natural gas transmission operator will schedule compressors by minimizing rates of energy consumption.

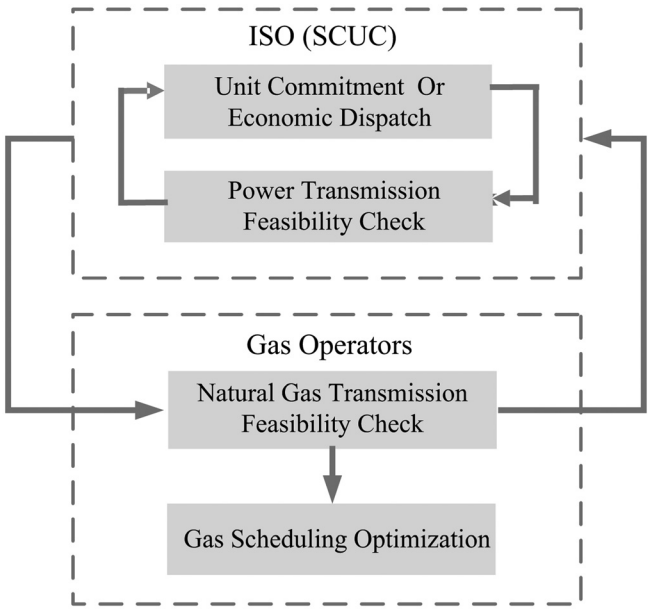


FIG. 1. Coordination scheme for electric power and natural gas infrastructures.

The rest of the paper is organized as follows. Section II proposes the transient-state model of natural gas transmission systems. Section III presents formulations of the coordinated scheduling model. Algorithms for solving the proposed model are discussed in Sec. IV. Numerical studies are given in Sec. V. The conclusion is drawn in Sec. VI.

## II. TRANSIENT FLOWS IN NATURAL GAS SYSTEMS

The dynamics of energy infrastructures could vary from milliseconds to hours, which indicates that energy transportation could occur in different frameworks. Electric energy travels almost instantaneously and cannot be stored economically in large quantities in current power systems. At the operation planning stage, once power injections and withdrawals at various buses are given, transmission line flows will satisfy steady-state algebraic equations that are independent on an hourly basis. Therefore, SCUC and security-constrained economic dispatch (SCED) commonly ignore

transients in the electricity infrastructure and focus on steady-state analyses.[15–17]

The natural gas pipeline flow would represent a much slower process. Such pipelines take longer to respond to disturbances. In particular, high-pressure interstate pipelines have much slower dynamics, and large sums of natural gas stored in the pipelines cannot be neglected. In this case, the steady-state assumption and the corresponding algebraic Weymouth equation for pipelines might be inappropriate for the numerical calculation of natural gas flows. If treated rigorously, natural gas flow simulations would require distributed parameters and the transient state model of pipelines.[18–23]

### A. Modeling of natural gas pipelines

Natural gas flows, driven by pressure through pipelines, are dependent on factors such as the length and the diameter of pipelines, operating temperature, composition of natural gas, altitude change over the transmission path, roughness of pipelines, and boundary conditions. The transient state of natural gas flow through a pipeline is described as a one-dimensional dynamics along the axis of the natural gas pipeline, which requires the use of distributed parameters and time-varying state variables. A set of PDEs is obtained by applying the laws of conservation of mass and energy, the laws of momentum. The PDEs for time and position, which are dependent natural gas density, mass flow, flow velocity, and pressure, are given in Eqs. (1)–(4)

$$\frac{\partial(\rho\cdot v)}{\partial z}=-\frac{\partial\rho}{\partial t}, \tag{1}$$

$$\frac{\partial(\pi+\rho\cdot v^2)}{\partial z}+\frac{2f_c\cdot\rho\cdot v^2}{d}+\frac{\partial(\rho\cdot v)}{\partial t}+\rho\cdot g_e\cdot\sin\alpha=0, \tag{2}$$

$$\frac{\partial[\rho\cdot(e+\frac{1}{2}v^2)]}{\partial t}+\frac{\partial[\rho\cdot v\cdot(h+\frac{1}{2}v^2)]}{\partial z}-\rho\cdot\Omega+\rho\cdot g_e\cdot v\cdot\sin\alpha=0, \tag{3}$$

$$\pi=\rho\cdot Z\cdot R_g\cdot T, \tag{4}$$

where $t$ represents time in the scheduling period; $\rho$ represents natural gas density; $\pi$ here denotes natural gas pressure; $v$ denotes natural gas axial velocity; $h$ denotes specific enthalpy; $z$ represents the length scale of the pipeline; $e$ denotes a specific internal energy of the gas pipeline; $\Omega$ represents the rate of heat transfer per unit time and unit mass of the gas; $Z$ represents a compressibility factor; and $T$ represents the temperature of gas in pipeline. $R_g$ is a gas constant; $g_e$ is gravitational acceleration; $\alpha$ is the elevation angle of the gas pipeline; $f_c$ is the friction factor of gas pipeline; $L$ is the total length of pipeline; and $d$ is the diameter of the pipeline.

The law of conservation states that mass can neither be created nor destroyed. Equation (1) indicates that the net mass rate of flow out of a differential volume of fluid is equal to the rate of decrease of mass within the differential volume. Equation (2) resulted from Newton's second law (law of momentum), which indicates that the sum of forces acting on the gas particles is equal to the rate of increase of momentum of natural gas particles at an instant in time. In Eq. (2), the terms $2f_c\cdot\rho\cdot v^2/d$, $\rho\cdot g_e\cdot\sin\alpha$, $\partial(\rho\cdot v)/\partial t$, and $\partial(\rho\cdot v^2)/\partial z$ define the hydraulic friction force, force of gravity, natural gas inertia, and dynamic pressure of flowing gas, respectively. In high-pressure gas pipelines, dynamics would take longer (hours). Accordingly, the convective acceleration terms, $\partial(\rho\cdot v)/\partial t$, $\partial(\rho\cdot v^2)/\partial z$, and $\rho\cdot g\cdot\sin\alpha$, contribute less than 1% to the solution of Eq. (2) under normal operating conditions.[20,22] Hence, such terms are neglected here for simplification.[18,19]

Equation (3) is derived from the law of conservation of energy. In order to solve Eqs. (1)–(4), it is required to know the value of $\Omega$. In practice, $\Omega\neq 0$, as there is no thermal equilibrium between a natural gas pipeline and its surroundings. Hence, we would need additional equations to model the heat conduction process. However, the assumption of isothermal flow is valid in the case of slow transients caused by fluctuations in demand and natural gas injections.[18–23] Accordingly, the pipeline would have sufficient time to reach its thermal equilibrium. The surrounding environment would dissipate natural gas temperature changes caused by the compression and expansion of natural gas. The natural gas temperature $T$ is assumed to be the same as that of its surroundings. So, Eq. (3) would become redundant if we are not concerned about the value of $\Omega$.

$$\pi=\rho\cdot Z_{avg}\cdot R_g\cdot T_{avg}. \tag{5}$$

In Eq. (4), the natural gas pressure is a function of the natural gas density, compressibility factor, and natural gas temperature. We use Eq. (5) instead of Eq. (4) under an isothermal process[20,22] in which the average temperature of gas pipeline $T_{avg}$ at time $t$ and the average compressor factor of gas pipeline $Z_{avg}$ are assumed to be constant.

After ignoring Eq. (3) and making reasonable approximations described above, we substitute the natural gas mass flow $Gf=\rho\cdot v\cdot S$, transient parameters of natural gas pipelines $K_1=\frac{Z_{avg}R_gT_{avg,t}}{S}$, $K_2=\frac{4f_cZ_{avg}R_gT_{avg,t}}{dS^2}$, and Eq. (5) into Eqs. (1) and (2), which result in Eqs. (6) and (7).[18,19] $S$ represents the area of the cross section of the gas pipeline. The following two equations are used hereafter:

$$\frac{\partial(\pi_{zt})}{\partial t}+K_1\frac{\partial(Gf_{zt})}{\partial z}=0, \tag{6}$$

$$\frac{\partial(\pi_{zt}^2)}{\partial z}+K_2\cdot Gf_{zt}^2=0. \tag{7}$$

If we use $Gf$ to represent gas mass flow, then, the steady-state Weymouth equation, $Gf_t^2=\mathrm{C}\sqrt{|\pi_{z=0,t}^2-\pi_{z=L,t}^2|}$, is obtained by integrating Eq. (7) over the length of pipeline, where $C$ is a constant that is equal to $\sqrt{1/K_2L}$.

### B. Modeling of compressors

A pressure loss occurs when the natural gas flow encounters pipeline resistance. Compressors are installed at intervals along the natural gas pipeline to compensate for the

pressure loss. The power of centrifugal compressor *cm* (the index of the compressor) is governed by the following:

$$CH_{cmt} = Gf_{cmt} \cdot (k2_{cm} \cdot PR_{cmt}^{k3_{cm}} - k1_{cm}), \tag{8}$$

where $CH_{cmt}$ represents power of compressor at time *t*. $k1_{cm}$, $k2_{cm}$, and $k3_{cm}$ are empirical parameters of compressors.[11,18,19,24,25] $Gf_{cmt}$ represents the natural gas mass flow through the compressor *cm*, where

$$CH_{\min,cm} \le CH_{cmt} \le CH_{\max,cm}. \tag{9}$$

The pressure ratio *PR* in Eq. (8) is within a feasible range given in Eq. (10), which is based on compressor characteristics. $\pi_{out}$ and $\pi_{in}$ represent pressures at the outlet and inlet of the compressor,

$$PR_{\min,cm} \le PR_{cmt} = \frac{\pi_{out,cmt}}{\pi_{in,cmt}} =\le PR_{\max,cm}. \tag{10}$$

Compressors can be driven by either natural gas or electricity. Natural gas compressors would consume additional natural gas that is withdrawn from either the inlet or outlet of the compressor to drive turbines. The amount of consumed natural gas is proportional to the power of the compressor $F_{cf,cm}(CH_{cmt})$.

### C. Nodal natural gas flow balance

Natural gas nodes are defined as junctions of pipelines and compressors where gas wells inject natural gas into the gas network and natural gas loads withdraw natural gas from the network. The natural gas pressure associated with each node is within a range stated by Eq. (11). The output of gas well *GP* and the natural gas load shedding *GSL* are restricted by Eqs. (12)–(13), where *na* represents an index of a node in the gas network, *gi* represents an index of the gas well, and *gl* represents an index of the gas load. *GL* denotes gas demand.

$$\pi_{\min,na} \le \pi_{nat} \le \pi_{\max,na}, \tag{11}$$

$$GP_{gi,\min} \le GP_{git} \le GP_{gi,\max}, \tag{12}$$

$$0 \le GSL_{glt} \le GSL_{\max,gl} \le GL_{gl}. \tag{13}$$

The nodal gas flow balance is modeled by Eq. (14), which indicates that the natural gas flow injected into a node *na* is equal to the natural gas withdrawn from the node *na*. $g_{na}()$ represents a gas flow mismatch of the node *na*.

$$g_{na}(\pi, \boldsymbol{CH}, \boldsymbol{GP}, \boldsymbol{GSL}, \boldsymbol{GL}) = -\sum_{nb\in na} Gf_{na\to nb,na} + \sum_{gi\in na} GP_{gi} - \sum_{gl\in na} GL_{gl} - GSL_{gl} - \sum_{cm\in na} F_{cf,cm}(CH_{cm}) = 0, \tag{14}$$

where $nb \in na$ means there is a pipeline or compressor between *na* and *nb*. $gi \in na$ and $gl \in na$ mean there is a gas well or gas load connected to *na*. $Gf_{na\to nb,na}$ is the gas mass flow injected to *na* through the branch between *na* and *nb*.

The boundary conditions for PDE (6) and (7) are stated as follows: at t = 0, initial values are given by various measures in the natural gas transmission system. At the beginning and the terminal ends of a pipeline, gas flows satisfy the nodal gas flow balance. If the pipeline flow from *na* to *nb* is positive, boundary conditions for the pipeline PDE are stated as in Eqs. (15) and (16),

$$\pi_{t,z=0} = \pi_{nat}, \pi_{t,z=\mathrm{L}} = \pi_{nbt}, \tag{15}$$

$$Gf_{t,z=0} = -Gf_{na\to nb,na}, Gf_{t,z=\mathrm{L}} = Gf_{na\to nb,nb}. \tag{16}$$

## III. FORMULATION OF COORDINATED SCHEDULING PROBLEM

### A. Scheduling model for electric power system

Traditionally, electric power and natural gas transmission systems are scheduled independently without any coordination. In electric power systems, the ISO executes the hourly SCUC to minimize the system operating costs in Eq. (17), while satisfying the prevailing UC constraints and power transmission network constraints in Eqs. (18)–(23). *I* is the binary indicator for generator ON/OFF status; *SU* and *SD* represent the startup and shutdown cost of generators; $\sigma$ represents fuel price; $F_{ef,i}()$ represents the fuel consumption of generators; and *P* is generation dispatch.

$$Min \sum_t \sum_i [\sigma_i \cdot F_{ef,i}(P_{it}) \cdot I_{it} + SU_{it} + SD_{it}] \tag{17}$$

*s.t.*

Power and load balance constraint (18)

System operating reserve requirements (19)

Individual generator limits (max / min capacity, ramp rate limits, and min on/off time[16,17,26]) (20)

Emission limits ($CO_2$, $SO_2$, and $NO_x$) (21)

Network constraints (alternating current [AC] or lossless linear power flow equations[10,14]) (22)

Fuel constraints (limits for usage of oil, coal, natural gas, and so on) (23)

### B. Scheduling model for natural gas system

The natural gas supply and transportation sectors were unbundled in the 1980s; a variety of contracts (as shown in Table I) appeared as the market evolved. Transportation services with different priority orders are described:[27]

- No-Notice: The customer can use natural gas, whether nominated or not, on a daily basis up to its firm entitlement without incurring any balancing or scheduling penalties.
- Firm: The customer should experience no interruptions (except for force majeure) but is responsible for paying penalties for using more natural gas then its nominated amount. This service can "bump" interruptible customers.

TABLE I. Natural gas transportation and supply contracts.

| Gas transportation contract | | | Supply contract | |
|---|---|---|---|---|
| No-notice | Firm | Interruptible | Take or pay | Flexible |

- Interruptible: The customer can be interrupted with little notice and can be bumped by the need to deliver higher-priority services. In most cases, gas-fired power plants sign interruptible contracts.

The natural gas transmission scheduling problem is to minimize the operating cost of compressors (24) while satisfying the constraints of transient transmission of natural gas and respecting natural gas transportation contracts and pressure requirements at receiving points. $\rho_{gas,cm}$ represents the gas price for compressors,

$$Min \sum_{t} \sum_{cm} \rho_{gas,cm} \cdot F_{cf,cm}(CH_{cmt}). \tag{24}$$

*s.t.* Transient-state natural gas transmission constraints (6)–(16)

The natural gas system is coupled with the electric power system by gas-fired generating units. The natural gas consumption rates of gas-fired generating units, $F_{ef,it}$, are equal to gas loads $GL_{gl,t}$ in the natural gas scheduling problem.

$$GL_{gl,t} = F_{ef,it}. \tag{25}$$

### C. Bi-level model for the coordinated scheduling problem

We propose a bi-level programming formulation in Eqs. (26)–(30) for the system coordination. The upper-level problem is to optimize the operating cost $EC(x)$ of the electric power system, and $\boldsymbol{x}$ and $\boldsymbol{y}$ in Eqs. (26)–(30) represent state and decision variables in the power system and natural gas optimizations, respectively. $\boldsymbol{x}_c$ is a subvector of $\boldsymbol{x}$ for representing natural gas consumption levels by power plants. Equations (27), (28), and (30) denote constraints on unit commitment, the power transmission network, and transient natural gas transmission, respectively. The lower-level problem in Eqs. (29)–(30) represents the natural gas scheduling optimization problem, which is embedded as a constraint into the upper-level optimization problem. $GC(\boldsymbol{y})$ denotes the operating cost of compressors. Technically, we can model the problem as a bi-level programming problem in reverse of which the upper level minimizes the natural gas operating cost. Because we model the scheduling problem from the ISO's viewpoint in this paper, we keep the electric power scheduling problem as the upper problem.

$$\underset{x}{Min}\, EC(\boldsymbol{x}) \tag{26}$$

$$s.t. \quad \boldsymbol{EU}(\boldsymbol{x}) \le 0 \tag{27}$$

$$\boldsymbol{EN}(\boldsymbol{x}) \le 0 \tag{28}$$

$$\underset{y}{Min}\; GC(\boldsymbol{y}) \tag{29}$$

$$s.t. \quad \boldsymbol{GN}(\boldsymbol{x}_c, \boldsymbol{y}) \le \boldsymbol{0}. \tag{30}$$

By ignoring Eq. (29), the bi-level programming problem will be transferred into Eq. (31). Here, *LB* provides a lower bound for the primal problem in Eqs. (26)–(30).

$$LB = EC(\boldsymbol{x}^*, \boldsymbol{y}^{\#}) = \underset{x}{Min}\{EC(\boldsymbol{x}) | (27), (28), (30)\}. \tag{31}$$

Electricity and natural gas markets are linked as vertically oriented markets, of which gas-fired power plants are the demand side of the gas market and the supply side of electric power market at the same time. In practice, natural gas operators would respect the contract or natural gas load requested from electric power plants unless delivering and supplying such an amount of natural gas by gas wells and pipelines is physically infeasible. Thus, the natural gas transmission operator seldom sheds natural gas loads (power plants) to reduce compressor costs. Such loads can only be mitigated by the other natural gas loads with higher transportation priorities when there is congestion.

Based on a fixed $\boldsymbol{x}_c^*$ provided by Eq. (31), we solve Eq. (32) to obtain an optimal solution $\boldsymbol{y}^*$. $EC(\boldsymbol{x}^*, \boldsymbol{y}^*)$ is an upper bound for Eqs. (26)–(30).

$$\boldsymbol{y}^* = \underset{y}{\text{Arg min}}\{GC(\boldsymbol{y}) | (30)\}. \tag{32}$$

Apparently, $UB = EC(\boldsymbol{x}^*, \boldsymbol{y}^*) = EC(\boldsymbol{x}^*, \boldsymbol{y}^{\#}) = LB$, so $(\boldsymbol{x}^*, \boldsymbol{y}^*)$ is the optimal solution.

The generalized L-shaped decomposition (Benders) is applied to decompose the optimization problem in Eq. (31) into the UC upper-level problem in Eq. (33), the power transmission network constraints check problem in Eq. (28), and the natural gas transmission network constraints check in the lower-level problem in Eq. (30).

$$\underset{x}{Min}\{EC(\boldsymbol{x}) | (27)\}. \tag{33}$$

### D. Coordinated scheduling scheme

Fig. 2 depicts the flowchart of the electricity and natural gas scheduling coordination. The integrated process is divided into the ISO and the natural gas operator problems, respectively. The ISO or the utility operator would calculate the hourly UC and dispatch that would satisfy the hourly electricity load forecast. The load shedding will be employed if the available generation would not be able to supply the electricity demand. Otherwise, based on the UC and dispatch solutions, the ISO conducts the security analysis to satisfy network constraints in contingencies. The power transmission check iterates with UC via the power transfer distribution factors (PTDFs) or Benders cuts to mitigate transmission violations.[18,20] If there is no violation in the power transmission network, the ISO determines the natural gas consumption of gas-fired generating units and submits the hourly gas demand to the natural gas operators.

The natural gas transmission operators would collect the information on the natural gas demands, gas contracts, natural gas transmission parameters, initial pressures, and

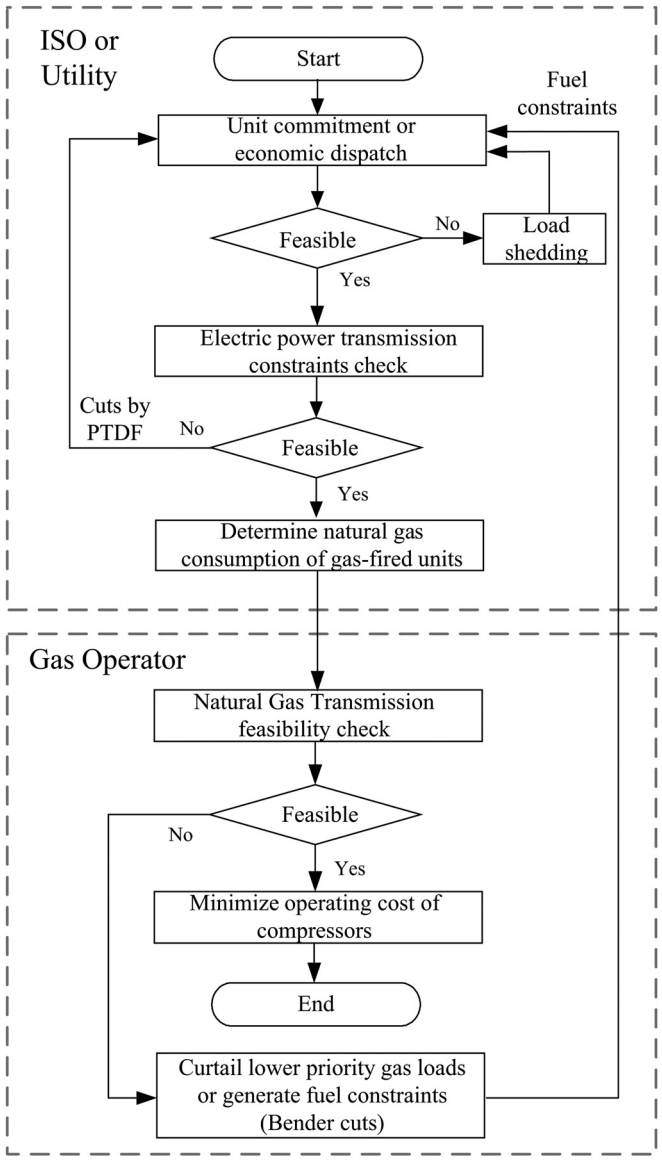


FIG. 2. Flowchart for the coordination of ISO and natural gas operator.

planned outages of natural gas pipelines. The natural gas feasibility check will examine the feasibility of the natural gas transmission system for serving the requested natural gas loads. If the natural gas transmission check is rendered infeasible, natural gas fuel constraints will be formed by cutting planes for gas-fired power plants and fed back to the ISO for the rescheduling of daily UC. The iterative process between SCUC and the natural gas transmission feasibility check will continue until the natural gas transmission flow is feasible. Accordingly, the SCUC solution will be fixed, and the natural gas transmission operator will continue to schedule compressors, storage facilities, and line pack resources by minimizing the operating cost of compressors.

## IV. SOLUTION OF THE COORDINATED SCHEDULING PROBLEM

### A. Solution of SCUC

The UC problem is a mixed-integer, nonlinear program that will be linearized and solved on the basis of the branch-and-cut method.[15,28,29] The power transmission feasibility check in the lower-level problem can be solved by linear programming (LP) and iterating with UC via PTDF or the Benders decomposition method.[15–17]

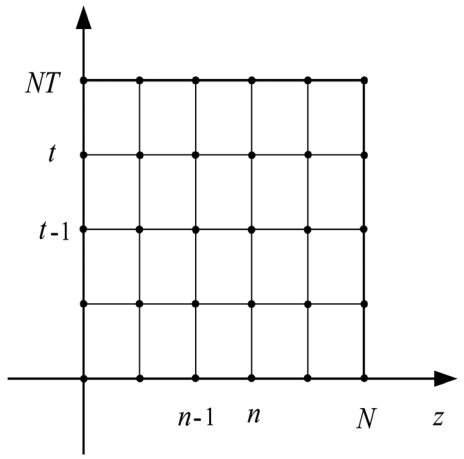


FIG. 3. Grid points in the finite difference scheme.

### B. Implicit finite difference approximation

The analytical method can provide the continuous solution for PDE by the compact mathematic expression if the region and boundary values of dependent variables are defined. Compared to the analytical method, numerical methods are available to evaluate the dependent variables at discrete points in a span of time and space as shown in Fig. 3. We adopt the Euler finite difference numerical method to approximate PDE in Eqs. (6)–(7) by replacing derivative expressions in space and time with equivalent difference quotients. Generally, implicit methods offer better numerical stability than do explicit methods, because explicit methods calculate dependent variables at a later time by using those at the current time, whereas implicit methods find a solution by solving an equation involving dependent variables in both the current time and the future. Equations (8)–(9) are obtained by applying the backward Euler method and the midpoint Euler method, which are applied according to implicit methods. A higher-order finite difference method, such as the Runge-Kutta method, may demonstrate more accurate results. However, using the Runge-Kutta method instead of the implicit Ruler method will not affect the effectiveness of our proposed model.

In Eqs. (34)–(35), the $n$ and $t$ indices correspond to different grid points. Obviously, increasing the number of points in Fig. 3 can enhance the numerical accuracy but will also entail longer computing times. We modify the number of grid points by adjusting the step size $\Delta z$ and $\Delta t$. The state variables at $t=0$ are given as initial values. In addition, Eq. (34) is replaced by Eqs. (36) and (37).

$$\frac{\pi_{t,n}-\pi_{t-1,n}}{\Delta t}=\frac{K_1}{2\Delta z}\left(Gf_{t,n-1}-Gf_{t,n+1}\right)$$
$$t\in\{1,2,...NT\},n\in\{1,2,...,N-1\}, \quad (34)$$

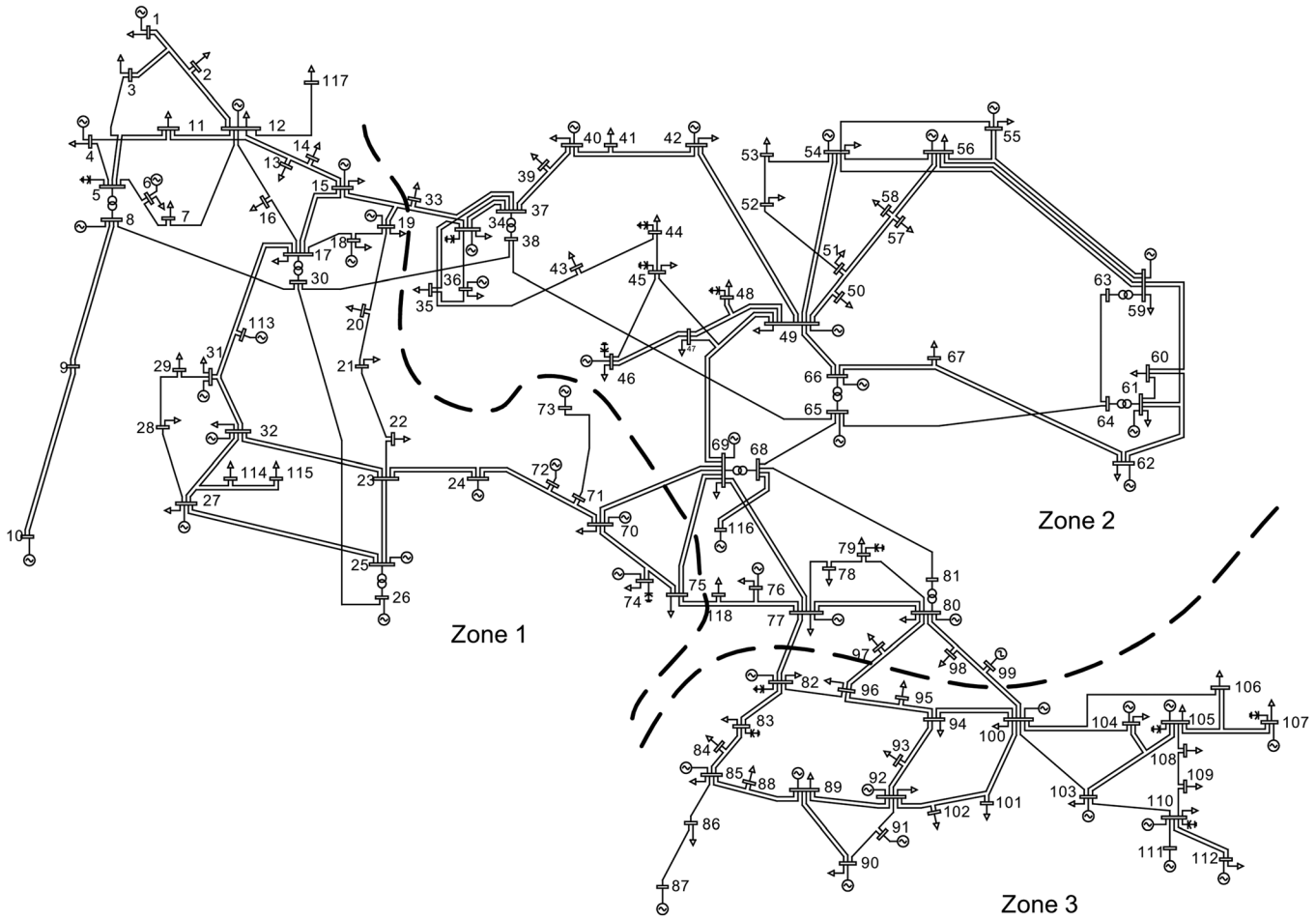


FIG. 4. 118-bus power system.

$$\frac{\pi_{t,n-1}^2 - \pi_{t,n+1}^2}{2\Delta z} = K_2 \cdot Gf_{t,n}^2 \quad t \in \{0, 1, ...NT\}, n \in \{1, 2, ..., N-1\}, \quad (35)$$

$$\frac{\pi_{t,n} - \pi_{t-1,n}}{\Delta t} = \frac{K_1}{\Delta z}(Gf_{t,n} - Gf_{t,n+1}) \quad t \in \{1, 2, ...NT\}, n = 0, \quad (36)$$

$$\frac{\pi_{t,n} - \pi_{t-1,n}}{\Delta t} = \frac{K_1}{\Delta z}(Gf_{t,n-1} - Gf_{t,n}) \quad t \in \{1, 2, ...NT\}, n = N. \quad (37)$$

As a result, PDEs are transformed into a set of algebraic equations in Eqs. (34)–(37), which are denoted in Eq. (38) for the sake of simplicity as

$$\boldsymbol{h}(\boldsymbol{Gf}, \pi) = 0. \quad (38)$$

### C. Natural gas transmission feasibility check

The natural gas transmission feasibility check in the lower-level problem will minimize the sum of slack variables $SL$ on each node, while satisfying the transient formulation of natural gas pipelines, pressure constraints, and compressor constraints, as well as complying with natural gas transportation contracts for the requested natural gas load $G\hat{L}$. The natural gas load shedding is implemented for the gas loads with lower priority. Here, $G\mathrm{SL}_{\max} = 0$ for loads with firm transportation contracts. We use the successive LP (Refs. 30 and 31) to solve the following optimization problem iteratively:

$$Min\ \omega(\boldsymbol{G\hat{L}}) = \sum_{na=1}^{NN} (SL), \quad (39)$$

TABLE II. Parameters of interstate pipeline.

| Maximum pressure | Minimum pressure | Parameter $K_1$ | Parameter $K_2$ | Parameter C | Length $L$ |
|---|---|---|---|---|---|
| 500 pounds per square inch gauge (psig) | 400 psig | 0.05 | $2 \times 10^{-6}$ | 50 | 200 miles |

TABLE III. Parameters of compressor and natural gas well.

| Gas compressor | | | | | | | | Gas well | |
|---|---|---|---|---|---|---|---|---|---|
| $F_{cf,cm}(CH_{cmt}) = cf + bf \cdot CH_{cmt} + af \cdot CH_{cmt}^2$ | | | | | | | | | |
| k1 | k2 | k3 | Min. power (horsepower [hp]) | Max. power (hp) | af (MBtu/hp$^2$h) | bf (MBtu/hph) | cf (MBtu/h) | Max. output (MBtu/h) | Min. output (MBtu/h) |
| 0.1 | 0.17 | 0.15 | 500 | 2000 | 0.0001 | 0.15 | 25 | 5000 | 20,000 |

*s.t.*

$$\nabla \boldsymbol{h}(\boldsymbol{Gf}, \pi) \cdot \begin{bmatrix} \Delta \boldsymbol{Gf} \\ \Delta \pi \end{bmatrix} = -\boldsymbol{h}(\boldsymbol{Gf}, \pi), \tag{40}$$

$$\begin{bmatrix} \dfrac{\partial \boldsymbol{g}}{\partial \pi} & \dfrac{\partial \boldsymbol{g}}{\partial \boldsymbol{CH}} & \boldsymbol{GA} & \boldsymbol{GB} \end{bmatrix} \cdot \begin{bmatrix} \Delta \pi \\ \Delta \boldsymbol{CH} \\ \Delta \boldsymbol{GP} \\ \Delta \boldsymbol{GSL} \end{bmatrix} + \boldsymbol{SL}$$

$$\boldsymbol{\mu} = -\boldsymbol{g}(\pi, \boldsymbol{CH}, \boldsymbol{GP}, \hat{\boldsymbol{GL}} - \boldsymbol{GSL}) \tag{41}$$

$$0 \le \boldsymbol{GSL} + \Delta \boldsymbol{GSL} \le \boldsymbol{GSL}_{\max} \le \hat{\boldsymbol{GL}}, \tag{42}$$

$$\pi_{\min} \le \pi + \Delta \pi \le \pi_{\max}, \tag{43}$$

$$\boldsymbol{GP}_{\min} \le \Delta \boldsymbol{GP} + \boldsymbol{GP} \le \boldsymbol{GP}_{\max}, \tag{44}$$

$$\boldsymbol{CH}_{min} \le \boldsymbol{CH} + \Delta \boldsymbol{CH} \le \boldsymbol{CH}_{max}, \tag{45}$$

$$\boldsymbol{PR}_{min}(\pi_{in} + \Delta \pi_{in}) \le \pi_{out} + \Delta \pi_{out} \le \boldsymbol{PR}_{max}(\pi_{in} + \Delta \pi_{in}), \tag{46}$$

$$0 \le \boldsymbol{SL}. \tag{47}$$

Then, we update variables by applying Eq. (48). The iterative process will continue until $\Delta \boldsymbol{\pi}^{(k)}$, $\Delta \boldsymbol{CH}^{(k)}$, $\Delta \boldsymbol{GP}^{(k)}$, $\Delta \boldsymbol{GL}^{(k)}$, and $\Delta \boldsymbol{GSL}^{(k)}$ are less than a specified $\varepsilon$, where $k$ represents the iteration number; $\boldsymbol{GA}$ is the node-gas supplier incidence matrix; $\boldsymbol{GB}$ represents node-gas load incidence matrix; $\boldsymbol{GK}$ is the node-node connection incidence matrix; and $\boldsymbol{GD}$ is the gas-withdrawing node-compressor incidence matrix.

Once the iterative process is completed, a non-negative objective function in Eq. (39) that is less than the specified tolerance indicates that the natural gas transmission network can support natural gas loads of electricity sectors. Otherwise, a natural gas fuel constraint (Benders cut) given in Eq. (49) will be generated and added to the SCUC formulation

$$\begin{bmatrix} \boldsymbol{\pi}^{(k+1)} \\ \boldsymbol{CH}^{(k+1)} \\ \boldsymbol{GP}^{(k+1)} \\ \boldsymbol{GSL}^{(k+1)} \end{bmatrix} = \begin{bmatrix} \boldsymbol{\pi}^{(k)} \\ \boldsymbol{CH}^{(k)} \\ \boldsymbol{GP}^{(k)} \\ \boldsymbol{GSL}^{(k)} \end{bmatrix} + \begin{bmatrix} \Delta \boldsymbol{\pi}^{(k)} \\ \Delta \boldsymbol{CH}^{(k)} \\ \Delta \boldsymbol{GP}^{(k)} \\ \Delta \boldsymbol{GSL}^{(k)} \end{bmatrix}, \tag{48}$$

$$\omega(\boldsymbol{GL}) = \omega(\hat{\boldsymbol{GL}}) + \boldsymbol{\mu}^T \cdot \boldsymbol{GB} \cdot (\boldsymbol{GL} - \hat{\boldsymbol{GL}}) \le 0, \tag{49}$$

where $\boldsymbol{\mu}$ is the dual variable vector obtained by solving LP in the last iteration.

The transient model of the natural gas transmission feasibility check in the lower-level problem is coupled on an hourly basis. However, that of the steady-state model is decoupled on an hourly basis, such that it can be solved by parallel processing. In addition, Eq. (40) represents many constraints and variables if the number of grid points in Fig. 3 is large. Therefore, the computing time of the transient model is usually higher than that of the steady-state model.

### D. Solution of natural gas scheduling problem

The natural gas scheduling problem is also solved by the successive LP. The natural gas transmission feasibility check in the lower-level problem can provide an initial value for the solution of the natural gas scheduling problem. In general, $F_{cf,cm}()$ is convex. The objective function in Eq. (39) is replaced by Eq. (50). However, pipeline and compressor equations may make the lower-level problem non-convex. Therefore, if the initial operating point of the natural gas problem is not close to the global optimal points, the solution

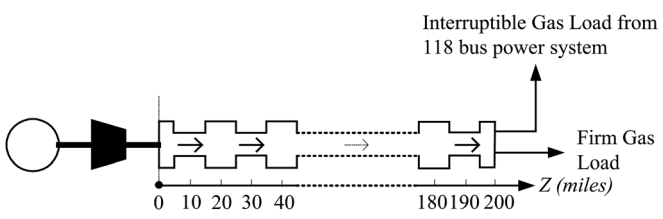


FIG. 5. Interstate pipeline.

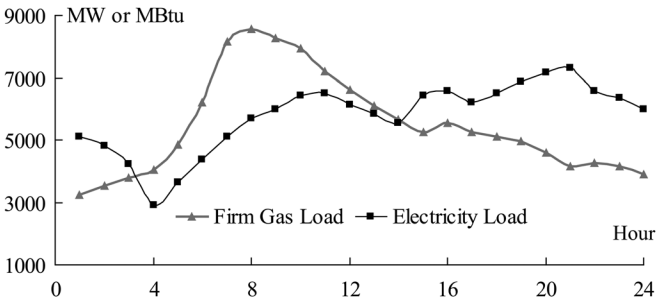


FIG. 6. Hourly natural gas and electricity load.

TABLE IV. Unit commitment in case 1.

| Unit | Hours (0–24) | | | | | | | | | | | | | | | | | | | | | | | | |
|---|---|---|---|---|---|---|---|---|---|---|---|---|---|---|---|---|---|---|---|---|---|---|---|---|---|
| 1013 | 1 | 0 | 0 | 0 | 0 | 0 | 0 | 0 | 0 | 0 | 0 | 0 | 0 | 0 | 0 | 0 | 0 | 0 | 0 | 0 | 1 | 0 | 0 | 0 |
| 1014 | 1 | 0 | 0 | 0 | 0 | 0 | 0 | 1 | 1 | 1 | 1 | 1 | 1 | 1 | 1 | 1 | 1 | 1 | 1 | 1 | 1 | 1 | 1 | 1 |
| 1019 | 1 | 0 | 0 | 0 | 0 | 0 | 0 | 0 | 0 | 1 | 1 | 1 | 1 | 1 | 1 | 1 | 1 | 1 | 1 | 1 | 1 | 1 | 1 | 1 |
| 1022–1023 | 1 | 0 | 0 | 0 | 0 | 0 | 0 | 0 | 0 | 1 | 1 | 1 | 1 | 1 | 1 | 1 | 1 | 1 | 1 | 1 | 1 | 1 | 1 | 1 |
| 1026 | 1 | 0 | 0 | 0 | 0 | 0 | 0 | 0 | 0 | 1 | 1 | 1 | 1 | 1 | 1 | 1 | 1 | 1 | 1 | 1 | 1 | 1 | 1 | 1 |
| 1034–1035 | 1 | 0 | 0 | 0 | 0 | 0 | 0 | 0 | 0 | 1 | 1 | 1 | 1 | 1 | 1 | 1 | 1 | 1 | 1 | 1 | 1 | 1 | 1 | 1 |
| 1047–1048 | 1 | 0 | 0 | 0 | 0 | 0 | 0 | 0 | 0 | 0 | 0 | 0 | 0 | 0 | 0 | 0 | 0 | 0 | 0 | 0 | 0 | 0 | 0 | 0 |
| 1051 | 1 | 0 | 0 | 0 | 0 | 0 | 0 | 0 | 0 | 0 | 0 | 0 | 0 | 0 | 0 | 0 | 0 | 1 | 1 | 1 | 1 | 1 | 1 | 0 |
| 1052 | 1 | 0 | 0 | 0 | 0 | 0 | 0 | 0 | 0 | 0 | 0 | 0 | 0 | 0 | 0 | 0 | 0 | 0 | 1 | 1 | 1 | 1 | 1 | 0 |
| 4001 | 0 | 0 | 0 | 0 | 0 | 0 | 0 | 0 | 0 | 0 | 0 | 0 | 0 | 0 | 0 | 0 | 0 | 1 | 1 | 3 | 3 | 1 | 1 | 0 |
| 4002 | 0 | 0 | 0 | 0 | 0 | 0 | 2 | 2 | 4 | 4 | 4 | 4 | 4 | 4 | 4 | 4 | 4 | 4 | 4 | 4 | 4 | 4 | 4 | 4 |
| 4003 | 0 | 1 | 1 | 0 | 0 | 0 | 1 | 1 | 3 | 3 | 4 | 4 | 4 | 4 | 4 | 4 | 4 | 4 | 4 | 4 | 4 | 4 | 4 | 4 |
| 4004 | 0 | 0 | 0 | 0 | 0 | 0 | 0 | 0 | 0 | 0 | 0 | 0 | 0 | 0 | 0 | 1 | 1 | 3 | 3 | 4 | 4 | 4 | 4 | 3 |
| 4005 | 0 | 0 | 0 | 0 | 0 | 0 | 2 | 2 | 4 | 4 | 4 | 4 | 4 | 4 | 4 | 4 | 4 | 4 | 4 | 4 | 4 | 4 | 4 | 4 |
| 4006 | 0 | 1 | 1 | 1 | 1 | 3 | 3 | 4 | 4 | 4 | 4 | 4 | 4 | 4 | 4 | 4 | 4 | 4 | 4 | 4 | 4 | 4 | 4 | 4 |
| 4007 | 0 | 2 | 2 | 2 | 4 | 4 | 4 | 4 | 4 | 4 | 4 | 4 | 4 | 4 | 4 | 4 | 4 | 4 | 4 | 4 | 4 | 4 | 4 | 4 |
| 4008–4009 | 0 | 1 | 1 | 1 | 3 | 3 | 3 | 4 | 4 | 4 | 4 | 4 | 4 | 4 | 4 | 4 | 4 | 4 | 4 | 4 | 4 | 4 | 4 | 4 |
| 4010 | 0 | 0 | 0 | 0 | 0 | 1 | 1 | 3 | 3 | 4 | 4 | 4 | 4 | 4 | 4 | 4 | 4 | 4 | 4 | 4 | 4 | 4 | 4 | 4 |
| 4011 | 0 | 0 | 0 | 1 | 1 | 3 | 3 | 3 | 4 | 4 | 4 | 4 | 4 | 4 | 4 | 4 | 4 | 4 | 4 | 4 | 4 | 4 | 4 | 4 |
| 4012 | 0 | 1 | 1 | 1 | 1 | 3 | 3 | 3 | 3 | 4 | 4 | 4 | 4 | 4 | 4 | 4 | 4 | 4 | 4 | 4 | 4 | 4 | 4 | 4 |
| 6002 | 0 | 1 | 1 | 0 | 0 | 0 | 0 | 1 | 1 | 1 | 1 | 1 | 1 | 1 | 0 | 1 | 1 | 1 | 1 | 0 | 0 | 0 | 1 | 0 | 0 |
| 6006 | 0 | 0 | 0 | 0 | 0 | 0 | 0 | 0 | 1 | 0 | 1 | 1 | 0 | 0 | 0 | 1 | 1 | 0 | 1 | 1 | 1 | 1 | 1 | 0 | 0 |

may be a local optima. Heuristic methods may be considered in this case to find the best possible solution.

$$Min \sum_{t=1}^{NT} \sum_{cm=1}^{NC} \rho_{gas,cm} \cdot \frac{\partial F_{cf,cm}(CH_{cmt})}{\partial CH_{cmt}} \cdot \Delta CH_{cmt}. \quad (50)$$

## V. CASE STUDIES

A modified Institute of Electrical and Electronics Engineers (IEEE) 118-bus system, as shown in Fig. 4, is used to study the coordinated scheduling. The power system has 54 fossil fuel units, 12 combined-cycle units, 7 hydro units, 186 branches, 14 capacitors, 9 tap-changing transformers, and 91 demand sides. Tables II and III show the parameters of the pipeline, compressor, and gas well. All 12 combined cycle units with interruptible transportation contracts are supplied by an interstate pipeline and a compressor, as shown in Fig. 5. Fuel prices are \$1.4 per one thousand British thermal units (MBtu) for natural gas and 1\$/MBtu for coal. The test data are given in motor.ece.iit.edu/data/Transient gastransmission_118test.xls. Fig. 6 shows the hourly electrical and firm natural gas loads supplied by interstate pipelines. In order to discuss the effectiveness of the proposed approach, as well as the impact of the transient-state natural gas flow model on SCUC and natural gas scheduling results, we solve the coordination model in three different cases. The program is coded in C++ and solved by CPLEX 9.0 on a 2.6-GHz personal computer.

### Case 1: Coordinated scheduling with steady-state natural gas transmission constraints

We calculate the hourly SCUC solution by considering both the dc transmission constraints and the steady-state natural gas transmission constraints. In the steady-state natural gas flow case, the maximum pipeline flow is 15 000 MBtu/h, which is based on the Weymouth equation. The natural gas usage of combined cycle units 4001–4012 is curtailed at certain hours to mitigate the natural gas

TABLE V. Daily scheduling coordination results in cases 1–3.

| Daily results | Case 1 | Case 2 | Case 3 |
|---|---|---|---|
| Operating cost of electric power system (\$) | 2 046 006 | 2 044 479 | 2 037 255 |
| Natural gas consumed by compressor (MBtu) | 8965 | 12 273 | 5056 |
| Natural gas well output (MBtu) | 322 031 | 408 621 | 201 383 |
| Gas delivered to power plants (MBtu) | 181 766 | 163 200 | 220 649 |
| Electric power generated by gas plants (megawatts [MW]) | 13 962 | 12 995 | 17 316 |

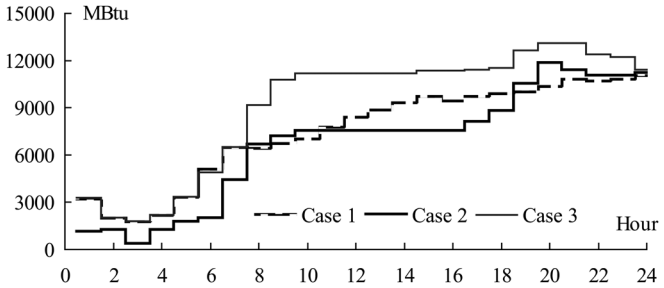


FIG. 7. Hourly natural gas delivered to power plants in cases 1–3.


FIG. 8. Hourly natural gas well output in cases 1–3.

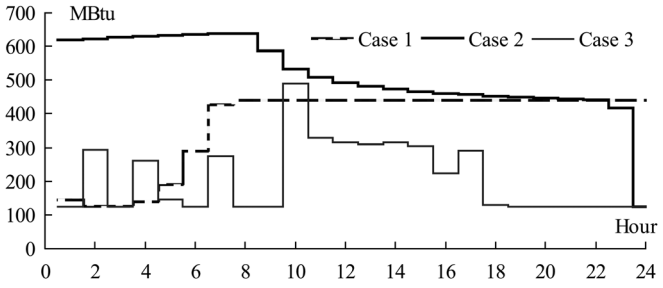


FIG. 9. Hourly natural gas consumed by compressor in cases 1–3.

TABLE VI. Initial parameters of interstate pipeline.

| Initial status of pipelines | Initial pressure (psig) | | Mass gas flow (MBtu) | |
|---|---|---|---|---|
| | Starting point | Ending point | Starting point | Ending point |
| Case 2 | 448 | 500 | 10 088 | 10 088 |
| Case 3 | 400 | 458 | 10 029 | 10 029 |

TABLE VII. Unit commitment in case 2.

| Unit | Hours (0–24) | | | | | | | | | | | | | | | | | | | | | | | | |
|---|---|---|---|---|---|---|---|---|---|---|---|---|---|---|---|---|---|---|---|---|---|---|---|---|---|
| 1013 | 1 | 1 | 1 | 1 | 1 | 1 | 1 | 1 | 1 | 1 | 1 | 1 | 1 | 1 | 1 | 1 | 1 | 1 | 1 | 1 | 1 | 1 | 0 | 0 | 0 |
| 1014 | 1 | 1 | 1 | 1 | 1 | 1 | 1 | 1 | 1 | 1 | 1 | 1 | 1 | 1 | 1 | 1 | 1 | 1 | 1 | 1 | 1 | 1 | 1 | 1 | 1 |
| 1019 | 1 | 0 | 0 | 0 | 0 | 0 | 0 | 0 | 1 | 1 | 1 | 1 | 1 | 1 | 1 | 1 | 1 | 1 | 1 | 1 | 1 | 1 | 1 | 1 | 1 |
| 1022–1023 | 1 | 0 | 0 | 0 | 0 | 0 | 0 | 0 | 1 | 1 | 1 | 1 | 1 | 1 | 1 | 1 | 1 | 1 | 1 | 1 | 1 | 1 | 1 | 1 | 1 |
| 1026 | 1 | 0 | 0 | 0 | 0 | 0 | 0 | 0 | 1 | 1 | 1 | 1 | 1 | 1 | 1 | 1 | 1 | 1 | 1 | 1 | 1 | 1 | 1 | 1 | 1 |
| 1034–1035 | 1 | 0 | 0 | 0 | 0 | 0 | 0 | 0 | 1 | 1 | 1 | 1 | 1 | 1 | 1 | 1 | 1 | 1 | 1 | 1 | 1 | 1 | 1 | 1 | 1 |
| 1047 | 1 | 0 | 0 | 0 | 0 | 0 | 0 | 0 | 0 | 0 | 1 | 1 | 1 | 1 | 1 | 1 | 1 | 1 | 1 | 1 | 1 | 1 | 1 | 1 | 0 |
| 1048 | 1 | 0 | 0 | 0 | 0 | 0 | 0 | 0 | 0 | 0 | 0 | 0 | 0 | 0 | 0 | 1 | 1 | 1 | 1 | 1 | 1 | 1 | 1 | 1 | 0 |
| 1051 | 1 | 0 | 0 | 0 | 0 | 0 | 0 | 0 | 0 | 0 | 0 | 0 | 0 | 0 | 0 | 1 | 1 | 1 | 1 | 1 | 1 | 1 | 1 | 1 | 0 |
| 1052 | 1 | 1 | 1 | 1 | 1 | 1 | 1 | 1 | 1 | 1 | 1 | 1 | 1 | 1 | 1 | 1 | 1 | 1 | 1 | 1 | 1 | 1 | 1 | 1 | 0 |
| 4001 | 0 | 0 | 0 | 0 | 0 | 0 | 0 | 0 | 0 | 0 | 0 | 0 | 0 | 0 | 0 | 0 | 0 | 0 | 0 | 0 | 1 | 1 | 0 | 0 | 0 |
| 4002 | 0 | 0 | 0 | 0 | 0 | 0 | 1 | 1 | 3 | 3 | 4 | 4 | 4 | 4 | 4 | 4 | 4 | 4 | 4 | 4 | 4 | 4 | 4 | 4 | 4 |
| 4003 | 0 | 1 | 1 | 0 | 0 | 0 | 0 | 2 | 2 | 4 | 4 | 4 | 4 | 4 | 4 | 4 | 4 | 4 | 4 | 4 | 4 | 4 | 4 | 4 | 4 |
| 4004 | 0 | 0 | 0 | 0 | 0 | 0 | 0 | 0 | 0 | 0 | 0 | 0 | 0 | 0 | 0 | 0 | 0 | 0 | 2 | 2 | 4 | 4 | 4 | 4 | 3 |
| 4005 | 0 | 0 | 0 | 0 | 0 | 0 | 0 | 0 | 0 | 0 | 0 | 0 | 0 | 0 | 2 | 2 | 4 | 4 | 4 | 4 | 4 | 4 | 4 | 4 | 4 |
| 4006 | 0 | 1 | 1 | 1 | 1 | 1 | 3 | 3 | 4 | 4 | 4 | 4 | 4 | 4 | 4 | 4 | 4 | 4 | 4 | 4 | 4 | 4 | 4 | 4 | 4 |
| 4007–4009 | 0 | 0 | 0 | 0 | 2 | 2 | 2 | 4 | 4 | 4 | 4 | 4 | 4 | 4 | 4 | 4 | 4 | 4 | 4 | 4 | 4 | 4 | 4 | 4 | 4 |
| 4010 | 0 | 0 | 0 | 0 | 0 | 0 | 0 | 0 | 0 | 0 | 0 | 0 | 0 | 0 | 0 | 0 | 0 | 0 | 0 | 0 | 0 | 0 | 0 | 0 | 0 |
| 4011 | 0 | 0 | 0 | 0 | 0 | 0 | 0 | 0 | 0 | 0 | 0 | 0 | 0 | 0 | 0 | 0 | 0 | 0 | 0 | 2 | 2 | 4 | 4 | 4 | 4 |
| 4012 | 0 | 0 | 0 | 2 | 2 | 2 | 2 | 4 | 4 | 4 | 4 | 4 | 4 | 4 | 4 | 4 | 4 | 4 | 4 | 4 | 4 | 4 | 4 | 4 | 4 |
| 6002 | 0 | 1 | 1 | 0 | 0 | 0 | 0 | 1 | 1 | 1 | 1 | 1 | 1 | 1 | 1 | 1 | 1 | 1 | 1 | 1 | 0 | 0 | 0 | 1 | 0 | 0 |
| 6006 | 0 | 0 | 0 | 0 | 0 | 0 | 0 | 0 | 0 | 1 | 1 | 1 | 0 | 0 | 0 | 1 | 1 | 0 | 1 | 1 | 1 | 1 | 1 | 0 | 0 |

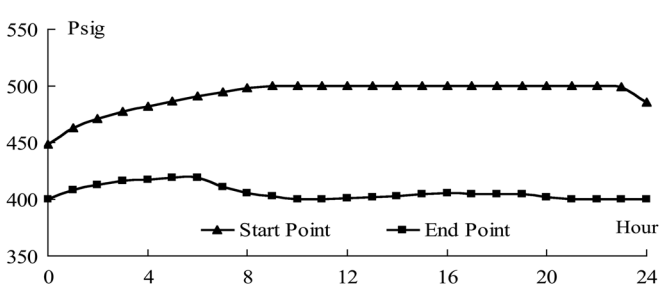


FIG. 10. Pressure at starting and ending points of the pipeline in case 2.

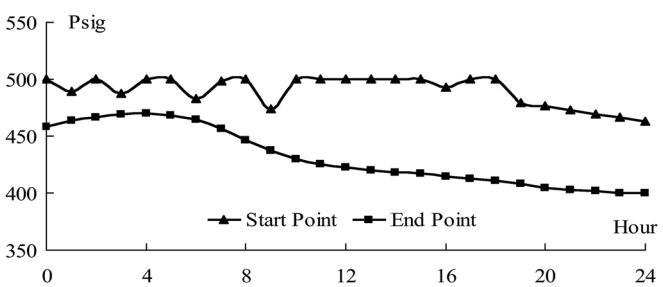


FIG. 11. Hourly pressure at starting/ending points of pipeline in case 3.

transmission congestion at hours 8–24. Table IV shows the hourly commitment in which the hour 0 represents the initial condition. Tables IV and VII list only the units with revised hourly commitment.

The daily operating cost of the power system is $2 046 006. After the power system schedule is set, we minimize the operating cost of the compressors, which is based on steady-state natural gas transmission constraints. Table V shows that the compressor will consume 8965 MBtu over the course of the next day. The hourly gas withdrawn from the pipeline, the hourly natural gas consumed by compressor, and the hourly gas well output consumed by the combined-cycle units are shown in Figs. 7–9.

### Case 2: Coordinated scheduling with transient natural gas flow model based on a lower initial line pack

We solve the generation scheduling problem again by considering the proposed transient-state model for natural gas flows. The pipeline is partitioned into several segments in its 200-mile length. The time interval is 1 h, and the length interval is 10 miles. Accordingly, PDEs of the pipeline with boundary conditions are transformed into a set of difference equations by the proposed implicit finite difference methodology. Table VI shows the initial pressures of the pipeline. The lower initial pressures in case 2 represent a smaller amount of natural gas contained in the pipeline after the previous day's operation. The hourly UC is given in Table VII, in which combined cycle units 4001–4012 generate less power (in MW) at many hours of the day as compared to case 1, and more coal units are committed. Fig. 7 shows that more natural gas is delivered to combined-cycle units in case 2 at h 19–23 when the electricity load is at peak. As a result, the daily operating cost of the power system is $2 044 476 in case 2, which is still lower than the cost realized in case 1. In order to satisfy peak hour natural gas demands at the ending point of the pipeline, the natural gas compressor has to charge the pipeline at the beginning hours of the period. Fig. 10 shows that the pressure level at the starting point of the pipeline increases gradually.

### Case 3: Coordinated scheduling with transient gas flow model based on a higher initial line pack

If the given initial pipeline pressure is higher, there will be more natural gas contained in the pipeline before the current operating day. Therefore, the pipeline can supply more natural gas to gas loads. Thus, even though the hourly UC results in cases 1 and 3 are the same, the dispatch in case 3 is more economical. The daily operating cost of the power system in case 3 is $2 037 255, which is lower than that of cases 1 and 2. In case 3, there is no violation in the natural gas transmission feasibility check in the lower-level problem. Fig. 11 shows that pressures at starting and ending points of the pipeline gradually decline, releasing the additional line pack resources to natural gas loads. The generation of combined-cycle units 4001–4012 is no longer limited by the natural gas transmission congestion. Table V shows that the total daily generating power is 17 316 MW, which is the highest in three cases. Figs. 8–9 show that the operating costs of compressor and the gas well output in case 3 are much lower than those found in cases 1 and 2 because of its higher initial line pack value. By comparing the results in three cases, we notice that the steady-state and transient-state models may yield two distinct results for the coordinated scheduling of power and natural gas systems.

## VI. CONCLUSIONS

This paper has developed a bi-level coordinated scheduling model for interdependent electricity and natural gas infrastructures. The transient model of natural gas flow is considered in the proposed model. The natural gas pipeline is modeled as a set of partial differential equations. An implicit finite difference method is introduced to transform the equations into difference equations. The paper shows that the proposed decomposition methodology and the coordination scheme can be applied to solve the proposed coordinated scheduling problem effectively. The case studies demonstrate that the applications of the steady-state and the transient-state models of natural gas flows would present different results for the coordinated scheduling of interdependent electricity and natural gas systems. It is also shown that the steady-state natural gas flow model, which would neglect the inherent storage capability of pipeline and the slower traveling speeds of natural gas flows, may result in impractical results and suboptimal schedules in short-term operation. The proposed coordinated scheduling model with the transient-state natural gas transmission formulation can be used in the daily operation scheduling, real-time operation, and post-contingency rescheduling.

[1]A. Helseth and A. T. Holen, Int. J. Electr. power Energy Syst. **31**, 531 (2009).
[2]S. V. Buldyrev, R. Parshani, G. Paul, H. E. Stanley, and S. Havlin, Nature **464**, 1025 (2010).
[3]J. Kavicky, E. Portante, S. Folga, and R. Fisher, Workshop on Grand Challenges in Modeling, Simulation, and Analysis for Homeland Security, Washington D.C., March 17–18, 2010.
[4]P. Hines, E. Cotilla-Sanchez, and S. Blumsack, Chaos **20**, 033122 (2010).
[5]M. Shahidehpour, Y. Fu, and T. Wiedman, Proc. IEEE **93**, 1042 (2005).
[6]T. Li and M. Shahidehpour, IEEE Trans. Power Syst. **20**, 1001 (2005).
[7]North American Electric Reliability Council, Reliability Assessment 2001–2011: The Reliability of Bulk Electric Systems in North America, (2002).
[8]R. G. Carter and H. H. Rachford, Jr., *Optimizing Line-pack Management to Hedge Against Future Load* (Pipeline Simulation Interest Group, Berne, Switzerland, 2003).
[9]R. R. Mercado, *Natural Gas Pipeline Optimization, Handbook of Applied Optimization* (Oxford University Press, 2002).
[10]C. Liu, M. Shahidehpour, Y. Fu, and Z. Li, IEEE Trans. Power Syst. **24**, 1523 (2009).
[11]S. An, Q. Li, and T. W. Gedra, "Natural gas and electricity optimal power flow," in *Proceedings of IEEE/PES Transmission and Distribution Conference and Exposition, Dallas, Texas, September, 2003*, Vol. 1, p. 7.
[12]C. Liu, M. Shahidehpour, and J. Wang, Application of augmented Lagrangian relaxation to coordinated scheduling of interdependent hydrothermal power and natural gas systems, IET Gener. Transm. Distrib. **4**, 1314 (2010).
[13]C. Unsihuay, J. W. M. Lima, and A. C. Zambroni de Souza, "Modeling the integrated natural gas and electricity optimal power flow," in Proceedings of IEEE/PES General Meeting, June 24–28, 2007.

[14]M. Geidl and G. Andersson, IEEE Trans. Power Syst. **22**, 145 (2007).
[15]M. Shahidehpour, H. Yamin, and Z. Li, *Market Operations in Electric Power Systems* (Wiley, New York, NY, 2002).
[16]A. J. Wood and B. F. Wollenberg, *Power Generation, Operation and Control*, 2nd ed. (Wiley, New York, 1996).
[17]Y. Fu, M. Shahidehpour, and Z. Li, IEEE Trans. Power Syst. **20**, 1001 (2005).
[18]P. J. Wong and R. E. Larson, IEEE Trans. Autom. Control **13**, 475 (1968).
[19]K. Ehrhardt and M. Steinbach. *Nonlinear Optimization in Gas Networks* (Konrad-Zuse-Zentrum fur Informationstechnik, Berlin, 2003).
[20]A. Herran-Gonzalez, J. M. De La Cruz, B. De Andres-Toro, J. L. Risco-Martin, Appl. Math. Model. **33**, 1584 (2009).
[21]A. J. Osiadacz, *Simulation and Analysis of Gas Pipeline Networks* (E. & F.N. Spon, London, 1987).
[22]A. J. Osiadacz, "Different transient models—Limitations, advantages, and disadvantages," in Proceedings of the PSIG, 28th Annual Meeting, San Francisco, CA, USA, Oct.23–25,1996.
[23]S. L. Ke and H. C. Ti, Chem. Eng. J. **76**, 169 (2000).
[24]G. P. Berard and B. G. Eliason, Soc. Pet. Eng. J. **18**, 389 (1978).
[25]M. A. Stoner, Soc. Pet. Eng. J. **12**, 115 (1972).
[26]C. Liu, M. Shahidehpour, Z. Li, and M. Fotuhi-Firuzabad, IEEE Trans. Power Syst. **24**, 976 (2009).
[27]ISO New England, CIGRE 2008 Case Study: Electric and Natural Gas Market Interdependencies within New England (2008).
[28]L. A. Wolsay, *Integer Programming* (Wiley, New York, 1998).
[29]R. G. Jeroslow, SIAM J. Control Optim. **18**, 264 (1980).
[30]R. P. O'Neill, M. Williard, B. Wilkins, and R. Pike, Oper. Res. **27**, 857 (1979).
[31]D. Wolf and Y. Smeers, Manage. Sci. **46**, 1454 (2000).

# Impact of Natural Gas System on Risk-Constrained Midterm Hydrothermal Scheduling

Cem Sahin, Zuyi Li, *Senior Member*, Mohammad Shahidehpour, *Fellow, IEEE, and* Ismet Erkmen[1]

***Abstract*—This paper studies the impact of natural gas (NG) contracts and constraints on a GENCO's midterm risk-constrained hydrothermal scheduling problem. The NG contracts and constraints are modeled as a set of linear equations. The proposed model utilizes the stochastic price-based unit commitment (PBUC). The PBUC hourly solution considers uncertainties of market prices for energy and ancillary services, uncertainties of natural water inflows, and random NG infrastructure interruptions in Monte-Carlo scenarios. Illustrative examples analyze the GENCO's risk levels when considering midterm schedules for generating units, target payoffs, and usages of water inflow, NG and other thermal resources. Simulation results show that a GENCO's midterm schedules and financial risks could be impacted significantly with the consideration of NG contracts and constraints.**

***Index Terms*—Interdependency of natural gas and electricity, financial and physical risks, generation companies, stochastic price-based unit commitment, natural gas contracts**

## NOMENCLATURE

**Indices:**

| | |
|---|---|
| $h$ | Index of hydro units |
| $i$ | Index of coal units |
| $j$ | Index of NG units |
| $k$ | Index of pumped-storage units |
| $l$ | Index of hydro catchments |
| $m$ | Index of pipelines |
| $n$ | Index of NG contracts |
| $p$ | Index of power plants |
| $r$ | Index of subareas |
| $s$ | Index of scenarios |
| $t$ | Index of time periods (hour) |
| $w$ | Index of NG storage facilities |

**Dimensions:**

| | |
|---|---|
| $NCM$ | Number of hydro catchments |
| $NCO$ | Number of coal units |
| $NGC$ | Number of NG gas contracts |
| $NGS$ | Number of NG gas storage facilities |
| $NH_l$ | Number of hydro units of a hydro catchment $l$ |
| $NNG$ | Number of NG units |
| $NPL$ | Number of NG plants |
| $NPP$ | Number of NG pipelines |
| $NPS$ | Number of pumped-storage hydro units |
| $NS$ | Number of scenarios |
| $NSA$ | Number of NG subareas |
| $NT$ | Number of time periods under study |

**Sets:**

| | |
|---|---|
| $SCT$ | Set of NG units utilizing a gas contract |
| $SFC$ | Set of firm NG contracts |
| $SIC$ | Set of interruptible NG contracts |
| $SPL$ | Set of NG units in a plant |
| $SPP$ | Set of gas contracts belonging to a pipeline |
| $SSA$ | Set of NG units in a subarea |
| $SST$ | Set of NG units sharing a NG storage facility |

**Variables:**

| | |
|---|---|
| $C_{ns}$ | Cost of NG usage from contract $n$ in scenario $s$ |
| $C_{ws}$ | Cost of NG usage from storage facility $w$ in scenario $s$ |
| $F$ | Fuel usage by unit |
| $OR$ | Operating reserve |
| $P$ | Power generation |
| $PF_s$ | GENCO's payoff in scenario $s$ |
| $q^{out}$ | NG withdrawn from storage facility $w$ |
| $q^{in}$ | NG injected to storage facility $w$ |
| $V_{wts}$ | Volume of NG in storage facility $w$ at time $t$ in scenario $s$ |
| $RISK_s$ | GENCO's downside risks in scenario $s$ |
| $SD$ | Shutdown cost |
| $SR$ | Spinning reserve |
| $SU$ | Startup cost |
| $\lambda$ | Lagrange multiplier |
| $\gamma_s$ | Lagrange multiplier for risk constraint in scenario $s$ |

**Constants:**

| | |
|---|---|
| $\alpha_n$ | Interruption rate of NG contract $n$ |
| $\beta_n$ | Restore rate of NG contract $n$ |
| $C_{0,n}$ | Fixed cost for firm NG contract $n$ |
| $\overline{EDR}$ | Expected downside risk tolerance |
| $F_{\max,\ jt}$ | Maximum NG usage allowed for unit $j$ at time $t$ |
| $F_{\max,\ j}$ | Maximum NG usage allowed for unit $j$ in one year |
| $p_s$ | Probability for a scenario $s$ |
| $T_0$ | Target payoff of a GENCO |
| $U_{nts}$ | Availability of NG contract $n$ at time $t$ in scenario $n$ |
| $V_{\max,\ w}$ | Maximum NG volume limit in storage facility $w$ |
| $V_{\min,\ w}$ | Minimum NG volume limit in storage facility $w$ |
| $V_{0,w}$ | Volume of NG in storage facility $w$ at time 0 |
| $V_{NT,w}$ | Volume of NG in storage facility $w$ at time $NT$ |
| $p_n$ | Steady-state availability of NG contract $n$ |

This work was supported in part by the NSF grant ECCS-0801853. Cem Sahin and Ismet ERKMEN are with the Department of Electrical and Electronic Engineering, Middle East Technical University (e-mail: cem.sahin@uzay.tubitak.gov.tr, erkmen@metu.edu.tr). Zuyi Li and Mohamamd Shahidehpour are with the Department of Electrical and Computer Engineering, Illinois Institute of Technology (e-mail: lizu@iit.edu, ms@iit.edu)

$q_n$ Steady-state unavailability of NG contract *n*

$\rho f_{its}$ Fuel price of coal unit *i* at time *t* in scenario *s*

$\rho g_{ts}$ Market price for energy at time *t* in scenario *s*

$\rho_n$ Price of one MMCF of interruptible NG contract *n*

$\rho or_{ts}$ Market price for operating reserve at time *t* in scenario *s*

$\rho sr_{ts}$ Market price for spinning reserve at time *t* in scenario *s*

$\rho_w$ Unit price of one MMCF of gas withdrawal from NG storage facility *w*

**Abbreviations:**

GENCO Generation Company
*MIP* Mixed Integer Program
*MMCF* Million cubic feet
*NG* Natural Gas
PBUC Price based unit commitment

## I. Introduction

GENCOs are responsible for the midterm operation planning which provides a basis for the optimal hourly bidding in a day-ahead market. The midterm operation planning will determine the optimal utilization of resources such as fuel, emission allowance, and natural water resources [1]-[3]. The modeling of NG contracts in midterm operation planning studies provides a more robust scheduling of hydrothermal assets when considering uncertainties related to market prices, NG interruptions, and water inflows.

Several approaches are available for the optimal midterm operation planning problem. A variable metric method was used in [4] to solve the dual maximization for achieving a good convergence property. A composite representation of thermal and hydro units was used in [5] for economic dispatch based on weekly and monthly requirements. A dual-decomposition of long-term planning problem was applied in [6],[7] for setting up easy-to-solve problems in subperiods. The framework in [8] is able to consider on and off-peak energy prices and user controlled multi-scenario water inflows. The interior point method is applied to solve the long-term scheduling problem, in which the hydro unit characteristics are linearly modeled. A two-stage dynamical programming (DP) method was proposed in [9] which is capable of handling nonconvex, nonlinear and stochastic characteristics of the problem. However, the DP technique might not be tractable in multi-reservoir systems due to the dimensionality problem. Reference [10] compared the stochastic dynamic programming and the deterministic optimization models with an inflow forecasting model for the long-term hydrothermal scheduling problem. The reference concludes that the two methods have similar performance and the deterministic model is superior in dry hydro periods. A two-phase nonlinear optimization model was proposed in [11] to model the integrated operation of NG network and power systems. In [12] and [13], a nonlinear optimization model was proposed by merging the traditional optimal power flow and NG network constraints. The short-term scheduling of integrated NG network and hydrothermal power system was solved in [14] by applying Lagrangian relaxation and dynamic programming. An integrated model was proposed in [15] for studying the interdependency of electricity infrastructure and NG system and the social sustainability of energy infrastructures. The integrated model considered NG network constraints as daily and hourly limits on pipelines, subareas, power plants, and generating units, and incorporated these constraints into the optimal solution of short-term security-constrained unit commitment.

In addition to the short-term NG scheduling, interdependencies were considered in midterm NG planning studies. A network-based stock and flow type model was created in [16] to analyze the NG network response to disruptions. The NG flows between regions were represented and stocks were the regional NG storages. The model was used to assess the NG network against transmission disruption scenarios. However, the model did not include contractual NG deliveries to other users which would likely worsen electric power supply scenarios. For example, there might be a sufficient transmission capacity available on a NG pipeline which would feed power plants. The NG flow can ramp up quickly in the event of a pipeline disruption elsewhere or an unseasonably cold weather. However, that capacity could have already been contracted to other users. Logically, such emergencies would take precedent, but legally there might be no way out of contractual agreements. An analytical framework was proposed in [17] to study physical and economic aspects of interdependent infrastructures such as electric power, petroleum, NG, water, and communications systems. A modeling and analyses tool was developed to capture interdependencies, evaluate potential effects of disruptions in one infrastructure, and suggest strategies to mitigate shortcomings.

This paper incorporates the NG infrastructure model presented in [15] to develop an extended framework for the risk-constrained stochastic midterm hydrothermal scheduling problem [18]. The main theme of this paper is to assess the impact of the NG infrastructure and contracts on the stochastic midterm planning of electric power systems. Consider a GENCO with hydro, thermal, and NG contacts for supplying its gas power plants. Since the residential NG demand is very high at certain seasons, NG suppliers in severe weather conditions could interrupt the supply to power plants. Such interruptions could have a significant impact on the GENCO's expected payoffs. In addition, when the risk is considered, the behavior of NG units could vary under different hydro conditions. For instance, NG units would tend to increase their generation output for lowering the total financial risk. This case could occur in scenarios with water supply shortages to prevent GENCOs from defaulting on their bilateral energy contracts. However, the NG output in practice could be constrained by physical limitations and contracts.

The availability of NG storage could facilitate lower risks in such cases. The storage capacity should be determined in such cases based on forecasted market prices, and duration and frequency of NG interruptions.

The hourly MIP solution of price-based hydrothermal system presented in [18] is considered here. The NG interruptions are also considered as uncertainties similar to those of hourly market prices and water inflows. The performances of individual units for risk reduction are studied and compared with the risk reduction performance of all units

considered together to evaluate possible alternatives in a GENCO's stochastic midterm scheduling.

This paper is organized as follows. The proposed model is formulated in Section II. Detailed simulation and solution methodologies are described in Section III. Examples are given in Section IV. Section V concludes this paper.

## II. Stochastic Modeling of NG Infrastructure

This section starts by defining the objective function of midterm PBUC problem, which includes revenues and expenses for coal, NG, cascaded hydro, and pumped-storage hydro units. Generating unit constraints are discussed and NG contracts and constraints are presented. Financial risk constraints are also discussed.

The proposed objective function (1) is to maximize the expected payoff with respect to power generations ($P$), spinning and operating reserves ($SR$ and $OR$) and unit commitment variables over all scenarios. The payoff of a scenario is defined as the difference between revenue and expense. The revenue (2) is due to sales of energy, spinning reserves, and operating reserves by coal, NG, cascaded hydro, and pumped-storage hydro units. The cost (3) includes that of i) fuel, startup, and shutdown for coal units; ii) NG contracts, storage, startup cost, and shutdown for NG units; iii) startup and shutdown for cascaded hydro units; and iv) startup cost and shutdown for pumped-storage units.

$$\text{Max:} \sum_{s=1}^{NS} p_s \cdot PF_s = \sum_{s=1}^{NS} p_s \cdot \{REVENUE_s - COST_s\} \quad (1)$$

where

$$\begin{aligned} REVENUE_s = & \sum_{i=1}^{NCO}\sum_{t=1}^{NT}\left[\rho g_{ts} \cdot P_{its} + \rho sr_{ts} \cdot SR_{its} + \rho or_{ts} \cdot OR_{its}\right] \\ & + \sum_{j=1}^{NNG}\sum_{t=1}^{NT}\left[\rho g_{ts} \cdot P_{jts} + \rho sr_{ts} \cdot SR_{jts} + \rho or_{ts} \cdot OR_{jts}\right] \\ & + \sum_{l=1}^{NCM}\sum_{h=1}^{NH_l}\sum_{t=1}^{NT}\left[\rho g_{ts} P_{hts} + \rho sr_{ts} \cdot SR_{hts} + \rho or_{ts} \cdot OR_{hts}\right] \\ & + \sum_{k=1}^{NPS}\sum_{t=1}^{NT}\left[\rho g_{ts} \cdot P_{kts} + \rho sr_{ts} \cdot SR_{kts} + \rho or_{ts} \cdot OR_{kts}\right] \end{aligned} \quad (2)$$

and

$$\begin{aligned} COST_s = & \sum_{i=1}^{NCO}\sum_{t=1}^{NT}\left[\rho f_{its} \cdot F_{its} + SU_{it} + SD_{it}\right] \\ & + \sum_{n=1}^{NGC} C_{ns} + \sum_{w=1}^{NGS} C_{ws} + \sum_{j=1}^{NNG}\sum_{t=1}^{NT}\left[SU_{jt} + SD_{jt}\right] \\ & + \sum_{l=1}^{NCM}\sum_{h=1}^{NH_l}\sum_{t=1}^{NT}\left[SU_{ht} + SD_{ht}\right] + \sum_{k=1}^{NPS}\sum_{t=1}^{NT}\left[SU_{kt} + SD_{kt}\right] \end{aligned} \quad (3)$$

A low-discrepancy Monte Carlo method, represented by Latin Hypercube, is used to generate a set of scenarios, which consider uncertainties in market prices, natural water inflows, and interruptions of NG interruptible contracts. The scenarios are then reduced based on backward and fast forward method. The probability $p_s$ assigned to each scenario reflects the possibility of occurrence [19]. The details of the modeling of market prices and natural water inflows are given in [18],[20]. A two-state continuous-time Markov chain model is used to represent available states of NG interruptible contracts [21]-[23]. The objective function defined in (1) is subject to the following generating unit and NG infrastructure constraints [18].

- **Coal Unit Constraints**

  a) Fuel consumption and emission allowance constraints for groups of coal units
  b) Energy and ancillary services supplied
  c) Minimum on/off time and ramping up/down constraints

- **NG Unit Constraints**

  NG units are subject to similar constraints to those of the coal units as well as the NG network constraints that will be discussed later in this section.

- **Cascaded Hydro Unit Constraints**

  a) Energy and ancillary services supplied
  b) Water-to-power conversion
  c) Operating regions (water discharge limits)
  d) Reservoir volume limits
  e) Initial and terminal reservoir volumes
  f) Water balance constraint
  g) Minimum on/off time and ramping up/down constraints

- **Pumped-storage Units Constraints**

The pumped-storage units are subject to the same constraints b, d, e and g of the cascaded hydro-unit constraints. The energy and ancillary services, operating regions and water balance constraints are extended to consider the pumping modes of the pumped-storage units.

- **NG Contracts and Constraints**

The eight NG units are fed from the NG transmission network as seen in Fig. 2. There are eight units related to Pipeline 1. Consequently, these units would be subject to limits on pipelines, contracts, and plants. Pipeline 2 is divided into two zones, and if Zone 1 is considered to be geographically far from gas well, the four units located in this zone would be able to access only a proportion of pipeline capacity due to subarea constraints. The units in Zone 3 of Pipeline 2 share a storage facility to which NG could be deposited. The stored NG could be withdrawn when necessary, i.e. the pipeline outage due to seasonal interruptions. The mathematical equations for NG contracts and network constraints are provided here which are used in the stochastic midterm operation planning problem.

NG contracts are modeled as firm (take-or-pay) or interruptible contracts with NG suppliers. Firm NG contracts have fixed costs. Interruptible NG contracts are utilized if it is either economical or required to satisfy certain constraints. The cost of a firm NG contract is specified as

$$C_{ns} = C_{0,n}, \ \forall n \in SFC, \forall s \quad (4)$$

An interruptible NG contract will have its own quantity and price. The cost of an interruptible NG contract depends on the gas usage

$$C_{ns} = \rho_n \sum_{t=1}^{NT} F_{nts}, \ \forall n \in SIC, \forall s \quad (5)$$

The NG usage from a specific NG contract at a specific scenario and time is limited by the availability of specific NG contracts defined by an integer availability variable $U_{nts}$.

$$F_{nts} \le F_{\max,\ nt}.U_{nts}\ ,\ \forall n, \forall t, \forall s \quad (6)$$

The NG usage from a firm contract *n* is equal to the contracted amount since it is prepaid.

$$\sum_{t=1}^{NT} F_{nts} = F_{\max,\ n}\ ,\ \forall n \in SFC\ , \forall s \quad (7)$$

The NG usage from an interruptible contract *n* cannot exceed the yearly contracted limit.

$$\sum_{t=1}^{NT} F_{nts} \le F_{\max,\ n}\ ,\ \forall n \in SIC\ , \forall s \quad (8)$$

Here, daily, weekly, and monthly contract limits may be included similarly.

The steady-state NG network equations define the nonlinear relationship between the gas flow and pressure. The pressures at network nodes and the gas flows in pipelines could be calculated based on the nodal balance approach with a large computation time. The linearized constraints would not calculate these parameters at each time step; however, the physical limitations of the network could still be enforced considering the maximum capacity of the network components at each time step with a significant drop in the computation time. The linearized approach is sufficient for the purpose of this paper since the algorithm aims to find the optimum fuel and resource scheduling rather than calculating the NG network parameters at each time step.

The modeling of storage is essential for a midterm study, since the storage facility could be used both for deposit and withdrawal purposes throughout the year. The storage model for the short-term study in [15] was simply represented by a gas inflow variable in the NG unit fuel balance equation. The short-term constraints considering capacity limits on pipelines, sub-areas, power plants, and units are adopted for the midterm stochastic model by increasing the time-span and introduction of *s* as scenario variables.

The hourly and yearly constraints are considered in this section. The daily, weekly, and monthly limits can be included similarly. The total NG usage from a contract *n* of pipeline *m* at time *t* in scenario *s* is equal to the sum of separate NG usages by individual NG units using that contract.

$$F_{nmts} = \sum_{j \in SCT\ (n)} F_{jnmts}\ ,\ \forall n, \forall m, \forall t, \forall s \quad (9)$$

A gas pipeline can be fed by several NG contracts. The total NG usage of pipeline *m* at time *t* in scenario *s* is equal to the sum of NG usage from all such contracts.

$$F_{mts} = \sum_{n \in SPP\ (m)} F_{nmts}\ ,\ \forall m, \forall t, \forall s \quad (10)$$

Generating units that are located far from NG pumping stations can only burn a certain percentage of available NG. Accordingly, a subarea is defined for the NG consumption of such units. The total NG usage at subarea *r* of pipeline *m* at time *t* in scenario *s* is equal to the sum of NG usages by individual NG units in that subarea.

$$F_{mrts} = \sum_{j \in SSA\ (r)} F_{jmrts}\ ,\ \forall m, \forall r, \forall t, \forall s \quad (11)$$

An NG unit *j* can be supplied by multiple contracts, pipelines, and NG storage facilities.

$$F_{jts} = \sum_{m=1}^{NPP} \sum_{n \in SPP\ (m)} F_{jnmts} + \sum_{w=1}^{NGS} \left( q_{jwts}^{out} - q_{jwts}^{in} \right),\ \forall j, \forall t, \forall s \quad (12)$$

where $q_{jwts}^{out}$ and $q_{jwts}^{in}$ are zero if the NG unit *j* is not connected to any storage facilities. The total NG injected into or withdrawn from the storage by individual units, which would share the same storage, is given as

$$q_{wts}^{in} = \sum_{j \in SST\ (w)} q_{jwts}^{in}\ ,\ \forall w, \forall t, \forall s \quad (13)$$

$$q_{wts}^{out} = \sum_{j \in SST\ (w)} q_{jwts}^{out}\ ,\ \forall w, \forall t, \forall s \quad (14)$$

The NG volume balance equation for the storage facility *w* is

$$V_{w(t+1)s} = V_{wts} + q_{wts}^{in} - q_{wts}^{out}\ ,\ \forall w, \forall t, \forall s \quad (15)$$

The term $V_{wts}$ is the volume of the NG storage *w* at time *t* and scenario *s*. This term could be obtained using the initial volume and the net injection and withdrawal amounts at each time step starting from the initial time 0 to time (*t*-1) as

$$V_{wts} = \sum_{j \in SCT\ (w)} \sum_{\tau=1}^{t-1} (q_{jw\tau s}^{in} - q_{jw\tau s}^{out}) + V_{w(0)s} \quad (16)$$

The NG storage volume constraint of the storage facility *w* is

$$V_{\min,\ w} \le V_{wts} \le V_{\max,\ w}\ ,\ \forall w, \forall t, \forall s \quad (17)$$

The initial and final volumes of the NG storage facility *w* are

$$V_{w(0)s} = V_{0,w}\ ,\ \forall w, \forall s \quad (18)$$

$$V_{w(NT)s} = V_{NT,w}\ ,\ \forall w, \forall s \quad (19)$$

The total cost of NG withdrawal from the storage facility *w* is

$$C_{ws} = \rho_w . \sum_{t=1}^{NT} q_{wts}^{out}\ ,\ \forall w, \forall s \quad (20)$$

The NG usage of unit *j* is subject to the following hourly and yearly limits

$$F_{jts} \le F_{\max,\ jt}\ ,\ \forall j, \forall t, \forall s \quad (21)$$

$$\sum_{t=1}^{NT} F_{jts} \le F_{\max,\ j}\ ,\ \forall j, \forall s \quad (22)$$

The NG units that belong to a specific power plant are subject to the following hourly and yearly limits

$$\sum_{j \in SPL\ (p)} F_{jts} \le F_{\max,\ pt}\ ,\ \forall p, \forall t, \forall s \quad (23)$$

$$\sum_{j \in SPL\ (p)} \sum_{t=1}^{NT} F_{jts} \le F_{\max,\ p}\ ,\ \forall p, \forall s \quad (24)$$

The NG usage of pipeline *m* is subject to the following hourly and yearly limits

$$F_{mts} \le F_{\max,\ mt}\ ,\ \forall m, \forall t, \forall s \quad (25)$$

$$\sum_{t=1}^{NT} F_{mts} \le F_{\max,\ m}\ ,\ \forall m, \forall s \quad (26)$$

The NG usage at subarea *r* is subject to the following hourly and yearly limits

$$F_{mrts} \le F_{\max,\ mrt}\ ,\ \forall m, \forall r, \forall t, \forall s \quad (27)$$

$$\sum_{t=1}^{NT} F_{mrts} \le F_{\max,\ mr}\ ,\ \forall m, \forall r, \forall s \quad (28)$$

- **Risk Constraints**

The stochastic formulation described above is a risk-neutral model that is only concerned with the optimization of expected payoff. However, a GENCO may also be concerned with its risk. A GENCO would set a target payoff $T_0$, and the risk associated with its decision is measured by the failure to

meet the target payoff. That is, if the payoff for a scenario is larger than the target, the associated downside risk is zero; otherwise, it is the difference between the payoff and its target value, which is expressed as

$$RISK_s = \max\{0, T_0 - PF_s\}, \ \forall s \quad (29)$$

The expected downside risk should be lower than a target risk level which is stated as

$$\sum_{s=1}^{NS} p_s . RISK_s \le \overline{EDR} \quad (30)$$

## III. Proposed Solution Methodology

### A. Decomposition procedure

The original problem is decomposed into subproblems for coal, NG, hydro, and pumped-storage units. The unit status indicators (I) are defined for each scenario separately. Bundle constraints are utilized to force the undistinguishable scenarios to have the same rendered decision variables, namely unit status indicators [18]. In this study, the unit status indicators are the same for every scenario. This formulation removes the necessity of using bundle constraints at the expense of a longer solution time since the decomposition is not among scenarios. The removal of bundle constraints reduces the number of Lagrange multipliers and simplifies the updating of multipliers.

### *A1. Decoupling expected downside risk constraint*

The expected downside risk constraint (30) is the only coupling constraint among different types of generating units. The constraint can be decoupled by relaxing it into the objective function by using the Lagrange multiplier $\gamma_s$. With the constant terms dropped, we have

$$Min \sum_{s=1}^{NS} p_s \cdot (-PF_s + \gamma_s . RISK_s) \quad (31)$$

Considering the definition of downside risk (29), we have

$$Min \sum_{s=1}^{NS} p_s \cdot (-PF_s + \gamma_s . \max\{0, T_0 - PF_s\}) \quad (32)$$

If the payoff of a scenario $s$ is higher than the target payoff,

$$-PF_s + \gamma_s . \max\{0, T_0 - PF_s\} = -PF_s \quad (33)$$

Otherwise,

$$-PF_s + \gamma_s . \max\{0, T_0 - PF_s\} = -(1+\gamma_s)PF_s + \gamma_s . T_0 \quad (34)$$

Here, (33) can be viewed as a special case of (34) where $\gamma_s = 0$. After relaxing the risk constraint, we proceed by decomposing different unit types to single unit problems.

### *A2. Decoupling constraints among coal units*

The coal unit subproblem is given in (35). Fuel allocation and emission allowance are considered by applying the Lagrangian relaxation [18]. The coal unit subproblem is further decomposed into single coal unit $i$ subproblems in (36).

$$Min \left\{ \sum_{i=1}^{NCO} \sum_{t=1}^{NT} \sum_{s=1}^{NS} p_s .(1+\gamma_s). \left\{ \begin{array}{l} -\left\lceil \rho g_{ks} \cdot P_{its} + \rho sr_{ts} \cdot SR_{its} \right\rceil \\ \left\lfloor + \rho or_{ts} \cdot OR_{its} \right\rfloor \\ + SU_{it} + SD_{it} + \rho f_{its} . F_{its} \end{array} \right\} \right\} \quad (35)$$

$$Min \left\{ \sum_{t=1}^{NT} \sum_{s=1}^{NS} p_s .(1+\gamma_s). \left\{ \begin{array}{l} -\left\lceil \rho g_{ks} \cdot P_{its} + \rho sr_{ts} \cdot SR_{its} \right\rceil \\ \left\lfloor + \rho or_{ts} \cdot OR_{its} \right\rfloor \\ + SU_{it} + SD_{it} + \rho f_{its} . F_{its} \end{array} \right\} \right\}, \quad \forall i \quad (36)$$

### *A3. Hydro subproblems for each catchment*

In order to avoid the decomposition of coupling constraints among hydro units in one catchment, we solve hydro subproblems for each catchment given in (37).

$$Min \left\{ \sum_{h=1}^{NH_l} \sum_{t=1}^{NT} \sum_{s=1}^{NS} p_s .(1+\gamma_s). \left\{ \begin{array}{l} -\left\lceil \rho g_{ts} \cdot P_{hts} + \rho sr_{ts} \cdot SR_{hts} \right\rceil \\ \left\lfloor + \rho or_{ts} \cdot OR_{hts} \right\rfloor \\ + SU_{ht} + SD_{ht} \end{array} \right\} \right\}, \quad \forall l \quad (37)$$

### *A4. Pumped-storage subproblems for each unit*

The pumped- storage hydro unit subproblem is given as

$$Min \left\{ \sum_{t=1}^{NT} \sum_{s=1}^{NS} p_s .(1+\gamma_s). \left\{ \begin{array}{l} -\left\lceil \rho g_{ks} \cdot P_{kts} + \rho sr_{ts} \cdot SR_{kts} \right\rceil \\ \left\lfloor + \rho or_{ts} \cdot OR_{kts} \right\rfloor \\ + SU_{kt} + SD_{kt} \end{array} \right\} \right\}, \quad \forall k \quad (38)$$

### *A5. NG subproblems for each unit*

The NG infrastructure constraints are coupling constraints that are relaxed by applying the Lagrangian relaxation method. The subproblems for NG units are given in (39), which are further decomposed into subproblems for each NG unit in (40). In (39), the first term is the expected revenue of selling energy and ancillary services minus the startup and shutdown costs for NG units. The second and third terms are the cost of NG usage from contracts and the NG withdraw from storage facilities, respectively. The fourth to seventh terms represent plant (24), pipeline (26), subarea (28), and max contracts for NG usage constraints (7) and (8) respectively. The last three terms relax upper and lower volume limits (17) and final volume (19) for gas storage facilities, respectively. Emission allowance constraints may be relaxed similarly [18].

$$\begin{aligned} Min & \left\{ \sum_{j=1}^{NNG} \sum_{t=1}^{NT} \sum_{s=1}^{NS} p_s .(1+\gamma_s) \left\{ \begin{array}{l} -\left\lceil \rho g_{ts} \cdot P_{jts} + \rho sr_{ts} \cdot SR_{jts} + \right. \\ \left\lfloor \rho or_{ts} \cdot OR_{jts} \right\rfloor \\ + SU_{jt} + SD_{jt} \end{array} \right\} \right\} \\ & + \sum_{m=1}^{NPP} \sum_{t=1}^{NT} \sum_{n \in SPP(m)} \sum_{j \in SCT(n)} \sum_{s=1}^{NS} p_s . \rho_n . F_{jnmts} \\ & + \sum_{w=1}^{NGS} \sum_{t=1}^{NT} \sum_{j \in SST(w)} \sum_{s=1}^{NS} p_s . \rho_w . q_{jwts}^{out} \\ & + \sum_{p=1}^{NPL} \sum_{s=1}^{NS} p_s . \left\{ \lambda_{\max, ps} \cdot \left( \sum_{j \in SPL(p)} \sum_{t=1}^{NT} F_{jts} - F_{\max, p} \right) \right\} \\ & + \sum_{m=1}^{NPP} \sum_{s=1}^{NS} p_s . \left\{ \lambda_{\max, ms} \cdot \left( \sum_{n \in SPP(m)} \sum_{j \in SCT(n)} \sum_{t=1}^{NT} F_{jnmts} - F_{\max, m} \right) \right\} \\ & + \sum_{r=1}^{NSA} \sum_{s=1}^{NS} p_s \cdot \left\{ \lambda_{\max, rs} \cdot \left( \sum_{j \in SSA(r)} \sum_{t=1}^{NT} F_{jts} - F_{\max, r} \right) \right\} \end{aligned}$$

$$+\sum_{m=1}^{NPP}\sum_{n\in SPP(m)}\sum_{s=1}^{NS} p_s\cdot\left\{\lambda_{\max,\ ns}\cdot\left(\sum_{j\in SCT(n)}\sum_{t=1}^{NT} F_{jnmts} - F_{\max,\ n}\right)\right\}$$

$$+\sum_{w=1}^{NGS}\sum_{s=1}^{NS} p_s\cdot\left\{\lambda_{\max,\ ws}\cdot\left(\sum_{t=1}^{NT} V_{wts} - V_{\max,\ w}\right)\right\}$$

$$-\sum_{w=1}^{NGS}\sum_{s=1}^{NS} p_s\cdot\left\{\lambda_{\min,\ ws}\cdot\left(\sum_{t=1}^{NT} V_{wts} - V_{\min,\ w}\right)\right\}$$

$$+\sum_{w=1}^{NGS}\sum_{s=1}^{NS} p_s\cdot\lambda_{NT,ws}\cdot\left(V_{wNTs} - V_{NT,w}\right)\Bigg\} \quad (39)$$

$$Min\left\{\sum_{t=1}^{NT}\sum_{s=1}^{NS}\left\{\begin{array}{l}p_s\cdot(1+\gamma_s)\cdot\left[\begin{array}{l}-(\rho g_{ts}\cdot P_{jts} + \rho sr_{ts}\cdot SR_{jts} + \\ \rho or_{ts}\cdot OR_{jts}) + SU_{jt} + SD_{jt}\end{array}\right] \\ +\left[p_s\cdot\left(\lambda_{\max,\ ps} + \lambda_{\max,\ rs}\right)\cdot F_{jts}\right]\end{array}\right\}\right.$$

$$+\sum_{m=1}^{NPP}\sum_{t=1}^{NT}\sum_{n\in SPP(m)}\sum_{s=1}^{NS} p_s\cdot\rho_n\cdot F_{jnmts} + \sum_{w=1}^{NGS}\sum_{t=1}^{NT}\sum_{s=1}^{NS} p_s\cdot\rho_w\cdot q^{out}_{jwts}$$

$$+\sum_{m=1}^{NPP}\sum_{s=1}^{NS} p_s\cdot\left\{\lambda_{\max,\ ms}\cdot\left(\sum_{n\in SPP(m)}\sum_{t=1}^{NT} F_{jnmts}\right)\right\}$$

$$+\sum_{m=1}^{NPP}\sum_{n\in SPP(m)}\sum_{s=1}^{NS} p_s\cdot\left\{\lambda_{\max,\ ns}\cdot\left(\sum_{t=1}^{NT} F_{jnmts}\right)\right\}$$

$$+\sum_{w=1}^{NGS}\sum_{s=1}^{NS} p_s\cdot\left\{\left(\lambda_{\max,\ ws} - \lambda_{\min,\ ws}\right)\cdot\left(\sum_{t=1}^{NT}\sum_{\tau=1}^{t-1}\left(q^{in}_{jw\tau s} - q^{out}_{jw\tau s}\right)\right)\right\}$$

$$+\sum_{w=1}^{NGS}\sum_{s=1}^{NS} p_s\cdot\left\{\lambda_{NT,ws}\cdot\left(\sum_{\tau=1}^{NT-1}\left(q^{in}_{jw\tau s} - q^{out}_{jw\tau s}\right)\right)\right\} \quad (40)$$

### *B. Proposed Solution Steps*

The algorithm flowchart is shown in Fig. 1. The subproblems for coal, NG, cascaded hydro, and pumped-storage hydro units are solved in parallel when the coupling risk constraint is relaxed. Each subproblem related to an individual unit is solved to maximize the expected payoff of all scenarios in the entire study horizon. For the NG unit subproblem in particular, coupling constraints are checked for constraints on NG contracts, pipelines, plants, subareas, and gas storage. The Lagrange multipliers are updated using the subgradient method and iterations continue until the difference between the objective functions in two consecutive iterations is smaller than a predefined threshold and an optimal or suboptimal solution is reached. After the solution of individual unit subproblems, the risk is calculated. If the risk aversion limit is met, the optimal solution is calculated. Otherwise, the Lagrange multipliers $\gamma_s$ is updated for the risk inequality constraint (30) and returned to recalculate individual unit subproblems. The risk Lagrange multipliers are initially set to zero for all scenarios and updated using the subgradient method afterwards [24].

The target risk and profit are essential factors, which could impact the convergence of the algorithm. A GENCO might calculate the factors based on the following steps:

1) The problem is solved by assuming an initial target profit and without considering risk constraints. The proposed algorithm would calculate the appropriate expected risk. Otherwise, go to step 2 if the risk is not within the GENCO's tolerance.

2) The proposed algorithm is implemented with risk constraints to calculate the optimum profit. If the target profit is too high and the target risk is not attainable, the GENCO would decrease its target profit and repeat this step.

## IV. Case Studies

A GENCO with 3 coal units, 12 NG units, 11 hydro units, and 3 pumped-storage units is considered to analyze the effect of NG constraints on the midterm hydrothermal scheduling problem. The scheduling horizon is one year with hourly intervals. The detailed generating unit data, market prices for energy and ancillary services are given in http://motor.ece.iit.edu/data/NGInfraPBUC.

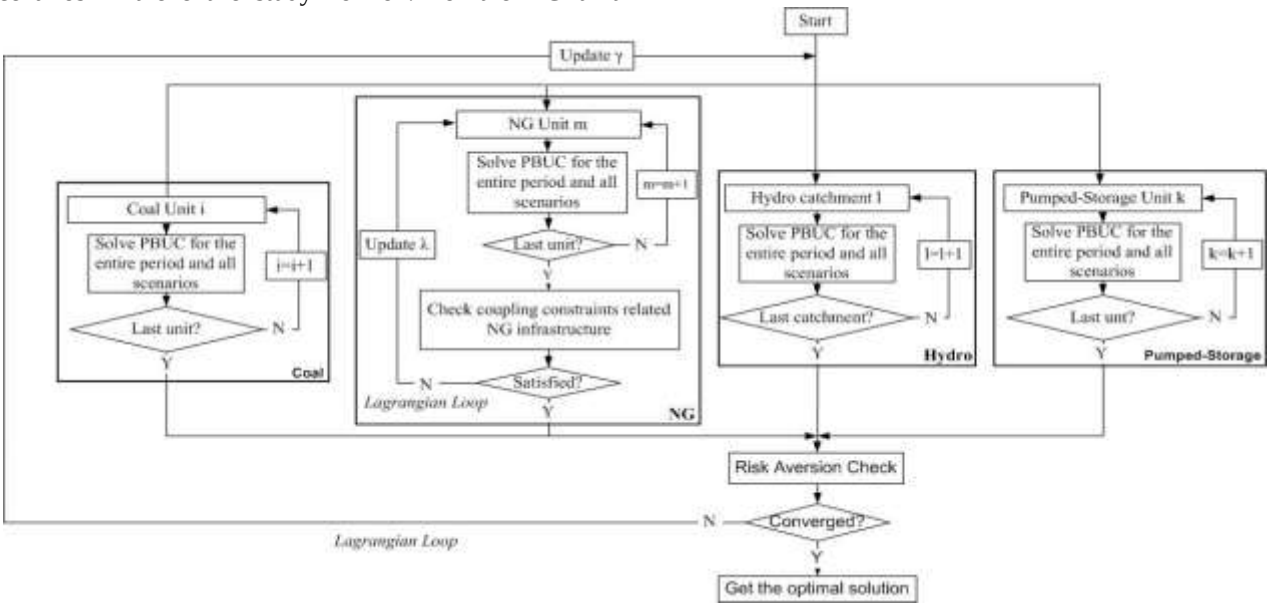


Fig. 1. Flowchart of the midterm stochastic hydrothermal scheduling

We assume uniform market clearing prices (MCPs) for all units. Locational marginal prices (LMPs) can be incorporated similarly. The NG infrastructure feeding NG units is shown in Fig. 2. Zone 1 is considered as a subarea since it is far from the NG supply. The yearly NG usage limit for Zone 1 is 37,200 MMCF (subarea limit).

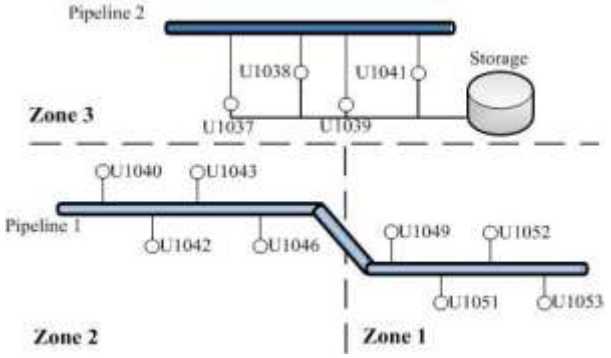


Fig. 2. NG units and infrastructure

In this study, NG storage facilities are not considered except in Case 4, where an NG storage facility with a capacity of 1,000 MMCF is located in Zone 3 for supplying NG units within Zone 3. The cost of utilizing the storage is $2,170 per MMCF. NG contracts are shown in Table I. Pipeline 1 has one firm and one interruptible contract while Pipeline 2 has one interruptible contract. The yearly pipeline constraints are 155,000 and 90,000 MMCF for Pipelines 1 and 2, respectively.

TABLE I
NG CONTRACTS

| Pipeline # | Contract # | Type | Amount (MMCF) | Cost or Price |
|---|---|---|---|---|
| 1 | 1 | Firm | 36,000 | $70,200,000 |
| 1 | 2 | Interruptible | 117,500 | $2,170 / MMCF |
| 2 | 3 | Interruptible | 88,400 | $2,100 / MMCF |

The following four cases are considered:

Case 1: Base case without any NG constraints or supply interruptions
Case 2: Effect of NG infrastructure constraints
Case 3: Effect of NG supply interruptions
Case 4: Effect of NG storage facilities

These cases are discussed as follows.

**Case 1: Base Case without any NG Constraints or Supply Interruptions:** This base case includes all the units but does not consider NG constraints or supply interruptions. This case is to be used as reference to show the effect of NG infrastructure and its interruptions in the following cases. The uncertainties in market price and natural water inflow are considered in the scenarios. The scenarios are reduced to 12 since the value of the objective function does not change much based on this number of scenarios [25]. The probability of each reduced scenario is given in Table II. A risk neutral model is considered first which aims to maximize the expected scenario payoffs. Scenarios 2 and 8 have lower payoffs as a function of market prices and natural water inflows. If the GENCO sets its target payoff at $485,849,996, which is the expected payoff for the risk neutral case, the corresponding probability for the set of scenarios below the target payoff is 0.46 (i.e., 0.11 + 0.02 + 0.07 + 0.1 + 0.05 + 0.11). The expected downside risk is $9,331,555. The expected downside risk would be decreased with the inclusion of risk constraints. Table III shows scenario payoffs for risk neutral and risk-constrained models (minimum risk). The downside risk is $8,309,323 with the inclusion of risk constraints, which shows a 10.95% less risk than that of the risk neutral case. However, the expected payoff decreases by 0.3% in the risk-constrained case. This is the cost of risk aversion. Table IV shows the NG usage of different contracts for risk neutral and risk-constrained cases. The firm NG contract is fully utilized in both cases and the interruptible NG is consumed when market prices are high. The interruptible NG contract usage decreases in all scenarios with the introduction of risk constraints. This is because NG units are shut down in specific hours to reduce the downside risk.

TABLE II
PROBABILITY OF EACH SCENARIO AFTER SCENARIO REDUCTION

| Scenario | 1 | 2 | 3 | 4 | 5 | 6 |
|---|---|---|---|---|---|---|
| **Probability** | 0.07 | 0.11 | 0.02 | 0.07 | 0.08 | 0.08 |
| **Scenario** | 7 | 8 | 9 | 10 | 11 | 12 |
| **Probability** | 0.1 | 0.05 | 0.09 | 0.09 | 0.13 | 0.11 |

TABLE III CASE 1 PAYOFF

| Scenario | Risk Neutral Payoff ($) | Risk Constrained Payoff ($) | Change (%) |
|---|---|---|---|
| 1 | 496,829,660 | 492,811,146 | -0.81 |
| 2 | 455,159,262 | 457,308,285 | 0.47 |
| 3 | 470,330,464 | 469,255,240 | -0.23 |
| 4 | 478,319,870 | 481,583,723 | 0.68 |
| 5 | 486,346,522 | 485,826,120 | -0.11 |
| 6 | 507,895,434 | 501,879,197 | -1.18 |
| 7 | 468,243,935 | 471,056,266 | 0.60 |
| 8 | 460,055,586 | 461,652,104 | 0.35 |
| 9 | 488,026,721 | 485,933,588 | -0.43 |
| 10 | 493,015,056 | 487,823,577 | -1.05 |
| 11 | 531,379,691 | 523,638,213 | -1.46 |
| 12 | 467,052,288 | 469,049,789 | 0.43 |
| **Expected Payoff ($)** | 485,849,996 | 484,407,904 | -0.30 |
| **Target ($)** | 485,849,996 | | - |
| **Downside Risk ($)** | 9,331,555 | 8,309,323 | -10.95 |

TABLE IV CASE 1 USAGE OF NG CONTRACTS

| Scenario | Contract 1 NG (MMCF) | | Contract 2 NG (MMCF) | | Contract 3 NG (MMCF) | |
|---|---|---|---|---|---|---|
| | Risk Neutral Case | Risk Cons. Case | Risk Neutral Case | Risk Cons. Case | Risk Neutral Case | Risk Cons. Case |
| 1 | 36,000 | 36,000 | 88,517 | 86,424 | 41,591 | 41,286 |
| 2 | 36,000 | 36,000 | 76,479 | 75,708 | 39,106 | 39,060 |
| 3 | 36,000 | 36,000 | 81,876 | 80,441 | 39,987 | 39,814 |
| 4 | 36,000 | 36,000 | 84,181 | 83,409 | 40,544 | 40,483 |
| 5 | 36,000 | 36,000 | 83,865 | 82,446 | 40,498 | 40,341 |
| 6 | 36,000 | 36,000 | 91,697 | 88,965 | 41,921 | 41,670 |
| 7 | 36,000 | 36,000 | 82,393 | 81,655 | 40,374 | 40,266 |
| 8 | 36,000 | 36,000 | 77,743 | 76,966 | 38,811 | 38,702 |
| 9 | 36,000 | 36,000 | 85,611 | 83,758 | 40,872 | 40,648 |
| 10 | 36,000 | 36,000 | 85,266 | 83,140 | 40,957 | 40,611 |
| 11 | 36,000 | 36,000 | 91,562 | 88,319 | 42,185 | 41,726 |
| 12 | 36,000 | 36,000 | 80,332 | 79,756 | 39,912 | 39,868 |
| **Exp. Value** | 36,000 | 36,000 | 84,429 | 82,827 | 40,661 | 40,462 |

**Case 2: Effect of NG Infrastructure Constraints: A**ll units and NG infrastructure constraints are used to show the effect of NG constraints on the midterm hydrothermal scheduling. These constraints, formulated in Section II, are on pipelines,

subareas, plants, and units. Table V shows scenario payoffs with risk neutral and risk-constrained model when considering NG infrastructure constraints. The downside risk is decreased by 11.96% against a drop in the expected payoff of 0.41%. When we adopt commitment decisions given in Case 1, the expected payoff changes to $481,881,658. The difference in the expected payoff is $282,486 (i.e., $482,164,144 - $481,881,658) which represents the cost of ignoring NG infrastructure constraints in decision-making.

TABLE V CASE 2 PAYOFF

| Scenario | Risk Neutral Payoff ($) | Risk Constrained Payoff ($) | Change (%) |
|---|---|---|---|
| 1 | 492,174,884 | 487,461,689 | -0.96 |
| 2 | 452,984,686 | 455,218,835 | 0.49 |
| 3 | 467,379,771 | 466,489,686 | -0.19 |
| 4 | 474,772,772 | 478,266,777 | 0.74 |
| 5 | 483,012,610 | 481,939,429 | -0.22 |
| 6 | 502,690,545 | 494,945,756 | -1.54 |
| 7 | 465,237,823 | 468,108,097 | 0.62 |
| 8 | 457,819,092 | 459,446,279 | 0.36 |
| 9 | 484,277,365 | 482,318,666 | -0.40 |
| 10 | 489,136,100 | 482,952,060 | -1.26 |
| 11 | 525,411,762 | 515,473,413 | -1.89 |
| 12 | 464,728,792 | 466,871,393 | 0.46 |
| **Expected Payoff ($)** | 482,164,144 | 480,180,559 | -0.41 |
| **Target ($)** | 482,164,144 | | - |
| **Downside Risk ($)** | 8,850,597 | 7,791,967 | -11.96 |

TABLE VI
ZONE GAS USAGES OF UNITS IN CASE 1 AND CASE 2 (RISK NEUTRAL CASE)

| Scenario | Zone 1 NG (MMCF) | | Zone 2 NG (MMCF) | | Zone 3 NG (MMCF) | |
|---|---|---|---|---|---|---|
| | Case 1 | Case 2 | Case 1 | Case 2 | Case 1 | Case 2 |
| 1 | 60,283 | 37,045 | 64,234 | 64,234 | 41,591 | 41,591 |
| 2 | 53,100 | 37,162 | 59,379 | 59,379 | 39,106 | 39,106 |
| 3 | 55,156 | 37,073 | 62,720 | 62,720 | 39,987 | 39,987 |
| 4 | 56,927 | 37,037 | 63,253 | 63,253 | 40,544 | 40,544 |
| 5 | 56,237 | 37,181 | 63,628 | 63,628 | 40,498 | 40,498 |
| 6 | 60,820 | 37,075 | 66,877 | 66,877 | 41,921 | 41,921 |
| 7 | 55,605 | 37,092 | 62,788 | 62,788 | 40,374 | 40,374 |
| 8 | 52,262 | 36,957 | 61,482 | 61,482 | 38,811 | 38,811 |
| 9 | 57,384 | 37,103 | 64,227 | 64,227 | 40,872 | 40,872 |
| 10 | 57,848 | 37,169 | 63,418 | 63,418 | 40,957 | 40,957 |
| 11 | 61,340 | 37,188 | 66,222 | 66,222 | 42,185 | 42,185 |
| 12 | 53,967 | 37,136 | 62,365 | 62,365 | 39,912 | 39,912 |
| **Exp. Value** | 56,968 | 37,116 | 63,460 | 63,460 | 40,661 | 40,661 |

TABLE VII
CASE 2 EXPECTED USAGES FROM NG CONTRACTS

| Contract 1 NG (MMCF) | | Contract 2 NG (MMCF) | | Contract 3 NG (MMCF) | |
|---|---|---|---|---|---|
| Risk Neutral | Risk Cons. | Risk Neutral | Risk Cons. | Risk Neutral | Risk Cons. |
| 36,000 | 36,000 | 64,577 | 62,157 | 40,661 | 40,465 |

Therefore, the target payoff in this case should not be the same as that in the previous case when the NG infrastructure constraints were not considered. The GENCO would experience a lower payoff than its expectation if it does not update the target payoff. The value of the downside risk is $8,850,597 for a target payoff $481,881,658. If the GENCO sets its target payoff at $485,849,996 as in Case 1, the probability for the set of scenarios below the target payoff would be 0.63 (i.e., 0.11 + 0.02 + 0.07 + 0.08 + 0.1 + 0.05 + 0.09 + 0.11) with an expected downside risk of $10,914,617. This indicates that ignoring NG constraints could affect the GENCO's midterm schedule and increases the financial risk. Table VI shows the total NG usage of generating units located in Zone 1 for Cases 1 and 2. We observe that the subarea constraint would limit the NG usage of units in Zone 1 to slightly lower than the upper limit (37,200 MMCF) even though the higher gas utilization in Zone 1 would lead to a higher payoff. The generating units in Zones 2 and 3 are unaffected since their NG usage remains within limits. The decrease in scenario payoffs is due to NG subarea limits. The expected NG usages from contracts for risk neutral and risk-constrained cases are given in Table VII. When compared with the risk neutral case in Case 1, we see that the NG usage from the interruptible contract of Pipeline 1 has decreased by 19,582 (i.e., 84,429 - 64,577) MMCF, which is due to binding subarea constraints in Zone 1. The units in Zone 1 would utilize the firm NG and the interruptible NG usage is limited by the subarea constraint. The interruptible contract in Pipeline 2 has not changed when compared to that in Case 1 since the midterm scheduling of units fed from Pipeline 2 does not violate the NG constraints.

It is cumbersome to represent the sensitivity of the risk with respect to the expected payoff analytically due to the complexity of the problem. Instead, the change of risk is evaluated for Case 2 by evaluating the minimum achievable risk at different target profits. The results are depicted in Fig. 3. The expected payoff for the risk neutral case was $482,164,144 with a downside risk of $8,850,597. The analysis for case 2 is repeated for the GENCO's target payoffs starting at $460,000,000 to $485,000,000 with a step of $5,000,000. The points are connected with linear curves to obtain 5 linear segments. The slopes of the curve segments given in Fig. 3 is calculated as 0.16, 0.33, 0.40, 0.45 and 0.53 from segment 1 to segment 5 respectively. This shows that the rate of change in the lowest achievable risk increases as the GENCO increases its target profit. Consider that the GENCO has two different target profits namely $460,000,000 and $480,000,000 with lowest achievable risks 0 and $6,730,647 respectively.

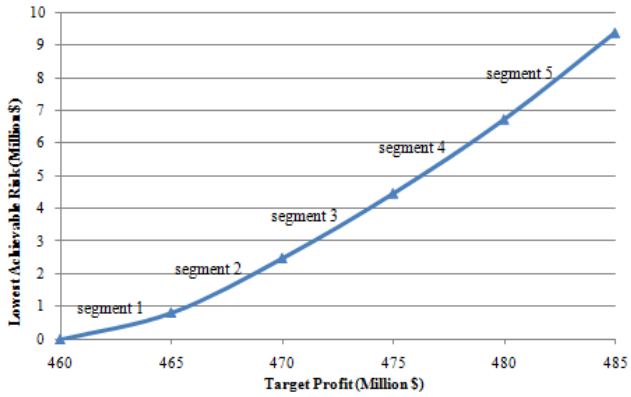


Fig. 3. Downside risk versus target payoff for Case 2

The $1,000,000 of increase in target profit will result $163,250 and $529,779 of increase in lowest achievable risk respectively. Consequently, the extra risk exposition increases when the GENCO updates its target profits in the ascending direction. A similar analysis is trivial when the GENCO updates its target profit in the descending direction. Even though the downside risk was decreased by 11.96% with the consideration of risk constraints in Case 2, the GENCO would

have to update the target payoff to $460,000,000 in order to reduce the risk to zero.

**Case 3: Effect of NG Supply Interruptions:** In this case, we study the effect of NG interruptions on the GENCO's payoff in a midterm scheduling. In severe weather conditions, the increasing NG demand for heating in residential areas is supplied by interruptible NG contracts. The interruption rate, which is defined as the ratio of the mean interruption time to the sum of mean interruption and mean available times [21], is taken as 0.1 for this case study and interruptions are simulated for the winter period. Table VIII depicts the scenario payoffs when considering NG interruptions and constraints for both risk neutral and risk-constrained conditions. If the GENCO determines a target payoff $465,492,606 for the risk neutral case, the downside risk probability is 0.46 (i.e., 0.11 + 0.02 + 0.07 + 0.1 + 0.05 + 0.11). The downside risk is $8,469,522 and the expected payoff is decreased by $16,671,538 (i.e., $482,164,144 - $465,492,606). This is the potential loss in the midterm stochastic hydrothermal scheduling due to NG interruptions. When compared with Case 1, the consideration of NG interruptions with NG infrastructure constraints further decreases the GENCO's expected payoff by $20,357,390 (i.e., $3,685,852-$16,671,538). The amount of decrease could change with the rate of the NG interruptions. If the GENCO sets its target payoff to $485,849,996 as in Case 1, the probability for the set of scenarios below the target payoff would be 0.87 (i.e., 0.07 + 0.11 + 0.02 + 0.07 + 0.08 + 0.08 + 0.1 + 0.05 + 0.09 + 0.09 + 0.11) with an expected downside risk of $23,126,635. This indicates that ignoring the NG network constraints could affect the GENCO's midterm schedule and further increases financial risks. With the consideration of risk constraints, the downside risk decreases by 12.19% against a drop in the expected payoff of 0.37%. Table IX gives the NG usage of gas contracts for each scenario for both risk neutral and risk considered cases. The NG contract utilization further decreases when compared with Case 2 due to NG interruptions. The NG usage does not decrease in Pipeline 1 with respect to Case 2 even if there are any NG interruptions. This is due to the fact that NG usage in Case 2 was already limited by subarea constraints and the unused gas at interrupted hours are shifted to other hours in Case 3. The decrease in gas usage from Contract 2 due to the interruptions is 10,575 MMCF (i.e., 40,661- 30,086).

TABLE VIII CASE 3 PAYOFF

| Scenario | Risk Neutral Payoff ($) | Risk Constrained Payoff ($) | Change (%) |
|---|---|---|---|
| 1 | 474,871,828 | 470,491,695 | -0.92 |
| 2 | 437,655,315 | 439,855,079 | 0.50 |
| 3 | 451,281,020 | 450,284,507 | -0.22 |
| 4 | 458,324,947 | 461,706,329 | 0.74 |
| 5 | 466,314,926 | 465,310,161 | -0.22 |
| 6 | 484,836,849 | 477,901,647 | -1.43 |
| 7 | 449,183,674 | 451,958,605 | 0.62 |
| 8 | 442,057,657 | 443,691,623 | 0.37 |
| 9 | 467,325,199 | 465,484,983 | -0.39 |
| 10 | 472,370,528 | 466,607,116 | -1.22 |
| 11 | 507,151,877 | 498,283,516 | -1.75 |
| 12 | 448,957,954 | 451,049,157 | 0.47 |
| **Expected Payoff ($)** | 465,492,606 | 463,761,550 | -0.37 |
| **Target ($)** | 465,492,606 | | - |
| **Downside Risk ($)** | 8,469,522 | 7,436,840 | -12.19 |

TABLE IX
CASE 3 EXPECTED USAGES FROM NG CONTRACTS

| Contract 1 NG (MMCF) | | Contract 2 NG (MMCF) | | Contract 3 NG (MMCF) | |
|---|---|---|---|---|---|
| Risk Neutral | Risk Cons. | Risk Neutral | Risk Cons. | Risk Neutral | Risk Cons. |
| 36,000 | 36,000 | 64,577 | 62,550 | 30,086 | 29,975 |

**Case 4: Effect of NG Storage Facility:** This case includes all the units, NG infrastructure constraints, NG interruption cases, and NG storage facilities. NG can be stored for use at constrained hours. In this case, the NG storage in Zone 3 is considered. The storage is assumed to be full prior to the study period and NG injection to the storage by units is assumed to be zero at all periods (i.e., $q^{in}_{wts}=0$, $\forall t$, $\forall s$). Table X depicts the scenario payoffs for both risk neutral and risk-constrained cases. Table XI gives the expected usage of NG contracts under risk neutral and risk-constrained cases. Fig. 4 depicts the expected payoff against the NG storage size.

TABLE X CASE 4 PAYOFF

| Scenario | Risk Neutral Payoff ($) | Risk Constrained Payoff ($) | Change (%) |
|---|---|---|---|
| 1 | 489,727,434 | 486,554,727 | -0.65 |
| 2 | 451,626,645 | 453,729,519 | 0.47 |
| 3 | 465,703,256 | 465,115,114 | -0.13 |
| 4 | 472,760,956 | 475,928,829 | 0.67 |
| 5 | 480,924,774 | 481,293,666 | 0.08 |
| 6 | 499,767,150 | 493,687,013 | -1.22 |
| 7 | 463,433,285 | 466,117,361 | 0.58 |
| 8 | 456,442,454 | 457,561,335 | 0.25 |
| 9 | 482,096,447 | 481,359,263 | -0.15 |
| 10 | 486,971,597 | 481,762,048 | -1.07 |
| 11 | 522,165,865 | 515,108,551 | -1.35 |
| 12 | 463,117,388 | 464,735,786 | 0.35 |
| **Expected Payoff ($)** | 480,028,588 | 478,840,621 | -0.25 |
| **Target ($)** | 480,028,588 | | - |
| **Downside Risk ($)** | 8,618,523 | 7,674,844 | -10.95 |

TABLE XI
CASE 4 EXPECTED USAGES FROM NG CONTRACTS

| Contract 1 NG (MMCF) | | Contract 2 NG (MMCF) | | Contract 3 NG (MMCF) | |
|---|---|---|---|---|---|
| Risk Neutral Case | Risk Cons. Case | Risk Neutral Case | Risk Cons. Case | Risk Neutral Case | Risk Cons. Case |
| 36,000 | 36,000 | 64,577 | 63,577 | 30,977 | 30,763 |

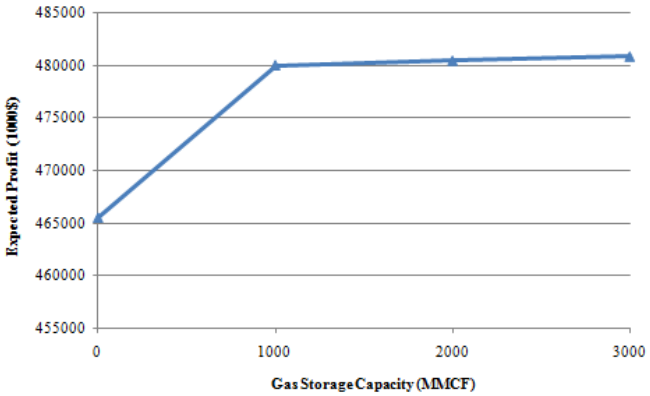


Fig. 4. NG Storage Capacity versus Expected payoff, risk neutral case

When there is no storage, the expected payoff is $465,492,606 as given in Case 3. The expected payoff is improved by 3.03% to $480,028,588 for the first 1,000 MMCF storage. However, the improvement is only 0.09% with a payoff of $480,456,556 for adding the second 1,000 MMCF of storage, and 0.08% with a payoff of $480,841,268 for the third 1,000 MMCF of storage. This is because the GENCO would choose to burn NG from the storage at the most profitable hours. The payoff improvement for the first 1,000 MMCF storage is higher than the next 2,000 MMCF since the GENCO uses the first 1,000 MMCF of additional NG at most profitable hours. The expected payoff is could be improved significantly with the addition of 1,000 MMCF of NG storage when compared with the no-storage Case 3. The downside risk for this case has decreased by 10.95% against a drop in the expected payoff of 0.25% with the addition of risk constraints.

The four cases are summarized in Table XII. The GENCO's expected payoff decreases when considering NG constraints and interruptions. Furthermore, the expected financial downside risk and downside risk probability increase if the GENCO does not update its midterm target payoff and uses the target payoff determined in the base case for Cases 2 and 3. Thus, the GENCO could run a risk free case when considering NG constraints and interruptions and then determine a suitable target payoff and reduce the risk, which would lead to a more realistic risk-constrained midterm scheduling results. A reduction of 10,575 MMCF of NG was observed for Contract 3 in Case 3 as compared to Case 2 due to an NG interruption. The interruption resulted in an expected payoff reduction of $16,671,538. However, the expected payoff increased to $14,535,982 when a 1,000 MMCF NG storage was considered in Zone 3. In other words, 87.2% of the reduction in expected payoff, which was due to the NG interruption, was recovered with the addition of storage. The NG storage was 9% of the interrupted NG. In this case, the GENCO utilized the stored NG at most profitable hours. Tables XIII and XIV list the results of optimizing the individual types of units separately or together for risk neutral and risk-constrained cases, respectively.

TABLE XII
COMPARISON OF RESULTS OF CASES 1-4 WITH RISK NEUTRAL SOLUTIONS

| | Case 1 | Case 2 | Case 3 | Case 4 |
|---|---|---|---|---|
| **Expected Payoff ($)** | 485,849,996 | 482,164,144 | 465,492,606 | 480,028,588 |
| **Downside Risk ($)** | 9,331,555 | 10,914,617 | 23,126,635 | 12,028,208 |
| **Down. Risk Probability** | 0.46 | 0.63 | 0.87 | 0.63 |
| **Target ($)** | 485,849,996 | | | |

TABLE XIII
COMPARISON OF RISK NEUTRAL CASES RESULTS

| Cases | Expected Payoff ($) | Downside Risk ($) | Target ($) |
|---|---|---|---|
| **5: Coal Units Only** | 22,423,534 | 1,101,054 | 22,423,534 |
| **6: NG Units Only** | 140,688,206 | 4,396,534 | 140,688,206 |
| **7: Hydro Units Only** | 232,620,703 | 2,178,677 | 232,620,703 |
| **8: PS Units Only** | 69,760,163 | 995,095 | 69,760,163 |
| **Sum of Cases 5-8** | 465,492,606 | 8,671,360 | 465,492,606 |
| **9: All Units Together** | 465,492,606 | 8,469,522 | 465,492,606 |
| **Change (%)** | 0.00 | 2.33 | 0.00 |

TABLE XIV
COMPARISON OF RISK REDUCTION OF CASES

| Cases | Expected Payoff ($) | Downside Risk ($) | Target ($) |
|---|---|---|---|
| **5: Coal Units Only** | 22,338,606 | 1,052,037 | 22,423,534 |
| **6: NG Units Only** | 140,117,126 | 4,231,735 | 140,688,206 |
| **7: Hydro Units Only** | 232,370,729 | 2,054,221 | 232,620,703 |
| **8: PS Units Only** | 69,464,139 | 551,639 | 69,760,163 |
| **Sum of Cases 5-8** | 464,290,600 | 7,889,632 | 465,492,606 |
| **9: All Units Together** | 463,761,550 | 7,436,840 | 465,492,606 |
| **Change (%)** | 0.11 | 5.74 | 0.00 |

The results of risk neutral case show that the scheduling of all units together with a target payoff that is equal to the sum of individual payoffs would result in a lower expected downside risk than the sum of those for individual risks. This could be explained by the fact that the variance of the sum of two normal distributed random variables is always less than or equal to the sum of their variances. Hence, a GENCO should determine a target by including all its units rather than considering them individually. For the risk-constrained case, the sum of lowest achievable risk for Case 3, which represents a combined solution of all generating units, is lower than the sum of separate downside risks of individual groups of units. The 5.75% improvement is because the consideration of all the units with a single total target payoff would provide more alternatives for risk reduction.

## V. CONCLUSIONS

In this paper, the NG infrastructure constraints are incorporate into the GENCO's risk-constrained hydrothermal scheduling. Test results show that besides uncertainties in market prices and water inflow, GENCOs must further consider the NG infrastructure limitations in the optimal midterm scheduling. The NG storage facilities would improve the expected payoff of the GENCO against NG interruptions by providing NG at interrupted hours. The effect of utilizing the NG storage on the expected payoff is analyzed and it is observed that a considerable improvement in the expected payoff would be attainable even by a limited storage capacity in comparison with any NG interruptions. In addition, the solution for the optimization of the individual types of units separately is compared with that of all units together. It is observed that the solution of all units together would provide a better chance for any risk reductions.

## REFERENCES


[1] M. Shahidehpour and Y. Wang, *Communication and Control of Electric Power Systems*, John Wiley and Sons, Jun. 2003

[2] M. Shahidehpour, H. Yamin, and Z.Y. Li, *Market Operations in Electric Power Systems, John Wiley &Sons, Inc.*, New York, 2002

[3] M. K. C. Marwali and M. Shahidehpour, "Coordination between longterm and short-term generation scheduling with network constraints, " *IEEE Trans. Power Syst.*, vol. 15, no. 3, pp. 1161–1167, Aug. 2000

[4] K. Aoki, M. Itoh, T. Satoh, K. Nara, and M. Kanezashi, "Optimal midterm unit commitment in large scale systems including fuel constrained thermal and pumped-storage hydro," *IEEE Trans. Power Syst.*, vol. 4, no. 3, pp. 1065-1073, Aug. 1989

[5] Z. Yu, F. Sparrow, and D. Nderitu, "Long-term hydrothermal scheduling using composite thermal and composite hydro representations," *IEE Proceedings on Generation, Transmission and Distribution*, vol. 145, no. 2, pp. 210-216, Mar. 1998

[6] Y. Fu, M. Shahidehpour and Z. Li, "Long-term security-constrained unit commitment: hybrid subgradient and Danzig-Wolfe decomposition," *IEEE Trans. Power Syst.*, vol. 20, no. 4, pp. 2093-2106, Nov. 2005
[7] E. Ni, X. Guan, and R. Li, "Scheduling hydrothermal power systems with cascaded and head-dependent reservoirs," *IEEE Trans. Power Syst.*, vol. 14, no. 3, pp. 1127–1132, Aug. 1999
[8] M. Christoforidis, M. Aganagic, B. Awobamise, S. Tong, A.F. Rahimi, "Long-Term/Mid-Term Resource Optimization of a Hydrodominant Power System Using Interior Point Method ," IEEE Transactions on Power Systems, Vol. 11, No. 1, pp. 287-294, February 1996
[9] R.W. Ferrero, J.F. Rivera, M. Shahidehpour, "A dynamic programming two-stage algorithm for long-term hydrothermal scheduling of multireservoir systems," IEEE Transactions on Power Systems, Vol. 13, No. 4, pp. 1534-1540, Nov. 1998
[10] L. Martinez and S. Soares, "Comparison Between Closed-Loop and Partial Open-Loop Feedback Control Policies in Long Term Hydrothermal Scheduling," IEEE Transactions on Power Systems, Vol. 17, No. 2, pp. 330-336, May 2002
[11] J. Munoz, N. Jimenez-Redondo, J. Perez-Ruiz, and J. Barquin, "Natural gas network modeling for power systems reliability studies," *Proceedings of IEEE/PES General Meeting*, vol. 4, pp. 23-26, Jun. 2003
[12] C. Unsihuay, J. W. Marangon Lima, and A.C. Zambroni de Souza, "Modeling the Integrated Natural Gas and Electricity Optimal Power Flow," *Proceedings of IEEE/PES General Meeting*, pp. 24-28, Jun. 2007
[13] S. An, Q. Li, and T. Gedra, "Natural gas and electricity optimal power flow," *Proceedings of IEEE/PES Transmission and Distribution Conference and Exposition*, vol. 1, pp. 7-12, 2003
[14] C. Unsihuay, J. Marangon Lima, and A. Zambroni de Souza, "Short-term operation planning of integrated hydrothermal and natural gas systems," *Proceedings of IEEE/PES Power Tech Conference*, 2007
[15] T. Li, M. Eremia, and M. Shahidehpour, "Interdependency of natural gas network and power system security," *IEEE Trans. Power Syst.*, vol. 23, no. 4, pp. 1817-1824, Nov. 2008
[16] J. Ellison, "Modeling the US natural gas network,", *Institute of Industrial Engineers (IIE) Transaction*, 39, 2007
[17] H. Min, W. Beyeler, T. Brown, Y. Son, and A. Jones, "Toward modeling and simulation of critical national infrastructure independencies," *Institute of Industrial Engineers (IIE) Transaction*, 39, pp. 57–71, 2007
[18] L. Wu, M. Shahidehpour, and Z. Li, "GENCO's risk-constrained hydrothermal planning," *IEEE Trans. Power Syst.* vol. 23, no. 4, pp. 1847 – 1858, Nov. 2008
[19] G. Paul, *Monte Carlo Method in Financial Engineering*. New York: Springer, 2003
[20] L. Wu, M. Shahidehpour, and T. Li, "Cost of reliability based on stochastic unit commitment," *IEEE Trans. Power Syst.* vol. 23, no. 3, pp. 1364 - 1374, Aug. 2008
[21] Billinton R., Allan N. R., *Reliability Evaluation of Power Systems*, *Plenum Press*, 1984
[22] L. Wu, M. Shahidehpour, and T. Li, "Stochastic security-constrained unit commitment," *IEEE Trans. Power Syst*., vol. 22, no. 2, pp. 800–811, May. 2007
[23] L. Wu, M. Shahidehpour, and T. Li, "GENCO's risk-based maintenance outage scheduling," *IEEE Trans. Power Syst.*, vol. 23, no. 1, pp. 127-136, Feb. 2008
[24] N. Z. Shor, *Minimization Methods for Non-Differentiable Functions*, ser. Springer in Computational Mathematics New York, 1985
[25] H. Heitsch, W. Romisch, " Scenario Reduction Algorithms in Stochastic Programming," Computational Optimization and Applications, Vol 24, Issue 2-3, pp. 187-206, Feb-March 2003

**Cem Sahin** received the B.S. and M.S. degrees in electrical engineering from Middle East Technical University (METU), Turkey, in 1999 and 2003, respectively. He is pursuing the Ph.D. degree at METU. He is a visiting research scholar at Illinois Institute of Technology, Chicago. His research interests include power systems optimization and power markets.

**Zuyi Li** (SM'09) received his BS degree in E.E. from Shanghai Jiaotong University in 1995, MS degree in E.E. from Tsinghua University, China, in 1998 and Ph.D degree in E.E. from Illinois Institute of Technology, USA, in 2002. Presently, he is an associate professor in the ECE Department.

**Mohammad Shahidehpour** (F'01) is the Bodine Professor in the Electrical and Computer Engineering Department at Illinois Institute of Technology. Dr. Shahidehpour is the VP for publication of the IEEE Power and Energy Society and the recipient an honorary doctorate form the Polytechnic University of Bucharest in Romania. He is an IEEE Distinguished Lecturer.

**Ismet Erkmen** is the Chairman in the Electrical and Computer Engineering Department at Middle East Technical University (METU), Ankara-TURKEY.

# Hourly Scheduling of DC Transmission Lines in SCUC with Voltage Source Converters

Azim Lotfjou, *Member IEEE,* Mohammad Shahidehpour, *Fellow, IEEE,* Yong Fu, *Member IEEE*[1]

***Abstract*— This paper presents the modeling of high voltage direct current (DC) transmission systems with voltage source converters (VSCs) in security-constrained unit commitment (SCUC). The impact of VSC-DC transmission system on the economics and the security of integrated AC/DC transmission systems is discussed. The nonlinear AC/DC equations are linearized and the Newton-Raphson method is utilized to solve the linearized network in the base case and contingencies. The SCUC solution will determine the optimal hourly schedule of controllable VSC-DC transmission systems in electricity markets. Numerical examples show the efficiency of the proposed model.**

***Keywords:*** *high voltage direct current transmission lines, voltage source converters, security-constrained unit commitment,*

## NOMENCLATURE

$b$ Index of AC buses
$c$ Superscript for contingency
$NB$ Number of AC buses
$E_h$ AC side voltage of the converter $h$
$h$ Index of DC converters
$i$ Index of units
$t$ Index of hour
*inj* Superscript for an injection
$I_{dc,h}$ DC current of converter $h$
$U_{it}$ on/off state of generating unit $i$ at time $t$
$\hat{U}_{it}$, $\hat{P}_{it}$ State and generation dispatch solution of unit $i$ at time $t$
$l$ Index of lines
$m$ Index of AC bus terminals connected with converters
*max, min* Subscript for maximum and minimum values
$M_h$ Modulation index of converter $h$
$P_{it}$ Generation dispatch of unit $i$ at time $t$
$P_h$ DC active power through converter $h$
$P_m$ Withdrawal real power at ac bus $m$
$P_{term,h}$ Active power injected into the converter $h$
$Q_h$ DC reactive power through the converter $h$
$Q_m$ Withdrawal reactive power at AC bus $m$
$Q_{term,h}$ Reactive power injected into converter $h$
$R_{dc}$ Resistance of DC line
$SP1_b$, $SP2_b$ Slack variables for real power mismatch at bus $b$ (>=0 )
$SQ1_b$, $SQ2_b$ Slack variables for reactive power mismatch at bus $b$ (>=0 )
$w$ Objective of SCUC subproblem
$X_h$ Leakage reactance of coupling transformer connected to converter $h$
$V_m$ AC voltage at bus $m$
$V_{dc,h}$ DC voltage of converter $h$
$\phi_h$ Power factor lagging/leading angle of converter $h$ ($0 \le \phi_h \le \frac{\pi}{2}$ for rectifier, $-\frac{\pi}{2} \le \phi_h \le 0$ for inverter)
$\Delta P_m$, $\Delta Q_m$ Active and reactive power mismatch at ac bus $m$
$\Delta R1_h$ $\Delta R2_h$, $\Delta R3_h$ Mismatches of DC power flow equations related to converter $h$
$\Delta_i$ Permissible real power adjustment for unit $i$
$\mathbf{A}$ Bus-unit incidence matrix
$\mathbf{G}_h$ Admittance matrix of DC network for converters $h$
$\mathbf{U}$ Generating unit state vector (0 or 1 values)
$\hat{\mathbf{U}}$, $\hat{\mathbf{P}}$ Generating unit state and economic dispatch solutions
$\mathbf{I_{dc}}$, $\mathbf{\Delta I_{dc}}$ Vector of DC current and its increment vector
$\mathbf{J1}$, $\mathbf{J2}$, $\mathbf{J3}$, $\mathbf{J4}$, $\mathbf{J5}$, $\mathbf{J6}$ Jacobian matrices
$\mathbf{M}$, $\mathbf{\Delta M}$ Modulation index vector and its increment vector
$\mathbf{M_0}$ Initial modulation index vector
$\mathbf{MP1}$, $\mathbf{MP2}$, $\mathbf{MQ1}$, $\mathbf{MQ2}$ Mismatch vectors
$\mathbf{P}$, $\mathbf{Q}$ Vector of real and reactive power generation of units
$\mathbf{V}$, $\mathbf{V_{dc}}$ AC and DC bus voltage vectors
$\mathbf{E}$, $\mathbf{\Delta E}$ Vector for AC side voltage of converters and its increment vectors
$\boldsymbol{\varphi}$, $\boldsymbol{\Delta\varphi}$ Power factor angle vector and its increment vector
$\boldsymbol{\delta}$, $\boldsymbol{\Delta\delta}$ Bus phase angle vector and its increment vector
$\mathbf{dP_0}$ Initial AC bus real power mismatch vector
$\mathbf{dQ_0}$ Initial AC bus reactive power mismatch vector
$\mathbf{dR1_0}$, $\mathbf{dR2_0}$, $\mathbf{dR3_0}$ Initial mismatch vectors of DC equations
$\pi$, $\underline{\psi}$, $\overline{\psi}$ Simplex multipliers vectors
$\mathbf{\Delta PL_{ac}}$, $\mathbf{\Delta PL_{dc}}$ Vector of AC and DC line flow Increments
$\mathbf{\Delta T}$ Vector of transformer tap increment
$\mathbf{\Delta\gamma}$ Vector of phase-shifter angle increment

## I. INTRODUCTION

Modern power systems introduce VSC-DC transmission systems to enhance the operation and the flexibility of AC transmission systems in electricity markets. VCS-DC transmission systems use insulated gate bipolar transistors (IGBTs) for transmitting remote energy resources reliably and economically to load centers [1-3]. VSC-DC links use pulse

[1] Azim Lotfjou and Mohammad Shahidehpour are with the ECE Department at Illinois Institute of Technology. Yong Fu is with the ECE Department at Mississippi State University. This work was supported in part by the U.S. Department of Energy Grants # DE-EE 0001380.000 and DE-EE 0002979.
.

width modulation (PWM) to set firing angles of IGBT switches in order to offer high speed controls.

In contrast to current source converter (CSC-DC) systems, VSC-DC transmission systems allow rapid and independent control of active and reactive power flows in all four quadrants by changing PWM firing patterns. VSC-DC transmission systems provide a full control to turn on/off IGBT switches for regulating DC voltages and power factors instantaneously and providing continuous and dynamic voltage regulations at AC transmission systems. Unlike CSCs, VSCs would not require active voltage commutations to switch off IGBTs, which enables them to feed isolated AC loads [4, 5]. Recently, VSC-DC taps were introduced to deliver energy to small loads located in the vicinity of DC lines [6, 7].

VSC-DC transmission systems were modeled as back-to-back links or similar configurations in power flow analyses [8-11]. Such studies utilized the Newton-Raphson method to solve nonlinear VCS-DC power flow equations. Two control actions, i.e., constant active power plus constant DC voltage (PV) and constant active power plus constant reactive power (PQ) were defined to maintain the secure operation of VSC-DC transmission systems. Also VSC-DC transmission constraints were included in the optimal power flow formulation by assuming that the total active power injection to a VSC-DC link was equal to power losses in the link.

In contrast to numerous publications on the modeling of phase shifters and FACTS devices in electricity markets [12-13], few studies investigated the optimal control of VSC-DC transmission systems in electricity markets. In this paper, we analyze the control and the scheduling of multi-terminal VSC-DC transmission systems and provide the optimal schedule for the control of VSC-DC transmission systems in the base case and contingencies.

We include the VSC-DC model in SCUC. As one of key tools for market clearing, the SCUC solution will provide the optimal hourly schedule of generating units and the optimal schedule of VSC-DC transmission systems for enhancing the security and economics. This paper uses sequential linear programming to find a feasible solution to the SCUC subproblem which may not guarantee a global optimal solution.

The rest of this paper is organized as follows. Section II discusses the DC modeling. The SCUC integrated with DC systems is presented in section III. The proposed model is tested with a 6-bus system and the IEEE 118-Bus system in section IV. We summarize our conclusion in section V.

## II. VSC-DC MODEL

### A. VSC-DC Transmission Model

We assume a balanced three phase conditions. In order to model the VSC $h$ which is connected to the AC terminal's bus $m$, five variables including the direct voltage $V_{dc,h}$, direct current $I_{dc,h}$, converter AC voltage $E_h$, PWM modulation index $M_h$ and the lagging/leading power factor angle $\varphi_h$, are defined in Fig. 1 [4]. $E_h$ is controlled by adjusting $M_h$ as

$$\begin{cases} E_h = \dfrac{M_h}{2\sqrt{2}} V_{dc,h} & \text{for rectifier} \\ E_h = -\dfrac{M_h}{2\sqrt{2}} V_{dc,h} & \text{for inverter} \end{cases} \quad (1)$$

where $0 \le M_h \le 1$. Also $P_{term,h}$ is controlled by adjusting $\varphi_h$,

$$\begin{cases} P_{term,h} = \dfrac{V_m E_h \sin(\varphi_h)}{X_h} & \text{for rectifier} \\ P_{term,h} = -\dfrac{V_m E_h \sin(\varphi_h)}{X_h} & \text{for inverter} \end{cases} \quad (2)$$

where $0 \le \phi_h \le \dfrac{\pi}{2}$ for rectifiers and $-\dfrac{\pi}{2} \le \phi_h \le 0$ for inverters. Assuming converter transformers, valves, and DC capacitors are lossless, the active power converted into DC is

$$P_{term,h} = P_h = V_{dc,h} I_{dc,h} \quad (3)$$

Combining (1)-(3), we obtain the second converter equation as

$$\begin{cases} I_{dc,h} = \dfrac{M_h V_m \sin(\varphi_h)}{2\sqrt{2} X_h} & \text{for rectifier} \\ I_{dc,h} = -\dfrac{M_h V_m \sin(\varphi_h)}{2\sqrt{2} X_h} & \text{for inverter} \end{cases} \quad (4)$$

The VSC in Fig. 1 generates $-Q_h$, where

$$Q_h = -\frac{E_h (E_h - V_m \cos(-\varphi_h))}{X_h} \quad (5)$$

The reactive power flow from bus $m$ to VSC-DC link is

$$Q_{term,h} = \frac{V_m (V_m - E_h \cos(\varphi_h))}{X_h} \quad (6)$$

The difference between $Q_{term,h}$ and $Q_h$ is the reactive power loss in the coupling transformer series reactance [14].

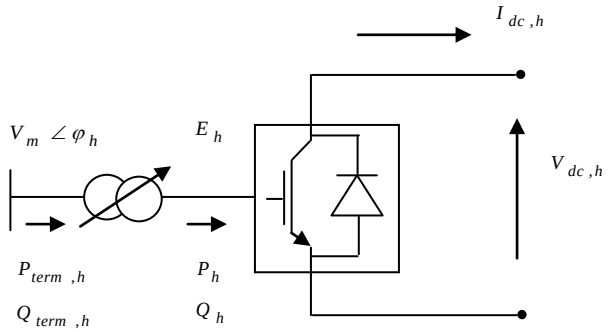


Fig 1. Schematic diagram of a VSC

### B. DC Transmission Line Model

In this paper, we model two-terminal DC transmission systems based on the converter model presented in section III.A. However, mathematical derivations can be easily expanded to any DC configurations with any number of VSCs. In Fig. 2, two VSCs are connected to AC buses $m1$ and $m2$ via coupling transformers. We assume that the converter $h1$ is a rectifier and converter $h2$ operates as an inverter. Converters $h1$ and $h2$ are connected by a DC transmission line with a resistance $R_{dc}$. Here, (7) represents the model for a two-terminal DC configuration

$$\begin{bmatrix} I_{dc,h1} \\ I_{dc,h2} \end{bmatrix} = \begin{bmatrix} \frac{1}{R_{dc}} & \frac{1}{R_{dc}} \\ \frac{1}{R_{dc}} & \frac{1}{R_{dc}} \end{bmatrix} \begin{bmatrix} V_{dc,h1} \\ V_{dc,h2} \end{bmatrix} \quad (7)$$

For a multi-terminal DC system, the equation in matrix form is

$$\mathbf{I_{dc}} = \mathbf{G.V_{dc}} \quad (8)$$

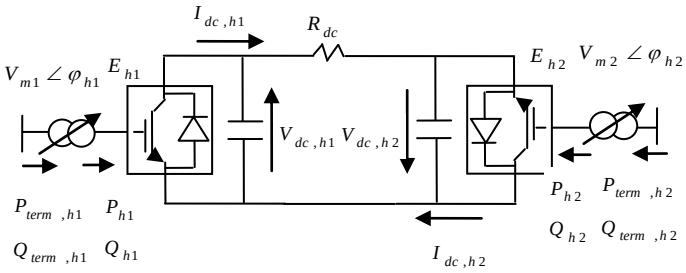


Fig 2. Schematic of a two-terminal VSC-DC system

### *C. Control Modes of DC Transmission*

DC links have two control modes including PV and PQ at their converter stations. In the PV control mode (9), VSC sets $P_h$ and $E_h$ at a specified level, while the PQ control mode (10) will keep a constant active power flow and reactive power flow. In each VSC-DC transmission link, at least one converter would operate in the PV mode to adjust DC voltages while others operate in PV or PQ mode.

$$P_h - P_h^{spec} = 0, \quad E_h - E_h^{spec} = 0 \quad (9)$$

$$P_h - P_h^{spec} = 0, \; Q_h - Q_h^{spec} = 0 \quad (10)$$

The PV control is used in VSC-DC transmission links to secure the transfer of scheduled active power while maintaining AC voltages against possible disturbances. VSC-DC injects a specific amount of reactive power into the AC system for satisfying reactive power requirements and increasing the available transfer capacity (ATC) of AC system in the PQ control mode. In this paper, we consider upper and lower limits of control variables for the optimal control of VSC-DC system in the SCUC solution.

A back-to-back VSC-DC link that connects two AC systems would have one station for both rectifier and inverter systems with a zero DC line resistance. In back-to-back VSC-DC systems, (11) and (12) will replace (3) and (8), respectively.

$$P_{h1} = P_{h2} \quad (11)$$

$$V_{dc,h1} = V_{dc,h2} \quad (12)$$

### *D. VSC-DC Power Flow Equations*

The nodal power balance at bus *m* which is connected to converter *h* is given as

$$\Delta P_m = P_m^{inj} - P_m - P_{term,h} = 0 \quad (13)$$

$$\Delta Q_m = Q_m^{inj} - Q_m - Q_{term,h} = 0 \quad (14)$$

where, $P_{term,h} = V_{dc,h} I_{dc,h}$ and $Q_{term,h} = \frac{V_m (V_m - E_h \cos(\varphi_h))}{X_h}$

The power flow in per-unit for converter *h* at the AC terminal bus *m* is given as

$$\begin{cases} \Delta R1_h = E_h - \frac{M_h}{2\sqrt{2}} V_{dc,h} = 0 & \text{for rectifier} \\ \Delta R1_h = E_h + \frac{M_h}{2\sqrt{2}} V_{dc,h} = 0 & \text{for inverter} \end{cases} \quad (15)$$

$$\begin{cases} \Delta R2_h = I_{dc,h} - \frac{M_h V_m \sin(\varphi_h)}{2\sqrt{2} X_h} = 0 & \text{for rectifier} \\ \Delta R2_h = I_{dc,h} + \frac{M_h V_m \sin(\varphi_h)}{2\sqrt{2} X_h} = 0 & \text{for inverter} \end{cases} \quad (16)$$

$$\Delta R3_h = f(\mathbf{V_{dc}}, I_{dc,h}) = I_{dc,h} - \mathbf{G_h V_{dc}} = 0 \quad (17)$$

## III. VSC-DC SYSTEM IN SCUC

Fig. 3 depicts the market clearing algorithm based on SCUC with AC/DC network constraints where market participants in AC systems (i.e., generation companies and customers) submit bids to the independent system operator (ISO). At the same time, transmission companies collect and send AC/DC network data to the ISO. The ISO executes the SCUC to clear the market with AC/DC transmission systems [15] in the base case and contingencies.

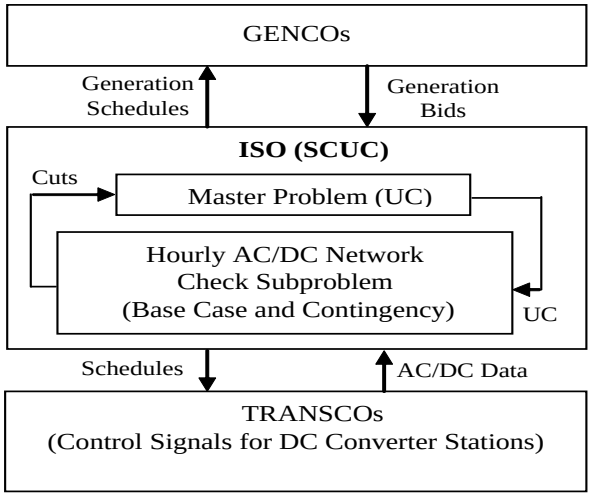


Fig. 3. Market clearing model with AC/DC network constraints

### *A. SCUC Formulation*

The SCUC with integrated AC/DC transmission systems is stated as the following nonlinear optimization problem:

$$\begin{aligned} &Min \quad f(\mathbf{x}) \\ &S.t. \\ &\quad \mathbf{g1(x)} \le \mathbf{b1} \\ &\quad \mathbf{ge1(x)} = \mathbf{be1} \\ &\quad \mathbf{g2(x)} \le \mathbf{b2} \\ &\quad \mathbf{ge2(x)} = \mathbf{be2} \end{aligned} \quad (18)$$

Variable $\mathbf{x}$ represents the on/off status and economic dispatch (ED) of generating units, startup/shut down indicators, and AC/DC control and state variables. The objective is to minimize the operating cost including generation and startup/ shutdown costs. In (18), the first set of inequality constraints, $\mathbf{g1(x)} \le \mathbf{b1}$, and equality constraints, $\mathbf{ge1(x)} = \mathbf{be1}$, represents UC constraints including power balance, generating

unit capacity, system spinning and operating reserve requirements, ramping up/down limits, minimum up/down time limits, maximum number of simultaneous on/offs in a plant, maximum number of on/offs of a generating unit in a given period, fuel and multiple emission limits. The second set of inequality constraints, $\mathbf{g2(x)} \le \mathbf{b2}$, and equality constraints $\mathbf{ge2(x)} = \mathbf{be2}$, include

- AC/DC power flow equations
- Limits on AC/DC control variables including real and reactive power generations, controlled shunt capacitors, tap-changing and phase-shifting transformers, modulation index and converter transformer tap ratios
- AC/DC network security constraints including AC/DC transmission flow and bus voltage limits, and limits to DC currents, voltages and power of converters
- Time limited corrective controls of contingencies such as permissible real power adjustment

### *B. SCUC Subproblem Formulation in Base Case*

DC transmission system constraints are included in the hourly AC/DC network check subproblem which minimizes the AC bus real and reactive power mismatch (19) based on the UC solution while satisfying network security constraints (20)-(35). In essence, AC/DC transmission violations appear as power mismatches at AC buses (20). The hourly subproblem (19)-(35) minimizes slack variables ($MP\_1$, $MP\_2$) and ($MQ\_1$, $MQ\_2$) which represent the amount of real and reactive power mismatch that should be added to corresponding buses to remove violations. (21) considers DC transmission flows. (22)-(35) represents limits on real and reactive power generations, real and reactive power withdrawals at AC converter terminals, AC and DC transmission flows, AC bus voltage magnitudes, transformer tap settings, phase shifter angles, DC converter voltages and currents, converter modulation index, AC converter voltages and power factor angles. The elements of Jacobian matrices $\mathbf{J1 - J6}$ are calculated in the Appendix A.

$$Min \quad w(\hat{\mathbf{U}}, \hat{\mathbf{P}}) = \sum_{b=1}^{NB} (MP\_1_b + MP\_2_b) + (MQ\_1_b + MQ\_2_b) \tag{19}$$

*s.t.*

$$\begin{bmatrix} \mathbf{A} \cdot \Delta\mathbf{P} \\ \mathbf{A} \cdot \Delta\mathbf{Q} \end{bmatrix} - [\mathbf{J1}] \begin{bmatrix} \Delta\boldsymbol{\delta} \\ \Delta\mathbf{V} \\ \Delta\mathbf{T} \\ \Delta\boldsymbol{\gamma} \\ \Delta\mathbf{V}_{\mathbf{dc}} \\ \Delta\mathbf{I}_{\mathbf{dc}} \\ \Delta\mathbf{E} \\ \Delta\boldsymbol{\varphi} \end{bmatrix} + \begin{bmatrix} \mathbf{MP1} \\ \mathbf{MQ1} \end{bmatrix} - \begin{bmatrix} \mathbf{MP2} \\ \mathbf{MQ2} \end{bmatrix} = \begin{bmatrix} \mathbf{dP}_{\mathbf{0}} \\ \mathbf{dQ}_{\mathbf{0}} \end{bmatrix} \tag{20}$$

$$-[\mathbf{J2}] \begin{bmatrix} \Delta\mathbf{V} \\ \Delta\mathbf{V}_{\mathbf{dc}} \\ \Delta\mathbf{I}_{\mathbf{dc}} \\ \Delta\mathbf{M} \\ \Delta\mathbf{E} \\ \Delta\boldsymbol{\varphi} \end{bmatrix} = \begin{bmatrix} \mathbf{dR1}_{\mathbf{0}} \\ \mathbf{dR2}_{\mathbf{0}} \\ \mathbf{dR3}_{\mathbf{0}} \end{bmatrix} \tag{21}$$

$$\Delta\mathbf{P} = \mathbf{0} \qquad \boldsymbol{\pi} \tag{22}$$

$$\Delta\mathbf{Q}_{\mathbf{min}} \le \Delta\mathbf{Q} \le \Delta\mathbf{Q}_{\mathbf{max}} \qquad \underline{\boldsymbol{\psi}}, \overline{\boldsymbol{\psi}} \tag{23}$$

$$\Delta\mathbf{P}_{\mathbf{dc,\,min}} \le \Delta\mathbf{P}_{\mathbf{dc}} = [\mathbf{J3}] \begin{bmatrix} \Delta\mathbf{V}_{\mathbf{dc}} \\ \Delta\mathbf{I}_{\mathbf{dc}} \end{bmatrix} \le \Delta\mathbf{P}_{\mathbf{dc,\,max}} \tag{24}$$

$$\Delta\mathbf{Q}_{\mathbf{dc,min}} \le \Delta\mathbf{Q}_{\mathbf{dc}} = [\mathbf{J4}] \begin{bmatrix} \Delta\mathbf{V}_{\mathbf{dc}} \\ \Delta\mathbf{I}_{\mathbf{dc}} \\ \Delta\boldsymbol{\varphi} \end{bmatrix} \le \Delta\mathbf{Q}_{\mathbf{dc,max}} \tag{25}$$

$$\Delta\mathbf{PL}_{\mathbf{ac,min}} \le \Delta\mathbf{PL}_{\mathbf{ac}} = [\mathbf{J5}] \begin{bmatrix} \Delta\boldsymbol{\delta} \\ \Delta\mathbf{V} \\ \Delta\mathbf{T} \\ \Delta\boldsymbol{\gamma} \end{bmatrix} \le \Delta\mathbf{PL}_{\mathbf{ac,max}} \tag{26}$$

$$\Delta\mathbf{PL}_{\mathbf{dc,min}} \le \Delta\mathbf{PL}_{\mathbf{dc}} = [\mathbf{J6}] \begin{bmatrix} \Delta\mathbf{V}_{\mathbf{dc}} \\ \Delta\mathbf{I}_{\mathbf{dc}} \end{bmatrix} \le \Delta\mathbf{PL}_{\mathbf{dc,max}} \tag{27}$$

$$\Delta\mathbf{V}_{\mathbf{min}} \le \Delta\mathbf{V} \le \Delta\mathbf{V}_{\mathbf{max}} \tag{28}$$

$$\Delta\mathbf{T}_{\mathbf{min}} \le \Delta\mathbf{T} \le \Delta\mathbf{T}_{\mathbf{max}} \tag{29}$$

$$\Delta\boldsymbol{\gamma}_{\mathbf{min}} \le \Delta\boldsymbol{\gamma} \le \Delta\boldsymbol{\gamma}_{\mathbf{max}} \tag{30}$$

$$\Delta\mathbf{V}_{\mathbf{dc,min}} \le \Delta\mathbf{V}_{\mathbf{dc}} \le \Delta\mathbf{V}_{\mathbf{dc,max}} \tag{31}$$

$$\Delta\mathbf{I}_{\mathbf{dc,\,min}} \le \Delta\mathbf{I}_{\mathbf{dc}} \le \Delta\mathbf{I}_{\mathbf{dc,\,max}} \tag{32}$$

$$\Delta\mathbf{M}_{\mathbf{min}} \le \Delta\mathbf{M} \le \Delta\mathbf{M}_{\mathbf{max}} \tag{33}$$

$$\Delta\mathbf{E}_{\mathbf{min}} \le \Delta\mathbf{E} \le \Delta\mathbf{E}_{\mathbf{max}} \tag{34}$$

$$\Delta\boldsymbol{\varphi}_{\mathbf{min}} \le \Delta\boldsymbol{\varphi} \le \Delta\boldsymbol{\varphi}_{\mathbf{max}} \tag{35}$$

The optimization of (19)-(35) is described as follows,

1. Initialize AC/DC state variables and settings. For example, $\delta = 0$ rad, $V = 1\ pu$, $V_{dc} = \pm 1\ pu$, $I_{dc} = 0$ amp, $M = 1$, $E = 1\ pu$ and $\varphi = 0$ rad. Calculate corresponding Jacobian matrices $\mathbf{J1 - J6}$, initial AC bus mismatch vectors $\mathbf{dP}_{\mathbf{0}}$ and $\mathbf{dQ}_{\mathbf{0}}$, and initial DC power mismatch $\mathbf{dR1}_{\mathbf{0}}$, $\mathbf{dR2}_{\mathbf{0}}$, $\mathbf{dR3}_{\mathbf{0}}$ based on the given UC solution.
2. Use LP to minimize (19) and calculate changes in AC/DC state and control variables (i.e., $\Delta\boldsymbol{\delta}$, $\Delta\mathbf{V}$, $\Delta\mathbf{T}$, $\Delta\boldsymbol{\gamma}$, $\Delta\mathbf{V}_{\mathbf{dc}}$, $\Delta\mathbf{I}_{\mathbf{dc}}$, $\Delta\mathbf{M}$, $\Delta\mathbf{E}$ and $\Delta\boldsymbol{\varphi}$).
3. Update state and control variables. Recalculate elements of Jacobian matrices and mismatch vectors.
4. Minimize (19) and calculate changes in AC/DC transmission system state and control variables. If the incremental change in objective values within the last two iterations is less than a specified tolerance (i.e., $\mathbf{dR1}, \mathbf{dR2}, \mathbf{dR3} \le \boldsymbol{\varepsilon}$), the DC power flow has converged; stop the iterative process. Otherwise, go back to Step 3.

If $w(\hat{\mathbf{U}}, \hat{\mathbf{P}})$ is larger than zero, ED cannot provide a feasible power flow solution to satisfy AC/DC flow constraints. Hence, a Benders cut (36) will be formed and added to the next iteration of UC problem.

$$w(\mathbf{U}, \mathbf{P}) = w(\hat{\mathbf{U}}, \hat{\mathbf{P}}) + \sum_{i=1}^{NG} (\overline{\pi}_{it} - \underline{\pi}_{it})(P_{it} - \hat{P}_{it}) + \sum_{i=1}^{NG} (\overline{\psi}_{it} Q_{\max,\,i} - \underline{\psi}_{it} Q_{\min,\,i})(U_{it} - \hat{U}_{it}) \le 0 \tag{36}$$

### C. Corrective and Preventive Actions for Managing Contingencies

In each contingency, sufficient corrective and preventive actions are considered based on $\left|P_{it} - \hat{P}_{it}^{0}\right| \le \Delta_i$ for managing AC/DC transmission violations [16]. $\Delta_i$ is equal to 1/6 of unit *i* hourly ramping which represents the physically accepted adjustment of generating unit in ten minutes. Corrective actions refer to the redispatch of generating units when satisfying transmission flow violations in real time. Preventive actions refer to day-ahead adjustments in the base case UC and ED when considering potential contingencies. Preventive actions cannot be implemented in real time when responding to power flow violations. The hourly AC/DC network check subproblem is formulated as

$$Min \quad w^c(\hat{\mathbf{U}}, \hat{\mathbf{P}}) = \sum_{b=1}^{NB} \left(MP\ 1_b^c + MP\ 2_b^c + MQ\ 1_b^c + MQ\ 2_b^c\right) \tag{37}$$

$$\begin{bmatrix} \mathbf{A}\cdot\Delta\mathbf{P}^c \\ \mathbf{A}\cdot\Delta\mathbf{Q}^c \end{bmatrix} - [\mathbf{J1}] \begin{bmatrix} \Delta\boldsymbol{\delta}^c \\ \Delta\mathbf{V}^c \\ \Delta\mathbf{T}^c \\ \Delta\gamma^c \\ \Delta\mathbf{V}_{\mathbf{dc}}^c \\ \Delta\mathbf{I}_{\mathbf{dc}}^c \\ \Delta\mathbf{E}^c \\ \Delta\boldsymbol{\varphi}^c \end{bmatrix} + \begin{bmatrix} \mathbf{MP1}^c \\ \mathbf{MQ1}^c \end{bmatrix} - \begin{bmatrix} \mathbf{MP2}^c \\ \mathbf{MQ2}^c \end{bmatrix} = \begin{bmatrix} \mathbf{dP}_{\mathbf{0}}^c \\ \mathbf{dQ}_{\mathbf{0}}^c \end{bmatrix} \tag{38}$$

$$-[\mathbf{J2}] \begin{bmatrix} \Delta\mathbf{V}^c \\ \Delta\mathbf{V}_{\mathbf{dc}}^c \\ \Delta\mathbf{I}_{\mathbf{dc}}^c \\ \Delta\mathbf{M}^c \\ \Delta\mathbf{E}^c \\ \Delta\boldsymbol{\varphi}^c \end{bmatrix} = \begin{bmatrix} \mathbf{dR1}_{\mathbf{0}}^c \\ \mathbf{dR2}_{\mathbf{0}}^c \\ \mathbf{dR3}_{\mathbf{0}}^c \end{bmatrix} \tag{39}$$

$$\left|\mathbf{P}^c - \hat{\mathbf{P}}^0\right| \le \boldsymbol{\Delta} \qquad \overline{\boldsymbol{\pi}}^c,\ \underline{\boldsymbol{\pi}}^c \tag{40}$$

$$\Delta\mathbf{Q}_{\mathbf{min}}^c \le \Delta\mathbf{Q}^c \le \Delta\mathbf{Q}_{\mathbf{max}}^c \qquad \underline{\boldsymbol{\psi}}^c,\ \overline{\boldsymbol{\psi}}^c \tag{41}$$

$$\Delta\mathbf{P}_{\mathbf{dc,\,min}}^c \le \Delta\mathbf{P}_{\mathbf{dc}}^c \le \Delta\mathbf{P}_{\mathbf{dc,\,max}}^c \tag{42}$$

$$\Delta\mathbf{Q}_{\mathbf{dc,\,min}}^c \le \Delta\mathbf{Q}_{\mathbf{dc}}^c \le \Delta\mathbf{Q}_{\mathbf{dc,\,max}}^c \tag{43}$$

$$\Delta\mathbf{PL}_{\mathbf{ac,\,min}}^c \le \Delta\mathbf{PL}_{\mathbf{ac}}^c \le \Delta\mathbf{PL}_{\mathbf{ac,\,max}}^c \tag{44}$$

$$\Delta\mathbf{PL}_{\mathbf{dc,\,min}}^c \le \Delta\mathbf{PL}_{\mathbf{dc}}^c \le \Delta\mathbf{PL}_{\mathbf{dc,\,max}}^c \tag{45}$$

$$\Delta\mathbf{V}_{\mathbf{min}}^c \le \Delta\mathbf{V}^c \le \Delta\mathbf{V}_{\mathbf{max}}^c \tag{46}$$

$$\Delta\mathbf{T}_{\mathbf{min}}^c \le \Delta\mathbf{T}^c \le \Delta\mathbf{T}_{\mathbf{max}}^c \tag{47}$$

$$\Delta\gamma_{\mathbf{min}}^c \le \Delta\gamma^c \le \Delta\gamma_{\mathbf{max}}^c \tag{48}$$

$$\Delta\mathbf{V}_{\mathbf{dc,\,min}}^c \le \Delta\mathbf{V}_{\mathbf{dc}}^c \le \Delta\mathbf{V}_{\mathbf{dc,\,max}}^c \tag{49}$$

$$\Delta\mathbf{I}_{\mathbf{dc,\,min}}^c \le \Delta\mathbf{I}_{\mathbf{dc}}^c \le \Delta\mathbf{I}_{\mathbf{dc,\,max}}^c \tag{50}$$

$$\Delta\mathbf{M}_{\mathbf{min}}^c \le \Delta\mathbf{M}^c \le \Delta\mathbf{M}_{\mathbf{max}}^c \tag{51}$$

$$\Delta\mathbf{E}_{\mathbf{min}}^c \le \Delta\mathbf{E}^c \le \Delta\mathbf{E}_{\mathbf{max}}^c \tag{52}$$

$$\Delta\boldsymbol{\varphi}_{\mathbf{min}}^c \le \Delta\boldsymbol{\varphi}^c \le \Delta\boldsymbol{\varphi}_{\mathbf{max}}^c \tag{53}$$

The objective function (37) is introduced for minimizing real and reactive power mismatches when calculating a converged power flow solution subject to transmission flow and bus voltage limits. If $w^c(\hat{\mathbf{U}}, \hat{\mathbf{P}})$ is larger than zero, a Benders cut (54) for contingency $c$ will be formed and added to UC for calculating the next iterative solution of master problem.

$$w^c(\hat{\mathbf{U}}, \hat{\mathbf{P}}) = \boldsymbol{\pi}^c(\mathbf{P} - \hat{\mathbf{P}}^0) + \overline{\boldsymbol{\psi}}^c\mathbf{Q}_{\max}(\mathbf{U} - \hat{\mathbf{U}}^0) - \underline{\boldsymbol{\psi}}^c\mathbf{Q}_{\min}(\mathbf{U} - \hat{\mathbf{U}}^0) \le 0 \tag{54}$$

## IV. Numerical Examples

We study a six bus system and a modified IEEE-118 bus system in the base case and contingencies.

### A. Six-bus System

The six-bus system shown in Fig. 4 has three generating units, seven AC transmission lines, two transformers and three loads. The slack bus is bus 1.

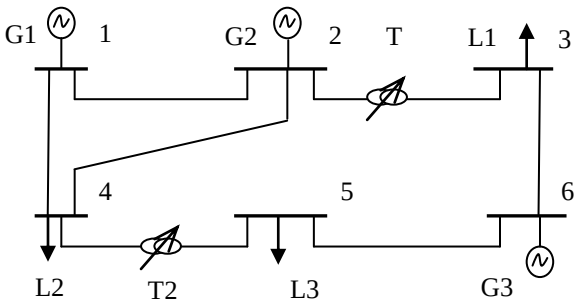


Fig. 4. Schematic diagram of six-bus system

The system data are presented in Appendix B. The following seven cases are tested in which Case 0 is for the UC problem (Base Case), Cases 1-3 consider SCUC with network constraints, and Cases 4-6 evaluate contingencies.

**Case 0:** UC without transmission constraints

**Case 1:** SCUC with AC transmission constraints

**Case 2:** SCUC with AC/DC transmission constraints in which the AC line 1-2 is replaced with a VSC-DC transmission link

**Case 3:** SCUC with AC/DC transmission constraints in which the AC line 1-2 is replaced with a CSC-DC transmission link.

**Case 4:** SCUC for Case 1 when the possible outage of unit 3 (CTGU3) is considered (preventive contingency)

**Case 5:** SCUC for Case 2 when the possible outage of unit 3 (CTGU3) is considered (corrective contingency)

**Case 6:** SCUC for Case 3 when the possible outage of unit 3 (CTGU3) is considered (corrective contingency)

In each case, base case and contingencies are considered to evaluate the system security and economics in different operating conditions. The results are presented as follows.

**Case 0:** When transmission constraints are ignored, the cheapest unit 1 will pick up the hourly base load and the more expensive unit 2 will be committed at hours 11-22 to supply partial loads. In this case, the most expensive unit 3 is not committed. The hourly UC is shown in Table I with a daily operating cost of $108,240.73.

**Case 1:** When AC transmission constraints are considered based on the UC solution in Case 0, we find power flow violations at hours 1 and 7-24. Accordingly, 19 Benders cuts at

violated hours are generated and added to the master problem for the next UC calculation. After four SCUC iterations, all violations are removed and the final UC results are shown in Table II in which the changes in comparison to Case 0 are presented in bold. Unit 2 was committed at hour 1, and though there is no violation at hour 2, unit 2 with a minimum on/off time of 2 hours will remain committed at hour 2. The total operating cost is $118,856.15.

TABLE I
UC RESULTS IN CASE 0

| | **Total Operation Cost = $108240.73** |
|---|---|
| **Unit** | **Hours (1-24)** |
| 1 | 1 1 1 1 1 1 1 1 1 1 1 1 1 1 1 1 1 1 1 1 1 1 1 1 |
| 2 | 0 0 0 0 0 0 0 0 0 0 0 1 1 1 1 1 1 1 1 1 1 1 0 0 |
| 3 | 0 0 0 0 0 0 0 0 0 0 0 0 0 0 0 0 0 0 0 0 0 0 0 0 |

TABLE II
UC RESULTS IN CASE 1

| | **Total Operation Cost = $ 118856.15** |
|---|---|
| **Unit** | **Hours (1-24)** |
| 1 | 1 1 1 1 1 1 1 1 1 1 1 1 1 1 1 1 1 1 1 1 1 1 1 1 |
| 2 | **1 1** 0 0 0 0 **1 1 1 1** 1 1 1 1 1 1 1 1 1 1 **1 1** |
| 3 | 0 0 0 0 0 0 0 0 0 0 **1 1 1 1 1 1 1 1 1 1 1 1** 0 0 |

TABLE III
UC RESULTS IN CASE 2

| | **Total Operation Cost = $ 113678.76** |
|---|---|
| **Unit** | **Hours (1-24)** |
| 1 | 1 1 1 1 1 1 1 1 1 1 1 1 1 1 1 1 1 1 1 1 1 1 1 1 |
| 2 | **0 0** 0 0 0 0 0 0 **0 0 0 0** 1 1 1 1 1 1 1 1 **0 0 0** |
| 3 | 0 0 0 0 0 0 0 0 0 0 0 1 1 1 1 1 1 1 1 1 1 1 0 0 |

**Case 2:** SCUC with AC/DC transmission constraints is calculated when the AC line 1-2 is replaced with a VSC-DC link with $R_{dc}$= 0.005 pu. We find power flow violations at hours 11-22 based on UC results in Case 0. Hence, 11 cuts are generated by (36) and added to the next UC calculation. All AC/DC violations are removed after three SCUC iterations. The final hourly UC is shown in Table III in which changes in comparison to Case 1 are presented in bold. In this case, the VSC-DC link transfers the additional generation of unit G1 from bus 1 to bus 2. For example, 141 MW flow on the DC transmission line 1-2 in this case is compared to 52.75 MW flow on the AC line 1-2 in Case 1 at hour 17. Consequently, the cheaper unit 1 generates 220 MW at peak hour 17 while it generated only 132.16 MW in Case 1. The expensive unit 2 is off at hours 1-2, 9-12 and 22-24 and the total operating cost is $113,678.76 which is less than that in Case 1. Tables IV and V show the optimal operating points of rectifier and inverter over 24 hours, respectively. The optimal control strategy of DC transmission line is determined according to the values in Tables IV and V. For instance, based on control criteria presented in section III.C, at hour 21, the rectifier will have a PV control mode ( $P = 141.46\ MW$ plus $V = 1.20\ pu$ ) and the inverter will have a PQ control mode ( $P = -140.76\ MW$ plus $Q = -70\ MVar$ ). For a two-terminal VSC-DC system, at least one converter should maintain the DC voltage.

**Case 3:** In this case, the SCUC solution with AC/DC transmission constraints is calculated in which the AC line 1-2 is replaced with a CSC-DC transmission link shown in Fig. 5. $\alpha$ and $T$ are the firing/extinction angle and the transformer

TABLE IV
RECTIFIER OPERATING POINT IN CASE 2

| **Hour** | **$P_{term}$ (MW)** | **$Q_{term}$ (MVAR)** | **$V_{dc}$ (pu)** | **$I_{dc}$ (pu)** | **M (pu)** | **E (pu)** |
|---|---|---|---|---|---|---|
| **1** | 100.91 | -50.36 | 1.20 | 0.84 | 0.87 | 1.05 |
| **2** | 90.75 | 15.79 | 1.17 | 0.77 | 0.81 | 0.95 |
| **3** | 84.18 | 11.10 | 1.20 | 0.70 | 0.83 | 1.00 |
| **4** | 80.16 | 44.93 | 1.20 | 0.67 | 0.91 | 1.09 |
| **5** | 80.51 | 40.89 | 1.20 | 0.67 | 0.86 | 1.03 |
| **6** | 85.99 | 66.71 | 1.20 | 0.72 | 0.84 | 1.01 |
| **7** | 99.13 | -55.69 | 1.16 | 0.85 | 0.90 | 1.05 |
| **8** | 103.32 | -52.05 | 1.17 | 0.88 | 0.82 | 0.96 |
| **9** | 112.53 | 29.68 | 1.20 | 0.94 | 0.90 | 1.08 |
| **10** | 132.91 | 30.53 | 1.20 | 1.11 | 0.90 | 1.08 |
| **11** | 141.19 | -31.28 | 1.16 | 1.22 | 0.85 | 0.98 |
| **12** | 141.28 | -15.45 | 1.15 | 1.23 | 0.86 | 0.98 |
| **13** | 141.28 | -52.82 | 1.20 | 1.18 | 0.85 | 1.02 |
| **14** | 141.34 | -36.60 | 1.20 | 1.18 | 0.90 | 1.08 |
| **15** | 141.25 | -36.07 | 1.20 | 1.18 | 0.92 | 1.11 |
| **16** | 141.26 | -55.41 | 1.20 | 1.18 | 0.90 | 1.08 |
| **17** | 141.00 | -55.45 | 1.20 | 1.18 | 0.90 | 1.08 |
| **18** | 141.03 | -50.61 | 1.20 | 1.18 | 0.85 | 1.02 |
| **19** | 141.06 | -40.97 | 1.17 | 1.20 | 0.84 | 0.99 |
| **20** | 141.19 | -41.55 | 1.20 | 1.18 | 0.81 | 0.98 |
| **21** | 141.46 | -41.56 | 1.20 | 1.18 | 0.81 | 0.98 |
| **22** | 141.88 | 6.97 | 1.17 | 1.21 | 0.83 | 0.97 |
| **23** | 121.77 | 41.63 | 1.20 | 1.01 | 0.87 | 1.05 |
| **24** | 121.41 | 1.39 | 1.20 | 1.01 | 0.91 | 1.09 |

TABLE V
INVERTER OPERATING STATUS IN CASE 2

| **Hour** | **$P_{term}$ (MW)** | **$Q_{term}$ (MVAR)** | **$V_{dc}$ (pu)** | **$I_{dc}$ (A)** | **M (pu)** | **E (pu)** |
|---|---|---|---|---|---|---|
| **1** | -100.56 | -20.63 | -1.20 | 0.84 | 0.76 | 0.90 |
| **2** | -90.45 | -48.97 | -1.17 | 0.77 | 0.80 | 0.94 |
| **3** | -83.94 | -63.26 | -1.20 | 0.70 | 0.89 | 1.06 |
| **4** | -79.93 | -38.51 | -1.20 | 0.67 | 0.90 | 1.08 |
| **5** | -80.29 | -41.14 | -1.20 | 0.67 | 0.86 | 1.03 |
| **6** | -85.73 | -51.33 | -1.20 | 0.72 | 0.87 | 1.04 |
| **7** | -98.76 | -18.95 | -1.16 | 0.85 | 0.78 | 0.90 |
| **8** | -102.93 | -65.01 | -1.17 | 0.88 | 0.84 | 0.99 |
| **9** | -112.09 | -53.62 | -1.20 | 0.94 | 0.90 | 1.08 |
| **10** | -132.30 | -54.52 | -1.19 | 1.11 | 0.89 | 1.06 |
| **11** | -140.44 | -70.00 | -1.15 | 1.22 | 0.83 | 0.96 |
| **12** | -140.52 | -70.00 | -1.14 | 1.23 | 0.84 | 0.96 |
| **13** | -140.58 | -70.00 | -1.19 | 1.18 | 0.80 | 0.95 |
| **14** | -140.65 | -32.17 | -1.19 | 1.18 | 0.77 | 0.92 |
| **15** | -140.56 | -70.00 | -1.19 | 1.18 | 0.91 | 1.08 |
| **16** | -140.57 | -70.00 | -1.19 | 1.18 | 0.87 | 1.04 |
| **17** | -140.30 | -70.00 | -1.19 | 1.18 | 0.87 | 1.04 |
| **18** | -140.34 | -70.00 | -1.19 | 1.18 | 0.80 | 0.96 |
| **19** | -140.34 | -70.00 | -1.17 | 1.20 | 0.83 | 0.96 |
| **20** | -140.50 | -70.00 | -1.19 | 1.18 | 0.81 | 0.96 |
| **21** | -140.76 | -70.00 | -1.19 | 1.18 | 0.81 | 0.96 |
| **22** | -141.14 | -70.00 | -1.17 | 1.21 | 0.82 | 0.96 |
| **23** | -121.25 | -58.17 | -1.19 | 1.01 | 0.88 | 1.05 |
| **24** | -120.90 | -58.20 | -1.19 | 1.01 | 0.91 | 1.09 |

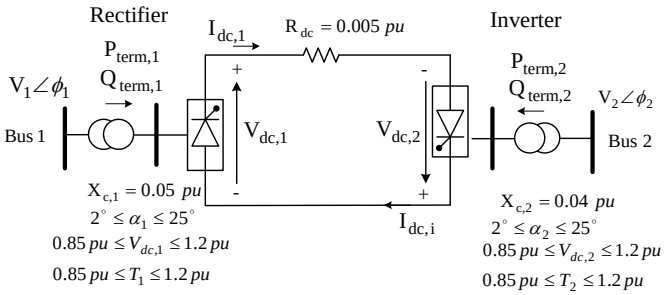


Fig. 5. Schematic diagram of the two-terminal CSC-DC link

tap ratio of rectifier/inverter terminals respectively. Similar to the VSC-DC transmission system, the CSC-DC system can have full control over its real power transmission.

Tables VI and VII show the operating status of CSC-DC transmission system over 24 hours. Comparing Cases 2 and 3, we learn that VSC-DC and CSC-DC systems would change the direction of real power flow to mitigate congestions. Here, $P_{term}$ in Tables IV and VI or Tables V and VII are quite similar. However, the CSC-DC transmission system consumes reactive power during the AC to DC power conversion (non-positive $Q_{term}$ in Tables VI and VII). Since the corresponding voltage profile is degraded, we would create additional cuts for voltage violations. Here, generating unit 2 is committed at hours 1-12, 22-24 to supply the reactive power for keeping the AC voltage at bus 2 within its limits. Table VIII shows that the expensive unit 3 is not committed at these hours when generating units 1 and 2 with a minimum on time of 2 hours will satisfy network constraints at hours 11 and 22 (compared with UC results presented in Table III). The total operating cost is $116,980.07 which is higher than that in Case 2.

TABLE VI
RECTIFIER OPERATION STATUS IN CASE 3

| Hour | $P_{term}$ (MW) | $Q_{term}$ (MVAR) | $V_{dc}$ (pu) | $I_{dc}$ (A) | α (Deg) | T (pu) |
|---|---|---|---|---|---|---|
| 1 | 93.84 | 23.52 | 1.17 | 257.25 | 4.04 | 1.10 |
| 2 | 85.30 | 20.68 | 1.13 | 242.87 | 2 | 1.06 |
| 3 | 82.32 | 21.39 | 1.08 | 244.54 | 4.31 | 1.08 |
| 4 | 74.93 | 19.65 | 0.99 | 243.54 | 2 | 1.01 |
| 5 | 74.59 | 18.00 | 1.06 | 225.37 | 2 | 1.05 |
| 6 | 80.05 | 18.73 | 1.13 | 228.23 | 2 | 1.06 |
| 7 | 94.04 | 23.10 | 1.17 | 257.92 | 2 | 1.10 |
| 8 | 99.09 | 25.17 | 1.17 | 272.46 | 2 | 1.10 |
| 9 | 108.22 | 28.46 | 1.18 | 293.43 | 2 | 1.12 |
| 10 | 96.99 | 24.28 | 1.17 | 266.14 | 2 | 1.10 |
| 11 | 81.64 | 18.72 | 1.16 | 226.59 | 2 | 1.08 |
| 12 | 94.33 | 23.13 | 1.17 | 257.86 | 2 | 1.10 |
| 13 | 88.77 | 21.16 | 1.17 | 244.18 | 2 | 1.10 |
| 14 | 87.30 | 20.64 | 1.17 | 240.43 | 2 | 1.09 |
| 15 | 82.97 | 19.13 | 1.16 | 229.45 | 2 | 1.09 |
| 16 | 78.02 | 17.46 | 1.15 | 217.00 | 2 | 1.08 |
| 17 | 77.83 | 17.41 | 1.15 | 216.61 | 2 | 1.08 |
| 18 | 84.65 | 19.70 | 1.16 | 233.62 | 2 | 1.09 |
| 19 | 85.29 | 19.94 | 1.16 | 235.36 | 2 | 1.09 |
| 20 | 93.20 | 22.72 | 1.17 | 255.03 | 2 | 1.10 |
| 21 | 93.24 | 22.74 | 1.17 | 255.13 | 2 | 1.10 |
| 22 | 77.60 | 17.35 | 1.15 | 216.19 | 2 | 1.08 |
| 23 | 54.03 | 10.19 | 1.10 | 157.07 | 2 | 1.05 |
| 24 | 103.83 | 26.89 | 1.18 | 283.64 | 2 | 1.11 |

**Case 4:** When the possible outage of unit 3 is considered (CTGU3), the UC results obtained in Case 1 for base case cannot supply the hourly load at hours 1-2 and 6-24. The hourly AC/DC network check subproblem solution presented in (37)-(53) generates Benders cuts related to existing violations for CTGU3. The final UC results presented in Table IX shows that this contingency is uncontrollable and preventive actions (i.e., additional commitment of unit 2 at hour 6) are necessary to maintain the system security in base case and contingency cases. In Table IX, commitment changes in comparison with Table II are shown in bold.

**Case 5:** Based on UC results obtained in Case 2, the system state can transfer to the base case by applying corrective actions (i.e., redispatch of units 1-2 and adjustments of phase-shifter angles, transformers tap ratios, and VSC controls). The total operating cost increases to $119456.27. In essence, $119456.27-$113678.76=$5777.51 is the cost of maintaining the system security in the event of CTGU3.

TABLE VII
INVERTER OPERATION STATUS IN CASE 3

| Hour | $P_{term}$ (MW) | $Q_{term}$ (MVAR) | $V_{dc}$ (pu) | $I_{dc}$ (A) | α (Deg) | T (pu) |
|---|---|---|---|---|---|---|
| 1 | -93.52 | 23.75 | 1.17 | 257.25 | 2 | 1.17 |
| 2 | -85.01 | 21.33 | 1.12 | 242.87 | 2 | 1.13 |
| 3 | -82.03 | 21.22 | 1.08 | 244.54 | 2 | 1.16 |
| 4 | -74.64 | 20.23 | 0.98 | 243.54 | 2 | 1.06 |
| 5 | -74.34 | 21.36 | 1.06 | 225.37 | 8.29 | 1.16 |
| 6 | -79.80 | 24.49 | 1.12 | 228.23 | 10.54 | 1.14 |
| 7 | -93.72 | 23.82 | 1.17 | 257.92 | 2 | 1.17 |
| 8 | -98.73 | 26.08 | 1.16 | 272.46 | 2.26 | 1.17 |
| 9 | -107.80 | 29.75 | 1.18 | 293.43 | 3.07 | 1.19 |
| 10 | -96.64 | 25.31 | 1.17 | 266.14 | 2.95 | 1.19 |
| 11 | -81.39 | 19.26 | 1.15 | 226.59 | 2 | 1.19 |
| 12 | -94.01 | 23.87 | 1.17 | 257.86 | 2 | 1.19 |
| 13 | -88.48 | 21.81 | 1.16 | 244.18 | 2 | 1.19 |
| 14 | -87.02 | 21.26 | 1.16 | 240.43 | 2 | 1.19 |
| 15 | -82.72 | 19.68 | 1.16 | 229.45 | 2 | 1.19 |
| 16 | -77.79 | 17.95 | 1.15 | 217.00 | 2 | 1.19 |
| 17 | -77.60 | 17.89 | 1.15 | 216.61 | 2 | 1.19 |
| 18 | -84.39 | 20.28 | 1.16 | 233.62 | 2 | 1.19 |
| 19 | -85.02 | 20.53 | 1.16 | 235.36 | 2 | 1.19 |
| 20 | -92.89 | 23.44 | 1.17 | 255.03 | 2 | 1.19 |
| 21 | -92.92 | 23.45 | 1.17 | 255.13 | 2 | 1.19 |
| 22 | -77.37 | 17.83 | 1.15 | 216.19 | 2 | 1.19 |
| 23 | -53.91 | 10.42 | 1.10 | 157.07 | 2 | 1.16 |
| 24 | -103.44 | 28.42 | 1.17 | 283.64 | 4.3528 | 1.19 |

TABLE VIII
UC RESULTS IN CASE 3

| | **Total Operation Cost = $ 116980.07** |
|---|---|
| **Unit** | **Hours (1-24)** |
| 1 | 1 1 1 1 1 1 1 1 1 1 1 1 1 1 1 1 1 1 1 1 1 1 1 1 |
| 2 | **1 1 1 1 1 1 1 1 1 1 1 1** 1 1 1 1 1 1 1 1 1 **1 1 1** |
| 3 | 0 0 0 0 0 0 0 0 0 0 **0** 1 1 1 1 1 1 1 1 1 1 **0** 0 0 |

TABLE IX
UC RESULTS IN CASE 4

| | **Total Operation Cost = $ 118856.15** |
|---|---|
| **Unit** | **Hours (1-24)** |
| 1 | 1 1 1 1 1 1 1 1 1 1 1 1 1 1 1 1 1 1 1 1 1 1 1 1 |
| 2 | 1 1 0 0 0 **1** 1 1 1 1 1 1 1 1 1 1 1 1 1 1 1 1 1 |
| 3 | 0 0 0 0 0 0 0 0 0 0 0 1 1 1 1 1 1 1 1 1 1 1 0 0 |

**Case 6:** Based on the UC results in Case 3, the system state cannot be transferred to another base case state in the event of CTGU3. In other word, the system does not have a sufficient supply of reactive power for satisfying the hourly load while maintaining the system security. The system operator would resort to load shedding in the event of CTGU3 to find a SCUC solution. The provision of additional reactive power would guarantee a feasible SCUC solution.

### *B. IEEE-118 Bus System*

A modified IEEE 118–bus system shown in Fig. 6 is tested. This system has 54 units, 186 branches, 14 capacitors, 9 tap-changing transformers and 91 demand sides. Zones 1 and 3 are connected by the AC tie line 23-24. Zones 2 and 3 are connected by AC tie lines 47-69, 49-69, and 65-68. In this example, we study the system performance for five cases. These cases include three zones which are operating

independently, interconnected with AC tie lines, or with VSC-DC lines. In each case, the system security is examined in different operating conditions. Furthermore, this example highlights the salient characteristics of VSC-DC transmission systems for enhancing the system security and economics. The 118-bus system data are given in http://motor.ece.iit.edu/DC/ VSC/ IEEE118.xls. The following cases are tested.

**Case 0:** UC for three separate zones (without flow constraints)

**Case 1:** UC for the entire system (without flow constraints)

**Case 2:** SCUC when three zones are connected by AC lines

**Case 3:** SCUC when three zones are connected by DC lines

**Case 4:** SCUC for Case 2 when the possible outage of unit 47 at Zone 2 is considered (preventive contingency)

**Case 5:** SCUC for Case 3 when the possible outage of unit 47 at Zone 2 is considered (corrective contingency)

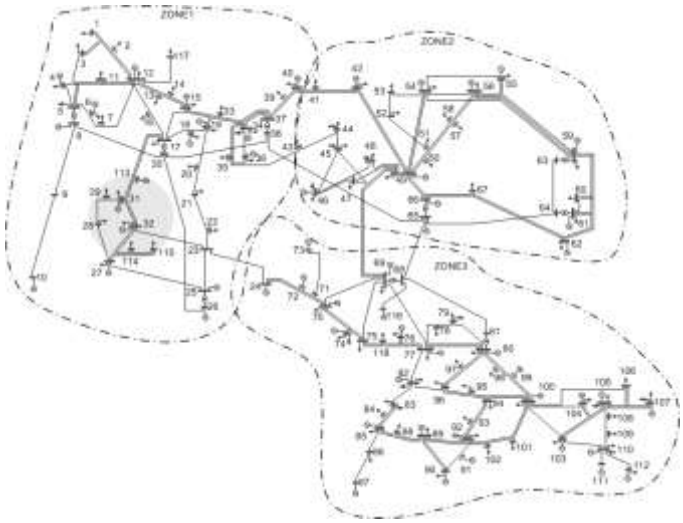


Fig. 6. Schematic diagram of IEEE 118-bus system

The details are given as follows.

**Case 0:** Since the generation in Zone 1is insufficient for supplying the load, the UC solution for this zone does not converge. In fact, Zone 1 imports power from the other two zones to supply its hourly load economically. The UC solutions converge in Zones 2 & 3 with a total operating cost of $496,426.1 and $659,534.06, respectively.

**Case 1:** In this case, the generation capacity in the 118-bus network is sufficient for supplying the hourly load. The final UC solution has a total operating cost of $1,727,165.

**Case 2:** The UC solution in Case 1 are used to analyze SCUC using (19)-(35). Accordingly, certain transmission violations occur which include peak-hour reactive power shortages at buses 21, 41 and 86. These three buses are PQ buses that would need the additional reactive power supply to keep their bus voltages within acceptable limits. Consequently, more expensive units are committed which increase the operating cost to $1,730,600.

**Case 3:** In this case, we replace AC tie lines with VSC-DC tie lines. We assume that converter terminals are similar to those listed in Table B.VI. Applying the UC results in Case 1, we find that there are violations at hours 1-7, 10-11, 14-16, and 18-23. Consequently, Benders cuts are generated using (36) and a new UC solution is calculated. The total operating cost is $1,728,242 that is less than that in Case 2. In this Case, the VSC-DC transmission system provides three additional degrees of flexibility (i.e., P, Q, and V) for security and economics. Consider AC and DC tie flows in Fig. 7 which represent the peak hour 17. The optimal loading will increase when the AC tie line 65-68 (in Case 2) is replaced with the DC tie line. The economical flows of other DC tie lines are adjusted similarly to minimize the total operating cost while enhancing the security margins in the base case. In other word, the DC control will optimize power exchanges among the three Zones. Table X compares the zonal operating costs at base case (Cases 0-3). Here, the operating costs in Zones 2&3 have increased in Case 3 as compared with that of Case 2; however, the total cost in this case is lower than that of Case 2 because of cost savings provided by Zone 1.

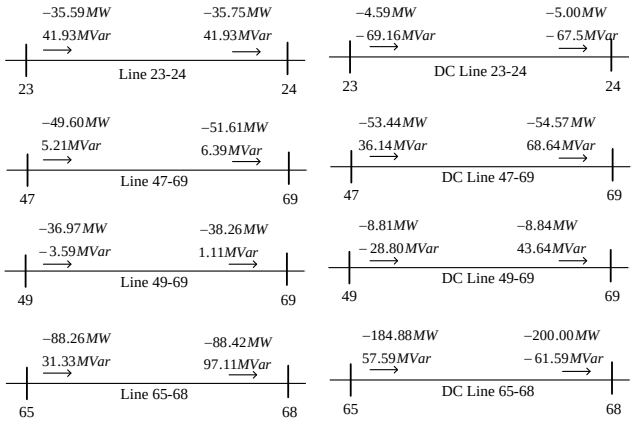


Fig. 7. AC flows (Case 2 on the left) and DC flows (Case 3 on the right)

TABLE X ZONAL OPERATING COSTS (BASE CASE)

| | Zone 1 ($) | Zone 2 ($) | Zone 3 ($) | Total ($) |
|---|---|---|---|---|
| **Case0** | - | 496,426.10 | 659,534.06 | - |
| **Case1** | 392,072.22 | 672,699.45 | 662,393.33 | 1,727,165.00 |
| **Case2** | 401,636.59 | 671,112.28 | 657,851.13 | 1,730,600.00 |
| **Case3** | 392,260.48 | 667,646.87 | 668,334.65 | 1,728,242.00 |

**Case 4:** When the possible outage of unit 47 is considered, the system state cannot be transferred to a new base case state by applying the UC solution in Case 2. Consequently, power flow violations appear and Benders cuts are generated to recalculate the UC solution in Case 2 (preventive actions). For instance, we observe that generating units 46 and 49 that were off in Case 2 are now committed to guarantee the system security. The difference in daily operation cost (i.e., $1,743,653-$1,730,600 = $13,053) is the cost of preventive action for maintaining the security when the outage of generating unit 47 is considered.

**Case 5:** This is a controllable contingency whereby corrective actions (i.e., ED based on physical ramping) will mitigate transmission violations. The total operating cost is $1,735,712 which is higher than that in Case 3.

## V. Conclusions

A VSC-DC transmission system is integrated into SCUC which is solved by the Benders decomposition method. The efficiency of the proposed model is examined in the base case and in contingency cases. In addition, the comparison of VSC-DC and CSC-DC systems emphasizes that CSC-DC systems would require reactive power compensations at converter stations to guarantee the system security. The presented model will expand the security margin by introducing preventive and corrective actions and transferring the AC/DC contingency state to a new base case state in the event of outages. The VSC-DC transmission systems can successfully control active and reactive power flows, increase the transfer capability of AC transmission, mitigate AC flow congestions, decommit expensive generating units, and improve the operating costs in the base case and contingencies.

## VI. References


[1] X. P. Zhang, "Multiterminal Voltage-Sourced Converter-Based DC Models for Power Flow Analysis," *IEEE Transactions on Power Systems*, Vol. 19, No. 4, pp. 1877-1884, Nov. 2004.

[2] R. L. Hendriks, J. H. D. Boon, G. C. Paap, W. L. Kling, "Connecting Offshore Wind Farms to (VSC-)DC Interconnections," *NORDIC Wind Power Conference*, May 2006.

[3] A. Lindberg, T. Larsson, "PWM and Control of Three Level Voltage Source Converters in an DC Back-to-Back Station," IEE proceeding on AC and dc Transmission, May 1996.

[4] M. P. Bahrman, J. G. Johansson, B. A. Nilsson, "Voltage Source Converter Transmission Technologies-The Right Fit for the Application," *IEEE Power Engineering Society General Meeting*, July, 2003.

[5] A. Lotfjou, M. Shahidehpour, Y. Fu, and Z. Li, "Security-Constrained Unit Commitment with AC/DC Transmission Systems," IEEE Transactions on Power System, vol. 25, no. 1, pp. 531-542, Feb 2010.

[6] M. Bahrman, M. Baker, J. Bowles, R. Bunch, J. Lemay, W. Long, J. McConnach, R. Menizies, J. Reeve, M. Szechtman, "Integration Of Small Taps Into (Existing) DC Links," *IEEE Transactions on Power Delivery*, Vol. 10, No.3 , pp. 1699-1706, July 1995.

[7] M. Aredes, C. Portela, F. C. Mechado, "A 25-MW Soft-Switching DC Tap for ±500-kV Transmission Lines," *IEEE Transactions on Power Delivery*, Vol. 19, No. 4, pp. 1835-1842, Oct. 2004.

[8] C. A. Camacho, O. L. Tortelli, E. Acha, C.R. F. Esquivel, "Inclusion of a high DC-Voltage Source Converter Model in a Newton-Raphson Power Flow Algorithm," *IEE Proceeding General Transmission Distribution*, Vol. 150, No. 6, Nov. 2003.

[9] L. Genyin, Z. Ming, H. Jie, L. Guangki, L. Haifeng, "Power Flow Calculation of Power Systems Incorporating VSC-DC," *IEEE International Conference On Power System Technology*, Singapore, Nov. 2005.

[10] X. Wei, J. H. Chow, B. Fardanesh, A. A. Edris, "A Common Modeling Framework of Voltage-Sourced Converters for Load Flow, Sensitivity, and Dispatch Analysis," *IEEE Transactions on Power Systems*, Vol. 19, No. 2, pp. 934-941, May 2004.

[11] A. Pizano-Martinze, C. R. Fuerte-Esquivel, H. Ambirz-Perez, E. Acha, "Modeling of VSC-Based DC Systems for a Newton-Raphson OPF Algorithm," *IEEE Transaction on Power System*, Vol. 22, No. 4, pp. 1794-1803, Nov. 2007.

[12] Y. Fu, M. Shahidehpour, Z. Li, "Security Constrained Unit Commitment with AC Constraints," *IEEE Transactions on Power Systems*, Vol. 20, No. 2, pp. 1001-1013, May 2005.

[13] G. Huang, S. C. Hsieh, "Fast Textured Algorithms for Optimal Power Delivery Problems in Restructured Environments," *IEEE Transactions on Power Systems*, Vol. 13, No. 2, pp. 493-500, May 1998.

[14] H. Saadat, "Power System Analysis," McGraw-Hill, 2002.

[15] M. Shahidehpour, H. Yamin, and Z. Y. Li, Market Operations in Electric Power Systems, Wiley, 2002.

[16] Y. Fu, M. Shahidehpour, and Z. Li, "AC contingency dispatch based on security-constrained unit commitment," *IEEE Transactions on Power System*, vol. 21, no. 2, pp. 897–908, May 2006.


## VII. Biographies

**Azim Lotfjou** received his BS and MS in E.E. from Sharif University of Technology, Tehran, in 2001 and 2004, respectively. He completed his PhD degree in 2009 in the ECE Department at Illinois Institute of Technology.

**Mohammad Shahidehpour** (F'01) is Bodine Professor in the Electrical and Computer Engineering Department at Illinois Institute of Technology. He also serves as the Director of the Center for Electricity Innovation at IIT. He was the recipient of an honorary doctorate from the Polytechnic University of Bucharest in 2009.

**Yong Fu** (M'05) received his BS and MS in E.E. from Shanghai Jiaotong University, China, in 1997 and 2002, respectively and PhD degree in E.E. from Illinois Institute of Technology in 2006. Presently, he is an assistant professor in the ECE Department at Mississippi State University.

## Appendix A: Jacobian Matrixes

The elements of Jacobian matrix $\mathbf{J}_1$ at the AC bus $m$ connected to the DC converter $h$ are formulated as

$$\frac{\partial \Delta P_{m,h}}{\partial V_{dc,h}} = -I_{dc,h} \tag{A.1}$$

$$\frac{\partial \Delta P_{m,h}}{\partial I_{dc,h}} = -V_{dc,h} \tag{A.2}$$

$$\frac{\partial \Delta Q_{m,h}}{\partial V_{m,h}} = -\frac{2V_{m,h} - E_h \cos(\phi_h)}{X_h} \tag{A.3}$$

$$\frac{\partial \Delta Q_{m,h}}{\partial E_h} = \frac{V_{m,h} \cos(\phi_h)}{X_h} \tag{A.4}$$

$$\frac{\partial \Delta Q_{m,h}}{\partial \varphi_h} = -\frac{V_{m,h} E_h \sin(\phi_h)}{X_h} \tag{A.5}$$

The elements of Jacobian matrix $\mathbf{J}_2$ at AC bus $m$ connected to the DC converter $h$ are formulated as

$$\frac{\partial \Delta R1_h}{\partial E_h} = 1 \tag{A.6}$$

$$\frac{\partial \Delta R1_h}{\partial M_h} = \begin{cases} -\dfrac{V_{dc,h}}{2\sqrt{2}} & \text{for rectifier} \\ \dfrac{V_{dc,h}}{2\sqrt{2}} & \text{for inverter} \end{cases} \tag{A.7}$$

$$\frac{\partial \Delta R1_h}{\partial V_{dc,h}} = \begin{cases} -\dfrac{M_h}{2\sqrt{2}} & \text{for rectifier} \\ \dfrac{M_h}{2\sqrt{2}} & \text{for inverter} \end{cases} \tag{A.8}$$

$$\frac{\partial \Delta R2_h}{\partial I_{dc,h}} = 1 \tag{A.9}$$

$$\frac{\partial \Delta R2_h}{\partial M_h} = \begin{cases} -\dfrac{V_{m,h} \sin(\phi_h)}{2\sqrt{2} X_h} & \text{for rectifier} \\ \dfrac{V_{m,h} \sin(\phi_h)}{2\sqrt{2} X_h} & \text{for inverter} \end{cases} \tag{A.10}$$

$$\frac{\partial \Delta R2_h}{\partial V_{m,h}} = \begin{cases} -\dfrac{M_h \sin(\phi_h)}{2\sqrt{2}X_h} & \text{for rectifier} \\ \dfrac{M_h \sin(\phi_h)}{2\sqrt{2}X_h} & \text{for inverter} \end{cases} \quad (A.11)$$

$$\frac{\partial \Delta R2_h}{\partial \phi_h} = \begin{cases} -\dfrac{M_h V_{m,h} \cos(\phi_h)}{2\sqrt{2}X_h} & \text{for rectifier} \\ \dfrac{M_h V_{m,h} \cos(\phi_h)}{2\sqrt{2}X_h} & \text{for inverter} \end{cases} \quad (A.12)$$

The partial derivatives of $\Delta R3_h$ will depend on the configuration of VSC-DC transmission system. For example, the partial derivatives of $\Delta R3_1$ for the two-terminal DC transmission system shown in Fig. 2 are listed as

$$\frac{\partial \Delta R3_1}{\partial I_{dc,1}} = 1, \frac{\partial \Delta R3_1}{\partial V_{dc,1}} = -\frac{1}{R_{dc}}, \frac{\partial \Delta R3_1}{\partial V_{dc,2}} = -\frac{1}{R_{dc}}$$

$$\frac{\partial \Delta R3_2}{\partial I_{dc,2}} = 1, \frac{\partial \Delta R3_2}{\partial V_{dc,1}} = -\frac{1}{R_{dc}}, \frac{\partial \Delta R3_2}{\partial V_{dc,2}} = -\frac{1}{R_{dc}}$$

The elements of Jacobian matrix $\mathbf{A}_2$ and $\mathbf{B}_2$ for the DC converter $v$ are formulated as

$$\frac{\partial \Delta P_h}{\partial V_{dc,h}} = -I_{dc,h} \quad (A.13)$$

$$\frac{\partial \Delta P_h}{\partial I_{dc,h}} = -V_{dc,h} \quad (A.14)$$

The elements of Jacobian matrix $\mathbf{A}_3$, $\mathbf{B}_3$ and $\mathbf{C}_3$ for the DC converter $v$ are formulated as

$$\frac{\partial \Delta Q_h}{\partial V_{m,h}} = -\frac{E_h \cos(-\phi_h)}{X_h} \quad (A.15)$$

$$\frac{\partial \Delta Q_h}{\partial E_h} = \frac{2E_h - V_h \cos(-\phi_h)}{X_h} \quad (A.16)$$

$$\frac{\partial \Delta Q_{m,h}}{\partial \varphi_h} = -\frac{E_h V_{m,h} \sin(-\phi_h)}{X_h} \quad (A.17)$$

## Appendix B: Network data for 6-Bus system

TABLE B.I
BUS DATA

| Bus No. | $V_{Max}$ (pu) | $V_{Min}$ (pu) |
|---|---|---|
| 1 | 1.10 | 0.95 |
| 2, 3,4,5,6 | 1.15 | 0.90 |

TABLE B.II
TRANSMISSION LINE DATA

| Line No. | From Bus | To Bus | R (pu) | X (pu) | Flow Limit (MW) |
|---|---|---|---|---|---|
| 1 | 1 | 2 | 0.0050 | 0.170 | 150 |
| 2 | 1 | 4 | 0.0030 | 0.258 | 75 |
| 3 | 2 | 4 | 0.0070 | 0.197 | 100 |
| 4 | 5 | 6 | 0.0020 | 0.140 | 90 |
| 5 | 3 | 6 | 0.0005 | 0.018 | 90 |

TABLE B.III
TAP CHANGING TRANSFORMER DATA

| Tap-Changing Transformers | From Bus | To Bus | X (pu) | Tap Max | Tap Min | Cap (MW) |
|---|---|---|---|---|---|---|
| T1 | 2 | 3 | 0.037 | 0.98 | 0.95 | 100 |
| T2 | 4 | 5 | 0.037 | 0.98 | 0.95 | 90 |

TABLE B. IV
HOURLY LOAD

| Hour | Pd (MW) | Qd (MVAR) | Hour | Pd (MW) | Qd (MVAR) |
|---|---|---|---|---|---|
| 1 | 175.19 | 50.28 | 13 | 242.18 | 69.51 |
| 2 | 165.15 | 47.40 | 14 | 243.60 | 69.91 |
| 3 | 158.67 | 45.54 | 15 | 248.86 | 71.42 |
| 4 | 154.73 | 44.41 | 16 | 255.79 | 73.41 |
| 5 | 155.06 | 44.50 | 17 | 256.00 | 73.47 |
| 6 | 160.48 | 46.06 | 18 | 246.74 | 70.81 |
| 7 | 173.39 | 49.76 | 19 | 245.97 | 70.59 |
| 8 | 177.60 | 50.97 | 20 | 237.35 | 68.12 |
| 9 | 186.81 | 53.61 | 21 | 237.31 | 68.11 |
| 10 | 206.96 | 59.40 | 22 | 232.67 | 66.78 |
| 11 | 228.61 | 65.61 | 23 | 195.93 | 56.23 |
| 12 | 236.10 | 67.76 | 24 | 195.60 | 56.14 |

TABLE B.V
GENERATOR DATA

| U | Bus No. | Unit Cost Coefficients | | | Pmax (MW) | Pmin (MW) | Qmax (MVAR) |
|---|---|---|---|---|---|---|---|
| | | A (MBtu) | b (MBtu/MWh) | c (MBtu/MW$^2$h) | | | |
| G1 | 1 | 176.9 | 13.5 | 0.1 | 220 | 100 | 100 |
| G2 | 2 | 176.9 | 17.6 | 0.1 | 100 | 10 | 50 |
| G3 | 6 | 176.9 | 32.6 | 0.1 | 30 | 10 | 10 |

TABLE B.V
GENERATOR DATA (CONTUNIED)

| Qmin (MVAR) | Ini. St. (h) | Min Down (h) | Min Up (h) | Ramp (MW/h) | Start Up (MBtu) | Fuel Price ($/MBtu) |
|---|---|---|---|---|---|---|
| -100 | 4 | 4 | 4 | 55 | 100 | 1.2469 |
| -40 | 2 | 2 | 3 | 50 | 200 | 1.2461 |
| -10 | 1 | 1 | 1 | 20 | 0 | 1.2462 |

TABLE B.VI
CONVERTERS DATA FOR THE TWO-TERMINAL DC SYSTEM

| Type | $X$ (pu) | $P_{min}$ (MW) | $P_{max}$ (MW) | $Q_{min}$ (MVAR) | $Q_{max}$ (MVAR) |
|---|---|---|---|---|---|
| Rec. | 0.02 | 0 | 150 | -70 | 70 |
| Inv. | 0.02 | 0 | 150 | -70 | 70 |

TABLE B.VI
CONVERTERS DATA FOR THE TWO-TERMINAL DC SYSTEM (CONTINUFES)

| $E_{min}$ (pu) | $E_{max}$ (pu) | $V_{dc,min}$ (pu) | $V_{dc,max}$ (pu) |
|---|---|---|---|
| 0.85 | 1.15 | 0.85 | 1.2 |
| 0.85 | 1.15 | -1.2 | -0.85 |

TABLE B.VII
STATIC LOAD DISTRIBUTION FACTORS

| L1 | L2 | L3 |
|---|---|---|
| 0.1 | 0.2 | 0.2 |

Published in IET Generation, Transmission & Distribution
Received on 27th February 2010
Revised on 2nd July 2010
doi: 10.1049/iet-gtd.2010.0151

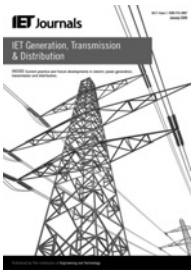

ISSN 1751-8687

# Application of augmented Lagrangian relaxation to coordinated scheduling of interdependent hydrothermal power and natural gas systems

*C. Liu*[1] *M. Shahidehpour*[1] *J. Wang*[2]

[1]*Electrical and Computer Engineering Department, Illinois Institute of Technology, Chicago, IL 60616 USA*
[2]*Decision and Information Sciences Division, Argonne National Laboratory, IL 64938 USA*
*E-mail: ms@iit.edu*

**Abstract:** This study proposes an optimisation model for the coordinated scheduling of interdependent electric power and natural gas transmission systems from a joint operator's viewpoint. The objective is to minimise the coordinated social cost while satisfying network and temporal constraints of the two interdependent systems. The joint operator will coordinate hourly schedules to supply natural gas to loads or generate electric power. The authors consider the application of Lagrangian relaxation (LR) or augmented LR to relax the coupling constraints of the two systems. The Lagrangian dual is decomposed into the security-constrained unit commitment subproblem with the hydro coordination and the natural gas allocation subproblem. The application of LR for solving the coordinated problem could cause oscillations in the dual solution which is due to the non-convex characteristics of the coordinated problem represented by integer variables and network constraints. Moreover, with slight changes in multiplier values, the linear cost function of the natural gas well may result in a cycling behaviour of the gas well output between its max and min limits. To avoid numerical oscillations and improve the solution quality, the augmented LR with a piecewise linear approximation of quadratic penalty terms and the block descent coordination technique are proposed. The authors consider the 6-bus with 7-node and the 118-bus with 14-node systems to verify that the applicability of the proposed method to the coordinated scheduling of electric power and natural gas transmission systems.

## Nomenclature

### *Index*

| | |
|---|---|
| $i, j$ | index of power unit |
| gi | index of gas supplier including gas wells, storages and liquefied natural gas tanks |
| cm | index of compressor |
| el, gl | index of electricity load and residual gas load |
| $t$ | index of hour |
| $k$ | index of iteration |
| $a$, $b$ | index of bus in power system |
| n$a$, n$b$ | index of node in gas network |
| $l$ | index of branch in power system |

### *Variables and functions*

| | |
|---|---|
| $I$ | status indicator of generating unit |
| $Y$, $Z$ | startup and shutdown indicator of unit |
| $P$ | generation of unit |
| $R$ | spinning reserve of unit |
| SU, SD | startup and shutdown cost of unit |
| $X_{it}^{\text{on}}$, $X_{it}^{\text{off}}$ | up/down time of unit $i$ at hour $t$ |

| | |
|---|---|
| GI | status indicator of gas well |
| $GI^{o}$, $GI^{I}$ | indicator of releasing status and charging status of storage |
| GP | net output of gas well, storage |
| $GP^{o}$, $GP^{I}$ | releasing and charging gas flow of storage |
| $F_{ec}$,() | unit's production cost function |
| $F_{gc}$,() | gas supplier's production cost function |
| $F_{ef}$,() | natural gas consumption of gas-fired unit |
| $F_{cf}$,() | natural gas consumption of compressor |
| $F_{h}$,() | power-water discharge function |
| SV, HV | volume of gas storage and hydro reservoir |
| ELS, GLS | not served electricity and residual gas load |
| EL, GL | scheduled electricity and gas load |
| $Pf_l$ | power flow through branch $l$ |
| PN | pressure of node in gas system |
| $GF_{nanb}$ | gas flow from node n$a$ to n$b$ |
| CH | horsepower of compressor |
| $\boldsymbol{\gamma}$ | control angel of phase shifter |
| $\theta$ | bus voltage angle |
| $q$ | water discharge of hydro unit |
| $s$ | spillage of hydro unit |
| $\eta$ | step size to update Lagrangian multiplier |
| $w$ | natural in flow to the reservoir of hydro unit |
| $\lambda$ | Lagrangian multiplier |
| $\omega$ | penalty factor |
| $\boldsymbol{x}$, $\boldsymbol{y}$ | vector of variables in power system and natural gas system |
| $\boldsymbol{x}_c$, $\boldsymbol{y}_c$ | sub-vector of $\boldsymbol{x}$, $\boldsymbol{y}$ representing variables in coupling constraints |
| $\boldsymbol{e}(\boldsymbol{x}_c)$, $\boldsymbol{g}(\boldsymbol{y}_c)$ | functions in coupling constraints |

### Constants

| | |
|---|---|
| $\rho$ | price of well-head of natural gas well, charging gas storage or releasing gas storage |
| $\sigma$ | price of not served electricity and gas load |
| $\alpha$, $\beta$ | parameters of augmented LR |
| $NT$ | scheduling period |
| $\boldsymbol{RC}$ | connection matrix for cascaded hydro reservoirs |
| $x_{ab}$ | reactance between buses $a$ and $b$ |
| $PF_{l,max}$ | power flow limits of branch $l$ |
| $EL_D$, $GL_D$ | estimated electricity and residual gas load |
| $R_D$ | required spinning reserve of system |
| $P_{Loss}$ | power transmission loss |
| GU | set of gas-fired units |
| GS | set of gas storages |
| UR, DR | max ramp up/down rate |
| $T^{on}$, $T^{off}$ | min on/off time of unit |
| $P_{min}$, $P_{max}$ | min/max capacity of a unit |
| $GP_{min}$, $GP_{max}$ | max/min net output of gas well and storage |
| $PN_{min}$, $PN_{max}$ | max/min pressure |
| $SV_{max}$, $SV_{min}$ | upper/lower volume limit of hydro reservoir |
| $HV_{max}$, $HV_{min}$ | upper/lower volume limits of storage |
| $PR_{min}$, $PR_{max}$ | max/min pressure ratio of compressor |
| $CH_{min}$, $CH_{max}$ | max/min horsepower of compressor |
| $\boldsymbol{A}$ | bus-generator incidence matrix |
| $\boldsymbol{B}$ | bus-electrical load incidence matrix |
| $\boldsymbol{C}$ | bus-branch incidence matrix |
| $\boldsymbol{GA}$ | node-gas supplier incidence matrix |
| $\boldsymbol{GB}$ | node-gas load incidence matrix |
| $\boldsymbol{GK}$ | node-gas branch incidence matrix |
| $\boldsymbol{GD}$ | gas withdrawing node-compressor incidence matrix |
| $\boldsymbol{GE}$ | gas load-power unit index incidence matrix |

## 1 Introduction

In the last few decades, the number of gas-fired generating unit installations in the world has grown dramatically, which is mostly based on three reasons [1]. First, new combined-cycle gas units demonstrate higher economics over other fossil generating units. Second, gas-fired units have lower environmental impacts. Third, the rapid growth and the installation of volatile and intermittent renewable generating units in electric power systems would require additional generation reserves provided by fast response gas-fired units. According to statistics, the installed natural gas-fired generating capacity in ERCOT, Florida and ISO New England represented 60, 51 and 38% of the total generation capacity, respectively [1, 2]. In Europe and South America, natural gas-fired generation would also account for a considerable proportion of the total generation capacity. The electricity and gas infrastructures are highly interdependent. Accordingly, the security and economics of electric power systems are influenced by the economic allocation of natural gas resources as well as the secure operation of natural gas transmission systems. The natural gas transmission systems are also influenced by the hourly scheduling and the optimal operation of electric power systems.

In [3] the interdependency of gas and electricity was addressed. In [4] a generalised network flow model of the

US integrated energy system was proposed considering natural gas, coal and power infrastructures. In [5] a non-linear continuous optimisation model was proposed for a coordinated flow in electricity and natural gas infrastructures. The short-term operation planning of integrated natural gas and hydrothermal power systems with linear gas transmission constraints was considered in [6], where the unit commitment (UC) problem was solved by Lagrangian relaxation (LR) and dynamic programming methods. The impact of the natural gas transmission system on electric power markets was discussed in [7]. Our previous paper [8] presented a comprehensive scheduling model by incorporating non-linear natural gas transmission constraints and contracts. The natural gas usage limits of gas-fired generating units were implicitly determined by the feasible adjustment range of the natural gas network and priority orders of gas load contracts. The Benders decomposition was used to apply the hourly UC results to separate blocks of electric power and natural gas transmission constraints. However, our previous model considered the viewpoints of the ISO and vertically integrated utility operators. Furthermore, operating costs of compressors and natural gas wells, and residual gas load models were not directly considered in the objective function.

In this paper, we propose a coordinated scheduling model from a joint operator's viewpoint as shown in Fig. 1. The coordination model is a mixed-integer non-linear optimisation problem in which the objective function will minimise the social cost of electric power and natural gas systems. In our proposed model, the joint operator is an independent organisation, which could operate outside the traditional jurisdictions of gas and electric power operators and would pursue the overall interest of coordinated energy systems. Natural gas resources will be allocated optimally to either supply gas loads or gas-fired generating units. The two systems have a decomposable structure and we consider the LR method as the decomposition strategy of the coordination problem. The coupling constraints between the electric power system and the natural gas transmission system are relaxed by Lagrangian multipliers and dualised into the objective function. The LR method is divided into two phases. The first phase is to solve the dual problem. However, the solution of phase one may not be feasible when considering the primal problem. Thus, the phase two of the dual problem will seek a feasible solution based on the solution of phase one as shown in Fig. 1. The relaxed primal problems are decomposed into security-constrained unit commitment subproblem with the hydro coordination (SCUC) and gas allocation subproblems that can be solved independently but in coordination. The methodologies for SCUC and natural gas allocation problems were developed in [9, 10], which incorporate the LR framework in our proposed model to solve the mixed-integer non-linear subproblems individually.

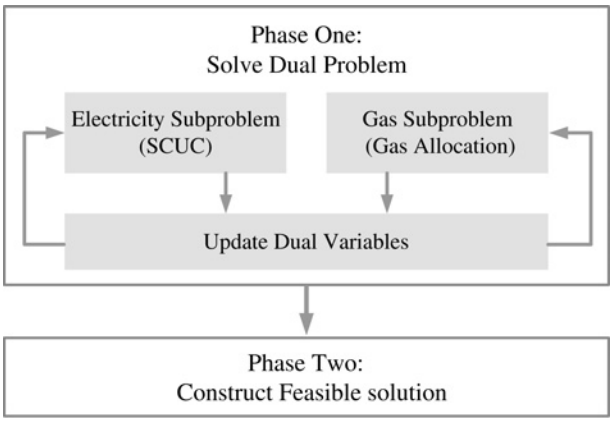


**Figure 1** *Augmented LR-based electricity-gas scheduling coordination*

We demonstrate that the LR approach in our coordination model will not exhibit a satisfactory convergence. The non-convex characteristics of the coordinated problem will result in the oscillation of dual solution, which is due to integer variables and network constraints. Moreover, with slight changes in the multipliers, the linear cost function of the natural gas well may lead to a cycling behaviour of gas well output between its max and min values. Accordingly, the violation of relaxed constraints cannot be alleviated iteratively. Hence, the augmented LR method with piecewise linear approximation of quadratic penalty term is used for preventing numerical oscillations and improving the quality of dual solution. The Lagrangian dual will no longer be decomposable after introducing inseparable penalty terms. So we use the block descent coordination (BDC) technique to deal with this problem and solve the decomposed SCUC and gas allocation subproblems sequentially.

The rest of the paper is organised as follows. Section 2 proposes formulations of integrated scheduling model. Section 3 presents the LR and augmented LR-based methodology to implement coordination procedures. Numerical cases are studied in Section 4. The conclusion is drawn in Section 5.

## 2 Scheduling coordination model

### 2.1 Modelling outline

Our proposed model focuses on the steady-state analyses of the electricity and the natural gas systems. Both include integer variables with non-linear constraints. The outline of our proposed model is described as the following optimisation problem

Max Social welfare or Min Social cost

s.t.

(a) Power balance and reserve requirements.

(b) Individual generator constraints (including min on/off time, min/max generation capacity, startup/ shutdown characteristics, ramp rate limits, etc.).




doi: 10.1049/iet-gtd.2010.0151

(c) Power transmission constraints.

(d) Gas source limits and gas storage constraints.

(e) Natural gas network constraints.

(f) Electricity – gas coupling constraints.

The objective function is to minimise the social cost, which is the sum of electricity and natural gas operating costs over the scheduling period as shown in (1)

$$\text{Min}(\text{EC} + \text{GC}) \tag{1}$$

In our proposed model, natural gas-fired generating units will consider maintenance and crew costs and fuel costs will be managed by the joint operator. Therefore EC in (2) represents all operating costs of non-gas-fired units, electricity load-not-served penalty as well as non-fuel operating costs of gas-fired units.

$$\begin{aligned}\text{EC} = &\sum_t \left[ \sum_{i \notin \text{GU}} F_{\text{ec},i}(P_{it}, I_{it}) + \text{SU}_{it} + \text{SD}_{it} \right] \\ &+ \sum_t \sum_{\text{el}} \sigma_{\text{el}} \text{ELS}_{\text{el}t} \\ &+ \sum_t \left[ \sum_{i \in \text{GU}} F_{\text{ec},i}(P_{it}, I_{it}) + \text{SU}_{it} + \text{SD}_{it} \right]\end{aligned} \tag{2}$$

The fuel cost of natural gas-fired units, which depends on the individual unit consumptions, will be implicitly considered in the natural gas allocation cost (GC). GC is represented in (3), which includes operating costs of gas well, liquefied natural gas (LNG) and gas storage as well as penalty costs for the residual natural gas load-not-served. $\sigma_{\text{gl}}$ is the penalty price corresponding to residual gas loads, indicating their incremental costs and priority orders.

$$\text{GC} = \sum_t \sum_{\text{gi}} F_{\text{gc,gi}}(\cdot) + \sum_t \sum_{\text{gl} \notin \text{GU}} \sigma_{\text{gl}} \text{GLS}_{\text{gl}t} \tag{3}$$

The joint operator will coordinate the operation schedule to pursue the overall interests of coupled electricity and natural gas systems. The optimal allocation of natural gas to residual loads or gas-fired generating units is determined by market demands and relative incremental costs. For instance, joint operators will supply more natural gas to power plants, if the proposed supply of fuel to gas-fired generating units will result in the additional commitment of expensive generators. Also, higher penalty costs for not supplying the residual gas loads will lead to a larger supply of natural gas to such loads. Here, we may consider gas-fired units to provide a generation service to the coordinated electricity and natural gas systems while being compensated for their maintenance or crew costs. The joint operator will then perform a coordination of fuel consumption by electric and natural gas systems.

## 2.2 Power system constraints

1. Power balance and reserve constraint

$$\sum_i P_{it} I_{it} + \sum_{\text{el}} \text{ELS}_{\text{el}t} = \sum_{\text{el}} \text{EL}_{D,\text{el}t} + P_{\text{Loss},t} \tag{4}$$

$$\sum_i R_{it} I_{it} \geq R_D \tag{5}$$

2. Individual unit constraints

*Min on/off time*

$$[X^{\text{on}}_{i(t-1)} - T^{\text{on}}_i]\,[I_{i(t-1)} - I_{it}] \geq 0 \tag{6}$$

$$[X^{\text{off}}_{i(t-1)} - T^{\text{off}}_i]\,[I_{it} - I_{i(t-1)}] \geq 0 \tag{7}$$

*Ramping rate limits*

$$P_{it} - P_{i(t-1)} \leq Y_{it}\, P_{\min,i} + (1 - Y_{it})\, \text{UR}_i \tag{8}$$

$$P_{i(t-1)} - P_{it} \leq Z_{it}\, P_{\min,i} + (1 - Z_{it})\, \text{DR}_i \tag{9}$$

*Max/Min power generation*

$$P_{\min,i}\, I_{it} \leq P_{it} \leq P_{\max,i}\, I_{it} - R_{it} \tag{10}$$

A more detailed formulation of such constraints including emission and fuel constraints is given in [9]. Either a mode or a component model [1] may be used for the simulation of combined-cycle generating units.

3. Hydro unit and reservoir constraints

*Power–water discharge conversion relationship*

$$P_{it} = F_{h,i}(q_{it}, I_{it}) \tag{11}$$

*Water discharge limits*

$$q_{i,\min}\, I_{it} \leq q_{it} \leq q_{i,\max}\, I_{it} \tag{12}$$

*Reservoir volume limits*

$$\text{HV}_{i,\min} \leq \text{HV}_{it} \leq \text{HV}_{i,\max} \tag{13}$$

$$\text{HV}_{i,t=0} = \text{HV}_{0,i}, \quad \text{HV}_{i,t=\text{NT}} = \text{HV}_{\text{NT},i} \tag{14}$$

*Water balance constraint for cascaded hydro units*

$$\text{HV}_{it} = \text{HV}_{i,t-1} - q_{it} - s_{it} + w_{it} + \boldsymbol{RC}_{ij}\, q_{j(t-\tau_j)} \tag{15}$$

where $q_{j(t-\tau)}$ represents the delayed water discharge to hydro unit $i$ from other hydro units $j$.

4. Power transmission constraints

$$\begin{aligned} &\boldsymbol{C}\cdot \mathrm{PF} = \boldsymbol{A}\cdot \boldsymbol{P} - \boldsymbol{B}\cdot(\mathrm{EL}-\mathrm{ELS}) \\ &\mathrm{PF}_l = \frac{\theta_a - \theta_b - \gamma_{ab}}{x_{ab}} \quad (a, b \in l) \\ &|\mathrm{PF}_l| \le \mathrm{PF}_{l,\max} \\ &\boldsymbol{\gamma}_{\min} \le \boldsymbol{\gamma} \le \boldsymbol{\gamma}_{\max} \\ &\theta_{\mathrm{ref}} = 0 \end{aligned} \tag{16}$$

## 2.3 Natural gas constraints

1. Gas well and storage constraints: The natural gas source is represented by gas well, gas storage and LNG tank, which demonstrate distinct prices and operating characteristics.

Cost of gas well is given as

$$F_{\mathrm{gc,gi}}(\cdot) = \rho_{\mathrm{gi}t}\ \mathrm{GP}_{\mathrm{gi}t}, \quad \forall \mathrm{gi} \notin \mathrm{GS} \tag{17}$$

Gas well and LNG source satisfy the following constraint

$$\mathrm{GI}_{\mathrm{gi}t}\ \mathrm{GP}_{\mathrm{gi,min}} \le \mathrm{GP}_{\mathrm{gi}t} \le \mathrm{GI}_{\mathrm{gi}t}\ \mathrm{GP}_{\mathrm{gi,max}}, \quad \forall \mathrm{gi} \notin \mathrm{GS} \tag{18}$$

Natural gas storage or LNG tank represents supplemental gas sources. The gas storage operation may switch among three exclusive modes, that is, releasing gas, charging gas and being off. When charging or releasing gas, additional operating costs will be considered as shown in (19)

$$F_{\mathrm{gc},gi}(\cdot) = \rho^{\mathrm{I}}_{\mathrm{gi}t}\ \mathrm{GP}^{\mathrm{I}}_{\mathrm{gi}t} + \rho^{\mathrm{O}}_{\mathrm{gi}t}\ \mathrm{GP}^{\mathrm{O}}_{\mathrm{gi}t}, \quad \forall \mathrm{gi} \in \mathrm{GS} \tag{19}$$

Max/Min flow rate while releasing or charging gas

$$\mathrm{GI}^{\mathrm{I}}_{\mathrm{gi}t}\ \mathrm{GP}^{\mathrm{I}}_{gi,\min} \le \mathrm{GP}^{\mathrm{I}}_{\mathrm{gi}t} \le \mathrm{GI}^{\mathrm{I}}_{\mathrm{gi}t}\ \mathrm{GP}^{\mathrm{I}}_{\mathrm{gi,max}}, \quad \forall \mathrm{gi} \in \mathrm{GS} \tag{20}$$

$$\mathrm{GI}^{\mathrm{O}}_{\mathrm{gi}t} \cdot \mathrm{GP}^{\mathrm{O}}_{\mathrm{gi,min}} \le \mathrm{GP}^{\mathrm{O}}_{\mathrm{gi}t} \le \mathrm{GI}^{\mathrm{O}}_{\mathrm{gi}t} \cdot \mathrm{GP}^{\mathrm{O}}_{\mathrm{gi,max}}, \quad \forall \mathrm{gi} \in \mathrm{GS} \tag{21}$$

Net output of gas storage is the difference between releasing and charging gas flow as shown in (22)

$$\mathrm{GP}^{\mathrm{O}}_{\mathrm{gi}t} - \mathrm{GP}^{\mathrm{I}}_{\mathrm{gi}t} = \mathrm{GP}_{\mathrm{gi}t}, \quad \forall \mathrm{gi} \in \mathrm{GS} \tag{22}$$

In addition, there is a volume balance constraint for each storage (e.g. hydro reservoir)

$$\mathrm{SV}_{\mathrm{gi}t} - \mathrm{SV}_{\mathrm{gi}(t+1)} = \mathrm{GP}_{\mathrm{gi}t}, \quad \forall \mathrm{gi} \in \mathrm{GS} \tag{23}$$

Volume of gas storage is restricted as

$$\mathrm{SV}_{\mathrm{gi,min}} \le \mathrm{SV}_{\mathrm{gi}t} \le \mathrm{SV}_{\mathrm{gi,max}}, \quad \forall \mathrm{gi} \in \mathrm{GS} \tag{24}$$

$$\mathrm{SV}_{i,t=0} = \mathrm{SV}_{0,i} \quad \mathrm{SV}_{i,t=\mathrm{NT}} = \mathrm{SV}_{\mathrm{NT},i} \tag{25}$$

2. Gas transmission constraints: A steady-state gas transmission model is built based on the nodal gas mass balance, which indicates that the gas flow injected to a node is equal to the gas flow out of the node as shown in (27). The natural gas pressure associated with each node is satisfied within a reasonable range (28).

$$\sum_{\mathrm{gi}} \mathrm{GA}_{\mathrm{n}a,\mathrm{gi}}\ \mathrm{GP}_{\mathrm{gi}} - \sum_{\mathrm{gl}} \mathrm{GB}_{\mathrm{n}a,\mathrm{gl}}(\mathrm{GL}_{\mathrm{gl}} - \mathrm{GLS}_{\mathrm{gl}}) - \sum_{\mathrm{n}b} \mathrm{GK}_{\mathrm{n}a,\mathrm{n}b}\ \mathrm{GF}_{\mathrm{n}a\mathrm{n}b} + \sum_{\mathrm{cm}} \mathrm{GD}_{\mathrm{n}a,\mathrm{cm}}\ F_{\mathrm{n}f,\mathrm{cm}}(\cdot) = 0 \tag{26}$$

The Weymouth equation [11] indicates the flow in a pipeline extending from gas node n$a$ to gas node n$b$ is modelled as

$$\mathrm{GF}_{\mathrm{n}a\mathrm{n}b} = \mathrm{sgn}(\mathrm{PN}_{\mathrm{n}a}, \mathrm{PN}_{\mathrm{n}b})\ C_{mn}\sqrt{|\mathrm{PN}^2_{\mathrm{n}a} - \mathrm{PN}^2_{\mathrm{n}b}|} \tag{27}$$

$$\mathrm{PN}_{\mathrm{min},\mathrm{n}a} \le \mathrm{PN}_{\mathrm{n}a} \le \mathrm{PN}_{\mathrm{max},\mathrm{n}a} \tag{28}$$

where $C_{mn}$ is the pipeline constant that depends on temperature, length, diameter, friction and gas composition.

For driving the natural gas flow from providers to gas loads, compressors are built at intervals along the gas pipeline to compensate the pressure loss [5, 11]. The gas flow through centrifugal compressor is governed by (30)–(32)

$$\mathrm{GF}_{\mathrm{n}a\mathrm{n}b} = \mathrm{sgn}(\mathrm{PN}_{\mathrm{n}a}, \mathrm{PN}_{\mathrm{n}b}) \cdot \frac{\mathrm{CH}_{\mathrm{cm}}}{k1_{\mathrm{cm}} - k2_{\mathrm{cm}}\mathrm{PR}^{k3_{\mathrm{cm}}}} \tag{29}$$

$$\mathrm{CH}_{\mathrm{min,cm}} \le \mathrm{CH}_{\mathrm{cm}t} \le \mathrm{CH}_{\mathrm{max,cm}} \tag{30}$$

$$\mathrm{PR}_{\min} \le \frac{\max(\mathrm{PN}_{\mathrm{n}a}, \mathrm{PN}_{\mathrm{n}b})}{\min(\mathrm{PN}_{\mathrm{n}a}, \mathrm{PN}_{\mathrm{n}b})} \le \mathrm{PR}_{\max} \tag{31}$$

where $k1_{\mathrm{cm}}$, $k2_{\mathrm{cm}}$ and $k3_{\mathrm{cm}}$ are empirical parameters corresponding to the compressor design.

## 2.4 Electricity–natural gas coupling constraints

A gas-fired power plant represents the linkage between natural gas and electricity systems. The gas consumption of a generation unit is a function of its hourly power generation stated as

$$\mathrm{GL}_{\mathrm{gl}t} = \sum_i \boldsymbol{GE}_{\mathrm{gl}i}\ F_{\mathrm{ef},i}(P_{it}, I_{it}), \quad \forall i \in \mathrm{GU} \tag{32}$$




doi: 10.1049/iet-gtd.2010.0151

# 3 Solution of coordinated scheduling model

## 3.1 Coordinated scheduling by LR

We try the LR method first. A group of equations in (32) represents the electricity–gas coordination problem. The two systems have a decomposable structure and we consider the LR method as the decomposition strategy of the coordination problem (1)–(32). The LR method is divided into two phases as shown in Fig. 1. For the sake of clarity, in Section 3 we use vectors $\boldsymbol{x}$ and $\boldsymbol{y}$ to represent electricity and natural gas system variables, respectively. The coupling constraints are expressed as in (33) instead of (32), in which $\boldsymbol{x}_c$, $\boldsymbol{y}_c$ are subvectors of $\boldsymbol{x}$ and $\boldsymbol{y}$ for representing variables in coupling constraints.

$$\boldsymbol{e}(\boldsymbol{x}_c) - \boldsymbol{g}(\boldsymbol{y}_c) = 0 \tag{33}$$

In the Lagrangian function (34), the coupling constraints (33) are relaxed and incorporated into the objective function using the following Lagrangian multipliers

$$\mathrm{L}(\boldsymbol{x}, \boldsymbol{y}, \boldsymbol{\lambda}) = \mathrm{EC}(\boldsymbol{x}) + \mathrm{GC}(\boldsymbol{y}) + \boldsymbol{\lambda}^{\mathrm{T}}\boldsymbol{e}(\boldsymbol{x}_c) - \boldsymbol{\lambda}^{\mathrm{T}}\boldsymbol{g}(\boldsymbol{y}_c) \tag{34}$$

The relaxed primal problem (35) is formulated in terms of minimising the Lagrangian function subject to constraints (4)–(32). In (35) $\phi(\boldsymbol{\lambda})$ is defined as the Lagrangian dual function with respect to $\boldsymbol{\lambda}$.

$$\phi(\boldsymbol{\lambda}) = \underset{x,y}{\mathrm{Min}}\{\mathrm{L}(\boldsymbol{x}, \boldsymbol{y}, \boldsymbol{\lambda}) | (4)\text{–}(31)\} \tag{35}$$

The resulting max–min problem is the following dual problem

$$\underset{\boldsymbol{\lambda}}{\mathrm{Max}}\ \underset{x,y}{\mathrm{Min}}\{\mathrm{L}(\boldsymbol{x}, \boldsymbol{y}, \boldsymbol{\lambda}) | (4)\text{–}(31)\} \tag{36}$$

The difference between the optimal objective function values of primal and dual problems (36) is the duality gap.

For a given $\boldsymbol{\lambda}^{(k)}$, the Lagrangian dual (35) of the primal problem is decomposed into the independent SCUC and the gas allocation subproblems as shown in (37) and (38).

$$\underset{x}{\mathrm{Min}}\{\mathrm{EC}(\boldsymbol{x}) + \boldsymbol{\lambda}^{(k)}\ \boldsymbol{e}(\boldsymbol{x}_c) | (4)\text{–}(16)\} \tag{37}$$

$$\underset{y}{\mathrm{Min}}\{\mathrm{GC}(\boldsymbol{y}) - \boldsymbol{\lambda}^{(k)}\ \boldsymbol{g}(\boldsymbol{y}_c) | (17)\text{–}(31)\} \tag{38}$$

Since $\boldsymbol{\lambda}^{(k)}$ may not be the optimal solution of the dual problem (36), the dual cost $\phi(\boldsymbol{\lambda}^{(k)})$ resulted from the solution of subproblems (37) and (38) will produce a lower bound for the optimal solution of the dual problem (36). According to the weak duality theory, (39) is satisfied where $\boldsymbol{x}^*$, $\boldsymbol{y}^*$ is the optimal solution of primal problem and $\lambda^*$ is the optimal solution of the dual problem.

$$\phi(\boldsymbol{\lambda}^{(k)}) \le \phi(\boldsymbol{\lambda}^*) \le \mathrm{EC}(\boldsymbol{x}^*) + \mathrm{GC}(\boldsymbol{y}^*) \tag{39}$$

The phase one procedure of LR is to update Lagrangian multipliers $\boldsymbol{\lambda}$ and then solve the resulting small-scale optimisation problem (37), (38) iteratively. The dual cost would increase gradually until changes of $\boldsymbol{\lambda}$ or $\boldsymbol{x}_c$ $\boldsymbol{y}_c$ are relatively small. The Lagrangian multipliers would be updated in the direction of the dual cost increment. The subgradient method shown in (40) is the most popular one. The parameter $\eta^{(k)}$ in (40) represents the step size that would satisfy (41) for convergence [12, 13]. Since $\phi(\boldsymbol{\lambda}^*)$ is generally unknown before the dual problem is solved, we use the estimated value of $\phi(\boldsymbol{\lambda}^*) - \phi(\boldsymbol{\lambda}^{(k)})$.

$$\boldsymbol{\lambda}^{(k+1)} = \boldsymbol{\lambda}^{(k)} + \eta^{(k)}[\boldsymbol{e}(\boldsymbol{x}_c) - \boldsymbol{g}(\boldsymbol{y}_c)] \tag{40}$$

$$0 < \eta^{(k)} < \frac{\phi(\boldsymbol{\lambda}^*) - \phi(\boldsymbol{\lambda}^{(k)})}{\|\boldsymbol{e}(\boldsymbol{x}_c) - \boldsymbol{g}(\boldsymbol{y}_c)\|^2} \tag{41}$$

where $\|\cdot\|$ represents Euclidian norm.

## 3.2 Coordinated scheduling by augmented LR

The proposed LR method has demonstrated a few drawbacks as follows. The linear production cost function of gas well and piecewise linear generator production cost function will make the electricity and gas subproblems oscillate between maximum and minimum outputs. Moreover, non-convex characteristics of our coordination problem with integer variables and non-linear network constraints will create a large duality gap, which will make it difficult to find a good dual solution. Based on our experience, a good dual solution with a lower degree of violation will result in an optimal primal solution. Furthermore, the LR application in our case will cause oscillations in the solution of dual problem, which is due to the linearity of the price function of gas wells, storage and contracts. A similar phenomenon is recognised in the solution of hydrothermal coordination problem [14, 15]. In the following, the augmented LR is used that introduces penalty terms to smooth out the dual function and alleviate numerical oscillations. We relax the coupling constraint (33) in an augmented Lagrangian fashion in (42), where $\omega$ is a positive penalty factor.

$$\mathrm{A}(\boldsymbol{x}, \boldsymbol{y}, \boldsymbol{\omega}, \boldsymbol{\lambda}) = \mathrm{EC}(\boldsymbol{x}) + \mathrm{GC}(\boldsymbol{y}) + \boldsymbol{\lambda}^{\mathrm{T}}[\boldsymbol{e}(\boldsymbol{x}_c) - \boldsymbol{g}(\boldsymbol{y}_c)] + \omega\|\boldsymbol{e}(\boldsymbol{x}_c) - \boldsymbol{g}(\boldsymbol{y}_c)\|^2 \tag{42}$$

The augmented Lagrangian function (42) cannot be decomposed as it contains an inseparable cross penalty term, whose variables belong to both power and gas constraints. To make this term separable, [16] uses the auxiliary problem principle to linearise the penalty term.

An alternative is to use the BCD method, which is a non-linear Gauss–Seidel-type method [13]. The BCD would solve the subproblems (43) and (44) sequentially. Here, when minimising one of the subproblems, the coupling variables of the other one appears in an inseparable penalty term, which will be fixed based on the latest solution $\tilde{\boldsymbol{x}}_c$, $\tilde{\boldsymbol{y}}_c$ of subproblems. In this paper, BCD method is adopted.

$$\underset{\boldsymbol{x}}{\text{Min}}\left\{\text{EC}(\boldsymbol{x})+\boldsymbol{\lambda}^{(k)\text{T}}\,\boldsymbol{e}(\boldsymbol{x}_c)+\frac{1}{2}\omega^{(k)}\|\boldsymbol{e}(\boldsymbol{x}_c)-\boldsymbol{g}(\tilde{\boldsymbol{y}}_c)\|^2\right\} \quad (43)$$

such that (4)–(16)

$$\underset{\boldsymbol{y}}{\text{Min}}\left\{\text{GC}(\boldsymbol{y})-\boldsymbol{\lambda}^{(k)\text{T}}\,\boldsymbol{g}(\boldsymbol{y}_c)+\frac{1}{2}\omega^{(k)}\|\boldsymbol{e}(\tilde{\boldsymbol{x}}_c)-\boldsymbol{g}(\boldsymbol{y}_c)\|^2\right\} \quad (44)$$

such that (17)–(31)

This procedure may create high-order terms for subproblems (43) and (44). In this paper, a piecewise linear approximation with respect to quadratic penalty terms is used. The dual problem is formulated as

$$\phi_\omega(\boldsymbol{\lambda}^*)=\underset{\boldsymbol{\lambda}}{\text{Max}}\{\underset{\boldsymbol{x},\boldsymbol{y}}{\text{Min}}\,\text{A}(\boldsymbol{x},\boldsymbol{y},\omega,\boldsymbol{\lambda})|(4)-(31)\} \quad (44)$$

The updating of Lagrangian multipliers can still use (40). The iterative solution steps for the augmented LR-based coordination algorithm are discussed as follows:

1. Initiate the Lagrangian multipliers $\boldsymbol{\lambda}^{(0)}$ and penalty factors $\omega^{(0)}$, $k=0$.

2. For the given $\boldsymbol{\lambda}^{(k)}\omega^{(k)}\tilde{\boldsymbol{y}}_c$, solve the electricity subproblem (43). Update $\tilde{\boldsymbol{x}}_c=\boldsymbol{x}_c^{(k)}$.

3. Solve the gas subproblem (45) based on $\boldsymbol{\lambda}^{(k)}$, $\omega^{(k)}$ and $\tilde{\boldsymbol{x}}_c$. Update $\tilde{\boldsymbol{y}}_c=\boldsymbol{y}_c^{(k)}$.

4. Update the Lagrangian multipliers $\boldsymbol{\lambda}$ based on the subgradient method (40).

5. If $\|\boldsymbol{e}(\boldsymbol{x}_c^{(k)})-\boldsymbol{g}(\boldsymbol{y}_c^{(k)})\|>\alpha\|\boldsymbol{e}(\boldsymbol{x}_c^{(k-1)})-\boldsymbol{g}(\boldsymbol{y}_c^{(k-1)})\|$ Update $\omega^{(k+1)}=\beta\omega^{(k)}$, $\beta>1$.

6. If $\|\boldsymbol{x}_c^{(k)}-\boldsymbol{y}_c^{(k)}\|\le\varepsilon$, the final primal-dual solution is calculated as $(\boldsymbol{x}^{(k)},\boldsymbol{y}^{(k)},\boldsymbol{\lambda}^{(k)})$. Otherwise, $k=k+1$.

7. If the iteration number $k$ is larger than the pre-specified number, go to step 8. Otherwise, go to step 2.

8. Construct the final feasible solution to the primal problem based on the obtained best solution to the dual problem.

## 3.3 Solution of SCUC and gas allocation subproblems

The common points of SCUC [9] and gas allocation [10] optimisation subproblems are represented by their types and structures. First, both are mixed-integer programming subproblems. Second, both have transmission network constraints and hold an L-shaped structure. For large-scale applications, the network security check is usually separated from the economic resource dispatch by either the Benders decomposition or the sensitivity analysis (i.e. power transfer distribution factor). The framework for the solution of SCUC or gas allocation subproblems is given in Fig. 2. More detailed formulations are provided in [8, 9]. The methodologies that may be engaged for the solution of SCUC or natural gas allocation subproblem do not change the overall framework of the proposed LR-based coordination strategy. Such methodologies can also be incorporated into our algorithm to solve the two subproblems [17, 18].

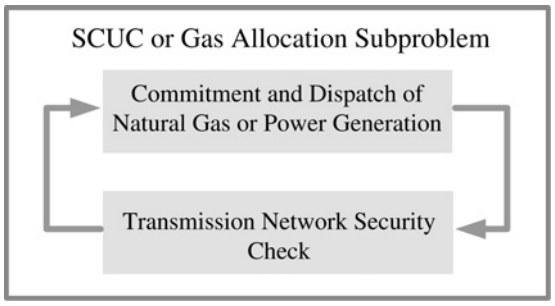


**Figure 2** *Framework for the solution of SCUC/gas allocation subproblem*

## 3.4 Calculation of feasible solution

In some cases, the convergence of dual problem is quick and fairly reliable, whereas in other cases the solution tends to exhibit a cycling behaviour, especially when using the LR approach. Usually, the iterative process is terminated after a pre-specified number of iterations. However, even the dual solution resulted from the last iteration may still be infeasible in the primal case, which is due to smaller violations of coupling constraints. Accordingly, we need to construct a feasible solution in the phase two of dual solution shown in Fig. 1. The feasible solution process could be heuristic or based on the approximate programming. In this paper, we adopt two steps to construct a feasible solution. First, based on the dual solution $\tilde{\boldsymbol{y}}_c$, we solve the SCUC problem (46) to obtain the power system schedule $\boldsymbol{x}^*$. In (46), $\boldsymbol{e}(\boldsymbol{x}_c)\le\boldsymbol{g}(\tilde{\boldsymbol{y}}_c)$ represents energy constraints or gas usage limits of gas-fired generating units. Then, we obtain a feasible solution $(\boldsymbol{x}^*,\boldsymbol{y}^*)$ by solving (47) based on the power system schedule $\boldsymbol{x}^*$.

$$\begin{aligned}&\boldsymbol{x}^*=\arg\min\text{EC}(\boldsymbol{x})\\&\text{such that (4)–(16)}\\&\boldsymbol{e}(\boldsymbol{x}_c)\le\boldsymbol{g}(\tilde{\boldsymbol{y}}_c)\end{aligned} \quad (45)$$



doi: 10.1049/iet-gtd.2010.0151

$$\begin{aligned} & y^* = \arg\min \mathrm{GC}(y) \\ & \text{such that (17)–(31)} \\ & g(y_c) = e(x_c^*) \end{aligned} \tag{46}$$

# 4 Case studies

In the 6-bus power system and the 7-node gas system, we mainly study the impact of gas storage and the network congestion on the coordinated scheduling results. The 118 bus with 14-nodes shows the impact of price incentives on the calculation of the least social cost and the coordinated schedule. The comparisons of augmented LR and LR methods are given in both cases.

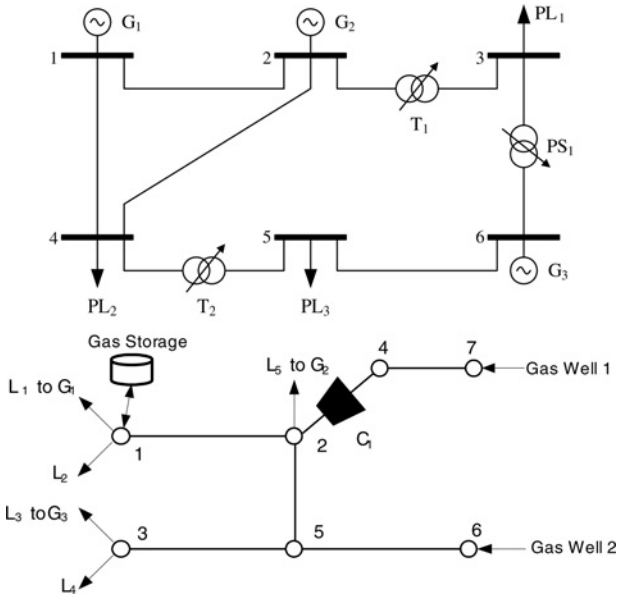


**Figure 3** *Six-bus power system and 7-node natural gas system*

**Table 1** Parameters of gas well

| Gas well | Node no. | Well-head price, $/kcf | Min output, kcf/h | Max output, kcf/h |
|---|---|---|---|---|
| 1 | 7 | 5.6 | 2000 | 5300 |
| 2 | 6 | 6 | 1000 | 6000 |

## 4.1 Six-bus power system and 7-node natural gas system

The 6-bus system and the 7-node natural gas system are depicted in Fig. 3. Parameters of the coupled power system and the natural gas system can be found in [8]. The cost information for the gas well and storage is given in Tables 1 and 2. Penalty prices for the electricity and the natural gas load not served are large as listed in Table 3. We apply the augmented LR and the LR methods to solve the following three cases.

*Case 1:* Base case without network or gas storage constraints

*Case 2:* Include network constraints

*Case 3:* Include network constraints and gas storage.

The augmented LR method is first applied to solve the three cases listed above. In Case 1, we ignore both electricity and natural gas transmission network constraints. Hence, there will be no congestion when scheduling the electricity and the natural gas systems. The hourly commitment of three gas-fired generating units is shown in Table 4. Fig. 4 shows the schedule of the gas well 2, which is the marginal gas well because of its higher well-head price. The social cost is $1 322 422, which is the lowest of all three cases. In Case 2, we consider the electricity and the natural gas transmission network constraints. The flow limits on power transmission line and the pressure limits on gas nodes through pipelines will result in the commitment of expensive generating units at additional hours. In comparison with those in Table 4, Table 5 shows

**Table 2** Parameters of gas storage in Case 3

| Storage node no. | Gas injection cost, $/kcf | Min. input, kcf/h | Max. input, kcf/h | Min. output, kcf/h | Max. output, kcf/h |
|---|---|---|---|---|---|
| 1 | 2.5 | 150 | 2500 | 0 | 2000 |

**Table 3** Electricity and gas load not served penalty price

| | |
|---|---|
| penalty price electricity load not served ($/MWh) | 2000 |
| penalty price of gas load not served ($/kcf) | 100 |

**Table 4** Hourly commitments of Case 1 based on augmented LR

| Unit | Hours (0–24) | | | | | | | | | | | | | | | | | | | | | | | |
|---|---|---|---|---|---|---|---|---|---|---|---|---|---|---|---|---|---|---|---|---|---|---|---|---|
| 1 | 1 | 1 | 1 | 1 | 1 | 1 | 1 | 1 | 1 | 1 | 1 | 1 | 1 | 1 | 1 | 1 | 1 | 1 | 1 | 1 | 1 | 1 | 1 | 1 |
| 2 | 1 | 0 | 0 | 0 | 0 | 0 | 0 | 0 | 0 | 0 | 0 | 0 | 1 | 1 | 1 | 1 | 1 | 1 | 1 | 1 | 1 | 1 | 0 | 0 | 0 |
| 3 | 0 | 0 | 0 | 0 | 0 | 0 | 0 | 0 | 0 | 0 | 1 | 1 | 1 | 1 | 1 | 1 | 1 | 1 | 1 | 1 | 1 | 1 | 1 | 0 | 0 |

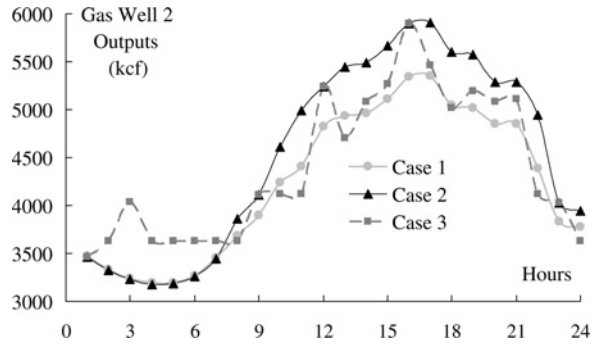


**Figure 4** *Gas well 2 in Cases 1, 2 and 3 based on augmented LR*

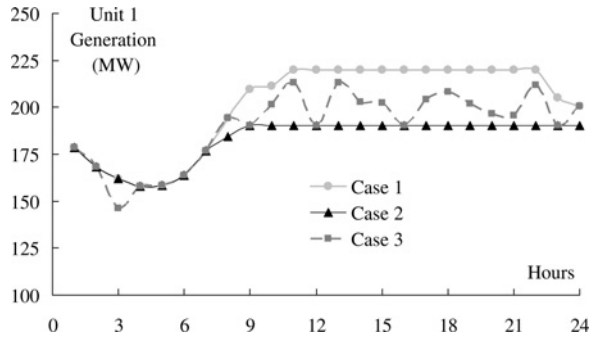


**Figure 5** *Unit 1 dispatches in Cases 1, 2 and 3 based on augmented LR*

that the unit 2 is committed at hours 10–11, 22, and the unit 3 is on at hours 8–9 and 23–24. Fig. 5 shows that the most efficient unit G1 would generate less in Case 2. The social cost is $1 366 196, which is higher than that in Case 1. In Case 3, the simulation includes a gas storage, which draws natural gas from the pipeline into the gas reservoir at off-peak hours 2–7, and releases the natural gas during peak hours 8–24. The figure shows that by using the stored gas, the efficient generation unit 1 will generate more during hours 1–24. Table 6 shows the hourly schedule of generation units. The social cost is $1 350 932, which includes the cost of gas well and the operation of gas storage.

We also solve the three cases by LR in order to compare the performances of the two methods. Table 7 shows the results. As presented in Section 3, using the LR algorithm will cause oscillations in the dual solution. A feasible solution based on the dual solution of LR by (45) will lead to electricity load shedding. The augmented LR algorithm, on the other hand, can avoid such oscillations and result in a better solution. To further illustrate the worst convergence of the dual problem by LR, the violation of constraints (32) against iterations is plotted in Fig. 6. The values of LR and augmented LR are shown in Fig. 7. Here, the violation of (32) is defined by the Manhattan norm $\|\boldsymbol{e}(\boldsymbol{x}_c) - \boldsymbol{g}(\boldsymbol{y}_c)\|_1$ of $\boldsymbol{e}(\boldsymbol{x}_c) - \boldsymbol{g}(\boldsymbol{y}_c)$. Obviously, the constraint violations cannot be mitigated in the LR method. However, the violations will approach zero by increasing the number of iterations in the augmented LR.

## 4.2 118-bus power system and 14-node natural gas system

The modified IEEE 118-bus power system has 54 fossil units, 12 gas-fired combined cycle units, 7 hydro units and 91 demand sides. The natural gas transmission system is composed of 14 nodes, 12 pipelines and 2 compressors. The electricity and natural gas transmission system data are found in motor.ece.iit.edu/data/Gastranssmion_118_14test.xls. Table 8 lists the well-head prices of natural gas as well as the penalty price of residual natural gas loads not served. Table 9 shows the social costs.

*Case 1: Base case solution:* We solve the coordinated scheduling problem as formulated in this paper to obtain the least social cost schedules for coupled power and natural gas system. The daily social cost based on augmented LR in this case is $2 350 957. Table 10 shows the daily generation and resource information. In addition, Fig. 8 shows the hourly generation for comparison. The congestion occurs in the 24-h gas transmission. The joint operators supply the residual gas loads 1–5 fully because of their higher penalty prices. However, the gas consumption of gas-fired units and residual gas loads 6–8 with lower priority are curtailed through optimisation iterations.

*Case 2: Impact of penalty price of residual gas loads:* We assume the penalty price of residual gas loads not served in Case 2 is decreased as shown in Table 10. The results show that residual gas loads can be interrupted or not supplied with a lower social cost as compared to Case 1. When considering the coordinated social cost, the joint operators would prefer to supply the additional natural gas to gas-fired units for power generation rather than supplying the residual gas loads. In other words, the social benefits of supplying gas-fired units are higher than providing the natural gas to residual gas loads. As shown in Table 10, the MWh generation fuelled by natural gas in Case 2 is higher than that in Case 1. The natural gas supplied to residual gas loads is reduced from 229 126 to 148 015 kcf in

**Table 5** Hourly commitments of Case 2 based on augmented LR

| Unit | Hours (0–24) | | | | | | | | | | | | | | | | | | | | | | | | |
|---|---|---|---|---|---|---|---|---|---|---|---|---|---|---|---|---|---|---|---|---|---|---|---|---|---|
| 1 | 1 | 1 | 1 | 1 | 1 | 1 | 1 | 1 | 1 | 1 | 1 | 1 | 1 | 1 | 1 | 1 | 1 | 1 | 1 | 1 | 1 | 1 | 1 | 1 | 1 |
| 2 | 1 | 0 | 0 | 0 | 0 | 0 | 0 | 0 | 0 | 0 | *1* | *1* | 1 | 1 | 1 | 1 | 1 | 1 | 1 | 1 | 1 | 1 | *1* | 0 | 0 |
| 3 | 0 | 0 | 0 | *0* | *0* | *0* | *0* | *0* | *1* | *1* | 1 | 1 | 1 | 1 | 1 | 1 | 1 | 1 | 1 | 1 | 1 | 1 | 1 | *1* | *1* |




doi: 10.1049/iet-gtd.2010.0151

**Table 6** Hourly commitments of Case 3 based on augmented LR

| Unit | Hours (0–24) | | | | | | | | | | | | | | | | | | | | | | | |
|---|---|---|---|---|---|---|---|---|---|---|---|---|---|---|---|---|---|---|---|---|---|---|---|---|
| 1 | 1 | 1 | 1 | 1 | 1 | 1 | 1 | 1 | 1 | 1 | 1 | 1 | 1 | 1 | 1 | 1 | 1 | 1 | 1 | 1 | 1 | 1 | 1 | 1 |
| 2 | 1 | 0 | 0 | 0 | 0 | 0 | 0 | 0 | 0 | 0 | *0* | *0* | 1 | 1 | 1 | 1 | 1 | 1 | 1 | 1 | 1 | 1 | *0* | 0 | 0 |
| 3 | 0 | 0 | 0 | *1* | *0* | *0* | *0* | *0* | *0* | *1* | 1 | 1 | 1 | 1 | 1 | 1 | 1 | 1 | 1 | 1 | 1 | 1 | 1 | *1* | *0* |

**Table 7** Comparison of augmented LR and standard LR based results

| | Case index | Case 1 | Case 2 | Case 3 |
|---|---|---|---|---|
| Augmented LR | dual cost ($) | 1 322 408 | 1 366 196 | 1 350 931 |
| | violation degree (kcf) | 2.3 | 3.1 | 3.6 |
| | feasible social cost ($) | 1 322 422 | 1 366 196 | 1 350 932 |
| | electricity load not served (MWh) | 0 | 0 | 0 |
| | gas load not served (kcf) | 0 | 0 | 0 |
| LR | dual cost ($) | 1 319 070 | 1 343 842 | 1 344 346 |
| | violation degree (kcf) | 14 642 | 12 162 | 12 491 |
| | feasible cost ($) | 1 525 986 | 2 0743 44 | 1 935 640 |
| | electricity load not served (MWh) | 76.2 | 396.4 | 319.2 |
| | gas load not served (kcf) | 0 | 0 | 0 |

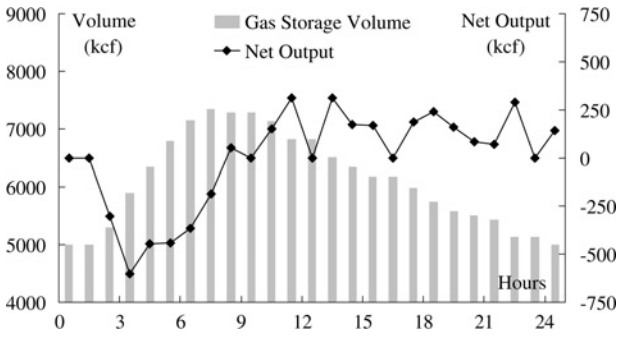


**Figure 6** *Gas storage volume and output based on augmented LR*

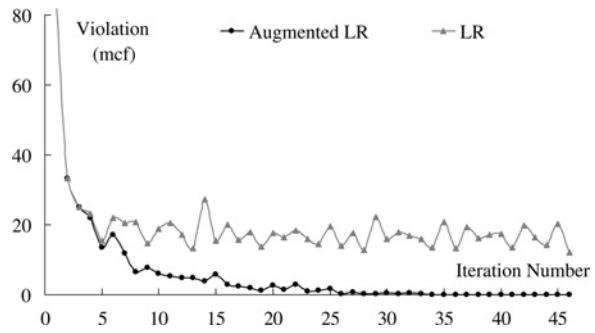


**Figure 7** *Violation of dual iterations in Case 2*

**Table 8** Well-head prices and gas load price incentives in Cases 1–3

| Price incentives | Case 1 | Case 2 | Case 3 |
|---|---|---|---|
| gas well 1 | 0.95 | 0.95 | 1.66 |
| gas well 2 | 0.90 | 0.90 | 1.58 |
| gas well 3 | 1.00 | 1.00 | 1.75 |
| penalty price of residual gas loads 1–3 not served | 3.00 | 1.20 | 3.00 |
| penalty price of residual gas loads 4–5 not served | 2.50 | 1.10 | 2.50 |
| penalty price of residual gas loads 6–8 not served | 1.10 | 0.90 | 1.80 |

Case 1. The social cost in Case 2 is $2 303 216. From Fig. 8, it is clear that the hourly coal generation in Case 1 is higher than that in Case 2.

*Case 3: Impact of well-head price of natural gas:* We increase the well-head price of natural gas wells by around 75% in comparison with that in Case 1 and solve the coordination scheduling problem by augmented LR. Table 10 shows that the power generation by natural gas in Case 1 is

**Table 9** Social costs based on LT and augmented LR in Cases 1–3

| Daily resources | Case 1 | Case 2 | Case 3 | |
|---|---|---|---|---|
| social cost ($) | augmented LR | 2 350 957 | 2 303 216 | 2 710 834 |
| | LR | 2 424 892 | 2 384 547 | 2 823 916 |

**Table 10** Summarised daily generation and resource based on augmented LR

| Daily resources | Case 1 | Case 2 | Case 3 |
|---|---|---|---|
| power generation by coal (MWh) | 120 796 | 114 312 | 131 724 |
| power generation by natural gas (MWh) | 14 689 | 21 178 | 3783 |
| hydro power generation (MWh) | 8308 | 8302 | 8286 |
| supplied gas to residual loads (kcf) | 229 126 | 148 015 | 305 526 |
| supplied gas to gas-fired units (kcf) | 190 270 | 275 309 | 48 907 |
| consumed gas by compressors (kcf) | 6374 | 6472 | 6186 |

replaced largely by coal generation because of the soaring natural gas price. The natural gas is no longer an economic choice for electricity generation in comparison with coal. Fig. 8 shows that in Case 3, natural gas units generate less than Case 1 and Case 2. Joint operators can dispatch more natural gas to residual gas loads. The daily social cost in Case 3 is $27 10 834, which is much higher than that in Case 1.

The daily and hourly hydro generation quantities are close in the three cases. The differences arise because the optimisation process will coordinate water resources to generate more during peak load hours or avoid committing more coal or gas-fired units while satisfying the hydro reservoir constraints.

We also solve the base case and the other two cases by LR. The social costs are given in Table 9. We draw a conclusion that the LR algorithm would result in a more expensive solution, whereas the augmented LR algorithm can avoid oscillations and lead to less expensive solutions. The computing time for obtaining dual solution of the LR method in Case 1 is 485 s with 20 iterations, whereas that based on augmented LR is 330 s with 15 iterations. The augmented Lagrangian decomposition and coordination method avoids the solution oscillation difficulties and speeds up algorithm convergence, thus augmented LR can obtain the solution more quickly than LR.

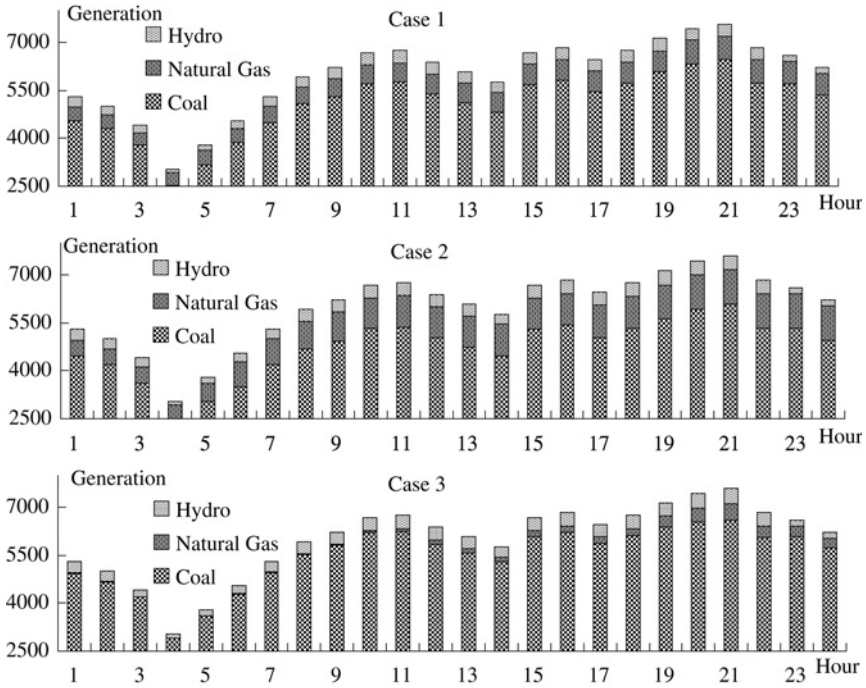


**Figure 8** *Hourly generation composition based on augmented LR*




doi: 10.1049/iet-gtd.2010.0151

## 5 Conclusions

This paper proposes a new model for the coordinated scheduling of the coupled electric power systems and natural gas transmission systems from a joint operator's viewpoint. The operator will coordinate the constrained resource scheduling and pursue the least social cost of energy system delivery. In this paper, the LR-based method is proposed initially to solve the problem. The augmented LR with the BDC technique is adopted to avoid numerical oscillations in this paper. Case studies verify that our proposed augmented LR method is effective in solving the coordinated energy scheduling model. Moreover, the augmented LR can avoid oscillations and improve the quality of the dual solution.

## 6 Acknowledgment

This work is supported in part by the US NSF grant # ECCS-0801853.

## 7 References

[1] LIU C., SHAHIDEHPOUR M., LI Z., FOTUHI-FIRUZABAD M.: 'Component & mode models for short-term scheduling of combined- cycle units', *IEEE Trans. Power Syst.*, 2009, **24**, pp. 976–990

[2] North American Electric Reliability Council: '2007/2008 Winter reliability assessment,' November 2007

[3] SHAHIDEHPOUR M., FU Y., WIEDMAN T.: 'Impact of natural gas infrastructure on electric power systems', *Proc. IEEE*, 2005, **93**, pp. 1042–1056

[4] QUELHAS A., GIL E., MCCALLEY J.D., RYAN S.M.: 'A multipeirod generalized network flow model of the U.S. integrated energy system: Part I-model description', *IEEE Trans. Power Syst.*, 2007, **22**, pp. 829–836

[5] AN S., LI Q., GEDRA T.W.: 'Natural gas and electricity optimal power flow'. Proc. IEEE/PES Transmission and Distribution Conf. and Exposition, 2003, vol. 1, pp. 7–12

[6] UNSIHUAY C., MARANGON LIMA J.W., ZAMBRONI DE SOUZA A.C.: 'Short-term operation planning of integrated hydrothermal and natural gas systems'. Proc. IEEE/PES Power Technical Conf., 2007

[7] MORAIS M.S., MARANGON LIMA J.W.: 'Natural gas network pricing and its influence on electricity and gas markets'. IEEE Bologna PowerTech Conf., Bologna, Italy, 23–26 June 2003

[8] LIU C., SHAHIDEHPOUR M., FU Y., LI Z.: 'Security-constrained unit commitment with natural gas transmission constraints', *IEEE Trans. Power Syst.*, 2009, **24**, pp. 1523–1536

[9] FU Y., SHAHIDEHPOUR M., LI Z.: 'Security-constrained unit commitment with ac constraints', *IEEE Trans. Power Syst.*, 2005, **20**, pp. 1001–1013

[10] O'NEILL R.P., WILLIARD M., WILKINS B., PIKE R.: 'A mathematical programming model for allocation of natural gas', *Oper. Res.*, 1979, **27**, (5), pp. 857–875

[11] BERARD G.P., ELIASON B.G.: 'An improved gas transmission system simulator', *Soc. Pet. Eng. J.*, 1978, **18**, (6), pp. 389–398

[12] ZHAO X., LUH P.B., WANG J.: 'Surrogate gradient algorithm for Lagrangian relaxation', *J. Optim. Theory Appl.*, 1999, **100**, (3), pp. 857–875

[13] BERTSEKAS D.P.: 'Nonlinear programming' (Athena Scientific, Belmont, MA, 1995)

[14] GUAN X., LUH P.B., ZHANG L.: 'Nonlinear approximation method in Lagrangian relaxation-based algorithms for hydrothermal scheduling', *IEEE Trans. Power Syst.*, 1995, **10**, pp. 772–778

[15] ZHANG L., LUH P.B., GUAN X., MERCHEL G.: 'Optimization-based inter-utility power purchase'. Proc. 1993 IEEE PICA Conf., Scottsdale, AZ, pp. 285–291

[16] COHEN G.: 'Auxiliary problem principle and decomposition of optimization problems', *J. Optim Theory Appl.*, 1980, **32**, pp. 277–305

[17] SHAHIDEHPOUR M., YAMIN H., LI Z.: 'Market operations in electric power systems' (Wiley, New York, NY, 2002)

[18] WOLF D., SMEERS Y.: 'The gas transmission problem solved by an extension of the simplex algorithm', *Manage. Sci.*, 2000, **46**, (11), pp. 1454–1465

# Transmission Switching in Security-Constrained Unit Commitment

Amin Khodaei and Mohammad Shahidehpour, *Fellow, IEEE*

***Abstract*—Transmission switching (TS) is introduced in security-constrained unit commitment (SCUC) for alleviating transmission violations and reducing operating costs. The SCUC problem is decomposed into the unit commitment (UC) master problem and the TS subproblem. The UC master problem finds the optimal hourly schedule of generating units. The TS subproblem uses this solution for transmission switching to find the optimal dispatch of units when considering network constraints. The TS subproblem also examines contingencies and identifies required changes to the UC master problem solution when contingencies cannot be mitigated in the TS subproblem. To propose a practical TS model, the standing phase angle difference limit is considered and relevant constraints are added to the TS subproblem. The case studies exhibit the effectiveness of the proposed approach.**

***Index Terms*—Benders decomposition, mixed-integer programming (MIP), security-constrained unit commitment, transmission switching.**

## NOMENCLATURE

*1) Indices:*

| | |
|---|---|
| $b, m, n$ | Index for bus . |
| $c$ | Index for contingency. |
| $i$ | Index for unit. |
| $l$ | Index for line. |
| $ns$ | Index for nonswitchable lines. |
| $s$ | Index for switchable lines. |
| $t$ | Index for time. |
| $\wedge$ | Index for given variables. |

*2) Sets:*

| | |
|---|---|
| $L_b$ | Set of lines connected to bus $b$. |
| $U_b$ | Set of units connected to bus $b$. |

*3) Parameters:*

| | |
|---|---|
| $F_{ci}$ | Production cost function of unit $i$. |
| $NB$ | Number of buses. |
| $NC$ | Number of contingencies. |
| $NL$ | Number of lines. |
| $NG$ | Number of units. |
| $NS$ | Number of switchable lines. |
| $NNS$ | Number of nonswitchable lines. |
| $NT$ | Number of time periods. |
| $D_t$ | System demand at time $t$. |
| $Pd_{bt}$ | Load at bus $b$ at time $t$. |
| $P_{i,\min}$ | Minimum power generation of unit $i$. |
| $P_{i,\max}$ | Maximum power generation of unit $i$. |
| $PL_{l,\max}$ | Maximum capacity of line $l$. |
| $UX_{it}^{c}$ | State of unit $i$ at time $t$ in contingency $c$. |
| $UY_{lt}^{c}$ | State of line $l$ at time $t$ in contingency $c$. |
| $x_l$ | Reactance of line $l$. |
| $\Delta_l$ | Maximum standing phase angle difference of line $l$. |

*4) Variables:*

| | |
|---|---|
| $I_{it}$ | Commitment state of unit $i$ at time $t$. |
| $P_{it}$ | Generation of unit $i$ at time $t$. |
| $PL_{lt}^{ns}$ | Power flow of nonswitchable line $l$ at time $t$. |
| $PL_{lt}^{s}$ | Power flow of switchable line $l$ at time $t$. |
| $SL_{bt,1}$, $SL_{bt,2}$ | Slack variables for power mismatch at bus $b$ at time $t$. |
| $v_t$ | Power mismatch at time $t$. |
| $w_t^c$ | Power mismatch at time $t$ and contingency $c$. |
| $z_{lt}$ | Switching state of line $l$ at time $t$. |
| $\pi_{it}$ | Marginal change in violations with increase in unit $i$ generation at time $t$. |
| $\delta_{mt}$ | Phase angle of bus $m$ at time $t$. |

## I. INTRODUCTION

ONE of the approaches for mitigating transmission flow violations is to switch power system elements. Corrective transmission switching (TS) can provide economic benefits when compared with other control methods such as generation unit rescheduling or load shedding [1], [2]. In [3], TS was considered by applying current sources at certain bus terminals in

Manuscript received May 01, 2009; revised August 19, 2009. Paper no. TPWRS-00320-2009.

The authors are with the Electrical and Computer Engineering Department, Illinois Institute of Technology, Chicago, IL 60616 USA (e-mail: akhodaei@iit.edu; ms@iit.edu).

Digital Object Identifier 10.1109/TPWRS.2010.2046344

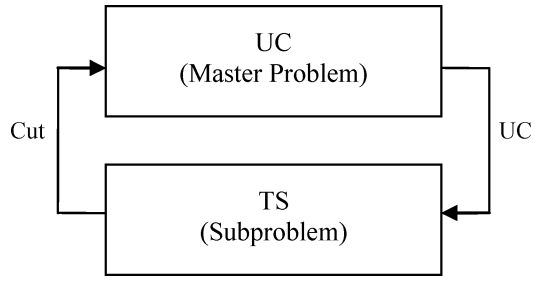


Fig. 1. SCUC using TS.

the base network. The injected currents were represented as control variables in the optimal TS subproblem. In [4], TS was employed as a corrective action to mitigate contingencies. Also, TS was used to model outages in optimal power flow. In [5], a TS method was devised for calculating $\mathrm{N}-1$ secure states. A linear switching model was applied to model control actions applied to contingency constraints. In [6], TS was considered as a means of mitigating violations in transmission flows and bus voltages. Also, practical issues related to switching operations were addressed. In these papers, transformer tap adjustments and static VAR compensators were recognized as a means of controlling the voltage problems [6]. In [7], a TS algorithm was developed for switching off lines and buses to mitigate contingencies. This TS algorithm was based on a sparse inverse technique and fast decoupled power flow. Also in [8], TS provided system operators with a congestion management tool.

These works showed that TS provides flexible control actions for voltage stability, congestion management, loss reduction, and system security. However, TS can provide economic benefits, where this concept was first introduced in a pioneering work by O'Neill *et al.* [9] in a market context. Moreover in [10] and [11], the problem of finding an optimal generation dispatch and transmission topology was investigated. In [10], the TS problem was solved only for the base case dispatch of the system, while in [11], the $\mathrm{N}-1$ contingency criterion was considered as well. A mixed-integer programming (MIP) model was used, which employed binary variables to represent the transmission line state. These papers found that TS could achieve large improvements in dispatch costs. The work in [12] was an extension of [10] which demonstrated that market participants are subject to system uncertainties when considering TS. The paper discussed ways that topology changes could affect nodal prices, load payments, generation revenues, congestion costs, and flowgate prices.

In this paper, the optimal TS for alleviating overloads is considered in SCUC that would take into account prevailing generating unit and transmission network constraints. Fig. 1 depicts the hierarchy for calculating SCUC by applying TS. The large-scale SCUC solution can represent a computation burden in power system operations. Since it is generally viewed as impractical to solve the generation unit and the entire set of network constraints together in SCUC, various decomposition approaches are considered by commercial SCUC packages.

The proposed decomposition applied to the SCUC problem in this paper consists of the UC master problem and the TS subproblem. Accordingly, Benders decomposition is utilized to decompose the SCUC problem into smaller and easier to solve subproblems. Benders decomposition is mathematically sound and can easily be applied to large-scale systems. The optimality of Benders decomposition as well as its applicability to power system problems in practical cases are discussed in [13]–[17].

The UC master problem in Fig. 1 will find the optimal schedule of units, considering the prevailing UC constraints. The initial optimal schedule of generating units is obtained based on the available market data. The UC solution is used in the TS subproblem to find the optimal hourly dispatch of units, considering transmission constraints and the switching capability of transmission lines.

The TS subproblem in Fig. 1 consists of three main blocks as shown in Fig. 2. The TS Feasibility Check inspects the UC result to find whether a feasible TS solution can be found in the base case (without considering contingencies). If violations persist, Benders cuts are generated and added to the UC master problem. After satisfying the TS feasibility, the Optimal TS Scheduling block will utilize the UC solution to find the optimal dispatch of generating units and the state of switchable lines in the base case and contingencies. The Transmission Contingencies Check block will then examine the Optimal TS Scheduling results as to whether a converged dc power flow solution can be obtained. The Transmission Contingencies Check block will also adjust the transmission flows to mitigate any existing bus mismatches. In the case of violations, Benders cuts are formed and added to the Optimal TS Scheduling block for the redispatch of generating units.

If a converged dc power flow solution can be found for a contingency considered in the TS subproblem, this contingency will be labeled as controllable. However, if a converged dc power flow solution does not exist after a certain number of iterations between the Optimal TS Scheduling and the Transmission Contingencies Check blocks, i.e., the violations still persist in the Transmission Contingencies Check block, the considered contingency will be labeled as uncontrollable. The controllable contingencies would not require any further processing as they can be handled by the existing UC solution. The uncontrollable contingencies, which cannot be handled in the TS subproblem, are sent back to the UC master problem to find a new (preventive) UC schedule. By labeling the contingencies, the controllable ones are considered first (corrective) and then uncontrollable ones are handled (preventive). In other words, the proposed approach examines less expensive corrective actions before resorting to the more expensive preventive actions.

One of the concerns in performing the TS in successive hours is the possibility of excessive standing phase angle difference across a switched line. If a line closing causes a loop closure, rapid changes may be required in the generation dispatch, which could otherwise impact the generator shaft. The corresponding torque induced in the rotor of a generator could cause generator fatigue and equipment failure [18]–[20]. This may happen to any generators irrespective of their connectivity to the closed line. So, it is required to limit the standing phase angle difference to safeguard the rotor shaft. Usually a generation redispatch upon line closures would bring the standing phase angles back to the safe region. Different approaches are proposed to obtain the minimum generation redispatch needed to achieve

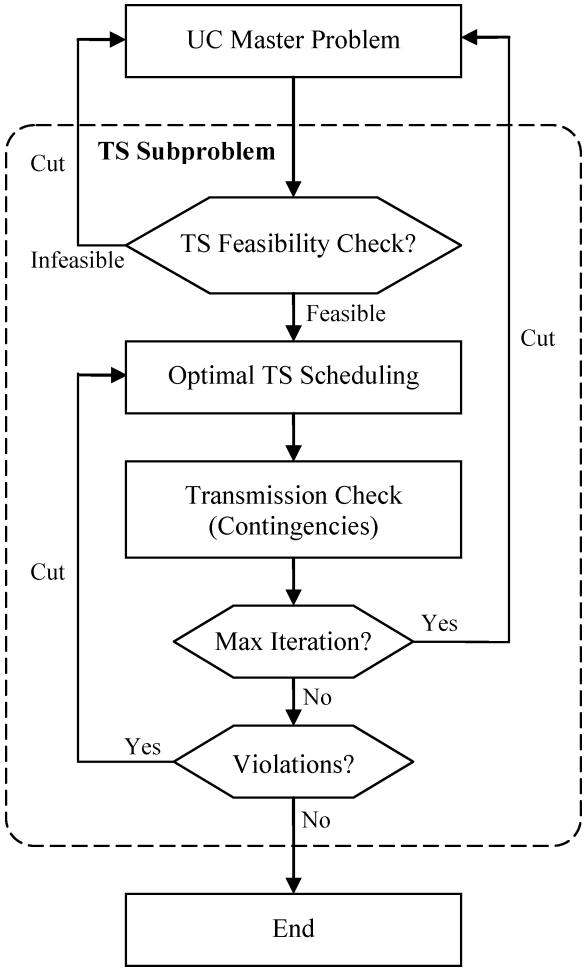


Fig. 2. Flowchart of SCUC using TS.

desired standing phase angles in a reasonable time [21]–[25]. This problem which is inevitable in restoration practices may also occur in the normal operation of power systems when attempting to reclose a single line that is a part of a transmission loop [20]. To present a practical TS model, the standing phase angle difference limit of switchable lines is formulated in our proposed model.

The rest of the paper is organized as follows. Section II presents the new proposed approach and formulates different parts of it. Section III conducts the numerical simulations and in detail discusses a six-bus system and the IEEE 118-bus system. Finally, concluding remarks are discussed in Section IV.

## II. SCUC Problem Formulation

The SCUC problem depicted in Fig. 2 is formulated as follows.

### A. UC Master Problem (Optimal Hourly Schedule of Units)

The objective of the UC master problem is to determine the day-ahead schedule of generating units in order to minimize the system operating cost while satisfying the prevailing constraints. A complete list of UC constraints and optimization techniques is found in [13].

### B. TS Subproblem

The TS subproblem consists of three parts, TS Feasibility Check, Optimal TS Scheduling, and Transmission Check as discussed below.

*1) TS Feasibility Check:* TS Feasibility Check which is a MIP problem would examine the possibility of a feasible TS solution. The objective is

$$Min \sum_{t=1}^{NT}\sum_{b=1}^{NB}(SL_{bt,1}+SL_{bt,2}). \tag{1}$$

The bus power mismatch is presented by (2), where $SL_{bt,1}$ and $SL_{bt,2}$ are surplus and deficit variables. The other constraints are power flow of switchable lines (3)–(6), power flow of nonswitchable lines (7)–(9), standing phase angle difference limits (10)–(11), and non-islanding constraint (12):

$$\sum_{i\in U_b} P_{it} - \sum_{l\in L_b} PL^{s}_{lt} - \sum_{l\in L_b} PL^{ns}_{lt} - Pd_{bt} + SL_{bt,1} - SL_{bt,2} = 0 \tag{2}$$
$$(b=1,\ldots,NB)(s=1,\ldots,NS)(ns=1,\ldots,NNS)$$

$$PL^{s}_{lt} - (\delta_{mt}-\delta_{nt})/x_l + M(1-z_{lt}) \geq 0 \tag{3}$$
$$(t=1,\ldots,NT)(l=1,\ldots,NL)(s=1,\ldots,NS)$$

$$PL^{s}_{lt} - (\delta_{mt}-\delta_{nt})/x_l - M(1-z_{lt}) \leq 0 \tag{4}$$
$$(t=1,\ldots,NT)(l=1,\ldots,NL)(s=1,\ldots,NS)$$

$$PL^{s}_{lt} \leq PL_{l,\max} z_{lt} \tag{5}$$
$$(t=1,\ldots,NT)(l=1,\ldots,NL)(s=1,\ldots,NS)$$

$$-PL^{s}_{lt} \leq PL_{l,\max} z_{lt} \tag{6}$$
$$(t=1,\ldots,NT)(l=1,\ldots,NL)(s=1,\ldots,NS)$$

$$PL^{ns}_{lt} = (\delta_{mt}-\delta_{nt})/x_l \tag{7}$$
$$(t=1,\ldots,NT)(l=1,\ldots,NL)(ns=1,\ldots,NNS)$$

$$PL^{ns}_{lt} \leq PL_{l,\max} \tag{8}$$
$$(t=1,\ldots,NT)(l=1,\ldots,NL)(ns=1,\ldots,NNS)$$

$$-PL^{ns}_{lt} \leq PL_{l,\max} \tag{9}$$
$$(t=1,\ldots,NT)(l=1,\ldots,NL)(ns=1,\ldots,NNS)$$

$$\delta_{mt}-\delta_{nt} \leq \Delta_l + Mz_{l(t-1)} + M(1-z_{lt}) \tag{10}$$
$$(t=1,\ldots,NT)(l=1,\ldots,NL)$$

$$\delta_{mt}-\delta_{nt} \geq -\Delta_l - Mz_{lt} - M(1-z_{l(t-1)}) \tag{11}$$
$$(t=1,\ldots,NT)(l=1,\ldots,NL)$$

$$\sum_{l\in L_b} z_{lt} \geq 1 \qquad (t=1,\ldots,NT) \tag{12}$$

where $M$ is a large positive number.

The TS constraints use a single binary variable $z_{lt}$. When this variable is equal to one, power flow constraints on switchable lines will be the same as those of other lines. In such a case, the line will be treated the same as other lines. When the line's binary variable is zero, (3)–(6) would impose a zero line flow and the line would be switched off. The direction of transmission flow is from bus $m$ to bus $n$. Constraints (10)–(11) consider the preset limits for the standing phase angle difference. The standing phase angle difference must be within its limits

before an attempt is made to close breakers. Using (10)–(11), standing phase angle difference limits are imposed when a line is switched on. Using (12), the islanding is prevented. This constraint guarantees that at least one line is connected to each bus when all corresponding lines are switchable.

If the TS Feasibility Check is infeasible, an LP problem is formed by setting the state of switchable lines to 1 and considering transmission constraints (2)–(9). This LP problem minimizes the bus power mismatches for 24 h and forms Benders cuts for the UC master problem. The LP problem applies the UC schedule using (13):

$$P_{it} = \hat{P}_{it}\hat{I}_{it} \leftrightarrow \pi_{it} \qquad (i = 1, \ldots, NG) \tag{13}$$

where $\hat{P}_{it}$ and $\hat{I}_{it}$ are fixed values calculated by the UC master problem. In (13), the arrow refers to the duality of the equality constraint, where $\pi_{it}$ is the dual variable (also known as simplex multiplier) of equality constraint (13). Mathematically, this multiplier represents the marginal increment/decrement of the objective value when $\hat{P}_{it}\hat{I}_{it}$ is changed. To form the Benders cut, this dual variable is needed. The solution of the LP problem will provide the hourly cuts for the UC master problem stated as

$$\hat{v}_t + \sum_{i=1}^{NG} \pi_{it}(P_{it}I_{it} - \hat{P}_{it}\hat{I}_{it}) \le 0. \tag{14}$$

In (14), the hourly bus power mismatch is noted as $\hat{v}_t$. The cut represents the coupled information on the unit generation dispatch and commitment state. The current violations can be mitigated by recalculating the hourly commitment states and the dispatch of generating units.

If the TS Feasibility Check solution is feasible, we will proceed to the Optimal TS Scheduling block as discussed next.

*2) Optimal TS Scheduling:* The Optimal TS Scheduling problem will calculate the optimal dispatch of generating units and the switchable line states in the base case and contingencies, given the hourly UC schedule

$$Min \sum_{i=1}^{NG}\sum_{t=1}^{NT} [F_{ci}(P_{it}^c)\hat{I}_{it}] \tag{15}$$

which is subject to unit and system constraints. The unit constraints include generation bids (prices), and power generation and ramp up/down rate limits. System constraints include power balance and spinning/operating reserve requirements, as well as fuel and emission constraints. A complete list of constraints can be found in [13]. The objective function (15) considers fixed unit commitment states which are calculated in the UC master problem. In the case of contingencies, the objective is also subject to load balance (16) and generation limit (17) constraints:

$$\sum_{i=1}^{NG} P_{it}^c = D_t \qquad (t = 1, \ldots, NT) \tag{16}$$

$$P_{i,\min}I_{it}UX_{it}^c \le P_{it}^c \le P_{i,\max}I_{it}UX_{it}^c \qquad (t = 1, \ldots, NT)(i = 1, \ldots, NG) \tag{17}$$

where $UX_{it}^c$ is the contingency state of unit $i$ at time $t$ in contingency $c$. Note that $c = 0$ represents base case. So, we would have $UX_{it}^0 = 1$. In (16), the load balance equation is satisfied for each contingency. According to (17), when a unit is on outage (contingency), its generation would be zero.

The Optimal TS Scheduling is a MIP problem because of the binary states of switchable lines. At the first iteration, there are no constraints on line flows or switchable lines states. So, any values could be assigned to these variables. But in the subsequent iterations, the Benders cuts from the Transmission Contingencies Check establish constraints on switchable line states.

*3) Transmission Check in Contingencies:* The solution of the Optimal TS Scheduling block will be checked in the Transmission Contingencies Check as to whether a converged dc power flow solution can be obtained. So, we would have

$$Min\ \ w_t^c = \sum_{b=1}^{NB} (SL_{bt,1}^c + SL_{bt,2}^c). \tag{18}$$

This objective is subject to transmission security constraints (19)–(32):

$$P_{it}^c = \hat{P}_{it}^c \leftrightarrow \pi_{it}^c (i = 1, \ldots, NG) \tag{19}$$

$$z_{lt}^c = \hat{z}_{lt}^c \leftrightarrow \mu_{lt}^c (l = 1, \ldots, NL) \tag{20}$$

$$\sum_{i\in U_b} P_{it}^c - \sum_{l\in L_b} PL_{lt}^{sc} - \sum_{l\in L_b} PL_{lt}^{nsc} - Pd_{bt} + SL_{bt,1}^c - SL_{bt,2}^c = 0 \quad (b = 1, \ldots, NB)(s = 1, \ldots, NS)(ns = 1, \ldots, NNS) \tag{21}$$

$$PL_{lt}^{sc} - (\delta_{mt}^c - \delta_{nt}^c)/x_l + M(1 - z_{lt}^c) + M(1 - UY_{lt}^c) \ge 0 \quad (l = 1, \ldots, NL)(s = 1, \ldots, NS) \tag{22}$$

$$PL_{lt}^{sc} - (\delta_{mt}^c - \delta_{nt}^c)/x_l - M(1 - z_{lt}^c) - M(1 - UY_{lt}^c) \le 0 \quad (l = 1, \ldots, NL)(s = 1, \ldots, NS) \tag{23}$$

$$PL_{lt}^{sc} \le PL_{l,\max} z_{lt}^c UY_{lt}^c (l = 1, \ldots, NL)(s = 1, \ldots, NS) \tag{24}$$

$$-PL_{lt}^{sc} \le PL_{l,\max} z_{lt}^c UY_{lt}^c (l = 1, \ldots, NL)(s = 1, \ldots, NS) \tag{25}$$

$$PL_{lt}^{nsc} - (\delta_{mt}^c - \delta_{nt}^c)/x_l + M(1 - UY_{lt}^c) \ge 0 \quad (l = 1, \ldots, NL)(ns = 1, \ldots, NNS) \tag{26}$$

$$PL_{lt}^{nsc} - (\delta_{mt}^c - \delta_{nt}^c)/x_l - M(1 - UY_{lt}^c) \le 0 \quad (l = 1, \ldots, NL)(ns = 1, \ldots, NNS) \tag{27}$$

$$PL_{lt}^{nsc} \le PL_{l,\max} UY_{lt}^c,\ (l = 1, \ldots, NL)(ns = 1, \ldots, NNS) \tag{28}$$

$$-PL_{lt}^{nsc} \le PL_{l,\max} UY_{lt}^c (l = 1, \ldots, NL)(ns = 1, \ldots, NNS) \tag{29}$$

$$\delta_{mt}^c - \delta_{nt}^c \le \Delta_l + M z_{l(t-1)}^c + M(1 - z_{lt}^c)(l = 1, \ldots, NL) \tag{30}$$

$$\delta_{mt}^c - \delta_{nt}^c \ge -\Delta_l - M z_{l(t-1)}^c - M(1 - z_{lt}^c)(l = 1, \ldots, NL) \tag{31}$$

$$\sum_{l\in L_b} z_{lt}^c \ge 1 (t = 1, \ldots, NT) \tag{32}$$

where $\hat{P}^c_{it}$ and $\hat{z}^c_{lt}$ are fixed values calculated by Optimal TS Scheduling. The power flow of switchable lines is obtained by (22)–(25). When a line is switched off, the line flow will be set to zero and removed from power flow equations. The power flow of nonswitchable lines is obtained by (26)–(29). In (22)–(29) the contingency state of line $l$ at time $t$ is considered by $UY^c_{It}$. Note that $c = 0$ represents base case. Therefore, we would have $UY^0_{lt} = 1$. Standing phase angle difference limits are considered by (30) and (31), and islanding is prevented using (32) for buses in which all corresponding lines are switchable. Here (30) and (31) use the given values of switchable states. So there is no time-based coupling in this problem.

If the total mismatch is zero, the proposed generation dispatch and switchable line schedule provide a feasible power flow solution which satisfies transmission security constraints. Otherwise, the Benders cut (33) will be added to the Optimal TS Scheduling block for mitigating the violations in the next iteration:

$$\hat{w}^c_t + \sum_{i=1}^{NG} \pi^c_{it}(P^c_{it} - \hat{P}^c_{it}) + \sum_{l=1}^{NL} \mu^c_{lt}(z^c_{lt} - \hat{z}^c_{lt}) \le 0. \quad (33)$$

This cut represents the coupled information on the unit generation dispatch and switchable line schedule. If the current UC solution cannot mitigate the contingency $c$ violations when the maximum number of iterations has reached, this contingency will be labeled as uncontrollable and the Benders cut (34) will be returned to the UC master problem for calculating a preventive generation schedule

$$\hat{w}^c_t + \sum_{i=1}^{NG} \pi^c_{it}(P_{it}I_{it} - \hat{P}^c_{it}\hat{I}_{it}) \le 0. \quad (34)$$

The controllable contingencies are handled by corrective actions in the Transmission Contingencies Check without requiring any revisions to the existing UC solution. The proposed solution procedure is given as follows.

Step 1) Solve the UC master problem.

Step 2) Given the UC schedule, check the TS feasibility. If the TS is feasible, then proceed to Step 4.

Step 3) Minimize bus power mismatches if the TS Feasibility Check is infeasible. Form the Benders cuts and go to Step 1.

Step 4) Use the Optimal TS Scheduling to calculate the generation dispatch and the switchable line states in the base case and contingencies.

Step 5) Use the Transmission Check block to minimize bus power mismatches by utilizing the Optimal TS Scheduling results. If the mismatch is not zero, add the Benders cuts to the Optimal TS Scheduling for the next iteration. The controllable contingencies are handled by Transmission Check block. However, the Benders cut for uncontrollable contingencies are added to Step 1 for the next UC iteration. Stop the process if the total mismatch is zero.

## III. Numerical Simulations

Two case studies for the six-bus system and the IEEE 118-bus system are analyzed to illustrate the performance of the proposed method. The proposed method was implemented on a 2.4-GHz personal computer using CPLEX 11.0 [26].

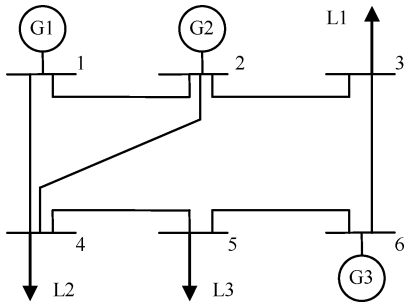


Fig. 3. Six-bus system.

### A. Six-Bus System

The six-bus system is shown in Fig. 3. The objective is to calculate the least cost of dispatch with an hourly fixed load. The characteristics of generators, lines, and the hourly load distribution over the 24-h horizon are given in Tables I–III, respectively. The load is distributed as 20%, 40%, and 40% among buses 3, 4, and 5, respectively. In Table I, the maximum sustained rate (MSR) and the quick start capability (QSC) of units are used to satisfy the reserve requirements of the system. The MSR and QSC are used to limit the spinning and operating reserves of the unit, respectively. The 10-min spinning reserve of a unit is the unloaded synchronized generation that can ramp up in 10 min. The spinning reserve of a unit cannot exceed the difference between its maximum capacity and current generation dispatch. This reserve is limited by the 10-min MSR. Operating reserve is the unloaded synchronized/unsynchronized generating capacity that can ramp up in 10 min. When a unit is on, its operating reserve is the same as spinning reserve. When a unit is off, its operating reserve is equal to its QSC. The following TS cases are considered:

Case 1: Base case UC (without contingencies)
Case 2: Outage of line 2–4 is considered in Case 1
Case 3: Outage of unit 2 is considered in Case 1
Case 4: Standing phase angle difference limits are considered in Case 1

The range of standing phase angle differences that a system can withstand mostly depends on the voltage level and is usually determined by steady-state and dynamic simulations. However in Cases 1, 2, and 3, it is assumed that the maximum standing phase angle is large enough to satisfy the associated constraints. In Case 4, the impact of standing phase angle difference on UC solution is examined.

*Case 1:* The UC with a subsequent dc network security check is used to find the results shown in Table IV. The cheaper unit 1 is on at all hours while unit 2 is used at peak hours to satisfy the remaining load and minimize the operating cost. Unit 2 is committed at hour 11 due to a load increase. The transmission network encounters flow violations on lines 1–4 and 4–5. Therefore, expensive unit 3 is turned on to help mitigate violations. Line 4–5 is congested at peak hours 15–19, which leads to a lower dispatch of unit 1 and a higher operating cost. The total operating cost is $125 465.

The TS application will result in a similar schedule, but unit 3 is not committed in the entire scheduling horizon. This UC schedule will satisfy the TS feasibility check. So, the

TABLE I
CHARACTERISTICS OF GENERATING UNITS

| Unit No. | | 1 | 2 | 3 |
|---|---|---|---|---|
| Bus No. | | 1 | 2 | 6 |
| Cost Coefficients | c ($/MW$^2$h) | 0.014 | 0.020 | 0.086 |
| | b ($/MWh) | 19.96 | 23 | 29.14 |
| | a ($) | 200 | 150 | 50 |
| Minimum Capacity (MW) | | 100 | 10 | 10 |
| Maximum Capacity (MW) | | 220 | 200 | 50 |
| Startup Cost ($) | | 50 | 40 | 0 |
| Shutdown Cost($) | | 100 | 200 | 0 |
| Minimum Up Time (h) | | 4 | 3 | 1 |
| Minimum Down Time (h) | | 4 | 2 | 1 |
| Ramp Up Rate (MW/h) | | 40 | 30 | 20 |
| Ramp Down Rate (MW/h) | | 50 | 35 | 20 |
| MSR (MW/min) | | 2 | 1.5 | 0.5 |
| QSC (MW) | | 15 | 10 | 10 |
| Initial Hour | | +4 | +3 | +1 |
| Initial Generation (MW) | | 140 | 20 | 10 |

TABLE II
CHARACTERISTICS OF TRANSMISSION LINES

| Line No. | From Bus | To Bus | X (pu) | Flow limit (MW) |
|---|---|---|---|---|
| 1 | 1 | 2 | 0.170 | 140 |
| 2 | 1 | 4 | 0.258 | 110 |
| 3 | 2 | 3 | 0.037 | 150 |
| 4 | 2 | 4 | 0.197 | 140 |
| 5 | 3 | 6 | 0.018 | 130 |
| 6 | 4 | 5 | 0.037 | 50 |
| 7 | 5 | 6 | 0.140 | 140 |

TABLE III
HOURLY LOAD DEMAND

| Hour | Load (MW) | Spinning Reserve (MW) | Operating Reserve (MW) |
|---|---|---|---|
| 1 | 175.19 | 2.63 | 12.26 |
| 2 | 165.15 | 2.48 | 11.56 |
| 3 | 158.67 | 2.38 | 11.10 |
| 4 | 154.73 | 2.32 | 10.83 |
| 5 | 155.06 | 2.33 | 10.85 |
| 6 | 160.48 | 2.40 | 11.23 |
| 7 | 173.39 | 2.60 | 12.14 |
| 8 | 177.60 | 2.85 | 13.33 |
| 9 | 186.81 | 3.09 | 14.39 |
| 10 | 206.96 | 3.26 | 15.20 |
| 11 | 228.61 | 3.43 | 16.00 |
| 12 | 236.10 | 3.54 | 16.52 |
| 13 | 242.18 | 3.63 | 16.95 |
| 14 | 243.60 | 3.66 | 17.05 |
| 15 | 248.86 | 3.73 | 17.42 |
| 16 | 255.79 | 3.84 | 17.91 |
| 17 | 256.00 | 3.84 | 17.92 |
| 18 | 246.74 | 3.70 | 17.27 |
| 19 | 245.97 | 3.69 | 17.22 |
| 20 | 237.35 | 3.56 | 16.62 |
| 21 | 237.31 | 3.56 | 16.62 |
| 22 | 232.67 | 3.41 | 15.90 |
| 23 | 195.93 | 3.02 | 14.07 |
| 24 | 195.60 | 2.95 | 13.78 |

model would proceed to the Optimal TS Scheduling block. Imposing fewer cuts in this case would result in a cheaper UC solution. Using TS, the total operating cost is slightly dropped

TABLE IV
UC SCHEDULE OF SIX-BUS SYSTEM IN CASE 1

| Unit | Hours (0-24) |
|---|---|
| 1 | 1 1 1 1 1 1 1 1 1 1 1 1 1 1 1 1 1 1 1 1 1 1 1 1 |
| 2 | 1 0 0 0 0 0 0 0 0 0 0 1 1 1 1 1 1 1 1 1 1 1 1 0 |
| 3 | 1 0 0 0 0 0 0 0 0 0 0 1 0 0 0 0 0 0 0 0 0 0 0 0 |

TABLE V
LINE SCHEDULE OF SIX-BUS SYSTEM IN CASE 1 USING TS

| Line | Hours (0-24) |
|---|---|
| 2-4 | - 1 1 1 1 1 1 0 0 0 0 0 0 0 0 0 1 1 0 0 0 0 0 0 0 |
| 4-5 | - 1 1 1 1 1 1 0 0 0 0 0 0 0 0 0 1 1 0 0 0 0 0 0 0 |

to $125 362. At hour 11 when lines 1–4 and 4–5 are congested, lines 2–4 and 4–5 are switched off instead of turning on unit 3. Here, there will be no transmission loop remaining in the system and the existing lines could increase the flows to their limits. Table V shows the state of switchable lines in which lines 2–4 and 4–5 are mostly switched off. At peak hours 16–17, the line flow constraints cannot be satisfied without placing back the lines 2–4 and 4–5. The standing phase angle differences for the two lines are 10.24 and 1.85 degrees, respectively.

*Case 2:* In this case, the outage of line 2–4 is considered. The UC in Case 1 cannot satisfy the dc network security check. The new UC is mostly the same as the schedule in Case 1, but unit 2 is committed at hours 10 and 24. This UC will mitigate the flow violations and satisfy the transmission security with a total operating cost of $125 848. The UC solution given in Case 1 will satisfy the optimal TS scheduling block with line switching. The unit schedule is the same as that of Case 1. The TS schedule is different from that of Case 1, where line 4–5 is in service at peak hours 16–17 and off otherwise. The standing phase angle difference of line 4–5 at hour 16 is 0.3 degree. The line 2–4 contingency is handled with a corrective action at the Transmission Contingencies Check block. The congestion of line 1–2 is mitigated at peak hours 16–17 with a total operating cost of $125 470 (i.e., 0.3% improvement)

*Case 3:* When unit 2 is on outage, unit 1 will not be able to satisfy the hourly load. Therefore, unit 3 is committed additionally. The preventive schedule without TS is shown in Table VI which is obtained with a more expensive daily operating cost of $126 413. However, the proposed TS approach provides a preventive UC schedule. Comparing the new schedule with that of Table VI, we learn that the unit 2 is committed at hour 13 instead of hour 20, and unit 3 is not committed at hour 10. The flow violations at this hour are mitigated by switching off lines 2–4 and 4–5. The operating cost with TS is $126 271. The state of switchable lines before outage of unit 2 is shown in Table VII. However, after the outage of unit 2, both switchable lines 2–4 and 4–5 will be switched off for the entire scheduling horizon.

In these three cases, all lines are considered as switchable. However, only lines 2–4 and 4–5 are switched in these cases. In Fig. 3, switching off any of lines 2–3, 3–6, 4–5, and 5–6 will remove the loop 2–3–4–5–6–2 with better results. Since line 4–5 has the lowest capacity, it is often subject to congestion which makes the line a good candidate for switching. This conclusion is consistent with the proposed results. By switching off line 4–5, the line flow in the loop, i.e., those of lines 2–3, 3–6,

TABLE VI
UC SCHEDULE OF SIX-BUS SYSTEM IN CASE 3 WITHOUT TS

| Unit | Hours (0-24) |
|---|---|
| 1 | 1 1 1 1 1 1 1 1 1 1 1 1 1 1 1 1 1 1 1 1 1 1 1 1 |
| 2 | 1 0 0 0 0 0 0 0 0 0 0 0 0 0 1 1 1 1 1 1 1 0 0 0 0 |
| 3 | 1 0 0 0 0 0 0 0 0 0 0 1 1 1 1 1 1 1 1 1 1 1 1 1 0 |

TABLE VII
LINE SCHEDULE OF SIX-BUS SYSTEM IN CASE 3 USING TS BEFORE OUTAGE OF UNIT 2

| Line | Hours (0-24) |
|---|---|
| 2-4 | - 1 1 1 1 1 1 1 1 1 1 1 1 1 0 1 1 1 1 1 1 1 1 0 1 |
| 4-5 | - 0 0 0 0 0 0 0 0 0 0 1 0 1 1 0 1 1 1 1 1 1 1 1 0 0 |

and 5–6, can be raised without affecting the flow on other lines. Next, one of lines in the other loop, i.e., lines 1–2, 1–4, and 2–4, could be a good choice for switching. Since unit 1 is the most economical and the largest unit, it will remain in service along with the attached lines. So, line 2–4 would be the best TS choice for this loop. With switching off both lines 2–4 and 4–5, there are still enough lines connected to bus 4 to supply its load. By considering lines 2–4 and 4–5 as switchable, loops would be relaxed while meeting the load balance requirements.

*Case 4:* In this case, the standing phase angle difference limits of the switchable lines are considered. The standing phase angle difference limit for switchable lines is considered to be 4 degrees. Imposing this limit, when the absolute value of the difference of phase angles in two sides of the switched line is less than its standing phase angle difference limit, the line cannot be switched back to the system.

In Case 1, both switchable lines 2–4 and 4–5 are switched back to the system at hour 16. The standing phase angle difference for these two lines is 10.24 and 1.85 degrees, respectively. Since the standing phase angle difference of line 2–4 is more than its limit, this line cannot be switched back at hour 16. Imposing this constraint to the problem, the switchable line 2–4 is switched back to the system one hour earlier, i.e., hour 15. At this hour, the line can be switched back to the system, since the standing phase angle difference is less than its limit. With this change in the state of switchable lines, the generation of unit 1 is decreased by 2.5 MW and the generation of unit 2 is increased by 2.5 MW. This change in dispatch leads to an insignificant increase in the total operating cost.

### B. IEEE 118-Bus System

A modified IEEE 118-bus system is used to study the SCUC with TS. The system has 118 buses, 54 units, and 186 branches. The data for this system are found in motor.ece.iit.edu/data/SCUC_118test.xls. Lines 30, 78, 90, 115, 151, 159, and 164 are considered switchable. Three cases are considered. The first case is the base case UC, and the second one is SCUC when considering contingencies. At the third case, the results of the proposed model are compared with those of an integrated model.

*Case 1:* In this case, the SCUC approach without TS is used to find the generating unit schedules with a total operating cost of $1 081 320.36. Using TS, seven lines are considered as switchable. The UC schedule found in the first iteration of the problem cannot satisfy the TS feasibility and Benders cuts are added to the UC problem. The feasible schedule is found after two iterations and shown in Table VIII. The TS schedule is shown in Table IX with a total operating cost of $1 078 155.86, which signifies a 0.30% improvement in the total operating cost as compared with the UC solution. The total execution time is 94 s.

TABLE VIII
UC SCHEDULE OF THE IEEE 118-BUS SYSTEM IN CASE 1 USING TS

| Unit | Hours (0-24) |
|---|---|
| 1-2 | 0 0 0 0 0 0 0 0 0 0 0 0 0 0 0 0 0 0 0 0 0 0 0 0 0 0 |
| 3 | 0 0 0 0 0 0 0 0 0 0 0 0 0 0 0 0 0 0 0 0 0 0 0 0 0 0 |
| 4-5 | 1 1 1 1 1 1 1 1 1 1 1 1 1 1 1 1 1 1 1 1 1 1 1 1 1 1 |
| 6 | 0 0 0 0 0 0 0 0 0 0 0 0 0 0 0 0 0 0 0 0 0 0 0 0 0 0 |
| 7 | 0 0 0 0 0 0 0 0 0 0 0 1 1 1 1 1 1 1 1 1 1 1 1 1 1 0 |
| 8 | 0 0 0 0 0 0 0 0 0 0 0 0 0 0 0 0 0 1 1 1 0 0 0 0 0 0 |
| 9 | 0 0 0 0 0 0 0 0 0 0 0 0 0 0 0 0 0 1 1 1 0 0 0 0 0 0 |
| 10-11 | 1 1 1 1 1 1 1 1 1 1 1 1 1 1 1 1 1 1 1 1 1 1 1 1 1 1 |
| 12 | 0 0 0 0 0 0 0 0 0 0 0 0 0 0 0 0 0 0 0 1 0 0 0 0 0 0 |
| 13 | 0 0 0 0 0 0 0 0 0 0 0 0 0 0 0 0 0 0 0 1 0 1 0 0 0 0 |
| 14 | 0 0 0 0 0 0 0 0 0 0 1 1 1 1 1 1 1 1 1 1 1 1 1 1 1 0 |
| 15 | 0 0 0 0 0 0 0 0 0 0 0 0 0 0 0 0 0 0 0 1 0 0 0 0 0 0 |
| 16 | 0 0 0 0 0 0 0 0 0 0 1 1 1 1 1 1 1 1 1 1 1 1 1 1 0 0 |
| 17 | 0 0 0 0 0 0 0 0 0 0 0 0 0 0 0 0 0 1 1 0 0 0 0 0 0 0 |
| 18 | 0 0 0 0 0 0 0 0 0 0 0 0 0 0 0 0 0 1 1 0 0 0 0 0 0 0 |
| 19 | 0 0 0 0 0 0 0 0 0 0 0 1 1 1 1 1 1 1 1 1 1 1 1 1 1 0 |
| 20-21 | 1 1 1 1 1 1 1 1 1 1 1 1 1 1 1 1 1 1 1 1 1 1 1 1 1 1 |
| 22 | 0 0 0 0 0 0 0 0 0 0 1 1 1 1 1 1 1 1 1 1 1 1 1 1 0 0 |
| 23 | 0 0 0 0 0 0 0 0 0 0 1 1 1 1 1 1 1 1 1 1 1 1 1 1 0 0 |
| 24-25 | 1 1 1 1 1 1 1 1 1 1 1 1 1 1 1 1 1 1 1 1 1 1 1 1 1 1 |
| 26 | 0 0 0 0 0 0 0 0 0 0 1 1 1 1 1 1 1 1 1 1 1 1 1 1 0 0 |
| 27-29 | 1 1 1 1 1 1 1 1 1 1 1 1 1 1 1 1 1 1 1 1 1 1 1 1 1 1 |
| 30 | 0 0 0 0 0 0 0 0 0 0 0 1 1 1 1 1 1 1 1 1 1 1 1 1 0 0 |
| 31 | 0 0 0 0 0 0 0 0 0 0 0 0 0 0 0 0 1 1 1 0 0 0 0 0 0 0 |
| 32 | 0 0 0 0 0 0 0 0 0 0 0 0 0 0 0 0 0 1 1 0 0 0 0 0 0 0 |
| 33 | 0 0 0 0 0 0 0 0 0 0 0 0 0 0 0 0 0 0 0 0 0 0 0 0 0 0 |
| 34-35 | 0 0 0 0 0 0 0 0 0 0 0 1 1 1 1 1 1 1 1 1 1 1 1 1 1 1 |
| 36 | 1 1 1 1 1 1 1 1 1 1 1 1 1 1 1 1 1 1 1 1 1 1 1 1 1 1 |
| 37 | 0 0 0 0 0 0 0 0 0 0 1 1 1 1 1 1 1 1 1 1 1 1 1 1 1 1 |
| 38 | 0 0 0 0 0 0 0 0 0 0 0 0 0 0 0 0 0 0 0 0 0 0 0 0 0 0 |
| 39 | 1 1 1 1 1 1 1 1 1 1 1 1 1 1 1 1 1 1 1 1 1 1 1 1 1 1 |
| 40 | 0 0 0 0 0 0 0 0 0 0 0 0 0 0 1 1 1 1 1 1 1 1 1 1 0 0 |
| 41-42 | 0 0 0 0 0 0 0 0 0 0 0 0 0 0 0 0 0 0 0 0 0 0 0 0 0 0 |
| 43 | 0 0 0 0 0 0 0 0 1 1 1 1 1 1 1 1 1 1 1 1 1 1 1 1 1 1 |
| 44-45 | 1 1 1 1 1 1 1 1 1 1 1 1 1 1 1 1 1 1 1 1 1 1 1 1 1 1 |
| 46 | 0 0 0 0 0 0 0 0 0 0 0 0 0 0 0 0 0 0 0 0 0 0 0 0 0 0 |
| 47 | 0 0 0 0 0 0 0 0 0 0 0 0 0 0 1 1 1 1 1 1 1 1 1 1 0 0 |
| 48 | 0 0 0 0 0 0 0 0 0 0 0 0 0 1 1 1 1 1 1 1 1 1 1 0 0 0 |
| 49 | 0 0 0 0 0 0 0 0 0 0 0 0 0 0 0 0 0 0 0 0 0 0 0 0 0 0 |
| 50 | 0 0 0 0 0 0 0 0 0 0 0 0 0 0 0 0 0 0 0 0 0 0 0 0 0 0 |
| 51 | 0 0 0 0 0 0 0 0 0 0 0 0 1 1 1 1 1 1 1 1 1 1 1 1 0 0 |
| 52 | 0 0 0 0 0 0 0 0 0 0 0 1 1 1 1 1 1 1 1 1 1 1 1 1 0 0 |
| 53 | 0 0 0 0 0 0 0 0 0 0 1 1 1 1 1 1 1 1 1 1 1 1 1 1 0 0 |
| 54 | 0 0 0 0 0 0 0 0 0 0 0 0 0 0 0 1 1 1 0 0 0 0 0 0 0 0 |

TABLE IX
LINE SCHEDULE OF THE IEEE 118-BUS SYSTEM IN CASE 1 USING TS

| Line | Hours (0-24) |
|---|---|
| 30 | - 1 1 0 0 0 1 1 0 0 0 0 0 1 0 1 0 0 0 0 0 0 1 1 0 1 1 |
| 78 | - 0 1 0 0 0 1 1 0 0 0 0 0 1 1 0 0 0 0 0 0 0 1 1 0 1 1 |
| 90 | - 1 1 0 0 0 1 1 0 0 0 1 1 1 1 1 1 1 1 1 1 0 0 0 1 1 |
| 115 | - 0 1 1 1 1 1 1 0 0 1 0 1 0 1 1 0 1 0 0 1 1 1 1 1 1 |
| 151 | - 1 1 1 1 1 1 1 0 0 0 1 1 0 0 1 1 1 1 1 1 0 0 1 1 1 |
| 159 | - 1 0 0 0 0 0 1 1 0 0 1 1 1 1 1 1 1 1 1 1 1 1 1 1 1 |
| 164 | - 0 0 0 0 0 0 0 0 0 0 0 0 0 0 0 0 0 0 0 0 0 0 0 0 0 |

*Case 2:* In this case, three simultaneous contingencies are considered. The contingencies include outages of unit 13, line 75–77, and line 85–89. Comparing the new schedule with that in Case 1, the states of 20 units have changed at different hours with a total operating cost of $1 081 898. To apply the proposed

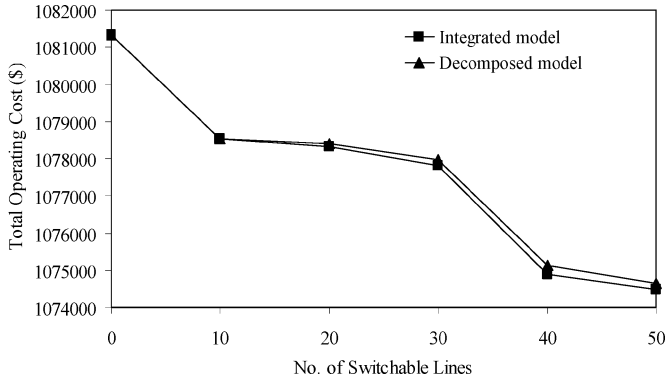


Fig. 4. Total operating cost comparison of integrated and decomposed models.

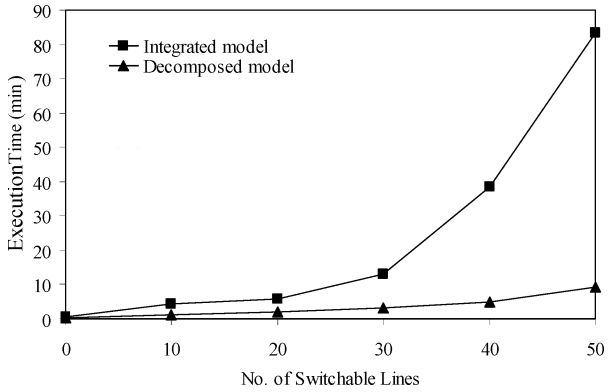


Fig. 5. Execution time comparison of integrated and decomposed models.

TS approach, the same lines as in Case 1 are considered switchable. The first UC result is feasible for the outage of line 75–77. So, the contingency of line 75–77 is controllable. Since the UC solution cannot lead to a feasible solution for the outages of unit 13 and line 85–89, these contingencies are uncontrollable. The obtained switchable line schedule is completely different from that in Case 1. The differences are highlighted in Table IX in comparison with those in Case 1. The corresponding UC solution is shown in Table VIII, where the highlighted values show the difference with Case 1. The total operating cost is $1 080 846, which shows a 0.09% improvement. This solution is obtained in 136 s.

*Case 3:* To show the effectiveness of the proposed model in handling a larger number of switchable lines, the TS cases with integrated and decomposed formulation are compared. The number of switchable lines is changed from 0 to 50 with step of 10. Zero means that no switchable line exists in the system, while 50 represents that more than one fourth of the transmission lines in the system are switchable. The default relative optimality gap of CPLEX, i.e., 0.01%, is used as the stopping criterion. The total operating cost and execution time for these two models for different numbers of switchable lines are obtained and shown in Figs. 4 and 5, respectively.

In Fig. 4, the decomposed model does not outperform the integrated model from optimality point of view. The integrated model always has a similar or better total operating cost. However, the difference between the total operating costs of two models is negligible. When there is no line switching in the system, the two models result in the same solution. Since the proposed model is an extension of the decomposed SCUC model, it is expected that in case of no line switching, the decomposed model finds the same solution as the integrated model. The worst case occurs at 40 switchable lines, where the difference is 0.02%.

In Fig. 5, for the small number of switchable lines, both models find the solution in a reasonable time. For instance for ten switchable lines, the decomposed model finds the solution in 1 min and the integrated model finds the solution in 4 min. However, as we increase the number of switchable lines, the execution time of the integrated model increases significantly, while that of decomposed model remains reasonable. In the case of 50 switchable lines, the solution of the decomposed model is obtained in 9 min, while that of integrated model is achieved in more than 80 min. This considerable increase in execution time is due to the large number of binary variables that should be handled by the integrated problem. However in the decomposed model, these binary variables are divided between the UC master problem and the TS subproblem. This division would help the large problems to find solutions in a reasonable execution time.

## IV. Conclusions

In this paper, TS was integrated with UC for solving the multi-interval optimal generation unit scheduling with security constraints. The Benders decomposition was employed to separate the problem into a UC master problem and a TS subproblem. The UC master problem minimizes the total operating cost and calculates the optimal hourly commitment and dispatch of generation units subject to power balance and reserve requirements. The TS subproblem adjusts the hourly unit schedules and optimizes the switching state of lines to mitigate transmission violations in the base case and controllable and uncontrollable contingencies. The features of the proposed approach are listed as follows.

- The TS model can be used for congestion management. The TS application will lead to adjustments in line flows and congestion levels.
- The number of switchable lines was limited here. This assumption is consistent with practical switching applications. If we increase the number of switchable lines, TS may find better SCUC solutions which could also converge at slower rates.
- The applications of Benders decomposition to SCUC and TS would make the proposed approach more applicable to large power systems.
- The proposed TS approach is an extension of the conventional SCUC. Hence, if we ignore the line switching in the proposed approach, the final SCUC solution will be the same as that of the conventional SCUC.
- The proposed approach allows for the utilization of corrective modes before resorting to more expensive preventive solutions.

The UC and the Optimal TS Scheduling blocks use the MIP format. MIP problems use a predefined gap to determine the optimality of solution. If this gap is set to zero, the problem will find the optimal solution with a longer computation time.

Otherwise, the problem will be terminated with a near-optimal solution in a reasonable time. Usually a near-optimal solution is considered in real-time applications in power systems. Additional points for improving the proposed TS approach are listed as follows.

- Numerical methods may be developed for identifying the optimal set of switchable lines. Such methods may include additional strategies for system operations. For example in the IEEE 118-bus system, line 164 would be a good prospect for switching since it is switched off periodically.
- Practical line switching strategies could be considered like how often and how long a line could be on/off.
- Switching states of lines are employed in the Optimal TS Scheduling by means of cuts. These binary variables will be adjusted more accurately if we use additional constraints to make stronger connections between the switchable lines states and the generation dispatch. The approach could help the TS subproblem find the optimal solution in fewer iterations [27].

## REFERENCES


[1] M. Shahidehpour, H. Yamin, and Z. Y. Li, *Market Operations in Electric Power Systems*. New York: Wiley, 2002.

[2] A. J. Conejo, E. Castillo, R. Mínguez, and R. García-Bertrand, *Decomposition Techniques in Mathematical Programming*. New York: Springer, 2006.

[3] R. Bacher and H. Glavitsch, "Network topology optimization with security constraints," *IEEE Trans. Power Syst.*, vol. 1, no. 4, pp. 103–111, Nov. 1986.

[4] G. Schnyder and H. Glavitsch, "Integrated security control using an optimal power flow and switching concepts," *IEEE Trans. Power Syst.*, vol. 3, no. 2, pp. 782–790, May 1988.

[5] G. Schnyder and H. Glavitsch, "Security enhancement using an optimal switching power flow," *IEEE Trans. Power Syst.*, vol. 5, no. 2, pp. 674–681, May 1990.

[6] J. G. Rolim and L. J. B. Machado, "A study of the use of corrective switching in transmission systems," *IEEE Trans. Power Syst.*, vol. 14, no. 1, pp. 336–341, Feb. 1999.

[7] W. Shao and V. Vittal, "Corrective switching algorithm for relieving overloads and voltage violations," *IEEE Trans. Power Syst.*, vol. 20, no. 4, pp. 1877–1885, Nov. 2005.

[8] G. Granelli, M. Montagna, F. Zanellini, P. Bresesti, R. Vailati, and M. Innorta, "Optimal network reconfiguration for congestion management by deterministic and genetic algorithms," *Elect. Power Syst. Res.*, vol. 76, pp. 549–556, Apr. 2006.

[9] R. P. O'Neill, R. Baldick, U. Helman, M. H. Rothkopf, and W. Stewart, "Dispatchable transmission in RTO markets," *IEEE Trans. Power Syst.*, vol. 20, no. 1, pp. 171–179, Feb. 2005.

[10] E. B. Fisher, R. P. O'Neill, and M. C. Ferris, "Optimal transmission switching," *IEEE Trans. Power Syst.*, vol. 23, no. 3, pp. 1364–1355, Aug. 2008.

[11] K. W. Hedman, R. P. O'Neill, E. B. Fisher, and S. S. Oren, "Optimal transmission switching with contingency analysis," *IEEE Trans. Power Syst.*, vol. 24, no. 3, pp. 1577–1586, Aug. 2009.

[12] K. W. Hedman, R. P. O'Neill, E. B. Fisher, and S. S. Oren, "Optimal transmission switching—sensitivity analysis and extensions," *IEEE Trans. Power Syst.*, vol. 23, no. 3, pp. 1469–1479, Aug. 2008.

[13] Y. Fu, M. Shahidehpour, and Z. Li, "Security-constrained unit commitment with AC constraints," *IEEE Trans. Power Syst.*, vol. 20, no. 3, pp. 1538–1550, Aug. 2005.

[14] M. Shahidehpour and Y. Fu, "Benders decomposition," *IEEE Power and Energy Mag.*, vol. 3, no. 2, pp. 20–21, Mar. 2005.

[15] M. Shahidehpour and V. Ramesh, "Nonlinear programming algorithms and decomposition strategies for OPF," in *IEEE/PES Tutorial on Optimal Power Flow*. Piscataway, NJ: IEEE Press, 1996.

[16] H. Ma and M. Shahidehpour, "Transmission constrained unit commitment based on Benders decomposition," *Elect. Power Energy Syst.*, vol. 20, no. 4, pp. 287–294, Apr. 1998.

[17] A. M. Geoffrion, "Generalized Benders decomposition," *J. Optim Theory Appl.*, vol. 10, no. 4, pp. 237–261, 1972.

[18] M. Adibi and R. Kafka, "Power system restoration issues," *IEEE Comput. Appl. Power*, vol. 4, no. 2, pp. 19–24, Apr. 1991.

[19] A. Ketabi and A. Ranjbar, "New approach to standing phase angle reduction for power system restoration," in *Proc. IEEE Elect. Power Eng., PowerTech Budapest, Hungary*, 1999.

[20] N. Martins, E. J. Oliviera, W. C. Moreira, J. L. R. Pereira, and R. M. Fontoura, "Redispatch to reduce rotor shaft impacts upon transmission loop closure," *IEEE Trans. Power Syst.*, vol. 23, no. 2, pp. 592–600, May 2008.

[21] T. Nagata, H. Sasaki, and R. Yokoyama, "Power system restoration by joint usage of expert system and mathematical programming approach," *IEEE Trans. Power Syst.*, vol. 10, no. 3, pp. 1473–1479, Aug. 1995.

[22] S. Wunderlich, M. M. Adibi, R. Fischl, and C. O. D. Nwankpa, "An approach to standing phase angle reduction," *IEEE Trans. Power Syst.*, vol. 9, no. 1, pp. 470–476, Feb. 1994.

[23] D. Hazarika and A. K. Sinhá, "Standing phase angle reduction for power system restoration," *Proc. Inst. Elect. Eng., Gen., Transm., Distrib.*, vol. 145, no. 1, pp. 82–88, Jan. 1998.

[24] D. Hazarika and A. K. Sinhá, "An algorithm for standing phase angle reduction for power system restoration," *IEEE Trans. Power Syst.*, vol. 14, no. 4, pp. 1213–1218, Nov. 1999.

[25] N. Martins, E. J. de Oliveira, J. L. R. Pereira, and L. C. A. Ferreira, "Reducing standing phase angles via interior point optimum power flow for improved system restoration," in *Proc. Power Systems Conf. Expo. 2004*, New York, Oct. 10–13, 2004.

[26] ILOG CPLEX ILOG CPLEX Homepage, 2009. [Online]. Available: http://www.ilog.com.

[27] J. Guo and Z. Li, "Network reduction with unknown transmission line status," in *Proc. 39th North Amer. Power Symp.*, 2007.



**Amin Khodaei** received the B.S. degree in electrical engineering from University of Tehran, Tehran, Iran, in 2005 and the M.S. degree in electrical engineering from Sharif University of Technology, Tehran, Iran, in 2007. He is currently pursuing the Ph.D. degree in the Electrical and Computer Engineering Department at the Illinois Institute of Technology, Chicago.

His research interests include operation and economics of power systems.

**Mohammad Shahidehpour** (F'01) is Bodine Chair Professor in the Electrical and Computer Engineering Department at Illinois Institute of Technology, Chicago. He is an Honorary Professor in the North China Electric Power University in Beijing and the Sharif University in Tehran. He is also the 2009 recipient of an Honorary Doctorate from the Polytechnic University of Bucharest.

Dr. Shahidehpour is the VP of Publications for the IEEE Power & Energy Society, an IEEE Distinguished Lecturer, Technical Program Chair for the 2010 IEEE Innovative Smart Grid Technologies Conference, and the Editor-in-Chief of the IEEE TRANSACTIONS ON SMART GRID.

# Security-Constrained Generation and Transmission Outage Scheduling With Uncertainties

Lei Wu, *Member, IEEE*, Mohammad Shahidehpour, *Fellow, IEEE*, and Yong Fu, *Member, IEEE*

***Abstract*—This study presents a stochastic model for the independent system operator's (ISO's) optimal coordinated long-term maintenance scheduling of generation units and transmission lines with short-term security-constrained unit commitment (SCUC). Random disturbances of power systems including forced outages of generation units and transmission lines, load forecast errors, and fuel price fluctuations are modeled as scenario trees using the Monte Carlo simulation. Lagrangian relaxation (LR) is applied to separate the coordinated optimization problem into long-term equipment maintenance (LTEM) and stochastic long-term SCUC (LTSCUC) subproblems. For the stochastic LTSCUC subproblem, scenario bundle constraints are relaxed via LR and the optimization problem is decomposed into deterministic LTSCUC problems. LR is applied to each deterministic LTSCUC to relax long-term fuel and emission limits and decompose the problem into short-term SCUC subproblems. The decomposition is further applied to short-term SCUC subproblems for separating hourly unit commitment and transmission network constraints. The unit commitment is formulated as a mixed-integer programming (MIP) problem and solved by the branch-and-cut method using CPLEX. The outcome of this study includes the hourly scheduling of outages of generation units and transmission lines, which corresponds to the optimal generation unit commitment and dispatch, and transmission flows. The hourly schedules minimize the total cost of operation and maintenance and satisfy long-term and short-term constraints of generation units and transmission network with the inclusion of power system uncertainty. A modified IEEE 118-bus system is used to exhibit the effectiveness of the proposed scheduling approach.**

***Index Terms*—Optimal coordination of generation and transmission outage scheduling, security-constrained unit commitment, stochastic modeling of power systems.**

## NOMENCLATURE

**Variables**:

| | |
|---|---|
| $F_{c,itp}(\cdot)$ | Production cost function of unit $i$ at time $t$ at weekly interval $p$. |
| $I^s_{itp}$ | Commitment state of unit $i$ at time $t$ at weekly interval $p$ in scenario $s$. |
| $J^s_{ltp}$ | State of line $l$ at time $t$ at weekly interval $p$ in scenario $s$. |
| $LOLE^s$ | Loss-of-load-expectation (LOLE) of scenario $s$. |
| $\overline{LOLE}$ | Expected quantity of loss-of-load-expectation for all $S$ scenarios. |
| $LS^s_{btp}$ | Load shedding at bus $b$ at time $t$ at weekly interval $p$ in scenario $s$. |
| $P^s_{itp}$ | Power generation dispatch of unit $i$ at time $t$ at weekly interval $p$ in scenario $s$. |
| $P^s_{btp}$ | System demand at bus $b$ at time $t$ at weekly interval $p$ in scenario $s$. |
| $q_{l\tau}, r_{l\tau}$ | Indicators for beginning and end maintenance of line $l$ at time $\tau$. |
| $SU(D)^s_{itp}$ | Startup/shutdown cost of unit $i$ at time $t$ at weekly interval $p$ in scenario $s$. |
| $VP$ | Objective value of a feasible solution of the original problem. |
| $VL_{EM}$ | Value of optimal LR function of the maintenance subproblem. |
| $VL^s$ | Value of optimal LR function of the SCUC subproblem in scenario $s$. |
| $VLP$ | Value of a feasible solution of the stochastic SCUC subproblem. |
| $VLL$ | Value of optimal LR function of the stochastic SCUC subproblem with relaxed bundle constraints. |
| $VLR$ | Sum of optimal LR function values of maintenance and stochastic SCUC subproblems with relaxed bundle constraints. |
| $X_{itp}$ | Maintenance status of unit $i$ at time $t$ at interval $p$, 0 if unit is offline for maintenance, otherwise 1. |
| $Y_{ltp}$ | Maintenance status of line $l$ at time $t$ at interval $p$, 0 if line is offline for maintenance, otherwise 1. |
| $\sigma_{LOLE}$ | Estimated standard deviation of LOLE. |
| $\eta, \pi, \theta, \alpha, \beta$ | Lagrangian multipliers. |
| $i, k, l, m, n, p, s, t, \tau$ | Indexes. |

**Constants**:

| | |
|---|---|
| $D_{itp}$ | Maintenance cost of unit $i$ at time $t$ at interval $p$. |
| $e_i, l_i$ | Starting and ending time for maintenance window of equipment $i$. |
| $E_{ltp}$ | Maintenance cost of line $l$ at time $t$ at interval $p$. |
| $MD$ | Maintenance duration. |
| $MN_{\max,l}$ | Partial maintenance number upper limit of line $l$. |

Manuscript received May 20, 2009; revised December 03, 2009. First published February 18, 2010; current version published July 21, 2010. Paper no. TPWRS-00366-2009.

The authors are with the Electrical and Computer Engineering Department, Illinois Institute of Technology, Chicago, IL 60616 USA (e-mail: lwu10@iit.edu; ms@iit.edu; fuyong@iit.edu).

Digital Object Identifier 10.1109/TPWRS.2010.2040124

| | |
|---|---|
| $MT^{off}_{\min,l}$ | Minimum time interval between two consecutive partial maintenances of line $l$. |
| $MT^{on}_{\min,l}$ | Minimum duration for partial maintenance of line $l$. |
| $NB$ | Number of buses. |
| $NG$ | Number of units. |
| $NL$ | Number of transmission lines. |
| $NP$ | Number of weeks under study. |
| $NT$ | Number of hours at each weekly interval (168 h). |
| $P^s$ | Weight of scenario $s$. |
| $P_{\min,i}$ | Minimum capacity of unit $i$. |
| $P_{\max,i}$ | Maximum capacity of unit $i$. |
| $P^s_{D,tp}$ | System demand at time $t$ at weekly interval $p$ in scenario $s$. |
| $pv^s_{btp}$ | Value of lost load (VOLL) of bus $b$ at time $t$ at weekly interval $p$ in scenario $s$. |
| $S$ | Total number of scenarios. |
| $\sigma_{fix}$ | Predefined standard deviation of LOLE. |
| $\varepsilon_1, \varepsilon_2$ | Predefined convergence threshold. |

## I. Introduction

RESTRUCTURED power systems signify generation and transmission participants that are unbundled as self-interested entities which are also responsible for their maintenance outage scheduling in a competitive environment. In such environments, generation companies (GENCOs) submit their maintenance plans and constraints to the independent system operator (ISO) including maintenance time windows, available maintenance resources, and generation price offers. Transmission companies (TRANSCOs) also submit their respective maintenance plans and constraints to the ISO. The ISO is responsible for the optimal coordination of maintenance for generation units and transmission lines which would ensure the security of power systems and maximize the social welfare [1]–[3].

The study in [4]–[7] focused on generation and transmission maintenance and their coordination. However, the subject of transmission security in restructured power systems was not considered. Furthermore, random outages of power systems were not included when maximizing planned outages in long-term operation planning studies.

Our proposed coordinated long-term generation and transmission maintenance scheduling intends to coordinate generation and transmission outage scheduling with short-term security-constrained generation scheduling. Random outages of generators and transmission lines, load forecast errors, and fuel price fluctuations are considered which could influence the optimal maintenance outage scheduling. Such a detailed security-constrained maintenance scheduling approach provides a wider range of options for managing short-term economics. Mathematically, the proposed problem is a stochastic, large-scale mixed-integer optimization problem and we introduce an effective decomposition and coordination strategy for its solution. The Lagrangian relaxation (LR) technique is applied to decompose such a stochastic and large mixed-integer programming (MIP) problem into tractable small-scale subproblems.

The proposed stochastic model could be applied to a vertically integrated utility. Here we consider fuel and emission constraints when scheduling the long-term operation of a utility. The same model can be utilized by centralized energy markets with ISOs. Here a combination of fuel and emission constraints used by traditional utilities, which is a quadratic function of power generation, represents the energy constraint for a GENCO. That is, GENCOs submit energy limits which indicate that the sum of daily generation for individual units, or the entire GENCO, would not exceed a prescribed level. The energy constraint is utilized by security-constrained unit commitment (SCUC) which is a market clearing tool in the day-ahead energy market.

The attributes of the proposed stochastic model, for the coordination of long-term generation and transmission maintenance schedules with the short-term SCUC, are presented in the following:

1) Coordination of generation maintenance with transmission maintenance. We introduce a binary variable for representing the transmission line status and adopt an optimization technique that applies to both generation and transmission maintenance scheduling.
2) LR is used to decompose the original stochastic problem into long-term equipment maintenance (LTEM) and long-term SCUC (LTSCUC) with fuel and emission subproblems, with unit commitment and transmission line status as coordinating (coupling) variables. The LTEM and LTSCUC subproblems are solved individually and violations are identified. Lagrangian multipliers are updated iteratively for subproblems until the stopping criterion is met.
3) Random outages of generators and transmission lines, load forecast errors, and fuel price fluctuations are simulated by the Monte Carlo method when solving the LTSCUC subproblem. The uncertainty could influence the maintenance schedule when updating Lagrangian multipliers. The scenario-based technique is used to solve the stochastic LTSCUC subproblem. Scenario reduction is adopted when solving the stochastic LTSCUC as a tradeoff between computation time and solution accuracy. The LR method is adapted to relax bundle constraints and a modified surrogate subgradient method is used for a faster convergence.
4) The chronological load profile is considered in the LTEM scheduling and its coordination with the short-term SCUC.

The rest of the paper is organized as follows. Section II describes the proposed model and its solution methodology. Section III presents the detailed formulation of maintenance and generation scheduling subproblems. The coordination and solutions methodologies are presented in Section IV. Section V presents and discusses a modified IEEE 118-bus system with 54 units and 91 loads. The conclusion is drawn in Section VI.

## II. Stochastic Model Description

In this paper, we analyze the optimal maintenance scheduling of a vertically integrated utility. The same methodology would also apply to restructured power systems. The utility's objective is to minimize the hourly cost of security-constrained short-term operation and long-term maintenance.

In applying (1) to a vertically integrated utility, the first two terms represent the cost of maintenance for generation and transmission equipment respectively. The remaining terms represent the production cost. We could consider a variable hourly maintenance cost coefficients ($D_{itp}$ and $E_{ltp}$) for each equipment. If the proposed model is used in restructured power systems, GENCOs and TRANSCOs would be independently responsible for generation and transmission maintenance, no equipment maintenance cost will appear in (1), and $D_{itp}$ and $E_{ltp}$ would be zero. The ISO would use the objective (1) to schedule equipment maintenance outages based on a GENCO's or a TRANSCO's preferred maintenance schedule. Accordingly, $D_{itp}$ and $E_{ltp}$ will be zero during the most preferred periods for maintenance of the corresponding equipment in order to increase the chance of maintenance during such periods:

$$\begin{aligned} Min \Bigg\{ & \sum_{p=1}^{NP}\sum_{t=1}^{NT}\sum_{i=1}^{NG} D_{itp}\cdot(1-X_{itp}) \\ & + \sum_{p=1}^{NP}\sum_{t=1}^{NT}\sum_{l=1}^{NL} E_{ltp}\cdot(1-Y_{ltp}) + \sum_{s=1}^{S} P^s \\ & \cdot \sum_{p=1}^{NP}\sum_{t=1}^{NT}\Bigg\{ \sum_{i=1}^{NG}\left[F_{c,itp}\left(P^s_{itp}\cdot I^s_{itp}\right) + SU^s_{itp} + SD^s_{itp}\right] \\ & + \sum_{b=1}^{NB} pv^s_{btp}\cdot LS^s_{btp} \Bigg\} \Bigg\}. \end{aligned} \tag{1}$$

Such objectives may not be easily realized by a one-step optimization technique due to the enormity of the maintenance scheduling problem. Thus, we schedule the long-term equipment maintenance and the short-term unit commitment problems separately, which are based on the decomposition technique depicted in Figs. 1–3. The distinct features of the proposed model include the way we introduce stochastic variables in the coordinated generation and transmission maintenance problem, handle scenario bundle constraints, and link maintenance and operation schedules. Fig. 1 shows the decomposition strategy of LTEM represented by (2)–(9) and LTSCUC constraints. Coupling constraints (11), (12) of LTEM and LTSCUC are relaxed using the LR method. LTEM and LTSCUC subproblems are solved individually before the coupling constraints are checked.

If the coupling constraints (11), (12) are not satisfied, Lagrangian multipliers $\eta$ and $\pi$ corresponding to the two constraints are updated and the pseudo price signals are fed back to the subproblems. We introduce $I$ as the unit commitment status variable and $J$ as the transmission line status variable, so that the transmission line maintenance can be treated the same way as that of generation units. The network security is checked in the deterministic LTSCUC subproblem and the same strategy is used for updating the Lagrangian multiplier $\eta$ and $\pi$.

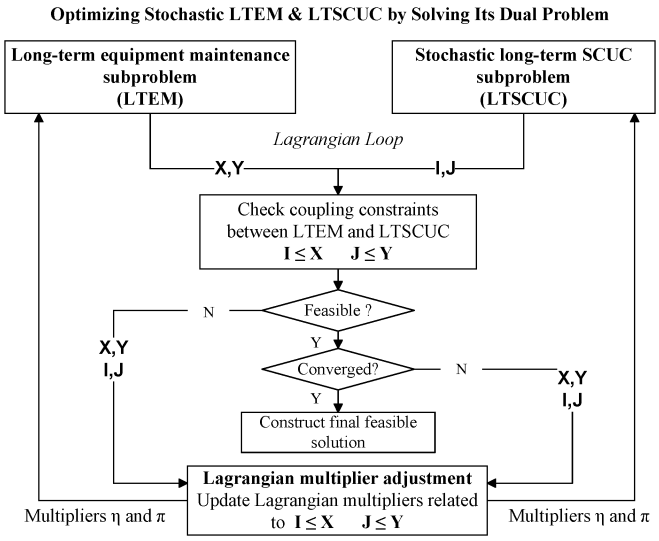


Fig. 1. Decomposition and coordination of LTEM and LTSCUC.

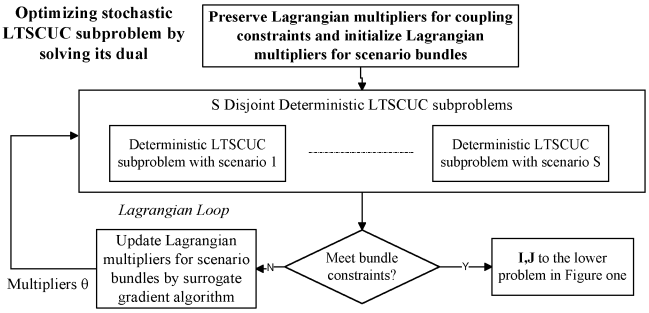


Fig. 2. Decomposition of scenario bundle constraints.

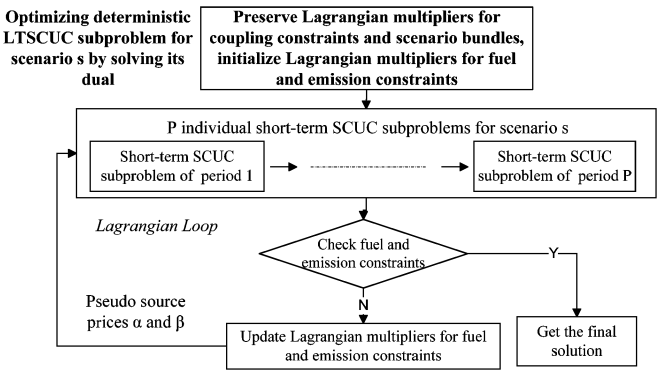


Fig. 3. Decomposition and coordination of deterministic LTSCUC.

Fig. 2 shows the decomposition strategy of the stochastic LTSCUC for managing the scenario bundle constraints (10). Scenario bundle constraints are relaxed by the LR method and the deterministic LTSCUC problem (shown in Fig. 3) is solved in each scenario. If the LTSCUC results in Fig. 2 do not satisfy the scenario bundle constraints, Lagrangian multipliers $\theta$ are updated and the corresponding pseudo price signals are fed back to scenarios for the next iterative solution. Since the problem is not convex, there is no guarantee that the bundle constraints would be entirely satisfied. Thus, the scenarios consider approximate solutions for fast convergence while maintaining a rel-

atively high level of accuracy. The iterative process will stop when the total violation of weighted bundle constraints is below a certain tolerance. A heuristic process is then used to obtain a feasible solution for satisfying the scenario bundle constraints. We use the modified surrogate subgradient method to improve the convergence. The solution details shown in the next section illustrate a tradeoff between the computation speed and the accuracy of solution.

Fig. 3 illustrates the decomposition of the deterministic LTSCUC into tractable subproblems. Fuel and emission constraints are relaxed with resource penalty prices represented by Lagrangian multipliers $\alpha$ and $\beta$. Based on the decomposition process, the individual short-term unit commitment problems will be solved without the fuel and emission constraints.

If the results do not satisfy the fuel and emission constraints, the Lagrangian multipliers $\alpha$ and $\beta$ are updated and the corresponding penalty resource prices are fed back to solve the short-term subproblems again [8], [9].

## III. Formulation of Subproblems

The LTEM and LTSCUC formulations, constraints, and coordination are summarized as follows.

*1) Generation Maintenance Constraints:* Generation maintenance windows: In the following, (2) shows starting and ending times when the maintenance is allowed. Also, (3) represents the total maintenance duration, and (4) shows that each unit could only be maintained once within the maintenance window:

$$\begin{aligned}
&X_{i\tau} = 0 \text{ or } 1 \text{ when } e_i \le \tau \le l_i;\\
&\text{otherwise } X_{i\tau} = 1 \ \forall i, \tau < e_i \text{ or } \tau > l_i \qquad (2)\\
&\sum_{\tau=e_i}^{l_i} (1 - X_{i\tau}) = MD_i \quad \forall\, i \qquad (3)\\
&\sum_{\tau=k}^{k+MD_i-1} (1 - X_{i\tau}) \ge MD_i \cdot \left[X_{i(\tau-1)} - X_{i\tau}\right]\\
&\quad \forall i, k = e_i, \cdots, l_i - MD_i + 1\\
&\sum_{\tau=k}^{l_i} \left\{1 - X_{i\tau} - \left[X_{i(k-1)} - X_{ik}\right]\right\} \ge 0\\
&\quad \forall i, k = l_i - MD_i + 2, \cdots, l_i. \qquad (4)
\end{aligned}$$

Generation maintenance resources and crew availability: The crew availability would limit the number of units that can be maintained simultaneously. For example, if units 1, 2 and 3 are to be maintained simultaneously, the constraint is represented as $X_{1\tau} = X_{2\tau} = X_{3\tau}$. Otherwise, for a single equipment, $(1 - X_{1\tau}) + (1 - X_{3\tau}) + (1 - X_{3\tau}) \le 1$. If unit 1 is maintained before unit 2, $\sum_{\tau=1}^{t}(1 - X_{1\tau}) - (1 - X_{2t}) \ge 0$. While $X_{1t} = X_{2t}$ indicates that unit 1 and 2 are to be on maintenance outage simultaneously. We can also represent limited resources for maintenance and crew availability at each location as $\sum_{i \in A} f_{Ri} \cdot (1 - X_{i\tau}) \le H_{R\tau}$ where $f_{Ri}$ is the resource needed for the maintenance of unit $i$ and $H_{R\tau}$ is the total resource quantity available at time $\tau$ for area A.

*2) Transmission Maintenance Constraints:* Partial maintenance is allowed for transmission lines. Hence

$$\begin{aligned}
&Y_{l\tau} = 0 \text{ or } 1 \text{ when } e_l \le \tau \le l_l;\\
&\text{otherwise } Y_{l\tau} = 1 \ \forall l, \tau < e_l \text{ or } \tau > l_l \qquad (5)\\
&\sum_{\tau=e_l}^{l_l} (1 - Y_{l\tau}) = MD_l \ \forall l \qquad (6)\\
&q_{l\tau} - r_{l\tau} = Y_{l(\tau-1)} - Y_{l\tau}, \quad q_{l\tau} + r_{l\tau} \le 1,\\
&1 \le \sum_{\tau=1}^{NT \cdot NP} r_{l\tau} \le MN_{\max,l} \ \forall l, \forall \tau \qquad (7)\\
&\sum_{\tau=k}^{k+MT^{on}_{\min,l}-1} (1 - Y_{l\tau}) \ge \left(Y_{l(\tau-1)} - Y_{l\tau}\right) \cdot MT^{on}_{\min,l}\\
&\quad \forall l, k = e_l, \cdots, l_l - MT^{on}_{\min,l} + 1\\
&\sum_{\tau=k}^{l_l} \left\{1 - Y_{l\tau} - \left[Y_{l(k-1)} - Y_{lk}\right]\right\} \ge 0\\
&\quad \forall l, k = l_l - MT^{on}_{\min,l} + 2, \cdots, l_l \qquad (8)\\
&\sum_{\tau=k}^{k+MT^{off}_{\min,l}-1} Y_{l\tau} \ge \left(Y_{l\tau} - Y_{l(\tau-1)}\right) \cdot MT^{off}_{\min,l}\\
&\quad \forall l, k = e_l, \cdots, l_l - MT^{off}_{\min,l} + 1\\
&\sum_{\tau=k}^{l_l} \left\{Y_{l\tau} - \left[Y_{lk} - Y_{l(k-1)}\right]\right\} \ge 0\\
&\quad \forall l, k = l_l - MT^{off}_{\min,l} + 2, \cdots, l_l. \qquad (9)
\end{aligned}$$

*3) Stochastic LTSCUC Constraints:* Short-term SCUC constraints presented in [18] are considered here in addition to

- Reliability constraints: An explicit reserve requirement constraint is not introduced. The optimal reserve requirement is implicitly determined because we add a penalty load shedding item to the objective function and include a LOLE constraint.
- Scenario bundle constraints: Scenario bundle constraints indicate that if two scenarios s and s' are indistinguishable from the beginning to time $(P, \tau)$ on the basis of information available at time $(P, \tau)$, then the generator commitment decisions rendered for the two scenarios must be identical from the beginning to time $\tau$. $B(s, P, \tau)$ represents a part of scenario s from the beginning to time $(P, \tau)$. In the scenario bundle constraints (10), the generator commitment decision $I$ rather than the line status $J$ is included. The line status $J$ is used as a state variable to relate the transmission maintenance decision and SCUC in (12). Based on (12), if a line is on maintenance, the line status $J$ for all scenarios would be zero; otherwise, $J$ would be one. The status of $J$ is determined by the optimization of LTSCUC because the line would be utilized in minimizing the operation cost. That is, it would not be necessary to include the line status in the scenario bundle constraints (10):

$$I^{s}_{itp} = I^{s'}_{itp}, \ for\ (p,t) \in \{(P,\tau) | B(s,P,\tau) = B(s',P,\tau)\}. \qquad (10)$$

The detailed formulation of LTSCUC constraints can be found in our previous works [20], [22].

*4) Coupling Constraints for LTEM and LTSCUC in Fig. 1:* Coupling constraints of generator maintenance $X$ and unit commitment status $I$ (11):

$$I^s_{itp} \le X_{itp} \qquad \forall s, \forall i, \forall t, \forall p. \tag{11}$$

Coupling constraints of transmission line maintenance $Y$ and transmission line status $J$ (12):

$$J^s_{ltp} \le Y_{ltp} \qquad \forall s, \forall l, \forall t, \forall p. \tag{12}$$

The proposed stochastic model differs from the deterministic one in several respects. First, the objective of the proposed stochastic model is to minimize the expected production cost of all scenarios, whereas the deterministic model would only minimize the production cost of a certain deterministic case. Second, the impact of the variance of uncertain variable on the maintenance schedule is considered. We also incorporate the coupling constraints of generator maintenance and unit commitment status (11) and the coupling constraints of transmission line maintenance and transmission lines status (12). Furthermore, there are scenario bundle constraints in the stochastic LTSCUC subproblem. Hence, the solution of stochastic model which includes a set of weighted scenarios is not simply the same as solving a deterministic model separately for each scenario.

## IV. Solution of Subproblems

### A. Coupling Constraints for LTEM and LTSCUC Subproblems

LR is employed to solve the coupling constraints (11), (12). Once constraints are relaxed and introduced into the LTEM and LTSCUC subproblems via the Lagrangian multipliers $\boldsymbol{\eta}$ and $\boldsymbol{\pi}$, the modified LTEM and LTSCUC subproblems at iteration $n$ are presented in (13) and (14), respectively:

$$\begin{aligned} &VL_{EM}(\eta^n, \pi^n) \\ &\quad = Min \sum_{p=1}^{NP}\sum_{t=1}^{NT}\sum_{i=1}^{NG}\left[D_{itp}\cdot(1-X_{itp}) - \left(\sum_s \eta^{s,n}_{itp}\right)\cdot X_{itp}\right] \\ &\qquad + \sum_{p=1}^{NP}\sum_{t=1}^{NT}\sum_{l=1}^{NL}\left[E_{itp}\cdot(1-Y_{ltp}) - \left(\sum_s \pi^{s,n}_{ltp}\right)\cdot Y_{ltp}\right] \end{aligned} \tag{13}$$

*S.t.* constraints (2)–(9)

$$\begin{aligned} Min \sum_{s=1}^{S}\sum_{p=1}^{NP}\sum_{t=1}^{NT}\Bigg\{ P^s \cdot \Bigg\{ &\sum_{i=1}^{NG}\left[F_{c,itp}\left(P^s_{itp}\cdot I^s_{itp}\right) + SU^s_{itp} + SD^s_{itp}\right] \\ &+ \sum_{b=1}^{NB} pv^s_{b,tp}\cdot LS^s_{b,tp}\Bigg\} \\ &+ \sum_{i=1}^{NG}\eta^{s,n}_{itp}\cdot I^s_{itp} + \sum_{l=1}^{NL}\pi^{s,n}_{ltp}\cdot J^s_{ltp}\Bigg\} \end{aligned} \tag{14}$$

*S.t.* stochastic LTSCUC constraints described in Section III.

After obtaining a solution for generator maintenance $\mathbf{X}$, transmission line maintenance $\mathbf{Y}$, as well as unit commitment $\mathbf{I}$ and transmission line status $\mathbf{J}$, we check the constraints and update the corresponding multipliers $\boldsymbol{\eta}$ and $\boldsymbol{\pi}$ by applying the subgradient method [19]. The Lagrangian iteration continues until a converged solution which would meet the stopping criterion is obtained:

If $\hat{I}^{s,n}_{itp} \ge \hat{X}^n_{itp}$,

$$\eta^{s,n+1}_{itp} = \eta^{s,n}_{itp} + S^{up,n}_G \cdot \left(\hat{I}^{s,n}_{itp} - \hat{X}^n_{itp}\right) \Big/ \left\|\hat{I}^{s,n}_{itp} - \hat{X}^n_{itp}\right\|$$

Otherwise

$$\eta^{s,n+1}_{itp} = \eta^{s,n}_{itp} + S^{down,n}_G \cdot \left(\hat{I}^{s,n}_{itp} - \hat{X}^n_{itp}\right) \Big/ \left\|\hat{I}^{s,n}_{itp} - \hat{X}^n_{itp}\right\|$$

If $\hat{J}^{s,n}_{ltp} \ge \hat{Y}^n_{ltp}$,

$$\pi^{s,n+1}_{ltp} = \pi^{s,n}_{ltp} + S^{up,n}_L \cdot \left(\hat{J}^{s,n}_{ltp} - \hat{Y}^n_{ltp}\right) \Big/ \left\|\hat{J}^{s,n}_{ltp} - \hat{Y}^n_{ltp}\right\|$$

Otherwise

$$\pi^{s,n+1}_{ltp} = \pi^{s,n}_{ltp} + S^{down,n}_L \cdot \left(\hat{J}^{s,n}_{ltp} - \hat{Y}^n_{ltp}\right) \Big/ \left\|\hat{J}^{s,n}_{ltp} - \hat{Y}^n_{ltp}\right\|$$

where $\|\cdot\|$ stands for a Euclidean norm, $S^{up,n}_G$, $S^{down,n}_G$, $S^{up,n}_L$ and $S^{down,n}_L$ are step sizes at iteration $n$ for updating multipliers of constraints (11), (12). Usually a constant step size or the one that decreases with iterations such as $(1+C)/(n+C)$ or $1/(C1+C2\cdot\sqrt{n})$ would be used, where $C$, $C1$, and $C2$ are pre-defined positive constants. In [23] the bundle method was also proposed to update Lagrangian multipliers in order to improve the updating process.

Concerning the coupling constraints (11), (12) for the LTEM and LTSCUC subproblems, the original problem is non-convex with integer variables. So additional heuristics strategies are applied to derive a feasible solution when a predefined number of Lagrangian iterations or the maximum execution time is reached. In this case, the LTSCUC solution would offer a feasible solution when generation and transmission maintenance schedules are assumed fixed according to their values in the current Lagrangian solution.

### B. Stochastic Simulation

We model forced outages of generation units and transmission lines as independent Markov processes, load forecast errors as uniform random variables, and fuel price fluctuations as Ornstein-Uhlenbeck processes. For an ISO model, we could replace the fuel price with bidding prices offered by market participants since the ISO does not deal with fuel prices. The solution process will still be the same as that discussed in this section. We introduce a set of scenarios in the Monte Carlo method for modeling the stochastic conditions. For stochastic programming, we assign a weight $P^s$ to each scenario that reflects the possibility of its occurrence.

A two-state continuous-time Markov chain model is used to represent available and unavailable states of generators and transmission lines. The parameters used for the Monte Carlo simulation are failure and repair rates of each power system component. Using failure and repair rates, forced outages are simulated for a specified time period with the assumption that the power system is at the base case at the beginning of the

period. Power system components are assumed independent in our scenario-based simulation and the simultaneous effects of outages are presented in scenario trees. For the simulation of load forecast errors, we divide the entire scheduling horizon into several time intervals. For each time interval we create additional scenarios based on historical data. The probabilities are assigned to hourly load quantities according to the likelihood of their occurrence. The proposed scenarios in each time interval reflect the representative days/hours chosen for each week/season.

The proposed approach makes it easy for a maintenance scheduler to include the relevant data of a certain week/season after assigning a suitable weight to each load scenario. It is desirable that one could shift the maintenance schedule to periods with higher fuel prices for mitigating higher operation cost associated with maintenance outages. We employ the Ornstein-Uhlenbeck process to simulate random fluctuations in fuel price [20], [21]. According to Fig. 4, we generate a set of scenarios, each representing possible fluctuations in fuel price, load forecast errors, as well as the availability of generation units and transmission lines.

In the proposed model, we use a low-discrepancy Monte Carlo method, Latin hypercube, to generate a set of scenarios. Weights for all scenarios in the initial scenario catalog generated by the Monte Carlo method are the same. Scenario reduction is adapted for a tradeoff between solution accuracy and computation speed, because computation requirements for solving scenario-based optimization models would depend on the number of scenarios [13], [14]. Here we use the following criterion for the stochastic LTSCUC subproblem while taking into account the solution accuracy:

$$\sigma_{LOLE}=\sqrt{\sum_{s=1}^{S}P^s\cdot(LOLE^s-\overline{LOLE})^2}\Bigg/\sqrt{S\cdot(S-1)}$$

$$\sigma_{LOLE}<\sigma_{fix}\quad \overline{LOLE}=\sum_{s=1}^{S}P^s\cdot LOLE^s. \tag{15}$$

The results are assumed to be reasonably accurate when the estimated standard deviation of LOLE, $\sigma_{LOLE}$, is less than the predefined boundary $\sigma_{fix}$.

### C. Scenario Bundle Constraints

The sample scenarios for representing the uncertainty are solved and a good combination of solution outcomes is selected to represent the stochastic solution. The solution outcome would satisfy the constraint that if two scenarios are indistinguishable from the beginning to time $\tau$ on the basis of information available at time $\tau$, then the decision rendered for two scenarios must be identical from the beginning to time $\tau$.

The LR method is adopted to relax the scenario bundle constraints. Thus the stochastic problem is divided into several tractable subproblems for each scenario. Once the scenario bundle constraints are relaxed, the LTSCUC subproblem for each scenario is represented as

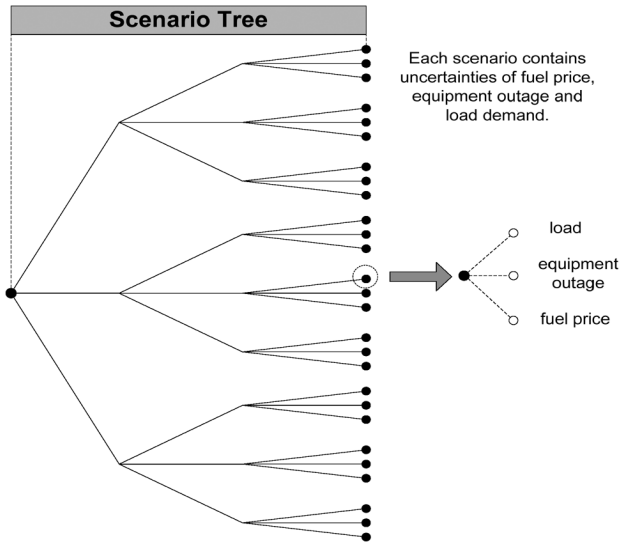


Fig. 4. Representation of uncertainty in a scenario tree.

$$\begin{aligned}VL^s(\theta^k)=Min\sum_{p=1}^{NP}\sum_{t=1}^{NT}\Bigg\{P^s\cdot\Bigg\{\sum_{i=1}^{NG}\left[F_{c,itp}\left(P^s_{itp}\cdot I^s_{itp}\right)\right.\\ \left.+SU^s_{itp}+SD^s_{itp}\right]\\ +\sum_{b=1}^{NB}pv^s_{b,tp}\cdot LS^s_{b,tp}\Bigg\}\\ +\sum_{i=1}^{NG}\eta^{s,n}_{itp}\cdot I^s_{itp}+\sum_{l=1}^{NL}\pi^{s,n}_{ltp}\cdot J^s_{ltp}\Bigg\}\\ +\sum_{p=1}^{NP}\sum_{t=1}^{NT}\sum_{s\in B(s,P,\tau)=\Omega_{P\tau}}\theta^{s,k}_{itp}\cdot I^s_{itp}\end{aligned} \tag{16}$$

*S.t.* stochastic LTSCUC constraints described in Section III except scenario bundle constraints.

The target $c_{itp}$, which is the weighted average of decision, is the same for all scenarios. Let $\theta^{s,k}_{itp}$ be the $k$th iteration of Lagrangian multiplier corresponding to $I^s_{itp}=c_{itp}$, $i=1\cdots NG$, $(p,t)\in\{P,\tau\}$. We obtain a new decision by calculating the expected value of $I^{s,k}_{itp}$ as $c^k_{itp}$, updating $\theta^{s,k+1}_{itp}$, and continuing the iteration. The iteration is terminated when the total weighted violation of bundle constraints, $\sum_{p=1}^{NP}\sum_{t=1}^{NT}\sum_{s\in B(s,P,\tau)=\Omega_{P\tau}}P^s\cdot|I^s_{itp}-c_{itp}|$, is below a certain threshold. Here, $|\cdot|$ denotes the absolute value. In order to accelerate the convergence, the surrogate gradient algorithm is adopted. The process starts by finding a scenario $s$ which has the largest weighted violation $\sum_{p=1}^{NP}\sum_{t=1}^{NT}P^s\cdot|I^s_{itp}-c_{itp}|$, updating multipliers, and calculating the scenario $s$ only. The detailed steps are given in Appendix A. The optimality conditions for the proposed dual solution via the surrogate subgradient method was provided in [15], [16]. Here, multipliers move iteratively closer to their global optimal.

In each scenario, the LR algorithm is adopted for the solution of deterministic long-term SCUC problem which deals

with fuel and emission constraints. The LR will divide the original problem into several tractable subproblems, i.e., short-term SCUC subproblems based on MIP. The Lagrangian multipliers are penalty price signals which optimize the allocation of fuel consumption and emission allowance based on a hybrid subgradient and Dantzig-Wolfe method [8], [17], [18].

The iteration will be terminated when the total weighted violation of bundle constraints is below a certain threshold. Accordingly, a heuristic process will be used to introduce a feasible solution with respect to the scenario bundle constraints. Here, we find the largest weighted violation $P^s \cdot |I^s_{itp} - c_{itp}|$ and adjust the multiplier $\theta^s_{itp}$ corresponding to hour $t$ at period $p$ of scenario $s$. The subproblem for the period $p$ of scenario $s$ is solved again and new $c_{itp}$ are computed. The process will be repeated for finding the next maximum violation and terminated within a finite number of iterations.

There are two main LR loops. $VL_{EM}(\eta^n, \pi^n)$ in (13) and $VL^s(\theta^k)$ in (16) are the optimal LR function values for the LTEM and LTSCUC subproblems in scenario $s$ at the current iteration. The optimal LR function of the stochastic LTSCUC subproblem with the relaxed bundle constraints $VLL$ at the current iteration is calculated by (17). The sum of optimal LR function values for the maintenance and the stochastic LTSCUC subproblems with relaxed bundle constraints $VLR$ at the current iteration is calculated by (18). The Lagrangian iterations will continue until the relative difference (duality gap) between $VP$ (upper bound) and $VLR$ (lower bound) of the optimal solution is within a pre-defined tolerance as stated in (19):

$$VLL = \sum_s VL^s(\theta^k) \tag{17}$$

$$VLR = VL_{EM}(\eta^n, \pi^n) + \sum_s VL^s(\theta^k) \tag{18}$$

$$|(VP - VLR)/VLR| \le \varepsilon_1. \tag{19}$$

Appendix B provides a proof for the validation of stopping criterion. The maximum number of iterations would have to be set since the duality gap could be intrinsic to the non-convex problem and would not be further reduced.

## V. Case Studies

A modified IEEE 118-bus system is considered in this section to demonstrate the proposed approach. The intention is to schedule the hourly maintenance, unit commitment, and generation economical dispatch over a 672-h (i.e., four weeks) horizon. The 118-bus system is composed of 54 thermal units, 186 branches, and 91 loads. The test data for the 118-bus system are given in http://motor.ece.iit.edu/data/coop. The annual peak load of the system is 6000 MW and the load trend over the study horizon is shown in Fig. 5.

For this system, three generators are considered for maintenance, each can be on maintenance at any hour. Only one transmission line L51 is considered for maintenance and a partial maintenance is acceptable. The maximum allowable number of partial maintenances for this line is two. The partial maintenance needs to last at least eight hours with a minimum of eight hours between two consecutive partial maintenances. The concern of this paper is to study the impact of uncertainties, on the coordinated maintenance scheduling of generation units and transmission lines with SCUC. Thus in the case study, emission limits and fuel consumption constraints are relaxed by introducing very large emission and fuel upper limits. The application of LR for relaxing emission and fuel consumption constraints, procedures for obtaining feasible solutions, and the performance of the system was discussed in [9] and [20].

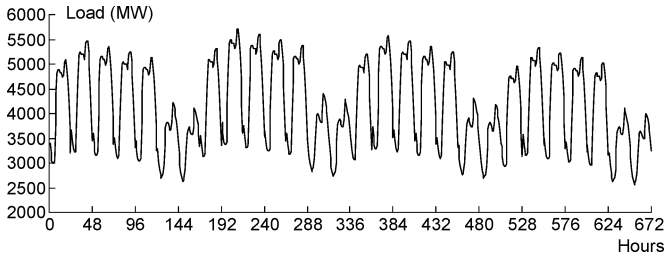


Fig. 5. Load profile in a 672-h horizon for the 118-bus system.

TABLE I
Generator Maintenance Limits for Cases 1–3

| Unit | At Bus | Windows | Duration (hours) | Cost ($/hour) |
|---|---|---|---|---|
| U10 | 25 | 1 – 624 | 24 | 1200 |
| U20 | 49 | 1 – 624 | 24 | 1000 |
| U34 | 76 | 1 – 624 | 24 | 400 |

TABLE II
Transmission Line Maintenance Limits for Cases 1–3

| Line | From Bus | To Bus | Windows | Duration (hours) | Cost ($/hour) |
|---|---|---|---|---|---|
| L51 | 38 | 37 | 1 – 336 | 18 | 5000 |
| **Maximum number of partial maintenances** | | **Minimum duration of partial maintenance (hours)** | | **Minimum interval between partial maintenances (hours)** | |
| 2 | | 8 | | 8 | |

We study four maintenance cases for a 672-h (four-week) period:

Case 1) Uncoordinated maintenance and unit commitment schedules.

Case 2) Coordinated generation unit and transmission line maintenance schedule without the consideration of uncertainty. We refer to this case as the expected value problem since expected values are used for load forecast and fuel price.

Case 3) Impact of uncertainty on the coordinated schedule.

Case 4) Same as Case 3 with a three-day maintenance duration.

For the first three cases, the equipment maintenance data listed in Tables I and II are used. In Case 4, the same data as those of Cases 1–3 are used except the maintenance duration is increased to 72 h. These cases are discussed as follows.

*Case 1:* LTEM and LTSCUC subproblems are not coordinated, so the optimal maintenance schedules are obtained individually for generators and transmission line maintenance subproblems as described in part one and two of Section III. The optimal maintenance schedule is shown in Fig. 6.

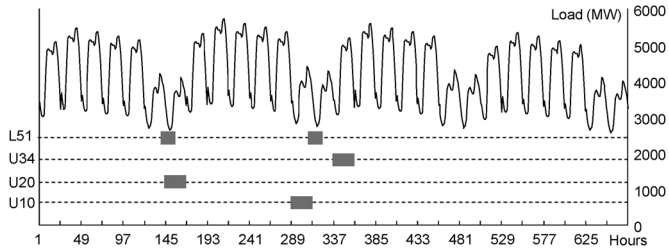


Fig. 6. Equipment maintenance in Case 1.

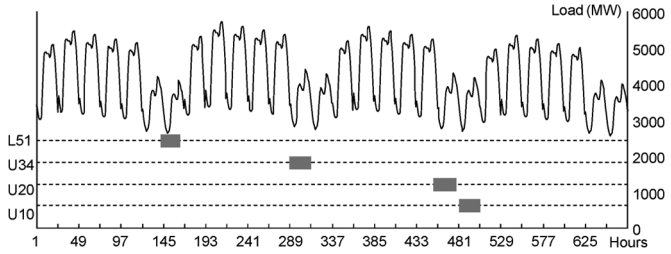


Fig. 7. Equipment maintenance in Case 2.

TABLE III
CLASSIFICATION OF UNITS

| Class | Units |
|---|---|
| Base | 4 5 10 11 20 21 24 25 27 28 29 36 39 40 43 44 45 |
| Intermediate | 1 2 3 6 12 13 31 32 38 42 50 54 |
| Peaking | 7 8 9 14 15 16 17 18 19 22 23 26 34 35 37 47 48 51 52 53 |
| Off | 30 33 41 46 49 |

TABLE IV
PROBABILITIES OF EACH SCENARIO AFTER SCENARIO REDUCTION

| **Scenario** | 1 | 2 | 3 | 4 | 5 | 6 |
|---|---|---|---|---|---|---|
| **Probability** | 0.01 | 0.01 | 0.28 | 0.01 | 0.01 | 0.39 |
| **Scenario** | 7 | 8 | 9 | 10 | 11 | 12 |
| **Probability** | 0.01 | 0.01 | 0.01 | 0.01 | 0.01 | 0.24 |

TABLE V
OPERATION COST FOR EACH SCENARIO ($)

| Scenario | Operation Cost | Scenario | Operation Cost |
|---|---|---|---|
| 1 | 40,767,940 | 7 | 39,288,403 |
| 2 | 40,202,328 | 8 | 41,929,654 |
| 3 | 40,984,806 | 9 | 41,345,839 |
| 4 | 39,963,756 | 10 | 41,724,055 |
| 5 | 40,717,038 | 11 | 41,637,338 |
| 6 | 40,581,050 | 12 | 41,283,492 |
| **EXP** | | 40,886,157±64,223 | |
| **Relative Error (%)** | | 0.157 | |

The maintenance of units U10, U20, and U34 are scheduled at hours of 289–312, 145–168, and 337–360, respectively. The maintenance of line L51 is scheduled at hours 144–152 and 312–320. Based on the above maintenance schedule, we optimize the hourly unit commitment schedule for 672 h without the consideration of system uncertainty. The total cost is $42 133 556, which includes the generator maintenance cost of $62 400, line maintenance cost of $90 000, and operation cost of $41 981 156. In the uncoordinated case, the unit commitment schedule is not considered in the maintenance problem. If the proposed maintenance schedule is used as input to the unit commitment problem, the commitment may be more expensive or could result in load shedding. For example in Fig. 6, L51 and U20 are both maintained during hours 145–152. An inefficient utilization of generators and lines at this period could increase the total cost and/or result in load shedding.

*Case 2:* This case coordinates the equipment maintenance outage and the unit commitment schedule without considering any uncertainty. Table III shows, based on the percentage of time, the units that are committed as base (committed more than 85% of the time in four weeks), intermediate (between 85% and 10% of time), peaking (less than 10% of time), and off units. The optimal maintenance schedule is shown in Fig. 7, in which much of the maintenance is scheduled near the minimum loading hours for maintaining the power systems reliability and economics. The maintenance of base units U10 and U20 is scheduled at the minimum loading hours of 481–504 and 457–480, respectively. Furthermore, the maintenance of line L51 is at hours 140–157, which shifts the maintenance of peaking unit U34 to the next available minimum loading hours of 289–312. The optimal cost is $40 176 827 which includes the generator maintenance cost of $62 400, line maintenance cost of $90 000, and operation cost of $40 024 427. Compared with the optimal cost of Case 1, a saving of $1 956 729 is achieved due to the simultaneous consideration of LTEM and LTSCUC subproblems.

*Case 3:* In this case, the power system uncertainty is considered for the coordination of LTEM and LTSCUC problems. At each hour, there are 461 decision variables and 2094 continuous variables. Thus the entire coordinated problem over a 672-h horizon contains 309 792 binary variables and 1 407 168 continuous variables. One hundred scenarios are created using the low-discrepancy Monte Carlo simulation method with each scenario representing forced outages of generation units and transmission lines, load forecast errors, and fuel price fluctuations. The scenario reduction method reduces the total number of scenarios from 100 to 12 as a tradeoff between the calculation speed and the solution accuracy. Table IV shows the scenario weights after reduction. Table V provides the operation cost of each scenario, the expected operation cost, and its variance. In Table V and thereafter, "EXP" is the expected value of all scenarios based on the 95% confidence interval, and the "Relative Error" is calculated as the ratio of 95% confidence interval to the expected value. The results presented in Tables V show that after 90% reduction, relative errors in operation costs are less than 1%.

Table VI compares maintenance cost, operation cost, and total cost for the above three cases. The coordination of LTEM and LTSCUC subproblems has reduced the total cost by $1 956 729 in Case 2 as compared with Case 1. This reduction is due to the coordination of LTEM and LTSCUC subproblems which avoids any unnecessary load shedding or the commitment of peaking units. It also shows that the uncertainty has increased the total operation cost by $861 730 in Case 3 as compared with Case 2. The inclusion of uncertainty would provide a more comprehensive coordination of maintenance outages and hourly unit commitment to satisfy the system security constraints.

TABLE VI
COST COMPARISON IN THREE CASES

| Case | Maintenance Cost ($) | Operation Cost ($) | Total Cost ($) |
|---|---|---|---|
| Case 1 | 152,400 | 41,981,156 | 42,133,556 |
| Case 2 | 152,400 | 40,024,427 | 40,176,827 |
| Case 3 | 152,400 | 40,886,157 | 41,038,557 |

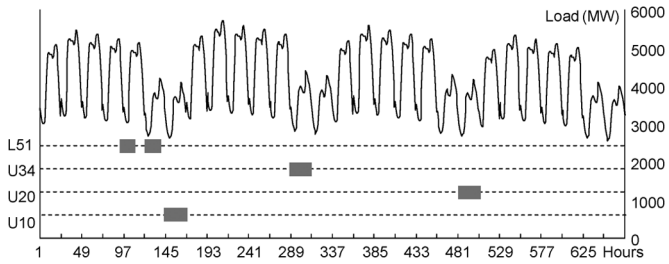


Fig. 8. Equipment maintenance in Case 3.

The optimal maintenance schedule is presented in Fig. 8. The load forecast in Fig. 8 is the same as that in Fig. 5. Among the simulated scenarios, the base unit U10 is on forced outage at hours 143–148 in scenario 6, and at hours 153–156 in scenario 10. Thus the optimal maintenance schedule of unit U10 is shifted to hours 145–168, and the maintenance of units U20 and U34 is shifted to hours 481–504 and 289–312, respectively.

Furthermore, the forced outage of transmission line L51 is simulated to be between hours 100–103 in scenario 3. Thus its maintenance outage is scheduled at periods of 97–105 and 126–134. The optimal cost is $41 038 557 which includes the generator maintenance cost of $62 400, the transmission line maintenance cost of $90 000, and the operation cost of $40 886 157.

To further evaluate the advantage of the stochastic model, a new set of scenarios is generated as shown in Table VII. We apply the stochastic problem solution (i.e., solution of Case 3) and the expected value problem solution (i.e., solution of Case 2) to each scenario. Tables VIII and IX show the operation costs for each scenario which are calculated by adopting the stochastic and the deterministic problem solutions of the maintenance and the unit commitment decision variables in each scenario. By comparison, the difference in the expected cost between stochastic and deterministic solutions is $543 397 (i.e., $41 491 977–$40 948 580), which shows the potential operation cost saving for utilizing the stochastic model. By comparison, the upper limit of the expected operation cost for the proposed stochastic solution (i.e., $\$40\,948\,580 + \$78\,305 = \$41\,026\,885$) is smaller than the lower limit of the expected operation cost of the deterministic decision (i.e., $\$41\,491\,977 - \$105\,887 = \$41\,386\,090$), which exhibits a potential saving when applying the stochastic model. The scenario costs in Table VIII are not necessarily smaller than those in Table IX for the deterministic solution. The costs for scenarios 6, 9, and 11 in Table VIII are higher than those in Table IX.

Fig. 9 shows the relationship between maintenance and MCPs calculated by the LTSCUC subproblem in a four-week horizon. The maintenance is likely to be scheduled when MCPs are low.

TABLE VII
PROBABILITIES OF EACH SCENARIO AFTER SCENARIO REDUCTION

| Scenario | 1 | 2 | 3 | 4 | 5 | 6 |
|---|---|---|---|---|---|---|
| Probability | 0.18 | 0.03 | 0.25 | 0.03 | 0.12 | 0.09 |
| Scenario | 7 | 8 | 9 | 10 | 11 | 12 |
| Probability | 0.01 | 0.03 | 0.04 | 0.04 | 0.02 | 0.16 |

TABLE VIII
OPERATION COSTS USING STOCHASTIC VALUE SOLUTION ($)

| Scenario | Operation Cost | Scenario | Operation Cost |
|---|---|---|---|
| 1 | 40,713,112 | 7 | 39,684,448 |
| 2 | 40,085,069 | 8 | 41,868,003 |
| 3 | 40,774,148 | 9 | 41,856,600 |
| 4 | 40,003,360 | 10 | 41,450,497 |
| 5 | 40,660,151 | 11 | 42,002,161 |
| 6 | 41,311,224 | 12 | 41,259,936 |
| EXP | | 40,948,580 ± 78,305 | |
| Relative Error (%) | | 0.191 | |

TABLE IX
OPERATION COSTS USING EXPECTED VALUE SOLUTION ($)

| Scenario | Operation Cost | Scenario | Operation Cost |
|---|---|---|---|
| 1 | 41,514,139 | 7 | 40,080,098 |
| 2 | 40,477,383 | 8 | 42,674,071 |
| 3 | 41,162,509 | 9 | 40,873,073 |
| 4 | 40,396,517 | 10 | 42,247,362 |
| 5 | 41,463,449 | 11 | 41,487,957 |
| 6 | 40,985,739 | 12 | 42,516,608 |
| EXP | | 41,491,977 ± 105,887 | |
| Relative Error (%) | | 0.255 | |

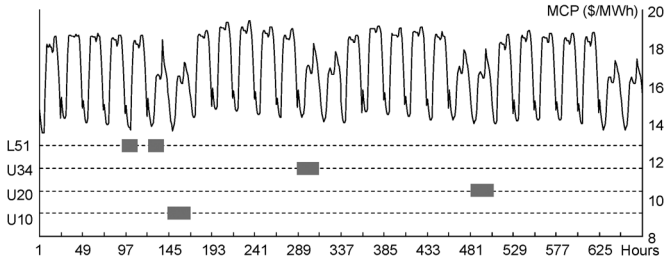


Fig. 9. Equipment maintenance in the stochastic case combined with MCP.

When units are on maintenance, expensive units have to be committed to meet system loads, which will increase certain hourly MCPs. The maintenance carried out at the low MCP periods could mitigate price risks in spot markets.

Figs. 10 and 11 show the iterative LR function values and the number of infeasible relaxed constraints (11) and (12), respectively. Fig. 11 shows that after 58 iterations of LTEM and LTSCUC, there are three violated coupling constraints corresponding to (11) and (12). We fix the maintenance schedule at iteration 58 and execute the LTSCUC to obtain a feasible and near-optimal solution of $41 038 557. Fig. 10 shows that at iteration 58, the relative difference between $VLR$ ($40 865 834) and $VP$ ($41 038 557) is 0.423% which satisfies the precision requirement. For the stochastic LTSCUC, we show the convergence of the last stochastic LTSCUC subproblem.

Figs. 12 and 13 show the iterative LR function values of (17) and the weighted violation of bundle constraints, respectively. Fig. 13 shows that after 27 iterations, the total

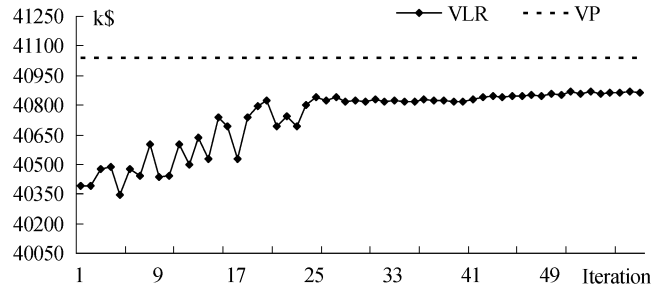


Fig. 10. Iterative LR function values in Case 3.

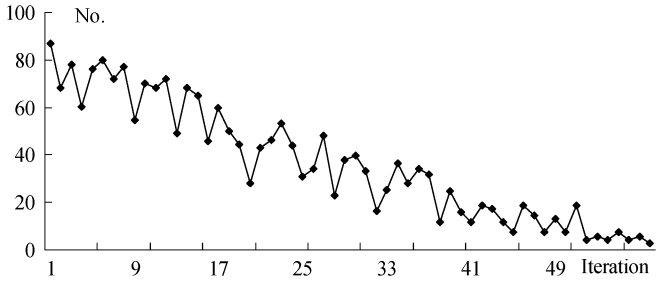


Fig. 11. Number of infeasible constraints (11), (12) in Case 3.

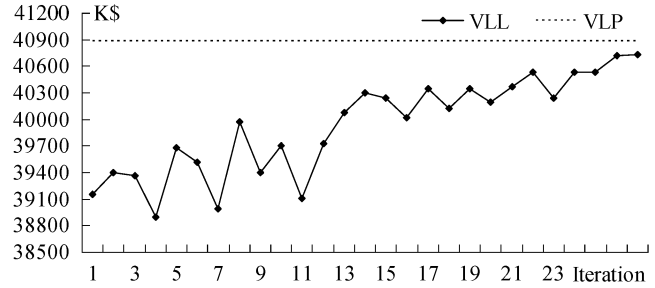


Fig. 12. Iterative LR values of (16) for one stochastic LTSCUC in Case 3.

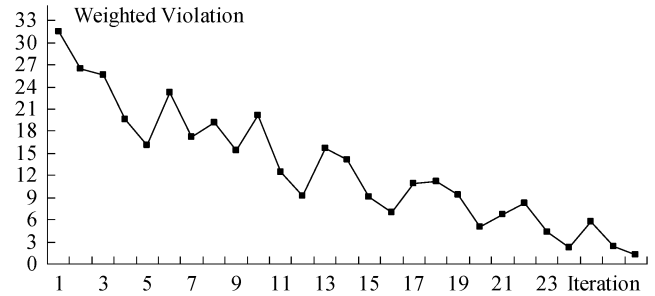


Fig. 13. Iterative weighted violation for one stochastic LTSCUC in Case 3.

weighted violation of bundle constraints is satisfied with a $VLL$ of \$40 731 316. Then, we apply the heuristic process to find a feasible solution with respect to the scenario bundle constraints. This process would require another 15 iterations and the relative difference between $VLL$ (\$40 731 316) and $VLP$ (\$40 886 157) is 0.380% as shown in Fig. 12.

*Case 4:* In this case, a three-day maintenance duration is studied. Other assumptions are the same as those of Cases 1–3. Also, the power system uncertainty is modeled in this case. First, we consider the uncoordinated solution for LTEM and LTSCUC. The optimal maintenance schedule is shown in Fig. 14. The total cost is \$42 951 648 which includes the

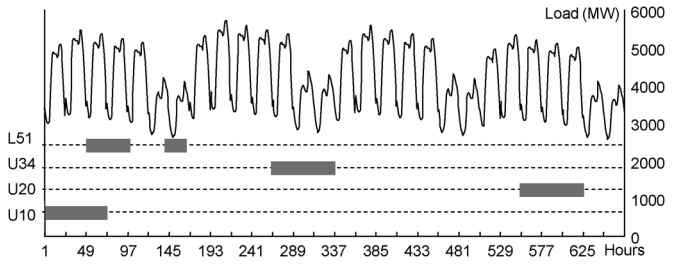


Fig. 14. Maintenance with uncoordinated LTEM and LTSCUC.

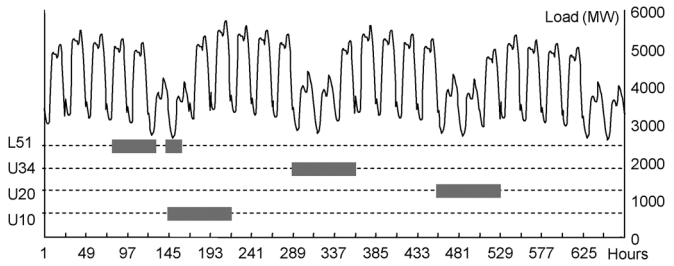


Fig. 15. Maintenance with coordinated LTEM and LTSCUC in Case 4.

generator maintenance cost of \$187 200, the line maintenance cost of \$360 000, and the operation cost of \$42 404 448. Note that the uncoordinated LTEM and LTSCUC solutions will result in the scheduling of maintenance at periods with higher loads and more expensive operation costs. Next we consider the coordination of LTEM and LTSCUC solutions. The optimal maintenance schedule is shown in Fig. 15. Thus the optimal maintenance of unit U10 is scheduled at hours 145–216, which do not coincide with the low-load period at hours 121–144, and maintenance of units U20 and U34 is scheduled at hours 457–528 and 288–360, respectively. The total cost is \$41 798 521 which includes the generator maintenance cost of \$187 200, the line maintenance cost of \$360 000, and the operation cost of \$41 251 321.

As we compare the coordinated and the uncoordinated results, a saving of \$1 153 127 (i.e., 42 951 648 − 41 798 521) occurs due to the coordination of LTEM and LTSCUC. Furthermore, the inclusion of uncertainty provides a more accurate coordination of maintenance outage and hourly generation unit commitment, satisfies the system security constraints, and makes a more efficient usage of fuel contracts.

The cases are tested on a 2.39-GHz server and the execution time is estimated based on parallel calculations with 12 CPUs. The CPU time of LTSCUC for one scenario is about 4 min, and the number of iterations for scenario bundle constraints is within 27 for the given accuracy. The heuristic process for obtaining a feasible LTSCUC solution requires another 15 iterations and $15 * 0.2$ minutes of computation. Thus the total CPU time for one iteration of LTEM and LTSCUC is about 1.9 h $(4 * 27 + 15 * 0.2 \text{ min})$, with the parallel processing of LTEM and stochastic LTSCUC subproblems. Notice that only the objective functions are changed in the following iterations, and the solutions obtained at previous iterations are still feasible which can be used as initial solutions in the current iteration. Furthermore, previous Benders cuts can also be used at the current LTSCUC calculation. Such strategies would reduce

the computation time. However, these strategies would not be suitable for the last iteration, which is a heuristic process for obtaining the feasibility solution by fixing the LTEM solutions and executing the LTSCUC. In Case 3, the total number of iterations between LTEM and LTSCUC is 58, and the total CPU time is about 57 h. However, if parallel computation is further adopted in each short-term SCUC calculation process, the total CPU time would be reduced to about 4.6 hours. In general, the computation time may not be a major concern since the proposed model is applied to the long-term evaluation. For a complex stochastic mixed-integer linear problem presented in the paper, the proposed decomposition methodology would provide a reliable solution with an acceptable duality gap within a reasonable CPU time.

## VI. Conclusions

Due to random events in power systems, a stochastic problem is proposed in this paper which coordinates LTEM and LTSCUC solutions with fuel and emission constraints. The approach considers the uncertainty in the availability of generation units and transmission lines, load forecast errors, as well as fuel price fluctuations, which are simulated as scenario trees by the Monte Carlo Method. LR is applied to decompose the original problem into maintenance and unit commitment subproblems, multipliers $\eta$ and $\pi$ corresponding to generator and line status coupling constraints are updated and fed back to the maintenance and unit commitment subproblems. The uncertainty is represented in the unit commitment scenarios, and LR is applied to solve the stochastic unit commitment problem with fuel allocation and emission allowance constraints. The solution results for the hourly maintenance and unit commitment subproblems represent the coordination of security, optimal unit commitment, resource allocation, and equipment maintenance in uncertain power systems. Compared with the expected value problem solution, the solution of the proposed stochastic model would provide potential savings in operation costs. The proposed approach can be applied to a vertically integrated utility as well as the ISO's operation in a restructured power system.

## Appendix A

The process starts by finding a scenario $s$ which has the largest weighted violation $\sum_{p=1}^{NP}\sum_{t=1}^{NT} P^s \cdot |I_{itp}^s - c_{itp}|$, updating multipliers, and calculating the scenario $s$ only. The steps are as follows:

*Step 0*: Calculate $I_{itp}^s$ for each scenario with $s = 1,\cdots,S$. Compute $c_{itp} = \sum_{s\in B(s,P,\tau)=\Omega_{P\tau}} P^s \cdot I_{itp}^s / \sum_{s\in B(s,P,\tau)=\Omega_{P\tau}} P^s$.

*Step 1*: Update multipliers. The multipliers are updated as $\theta_{itp}^{s,k+1} = \theta_{itp}^{s,k} + r^k \cdot d_{itp}^{s,k}$, where $r^k$ is the step size which satisfies $0 \le r^k \le (L^* - L^k)/\|d^k\|^2$ and $d_{itp}^{s,k}$ is the modified surrogate subgradient, which is given by

$$d_{itp}^{s,0} = I_{itp}^{s,0} - c_{itp}^0$$
$$d_{itp}^{s,k} = \left[I_{itp}^{s,k} - c_{itp}^k\right] + \gamma_{itp}^{s,k} \cdot \left[I_{itp}^{s,k-1} - c_{itp}^{k-1}\right]$$

where $\gamma_{itp}^{s,k} = \max\{0, -\varsigma \cdot (I_{itp}^{s,k} - c_{itp}^k)/d_{itp}^{s,k-1}\} \varsigma \in [1,2]$.

*Step 2*: Use new multipliers to recalculate the problem, get new solutions for $I_{itp}^s$.

*Step 3*: Check the stopping criteria. If the criterion given by $\sum_{s\in B(s,P,\tau)=\Omega_{P\tau}} P^s \sum_{p=1}^{NP}\sum_{t=1}^{NT} |I_{itp}^s - c_{itp}| \le \varepsilon_2$ is met, then stop; otherwise, go to Step 1.

## Appendix B

*Proof for Stopping Criterion:* The original optimization problem is defined as

$$\begin{aligned} VP^* = Min & \left\{ f(x) + \sum_s g(y^s) \right\} \\ S.t. \quad & x \in X \quad y^s \in Y^s \\ & y^s \le x \quad \forall s \\ & y^s = y^{s'} \quad for \quad s \in B(s,P,\tau) = \Omega_{P\tau}. \end{aligned} \tag{B1}$$

The Lagrangian dual of the primal problem (B1) is written as

$$VL^* = \underset{\eta^s \ge 0}{Max} \left\{ \underset{\substack{x\in X, y^s\in Y^s, y^s = y^{s'} \\ for\ s\in B(s,P,\tau)=\Omega_{P\tau}}}{Min} \left[ f(x) + \sum_s g(y^s) + \sum_s \eta^s \cdot (y^s - x) \right] \right\}. \tag{B2}$$

We minimize the following Lagrangian function (B3) at the current iteration $n$ which is a lower bound of (B2)

$$VL = \underset{\substack{x\in X, y^s\in Y^s, y^s = y^{s'} \\ for\ s\in B(s,P,\tau)=\Omega_{P\tau}}}{Min} \left[ f(x) + \sum_s g(y^s) + \sum_s \eta^{s,n} \cdot (y^s - x) \right]. \tag{B3}$$

Let $VP$ be the objective value of a feasible solution of the original problem (B1), which is the upper bound of $VP^*$. Based on the above discussions

$$VL \le VL^* \le VP^* \le VP. \tag{B4}$$

(B3) is further decomposed into two subproblems as (B5) and (B6) corresponding to $x$ and $y$, respectively:

$$VL_x = \underset{x\in X}{Min} \left[ f(x) - \sum_s (\eta^{s,n} \cdot x) \right] \tag{B5}$$

$$\begin{aligned} VL_y = & Min \left[ \sum_s g(y^s) + \sum_s (\eta^{s,n} \cdot y^s) \right] \\ S.t. \quad & y^s \in Y^s \\ & y^s = y^{s'} \quad for \quad s \in B(s,P,\tau) = \Omega_{P\tau}. \end{aligned} \tag{B6}$$

Based on the discussion in Section IV-C, the Lagrangian dual of (B6) is

$$VLL_y^* = \underset{\theta^s}{Max} \left\{ \underset{y^s\in Y^s}{Min} \left[ \sum_s g(y^s) + \sum_s (\eta^{s,n} \cdot y^s) + \sum_{s\in B(s,P,\tau)=\Omega_{P\tau}} (\theta^s \cdot y^s) \right] \right\}. \tag{B7}$$

In this paper, we minimize the following Lagrangian function at the current iteration $k$ which is the lower bound of (B7):

$$VLL_y = \underset{y^s \in Y^s}{Min} \left[ \sum_s g(y^s) + \sum_s \eta^{s,n} \cdot y^s + \sum_{s \in B(s,P,\tau) = \Omega_{P\tau}} (\theta^{s,k} \cdot y^s) \right]. \quad \text{(B8)}$$

Accordingly

$$VLL_y \le VLL_y^* \le VL_y. \quad \text{(B9)}$$

Combining (B4)–(B6) and (B9), we get

$$VLL_y + VL_x \le VLL_y^* + VL_x \le VL_y + VL_x = VL \le VL^* \le VP^* \le VP. \quad \text{(B10)}$$

Thus the stopping criterion (B11) is used to terminate the iterative process since the unknown optimal solution $VP^*$ is between $(VLL_y + VL_x)$ and $VP$:

$$\frac{|VP - (VLL_y + VL_x)|}{(VLL_y + VL_x)} \le \varepsilon_1. \quad \text{(B11)}$$

## REFERENCES


[1] M. Shahidehpour and Y. Wang, *Communication and Control of Electric Power Systems*. New York: Wiley, Jun. 2003.

[2] M. Shahidehpour, H. Yamin, and Z. Y. Li, *Market Operations in Electric Power Systems*. New York: Wiley, 2002.

[3] M. Shahidehpour and M. Marwali, *Maintenance Scheduling in Restructured Power Systems*. Norwell, MA: Kluwer, 2000.

[4] E. L. Silva, M. Morozowski, L. G. S. Fonseca, G. C. Oliveira, A. C. G. Melo, and J. C. O. Mello, "Transmission constrained maintenance scheduling of generating units: A stochastic programming approach," *IEEE Trans. Power Syst.*, vol. 10, no. 2, pp. 695–701, May 1995.

[5] R. Billinton and A. Abdulwahab, "Short-term generating unit maintenance scheduling in a restructured power system using a probabilistic approach," *Proc. Inst. Elect. Eng., Gen., Transm., Distrib.*, vol. 150, no. 4, pp. 463–468, Jul. 2003.

[6] A. J. Conejo, R. Garcia-Bertrand, and M. Diaz-Salazar, "Generation maintenance scheduling in restructured power systems," *IEEE Trans. Power Syst.*, vol. 20, no. 2, pp. 984–992, May 2005.

[7] T. Geetha and K. S. Swarup, "Coordinated maintenance scheduling of Gencos and Transcos in restructured power systems," in *Proc. IEEE Power India Conf.*, 2006.

[8] M. K. C. Marwali and M. Shahidehpour, "Coordination between long-term and short-term generation scheduling with network constraints," *IEEE Trans. Power Syst.*, vol. 15, no. 3, pp. 1161–1167, Aug. 2000.

[9] Y. Fu, M. Shahidehpour, and Z. Li, "Long-term security-constrained unit commitment: Hybrid subgradient and Danzig-Wolfe decomposition," *IEEE Trans. Power Syst.*, vol. 20, no. 4, pp. 2093–2106, Nov. 2005.

[10] J. Lenzuela and M. Mazumdar, "Monte Carlo computation of power generation production costs under operating constraints," *IEEE Trans. Power Syst.*, vol. 16, no. 4, pp. 671–677, Nov. 2001.

[11] P. Glasserman, *Monte Carlo Method in Financial Engineering*. New York: Springer, 2003.

[12] Y. Yamamoto and T. Tezuka, "Optimal investment in power plant under price uncertainty," in *Proc. 41st SICE Annu. Conf. (SICE 2002)*, Aug. 2002, vol. 2, pp. 1302–1305.

[13] J. Dupăová, N. Gröwe-Kuska, and W. Römisch, "Scenario reduction in stochastic programming: An approach using probability metrics," *Math. Program.*, ser. A, vol. 95, pp. 493–511, 2003.

[14] R. T. Rockafellar and R. J.-B. Wets, "Scenarios and policy aggregation in optimization under uncertainty," *Math. Oper. Res.*, vol. 16, no. 1, pp. 119–147, 1991.

[15] X. Zhao, P. B. Luh, and J. Wang, "Surrogate gradient algorithm for lagrangian relaxation," *J. Optim. Theory Appl.*, vol. 100, no. 3, pp. 699–712, Mar. 1999.

[16] P. Camerini, L. Fratta, and F. Maffioli, "On improving relaxation methods by modified gradient techniques," in *Mathematical Programming Study*. Amsterdam, The Netherlands: North Holland, 1975, vol. 3, pp. 26–34.

[17] M. Shahidehpour, Y. Fu, and T. Wiedman, "Impact of natural gas infrastructure on electric power systems," *Proc. IEEE*, vol. 93, no. 5, pp. 1042–1056, May 2005.

[18] Y. Fu, M. Shahidehpour, and Z. Li, "Security-constrained unit commitment with AC constraints," *IEEE Trans. Power Syst.*, vol. 20, no. 3, pp. 1538–1550, Aug. 2005.

[19] D. P. Bertsekas, *Nonlinear Programming*. Belmont, CA: Athena Scientific, 1999.

[20] L. Wu, M. Shahidehpour, and T. Li, "Stochastic security-constrained unit commitment," *IEEE Trans. Power Syst.*, vol. 22, no. 2, pp. 800–811, May 2007.

[21] L. Wu, M. Shahidehpour, and Z. Li, "GENCO's risk-constrained hydrothermal scheduling," *IEEE Trans. Power Syst.*, vol. 23, no. 4, pp. 1847–1858, Nov. 2008.

[22] L. Wu, M. Shahidehpour, and T. Li, "Cost of reliability analysis bases on stochastic unit commitment," *IEEE Trans. Power Syst.*, vol. 23, no. 3, pp. 1364–1374, Aug. 2008.

[23] Y. Fu, Z. Li, M. Shahidehpour, T. Zheng, and E. Litvinov, "Coordination of midterm outage scheduling with short-term security-constrained unit commitment," *IEEE Trans. Power Syst.*, vol. 24, no. 4, pp. 1818–1830, Nov. 2009.

[24] J. R. Birge and F. V. Louveaux, *Introduction to Stochastic Programming*. New York: Springer, 1997.



**Lei Wu** (M'07) received the B.S. and M.S. degrees in electrical engineering from Xi'an Jiaotong University, Xi'an, China, in 2001 and 2004, respectively, and the Ph.D. degree in electrical engineering from the Illinois Institute of Technology, Chicago, in 2008.

Presently, he is a Visiting Professor at Illinois Institute of Technology. His research interests include power systems restructuring, reliability, and economics.

**Mohammad Shahidehpour** (F'01) is Bodine Chair Professor in the Electrical and Computer Engineering Department at Illinois Institute of Technology, Chicago. He is an Honorary Professor in the North China Electric Power University in Beijing and the Sharif University in Tehran. He is also the 2009 recipient of an Honorary Doctorate from the Polytechnic University of Bucharest.

Dr. Shahidehpour is the VP of Publications for the IEEE Power & Energy Society, an IEEE Distinguished Lecturer, Technical Program Chair for the 2010 IEEE Innovative Smart Grid Technologies Conference, and the Editor-in-Chief of the IEEE TRANSACTIONS ON SMART GRID.

**Yong Fu** (M'05) received the B.S. and M.S. degrees in electrical engineering from Shanghai Jiaotong University, Shanghai, China, in 1997 and 2002, respectively, and the Ph.D. degree in electrical engineering from the Illinois Institute of Technology, Chicago, in 2006.

Presently, he is an Assistant Professor in the Electrical and Computer Engineering Department at the Mississippi State University. His research interests include power systems restructuring and reliability.

# Transmission Switching in Expansion Planning

Amin Khodaei, Mohammad Shahidehpour, *Fellow, IEEE,* and Saeed Kamalinia, *Member, IEEE*

***Abstract*— Transmission switching (TS) is introduced to add flexibility to the transmission and generation capacity expansion planning problem. TS could improve the performance of the capacity expansion planning model and reduce the total planning cost. The capacity expansion planning problem is decomposed into a master problem and two subproblems. The master problem utilizes the candidate set for additional generating unit and transmission capacity investments to find the optimal plan throughout the planning horizon. The subproblems use the optimal plan, apply transmission switching to relieve any transmission flow violations, and calculate the optimal dispatch of generating units. The transmission network contingencies are also considered in the subproblems. The case studies exhibit the effectiveness of the proposed expansion planning approach.**

***Index Terms*—Transmission and generation capacity expansion planning, transmission switching, mixed integer linear programming, Benders decomposition.**

## NOMENCLATURE

***Indices:***

| | |
|---|---|
| $b$ | Index for a load block |
| $C$ | Index for a candidate generating unit or transmission line |
| $E$ | Index for an existing generating unit or transmission line |
| $h$ | Index for a bus |
| $i$ | Index for a generating unit |
| $j$ | Index for a transmission line |
| $t$ | Index for a year |
| $\wedge$ | Index for the known variables |

***Sets:***

| | |
|---|---|
| $J_h$ | Set of transmission lines connected to bus $h$ |
| $I_h$ | Set of generating units connected to bus $h$ |

***Parameters:***

| | |
|---|---|
| $CI$ | Investment cost for candidate generating unit or transmission line |
| $d$ | Discount rate |
| $DT_{bt}$ | Duration of the load block $b$ in year $t$ |
| $GCI_t$ | Capital generating unit investment in year $t$ |
| $GCT_i$ | Required time for the construction of unit $i$ |
| $GUC_t$ | Maximum added generating capacity in year $t$ |
| $GUN_t$ | Maximum number of generating units added in year $t$ |
| $LCI_t$ | Capital transmission line investment in year $t$ |
| $LCT_j$ | Required construction time for the transmission line $j$ |
| $LUC_t$ | Maximum transmission line capacity to be added in year $t$ |
| $LUN_t$ | Maximum added number of transmission lines in year $t$ |
| $NB$ | Number of load blocks |
| $NCG$ | Number of candidate generating units |
| $NCL$ | Number of candidate transmission lines |
| $NEG$ | Number of existing generating units |
| $NEL$ | Number of existing transmission lines |
| $NH$ | Number of buses |
| $NT$ | Number of years |
| $OC_{ibt}$ | Operating cost of the generating unit $i$ at load block $b$ in year $t$ |
| $PD_{hbt}$ | Load demand at bus $h$ at load block $b$ in year $t$ |
| $UX_{ibt}$ | Contingency state of the generating unit $i$ at load block $b$ in year $t$ |
| $UY_{jbt}$ | Contingency state of the transmission line $j$ at load block $b$ in year $t$ |
| $\gamma_j$ | Susceptance of the transmission line $j$ |
| $\varepsilon$ | Small positive and predefined threshold |

***Variables:***

| | |
|---|---|
| $PG_{ibt}$ | Dispatched capacity of the generating unit $i$ at load block $b$ in year $t$ |
| $PL_{jbt}$ | Power flow on the transmission line $j$ at load block $b$ in year $t$ |
| $SL_{hbt,1}, SL_{hbt,2}$ | Non-negative Slack variables for power mismatch at bus $h$ at load block $b$ in year $t$ |
| $X_{it}$ | Investment state of the generating unit $i$ in year $t$ |
| $Y_{jt}$ | Investment state of transmission line $j$ in year $t$ |
| $Z_{jbt}$ | Switching state of the transmission line $j$ at load block $b$ in year $t$ |
| $\delta_{mbt}$ | Voltage angle of bus $m$ at load block $b$ in year $t$ |
| $\lambda, \mu, \pi$ | Dual variables. |

The authors are with Electrical and Computer Engineering Department, Illinois Institute of Technology, Chicago, IL 60616 USA (e-mail: akhodaei@iit.edu; ms@iit.edu; skamalin@iit.edu).

## I. INTRODUCTION

SWITCHING of power system elements can help ISOs maintain the system security and reduce operation costs. In comparison with existing control methods such as generating unit rescheduling or load shedding [1,2], transmission switching (TS) can provide additional economical advantages. Several TS approaches were presented in the literature to encompass various operational modes of

power systems. In [3], TS was used as a corrective action to mitigate transmission flow violations. In [4]-[7], TS was used to model the power system security in contingency cases. TS was used in [8] as a congestion management tool. However, TS can provide economic benefits which was first introduced in [9] in a market context. The application of TS in reducing the production cost was investigated in [10], and was further developed in [11] to examine the effects of network topology changes on nodal prices, load payments, generation revenues, congestion costs, and flowgate prices. In [12] a model was proposed to add contingencies to the model in [10]. These studies indicated that the switching could provide additional control actions for voltage stability, congestion management, transmission loss reduction, production cost minimization, and the enhancement of system security. However, the TS applicability to the power system planning was not addressed.

Power system planning is the science of determining the optimal place, size, and time for adding new resources to power systems. Previous studies investigated generation and transmission expansion planning methodologies in competitive market environments. The most common planning methods are based on mathematical optimization such as branch and bound, linear programming, and Benders decomposition [13]-[21]. Also heuristic approaches, such as genetic algorithms, fuzzy-sets, simulated annealing, expert systems, and game-theoretic methods [22]-[30] were used to solve the expansion planning problem. The market-based planning in power systems considers economics, security, and reliability constraints and analyzes the risk of planning strategies based on uncertainties [31]-[35]. Using Lagrangian relaxation and Benders decomposition, the impact of transmission security on generation resource planning was discussed [36]. The coordination of transmission expansion planning with the competitive generation capacity planning was presented in [37]. In [38], a very constructive proposal was offered on the interaction of generation and transmission investments in transmission planning. In [39], the long-term transmission expansion planning problem in a competitive pool-based electricity market was modeled. In this model, a number of scenarios based on the future system demand were defined and the optimal expansion planning was simulated by the maximization of the aggregated social welfare. A bilevel model for transmission expansion planning within a market environment was proposed in [40]. The minimization of the network investment was considered in the upper level, while the lower level included pool trading constraints.

The objective of a generation company (GENCO) or a transmission company (TRANSCO) is to maximize its profit over the planning horizon. However, when the ISO performs the planning, the objective will be replaced by the minimization of investment and operating costs. In this paper, it is assumed that the GENCOs and TRANSCOs have already submitted their candidate expansion proposals to the ISO. The ISO will solve the expansion planning problem to satisfy the system constraints based on the candidate set of components submitted by the participating companies.

This paper presents a TS coordinated expansion planning model. The planning is a long-term problem that is solved over an extended period of time. TS is a short-term operation problem. The two problems are solved separately, considering the associated time periods. The important point is to link these two problems in a way that the impact of TS on planning can be observed. This task is accomplished by using the security check and the optimal operation subproblems in Fig. 1. The TS application could reduce the total planning cost and possibly defer the planning of the candidate units and transmission lines. In this situation the transmission congestion in the system can vary. A corrective/preventive scheme is used to handle transmission line and generating unit contingencies. The security check subproblem performs corrective actions, while the preventive actions are considered in the master problem. Our proposed approach uses a deterministic criterion to consider contingencies. A future stochastic market-based expansion planning study will explore the effect of random outages of generating units and transmission lines in addition to the long-term load forecast errors, where the Monte Carlo simulation will be used to identify scenarios and the proposed deterministic model will be solved in each scenario.

The rest of the paper is organized as follows. Section II presents the model outline of the proposed approach, while Section III formulates different parts of it. Section IV conducts the numerical simulations and in detail discusses a six-bus, the IEEE 118-bus and an 1168-bus systems. Finally, concluding remarks are presented in Section V.

## II. Proposed Model Outline

Fig. 1 depicts the proposed coordinated generation and transmission expansion planning model. The objective of this problem is to minimize the investment cost, for new generating units and transmission lines, in addition to operating costs. This objective is subject to different security-based planning and operation constraints.

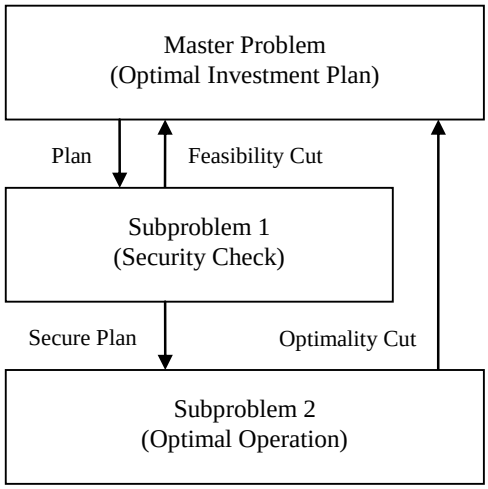


Fig. 1 Proposed expansion planning using TS

In this paper, Benders decomposition is used to decompose the expansion planning problem. Benders decomposition is mathematically sound and can easily be applied to large-scale systems. The optimality of Benders decomposition as well as its applicability to power system problems in practical cases are discussed in [41]-[44]. Also in [2], the practical

applications of Benders decomposition are discussed in detail, where it is explained that the most suitable approach to solve the multi-period expansion planning problem is to use the Benders decomposition. The Benders decomposition provides the iterative solution of the mixed integer linear programming problem in a distributed manner. The decomposed planning model includes the optimal investment plan as the master problem, and the security and the optimal operation of the system as the two subproblems. The master problem utilizes the candidate set of generating units and transmission lines to find the optimal investment plan. The security check subproblem examines this plan for satisfying the base case and the security constraints. The optimal operation subproblem inspects the operating cost of the plan. TS is used in the security check and the optimal operation subproblems to enhance the feasibility and the optimality of the proposed problem, respectively. Integer linear programming (ILP) is used to model the master problem, while the subproblems are LP models. A typical set of planning constraints includes

- Capital investment funds
- Projected resource and line capacity
- Maximum number of generating units and transmission lines to be added
- Construction time of the candidate investments

A typical set of operation constraints includes

- Power balance
- Transmission line flow limits
- Generation limits

The approach is presented as follows.

### *A. Master problem*

The master problem calculates the investment plan for generating units and transmission lines based on the initial set of candidates when considering generation and transmission expansion constraints. The lower bound for the original MIP planning problem is determined by the value of the master problem objective at each iteration. The variables in the master problem are binary and constraints are linear. So the master problem is in the ILP format.

### *B. Subproblems*

The investment plan calculated in the master problem is submitted to the subproblems. The security check subproblem checks whether the proposed plan satisfies the operation constraints. This subproblem would satisfy the power balance at every bus while preserving base case and contingency constraints. If any of the constraints are violated, a feasibility cut is formed and added to the master problem for the solution of the next iteration of the expansion planning problem. This iterative process will continue until a secure plan is achieved.

The optimal operation subproblem is used to check the minimum cost of solution. This subproblem checks the optimality by calculating the upper bound of the original MIP planning problem's objective function and comparing it with its lower bound, which is already calculated in the master problem. If the proposed plan is not optimal, Benders cuts will be formed and added to the master problem for solving the next iteration.

### *C. TS*

TS is used in both subproblems to minimize the operating costs as well as the transmission security violations. The TS binary variables are determined in the master problem and treated as constants in the subproblems. The utilization of TS states in the proposed cuts will help utilize candidate generating units and transmission lines in the planning options. The switchable line states appear as variables in the master problem, but they are governed by dual values in the subproblems.

### *D. Cuts*

In the proposed approach two types of cuts are used. The first one is a feasibility cut which is generated in the security check subproblem. The feasibility cut indicates that the security violations can be mitigated by readjusting the investment plan in each planning year as well as the state of switchable lines in the operation periods. This cut represents the coupling of the proposed investment plan and adjustments in the state of switchable lines. The dual variables in the feasibility cut are the incremental reduction in the load balance violations. The second one is an optimality cut that is generated in the optimal operation subproblem. The optimality cut would limit the range of master problem objective to make it closer to the objective function of the expansion planning problem calculated prior to the decomposition. The optimality cut indicates that the objective value of the expansion planning problem can be decreased by modifying the investment plan in addition to the state of switchable lines. Similar to the feasibility cut, this cut represents the coupling of adjustments in the proposed investment plan and the state of switchable lines. The dual variables in the optimality cut are the incremental reduction in the objective function of the optimal operation subproblem.

### *E. Solution Procedure*

The binary switching variables in the master problem are governed by Benders cuts generated in the subproblems. On the other hand, the switching variables affect the investment plans. So the solution of the larger time scale is guided by the smaller time scale problem, and the solution of the smaller time scale problem is guided by the cuts produced at each iteration. The planning solution procedure is given as follows.

1) Solve the planning master problem by considering candidate generating units and transmission lines. There will be no Benders cut in the first iteration of the master problem.
2) Given the proposed plan in the master problem, check the feasibility of system constraints. If the subproblem is feasible, proceed to Step 3. Otherwise, form the Benders cut and return to the master problem.
3) Minimize the operating cost by considering the system constraints. Compare the solution value, i.e., an upper bound, with the objective of master problem, i.e. a lower bound. If the difference is larger than a predefined threshold, form the Benders cuts and return to the master problem for the next iteration. Otherwise, consider the proposed plan as optimal.

## III. Problem Formulation

The objective of the expansion planning problem is to minimize the total cost of the system while satisfying the system security and reliability constraints. The total cost includes the investment cost of new generating units and transmission lines plus the system operating cost. This objective is formulated as (1), and is subject to planning and operation constraints.

$$\begin{aligned} Min \quad PP = & \sum_{t=1}^{NT}\sum_{i=1}^{CG}\frac{CI_{it}(X_{it}-X_{i(t-1)})}{(1+d)^{(t-1)}} \\ & +\sum_{t=1}^{NT}\sum_{j=1}^{CL}\frac{CI_{jt}(Y_{jt}-Y_{j(t-1)})}{(1+d)^{(t-1)}} \\ & +\sum_{t=1}^{NT}\sum_{b=1}^{NB}\sum_{i=1}^{NG}\frac{DT_{bt}OC_{ibt}PG_{ibt}}{(1+d)^{(t-1)}} \end{aligned} \tag{1}$$

The solution of this problem would determine the size, the location, and the time for adding new generating units and transmission lines in an economical way that ensures the system capability to meet the anticipated load growth in the future. Using the Benders decomposition, the problem is decomposed into a master problem and two subproblems. The master problem provides the optimal plan and the subproblems provide solutions for the security check and the optimal operation.

### A. Optimal Plan

The objective of the optimal investment planning problem is to minimize the investment cost of new generating units and transmission lines.

$$Min \quad MP$$

$$MP \ge \sum_{t=1}^{NT}\sum_{i=1}^{CG}\frac{CI_{it}(X_{it}-X_{i(t-1)})}{(1+d)^{(t-1)}}+\sum_{t=1}^{NT}\sum_{j=1}^{CL}\frac{CI_{jt}(Y_{jt}-Y_{j(t-1)})}{(1+d)^{(t-1)}} \tag{2}$$

This objective is subject to the planning constraints (3)-(12). The generating unit constraints include capital investment funds in a planning year (4), anticipated resource capacity in a planning year (5), maximum number of generating units to be added at a planning year (6), and the construction time of the candidate investment (7). Similarly, the transmission line constraints are capital investment funds in a planning year (9), anticipated transmission line capacity in a planning year (10), maximum number of transmission lines to be added at a planning year (11), and the construction time of the candidate investment (12). Constraint (3) specifies that once a generating unit is in place, its investment state will be 1 in the following years. The same constraint exists for transmission lines, which is presented by (8).

$$X_{i(t-1)} \le X_{it} \qquad (i=1,...,NCG)(t=2,...,NT) \tag{3}$$

$$\sum_{i=1}^{CG} CI_{it}(X_{it}-X_{i(t-1)}) \le GCI_t \qquad (t=1,...,NT) \tag{4}$$

$$\sum_{i=1}^{CG} Cap_i(X_{it}-X_{i(t-1)}) \le GUC_t \qquad (t=1,...,NT) \tag{5}$$

$$\sum_{i=1}^{CG} (X_{it}-X_{i(t-1)}) \le GUN_t \qquad (t=1,...,NT) \tag{6}$$

$$X_{it} = 0 \ \text{if} \ t < GCT_i \qquad (i=1,...,NCG)(t=1,...,NT) \tag{7}$$

$$Y_{j(t-1)} \le Y_{jt} \qquad (j=1,...,NCL)(t=2,...,NT) \tag{8}$$

$$\sum_{j=1}^{CL} CI_{jt}(Y_{jt}-Y_{j(t-1)}) \le LCI_t \qquad (t=1,...,NT) \tag{9}$$

$$\sum_{j=1}^{CL} Cap_j(Y_{jt}-Y_{j(t-1)}) \le LUC_t \qquad (t=1,...,NT) \tag{10}$$

$$\sum_{j=1}^{CL} (Y_{jt}-Y_{j(t-1)}) \le LUN_t \qquad (t=1,...,NT) \tag{11}$$

$$Y_{jt} = 0 \ \text{if} \ t < LCT_j \qquad (j=1,...,NCL)(t=1,...,NT) \tag{12}$$

The master problem will determine the optimal investment plan and the lower bound for the original MIP planning problem. The optimality cuts will help minimize investment and operation costs in the master problem. The states of switchable transmission lines are also examined in this problem. Here, the Benders cuts provide the state of switchable lines to the master problem.

### B. Security Check

Given the proposed plan in the master problem, as well as the state of switchable lines, the security check subproblem minimizes the potential system violations. This task is accomplished by introducing slack variables in the power balance equation at each bus. The objective is to minimize the sum of non-negative slack variables.

$$Min \quad v_t = \sum_{b=1}^{NB}\sum_{h=1}^{NH}(SL_{hbt,1}+SL_{hbt,2}) \tag{13}$$

$$\sum_{i\in I_h} PG^{E}_{ibt} + \sum_{i\in I_h} PG^{C}_{ibt} - PD_{hbt} - \sum_{j\in J_h} PL^{E}_{jbt} - \sum_{j\in J_h} PL^{C}_{jbt} + SL_{hbt,1} - SL_{hbt,2} = 0 \tag{14}$$

$$(h=1,...,NH)(b=1,...,NB)(t=1,...,NT)$$

Equation (14) shows the power mismatch at bus *h*. In this equation, existing and candidate lines are shown with superscripts *E* and *C*, respectively. Set $J_h$ includes the lines connected to bus *h* which are labeled as either the 'to bus' or the 'from bus' in the set.

This problem is subject to existing and candidate generating unit and transmission line constraints. These constraints represent the capacity of existing and candidate generating units (18)-(19), existing transmission line flows (20)-(23), candidate transmission line flows (24)-(27), and phase angle of reference bus (28).

$$X_{it} = \hat{X}_{it} \qquad (i=1,...,NCG)(t=1,...,NT) \tag{15}$$

$$Y_{jt} = \hat{Y}_{jt} \qquad (j=1,...,NCL)(t=1,...,NT) \tag{16}$$

$$Z_{jbt} = \hat{Z}_{jbt} \qquad (j=1,...,NEL)(b=1,...,NB)(t=1,...,NT) \tag{17}$$

$$0 \le PG^{E}_{ibt} \le PG^{\max,E}_{i} UX^{E}_{ibt} \qquad (i=1,...,NEG)(b=1,...,NB)(t=1,...,NT) \tag{18}$$

$$0 \le PG^{C}_{ibt} \le PG^{\max,C}_{i} X_{it} UX^{C}_{ibt} \qquad (i=1,...,NCG)(b=1,...,NB)(t=1,...,NT) \tag{19}$$

$$PL^{E}_{jbt} - \gamma_j(\delta^{E}_{mbt} - \delta^{E}_{nbt}) - M^{E}_{j}(1 - Z_{jbt}) - M^{E}_{j}(1 - UY^{E}_{jbt}) \le 0 \quad (j = 1,..., NEL)(b = 1,..., NB)(t = 1,..., NT) \tag{20}$$

$$PL^{E}_{jbt} - \gamma_j(\delta^{E}_{mbt} - \delta^{E}_{nbt}) + M^{E}_{j}(1 - Z_{jbt}) + M^{E}_{j}(1 - UY^{E}_{jbt}) \ge 0 \quad (j = 1,..., NEL)(b = 1,..., NB)(t = 1,..., NT) \tag{21}$$

$$PL^{E}_{jbt} \le PL^{\max,E}_{j} Z_{jbt} UY^{E}_{jbt} \quad (j = 1,..., NEL)(b = 1,..., NB)(t = 1,..., NT) \tag{22}$$

$$-PL^{E}_{jbt} \le PL^{\max,E}_{j} Z_{jbt} UY^{E}_{jbt} \quad (j = 1,..., NEL)(b = 1,..., NB)(t = 1,..., NT) \tag{23}$$

$$PL^{C}_{jbt} - \gamma_j(\delta^{C}_{mbt} - \delta^{C}_{nbt}) - M^{C}_{j}(1 - Y_{jt}) - M^{C}_{j}(1 - UY^{C}_{jbt}) \le 0 \quad (j = 1,..., NCL)(b = 1,..., NB)(t = 1,..., NT) \tag{24}$$

$$PL^{C}_{jbt} - \gamma_j(\delta^{C}_{mbt} - \delta^{C}_{nbt}) + M^{C}_{j}(1 - Y_{jt}) + M^{C}_{j}(1 - UY^{C}_{jbt}) \ge 0 \quad (j = 1,..., NCL)(b = 1,..., NB)(t = 1,..., NT) \tag{25}$$

$$PL^{C}_{jbt} \le PL^{\max,C}_{j} Y_{jt} UY^{C}_{jbt} \quad (j = 1,..., NCL)(b = 1,..., NB)(t = 1,..., NT) \tag{26}$$

$$-PL^{C}_{jbt} \le PL^{\max,C}_{j} Y_{jt} UY^{C}_{jbt} \quad (j = 1,..., NCL)(b = 1,..., NB)(t = 1,..., NT) \tag{27}$$

$$\delta_{ref} = 0 \tag{28}$$

In the above formulation, the constraints on candidate generating units and transmission lines include the associated binary variable, which is already determined in the master problem. The state of switchable transmission lines is included in the existing transmission flow constraints (20)-(23). So, whenever a transmission line is switched off its associated switchable state is zero and the transmission line will be completely removed from the network. A subset of existing transmission lines is usually considered as switchable. Therefore, for the remaining and non-switchable lines the switching state (binary variable) will be equal to 1 in the expansion planning problem. The transmission line $j$ is between buses $m$ and $n$ with a transmission flow from bus $m$ to bus $n$. In constraints (20), (21), (24) and (25), a large constant value, i.e. $M$, is used to satisfy the relaxation of associated constraints when they would be eliminated. This disjunctive parameter would be larger than a minimum value and should not be very large. The solution of the planning problem is sensitive to the value of this parameter, where in [45] it is shown that large values of disjunctive parameter could limit the validity of the Benders decomposition results. In [21], an effective approach is presented to calculate this parameter, where the disjunctive parameter is increased along the Benders iterations. However in this paper, it is assumed that the disjunctive parameter of each line has a constant value, which is equal to its minimum allowable value. In Appendix, the minimum allowable values of disjunctive parameters are calculated for transmission lines.

The security check subproblem is solved for the base case and contingencies. During the contingencies, transmission lines can operate at their emergency ratings. So, $PL_j^{max}$ will be adjusted accordingly. The contingency state of the element that is on outage will be zero. In the base case, this parameter will be one. The security check subproblem performs corrective actions to mitigate the violations. Those contingencies that cannot be mitigated with corrective actions are dealt with by preventive actions in the next iteration of the master problem.

If the proposed objective is zero, the problem will proceed to the optimal operation subproblem. Otherwise, the Benders cut (29) will be formed and added to the master problem for the next iteration.

$$v_t + \left\{ \begin{array}{l} \left| \sum_{i=1}^{CG} \lambda_{it}(X_{it} - \hat{X}_{it}) + \sum_{j=1}^{CL} \mu_{jt}(Y_{jt} - \hat{Y}_{jt}) \right| \\ \left| + \sum_{j=1}^{NS} \sum_{b=1}^{NB} \pi_{jbt}(Z_{jbt} - \hat{Z}_{jbt}) \right| \end{array} \right\} \le 0 \tag{29}$$

where $\lambda$, $\mu$, and $\pi$ are dual values of constraints (15), (16) and (17), respectively. This cut points out that the stated violations could be mitigated by changing the investment plan in addition to the state of switchable lines. In fact, this cut calculates the capacity signals for the investment of new generating units and transmission lines in case the existing ones cannot satisfy the system feasibility. The Benders cut will be formed for each violated case and added to the master problem. The iterative procedure continues until a secure plan that satisfies the system feasibility is achieved in the base case and contingencies.

### *C. Optimal Operation*

After satisfying the feasibility of the plan due to system constraints, the optimal operation will check the optimality of the solution cost. The objective of the optimal operation problem is to minimize the operating cost for every year and load block as

$$Min \quad w_{bt} = \sum_{i=1}^{NG} \frac{DT_{bt} OC_{ibt} PG_{ibt}}{(1 + d)^{(t-1)}} \tag{30}$$

This objective is subject to (15)-(28). The problem is solved for the base case in which contingency parameters are equal to 1. The solution provides the upper bound of the objective function of expansion planning. This upper bound is used to check the optimality of the solution. So the stopping criterion is defined based on this solution. If the proposed plan is not optimal, a Benders cut will be formed and added to the master problem for the next iteration. The proposed Benders cut (31) would restrict the lower bound of objective function in the master problem. Here, $\lambda$, $\mu$, and $\pi$ are dual values of (15), (16), and (17), respectively.

The iterative process between the master problem and subproblems will continue until an optimal solution of the expansion planning problem is calculated. The problem feasibility is ensured via the security check subproblem, while the optimality is guaranteed by comparing the solutions of the master problem and the optimal operation subproblem at each iteration. The solution of the master problem is the lower bound of the optimal solution. The upper bound of the optimal solution is found by using the results of optimal operation subproblem. The optimal solution is obtained when lower and upper bounds are close enough. These bounds are utilized to form an effective convergence criterion in (32).

$$MP \geq \sum_{t=1}^{NT}\sum_{b=1}^{NB} \hat{w}_{bt} + \sum_{t=1}^{NT}\sum_{i=1}^{CG} \frac{CI_{it}(X_{it} - X_{i(t-1)})}{(1+d)^{(t-1)}} + \sum_{t=1}^{NT}\sum_{j=1}^{CL} \frac{CI_{jt}(Y_{jt} - Y_{j(t-1)})}{(1+d)^{(t-1)}} + \sum_{t=1}^{NT}\sum_{i=1}^{CG} \lambda_{it}(X_{it} - \hat{X}_{it}) + \sum_{t=1}^{NT}\sum_{j=1}^{CL} \mu_{jt}(Y_{jt} - \hat{Y}_{jt}) + \sum_{t=1}^{NT}\sum_{j=1}^{NS}\sum_{b=1}^{NB} \pi_{jbt}(Z_{jbt} - \hat{Z}_{jbt}) \quad (31)$$

$$\frac{PP - MP}{PP + MP} < \varepsilon \quad (32)$$

The planning stage is performed yearly while the operation stage is carried out for load blocks. The contingencies would last for the entire load block in a year. However, there are no limitations on the length of load blocks which can be chosen as any period of time from hours to months. The choice will be a tradeoff between the accuracy and the simplicity in the execution of the proposed model. However, the choice of load blocks would play an important role in the proposed model. This issue will be addressed in our future study.

## IV. Numerical Simulations

Three case studies consisting of a six-bus system, the IEEE 118-bus system and an 1168-bus system are analyzed. The proposed method was implemented on a 2.4-GHz personal computer using CPLEX.

### *A. Six-Bus System*

The six-bus system is shown in Fig. 2. A 10-year planning horizon is considered. The system data for generating units and transmission lines are given in Tables I and II, respectively. In Table III the forecasted yearly peak load is listed. This load is distributed at the rate of 40%, 30% and 30% among buses 3, 4 and 5, respectively. To simplify the calculations, four load blocks are considered annually. The duration and quantity of load blocks in the first year are given in Table IV. The load blocks in subsequent years will change in proportion to those in Year 1. A set of 4 candidate generating units and 4 candidate transmission lines are considered as planning options in Tables I and II. The construction time for generating units is considered to be 3 years, while it is less than one year for the transmission lines. It is assumed that there are no annual limitations on capital investments or the number of generating units and transmission lines. The discount rate is assumed to be 0. Three transmission lines 1-4, 2-4, and 4-5 are considered as switchable in the following four planning cases:

Case 1: Base case planning
Case 2: Transmission line 5-6 outage in load block 3 of year 4
Case 3: Generating unit 3 outage in load block 1 of year 6
Case 4: Simultaneous outages considered in Cases 2 and 3

The cases are discussed next.

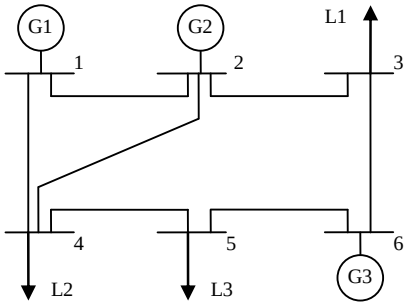


Fig. 2 Six-bus system

TABLE I
GENERATING UNIT DATA OF SIX-BUS SYSTEM

| Unit No. | Bus No. | Generating Capacity (MW) | Investment Cost ($/kW) | Operation Cost ($/MWh) |
|---|---|---|---|---|
| 1 | 1 | 100 | Existing | 15 |
| 2 | 2 | 100 | Existing | 18 |
| 3 | 6 | 50 | Existing | 23 |
| 4 | 1 | 100 | 200 | 15 |
| 5 | 2 | 80 | 270 | 21 |
| 6 | 2 | 60 | 250 | 24 |
| 7 | 3 | 20 | 250 | 24 |

TABLE II
TRANSMISSION LINE DATA OF SIX-BUS SYSTEM

| Line No. | From Bus | To Bus | X (p.u.) | Capacity (MW) | Investment Cost ($/kW) |
|---|---|---|---|---|---|
| 1 | 1 | 2 | 0.17 | 80 | Existing |
| 2 | 2 | 3 | 0.037 | 70 | Existing |
| 3 | 1 | 4 | 0.258 | 140 | Existing |
| 4 | 2 | 4 | 0.197 | 100 | Existing |
| 5 | 4 | 5 | 0.037 | 50 | Existing |
| 6 | 5 | 6 | 0.14 | 140 | Existing |
| 7 | 3 | 6 | 0.018 | 130 | Existing |
| 8 | 1 | 2 | 0.17 | 80 | 20 |
| 9 | 2 | 3 | 0.037 | 70 | 24 |
| 10 | 1 | 4 | 0.258 | 140 | 30 |
| 11 | 5 | 6 | 0.14 | 140 | 14 |

TABLE III
YEARLY PEAK LOAD FORECAST OF SIX-BUS SYSTEM

| Year | 1 | 2 | 3 | 4 | 5 |
|---|---|---|---|---|---|
| Peak (MW) | 209 | 225 | 231 | 243 | 269 |
| Year | 6 | 7 | 8 | 9 | 10 |
| Peak (MW) | 297 | 307 | 315 | 324 | 330 |

TABLE IV
LOAD BLOCKS IN THE FIRST YEAR

| Block | 1 | 2 | 3 | 4 |
|---|---|---|---|---|
| Duration (h) | 87 | 2541 | 4380 | 1752 |
| Load (MW) | 209 | 192 | 167 | 150 |

**Case 1:** The 10-year expansion planning is considered without considering the TS. According to this plan, line 2-3 is installed in the first year. Also, generating units 6 and 7 are added in years 5 and 8, respectively. At the first year, existing units 1,2,3 try to satisfy the system load while maintaining the feasibility of transmission flows. Here, cheaper units 1 and 2

are dispatched at their maximum capacity and the remaining load is supplied by unit 3. However, due to the congestion of line 2-3, unit 2 cannot increase its generation to its capacity. So the more expensive unit 3 would increase its generation, which increases the operating cost. Accordingly, the candidate line 2-3 is installed at the first year. This installation leads to an increase in the transmission capacity between buses 2 and 3, which allows unit 2 to increase its generation to its capacity in subsequent years.

The new system topology satisfies the system load while the system load is less than the total installed capacity in the system, i.e., years 1-4. In year 5 the system would need to install a new generation capacity to help satisfy the additional load. So, unit 6 is placed at bus 2 which can transfer more power in conjunction with the installation of line 2-3. Two options (i.e. either candidate unit 5 or 6) are available for the installation of a unit in bus 2. Unit 5 is more economical while unit 6 requires a less investment cost. Considering the remaining 5 years, the algorithm chooses unit 6. Similarly in year 8, another unit is installed. The cheapest generating candidate from the operation viewpoint is unit 4, and the one from the planning viewpoint is unit 7. However, considering the remaining two years in the planning horizon, unit 7 is selected as being more economical. In this case, unit 5 is not a good option since the larger generation in bus 2 may lead to the congestion on line 2-3. The total cost in this case is $366.3M.

TABLE V
CANDIDATE UNIT INSTALLATION YEAR OF SIX-BUS SYSTEM

| Candidate Unit | Case 1 | Case 2 | Case 3 | Case 4 |
|---|---|---|---|---|
| 4 | - | 5 | 6 | 6 |
| 5 | - | - | - | - |
| 6 | 5 | - | - | - |
| 7 | 8 | - | 5 | 5 |

TABLE VI
CANDIDATE UNIT INSTALLATION YEAR OF SIX-BUS SYSTEM USING TS

| Candidate Unit | Case 1 | Case 2 | Case 3 | Case 4 |
|---|---|---|---|---|
| 4 | 5 | 5 | 6 | 6 |
| 5 | - | - | - | - |
| 6 | - | - | - | - |
| 7 | - | - | 5 | 5 |

TABLE VII
CANDIDATE LINE INSTALLATION YEAR OF SIX-BUS SYSTEM

| Candidate Line | Case 1 | Case 2 | Case 3 | Case 4 |
|---|---|---|---|---|
| 1-2 | - | - | 6 | - |
| 2-3 | 1 | 1 | 1 | 1 |
| 1-4 | - | 7 | 6 | 6 |
| 5-6 | - | 4 | - | 4 |

TABLE VIII
CANDIDATE LINE INSTALLATION YEAR OF SIX-BUS SYSTEM USING TS

| Candidate Line | Case 1 | Case 2 | Case 3 | Case 4 |
|---|---|---|---|---|
| 1-2 | - | - | - | - |
| 2-3 | 1 | 1 | 1 | 1 |
| 1-4 | 9 | 7 | 6 | 6 |
| 5-6 | - | 4 | - | 4 |

The TS application in Case 1 will result in a different expansion plan, where unit 4 is installed at year 5 and lines 2-3 and 1-4 are installed at years 1 and 9, respectively. The installation of line 2-3 at year 1 will again relieve the congestion on line 2-3 and increase the dispatchability of units at buses 1 and 2. At year 5, unit 4 is chosen when the system needs to install additional generation capacity. This unit is the most economical candidate unit from operation viewpoint. With the installation of unit 4 at bus 1, most of the system load will be supplied. The additional dispatch at bus 1 would lead to an increase in line flows with a possible congestion. TS is used to mitigate the congestion. For example when the load in year 5 is higher than 215 MW, the feasibility constraints cannot be satisfied. The constraints are satisfied with the switching of line 2-4. Here, the total cost is dropped by 5.56% to $345.9M.

**Case 2:** In this case, the outage of line 5-6 in year 4 is considered. Similar to Case 1, line 2-3 is installed at year 1. With the possible outage of line 5-6, the installation of candidate line 5-6 will be necessary. Furthermore, the candidate line 1-4 is installed in year 7 with the largest investment cost among candidate lines. However, the line will enhance the dispatch of energy generated by cheap units at bus 1. The total cost in this Case is $347.9M which is higher than that in Case 1.

Using TS, a similar expansion plan is proposed, i.e., the installation of unit 4 at year 5 and lines 2-3, 1-4, and 5-6 in years 1, 7, and 4, respectively. The line switching does not change the proposed plan in this case. However, the total cost is reduced to $346.4M. The lower total cost is mainly due to the switching of line 2-4. When the line is switched off, the flows on lines 1-2 and 1-4 will be less dependent on one another. So both lines can transfer more power, which would result in the additional dispatch of units at bus 1. Since the cheapest units are at bus 1, the additional dispatch of these units will reduce the total cost.

**Case 3:** The outage of unit 3 at year 6 would change the proposed plan in Case 1. Like previous cases, new generation capacity is added at year 5. The proposed plan requires the installation of unit 7 at year 5 and subsequently unit 4 at year 6. The installation of unit 4 would increase the installed capacity. Also, unit 7 is added to satisfy the loads in buses 3 and 5. The installation of unit 7 is a preventive action to handle the outage of unit 3. The installed lines are 1-2, 2-3 and 1-4 in years 6, 1 and 6, respectively. Line 2-3 is installed to increase the dispatchability of units at buses 2 and 3, while lines 1-2 and 1-4 are installed to enhance the dispatchability of units at bus 1. The TS application would eliminate the previous installation of line 1-2 at year 6. The previous line flow violations that required the installation of line 1-2 are alleviated by the switching of lines 2-4 and 4-5. The total cost is $350.6M, which is 0.4% cheaper when using TS. This improvement is due to the elimination of candidate line 1-2 in the planning horizon as well as a decrease in the operating cost. This study demonstrates that the application of TS could result in a similar but cheaper expansion planning.

**Case 4:** The expansion plan will not be influenced by TS when

considering simultaneous outages of line 5-6 in year 4 and unit 3 in year 6. The expansion plan includes the installation of unit 4 at year 6, unit 7 at year 5, and lines 2-3, 1-4 and 5-6 at years 1, 6, and 4, respectively. The installation of unit 7 is a preventive action for the possible outage of unit 3, while the installation of line 11 is a preventive action for the possible outage of line 5-6. The TS application will not alter the proposed expansion plan, but will reduce the total cost by 0.5%.

### *B. IEEE 118-Bus System*

A modified IEEE 118-bus system is used to study the expansion planning problem with TS. The system has 118 buses, 54 units and 186 branches. The data is given in motor.ece.iit.edu/data/Planning_118.xls. The candidate units and lines data are presented in Tables IX and X, respectively. The load growth rate is at 7%. The following three cases are analyzed:

Case 1: Base case planning

Case 2: Effect of discount rate on the planning solution

Case 3: Effect of the number of switchable lines on the planning solution

In Cases 1 and 3, the discount rate is assumed to be 10%, while in Case 2 the discount rate is changed to investigate its effect on the planning solution. In Cases 1 and 2 the effect of TS on planning is analyzed, where ten lines are considered as switchable. The list of these switchable lines is presented in Table XI. In Case 3 the planning problem is solved for a variable number of switchable lines.

TABLE IX
CANDIDATE UNIT DATA OF IEEE 118-BUS SYSTEM

| Unit No. | Bus No. | Generating Capacity (MW) | Investment Cost ($/kW) | Operation Cost ($/MWh) |
|---|---|---|---|---|
| 1 | 10 | 200 | 15 | 250 |
| 2 | 12 | 200 | 15 | 250 |
| 3 | 25 | 200 | 15 | 250 |
| 4 | 26 | 200 | 15 | 250 |
| 5 | 80 | 200 | 15 | 250 |
| 6 | 89 | 200 | 15 | 250 |
| 7 | 18 | 100 | 18 | 120 |
| 8 | 32 | 100 | 18 | 120 |
| 9 | 55 | 100 | 18 | 120 |
| 10 | 56 | 100 | 18 | 120 |
| 11 | 62 | 100 | 18 | 120 |
| 12 | 74 | 20 | 38 | 50 |
| 13 | 74 | 20 | 38 | 50 |
| 14 | 90 | 20 | 38 | 50 |
| 15 | 103 | 20 | 38 | 50 |
| 16 | 103 | 20 | 38 | 50 |

TABLE X
CANDIDATE TRANSMISSION LINE DATA OF IEEE 118-BUS SYSTEM

| Line No. | From Bus | To Bus | X (p.u.) | Capacity (MW) | Investment Cost ($/kW) |
|---|---|---|---|---|---|
| 1 | 30 | 38 | 0.054 | 100 | 30 |
| 2 | 77 | 82 | 0.0853 | 100 | 30 |
| 3 | 110 | 111 | 0.0755 | 100 | 30 |
| 4 | 20 | 21 | 0.0849 | 100 | 30 |
| 5 | 17 | 113 | 0.0301 | 100 | 30 |

TABLE XI
SWITCHABLE LINE DATA OF IEEE 118-BUS SYSTEM

| Switchable Line No. | Line No. | From Bus | To Bus | X (p.u.) | Capacity (MW) |
|---|---|---|---|---|---|
| 1 | 30 | 23 | 24 | 0.0492 | 100 |
| 2 | 54 | 30 | 38 | 0.0540 | 100 |
| 3 | 65 | 47 | 49 | 0.0625 | 100 |
| 4 | 115 | 70 | 75 | 0.1410 | 100 |
| 5 | 151 | 80 | 97 | 0.0934 | 100 |
| 6 | 159 | 99 | 100 | 0.0813 | 100 |
| 7 | 164 | 100 | 104 | 0.2040 | 100 |
| 8 | 78 | 54 | 56 | 0.0096 | 100 |
| 9 | 90 | 60 | 61 | 0.0135 | 500 |
| 10 | 184 | 12 | 117 | 0.1400 | 100 |

**Case 1:** The base case planning for the IEEE-118 bus system is solved as a coordinated generation and transmission expansion planning problem. At first we disregard the TS option. The proposed plan is shown in Tables XII and XIII for unit and line installations, respectively. In the first four years of planning, loads are satisfied and there is no need to install any new units or lines. The installed generation capacity of the system is 5,850 MW. In these four years, the congestion occurs in lines 8 and 96. However at year 5, due to the congestion in line 38 the system cannot satisfy its load, though the system has enough installed capacity. To alleviate this congestion and transfer the required power to the loads, the candidate units 2 and 4 are installed. The installations will mitigate the congestion of lines 8, 96 and 38 and the system will be able to meet the load. At the subsequent years 6 and 7, candidate units 5 and 3 are installed, respectively.

TABLE XII
CANDIDATE UNIT INSTALLATION YEAR FOR IEEE 118-BUS SYSTEM IN CASE 1

| Candidate Unit | Ignoring TS | Considering TS |
|---|---|---|
| 1 | - | 7 |
| 2 | 5 | 5 |
| 3 | 7 | 6 |
| 4 | 5 | - |
| 5 | 6 | 5 |
| 6 | - | - |
| 7 | - | - |
| 8 | 10 | - |
| 9 | 9 | 10 |
| 10 | 10 | 10 |
| 11 | - | 10 |
| 12 | 10 | 10 |
| 13 | 10 | 10 |
| 14 | 10 | 10 |
| 15 | - | - |
| 16 | - | - |

TABLE XIII
CANDIDATE LINE INSTALLATION YEAR FOR IEEE 118-BUS SYSTEM IN CASE 1

| Candidate Line | Ignoring TS | Considering TS |
|---|---|---|
| 1 | 7 | - |
| 2 | - | - |
| 3 | - | - |
| 4 | - | - |
| 5 | 10 | - |

The installation of unit 5 at year 6 offers physical and economical advantages. On the other side, the installation of unit 3 at year 7 will mitigate the congestion in lines 31, 38 and 51. The candidate units 2, 4 and 5 represent expensive investments, but are necessary to provide sufficient generation capacity and transmission flow feasibility. Also the candidate line 1 is installed at year 7 to mitigate the congestion. Accordingly, there will be no need to install new components at year 8. However, at year 9 the candidate unit 9 is installed and subsequently the units 8, 10, 12, 13 and 14 are installed at the last planning year. Also, the candidate line 5 is installed to increase the transfer capacity of the system. Considering the results, we conclude that the system is well-designed and the transmission lines offer a sufficient capacity to transfer the generated power most often.

TS provides quite different results. The candidate units 5 and 3 are installed one year earlier. The candidate units 4 and 8 are not installed and instead units 1 and 11 are installed at years 7 and 10, respectively. Also, the installation of unit 9 is delayed by one year, while the installation of other candidate units is remained the same, i.e. unit 2 is installed at year 5 and units 10, 12, 13 and 14 are installed at year 10. Accordingly, the generation investment cost is decreased by 0.35%. The use of TS eliminates the line investment in this case, as shown in Table XIII. Also, TS enhances the power transfer capability by allowing existing transmission lines to transfer additional power. Here, the lines 7, 8, 9 and 36 are congested at years 7 to 10. Also line 96 is congested at years 1 to 5. The TS applications at certain load blocks will mitigate the congestions and enhances the system feasibility. Accordingly, the operating cost of the system is slightly increased. However, the proposed TS plan will reduce the total cost by 0.04%. As noted in the Introduction, TS may defer generation and transmission investments. Considering the obtained results, the installation of candidate unit 9 is deferred, while the candidate units 3 and 5 are installed earlier than the base case solution.

**Case 2:** The sensitivity of the proposed plan to the discount rate is investigated. Generally, the discount rate is used in the calculation of the net present value and capacity payment for new generating unit and transmission line investments. It is clear when the discount rate is higher the investment candidates with higher capital costs become inferior. In the real world, investors may use different discount rates in their planning studies which would depend on their financial situation and business strategies. However, in this case the discount rate is assumed to be the same for all candidate units and lines. The discount rates of 10%, 5% and 0% are considered. The candidate units and lines are the same as those of Case 1.

The plan with a 10% discount rate was obtained in Case 1. By decreasing the discount rate to 5%, it is expected that the candidate units with higher capital costs, i.e. units 1 to 6, become inferior. So, units 1 and 3 are not installed and installation of unit 5 is delayed by one year. However, Table XIV shows that cheaper units are installed in this case, in which the units 7 and 8 are installed at year 10 and units 9 and 10 are planned at year 9. In addition, similar to the 10% discount solution, there would be no need to install new transmission lines when TS is applied and the discount rate is 5%. Accordingly, the investment cost and total planning cost are increased by 14.4% and 0.63%, respectively.

If we further decrease the discount rate and set it to zero, a quite different investment plan, as shown in last column of Table XIV, will be obtained. The discount rate of 0% means that there is no difference on the installation year of the candidate unit or line, since the investment cost will not change with time.

From the optimization viewpoint, all units are installed at the first year that they are required. Again using TS, there is no requirement for new transmission line investments, since TS satisfies the system feasibility. In comparison with the 10% discount rate, the investment cost and the total planning cost are increased by 47.8% and 1.36%, respectively when the discount rate is assumed to be zero.

TABLE XIV
CANDIDATE UNIT INSTALLATION YEAR FOR IEEE 118-BUS SYSTEM IN CASE 2

| Candidate Unit | Discount Rate (%) | | |
|---|---|---|---|
| | 10 | 5 | 0 |
| 1 | 7 | - | - |
| 2 | 5 | 4 | 4 |
| 3 | 6 | - | - |
| 4 | - | 5 | 4 |
| 5 | 5 | 6 | 4 |
| 6 | - | - | - |
| 7 | - | 10 | 4 |
| 8 | - | 10 | 4 |
| 9 | 10 | 9 | 4 |
| 10 | 10 | 9 | 4 |
| 11 | 10 | 10 | 4 |
| 12 | 10 | 10 | 4 |
| 13 | 10 | 10 | 4 |
| 14 | 10 | 10 | 4 |
| 15 | - | - | - |
| 16 | - | - | - |

**Case 3:** In order to examine the impact of TS on the planning results more comprehensively, the expansion planning problem in Case 1 is solved for a variety of switchable lines. The number of switchable lines is varied here form 0 to 40, which 0 means that no line in the system has the switching capability, and 40 means that more than one fifth of transmission system is considered as switchable. Discount rate of 10% is considered for all cases.

The installation year of candidate units as a function of the number of switchable lines is shown in Table XV. The investment plan is a function of the number of switchable lines. However, no transmission line is installed when TS is applied. The investment cost is shown in Fig. 3. This figure shows that the investment cost is a function of the number of switchable lines. In the case of the no line switching capability, the investment cost includes the installation costs of units and lines; however, with the TS capability, the investment cost is only that of unit installations.

The operating cost of the system is shown in Fig. 4. By increasing the number of switchable lines from 0 to 30, the operating cost is decreased. However, the operating cost of the 40 switchable lines is higher than that of 30.

TABLE XV
CANDIDATE UNIT INSTALLATION YEAR FOR IEEE 118-BUS SYSTEM IN CASE 3

| Candidate Unit | Number of Switchable Lines | | | | |
|---|---|---|---|---|---|
| | 0 | 10 | 20 | 30 | 40 |
| 1 | - | 7 | 5 | 5 | 7 |
| 2 | 5 | 5 | 7 | 7 | 5 |
| 3 | 7 | 6 | 6 | 6 | - |
| 4 | 5 | - | - | - | 6 |
| 5 | 6 | 5 | 5 | 5 | 5 |
| 6 | - | - | - | - | - |
| 7 | - | - | - | - | - |
| 8 | 10 | - | - | - | - |
| 9 | 9 | 10 | 10 | 10 | 10 |
| 10 | 10 | 10 | 10 | 10 | 10 |
| 11 | - | 10 | 10 | 10 | 10 |
| 12 | 10 | 10 | - | 10 | - |
| 13 | 10 | 10 | 10 | 10 | - |
| 14 | 10 | 10 | 10 | 10 | 10 |
| 15 | - | - | - | - | - |
| 16 | - | - | - | - | - |

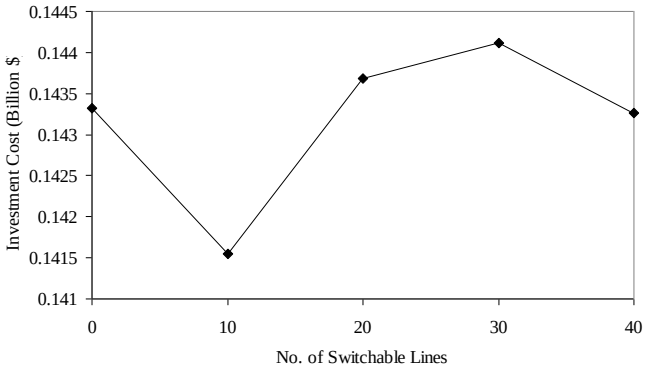


Fig. 3 Investment cost in Case 3

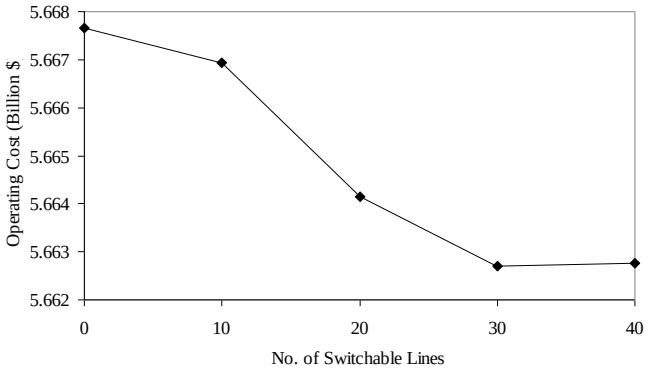


Fig. 4 Operating cost in Case 3

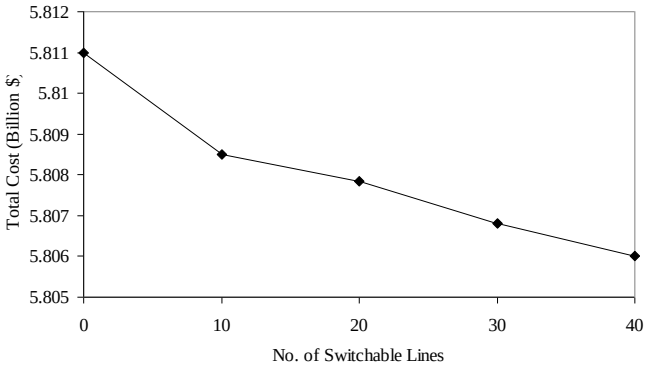


Fig. 5 Total planning cost in Case 3

So, by increasing the number of switchable lines the operating cost of the system does not decrease monotonically.

The objective of the investment planning problem is to minimize the total planning cost, which is the sum of the investment and the operating costs. The total cost is depicted in Fig. 5. As expected, by increasing the number of switchable lines, the total cost is decreased uniformly. The reduction in the total planning cost for 10, 20, 30 and 40 switchable lines, as compared to the case with no switching, is 0.043%, 0.054%, 0.072% and 0.086%, respectively. These increments would amount to large savings in the case of large-scale power systems.

### *C. 1168-Bus System*

As a large-scale power system, the 1168-bus system is used to compare the effectiveness of the proposed decomposition approach with that of the integrated model. This system has 149 units, 1474 branches, and 568 demand sides. 20 units are considered as candidate investments. The discount rate for candidate units is assumed to be 10%. The transmission flow limit is increased to alleviate the need for any transmission expansions. To obtain the solution in a reasonable time a planning horizon of three years is considered. 100 transmission lines are assumed to be switchable. The total planning costs as a function of execution time is depicted in Fig. 6. The solution of the integrated model is achieved using the CPLEX, where the total planning cost is the best current integer solution of the problem. In the decomposed model the total planning cost is the upper bound of the MIP planning problem, i.e. current solution of the decomposed problem.

As shown in Fig. 6, the integrated model finds a better solution initially, and is better than that of decomposed model for the next 14 hours. Also, it reaches a near optimal solution in just 3.5 hours. However, this near optimal solution cannot be improved further. On the other hand, the decomposed model would require an additional computation time but is able to reach a cheaper solution. After 15 hours, the solution of the decomposed model is 0.17% better than that of the integrated model. We continued with the execution of the two models for another 12 hours and learned that the solution of the integrated model did not change. However, the duality gap of the CPLEX solution continued to drop which is because of the increment in the best current node of the solution.

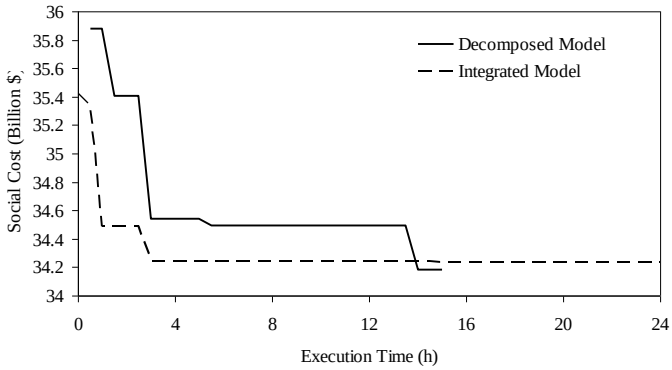


Fig. 6 Comparison of integrated and decomposed planning models

## V. Conclusions

The TS application was investigated in the expansion planning of power systems. The expansion planning problem was decomposed into a master problem and two subproblems. The master problem found the optimal expansion plan by considering candidate units and lines. The subproblems utilized the proposed plan to satisfy the feasibility and check the possibility of optimal operation. The TS application for enhancing the system security and economics was considered in the subproblems while the role of TS for enhancing the expansion plan was taken into account in the master problem. The proposed approach was analyzed further through numerical examples introduced in the paper. The proposed TS approach can be utilized as an ISO model for coordinating the transmission expansion planning with the competitive generation capacity planning by representing an iterative process for representing the interactions among generation companies, transmission companies and the ISO, while considering the switching capability of lines.

## Appendix

Suppose that we have the following conditional statement,

$$\text{If } v = 1 \text{ then } \sum_i a_i x_i = b \,, \tag{A1}$$

where $v$ is a binary variable, $x_i$ is a continuous variable, and $a_i$ and $b$ are constant parameters. To model this statement in MIP format (A2) and (A3) are used.

$$\sum_i a_i x_i - b \le M\,(1 - v) \tag{A2}$$

$$\sum_i a_i x_i - b \ge m\,(1 - v) \tag{A3}$$

Similarly, if we have the following conditional statement

$$\text{If } v = 0 \text{ then } \sum_i a_i x_i = b \,, \tag{A4}$$

We can represent (A5) and (A6) in the MIP format,

$$\sum_i a_i x_i - b \le Mv \tag{A5}$$

$$\sum_i a_i x_i - b \ge mv \tag{A6}$$

The constant values $M$ and $m$ are disjunctive parameters of the associated inequality constraint. Usually, $M$ would not be less a specific value which is given as

$$M = \max \left\{ \sum_i a_i x_i - b \right\} \tag{A7}$$

Similarly, $m$ should not be larger than a specific value

$$m = \min \left\{ \sum_i a_i x_i - b \right\} \tag{A8}$$

So, $M$ and $m$ are upper and lower bounds of the expression $\sum_i a_i x_i - b$, respectively.

These MIP representations of conditions can simply be extended to cases with more than one binary variable. The proposed formulations for line flows, considering the installation state and switching state as binary variables, are obtained similarly. So, disjunctive parameters of line flow constraints are

$$M_j^E = 2\,PL_j^{\max,\,E} \tag{A9}$$

$$m_j^E = -2\,PL_j^{\max,\,E} \tag{A10}$$

$$M_j^C = 2\,PL_j^{\max,\,C} \tag{A11}$$

$$m_j^C = -2\,PL_j^{\max,\,C} \tag{A12}$$

## References


[1] M. Shahidehpour, H. Yamin, and Z. Y. Li, *Market Operations in Electric Power Systems*. New York: Wiley, 2002.

[2] A.J. Conejo, E. Castillo, R. Mínguez, and R. García-Bertrand, *Decomposition Techniques in Mathematical Programming*, Springer, 2006.

[3] R. Bacher and H. Glavitsch, "Network topology optimization with security constraints," *IEEE Trans. Power Syst.*, vol. 1, pp. 103-111, Nov. 1986.

[4] G. Schnyder and H. Glavitsch, "Integrated security control using an optimal power flow and switching concepts," *IEEE Trans. Power Syst.*, vol. 3, pp. 782-790, May 1988.

[5] G. Schnyder and H. Glavitsch, "Security enhancement using an optimal switching power flow," *IEEE Trans. Power Syst.*, vol. 5, pp. 674-681, May 1990.

[6] J. G. Rolim and L. J. B. Machado, "A study of the use of corrective switching in transmission systems," *IEEE Trans. Power Syst*., vol. 14, pp. 336-341, Feb. 1999.

[7] W. Shao and V. Vittal, "Corrective switching algorithm for relieving overloads and voltage violations," *IEEE Trans. Power Syst*., vol. 20, no. 4, pp. 1877-1885, Nov. 2005.

[8] G. Granelli, M. Montagna, F. Zanellini, P. Bresesti, R. Vailati and M. Innorta, "Optimal network reconfiguration for congestion management by deterministic and genetic algorithms," *Electr. Power Syst. Res.*, vol. 76, pp. 549-556, Apr. 2006.

[9] R. P. O'Neill, R. Baldick, U. Helman, M. H. Rothkopf, and W. Stewart, "Dispatchable transmission in RTO markets," *IEEE Trans. Power Syst.*, vol. 20, no. 1, pp. 171–179, Feb. 2005.

[10] E. B. Fisher, R. P. O'Neill, and M. C. Ferris, "Optimal transmission switching," *IEEE Trans. Power Syst.*, vol. 23, no. 3, pp. 1364-1355, Aug. 2008.

[11] K. W. Hedman, R. P. O'Neill, E. B. Fisher, S. S. Oren, "Optimal transmission switching – sensitivity analysis and extensions," *IEEE Trans. Power Syst.*, vol. 23, no. 3, pp. 1469-1479, Aug. 2008.

[12] K. W. Hedman, R. P. O'Neill, E. B. Fisher and S. S. Oren, "Optimal transmission switching with contingency analysis," *IEEE Trans. Power Syst.*, vol. 24, no. 3, pp. 1577-1586, Aug. 2009.

[13] L. L. Garver, "Transmission network estimation using linear programming," *IEEE Trans. Power App. Syst*., vol. PAS-89, no. 7, pp.1688–1697, Sept./Oct. 1970.

[14] S. T. Y. Lee, K. L. Hocks, and E. Hnyilicza, "Transmission expansion of branch-and-bound integer programming with optimal cost-capacity curves," *IEEE Trans. Power App. Syst.*, vol. PAS-93, pp. 1390–1400, Aug. 1974.

[15] J. Choi, A. A. El-Keib and T. Tran, "A fuzzy branch and bound-based transmission system expansion planning for the highest satisfaction level of the decision maker," *IEEE Trans. Power Syst*, vol. 20, pp. 476-484, Feb. 2005.

[16] J.Choi, T.Tran, A. A. El-Keib, R. Thomas, H.S. Oh and R. Billinton, " A method for transmission expansion system expansion planning considering probabilistic reliability criteria," *IEEE Trans. Power Syst*., vol. 20, pp. 1606-1615, Aug. 2005.

[17] M. Lu, Z. Y. Dong and T. K. Saha, "A Framework for Transmission Planning in a Competitive Electricity Market," *Transmission and Distribution Conference and Exhibition*, Asia and Pacific, pp. 1-6, Aug. 2005.

[18] G. B. Shrestha and P. A. J. Fonseka, "Congestion-driven transmission expansion in competitive power markets," *IEEE Trans. Power Syst.*, vol. 19, pp. 1658-1665, Aug. 2004.

[19] O. B. Tor, A. N. Guven, M. Shahidehpour, "Congestion-Driven Transmission Planning Considering the Impact of Generator Expansion," *IEEE Trans. Power Syst.*, vol. 23, no.2, pp. 781-789, May. 2008.

[20] R. Romero A. Monticelli , "A zero-one implicit enumeration method for optimizing investments in transmission expansion planning," *IEEE Trans. Power Syst.*, vol. 9, pp. 1385–1391, Aug. 1994.
[21] S. Binato, M. V. Pereira, and S. Granville, "A new benders decomposition approach to solve power transmission network design problems," *IEEE Trans. Power Syst.*, vol. 16, pp. 235–240, May 2001.
[22] P. Sánchez-Martín, A. Ramos and J. F. Alonso, " Probabilistic Midterm Transmission Planning in a Liberalized Market," *IEEE Trans. Power Syst.*, vol. 20, no. 4, pp. 2135-2142, Nov. 2005.
[23] E. L. Silva, H. A. Gil, and J. M. Areiza, "Transmission network expansion planning under an improved genetic algorithm," *IEEE Trans. Power Syst.*, vol. 15, pp. 1168–1175, Aug. 2000.
[24] H. B. Sun and D. C. Yu, "A multiple-objective optimization model of transmission enhancement planning for independent transmission company (ITC)," in Proc. *IEEE Power Eng. Soc. Transmission and Distribution Conf*, Jul. 2000, vol. 4, pp. 2033-2038.
[25] A. S. D. Braga and J. T. Saraiva, "A multiyear dynamic approach for transmission expansion planning and long-term marginal costs computation," *IEEE Trans. Power Syst.*, vol. 20, pp. 1631-1639, Aug. 2005.
[26] M. S. Kandil, S. M. El-Debeiky and N. E. Hasanien, "A hybrid mathematical and rule-based system for transmission network planning in a deregulated environment," in Proc. *IEEE Power Eng. Soc. Transmission and Distribution Conf.*, Jul. 2001, pp. 1451-1456.
[27] N. Yang and F. S. Wen, "A chance constrained programming approach to transmission system expansion planning," *Electric Power Systems Research*, vol. 75, pp. 171-177, Aug. 2005.
[28] J. Contreras and F. F. Wu, "Coalition formation in transmission expansion planning," *IEEE Trans. Power Syst.*, vol. 14, pp. 1144-1152, 1999.
[29] T. De la Torre, J. W. Feltes, T. G. S. Roman and H. M. Merril, "Deregulation, privatization, and competition: Transmission planning under uncertainty," *IEEE Trans. Power Syst.*, vol. 14, pp. 460-465, May 1999.
[30] E. E. Sauma and S. S. Oren, "Economic Criteria for Planning Transmission Investment in Restructured Electricity Markets," *IEEE Trans. Power Syst.*, vol. 22, no.4, pp. 1394-1405, 2007.
[31] M. Buygi, G. Balzer, H. Shanechi, and M. Shahidehpour, "Market-Based Transmission Expansion Planning", *IEEE Trans. Power Syst.*, vol. 19, no. 4,2060-2067, Nov. 2004
[32] M. O. Buygi, M. Shahidehpour, H. M. Shanechi and G. Balzer, "Market based transmission expansion planning: Stakeholders' desires," in Proc. 2004 *IEEE Int. Conf: on Electric Utility Deregulation, Restructuring and Power Technologies*, vol. 2, pp. 433-438.
[33] M. O. Buygi, M. Shahidehpour, H. M. Shanechi and G. Balzer, "Market based transmission planning under uncertainties," *Int. Conf: on Probabilistic Methods Applied to Power Syst.*, pp. 563-568, Sep. 2004.
[34] M. O. Buygi, M. Shahidehpour, H. M. Shanechi and G. Balzer, "Market based transmission expansion planning: Fuzzy risk assessment," in Proc. 2004 *IEEE Int. Conf: on Electric Utility Deregulation, Restructuring and Power Technologies*, vol. 2, pp. 427-432.
[35] J. Buechler, "Transmission planning in a market based environment," In Proc. 2005 *IEEE Power Eng. Soc. General Meeting*, pp.1850-1852.
[36] J. H. Roh, M. Shahidehpour, and Y. Fu, "Security-Constrained Resource Planning in Electricity Markets," *IEEE Trans. Power Syst.*, Vol. 22, No. 2, pp. 812-820, May 2007.
[37] J.H. Roh, M. Shahidehpour and Y. Fu, "Market-Based Coordination of Transmission and Generation Capacity Planning," *IEEE Trans. Power Syst.*, Vol. 22, No. 4, pp.1406-1419, Nov. 2007.
[38] E. Sauma and S. Oren, "Proactive Planning and Valuation of Transmission Investments in Restructured Electricity Markets," *Journal of Regulatory Econ*., Vol. 30, pp261-290, Sep. 2006.
[39] S. de la Torre, A.J. Conejo and J. Contreras, "Transmission expansion planning in electricity markets," *IEEE Trans. Power Syst*., vol. 23, no. 1, pp. 238-248, Feb. 2008.
[40] L.P. Garces, A.J. Conejo, R. Garcia-Bertrand and R. Romero, "A bilevel approach to transmission expansion planning within a market environment" *IEEE Trans. Power Syst*., vol. 24, no. 3, pp. 1513-1522, Aug.. 2009.
[41] M. Shahidehpour and Y. Fu, "Benders Decomposition," *IEEE Power and Energy Magazine*, Vol. 3, No. 2, pp. 20-21, March 2005.
[42] M. Shahidehpour and V. Ramesh, "Nonlinear programming algorithms and decomposition strategies for OPF," in *IEEE/PES Tutorial on Optimal Power Flow*. Piscataway, NJ: IEEE Press, 1996.
[43] H. Ma and M. Shahidehpour, "Transmission constrained unit commitment based on benders decomposition," *Elect. Power Energy Syst.*, vol. 20, no. 4, pp. 287–294, Apr. 1998.
[44] A. M. Geoffrion, "Generalized Benders decomposition," *J. Optim Theory Appl.*, vol. 10, no. 4, pp. 237–261, 1972.
[45] Granville S, Pereira MVF, "Analysis of the linearized power flow model in Benders decomposition." *Technical Report* SOL 85-04, *Stanford University*; 1985.

## BIOGRAPHIES

**Amin Khodaei** obtained the B.S. degree in electrical engineering from University of Tehran, Tehran, Iran, in 2005 and M.S. degree in electrical engineering from Sharif University of Technology, Tehran, Iran, in 2007. He is currently a Ph.D. student in the Electrical and Computer Engineering Department at the Illinois Institute of Technology, Chicago. His research interests include operation and economics of power systems.

**Mohammad Shahidehpour** (F'01) is Carl Bodine Distingusihed Professor in the Electrical and Computer Engineering Department at Illinois Institute of Technology, Chicago. He is an Honorary Professor at Sharif University of Technology and the North China Electric Power University. He is the recipient of the 2009 Honorary Doctorate from the Polytechnic University of Bucharest. Dr. Shahidehpour is the VP of Publications for the IEEE Power & Energy Society.

**Saeed Kamalinia** (M'07) received the BS and MS in E.E. from University of Tehran, Iran, in 2005 and 2007, respectively. Presently, he is pursuing a Ph.D degree at Illinois Institute of Technology, USA. His research interests include restructured power system generation and transmission planning.

# Promoting the Investment on IPPs for Optimal Grid Planning

Osman Bulent Tor, *Student Member, IEEE,* Ali Nezih Guven, *Senior Member, IEEE*
Mohammad Shahidehpour, *Fellow, IEEE*

***Abstract*—This paper presents a transmission expansion planning (TEP) model which coordinates investment decisions in monopolistic transmission and decentralized generator sectors. The proposed planning approach gauges transmission congestion and security constraints with respect to transmission investments while promoting investments on independent power produces (IPPs) through incentive payments. The paper includes discussions on incentive mechanisms and prioritization among qualified IPPs for several planning scenarios. Such incentives might be necessary to trigger investments on IPPs earlier than those projected by the decentralized generation system, when the power system security is threatened. The proposed planning approach would optimize the sum of transmission investments, incentive payments to IPPs, and congestion costs along the planning horizon. The case studies illustrate how the proposed planning algorithm could be utilized in order to determine incentive payments to candidate generators when necessary, and prioritize such incentives among multiple IPP candidates.**

***Index Terms* - Transmission expansion planning, IPP investments, incentive payments, transmission security, transmission congestion.**

## NOMENCLATURE

| | |
|---|---|
| $b$ | Index for subperiod |
| $d$ | Discount rate |
| $i$ | Index for generator (existing and candidate) |
| $k$ | Index for line (from bus $m$ to bus $n$) |
| $q$ | Single contingency index |
| $t$ | Year index |
| $CL$ | Number of candidate transmission lines |
| $NCG$ | Number of candidate generators |
| $NS$ | Number of subperiods |
| $NT$ | Number of planning year |
| $CI_{kt}$ | Capital investment cost of transmission line $k$ in year $t$ ($/yr) |
| $R_{C,ibt}$ | Forecasted energy sales price of candidate IPP $i$ at subperiod $b$ in year $t$ ($/MWh) |
| $\alpha_i$ | Profit coefficient of IPP $i$ (%) |
| $CI_{it}$ | Capital investment cost of IPP $i$ in year $t$ ($/yr) |
| $P_{GC,ibt}$ | Dispatched capacity of candidate generator $i$ at subperiod $b$ in year $t$ (MW) |
| $IP_{it}$ | Incentive payment required by IPP $i$ in year $t$ ($/yr) |
| $OC_{GC,ibt}$ | Operating costs of candidate IPP $i$ at subperiod $b$ in year $t$ ($/MWh) |
| $AOCC_{bt}$ | Additional operation cost due to congestion at subperiod $b$ in year $t$ ($/yr) |
| $X_{it}$ | Installation status of candidate generator of IPP $i$ in year $t$, 1 if installed, otherwise 0 |
| $X_{kt}$ | Investment status of candidate line $k$ in year $t$ |

O.B. Tor is with the Power Systems Department of TUBITAK UZAY, METU Campus, Ankara, 06531, Turkey (e-mail: osman.tor@uzay.tubitak.gov.tr). A.N. Guven is with the Department of Electrical and Electronics Engineering, Middle East Technical University, Ankara, 06531, Turkey (e-mail: guven@metu.edu.tr). M. Shahidehpour is with the Department of Electrical and Computer Engineering, Illinois Institute of Technology, Chicago, IL, 60616, USA (e-mail: ms@iit.edu).

## I. INTRODUCTION

The liberalization and restructuring processes worldwide have introduced new complexities to the transmission expansion problem (TEP) [1]-[5]. This movement has introduced competition at the two extreme points of the industry infrastructure (i.e., generation and retailing) while keeping transmission and distribution sectors as natural monopolies. TEP is presented as a process which is decoupled from generation and distribution planning despite their natural and indispensable dependencies. This means that, in some ways, the transmission network will have to solicit users' involvement both at the generation and the demand sides which would introduce a new level of the TEP uncertainty.

This paper presents a new model for the coordination of TEP and decentralized generation investment planning. The model gauges the level of transmission congestion and security with respect to transmission investments while promoting generation investments through incentive payments to mitigate the operation risks when necessary. For the purpose of maintaining the system security such incentives which would trigger generation investments could be paid earlier than the IPPs' projected investment date.

The generation capacity market and the institution of capacity signals have been a controversial issue in the electricity industry restructuring. Many experts argue that the capacity mechanism is essential for encouraging the investment in the new capacity [6]. In theory, energy and ancillary services markets should provide incentives for such investments. However, most peaking units may not recover their fixed costs of investment without market price spikes. Thus, significant price volatilities may be necessary to make such investments feasible in the absence of capacity payments [7]. Given the political realities of electricity markets, prices may fluctuate insufficiently to induce investments when the available capacity is tightened; then an explicit capacity mechanism would be needed to signal capacity shortages and induce investments on generation [8].

The coordination between transmission and generation resource planning was addressed previously. Roh *et al* proposed a model that brings transmission and electricity

market into the sphere of long-term generation resource planning [9]. Security payments to generation companies (GENCOs) by the ISO are proposed for supplying the load and satisfying the network security. The study shows that a proper expansion of transmission capacity could lower the ISO's security payment to GENCOs. Our planning approach considers this fact inherently by coordinating transmission and generation planning decisions. Botterud *et al* presented a stochastic dynamic generator investment model which offers a comprehensive treatment of long-term uncertainties and their influence on optimal generator investment decisions [10]. The proposed model assesses optimal investment strategies when the increase in demand, and thereby future prices, are uncertain. However, it considers only the generator investment decision and ignores its close linkage with transmission expansion. The interaction between transmission and generation in TEP was also investigated recently in [11]. The objective of TEP is to maximize the social welfare based on a valuation methodology outlined as proactive transmission network planning. It is assumed that network planner anticipates the way that generation investment and operations would react.

This study proposes an enhancement to the planning model given in [12] by considering incentive payments to IPPs to trigger generation investments when necessitated by the system security. The proposed coordinated planning model in [12] provides the best combination of transmission and generation investment planning, although there is no guarantee that profit-making IPPs will follow the proposed options which would maximize the social-welfare. Our approach is unique as it proposes an incentive mechanism to IPPs that considers this situation within a coordinated transmission planning problem.

Fig. 1 depicts the flowchart of the proposed method. The main distinction in this study is the integration of the IPP investment planning decisions with TEP when considering the system security in long-term planning studies. Thus generator investments which contribute to the optimal system planning (considering the network security) but might be delayed by IPPs for various reasons are considered in the proposed planning algorithm by including incentive mechanisms. For example, those IPPs which are essential for maintaining the system security during on-peak periods might require additional incentives due to the insufficient dispatch of their units during off-peak periods. We propose such an incentive mechanism within the context of coordinated planning performed by a central entity, which is assumed to be a state-owned transmission company. Accordingly, the planning concern as to whether profit-making IPPs will follow the coordinated planning option is taken into account in this paper.

The rest of the paper is organized as follows. The proposed planning model and the solution methodology are described in Section II which also presents the IPPs' investment problem and the interaction between the transmission company and IPPs during the planning process. Section III presents the case study of a two-bus system which enables easy understanding of the contribution of this paper, and application of the approach to modified IEEE 30 bus system. Prioritization among multiple IPPs that qualified for incentive payment and determination of the incentive mechanism are also discussed in Section III. The conclusion drawn from the study is provided in Section IV.

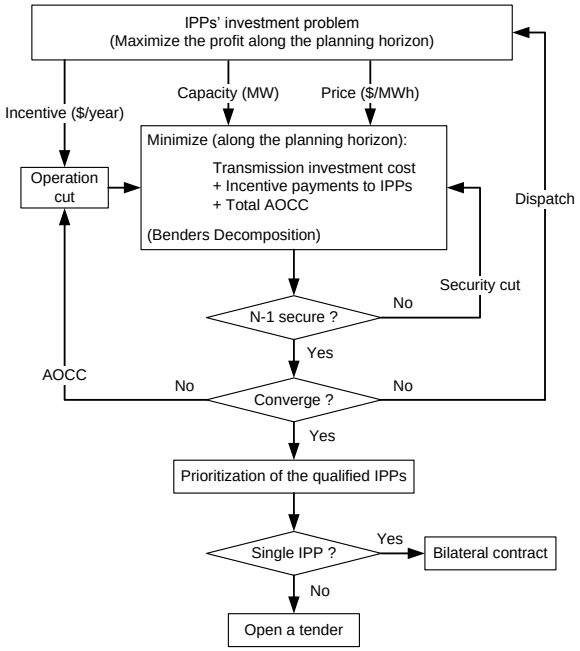


Fig. 1. Integration of IPPs' investment planning decisions with TEP

## II. Planning Model and Incentive Mechanism

### A. Centralized Transmission Expansion Planning Problem

The objective of the proposed planning problem is to optimize the transmission investment cost, the incentive payments to IPPs which contribute to the optimal solution, and the total additional operation cost due to congestion (AOCC), in the planning horizon while satisfying the system security based on the single contingency (i.e., N-1) criterion. The objective function is formulated as

$$Min \left\{ \sum_{t=1}^{NT} \sum_{k=1}^{CL} \left\lceil \frac{CI_{kt} * X_{kt}}{(1+d)^{(t-1)}} \right\rceil + \sum_{t=1}^{NT} \sum_{i=1}^{NCG} \frac{IP_{it} * X_{it}}{(1+d)^{(t-1)}} + \sum_{t=1}^{NT} \sum_{b=1}^{NS} \frac{AOCC_{bt}}{(1+d)^{(t-1)}} \right\} \quad (1)$$

where AOCC is the difference between generation dispatch costs when ignoring and considering transmission constraints along the planning horizon. The objective function is decomposed into security and operation problems and the DC power flow model [13] is utilized in the formulation of Benders cuts as illustrated in Fig. 1. Security cuts ensure the load curtailment criteria while meeting the N-1 contingency along the planning horizon. On the other hand, operation cuts force the planning algorithm to search for a better solution that would result in more economic dispatch solutions (i.e., minimize the AOCC). Thereby, transmission investment cost, congestion cost and incentive payments to the qualified IPPs are optimized iteratively. Here, the generator investment costs in the planning algorithm proposed in [12] are replaced by incentive payments to IPPs.

### B. Decentralized Generator Investment Planning Problem

The main objective of a generation planning problem executed by IPPs (i.e., non-utility generators) is to maximize the profit based on investments. A generation investment project is profitable if the discounted project return is positive. The internal rate of return (IRR) is a popular concept for measuring the discounted project returns [14].

It is assumed here that there are no coupling constraints among IPPs for investment decisions. Accordingly, the investment planning problem of IPP for each generation candidate is to maximize the profit based on the corresponding investment along the planning horizon:

$$Max \left\{ \sum_{t=1}^{NT} \sum_{b=1}^{NS} \frac{DT_{bt}}{(1+d)^{(t-1)}} * \begin{pmatrix} R_{C,ibt} * P_{GC,ibt} \\ -OC_{GC,it} * P_{GC,ibt} \end{pmatrix} - \sum_{t=1}^{NT} \frac{CI_{it} * X_{it}}{(1+d)^{(t-1)}} \right\} \quad (2)$$

where $R_{C,ibt} = \alpha_i * OC_{GC,ibt}$ (3)

### C. Incentive Requirement of IPPs

An investment decision for a specific IPP depends on its forecasted profit, which is a function of expected energy production (2). For a fixed energy sale price, $R_C$, the expected profit depends solely on the energy production. If an IPP could forecast the level of energy sales (i.e., dispatch level) for a predefined level of energy sale price, then its investment decision would be as simple as calculating the IRR based on procurements. Therefore, the expected dispatch level is a critical component of a candidate's investment decision which gives an important signal to the IPPs on their forecasted energy price. The IPP would presumably make no investments unless its deficiency is compensated. Essentially, the correct time for making any investment is when the discounted project return is positive. Accordingly, the minimum incentive payment required by candidate *i* in year *t* is assumed to be the difference between the annual investment and the expected profit form energy sales stated as

$$IP_{it} = \frac{CI_{it} * X_{it}}{(1+d)^{(t-1)}} - \sum_{b=1}^{NS} \frac{DT_{bt}}{(1+d)^{(t-1)}} * \begin{pmatrix} R_{C,ibt} * P_{GC,ibt} \\ -OC_{GC,it} * P_{GC,ibt} \end{pmatrix} \quad (4)$$

When (4) is negative, the investments are profitable, the required incentive is assumed to be zero, and the IPP's investment could manipulate the mechanism.

The proposed incentive mechanism may encourage IPPs to game the market by manipulating the incentives and requiring additional payments. However, the additional incentives will be rejected by the proposed algorithm if an alternative option is available. Such alternatives may include either transmission enforcements or the selection of another IPP with more reasonable incentive requirements. The selection of more economical alternatives among candidates is made possible by Benders cuts. On the other hand, when alternative candidates are not available (due to locational importance), an IPP whose commitment is critical to the system security may essentially abuse the situation. That is, security cuts generated during the iterative planning process may force such investments regardless of their costs (i.e., incentive requirements). The proposed planning model can be utilized by the authorities to identify such opportunities by applying sensitivity analyses and investigating the impact of energy prices on planning alternatives.

### D. Interaction between Transmission Company and IPPs

In the proposed approach, each IPP provides the energy sale price of the corresponding generation investment to the ISO. The ISO calculates the expected economic dispatch along the planning horizon. Accordingly, each IPP determines its annual incentive requirements for investments. These incentive requirements are utilized as payments in determining the operation cuts which are iteratively included as constraints of the objective problem (1). The interaction between the transmission company and IPPs which is managed by the ISO is illustrated in Fig. 2. Fig. 1 shows a more detailed information exchange which continues until an optimal planning solution is found.

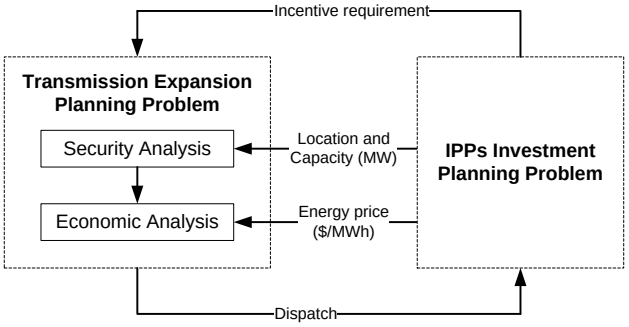


Fig. 2. Information exchange between the transmission company and IPPs

## III. Case Studies

The case studies include a two-bus system and the IEEE 30-bus system as discussed below.

### A. Two-bus system

The two-bus system depicted in Fig. 3 shows two generators that can supply the loads at two different buses. It is assumed that G1, which is located at a distance from the large load at Bus 2, is cheaper than G2 (i.e., closer unit). The solid lines correspond to existing transmission lines and the dashed lines correspond to the transmission reinforcement. The dashed generator at Bus 2 corresponds to a candidate investment by an IPP. The annual load growth rate is 5% at Bus 1 and 8% at Bus 2. The transmission investment cost is 800 $/MW-mile. A 5% annual interest rate based on a 10-year loan is utilized to calculate the annual capital investment for transmission line and generator.

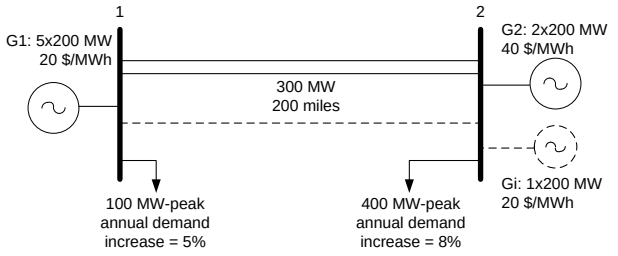


Fig. 3. Two-bus system

The generation investment data are given in Table 1.

Provided that the candidate generator is operated at full capacity (i.e., 8,760*200=1,752 GWh per year), the discounted annual profit based on its investment is approximately 2 $M/year. The profit will decrease along the planning horizon if the unit is operated at less than the full capacity.

TABLE 1
TWO-BUS SYSTEM CANDIDATE GENERATOR DATA ($G_I$)

| Capacity (MW) | Capital investment cost ($M/MW) | Forecasted energy sale price ($/MWh) | Profit in energy sales (%) |
|---|---|---|---|
| 200 | 0.75 | 20 | 60 |

The following cases are studied for the two-bus system:

*Case 1 – Without Promoting IPP Investment*

The TEP problem is solved without considering the candidate generator. According to the given demand forecasts, the total demand to be supplied in two buses will be approximately 1,025 MW in year 10. The existing generators could not supply this demand unless the transmission line enforcement would take place. The planning problem in this case will only determine the optimal timing for transmission investment. The TEP results are given in Table 2. The transmission enforcement will take place in year 7 despite the congestion in year 6. It is obvious as the $6.09M AOCC in year 6 is smaller than the annual transmission investment (i.e., $6.11M). On the other hand, given the high annual peak demand increase, the AOCC would be $14.9M unless the transmission investment would take place in year 7. The 25 MW of total demand is supplied by the expensive generator G2 in year 10 since G1 is already fully loaded. According to the definition, the total AOCC is zero in year 10.

*Case 2 - Promoting the IPP Investment*

The candidate generator investment at Bus 2 is considered. Table 3 shows that the transmission line enforcement is deferred by 4 years provided that the candidate generation investment is procured in year 7. Although the candidate generator is fully loaded in year 10, the transmission investment mitigates the possible congestion by enabling the dispatch of cheaper generator G1. The $6.09M AOCC is again due to the congestion in year 6 as in Case 1. The annual incentives to trigger generation investments are given in Table 4. Since no generation dispatch is required in years 1-6, the incentive requirement is the same as the annual capital cost of the generator. The incentives provided in years 7 and 8 would compensate the IPP's deficit which is due to low dispatch. Note that even though the energy sale prices of the existing generator G1 and candidate generator Gi are the same, the dispatch priority is given to G1. It is assumed that the existing generator G1 already has long-term contracts and therefore deserves the priority, which is a reasonable assumption.

TABLE 2
TWO-BUS SYSTEM - CASE 1 RESULTS

| Transmission investment | TTIC * ($M) | AOCC ($M) | TC ** ($M) |
|---|---|---|---|
| Year 7 | 24.44 | 6.09 | 30.53 |

* TTIC: Total transmission investment cost
** TC: Total cost along the planning horizon

TABLE 3
TWO-BUS SYSTEM CASE 2 RESULTS

| Transmission investment year | Generator investment year | TTIC ($M) | TIP* ($M) | AOCC ($M) | TC ($M) |
|---|---|---|---|---|---|
| 10 | 7 | 6.11 | 14.44 | 6.09 | 26.64 |

* TIP: Total incentive payment to the IPP

TABLE 4
TWO-BUS SYSTEM CASE 2 INCENTIVE PAYMENTS

| Year | 1-6 | 7 | 8 | 9 | 10 |
|---|---|---|---|---|---|
| Dispatch (MW) | 0 | 85.53 | 140.37 | 199.6 | 200 |
| Incentive payment ($M) | 19.1 | 10.1 | 4.34 | 0 | 0 |
| Investment status of Gi * | 0 | 1 | 1 | 1 | 1 |

* If installed: 1, otherwise: 0

This example shows the effectiveness of promoting the generation investments in the optimal TEP. The incentive payments are required to trigger generation investments earlier than envisaged by IPPs. When there are multiple candidate generators, those which contribute significantly to the system security and optimal operation are given the priority. The security and operational cuts in the proposed planning approach satisfy this criterion when considering the marginal effects of generation investments on the system security and optimal operation.

Table 5 compares the results of Cases 1 and 2 from the consumers' viewpoint in which Case 2 provides a more economic solution. The difference in the total cost between the two cases is $3.89M from the transmission company's viewpoint (see Tables 2 and 3) and $8.52M from the consumers' viewpoint (see Table 5).

TABLE 5
TWO-BUS SYSTEM - CONSUMER POINT OF VIEW

| Case | TIRC * ($M) | TEC ** ($M) | TC ($M) |
|---|---|---|---|
| 1 | 24.44 | 1426.14 | 1450.58 |
| 2 | 20.55 | 1421.51 | 1442.06 |

* TIRC: Total investment related cost (TTIC + TIP)
** TEC: Total energy cost

In Case 1, the dispatch of expensive generator G2 is inevitable in the last year as G1 is fully dispatched and there is no other supplier available. Although the AOCC by definition is zero in year 10, the operation of G2 increases the cost to consumers by $8.52M - $3.89M = $4.63M. Consequently, the utilization of AOCC approach provides the optimal planning solution while assessing the annual investment/profit against congestion cost.

One of the transmission planner's main concerns in promoting multiple market players is the inability to institute a fair incentive mechanism in the market. In the example, G2 at Bus 2 might consider that the incentives will provide unfair advantages to Gi when contributing to the transmission system security. Indeed, both G2 and Gi have the same marginal effects on security, although Gi contributes to the economic dispatch additionally. On the other hand, if G2 benefits from the promotion as well, then the cost of planning may not be optimal.

The Gi in Case 2 deserves an incentive due to its contribution to the system security and optimal operation. Before proposing an incentive plan, it is better to analyze the two-bus example further. Table 4 shows that the additional cost of energy due to the incentive payment in year 7 is 13.48 $/MWh (i.e., $10.1M/85.53MW/8760h). Accordingly, the

breakpoint energy sale price for the IPP's investment on Gi in year 7 is 33.48 $/MWh (i.e., 20 + 13.48). In order to be fair, a tender could be opened in the initial year to buy 85.53 MW x 8760h ≈ 750GWh energy at 33.48 $/MWh in year 7 and 140.37MW x 8760 h ≈ 1230GWh at 23.53 $/MWh in year 8. If the existing generator G2 signs a contract to sell energy at those predefined prices, then there would be no need to promote the investment. It should be noted that this amount of advance energy purchase agreement with G2 will delay the transmission enforcement by 2 years unless the investment of G2 takes place in year 9. On the other hand, the IPP is expected to make the investment. Otherwise G2 will hold its market power unless the transmission enforcement would take place.

Given the feasibility of investing on Gi in year 7 with additional incentives, the existing generator G2 is clearly competitive as its energy sale price (40 $/MWh) is higher than that of Gi even after paying the incentive (i.e., 33.48 $/MWh). So our approach not only ensures the system security but also enables the appraisal at expected energy sale prices. Thereby, the regulatory authority would have additional ideas on the competition level and market power.

This simple example illustrates how the candidate investments, which contribute to the planning problem (1) at most, are successfully selected by the proposed planning methodology. In a specific case when several IPPs are willing to invest in a same bus, the operation cut considers the incentive payments to all candidate generators as well as investment cost of transmission lines and AOCC. This is essential as the candidate generators willing to connect to the same bus will have the same incremental contribution to the security (i.e., load curtailment). Note that, the candidate generator Gi in the simple 2-Bus example deserves an incentive payment despite that G2 is connected to the same bus. The reason is that the contribution of Gi to reducing the AOCC is higher than its incentive requirement along the planning horizon. The next example illustrates the performance of the proposed approach when there is more than one candidate generator considered for investment.

### *B. IEEE 30-Bus system*

The proposed planning approach is applied to the modified IEEE 30-bus system, depicted in Fig. 4, to analyze the performance of the proposed approach when there are several candidate generators. The existing transmission grid satisfies the single contingency security criterion at the initial year. The possible transmission enforcements are shown in Fig. 4. The initial set of candidate transmission lines are determined based on preliminary load flow analyses. The lines which are loaded more than 50% in the initial year are selected as candidates for investment. The initial grid consists of 50 transmission lines, 15 candidate transmission lines, 21 demand buses, 7 existing power plants and 8 candidate generators. The length of each transmission line (in miles) is indicated in Fig. 4. Buses with relatively higher load densities are indicated by bold arrows. The modified IEEE 30-bus system data which include transmission lines, generators, and forecasted load are given in http://motor.ece.iit.edu/Data/IEEE_30bus_modified.xls. It is assumed for simplicity that the construction time for each transmission lines or generator is one year.

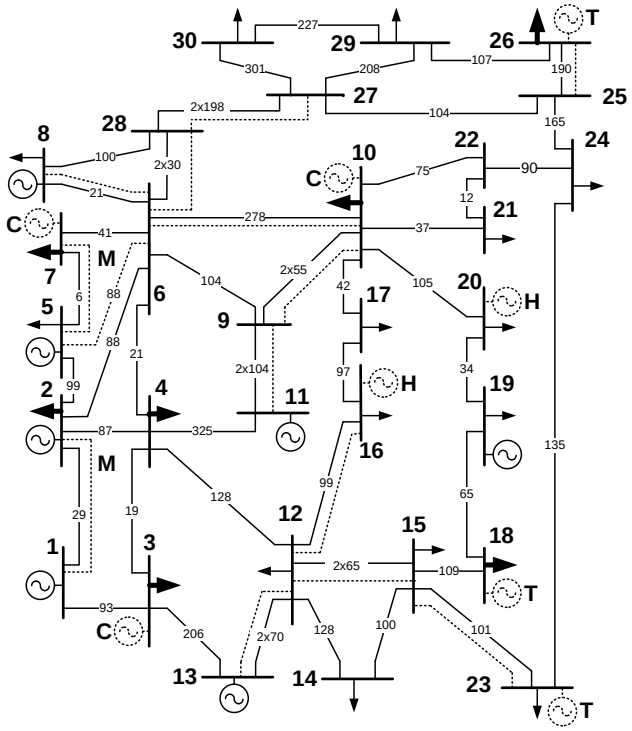


Fig. 4 . Modified IEEE 30-bus System

TABLE 6
IEEE-30 BUS SYSTEM CANDIDATE GENERATOR TYPES

| Type [1] | Capacity (MW) | Capital investment cost ($M/MW) | Loan schedule | ESP [2] ($/MWh) | Profit [3] (%) |
|---|---|---|---|---|---|
| H | 300 or 100 | 1 | 20 years | 18 | 70 |
| T | (see the | 0.6 | | 20 | 40 |
| C | Case studies) | 0.5 | 7% | 22 | 30 |

[1] H: Hydro plant; T: Coal fired thermal plant; C: Natural gas combined cycle plant. [2] ESP: Energy sale price. [3] Profit based on energy sale price

The candidate investment pool includes 3 types of generators as illustrated in Table 6. For simplicity, generator capacities are all assumed to be same. In this table, the capital investment on hydro generators is the highest. The hydro energy sale price is the lowest which provides the highest profit among the candidate generators for the given energy sale price. It is assumed that all candidate generators provide the same annual profit when operating in full capacity.

Buses with higher load distribution factors (bold arrows in Fig. 4) are connected in metropolitan regions so that capital investments for enforcing transmission lines in those regions would be higher than the others. Such regions are indicated by "M" (representing Metropolitan) in Fig. 4.

A planning year is divided into 4 subperiods representing seasonal load patterns. We consider the following four cases to analyze the performance of the proposed planning model. The planning horizon is assumed to be 10 years in all scenarios. The results are summarized in Table 7.

#### *Case 1 – Without Promoting IPP Investment*

The annual peak demand increase is 2% in all seasons along the planning horizon. In this case the existing generators are

sufficient to supply the forecasted demand. Given the low demand increase ratio, the planning model does not provide any incentives to IPPs. Transmission investments shown in Table 7 are already sufficient to satisfy the security criterion while minimizing the investment cost and the transmission congestion level along the planning horizon. In other words, incentive payments required by IPPs are considerably high as compared to transmission investments.

TABLE 7
30-BUS SYSTEM RESULTS SUMMARY

| Case | API * | Investment ** | TTIC ($M) | TIP ($M) | AOCC ($M) | TC ($M) |
|---|---|---|---|---|---|---|
| 1 | 2% | $L_{9\text{-}10}$; $Y_1$<br>$L_{5\text{-}7}$; $Y_2$<br>$L_{9\text{-}11}$; $Y_3$ | 31.19 | - | 24.64 | 55.83 |
| 2 | 2% | $L_{9\text{-}10}$; $Y_4$<br>$L_{5\text{-}7}$; $Y_5$<br>$L_{9\text{-}11}$; $Y_6$<br>$G_{H,16}$; $Y_1$ | 20.45 | ≈ 5 | 21.40 | 46.85 |
| 3 | 5% | $L_{5\text{-}6}$; $Y_1$<br>$L_{5\text{-}7}$; $Y_1$<br>$L_{9\text{-}10}$; $Y_6$<br>$L_{9\text{-}11}$; $Y_9$<br>$L_{12\text{-}16}$; $Y_{10}$<br>$L_{15\text{-}23}$; $Y_{10}$<br>$G_{H,16}$; $Y_2$<br>$G_{H,20}$; $Y_7$ | 53.65 | 40.56 | ≈ 0 | 94.21 |
| 4 | 7% | $L_{5\text{-}6}$; $Y_1$<br>$L_{5\text{-}7}$; $Y_1$<br>$L_{9\text{-}10}$; $Y_8$<br>$L_{9\text{-}11}$; $Y_7$<br>$G_{T,26}$; $Y_7$<br>$G_{T,23}$; $Y_{10}$<br>$G_{H,16}$; $Y_5$<br>$G_{H,20}$; $Y_2$ | 51.52 | 100.85 | ≈ 0 | 152.37 |

* API: Annual peak demand increase (%)
** $L_{i\text{-}j}$: Investment on Transmission line from bus *i* to bus *j*; $Y_i$: Year *i*; $G_{X,i}$: Candidate generator at bus *i* (X: generator type index)

*Case 2 - Promoting IPP Investment (Providing a more Economical Solution)*

In Table 6, the capacity of candidate generators is reduced from 300 MW to 100 MW so that the annual incentives are comparable with transmission investments. The other financial figures are fixed in Table 6. The planning result in Table 7 shows that the investment on hydro generator at Bus 16 (i.e., $G_{H,16}$) in year 1 defers the transmission investment proposed in Case 1 while satisfying the security criterion with a reduced AOCC along the horizon.

The proposed dispatch for $G_{H,16}$ along the horizon and corresponding annual incentives are given in Table 8. The generator is fully dispatched during peak demand seasons (i.e., $S_2$ and $S_4$) in each year which is not the case during the off-peak seasons. For the same energy sale price, the dispatch priority is given to existing generators considering their possible long-term contracts. Consequently, the incentive in initial years is due to the partial operation of $G_{H,16}$ during the off-peak seasons. An energy purchase agreement could be made in advance with the corresponding IPP to trigger the investment on $G_{H,16}$ in year 1. Table 8 shows the financial attributes of such agreements when considering the proposed method.

TABLE 8
30-BUS SYSTEM CASE 2 : DISPATCH AND INCENTIVE PAYMENTS FOR $G_{H,16}$

| Years | | $Y_1$ * | $Y_2$ | $Y_3$ | $Y_4$ | $Y_5$ | $Y_6$ | $Y_7$ | $Y_8$ | $Y_{9\text{-}10}$ |
|---|---|---|---|---|---|---|---|---|---|---|
| Dispatch (MW) | $S_1$ ** | 0 | 0 | 0 | 67 | 89 | 79 | 89 | 99 | 100 |
| | $S_2$ | 100 | 100 | 100 | 100 | 100 | 100 | 100 | 100 | 100 |
| | $S_3$ | 30 | 100 | 100 | 100 | 100 | 100 | 100 | 100 | 100 |
| | $S_4$ | 100 | 100 | 100 | 100 | 100 | 100 | 100 | 100 | 100 |
| Incentive ($M) | | 2.95 | 1.03 | 1.03 | 0 | 0 | 0 | 0 | 0 | 0 |
| Advance contracts | $/MWh | 24 | 19 | 19 | 0 | 0 | 0 | 0 | 0 | 0 |
| | GWh | 500 | 650 | 650 | 0 | 0 | 0 | 0 | 0 | 0 |

* $Y_i$: Year along the planning horizon
** $S_i$: Season in a year

*Case 3 & 4 - Promoting the IPP Investment (Supply / Demand Adequacy)*

The annual peak demand increase is assumed to be 5% in Case 3 so the total capacity of existing generators would not be sufficient to supply the forecasted demand along the planning horizon. Contrary to the previous cases, the generation investment is inevitable for satisfying the system security criterion. Assuming that the capacity of all candidate generators is again 300 MW, our planning model proposes a combination of transmission and generation investments shown in Table 7, which optimizes the TEP problem. Given their lowest energy sale prices, the hydro generators are given the priority not only for security concerns but also minimizing the congestion along the planning horizon. Indeed, the expected AOCC is zero under the proposed investments, as shown in Table 7.

The higher energy sale prices would promote investments on other types of candidate generators only if such investments contribute to the system security. In Case 4, the 7% annual peak demand increase would promote investments on thermal generators at buses 23 and 26 in addition to hydro generators to compensate for supply deficiency. Table 7 shows the optimal investments and corresponding total costs along the planning horizon.

*Further Discussions on the IEEE 30-Bus System*

The IEEE modified 30-Bus system example shows how incentives are prioritized among candidate generators to satisfy the system security and optimize TEP. The optimal investment which satisfies the system security criterion could also mitigate the transmission congestion along the planning horizon (Cases 3 and 4). On the other hand, when the installed capacity is sufficient, the investment on candidate generators would be promoted only if the incentives are comparable with transmission investments (Cases 1 and 2).

In the case of a single generator investment, bilateral energy purchase contracts are the obvious incentive mechanism as proposed in Case 2. Incentive payments are essentially based on the proposed energy sale prices of the corresponding IPPs. On the other hand, a tender could be opened in the case of multiple generators. The existing peaking generators in a region would contribute to the security and should be considered equally.

As shown in Cases 3 and 4, the incentive mechanism is more challenging when the candidate generators are at different regions and/or deserve incentive in different years. In

Case 3 (with a 5% annual demand increase), both $G_{H,16}$ and $G_{H,20}$ contribute to the supply deficiency problem, although $G_{H,16}$ is promoted just two years after the initial year. In Case 4 (with a 7% annual demand increase), $G_{H,20}$ is promoted from the second year on. In Case 4, two more generators ($G_{T,23}$ and $G_{T,26}$) are proposed during the second half of the planning horizon. A tender may be opened based on the following considerations:

- The difference in the annual demand increase is just 2% between Cases 3 and 4. Therefore, the incentive mechanism should consider the Case 4 which is the worse Case in the sense of security concern.
- $G_{H,16}$ and $G_{H,20}$ should be considered equally given that they are in the same region (i.e., equal marginal contribution to security) and their energy sale price - and accordingly incentive requirements - are equal under the same dispatch.
- The incentive payment to $G_{T,23}$ and $G_{T,26}$ could be postponed since it is proposed after the seventh year (see Table 7, Case 4). That is, the incentive payment to the designated IPPs could be decided later. The load growth uncertainty along the planning horizon also supports this idea.

Consequently, the tender could be opened to sign contracts with IPPs of $G_{H,16}$ and $G_{H,20}$ for an investment in year 2. Table 9 shows the financial aspects of such a tender. Note that the average energy purchase price is 20.5 \$/MWh which is higher than the 18 \$/MWh energy sale price envisaged by the IPPs to compensate the early investment. Furthermore,

- The 20.5 \$/MWh average energy price in Table 9 ensures the required IPPs incentive for the 280 MW operation in 7 years. The IPP could also participate in the ancillary service market and/or fulfill its reserve requirement by the remaining 20 MW capacity in Cases 3 and 4.
- Averaging the incentive mechanism to 7 years is due to the fact that no additional investment is made by the market forces. Meanwhile, it will be necessary to open a second tender to ensure the security of the system under the worse annual load growth scenario.
- If both IPPs intend to make the contract shown in Table 9, an auction could be considered and the IPP which accepts the lower energy purchase price would take the higher risk.

TABLE 9
FINANCIAL ASPECTS OF THE PROPOSED TENDER BETWEEN $G_{H,16}$ AND $G_{H,20}$

| | | |
|---|---|---|
| Incentive duration (years) | | 7 |
| Total incentive along the planning horizon (\$M) | | 43.5 |
| Advance contract | MW | 280 |
| | TWh/year | 2.25 |
| | \$/MWh | 20.5 |

## IV. CONCLUSIONS AND REMARKS

In this paper, a multi-year TEP model is proposed which possible incentive payments to IPPs to trigger candidate generation investments. The purpose is to get an optimal planning solution when considering the system security and congestion along the planning horizon after the restructuring of power systems. The proposed approach would successfully to optimize the sum of investment cost of transmission lines, incentive payments to IPPs, and forecasted operation costs due to congestion along the planning horizon. The results of numerical examples (two-bus and the IEEE 30-bus systems) show the effectiveness of the proposed model.

The necessity of incentives to trigger IPP investments was evaluated within the TEP problem concerning the security and the congestion of grid along the planning horizon. The main idea is to trigger investments on IPPs earlier than those projected by the decentralized generation system, when the power system security is threatened. The case studies illustrate how the proposed planning algorithm could be utilized in order to determine incentive payments to candidate generators when necessary, and prioritize such incentives among multiple IPP candidates. The proposed planning model is applicable to restructured power systems, particularly during the market development phase when inherent uncertainties in existing policies and electricity prices due to the considerable share of state-owned generation companies could signal delays in investment decisions by IPPs.

The incentive offers to IPPs for advancing their generator investment plan is conceivable particularly when such investments are subject to low dispatch levels during initial years. For instance, peaking generators could contribute to the grid reliability, particularly during on-peak periods. Although they are expensive, system operators would appreciate the availability and the commitment of such units in emergency conditions. A considerable share of consumers would also prefer to pay extra instead of facing any interruptions. Accordingly, the following incentive mechanism could be proposed: either make a direct energy purchase contract with IPPs or open a tender among IPPs when fairness is a concern. Both incentive mechanisms should take into account the fact that incentive payments proposed by our planning algorithm depend on the energy sale prices provided by IPPs, as illustrated in Table 8.

The proposed planning algorithm would be utilized by an independent authority that is responsible for the long-term security of the power system. Such an institution is assumed to be a state-owned transmission company in this paper, which is indeed common in most EU countries. The IPP decisions would be reviewed and regulated by the authority as an independent entity. Accordingly, the authority is responsible for both determining and offering the incentives or making direct energy purchase contracts with the qualified IPPs. The planning uncertainties including energy sale prices and the role of monopolistic state-owned transmission company are among IPPs' risk factors that could result in delays on generation investment decisions.

Given their contribution to both power system security and transmission investment cost reduction (not only by postponing the transmission investment but also by ensuring the optimum transmission/generation expansion planning), such incentive payments to IPPs should be recovered from consumer payments. Accordingly, the incentive payments could be considered as a parameter in calculating the transmission usage charge by consumers. They could also be considered as capacity payments by consumers, like the ancillary services payments which are also related to the system security. The distribution of incentive payments among

the consumers is beyond the scope of this paper, and will be discussed in detail in a future study.

Although the proposed incentive mechanism may encourage IPPs to game the market by manipulating the incentive requirements, those payments will be rejected in the proposed algorithm by means of Benders cuts if better alternatives (transmission lines or IPPs) could be identified. On the other hand, the proposed planning model could be utilized to reveal market manipulations and measure the level of market competition, as illustrated in Section 2 (Two-Bus system, Case 2). Such issues should indeed be among the regulatory authority's main concerns when considering the system security. When the manipulation of incentives is a concern, the authority could make additional sensitivity analyses to evaluate the impact of energy price on the planning solution.

The numerical examples also illustrated how the risk of generator investments - due to low dispatch levels during initial years of the investment - could signal delays in IPP investments. The risk is demonstrated by providing IPPs the expected dispatch levels of the investments based on their envisaged energy sale prices. This indicator would essentially provide IPPs with important signals on their forecasted energy price and cover investment uncertainties considerably.

A future study could consider the impact of electricity price forecast uncertainties in electricity markets. The planning algorithm could be improved by considering the demand side management and load curtailment costs. In addition, generator planning criteria could be improved further by considering more sophisticated financial models. The net present value (NPV) approach considered in this paper would ensure a profit; however, it does not consider investment opportunities. The NPV could be positive while there is no optimal time for investment as there might be a chance to get larger NPVs by delaying the proposed investments.

## REFERENCES


[1] R. Baldick and E. Kahn, "Transmission Planning Issues in a Competitive Economic Environment," *IEEE Trans. on Power Systems*, vol. 8, no. 4, pp. 1497-1503, Nov. 1993.

[2] A. K. David and F. Wen, "Transmission Planning and Investment under Competitive Electricity Market Environment," in *Proc. of the IEEE PES Summer Meeting*, vol. 3, pp. 1725-1730, July 2001.

[3] R. J. Thomas, J. T. Whitehead, H. Outhred, T. D. Mount, "Transmission System Planning – The Old World Meets the New," in *Proc. of the IEEE*, vol. 93, no. 11, pp. 2026-2034, Nov. 2005.

[4] A. S. D. Braga and J. T. Saraiva, "A Multiyear Dynamic Approach for Transmission Expansion Planning and Long-Term Marginal Costs Computation," *IEEE Trans. on Power Systems*, vol. 20, no. 3, pp. 1631-1639, Aug 2005.

[5] P. Gribik, D. Shirmohammadi, J. Graves, and J. Kritikson, "Transmission rights and transmission expansions," IEEE Trans. Power Syst., vol. 20, no. 4, pp. 1728–1737, Nov. 2005.

[6] P. Cramton and S. Stoft, "A capacity market that makes sense," in Proc. IEEE Power Eng. Soc. Gen. Meeting, Jun. 2005, pp. 3022–3034.

[7] B. J. Gail, J. G Farr, and S. F. Tierney, "The political economy of longterm generation adequacy: Why an ICAP mechanism is needed as part of standard market design," *Electricity J.*, vol. 15, no. 7, pp. 53–62, Aug./Sep. 2002.

[8] J. H. Roh, M. Shahidehpour and Y. Fu, "Market-Based Coordination of Transmission and Generation Capacity Planning," *IEEE Trans. on Power Systems*, vol. 22, pp. 1406-1419, Nov. 2007.

[9] J. H. Roh, M. Shahidehpour and Y. Fu, "Security-Constrained Resource Planning in Electricity Markets," *IEEE Trans. on Power Systems*, vol. 22, pp. 812-820, May 2007.

[10] A. Botterud, M. D. Ilic, and I. Wangensteen, "Optimal investments in power generation under centralized and decentralized decision making," IEEE Trans. Power Syst., vol. 20, no. 1, pp. 254–263, Feb. 2005.

[11] E. Sauma and S. Oren, "Proactive planning and valuation of transmission investments in restructured electricity markets," J. Regul. Econ., vol. 30, pp. 261–290, Sep. 2006.

[12] O. B. Tor, A. N. Guven, M. Shahidehpour, "Congestion-Driven Transmission Planning Considering the Impact of Generator Expansion," *IEEE Trans. on Power Systems*, vol. 23 no. 2, pp. 781-789, May 2008.

[13] R. Romero, A. Monticelli, A. Gercia, S. Haffner, "Test Systems and Mathematical Models for Transmission Network Expansion Planning," *Proc. of the IEE Gener. Transm. Distrib.*, vol. 149, no. 1, pp. 27-36, Jan 2002.

[14] E. Kahn, "Electric Utility Planning and Regulation," Washington, DC: American Council for an Energy-Efficiency Economy, 1991.


## BIOGRAPHIES

**Osman Bulent Tor** (S'04) received the B.S., M.S. and Ph.D. degrees from Middle East Technical University (METU), Turkey, in 1998, 2001 and 2008, respectively. He is working as a Chief Researcher at the Power Systems Department of Space Technologies Research Institute of the Scientific and Technological Research Council of Turkey (TUBITAK). He is the leader of the Power System Analysis Project Group.

**Ali Nezih Guven** (SM'00) received the B.S. degree from Middle East Technical University (METU), Turkey, in 1979, and the M.S. and Ph.D. degrees from the Ohio State University, USA, in 1981 and 1984, respectively. He is a professor in the Department of Electrical and Electronics Engineering at METU, Ankara, Turkey now. His research interests are the analysis, design and operation of power systems, and distribution automation.

**Mohammad Shahidehpour** (F'01) is Bodine Distinguished Professor in the Electrical and Computer Engineering Department at Illinois Institute of Technology. He is the VP of Publications and a Distinguished Lecturer for the IEEE Power and Energy Society. He is also the recipient of Honorary Doctorate from the Polytechnic University of Bucharest. Dr. Shahidehpour is an Honorary Professor in the North China Electric Power University in Beijing and Sharif University in Tehran.

# A Hybrid Model for Day-Ahead Price Forecasting

Lei Wu, *Member, IEEE*, and Mohammad Shahidehpour, *Fellow, IEEE*

***Abstract*—This paper presents a hybrid time-series and adaptive wavelet neural network (AWNN) model for the day-ahead electricity market clearing price forecast. Instead of using price series, one-period continuously compounded return series is used to achieve more attractive statistical properties. The autoregressive moving average with exogenous variables (ARMAX) model is used to catch the linear relationship between price return series and explanatory variable load series, the generalized autoregressive conditional heteroscedastic (GARCH) model is used to unveil the heteroscedastic character of residuals, and AWNN is used to present the nonlinear, nonstationary impact of load series on electricity prices. The Monte Carlo method is adopted to generate more evenly distributed random numbers used for time series and AWNN models to accelerate the convergence. Several criteria such as average mean absolute percentage error (AMAPE) and the variance of forecast errors are used to assess the model and measure the forecasting accuracy. Illustrative price forecasting examples of the PJM market are presented to show the efficiency of the proposed method.**

***Index Terms*—AMAPE, ARMAX, AWNN, day-ahead price forecast, GARCH, Monte Carlo, time series method, variance of forecast errors.**

## NOMENCLATURE

**Variables:**

| | |
|---|---|
| $a_t$ | Noise process. |
| $a_{ij}$, $b_{ij}$ | Translation and dilation parameters of wavelets. |
| $c$ | Constant item in the GARCH model. |
| $d$ | Differential order. |
| $e$ | Bias of the output node in AWNN. |
| $h_t$ | Conditional variance of residual series at time $t$. |
| $i$, $j$ | Index. |
| $k$ | AWNN training iteration index. |
| $m$ | Number of input layer of AWNN. |
| $MSE_T^k$ | Mean squared error (MSE) on testing set at iteration $k$ for AWNN. |
| $MSE_V^k$ | MSE on validation set at iteration $k$ for AWNN. |
| $\overline{MSE}_V^k$ | Average MSE on validation set until iteration $k$ for AWNN. |
| $n$ | Number of hidden nodes of AWNN. |
| $O_t$ | Forecast electricity price at time $t$. |
| $p$, $b$, $q$ | Orders of time series models. |
| $W_i$, $W_j$, $W_{ij}$ | Weights of AWNN. |
| $\overline{R(d)}$ | Average value of $R_t(d)$ series. |
| $t$, $\tau$ | Index of time series. |
| $\alpha_i$, $\beta_i$ | GARCH coefficients. |
| $\phi(B)$ | Coefficient function for price series. |
| $\varphi(B)$ | Coefficient function for load series. |
| $\theta(B)$ | Coefficient function for noise process. |
| $\rho_k$ | Sample autocorrelation value of lag $k$. |
| $\varepsilon_t$ | Residual at time $t$. |
| $\gamma^k$ | Generalization factor of iteration $k$ for AWNN. |
| $\overline{\gamma}^k$ | Average generalization factor until iteration $k$ for AWNN. |
| $\sigma_E^2$ | Variance of forecast errors. |
| $\sigma_V^k$ | Standard deviation (STD) of MSE on validation set until iteration $k$ for AWNN. |
| $\sigma_\gamma^k$ | STD of generalization factor until iteration $k$ for AWNN. |

**Constants:**

| | |
|---|---|
| $B$ | Backshift operator, means $B^p \cdot P_t = P(t-p)$. |
| $F^{-1}(\cdot)$ | Inverse probability distribution function. |
| $L_t$ | Load at time $t$. |
| $P_t$ | Electricity price at time $t$. |
| $R_t$ | One-period log return at time $t$. |
| $R_t(\tau)$ | Log return of $\tau$-period at time $t$. |
| $T$ | Study period. |

## I. INTRODUCTION

WITH the introduction of restructuring to the electric power industry, the price of electricity is becoming the focus of all activities in electricity markets. Price forecasting

Manuscript received December 19, 2008; revised June 21, 2009. Paper no. TPWRS-01020-2008.

The authors are with the Electrical and Computer Engineering Department, Illinois Institute of Technology, Chicago, IL 60616 USA (e-mail: lwu10@iit.edu; ms@iit.edu).

Digital Object Identifier 10.1109/TPWRS.2009.2039948

techniques are used for bidding purposes and hedging against volatilities. With a good next-day market clearing price forecast, a market participant would be able to delineate better financial decisions. That is, a power producer can develop appropriate strategies to maximize its payoff and a consumer can minimize its utilization cost [1].

Electricity has distinct characteristics as compared to other commodities; it cannot be stored economically and transmission congestion may prevent a free exchange of power among control areas. Thus, electricity price series can exhibit a major volatility and the application of forecasting methods prevailed in other commodities can pose large errors in electricity price forecasting. For different applications, price forecasting can be categorized into very short-term (several minutes to few hours), short-term (few days), midterm (few months) and long-term (few years). In this paper, we focus on the day-ahead market clearing price forecasting in electricity markets. A reasonable forecasting algorithm could capture important properties of electricity prices such as spikes, mean reversion, seasonality, and fat tails.

There are several possible methods for the day-ahead electricity price forecasting. The first approach is based on fundamental models, which is to simulate the exact physical model of power system components and apply algorithms which consider physical characteristics of power networks. Such an approach would express electricity prices based on marginal generation costs with the consideration of transmission congestion, losses, and other ancillary service requests in power markets [1], [2]. Fundamental models account for the impact of physical capacity of power plants and transmission lines, and demand characteristics and fluctuations. The most difficult issue here is that a fundamental model may require significant amounts of real-time data on power systems which can result in a complex computation process.

The second approach is based on mathematical finance models which were originally developed and widely used for stock and interest rate markets. Skantze *et al.* [3] developed a dynamic model to describe price series based on interactions of supply bids and load demands, which are simulated as mean reverting processes and exponential functions, respectively. The market clearing price was calculated as the cross section of aggregated supply and demand bid curves. A diffusion model for electricity prices, based on stochastic models for supply and demand curves, was proposed by Barlow [4] to exhibit price spikes. By fitting to historical data with the maximum likelihood estimation, Barlow concluded that the proposed diffusion model could provide a better fit than models with jumps. The finance models reflect the electricity price volatility caused by supply and demand, thus are suitable for option valuation and risk assessment purposes. The drawback is that it is very difficult to incorporate physical characteristics of power systems, such as transmission congestions, network losses, and contingencies, into mathematical finance models which may cause a discrepancy between the finance model solution and the real-time status of power systems.

The third approach is based on game theory models, which are particularly focused on the impact of bidders' strategic behavior on electricity prices. Bolle [5] used supply and demand functions as instruments to determine market equilibria. It showed that under a certain condition, an equilibrium exists for every finite spread of autonomous demand, including small, nonstrategically acting consumers. Lower bounds of market prices were also computed. Ruibal *et al.* [32] used three oligopoly models, Bertrand, Cournot, and supply function equilibrium, to obtain closed form expressions for expected values and variances of hourly electricity prices as well as average prices, with the consideration of hourly demand volatility and random outages of generating units. It concluded that the introduction of competition may decrease expected prices but variances may actually increase. Li *et al.* [6] used the incomplete information game theory to analyze competitions among transmission-constrained GENCOs. Based on the solution of incomplete information game, the Bayesian Nash equilibrium which represents locational marginal prices (LMPs) was calculated using the ISO's security-constrained economic dispatch (i.e., a market clearing model). The problem was an iterative bilevel process, with the upper process representing individual GENCOs' bidding strategies to maximize payoffs and the lower process solving the ISO's market clearing problem for calculating LMPs. One presumption in the game theory is that all players are rational, which is not always the case in electricity markets. Other drawbacks are represented by time-consuming processes for calculating Nash equilibria.

The fourth method is based on regression models, which include time-series, and artificial intelligence models such as artificial neural network (ANN) and fuzzy logic. Regression models relate electricity price fluctuations to historical prices and other explanatory factors such as temperature, time of day, load demand, etc. The autoregressive integrated moving average (ARIMA) time series was applied to load forecasting [7], [8]. Contreras *et al.* [9] proposed an ARIMA model for the day-ahead electricity price forecasting, with examples from the Spanish electricity market and the PJM electricity market. Backshift factors were introduced into the ARIMA model for reflecting the seasonality of prices. In addition, it reported that the inclusion of explanatory variables, such as demand and available daily production of hydro units, may improve price forecasts with large spikes. Conejo *et al.* [10] proposed a hybrid wavelet transform and ARIMA model to forecast day-ahead electricity prices. Wavelet transform was used to decompose historically ill-behaved price series into a set of well-behaved constitutive series. Then, ARIMA was adopted for each constitutive series and the inverse wavelet transform was used to reconstruct a better forecast result. Gao *et al.* [11] used a three-layer back propagation network to forecast day-ahead market clearing prices (MCPs) and market clearing quantities (MCQs). Historical MCPs and MCQs, system loads, fuel prices, power exchanges, weather, and season indices that influenced market prices were used for network training, validating, and forecasting. Holiday data were pretreated as weighted average of following normal days. Price spikes were truncated for a better accuracy of normal prices. Mandal *et al.* [31] explored an ANN model based on similar days method to forecast day-ahead electricity prices in the PJM market. The impact factors were historical loads and price series of the days similar to those of the forecast day. Pindoriya *et al.* [33]

proposed an adaptive wavelet-ANN by using the Mexican hat wavelet as the activation function for hidden-layer neurons of feed-forward ANN. The forecast results showed good accuracy compared to ARIMA, multi-layer perceptrons, radial basis functions, and fuzzy neural networks. Swanson *et al.* [29] compared various adaptive and nonadaptive, linear and potentially nonlinear models, and concluded that the hybrid models, by grouping the multivariate adaptive linear and nonlinear models, dominate other models and provide least confused forecasts. The regression method is simple and computationally efficient. It requires detailed and correct historical data and proper model (orders of time series model, details of layer structure of artificial intelligence model) for adaptation and forecasting.

Price spikes were addressed regularly in electricity price forecasting. Previously proposed models preprocess, ignore, or truncate price spikes in order to get better forecasts for hourly electricity prices. Zhao *et al.* [30] developed a data mining based approach to forecast price spikes. Feature selection techniques were described to identify attributes relevant to the occurrence of spikes, including system demand, system supply, seasonality, scheduled interchanges, and dispatchable loads. Two algorithms, i.e., support vector machine and probability classifier, were applied as spike occurrence predictors. Guan *et al.* [12] proposed that price spikes might be the result of power suppliers' strategic gaming behavior. A prisoner's dilemma matrix game was formulated, and the notion of opportunistic tacit collusion was introduced to explain strategic bidding behaviors in which suppliers withhold a generation capacity from the market to drive prices up.

This paper focuses on day-ahead electricity market clearing price forecasts with large volatilities. Return series is used instead of original price series to capture statistical properties. The ARMAX model is used to seize the linear relationship between price return series and load series, the GARCH model is used to present heteroscedastic characteristics of residuals, and AWNN is used to show nonlinear and nonstationary impacts of system loads on electricity prices. Our proposed hybrid model provides a 24-h MCP forecast of the next day based on historical data and forecast explanatory factors. To illustrate our model, price forecasts in the PJM electricity market [13] are calculated and discussed.

The rest of the paper is organized as follows. Section II describes the proposed model and its solution methodology. Section III presents illustrative examples to show the proposed model applied to the PJM electricity market. Conclusions are provided in Section IV.

## II. Forecasting Methodologies

In competitive power markets, electricity prices appear to be highly volatile with nonstationary means and variances. The prices correspond to seasonality, weekdays, weekends, and holidays. Furthermore, power system loads as an explanatory factor would impact electricity prices. Here, we propose a hybrid model that uses ARMAX time series to forecast linear relationships between electricity price return series and system load series, followed by GARCH to simulate nonconstant variances of residuals, and applies AWNN to forecast nonlinear and nonstationary impacts of system loads on electricity prices as shown in Fig. 1. In Fig. 1, the ARMAX model is first applied for forecast using historical prices and other explanatory data. Then, forecast results from the ARMAX model are used as input to the GARCH model. The GARCH model output includes nonconstant residuals. The ARMAX and GARCH results are combined and used as input to AWNN. The AWNN output is the final price forecast.

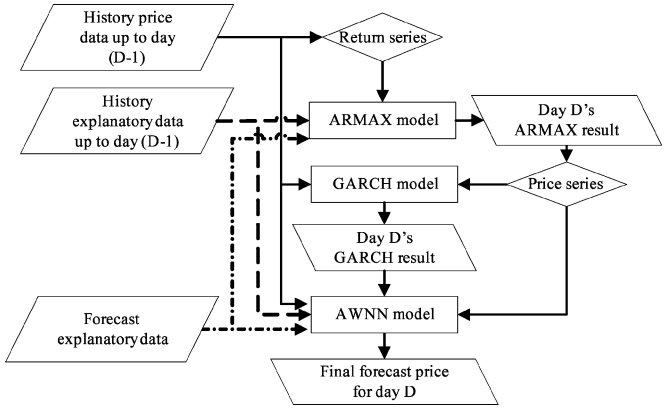


Fig. 1. Flowchart of the proposed forecasting procedure.

### A. Price Data Preprocess

A key feature that distinguishes the electricity price series from other time series lies on the assumption that the electricity price is very volatile. Return series has more attractive statistical properties and thus is easier to handle than price series [14]. There are several common definitions of asset return [15]. In this paper, we use the continuously compounded return, also called log return. The one-period continuously compounded return series is defined as

$$R_t = \ln(P_t) - \ln(P_{t-1}) = \ln\left(\frac{P_t}{P_{t-1}}\right). \tag{1}$$

The continuously compounded return enjoys several advantages over the price series. First, the multiperiod return is simply the sum of one-period continuously compounded returns in (2):

$$\begin{aligned} R_t(\tau) &= \ln(P_t) - \ln(P_{t-\tau}) = \sum_{j=0}^{\tau-1} [\ln(P_{t-j}) - \ln(P_{t-j-1})] \\ &= R_t + R_{t-1} + \cdots R_{t-(\tau-1)}. \end{aligned} \tag{2}$$

Second, statistical properties of the continuously compounded return are more tractable. Fig. 2 shows the hourly electricity prices from January 1, 2006 to May 31, 2006 of the PJM market [13]. Fig. 3 shows the return series during the same period. Comparing the two figures, we learn that the mean value of return series is close to zero and the variability of return series over time looks more homogeneous than that of price series. Thus, statistical characteristics of return series may be better comprehended than those of price series. Therefore, we study the return series of assets in the stationary ARMAX model instead of price series. In the following, we refer to return series as the one-period continuously compounded return as in (1).

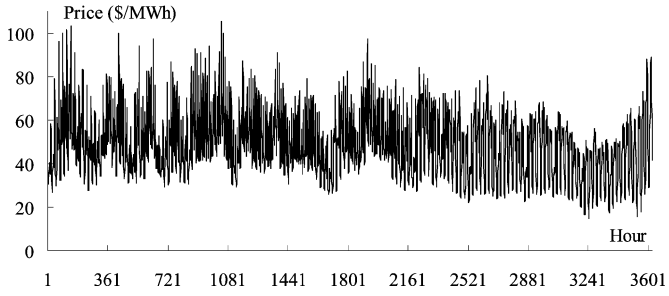


Fig. 2. Price series of PJM market from January 1, 2006 to May 31, 2006.

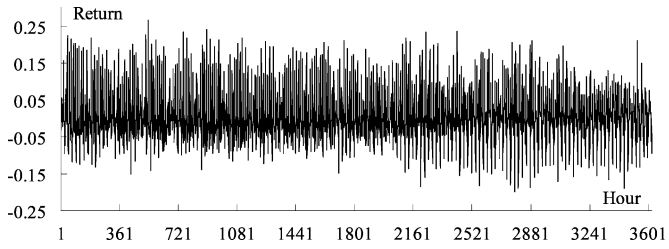


Fig. 3. Return series of PJM market from January 1, 2006 to May 31, 2006.

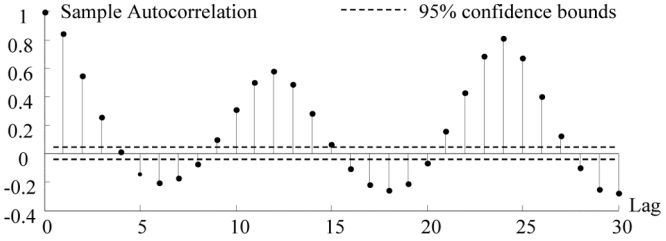


Fig. 4. ACF of price series of PJM market from January 1, 2006 to May 31, 2006.

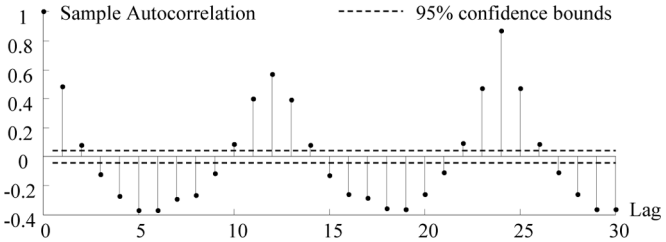


Fig. 5. ACF of return series of PJM market from January 1, 2006 to May 31, 2006.

### *B. ARMAX Time Series Model*

ARMAX is a class of stationary stochastic model. The series in Fig. 2 shows nonequilibrium at a constant mean level, which means the original price series is nonstationary. Using suitable differences, a homogeneous nonstationary time series is transferred to stationary mixed autoregressive-moving average process shown in (3):

$$\phi(B)\cdot(1-B)^{d}\cdot\ln(P_t)=\varphi(B)\cdot L_t+\theta(B)\cdot a_t \qquad (3)$$

where $a_t$ is a Gaussian $N\left(0,\sigma_a^2\right)$ white noise process, $\phi(B)=1-\phi_1\cdot B-\cdots-\phi_p\cdot B^p$, $\varphi(B)=1-\varphi_1\cdot B-\cdots-\varphi_b\cdot B^b$, and $\theta(B)=1-\theta_1\cdot B-\cdots-\theta_q\cdot B^q$.

A homogeneous nonstationary time series is transferred to a stationary time series by taking a proper degree of differencing. From (3), $\ln(P_t)$ is a homogeneous nonstationary time series. By applying a suitable difference of order $d$, i.e., $R_t(d)=(1-B)^{d}\cdot\ln(P_t)$, the new return series $R_t(d)$ is transferred to a stationary stochastic process and fitted in a standard ARMAX $(p,q,b)$ model as

$$\phi(B)\cdot R_t(d)=\varphi(B)\cdot L_t+\theta(B)\cdot a_t. \qquad (4)$$

The general ARMAX scheme is described as follows:

*1) Model Identification:* Use the autocorrelation function (ACF) and partial autocorrelation function (PACF) to identify the order of ARMAX $(p,q,b)$ and the suitable difference order $d$. The autocorrelation of lag $k$ is given as

$$\rho_k=\frac{\sum_{t=1}^{T-k}\left[R_t(d)-\overline{R(d)}\right]\cdot\left[R_{t+k}(d)-\overline{R(d)}\right]}{\sum_{t=1}^{T}\left[R_t(d)-\overline{R(d)}\right]^2}. \qquad (5)$$

The stationary property implies that zeros of $\phi(B)$ lie outside the unit circle, which means that the ACF will die out quickly and rather linearly. Figs. 4 and 5 show the ACF of price series and return series from January 1, 2006 to May 31, 2006 in the PJM market, respectively. Dashed lines indicate the approximate upper and lower confidence bounds. That is, if the ACF at a certain lag is smaller than the 95% confidence bound, we assume there is no significant autocorrelation at that lag. After the first order difference (which is carried out in return series), the ACF dies out quickly after lag 2 with a damping sine-cosine wave; so the price series may follow the process with $d=1$, which is the one-period return series as defined in (1). Thus inputs and outputs of ARMAX model are all price return series. Furthermore, $(p,q,b)$ orders are determined by lags where ACF and PACF die out.

There are two alternatives to the ARMAX model to forecast a day-ahead electricity price return series. One is to build a single ARMAX model based on the entire series, and then consider a 24-step forecast for the next day. The other is to consider different hourly models. That is, dividing the entire series into 24 sets corresponding to different hours of a day, building ARMAX models based on different hourly series, and forecasting a one step ahead for each ARMAX model. The forecast results of the 24 ARMAX models constitute the day ahead forecast. Figs. 6–8 show the ACF of return series for the first hour and two peak hours, i.e., hours 10 and 20, of each day in the PJM market from January 1, 2006 to May 31, 2006. Comparing Figs. 6–8 with 5, we learn that, although hourly ACFs are not exactly the same, the return series ACF of the same-hour dies out more quickly than the return series of the entire day. Hence by considering the hourly-based series, the ARMAX model can better fit a series with proper AR and MA orders. Here we consider different hourly ARMAX models instead of a single ARMAX model for the entire series.

*2) Parameter Estimation:* After identifying a tentative model, the next step is to estimate the model parameters. The ordinary least squares (OLS) estimation is efficiently used to make inferences about parameters conditional on the adequacy

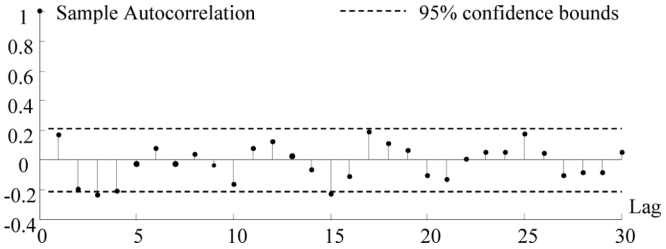


Fig. 6. ACF of return series for the daily hour 01:00 from January 1, 2006 to May 31, 2006.

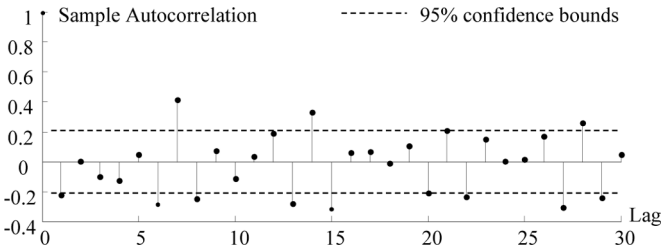


Fig. 7. ACF of return series for the daily hour 10:00 from January 1, 2006 to May 31, 2006.

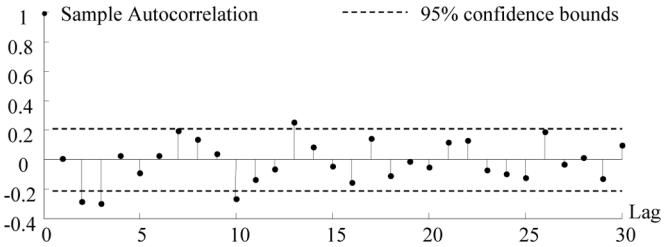


Fig. 8. ACF of return series for the daily hour 20:00 from January 1, 2006 to May 31, 2006.

of the model. Tray *et al.* proposed an iterative regression process to estimate parameters for stationary and nonstationary ARMA models [16].

*3) Diagnostic Checking:* Once parameters are estimated, we check the model adequacy for representing the series which is intended to reveal model inadequacies and consider improvements. One technique that can be used for diagnostic checking is overfitting, i.e., fitting a more elaborate model to show whether additions are needed. The other is the diagnostic check applied to residuals to show if there are any autocorrelations or partial autocorrelations among residuals. If the current model is inadequate, we return to step one and repeat the iterative procedure.

In conclusion, the time series model building is an iterative procedure. It starts with the model identification and the parameter estimation. After the parameter estimation which is used to analyze the adequacy of the model by diagnostic checking, iterative steps of the model building are repeated until a satisfactory model is obtained. One issue that needs to be considered here is that the fit of a regression model to the new data is nearly always worse than its fit to the original data. In this paper, the task is accomplished by separating the series into two parts, with the first portion of the data used for the model construction and the remaining portion for the evaluation of forecasting

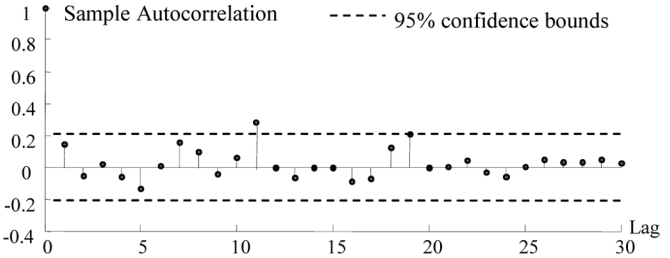


Fig. 9. ACF of residuals after the ARMAX is fit to the PJM market from January 1, 2006 to May 31, 2006.

capability. Copas [17] proposed the preshrunk predictor which anticipates the overfitting and gives predictions with a uniformly lower mean squared error.

### C. GARCH—Conditional Heteroscedastic Model

It is generally agreed that both price series and return series present nonconstant deviations over time as demonstrated in Figs. 2 and 3. Thus the OLS estimator of ARMAX model coefficients is no longer asymptotically unbiased and consistent, when error terms are autocorrelated. Thus, the residual analysis is an important step in the regression analysis. GARCH models are widespread tools to deal with series conditional standard deviations [18]. A $\mathrm{GARCH}\,(p,q)$ is modeled as (6) where $\nu_t$ is a Gaussian $N\,(0,1)$ white noise process and $h_t = Var\,(\varepsilon_t|\varepsilon_{t-1})$ represents the conditional variance of time $t$ based on time $(t-1)$:

$$h_t = c + \sum_{i=1}^{p} \alpha_i \cdot h_{t-i} + \sum_{i=1}^{q} \beta_i \cdot \varepsilon_{t-i}^2$$
$$\varepsilon_t^2 = \nu_t^2 \cdot h_t. \tag{6}$$

The proposed GARCH model described in (6) can forecast beyond one day out. The input series, $\varepsilon_t$, considers the residual of ARMAX model as the actual price minus the forecast from the ARMAX process when the actual price is known, or forecast residual values from the GARCH model when foresting beyond one day out and the actual price is unknown. The prediction quality deteriorates as the number of predicted hours increases. After combining the results of ARMAX and GARCH models, forecast results incorporate the possibility of nonconstant error variance. The application of GARCH model is an iterative procedure which is similar to the ARMAX model. It includes iteratively order determination, parameter estimation, and model diagnostic checking [19].

Fig. 9 shows the ACF of residual series after the ARMAX model is fit to the PJM market from January 1, 2006 to May 31, 2006. This ACF figure suggests that the residual series fails to have a significant serial correlation. Fig. 10 shows the ACF of squared residuals. The autocorrelations at several lags are larger than bounds, which suggest that the residual series may have a conditional heteroscedasticity.

### D. Adaptive Wavelet Neural Network (AWNN)

Considering nonlinear and nonstationary impacts of system loads on price does help improve predictions based on time se-

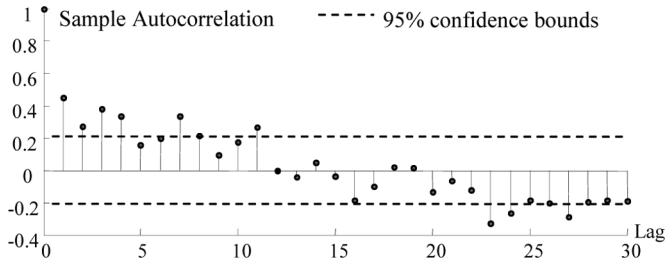


Fig. 10. ACF of squared residuals after the ARMAX is fit to the PJM market from January 1, 2006 to May 31, 2006.

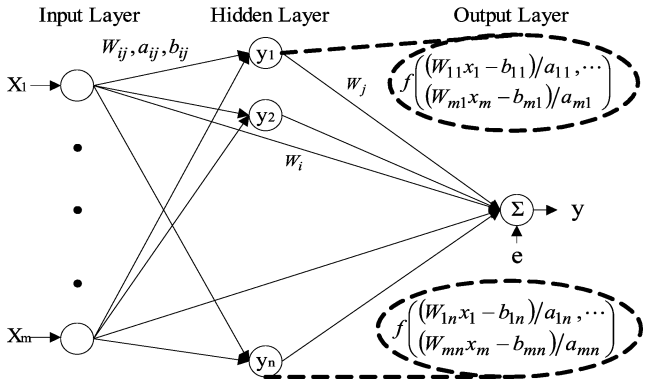


Fig. 11. AWNN model.

ries techniques, especially in the case of sky-high price spikes. AWNN represents a more modern estimation technique for a nonlinear relationship between electricity prices and system loads. AWNN introduces wavelets as activation functions of hidden neurons in traditional feed-forward neural networks with a linear output neuron. The unknown parameters of network include weights and dilation/translation factors which can be learned by gradient-type algorithms. The success of this configuration dwells on the fact that the wavelet network has universal and $L^2$ approximation properties and is a consistent function estimator [21], [22]. The AWNN structure is shown in Fig. 11.

The output of AWNN is computed as (7) where the multidimensional wavelet function $f(\,)$ is calculated by the tensor product of one-dimensional wavelets or some radial functions, and $b_{ij}$, $a_{ij}$ are translation and dilation parameters:

$$y = \sum_{j=1}^{n} W_j \cdot f\left(\frac{(W_{1j}\cdot x_1 - b_{1j})}{a_{1j}}, \ldots, \frac{(W_{mj}\cdot x_m - b_{mj})}{a_{mj}}\right) + \sum_{i=1}^{m} W_i \cdot x_i + e. \quad (7)$$

The morlet wavelet shown in (8) is used here as the mother wavelet, and other wavelet functions are dilations and translations derived from this prototype mother wavelet. We compared two most popular mother wavelets given in the literature with numerical tests: Morlet and Mexican Hat. We found that Morlet always gives a better forecast solution. Since dilation parameters $a_{1j}, \ldots, a_{mj}$ in (7) are already included for each input, the usage of 1.75 in (8) is an arbitrary coefficient which will not impact the forecasting accuracy. Multidimensional wavelet function is calculated by the tensor product in (9) and by the radial function in (10):

$$f(x) = \cos(1.75x)\cdot \exp\left(-x^2/2\right) \quad (8)$$

$$f\left((W_{1j}\cdot x_1 - b_{1j})/a_{1j}, \ldots, (W_{mj}\cdot x_m - b_{mj})/a_{mj}\right) = \prod_{i=1}^{m} \cos\left[1.75\cdot (W_{ij}\cdot x_i - b_{ij})/a_{ij}\right] \cdot \exp\left\{-\left[(W_{ij}\cdot x_i - b_{ij})/a_{ij}\right]^2/2\right\} \quad (9)$$

$$f\left((W_{1j}\cdot x_1 - b_{1j})/a_{1j}, \ldots, (W_{mj}\cdot x_m - b_{mj})/a_{mj}\right) = \cos\left(1.75\sqrt{\sum_{i=1}^{m}\left[(W_{ij}\cdot x_i - b_{ij})/a_{ij}\right]^2}\right) \cdot \exp\left(-\sum_{i=1}^{m}\left[(W_{ij}\cdot x_i - b_{ij})/a_{ij}\right]^2/2\right). \quad (10)$$

In the training process, the network learns by adjusting weights as well as translation and dilation parameters by using the product of gradient and learning rate. Two parameters, i.e., learning rate and momentum, are adjusted to accelerate the learning process [19]. The learning rate controls the size of each step for minimizing the objective function. The calculation of momentum term is to average the changes and determine the proportion of past changes that should be used for new values. Thereby, the term ensures that the search path on the average is in the downhill direction.

One of the critical issues in network training is overfitting which means that the network memorizes the training patterns and consequently loses the ability to generalize. That is, it fits the training set but cannot predict the fit for new data sets. Overfitting is especially a serious problem for price forecasting since there are many price spikes which are blended into historical prices.

In the training process, there is a point at which the training error continues to decrease while the generalization error starts to increase. The training process should stop at this point to avoid overfitting. Accordingly, in order to detect overfitting, the original data set is divided into three disjoint sets, i.e., training set, validation set, and generalization set. The training set is used to train the network model, and the validation set is used to estimate the generalization error while the generalization set is for forecasting. In this paper, two indicators are considered together to detect the point of overfitting. One is to check whether the MSE in each training iteration exceeds the average MSE plus its standard deviation, as expressed in (11):

$$MSE = \frac{1}{T}\sum_{t=1}^{T}(O_t - P_t)^2$$
$$MSE_V^k > \overline{MSE}_V^k + \sigma_V^k. \quad (11)$$

MSE implies an underlying quadratic loss function. It is the assumed loss function for which the conditional mean is the best, i.e., it is the minimum MSE forecast. The other is to measure the generalization factor, given in (12). Overfitting is detected at the training iteration $k$ where $\gamma^k > \chi_\gamma^k$ with $\chi_\gamma^k$ given in (13).

This test always ensures that $\gamma^k \leq 1.0$ before overfitting occurs to make sure that the validation error is smaller than the testing error [22]:

$$\gamma^k = \frac{MSE_V^k}{MSE_T^k} \tag{12}$$

$$\chi_\gamma^k = \min\left\{\chi_\gamma^{k-1}, \overline{\gamma}^k + \sigma_\gamma^k, 1.0\right\}. \tag{13}$$

ARMAX considers different models for different hours. However, it is not the case for WANN. Two AWNN models are used for weekday and weekend forecasts. Both AWNNs for PJM price forecast studies contain 16 hidden nodes and one output. There are two AWNN input structures, one for predicting weekday prices and the other for weekend prices. For weekday forecasts, nine input data are used at hour $t$ on day D, which are loads at hours $(t-1)$, $t$ and $(t+1)$ on day D, historical prices at hour $t$ on days (D-1) and (D-2), and forecast prices at $(t-3)$, $(t-2)$, $(t-1)$ and $t$ based on the forecast results from ARMAX&GARCH models. For weekend forecasts, 14 input data are used at hour $t$ on day D, which are loads at hours $(t-1)$, $t$ and $(t+1)$ on day $D$, historical prices at hour $t$, $(t+1)$ and $(t+2)$ on day (D-1), historical prices at hour $(t-3)$, $(t-2)$, $(t-1)$ and $t$ on day (D-2), and forecast prices at $(t-3)$, $(t-2)$, $(t-1)$ and $t$ based on the forecast results from ARMAX and GARCH models. The selection of input features is based on correlation analysis, and the number of hidden nodes, 16, is based on the forecasting experience in the PJM market, which are all system specific.

The utilization and analysis of large data sets often represent a complex forecasting task. The process of feature selection is regarded as a reduction in dimensionality by choosing a subset of variables as features which are more relevant than others. It is likely that statistically less important components arise from noise which are not relevant to the intrinsic nature of the data. The dimensionality can be reduced by using statistical-based and artificial intelligence algorithms as principal component analysis, factor analysis, feature clustering, etc. [26], [27]. ARMAX considers hourly model structures on each day. However, the only two AWNN models are for weekdays and weekends, respectively.

### *E. Assessment of Forecasting*

Several measurements are used to examine the accuracy of forecast results. The mean absolute percentage error (MAPE) index in (14) is considered here to evaluate the performance of forecast results. MAPE represents the absolute average prediction error between predictions and actual targets:

$$\text{MAPE} = \left(\frac{1}{T}\cdot\sum_{t=1}^{T}\frac{|O_t - P_t|}{P_t}\right)\cdot 100\%. \tag{14}$$

If the actual value is small, (14) will contribute large terms to MAPE even if the difference between actual and forecast values is small. In addition, if the forecast value is small and actual value is large, the absolute percentage error will be close to 100% [28]. In order to avoid the adverse effect of very small prices, the AMAPE defined in (15) is adopted and compared with those in the literature. For (14) and (15), period $T$ could be hourly, daily, or weekly:

$$\text{AMAPE} = \left(\frac{1}{T}\cdot\sum_{t=1}^{T}\left[\frac{|O_t - P_t|}{\left(\frac{1}{T}\cdot\sum_{t=1}^{T}P_t\right)}\right]\right)\cdot 100\%. \tag{15}$$

Before using a single model or a combination of models to predict the future, we assume implicitly that there is a true model or a combination of models for a given series. However, the assumption is rarely accurate. Even if it is true, there is no guarantee that it will be selected as the best fit to the data. Thus the impact of model uncertainty on forecasts needs to be measured [23]. In this paper, we use the variance of forecast errors to measure this uncertainty. The smaller the variance, the less uncertain is the model or more accurate is the forecast results. The variance of error in a time span $T$ is defined as

$$\sigma_E^2 = \frac{1}{T}\cdot\sum_{t=1}^{T}\left(\left[\frac{|O_t - P_t|}{\left(\frac{1}{T}\cdot\sum_{t=1}^{T}P_t\right)}\right] - \text{AMAPE}\right)^2. \tag{16}$$

### *F. Monte Carlo Random Number Generator*

Series $a_t$ in the ARMAX model, series $\nu_t$ in the GARCH model, and noise $e$ in AWNN are regarded as Gaussian processes. Also, gradient algorithms used for the training of AWNN may be sensitive to initial conditions (i.e., weights, translation, and dilation factors). Evenly distributed random numbers would improve the universal search and the convergence process for the training of ARMAX, GARCH, and AWNN models. In this subsection, we describe the application of Monte Carlo method for generating more evenly distributed random numbers. We adopt antithetic variates, a variance reduction technique, to accelerate the convergence of results. A low-discrepancy Monte Carlo simulation method (lattice) is adopted with the possibility of accelerating the convergence rate. Random numbers in the lattice method are more evenly distributed. An $n$-point lattice rule of rank-$r$ in dimension $d$ is defined as

$$\left\{\sum_{i=1}^{r}\frac{k_i}{n_i}v_i \bmod 1,\ k_i = 0,1,\ldots,n_i - 1\ i = 1,\ldots r\right\} \tag{17}$$

where $v_1,\ldots,v_r$ are linearly independent $d$-vector of integers. If we draw $N$ independent samples according to the Monte Carlo simulation method, the iteration ends when the relative standard deviation is less than a predefined value (e.g., 95% relative standard deviation is given as $1.96\cdot\sigma/\sqrt{N}$ where $\sigma$ is the standard deviation and $N$ is number of simulations). Usually $N$ exceeds several thousands for a relatively small standard deviation. If the low-discrepancy method is used, the convergence will be accelerated from $O\left(1/\sqrt{N}\right)$ to nearly $O(1/N)$ and we can use a relatively smaller number of samples to reach the same convergence [24], [25]. The method of antithetic variates is a commonly used control variance method. It attempts to reduce the variance by introducing the negative dependence between pairs of replications. It is based on the observation that $Y_i = F^{-1}(U_i)$ and $\tilde{Y}_i = F^{-1}(1-U_i)$ have a distribution $F$ but are antithetic to each other. The basic idea is that the variance

after including the pair $\left(Y_i, \tilde{Y}_i\right)$ is smaller than just using the same size of random numbers generated by the ordinary Monte Carlo method [24], [25]. The emphasis on using the low-discrepancy method and the control variance method, lattice and antithetic variates, will generate more evenly distributed random numbers and accelerate the convergence.

## III. Case Studies

The proposed model is applied to predict electricity prices for the PJM market. It is trained and tested using the data set from January 1, 2005 to December 31, 2006. Price data and other supporting information are given in [13]. In all case studies, for the day D's price forecast, the training set includes actual price and load data up to the day before day D. Also, the demand up to one hour ahead the price forecast hour are assumed known. As reported in the literature [34], [35], short-term load forecasting has reached a comfortable state of performance with 1%–2% error. Thus load forecast errors will have very limited impacts on price forecast errors reported in the paper. The cases are listed as follows:

- Case 1) Five single days, selected for each month from January to May 2006 including weekdays and weekends, are forecast and compared with those in [31].
- Case 2) Two weeks, February 1–7, 2006 representing a low load demand week and February 22–28, 2006 representing a high load demand week, are studied and compared with results reported in [31]. Furthermore, in order to investigate the trend in the prediction quality degradation as we increase the number of predicted hours, the forecast is studied based on day-ahead and represented for the whole month of February 2006. The same hybrid model is used for the entire month.
- Case 3) Four one-week periods, the first seven days in each month of February, May, August, and November representing different seasons in 2006, are studied.

The cases are discussed as follows.

*1) Case 1:* Five single days

For a fair comparison, same five test days used in [31] are considered, which includes January 20, February 10, March 5, April 7, and May 13 in 2006. Five individual models are developed and forecast prices for those five days, respectively. The forecasts are presented in Table I and compared with those in [31]. The AMAPE given in (15) that is also used in [31] is considered for the results in Table I. In Table I and thereafter, the improvement is calculated as: (the difference between the forecast results reported in [31] and the forecast results reported in this paper) divided by (the forecast results reported in [31]). A lower forecast error indicates that results are more accurate. Table I shows the daily AMAPE for selected days. Comparing the daily AMAPE of the proposed forecasts with those in [31], we learn that the consideration of price series deviations and nonlinear characteristics would help improve the forecast accuracy. Table II shows the variance of forecast errors as a measure of the model uncertainty. The smaller the variance, the less uncertain is the model, thus the more accurate are the forecasts. Notable improvements in AMAPEs and error variances of the proposed method as compared to [31] are shown in the last column of Tables I and II. Table III compares the forecast results on April 7 using the proposed method and the method excluding GARCH (that is, only ARMAX and AWNN are used and GARCH is bypassed). Better results are obtained at most hours with GARCH, and the best one occurs at hour 12 with the actual price of 70.37$/MWh, which is 71.90$/MWh as compared to 66.20$/MWh without GARCH. The forecast results with GARCH are slightly worse at hours 4,7, 14,15, 23, and the worst one occurs at hour 15, with the actual price of 59.00 $/MWh, which is 51.29$/MWh as compared to 53.32$/MWh without GARCH. The final daily AMAPE of the proposed model is 4.17% as compared with the one without GARCH 4.72%, which indicates that by including GARCH, the final AMAPE for the whole day is improved by about 13.19% (i.e., $(4.72\% - 4.17\%)/4.17\%$).

TABLE I
Comparison of Daily AMAPEs for Case 1

| Day in 2006 | Proposed Method | Results in [31] | Improvement |
|---|---|---|---|
| Jan. 20th | 3.71% | 6.93% | 46.46% |
| Feb. 10th | 2.85% | 7.96% | 64.20% |
| Mar. 5th | 5.48% | 7.88% | 30.46% |
| Apr. 7th | 4.17% | 9.02% | 53.77% |
| May 13th | 4.06% | 6.91% | 41.24% |

TABLE II
Comparison of Daily Error Variances for Case 1

| Day in 2006 | Proposed Method | Results in [31] | Improvement |
|---|---|---|---|
| Jan. 20th | 0.0010 | 0.0034 | 70.59% |
| Feb. 10th | 0.0015 | 0.0050 | 70.00% |
| Mar. 5th | 0.0033 | 0.0061 | 45.90% |
| Apr. 7th | 0.0013 | 0.0038 | 65.79% |
| May 13th | 0.0015 | 0.0049 | 69.39% |

TABLE III
Comparison for April 7 for the Effect of GARCH ($/MWh)

| Hour | Actual Price | Proposed method | Without GARCH | Hour | Actual Price | Proposed method | Without GARCH |
|---|---|---|---|---|---|---|---|
| 1 | 34.33 | 35.76 | 35.79 | 13 | 64.92 | 61.91 | 61.90 |
| 2 | 31.85 | 35.38 | 35.92 | 14 | 62.50 | 57.80 | 58.80 |
| 3 | 31.09 | 34.49 | 36.36 | 15 | 59.00 | 51.29 | 53.32 |
| 4 | 30.32 | 32.24 | 32.23 | 16 | 53.05 | 51.10 | 50.82 |
| 5 | 31.59 | 31.28 | 30.67 | 17 | 50.13 | 47.27 | 47.27 |
| 6 | 38.02 | 42.41 | 43.30 | 18 | 45.95 | 45.95 | 45.85 |
| 7 | 60.59 | 66.46 | 65.99 | 19 | 49.77 | 50.38 | 50.92 |
| 8 | 67.06 | 68.60 | 68.88 | 20 | 62.25 | 62.25 | 62.86 |
| 9 | 68.91 | 68.82 | 70.09 | 21 | 69.08 | 69.88 | 70.57 |
| 10 | 68.72 | 67.50 | 67.40 | 22 | 63.33 | 60.96 | 60.76 |
| 11 | 66.15 | 66.97 | 66.97 | 23 | 46.45 | 46.05 | 46.70 |
| 12 | 70.37 | 71.90 | 66.20 | 24 | 42.44 | 40.06 | 39.87 |

Figs. 12 and 13 show the day-ahead price forecasts for chosen days of April 7 and May 13, 2006. It is reported in [31] that the prediction is particularly inaccurate for the morning and evening peaks of April 7, 2006. Fig. 12 shows that the prediction is improved by applying the proposed method for the morning and evening peaks, and the daily AMAPE is improved from 9.02% to 4.17%, with a 53.77% improvement. In Fig. 13, the prediction is improved for the daily and evening peaks especially at hours 9:00 and 21:00. The forecast inaccuracy is improved here especially for very large peaks, which are essential to GENCOs' bidding strategies.

*2) Case 2:* Two weeks with low and high load demands

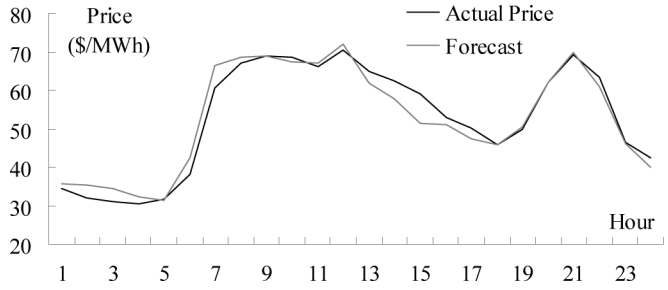


Fig. 12. Actual and forecast prices for April 7, 2006.

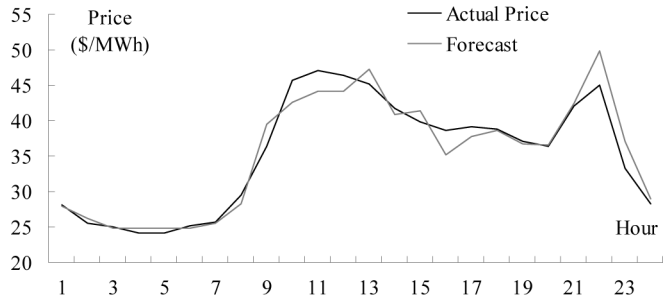


Fig. 13. Actual and forecast prices for May 13, 2006.

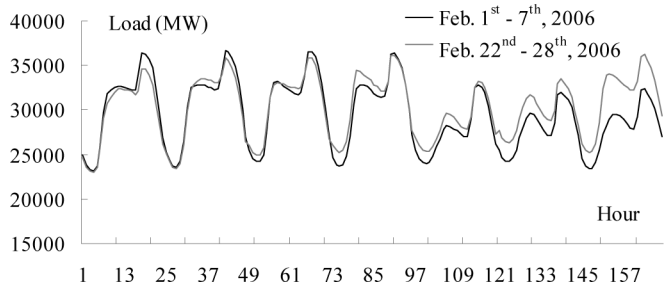


Fig. 14. Actual load profile for February 1–7 and February 22–28, 2006.

Two weeks, February 1–7, 2006 representing a low demand week and February 22–28, 2006 representing a high demand week, are studied. Load profiles for these two weeks are shown in Fig. 14.

Tables IV and V compare the performance of the proposed method with that of [31]. For these two weeks, both the AMAPE and error variance are notably improved. Especially in the week of February 22–28, 2006, the AMAPE is decreased from 8.88% to 5.01%, which is improved by 43.58%. With the proposed forecasting method, the maximal daily AMAPE of 8.25% is even smaller than the weekly AMAPE of 8.88% as reported in [31]. These forecasts are based on day-ahead and represented for one week. That is, the actual prices of the PJM market on February 1, 2006 are used as inputs to forecast the price on February 2, 2006 and so on; however, only one hybrid model is used for the entire week.

The weekly forecasts for February 1–7, 2006 are presented in Fig. 15 which shows price forecasts obtained from the proposed model follow the trend of actual market prices. When price spikes appear during peak hours in the last three days of this week, the proposed model outperforms that in [31] by capturing actual prices more closely as highlighted in Fig. 15. The weekly AMAPE proposed by the hybrid model is 5.27%

TABLE IV
COMPARISON OF WEEKLY AMAPES FOR CASE 2

| Week (2006) | | Proposed Method | Results in [31] | Improvement |
|---|---|---|---|---|
| Feb. 1st 7th | Max. Daily AMAPE | 8.21% | 11.32% | 27.47% |
| | Min. Daily AMAPE | 2.98% | 5.94% | 49.83% |
| | Weekly AMAPE | 5.27% | 7.66% | 31.20% |
| Feb. 22nd-28th | Max. Daily AMAPE | 8.25% | 12.37% | 33.31% |
| | Min. Daily AMAPE | 2.11% | 5.66% | 62.72% |
| | Weekly AMAPE | 5.01% | 8.88% | 43.58% |

TABLE V
COMPARISON OF WEEKLY ERROR VARIANCES FOR CASE 2

| Week (2006) | Proposed Method | Results in [31] | Improvement |
|---|---|---|---|
| Feb. 1st 7th | 0.0037 | 0.0066 | 43.94% |
| Feb. 22nd-28th | 0.0025 | 0.0047 | 46.81% |

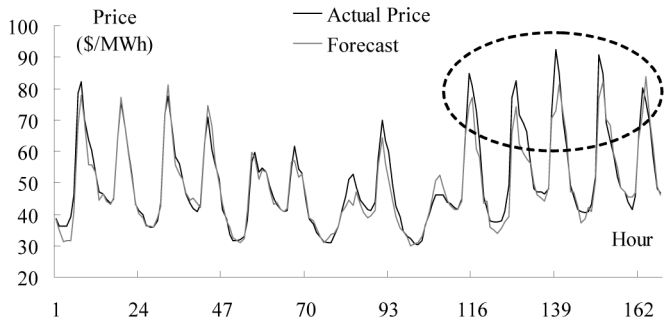


Fig. 15. Actual and forecast prices for February 1–7, 2006.

as compared to 7.66% reported in [31], which shows a 31.20% improvement.

Similarly, weekly forecasts of February 22–28, 2006 are presented in Fig. 16. According to Fig. 14, load patterns for the first five days are similar in these two weeks. Large loads occur in later days of the week, which increase electric prices. In comparison with [31], the proposed weekly AMAPE is decreased from 8.88% to 5.01%, with a 43.58% improvement. Also, the proposed accuracy of forecasts is improved especially for the last day of the week as highlighted. The quality of prediction may deteriorate as the number of predicted hours increases since the same set of hybrid models will be used to for the entire week instead of developing a set of new models for each day.

Table VI gives the forecast error variance, corresponding to the same hours on different days of the week of February 1–7, 2006, to measure the model uncertainty. The smaller the variance, the less uncertain is the model and the more accurate are the forecasts. Variances for off-peak hours are much less than those of peak hours. The largest variances, which are less than 0.008, occur during hours 5–7. The second largest variances of 0.005 occur during hours 19–21 which are the evening. Variances less than 0.002 occur at off-peak hours.

The prediction quality deteriorates gradually as the number of predicted hours increases. In order to show the degradation of the forecast based on the increasing number of predicted hours, forecasts based on the single day-ahead model for the whole month of February 2006 are presented in Fig. 17 and Table VII. The results show that the forecast performance deteriorates slowly as the number of predicted hours increases. As

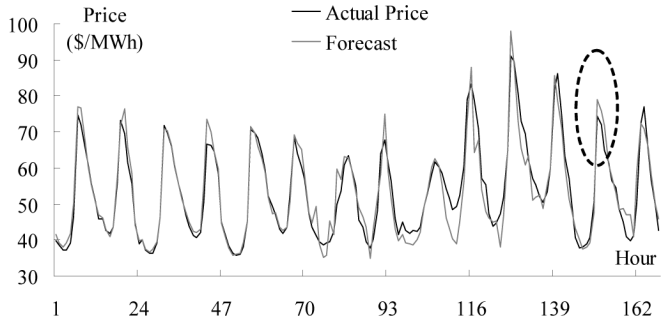


Fig. 16. Actual and forecast prices for February 22–28, 2006.

TABLE VI
VARIANCE OF HOURLY FORECAST ERRORS FOR FEBRUARY 1–7, 2006 IN CASE 2

| Hour | Variance | Hour | Variance | Hour | Variance |
|---|---|---|---|---|---|
| 1 | 0.00042 | 9 | 0.00202 | 17 | 0.00024 |
| 2 | 0.00133 | 10 | 0.00242 | 18 | 0.00023 |
| 3 | 0.00254 | 11 | 0.00374 | 19 | 0.00566 |
| 4 | 0.00199 | 12 | 0.00044 | 20 | 0.00175 |
| 5 | 0.00436 | 13 | 0.00031 | 21 | 0.00492 |
| 6 | 0.00559 | 14 | 0.00029 | 22 | 0.00084 |
| 7 | 0.00759 | 15 | 0.00052 | 23 | 0.00062 |
| 8 | 0.00145 | 16 | 0.00120 | 24 | 0.00067 |

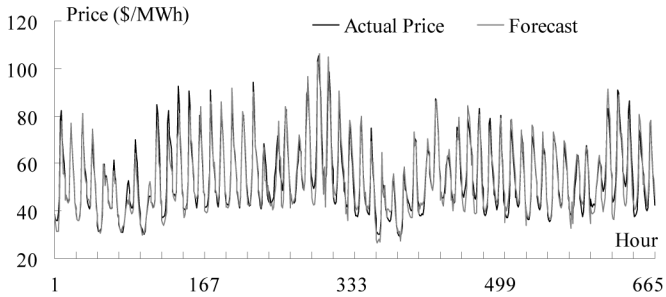


Fig. 17. Actual and forecast prices for February 1–28, 2006.

TABLE VII
COMPARISON OF MAPES FOR THE MONTH OF FEBRUARY 1–28, 2006

| Test Week (2006) | Feb. 1st -7th | Feb. 8th -14th | Feb. 15th-21st | Feb. 22nd-28th |
|---|---|---|---|---|
| Weekly AMAPE | 5.27% | 6.09% | 6.26% | 6.70% |

shown in Table IV, with a newly developed model for the week of February 22–28, 2006, the weekly AMAPE is 5.01%. In comparison, the same period results based on the monthly forecast would increase to 6.70% as shown in Table VII. This test shows that a single model can be applied to several weeks.

The hybrid model would be updated as required if the current forecasting model is not accurate enough. Accordingly, we train the new model offline using the historical data. The technology of incremental learning would be applied for reducing the frequency of developing the new model. The technology would update the existing model in an incremental fashion to accommodate the new data without compromising the performance [36].

*3) Case 3:* Four one-week periods for seasons in 2006

In this case, four weeks, the first seven days in each month of February, May, August, and November representing different

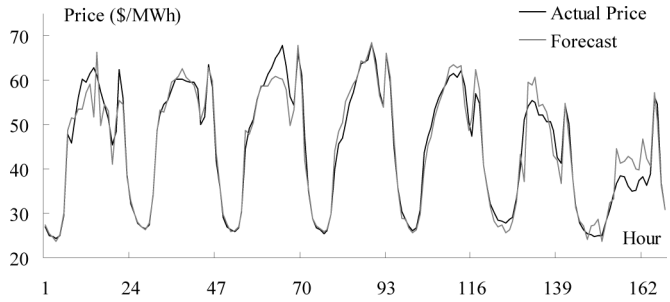


Fig. 18. Actual and forecast prices for May 1–7, 2006.

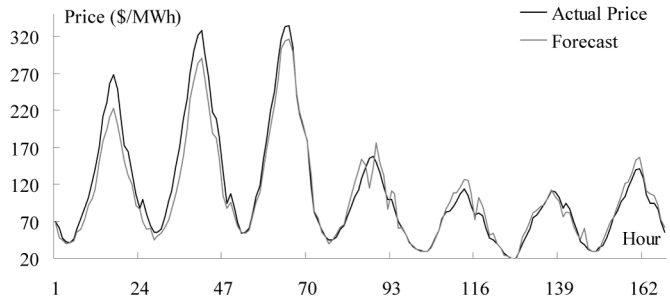


Fig. 19. Actual and forecast prices for August 1–7, 2006.

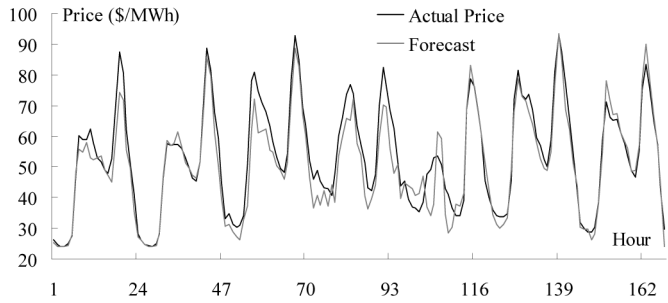


Fig. 20. Actual and forecast prices for November 1–7, 2006.

TABLE VIII
FORECAST RESULTS OF WEEKLY FORECAST PERFORMANCE OF CASE 3

| Test Week (2006) | Feb. | May | Aug. | Nov. |
|---|---|---|---|---|
| Weekly AMAPE | 5.27% | 4.64% | 11.28% | 7.70% |
| Max. Daily AMAPE | 8.21% | 8.75% | 16.04% | 11.94% |
| Min. Daily AMAPE | 2.98% | 1.79% | 5.59% | 3.63% |
| Error Variance | 0.0047 | 0.0026 | 0.0126 | 0.0050 |

seasons in year 2006, are studied. Table VIII shows the forecasts. The smallest weekly AMAPE occurs in the week of May, and the largest occurs in the week of August, which is mainly due to large spikes occurring during that week. Figs. 18–20 show price forecasts for weeks of May, August, and November. The different price curves show seasonal variant volatilities for the PJM electricity market. Daily prices in May and November appear to be more periodic than those in August, and the two weekly forecasts follow the actual prices more closely.

In the week of August 2006, spikes as large as over 350$/MWh occur on August 3, 2006. Another two spikes occur on peak hours of August 1 and 2, 2006. Fig. 19 shows that the proposed price forecasts follow the trend of actual market price spikes when spikes are directly related to the load values,

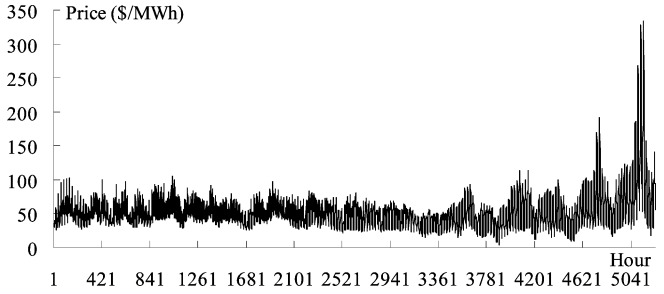


Fig. 21. Actual price from January 1, 2006 to August 7, 2006.

TABLE IX
FORECAST FOR THREE LARGE SPIKES FOR THE WEEK OF AUGUST 1–7, 2006

| Hour | Actual price ($/MWh) | Forecast price($/MWh) | Error |
|---|---|---|---|
| 17:00 on Aug. 1st, 2006 | 267.99 | 223.02 | 16.78% |
| 17:00 on Aug. 2nd, 2006 | 328.04 | 289.83 | 11.65% |
| 17:00 on Aug. 3rd, 2006 | 333.91 | 316.61 | 5.18% |

although the spike quantity is not predicted very accurately. Fig. 21 shows the actual price series from January 1, 2006 to August 7, 2006. The spikes, as large as 267.99$/MWh, occurring on August 1, 2006 are the first large spikes in 2006. Thus, spike forecasts for August 1, 2006 would hardly capture actual spikes, which is mainly due to the lack of historical spike information when the model is built. Although forecast spike magnitudes are smaller than those of actual prices, the proposed algorithm does predict the spike vertex to some level of accuracy. Reference [31] did not report any results on such large spikes in the PJM market. In fact, the literature on price spike forecasts is very limited. Zhao *et al.* [30] forecasted price spikes of the Queensland Electricity market in June 2004 with forecast errors of 20%. Table IX gives the hourly forecasts at peak hours on the first three days. The largest hourly spike forecast error, which is 16.78%, occurs at 17:00 on August 1, 2006, and the smallest, as low as 5.18%, occurs at 17:00 hours on August 3, 2006.

Compared with [30], the accuracy of the proposed price spike forecasts is sufficiently good considering the extreme volatility of spike signals. Furthermore, forecasts capture actual prices very well when prices suddenly drop by about 50% on August 4, 2006 from over 350$/MWh to as low as 157$/MWh. Other explanatory factors that may affect electricity prices such as weather, available ancillary services, power exchanges, and the availability of generators and transmission lines are not included in the proposed day-ahead price forecasting model. Such factors are less important for price forecasting in most situations, and their inclusion may cause overfitting or even deteriorate the accuracy of the forecasting method. With modern SCADA/EMS systems, one can monitor/evaluate the power system status and perform very short-time price forecasts with the proposed model, which improves the forecasting of spikes.

## IV. CONCLUSIONS

Several case studies are chosen for the PJM electricity market with various levels of price spikes to test and validate the proposed model. The proposed hybrid time-series and AWNN model, composed of linear and nonlinear relationships of prices and explanatory variables, improves the performance of forecast results. The usage of one-period continuously compounded return series and AWNN has an advantage of modeling nonstationary electricity prices, especially price spikes. The use of AWNN as a consistent function estimator and two overfitting detection indications diminishes the overfitting issue when including history spikes in the training data set for price spikes forecasting. It is observed that the proposed hybrid model outperforms the literature, and considering the extreme volatility of the spike signal, the price spike forecast accuracy level of the proposed model is sufficiently good as compared with those reported in the literature.

## REFERENCES

[1] M. Shahidehpour, H. Yamin, and Z. Y. Li, *Market Operations in Electric Power Systems*. New York: Wiley, 2002.
[2] Y. Fu and Z. Li, "Different models and properties on LMP calculations," in *Proc. IEEE Power Eng. Soc. General Meeting*, Montreal, QC, Canada, Jun. 2006.
[3] P. Skantze, M. Ilic, and J. Chapman, "Stochastic modeling of electric power prices in a multi-market environment," in *Proc. IEEE Power Eng. Soc. Winter Meeting*, Singapore, Jan. 2000, pp. 1109–1114.
[4] M. T. Barlow, "A diffusion model of electricity prices," *Math. Fin.*, vol. 12, pp. 287–298, 2002.
[5] F. Bolle, "Competition with supply and demand functions," *Energy Econ.*, vol. 23, pp. 253–271, 2001.
[6] T. Li and M. Shahidehpour, "Strategic bidding of transmission-constrained GENCOs with incomplete information," *IEEE Trans. Power Syst.*, vol. 20, no. 1, pp. 437–447, Feb. 2005.
[7] G. Gross and F. D. Galiana, "Short-term load forecasting," *Proc. IEEE*, vol. 75, no. 12, pp. 1558–1573, Dec. 1987.
[8] M. T. Hagan and S. M. Behr, "The time series approach to short term load forecasting," *IEEE Trans. Power Syst.*, vol. 2, no. 3, pp. 785–791, Aug. 1987.
[9] J. Contreras, R. Espínola, F. J. Nogales, and A. J. Conejo, "ARIMA models to predict next-day electricity prices," *IEEE Trans. Power Syst.*, vol. 18, no. 3, pp. 1014–1020, Aug. 2003.
[10] A. J. Conejo, M. A. Plazas, R. Espínola, and A. B. Molina, "Day-ahead electricity price forecasting using the wavelet transform and ARIMA models," *IEEE Trans. Power Syst.*, vol. 20, no. 2, pp. 1035–1042, May 2005.
[11] F. Gao, X. H. Guan, X. -R. Cao, and A. Papalexopoulos, "Forecasting power market clearing price and quantity using a neural network method," in *Proc. IEEE Power Eng. Soc. Summer Meeting*, Seattle, WA, Jul. 2000, pp. 2183–2188.
[12] X. Guan, Y. C. Ho, and D. L. Pepyne, "Gaming and price spikes in electric power markets," *IEEE Trans. Power Syst.*, vol. 16, no. 3, pp. 402–408, Aug. 2001.
[13] PJM Electricity Market Data. [Online]. Available: http://www.pjm.com/.
[14] J. Y. Campbell, A. W. Lo, and A. C. MacKinlay, *The Econometrics of Financial Markets*. Princeton, NJ: Princeton Univ. Press, 1997.
[15] R. S. Tsay, *Analysis of Financial Time Series*, 2nd ed. New York: Wiley, 2005.
[16] R. S. Tsay and G. C. Tiao, "Consistent estimates of autoregressive parameters and extended sample autocorrelation function for stationary and nonstationary ARMA models," *J. Amer. Statist. Assoc.*, vol. 79, no. 385, pp. 84–96, Mar. 1984.
[17] J. B. Copas, "Regression, prediction and shrinkage," *J. Roy. Statist. Soc.*, ser. B 45, no. 3, pp. 311–354, 1983.
[18] T. Bollerslev, "Generalized autoregressive conditional heteroscedasticity," *J. Econ.*, vol. 31, pp. 307–327, 1986.
[19] A. P. Engelbrecht, *Computational Intelligence: An Introduction*. New York: Wiley, 2002.
[20] Q. Zhang and A. Benveniste, "Wavelet networks," *IEEE Trans. Neural Netw.*, vol. 3, no. 6, pp. 889–898, Nov. 1992.
[21] J. Zhang, G. G. Walter, Y. Miao, and W. N. W. Lee, "Wavelet neural networks for function learning," *IEEE Trans. Signal Process.*, vol. 43, no. 6, pp. 1485–1497, Jun. 1995.

[22] A. Röbel, The Dynamic Pattern Selection Algorithm: Effective Training and Controlled Generalization of Backpropagation Neural Networks, Tech. Univ. Berlin, Berlin, Germany, 1993, Tech. Rep. 93–23.
[23] C. Chatfield, *Time-Series Forecasting*. London, U.K.: Chapman & Hall/CRC, 2000.
[24] L. Wu, M. Shahidehpour, and T. Li, "Stochastic security-constrained unit commitment," *IEEE Trans. Power Syst.*, vol. 22, no. 2, pp. 800–811, May 2007.
[25] G. Paul, *Monte Carlo Simulation Method in Financial Engineering*. New York: Springer, 2003.
[26] I. Guyon and A. Elisseeff, "An introduction to variable and feature selection," *J. Mach. Learn. Res.*, vol. 3, pp. 1157–1182, Mar. 2003.
[27] A. Jain and D. Zongker, "Feature selection: Evaluation, application, and small sample performance," *IEEE Trans. Pattern Anal. Mach. Intell.*, vol. 19, no. 2, pp. 153–158, Feb. 1997.
[28] H. Y. Yamin, S. M. Shahidehpour, and Z. Li, "Adaptive short-term electricity price forecasting using artificial neural networks in the restructured power markets," *Elect. Power Energy Syst.*, vol. 26, pp. 571–581, 2004.
[29] N. R. Swanson and H. White, "A model selection approach to real-time macroeconomic forecasting using linear models and artificial neural networks," *Rev. Econ. Statist.*, vol. 79, no. 4, pp. 540–550, Nov. 1997.
[30] J. Zhao, Z. Dong, X. Li, and K. Wong, "A framework for electricity price spike analysis with advanced data mining methods," *IEEE Trans. Power Syst.*, vol. 22, no. 1, pp. 376–385, Feb. 2007.
[31] P. Mandal, T. Senjyu, N. Urasaki, T. Fundabashi, and A. K. Srivastava, "A novel approach to forecast electricity price for PJM using neural network and similar days method," *IEEE Trans. Power Syst.*, vol. 22, no. 4, pp. 2058–2065, Nov. 2007.
[32] C. M. Ruibal and M. Mazumdar, "Forecasting the mean and the variance of electricity prices in deregulated markets," *IEEE Trans. Power Syst.*, vol. 23, no. 1, pp. 25–32, Feb. 2008.
[33] N. M. Pindoriya, S. N. Singh, and S. K. Singh, "An adaptive wavelet neural network-based energy price forecasting in electricity markets," *IEEE Trans. Power Syst.*, vol. 23, no. 3, pp. 1423–1432, Aug. 2008.
[34] T. Senjyu, P. Mandal, K. Uezato, and T. Funabashi, "Next day load curve forecasting using hybrid correction method," *IEEE Trans. Power Syst.*, vol. 20, no. 1, pp. 102–109, Feb. 2005.
[35] D. W. Bunn, "Forecasting loads and prices in competitive power markets," *Proc. IEEE*, vol. 88, no. 2, pp. 163–169, Feb. 2000.
[36] R. Polikar, L. Udpa, S. S. Udpa, and V. Honavar, "Learn++: An incremental learning algorithm for supervised neural networks," *IEEE Trans. Syst., Man, Cybern. C. Appl. Rev.*, vol. 31, no. 4, pp. 497–508, Nov. 2001.

**Lei Wu** (M'07) received the Ph.D. degree in electrical engineering from Illinois Institute of Technology, Chicago, in 2008.

Presently, he is a visiting Professor at Illinois Institute of Technology. His research interests include power systems restructuring, reliability, and economics.

**Mohammad Shahidehpour** (F'01) is the Bodine Distinguished Professor in the Electrical and Computer Engineering Department at Illinois Institute of Technology (IIT), Chicago. He is an honorary professor at the North China Electric Power University and the Sharif University in Iran.

Dr. Shahidehpour is the VP for Publications of the IEEE Power & Energy Society. He is the recipient of an honorary doctorate from the Polytechnic University of Bucharest.

*ISSN 1868-3967, Volume 1, Number 3*

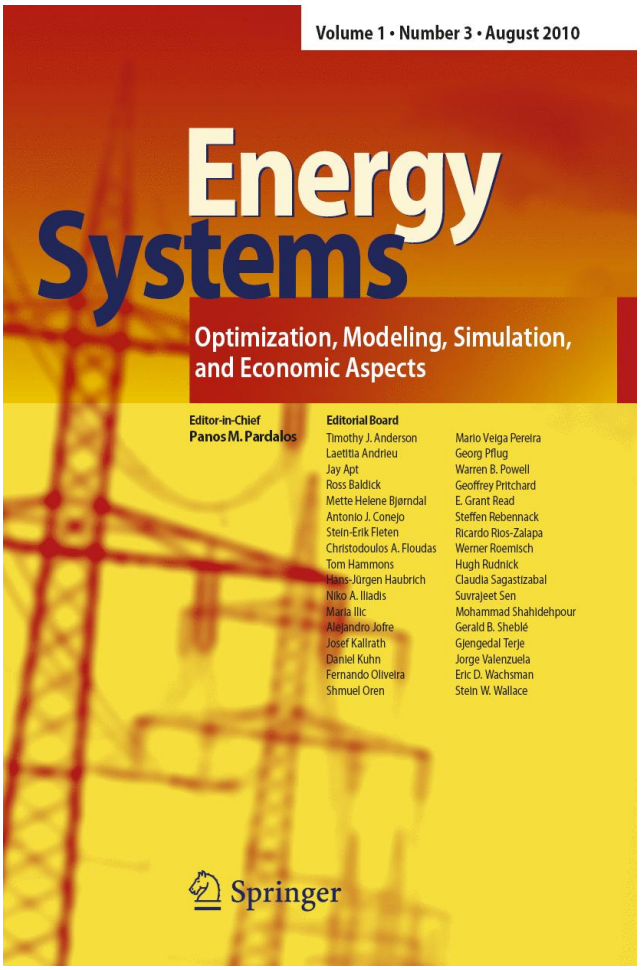

Energy Syst (2010) 1: 339–376
DOI 10.1007/s12667-010-0015-4



ORIGINAL PAPER

# Accelerating the Benders decomposition for network-constrained unit commitment problems

**Lei Wu · Mohammad Shahidehpour**

Received: 21 February 2010 / Accepted: 31 May 2010 / Published online: 16 June 2010


**Abstract** This paper presents an optimization method by generating multiple strong Benders cuts for accelerating the convergence of Benders Decomposition (BD) when solving the network-constrained generation unit commitment (NCUC) problem. In NCUC, dc transmission network evaluation subproblems are highly degenerate, which would lead to many dual optimal solutions. Furthermore, the classical BD cuts are often low-density which involve only a limited number of decision variables in the master problem. Therefore, the dual optimal solutions and the corresponding Benders cuts are of crucial importance for improving the efficiency of the BD algorithm. The proposed method would generate multiple strong Benders cuts, which are pareto optimal, among candidates from multiple dual optimal solutions. Such cuts would be high-density in comparison with low-density cuts produced by the classical BD. The proposed multiple strong Benders cuts are efficient in terms of reducing the total iteration number and the overall computing time. The high-density cuts may restrict the feasible region of the master unit commitment (UC) problem in each iteration as they incorporate more decision variables in each Benders cut. The multiple strong Benders cuts would accordingly reduce the iteration number and overall computing time. Numerical tests demonstrate the efficiency of the proposed multiple strong Benders cuts method in comparison with the classical BD algorithm and the linear sensitivity factors (LSF) method. The proposed method can be extended to other applications of BD for solving the large-scale optimization problems in power systems operation, maintenance, and planning.

This work is supported in part by the National Science Foundation grants ECCS-0725666 and ECCS-0801853.

L. Wu · M. Shahidehpour (✉)
Electrical and Computer Engineering Department, Illinois Institute of Technology, Chicago, IL 60616, USA
e-mail: ms@iit.edu

L. Wu
e-mail: lwu10@iit.edu

**Keywords** Electric power systems · Network-constrained unit commitment · Benders decomposition · Multiple strong Benders cuts · Degenerate · Multiple optimal dual solutions · Low-density · Pareto optimal · LSF

**Nomenclature**

*Indices*

| | |
|---|---|
| $a, b, m, n$ | Denote a bus |
| $d, d'$ | Denote a BD iteration |
| $i, j$ | Denote a unit |
| $k$ | Denote a segment of a cost curve function |
| $l, l'$ | Denote a transmission line |
| $o, o'$ | Denote a subset |
| $p$ | Denote a phase shifter |
| $t, \tau$ | Hourly index |

*Sets and vectors*

| | |
|---|---|
| $\mathbf{B}, \mathbf{B}_o, \mathbf{B}_{o'}$ | Set/subsets of buses |
| $\mathbf{f}(b), \mathbf{t}(b)$ | Set of transmission lines starting from bus $b$/ending at bus $b$ |
| $\mathbf{PL}_t$ | Vector of power flow variables at hour $t$ |
| $\mathbf{PL}^{\max}$ | Vector of power flow upper limit |
| $\mathbf{U}(b)$ | Set of generators located at bus $b$ |
| $\mathbf{Z}, \mathbf{Z}^c, \mathbf{SZ}_o, \mathbf{SZ}_{o'}$ | Sets of buses |
| $\gamma(m)$ | Denote a set of buses, for each bus n in the set, there is a phase shifter at line m to $n$, and $m$ is the tap side and $n$ is the non-tap side |
| $\gamma_t$ | Vector for phase shifter at hour $t$ |
| $\gamma^{\min}, \gamma^{\max}$ | Vector of phase shifter lower/upper limits |

*Variables*

| | |
|---|---|
| $DT_i, UT_i$ | Number of hours unit $i$ must be initially offline/online due to its minimum off/on time limits |
| $G$ | Objective value of the global optimal solution to the original problem |
| $I_{it}, P_{it}$ | Unit commitment decision/generation dispatch of unit $i$ at hour $t$ |
| $LB_d, UB_d$ | Lower/upper bound of the original problem objective value obtained at BD iteration $d$ |
| $LB_{best}, UB_{best}$ | Best obtained lower/upper bounds for the objective value to the original problem |
| $offset$ | Offset term in the linear expression of the power loss |
| $OR_{it}, SR_{it}$ | Non-spinning/spinning reserve provided by unit $i$ at hour $t$ |
| $P_{ikt}$ | Generation dispatch of unit $i$ at hour $t$ at segment $k$ |
| $P_{Losst}$ | System loss at hour $t$ |
| $PL_{lt}$ | Power flow of transmission line $l$ at hour $t$ |
| $q, q_1, q_2, Q$ | Dual variables for the dual problem |
| $s$ | Slack variable |
| $SD_{it}, SU_{it}$ | Shutdown/startup cost of unit $i$ at hour $t$ |
| $\theta_{at}, \theta_{bt}$ | Phase angle of bus $a$ and bus $b$ at hour $t$ |
| $\theta_{ref}$ | Phase angle of the reference bus |

  

| | |
|---|---|
| $\gamma_{abt}$ | Phase shifter value on the line from bus $a$ to bus $b$ at hour $t$ |
| $\lambda, \kappa, \pi$ | Dual variables for the primal problem |
| $\|\mathbf{Z}\|$ | Number of buses that belong to set $\mathbf{Z}$ |
| $\hat{\cdot}, \tilde{\cdot}$ | Value for variables calculated at previous BD iterations |

*Constants*

| | |
|---|---|
| $c$ | A constant integer number determined during the algorithm |
| $C_b$ | Loss distribution factor corresponding to bus $b$ |
| $c_{ik}, N_i$ | Incremental cost for segment $k$ and no-load cost of unit $i$ |
| $D_{bt}$ | System load at bus $b$ hour $t$ |
| $DP_i, UP_i$ | Shutdown/startup ramp limits of unit $i$ |
| $DR_i, UR_i$ | Ramping down/ramping up limits of unit $i$ |
| $LF_b$ | Loss factor related to bus $b$ |
| $LSF_{ab}^m$ | The sensitivity of the power flow on line $l$ (from bus $a$ to bus $b$) to power injection at bus $m$ |
| $M, \varepsilon$ | Very large/small positive number |
| $MSR_i$ | Spinning reserve that can be provided by unit $i$ in one minute |
| $NB$ | Number of buses |
| $NT$ | Number of hours under study |
| $P_{Dt}, P_{Lt}$ | System load/loss at hour $t$ |
| $P_i^{\min}, P_i^{\max}$ | Minimum/maximum capacity of unit $i$ |
| $P_{ik}^{\max}$ | Maximum capacity of unit $i$ of segment $k$ |
| $QSC_i$ | Quick start capacity of unit $i$ |
| $R_{Ot}, R_{St}$ | System non-spinning/spinning reserve requirements at hour $t$ |
| $T_i^{on}, T_i^{off}$ | Minimum on/off time limits of unit $i$ |
| $x_{ab}$ | Line reactance between bus $a$ and bus $b$ |
| $X_{i0}^{on}, X_{i0}^{off}$ | On/off time counter of unit $i$ at the initial status |

## 1 Introduction

In restructured power systems, self-interested entities, including generation companies (GENCOs), transmission companies (TRANSCOs), and distribution companies (DISCOs), are to maximize their own profits and minimize potential risks when participating in power markets. The independent system operator (ISO) coordinates market participants and operates the competitive market efficiently for ensuring a secure and economic operation. Such decisions corresponding to the power system operation, maintenance, and planning are to be made via efficient optimization models and methodologies [1]. Efficient decomposition methods are utilized in large power system optimization problems since most of the optimization problems belong to non-deterministic polynomial-time hard (NP-hard) problems and the solution to the original problem in such cases would be an intractable task without decomposition.

The BD algorithm was first introduced by J.F. Benders [2] for solving large-scale, mixed-integer programming (MIP) problems. BD is a common technique for separating large scale power system problems into several easy-to-solve subproblems. The algorithm is widely adopted in various power system optimization problems including security-constrained unit commitment (SCUC) and security-constrained optimal

power flow (SCOPF) [3–9]. Reference [3] applied BD to SCUC problems for separating the unit commitment (UC) in the master problem from the hourly network security check in subproblems. The subproblems checked the ac network security constraints based on the UC solution to determine whether a converged and secure ac power flow solution would be feasible. If the feasibility conditions could not be satisfied, the feasibility Benders cuts were fed back to the master UC problem for seeking a feasible UC solution based on the added cuts. Reference [4] considered BD applications to generation and transmission planning problems by decoupling the master planning problems from the network evaluation and network security checking subproblems. Reference [5] used the feasibility theorem of BD to derive an analytical condition for determining whether feasible solutions of the original SCUC problems could be obtained from the current dual solution of Lagrangian Relaxation. Reference [6] proposed a BD-based algorithm for calculating a preventive dispatch solution based on a full ac power flow. It solved the optimal power flow in the master problem, and then minimized the real and reactive power by fictitious sources in subproblems. Reference [7] used the generalized BD to solve the large-scale multiperiod optimal power flow problem. The problem considered the start-up and shutdown characteristics of thermal units, the transmission network model, and hydraulic equations for integrated hydroelectric plants in a river system. Optimality cuts generated at each iteration provided a lower estimate of total operation cost in the Benders subproblem. Reference [8] applied generalized feasibility Benders cuts for optimizing the post-contingency corrective action in SCUC, which accurately formulated the hourly UC of quick-start units in post-contingency corrective actions via a MIP subproblem instead of linear programming (LP). Reference [9] discussed a general structure of BD for power system decision making applications. Three categories of decision-making problems in power systems for economic, reliability, and risk evaluations were mapped onto Benders subproblems. The applications demonstrated the potential use of BD for solving special structured MIP problems in power systems.

The classical BD algorithm often converges slowly, i.e., the slow convergence would introduce major computational bottlenecks for a MIP problem which has to be solved repeatedly in practical cases. Several studies discussed possible improvements for accelerating the BD convergence. Reference [10] discussed several ways of improving the performance of BD including a judicious selection of optima from the Benders subproblems to generator strong cuts and properly formulate the subsequent BD problems. Reference [11] proposed to generate cuts from the solution of a LP-approximated master problem by relaxing the integrality request for the first several iterations. Similarly, [12] discussed that only a feasible, rather than an optimal, solution of master problem was necessary for subproblems to generate cuts. Therefore, heuristic methods were sought, in place of the optimal solution of master problem, to quickly locate feasible solutions for generating cuts. In this situation, the convergence was not guaranteed since the cuts were only associated with a set of feasible master solutions. On the other hand, [13] proposed to generate inexact cuts which were to derive a good enough dual solution, instead of the optimal dual solution, for subproblems. In such cases, subproblems were very large-scale LP problems which required a substantial computation time to get the solution. Reference [14] applied the subsystems of an infeasible LP to generate feasibility cuts, and computational results

  

showed that the method converged faster than that with feasibility cuts generated via extreme rays located by the simplex method. Recently, [15] proposed an algorithm to accelerate the BD by exploring the local branching in the neighborhood of the master problem solution. The lower and the upper bounds were simultaneously improved via local branching in which each located feasible solution was used to generator optimality/feasibility cuts.

This paper proposes multiple strong Benders cuts at each iteration to accelerate the convergence of the NCUC problem. The experiments have shown that the drawback of classical BD algorithm resides in the slow convergence for large-scale power system applications [4]. As will be proved in this paper, each strong Benders cut generated through the proposed algorithm is a pareto optimal cut, and the proposed method reduces the number of Benders iterations as well as the overall computing time. The proposed BD strategy can be easily extended to other large-scale optimization problems in power systems.

The rest of the paper is organized as follows. Section 2 presents the NCUC model and the classical BD algorithm. Section 3 proposes two methods for generating multiple strong cuts at each iteration for accelerating convergence, and in the appendix we prove that each generated cut is pareto optimal. Section 4 presents three cases to discuss the effectiveness of the proposed method. The conclusions are drawn in Sect. 5.

## 2 NCUC problem formulation and solution methodology

The NCUC problem is formulated as a MIP problem shown in (1)–(8). The objective function is to minimize the total operation cost, including incremental cost, no-load cost, and startup/shutdown cost, as shown in (1), subject to a set of system and generating unit constraints. System constraints include the system power balance in (2), and the system spinning and non-spinning reserve requirements in (3). Unit constraints include ramping up/down limits as well as startup/shutdown ramping for individual units in (4), minimum on and off time constraints in (5), real power generation limits in (6), and constraints on spinning and non-spinning reserves provided by individual generators in (7). Only thermal units are modeled in (4)–(7). The formulation of other types of generating units including combined-cycle, cascaded hydro, and pumped storage, is discussed in the authors' previous work [19]. Here, (8) represents the dc network evaluation constraints, which include power balance for each bus $b$, power flow equation for each transmission line $l$, and phase shifter and transmission power flow limits. For simplicity, $P_{Losst}$ is given initially as an input which is estimated as a percentage of the system load $P_{Dt}$. A more accurate loss formulation is given in (9) if the loss factor $LF_b$ is known, which represents the sensitivity of power loss to the bus power injection

$$G = \text{Min} \sum_t \sum_i \left[ \sum_k c_{ik} \cdot P_{ikt} + N_i \cdot I_{it} + SU_{it} + SD_{it} \right] \tag{1}$$

$$\text{S.t.} \quad \sum_i P_{it} = P_{Dt} + P_{Losst} \tag{2}$$

$$\sum_i SR_{it} \geq R_{St}$$
$$\sum_i OR_{it} \geq R_{Ot} \tag{3}$$

$$P_{it} - P_{i(t-1)} \leq UR_i \cdot I_{i(t-1)} + UP_i \cdot (I_{it} - I_{i(t-1)}) + P_i^{\max} \cdot (1 - I_{it})$$
$$P_{i(t-1)} - P_{it} \leq DR_i \cdot I_{it} + DP_i \cdot (I_{i(t-1)} - I_{it}) + P_i^{\max} \cdot (1 - I_{i(t-1)}) \tag{4}$$

$$\sum_{t=1}^{UT_i} (1 - I_{it}) = 0, \quad \text{where } UT_i = \max\{0, \min[NT, (T_i^{on} - X_{i0}^{on}) \cdot I_{i0}]\}$$
$$\sum_{\tau=t}^{t+T_i^{on}-1} I_{i\tau} \geq T_i^{on} \cdot (I_{it} - I_{i(t-1)}), \quad \forall t = UT_i + 1, \ldots, NT - T_i^{on} + 1$$
$$\sum_{\tau=t}^{NT} [I_{i\tau} - (I_{it} - I_{i(t-1)})] \geq 0, \quad \forall t = NT - T_i^{on} + 2, \ldots, NT$$
$$\sum_{t=1}^{DT_i} I_{it} = 0, \quad \text{where } DT_i = \max\{0, \min[NT, (T_i^{off} - X_{i0}^{off}) \cdot (1 - I_{i0})]\} \tag{5}$$
$$\sum_{\tau=t}^{t+T_i^{off}-1} (1 - I_{i\tau}) \geq T_i^{off} \cdot (I_{i(t-1)} - I_{it}),$$
$$\forall t = DT_i + 1, \ldots, NT - T_i^{off} + 1$$
$$\sum_{\tau=t}^{NT} [1 - I_{i\tau} - (I_{i(t-1)} - I_{it})] \geq 0, \quad \forall t = NT - T_i^{off} + 2, \ldots, NT$$

$$P_{it} = P_i^{\min} \cdot I_{it} + \sum_k P_{ikt}$$
$$0 \leq P_{ikt} \leq P_{ik}^{\max} \cdot I_{it} \tag{6}$$
$$P_i^{\min} \cdot I_{it} \leq P_{it} \leq P_i^{\max} \cdot I_{it}$$
$$P_{it} + SR_{it} \leq P_i^{\max} \cdot I_{it}$$
$$SR_{it} \leq 10 \cdot MSR_i \cdot I_{it} \tag{7}$$
$$OR_{it} = SR_{it} + (1 - I_{it}) \cdot QSC_i$$

$$\sum_{l \in \mathbf{f}(b)} PL_{lt} - \sum_{l \in \mathbf{t}(b)} PL_{lt} = \sum_{i \in \mathbf{U}(b)} P_{it} - D_{bt} - C_b \cdot P_{Losst}$$
$$PL_{lt} - (\theta_{at} - \theta_{bt} - \gamma_{abt})/x_{ab} = 0 \quad \text{line } l \text{ is from bus } a \text{ to bus } b \tag{8}$$
$$\gamma^{\min} \leq \gamma_t \leq \gamma^{\max}$$

  

$$
\begin{aligned}
&-\mathbf{PL}^{\max} \le \mathbf{PL}_t \le \mathbf{PL}^{\max} \\
&\theta_{ref} = 0 \\
&P_{Lt} - \sum_b LF_b \cdot \left( \sum_{i \in \mathbf{U}(b)} P_{it} - D_{bt} \right) - offset = 0
\end{aligned} \tag{9}
$$

BD is employed to solve the large-scale NCUC problem with a large number of constraints including those in the hourly network evaluation subproblems (8). In applying BD, the original problem described as (1)–(8) is decomposed into a master UC problem (10) and several hourly network evaluation subproblems (11). The master is a MIP problem and subproblems are LP problems. The subproblems examine the master problem solution for satisfying the network constraints. If the subproblem at hour $t$ is infeasible, the corresponding Benders cut in (12) is generated and added to the next iteration of the master UC problem. The iterative process will continue by successively adding Benders cuts until network violations are mitigated. In (11) a unique non-negative slack variable $s_t$ is introduced for all buses. The physical interpretation of a single non-negative slack variable is to diminish the most violated bus power balance iteratively. Reference [16] reported that a single non-negative slack variable strategy would outperform multiple non-negative slack variables at different buses by reducing the overall number of iterations

$$
LB = \text{Min} \sum_t \sum_i \left[ \sum_k c_{ik} \cdot P_{ikt} + N_i \cdot I_{it} + SU_{it} + SD_{it} \right]
$$

$$
\text{S.t.} \quad \text{Equations (2)–(7)} \tag{10}
$$

$$
\text{Benders cuts from all previous iterations}
$$

$$
\begin{aligned}
\text{Min} \quad & s_t \\
\text{S.t.} \quad & \sum_{l \in \mathbf{f}(b)} PL_{lt} - \sum_{l \in \mathbf{t}(b)} PL_{lt} - s_t \le \sum_{i \in \mathbf{U}(b)} P_{it} - D_{bt} - C_b \cdot P_{Losst} && \lambda_{1,bt} \\
& - \sum_{l \in \mathbf{f}(b)} PL_{lt} + \sum_{l \in \mathbf{t}(b)} PL_{lt} - s_t \le - \sum_{i \in \mathbf{U}(b)} P_{it} + D_{bt} + C_b \cdot P_{Losst} && \lambda_{2,bt} \\
& PL_{lt} - (\theta_{at} - \theta_{bt} - \gamma_{abt})/x_{ab} = 0 && \kappa_{lt} \\
& \gamma_{pt} \le \gamma_p^{\max} && \pi_{1,pt} \\
& -\gamma_{pt} \le -\gamma_p^{\min} && \pi_{2,pt} \\
& PL_{lt} \le PL_l^{\max} && \pi_{3,lt} \\
& -PL_{lt} \le PL_l^{\max} && \pi_{4,lt} \\
& \theta_{ref,t} = 0 && \pi_t \\
& 0 \le s_t
\end{aligned} \tag{11}
$$

If the optimal objective value $\hat{s}_t$ in (11) is larger than the predefined threshold $\varepsilon$, the feasibility Benders cut represented by (12) will be utilized by grouping generators that are located at the same bus

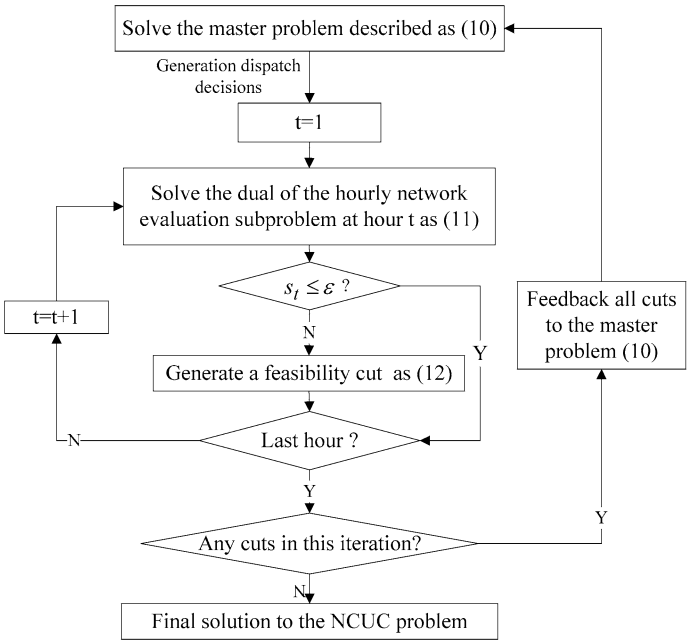


**Fig. 1** NCUC procedure with the classical BD method

$$\sum_{b=1}^{NB} \sum_{i \in \mathbf{U}(b)} (\hat{\lambda}_{1b,t} - \hat{\lambda}_{2b,t}) \cdot (P_{it} - \hat{P}_{it}) + \hat{s}_t \le 0 \tag{12}$$

$\mathbf{U}(b)$ represents the set of generators located at the same bus $b$ that shares the same dual variables $\hat{\lambda}_{1b,t}$ and $\hat{\lambda}_{2b,t}$, and $\hat{s}_t$ is the current optimal objective value of (11). Figure 1 shows the flowchart of the NCUC problem with the classical BD method. The master UC problem (10) is solved and the dispatch solution $\hat{P}_{it}$ is passed on to the hourly network evaluation subproblems (11). If there is any network violations (i.e. $s_t > \varepsilon$), a feasibility cut in (12) corresponding to the violated hour is generated and fed back to the master UC problem for further iterations. The procedure stops when $s_t \le \varepsilon$ is satisfied at all hours, no more feasibility Benders cuts are generated, and the final solution to the original NCUC problem is obtained. At each Benders iteration $d$, the objective value of (10) provides a lower bound $LB_d$ to the original problem, and $UB_d = LB_d + M \cdot \sum_t s_{dt}$ provides an upper bound to the original problem where $s_{dt}$ is the solution of (11) representing the violation at hour $t$ at Benders iteration $d$. It is noted that by successively appending feasibility cuts to (10) the lower bound obtained at each iteration will be monotonically increasing, i.e. $LB_{d-1} \le LB_d \le G$ and $LB_{best} = LB_d$, but that will not be the case with the upper bound. The upper bound for the current iteration may be lower or higher than that in previous iterations, and the best upper bound is the minimum of all obtained values, i.e. $G \le UB_{best} = \min_d\{UB_d\}$. Assuming the current Benders iteration is $d$, and the best upper bound is obtained at iteration $d'$, the stopping criterion $s_t \le \varepsilon$ is $\frac{UB_{best} - LB_{best}}{LB_{best}} = \frac{(LB_{d'} + M \cdot \sum_t s_{d't}) - LB_d}{LB_d} \le \frac{M}{LB_d} \cdot NT \cdot \varepsilon$ where $s_{d't}$ is the violation at hour

  

$t$ obtained at the Benders iteration $d'$. That is, with a small enough $\varepsilon$, the stopping criterion will force $LB_{best}$ and $UB_{best}$ to be close, which will restrict the final solution to be close enough to the global optimal solution of the original problem. Here, $s_t$ in (11) represents the maximum power imbalance among all buses at hour $t$; thus a non-zero $s_t$ means the final solution is not strictly feasible to the original NCUC problem in the sense that there will be at most $\varepsilon$ MW violation at each bus. The $\varepsilon$ values of 0.01–0.1 are used in our case studies. For power systems with peak loads of thousands to tens of thousands of MW, the violation of less than 0.01–0.1 MW is tolerable and practical. The NCUC is used to determine day-head UC schedules (i.e. 24 hours), and small violations less than 0.01–0.1 MW can be handled by the real-time power system operation with automatic generation control schemes [1].

The linear sensitivity factor (LSF) method could also be used to solve the NCUC problem [1], which replaces (8) with (13). LSF represents the sensitivity of line flows to the bus power injection. The power flow in each line can be calculated by (13), where $LSF_{ab}^{m}$ represents the sensitivity of power flow of line $l$ (from bus $a$ to bus $b$) to power injection at bus $m$. The detailed calculation procedure of $LSF_{ab}^{m}$ is discussed in [1]. Here, $(\sum_{i:i\in \mathbf{U}(m)} P_{it} - D_{mt} - C_m \cdot P_{Losst} + \sum_{n:n\in\gamma(m)} \gamma_{mn}/x_{mn} - \sum_{n:m\in\gamma(n)} \gamma_{mn}/x_{mn})$ represents the total power injection to bus $m$, where items represent total generation, load demand, losses distributed at bus $m$, and equivalent power injection from phase shifters to bus $m$, respectively. Using the LSF method for the solution of NCUC problem, the UC problem described as (1)–(7) is solved first, then we check the power flow on each transmission line at each hour using (13), and append the violated (13) back to the master UC problem for mitigating violations. The procedure will stop when (13) is satisfied for all lines at all hours, and no transmission power flow violation exists. In the case study section, we will see that the LSF method may be efficient for small systems. However, since there is one constraint for each violated transmission line at each hour, LSF may introduce many more constraints than the BD method for large-scale power systems, which makes the UC problem difficult to solve in real time. Thus, decomposition is the only viable option for the solution of the large-scale NCUC problem in real time

$$-PL_l^{\max} \le PL_{lt} = \sum_m LSF_{ab}^{m} \cdot \Bigg( \sum_{i\in \mathbf{U}(m)} P_{it} - D_{mt} - C_m \cdot P_{Losst} + \sum_{n\in\gamma(m)} \gamma_{mn}/x_{mn} - \sum_{m\in\gamma(n)} \gamma_{mn}/x_{mn} \Bigg) \le PL_l^{\max} \tag{13}$$

## 3 Accelerating BD via multiple strong Benders cuts

The drawback of the classical BD algorithm presented in Sect. 2 resides in its slow convergence. In this section, we discuss our methodology for accelerating the BD procedure via multiple strong Benders cuts at each iteration. The proposed methodology for generating multiple strong Benders cuts reduces the number of Benders iterations as well as the overall computing time.

3.1 Generate multiple strong Benders cuts from multiple optimal dual solutions

The dual problem of (11) is formulated as (14) which is highly degenerate. In this case, there are many zeros on the right-hand-side with multiple optimal solutions. If one or more of the variables in the basis of a LP problem is zero, the basis is called degenerate. And the LP is highly degenerate if there are many vertices of the feasible region for which the associated basis is degenerate. Since the coefficients of Benders cut (12) are generated using the optimal dual solution of (14), the proper choice of the optimal dual solution and the corresponding Benders cuts would be of crucial importance for the efficiency of the BD algorithm

$$
\begin{aligned}
\text{Max}\quad & \sum_{b}\Bigg(\sum_{i\in\mathbf{U}(b)} P_{it} - D_{bt} - C_b\cdot P_{Losst}\Bigg)\cdot(\lambda_{1,bt}-\lambda_{2,bt}) \\
& +\sum_{p}(\gamma_p^{\max}\cdot\pi_{1,pt}-\gamma_p^{\min}\cdot\pi_{2,pt})+\sum_{l}PL_l^{\max}\cdot(\pi_{3,lt}+\pi_{4,lt}) \\
\text{S.t.}\quad & (\lambda_{1,at}-\lambda_{2,at})+(-\lambda_{1,bt}+\lambda_{2,bt})+\kappa_{lt}+\pi_{3,lt}-\pi_{4,lt}=0 \\
& \quad \text{line } l \text{ is from bus } a \text{ to } b \\
& \sum_{a}\kappa_{lt}/x_{am}-\sum_{b}\kappa_{l't}/x_{mb}=0 \\
& \quad \text{line } l \text{ is from bus } a \text{ to } m, \text{ line } l' \text{ is from bus } m \text{ to } b, \\
& \quad m \text{ is not reference bus} \\
& \sum_{a}\kappa_{lt}/x_{am}-\sum_{b}\kappa_{l't}/x_{mb}+\pi_t=0 \qquad (14) \\
& \quad \text{line } l \text{ is from bus } a \text{ to } m, \text{ line } l' \text{ is from} \\
& \quad \text{bus } m \text{ to } b, m \text{ is reference bus} \\
& \kappa_{lt}/x_{ab}+\pi_{1,pt}-\pi_{2,pt}=0 \\
& \quad \text{phase shifter } p \text{ is located at line } l, \text{ which is from bus } a \text{ to } b \\
& -\sum_{b=1}^{NB}(\lambda_{1b,t}+\lambda_{2b,t})\le 1 \\
& \lambda_{1,bt},\lambda_{2,bt},\pi_{1,pt},\pi_{2,pt},\pi_{3,lt},\pi_{4,lt}\le 0, \quad \kappa_{lt},\pi_t \text{ free}
\end{aligned}
$$

All buses are divided into exclusive subsets $\mathbf{B}_o$ that satisfy $\bigcup_o \mathbf{B}_o=\mathbf{B}$ and $\mathbf{B}_o\cap\mathbf{B}_{o'}=\mathbf{\Phi}$, where $\mathbf{B}$ is the set of all buses in the system. A set of new subproblems (15) is generated corresponding to each subset $\mathbf{B}_o$. The idea behind (15) is to find an optimal dual solution which can generate a cut for restricting the feasible region of $P_i$ $i\in\mathbf{U}(b)$ and $b\in\mathbf{B}_o$ to the highest possible extent. An optimal solution of (15) is also an optimal solution to the dual problem (14) since all constraints in (14) are included in (15) and the fifth constraint in (15) would force the objective value to be

  

equal to its optimal value $\hat{s}$, calculated by (11)

$$\begin{aligned}
\text{Max} \quad & \sum_{b\in\mathbf{B}_o}\sum_{i\in\mathbf{U}(b)}(P_i^{\max}-\varepsilon)\cdot(\lambda_{1b,t}-\lambda_{2b,t}) \\
& +\sum_{b\notin\mathbf{B}_o}\sum_{i\in\mathbf{U}(b)}(P_i^{\min}+\varepsilon)\cdot(\lambda_{1b,t}-\lambda_{2b,t}) \\
\text{S.t.} \quad & (\lambda_{1,at}-\lambda_{2,at})+(-\lambda_{1,bt}+\lambda_{2,bt})+\kappa_{lt}+\pi_{3,lt}-\pi_{4,lt}=0 \\
& \quad \text{line } l \text{ is from bus } a \text{ to } b \\
& \sum_a \kappa_{lt}/x_{am}-\sum_b \kappa_{l't}/x_{mb}=0 \\
& \quad \text{line } l \text{ is from bus } a \text{ to } m, \text{ line } l' \text{ is} \\
& \quad \text{from bus } m \text{ to } b, m \text{ is not reference bus} \\
& \sum_a \kappa_{lt}/x_{am}-\sum_b \kappa_{l't}/x_{mb}+\pi_t=0 \qquad (15) \\
& \quad \text{line } l \text{ is from bus } a \text{ to } m, \text{ line } l' \text{ is from bus } m \text{ to } b, m \text{ is reference bus} \\
& \kappa_{lt}/x_{ab}+\pi_{1,pt}-\pi_{2,pt}=0 \\
& \quad \text{phase shifter } p \text{ is located at line } l, \text{ which is from bus } a \text{ to } b \\
& \sum_b\left(\sum_{i\in\mathbf{U}(b)}P_{it}-D_{bt}-C_b\cdot P_{Losst}\right)\cdot(\lambda_{1,bt}-\lambda_{2,bt}) \\
& \quad +\sum_p(\gamma_p^{\max}\cdot\pi_{1,pt}-\gamma_p^{\min}\cdot\pi_{2,pt})+\sum_l PL_l^{\max}\cdot(\pi_{3,lt}+\pi_{4,lt})=\hat{s}_t \quad Q \\
& -\sum_{b=1}^{NB}(\lambda_{1b,t}+\lambda_{2b,t})\le 1 \\
& \lambda_{1,bt},\lambda_{2,bt},\pi_{1,pt},\pi_{2,pt},\pi_{3,lt},\pi_{4,lt}\le 0, \quad \kappa_{lt},\pi_t \text{ free}
\end{aligned}$$

The new cut (16) is generated from the optimal solution of (15).

$$\sum_{b=1}^{NB}\sum_{i\in\mathbf{U}(b)}(\tilde{\lambda}_{1,bt}-\tilde{\lambda}_{2,bt})\cdot P_{it}+\hat{s}_t\le 0 \qquad (16)$$

where $\tilde{\lambda}$ is the new optimal solution to (15).

**Definition 1** (See also Magnanti and Wong 1981 [10]) A cut for the minimization of (1)–(8) as $\sum_{b=1}^{NB}\sum_{i\in\mathbf{U}(b)}(\lambda_{1b,t}-\lambda_{2b,t})\cdot(P_{it}-\hat{P}_{it})+\hat{s}_t\le 0$ would dominate or is stronger than $\sum_{b=1}^{NB}\sum_{i\in\mathbf{U}(b)}(\lambda'_{1b,t}-\lambda'_{2b,t})\cdot(P_{it}-\hat{P}_{it})+\hat{s}_t\le 0$ as another cut, if for all $\mathbf{P}_t$ in their domain $\{\mathbf{0},[\mathbf{P}^{\min},\mathbf{P}^{\max}]\}$, (17) is satisfied with a strict inequality for

any point in the feasible region.

$$\left[\sum_{b=1}^{NB}\sum_{i\in\mathbf{U}(b)}(\lambda'_{1b,t}-\lambda'_{2b,t})\cdot(P_{it}-\hat{P}_{it})+\hat{s}_t\right] - \left[\sum_{b=1}^{NB}\sum_{i\in\mathbf{U}(b)}(\lambda_{1b,t}-\lambda_{2b,t})\cdot(P_{it}-\hat{P}_{it})+\hat{s}_t\right]\le 0 \tag{17}$$

**Definition 2** (See also Magnanti and Wong 1981 [10]) A cut is pareto optimal if no other cut could dominate it.

**Theorem 1** *The cut* (16) *generated via multiple optimal dual solutions is pareto optimal.*

The proof of Theorem 1 is provided in Appendix A. The problem considered in Magnanti and Wong 1981 [10] is a convex hull, and the points $\mathbf{P}_t$ we discuss here belong to a non-convex set $\{\mathbf{0}, [\mathbf{P}^{\min}, \mathbf{P}^{\max}]\}$. The dual to (15), which corresponds to the primal form of the original problem (11), is given in (18). Since dual problems (14)–(15) would introduce many more variables than the primal problem (11), we have experienced that it is more efficient to solve the NCUC problem in its primal form (11) and (18) than its dual form (14)–(15). Furthermore, subproblems (11) and (18) are large and sparse and could experience a higher convergence speed by using a primal-dual logarithmic barrier algorithm provided by CPLEX [17]. This algorithm is suitable for large LP problems with dense columns; that is, a relatively high number of nonzero entries in each column

$$\begin{aligned}
\text{Min}\quad & \hat{s}_t\cdot Q+s_t\\
\text{S.t.}\quad & \sum_{l\in\mathbf{f}(b)}PL_{lt}-\sum_{l\in\mathbf{t}(b)}PL_{lt}-s_t+\left(\sum_{i\in\mathbf{U}(b)}P_{it}-D_{bt}-C_b\cdot P_{Losst}\right)\cdot Q\\
& \quad\le RQ1_{bt}\\
& -\sum_{l\in\mathbf{f}(b)}PL_{lt}+\sum_{l\in\mathbf{t}(b)}PL_{lt}-s_t-\left(\sum_{i\in\mathbf{U}(b)}P_{it}-D_{bt}-C_b\cdot P_{Losst}\right)\cdot Q\\
& \quad\le RQ2_{bt}\\
& PL_{lt}-(\theta_{at}-\theta_{bt}-\gamma_{abt})/x_{ab}=0\\
& \gamma_{pt}+\gamma_p^{\max}\cdot Q\le\gamma_p^{\max}\\
& -\gamma_{pt}-\gamma_p^{\min}\cdot Q\le-\gamma_p^{\min}\\
& PL_{lt}+PL_l^{\max}\cdot Q\le PL_l^{\max}\\
& -PL_{lt}+PL_l^{\max}\cdot Q\le PL_l^{\max}\\
& \theta_{ref,t}=0\\
& 0\le s_t,\quad Q\ \text{free}
\end{aligned} \tag{18}$$

  

where

$$RQ1_{bt} = \begin{cases} \sum_{i \in \mathbf{U}(b)} (P_i^{\max} - \varepsilon), & b \in \mathbf{B}_o \\ \sum_{i \in \mathbf{U}(b)} (P_i^{\min} + \varepsilon), & b \notin \mathbf{B}_o \end{cases} \quad \text{and}$$

$$RQ2_{bt} = \begin{cases} -\sum_{i \in \mathbf{U}(b)} (P_i^{\max} - \varepsilon), & b \in \mathbf{B}_o \\ -\sum_{i \in \mathbf{U}(b)} (P_i^{\min} + \varepsilon), & b \notin \mathbf{B}_o \end{cases}$$

In the implementation of (18), a strong Benders cut (16) is generated for each subset $\mathbf{B}_o$. We should point out that different forms of subsets $\mathbf{B}_o$ might conceivably generate different pareto optimal cuts. The number of subsets may also impact the convergence. More pareto optimal cuts generated in each iteration could result in fewer iterations between the master UC and network evaluation subproblems. However, the solution of the master problem may take longer because of the large number of cuts. Here, the optimal number of subsets would be a tradeoff between the computational burden of solving the master problem and the number of iterations. We use 2 subsets for off peak hours and 6 for peak hours in our case studies. Also, buses that are geographically close are placed into the same subset $\mathbf{B}_o$. In practice, the parameter tuning will be necessary in order to reduce the number of iterations and the overall computing time.

### 3.2 Generate multiple strong Benders cuts by enhancing the density of cuts

For an optimal dual solution of (14), $\hat{\lambda}_{1,bt}, \hat{\lambda}_{2,bt}, \hat{\pi}_{1,pt}, \hat{\pi}_{2,pt}, \hat{\pi}_{3,lt}, \hat{\pi}_{4,lt}, \hat{\kappa}_{lt}, \hat{\pi}_t$, all buses are divided into two subsets $\mathbf{Z}$ and $\mathbf{Z}^c$, with $\mathbf{Z}$ representing the set of buses $b$ that satisfy $(\hat{\lambda}_{1,bt} - \hat{\lambda}_{2,bt}) = 0$, and $\mathbf{Z}^c$ representing the set of all other buses. Usually the Benders cut (12) is low density which means that a small number of decision variables $\mathbf{P}_t$ is involved. That is, very few coefficients of $\mathbf{P}_t$ are nonzero, which would limit the contribution of Benders cut (12) to strengthening the feasible region of the master UC problem. The idea here is to generate strong Benders cuts for strengthening the master UC problem at each iteration and incorporating more decision variables $\mathbf{P}_t$ at each Benders cut for reducing the number of iterations and the overall computing time.

Based on this idea, we divide the set $\mathbf{Z}$ into exclusive subsets $\mathbf{SZ}_o$, which satisfy $\bigcup_o \mathbf{SZ}_o = \mathbf{Z}$ and $\mathbf{SZ}_o \bigcap \mathbf{SZ}_{o'} = \mathbf{\Phi}$. Here buses in the set $\mathbf{Z}$ that are geographically close are included in the same subset $\mathbf{SZ}_o$. Different partitioning subsets may result in deriving different high density cuts and different convergence performances, which would require more research. A new LP optimization problem (19) is formulated corresponding to each subset $\mathbf{SZ}_o$ for generating high-density Benders cuts. The last inequality constraint in (19) is to guarantee that the problem (19) is bounded. We experience that the value of $2 \cdot |\mathbf{Z}|$ used in problem (19) does not impact the convergence performance of the proposed method significantly as illustrated in Case study 4.2 in which we replace $2 \cdot |\mathbf{Z}|$ with 1. The optimal solution of (19), $\hat{\lambda}_{1,bt} \hat{\lambda}_{2,bt}$ for $b \in \mathbf{Z}^c$ and $\bar{\lambda}_{1,bt} \bar{\lambda}_{2,bt}$ for $b \in \mathbf{Z}$, is not feasible for the network evaluation problem (11) or its dual (14) as it violates $-\sum_{b=1}^{NB} (\lambda_{1,bt} + \lambda_{2,bt}) \leq 1$ in (14). Thus (20) is solved to get the final high-density Benders cut given in (21), where $c = \sum_{b \in \mathbf{Z}^c} (-\hat{\lambda}_{1,bt} - \hat{\lambda}_{2,bt}) + 2 \cdot |\mathbf{Z}|$

is constant with the given $\hat{\lambda}_{1,bt}$ and $\hat{\lambda}_{2,bt}$ for $b \in \mathbf{Z}^c$

$$
\begin{aligned}
\text{Max} \quad & \sum_{b\in\mathbf{SZ}_o}\sum_{i\in\mathbf{U}(b)}(P_i^{\max}-\varepsilon)\cdot(\lambda_{1b,t}-\lambda_{2b,t}) \\
& +\sum_{b\in\{\mathbf{Z}-\mathbf{SZ}_o\}}\sum_{i\in\mathbf{U}(b)}(P_i^{\min}+\varepsilon)\cdot(\lambda_{1b,t}-\lambda_{2b,t}) \\
\text{S.t.} \quad & (\lambda_{1,at}-\lambda_{2,at})+(-\lambda_{1,bt}+\lambda_{2,bt})+\kappa_{lt}+\pi_{3,lt}-\pi_{4,lt}=0 \\
& \text{line } l \text{ is from bus } a \text{ to } b \\
& \sum_a \kappa_{lt}/x_{am}-\sum_b \kappa_{l't}/x_{mb}=0 \\
& \text{line } l \text{ is from bus } a \text{ to } m, \text{ line } l' \text{ is from} \\
& \text{bus } m \text{ to } b, \ m \text{ is not reference bus} \\
& \sum_a \kappa_{lt}/x_{am}-\sum_b \kappa_{l't}/x_{mb}+\pi_t=0 \\
& \text{line } l \text{ is from bus } a \text{ to } m, \text{ line } l' \text{ is} \\
& \text{from bus } m \text{ to } b, \ m \text{ is reference bus} \\
& \kappa_{lt}/x_{am}+\pi_{1,pt}-\pi_{2,pt}=0 \\
& \text{phase shifter } p \text{ is located at line } l, \text{ which is from bus } a \text{ to } b \\
& \sum_b\left(\sum_{i\in\mathbf{U}(b)}P_{it}-D_{bt}-C_b\cdot P_{Losst}\right)\cdot(\lambda_{1,bt}-\lambda_{2,bt}) \\
& +\sum_p(\gamma_p^{\max}\cdot\pi_{1,pt}-\gamma_p^{\min}\cdot\pi_{2,pt})+\sum_l PL_l^{\max}\cdot(\pi_{3,lt}+\pi_{4,lt})=\hat{s}_t \quad Q \\
& \lambda_{1,bt}=\hat{\lambda}_{1,bt}, \quad b\in\mathbf{Z}^c, \quad q_{1,bt} \\
& \lambda_{2,bt}=\hat{\lambda}_{2,bt}, \quad b\in\mathbf{Z}^c, \quad q_{2,bt} \\
& \sum_{b\in\mathbf{Z}}(-\lambda_{1,bt}-\lambda_{2,bt})\le 2\cdot|\mathbf{Z}| \quad q \\
& \lambda_{1,bt},\lambda_{2,bt},\pi_{1,pt},\pi_{2,pt},\pi_{3,lt},\pi_{4,lt}\le 0, \quad \kappa_{lt},\pi_t \text{ free}
\end{aligned}
\tag{19}
$$

$$
\begin{aligned}
\text{Max} \quad & \breve{s}_t=\sum_b\left(\sum_{i\in\mathbf{U}(b)}P_{it}-D_{bt}-C_b\cdot P_{Losst}\right)\cdot(\lambda_{1,bt}-\lambda_{2,bt}) \\
& +\sum_p(\gamma_p^{\max}\cdot\pi_{1,pt}-\gamma_p^{\min}\cdot\pi_{2,pt})+\sum_l PL_l^{\max}\cdot(\pi_{3,lt}+\pi_{4,lt})
\end{aligned}
$$

  

$$
\begin{aligned}
\text{S.t.}\quad & (\lambda_{1,at}-\lambda_{2,at})+(-\lambda_{1,bt}+\lambda_{2,bt})+\kappa_{lt}+\pi_{3,lt}-\pi_{4,lt}=0 \\
& \quad \text{line } l \text{ is from bus } a \text{ to } b \\
& \sum_{a}\kappa_{lt}/x_{am}-\sum_{b}\kappa_{l't}/x_{mb}=0 \\
& \quad \text{line } l \text{ is from bus } a \text{ to } m, \text{ line } l' \text{ is from} \\
& \quad \text{bus } m \text{ to } b, m \text{ is not reference bus} \\
& \sum_{a}\kappa_{lt}/x_{am}-\sum_{b}\kappa_{l't}/x_{mb}+\pi_{t}=0 \\
& \quad \text{line } l \text{ is from bus } a \text{ to } m, \text{ line } l' \text{ is} \\
& \quad \text{from bus } m \text{ to } b, m \text{ is reference bus} \\
& \kappa_{lt}/x_{am}+\pi_{1,pt}-\pi_{2,pt}=0 \\
& \quad \text{phase shifter } p \text{ is located at line } l, \text{ which is from bus } a \text{ to } b \\
& -\sum_{b=1}^{NB}(\lambda_{1,bt}+\lambda_{2,bt})\le 1 \\
& \lambda_{1,bt}=\hat{\lambda}_{1,bt}/c, \quad \lambda_{2,bt}=\hat{\lambda}_{2,bt}/c, \quad b\in\mathbf{Z}^c, \quad q_{1,bt}, q_{2,bt} \\
& \lambda_{1,bt}=\bar{\lambda}_{1,bt}/c, \quad \lambda_{2,bt}=\bar{\lambda}_{2,bt}/c, \quad b\in\mathbf{Z}, \quad q_{1,bt}, q_{2,bt} \\
& \lambda_{1,bt}, \lambda_{2,bt}, \pi_{1,pt}, \pi_{2,pt}, \pi_{3,lt}, \pi_{4,lt}\le 0, \quad \kappa_{lt}, \pi_{t} \text{ free}
\end{aligned}
\tag{20}
$$

**Theorem 2** *The cut* (21) *is pareto optimal, given the fixed coefficients* $\hat{\lambda}_{1,bt}$ *and* $\hat{\lambda}_{2,bt}$ *corresponding to all buses in the subset* $b\in\mathbf{Z}^c$, *which is the optimal solution of* (14).

$$
\sum_{b\in\mathbf{Z}^c}\sum_{i\in\mathbf{U}(b)}(\hat{\lambda}_{1,bt}/c-\hat{\lambda}_{2,bt}/c)\cdot(P_{it}-\hat{P}_{it})+\sum_{b\in\mathbf{Z}}\sum_{i\in\mathbf{U}(b)}(\bar{\lambda}_{1,bt}/c-\bar{\lambda}_{2,bt}/c)\cdot P_{it}+\breve{s}_t\le 0 \tag{21}
$$

The proof of Theorem 2 is provided in Appendix B. The duals to (19)–(20), which correspond to the primal form of the original problem (11), are given in (22)–(23). Similar to (14)–(15), the dual forms (19)–(20) introduce many more variables than their corresponding primal forms (22)–(23). Thus a higher efficiency could be achieved by solving primal problems (22)–(23)

$$
\begin{aligned}
\text{Min}\quad & \hat{s}_t\cdot Q+\sum_{b\in\mathbf{Z}^c}(\hat{\lambda}_{1,bt}\cdot q_{1,bt}+\hat{\lambda}_{2,bt}\cdot q_{2,bt})+2\cdot|\mathbf{Z}|\cdot q \\
\text{S.t.}\quad & \sum_{l\in\mathbf{f}(b)}PL_{lt}-\sum_{l\in\mathbf{t}(b)}PL_{lt} \\
& +\left(\sum_{i\in\mathbf{U}(b)}P_{it}-D_{bt}-C_b\cdot P_{Losst}\right)\cdot Q+Q1_{bt}\le RQ1_{bt}
\end{aligned}
$$

$$
\begin{aligned}
&-\sum_{l\in\mathbf{f}(b)} PL_{lt}+\sum_{l\in\mathbf{t}(b)} PL_{lt}\\
&-\left(\sum_{i\in\mathbf{U}(b)} P_{it}-D_{bt}-C_b\cdot P_{Losst}\right)\cdot Q+Q2_{bt}\le RQ2_{bt}\\
&PL_{lt}-(\theta_{at}-\theta_{bt}-\gamma_{abt})/x_{ab}=0\\
&\gamma_{pt}+\gamma_p^{\max}\cdot Q\le 0\\
&-\gamma_{pt}-\gamma_p^{\min}\cdot Q\le 0\\
&PL_{lt}+PL_l^{\max}\cdot Q\le 0\\
&-PL_{lt}+PL_l^{\max}\cdot Q\le 0\\
&\theta_{ref,t}=0\\
&0\le q,\quad Q,q_{1,bt},q_{2,bt}\text{ free}
\end{aligned}
\tag{22}
$$

where

$$
RQ1_{bt}=\begin{cases}\sum_{i\in\mathbf{U}(b)}(P_i^{\max}-\varepsilon), & b\in\mathbf{SZ}_o,\\ \sum_{i\in\mathbf{U}(b)}(P_i^{\min}+\varepsilon), & b\in\mathbf{Z}-\mathbf{SZ}_o,\\ 0, & b\in\mathbf{Z}^c,\end{cases}\qquad RQ2_{bt}=-RQ1_{bt}
$$

$$
Q1_{bt}=\begin{cases}-q, & b\in\mathbf{Z},\\ q_{1,bt}, & b\in\mathbf{Z}^c,\end{cases}\qquad Q2_{bt}=\begin{cases}-q, & b\in\mathbf{Z}\\ q_{2,bt}, & b\in\mathbf{Z}^c\end{cases}
$$

$$
\begin{aligned}
\text{Min}\quad & s_t+\sum_{b\in\mathbf{Z}^c}(\hat{\lambda}_{1,bt}\cdot q_{1,bt}+\hat{\lambda}_{2,bt}\cdot q_{2,bt})/c+\sum_{b\in\mathbf{Z}}(\hat{\lambda}_{1,bt}\cdot q_{1,bt}+\hat{\lambda}_{2,bt}\cdot q_{2,bt})/c\\
\text{S.t.}\quad & \sum_{l\in\mathbf{f}(b)} PL_{lt}-\sum_{l\in\mathbf{t}(b)} PL_{lt}-s_t+q_{1,bt}\le\sum_{i\in\mathbf{U}(b)} P_{it}-D_{bt}-C_b\cdot P_{Losst}\\
& -\sum_{l\in\mathbf{f}(b)} PL_{lt}+\sum_{l\in\mathbf{t}(b)} PL_{lt}-s_t+q_{2,bt}\le-\sum_{i\in\mathbf{U}(b)} P_{it}+D_{bt}+C_b\cdot P_{Losst}\\
& PL_{lt}-(\theta_{at}-\theta_{bt}-\gamma_{abt})/x_{ab}=0\\
& \gamma_{pt}\le\gamma_p^{\max}\\
& -\gamma_{pt}\le-\gamma_p^{\min}\\
& PL_{lt}\le PL_l^{\max}\\
& -PL_{lt}\le PL_l^{\max}\\
& \theta_{ref,t}=0\\
& 0\le s_t,\quad q_{1,bt},q_{2,bt}\text{ free}
\end{aligned}
\tag{23}
$$

In the implementation of (22)–(23), there is one high-density Benders cut (14) corresponding to each subsets $\mathbf{SZ}_o$, and different divisions of subsets $\mathbf{SZ}_o$ may conceivably generate different cuts. The number of subsets may also impact the convergence. The more cuts added to each iteration would result in fewer iterations between

  

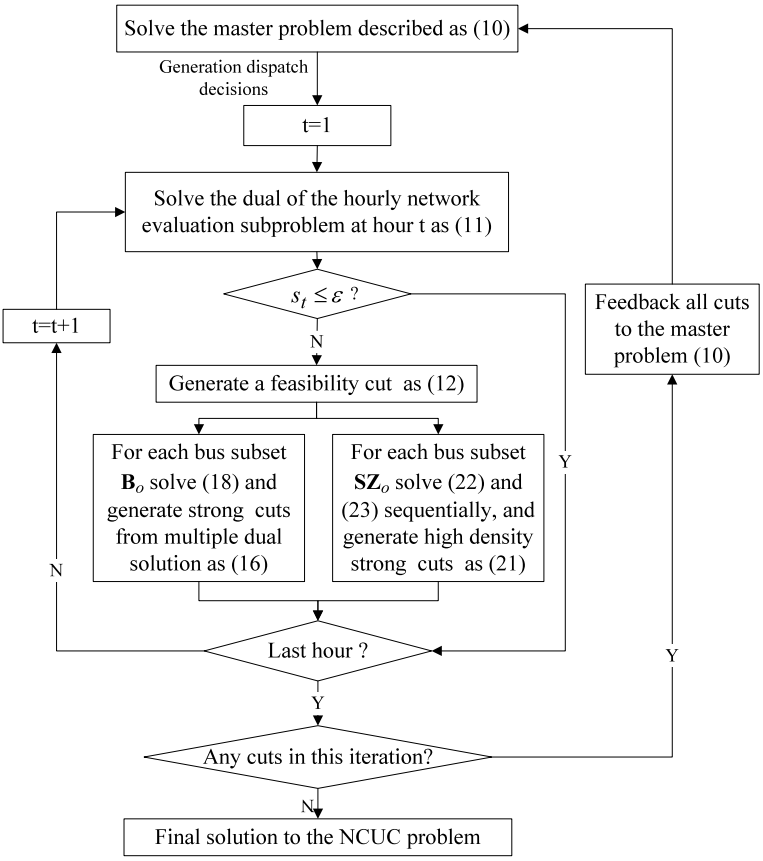


**Fig. 2** NCUC procedure with the proposed accelerating BD algorithm

master UC and network evaluation subproblems, but the solution of master problem may take longer because of the large number of added cuts. Here, 5 subsets are used in our case studies.

The overall computing time is the time for solving the master UC problem and a series of network evaluation subproblems iteratively. Fewer iterations would result in a significant reduction in computing time. However, the calculation of additional cuts could be time consuming. Here subproblems (18) and (22)–(23) with respect to disjunctive subsets would be solved in parallel since they are independent, which will reduce the overall computing time.

Figure 2 shows the flowchart for solving the NCUC problem with the proposed accelerating BD method. In comparison to Fig. 1, if there is a network violation (i.e. $s_t > \varepsilon$), besides the feasibility cuts obtained in (12), we also solve a set of subproblems and generate strong Benders cuts for accelerating the BD algorithm. We solve (18) for each subset $\mathbf{B}_o$ and generate strong cuts from multiple dual solutions as in (16). Concurrently, we also solve (22)–(23) for each subset $\mathbf{SZ}_o$ and generate high density strong cuts as (21). Here, (18) corresponding to different subsets $\mathbf{B}_o$ and

(22)–(23) corresponding to different subset $\mathbf{SZ}_o$ can be solved in parallel. All cuts from (12), (16) and (21) are fed back to the master UC problem for further iterations. The same stopping criterion as that of the classical BD discussed in Sect. 2 is used. This paper does not intend to prove that high density cuts (21) are tighter than cuts (12) generated by the classical BD method. In fact, cuts (16) and (21) generated by the proposed method and the cut (12) generated from the classical BD are all pareto; that is, non of them dominates the others. We observed that the classical BD usually generates low density cuts which involve a small number of decision variables $\mathbf{P}_t$. That is, very few coefficients of $\mathbf{P}_t$ are nonzero. These cuts may not restrict significantly the feasible region of the master UC problem, thus more iterations may be needed. The idea here is to generate additional strong Benders cuts for incorporating more decision variables $\mathbf{P}_t$ at each generated Benders cut and strengthening the master UC problem at each iteration. As shown in numerical examples, the incorporation of multiple strong Benders cuts proposed here can strengthen the master UC problem at each iteration as compared with the single cut generated by the classical BD, and reduce the iteration number and overall computing time.

## 4 Case studies

Three cases are studied in this section to demonstrate the effectiveness of the proposed strong Benders cuts approach in terms of offering fewer Benders iterations and a shorter CPU time. The first case is a mathematical example which shows how Benders cuts are generated for multiple optimal dual solutions, which is common in large-scale power systems. The second one is a 3-bus power system which shows the effectiveness of high-density cuts. The third example is a large-scale 5663-bus system which shows both aspects of the previous examples. All cases are solved using CPLEX 11.0.0 on a 2.4 GHz personal computer.

### 4.1 Mathematical example

The problem is described as:

$$
\begin{aligned}
\text{Min} \quad & 6 \cdot P_1 + 8 \cdot P_2 + 10 \cdot P_3 \\
\text{S.t.} \quad & 1 \cdot I_1 \le P_1 \le 10 \cdot I_1, \qquad 1 \cdot I_2 \le P_2 \le 10 \cdot I_2, \qquad 1 \cdot I_3 \le P_3 \le 10 \cdot I_3 \\
& P_1 + P_2 + P_3 = 10, \qquad 2 \cdot x_1 + x_2 - 4 \cdot x_4 + P_1 \le 13 \\
& x_1 + x_3 - 0.5 \cdot P_2 \le 2, \qquad 3 \cdot x_2 + 0.5 \cdot x_3 + x_4 + P_3 \le 12.5 \\
& -x_1 - x_2 - x_3 \le -7, \qquad 0 \le x_1 \le 5, \qquad 0 \le x_2 \le 4, \qquad 0 \le x_3 \le 3 \\
& 0 \le x_4 \le 2, \qquad I_1, I_2, I_3 \in \{0, 1\}
\end{aligned}
$$

Table 1 shows the solution procedure with the classical BD algorithm. The optimal solution is reached after 3 iterations. The primal and dual subproblems for the first iteration are presented in Table 2. By solving the primal subproblem, we get an optimal dual solution of $\lambda_1 = 0, \lambda_2 = -1, \lambda_3 = 0$ with a feasibility Benders cut of $-P_2 \le -2$.

  

**Table 1** Solution procedure with the classical BD algorithm

| Iteration | Solution | | | | | | Benders cuts |
|---|---|---|---|---|---|---|---|
| | $I_1$ | $I_2$ | $I_3$ | $P_1$ | $P_2$ | $P_3$ | |
| 1 | 1 | 0 | 0 | 10 | 0 | 0 | $-P_2 \le -2$ |
| 2 | 1 | 1 | 0 | 8 | 2 | 0 | $0.0625 \cdot P_1 - 0.34375 \cdot P_2 + 0.25 \cdot P_3 \le -0.375$ |
| 3 | 1 | 1 | 0 | 7.538 | 2.462 | 0 | – |

**Table 2** Primal and dual subproblems in the first iteration

| Subproblem in the primal form | | | Subproblem in the dual form | |
|---|---|---|---|---|
| Min | $s$ | | Max | $3 \cdot \lambda_1 + 2 \cdot \lambda_2 + 12.5 \cdot \lambda_3 - 7 \cdot \pi_1 + 5 \cdot \pi_2$ |
| S.t. | $2 \cdot x_1 + x_2 - 4 \cdot x_4 - s \le 13 - \hat{P}_1$ | $\lambda_1$ | | $+ 4 \cdot \pi_3 + 3 \cdot \pi_4 + 2 \cdot \pi_5$ |
| | $x_1 + x_3 - s \le 2 + 0.5 \cdot \hat{P}_2$ | $\lambda_2$ | S.t. | $2 \cdot \lambda_1 + \lambda_2 - \pi_1 + \pi_2 \le 0$ |
| | $3 \cdot x_2 + 0.5 \cdot x_3 + x_4 - s \le 12.5 - \hat{P}_3$ | $\lambda_3$ | | $\lambda_1 + 3 \cdot \lambda_3 - \pi_1 + \pi_3 \le 0$ |
| | $-x_1 - x_2 - x_3 \le -7$ | $\pi_1$ | | $\lambda_2 + 0.5 \cdot \lambda_3 - \pi_1 + \pi_4 \le 0$ |
| | $0 \le x_1 \le 5$ | $\pi_2$ | | $-4 \cdot \lambda_1 + \lambda_3 + \pi_5 \le 0$ |
| | $0 \le x_2 \le 4$ | $\pi_3$ | | $-\lambda_1 - \lambda_2 - \lambda_3 \le 1$ |
| | $0 \le x_3 \le 3$ | $\pi_4$ | | $\lambda_1, \lambda_2, \lambda_3, \pi_1, \pi_2, \pi_3, \pi_4, \pi_5 \le 0$ |
| | $0 \le x_4 \le 2$ | $\pi_5$ | | |
| | $0 \le s$ | | | |

The dual subproblem in Table 2 has multiple optimal solutions and the above solution is the one chosen by the LP solver. Based on the LP theory, there are infinite optimal solutions for this dual subproblem because the linear combination of any two optimal solutions is also an optimal solution. According to (18), we optimize two extra problems (i.e., subset $\mathbf{B}_1$ including all three buses, and subset $\mathbf{B}_2$ including non) as presented in Table 3. When shifted to the right-hand side, coefficients of $P_1$ and $P_3$ are negative and coefficients of $P_2$ is positive, by considering the $\mathbf{B}_1$ subset the most strict feasibility region of $P_2$ is found that can be fed back to the master problem. Similarly, by considering non in $\mathbf{B}_2$ subset, we find the most restrict feasibility region of $P_1$ and $P_3$. Accordingly, a new dual optimal solution is obtained for both problems as $\lambda_1 = -0.0625, \lambda_2 = -0.6875, \lambda_3 = -0.25$ with the corresponding cut of $0.0625 \cdot P_1 - 0.34375 \cdot P_2 + 0.25 \cdot P_3 \le -0.375$. The problem is solved in two iterations with multiple strong Benders cuts generated via multiple dual optimal solutions and shown in Table 4. Here, a reduction of 33.3% is achieved in the number of iterations while the same global optimal solution is obtained. For comparison, this problem is solved directly by CPLEX without decomposition. The computation time with CPLEX is 0.11 second, with the global optimal solution of $P_1 = 7.538, P_2 = 2.462, x_1 = 3.231, x_2 = 3.769, x_4 = 1.192, I_1 = I_2 = 1$ which is the same as that obtained by the proposed accelerating BD algorithm.

**Table 3** Subproblems for obtaining multiple dual optimal solutions as shown in (18)

| Subproblem corresponding to subset $\mathbf{B}_1$ | | Subproblem corresponding to subset $\mathbf{B}_2$ | |
|---|---|---|---|
| Min | $s+Q$ | Min | $s+Q$ |
| S.t. | $2\cdot x_1+x_2-4\cdot x_4-s+3\cdot Q\le -9.99$ | S.t. | $2\cdot x_1+x_2-4\cdot x_4-s+3\cdot Q\le -1.01$ |
| | $x_1+x_3-s+2\cdot Q\le 4.995$ | | $x_1+x_3-s+2\cdot Q\le 0.505$ |
| | $3\cdot x_2+0.5\cdot x_3+x_4-s+12.5\cdot Q\le -9.99$ | | $3\cdot x_2+0.5\cdot x_3+x_4-s+12.5\cdot Q\le -1.01$ |
| | $-x_1-x_2-x_3-7\cdot Q\le 0$ | | $-x_1-x_2-x_3-7\cdot Q\le 0$ |
| | $x_1+5\cdot Q\le 5$ | | $x_1+5\cdot Q\le 5$ |
| | $x_2+4\cdot Q\le 4$ | | $x_2+4\cdot Q\le 4$ |
| | $x_3+3\cdot Q\le 3$ | | $x_3+3\cdot Q\le 3$ |
| | $x_4+2\cdot Q\le 2$ | | $x_4+2\cdot Q\le 2$ |
| | $0\le x_1,x_2,x_3,x_4,s$ $Q$ free | | $0\le x_1,x_2,x_3,x_4,s$ $Q$ free |

**Table 4** Solution procedure using the proposed multiple cuts from multiple optimal dual solutions

| Iteration | Solution | | | | | | Benders cuts |
|---|---|---|---|---|---|---|---|
| | $I_1$ | $I_2$ | $I_3$ | $P_1$ | $P_2$ | $P_3$ | |
| 1 | 1 | 0 | 0 | 10 | 0 | 0 | $-P_2\le -2$ |
| | | | | | | | $0.0625\cdot P_1-0.34375\cdot P_2+0.25\cdot P_3\le -0.375$ |
| 2 | 1 | 1 | 0 | 7.538 | 2.462 | 0 | – |

## 4.2 3-bus system

A 3-bus system shown in Fig. 3 with three generators, three transmission lines, and one load is studied. Three generators are located at three buses respectively, with parameters listed in Table 5. Transmission line capacities are also given in Fig. 3. Reactance of all lines is 0.1 p.u. and bus 1 is the reference bus. A one-hour NCUC problem described by (1)–(2), (6) and (8) is considered to find the optimal UC decisions and generation dispatch with minimum operation cost, while satisfying the system load of 450 MW located at bus 3. For this one-hour case study, other constraints, such as reserve requirement, system losses, generator minimum on/off time constraints, and ramping up/down limits, are relaxed for the sake of discussion. The problem is formulated as follows with constraints in each row representing the system load balance, generation capacity limits for each unit, power balance for each bus, dc power flow equation for each transmission line, power flow capacity limits for each line, and the reference bus identification

$$\begin{aligned}
\text{Min}\quad & 10\cdot P_{11}+11\cdot P_{21}+12\cdot P_{31}\\
\text{S.t.}\quad & P_{11}+P_{21}+P_{31}=450\\
& 100\cdot I_{11}\le P_{11}\le 500\cdot I_{11},\qquad 90\cdot I_{21}\le P_{21}\le 400\cdot I_{21}\\
& 30\cdot I_{31}\le P_{31}\le 200\cdot I_{31}\\
& PL_{11}+PL_{31}=P_{11},\qquad PL_{21}-PL_{11}=P_{21}
\end{aligned}$$

  

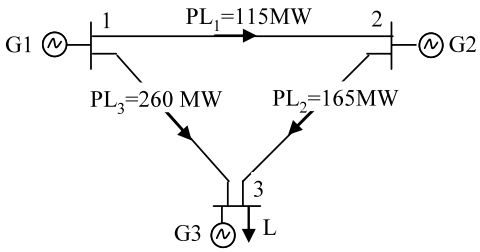


**Fig. 3** One-line diagram of the 3-bus system

**Table 5** Generator parameters

| Generator | $P^{\min}$ (MW) | $P^{\max}$ (MW) | Cost function ($/MWh) |
|---|---|---|---|
| 1 | 100 | 500 | 10 |
| 2 | 90 | 400 | 11 |
| 3 | 30 | 200 | 12 |

**Table 6** Solution procedure using classical BD algorithm

| Iteration | UC solution (MW) | | | Benders cuts |
|---|---|---|---|---|
| | $P_{11}$ | $P_{21}$ | $P_{31}$ | |
| 1 | 450 | 0 | 0 | $P_{11} \le 375$ |
| 2 | 360 | 90 | 0 | $-P_{31} \le -25$ |
| 3 | 375 | 0 | 75 | $P_{11} - P_{21} \le 345$ |
| 4 | 330 | 90 | 30 | $P_{21} - P_{31} \le 45$ |
| 5 | 315 | 90 | 45 | – |

$$-PL_{21} - PL_{31} = P_{31} - 450$$
$$PL_{11} - (\theta_{11} - \theta_{21})/0.1 = 0, \qquad PL_{21} - (\theta_{21} - \theta_{31})/0.1 = 0$$
$$PL_{31} - (\theta_{11} - \theta_{31})/0.1 = 0$$
$$-115 \le PL_{11} \le 115, \qquad -165 \le PL_{21} \le 165, \qquad -260 \le PL_{31} \le 260$$
$$\theta_{11} = 0, \qquad I_{11}, I_{21}, I_{31} \in \{0, 1\}$$

Applying the classical BD algorithm as described by (10)–(12), we would need 5 iterations between the master UC and the network evaluation subproblems with only 3 transmission lines to eliminate the network violations. Four feasibility Benders cuts are generated as shown in the last row of Table 6. The final optimal solution is to commit all three generators with a dispatch of 315 MW, 90 MW and 45 MW. This example shows the drawback of the classical BD algorithm, which is partly due to the low-density cuts generated in the first two iterations. That is, only one variable is incorporated in each cut, which would limit the algorithm's capability for reducing the feasible region of the master problem.

Next, we show that the proposed method would generate high-density strong Benders cuts for reducing the number of Benders iterations to 3 and the overall computing time. First the network evaluation subproblem (11) is solved, which is shown in the first row of Table 7. We obtain a feasibility Benders cut $P_{11} \le 375$ with the opti-

**Table 7** Subproblems (11), (22)–(23) corresponding to $\mathbf{SZ}_1 = \{2\}$

| | | |
|---|---|---|
| Subproblem (11) | Min | $s_1$ |
| | S.t. | $PL_{11} + PL_{31} - s_1 \le 450 \quad \lambda_{1,11}$ |
| | | $-PL_{11} - PL_{31} - s_1 \le -450 \quad \lambda_{2,11}$ |
| | | $PL_{21} - PL_{11} - s_1 \le 0 \quad \lambda_{1,21}$ |
| | | $-PL_{21} + PL_{11} - s_1 \le 0 \quad \lambda_{2,21}$ |
| | | $-PL_{21} - PL_{31} - s_1 \le -450 \quad \lambda_{1,31}$ |
| | | $PL_{21} + PL_{31} - s_1 \le 450 \quad \lambda_{2,31}$ |
| | | $PL_{11} - (\theta_{11} - \theta_{21})/0.1 = 0 \quad \kappa_{11}, \quad PL_{21} - (\theta_{21} - \theta_{31})/0.1 = 0 \quad \kappa_{21}$ |
| | | $PL_{31} - (\theta_{11} - \theta_{31})/0.1 = 0 \quad \kappa_{31}$ |
| | | $PL_{11} \le 115 \quad \pi_{3,11}, \quad -PL_{11} \le 115 \quad \pi_{4,11}$ |
| | | $PL_{21} \le 165 \quad \pi_{3,21}, \quad -PL_{21} \le 165 \quad \pi_{4,21}$ |
| | | $PL_{31} \le 260 \quad \pi_{3,31}, \quad -PL_{31} \le 260 \quad \pi_{4,31}$ |
| | | $\theta_{11} = 0 \quad \pi_1, \quad 0 \le s_1$ |
| Subproblem (22) | Min | $75 \cdot Q + 0 \cdot q_{1,11} + (-1) \cdot q_{2,11} + 4 \cdot q$ |
| | S.t. | $PL_{11} + PL_{31} + 450 \cdot Q + q_{1,11} \le 0 \quad \lambda_{1,11}$ |
| | | $-PL_{11} - PL_{31} - 450 \cdot Q + q_{2,11} \le 0 \quad \lambda_{2,11}$ |
| | | $PL_{21} - PL_{11} + 0 \cdot Q - q \le 399.99 \quad \lambda_{1,21}$ |
| | | $-PL_{21} + PL_{11} - 0 \cdot Q - q \le -399.99 \quad \lambda_{2,21}$ |
| | | $-PL_{21} - PL_{31} + (-450) \cdot Q - q \le 30.01 \quad \lambda_{1,31}$ |
| | | $PL_{21} + PL_{31} - (-450) \cdot Q - q \le -30.01 \quad \lambda_{2,31}$ |
| | | $PL_{11} - (\theta_{11} - \theta_{21})/0.1 = 0, \quad PL_{21} - (\theta_{21} - \theta_{31})/0.1 = 0$ |
| | | $PL_{31} - (\theta_{11} - \theta_{31})/0.1 = 0$ |
| | | $PL_{11} + 115 \cdot Q \le 0, \quad -PL_{11} + 115 \cdot Q \le 0$ |
| | | $PL_{21} + 165 \cdot Q \le 0, \quad -PL_{21} + 165 \cdot Q \le 0$ |
| | | $PL_{31} + 260 \cdot Q \le 0, \quad -PL_{31} + 260 \cdot Q \le 0$ |
| | | $\theta_{ref,t} = 0$ |
| | | $0 \le q, \quad Q, q_{1,11}, q_{2,11}$ free |
| Subproblem (23) | Min | $s_1 + (-1/5) \cdot q_{2,11} + (-1.263/5) \cdot q_{2,21} + (-2.737/5) \cdot q_{2,31}$ |
| | S.t. | $PL_{11} + PL_{31} - s_1 + q_{1,11} \le 450 \quad \lambda_{1,11}$ |
| | | $-PL_{11} - PL_{31} - s_1 + q_{2,11} \le -450 \quad \lambda_{2,11}$ |
| | | $PL_{21} - PL_{11} - s_1 + q_{1,21} \le 0 \quad \lambda_{1,21}$ |
| | | $-PL_{21} + PL_{11} - s_1 + q_{2,21} \le 0 \quad \lambda_{2,21}$ |
| | | $-PL_{21} - PL_{31} - s_1 + q_{1,31} \le -450 \quad \lambda_{1,31}$ |
| | | $PL_{21} + PL_{31} - s_1 + q_{2,31} \le 450 \quad \lambda_{2,31}$ |
| | | $PL_{11} - (\theta_{11} - \theta_{21})/0.1 = 0 \quad \kappa_{11}, \quad PL_{21} - (\theta_{21} - \theta_{31})/0.1 = 0 \quad \kappa_{21}$ |
| | | $PL_{31} - (\theta_{11} - \theta_{31})/0.1 = 0 \quad \kappa_{31}$ |
| | | $PL_{11} \le 115 \quad \pi_{3,11}, \quad -PL_{11} \le 115 \quad \pi_{4,11}$ |
| | | $PL_{21} \le 165 \quad \pi_{3,21}, \quad -PL_{21} \le 165 \quad \pi_{4,21}$ |
| | | $PL_{31} \le 260 \quad \pi_{3,31}, \quad -PL_{31} \le 260 \quad \pi_{4,31}$ |
| | | $\theta_{ref,t} = 0$ |
| | | $0 \le s_1, \quad q_{1,11}, q_{2,11}, q_{1,21}, q_{2,21}, q_{1,31}, q_{2,31}$ free |

  

**Table 8** Solution procedure using the proposed high-density cuts

| Iteration | UC solution (MW) | | | Benders cuts |
|---|---|---|---|---|
| | $P_{11}$ | $P_{21}$ | $P_{31}$ | |
| 1 | 450 | 0 | 0 | $P_{11} \leq 375$ |
| | | | | $0.2 \cdot P_{11} + 0.253 \cdot P_{21} - 0.547 \cdot P_{31} \leq 75$ |
| | | | | $0.2 \cdot P_{11} - 0.0875 \cdot P_{21} + 0.0571 \cdot P_{31} \leq 75$ |
| 2 | 330 | 90 | 30 | $P_{21} - P_{31} \leq 45$ |
| 3 | 315 | 90 | 45 | – |

mal dual solution of $\lambda_{2,11} = \pi_{3,11} = \pi_{3,31} = -1$, all others are zero, and $\hat{s} = 75$, which is a low density cut that only contains variable $P_{11}$. Thus at the first iteration, the set $\mathbf{Z}$ contains two buses 2 and 3, and set $\mathbf{Z}^c$ contains bus 1, since the corresponding dual variables for generators 2 and 3 (i.e., $\lambda_{1,21}, \lambda_{2,21}, \lambda_{1,31}, \lambda_{2,31}$) are all zero. $\varepsilon$ is assumed to be 0.01 in (22). Two optimization subproblems are constructed according to the primal form (22) with $\mathbf{SZ}_1 = \{2\}$ and $\mathbf{SZ}_2 = \{3\}$ respectively for the fixed $\lambda_{1,11} = 0, \lambda_{2,11} = -1, \hat{s}_t = 75$. The two solutions are $\lambda_{1,21} = 0, \lambda_{2,21} = -1.263, \lambda_{1,31} = -2.737, \lambda_{2,31} = 0$ and $\lambda_{1,21} = -0.429, \lambda_{2,21} = 0, \lambda_{1,31} = 0, \lambda_{2,31} = 0.286$. We apply these to the primal problem (23) which would generate the following two high-density cuts: $0.2 \cdot P_{11} + 0.253 \cdot P_{21} - 0.547 \cdot P_{31} \leq 75$ and $0.2 \cdot P_{11} - 0.0875 \cdot P_{21} + 0.0571 \cdot P_{31} \leq 75$. Here $c$ is equal to 5. In Table 7, we give the detailed mathematical formulations for subproblems (22)–(23) corresponding to $\mathbf{SZ}_1 = \{2\}$.

These two cuts are high density because decision variables in the master problem, $P_{11}$, $P_{21}$ and $P_{31}$, are all incorporated in these two cuts; thus they can better restrict the feasible region of the master problem. Appending these three feasibility cuts to the master problem, a solution of 330 MW, 90 MW and 30 MW is obtained. Repeating the above procedures by solving the network evaluation subproblem (11), we obtain the feasibility Benders cut $P_{21} - P_{31} \leq 45$ for the second iteration, with $\lambda_{2,21} = \lambda_{1,31} = \kappa_{31} = -0.5, \kappa_{11} = \kappa_{21} = 0.5, \pi_{3,21} = -1.5$, all others are zero, and $\hat{s} = 7.5$. Thus, at this iteration, the set $\mathbf{Z}$ contains only bus 1 and set $\mathbf{Z}^c$ contains buses 2 and 3. Here, one optimization problem is constructed according to the primal form (22), with $\mathbf{SZ}_1 = \{1\}$, for the fixed $\lambda_{1,21} = 0, \lambda_{2,21} = -0.5, \lambda_{1,31} = -0.5, \lambda_{2,31} = 0, \hat{s}_t = 7.5$. The solution is $\lambda_{1,11} = 0, \lambda_{2,11} = 0$, which means no more high-density cuts can be generated at this iteration, and there is no need to further optimize the primal form (23). If we append the feasibility cut $P_{21} - P_{31} \leq 45$ obtained in this iteration to the master problem, a solution of 315 MW, 90 MW and 45 MW is obtained.

If we repeat the above procedure, the optimal objective value of (11) will be equal to zero which means that there will be no more violations in the network evaluation subproblem. Thus the current solution is optimal and the BD procedure stops. The procedure is shown in Table 8.

Benders cuts presented in the last column of Tables 6 and 8 are mapped onto the $P_{21} - P_{31}$ plane for comparison, which are shown in Figs. 4 and 5, respectively. The mapping is processed by substituting $P_{11}$ with $450 - P_{21} - P_{31}$, which is derived from the system power balance constraint. The domains of $P_{21}$ and $P_{31}$, $\{P_{21} =$

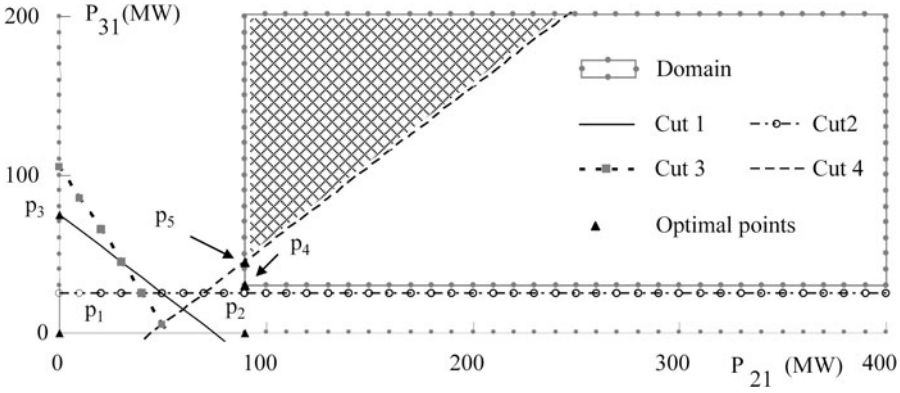


**Fig. 4** Benders cuts from the classical BD algorithm mapped onto $P_{21} - P_{31}$ plane

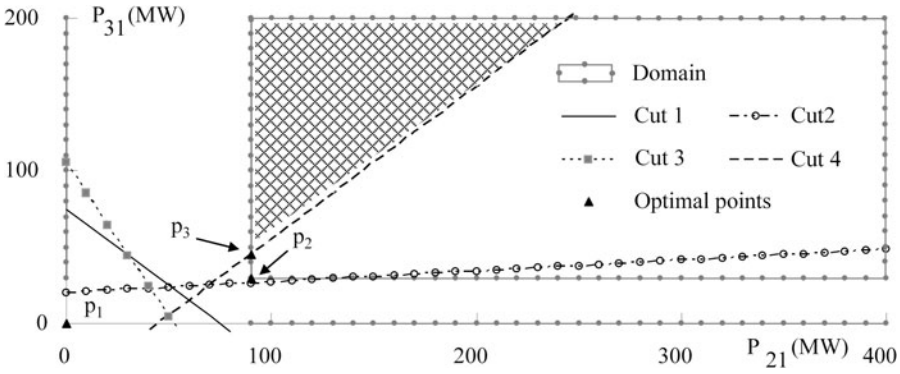


**Fig. 5** Benders cuts from the proposed method mapped onto $P_{21} - P_{31}$ plane

$0, P_{31} = 0\} \cup \{90 \leq P_{21} \leq 400, P_{31} = 0\} \cup \{P_{21} = 0, 30 \leq P_{31} \leq 200\} \cup \{90 \leq P_{21} \leq 400, 30 \leq P_{31} \leq 200\}$, are also shown in Figs. 4 and 5. The Benders cuts 1–4 correspond to the four cuts in Tables 6 and 8 respectively. The optimal points $p_1 - p_5$ obtained at each iteration in Table 6 and optimal points $p_1 - p_3$ at each iteration in Table 8 are also shown. Here, Cuts 1 and 4 are the same in both methods. The Cut 3 coincides in the two methods, i.e., by substituting $P_{11}$ with $450 - P_{21} - P_{31}$, the Cut 3 in Table 6 becomes $2P_{21} + P_{31} \geq 105$ and the Cut 3 in Table 8 becomes $0.2875P_{21} + 0.1429P_{31} \geq 15$, which is $2.0119P_{21} + P_{31} \geq 104.9685$. The Cut 2 from Table 8 provides a tighter formulation than Cut 2 from Table 6, i.e., it passes through the domain boundary $\{90 \leq P_{21} \leq 400, P_{31} = 0\}$ and restricts a tighter feasibility region. The meshed areas in Figs. 4 and 5 show the feasibility regions at the final iteration bounded by Benders cuts and the domain. In Fig. 5, the high density Cuts 2 and 3 generated at the first iteration would tighten the feasibility region of the master problem. These two high density cuts would eliminate the two feasible solutions obtained in the classical BD algorithm and shown as $p_2$ and $p_3$ in Fig. 4; thus they would reduce the number of iterations by two as compared with that of the classical BD algorithm. By comparison, the proposed method outperforms the classical BD

  

**Table 9** Solution procedure using the proposed method with tuning parameter

| Iteration | UC Solution (MW) | | | Benders cuts |
|---|---|---|---|---|
| | $P_{11}$ | $P_{21}$ | $P_{31}$ | |
| 1 | 450 | 0 | 0 | $P_{11} \leq 375$ |
| | | | | $0.2 \cdot P_{11} + 0.0947 \cdot P_{21} - 0.1053 \cdot P_{31} \leq 75$ |
| | | | | $0.2 \cdot P_{11} - 0.0875 \cdot P_{21} + 0.0571 \cdot P_{31} \leq 75$ |
| 2 | 330 | 90 | 30 | $P_{21} - P_{31} \leq 45$ |
| 3 | 315 | 90 | 45 | – |

algorithm in the sense that it would offer the same reduced feasible region in fewer iterations and smaller overall computing time.

In the above study, $2 \cdot |\mathbf{Z}|$ is used as the right-hand-side for the last inequality constraint in (22) to guarantee that the problem (22) is bounded. In comparison, we use 1 instead of $2 \cdot |\mathbf{Z}|$ to show the impact of this parameter on convergence. Table 9 shows that the problem is solved in three iterations and the same global optimal solution is derived. As compared with Table 8, when using 1 instead of $2 \cdot |\mathbf{Z}|$, the strong cuts are not exactly the same but the UC solution at iteration 2 is the same as that in Table 8. The total number of iterations and generated cuts are the same in the two cases with the same final solution, which shows that the parameter $2 \cdot |\mathbf{Z}|$ does not significantly impact the convergence in this case. This small problem is also directly solved by CPLEX with the computation time of 0.04 second and the global optimal solution of $P_{11} = 315$, $P_{21} = 90$, $P_{31} = 45$, $I_{11} = I_{21} = I_{31} = 1$, $PL_{11} = 75$, $PL_{21} = 165$, $PL_{31} = 240$, $\theta_{11} = 0$, $\theta_{21} = -7.5$, and $\theta_{31} = -24$, which is the same as that obtained by the proposed accelerating BD algorithm. For Cases 4.1 and 4.2, the purpose of reporting the solutions with CPLEX is to show the effectiveness of the proposed accelerating BD algorithm. In the following Case 4.3, we will see that the NCUC problem for large-scale power systems may take much longer to be solved directly by CPLEX, and the proposed accelerating BD algorithm can efficiently solve the problem by delivering good enough solutions within acceptable time frames.

### 4.3 5663-bus system

A large-scale system with 599 generators, 5663 buses, 7036 transmission lines, and 251 phase shifters is used to illustrate the effectiveness of the proposed methodology. A 24-hour NCUC problem is considered to find the optimal UC decisions and generation dispatch with the minimum operation cost, while satisfying the system loads, reserve requirements, and losses for a 24-hour horizon shown in Fig. 6. All UC and dc transmission network constraints described by (2)–(8) are considered in this case. Table 10 shows the complexity of the large-scale power system optimization problem. It is noted that the number of dc network constraints in (8) (excluding upper and lower limits for phase shifters and transmission flow variables) is even larger than the number of UC constraints in (2)–(7), which indicates that the decomposition is the only option for handling large-scale power system optimization problems with a substantial network structure.

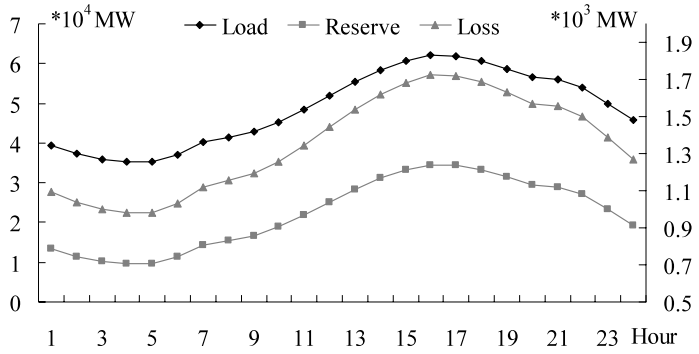


**Fig. 6** System loads, reserves, and losses for a 24-hour horizon

**Table 10** Complexity of the 5663-bus system

| | # of binary variables | # of continuous variables | # of UC constraints in (2)–(7) | # of dc network constraints in (8) |
|---|---|---|---|---|
| Peak hour problem | 1,797 | 19,318 | 10,323 | 12,700 |
| 24-hour problem | 43,128 | 457,608 | 274,268 | 304,800 |

- Case 1: Comparison of the proposed method with the classical BD algorithm at the peak hour 16 with a peak load of 62,000 MW.
- Case 2: Comparison of the proposed method with the classical BD algorithm for the 24-hour study.
- Case 3: Appending the initial cuts and studying its impact on convergence.

*Case 1*: The peak hour is studied using the classical BD algorithm (12) and the proposed strong Benders cuts (16) and (21). Figure 7 shows the NCUC convergence. The proposed method would give a steeper ascent to the violation and speed up the convergence. Table 11 compares the number of iterations and cuts, total CPU time, and the operation cost between the classical BD algorithm and the proposed strong Benders cuts method. We also provide the solution by using the LSF for comparison. The CPU time is based on multiple CPUs, which enables the parallel calculation of hourly network checking subproblems, and the parallel calculation of (18) for all subset $\mathbf{B}_o$ and (22)–(23) for all subset $\mathbf{SZ}_o$. The classical BD algorithm would need 18 iterations with a total of 17 cuts and a total CPU time of 118 s, most of which is consumed by iterations between UC and hourly network evaluation subproblems. In comparison, with the proposed strong Benders cuts, only 8 iterations are needed and the total CPU time is 25 s, which is almost one-fifth of the time used by the classical BD algorithm. A total of 23 cuts are generated in which 13 are from multiple optimal dual solutions and another 3 for enhancing the cut density. For this case, the difference between the proposed method and the classical BD algorithm is even more evident. The proposed method converges more rapidly in terms of the total number of iterations by restricting the feasible region of the master problem at each iteration via strong Benders cuts.

  

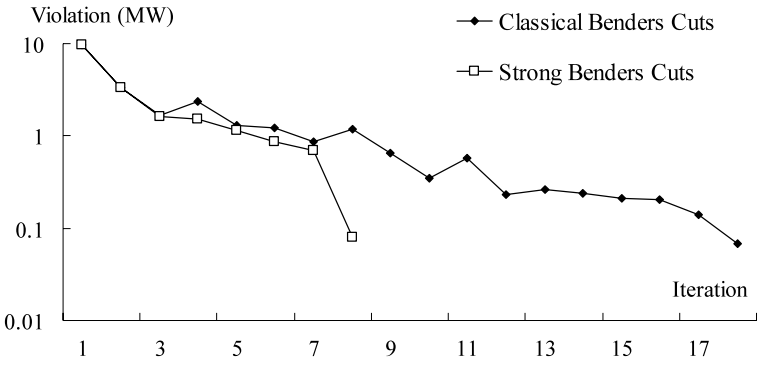


**Fig. 7** Classical and multiple strong Benders cuts for the peak hour

**Table 11** Comparison of the results in Case 1

| | # of iterations | # of cuts | CPU time (s) | Operation cost ($) |
|---|---|---|---|---|
| Classical BD algorithm | 18 | 17 | 118 | 1,745,451.8 |
| LSF | 4 | 129 | 11 | 1,747,353.5 |
| Multiple strong Benders cuts | 8 | 23 | 25 | 1,777,264.2 |
| CPLEX Directly | – | – | 67 | 1,747,360.4 |

The violation threshold of 0.1 MW is used here. The LSF uses fewer iterations and less CPU time than the strong Benders cuts method for this one-hour NCUC problem. However, LSF introduces many more network evaluation constraints than the strong Benders cuts method, which will cause a longer study period for the master UC problem since the master UC is a NP-hard problem. As shown in Cases 2–3, the CPU time for LSF and strong Benders cuts are comparable. The last row of Table 11 shows the operation cost for the three methods. The three solutions are suboptimal since the problem is NP-hard. In this case, the operation cost based on the proposed multiple strong Benders cuts is about 1.82% (i.e. $(1,777,264.2-1,745,451.8)/1,745,451.8$) higher than that of the classical BD algorithm. However, the proposed multiple strong Benders cut method reduces of the number of iterations by 55.56% and the CPU time by 78.81%, and provides a similar operation cost as compared to the classical BD algorithm. Hence the proposed method outperforms the classical BD algorithm by providing a good enough solution with a much smaller computation time. This peak hour NCUC problem can be directly solved by CPLEX in 67 seconds. The objective is $1,747,360.4 with the MIP gap tolerance of 0.05%. In comparison to the solutions given in Table 11, the proposed multiple strong Benders cuts obtained an operation cost that is 1.71% (i.e. $(1,777,264.2-1,747,360.4)/1,747,360.4$) higher than that of CPLEX, while saving a computation time of more than 62.69% (i.e. $(67-25)/67$).

*Case 2*: In this case, the system is studied for a 24-hour period. Figure 8 compares the NCUC convergence of the classical BD with that of the proposed strong Benders cuts method. The classical BD algorithm takes 27 iterations vs. 16 for the proposed

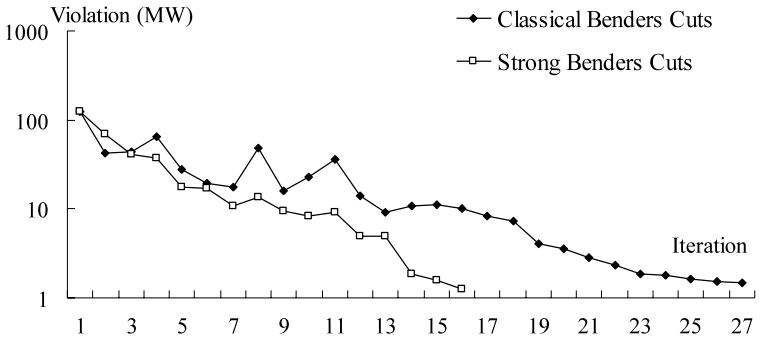


**Fig. 8** Classical and strong Benders cuts for the 24-hour case study

**Fig. 9** CPU time at each iteration in Case 2

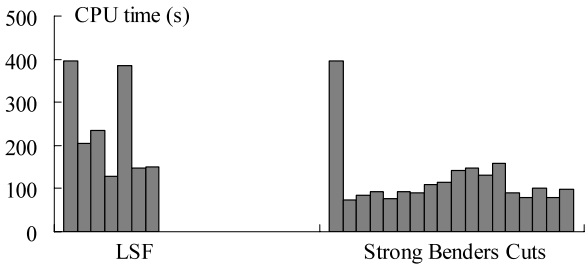


**Table 12** Comparison of the results for the 24-hour study

| | # of iterations | # of cuts | CPU time (s) | Operation cost ($) |
|---|---|---|---|---|
| Classical BD algorithm | 27 | 409 | 3008 | 28,652,220.7 |
| LSF | 7 | 1693 | 1713 | 28,607,073.8 |
| Multiple strong Benders cuts | 16 | 881 | 2159 | 28,660,027.6 |

strong Benders cuts method. A total of 881 cuts are generated for limiting the feasible region of the master problem during the iterative process in which 491 strong cuts are derived from the multiple optimal dual solutions and another 110 for enhancing the cut density. Table 12 compares the number of iterations and cuts, total CPU time, and the operation cost of the classical BD algorithm, the strong Benders cuts, and the LSF method. The proposed strong Benders cuts method reduces the number of iterations by 40.74% (i.e. $(27-16)/27$) and saves the CPU time by 28.22% (i.e. $(3008-2159)/3008$) as compared to the classical BD algorithm. In this case, the operation cost obtained by LSF is the lowest, and the cost by multiple strong Benders cuts is about 0.027% (i.e. $(28,660,027.6-28,652,220.7)/28,652,220.7$) higher than that of the classical BD algorithm. Figure 9 shows that it takes more time to solve the master UC at each iteration with the LSF method since the LSF introduces many more constraints than the strong Benders cuts method. The LSF introduces 1,693 network evaluation constraints vs. 812 in the strong Benders cuts method. Although LSF takes 7 iterations, which is less than half of the 16 for the strong Benders cuts

  

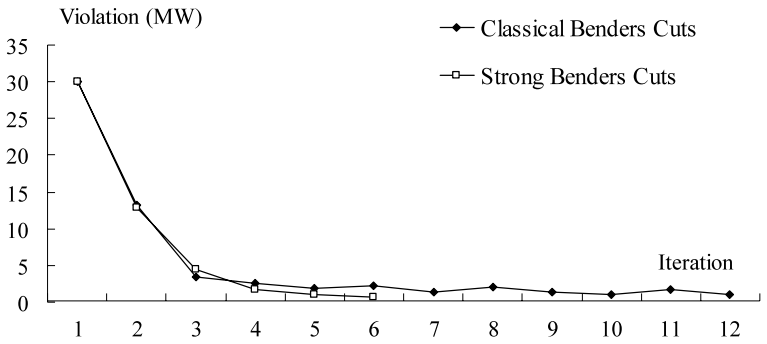


**Fig. 10** Classical and strong Benders cuts for the 24-hour study with initial cuts

method, the required CPU time of LSF is only 20.66% (i.e. $(2159 - 1713)/2159$) smaller than that of the strong Benders cuts method. When solving the master UC problem successively, the solution at the previous iteration can be used as a starting point for the existing UC. Figure 9 shows that a smaller CPU time is used progressively at each iteration of the BD algorithm since only a limited number of Benders cuts are introduced into the master problem at each iteration and the solution at the previous iteration always provides a good starting point. In contrast, the LSF method introduces more constraints at each iteration, all generation dispatch decision variables are considered which would make the problem more difficult to be solved, and the solution of previous iteration may not be used as the starting point. Hence, the CPU time for each LSF iteration is not dramatically reduced as compared with that of the BD algorithm. This 24-hour NCUC problem can not be solved without decomposition by the current version of CPLEX. It takes 2,389 seconds to just solve the root node LP problem, which is generated by relaxing integrality requests of the NCUC problem. Furthermore, after running for more than 3 hours, the CPLEX could not locate a feasible solution to the NCUC problem at any MIP gap level.

*Case 3*: A good set of effective initial Benders cuts could reduce the number of iterations between the master problem and subproblems [10]. In this case, the hourly NCUCs are first solved in parallel while ignoring startup and shutdown costs and coupling constraints among UC hours (e.g. min on/off time and ramping up/down rate limits) to generate an initial set of Benders cuts [18]. The Benders cuts resulting from the hourly NCUC solution are considered as initial Benders cuts for the 24-hour NCUC solution. Figure 10 shows the NCUC convergence for the classical BD and the strong Benders cuts methods with 603 initial Benders cuts generated by solving the hourly NCUC. The classical BD algorithm takes 12 iterations with a total of 90 cuts. The strong Benders cuts method takes 6 iterations with a total of 294 cuts in which 185 strong cuts are derived from the multiple optimal dual solutions and another 26 are high-density cuts. For a fair comparison, the same set of initial Benders cuts are adopted in the LSF method. The difference between the three operation costs is less than 1% (i.e., $28,566,540.3 - 28,548,341.2)/28,548,341.2 = 0.064\%$). Compared with the solutions given in Tables 12, 13 shows that the inclusion of initial Benders cuts would dramatically reduce the number of iterations and cuts for both the classical BD algorithm and the strong Benders cuts methods.

**Table 13** Comparison of the results for the 24-hour study with initial cuts

| | # of iterations | # of cuts | CPU time (s) | Operation cost ($) |
|---|---|---|---|---|
| Classical BD algorithm | 12 | 90 | 2797 | 28,548,341.2 |
| LSF | 5 | 711 | 1665 | 28,566,540.3 |
| Strong Benders cuts | 6 | 294 | 1584 | 28,554,679.8 |

The number of iterations is reduced by 55.56% and 62.5% respectively (i.e., $(27-12)/27$ and $(16-6)/16$), and the number of cuts is decreased by about 78.00% (i.e., $(409-90)/409$) for the classical BD algorithm and 66.63% (i.e., $(881-294)/881$) for the strong Benders cuts. However, the total CPU time for the classical BD algorithm is decreased only by about 7% (i.e., $(3008-2797)/3008$) and 21.63% (i.e., $(2159-1584)/2159$) for the strong Benders cuts. Here, the total CPU time reduction is not significant as may be expected because by appending 603 initial cuts, the required CPU time for each UC master problem would be longer which would diminish the saving in time when initial cuts are used. With initial cuts, the LSF takes 5 iterations as compared with 6 for the strong Benders cuts method, and the CPU time for these two methods are comparable in this case. The strong Benders cuts method would take 4.86% (i.e., $(1665-1584)/1665$) less CPU time than the LSF method.

## 5 Conclusions

This paper proposed a method for generating multiple strong Benders cuts to accelerate the convergence of NCUC with BD. The generated strong Benders cuts are proved to be pareto optimal. Numerical tests show that as compared to the classical BD algorithm, multiple strong Benders cuts generated by the proposed method result in a significant reduction in terms of total number of iterations and the CPU time. For large systems, the proposed multiple strong Benders cuts method and the LSF method are comparable in terms of good enough solutions and CPU time. The proposed multiple strong Benders cuts method also requires fewer cuts than that of the LSF methods. The proposed strong Benders cuts method can be easily extended to other applications of BD on large-scale optimization problems in power systems operation, maintenance and planning.

## Appendix A

*Proof for Theorem 1* Suppose to the contrary that (16) is not pareto optimal. That is, there exists a cut (A.1) that dominates (16)

$$\sum_{b=1}^{NB} \sum_{i \in \mathbf{U}(b)} (\lambda'_{1,bt} - \lambda'_{2,bt}) \cdot P_{it} + \hat{s}_t \leq 0 \tag{A.1}$$

  

Then from Definition 2, it is true that for all $\mathbf{P}_t$ in their domain of $\{\mathbf{0}, [\mathbf{P}^{\min}, \mathbf{P}^{\max}]\}$

$$\left\{\left[\sum_{b=1}^{NB}\sum_{i\in\mathbf{U}(b)}(\tilde{\lambda}_{1,bt}-\tilde{\lambda}_{2,bt})\cdot P_{it}+\hat{s}_t\right]-\left[\sum_{b=1}^{NB}\sum_{i\in\mathbf{U}(b)}(\lambda'_{1,bt}-\lambda'_{2,bt})\cdot P_{it}+\hat{s}_t\right]\right\}\leq 0 \tag{A.2}$$

Thus (A.2) is true for $P_{it}=P_i^{\max}-\varepsilon, \forall i\in\mathbf{U}(b), b\in\mathbf{B}_o$, and $P_{it}=P_i^{\min}+\varepsilon, \forall i\in\mathbf{U}(b), b\notin\mathbf{B}_o$, which is

$$\left\{\begin{array}{l}\left[\sum_{b\in\mathbf{B}_o}\sum_{i\in\mathbf{U}(b)}(\tilde{\lambda}_{1,bt}-\tilde{\lambda}_{2,bt})\cdot(P_i^{\max}-\varepsilon)\right.\\ \left.+\sum_{b\notin\mathbf{B}_o}\sum_{i\in\mathbf{U}(b)}(\tilde{\lambda}_{1,bt}-\tilde{\lambda}_{2,bt})\cdot(P_i^{\min}+\varepsilon)\right]\\ -\left[\sum_{b\in\mathbf{B}_o}\sum_{i\in\mathbf{U}(b)}(\lambda'_{1,bt}-\lambda'_{2,bt})\cdot(P_i^{\max}-\varepsilon)\right.\\ \left.+\sum_{b\notin\mathbf{B}_o}\sum_{i\in\mathbf{U}(b)}(\lambda'_{1,bt}-\lambda'_{2,bt})\cdot(P_i^{\min}+\varepsilon)\right]\end{array}\right\}\leq 0 \tag{A.3}$$

However, solving the maximization problem (15), we obtain the optimal objective value as $\sum_{b\in\mathbf{B}_o}\sum_{i\in\mathbf{U}(b)}(\tilde{\lambda}_{1,bt}-\tilde{\lambda}_{2,bt})\cdot(P_i^{\max}-\varepsilon)+\sum_{b\notin\mathbf{B}_o}\sum_{i\in\mathbf{U}(b)}(\tilde{\lambda}_{1,bt}-\tilde{\lambda}_{2,bt})\cdot(P_i^{\min}+\varepsilon)$, which means

$$\left\{\begin{array}{l}\left[\sum_{b\in\mathbf{B}_o}\sum_{i\in\mathbf{U}(b)}(\tilde{\lambda}_{1,bt}-\tilde{\lambda}_{2,bt})\cdot(P_i^{\max}-\varepsilon)\right.\\ \left.+\sum_{b\notin\mathbf{B}_o}\sum_{i\in\mathbf{U}(b)}(\tilde{\lambda}_{1,bt}-\tilde{\lambda}_{2,bt})\cdot(P_i^{\min}+\varepsilon)\right]\\ -\left[\sum_{b\in\mathbf{B}_o}\sum_{i\in\mathbf{U}(b)}(\lambda'_{1,bt}-\lambda'_{2,bt})\cdot(P_i^{\max}-\varepsilon)\right.\\ \left.+\sum_{b\notin\mathbf{B}_o}\sum_{i\in\mathbf{U}(b)}(\lambda'_{1,bt}-\lambda'_{2,bt})\cdot(P_i^{\min}+\varepsilon)\right]\end{array}\right\}\geq 0 \tag{A.4}$$

Using (A.3) and (A.4), we have

$$\left\{\begin{array}{l}\left[\sum_{b\in\mathbf{B}_o}\sum_{i\in\mathbf{U}(b)}(\tilde{\lambda}_{1,bt}-\tilde{\lambda}_{2,bt})\cdot(P_i^{\max}-\varepsilon)\right.\\ \left.+\sum_{b\notin\mathbf{B}_o}\sum_{i\in\mathbf{U}(b)}(\tilde{\lambda}_{1,bt}-\tilde{\lambda}_{2,bt})\cdot(P_i^{\min}+\varepsilon)\right]\\ -\left[\sum_{b\in\mathbf{B}_o}\sum_{i\in\mathbf{U}(b)}(\lambda'_{1,bt}-\lambda'_{2,bt})\cdot(P_i^{\max}-\varepsilon)\right.\\ \left.+\sum_{b\notin\mathbf{B}_o}\sum_{i\in\mathbf{U}(b)}(\lambda'_{1,bt}-\lambda'_{2,bt})\cdot(P_i^{\min}+\varepsilon)\right]\end{array}\right\}=0 \tag{A.5}$$

Since (A.1) dominates (16), according to Definition 1 there must exits a $\tilde{\mathbf{P}}$ in the domain of $\{\mathbf{0}, [\mathbf{P}^{\min}, \mathbf{P}^{\max}]\}$ by which the strict inequality of (A.2) is satisfied as shown in (A.6)

$$\left\{\left[\sum_{b=1}^{NB}\sum_{i\in\mathbf{U}(b)}(\tilde{\lambda}_{1,bt}-\tilde{\lambda}_{2,bt})\cdot\tilde{P}_i\right]-\left[\sum_{b=1}^{NB}\sum_{i\in\mathbf{U}(b)}(\lambda'_{1,bt}-\lambda'_{2,bt})\cdot\tilde{P}_i\right]\right\}<0 \quad \text{(A.6)}$$

Next we show that there exits a scalar $\theta > 1$ such that $\theta\cdot(P_i^{\max}-\varepsilon)+(1-\theta)\cdot\tilde{P}_i$ and $\theta\cdot(P_i^{\min}+\varepsilon)+(1-\theta)\cdot\tilde{P}_i$ are both in the range of $\{\mathbf{0}, [\mathbf{P}^{\min}, \mathbf{P}^{\max}]\}$.

1. If $\tilde{P}_i = 0, \theta\cdot(P_i^{\max}-\varepsilon)+(1-\theta)\cdot\tilde{P}_i = \theta\cdot(P_i^{\max}-\varepsilon)$ and $\theta\cdot(P_i^{\min}+\varepsilon)+(1-\theta)\cdot\tilde{P}_i = \theta\cdot(P_i^{\min}+\varepsilon)$. Thus for small $0\le\varepsilon$ and $1<\theta\le\min\{\frac{P_i^{\max}}{P_i^{\max}-\varepsilon}, \frac{P_i^{\max}}{P_i^{\min}+\varepsilon}\}$, $\theta\cdot(P_i^{\max}-\varepsilon)+(1-\theta)\cdot\tilde{P}_i$ and $\theta\cdot(P_i^{\min}+\varepsilon)+(1-\theta)\cdot\tilde{P}_i$ are both in the range of $[\mathbf{P}^{\min}, \mathbf{P}^{\max}]$.
2. If $\tilde{P}_i \in [P_i^{\min}, P_i^{\max}]$, for $\theta$ that satisfies $1<\theta\le\frac{P_i^{\max}-P_i^{\min}}{P_i^{\max}-P_i^{\min}-\varepsilon}$, we have $\frac{\theta}{\theta-1}\cdot\varepsilon\ge P_i^{\max}-P_i^{\min}$. Thus $\frac{\theta}{\theta-1}\cdot\varepsilon\ge P_i^{\max}-P_i^{\min}\ge P_i^{\max}-\tilde{P}_i$, and we have $\theta\cdot(P_i^{\max}-\varepsilon)+(1-\theta)\cdot\tilde{P}_i-P_i^{\max}=(\theta-1)\cdot(P_i^{\max}-\tilde{P}-\frac{\theta}{\theta-1}\cdot\varepsilon)\le 0$, which derives $\theta\cdot(P_i^{\max}-\varepsilon)+(1-\theta)\cdot\tilde{P}_i\le P_i^{\max}$. For small $0\le\varepsilon$, it usually holds that $P_i^{\max}-P_i^{\min}-\varepsilon\ge\varepsilon$ since $P_i^{\max}$ and $P_i^{\min}$ are usually in tens and hundreds of MW range, and an $\varepsilon$ of 0.01–0.1 MW is used in this paper. Thus $1<\theta\le\frac{P_i^{\max}-P_i^{\min}}{P_i^{\max}-P_i^{\min}-\varepsilon}\le\frac{P_i^{\max}-P_i^{\min}}{\varepsilon}$, and we have $\theta\cdot(P_i^{\max}-\varepsilon)+(1-\theta)\cdot\tilde{P}_i-P_i^{\min}\ge\theta\cdot(P_i^{\max}-\varepsilon)+(1-\theta)\cdot P_i^{\max}-P_i^{\min}=P_i^{\max}-P_i^{\min}-\theta\cdot\varepsilon\ge 0$, which derives $P_i^{\min}\le\theta\cdot(P_i^{\max}-\varepsilon)+(1-\theta)\cdot\tilde{P}_i$. Similarly, we derive that $\theta\cdot(P_i^{\min}+\varepsilon)+(1-\theta)\cdot\tilde{P}_i$ is in the range of $[\mathbf{P}^{\min}, \mathbf{P}^{\max}]$.

Based on the above discussion, we multiply (A.5) by $\theta$ and (A.6) by $(1-\theta)$ which is negative and preserves the inequality, and add them up to derive

$$\begin{aligned}
&\sum_{b\in\mathbf{B}_o}\sum_{i\in\mathbf{U}(b)}(\tilde{\lambda}_{1,bt}-\tilde{\lambda}_{2,bt})\cdot[\theta\cdot(P_i^{\max}-\varepsilon)+(1-\theta)\cdot\tilde{P}_i]\\
&\quad+\sum_{b\notin\mathbf{B}_o}\sum_{i\in\mathbf{U}(b)}(\tilde{\lambda}_{1,bt}-\tilde{\lambda}_{2,bt})\cdot[\theta\cdot(P_i^{\min}+\varepsilon)+(1-\theta)\cdot\tilde{P}_i]\\
&>\sum_{b\in\mathbf{B}_o}\sum_{i\in\mathbf{U}(b)}(\lambda'_{1,bt}-\lambda'_{2,bt})\cdot[\theta\cdot(P_i^{\max}-\varepsilon)+(1-\theta)\cdot\tilde{P}_i]\\
&\quad+\sum_{b\notin\mathbf{B}_o}\sum_{i\in\mathbf{U}(b)}(\lambda'_{1,bt}-\lambda'_{2,bt})\cdot[\theta\cdot(P_i^{\min}+\varepsilon)+(1-\theta)\cdot\tilde{P}_i] \qquad \text{(A.7)}
\end{aligned}$$

According to (A.7)

$$P_{it}=\begin{cases}\theta\cdot(P_i^{\max}-\varepsilon)+(1-\theta)\cdot\tilde{P}_i, & \forall i\in\mathbf{U}(b), b\in\mathbf{B}_o\\ \theta\cdot(P_i^{\min}+\varepsilon)+(1-\theta)\cdot\tilde{P}_i, & \forall i\in\mathbf{U}(b), b\notin\mathbf{B}_o\end{cases}$$

  

$$\left\{\begin{array}{l}\left[\sum\limits_{b\in\mathbf{B}_o}\sum\limits_{i\in\mathbf{U}(b)}(\hat{\lambda}_{1,bt}-\hat{\lambda}_{2,bt})\cdot(P_{it}-\hat{P}_{it})\right.\\ \left.\quad+\sum\limits_{b\notin\mathbf{B}_o}\sum\limits_{i\in\mathbf{U}(b)}(\tilde{\lambda}_{1,bt}-\tilde{\lambda}_{2,bt})\cdot P_{it}+\hat{s}_t\right]\\ -\left[\sum\limits_{b\in\mathbf{B}_o}\sum\limits_{i\in\mathbf{U}(b)}(\hat{\lambda}_{1,bt}-\hat{\lambda}_{2,bt})\cdot(P_{it}-\hat{P}_{it})\right.\\ \left.\quad+\sum\limits_{b\notin\mathbf{B}_o}\sum\limits_{i\in\mathbf{U}(b)}(\lambda'_{1,bt}-\lambda'_{2,bt})\cdot P_{it}+\hat{s}_t\right]\end{array}\right\}>0$$

which is inconsistent with (A.2). Hence our assumption of (16) not being pareto optimal is untenable. Thus (16) is pareto optimal. □

## Appendix B

The following Theorem B.1 is a prerequisite for the proof of Theorem 2.

**Theorem B.1** *Let* $\{\hat{\lambda}_{1,bt}/c, \hat{\lambda}_{2,bt}/c, b\in\mathbf{Z}^c, \bar{\lambda}_{1,bt}/c, \bar{\lambda}_{2,bt}/c, b\in\mathbf{Z}\}$ *together with* $\{\bar{\pi}_{1,pt}, \bar{\pi}_{2,pt}, \bar{\pi}_{3,lt}, \bar{\pi}_{4,lt}, \bar{\pi}_t, \bar{\kappa}_{lt}\}$ *be an optimal solution of* (20) *with the objective value of* $\breve{s}_t$. *Thus* $\hat{s}\le c\cdot\breve{s}_t$ *is satisfied, where* $\hat{s}_t$ *is the optimal objective value of* (11) *used in* (19).

*Proof for Theorem B.1* First let us show that the following problem (B.1) has the optimal objective value of $c\cdot\breve{s}_t$. Assume the optimal objective value of (B.1) is $O$

$$\begin{aligned}
\text{Max}\quad & \sum_b\left(\sum_{i\in\mathbf{U}(b)}P_{it}-D_{bt}-C_b\cdot P_{Losst}\right)\cdot(\lambda_{1,bt}-\lambda_{2,bt})\\
& +\sum_p(\gamma_p^{\max}\cdot\pi_{1,pt}-\gamma_p^{\min}\cdot\pi_{2,pt})+\sum_l PL_l^{\max}\cdot(\pi_{3,lt}+\pi_{4,lt})\\
\text{S.t.}\quad & (\lambda_{1,at}-\lambda_{2,at})+(-\lambda_{1,bt}+\lambda_{2,bt})+\kappa_{lt}+\pi_{3,lt}-\pi_{4,lt}=0\\
& \quad l \text{ is from bus } a \text{ to bus } b\\
& \sum_a\kappa_{lt}/x_{am}-\sum_b\kappa_{l't}/x_{mb}=0\\
& \quad l \text{ is from bus } a \text{ to bus } m, l' \text{ is from bus } m \text{ to bus } b,\\
& \quad m \text{ is not reference bus}\\
& \sum_a\kappa_{lt}/x_{am}-\sum_b\kappa_{l't}/x_{mb}+\pi_t=0\\
& \quad l \text{ is from bus } a \text{ to bus } m, l' \text{ is from bus } m \text{ to bus } b,\\
& \quad m \text{ is reference bus}\\
& \kappa_{lt}/x_{ab}+\pi_{1,pt}-\pi_{2,pt}=0\\
& \quad \text{phase shifter } p \text{ is located at line } l, \text{ which is from bus } a \text{ to bus } b\\
& -\sum_{b\in Z}(\lambda_{1,bt}+\lambda_{2,bt})\le 2\cdot|\mathbf{Z}|
\end{aligned}\tag{B.1}$$

$$\lambda_{1,bt} = \hat{\lambda}_{1,bt}, \quad \lambda_{2,bt} = \hat{\lambda}_{2,bt}, \quad b \in \mathbf{Z}^c$$
$$\lambda_{1,bt} = \bar{\lambda}_{1,bt}, \quad \lambda_{2,bt} = \bar{\lambda}_{2,bt}, \quad b \in \mathbf{Z}$$
$$\lambda_{1,bt}, \lambda_{2,bt}, \pi_{1,pt}, \pi_{2,pt}, \pi_{3,lt}, \pi_{4,lt} \le 0, \quad \kappa_{lt}, \pi_t \text{ free}$$

It is obvious that $\{\hat{\lambda}_{1,bt}, \hat{\lambda}_{2,bt}, b \in \mathbf{Z}^c, \bar{\lambda}_{1,bt}, \bar{\lambda}_{2,bt}, b \in \mathbf{Z}\}$ together with $\{c \cdot \bar{\pi}_{1,pt}, c \cdot \bar{\pi}_{2,pt}, c \cdot \bar{\pi}_{3,lt}, c \cdot \bar{\pi}_{4,lt}, c \cdot \bar{\pi}_t, c \cdot \bar{\kappa}_{lt}\}$ is a feasible solution of (B.1), with the objective value of $c \cdot \breve{s}_t$. Thus the optimal objective value of (B.1) is not less than $c \cdot \breve{s}_t$, i.e.,

$$O \ge c \cdot \breve{s}_t \tag{B.2}$$

Assume $\{\hat{\lambda}_{1,bt}, \hat{\lambda}_{2,bt}, b \in \mathbf{Z}^c, \bar{\lambda}_{1,bt}, \bar{\lambda}_{2,bt}, b \in \mathbf{Z}\}$ together with $\{\pi'_{1,pt}, \pi'_{2,pt}, \pi'_{3,lt}, \pi'_{4,lt}, \pi'_t, \kappa'_{lt}\}$ is the optimal solution of (B.1) with the optimal objective value of $O$. Thus it is obvious that $\{\hat{\lambda}_{1,bt}/c, \hat{\lambda}_{2,bt}/c, b \in \mathbf{Z}^c, \bar{\lambda}_{1,bt}/c, \bar{\lambda}_{2,bt}/c, b \in \mathbf{Z}\}$ together with $\{\pi'_{1,pt}/c, \pi'_{2,pt}/c, \pi'_{3,lt}/c, \pi'_{4,lt}/c, \pi'_t/c, \kappa'_{lt}/c\}$ is a feasible solution of (20) with the objective value of $O/c$. Since the optimal objective value to (20) is $\breve{s}_t$, we have

$$O/c \le \breve{s}_t \tag{B.3}$$

Using (B.2) and (B.3), we conclude that $O = c \cdot \breve{s}_t$. That is the optimal objective value of (B.1) $O$ is equal to $c \cdot \breve{s}_t$. Comparing (B.1) with (19), the optimal solution of (19), which is $\hat{\lambda}_{1,bt}\hat{\lambda}_{2,bt}$ for $b \in \mathbf{Z}^c$ and $\bar{\lambda}_{1,bt}\bar{\lambda}_{2,bt}$ for $b \in \mathbf{Z}$ together with the corresponding $\{\pi'_{1,pt}, \pi'_{2,pt}, \pi'_{3,lt}, \pi'_{4,lt}, \pi'_t, \kappa'_{lt}\}$ is a feasible solution to (B.1) as this solution set satisfies all constraints in (B.1) with the objective value of $\hat{s}_t$. Thus, $\hat{s}_t$ is no larger than the optimal objective value $c \cdot \breve{s}_t$, that is $\hat{s} \le c \cdot \breve{s}_t$. □

*Proof for Theorem 2* Suppose that contrary to our assumption, (21) is not pareto optimal. That is, there exists a cut (B.4) that dominates (21)

$$\sum_{b \in \mathbf{Z}^c} \sum_{i \in \mathbf{U}(b)} (\hat{\lambda}_{1,bt}/c - \hat{\lambda}_{2,bt}/c) \cdot (P_{it} - \hat{P}_{it}) + \sum_{b \in \mathbf{Z}} \sum_{i \in \mathbf{U}(b)} (\lambda'_{1,bt} - \lambda'_{2,bt}) \cdot P_{it} + \breve{s}_t \le 0 \tag{B.4}$$

Then from Definition 2, it is true that for all $\mathbf{P}_t$ in the domain of $\{\mathbf{0}, [\mathbf{P}^{\min}, \mathbf{P}^{\max}]\}$, we have

$$\left\{ \begin{array}{l} \left[ \sum\limits_{b \in \mathbf{Z}^c} \sum\limits_{i \in \mathbf{U}(b)} (\hat{\lambda}_{1,bt}/c - \hat{\lambda}_{2,bt}/c) \cdot (P_{it} - \hat{P}_{it}) \right. \\ \quad \left. + \sum\limits_{b \in \mathbf{Z}} \sum\limits_{i \in \mathbf{U}(b)} (\bar{\lambda}_{1,bt}/c - \bar{\lambda}_{2,bt}/c) \cdot P_{it} + \breve{s}_t \right] \\ - \left[ \sum\limits_{b \in \mathbf{Z}^c} \sum\limits_{i \in \mathbf{U}(b)} (\hat{\lambda}_{1,bt}/c - \hat{\lambda}_{2,bt}/c) \cdot (P_{it} - \hat{P}_{it}) \right. \\ \quad \left. + \sum\limits_{b \in \mathbf{Z}} \sum\limits_{i \in \mathbf{U}(b)} (\lambda'_{1,bt} - \lambda'_{2,bt}) \cdot P_{it} + \breve{s}_t \right] \end{array} \right\} \le 0 \tag{B.5}$$

Thus (B.5) is true for $P_{it} = \hat{P}_{it}, \forall i \in \mathbf{U}(b), b \in \mathbf{Z}^c$, $P_{it} = P_i^{\max} - \varepsilon, \forall i \in \mathbf{U}(b), b \in \mathbf{SZ}_o$, and $P_{it} = (P_i^{\min} + \varepsilon), \forall i \in \mathbf{U}(b), b \in \{\mathbf{Z} - \mathbf{SZ}_o\}$, which indicates that

  

$$\left\{\begin{array}{l}\left[\sum\limits_{b\in\mathbf{SZ}_o}\sum\limits_{i\in\mathbf{U}(b)}(\bar{\lambda}_{1,bt}/c-\bar{\lambda}_{2,bt}/c)\cdot(P_i^{\max}-\varepsilon)\right.\\ \quad\left.+\sum\limits_{b\in\{\mathbf{Z}-\mathbf{SZ}_o\}}\sum\limits_{i\in\mathbf{U}(b)}(\bar{\lambda}_{1,bt}/c-\bar{\lambda}_{2,bt}/c)\cdot(P_i^{\min}+\varepsilon)\right]\\ -\left[\sum\limits_{b\in\mathbf{SZ}_o}\sum\limits_{i\in\mathbf{U}(b)}(\lambda'_{1,bt}-\lambda'_{2,bt})\cdot(P_i^{\max}-\varepsilon)\right.\\ \quad\left.+\sum\limits_{b\in\{\mathbf{Z}-\mathbf{SZ}_o\}}\sum\limits_{i\in\mathbf{U}(b)}(\lambda'_{1,bt}-\lambda'_{2,bt})\cdot(P_i^{\min}+\varepsilon)\right]\end{array}\right\}\leq 0 \qquad \text{(B.6)}$$

With (B.4), $\{\hat{\lambda}_{1,bt}/c, \hat{\lambda}_{2,bt}/c, b\in\mathbf{Z}^c, \lambda'_{1,bt}, \lambda'_{2,bt}, b\in\mathbf{Z}\}$ together with $\{\pi'_{1,pt}, \pi'_{2,pt}, \pi'_{3,lt}, \pi'_{4,lt}, \pi'_t, \kappa'_{lt}\}$ is an optimal solution of (20) since its corresponding objective value is also $\breve{s}_t$. According to Theorem B.1, $\hat{s}\leq c\cdot\breve{s}_t$, thus there must exit a solution of $\{\hat{\lambda}_{1,bt}/c, \hat{\lambda}_{2,bt}/c, b\in\mathbf{Z}^c, \lambda'_{1,bt}, \lambda'_{2,bt}, b\in\mathbf{Z}\}$ together with $\{\pi''_{1,pt}, \pi''_{2,pt}, \pi''_{3,lt}, \pi''_{4,lt}, \pi''_t, \kappa''_{lt}\}$ for (20), which has the objective value of $\hat{s}/c$. Thus $\{\hat{\lambda}_{1,bt}, \hat{\lambda}_{2,bt}, b\in\mathbf{Z}^c, c\cdot\lambda'_{1,bt}, c\cdot\lambda'_{2,bt}, b\in\mathbf{Z}\}$ together with $\{c\cdot\pi''_{1,pt}, c\cdot\pi''_{2,pt}, c\cdot\pi''_{3,lt}, c\cdot\pi''_{4,lt}, c\cdot\pi''_t, c\cdot\kappa''_{lt}\}$ is a feasible solution of (19).

Since $\{\hat{\lambda}_{1,bt}, \hat{\lambda}_{2,bt}, b\in\mathbf{Z}^c, \bar{\lambda}_{1,bt}, \bar{\lambda}_{2,bt}, b\in\mathbf{Z}\}$ is the optimal solution of (19), and $\{\hat{\lambda}_{1,bt}, \hat{\lambda}_{2,bt}, b\in\mathbf{Z}^c, c\cdot\lambda'_{1,bt}, c\cdot\lambda'_{2,bt}, b\in\mathbf{Z}\}$ is one of its feasible solutions, we learn that

$$\left\{\begin{array}{l}\left[\sum\limits_{b\in\mathbf{SZ}_o}\sum\limits_{i\in\mathbf{U}(b)}(\bar{\lambda}_{1,bt}-\bar{\lambda}_{2,bt})\cdot(P_i^{\max}-\varepsilon)\right.\\ \quad\left.+\sum\limits_{b\in\{\mathbf{Z}-\mathbf{SZ}_o\}}\sum\limits_{i\in\mathbf{U}(b)}(\bar{\lambda}_{1,bt}-\bar{\lambda}_{2,bt})\cdot(P_i^{\min}+\varepsilon)\right]\\ -\left[\sum\limits_{b\in\mathbf{SZ}_o}\sum\limits_{i\in\mathbf{U}(b)}(c\cdot\lambda'_{1,bt}-c\cdot\lambda'_{2,bt})\cdot(P_i^{\max}-\varepsilon)\right.\\ \quad\left.+\sum\limits_{b\in\{\mathbf{Z}-\mathbf{SZ}_o\}}\sum\limits_{i\in\mathbf{U}(b)}(c\cdot\lambda'_{1,bt}-c\cdot\lambda'_{2,bt})\cdot(P_i^{\min}+\varepsilon)\right]\end{array}\right\}\geq 0 \qquad \text{(B.7)}$$

Multiplying both sides of (B.7) by $c$, we get (B.8) where $c=\sum_{b\in\mathrm{NZ}}(-\hat{\lambda}_{1,bt}-\hat{\lambda}_{2,bt})+2\cdot|\mathbf{Z}|$ is a positive constant

$$\left\{\begin{array}{l}\left[\sum\limits_{b\in\mathbf{SZ}_o}\sum\limits_{i\in\mathbf{U}(b)}(\bar{\lambda}_{1,bt}/c-\bar{\lambda}_{2,bt}/c)\cdot(P_i^{\max}-\varepsilon)\right.\\ \quad\left.+\sum\limits_{b\in\{\mathbf{Z}-\mathbf{SZ}_o\}}\sum\limits_{i\in\mathbf{U}(b)}(\bar{\lambda}_{1,bt}/c-\bar{\lambda}_{2,bt}/c)\cdot(P_i^{\min}+\varepsilon)\right]\\ -\left[\sum\limits_{b\in\mathbf{SZ}_o}\sum\limits_{i\in\mathbf{U}(b)}(\lambda'_{1,bt}-\lambda'_{2,bt})\cdot(P_i^{\max}-\varepsilon)\right.\\ \quad\left.+\sum\limits_{b\in\{\mathbf{Z}-\mathbf{SZ}_o\}}\sum\limits_{i\in\mathbf{U}(b)}(\lambda'_{1,bt}-\lambda'_{2,bt})\cdot(P_i^{\min}+\varepsilon)\right]\end{array}\right\}\geq 0 \qquad \text{(B.8)}$$

Using (B.6) and (B.8), we have

$$\left\{\begin{array}{l}\Bigg[\sum\limits_{b\in\mathbf{SZ}_o}\sum\limits_{i\in\mathbf{U}(b)}(\bar{\lambda}_{1,bt}/c-\bar{\lambda}_{2,bt}/c)\cdot(P_i^{\max}-\varepsilon)\\ \quad+\sum\limits_{b\in\{\mathbf{Z}-\mathbf{SZ}_o\}}\sum\limits_{i\in\mathbf{U}(b)}(\bar{\lambda}_{1,bt}/c-\bar{\lambda}_{2,bt}/c)\cdot(P_i^{\min}+\varepsilon)\Bigg]\\ -\Bigg[\sum\limits_{b\in\mathbf{SZ}_o}\sum\limits_{i\in\mathbf{U}(b)}(\lambda'_{1,bt}-\lambda'_{2,bt})\cdot(P_i^{\max}-\varepsilon)\\ \quad+\sum\limits_{b\in\{\mathbf{Z}-\mathbf{SZ}_o\}}\sum\limits_{i\in\mathbf{U}(b)}(\lambda'_{1,bt}-\lambda'_{2,bt})\cdot(P_i^{\min}+\varepsilon)\Bigg]\end{array}\right\}=0 \tag{B.9}$$

Since (B.4) dominates (21), according to the Definition 1 there must exits a $\tilde{\mathbf{P}}$ in the domain of $\{\mathbf{0},[\mathbf{P}^{\min},\mathbf{P}^{\max}]\}$ which satisfies the strict inequality of (B.5) as shown in (B.10)

$$\left\{\begin{array}{l}\Bigg[\sum\limits_{b\in\mathbf{Z}^c}\sum\limits_{i\in\mathbf{U}(b)}(\hat{\lambda}_{1,bt}/c-\hat{\lambda}_{2,bt}/c)\cdot(\tilde{P}_i-\hat{P}_{it})\\ \quad+\sum\limits_{b\in\mathbf{Z}}\sum\limits_{i\in\mathbf{U}(b)}(\bar{\lambda}_{1,bt}/c-\bar{\lambda}_{2,bt}/c)\cdot\tilde{P}_i+\breve{s}_t\Bigg]\\ -\Bigg[\sum\limits_{b\in\mathbf{Z}^c}\sum\limits_{i\in\mathbf{U}(b)}(\hat{\lambda}_{1,bt}/c-\hat{\lambda}_{2,bt}/c)\cdot(\tilde{P}_i-\hat{P}_{it})\\ \quad+\sum\limits_{b\in\mathbf{Z}}\sum\limits_{i\in\mathbf{U}(b)}(\lambda'_{1,bt}-\lambda'_{2,bt})\cdot\tilde{P}_i+\breve{s}_t\Bigg]\end{array}\right\}<0 \tag{B.10}$$

Applying $\tilde{\mathbf{P}}$ to (B.9), we get

$$\left\{\begin{array}{l}\Bigg[\sum\limits_{b\in\mathbf{Z}^c}\sum\limits_{i\in\mathbf{U}(b)}(\hat{\lambda}_{1,bt}/c-\hat{\lambda}_{2,bt}/c)\cdot(\tilde{P}_i-\hat{P}_{it})\\ \quad+\sum\limits_{b\in\mathbf{SZ}_o}\sum\limits_{i\in\mathbf{U}(b)}(\bar{\lambda}_{1,bt}/c-\bar{\lambda}_{2,bt}/c)\cdot(P_i^{\max}-\varepsilon)\\ \quad+\sum\limits_{b\in\{\mathbf{Z}-\mathbf{SZ}_o\}}\sum\limits_{i\in\mathbf{U}(b)}(\bar{\lambda}_{1,bt}/c-\bar{\lambda}_{2,bt}/c)\cdot(P_i^{\min}+\varepsilon)\Bigg]\\ -\Bigg[\sum\limits_{b\in\mathbf{Z}^c}\sum\limits_{i\in\mathbf{U}(b)}(\hat{\lambda}_{1,bt}/c-\hat{\lambda}_{2,bt}/c)\cdot(\tilde{P}_i-\hat{P}_{it})\\ \quad+\sum\limits_{b\in\mathbf{SZ}_o}\sum\limits_{i\in\mathbf{U}(b)}(\lambda'_{1,bt}-\lambda'_{2,bt})\cdot(P_i^{\max}-\varepsilon)\\ \quad+\sum\limits_{b\in\{\mathbf{Z}-\mathbf{SZ}_o\}}\sum\limits_{i\in\mathbf{U}(b)}(\lambda'_{1,bt}-\lambda'_{2,bt})\cdot(P_i^{\min}+\varepsilon)\Bigg]\end{array}\right\}=0 \tag{B.11}$$

Theorem 1 points out that there exits a scalar $\theta>1$ such that $\theta\cdot(P_i^{\max}-\varepsilon)+(1-\theta)\cdot\tilde{P}_i$ and $\theta\cdot(P_i^{\min}+\varepsilon)+(1-\theta)\cdot\tilde{P}_i$ are in the range of $\{\mathbf{0},[\mathbf{P}^{\min},\mathbf{P}^{\max}]\}$. Thus multiplying (B.11) by $\theta$ and (B.10) by $(1-\theta)$ which is negative and preserves the inequality,

  

and adding the two quantities up, we get

$$\begin{aligned}
&\sum_{b\in\mathbf{Z}^c}\sum_{i\in\mathbf{U}(b)}(\hat{\lambda}_{1,bt}/c-\hat{\lambda}_{2,bt}/c)\cdot(\tilde{P}_i-\hat{P}_{it})\\
&\quad+\sum_{b\in\mathbf{SZ}_o}\sum_{i\in\mathbf{U}(b)}(\bar{\lambda}_{1,bt}/c-\bar{\lambda}_{2,bt}/c)\cdot[\theta\cdot(P_i^{\max}-\varepsilon)+(1-\theta)\cdot\tilde{P}_i]\\
&\quad+\sum_{b\in\{\mathbf{Z}-\mathbf{SZ}_o\}}\sum_{i\in\mathbf{U}(b)}(\bar{\lambda}_{1,bt}/c-\bar{\lambda}_{2,bt}/c)\cdot[\theta\cdot(P_i^{\min}+\varepsilon)+(1-\theta)\cdot\tilde{P}_i]\\
&>\sum_{b\in\mathbf{Z}^c}\sum_{i\in\mathbf{U}(b)}(\hat{\lambda}_{1,bt}/c-\hat{\lambda}_{2,bt}/c)\cdot(\tilde{P}_i-\hat{P}_{it})\\
&\quad+\sum_{b\in\mathbf{SZ}_o}\sum_{i\in\mathbf{U}(b)}(\lambda'_{1,bt}-\lambda'_{2,bt})\cdot[\theta\cdot(P_i^{\max}-\varepsilon)+(1-\theta)\cdot\tilde{P}_i]\\
&\quad+\sum_{b\in\{\mathbf{Z}-\mathbf{SZ}_o\}}\sum_{i\in\mathbf{U}(b)}(\lambda'_{1,bt}-\lambda'_{2,bt})\cdot[\theta\cdot(P_i^{\min}+\varepsilon)+(1-\theta)\cdot\tilde{P}_i] \qquad \text{(B.12)}
\end{aligned}$$

Equation (B.12) indicates that

$$P_{it}=\begin{cases}\tilde{P}_i & \forall i\in\mathbf{U}(b), b\in\mathbf{Z}^c\\ \theta\cdot(P_i^{\max}-\varepsilon)+(1-\theta)\cdot\tilde{P}_i, & \forall i\in\mathbf{U}(b), b\in\mathbf{SZ}_o\\ \theta\cdot(P_i^{\min}+\varepsilon)+(1-\theta)\cdot\tilde{P}_i, & \forall i\in\mathbf{U}(b), b\in\{\mathbf{Z}-\mathbf{SZ}_o\}\end{cases}$$

then

$$\left\{\begin{aligned}
&\Bigg[\sum_{b\in\mathbf{Z}^c}\sum_{i\in\mathbf{U}(b)}(\hat{\lambda}_{1,bt}/c-\hat{\lambda}_{2,bt}/c)\cdot(P_{it}-\hat{P}_{it})\\
&\quad+\sum_{b\in\mathbf{Z}}\sum_{i\in\mathbf{U}(b)}(\bar{\lambda}_{1,bt}/c-\bar{\lambda}_{2,bt}/c)\cdot P_{it}+\breve{s}_t\Bigg]\\
&\quad-\Bigg[\sum_{b\in\mathbf{Z}^c}\sum_{i\in\mathbf{U}(b)}(\hat{\lambda}_{1,bt}/c-\hat{\lambda}_{2,bt}/c)\cdot(P_{it}-\hat{P}_{it})\\
&\quad+\sum_{b\in\mathbf{Z}}\sum_{i\in\mathbf{U}(b)}(\lambda'_{1,bt}-\lambda'_{2,bt})\cdot P_{it}+\breve{s}_t\Bigg]
\end{aligned}\right\}>0$$

which is inconsistent with (B.5) and shows that our assumption that (21) is not pareto optimal is untenable. Thus (21) is pareto optimal. □

## References


1. Shahidehpour, M., Yamin, H., Li, Z.: Market Operations in Electric Power Systems. Wiley, New York (2002)
2. Benders, J.F.: Partitioning procedures for solving mixed-variables programming problems. Numer. Math. **4**, 238–252 (1962)
3. Fu, Y., Shahidehpour, M., Li, Z.: Security-constrained unit commitment with ac constraints. IEEE Trans. Power Syst. **20**, 1538–1550 (2005)

4. Shahidehpour, M., Fu, Y.: Benders decomposition—applying Benders decomposition to power systems. IEEE Power Energy Mag. **3**, 20–21 (2005)
5. Guan, X., Guo, S., Zhai, Q.: The conditions for obtaining feasible solutions to security-constrained unit commitment problems. IEEE Trans. Power Syst. **20**, 1746–1756 (2005)
6. Martínez-Crespo, J., Usaola, J., Fernández, J.L.: Security-constrained optimal generation scheduling in large-scale power systems. IEEE Trans. Power Syst. **21**, 321–332 (2006)
7. Alguacil, N., Conejo, A.J.: Multiperiod optimal power flow using Benders decomposition. IEEE Trans. Power Syst. **15**, 196–201 (2000)
8. Wu, L., Shahidehpour, M., Liu, C.: MIP-based post-contingency corrective action with quick-start units. IEEE Trans. Power Syst. **24**, 1898–1899 (2009)
9. Li, Y., McCalley, J.D.: A general Benders decomposition structure for power system decision problems. In: EIT 2008 IEEE International Conference, pp. 72–77 (2008)
10. Magnanti, T.L., Wong, R.T.: Accelerating Benders decomposition: algorithmic enhancement and model selection criteria. Oper. Res. **29**, 464–484 (1981)
11. McDaniel, D., Devine, M.: A modified Benders' partitioning algorithm for mixed integer programming. Manag. Sci. **24**, 312–319 (1977)
12. Côté, G., Laughton, M.A.: Large-scale mixed integer programming: Benders-type heuristics. Eur. J. Oper. Res. **16**, 327–333 (1984)
13. Zakeri, G., Philpott, A.B., Ryan, D.M.: Inexact cuts in Benders decomposition. SIAM J. Optim. **10**, 643–657 (2000)
14. Fischetti, M., Salvagnin, D., Zanette, A.: Minimal infeasible subsystems and Benders cuts. http://www.dei.unipd.it/~fisch/papers/Benders.pdf (2010). Accessed 12 April 2010
15. Rei, W., Gendreau, M., Cordeau, J.F., Soriano, P.: Accelerating Benders decomposition by local branching. Informs J. Comput. **21**, 333–345 (2009)
16. Fu, Y., Li, Z., Shahidehpour, M.: Accelerated Benders decomposition in SCUC. IEEE Tran. Power Syst. (2010)
17. CPLEX 11.0. User's manual. http://www-01.ibm.com/software/integration/optimization/cplex/ (2010). Accessed 12 April 2010
18. Fu, Y., Shahidehpour, M.: Fast SCUC for large-scale power systems. IEEE Trans. Power Syst. **22**, 2144–2151 (2007)
19. Li, T., Shahidehpour, M.: Price-based unit commitment: a case of Lagrangian relaxation versus mixed integer programming. IEEE Trans. Power Syst. **20**, 2015–2025 (2005)

# Extended Benders Decomposition for Two-Stage SCUC

Cong Liu, *Student Member*, *IEEE*, Mohammad Shahidehpour, *Fellow*, *IEEE*, Lei Wu, *Member*, *IEEE*

***Abstract*—**This paper presents the solution of a two-stage security-constrained unit commitment (SCUC) problem. The proposed SCUC model could include integer variables at the second stage. A framework of extended Benders decomposition with linear feasibility and optimality cuts is proposed for the solution of mixed-integer programming (MIP) problems at both stages. Test results show the effectiveness of the proposed methodology.

***Index Terms*- SCUC, MIP, L-shaped decomposition.**

## I. Nomenclature

| | |
|---|---|
| $\boldsymbol{A},\boldsymbol{b},\boldsymbol{c},\boldsymbol{d},\boldsymbol{E},\boldsymbol{F},\boldsymbol{g}$ | Coefficients vector, matrix of MIP problem |
| $\mathbf{e},\mathbf{I}$ | Vector of ones and identity matrix |
| $i, j, k, s$ | Index of nodes in branch and bound trees, iterations and scenarios |
| $m_1, n_1, m_2^s, n_2^s$ | Dimension of first/second stage problems |
| $O(\ ), IF(\ ), Q(\ )$ | Dual price function of MIP problem |
| $OR(\ ), IFR(\ )$ | Dual price function of LP-Relaxation of MIP |
| $S, p^s$ | Number of scenarios and their probabilities |
| $\boldsymbol{t},\boldsymbol{x},\boldsymbol{y}$ | First stage, second stage and slack variables |
| $\mathbf{X},\mathbf{Y}$ | Spanning space of $x$ and $y$ variables |
| $z,\theta$ | Variables represent objective function values |
| $\delta_{OR}, \delta_{IFR}$ | Ancillary binary variables |
| $\mu,\pi$ | Dual variables |
| $\varepsilon, M$ | Predefined tolerance and a large number |

## II. Proposed MIP Problem

The SCUC problem shown in Table I is solved in two stages according to its specific structure. Generally, the first stage corresponds to an optimal decision, while the second stage would examine the viability of first stage decisions.

TABLE I SCUC Decomposition Strategies

| Problem | First Stage | Second Stage |
|---|---|---|
| UC with network constraints | UC | Transmission constraints |
| Contingency-based SCUC | UC with pre-contingency transmission constraints | Post- contingency transmission constraints |
| Two-stage stochastic SCUC | Decision costs and constraints | Recourse costs and constraints |

Benders cut applications are based on a prerequisite that the subproblem corresponding to the second stage is LP or convex NLP [1]. In practice, variables in the second stage can be integer or semi-continuous. Consider the following examples:

1. Integer variables in power transmission control.
2. Status of quick start units in post-contingency evaluation.

We have developed an extended Benders decomposition method which can be applied to such SCUC problems. The SCUC problem is represented as a MIP formulation (1)-(4). Decision variables $x$ at the first stage and $y$ at the second stage in P could be either integer or continuous. The constraint structure is L-shaped and no coupling among subproblems.

$$\text{P:}\quad Min\ \ z=\left\{\boldsymbol{c}\cdot\boldsymbol{x}+\sum_{s}p^s\cdot\boldsymbol{d}^s\cdot\boldsymbol{y}^s\right\} \tag{1}$$

$$s.t.\quad \boldsymbol{A}\cdot\boldsymbol{x}\geq\boldsymbol{b} \tag{2}$$

$$\boldsymbol{E}^s\cdot\boldsymbol{x}+\boldsymbol{F}^s\cdot\boldsymbol{y}^s\geq\boldsymbol{g}^s\qquad\forall s\in\{1,2,\cdots,S\} \tag{3}$$

$$\boldsymbol{x}\in\mathbf{X}=span\ \left\{\boldsymbol{R}^{m_1}\times\{0,1\}^{n_1}\right\},\ \boldsymbol{y}^s\in\mathbf{Y}=span\ \left\{\boldsymbol{R}^{m_2^s}\times\{0,1\}^{n_2^s}\right\} \tag{4}$$

Nonlinear feasibility and optimality cuts were developed in [3] via the general duality theory and showed that an L-shaped decomposition can converge within a finite time. The formulation of optimality and feasibility cuts are given in (12)-(13). After introducing integer variables, the linear feasibility and optimality cuts (21)-(23) would transform the two-stage SCUC problem into a MIP set, which can be incorporated into the master problem and lead to the global optimal solution.

As to the extended Benders decomposition, the mixed-integer master problem (BD-MP) and subproblems (BD-SP) are given in (5)-(8) and (9), respectively.

$$\text{BD-MP:}\quad z_{LB}=\underset{x,\theta^s}{Min}\left\{\boldsymbol{c}\cdot\boldsymbol{x}+\sum_{s}p^s\cdot\theta^s\right\} \tag{5}$$

$$s.t.\quad \boldsymbol{A}\cdot\boldsymbol{x}\geq\boldsymbol{b}\quad\boldsymbol{x}\in\mathbf{X},\ \ \theta^s\in\boldsymbol{R}^1 \tag{6}$$

$$O^s(\boldsymbol{x})-\theta^s\leq 0 \tag{7}$$

$$IF^s(\boldsymbol{x})\leq 0 \tag{8}$$

$$\text{BD-SP:}\quad \underset{y^s}{Min}\left\{\boldsymbol{d}^s\cdot\boldsymbol{y}^s\ \middle|\ \boldsymbol{F}^s\cdot\boldsymbol{y}^s\geq\boldsymbol{g}^s-\boldsymbol{E}^s\cdot\hat{\boldsymbol{x}},\ \boldsymbol{y}^s\in\mathbf{Y}\right\} \tag{9}$$

Here, $\hat{x}$ is the current BD-MP solution. In addition, (7)-(8) represent optimality and feasibility cuts, respectively, which are formed by solving BD-SP. The BD-MP solution provides a lower bound while a feasible BD-SP solution leads to an upper bound. The optimal solution of P is calculated when upper and lower bounds are sufficiently close according to (10),

$$(z_{UB}-z_{LB})/z_{UB}\leq\varepsilon \tag{10}$$

We form feasibility and optimality cuts by the dual price function when BD-SP is a MIP problem. BD-SP is nonconvex so its dual problem (BD-DSP) is given in (11) which is based on the general duality theory:

$$\underset{Q^s\geq 0}{Max}\left\{Q^s\left(\boldsymbol{g}^s-\boldsymbol{E}^s\cdot\hat{\boldsymbol{x}}\right)\middle|\ Q^s(\boldsymbol{F}^s\cdot\boldsymbol{y}^s)\leq\boldsymbol{d}^s\cdot\boldsymbol{y}^s,\ \forall\ \boldsymbol{y}^s\in\mathbf{Y}\right\} \tag{11}$$

This problem is considered as finding MIP sensitivities of (9) corresponding to the right-hand side of $\left(\boldsymbol{g}^s-\boldsymbol{E}^s\cdot\boldsymbol{x}\right)$. According to [2], a lower bound at a non-terminal node, which is based on branch and bound, is proposed in (12),

$$O_i^s(\boldsymbol{x})=Max\ \left\{OR_i^s(\boldsymbol{x}),Min\ \left\{O_{i,LB}^s(\boldsymbol{x}),O_{i,UB}^s(\boldsymbol{x})\right\}\right\} \tag{12}$$

where $OR_i^s(\boldsymbol{x})$ is the dual price function of the LP-relaxation of MIP (9) at the current node $i$. $O_{i,LB}^s(\boldsymbol{x})$, $O_{i,UB}^s(\boldsymbol{x})$ are dual

The authors are with ECE Department, Illinois Institute of Technology, Chicago, IL, USA. (E-mail: cliu35@iit.edu, ms@iit.edu, lwu10@iit.edu).

price functions of lower and upper partition nodes of current $i$. If the relaxed LP at current node is infeasible, $OR_i^s(x) = +\infty$ is set and the feasibility cut (13) is added,

$$IFR_i^s(x) \le 0 \tag{13}$$

If the current node is a root node of branch and bound tree, the optimality cuts and feasibility cuts based on (12) and (13) are fed back to BD-MP. Reference [2] offers another dual price function (14) where node $i$ belongs to the set of feasible terminal nodes in the tree generated by branch and bound. Coefficients in (15) are determined by solving the LP primal-dual problem (16)-(18)

$$O^s(x) = \underset{i}{Min}\left\{ OR_i^s(x) \,\middle|\, i \in \text{set of feasible terminal nodes} \right\} \tag{14}$$

$$OR_i^s(x) = \boldsymbol{\mu}_i^s \cdot \left(\boldsymbol{g}^s - \boldsymbol{E}^s \cdot \boldsymbol{x}\right) + \bar{\boldsymbol{\pi}}_i^s \cdot \bar{\boldsymbol{y}}^s + \underline{\boldsymbol{\pi}}_i^s \cdot \underline{\boldsymbol{y}}^s \tag{15}$$

$$Min \quad \boldsymbol{d}^s \cdot \boldsymbol{y}^s \tag{16}$$

$$s.t. \quad \boldsymbol{F}^s \cdot \boldsymbol{y}^s \ge \boldsymbol{g}^s - \boldsymbol{E}^s \cdot \hat{\boldsymbol{x}} \qquad \boldsymbol{\mu}_i^s \ge 0 \tag{17}$$

$$\bar{\boldsymbol{y}}_i^s \ge \boldsymbol{y}^s \ge \underline{\boldsymbol{y}}_i^s \qquad \bar{\boldsymbol{\pi}}_i^s \le 0, \underline{\boldsymbol{\pi}}_i^s \ge 0 \tag{18}$$

If a terminal node $j$ of a BD-SP scenario is infeasible, we add a slack vector to the LP (19) corresponding to the terminal node. We form feasibility cuts (20) the same way as optimality cuts by finding the dual price function of (19). Compared to (12), the combination of (14) and (20) is a weaker bound which leads to a global optimal solution within a finite time [3].

$$\underset{\boldsymbol{t}^s, \boldsymbol{y}^s}{Min}\left\{ \boldsymbol{e}^s \cdot \boldsymbol{t}^s \,\middle|\, \boldsymbol{F}^s \cdot \boldsymbol{y}^s + \boldsymbol{I}^s \cdot \boldsymbol{t}^s \ge \boldsymbol{g}^s - \boldsymbol{E}^s \cdot \hat{\boldsymbol{x}}, \bar{\boldsymbol{y}}_j^s \ge \boldsymbol{y}^s \ge \underline{\boldsymbol{y}}_j^s \right\} \tag{19}$$

$$IF^s(x) = \underset{j}{Min}\left\{ IFR_j^s(x) \,\middle|\, j \in \text{set of infeasible terminal nodes} \right\} \tag{20}$$

Substituting (14) and (20) into (7) and (8), respectively, the BD-MP becomes a mixed-integer bilevel optimization problem. We introduce additional integer variables $\delta$ in the BD-SP so that (21)-(23) can be used instead of (7)-(8).

$$OR_i^s(x) - \theta^s - \left(1 - \delta_i^s\right) \cdot M \le 0 \quad i \in \text{set of feasible terminal nodes} \tag{21}$$

$$IFR_j^s(x) - \left(1 - \delta_j^s\right) \cdot M \le 0 \quad j \in \text{set of infeasible terminal nodes} \tag{22}$$

$$\sum_i \delta_i^s + \sum_j \delta_j^s = 1 \quad \delta_i^s, \delta_j^s \in \{0,1\} \tag{23}$$

The decomposition solution in Fig. 1 is summarized as follows:

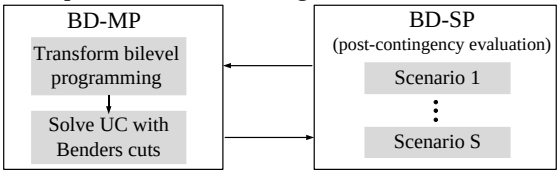


Fig. 1. Decomposition framework

Step 0: Set the lower bound $z_{LB} = 0$, $z_{UB} = +\infty$. Initialize the iteration counter of outer loop $k = 1$ and tolerance $\varepsilon$.

Step 1: Introduce (21)-(23) instead of (7) and (8) for Benders cuts and solve the MIP-based BD-MP.

Step 2: Go to Step 2.1 if BD-SPs are feasible for all scenarios, based on the solution of BD-MP. Otherwise, go to Step 2.2.

Step 2.1: For each scenario, form an optimality cut (7) by branch and bound. Update $z_{UB}$. If (10) is satisfied, stop the procedure. Else, go to Step 1 and set $k = k + 1$.

Step 2.2: For infeasible scenarios, use branch and bound to form feasibility cuts (8). Go to Step 1 and set $k = k + 1$.

## III. Numerical Example

Three generators are scheduled by a two-stage stochastic UC to supply a load with uncertainty levels shown in Table II. Unit 1 is a coal unit without a quick start capacity; thus its commitment decision can only be made at the first stage. However, units 2 and 3 have quick start capability and their commitment can be adjusted quickly at the second stage. The second stage is comprised of two parallel MIP subproblems corresponding to two scenarios with commitment decisions for units 2 and 3. The problem is solved by applying the proposed extended Benders decomposition. Table II shows the second-stage solution of the stochastic UC by the proposed method, which is the same as that of solving the MIP problem without decomposition by applying CPLEX. The first stage solution shows that unit 1 is committed in both scenarios. The second stage solution shows that Unit 2 is committed only at hour 2 in scenario 1. Two iterations between BD-MP and BD-SP are executed, and two feasibility cuts (21) and two optimality cuts (22) are generated before (10) is satisfied. More information on this example is presented in http://motor.ece.iit.edu/data/bds_example.doc.

TABLE II Second-Stage Stochastic UC Solution (MW)

| Scenario | Probability | Period | Load | Unit 1 | Unit 2 | Unit 3 |
|---|---|---|---|---|---|---|
| 1 | 0.5 | T=1 | 90 | 90 | 0 | 0 |
| | | T=2 | 110 | 100 | 10 | 0 |
| 2 | 0.5 | T=1 | 95 | 95 | 0 | 0 |
| | | T=2 | 105 | 100 | 0 | 0 |

## IV. Discussions and Summary

The SCUC problem is solved by introducing the decomposition presented in Table I for practical systems with a large number of scenarios/contingencies. The deterministic SCUC problems in Table I, which require no optimality cuts, can be solved by a limited number of feasibility cuts. With N1 quick-start units, S contingencies, and N2 discrete network equipment, the number of the second-stage integer variables is S*(N1+N2), which could be a large number and make it impossible to solve the problem without decomposition. In the proposed method, the number of feasibility cuts (22) is much less than S*(N1+N2) which can be solved easily for large systems. The stochastic SCUC in Table I, which considers recourse costs, would require optimality and feasibility cuts formed in every scenario. For a global optimization, $2^{(N1+N2)\cdot S}$ integer variables would be introduced into the master problem as shown in (21)-(23). The type 1 Special Ordered Set (23) facilitates the branching process of branch-and-bound method for a faster convergence. The potential future studies could seek better methodologies for implementing (12), (13), (14) and (20) such that a few terminal nodes in the tree can be excluded in (14) and (20). Heuristic algorithms may be embedded into the proposed framework to provide a tradeoff between the computing time and the accuracy.

## References

[1] A. J. Conejo, et al, "Decomposition Techniques in Mathematical programming," Springer, 2006.

[2] L. Schrage, L.A. Wolsey, "Sensitivity analysis for branch and bound integer programming," *Operations Research* 33 (1985) 1008-1023.

[3] C. Carøe "L-shaped Decomposition of Two-stage Stochastic Programs with Integer Recourse," *Mathematical Programming* 83 (1998) 451-464.

# Capacity Adequacy Calculation by Considering Locational Capacity Prices

Saeed Kamalinia and Mohammad Shahidehpour
Electrical and Computer Engineering Department
Illinois Institute of Technology

ABSTRACT

A proper investment mechanism is required in restructured power systems to secure the adequacy of installed capacity by encouraging investments on generation and transmission expansions. In this paper, we propose a locational capacity price (LCP) model along with multi-level load bidding curves, which reflect the effectiveness of the market-based capacity payment and at the same time, prohibits the capacity withholding and the exercising of market power. The purpose of capacity expansion decision is analyzed and compared with three other market design options, i.e., energy only, capacity payment, and installed capacity. The case studies show that the proposed LCP method provides proper investment signals in capacity-constrained locations. The proposed LCP method also provides signals to system operators to alleviate transmission congestions economically using proper operation strategies in power systems.

## 1. NOMENCLATURE

The symbols used in this paper are classified into indices, parameters, variables and Matrices and Vectors as follows.

**Indices:**

| | |
|---|---|
| max | Subscript index for upper bound |
| min | Subscript index for lower bound |
| $g$ | Subscript for GENCO |
| * | Superscript for optimal value |

**Parameters:**

| | |
|---|---|
| $CUR$ | Capacity usage rate |
| $E[\cdot]$ | Expected value |
| $FOR$ | Forced outage rate |
| $F(V)$ | Value of postponed investment |
| $I$ | Investment cost |
| $LMP$ | Locational marginal price |
| $Load_{lijt}$ | Forecasted bidding quantity of the load $l$ at segment $i$ and alternative $j$ at time $t$ |
| $L_{peak}$ | Peak load |
| $lft$ | Expected life time of the project |
| $N_g$ | Number of generator's bidding segments |
| $NS_{lt}$ | Number of bidding segments of load $l$ at time $t$ |
| $NA_{lit}$ | Number of alternatives at the bidding segment $i$ of load $l$ at time $t$ |
| $OC$ | Average operating cost |
| $P_{g,t}$ | Dispatched power of generator $g$ at time $t$ |
| $\Pr_t$ | Generator profit function |

| | |
|---|---|
| $T$ | Investment time parameter |
| $wf$ | Weighting Factor |
| $\alpha$ | Project value factor |
| $\rho$ | Discount rate |
| $\theta$ | Bus angel |
| $\lambda, \boldsymbol{\kappa}, \pi, \mu$ | Lagrangian multipliers |

**Variable:**

| | |
|---|---|
| $t$ | Planning time variable |
| $L_{ij,t}$ | Accepted load quantity at the bidding segment *i* and alternative *j* at time *t* |
| $V$ | Value of the project |
| $U_{ij,t}$ | Load quantity binary integer variable at the bidding segment *i* and alternative *j* at time *t*; equal to 1 when the load bid is accepted and 0 when the bid is not accepted by the market |

**Matrices and Vectors:**

| | |
|---|---|
| **A** | Bus-unit incidence matrix |
| **B** | Bus-load incidence matrix |
| **b** | Bidding price vector of buyers |
| **c** | Bidding price vector of buyers |
| **H** | Bus-angel incidence matrix |
| **K** | Bus-branch incidence matrix |
| **P** | Bidding energy vector of sellers |
| $\mathbf{P_D}$ | Bidding energy vector of buyers |
| **PL** | Real power flow in vector form |
| **X** | Line reactance vector |

## 2. INTRODUCTION

Adequacy analyses would investigate the ability of power systems to provide a reliable supply of energy [1,2]. In theory, the capacity adequacy is managed by market participants in a perfectly competitive market with provisions for the allocation of risks to consumers and suppliers [2]. However, the California market crisis showed that the market alone may not produce sufficient investment signals to guarantee the capacity adequacy. The main reasons which impede electricity markets from generating such investment signals include, but may not be limited to, flaws in the demand response, market power, excessive investment risks, and ill-designed capacity markets [2,3]. An exertion of market power is made possible by monitoring the gap between the marginal cost and real market prices [4,5]. Insufficient energy market revenues to compensate capacity investments resulted in other market mechanisms, which included "installed capacity" (ICAP) and capacity payment (CP) [2]. ICAP deficiencies would include a lack of representation of locational- or temporal-based market prices. Furthermore, ICAP could provide a revenue source for generating units that are seldom committed or have only contributed to generation supply in peak periods. Such units may submit bids that are as high as price caps so that they do not participate in energy supply and get paid by ICAP [3,6]. The CP mechanism may encourage market participants to exercise market power as insecure markets would tend to supply more CPs, i.e. capacity payments could be the same as the value of lost load (VOLL) (i.e., market price cap) times a reliability index (e.g., loss of load probability). So generators would find it more profitable to pose artificial capacity deficiencies. In recent years, US electricity markets have reformed the capacity adequacy calculation mechanisms, which include the PJM's reliability pricing model (RPM), the ISO-NE's locational installed capacity (LICAP) model, and the demand curve model considered in NYISO and MISO [7,8]. There are other approaches to the capacity market, e.g., call option [9,10] and capacity subscription [11,12], which are not widely

implemented in electricity markets.

Our previous studies on the system capacity expansion [13-15] showed that a market-based signal would ensure sufficient and optimal investments in generation and transmission. Market mechanisms for the capacity adequacy were compared in [7] and concluded that a capacity mechanism is needed for resource adequacy, both in power pools and in transmission-constrained regions. Studies on energy only market models for supplying an adequate capacity concluded that a greater transparency into market behaviors, supply and demand forecasts, and higher system-wide offer caps is needed to ensure the market success [16]. It also discussed that low price cap could result in under-investment in generation capacity [17]. Resource adequacy is a critical part of the reliability when demand response is insufficient or non-existent. Resource adequacy problems in several existing power markets were thoroughly discussed in [18]. In the literature, resource adequacy is classified into two main categories including short-term and long-term problems. Different aspect of the short-term capacity adequacy was elaborated in [19-21] and the long-term capacity mechanism was addressed in [22-24]. Another study showed that generation investment decisions could be evaluated based on the real options theory [24]. The real options theory presents new alternatives in investment strategies since it considers market uncertainties and options to invest when evaluating the value of project delays [26,27].

In this paper, we utilize the real options theory for the modeling of investments under uncertainties. Such uncertainties include financial and physical risks pertaining to the time and the location of new capacity expansions. The proposed method compares net cash flows in two possible investment modes: 1) invest right after net present value (*NPV*) of the project becomes positive (instant decision), and 2) consider a delay in investment to achieve the maximum profit (postponed decision). The rest of this paper is organized as follows. Section 3 discusses real options theory and its application in capacity expansion problem. Section 4 presents the proposed methodology and mathematical formulation. Section 5 in detail discusses the effectiveness of proposed approach in a sample two-bus system with three units and IEEE 118-bus system with 54 units. Section 6 provides the conclusions drawn from the proposed studies.

## 3. Investment in Capacity with Uncertainty

The capacity expansion mechanism introduces optimal the size, location, algorithm, and time for new investments in power generation. Capacity investors consider the time for the implementation of new projects, a flexible item as compared to other decision attributes. Therefore, we consider the investment time as a decision variable. We assume that the investment cost, $I$, is given. The finance theory indicates that the *NPV* is the best measure for evaluating new investments, which signals to invest as long as the $V$ is larger than the discounted $I$, i.e., the sum of discounted cash flows from the project is positive. However, this would lead to an incorrect result because the static *NPV* assessment does not consider the choice of deferring the investment. While future values of $V$ are unknown, there is always an opportunity cost for investing today. Hence, the optimal investment rule is stated as make the investment when $V$ is larger than a critical value $V^*$ [26-28]. The value of investment opportunity, $F(V)$, in dollars is given as in (1), where $V$ is the value of the project and a function of the planning time variable, $t$. On the other hand, the planning period includes the investment time and the lifetime of installed unit.

$$F(V) = \max_{t} \quad E[(V - I) \cdot \exp(-\rho t)] \tag{1}$$

where,

$$V = V_0 \exp(\alpha t) \tag{2}$$

$$\text{and } V_0 = \frac{V}{(1+\rho)^t} \tag{3}$$

Using (2) and (3), we obtain $\alpha$ as

$$\alpha = \ln(1+\rho) \tag{4}$$

in which $0 < \alpha < \rho$. In a deterministic model, the expectation function give in (1) would be eliminated. Therefore to maximize *F(V)* with respect to *t* in (1), the first order condition would be

$$\frac{dF(V)}{dt} = -(\rho - \alpha)V_0 \exp(-(\rho - \alpha)t) + \rho I \exp(-\rho t) = 0 \tag{5}$$

where $0 \le t \le T + lft$ ; which implies that the optimal investment time is

$$T^* = \max \{\frac{1}{\alpha} \ln[\frac{\rho I}{(\rho - \alpha)V}] \ , \ 0\} \tag{6}$$

Accordingly, the decision to invest is made readily if *V* is sufficiently larger than *I*; otherwise $T^* > 0$ denotes the optimal investment time. The value of *V**, which corresponds to an immediate investment, is obtained by setting $T^* = 0$ in (4). So,

$$V^* = \frac{\rho I}{(\rho - \alpha)} > I \tag{7}$$

Finally, by substituting (6) in (1), we obtain,

$$F(V) = \begin{cases} [\alpha I / (\rho - \alpha)]\{(\rho - \alpha)V_0 / \rho I\}^{\rho/\alpha} & V \le V^* \\ V - I & V \ge V^* \end{cases} \tag{8}$$

and the NPV of the project, *N(V)*, is obtained as

$$N(V) = -\frac{I}{(1+\rho)^T} + \sum_{t=T}^{T+lft} \frac{V}{(1+\rho)^t} \tag{9}$$

The planning period, *t*, starts from the initial point of study and finishes at the end of the project lifetime. However, only a certain time in the planning period, *t*, is candidate for investment, *T*.

It is shown in Fig. 1, that the optimal investment time (6) is the intersection of (8) and (9). The intersection of *F(V)* and *N(V)* in Fig. 1 would determine $V^*$ (or equivalently $T^*$), which is the optimal value and the time of the investment. In the following, we discuss the optimal investment and the time for capacity expansion.

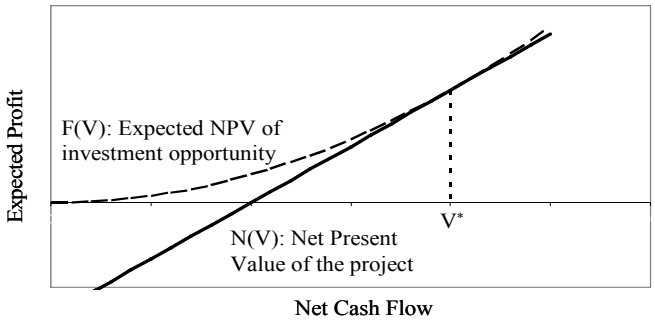


**Figure 1** *Optimal investment time and value based on the real options theory*

## 4. PROPOSED CAPACITY MECHANISM AND FORMULATION

In order to determine the optimal investment threshold, the market is simulated while the load is progressively increased during the lifetime of the installed generation unit. Here, we calculate the discounted project value (NPV) and determine the value of deferring the investment (forwarding value). The static NPV rule recommends that investors proceed with the project when *N(V)* turns positive. However, we consider a more restrictive investment strategy by considering the option to wait for maximizing the profit and minimizing the risk. Fig. 2 shows the proposed capacity investment decision process using the real options theory. The flowchart simulates the market for the entire planning period (t). *N (V)* is calculated in each year for the expected lifetime of generation unit and compared to *F(V)*. The optimal investment time occurs when *N(V)* exceeds *F(V)*. If *N(V)* is higher than *F(V)* at the starting point, the investment decision can be made immediately. However, if the two curves do not intersect, the investment will not be profitable.

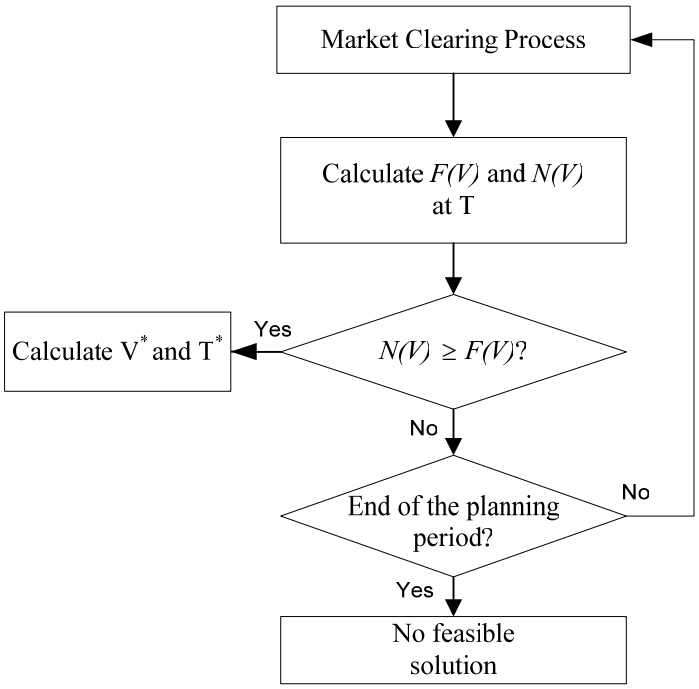


**Figure 2** *Capacity expansion procedure using the real options theory*

The market-clearing model in Fig. 2 could represent energy only, installed capacity, capacity payment, or the proposed locational capacity price approach. Regardless of the market mechanism, the objective is to maximize the

social welfare (10) based on the prevailing power flow constraints including power balance (11), dc power flow (12), line flow limits (13), generation limits (14), demand range (15) and the reference bus angel constraint (16) [29].

$$Max \quad \mathbf{b}^T \mathbf{P_D} - \mathbf{c}^T \mathbf{P} \tag{10}$$

*S.t.*

$$\mathbf{K} \cdot \mathbf{PL} - \mathbf{A} \cdot \mathbf{P} + \mathbf{B} \cdot \mathbf{P_D} = \mathbf{0} \qquad \boldsymbol{\lambda} \tag{11}$$

$$\mathbf{PL} = \mathbf{X}^{-1}\mathbf{K}^T \boldsymbol{\theta} \qquad \boldsymbol{\kappa} \tag{12}$$

$$-\mathbf{PL_{max}} \le \mathbf{PL} \le \mathbf{PL_{max}} \qquad \underline{\boldsymbol{\pi}}, \bar{\boldsymbol{\pi}} \tag{13}$$

$$\mathbf{P_{min}} \le \mathbf{P} \le \mathbf{P_{max}} \qquad \underline{\boldsymbol{\mu}}_P, \bar{\boldsymbol{\mu}}_P \tag{14}$$

$$\mathbf{P_{Dmin}} \le \mathbf{P_D} \le \mathbf{P_{Dmax}} \qquad \underline{\boldsymbol{\mu}}_L, \bar{\boldsymbol{\mu}}_L \tag{15}$$

$$\theta_{ref} = 0 \qquad \mu_{ref} \tag{16}$$

The generator revenue depends on the market structure and operation. We simulate the capacity expansion process using four models, including energy only, installed capacity, capacity payment, and locational capacity price. We compare the corresponding investment efficiencies including the value and the time of project investment. The bus LCP is a positive (or zero) value which is obtained from the base generator's maximum power capacity at a given bus. The base generator at a bus is the one with the lowest bidding price and the highest capacity usage rate. The capacity usage rate is given as

$$CUR_{gt} = \frac{P_{gt}}{P_{g,\max}} \tag{17}$$

Using (10)-(16), the Lagrange function is

$$\begin{aligned} L = {} & \mathbf{c}^T \mathbf{P} - \mathbf{b}^T \mathbf{L} + \boldsymbol{\lambda}^T (\mathbf{K} \cdot \mathbf{PL} - \mathbf{A} \cdot \mathbf{P} + \mathbf{B} \cdot \mathbf{L}) + \boldsymbol{\kappa}^T (\mathbf{PL} - \mathbf{X}^{-1}\mathbf{H}^T \boldsymbol{\theta}) + \bar{\boldsymbol{\pi}}^T (\mathbf{PL} - \mathbf{PL_{max}}) + \underline{\boldsymbol{\pi}}^T (-\mathbf{PL_{max}} - \mathbf{PL}) \\ & + \bar{\boldsymbol{\mu}}_P (\mathbf{P} - \mathbf{P_{max}} - \mathbf{\Delta P_{max}}) + \underline{\boldsymbol{\mu}}_P (\mathbf{P_{min}} - \mathbf{P}) + \bar{\boldsymbol{\mu}}_L^T (\mathbf{L} - \mathbf{L_{max}}) + \underline{\boldsymbol{\mu}}_L^T (\mathbf{L_{min}} - \mathbf{L}) + \mu_{ref} \theta_{ref} \end{aligned} \tag{18}$$

The bus LCP, which is the shadow capacity price of the base generator, is given as

$$LCP = -\frac{\partial F}{\partial \mathbf{\Delta P_{max}}} = \bar{\boldsymbol{\mu}}_P \tag{19}$$

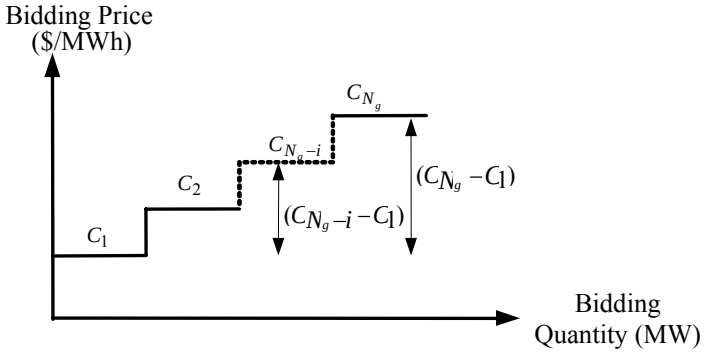


**Figure 3** *Generators' biding price and change in the social welfare*

The rationale for using LCP as a capacity signal is that by increasing the number of fully-loaded units in a bus, the

Lagrange multiplier corresponding to the base generator's capacity constraint will increase. Assume that bids of $N_g$ generators are $C_1, C_2, ..., C_{N_g-i}, ..., C_{N_g}$ where $C_1 < C_2 < ... < C_{N_g-i} < ... < C_{N_g}$. By disregarding the operating constraints and assuming that the generation units bid at their maximum capacity, when $N_g$ generators are in service, at least $(N_g - 1)$ generators are at their capacity and only the most expensive generator may be loaded partially. So by adding one MW to the capacity of generator 1, $P_{N_g}$ will decrease by one MW and $P_1$ will increase by one MW. Accordingly, the change in social welfare will be $(C_{N_g} - C_1)$. Hence, the change in the social welfare ($\bar{\boldsymbol{\mu}}_P = \mathbf{LCP}$) is larger when there are $N_g$ generators as compared to $(N_g - i)$, i.e. $(C_{N_g} - C_1) > (C_{N_g-i} - C_1)$. Hence, LCP is a capacity signal. The higher the LCP, the more capacity constrained the system will be at a bus, which encourages a capacity investment to relieve capacity scarcity. The generators' bidding value and the changes in social welfare for each mode are shown in Fig. 3.

In the locational capacity model, generators would have income for selling electricity at LMP in addition to earning revenues equal to the LCP times the available capacity (20).

$$\mathrm{Pr}_{gt} = \sum_{t=T}^{T+lft} [(LMP_t - OC_{gt}) \cdot P_{gt} + wf \cdot LCP_t \cdot P_{\max} \cdot (1 - FOR_g)] \tag{20}$$

Here, we assume $P_{\max} \cdot (1 - FOR_g)$ is the available capacity of generating unit. A weighting factor is considered in (20) to limit the over-payment by consumer and prevent unacceptable reductions in consumptions as a result of higher prices.

## 5. Case Study and Discussions

In this section, the capacity expansion problem is analyzed in a two-bus system and investment conditions are discussed in various market structures, including the proposed LCP model. An IEEE 118-bus system is also used to evaluate the effectiveness of proposed approach.

### *A. Two-bus system*

A two-bus system with two existing generators, one candidate generator, and a single load point is considered to illustrate the case. The simplicity and the limited number of elements in the two-bus system, would make it much easier to analyze the effect of market structure on investment decisions, which is the main contribution of this paper. Fig. 4 shows a single diagram of the test system. Generation data are provided in Table 1. The 1900 MW load located in bus 2 will increases at a fixed annual rate of 5%. The transmission constraint is not considered. Investment period is 10 years ($T \in \{1,2,3,...,10\}$) and the unit expected lifetime is assumed to be 15 years. Therefore, the maximum planning time would be 25 years. It is assumed that the new installed unit comes to operation at $T$ and the construction time is one year. So the earliest time for a unit to come into service would be one year after the planning period has started, i.e., $T$=1. Table 2 presents the initial generation and the loading condition and price bids. It is assumed that generating units would bid at their marginal price level, which is known.


**Figure 4** *Single diagram of the 2-bus system*

**Table 1** GENERATORS DATA

| Bus No. | Investment Cost ($/MW/year) | Capacity (MW) | FOR (%) | Existing (E) or Candidate (C)? |
|---|---|---|---|---|
| 1 | - | 2000 | 0.1 | E |
| 2 | - | 2000 | 0.1 | E |
| 2 | 220,000 | 2000 | 0.1 | C |

**Table 2** GENERATORS AND LOAD BIDDING DATA

| Unit Name | Bidding Segment No. | MW | Bidding Price ($/MWh) |
|---|---|---|---|
| G1 | 1 | 1000 | 20 |
| G1 | 2 | 600 | 25 |
| G1 | 3 | 400 | 35 |
| G2 | 1 | 1000 | 38 |
| G2 | 2 | 600 | 40 |
| G2 | 3 | 400 | 45 |
| G3 | 1 | 1000 | 30 |
| G3 | 2 | 600 | 36 |
| G3 | 3 | 400 | 39 |
| Load | 1 | $L_{peak,t}$ / 2 | 51 |
| Load | 2 | $L_{peak,t}$ / 3 | 47 |
| Load | 3 | $L_{peak,t}$ / 6 | 44 |

*A.1.Energy only model*

In the energy only model, the market is supposed to provide sufficient incentives to ensure optimal investments in generation expansion. While in theory, an ideal competitive spot market along with ancillary services must identify the key elements necessary for securing the short-term grid operations while maintaining the long-term grid reliability. The power markets in Scandinavia, United Kingdom, Australia, ERCOT and MISO have implemented such models. The latter two markets consider scarcity pricing while developing bilateral forward contracts through energy only markets and legislating proper rules to ensure the active participations of demand side in wholesale markets.

In the energy only model, electricity sales are the only sources of revenue and the capacity scarcity premium is not paid to generation owners. In our study, the market is simulated during the expected lifetime of a new generation. In this market, generators seek to be compensated for high investment costs through price spikes. However, price spikes may not occur often and as expected, which could increase the investor's financial risks. In such cases, generators can benefit from market volatilities which themselves are impediments for investment.

In this case, VOLL is assumed to be 1000 $/MWh and no price cap is considered. Therefore, the price can jump up to the VOLL in scarcity periods [30]. The profit function, $\Pr_t$ , is given in (21). The market objective is to maximize

the social welfare, while in a competitive market a more appropriate objective for individual investors is to maximize the expected profit. However, in a perfect power market, investment decisions based on a centralized social welfare maximization and a decentralized profit maximization would lead to the same results [31].

$$\mathrm{Pr}_{gt} = \sum_{t=T}^{T+lft} (LMP_t - OC_{gt}) * P_{gt} \tag{21}$$

Fig. 5 shows that $V^*$=\$83.317 million and $T^*$=4.021 years. Hence, $T$ is an integer parameter, and a linear approximation is applied to find the optimal investment time. The project *NPV* becomes positive at 3.421 years. If an investor applies the static *NPV* assessment, instead of the real options approach, the investment will be possible as soon as the *NPV* is positive [32]. However, the investment will be more profitable at $T^*$.

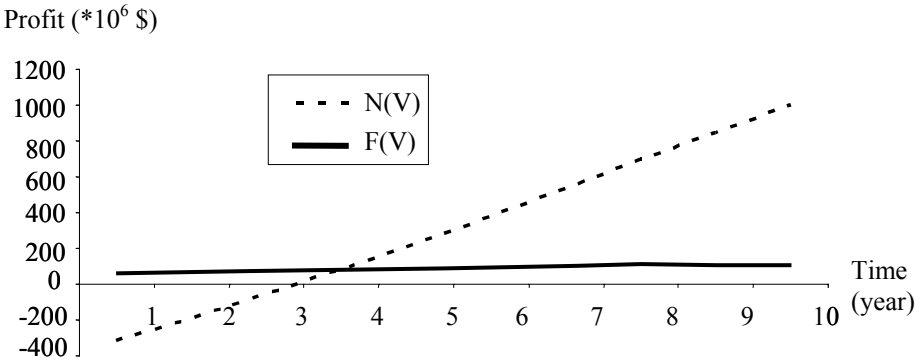


**Figure 5** *Expected profit with F(V) and N(V) models in energy only market*

*A.2. Installed capacity model*

The application of ICAP in a installed capacity model requires the load serving entities (LSEs) to buy more power than their expected peak capacity in a long-term market, so that they can guarantee a prescribed level of generation capacity. ICAP showed market deficiencies such as providing revenues to the generating units that rarely (or never) were committed. The ICAP model is not affected by the location or time, i.e., late nights and weekends are treated the same as peak hours in hot summers. In essence, there is an incentive for the generation investment in areas with high LMPs. However, ICAP payment can eliminate locational differences in energy prices [33]. This model was adopted in PJM, NY-ISO and NE-ISO before such markets reconsidered the process. Fig. 6 shows the ICAP study results. In this model, LSEs are required to buy 10% more than their expected peak load. The price of ICAP is determined administratively or based on long-term capacity markets. In this case, $V^*$= \$111.26 million and $T^*$=3.267 while the *NPV* of project becomes positive at 2.637 years. The dynamic investment assessment [32] would result in postponing the investment decision. However, when the demand is increased in the ICAP model, the system becomes capacity constrained earlier as compared to energy only market and it will be more profitable for generators to make early investments. The project value is increased since there is a revenue source for the installed capacity.

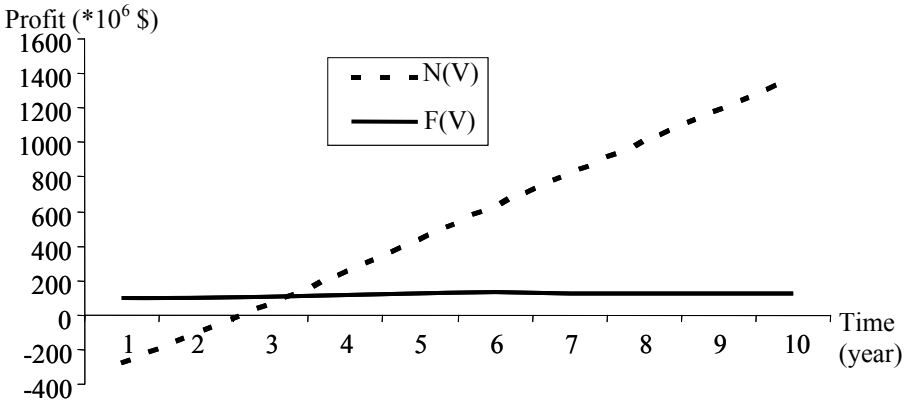


**Figure 6** *Expected profit with F(V) and N(V) models in ICAP market*

*A.3. Capacity payment model*

Generators in the capacity payment model have an opportunity to earn revenues through regulatory mechanisms as well as energy markets. The additional payment is based on LOLP and VOLL. In this model, there is a regulatory price cap to hedge price spikes, which is significantly smaller than VOLL. Spain, Argentina, Colombia and Chile applied this market model. The main drawback of this model is that generators are inclined to pose artificial outages and exercise market power (e.g., delay the completion of scheduled maintenances or declare artificial outages).

One of the problems with the capacity payment method is that, similar to the ICAP model, the payment is not based on locational attributes. In other words, an increase in LOLP will boost the capacity payment for all generators even those which do not contribute to the system reliability or are located at a distance from capacity-constrained areas. Due to the transmission constraints, remote generating units may not contribute to generation shortages. Therefore, the capacity payment incentive should follow a flexible paradigm (i.e., market-based) rather than providing a uniform revenue for the generating capacity which does not encourage contributions to hedge power shortage. Capacity payment is distributed among generators according to their market contributions. However, at times, a small generation in a strategic location could be more vital than hundreds of megawatt in remote areas. Furthermore, in most cases VOLL is more of an administrative value, which may not show the willingness to pay off the loads and cannot be assumed as a decent signal for the capacity expansion.

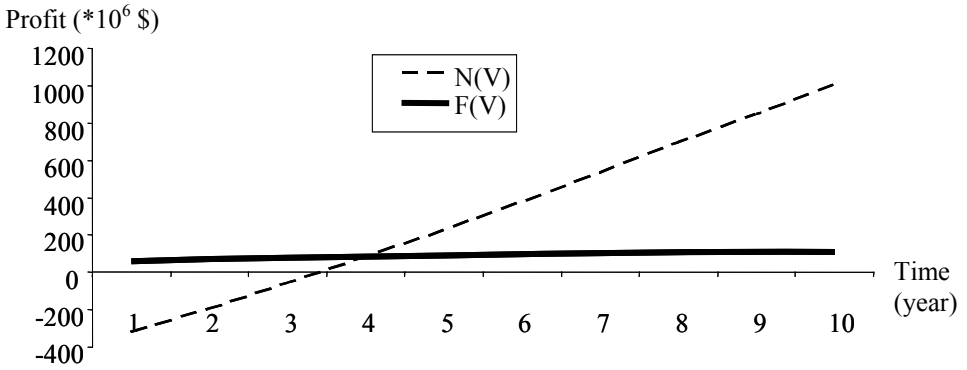


**Figure 7** *Expected profit with F(V) and N(V) models in the CP market*

Fig. 7 shows the result for the capacity payment model. The capacity payment is paid here to the available units according to their installed capacity. In this case, $V^*$=\$83.985 millions and $T^*$=4.012 years while the *NPV* of project

becomes positive in 3.411 years. Here generators earn extra revenues from the capacity market. However, the market price cap would limit the value of project which is almost the same as that of the energy only market model. Determining the price cap in markets with capacity payment is a challenging task which can limit generator revenues. In an ideal market if the price cap is equal to the average VOLL, an optimal investment along with the acceptable frequency of interruption will occur [34]. However, the average VOLL (e.g. 10,000 $/MWh) is still significantly higher than the average electricity price (e.g., 50 $/MWh). Therefore, price caps as high as VOLL may not hedge price spikes. On the other hand, markets with low price caps may not be able to compensate generators, especially peaking units, for their fixed and variable costs.

*A.4. Locational capacity price model*

In this model, the LCP obtained from (19) is paid to generators as additional revenue. Fig. 8 shows the optimal investment time and value for the LCP approach. Comparing with the first three market models, we learn that the optimal investment occurs earlier, T*=4.021 and V*=$83.317 million. However, the static NPV rule proposes to invest even earlier at T=3.421 year. The interesting result is that, compared to other capacity market mechanisms, the additional revenues in this framework would not obligate the investment to occur prematurely at earlier periods. Another common problem in markets with a capacity mechanism is that, over-investment may occur due to excessive incentive for new expansions. However, the LCP approach does not allow capacity incentives to unnecessarily increase the project value or consumer payments when the system does not require any capacity expansion. In this model, generation units can only get incremental profits by offering additional generation when the system becomes capacity constrained, i.e., LCP is the dual variable of the capacity constraint which is zero when the capacity is still available and the constraint is not binding. For instance, in year 7, the project value increases by about $100M which means the system is confronting capacity shortages. It is desirable to see the expansion at the right time before scarcity periods; however, when the system security is threatened by generation capacity shortages, LCP increases significantly which raises consumer charges as compared to those in the energy only market. However, in the long-term LCP can ensure the adequacy of capacity which would benefit the system reliability along with consumer satisfactions.

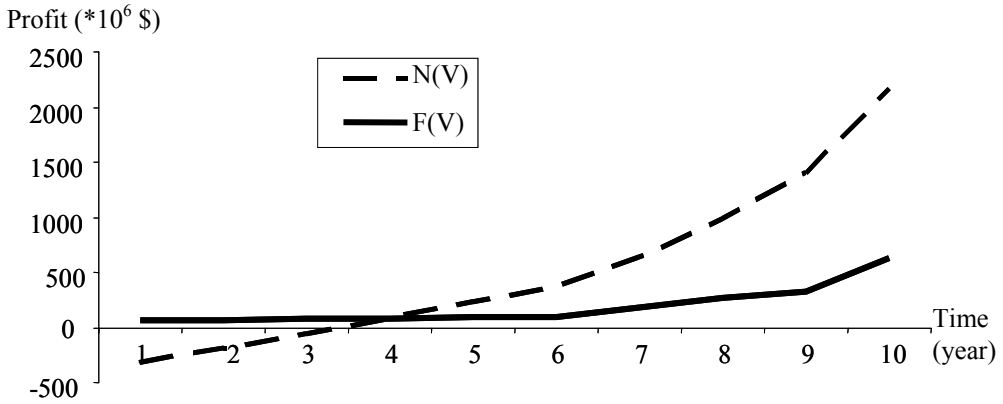


**Figure 8** *Expected profit with F(V) and N(V) models in the LCP market*

In all the case studies, the discount rate $\rho = 0.1$. A sensitivity analysis is performed to show the correlation between

the results (i.e., optimal investment time and value) and discount rates. As Table 3 shows that the investment time is delayed and the value of project is decreased by increasing the discount rate.

**Table 3** SENSITIVITY ANALYSIS ON DISCOUNT RATE

| Discount rate (ρ) | 0.01 | 0.05 | 0.10 | 0.15 | 0.20 | 0.25 |
|---|---|---|---|---|---|---|
| T* (Year) | 2.78 | 3.30 | 4.02 | 4.72 | 5.35 | 5.87 |
| V* ($) | 2.79E+08 | 1.62E+08 | 8.33E+07 | 4.29E+07 | 2.23E+07 | 1.17E+07 |

*A.4.1. Multi-level load bidding*

In this model, multi-level load bidding is considered. In Fig. 9 each load (or group of loads) submits a set of bids to the market according to its preferred demand level. The capacity index is introduced as a deduction margin below the peak demand for serving load. For instance, a 100 MW load with a capacity index of 0.1 is presented as 90 MW. This addresses the problem of demand overpayments in real markets when there is a limited number of cheap units or generation capacity in general. Here, the overpayment refers to a case when a load would bid a certain MW value; however, when the market is cleared, the load is partially supplied at a high rate. A multi-level load bid allows loads to pay lower rates if they are partially supplied. In Fig. 9, solid line represents the load's first priority to be served fully (Alternative 1), dashed line shows the load tendency to stay in the market at 90 percent of its initial schedule (Alternative 2), and gray color line shows the load to be served at 80 percent (Alternative 3).

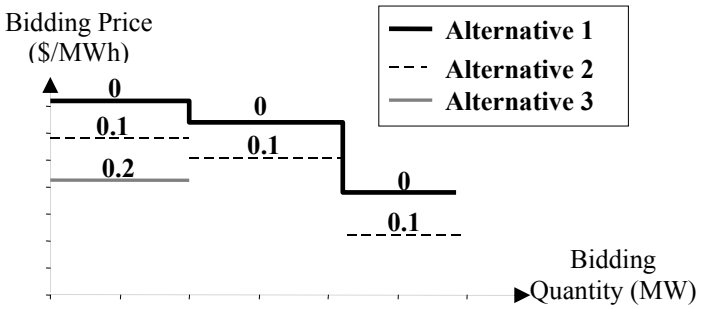


**Figure 9** *Multi-level load bidding*

This forms an MIP problem in which the loads have *i* bidding segments and each segment has *j* alternatives that at most, one of these alternatives can be served in full or zero quantity.

$$L_{ijt} = \sum_{l}\sum_{i}\sum_{j} U_{lijt} * Load_{lijt} \tag{22}$$

$$\sum_{j} U_{lijt} \le 1 \qquad \forall i = 1,2,..., NS_{lt} \quad , \quad \forall j = 1,2,..., NA_{lit} \tag{23}$$

Fig. 10 shows the market simulation results when the loads bid more than a single price at each segment. Here the optimal investment time and project value are the same as Case A.4. However, as shown in Fig. 10, when the system is on the verge of becoming capacity-constrained, the project value would change dramatically as the demand would provide more information on its tendency to be shed or not, i.e. different level of price bids to minimize the load loss. As shown in Figs. 8 and 10, the trend in the project value would be different when we use the LCP rather than the

other three approaches (Figs. 5-7). The major distinction in the LCP model is that the slope changes (increases) significantly, closer to the end of planning period, i.e. scarcity periods. This makes sense, because generators are getting paid by LCP only if they reach their capacity limits. Since, the demand increases during the planning period, the chance of that new generator works at full capacity in ending years will be higher, and the value of the project is larger accordingly.

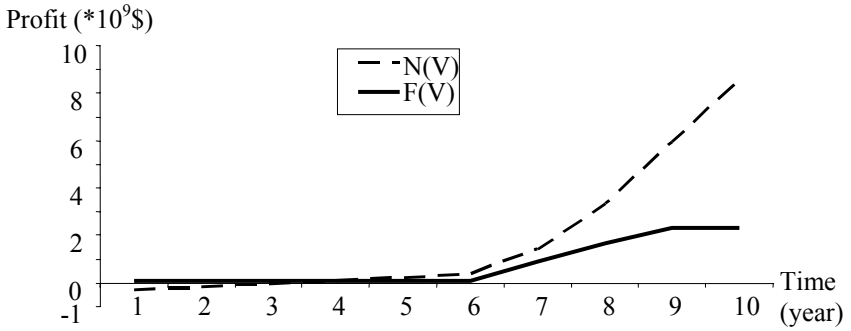


**Figure 10** *Expected profit with F(V) and N(V) models in the LCP market with multi-level load bidding*

*B. IEEE 118- Bus System*

A modified IEEE 118 bus system is used to study the proposed LCP approach. The system has 54 units, 186 branches, nine tap-changing transformers, and 91 demand sides. The peak load is 3,733 MW. The test data for the 118-bus system are given in motor.ece.iit.edu/data/SCUC_118test.xls. Fig. 11 shows the LMP results using the optimal power flow (DC-OPF). Here, bus 56 shows the highest LMP where there is an incentive to install new generating units [35]. Therefore, we select bus 56 as a first candidate site for generation expansion. However, to investigate the effectiveness of LCP, we select buses 95 and 83 that represent an average and the lowest LMPs, respectively. Furthermore, buses 59 and 89 are considered as they have the largest installed load (277 MW) and transmission capacity accessibility (2600 MW), respectively. Similar to the study in section IV.A, we simulate market operations for the expected life of the new generation and investigate the optimal timing and value for the expansion project. The new unit has the capacity of 200 MW and an operating marginal cost of 12.64 $/MWh. The load growth rate is assumed to be one percent over the lifetime of the project and the investment cost is the same as that in section IV.A.

Table 4 shows the results for installing the new unit in different sites using the LCP and the energy only market models. The investment here occurs in the earliest time and with the highest value of return. The investment in year zero means that there is no reason to delay the expansion as soon as other constraints such as land acquisitions and project permits are met. As expected, it is not profitable to add any generation capacity in bus 83 with the lowest LMP. Bus 59 is a suitable candidate especially in transmission-constrained systems as it shows two positive factors including a high LMP and a large demand quantity. It is also profitable to choose bus 95 using the LCP approach. However, in all cases, the generation expansion would occur in earlier years if the locational capacity mechanism is considered in the market structure. Furthermore, investments would have a true market-based signal to find the best location for their expansion projects.

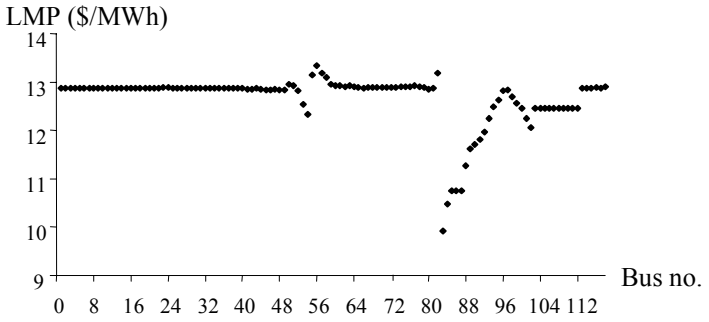


**Figure 11** *Bus LMPs in the IEEE 118-bus*

Table 4: OPTIMAL INVESTMENT TIME AND VALUE

| Bus No. | LMP ($/MWh) | LCP Model | | | Energy Only Model | | |
|---|---|---|---|---|---|---|---|
| | | Optimal Investment Time (year) | | Optimal Project Value (M$) | Optimal Investment Time (year) | | Optimal Project Value (M$) |
| | | F(V) | N(V) | | F(V) | N(V) | |
| 56 | 13.33 | 0 | 0 | 208.504 | 5.03 | 4.49 | 0.938 |
| 59 | 12.96 | 0 | 0 | 207.69 | 5.04 | 4.50 | 0.936 |
| 83 | 9.92 | NI* | NI | (3.084) | NI | NI | (3.084) |
| 89 | 11.63 | NI | NI | (3.084) | NI | NI | (3.084) |
| 95 | 12.64 | 6.98 | 6.48 | 0.639 | NI | NI | (3.029) |

* No investment

## 6. CONCLUSIONS

It was shown that with low VOLL values, the energy only market model might not guarantee the capacity adequacy in power systems. Therefore, it is essential to have a capacity mechanism to ensure that there will be enough capacity available to prevent the scarcity as the system load grows. Capacity payment and installed capacity models have shown planning deficiencies because they do not include locational and temporal variables. Furthermore, the aforementioned capacity mechanisms may incur burdensome and excessive payments at demand side. The proposed LCP model provides an efficient solution for a market-based capacity mechanism while would not increase load payments if the new expansion has occurred at the right time, i.e. before scarcity period. LCP brings about the following benefits:

- Allows cost effective investments at earlier years before capacity shortages occur.
- Enables the creation of true capacity markets as it follows market trends and provides market-based investment signals.
- Provides generation companies with additional revenues to hedge investment risks.
- Encourages generation units to declare the available capacity in the market rather than exercising any market power.
- Is easily adapted to various market structures.
- Would not increase load payments in normal operation conditions.

Furthermore, the value of project provides investment signals when the system is on the verge of facing capacity

shortages while risks are borne by investors rather than consumers. The installed capacity model would lead to additional capacity investments while transferring considerable revenues, as capacity incentive payments, from consumers to suppliers. However, the LCP, along with multi-level load bidding would result in efficient capacity investments as well as a higher social welfare since it highlights consumer preferences for an uninterrupted supply. In the long-term, the proposed model will contribute to healthier electricity market designs and fewer administrative regulations in favor of robust capacity adequacy options.

## 7. REFERENCES


[1] Wang, X., Song, Y., and Irving, M., 'Modern power System Analysis' (Springer, New York, 2009)

[2] De Vries, L.J., 'Securing the public interest in electricity generation markets,' PhD Thesis, Technical University of Delft, the Netherlands, 2004

[3] Chao, H., 'Capacity Markets in NYISO & ISO-NE,' IEEE PES General Meeting, 2007, pp. 1-4

[4] Wang, J., Botterud, A., Conzelmann, G., and Koritarov, V., 'Market Power Analysis in the EEX Electricity Market: An Agent-Based Simulation Approach,' IEEE PES General Meetings, 2008, pp.1 - 8

[5] Wang, J., 'Conjectural Variation-Based Bidding Strategies with Q-learning in Electricity Markets,' The 42nd Annual Hawaii International Conference on System Sciences (HICSS 2009), 2009, pp. 1-10

[6] Cramton, P., and Stoft, S., 'A capacity Market that Makes Sense,' Electricity Journal, 2005, **18**, (7), pp. 43-54.

[7] Stoddard, R., and Adamson, S., 'Comparing Capacity Market and Payment Designs for Ensuring Supply Adequacy,' Proceedings of the 42nd Hawaii International Conference on System Sciences, 2009, pp.1-8

[8] Crampton, P., and Stoft, S., 'The Convergence of Market Designs for Adequate Generating Capacity with Special Attention to the CAISO's Resource Adequacy Program,' White Paper for California's Electricity Oversight Board, 2006

[9] Vazquez, C., Rivier, M., and Perez-Arriaga, I.J., 'A Market Approach to Long-term Security of Supply,' IEEE Trans. Power Syst., 2002, **17**, (2), pp. 349-357

[10] Oren, S.S., 'Generation Adequacy via Call Options Obligations: Safe Passage to the Promised Land,' The Electricity Journal, 2005, **18**, (9), pp. 28-42

[11] Doorman, G.L., 'Capacity Subscription: Solving the Peak Demand Challenge in Electricity Markets,' IEEE Trans. Power. Syst., 2005, **20**, (1), pp. 239-245.

[12] Doorman, G.L, Botterud, A., 'Analysis of Generation Investment under Different Market Designs,' IEEE Trans. Power. Syst., 2008, **23**, (3), pp. 859-867.

[13] Fu, Y., Li, Z., and Shahidehpour, M., 'Profit-based Generation Resource Planning,' IMA Journal of Management Mathematics, 2004, **15**, (4), pp. 273-289

[14] Roh, J.H., Shahidehpour, M., and Fu, Y., 'Security-Constrained Resource Planning in Electricity Markets,' IEEE Trans. Power Syst., 2007, **22**, (2), pp. 812-820

[15] Roh, J.H., Shahidehpour, M., and Fu, Y., 'Market-Based Coordination of Transmission and Generation Capacity Planning,' IEEE Trans. Power Syst., 2007, **22**, (4), pp.1406-1419

[16] Siddiqi, S.N., 'Resource Adequacy in the Energy-Only ERCOT Market,' IEEE PES General Meeting, 2007, pp. 1-3

[17] Woychik, E., 'Capacity" for the Energy Only Market: Demand Response to Educate Customers, Hedge Market Power, and Ensure Resource Adequacy,' White Paper, Electric Reliability Council of Texas and the Public Utilities Commission of Texas, 2006

[18] Tezak, C., 'Resource Adequacy — Alphabet Soup,' Stanford Washington Research Group, Jun 2005.

[19] Ruiz, P. A., and Gross, G., 'An Analytical Framework for Short-Term Resource Adequacy in Competitive Electricity Markets,' Proceedings of the IX Probabilistic Methods Applied to Power Systems (PMAPS) Conference, Stockholm, 2006, pp. 1-6

[20] Ruiz, P. A., and Gross, G., 'Short-Term Resource Adequacy in Electricity Market Design,' IEEE Trans. Power Syst.., 2008, **23**, (3), pp. 916-926

[21] 'Short-Term Resource Adequacy,' Ontario Independent System Operator (IESO), Market Evolutionary Program, 2003.

[22] De Vries, L.J., and Hakvoort, R.A., 'The question of generation adequacy in liberalized electricity markets,' Proc. 26th IAEE International Conference, Prague, 2003

[23] Botterud., A, Ilic, M.D., and Wangensteen, I., 'Optimal Investments in Power Generation under Centralized and Decentralized Decision Making,' IEEE Trans. Power Syst., 2005, **20**, (1), pp. 254-263

[24] Botterud, A., Mahalik, M. R., Veselka, T. D., Ryu, H-S., and Sohn, K-W., 'Multi-Agent Simulation of Generation Expansion in Electricity Markets,' Proceedings IEEE PES General Meeting, Tampa, Florida, 2007, pp. 1-8

[25] Botterud, A., and Korpas, M., 'Modeling of power generation investment incentives under uncertainty in liberalized electricity markets,' presented at 6th IAEE European Conference, Zurich, Switzerland, 2000

[26] Dixit, A., and Pindyck, R. S., 'Investment under Uncertainty' (Princeton University Press, New Jersey, 1996)

[27] Ciaran, D., and David, M., 'Investment, Expectations and Uncertainty' (Oxford: Blackwell Publishers, 1992)

[28] Brennan, M.J., Trigeorigis L., 'Real Options: Development and New Contributions,' in "Project Flexibility, Agency and Competition", edited by M.J. Brennan and L. Trigeorgis, Oxford University Press, 2000

[29] Fu, Y., and Li, Z., 'Different models and properties on LMP calculations' IEEE PES Conference, 2006, pp: 1-11.

[30] Oren, S. S., 'Capacity Payments and Supply Adequacy in Competitive Electricity Markets' VII Symposium of Specialists In Electric Operational And Expansion Planning, Curitiba, Brazil, 2000

[31] Botterud, A., 'Long-Term Planning in Restructured Power Systems,' PhD Thesis, The Norwegian University of Science and Technology (NTNU), 2003

[32] Botterud, A., and Korpas, M., 'A Stochastic Dynamic Model for Optimal Timing of Investments in New Generation Capacity in Restructured Power Systems,' International Journal of Electrical Power & Energy Systems, Published by Elsevier, 2007, **29**, (2), pp. 163-174

[33] Singh, H., and Jacobs, J., 'ISO Markets and Capacity Products,' 5th Annual Power Conference, UC Berkeley California, 2000

[34] Stoft, S., 'Power System Economics: Designing Markets for Electricity' (John Wiley and Sons, New York, 2002)

[35] Buygi, M., Balzer, G., Shanechi, H., and Shahidehpour, M., 'Market-based transmission expansion planning", IEEE Trans. Power Syst., 2004, **19**, (4), pp. 2060-2067

## 8. BIOGRAPHIES

**Saeed Kamalinia** received his BS and MS in E.E. from University of Tehran, Iran, in 2005 and 2007, respectively. Presently, he is pursuing his Ph.D degree at Illinois Institute of Technology, USA. His research interests include restructured power system generation and transmission planning.

**Mohammad Shahidehpour** is the Bodine Distinguished Professor in the ECE Department at Illinois Institute of Technology. He is the recipient of an honorary doctorate from the Polytechnic University of Bucharest in 2009. He is the Vice President of Publication for the IEEE Power and Energy Society. Dr. Shahidehpour is an honorary professor in the North China Electric Power University in China and Sharif University of Technology in Iran. He is a Fellow of IEEE.

# Security-Constrained Unit Commitment with AC/DC Transmission Systems

Azim Lotfjou, *Member, IEEE,* Mohammad Shahidehpour, *Fellow, IEEE,*
Yong Fu, *Member, IEEE, and* Zuyi Li, *Member, IEEE*

***Abstract*—This paper presents the solution to the security-constraint unit commitment (SCUC) problem with a detailed representation of high voltage direct current (DC) transmission system with current source converters (CSCs). The SCUC problem is decomposed into a master problem for solving unit commitment (UC) problem and hourly transmission security check subproblems that evaluate branch flows and bus voltages of integrated AC/DC transmission systems. The solution of the transmission security check subproblem is based on a linear programming (LP) formulation that minimizes AC bus mismatches subject to AC/DC transmission constraints. The final SCUC solution prescribes an economic and secure operation and control strategy for AC/DC transmission systems and coordinates DC power transfers for enhancing the economics and the security of AC transmission systems. Numerical tests illustrate the efficiency of the proposed AC/DC transmission model.**

***Index Terms*—AC/DC transmission systems, current source converters, security-constrained unit commitment, Benders decomposition.**

## NOMENCLATURE

$b$ Index for AC buses
$c$ Index for contingencies
$h$ Index for DC converters
$i$ Index for generating units
$l$ Index for transmission lines
$m$ Index for AC bus terminals connected to converters
$I_{dc,h}$ DC current of converter $h$
$MP_{b,1}$, $MP_{b,2}$ Slack variables for the real power mismatch at bus $b$ (>=0)
$MQ_{b,1}$, $MQ_{b,2}$ Slack variables for the reactive power mismatch at bus $b$ (>=0)
$NB$ Number of ac buses
$P_m$, $Q_m$ Real and reactive power withdrawals at bus $m$
$P_m^{inj}$, $Q_m^{inj}$ Real and reactive power injections at bus $m$
$P_{term,h}$, $Q_{term,h}$ Real and reactive power of converter $h$
$R_{dc}$ Resistance of DC line
$T_h$ Off-nominal tap ratio of the transformer connected to converter $h$
$V_{dc,h}$ DC voltage of converter $h$
$V_m$ AC bus voltage at bus $m$
$w$ Objective value of SCUC subproblem
$X_{c,h}$ Commutation reactance of converter $h$
$\alpha_h$ Firing/extinction angle of converter $h$
$\phi_h$ Power factor angle of converter $h$ ($0 \le \phi_h \le \frac{\pi}{2}$ for rectifier, $-\frac{\pi}{2} \le \phi_h \le 0$ for inverter)
$\Delta P_m$ Real power mismatch at bus $m$
$\Delta Q_m$ Reactive power mismatch at bus $m$
$\Delta R1_h$ $\Delta R2_h$, $\Delta R3_h$ DC mismatches of converter $h$
$\Delta_i$ Permissible real power adjustment for unit $i$
$\mathbf{A}$ Bus-unit incidence matrix
$\mathbf{G}_h$ Admittance matrix of DC transmission system for converters $h$
$\mathbf{I}$ Unit state vector
$\mathbf{I_{dc}}$, $\mathbf{\Delta I_{dc}}$ DC current vector and its incremental vector
$\mathbf{J1}$, $\mathbf{J2}$, $\mathbf{J3}$, $\mathbf{J4}$ Jacobian matrices
$\mathbf{MP1}$, $\mathbf{MP2}$ Mismatch vector for real power slack variables
$\mathbf{MQ1}$, $\mathbf{MQ2}$ Mismatch vector for reactive power slack variables
$\mathbf{P}$, $\mathbf{\Delta P}$ Real power generation vector and its increment
$\mathbf{Q_{max}}$, $\mathbf{Q_{min}}$ Upper and lower limit vectors for reactive power generation
$\mathbf{V}$, $\mathbf{V}_{dc}$ AC and DC bus voltage vectors
$\mathbf{x}$ Vector of SCUC variables
$\boldsymbol{\varphi}$, $\boldsymbol{\Delta\varphi}$ Power factor angle vector and its increment
$\boldsymbol{\alpha}$, $\boldsymbol{\Delta\alpha}$ Firing/extinction angle vector and its increment
$\boldsymbol{\delta}$, $\boldsymbol{\Delta\delta}$ Bus phase angle vector and its increment
$\boldsymbol{\pi}$, $\boldsymbol{\psi}$, $\boldsymbol{\overline{\psi}}$ Simplex multiplier vectors
$\mathbf{dP_0}$ Initial AC bus real power mismatch vector
$\mathbf{dQ_0}$ Initial AC bus reactive power mismatch vector
$\mathbf{dR1_0}$, $\mathbf{dR2_0}$, $\mathbf{dR3_0}$ Initial mismatch vectors for DC equations
$\mathbf{\Delta I_{dc,max}}$, $\mathbf{\Delta I_{dc,min}}$ Upper and lower limit vectors for incremental converter currents
$\mathbf{\Delta PL_{ac}}$, $\mathbf{\Delta PL_{dc}}$ Increment vectors for AC and DC line flows
$\mathbf{\Delta PL_{ac,max}}$, $\mathbf{\Delta PL_{ac,min}}$ Upper and lower limit vectors for incremental AC line flows
$\mathbf{\Delta PL_{dc,max}}$, $\mathbf{\Delta PL_{dc,min}}$ Upper and lower limit vectors for incremental DC line flows
$\mathbf{\Delta Q}$ Incremental vector of reactive power generation
$\mathbf{\Delta Q_{max}}$, $\mathbf{\Delta Q_{min}}$ Upper and lower limit vectors for incremental unit reactive power
$\mathbf{\Delta T}$ Increment vector for transformer taps
$\mathbf{\Delta T_{max}}$, $\mathbf{\Delta T_{min}}$ Upper and lower limit vectors for incremental transformer taps
$\mathbf{\Delta V}$, $\mathbf{\Delta V_{dc}}$ Increment vectors for AC and DC bus voltages

$\Delta V_{max}$ , $\Delta V_{min}$ Upper and lower limit vectors for incremental AC voltages

$\Delta\gamma$ Increment vector for phase-shifter angles

$\Delta\gamma_{max}$ , $\Delta\gamma_{min}$ Upper and lower limit vectors for incremental phase shifter angles

$\Delta\alpha_{max}$ , $\Delta\alpha_{min}$ Upper and lower limit vectors for incremental firing/extinction angles

$\Delta\varphi_{max}$ , $\Delta\varphi_{min}$ Upper and lower limit vectors for incremental power factor angles

## I. Introduction

DC transmission systems are often considered for delivering bulk power via long distances. The attributes of DC transmission systems include low capacitance, low average transmission cost in long distances, ability to prevent cascaded outages in AC transmission systems, rapid adjustments for direct power flow controls, ability to improve the stability of AC transmission systems, mitigation of transmission congestion, enhancement of transmission capacity, rapid frequency control following a loss of generation, ability to damp out regional power oscillations following major contingencies, and offering major economic incentives for supplying loads [1-4]. Flexible and fast DC controls provide efficient and desirable performance for a wide range of AC transmission systems [5].

Proper control modes applied to rectifiers (source) and inverters (sink) could maintain DC voltages near rated values and set power factors as high as possible. DC transmission system would require two control modes out of five for source and sink operations. The control modes include fixed firing/ extinction advance angles, tap setting of converter transformers, DC currents, DC voltages, and DC power [6,7]. The selection of DC control modes depends on the nature of specific applications for enhancing the economic and security.

DC transmission system configurations include monopolar, bipolar, tripolar, and multi-terminal which are used in diverse applications including the reinforcement of AC transmission flows and the interconnection of several AC transmission systems with different operating frequencies [8].

In the past, DC transmission systems were modeled in the optimal power flow (OPF) problem to analyze the impact of DC transmission systems on the operation of AC transmission systems [9,10]. Several numerical techniques such as unified and sequential methods were considered for solving integrated AC/DC transmission flow equations [11-13]. The unified method solves AC and DC power flow equations simultaneously. The sequential method applies an iterative procedure between AC and DC transmission systems.

With the advent of electricity restructuring, DC transmission systems were utilized to maintain the system security and decrease social costs. The simplest approach to consider DC transmission systems in SCUC was to regard DC terminals as constant power injections or withdrawals in AC transmission systems [14-16]. However, such simplified models in SCUC may ignore the dependency of AC power flows to DC transmission variables.

Fig. 1 depicts the market clearing process for AC/DC transmission systems. The AC system includes AC generators, loads, and transmission lines. The DC transmission system is composed of converter terminals and DC transmission lines. At first, the independent system operator (ISO) receives supply/demand bids and collects AC/DC transmission data provided by transmission companies (TRANSCOs). Once the market is cleared, the ISO will send hourly schedules (unit commitment, generation dispatch, and load schedules) to the AC system and optimal control strategies to the TRANSCOs which will activate control signals (tap-changing and phase-shifting transformers, adjustable shunt capacitors, firing angles of thyristors, and taps of converter transformers) to operate AC/DC transmission systems.

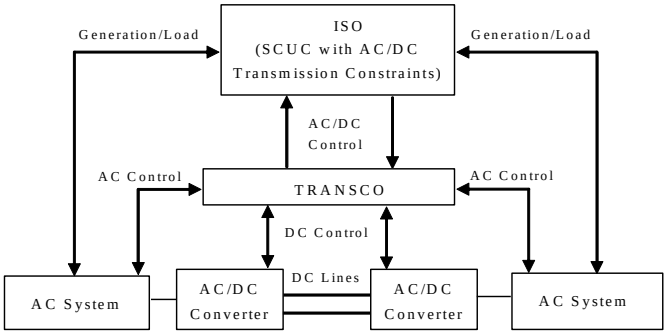


Fig. 1. Market clearing process with AC/DC transmission

Since most DC transmission installations in the world use a line-commutation based current source converter (CSC) [17], we study in this paper the application of CSC-DC transmission system. The other option for the modeling of DC transmission system is based on the voltage source converter (VSC-DC) [18-20]. The application of VSC-DC to SCUC is under investigation and will appear in our subsequent publications. The proposed SCUC model would secure the power flow solution and optimize the hourly UC by a set of proper control strategies of AC/DC transmission systems. The SCUC solution for handling AC/DC transmission constraints applies Benders decomposition for mitigating transmission congestion and improving power system economics while satisfying system security constraints including transmission flow and bus voltage limits. Once a credible contingency occurs on AC/DC transmission lines or generating units, contingency subproblems will minimize transmission violations. In such cases, preventive actions will accommodate uncontrollable contingencies by transferring the base case operating point to a secure state. A corrective action will otherwise be considered for accommodating controllable contingencies [21].

The rest of the paper is organized as follows. Section II models the CSC (DC terminal) and power flow equations for the DC transmission system. The SCUC formulation with AC/DC transmission constraints and Benders decomposition based solution are presented in Section III. The proposed algorithm is tested with the IEEE 14-bus and IEEE 118-bus systems in Section IV. We summarize the conclusion in Section V.

## II. DC Transmission System Model

DC transmission systems consist of at least two converters (i.e., rectifiers and inverters) and overhead lines that link converters. In order to eliminate harmonics generated by AC/ DC systems, AC filters are installed on the AC side of DC terminals. In this section, we review DC transmission systems and corresponding DC power flow equations for our SCUC formulation.

### A. CSC Model

Fig. 2 presents a typical CSC system which is connected to AC bus $m$ through a coupling transformer. In order to model the CSC $h$ which is linked to the AC bus *m*, five converter variables, i.e., $V_{dc,h}$ , $I_{dc,h}$ , $T_h$ , $\alpha_h$ , and $\phi_h$ are considered in Fig. 2. These variables determine the DC line operating state.

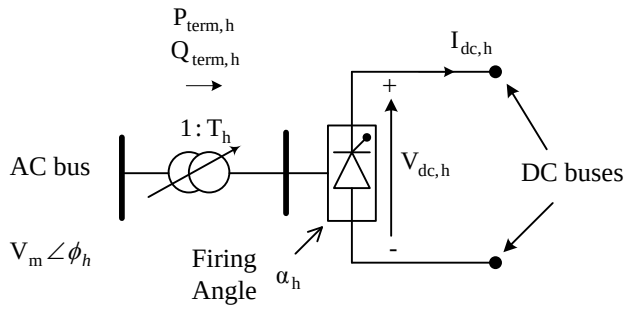


Fig. 2. Schematic Diagram of a CSC-DC system

A converter, either a rectifier or an inverter, is modeled by (1)-(3). The converter equations (1) and (2) express $V_{dc,h}$ in terms of $V_m$ and other converter variables while the coupling transformer is assumed to be lossless. The converter equation (3), which can be expressed using a nodal-mesh procedure, represents the DC voltage-current relationship which depends on the DC transmission system configuration (i.e., monopole, bipole, tri-pole, or a multi-terminal link).

$$V_{dc,h} = \frac{3\sqrt{2}}{\pi} T_h V_m \cos\alpha_h - \frac{3}{\pi} X_{c,h} I_{dc,h} \quad \text{rectifier}$$
$$V_{dc,h} = -\frac{3\sqrt{2}}{\pi} T_h V_m \cos\alpha_h + \frac{3}{\pi} X_{c,h} I_{dc,h} \quad \text{inverter} \tag{1}$$

$$V_{dc,h} = 0.995 \frac{3\sqrt{2}}{\pi} T_h V_m \cos\phi_h \quad \text{rectifier}$$
$$V_{dc,h} = -0.995 \frac{3\sqrt{2}}{\pi} T_h V_m \cos\phi_h \quad \text{inverter} \tag{2}$$

$$f(\mathbf{V_{dc}}, I_{dc,h}) = 0 \tag{3}$$

Here, (3) for converter *h* is rewritten as (4) in a matrix form,

$$I_{dc,h} - \mathbf{G}_h \cdot \mathbf{V_{dc}} = \mathbf{0} \tag{4}$$

where, $\mathbf{G}_h$ is the admittance matrix of DC transmission system for converter *h*. A DC terminal is selected as slack bus in each DC transmission system. Similar to that in an AC transmission system, the slack bus balances the real power among DC terminals in the DC transmission system [22].

### B. Control Modes of DC Transmission Systems

Each CSC (rectifier or inverter) is regulated by two out of five control modes. The modes are.

1) Constant current (CC)

$$I_{dc,h} = const$$

2) Constant voltage (CV)

$$V_{dc,h} = const$$

3) Constant power (CP)

$$P_{term,h} = V_{dc,h} I_{dc,h} = const$$

4) Constant firing/extinction angle (CFA/CEA)

$$\alpha_h = const$$

5) Constant transformer tap ratio (CTR)

$$T_h = const$$

The selection of two control modes would maximize the economic benefits of DC transmission systems while keeping all variables within their limits. The rules for selecting effective CSC control modes are given below [1-3],

Rule 1: At least one converter in each DC transmission system would select CV as the first control mode; other converters would maintain CC as the first control mode. If converters are not operating at their minimum firing/extinction angles, CP may be applied as the second control mode.

Rule 2: If a rectifier is not operating at its minimum firing angle, the rectifier would be operated as (CC/CP plus CV). For an inverter which is not operating at its minimum extinction angle, (CC/CP/CV plus CEA) is selected.

Rule 3: Once the minimum firing angle of rectifier is reached, the rectifier would switch from (CC plus CV) to (CFA plus CTR). In this case, the inverter would maintain CC plus CEA.

Rule 4: If an inverter is operating at its minimum extinction advance angle, it would switch to (CC/CP/CV plus CTR).

### C. Power Flow Equations of DC Transmission Systems

Using the per-unit system given in Appendix A, nodal power balance equations at the AC bus *m* that is linked to converter *h* are listed as

$$\Delta P_m = P_m^{inj} - P_m - P_{term,h} = 0 \tag{5}$$

$$\Delta Q_m = Q_m^{inj} - Q_m - Q_{term,h} = 0 \tag{6}$$

where,

$$P_{term,h} = V_{dc,h} I_{dc,h} \tag{7}$$

$$Q_{term,h} = V_{dc,h} I_{dc,h} \tan\phi_h \tag{8}$$

CSC always consumes reactive power and $Q_{term,h}$ is non-negative. Similarly, (1), (2) and (4) are replaced in pu as

$$\begin{cases} \Delta R1_h = V_{dc,h} - T_h V_m \cos\alpha_h + X_{c,h} I_{dc,h} = 0 & \text{rectifier} \\ \Delta R1_h = V_{dc,h} + T_h V_m \cos\alpha_h - X_{c,h} I_{dc,h} = 0 & \text{inverter} \end{cases} \tag{9}$$

$$\begin{cases} \Delta R2_h = V_{dc,h} - 0.995\, T_h V_m \cos\phi_h = 0 & \text{rectifier} \\ \Delta R2_h = V_{dc,h} + 0.995\, T_h V_m \cos\phi_h = 0 & \text{inverter} \end{cases} \tag{10}$$

$$\Delta R3_h = I_{dc,h} - \mathbf{G_h V_{dc}} = 0 \tag{11}$$

In the next section, we will apply the Newton-Raphson method that utilizes the linearized version of (5)-(11) for the network

security violation checking in base case and contingency conditions.

## III. SCUC WITH DC CONSTRAINTS

### A. Formulation of SCUC with AC/DC Constraints

SCUC is generalized in (12) where $f(\mathbf{x})$ is composed of production cost, and start up and shut down costs of individual units for the study horizon [21, 23-25].

$$\begin{aligned} &Min \quad f(\mathbf{x}) \\ &S.t. \\ &\quad \mathbf{g1(x)} \le \mathbf{b1} \\ &\quad \mathbf{ge1(x)} = \mathbf{be1} \\ &\quad \mathbf{g2(x)} \le \mathbf{b2} \\ &\quad \mathbf{ge2(x)} = \mathbf{be2} \end{aligned} \tag{12}$$

where $\mathbf{x}$ is composed of on/off status and generation of generating units, startup and shutdown indicators, and AC/DC transmission system variables. The first set of inequality constraints $\mathbf{g1(x)} \le \mathbf{b1}$ and equality constraints $\mathbf{ge1(x)} = \mathbf{be1}$ represents UC constraints such as,

1. Power balance
2. Generating unit capacity
3. System spinning and operating reserve requirements
4. Ramping up/down limits
5. Minimum up/down time limits
6. Maximum number of simultaneous on/offs in a plant
7. Maximum number of on/offs of a unit in a given period
8. Fuel and multiple emission limits

The second set of inequality constraints $\mathbf{g2(x)} \le \mathbf{b2}$ and equality constraints $\mathbf{ge2(x)} = \mathbf{be2}$ includes

9. AC/DC power flow equations
10. Limits on AC/DC control variables including real and reactive power generations, controlled shunt capacitors, tap-changing and phase-shifting transformers, firing/ extinction angles and coupling transformer tap ratios of converters
11. AC/DC network security constraints including AC/DC transmission flow and bus voltage limits, and limits to DC currents, voltages and power of converters
12. Time limited corrective controls, such as permissible real power adjustments, for handling contingencies

### B. Solution of SCUC with AC/DC Constraints

We apply the Benders decomposition to solve the SCUC with AC/DC transmission systems as depicted in Fig. 3. The master problem applies MIP for solving the UC problem. The Newton-Raphson based subproblem is utilized to check transmission flows and bus voltages in base case and contingency conditions. The SCUC subproblem considers both real and reactive power mismatches at AC buses which are minimized based on optimal adjustments of scheduled power generation, tap-changing transformers, and phase shifters in the AC system, and by adjusting DC transmission controls (e.g. converter firing/extinction advance angles and transformer tap settings). The subproblem generates Benders cuts for the next UC iteration once the mismatch exists in either base case or contingencies. This iterative procedure will continue until all mismatches are removed.

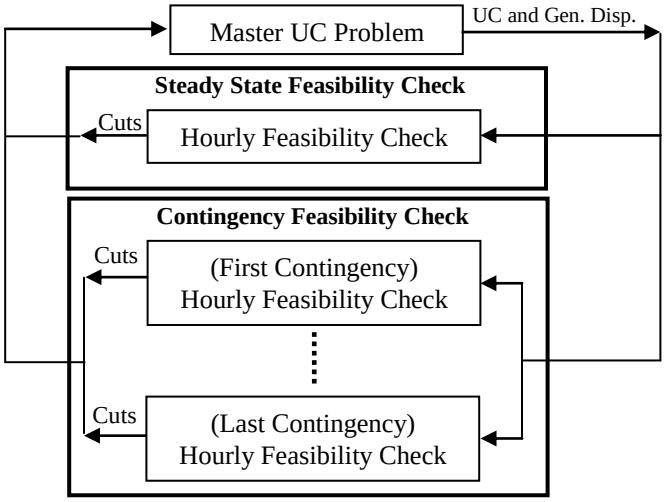


Fig. 3 SCUC with AC/DC transmission systems

### C. SCUC Subproblem for Base Case

The subproblem for base case is formulated as (13)-(26). (14)-(26) represents AC/DC power flow equations, limits on real and reactive power generations, AC and DC line flows, real power withdrawals at AC converter buses, AC bus voltages magnitudes, transformer tap settings, phase shifter angles, DC bus voltages, DC voltages and currents of converters, converter firing/extinction advance angles, and converter power factor (lagging/leading) angles, respectively. Note that (15) is for all generating units except the ones at the slack bus. Appendix B lists the elements of Jacobian matrices $\mathbf{J1}$, $\mathbf{J2}$, $\mathbf{J3}$, and $\mathbf{J4}$ for DC transmission systems.

$$Min \quad w = \sum_{b=1}^{NB} (MP\,1_b + MP\,2_b + MQ\,1_b + MQ\,2_b) \tag{13}$$

$$\begin{bmatrix} \mathbf{A}\cdot\Delta\mathbf{P} \\ \mathbf{A}\cdot\Delta\mathbf{Q} \\ \mathbf{0} \\ \mathbf{0} \\ \mathbf{0} \end{bmatrix} - [\mathbf{J1}] \begin{bmatrix} \Delta\delta \\ \Delta V \\ \Delta T \\ \Delta\gamma \\ \Delta V_{dc} \\ \Delta I_{dc} \\ \Delta\alpha \\ \Delta\varphi \end{bmatrix} + \begin{bmatrix} \mathbf{MP1} \\ \mathbf{MQ1} \\ \mathbf{0} \\ \mathbf{0} \\ \mathbf{0} \end{bmatrix} - \begin{bmatrix} \mathbf{MP2} \\ \mathbf{MQ2} \\ \mathbf{0} \\ \mathbf{0} \\ \mathbf{0} \end{bmatrix} = \begin{bmatrix} dP_0 \\ dQ_0 \\ dR1_0 \\ dR2_0 \\ dR3_0 \end{bmatrix} \tag{14}$$

$$\Delta\mathbf{P} = \mathbf{0} \qquad \pi \tag{15}$$

$$\Delta\mathbf{Q}_{min} \le \Delta\mathbf{Q} \le \Delta\mathbf{Q}_{max} \qquad \underline{\psi}, \overline{\psi} \tag{16}$$

$$\Delta\mathbf{PL}_{ac,\,min} \le \Delta\mathbf{PL}_{ac} = [\mathbf{J2}] \begin{bmatrix} \Delta\delta \\ \Delta V \\ \Delta T \\ \Delta\gamma \end{bmatrix} \le \Delta\mathbf{PL}_{ac,\,max} \tag{17}$$

$$\Delta\mathbf{PL}_{dc,\,min} \le \Delta\mathbf{PL}_{dc} = [\mathbf{J3}] \begin{bmatrix} \Delta V_{dc} \\ \Delta I_{dc} \end{bmatrix} \le \Delta\mathbf{PL}_{dc,\,max} \tag{18}$$

$$\Delta\mathbf{P}_{term,\,min} \le \Delta\mathbf{P}_{term} = [\mathbf{J4}] \begin{bmatrix} \Delta V_{dc} \\ \Delta I_{dc} \end{bmatrix} \le \Delta\mathbf{P}_{term,\,max} \tag{19}$$

$$\Delta V_{min} \le \Delta V \le \Delta V_{max} \quad (20)$$

$$\Delta T_{min} \le \Delta T \le \Delta T_{max} \quad (21)$$

$$\Delta\gamma_{min} \le \Delta\gamma \le \Delta\gamma_{max} \quad (22)$$

$$\Delta V_{dc,min} \le \Delta V_{dc} \le \Delta V_{dc,max} \quad (23)$$

$$\Delta I_{dc,min} \le \Delta I_{dc} \le \Delta I_{dc,max} \quad (24)$$

$$\Delta\alpha_{min} \le \Delta\alpha \le \Delta\alpha_{max} \quad (25)$$

$$\Delta\varphi_{min} \le \Delta\varphi \le \Delta\varphi_{max} \quad (26)$$

The steps for solving the SCUC subproblem include,

Step 1: Calculate elements of corresponding Jacobian matrices **J1**, **J2**, **J3**, and **J4**, initial AC bus mismatch vectors $\mathbf{dP}_0$ and $\mathbf{dQ}_0$, and initial DC power mismatch $\mathbf{dR1}_0$, $\mathbf{dR2}_0$ and $\mathbf{dR3}_0$. The calculation is based on the initial UC solution and the given AC/DC transmission system state.

Step 2: Use LP to minimize (13) and calculate changes in the AC/DC transmission state and control variables.

Step 3: Update state and control variables. Recalculate elements of Jacobian matrices and mismatch vectors.

Step 4: Minimize (13) and calculate changes in AC/DC transmission system state and control variables. If the difference between the last two iterative changes is less than a specified tolerance, stop the process. Otherwise, go back to Step 3.

If $w$ is larger than zero, a mismatch Benders cut (27) will be formed and added to the UC problem for calculating the next iterative solution of master problem.

$$w + \boldsymbol{\pi}(\mathbf{P} - \hat{\mathbf{P}}) + \overline{\boldsymbol{\psi}}\mathbf{Q}_{max}(\mathbf{I} - \hat{\mathbf{I}}) - \underline{\boldsymbol{\psi}}\mathbf{Q}_{min}(\mathbf{I} - \hat{\mathbf{I}}) \le 0 \quad (27)$$

where $\hat{\mathbf{I}}$ and $\hat{\mathbf{P}}$ are the UC and generation dispatch results in the current iteration, respectively.

### *D. SCUC Subproblem for Contingencies*

The subproblem for a contingency $c$ is formulated in (28)-(41). The objective function (28) is introduced according to the Newton-Raphson method for minimizing real and reactive bus power mismatches and calculating a converged AC power flow solution subject to transmission flow and bus voltage limits.

In each contingency case, corrective and preventive actions are considered for managing AC/DC violations. Corrective actions refer to the redispatch of generating units and adjustments of transmission flow controls for mitigating transmission flow violations in real time. Preventive actions refer to day-ahead adjustments of transmission flows by applying transformer controls, as well as UC and economic dispatch (ED) of generating units. Preventive actions will be applied if corrective actions are not feasible in real time. (30) represents the physically acceptable corrective action for generating units [25].

$$Min \quad w^c = \sum_{b=1}^{NB}\left(MP\,1_b^c + MP\,2_b^c + MQ\,1_b^c + MQ\,2_b^c\right) \quad (28)$$

$$\begin{bmatrix} \mathbf{A}\cdot\Delta\mathbf{P}^c \\ \mathbf{A}\cdot\Delta\mathbf{Q}^c \\ \mathbf{0} \\ \mathbf{0} \\ \mathbf{0} \end{bmatrix} - [\mathbf{J1}] \begin{bmatrix} \Delta\delta^c \\ \Delta V^c \\ \Delta T^c \\ \Delta\gamma^c \\ \Delta V_{dc}^c \\ \Delta I_{dc}^c \\ \Delta\alpha^c \\ \Delta\varphi^c \end{bmatrix} + \begin{bmatrix} \mathbf{MP1}^c \\ \mathbf{MQ1}^c \\ \mathbf{0} \\ \mathbf{0} \\ \mathbf{0} \end{bmatrix} - \begin{bmatrix} \mathbf{MP2}^c \\ \mathbf{MQ2}^c \\ \mathbf{0} \\ \mathbf{0} \\ \mathbf{0} \end{bmatrix} = \begin{bmatrix} \mathbf{dP}_0^c \\ \mathbf{dQ}_0^c \\ \mathbf{dR1}_0^c \\ \mathbf{dR2}_0^c \\ \mathbf{dR3}_0^c \end{bmatrix} \quad (29)$$

$$\left|\mathbf{P}^c - \hat{\mathbf{P}}^0\right| \le \Delta \qquad \overline{\boldsymbol{\pi}}^c, \underline{\boldsymbol{\pi}}^c \quad (30)$$

$$\Delta\mathbf{Q}_{min}^c \le \Delta\mathbf{Q}^c \le \Delta\mathbf{Q}_{max}^c \qquad \underline{\boldsymbol{\psi}}^c, \overline{\boldsymbol{\psi}}^c \quad (31)$$

$$\Delta PL_{ac,min}^c \le \Delta PL_{ac}^c \le \Delta PL_{ac,max}^c \quad (32)$$

$$\Delta PL_{dc,min}^c \le \Delta PL_{dc}^c \le \Delta PL_{dc,max}^c \quad (33)$$

$$\Delta P_{term,min}^c \le \Delta P_{term}^c \le \Delta P_{term,max}^c \quad (34)$$

$$\Delta V_{min}^c \le \Delta V^c \le \Delta V_{max}^c \quad (35)$$

$$\Delta T_{min}^c \le \Delta T^c \le \Delta T_{max}^c \quad (36)$$

$$\Delta\gamma_{min}^c \le \Delta\gamma^c \le \Delta\gamma_{max}^c \quad (37)$$

$$\Delta V_{dc,min}^c \le \Delta V_{dc}^c \le \Delta V_{dc,max}^c \quad (38)$$

$$\Delta I_{dc,min}^c \le \Delta I_{dc}^c \le \Delta I_{dc,max}^c \quad (39)$$

$$\Delta\alpha_{min}^c \le \Delta\alpha^c \le \Delta\alpha_{max}^c \quad (40)$$

$$\Delta\varphi_{min}^c \le \Delta\varphi^c \le \Delta\varphi_{max}^c \quad (41)$$

If $w_c$ is larger than zero, a mismatch Benders cut (42) for contingency $c$ will be formed and added to the master UC problem for calculating the next iterative solution.

$$w^c + \boldsymbol{\pi}^c(\mathbf{P} - \hat{\mathbf{P}}^0) + \overline{\boldsymbol{\psi}}^c\mathbf{Q}_{max}(\mathbf{I} - \hat{\mathbf{I}}^0) - \underline{\boldsymbol{\psi}}^c\mathbf{Q}_{min}(\mathbf{I} - \hat{\mathbf{I}}^0) \le 0 \quad (42)$$

## IV. Numerical Examples

The modified IEEE 14-bus system and the IEEE 118-bus system are studied. Optimal control strategies for DC transmission systems are determined based on SCUC results. We set the mismatch tolerance at 0.001 pu (or 0.1 MVA). Numerical examples presented in this section are mainly to show the economic benefits of DC system while maintaining the system security in base case and contingency conditions.

### *A. IEEE-14 Bus System*

The IEEE-14 bus system depicted in Fig. 4 is considered with pertinent data listed in Appendix C. This system has 5 generating units, 20 branches, 11 loads and 3 transformers. Bus 1 is selected as slack bus. The following cases are considered to examine the efficiency of the proposed model.

**Case 0:** UC solution without transmission constraints

**Case 1:** SCUC solution with AC transmission constraints

**Case 2:** ED solution when line 1-5 is replaced with a two-terminal DC line

**Case 3:** SCUC solution for Case 2

**Case 4:** SCUC for Case 1 considering the outage of line 2-3

**Case 5:** SCUC for Case 3 considering the outage of line 2-3

**Case 6:** SCUC for Case 3 with a simplified DC model (fixed power injection model).

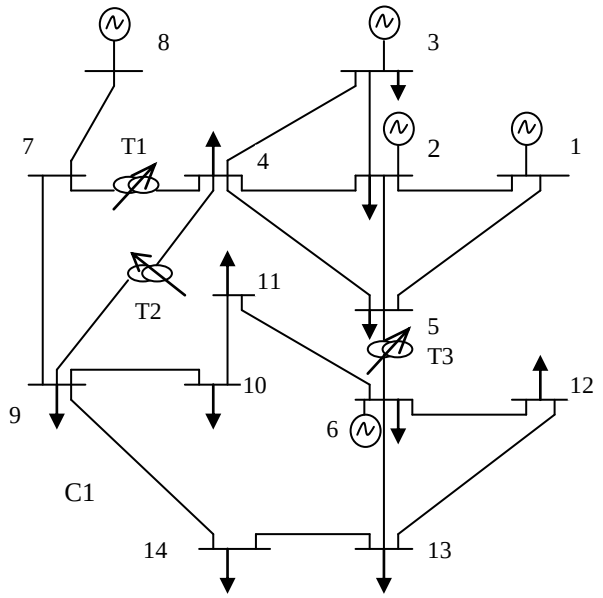


Fig. 4. IEEE 14-bus system

The above cases are discussed as follows:

**Case 0:** When AC transmission constraints are not considered, the cheapest generating unit 1 is committed at all hours to supply the base load. The cheap units 2 and 3 with higher bidding prices of 10$/MW and 18$/MW are committed at certain hours to serve system loads. The expensive units 4 and 5 are always off. The corresponding hourly UC and ED results are listed in Tables I and II with an operating cost of $45,666.28.

**Case 1:** In this case, the impact of AC transmission constraints on UC results is studied. The network security checking subproblem (13)-(26) is solved over 24 hours. The final SCUC solution is obtained after 6 iterations between master UC problem and network security checking subproblem. Tables III and IV show the hourly UC and ED in which UC changes in comparison to Case 0 are shown in bold. For example, the expensive generating unit 4 is committed at hours 1,2,7-24 to remove violations. We observed that the AC line 1-2 is the most congested line at peak-load hours because the cheapest unit 1 is dispatched at its maximum. In Table IV, unit 1 will pick up system losses. For example, at hour 1, the total generation dispatch is 184.16 MW which satisfies the system load of 181.3 MW and the loss of 2.86 MW. The operating cost in this case increases to $64,086.07.

**Case 2:** In this case, line 1-5 is replaced with a two-terminal DC line shown in Fig. 5. The DC transmission data are listed in Tables C.6-C.8. We solve the ED problem based on UC results in Case 1 and find that a feasible ED cannot be obtained at certain hours. For instance, at hour 10, there is a reactive power mismatch of 2.14 MVar at bus 8. One possible reason is that the DC converters in this case consume additional reactive power and the committed units cannot provide enough reactive power. One option for calculating a feasible ED is to commit the most expensive unit 5 at bus 8 to supply additional reactive power. A new UC is calculated in Case 3.

TABLE I
UC IN CASE 0

| Unit | Hours (1-24) |
|---|---|
| **1** | 1 1 1 1 1 1 1 1 1 1 1 1 1 1 1 1 1 1 1 1 1 1 1 1 |
| **2** | 1 1 1 0 0 1 1 1 1 1 1 1 1 1 1 1 1 1 1 1 1 1 1 1 |
| **3** | 0 0 0 0 0 0 0 1 1 1 1 1 1 0 1 1 1 1 1 1 1 1 1 1 |
| **4** | 0 0 0 0 0 0 0 0 0 0 0 0 0 0 0 0 0 0 0 0 0 0 0 0 |
| **5** | 0 0 0 0 0 0 0 0 0 0 0 0 0 0 0 0 0 0 0 0 0 0 0 0 |

TABLE II
UNIT GENERATION DISPATCH IN CASE 0

| Hour | Unit 1 | Unit 2 | Unit 3 | Unit 4 | Unit 5 |
|---|---|---|---|---|---|
| 1 | 150.00 | 31.30 | 0.00 | 0.00 | 0.00 |
| 2 | 150.00 | 20.94 | 0.00 | 0.00 | 0.00 |
| 3 | 130.22 | 20.00 | 0.00 | 0.00 | 0.00 |
| 4 | 103.60 | 0.00 | 0.00 | 0.00 | 0.00 |
| 5 | 129.50 | 0.00 | 0.00 | 0.00 | 0.00 |
| 6 | 135.40 | 20.00 | 0.00 | 0.00 | 0.00 |
| 7 | 150.00 | 31.30 | 0.00 | 0.00 | 0.00 |
| 8 | 150.00 | 40.02 | 12.00 | 0.00 | 0.00 |
| 9 | 150.00 | 50.00 | 12.38 | 0.00 | 0.00 |
| 10 | 150.00 | 50.00 | 27.92 | 0.00 | 0.00 |
| 11 | 150.00 | 50.00 | 30.51 | 0.00 | 0.00 |
| 12 | 150.00 | 50.00 | 17.56 | 0.00 | 0.00 |
| 13 | 150.00 | 45.20 | 12.00 | 0.00 | 0.00 |
| 14 | 150.00 | 46.84 | 0.00 | 0.00 | 0.00 |
| 15 | 150.00 | 50.00 | 27.92 | 0.00 | 0.00 |
| 16 | 150.00 | 50.00 | 33.10 | 0.00 | 0.00 |
| 17 | 150.00 | 50.00 | 20.15 | 0.00 | 0.00 |
| 18 | 150.00 | 50.00 | 30.51 | 0.00 | 0.00 |
| 19 | 150.00 | 50.00 | 43.46 | 0.00 | 0.00 |
| 20 | 150.00 | 50.00 | 53.82 | 0.00 | 0.00 |
| 21 | 150.00 | 50.00 | 59.00 | 0.00 | 0.00 |
| 22 | 150.00 | 50.00 | 33.10 | 0.00 | 0.00 |
| 23 | 150.00 | 50.00 | 25.33 | 0.00 | 0.00 |
| 24 | 150.00 | 50.00 | 12.38 | 0.00 | 0.00 |

TABLE III
UC IN CASE 1

| Unit | Hours (1-24) |
|---|---|
| **1** | 1 1 1 1 1 1 1 1 1 1 1 1 1 1 1 1 1 1 1 1 1 1 1 1 |
| **2** | 1 1 1 **1 1** 1 1 1 1 1 1 1 1 1 1 1 1 1 1 1 1 1 |
| **3** | **1 1 1** 0 **1 1 1** 1 1 1 1 1 **1** 1 1 1 1 1 1 1 1 1 |
| **4** | **1 1** 0 0 0 0 **1 1 1 1 1 1 1 1 1 1 1 1 1 1 1 1 1 1** |
| **5** | 0 0 0 0 0 0 0 0 0 0 0 0 0 0 0 **1** 0 0 **1 1 1 1** 0 0 |

TABLE IV
UNIT GENERATION DISPATCH IN CASE 1

| Hour | Unit 1 | Unit 2 | Unit 3 | Unit 4 | Unit 5 |
|---|---|---|---|---|---|
| 1 | 83.21 | 50.00 | **40.95** | **10.00** | 0.00 |
| 2 | 82.54 | 50.00 | **31.09** | **10.00** | 0.00 |
| 3 | 82.65 | 50.00 | **20.26** | 0.00 | 0.00 |
| 4 | 77.14 | **28.44** | 0.00 | 0.00 | 0.00 |
| 5 | 80.11 | **39.68** | **12.00** | 0.00 | 0.00 |
| 6 | 82.98 | 50.00 | **25.15** | 0.00 | 0.00 |
| 7 | 80.11 | 50.00 | **40.95** | **10.00** | 0.00 |
| 8 | 84.50 | 50.00 | 60.60 | **10.00** | 0.00 |
| 9 | 85.20 | 50.00 | 70.38 | **10.00** | 0.00 |
| 10 | 82.76 | 50.00 | 68.29 | **30.21** | 0.00 |
| 11 | 82.43 | 50.00 | 68.37 | **33.08** | 0.00 |
| 12 | 84.08 | 50.00 | 73.21 | **13.59** | 0.00 |
| 13 | 84.87 | 50.00 | 65.41 | **10.00** | 0.00 |
| 14 | 84.17 | 50.00 | **55.64** | **10.00** | 0.00 |
| 15 | 82.76 | 50.00 | 68.29 | **30.21** | 0.00 |
| 16 | 85.20 | 50.00 | 80.00 | **11.03** | **10.00** |
| 17 | 83.93 | 50.00 | 69.02 | **20.43** | 0.00 |
| 18 | 82.43 | 50.00 | 68.37 | **33.08** | 0.00 |
| 19 | 83.91 | 50.00 | 80.00 | **22.77** | **10.00** |
| 20 | 82.64 | 50.00 | 80.00 | **34.48** | **10.00** |
| 21 | 82.00 | 50.00 | 80.00 | **40.36** | **10.00** |
| 22 | 85.20 | 50.00 | 80.00 | **11.03** | **10.00** |
| 23 | 83.25 | 50.00 | 69.11 | **26.30** | 0.00 |
| 24 | 85.20 | 50.00 | 70.38 | **10.00** | 0.00 |

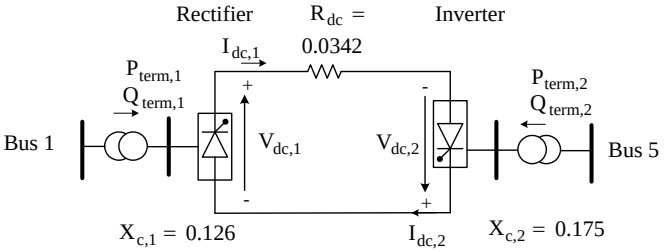


Fig. 5. Two-terminal DC transmission line

**Case 3:** A new SCUC is calculated to examine the impact of the DC line flows. Tables V and VI show the UC and ED results. The bold numbers show the difference between Cases 3 and 1. Compared with Case 1, the more expensive unit 3 is off at hours 3 and 6 to reduce the operating cost since the DC transmission system allows the cheapest unit 1 to increase its generation. In fact, the DC line can transfer additional power (compared to the AC line 1-5 flow in Case 1) from bus 1 to bus 5 which results in the mitigation of congestion on line 1-2 and the additional dispatch of cheapest unit 1. Consequently, it is not necessary to turn on the more expensive unit 3 for supplying the load at hour 3. In addition, the expensive units 4 & 5 are committed to maintain bus voltages within their limits. In this case, the system operating cost drops to $61,212.71 which is reduced by $64,086.07 - $61,212.71 = $2,873.36 as compared with Case 1.

TABLE V
UC IN CASE 3

| Unit | Hours (1-24) |
|---|---|
| **1** | 1 1 1 1 1 1 1 1 1 1 1 1 1 1 1 1 1 1 1 1 1 1 1 1 |
| **2** | 1 1 1 1 1 1 1 1 1 1 1 1 1 1 1 1 1 1 1 1 1 1 1 1 |
| **3** | 1 1 **0** 0 1 **0** 1 1 1 1 1 1 1 1 1 1 1 1 1 1 1 1 |
| **4** | 1 1 **1** 0 0 **1** 1 1 1 1 1 1 1 1 1 1 1 1 1 1 1 1 |
| **5** | 0 0 0 0 0 0 0 **1 1 1 1 1 1** 0 **1** 1 **1 1** 1 1 1 1 **1 1** |

TABLE VI
GENERATION DISPATCH IN CASE 3

| Hour | Unit 1 | Unit 2 | Unit 3 | Unit 4 | Unit 5 |
|---|---|---|---|---|---|
| 1 | 94.69 | 50.00 | 17.56 | 22.43 | 0.00 |
| 2 | 100.20 | 50.00 | 14.18 | 10.00 | 0.00 |
| 3 | 90.35 | 50.00 | **0.00** | **13.09** | 0.00 |
| 4 | 85.62 | 20.00 | 0.00 | 0.00 | 0.00 |
| 5 | 93.61 | 26.32 | 12.00 | 0.00 | 0.00 |
| 6 | 96.67 | 50.00 | **0.00** | **12.32** | 0.00 |
| 7 | 94.69 | 50.00 | 17.56 | 22.43 | 0.00 |
| 8 | 104.99 | 50.00 | 30.45 | 10.00 | **10.00** |
| 9 | 106.28 | 50.00 | 39.61 | 10.00 | **10.00** |
| 10 | 108.22 | 50.00 | 53.28 | 10.00 | **10.00** |
| 11 | 108.49 | 50.00 | 55.63 | 10.00 | **10.00** |
| 12 | 106.93 | 50.00 | 44.16 | 10.00 | **10.00** |
| 13 | 105.64 | 50.00 | 35.04 | 10.00 | **10.00** |
| 14 | 96.07 | 50.00 | 43.98 | 10.00 | 0.00 |
| 15 | 108.22 | 50.00 | 53.28 | 10.00 | **10.00** |
| 16 | 108.86 | 50.00 | 57.86 | 10.00 | **10.00** |
| 17 | 107.20 | 50.00 | 46.50 | 10.00 | 10.00 |
| 18 | 108.49 | 50.00 | 55.63 | 10.00 | **10.00** |
| 19 | 110.09 | 50.00 | 67.08 | 10.00 | **10.00** |
| 20 | 109.34 | 50.00 | 75.06 | 13.19 | 10.00 |
| 21 | 106.80 | 50.00 | 77.72 | 18.20 | 10.00 |
| 22 | 108.86 | 50.00 | 57.86 | 10.00 | 10.00 |
| 23 | 107.85 | 50.00 | 51.06 | 10.00 | **10.00** |
| 24 | 106.28 | 50.00 | 39.61 | 10.00 | **10.00** |

Table VII shows the hourly bus power mismatch per iteration. Bus power mismatches have decreased significantly at the second SCUC iteration in comparison with those at the first iteration. At the third SCUC iteration, the bus power mismatch at certain hours is smaller than the tolerance of 0.1 MVA. Consequently, no Benders cut are generated at those hours and the number of cuts have decreased from 24 at iteration 1 to 7 at iteration 5. There are no mismatches after 7 iterations. The economic control strategy of DC transmission system is devised based on the optimal operation of converters shown in Tables VIII and IX. This control scheme would be specified for each rectifier/inverter terminal in order to maintain two out of five control modes. Table X shows a set of 24-hour control strategies for the DC transmission system. At hour 1, the rectifier is operating at its minimum firing angle of $\alpha_r$ = 5 Deg (in Table VIII) and, according to Rules 1 and 3, the first control mode is CFA=5 Deg and the rectifier maintains CTR=1.09 pu. At this hour, the inverter maintains CC=129 A and CV=-1.10 pu.

TABLE VII
HOURLY NODAL MISMATCH PER ITERATION OF SCUC (MVA) IN CASE 3

| Hour | Iter1 | Iter2 | Iter3 | Iter4 | Iter5 | Iter6 | Iter7 |
|---|---|---|---|---|---|---|---|
| 1 | 106.00 | 28.34 | 13.24 | 3.09 | 0.28 | <0.1 | <0.1 |
| 2 | 41.90 | 45.43 | 17.97 | <0.1 | 4.21 | <0.1 | <0.1 |
| 3 | 67.29 | 11.05 | 4.38 | 13.37 | <0.1 | 3.59 | <0.1 |
| 4 | 0.35 | <0.1 | <0.1 | <0.1 | <0.1 | <0.1 | <0.1 |
| 5 | 22.75 | 5.32 | 3.31 | 6.63 | 2.77 | 0.28 | <0.1 |
| 6 | 27.87 | 25.70 | 5.36 | 15.48 | 1.55 | <0.1 | <0.1 |
| 7 | 106.00 | 28.34 | 13.24 | 3.09 | 0.28 | <0.1 | <0.1 |
| 8 | 44.61 | 10.33 | 20.10 | 8.41 | <0.1 | <0.1 | <0.1 |
| 9 | 47.99 | 29.36 | 10.25 | 0.17 | <0.1 | <0.1 | <0.1 |
| 10 | 50.44 | 25.74 | 13.46 | 0.15 | <0.1 | <0.1 | <0.1 |
| 11 | 50.91 | 24.92 | 14.19 | 0.24 | <0.1 | <0.1 | <0.1 |
| 12 | 48.88 | 28.27 | 10.60 | 0.19 | <0.1 | <0.1 | <0.1 |
| 13 | 46.30 | 33.25 | 15.13 | 15.22 | 0.47 | 0.42 | <0.1 |
| 14 | 56.33 | 42.80 | 15.18 | 17.70 | <0.1 | <0.1 | <0.1 |
| 15 | 50.44 | 25.74 | 13.46 | 0.15 | <0.1 | <0.1 | <0.1 |
| 16 | 51.38 | 24.21 | 14.90 | 0.12 | <0.1 | <0.1 | <0.1 |
| 17 | 49.34 | 27.62 | 11.31 | 0.31 | <0.1 | <0.1 | <0.1 |
| 18 | 50.91 | 24.92 | 14.19 | 0.24 | <0.1 | <0.1 | <0.1 |
| 19 | 53.33 | 21.02 | 18.42 | 0.18 | <0.1 | <0.1 | <0.1 |
| 20 | 55.05 | 18.28 | 18.34 | 0.23 | 0.16 | <0.1 | <0.1 |
| 21 | 58.34 | 22.78 | 0.78 | 0.35 | <0.1 | <0.1 | <0.1 |
| 22 | 51.38 | 24.21 | 14.90 | 0.12 | <0.1 | <0.1 | <0.1 |
| 23 | 49.97 | 26.55 | 12.75 | 0.12 | <0.1 | <0.1 | <0.1 |
| 24 | 47.99 | 29.36 | 10.25 | 0.17 | <0.1 | <0.1 | <0.1 |

TABLE VIII
RECTIFIER OPERATION STATUS IN CASE 3

| Hour | $P_{term}$ (MW) | $Q_{term}$ (MVar) | $V_{dc}$ (pu) | $I_{dc}$ (A) | α (Deg) | T (pu) |
|---|---|---|---|---|---|---|
| 1 | 44.69 | 13.42 | 1.11 | 129 | 5.00 | 1.09 |
| 2 | 50.20 | 16.00 | 1.12 | 145 | 5.00 | 1.10 |
| 3 | 40.35 | 11.93 | 1.07 | 121 | 5.00 | 1.05 |
| 4 | 35.62 | 9.56 | 1.11 | 104 | 5.00 | 1.08 |
| 5 | 43.59 | 13.60 | 1.08 | 130 | 6.08 | 1.06 |
| 6 | 46.67 | 14.32 | 1.11 | 135 | 5.00 | 1.09 |
| 7 | 44.69 | 13.42 | 1.11 | 129 | 5.00 | 1.09 |
| 8 | 54.99 | 18.51 | 1.11 | 160 | 5.00 | 1.10 |
| 9 | 56.28 | 19.22 | 1.11 | 164 | 5.00 | 1.10 |
| 10 | 58.22 | 20.32 | 1.10 | 170 | 5.00 | 1.10 |
| 11 | 58.48 | 20.55 | 1.10 | 171 | 5.39 | 1.10 |
| 12 | 56.94 | 19.58 | 1.10 | 166 | 5.00 | 1.10 |
| 13 | 55.63 | 18.93 | 1.10 | 162 | 5.00 | 1.10 |
| 14 | 46.07 | 14.05 | 1.11 | 133 | 5.00 | 1.09 |
| 15 | 58.22 | 20.32 | 1.10 | 170 | 5.00 | 1.10 |
| 16 | 58.87 | 20.68 | 1.10 | 172 | 5.00 | 1.10 |
| 17 | 57.20 | 19.77 | 1.11 | 166 | 5.28 | 1.10 |
| 18 | 58.48 | 20.55 | 1.10 | 171 | 5.39 | 1.10 |
| 19 | 60.09 | 21.35 | 1.10 | 176 | 5.00 | 1.10 |
| 20 | 59.33 | 20.86 | 1.10 | 173 | 5.00 | 1.10 |
| 21 | 56.80 | 19.45 | 1.11 | 165 | 5.00 | 1.10 |
| 22 | 58.87 | 20.68 | 1.10 | 172 | 5.00 | 1.10 |
| 23 | 57.84 | 20.15 | 1.10 | 169 | 5.30 | 1.10 |
| 24 | 56.28 | 19.22 | 1.11 | 164 | 5.00 | 1.10 |

TABLE IX
INVERTER OPERATION STATUS IN CASE 3

| Hour | $P_{term}$ (MW) | $Q_{term}$ (MVar) | $V_{dc}$ (pu) | $I_{dc}$ (A) | α (Deg) | T (pu) |
|---|---|---|---|---|---|---|
| 1 | -44.14 | 10.16 | -1.10 | 129 | 5.00 | 1.12 |
| 2 | -49.51 | 12.10 | -1.10 | 145 | 5.00 | 1.13 |
| 3 | -39.86 | 9.01 | -1.06 | 121 | 5.00 | 1.07 |
| 4 | -35.26 | 7.68 | -1.10 | 104 | 5.00 | 1.12 |
| 5 | -43.03 | 11.03 | -1.07 | 130 | 6.08 | 1.09 |
| 6 | -46.07 | 10.84 | -1.10 | 135 | 5.00 | 1.13 |
| 7 | -44.14 | 10.16 | -1.10 | 129 | 5.00 | 1.12 |
| 8 | -54.14 | 14.00 | -1.09 | 160 | 5.00 | 1.12 |
| 9 | -55.40 | 14.53 | -1.09 | 164 | 5.00 | 1.12 |
| 10 | -57.26 | 15.36 | -1.08 | 170 | 5.00 | 1.12 |
| 11 | -57.52 | 15.45 | -1.08 | 171 | 5.39 | 1.12 |
| 12 | -56.03 | 14.80 | -1.09 | 166 | 5.00 | 1.12 |
| 13 | -54.76 | 14.31 | -1.09 | 162 | 5.00 | 1.11 |
| 14 | -45.49 | 10.63 | -1.10 | 133 | 5.00 | 1.12 |
| 15 | -57.26 | 15.36 | -1.08 | 170 | 5.00 | 1.12 |
| 16 | -57.89 | 15.63 | -1.08 | 172 | 5.00 | 1.11 |
| 17 | -56.29 | 14.89 | -1.09 | 166 | 5.28 | 1.12 |
| 18 | -57.52 | 15.45 | -1.08 | 171 | 5.39 | 1.12 |
| 19 | -59.07 | 16.13 | -1.08 | 176 | 5.00 | 1.11 |
| 20 | -58.35 | 15.76 | -1.09 | 173 | 5.00 | 1.12 |
| 21 | -55.90 | 14.70 | -1.09 | 165 | 5.00 | 1.12 |
| 22 | -57.89 | 15.63 | -1.08 | 172 | 5.00 | 1.11 |
| 23 | -56.91 | 15.16 | -1.09 | 169 | 5.30 | 1.12 |
| 24 | -55.40 | 14.53 | -1.09 | 164 | 5.00 | 1.12 |

TABLE X
CONTROL STRATEGIES FOR DC TRANSMISSION SYSTEM IN CASE 3

| Hr. | Rectifier | | | | Inverter | | | |
|---|---|---|---|---|---|---|---|---|
| | First Control | | Second Control | | First Control | | Second Control | |
| | Mode | Value | Mode | Value | Mode | Value | Mode | Value |
| 1 | CFA | 5.00 Deg | CTR | 1.09 pu | CC | 129 A | CV | -1.10 pu |
| 2 | CFA | 5.00 Deg | CTR | 1.10 pu | CC | 145 A | CV | -1.10 pu |
| 3 | CFA | 5.00 Deg | CTR | 1.05 pu | CC | 121 A | CV | -1.06 pu |
| 4 | CFA | 5.00 Deg | CTR | 1.08 pu | CC | 104 A | CV | -1.10 pu |
| 5 | CC | 130 A | CV | 1.08 pu | CAE | 6.08 Deg | CP | -43.03MW |
| 6 | CFA | 5.00 Deg | CTR | 1.09 pu | CC | 135 A | CV | -1.10 pu |
| 7 | CFA | 5.00 Deg | CTR | 1.09 pu | CC | 129 A | CV | -1.10 pu |
| 8 | CFA | 5.00 Deg | CTR | 1.10 pu | CC | 160 A | CV | -1.09 pu |
| 9 | CFA | 5.00 Deg | CTR | 1.10 pu | CC | 164 A | CV | -1.09 pu |
| 10 | CFA | 5.00 Deg | CTR | 1.10 pu | CC | 170 A | CV | -1.08 pu |
| 11 | CC | 171 A | CP | 58.48MW | CAE | 5.39 Deg | CV | -1.08 pu |
| 12 | CFA | 5.00 Deg | CTR | 1.10 pu | CC | 166 A | CV | -1.09 pu |
| 13 | CFA | 5.00 Deg | CTR | 1.10 pu | CC | 162 A | CV | -1.09 pu |
| 14 | CFA | 5.00 Deg | CTR | 1.09 pu | CC | 133 A | CV | -1.10 pu |
| 15 | CFA | 5.00 Deg | CTR | 1.10 pu | CC | 170 A | CV | -1.08 pu |
| 16 | CFA | 5.00 Deg | CTR | 1.10 pu | CC | 172 A | CV | -1.08 pu |
| 17 | CC | 166 A | CP | 57.20MW | CAE | 5.28 Deg | CV | -1.09 pu |
| 18 | CC | 171 A | CV | 1.10 pu | CAE | 5.39 Deg | CP | -57.52MW |
| 19 | CFA | 5.00 Deg | CTR | 1.10 pu | CC | 176 A | CV | -1.08 pu |
| 20 | CFA | 5.00 Deg | CTR | 1.10 pu | CC | 173 A | CV | -1.09 pu |
| 21 | CFA | 5.00 Deg | CTR | 1.10 pu | CC | 165 A | CV | -1.09 pu |
| 22 | CFA | 5.00 Deg | CTR | 1.10 pu | CC | 172 A | CV | -1.08 pu |
| 23 | CC | 169 A | CV | 1.10 pu | CAE | 5.30 Deg | CP | -56.91MW |
| 24 | CFA | 5.00 Deg | CTR | 1.10 pu | CC | 164 A | CV | -1.09 pu |

The control mode at hours 2-4 is the same as that at hour 1. At hour 5, neither the rectifier firing angle nor the inverter extinction angle reaches its minimum. According to Rules 1 and 2, the rectifier would maintain CC=130 A. The second rectifier control mode is CV=1.08 pu. At this hour, the first inverter control mode is CAE=6.08 Deg and its second control mode is CP=-43.03 MW. The alternative second inverter control modes are CTR=1.09 pu or CV=-1.07 pu.

**Case 4:** Using the UC results in Table III, the system state can be transferred from base case to a new state in the event of line 2-3 outage (CTGL2-3) without any changes in UC. Only the generating unit dispatch is changed in accordance with (30). This is a controllable contingency and only corrective actions (changing the generation dispatch based on units physical ramping) are required in real time to mitigate violations. The total operating cost is $64,849.43 which is higher than that without the contingency (Case 1).

**Case 5:** If CTGL2-3 occurs in the AC/DC transmission system described in Case 2, the system security would not be satisfied based on the UC results in Table V. The bus mismatches at hours 3,4, and 6 cannot be eliminated by only changing the generation dispatch (corrective actions). Consequently, 3 Benders cuts (42) are generated to change the UC results. In this case, generating unit 3 is committed (preventive actions) at hours 3,4 and 6 to satisfy the system security in the event of CTGL2-3. In Table XI, the UC changes in comparison to that in Case 3 are shown in bold. The total operating cost increases to $64,269.91.

**Case 6:** In this case, we run the SCUC when the DC system is a fixed injection at buses 1 and 5 at all hours. We also assume that the power factor at rectifier and inverter terminals is 0.98 and the DC line has no losses. Fig. 6 shows the total operating cost when the DC transmission system is modeled with different injections between 30 MW and 55 MW. It is obvious that the proposed model would result in lower costs. There is no feasible SCUC solution when power flow injections are smaller than 30 MW or higher than 55 MW.

TABLE XI
UC IN CASE 5

| Unit | Hours (1-24) |
|---|---|
| **1** | 1 1 1 1 1 1 1 1 1 1 1 1 1 1 1 1 1 1 1 1 1 1 1 1 |
| **2** | 1 1 1 1 1 1 1 1 1 1 1 1 1 1 1 1 1 1 1 1 1 1 1 1 |
| **3** | 1 1 **1 1** 1 **1** 1 1 1 1 1 1 1 1 1 1 1 1 1 1 |
| **4** | 1 1 1 0 0 1 1 1 1 1 1 1 1 1 1 1 1 1 1 1 1 1 1 1 |
| **5** | 0 0 0 0 0 0 0 1 1 1 1 1 1 0 1 1 1 1 1 1 1 1 1 1 |

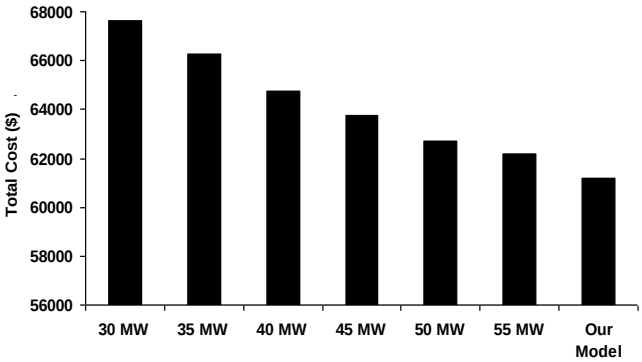


Fig. 6. Total generation costs for DC system with fixed injections

### *B. IEEE 118- Bus System*

We consider a modified IEEE 118-bus system shown in Fig. 7 to study the proposed model. This system has 54 units, 186 branches, 14 capacitors, 9 tap-changing transformers, and 91 demand sides. The peak load of the system is 6000 MW that

occurs at hour 21. The 118-bus system data are given at http://motor.ece.iit.edu/DC/CSC/IEEE118.xls.

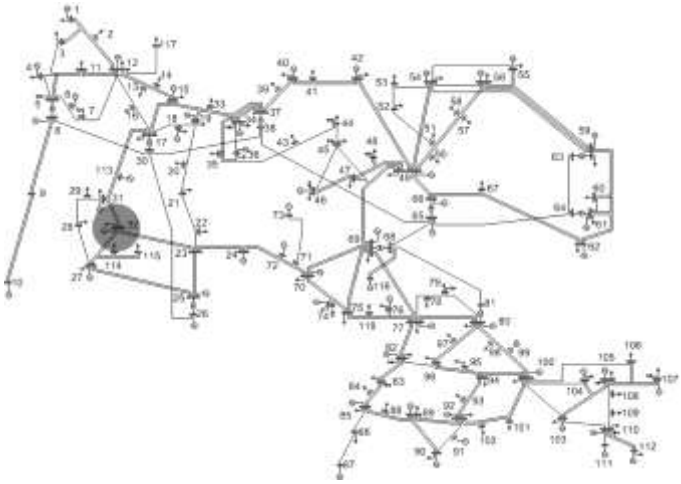

Fig. 7. IEEE 118-bus system

The following cases are tested.

**Case 0:** Base case without transmission constraints
**Case 1:** SCUC solution with AC transmission constraints
**Case 2:** SCUC solution when the AC line 32-113 is replaced with a two-terminal DC transmission system. The rectifier terminal is connected to bus 113 and the inverter terminal to bus 32 with the same parameters as those in Table C.6. This DC system is installed in the congested area based on SCUC results obtained in Case 1. The congested area is highlighted in Fig. 7.

The operating cost of UC in Case 0 is $1,727,170 which increases to $1,732,274 when the AC transmission constraints are considered in Case 1. The additional $5,103.64 cost is mainly due to the congestion of AC line 23-32 at peak hours which causes the commitment of expensive units. Case 2 replaces the AC line 32-113 with a two-terminal DC transmission line which results in an operating cost of $1,729,950. The DC transmission flow has decreased the transmission congestion cost of AC line 23-32 from $5,103.64 to $2,780 when it transfers more power from bus 113 to bus 32. In Case 2, at the peak hour, the flow on DC transmission line 32-113 increases to 38.22 MW in comparison to 3 MW in Case 1.

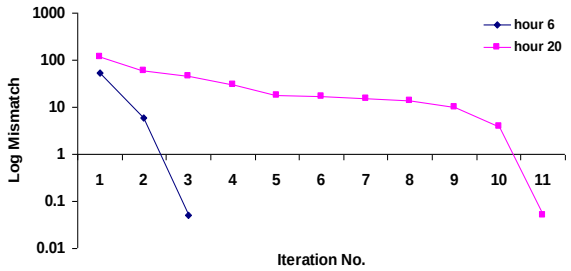


Fig. 8. Total hourly nodal mismatch in case 2

Fig. 8 shows the convergence results for Case 2 at hours 6 and 20. Here additional iterations are required for SCUC to converge at higher load hours (11 iterations at hour 20) as compared to those at low-load hours (3 iterations at hour 6).

## V. Conclusions

In this paper, controllable DC transmission systems are modeled in SCUC along with AC transmission systems. Benders decomposition is applied to effectively handle both AC and DC transmission constraints. The SCUC solution determines the optimal selection of DC control strategies and optimal hourly DC transmission schedule at the minimum cost while maintaining the system security. A set of optimal controls for DC transmission systems can successfully mitigate the AC transmission flow congestion and enhance power system economics. We compared the proposed model with a simplified DC transmission system model with fixed power flow injections/withdrawals that was widely used in SCUC. The simplified DC model may not provide a feasible SCUC solution while the proposed SCUC model guarantees the convergence. The test results also indicate that a given UC solution for an AC transmission system may not result in a feasible once the AC lines are partly replaced by DC lines. Additional adjustments in UC and ED, and transmission control are needed to ensure the feasibility.

## VI. References


[1] K.R. Padiyar, *HVDC Power Transmissions, New York*, Wiley, 1990.
[2] A.E. Hammad and W.F. Long, "Performance and economic comparisons between point-to-point HVDC transmission and hybrid back-to-back HVDC/AC transmission," *IEEE Transaction on Power Delivery*, Vol. 5, No. 2, pp. 1137 - 1144, April 1990.
[3] S. Wang, J. Zhu, L. Trinh, and J. Pan, "Economic assessment of HVDC project in deregulated energy markets," *Third Int. Conf. on Electric Utility Deregulation and Restructuring and Power Technologies*, China, April 2008.
[4] X.P. Zhang and L. Yao, "A vision of electricity network congestion management with FACTS and HVDC," *Third Int. Conf. on Electric Utility Deregulation and Restructuring and Power Technologies*, China, April 2008.
[5] E.W. Kimbark, *Direct Current Transmission*, Wiley, 1971.
[6] M. Ishikawa, S. Horiuchi, S. Hirose, T. Sakai, and T. Horiuchi, "HVDC transmission control equipment with high reliability", *IEEE Transaction on Power Systems*, Vol. PWRD-1, No. 2, pp. 254-263, April 1986.
[7] P. Kundur, *Power System Stability and Control*, McGraw- Hill, 1994.
[8] J. Arrillaga, Y.H. Liu, and N.R. Watson, *Flexible Power Transmission: The HVDC options*, Wiley, 2007.
[9] C.N. Lu, S.S. Chen, and C.M. Ong, "The incorporation of HVDC equations in optimal power flow methods using sequential quadratic programming technique," *IEEE Trans. Power Systems*, Vol. 3, No. 3, pp. 1005-1011, Aug. 1988.
[10] H. Ambriz-Perez, E. Acha, and C.R. Fuerte-Esquivel, "High voltage direct current modelling in optimal power flows," *Electrical Power & Energy Systems*, (30) 2008, 157-168.
[11] M.M. El-Marsafawy and R.M. Mathur, "A new, fast technique for load flow solution of integrated multi-terminal DC/AC systems," *IEEE Trans. on PAS*, Vol. PAS-99, No. 1, pp. 246-255, Jan/Feb 1980.
[12] J. Reeve, G. Fahny, and B. Stott, "Versatile load flow method for multi-terminal HVDC systems," *IEEE Trans. Power Apparatus and Systems*, Vol. PAS-96, No. 3, pp. 925-933, May/June 1977.
[13] T. Smed, G. Anderson, G.B. Sheble, and L.L. Grigsby, "A new approach to AC/DC power flow," *IEEE Trans. Power Systems*, Vol. 6., No. 3, pp. 1238-1244, August 1991.
[14] V. Sarkar and S.A. Khaparde, "Implementation of LMP-FTR mechanism in an AC-DC system," *IEEE Trans. Power Systems*, Vol. 23, No. 2, pp. 737-746, May 2008.
[15] Z. Li and M. Shahidehpour, "Security-constrained unit commitment for simultaneous clearing of energy and ancillary services markets," *IEEE Trans. Power Systems*, Vol. 20, No. 2, pp. 1079-1088 May 2005.
[16] S. Harvey, "Internal NYISO HVDC controllable line scheduling: concept of operation," *http://www.nyiso.com*, May 2004.

[17] N. Stretch, M. Kazerani, and R.E. ShatShat, "A current-sourced converter based HVDC light transmission system," *IEEE Int. Symp. on Industrial Electronics, Vol. 3, July 2006.*

[18] A. Pizano-Martinze, C.R. Fuerte-Esquivel, H. Ambirz-Perez, E. Acha, "Modeling of VSC-Based DC Systems for a Newton-Raphson OPF Algorithm," *IEEE Transaction on Power System*, Vol. 22, No. 4, pp. 1794-1803, Nov. 2007.

[19] X.P. Zhang, "Multiterminal Voltage-Sourced Converter-Based DC Models for Power Flow Analysis," *IEEE Transactions on Power Systems*, Vol. 19, No. 4, pp. 1877-1884, Nov. 2004.

[20] X. Wei, J.H. Chow, B. Fardanesh, A.A. Edris, "A Common Modeling Framework of Voltage-Sourced Converters for Load Flow, Sensitivity, and Dispatch Analysis," *IEEE Transactions on Power Systems*, Vol. 19, No. 2, pp. 934-941, May 2004.

[21] Y. Fu, M. Shahidehpour, and Z. Li, "AC contingency dispatch based on security-constrained unit commitment," *IEEE Transactions on Power System*, vol. 21, no. 2, pp. 897-908, May 2006.

[22] D.A. Braunagel, L.A. Kraft, and J. L. Whysong, "Inclusion of DC converter and transmission equations directly in a Newton power flow,", *IEEE Trans. on Power Apparatus and Systems*, Vol. PAS-95, No. 1, pp. 76-88, 1976.

[23] M. Shahidehpour, H. Yamin, and Z. Li, *Market Operations in Electric Power Systems*, Wiley, 2002.

[24] Y. Fu, M. Shahidehpour, "Fast SCUC for large-scale power systems," *IEEE Trans. Power Systems*, Vol. 22, pp. 2144-2151, Nov 2007.

[25] Y. Fu, M. Shahidehpour, and Z. Li, "Security constrained unit commitment with AC Constraints," *IEEE Trans. Power Systems*, Vol. 20, No. 2, pp. 1001-1013, May 2005.


## BIOGRAPHIES

**Azim Lotfjou** received his BS and MS in E.E. from Sharif University of Technology, Tehran, in 2001 and 2004, respectively. Presently, he is a research assistant while completing his Ph.D degree at Illinois Institute of Technology.

**Mohammad Shahidehpour** (F'01) is a Carl Bodine Professor in the Electrical and Computer Engineering Department at Illinois Institute of Technology (IIT). He is Vice President of Publication for the IEEE Power and Energy Society of IEEE.

**Yong Fu** (M'05) received his BS and MS in E.E. from Shanghai Jiaotong University, China, in 1997 and 2002, respectively and Ph.D degree in E.E. from Illinois Institute of Technology, USA, in 2006.

**Zuyi Li** (M'01) is an Associate Professor in the Electrical and Computer Engineering Department at Illinois Institute of Technology.

## Appendix A: Base for Per Unit Values

The base values for AC/DC transmission systems are listed in Table A.1.

TABLE A.1
AC AND DC BASE VALUES

| AC Base | DC Base |
|---|---|
| $V_{base}$ (kV) | $V_{dc,base} = \frac{3\sqrt{2}}{\pi} V_{base}$ (kV) |
| $S_{base}$ (MVA) | $P_{dc,base} = V_{dc,base} I_{dc,base} = S_{base}$ (MW) |
| $I_{base} = \frac{S_{base}}{\sqrt{3} V_{base}}$ (kA) | $I_{dc,base} = \frac{\pi}{\sqrt{6}} I_{base}$ (kA) |
| $Z_{base} = \frac{V_{base}^2}{S_{base}} = \frac{V_{base}}{\sqrt{3} I_{base}}$ ($\Omega$) | $Z_{dc,base} = \frac{V_{dc,base}}{I_{dc,base}} = \frac{18}{\pi^2} Z_{base}$ ($\Omega$) |
| | $X_{c,base} = \frac{6}{\pi} Z_{base}$ ($\Omega$) |

## Appendix B: AC/CSC-DC Jacobian Matrices

Reference [21] provides the Jacobian matrices **J1** and **J2** related to the AC system. The non-zero elements of Jacobian matrix **J1** related to the DC transmission system are

$$\frac{\partial \Delta P_m}{\partial V_{dc,h}} = -I_{dc,h}, \quad \frac{\partial \Delta P_m}{\partial I_{dc,h}} = -V_{dc,h}, \quad \frac{\partial \Delta Q_m}{\partial V_{dc,h}} = -I_{dc,h} \tan \phi_h$$

$$\frac{\partial \Delta Q_m}{\partial I_{dc,h}} = -V_{dc,h} \tan \phi_h, \quad \frac{\partial \Delta Q_m}{\partial \phi_h} = -V_{dc,h} I_{dc,h} \left(\frac{1}{\cos \phi_h^2}\right)$$

$$\frac{\partial \Delta R1_h}{\partial V_m} = \begin{cases} -T_h \cos \alpha_h & \text{for rectifier} \\ +T_h \cos \alpha_h & \text{for inverter} \end{cases}$$

$$\frac{\partial \Delta R1_h}{\partial V_{dc,h}} = 1, \quad \frac{\partial R1_h}{\partial I_{dc,h}} = \begin{cases} -X_{c,h} & \text{for rectifier} \\ +X_{c,h} & \text{for inverter} \end{cases}$$

$$\frac{\partial \Delta R1_h}{\partial T_h} = \begin{cases} +V_m \cos \alpha_h & \text{for rectifier} \\ -V_m \cos \alpha_h & \text{for inverter} \end{cases}$$

$$\frac{\partial \Delta R1_h}{\partial \alpha_h} = \begin{cases} +T_h V_m \sin \alpha_h & \text{for rectifier} \\ -T_h V_m \sin \alpha_h & \text{for inverter} \end{cases}$$

$$\frac{\partial \Delta R2_h}{\partial V_m} = \begin{cases} -0.995\, T_h \cos \phi_h & \text{for rectifier} \\ +0.995\, T_h \cos \phi_h & \text{for inverter} \end{cases}, \quad \frac{\partial \Delta R2_h}{\partial V_{dc,h}} = 1$$

$$\frac{\partial \Delta R2_h}{\partial T_h} = \begin{cases} -0.995\, V_m \cos \phi_h & \text{for rectifier} \\ +0.995\, V_m \cos \phi_h & \text{for inverter} \end{cases}$$

$$\frac{\partial \Delta R2_h}{\partial \phi_h} = \begin{cases} +0.995\, T_h V_m \sin \phi_h & \text{for rectifier} \\ -0.995\, T_h V_m \sin \phi_h & \text{for inverter} \end{cases}$$

The partial derivatives of $\Delta R3_h$ depend on the of the DC configuration. For example, the partial derivatives of $\Delta R3_h$ for the two-terminal DC system shown in Fig. 5 are

$$\frac{\partial \Delta R3_1}{\partial I_{dc,1}} = 1, \frac{\partial \Delta R3_1}{\partial V_{dc,1}} = -\frac{1}{R_{dc}}, \frac{\partial \Delta R3_1}{\partial V_{dc,2}} = -\frac{1}{R_{dc}}$$

$$\frac{\partial \Delta R3_2}{\partial I_{dc,2}} = 1, \frac{\partial \Delta R3_2}{\partial V_{dc,1}} = -\frac{1}{R_{dc}}, \frac{\partial \Delta R3_2}{\partial V_{dc,2}} = -\frac{1}{R_{dc}}$$

where the subscribe 1 represents the rectifier, 2 for the inverter. Similarly, since the elements of Jacobian matrix **J3** depend on the DC configuration, we list non-zero elements of **J3** for the two-terminal DC transmission system shown in Fig. 5 as

$$\frac{\partial \Delta PL_{dc,1-2}}{\partial V_{dc,1}} = I_{dc,1}, \frac{\partial \Delta PL_{dc,1-2}}{\partial I_{dc,1}} = V_{dc,1}$$

$$\frac{\partial \Delta PL_{dc,2-1}}{\partial V_{dc,2}} = -I_{dc,2}, \frac{\partial \Delta PL_{dc,2-1}}{\partial I_{dc,2}} = -V_{dc,2}$$

where the subscribe 1 represents the rectifier, 2 for the inverter. The elements of Jacobian matrix **J4** are listed as,

$$\frac{\partial \Delta P_{term,h}}{\partial V_{dc,h}} = I_{dc,h}, \quad \frac{\partial \Delta P_{term,h}}{\partial I_{dc,h}} = V_{dc,h}$$

## Appendix C: IEEE 14-Bus System Data

TABLE C.1 UNIT DATA

| Unit | Bus No. | Bid ($/MW) | Pmin (MW) | Pmax (MW) | Qmin (MVar) | Qmax (MVar) | Min On/Off (h) |
|---|---|---|---|---|---|---|---|
| 1 | 1 | 8 | 50 | 150 | -100 | 100 | 1 |
| 2 | 2 | 10 | 20 | 50 | -50 | 50 | 1 |
| 3 | 3 | 18 | 12 | 80 | -60 | 100 | 1 |
| 4 | 6 | 25 | 10 | 45 | -30 | 30 | 1 |
| 5 | 8 | 40 | 10 | 45 | -30 | 30 | 1 |

TABLE C.2 BUS DATA

| Bus No. | Min Voltage (pu) | Max Voltage (pu) | Bus No. | Min Voltage (pu) | Max Voltage (pu) |
|---|---|---|---|---|---|
| 1 | 1.04 | 1.07 | 8 | 1.02 | 1.10 |
| 2 | 1.03 | 1.05 | 9 | 1.00 | 1.03 |
| 3 | 1.00 | 1.02 | 10 | 1.00 | 1.05 |
| 4 | 1.00 | 1.03 | 11 | 0.98 | 1.05 |
| 5 | 1.00 | 1.04 | 12 | 1.04 | 1.07 |
| 6 | 1.05 | 1.10 | 13 | 1.01 | 1.07 |
| 7 | 1.01 | 1.05 | 14 | 0.98 | 1.07 |

TABLE C.3 AC BRANCH DATA

| Line No. | From Bus | To Bus | R (pu) | X (pu) | Charging Shunt (pu) | Flow Limit (MW) |
|---|---|---|---|---|---|---|
| 1 | 1 | 2 | 0.0194 | 0.0592 | 0.0264 | 50 |
| 2 | 1 | 5 | 0.0540 | 0.2230 | 0.0246 | 65 |
| 3 | 2 | 3 | 0.0470 | 0.1980 | 0.0219 | 60 |
| 4 | 2 | 4 | 0.0581 | 0.1763 | 0.0187 | 60 |
| 5 | 2 | 5 | 0.0570 | 0.1739 | 0.0170 | 60 |
| 6 | 3 | 4 | 0.0670 | 0.1710 | 0.0173 | 60 |
| 7 | 4 | 5 | 0.0134 | 0.0421 | 0.0064 | 40 |
| 8 | 4 | 7 | 0.0000 | 0.2091 | 0.0000 | 65 |
| 9 | 4 | 9 | 0.0000 | 0.5562 | 0.0000 | 40 |
| 10 | 5 | 6 | 0.0000 | 0.2520 | 0.0000 | 65 |
| 11 | 6 | 11 | 0.0950 | 0.1989 | 0.0000 | 50 |
| 12 | 6 | 12 | 0.1229 | 0.1558 | 0.0000 | 50 |
| 13 | 6 | 13 | 0.0662 | 0.1303 | 0.0000 | 50 |
| 14 | 7 | 8 | 0.0000 | 0.1762 | 0.0000 | 50 |
| 15 | 7 | 9 | 0.0000 | 0.1100 | 0.0000 | 30 |
| 16 | 9 | 10 | 0.0318 | 0.0845 | 0.0000 | 50 |
| 17 | 9 | 14 | 0.1271 | 0.2704 | 0.0000 | 50 |
| 18 | 10 | 11 | 0.0821 | 0.1921 | 0.0000 | 50 |
| 19 | 12 | 13 | 0.2209 | 0.1999 | 0.0000 | 50 |
| 20 | 13 | 14 | 0.1709 | 0.3480 | 0.0000 | 50 |

TABLE C.4 DISTRIBUTION FACTORS OF LOADS AT DIFFERENT BUSES

| Load | At Bus | MW Load Factor | MVar Load Factor |
|---|---|---|---|
| 1 | 2 | 0.0838 | 0.1728 |
| 2 | 3 | 0.3637 | 0.2585 |
| 3 | 4 | 0.1846 | -0.0531 |
| 4 | 5 | 0.0293 | 0.0218 |
| 5 | 6 | 0.0432 | 0.1020 |
| 6 | 9 | 0.1139 | 0.2259 |
| 7 | 10 | 0.0347 | 0.0789 |
| 8 | 11 | 0.0135 | 0.0245 |
| 9 | 12 | 0.0236 | 0.0218 |
| 10 | 13 | 0.0521 | 0.0789 |
| 11 | 14 | 0.0575 | 0.0680 |

TABLE C.5 HOURLY LOAD DISTRIBUTION

| Hour | MW | MVar | Hour | MW | MVar |
|---|---|---|---|---|---|
| 1 | 181.30 | 51.45 | 13 | 207.20 | 58.80 |
| 2 | 170.94 | 48.51 | 14 | 196.84 | 55.86 |
| 3 | 150.22 | 42.63 | 15 | 227.92 | 64.68 |
| 4 | 103.60 | 29.40 | 16 | 233.10 | 66.15 |
| 5 | 129.50 | 36.75 | 17 | 220.15 | 62.48 |
| 6 | 155.40 | 44.10 | 18 | 230.51 | 65.42 |
| 7 | 181.30 | 51.45 | 19 | 243.46 | 69.09 |
| 8 | 202.02 | 57.33 | 20 | 253.82 | 72.03 |
| 9 | 212.38 | 60.27 | 21 | 259.00 | 73.50 |
| 10 | 227.92 | 64.68 | 22 | 233.10 | 66.15 |
| 11 | 230.51 | 65.42 | 23 | 225.33 | 63.95 |
| 12 | 217.56 | 61.74 | 24 | 212.38 | 60.27 |

TABLE C.6 CONVERTER DATA FOR THE DC TRANSMISSION SYSTEM

| Type | $X_c$ (pu) | $\alpha_{\min}$ (Deg) | $\alpha_{\min}$ (Deg) | $V_{dc,\min}$ (pu) | $V_{dc,\max}$ (pu) | Min Tap | Max Tap |
|---|---|---|---|---|---|---|---|
| Rec. | 0.126 | 5 | 30 | 0.95 | 1.20 | 0.9 | 1.1 |
| Inv. | 0.175 | 5 | 30 | 0.90 | 1.10 | 0.9 | 1.5 |

TABLE C.7 DC BUS DATA FOR THE DC TRANSMISSION SYSTEM

| Bus No. | Min Voltage (pu) | Max Voltage (pu) |
|---|---|---|
| 1 | 0.95 | 1.20 |
| 2 | 0.90 | 1.10 |

TABLE C.8 DC BRANCH DATA

| Line No. | From DC Bus | To DC Bus | R (pu) | Flow Limit (MW) |
|---|---|---|---|---|
| 1 | 1 | 5 | 0.0342 | 65 |

# Transmission Congestion Analysis in the Eastern Interconnection using POMS

Wei Tian, *Student Member*, Zuyi Li, *Senior Member*, and Mohammad Shahidehpour, *Fellow, IEEE*

***Abstract*—A methodology based on the security-constrained unit commitment (SCUC) is applied to analyze the transmission congestion in the Eastern Interconnection of the United States for 2008 and 2018. The proposed SCUC tool for this study is referred to as the POwer Market Simulator (POMS). The identified congestions are visualized along with the Geographical Information System (GIS) data and compared with the results published by the U.S. Department of Energy's National Electric Transmission Congestion Study (NETCS) in 2006. The POMS study also provides the locational marginal price (LMP) information in the Eastern Interconnection, which is not available in the NETCS report. The POMS simulation results for representing congested branches and LMPs could be applied to the future transmission expansion planning studies.**

***Index Terms*—Transmission Congestion, SCUC, LMP, National Electric Transmission Congestion Study, Eastern Interconnection in the United States**

## I. Introduction

THE identification of possible congestion sites is the first step in any grid expansion and reinforcement studies. The Federal Power Act (FPA) 216(a) resulted in a study of the electric transmission congestion in the United States [1]. The first congestion study report, known as the National Electric Transmission Congestion Study (NETCS) and issued in August 2006, identified congestions and constraints in the Eastern and the Western Interconnections [2]. The NETCS report included the review of the available information on historical congestion, the simulation of future congestions, and the comparison of simulation results with the historical information. Another published report analyzes the available 2007 data for assessing the transmission congestion in the Eastern Interconnection [3]. For the purpose of comparison, this paper will focus on the NETCS in 2006.

This paper focuses on the congestion studies in the Eastern Interconnection of the U.S. by applying SCUC. In addition, the congestion and LMP results are visualized along with the GIS data. The rest of this paper is organized as follows. Section II describes the proposed methodology for indentifying congestions and presents the congestion study results for the Eastern Interconnection in 2008 and 2018. The study results of 2008 are also compared with the results in the NETCS report. Section III concludes this paper.

## II. Methodology for Identifying Congestion

### A. Congestion Simulation

The tool used for this study is called POwer Market Simulator (POMS), which has been used extensively for power system studies for decades. The methodology in POMS simulates the hourly electricity market operation based on SCUC for identifying possible congestions[1]. The POMS simulation results have several advantages over those of the optimal power flow (OPF). A POMS simulation study considering the commitment and the redispatch of generating units will provide a more realistic picture of possible scenarios. In essence, it may be necessary to consider potential changes in the hourly unit commitment to satisfy certain constraints.

The POMS applications to the Eastern Interconnection simulation consider a decomposition and coordination strategy shown in Fig. 1. A similar procedure is followed for considering contingencies [4]-[7].

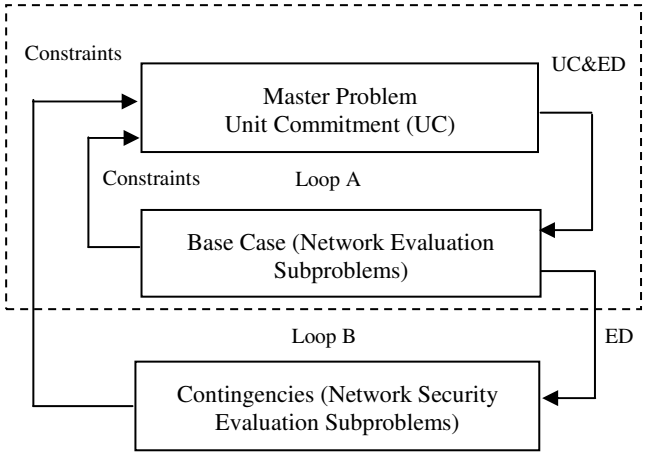


Fig. 1 SCUC Solution for the Eastern Interconnection

In this section, we utilize POMS to simulate the congestions in the Eastern Interconnection based on the 2008 and 2018 data. We compare the POMS simulation results with those in the NETCS report, referred to as NETCS results thereafter, and analyze the variations in the POMS simulation results from 2008 to 2018. Note that there are about 70,000 branches at all voltage levels in the Eastern Interconnection. We consider in the POMS simulation only those branches that are above 200kV along with 1,000 flowgates.

### B. POMS Simulation Results for 2008

In this case, POMS is applied to simulate the 8,760 hours of generation dispatch and transmission flows in the Eastern Interconnection in 2008. The pertinent definitions are provided in Appendix A.

This study is funded by the U.S. Department of Energy Grants # DE-EE 0002979 and DE-EE 0001380.000. The authors are with the Electrical and Computer Engineering Department, Illinois Institute of Technology, Chicago, IL 60616 USA. (E-mail:wtian3@iit.edu, lizu@iit.edu, ms@iit.edu).

[1] The congestion in this paper is defined as a state in which the flow on a branch has reached the branch capacity.

*B1) Transmission Congestions based on the Binding Hours Metric*

The POMS simulation results show that in 2008 there are 1,325 congested branches[2], 270 of which are congested in all hours. The most congested branches are in the New York and the Chicago regions. There are also several congested branches in the boundary between Georgia and Florida. Fig. 2 shows the zoomed-out version of the congested branches based on the binding hours metric.

*B2) Constrained Branches based on the U90 Hours Metric*

As expected, more transmission branches are constrained based on the U90 hours metric. There are 2,497 U90 branches[3], 483 of which are continuously loaded above 90% of their capacities. The U90 branches are again concentrated in the New York region, the Chicago region, and the boundary between Georgia and Florida. Fig. 3 shows the zoomed-out version of constrained branches based on the U90 hours metric.

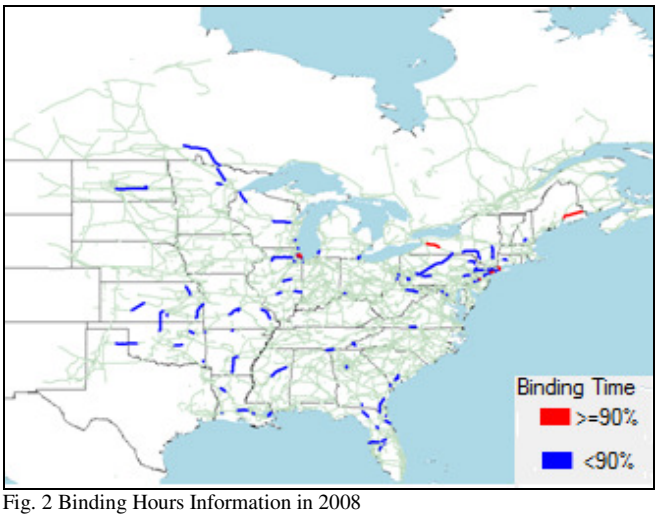


Fig. 2 Binding Hours Information in 2008

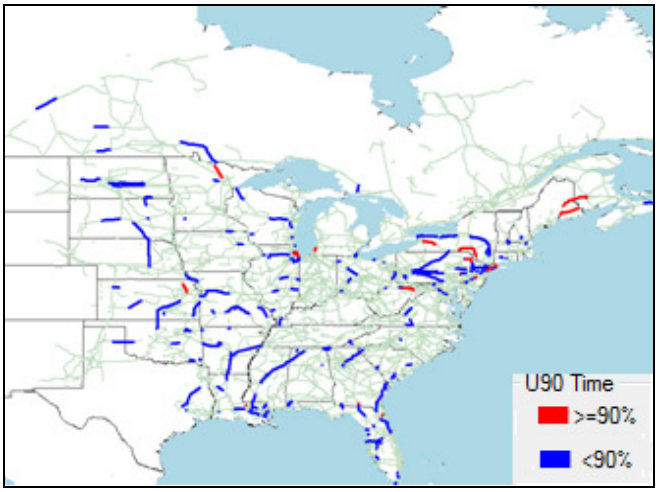


Fig. 3 U90 Hours Information in 2008

*B3) Number of Constrained Branches*

Fig. 4 shows the number of constrained branches as a percentage of time. There are 1,325 congested branches and 439 (i.e. 33%) of these branches are congested in more than 80% of the annual hours and 600 (i.e. 45%) are congested in less than 20% of the annual hours. The U90 curve in Fig. 4 has a similar trend except that more branches are constrained based on the U90 metric. It is expected that more branches would be constrained if U75 was used as the metric.

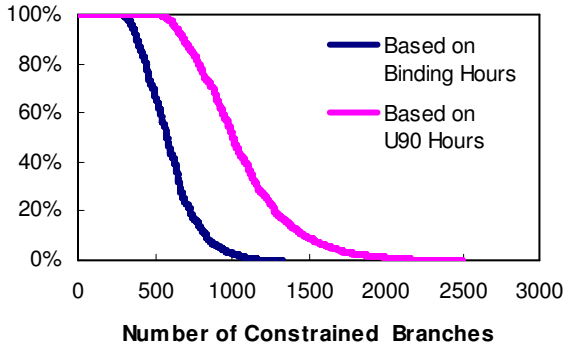


Fig. 4 Constrained Branches as a Function of Time in 2008

*B4) Locational Marginal Prices*

Fig. 5 shows the 2008 annual average LMPs based on the POMS simulation results. The New York region shows the highest LMPs in the Eastern Interconnection because of its limited generation capacity. Due to the existing transmission congestions, much of the low cost power from neighboring regions cannot be transmitted to the New York region. So, the LMPs in the New York region are high due to its dependence on local expensive units such as gas units and oil units for supplying the local load. The LMPs in New England and Florida are relatively high for similar reasons. Even though the Chicago region also exhibits transmission congestion, the LMPs are not as high which is partly due to the cheap coal-fired and nuclear power generation close to the load centers. Large wind developments in the Midwest could provide large sums of low cost energy to the Midwest energy markets. So, LMPs in the northwest region of the Midwest are relatively low.

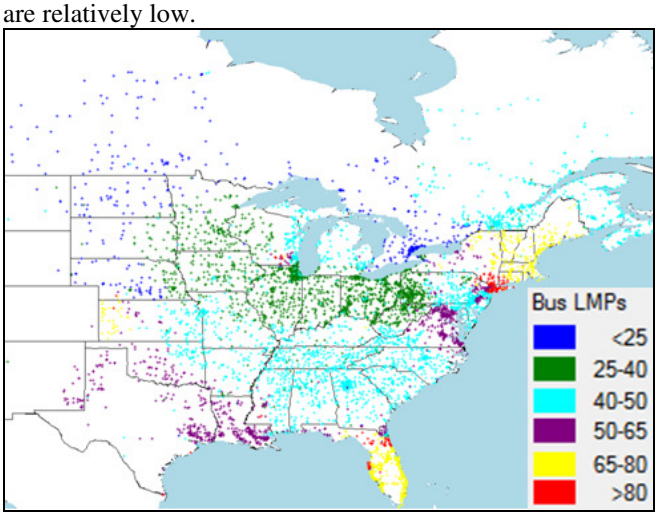


Fig. 5 Annual Average of LMPs in 2008

*B5) Cost of Served Load and Congestion Cost*

Based on the 2008 POMS simulation, the total cost of served load is about $172.3 billion. The total congestion cost is about $13 billion which is about 7.5% of the total cost of served load. The total production cost is about $75.3 billion. Fig. 6 shows that the production cost as a function of the

[2] A congested branch is a branch with a non-zero binding hour.
[3] A U90 branch is branch with a non-zero U90 hour.

hourly load. A higher production cost would appear in hours 5000-5500 (July and August), which are consistent with higher loads experienced during this time.

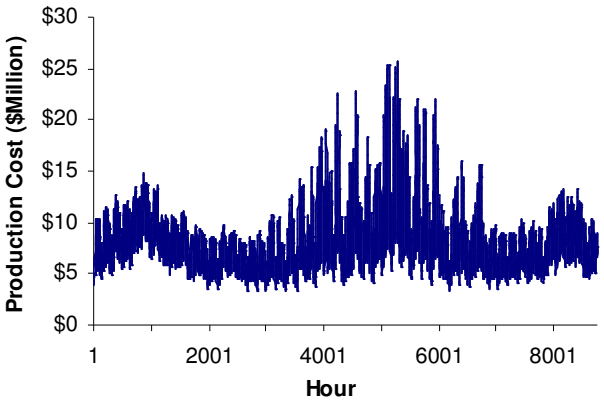


Fig. 6 Production Cost in 2008

### C. POMS Simulation Results for 2018

The Eastern Interconnection is simulated in 2018 using POMS. The input data are based on the forecasts in the MISO MTEP 2008 study [8]. The loads are assumed to increase at an annual rate of 1.0128% based on the 2008 loads. The fuel prices are assumed to increase at an annual escalation rate of 4% for oil and gas, 2% for coal, and 3% for nuclear fuels. The transmission and generation projects that are under construction or are planned by 2018 in the Eastern Interconnection are incorporated in the 2018 simulation. New England and Florida, which were not included in the MISO MTEP 2008 study, are excluded from the POMS simulation.

#### *C1) Transmission Congestion based on the Binding Hours Metric*

The simulated 2018 congestion is shown in Fig. 7. There are 2,665 branches that are congested for at least one hour and 314 of those branches are always congested in 2018. Most of the congested branches are in the New York and the PJM interconnections. Certain branches in the west side of the SERC region are also congested.

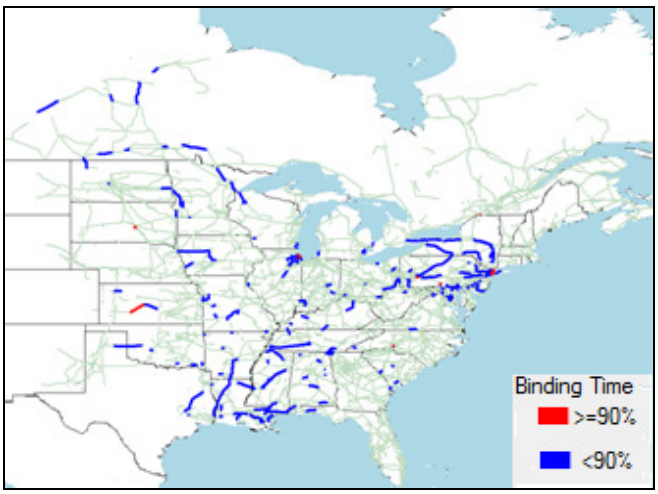


Fig. 7 Binding Hours Information in 2018

#### *C2) Constrained Branches based on the U90 Hours Metric*

Fig. 8 shows constrained branches based on the U90 metric. There are 4,239 constrained branches based on U90 and 472 of those branches are continuously loaded in excess of 90% of their capacities. Such branches are mainly located in New York and in certain parts of the PJM system (including Chicago). A few branches are also constrained in the west side of the SERC region.

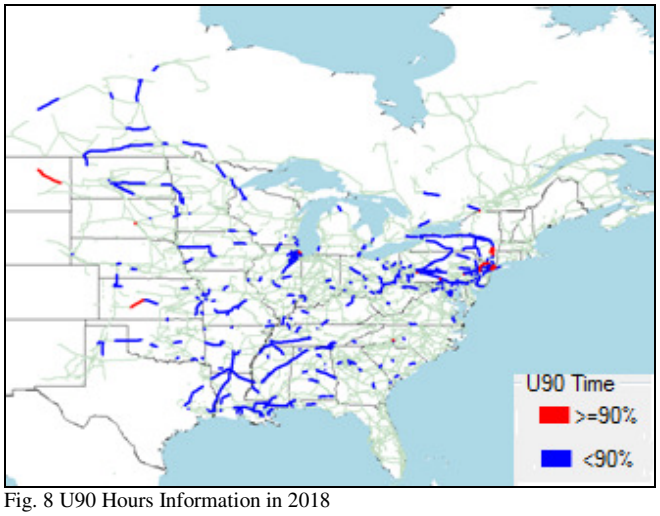


Fig. 8 U90 Hours Information in 2018

#### *C3) Number of Constrained Branches*

Fig. 9 shows the number of constrained branches as a percentage of time. Out of 2,665 branches that are congested in at least one hour, 524 (i.e. 20%) remain congested in at least 80% of the annual hours and 1,599 (i.e., 60%) are congested in less than 20% of the annual hours. Based on the U90 metric, there are 4,239 branches that are constrained, 710 (i.e., 15%) of such branches remain constrained in at least 80% of annual hours, and 2,715 (i.e., 65%) are constrained in less than 20% of the annual hours. The two curves have similar trends except that more branches are constrained based on the U90 metric.

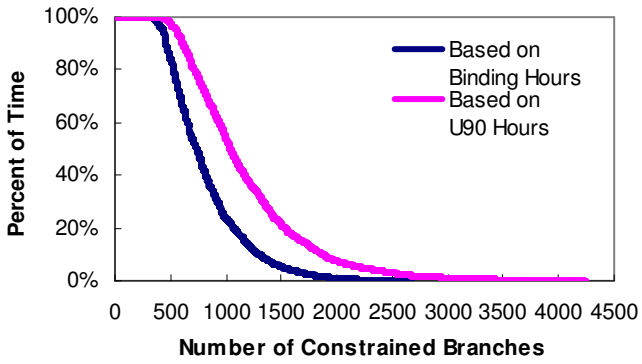


Fig. 9 Constrained Branches as a Function of Time in 2018

#### *C4) Locational Marginal Prices*

The annual average LMPs based on the 2018 simulation are shown in Fig. 10. New York has the highest LMPs in the Eastern Interconnection. The LMPs in the East Coast are generally higher than those in other regions. High LMPs are also encountered in Louisiana and Mississippi indicating transmission congestions. LMPs in Illinois and Indiana are lower than those in the East Coast because there are cheap

coal-fired and nuclear power plants close to load centers. LMPs in the Northwester region of the Midwest are significantly lower than those in other regions due to expected high penetration of wind power.

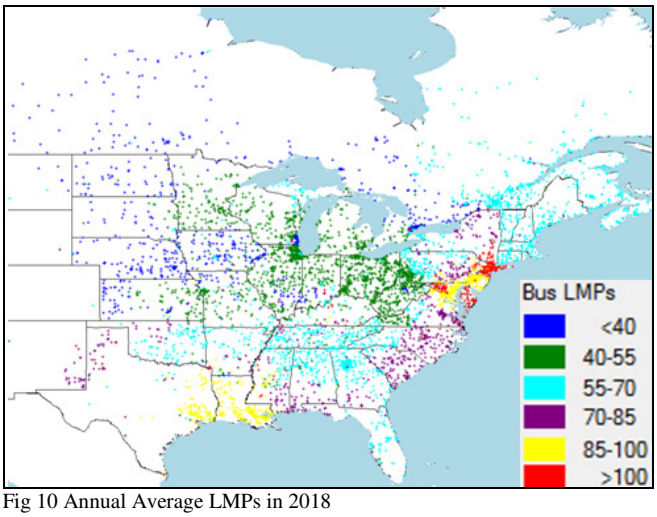


Fig 10 Annual Average LMPs in 2018

*C5) Cost of Served Load and Congestion Cost*

The total cost of served load in 2018 is about $230.9 billion and the total congestion cost is about 10% of the total cost of served load. The total production cost in 2018 is $83.6 billion with the hourly costs shown in Fig. 11, where higher hourly production costs appear in July and August.

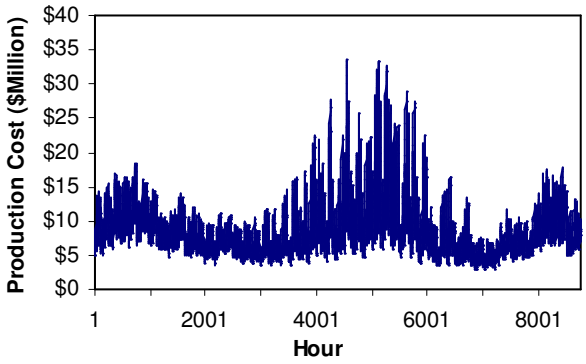


Fig. 11 Production Cost in 2018

## D. Comparison of POMS and NETCS Results in 2008

In this section, we compare the 2008 POMS simulation results with the NETCS results. The NETCS report reviewed the historical congestions and analyzed the 2008 congestion in the Eastern Interconnection using the optimal power flow (OPF) model [2].

*D1) Regional Congestion*

The POMS and the NETCS simulation results show that congestions are concentrated in the New York and the PJM regions (including Chicago). In addition, congestions are identified at the border between Georgia and Florida. With high LMPs in Florida, the cheaper energy is imported to the state which leads to congestions at the border. These congestions were not presented in the review of historical information in the NETCS report because the actual transactions between Florida and Georgia are based on long term contracts which would limit the power flow across the Georgia-Florida border.

*D2) Number of Congested Paths/Branches*

In NETCS, 58 historically congested paths were identified with the detailed geographical information given in [2]. In the simulation results presented in NETCS, 171 congested transmission paths were identified in 2008. In comparison, the POMS simulation results for 2008 identified 270 congested branches that always constrained based on the binding hours metric. The difference is due to the fact that one transmission path in the NETCS report may represent several branches although the details are not given in the NETCS report.

One notable point is that both the NETCS and the POMS simulation results identify more congestions than what is reported by the historical data. This is due to the assumption in both simulations that economic transactions occur whenever is possible. A two-bus example presented in the Appendix B illustrates how economic transactions could cause additional congestions. It should be pointed out that almost all historical congestions have also been identified in the NETCS simulation results and the POMS simulation results.

*D3) Constrained Transmission Capacities*

Fig. 12 shows the percentage of constrained transmission capacity as a function of time and Fig. 13 shows the constrained capacity (GW) as a function time in 2008. In particular, it is shown in Fig. 12 that about 23% of the constrained transmission capacity is congested more than 80% of the annual hours based on the Binding Hours curve, and about 30% of the constrained transmission capacity is constrained more than 80% of annual hours based on the U90 Hours curve. Note that the U90 branches will always include the congested branches and that is why the U90 Hours curve is above the Binding Hours curve in Figs. 12 and 13.

In NETCS, heavy congestion occurs in only a few hours per year. For instance, 80% of the congestion occurs for less than 20% of the annual hours [2]. In comparison, the POMS simulation results in Fig. 12 show more congestion. In the latter case, 50% of the congestion occurs in less than 20% of the annual hours.

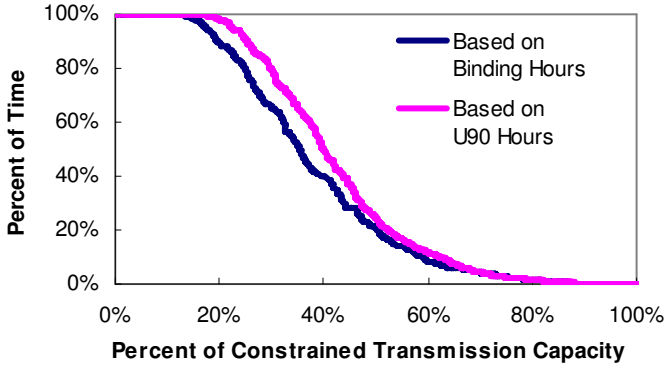


Fig. 12 Constrained Transmission Capacity (%) as a function of Time in 2008

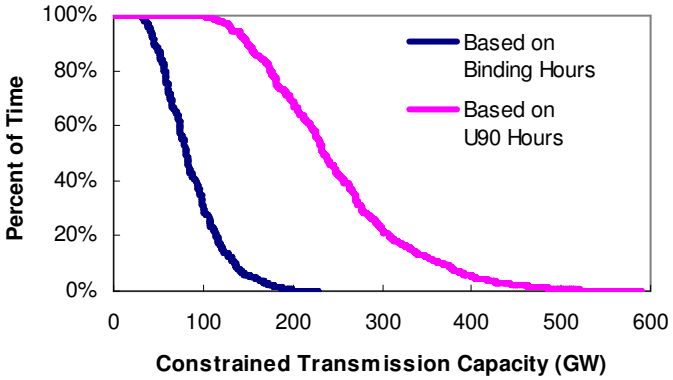


Fig. 13 Constrained Transmission Capacity (GW) as a function of Time in 2008

This difference can be attributed to the differences in the input data and the modeling details. For instance, both branch flowgate limits are taken into account in the POMS simulation, while only branch limits are monitored in the NETCS. In addition, the NETCS was completed in 2006. Thus, some transmission projects that were completed since then might not be included in the NETCS simulation. It is also possible that certain transmission projects that were assumed in the NETCS are not built and thus not included in the simulation in this paper.

In Fig. 12, the two curves coincide beyond the 60% constrained transmission capacity point, i.e., about 40% of constrained transmission capacity is constrained less than 10% of the time. The difference between the two curves is more obvious in Fig. 13. 228 GW of transmission capacity is congested based on Binding Hour metric and 588 GW is constrained based on the U90 Hour metric.

Fig. 14 also shows the constrained transmission capacity as a function of time. However, only the congested transmission branches are considered in calculating the constrained transmission capacity in both cases. In contrast to Fig. 12, the two curves in Fig. 14 are more distinguishable. For instance, 40% of the congested transmission capacity is congested as least 40% of the binding time. The same transmission capacity will be loaded to 90% or more at 70% of the time.

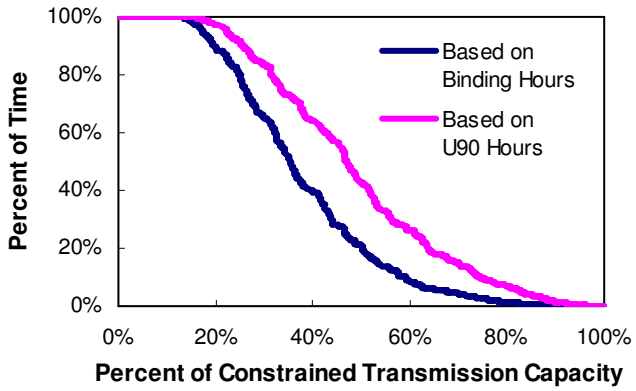


Fig. 14 Constrained Transmission Capacity as a function of Time in 2008 (congested capacity is used as base)

*D4) Congestion Costs*

In the POMS simulation results for 2008, the total cost of served load is $172.3 billion and the congestion cost is about 7.5% of the total cost. In comparison, in the NETCS report, the total cost of served load is about $171 billion and the congestion cost is about 4.7% of the total cost. That is, the total costs in two cases are almost the same but the POMS simulation results show more congestion. Fig. 15 shows the relationship between the congestion cost and the constrained transmission capacity for the POMS simulation in 2008 and 2018. For the 2008 case, 20% of the constrained transmission capacity accounts for about 73% of the total congestion cost and 50% of the constrained transmission capacities account for 97% of the total congestion cost. For the 2008 case in the NETCS report, 20% of the constrained transmission capacity accounts for 60% of the total congestion cost and 50% of the constrained transmission capacity accounts for 95% of the total congestion cost [2]. The POMS simulation results are similar to those of the NETCS in this case.

The POMS simulation results in Fig. 15 also show that the congestion cost is caused by a small number of constrained branches. The POMS results are similar to the NETCS results. Since the congestion cost is ultimately passed through to consumers, this also means that the planning of a relatively small number of transmission projects along constrained transmission paths could lead to a significant reduction in congestion costs and introduce a major economic benefit to consumers.

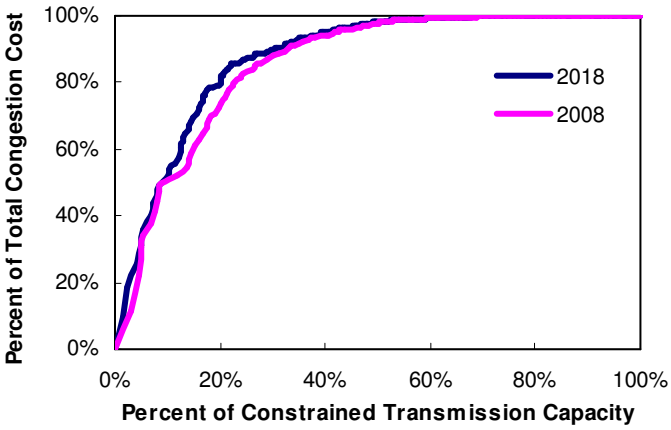


Fig. 15 Congestion Cost and the Constrained Transmission Capacity

*E. Comparison of POMS Results in 2008 and 2018*

In this section, we compare the POMS simulation results for 2008 and 2018.

*E1) Locational Marginal Prices*

Figs. 5 and 10 show that LMPs in 2018 are higher than those in 2008. In fact, the average load-weighted LMP in the Eastern Interconnection increases from $48.85/MWh in 2008 to $65.93/MWh in 2018. The higher LMPs could be attributed to increasing loads and fuel prices.

*E2) Production and Congestion Costs*

The total production cost in 2008 is about $75.3 billion as compared to $83.6 billion in 2018. The hourly production costs in 2018 (Fig. 11) and 2008 (Fig. 6) are similar. In both cases, higher production costs appear in the summer months (July and August). As expected, the hourly production costs in 2018 are higher than those in 2008 due to the load growth and fuel price escalations. Even though the New England and the Florida are not considered in the 2018 simulation, the total cost of served load increases from $172.3 billion in 2008

to $230.9 billion in 2018. It is interesting to note that the total cost of served load increases by 34% while the total production cost increases by 11%. This phenomenon can be explained using a two-bus example presented in Appendix C.

The congestion cost as a percentage of the cost of supplying the load increases from 7.5% in 2008 to 10% in 2018, which shows that the system is more congested in 2018 due to the load growth and higher fuel prices. The results would also point out that sufficient generation and transmission projects investments may not have been planned within the 10-year period.

Fig, 15 shows that the 2018 curve is a little higher than the 2008 curve, 20% of the congested transmission capacity accounts for about 73% of the total congestion cost in 2008 while 20% of the congested transmission capacity accounts for 83% of the total congestion cost in 2018. This means that congestion costs are more concentrated on a small percentage of constrained transmission capacity in 2018 than in 2008. Fig. 15 also shows that 50% of the congested transmission capacity accounts for 97% of the total congestion cost in 2008 and that 50% of the congested transmission capacity accounts for 98% of the total congestion cost in 2018. This means that the congestion cost is attributed to half of the congested capacity. In Fig. 15, the two curves almost coincide above the 50% of congested transmission capacity, which shows that the other 50% of the congested transmission capacity has very small impact on the congestion cost in both 2008 and 2018.

*E3) Constrained Transmission Capacity as a Function of Time*

Fig. 16 shows the percentage of constrained transmission capacity as a function of time. Fig. 17 shows the MW constrained transmission capacity as a function of time in 2018. In 2018, about 549GW of transmission capacity is congested, 4.9% of which is continuously congested and 66% is congested less than 20% of the time in one year. Based on the U90 metric, about 944GW of the transmission capacity is constrained, about 5.4% of which is constrained continuously in one year. In 2008, 228GW of transmission capacity is congested, about 11% of which is congested continuously for the entire year and 50% is congested less than 20% of the time in one year. Based on the U90 metric, about 588GW transmission capacity is constrained in 2008, about 15% of which is constrained continuously for the entire year.

In Fig. 16, the two curves are closer in comparison to Fig. 12. This means that the transmission capacities that are identified as constrained by the U90 metric would be more often constrained in 2018 than in 2008. In Fig. 16, the two curves coincide beyond the 40% constrained transmission capacity which account for about 15% of the time, so about 60% of constrained transmission capacity is constrained only in a few hours for the one year. Again we see that the congestion would be more confined to a small percentage of constrained transmission capacities in 2018 as compared with those in 2008.

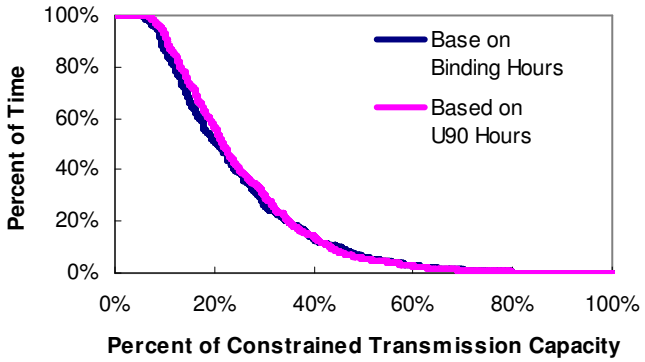


Fig. 16 Constrained Transmission Capacity as a Function of Time in 2018

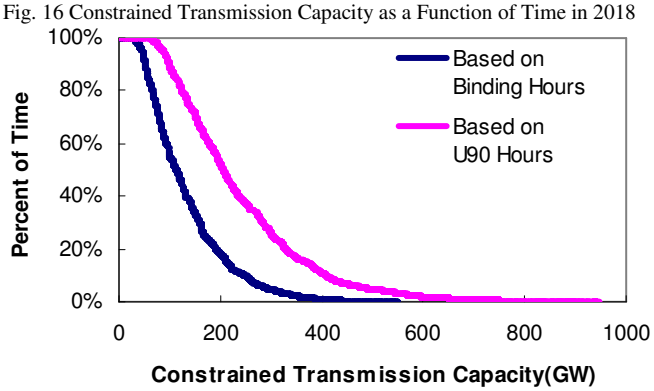


Fig. 17 Percent of Time and Constrained Transmission Capacity in 2018

## III. Conclusions

In this paper, a SCUC methodology is proposed in POMS for the congestion analysis in the U.S. Eastern Interconnection for 2008 and 2018. The POMS simulation results are compared with those in the NETCS report. The simulation results are integrated with GIS data to offer a comprehensive and intuitive understanding of transmission constraints and LMPs. We envision that the proposed POMS methodology and the result can provide valuable information for transmission expansion studies.

## Appendix

### A. Congestion Metrics

In NETCS, five metrics were defined to assess the magnitude of transmission congestion, including binding hours, U90, all-hour shadow prices, binding hour shadow prices, and congestion rents. The metrics used in this paper include binding hours, U90 hours, constrained transmission capacity, LMPs, cost of served load, and congestion cost.

*1) Binding Hours and U90 Hours*

Those branches on which the flows have reached their limits are identified as congested branches. In addition, branches with flows above 90% of the flow limits are identified as U90 branches. In this paper, two congestion metrics including the binding hours and the U90 hours [2] [9] are defined as follows which are based on a long term (e.g., 8,760 hours) POMS simulation.

$$\text{Binding hours of branch } l = \sum_{t=1}^{NT} x_{l,t} \quad (1)$$

$$x_{l,t} = \begin{cases} 1 \text{ if branch } l \text{ is congested at period } t \\ 0 \qquad\qquad\qquad \text{otherwise} \end{cases}$$

$$\text{U90 hours of branch } l = \sum_{t=1}^{NT} y_{l,t} \tag{2}$$

$$y_{l,t} = \begin{cases} 1 \text{ if branch } l \text{ is loaded above 90\%} \\ \qquad\qquad \text{of its capcity at period } t \\ 0 \qquad\qquad\qquad \text{otherrwise} \end{cases}$$

where $NT$ represents the number of time periods (e.g., 8,760). These two definitions are similar to those in the NETCS report.

Similar to U90 hours, other metrics such as U75 hours or U60 hours can also be defined in order to assess the degree of congestion. These metrics can be used to classify and rank the identified congestions.

*2) Constrained Transmission Capacity*

The constrained transmission capacity of a system is the sum of the transmission capacity of all branches that are constrained at least in one hour during the study horizon. The constrained transmission capacity could be different when different congestion metrics are used, e.g., binding hours and U90 hours. If binding hours is applied to identify congestions, the constrained transmission capacity is formulated as follows.

$$\text{Constrained transmission capacity} = \sum_{l=1}^{NB} z_{l,1} * PL_{l,\max} \tag{3}$$

$$z_{l,1} = \begin{cases} 1 \text{ if binding hours of branch } l > 0 \\ 0 \text{ if binding hours of branch } l = 0 \end{cases}$$

where $NB$ represents the number of branches and $PL_{l,\max}$ is the capacity of branch $l$. Similarly, if U90 hours is applied to identify congestions, the constrained transmission capacity is formulated as follows.

$$\text{Constrained transmission capacity} = \sum_{l=1}^{NB} z_{l,2} * PL_{l,\max} \tag{4}$$

$$z_{l,2} = \begin{cases} 1 \text{ if U90 hours of branch } l > 0 \\ 0 \text{ if U90 hours of branch } l = 0 \end{cases}$$

*3) LMPs*

LMPs at individual buses are calculated as part of the outputs from the SCUC based simulation. Since LMP differences in a system are caused by congestions, an LMP map would provide an intuitive way of visualizing congestions across the system. LMP information is not discussed in the NETCS report.

*4) Cost of Served Load*

The cost of served load is the total payment made by all loads in the system, which is calculated as,

$$\text{Cost of served load} = \sum_{t=1}^{NT} \sum_{j=1}^{ND} LMP_{j,t} * D_{j,t} \tag{5}$$

where $ND$ represents the number of load buses; $LMP_{j,t}$ represents the LMP of load bus $j$ at period $t$; $D_{j,t}$ represents the load at bus $j$ at period $t$.

*5) Congestion Cost*

The congestion cost was calculated as the increase in the production cost due to the re-scheduling of units to alleviate congestions [10]. In this paper, the congestion cost is defined as the difference between the load payment and the generation credit based on LMPs,

$$\text{Congestion cost} = \sum_{t=1}^{NT} \sum_{j=1}^{ND} LMP_{j,t} * D_{j,t} - \sum_{t=1}^{NT} \sum_{i=1}^{NG} LMP_{i,t} * P_{i,t} \tag{6}$$

where $NG$ represents the number of generator buses; $LMP_{i,t}$ represents the LMP at generator bus $i$ at period $t$; $P_{i,t}$ represents the generation at bus $i$ at period $t$.

The congestion cost metric defined as (6) is similar to the congestion rent defined in the NETCS report [2]. Congestion cost as a percentage of the cost of served load could indicate the magnitude of congestion of the entire system.

## B. Congestion Analysis

The one-line diagram of a two-bus system with two generators and two loads is shown in Fig. 18. G1 and L1 are located at Bus 1 and G2 and L2 are located at Bus 2. The capacities for both generators are 800MW and the incremental cost is 10$/MWh for G1 and 20$/MWh for G2. L1 is 400MW and L2 is 600MW. Bus 1 and Bus 2 are connected through one transmission line with a capacity of 300MW. In the ideal case, G1 and G2 will be dispatched to 700MW and 300MW, respectively. The economic transaction between Bus 1 and Bus 2 will be 300MW. Accordingly, the flow on the line will be 300MW, which makes the line congested. However, if we intentionally limit the transaction between Bus 1 and Bus 2 to 100MW, there will be no congestion on the line. This shows that economic transactions could cause congestions that are not present without the economic transactions

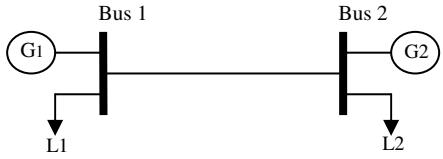


Fig. 18 Two-Bus System

## C. Operation and Congestion Costs Analysis

The system is the same as the two-bus system in B. We assume the L1 is 250MW and L2 is 250MW at first. So the system will have no congestion. All the loads will be supplied by G1 and the production cost is $5,000 and the cost of served load is $5,000. If L1 and L2 are both increased by 50MW, the power flow on the transmission line will reach its limit 300MW). G2 will be the marginal generator at Bus 2 and the LMP at Bus 2 will be $20/MWh. The production cost

is $6,000, and the cost of served load is $9,000. That is, the production cost increases by about 20% and the cost of served load increases by about 80% owing to the growth of loads.

## REFERENCES


[1] Section 1221(a) of the Energy Policy Act of 2005. http://www.oe.energy.gov/epa_sec1221.htm.

[2] U.S. Department of Energy, *National Electric Transmission Congestion Study. August 2006*. Available online at http://nietc.anl.gov/congestionstudy/index.cfm

[3] Assessment of historical transmission congestion in the Eastern Interconnection. http://congestion09.anl.gov/documents/docs/EasternInterconnection.pdf

[4] Y. Fu, M. Shahidehpour, and Z. Li, "Security-constrained unit commitment with AC constraints," IEEE Trans. Power Syst., vol. 20, no. 3, pp. 1538–1550, Aug. 2005.

[5] Y. Fu, M. Shahidehpour, and Z. Li, "AC contingency dispatch based on security-constraints unit commitment," IEEE Trans. Power Syst., vol. 21, no. 2, pp. 897-908, May 2006.

[6] Y. Fu, M. Shahidehpour, and Z. Li, "Long-term security-constrained unit commitment: hybrid Dantzig–Wolfe decomposition and subgradient approach," IEEE Trans. Power Syst., vol. 20, no. 4, pp. 2093-2106. Nov. 2005.

[7] M. Shahidehpour, H. Yamin, and Z. Li, *Market Operations in Electric Power Systems.* New York, NY: Wiley, 2002.

[8] Midwest ISO Planning. Available online at http://www.midwestiso.org/page/Expansion+Planning

[9] A. Rudkevich, K. Egilmez, M. Liu, P. Murti, and T. Overbye, "Identification and congestion analysis of transmission corridors of the Eastern Interconnection," in Proc. of the 40th Hawaii International Conference on System Sciences, 2007.

[10] G. Hamoud and I. Bradley, "Assessment of transmission congestion cost and locational marginal pricing in a competitive electricity market," IEEE Trans. Power Syst., vol. 19, no. 2, pp. 769-775, May 2004.



**Wei Tian** (S'08) received his BS degree in mathematics from Shandong University in 2001, MS degree in system engineering from Xi'an Jiaotong University, China in 2004. Presently, he is pursuing the Ph.D. degree at the Illinois Institute of Technology, Chicago. His research interests include power systems restructuring and planning.

**Zuyi Li** (SM'09) received his BS degree in E.E. from Shanghai Jiaotong University, China, in 1995, MS degree in E.E. from Tsinghua University, China, in 1998, and Ph.D degree in E.E. from Illinois Institute of Technology, USA, in 2002. Presently, he is an assistant professor in the ECE Department.

**Mohammad Shahidehpour** (F'01) is the Carl Bodine Distinguished Professor and Chairman in the ECE Department at Illinois Institute of Technology. He is the recipient of the 2005 IEEE/PES Prize Paper Award and 2006 IEEE/PSO Prize Paper Award.

Fourth International Meeting on Wind Turbine Noise

Rome Italy 12-14 April 2011

# Test bed for acoustic assessment of small wind turbine drive-trains

**Ganesh Raman, Mahesh Krishnamurthy, Rakesh C Ramachandran, Clement Pereira, Xiaodong Shi and Yong Jiang**
**Illinois Institute of Technology, Chicago, IL, USA.**
**raman@iit.edu, kmahesh@ece.iit.edu**

**Martin Price and Matthew Arnold**
**Viryd Technologies, Austin, TX, USA**

## Abstract

This paper describes a test facility for acoustic assessment of small wind turbine drive trains. The wind turbine drive train chosen for our facility was that of a 8 kW horizontal axis wind turbine (Viryd 8000). The facility has a drive side and a turbine side. On the drive side, a drive motor is connected through a gearbox to a flywheel that compensates for the absence of the blades. The turbine side includes the entire driveline of the wind turbine. The system can simulate inflow wind speed and turbulence. The system also includes accelerometers and torque sensors. For the acoustic assessment both single microphones and an array of 24 microphones were used. Various beamforming algorithms were used for source localization. These include classical beamforming (FDBF), deconvolution approaches for mapping acoustic sources (DAMAS2), CLEAN based on source coherence (CLSC) and TIDY. The array was calibrated and validated for both coherent and incoherent sources. Acoustic measurements from the fully functional drive train test facility are presented for a few operating conditions. Further tests in the facility will be conducted to assess wind turbine drive train acoustics and vibration for various wind velocities and turbulence levels. The facility will also be used to develop techniques for the minimization of sound and vibration from small wind turbine drive trains.

## Introduction

Wind turbines generate both aerodynamic and mechanical noise from its various components. Aerodynamic noise includes low-frequency sound, in-flow turbulence sound, and airfoil self- noise. The cylindrical tower can produce additional noise due to vortex shedding in various regimes. Mechanical sources include sound from the gearbox, generator, yaw drives, cooling fans, and hydraulics. Even though wind turbines have become much quieter over the years, their sound is still important because noise is a measure of the inefficiency of a machine. Clearly, excessive noise indicates that energy is being wasted. Mechanical sounds originate from the relative motion of mechanical components and dynamic response among them. Examples of mechanical sound sources include the gear box that houses gears that connect the low speed shaft to the high speed shaft. Typically the rotor blade rotations occur at 30-60 rotations per minute (rpm). These rotations are transmitted

to the high speed shaft at 1000-1800 rpm and during the process noise is produced by the gears and the high speed shaft.

The work presented in this paper represents a collaborative multidisciplinary effort between the Electrical and Computer Engineering (ECE) department and the Mechanical, Materials and Aerospace (MMAE) department at the Illinois Institute of Technology, IL. In this paper we describe the test bed that was developed for the acoustic assessment of the drive trains of small wind turbines. The drive side of the facility can simulate various wind speeds and turbulence levels whereas the turbine side includes the entire driveline of the wind turbine. The acoustic measurements presented in this paper include both single microphone and phased array measurements that can localize sources. The eventual goal of this effort is to develop technologies to minimize sound and vibration from wind turbine drive trains.

The work encompasses both a research component as well as an educational component intended to focus on work force development for the next generation of engineers.

## Experimental Details

## Drive Train

The wind turbine drive train chosen was that of a Viryd 8000 horizontal axis wind turbine (see Fig. 1(a)). The wind turbine incorporates a proprietary continuously variable planetary (CVP) gearbox that provides the benefits of using a grid tied induction generator without the costly and unreliable inverter. This one of its kind wind turbine drive test bed facility houses two sides: a drive side and the turbine side. On the drive side, a drive motor is attached through a gear box to an inertia wheel that compensates for the absence of blades. The drive side also houses a torque transducer. The turbine side of the test bed contains the entire turbine driveline, with the addition of a torque transducer. The turbine software simulates the system response to input wind speed and power similar to that for a production model. The drive side software controls the turbine side by feeding it these inputs, and monitoring its performance and safety. The turbine side can be manipulated to run as a production turbine or as a multi-purpose research test bed. Some of the important software parameters are shown in Table 1. One of the unique features of this test facility is that, different scenarios of realistic operating conditions can be simulated from torque values derived from an analytical model developed by Viryd. In the simulation mode, the user can input a value of wind speed either by a slider input or an input file. As the turbine side changes rotor speed to optimize the power at that given wind speed, the rotor speed and wind speed are used to calculate the amount of input torque required from the drive motor in open loop control. There are also various sensors such as accelerometers and torque sensors to monitor the system safety and performance. Speed and torque are measured at low speed shaft torque transducer on the drive side. On the turbine side, torque and speed are also measured to calculate mechanical power going into the generator. Vibration can be measured at two locations on the test stand using accelerometers on the turbine side. The temperature of the system is also monitored at four different locations and the lube pressure is monitored using pressure transducers.

## Phased Array and Beamforming Algorithms

Various beamforming algorithms have been developed over the years (see Ref [1] – [5]). General aspects of measurement of noise from wind turbines are covered iin Refs [6,7]. The very first step after acquiring data from the phased array system for every beamforming algorithm considered is the computation of a cross spectral matrix (CSM). The pressure time series of each microphone is divided into blocks and the FFT of each block is computed after applying a suitable spectral window. Then each element of the CSM is calculated via sample averaging. Since the locations of the sources are unknown in practice, a scanning grid that covers a region of interest with a certain resolution is formed and every point of this grid is considered as a potential source whose corresponding sound pressure level at the array center is estimated. This results in a beam forming map representing the acoustic source distribution in the region of interest. DAMAS attempts to estimate the true signal power from the contaminated DAS results by constructing a linear system of equations that relate the DAS estimates at every scanning point to the signal powers at every scanning point. It utilizes the iterative Gauss-Seidel method. A potential drawback of this is computation time. DAMAS2 solves this problem by calculating the point spread function only once and using the same for all the points in the scanning grid. Another widely used method is the CLEAN-SC which iteratively builds up the beamform maps corresponding to the dominant sources using the previously estimated signal powers. TIDY is philosophically similar to CLEAN-SC, but it works in the time domain using the cross correlation matrix (CCM) instead of the frequency domain with CSM.

The use of phased arrays to measure wind turbine noise is not new (see Oerlemans et al. [5]). Our goal in this paper is to describe the creation of a small wind turbine drive train facility for acoustic performance evaluation using a compact phased array that employs sophisticated beamforming algorithms.

## Calibration of Phased Array

The calibration experimental setup consisted of three 4 ohm dual cone speaker with a maximum power of 60 W connected to a dedicated amplifier which received input from a white noise generator. The speakers were mounted on a rectangular frame support which had 21 different mounting locations each separated by a distance of one inch (see Fig. 1(b)). One speaker was mounted at the center most location on the frame, referred to as the $0^{th}$ position. The other two speakers were mounted on the frame at a distance of 9 inches, both to the left and right of the $0^{th}$ position, and the setup was referred to as 9_0_9. The amplitude of the speakers were individually controlled by dedicated amplifiers. Before the experiments were conducted three different amplitude levels were selected, a low amplitude (69-71 dB), one mid amplitude (75-77 dB) and a high amplitude (82-84 dB). For ease of reference these three amplitude cases were assigned a number; low amplitude case- ‘2’, mid amplitude case- ‘4’ and high amplitude case- ‘6’. The speaker switched off case was assigned a ‘0’. For example, if the center speaker was fed with high amplitude input and the other two speakers were switched off then the configuration was referred to as 9.0_0.6_9.0. Similarly if the right and left speaker were fed with high amplitude input and the center one was switched off then it was referred to as 9.6_0.0_9.6. This nomenclature will be used throughout the paper. A Coherent source scenario was

created by feeding the three amplifiers with input from the same white noise generator whereas three different white noise generators were used to feed the amplifiers in the incoherent case. OptiNav's 24 microphone array system with integral preamps and a built-in camera was used for the experiments (see Fig. 1(c)). The signal from the microphone array is acquired by an A/D converter which has 24 I/O audio interfaces. A MAGMA express box handles the task of interfacing the PCI 424 card to the computer. A USB cable connects the camera to a USB port on the computer. The data acquired from the microphone array was then processed through four different beamforming algorithms namely the Frequency Domain Beamforming (FDBF), DAMAS (DMS2), CLEAN-SC (CLSC) and TIDY. A single 0.25" B&K 4939 microphone with a flat response from 1 Hz - 100 kHz was used for acquiring the acoustic data for comparing the results with that of the microphone array. The microphone was positioned such that it was located exactly at the center of the microphone array. The calibration of the microphone was done using a piston phone which emits sound at 250 Hz at an amplitude of 124 dB.

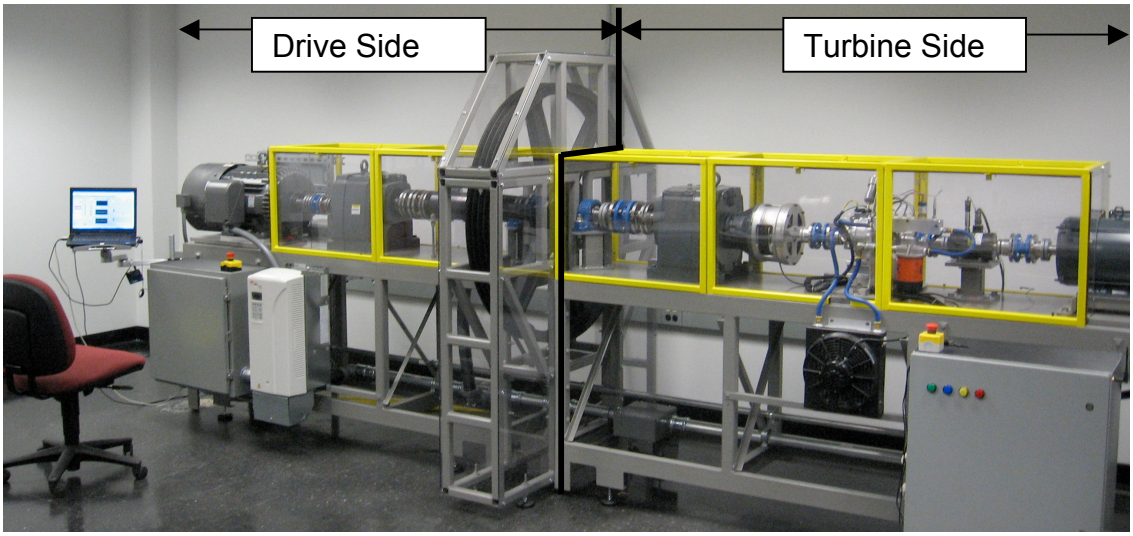


(a)

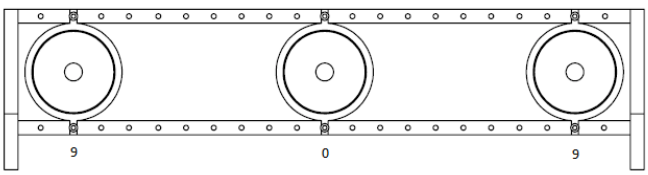


(b)


(c)

**Figure 1. Schematic of : (a) Viryd 8000 horizontal axis wind turbine drive train test facility; (b) the speaker arranged on the rectangular frame support at the 9_0_9 position and (c) the microphone array.**

**Table 1. Software parameters for the turbine software.**

| | |
|---|---|
| Cut In Wind Speed | 5.0 m/s |
| Cut Out Wind Speed (Low) | 4.0 m/s |
| Cut Out Wind Speed (High) | 25 m/s |
| Power Regulation | 6000 Watts |

## Results and Discussion

We begin by using synthetic sound sources from small speakers to evaluate the phased array. Various beamforming algorithms are considered for the evaluation. The results of the 9.0_0.6_9.0 case are shown in Fig. 2(a), 2(b) and 2(c). Fig. 2(a) shows the beamform map of narrow band frequency 972.5-1028.3 Hz. We observe that even though FDBF and DMS2 locate the source they fail to produce a clean map, whereas the CLSC and TIDY locate the source close to the center of the speaker and also produce a clean map of the source. As we increase the frequency band to 2174.6-2299.3 Hz we observe that all the algorithms produce a cleaner map (see Fig. 2(b)). A similar trend is observed as we increase the narrowband frequency to the range from 5777-6120.6 Hz. For all the above beamform maps the dynamic range was set to 5 dB with the upper limit as 69.5, 87 and 82 dB respectively. In order to check the amplitude values, the beamform amplitude values were compared with that of calibrated single microphone values. These values are shown in Table 2. We observe that the integral amplitude values of the FDBF match closely with the integral values of the single microphone value. The peak amplitude values of the CLSC are close to the peak amplitude values of the single microphone. The rest of the amplitude values differ from the single microphone values in the order of 4 to 5 dB.

**Table 2. Comparison of beamform amplitude values with the calibrated single microphone values.**

| Position | Frequency | Single Microphone | | Microphone Array | | BF-Algorithm |
|---|---|---|---|---|---|---|
| | (Hz) | Peak (dB) | Integral (dB) | Peak (dB) | Integral (dB) | |
| | | | | | | |
| 9.0_9.2_9.0 | 2174-2299 | 64.33 | 69.96 | 67.3 | 70.4 | FDBF |
| | | | | 68.6 | 66.7 | TIDY |
| | | | | 65.0 | 65.6 | CLSC |
| | | | | 67.8 | 68.1 | DMS2 |
| 9.0_9.4_9.0 | 2174-2299 | 77.95 | 83.35 | 80.7 | 83.4 | FDBF |
| | | | | 81.2 | 79.9 | TIDY |

| | | | | | | |
|---|---|---|---|---|---|---|
| | | | | 79.0 | 79.0 | CLSC |
| | | | | 81.2 | 81.4 | DMS2 |
| 9.0_9.6_9.0 | 2174-2299 | 82.8 | 88.53 | 87.4 | 90.1 | FDBF |
| | | | | 87.1 | 86.6 | TIDY |
| | | | | 85.7 | 85.7 | CLSC |
| | | | | 87.9 | 88.1 | DMS2 |

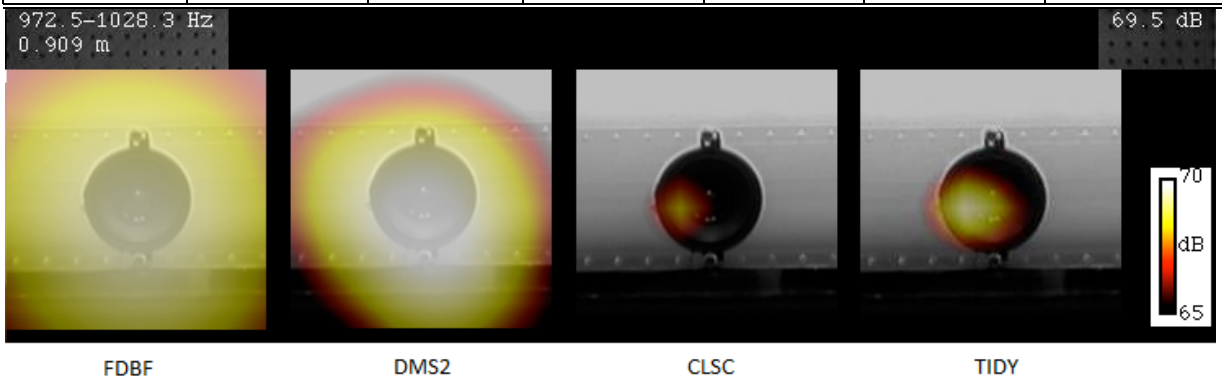


(a)

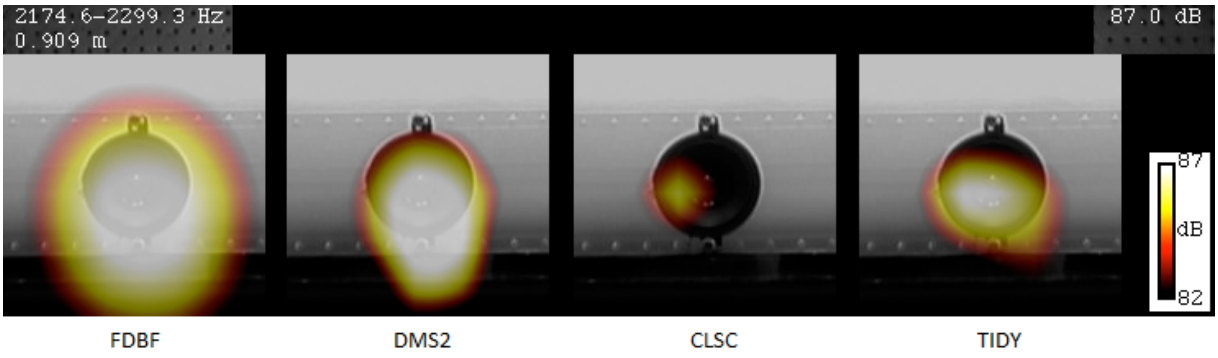


(b)

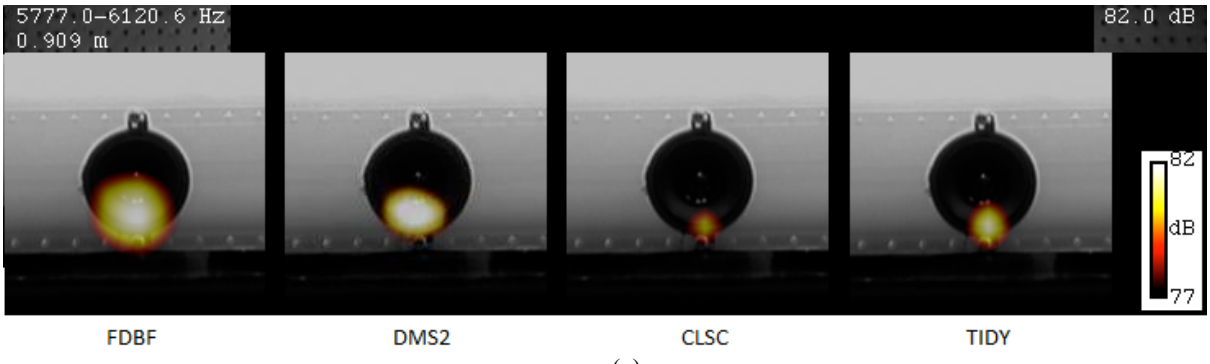


(c)

**Figure 2. Beamform maps of narrowband frequency ranging between: (a) 972.5-1028.3 Hz, (b) 2174.6-2299.3 Hz and (c) 5777-6120.6 Hz.**

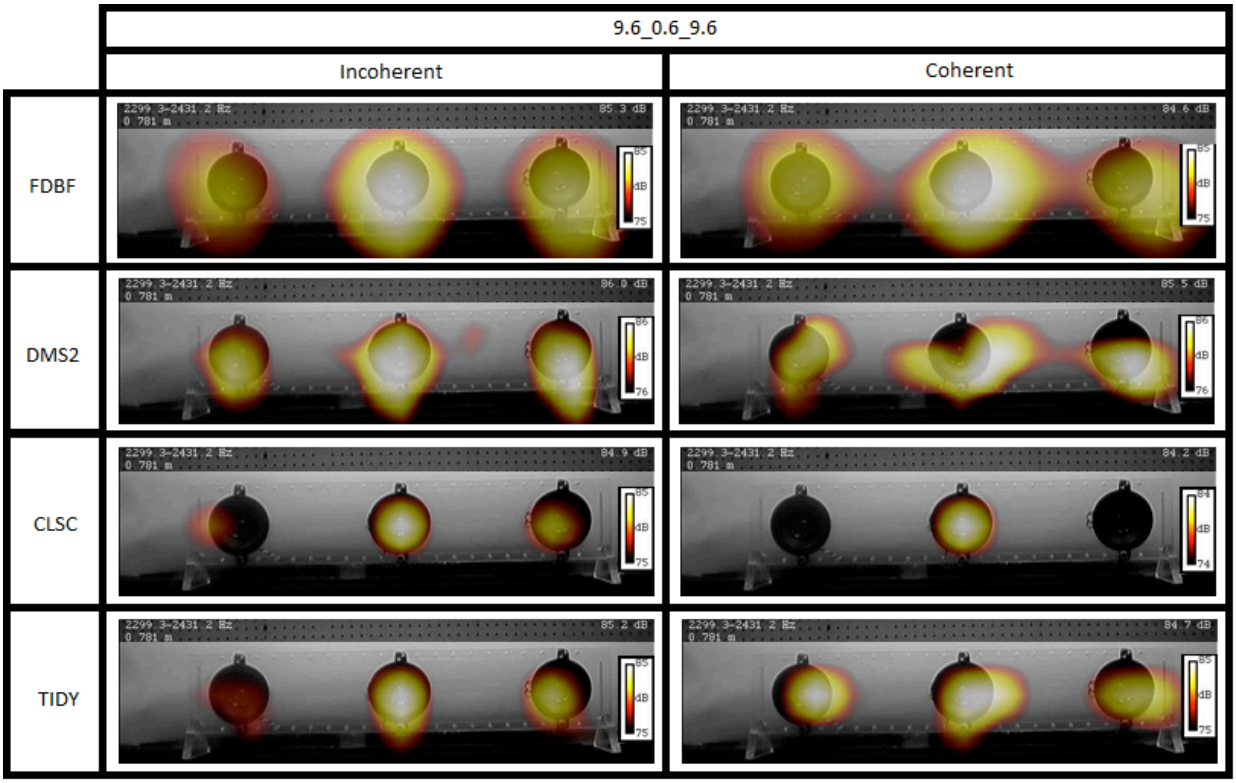


**Figure 3. Comparison of beamform maps obtained from FDBF, DMS2, CLSC and TIDY for three incoherent and coherent sources of the same amplitude (9.6_0.6_9.6).**

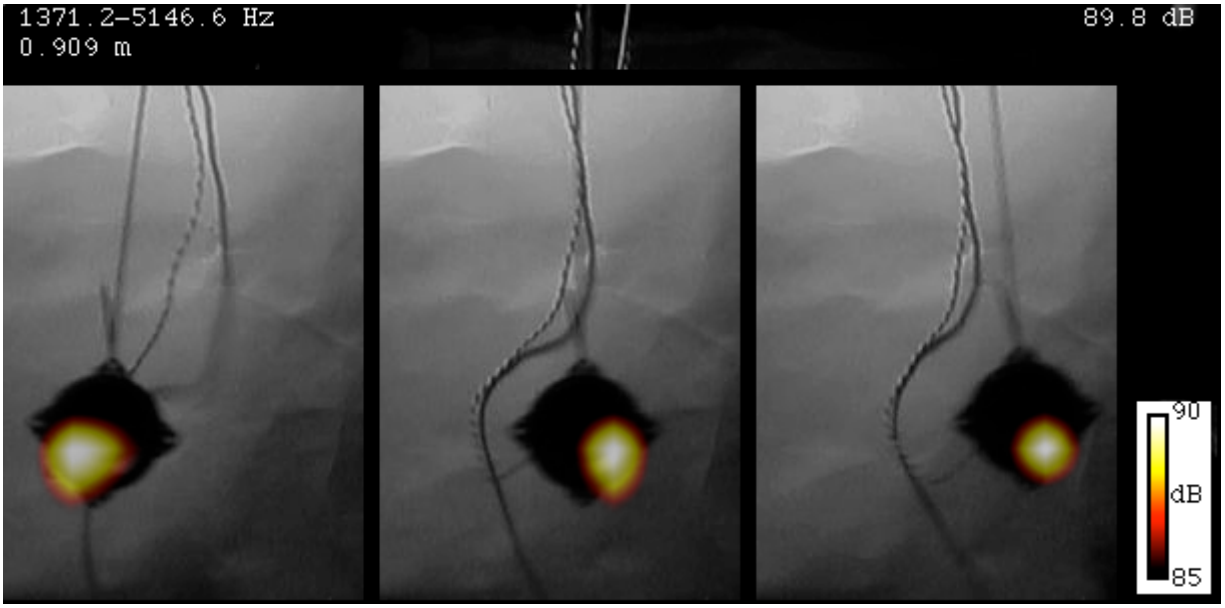


**Figure 4. Beamform map of a single oscillating source at three different positions during oscillation obtained using TIDY.**

Fig. 3 shows the beamform maps of three coherent and incoherent sources set at the same amplitude (9.6_0.6_9.6). Even though the FDBF and DMS2 were developed to resolve incoherent sources, they were successful in locating the three sources in both the coherent and the incoherent cases. However the difference in the formulation of the CLSC is clearly visible as it locates the maximum amplitude source with pin point accuracy and neglects the lower amplitude coherent sources. In the

incoherent case the CLSC is able to locate all the three sources. TIDY also does a good job in locating all the three sources in both coherent and incoherent cases. The main disadvantage with the FDBF, DMS2 and CLSC are that they are limited to a narrow band formulation. Thus larger bandwidth noise cannot be located using these algorithms. TIDY however is not limited in frequency bandwidth. This gives TIDY an advantage over the other beamforming algorithms and makes it a good choice for the wind turbine application. The effectiveness of TIDY in detecting a larger bandwidth moving white noise signal was also tested. The results are shown in Fig. 4.

After conducting calibration experiments, the phased array was used to locate the sources of noise generated by the wind turbine drive train. The test was run at 3 different conditions which corresponds to 3 different wind speeds. Table 3 gives details of the 3 different tests conducted in this study. The phased array was placed at 3.125 m away from the drive train and at the center, so that it covers both the driver part and the driven part of the drive train. The microphone was placed such that it's equivalent to placing a microphone at the centre of the phased array. Fig. 5 shows the different rpm of the driver motor and the generator for all the three cases. The Frequency spectrum from both the phased array and the single microphone for all three cases are shown in Fig. 6 and Fig. 7, respectively. We observe that the frequency spectra of both the phased array and the single microphone are similar in nature. The peak amplitude is about 4 dB higher than the single microphone values as observed earlier in the calibration experiments. Fig. 8 shows the beamform maps obtained for the three different test cases. For narrowband width the beamforming algorithm used was DMS2 and for broadband cases TIDY was used. We observe that at higher frequencies the algorithms are able to locate the noise generated by the gearboxes and the CVP. However the low frequency noise was not successfully located using these algorithms. In order to locate the sources at low frequency we will have to use a bigger array or use super resolution algorithms such as the MUSIC algorithm. Further, by using a combination of a single microphone and the phased array the low frequency noise could be effectively studied.

**Table 3. Parameters for the three test cases used in this study.**

| Parameters | Test 1 | Test 2 | Test 3 |
|---|---|---|---|
| Wind speed (m/s) | 20 | 12 | 6 |
| Turbulence | 0 | 0 | 0 |
| Input torque (Nm) | 400 | 400 | 400 |
| Transmission ratio | 0.8 | 1.195 | 1.5 |
| Power factor | ON | ON | ON |
| Power (kW) | 3.7 | 2.1 | 1.5 |

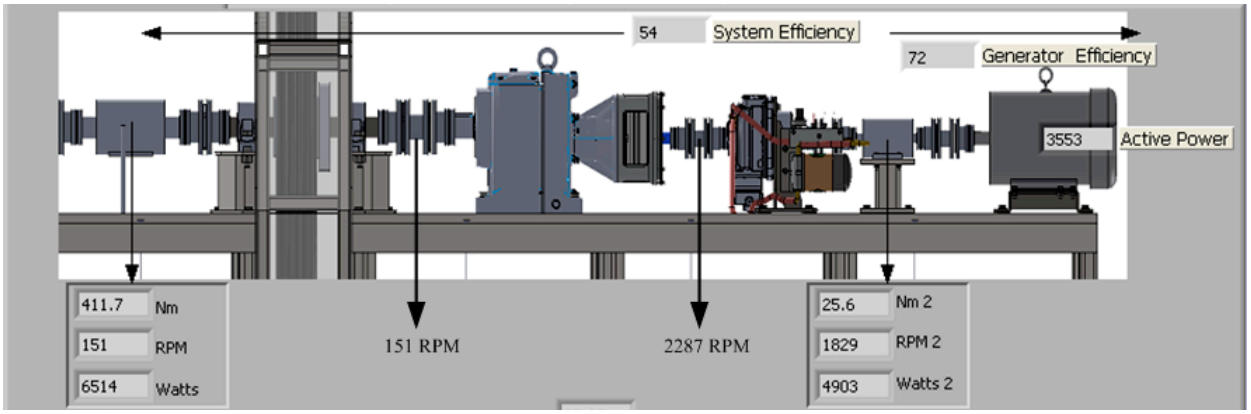


(a)

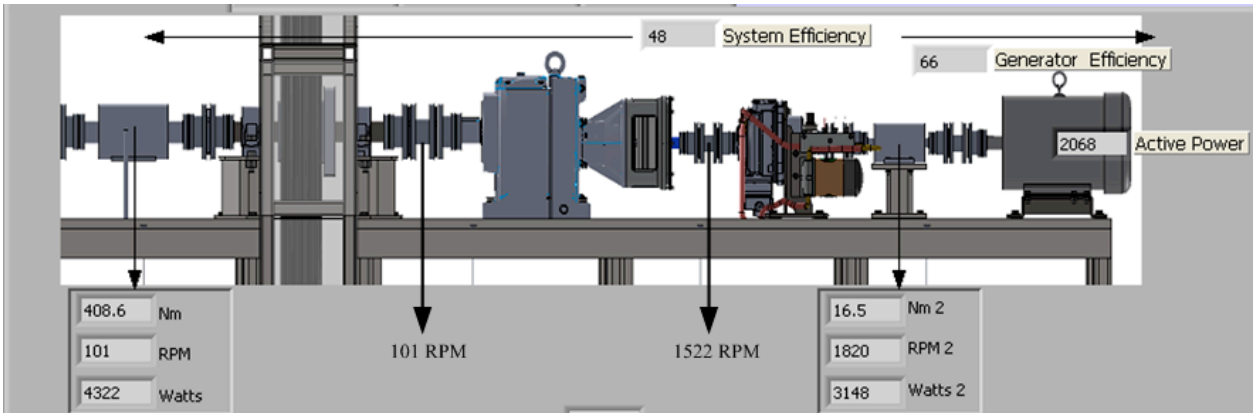


(b)

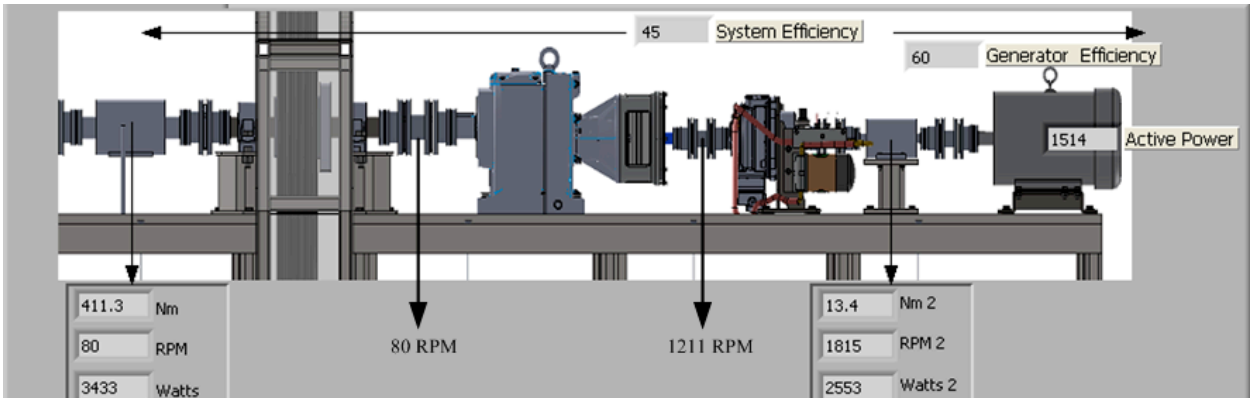


(c)

**Figure 5. Operating parameters for the wind turbine drive train (a) Test 1; (b) Test 2; (c) Test 3.**

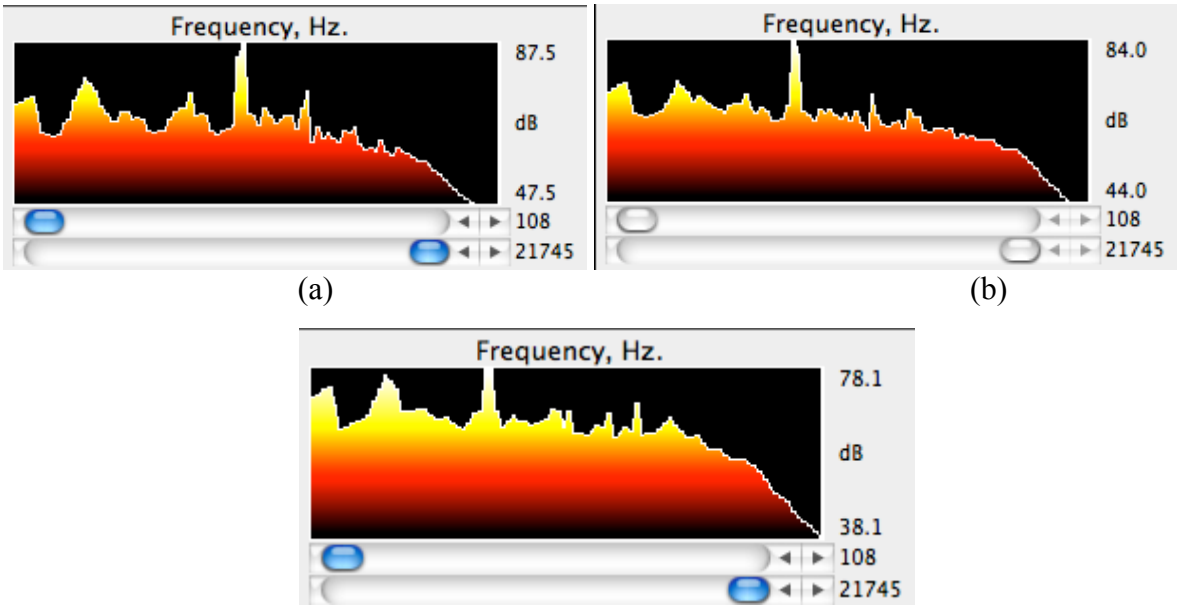


**Figure 6. Frequency spectrum obtained using the phased array: (a) Test 1; (b) Test 2; (c) Test 3.**

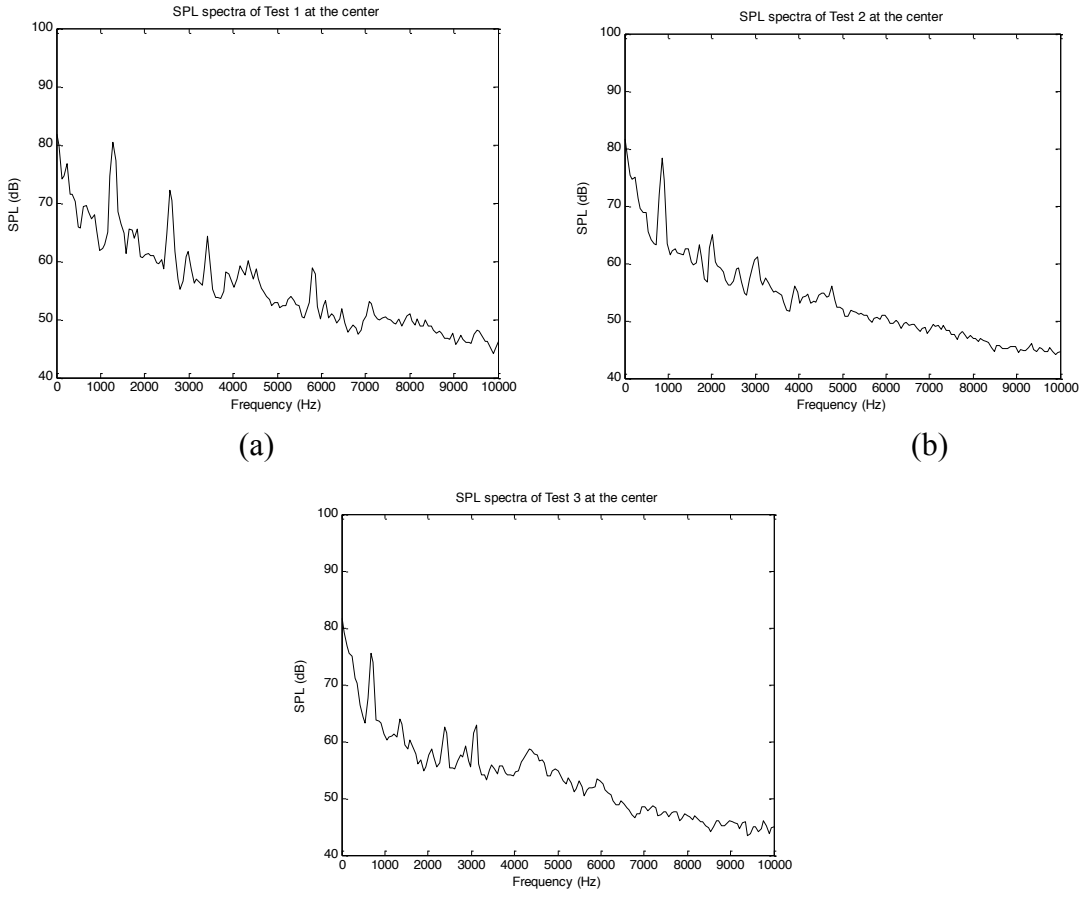


**Figure 7. Frequency spectrum obtained using a single microphone: (a) Test 1; (b) Test 2; (c) Test 3.**

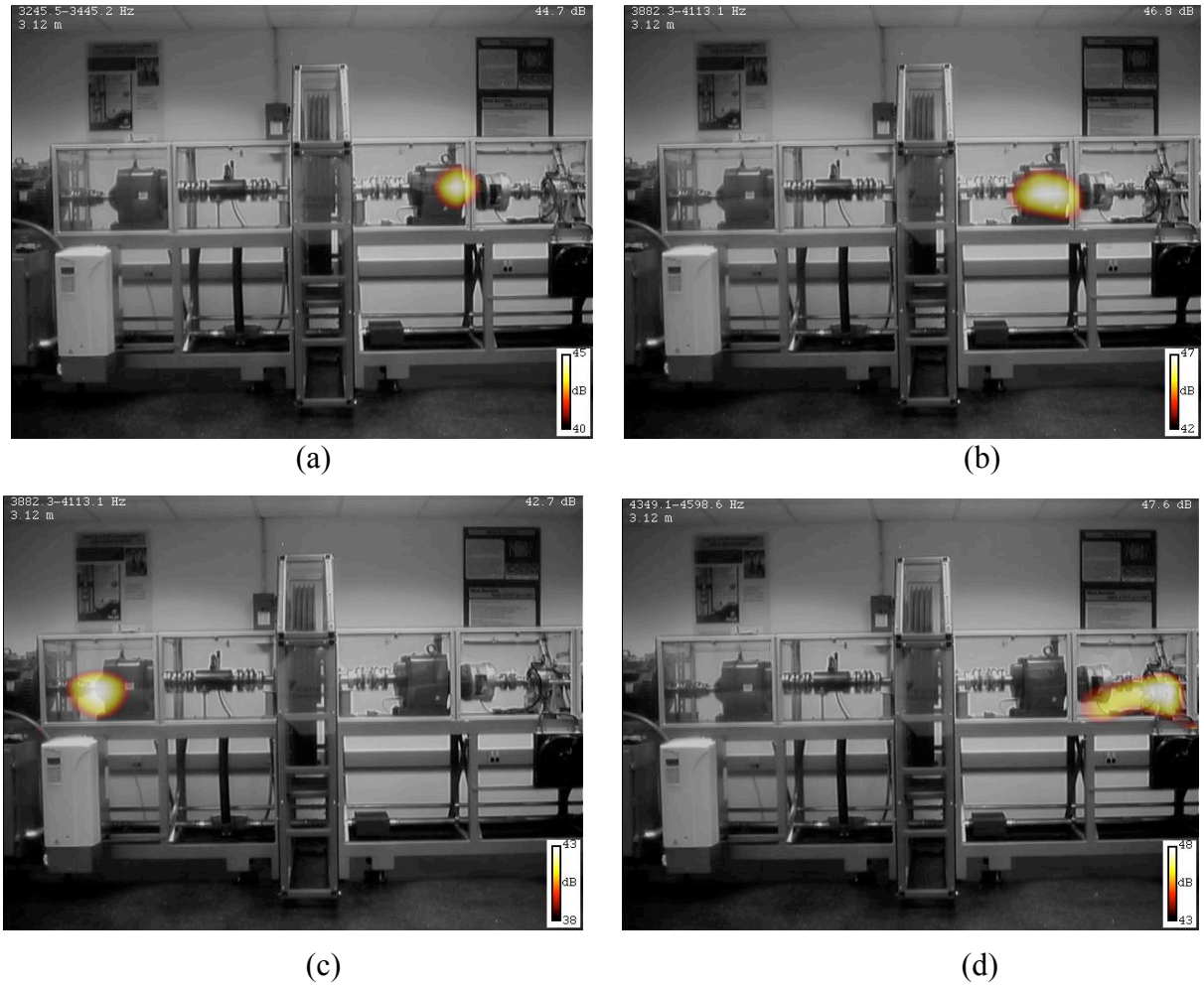


**Figure 8. Beamform plots of; (a) turbine side gearbox noise of Test 1; (b) turbine side gearbox noise of Test 2; (c) drive side gearbox of Test 2; (d) turbine side CVP noise of Test 3.**

## Conclusions

In this paper we described a new test bed created at the Illinois institute of Technology that is capable of conducting an acoustic assessment of small wind turbine drive trains. The facility allows one to vary inflow speeds and turbulence. Acoustic measurements were made using a single microphone and a phased array. The phased array was initially calibrated using three 4 ohm dual cone speakers. The beamforming algorithms were able to locate the source/sources when they were subjected to a broadband white noise. We observed that although the FDBF, DMS2 and TIDY are formulated for incoherent sources, they were able to locate the sources in the coherent cases as well. The formulation of CLSC was clearly evident as it picks only the highest amplitude coherent source from the beamform map. While algorithms FDBF, DMS2 and CLSC are limited to a small bandwidth analysis, TIDY can analyze large bandwidth. The algorithms also located the source in case of moving sources. From the experiments we learn that for high frequency broadband noise TIDY is a good algorithm to use and for low frequencies super resolution algorithms such as MUSIC have to be used to effectively locate the sources.

Although our study provides some guidance on beamforming algorithm choice, further studies are necessary to determine the best suited algorithm for wind turbine applications.

## Acknowledgement

The work described in this paper was funded by the US Department of Energy (DOE) with Mr. Brian Connor as Program Manager. The authors appreciate the guidance and technical support provided by Dr. Robert Dougherty of OptiNav Inc.

## References

[1] P. Sijtsma, “CLEAN based on spatial source coherence”, *International Journal of Aeroacoustics* 6 (4) (2007), pp. 357–374.

[2] T. F. Brooks and W. M. Humphreys, “A deconvolution approach for the mapping of acoustic sources (DAMAS) determined from phased microphone arrays”, *Journal of Sound and Vibration*, vol. 294, pp. 856–879, Jul. 2006.

[3] Dougherty, R.P, “Extensions of DAMAS and benefits and limitations of deconvolution in beamforming,” AIAA–2005–2961.

[4] Dougherty, R.P. and G.G. Podboy, “Improved phased array imaging of a model jet,” AIAA Paper 2009-3186, Miami, FL, May 2009.

[5] Oerlemans, S., Sijtsma, P., and Mendez Lopez, B., “Location and quantification of noise sources on a wind turbine,” Journal of Sound and Vibration, Vol. 299, pp. 869-883, 2007.

[6] Ganesh Raman, “Wind turbines: clean, renewable and quiet?”, Noise & Vibration Worldwide, vol. 40, pp. 15-21, Nov. 2009.

[7] Ganesh Raman, “Advances in measuring noise from wind turbines”, Noise & Vibration Worldwide, vol. 41, pp. 19-25, Apr. 2010.

# A Back EMF-based Rotor Position Prediction in Permanent Magnet Machines for Survivable Wind Generator Systems

Xiaodong Shi, Jorge Pineiro Serradilla and Mahesh Krishnamurthy
Electric Drives & Energy Conversion Lab
Illinois Institute of Technology
3301 S Dearborn Street
Chicago, IL 60616 USA
EML: kmahesh@ece.iit.edu; URL: http://drives.ece.iit.edu

***Abstract*-In wind power generators, position information is often required for tracking maximum power point as well as implementing control strategies for the Permanent Magnet (PM) generator. For such a system, failure of position sensor could potentially lead to major fault or require the system to be shut down. This could cause significant economic losses and also require unscheduled maintenance. This paper proposes a new sensorless position estimation approach to track position of the PM machine using the back EMF if the position sensor fails. This technique can also be used to provide initial rotor position for the proper implementation of a fall-back strategy. This technique can also be extended to detect position information at low speeds. Simulation and experimental results have been presented showing the effectiveness the proposed scheme and validate the claims presented.**

***Keywords: PM Machines, Position Estimation, Survivable Drives, Wind Generation***

## I. INTRODUCTION

Permanent Magnet (PM) machines have been frequently used in wind power generation due to their compactness, reliability, high torque density, high efficiency and structural simplicity [1], [3], [4]. They can operate at a fixed speed to obtain synchronous power [2]. These systems typically require information regarding shaft position and speed in order to control it properly and employing Maximum Power Point Tracking (MPPT) schemes. Researchers have typically used two methods to detect the rotor position. One method is to install position sensors to PM machines such as optical encoders or hall sensors. The advantage of these position sensors is that they are usually very accurate. For such systems, in the event of a failure of the position sensor, the system usually has to be turned off. Another method to get the position information is sensorless prediction. Sensorless prediction can be cost-effective compared to the use of position sensors if the algorithm uses information already available from feedback sensors. Therefore, several sensorless techniques have been developed over the last two decades for motoring and generating applications [5].

This paper presents a new approach for the detection of rotor positions in PM machines in the event of failure of the position sensor in generators for wind power systems. The technique can be broadly described using three operating periods. During "Normal Operation Period", position sensor is used to detect the shaft position for controlling the generator. In case the position sensor fails, power is removed immediately by turning off all the six switches of the inverter. During this period, the PM machine continues to spin down due to inertia and the operation of the PM machine enters a "Transition Period". During this period, the proposed back EMF based sensorless prediction is employed to keep tracking the position of the rotor shaft. Using this information, the machine can be turned on again at certain desired commutation point and the operation of the PM machine reaches to the "Revival Period". During this period, the PM machine could be controlled by a relatively simple control strategy, such as digital control [6] to meet the minimum requirement of the wind power generation based on the second sensorless technique proposed in this paper. Two sensorless techniques have been proposed and implemented during the "Transition Period" and "Revival Period". Simulation and experimental results are included to prove the practicality of the proposed approach.

## II. REVIEW OF ROTOR POSITION PREDICTION TECHNIQUES FOR PM MACHINES USING BACK EMF

Sensorless rotor position prediction for PM machines has received increasing attention over the last decade. Many methods have been proposed by researchers. These methods could be divided into three different categories: Motional-EMF based prediction [7], Inductance variation based prediction [8] and Flux-Linkage variation based prediction [5]. Back-EMF based sensorless control techniques are very popular due to the direct relation between the back EMF waveforms and the rotor position. Some Back EMF based techniques are briefly discussed in this section.

### *A. Terminal voltage sensing*

This method estimates commutation points by looking at the BLDC back EMF and phase current signals [7]. For ideal operation of the BLDC machine, the phase current and back EMF should be aligned in phase to generate a constant torque. Therefore, the current commutation point can be estimated by the zero crossing point of the back EMFs and a proper degree phase shift. A disadvantage of this method is

that only commutation points could be measured and the position information is not continuous.

*B. Back EMF integration*

This technique uses the integration of the back EMF of the silent phase to determine the commutation points [9]. The integrated area of the back EMF is approximately the same for different speed values. Therefore the commutation point will be at the same value. When the integrated area reaches this value the current is then commutated. This method is also focused on the commutation points instead of continuous position information.

*C. Third harmonic of the back EMF*

Using third harmonic signals of the back EMF is another possible way to determine the current commutation instants [10]. As the third harmonic has three times greater frequency, it makes this method less sensitive to time delay of a low power filter. External hardware is necessary to measure the third harmonics. Mathematically, it has been demonstrated that the zero crossings of the integrated third harmonic flux linkage are commutation points. This method has wider speed range than the previous two methods. But the position information is also not continuous.

*D. Freewheeling diode conduction*

This technique is based on letting current flow through a freewheeling diode in silent phase [11]. Every time back EMF crosses zero, a small current flows through the freewheeling diode during the period when the active phase switches are turned off under a switching control. The main drawback of this method is the need of using six isolated power sources for the comparator circuit in order to detect each of the freewheeling currents.

## III. PROPOSED SENSORLESS ROTOR POSITION ESTIMATION

*A. Back EMF based sensorless technique during transition period*

During "Transition Period", as mentioned in the introduction, no power is extracted from or supplied to the PM machine. As a result, there is no armature reaction during this period. Under this condition, three back EMF signals can be easily obtained by measuring the stator voltage of the PM machine. In addition, while the rotor speed begins to decrease, it still spins at a relative high speed due to inertia. Therefore, Back EMF based sensorless position estimation can be accurate during this period before the shaft speed goes to very low velocity.

Back EMF waveforms of a PM machine are directly related to the rotor position. Therefore, an algorithm can be created to deduce the rotor position from reading back EMF signals in every instant. In Fig. 1, the measured voltages are first to divided the electrical cycle (360 degrees) into six equivalent areas or zones corresponding to 60 degrees each. Every area is delimited by comparing the voltage values of the three back EMF signals. In other words, every point in which the voltage value of one back EMF signal becomes identical to the other one, a new area begins. Therefore, there are six points in all, delimiting six different areas. These points correspond with 0, 60, 120, 180, 240 or 300 electrical degrees respectively. Representation of the six different areas (from 0 to 360) for sinusoidal back EMF signals is shown in Fig. 1. The rotor position is then estimated by using interpolation of the known position of the two points that delimit the area.

For a complete electrical cycle there are six different combinations to order the back EMF signals from highest to lowest. For our case it can be seen that each of the bounded areas is defined by one of the six possible combinations described in Table I.

From Fig. 1 we observe that the intermediate back EMF signal, which has the highest absolute slope, is characterized by an approximately constant slope from the beginning to the end of the area. That means this signal can be interpreted as a straight line for this interval. The algorithm uses the instantaneous value of this signal to calculate the position using interpolation with the limits of the corresponded area.

This algorithm can be explained using flow charts shown in Fig. 2 and Fig. 3. The first part of the algorithm is shown in Fig.2. It captures input voltages Va, Vb & Vc and identifies the phase with the intermediate value. This value is assigned to $V_{ch}$, which is used to calculate the position and also for the next iteration. Additionally the variable 'abc' is equated to either 1,2, or 3 depending on the voltage assigned in the previous state, Va, Vb or Vc, respectively.

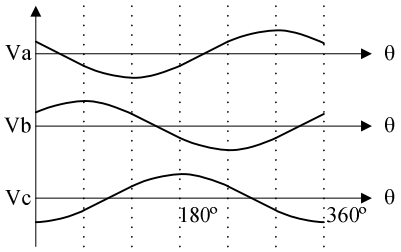


Fig. 1. Sinusoidal back EMF signals separated in six equivalent areas

TABLE I

COMBINATIONS OF VOLTAGES FOR EACH AREA

| Zone | Combination | Highest | Lowest | Middle (Vch) |
|---|---|---|---|---|
| 1 (0-60) | Vb>Va>Vc | Vb | Vc | Va |
| 2 (60-120) | Vb>Vc>Va | Vb | Va | Vc |
| 3 (120-180) | Vc>Vb>Va | Vc | Va | Vb |
| 4 (180-240) | Vc>Va>Vb | Vc | Vb | Va |
| 5 (240-300) | Va>Vc>Vb | Va | Vb | Vc |
| 6 (300-360) | Va>Vb>Vc | Va | Vc | Vb |

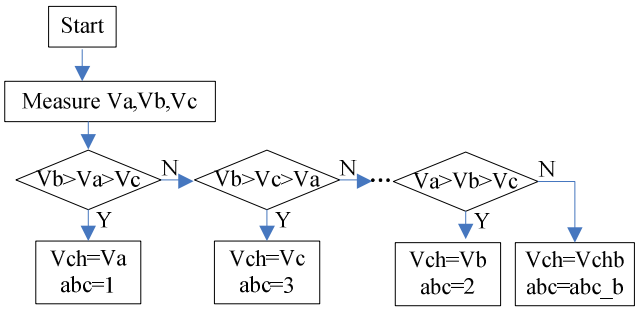


Fig. 2. First part of the algorithm which captures the intermediate voltage

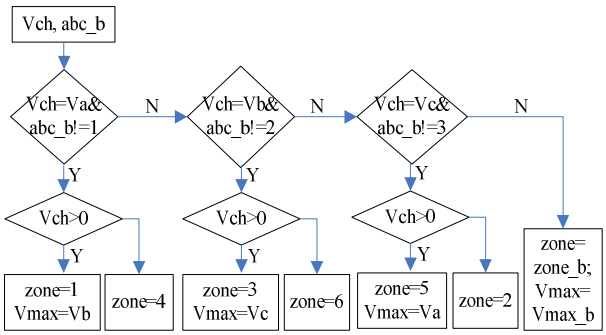

Fig. 3. Second part of the algorithm calculates the zone number and Vmax

The second part of the algorithm is shown in Fig.3. Here the variable 'abc' is used for the next iteration as 'abc_b' to predict if the area has changed with the new value. In other words, if 'abc' is not the same as 'abc_b', it implies that the zone has changed and this point is a maximum or minimum voltage value for $V_{ch}$. If we are at the maximum value ($V_{ch}$ positive), the value is saved in another variable called $V_{max}$, which is used to store the maximum value of $V_{ch}$ to later interpolate the measured voltage and obtain the rotor position. $V_{max}$ is also delayed and fed back to the algorithm so if we are not at the maximum point the value stay constant. This method of calculating the maximum point is useful for cases we change the rotor speed thus the frequency and hence the maximum value of the back EMF also changes.

The rotor position is calculated finally based on the zone and voltage magnitude which is known. Using equation (1), the electrical rotor angle position $\theta$ can be obtained. It must be noted that $\theta$ is always a value between 0 and 360 degrees as it can be seen from the equation used.

$$\theta = 30 + 30*(Z-1) - 30*\frac{Vch}{V\max}*(2*rem(Z,2)-1) \qquad (1)$$

Where $\theta$ is the estimated electrical rotor position in degrees, Z is the zone number, $V_{ch}$ is the instantaneous voltage value of the intermediate back EMF signals, $V_{max}$ is the maximum voltage value at the boundary of each zone.

*B. Back EMF based sensorless technique during survival period*

During "Survival Period", the PM machine needs to turn ON again at a desired commutation point. If we need to control the PM machine and let it operate at fix speed, a "six-step" method is assumed to be used. The initial operation of these six switches of the inverter at this commutation point is given by the previous sensorless technique.

After the machine is powered on, three Back EMF signals can not be obtained easily at the same time due to armature reaction. Therefore, the previous sensorless method can not be used in this period. In order to continue tracking the position information during this period, another Back EMF based sensorless technique is designed and implemented. This algorithm is very similar to the previous one. First, the electrical cycle (360 degrees) is also divided into six equivalent areas, as shown in Fig.1. But in this case, every area is delimited by status of the six switches of the inverter in Fig.4. Every time, when the status of the six switches changes, a new area begins. Therefore, by checking the switch status at each instant, we can identify the area that the rotor enters and a corresponding "idle" phase. Subsequently the back EMF of this "idle" phase can be used to predict the rotor position in this area. Based on the estimated rotor position, the moment at which the rotor position reaches the boundary of the current area can be detected and then the switch status can be changed accordingly.

For a complete electrical cycle there are six different combinations of switch status and back EMF. These combinations could be listed in Table II. Similar to the previous algorithm, the back EMF signal of the unexcited phase can be mathematically expressed by a straight line in each region. At the same time, the voltage values of the extreme points of every area need to be recorded for the interpolation calculation. This value is measured when switch status changes. After that, this algorithm uses the instantaneous value of this signal and the recorded boundary values to calculate the position. This algorithm is explained in detail in the flow charts in Fig.5 and Fig.6.

In Fig.5, we find that this algorithm first captures the back EMF signal of the unexcited phase and zone number by examine the switch status. The voltage value of the back EMF is assigned to $V_{ch}$, which is used to calculate the position. Fig.6 shows the algorithm for capturing the boundary voltage value at the moment when current switch status is different from previous switch status. In other words, if $V_{ch}$=Va, current switch status should be T3=T6=1 or T4=T5=1. If the previous switch status is T1_b=T6_b=1. It reflects a zone change and this point is a maximum or minimum voltage value for $V_{ch}$ value. This value is saved in $V_{max}$ and will be used to interpolate the measured voltage and obtain the rotor position. The rotor position is finally calculated using equation (1) as described in the previous section.

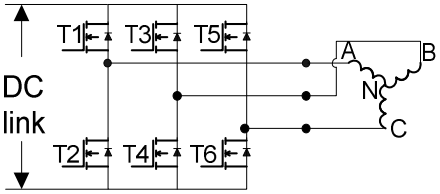

Fig. 4. Back EMF based Simulink Rotor Position Estimation Model

TABLE II
COMBINATIONS OF SWITCH STATUS AND BACK EMF OF UNEXCITED PHASE

| Zone | Switch Status (ON) | Unexcited (Vch) |
|---|---|---|
| 1 (0-60) | T3 T6 | Va |
| 2 (60-120) | T2 T3 | Vc |
| 3 (120-180) | T2 T5 | Vb |
| 4 (180-240) | T4 T5 | Va |
| 5 (240-300) | T1 T4 | Vc |
| 6 (300-360) | T1 T6 | Vb |

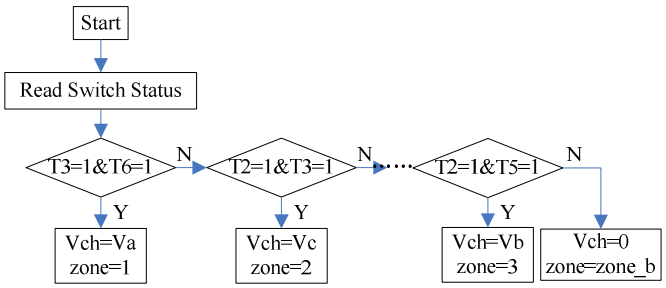


Fig. 5. First part of the algorithm which capture the back EMF of the unexcited phase and calculate the zone number based on switch status.

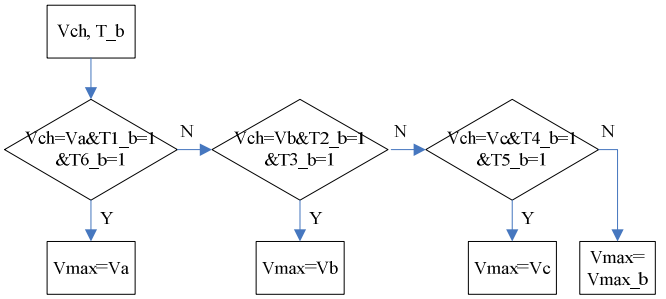


Fig. 6. Second part of the algorithm which captures the boundary voltage value at the moment when the current switch status and previous switch status are different

## IV. SIMULATION AND EXPERIMENTAL RESULTS

### *A. Sensorless technique during "Transition Period"*

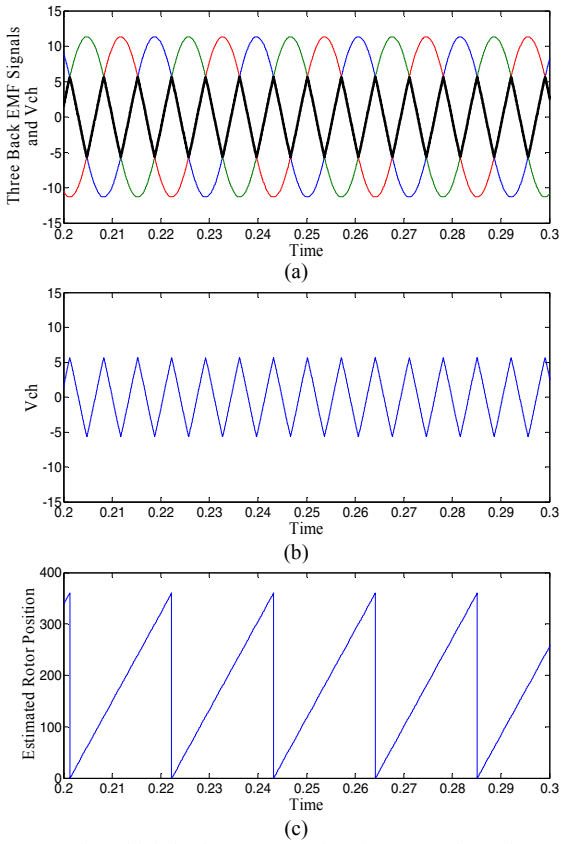


Fig. 7. (a)Sinusoidal back EMFs and reference voltage.(b) Reference waveform Vch. (c) Rotor position estimated in degrees from 0 to 360

During the "Transition Period", power supplied to the machine is removed and the machine spins due to its inertia. Therefore, three back EMF signals can be utilized to predict the rotor position. In this simulation, we made an assumption that the spinning speed of the machine is constant.

This simulation deals with the performance of the first algorithm when three sinusoidal back EMFs generated in Simulink are applied as system input. These waveforms are shown in Fig. 7(a). As mentioned in section III, the first step of the algorithm is to identify the signal which serves as the phase voltage for the rotor position estimation. This signal is formed by the intermediate voltage values of the three back EMF signals. In order to see the behavior of the algorithm in this stage this reference voltage is plotted over the other three voltage signals in Fig. 7(a).

The reference signal $V_{ch}$ is extracted and used for the rotor position estimation. Fig. 7(b) shows the extracted $V_{ch}$. The next step involves comparison of the reference voltage value with every phase voltage to identify the range (zone) for the rotor position. Once the zone is established, the rotor position is estimated using the equation for the back EMF for the idle phase. Fig. 7(c) represents the rotor position (theta) estimated for every point from 0.2 to 0.3 seconds.

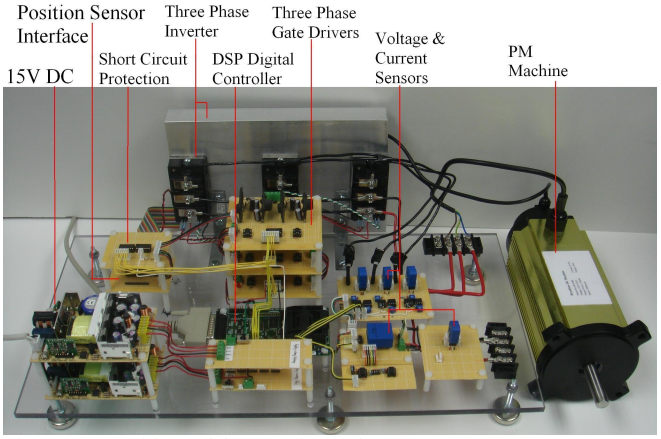


Fig. 8. Compositions of the Experimental setup

Three back EMF signals were sampled from the PM machine which was driven by a prime mover at a constant speed. Reference voltage was captured using the algorithm and plotted over these back EMF signals, as shown in Fig. 9(a). The input signals in this case are not perfectly sinusoidal and change slightly their magnitudes along time. The extracted reference voltage is then used to estimate position of the rotor. The results are shown in Fig.9 (b), which shows a very good estimation of the rotor position at each instant.

The next test was conducted to test the algorithm during the transition period, when the machine spins down due to inertia. This measurement is shown in Fig. 10(a). During this period, the magnitude of back EMF signals keeps decreasing, as expected. The reference voltage was captured using the algorithm and plotted over these three back EMF signals, as

shown by the bold lines in Fig. 10(a). The result of the rotor position estimation in this case is shown in Fig. 10(b). These experimental results verify the accuracy of the proposed sensorless estimation method during transition period.

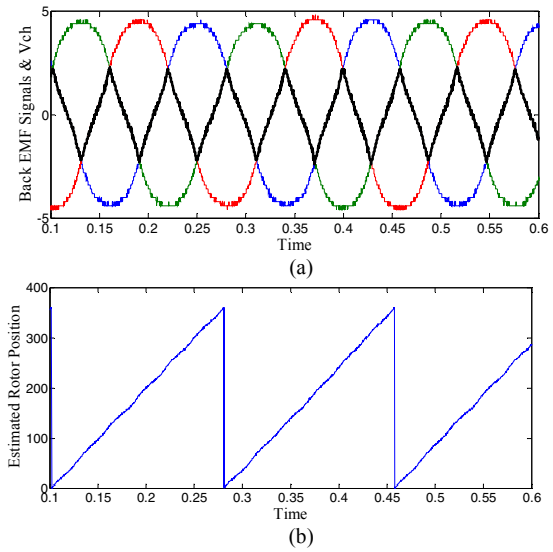


Fig.9. (a) Experimental back EMF signals and Vch. (b) Estimated rotor position in degrees for constant speed

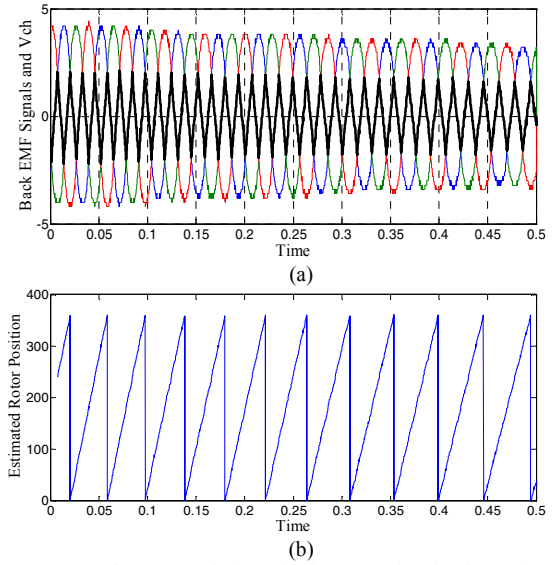


Fig.10. (a) Vch Extracted from back EMF signals (b) Estimated rotor position in degrees during spin down in the event of sensor failure

### *B. Sensorless technique during "Survival Period"*

During this period, the PM machine is turned on again. Therefore, the previous sensorless technique can not be used because these three back EMF signals can not be obtained easily due to armature reaction. This method is based on the back EMF of the unexcited phase of the machine every time by examine the switch status of the inverter. Fig. 11(a) shows the back EMF signals of the unexcited phases. Similar to the previous method, the rotor position can be calculated using equation (1) and its simulation result is shown in Fig. 11(b).

Experimental results are shown in Fig. 12. The PM machine is operated at a constant speed of 500rpm with its current rms value equals to 0.5A. Three phase voltages could be easily obtained by measuring the terminal-to-neutral voltages. As shown in Fig. 12(a) the reference voltage $V_{ch}$ is captured according to the switch status in Fig. 12(b) (Table II) and plotted over these phase voltages. The reference voltage $V_{ch}$ represents the unexcited phase of the PM machine in operation. Based on reference voltage, the rotor potion can be estimated and its result is shown in Fig. 12(c). Fig. 12(d) shows the error of position estimation compared to the actual position from a position sensor. The maximum position error is 10 electrical degrees which is an acceptable value for the operation of the PM generator.

It must be noted that this sensorless technique has some limitations. Line-to-neutral (phase) voltages are not easy to sense due to the unavailability of the neutral point. Phase voltages will be greatly distorted and phase-shifted in high current application due to the strong effect of armature reaction. Therefore, this sensorless technique has been found to be most suitable for low current and low speed application. However, this method meets the operation requirement of the PM generator in wind power applications under position sensor failure.

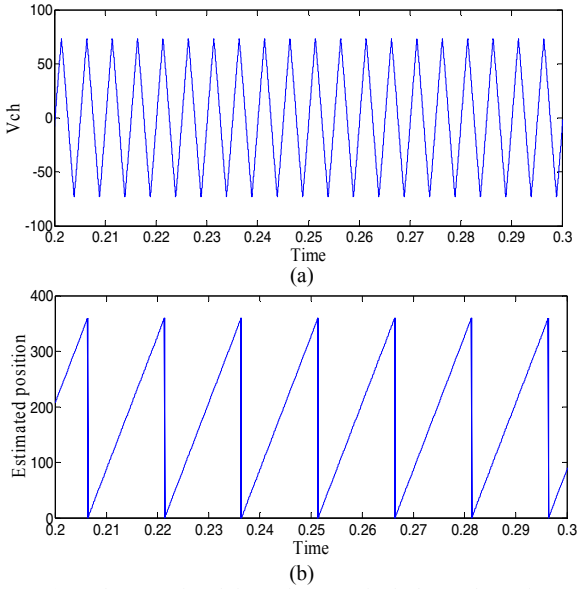


Fig.11. (a) Back EMF signal from the unexcited phase. (b) Estimated rotor position in degrees

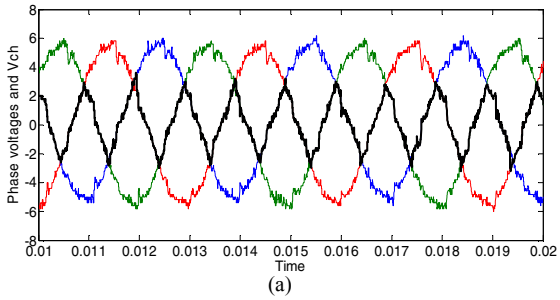

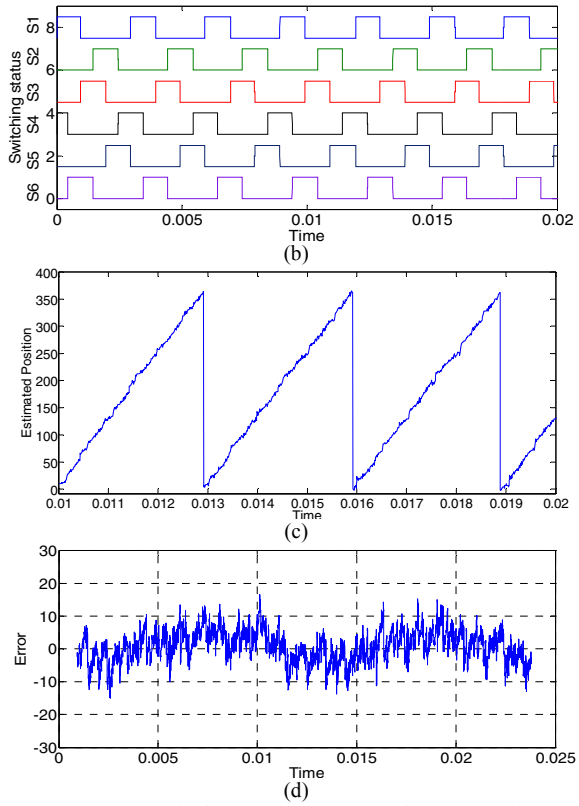


Fig.12 (a) Experimental phase voltages and Vch. (b) Switch status. (c) Estimated rotor position in degrees. (d) Position error in degrees.

### C. *Sensitivity of the proposed techniques to sampling frequency*

The two proposed sensorless techniques are based on the measured back EMF signals and phase voltages. Therefore, voltage sampling frequency is an important factor which determines the accuracy of position prediction. Fig. 13 shows the relationship between sampling frequency and rotor position estimation error. In order to get the best performance of the proposed sensorless estimation methods, sampling frequency above 50 kHz has been recommended.

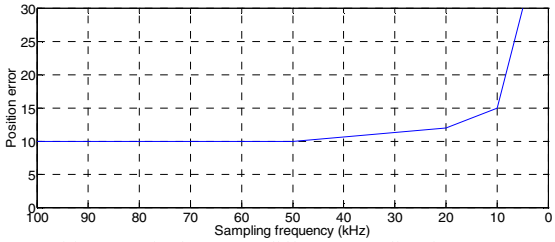


Fig. 13. Position error in degrees at different sampling frequency

## V. CONCLUSION

In this paper, a new approach has been presented for the detection of the PM machines' rotor position under fault conditions in wind power generation. Two sensorless position estimation methods are used to predict the rotor position in two different periods after faults occur. One sensorless position estimated method is design based on the three back EMF signals during transition period when PM machine is powered off. This method can track the rotor position in every instant and could provide the initial position information to the second sensorless method. The second sensorless method is similar, but is based on the back EMF signals of the unexcited phase when machine is powered on again using "six-step" methods. The extraction of the back EMF of the unexcited phase is based on the switch status. Simulation and experiment results have been presented in this paper to validate the effectiveness of these two sensorless position estimation methods, which make the operation of PM machine during fault condition possible.

## ACKNOWLEDGEMENT

Authors would like to thank the U.S. Department of Energy grant number # DE-EE 0002979: "A World-Class University-Industry Consortium for Wind Energy Research, Education, and Workforce Development" for funding this project.

## REFERENCES

[1] Z.Chen, J.M.Guerrero and F.Blaabjerg, "A Review of the State of the Art of Power Electronics for Wind Turbines", *IEEE Trans. Power Electronics*, Vol.24, No.8, Aug, 2009, pp: 1859-1875

[2] R. Poore and T. Lettenmaier, "Alternative design studyreport: WindPACT advanced wind turbine drive train designs study", NREL, Golden, CO, Rep. Number NREL/SR-500-33196, 2003, Available: http://www.nrel.gov/docs/fy03osti/33196.pdf

[3] H.Polinder, F.A.van der Pijl, G.de Vilder and P.J.Tavner, "Comparison of Direct-Drive and Geard Generator Concepts for Wind Turbines", *IEEE Trans. Energy Conversion*, Vol.21, No.3, Sep.2006, pp: 725-733

[4] M.E.Haque, M.Negnevitsky and K.M.Muttaqi, "A Novel Control Strategy for a Variable-Speed Wind Turbine with a Permanent-Magnet Synchronous Generator", *IEEE Trans. Industry Application*, Vol.46, No.1, Jan/2010, pp: 331-339

[5] P. P. Acarnley and J. F. Watson, "Review of Position-Sensorless Operation of Brushless Permanent-Magnet Machines", *IEEE Trans. Industrial Electronics*, Vol.53, No.2, April, 2006, pp:352-362

[6] A.Sathyan, N. Milivojevic, Y. Lee, and M. Krishnamurthy, "An FPGA-Based Novel Digital PWM Control Scheme for BLDC Motor Drives", *IEEE Trans. Industrial Electronics*, Vol.56, No.8,Aug.2009, pp: 3040-3049

[7] K.Iizuka, H. Uzuhashi, M. Kano, T. Endo and K. Mohri "Microcomuter Control for sensorless Brushless Motor", *IEEE Trans. Industry Applications*, Vol.IA-21, No.4,May.1985, pp: 595-601

[8] M.Krishnamurthy, C. S. Edrington and B. Fahimi, "Prediction of Rotor Position at Standstill and Rotating Shaft Condition in Switched Reluctance Machines", *IEEE Trans. Power Electronics*, Vol.21, No.1, Jan.2006, pp:225-233

[9] T.M. Jahns, R.C. Becerra, and M.Ehsani, "Integrated current regulation for a brushless ECM drive," *IEEE Trans. Power Electron*., vol. 6, Jan. 1991, pp.118–126.

[10] J. C. Moreira, "Indirect sensing for rotor flux position of permanent magnet AC motors operating over a wide speed range," *IEEE Trans. Ind*. Appl., vol. 32, no. 6, pp. 1394–1401, Nov./Dec. 1996.

[11] S.Ogasawara and H.Akagi, "An approach to position sensorless drive for brushless dc motors," *IEEE Trans. Ind. Applicat*., vol. 27,Sep./Oct.1991, pp:928–933

# Concept and Implementation of a Simplified Speed Control Strategy for Survivable Induction Motor Drives

Xiaodong Shi, *Student Member*, *IEEE* and Mahesh Krishnamurthy, *Member*, *IEEE*
Electric Drives & Energy Conversion Lab
Electrical and Computer Engineering Department,
Illinois Institute of Technology
3301 S Dearborn Street, Chicago, IL 60616 USA
EML: kmahesh@ece.iit.edu, URL: http://drives.ece.iit.edu

***Abstract*-Induction machine is one of the most widely used machines in residential and industrial applications. Traditional drive methods for induction machines such as vector control usually require complex control routines, fast processing unit and multiple system status feedbacks. The complexity of these methods greatly reduces the reliability of the system since the failure of the sensor or even the drift of system parameters could potentially result in system malfunction. This creates the need for a simple, cost-effective and reliable control strategy as a backup to continue operation of the system in case of failure of current and voltage feedback sensors. In this paper, an effective, yet simple and low-cost state switching control technique is proposed and implemented for a three phase squirrel cage induction machine system. This state switching control operates at two specific duty cycles of PWM which produces phase voltages with different magnitudes across the phase windings. At the same time, the frequency of phase voltages is derived from the reference speed. By switching between these two states, precise speed regulation can be achieved. This new control method makes the controller extremely simple in design and implementation for induction machine. Simulation and experimental results are included in this paper to validate our claims.**

***Keywords: Induction Machines (IM), State Switching Control, Survivable Drive, Pulse Width Modulation (PWM)***

## I. INTRODUCTION

Induction machines (IM) have been widely used in a variety of industrial and residential applications. This is primary due to their compactness, reliability, and low costs. In order to control induction machine properly and efficiently, different kinds of control strategies emerged in the past. Among these control strategies, most commonly used control strategies are constant V/f control and vector control.

Constant V/f control [1], [2] is popular for induction machine mainly because of its simplicity. In general purpose applications, most constant V/f controls are open-looped and control the voltage and frequency proportionally. By applying a specific phase voltage and frequency to induction machine, it can settle down at a desired speed. However, the speed control of conventional constant V/f controls lacks accuracy due to the existence of the rotor slip. When load increases or frequency decreases, rotor slip increases. This results in the increase of error between reference speed and actual speed. In order to deal with these problems, stator voltage boost [3]-[5] and slip compensation methods [4], [5] are often used. However, these methods increase the complexity of the system and require additional voltage or current sensors.

Vector control strategy [6]-[8] has gained popularity over the last three decades due to its high efficiency and better transient performance. This method controls the flux and torque of induction machine separately and hence enables an easy and effective control as for DC-machines. Vector control turns out to be the most efficient and promising control strategy for induction machine. However, the practical implementation of vector control is complicated and expensive. Fast processing devices, such as DSP and even computer, are often required to perform complex calculations including Clark, Park transformation and Rotor Flux Estimation with the knowledge of induction machine parameters. In addition, at least two current sensors and one position sensor is necessary to meet the minimum feedback requirements of vector control. As a result, the failure of the sensor or even the drift of system parameters could potentially result in system malfunction.

The possibility of system failure when advanced control methods are utilized creates the need for a simple, cost-effective and reliable control strategy as a backup control strategy to continue operate the system in case of failure of current and voltage feedback sensors. One of the techniques that have shown promising performance in recent years is "Digital Control" [9]-[12]. This control method has been shown to be simple and effective for several applications, such as BLDC & SRM control and DC-DC converter control. This technique requires no additional hardware and is not computationally intensive, which also makes it ideal for FPGA implementation. Therefore, use of such a control technique as a backup control strategy to continue operate the induction generator when fault happens, system would become much more reliable and fault tolerant.

This paper presents the concept and implementation of state switching control technique for induction machine based on the principle of digital control but specifically designed for induction machine. Specific gate signals for inverter are derived from six-step drive method [1] by integrating PWM signals to conventional gate signals of six-step drive. This enables the change of phase voltage magnitude by manipulating the duty cycle of PWM signal. Meanwhile, frequency of phase voltage is directly calculated from reference speed. As a result, by applying state switching control, the induction generator system is only allowed to operate at two different duty cycles of PWMs which are given to the inverter and produce phase voltages with different

magnitudes. Speed regulation is achieved by switching between these two different PWM duty cycles with the frequency of the phase voltage directly obtained from the given reference speed. Therefore, this controller is extremely simple in implementation and only speed sensor is required for speed regulation. This enhances reliability of the control technique and reduces complexity in hardware implementation. While phase current distortion is a challenge due to the lack of current observation, the overall performance of this method is highly acceptable and thus can be used as a backup control strategy. Simulation and experiment results presented in this paper prove the effectiveness of the proposed approach.

## II. Six-step Drive Method For Induction Machine

For a three phase induction machine, the most frequently used driver topology is the three phase inverter which can be illustrated in Fig.1. This inverter includes six switches (MOSFETs or IGBTs) and six freewheeling diodes. By applying specific signals to these switches, induction machine can be operated properly.

Six-step drive method [1] is one of the simplest methods to drive the induction machine. Gate signals from the inverter are shown in Fig.2. In every electrical circle, each switch is turned on for 180 electrical degrees. The switching status of the upper and lower switches of each phase is always complementary in order to avoid short circuit. At the same time, for different phases, switching statuses are 120 electrical degrees phase shifted from each other. In other words, only three switches are turned on for every 60 electrical degrees. Two in high side and one in low side, or one in high side and two in low side. Therefore, for a wye-connected three phase induction machine, three six-stepped and quasi-sine phase voltages can be formed in the stator winding of the induction machine. These phase voltages are illustrated in Fig.2.

The implementation of the six-step drive method is also very simple. The electrical cycle is first divided into six equivalent regions with 60 degrees each. Each region corresponds to a specific combination of switching status. These combinations can be described in Table I. Finally, by generating these gate signals and applying them to the inverter with proper frequency, the induction machine can be operated.

## III. Proposed State Switching Control Method For Induction Machine

### *A. Principle of State Switching Control of Induction Machine*

Speed control of induction machine involves two parameters--the magnitude and frequency of the applied voltage across the phase winding. The frequency of the applied phase voltage mainly determines the shaft speed of the induction machine. This relationship can be explained in the following equations.

$$\omega_s = \frac{2\pi f_s}{P} \tag{1}$$

$$\omega_r = \omega_s(1-s) \tag{2}$$

where $\omega_s$ is the synchronous speed of the induction machine in rad/s, $f_s$ is the frequency of the applied phase voltage in Hz, $P$ is the number of pole pairs, $\omega_r$ is the speed of the shaft in rad/s and s is the slip rate.

By changing the frequency of the phase voltage, synchronous speed can be changed. At the same time, the variation of the synchronous speed results in the change of the shaft speed since shaft speed is very close to the synchronous speed at steady-state. Therefore, the shaft speed can be determined mainly by the frequency of the phase voltage. On the other hand, if the reference speed of the shaft is defined, frequency of the applied phase voltage can also be determined using equation (1) and (2).

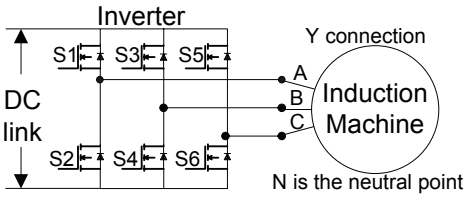


Fig.1. Inverter for induction machine

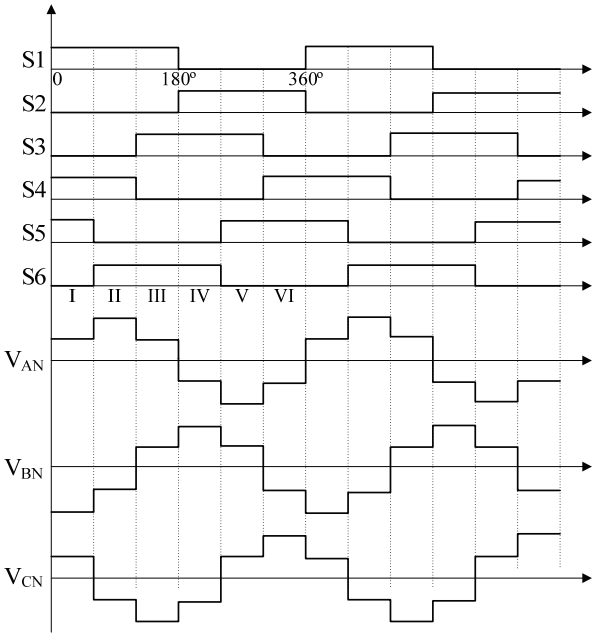


Fig.2. Six-Step waveform

TABLE I
Switching Status for Different Regions of Six-step Drive Method

| Region No. | Switch Status | | | | | |
|---|---|---|---|---|---|---|
| | S1 | S2 | S3 | S4 | S5 | S6 |
| I | ON | OFF | OFF | ON | ON | OFF |
| II | ON | OFF | OFF | ON | OFF | ON |
| III | ON | OFF | ON | OFF | OFF | ON |
| IV | OFF | ON | ON | OFF | OFF | ON |
| V | OFF | ON | ON | OFF | ON | OFF |
| VI | OFF | ON | OFF | ON | ON | OFF |

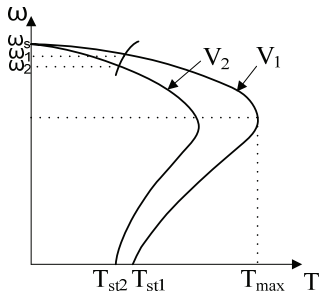

Fig.3 Speed torque characteristics at different voltage level

The magnitude of applied phase voltage is also a factor which could affect the shaft speed. This relationship is shown in Fig.3 [13]. If the magnitude of the applied phase voltages is increased (V1>V2), the torque performance of the induction machine will be changed, as a result, the shaft speed will increase slightly (ω1>ω2), but the synchronous speed will be the same.

Based on the above analysis as well as the six-step drive method, a state switching control technique can be designed and expressed in Fig.4. Based on the reference speed ($\omega_{ref}$), the applied phase frequency can be defined using equation (1) and (2) if slip is approximated to be constant (5% in this case). By applying this frequency to the induction machine with proper magnitude of the phase voltage, shaft speed can be obtained, which is close to the reference. Then, by comparing the actual speed to the reference speed, the magnitude of the phase voltage can be switched between high voltage level ($V_H$) and low voltage level ($V_L$). As a result, the actual speed ($\omega_{act}$) of the induction machine can be regulated accurately. In other words, the definition of the synchronous frequency achieves the coarse tuning of the shaft speed while the switching between two PWM duty cycles accomplishes the fine tuning of the shaft speed.

The change of the magnitude of the applied phase voltage is done by a new drive method—PWM six-step drive method. As shown in Fig.5 and Table II, compared to traditional six-step drive method which is shown in Fig.2, switches are given PWM gate signals instead of turning them "ON" all the time for 60 electrical degrees. As a result, in Fig.5, the phase voltages are also PWM shaped if the load is resistive. Therefore, by changing the duty cycle of the PWM, the magnitude of the phase voltage of the induction machine can be changed.

Therefore, the principle of the state switching control of induction machine can be shown in Fig.6 and concluded as follow:

1. The reference speed determines the frequency of the applied phase voltage. In our case, it determines the frequency of the six-step waveform.
2. The duty cycle ($d_L$ or $d_H$) of the PWM is determined by comparing the actual speed ($\omega_{act}$) with the reference speed ($\omega_{ref}$). The frequency of the PWM is set to 5 kHz in our case.

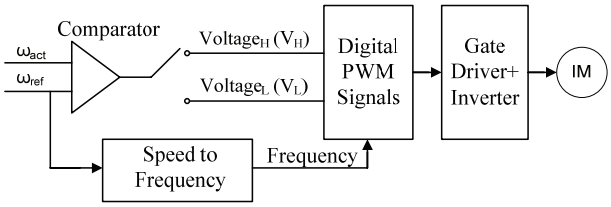

Fig.4 Principle of state switching control of induction machine

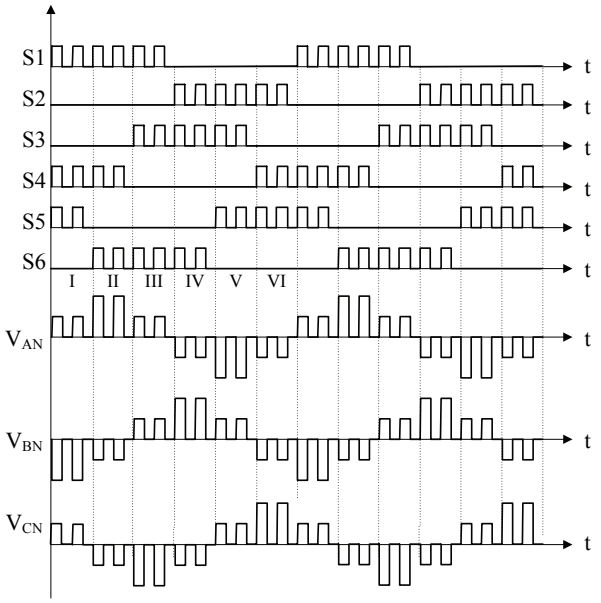

Fig.5 PWM six-step waveform

TABLE II
SWITCHING STATUS OF PWM SIX-STEP DRIVE METHOD

| Region No. | Switch Status | | | | | |
|---|---|---|---|---|---|---|
| | S1 | S2 | S3 | S4 | S5 | S6 |
| I | PWM | OFF | OFF | PWM | PWM | OFF |
| II | PWM | OFF | OFF | PWM | OFF | PWM |
| III | PWM | OFF | PWM | OFF | OFF | PWM |
| IV | OFF | PWM | PWM | OFF | OFF | PWM |
| V | OFF | PWM | PWM | OFF | PWM | OFF |
| VI | OFF | PWM | OFF | PWM | PWM | OFF |

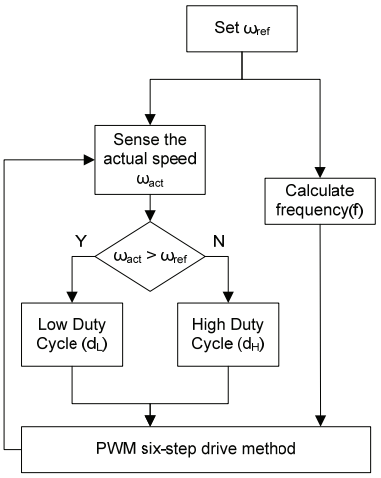

Fig.6 Principle of state switching control of induction machine

### B. *Controller Design of State Switching Control of Induction Machine*

From the torque equation, we have

$$T_e = J\frac{d\omega_m}{dt} + b\omega_m + T_L \tag{3}$$

Where *Te* is the generated electromagnetic torque, $\omega_m$ is the rotor speed in rad/s, *J* is the rotor moment of inertia, *b* is the viscous friction constant and $T_L$ is the load torque.

The rotor induced torque [14] of the induction machine is

$$T_e = \frac{3V_s^2 R_2 / s}{\omega_s\left[\left(R_1 + R_2/s\right)^2 + \left(X_1 + X_2\right)^2\right]} \tag{4}$$

Where $V_s$ is the magnitude of the applied phase voltage, $\omega_s$ is the synchronous speed of the induction machine in rad/s, *s* is the slip, $R_1$ and $X_1$ refers to the stator impedance, $R_2$ and $X_2$ refers to the rotor impedance.

Substituting (4) into (3), we get

$$\frac{3V_s^2 R_2 / s}{\omega_s\left[\left(R_1 + R_2/s\right)^2 + \left(X_1 + X_2\right)^2\right]} = J\frac{d\omega_m}{dt} + b\omega_m + T_L \tag{5}$$

At steady state, the shaft speed $\omega_s$ and the slip s is constant. Meanwhile, stator and rotor impedances are also constant. As a result, equation (5) can be simplified as

$$kV_s^2 = b\omega_{mss} + T_L \tag{6}$$

Where $\omega_{mss}$ is the rotor steady state speed and $k = \frac{3R_2 / s}{\omega_s\left[\left(R_1 + R_2/s\right)^2 + \left(X_1 + X_2\right)^2\right]}$.

Therefore, the relationship between voltage magnitude and rotor speed can be obtained as

$$V_s = \sqrt{\frac{b\omega_{mss} + T_L}{k}} \tag{7}$$

In six step method, the magnitude of the applied phase voltage $V_s$ is 2/3 of the DC link voltage $V_{DC}$. If the duty cycle of the PWM is *d*, we get

$$\frac{2}{3}dV_{DC} = \sqrt{\frac{b\omega_{mss} + T_L}{k}} \tag{8}$$

Therefore, the relationship between the duty cycle and the rotor speed of the induction machine can be expressed as

$$d = \frac{3\sqrt{\frac{b\omega_{mss} + T_L}{k}}}{2V_{DC}} \tag{9}$$

Meanwhile, the frequency of the applied voltage can be calculated using equation (10) which is derived from equation (1) and (2). Slip is considered as a constant which equals to 5% in our simulation and experiment.

$$f = \frac{\omega_{ref} P}{2\pi(1-s)} \tag{10}$$

## IV. SIMULATION RESULTS

In order to verify the feasibility of the proposed state switching control of induction machine, simulation is implemented in Matlab/Simulink. The block diagram of the proposed state switching control of induction machine in simulation is shown in Fig.7, in which a 60Hz, 4 pole induction machine is used with a rated speed of 1725rpm.

Fig.8 shows the speed response of the proposed digitally controlled induction machine. Although the actual speed has a little oscillation during starting period, it quickly settles down and precisely tracks the reference speed.

Fig.9 and Fig.10 are simulation results in steady-state. Fig.9 shows the steady-state speed of the induction machine. The speed error between reference speed and actual speed is very small due to high sampling rate of actual speed. Fig.10 shows the change of duty cycle during steady-state.

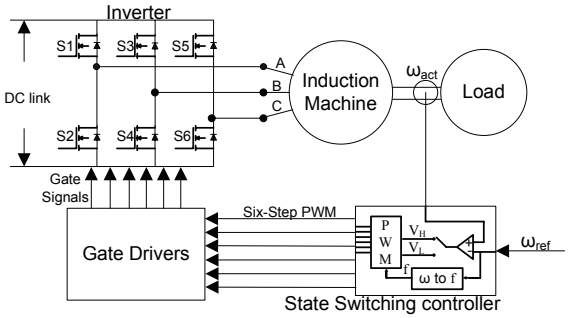


Fig.7 Block diagram of the state switching control of Induction Machine

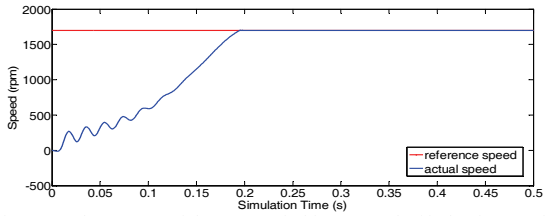


Fig.8 Speed response of the state switching control of induction machine

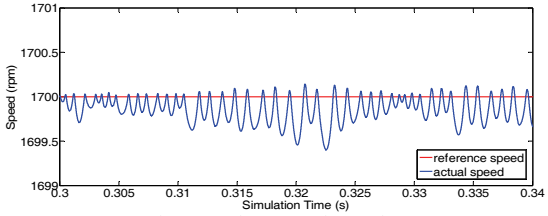


Fig.9 Speed response in steady-state

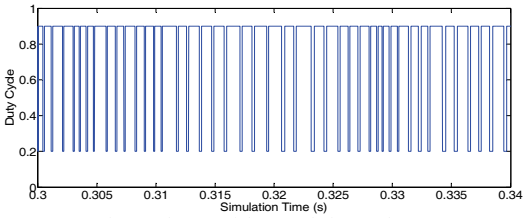


Fig.10 Change of duty cycle in steady-state

## V. EXPERIMENTAL VERIFICATION

In order to verify the effectiveness of the proposed state switching control method for induction machine as well as its simulation results, an experimental setup has been developed which is shown in Fig.11. It includes a 3.9kW DC power supply, a TMS320F2812 based DSP controller, three phase inverter and gate drivers, a 2.2kW induction machine and a 3kW PM DC Load. Specifications regarding the induction machine and the PM DC load are listed in Table III.

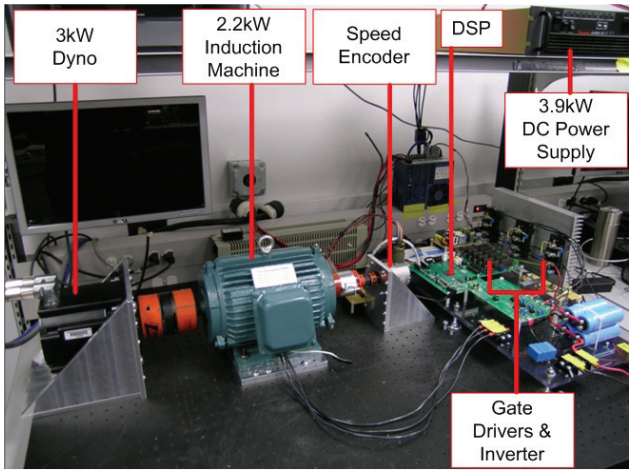


Fig.11 Hardware setup for experimental verification of proposed state switching control strategy of an Induction Machine

TABLE III
PARAMETERS OF THE INDUCTION MACHINE AND PM DC LOAD

| | Induction Machine | PM Dyno |
|---|---|---|
| Rated Power | 2.2kW | 3 kW |
| Rated RPM | 1420 | 6000 |
| Rated Volts | 380/Y Conn. | 640DC |
| Rated Current | 5A/phase | 12.4A/phase |
| No. of poles | 4 | N/A |
| No. of phases | 3 | 3 |

Fig.12 to Fig.19 show experimental results obtained from the setup under different operating conditions. Fig.12 shows the speed response of the induction machine when reference speed is 1025rpm and load torque is 1Nm. It can be seen that the actual speed of the induction machine quickly settles down to the reference and tracks it precisely without any overshoots, which shows fast dynamic response of this control method. Fig.13 shows the phase current profile and the change of PWM duty cycle between $D_H$ and $D_L$. The phase current is distorted with harmonics which is the main trade-off in the implementation of this control technique.

Similarly, Fig.14 and Fig.15 show results when reference speed is 366rpm and load is 1Nm. From these figures, it can be noticed that the proposed state switching control method also has a wide range of speed regulation capability.

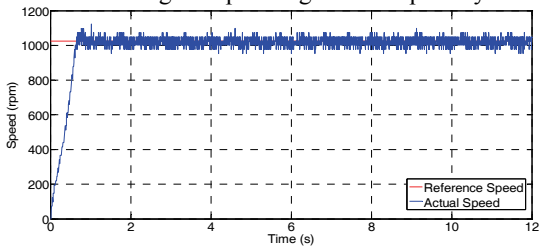


Fig.12 Speed response when reference speed is 1025rpm and load torque is 1Nm

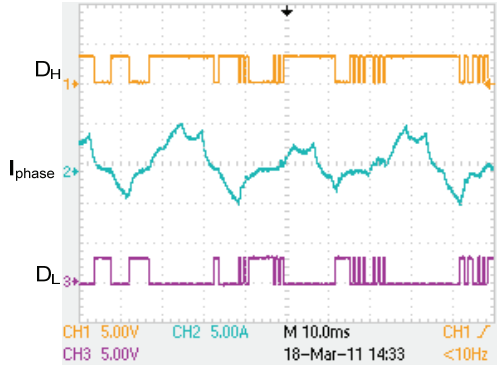


Fig.13 Phase current and change of PWM duty cycle when reference speed is 1025rpm

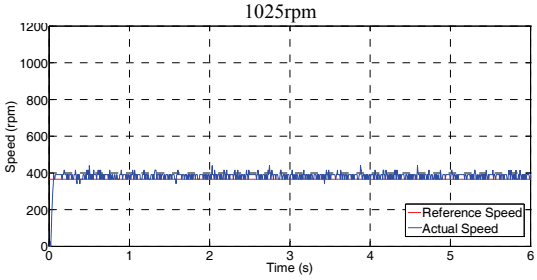


Fig.14 Speed response when reference speed is 366rpm and load torque is 1Nm

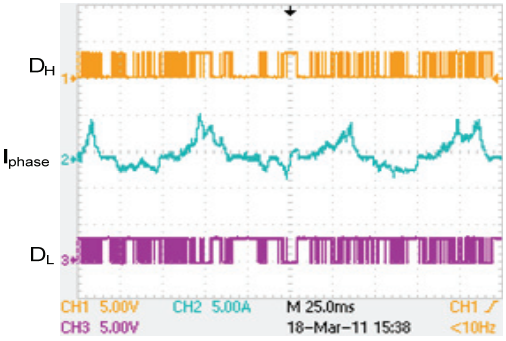


Fig.15 Phase current and change of PWM duty cycle when reference speed is 366rpm

In order to test the performance of the control strategy for sensitivity to change in operating conditions, a step change in load torque and reference speed was applied to the machine. Fig.16 shows the speed response of the induction machine when load torque was changed from 0.5Nm to 1.5Nm. Fig.17 and Fig.18 shows the phase current, change of PWM duty cycle before and after torque change respectively. Fig.19 shows the speed response of the induction machine when

reference speed was changed from 1025rpm to 366rpm (load torque is 1Nm). System can responds to any change in speed command within an acceptable time period.

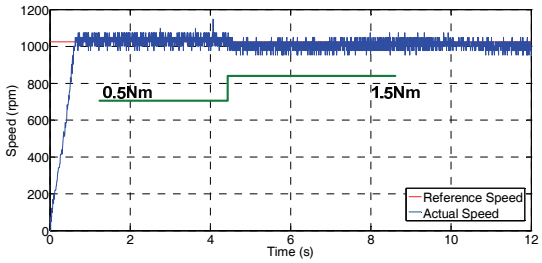


Fig. 16 Speed response when reference speed is 1025rpm and load torque changes from 0.5Nm to 1.5Nm

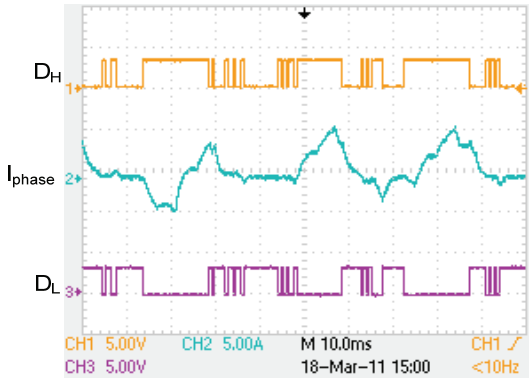


Fig. 17 Phase current and change of PWM duty cycle when load torque is 0.5Nm

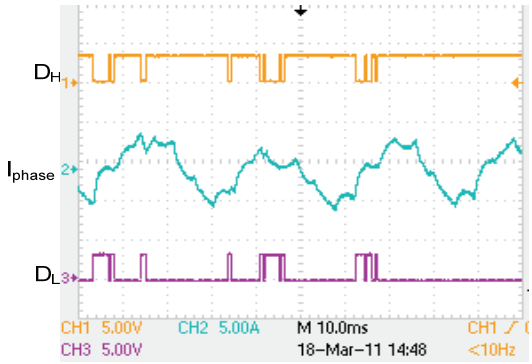


Fig.18 Phase current and change of PWM duty cycle when load torque is 1.5Nm

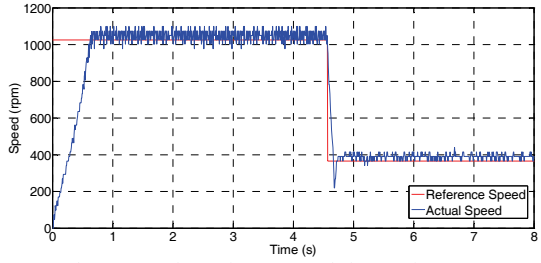


Fig.19 Speed response when reference speed changes from 1025rpm to 366rpm

## VI. CONCLUSIONS

This paper presents a simple, low-cost and effective state switching control technique which has wide speed regulation capability and can be used as backup control strategy in the event of sensor failure. This method is based on PWM six-step drive method, in which two different PWM duty cycles are predefined. At the same time, the frequency of the phase voltage is directly derived from the reference speed. By switching between two PWM duty cycles, the shaft speed of the induction machine can be accurately regulated. Owing to its simplicity, this strategy can be implemented on device with low computational capability and therefore requires no additional hardware. In addition, only speed feedback is necessary for this method, which significantly enhances the reliability of the system with highly acceptable performance. Simulation and experiment results presented in this paper demonstrate feasibility of the proposed approach.

## ACKNOWLEDGEMENT

The authors would like to thank the financial support provided by the Department of Energy (Grant No. DE-EE 0002979) for conducting this research.

## REFERENCES

[1] R. Krishnan, *Electric Motor Drives--Modeling, Analysis, and Control.* New Delhi: Prentice/Hall of India, 2007, pp. 317-345

[2] R. Ueda, T. Sonoda, K, Koga and M. Ichikawa, Stability Analysis in Induction Motor Driven by V/f Controlled General-Purpose Inverter, *IEEE Trans. Ind. App.*, Vol. 28, No. 2, Mar/Apr. 1992, pp 472-481

[3] R. Yang, W. Chen, Y. Yu and D. Xu, A Novel V/f Control System Based on Stator Voltage Oriented Method, *IEEE Conf. Electrical Machines and Systems*, 2008, pp. 83-87

[4] A. Munoz-Garcia, T. A. Lipo and D. W. Novotny, A New Induction Motor V/f Control Method Capable of High-Performance Regulation at Low Speeds, *IEEE Trans. Ind. App.*, Vol. 34, No. 4, Jul/Aug. 1998, pp. 813-821

[5] M. Tsuji, S. Chen, S. Hamasaki, X. Zhao and E. Yamada, A Novel V/f Control of Induction Motors for Wide and Precise Speed Operation, *IEEE Conf. Power Electronics, Electrical Drives, Automation and Motion*. 2008, pp. 1130-1135

[6] J. A. Santisteban and R. M. Stephan, Vector Control Methods for Induction Machines: An Overview, *IEEE Trans. Education*, Vol. 44, No, 2, May, 2001, pp. 170-175

[7] S. Wade, M. W. Dunnigan and B. W. Williams, Modeling and simulation of induction machine vector control with rotor resistance identification, IEEE Trans. Power Electron., Vol. 12, No. 3, May, 1997, pp. 495-506

[8] Y. Lai, Machine Modeling and Universal Controller for Vector-Controlled Induction Motor Drives, IEEE Trans. Energy Conversion, Vol. 18, No.1, Mar.2003, pp.23-32

[9] A. Sathyan, N. Milivojevic, Y. Lee, M. Krishnamurthy and A. Emadi, "An FPGA-Based Novel Digital PWM Control Scheme for BLDC Motor Drives", *IEEE Trans. Ind. Electron.*, Vol. 56, No.8, pp. 3040-3048, Aug.2009

[10] F. Rodriguez and A. Emadi, "A Novel Digital Control Technique for Brushless DC Motor Drives", *IEEE Tans. Ind. Electron.*, Vol. 54, No. 5, Oct. 2007

[11] A. Khaligh, A. M. Rahimi, Y. J. Lee, J. Cao, A. Emadi, S. D. Andrews, C. Robinson, and C. Finnerty, "Digital control of an isolated active hybrid fuel cell/Li-ion battery power supply," IEEE Trans. Vehicular Tech., vol. 56, pp. 3709 - 3721, Nov. 2007.

[12] A. Khaligh and A. Emadi, Pulse Adjustment, a Novel Digital Control Technique, for Control of a DC-DC Buck-Boost Converter Operating in Discontinuous Conduction Mode and Driving Constant Power Loads, *IEEE conf. Vehicle Power and propulsion*, 2006, pp.1-5

[13] M. A. El-Sharkawi, *Fundamental of Electric Drives.* Toronto: Cengage Learning, 2000, pp. 138-143

[14] S. J. Chapman, *Electric Machinery and Power System Fundamentals.* New York: McGraw-Hill, 2002, pp. 309-313

# Health Monitoring, Fault Diagnosis and Failure Prognosis Techniques for Brushless Permanent Magnet Machines

Yao Da, *Student Member*, *IEEE*, Xiaodong Shi, *Student Member*, *IEEE* and Mahesh Krishnamurthy, *Member*, *IEEE*

Electric Drives and Energy Conversion Laboratory, Electrical and Computer Engineering Department,
Illinois Institute of Technology, 3301 S. Dearborn St., Chicago, IL 60616
*E-mail:* kmahesh@ece.iit.edu , *URL:* http://www.drives.ece.iit.edu/

***Abstract*—** Over the past few years, many researchers have been attracted by the challenges of electrical machines' fault diagnosis and condition monitoring, which provide early warnings that could help schedule necessary maintenance to avoid catastrophic consequence. With advancements in the use of rare-earth magnets, Brushless Permanent Magnet Machines are widely used in industry recently, which has led to the development of numerous fault diagnosis techniques. Considerable papers have presented reviews and compared condition monitoring and fault diagnosis methods for induction machines, but none for Brushless Permanent Magnet Machines. To make a difference, this paper presents a comprehensive survey of modern research advancements and state-of-the-art in health monitoring, fault diagnosis and prognosis techniques for Brushless Permanent Magnet Machines. The symptoms of each type of fault and the principles of diagnosis process are also described and discussed.

***Keywords—Brushless permanent magnet machine, Health monitoring, Fault diagnosis.***

## I. INTRODUCTION

Over the past decade, Permanent Magnet Synchronous Machines (PMSMs) and Brushless DC machines (BLDCs) have gained significant popularity in the industry, especially where high performance is required, owing to higher efficiency, high output power to volume ratio, high torque to current ratio, etc. Some of the commonly occurring faults in PMSMs are eccentricity, bearing failure, demagnetization of permanent magnets, short circuit in the stator or armature winding, etc. Health monitoring and fault diagnosis of the machine could help in scheduling preventive maintenance to length their lifespan and avoid catastrophic system failure. Basic steps for a machine diagnosis scheme are illustrated in Fig.1, where dashed lines indicate non-necessary steps. Considerable papers have presented reviews and compared condition monitoring and fault diagnosis methods for induction machines [1]-[4], but none for Brushless Permanent Magnet Machines. The goal of this paper is to provide a comprehensive review in this area to help fellows to consider what have been done, where we are now, and which direction we might go.

This paper is organized as follows. In Section II, the classification of the common faults is presented. Their causes are explained and their influence on machine parameters is discussed. In Section III, various signatures extraction schemes are presented, analyzing their pros and cons. Section IV discusses various artificial intelligence algorithms for distinguishing different signatures. In Section V, the concept of prognosis is introduced. The summary and conclusions are presented in Section VI.

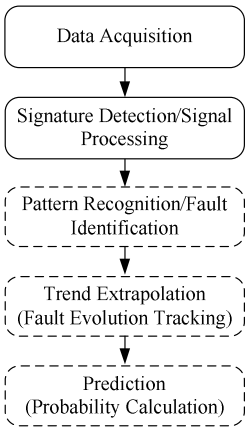


Fig. 1. Basic steps for electric machine diagnosis

## II. TYPES OF FAULTS IN PM MACHINES

In an electric machine, faults can occur in the rotor/field, stator/armature, inverter, or mechanical components connected to it. This paper discusses a permanent magnet machine without focusing on associated inverter faults and bearing faults. Fig. 2 illustrates the most frequently encountered problems for electric machines [5]. Their causes and symptoms are presented in this section.

### *A. Armature Faults*

Armature faults are usually caused by winding insulation failure, which frequently happens in the regions where end windings enter the slots. The reasons which cause insulation

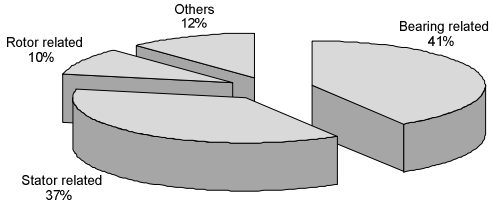


Fig. 2. Failure of components

978-1-61284-247-9/11/$26.00 ©2011 IEEE

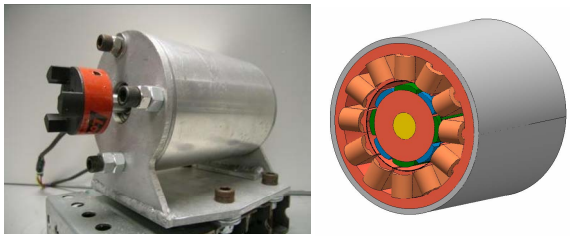

Fig. 3. Test brushless permanent magnet machine and its FEA model

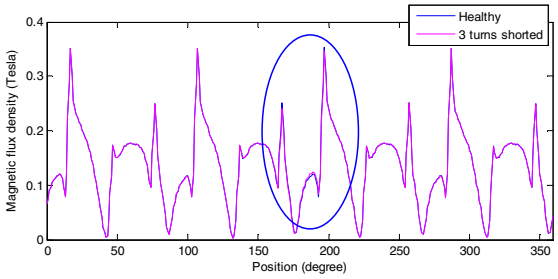


Fig. 4. Magnetic flux density around the air-gap with winding short circuit

failure could be

1) Manufacturing defect
2) High operation temperature/Cooling system malfunction
3) Machine overloading
4) Transient high voltage
5) Vibration caused rubbing

This fault usually starts as an incipient turn-to-turn short circuit and could grow to a ground-to-phase or phase-to-phase short circuit if no preventive maintenance is done. A bolted turn-to-turn short circuit behaves similar to a same system with less number of turns. To illustrate multi-faults' effect on the magnetic flux in air-gap, finite element analysis (FEA) is used to simulate a three phase eight pole brushless permanent magnet machine shown as Fig. 3. Figure 4 shows the difference of flux density in the air gap for a healthy machine and a machine with three turn shorted respectively, under a condition that 30% rated load is applied. It can be seen that the difference is very small and not obvious. The notches in this figure are caused by slot effect.

From the electromagnetic perspective, change in the number of turns affects phase self-inductance, phase-to-phase mutual inductance, winding resistance, and back EMF of a PMSM. For both the inductor models as Fig.5, the relationship between inductances and number of turns are described as

$$L_s = \frac{N^2}{R + R_m} \tag{1}$$

where $L_s$ is phase self inductance, $R$ is reluctance of the back iron, $R_m$ is the reluctance of the permanent magnet. And

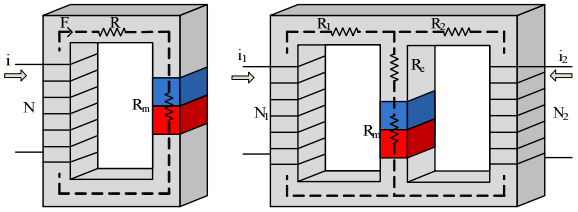


Fig. 5. Model of self-inductance and mutual inductance in a PM machine

$$L_m = \frac{N_1 N_2 R_c}{R_1 R_2 + R_1(R_c + R_m) + R_2(R_c + R_m)} \tag{2}$$

where $L_m$ is mutual inductance, the $R_1$ and $R_2$ are reluctance of each phases and $R_c$ is reluctance of their common path. It can be seen from above equations that self inductance is proportional to the square of number of turns, while mutual inductance is proportional to the number of turns, under ideal conditions.

### *B. Permanent Magnetic Faults*

For permanent magnet machines, field fault typically refers to a failure in the permanent magnets, where demagnetization is the most common issue. The demagnetization could be uniform over all poles or partial over certain region or poles. Conditions that could cause permanent magnets in a PMSM to demagnetize include

1) High operation temperature/Cooling system malfunction
2) Aging of magnets
3) Corrosion of magnets
4) Inappropriate armature current

Commonly used sintered rare-earth magnet materials such as NdFeB and SmCo have straight demagnetization curves in the second quadrant in their B-H loops. Influence of temperature on the magnetic remanence is approximately linear below Curie temperature [6] expressed in equation (3)

$$B_r(T) = B_r(T_0)[1 + \Delta_B(T - T_0)] \tag{3}$$

where $T$ is magnet's operation temperature, $T_0$ is the preferred temperature, $B_r(T_0)$ is the remanence at $T_0$, and $\Delta_B$ is the reversible temperature coefficient, which is a negative number. The moving of operating point due to increasing temperature is illustrated in Fig. 6.

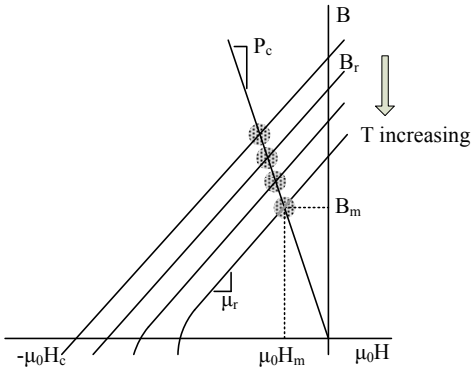


Fig. 6. Effect of increasing temperature on the operating point

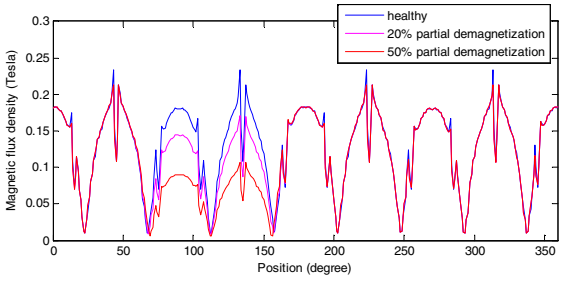


Fig. 7. Magnetic flux density around the air-gap with demagnetization

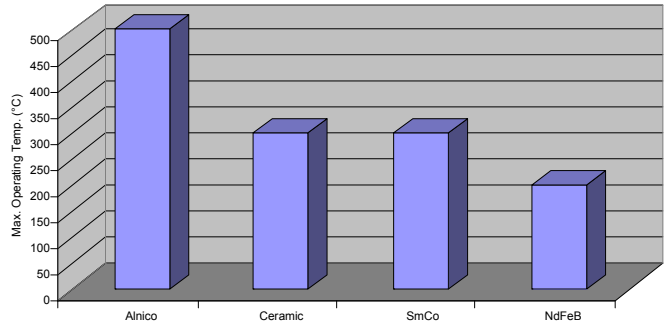

Fig. 8. Maximum operating temperature of different magnet materials

Magnet's permeance coefficient $P_c$ is a function of magnet length, air gap length, and armature current. It is usually greater than one to keep the operation point far away from the knee point. Operation around the knee area will cause irreversible demagnetization. A partial demagnetization FEA simulation result is illustrated in Fig. 7, which shows the changes of flux density with 20% and 50% demagnetization respectively.

The approximate maximum operation temperature of commercial magnets is illustrated in Fig. 8. To evaluate the effect on the parameters of the machines under demagnetization conditions, various analytical models have been proposed [7]-[11], which are discussed in Section III.

### C. Mechanical Faults

Mechanical faults typically refer to bearing failure and eccentricity in most machines. Bearing is a mechanical component which consists of two rings and a set of balls rolling between them and it has been recorded as one of the dominant causes for electric machine failure [5]. It could be caused by

1) Metal fatigue
2) Unbalanced stress
3) Improper installation
4) Corrosion/Contamination

These problems could result in vibrations and noise during machine operation, which are usually measured and processed as diagnosis indicators [12]. Since bearing fault manifest itself as a vibration of rotor and unbalance air gap length, it is sometimes also classified in the eccentricity category. However, it has its own frequency signatures related to its number of balls, ball diameter and ball pitch [13], which is not the same as eccentricity. This is a common issue to all machines with similar effects on performance. Nandi *et al.* [1], [2] have presented a review of fault diagnosis in an induction machine, therefore it has not been discussed in detail in this paper to avoid repetition.

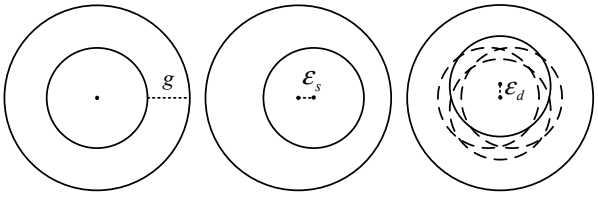

Fig. 9. The air-gap of a healthy machine, a static eccentricity machine and dynamic eccentricity machine

Eccentricity in a machine is a condition of uneven air-gap between the stator and rotor. If the condition is severe, the Unbalanced Magnetic Pull (UMP) could cause stator and rotor contact [14]. Generally, eccentricity is classified into three types: Static eccentricity, dynamic eccentricity and mixed eccentricity. Static eccentricity is the case where there is a displacement in the axis of rotation. This could be caused by an oval stator or misaligned mounting of bearings, rotors or stators. In this case, the air gap is length is fixed in space. Static eccentricity ratio is defined as [15]

$$\vec{e}_s = \frac{\vec{\varepsilon}_s}{g} \tag{4}$$

where $\varepsilon_s$ is the radial distance between rotor axis and stator axis, and g is the uniform air-gap length.

Dynamic eccentricity is the condition in which the stator axis and the rotor rotation axis are identical, but the rotor's axis is displaced to some extent. Therefore the minimum air-gap length position rotates around. This case is usually caused by bent shaft, misaligned mounting of bearings, etc. Similarly, the dynamic eccentricity ratio is defined as

$$\vec{e}_d = \frac{\vec{\varepsilon}_d}{g} = \frac{|\vec{\varepsilon}_d| \angle \omega t}{g} \tag{5}$$

where $\varepsilon_d$ is the radical distance between rotor's axis and stator's axis. Combination of both static and dynamic eccentricities is called mixed eccentricity. Their vector sum can be expressed by equation (6) and (7).

$$|\vec{e}_m| = \left| \frac{\vec{\varepsilon}_s}{g} + \frac{\vec{\varepsilon}_d}{g} \right| = \sqrt{|\vec{e}_s|^2 + |\vec{e}_d|^2 + 2|\vec{e}_s||\vec{e}_d|\cos(\omega t)} \tag{6}$$

$$\angle\varphi = \angle\vec{e}_m = \tan^{-1} \frac{|\vec{e}_d|\sin(\omega t)}{|\vec{e}_s| + |\vec{e}_d|\cos(\omega t)} \tag{7}$$

where $\varphi$ is the angle of the mixed eccentricity, with a reference to static eccentricity direction. It is a time dependent variant with the same period as the rotor's mechanical speed. Thus, the air-gap length $l$ can be calculated as

$$l_{air}(\zeta, t) = R_s - |\vec{e}_m| g \cos(\zeta - \varphi) - \sqrt{R_r^2 - |\vec{e}_m|^2 g^2 \sin^2(\zeta - \varphi)} \tag{8}$$

where $\zeta$ is the position around the air-gap, from 0 to 360 degree.

In a machine's magnetic circuit, reluctance is a function of the air-gap length and back iron equivalent length $l_{iron}$. Therefore magnetic flux is given by equation 9.

$$\Phi(\zeta, t) = \frac{F}{R_{air} + R_{iron}} = \frac{F}{\frac{l_{air}(\zeta, t)}{\mu_o A_{air}} + \frac{l_{iron}}{\mu_o \mu_r A_{iron}}} \tag{9}$$

where $\Phi$ is magnetic flux through a search coil, $F$ is MMF produced by permanent magnets, $R_{air}$ and $R_{iron}$ are reluctance of air-gap and back iron respectively, and $\mu_o$ is the permeability of the air, $\mu_r$ is the relative permeability of the back iron. If only static eccentricity exists, $l_{air}$ is just a function of position, so $\Phi$ is also time irrelevant. If dynamic

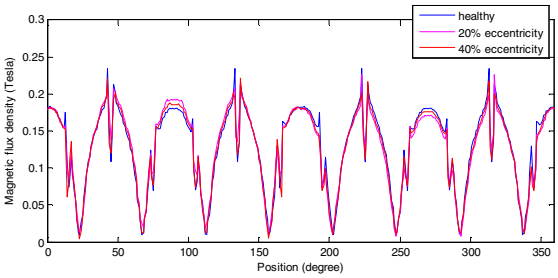


Fig. 10. Magnetic flux density around the air-gap with eccentricity

eccentricity exists, $\Phi$ will be a function of both position and time.

Figure 10 shows the magnetic flux density distribution around the air gap with 20% and 40% eccentricity in the FEA model, from which the unbalance can be found. Besides of FEA, instantaneous magnetic flux density distribution in air gap region can also be calculated by solving the governing Laplacian/quasi-Poissonian field equations and associated boundary conditions with analytical methods. Zhu *et al.* [16] reported a 2D analytical method to predict magnetic flux density of PMSM under different scenarios. Kim *et al.* [17] also presented a perturbation method to predict the air gap magnetic flux density distribution to analyze eccentricity faults based on a model in polar coordinated, with and without considering slotting effect, where analytically calculated results were verified by corresponding FEA results.

## III. FAULT SIGNATURE DETECTION TECHNIQUES

### A. Frequency Signature Analysis

Stator current frequency analysis is the most frequently used technique for machine fault diagnosis. It is usually called Motor Current Signature Analysis (MCSA). Fast Fourier transform (FFT) method is widely used for frequency analysis. Some specific harmonics in the stator winding current spectrum can be detected as a signature of specific fault. Since only current measurement is required, this method can be used for simultaneous multi-fault detection. In addition, this technique is also non-invasive, and cost-effective.

In dynamic eccentricity case, frequency components in the order of 1/P exist in the inductance versus position profile, where P is the number of pole pairs. Since the position of minimum air gap rotates, harmonics can be found in the stator current spectrum. The frequencies due to dynamic eccentricity are given in equation (10)

$$f = f_e(1 \pm \frac{k}{P}) \tag{10}$$

where $f_e$ is the electrical fundamental frequency, and k is an integer.

It has been observed in [18] that the additional frequencies due to partial demagnetization are as same as dynamic eccentricity signature frequencies given by equation (10), and they cannot be distinguished. In the case of demagnetization, a machine's inductance profile does not contain any new spectral contents, since the permeance of permanent magnet is approximately one. However, the flux profile contains the 1/P component; therefore the integer multiples k/P can also be found. In reality not only partial demagnetization, but also other asymmetric problems like load unbalance, misalignment, or oscillating load can produce the same harmonics [19].

Since FFT doesn't contain the information about time, for non-stationary operated machine, short time Fourier Transform (STFT) can be applied. However, the selection of suitable FFT window type and window size is still a critical issue for STFT. A fixed length of window will provoke an inconsistent treatment of different current frequencies [20], and changing motor speed makes it harder to determine harmonic orders, therefore STFT has limitation for non-stationary operated machines.

To overcome the tradeoff between time and frequency resolution of STFT, Rajagopalan *et al.* applied other algorithms such as Windowed Fourier Ridges, Wigner-Ville Distributions, [21], Choi–Williams distribution, Born–Jordan distribution and the Zhao–Atlas–Marks distribution [22] to improve the readability of the time-frequency spectrum. These transformations has a general form as

$$D(t,\omega) = \iiint e^{j(\xi\mu-\tau\omega-\xi t)}\varphi(\xi,\tau) \times f(\mu+\frac{\tau}{2})f^*(\mu-\frac{\tau}{2})d\mu d\tau d\xi \tag{11}$$

where $t$ is the instantaneous time, $\omega$ is the instantaneous frequency; $\tau$, $\xi$ and $\mu$ are variables for integration; and $\varphi(\xi, \tau)$ is a kernel which is given by Table I. In this table, $h(\tau)$ is a window, and $\sigma$ is a constant.

TABLE I
COMPARISON OF TIME–FREQUENCY REPRESENTATION ALGORITHMS

| Distributions | Kernel |
|---|---|
| Wigner-Ville | 1 |
| Windowed WV | $h(\tau)$ |
| Choi–William | $e^{-\xi^2\tau^2/\sigma}$ |
| Born–Jordan | $\varphi_1(\tau)\frac{\sin(\xi\lvert\tau\rvert/a)}{\xi/2}$ |
| Zhao–Atlas–Marks | $\frac{\sin(\xi\tau)}{\xi/2}$ |

For machines operated with a rapidly changing speed profile, wavelet analysis is another option to avoid the dilemma between time resolution and frequency resolution. Rosero *et al.* [20] applied both continuous wavelet transform (CWT) and discrete wavelet transform (DWT) to detect demagnetization faults in machine running under non-stationary condition. Similar method is also used to detect dynamic eccentricity in PMSM and to monitor their health condition [23].

Similarly to current frequency, indications of several faults are also found to be hidden in other spectrums, such as noise, vibration and torque, etc [24]-[26]. However, due to the high

cost of accelerometer or torque meter, they are usually implemented in relative larger machines.

The limitations of these frequency analysis based algorithms are relatively time consuming to some certain extent, and it is too hard to determine the source of specific harmonics, so it cannot discriminate faults that have the same signature frequencies, like partial demagnetization, dynamic eccentricity and unbalanced load.

### *B. Model Based Methods*

For model based machine diagnosis methods, an accurate machine model is required. Modeling of a balanced three-phase healthy PMSM is widely recognized, as presented by researchers in [27]

$$\begin{cases} u_d = R_s i_d + L_d \dfrac{di_d}{dt} - \omega L_q i_q \\ u_q = R_s i_q + L_q \dfrac{di_q}{dt} + \omega L_d i_d + \omega \psi_{PM} \end{cases} \tag{12}$$

$$T_e = \frac{3}{2} p i_q [\psi_{PM} + (L_d - L_q) i_d] \tag{13}$$

where $u_d$, $u_q$ and $i_d$, $i_q$ are stator winding voltage and current in d-q coordinate system respectively; $R_s$ is the stator winding resistance; $L_d$ and $L_q$ are the $d$, $q$ axis stator winding inductances; $\Psi_{PM}$ is the permanent magnetic flux linkage; ω is the angular speed of the rotor; $T_e$ is electromagnetic torque. In faulty cases, specific parameters changes accordingly.

Negative/zero current [28], negative/zero impedance [29], or negative/zero voltage [30] are utilized as indicators for fault detection. These indicators are sensitive to machine asymmetry so that faults due to unbalance signals can be discriminated. However, any asymmetry caused by the machine structure or the power supply's unbalance could also influence the fault detection.

Parameter estimation is another scheme that can be used for online fault diagnosis through detecting abnormal physical parameters. Usually current, voltage and speed are measured, while other parameters are estimated so that faults can be found from any change in magnitude or asymmetry. For parameter estimation, various algorithms are used in literatures. X. Liu *et al.* [31] utilized least-squares method to estimate the stator resistance, inductance, rotor inertia, friction, and back EMF constant from a liberalized PMSM model for multi fault detection. W. le Roux *et al.* [32] determined the strength of the permanent magnets to distinguish rotor magnet defect from dynamic eccentricity, by estimating the mean value of the torque constant. Liu *et al.* [33] implemented an evolutionary computation technique, called particle swarm optimization approach, to estimate two parameters which indicate stator winding inter-turn short circuit fault severity and fault location.

Besides frequency based and model based methods, pros and cons of some other types of methods are compared in Table II.

## IV. FAULT IDENTIFICATION TECHNIQUES

Sometime, extracted fault features are not easily distinguished from fault-free cases or other fault types, especially when disturbances and noise are not negligible. Therefore, several researchers have reported artificial intelligence (AI) algorithms for faults isolation. This approach maps extracted features to specific fault categories. Some frequently used fault identification tools are: artificial neural network (ANN), fuzzy logic, expertise system, support vector machine, etc.

ANN mimics the structure of human brain, which consists of numerous processing unit-neurons, to form a complex adaptive network to perform multi-input/multi-output mapping, even though every neuron has a very simple function. Usually, complex systems will have many hidden layers or feedbacks to enhance the ANN performance. However, the main challenges are that such a system often requires massive computational device and large storage memory. In real application, commonly used ANNs in literatures are three layers feed forward structure in order to simplify the implementation and lower the hardware requirements. Various ANN structures are approved successful in brushless permanent magnet machine fault diagnosis [31], [34]-[39]. For machine condition monitoring and faults identification, the input could be current, voltage, vibration signals, or other estimated parameters. To perform this task, a training data which covers different operating conditions from simulation or experiments are applied to ANN for the offline training procedure to determine the weighting coefficients. After being trained, ANNs need to be tested at some operating points with the testing data from either the training data set or other data sets. Once the offline training and tests are finished, the ANNs can be implemented on hardware to perform fault identification tasks. Besides fault identification, ANNs' nonlinear mapping ability is also implemented for parameter estimation in a supervised learning environment [31], [40], [41].

Fuzzy logic is another AI tool in pattern recognition field. In contrast to crisp logic, it has a truth value between 0 and 1. For machine fault identification, it works as an inferential engine for classification based on a mother function set and

TABLE II
COMPARISON OF CLASSES OF DIAGNOSIS TECHNIQUES

| Types of methods | Types of Failures | | | | Hardware Requirement | Drawbacks |
|---|---|---|---|---|---|---|
| | Bearing | Eccentricity | Winding short circuit/open circuit | Partial Demagnetization | | |
| Current frequency Analysis | √ | √ | √ | √ | Current sensor, Raster encoder | Not good for various speed operated machines. Eccentricity and demagnetization have same frequency signature. |
| Vibration/Noise frequency Analysis | √ | √ | | | Accelerometer/Sound recorder, Raster encoder | |
| Parameter estimation based on current and voltage monitoring | | | √ | √ | Current sensor, Raster encoder | Fault-free machine accurate parameters are required. |
| Temperature Monitoring | | | √ | | Thermograph | Temperature is affected by many factors. |
| Direct Flux Monitoring | | √ | √ | √ | Search coils, Raster encoder | Additional built-in flux sensors are required. |

an if-then rule set [42]-[44]. These sets are needed to be formed before the diagnosis process by expertise based on experience. To make it more adaptive to achieve more accurate solutions under different operation conditions, hybrid neural/fuzzy machine fault detectors are also under research [45]-[48], which take advantage of the learning capability of ANNs to optimize fuzzy sets.

## V. Failure Prognosis Techniques

With emerging applications in hybrid electric vehicles and renewable energy systems, failure prognosis has become an active area of interest for electric machines and drives. S.J. Engel *et al.* [49] have defined this word as follows: *Prognostics is the capability to provide early detection of precursor and/or incipient fault condition (very "small" fault) of a component and to have the technology and means to manage and predict the progression of this fault condition to component failure. However, so far, understanding of this word is still diverse.* Some papers define "*prognosis*" as the estimation of Remaining Useful Life (RUL) [49], [50]. Since fault evolution is a stochastic process influenced by factors which could have unknown future values, it is impossible for one to know exactly when a component will fail. However, one can find an extrapolated trend of fault evolution, or a Probability Density Function estimating the failure time's probability.

In [51]-[54], prognosis is defined as the prediction/forecasting of future state during the evolution of a fault. In these papers, state prediction algorithms such as Kalman Filter, Hidden Markov Model, are utilized for state prediction based on known state conditions. However, the state transition matrix is assumed to remain same throughout the progression of the fault, which might not be true in reality. In [55], [56], prognosis is defined as small transient signal detection. It must be noted that there is no prediction process that has been specifically cited in these papers. They refer to prognosis since the faults detected are transient signal existing during a short time, which can be considered as incipient fault. It is based on an assumption that specific conditions leading to faults produce short transients on the currents of electrical motors. The analysis and transient fault detection tools developed in these papers might better fall into diagnosis category rather than prognosis.

## VI. Conclusion

A brief review of armature, field and mechanical faults occurs to PMSM and their diagnosis schemes have been presented in this paper. So far spectrum signature analysis based methods and machine model based methods are the mostly preferred. Apart from Fourier Transform based techniques, other spectrum manipulation algorithms, such as higher order spectrum, wavelet transforms show better performance for various speed conditions. Artificial intelligence algorithms are also discussed in this paper, which is necessary to distinguish the fault signatures. This paper also discusses the concept of prognosis, which holds the potential for machine life time estimation and incipient fault warning.

## References


[1] S. Nandi, H. Toliyat, and Xiaodong Li, "Condition monitoring and fault diagnosis of electrical motors-a review," *Energy Conversion, IEEE Transactions on*, vol. 20, no. 4, pp. 719-729, 2005.

[2] D. Basak, A. Tiwari, and S. Das, "Fault diagnosis and condition monitoring of electrical machines - A Review," in *Industrial Technology, 2006. ICIT 2006. IEEE International Conference on*, pp. 3061-3066, 2006.

[3] M. El Hachemi Benbouzid, "A review of induction motors signature analysis as a medium for faults detection," *Industrial Electronics, IEEE Transactions on*, vol. 47, no. 5, pp. 984-993, 2000.

[4] M. Awadallah and M. Morcos, "Application of AI tools in fault diagnosis of electrical machines and drives-an overview," *Energy Conversion, IEEE Transactions on*, vol. 18, no. 2, pp. 245-251, 2003.

[5] "Report of Large Motor Reliability Survey of Industrial and Commercial Installations, Part I," *Industry Applications, IEEE Transactions on*, vol. 21, no. 4, pp. 853-864, 1985.

[6] D. C. Jiles, *Introduction to Magnetism and Magnetic Materials, Second Edition*, 2nd ed. CRC Press, 1998.

[7] M. Rosu, J. Saitz, and A. Arkkio, "Hysteresis model for finite-element analysis of permanent-magnet demagnetization in a large synchronous motor under a fault condition," *Magnetics, IEEE Transactions on*, vol. 41, no. 6, pp. 2118-2123, 2005.

[8] S. Ruoho, E. Dlala, and A. Arkkio, "Comparison of Demagnetization Models for Finite-Element Analysis of Permanent-Magnet Synchronous Machines," *Magnetics, IEEE Transactions on*, vol. 43, no. 11, pp. 3964-3968, 2007.

[9] Jung Ho Lee and Jung Pyo Hong, "Permanent Magnet Demagnetization Characteristic Analysis of a Variable Flux Memory Motor Using Coupled Preisach Modeling and FEM," *Magnetics, IEEE Transactions on*, vol. 44, no. 6, pp. 1550-1553, 2008.

[10] J. Farooq, S. Srairi, A. Djerdir, and A. Miraoui, "Use of permeance network method in the demagnetization phenomenon modeling in a permanent magnet motor," *Magnetics, IEEE Transactions on*, vol. 42, no. 4, pp. 1295-1298, 2006.

[11] T. H. Kim and J. Lee, "Effect of design variables on irreversible magnet demagnetization in brushless dc motor," *Journal of Applied Physics*, 2005. [Online]. Available: 10.1063/1.1855272. [Accessed: 12-Sep-2010].

[12] S. McInerny and Y. Dai, "Basic vibration signal processing for bearing fault detection," *Education, IEEE Transactions on*, vol. 46, no. 1, pp. 149-156, 2003.

[13] P. Vas, *Parameter Estimation, Condition Monitoring, and Diagnosis of Electrical Machines*, Illustrated edition. Oxford University Press, USA, 1993.

[14] C. Kral, T. Habetler, and R. Harley, "Detection of mechanical imbalances of induction machines without spectral analysis of time-domain signals," *Industry Applications, IEEE Transactions on*, vol. 40, no. 4, pp. 1101-1106, 2004.

[15] B. Ebrahimi, J. Faiz, and M. Roshtkhari, "Static-, Dynamic-, and Mixed-Eccentricity Fault Diagnoses in Permanent-Magnet Synchronous Motors," *Industrial Electronics, IEEE Transactions on*, vol. 56, no. 11, pp. 4727-4739, 2009.

[16] Z. Zhu, D. Howe, and C. Chan, "Improved analytical model for predicting the magnetic field distribution in brushless permanent-magnet machines," *Magnetics, IEEE Transactions on*, vol. 38, no. 1, pp. 229-238, 2002.

[17] U. Kim and D. Lieu, "Magnetic field calculation in permanent magnet motors with rotor eccentricity: with slotting effect considered," *Magnetics, IEEE Transactions on*, vol. 34, no. 4, pp. 2253-2266, 1998.

[18] S. Rajagopalan, W. Roux, T. Habetler, and R. Harley, "Dynamic Eccentricity and Demagnetized Rotor Magnet Detection in Trapezoidal Flux (Brushless DC) Motors Operating Under Different Load Conditions," *Power Electronics, IEEE Transactions on*, vol. 22, no. 5, pp. 2061-2069, 2007.

[19] Jongman Hong, Doosoo Hyun, Sang Bin Lee, Jiyoon Yoo, and

Kwangwoon Lee, "Automated monitoring of magnet quality for permanent magnet synchronous motors at standstill," in *Energy Conversion Congress and Exposition, 2009. ECCE 2009. IEEE*, pp. 2326-2333, 2009.

[20] J. Ruiz, J. Rosero, A. Espinosa, and L. Romeral, "Detection of Demagnetization Faults in Permanent-Magnet Synchronous Motors Under Nonstationary Conditions," *Magnetics, IEEE Transactions on*, vol. 45, no. 7, pp. 2961-2969, 2009.

[21] S. Rajagopalan, J. Aller, J. Restrepo, T. Habetler, and R. Harley, "Detection of Rotor Faults in Brushless DC Motors Operating Under Nonstationary Conditions," *Industry Applications, IEEE Transactions on*, vol. 42, no. 6, pp. 1464-1477, 2006.

[22] S. Rajagopalan, J. Restrepo, J. Aller, T. Habetler, and R. Harley, "Nonstationary Motor Fault Detection Using Recent Quadratic Time–Frequency Representations," *Industry Applications, IEEE Transactions on*, vol. 44, no. 3, pp. 735-744, 2008.

[23] Wenxian Yang, P. Tavner, and M. Wilkinson, "Condition monitoring and fault diagnosis of a wind turbine with a synchronous generator using wavelet transforms," in *Power Electronics, Machines and Drives, 2008. PEMD 2008. 4th IET Conference on*, pp. 6-10, 2008.

[24] Gyu-Hong Kang, Young-Dae Son, and Gyu-Tak Kim, "The Noise and Vibration Analysis of BLDC Motor Due to Asymmetrical Permanent-Magnet Overhang Effects," *Industry Applications, IEEE Transactions on*, vol. 44, no. 5, pp. 1569-1577, 2008.

[25] Taeyong Yoon, "Magnetically induced vibration in a permanent-magnet brushless DC motor with symmetric pole-slot configuration," *Magnetics, IEEE Transactions on*, vol. 41, no. 6, pp. 2173-2179, 2005.

[26] Hong-Seok Ko and Kwang-Joon Kim, "Characterization of noise and vibration sources in interior permanent-magnet brushless DC motors," *Magnetics, IEEE Transactions on*, vol. 40, no. 6, pp. 3482-3489, 2004.

[27] R. Krishnan, *Electric Motor Drives: Modeling, Analysis, and Control*, United States ed. Prentice Hall, 2001.

[28] G. Kliman, W. Premerlani, R. Koegl, and D. Hoeweler, "A new approach to on-line turn fault detection in AC motors," in *Industry Applications Conference, 1996. Thirty-First IAS Annual Meeting, IAS '96., Conference Record of the 1996 IEEE*, vol. 1, pp. 687-693 vol.1, 1996.

[29] J. Sottile and J. Kohler, "An on-line method to detect incipient failure of turn insulation in random-wound motors," *Energy Conversion, IEEE Transactions on*, vol. 8, no. 4, pp. 762-768, 1993.

[30] M. Cash, T. Habetler, and G. Kliman, "Insulation failure prediction in AC machines using line-neutral voltages," *Industry Applications, IEEE Transactions on*, vol. 34, no. 6, pp. 1234-1239, 1998.

[31] Xiang-Qun Liu, Hong-Yue Zhang, Jun Liu, and Jing Yang, "Fault detection and diagnosis of permanent-magnet DC motor based on parameter estimation and neural network," *Industrial Electronics, IEEE Transactions on*, vol. 47, no. 5, pp. 1021-1030, 2000.

[32] W. le Roux, R. G. Harley, and T. G. Habetler, "Detecting Rotor Faults in Low Power Permanent Magnet Synchronous Machines," *Power Electronics, IEEE Transactions on*, vol. 22, no. 1, pp. 322-328, 2007.

[33] Li Liu, D. Cartes, and Wenxin Liu, "Application of Particle Swarm Optimization to PMSM Stator Fault Diagnosis," in *Neural Networks, 2006. IJCNN '06. International Joint Conference on*, pp. 1969-1974, 2006.

[34] Byung-Geun Hyun and Kwanghee Nam, "Faults diagnoses of rotating machines by using neural nets: GRNN and BPN," in *Industrial Electronics, Control, and Instrumentation, 1995., Proceedings of the 1995 IEEE IECON 21st International Conference on*, vol. 2, pp. 1456-1461 vol.2, 1995.

[35] F. Filippetti, G. Franceschini, and C. Tassoni, "Neural networks approach to electric machine on-line diagnostics," in *Power Electronics and Applications, 1993., Fifth European Conference on*, pp. 213-218 vol.4, 1993.

[36] B. Li, M. Chow, Y. Tipsuwan, and J. Hung, "Neural-network-based motor rolling bearing fault diagnosis," *Industrial Electronics, IEEE Transactions on*, vol. 47, no. 5, pp. 1060-1069, 2000.

[37] M. Chow, R. Sharpe, and J. Hung, "On the application and design of artificial neural networks for motor fault detection. I," *Industrial Electronics, IEEE Transactions on*, vol. 40, no. 2, pp. 181-188, 1993.

[38] M. Chow, R. Sharpe, and J. Hung, "On the application and design of artificial neural networks for motor fault detection. II," *Industrial Electronics, IEEE Transactions on*, vol. 40, no. 2, pp. 189-196, 1993.

[39] Mo-Yuen Chow and P. Goode, "The advantages and challenges of machine fault detection using artificial neural network and fuzzy logic technologies," in *Circuits and Systems, 1993., Proceedings of the 36th Midwest Symposium on*, pp. 708-711 vol.1, 1993.

[40] M. Calvo and O. Malik, "Synchronous Machine steady-State parameter estimation using neural networks," *Energy Conversion, IEEE Transactions on*, vol. 19, no. 2, pp. 237-244, 2004.

[41] I. El-Arabawy, H. Yousef, M. Mostafa, and H. Abdulkader, "Parameters estimation of nonlinear models of DC motors using neural networks," in *Industrial Electronics Society, 2000. IECON 2000. 26th Annual Confjerence of the IEEE*, vol. 3, pp. 1997-2000 vol.3, 2000.

[42] I. Lasurt, A. Stronach, and J. Penman, "A fuzzy logic approach to the interpretation of higher order spectra applied to fault diagnosis in electrical machines," in *Fuzzy Information Processing Society, 2000. NAFIPS. 19th International Conference of the North American*, pp. 158-162, 2000.

[43] C. Combastel, S. Gentil, and J. Rognon, "A symbolic reasoning approach to fault detection and isolation applied to electrical machines," in *Control Applications, 1998. Proceedings of the 1998 IEEE International Conference on*, vol. 1, pp. 475-479 vol.1, 1998.

[44] G. Goddu, Bo Li, Mo-Yuen Chow, and J. Hung, "Motor bearing fault diagnosis by a fundamental frequency amplitude based fuzzy decision system," in *Industrial Electronics Society, 1998. IECON '98. Proceedings of the 24th Annual Conference of the IEEE*, vol. 4, pp. 1961-1965 vol.4, 1998.

[45] M. Awadallah, M. Morcos, S. Gopalakrishnan, and T. Nehl, "A neuro-fuzzy approach to automatic diagnosis and location of stator inter-turn faults in CSI-fed PM brushless DC motors," *Energy Conversion, IEEE Transactions on*, vol. 20, no. 2, pp. 253-259, 2005.

[46] S. Altug, Mo-Yuen Chen, and H. Trussell, "Fuzzy inference systems implemented on neural architectures for motor fault detection and diagnosis," *Industrial Electronics, IEEE Transactions on*, vol. 46, no. 6, pp. 1069-1079, 1999.

[47] M. Chow, *Methodologies of Using Neural Network and Fuzzy Logic Technologies for Motor Incipient Fault Detection*. World Scientific Publishing Company, 1998.

[48] P. Frank, "Residual evaluation for fault diagnosis based on adaptive fuzzy thresholds," in *Qualitative and Quantitative Modelling Methods for Fault Diagnosis, IEE Colloquium on*, pp. 4/1-411, 1995.

[49] S. Engel, B. Gilmartin, K. Bongort, and A. Hess, "Prognostics, the real issues involved with predicting life remaining," in *Aerospace Conference Proceedings, 2000 IEEE*, vol. 6, pp. 457-469 vol.6, 2000.

[50] B. Satish and N. Sarma, "A fuzzy BP approach for diagnosis and prognosis of bearing faults in induction motors," in *Power Engineering Society General Meeting, 2005. IEEE*, pp. 2291-2294 Vol. 3, 2005.

[51] S. Zaidi, S. Aviyente, M. Salman, K. Shin, and E. Strangas, "Failure prognosis of DC starter motors using hidden Markov models," in *Diagnostics for Electric Machines, Power Electronics and Drives, 2009. SDEMPED 2009. IEEE International Symposium on*, pp. 1-7, 2009.

[52] Xin Wu, Yaoyu Li, T. Lundell, and A. Guru, "Integrated prognosis of AC servo motor driven linear actuator using Hidden Semi-Markov models," in *Electric Machines and Drives Conference, 2009. IEMDC '09. IEEE International*, pp. 1408-1413, 2009.

[53] W. Wang, "Modelling the probability assessment of system state prognosis using available condition monitoring information," *IMA Journal of Management Mathematics*, vol. 17, no. 3, pp. 225 -233, Jul. 2006.

[54] R. Chinnam and P. Baruah, "Autonomous diagnostics and prognostics through competitive learning driven HMM-based clustering," in *Neural Networks, 2003. Proceedings of the International Joint Conference on*, vol. 4, pp. 2466-2471 vol.4, 2003.

[55] W. Zanardelli, E. Strangas, H. Khalil, and J. Miller, "Comparison of wavelet-based methods for the prognosis of failures in electric motors," in *Power Electronics in Transportation, 2002*, pp. 61-67,.

[56] E. Strangas, S. Aviyente, and S. Zaidi, "Time–Frequency Analysis for Efficient Fault Diagnosis and Failure Prognosis for Interior Permanent-Magnet AC Motors," *Industrial Electronics, IEEE Transactions on*, vol. 55, no. 12, pp. 4191-4199, 2008.

# A Simplified State Switching Control Strategy for Survivable Variable-Speed Induction Generators

Xiaodong Shi, *Student Member*, *IEEE* and Mahesh Krishnamurthy, *Member*, *IEEE*
Electric Drives & Energy Conversion Lab
Department of Electrical and Computer Engineering,
Illinois Institute of Technology
3301 S Dearborn Street, Chicago, IL 60616 USA
EML: kmahesh@ece.iit.edu, URL: http://drives.ece.iit.edu

***Abstract*-Induction machines are one of the most widely used electric machines in wind power applications. However, the control of an induction generator is complicated if advanced control strategy is employed in order to maximize the performance. Also, the complexity of advanced control strategies and their high demand on hardware and sensors can lower the overall reliability of the generator system and potentially result in system malfunction, leading to unscheduled maintenance and power yield reduction. In this paper, an effective, yet simple and low-cost state switching control technique is proposed and implemented as a backup control strategy in case of control or sensor failure. This state switching control system is only allowed to operate at two different duty cycles of PWM which produces phase voltages with different magnitudes. At the same time, the frequency of the phase voltages is derived from the reference speed. By switching between these two states, precise speed regulation can be achieved. Owing to its simplicity, the control strategy can be implemented on a low cost FPGA or embedded into existing controllers for use as a backup strategy. In addition since it does not require the use of current sensors, it is very suitable for survivable operation. Simulation and experimental results are included to validate our claims.**

***Keywords: Induction Generator (IG), State Switching Control, Pulse Width Modulation (PWM)***

## I. INTRODUCTION

Due to robustness, simple construction and low cost, induction machines (IM) have been prime candidates for a variety of generator applications. With increasing popularity of wind energy in recent years [1], [2], induction generators (IG) have become one of the most common generators used in wind turbines. Squirrel cage induction machines are often utilized for low power-level wind turbines. For medium and high power-level wind applications, wound rotor induction machines (or Double Fed Induction Machine) are often employed. In addition to wind generators, induction machines have also been a popular choice in hydropower and hybrid electric and electric vehicle applications.

In order to obtain the maximum power output from the induction generator, many sophisticated control methods have been proposed to control it in variable-speed operation mode. Among these methods, Vector Control and Direct Torque Control (DTC control) are the most widespread control strategies. Vector control [3]-[5] has gained popularity over the last three decades due to its high efficiency and superior transient performance. It is also one of the most efficient and promising control strategies for induction machine. However, the implementation of vector control is complicated and expensive. It not only requires fast processing devices to meet its large computational requirements and perform accurate identification of machine parameters, but also needs multiple sensors to provide necessary feedback information including phase currents and rotor position. DTC control [6], [7] is simpler than vector control due to the absence of PI controller, coordinate transformations and current regulators. However, similar drawbacks also exist in hardware requirement and implementation. Failure of current sensor or even the drift of system parameters may result in system malfunction. Therefore, while vector control and DTC control are efficient control strategies, they are not usually most reliable. The complex control strategy and the requirement of additional devices reduce reliability of the system and increase its cost. This makes it necessary to implement a simple, cost-effective and reliable control strategy as a backup control strategy to make the system fault tolerant.

In recent years, digital control has been proposed in literature [8]-[11]. This control method is extremely simple and effective for many applications, such as BLDC control and DC-DC converter control. In this method, two different states (state "High" and state "Low") are predefined, these states can be voltage, current and PWM duty cycle. Then, state is switched between these two values by comparing the actual output value with the reference. This allows the machine to be treated as a digital system and the system output can be well regulated. Therefore, there is no need for major computation controllers or even PI controllers. Reduction of feedback sensors also improves reliability of this method.

In this paper, an effective, yet simple and low-cost State Switching Control technique is proposed and implemented for a three phase induction generator system. This control method is based on the principle of digital control specifically designed for an induction machine. By applying state switching control, two specific PWM duty cycles are applied to the converter and produce excitation phase voltages with different magnitudes. Speed regulation is achieved by switching between these two different PWM duty cycles with the frequency of the excitation phase voltage directly derived from the given reference speed. Therefore, this controller is extremely simple in implementation and only speed sensor is required for speed regulation. This enhances reliability of the control technique and reduces complexity in hardware implementation. While phase current distortion is a challenge

due to the lack of current observation, the overall performance of this method is highly acceptable and thus can be used as a backup control strategy.

## II. FUNDAMENTALS OF INDUCTION GENERATOR

In order to operate the induction machine in generating mode, reactive power is needed for the excitation of its magnetic field. There are two excitation methods which are often used to initially start the induction generator, self-excitation and source excitation. Self excitation [12] is often utilized by standalone induction generators with their output connected with capacitors in parallel. Due to the residual magnetism on the rotor, the rotation of the rotor gradually builds up a terminal voltage on the stator winding. However, in this method, the output voltage and frequency is a complex function of several parameters, which makes it challenging to be controlled if the shaft speed changes. Source excitation method is often used when induction generator is connected to the grid or other power sources. In this case, magnetizing current is drawn from the source and therefore the phase voltage and frequency can be controlled.

For a three phase induction machine, the most frequently used active converter topology for source excited induction generator is illustrated in Fig.1. This converter includes six switches (MOSFETs or IGBTs) and six anti-parallel diodes. By applying specific switching signals to these switches, the magnitude and the frequency of the phase voltage can be fully controlled.

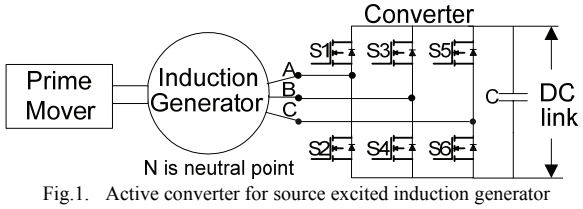


Fig.1. Active converter for source excited induction generator

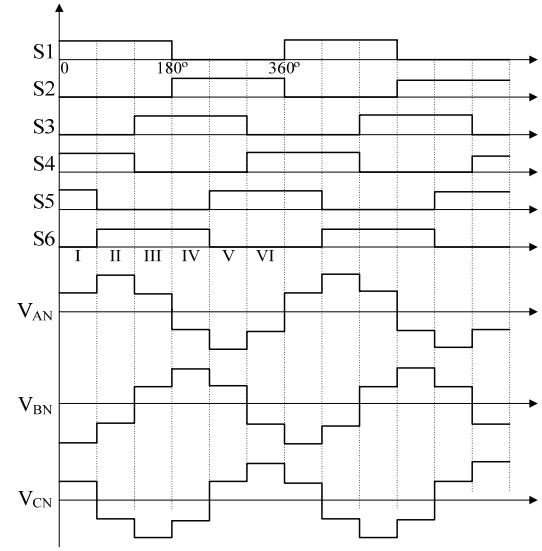


Fig.2. Six-Step waveform

Six-step method [13] is one of the simplest methods to excite the induction generator. Gate signals for the converter are shown in Fig.2. In every electrical cycle, a switch is turned on for 180 electrical degrees and only three switches are turned on for every 60 electrical degrees. For a wye-connected three phase induction machine, three six-stepped and quasi-sine phase voltages can be formed in the stator winding as illustrated in Fig.2. Therefore, by applying these gate signals to the converter with proper frequency, the induction generator can be controlled.

## III. PROPOSED STATE SWITCHING CONTROL METHOD FOR INDUCTION GENERATOR

### *A. Principle of State Switching Control of Induction Generator*

It is well known that by applying phase voltages with proper magnitude and frequency to the stator windings, an IM can be operated in motoring mode when its shaft speed is lower than synchronous speed. Under this condition, if a negative torque from the prime mover is applied to the shaft of the induction machine, the shaft speed increases to super-synchronous speed, which enables the induction machine to work as a generator. Therefore, if the torque of the prime mover is constant, speed regulation of the induction generator mainly involves two parameters--the magnitude and the frequency of the applied voltage across the phase winding. The frequency of the applied phase voltage mainly determines the shaft speed of the induction machine. This relationship can be explained in the following equations.

$$\omega_s = \frac{2\pi f_s}{P} \tag{1}$$

$$\omega_r = \omega_s(1+s) \tag{2}$$

where $\omega_s$ is the synchronous speed of the induction machine in rad/s, $f_s$ is the frequency of the applied phase voltage in *Hz*, $P$ is the number of pole pairs, $\omega_r$ is the speed of the shaft in rad/s and $s$ is the slip rate.

If the frequency of the phase voltage is defined, the synchronous speed is set according to equation (1). By changing the frequency of the phase voltage, the synchronous speed can be changed. At the same time, the variation of synchronous speed causes a change of the shaft speed since shaft speed is a slightly higher than the synchronous speed at steady-state in generating mode. Therefore, the shaft speed can be determined mainly by the frequency of the phase voltage. Additionally, if the reference speed of the shaft is defined, frequency of phase voltages that should be applied to the induction generator can be calculated using equations (1) and (2).

The magnitude of applied phase voltage is a factor which can also affect the shaft speed of IM in generating mode. This relationship is shown in Fig.3. If magnitude of the applied phase voltages is increased (V1>V2), electromagnetic torque of the IG (opposing the prime mover torque) increases as well. As a result, shaft speed decreases slightly ($\omega 1 < \omega 2$), but the synchronous speed remains the same.

Based on the above analysis as well as the six-step method, a state switching control technique can be designed and expressed in Fig.4. According to the reference speed ($\omega_{ref}$), the applied phase voltage frequency can be calculated using equation (1) and (2) with a constant slip (5% in our case). By applying this frequency to the induction machine, the shaft

speed will settle down to a value close to the reference. Then, by comparing the actual speed to the reference speed, the magnitude of the phase voltage can be switched between high voltage level ($V_H$) and low voltage level ($V_L$). This allows the actual speed ($\omega_{act}$) of the IG to be precisely regulated.

The magnitude of applied phase voltages can be changed by PWM-integrated six-step excitation method. As shown in Fig. 5, compared to traditional six-step method which is shown in Fig.2, switches are given PWM signals instead of turning them "ON" all the time for 60 electrical degrees. Therefore, by changing the duty cycle of the PWMs, the magnitude of the phase voltages can be changed. As a result, the operating principle of state switching control of an IG is shown in Fig. 6.

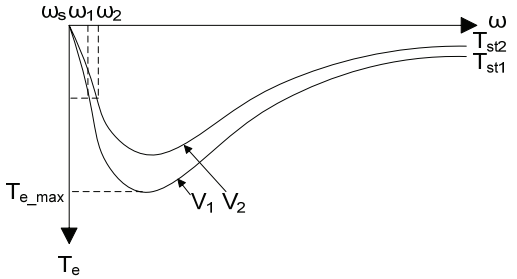

Fig.3 Speed torque characteristics of IG at different voltage level

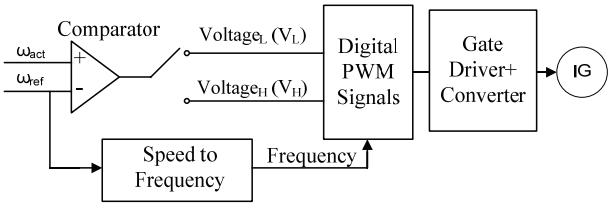

Fig.4 Principle of state switching control of induction generator

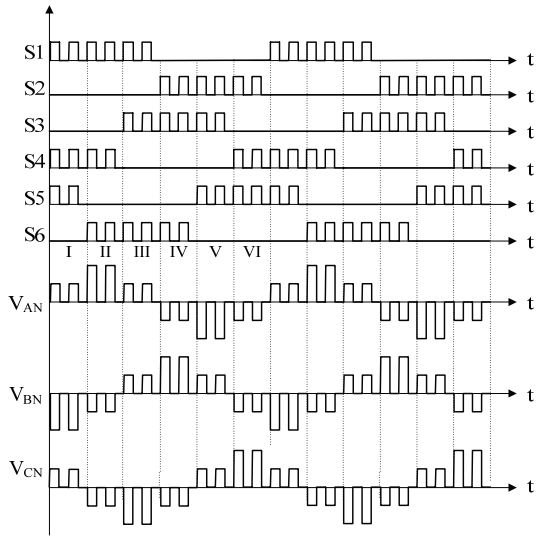

Fig.5 PWM-integrated six-step waveform

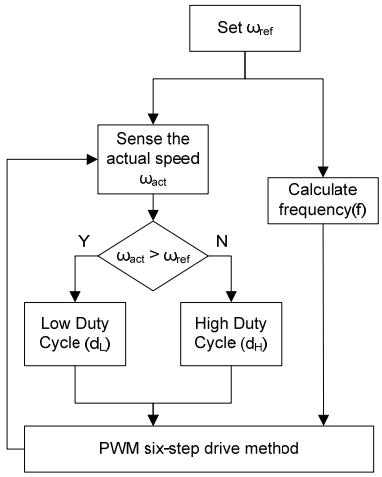

Fig.6 Principle of state switching control of induction generator

*B. Controller Design of State Switching Control of IG*

From the generator torque equation, we have

$$T_L = J\frac{d\omega_m}{dt} + b\omega_m + T_e \tag{3}$$

Where $T_e$ is the generated electromagnetic torque, $\omega_m$ is the rotor speed in rad/s, $J$ is the rotor moment of inertia, $b$ is the viscous friction constant and $T_L$ is the load torque.

The rotor induced torque [14] of the induction machine is

$$T_e = \frac{3V_s^2 R_2 / s}{\omega_s\left[\left(R_1 + R_2/s\right)^2 + \left(X_1 + X_2\right)^2\right]} \tag{4}$$

Where $V_s$ is the magnitude of the applied phase voltage, $\omega_s$ is the synchronous speed of the induction machine in rad/s, $s$ is the slip, $R_1$ and $X_1$ refers to the stator impedance, $R_2$ and $X_2$ refers to the rotor impedance.

Substituting (4) into (3), we get

$$T_L = J\frac{d\omega_m}{dt} + b\omega_m + \frac{3V_s^2 R_2 / s}{\omega_s\left[\left(R_1 + R_2/s\right)^2 + \left(X_1 + X_2\right)^2\right]} \tag{5}$$

At steady state, the shaft speed $\omega_s$ and the slip $s$ is constant. Meanwhile, stator and rotor impedances are also constant. As a result, equation (5) can be simplified as

$$T_L = b\omega_{mss} + kV_s^2 \tag{6}$$

Where $\omega_{mss}$ is the rotor steady state speed and $k = \dfrac{3R_2 / s}{\omega_s\left[\left(R_1 + R_2/s\right)^2 + \left(X_1 + X_2\right)^2\right]}$.

Therefore, the relationship between voltage magnitude and rotor speed can be obtained as

$$V_s = \sqrt{\frac{T_L - b\omega_{mss}}{k}} \tag{7}$$

In six step method, the magnitude of the applied phase voltage $V_s$ is 2/3 of the DC link voltage $V_{DC}$. If the duty cycle of the PWM is $d$, we get

$$\frac{2}{3}dV_{DC} = \sqrt{\frac{T_L - b\omega_{mss}}{k}} \tag{8}$$

Therefore, the relationship between the duty cycle and the rotor speed of the induction generator can be expressed as

$$d = \frac{3\sqrt{\frac{T_L - b\omega_{mss}}{k}}}{2V_{DC}} \tag{9}$$

Meanwhile, the frequency of the applied voltage can be calculated using equation (10) which is derived from equation (1) and (2). A constant slip of 5% is considered in all simulations and experiments.

$$f = \frac{\omega_{ref} P}{2\pi(1+s)} \tag{10}$$

## IV. Simulation Results

In order to verify the feasibility of the proposed state switching control of induction generator, the control strategy was implemented in Matlab/Simulink. The block diagram of the proposed state switching control of induction generator in simulation is shown in Fig.7, in which a 60Hz, 4 pole induction machine is used with the rated speed is 1725rpm. Two PWM duty cycles are defined at 30% and 90%.

Simulation results are shown in figures 8 to 10. Fig.8 shows the speed response of the IG controlled by the proposed state switching technique. It can be observed that transients quickly settle down and the reference speed is precisely tracked. Fig.9 shows the steady-state speed error between reference speed, actual speed and the corresponding duty cycle adjustment. Fig.10 shows the DC-link current flowing into the power source. The average DC-link current is positive, which indicates that the induction machine is working in generating mode and supplying power to the source.

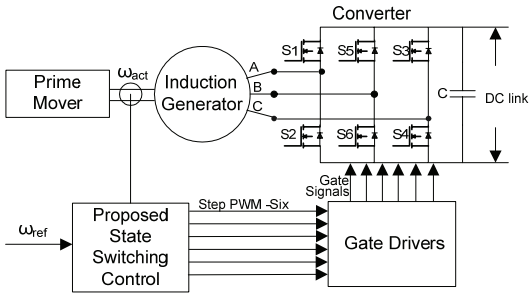


Fig.7 Block diagram of the proposed state switching control of IG

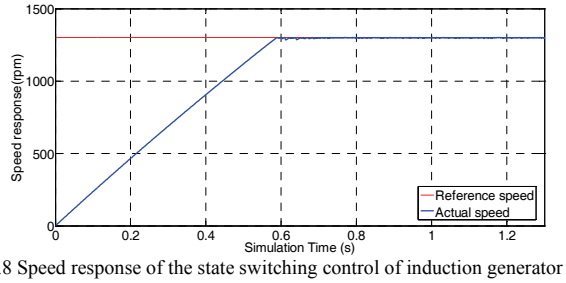


Fig.8 Speed response of the state switching control of induction generator

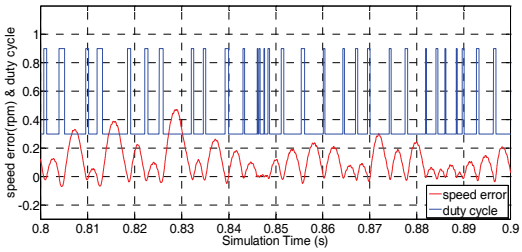


Fig.9 Steady state error and change of duty cycle

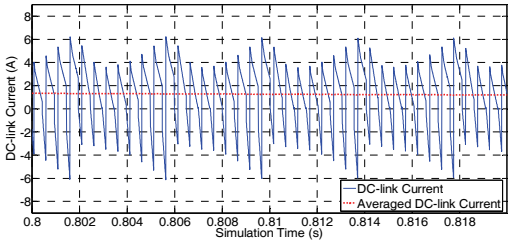


Fig.10 DC-link current flowing into the source

## V. Experimental Verification

In order to verify the effectiveness of the proposed state switching control method for induction generator, an experimental setup has been developed as shown in Fig.11. It includes a 3.9kW DC power source connected to a 2.2kW induction machine, a 3kW permanent magnet DC programmable dynamometer used as a prime mover, a TMS320F2812 based DSP controller, three phase converter and gate drivers, speed sensor, and a dump resistor. Specifications regarding the induction machine and the PM DC machine are listed in Table I.

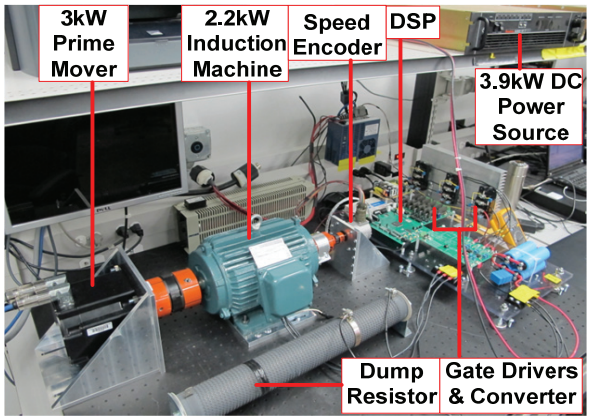


Fig.11 Hardware setup for experimental verification of proposed state switching control strategy of an Induction Generator

TABLE I

Property of the Induction Generator and PM DC Load

| | Induction Machine | PM Dyno |
|---|---|---|
| Rated Power | 2.2kW | 3 kW |
| Rated RPM | 1420 | 6000 |
| Rated Volts | 380/Y Conn. | 640DC |

| Rated Current | 5A/phase | 12.4A/phase |
|---|---|---|
| No. of poles | 4 | N/A |
| No. of phases | 3 | 3 |

Figures 12 to 20 show experimental results obtained from the setup under different operating conditions. Fig.12 shows the speed response of the induction generator when reference speed is set to 1025rpm and the torque of prime mover is 1Nm. Since the prime mover is turned on before starting the induction generator, initial speed at startup increases to 1500rpm. Once the induction generator is started and state switching control is applied, speed quickly settles down to the reference speed with a steady state error lower than 7%. Fig.13 shows the generated DC link voltage and DC link current flowing into the dump resistor and the change of duty cycle between $D_H$ and $D_L$. It is clear that the average DC link current is positive which confirms the operation of the IM in generating mode. Fig.14 shows the steady state phase current as well as the change of duty cycle. It can be observed that the phase current has significant harmonics which is the main trade-off in the implementation of this control technique.

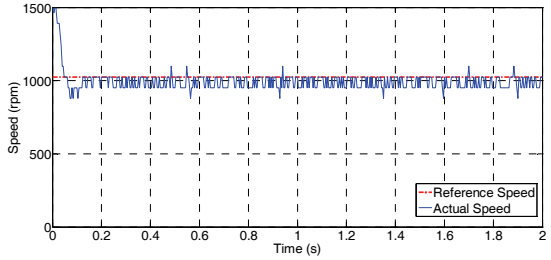

Fig.12 Speed response when reference speed is 1025 rpm

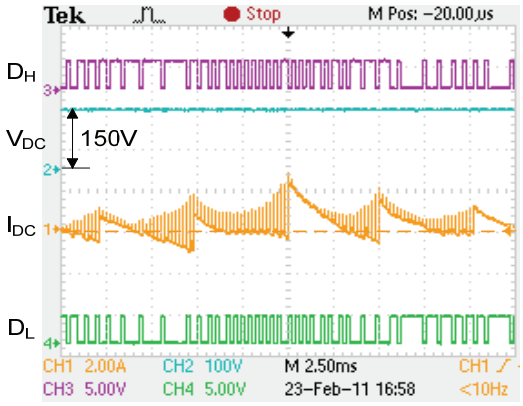

Fig.13 DC link voltage, current and change of duty cycle

Figures 15 to 17 show results when the reference speed is 586rpm and the prime mover torque is 1Nm. Fig.15 shows the speed response of the induction generator. The initial speed is 1150rpm before exciting the induction generator. After the induction generator is excited, shaft speed quickly goes down and tracks the reference speed. Fig.16 shows the DC link voltage and DC link current flowing into the dump resistor and the change of duty cycle. Fig.17 shows the steady state phase current and the change of duty cycle. From these figures, it can be noticed that the proposed state switching control method also has a good speed tracking performance at relatively low speeds.

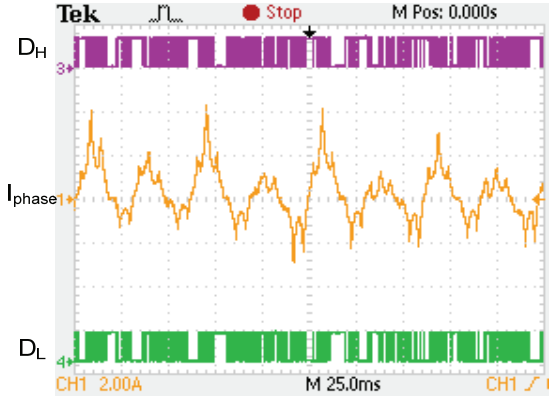

Fig.14 Phase current and change of duty cycle

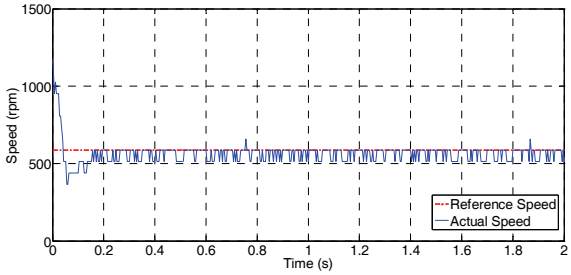

Fig.15 Speed response when reference speed is 586rpm

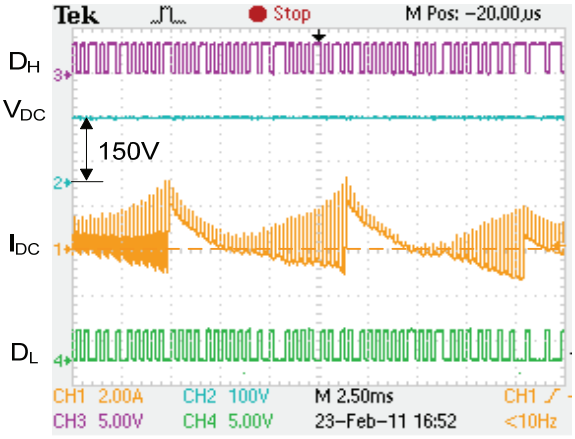

Fig.16 DC link voltage, current and change of duty cycle

The generated DC link voltage and current for a step change in torque from 1Nm to 2Nm from the prime mover are shown in Fig.19. It is clear that when the prime mover torque becomes larger, more power is generated and transmitted to the dump resistor. In addition, a step change of reference speed is also applied to the machine. Fig.20 shows the speed response of the induction generator when reference speed changes from 1025rpm to 586rpm. The actual speed again can track the reference speed precisely.

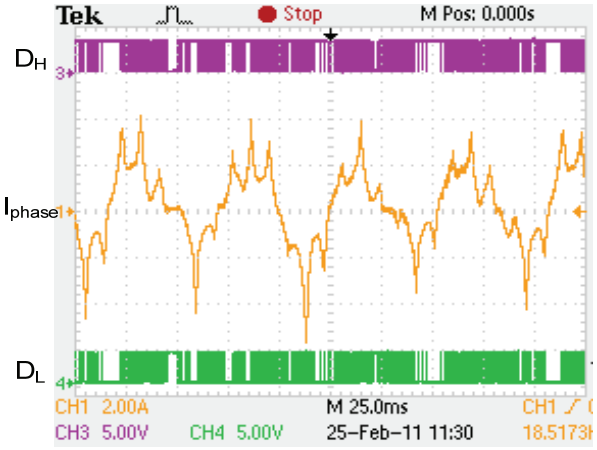


Fig.17 Phase current and change of duty cycle

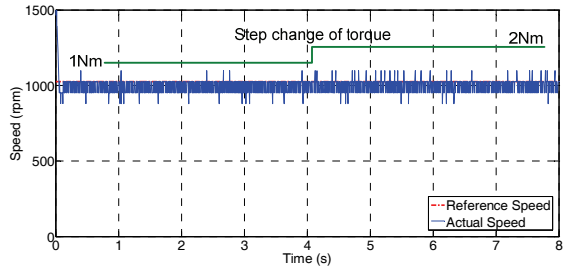


Fig.18 Speed response under step change of prime mover torque

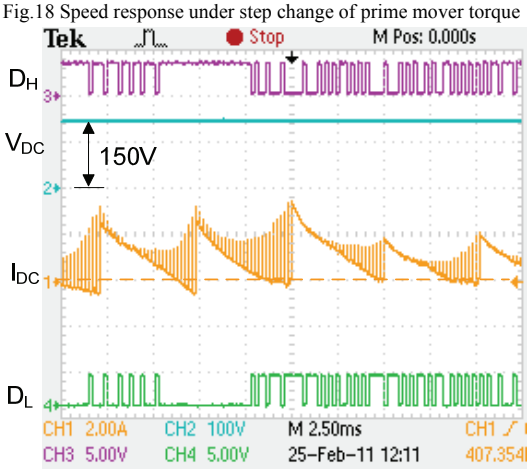


Fig.19 DC link voltage, current and change of duty cycle at 2Nm

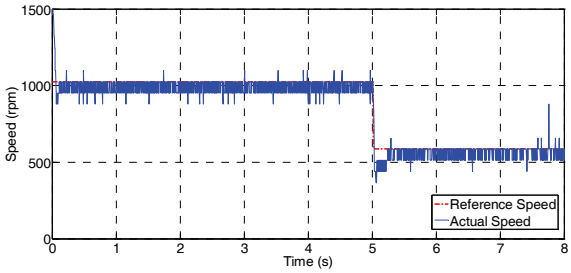


Fig.20 Speed response under step change of reference speed

From the results obtained, it can be seen that the speed ripple was found in an acceptable range under different conditions. This shows the effectiveness of the control scheme.

## VI. CONCLUSION

This paper presents a simple, low-cost and effective state switching control technique for the speed regulation of the induction generator. Owing to its simplicity, this method can significantly enhance the reliability of the drive system with highly acceptable speed tracking performance. It does not need any current sensors and requires very little computational capacity. This enables implementation of the control strategy on a low-cost FPGA. Therefore, this technique can be used as a backup control strategy for induction generators in the event of failure of sensors used in or advanced control methods. Challenges of this control method are the distortion of phase currents and the torque ripple. But as a backup control strategy, this method is very effective and shows acceptable performance. Simulation and experiment results verify the feasibility of the proposed approach.

## ACKNOWLEDGEMENT

The authors would like to thank the financial support provided by the Department of Energy (Grant No. DE-EE 0002979) for conducting this research.

## REFERENCES

[1] US Department of Energy, *20% Wind Energy by 2030: Increasing Wind Energy's Contribution to U.S. Electricity Supply*, Jul. 2008.

[2] Us Department of Energy, *2009 Wind Technologies Market Report*. Aug. 2010.

[3] J. A. Santisteban and R. M. Stephan, Vector Control Methods for Induction Machines: An Overview, *IEEE Trans. Education*, Vol. 44, No, 2, May, 2001, pp. 170-175

[4] S. Wade, M. W. Dunnigan and B. W. Williams, Modeling and simulation of induction machine vector control with rotor resistance identification, IEEE Trans. Power Electron., Vol. 12, No. 3, May, 1997, pp. 495-506

[5] Y. Lai, Machine Modeling and Universal Controller for Vector-Controlled Induction Motor Drives, IEEE Trans. Energy Conversion, Vol. 18, No.1, Mar.2003, pp.23-32

[6] M. Depenbrok, Direct self-control (DSC) of inverter-fed induction machine, *IEEE Trans. Power Electron.* Vol. 3, 1988, pp. 420–429

[7] I. Takahashi and Y. Ohmori, High-performance direct torque control of an induction motor, *IEEE Trans. Ind. Applicat.* Vol. 25, 1989 pp. 257–264.

[8] A. Sathyan, N. Milivojevic, Y. Lee, M. Krishnamurthy and A. Emadi, "An FPGA-Based Novel Digital PWM Control Scheme for BLDC Motor Drives", *IEEE Trans. Ind. Electron.*, Vol. 56, No.8, pp. 3040-3048, Aug.2009

[9] F. Rodriguez and A. Emadi, "A Novel Digital Control Technique for Brushless DC Motor Drives", *IEEE Tans. Ind. Electron.*, Vol. 54, No. 5, Oct. 2007

[10] A. Khaligh, A. M. Rahimi, Y. J. Lee, J. Cao, A. Emadi, S. D. Andrews, C. Robinson, and C. Finnerty, "Digital control of an isolated active hybrid fuel cell/Li-ion battery power supply," *IEEE Trans. Vehicular Tech.*, vol. 56, pp. 3709 - 3721, Nov. 2007.

[11] A. Khaligh and A. Emadi, Pulse Adjustment, a Novel Digital Control Technique, for Control of a DC-DC Buck-Boost Converter Operating in Discontinuous Conduction Mode and Driving Constant Power Loads, *IEEE conf. Vehicle Power and propulsion*, 2006, pp.1-5

[12] R. C. Bansal, Three-Phase Self-Excited Induction Generators: An Overview, *IEEE Trans. Energy Conv.*, vol. 20, No. 2, pp. 292-299, June 2005

[13] R. Krishnan, *Electric Motor Drives--Modeling, Analysis, and Control.* New Delhi: Prentice/Hall of India, 2007, pp. 317-345

[14] S. J. Chapman, *Electric Machinery and Power System Fundamentals.* New York: McGraw-Hill, 2002, pp. 309-313